COBEE 2025 – Proceedings

MONDAY

Pandemic and Epidemic (11:00-12:30 h)

6th International Conference on Building Energy and Environment
Eindhoven University of Technology, The Netherlands
6 - 10 July 2025

Development of a breath-taking hood for airborne diseases

Sheng-Hsiu Huang[1], Yu-Mei Kuo[2], Chih-Wei Lin[3], Chih-Chieh Chen[4]

[1]National Taiwan University, Taipei, Taiwan, shhuangieh@ntu.edu.tw
[2]Chung Hwa University of Medical Technology, Tainan, Taiwan, kuoyumei@gmail.com
[3]National Taiwan University, Taipei, Taiwan, chihweilin1981@gmail.com
[4]National Taiwan University, Taipei, Taiwan, ccchen@ntu.edu.tw

SUMMARY
In terms of epidemic prevention and control, although biomedical means are crucial to combating the epidemic, they can only serve as a second line of defense due to their late appearance. Engineering controls are more timely and preventative, but these tools are imperfect, as the protracted COVID-19 pandemic has shown. Source control is always more effective than the recipient and pathway control based on the control hierarchy. Preventing the particles exhaled by infected persons from contaminating the environment plays a crucial role in breaking the chain of transmission of viral aerosols. This study aims to develop a personal breath-responsive breath-taking hood (BR-BTH) to efficiently capture exhaled particles without burdening the wearer's breath.

Keywords: suction hood, source control, capture efficiency, negative pressure.

GENERAL INSTRUCTIONS

The coronavirus spreads like a forest fire. It won't end until the entire forest burns down naturally. Current approaches to combating airborne diseases can be divided into biomedical and engineering tools. Biomedical tools often have belated flaws despite their critical role in fighting viruses. Thus, they can only be used as a second line of defense. For example, mRNA vaccines took most manufacturers over ten months to develop and were used under Emergency Use Authorization (EUA) during the COVID-19 pandemic. Infection control and prevention experts tend to focus only on vaccines. Vaccines are critical in combating infectious airborne microorganisms, but vaccines alone cannot stop the spread of disease.

On the other hand, engineering control tools are more readily available and, therefore, more preventative, making them ideal for frontline defense. However, the combination of biomedical and engineering tools still failed to stop the spread of the virus, suggesting that the two tools combined are still not enough. Therefore, we need new engineering control tools, such as fire extinguishers, to snuff out sparks or small fires to prevent them from spreading and getting out of control. This study aims to develop a source control device called a Breath-Taking Hood (BTH) for infected persons to capture all exhaled aerosol particles and prevent them from contaminating the environment.

METHODS

The BTH consisted of a capture hood with a shield connected via a flexible connecting tube to a filter unit connected to a battery-operated extractor fan, as shown in Figure 1. The filter, fan, and

battery were designed to attach to the waist belt for comfort. The main body of the capture hood consisted of a triangular curved groove (TCG) connecting to a shield, a particle mixing reducer, and a strip. A 3D drafting software and a 3D printer were used to fabricate the hood. The

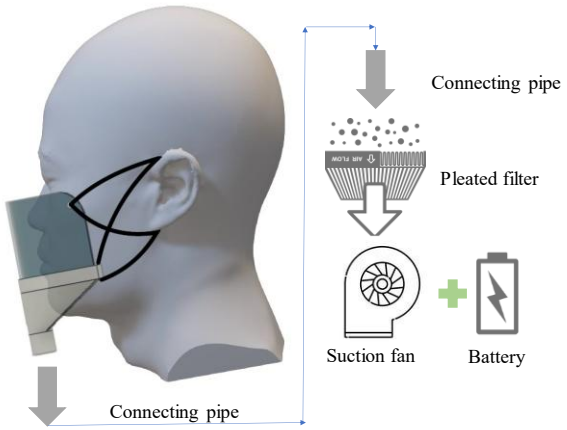

Figure 1. Schematic diagram of wearing a breath-taking hood.

shielding sheet was made of polycarbonate (PC) film. Polyurethane (PU) foams with different porosity and thickness were used as particle mixing reducers, and elastic adjustable cotton threads were used as ear or head strips.

Structural parameters were optimized based on capture efficiency as a function of suction flow rate. The capture Efficiency testing system consisted mainly of a clean air generation system, an exhaled particle generation system, an air extraction device, and a particle measurement instrument. The test chamber dimensions were 60 x 60 x 136.5 cm, and the BTH was worn on a manikin and tested inside the chamber. The aerosol testing chamber was slightly pressurized to prevent external particle contamination. The filtered air with an aerosol number concentration of less than 0.01 #/cm^3 was used to purge the aerosol chamber to minimize the measurement noise. Ultra-clean air was necessary to achieve 99.99% capture efficiency with reasonable accuracy and precision. The flow rate supplied to the chamber also varied to study the effect of approaching velocity on BTH capture efficiency. A nebulizer was used to generate sub-micrometer-sized oil droplets (di-ethylhexyl sebacate, DEHS) to simulate exhaled particles with the count medium diameter around 0.3 μm.

Challenge aerosols were generated using a fixed cyclic breathing flow (15 L/min) of different breathing patterns and the constant suction flow rate of 23.6 L/min, which was the peak flow of the cyclic breathing patterns, to study the effects of respiratory flow and breathing patterns on capture efficiency. A condensation particle counter was used to measure the concentration at the chamber outlet. The capture efficiency was determined by taking the ratio of aerosol concentrations when the suction fan was turned on and off. The target capture efficiency was set at 99.99%.

RESULTS / DISCUSSION

The optimal height, width, and thickness of BTH were 3, 10, and 2 cm, respectively. BTH capture efficiency increased with increasing suction flow rate. The opening area between the top edge of the BTH and the wearer's face significantly affected the suction flow required to achieve 99.99%

capture efficiency. The fixed inspiratory flow rate of 40 L/min applied only when the average respiratory rate was less than 15 L/min and the slot opening area was not greater than 20 cm^2. The PU foam filters, as mixing reducers, effectively reduced the escaping aerosols and the required suction flow rate. The use of foam filter also helped fix the opening area.

The cross-sectional area between the top edge of the hood and the wearer's face was critical to capture efficiency and greatly affected the required suction flow rate. However, as shown in Figure 2, the cross-sectional area varied and was difficult to control. Another disadvantage of the invention was that the connecting tube between the hood and the suction fan and filter unit might disturb the wearer's daily operation unless the tube was tightly secured to the clothing.

Figure 2. Schematic diagram of a human body wearing a BTH.

CONCLUSIONS AND RECOMMENDATIONS

Overall, this constant suction BTH is comfortable to wear has high capture efficiency and can prevent exhaled particles from polluting the environment. High respiratory flows require increased inspiratory flow to maintain high capture efficiency. In this case, a larger fan, battery, and filter are needed to maintain adequate negative pressure in the hood during exhalation.

To further improve the performance of this new device, we propose to attach the filter, fan, auto-feedback control unit, and battery directly to the mask, making it look like a regular elastomeric half-mask respirator. Its appearance resembles commercially available breath-responsive powered air-purifying respirators, but the exhalation valve and inhalation fan directions are reversed. After such adjustment, the suction mask should be able to maintain a slight negative pressure during the breathing cycle. The breath-responsive BTH is designed to hold a slight negative pressure within the hood and is still under development.

International and national health authorities responsible for infection prevention and control have not learned enough lessons from past COVID-19 outbreaks and continue to rely too much on biomedical tools while neglecting the importance and necessity of engineering control tools. Medical students need to learn more about aerosol science and technology. The infection control and prevention course syllabus should include the basic knowledge of aerosol generation mechanisms, aerosol size dependency, aerosol transmission characteristics, and aerosol removal principles to eliminate the knowledge gaps and control strategy differences during the recent epidemic.

Source control is the most effective approach compared to receptor and pathway control measures. Personal BTH can play a role in stopping the spread of an outbreak in its early stages,

just like a fire extinguisher puts out a small fire. If education and training programs are well promoted and implemented, this novel source control device could make quarantines and lockdowns meaningless and redundant.

ACKNOWLEDGEMENTS

This study was sponsored by the National Science and Technology Council of Taiwan under grants JC/2102, MOST 111-2221-E-002-045 and MOST 111-2221-E- 273-002.

REFERENCES

Jayaweera, M., Perera, H., Gunawardana, B., & Manatunge, J. (2020, Sep). Transmission of COVID-19 virus by droplets and aerosols: A critical review on the unresolved dichotomy. Environmental Research, 188, 109819.

Lindsley, W. G., Blachere, F. M., Law, B. F., Beezhold, D. H., & Noti, J. D. (2021). Efficacy of face masks, neck gaiters and face shields for reducing the expulsion of simulated cough-generated aerosols. Aerosol Science and Technology, 55(4), 449-457.

Morawska, L., & Cao, J. (2020, Jun). Airborne transmission of SARS-CoV-2: The world should face the reality. Environ Int, 139, 105730.

Morawska, L., & Milton, D. K. (2020, Dec 3). It Is Time to Address Airborne Transmission of Coronavirus Disease. Clin Infect Dis, 71(9), 2311-2313.

6th International Conference on Building Energy and Environment
Eindhoven University of Technology, The Netherlands
6 - 10 July 2025

How CO_2 concentration and window opening in classrooms of elementary/secondary schools changed during COVID-19 pandemic period in Tokyo, based on governmental hygienic inspection data

Go Iwashita [1]

[1]*Department of Architecture, Tokyo City University, Tokyo, Japan, iwashita@tcu.ac.jp*

SUMMARY
The time series changes in air environment during winter and summer periods in elementary/secondary schools located in Tokyo was analysed by using the local governmental hygienic inspection data. The period of analysis was set from 2007 to 2021.
1) Before the coronavirus outbreak in 2020, the 50th percentile of indoor CO2 concentration in elementary school classrooms was below 1000ppm, while the 95th percentile was around 2000 to 2500ppm, which exceeded the school environmental hygiene standard of 1500ppm. During and after the coronavirus pandemic that occurred in 2020, the 95th percentile value decreased to below 1,500 ppm.
2) Before 2019, the 50th percentile of indoor CO_2 concentration in secondary school classrooms during the winter and summer was between 1000 and 1500ppm, while the 95th percentile was approximately 2500ppm. During and after the coronavirus pandemic in 2020, the 95th percentile of CO_2 decreased to below 1500ppm in secondary school as well.

Keywords: school classroom, CO_2 concentration, coronavirus outbreak

1. 1. INTRODUCTION

In Japan, based on the ``School Health and Safety Act'', environmental health inspections are required to be conducted regularly in school classrooms. Most of the regular inspections are conducted by school pharmacists. The School Health and Safety Act (Ministry of Education, Culture, Sports, Science and Technology, 2018) requires a school principal to take necessary measures to improve each school's environmental health problems based on the school environmental hygiene standards, or otherwise to report on the situation to the local officer in charge of the school management so that the problem can be dealt with. When considering control measures for the indoor air quality in classrooms, such as measures against influenza and COVID-19 infections, it is important to understand the actual situation of the air environment in school classrooms. Therefore, it is useful to obtain and analyse each school's environmental health inspection results mentioned above. However, the inspection results are not made public except by some local governments, making it difficult for the general public to know actual situations of each school's environmental hygiene.
As the COVID-19 infection gradually spread across the country, public elementary and secondary schools in X City started to cancel classes in March 2020, and the school closure continued for three months. In this study, we will examine the impact of new coronavirus infection control measures on the school air environment based on the ``School Environmental Hygiene Inspection Report of X city'', which is a survey of all schools in X city, rather than the limited measurement school studies mentioned above.

2. METHOS

2.1 Survey target area and survey year

The survey target area is X city in the Tokyo metropolitan area. In school year of 2021, there were 62 public elementary schools and 28 public secondary schools in X city. Classrooms in public elementary and secondary schools in X city are equipped with heat pump air conditioner. Since the report on X city used in this study did not mention the installation and operation status of ventilation equipment at the time of inspection, the influence of mechanical ventilation equipment is not considered in the analysis. The survey had been conducted for a period of 15 years from 2007 to 2021. However, the inspection was not conducted in 2013, thus the data only covers 14 years. From 2007 to 2009, school pharmacists of each school conducted an inspection of CO_2 concentration, air temperature, and relative humidity in classrooms once a year during winter. A school principal designated two measurement classrooms in each target school, and school pharmacists conducted measurements in the classrooms. From 2010 to 2021, measurements were conducted once during the summer and once during the winter, and just one classroom was surveyed for each school. Summer inspections were conducted from June to September, while winter inspections were conducted from December to February.

2.2 Inspection method

The classroom air inspection procedures for CO_2 concentration, air temperature, and relative humidity performed by school pharmacists are as follows:

(1) Air sampling 5 to 15 minutes after a class starts
(2) Air sampling 15 to 25 minutes after a class starts
(3) Air sampling 30 to 40 minutes after a class starts

Test items were measured also in the adjacent corridor before or after the measurements in the classrooms (1) to (3), while the outside air temperature was taken with the outside air. In addition to the above inspection items, the following items were measured: number of teachers, number of students, number of inspectors, operating status of cooling/heating equipment, opening status of exterior window, corridor-side door, and corridor-side transom, and so forth.

3. Results

3.1 Winter CO_2 measurement results

Figure 1 shows the time series changes in CO_2 concentration in all measured elementary school classrooms during winter inspections from 2007 to 2021. Figure 1 shows the CO_2 concentration in the 95th percentile, 75th percentile, and 50th percentile for each year in approximately 60 public elementary schools in X city. The numbers shown above the upper abscissa are the numbers of measurement data for each year. The CO_2 concentration used in this figure was the result of air sampling data measured 30 to 40 minutes after a class starts. It can be seen that the CO_2 concentration has decreased significantly since 2020, when COVID-19 infections spread nationwide. There is a significant difference in the CO_2 concentration between a period of two years before the COVID-19 (2018, 2019) and a period of two years during the COVID-19 spread (2020, 2021) ($p<0.0001$).

Figure 2 shows the time series changes in CO_2 concentration in the secondary school classrooms during winter inspections from 2007 to 2021. It shows the CO_2 concentration in the 95th percentile, 75th percentile, and 50th percentile for each year in approximately 30 public secondary schools in X city. As seen in Figure 1, it can be found that the CO_2 concentration has also decreased significantly in secondary schools after 2020, when COVID-19 infections spread. There

is a significant difference in the CO_2 concentration between before and after the COVID-19 pandemic ($p<0.0001$).

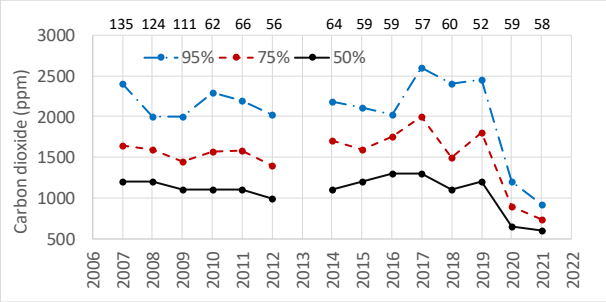

Figure 1. CO_2 concentration in the elementary school classrooms during winter inspections from 2007 to 2021. (CO_2 concentration in the 95th percentile, 75th percentile, and 50th percentile of winter measurements for each year)

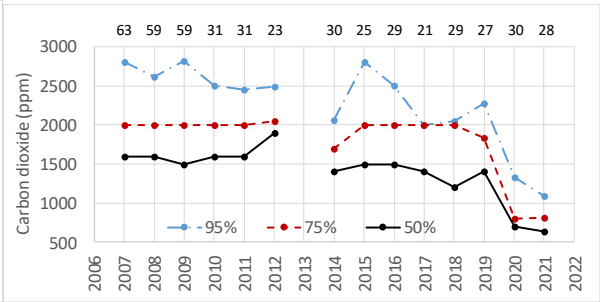

Figure 2. CO_2 concentration in the secondary school classrooms during winter inspections from 2007 to 2021. (CO_2 concentration in the 95th percentile, 75th percentile, and 50th percentile of winter measurements for each year)

3.2 Changes over time in the opening length while windows and doors are remaining open

In the school air inspection conducted for this study, opening length while classroom windows, transom windows and doors were remaining open was recorded when measuring CO_2 concentration, temperature, humidity, etc. The windows, transom windows, and doors in the target elementary and secondary school classrooms in X city are mainly sliding type, so the degree of opening of the windows and doors is recorded in centimetres (cm). The types of opening sections include exterior windows, exterior transom windows, corridor-side doors, and corridor-side transom windows.

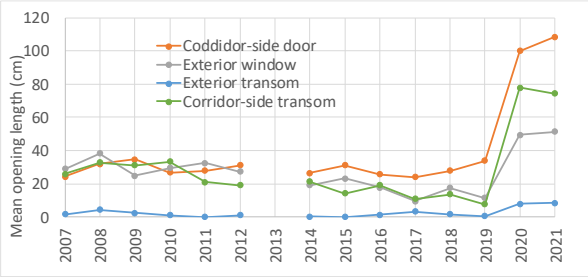

Figure 3 Mean opening length of the elementary school classrooms during winter inspections from 2007 to 2021

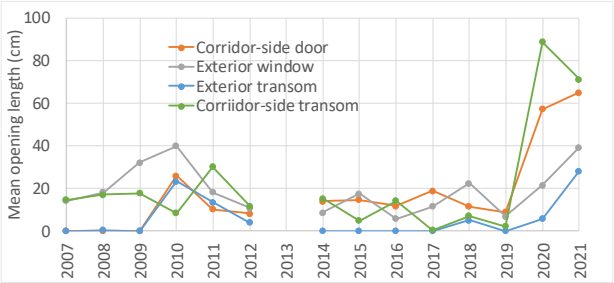

Figure 4 Mean opening length of the secondary school classrooms during winter inspections from 2007 to 2021

Figures 3 and 4 show the changes over time in the average opening length of each opening section observed in elementary school classrooms and secondary school classrooms, respectively, in the winter inspection. Before the COVID-19 outbreak in 2020, all opening sections in the elementary and secondary schools remained open with short length during the winter, while the exterior transoms were usually closed. Apparently, this was due to a risk prevention for falling from open windows, and difficulty of opening the windows. After 2020, the opening length of all opening sections has increased, especially, the corridor-side doors and corridor-side transoms were kept open more widely. On the other hand, the opening length of the exterior transoms in elementary school classrooms did not increase much even during the COVID-19 period.

4. DISCUSSION

When schools reopened during the coronavirus pandemic in June of 2020, the Ministry of Education, Culture, Sports, Science and Technology (MEXT) made a request that each school make sure to maintain an adequate ventilation rate to avoid closed spaces. For elementary and secondary school teachers who are not experts in HVAC, it was not obvious whether their school buildings had mechanical ventilation equipment or not, and even if the buildings were equipped with adequate ventilation system, they were not certain about the capabilities of the equipment. Therefore, it was assumed that they should always keep the windows open for cross ventilation even if their school buildings had mechanical ventilation. In addition, the above-mentioned request by MEXT required thorough ventilation even during the period when air conditioner was operated, therefore, it was thought the ventilation by opening the windows was used while operating air conditioner during heating or cooling period. During the COVID-19 pandemic, there is a risk that heating will become less efficient and room temperature will drop due to the windows being open to heat the room.

5. CONCLUSION

Using the air inspection results from the school environmental hygiene survey in X city, a local government in the Tokyo metropolitan area, we investigated changes over time in CO_2 concentration, room temperature, and openings. As a result, the following findings were obtained.

1) Before the coronavirus outbreak in 2020, the 50th percentile of indoor CO_2 concentration in elementary school classrooms during winter was below 1000ppm, while the 95th percentile was around 2000 to 2500ppm, which exceeded the school environmental hygiene standard of 1500ppm. During and after the coronavirus pandemic in 2020, the 95th percentile value decreased to below 1,500 ppm.

2) Before 2019, the 50th percentile of indoor CO_2 concentration in secondary school classrooms during winter was between 1000 and 1500ppm, while the 95th percentile was approximately 2500ppm. During and after the coronavirus pandemic in 2020, even the 95th percentile of CO_2 has been below 1500ppm.

3) The decrease in CO_2 concentrations during the COVID-19 pandemic was probably due mainly to ventilation through open windows and doors.

4) On the other hand, consideration must be given to the deterioration of the thermal environment due to reduced heating and cooling efficiency caused by opening windows for ventilation.

ACKNOWLEDGEMENTS

This work was supported by JSPS KAKENHI Grant (22H01655).

REFERENCES

Ministry of Education, Culture, Sports, Science and Technology: School Health and Safety Act Enforcement Regulations, School environmental hygiene management manual, https://www.mext.go.jp/content/20230817-mext_kenshoku-100000613_2.pdf, 2018.5(in Japanese)

6th International Conference on Building Energy and Environment
Eindhoven University of Technology, The Netherlands
6 - 10 July 2025

Inversion identification of heavy gas source strength and dispersion in enclosed workplaces based on a three-dimensional computational fluid dynamics and iterative ensemble Kalman filter model

Shasha Wang [1], Xing Zheng [1], S. Thomas Ng [1]

[1] *Department of Architecture and Civil Engineering, City University of Hong Kong, Kowloon Tong, Hong Kong, China.*

SUMMARY
In the early stages of gas leak accidents, accurately estimating the source strength is crucial for formulating effective rescue strategies. However, CFD modeling methods typically provide reasonable concentration predictions when source information is known. This paper proposes a model that integrates three-dimensional (3D) computational fluid dynamics (CFD) with iterative ensemble Kalman Filtering (IEnKF) to identify the strength and dispersion of heavy gas sources in enclosed workplaces. The developed model can iteratively correct uncertainties of input parameters using limited observational data and then enable accurate estimation of source information. For the case study of hydrogen sulfide (H_2S) leakage in a confined space, the proposed CFD-based IEnKF model can provide reasonable estimates of the H_2S leakage velocity, fresh air supply velocity, and concentration distribution after only two assimilation time steps. The results provide valuable insights for consequence assessment and emergency response in indoor pollutant leakage incidents.

Keywords: Inversion identification, Heavy gas leakage, Iterative ensemble Kalman filter.

1. INTRODUCTION

Indoor environments are crucial for human safety, especially in spaces like biochemical labs, which are at high risk of toxic gas leakage. Most toxic gases have a higher molecular weight than air and are classified as heavy or dense gases. These gases tend to accumulate near the ground or in occupied areas, posing a significant threat to human health. Therefore, accurately predicting the leakage of toxic heavy gases in enclosed workspaces is essential for human safety and effective consequence assessment.

Various studies have investigated the leakage and dispersion behaviours of heavy gases in indoor environments using field experiments, wind tunnel experiments, mathematical and CFD models(Han et al., 2020; Wang et al., 2013). These studies generally focus on forward modeling with known source parameters. However, in most leakage incidents, unknown source parameters present huge challenges. Data assimilation techniques, such as ensemble Kalman Filter (EnKF) and its iterative version (IEnKF), are effective for addressing this issue by using observational data to correct initial uncertainties of input parameters.

Table 1 provides a non-exhaustive overview of EnKF/IEnKF studies on source parameter estimation in various fields. Records were retrieved from Web of Science and Scopus for the period 2000 – 2024 using the query ("Ensemble Kalman Filter" OR "Iterative EnKF") AND ("source

term" OR "source parameter" OR "source inversion"). After retrieval, papers were screened manually by title, abstract and conclusions to exclude irrelevant works; only English-language publications were retained. Owing to space limitations, Table 1 discusses the most pertinent contributions. Key findings include: (1) EnKF is the commonly used method for estimate source parameter, with limited use of IEnKF. (2) While EnKF/IEnKF has been applied across various fields, studies on the inversion of indoor source parameters remain limited. (3) Most studies use simplified dispersion models, with only a few employing complex 3D CFD models. (4) Twin experiments are the most common validation method, with some studies also using field tracer experiments.

This study aims to propose a 3D CFD-IEnKF model for the inversion and identification of heavy gas source strength and dispersion in enclosed workspaces to fill the above gap. The reliability of the proposed model is evaluated through a case study of H_2S leakage in an enclosed workspace.

Table 1. Summary of EnKF/IEnKF studies on source parameter estimation in various scenarios.

Reference	Field	Source	Interested source parameters	Dispersion model	Inversion method	Temporal release	Validation method
(Zhang and Huang, 2017)	River	RWT	SRR	1D-ADE	EnKF	Yes	TE, FE
(Jing et al., 2023)	Water	RB	SL, SRT, SRM	2D-ADE	RC-EnKF	Yes	FE
(Yuan et al., 2019)	Tunnel	CH_4	SRR	1D-ADE	EnKF	Yes	TE
(Cai et al., 2022)	Tunnel	CH_4	SRV	3D-CFD	EnKF	Yes	TE
(Qian et al., 2022)	Indoor	N/A	BC	3D-CFD	EnKF	No	SE
(Qian et al., 2024)	Indoor	N/A	BC	3D-CFD	EnKF	No	TE
(Lin and Wang, 2013)	Indoor	SF_6	N/A	MBM	EnKF	Yes	TE
(Zhang et al., 2014)	Atmosphere	^{137}Csc	SRR, PRH	LPM	IEnKF	Yes	TE
(Zhang et al., 2015)	Atmosphere	SF_6	SRR	LPM	IEnKF	Yes	FE
(Wu et al., 2023)	Tunnel	CH_4	SRR,SL	1D-ADE	IEnKF	Yes	TE

RWT = Rhodamine WT dye; RB = Rhodamine B dye; CH_4 = Methane; SF_6= Sulfur hexafluoride; ^{137}Csc = Cesium-137; SRR = Source Release Rate; SL = Source location; SRT = Source release Time; SRM = Source release mass; SRV = Source release velocity; BC = Boundary conditions; PRH = Plume rise height; 1D/2D-ADE = One/Two-dimensional advection-dispersion equation; 3D-CFD = Three-dimensional CFD-based gas dispersion model; MB = Mass balance model; LPM = Lagrangian puff model; EnKF = Ensemble Kalman filter; RC-EnKF = Improved EnKF based on relation coefficient assimilation; IEnKF = Iterative EnKF; TE = Twin experiments; FE = Field tracer experiments; SE = Reduced-scale model experiments.

2. METHODS

Firstly, a 3D CFD model is developed and validated through grid independence analysis and comparison with existing experimental data. This CFD model is then integrated with the Iterative Ensemble Kalman Filtering (IEnKF) method to estimate the H_2S leakage velocity, air supply velocity, and predict the concentration distribution in enclosed workspaces. To assess the

reliability of the proposed model, the twin experiment approach is employed, which involving comparing three sets: the control set, where assumed true values are used as inputs and serve as the ground truth; the data assimilation (DA) set, where initial guess distributions are corrected using the IEnKF method; and the reference set, where initial guess distributions are applied without IEnKF correction. Due to space limitations, only a concise overview of the methodology is presented here. For a detailed description of the methodology, see (Wang et al., 2024).

3. RESULTS & DISCUSSION

The proposed model provides time-series estimations of the H_2S leakage velocity and air supply velocity, as shown in Fig. 1. (a) and (b). The results demonstrate that accurate estimates can be obtained after only two assimilation time steps (2 s): the estimated H_2S leakage velocity (18.2 m/s) has a relative error of less than 7.06% compared to the assumed true value (17 m/s); the estimated air supply velocity (0.89 m/s) has a relative error of less than 11.25% compared to the assumed true value (0.8 m/s). After 13 assimilation steps, the estimated H_2S leakage velocity (17.2 m/s) is nearly identical to the assumed true value.

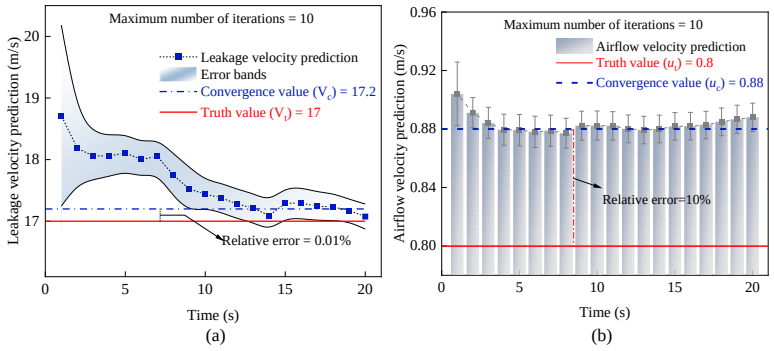

Figure 1. Time-series estimations of (a) H_2S leakage velocity and (b) air supply velocity.

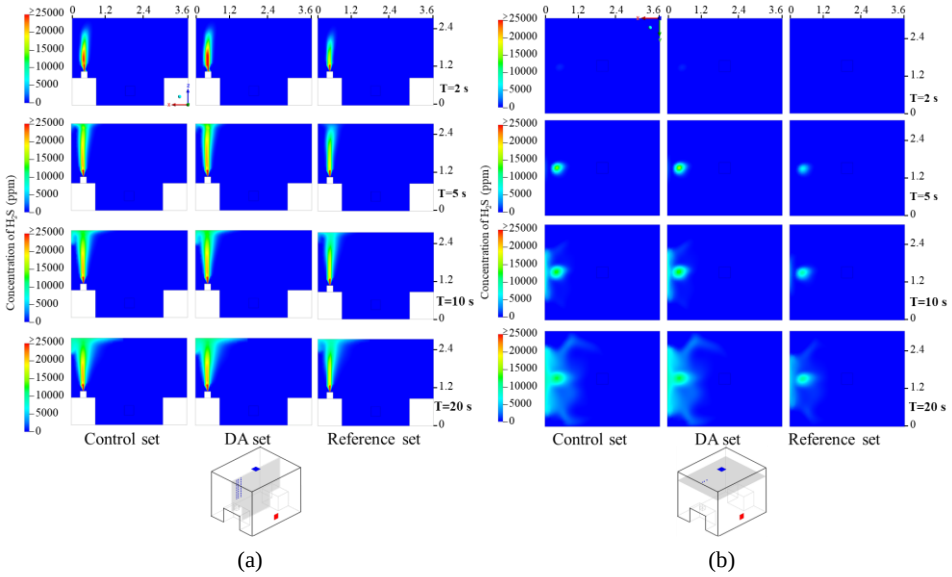

Figure 2. Gas concentration distribution at (a) Y = 1.5 m plane; (b) Z = 2.5 m plane.

4. CONCLUSION

In this study, a 3D CFD-IEnKF coupled model was developed to enable the rapid and accurate estimation of indoor heavy gas leakage source parameters and provide detailed predictions of concentration distributions. The reliability of the proposed model was validated through a case study of H_2S leakage in an enclosed workspace using the twin experiment method. This model can be effectively applied in the initial stages of indoor leakage incidents to offer managers timely feedback on leakage source information and provide valuable guidance for emergency response.

REFERENCES

Cai, J., Wu, J., Yuan, S., Kong, D., Zhang, X., 2022. Prediction of gas leakage and dispersion in utility tunnels based on CFD-EnKF coupling model: A 3D full-scale application. Sustainable Cities and Society 80, 103789.

Han, O., Zhang, Y., Li, A., Li, J., Li, Y., Liu, H., 2020. Experimental and numerical study on heavy gas contaminant dispersion and ventilation design for industrial buildings. Sustainable Cities and Society 55, 102016.

Jing, L., Kong, J., Wang, J., Xu, T., Pan, M., Chen, W., 2023. Joint identification of contaminant source based on the ensemble Kalman filter integrated with relation coefficient. Journal of Hydrology 617, 129057.

Lin, C.-C., Wang, L. (Leon), 2013. Forecasting simulations of indoor environment using data assimilation via an Ensemble Kalman Filter. Building and Environment 64, 169–176.

Qian, W., Gao, H., Lu, Y., Lyu, S., Zhuang, L., Hu, S., Wang, L., Liu, J., 2024. Optimizing measurement schemes to improve indoor airflow and temperature CFD–EnKF joint simulation. Building and Environment 248, 111070.

Qian, W., Tang, M., Gao, H., Dong, J., Liang, J., Liu, J., 2022. Improving indoor air flow and temperature prediction with local measurements based on CFD-EnKF data assimilation. Building and Environment 223, 109511.

Wang, S., Zheng, X., Ng, S.T., Bao, Z., 2024. An innovative three-dimensional computational fluid dynamics-iterative ensemble Kalman filter model for the prediction of heavy gas leakage and dispersion in enclosed workplaces: Case study for hydrogen sulfide leakage. Physics of Fluids 36.

Wang, Z., Hu, Y., Jiang, J., 2013. Numerical investigation of leaking and dispersion of carbon dioxide indoor under ventilation condition. Energy and Buildings 66, 461–466. https://doi.org/10.1016/j.enbuild.2013.06.031

Wu, J., Cai, J., Liu, Z., Yuan, S., Bai, Y., Zhou, R., 2023. BI-IEnKF coupling model for effective source term estimation of natural gas leakage in urban utility tunnels. Tunnelling and Underground Space Technology 136, 105080.

Yuan, S., Wu, J., Zhang, X., Liu, W., 2019. EnKF-based estimation of natural gas release and dispersion in an underground tunnel. Journal of Loss Prevention in the Process Industries 62, 103931.

Zhang, X., Huang, M., 2017. Ensemble-based release estimation for accidental river pollution with known source position. Journal of Hazardous Materials 333, 99–108.

Zhang, X.L., Su, G.F., Chen, J.G., Raskob, W., Yuan, H.Y., Huang, Q.Y., 2015. Iterative ensemble Kalman filter for atmospheric dispersion in nuclear accidents: An application to Kincaid tracer experiment. Journal of Hazardous Materials 297, 329–339.

Zhang, X.L., Su, G.F., Yuan, H.Y., Chen, J.G., Huang, Q.Y., 2014. Modified ensemble Kalman filter for nuclear accident atmospheric dispersion: Prediction improved and source estimated. Journal of Hazardous Materials 280, 143–155.

6th International Conference on Building Energy and Environment
Eindhoven University of Technology, The Netherlands
6 - 10 July 2025

New Insights into the Dynamics of Dental Atomization Procedures for Healthier and Cleaner Future Environments

Xiujie LI [1], Cheuk Ming Mak [2], Kuen Wai Ma [3], Siqi Zhou [4], Hai Ming Wong [5]

[1]*Department of Building Environment and Energy Engineering, The Hong Kong Polytechnic University, Hong Kong, xiujie.li@connect.polyu.hk*
[2]*Department of Building Environment and Energy Engineering, The Hong Kong Polytechnic University, Hong Kong, cheuk-ming.mak@polyu.edu.hk*
[3] *Department of Building Environment and Energy Engineering, The Hong Kong Polytechnic University, Hong Kong, kuen-wai.ma@polyu.edu.hk*
[4] *Department of Building Environment and Energy Engineering, The Hong Kong Polytechnic University, Hong Kong, 21039114r@connect.polyu.hk*
[5]*Faculty of Dentistry, The University of Hong Kong, Hong Kong, wonghmg@hku.hk*

SUMMARY
Emerging respiratory infectious disease agents, like SARS-CoV-2 and influenza, have significantly impacted public health and the provision of medical services. Dental environments have been widely regarded as one of the most vulnerable healthcare facilities owing to the continued ejection of contaminated droplets and aerosol particles in the atomization procedures. The present study aims to combine the Particle Image Velocity measurement and fast Large-eddy Simulation to assess dental spray dynamics, further evaluating the particle removal performance of high-volume suction (HVS). The results are analysed from the contamination areas and fallow time. The dental droplets with a diameter threshold of $72.6\,\mu m$ can escape from the spray core region under the air entrainment, along with two distinctive final fates: suspension and deposition. The placement location of the HVS at the different spray regions can directly affect the particle removal efficiency, fluctuating at around 60%. The average residence time for the dehydrated droplet nuclei and aerosol can be achieved in 6 min. Entering the surgery room early without waiting for fallow time can induce a high exposure index. The results can thus provide suggestions for updating dental guidelines and better prevention for the next respiratory infectious disease, "Disease X" in medical environments.

Keywords: Dental spray dynamics, Particle Image Velocimetry, Large-eddy simulation, Droplet.

1. GENERAL INSTRUCTIONS

Understanding the interaction between humans and the environment, particularly about fluid flow and disease transmission, has long been a focus of research (Prather et al., 2020). Among healthcare facilities, dental clinics are widely regarded as some of the most vulnerable environments. During dental procedures, a contaminated liquid mixture, including mucosalivary fluid and microbiomes, can be aerosolized. Once dental professionals and patients inhale the pathogen-carrying particles, the transmission of infectious diseases would occur. The suspended particles have already instilled fear and uncertainty about cross-infection in healthcare facilities, posing significant threats to the provision of medical services. Investigating the dynamics of dental spray is crucial for creating healthier and cleaner future environments, especially given the aging patient population in urban areas (Guida et al., 2021).

During the COVID-19 pandemic, various mitigation measures and equipment have been developed to reduce human exposure to suspended aerosols. Compared to other engineering control methods, source-control measures can directly reduce the generation and ejection of contaminated droplets. Recent studies have evaluated the particle removal performance of high-volume suction (HVS) systems and air cleaners (Li et al., 2021a). They indicated that this equipment only removes the vortices at the spray surroundings and the ambient small droplets. Due to the limited research on the structures and dynamics of dental sprays, the mitigation measures have not been effectively developed to meet targeted objectives. The advances in computational resources and the development of high-speed cameras promote the investigation of the droplet aerosolization and transmission process. A recent study experimentally captured the formation of multi-phase turbulent clouds during human coughs (Bourouiba et al., 2020). From the Particle Image Velocimetry (PIV) investigation, clusters of larger droplets swirling within the clouds could be transported for 1-2 meters. Additionally, Direct Numerical Simulation (DNS) and Large Eddy Simulation (LES) can provide more comprehensive insights into the flow and development of droplet clouds. However, there is limited research focused on specific dental surgery environments due to the challenges in accurately characterizing droplet properties in these settings.

The present study aims to integrate PIV measurements with LES techniques to gain a new insight into the dental spray structures and dynamics. The findings are expected to update the dental guidelines and enhance prevention strategies for future respiratory infectious diseases in medical environments. The second section of this study introduces the experimental and numerical methods. The third section shows the results and discussion.

2. METHODOLOGY

Figure 1 presents a schematic figure combining the Particle Image Velocimetry (PIV) measurement and large eddy simulation techniques. The ultrasonic scaling, high-speed drilling, and 3-in-1 spraying are conducted on the manikin model, and the ejected droplets can be illuminated by the laser light sheet (Figure 1a). The dental spray core region can be further determined by the angle (red dashed line shown in Figure 1b), which covers the vast majority of ejected droplets. The droplet characteristics, including size range: 5−250 μm; velocity: 2.5 m/s, and distribution angle: 30 degrees, could be obtained from the recorded image sequence analysis by the Image J software. The measured geometric diameter was in line with the aerodynamic diameter (Li et al., 2024), since the density of dental-emitted droplets was also kept at 1 g/cm^3. The computational domain is designed to include two dental professionals and one patient. The droplet characteristics identified in the PIV experiment are used as boundary conditions for the LES modeling. This approach allows for to determination of the spatial distribution of contaminated droplets, the contamination caused by deposition, and the residence time of suspended particles in surgical environments. Detailed descriptions of the experimental and numerical methods are available in our previous studies (Li et al., 2021b; Li et al., 2023a; Li et al., 2023b).

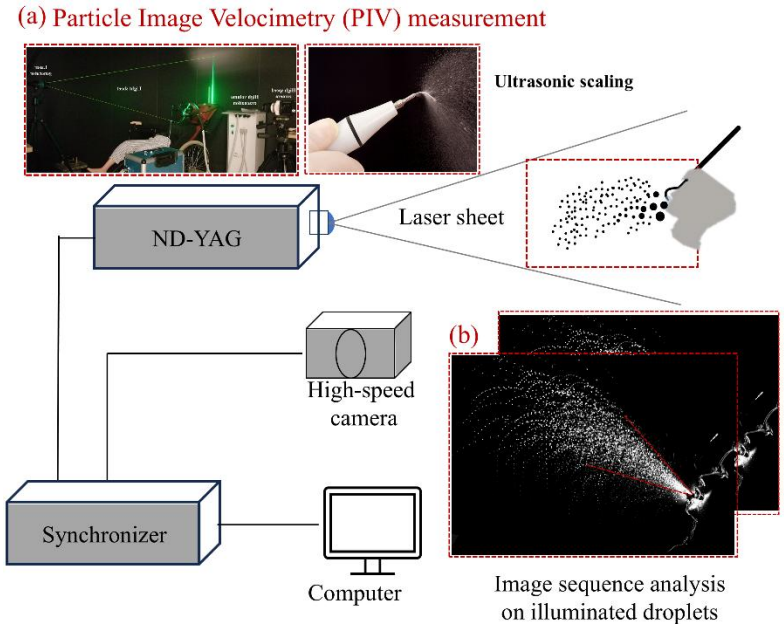

Figure 1. Schematic diagram of the assessment on dental spray dynamics: (a) the Particle Image Velocimetry (PIV) measurement on the illuminated droplets; (b) the droplet characteristics identified in image sequence analysis further serve as boundary conditions for fast large-eddy simulation.

2.1. Particle Image Velocimetry (PIV) Measurement

The PIV measurements and dental atomization procedures were carried out in the experimental chamber at the Hong Kong Polytechnic University. A thermal manikin, featuring 24 individually controlled body segments, was positioned on the dental chair. The surface area and sitting body height of the manikin were $1.6\,m^2$ and $1.35\,m$, respectively. A laser light sheet was projected across the dental treatment area, with a high-speed camera positioned perpendicularly to capture the interaction. Synchronization between the high-speed camera and the laser generator ensured precise timing. The captured image sequences were initially analysed using an adaptive PIV algorithm to determine droplet velocity patterns. Subsequently, Image J software was utilized to assess droplet size distribution and identify the core of the dental spray. Further analysis details can be found in our previous study (Li et al., 2021b). Overall, the dental-contaminated droplets are generally located in the range from $5-250\,\mu m$, while the velocity fluctuates at around $2.5\,m/s$. The droplet composition model can be regarded as the combination of 98.92% water, 0.9% glycerin, and 0.18% salt (Li et al., 2025a).

2.2. Large Eddy Simulation

To accurately simulate the transmission patterns, it is essential to consider the evaporation process and the composition of dental-contaminated droplets in the present study. Firstly, the dental liquid mixture was assumed to be well-mixed during the dental atomization procedures, with a mean stimulated salivary flow rate of $1.4\,mL/min$ and a water supply flow rate of $60\,mL/min$. As droplets evaporate, their non-volatile components form droplet nuclei that can remain suspended in the clinical environment for extended periods. The following equations describe the nondimensional evaporation rate of the l-th droplet:

$$\frac{dm_{p,i}}{dt} = -\pi d_i Nu \ ln\left(1 + B_{m,i}\right) \frac{1-\psi_i}{Re_{in}Sc} \quad (1)$$

$$Nu = \frac{hd_p}{k_\infty} = 2.0 + 0.6Re_d^{1/2}Pr^{1/3} \quad (2)$$

$$B_{m,i} = (Y_{p,i} - Y_{f,i})/(1 - Y_{p,i}) \quad (3)$$

where, $m_{p,i}$ is the mass of i-th droplet. Nu refers to the Nusselt number. k_∞ and Pr are the thermal conductivity and Prandtl number of the continuous phase (air), respectively. h is the heat transfer coefficient, which is defined based on the Ranz-Marshall model (Ranz et al., 1952). Owing to the small variation in the air temperature, the thermodynamic characteristics of the air were treated to be constant. $B_{m,i}$ indicates the Spalding mass number. $Y_{p,i}$ and $Y_{f,i}$ are the mass fractions of water vapor in the droplet and the surrounding air, respectively. Sc is the Schmidt number. The heat balance between the droplet and gas phases related to the convective and latent heat transfer can be obtained as follows:

$$m_p c_p \frac{dT_p}{dt} = hA_p\left(T_g - T_p\right) - L\frac{dm_p}{dt} \quad (4)$$

where c_p and A_p refer to the specific heat and surface area of the droplet, respectively. T_p and T_g indicate the droplet and gas temperature, respectively [Li et al., 2022a; Li et al., 2022b].

3. RESULTS AND DISCUSSION

3.1. Human Micro-environment and Airflow Patterns

Figure 2 illustrates the velocity streamlines and airflow patterns in the dental surgery environment. Cooling air exits from the ventilation inlet and travels along the ceiling surface. Airflow separations occur due to impingement with the room walls. After interacting with the human thermal plume and respiratory flow, the mixed air is expelled through the ceiling exhaust. The maximum velocity for the mannikin thermal plume is around $0.23\ m/s$. To accurately assess the human exposure index, it is essential to precisely simulate airflow interactions within the human micro-environment.

Figure 3 presents the local mesh refinement in the human breathing zone, highlighting nasal inhalation and exhalation characteristics. To unravel the temporal evolution of the multi-phase turbulent cloud during the ultrasonic atomization procedure, the mesh refinement near the dental treatment region is created with the finest cell size maintained at around 0.0008 m. Five layers of prismatic cells are created to guarantee that the y+ value remains below 1. The aforementioned grid can provide a good resolution for unravelling the dental spray dynamics. Nasal exhalation flows can disrupt the rising thermal plume, while ambient particles may be drawn into the inhalation flow. These localized airflow patterns significantly influence the distribution of suspended droplets and aerosol particles, particularly those with small aerodynamic sizes. The following sections will evaluate the relationship between droplet propagation patterns and flow field characteristics.

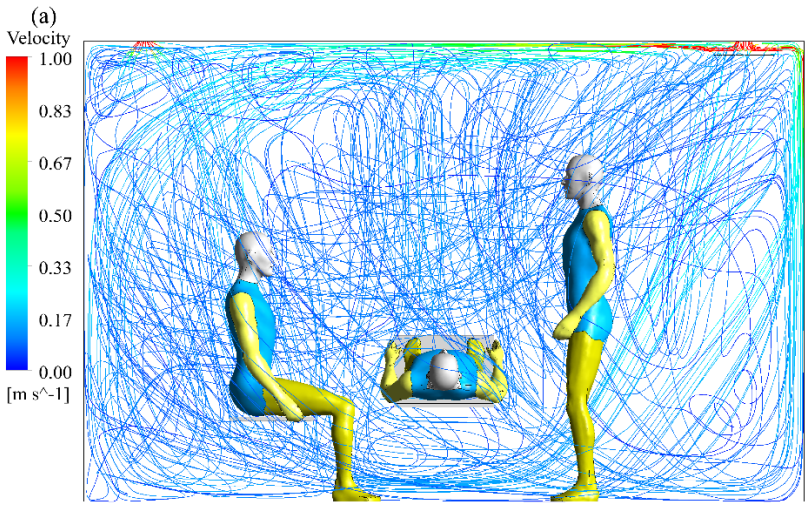

Figure 2. Velocity streamlines and airflow patterns in the dental surgery environment, streamlines colored by the velocity magnitude

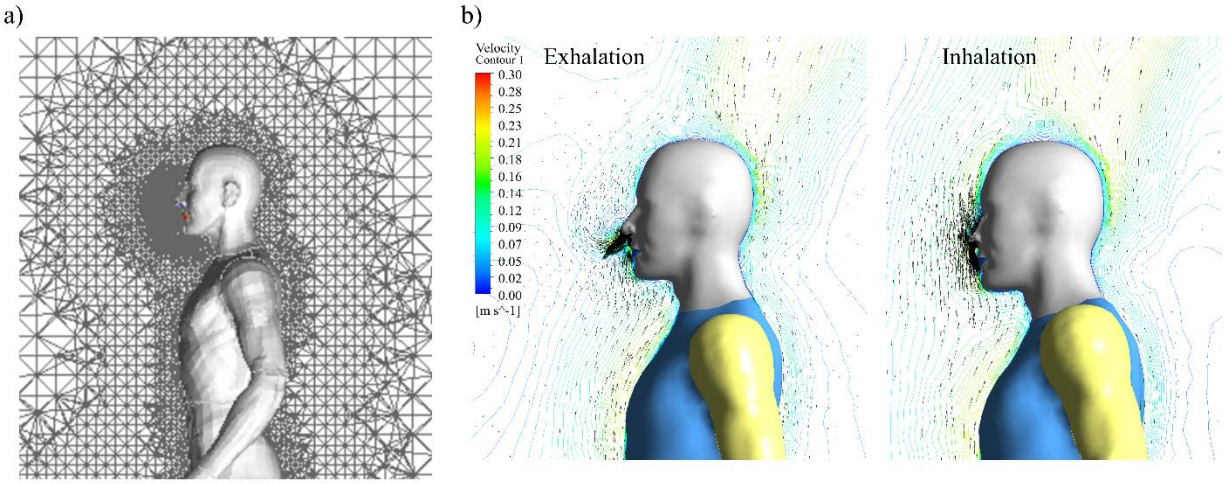

Figure 3. Local mesh and the nasal inhalation/exhalation characteristics

3.2. Dental Spray Dynamics and Residence Time

Figure 4 illustrates the spatial-temporal distribution patterns of contaminated droplets during the ultrasonic procedure. The red triangular area indicates the dental spray core, as determined by PIV visualization. At the moment of $T = 3s$, some small particles, depicted in blue, can escape from the core region of the dental spray and form a surrounding shear layer. The maximum size of these escaped particles is identified as $15.4\,\mu m$. Based on the mass fraction ratio of the dental-contaminated droplets and the corresponding equivalent size ratio (21.2%), the initial droplet size can be calculated as $15.4 \div 21.2\% = 72.6\,\mu m$. Consequently, dental droplets with a diameter threshold of $72.6\,\mu m$ can escape from the spray core region due to air entrainment, leading to two distinct final fates: suspension in the air or deposition on surfaces. The droplets swirling within the cloud will gradually lose their water content, forming stable droplet nuclei. The roll-up effect of small droplets is noticed at T=6.0 s, with the high-velocity magnitude. This region can be referred to as the recirculation area, and the surrounding airflow entraining the pathogen-carrying

droplets can lead to contamination near the patient's head. The placement region of the HVS significantly affects particle removal efficiency, particularly in the spray core region and the surrounding shear layer. Our previous PIV visualization indicated that the removal efficiency fluctuated around 60% (Malmgren et al., 2021; Li et al., 2024; Li et al., 2025a) when the HVS was placed near the surrounding shear layer. Plenty of droplets in the core region cannot be removed, especially for those with high velocity and larger diameters. Therefore, the development of targeted mitigation measures should be based on the identified dental spray dynamics, along with the detailed guidelines. The results obtained in the present study can inform updates to dental guidelines during atomization procedures to enhance safety and effectiveness.

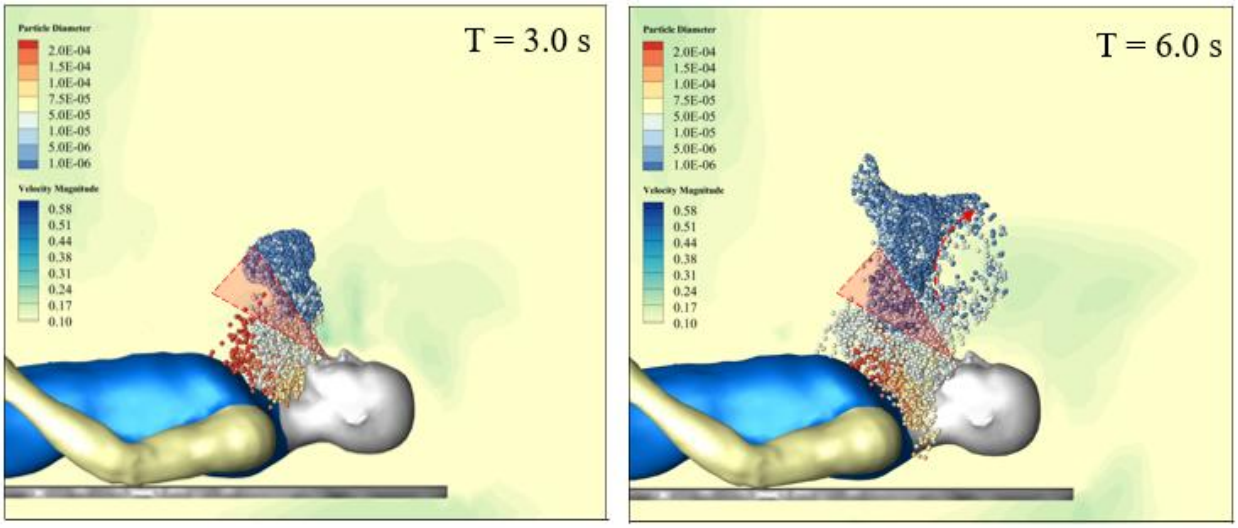

Figure 4. Dental spray dynamics and the dispersion patterns of contaminated droplets during the atomization procedures

Figure 5 illustrates the average residence time of droplets across different size distributions. For large droplets (greater than $100\ \mu m$), the residence time is generally less than 1.0 second. In contrast, aerosol particles smaller than $10\ \mu m$ can remain suspended for over $300\ s$, with a 50% increase in residence time for particles of $10-20\ \mu m$ ($200\ s$). Due to the prolonged airborne lifetime of these suspended particles, entering the surgery room prematurely, without allowing for adequate fallow time, can result in a high exposure index. Determining the proper fallow time based on the discrepancies between dental procedures and environmental conditions is also the warrant for future research (Li et al., 2021c). The results on the residence time of suspended particles are obtained based on a single realization, only for the ultrasonic scaling in a single dental surgery. Different medical procedures, ventilation rates, and clearance mechanisms can also lead to discrepancies in the particle residence time and human infection risks. The default Discrete Random Walk stochastic model in the ANSYS-Fluent code can induce time-varying deposition velocities and overestimate deposition rate, accounting for the discrepancy in the settling of micron-sized nuclei in the present study (Mofakham et al., 2020). Future research should consider a large number of droplets and numerous realizations to account for the turbulent flow and chaotic nature. The continuous random walk model based on the normalized Langevin equation is also warranted to further assess the particle dispersion and deposition in dental surgery environments.

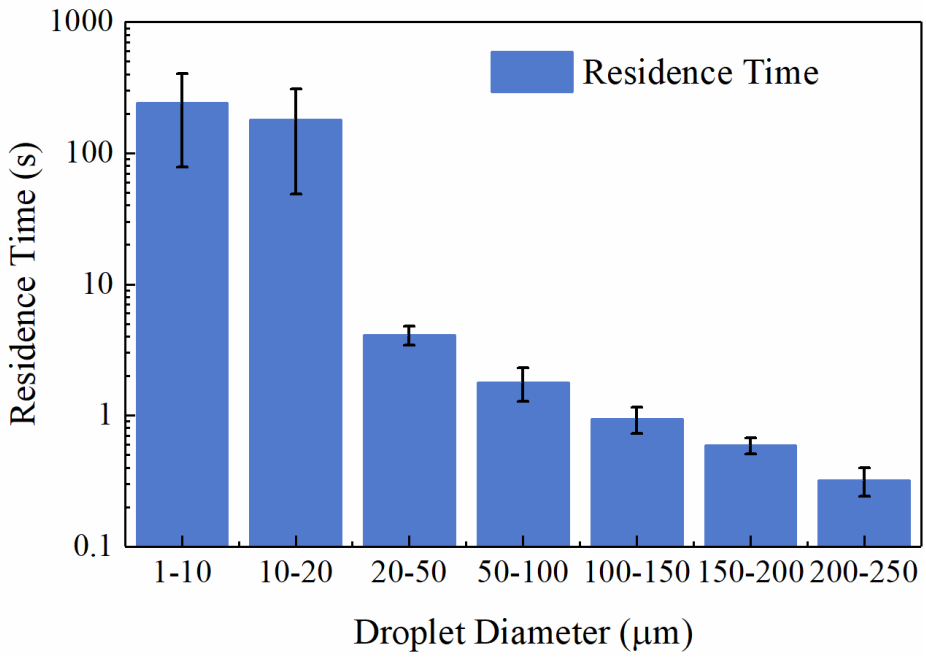

Figure 5. Average residence time of droplets in different size distributions

4. CONCLUSIONS

The contaminated liquid mixture, which includes mucosalivary fluid and microbiome, can become atomized during medical procedures. The presence of suspended particles has raised concerns about potential airborne transmission between subsequent appointments. Providing new insights into the dynamics of dental atomization can contribute to creating cleaner and healthier future environments. Droplets with a maximum size of $72.6\,\mu m$ can escape the core region, with two distinctive final fates: deposition or suspension. Source-control measures should be target-developed based on the analyzed spray dynamics. This study aims to support the development of evidence-based guidelines for dental environments, enhancing prevention strategies for future respiratory infectious diseases, such as the hypothetical "Disease X."

ACKNOWLEDGEMENTS

The work described in this paper was fully supported by a grant from the Research Grants Council of the Hong Kong Special Administrative Region, China (Project No PolyU 15209723).

REFERENCES

Prather, K. A., Wang, C. C., & Schooley, R. T. (2020). Reducing transmission of SARS-CoV-2. Science, 368(6498), 1422-1424.

Guida, C., & Carpentieri, G. (2021). Quality of life in the urban environment and primary health services for the elderly during the Covid-19 pandemic: An application to the city of Milan (Italy). Cities, 110, 103038.

Li X, Mak CM, Ma KW, Wong HM. (2021a). How the high-volume evacuation alters the flow-field and particle removal characteristics in the mock-up dental clinic. Building and Environment. 205:108225

Bourouiba L. (2020). Turbulent gas clouds and respiratory pathogen emissions: potential implications for reducing transmission of COVID-19. Jama, 323(18):1837-1838.

Li X, Mak CM, Ma KW, Wong HM. Evaluating flow-field and expelled droplets in the mockup dental clinic during the COVID-19 pandemic. Physics of Fluids 2021b, 33(4).

Li, X., Mak, C. M., Ai, Z., Ma, K. W., & Wong, H. M. (2023a). Numerical investigation of the impacts of environmental conditions and breathing rate on droplet transmission during dental service. Physics of Fluids, 35(4).

Li X, Mak CM, Ai Z, Ma KW, Wong HM. (2023b). Cross-infection risk assessment in dental clinic: Numerical investigation of emitted droplets during different atomization procedures. Journal of Building Engineering, 75:106961.
Ranz WE. (1952). Evaporation from drops. Chemical Engineering Progress, 48:142-180.
Li, X., Ai, Z., Ye, J., Mak, C. M., & Wong, H. M. (2022a). Airborne transmission during short-term events: Direct route over indirect route. Building Simulation. 15, 2097-2110.
Li, X., Mak, C. M., Ai, Z., & Wong, H. M. (2022b). Airborne transmission of exhaled pollutants during short-term events: Quantitatively assessing inhalation monitor points. Building and Environment, 223, 109487.
Malmgren R, Välimaa H, Oksanen L, Sanmark E, Nikuri P, Heikkilä P, Hakala J, Ahola A, Yli-Urpo S, Palomäki V. (2023). High-volume evacuation mitigates viral aerosol spread in dental procedures. Scientific Reports, 13(1):18984.
Li X, Mak CM, Ai Z, Ma KW, Wong HM. (2024). Propagation and Evaporation of Contaminated Droplets, Emission and Exposure in Surgery Environments Revealed by Laser Visualization and Numerical Characterization. Journal of Hazardous Materials. 135338.
Li, X., Mak, C. M., Ma, K. W., & Wong, H. M. (2025a). Large eddy simulation study on dental spray dynamics and infection during ultrasonic atomization. Journal of Building Engineering, 103, 112164.
Li, X., Mak, C. M., Ai, Z., Ma, K. W., & Wong, H. M. (2025b). Composition effect of the dental liquid mixture on droplet evaporation and deposition. Indoor and Built Environment, 1420326X251319480.
Mofakham, A. A., & Ahmadi, G. (2020). On random walk models for simulation of particle-laden turbulent flows. International Journal of Multiphase Flow, 122, 103157.
Li X, Mak CM, Ma KW, Wong HM. (2021c). Restoration of dental services after COVID-19: The fallow time determination with laser light scattering. Sustainable Cities and Society, 74:103134.

Building Physics, Building Envelope and Materials (11:00-12:30 h)

6th International Conference on Building Energy and Environment
Eindhoven University of Technology, The Netherlands
6 - 10 July 2025

Exploratory hydrovoltaic cement generator

Mostafa Yossef[1,2], Tanja Kallio[3], and Jari Puttonen[4]

[1]*Department of Civil Engineering, Aalto University, Espoo, Finland, mostafa.yossef@aalto.fi*
[2]*Department of Construction and Building Engineering, Arab Academy for Science, Technology and Maritime Transport, Cairo, Egypt, moyssef@aast.edu*
[3]*Department of Chemistry and Materials Science, Aalto University, Espoo, Finland, tanja.kallio@aalto.fi*
[4]*Department of Civil Engineering, Aalto University, Espoo, Finland, Jari.puttonen@aalto.fi*

SUMMARY
Combining water and cement, which are the most used materials worldwide, can support the development of sustainable energy-harvesting applications. This study demonstrates a hydrovoltaic device based on the building material that generates electricity utilizing humidity difference between surfaces of cement samples for hydrovoltaic energy generation. The moisture flow inside the electrode nanochannels of the cement supercapacitors composed of nickel foam (NF) with carbon nanotubes (CNTs) can generate a voltage difference of up to 40.1 mV for a surface area of only 6.25 cm^2. Such a device can bring the idea of a positive energy balance of buildings and structures into reality.

Keywords: cement, CNT, hydrovoltaic, Nickel foam, relative humidity

1. INTRODUCTION

Recently, a new emerging type of energy known as “hydrovoltaic power generation”, which can be scaled from small to large spaces, has attracted much attention as an alternative way to power low-power electronics and Internet of Things (IoT) devices. Hydrovoltaic generators produce electrical energy from water or moisture flow through hygroscopic substances and active materials (Jiao et al., 2022; Lim et al., 2024). The hygroscopic substance is a hydrophilic material that absorbs water from surroundings, such as salts (H. Li et al., 2023), hydrogels (C. Liu et al., 2022; Yossef et al., 2024), and silica aerogel (Tian et al., 2024). Active materials can be carbon-based nanomaterials such as carbon nanotubes (CNTs) (Ding et al., 2017a; Z. Zhang et al., 2018), carbon nanofibers (Tabrizizadeh et al., 2021), carbon black (Xue et al., 2017) and graphene [23–25], and their active research area extents to metal oxides (Ji et al., 2019; Jin et al., 2020), organic metal frameworks (MOFs) (Z. Li et al., 2021; Q. Ma et al., 2020; X. Ma et al., 2021) and conductive polymers (Xie et al., 2022).

As shown in Table 1, hydrovoltaic energy generation has many applications, including sensors (Hui et al., 2020), electronics (Yun et al., 2019) and environmental aspects (Chen et al., 2024). However, hydrovoltaic energy generation has not been applied to building applications yet.

Table 1. Hydrovoltaic Generators Applications

Category	Specific Application	Reference
Sensors	Liquid Detection Protection	(Hui et al., 2020)
	Light-Controlled Switch	(Ji et al., 2019)
	Wearable Sweat Sensor	(L. Li et al., 2021)

	Respiratory Monitoring	(Yang et al., 2024)
	Motion & Physical Activity Tracking	(X. Zhang et al., 2023)
	Location Identification	(X. Zhang et al., 2023)
	Human Respiration Monitoring	(F. Zhao et al., 2015)
	Environmental Temperature Monitoring	(L. Li et al., 2022)
	Microcystin detection	(Bian et al., 2025)
	Wireless Sensor Nodes	(Yao et al., 2024)
Electronics	LED Lighting	(Hu et al., 2022)
	LCD Display	(Xue et al., 2017)
	Electrodeposition	(Ding et al., 2017b)
	Calculator	(Gong et al., 2020)
	Smartphone	(Tan et al., 2022)
Environments	Seawater Desalination	(Chen et al., 2024)
	Pollutant Degradation	(Ding et al., 2018)
	Self-Powered Environmental Sensing	(Lin et al., 2024)
	Soil Remediation	(X. Liu et al., 2022)
	Methane Production	(HU et al., 2023)
	Hydrogen Production	(L. Zhao et al., 2024)

This study aims to develop a hydrovoltaic device based on cementitious material as a hygroscopic substance and CNTs as an electrically active material for construction applications. The roles of the NF and deposition of CNTs are investigated, and a discussion of the hydrovoltaic energy generation in cement material is outlined in this paper.

2. SAMPLE PREPARATION

In this study, the components and materials used are a 1.6 mm thick sheet of porous nickel foam (Ni-foam, MSE Supplies LLC, USA), single-walled carbon nanotubes (SWCNTs, Tuball OCSiAl, Luxembourg), isopropanol (99.8% purity, Merck), acetone (Avantor), hydrochloric acid (37% purity, Avantor/VWR), and Pika cement (Finncement, Finland).

The nickel foam sheets (NFs) were cut into 25 x 25 mm^2 electrodes and divided into three groups (A, B, and C). The process of electrode preparation was meticulous. First, NF sheets were cleaned using 1 mol hydrochloric acid (HCl) for 55 minutes, then washed with acetone and distilled water multiple times. Then the sheets were labeled, and their weights were measured. The A group represented bare nickel foam electrodes without any additional active material. For the needs of the B and C groups, CNT/isopropanol solution was dispersed using ultrasonication for 10 minutes, rested for another 10 minutes, and the treatment was repeated twice. In the B group, the NF sheets were directly drop-cast into CNT/isopropanol solution, while in group C, the solution was sprayed into NF using an airbrush using the dry and spray method, where the NF sheet was sprayed, left to dry, and then sprayed and dried again. Upon preparation, all samples were left overnight in a vacuum chamber. Then, the weight of the sample was measured again to determine the mass of the active material.

Electrodes were placed in a 3D-printed mold of thermoplastic polyurethane (TPU) with NF electrodes placed on the sides, and the mold was opened from the top to cast cement paste in a 5mm thick grove while tape held the NF sheets in their places during casting. After casting, two wooden plates kept the NF sheets in their place as shown in Figure 1. The output samples with a thickness of 5 mm should match the dimensions of the NF sheets (25 mm x 25 mm). Cement paste

was prepared using a 0.45 water/cement ratio and placed using a small spatula with the same thickness. The samples were wrapped with a plastic sheet and left to cure overnight, then they were un-molded and cured in 95% RH until testing.

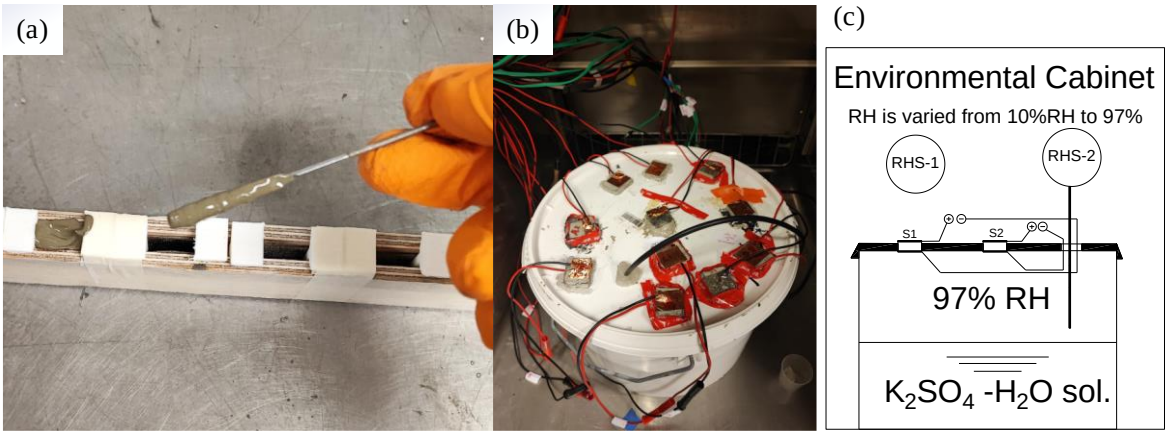

Figure 1. (a) 3DP TPU mold with taped nickel foam sheets during cement paste casting, relative humidity test setup showing (b) sample placement and (c) schematic diagram of the test setup, relative humidity sensor (RHS), and samples represented by S.

3. EXPERIMENTAL SETUP AND CHARACTERIZATION

A representative electrode was selected from each group and investigated using Raman Spectroscopy (Renishaw inVia™ Confocal Raman Microscope). The samples were examined using a 523 nm laser and a 20x microscope. Scanning of the samples was made under a focus track with a laser intensity of 1%. Electrode morphology was investigated using a Scanning Electron Microscope (SEM) (Quanta FEG 450) equipped with an ETD and CBS detector. The voltage was set to 10 kV, and the magnification varied up to 10000x. Samples were tested under differential humidity from both sides. A container was filled with K_2SO_4 solution to provide relative humidity (RH) of around 97% RH (Carotenuto & Dell'Isola, 1996). The samples were placed in existing holes, and their sides were tightened with a double tape that is resistant to temperature and moisture. The container was placed inside the environmental cabinet, and coupled temperature and humidity sensors were placed inside and outside the container. The relative humidity of the environmental cabinet varied from 97% RH to 10% RH. The voltage readings were recorded and plotted as a function of the difference between relative humidity values in the container and in the cabinet.

4. RESULTS

Raman spectroscopy results for group A, B, and C electrodes are shown in Figure 2. The results show that group A (NF) is treated well with HCl without any oxide layers, while groups B and C show peaks related to CNTs. It can be shown that the D-band (around 1350 cm^{-1}) is barely noticeable while G-band reaching around 11844 and 27927 (a.u) for dispersed and undispersed CNTs, respectively. The high G/D ratio >90 indicates that these CNTs are pristine with no signs for surface functionalization. NF is not showing any signs of oxidation, which implies that the CNTs are the driving force for hydrovoltaic energy generation.

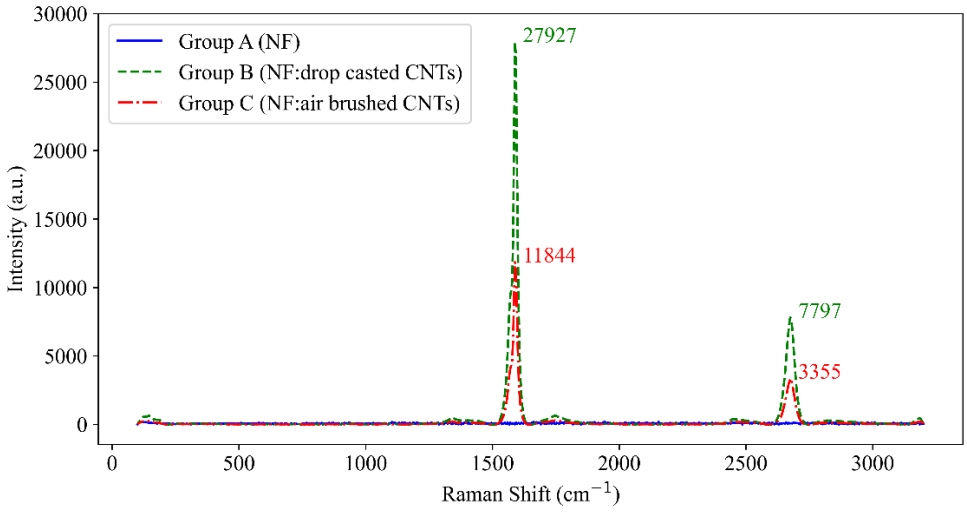

Figure 2. Raman Spectroscopy for bare NF and NF with drop cast and air brushed CNTs

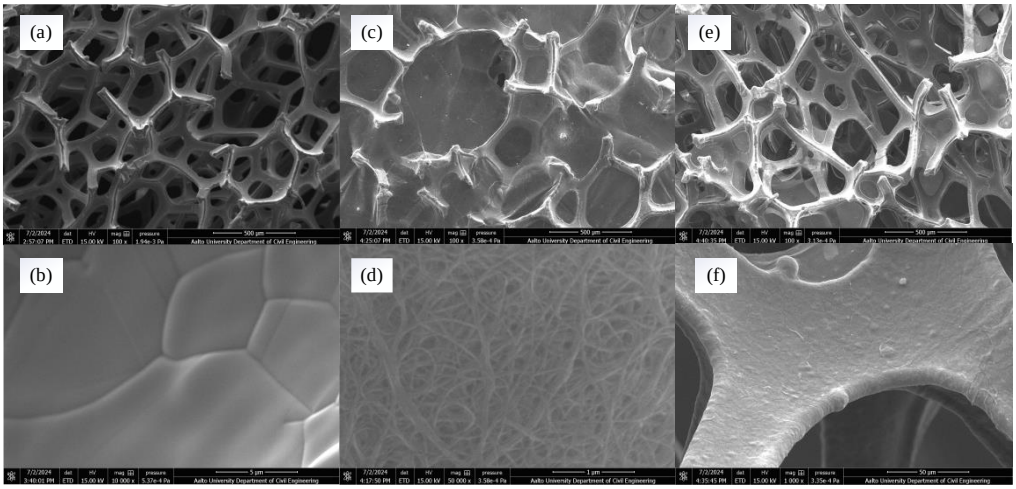

Figure 3. SEM images showing (a,b) bare NF, (c,d) NF with drop cast CNTs, and (e,f) NF with airbrushed CNTs

The morphology of the CNTs was investigated using SEM, as shown in Figure 3 (a-f). The morphology shows that the CNTs tend to form a "spider-network" like network when transferred by drop casting, which blocks the 3D NF pore structure, as shown in Figure 3(c), where the CNTs are interlocked, as shown in Figure 3 (d). In the case of spraying CNTs using an airbrush, the CNTs are mostly settled on the NF stems, as shown in Figure 3(e and f). Bare NF is displayed in Figure 3 (a and b) for comparison, showing no sign of CNTs.

Figure 4 shows that sample A, which represents the bare NF, has an insignificant potential of 2.8 mV, while sample C, which represents the NF with airbrushed CNTs, has a slightly higher potential of 6.4 mV. The drop cast CNTs samples, noted as B, show a potential difference of up to 40.1 mV for a surface area of only 6.25 cm^2. These results show that the CNTs have a significant role in generating the potential difference, while the method of deposition of CNTs has a critical role on hydrovoltaic energy generation.

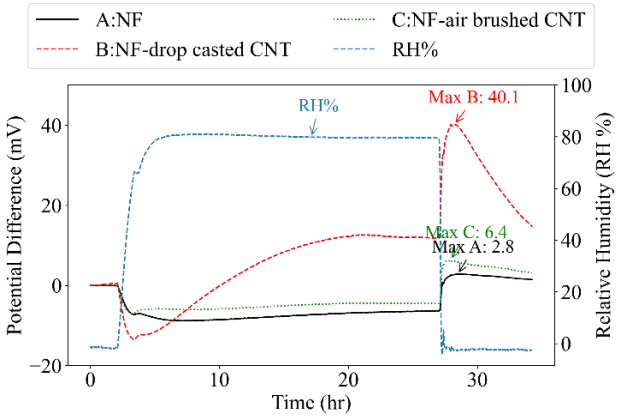

Figure 4. Hydrovoltaic test results at 87% relative humidity difference

5. DISCUSSION

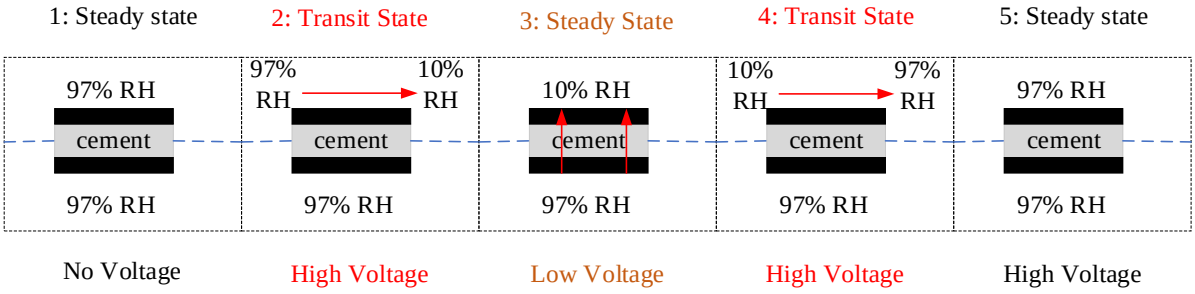

Figure 5. Schematic diagram showing different stages

Figure 5 shows different stages for the hydrovoltaic energy generation. Stage 1 shows a steady state where the same relative humidity (97% RH) is set to both sides, and no voltage is induced as a result of still water molecules. During variation of the ambient of the upper electrode from 97% RH to 10% RH, i.e., in transient state, a pressure gradient is formed between low and high humidity regions, which forces the water molecules to evaporate from the surface of the CNTs, causing an increase in local electrons at the upper electrode. The electrons interact with water molecules and oxygen and produce OH^-, which migrate to the lower electrode inducing a voltage difference between the upper and lower electrode (Yu et al., 2023). The results in Figure 4 show that CNTs transferred by drop casting tend to have a more extensive network of interconnected channels for water molecules, inducing a higher hydrovoltaic potential than air-brushed CNTs. The water molecules remain still when the environmental cabinet is steady at 10% RH in stage 3. Thus, no voltage is created from the motion of the water across the width of a single electrode. However, due to the diffusion of water vapor and liquid water l from one side to the other, low voltage is formed due to the moving of water molecules within the CNT nanochannels across the thickness of the electrode. Similarly to the stage 2, the stage 4 shows the moisture change by an increase in the humidity chamber from 10% to 97% RH. Thus, more moisture comes in contact with the CNTs, and a high voltage is induced. Finally, stage 5 shows the steady state where the water is no longer in motion and no voltage is induced.

6. CONCLUSION

This study presents a novel idea for generating electricity from the internal humidity difference of a building material. Hydrovoltaic energy generation of cement paste samples enclosed by two electrodes composed of NF sheets and CNTs is presented by investigating also the role of the porous NF sheet and its deposition by CNTs. The results can be summarized as:

1. Method of deposition of CNTs has a significant effect on the hydrovoltaic energy generated, as a uniform distribution of the CNTs on the walls of porous NF produced by airbrushing results in a lower contact between moisture and CNTs than the drop-casting method in which CNTs block the pores of the foam.
2. Bare NF sheet induces the least potential of 2.8 mV, followed by 6.4 mV received with air-brushed CNTs, and finally, NF sheet with drop-cast CNTs gave a potential of 40.1 mV at a relative humidity difference of around 87% RH.
3. Hydrovoltaic energy is mainly generated by the separation of water molecules from the surface of CNTs driven by moisture gradient between the electrodes and at their surfaces, which occurs along with a change in the surrounding relative humidity.

Based on conclusions, hydrovoltaic energy generation shows a promising path towards generating electricity in buildings from the variation of the relative humidity. Future recommendations include full-scale implantation of the hydrovoltaic energy on roof and wall façades.

ACKNOWLEDGEMENTS

The first author would like to thank the Research Council of Finland (Academy of Finland) for postdoctoral academy funding (#348611).

REFERENCES

Bian, Y., Jiang, D., Du, X., Wang, Y., Shan, X., Wang, W., Shiigi, H., & Chen, Z. (2025). Portable self-powered electrochemical aptasensor for ultrasensitive and real-time detection of microcystin-RR based on hydrovoltaic-photothermal coupling effect. *Biosensors and Bioelectronics*, *267*. https://doi.org/10.1016/j.bios.2024.116834

Carotenuto, A., & Dell'Isola, M. (1996). An experimental verification of saturated salt solution-based humidity fixed points. *International Journal of Thermophysics*, *17*(6), 1423–1439. https://doi.org/10.1007/BF01438677

Chen, Y., He, J., Ye, C., & Tang, S. (2024). Achieving Ultrahigh Voltage Over 100 V and Remarkable Freshwater Harvesting Based on Thermodiffusion Enhanced Hydrovoltaic Generator. *Advanced Energy Materials*, *14*(24). https://doi.org/10.1002/aenm.202400529

Ding, T., Liu, K., Li, J., Xue, G., Chen, Q., Huang, L., Hu, B., & Zhou, J. (2017a). All-Printed Porous Carbon Film for Electricity Generation from Evaporation-Driven Water Flow. *Advanced Functional Materials*, *27*(22). https://doi.org/10.1002/adfm.201700551

Ding, T., Liu, K., Li, J., Xue, G., Chen, Q., Huang, L., Hu, B., & Zhou, J. (2017b). All-Printed Porous Carbon Film for Electricity Generation from Evaporation-Driven Water Flow. *Advanced Functional Materials*, *27*(22). https://doi.org/10.1002/adfm.201700551

Ding, T., Liu, K., Zhou, J., Xue, G., Li, J., Chen, Q., & Yang, P. (2018). Evaporation induced electricity generation in freestanding and flexible carbon-based hybrid film. *Chinese Science Bulletin*, *63*(27), 2846–2852. https://doi.org/10.1360/N972018-00675

Gong, F., Li, H., Zhou, Q., Wang, M., Wang, W., Lv, Y., Xiao, R., & Papavassiliou, D. V. (2020). Agricultural waste-derived moisture-absorber for all-weather atmospheric water collection and electricity generation. *Nano Energy*, *74*, 104922. https://doi.org/10.1016/j.nanoen.2020.104922

Hu, Q., Ma, Y., Ren, G., Zhang, B., & Zhou, S. (2022). Water evaporation–induced electricity with Geobacter sulfurreducens biofilms. *Science Advances*, *8*(15). https://doi.org/10.1126/sciadv.abm8047

HU, Q., QIU, Y., LIN, X., REN, G., & ZHOU, S. (2023). Biofilm-based hygroelectric generator: Research on the fabrication and performance of a large-area device. *SCIENTIA SINICA Technologica*, *53*(12), 2164–2174. https://doi.org/10.1360/SST-2022-0133

Hui, Z., Xiao, M., Shen, D., Feng, J., Peng, P., Liu, Y., Duley, W. W., & Zhou, Y. N. (2020). A Self-Powered Nanogenerator for the Electrical Protection of Integrated Circuits from Trace Amounts of Liquid. *Nano-Micro Letters*, *12*(1), 5. https://doi.org/10.1007/s40820-019-0338-1

Ji, B., Chen, N., Shao, C., Liu, Q., Gao, J., Xu, T., Cheng, H., & Qu, L. (2019). Intelligent multiple-liquid evaporation power generation platform using distinctive Jaboticaba-like carbon nanosphere@TiO2 nanowires. *Journal of Materials Chemistry A*, *7*(12), 6766–6772. https://doi.org/10.1039/C8TA12328D

Jiao, S., Liu, M., Li, Y., Abrha, H., Wang, J., Dai, Y., Li, J., Kang, N., Li, Y., & Liu, X. (2022). Emerging hydrovoltaic technology based on carbon black and porous carbon materials: A mini review. In *Carbon* (Vol. 193, pp. 339–355). Elsevier Ltd. https://doi.org/10.1016/j.carbon.2022.03.047

Jin, H., Yoon, S. G., Lee, W. H., Cho, Y. H., Han, J., Park, J., & Kim, Y. S. (2020). Identification of water-infiltration-induced electrical energy generation by ionovoltaic effect in porous CuO nanowire films. *Energy & Environmental Science*, *13*(10), 3432–3438. https://doi.org/10.1039/D0EE02190C

Li, H., Li, X., Li, X., Chong, C., Jin, J., Wu, Z., Wang, H., Huang, J., Han, J., & Lee, H. K. (2023). Multifunctional smart mask: Enabling self-dehumidification and self-powered wearables via transpiration-driven electrokinetic power generation from human breath. *Chemical Engineering Journal*, *461*, 142083. https://doi.org/10.1016/j.cej.2023.142083

Li, L., Feng, S., Bai, Y., Yang, X., Liu, M., Hao, M., Wang, S., Wu, Y., Sun, F., Liu, Z., & Zhang, T. (2022). Enhancing hydrovoltaic power generation through heat conduction effects. *Nature Communications*, *13*(1). https://doi.org/10.1038/s41467-022-28689-8

Li, L., Gao, S., Hao, M., Yang, X., Feng, S., Li, L., Wang, S., Xiong, Z., Sun, F., Li, Y., Bai, Y., Zhao, Y., Wang, Z., & Zhang, T. (2021). A novel, flexible dual-mode power generator adapted for wide dynamic range of the aqueous salinity. *Nano Energy*, *85*, 105970. https://doi.org/10.1016/j.nanoen.2021.105970

Li, Z., Ma, X., Chen, D., Wan, X., Wang, X., Fang, Z., & Peng, X. (2021). Polyaniline-Coated MOFs Nanorod Arrays for Efficient Evaporation-Driven Electricity Generation and Solar Steam Desalination. *Advanced Science*, *8*(7). https://doi.org/10.1002/advs.202004552

Lim, H., Kim, M. S., Cho, Y., Ahn, J., Ahn, S., Nam, J. S., Bae, J., Yun, T. G., & Kim, I. D. (2024). Hydrovoltaic Electricity Generator with Hygroscopic Materials: A Review and New Perspective. In *Advanced Materials* (Vol. 36, Issue 12). John Wiley and Sons Inc. https://doi.org/10.1002/adma.202301080

Lin, J., Zhang, Z., Lin, X., Cai, X., Fu, S., Fang, X., Ding, Y., Wang, X., Sèbe, G., & Zhou, G. (2024). All Wood-Based Water Evaporation-Induced Electricity Generator. *Advanced Functional Materials*, *34*(30). https://doi.org/10.1002/adfm.202314231

Liu, C., Wang, S., Wang, X., Mao, J., Chen, Y., Fang, N. X., & Feng, S.-P. (2022). Hydrovoltaic energy harvesting from moisture flow using an ionic polymer–hydrogel–carbon composite. *Energy & Environmental Science*, *15*(6), 2489–2498. https://doi.org/10.1039/D2EE00030J

Liu, X., Wang, Z., Liang, H., Li, Y., Liu, T., Guo, Q., Wang, L., Yang, Y., & Chen, N. (2022). Solar-Driven Soil Remediation along with the Generation of Water Vapor and Electricity. *Nanomaterials*, *12*(11), 1800. https://doi.org/10.3390/nano12111800

Ma, Q., He, Q., Yin, P., Cheng, H., Cui, X., Yun, Q., & Zhang, H. (2020). Rational Design of MOF-Based Hybrid Nanomaterials for Directly Harvesting Electric Energy from Water Evaporation. *Advanced Materials*, *32*(37). https://doi.org/10.1002/adma.202003720

Ma, X., Li, Z., Deng, Z., Chen, D., Wang, X., Wan, X., Fang, Z., & Peng, X. (2021). Efficiently cogenerating drinkable water and electricity from seawater via flexible MOF nanorod arrays. *Journal of Materials Chemistry A*, *9*(14), 9048–9055. https://doi.org/10.1039/D0TA11870B

Tabrizizadeh, T., Wang, J., Kumar, R., Chaurasia, S., Stamplecoskie, K., & Liu, G. (2021). Water-Evaporation-Induced Electric Generator Built from Carbonized Electrospun Polyacrylonitrile Nanofiber Mats. *ACS Applied Materials & Interfaces*, *13*(43), 50900–50910. https://doi.org/10.1021/acsami.1c13487

Tan, J., Fang, S., Zhang, Z., Yin, J., Li, L., Wang, X., & Guo, W. (2022). Self-sustained electricity generator driven by the compatible integration of ambient moisture adsorption and evaporation. *Nature Communications*, *13*(1), 3643. https://doi.org/10.1038/s41467-022-31221-7

Tian, Z., Chang, Q., Liu, Z., Xue, C., Li, N., Jia, S., Fan, X., Yang, J., & Hu, S. (2024). Electricity Harvesting from Water Evaporation on Hierarchical Pore Gradient Silica Aerogel-Based Generators. *ACS Applied Materials & Interfaces*, *16*(32), 42468–42475. https://doi.org/10.1021/acsami.4c07729

Xie, J., Wang, Y., & Chen, S. (2022). Textile-Based Asymmetric Hierarchical Systems for Constant Hydrovoltaic Electricity Generation. *Chemical Engineering Journal*, *431*, 133236. https://doi.org/10.1016/j.cej.2021.133236

Xue, G., Xu, Y., Ding, T., Li, J., Yin, J., Fei, W., Cao, Y., Yu, J., Yuan, L., Gong, L., Chen, J., Deng, S., Zhou, J., & Guo, W. (2017). Water-evaporation-induced electricity with nanostructured carbon materials. *Nature Nanotechnology*, *12*(4), 317–321. https://doi.org/10.1038/nnano.2016.300

Yang, Y., Wang, J., Wang, Z., Shao, C., Han, Y., Wang, Y., Liu, X., Sun, X., Wang, L., Li, Y., Guo, Q., Wu, W., Chen, N., & Qu, L. (2024). Moisture-Electric–Moisture-Sensitive Heterostructure Triggered Proton Hopping for Quality-Enhancing Moist-Electric Generator. *Nano-Micro Letters*, *16*(1), 56. https://doi.org/10.1007/s40820-023-01260-w

Yao, Y., Lu, X., Fu, C., Zhang, Y., Fang, J., Qin, J., He, Q., & Yang, T. (2024). Patterned Coating of Ionic Diode Arrays Toward Flexible Moist-Electric Generators to Power Wireless Sensor Nodes. *Advanced Functional Materials*, *34*(9). https://doi.org/10.1002/adfm.202311465

Yin, J., Zhang, Z., Li, X., Yu, J., Zhou, J., Chen, Y., & Guo, W. (2014). Waving potential in graphene. *Nature Communications*, *5*(1), 3582. https://doi.org/10.1038/ncomms4582

Yossef, M., Baniasadi, H., Kallio, T., Perry, M., & Puttonen, J. (2024). Ionic thermoelectricity of salt-free PVA-hydrogel. *Applied Materials Today*, *38*, 102240. https://doi.org/10.1016/j.apmt.2024.102240

Yu, F., Li, J., Jiang, Y., Wang, L., Yang, X., Yang, Y., Li, X., Jiang, K., Lü, W., & Sun, X. (2023). High Hydrovoltaic Power Density Achieved by Universal Evaporating Potential Devices. *Advanced Science*, *10*(30). https://doi.org/10.1002/advs.202302941

Yun, T. G., Bae, J., Rothschild, A., & Kim, I.-D. (2019). Transpiration Driven Electrokinetic Power Generator. *ACS Nano*, *13*(11), 12703–12709. https://doi.org/10.1021/acsnano.9b04375

Zhang, X., Wang, M., Wu, Y., Chen, X., Wu, K., Fu, Q., & Deng, H. (2023). Biomimetic Aerogel for Moisture-Induced Energy Harvesting and Self-Powered Electronic Skin. *Advanced Functional Materials*, *33*(7). https://doi.org/10.1002/adfm.202210027

Zhang, Z., Li, X., Yin, J., Xu, Y., Fei, W., Xue, M., Wang, Q., Zhou, J., & Guo, W. (2018). Emerging hydrovoltaic technology. *Nature Nanotechnology*, *13*(12), 1109–1119. https://doi.org/10.1038/s41565-018-0228-6

Zhao, F., Cheng, H., Zhang, Z., Jiang, L., & Qu, L. (2015). Direct Power Generation from a Graphene Oxide Film under Moisture. *Advanced Materials*, *27*(29), 4351–4357. https://doi.org/10.1002/adma.201501867

Zhao, L., Chen, Y., Zeng, X., Fang, W., He, X., Du, X., Li, W., Wang, D., Chen, H., Guo, Z., & Liu, W. (2024). Laplace pressure assisted hydrovoltaic effect in-situ enhancing photocatalytic water splitting. *Ceramics International*, *50*(5), 8539–8545. https://doi.org/10.1016/j.ceramint.2023.12.155

This publication was produced in the context of PhD research co-financed by the Ministerial Decree no. 352 of 9th April 2022, based on the NRRP - funded by the European Union - NextGenerationEU - Mission 4 "Education and Research", Com-ponent 2 "From Research to Business", Investment 3.3, and by the EURAC Research.

REFERENCES

Attia, Shady, Ramin Rahif, Vincenzo Corrado, Roonen Levinson, Aziz Laouadi, Leon Wang, Behzad Sodagar, Anais Machard, Rajat Gupta, and Bjarne Olesen. 2021. “Framework to Evaluate the Resilience of Different Cooling Technologies.”

Bastos, Joana, Fabio Monforti-Ferrario, and Giulia Melica. 2024. “Covenant of Mayors for Climate and Energy: Greenhouse Gas Emission Factors for Local Emission Inventories.”

Bordignon, Sara, Jeffrey D. Spitler, and Angelo Zarrella. 2024. “Simplified Water-Source Heat Pump Models for Predicting Heat Extraction and Rejection.” *Renewable Energy* 220 (January):119701. https://doi.org/10.1016/j.renene.2023.119701.

“Climate Pledges Explorer – Data Tools.” n.d. *IEA*. https://www.iea.org/data-and-statistics/data-tools/climate-pledges-explorer.

“Directive (EU) 2024/1275 of the European Parliament and of the Council.” 2024. https://eur-lex.europa.eu/eli/dir/2024/1275/oj#document1.

Fakhari, Maryam, Riccardo Pinotti, and Roberto Lollini. 2023. “Report Presenting Proposal for New Baselines for IWG Targets: IWG5-CSA Deliverable D2.3.” Brussels: Funded by the European Union, Horizon 2020 Programme. https://cordis.europa.eu/project/id/101075700.

Fundamentals, ASHRAE. 2017. “ASHRAE Handbook 2017 Fundamentals SI; 2017.”

Heiranipour, Milad, Miren Juaristi, Stefano Avesani, Fabio Favoino, and Valentina Serra. 2025. “Contrasting Building Performance and Thermal Resiliency: A Simulation-Based Quantitative Evaluation Framework for Evaluating the Impact of Building Envelope Technologies.” In , 432–37. https://doi.org/10.1007/978-981-97-8313-7_60.

International Energy Agency. 2024. “Greenhouse Gas Emissions from Energy.” Paris: International Energy Agency.

ISO. 2016. *ISO 18523-1: Energy Performance of Buildings — Schedule and Condition of Building, Zone and Space Usage for Energy Calculation — Part 1. Non-Residential Buildings, Geneva, Switzerland (2016)*.

Karimpour, Mahsa, Martin Belusko, Ke Xing, John Boland, and Frank Bruno. 2015. “Impact of Climate Change on the Design of Energy Efficient Residential Building Envelopes.” *Energy and Buildings* 87 (January):142–54. https://doi.org/10.1016/j.enbuild.2014.10.064.

Khan, Sahil Ali, Tabish Alam, Mohammad Saaim Khan, Paolo Blecich, Mohammad Arif Kamal, Naveen Kumar Gupta, and Anil Singh Yadav. 2022. “Life Cycle Assessment of Embodied Carbon in Buildings: Background, Approaches and Advancements.” *Buildings* 12 (11): 1944. https://doi.org/10.3390/buildings12111944.

Kiamili, Christina, Alexander Hollberg, and Guillaume Habert. 2020. “Detailed Assessment of Embodied Carbon of HVAC Systems for a New Office Building Based on BIM.” *Sustainability* 12 (8): 3372. https://doi.org/10.3390/su12083372.

Machard, Anaïs, Agnese Salvati, Mamak P. Tootkaboni, Abhishek Gaur, Jiwei Zou, Liangzhu Leon Wang, Fuad Baba, et al. 2024. “Typical and Extreme Weather Datasets for Studying the Resilience of Buildings to Climate Change and Heatwaves.” *Scientific Data* 11 (1): 531. https://doi.org/10.1038/s41597-024-03319-8.

Rouws, A.L., R.C.G.M. Loonen, and J.L.M. Hensen. 2024. “The Role of the Electricity Grid in Operation-Induced Greenhouse Gas Emissions by a Residential Building: A Multi-Year Retrospective Simulation Study.” *Energy and Buildings* 324 (December):114870. https://doi.org/10.1016/j.enbuild.2024.114870.

Soudian, Shahrzad, and Umberto Berardi. 2025. “Impact of Future Climate Scenarios on Thermal Performance and Resilience of Building Façades: Canadian Climate Case Study.” *Building and Environment* 267 (January):112245. https://doi.org/10.1016/j.buildenv.2024.112245.

Tettey, Uniben Yao Ayikoe, Ambrose Dodoo, and Leif Gustavsson. 2017. “Energy Use Implications of Different Design Strategies for Multi-Storey Residential Buildings under Future Climates.” *Energy* 138 (November):846–60. https://doi.org/10.1016/j.energy.2017.07.123.

6th International Conference on Building Energy and Environment
Eindhoven University of Technology, The Netherlands
6 - 10 July 2025

Supporting early-stage Façade Design in Climate Change Scenarios: the impact of Grid Decarbonization and HVAC performance models

Milad Heiranipour [1,2,3], Stefano Avesani [2], Marzieh Zarei[2], Miren Juaristi [2], Fabio Favoino [1]
[1]*Energy Department, Politecnico di Torino, Corso Duca degli Abruzzi 24, Turin, Italy, Milad.heiranipour@polito.it and Fabio.favoino@polito.it*
[2]*EURAC Research, Institute for Renewable Energy, Viale Druso 1, I-39100, Bolzano, Italy, miren.juaristigutierrez@eurac.edu, stefano.avesani@eurac.edu, and marzieh.zarei@eurac.edu*
[3]Scuola Universitaria Superiore IUSS Pavia, Italy.

SUMMARY
This study investigates the impact of methodological assumptions in building performance modelling to select façade design strategy based on the expected Greenhouse Gass Emissions (GHG). A parametric simulation framework was employed to examine the effects of varying COP (Coefficient of Performance) and SEER (Seasonal Energy Efficiency Ratio) calculations, embodied emissions considerations, future climate scenarios, and decarbonization pathways on façade optimization decisions. The framework was applied to case studies in Turin, Italy, and Eindhoven, Netherlands, revealing significant geographical variations in emissions reduction potential. The study shows substantial reductions in combined operational and envelope-related embodied GHG emissions when considering variable COP with progressive decarbonization pathways - up to 61.8% in Italy and 50.3% in the Netherlands. Key findings indicate that while absolute emission values exhibit substantial variation across methodologies, the relative ranking of façade design strategies remains predominantly consistent, particularly for wall configurations with performance variations typically limited to 2-4%. This observation suggests that simplified approaches, despite overestimating absolute emissions, can offer reliable guidance for comparing façade design alternatives during early-stage decision-making.
Keywords: Thermal Resilience, Lifecycle Assessment, Building Envelope, Parametric Simulation-based Framework, Dynamic Carbon Assessment.

1. INTRODUCTION

Climate change creates challenges for buildings: they must adapt to extreme weather while maintaining comfort and reducing emissions. Building resilience - the ability to maintain performance under changing conditions while minimizing environmental impact - has become crucial for the building sector (Attia et al. 2021). The building façade, acting as the barrier between inside and outside, shapes thermal performance and impacts energy use, comfort, and emissions (Soudian & Berardi 2025). The connection between resilience and emissions is key as buildings must adapt to extreme weather while reducing their climate impact. Research shows façade design strongly influences future building resilience. Tettey et al. (Tettey et al. 2017) found that orientation, Window-to-Wall Ratio, and glazing significantly affect future energy performance. Karimpour et al. (Karimpour et al. 2015) showed Mediterranean buildings will shift from balanced heating-cooling to mainly cooling needs by 2070. Building resilience involves more than weather patterns - it includes interactions between building systems, energy grids, and environment. Therefore, understanding how building envelope design affects resilience requires evaluating both immediate performance and long-term environmental impacts, making emissions assessment crucial for resilient design strategies. Previous research demonstrated the importance of future weather data for assessing building resilience (Heiranipour et al. 2025). However, this approach often overlooks other climate-influenced factors affecting emissions, like grid decarbonization and

building system efficiencies. This might therefore ignore the complex interdependencies between different aspects of performance, leading to strategies that may not be robust under evolving climate scenarios (Rouws et al. 2024). On the other side future operational GHG emissions could be reduced by higher penetration of renewable energy generation in the electrical grid, while embodied carbon emissions could become more significant, thus influencing building envelope related design choices.

Considering the above, this study focuses on the following research questions: *to what extent do simplifications in methodological assumptions related to building system and building-to-grid interaction —such as variability in COP (Coefficient of Performance) and SEER (Seasonal Energy Efficiency Ratio), consideration of embodied emission and of decarbonization pathways — may impact on façade design strategy selection for building heat resiliency?* These methodological considerations - such as varying HVAC performance and grid decarbonization pathways - are fundamental for developing façade design guidelines that remain effective under future climate and energy scenarios. To address this, a parametric simulation-based framework was improved with the aim of testing these assumptions systematically. By comparing the effects of these factors on façade strategy rankings across different climates, this study aims to determine whether these methodological variations critically influence decision-making or if a simplified approach could still yield reliable results. Subsequent sections present the methodology, analyse results, and discuss implications for sustainable façade design, concluding with recommendations for developing climate-resilient, low-carbon buildings.

2.METHODOLOGY

The building resilience evaluation framework previously developed (Heiranipour et al. 2025) has been enhanced to be able to consider the following three key methodological variants: (i) future climate evolution scenarios (already featured), (ii) heating-cooling system performance modelling approach (constant versus climate-dependent COP/SEER), and (iii) future potential decarbonization pathways for national electricity mix (Scenarios 1, 2, and 3). While the original framework assessed multiple Key Performance Indicators (KPIs), for sake of simplicity this study focuses only on GHG emissions during operation (Op) and envelope-related embodied emissions (Env.Emb), expressed as t_CO2_eq.

This paper methodology explores interactions between façade design strategies, HVAC system efficiency, and GHG emission scenarios over a 30-year building lifetime. Two current and future weather datasets have been produced considering Turin (Italy) and Eindhoven (the Netherlands), based on the dynamical downscaling methodology (Machard et al. 2024) considering RCP 8.5 scenario. The dynamic Coefficient of Performance (COP) and Seasonal Energy Efficiency Ratio (SEER) are based on Eq. (1). and Eq. (2)., validated for air-to-water systems against both manufacturer specifications and experimental data (Bordignon et al. 2024).

$$COP = 0.6261 + 0.0528 * (Tair + 273.15) - 0.0391 * (T\ load, out\ heating + 273.15) \quad (1)$$

$$SEER = 12.7264 - 0.0404 * (Tair + 273.15) + 0.158 * (Tload, out\ cooling + 273.15) \quad (2)$$

- T_{air} is the outdoor air temperature in degrees Celsius.
- $T_{load,out\ heating}$ and $T_{load,out\ cooling}$ are the temperatures of the water used for heating and cooling, respectively, in degrees Celsius (for cooling set on 7°C and for heating set on 40 °C).

The GHG emissions calculation considers both operational and envelope-related embodied carbon over a 30-year building life (2025-2055). The operational ones are calculated based on energy calculations of two 15-years intervals: 2025-2040 using current EPW results and 2040-2055 for mid-future EPW results (Figure 1). Moreover, a static baseline scenario was established using current weather data for the entire building lifetime, maintaining constant emission factors and fixed HVAC system efficiencies. This approach represents conventional practice that does not account for climate change effects, providing a reference point for comparing more sophisticated methodological variants. Different emissions factors definition methods are used to convert electrical delivered energy use to GHG emissions. As a benchmark, a constant emission factor has been implemented using the current location-specific factors from the Covenant of Mayors for Climate and Energy (Bastos et al. 2024). Afterwards, three different decarbonization scenarios have been established: Scenario 1 implements an aggressive linear reduction pathway aiming for carbon neutrality by 2050 (International Energy Agency 2024); Scenario 2 follows the European Environment Agency's projections with a two-step approach, initially aiming for a reduction to 82% of 2023 levels by 2030, followed by a linear decline to zero emissions ("Climate Pledges Explorer – Data Tools," n.d.); Scenario 3 is derived from historical emission reduction trends (2002-2023) documented in the Energy Performance of Buildings Directive (EPBD) reports ("Directive (EU) 2024/1275 of the European Parliament and of the Council" 2024). A combination of these operational and envelope-related embodied emissions has been then obtained summing the two-contribution expressed as tCO2-eq per 30-year. For the embodied carbon assessment, the calculation focuses exclusively on the envelope materials for stages A1-A3, and it is based on the EcoInvent 3.9 database and building archetype quantities, with calculations performed using openLCA 2.2 software and the EF3.1 impact assessment method.

The building model uses Grasshopper 1.0.0007 within Rhino 7 (SR31) coupled to Ladybug Tools 1.8.0, with thermal energy assessments conducted using EnergyPlus under dynamic yearly conditions. The case study is a single-family house archetype representative of typical European residential construction based on the archetype defined by (Fakhari et al. 2023) while complying with local regulations. The HVAC system accounts for 8-15% of total building embodied emissions. For this case study the HVAC system contributes 9.516 tCO2eq in total embodied emissions (0.183 tCO2eq/m²) (Kiamili et al. 2020). The load-bearing structure represents 20-30% of total embodied emissions, with contributions varying significantly based on construction method (Khan et al. 2022): a reinforced concrete structure is responsible for 46.8 tCO2eq (0.450 tCO2eq/m²), whereas a steel structure would result in 83.2 tCO2eq (0.800 tCO2eq/m²). A timber structure results in 46.0 tCO2eq (0.442 tCO2eq/m²) and 89.9 tCO2eq (0.864 tCO2eq/m²) if a prefabricated modular system is used. However, in this research, both embodied emissions related to HVAC and building structure are intentionally excluded to emphasize the envelope design strategies (which together would account for approximately 55-100 tCO2eq).

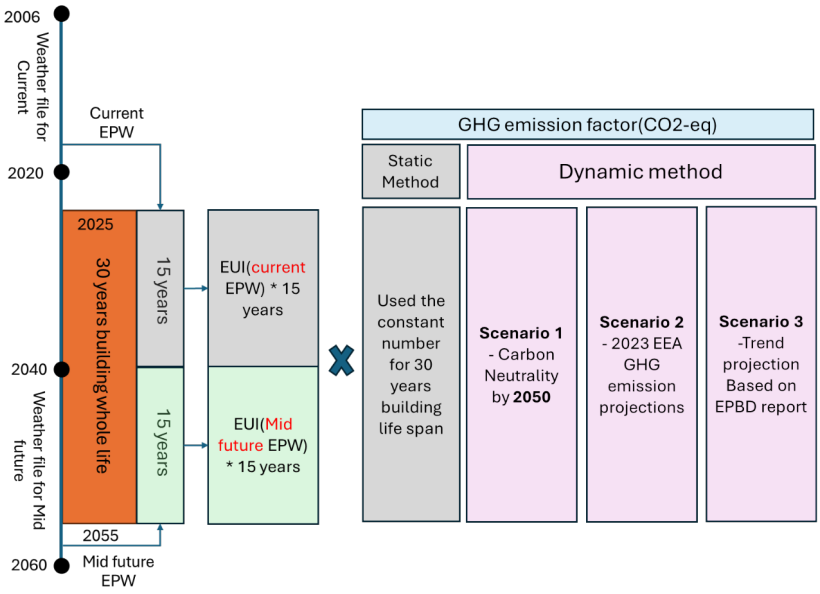

Figure 1. Framework of total GHG emission of whole life of building with emission scenarios.

Table 1. Building simulation characteristic

Building parameters		Values	Ref
Geometry parameter	Number of storeys	2	(Fakhari et al. 2023)
	Building width/depth (m)	8*6.5	
	Area per storey (m^2)	52	
	Glazing ratio (%)	[Parametric]	
Internal heat gain	No. of occupants(N/m^2)- schedule	0.07- Residential	(ISO 2016)
	Metabolic rate (Met)	1.2	
	Lighting density (W/m^2)- schedule	7- Residential	
	Equipment load (W/m^2)- schedule	3.125- Residential	
Thermal characterizes	Ground floor thermal transmittance (W/m^2K)	0.517	(Fakhari et al. 2023)
	External roof thermal transmittance (W/m^2K)	0.193	
	Wall thermal transmittance (W/m^2K)	0.330	
	Window thermal transmittance (W/m^2K), SHGC, Tvis	1.70, 0.55, 0.70	
Infiltration and ventilation parameters	Infiltration rate (m^3/s per m^2 facade)	0.005	(Fundamentals 2017)
	Mechanical ventilation rate (ACH)	0. 35	
HVAC characterizes	Heating setpoint (°C)	20	
	Cooling setpoint (°C)	26	
	HVAC system	Ideal air load	

Table 2. Facade design strategies considered (first row is the benchmark, compliant with local regulation).

WWR	Wall number	Type of wall	Thermal characteristics for different façade designs
40 %	Wall_3	Plaster (2cm),Insulation (15cm), Brick (25cm), Gypsum (1cm)	(U=0.23 W/m^2K) (Y=0.021 W/m^2K)
20 %	Wall_1	Plaster (2cm),Brick (25cm), Gypsum (1cm)	(U=1.63 W/m^2K) (Y=0.498 W/m^2K)

60%	Wall_2	Plaster (2cm),Insulation (5cm), Brick (25cm), Gypsum (1cm)	(U=0.55 W/m^{2}K) (Y=0.061 W/m^{2}K)
	Wall_4	Plaster (2cm),Insulation (25cm), Brick (25cm), Gypsum (1cm)	(U=0.15 W/m^{2}K) (Y=0.012 W/m^{2}K)

To assess methodological impacts, two exemplary building envelope parameters were selected based on previous findings (Heiranipour et al. 2025): the WWR and opaque wall configurations in terms of insulation thickness. These parameters were chosen as they significantly influence both the building's energy balance and the trade-offs between heating, cooling, and lighting energy use, hence controlling the overall dynamic heat transfer (Table 2). In this study, all possible combinations of WWR with each insulation thickness configuration were examined to comprehensively evaluate the interaction effects between these design parameters.

3. RESULTS

The analysis of the baseline energy distribution reveals that grid decarbonization scenarios and HVAC performance models impact the calculation of GHG emissions related to different façade strategies differently based on the location. In the Italian context, for the benchmark case (WWR=40%, insulation thickness=15cm) with constant COP and no future climate consideration, a more balanced energy profile was obtained, with heating accounting for 49.5%, cooling 11.3% and equipment and lighting 39.2%. In contrast, the Netherlands shows a heating dominated profile with heating accounting for 63.2%, cooling negligible at 0.20% and equipment and lighting 36.6%. Considering only future climate scenarios with constant COP, Italy shows a 6.2% decrease in heating emissions and a 18.7% increase in cooling emissions, resulting in a net decrease of 4.2% in total energy use, while the Netherlands shows a 2.3% decrease in heating emissions and a 170% increase in cooling emissions, leading to a net increase of 1.8% in total energy use. Despite the dramatic percentage increase in cooling demand for the Netherlands, its impact on total energy use remains moderate due to the very low baseline cooling energy consumption. The introduction of temperature-dependent COP/SEER calculations, together with the consideration of future climate leads to further significant changes: Italy's heating emissions decrease by an additional 16.1% and cooling emissions by 29.4%, while the Netherlands shows an additional 16.0% reduction in heating emissions and a 32.8% reduction in cooling emissions. Based on Figure 2, average COP values for Italy range from 2.6-3.3, while the Netherlands shows a slightly higher and narrower range of 2.8-3.4, reflecting the difference in winter temperature distributions between the locations. Under future climate scenarios, both locations show improved COP values due to warmer winter conditions. SEER values demonstrate more pronounced geographical variations, with Italy maintaining relatively stable values around 4.8 despite future temperature increases, while the Netherlands shows a significant decrease from current values around 5.2 to future values around 4.6, though this efficiency reduction has limited impact on total emissions due to the Netherlands' predominantly heating-dominated energy profile.

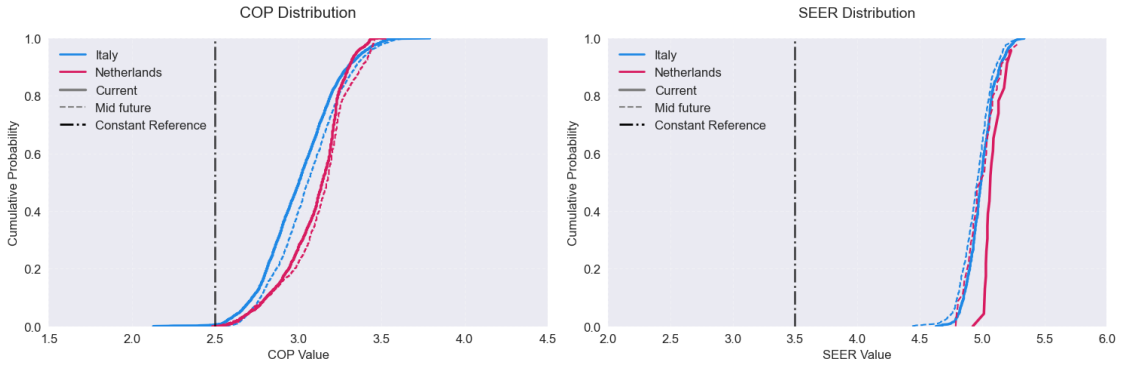

Figure 2-Variable COP and SEER for Italy and Netherland in current and mid future.

Table 3-Result of simulation

Op+Env_Emb GHG emissions [tCO-eq/30y]-Italy

façade strategies	W_20_w_1	W_20_w_2	W_20_w_3	W_20_w_4	W_40_w_1	W_40_w_2	W_40_w_3	W_40_w_4	W_60_w_1	W_60_w_2	W_60_w_3	W_60_w_4
Constant COP and GHG_noFutureClimate	169.52	149.29	142.49	140.75	162.21	148.08	144.51	142.09	157.60	148.91	145.85	145.05
Constant_COP_GHG_FutureClimate	168.08	148.38	141.73	140.04	160.97	147.30	143.34	141.57	156.64	148.37	145.43	144.66
VAR_COP_constant GHG	153.74	137.23	131.72	130.35	146.38	134.89	131.12	130.18	141.07	134.00	131.46	130.87
Constant_COP_GHG Sc_1	86.54	79.18	76.90	76.49	81.87	76.75	75.55	74.92	78.22	75.10	74.10	73.94
Constant_COP_GHG Sc_2	115.55	103.80	99.96	99.10	110.02	101.85	99.67	98.62	106.12	101.16	99.47	99.09
Constant_COP_GHG Sc_3	67.96	63.43	62.15	62.05	63.86	60.71	60.11	59.78	60.39	58.47	57.92	57.89
VA_COP_GHG_Sc_1	81.34	75.10	73.28	72.98	76.58	72.25	70.96	70.78	72.66	69.98	69.14	69.04
VA_COP_GHG_Sc_2	107.11	97.21	94.07	93.40	101.42	94.54	92.37	91.91	97.01	92.76	91.32	91.04
VA_COP_GHG_Sc_3	64.78	60.93	59.94	59.90	60.62	57.96	57.26	57.25	57.01	55.36	54.91	54.93

Op+Env_Emb GHG emissions [tCO-eq/30y]-Netherland

façade strategies	W_20_w_1	W_20_w_2	W_20_w_3	W_20_w_4	W_40_w_1	W_40_w_2	W_40_w_3	W_40_w_4	W_60_w_1	W_60_w_2	W_60_w_3	W_60_w_4
Constant COP and GHG_noFutureClimate	187.24	159.94	151.20	148.97	179.74	158.67	152.07	148.50	172.54	157.79	153.28	152.16
Constant_COP_GHG_FutureClimate	185.32	158.63	150.09	147.90	178.08	157.52	151.07	148.49	171.08	156.69	152.29	151.20
VAR_COP_constant GHG	170.11	147.77	140.68	138.91	163.47	146.25	140.89	139.58	157.06	144.98	141.32	140.42
Constant_COP_GHG Sc_1	93.13	83.13	80.13	79.54	88.40	80.68	78.42	77.40	83.77	78.37	76.83	76.54
Constant_COP_GHG Sc_2	125.66	109.77	104.81	103.66	120.04	107.79	104.05	102.46	114.57	106.00	103.45	102.88
Constant_COP_GHG Sc_3	103.90	91.94	88.29	87.52	98.87	89.65	86.90	85.69	93.96	87.51	85.64	85.26
VA_COP_GHG_Sc_1	86.72	78.57	76.18	75.76	82.26	75.97	74.17	73.87	77.89	73.47	72.24	72.04
VA_COP_GHG_Sc_2	116.10	102.95	98.91	98.01	110.87	100.73	97.68	97.02	105.78	98.67	96.58	96.13
VA_COP_GHG_Sc_3	96.44	86.63	83.70	83.12	91.73	84.16	81.94	81.53	87.12	81.81	80.29	80.01

Op GHG emissions [tCO-eq/30y]-Italy

façade strategies	W_20_w_1	W_20_w_2	W_20_w_3	W_20_w_4	W_40_w_1	W_40_w_2	W_40_w_3	W_40_w_4	W_60_w_1	W_60_w_2	W_60_w_3	W_60_w_4
Constant COP and GHG_noFutureClimate	132.13	111.70	104.52	102.40	127.95	113.68	109.81	107.09	126.48	117.69	114.42	113.40
Constant_COP_GHG_FutureClimate	130.68	110.79	103.76	101.69	126.72	112.89	108.63	106.58	125.52	117.14	113.99	113.02
VAR_COP_constant GHG	116.34	99.64	93.75	92.00	112.12	100.49	96.42	95.18	109.95	102.77	100.03	99.22
Constant_COP_GHG Sc_1	49.15	41.59	38.93	38.14	47.62	42.34	40.85	39.92	47.10	43.87	42.67	42.29
Constant_COP_GHG Sc_2	78.16	66.21	61.99	60.74	75.76	67.44	64.97	63.63	75.00	69.93	68.03	67.45
Constant_COP_GHG Sc_3	30.57	25.85	24.19	23.70	29.61	26.31	25.41	24.79	29.27	27.24	26.48	26.25
VA_COP_GHG_Sc_1	43.94	37.52	35.31	34.63	42.32	37.84	36.26	35.78	41.54	38.75	37.71	37.40
VA_COP_GHG_Sc_2	69.71	59.63	56.11	55.05	67.16	60.13	57.66	56.91	65.89	61.53	59.89	59.40
VA_COP_GHG_Sc_3	27.38	23.35	21.98	21.55	26.36	23.55	22.55	22.25	25.88	24.13	23.48	23.28

Op GHG emissions [tCO-eq/30y]-Netherland

façade strategies	W_20_w_1	W_20_w_2	W_20_w_3	W_20_w_4	W_40_w_1	W_40_w_2	W_40_w_3	W_40_w_4	W_60_w_1	W_60_w_2	W_60_w_3	W_60_w_4
Constant COP and GHG_noFutureClimate	149.85	122.36	113.23	110.62	145.48	124.27	117.37	113.50	141.42	126.56	121.84	120.51
Constant_COP_GHG_FutureClimate	147.93	121.04	112.12	109.55	143.82	123.12	116.36	113.49	139.96	125.47	120.86	119.55
VAR_COP_constant GHG	132.71	110.18	102.71	100.56	129.21	111.85	106.19	104.58	125.94	113.75	109.88	108.78
Constant_COP_GHG Sc_1	55.73	45.54	42.16	41.19	54.14	46.28	43.72	42.40	52.64	47.14	45.39	44.90
Constant_COP_GHG Sc_2	88.27	72.18	66.84	65.31	85.78	73.38	69.35	67.46	83.45	74.77	72.01	71.23
Constant_COP_GHG Sc_3	66.50	54.36	50.33	49.17	64.61	55.25	52.20	50.69	62.84	56.28	54.20	53.61
VA_COP_GHG_Sc_1	49.33	40.98	38.21	37.41	48.00	41.56	39.46	38.87	46.77	42.25	40.80	40.39
VA_COP_GHG_Sc_2	78.71	65.37	60.94	59.66	76.62	66.33	62.98	62.02	74.66	67.44	65.14	64.48
VA_COP_GHG_Sc_3	59.05	49.05	45.73	44.77	57.47	49.75	47.24	46.53	55.99	50.58	48.86	48.36

Embodied Emission [tCO-eq/m2]

façade strategies	wall _1	wall _2	wall _3	wall _4
Embodied part (Wall)	0.165	0.166	0.169	0.172
Embodied part (Window)	0.065			

Transitioning from a constant COP with static GHG emissions to temperature-dependent HVAC performance consistently lowers absolute emissions in both locations. Within each WWR category, increasing insulation thickness progressively minimizes these methodological differences. In Italy, Scenario 3 (targeting carbon neutrality by 2042) achieves the most significant reductions, with total emissions decreasing by up to 61.8% when combined with a variable COP. Conversely, in the Netherlands, Scenario 1 (aiming for carbon neutrality by 2050) yields optimal results, reaching a 50.3% reduction. These geographical variations reflect differences in energy demand patterns and grid decarbonization trajectories between the two regions. Notably, the relationship between operational and total emissions (Op+Env) remains consistent across scenarios for each design strategy, maintaining proportional differences regardless of the calculation methodology.

As WWR increases, embodied carbon consistently decreases, with a 16.8% reduction for the same wall configurations. Conversely, within each WWR category, increasing insulation thickness results in a steady 2.6% increase in embodied carbon. The analysis reveals distinct optimal configurations across locations: in Italy, the configuration with 20% WWR and Wall_4 achieves minimum GHG emissions, while 20% WWR with Wall_1 results in the highest emissions. Interestingly, the Netherlands shows a different optimal configuration, with 40% WWR and Wall_4 performing best, though it shares the same worst-performing configuration as Italy. In this research, the transparent facade had lower embodied carbon than the opaque part, as it was modelled as a residential window. For tertiary buildings, curtain walls with the same WWR would have higher embodied carbon. While absolute emission values show substantial variation between different calculation approaches, the relative ranking of façade design strategies remains remarkably consistent, especially for wall configurations where performance variations typically stay within 2-4%. Consequently, simpler methodologies—though potentially overestimating absolute emissions—can still provide reliable insights for comparing façade design strategies in early-stage decision-making.

4.CONCLUSION

This study demonstrates that methodological choices in building performance modelling significantly influence GHG emissions predictions related to different façade design strategies across two geographic regions. In Itay, reductions of up to 61.8% when combining variable COP with advanced decarbonization pathways, while the Netherlands shows more moderate but still significant reductions of up to 50.3%, reflecting its more stable climate conditions. Temperature-dependent HVAC performance modeling reveals climate-specific patterns, with Italy's broader COP distribution reflecting its variable winter temperatures, compared to the Netherlands' narrower range. Our research addresses a critical gap in façade design literature by quantifying how methodological simplifications in HVAC modeling and grid decarbonization impact decision-making. Previous studies overlooked these interdependencies, focusing on weather patterns without considering relationships between envelope performance, system efficiency, and grid emissions. By examining these factors across geographical contexts, we resolve uncertainty about when comprehensive modeling approaches are necessary for early design decisions.

Notably, while these methodological refinements substantially affect absolute emission values, the relative ranking of façade design strategies is constant, with performance variations typically remaining within 2-4%. However, in locations where cooling energy represents a substantial portion of total energy use, the consideration of temperature-dependent SEER becomes crucial for façade design optimization, as cooling efficiency shows greater sensitivity to climate change impacts. The result of this paper suggests that simplified methodological approaches, though overestimating absolute emissions, can provide reliable guidance for comparing façade design alternatives during early-stage decision-making, particularly in temperate climates, while comprehensive frameworks incorporating variable HVAC performance and grid decarbonization remain essential for accurate absolute predictions.

ACKNOWLEDGEMENTS

This publication was produced in the context of PhD research co-financed by the Ministerial Decree no. 352 of 9th April 2022, based on the NRRP - funded by the European Union - NextGenerationEU - Mission 4 "Education and Research", Com-ponent 2 "From Research to Business", Investment 3.3, and by the EURAC Research.

REFERENCES

Attia, Shady, Ramin Rahif, Vincenzo Corrado, Roonen Levinson, Aziz Laouadi, Leon Wang, Behzad Sodagar, Anais Machard, Rajat Gupta, and Bjarne Olesen. 2021. “Framework to Evaluate the Resilience of Different Cooling Technologies.”

Bastos, Joana, Fabio Monforti-Ferrario, and Giulia Melica. 2024. “Covenant of Mayors for Climate and Energy: Greenhouse Gas Emission Factors for Local Emission Inventories.”

Bordignon, Sara, Jeffrey D. Spitler, and Angelo Zarrella. 2024. “Simplified Water-Source Heat Pump Models for Predicting Heat Extraction and Rejection.” *Renewable Energy* 220 (January):119701. https://doi.org/10.1016/j.renene.2023.119701.

“Climate Pledges Explorer – Data Tools.” n.d. *IEA*. https://www.iea.org/data-and-statistics/data-tools/climate-pledges-explorer.

“Directive (EU) 2024/1275 of the European Parliament and of the Council.” 2024. https://eur-lex.europa.eu/eli/dir/2024/1275/oj#document1.

Fakhari, Maryam, Riccardo Pinotti, and Roberto Lollini. 2023. “Report Presenting Proposal for New Baselines for IWG Targets: IWG5-CSA Deliverable D2.3.” Brussels: Funded by the European Union, Horizon 2020 Programme. https://cordis.europa.eu/project/id/101075700.

Fundamentals, ASHRAE. 2017. “ASHRAE Handbook 2017 Fundamentals SI; 2017.”

Heiranipour, Milad, Miren Juaristi, Stefano Avesani, Fabio Favoino, and Valentina Serra. 2025. “Contrasting Building Performance and Thermal Resiliency: A Simulation-Based Quantitative Evaluation Framework for Evaluating the Impact of Building Envelope Technologies.” In , 432–37. https://doi.org/10.1007/978-981-97-8313-7_60.

International Energy Agency. 2024. “Greenhouse Gas Emissions from Energy.” Paris: International Energy Agency.

ISO. 2016. *ISO 18523-1: Energy Performance of Buildings — Schedule and Condition of Building, Zone and Space Usage for Energy Calculation — Part 1. Non-Residential Buildings, Geneva, Switzerland (2016)*.

Karimpour, Mahsa, Martin Belusko, Ke Xing, John Boland, and Frank Bruno. 2015. “Impact of Climate Change on the Design of Energy Efficient Residential Building Envelopes.” *Energy and Buildings* 87 (January):142–54. https://doi.org/10.1016/j.enbuild.2014.10.064.

Khan, Sahil Ali, Tabish Alam, Mohammad Saaim Khan, Paolo Blecich, Mohammad Arif Kamal, Naveen Kumar Gupta, and Anil Singh Yadav. 2022. “Life Cycle Assessment of Embodied Carbon in Buildings: Background, Approaches and Advancements.” *Buildings* 12 (11): 1944. https://doi.org/10.3390/buildings12111944.

Kiamili, Christina, Alexander Hollberg, and Guillaume Habert. 2020. “Detailed Assessment of Embodied Carbon of HVAC Systems for a New Office Building Based on BIM.” *Sustainability* 12 (8): 3372. https://doi.org/10.3390/su12083372.

Machard, Anaïs, Agnese Salvati, Mamak P. Tootkaboni, Abhishek Gaur, Jiwei Zou, Liangzhu Leon Wang, Fuad Baba, et al. 2024. “Typical and Extreme Weather Datasets for Studying the Resilience of Buildings to Climate Change and Heatwaves.” *Scientific Data* 11 (1): 531. https://doi.org/10.1038/s41597-024-03319-8.

Rouws, A.L., R.C.G.M. Loonen, and J.L.M. Hensen. 2024. “The Role of the Electricity Grid in Operation-Induced Greenhouse Gas Emissions by a Residential Building: A Multi-Year Retrospective Simulation Study.” *Energy and Buildings* 324 (December):114870. https://doi.org/10.1016/j.enbuild.2024.114870.

Soudian, Shahrzad, and Umberto Berardi. 2025. “Impact of Future Climate Scenarios on Thermal Performance and Resilience of Building Façades: Canadian Climate Case Study.” *Building and Environment* 267 (January):112245. https://doi.org/10.1016/j.buildenv.2024.112245.

Tettey, Uniben Yao Ayikoe, Ambrose Dodoo, and Leif Gustavsson. 2017. “Energy Use Implications of Different Design Strategies for Multi-Storey Residential Buildings under Future Climates.” *Energy* 138 (November):846–60. https://doi.org/10.1016/j.energy.2017.07.123.

6th International Conference on Building Energy and Environment
Eindhoven University of Technology, The Netherlands
6 - 10 July 2025

Influence of moisture transfer on the U-value measurement of insulated timber frame walls

Machhour EL ASSAAD [1], Yohan PLANTEC [1,2], Thibaut LECOMPTE[1], Thibaut COLINART [1*]

[1]*Univ. Bretagne Sud, UMR CNRS 6027, IRDL, F-56100 Lorient, France*
[2]*Cellaouate, 29600 Saint Martin des Champs, France*
[*] *Corresponding author: thibaut.colinart@univ-ubs.fr*

SUMMARY
This research explores how moisture transfer affects the thermal transmittance (U-value) of timber frame walls using experimental and numerical methods. Six wall systems with different insulation materials and finishing layers were analyzed. Results show that moisture flow increases the U-value when aligned with the heat flux, with more significant effects in highly permeable systems. The study also highlights the limitations of the Heat Flow Meter (HFM) method, which inaccurately measures U-values by blocking moisture flow. The findings emphasize the need to account for moisture effects in energy performance assessments and to develop advanced measurement techniques for accurate evaluations.

Keywords: Moisture transfer, Thermal transmittance (U-value), Heat flow meter method (HFM).

1. INTRODUCTION

The thermal transmittance coefficient of a wall (or U-value) is a crucial parameter for assessing heat loss and determining a building's energy needs. It can be theoretically evaluated following the methodology outlined in ISO 6946 or measured experimentally through in situ methods such as the Heat Flow Meter (HFM) method (Gaspar et al., 2018; Ficco et al., 2015), the thermometric method (Bienvenido-Huertas et al., 2018), or quantitative infrared thermography (Albatici and Tonelli, 2010; François et al., 2021). Due to its simplicity, the HFM method, described in ISO 9869-1, is the most widely used. This method involves measuring heat flux with heat flux sensors and surface temperatures using two thermocouples. It has been extensively tested on walls made of non-hygroscopic materials. Several factors have been shown to influence the accuracy of this method, including heat flux deflection caused by the heat flux sensor (Cucumo et al., 2018), the emissivity of the sensor relative to the wall's surface (Cesaratto et al., 2011), the positioning of the thermocouple, as well as the size, shape, and orientation of the heat flow meter sensor (Meng et al., 2015), the contact quality between the sensor and the wall (Ficco et al., 2015) and the temperature gradient across the wall (Ficco et al., 2015; Albatici and Tonelli, 2010; Gori and Elwell, 2018; Desogus et al., 2011). All these studies showed that thermal transmittance can be evaluated with an uncertainty ranging between 14 to 30 %. Recent studies have highlighted the emergence of walls more open to moisture transfer, attributed to better moisture management within walls (McClung et al., 2014; Mlakar and Štrancar, 2013; Lstiburek, 2004) or lower indoor relative humidity levels (Mlakar and Štrancar, 2013), while maintaining significant drying potential (Lstiburek, 2004). These new walls often incorporate bio-based concretes (Shea et al., 2012; Evrard and De Herde, 2010; Piot et al. 2017; Lelievre et al., 2014). Coupled heat and moisture transfers occurs such walls, which can influence their thermal transmittance coefficient.

Nevertheless, literature studies concerning the effects of moisture on the in situ thermal transmittance measurements are scarce. Nicolajsen (Nicolajsen, 2005) compared the thermal transmittance of a facade insulated with cellulose wadding to one with rock wool in a real Danish climate. The results showed that moisture content, reaching up to 18% in winter, had no significant impact on measured values. Latif et al. (Latif et al., 2014) compared panels with hemp and rock wool insulation of similar theoretical transmittance under different conditions. They found that thermal transmittance increased with rising moisture content, with a slightly greater increase for hemp-insulated panels. In another study, they compared three panels with identical theoretical U-values under winter conditions (Latif et al., 2018). Results indicated that the bio-based panel had higher U-values than the traditional ones, highlighting the influence of moisture on hygroscopic materials. These studies only consider the rise in U-value resulting from the increase in moisture content. However, the situation is more intricate, as moisture can have additional effects on the measurements like latent heat transfer on the surface. This research focuses therefore on the influence of moisture transfer on the thermal transmittance (U-value) of timber frame walls through a combination of experimental and numerical analyses. Additionally, the study evaluates the accuracy of the Heat Flow Meter (HFM) method in capturing the full effects of moisture transfer.

2. MATERIALS AND METHODS

In the present study, six distinct wood frame walls are studied (see Fig. 1). The frames are 880 mm wide and 970 mm high (corresponding to a surface of 0.85 m^2) and their thickness is 220 mm, which corresponds to the thickness of the insulation layer. The tested walls are:

- LE-1: dried projected light earth without any finishing layer.
- LE-2: dried projected light earth with a rain barrier outside and earthen plaster inside.
- LE-3: dried projected light earth with a rain barrier outside and a vapor retarder inside.
- CW-1: dried projected cellulose with a rain barrier outside and a vapor retarder inside.
- CW-2: blown dry loose fill cellulose with a rigid rain barrier outside and OSB inside.
- GW: glass fiber with a rain barrier outside and with a vapor retarder inside. GW wall is non-hygroscopic, meaning moisture should have no significant influence on it and can be taken as a reference.

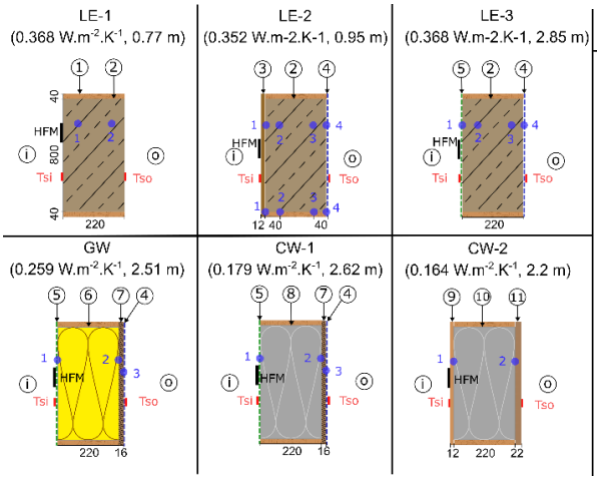

Layer	Material	Thickness [mm]
1	Wooden frame	40
2	Light earth	220
3	Earthen plaster	12
4	Rain barrier (Dorken Delta-XX SD = 0.08 m)	
5	Vapor retarder (Isocell SD = 2 m)	
6	Glass fiber cellulose (ISOMOB35R)	220
7	Medium-density fibre board	16
8	Wet projected cellulose	220
9	Oriented strand board	12
10	Dry blown cellulose	220
11	Rigid rain barrier (Pavatex)	22
–	Thermocouples	
•	Thermohygrometers	
—	Heat flow sensor	

Figure 1. Schematic view of the studied walls, their theoretical U-values and Sd values, their composition, and the sensors placement.

The materials' properties are either measured in the lab or taken from the manufacturer. They are presented in Table 1 (sorption isotherms are characterized by GAB parameters). Using these properties, the tested walls have theoretical thermal transmittance ranging from 0.16 to 0.37 $W.m^{-2}.K^{-1}$ and Sd values ranging from 0.77 to 2.85 m.

Table 1. Material's hygrothermal properties.

Materials	ρ [$kg.m^{-3}$]	λ(w) [$W.m^{-1}.K^{-1}$]	μ [-]	Sd [m]	c_p [$J.kg^{-1}.K^{-1}$]	GAB parameter		
						W_m[-]	K [-]	C [-]
Cellulose	50	0.01w + 0.041	1.5	0.33	1250	0.0499	0.87	14.42
Glass wool	50	0.036	1	0.22	840	0.0125	0.79	1086
Light earth	260	0.23w + 0.081	3.5	0.77	1003	0.026	0.87	8.15
OSB	600	0.13	150	1.8	2100	0.055	0.792	7.04
Earthen plaster	500	0.1	8	0.1	1003	0.0063	0.91	18.7
Rigid RB	200	0.044	3	0.07	1300	0.0489	0.84	8.34
MDF	550	0.09	13	0.21	1300	0.0516	0.8	7.51
VR		N/A		2		N/A		
RB				0.08				

The walls are instrumented with temperature and relative humidity sensors (SHT85 sensors with accuracy of ±0.1 °C and ±1.5% rh). These sensors are embedded within light earth at 40 mm from the surfaces, at the interfaces between different materials, and in the indoor and outdoor environments. K-type thermocouples are placed on the interior and exterior surfaces. Thin, square (50 x 50 mm^2), and rigid heat flux meters HFM (C50 Captec sensor) are fixed to the interior surface using double-sided adhesive tape. They are covered with either black tapes or vapor retarders (depending on the finishing layers of each system) so that the sensors emissivity is similar to walls surface ones. Data are recorded at 5-minute intervals. The instrumented walls are installed in a bi-climatic chamber, where temperature and relative humidity is controlled independently.

To further analyse the results, experiments are simulated using 2D heat and moisture transfer model. Materials properties are those presented in Table 1. The total heat transfer coefficient at the surface which includes both radiation and convection in the enclosure ranges between 8 and 10 $W.m^{-2}.K^{-1}$ for indoor surfaces (depending on wall's surface emissivity) and is set to 10 $W.m^{-2}.K^{-1}$ for outdoor surfaces. Convective moisture transfer coefficient is determined by Lewis relation. Measured ambient temperature and relative humidity are used to assess boundary conditions while temperature and relative humidity measured within the material are extrapolated over the wall's thickness to assess initial conditions.

3. RESULTS AND DISCUSSION

3.1. Analysis of experimental results

The applied experimental protocol consists in fixing a temperature gradient while varying the vapor pressure gradient. Here, two tests are performed: almost no vapor pressure gradient (Test 1) and significant vapor pressure gradient flowing from outdoor to indoor, aligning with the direction of heat flow (Test 2). Temperature and vapor pressure variations in the indoor and outdoor chambers are presented in Fig. 2. Conditions in outdoor chamber are controlled with HVAC systems and setting points are correctly regulated. On the other hand, controlling conditions in indoor chamber with HVAC systems has led to large perturbation on surface heat flux measurement. Therefore, indoor conditions are uncontrolled and equal to those of the lab (which

is more realistic). Indoor temperature fluctuates between 20 and 25 ± 2 °C leading to temperature difference between outdoor and indoor ranging between 10 and 15 °C throughout the experiment. Indoor vapor pressure fluctuates around 1500 ± 500 Pa throughout the test: limited vapor pressure difference is noted for Test 1 (< 300 Pa) while large vapor pressure difference between outdoor and indoor is maintained for Test 2 (> 2600 Pa). Both tests last 7 weeks so that hygrothermal steady state can be reached in all walls at the end of each test.

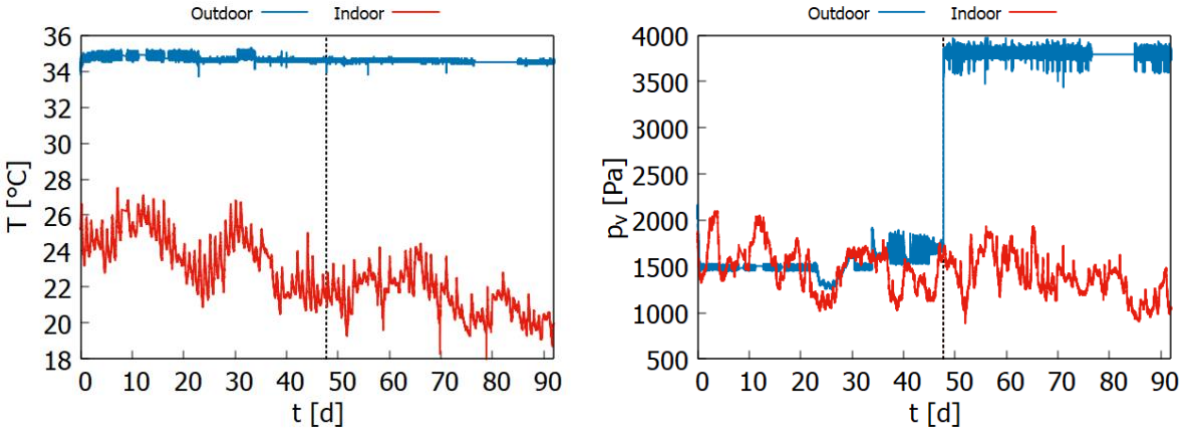

Figure 2. Temporal evolution of the outdoor and indoor temperature and vapor pressures.

Experimental U-values U_{exp} are calculated for all walls using the average method proposed by ISO 9869-1 considering data from the last 5 days of each test:

$$U_{Average} = \frac{\sum_{j=1}^{n} \varphi_j}{\sum_{j=1}^{n} (T_{sej} - T_{sij})} \quad (1)$$

The experimental U-values U_{exp} are plotted in Fig. 3 for light earth walls and in Fig. 4 for walls made with light insulation material. In absence of vapor pressure gradient (Test 1), less than 10% of difference is noted between U_{exp} and the theoretical U-value U_{th} (except for LE-1). These differences are due to assumption when calculating U_{th} (dry thermal conductivity is used, while walls are not dry during Test 1) and to experimental uncertainties. Here, an uncertainty of ± 5.1% is determined using the error propagation method, accounting for 5% uncertainty in the heat flux measurement and 1% uncertainty in temperature measurements (Gloriant et al., 2021). In presence of vapor pressure gradient (Test 2), U_{exp} tend to increase (except for LE-1), slightly for light earth walls (by 7 % and 17 % for LE-2 and LE-3 respectively) and significantly for other walls (almost by 50%).

To explain these increases, hygrothermal simulations are performed considering the physical presence of HFM. The latter is modelled by adding a 50 mm-width moisture-tight layer on the inner side of the wall. Simulated U-values U_{sim} are calculated according to Eq. (1) using simulated surface temperatures below the HFM and heat flux simulated at HFM surface. The results are included in Fig. 3 and Fig. 4. An uncertainty analysis performed for all materials hygrothermal properties has shown logically that thermal conductivity of insulation materials is the most influencing parameter (El Assaad, 2024). Assuming simulation uncertainties of ±10% (due to uncertainty of ±10% in the input thermal conductivity (El Assaad et al., 2024), U_{sim} agree with

U_{exp}, except for two cases. First, U_{exp} present lower values than U_{sim} for LE-1 wall. These errors are attributed to imperfect thermal contact between HFM and light earth wall, which has rugged surface. Second, U_{exp} is much higher than U_{sim} for GW wall for Test 2. In this case, simulation indicates high relative humidity behind the vapor retarder. Nevertheless, simulated are performed with dry thermal conductivity for the GW wall, neglecting therefore its increases at high moisture content and thus lowering U_{sim}.

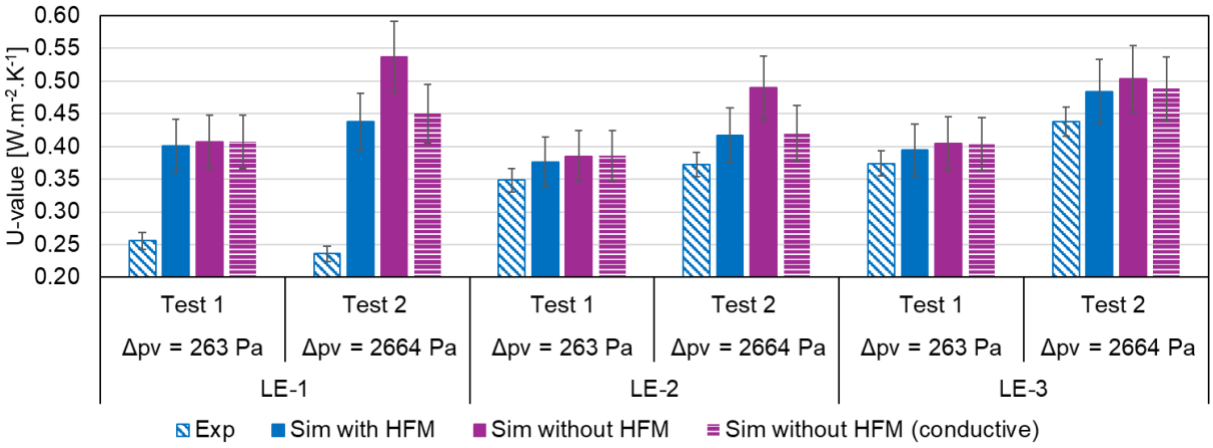

Figure 3. The total U-values simulated under the HFM, the total and conductive U-values without HFS and the experimental values for the light earth systems.

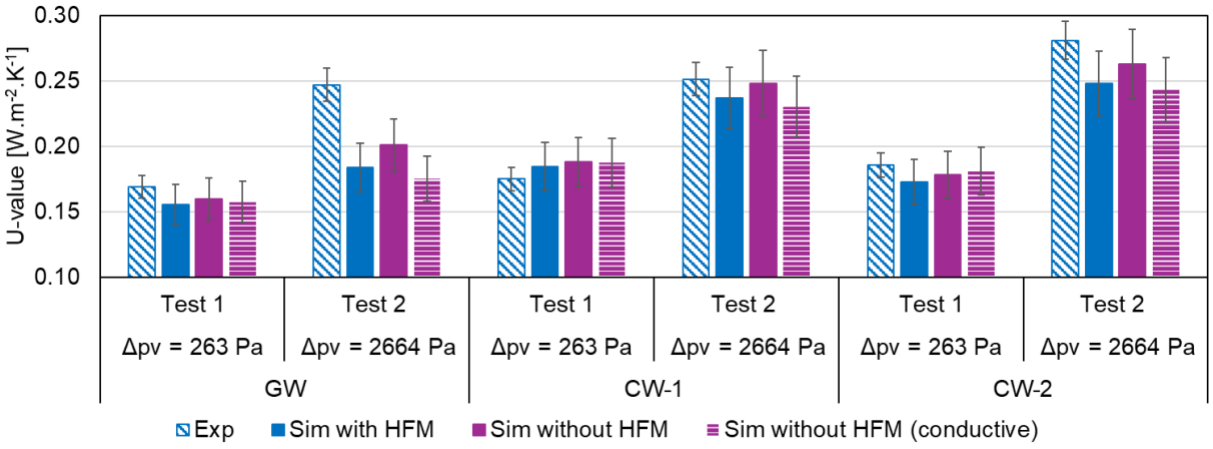

Figure 4. The total U-values simulated under the HFM, the total and conductive U-values without HFS and the experimental values for the conventional systems.

Besides, the simulations of Test 2 show that moisture is blocked behind HFM, which highlights that adding HFM on wall's surface interferes with the wall's hygrothermal behavior. To assess the influence of HFM on U-value evaluation, additional hygrothermal simulations are carried out without HFM. In this case, simulated surface heat flux includes both heat conduction and latent effects of moisture transfer as expressed in Eq. (2):

$$\varphi_{tot} = -\lambda \nabla T + Lv\left(D_v^{\phi} \nabla \phi + D_v^{T} \nabla T\right) \quad (2)$$

To assess the contribution of latent heat transfer to U_{sim}, conductive U-values U_{cond} are calculated using the conductive heat flux described in Eq. (3):

$$\varphi_{cond} = -\lambda \nabla T \quad (3)$$

During Test 1, simulated U-values U_{sim} with and without HFM are logically similar, the differences being lower than 3% (see Table 2). In absence of vapor pressure gradient, moisture flow and thus surface latent heat flux cancel out. During Test 2, U_{sim} without HFM are higher from 3.8% to 18% than U_{sim} with HFM (see Table 2). The more permeable the wall, the higher difference. However, U_{sim} with HFM match well with U_{cond}.

Table 2. Difference between the simulated U-values U_{sim} with and without the presence of HFM.

Wall	Difference [%]		Sd [m]
	Test 1 (Δp_v < 300 Pa)	Test 2 (Δp_v > 2600 Pa)	
LE-1	1.5	18.5	0.77
LE-2	2.3	14.8	0.95
LE-3	2.6	3.8	2.85
GW	2.9	8.5	2.51
CW-1	1.8	4.6	2.62
CW-2	3	5.7	2.2

Finally, when comparing simulations performed without HFM for Test 1 and Test 2, one observes that U_{sim} increase with vapor pressure gradient whatever the wall. For the less permeable walls, this increase is mainly due to the increase of wall's moisture content, which increase the mean thermal conductivity of hygroscopic building insulation material and thus U_{cond}. On the other hand, for the most permeable walls (LE-1 and LE-2), the contribution of surface latent heat flux to the increase in U_{sim} is more significant (up to 18.5 %).

3.2. Extended numerical analysis of the influence of moisture transfer on U-value

This previous finding of the influence of moisture transfer on U-value is extended by running four additional simulations. The simulation conditions are summarized in Table 3. For three cases, heat flows from outdoor to indoor (with a constant temperature difference of 9 °C) and vapor pressure differences between outdoor and indoor vary from negative values (vapor flow opposite to heat flux) to positive values (vapor flow in the same direction as heat flux). For the fourth case, vapor pressure difference is negative, but with the vapor flow is in the same direction as the heat flux (from indoor to outdoor).

Table 3. Indoor and outdoor conditions and vapor pressure difference set for the simulations.

Case	Indoor		Outdoor		Δp_v [Pa]
	T [°C]	Φ [%rh]	T [°C]	Φ [%rh]	
1	21	61	30	29	-300
2			30	36	0
3			30	73	1500
4			10	73	-590

For all walls, U-values U_{sim} are calculated using Eq. (1) once steady-state is reached for each case and compared to U_{sim} calculated for case 2 (i.e. in absence of vapor pressure difference) to evaluate the latent effects on U-value. This latent effect is plotted in Fig. 5 as function of vapor pressure difference between outdoor and indoor multiplied by the sign of heat flux (positive when heat

flows from outside to inside and negative otherwise). The latent effect is positive (i.e. vapor flow increases the U-value) when it aligns with the direction of the heat flux (both in summer and winter conditions) and negative when vapor flows in the opposite direction of the heat flux. A quasi-linear increase is observed whatever the wall, but no correlation is currently found between the slope and the materials or wall properties.

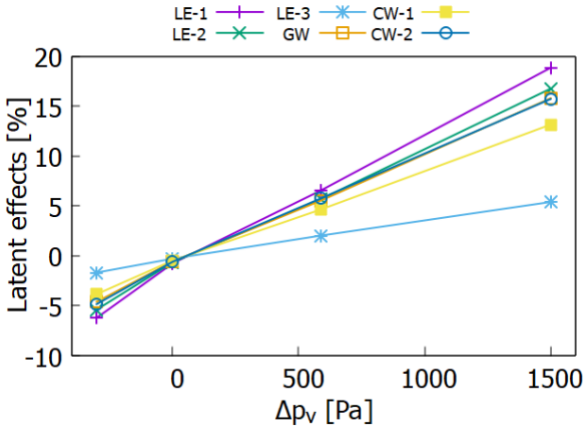

Figure 5. Latent effects due to vapor flow on simulated U-values U_{sim} with respect to the vapor pressure difference multiplied by the sign of heat flux (positive when heat flows from outside to inside and negative otherwise).

4. CONCLUSIONS

This study investigated the influence of moisture transfer on the thermal transmittance (U-value) of insulated timber frame walls, combining experimental and numerical analyses. Six instrumented walls with various designs were tested in a bi-climatic chamber. U-value is measured with HFM by imposing almost constant temperature gradient and by varying vapor pressure gradient. Hygrothermal simulations, including or not the presence of HFM, were carried out to support the experimental data. The key findings from this study are as follows:

- In absence of vapor pressure gradient, measured U-value match with theoretical and simulated U-values considering the experimental and numerical uncertainties and the experimental complexity.
- In the presence of vapor pressure gradient in the direction of temperature gradient (flowing from the outside to the inside), measured and simulated U-value increased up to 50 % due to the moisture accumulation in the less permeable walls and also due to the surface latent heat flow for the more permeable walls. This analysis should be extended to a broader range of materials and configurations to derive a universal equation that accurately defines the contribution of latent effects to the U-value.
- Adding moisture-tight HFM on the indoor surface to measure heat flux inherently blocks moisture transfer at the wall's surface in the presence of vapor pressure gradient. Only conductive contribution to U-value can be therefore measured and errors up to 18% can be made on U-value measurement. Further development of advanced testing methods that can fully capture the latent effects of vapor flow is welcome.

ACKNOWLEDGEMENTS

This work received financial support from ADEME through the Locabati project. Special thanks are extended to the Cellaouate company for providing the cellulose used in this study.

REFERENCES

Albatici R., Tonelli A.M., 2010. Infrared Thermovision Technique for the Assessment of Thermal Transmittance Value of Opaque Building Elements on Site. Energy and Buildings 42, 2177–83.

Bienvenido-Huertas D., Rodríguez-Álvaro R., Moyano J.J., Rico F, Marín D., 2018. Determining the U-Value of Façades Using the Thermometric Method: Potentials and Limitations. Energies 11 ; 360.

Cesaratto P.G., De Carli M., Marinetti S., 2011. Effect of Different Parameters on the in Situ Thermal Conductance Evaluation. Energy and Buildings 43, 1792–1801.

Cucumo M., Ferraro V., Kaliakatsos D., Mele M., 2018. On the Distortion of Thermal Flux and of Surface Temperature Induced by Heat Flux Sensors Positioned on the Inner Surface of Buildings. Energy and Buildings 158, 677–83.

Desogus G., Mura S., Ricciu R., 2011. Comparing Different Approaches to in Situ Measurement of Building Components Thermal Resistance. Energy and Buildings 43, 2613–20.

El Assaad M., Plantec Y., Colinart T., Lecompte T., 2024. Influence of moisture transfer on thermal conductivity measurement by HFM: Measurement accuracy on insulation materials and consequences on building energy assessments. Energy & Buildings 320 114635

El Assaad M., 2024. Toward estimation of real consumption of building: influence of moisture on thermal transmission coefficient of walls, Phd Thesis, Université Bretagne Sud

Evrard A., A. De Herde, 2010. Hygrothermal Performance of Lime-Hemp Wall Assemblies. Journal of Building Physics 34, 5–25.

Ficco G., Iannetta F., Ianniello E., d'Ambrosio Alfano F.R., Dell'Isola M., 2015. U-Value in Situ Measurement for Energy Diagnosis of Existing Buildings. Energy and Buildings 104; 108–21.

François A., Ibos L., Feuillet V., Meulemans J., 2021. In Situ Measurement Method for the Quantification of the Thermal Transmittance of a Non-Homogeneous Wall or a Thermal Bridge Using an Inverse Technique and Active Infrared Thermography. Energy and Buildings 233, 110633.

Gaspar K., Casals M., Gangolells M., 2018. In Situ Measurement of Façades with a Low U-Value: Avoiding Deviations. Energy and Buildings 170, 61–73.

Gloriant F., Joulin A., Tittelein P., Lassue S. (2021). Using heat flux sensors for a contribution to experimental analysis of heat transfers on a triple-glazed supply-air window. Energy, 215, 119154.

Gori V., Elwell C.A., 2018. Estimation of Thermophysical Properties from In-Situ Measurements in All Seasons: Quantifying and Reducing Errors Using Dynamic Grey-Box Methods. Energy and Buildings 167, 290–300.

Latif E., Lawrence M., Shea A.D., Walker P., 2018. An Experimental Investigation into the Comparative Hygrothermal Performance of Wall Panels Incorporating Wood Fibre, Mineral Wool and Hemp-Lime. Energy and Buildings 165, 76–91.

Latif E., Ciupala M.A., Wijeyesekera D.C. 2014. The Comparative in Situ Hygrothermal Performance of Hemp and Stone Wool Insulations in Vapour Open Timber Frame Wall Panels. Construction and Building Materials 73, 205–13.

Lelievre D., Colinart T., Glouannec P., 2014. Hygrothermal Behavior of Bio-Based Building Materials Including Hysteresis Effects: Experimental and Numerical Analyses. Energy and Buildings 84, 617–27.

Lstiburek J.W., 2004. Understanding Vapor Barriers. ASHRAE Journal.

McClung R., Ge H., Straube J., Wang J., 2014. Hygrothermal Performance of Cross-Laminated Timber Wall Assemblies with Built-in Moisture: Field Measurements and Simulations. Building and Environment 71, 95–110.

Meng X., Yan B., Gao Y., Wang J., Zhang W., Long E., 2015. Factors Affecting the in Situ Measurement Accuracy of the Wall Heat Transfer Coefficient Using the Heat Flow Meter Method. Energy and Buildings 86, 754–65.

Mlakar J., Štrancar J., 2013. Temperature and Humidity Profiles in Passive-House Building Blocks. Building and Environment 60, 185–93.

Nicolajsen A., 2005. Thermal Transmittance of a Cellulose Loose-Fill Insulation Material. Building and Environment 40, 907–14.

Piot A., Béjat T., Jay A., Bessette L., Wurtz E., Barnes-Davin L., 2017. Study of a Hempcrete Wall Exposed to Outdoor Climate: Effects of the Coating. Construction and Building Materials 139, 540–50.

Shea A., Lawrence M., Walker P., 2012. Hygrothermal Performance of an Experimental Hemp–Lime Building. Construction and Building Materials 36, 270–75.

6th International Conference on Building Energy and Environment
Eindhoven University of Technology, The Netherlands
6 - 10 July 2025

An analytical study of the impact of glazed vs diffuse facades on solar trapping with detailed directional radiation model

Delia Valledor[1,2,3], Georgios Kyriakodis[2], Anne Penillard[1], Emmanuel Bozonnet[3]

[1] *Saint-Gobain, Paris, France, delia.valledor@saint-gobain.com*
[2] *CSTB, Sophia-Antipolis, France, georgios.kyriakodis@cstb.fr*
[3] *LaSIE UMR CNRS 7356, La Rochelle, France, emmanuel.bozonnet@univ-lr.fr*

SUMMARY

The optical properties of building envelopes govern the inward and outward energy fluxes of a city; and therefore play a major role in urban overheating due to solar trapping. High reflectance (cool) materials have demonstrated a reduction in surface temperature of roofs with a high sky view factor, but their effects are limited to the upper floors of the buildings. To address the root cause of solar trapping, we must focus our attention on facades and roads, as these are the surfaces that contribute to multireflections in densely populated areas. We will showcase the interrelation between the shortwave optical properties of facades and the leading reflections within the canyon.

We have developed an analytical urban canyon model that integrates a detailed angular shortwave radiation description of materials. We aim to quantify the impact of the optical properties of building facades on solar trapping by analyzing the directionality of their reflections. We track the irradiance reflected toward the road and toward the buildings, as they will affect pedestrian thermal comfort and building cooling needs, respectively. We consider traditional materials (lambertian and specular) to evaluate the current situation, and innovative materials (retroreflective) to envision solar trapping mitigation strategies. Simulations are performed with an hourly time step for a year time period.

To verify the consistency of the model, we present the results for a mediterranean compact midrise neighborhood (H/W=1). During summer, for East-West facade orientations, glazed facades contribute to a 15 % increase of ground peak irradiance (equivalent to 85 W/m^2) compared to typical lambertian facades. The contribution of solar irradiance to thermal stress is evaluated with temperature sol-air indicator. Specular canyons result in a rise of 2°C in peak sol-air temperature. For a typical meteorological year, specular facades increase by 11 % (155) the sol-air degree-hours above 26°C, and increase by 132 % (145) the degree-hours above 40°C compared to lambertian facades. Future studies will focus on measuring the impact on thermal comfort and building energy performance at neighborhood scale.

Keywords: urban canyon model, urban radiative model, solar trapping.

1. INTRODUCTION

Urban overheating is a major problem in densely populated areas, leading to the degradation of thermal comfort and and increase in health problems (Santamouris, 2020). This positive energy balance is primarily driven by a radiative solar trapping phenomenon, resulting from a combination of multiple factors: (1) narrow and deep canyons, which facilitate shortwave multireflections and limit longwave cooling exchanges with the sky, and (2) high-capacity materials that store energy during the day and release it at night. Anthropogenic heat release (urban traffic and other contributions such as air conditioners), and the scarcity of green areas contribute to urban overheating.

High reflectance (cool) materials have proven to be an effective mitigation strategy to cool down surfaces with a high sky view factor (roofs). However, when applied to other urban surfaces (i.e. vertical facades), they increase the multireflections, what consequently penalize neighboring buildings and pedestrian comfort. In recent years, researchers have started to focus their attention toward retroreflective materials. These materials are engineered in such a way that they reflect the incoming shortwave radiation back toward the source and limit the multireflections with surrounding surfaces, hence solar trapping. Retroreflective materials have shown promising results when applied to urban facades both experimentally (Rossi et al., 2015) and numerically (Kyriakodis, Schiavoni, et al., 2023). They have proven to lower ground surface temperature, to improve in pedestrian thermal comfort and to reduce energy consumption.

This article aims to isolate shortwave radiation from other heat transfer mechanisms in order to build a fundamental understanding of how the shortwave directional properties of urban materials—lambertian, specular, and retroreflective—impact irradiance within an urban canyon. To achieve this, we have developed an analytical bidimensional urban canyon model.

2. METHODOLOGY

This section describes an bidimensional urban canyon model that we have developed.

2.1. Shortwave radiation model

This model describes the dynamics of shortwave radiation in an urban canyon. The total solar irradiance on a surface (E) is the result of the combination of the direct (beam) irradiance (E_b), the diffuse irradiance (E_d), as well as the multireflections between the surfaces (E^*), as described in Equation 1 (Duffie and Beckman, 2013).

$$E = E_\mathrm{b} + E_\mathrm{d} + E^* \tag{1}$$

Surface material properties are defined by their angular reflectance $\rho^\mathrm{mat}(\theta)$, which allows to compute the angular reflected irradiance of a material by considering the instantaneous beam irradiance. The novelty of this model is the explicit calculation of the first beam reflection $E_\mathrm{rb}^\mathrm{mat}$ as a function of the angular reflectance of the material (Equation 2). This allows to track the amount and the direction of this reflected radiation (material models explained in 2.1.3). The following reflections are computed following the radiosity model (Gros et al., 2011).

$$E_\mathrm{rb}^\mathrm{mat}(\theta) = \rho^\mathrm{mat}(\theta) \times E_\mathrm{b} \tag{2}$$

The sun position is defined by the solar elevation angle h_{sun} and the solar azimuth ϕ_{sun}. The urban canyon geometry is defined by the building height (H) and the street width (W). Each urban

surface is characterized by the tilt angle χ_{surf} measured with respect to the horizontal plane and an azimuth angle ϕ_{surf} defined clockwise with respect to the North. Solar masks link solar position with surface position, indicating for a given surface whether the surface is being irradiated or not for every time step. As observed in Equation 3, solar masks are defined as boolean Ψ_{surf} that are true if the surface is irradiated.

$$\Psi_{\text{surf}} = \sin h_{\text{sun}} \times (\cos(\phi_{\text{sun}} - \phi_{\text{surf}}) \times \sin \chi_{\text{surf}} + (h_{\text{sun}} > \arctan(H/W)) \times \cos \chi_{\text{surf}}) > 0 \tag{3}$$

For an irradiated surface, the total angle of incidence of the solar irradiance θ_{i} is computed with Equation 4. The angle of incidence is 0° if normal to the surface, and 90° if tangent.

$$\cos \theta_{\text{i}} = \cos h_{\text{sun}} * \cos(\phi_{\text{sun}} - \phi_{\text{surf}}) * \sin \chi_{\text{surf}} + \sin h_{\text{sun}} * \cos \chi_{\text{surf}} \tag{4}$$

The irradiated surface per meter depth of canyon of a vertical building facade ($x_{\text{s}}^{\text{bld}}$) and the street pavement ($x_{\text{s}}^{\text{pav}}$) are computed as a function of solar elevation and the canyon dimensions with Equations 5 and 6 respectively.

$$x_{\text{s}}^{\text{bld}} = \min(|W * \tan h_{\text{sun}}|, H) \tag{5}$$

$$x_{\text{s}}^{\text{pav}} = W - \min\left(\left|\frac{H}{\tan h_{\text{sun}}}\right|, W\right) \tag{6}$$

2.1.1. Reflection of building facades

When considering a vertical building facade, one can compute the total reflected irradiance in W/m (per meter of depth) toward the street and the building, as shown in Equations 7 and 8.

$$x_{\text{s}}^{\text{bld}}(t) * E_{\text{rb}}^{\text{bld}\to\text{pav}}(t) = \int_0^{x_{\text{s}}} \int_{-90}^{\theta_{\text{pav-bld}}} E_{\text{rb}}(\theta, t)\, d\theta\, dx \tag{7}$$

$$x_{\text{s}}^{\text{bld}}(t) * E_{\text{rb}}^{\text{bld}\to\text{bld}}(t) = \int_0^{x_{\text{s}}} \int_{\theta_{\text{pav-bld}}}^{\theta_{\text{bld-sky}}} E_{\text{rb}}(\theta, t)\, d\theta\, dx \tag{8}$$

Where the integration limits can be calculated with Equations 9 and 10. Note that the integration limits are computed at x, that stands for each of the 10 discretized elements of x_{s}.

$$\theta_{\text{pav-bld}}^{\text{bld}} = -90 + \arctan\frac{W}{H - x} \tag{9}$$

$$\theta_{\text{bld-sky}}^{\text{bld}} = 90 - \arctan\frac{W}{x} \tag{10}$$

2.1.2. Reflection on pavement

Similarly, when considering a horizontal pavement, one can compute the total reflected irradiance in W/m (per meter of depth) toward the building on the right with Equation 11.

$$x_s(t) * E_{rb}^{\text{pav}\rightarrow\text{bld right}}(t) = \int_0^{x_s} \int_{-90}^{\theta_{\text{bld right}}} E_{rb}(\theta, t)\, d\theta\, dx \tag{11}$$

Equation 12 computes the integration limit of the equation above. Note that the integration limit is computed at x, that stands for each of the 10 discretized elements of x_s.

$$\theta_{\text{bld right-sky}}^{\text{pav}} = \begin{cases} -90 + \arctan\frac{H}{W-x}, & \text{if } \cos(\phi_{\text{sun}} - \phi_{\text{bld left}}) \geq 0 \\ 90 - \arctan\frac{H}{x}, & \text{otherwise} \end{cases} \tag{12}$$

2.1.3. Material models for first direct (beam) reflection

The definition the angular reflection material models is the key of this model. The three material models used in this study can be visualized in Figure 1: lambertian, specular and retroreflective.

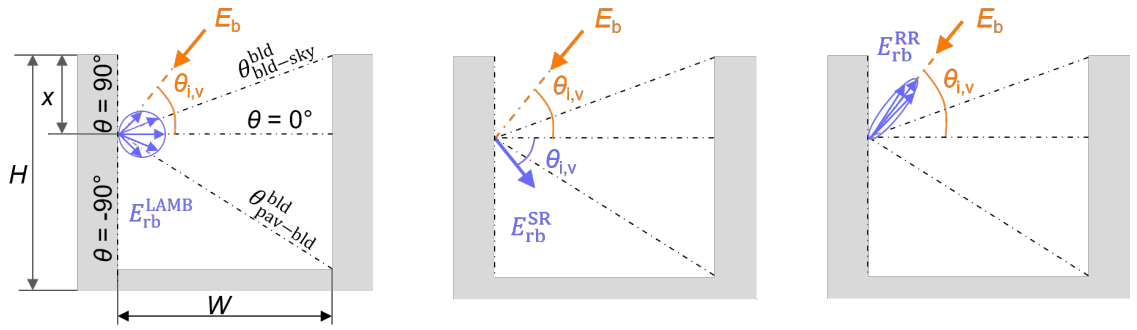

(a) Lambertian (LAMB) **(b)** Specular Reflective (SR) **(c)** Diffuse Retroreflective (RR)

Figure 1. Schematic of the beam first reflection for urban canyons with (a) lambertian, (b) specular and (c) retroreflective facades.

Lambertian (LAMB, Figure 1a) model represents matte or rough diffuse surfaces such as concrete or paintings. The reflected irradiance directs toward every point in the space, as described by Equation 13.

$$E_{rb}^{LAMB} = E_b \int \rho^{LAMB} \cos\theta\, d\theta \tag{13}$$

Specular Reflective (SR, Figure 1b) model represents very smooth materials such as glazing. The reflected irradiance presents a form of a point ray in a direction that is symmetrical to the angle of incidence with respect to the facade, as described by Equation 14.

$$E_{rb}^{SR} = E_b \int \rho^{SR} \delta(\theta - \theta_i)\, d\theta \tag{14}$$

Diffuse Retroreflective (RR, Figure 1c) model represents innovative materials that reflect radiation mostly in the direction of incidence. The reflection follow a Lafortune lobe (with concentration factor $n = 15$), as described by Equation 15.

$$E_{rb}^{RR} = E_b \int \rho^{RR} \cos(\theta - \theta_i)^n\, d\theta \tag{15}$$

2.2. Metric for thermal stress

Temperature sol-air ($T_{\text{sol-air}}$) is the chosen indicator to measure the contribution of irradiance to thermal stress. This is a standard equivalent temperature that includes both convective and radiative heat transfer to calculate the temperature of the considered surface using the overall irradiance. It is calculated with Equation 16:

$$T_{\text{sol-air}} = T_{\text{amb}} + \frac{\alpha \times E}{h_{\text{e}}} \tag{16}$$

Where T_{amb} stands for the air temperature from the weather file, α is the material shortwave absorptivity and h_{e} is the equivalent (convective and radiative) heat transfer coefficient. According to the Standard EN ISO 6945 h_{e} is set to 25 W/Km^2.

2.3. Case study

This study analyzes an infinite urban canyon along the axis North-South located in a compact midrise neighborhood (H/W=1) with mediterranean climate (Nice, South of France) for a typical meteorological year. We aim to evaluate the impact of the optical properties of the urban surfaces (facades) on the solar irradiance distribution within the canyon and the pedestrian thermal stress. More specifically, we will compare lambertian reflection representing residential buildings with low window-to-wall ratio; specular reflection, representing glazed facade buildings of financial districts; and retroreflection, representing innovative facades with diffuse retroreflective properties.

To compare these three reflective properties in realistic conditions, typical material properties have been chosen according to Saint-Gobain database. lambertian facades are defined with 30 % albedo. Specular facades present an angular dependent albedo varying between 40 and 90 %, with average value of 50 % and an average absorption of 26 %. Retroreflective materials present an albedo of 60 %. The street presents an albedo of 15 % (Kyriakodis and Santamouris, 2018).

3. RESULTS

This section presents the results of irradiance and temperature sol-air for a North-South urban canyon (H/W=1) with a mediterranean climate.

3.1. Daily solar irradiance

June 23 has been selected as a representative day in summer, the closest to the summer equinox with high sky clearance. Figure 2 shows the total solar irradiance on a West facade and the ground analyzed on an hourly basis for the three materials examined in this study. Irradiance values are normalized by the area of the respective surfaces. Yellow shaded areas represent the solar direct and diffuse irradiance; dark and light pink shaded areas stand for the reflected radiation from the East and West facades respectively; green shaded areas represent the reflected radiation from the ground; and gray areas represents multireflections.

We can observe that the direct and diffuse irradiance components are consistent across all West facades and the ground. Peak irradiance occurs at 17:00 for the West facade and at 13:00 for the ground. The daily direct and diffuse radiant exposure amounts to 1800 Wh/m^2 for the West facade and 2900 Wh/m^2 for the ground.

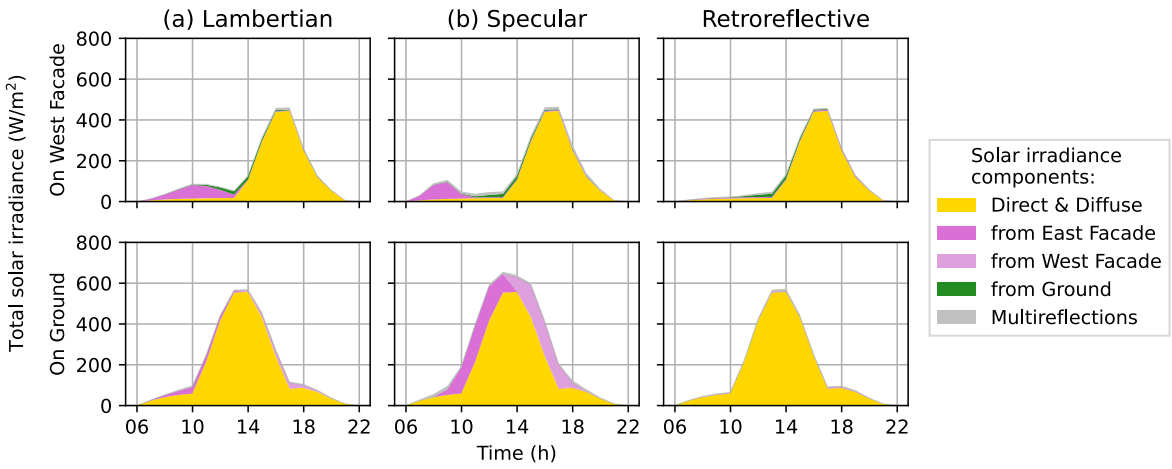

Figure 2. Total shortwave irradiance on West facade (first row) and ground (second row) on June 23 for a H/W=1 urban canyon with (a) lambertian, (b) specular and (c) retroreflective facades.

West facades in both lambertian and specular canyons experience a 230 Wh/m^2 (10 %) increase in radiant exposure compared to retroreflective canyons, primarily due to reflections from the east-facing facades. Specular East facades reflect solar irradiance toward the West facade in the early morning (before 10h), while lambertian east facades reflect irradiance until 13h. Peak irradiance remains equal for the three canyons. The contribution from the ground represents 3 % of the total daily irradiance.

The radiant exposure on the ground of a specular canyon is 970 Wh/m^2 higher than lambertian canyon and 1140 Wh/m^2 higher than a retroreflective canyon. Specular reflection by the East facade increases by 40 % the total daily irradiance on the ground compared to retroreflective canyons. Peak irradiance increases by 85 W/m^2 (15 %) due to specular reflection compared to canyons with lambertian and retroreflective facades.

3.2. Annual solar irradiance on facades

The total solar irradiance on the West facade for a typical meteorological year is presented in Figure 3 in terms of W/m^2 for every hour of the year for a H/W=1 urban canyon with lambertian, specular and retroreflective facades. Total irradiance includes direct, diffuse and reflections from the surrounding surfaces (East facade and Ground). White areas indicate no irradiance, dark intensity indicates higher irradiance.

We can observe that all lambertian, specular and retroreflective facades are irradiated between 13h and 20h, this corresponds to direct and diffuse irradiance, and reflection from the ground. Unlike retroreflective facades, that are only irradiated during these period, lambertian and specular facades are also irradiated between 6h and 13h due to reflections from the East facade. Specular facades present a thinner irradiated region during the morning period. Annual peak irradiance is up to 589 W/m^2 in both lambertian and specular canyons, 1.5 % higher than retroreflective facades. Regarding the daily radiant exposure for the year period, specular canyons increase the annual peak by 9 % compared to retroreflective canyons.

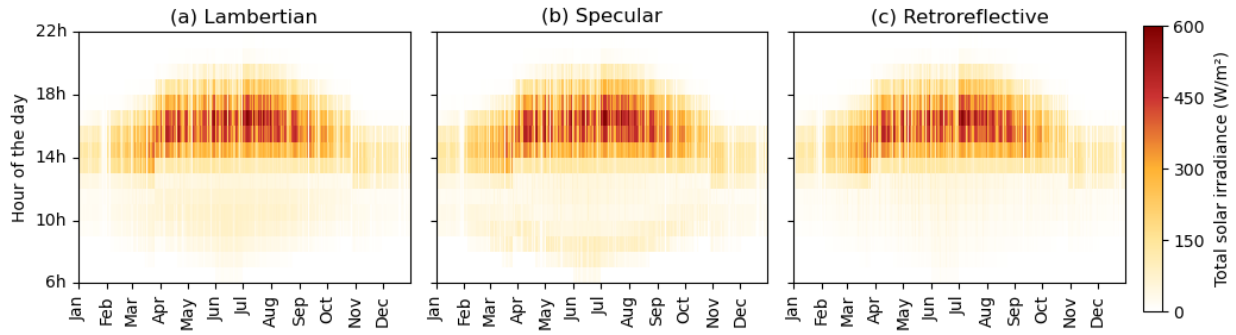

Figure 3. Total shortwave irradiance on West facade (direct, diffuse and reflections) for a H/W=1 urban canyon with (a) lambertian, (b) specular and (c) retroreflective facades.

3.3. Irradiance contribution to thermal stress

The temperature sol-air for the ground for a typical meteorological year is presented in Figure 4 for every hour of the year for canyons with lambertian, specular and retroreflective facades.

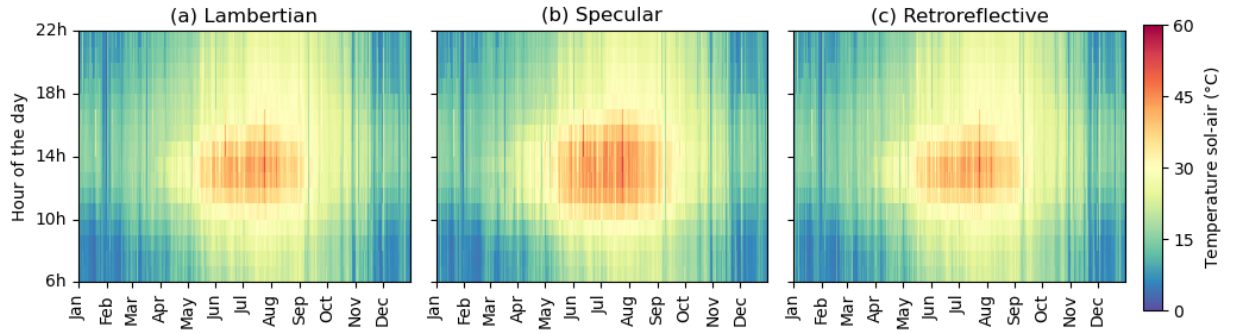

Figure 4. Temperature sol-air on ground for a H/W=1 urban canyon with (a) lambertian, (b) specular and (c) retroreflective facades.

Specular canyons lead to a maximum annual temperature sol-air of 54°C, that is 2°C higher than lambertian and retroreflective canyons. Specular canyons lead to 1555 degree-hours/year of temperature sol-air above 26°C, that is 155 degree-hours (11 %) more than lambertian canyons and 210 degree-hours (16 %) more than retroreflective canyons. Sol-air temperatures above 26°C occur between April and October.

Specular canyons result in 255 degree-hours per year of sol-air temperatures exceeding 40°C, which is 145 degree-hours (132 %) higher than lambertian canyons and 150 degree-hours (143 %) higher than retroreflective canyons. These sol-air temperatures above 40°C are observed between May and August.

4. CONCLUSIONS AND PERSPECTIVES

This study aims to improve our understanding of shortwave irradiance and interreflections between surfaces by examining typical materials—Lambertian, specular, and retroreflective. To achieve this, we developed a bidimensional urban canyon model that accounts for the angular reflectance of these materials. Our findings demonstrate consistent differences between the three models, emphasizing the need for caution when using radiosity algorithms to model all surfaces within a neighborhood, especially in the presence of large specular surfaces.

For an urban canyon with a height-to-width ratio of $H/W = 1$ in a Mediterranean climate (Nice, South of France), specular facades (with angular-dependent albedo ranging from 40 % to 90 %) result in a 15 % increase in peak irradiance on the ground (85 W/m^2) compared to lambertian (30 % albedo) and retroreflective (60 % albedo) canyons. This increase in peak irradiance contributes to a higher thermal stress, measured using the sol-air temperature indicator. Specifically, specular canyons lead to an increase of 225 degree-hours per year (+143 %) above 40°C compared to lambertian canyons. This study highlights the strong correlation between shortwave radiation directionality and thermal stress.

Beyond this first approach to demonstrate the issues of specular materials in dense cities and the potential of innovative retroreflective materials, we will exploit this fast analytical model (1 minute calculation time for an annual analysis) to perform an extensive parametric analysis on aspect ratio, street orientation and geolocation for different materials. Besides we are conducting an experimental validation and intermodel comparisons that will be published soon. Then, we will develop a three-dimensional multiphysics model to asses neighborhood configurations and quantify the impact of urban surfaces on thermal comfort and building energy performance, building upon the promising results presented by Kyriakodis, Schiavoni, et al. (2023).

ACKNOWLEDGMENTS

The authors would like to thank the ANRT for supporting the contract CIFRE 2023/1818.

REFERENCES

Duffie J. A. and Beckman W. A., 2013. Solar Engineering of Thermal Processes. John Wiley & Sons, Ltd.

Gros A., Bozonnet E., and Inard C., May 2011. Modelling the Radiative Exchanges in Urban Areas: A Review. Advances in Building Energy Research 5, 163–206.

Kyriakodis G.-E., Schiavoni M., Riederer P., Bozonnet E., Anne P., and Xavier C., Dec. 2023. Impact of retro-reflective windowpanes on building energy demand and pedestrian thermal comfort under various neighborhood settlements. Proceedings of 6th International Conference on Countermeasures to Urban Heat Islands (IC2UHI). Ed. by P. Rajagopalan, V. Soebarto, and H. Akbari. RMIT University. Melbourne (AUS), Australia, 1097–1106.

Kyriakodis G.-E. and Santamouris M., June 2018. Using Reflective Pavements to Mitigate Urban Heat Island in Warm Climates - Results from a Large Scale Urban Mitigation Project. Urban Climate 24, 326–339.

Rossi F., Morini E., Castellani B., Nicolini A., Bonamente E., Anderini E., and Cotana F., Oct. 2015. Beneficial Effects of Retroreflective Materials in Urban Canyons: Results from Seasonal Monitoring Campaign. Journal of Physics: Conference Series 655, 012012.

Santamouris M., Jan. 2020. Recent Progress on Urban Overheating and Heat Island Research. Integrated Assessment of the Energy, Environmental, Vulnerability and Health Impact. Synergies with the Global Climate Change. Energy and Buildings 207, 109482.

6th International Conference on Building Energy and Environment
Eindhoven University of Technology, The Netherlands
6 - 10 July 2025

Developing calibrated building energy and hygrothermal models to assess deep energy retrofits

Myles Freeman Zagar [1], Cynthia A. Cruickshank [2], Daniel Chung[3]

[1]*Carleton University, Ottawa, Canada, myleszagar@cmail.carleton.ca*
[2]*Carleton University, Ottawa, Canada, cynthiacruickshank@cunet.carleton.ca*
[3]*University of Toronto, Toronto, Canada, danielh.chung@daniels.utoronto.ca*

SUMMARY
To accurately evaluate the performance of deep energy retrofits in future climates, validated building energy models are required. In this study, energy and hygrothermal models representing a pilot deep energy retrofit were created using EnergyPlus 23.1 and DELPHIN 6.1, respectively. Base case models were created using building specifications and conservative assumptions. Using data for both measured energy use and envelope conditions from the building as well as previous models, the initial model variables were manually tuned such that energy use, envelope temperature and moisture were calibrated. Energy models were assessed using established thresholds for Normalized Mean Bias Error (NMBE) and Coefficient of Variation of Root Mean Square Error (CV(RMSE)). Hygrothermal models were assessed visually and with previously proposed thresholds for Mean Absolute Error (MAE) and Pearson Correlation Coefficient (r). Final calibration levels for the energy models and preliminary calibration levels for the hygrothermal models are presented. The models can be used to assess this retrofit type under different future weather scenarios as well as to develop a co-simulated energy-hygrothermal model that streamlines the modelling process.

Keywords: energy modelling, hygrothermal modelling, calibration

1. INTRODUCTION

Building energy and hygrothermal models can be effective tools in assessing the performance of deep energy retrofits, through predictions of energy savings and improvements to occupant comfort as well as evaluating any durability risks in the new envelope. However, confidence in model predictions is limited if the models are not calibrated (Huerto-Cardenas et al. 2020; Dang et al. 2023). This is often achieved by comparing model outputs with measured outputs from the building using established metrics and thresholds. Common outputs include utility usage for energy models, or temperature and moisture measurements in the wall assembly for hygrothermal models. The level of calibration required for energy models is set out in several standards, while no current standard exists for hygrothermal models (Huerto-Cardenas et al. 2020).

The motivation for this study was to develop calibrated energy and hygrothermal models of the same building by applying existing calibration strategies. The calibrated models can then be used to assess the future performance of the design under various environmental conditions. To achieve this, multi-zone energy and one-dimensional hygrothermal models in EnergyPlus 23.1 and DELPHIN 6.1 representing a retrofitted semi-detached residential building were created. Measured utility data was used to calibrate the energy models, with ASHRAE Guideline 14 thresholds serving as the calibration standard (ASHRAE 2014). The hygrothermal models utilized recently proposed metrics and thresholds that have been applied in a guarded hot box calibration

experiment (Huerto-Cardenas et al. 2020; Hilbrecht 2024). To reach calibration, input variables of the models with uncertainty were manually tuned in a stepwise manner.

2. METHODOLOGY

2.1. Case Study Building

The building is a retrofitted community housing unit in Ottawa, Canada, shown in Fig. 1. The east unit (rightmost, Fig. 1) was modelled, with an above grade volume of approximately 6.89m x 7.95m x 5.85m. It was selected for the available data on the project that could be used to calibrate the model. Four years of pre-retrofit electricity usage data (on an hourly basis), and two years of natural gas usage via monthly billing data were available. Post-retrofit, sub-divided usage of the new HVAC, water heating, and plug loads were available at hourly intervals. The cross section of the pre and post retrofit wall assemblies are shown in Fig. 2. Sensors were installed in various layers of the exterior retrofitted envelope to record temperature, moisture content and relative humidity (RDH Building Science 2021, Carver and Dicaire 2021).

Figure 1. Case study building before and after retrofit (Dicaire and Carver 2023).

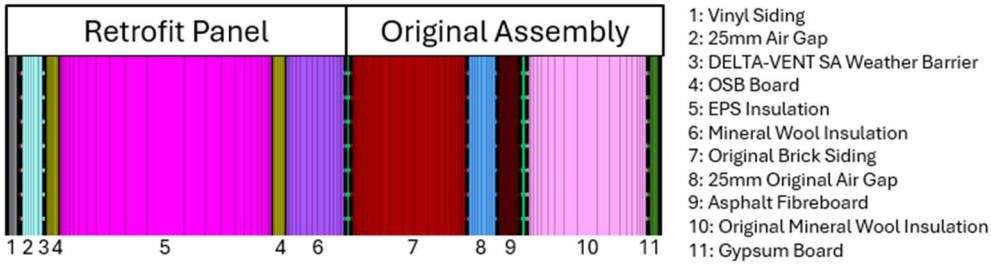

Figure 2. Cross section of pre (right) and post (left) retrofit wall assemblies.

The original building envelope was a brick veneer, wood framed construction built in 1960. It was heated by a central air natural gas furnace with no central cooling; however, most units had installed window-mounted air conditioning units for cooling. Domestic hot water (DHW) was heated by natural gas.

The deep energy retrofit used an exterior, prefabricated panelized construction (layers 1-6 in Fig. 2). A new roof was also installed, coupled with solar PV added to the south facing roof. Cold climate air source heat pumps replaced the furnace and included a backup electrical resistance furnace. The DHW was upgraded to a heat pump water heater, also air source.

2.2. Energy Models

Monthly electrical and natural gas usage in the models were assessed against the measured data using the NMBE and CV(RMSE) as shown in Eq. 1 and Eq. 2 (ASHRAE 2014). Although the measured electrical usage was provided on an hourly basis, it was summed for each month. This was done to reduce variability in plug loads related to occupancy, since the small number of people living in the building would have an outsized effect on total usage. Next, although four years of data was available for the electrical usage, it was apparent that a vacancy and change in occupancy significantly altered the usage in the building during periods of time. Thus, 2017 was used for calibration since it showed consistent occupancy and aligned with the only full calendar year of natural gas data provided.

$$NMBE(\%) = \frac{1}{\bar{m}} \frac{\sum_{i=1}^{n}(m_i - s_i)}{n-p} \times 100 \quad (1)$$

$$CV(RMSE) = \frac{1}{\bar{m}} \sqrt{\frac{\sum_{i=1}^{n}(m_i - s_i)^2}{n-p}} \times 100 \quad (2)$$

Occupancy preferences, weather files, air infiltration and ground heat transfer are some of most significant factors affecting energy model outputs (Beausoleil-Morrison 2020; Mahdavi and Tahmasebi 2019; Chen 2015). Building airtightness was tested pre- and post-retrofit through a blower door test. The infiltration at 50 Pa retrieved from the testing was scaled down to natural air pressures to extract values used by EnergyPlus to calculate a wind dependant infiltration rate. Ground heat transfer was calculated using KIVA, which has been shown to produce reliable results (Kruis and Krarti 2017). To reduce uncertainty in exterior conditions, actual year weather files (AMY) were created using data from Environment and Climate Change Canada and NASA Power databases for the calibration year.

Remaining variables with large uncertainty were occupant influenced. This included water use, thermostat setpoint, and internal heat and moisture gains from occupancy presence and appliance use. The water use schedule was selected from published averaged data (Edwards et al. 2013). Water use quantity was then tuned for natural gas usage until the annual water usage approached estimates from the pre-retrofit energy audit data. Thermostat setpoints were used to further calibrate natural gas consumption, since no information regarding setpoints were available. Occupancy schedules were first set with profiles from Mitra et al. 2020 but were changed to seasonal daily averaged profiles of the usage data. Internal gains magnitude was a summed amount of appliance values taken from the ASHRAE Handbook of Fundamentals (ASHRAE 2023).

For the post-retrofit model, envelope layers were added to reflect the exterior panels installed. Infiltration inputs were updated based on the second blower door test results. HVAC and DHW system models were revised to represent post-retrofit electrification. Since the post-retrofit usage data was sub divided into HVAC, water heating, and plug loads, the electrical usage of each device was output monthly and compared to the measured data.

2.3. Hygrothermal Models

2.3.1 Pre-Retrofit Model

The pre-retrofit hygrothermal model was not calibrated using statistical metrics like Eq. 1 and Eq. 2 since there was no temperature and moisture data for the original wall. Thus, an inter-model comparison was used to assess model calibration (Dang et al. 2023). A base case of the pre-retrofit assembly was created in DELPHIN 6.1, then simulated and compared to previous models of the same construction in WUFI Pro 6 (McNally 2022).

Materials were taken from the closest material in the DELPHIN database, with a focus on similar default values of thermal conductivity and water absorption coefficient, and numerical properties were changed to match the WUFI database materials to be consistent with previous models (McNally 2022; Natural Resources Canada, 2023). Existing moisture functions were automatically scaled by DELPHIN based on the numerical value changes. Air and moisture sources were applied to layers of the assembly using best practices for hygrothermal modeling and ASHRAE Guideline 160 (Wright et al. 2021). This included exterior air infiltration in the original air gap (layer 8, Fig. 2) of $10\frac{1}{h}$, 1% of wind driven rain (WDR) applied to the interior elements of the brick (layer 7, Fig. 2), and 0.01% WDR applied to the exterior elements of the fibreboard (layer 9, Fig. 2). The model was run for four years with the ASHRAE Year Three moisture reference year weather file for Ottawa. The moisture content in the brick and fibreboard were compared to previous WUFI models to see if quantities and trends were the same.

2.3.2. Post Retrofit Model

The post-retrofit model added layers 1-6 in Fig. 2 to the pre-retrofit model and included new sources of air and moisture exchange. A multi-run process was used for calibration that has been previously applied to WUFI models (Lstiburek et al. 2016; McNally 2022).

Pre-retrofit rain sources in layers 7 and 9 were removed since rain no longer penetrated these layers. Air infiltration in layer 8 was removed to reflect the air sealing that occurred. New exterior infiltration was placed in the layer 2 air gap behind the vinyl cladding. An additional infiltration source was placed between layers 6 (mineral wool) and 7 (brick) via a 5 mm air gap. WDR sources of 1% and 0.01% were added just behind layers 1 and 4. The vinyl rain source was facilitated using a thin brick layer, consistent with previously calibrated models (McNally 2022). An interior infiltration source was applied between the original fibreboard and mineral wool layers.

Initial conditions were determined from the end of a one-year simulation using a 2021 AMY weather file and moisture content taken from the end of the construction period calibration process completed in WUFI Pro 6. The calibration period comprised of a one-year simulation using a 2022 AMY weather file. Calibration was achieved using an approach based on previous work by McNally 2022. This was selected for its novel application of tuning infiltration source levels variables via the multi-run methodology in WUFI. Ranges of infiltration rates for each air gap were selected from experimental data by Finch and Straube 2007. Here, DELPHIN's scripting capability allowed for all combinations of each infiltration rate to be simulated quickly, the calibration metrics were calculated for each variant. The best variants selected for further refined runs with narrower gaps between infiltration values. The methodology could later be adapted to work within an optimization framework using calibration statistical metrics.

The inner OSB layer was expected to be an at-risk material and was the primary focus of the

calibration. First, measured and modelled moisture content curves were plotted to see if they showed similar magnitudes and trends over the calibration period. Next Eq. 3 and Eq. 4 were computed to assess model calibration (Huerto-Cardenas et al. 2020). These metrics have been shown to better articulate the accuracy of hygrothermal models, compared to the metrics used for assessing energy models (Huerto-Cardenas et al. 2020).

Model output of the moisture mass density (kg/m^3) in the inner OSB, $MC_{\text{OSB-abs}}$, was converted to a percentage, $MC_{OSB}\,(\%)$, using Eq. 5 for easy comparison to the calibration thresholds. The density of the material, ρ_{OSB} (kg/m^3), was taken from the material data file. Once Eq. 3 and Eq. 4 approached the threshold values, the outer OSB, new batt insulation, and rainscreen layers were examined to verify overall model agreement.

$$MAE = \frac{\sum_{i=1}^{n}|m_i - s_i|}{n} \tag{3}$$

$$r = \frac{\sum_{i=1}^{n}(m_i - \bar{m})\times(s_i - \bar{s})}{\sqrt{\sum_{i=1}^{n}(m_i - \bar{m})^2}\times\sqrt{\sum_{i=1}^{n}(s_i - \bar{s})^2}} \tag{4}$$

$$MC_{OSB}(\%) = \frac{MC_{OSB-a}}{\rho_{OSB}} \times 100\% \tag{5}$$

3. RESULTS

3.1 Energy Models

Calibration was considered complete as soon as model outputs met ASHRAE Guideline 14 thresholds. Table 1 shows the achieved level of calibration in electrical and natural gas energy against the threshold value for select metrics, and Fig. 3 and Fig. 4 provide monthly insight into the month-by-month comparison of the models predicted usage versus the measured actual use.

Table 1. Final values of calibration metrics achieved for energy models.

Metric	ASHRAE Threshold	Pre retrofit electricity	Pre retrofit natural gas	Post retrofit heating and cooling	Post retrofit hot water
NMBE (%)	±5	0.42	-3.18	-4.3	-1.14
CV(RMSE) %	15	14.43	12.88	14.98	8.53

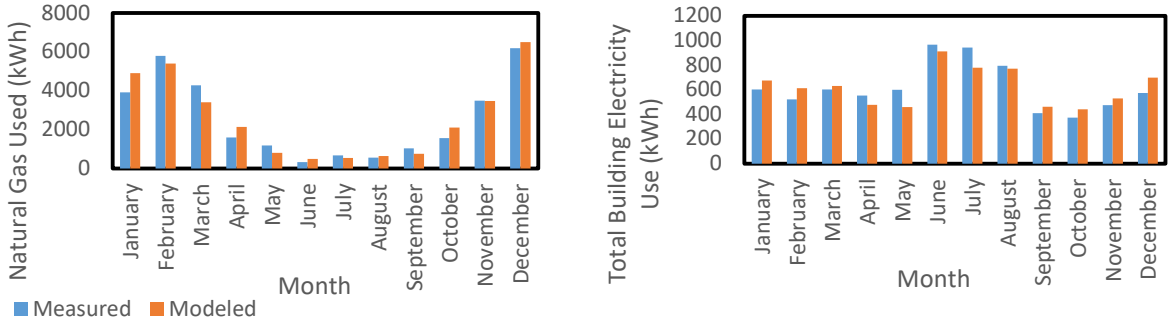

Figure 3. Monthly energy usage of building pre retrofit. Natural gas (left) and electricity (right).

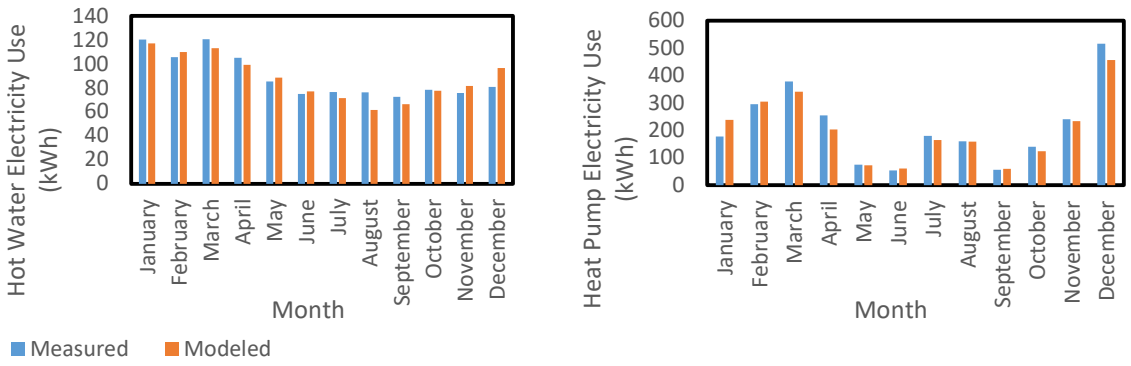

Figure 4. Post retrofit hot water (left) and heat pump (right) electricity usage.

3.2. Hygrothermal Models

The moisture content of the fibreboard and brick layers over the pre-retrofit simulation are shown on Fig. 5. Compared to previous WUFI models, the fibreboard moisture content profile shows similar cyclic behaviour of wetting and drying year on year in magnitude and timing (McNally 2022). The brick moisture content profiles also show similar behaviour through the simulation, but the DELPHIN model predicts lower moisture contents by 20-30kg/m^3. This likely results from limitations in transferring the customized moisture functions of the brick material into DELPHIN. Given the air sealing that occurred as part of the retrofit, if moisture levels in the brick do not increase, this deviation is acceptable as there was no mould risk at the brick interface in either model. While this cannot be considered full calibration, given the lack of in-situ data available pre-retrofit, equivalent results between this model and the previous WUFI model represent a strong likelihood of model conditions and behaviour in the envelope that matched the original building.

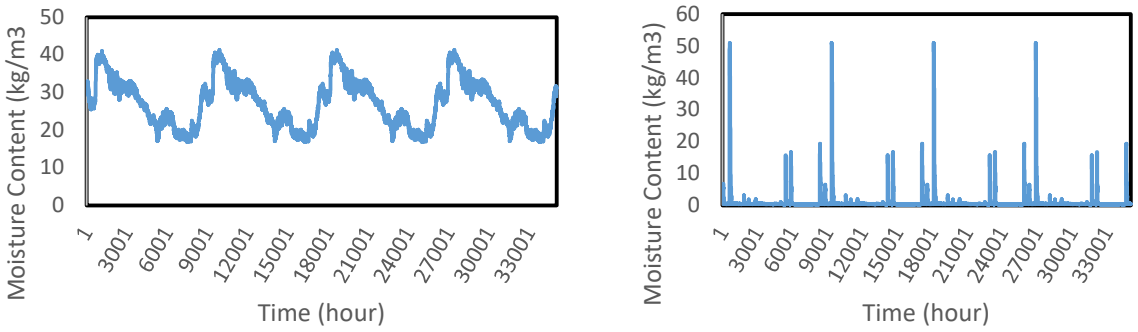

Figure 5. Year on year moisture content in fibreboard (left) and brick (right) layers pre retrofit.

Table 2 summarizes the calibration level in each layer of the post-retrofit assembly. Only the lower threshold was reached for MAE, while all layers met the single threshold for R-value with differing degrees of success. Note, the model with the lowest MAE for the inner OSB was not selected as the best case due to poorer performance among other layers. The model outputs are compared to

the measured levels in Fig. 6. Despite the satisfactory level of performance of Table 2 metrics, the difference in trends of the moisture content in OSB layers suggests the level of calibration can be improved upon. Thus, these results are presented as a preliminary level of calibration. It is estimated that uncertainty in material properties is a possible cause, since both the DELPHIN and WUFI libraries contain multiple OSB material files. Although the infiltration rates are constant, which does not reflect changing conditions in the wall, previous work has shown static infiltration rates can result in good calibration. Here, a static infiltration rate in the air gap placed next to the Squishy insulation layer resulted in an excellent result.

Table 2. Model details and calibration level achieved for calibrated model.

Metric	Proposed LV 1 Threshold	Proposed LV 2 Threshold	Inner OSB Moisture Content (%)	Outer OSB Moisture Content (%)	Squishy Insulation RH (%)	Rainscreen RH (%)
MAE	< 5%	< 10%	6.34	5.89	5.07	10.94
r	> 0.5	N/A	0.80	0.78	0.69	0.53

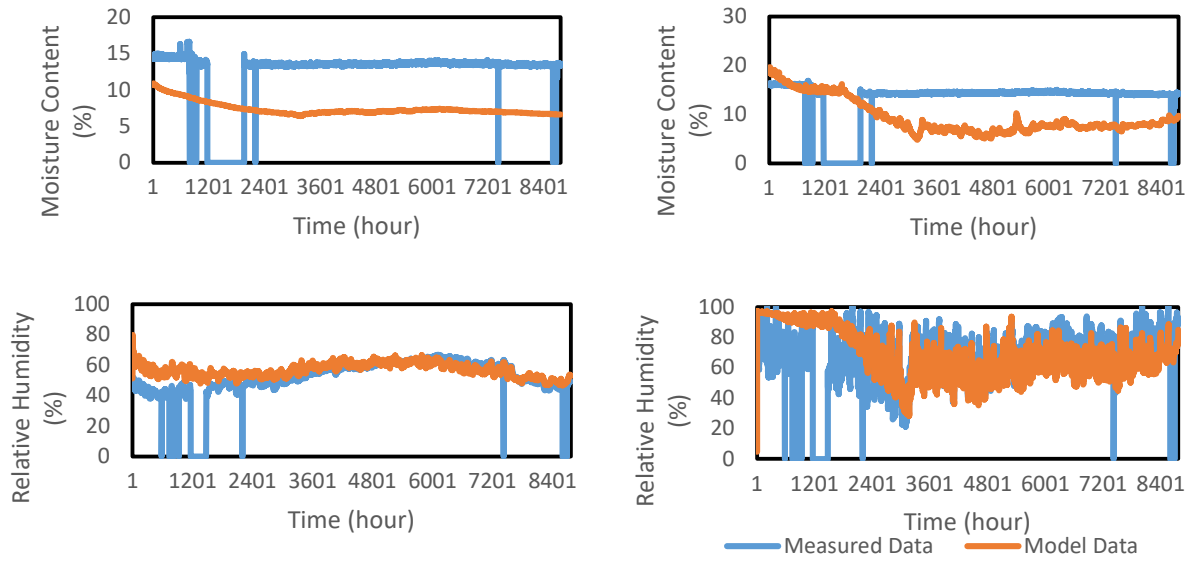

Fig 6. Moisture content and relative humidity of inner (top left), outer (top right) OSB layers, mineral wool (bottom left) and rainscreen (bottom right).

4. CONCLUSIONS AND FUTURE WORK

This study outlined the calibration process for energy and hygrothermal models of a pilot project undertaken in Ottawa, Canada. Both energy models met established thresholds by varying building variables with greatest uncertainty, while the hygrothermal models applied proposed thresholds and a recently developed calibration methodology with moderate success.

Improvement to hygrothermal model calibration will be attempted using different OSB material options in the DELPHIN database. Given the uncertainty of material properties from different sources and locations, and the potential for different amounts of infiltration in the assembly due to

poor assembly or lack of maintenance, future hygrothermal calibration may benefit from increased use of stochastic modelling techniques. This way, uncertainty in the calibration can be quantified. Finally, all models will be simulated under future weather conditions to assess whether climate change reduces the effectiveness or durability of the retrofit.

ACKNOWLEDGEMENTS

The authors would like to thank their colleagues at the Centre for Advanced Building Envelope Research (CABER) at Carleton University and their New Frontiers in Research Fund (NFRF) collaborators for their support and insights that helped accomplish this work.

REFERENCES

ASHRAE, ANSI/ASHRAE 14-Measurement of Energy, Demand, and Water Savings. Atlanta, GA, USA: American Society of Heating, Refrigerating and Air-Conditioning Engineers (ASHRAE), 2014.

ASHRAE, 2023 ASHRAE Handbook of Fundamentals – HVAC Applications (SI Edition). Atlanta, GA, USA: American Society of Heating, Refrigerating and Air-Conditioning Engineers (ASHRAE), 2023.

Beausoleil-Morrison I. Fundamentals of Building Performance Simulation. New York, USA. Routledge, 2020.

Carver M., Dicaire D. OCH PEER Pilot Monitoring Plan V1.4. Ottawa, ON, CAN: City of Ottawa, 2021.

Chen Z., Wen J., Bushby S. T., Lo L. J., O'Neill O., Payne W. V., Pertzborn A., Calfa C., Fu Y., Grajewski G., Li Y., Yang Z., 2022. An analysis of the hybrid internal mass modeling approach in EnergyPlus. In: Proceedings of eSim 2022: 12th Conference of IBPSA-Canada, Ottawa.

Chen D., 2015. Three-dimensional steady-state ground heta transfer for multi-zone buildings, Journal of Building Performance Simulation 8(2), 866696.

Dang X., Janssen H., Roels S., 2023. Hygrothermal modelling of one-dimensional wall assemblies: inter-model validation between WUFI and DELPHIN. Journal of Physics: Conference Series 2654, 012040.

Dicaire D., Carver M. Ottawa Community Housing Pilot – IURC Presentation. Ottawa, ON, CAN: Ottawa Community Housing (OCH), 2023.

Edwards S., Beausoliel-Morrison I., Laperriere A., 2015. Representative hot water draw profiles at high temporal resolution for simulating the performance of solar thermal systems. Solar Energy 111, pp 43-52.

Finch G., Straube J., 2009. Ventilated Wall Claddings: Review, Field Performance, and Hygrothermal Modeling. Westford, MA, USA: Building Science Corporation.

Hilbrecht R.F. Development of a hygrothermal model validation methodology using a two-storey guarded hot box. MASc. thesis, Carleton University, 2024.

Huerto-Cardenas H. E., Leonforte F., Aste N., Del Pero C., Evola G., Costanzo V., Lucchi E., 2020. Validation of Dynamic Hygrothermal Simulation Models for Historical Buildings: State of the Art, Research Challenges and Recommendations. Building and Environment 180, 107081.

Kruis N., Krarti M., 2017. Three-dimensional accuracy with two-dimensional computation speed: using the Kiva numerical framework to improve foundation heat transfer calculations. Journal of Building Performance Simulation 10(2), 1211177.

Li W., Tian Z., Lu Y., Fu F., 2018. Stepwise Calibration for Residential Building Thermal Performance Model Using Hourly Heat Consumption Data. Energy and Buildings, 181, pp. 10-25.

Lstiburek J, Ueno K., Musunuru S., Strategy Guideline: Modeling Enclosure Design in Above-Grade Walls. Westford, MA, USA: Building Science Corporation, 2016.

Mahdavi A., Tahmasebi F. Building Performance Simulation for Design and Operation. Abingdon, UK. Routledge, 2019.

McNally J., 2022. PEER Hygrothermal Model Validation: Final Report. Ottawa, ON, CAN: Natural Resources Canada.

Mitra D., Steinmetz N., Chu Y., Cetin K. S., 2020. Typical occupancy profiles and behaviors in residential buildings in the United States. Energy and Buildings, 210, 109713.

NR-CAN, Prefabricated Exterior Energy Retrofit (PEER) Project Guide. Ottawa, ON, CAN: Natural Resources Canada, 2023.

RDH, PEER Modeling and Monitoring Protocols. Courtenay, BC, CAN: RDH Building Science, 2021.

Wilson E., Engebrecht Metzger C., Horowitz S., Hendron R., 2014. 2014 Building America House Simulation Protocols. Golden, CO, USA: National Renewable Energy Laboratory, 2014.

Wright G. S., Ferreira P., Richman R., Moisture Risk Analysis and Assessment using WUFI. Chicago, IL, USA: PHIUS, 2021.

6th International Conference on Building Energy and Environment
Eindhoven University of Technology, The Netherlands
6 - 10 July 2025

Hygrothermal performance and dynamic behavior of a panel-based exterior retrofitting wall system: post-retrofit measurements and analysis

Shayan Mirzabeigi [1,2], Sameeraa Soltanian-Zadeh [3], Bess Krietemeyer [4], Jianshun Zhang [5,6]

[1]*SUNY College of Environmental Science and Forestry, Syracuse, NY, USA, smirzabeigi@esf.edu*
[2]*Syracuse University, Syracuse, NY, USA, smirzabei@syr.edu*
[3]*Syracuse University, Syracuse, NY, USA, ssoltani@syr.edu*
[4]*Syracuse University, Syracuse, NY, USA, eakriete@syr.edu*
[5]*Syracuse University, Syracuse, NY, USA, jszhang@syr.edu*
[6]*Syracuse Center of Excellence in Environmental and Energy Systems, Syracuse, NY, USA*

SUMMARY
Improving the building envelope's thermal insulation can lead to significant thermal load reduction and save energy. Prefabricated insulated panels are often applied to the exterior surfaces of the existing building facade in a deep building energy retrofit. However, few studies have been done to assess the hygrothermal performance of the retrofitted assembly in an occupied building. Considering the airtightness level of the panel-to-panel seams, the presence of an air gap between the existing façade and the new insulation panels can lead to increased heat loss through exfiltration, risk of moisture condensation and significant reduction in the effective thermal resistance of the building envelope if the air leakage and vapor transport are not controlled properly in the wall assembly. There is a need to quantify air and airflow conditions in these air gaps and how they impact the overall panel performance under different climatic conditions in order to better define requirements for retrofitting material system design and building operation. This paper presents a post-retrofit hygrothermal analysis to evaluate the performance of a retrofit assembly consisting of insulated Expanded Polystyrene insulation foam panels. The new panel system was installed at a dormitory building at Syracuse University's campus. The existing external enclosure includes pre-cast concrete and wood-framed wall assemblies. Measurements included heat flux, surface temperature, relative humidity, and air temperature and humidity on both the interior side of the existing assembly and exterior of the new insulated panels, as well as the air temperature and relative humidity inside the air cavity. The study investigates the hygrothermal performance of the entire assembly using data collected from September to December 2024. Results show that the mean effective R-value of the whole assembly after retrofit was 6.02 $m^2 \cdot K/W$, representing 5.44 times increase over the pre-retrofit condition on average. The air cavity data analysis revealed an average temperature difference of 4.01°C (summer) and 9.47°C (winter) for the top and base sections for the concrete wall, and 3.17°C (summer) and 9.76°C (winter) for the top and base sections for the wood-framed wall, indicating a significant vertical temperature gradient due to little to no air mixing inside the wall cavity. The local hygrothermal analysis showed that the new insulation material absorbed less moisture at low temperature winter days indicating vapor diffusion capability of the retrofitting panel but under warm temperature summer condition, the panels adsorbed more moisture from the outside air at the night and released them into the indoor space during the day. These findings contribute to the understanding of the hygrothermal dynamics in retrofit panel systems and provide valuable insights for optimizing future building envelope retrofits, improving performance across varying climatic conditions.

Keywords: Hygrothermal performance, External wall insulation system, Building envelope.

1. INTRODUCTION

In the United States, buildings account for more than 70% of total electricity consumption and they are a major source of carbon emissions (IEA, 2018). Older residential buildings, particularly those constructed before 1950, dedicate 54% of their energy usage to space conditioning, in

contrast to 43% for homes built between 2000 and 2009 (EIA, 2009). With ambitious climate goals to reduce greenhouse gas emissions, the United States has aligned on the vision to reach a net-zero-energy building stock by 2050 (Biega & Krarti, 2024). Achieving this goal will necessitate significant advancements in energy efficiency for both new constructions and existing buildings. In particular, the retrofit effort will require a blend of strategies, including the broader adoption of energy efficient electrification technologies, the development of grid-interactive communities, as well as building envelope upgrades. Improving the building envelope's thermal insulation can lead to remarkable energy savings in existing buildings. One of the most promising technologies for building envelope energy retrofitting is prefabricated panelized exterior insulated envelope systems (Mirzabeigi et al., 2023). While prefabricated insulated wall assemblies are widely available for new construction, the market offers very few options specifically designed for retrofit applications. Exterior insulated retrofit panels can be applied on the exterior envelope of existing buildings to considerably improve insulation and airtightness while also offering potential aesthetic improvements. These improvements are essential for achieving better-performing residential buildings. Given the pivotal role of the building envelope in retrofit strategies, evaluating their hygrothermal performance is essential for understanding pre-retrofit conditions and validating improvements made through retrofitting (Recart & Sturts Dossick, 2022). The term hygrothermal refers to the movement of heat and moisture through buildings. However, there are few studies that have assessed their hygrothermal performance in an occupied building (Choi et al., 2023). Considering the airtightness level of the panel-to-panel seams, the presence of an air gap between the existing assembly and the new insulation represents hygrothermal advantages and disadvantages (Recart et al., 2023). Therefore, there is a need to quantify air gap conditions and the overall panel performance under different climatic conditions (Byrne et al., 2016). This paper presents a post-retrofit hygrothermal analysis to evaluate the performance of an integrated energy efficiency retrofit assembly with exterior insulated insulation foam panels.

2. DESCRIPTION OF THE CASE STUDY

The case study is a two-story multifamily townhouse-style building, that consists of 8 units and is located on Syracuse University's South Campus. It was originally constructed in 1972-1973. The exterior walls consist of pre-cast concrete and wood-framed walls. The pre-cast walls have 1-inch closed-cell extruded polystyrene foam for a wall area of 175.98 m^2. The 2 by 4 wood-framed walls have 3.5 inches of fiberglass batt insulation for a wall area of 205.46 m^2. Fig. 1 shows the exterior view of the pre- and post-retrofit condition of the building and monitoring locations on the architectural plans.

The project's whole-building retrofit approach includes highly insulated prefabricated exterior building envelope panels for improved thermal performance and airtightness at the walls, roof, and foundation, and high-efficiency integrated mechanical pod solution with real-time performance monitoring for heating, cooling, ventilation, and domestic hot water. In particular, the building envelope panels are prefabricated, reinforced, insulated Expanded Polystyrene (EPS) foam exterior panel system with air-sealing at seams and penetrations for mechanicals, windows, doors, foundation, and sealant and backer rod for continuous seal for air and moisture barrier. The system provides varying thicknesses (6"-7-1/2") for integration with existing wall construction. Fig. 2 shows the panel composition with typical vertical and horizontal connection sections.

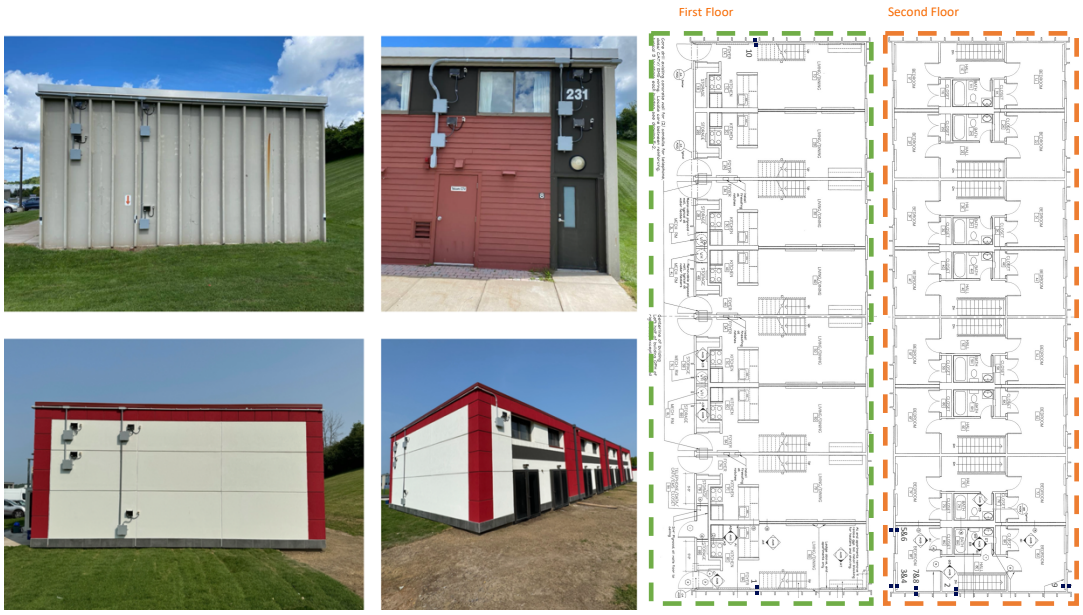

Figure 1. Exterior views of the pre- and post-retrofit condition of the case study building (left) and monitoring locations on the architectural plans (right).

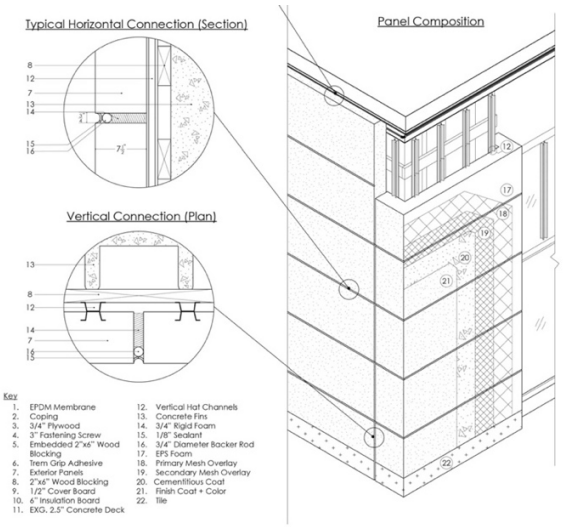

Figure 2. Panel composition with typical vertical and horizontal connection sections.

3. METHODS

This section is divided into: (1) the description of the sensing method, which combines the integration of in-house developed interior and exterior sensor packages and the wireless LoRa sensors for measuring temperature and humidity inside the air gap; and (2) the explanation about the framework the approach for quantification of the R-value of the post-retrofit whole assembly.

3.1. Sensing Method

For each monitoring location shown in Fig. 1, there are three measurement spots including interior surface of the existing wall, inside the air gap, and exterior surface of the newly added insulation panel. For the interior and exterior wall measurements, we developed custom sensor packages

(Mirzabeigi et al., 2025). The full description of the experimental setup and data collection method is provided in Mirzabeigi et al., (2025). Each monitoring location (interior and exterior) is equipped with an Arduino micro-controller, Wi-Fi radio, analog-to-digital converter, power module, and sensor module. Two sensor modules are a mated pair through the Bluetooth radio configuration. There is also one central sensor gateway that is responsible for monitoring and controlling the package communication, in addition to pushing data to the database for storing purposes. The sensor module consists of a heat flux thermocouple pile (with Sensitivity of 1 μV/(W/m^2)), type T thermocouples (±1°C or ±0.75%), surface Relative Humidity (RH) (± 3.5%), and a BME 688 environmental sensor (for monitoring local air temperature (±1°C) and RH ((± 3.5%)). Interior packages were powered by wall outlets. For measuring the air temperature and humidity, LHT65N Dragino sensors (±0.3 °C with 0.1°C resolution for temperature measurement and ±3% RH with 0.5% RH resolution) are utilized that are connected to a central gateway for sending the data to the cloud for storing purposes. In addition to measuring interior surface, inside air gap, and exterior surface of those ten monitoring locations (used for pre- and post-retrofit), more sensors were utilized to characterize the air gap conditions at four height levels. Fig. 3 highlights the location of these sensors on two vertical sections of pre-cast concrete and wood-framed walls on the south and west elevation of the building.

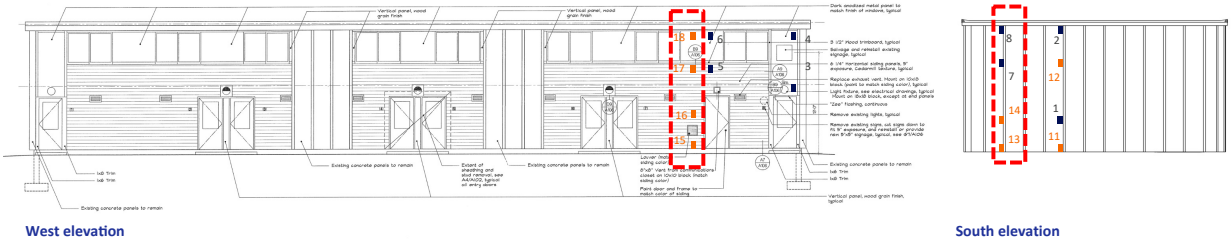

Figure 3. Location of air gap sensors for two vertical sections of pre-cast concrete and wood-framed walls on the west and south elevation of the case study building.

3.2. R-value Calculation Method

The calculation of R-value is in accordance with the ASTM C1155-95 - Standard Test Method for Determining Thermal Resistance of Building Envelope Components from the In-Situ Data (ASTM, 2021). The effective thermal resistance will be calculated from measured in-situ temperature difference among interior and exterior surface temperatures and interior heat flux data by using summation technique over time. The estimation of the effective thermal resistance is calculated by using summation technique (see Eq. (1)).

$$R_e = \frac{\sum_{k=1}^{M} \Delta T_k}{\sum_{k=1}^{M} q_k} \tag{1}$$

In this equation, R_e is thermal resistance ($m^2 \cdot K/W$); M is number of values of ΔT and q in the source data; ΔT is difference in temperature between interior and exterior surface (K); k is counter for summation of time-series data, and q is heat flux (W/m^2). To determine the time to compute the estimate thermal resistance, the convergence factor (CR_n) is calculate from Eq. (1), with n time units. At selected time, CR_n remains below 0.1 for at least 3 periods of length n to evaluate if the calculated thermal resistance of the building component is acceptable or not

$$CR_n = \frac{R_e(t) - R_e(t-n)}{R_e(t)} \quad (2)$$

4. RESULTS AND DISCUSSION

A detailed analysis of the post-retrofit performance of the integrated exterior building envelope retrofitting system was performed, incorporating field-measured data collected from the case study. The hygrothermal performance of the system was assessed by measuring key parameters such as interior and exterior surface temperature, RH and heat flux and air temperature and RH inside the air gap across various locations for both pre- and post-retrofit conditions. The analysis is focused on the post-retrofit performance of the whole assembly with the insulated panel system.

4.1. Temperature and Humidity Conditions in the Air Gap

For the air gap, a detailed analysis was performed for two vertical sections of pre-cast concrete (location 7, 8, 13, and 14) and wood-framed walls (location 15, 16, 17, and 18) of the building. A detailed analysis of the temperature, absolute humidity and RH for the pre-cast concrete wall for summer (September 1 - 7) and winter (December 1-7) was provided in Fig. 4. The analysis reveals that the air gap behaves differently at various elevations, with the top section generally exhibiting higher temperatures and lower RH values compared to the base section. In warm conditions, daytime temperature differences between the top and base of the concrete wall averaged 4.01 °C, and nighttime differences averaged 3.73 °C. For the wood-framed wall, these differences were smaller, with daytime values of 3.17 °C and nighttime values of 3.15 °C. By contrast, in cold conditions, daytime temperature differences increased to 9.47°C for the concrete wall and 9.76 °C for the wood-framed wall. Nighttime differences were slightly higher at 9.80 °C for the concrete wall and 10.05 °C for the wood-framed wall, reflecting stronger vertical gradients during colder conditions. This stratification, especially under colder conditions, suggests the presence of natural convection within the cavity. However, as air velocity was not directly measured in this study, this remains a hypothesis that should be validated in future investigations. Additionally, thermal bridging at panel joints and penetrations may have influenced localized heat flow and further analysis is needed to quantify that effect. Future acknowledged modeling work will incorporate these variables to assess their long-term impact on hygrothermal performance. Outdoor air shows consistently lower absolute humidity values overall. The concrete top layer generally shows higher temperatures and absolute humidity, but lower relative humidity compared to other layers, indicating it absorbs and retains more heat and moisture. In summer, absolute humidity differences between the top and base sections were 1.01 g/m³ during the day and 1.12 g/m³ at night for the concrete wall, while the wood-framed wall exhibited values of 0.87 g/m³ and 1.12 g/m³, respectively. In winter, these differences were smaller, with values of 0.96 g/m³ (day) and 0.99 g/m³ (night) for the concrete wall, and 0.41 g/m³ for both day and night for the wood-framed wall. The Concrete base layer remains cooler and more humid, likely due to due to air behavior, the proximity to the ground and the insulating effect of the building's foundation.

Day and night dynamics provide further insights into the hygrothermal performance of the system. During warm summer nights, cooler external air led to moisture adsorption by the insulation material, as seen in rising absolute humidity values inside the air gap. During the day, solar radiation and increased cavity temperatures facilitated desorption, releasing moisture into the cavity air. By contrast, in winter, lower ambient temperatures and reduced vapor pressures resulted in reduced moisture exchange, with moisture gradients remaining relatively stable throughout the day. This temperature and moisture retention pattern, particularly in the concrete walls, supports the hypothesis that the air cavity plays a significant role in the overall hygrothermal performance of the system. The air cavity, a critical feature of the retrofitted system, showed notable temperature and humidity gradients across different sections. An interesting observation was made

regarding the moisture dynamics inside the air cavity. The moisture retention properties of the insulation material varied with temperature. At lower temperatures, the new insulation material absorbed less moisture, likely due to the reduced moisture vapor in the air. However, at higher temperatures, the material released more moisture into the cavity air, highlighting the material's dynamic interaction with the hygrothermal environment.

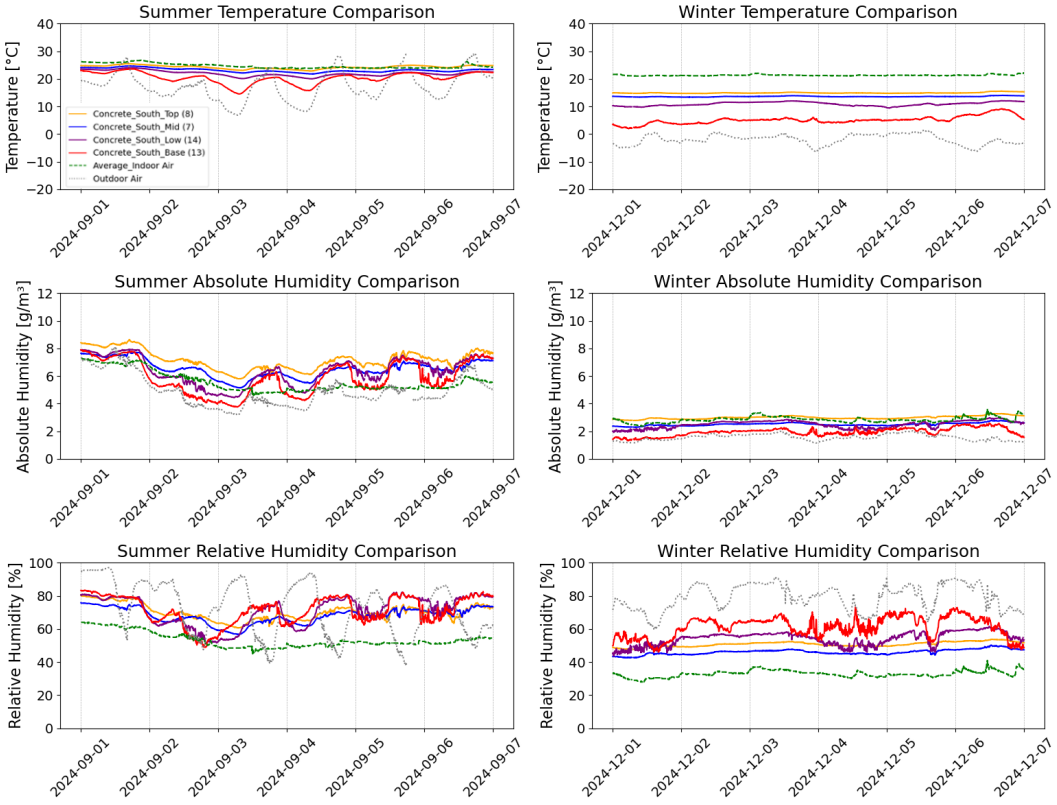

Figure 4. Temperature, absolute humidity and RH for air gap.

4.2. Hygrothermal Performance and R-value Assessment

The analysis of the hygrothermal performance focused on two period of September 1 - 19 (Fig. 5) and November 1 - 15 (Fig. 6) for the selected monitoring locations (representing various orientation and construction materials). Surface temperature, as shown in Figure 5, reveal a clear impact of solar radiation on the wall assembly. During peak solar exposure periods, interior surface temperatures of the whole assembly increase too. This effect is particularly pronounced on the southwest and west walls, where solar radiation is highest. When the intensity of solar irradiation is reduced the observed difference between southwest and north is not very significant. Overall, internal surface temperatures remain more constant, illustrating the walls' impact on temperature stabilization. However, this stability is also influenced by the building's indoor space conditioning system, which regulates interior temperatures. The interaction between the wall assembly's thermal resistance and the space conditioning system contributes to the observed stabilization of internal surface temperatures. Additionally, indoor RH trend showed relatively stable values compared to the fluctuating outdoor RH. While outdoor RH exhibited considerable daily variation due to temperature changes and weather conditions, the indoor RH remained more consistent.

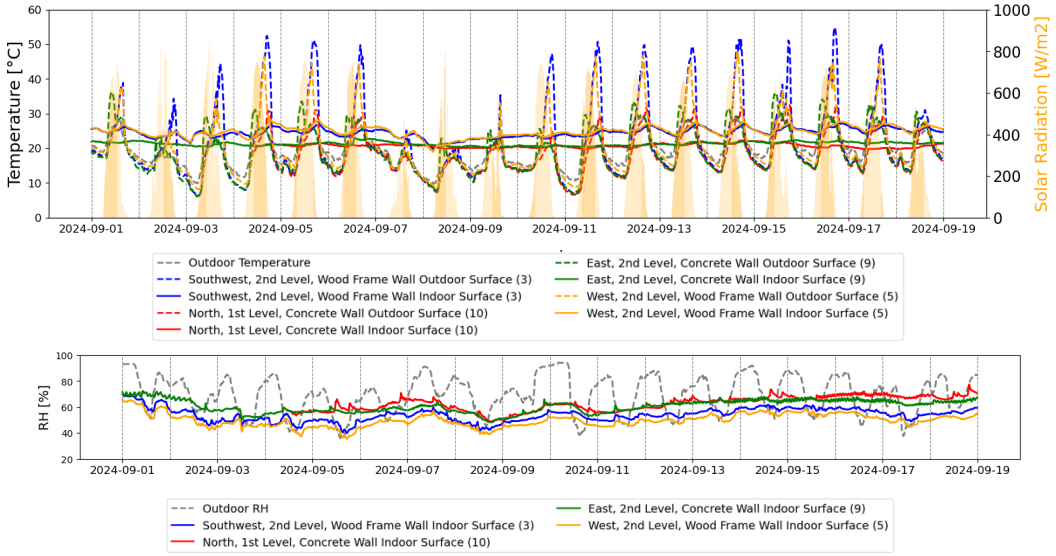

Figure 5. Surface temperature variations (top) Indoor humidity variation (bottom) and of selected walls.

Fig. 6 shows the interior surface temperatures are relatively constant compared to the exterior temperatures. There is a considerable temperature drop between the exterior and interior side of the insulation panel (air gap layer) for all locations (relative difference between air gap and outdoor vs. air gap and indoor), showcasing the retrofit panel effectiveness. When it is colder this difference is more pronounced (better insulation and more airtight compared to pre-retrofit).

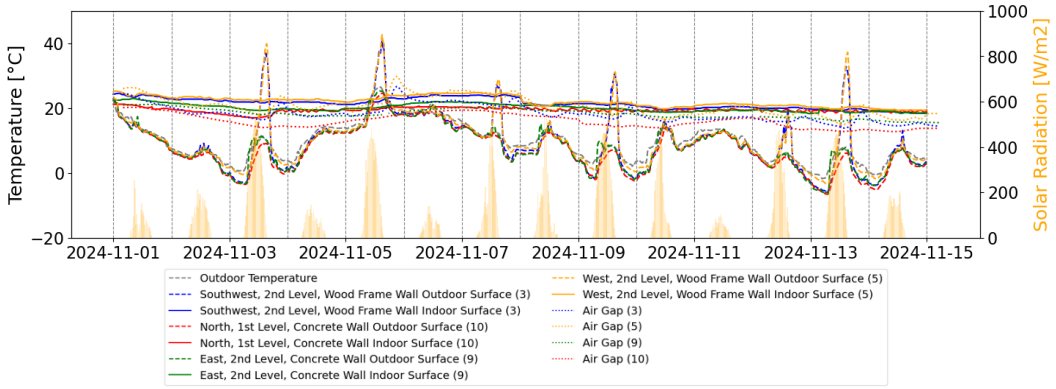

Figure 6. Temperature variations across the assembly for the selected locations.

R-value assessments were performed in accordance with the methodology for determining the thermal resistance of building envelope components based on in-situ measurements. It should be noted that for the design values, the summation of existing wall, air gap and newly insulation layer was considered (conduction only). Table 1 provides a detailed breakdown of the R-value calculations for both concrete and wood-framed walls. These calculated values show the retrofit's role in significantly enhancing the thermal barrier properties of the building's envelope, ultimately leading to reduced heat transfer and improved energy efficiency. Measured R-values align with design specifications. These values fall within the broader performance range of exterior retrofitting systems, which reported thermal resistances from 2-6.67 $m^2 \cdot K/W$ for systems with thicknesses between 7-64 cm (Mirzabeigi et al., 2023). This confirms that the retrofit solution applied here performs near the upper end of the spectrum in terms of R-value.

Table 1. Summary of R-values.

Post-retrofit R-value Assessment	Wood Frame Design	Wood Frame Measured	Deviation between R-values	Concrete Design	Concrete Measured	Deviation between R-values
Mean R-value(m^2·K/W)	6.52	6.30	3.4%	5.86	5.69	2.9%
Standard Deviation	-	1.10	-	-	1.14	-
Coefficient of Variation	-	17.4%	-	-	19.9%	-

5. CONCLUSION

This study presents a detailed post-retrofit hygrothermal assessment of an integrated exterior building envelope retrofitting system, focusing on the impact of insulation foam panels with an air cavity. The results highlight considerable improvements in thermal performance and heat loss reduction, with the whole retrofitted system achieving an average effective R-value of 6.08 m^2·K/W. In warm conditions, the air cavity mitigated heat gain and facilitated moisture redistribution through adsorption and desorption cycles driven by solar radiation and temperature gradients. The insulation absorbed less moisture during cold conditions, indicating its vapor diffusion capability, while in warm conditions, it exhibited higher moisture dynamics, absorbing moisture from external air at night and releasing it during the day. The analysis of temperature and humidity variations within the air gap revealed insights for further considerations and used in hygrothermal model development for a more detailed analysis. Furthermore, the R-value assessments confirmed the role of the new insulation in enhancing the building's thermal resistance, leading to reduced energy consumption. These findings underscore the potential of prefabricated exterior insulation systems for improving the energy efficiency of existing buildings in cold climates, offering valuable insights for future retrofit strategies.

ACKNOWLEDGEMENTS

This work was conducted under the project "Integrated Whole-Building Energy Efficiency Retrofit Solution for Residences in Cold/Very Cold Climates" Award Number DE-EE0009060 funded by the U.S. Department of Energy under the Advanced Building Construction with Energy Efficient Technologies and Practices (ABC) initiative.

REFERENCES

ASTM. (2021). *C1155-95 - Standard Practice for Determining Thermal Resistance of Building Envelope Components from the In-Situ Data*. https://doi.org/10.1520/C1155-95R21

Biega, K., & Krarti, M. (2024). Evaluation of Exterior Insulated Panels for Residential Deep Energy Retrofits. *Energies*, *17*(16). https://doi.org/10.3390/en17163988

Byrne, A., Byrne, G., O'Donnell, G., & Robinson, A. (2016). Case studies of cavity and external wall insulation retrofitted under the Irish Home Energy Saving Scheme: Technical analysis and occupant perspectives. *Energy and Buildings*, *130*, 420–433. https://doi.org/10.1016/j.enbuild.2016.08.027

Choi, D. S., Lee, Y. J., Moon, J. H., Kim, Y. S., & Ko, M. J. (2023). Estimating In-Situ R-Value of Highly Insulated Building Walls Based on the Measurement of Temperature and Heat Flux Inside the Wall. *Energies*, *16*(15).

EIA. (2009). *2009 RECS Survey Data*. https://www.eia.gov/consumption/residential/data/2009/

IEA. (2018). *Towards a zero-emission, efficient and resilient buildings and construction sector*. www.iea.org

Mirzabeigi, S., Soltanian-Zadeh, S., Carter, B., Krietemeyer, B., & Zhang, J. "Jensen." (2025). Networked Sensors for In-Situ Real-Time Monitoring of the Local Hygrothermal Conditions and Heat Fluxes Across a Building Enclosure Before and After a Building Retrofit. In U. Berardi (Ed.), *Multiphysics and Multiscale Building Physics* (pp. 527–532). Springer Nature Singapore.

Mirzabeigi, S., Zhang, J., & Razkenari, M. (2023). Exterior Retrofitting Systems for Energy Conservation and Efficiency in Cold Climates: A Systematic Review. *Environmental Science and Engineering*, 413–422.

Recart, C., Dossick, C. S., & Echenagucia, T. M. (2023). Impacts of Air Cavities on Hygrothermal Performance of Retrofitted Timber Frame Assemblies in Six US Climates. In *Computing in Civil Engineering 2023*.

Recart, C., & Sturts Dossick, C. (2022). Hygrothermal behavior of post-retrofit housing: A review of the impacts of the energy efficiency upgrade strategies. In *Energy and Buildings* (Vol. 262). Elsevier Ltd.

6th International Conference on Building Energy and Environment
Eindhoven University of Technology, The Netherlands
6 - 10 July 2025

Integrating ensemble-based machine learning method in developing data-driven residential archetypes

Arash B. Naamrudi [1], Brian Corcoran[2], Reihaneh Aghamolaei [3]

[1] *School of Mechanical & Manufacturing Engineering, Faculty of Engineering and Computing, Dublin City University, Whitehall, Dublin 9, Ireland, Arash.naamrudi2@mail.dcu.ie*
[2] *School of Mechanical & Manufacturing Engineering, Faculty of Engineering and Computing, Dublin City University, Whitehall, Dublin 9, Ireland, brian.corcoran@dcu.ie*
[3] *School of Mechanical & Manufacturing Engineering, Faculty of Engineering and Computing, Dublin City University, Whitehall, Dublin 9, Ireland, reihaneh.aghamolaei@dcu.ie*

SUMMARY
Developing building archetypes is a crucial preliminary step in bottom-up Urban Building Energy Modelling (UBEM), where buildings with shared characteristics are grouped together. Selecting the most important set of features is vital for accurate energy performance analysis, as it directly impacts energy usage predictions and model accuracy. However, existing engineering-based and statistical feature selection methods often oversimplify complex interactions or face challenges with multicollinearity. Additionally, conventional data-driven approaches such as wrapper and embedded methods are often prone to bias and lack robustness and reliability.
This study introduces a novel ensemble-based methodology to select important features for developing residential building archetypes that are both reliable and robust while maintaining computational efficiency. A multistage ensemble data-driven feature selection technique, along with a single embedded feature selection method, is compared for four different scenarios from four perspectives: selection accuracy, stability and robustness, performance, and reliability.
The results indicate that ensemble feature selection outperforms embedded methods in terms of selection accuracy, robustness, and reliability. Regarding classification accuracy, the ensemble method surpasses embedded only for minimal and balanced models (5 and 10 features), achieving 74% and 87% compared to 72% and 77%, respectively. However, as the number of selected features increases (for the detailed model with 20 features and for the high-complex model with 30 features), embedded performs better, with classification accuracies of 92% and 93%, compared to 89% and 89.1% for the ensemble method. In the ensemble method, the high-complex model achieved superior reliability and robustness scores of 1, along with PSFI and PIFS values of 0.33 and 0.38, respectively. By focusing on important variables and eliminating irrelevant information, this approach helps stakeholders better understand energy consumption factors and identify effective retrofit measures.

Keywords: Archetypes, Urban Building Energy Modelling (UBEM), Data-Driven Approach, Feature Selection.

1. INTRODUCTION AND LITERATURE REVIEW

Energy analysis and evaluation of residential buildings on large scales can be achieved by Urban Building Energy Modelling (UBEM) (Kong et al. 2023). Nonetheless, simulating numerous buildings at the urban scale quickly becomes computationally expensive. This challenge in urban-scale building energy simulations is often addressed using various clustering and grouping techniques (Dahlström et al. 2024). Instead of collecting data and characterizing each individual building, a subset of representative buildings (archetypes) is created for upscaling.
Identifying the most important set of features for archetype development can be done based on

three approaches: engineering, data-driven, and hybrid. In the engineering approach, features are selected based on the existing literature. A review of the existing UBEMs shows that the choice of feature configuration is made based on the engineering method (Johari et al. 2022; Ferrando et al. 2022). Despite the popularity of this method, it has some disadvantages. First, choosing features is arbitrary and there are some discrepancies in the selected features. Second, this method is unsuitable for high-dimensional datasets such as building stock datasets.

In the data-driven approach, statistics or machine learning algorithms aid in finding key features. This approach is well-suited for high-dimensional datasets, as they often contain irrelevant and redundant features. Based on the search strategy for finding the key features in this method, the feature selection is classified into filter-based, wrapper-based, embedded-based, and ensemble-based techniques (Barbieri et al., 2024). The filter method, also referred to as the correlation-based method, is the most common approach for feature selection. The second method, wrapper-based, identifies the optimal feature subset by generating various possible subsets and comparing their prediction or classification performance. Compared to the filter method, this method typically provides better prediction accuracy, but this comes with the drawback of higher computational costs (Eskandari et al., 2024). The third method, the embedded-based method, integrates feature selection into the training process, and this is the key distinction of the embedded method compared to the filter and wrapper methods (Moslemi, 2023). Finally, the ensemble method involves combining multiple models, rather than relying on a single model, to identify and select important features resulting in greater stability compared to other methods (Pes, 2020). Despite the advantages of the ensemble method, it has rarely been used to select key features that influence building energy ratings, which can ultimately aid in archetype development.

Identifying and selecting important features for archetype development significantly impacts the quality and accuracy of the resulting archetypes. In most existing UBEM studies, engineering-based feature selection remains the dominant approach. However, this method is inherently biased—if past studies have overlooked a feature, it is likely to be excluded again. Moreover, superior advantages of ensemble feature selection such as the ability to increase stability and robustness, improve interpretability, and decrease risk of overfitting have not been tested on the available dataset for archetype development.

The aim of this research is to evaluate the effectiveness of a novel ensemble-based feature selection method for archetype development from multiple perspectives, including selection accuracy, reliability, stability and robustness, and performance. The proposed method is compared against embedded methods using the aforementioned criteria.

This paper is organized as follows: Section 2 details the methodology developed, including a description of the steps taken to extract key features. Section 3 presents and discusses the results of the Irish case study. Finally, Section 4 concludes with a summary of challenges and suggestions for future work.

2. METHODOLOGY

The development of residential building archetypes involves four key steps, as illustrated in Fig. 1. The first step is data collection from the existing building stock dataset. This is followed by the pre-processing step, which uses data-driven techniques to enhance the quality of the building stock data. The third step, feature selection, identifies the critical features that influence the energy rating of existing buildings. This rating encompasses space heating, ventilation, water heating and lighting under standardized operating conditions.

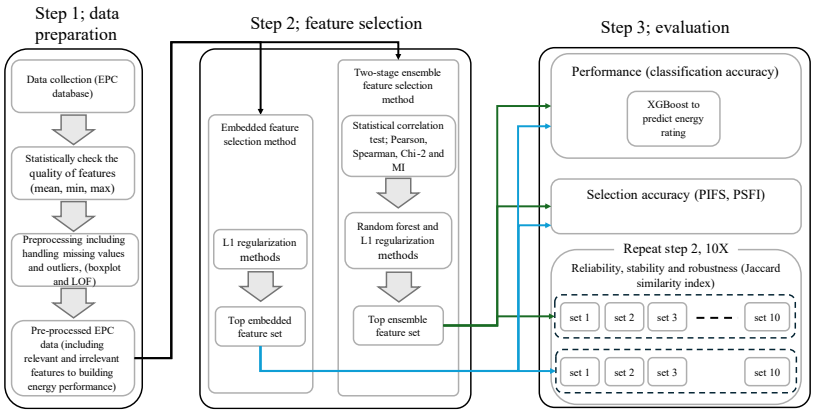

Figure 1. Overarching methodology for ensemble-based machine learning feature selection method.

2.1 Data collection and preparation

Energy Performance Certificate (EPC) databases are a valuable resource as they provide detailed data on building features, including U-values, heating systems, and construction types, which are essential for defining building archetypes. This data source supports data-driven feature selection, as it includes normalized annual energy consumption and energy rating for each building, serving as a valuable target variable for identifying the most impactful features.

Building stock dataset pre-processing takes place after data collection and includes an initial statistical analysis, data pre-processing, and outlier detection. The initial sub-step consists of a preliminary statistical analysis of the building stock dataset. Then, data pre-processing addresses the identified inconsistencies with the following steps: data cleaning for addressing missing or zero values, data reduction for eliminating irrelevant attributes, and finally data discretization for converting attributes format. In the third sub-step, methods such as the Local Outlier Factor (LOF), further improve data quality by removing outliers.

2.2 Feature selection

The focus of this research is on feature selection where a novel two-stage ensemble-based machine learning method is implemented to select the most impactful features of the energy rating of buildings in the EPC database. The contribution of each feature to predictive accuracy of the model is the key criteria for selection. This study compares the proposed methodology with the embedded data-driven feature selection method. Figure 2 shows the schematic of the proposed methodology. In this research, four filter-based feature selections are used. For numerical variables, Spearman and Pearson, and for categorical data, Chi-square (Chi-2) and mutual information (MI) are selected. This combination can capture a wider spectrum of linear, monotonic, and non-linear relationships, ensuring more robust feature relevance detection. Moreover, it can reduce the risk of overlooking important factors, leading to improved model performance and generalization.

Filter- and embedded-based methods are combined via intersection and union to form two aggregated subsets. The primary reasons for selecting these four Filter-based methods are: 1) They offer a reasonable combination of different FS categories, 2) They are among the most widely used FS methods in literature (Ali et al., 2020; Eskandari et al., 2024; Zhang et al., 2023). The resulting subsets of these four methods are then intersected to form the first aggregated subset. Following this stage, two well-known embedded-based feature selection techniques namely LASSO (Least

Absolute Shrinkage and Selector Operator) Regression or L1 Regularization, and Random Forests which is a Tree-Based method are implemented to create the second aggregated subset using union.

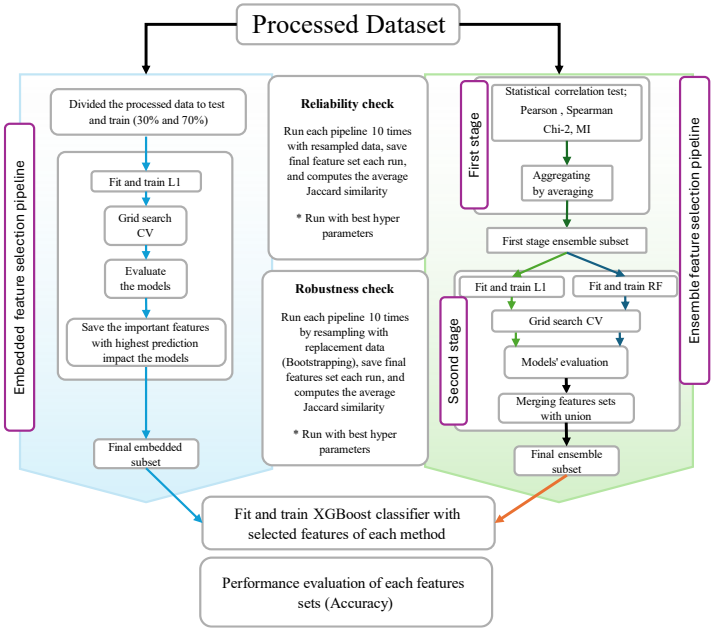

Figure 2. A schematic of the methodology used for feature selection and evaluation of the selected features

Alongside this ensemble-based feature selection pipeline, an embedded method is used to identify the most important features of the EPC database. For this standalone feature selection pipeline, L1 regularization is applied, as its results were deemed acceptable in a study conducted by Neale et al. (Neale et al., 2022). Additionally, this method has better computational costs than the wrapper method (Barbieri et al., 2024).

2.3 Evaluation

To evaluate the impact of feature selection on archetype development, four scenarios are considered. The minimal model (Top 5) includes only the most essential features, while the balanced model (Top 10) expands the selected features. The detailed model (Top 20) and high-complex model (Top 30) further incorporate additional features, increasing depth and complexity for a more refined analysis. For both methods, these scenarios are evaluated based on four criteria: reliability, classification performance, stability and robustness, and feature selection accuracy. Feature selection accuracy is assessed using two metrics: the Percentage of Informative Features Selected (PIFS) and the Percentage of Selected Features that are Informative (PSFI). Performance is measured by classification accuracy, while stability and robustness are evaluated using the Jaccard similarity index.

3. RESULTS AND DISCUSSION

The cleaned EPC dataset of Ireland was downloaded from (Raushan, 2023). This dataset provides detailed information on 701,898 residential buildings in Ireland. Despite being cleaned, the dataset still contains outliers and zero values. Data cleaning was performed by imputing missing values with simple mean imputation and applying the LOF method. Additionally, features with more than

99% missing values or those irrelevant to energy consumption, such as assessment dates and building IDs, were removed from the dataset. In the next step, focusing on Dublin City, because it has the highest proportion of the cleaned EPC dataset, and filtering for houses with existing energy ratings reduced the dataset to 16,940 houses with 165 features.

To evaluate selection accuracy and identify the most important features for building energy performance, it is first necessary to determine the key parameters for archetype development. Since not all features in the EPC dataset are relevant (Neale et al., 2022), a list of common features shared between the EPC dataset and previous literature (Ali et al., 2020, 2024; Egan et al., 2018; Neale et al., 2022) is compiled. Following this, selected features for different final subset sizes in both methods are presented in Figure 3.

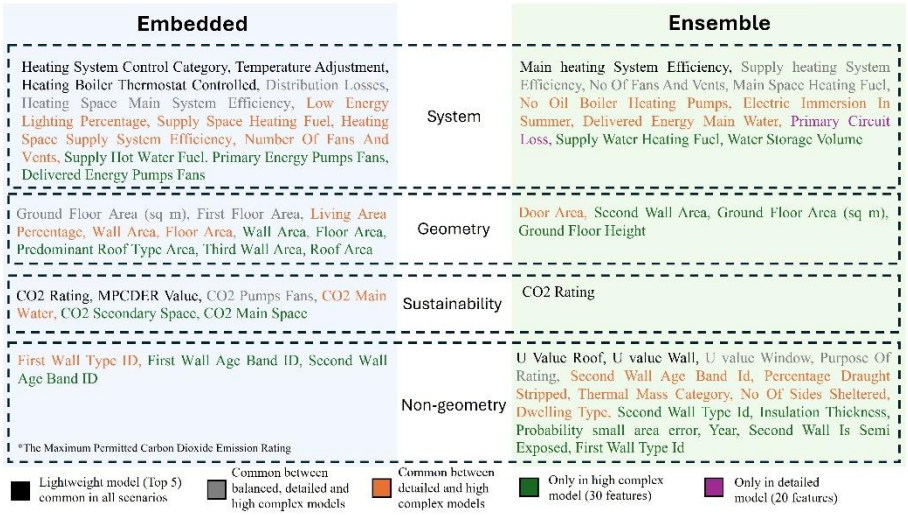

Figure 3. Selected features by embedded and ensemble methods, for various final subset size

The comparison between embedded and ensemble feature selection methods highlights differences in variable prioritization. System-related features remain important in data-driven approaches, even though they receive less attention in traditional engineering models. Key parameters such as heating system efficiency, supply heating fuel, and ventilation consistently appear, demonstrating their strong influence on energy performance. While ensemble methods apply correlation thresholds, their "or" condition for Pearson and Spearman correlations allows redundant features like CO2 rating to persist. Additionally, ensemble methods tend to capture more system-related and geometric dependencies as model complexity increases, whereas embedded methods focus more on primary efficiency indicators. This broader feature selection may enhance predictive performance but also raises the risk of overfitting.

Feature selection accuracy of embedded and ensemble methods is compared in Figure 4. The results indicate a clear advantage of the ensemble method over the embedded method in terms of both PSFI and PIFS. For instance, when selecting the top 5 important features, the ensemble method achieves a PSFI of 80% and a PIFS of 15%, compared to 0% PSFI and PIFS for the embedded approach, demonstrating its superior capability to identify and prioritize significant features even with a small feature set. As the number of selected features increases, PIFS values rise for both methods; however, the ensemble method consistently outperforms the embedded method. This suggests that the ensemble approach not only captures a larger proportion of truly informative features but also selects features more precisely, likely due to its ability to aggregate information from multiple models, reduce variability, and better handle correlated features.

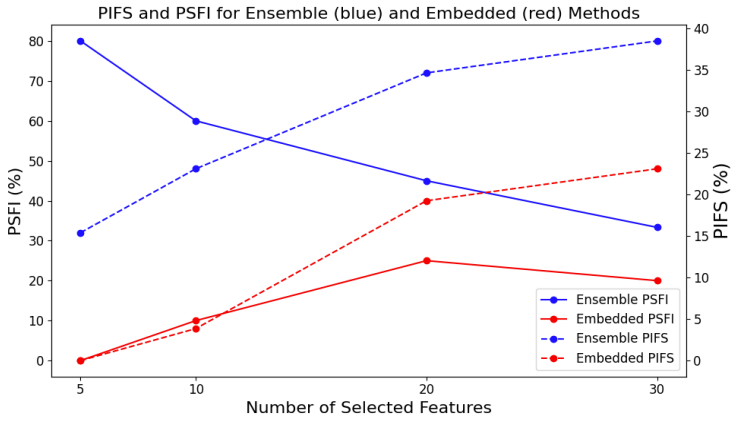

Figure 4. Comparison of selection accuracy based on PIFS and PSFI for ensemble and embedded methods with respect to the number of final feature subsets.

The classification accuracy results (Figure 5) highlight key trade-offs between feature selection methods across different model complexities. At lower feature counts, the ensemble method outperforms the embedded method, making it a strong choice for minimal and balanced models, where selecting the most dominant predictors is crucial. However, as the feature count increases, the embedded method surpasses the ensemble approach at 20 and 30 features, suggesting that it better captures higher-order feature interactions in detail and high-complex model scenarios. The ensemble method's reliance on correlation-based filtering may explain its stagnation beyond 20 features, as redundant but individually significant features can limit further accuracy improvements. In contrast, the embedded method benefits from dynamic selection, optimizing performance as more features are introduced. These results indicate that ensemble selection is ideal for constrained models requiring efficiency and stability, while embedded methods are better suited for complex, feature-rich environments.

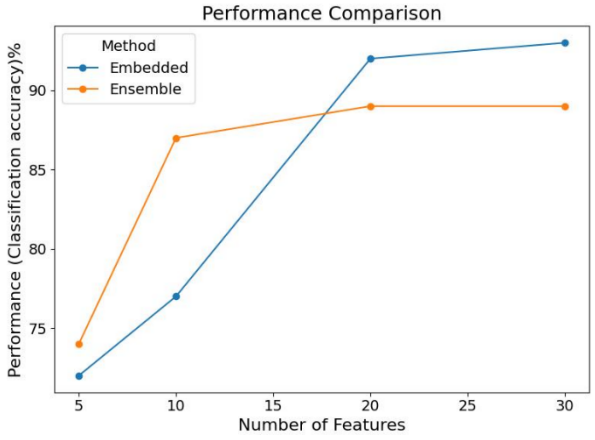

Figure 5. Classification accuracy of the XGBoost model using final sets of ensemble and embedded methods

The Jaccard similarity index measures the reliability of feature selection by assessing the consistency of selected sets over 10 runs. The ensemble method demonstrates high reliability, achieving a perfect similarity score of 1 for minimal, detailed, and high-complex models, and 0.93 for the balanced model. A noticeable drop in similarity at the 10-feature set suggests increased sensitivity to data variations, particularly in the embedded method, which appears more dependent

on algorithmic factors. This instability may result from interchangeable features with similar predictive power. However, as the number of selected features increases to 20 and 30, selection stabilizes, reducing inconsistency and reinforcing the reliability of ensemble methods.
The ensemble method also outperforms embedded methods in robustness, making it a more reliable choice for models that need to generalize across different data variations. The embedded method's instability at 10 features highlights the need for additional validation when selecting a balanced model. A decline in robustness at 20 features suggests the introduction of less dominant features, increasing variability. However, by 30 features, selection stabilizes again, emphasizing the importance of carefully evaluating mid-sized feature sets for robustness, particularly when using ensemble methods.

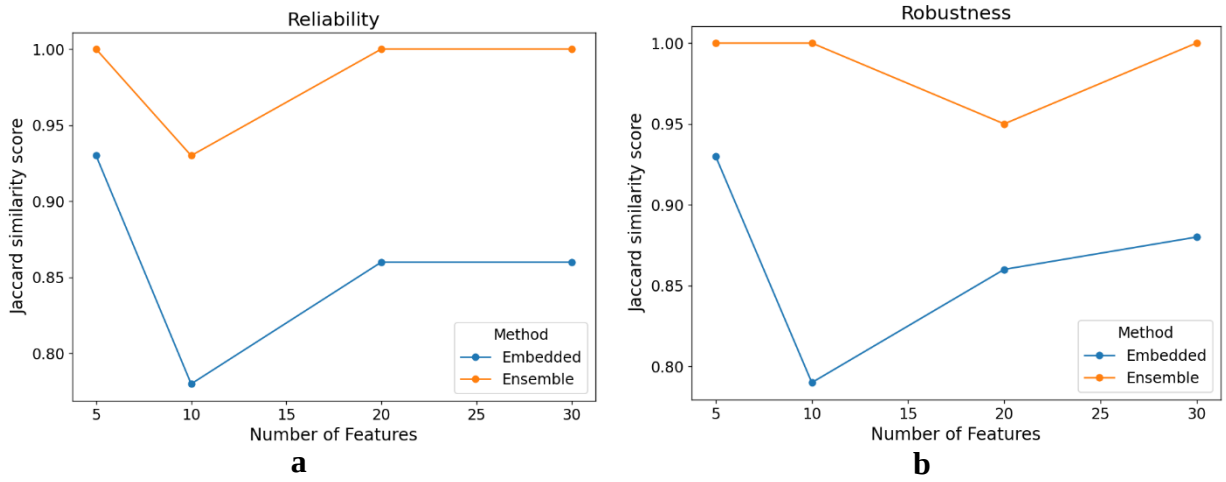

Figure 6. Average Jaccard similarity score for 10 runs for ensemble and embedded methods, a) bootstrapping without replacement for reliability. b) bootstrapping with a replacement for stability and robustness.

4. CONCLUSION

This study presents an innovative ensemble-based approach for selecting key features to develop reliable and robust residential building archetypes. The study compares a multistage ensemble data-driven feature selection technique with a single embedded method across four dimensions: selection accuracy, stability and robustness, performance, and reliability. This research demonstrates that an ensemble-based methodology for developing residential building archetypes provides a robust and reliable feature set.
The study reveals that ensemble feature selection outperforms the embedded approach in all evaluated aspects except classification accuracy. The number of selected features impacts various evaluation criteria, including selection and classification accuracy, reliability, and robustness. Furthermore, for the ensemble method, the high-complex model with 30 features performed better in reliability and robustness with scores of 1, PSFI and PIFS values of 0.33 and 0.38, respectively. However, the classification accuracy of this model was equal to the detailed model with 20 feature subsets with 89% accuracy. In conclusion, ensemble-based feature selection demonstrates strong potential for selecting reliable and robust features that are important in energy rating. This characteristic can aid archetype development by enhancing model consistency, reproducibility, and trustworthiness. This approach not only helps domain expert confidence but also supports practical and interpretable models.
This study highlights several opportunities for future research, particularly in optimizing feature

selection methods. For instance, wrapper feature selection was not employed due to its high computational costs, an issue that future work should address. Additionally, execution time should be incorporated as a critical evaluation criterion when comparing feature selection techniques.

ACKNOWLEDGEMENTS

This publication has emanated from research supported partly by a grant from the Sustainable Energy Authority of Ireland (SEAI) under the Funding Program Grant No. 22/RDD/822. The opinions, findings, conclusions or recommendations expressed here are those of the author(s) and do not necessarily reflect the views of the SEAI.

REFERENCES

Ali, U., Bano, S., Shamsi, M. H., Sood, D., Hoare, C., Zuo, W., Hewitt, N., & O'Donnell, J. (2024). Urban building energy performance prediction and retrofit analysis using data-driven machine learning approach. Energy and Buildings, 303, 113768. https://doi.org/10.1016/J.ENBUILD.2023.113768

Ali, U., Shamsi, M. H., Bohacek, M., Hoare, C., Purcell, K., Mangina, E., & O'Donnell, J. (2020). A data-driven approach to optimize urban scale energy retrofit decisions for residential buildings. Applied Energy, 267, 114861. https://doi.org/10.1016/J.APENERGY.2020.114861

Ali, U., Shamsi, M. H., Bohacek, M., Purcell, K., Hoare, C., Mangina, E., & O'Donnell, J. (2020). A data-driven approach for multi-scale GIS-based building energy modeling for analysis, planning and support decision making. Applied Energy, 279, 115834. https://doi.org/10.1016/J.APENERGY.2020.115834

Barbieri, M. C., Grisci, B. I., & Dorn, M. (2024). Analysis and comparison of feature selection methods towards performance and stability. In Expert Systems with Applications (Vol. 249). Elsevier Ltd. https://doi.org/10.1016/j.eswa.2024.123667

Dahlström, L., Johari, F., Broström, T., & Widén, J. (2024). Identification of representative building archetypes: A novel approach using multi-parameter cluster analysis applied to the Swedish residential building stock. Energy & Buildings, 303, 113823. https://doi.org/10.1016/j.enbuild.2023.113823

Ding, Y., Fan, L., & Liu, X. (2021). Analysis of feature matrix in machine learning algorithms to predict energy consumption of public buildings. Energy and Buildings, 249, 111208. https://doi.org/10.1016/j.enbuild.2021.111208

Egan, J., Finn, D., Deogene Soares, P. H., Rocha Baumann, V. A., Aghamolaei, R., Beagon, P., Neu, O., Pallonetto, F., & O'Donnell, J. (2018). Definition of a useful minimal-set of accurately-specified input data for Building Energy Performance Simulation. Energy and Buildings, 165, 172–183. https://doi.org/10.1016/j.enbuild.2018.01.012

Eskandari, H., Saadatmand, H., Ramzan, M., & Mousapour, M. (2024). Innovative framework for accurate and transparent forecasting of energy consumption: A fusion of feature selection and interpretable machine learning. Applied Energy, 366. https://doi.org/10.1016/j.apenergy.2024.123314

Ferrando, M., Ferroni, S., Pelle, M., Tatti, A., Erba, S., Shi, X., & Causone, F. (2022). UBEM's archetypes improvement via data-driven occupant-related schedules randomly distributed and their impact assessment. Sustainable Cities and Society, 87, 104164. https://doi.org/10.1016/J.SCS.2022.104164

Johari, F., Munkhammar, J., Shadram, F., & Widén, J. (2022). Evaluation of simplified building energy models for urban-scale energy analysis of buildings. https://doi.org/10.1016/j.buildenv.2021.108684

Kong, D., Cheshmehzangi, A., Zhang, Z. et al. Urban building energy modeling (UBEM): a systematic review of challenges and opportunities. Energy Efficiency 16, 69 (2023). https://doi.org/10.1007/s12053-023-10147-z

Moslemi, A. (2023). A tutorial-based survey on feature selection: Recent advancements on feature selection. In Engineering Applications of Artificial Intelligence (Vol. 126). Elsevier Ltd. https://doi.org/10.1016/j.engappai.2023.107136

Neale, J., Shamsi, M. H., Mangina, E., Finn, D., & O'Donnell, J. (2022). Accurate identification of influential building parameters through an integration of global sensitivity and feature selection techniques. Applied Energy, 315, 118956. https://doi.org/10.1016/J.APENERGY.2022.118956

Pes, B. (2020). Ensemble feature selection for high-dimensional data: a stability analysis across multiple domains. Neural Computing and Applications, 32(10), 5951–5973. https://doi.org/10.1007/s00521-019-04082-3

Raushan, K. (2023). Cleaned and validated Irish EPC database. 1. https://doi.org/10.17632/5VNNBF8HD6.1

SEAI. (2024). Domestic Energy Assessment Procedure (DEAP) Manual. https://www.seai.ie/ber/support-for-ber-assessors/

Zhang, Y., Liu, J., Li, W., & Liang, S. (2023). A Proposed Ensemble Feature Selection Method for Estimating Forest Aboveground Biomass from Multiple Satellite Data. Remote Sensing, 15(4). https://doi.org/10.3390/rs15041096

6th International Conference on Building Energy and Environment
Eindhoven University of Technology, The Netherlands
6 - 10 July 2025

Effects of the design parameters of monitor roofs on hybrid natural ventilation

Yi-Pin Lin [1], Sein Lae Yi Win [2], Chi-Ming Li [3]

[1]*Department of Creative Design, National Yunlin University of Science and Technology, Taiwan, linyp@yuntech.edu.tw*
[2]*Department of Civil Engineering, National Cheng Kung University, Tainan, Taiwan, seinlae07@gmail.com*
[3]*Department of Civil Engineering, National Cheng Kung University, Tainan, Taiwan, cmlai@mail.ncku.edu.tw*

SUMMARY
This study investigated the influence of design parameters on the efficiency of hybrid natural ventilation facilitated by monitor roofs (with and without rain shelters) using computational fluid dynamics (CFD). The design parameters of monitor roofs include the width S, height H, and eave overhang E. In consideration of engineering practices, the parameter ranges were set as follows: S=1.2, 1.8, 2.4, and 3 m; H=0.3, 0.6, 0.9, and 1.2 m; and E=0, 0.3, and 0.6 m. The set wind speed (0.01–3 m/s) refers to the wind speed at a height of 10 m. The results show that for a larger monitor roof (width =3 m, height =1.2 m), the presence of outdoor wind combined with thermal buoyancy increased the ventilation rate to 1.5-3.5 times that found when only buoyancy was present. After rain shelter installation, a rain protection effect was achieved, and the ventilation rate increased because of flow structure conformity, with an overall average effectiveness of 1.02.

Keywords: ventilation, monitor roof, rain shelter, roof, building.

1. INTRODUCTION

Natural ventilation involves the use of natural forces, such as wind and/or thermal buoyancy, to introduce fresh air into indoor spaces without the use of mechanical energy. These natural forces usually affect the natural ventilation performance. Notably, natural forces can be isolated, opposed, or mutually reinforcing, and occasionally, they can act synergistically. As a common means of building ventilation, monitor roofs (or a ridge vent of a smaller size) with or without rain shelter have been employed to introduce indoor airflow via thermal buoyancy and/or wind.

Taiwan is located in a tropical area. Various types of monitor roofs are often installed at the roof ridges of buildings (as shown by the red dotted line in Fig. 1(a)) to increase the effectiveness of indoor ventilation in the spaces below, and their ability to induce ventilation is widely recognized. However, people have different evaluations of their ability to induce natural ventilation. What is the ventilation rate? Are there any appropriate design parameters? To date, these details have not been unveiled in the literature. The available data on design details are relatively limited, and only our previous studies focused on such topics (Chen et al., 2022)(Lin et al., 2023)(Win et al., 2024). Moreover, to prevent rainwater from entering the building via the monitor roof, a rain shelter can be installed (hereafter referred to as the modified monitor roof), as shown by the blue dotted line area in Fig. 1(b). How design parameters affect the efficiency of hybrid natural ventilation caused by monitor roofs is an issue that needs to be clarified. Thus those issues have become the motivation for this study.

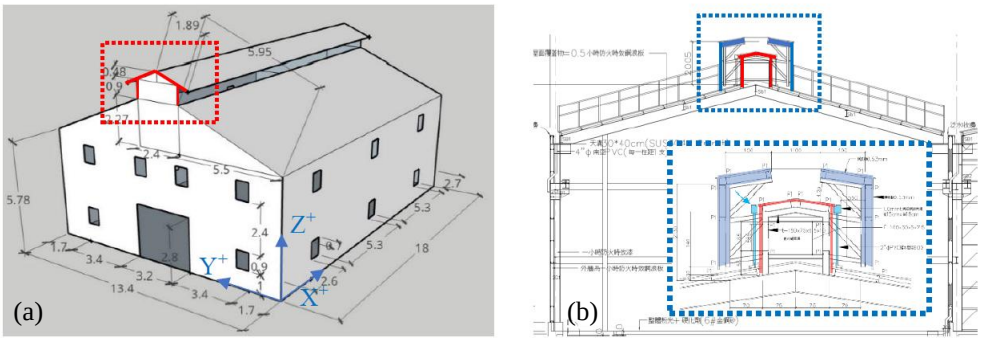

Figure 1. The illustration of a monitor roof (red line) and the addition of a rain shelter (blue line) (Win et al., 2024).

2. RESEARCH METHOD

The considered monitor roof design parameters are the width (S), height (H), and eave overhang (E), as shown in Fig. 2(a). The length range of each parameter is as follows: S, 1.2–3 m; H, 0.3–1.2 m; and E, 0–0.6 m; these ranges were derived from engineering practice and confirmed in our previous study (Chen et al., 2022). In the second part of this study, a common monitor roof with the rain shelter was investigated, and its dimensions are as follows: S = 1.2 m, H = 1.2 m, E = 0 and 0.3 m. The rain shelter is shown as a blue structure in Figs. 1(b), 2(b).

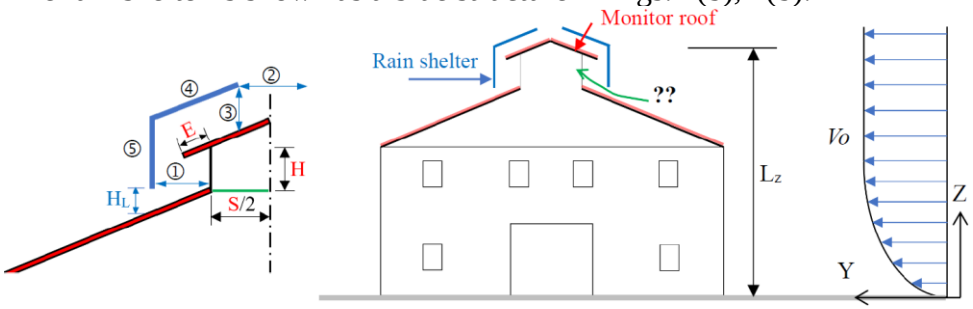

(b) Design parameters of the modified monitor roof

(a) Modified monitor roof, pitched roof and the space below

Figure 2. Physical model used in this study (not to scale; unit: m).

The design procedure for the rain shelter is as follows: the distance between the vertical plates of the rain shelter and that of the existing monitor roof (① in Fig. 2(d)), 1 m in this study) is determined; the width of the horizontal outlet of the rain shelter (②, 1 m) is obtained; the distance between the top of the rain shelter and the upper roof panel of the existing monitor roof (③, 0.7 m) is measured; the inclination angle of the roof panel of the rain shelter is matched to that of the monitor roof; the length of the roof panel (④) is determined; the length of the vertical panel of the rain shelter (i.e., the side flow opening H_L (= 0.4 m, 0.6 m)) is obtained; and the length of eave overhang is calculated (E = 0 and 0.3 m).

Finite-volume CFD code PHOENICS was used to simulate fluid flow and heat transfer. The detailed information of the used numerical methods and parameter settings are detailed in (Win et al., 2024). The governing equations solved by PHOENICS include a three-dimensional incompressible Navier–Stokes equation, a time-independent convection diffusion equation and the

LVEL turbulence model. Their formulations can be found in the PHOENICS manual. Iterative calculations were conducted until all field variables in the problem satisfied the specified relative convergence value of 10^{-3}.

3. RESULTS AND DISCUSSION

3.1 Ventilation performace of the monitor roofs (without rain shelter)

Figure 3(a) shows when the outdoor wind is very weak (Gr/Re^2>1.5), the ventilation airflow is dominated by the buoyant effect (via solar heating), and the ventilation rate does not change dramatically with a change in Gr/Re^2 for a fixed direction of the incoming wind. As the outdoor wind speed increases, Gr/Re^2 decreases accordingly. When Gr/Re^2=0.84-1.5, the ventilation rate first increases and then decreases, as shown in the dashed-line box. When Gr/Re^2<0.84, the trend of the ventilation rate at various incoming wind directions is different. When the incoming wind direction is 0°, the ventilation rate slightly increases as Gr/Re^2 decreases; however, when the incoming wind direction is 45° or 90°, the ventilation rate increases significantly as Gr/Re^2 decreases, suggesting that outdoor wind under these conditions can effectively increase the ventilation rate.

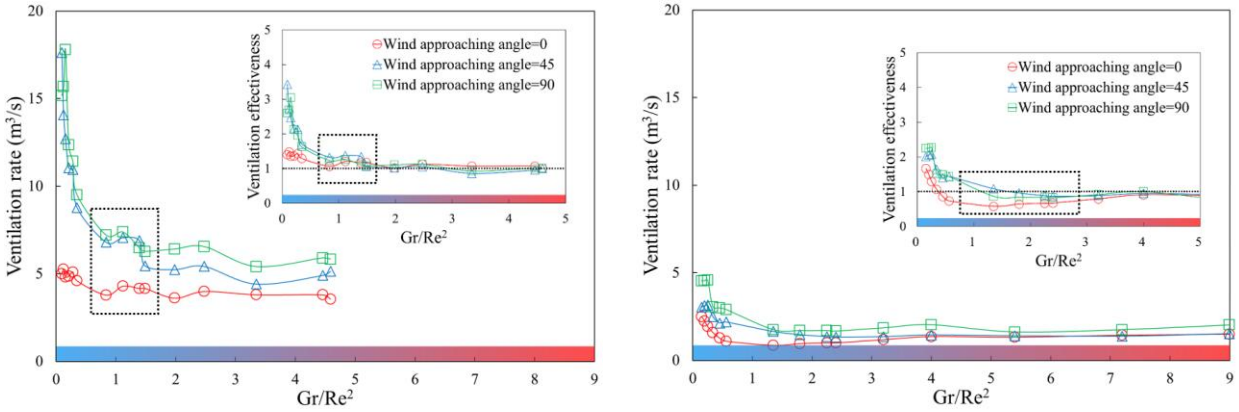

(a) S =3 m, H =1.2 m, E =0.3 m (b) S =1.2 m, H =0.3 m, E =0.3 m

Figure 3 Effect of Gr/Re^2 on the hybrid ventilation rate of the monitor roof under different incoming wind directions

Figure 3(b) shows when the width and height of the monitor roof decrease (S=1.2 m, H=0.3 m, and E=0.3 m), the ventilation efficiency caused by thermal buoyancy and outdoor wind is lower than that of the larger monitor roof (S=3, H=1.2, E=0.3). When the incoming wind direction is 45° or 90° and Gr/Re^2=1.4-3.2, the ventilation rate first decreases and then increases. In this Gr/Re^2 range, the presence of outdoor wind has a negative effect on the ventilation efficiency. At an incoming wind direction of 0°, the ventilation rate first decreases and then increases over Gr/Re^2=0.45-3.2, indicating a larger range of Gr/Re^2 over which the outdoor wind negatively impacts the ventilation rate. Thus, Gr/Re^2=1 is not suitable as a criterion for when the outdoor wind starts to impact the ventilation rate.

3.2 Ventilation performance of the monitor roofs with rain shelter

In general, after rain shelter (H_L = 0.4 m) installation on the monitor roof, the average effectiveness reached 1.02. Figure 4 shows that a rain protection effect could be achieved, and the ventilation

rate increased by 2% because of flow structure conformity. As shown by the green dotted line area, when there is no wind or when a low wind speed occurs (0.01 m/s), the driving force of the ventilation airflow is the thermal buoyancy force generated by the heated roof slab. Moreover, for both the monitor roof and the modified monitor roof, their geometric shapes allow the thermal buoyancy airflow to first move upward and then exit the roof. Therefore, both the monitor roof and the modified monitor roof provided similar ventilation performance levels, and the effectiveness approached 1.

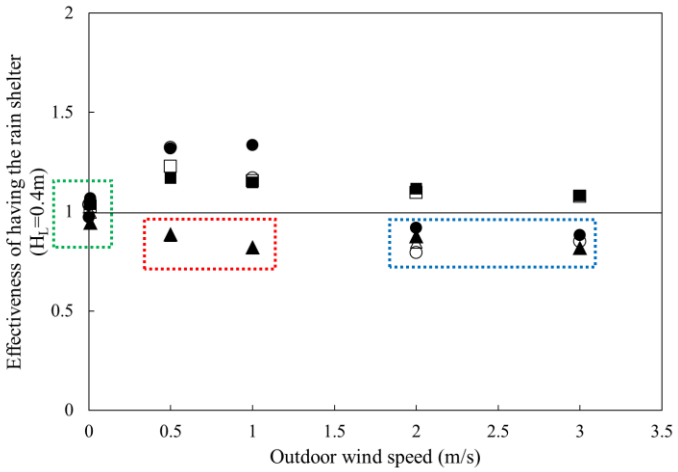

Figure 4. Physical Relationships between the effectiveness of the rain shelter (HL = 0.4 m) and the outdoor wind speed, wind direction, and presence of eaves.

When the wind speed increased to 0.5–1 m/s, due to the flow structure, the ventilation performance of the modified monitor roof was better than that of the monitor roof under wind angles of 0° and 45°. Under a wind angle of 90°, owing to the large area of the gable, the airflow was obstructed. The opening of the modified monitor roof is located in the wake area downstream of the gable, so it cannot efficiently guide the indoor airflow outward, and the ventilation effectiveness is lower than that of the monitor roof, yielding an effectiveness less than 1, as shown by the red dotted area.

4. CONCLUSION

For a larger monitor roof (width =3 m, height =1.2 m), the presence of outdoor wind combined with thermal buoyancy increased the ventilation rate to 1.5-3.5 times that found when only buoyancy was present. For a smaller monitor roof (width =1.2 m, height =0.3 m), Gr/Re^2=0.45-3.2 was the transition range over which the presence of outdoor wind decreased the ventilation rate below that found when only buoyancy was present. After installing a rain shelter (side flow opening H_L = 0.4 m) on the monitor roof, rain protection was achieved, and the ventilation rate increased owing to flow structure conformity, with an overall average effectiveness of 1.02.

REFERENCES

Chen C.M., Lin Y.P., Chung S.C., Lai C.M., 2022, Effects of the Design Parameters of Ridge Vents on Induced Buoyancy-Driven Ventilation, Buildings 12, 112

Lin Y.P., Huang Z.L., Chung S.C., Lai C.M., 2023, Effect of outdoor wind on the hybrid natural ventilation performance of monitor roofs. Alexandria Engineering Journal 80, 584-593

Win S.J.Y., Chiang Y.C., Lin Y.P., Lai C.M., 2024, Effect of rain shelter installation on the natural ventilation performance of monitor roofs. International Journal of Ventilation (in press)

6th International Conference on Building Energy and Environment
Eindhoven University of Technology, The Netherlands
6 - 10 July 2025

Adaptive Insulation System with thermochemical Actuation for thermally activated Building Structures (TABS)

Jonina Felbinger [1], Marc Linder [1]

[1]*German Aerospace Center, Institute of Engineering Thermodynamics, Stuttgart, Germany, jonina.felbinger@dlr.de*

SUMMARY
A novel adaptive insulation system, actuated by thermochemical gas pressure control, was developed and successfully demonstrated in laboratory experiments. The system consists of an open-pored vacuum insulation panel coupled with a metal hydride reactor to precisely and reversibly adjust the thermal conductivity by varying the internal gas pressure. Experiments demonstrated that the insulation system allows for effective control of the heat transport, and thus, activating massive building components such as screed or concrete as thermal energy storage. This makes it possible to charge building masses to higher temperatures, utilizing existing storage capacity and offering options for minimally invasive retrofitting and flexible energy management in existing buildings.

Keywords: Variable conductance envelope, Thermochemical reactions, Thermal energy storage, Building retrofit

1. INTRODUCTION

According to the 2020 Global Status Report of the United Nations Environment Programme (United Nations, 2020), the building and buildings construction sector collectively contribute to more than one-third of global final energy consumption and nearly 40% of the total direct and indirect CO2 emissions. There is clearly a significant potential for innovative and resource-efficient thermal management for buildings. Traditional insulation materials offer low – but constant – values of thermal conductivity and thus play a significant but only passive role for the heat flows in buildings. However, if insulating materials are variable in their thermal transmittance, heat flows can be adapted to fluctuating internal (heating/cooling comfort, number of people and electronic devices, etc.) and external (seasons, weather, day/night cycles, etc.) conditions, and further, building components could be made active components of the energy system.

Firstly, adaptive building envelopes are capable of contributing to significant energy savings, according to a referred study in a comment (Henry,2020) in Nature Energy, which declares variable conductance buildings envelopes to be one of the five grand challenges for thermal energy decarbonization. This would allow solar heat to be gained temporally and partially in winter and transitional seasons as needed. Most importantly, variable conductance building envelopes can reduce the energy consumption of air-conditioning in non-residential buildings by taking advantage of the passive cooling effect by night during hot summer periods.

Another scenario for controllable insulation in buildings is the utilization of existing high-capacity building components as thermal energy storage and thereby transforming buildings into active players for load shifting and grid flexibility. Provided the heat flux through an insulation layer can be controlled in terms of time and amplitude, thus thermally activated building components (TABS), charged by excess energy, are able to contribute to space heating/cooling and peak shaving. Figure 1 depicts schematically the implementation potential of controllable

insulation systems in buildings.
This contribution presents the development, experimental investigation, and application perspectives of a thermally controllable insulation system with gas-solid reactions as actuation mechanism for the heat switch, developed at the German Aerospace Center (DLR).

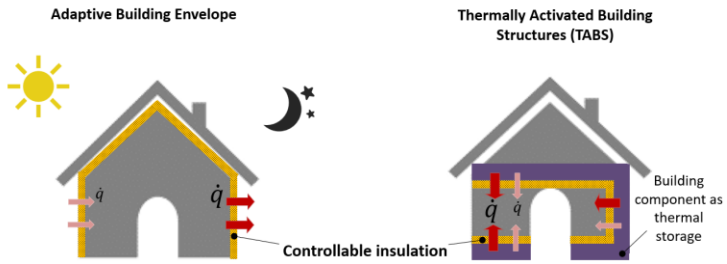

Figure 1. Schematic visualization of application scenarios of controllable insulation systems in buildings.

2. METHODS

2.1. Concept

The working principle of the controllable insulation layer is to adjust the gas pressure in open-pored insulation panels to control thermal conductivity along an S-shaped curve (Knudsen effect). This can be achieved by using thermochemical materials by precisely setting the temperature of the reaction material and thus the gas pressure can be adjusted reversibly along the equilibrium line. By coupling the thermochemical reaction with an open-pored panel, an insulation system with adjustable thermal conductance is realized. Figure 2 gives a schematic overview.

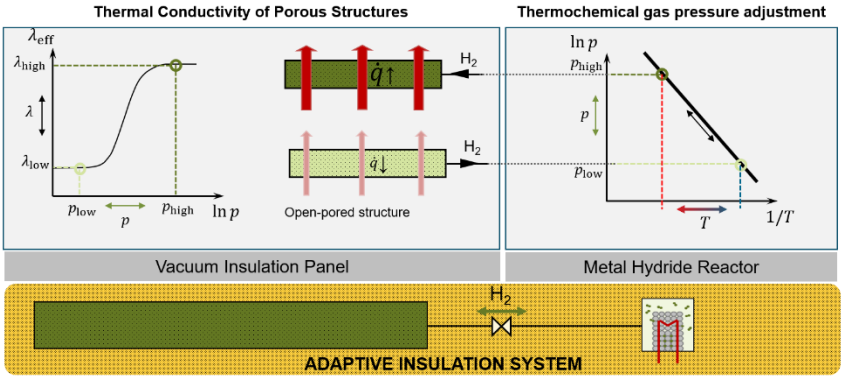

Figure 2. Representation of the concept and fundamentals of the controllable thermal insulation system, with the Knudsen effect (left) and the Van't Hoff equilibrium plot of thermochemical materials (right).

The two core components of the adaptive insulation system are the enveloped open-pored vacuum insulation panel and the metal hydride reactor for the hydrogen gas pressure adjustment in the panel. These units are physically linked, meaning that the temperature setting of the metal hydride is directly related to the gas pressure and, as a result, to the thermal conductivity of the insulation panel.

2.2. Experimental Setup

A prototype vacuum insulation panel was developed using open-pored core materials and

enclosed in multi-layer laminates. For gas pressure regulation, metal hydride materials were studied (Felbinger,2023; Felbinger,2024), and an additively manufactured reactor was designed and its operational behavior characterized. Figure 3b-c) shows such a custom-made vacuum insulation panel with a 30 cm edge length, as well as a developed metal hydride reactor for gas pressure control. To experimentally verify the function of the lab-scale 30x30x2 cm controllable insulation system – with fibre mat as core material -, a dedicated test bench was constructed. This setup enables both the actuation of the reactor and the measurement of gas pressure on the reactor side, as well as the assessment of the resulting thermal performance on the panel side. The test bench is illustrated in Figure 3c). Gas pressure is intended to be varied between approximately 1 and 1000 mbar. The system is equipped with multiple temperature sensors, pressure transducers, a heat flux meter, and an infrared camera to monitor the insulation system's response under controlled laboratory conditions. In a second approach, a laboratory setup was built, combining the controllable insulation with an electrically charged massive concrete screed layer, to investigate a TABS floor heating application. Here, the heat flux into the room during charging and discharging are managed by the adaptive insulation, demonstrating the system's potential for building integration. Figure Figure 3d) shows the experimental layer structure. The 30x30x6 cm screed layer is heated by an electrical heating mat (120 W/m²), while the adaptive insulation minimizes heat flow into the room in its 'OFF' state. After 6 hours, the heating mat is switched off and the adaptive insulation is turned 'ON' to increase space heating, continuing until the thermal storage layer is fully discharged.

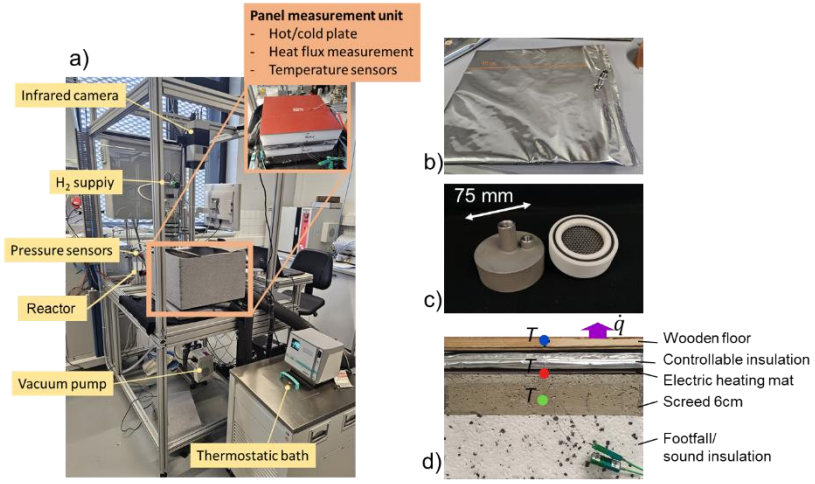

Figure 3. Experimental setup for investigating adaptive insulation system (a), custom-made insulation panel with gas connection (b) and metal hydride reactor (c).

3. RESULTS

3.1. Proof of Function

The proof of function experiments demonstrated that the thermal conductivity of the insulation system can be modulated in a reversible and precisely controlled manner. As a first step, the gas pressure-dependent thermal conductivity of the porous insulation element was measured. Figure 4a) illustrates the characteristic S-shaped curve of the fibre-core insulation panel, achieved by varying the hydrogen gas pressure. The results show that, when the gas pressure is changed from 1 (or less via vacuum pump) to 1000 mbar, a switching ratio (SR) (defined as the ratio of maximum to minimum thermal conductivity) of approximately 15 is obtained.

3.2. Application for Thermally Activated Building Components

The initial experimental investigations of the targeted activation of building structures, using adaptive insulation, have yielded promising results. Figure 4b) illustrates the results of the described experiment. During the first 6 hours, the charging phase takes place, with the storage mass heated by an electric mat. To minimize heat losses during this period, the adaptive insulation is set to its insulating state, meaning the gas pressure is kept as low as possible. As a result, the heat flux into the room (violet line) remains below 15 W/m², and the floor surface temperature (blue line) does not exceed 25 °C, even though the charging phase leads to an average screed temperature (green line) of 48 °C. At the 6-hour mark, marking the end of the charging period, the insulation system is switched to the 'ON' state by increasing the gas pressure (as shown by the grey line). This results in a sudden increase in heat flow into the room and a gradual discharge of the storage layer for the next 18 h. The discharge process proceeds in an uncontrolled manner; the gas pressure—and thus the thermal conductivity of the insulation layer by factor 10—was increased only once. The experiment successfully demonstrated that thermal activation of massive building components using controllable insulation is feasible. By regulating the heat flow into the room, it becomes possible to charge building masses to higher temperatures, which significantly increases the storage density.

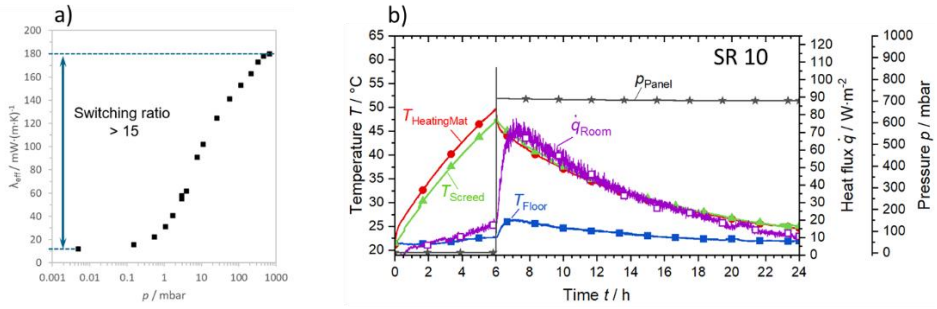

Figure 4. Experimental results of gas pressure-dependent thermal conductivity for insulation system (a), thermal activation of massive components by applying adaptive insulation (b).

4. CONCLUSIONS

A proof of concept for adaptive insulation actuated by thermochemical gas pressure control has been demonstrated, showing its potential for use in building component activation. The approach of using insulation with controllable heat flux enables the electrification of existing buildings through minimally invasive retrofitting, such as with electric heating mats. The – already existing - high thermal storage capacity of screed or concrete allows buildings to contribute to the energy grid and increases operational flexibility. Further research, particularly on advanced control strategies, will be necessary in the future.

REFERENCES

Felbinger J., 2023. Novel temperature-driven technique to characterize hydrogen sorption properties under vacuum conditions: Method development, experimental setup, and demonstration on the AB5-type metal hydride LaNi4.1Al0.52Mn0.38. Int. Journal of Hydrogen Energy, Vol. 48, 36849

Felbinger J., 2024. Thermodynamic characterisation and application of the ZrNi–H metal hydride system in the low-pressure regime. Journal of Materials Chemistry A, Vol. 12, pp. 6075-6086

Henry, A., Prasher, R., Majumdar, A., 2020. Five thermal energy grand challenges for decarbonization. Nature Energy, Vol.5, pp.635-637.

United Nations Environment Programme, 2020. 2020 Global Status Report for Buildings and Construction: Towards a Zero-emission, Efficient and Resilient Buildings and Construction Sector.

Occupant-Centric Building Design and Controls (11:00-12:30 h)

6th International Conference on Building Energy and Environment
Eindhoven University of Technology, The Netherlands
6 - 10 July 2025

Campus-wide indoor environmental quality (IEQ) assessment for MVAC optimization

Tsang Tsz Wun [1], Mui Kwok Wai [1], Wong Ling Tim [1], Liu Bian [1]

[1]*Department of Building Environment and Energy Engineering, The Hong Kong Polytechnic University, Hong Kong, China, hayley.tsang@polyu.edu.hk*

SUMMARY
In this study, both passive and active approaches were adopted to evaluate indoor environmental quality (IEQ) on a university campus, ultimately aiming to optimize MVAC energy consumption. An IoT-based IEQ sensor grid was deployed in air-conditioned spaces throughout the campus, monitoring a total of 10 IEQ indicators, representing thermal comfort, indoor air quality (IAQ), aural comfort, and visual comfort. In selected classrooms, 383 feedback from occupants regarding the thermal, aural, and visual environments, air quality, and overall IEQ was collected. Findings indicated a misalignment between the provided IEQ and occupants' expectations, highlighting issues such as over-cooling and stuffiness. Approximately 20% of occupants were dissatisfied with the perceived thermal conditions and air quality. Based on the thermal response and the Humanized Adaptive Baseline Information Technology (HABIT) algorithm developed earlier, the control parameters for optimal set-point temperature were defined. This paper presents a practical solution to achieve occupant-centric set-point temperature control.

Keywords: occupant-centric, energy optimization, indoor environmental quality

1. INTRODUCTION

Indoor environmental quality (IEQ) is a critical factor significantly impacting the health, well-being, and productivity of building occupants, as well as influencing energy consumption in buildings (Zhang et al., 2023). Among the four key aspects of IEQ—thermal comfort, indoor air quality (IAQ), visual comfort, and acoustic comfort—dissatisfaction predominantly arises from complaints regarding thermal conditions (Wong et al., 2008a). This often indicates a misalignment between building design, operation, and occupant expectations. Notably, overcooling of buildings accounts for an average of 17% of thermal sensation votes in warm climates, corresponding to about 12% of cooling energy wasted in buildings (Alnuaimi et al., 2022).

While building operation predominantly relies on established IEQ or thermal comfort models to assess occupant preferences and determine optimal environmental settings, these models often overlook the importance of integrating occupant perceptions of the environment into building control. Understanding occupant preferences for environmental conditions typically requires collecting feedback through field surveys. When combined with the implementation of set-point control policies to achieve healthy indoor environments and meet occupant expectations at a set-point temperature range of 20 to 25.5°C, annual carbon dioxide (CO_2) emissions from Mechanical Ventilation and Air Conditioning (MVAC) energy consumption could be reduced by 2% to 9% (Wong et al., 2008b). Other research has also suggested that minor adjustments in thermal settings can yield substantial energy savings; for example, increasing the set-point temperature by 1°C can result in an average energy saving of approximately 6% (Yamtraipat et al., 2005; Zhang et al.,

2017).

Although field surveys provide valuable insights into occupant preferences for establishing operational strategies, achieving smart building control automation that accommodates occupant needs requires facility management to adopt both passive and active engagement approaches. Passive engagement involves constant monitoring of environmental parameters through the implementation of a sensing network. This network allows for the monitoring of temporal and spatial variations in environmental conditions resulting from human activities and external factors. When conditions fall below standards, swift responses can be made to restore IEQ. Active engagement, on the other hand, adopts a human-centric approach that allows occupants to "actively" participate in the decision-making process to determine optimal environmental conditions. Where technically feasible, this dual approach leverages both occupant comfort sensation data and corresponding physical environmental condition data to enable (almost) real-time control of the MVAC system, prioritizing the provision of a satisfying and preferred perceived environment.

This study demonstrates the use of such dual approaches for set-point temperature optimization. An IoT-based IEQ sensor grid was deployed in nine air-conditioned classrooms and lecture theatres to monitor crucial surrogate indicators. Feedback from occupants regarding thermal, aural, and visual environments, air quality, and overall IEQ was collected. Based on the subjective and objective measurement results, the Humanized Adaptive Baseline Information Technology (HABIT) framework was adopted to determine the optimal indoor set-point temperature. This study highlights the significance of embracing an occupant-centric approach for environmental comfort and enhancing energy efficiency, paving the way for a new era of building control practices.

2. METHODOLOGY

2.1. Field measurement

2.1.1. Physical measurement of IEQ parameters

The physical measurement is part of a larger campaign conducted across the entire campus to establish a comprehensive continuous environmental monitoring network for evaluating Indoor IEQ performance. For this purpose, an IoT-based IEQ sensing device was developed to measure indoor air temperature, radiant temperature, relative humidity, air velocity, CO_2 levels, particulate matter (PM_{10} and $PM_{2.5}$) levels, total volatile organic compounds (TVOC), horizontal illuminance levels, and sound pressure levels. These parameters serve as representative surrogate indicators for thermal comfort, IAQ, as well as aural and visual comfort.

With a rapid response time and a sampling interval of 10 seconds, minute-average data is transmitted wirelessly via a Wi-Fi network and stored on a backend cloud server maintained by the University. By implementing multiple sensors simultaneously at various locations, the sensing network captures instantaneous environmental variations induced by human activities. This setup also offers spatial characterization and temporal insights into the environment, aiding in the identification of discomfort sources and mitigation strategies. Figure 1 shows the measurements conducted in one of the investigated classrooms.

(a) (b)

Figure 1. (a) A typical air-conditioned classroom investigated during the measurement campaign; and (b) the IoT-based indoor environmental quality (IEQ) sensor deployed for IEQ assessment.

2.1.2. Subjective responses on perceived IEQ

Surveys assessing perceived IEQ aspects and overall IEQ were conducted in nine selected classrooms and lecture theatres. The target participants of the survey were students, who are the primary users of the campus buildings. The survey collected demographic information and subjective assessments of perceived IEQ. Specifically, the 7-point ASHRAE thermal sensation was employed to evaluate perceived thermal comfort (ASHRAE, 2013), while a 5-point scale was used for assessing perceived IAQ. A scoring system was adopted for visual, aural, and overall comfort, and a dichotomous question was included to assess occupant satisfaction with the environment.

2.2. Humanized Adaptive Baseline Information Technology (HABIT) framework

The Humanized Adaptive Baseline Information Technology (HABIT) framework was proposed to determine the optimal indoor set-point temperature based on the best available information regarding thermal demand (Wong et al., 2006). Figure 2 is the schematic representation of the workflow of the HABIT framework.

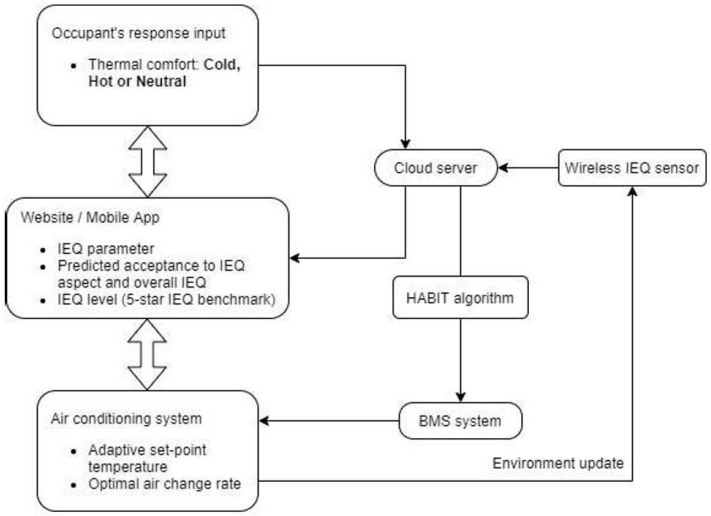

Figure 2. Proposed MVAC system feedback control using the Humanized Adaptive Baseline Information Technology (HABIT) system

The HABIT algorithm can be expressed by Eq. (1), where $T_{a,0}$ (°C) is the set-point temperature at the minimum predicted percentage dissatisfaction D, which is determined by the expected values of an acceptable thermal comfort temperature from occupants within a controllable range of temperatures T_1 (°C) and T_2 (°C).

$$T_{a,0} = \langle \widehat{T_a} \rangle = \langle \int_{T_1}^{T_2} f(T_a) dT_a \rangle ; \frac{\partial D}{\partial T_a} = 0 \quad (1)$$

While students are not permitted to adjust the set-point temperature via the control panel, they are encouraged to provide feedback on their thermal comfort through an online survey. With occupant feedback indicating 'Hot' ($T=T^+$) or 'Cold' ($T=T^-$) regarding the thermal environment at temperature T (°C), the step function ξ(T) shown in Eq. (2) is utilized to update the set-point temperature for occupant satisfaction ξ in the environment, at a selected control constant $0.5 \leq \lambda < 0.5$ and a temperature control range of k=5–10°C.

$$\xi(T) = \begin{cases} 1-\lambda ; & T<T^+; T>T^- \\ \lambda ; & T \geq T^+; T \leq T^- \end{cases} \quad (2)$$

Based on prior knowledge of the temperature distribution that satisfied the majority at the minimum predicted percentage dissatisfied (PPD), i.e., prior mean $\upsilon = 23.2$ and prior standard deviation $\tau = 3.7$, as adopted in design guidelines, a Bayesian approach is used to update this prior understanding with the given complaints, as shown in Eq. (3). The posterior distribution of the set-point temperature T_s can be approximated by a normal distribution with mean θ and variance σ^2, $(\theta|T) \sim N(\upsilon, \tau^2)$. Thermal comfort can thus be maintained by adjusting the set-point temperature when complaints arise due to a set-point temperature falling outside the comfort zone for the target occupants.

$$(\theta|T_s, \sigma^2, \upsilon, \tau^2) \sim N(\theta_1, \tau_1^2); \begin{cases} \theta_1 = \frac{\sigma^2 \upsilon + \tau^2 T_s}{\sigma^2 + \tau^2} \\ \tau_1^2 = \frac{\sigma^2 \tau^2}{\sigma^2 + \tau^2} \end{cases} \quad (3)$$

After determining the neutral temperature based on survey feedback, a simulation was conducted to demonstrate how the HABIT algorithm would adjust the set-point temperature in response to simulated complaints generated by the Monte Carlo sampling technique. Additionally, the settings of parameters such as the control constant λ and temperature control range k were assessed.

3. RESULTS AND DISSCUSSION

3.1. Field measurement results

3.1.1. Environmental conditions

Physical IEQ measurements indicated that environmental control in the measured classrooms and lecture theatres was consistent and stable. As shown in Table 1, thermal parameters were maintained within a narrow range of acceptable levels, in accordance with established guidelines. IAQ parameters also remained within acceptable levels according to the exposure standards set by the IAQ Certification Scheme, except for TVOC, which exhibited elevated average levels. While the horizontal illuminance levels could be considered low for teaching and learning environments, it is believed that the positioning of the IEQ devices requires adjustment to ensure appropriate measurement protocols for visual comfort. Given that the aural environment is regarded as the

most critical aspect for learning activities, the measured sound pressure levels were deemed acceptable (Lee et al., 2012).

Table 1. Environmental conditions in measured classrooms and lecture theatres.

	Operative temperature (°C)	Air velocity (m/s)	Relative humidity (%)	CO_2 (ppm)	TVOC (ppb)	PM_{10} ($\mu g/m^3$)	$PM_{2.5}$ ($\mu g/m^3$)	Horizontal illuminance level (lux)	Sound pressure level (dBA)
Mean	22.4	0.1	62.0	704	564	18.4	14.4	50	46.5
Min	21.5	0.0	36.1	404	0	0.4	0.1	9	23.7
Max	23.5	0.3	89.3	1054	1288	65.2	62.6	145	59.8
Std	0.5	0.1	12.1	131	354	11.4	9.7	22	11.2

3.1.2. Subjective responses and satisfaction

A total of 383 survey responses were collected from students attending classes in the nine selected classrooms and lecture theatres. Among the participants, the gender distribution was balanced, with 93% falling within the age range of 16 to 30. Significant differences in thermal sensation votes between genders were observed ($p = 0.007 < 0.05$, chi-square); however, no such differences were found among different age groups ($p = 0.472 > 0.05$, chi-square). 79.6% reported satisfaction with the perceived thermal environment, with thermal sensation votes skewed towards the cooler side. Votes within the range of $-1 \leq TSV \leq +1$ accounted for 68.7% of the total responses, which was lower than the overall thermal satisfaction rating. This suggests that some respondents may still feel satisfied with the thermal environment even when they experience a sub-optimal or extreme thermal sensation. This finding aligns with a review by Mui et al. (2020), which indicates that thermal preferences may cover a broader range of acceptance than predicted by the traditional PMV-PPD model, possibly due to thermal tolerance and adaptation. Figure 3 illustrates the average percentage and thermal satisfaction corresponding to thermal sensation votes.

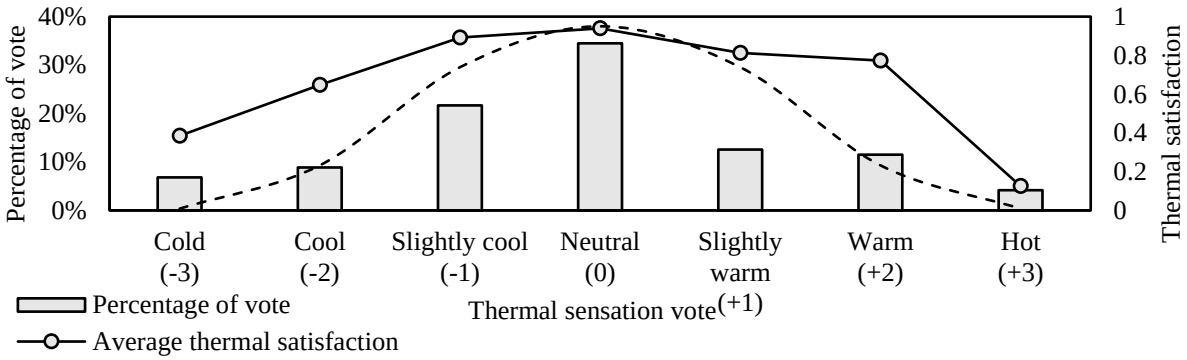

Figure 3. Average percentage of vote and average thermal satisfaction at various thermal sensation votes.

With a narrow range of observable operative temperatures from 21.5°C to 23.5°C, as shown in Figure 4, a linear relationship ($R^2 = 0.38$) was identified between thermal sensation votes and operative temperature, with the neutral temperature found to be 23.4°C. Although no significant trend was observed between operative temperature and thermal satisfaction, the highest level of satisfaction occurred at the warmer end of the thermal conditions (i.e., at 23.25°C).

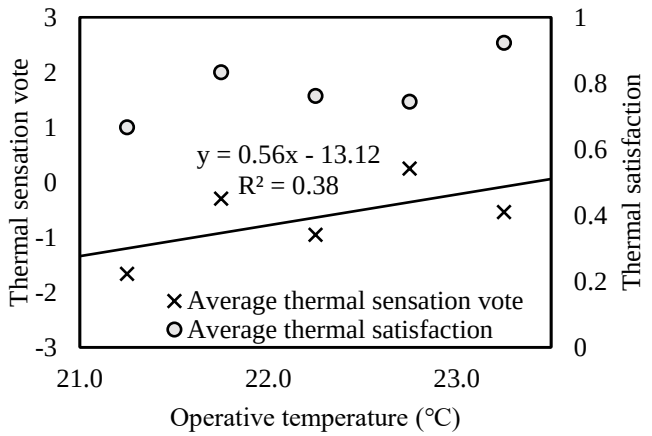

Figure 4. Average thermal sensation vote and average thermal satisfaction at observable operative temperature range.

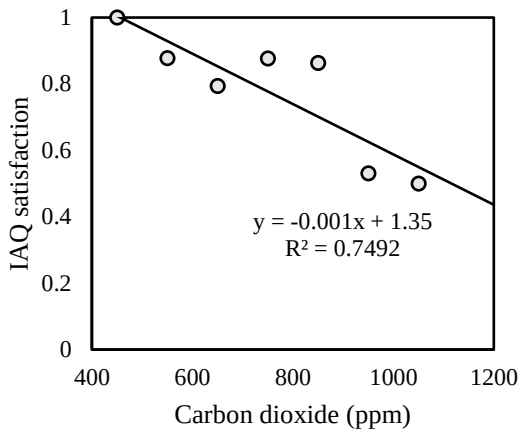

Figure 5. Average IAQ satisfaction at observable range of carbon dioxide levels.

Similar to thermal comfort, up to 81.2% of respondents expressed dissatisfaction with the IAQ. Despite a neutral rating towards IAQ, 18.5% of respondents reported dissatisfaction, indicating that students expect higher than acceptable IAQ levels. No significant association was found between IAQ satisfaction and gender ($p = 0.839 > 0.05$, chi-square) or age group ($p = 0.326 > 0.05$, chi-square). While CO_2 concentrations were maintained below 1000 ppm most of the time, a correlation between IAQ satisfaction and CO_2 concentration was found, as shown in Figure 5. Although it falls outside the scope of this study, this observation of correlation suggests the potential for using subjective evaluations to assess IAQ performance or for ventilation control purposes. No significant correlation was observed between IAQ satisfaction and PM10, PM2.5, or TVOC levels. For visual, aural, and overall IEQ comfort, satisfaction levels reached 88.5%, 90.9%, and 89.5%, respectively, indicating a high standard of perceived environmental quality.

3.2. Optimal set-point temperature determination by the HABIT algorithm

Based on the thermal preferences identified from the field survey, control parameters for optimizing the set-point temperature using the HABIT framework were tested. Utilizing the Monte Carlo sampling technique, both cold and hot complaints were generated from the surveyed distribution of temperature that could lead to thermal complaints. These complaint temperatures served as the initial set-point temperatures to evaluate the progression of the set-point temperature within control ranges of 20–25°C and 18–28°C, i.e., k=5 or k=10°C, after rounds of complaints.

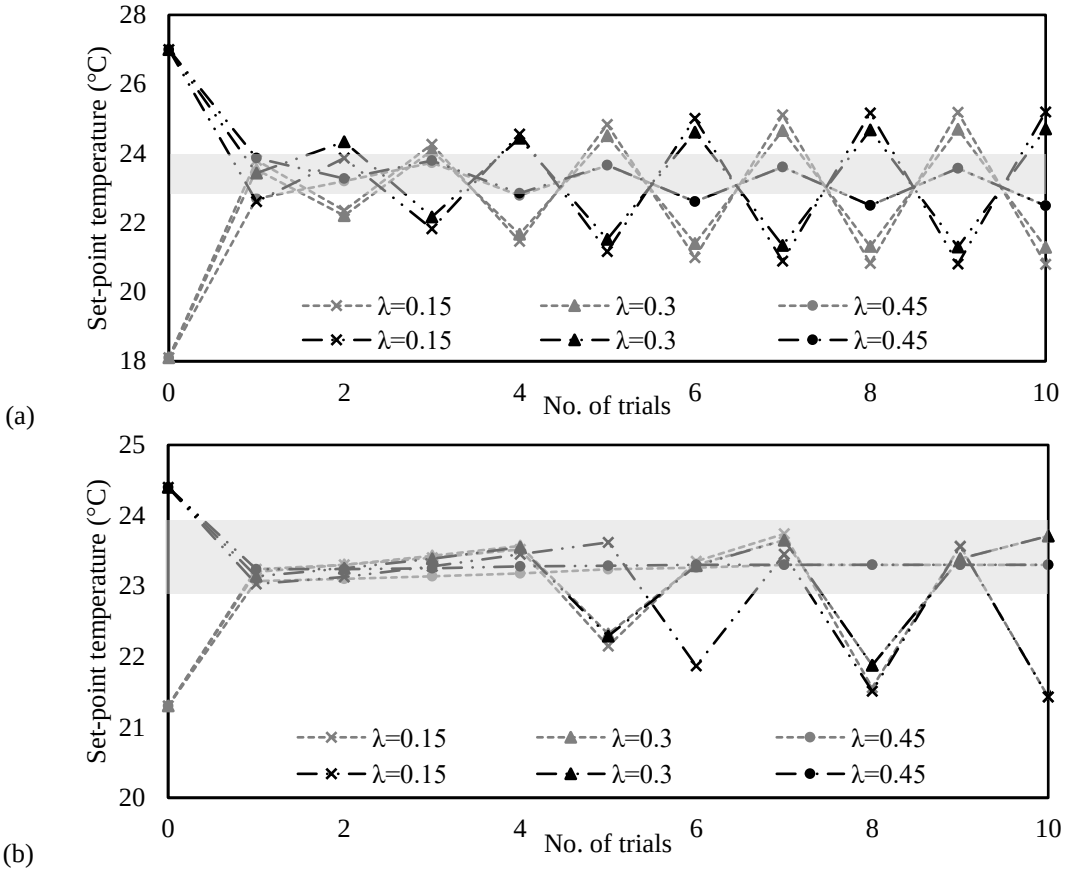

Figure 6. (a) Set-point temperature adjustment using the HABIT algorithm after trials of thermal complaints with (a) k=5℃; and (b) k=10℃. The ideal temperature range of 22.9–23.9°C, derived from the field survey, is highlighted in grey.

Ideally, the set-point temperature would approach the expected neutral temperature of 23.4°C, as indicated by the surveyed. Practically, a temperature range of ±1°C is acceptable. As shown in Figure 6, a small λ, which defines the magnitude of the step change when a complaint is received, resulted in significant fluctuations in the set-point temperature as the optimization process progressed. In some cases, particularly with k=5℃, the set-point temperature not only fell outside the ideal temperature zone but also failed to converge. In contrast, a larger k=10°C mitigated the convergence issue; however, a smaller λ still led to fluctuations in the set-point temperature of up to 4.4℃. Overall, a λ=0.45 is recommended to ensure the stability of the optimization process.

4. CONCLUSION

Indoor environmental quality (IEQ) plays a critical role in influencing the health, comfort, and productivity of building occupants, while also impacting the energy efficiency of buildings. A field study was conducted on campus to measure objective IEQ conditions in air-conditioned classrooms and lecture theatres and gather responses from building occupants. The results indicated occupants were generally satisfied with the perceived environmental conditions. Consistent with findings from previous studies, a broader range of thermal satisfaction was observed compared to the PMV-PPD model. A neutral temperature of 23.4℃ was identified, at which the highest satisfaction level was reported. A negative correlation was found between indoor air quality (IAQ) satisfaction and carbon dioxide (CO_2) concentration, suggesting that satisfaction

could potentially be used as an indicator of IAQ performance. Additionally, high satisfaction levels were noted for lighting, acoustic conditions, and overall IEQ.

Based on the collected data, a dual passive-active approach was adopted, leveraging both occupant thermal sensation data and corresponding physical environmental condition data to determine the optimal indoor set-point temperature within the Humanized Adaptive Baseline Information Technology (HABIT) framework.

Using a Bayesian approach to update the distribution of thermal satisfaction across a fixed range of set-points temperature controls, with observations of thermal complaints, the calculations suggest that, with appropriate implementation of control parameters, the set-point temperature adjusted by the HABIT framework aligns closely with the expected neutral temperature derived from on-site measurements. A small control constant (λ) and temperature control range (k) may lead to significant fluctuations in the set-point temperature, causing it to fall outside the ideal temperature zone and fail to converge. To ensure stability in the calculation process, a control constant λ of 0.45 and temperature control range k of 10℃ are recommended.

This study assessed the efficiency of the HABIT framework based on field study results and simulated complains regarding the thermal condition. Besides, it defined the optimal control parameter for the HABIT algorithm implementation, providing valuable insights into its application for on-site operation in actual building systems with occupant-centric set-point temperature control.

ACKNOWLEDGEMENTS

This research was jointly funded by the Carbon Neutrality Funding Scheme, PolyU (project no. WZ2N), Start-up Fund for RAPs under the Strategic Hiring Scheme, PolyU (project no. 1-BDWZ), and Philip K. H. Wong Foundation (Donation) (project no. 1-52UD).

REFERENCES

Alnuaimi A., Natarajan S., Kershaw T., 2022. The comfort and energy impact of overcooled buildings in warm climates. Energy and Buildings 260, 111938.

ASHRAE, ANSI/ASHRAE 55-Thermal Environmental Conditions for Human Occupancy. Atlanta, GA, USA: American Society of Heating, Refrigerating and Air-Conditioning Engineers (ASHRAE), 2013.

Lee M.C., Mui K.W., Wong L.T., Chan W.Y., Lee E.W.M., Cheung C.T., 2012. Student learning performance and indoor environmental quality (IEQ) in air-conditioned university teaching rooms. Building and Environment 49, 238–244.

Mui K.W., Tsang T.W., Wong L.T., 2020. Bayesian updates for indoor thermal comfort models. Journal of Building Engineering 29, 101117.

Wong L.T., Mui K.W., Fong N.K., 2006. A humanized adaptive baseline information technology (HABIT) algorithm for a building management system. Building Services Engineering Research and Technology 27(4), 341–347.

Wong L.T., Mui K.W., Hui P.S., 2008a. A multivariate-logistic model for acceptance of indoor environmental quality (IEQ) in offices. Building and Environment 43, 1–6.

Wong L.T., Mui K.W., Shi K.L., 2008b. Energy impact of indoor environmental policy for air-conditioned offices of Hong Kong. Energy Policy 36, 714–721.

Yamtraipat N., Khedari J., Hirunlabh J., 2005. Thermal comfort standards for air conditioned buildings in hot and humid Thailand considering additional factors of acclimatization and education level. Solar Energy, Sustainable Energy and Green Architecture 78, 504–517.

Zhang D., Mui K.W., Wong L.T., 2023. Ten Questions Concerning Indoor Environmental Quality (IEQ) Models: The Development and Applications. Applied Sciences 13, 3343.

Zhang S., Cheng Y., Fang Z., Huan C., Lin Z., 2017. Optimization of room air temperature in stratum-ventilated rooms for both thermal comfort and energy saving. Applied Energy 204, 420–431.

6th International Conference on Building Energy and Environment
Eindhoven University of Technology, The Netherlands
6 - 10 July 2025

An occupancy-based framework for efficient heating, ventilation, and air conditioning (HVAC) system control in light commercial buildings

Alexandre Cruz [1*], Mohamed Ouf [1], Mazdak Nik-Bakht, Pierre Paquette[2], Steve Lupien [2]

[1]*Concordia University, Montreal, Canada, alexandre.cruz@mail.concordia.ca*
[2]*Strato Automation, Montreal, Canada*

SUMMARY
This study presents a framework for optimizing HVAC scheduling and setpoint selection through occupancy forecasting. Designed as a generalizable algorithm with adjustable parameters, it adapts to various occupancy patterns. The novelty lies in integrating Kernel Density Estimation (KDE), Random Forest (RF), and Cumulative Relative Frequency (CRF) to predict arrival and departure times, defining three operation modes: occupied, unoccupied, and standby. By leveraging historical and real-time data, the method enhances HVAC control for energy conservation. The framework is evaluated against schedule-based operations in a Montreal case study and validated with an additional case in Vienna. Results highlight the proposed method's effectiveness in predicting arrivals and detecting early departures, reducing standby hours by initiating and shutting down the system later or earlier than the schedule-based operation mode.

Keywords: Occupant-centric control, Energy efficiency, Machine learning, HVAC.

1. INTRODUCTION

Energy demand has reached unprecedented levels, raising growing concerns about environmental sustainability. Buildings play a pivotal role in this debate, accounting for approximately 40% of global energy consumption and one-third of greenhouse gas emissions (Lucon et al., 2023). Heating, Ventilation, and Air Conditioning (HVAC) systems are crucial for maintaining thermal comfort but can consume over 50% of a building's total energy use (World Energy Outlook, 2022). Therefore, optimizing HVAC control sequences presents a key opportunity to reduce energy consumption and support low-carbon transitions.

Advances in smart building technologies, driven by declining sensor and data costs, enhance building performance and enable advanced control strategies (Kim et al., 2023). The Internet of Things (IoT) utilizes sensors to collect real-time data on parameters such as temperature, humidity, carbon dioxide (CO_2) levels, motion (via Passive Infrared - PIR sensors), and Bluetooth or Wi-Fi connections (Van Thillo et al., 2022). Subsequently, control methods can leverage this information to optimize HVAC operations by dynamically adjusting setpoints and ventilation rates based on the number of occupants or eliminating energy use in unoccupied spaces (Qiang et al., 2023). Finally, incorporating occupant behaviour insights into HVAC scheduling can improve thermal comfort, reduce energy use and lower carbon emissions.

1.1 Literature review

Occupant-centric control (OCC) is an indoor climate management approach that integrates occupant-related data, such as presence and comfort preferences, into HVAC system operations (Burak Gunay et al., 2021; O'Brien et al., 2020; Xie et al., 2020). A typical OCC framework consists of three key components: 1) Sensing, where sensors capture occupant-related data; 2) Learning, which identifies patterns, preferences, and behaviors from the data; and 3) Integrating, where these insights inform HVAC control strategies to enhance efficiency (O'Brien et al., 2020). Occupant data modeling is an approach that captures, analyzes, and predicts occupant behavior, preferences, and interactions within built environments. By leveraging data from various sources, these models provide valuable insights for optimizing building operations. For instance, Hobson et al. (2019) developed an Artificial Neural Network (ANN) for occupancy counting system using sensor fusion (Wi-Fi, CO_2 sensors, motion detectors, and electricity load meters) with 83% accuracy. Similarly, Mutis et al. (2020) proposed a vision-based ANN system to estimate occupant numbers and activities with 85% accuracy. Sheikh Khan et al., (2021) used desk-mounted PIR sensors in office spaces, achieving 87.5% accuracy to estimate occupant presence. These occupant data models enable the development of predictive control strategies that enhance energy efficiency while maintaining occupant comfort. Taheri & Razban (2021) used a Multilayer Perceptron algorithm to model CO_2 concentrations and optimize ventilation rates, reducing HVAC fan energy use by 50%. Choi et al. (2021) applied vision-based occupancy counting with a Support Vector Machine (SVM), achieving an 11% reduction in annual HVAC energy for small offices. Wang et al. (2022) used a vision-based camera with an ANN for occupant prediction, potentially lowering HVAC energy demand by 40%. Li et al. (2020) developed an HVAC control approach that adjusts indoor temperatures based on occupancy, saving up to 60% of cooling energy during unoccupied hours. Yang & Becerik-Gerber (2014b, 2014a) explored ANN-based start/stop schedules for office HVAC systems, reducing energy use by 10% through occupancy-driven scheduling.

1.2. Problem statement and main contribution

Although numerous studies acknowledge the importance of occupancy-based control, very few focused on developing generalizable algorithms that integrate occupancy pattern predictions with control sequences for HVAC systems. This study presents a framework for optimizing HVAC scheduling and setpoint selection through occupancy forecasting. Designed as a generalizable algorithm with adjustable parameters, it adapts to various occupancy patterns. The novelty lies in integrating Kernel Density Estimation (KDE), Random Forest (RF), and Cumulative Relative Frequency (CRF) to predict arrival and departure times, defining three operation modes: occupied, unoccupied, and standby. By leveraging historical and real-time data, the method enhances HVAC control for energy conservation. The framework is evaluated against schedule-based operations in a Montreal case study and validated with an additional case in Vienna.

2. METHODOLOGY

2.1. Data description and preprocessing steps

The dataset used in this study is collected from an office located in Montreal, Canada. The office space with approximately 200 m^2 is divided into four main zones: an open-concept office, two small shared offices, and a meeting room (see Figure 1). The dataset consists of motion sensor data gathered from PIR devices installed in each zone, spanning 15 months from January 2022 to March 2023.

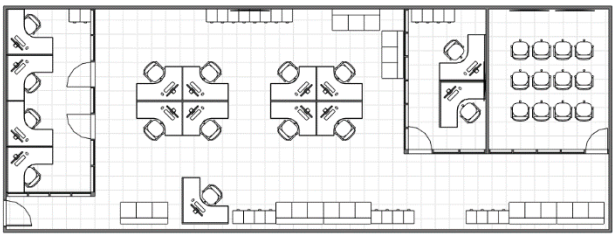

Figure 1. Case study floor plan.

PIR sensors detect movement in 15-minute intervals, providing a binary occupancy status but may miss immobile occupants. To refine occupancy data, zero-motion periods during the first and last daily occupancy events are analyzed. A percentile-based threshold identifies false non-occupancy intervals, which are then corrected to reflect actual occupancy. Furthermore, to facilitate comprehensive data analysis, various statistical methods are applied. Specifically, the analysis included calculating the density distributions of arrivals, and departures.

2.2. Modelling procedure

A total of three techniques are considered—KDE, RF, and CRF—to develop a robust modeling procedure. In this study, KDE is applied to identify dense periods when arrivals and departures are most likely to occur by filtering outliers. Furthermore, this study develops a RF model that predicts daily arrival times leveraging features such as hour, minute, and day of the week. Finally, CRF is applied to estimate the earliest and latest typical arrival and departure times.

2.3. The proposed method

The proposed method defines three distinct HVAC operation modes—occupied, unoccupied, and standby—each with a specific temperature range. By leveraging historical and real-time data, the method enhances HVAC control to promote energy conservation and operational efficiency. Figure 2 presents the flowchart illustrating the proposed method in detail. The KDE method filters the data that will be used by the RF algorithm and the CRF approach, leading to the models being referred to as the KDE-RF model and the KDE-CRF model, respectively.

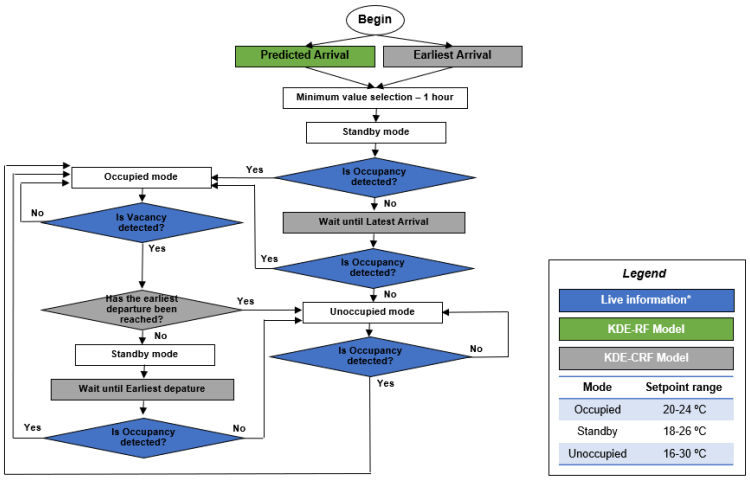

Figure 2. The flowchart of the proposed method.

The proposed method begins by selecting the minimum value from either the KDE-RF model or the KDE-CRF model to initiate standby mode 1 hour prior. This strategy, known as pre-heating or pre-cooling, is designed to prevent discomfort upon occupants' arrival. If occupancy is detected during this period, the system transitions to occupied mode. Otherwise, it remains in standby mode until the latest predicted arrival time, after which it switches to unoccupied mode if no occupancy is detected. Once in occupied mode, the system monitors for vacancy. If a vacancy is detected, it checks whether the earliest departure time has been reached. If so, the system transitions to unoccupied mode; otherwise, it reverts to standby mode, waiting for either the detection of occupancy or the earliest departure time. The framework assumes daily occupancy of the commercial space, meaning it does not account for the ability to predict whether the office space will be occupied or unoccupied on the following day.

2.4. Main algorithm settings

The proposed method is a generalizable algorithm and incorporates seven key parameters: forecasted time range, day selection, training window, dense period threshold, CRF grouping, and arrival/departure percentiles. These parameters define arrival and departure intervals, operating days (weekdays, weekends, or both), modeling period, and common arrival/departure times while filtering outliers. CRF grouping analyzes arrivals and departures by weekday or overall, and percentiles determine the earliest/latest arrivals and earliest departures based on data distribution. Finally, to identify the optimal algorithm settings, a loop is implemented in the proposed method to analyze the output across different thresholds for the latest arrivals and earliest departures, based on the number of weeks.

2.5. Performance evaluation criteria

To evaluate the proposed method, three metrics are established. Table 1 provides an overview of these metrics, including their descriptions and the criteria used for assessment.

Table 1. Evaluation metrics for the proposed method.

Index	Metric	Description	Criteria
1	Arrival accuracy	Measures the accuracy of predicted arrival times.	• Deviation: ±15min and ±30min • Remove days with no occupancy • Remove outliers (KDE)
2	Late arrival frequency	Tracks how often actual arrivals occur after the latest predicted time.	• Deviation: +15min • Remove days with no occupancy • Remove outliers (KDE)
3	Early departure frequency	Measures how often departures occur before the earliest predicted time.	• Deviation: -15min • Remove days with no occupancy • Remove outliers (KDE)

2.6. Comparison of operation modes

To estimate potential energy savings, the proposed method is benchmarked with two operation modes: the current operational system and an idealized optimal operating scenario. The current operational system operates on a predefined schedule. Standby mode begins daily at 6:00 AM to accommodate arrivals, transitioning to occupied mode upon detecting occupancy. For departures, the system remains in standby mode until 5:30 PM or five minutes after the last motion is detected. In contrast, the optimal operating scenario, though idealized and somewhat unrealistic, assumes that standby mode starts exactly one hour before actual arrivals, unoccupied mode begins immediately after the last actual departure, and vacancy days are predicted with perfect accuracy.

While this optimal scenario is unlikely to be fully achievable in practice, it serves as a valuable benchmark for assessing the energy savings potential of the proposed method.

Furthermore, to calculate energy savings, four metrics are established: total savings, arrival savings and departure savings. Total savings metric measures total standby hours saved when using the proposed method, and arrival and departure savings metrics calculates standby hours saved at the start or end of the day, when using the proposed method, respectively.

2.7. Validation of proposed method

To validate the proposed method, a dataset from a university office in Vienna, Austria, is used. The 200 m² space includes six zones: a kitchen, a meeting room, two open-concept offices, and a single office. Motion sensor data was collected from January to December 2013. All previously described steps are replicated for validation.

3. RESULTS

3.1. Data analysis

Figure 3 presents the analysis of arrivals and departures, highlighting distributions using the KDE approach, and weekday-based distributions using the CRF method.

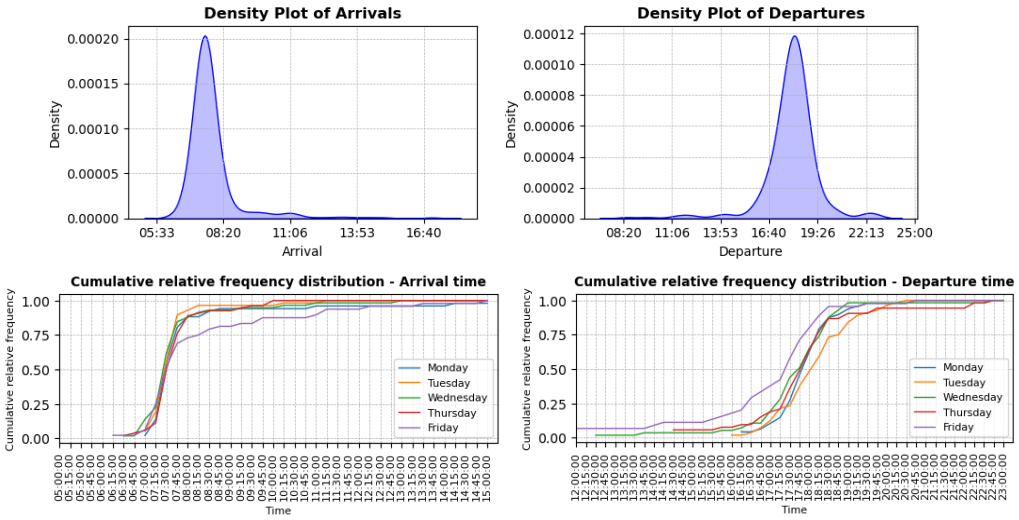

Figure 3. Overview of the dataset.

Figure 3(a) shows that arrivals are concentrated within a narrow time interval, with a sharp peak around 7:00 and 8:00 AM and a few scattered occurrences outside this range. Figure 3(b) presents the CRF curve with arrival distributions remaining consistent across most weekdays, except on Fridays. In contrast, departure events exhibit greater variability, spanning up to five hours compared to the two-hour arrival window. Additionally, departure distributions vary significantly across weekdays, highlighting their more dynamic nature.

3.2. Performance evaluation results

To illustrate the dynamics of the proposed method, Figure 4(a) presents the predicted (blue dots), latest arrivals (red dots), and actual arrivals (green dots), while Figure 4(b) displays the earliest departures (blue dots) and actual departures (red dots).

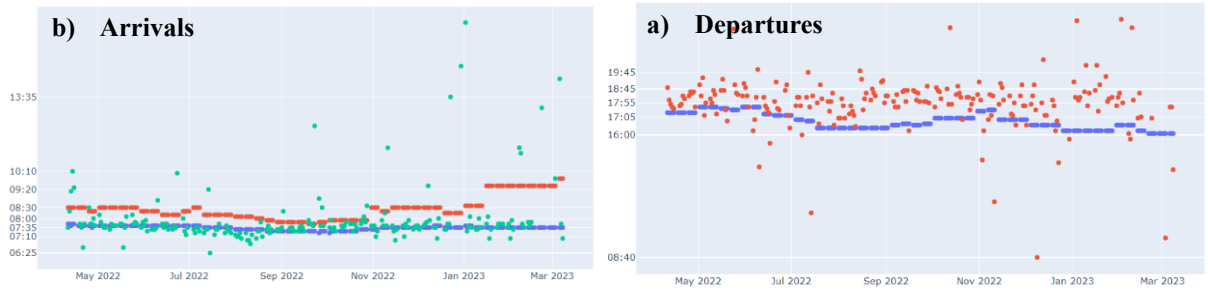

Figure 4. Performance evaluation results: a) Arrivals and b) Departures.

Figure 4 provides valuable insights into arrival and departure patterns over 12 weeks of training. The arrival accuracy shows strong performance, with 98% predicted arrivals falling within ±30 minutes of the actual time and 78% within ±15 minutes, demonstrating the model's reliability. The late arrival frequency of 10%, determined at the 98th percentile, indicating a few occasional discrepancies. For departures, the model shows an early departure frequency of 12%, based on the 10th percentile, highlighting some inconsistencies in early departure events. These results underscore the method's strengths in arrival predictions and identifying early departure events.

3.3 Comparison of operation modes

To estimate potential energy savings, the proposed method is compared with two operation modes. To illustrate the dynamics of each operation mode, Figure 5(a) shows the start times for the optimal operating scenario (blue dots), the current operational system (red dots), and the proposed method (green dots), while Figure 5(b) presents their respective end times.

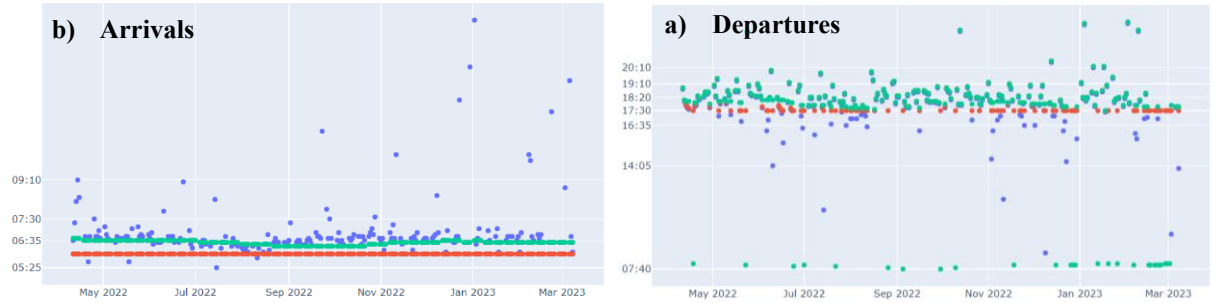

Figure 5. Comparison of operations modes: a) Arrivals and b) Departures.

Figure 5(a) demonstrates that the points corresponding to the proposed method closely overlap with those of the optimal operating scenario for most instances, indicating an efficient and accurate starting time for the HVAC system. In contrast, a noticeable shift is observed between the dots representing the current operating system and those of the other two modes, attributed to the conservative assumptions of building operators. This difference highlights the energy-saving potential achievable when incorporating occupant data into HVAC operation. Similarly, Figure 5(b) reveals instances where the proposed method ends operation early in the day, aligning with

the latest arrival time. On vacant days, the system remains in standby mode until the latest arrival time, and if no occupancy is detected, it transitions to the unoccupied mode. Additionally, the proposed method effectively captures most early departures, allowing the system to switch to unoccupied mode before the default time of 5:30 PM. These results demonstrate how promising the proposed method is for promoting energy efficiency and enhancing HVAC operations. When evaluating total savings, the proposed method reduces standby hours by 57%, equivalent to 299 hours. Of these, 230 hours are saved during arrivals, and 69 hours during departures. However, it is crucial to compare these results with the optimal operating scenario, which, while unrealistic, provides a valuable benchmark for assessing the energy-saving potential of the proposed method. The optimal operating scenario achieves savings of 336 hours during arrivals and 170 hours during departures. Consequently, the proposed method achieves 68% of the savings for arrivals and 41% for departures compared to the optimal operating scenario.

3.4. Algorithm validation

To validate the proposed method, a dataset from a university office in Vienna, Austria, is used, replicating all described steps. Occupants typically arrive between 7:45 and 09:15 AM and depart between 18:00 and 20:45 PM. Moreover, when evaluating the method within this new dataset, arrival predictions achieve 85% accuracy with a 30-minute deviation, late arrivals occur 12% of the time, with an average delay of 95 minutes, and early departures occur 7% of the time, with an average lead time of 38 minutes. Finally, when evaluating total savings, the proposed method reduces standby hours by 47%, equivalent to 472 hours. Furthermore, the optimal operating scenario achieves savings of 553 hours during arrivals and 147 hours during departures. Consequently, the proposed method achieves 71% of the savings for arrivals and 63% for departures compared to the optimal operating scenario. These validation results prove the potential of the proposed method as a generalizable algorithm for promoting energy efficiency and enhancing HVAC operations.

4. CONCLUSION

This investigation proposed a framework to address the stochastic nature of occupancy by analyzing and integrating it into the control sequences of HVAC systems. The framework is designed as a generalizable algorithm with adjustable parameters, enabling it to adapt to diverse occupancy patterns. The results highlight the proposed method's effectiveness in predicting arrivals and detecting early departures for the case study located in Montreal, reducing standby hours by 57% by initiating and shutting down the system later or earlier than the schedule-based operation mode. Additionally, as for the case study located in Vienna, the validation results reported standby hours reduction by 47%, proving the potential of the proposed method as a generalizable algorithm for promoting energy efficiency and enhancing HVAC operations. Future work includes validating the algorithm with new datasets, developing automation strategies to optimize adjustable parameters, creating a framework to capture zone-level dynamics, and deploying it in a real-world case study.

5. REFERENCES

Burak Gunay, B., Member Ashrae, A., Nagy, Z., Miller, C., Ouf, M., & Dong, B. (2021). *Using Occupant-Centric Control for Commercial HVAC Systems TECHNICAL FEATURE*. https://www.ashrae.org/technical-resources/ashrae-journal/featured-articles/using-occupant-centric-control-for-commercial-hvac-systems

Choi, H., Um, C. Y., Kang, K., Kim, H., & Kim, T. (2021). Application of vision-based occupancy counting method using deep learning and performance analysis. *Energy and Buildings*, *252*. https://doi.org/10.1016/j.enbuild.2021.111389

Hobson, B. W., Lowcay, D., Gunay, H. B., Ashouri, A., & Newsham, G. R. (2019). Opportunistic occupancy-count estimation using sensor fusion: A case study. *Building and Environment*, *159*. https://doi.org/10.1016/j.buildenv.2019.05.032

Kim, H., Kang, H., Choi, H., Jung, D., & Hong, T. (2023). Human-building interaction for indoor environmental control: Evolution of technology and future prospects. In *Automation in Construction* (Vol. 152). Elsevier B.V. https://doi.org/10.1016/j.autcon.2023.104938

Li, W., Koo, C., Hong, T., Oh, J., Cha, S. H., & Wang, S. (2020). A novel operation approach for the energy efficiency improvement of the HVAC system in office spaces through real-time big data analytics. *Renewable and Sustainable Energy Reviews*, *127*. https://doi.org/10.1016/j.rser.2020.109885

Lucon, O., Zain Ahmed, A., Akbari USA, H., Bertoldi, P., Cabeza, L. F., Graham, P., Brown, M., Henry Abanda, F., Korytarova, K., Ürge-Vorsatz, D., Zain Ahmed, A., Akbari, H., Bertoldi, P., Cabeza, L. F., Eyre, N., Gadgil, A., D Harvey, L. D., Jiang, Y., Liphoto, E., … Minx, J. (2023). Buildings. In *Climate Change 2022 - Mitigation of Climate Change* (pp. 953–1048). Cambridge University Press. https://doi.org/10.1017/9781009157926.011

Mutis, I., Ambekar, A., & Joshi, V. (2020). Real-time space occupancy sensing and human motion analysis using deep learning for indoor air quality control. *Automation in Construction*, *116*. https://doi.org/10.1016/j.autcon.2020.103237

O'Brien, W., Wagner, A., Schweiker, M., Mahdavi, A., Day, J., Kjærgaard, M. B., Carlucci, S., Dong, B., Tahmasebi, F., Yan, D., Hong, T., Gunay, H. B., Nagy, Z., Miller, C., & Berger, C. (2020). Introducing IEA EBC annex 79: Key challenges and opportunities in the field of occupant-centric building design and operation. *Building and Environment*, *178*. https://doi.org/10.1016/j.buildenv.2020.106738

Qiang, G., Tang, S., Hao, J., Di Sarno, L., Wu, G., & Ren, S. (2023). Building automation systems for energy and comfort management in green buildings: A critical review and future directions. In *Renewable and Sustainable Energy Reviews* (Vol. 179). Elsevier Ltd. https://doi.org/10.1016/j.rser.2023.113301

Sheikh Khan, D., Kolarik, J., Anker Hviid, C., & Weitzmann, P. (2021). Method for long-term mapping of occupancy patterns in open-plan and single office spaces by using passive-infrared (PIR) sensors mounted below desks. *Energy and Buildings*, *230*. https://doi.org/10.1016/j.enbuild.2020.110534

Taheri, S., & Razban, A. (2021). Learning-based CO2 concentration prediction: Application to indoor air quality control using demand-controlled ventilation. *Building and Environment*, *205*. https://doi.org/10.1016/j.buildenv.2021.108164

Van Thillo, L., Verbeke, S., & Audenaert, A. (2022). The potential of building automation and control systems to lower the energy demand in residential buildings: A review of their performance and influencing parameters. In *Renewable and Sustainable Energy Reviews* (Vol. 158). Elsevier Ltd. https://doi.org/10.1016/j.rser.2022.112099

Wang, Z., Calautit, J., Wei, S., Tien, P. W., & Xia, L. (2022). Real-time building heat gains prediction and optimization of HVAC setpoint: An integrated framework. *Journal of Building Engineering*, *49*. https://doi.org/10.1016/j.jobe.2022.104103

World Energy Outlook 2022. (n.d.). www.iea.org/t&c/

Xie, J., Li, H., Li, C., Zhang, J., & Luo, M. (2020). Review on occupant-centric thermal comfort sensing, predicting, and controlling. In *Energy and Buildings* (Vol. 226). Elsevier Ltd. https://doi.org/10.1016/j.enbuild.2020.110392

Yang, Z., & Becerik-Gerber, B. (2014a). Modeling personalized occupancy profiles for representing long term patterns by using ambient context. *Building and Environment*, *78*, 23–35. https://doi.org/10.1016/j.buildenv.2014.04.003

Yang, Z., & Becerik-Gerber, B. (2014b). The coupled effects of personalized occupancy profile based HVAC schedules and room reassignment on building energy use. *Energy and Buildings*, *78*, 113–122. https://doi.org/10.1016/j.enbuild.2014.04.002

6th International Conference on Building Energy and Environment
Eindhoven University of Technology, The Netherlands
6 - 10 July 2025

Influence of environmental control behavior on the air environment in open-plan classrooms of an elementary school in Tokyo

Ayumi Sakuma [1], Go Iwashita [2], Mine Taguchi[3]

[1]*Department of Architecture, Tokyo, Japan, g2481621@tcu.ac.jp*
[2]*Department of Architecture, Tokyo, Japan, iwashita@tcu.ac.jp*
[3]*Department of Architecture, Tokyo, Japan, g2531308@tcu.ac.jp*

SUMMARY
A study on the thermal and air environment of open-plan classrooms in an elementary school in Tokyo, Japan, has been conducted. With the subsidence of the COVID-19 pandemic, it became possible to visit schools during the times when students are present. Therefore, a field survey was conducted where the status of window and door openings, the operation of heating, cooling, and ventilation systems, and the number of students were visually inspected over a full day. By comparing the results of the field survey with the data obtained from monitoring instruments, it was confirmed that differences in window openings had a significant impact on CO_2 concentration. Additionally, despite the air conditioner switches being centralized in one location, it was found that the operation of the air conditioners varied between classrooms.

Keywords: window opening, environmental control behavior, open-plan classrooms

1. INTRODUCTION

In Japan, there are few studies on thermal and air environments in open-plan classrooms. During the COVID-19 pandemic, air environment measurements in school classrooms were primarily conducted through remote monitoring using IoT devices, as visits during times when students were present were avoided. However, in May 2023, with the reclassification of COVID-19 to Category 5, same category as influenza under the Infectious Disease Control Law, restrictions were eased, allowing visits during the hours when students were in the classroom. Consequently, a field survey was conducted with the aim of understanding the relationship between environmental adjustment behavior and the thermal and air environment in open-plan elementary school classrooms.

2. OVERVIEW OF THE MEASUREMENT

The target of the field measurements was three classrooms located on the second floor of F Elementary School (a four-story, reinforced concrete building) in Tokyo. These are open-plan classrooms with no partition walls between the classrooms and the hallway (Figure 1). The air conditioning remote controls and mechanical ventilation system switches are installed on the wall of the open space. The ventilation system is an exhaust-type mechanical ventilation system, allowing only control of airflow (high or low settings). In principle, the system is instructed to operate on high while the room is occupied and on low even when unoccupied, running 24 hours a day. Moreover, the mechanical ventilation system is not operated individually for each classroom

but is controlled collectively for the three classrooms. In Figure 1, the classrooms are labeled U161, U162, and U163 from left to right. The instruments (RTR576, T&D) for CO_2 concentration, room temperature and relative humidity were installed above the blackboard in each classroom. Continuous monitoring using these instruments was conducted at one-minute intervals throughout the year. Long-term continuous measurements of CO2 concentrations showed no significant differences in CO2 concentrations in the three classrooms. The percentage of time that the CO2 concentration standard of 1000 ppm set by the Building Management Act met in December 2023 would be 93.8% for U161, 92.3% for U162, and 90.7% for U163. Since remote measurements without a visit cannot reveal actual residential conditions, we planned to conduct the on-site survey. In the on-site survey, we stayed at the school for a full day and conducted a visual survey of the window and door opening/closing conditions, the operation status of heating, cooling, and ventilation systems, and the number of students in each classroom. The results of this on-site survey were compared with the data obtained from monitoring equipment. The on-site survey was conducted on December 14, 2023. The three classrooms subject to the field measurement were sixth-grade classrooms. The open-plan classrooms being measured had sliding windows, mid-height windows, and transom windows facing the balcony on the south side, and mid-height windows facing the north-side balcony (Figure 2).

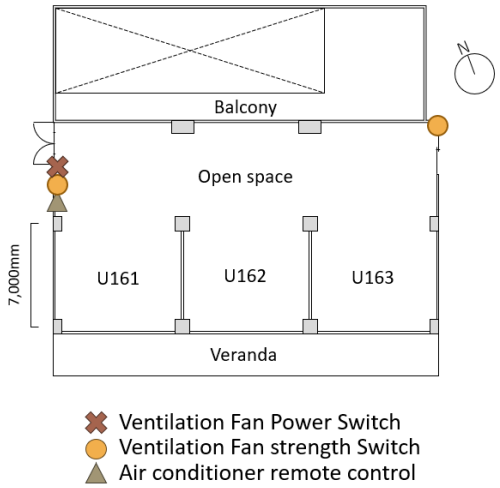

Figure 1. Open-plan classrooms of measurement target

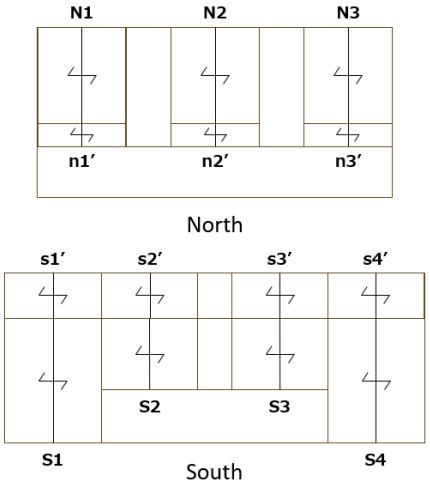

Figure 2. Interior elevation of the windows

3. RESULTS AND DISCUSSION

Table 1 shows the timetable for the day of the on-site survey and the number of students present during class in each classroom. Figure 3 illustrates the window opening ratio for each classroom, and Figure 4 shows the changes in CO_2 concentration over time in each classroom. In Figure 4, a significant difference in the variation of CO_2 concentration between classes and the influence of adjacent classrooms were observed. On the day of the on-site survey, the mechanical ventilation system was continuously operating on high mode, and the doors connecting to the hallway were kept open at all times. One possible factor contributing to the differences in CO_2 concentration between the classes is the variation in window opening ratio. The window opening ratio was defined as the proportion of the window surface area that was open, considering the windows on both the south and north sides, as shown in Figure 2. A window opening ratio of "1" indicates that

all openings were fully open, while a ratio of "0" means that all openings were closed. When looking at the CO_2 concentration trend during the second period in Figure 4, even though both U161 classroom and U162 classroom were unoccupied, there was a noticeable difference in their CO_2 concentrations. The faster decay of CO_2 concentration in U161 can be attributed to its higher window opening ratio, while the higher CO_2 concentration in U162 is likely influenced by its proximity to U163, which had students present. During the third period, when all three classrooms were occupied, the window opening ratio decreased in the order of U161, U162, and U163. Correspondingly, the CO_2 concentration increased in the same order, with U161 having the lowest concentration and U163 the highest. Since the same lesson (theme) was being conducted in all three classrooms during the third period, and the students' activity levels and the number of occupants were similar, it can be inferred that the differences in window opening ratio were a significant factor contributing to the variations in CO_2 concentration. This trend was similar to the difference in the rate of fulfilment of CO2 concentration standards between classrooms obtained from the long-term measurements mentioned above. The on-site survey is useful for investigating the actual situation of window opening and closing

Table 1. Timetable and number of students in the room during the class

Period		1	2	3	4			5	6	
Time	8:25 - 8:40	8:40 - 9:25	9:40 -10:25	10:40 - 11:25	11:40 - 12:25	12:25 - 13:10	13:25 - 13:40	13:40 - 14:25	14:30 - 15:15	15:15 - 15:30
U161	Morning meeting	34	0	34	0	Lunch time	Module learning	34	34	Leaving meeting
U162		0	0	32	0			32	32	
U163		33	33	33	0			33	33	

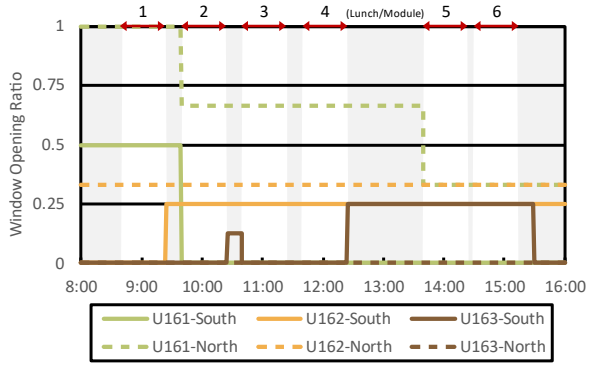

Figure 3. Opening ratio of the south and north windows in three classrooms

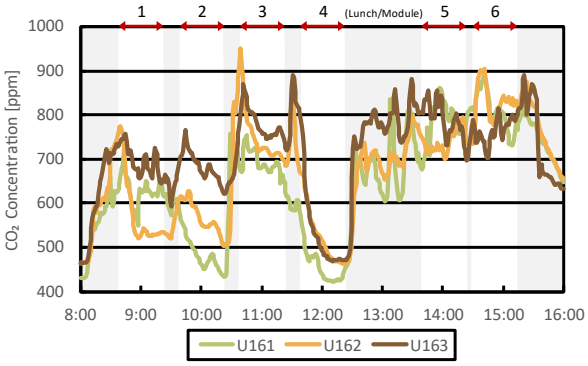

Figure 4. CO_2 concentration in three classrooms

Figure 5 shows the changes in room temperature and outside temperature over time for each classroom, while Figure 6 shows the changes in the set point temperature of the air conditioner for heating (AC) over time for each classroom. From Figure 6, it was confirmed that there were differences in how the AC was operated in each classroom. As shown in Figure 1, the AC switches are grouped together in one location for the three classrooms. Therefore, it was assumed that the air conditioning in the open-plan classrooms was centrally managed until the field survey were conducted. However, in practice, students frequently operated the AC during class in U161, which is the classroom closest to the switch, highlighting a difference in the frequency of AC operation due to the switch's location. Additionally, the results suggest that, in winter, the fluctuation in room temperature is more influenced by the AC set temperature than by the outside temperature. In

U162, where the AC was turned off after the third period, the room temperature remained around 26°C, even though the windows were open. The room temperature shown here was measured at the top of the blackboard (2 meters above the floor), but the air temperature at 10 cm above the floor in U162 also remained within the range of 20-21°C, even after the AC was turned off. Since the recommended room temperature range during winter, according to the School Environmental Health Management Manual (MEXT, 2018), is 18-20°C, it can be considered that the thermal environment is not uncomfortable. One reason the temperature in U162 remained at around 26°C, even with the windows open and the AC off, could be that the AC set temperatures in the adjacent classrooms were 30°C, and air from those classrooms flowed into U162. Furthermore, all three classrooms experienced periods when the room temperature was too high for the winter season, creating an environment unsuitable for learning. To improve the thermal environment, it is important to communicate room temperature conditions to the occupants and to position the AC switches in a location where they can be easily operated by each classroom independently.

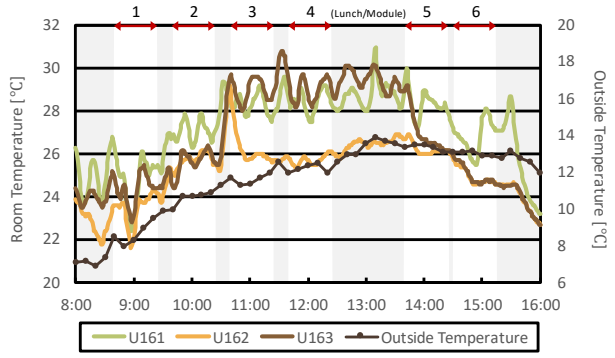

Figure 5. The room temperature in three classrooms with the outside temperature

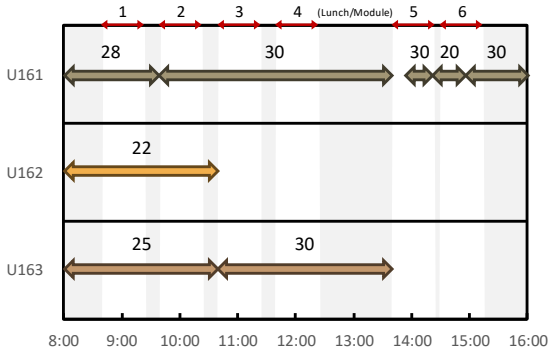

Figure 6. The set point temperature (°C) of the air conditioner for heating in three classrooms

4. CONCLUSIONS

The on-site survey revealed that the frequency of windows open/close had a large impact on the difference among the CO2 concentrations in the three classrooms, even these classrooms had the same floor plan and shared a ventilation system. Additionally, it was found that the frequency of temperature setting changes was affected by the difference in distance from each classroom to the air conditioning switch.

Previous long-term remote measurements have relied solely on measurement data using physical measurement instruments, making it unclear how occupants' behavior affects the indoor air environment. However, the on-site survey of living conditions enabled to understand the impact of occupant behavior on the air environment, complementing the analysis that was unclear during the long-term remote survey.

ACKNOWLEDGEMENTS

This work was supported by JSPS KAKENHI Grant (22H01655).

REFERENCES

Ministry of Education, Culture, Sports, Science and Technology (MEXT): School Health and Safety Act Enforcement Regulations, School environmental hygiene management manual, https://www.mext.go.jp/content/20230817-mext_kenshoku-100000613_2.pdf, 2018.5 (in Japanese)

6th International Conference on Building Energy and Environment
Eindhoven University of Technology, The Netherlands
6 - 10 July 2025

A fast prediction model for indoor temperature distribution based on adaptive spatio-temporal graph convolutional network with limited sensors

Shuqing Wen [1], Weirong Zhang [1]

[1] *Key Laboratory of Green Built Environment and Energy Efficient Technology, Beijing, China, wenshuqing@emails.bjut.edu.cn*
[1] *Key Laboratory of Green Built Environment and Energy Efficient Technology, Beijing, China, zhangwr@bjut.edu.cn*

ABSTRACT
The implementation of non-uniform indoor thermal environments serves as an effective approach to simultaneously enhancing occupant thermal comfort and building energy efficiency. The core of this process lies in the real-time prediction of indoor temperature field. To enable real-time prediction of indoor temperature distribution, this study introduces an adaptive Spatio-temporal Graph Convolutional Network (ASTGCN) model, which operates efficiently with limited sensors. A case study was conducted in an office room in Beijing, where data were collected from 39 measurement points at various spatial locations over a 10-day period. Experimental results indicate that the proposed model, during its operational phase, can accurately reconstruct the temperature distribution across the remaining 32 locations within the space using only 7 fixed sensors. The model achieves a mean absolute error (MAE) of 0.34 °C and an average computation time of 8 s, demonstrating both high accuracy and computational efficiency.

Keywords: temperature distribution, temperature prediction, sensor network, graph convolutional network

1. INTRODUCTION
1.1 Background
A comfortable indoor environment significantly impacts work efficiency and occupant health. Temperature is the most directly perceptible parameter in the indoor environment for occupants and plays a significant role in human comfort. Traditional temperature control methods are based on the assumption of uniformly distributed temperature across the entire space, employing a constant target temperature for regulation[1]. However, due to the influence of factors such as outdoor environmental conditions, building layout, occupant activities, and equipment operation, the actual indoor temperature distribution is non-uniform. Traditional temperature control methods are unable to accurately capture temperature variations in different zones, potentially leading to localized overheating or underheating, thereby compromising occupant comfort. Moreover, traditional control modes typically adjust the entire space uniformly, which may result in significant energy waste. In summary, a single uniform temperature control strategy is insufficient to meet the diverse comfort requirements of occupants and the sustainability goals of buildings. he creation of a non-uniform indoor thermal environment represents an effective strategy for

addressing occupants' personalized comfort needs while enhancing energy efficiency. By selectively regulating the temperature in specific zones, it can effectively meet the comfort requirements of occupants in different areas. Furthermore, by avoiding excessive regulation of the entire space, it significantly enhances building energy efficiency. The key to achieving this goal lies in the acquisition, prediction, and control of indoor temperature parameters. Through precise real-time temperature regulation, it is possible to enhance indoor comfort while minimizing energy waste. Among these, rapidly understanding the patterns of indoor temperature distribution serves as a critical foundation for realizing real-time temperature control.

1.2 Related works

Indoor temperature distribution prediction methods primarily include numerical simulation-based, mathematical model-based, and data-driven approaches. Computational Fluid Dynamics (CFD) employs numerical techniques to simulate physical processes such as airflow, heat conduction, and radiative heat transfer, thereby providing high-precision predictions of temperature distributions. In 1974, Nielsen from Denmark first applied CFD technology in the field of heating, ventilation, and air conditioning (HVAC); since then, CFD has been progressively developed and widely utilized in simulation studies of indoor thermal environments in buildings [2]. For instance, Li et al. [3] used CFD methods to evaluate the indoor thermal environment of a station under three different air conditioning design schemes. Their study assumed a relatively fixed distribution and activity pattern of occupants within the station, although in practical scenarios, occupant distribution and behavior are often dynamic. Nonetheless, when applied to large spaces, CFD is limited by its substantial computational burden and the insufficient availability of field data for validation.

Mathematical models, by employing simplified equations and assumptions, can accelerate temperature prediction and reduce computational costs. In 2009, Zuo and Chen [4] firstly proposed the Fast Fluid Dynamics (FFD) model, which is about 50 times faster than the traditional CFD method. Kato et al. [5] proposed the Contribution Ratio of Indoor Climate (CRI), a metric designed to quantify the contributions of various heat sources and sinks to indoor temperature distribution under steady-state conditions. On this basis, Zhao et al. [6] developed a rapid prediction method for indoor temperature distribution by combining mobile sensors with the CRI methodology. However, their study considered only variations in heat source intensity, limiting its applicability to real-world settings where occupant activities dynamically influence thermal conditions. Furthermore, since the model relies on CFD computations to obtain the CRI, any changes in boundary conditions or heat sources necessitate recalculations, thereby compromising its real-time performance.

With the rapid advancements in computer and sensor network technologies, data-driven algorithms have substantially propelled the field of indoor temperature distribution prediction. Li et al. [7] developed a Room Thermal Reaction Model (RTRModel) and an Airflow Prediction Model (AFPModel). However, since these models were developed using CFD-derived datasets, they might not encompass all possible indoor operating conditions. Minassian et al. [8] deployed microclimate sensors on a university campus in Sydney and, based on the substantial data collected, compared the performance of CNN, LSTM, and CNN-LSTM models for indoor temperature prediction. It is important to note that this study relied solely on indoor sensor data for model training and did not account for the impact of external climatic conditions, occupant

movement, or equipment usage on the indoor temperature distribution. Consequently, data-driven temperature prediction methods, which depend on extensive historical data, may face challenges in practical applications due to the difficulty of acquiring large-scale, high-quality multivariate datasets.

1.3 Research gaps and objectives

In summary, existing research and technologies on predicting non-uniform indoor temperature distribution still face the following research gaps in practical applications. Firstly, Previous studies on indoor temperature distribution prediction are typically based on steady-state indoor environments. The influence of complex internal and external factors on temperature distribution is often overlooked. Secondly, Current data-driven temperature prediction models require extensive historical data to ensure accuracy. However, deploying numerous sensors in practical engineering applications is often infeasible. Therefore, achieving efficient and accurate temperature field prediction with limited sensors remains a critical unresolved issue.

This study aims to provide a solution that enables fast and accurate indoor temperature field prediction while ensuring practical applicability. The main contributions of this study are as follows:

(1) An adaptive spatio-temporal graph convolutional network (ASTGCN) based on limited sensors is proposed for rapid indoor temperature field prediction.

(2) For the first time, an adaptive graph learning-based GCN method is applied to optimal sensor selection for temperature field prediction. The approach dynamically adjusts the sensor network topology through adaptive graph learning and identifies key sensor nodes that contribute significantly to prediction accuracy. During building operation, this method enables high-resolution temperature field prediction using only a limited number of sensors.

2. METHODOLOGY

Indoor temperature is influenced by various thermal disturbances from both inside and outside the building, including solar radiation, outdoor temperature, air conditioning airflow, indoor occupants, and equipment. Spatially, the indoor temperature field is divided into several regular grids, with the temperature within each grid assumed to be uniform. Heat exchange occurs between different grids, and temperature fluctuations in one grid can affect the temperature of adjacent grids. Additionally, the temperature within each grid changes over time. Therefore, indoor temperature distribution exhibits both temporal and spatial dependencies. In this study, sensors are deployed in each grid to investigate the spatiotemporal patterns of indoor temperature distribution under complex thermal disturbances based on long-term monitoring data from these sensors.

2.1 Modeling Framework

In this study, we propose an adaptive spatiotemporal graph convolutional network model that integrates Graph Convolutional Networks (GCN) and Gated Recurrent Units (GRU) for the reconstruction and prediction of indoor temperature distributions, as depicted in the Fig. 1. The overall data processing workflow is divided into three main steps.

Step 1 is data preprocessing. Acquire the time-series data from sensors along with their spatial locations, and perform data preprocessing.

Step 2 is ASTGCN learning module. First, construct the graph structure for all sensor nodes, dynamically adjusting the relationships between nodes based on an adaptive adjacency matrix. Utilize multi-layer Graph Convolutional Networks to aggregate neighborhood information and update node features. Subsequently, based on the graph information generated by the GCN, the historical temperature data of each sensor is fed into a GRU module for temporal feature modeling.

During the model training process, compute the contribution value of each node in the adaptive adjacency matrix, and select nodes with higher contribution rankings. The selected sensors, along with additional sensors, are reintroduced as new input variables into the GCN.

Step 3 is temperature distribution prediction. Fuse the spatial features from the GCN and the temporal features from the GRU, and predict the values of target nodes through a fully connected layer. By consolidating the prediction results of all target nodes, the overall temperature field is obtained.

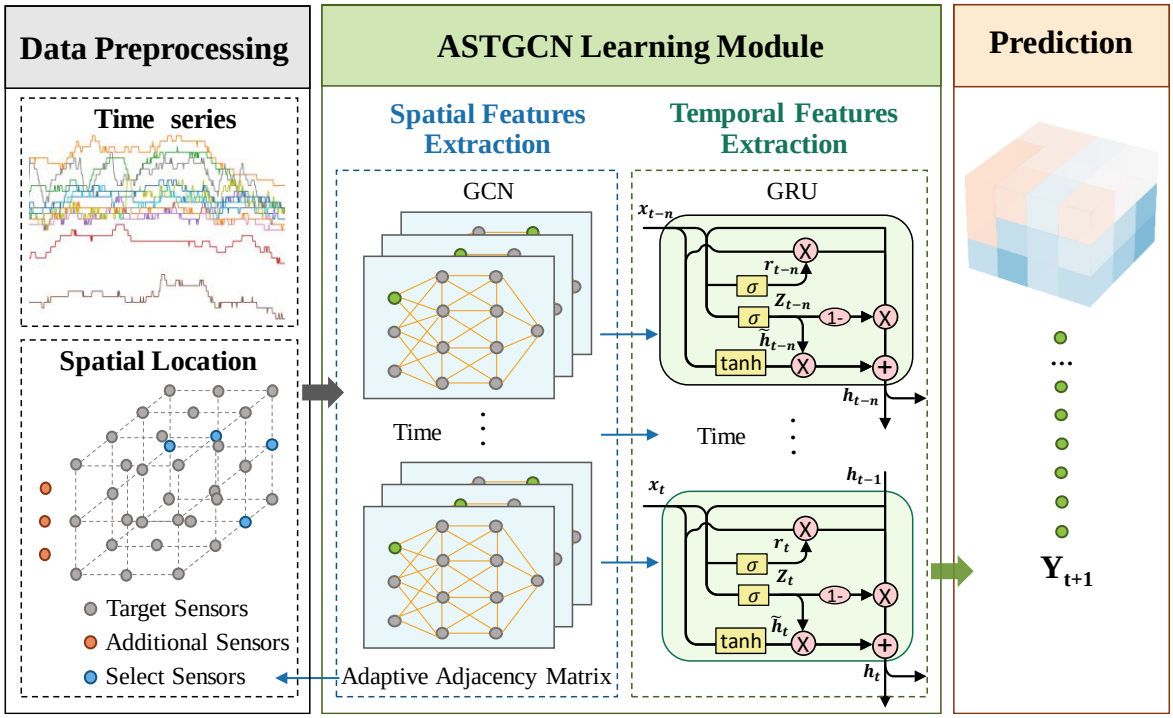

Figure 1. ASTGCN model framework.

2.2 Evaluation Metrics

Three metrics are used to evaluate the performance of the model: Mean Absolute Error (MAE), Mean Squared Error (MSE) and Root Mean Squared Error (RMSE). Their mathematical formulations are given by Eq. (1)-(3).

$$MAE = \frac{1}{n}\sum_{i=1}^{n}\left|y_i - \hat{y}_i\right| \tag{1}$$

$$MSE = \frac{1}{n}\sum_{i=1}^{n}(y_i - \hat{y}_i)^2 \quad (2)$$

$$RMSE = \sqrt{\frac{1}{n}\sum_{i=1}^{n}(y_i - \hat{y}_i)^2} \quad (3)$$

where, y_i represents the actual values, $\hat{y}_i$ represents the predicted values, and n is the number of samples.

3. CASE STUDY

3.1 Experimental settings

The experiment was conducted in an office located in Beijing, with dimensions of 5.4m × 5.2m × 3.4m (length × width × height), which includes two south-facing windows. The internal disturbances of the room include personnel, monitors, a main computer, and a standalone air conditioner. The external disturbances include solar radiation and outdoor temperature. The room was divided into a three-dimensional grid, consisting of 12 points on the horizontal plane and 3 height levels (0.6m, 1.2m, and 2.4m). All these sensors have been measured, calibrated, and assigned unique identification numbers. The Fig. 2 shows the layout details of the measurement points. A total of 39 temperature measurement points were monitored over a 10-day period (from August 30 to September 8), with measurements taken daily from 08:30 to 21:30 at 1minute intervals.

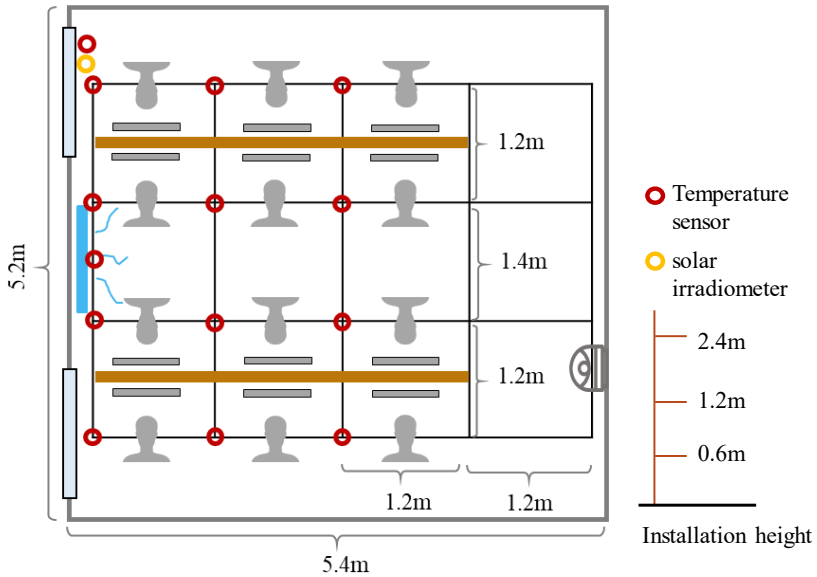

Figure 2. Schematic diagram of sensor installation location.

3.2 Dataset

First, data preprocessing was performed on the dataset, followed by basic visual analysis. Fig. 3 shows the temperature distribution across different height sections of the indoor space at a specific moment. It can be observed that non-uniform temperature distribution exists within the space, with a maximum temperature difference of 2.6 °C. The temperature distribution at the 0.6m

and 1.2m height sections exhibits significant non-uniformity, while the temperature distribution at the 2.4m height section tends to be more uniform. This is because, at the 0.6m and 1.2m heights, the primary heat sources are human occupants and equipment, and human activities have a considerable impact on temperature distribution. At the 2.4m height, the primary heat source is lighting, which is uniformly distributed and typically turned on and off collectively, resulting in a more uniform temperature distribution.

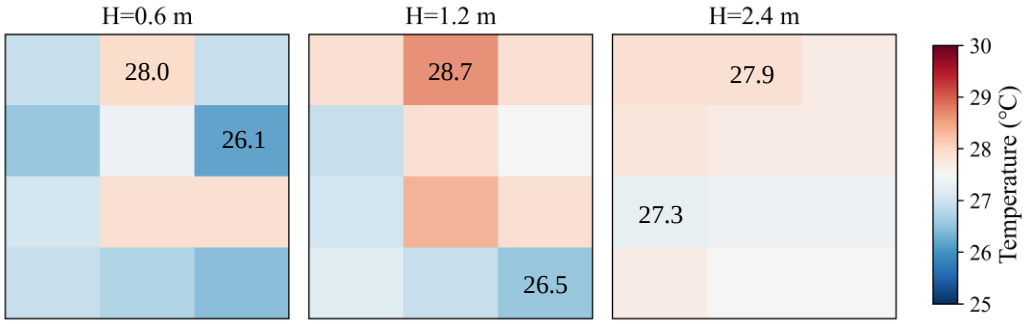

Figure 3. Temperature distribution at different altitudes.

4. RESULTS

4.1 Determination of the number of sensors

To determine the optimal number of sensors required for temperature distribution reconstruction, this study evaluated the model performance using the top 5-10 most contributive sensors as inputs. The model's prediction results are shown in Table 1 and Fig. 4. It can be observed that when 7 sensors were selected, the model achieved the highest average prediction accuracy and the smallest maximum root mean square error, indicating greater stability in the model's predictions. Furthermore, Figure. 3 illustrates that the model also performed well in terms of overall spatial prediction, with the maximum prediction error not exceeding 1.2°C. Therefore, using the historical data from 7 fixed sensors as input to the ASTGCN model yielded the best performance. Subsequent result analysis is based on this model.

Table1. Comparison of prediction results of different sensor numbers

Nodes	MAE (°C)	MSE ($°C^2$)	RMSE (°C)	Max MAE (°C)	Max MSE ($°C^2$)	Max RMSE (°C)
5	0.47	0.32	0.49	1.22	1.5	1.23
6	0.45	0.3	0.47	1.23	1.5	1.23
7	**0.34**	**0.17**	**0.36**	**0.96**	**0.93**	**0.97**
8	0.35	0.18	0.37	0.99	0.99	0.99
9	0.43	0.3	0.45	1.18	1.8	1.34
10	0.43	0.27	0.43	1.17	1.36	1.17

4.2 The predictive performance of the model at different heights

To further analyze the model's prediction performance, comparison charts of prediction accuracy and prediction error heatmaps at different heights were plotted. As shown in Fig. 5, the model exhibits higher prediction accuracy for sensors at a height of 2.4m, while at 0.6m and 1.2m heights, the prediction accuracy for certain sensors is lower. This is likely due to the greater influence of personnel on temperature distribution at 0.6m and 1.2m, leading to larger temperature fluctuations

at different locations. In contrast, the temperature distribution at 2.4m is less affected by heat disturbances, resulting in smaller temperature fluctuations. This is consistent with the characterization of the dataset in Section 3.2.

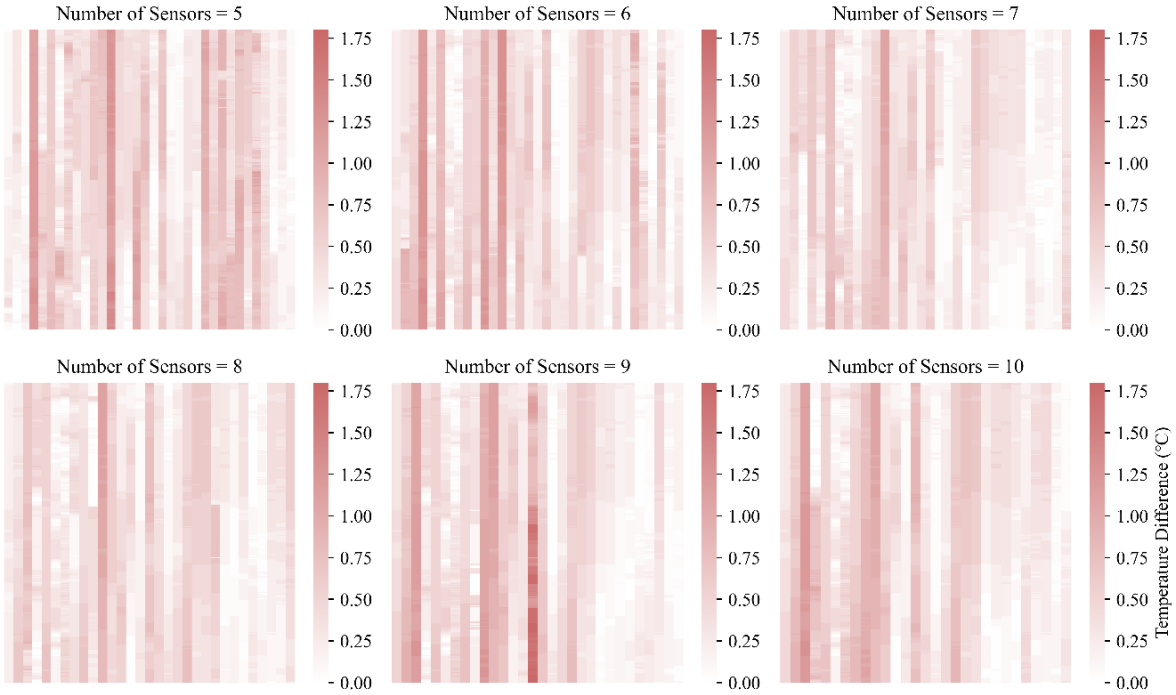

Figure 4. The heatmap of prediction errors for the model under different sensor quantities.

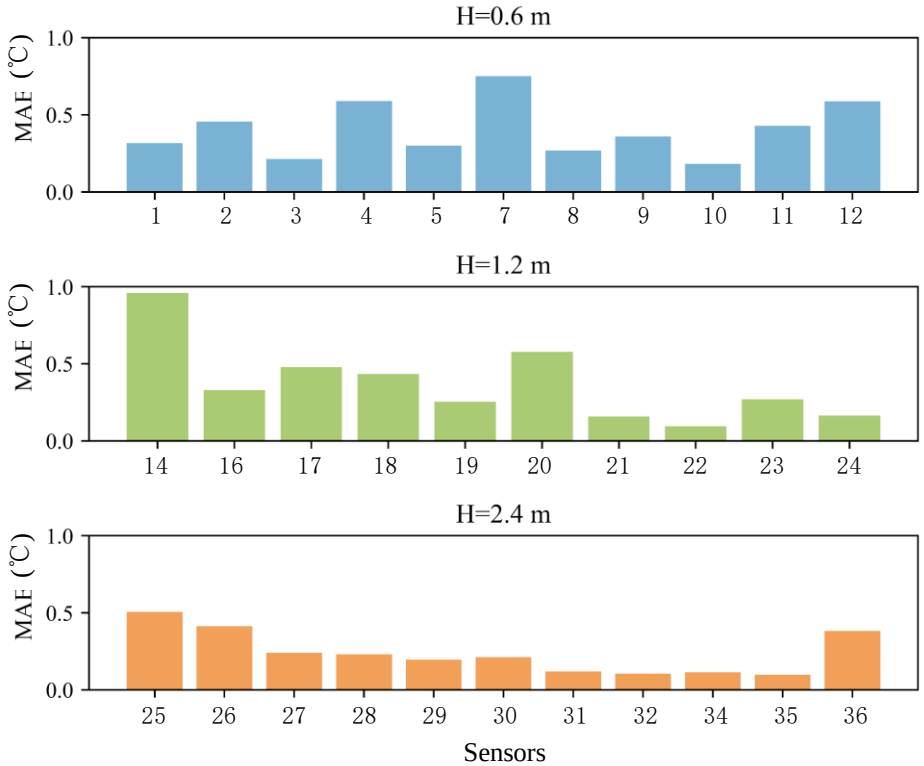

Figure 5. The prediction accuracy of the model at different heights.

5. CONCLUSIONS

This study proposes an ASTGCN model based on a limited sensors to achieve fast and accurate predictions of non-uniform indoor temperature field. First, the ASTGCN module employs an adaptive graph learning mechanism to capture spatial dependencies among sensors. By ranking node weights in the adaptive adjacency matrix, four sensors with significant contributions to temperature field prediction are selected and combined with three additional sensors as model inputs. Subsequently, a GCN is applied at each time step to perform graph convolution operations on the sensor network data, extracting spatial features. The outputs of the GCN are then fed into a GRU to model the temporal evolution of sensor data. Finally, a fully connected layer generates the predicted values for target nodes, reconstructing the indoor temperature field. The performance of the model was validated in a real office building.

The ASTGCN model can automatically identify key sensors that capture thermal sources and boundary conditions from historical data, enabling temperature estimation at unobserved locations based on a limited number of sensors. In the case study office, the model accurately predicted temperatures at 32 unmeasured locations using only 7 fixed sensors. This approach reduces the number of sensors by 82% while achieving high spatial resolution in temperature field reconstruction. Furthermore, compared to the POD-RBF and POD-STGCN models, the proposed model demonstrates superior prediction accuracy and robustness. For the case study office, the model achieves a MAE of 0.34°C. By comparing prediction performance across different heights and locations, the proposed model exhibits greater stability. Therefore, the model effectively addresses indoor environmental challenges under complex and dynamic thermal disturbances.

REFERENCES

[1] Nguyen A T, Pham D H, Oo B L, et al. Modelling building HVAC control strategies using a deep reinforcement learning approach. Energy and Buildings, 2024, 310: 114065.

[2] Li Y, Nielsen P V. CFD and ventilation research. Indoor air, 2011, 21(6): 442-453.

[3] Q. Li, H. Yoshino, A. Mochida, CFD study of the thermal environment in an air-conditioned train station building, Build Environ (2009), pp. 1452-1465.

[4] W. Zuo, Q. Chen, Real-time or faster-than-real-time simulation of airflow in buildings, Indoor Air 19 (2009) 33–44.

[5] S. Kato, S. Murakami, H. Kobayashi, New scales for assessing contribution of heat sources and sinks to temperature distributions in room by means of numerical simulation, in: Proceedings of ROOMVENT'94, fourth international conference on air distribution in rooms, Poland, Krakow, 1994, pp. 539–557.

[6] Y. Zhao, Z. Zang, W. Zhang, S. Wei, Y. Xuan, Predicting indoor temperature distribution based on contribution ratio of indoor climate (CRI) and mobile sensors, Buildings 11 (2021) 458.

[7] Li Y, Pan Y, Huang Z, et al. Numerical modeling of non-uniform indoor temperature distribution for coordinated air flow control. Journal of Building Engineering, 2024, 82: 108246.

[8] Minassian R, Mihăiţă A S, Shirazi A. Optimizing indoor environmental prediction in smart buildings: A comparative analysis of deep learning models. Energy and Buildings, 2025, 327: 115086.

6th International Conference on Building Energy and Environment
Eindhoven University of Technology, The Netherlands
6 - 10 July 2025

Exploring physiological stress responses to different speaking behaviours across various indoor thermal environments

Xuange Zhang [1], Minhyun Lee [1] (CORRESPONDING AUTHOR), Junjiang Luo [1], Xue Cui [1], Mohammad Nyme Uddin [1], Lijie Huang [1], Ruixiaoxiao Zhang [1], Wenjun Gao [1]

[1]*The Hong Kong Polytechnic University, Hong Kong SAR, China, xuange-dante.zhang@connect.polyu.hk*

SUMMARY
To understand the variations in stress levels accompanying changes in thermal environments for different behaviours, this study took speech (continuous speaking) and conversation (intermittent speaking) as examples and conducted an experiment to detect the skin conductance level and skin conductance level fluctuation, which are two objective physiological parameters reflecting stress level, in different thermal sensations across speech and conversation. During the experiment, 30 subjects performed speech and conversation at three temperature settings, and reported their thermal sensation. Mann-Whitney U test was used to analyse the differences in stress levels between speech and conversation. Fitted curves for the two speaking behaviours under changes in thermal sensation were calculated. The results showed significant differences in stress levels between speaking behaviours under some specific thermal sensations, and the fitted curves show different trends in stress levels. The findings contribute to our understanding of the relationship between stress level, thermal comfort and speaking behaviours.

Keywords: Thermal comfort, occupant behaviour, stress level, electrodermal activity

1. INTRODUCTION

Stress has a negative impact on humans' physical and mental health as well as cognitive functions (Marin et al., 2011), and it has been regarded as one of the factors that seriously affect human life in the present generation (Whiteford et al., 2013). Today, human beings face increasing pressure from all walks of life, and more and more scholars are devoted to research on improving stressful situations from different perspectives.

There are many factors that affect stress, with many studies found that there is a relationship between the environment and stress levels, especially in indoor environments (Elsadek & Liu, 2021). As one of the significant perspectives of indoor environments (Wierzbicka et al., 2018), thermal comfort is an essential factor influencing the stress level of the occupants (Yang et al., 2022). In order to explore the stress levels under different thermal environment, many studies have been conducted (Choi et al., 2015; M. Kim et al., 2017). While thermal environmental factors are important, occupant behaviour and mood also influence stress (Koo & Kim, 2018; Lawanont & Inoue, 2018). Most prior studies focused on static conditions, neglecting the impact of occupant behaviours, which limits their real-world applicability. Speaking, a common indoor activity, has been shown to affect thermal comfort (Zhang et al., 2024). This research addresses the gap by analysing stress level variations under different speaking behaviours (continuous speaking and intermittent speaking) across thermal environments.

Stress levels can be measured through subjective questionnaires (Alkatheri et al., 2020; Dogan et al., 2019). or objective physiological signals. Physiological signals, collected using wearable, non-invasive devices, are increasingly favoured for stress measurement. EDA, particularly its tonic component (SCL), has proven effective in detecting stress due to its positive correlation with stress levels (Liu et al., 2020).

This study examines stress variations across thermal sensations during different speaking behaviours (speech and conversation) by analysing SCL, measured via smart wristbands, alongside thermal sensation votes (TSV). Statistical analyses and regression models were employed to explore the relationship between stress and thermal sensations. The findings provide insights into reducing stress in communication-intensive settings and designing low-stress indoor environments.

2. METHODOLOGY

2.1 Data collection

2.1.1. Experimental design and setup

In this study, an experiment has been designed and conducted to collect thermal sensations and their corresponding EDA between speech and conversation behaviours. In order to collect a variety of thermal sensations, this experiment set different temperatures in three identical office rooms quipped with an HVAC system to simulate different thermal environments during autumn. The room simulating the cold environment was set to 20°C, neutral was set to 24°C, and hot was set to 28°C, respectively, according to the room temperature set in the previous study (H. Kim et al., 2022; Shan et al., 2020; Xu et al., 2021). The subjects were asked to simulate continuous speaking (speech) and intermittent speaking (conversation). Environmental factors like air humidity (~55%), air speed (<0.10 m/s), and CO2 concentration (<880 ppm) were strictly controlled, with windows closed and covered for consistency. The neutral room (24°C) served as the preparation and rest area, while the other rooms were set to 20°C (Room 1), 24°C (Room 2), and 28°C (Room 3) based on the experimental design.

A total of 30 volunteers were recruited to participate in the experiment as subjects. The Anthropometrics information of the subjects is shown in Table 1. The subjects were asked to wear a long-sleeved top and trousers, with insulation of 0.61clo according to the ASHRAE 55 standard (American National Standards Institute, 2023) to standardise the clothing insulation level among subjects. Furthermore, to uphold the study's credibility.

Table 1. Anthropometrics of subjects

Variables	Average ± std	Minimum	Maximum
Age (years old)	29.5 ± 14.4	18	56
Body height (cm)	168.8 ± 9.7	153	188
Body weight (kg)	63.6 ± 13.9	43	100
BMIa(kg/m2)	22.1 ± 3.3	15.2	30.9

a BMI: Body mass index = Weight/Height2 (kg/m2)

During the experiment, the subjects were asked to simulate speech and conversation scenarios by reading the speaking materials provided by the organiser. To minimise any potential emotional influence from the content, the materials for both scenarios were kept identical for all subjects.

During the experimental setup, each participant was asked to read aloud from a script provided in the speech materials, simulating a speech context. Meanwhile, pairs of participants were instructed to read through a dialogue from the conversation materials, simulating a conversational context. When simulating the speaking behaviour, the subjects were asked to wear an Empatica E4 wristband to collect the EDA data with the sampling frequency of 4Hz. In the meantime, they were asked to report their thermal sensation regularly by ticking the TSV which is a Likert Scale from -3 to +3, representing cold, cool, slightly cool, neutral, slightly warm, warm, and hot, respectively. This TSV is suggested in ASHRAE 55 to evaluate thermal sensation (American National Standards Institute, 2023).

2.1.2. Experimental procedure

The experimental procedure is outlined in Figure 1. Subjects were paired and, on the experiment day, arrived at a pre-experiment room for 10 minutes of preparation. During this time, their clothing was checked, identification numbers assigned, and instructions provided on the procedure, precautions, and use of the Empatica E4 wristband. Subjects signed consent forms, completed a pre-experiment questionnaire, and randomly selected the order of room temperatures (20°C, 24°C, 28°C).

Figure 1. Experimental procedure timetable

Each subject completed the experiment in three temperature-controlled rooms, with each session lasting 105 minutes. Upon entering a room, subjects underwent 60 minutes of acclimation to stabilize their physiological state, during which the wristband was properly fitted. The order of speaking behaviors (speech and conversation) was also randomly assigned. Subjects then simulated their assigned behavior for 15 minutes, reporting thermal sensation (TSV) every 3 minutes, resulting in five TSVs per behavior. A 20-minute acclimation period separated the two behaviors to allow physiological recovery, after which the second behavior was performed under the same conditions.

After completing both behaviors in one room, subjects returned to the preparation room for a 1-hour break, during which they could remove the wristband and leave briefly if needed. They then repeated the same procedure in the next temperature-controlled room, following the same cycle:

acclimation, two 15-minute behaviors with TSV reporting, and rest periods between transitions. This process continued until all subjects completed the experiment in all three thermal environments.

This procedure ensured the collection of EDA data during speech and conversation under varying thermal sensations across different environments.

2.2 Data processing

A total of 30 subjects contributed to 90 series of EDA samples and 450 TSV results in three temperature settings. The SCL need to be extracted from the EDA data. The Neurokit 2 Python Tool (Makowski et al., 2021) was applied to extract the SCL from EDA data. The fluctuation data of SCL (SCLF) was also obtained by this tool. Then, the interquartile range (IQR) approach was applied to identify outliers, which were then substituted with the average values for that specific subject in that particular state. Since EDA data, as well as SCL data, have significant individual differences, the SCL and SCLF were log-transformed to alleviate this variation.

2.3 Statistical analysis

Statistical analysis was applied to test the differences in SCL and SCLF under different speaking behaviours. The SCL and SCLF were categorised according to the TSV. Firstly, the normality of TSV was tested by the frequency histogram. The results show that the TSV is normally distributed. The Shapiro-Wilk test was applied to test the normality of SCL and SCLF. All the SCL and SCLF data tested by the Shapiro-Wilk test resulted in p-values below 0.05 which rejected the null hypothesis (H_0: The SCL and SCLF data are normally distributed).

Due to the normal distribution situation of SCL and SCLF, the Mann-Whitney U test was used to assess the difference across different thermal sensations. If the Mann-Whitney U tests result in a p-value below 0.05, the alternative hypothesis (H_1: There are significant differences in SCL and SCLF between different speaking behaviours) will be retained. Otherwise, retain the null hypothesis (H_0: There are no significant differences in SCL and SCLF between different speaking behaviours). In addition, polynomial regression fitted curves of SCL and SCLF based on their distribution for 30 subjects under seven scales of thermal sensations have been derived.

3. RESULTS

3.1 Non-parametric test results

Table 2 presents the results of the Mann-Whitney U test, a non-parametric approach to comparing speech and conversation in SCL and SCLF. It has been found that there are significant differences between speech and conversation in some specific thermal sensation levels. To be specific, the p-values of SCL are lower than 0.05 at the thermal sensation levels of -3, -1 and +2, which means that at these levels, the H_1 (There are significant differences in SCL between speech and conversation) was retained. The results of SCL, at other levels of thermal sensation (-2, 0, +1 and +3), retained the H_0 (There are not significant differences in SCL between speech and conversation). For SCLF, the H_1 (There are significant differences in SCLF between speech and

conversation) was retained at the level of -2, -1 and +2 and was rejected at the level of -3, 0, +1 and +3. These results indicate that SCL and SCLF exhibit differently during speech and conversation at various thermal sensation levels. However, significant differences were not observed at all thermal sensation levels. These imply that the thermal sensation levels that minimise SCL or SCLF are different during speech and conversation.

Table 2. Mann-Whitney U test results of SCL and SCLF

	TSV	Group	N	Mean rank	Sum of ranks	Mann-Whitney U	Z	p (2-tailed)
SCL	-3	Speech	28	22.14	620	214	-2.241	0.025*
		Conversation	24	31.58	758			
	-2	Speech	64	52.02	3328	1249	-1.848	0.065
		Conversation	49	63.51	3112			
	-1	Speech	80	96.70	7736	3144	-3.905	0.000*
		Conversation	83	67.83	5630			
	0	Speech	144	143.31	20637	9819	-0.275	0.784
		Conversation	139	140.64	19549			
	+1	Speech	84	78.73	6613	2921	-0.219	0.826
		Conversation	71	77.14	5477			
	+2	Speech	46	46.00	2116	1035	-2.958	0.003*
		Conversation	67	64.55	4325			
	+3	Speech	4	13.25	53	25	-0.806	0.420
		Conversation	17	10.47	178			
SCLF	-3	Speech	28	25.79	722	316	-0.367	0.714
		Conversation	24	27.33	656			
	-2	Speech	64	48.78	3122	1042	-3.048	0.002*
		Conversation	49	67.73	3319			
	-1	Speech	80	95.21	7617	2263	-3.511	0.000*
		Conversation	83	69.27	5749			
	0	Speech	144	140.44	20223	9783	-0.327	0.744
		Conversation	139	143.62	19963			
	+1	Speech	84	71.93	6042	2472	-1.833	0.067
		Conversation	71	85.18	6048			
	+2	Speech	46	45.28	2083	1002	-3.151	0.002*
		Conversation	67	65.04	4358			
	+3	Speech	4	12.75	51	27	-0.627	0.531
		Conversation	17	10.59	180			

Note: * indicates significance level (*p < 0.05). The significance level is based on a 2-tailed Mann-Whitney U between speech and conversation.

3.2 Distribution situation and fitted curves

In order to further explore the statistics results of SCL and SCLF, the data distribution of SCL and SCLF of 30 subjects was plotted separately in the form of boxplots. Based on these data, the multiple linear regression fitted curves of SCL and SCLF following the changes in thermal sensation levels were plotted separately. Figure 2 showed the boxplots and fitted curves of SCL and SCLF.

(a) Skin conductance level of speech and conversation under different thermal sensations and the polynomial regression fitted curves

(b) Skin conductance level fluctuation of speech and conversation under different thermal sensations and the polynomial regression fitted curves

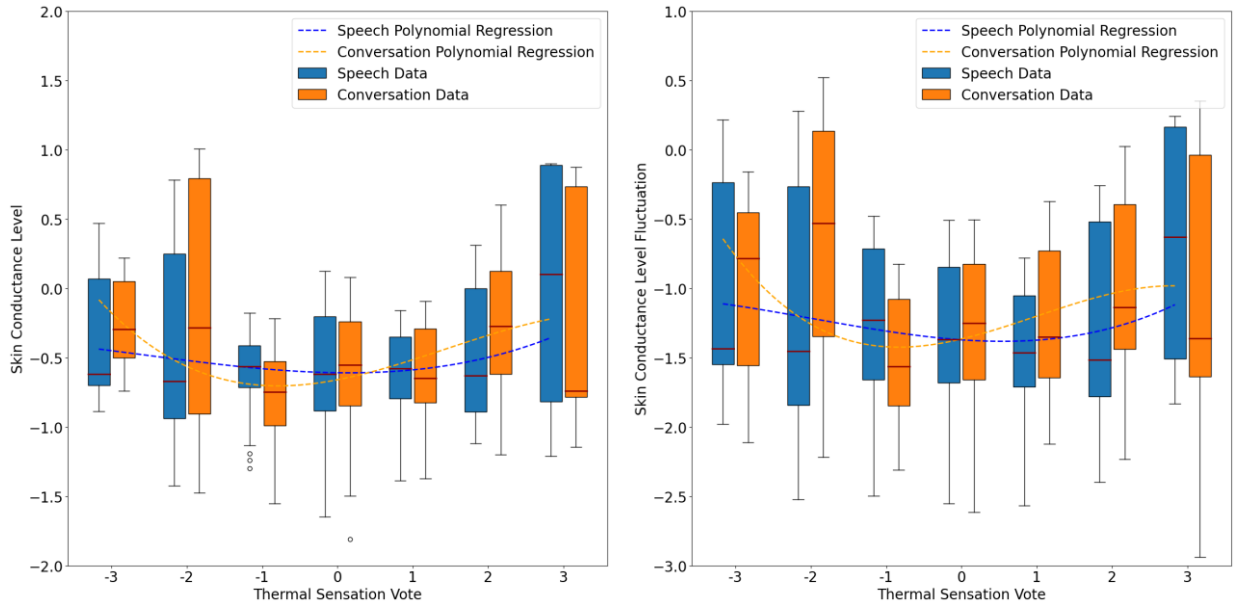

Figure 2. Boxplots and fitted cures of skin conductance level and skin conductance level fluctuation

3.2.1. Data distribution

The box plots provide insights into the distribution of SCL and SCLF across different thermal sensation levels during speech and conversation. For SCL, the IQRs are smaller for thermal sensation levels between -1 and 1, indicating lower variability and more consistent physiological responses near neutral conditions. In contrast, IQRs are larger at extreme levels (-2, +3), showing greater variability in skin conductance. Outliers are more frequent at these extremes, reflecting diverse responses. Median SCL values also vary, with more pronounced differences between speech and conversation at extreme levels (-3, -2, +3), suggesting distinct physiological responses under these conditions.

Similarly, SCLF shows smaller IQRs near neutral sensations (-1 to 1), indicating stable responses during speech and conversation. However, variability increases at extremes (-3, -2, +3), with frequent and more extreme outliers, suggesting heightened sensitivity to thermal extremes. Median SCLF differences between speech and conversation are noticeable at levels -2, 0, and +2, highlighting distinct responses based on activity. Overall, both SCL and SCLF demonstrate reduced variability near neutral conditions and increased variability under extreme thermal sensations, with notable differences between speech and conversation.

3.2.2. Polynomial regression fitted curves

For the SCL fitted curves, the equations represent the relationship between thermal sensation levels and SCL during speech ($\boldsymbol{y_{1s}}$) and conversation ($\boldsymbol{y_{1c}}$) within the -3 to +3 range.

The fitted curve for SCL during speech ($\boldsymbol{y_{1s}}$) is described by Equation (1). The fitted curve for SCL during conversation ($\boldsymbol{y_{1c}}$) is described by the Equation (2).

$$y_{1s} = -0.607 - 0.016x + 0.023x^2 + 0.003x^3 \quad (1)$$

$$y_{1c} = -0.675 + 0.086x + 0.058x^2 - 0.012x^3 \quad (2)$$

For the SCLF fitted curves, the equations represent the relationship between thermal sensation levels and SCL during speech ($\boldsymbol{y_{2s}}$) and conversation ($\boldsymbol{y_{2c}}$) within the -3 to +3 range. The fitted curve for SCLF during speech ($\boldsymbol{y_{2s}}$) is described by the Equation (3). The fitted curve for SCLF during conversation ($\boldsymbol{y_{2c}}$) is described by the Equation (4).

$$y_{2s} = -1.364 - 0.047x + 0.028x^2 + 0.005x^3 \quad (3)$$
$$y_{2c} = -1.385 + 0.109x + 0.064x^2 - 0.018x^3 \quad (4)$$

4. DISCUSSION

This study investigated variations in SCL and SCLF across thermal sensation levels during speech and conversation to understand how stress levels change with thermal sensations and speaking behaviours.The Mann-Whitney U test revealed significant differences in SCL at thermal sensation levels of -3, -1, and +2, indicating that speech and conversation elicit different stress responses. Similarly, SCLF showed significant differences at levels -2, -1, and +2, suggesting that verbal activity affects the stability of stress responses. Higher SCLF values imply greater instability and emotional reactivity. Data analysis showed that SCL variability (IQR) was wider at extreme thermal sensations, except at -3, and narrower near neutral levels (-1, 0, +1). Notably, the IQR at 0 was wider than at -1 or +1, indicating more individual differences at neutral sensations. For speech, individual differences were smaller at -2, while for conversation, they were smaller at +3. Both behaviours had the lowest variability at -1. For SCLF, variability was also lower between -1 and +1, with the lowest variability for speech at +1 and for conversation at -1. Fitted curves showed that SCL and SCLF changed more rapidly during conversation, especially when transitioning from cold to slightly cool. Stress levels and fluctuations were lowest during speech in the slightly warm to neutral range, but for conversation, they were lowest in the slightly cool to neutral range. This highlights that optimal thermal sensations for minimizing stress vary by speaking behaviour.

5. CONCLUSION

Through an experimental investigation, this study reveals significant differences in physiological stress responses, measured through SCL and SCLF, between speech and conversation across various thermal sensation levels. The findings indicate that stress levels in speech and conversation change differently along with the thermal sensation levels. Speech and conversation reach the minimum stress levels and stress level fluctuations at different thermal sensation levels. The individual differences in stress responses are notable depending on thermal sensations. These insights have important implications for designing more comfortable and stress-reducing environments in workplaces and educational settings. By understanding how thermal conditions and communication contexts impact stress, interventions can be tailored to improve well-being and performance of occupants. Further research should explore stress levels at different thermal sensation levels among a wider range of behaviours and activities. Additional perspectives on stress levels and behaviours can be considered in the design of thermal environments.

REFERENCES

Alkatheri, A. M., Bustami, R. T., Albekairy, A. M., Alanizi, A. H., Alnafesah, R., Almodaimegh, H., Alzahem, A., Aljamaan, K., Zurnuq, S., & Qandil, A. M. (2020). Quality of Life and Stress Level Among Health Professions Students. *Health Professions Education*, *6*(2), 201–210. https://doi.org/10.1016/j.hpe.2019.11.004

American National Standards Institute. (2023). Thermal Environmental Conditions for Human Occupancy. In *American Society of Heating, Refrigerating and Air-Conditioning Engineers* (2023rd ed., Vol. 55).

Choi, Y., Kim, M., & Chun, C. (2015). Measurement of occupants' stress based on electroencephalograms (EEG) in twelve combined environments. *Building and Environment*, *88*, 65–72. https://doi.org/10.1016/j.buildenv.2014.10.003

Dogan, D., Bogosyan, S., & Acarman, T. (2019). Evaluation of driver stress level with survey, galvanic skin response sensor data, and force-sensing resistor data. *Advances in Mechanical Engineering*, *11*(12), 168781401989155. https://doi.org/10.1177/1687814019891555

Elsadek, M., & Liu, B. (2021). Effects of viewing flowering plants on employees' wellbeing in an office-like environment. *Indoor and Built Environment*, *30*(9), 1429–1440. https://doi.org/10.1177/1420326X20942572

Kim, H., Jung, D., Choi, H., & Hong, T. (2022). Advanced prediction model for individual thermal comfort considering blood glucose and salivary cortisol. *Building and Environment*, *224*, 109551. https://doi.org/10.1016/j.buildenv.2022.109551

Kim, M., Chong, S. C., Chun, C., & Choi, Y. (2017). Effect of thermal sensation on emotional responses as measured through brain waves. *Building and Environment*, *118*, 32–39. https://doi.org/10.1016/j.buildenv.2017.03.023

Koo, K.-M., & Kim, C.-J. (2018). The effect of the type of physical activity on the perceived stress level in people with activity limitations. *Journal of Exercise Rehabilitation*, *14*(3), 361–366. https://doi.org/10.12965/jer.1836164.082

Lawanont, W., & Inoue, M. (2018). An unsupervised learning method for perceived stress level recognition based on office working behavior. *2018 International Conference on Electronics, Information, and Communication (ICEIC)*, 1–4. https://doi.org/10.23919/ELINFOCOM.2018.8330700

Liu, X., Shan, Y., Peng, M., Chen, H., & Chen, T. (2020). Human Stress and StO2: Database, Features, and Classification of Emotional and Physical Stress. *Entropy*, *22*(9), 962. https://doi.org/10.3390/e22090962

Makowski, D., Pham, T., Lau, Z. J., Brammer, J. C., Lespinasse, F., Pham, H., Schölzel, C., & Chen, S. H. A. (2021). NeuroKit2: A Python toolbox for neurophysiological signal processing. *Behavior Research Methods*, *53*(4), 1689–1696. https://doi.org/10.3758/s13428-020-01516-y

Marin, M.-F., Lord, C., Andrews, J., Juster, R.-P., Sindi, S., Arsenault-Lapierre, G., Fiocco, A. J., & Lupien, S. J. (2011). Chronic stress, cognitive functioning and mental health. *Neurobiology of Learning and Memory*, *96*(4), 583–595. https://doi.org/10.1016/j.nlm.2011.02.016

Shan, C., Hu, J., Wu, J., Zhang, A., Ding, G., & Xu, L. X. (2020). Towards non-intrusive and high accuracy prediction of personal thermal comfort using a few sensitive physiological parameters. *Energy and Buildings*, *207*, 109594. https://doi.org/10.1016/j.enbuild.2019.109594

Whiteford, H. A., Degenhardt, L., Rehm, J., Baxter, A. J., Ferrari, A. J., Erskine, H. E., Charlson, F. J., Norman, R. E., Flaxman, A. D., Johns, N., Burstein, R., Murray, C. J., & Vos, T. (2013). Global burden of disease attributable to mental and substance use disorders: findings from the Global Burden of Disease Study 2010. *The Lancet*, *382*(9904), 1575–1586. https://doi.org/10.1016/S0140-6736(13)61611-6

Wierzbicka, A., Pedersen, E., Persson, R., Nordquist, B., Stålne, K., Gao, C., Harderup, L.-E., Borell, J., Caltenco, H., Ness, B., Stroh, E., Li, Y., Dahlblom, M., Lundgren-Kownacki, K., Isaxon, C., Gudmundsson, A., & Wargocki, P. (2018). Healthy Indoor Environments: The Need for a Holistic Approach. *International Journal of Environmental Research and Public Health*, *15*(9), 1874. https://doi.org/10.3390/ijerph15091874

Xu, Q., Chen, L., Chen, H., & Julien Dewancker, B. (2021). Exercise Thermal Sensation: Physiological Response to Dynamic–Static Steps at Moderate Exercise. *International Journal of Environmental Research and Public Health*, *18*(8), 4239. https://doi.org/10.3390/ijerph18084239

Zhang, X., Lee, M., Cui, X., Huang, L., Zhang, R., & Uddin, M. N. (2024). Thermophysiological responses and thermal comfort of occupants in indoor spaces under different speaking and non-speaking conditions. *Building and Environment*, *260*, 111682. https://doi.org/10.1016/j.buildenv.2024.111682

6th International Conference on Building Energy and Environment
Eindhoven University of Technology, The Netherlands
6 - 10 July 2025

A Comparative Analysis of Pre- and Post-Retrofit Indoor Environmental Quality (IEQ) Conditions and the Impact of Occupant Activities

Sameeraa Soltanian-Zadeh [1], Shayan Mirzabeigi [2,3], Bess Krietemeyer [4], Jianshun Zhang [5,6]

[1]*Syracuse University, Syracuse, NY, USA, ssoltani@syr.edu*
[2]*Syracuse University, Syracuse, NY, USA, smirzabei@syr.edu*
[3]*SUNY College of Environmental Science and Forestry, Syracuse, NY, USA, smirzabeigi@esf.edu*
[4]*Syracuse University, Syracuse, NY, USA, eakriete@syr.edu*
[5]*Syracuse University, Syracuse, NY, USA, jszhang@syr.edu*
[6]*Syracuse Center of Excellence in Environmental and Energy Systems, Syracuse, NY, USA*

SUMMARY
Indoor air quality (IAQ) and ventilation are critical for maintaining healthy and comfortable living environments. Building energy retrofits, typically aimed at reducing energy consumption, must also address the impacts on IAQ, thermal comfort, and occupant behavior. In dormitories and similar residential settings, managing IAQ is particularly challenging due to diverse occupant activities and behavior. Existing ventilation systems, often designed for lower occupancy rates and less airtight building enclosures, may not meet current standards for air exchange and pollutant control. This study examines IAQ and ventilation performance before and after a comprehensive energy retrofit of a two-story multifamily townhouse-style building in Syracuse, New York, USA. By integrating environmental monitoring with occupancy data, the study evaluates the interactions between human behavior and indoor environmental conditions. The objectives are to: (1) assess IAQ and thermal comfort pre- and post-retrofit, (2) analyze the influence of occupant behavior, and (3) provide recommendations for future retrofits. Results show reduced CO_2 levels, changes in PM 2.5 concentrations, and altered window-opening behaviors, highlighting the importance of occupant-centered retrofit strategies.

Keywords: Indoor Air Quality, Thermal Comfort, Building Retrofit.

1. INTRODUCTION

Indoor air quality (IAQ) and thermal comfort are fundamental components of creating healthy, productive, and sustainable living environments, particularly in university dormitories where diverse occupant behaviors introduce unique challenges. Poor IAQ and thermal dissatisfaction have been linked to adverse health outcomes, including respiratory issues and mental discomfort (Coggins et al., 2024). Energy retrofits have gained prominence as a strategy for improving building sustainability by reducing energy consumption. However, these retrofits also have a profound impact on indoor environmental quality (IEQ), influencing factors such as air quality, thermal comfort (Coombs et al., 2016; Synnefa et al., 2017), and ventilation effectiveness. Studies show that retrofits can enhance occupant health and comfort by stabilizing indoor temperatures and reducing exposure to pollutants. Yet, the success of these interventions is intricately tied to occupant behavior, preferences, and activities, which often go overlooked in retrofit design and evaluation (Liu et al., 2022).

Existing ventilation systems in older dormitory buildings often fail to meet the needs of modern occupancy patterns and activities (Mannan & Al-Ghamdi, 2021). Behaviors such as window opening, vent blocking, and smoking can significantly alter air exchange rates, pollutant concentrations, and energy performance (Elsayed et al., 2023). For instance, studies have shown that 87% of air change rate (ACR) variability in residential settings can be attributed to occupant actions like opening doors and windows (Ortiz et al., 2020). These findings underscore the need for the analysis of retrofit strategies that account for the dynamic interplay between human behavior and building systems to achieve holistic improvements in IAQ and thermal comfort.

This study investigates the impact of energy retrofits on IAQ and thermal comfort in a university dormitory in Syracuse, NY. By comparing pre- and post-retrofit conditions and incorporating data on occupant behaviors, the research aims to provide a comprehensive understanding of how human activity shapes indoor environments of retrofitted buildings. The objectives are threefold: 1) to assess IAQ and thermal comfort before and after retrofits; 2) to analyze the influence of occupancy patterns and occupant behaviors on these conditions; and 3) to develop recommendations for retrofit strategies that promote both energy efficiency and occupant health. By bridging the gap between technical retrofit measures and behavioral insights, this study contributes to the development of strategies for optimizing IAQ and thermal comfort in residential environments. The findings will help inform future retrofits, ensuring they are designed with a holistic understanding of the complex interactions between building systems, occupant activities, and environmental conditions.

2. METHODS

This study focuses on the analysis of a two-story multifamily townhouse-style building located at Syracuse University's South Campus. The building was originally constructed between 1972 and 1973 and comprises eight two-bedroom units. Each unit accommodates two students, resulting in a total occupancy of 16 students. It was equipped with baseboard heaters and had no air conditioning (AC) nor mechanical ventilation before the retrofit. The building was retrofitted with exterior insulation and air-sealing, ceiling-mounted fan coil units in each living room and bedroom to replace the baseboard heaters and provide both heating and cooling, and energy recovery ventilation (ERV) systems in each unit.

Figure 1 illustrates the diagram for real-time building performance monitoring system which was installed during the pre-retrofit stage of the research (Mirzabeigi et al., 2024). The full description of this approach is provided in Mirzabeigi et al., (2024). The monitoring system includes unit-level interior monitoring for all apartments, measuring IAQ parameters, air temperature, humidity, and motion. Additionally, two units were equipped with detailed monitoring of window and door opening activities; these units are referred to as "research units" throughout the study. Weather data was also collected to provide additional context.

Indoor sensors were installed to measure air temperature, Relative Humidity (RH), concentrations of CO_2, TVOC, and PM 2.5, PM 10, motion, and door/window open and close status. Additionally, we collected various outdoor physical parameters including air temperature, RH, solar radiation and wind intensity and direction, CO_2, TVOC, and PM 2.5, PM 10. IAQ data was collected at 5-minute intervals, and window/door status was recorded based on the exact time of each opening/closing event using magnetic sensors. Motion sensor data was collected at 5-minute intervals, with immediate data transmission triggered upon motion detection. Measurements began

one year prior to retrofitting, with the building undergoing retrofits during the summer of 2024. Monitoring is planned to continue for at least one year following the retrofit to assess changes in indoor environmental quality and building performance.

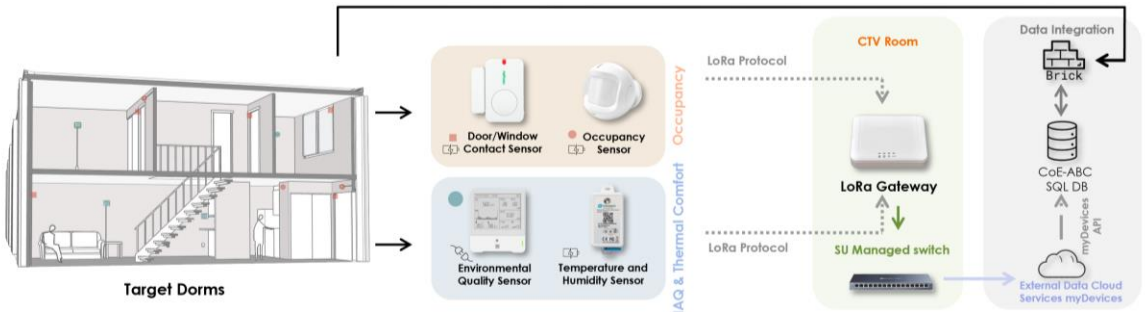

Figure 1. Conceptual diagram for real-time performance monitoring.

The data was analyzed using the Python environment, utilizing various packages and libraries such as NumPy (Harris et al., 2020), scikit-learn (Baranwal et al., 2019) and SciPy libraries. To assess the impact of the retrofit on indoor environmental quality, independent sample t-tests (Welch's t-tests) were conducted to compare pre- and post-retrofit hourly averaged data for CO_2 concentration, PM 2.5 levels, indoor air temperature, and relative humidity. Analyses were performed for two groups: (1) selected spaces in two representative research units (A-7 and A-8), and (2) all living rooms across the monitored units (A-1 through A-8). Welch's t-test was used to account for unequal variances between groups. A p-value threshold of 0.05 determined statistical significance. For the preliminary analysis of occupant thermal comfort, indoor temperature and humidity data were examined. A temperature range of 20–23 °C for winter and 23–26 °C for summer was used as the comfort quantification criteria, while a range of 35–55% for winter and 40–60% for summer was applied for humidity per ASHRAE Standard 55. For data from the window/door contact sensors, a post-processing step converted the data into a time series format indicating open and closed conditions. Then, we looked at the correlation on how the window/door status activity changed the indoor environment (e.g., CO_2 as an indication of ventilation). We looked at patterns of change of CO_2 during the day (weekdays and weekends) to understand how occupant activities affected various indoor air quality. For comparing PM 2.5 concentration for the pre- and post-retrofit, the data were categorized into six pre-defined classes based on EPA guidelines, enabling a clearer comparison of changes.

3. RESULTS AND DISCUSSION

The data analysis presented in this section represents a subset from the overall data collection period. Selected time periods are shown as examples, as post-retrofit data collection is still ongoing. A comprehensive analysis of the full dataset is beyond the scope of this paper. The analysis compared pre- and post-retrofit conditions to evaluate changes in thermal comfort, IAQ, and occupant behavior. Figure 2 shows the pre- and post-retrofit measured data from various spaces of two research units, during the warm and cold seasons, represented on the psychrometric chart. During warm weather, pre-retrofit temperatures reached up to 24 °C, while for the post-retrofit, the temperatures remained mostly within the comfort range. In cold weather, pre-retrofit temperatures reached close to 31 °C, indicating overheating. In contrast, post-retrofit temperatures were more comfortable. Overall, pre-retrofit conditions exhibited higher variability in temperature and humidity for both summer and winter scenarios, whereas post-retrofit conditions were more stable and controlled.

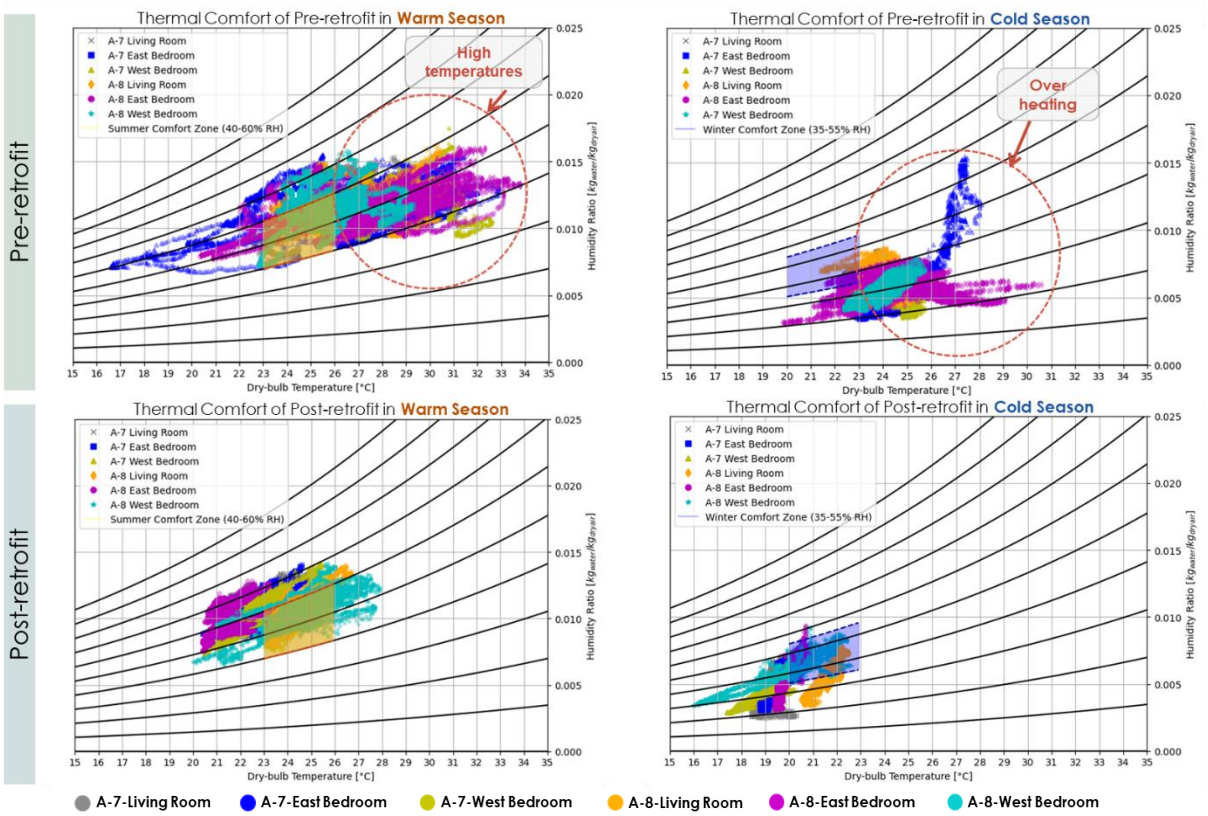

Figure 2. Indoor thermal condition for pre- and post-retrofit.

Figure 3 shows the average hourly CO_2 concentration for the two research units, categorized by weekdays and weekends. Higher concentrations were observed in the bedrooms compared to the living room, with elevated levels were also noted during weekends when occupants spent more time in their units.

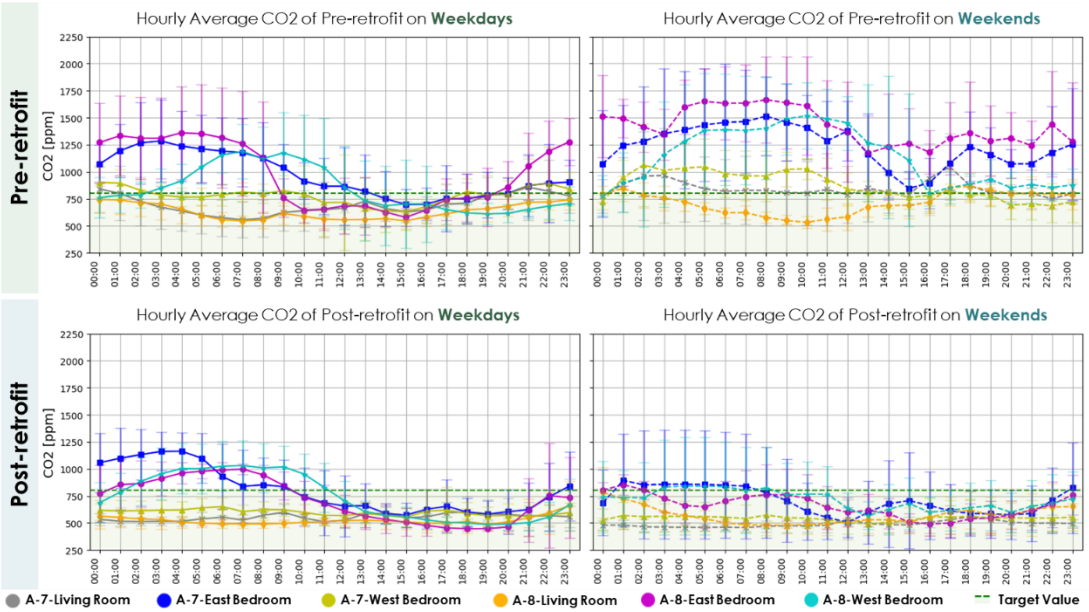

Figure 3. Hourly average CO_2 for pre- and post-retrofit (the whisker lines show the data variability).

During sleep hours, pre-retrofit CO_2 concentrations in one of the bedrooms exceeded 2000 ppm. However, post-retrofit, these concentrations have significantly decreased to below 1400 ppm.

Figure 4 shows the sample of PM 2.5 concentrations in the living rooms of three units before and after the retrofit. Each cell represents the average hourly PM 2.5 concentration. Concentration patterns varied among the units due to differences in indoor activities and occupant behavior. Additionally, as shown in Figure 5, overall PM 2.5 concentrations were lower following the retrofit, with an increased frequency of PM 2.5 levels falling within the 0–12 μg/m³ range. This improvement is attributed to enhanced ventilation, which helps reduce indoor PM 2.5 concentrations, particularly when the pollutant source is indoors, and the ventilation air is filtered. Occupant behavior also played a significant role, as different individuals occupied the units before and after the retrofit. Outdoor PM 2.5 concentrations were also considered in the analysis. Furthermore, it has been observed that the PM 2.5 decay rate has increased post-retrofit, which may impact the overall indoor air quality and its ability to recover after exposure to elevated pollutant levels.

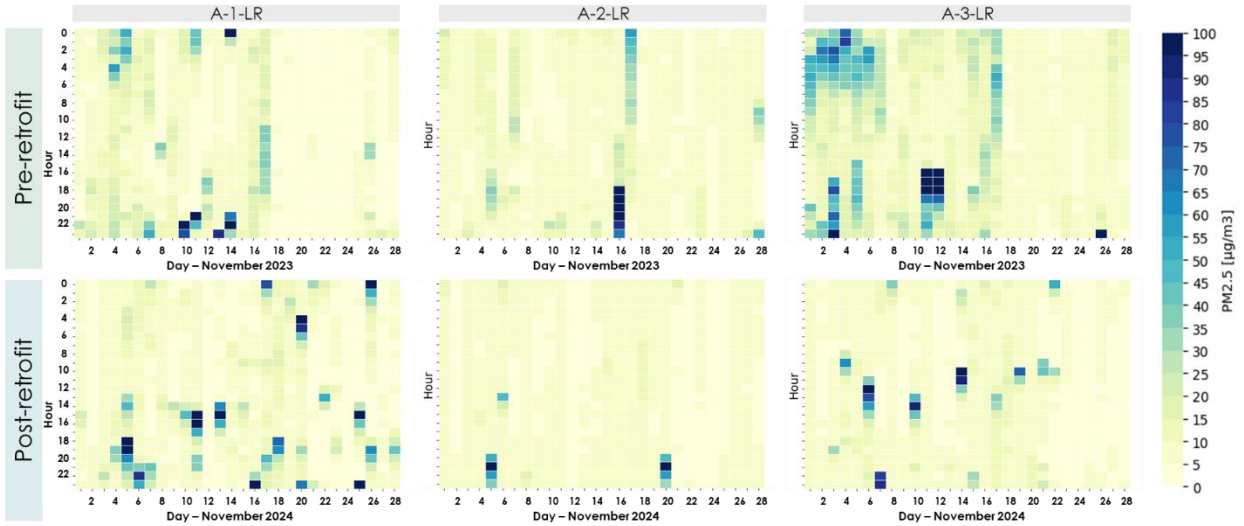

Figure 4. Sample data plots of PM 2.5 concentrations across three units pre- and post-retrofit for November.

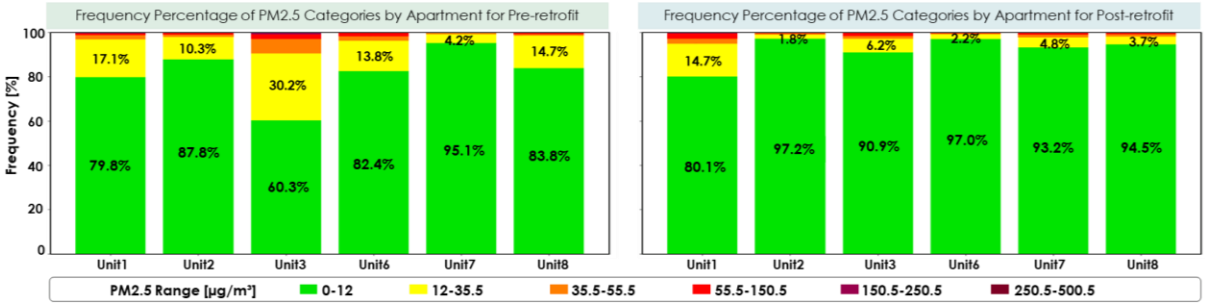

Figure 5. Frequency percentage of PM 2.5 categories by apartment for pre- and post-retrofit.

Figure 6 presents an example of window-opening behavior for two bedrooms in one of the monitored units. Pre-retrofit data are represented in green, while post-retrofit data are shown in blue. The size of each bubble indicates the duration for which the window remained open. During

the pre-retrofit period, occupants tended to open windows more frequently and for longer durations, particularly at higher indoor and outdoor temperatures, compared to the post-retrofit period. This behavior change suggests that the retrofit reduced the need for occupants to rely on window openings for cooling or ventilation. A similar trend was observed in the second research unit, where contact sensors monitored window activity.

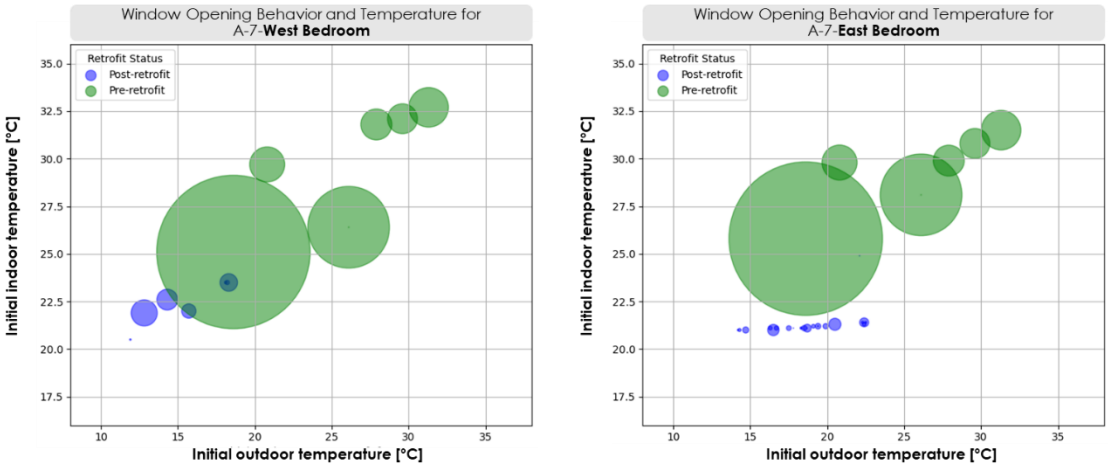

Figure 6. Window opening behavior pre-retrofit (green) and post-retrofit (Blue)

The air change rate (ACR) in the east bedroom was calculated using the decay method for both closed and open window scenarios during the pre-retrofit period. ACR was analyzed for one of the bedrooms under both pre- and post-retrofit conditions. For the pre-retrofit, window-opening behavior significantly influenced the ACR. Approximately 64% of the total ACR when the window is open is attributable to occupant window opening, highlighting the pivotal role of occupant actions in enhancing natural ventilation. For the post-retrofit, the average ACR increased by 87% compared to the pre-retrofit period, primarily due to the addition of mechanical ventilation systems, which provided consistent airflow and improved overall ventilation. Additional data collection is required to calculate the ACR for post-retrofit periods with open windows. This would allow for a direct comparison of the effect of occupant window-opening behavior on ACR in post-retrofit conditions, further clarifying the interplay between mechanical ventilation and natural ventilation.

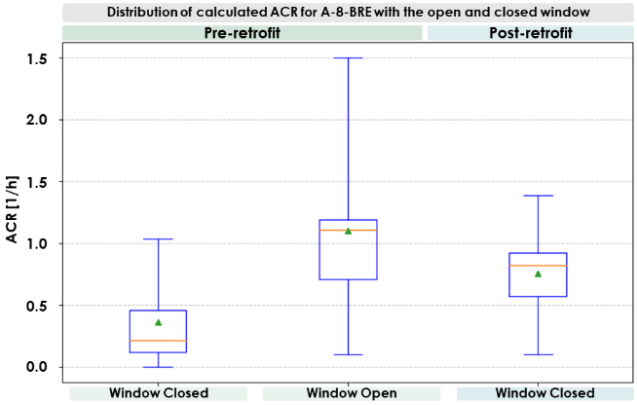

Figure 7. Calculated ACR for one bedroom and the effect of window opening.

Independent sample t-tests were conducted to compare pre- and post-retrofit indoor environmental quality parameters (CO_2, temperature, humidity, and PM 2.5) across two groups of residential spaces (spaces in research units and A-1 to A-8 living rooms). The results showed statistically significant differences ($p < 0.05$) for all parameters in both groups, indicating that the retrofit measures had a substantial impact on changing indoor air quality and thermal conditions.

4. CONCLUSION

This study highlights the critical role of energy retrofits in improving IAQ and thermal comfort in university dormitories, while also emphasizing the importance of integrating occupant behaviors into retrofit strategies. By comparing pre- and post-retrofit conditions in the dormitory building in Syracuse, NY, we observed notable improvements in IAQ and thermal comfort, including reduced CO_2 levels, lower PM 2.5 concentrations, and more consistent temperature and humidity levels. The results also reveal the significant influence of occupant activities on IAQ outcomes. Variations in window-opening behavior were closely linked to changes in ventilation rates, and this behavior changed before and after the retrofit. For instance, while retrofits improved baseline IAQ metrics, occupant behaviors such as extended window openings during specific temperature ranges had a profound impact on air exchange rates and pollutant dynamics. These findings align with prior research indicating that retrofit benefits are limited without addressing occupant-related factors (Luo et al., 2019; Zhong & Ridley, 2020). The analysis demonstrates that achieving optimal IAQ and thermal comfort in residential environments requires a holistic approach that combines technical interventions with behavioral insights. Retrofit designs that focus solely on building envelope and mechanical improvements risk unintended consequences, such as inadequate pollutant control or thermal dissatisfaction, if occupant behavior is not adequately accounted for. To maximize the benefits of energy retrofits, future efforts should incorporate the following recommendations:

1. Retrofit strategies must consider the preferences and habits of occupants, particularly regarding ventilation and window usage, to enhance overall effectiveness. For example, conducting pre-retrofit surveys and collecting measured data can reveal how often occupants open windows and their preferred ventilation practices. This information allows designers to tailor interventions—such as optimizing mechanical ventilation settings or improving natural airflow—that align with actual occupant behavior, ultimately balancing energy efficiency with comfort.
2. Promoting awareness among residents about the impact of their behaviors on IAQ can lead to better outcomes, as seen in prior studies that reduced pollutant exposure through targeted education (Noris et al., 2013). For example, engaging residents before and after the retrofit—through workshops, surveys, and interactive sessions—can educate them about how their daily actions (such as window usage, cleaning practices, or product choices) affect IAQ. This proactive approach not only informs residents but also gives them a sense of ownership over the process, leading to sustained improvements in air quality.
3. Continuous monitoring of IAQ, thermal comfort, and occupant activities can provide real-time feedback to guide adaptive management and improve building performance over time. Continuous monitoring should ideally span a minimum of one year. This timeframe ensures that seasonal variations in indoor air quality, thermal comfort, and occupant activities are captured, providing a comprehensive dataset for adaptive management and performance improvement.
4. Combining expertise from architecture, engineering, environmental science, and behavioral studies—and importantly budgeting the time and cost to integrate expert input early on—will enable the development of retrofits that align energy efficiency goals with occupant health and comfort.

In conclusion, while energy retrofits enhance building performance, their success depends on addressing the complex interplay between human behavior, building systems, and environmental conditions. By bridging this gap, future building energy retrofit initiatives can create healthier, more comfortable, and sustainable living environments that meet the diverse needs of occupants.

Acknowledgments

"This research was performed under an appointment to the Building Technologies Office (BTO) IBUILD- Graduate Research Fellowship administered by the Oak Ridge Institute for Science and Education (ORISE) and managed by Oak Ridge National Laboratory (ORNL) for the U.S. Department of Energy (DOE). ORISE is managed by Oak Ridge Associated Universities (ORAU), and ORNL is managed by UT-Battelle LLC. All opinions expressed in this paper are the author's and do not necessarily reflect the policies and views of DOE, EERE, BTO, ORISE, ORAU, ORNL or UT-Battelle. ORISE is managed by ORAU under DOE contract number DE-SC0014664, and ORNL is managed by UT-Battelle LLC under DOE contract number DE-AC05-00OR22725" and the data analyzed for this presentation is collected under the project "Integrated Whole-Building Energy Efficiency Retrofit Solution for Residences in Cold/Very Cold Climates" Award Number DE-EE0009060 funded by the U.S. Department of Energy under the Advanced Building Construction with Energy Efficient Technologies and Practices (ABC) initiative.

REFERENCES

Baranwal, A., Bagwe, B. R., & M, V. (2019). Machine Learning in Python. 12, 128–154. https://doi.org/10.4018/978-1-5225-9902-9.ch008

Coggins, A. M., Hogan, V., Mishra, A. K., Norton, D., Foster, D., Wemken, N., Cowie, H., & Doherty, E. (2024). Energy retrofits: Factors affecting a just transition to better indoor air quality. *Indoor Environments*, *1*(4), 100058. https://doi.org/10.1016/j.indenv.2024.100058

Coombs, K. C., Chew, G. L., Schaffer, C., Ryan, P. H., Brokamp, C., Grinshpun, S. A., Adamkiewicz, G., Chillrud, S., Hedman, C., Colton, M., Ross, J., & Reponen, T. (2016). Indoor air quality in green-renovated vs. non-green low-income homes of children living in a temperate region of US (Ohio). *Science of the Total Environment*, *554–555*, 178–185. https://doi.org/10.1016/j.scitotenv.2016.02.136

Elsayed, M., Romagnoni, P., Pelsmakers, S., Castaño-Rosa, R., & Klammsteiner, U. (2023). The actual performance of retrofitted residential apartments: post-occupancy evaluation study in Italy. *Building Research and Information*, *51*(4), 411–429. https://doi.org/10.1080/09613218.2022.2121908

Harris, C. R., Millman, K. J., van der Walt, S. J., Gommers, R., Virtanen, P., Cournapeau, D., Wieser, E., Taylor, J., Berg, S., Smith, N. J., Kern, R., Picus, M., Hoyer, S., van Kerkwijk, M. H., Brett, M., Haldane, A., del Río, J. F., Wiebe, M., Peterson, P., … Oliphant, T. E. (2020). Array programming with NumPy. Nature, 585(7825), 357–362. https://doi.org/10.1038/s41586-020-2649-2

Liu, S., Jian, Y., Liu, J., Guo, R., & Zhu, W. (2022). Associating occupants' interaction with windows with air change rate –One case study. *Building and Environment*, *222*. https://doi.org/10.1016/j.buildenv.2022.109387

Luo, N., Weng, W., Xu, X., Hong, T., Fu, M., & Sun, K. (2019). Assessment of occupant-behavior-based indoor air quality and its impacts on human exposure risk: A case study based on the wildfires in Northern California. *Science of the Total Environment*, *686*, 1251–1261. https://doi.org/10.1016/j.scitotenv.2019.05.467

Mannan, M., & Al-Ghamdi, S. G. (2021). Indoor air quality in buildings: A comprehensive review on the factors influencing air pollution in residential and commercial structure. In *International Journal of Environmental Research and Public Health* (Vol. 18, Issue 6, pp. 1–24). MDPI AG. https://doi.org/10.3390/ijerph18063276

Mirzabeigi, S., Soltanian-Zadeh, S., Krietemeyer, B., Dong, B., Wilson, N., Carter, B., & Zhang, J. (2024). Towards Occupant-Centric Building Retrofit Assessments: An Integrated Protocol for Real-time Monitoring of Building Energy Use, Indoor Environmental Quality, and Enclosure Performance in Relationship to Occupant Behaviors. *ASHRAE Annual Conference 2024*.

Noris, F., Adamkiewicz, G., Delp, W. W., Hotchi, T., Russell, M., Singer, B. C., Spears, M., Vermeer, K., & Fisk, W. J. (2013). Indoor environmental quality benefits of apartment energy retrofits. *Building and Environment*, *68*, 170–178. https://doi.org/10.1016/j.buildenv.2013.07.003

Ortiz, M., Itard, L., & Bluyssen, P. M. (2020). Indoor environmental quality related risk factors with energy-efficient retrofitting of housing: A literature review. *Energy and Buildings*, *221*. https://doi.org/10.1016/j.enbuild.2020.110102

Synnefa, A., Vasilakopoulou, K., Kyriakodis, G. E., Lontorfos, V., De Masi, R. F., Mastrapostoli, E., Karlessi, T., & Santamouris, M. (2017). Minimizing the energy consumption of low income multiple housing using a holistic approach. *Energy and Buildings*, *154*, 55–71. https://doi.org/10.1016/j.enbuild.2017.07.034

Zhong, X., & Ridley, I. A. (2020). Verification of behavioural models of window opening: The accuracy of window-use pattern, indoor temperature and indoor PM2.5 concentration prediction. *Building Simulation*, *13*(3), 527–542. https://doi.org/10.1007/s12273-020-0615-4

6th International Conference on Building Energy and Environment
Eindhoven University of Technology, The Netherlands
6 - 10 July 2025

Resident-oriented energy saving measures: performance assessment of a warm room for apartment buildings

Iris Loche [1], Carolina Recart [1], Lenneke Kuijer [2], Roel Loonen [1]

[1] *Department of the Built Environment, Eindhoven University of Technology, The Netherlands, i.m.costa.fajardo.werneck.loche@tue.nl*
[2] *Department of Industrial Design, Eindhoven University of Technology, The Netherlands*

SUMMARY
This study quantifies the energy-saving potential of the warm room strategy, focusing renovation efforts on the living room of an apartment building. The warm room strategy proved most beneficial for corner apartments on the top floor, reducing heating loads by up to 41%, depending on residents' setpoint preferences. Results confirm that the warm room strategy can be viable when aligned with residents' heating practices, despite its effectiveness being often dismissed when decisions rely on standard occupancy. Future research could explore the impact of lower indoor temperatures on unheated rooms and assess residents' receptiveness to the warm room concept to expand its potential application in renovation projects.

Keywords: energy transition, thermal compartmentation, occupant behaviour, building performance simulation

1. INTRODUCTION

Efforts to integrate dwellings into the energy transition face significant challenges, primarily due to the mismatch between retrofit technologies and the diverse energy practices of residents (Furman; Hadjri, 2025). Current renovation strategies prioritize deep envelope insulation and upgrading of ventilation and heating systems, in line with European and national energy efficiency standards (European Commission, 2024; NTA 8800:23, 2024; RVO, 2021). However, these approaches often rely on standardized assumptions about thermal comfort, neglecting the variability in residents' heating practices. This oversight leads to energy savings that tend to be lower than expected after renovations, driven by prebound and rebound effects, undermining the effectiveness of energy renovations in achieving sustainability goals (van de Brom et al., 2019).

Recent research highlights a disparity between professional assumptions of uniform indoor heating norms and the diverse heating practices of residents (de Koning et al., 2024; van Wieringen et al., 2025). Field studies conducted with households in two Dutch municipalities by de Koning et al. (2024) and van Wieringen et al. (2025) highlight the importance of residents' know-how and preferences in keeping themselves warm. Residents reported that, instead of heating the entire dwelling, they prefer to keep the living room as a warm space for relaxation, while rarely heating the bedroom. They enjoy sleeping in a cooler, "fresh" environment, as it creates a pleasant contrast with the warmth of their blankets (De Koning et al., 2024; van Wieringen et al., 2025). Understanding residents' heating practices allows for a revaluation of space usage by distinguishing between areas with higher comfort demands and those with lower comfort requirements (Verbeeck; Bosserez, 2021).

The concept of energy sufficiency has emerged as an alternative to energy efficiency, suggesting a shift from a building-centred to a resident-oriented approach. It emphasizes providing sufficient

energy services that align with residents' heating practices, while avoiding unnecessary oversupply (Fawcett; Darby, 2018). Considering the residents' preference for warmer living rooms and cooler bedrooms, focusing renovation efforts on the living room to create a warm room offers a promising strategy for advancing energy sufficiency in renovation projects. The approach of warm room was previously tested by Rovers et al. (2020) in a field study involving three Dutch terraced houses, demonstrating improved thermal performance of the dwelling after renovating the living area. Building on this, the current study aims to quantify the energy-saving potential of applying the warm room strategy to an apartment building. This study considers two types of apartments (corner and middle) across three levels (ground floor, middle floor, and top floor), considering three profiles of heating practices (only the living room heated pre-retrofit and a wider range of setpoint preferences).

2. METHODS

1.1 Reference building

A 'typical' medium-rise apartment was selected as a reference building, based on Guerra-Santin et al. (2017) (Figure 1a). The representative building consists of three floors: ground (with a crawl space), intermediate, and top. It includes two apartment types: corner units and central units (Figure 1b). Constructed in the 1960s, the building was poorly insulated at the time of construction, The building envelope characteristics were selected based on the Voorbeeldwoningen 2022 (RVO, 2022), described on Figure 1c.

a) Reference building

b) Apartment floor plan

Envelope component	U-value (W/m².K)
External walls	1.64
Flat roof	1.55
Internal wall	1.69
Ventilation type	Natural ventilation
Infiltration	0.7 ACH

c) Construction characteristics

Figure 1: Reference building based on Guerra-Santin et al. (2017).

1.2 Warm room and residents' heating practices

The initial concept of thermal compartmentation, proposed by Rovers et al. (2020), involved insulating both external and internal walls of the living room to isolate it from all the neighbouring rooms within the dwelling. However, an important finding from the building performance simulations conducted in the present study is that insulating internal walls results in negligible energy savings, and heat in the living room can be retained by simply closing doors. Additionally, modest heat flow between the heated living room and the rest of the dwelling can be considered as beneficial. From a technical perspective, we proposed cavity insulation for the main external walls of the living room and bedroom, interior insulation along the living room's external wall in corner apartments, and the replacement of single-pane windows with triple-glass windows exclusively in the living room, as detailed in Figure 2a and 2b.

To capture the variability in residents' heating practices in Dutch social housing, quantitative data was extracted from the Energy Module of the national WoON2018 database (BZK, 2018). Residents were considered to heat only their living room, as 60% of the residents in the database reported that bedrooms are cooler spaces and are rarely heated. Three setpoint preferences were selected to represent (i) high temperatures throughout the whole day, (ii) evening peak, and (iii) a case with lower setpoints (Figure 2c) .

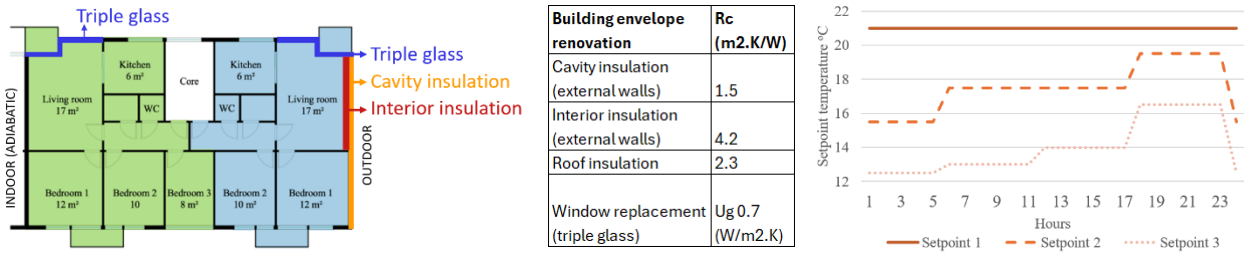

Building envelope renovation	Rc (m2.K/W)
Cavity insulation (external walls)	1.5
Interior insulation (external walls)	4.2
Roof insulation	2.3
Window replacement (triple glass)	Ug 0.7 (W/m2.K)

a) Warm room b) Thermal properties c) Setpoint preferences

Figure 2: Warm room setting and setpoint preferences

1.3 Building performance simulations

Building performance simulations were performed using EnergyPlus. The envelope materials for the reference case and the energy saving measures were modelled as described in Figures 1 and 2. Annual building simulations were performed using a typical meteorological year derived from the period between 1996 and 2015 in De Bilt, the Netherlands (NEN 5060, 2018) Two key performance metrics were defined to evaluate the efficiency of the warm room: heating demands (kWh/m^2.year) and reduction in heating demands (%).

3. RESULTS

The warm room strategy showed to be more beneficial for the corner apartment on the top floor, with greater opportunities for insulation improvements in the living room. In this apartment, the warm room concept reduced heating load by 35% for setpoint 1 and 2 and 41% for setpoint 3. For apartments on the ground and 1st floor, the percentage of reduction in heating demands was similar for all three setpoints, with improvements ranging from 17% to 22% for central apartments and 29% to 32% for corner apartments. The heating loads required to heat the living room is strongly influenced by residents' setpoint preferences. For instance, heating loads for setpoint 1 is three times higher than for setpoint 3, both before and after renovations.

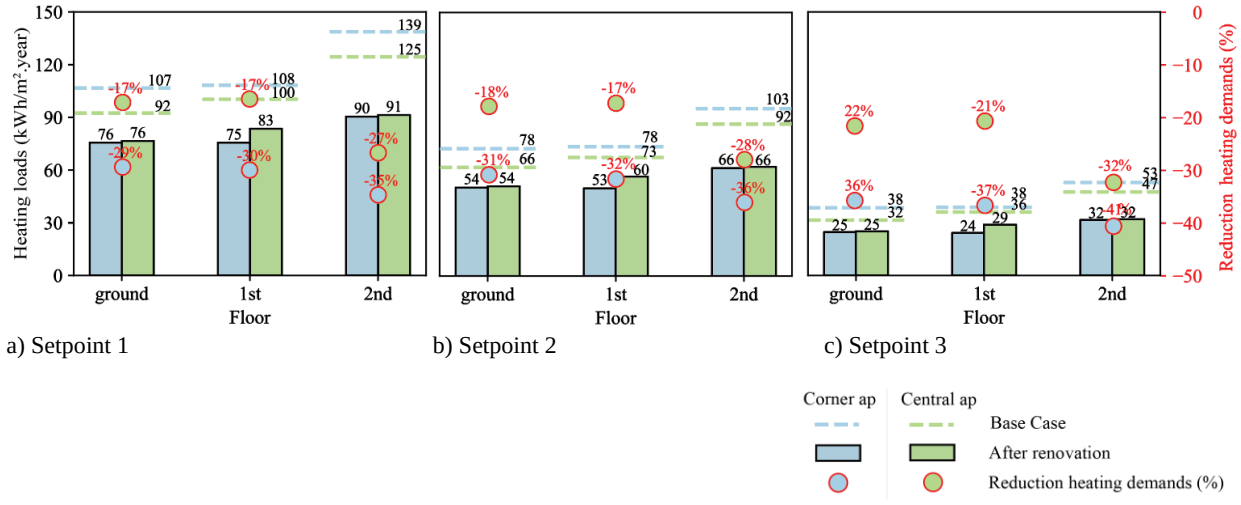

a) Setpoint 1 b) Setpoint 2 c) Setpoint 3

Figure 3: Heating loads and energy savings

These findings suggest that, even though the warm room can achieve up to 41% in reduction of

heating loads, the setpoint preferences also plays an important role in energy savings. Additionally, although energy renovations focused on the entire apartment are more likely to lead to heating in other rooms, the warm room strategy can be considered as a measure against less conscious heating behaviours, that could lead to rebound effects.

4. CONCLUSIONS

This study aimed to quantify the energy-saving potential of the warm room strategy for an apartment building, considering two apartment types (corner and middle) across three levels (ground floor, middle floor, and top floor), and exploring three profiles (living room heated only pre-retrofit, and a broader range of setpoint preferences). This study identified an optimal configuration for the warm room: cavity insulation in the external wall, interior insulation in the living room's external wall, window replacement with triple glazing in the living room, and no insulation for the internal walls, as it was found to have a negligible effect on energy savings. The warm room strategy was shown to be an effective and more sustainable solution when aligned with residents' heating practices. However, it is often dismissed as a viable solution when decisions are based on standard occupancy and uniformly heated dwellings, therefore not complying with insulation regulations. The efficiency of this approach depends on residents' behaviour, being effective if other rooms in the house remain unheated. Future research could explore the impact of lower indoor temperatures on the hygrothermal performance of unheated rooms and assess residents' receptiveness to the warm room concept, thereby expanding its potential application in renovation projects.

ACKNOWLEDGEMENTS

This research is part of the Just Prepare project funded by the Dutch Research Council (NWO) in the KIC-call ‘Energietransitie als maatschappelijk-technische uitdaging’. Project Number KrcH 1. ED03.20.001.

REFERENCES

BZK, 2018. Energiemodule woON 2018.

De Koning, P. et al, 2024. Close a door to open a window: Unpacking strategies and know-how in making comfortable. In: DIS’24, Copenhagen, Denmark, pp. 3129-3144.

European Commission, 2024. Energy Performance of Buildings Directive, https://energy.ec.europa.eu/topics/energy-efficiency/energy-efficient-buildings/energy-performance-buildings-directive_en, last accessed 2025/01/13.

Fawcett, T., Darby, S., 2018. Energy sufficiency-an introduction: A concept paper for ECEEE. Technical Report.

Furman, S., Hadjri, K., 2025. Wasted expertise: Why retrofit should include residents. Energy Research and Social Science, 119.

Guerra-Santin, O. et al., 2017. Designing for residents: Building monitoring and co-creation in social housing renovation in the Netherlands. Energy Research & Social Science, 32.

NEN 5060:2018, 2018. Hygrothermal performance of buildings: Climatic reference data. Stand-ard, 2018

NTA 8800:23, 2024. NTA 8800:2024. Energy Performance of buildings – Determination method. Standard, 2024.

Rovers, T. et al., 2020. Towards the evaluation of a thermal compartmentation renovation concept through in-situ measurements. In: 12th Nordic Symposium on Building Physics (NSB 2020), Tallinn, Estonia, pp. 1-4.

RVO, 2021. Standaard en streefwaarden voor woningisolatie, https://www.rvo.nl/onderwerpen/wetten-en-regels-gebouwen/standaard-streefwaarden-woningisolatie, last accessed 2025/01/13.

RVO, 2022. Voorbeeldwoningen 2022: bestaande bouw. Report, 2022.

Van den Brom P, et al., 2019. Actual energy saving effects of thermal renovations in dwellings. Energy Build.

Van Wieringen S et al. Spatial Justice in Dutch Social Housing. Energy Res. Soc. Sci. 2025 (Pre-print).

Verbeeck, G., Bosserez, A., 2021. A Design Process for a Resident-Oriented, Sufficiency-Based Energy Renovation Approach for Dwellings. In: eceee Summer Study on energy efficiency, Stockholm, pp. 1-12.

6th International Conference on Building Energy and Environment
Eindhoven University of Technology, The Netherlands
6 - 10 July 2025

A Novel Personal Environment Control System (PECS) Survey Tool

Sahan Atulugama [1], Mohamed Karzan [1], Luo Wei [1], Shalika Walker [2], Rick Kramer [1]

[1] *Technical University of Eindhoven, Eindhoven, Netherlands, s.w.atulugama@tue.nl / r.p.kramer@tue.nl*
[2] *Kropman Installatietechniek BV, Breda, Netherlands, shalika.walker@kropman.nl*

SUMMARY
The PECS survey tool is a novel desktop application designed to gain feedback and enhance personalized thermal comfort in indoor office environments through high quality occupant feedback. Integrated with a Personal Environmental Control System (PECS), the survey tool enables obtaining subjective occupant feedback to provide an optimal microclimate to its user through machine learning methods. To address the limitations of conventional survey tools related to survey fatigue, user engagement, and data quality, the tool has several features such as dynamic unfolding questionnaires that adapt based on user response, automated reminders, and gamification through a leaderboard-based point system. This tool was deployed on 23 users' workstations for 14 days obtaining hourly feedback from users to test its performance. While the current use-case is data collection, future versions will enable real-time PECS control. This paper presents the features, design, and the experiment outcomes of PECS survey tool.

Keywords: Survey Tool, Subjective Feedback, Personal Comfort, Indoor Environmental Quality.

1. INTRODUCTION

Human beings spend around 80% of their lifetime indoors (Zhao et al., 2004). Hence Indoor Air Quality (IAQ) and Thermal Comfort (TC) are fundamental to their well-being, productivity, and the overall quality of life. Heating, Ventilation, and Air Conditioning (HVAC) systems help to maintain IAQ and TC levels in favourable conditions. However, HVAC systems consume 10-20% of total energy demand in Europe and USA (Verhaart et al., 2015). This makes HVAC sector a significant energy demand factor. Despite the high energy demand for HVAC sector, the studies indicate that only 11% of the buildings meet the standard thermal comfort requirements, which require an 80% satisfaction rate among occupants (Katić et al., 2020).

One of the challenges faced by conventional HVAC systems are the individual differences among the users. Conventional HVAC systems are designed to operate as a centralized thermal comfort solution for all individuals (one-size-fits-all approach) while individual thermal preference varies among individuals substantially. Hence a single temperature setting does not provide the optimal thermal comfort to all. Despite the high energy consumption, HVAC systems fail to meet the standard thermal satisfaction rate (80%) making it highly inefficient.

Personal Environment Control System (PECS) is developed to address the inefficiencies in conventional HVAC systems. PECS can offer individualized thermal comfort through a combination of personalized ventilation and heating.

PECS has three main parts. The hardware system including the personal ventilation

system and heated seat, the user interface (survey tool), and the system backend consisting of the Application Programming Interface (API), the database, business logic, and machine learning modules.

PECS operates by obtaining subjective (occupant feedback) data and objective data (temperature, relative humidity) to learn the thermal preference of the user using a machine learning algorithm. Based on the learned personal thermal preferences, the PECS will predict the settings for personalized ventilation and heated seating to provide the optimal thermal comfort to its user.

In this process, obtaining subjective data from the users is critical for prediction of personal thermal comfort. Hence, the quality of PECS automation depends especially on the quality of subjective feedback obtained from the user. However, traditional surveys often suffer from low response rates and poor user engagement due to negative sentiments towards answering repetitive questions. PECS survey tool is designed and developed to overcome the issues and improve the overall quality and consistency of subjective data gathering.

This paper presents the design and key features and their performance of the PECS Survey Tool, explaining how it enhances the user engagement and data quality to support improved indoor climate personalization.

1.1. Related Work

Existing survey tools, such as the web application developed by Zagreus et al. (2004) which is one of the first large-scale web based Indoor Environmental Quality (IEQ) surveys, have suffered from low user engagement due to survey fatigue. Further, Peretti and Schiavon (2011) highlights the importance of improving the user experience of the application to uplift user engagement. Based on this, Wargocki and Da Silva (2015) shows that timely prompts can increase the user engagement of the application. Additionally, Laign and Kuhl (2020) shows that integrating gamification into thermal feedback tools can significantly improve the user engagement of survey applications.
Our work addresses designing a user-centric application tailored to integrate seamlessly user workflows to improve the user engagement and data quality.

2. METHODOLOGY

2.1. Requirement Analysis

The proposed application enables the collection of subjective data from the PECS users. The first phase of application development was requirement gathering and analysis.

A third-party mobile software tool was utilized in the older PECS version to get users' feedback. However, data that could be collected from the experiments through this third-party tool was limited due to users not using the application regularly.

To identify the issues related to the data collection process, several interview sessions were arranged with users and the surveyors who have been working on the PECS project previously. The interviews identified following pain points in the user's experience and data quality.

- Too many questions
- Lengthy user flow
- Mobile apps being seldom used while working
- Users forgetting to answer
- Uninviting user interface

Considering the above issues, several decisions were made before developing the application. Special attention was given to the user

experience of the application. Listed below are the key design decisions made before developing the application.

- **Develop a desktop application** : Since the office users seldom use mobiles while working, it was decided to develop a desktop application. PECS survey tool expects the users to send feedback from the location where PECS is installed. The PECS are usually installed at the users' workstations. Therefore, a desktop application is more suitable compared to a mobile application.
- **Develop a Windows application** : Since all users that contribute to the experiments in the living lab are using the Windows operating system, it was decided to develop a windows application. But the codebase must be compatible to build the application for other platforms such as MacOS.
- **Introduce an Unfolding Questionnaire** : This is a new concept introduced in obtaining subjective feedback from users. Unfolding questionnaire unfolds the questions based on previous responses from the user. In this way, the number of questions asked can be substantially reduced and only ask the most relevant follow-up questions from the user. Adaptive surveys such as unfolding questionnaires are proven to reduce survey fatigue and improve response quality (Van der Zanden et al., 2015).
- **Triggering Windows notifications** : Triggering windows notifications to remind the user to answer and submit a given survey at a specific time. The application is added to the startup processes in Windows and will run as a background process so that users don't have to open the application every time they want to send feedback.
- **Minimalistic user interface** : Improve the user interface in such a way that users can easily understand the user flow and submit the surveys. Users can also communicate with the admins regarding any problem related to PECS through the application. In addition, a better user interface can make the application more appealing to the user.
- **Introduce a Leaderboard** : Leaderboard keeps track of the number of surveys and questions answered by each user. For each survey completed, some contribution points will be added to the user account. Based on the contribution points, users will be ranked. This feature is added to introduce some sense of competition between users and reduce the survey fatigue.

The above decisions made on the design of the application to improve its user experience.

2.2. Design and Development

2.2.1. Frameworks Utilized

Two frameworks were utilized to develop the PECS survey tool. Flutter framework was utilized for the frontend and Django framework for the backend system. Both frameworks are robust and scalable solutions.

2.2.2. Flutter (Frontend Development)

Flutter is an open-source user interface (UI) development framework created by Google. Flutter allows the developers to create natively compiled applications for mobile, web, and desktop applications. All of this is using a single codebase using the dart programming language.

Flutter offers following advantages:

- **Cross platform development** : Allows the developer to use the same codebase to deploy the application across multiple platforms with the same performance and UI.
- **Rich UI components** : Flutter consists of a comprehensive set of customizable widgets that can be utilized in building a UI with high responsiveness and visual appeal.

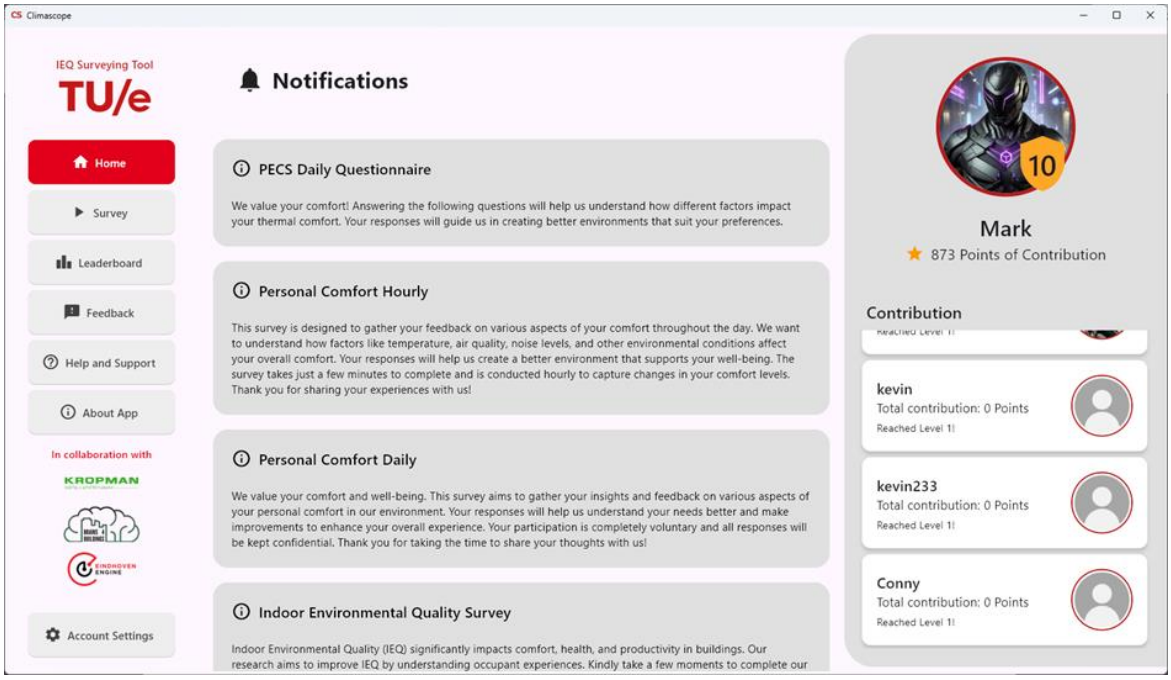

Figure 1. User Interface Home Page of PECS Survey Tool

- **High performance**: Compiles to native machine code allowing fast rendering and smooth performance.

2.2.3. Django (Backend Development)

Django is a robust high level python web framework that encourages rapid development utilizing Model-View-Controller (MVC) architecture. This architectural pattern offers a clear segregation between data management, UI, and business logic.

Django offers following advantages:

- **Rapid development** : Availability of built in features and modules speed up the backend development process
- **Scalable** : Django can handle high traffic loads making it suitable for large scale applications
- **Security** : Built in security features against vulnerabilities such as SQL injection, cross-site scripting, cross-site request forgery offers extra protection.
- **Support for Machine Learning** : Availability of libraries that can cater for machine learning requirements making it suitable for high-tech applications.

2.2.4. MVC Architecture in the PECS Tool

Both the frontend and the backend of PECS survey tool is built according to the Model-View-Controller (MVC) architecture.

- Model : Manages data and business rules of the application.
- View: Views are used to display data to the user.
- Controller: Controller acts as the mediator between the Model and the View. It handles the business logic of the application as well as the application state.

2.3. Description of PECS Survey Tool Features

The PECS survey tool was developed with the objective of collecting high-quality subjective feedback and maximizing the user

engagement. To achieve these requirements, the application was developed with following innovative features:

2.3.1. Dynamic Unfolding Questionnaire

The survey records all the answers given by the user to selectively ask only relevant follow-up questions based on the answers provided. This feature allows the user to provide the feedback in the shortest possible time and with minimal effort. Hence this feature is designed specifically to reduce the survey fatigue and improve the quality of data collected.

2.3.2. Notification and Reminder System

Survey tool is designed to send automated notifications at predefined intervals. Whenever a survey is being triggered at a set time, a notification is popped up in the screen. When the notification is clicked, it routes to the active survey. Notifications feature is included in the application to remind the user to engage with the active surveys. This feature enables the user to access the survey swiftly and engage with the survey smoothly.

2.3.3. Gamification Elements

Integration of leaderboard and a point-based system for users is to boost the user engagement by introducing an element of gamification into the survey tool. It's designed in such a way that the users will earn contribution points for each completed survey, which will ultimately affect their rank. This gamified approach is proven to positively influence the user engagement, especially in non-entertainment contexts such as IEQ surveys (Deterding et al., 2011).

2.3.4. Integration into User's Work Routine

The application is designed in such a way that the user doesn't have to learn any new skills to interact with it. The minimalistic user interface makes it self-intuitive for the users to understand the workflow of the application. When the user installs the application and logs in, it will save the logged in status even after restarting the operating system. User also can close the application if it hinders the daily work routine. The application is developed to run in the background in Windows operating system. It will notify the user only when there is a survey triggered for submission. These features are available in the application to reduce the friction in integrating a new application into the daily work routine of users. Further, the users are also able to provide feedback or request support through the application itself.

2.3.5. Example User Flow of PECS Survey

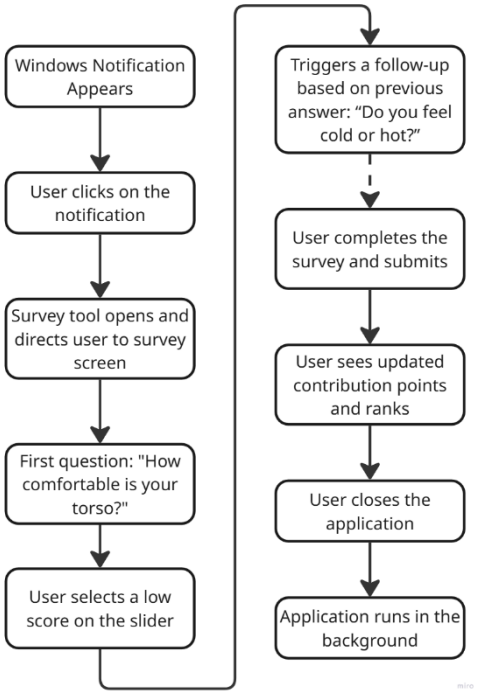

Figure 1: User flow of PECS session

2.4. Experimental Setup to Test PECS

The effectiveness of the PECS survey tool was tested by utilizing the survey tool in an experiment to evaluate indoor environment quality targeting users in an office environment. The study was conducted to gather feedback on user's perceptions of indoor environment quality while analysing

user engagement patterns.

2.4.1. The Participation and Duration of the Study

The PECS survey tool was installed in 23 users' computers. The survey was conducted for 14 consecutive days allowing to analyse user trends and response behaviours over time. The users were initially notified of the development status of the application. Furthermore, users were provided with a user guide to reduce any confusion in the workflow of the application.

2.4.2. Survey Time Slots and Trigger Strategy

Three time slots were selected to prompt the survey to users each day.

- 1st Time Slot - 09:30 to 10:30
- 2nd Time Slot - 11:30 to 12:30
- 3rd Time Slot - 14:30 to 15:30

If the users missed the survey within the designated timeslot, the same survey will be triggered again just after each time slot to ensure that the feedback was gathered consistently. After the survey was triggered for the second time, the users were notified in person to remind them of the survey.

2.4.3. Subjective Data Collection

The survey tool is used to capture subjective feedback on occupants' perceptions of the indoor environment. Users responded to quantitative questions with Graphical Rating Scales (GRS) numbered from 0 to 100. The responses are analysed to determine overall response patterns across time slots and days.

3. RESULTS

3.1. Overall Submission Pattern Overtime

The overall submission pattern (Figure 2) shows the number of submissions gathered on each day of the experiment. The chart shows daily fluctuations in user engagement. The 5th and 10th of February shows the peaks of user

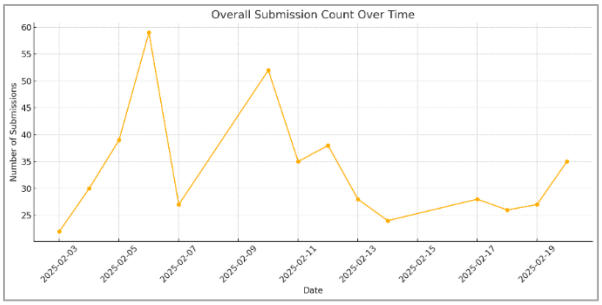

Figure 2: Plot of overall submission pattern overtime

engagement with 59 and 52 engagements respectively. The number of submissions significantly decreased after 12th February. There is a significant dip on the 7th of February depicting a significant variation from the general trend. This is because the experiment was not conducted on this day but the survey tool was programmed to run continuously.

3.2. Main Slot vs Second Trigger Responses

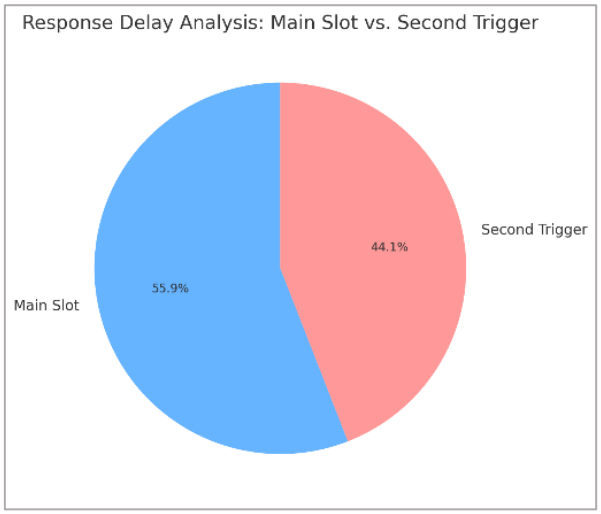

Figure 3: Responses in main slot vs second slot

The percentage of responses gathered in the main time slot and second trigger is presented in Figure 3. A total of 55.9% of the responses were collected in the first trigger in the main time slot by the help of notifications generated

by the application. 44.1% of the responses were gathered through second triggers which included both automated reminders and human follow-ups.

3.3. Responses by Time Slot

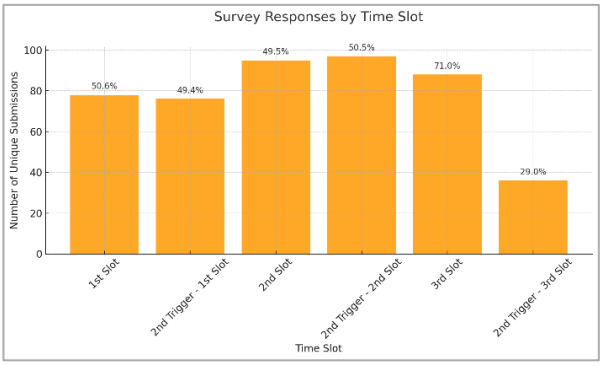

Figure 4: Responses by time slot

The number of submissions gathered across time slots is represented in the chart given in Figure 4. The first two time slots show a response distribution of around 50% between the main trigger and the second trigger. But the responses in the third time slot have gathered 71% of the responses in the first trigger and 29% submission in the second trigger.

3.4. User Engagement Heat Map Across the Experiment

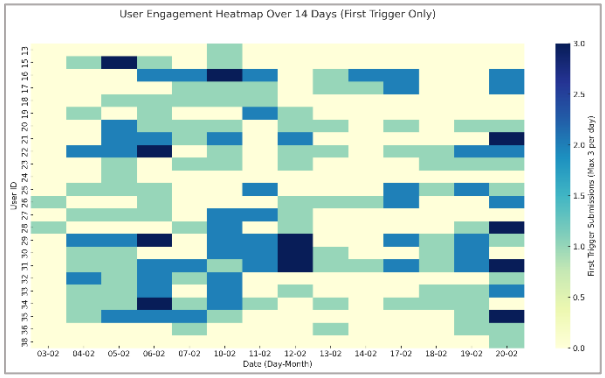

Figure 5: User engagement heat map

Figure 5 shows a heatmap of the user engagement across a total period of the experiment. The heatmap was created by the responses gathered in the main time slot (through app notifications) only. A significant reduction of the engagement can be noticed in 13th and 14th of February. Overall decrease can also be noticed after the 12th of February.

4. ANALYSIS AND DISCUSSION

Meaningful insights into user engagement were derived from the data collected over the 14-day experiment period.

4.1. User engagement variability

The standard deviation of total submissions per participant is 10.49 showing a high variability in user engagement across participants. This means that some participants were consistently responsive while others engaged with the survey less frequently. To evaluate the difference between user engagement, the users were divided into two groups. High engagement group are the participants with submissions above the median while the low submission group is the participants with submissions below the median. A two-sample t-test resulted in a t-statistic of 6.12 with a p value of 9.99×10^{-6}, which is lower than the significance threshold 0.05. This suggests that there is a statistically significant difference between engagement level of the two groups.
It confirms that the differences in participation rates are not due to random variation but are influenced by external factors such as work schedules, site visits, workload, technical issues, or reduced motivation levels.

4.2. Effectiveness of Notifications

The bar chart shown in Figure 3 and 4 depicting the survey responses by time slots shows important patterns related to the effectiveness of the application's notification system. It shows a higher engagement for the first trigger in the main time slots compared to the second trigger. This demonstrates the effectiveness of the notification system. In

addition, the reliance on the notification system was also observed when some participants reporting technical issues related to Windows notifications which led to miss the survey in the main time slot.

4.3. Remarks on Ease of Use

Daily submissions (Figure 2) show a high positive gradient in the first three days of the experiment with a peak on February 6th registering the maximum number of submissions per day within the 14-day period. This suggests that the participants adapted to the application within two days. This highlights the intuitiveness and the ease of use of the application.

4.4. Low Engagement on Fridays

Reduced activity towards the end of the week (Fridays – 7th and 14th February) of all participants is also noticeable in the heatmap.

5. CONCLUSION

This study evaluated the effectiveness of PECS survey tool that has unique features designed to collect subjective feedback on indoor environmental quality. The field study highlights the automated notification feature effectively prompted surveys during the designated time slots. Recording the highest number of survey responses after three days of use indicates the intuitiveness and ease of use of the application.

The higher engagement in main time slots and user consistency confirms that the features included in the application (dynamic unfolding questionnaire, leaderboard, and notification system) has positively impacted on user experience.

6. ACKNOWLEDGEMENT

The authors would like to thank Team TCC and Team Breda from Kropman B.V. for their continuous support for making the experiments a success. The authors would also like to express their gratitude to the Netherlands Enterprise Agency (‘Brians 4 Buildings’ project number MOOI32004 and ‘Brains for Buildings, Eindhoven Engine, APK 2.0 Project’ with project number RT104151) for their financial support.

7. REFERENCES

Zhao, R., Sun, S. and Ding, R. (2004). Conditioning strategies of indoor thermal environment in warm climates. Energy and Buildings, 36(12), pp.1281–1286. doi:https://doi.org/10.1016/j.enbuild.2003.07.002.

Verhaart, J., Veselý, M. and Zeiler, W. (2015). Personal heating: effectiveness and energy use. *Building Research & Information*, 43(3), pp.346–354. doi:https://doi.org/10.1080/09613218.2015.1001606.

Katić, K., Li, R. and Zeiler, W. (2020). Machine learning algorithms applied to a prediction of personal overall thermal comfort using skin temperatures and occupants’ heating behavior. Applied Ergonomics, 85, p.103078. doi:https://doi.org/10.1016/j.apergo.2020.103078.

Zagreus, L., Huizenga, C., Arens, E. and Lehrer, D. (2004). Listening to the occupants: A Web-based indoor environmental quality survey. Indoor Air, 14(Suppl 8), pp.65–74. doi: https://doi.org/10.1111/j.1600-0668.2004.00301.x.

Peretti, C. and Schiavon, S. (2011). Indoor environmental quality surveys: A brief literature review. Energy and Buildings, 43(10), pp.2161–2167. doi: https://doi.org/10.1016/j.enbuild.2011.04.032.

Laing, S., & Kühl, N. (2020). Comfort-as-a-Service: Designing a User-Oriented Thermal Comfort Artifact for Office Buildings. arXiv preprint arXiv:2004.03323. https://arxiv.org/abs/2004.03323

Wargocki, P. and Da Silva, N.A. (2015). Use of visual prompts to enhance use of environmental controls in offices. Building and Environment, 92, pp.185–193.

DOI: https://doi.org/10.1016/j.buildenv.2015.04.013

Van der Zanden, P.J., Denessen, E., Cillessen, A.H. and Meijer, P.C. (2015). Domains and predictors of first-year student success: A systematic review. *Educational Research Review*, 10, pp.1–23.

Deterding, S., Dixon, D., Khaled, R. and Nacke, L. (2011). From game design elements to gamefulness: Defining “gamification”. In *Proceedings of the 15th International Academic MindTrek Conference: Envisioning Future Media Environments*, pp.9–15.

Building Renewables, Solar Buildings and Smart Grid (11:00-12:30 h)

6th International Conference on Building Energy and Environment
Eindhoven University of Technology, The Netherlands
6 - 10 July 2025

Retrofit existing commercial buildings towards nearly zero energy - a case study in Kaohsiung, Taiwan

Hung-Chi Chiu [1], Wei-An Chen [2], Ruey-Lung Hwang [3]

[1] *Department of Industrial Technology Education, National Kaohsiung Normal University, Kaohsiung, Taiwan, 411171203@mail.nknu.edu.tw*
[2] *Department of Multidisciplinary Engineering, Texas A&M University, College Station, TX U.S.A., weian.chen@tamu.edu*
[3] *Department of Industrial Technology Education, National Kaohsiung Normal University, Kaohsiung, Taiwan, rueylung@nknu.edu.tw*

ABSTRACT
Taiwan's existing buildings make up 97% of its total stock, playing a vital role in achieving near-zero carbon goals and the 2050 net-zero emissions target. This study explores retrofitting a bank branch into a nearly zero-energy building. Using EnergyPlus, a baseline energy model was created and validated with utility data, on-site surveys, and performance checks. Energy Efficiency Strategies included upgrading lighting and HVAC systems, paired with solar photovoltaics and green electricity purchases. The results showed that Energy Efficiency Strategies reduced the Energy Use Intensity, contributing 56% of the targeted energy savings, while Renewable Energy Technologies provided the remaining 44%, surpassing the near-zero energy target of 72 kWh/m²·year. Overall, the combination of proven Energy Efficiency Strategies and Renewable Energy Technologies successfully transformed the existing building into a near-zero carbon building. This case provides valuable insights and a reference model for retrofitting existing buildings in Taiwan to support sustainable development goals.

Keywords: Energy Use Intensity, Energy Efficiency Strategies, Renewable Energy Technologies, nearly zero-energy buildings.

1. INTRODUCTION

Zero-Energy Buildings (ZEB) are increasingly prioritized. In March 2022, Taiwan announced its "2050 Net-Zero Emissions Strategy" for the building sector. By 2030, all new public buildings must meet nearly zero-energy (nZEB) standards. By 2040, 50% of existing buildings will be retrofitted, and by 2050, all new buildings and over 85% of existing ones will comply. With 97% of Taiwan's buildings being older, privately owned structures, retrofitting poses challenges. The government has adopted a phased approach, requiring public building retrofits and offering subsidies to incentivize private owners. The plan requires over 50% of energy reductions through Energy Efficiency Strategies (EES), with the rest from Renewable Energy Technologies (RET). Since 2023, pilot projects have retrofitted buildings using cost-effective EES, such as envelope and system upgrades (HVAC, lighting, hot water), and RET, including photovoltaics (PVs), wind turbines, solar thermal, and green electricity.

Existing buildings must prioritize cost-effective EES before adding renewable energy. Retrofitting them for nZEB is more complex than designing new ones, with most research focusing on residential and new buildings, leaving retrofits of commercial and governmental buildings

underexplored. A 40% energy reduction was achieved in an Italian office through retrofits and onsite renewables (Ferrari, 2017). Investigated the retrofitting of a Kuwaiti university building using EES and building-integrated solar systems, achieving experimental feasibility for a nZEB (AlAjmi, 2016). Achieved a 45% energy demand reduction in Canada through airtightness and insulation improvements, with solar panels facilitating net-zero energy (Charles, 2019). Demonstrated a 60% energy savings in a U.S. office building using EES, with PV supplying 31.4% of the remaining demand (Alajmi, 2020). Similarly, Analyzed retrofitting a typical administrative building in Cairo into an nZEB, showing EES could reduce energy use by 11.9% and PV by 29.5% (El-Sherif, 2020). Upgrades to a Cairo educational building showed a 36% energy savings through envelope improvements and 50% through HVAC systems, with PV panels covering the remaining demand (Emil, 2021).

This paper explores the nZEB retrofit of a bank branch in Kaohsiung, Taiwan, as part of the net-zero carbon initiative. The project, in construction and testing, involves two stages: validating the EnergyPlus model with pre-retrofit data and applying EES, followed by integrating solar systems and green electricity. This study demonstrates the feasibility of transforming a high-energy-consuming building into an nZEB under Taiwan's hot and humid climate.

2. RESEARCH METHODOLOGY

2.1. Description of the Building

The investigated case is located in Kaohsiung City, southern Taiwan, with a climate featuring a maximum temperature of 36.8°C, a minimum of 18.8°C, an average of 24.8°C, and 79.1% relative humidity. With a cooling degree-hour of 25,680°C·hours (based on 23°C), air conditioning is needed year-round. The branch, occupying 630.8 m² across the first and second floors of a 2013 commercial building, faces east-northeast at 20° and features concrete walls, low-emissivity glass windows (SHGC = 0.5), and a 0.16 window-to-wall ratio. Internal heat sources include lighting, equipment, and occupant activities.

The HVAC system, lighting, and equipment operate from 8:00 AM to 6:00 PM, Monday to Friday. Before the retrofit, lighting used 20W and 40W T8 fluorescent lamps, consuming 7.9 kW with a lighting power density (LPD) of 12.5 W/m². The HVAC system includes a chiller, cooling tower, and water pumps on the rooftop, with fan coil units and two fresh air systems in the office. HVAC specifications and performance details before the retrofit are in Table 1. A site survey of equipment revealed a plug load of approximately 16 W/m². In 2023, monthly electricity consumption ranged from 7,335 kWh in January to 11,137 kWh in August, totaling 112,155 kWh annually, with an EUI of 178 kWh/m²·year (Figure 1).

2.2. Retrofit Strategies

For the retrofit, proven technologies approved by the bank were implemented, including advanced lighting, HVAC upgrades, a PV system, and green electricity. Regarding lighting systems, energy-efficient LED fixtures replaced 20W and 40W T8 fluorescent lamps, reducing power to 14W and 28W, with excess fixtures removed. These upgrades lowered total lighting power to 4.1 kW and the LPD to 6.5 W/m².

The HVAC retrofit included replacing the chiller with an Energy Efficiency Class 1 variable

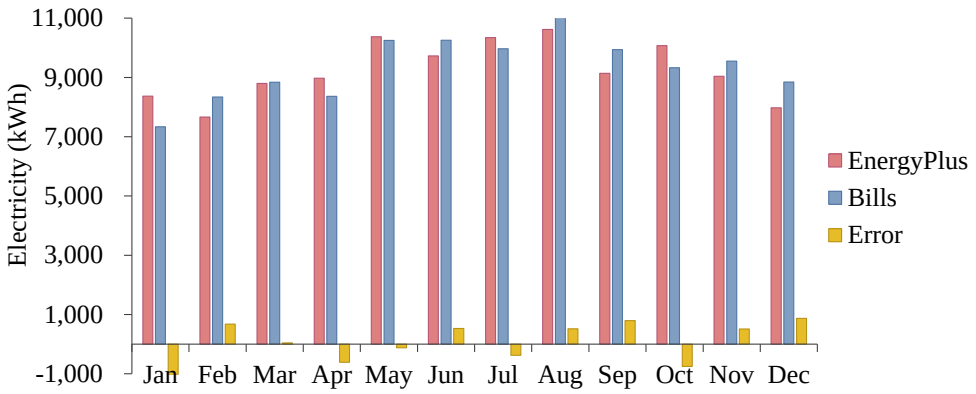

Figure 1. Monthly Actual Electricity Consumption of the Bank Branch

Table 1. Specifications and Performance of the HVAC System Before and After Retrofit

Equipment Name	Pre-retrofit	Post-retrofit
Chiller	Two scroll chillers with total cooling capacity of 60 RT and total input power of 51.2 kW.	One screw chiller with a cooling capacity of 50 RT and an input power of 34.1 kW, with VFD.
Cooling Tower	Two cooling towers with 80 RT heat rejection capacity and 1.5 kW input power, without VFD.	One cooling tower Two cooling towers with a heat rejection capacity of 80 RT and a 1.5 kW VFD fan.
Cooling Water Pump	Two pumps with a total flow rate of 630 LPM and 7.5 kW total input power.	One pump with a flow rate of 650 LPM and a power input of 3.7 kW.
Chilled Water Pump	Two pumps with a total flow rate of 504 LPM and total power input of 7.5 kW.	One pump with a flow rate of 500 LPM and total power input of 3.7 kW.
Fan-Coil Unit	21 units, each with an airflow of 680 to 1,360 CMH and a total power input of 2.2 kW.	Same as pre-retrofit
Outdoor Air	Two DOAS units with a total airflow of 1,600 CMH and a power input of 1.16 kW, without heat recovery.	Two DOAS units with 1,600 CMH airflow and 1.16 kW power input, featuring heat recovery and CO2 DCV.

frequency model, reducing capacity from 60 RT to 50 RT to match demand. A high-efficiency cooling tower with variable frequency drive fans was installed to lower the outlet water temperature and improve chiller efficiency. The fresh air system was upgraded with an enthalpy heat exchanger and CO_2-based volume control to optimize air quality. An Energy Management System (EMS) was implemented to monitor, and analyze energy use, supporting the net-zero energy target. The specifications and performance of the retrofitted HVAC system are in Table 1.

Based on the availability of renewable energy, a rooftop PV system was installed, covering 51.2 m^2 with a 9.6 kWp capacity, generating 12,916 kWh annually. Due to the limited rooftop area, the electricity generated by the system is insufficient to fully meet the requirements of a nZEB. Therefore, an additional 28,338 kWh of green electricity is purchased annually from the utility company.

2.3. Measurement and Verification of Building Retrofit

The Measurement and Verification (M&V) process for building retrofits consists of two phases: pre-retrofit and post-retrofit. Pre-retrofit M&V calibrates the energy model by comparing simulated data with actual consumption. Post-retrofit M&V, conducted after the retrofit, is beyond

the scope of this study, as the project is still under construction. This study uses a calibrated energy model to simulate and predict energy savings from the proposed EES. The model incorporates building geometry, orientation, façade structure, window specifications, lighting, equipment, HVAC systems, interior layout, occupant schedules, and climate data. Variables such as plug loads, lighting intensity and schedules, and indoor temperature setpoints were adjusted based on site visits, architectural documentation, and feedback from facility management personnel. A one-week field measurement campaign recorded power consumption with analyzers and chilled water flow/temperature differences with thermal meters, providing insights into cooling needs and system performance. The EnergyPlus V22.2 simulation program, using local weather data, was employed to simulate the model and produce 12 months of energy usage results. Monthly consumption calibration was performed with 2023 data, adjusting the model until power consumption fell within an acceptable error range. Calibration is considered successful if the Mean Bias Error (MBE) and the Coefficient of Variation of the Root Mean Square Error (CV(RMSE)) are within ±5% and ±15%, respectively, as per ASHRAE Guideline 14. The calculations for MBE and CV(RMSE) are shown in equations (1)-(3).

$$MBE(\%) = \frac{\sum_{i=1}^{n} S_i - M_i}{n} \times 100 \quad (1)$$

$$RMSE = \sqrt{\frac{\sum_{i=1}^{n} (S_i - M_i)^2}{n}} \quad (2)$$

$$Cv(RMSE) = \frac{RMSE}{M_{avg}} \times 100 \quad (3)$$

Where n represents the period, S_i and M_i are the simulated and measured energy consumptions, respectively, and M_{avg} is the average measured energy consumption.

3. RESULTS AND DISCUSSION

3.1. Chiller Measurement Results

To further analyze the cooling demand of the building and the operational status of the chiller system, this study monitored a five-day period from May 20 to May 24, 2024. The results are presented in Figure 2 During this period, the total electricity consumption of the chiller system was 1,215 kWh, with daily consumption ranging from 225 kWh to 262 kWh. The analysis revealed that the energy consumption distribution of the chiller system remained relatively stable, with the chiller compressor accounting for 69%, the cooling tower for 3%, the chiller pump for 13%, and the cooling water pump for 15%. The total cooling load was 697 RTh, averaging 139 RTh/day. Chiller efficiency ranged from 1.10 to 1.25 kW/RT (average 1.21 kW/RT), while overall system efficiency ranged from 1.67 to 1.80 kW/RT (average 1.74 kW/RT). These findings provide key insights into system performance and validate the energy model.

3.2. Analysis of Calibration Results

The building energy simulation model was developed using EnergyPlus, a comprehensive program for building energy simulation. The design of each floor's structural elements, including floors, exterior walls, internal partitions, and windows, was based on the as-built construction drawings.

Specifications for HVAC equipment, lighting, and plug loads were derived from on-site

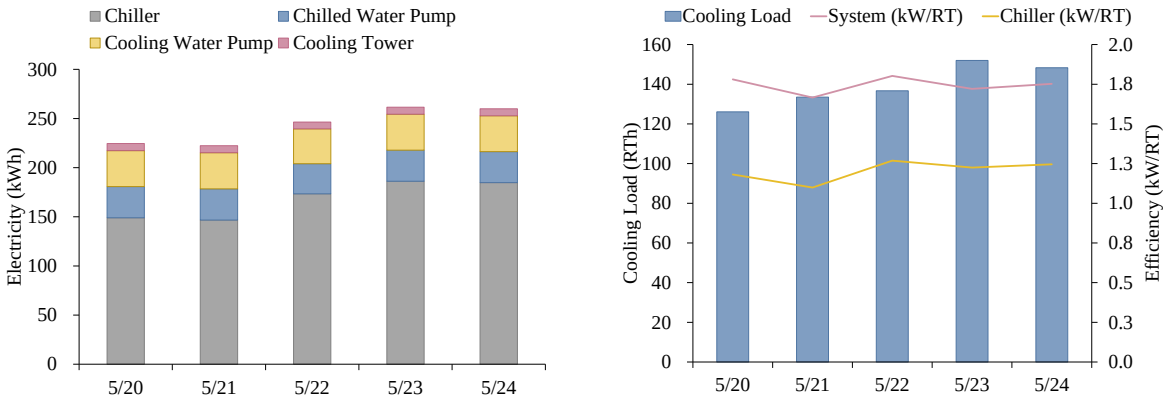

Figure 2. (a) Total electricity consumption of the chiller system and (b) cooling load demand and efficiency during five typical working days in May 2024.

observations. The efficiency of the HVAC system, measured on-site, was incorporated into the simulation model as input data. Additionally, the weather data file used for the simulation was based on the Typical Meteorological Year (TMY) rather than the actual meteorological year, a common practice in building energy modeling.

Lacking a sub-metering system, the building energy model calibration relied on total electricity consumption data from the utility. Figure 1 compares EnergyPlus estimated and actual monthly electricity consumption. The simulation's predicted annual electricity consumption is 111,105 kWh (176 kWh/m²·year), while the actual building's annual consumption is 112,155 kWh (178 kWh/m²·year), with the simulated prediction being 99% of the actual consumption. The error between actual and simulated monthly consumption ranges from -14% to 10%, caused by discrepancies in weather data, occupancy rate estimation, and uncertainties in plug load power and usage. In the calibration based on monthly data, the normalized mean bias error (NMBE) and the coefficient of variation of the root mean square error (CV(RMSE)) for the simulation model are 1% and 7%, respectively. The results meet the ASHRAE Guideline 14 criteria of 5% NMBE and 15% CV(RMSE), confirming the simulation model's high accuracy for energy analysis. The calibrated model shows the bank branch's pre-retrofit annual electricity consumption (Figure 3): HVAC at 70,829 kWh (64%), lighting at 17,665 kWh (16%), and plug loads at 22,611 kWh (20%).

3.3. The effect of Energy Efficiency Strategies

The lighting system was upgraded from T8 fluorescents to LEDs, reducing wattage from 7.9 kW to 4.1 kW and annual energy use by 48% (from 17,665 kWh to 9,115 kWh). HVAC, which accounts for 76% of energy use, underwent significant upgrades: the old chiller (1.21 kW/RT) was replaced with a more efficient model (0.68 kW/RT), and a DOAS with energy recovery and CO_2 control was added. Figure 4 shows HVAC energy consumption decreased by over 2,800 kWh/month (40%) during peak months and 1,800 kWh/month (41%) in cooler months, totaling 27,624 kWh annually (39%), making the upgrade essential for achieving nZEB. Figure 3(b) shows a significant EUI drop after the retrofit, with lighting EUI reduced by 14 kWh/m²·year and HVAC by 69 kWh/m²·year. The branch's EUI fell from 176 to 119 kWh/m², achieving 32% total energy savings, advancing toward NZEB.

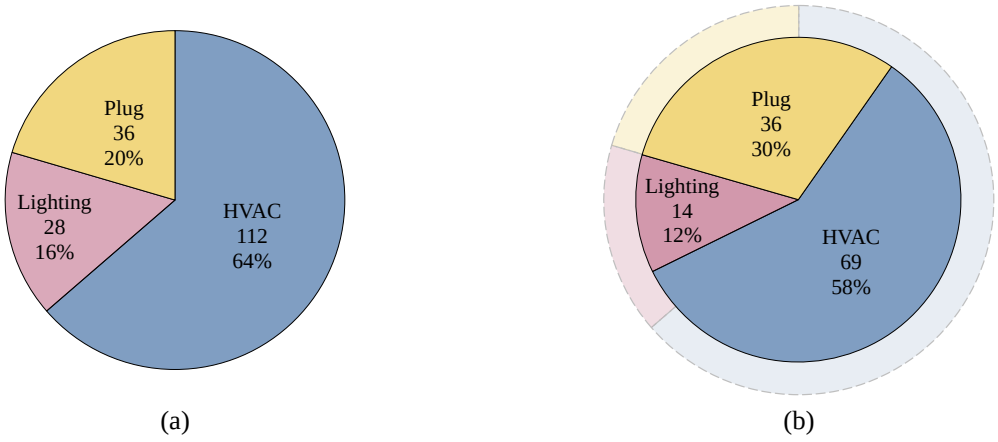

Figure 3. The sub-metered EUI of the bank branch (a) before and (b) after the retrofit.

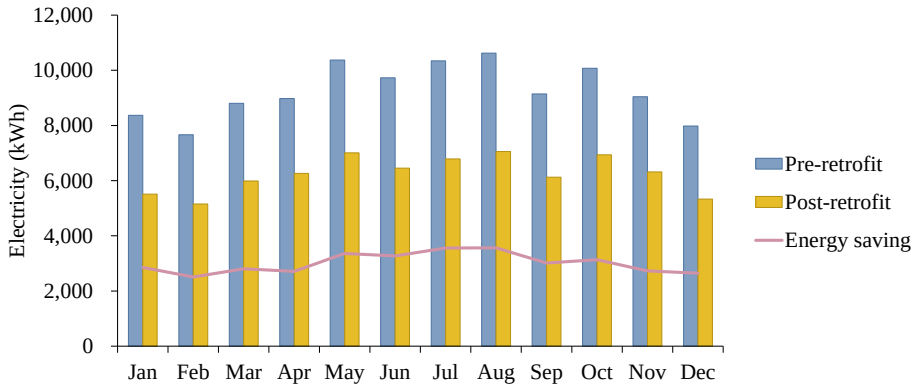

Figure 4. Comparison of monthly electricity consumption before and after HVAC retrofit.

3.4. Renewable energy system

The 51.2 m² rooftop PV system, rated at 18% efficiency by the manufacturer and 15% in simulation considering effective area and inverter efficiency, supplies power directly on working days and stores holiday excess in batteries for later use.

The solar PV system's performance was evaluated using TMY data to convert horizontal solar radiation to the collector array, predicting power generation. The total solar radiation in Kaohsiung is 1.492 MWh/m² annually. Figure 5 shows monthly performance, peaking at 1,325 kWh in July with lower output in winter. The system is expected to generate 12,916 kWh annually (17% of total consumption), with the bank purchasing 28,388 kWh/year of green electricity (38%) during non-summer months (October to April), accounting for 38% of the total electricity usage.

3.5. Post-retrofit nZEB Performance

Figure 6 compares monthly electricity consumption and renewable energy production, showing a shortfall in offsetting the building's usage. The peak energy deficit occurs from May to October, requiring additional non-renewable energy. August's 3,200 kWh deficit suggests doubling the PV area to 135 m² for net-zero energy.

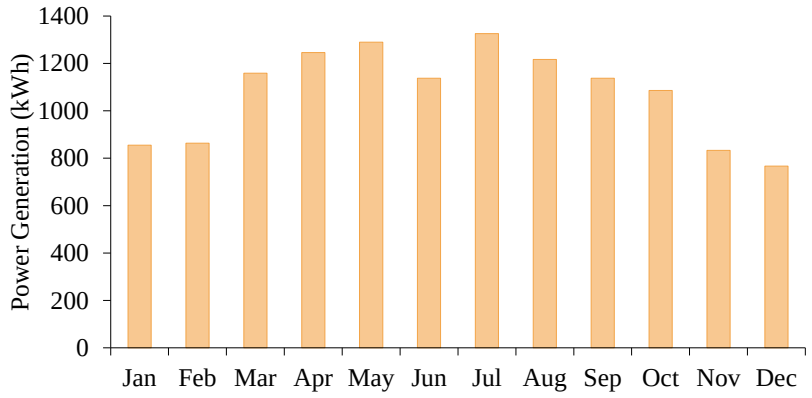

Figure 5. Monthly power generation of the solar PV system.

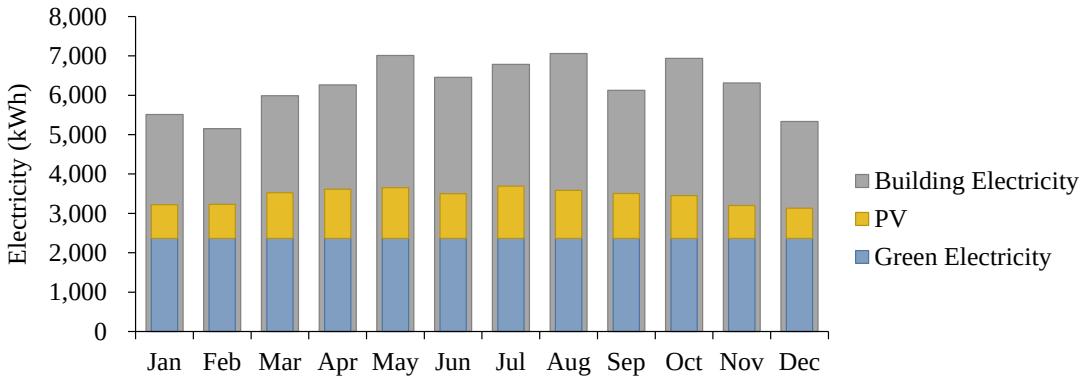

Figure 6. Comparison of Monthly Electricity Consumption and Renewable Energy Generation of the pre-retrofit.

Figure 7 illustrates the path to nZEB, with EES lowering the EUI from 176 to 119 kWh/m²·year. Lighting EES saved 14 kWh/m²·year, and HVAC EES cut 44 kWh/m²·year. The proposed EES measures achieved 56% of the total energy savings, reducing EUI from 176 to 73 kWh/m²·year. This fulfills the requirement for EES to provide over 50% of savings, but the branch still falls short of Taiwan's nZEB standard, requiring RET to meet the remaining demand.

Integrating RETs reduced the EUI to 55 kWh/m²·year, with PV providing 20 kWh/m²·year and green power contributed an additional reduction of 44 kWh/m²·year, meeting the nZEB target. This renovation underscores the importance of practical technologies in cutting energy use, modernizing Taiwan's buildings, and achieving near-zero energy goals.

4. Conclusion

This study evaluated the accuracy of the pre-retrofit building energy model and analyzed the impact of EES and RET on energy consumption. The project successfully converted an existing bank branch office into an nZEB. The following conclusions were drawn:

- The simulated pre-retrofit EUI of 176 kWh/m²·year closely aligned with the measured 178 kWh/m²·year, achieving an NMBE of 1% and a CV(RMSE) of 7%, meeting ASHRAE Guideline 14 criteria and confirming model accuracy.

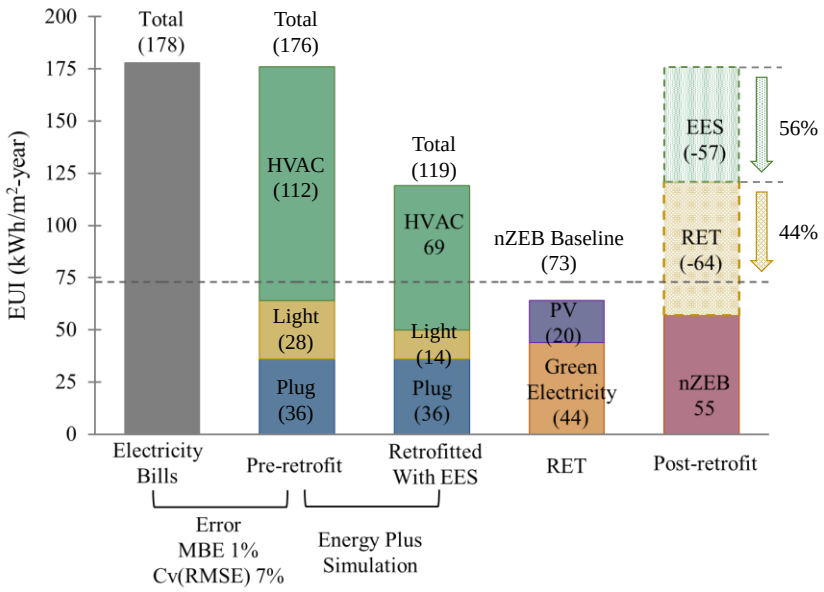

Figure 7. Pathways to achieving nZEB for the bank branch.

- Lighting system optimization reduced the building's EUI by 14 kWh/m²·year, while HVAC efficiency improvements reduced energy consumption by 44 kWh/m²·year. EES provided 56% of the target energy savings.
- Two RETs were introduced: a PV system and green electricity purchase, supplying 64 kWh/m²·year of green energy. The PV system generated 20 kWh/m²·year annually, and 44 kWh/m²·year was purchased from the grid.
- After implementing EES and RET, the building's EUI was reduced from 176 kWh/m²·year pre-retrofit to 55 kWh/m²·year post-retrofit, significantly below the 73 kWh/m²·year benchmark, achieving substantial energy savings.

In conclusion, retrofitting existing buildings to nZEB standards is technically feasible and provides valuable insights for advancing sustainable development goals. This area merits further research and greater emphasis from policymakers to accelerate its implementation.

REFERENCES

Ferrari S., Beccali M., 2017. Energy-environmental and cost assessment of a set of strategies for retrofitting a public building toward nearly zero-energy building target. Sustainable Cities and Society 32, 226-234.

AlAjmi A. et al., 2016. Achieving annual and monthly net-zero energy of existing building in hot climate. Applied Energy 165, 511-521.

Charles A., Maref W., Ouellet-Plamondon C.M., 2019. Case study of the upgrade of an existing office building for low energy consumption and low carbon emissions. Energy and Buildings 183, 151-160.

Alajmi A. et al., 2020. Detailed energy efficiency strategies for converting an existing office building to NZEB: a case study in the Pacific Northwest. Energy Efficiency 13, 1089–1104.

El-Sherif M.O. et al., 2020. Implementing the Net Zero Energy Building "nZEB" Strategies on an Existing Administration Building in Egypt. Engineering Research Journal 168, 146-171.

Emil F., Diab A., 2021. Energy rationalization for an educational building in Egypt: Towards a zero energy building. Journal of Building Engineering 44, 103247.

ASHRAE, ASHRAE Guideline 14-2023: Measurement of energy and demand savings - Measurement of Energy, Demand and Water Savings. Atlanta, GA, USA: American Society of Heating, Refrigerating and Air-Conditioning Engineers (ASHRAE), 2023.

6th International Conference on Building Energy and Environment
Eindhoven University of Technology, The Netherlands
6 - 10 July 2025

Adsorption Chiller-Based Waste Heat Recovery Calculation for Heat Recovery Data Center

Joo Hyun Moon[1], Jinkyun Cho[2,3]

[1]Hanbat National University, Daejeon, Republic of Korea, jhmoon9@hanbat.ac.kr
[2]Hanbat National University, Daejeon, Republic of Korea, jinkyun.cho@hanbat.ac.kr
3Corresponding Author, jinkyun.cho@hanbat.ac.kr

SUMMARY
The rapid growth of data centers has led to substantial energy consumption and waste heat production, creating both environmental challenges and opportunities for energy recovery. This study aims to investigate how adsorption heat pumps can utilize low-grade waste heat from data centers to improve overall energy efficiency and reduce the environmental footprint. A numerical analysis is performed using a Linear Driving Force (LDF) model on a two-bed adsorption chiller (e.g., silica gel-water pair). Key parameters (inlet temperature range of 53°C–73°C, chilled water temperature of 25°C–20°C) are optimized for typical data center conditions. Results show that the proposed system significantly enhances cooling efficiency and can achieve a reasonable coefficient of performance (COP) when applied to time-varying data center loads. Waste heat from immersion-cooled servers was successfully converted into usable cooling capacity for additional air-cooled racks, thereby reducing the electricity demand of the data center. Adsorption chillers, when integrated with immersion cooling systems, offer a promising pathway for waste heat recovery in data centers. This integrated solution supports sustainable development by reducing both operational costs and environmental impact.
Keywords: Data Center, Adsorption Chiller, Immersion Cooling, Calculation.

1. GENERAL INSTRUCTIONS

With the rapid expansion of information and communication technology (ICT) and the surge in data processing requirements, constructing large-scale data centers has emerged as a core development strategy for major economies (Masanet et al. 2020; Cho and Lee 2024). Driven by the so-called ABC technologies—artificial intelligence, big data, and cloud computing—both current and future data centers are reshaping not only the ICT sector and newly emerging industries, but also the service landscape of established fields (Cho et al. 2022). Traditional areas such as manufacturing, agriculture, and fisheries are likewise undergoing profound changes through digital transformation.

IT equipment (ITE) can demand power densities of 50 kW per rack or higher, depending on workload and equipment performance. Although the average density generally remains below 10 kW per rack, data centers with IT capacities of 5 MW or more often see higher values (Davis et al. 2022). Nearly all power consumed by ITE is eventually converted into heat, and the majority of new and existing data centers worldwide rely on air-cooled ITE. However, with rising rack-level heat loads—driven by generative AI and other applications—many data centers are approaching the limits of airflow and cooling capacity (Zhang et al. 2014; Sohel Murshed and Nieto de Castro 2017). As a result, more efficient cooling approaches are needed, and liquid cooling has emerged as one of the most promising alternatives. By transferring waste heat through the liquid refrigerant to a utility heat source, liquid cooling can significantly reduce the airflow needed in racks and may further enhance ITE performance by lowering operating temperatures (Cho and Lim 2023).

In this context, the present study proposes new data center concept of cooling system that integrates an immersion cooling system, addressing the heightened demand and power density of ITE, with an adsorption heat pump. Crucially, the adsorption heat pump recovers a large portion of cooling waste heat and repurposes it as a secondary cooling source, thus enabling a shift from existing air-based cooling systems. To validate this concept, the study provides an optimal design of the adsorption heat pump employing waste heat and offers a quantitative assessment of the overall energy efficiency for the proposed data center cooling solution.

2. METHODOLOGY

2.1. System Description

A key requirement for implementing liquid cooling is having liquid-cooled IT equipment (ITE). Because such ITE is not yet widely adopted, designing liquid cooling systems can involve uncertainty about cooling needs. In this study, a 200 kW ITE load is cooled via immersion cooling and a 50 kW adsorption heat pump, which together provide cooling to air-cooled ITE through a 20 kW rear door heat exchanger (RDHx). Waste heat from the immersion process supplies hot water to the adsorption heat pump; the pump's output, in turn, cools the RDHx. The central challenge lies in establishing suitable operating conditions for the integrated components. Optimizing the adsorption heat pump requires examining adsorbents such as silica gel, MIL-101Cr, or SAPO-34, and considering hot water temperatures between 53°C and 73°C to achieve an adequate coefficient of performance (COP).

Standard metrics like power usage effectiveness (PUE) are not ideal for liquid cooling because they alter both total data center power and ITE power (Avelar et al. 2012). Alternative measures, such as total usage effectiveness (TUE) (Patterson et al. 2013), can be more informative. Conventional data centers often use air cooling, generating low-temperature waste heat of limited reuse value (Jang and Cho 2024). Liquid cooling, however, can recover higher-grade waste heat without extra heating requirements.

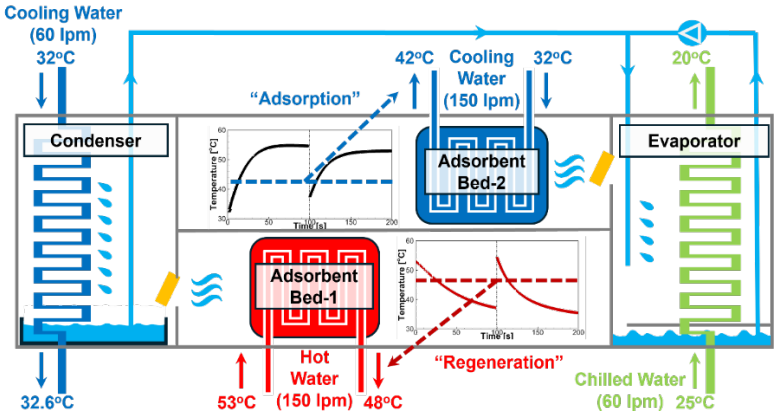

Figure 1. Adsorption chiller concept for data center with waste heat recovery

In this study, 50 kW of the 200 kW immersion-cooling waste heat is directed to an adsorption heat pump that provides chilled water for the RDHx. Two coolant distribution units (CDUs), each with six 34 kW immersion tanks, handle the 200 kW total load. The CDU system is split into two units: one providing 50 kW for the adsorption heat pump and the other managing the remaining 150 kW via a cooling tower. The RDHx cools a rack at 18 kW/rack, with a 10°C air differential and 100 m^3/min airflow. Chilled water is circulated at 20 kW (110% of RDHx capacity), at a 20°C outlet from the adsorption heat pump, with a 6.6 m^3/h flow at a 5°C temperature difference. Lastly, the

condenser water loop is sized for 38.4 m³/h at a 32°C tower outlet temperature; two parallel pumps circulate 28.8 m³/h for immersion cooling and 12.6 m³/h for the adsorption heat pump plus RDHx.

2.2. Model Description

Figure 1 illustrates a simplified schematic of a two-bed adsorption cooling system, comprising an adsorber, a desorber (or regenerator), a condenser, and an evaporator. As adsorption is exothermic, a cooling water supply removes heat from the adsorber, maintaining the cooling effect while the refrigerant is adsorbed. The vapor then condenses and feeds into the evaporator, ensuring continuous cooling (Al-Mousawi et al. 2016; Gediz et al. 2021). The subsequent focus is on the adsorbent bed, where the Linear Driving Force (LDF) model is applied. The LDF model (Linear Driving Force) is adopted to describe the transient adsorption/desorption rates. Let q be the instantaneous adsorbate concentration, and $q*$ be the equilibrium concentration. The governing equation is expressed as

$$\frac{dq}{dt} = k_{\mathrm{LDF}}(q^* - q) \tag{1}$$

where k_{LDF} is the overall mass transfer coefficient. This formulation assumes the adsorption process is primarily controlled by macropore diffusion rather than micropore diffusion. Additionally, isothermal conditions are assumed within each bed layer, and the bed thermal capacity is accounted for by coupling with energy balance equations.

3. RESULTS

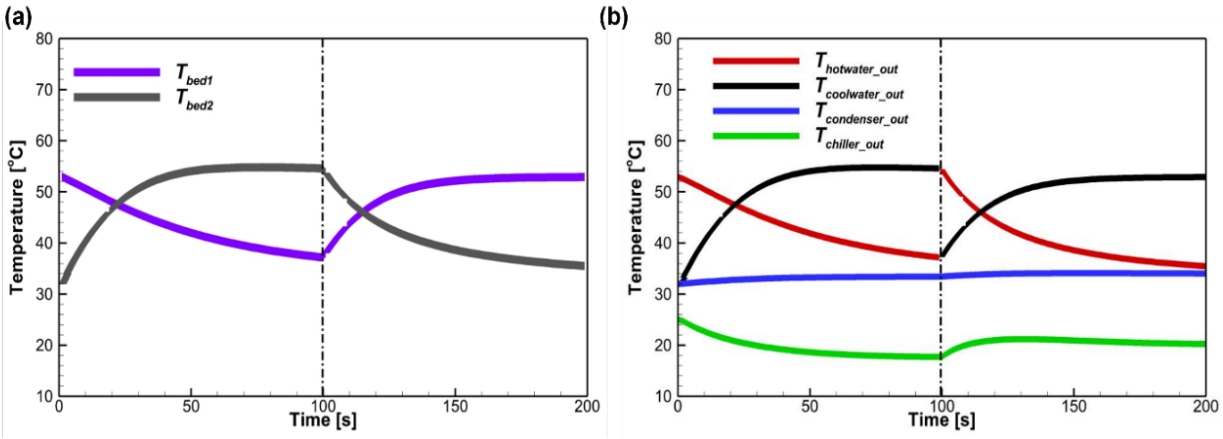

Figure 2. (a) Two beds temperature for Silica gel-water and (b) liquid output temperature at each component.

Figure 2(a) displays the temperatures in each adsorbent bed, illustrating how one bed absorbs while the other regenerates. Both beds receive water initially heated to 53.0°C for regeneration and water at 32.0°C for adsorption. Figure 2(b) shows outlet temperatures after heat exchange in the beds, indicating that a short cycle time of about 200 seconds is required at 53.0°C/32.0°C. The condenser temperature remains stable between 32.0°C and 33.5°C. Globally, data centers relying on air cooling have maintained a PUE of 1.55–1.59 since 2020 (Davis et al. 2022). A 200 kW immersion-cooled data center would consume 210.16 kWh total power (cooling: 10.16 kWh), producing a $\mathrm{PUE}_{\mathrm{cooling}}$ of 1.051. When adding an adsorption heat pump plus 18 kW of air-cooled ITE, total power climbs to 232.16 kWh (cooling: 14.16 kWh), yielding a $\mathrm{PUE}_{\mathrm{cooling}}$ of 1.064. Although slightly higher, the extra 18 kW of cooling energy can be more effectively utilized. The TUE metric shows a starker difference: 2.131 for a pure air-cooled approach and 1.345 for immersion

cooling alone. With the combined waste heat recovery system, the $TUE_{cooling}$ is 1.367, a marginal increase but one offset by the advantages of recovering waste heat.

4. CONCLUSIONS

This study introduces an innovative system that pairs immersion cooling with an adsorption heat pump, converting waste heat into a secondary cooling source. Three main goals are addressed: (1) designing an integrated 200 kW waste heat recovery system, (2) determining optimal conditions for operating the adsorption heat pump on immersion-cooling waste heat, and (3) assessing energy efficiency via PUE/TUE. Two adsorbents were tested under the LDF model for adsorber, desorber, evaporator, and condenser energy balances. Silica gel achieved a higher COP at 53.0°C, while MIL101Cr recorded a COP near 0.4, indicating good regeneration potential. For a 200 kW immersion-cooled ITE load plus 18 kW of air-cooled ITE, power usage reached 232.16 kWh, corresponding to a $PUE_{cooling}$ of 1.064. Separating liquid- and air-cooled loads yielded a $TUE_{cooling}$ of 1.367—slightly above immersion cooling alone, yet still advantageous for waste heat recovery. Future research should address stable adsorption cycle operation and low efficiency while considering real-world variables such as cooling tower availability. Developing real-time control algorithms for adsorption cycle phases could optimize both throughput and energy efficiency. Also, investigating next-generation adsorbents, such as metal-organic frameworks (MOFs) and advanced composites, to improve regeneration under moderate-temperature inputs. Lastly, evaluating how surplus heat could be fed into local district heating networks, thus expanding the beneficial re-use of waste heat beyond the data center itself.

ACKNOWLEDGEMENTS

This work was supported by the Korea Institute of Energy Technology Evaluation and Planning (KETEP) and the Ministry of Trade, Industry and Energy (MOTIE) of the Republic of Korea (No. RS-2024-00421998).

REFERENCES

Al-Mousawi F.N., Al-Dadah R., Mahmoud S., 2016. Low grade heat driven adsorption system for cooling and power generation using advanced adsorbent materials. Energy Conversion and Management 126, pp. 373-384.

Avelar V., Azevedo D., French A., 2012. PUE™: A comprehensive examination of the metric. The Green Grid White Paper #49. The Green Grid Technical Committee.

Cho J., Lee J., 2024. Higher-efficiency redundancy strategy for data center cooling. ASHRAE Journal 66, pp. 34-46.

Cho J., Lim S.-B., 2023. Balanced comparative assessment of thermal performance and energy efficiency for three cooling solutions in data centers. Energy 285, pp. 129370.

Cho J., Park B., Jang S., 2022. Development of an independent modular air containment system for high-density data centers: Experimental investigation of row-based cooling performance and PUE. Energy 258, pp. 124787.

Davis J., Bizo D., Lawrence A., Rogers O., Smolaks M., Simon L., Donnellan D., 2022. Uptime institute global data center survey 2022. Uptime Institute Intelligence.

Gediz Ilis G., Demir H., Saha B.B., 2021. Analysis of operation and construction parameters for adsorption chiller performance with Matlab/Simulink simulation. Applied Thermal Engineering 198, pp. 117499.

Jang S., Cho J., 2024. Waste heat recovery from data center cooling systems for district heating. ASHRAE Transactions 130, pp. 1063-1071.

Masanet E., Shehabi A., Lei N., Smith S., Koomey J., 2020. Recalibrating global data center energy-use estimates. Science 367, pp. 984-986.

Patterson M.K., Poole S.W., Hsu C.-H., Maxwell D., Tschudi W., Coles H., Martinez D.J., Bates N., 2013. TUE, a new energy-efficiency metric applied at ORNL's Jaguar. Lecture Notes in Computer Science 7905, pp. 372-382.

Sohel Murshed S.M., Nieto de Castro C.A., 2017. A critical review of traditional and emerging techniques and fluids for electronics cooling. Renewable and Sustainable Energy Reviews 78, pp. 821-833.

Zhang H., Shao S., Xu H., Zou H., Tian C., 2014. Free cooling of data centers: A review. Renewable and Sustainable Energy Reviews 35, pp. 171-182.

6th International Conference on Building Energy and Environment
Eindhoven University of Technology, The Netherlands
6 - 10 July 2025

Investigation on Thermal Performance of the Phase Change Material-assisted Earth-to-Air Heat Exchanger Based on Recurrent Neural Networks

Zehui Yang [1], Weilan Wu [2], Tiecheng Zhou [3], Huating Zhang [4], Yimin Xiao [5*]

[1]College of Civil Engineering, Chongqing University, China, 958732868@qq.com
[2]CMCU Engineering Co., Ltd, China, wwl1971123@126.com
[3] CMCU Engineering Co., Ltd, China, ztc18875207580@126.com
[4]CMCU Engineering Co., Ltd, China, 20231601115G@stu.cqu.edu.cn
[5]College of Civil Engineering, Chongqing University, China, xiaoyimin@cqu.edu.cn(Corresponding author)

SUMMARY
This study aims to develop a predictive model based on recurrent neural networks for the rapid and accurate prediction of the complex heat transfer processes within PCM earth-to-air heat exchangers (PCM-EAHE), thereby facilitating system design. Recurrent neural networks, long short-term memory networks, gated recurrent units, and bidirectional recurrent neural networks were primarily employed to assess the performance of various neural network architectures in predicting the heat transfer performance of PCM-EAHE. The model can rapidly and accurately predict the outlet air temperature by using the inlet air temperature, pipe geometry, and inlet air velocity as inputs. A validated numerical model of the PCM-EAHE was developed, and datasets for neural network training were generated based on variations in geometries, inlet air velocities, and inlet air temperatures. After training various neural networks, the bidirectional gated recurrent unit demonstrated the best predictive performance following hyperparameter optimization, achieving an RMSE of 0.9944, an R^2 of 0.8781, and an MAE of 0.6726.

Keywords: Phase Change Material (PCM), Earth-to-air Heat Exchanger, Recurrent Neural Network (RNN), Long Short-Term Memory Network (LSTM), Gated Recurrent Unit Network (GRU, Heat Transfer Prediction.

1. GENERAL INSTRUCTIONS

In modern energy management and sustainable building design, the integration of phase change materials (PCM) with soil-air heat exchangers can form PCM-EAHE systems. This system utilizes phase change materials to facilitate the spatiotemporal transfer of natural energy stored in outdoor air, thereby enhancing the preconditioning effect of fresh air within the system. In recent years, research in this field has grown rapidly (Ren et al., 2024b). However, the complex heat transfer processes within PCM-earth-to-air heat exchangers (PCM-EAHE), involving mechanisms such as phase change and convection, pose challenges for traditional computational fluid dynamics (CFD) methods, which are computationally expensive and time-consuming. With the development of machine learning, particularly neural network technologies, researchers have begun exploring their application in predicting the heat transfer performance of PCM soil-air heat exchangers to enhance prediction efficiency and accuracy (Wang and Wang, 2021).

In recent years, neural networks have found increasing applications in fluid mechanics and heat transfer problems. Deep learning frameworks, such as convolutional neural networks (King et al., 2024), long short-term memory networks (G. Li et al., 2024), feedforward backpropagation

artificial neural networks (Ermis et al., 2007), and physics-informed neural networks (Eivazi et al., 2022), have been successfully applied to model and predict various fluid heat transfer problems, including natural and forced convection. Particularly with the aid of computational fluid dynamics (CFD), neural networks can approximate complex nonlinear heat conduction and fluid flow equations by learning from large datasets of simulation or experimental data, enabling rapid and accurate predictions of heat transfer performance (Wang et al., 2023; Yue et al., 2024).

Although neural networks have seen extensive applications in computational fluid dynamics and heat transfer prediction, research on their application in predicting the heat transfer performance of PCM-EAHE systems remains limited. This study first developed an experimentally validated numerical model of a PCM-EAHE to generate the requisite datasets for training. Various models were then trained on the same dataset to evaluate their predictive performance, aiming to promote the application and adoption of this technology in practical engineering.

2. NUMERICAL MODELS

2.1. Physical model description

This study focuses on an EAHE integrated with PCM, where cylindrical PCM materials are placed inside the pipes of the soil-air heat exchanger. This pipe system is primarily used in summer to precondition fresh air for air conditioning. As air flows through the pipes, it exchanges heat with the PCM materials and the surrounding soil, thereby preconditioning the air, reducing the fresh air load during the summer, and lowering air conditioning energy consumption, as illustrated in Figure 1.

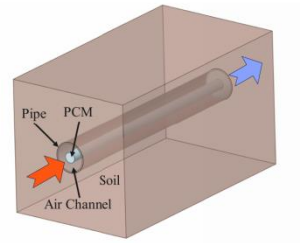

Figure 1. Schematic diagram of CPCM-EAHE（cylindrical phase change material -filled earth-air heat exchanger) device shape.

2.2. Control Equations

The numerical model of the PCM-EAHE was developed using the finite volume method. To facilitate subsequent computational analysis, it is assumed that the air is incompressible, and that the effect of moisture content variation inside the shaft on heat transfer is neglected. Only sensible heat exchange in the buried pipe is considered. The soil and PCM are treated as isotropic materials, and thermal contact resistance within the system is neglected. The effects of pipe wall thickness and air gravity are also disregarded. Additionally, it is assumed that the PCM-soil air heat exchanger is buried in a region where the soil temperature is constant throughout the year.

The computational domain of the model encompasses the air, phase change material, and soil regions. The air region is divided into uniform blocks, with a grid size of dz and a total number of grids equal to Z/dz. Radially, the air is assumed to be uniformly distributed, and no radial grid division is performed. The phase change material (PCM) has a radius of r_p and is uniformly divided into M radial layers, with a radial grid size of $\Delta r_p = r_p/M$. The axial grid size is consistent

with that of the air region. The soil region has an inner radius of r_{s1} and an outer radius of r_{s2}, with J radial grids and a radial grid size of $\Delta r_s = (r_{s2} - r_{s1})/J$. The axial grid size is consistent with that of the air region.

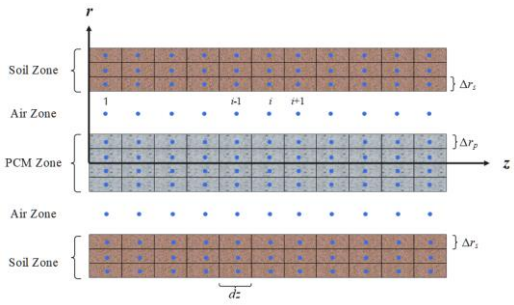

Figure 2. Grid division and structure diagram of CPCM-EAHE system.

The detailed parameters of the phase change material (PCM) are provided in Table 1.

Table 1. Thermophysical parameters of phase change materials.

Characteristics	Phase change materials
$\lambda(\mathrm{W \cdot m^{-1} \cdot ^{\circ}C^{-1}})$	5.43(s)/3.26(l)
$\rho(\mathrm{kg \cdot m^{-3}})$	904.5
$c_p(\mathrm{J \cdot kg^{-1} \cdot ^{\circ}C^{-1}})$	1750
$T_m(^{\circ}\mathrm{C})$	28.16-32.68
$L_p(\mathrm{kJ \cdot kg^{-1}})$	135.7

2.1.1. Energy governing equation of the air layers

Based on the energy conservation equation and the mathematical model, the energy governing equation for the air region, as shown in Equation (1). From left to right, the terms represent the unsteady term, convective term, diffusion term, and convective source term, respectively.

$$\pi(r_a^2 - r_p^2)\rho_a \frac{\partial T_a}{\partial \tau} + \pi(r_a^2 - r_p^2)\rho_a u \frac{\partial T_a}{\partial z} = \pi(r_a^2 - r_p^2)\frac{\lambda_a}{C_a}\frac{\partial^2 T_a}{\partial z^2} + \frac{S_c}{C_a} \quad (1)$$

In the above equation, r_a represents the equivalent radius of the vertical shaft channel; ρ_a is the air density; C_a denotes the specific heat capacity of air; λ_a is the thermal conductivity of air; T_a represents the air temperature; u is the airflow velocity; and S_c denotes the source term for convective heat and mass transfer in air.

2.1.2. Energy governing equation of the phase change material layers

Similarly, based on the energy conservation equation, the energy governing equation for the PCM region, as shown in Equation (2).

$$\rho_p C_p \frac{\partial T_p}{\partial \tau} = \lambda_p\left(\frac{\partial^2 T_p}{\partial r^2} + \frac{1}{r}\cdot\frac{\partial T_p}{\partial r} + \frac{\partial^2 T_p}{\partial z^2}\right) \quad (2)$$

In the equation, C_p represents the specific heat capacity of the phase change material (PCM); ρ_p is the density of the PCM; and T_p denotes the central temperature of the PCM layer..

2.1.3. Energy governing equation of the soil layers

Based on the energy conservation equation, the energy governing equation for the soil region, as shown in Equation (3).

$$\rho_s C_s \frac{\partial T_s}{\partial \tau} = \lambda_r \left(\frac{\partial^2 T_s}{\partial r^2} + \frac{1}{r} \cdot \frac{\partial T_s}{\partial r} + \frac{\partial^2 T_s}{\partial z^2}\right) \tag{3}$$

In the equation, C_s represents the specific heat capacity of the soil; ρ_s is the density of the soil; and T_s denotes the central temperature of the soil layer.

2.2. Experimental Validation

The experimental parameters from Zhou (Zhou et al., 2020) for the PCM-soil-air heat exchanger are applied to the numerical model in this study. The results from the numerical model are compared with the experimental data. As shown in Figure 3, the final results demonstrate that the numerical model achieves good agreement with the experimental data. The average absolute error in outlet air temperature is 0.46°C, with a maximum absolute error of 1.1°C and a maximum relative error of 1.79%.

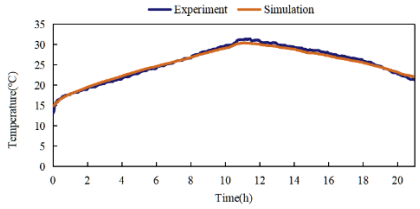

Figure 3. Comparison of numerical model calculations with experimental data.

3. NEURAL NETWORK MODEL

3.1. Neural Network Architecture

3.1.1. Recurrent Neural Network (RNN)

Recurrent Neural Networks (RNNs) are a type of artificial neural network designed for sequence modeling. Unlike traditional feedforward neural networks, RNNs allow data to flow horizontally between neurons, capturing the correlation between data points. The distinctive feature of RNNs lies in the interconnections among neurons in the hidden layer, which enable the sequential transmission of time-dependent input data within a sliding window. Its mathematical expression is provided in Equation (4) (King et al., 2024).

$$Y_t = tanh(Ux_t + WY_{t-1} + b_h) \tag{4}$$

In the equation: Y represents the state value at each time step; U is the weight of the input at time t; W is the weight of the state at time $t-1$; b_{h} is the bias term.

3.1.2. Long Short-Term Memory Neural Network (LSTM)

Although RNNs can effectively process nonlinear time series, they suffer from the vanishing gradient and exploding gradient problems, which limit their ability to handle time series with excessively long sliding windows. Moreover, training an RNN model requires a predefined window length, which is challenging to optimize automatically in practical applications. To

address these issues, the LSTM model introduces a mechanism called the "cell state," which effectively captures long-term dependencies. Its forward computation can be expressed as follows (Wan, 2024):

$$i_t = \sigma(W_{xi}x_t + W_{hi}Y_{t-1} + b_i) \quad (5)$$
$$f_t = \sigma\left(W_{xf}x_t + W_{hf}Y_{t-1} + b_f\right) \quad (6)$$
$$c_t = f_t c_{t-1} + i_t tanh(W_{xc}x_t + W_{hc}Y_{t-1} + b_c) \quad (7)$$
$$o_t = \sigma(W_{xo}x_t + W_{ho}Y_{t-1} + W_{co}c_t + b_o) \quad (8)$$
$$Y_t = o_t tanh(c_t) \quad (9)$$

In the equation: i_t, f_t, c_t, and o_t represent the input gate, forget gate, cell state, and output gate, respectively; W and b denote the corresponding weight matrices and bias terms; σ and tanh represent the Sigmoid and hyperbolic tangent activation functions, respectively.

3.1.3. Gated Recurrent Unit (GRU)

The GRU model is a simplified version of the LSTM model, retaining its long-term memory capabilities. The primary modification involves replacing the input gate, forget gate, and output gate in the LSTM cell with an update gate and a reset gate. By introducing this gating mechanism, the GRU controls the flow of information and captures long-term dependencies more effectively. Its mathematical expression is provided in the equation (Sui et al., 2024):

$$z_t = \sigma(W_z h_{t-1} + U_z x_t + b_z) \quad (10)$$
$$r_t = \sigma(W_r h_{t-1} + U_r x_t + b_r) \quad (11)$$
$$\tilde{Y}_t = tanh(W_h x_t + U_h(r_t Y_{t-1}) + b_h) \quad (12)$$
$$Y_t = (1 - z_t)h_{t-1} + z_t \tilde{Y}_t \quad (13)$$

In the equation: r_t represents the output of the reset gate; z_t represents the output of the update gate; $\tilde{Y}_t$ denotes the hidden state at the current time step; W_{r} and U_{r} are the weights of the reset gate to the hidden state and input, respectively; W_{z} and U_{z} are the weights of the update gate to the hidden state and input, respectively; U_{h} and W_{h} represent the weights of the hidden state to itself and to the cell input, respectively; b_{r} and b_{z} are the biases of the reset and update gates. σ denotes the Sigmoid function, and tanh denotes the hyperbolic tangent function.

3.1.4. Bidirectional Recurrent Neural Network (Bi-RNN)

If a complete sequence is available during training, a Bidirectional Recurrent Neural Network (Bi-RNN) can be constructed. Traditional RNNs process sequential data in a unidirectional manner, from past to future, whereas Bi-RNNs capture contextual information from both the past and the future at each time step, leading to improved performance in many tasks. The hidden states are computed for both the backward and forward directions (F. Li et al., 2024). In this study, the Bi-RNN will be applied to both the GRU and LSTM models to construct Bidirectional Gated Recurrent Unit (Bi-GRU) and Bidirectional Long Short-Term Memory (Bi-LSTM) networks, and their performance will be compared.

3.2. Hyperparameter Fine-tuning

The hyperparameters of the neural network are determined using a grid search method, with the specific settings listed in Table 2. This study employs Python as the programming environment and PyTorch as the deep learning framework for training and prediction.

Table 2. Setting of hyperparameters.

Learning rate	Iterations	Batches	Layers	Neurons
0.0005	100	4	4	16
0.001	500	8	5	32
0.005	1000	16	6	64

3.3. Evaluation Index for Network

This study primarily employs three key performance metrics: $RMSE$, R^2, and MAE, to evaluate the model. The specific calculation formulas are as follows:

$$R^2 = 1 - \frac{\sum_{i=0}^{m}(y_i - \hat{y}_i)^2}{\sum_{i=0}^{m}(y_i - \bar{y})^2} \tag{14}$$

$$RMSE = \sqrt{\frac{1}{m}\sum_{i=1}^{m}(y_i - \hat{y}_i)^2} \tag{15}$$

$$MAE = \frac{1}{m}\sum_{i=1}^{m}|y_i - \hat{y}_i| \tag{16}$$

In the equation: y_i is the true value, $\hat{y}$ is the predicted value, and m is the number of samples.

4. DATA SETS

Based on the design parameters of the PCM soil-air heat exchanger in practical applications, five variables were defined: PCM pipe diameter, ventilation pipe diameter, pipe length, inlet temperature, and inlet air velocity. Considering the actual diameter of PCM ventilation pipes, the PCM pipe diameter and ventilation pipe diameter were set between 0.05 m and 0.3 m, while the pipe length ranged from 10 m to 45 m. The inlet temperature was selected from hourly temperature measurements during the summer months (May to September) in a typical meteorological year in Chongqing (Ren et al., 2024a), and the inlet air velocity was set between 0.5 m/s and 2.5 m/s. The specific training and test sets are presented in Tables 3 and 4.

Recurrent neural networks require input time series data for computation. In this study, the time series for all models was set to 15 days, comprising 360 hours of temperature data. The 360-hour temperature data, along with the PCM pipe diameter, ventilation pipe diameter, and pipe length, were organized into a (360, 5) matrix as input data for the model. A corresponding (360, 1) matrix containing the 360-hour outlet temperature data served as the output data.

Table 3. Parameters for the experimental setup of the training dataset.

Level	PCM pipe diameter (m)	Ventilation pipe diameter (m)	Pipe length (m)	Inlet air velocity (m/s)	Inlet temperature date
1	0.05	0.05	10	0.5	May 16 - May 30
2	0.12	0.17	28	1.5	May 31-June 14
3	0.2	0.3	45	2.5	June 15 - June 29

Table 4. Parameters for the experimental setup of the test dataset.

Level	PCM pipe diameter (m)	Ventilation pipe diameter (m)	Pipe length (m)	Inlet air velocity (m/s)	Inlet temperature date
1	0.08	0.07	15	0.8	July 30-August 13
2	0.14	0.18	24	1.3	August 13-August 28

3	0.18	0.25	40	2.4	August 29-September 12

5. ANALYSIS OF RESULTS

Firstly, the dataset and initial hyperparameters described earlier were used to train each model. The initial hyperparameters are shown in Table 6. After training, the prediction accuracy of each model was obtained before hyperparameter tuning. Then, hyperparameter tuning was performed for each model, and the prediction errors after tuning were obtained. The prediction performance of each model was evaluated using three metrics (RMSE, R^2, and MAE), as shown in Table 7. The final results indicate that the prediction performance of all models improved by an average of 17% after hyperparameter tuning. The BiGRU model demonstrated the best prediction accuracy, with an RMSE of 0.9944, R^2 of 0.8781 and MAE of 0.6726 after hyperparameter tuning.

Table 5. Initial hyperparameters for each model.

Learning rate	Iterations	Batches	Layers	Neurons
0.005	500	8	4	64

Table 6. Accuracy of the models' predictions.

	Before/after hyperparameter tuning		
Model	$RMSE$	R^2	MAE
RNN	2.1947/1.4309	0.4064/0.7477	1.6593/1.0581
LSTM	1.4468/1.2216	0.7420/0.8161	1.0498/0.8324
GRU	1.5245/1.0217	0.7136/0.8714	1.2225/0.7424
BiLSTM	1.4960/1.2638	0.7242/0.8031	1.0690/0.9144
BiGRU	1.2206/**0.9944**	0.8164/**0.8781**	**0.9165/0.6726**

Furthermore, to provide a more intuitive analysis of the prediction results from different models and verify their prediction accuracy, all models, after hyperparameter tuning, were tested using a 360-hour dataset. The comparison between predicted and actual results is presented in Figure 4. As shown in the figure, all models effectively captured the output temperature variation trend, with their predictions closely following the actual values. The Bi-GRU model produced predictions that were closest to the actual values, consistent with the accuracy evaluation metrics.

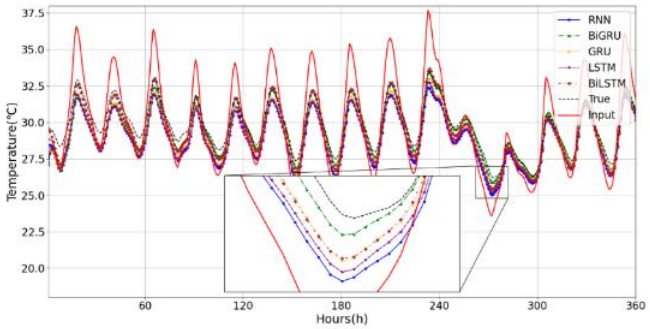

Figure 4. Comparison of the predicted results of the models with the true results.

6. CONCLUSION

To efficiently and accurately predict the heat transfer performance of PCM-soil-air heat exchangers, this study proposes a prediction model based on recurrent neural networks (RNNs). By comparing different RNN models and conducting an exhaustive hyperparameter search, the model's full potential was explored. The following conclusions were drawn: five different types of recurrent neural networks were trained using the original dataset. After hyperparameter tuning, the best-performing model was the Bi-GRU, which achieved an RMSE of 0.9944, R^2 of 0.8781, and MAE of 0.6726. The results indicate that RNNs can effectively predict the heat transfer performance of PCM-soil-air heat exchangers. However, due to limitations in the training dataset size and input parameters, the overall prediction accuracy of the neural network remains suboptimal. Future work should focus on further enhancing the training dataset to identify more robust datasets and comprehensively improve model performance.

ACKNOWLEDGMENT

This work was supported by Graduate Research and Innovation Foundation of Chongqing, China (No. CYB240037).

REFERENCES

Eivazi, H., Tahani, M., Schlatter, P., Vinuesa, R., 2022. Physics-informed neural networks for solving Reynolds-averaged Navier–Stokes equations. Physics of Fluids 34, 075117.

Ermis, K., Erek, A., Dincer, I., 2007. Heat transfer analysis of phase change process in a finned-tube thermal energy storage system using artificial neural network. International Journal of Heat and Mass Transfer 50, 3163–3175.

King, M., Woo, S.I., Yune, C.-Y., 2024. Utilizing a CNN-RNN machine learning approach for forecasting time-series outlet fluid temperature monitoring by long-term operation of BHEs system. Geothermics 122, 103082.

Li, G., Wang, Y., Xu, C., Wang, J., Fang, X., Xiong, C., 2024. BO-STA-LSTM: Building energy prediction based on a Bayesian optimized spatial-temporal attention enhanced LSTM method. Developments in the Built Environment 18, 100465.

Ren, Z., Ren, Y., Zhou, T., Wang, T., Gao, X., Yang, Z., Xiong, Q., Chen, S., Xiao, Y., 2024a. Investigating the dynamic thermal performance of a novel PCM to earth-air heat exchanger: Developing numerical model and comparing thermal performance. Journal of Building Engineering 97, 110718.

Ren, Z., Ren, Y., Zhou, T., Xiao, Y., Zeng, Z., 2024b. The effect of operation modes on the thermal performance of a novel multi-tubular phase change material-filled earth-air heat exchanger. Renewable Energy 237, 121887.

Sui, L., Sun, W., Liu, W., Xiong, W., 2024. A sparse regularized soft sensor based on GRU and self-interpretation double nonnegative garrote: From variable selection to structure optimization. Control Engineering Practice 153, 106074.

Wan, S., 2024. Improved whale optimization algorithm towards precise state-of-charge estimation of lithium-ion batteries via optimizing LSTM. Energy.

Wang, B., Wang, J., 2021. Application of Artificial Intelligence in Computational Fluid Dynamics. Industrial & Engineering Chemistry Research.

Wang, Y., Ma, Y., Chao, H., 2023. Machine learning and computational fluid dynamics based optimization of finned heat pipe radiator performance. Journal of Building Engineering 78, 107612.

Yue, Y., Yan, Z., Ni, P., Lei, F., Yao, S., 2024. Machine learning-based multi-performance prediction and analysis of Earth-Air Heat Exchanger. Renewable Energy 227, 120550.

Zhou, T., Xiao, Y., Huang, H., Lin, J., 2020. Numerical study on the cooling performance of a novel passive system: Cylindrical phase change material-assisted earth-air heat exchanger. Journal of Cleaner Production 245, 118907.

6th International Conference on Building Energy and Environment
Eindhoven University of Technology, The Netherlands
6 - 10 July 2025

Performance Analysis of a Heat Pump System for a PV integrated Building in Hot-summer and Cold-winter Region in China

Yilin Li [1,2,3], Hao Lu[1], Tianhang Wang [1], Shiji Zong [1], Yang Lu [1]

[1] *University of Shanghai for Science and Technology, Shanghai, China, yilin.li@usst.edu.cn*
[2] *Jiangsu Province Engineering Research Center of Construction Carbon Neutral Technology, Suzhou University of Science and Technology, Suzhou, China*
[3] *Key Laboratory of Ecology and Energy Saving Study of Dense Habitat, Ministry of Education, China*

ABSTRACT
With the wide application of building integrated PV systems, there is an increasing demand for DC inverter heat pumps in buildings. In this paper, the performance of a DC inverter heat pump system for integration in a PV integrated building was analyzed. The PV power fluctuation and demand-side load characteristics were first analyzed based on the operational data obtained from two case study buildings located in hot-summer and cold-winter regions in China. Then, the numerical models for the heat transfer and energy conservation of the integrated system in a reference building were developed. A control strategy for the heat pump was proposed accounting for the characteristics of PV power generation and demand-side heating load. By using MATLAB software, the performance of the integrated system was simulated. The simulation results indicate that the proposed strategy can achieve stable operational characteristics of the DC inverter heat pump while maintaining the thermal comfort level of the indoor thermal environment. Therefore, the heat pumps employ a start-up and standby control strategy. Adjusting the setting range of the room temperature can significantly affect the allowable standby time of heat pumps. The standby time duration of heat pumps can be extended to about 20~30% by reducing the room temperature from Class I to Class II comfort criteria in Chinese national standards.

Keywords: DC inverter heat pump, PV power fluctuation, Demand-side characteristic, performance analysis.

1. INTRODUCTION

Climate change and energy crises are major global challenges. With population growth and rapid increase in energy demand, traditional energy consumption and environmental pollution are becoming increasingly serious (Tan et al. 2022) (Wang et al. 2023). China is committed to achieving a "carbon peak" by 2030 and "carbon neutrality" by 2060 (Chen et al. 2022), and building energy consumption accounts for 45.6% of the country's total energy consumption, with the power sector and the building sector accounting for about 21% and 59% of carbon emissions, respectively (Lin et al. 2022). Therefore, energy saving and carbon reduction in the power industry and buildings are urgent. As a renewable energy source, solar energy is clean and economical, allowing it to be exploited for a variety of applications, including power generation and heating for domestic and industrial processes (Krishnan et al. 2023). In order to meet the needs of carbon neutrality, Jiang proposed the “Photovoltaics, Energy storage, Direct current and flexibility” (PEDF) technology. It connects photovoltaic systems directly to building DC buses, reducing energy conversion losses, and allows buildings to flexibly adjust their energy supply and demand, participating in grid dispatch. (Liu et al. 2022; Jiang 2021). However, the indirectness, randomness,

volatility of new energy generation and the uncertainty of building user loads have led to prominent supply and demand balance problems in the power system (Wang et al. 2019; Zhu et al. 2023), and there is an exigent need to research and develop DC power equipment and related regulation strategies that can be used in PEDF buildings (Notton et al. 2018).

DC inverter heat pump systems have become an important part of energy-efficient technologies for buildings due to their high energy efficiency and flexibility. These systems can directly utilize building-generated DC power, omitting energy conversion losses and improving the efficiency of energy use (Liu et al. 2022). However, the operation of DC inverter heat pump systems is affected by fluctuations in photovoltaic (PV) power generation and demand-side load characteristics, and flexible operation strategies need to be developed to accommodate these variations (Liu et al. 2022). In hot-summer and cold-winter regions, these systems not only have to cope with the heat load demand under extreme climatic conditions but also have to take into account the seasonal and intra-day fluctuations of PV power generation, as well as the uncertainty of building occupant loads (Wang et al. 2019).

Although some studies have explored regulation strategies for heat pump systems based on source-side and load-side characteristics, few focus on DC heat pump systems in PEDF buildings. Given the instability of new energy generation and the uncertainty of building occupant loads, combining unit power regulation and indoor temperature regulation to develop a reasonable DC heat pump system strategy is crucial for safe and reliable system operation (Jiang 2021). Currently, theoretical and practical applications of such heat pump systems in PEDF buildings are limited, mostly based on demonstration projects (Chen et al. 2021).

The research is motivated by the urgent need for energy-saving and carbon reduction in the power and building industries. PEDF buildings, as a key solution, require effective regulation strategies for their DC heat pump systems to balance the instability of power generation with load-side consumption characteristics. Fig. 1 shows the schematic diagram of the DC inverter heat pump system. The research aims to address the energy-saving and carbon-reduction needs in power and building sectors by developing effective regulation strategies for DC heat pump systems in PEDF buildings, balancing power generation instability with load-side consumption.

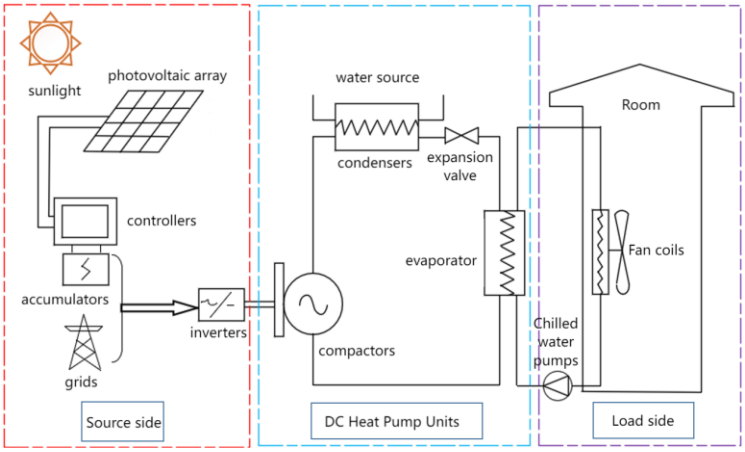

Figure 1. DC heat pump system composition schematic

2. METHODOLOGY

2.1 Case Study Buildings

Two case buildings located in hot-summer and cold-winter regions were selected for analyzing the power generation and demand-side characteristics. Both of them are office buildings, and located in industrial parks Shanghai, and Suzhou respectively, as shown in Fig. 2. In summer, the region has sufficient solar radiation and continuous sunshine hours, and the PV power generation is sufficient; while in winter, the number of sunshine hours is significantly reduced, and the solar radiation time is greatly shortened, compared with the summer PV power generation decreased significantly.

Figure 2. Conceptual overview of office buildings (left) and distributed photovoltaic systems (right)

2.2 Modeling of DC heat pump system

Based on the fluctuating characteristics of bus voltage, experiments were conducted on the rated operating conditions of the unit at different bus voltages to study the effect of variable bus voltage on the rated heating and cooling capacity of the DC heat pump unit. The performance of the heat pump unit under rated bus voltage conditions is investigated for different partial load rates, customer-side inlet water temperatures, and water-side outlet pump temperatures. Then, the variable operating condition performance experiment of the unit under fixed voltage is carried out. Based on the analysis of the experimental data, the performance model of the DC heat pump unit under different operating conditions is constructed, which provides a basis for the establishment of the overall model of the subsequent system.

2.3 Numerical modeling of heat transfer and energy conservation

A standard office building model was established, with an office building in Shanghai as a prototype. Energy Plus software was used to simulate the building load and energy consumption, and an equivalent RC model was established for the standard building.

According to the analysis of each node in Fig. 3, the indoor and outdoor heat balance equations of the building are shown in Eq. (1); the amount of cold and heat delivered by the HVAC system for the interior of the building is shown in Eq. (2); and the hour-by-hour solar radiation heat gain approximation replaces the heat gain through solar radiation illuminance calculations is shown in Eq. (3). The unknown parameters of the RC model were identified using a genetic algorithm with the data obtained from the simulation in Energy Plus as the driving source, and a load prediction

model was obtained for the building. On this basis, load calculations and predictions for a standard building model are obtained, which have an important impact on the regulation of the DC heat pump system. In this way, the control strategy of the heat pump can be proposed taking into account the characteristics of PV power generation and demand side heat load.

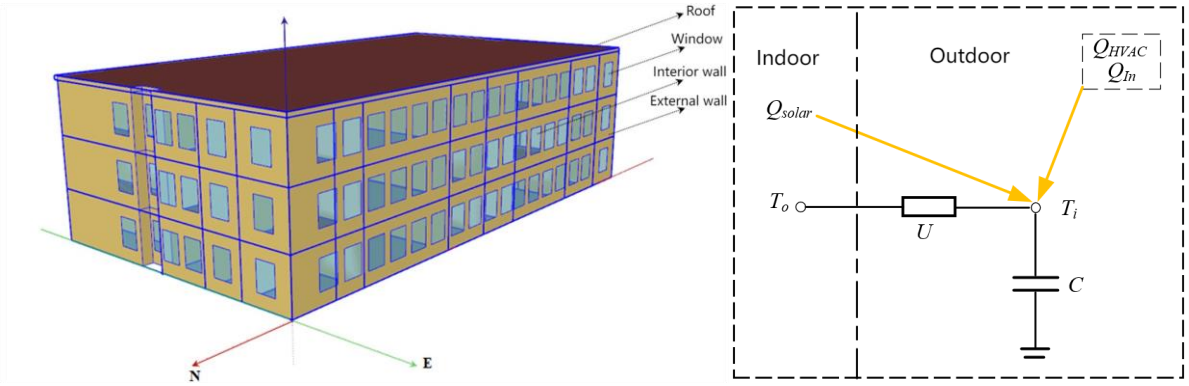

Figure 3. Office building 3D model schematic (left) and First-order equivalent RC model of a building(right)

$$C\frac{dT_i(t)}{dt} = \frac{(T_o(t)-T_i(t))}{R} + Q_{HVAC}(t) + Q_{\text{mn}}(t) + Q_{\text{solar}}(t) \quad (1)$$

$$Q_{HVAC} = \rho m c_p(\triangle T) \quad (2)$$

$$Q_{\text{Solar}}(t) = pI(t) \quad (3)$$

$$Q_{\text{load}} = Q_{HVAC} \quad (4)$$

Where T_O(℃) is outdoor air temperature node,T_i(℃) is indoor air temperature node, C(J/K) is Combined equivalent heat capacity of the whole building, R(K/W) is the combined thermal resistance of the building, the reciprocal of which is the combined heat transfer coefficient of the building, Q_{HVAC}(W) is Cooling/heating provided by the air conditioning system to the interior of the building, as negative/positive values, Q_{Solar}(W) is Heat gained by buildings through solar radiation, Q_{in}(W) is indoor heat, ρ(kg/m³) is density of water, m(m³/s) is water flow, $C_P(J/(kg \cdot K))$ is Constant pressure specific heat capacity of water, ΔT(℃) is Inlet and outlet water temperature difference, Q_{load}(W) is Building load, I(W/m^2) is solar radiation intensity, P(m^2) is Aggregate coefficients related to building surface area, absorptivity, reflectivity, etc.

2.4 Heat pump control strategy and simulation

The indoor design temperature has a direct impact on the power of the DC heat pump unit, and in PEDF buildings, the upper limit temperature of comfort level I is selected as the maximum PV consumption temperature, and the lower limit temperature of comfort level II is selected as the peaking temperature. In view of the fact that PEDF buildings can observe the state of the building power system through the bus voltage, a method of indoor design temperature setting based on the bus voltage is proposed. Table 1 shows the indoor temperature setting table designed based on the above principles, and the current heat pump operating mode and indoor temperature setting value are determined by the interval of the determined bus voltage.

Table 1. Indoor temperature setpoint based on bus voltage

Model name	Heat pump unit operation status	Bus voltage	Winter indoor temperature setting	Summer indoor temperature setting	comfort level
Down Frequency mode	Down Frequency	DC500V-DC576V DC656V-DC676V	18℃	28℃	Level II
Normal mode	Energy-saving	DC576V-DC596V	18℃	28℃	Level II
	Normal	DC596V-DC636V	22℃	26℃	Level I
	Overlimit	DC636V-DC656V	24℃	24℃	Level I
Standby mode	Shutdown	Less thanDC500V More thanDC676V	N/A	N/A	N/A

- When the bus voltage is at DC576 V~DC596 V, the electricity consumption of the building is mainly supplied through the utility power supply, and in order to minimize the electricity consumption of the HVAC system, the indoor temperature should be set to the lower bound of the comfort degree of level II;
- When the bus voltage is DC596 V~DC636 V, the photovoltaic power generation system normally supplies power for the building users, and the indoor temperature shall be set to the lower bound of Level I comfort;
- When the bus voltage is DC636 V~DC656 V, the PV power generation resources are relatively abundant, and the indoor temperature should be set as the upper limit of level I comfort in order to maximize the consumption of PV resources;
- When the bus voltage is DC500 V~DC576 V or DC656 V~DC676 V, the PV resources are extremely scarce or abundant, and too low or too high a voltage may lead to the burnout of the DC heat pump unit, and at this time, the power of the heat pump should be reduced to protect its safety;
- When the busbar voltage is at DC0 V~DC500 V or greater than DC676 V, it has exceeded the working range of the heat pump, and at this time, the DC heat pump unit should be temporarily shut down.

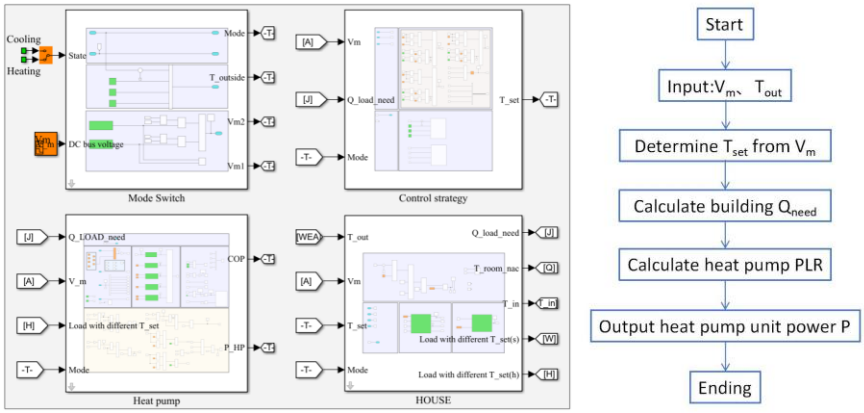

Figure 4. DC Heat Pump System Model (left) and DC heat pump unit control logic (right)

Then, the performance of the integrated system was simulated using MATLAB software. Fig. 4 illustrates some of the operational processes. The simulation model combines the developed numerical model and the proposed control strategy to evaluate the performance of the system in different scenarios.

3. RESULTS

3.1 Analysis of PV power fluctuation and demand-side load characteristics

By analyzing the PV power fluctuation and demand-side load characteristics of the case building, the instability of PV power generation is mainly caused by weather changes, seasonal differences, and intraday fluctuations. In terms of intraday fluctuations, the PV power is affected by the weather, and the maximum difference can be up to 260.1 kW, which poses a challenge to the safety and stability of the building's power equipment. Moreover, the energy consumption of the HVAC system of the office building accounts for a large proportion of the total energy consumption of the building, which is 61.71% and 39.36% on weekdays and days off, respectively. This high percentage of energy consumption and the intermittent mode of operation of the air conditioning system provide significant load regulation potential for the building.

3.2 Analysis of building load forecasting effects

Load calculations and forecasts have a significant impact on the regulation of DC heat pump systems. Load prediction is carried out for the data of the winter working week and the summer working week, respectively, and the results are shown in Fig. 5. The maximum heat load value of the building in winter is 105.81 kW at point 7 and the maximum cold load value of the building in summer is 156.88 kW at point 15. The results show that the MBE indicator of the winter load forecast value is 3.28 % and the RMSE indicator is 11.37 %, while the MBE indicator of the summer load forecast value is 4.78 % and the RMSE indicator is 14.19 %, which has a good forecasting effect.

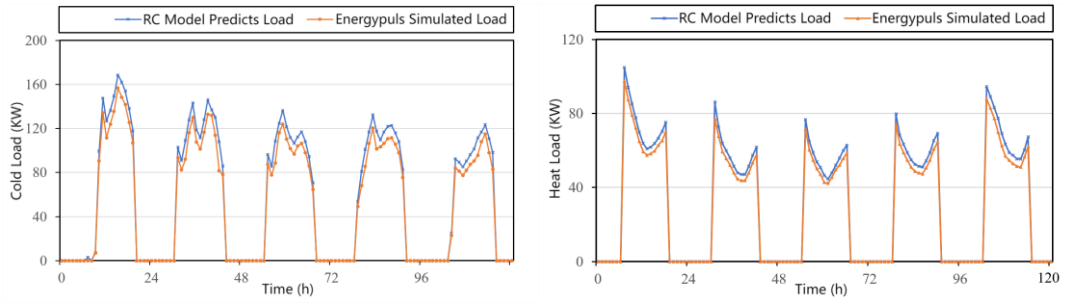

Figure 5. Building load forecast results for summer (left) and winter (right)

3.3 Analysis of model energy efficiency

In the normal bus voltage range, the strategy based on bus voltage compared with the traditional indoor temperature setting strategy can provide 9.29% and 14.32% of the additional photovoltaic consumption in the heating season and cooling season, and 22.81% and 11.98% of the power consumption reduction when the photovoltaic power generation is small. The variation curves of bus voltage, heat pump power, and outdoor temperature for heating conditions and cooling conditions are shown in Fig. 6. Compared with the basic working conditions, the heating season

and the cooling season can reduce the electricity consumption demand by 21.88% and 13.26% on the source side, respectively. In addition, the adjustment of the room temperature setting significantly affects the standby time of the heat pump. By gradually lowering the room temperature from level 1 comfort to level 2, the standby time can be extended to about 20~30%, making the heat pump operation more flexible and effectively reducing energy consumption during periods of low demand while maintaining the comfort level of the occupants.

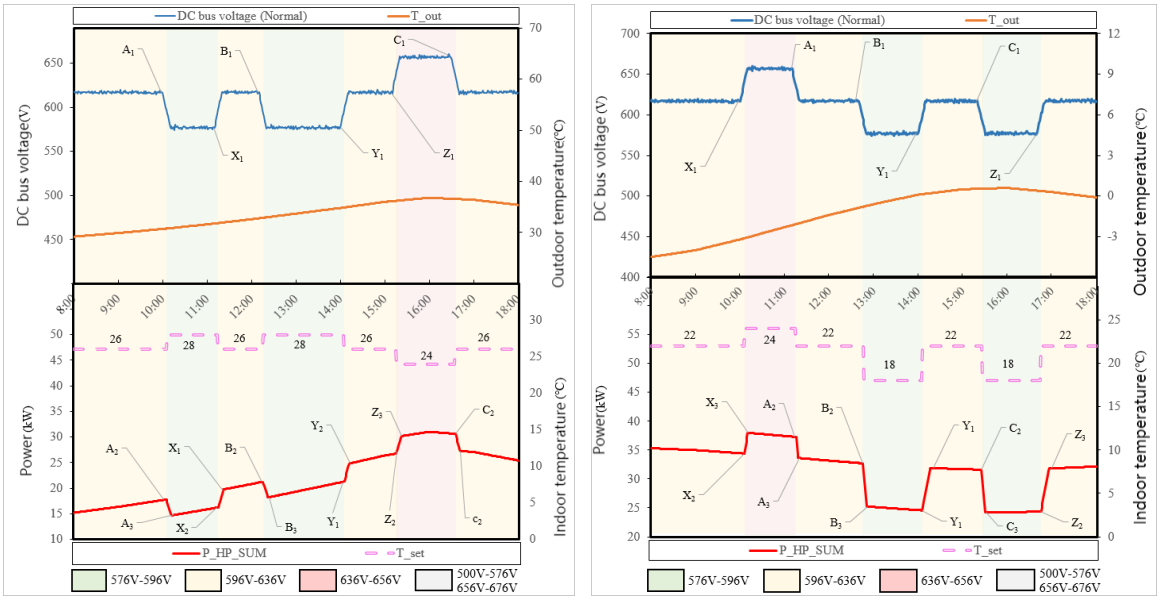

Figure 6. The variation curves of bus voltage, heat pump power, and outdoor temperature for heating condition (left) and cooling condition (right)

4. DISCUSSION

While the traditional strategy uses a constant indoor temperature setting (22~24°C in winter and 24~26°C in summer), this strategy dynamically adjusts the indoor temperature setting according to the fluctuation of the bus voltage and extends the standby time to reduce the start-stop time, reduce the energy consumption of the heat pump, and improve its safety. However, the strategy has only been studied by theoretical simulation, and experiments have not verified its effectiveness. Future research can further optimize the safe heating and cooling capabilities of the heat pump, propose a more effective control strategy by combining multiple climate zones and thermal comfort indicators, and verify the strategy's effectiveness through experiments.

5. CONCLUSIONS

This study takes the DC heat pump system as the research object, and based on the analysis of the characteristics of the source-side power supply and load-side power consumption of the actual PEDF building, it proposes a DC heat pump system regulation strategy that can adapt to the fluctuating bus voltage and meet the indoor comfort demand. The main research results are as follows:

- Substantial load regulation potential in the HVAC system of the case study buildings. The load

forecasting model showed good accuracy, with MBE and RMSE values indicating reliable predictions for both winter and summer periods.

- The proposed control strategy based on bus voltage demonstrated significant energy efficiency improvements. Compared to traditional indoor temperature setting methods, it increased PV consumption by 9.29% in the heating season and 14.32% in the cooling season. Additionally, it reduced power consumption by 22.81% in the heating season and 11.98% in the cooling season.
- Adjusting the indoor temperature settings from level I to level II comfort criteria significantly extended the allowable standby time of the heat pumps by approximately 20% to 30%.

In conclude, this strategy effectively balances the fluctuating PV power generation with the varying demand-side heating and cooling loads, ensuring stable operation of the heat pump system while maintaining indoor thermal comfort. The innovation of the strategy lies in its ability to dynamically adjust the room temperature setting range, thereby extending the heat pump's standby time and improving PV utilization. Future research should explore different priorities and weights for factors like energy use, comfort, and system stability to enhance the strategy's versatility and effectiveness.

ACKNOWLEDGEMENTS

This research was supported by Jiangsu Province Engineering Research Centre of Construction Carbon Neutral Technology (Grant No. JZTZH2023-0201), Key Laboratory of Ecology and Energy Saving Study of Dense Habitat, Ministry of Education (Grant No. 20230102), National Natural Science Foundation of China (Grant No. 52008245), Shanghai Sailing Program (Grant No. 20YF1432000).

REFERENCES

Tan X, Sun Q, Wang M, Cheong TS, Shum WY, Huang J, 2022. Assessing the effects of emissions trading systems on energy consumption and energy mix. Appl Energy; 310:118583.

Wang Z, Wei L, Zhang X, et al, 2023. Impact of demographic age structure on energy consumption structure: Evidence from population aging in mainland China[J]. Energy, 273: 127226

Chen W H, You F, 2022. Sustainable building climate control with renewable energy sources using nonlinear model predictive control[J]. Renewable and Sustainable Energy Reviews, 168: 112830.

Lin B, Chen Z, 2022. Net zero energy building evaluation, validation, and reflection – A successful project application[J]. Energy and Buildings, 261: 111946.

Krishnan N, K. Ravi Kumar, Chandrapal Singh Inda,2023. How solar radiation forecasting impacts the utilization of solar energy: A critical review[J]. Journal of Cleaner Production,388: 135860.

Liu X, Zhang T, Liu X, Jiang Y, 2022. “Development statuses and research prospects of PEDF (photovoltaics, energy storage, direct current and flexibility) building energy systems [J]. Heating Ventilating & Air Conditioning, 2022, 52(8): 1-9+82.

Jiang Y, 2021. PSDF(photovoltaic, storage, DC, flexible)—A new type of building power distribution system for zero carbon power system [J]. Heating Ventilating & Air Conditioning, 2021, 51(10): 1-12.

Wang X, Virguez E, Xiao W, et al, 2019. Clustering and dispatching hydro, wind, and photovoltaic power resources with multiobjective optimization of power generation fluctuations: A case study in southwestern China[J]. Energy, 189: 116250.

Zhu J, Li M, Luo L, et al, 2023. Short-term PV power forecast methodology based on multi-scale fluctuation characteristics extraction[J]. Renewable Energy, 208: 141-151.

Notton G, Nivet M L, Voyant C, et al, 2018. Intermittent and stochastic character of renewable energy sources: Consequences, cost of intermittence and benefit of forecasting[J]. Renewable and Sustainable Energy Reviews, 87: 96-105.

Chen W, Hao B, 2021. Analysis of Rural PEDF System toward Carbon Neutral—Case study of Dongyao Village, Ruicheng County, Shanxi Province [J]. Construction Science and Technology, (7): 86-89.

Urban & Building Energy (13:30-15:00 h)

6th International Conference on Building Energy and Environment
Eindhoven University of Technology, The Netherlands
6 - 10 July 2025

Heating energy use analysis based on virtual energy meters: results from a Canadian institutional building

Qiwei Qin [1], Guy Labelle [1], Etienne Saloux [1]

[1]*CanmetENERGY, Natural Resources Canada, Varennes, QC, Canada*

SUMMARY
Virtual meters offer a cost-effective alternative to physical meters by using models that estimate energy usage from readily available data. This study aims at developing different virtual energy meters based on building automation system data to provide key insights on heating usage at sub-system level. It focusses on air handling units, variable air volume boxes, hydronic perimeter units and heat recovery systems and uses an existing Canadian institutional building as a case study. Building operators and facility managers can then make informed decisions to improve building energy efficiency, and to prioritize the implementation of retrofit measures for decarbonizing the built environment. This work highlights the potential of virtual energy meters for improving building operation, contributing to broader goals of energy conservation and climate change mitigation.

Keywords: virtual energy meter, data-driven model, heating load, building automation system.

1. INTRODUCTION

Energy use in buildings represents a significant portion (~30%) of global energy consumption and institutional buildings account for nearly 30% of this amount, making energy use estimates critical for improving energy efficiency and reducing greenhouse gas emissions (Intergovernmental Panel on Climate Change (IPCC), 2023). Energy mapping can help building operators better understand energy flows in different sub-systems, detect inefficiencies and optimize control strategies. Building automation systems (BAS) rely on a monitoring infrastructure that has been mainly used for local controls or fault detection diagnostics but that can now provide an untapped opportunity for energy mapping as operational data becomes increasingly available (Saloux et al., 2023). Unlike simulation studies that estimate full-scale building energy use based on simulation parameters and energy balance equations, virtual energy meters leverage readily available data to estimate specific quantities while taking into account sensor uncertainty and missing variables. Indeed, not all key energy variables are directly measured or readily available. Installing physical meters may be expensive and bring practical challenges, and virtual meters have emerged as a cost-effective and scalable solution for analyzing building energy performance.

The application of virtual sensors and virtual energy meters (VEMs) has gained significant attention in recent years due to their ability to provide granular insights into building energy performance. (Li et al., 2011) conducted a comprehensive review of virtual sensors across a wide range of applications, emphasizing their critical role in enabling cost-effective and robust optimal control strategies. When applied to specific system components, (McDonald and Zmeureanu, 2015) developed a virtual flow meter (VFM) for monitoring the energy performance of a cooling plant. Furthermore, a detailed investigation of cooling energy usage of a large commercial building was conducted in (Saloux and Zhang, 2022). Their subsequent work (Saloux and Zhang, 2023)

delved into the applications of VEMs for improving building controls as well as the uncertainties associated with these meters, highlighting the importance of understanding and mitigating potential inaccuracies in virtual energy metering applications. Virtual flow meters that rely on BAS data were investigated in (Cotrufo and Zmeureanu, 2018) for estimating outdoor air flow rate in air handling units (AHU). Similarly, a virtual flow meter was developed in (Yu et al., 2011) for supply air flow rate in rooftop air-conditioning units. Virtual energy meters based on steady-state and transient inverse grey-box model, and water-side load disaggregation were proposed by (Darwazeh et al., 2021) to calculate heat supplied by hydronic perimeter units. Based on these VEM, a visualization tool (Darwazeh et al., 2022) was developed for showing energy flows in AHU systems, which can help support decision-making and improve building performance.

This paper provides two main contributions. (1) It applies virtual energy meter methods in a real-world institutional building, offering a detailed visualization of energy flows across components at seasonal and hourly levels. These insights help identify inefficiencies and optimization opportunities, bridging the gap between theory and practice in energy management. (2) It provides a comprehensive comparison of different VEM to assess strengths and limitations in terms of accuracy, scalability, monitoring infrastructure, computational resources, and applications.

2. DEVELOPMENT OF VIRTUAL ENERGY METERS (VEM)

2.1 Case study building

Virtual energy meters were developed for a typical heating system in a 5,257 m² institutional building in Varennes, Quebec (climate zone 7A). The system serves a 330-m² section built in 2017, with hot water supplied by a dual-fuel heating plant. During non-occupied periods, the ventilation system is off, and only perimeter units provide heating. In contrast, during occupied periods (5:30-17:30, Monday-Friday), fresh air is preheated via a heat recovery system, mixes with return air, is heated up by a water-based heating coil in the AHU and distributed to variable air volume (VAV) boxes. Electric reheat coils located in VAV boxes can eventually fulfill the demand while heating is also provided by water-based perimeter units. Data for three winter seasons (Nov-Mar, 2020-2023), available at 5-min intervals, are used for analysis.

2.2 Applications and limitations of virtual energy meters

Although VEMs can be used for various applications such as inefficiency detection and optimization, this paper focuses on performance tracking and energy mapping. VEMs can provide a comprehensive energy mapping, tracing energy flows from sources to end-uses and visualizing heating energy distribution. This helps operators pinpoint energy-intensive components, sources of heat losses, and potential energy savings of control strategies. It is worth mentioning that in simulation studies, calculations are compared with the measured performance, which is considered as the reference. In contrast, VEMs aim to estimate this reference, and different methods can be used to cross-compare and validate results. VEMs address among others sensor instrumentation, bias and random errors, operating conditions, error propagation and uncertainties, which all impact the accuracy of estimations. VEMs provide a cost-effective alternative to physical sensors and leverage existing data to extract operational insights. Their scalability depends on sensor availability and quality, which vary across buildings. To ensure broad applicability, especially in diverse Canadian buildings, VEMs prioritize adaptability, build upon readily available datasets and leverage manufacturer information and building plans. Missing data is inferred from

assumptions or virtual sensors, focusing on its impact on energy predictions. Balancing simplicity, accuracy, and monitoring needs, VEMs validate both detailed and simple methods, ensuring practical scalability while maintaining performance insights tailored to specific applications.

2.3 Mechanical ventilation system

Fig. 1 illustrates the simplified schematic of the mechanical ventilation system. In commercial buildings, standards like ASHRAE 62.1 ASHRAE, 2022) require minimum fresh air during occupied periods, causing heat losses as cold fresh air is introduced. However, fresh air flow rates are rarely measured, but can be estimated using mass and energy balance equations:

$$\rho_a \dot{V}_f = \rho_a \dot{V}_s - \rho_a \dot{V}_r \Rightarrow \dot{V}_f = \dot{V}_s - \dot{V}_r \quad (1)$$

$$\rho_a \dot{V}_f (T_r - T_{f2}) = \rho_a (T_r - T_m) \dot{V}_s \Longrightarrow \dot{V}_f = \frac{T_r - T_m}{T_r - T_{f2}} \dot{V}_s \quad (2)$$

Eq. (1) uses mass balance equation, expressed using volumetric flow rates (which are typically measured), and requires flow rate sensors for both supply and return air; however, in some cases, only one of these sensors may be available. To overcome this, (Cotrufo and Zmeureanu, 2018) have successfully applied energy balance equation and proposed Eq. (2). This equation has been used in (Zmeureanu and Vandenbroucke, 2015) and its validity is evaluated for this case study.

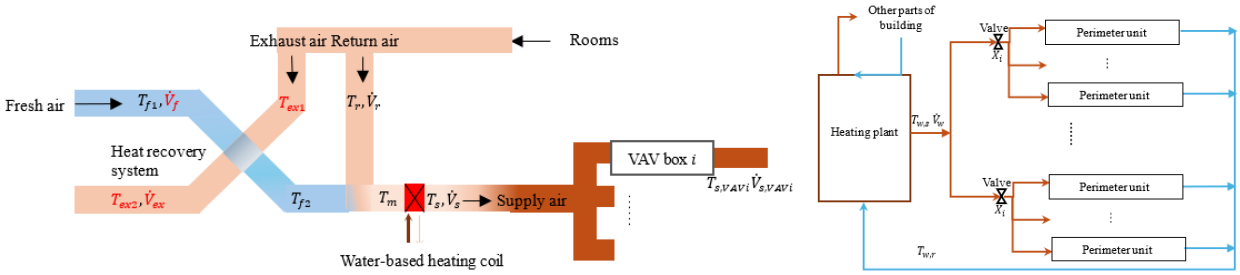

Figure 1. Simplified schematic of ventilation system (left) and water-loop of perimeter units (right). *T* means temperature (℃), *V* is flow rate (L/s) and X_i is valve opening (%); unmeasured variables are marked in red.

Heat recovered from return air in the heat exchanger can be calculated using fresh air flow rate and energy balance equation:

$$\dot{Q}_{heat\ recovery} = c_a \rho_a \dot{V}_f (T_{f2} - T_{f1}) \quad (3)$$

Heat losses associated with mechanical ventilation (i.e. incorporating fresh air in the building) is calculated as the enthalpy difference between exhaust and fresh air. Since there is no dehumidification in winter, air humidity is neglected. Exhaust air flow rate is assumed equal to that of fresh air to ensure pressure balance in the building. The following VEM is used for evaluating heat losses due to mechanical ventilation:

$$\dot{Q}_v = c_a \rho_a \dot{V}_f (T_r - T_{f1}) - \dot{Q}_{heat\ recovery} \quad (4)$$

The first term of Eq. (4) represents heat losses due to ventilation in the absence of a heat recovery system and represents the energy required for heating cold fresh air up to the room air temperature (assumed equal to the return temperature). Eq. (4) can then be used to evaluate the contribution of

heat recovery systems.

2.4 Water-based heating coil in the air handling unit

During occupied period, a water-based heating coil (see Fig. 1) is used to increase air temperature up to the required setpoint. Heating coil power can be calculated using enthalpy difference applied to air-side measurements or water-side measurements. Since there are typically no measurements for water flow rate and return water temperature, air-side measurements are used:

$$\dot{Q}_{AHU_coil} = c_a \rho_a \dot{V}_s (T_s - T_m) \tag{5}$$

Depending on the application, other models could be developed using only water-side measurements (e.g. valve modulation) or both air-side and water-side measurements.

2.5 Electric reheat coil in variable air volume boxes

Electric reheat coils installed in VAV boxes adjust air conditions to local needs before being distributed to the rooms. Applying the enthalpy difference method to air yields to:

$$\dot{Q}_{e_coil} = \sum_{i=1}^{N} c_a \rho_a \dot{V}_{s,VAVi} \left(T_{s,VAVi} - T_s\right) \tag{6}$$

Another VEM can be developed to calculate electric reheat coil power from the coil modulation:

$$\dot{Q}_{e_coil} = \sum_{i=1}^{N} X_{e_coil,i} C_{n_coil,i} \tag{7}$$

where $X_{e_coil,i}$ is the modulation (%) and $C_{n_coil,i}$ is the nominal capacity of electric coil *i*. Eq. (6) requires measurements for air flowrate ($\dot{V}_{s,VAVi}$), inlet and outlet temperature ($T_{s,VAVi}$) for each VAV box. In the case study, inlet temperatures before electric coils are not measured and are assumed to be equal to AHU supply temperature (T_s). Eq. (6) depends on 3 sensors, which increases uncertainty whereas Eq. (7) only relies on the coil modulation but may not account for electric coil performance degradation with time.

2.6 Water based perimeter units

The hydronic heating system supplies 29 perimeter units and the AHU heating coil (see Fig. 1), all connected in parallel. The perimeter units are divided into 9 distinct groups supplying different thermal zones. For each group, one valve controls the hot water flow rate. Only one flow meter is installed on the main water supply branch ($\dot{V}_w$) along with supply ($T_{w,s}$) and return ($T_{w,r}$) water temperature sensors to measure heating energy delivered to the 330-m² building section (see Section 2.1). The total heat supplied to the 29 units is determined as follows:

$$\dot{Q}_{perimeter\ units} = c_w \rho_w \dot{V}_w \left(T_{w,s} - T_{w,r}\right) - \dot{Q}_{AHU_coil} \tag{8}$$

While the first term represents the total heat supplied to the building section through the hydronic loop, the second term is the AHU heating coil power from Eq. (5). Eq. (8) is based on enthalpy difference and depends on 6 air-side and water-side sensors, which increases uncertainty while being less scalable. Moreover, (Darwazeh et al., 2021) proposed a multi-linear regression (MLR)

model to calculate heating power in each perimeter unit group; the authors highlighted that the model error increases with the number of perimeter units. This approach was tested in this case study and heating power is calculated as follows:

$$\dot{Q}_{perimeter\ units} = \sum_{i=1}^{n} (a_i X_i) + e \tag{9}$$

where X_i is the valve position of each individual group. Coefficients a_i are calibrated using Eq. (8) and e is the error. Although Eq. (9) requires Eq. (8) for calibration, its advantage is its ability to disaggregate total energy use into individual groups, enabling additional distribution insights.

2.7 Other parts of the Sankey diagram

The remaining sections of the Sankey diagram are derived from energy conservation principles. The heating energy supplied to the AHU and perimeter units comes from a dual energy heating system, composed of electric and natural gas boilers. It is worth reminding that the Sankey diagram only covers a single section of the entire building.

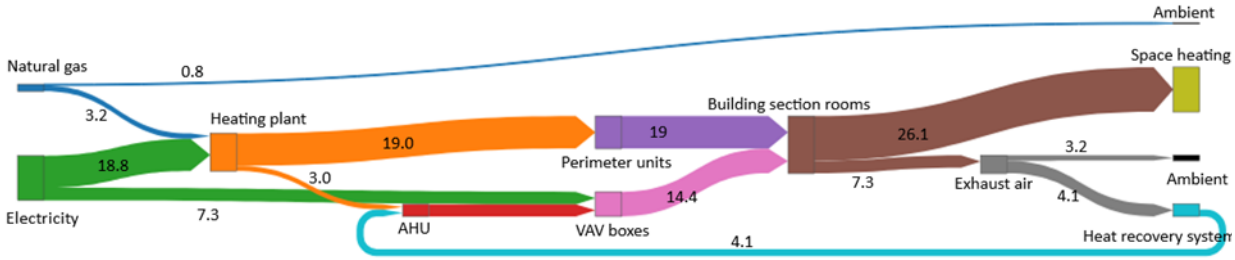

Figure 2. Sankey diagram of thermal energy flows for the case study building in winter (units: MWh/season)

3. ENERGY USE ANALYSIS AND VIRTUAL ENERGY METER COMPARISON

3.1 Sankey diagram

The Sankey diagram provides a detailed visualization of energy flows (average values calculated from three winter seasons) for the building section, showcasing the interactions between primary energy sources, heating plant, and building systems. Heating energy is distributed through perimeter units, AHUs and electric reheat coils in VAV boxes. The AHU and VAV boxes supply 14.4 MWh/season of heat, with 4.1 MWh/season from the heat recovery system, reducing by 58% the AHU heating coil contribution (3.0 MWh/season). While the AHU operates only during occupied hours (33% of the time), perimeter units are continuously in operation to maintain indoor air temperature setpoints and supply 57% of the whole heating demand (19 MWh/season). Only 3.2 MWh/season is associated with ventilation losses, an amount that could have reached 7.3 MWh/season without a heat recovery system. The Sankey diagram underscores the importance of space heating and the added value of heat recovery system for improving building performance.

3.2 Hourly heating usage distribution

Fig. 3 shows the hourly average distribution of heating among the different heating sub-systems. The heating demand on weekdays shows a morning peak (particularly during 6:00-9:00), which is mainly caused by the transition from nighttime to daytime conditions. On weekends, heating demand is predominantly from perimeter units, with no contribution from the AHU and VAV

boxes, as they remain inactive. As shown in Fig. 4 (left), the heat recovery system reduces heating demand by 12%, contributing only during AHU operation and being particularly effective from mid-morning to early afternoon. While the heat supplied to the building and the heat losses due to ventilation have been calculated, other energy terms related to space heating –heat losses through the envelope, solar gains, internal heat gains from plug loads and occupants, and room conditioning (indoor temperature variations)– cannot be easily separated. They would require additional modelling with potential challenges in terms of model structure (e.g. Resistance-Capacitance thermal network; electric load disaggregation) and accuracy, which is beyond the scope of this paper. However, Fig. 4 (right) still provides valuable insights. By comparing nights (22:00 to 4:00) and working hours (9:00 to 16:00) when indoor temperature remains rather constant, space heating is notably lower during the day despite higher room temperatures, which could be attributed to higher solar gains and internal gains (equipment, occupancy), coupled with reduced temperature differences between indoor and outdoor environments. In turn, the morning peak is mainly driven by the heating demand required to increase indoor temperatures to meet daytime conditions.

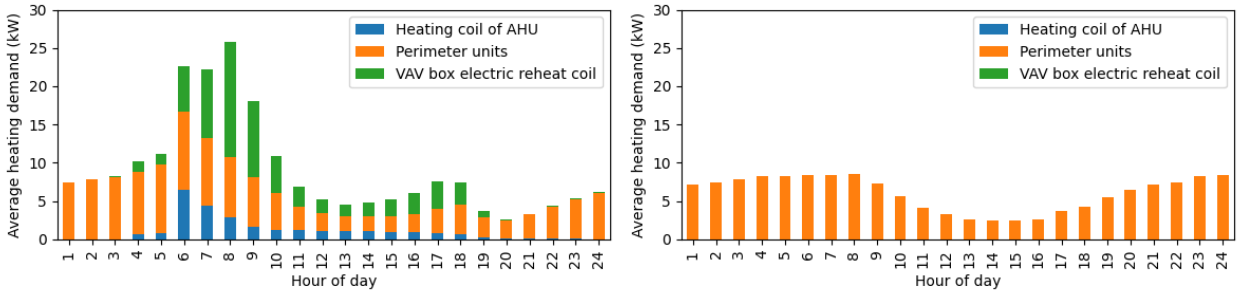

Figure 3. Hourly average heating demand provided by the different heating sub-systems against hour of day: on weekdays (left) and weekends (right)

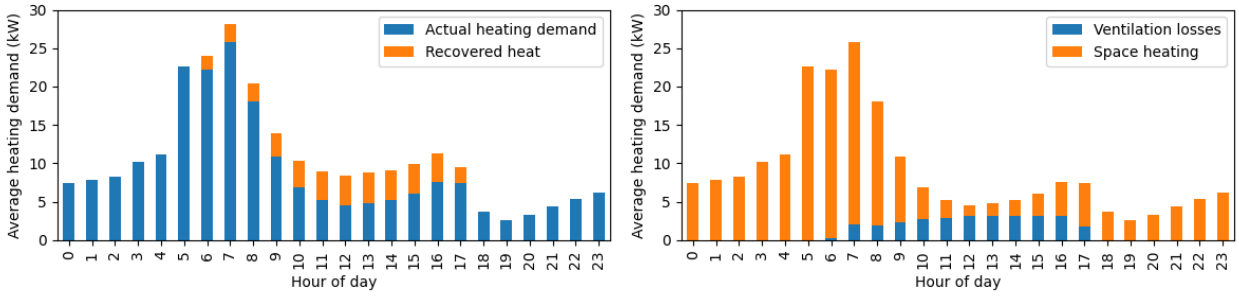

Figure 4. Hourly average distribution against hour of day: actual heating demand vs recovered heat (left) and ventilation losses vs space heating (right)

3.3 Comparison between different methods

Instrumentation level, sensor quality, and operational scenarios vary from one building to another, and several VEMs could be used to cross compare results for a given variable and to validate and increase confidence in the approach. The diversity of VEMs ensures adaptability in different contexts while enhancing robustness and reliability. Eqs (1)-(2) estimate fresh air flow rate, which is critical for virtual energy metering of heat recovery system and ventilation losses. According to the control sequence document, the fresh air flowrate is set at 400 L/s. Using Eq. (1), an average value of 398 L/s is obtained (95% of the data is among 350-450 L/s) and is consistent with the control sequence document. However, although successfully applied in previous studies, Eq. (2) shows significant discrepancies, which may be attributed to the uncertainty of temperature sensors

while the fresh air flow rate is rather low (~25%) compared with supply air flow rate. In previous studies, this ratio could be 80% (Cotrufo and Zmeureanu, 2018). Fig. 5 shows the uncertainty of Eqs (1)-(2) with bias errors of ± 0.45°C for temperature and ± 5% of the mean value for flow rate, and highlights the limitations of using Eq. (2) under specific operational conditions.

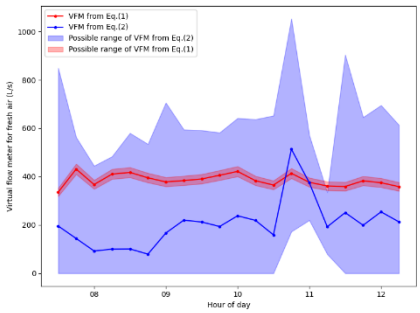

Figure 5. Comparison between VFM from Eq. (1) and Eq. (2)

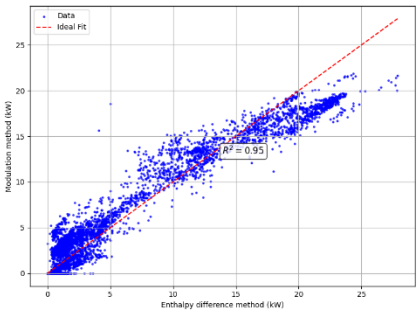

Figure 6. Enthalpy difference method vs modulation method for VAV box electric coils

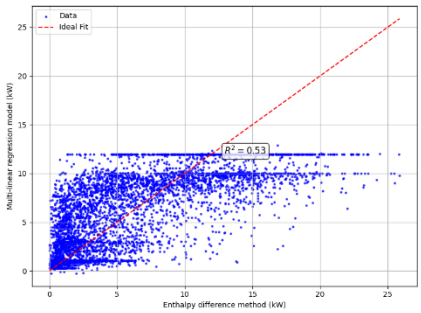

Figure 7. Enthalpy difference method vs. multi-linear regression model for perimeter units

For VAV box electric reheat coils, Fig. 6 compares estimates using the modulation method (Eq. (7)) and the enthalpy difference method (Eq. (6)), and demonstrates strong agreement between both methods, with an R^2 score of 0.95, indicating a high degree of similarity. This suggests that both methods are effective for estimating aggregate power consumption across all VAV boxes. However, when examining individual coils, the errors can be more significant, highlighting the need for further investigation into the sources of discrepancies. Understanding and addressing these errors will improve the reliability of the methods for more granular energy modelling.

Finally, Fig. 7 compares the results from Eq. (8) and Eq. (9) for perimeter units, revealing a weak correlation with an R^2 score of 0.53. It is worth reminding that Eq. (9) has been calibrated with Eq. (8). While the model demonstrated good performance in (Darwazeh et al., 2021), its practical application in this case study shows significant discrepancies. (Darwazeh et al., 2021) applied their method to 3-15 perimeter units but they acknowledged that the model performance rapidly declines with the number of perimeter units. This case study has 29 perimeter units, which may explain the loss of model accuracy. Furthermore, in (Markus et al., 2025), the assumption of linear relationship between perimeter unit power and valve position, may result in an overestimation of heat output, which is also observed here (MLR shows higher results 60% of the time). Finally, Eq. (8), which was used to calibrate Eq. (9), depends on six air-side and water-side variables, which also increase uncertainty. This comparison underscores the need for further model refinement or alternative approaches for such systems, especially in situations where there is a lack of instrumentation.

3.4 Opportunities highlighted by virtual energy meters

Through the case study presented, Virtual Energy Meters (VEMs) demonstrate significant potential for improving building energy performance and operational efficiency. During the morning peak on weekdays, 34% of the heating load comes from electrical reheat coils, a reliance that could be optimized through AHU heating coil supply temperature setpoints, particularly during demand response events and depending on the central heating plant equipment (boilers vs. heat pumps). For ventilation, VEMs reveal opportunities for energy savings by adjusting ventilation rates based on actual occupancy instead of nominal values. This adjustment could save 1.4-1.8 MWh/winter, equivalent to 80-103 $/winter (0.24-0.32 $/m^2), and 61-80 kg$CO_{2eq}$/winter

(0.18-0.24 $kgCO_{2eq}/m^2$), numbers rather low due to the heat recovery system. Additionally, VEMs allow to quantify the impact of heat recovery systems in reducing ventilation-related losses; savings of 188 \$/winter (0.56 $\$/m^2$), and 141 $kgCO_{2eq}$/winter (0.42 $kgCO_{2eq}/m^2$) are achieved in this case study. Furthermore, VEMs could play a critical role in fault detection and diagnostics by comparing outputs from different methods to identify sensor errors or equipment malfunctions. These insights highlight the potential of VEMs for making informed decisions, improving efficiency, and advancing sustainable building practices.

4. CONCLUSION AND FUTURE WORK

This work demonstrates the potential of applying virtual energy meters for typical heating systems in commercial and institutional buildings. Insights gained from virtual energy meters provide a comprehensive understanding of energy usage and losses within the building, which can be used for designing more efficient HVAC operations. These calculations help quantify energy-intensive components and identify opportunities for optimization, ensuring that energy usage aligns with actual occupancy and operational needs. Future work includes the improvement of existing models, the testing of new methods, extending the analysis to the whole building and replication to other buildings, equipped with different heating and cooling systems.

ACKNOWLEDGEMENTS

The financial support of Natural Resources Canada through the Office of Energy Research and Development (OERD) is gratefully acknowledged. The authors would like to thank internal and external reviewers for their useful comments.

REFERENCES

American Society of Heating, Refrigerating and Air-Conditioning Engineers, 2022. ANSI/ASHRAE Standard 62.1: Ventilation for Acceptable Indoor Air Quality, 2022nd ed. ASHRAE, Atlanta, GA.

Cotrufo, N., Zmeureanu, R., 2018. Virtual outdoor air flow meter for an existing HVAC system in heating mode. Autom. Constr. 92, 166–172.

Darwazeh, D., Duquette, J., Gunay, B., 2021. Virtual metering of heat supplied by zone-level perimeter heaters: An investigation with three inverse modelling approaches. Energy Build. 240, 110867.

Darwazeh, D., Gunay, B., Duquette, J., O'Brien, W., 2022. A virtual meter-based visualization tool to present energy flows in multiple zone variable air volume air handling unit systems. Build. Environ. 221, 109275.

Intergovernmental Panel on Climate Change (IPCC) (Ed.), 2023. Buildings, in: Climate Change 2022 - Mitigation of Climate Change: Working Group III Contribution to the Sixth Assessment Report of the Intergovernmental Panel on Climate Change. Cambridge University Press, Cambridge, pp. 953–1048.

Li, H., Yu, D., Braun, J.E., 2011. A review of virtual sensing technology and application in building systems. HVACR Res. 17, 619–645.

Markus, A.A., Bursill, J., Gunay, H.B., Hobson, B.W., 2025. Projecting and estimating HVAC energy savings from correcting control faults: Comparison between physical and virtual metering approaches. Energy Build. 328, 115169.

McDonald, E., Zmeureanu, R., 2015. Development and Testing of a Virtual Flow Meter Tool to Monitor the Performance of Cooling Plants. Energy Procedia 78, 1129–1134.

Saloux, E., Zhang, K., 2023. Towards integration of virtual meters into building energy management systems: Development and assessment of thermal meters for cooling. J. Build. Eng. 65, 105785.

Saloux, E., Zhang, K., 2022. Virtual energy metering of whole building cooling load from both airside and waterside measurements, 12th Conference of IBPSA-Canada, eSim, Vancouver, Canada.

Saloux, E., Zhang, K., Candanedo, J.A., 2023. A Critical Perspective on Current Research Trends in Building Operation: Pressing Challenges and Promising Opportunities. Buildings 13.

Yu, D., Li, H., Yang, M., 2011. A virtual supply airflow rate meter for rooftop air-conditioning units. Build. Environ. 46, 1292–1302.

Zmeureanu, R., Vandenbroucke, H., 2015. Use of Trend Data from BEMS for the Ongoing Commissioning of HVAC Systems. 6th Int. Build. Phys. Conf. IBPC 2015 78, 2415–2420.

6th International Conference on Building Energy and Environment
Eindhoven University of Technology, The Netherlands
6 - 10 July 2025

Evaluating the Influence of Urban Wind Environment on Energy Performance of Mid-Rise Buildings in Amman

Paria Saadatjoo [1], Hamed Moradi [2], Mohammad Hamdan [3,4], Mahmoud Murtala Farouq [3,5], Parham Mirzaei [6]

[1] *Department of Architecture, Faculty of Civil Engineering, University of Tabriz, Tabriz, Iran, paria.saadatjoo@tabrizu.ac.ir*
[2] *Department of Construction, Faculty of Architecture and Urban Planning, Shahid Beheshti University, Tehran, Iran, hamy194045@gmail.com*
[3] *Department of Architecture and Built Environment, Faculty of Engineering, University of Nottingham, Nottingham, England.*
[4] *Department of Architecture, Faculty of Engineering and Design, Middle East University, Amman, Jordan, Mohammad.hamdan@nottingham.ac.uk*
[5] *Department of Engineering, Aliko Dangote University of Science and Technology, Wudil, Nigeria, mahmoudmurtala@kustwudil.edu.ng*
[6] *Department of Civil and Architectural Engineering - Building Science, Aarhus University, Aarhus, Denmark, parhammir@cae.au.dk*

SUMMARY
Rapid urbanization has led to compact cities with vertical structures and complex configurations. The urban wind environment (UWE), shaped by urban morphology, influences building energy consumption, yet current building energy simulation (BES) tools cannot fully account for its impact. This study examines how urban configuration affects energy performance in a mid-rise district in Amman, Jordan. A target building was analysed within five sub regions, each with distinct physical characteristics. Computational Fluid Dynamics simulations measured wind velocity, pressure coefficients, and convective heat transfer coefficients (CHTC) around the building. These data were integrated into DesignBuilder 7.3 to assess UWE's impact on energy performance. The findings show a significant discrepancy in measured wind velocity (up to 1.73 m/s) and CHTC values across zones, demonstrating the built environment's effect on UWE. Comparing the base case (without CHTC) to scenarios with CHTC revealed discrepancies of up to 49%, emphasizing urban morphology's role in energy demand.

Keywords: Urban wind environment, Building energy performance, Urban configuration, Computational Fluid Dynamics (CFD).

1. INTRODUCTION

Rapid urbanization has transformed natural landscapes into densely built environments, creating compact cities with high-density buildings that significantly impact the urban microclimate (Bhalindar Singh, 2020). These dense cityscapes disrupt wind flows, reduce ventilation, and create turbulent air patterns, affecting pedestrian comfort, air quality, and pollutant dispersion (Al Labbad et al., 2022, Xia et al., 2015). Urban microclimates significantly influence building energy performance (BEP) by affecting ventilation, infiltration, and convective heat transfer across building surfaces (Pfafferott et al., 2021, Mirzaei, 2022). The convective heat transfer coefficient (CHTC), which measures the heat exchange between a building's exterior and the surrounding air, is shaped by factors such as wind speed, direction, and temperature differences air (Xue et al.,

2022; Yang et al., 2017). Additionally, variations in wind pressure influence infiltration and natural ventilation, which in turn affect heating and cooling demands (Cóstola et al., 2009; Younes et al., 2012). Other microclimate elements, including the urban heat island effect, greenery, wind-driven rain, and pedestrian wind comfort, also contribute to energy consumption in buildings (Kubilay et al., 2018; Li et al., 2019; Priya & Senthil, 2021). Although the influence of microclimate on BEP is well-documented, current Building Performance Simulation (BPS) tools typically rely on generic meteorological data, often overlooking localized urban conditions, resulting in significant inaccuracies in energy assessments (Hadavi & Pasdarshahri, 2021b, Pei et al., 2023). A promising approach to integrating urban microclimate into BEP analysis is the coupling of computational fluid dynamics (CFD) with BPS tools (Bouyer et al., 2011). This integration can be performed through one-way coupling, where either BPS data informs CFD simulations (Type A) (Hadavi & Pasdarshahri, 2021b) or vice versa (Type B) (Brozovsky et al., 2022), or through two-way dynamic coupling (Type C) (Zhang & Mirzaei, 2021b, Zhang & Mirzaei, 2021a), which provides higher accuracy but is computationally intensive. Several studies have successfully used CFD-BPS coupling to enhance urban energy simulations (Shirzadi et al., 2019b, Gobakis & Kolokotsa, 2017). Other studies have used CFD to compare standard weather data with localized microclimate data, highlighting substantial variations in energy consumption predictions (Kyriakodis et al., 2019). Additionally, research has examined how urban form influences microclimate and energy demand, showing that factors like urban density, building orientation, and vegetation can mitigate cooling loads (Brozovsky et al., 2022; Javanroodi & Nik, 2019). Despite advances in CFD-BPS coupling, challenges remain, including high computational costs, complex modelling requirements, and limited experimental validation datasets (Mirzaei, 2021). Many studies rely on simplified models that fail to capture the full complexity of urban environments, and large-scale research integrating CFD-based microclimate data into BPS remains limited. This research aims to systematically address the building energy performance gap related to their surrounding wind environment. A densely populated neighbourhood in Amman, subdivided into five distinct zones, serves as the case study. By situating an identical reference building in each zone, the research investigates how urban morphology shapes microclimatic conditions and energy consumption. Validated CFD simulations will be employed to evaluate wind flow patterns and surface pressure coefficients, which will then be incorporated into Design Builder for energy modelling.

2. METHODOLOGY

This study examines a high-density urban district in Amman, subdivided into five zones with distinct morphological characteristics, including variations in density, block arrangement, height-to-width ratios, and occupied area. A representative building, reflecting the district's predominant typology, was placed at the center of each zone to assess the impact of urban form on wind behavior and energy performance. CFD simulations were conducted for eight wind directions and three wind speeds (maximum, minimum, and median) based on Amman's meteorological data. Wind velocity was measured at 256 points along four logging axes positioned two meters from the building façades, while additional parameters such as Cp and CHTCs were recorded. The results were integrated into Design Builder Version 7.3 for BPS, quantifying the impact of urban wind environments on energy performance by evaluating how urban configurations influence local wind conditions and building energy consumption.

2.1. Case Study Area

This study focuses on Basman, a densely populated district in central Amman, located about 5 km from the city's official meteorological station in Marka. Positioned at latitude 31.96° N and longitude 35.95° E, Amman experiences high solar radiation, with around 320 sunny days annually (Alrwashdeh, 2021). The city's climate is characterized by hot, dry summers (28–32°C) and cool winters with occasional snowfall (UN-Habitat, 2022). The case study area is Basman, spans 141,424 m, and has a predominantly northeast orientation. It consists of 132 residential blocks with building heights ranging from 4 to 16 meters. Buildings range from those built in the 1980s to recent constructions in 2024, with stone as the main material. The study area was divided into 200×200 meter zones to analyze the impact of urban morphology on wind dynamics and building performance. These zones were selected to minimize overlap while capturing key physical variations (Fig. 1).

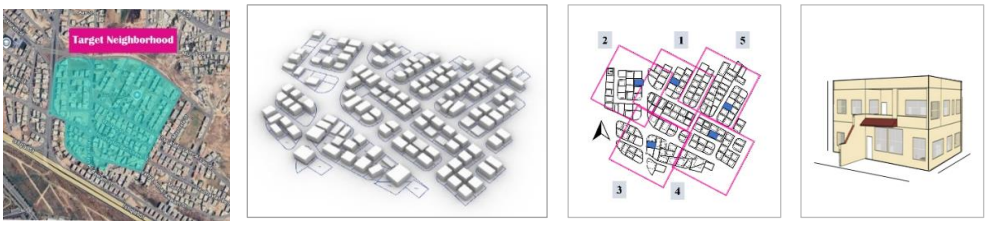

(a) (b) (c) (d)

Figure 1. a) The map of target neighbourhood, b) perspective of target district, c) location of five sub regions, d) two-story target building

A representative building, reflecting the district's common architectural features, was placed in each zone to assess how different urban configurations influence wind behavior and energy performance. One the buildings in each zone was selected randomly and replaced by representative building. Building configurations and simulation settings are presented in Table 1.

Table 1. Building energy simulation settings

Building characteristics	Location	Function	Building Area (m^2)	Occupancy density ($People/M^2$)
	$N31°58'23.28$, $E35°56'28.78$		450	9 persons, 0.0156
Envelope Properties	Infiltration (ac/h)	R ($m^2\,K/W$)-Wall	U (W/m^2K)-Wall	U (W/m^2K)-Roof
	1.2	0.473	2.11	1.02
Systems & Operations	HVAC Systems	Heating set point-set back (℃)	Cooling set point/ set back (℃)	Internal Heat Gains (w)
	Direct Expansion (DX) systems	21/12	25- 27	2,897

2.2. CFD-BPS Coupling

This study adopts a one-way coupling approach (Type B) to examine how urban microclimate affects building energy performance by integrating CFD (ANSYS Fluent 2022 R1) with Design Builder Version 7.3. The CFD outputs serve as inputs for Design Builder Version 7.3 to assess the energy demand of the target building in the hottest day. Simulations were conducted for eight wind directions and three wind speeds, determined from meteorological data spanning the past decade. Additionally, steady-state simulations were performed for the four prevailing wind directions. Microclimate conditions were recorded along vertical lines positioned near the building façades, with logging points capturing wind speed variations (Fig. 2). The collected data were used to

generate weather files for energy simulations. Key parameters, including pressure coefficients (Cp) and convective heat transfer coefficients (CHTC) for all façades and the roof, were analyzed, and floor-by-floor pressure distributions were calculated. These results were then integrated into Design Builder for a comprehensive energy performance evaluation.

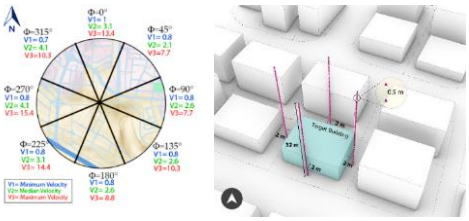

(a) (b)

Figure 2. (a) Minimum, median and maximum windspeed from eight directions in Amman city, and (b) location of logging points around the target building

3. CFD SIMULATION SETTINGS

3.1. Computational Domain and Grid

Fluid flow characteristics were analyzed across various scenarios, ensuring residual errors remained below the threshold. Average pressure coefficients and convective heat transfer rates were determined for each building surface under four wind directions. The urban district was modeled at Level of Detail 1.0 within a 453m × 453m grid. Following COST and AIJ guidelines, the CFD domain extended 15 times the tallest building (H = 16m) on each side, resulting in a 933m × 933m × 255m domain. The polyhedral grid contained 1,190,976 cells, with skewness and non-orthogonality below 0.5 (Fig. 3).

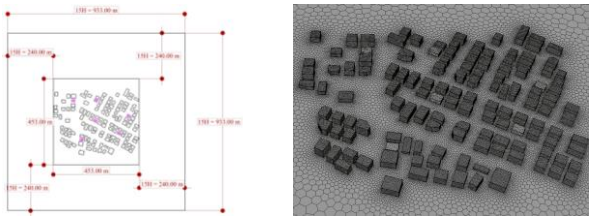

(a) (b)

Figure 3. (a) Case study domain size, b) grid of case study area

3.2. Grid Sensitivity Analysis

A grid independence study with three mesh sets was performed using the Grid Convergence Index (GCI). According to the results, the GCI results for the level 2 refinement grid were below 5%, aligning with previous research recommendations. A wind speed ratio comparison across different mesh refinement levels revealed significant differences between level 1 and levels 2 and 3. However, the discrepancy between levels 2 and 3 was minimal, indicating that further refinement would provide only marginal improvements. Consequently, level 2 mesh settings were selected for data generation (Table 2).

Table 2. CGI value for different mesh refinement levels

level of refinement	Number of Cells	r value	CGI For pressure field	CGI For velocity field
1	606,901	1.25	1.80%	6.00%

2	1,190,976	1.25	1.40%	4.43%
3	2,346,433	-	-	-

4. RESULTS

The research results are divided into two phases. The first phase presents CFD simulation outcomes, including wind velocities, wind speed at building height, CHTC, and Cp for the main facades across five urban zones. The second phase focuses on the energy simulation results for the target building.

4.1. Wind Behavior Comparison

Wind speed was measured at 7.11m on five 7m buildings to evaluate urban impacts on wind flow. Figure 4 shows the significant influence of surrounding structures, with notable velocity differences across wind directions. For example, in the North wind direction (D1), wind speeds at the West logging point ranged from 1.83 m/s to 0.10 m/s, a discrepancy of 1.73 m/s (1730% difference). Likewise, at the South logging point, wind speeds ranged from 0.15 m/s to 0.92 m/s, showing a discrepancy of 0.70 m/s (513.33% difference). In the East wind direction (D2), the South logging point exhibited the greatest difference of 0.72 m/s, ranging from 0.81 m/s to 0.09 m/s. For the South wind direction (D3), wind velocities at the South logging point varied significantly, with a maximum of 1.61 m/s and a minimum of 0.18 m/s, yielding a discrepancy of 1.43 m/s (794% difference), while the East logging point displayed a 0.44 m/s difference. Lastly, in the West wind direction (D4), the East logging point showed wind speeds between 0.22 m/s and 0.56 m/s, with a discrepancy of 0.34 m/s (154% difference), while the West logging point ranged from 0.15 m/s to 0.63 m/s, showing a 0.48 m/s discrepancy (320% difference). These findings emphasize the considerable influence of urban form on wind behavior, with some discrepancies exceeding 1700%, highlighting the critical importance of considering the urban context in wind flow analyses.

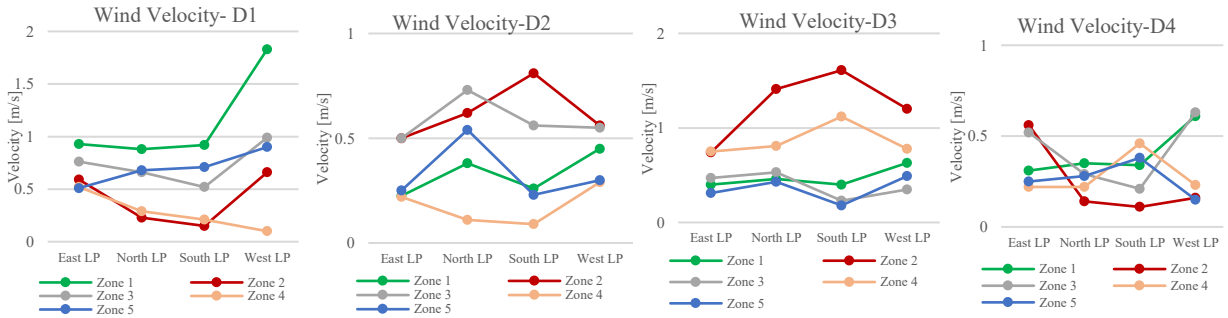

Figure 4. Velocity at logging points at the height of target buildings in five zones for four wind directions

4.2. CHTC and Cp Variations Across Facades

Measured values of CHTC on the facades are illustrated in Figure 5. These results indicate that across all wind directions and for each of the five facades, the "Isolated" scenario persistently exhibits the highest CHTC values. This pattern arises due to the absence of adjacent structures, which allows uninterrupted wind flow around the building. Consequently, elevated wind velocities enhance convective heat transfer rates across all surfaces. The magnitude of this effect is particularly striking in certain cases. For instance, under the north wind condition (D4), the western facade experiences the most pronounced discrepancy, with a CHTC of 16.63 W/m²·K in the "Isolated" case, compared to just 5.12 W/m²·K in Zone 5—an increase of 224.80%. Even within the urban setting, disparities in CHTC values across various zones highlight the crucial role of

environmental parameters. For example, under the west wind direction (D4), the western facade exhibits CHTC values ranging from 5.12 W/m²·K to 11.60 W/m²·K, reflecting a variation of 126.56%. These discrepancies stem from factors such as urban configuration, building density, and the spatial distribution of adjacent structures, all of which modulate local wind patterns and, in turn, surface heat dissipation. Examining the influence of facade orientation in relation to the prevailing wind direction within each urban zone indicates that the degree of exposure to wind currents dictates the extent of convective heat transfer. Windward facades, directly confronting the airflow, experience heightened wind pressures, leading to intensified heat transfer rates. In contrast, leeward facades and those aligned perpendicular to the wind direction are more sheltered, resulting in diminished wind velocities and consequently lower CHTC values. Additionally, the roof consistently registers higher CHTC values than vertical facades, as it remains fully exposed to wind flow across all wind conditions, thereby facilitating greater thermal exchange. These findings emphasize that, beyond the influence of urban morphology, facade orientation is a fundamental determinant in the spatial distribution of CHTC across the building envelope (Fig. 5).

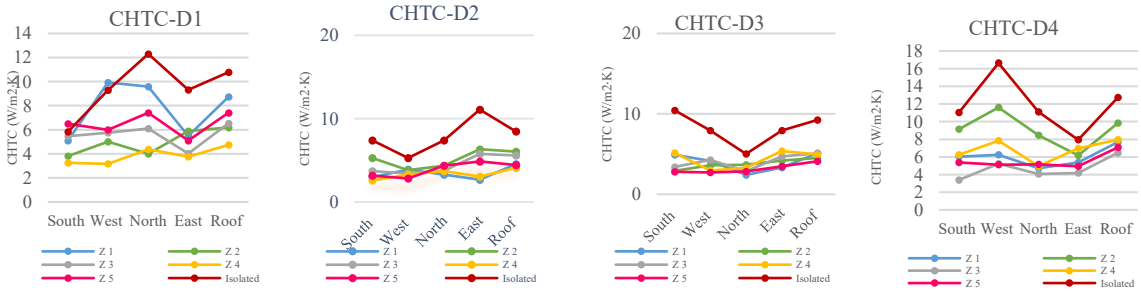

Figure 5. CHTC values on the four facades of the target building across five zones for four wind directions

4.3. Building Energy Consumption

It has been demonstrated that the built environment and urban configurations influence wind conditions, leading to variations in CHTC and Cp. These variations affect the heat exchange rate and natural ventilation potential of buildings, ultimately impacting overall building energy consumption. To assess the impact of urban context on building energy consumption, CHTC and Cp values obtained from CFD simulations are integrated into energy simulations in Design Builder, and the results are compared. The target building is a two-story residential building.

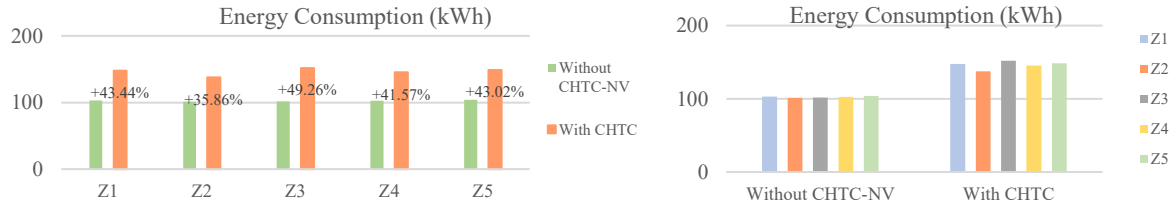

Figure 6. Energy consumption of the target building in July 28, 2016

The above chart illustrates energy consumption over a 12-hour period (8 AM to 8 PM) on the hottest day of the year, July 28, 2016. In these simulations, CHTC obtained from CFD wind simulations were applied to all five building façades within Design Builder. The results demonstrate a significant difference in energy consumption when CHTC values are considered compared to when they are ignored. In conventional energy simulations that do not account for the surrounding environment, the predicted energy consumption is considerably lower. However, incorporating the urban context and CFD-derived CHTC values leads to a substantial shift in

simulation results. Notably, the scenario where only ventilation heat exchange with the environment (CHTC) is accounted for exhibits the highest energy consumption. In some cases, the discrepancy between this scenario and the baseline reaches up to 49%. Furthermore, when comparing energy consumption among target buildings located in five different zones under similar conditions (with and without CHTC), notable differences emerge. In the absence of CHTC, variations in energy consumption are minimal and primarily influenced by differences in building orientation and rotational angles relative to geographic north and south. However, when CHTC is considered, the same buildings with identical characteristics exhibit significant differences in energy consumption due to variations in their surrounding urban configurations. A comparison of different zones reveals that the target building in Zone 2 experiences the lowest energy consumption, while the target building in Zone 3 shows the highest energy demand.

5. CONCLUAION

In conclusion, this study highlights the significant impact of urban morphology on the UWE and building energy performance, particularly in densely populated, high-rise urban areas. Through a comprehensive analysis of various urban configurations in a case study from Amman, Jordan, this research underscores the need for a more nuanced approach to urban design that incorporates the effects of UWE on energy consumption. The CFD with BPS tools, such as Design Builder, has provided valuable insights into how urban form, including building density, block proportions, and spatial layout, influences wind behavior and natural ventilation. The findings demonstrate that modifications in urban design, such as changes in building proportions and configurations, can significantly alter convective heat transfer, wind pressure, and ventilation patterns, leading to variations in heating and cooling demands. The results indicate that urban microclimate factors, often overlooked in conventional energy performance simulations, play a crucial role in shaping energy consumption patterns. This study reveals that localized microclimate data, when incorporated into building energy simulations, can significantly improve the accuracy of energy performance assessments. The coupling of CFD and BPS tools, though computationally intensive, offers a promising pathway to more accurate, site-specific energy simulations.

References

Al Labbad, M., Wall, A., Larose, G. L., Khouli, F., & Barber, H. (2022). Experimental investigations into the effect of urban airflow characteristics on urban air mobility applications. *Journal of Wind Engineering and Industrial Aerodynamics*, *229*, 105126. https://doi.org/https://doi.org/10.1016/j.jweia.2022.105126

Alrwashdeh, S. (2021). Investigation of the energy output from PV panels based on using different orientation systems in Amman-Jordancorlowast. *Case Studies in Thermal Engineering*, *28*, 101580.

Bhalindar Singh, C. S. (2020). Monitoring Urban Growth and Detection of Land Use/ Land Cover Change in Silchar City, Assam and Balurghat City, West Bengal. *International Journal of Innovative Technology and Exploring Engineering (IJITEE)*, *9*(8).

Bouyer, J., Inard, C., & Musy, M. (2011). Microclimatic coupling as a solution to improve building energy simulation in an urban context. *Energy and Buildings*, *43*(7), 1549–1559. https://doi.org/https://doi.org/10.1016/j.enbuild.2011.02.010

Brozovsky, J., Radivojevic, J., & Simonsen, A. (2022). Assessing the impact of urban microclimate on building energy demand by coupling CFD and building performance simulation. *Journal of Building Engineering*, *55*, 104681. https://doi.org/https://doi.org/10.1016/j.jobe.2022.104681

Cóstola, D., Blocken, B., & Hensen, J. L. M. (2009). Overview of pressure coefficient data in building energy simulation and airflow network programs. *Building and Environment*, *44*(10), 2027–2036. https://doi.org/https://doi.org/10.1016/j.buildenv.2009.02.006

Gobakis, K., & Kolokotsa, D. (2017). Coupling building energy simulation software with microclimatic simulation for the evaluation of the impact of urban outdoor conditions on the energy consumption and indoor

environmental quality. *Energy and Buildings*, *157*, 101–115. https://doi.org/10.1016/j.enbuild.2017.02.020
Hadavi, M., & Pasdarshahri, H. (2021). Investigating effects of urban configuration and density on urban climate and building systems energy consumption. *Journal of Building Engineering*, *44*, 102710. https://doi.org/https://doi.org/10.1016/j.jobe.2021.102710
Javanroodi, K., & Nik, V. M. (2019). Impacts of Microclimate Conditions on the Energy Performance of Buildings in Urban Areas. In *Buildings* (Vol. 9, Issue 8). https://doi.org/10.3390/buildings9080189
Kubilay, A., Derome, D., & Carmeliet, J. (2018). Coupling of physical phenomena in urban microclimate: A model integrating air flow, wind-driven rain, radiation and transport in building materials. *Urban Climate*, *24*, 398–418. https://doi.org/https://doi.org/10.1016/j.uclim.2017.04.012
Kyriakodis, G. E., Bozonnet, E., & Riederer, P. (2019). Quantifying the impact of urban microclimate in detailed urban building energy simulations. *Building Simulation Conference Proceedings*, *6*, 3714–3721. https://doi.org/10.26868/25222708.2019.211137
Li, X., Zhou, Y., Yu, S., Jia, G., Li, H., & Li, W. (2019). Urban heat island impacts on building energy consumption: A review of approaches and findings. *Energy*, *174*. https://doi.org/10.1016/j.energy.2019.02.183
Mirzaei, P. (2022a). *Applications of Fluid Mechanics in Buildings* (pp. 93–156). https://doi.org/10.1002/9781119815099.ch3
Mirzaei, P. (2022b). *Fundamental of Computational Fluid Dynamics – A Finite Volume Approach* (pp. 413–488). https://doi.org/10.1002/9781119815099.ch10
Mirzaei, P. A. (2021). CFD modeling of micro and urban climates: Problems to be solved in the new decade. *Sustainable Cities and Society*, *69*, 102839. https://doi.org/https://doi.org/10.1016/j.scs.2021.102839
Parham A. Mirzaei. (2022). *Computational Fluid Dynamics and Energy Modelling in Buildings: Fundamentals and Applications*. WILEY Blackwell.
Pei, L., Schalbart, P., & Peuportier, B. (2023). Quantitative Evaluation of the Effects of Heat Island on Building Energy Simulation: A Case Study in Wuhan, China. In *Energies* (Vol. 16, Issue 7). https://doi.org/10.3390/en16073032
Pfafferott, J., Rißmann, S., Sühring, M., Kanani-Sühring, F., & Maronga, B. (2021). Building indoor model in PALM-4U: indoor climate, energy demand, and the interaction between buildings and the urban microclimate. *Geoscientific Model Development*, *14*(6), 3511–3519. https://doi.org/10.5194/gmd-14-3511-2021
Priya, U. K., & Senthil, R. (2021). A review of the impact of the green landscape interventions on the urban microclimate of tropical areas. *Building and Environment*, *205*, 108190. https://doi.org/https://doi.org/10.1016/j.buildenv.2021.108190
Shirzadi, M., Naghashzadegan, M., & Mirzaei, P. A. (2019). Developing a framework for improvement of building thermal performance modeling under urban microclimate interactions. *Sustainable Cities and Society*, *44*, 27–39. https://doi.org/10.1016/j.scs.2018.09.016
Tominaga, Y., Mochida, A., Yoshie, R., Kataoka, H., Nozu, T., Yoshikawa, M., & Shirasawa, T. (2008). AIJ guidelines for practical applications of CFD to pedestrian wind environment around buildings. *Journal of Wind Engineering and Industrial Aerodynamics*, *96*(10–11), 1749–1761. https://doi.org/10.1016/j.jweia.2008.02.058
UN-Habitat. (2022). *Amman Spatial profile*. *March*. https://unhabitat.org/sites/default/files/2022/04/220411-final_amman_profile.pdf
Xia, Q., Liu, X., Niu, J., & Kwok, K. C. S. (2015). Effects of building lift-up design on the wind environment for pedestrians. *Indoor and Built Environment*, *26*(9), 1214–1231. https://doi.org/10.1177/1420326X15609967
Xue, X., Han, S., Guo, D., Zhao, Z., Zhou, B., & Li, F. (2022). Study of the Convective Heat Transfer Coefficient of Different Building Envelope Exterior Surfaces. In *Buildings* (Vol. 12, Issue 6). https://doi.org/10.3390/buildings12060860
Yang, W., Zhu, X., & Liu, J. (2017). Annual experimental research on convective heat transfer coefficient of exterior surface of building external wall. *Energy and Buildings*, *155*, 207–214. https://doi.org/https://doi.org/10.1016/j.enbuild.2017.08.075
Younes, C., Abishdid, C., & Bitsuamlak, G. (2012). Air infiltration through building envelopes: A review. *Journal of Building Physics - J BUILD PHYS*, *35*, 267–302. https://doi.org/10.1177/1744259111423085
Zhang, R., & Mirzaei, P. A. (2021a). Fast and dynamic urban neighbourhood energy simulation using CFDf-CFDc-BES coupling method. *Sustainable Cities and Society*, *66*, 102545. https://doi.org/https://doi.org/10.1016/j.scs.2020.102545
Zhang, R., & Mirzaei, P. A. (2021b). Virtual dynamic coupling of computational fluid dynamics-building energy simulation-artificial intelligence: Case study of urban neighbourhood effect on buildings' energy demand. *Building and Environment*, *195*, 107728. https://doi.org/https://doi.org/10.1016/j.buildenv.2021.107728

6th International Conference on Building Energy and Environment
Eindhoven University of Technology, The Netherlands
6 - 10 July 2025

Improving energy efficiency across building portfolios: Disaggregating bulk meter data using XGBRegressor)

Narges Zaeri[1] and Darwish Darwazeh[2]

[1] *National Research Council Canad, Ottawa, Canada, Narges.ZaeriEsfahani@nrc-cnrc.gc.ca*
[2] *National Research Council Canad, Ottawa, Canada, Darwish.Darwazeh@nrc-cnrc.gc.ca*

SUMMARY
Energy disaggregation is a critical tool for improving energy efficiency in building management, yet most current methods focus on single buildings with submeter data, leaving a gap in scalable solutions for large building portfolios using only bulk meter data. This research addresses that gap by developing a model to disaggregate electricity consumption across a portfolio of buildings. Using the ASHRAE Kaggle dataset, which includes extensive building metadata (e.g., primary use, square footage, year built, floor count) and weather features (e.g., air temperature, wind speed, cloud coverage), we incorporate time-series features data and explore eXtreme Gradient Boosting (XGBRegressor) to enhance the model's ability to generalize to unseen building portfolios. Submeter data will be used for evaluation, ensuring accuracy and robustness in disaggregation. This approach aims to provide actionable insights for energy optimization at scale, paving the way for better-informed policy decisions and improved energy management practices.

Keywords: Energy disaggregation, Building Portfolio, Submetering, Regression-based model.

1. INTRODUCTION

In the quest for sustainability, enhancing energy efficiency in buildings has become a critical objective for both policymakers and facility managers. A key strategy in achieving this goal is energy disaggregation, which involves breaking down total energy consumption into its components. This allows for targeted interventions that can significantly reduce energy waste. However, the current methods for energy disaggregation primarily focus on individual buildings with detailed sub-meter data, leaving a substantial gap when it comes to applying these techniques across larger portfolios of buildings that rely solely on bulk meter data.

Non-intrusive load monitoring (NILM) methods have become increasingly popular for their capability to break down energy consumption by specific appliances, promoting better energy management and possible cost reductions. These techniques have primarily been applied within residential buildings, mainly because household appliance data is easily accessible and there are several public datasets available. Although NILM has been effective in residential areas, implementing these techniques in large office buildings is notably challenging. This is due to restricted access to data

and the significant differences between residential, office, and industrial sites (Adabi et al., 2015; Yaniv and Beck, 2025).

The potential benefits of implementing disaggregation techniques in large buildings are significant, both economically and environmentally. Many buildings spend thousands of dollars or more annually on electricity and are often required by regulations in various countries to reduce their energy consumption. Beyond financial savings, large buildings represent a major share of global energy use, so even small gains in energy efficiency facilitated by disaggregation insights can lead to considerable reductions in carbon emissions. This underscores the importance of industries in sustainable development and environmental protection (Calvo et al., 2021).

The behavior of heating/cooling systems, lighting plug loads, and appliances is quite different from that of household devices. Large office and commercial buildings host a wide array of equipment, while household appliances typically fall into a few standard categories such as ovens, toasters, and air conditioners. Additionally, the operation of some industrial machines can be highly complex compared to the relatively simple functions of most home appliances. The operational schedules in this sector are distinct as well; while residential electricity usage follows predictable patterns based on time of day, weekends, seasons, and holidays, industrial operations often adhere to specific shift schedules, requiring coordination with shift managers to understand each facility's timetable.

Federal buildings, which often lack comprehensive sub-metering systems, highlight the challenges associated with bulk meter data. These buildings frequently have either no sub-meter data or data that is riddled with gaps and inaccuracies. Even when available, sub-meter data typically spans only a limited timeframe, such as a year or less, which impedes effective long-term energy management. This lack of detailed data prevents energy managers from accurately identifying inefficiencies and implementing improvements on a broader scale.

Disaggregation techniques play an important role in optimizing energy consumption in buildings. These methods, categorized into supervised and unsupervised approaches, offer valuable alternatives for different data availability scenarios. In supervised methods, optimization algorithms are utilized, but their main drawback is the requirement of a labeled dataset (e.g., refrigerator, air conditioner, washing machine). Acquiring labeled data can increase the setup costs of NILM systems, making unsupervised methods more favorable in some cases (García et al., 2018). Using an unsupervised disaggregation method, García et al., 2018, presented an interactive web tool for exploring NILM results. Using non-negative matrix factorization (NMF) methods, it analyzes power demand data from a hospital complex. The tool integrates user knowledge through visual analytics, allowing expert users to interpret NMF components and identify demand patterns and inefficiencies. In a previous study presented by Brucke et al., 2020, a fully unsupervised approach using particle swarm optimization was introduced for energy disaggregation. However, its application was limited to power data from two industrial consumers, making comparisons with other research challenging.

Zaeri, Ashouri, et al., 2022, proposed a regression-based approach using BAS trend data to disaggregate heating and electricity consumption in commercial buildings. This method, which employs genetic algorithms and least-square solvers, demonstrated its accuracy using data from an

academic office building in Ottawa, Canada. Additionally, A. A. Narges Zaeri Esfahani B. G. and Rizvi, 2023; Zaeri, Gunay, et al., 2022 investigated the impact of submeter density and configuration on disaggregation accuracy, highlighting critical factors for optimizing submeter deployment in commercial buildings. Moreover, H. B. G. Narges Zaeri Esfahani A. A. and Bahiraei, 2024 proposed a time-series decomposition-based method for unsupervised energy disaggregation, which was validated using submeter data from ten office buildings. This method provides insight into lighting and thermal scheduling variations at different temporal scales.

The limitation of current energy disaggregation methods in addressing large-scale applications creates a significant knowledge gap. Traditional models require granular data inputs that bulk meters do not provide, making it difficult to derive actionable insights for large building portfolios. This gap underscores the need for innovative approaches that can leverage existing bulk meter data to provide meaningful energy usage breakdowns.

Driven by these challenges, our research seeks to bridge this gap by developing a scalable model capable of disaggregating electricity consumption across multiple buildings. Using the ASHRAE Kaggle dataset, which includes extensive metadata and weather features, we employ eXtreme Gradient Boosting (XGBRegressor) to enhance the model's generalization to unseen building portfolios. By evaluating the model against available sub-meter data, we ensure its accuracy and robustness, providing a reliable tool for energy optimization. Our approach not only addresses the immediate data availability issues but also aims to transform how energy consumption is managed across large building portfolios. By providing more precise insights, this model supports better-informed policy decisions and improved energy management practices, contributing to the overarching goal of sustainability in the built environment.

Through visual representations, users can easily spot anomalous values, detect malfunctioning or poorly commissioned systems, and observe energy consumption patterns. This visualization-based approach enhances the ability to analyze and interpret energy data, enabling more effective decision-making and interventions to optimize energy usage within buildings (Meyers et al., 1996).

2. METHODOLOGY

In this paper, we developed five separate XGBoost regressors, one for each building use portfolio, leveraging bulk meter data, weather data, and time-series characteristics of the bulk meters. Each model is trained on a complete year of data for a given building, and subsequently, the models can be saved and used to predict missing or faulty submeter data during other time periods. Additionally, we performed feature importance analysis to identify the most correlated predictors, helping to understand the key variables influencing the model's predictions.

2.1. Portfolio disaggregation model

2.2. XGBRegressor

We selected the XGBoost model due to its capability to handle complex, non-linear relationships and its robustness against overfitting. XGBoost provides insights into feature importance, which is valuable for understanding the factors influencing energy consumption. XGBoost is an ensemble learning method based on decision tree algorithms. It utilizes gradient boosting to optimize the predictive power. The model iteratively improves by minimizing the objective function, which is

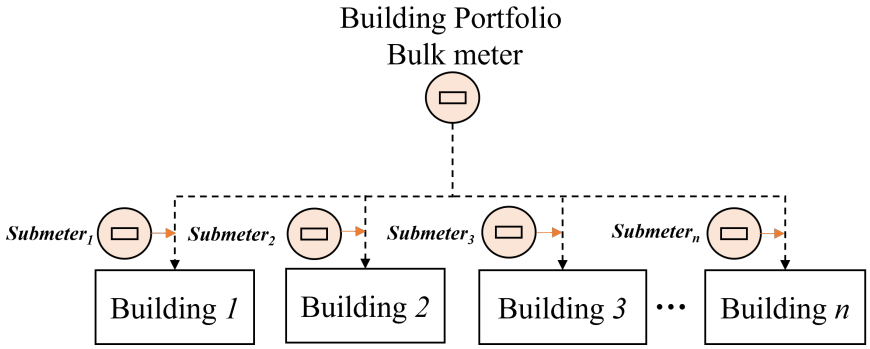

Figure 1. Example of figure.

composed of a differentiable loss function and a regularization term. The model can be mathematically described as follows:

$$L(\phi) = \sum_{i=1}^{n} l(y_i, \hat{y}i) + \sum k = 1^{K} \Omega(f_k) \tag{1}$$

where $L\phi$ is the overall objective function, l is a differentiable loss function measuring the difference between the prediction $\hat{y}_i$ and the true value y_i, and $\Omega(f_k)$ is a regularization term that penalizes the complexity of the model. The regularization term can be expressed as:

$$\Omega(f) = \gamma T + \frac{1}{2}\lambda \sum_{j=1}^{T} w_j^2 \tag{2}$$

where γ and λ are hyperparameters controlling the model complexity, T is the number of leaves in the tree, and w_j is the weight of leaf j.

The model was implemented using the XGBoost library in Python. We conducted extensive hyperparameter tuning to optimize performance, focusing on parameters such as the learning rate, maximum tree depth, and number of estimators. The input data was preprocessed to handle missing values and normalize features.

2.3. Case study and dataset

The ASHRAE Great Energy Predictor III competition dataset is a comprehensive collection used to advance machine learning methodologies for predicting energy usage in buildings. It includes over 20 million data points from 2,380 energy meters across 1,448 buildings, collected from diverse sites worldwide (Miller et al., 2020). The dataset provides three years of hourly meter readings and is instrumental in developing counterfactual models that predict energy consumption without retrofits. This allows for the calculation of energy savings post-retrofit, supporting better market incentives and reducing financing costs by demonstrating the value of energy efficiency improvements. For this study, we focused on a case study involving five buildings from this dataset, all

located at site_id 14. By selecting buildings within the same region, we ensured similar weather conditions, which aids in creating consistent and reliable models. These buildings, categorized as either office or education facilities, serve as a practical example of how the dataset can be utilized to develop models that disaggregate electricity consumption. This approach demonstrates the scalability of the models across building portfolios and their potential impact on energy management practices.

2.4. Exploratory data analysis

The analysis of feature importance across various buildings shows that '*total_Elec*' consistently stands out as a significant predictor of electricity consumption. It emerges as the most crucial feature for Buildings 1260, 1251, and 1287, underscoring its role in capturing historical consumption patterns that aid in future predictions. Temporal features such as '*week_of_year*', '*hour*', and '*day_of_week*' also prove important across different buildings, indicating the impact of time-based patterns on energy usage. For instance, '*week_of_year*' is the leading feature for Building 1296, while '*hour*' is vital for Building 1242. Weather-related features, like '*dew_temperature*' and '*air_temperature*', although less dominant compared to temporal or historical consumption data, modestly enhance the model's predictive power, particularly for Building 1251, where '*dew_temperature*' holds a significant importance score.

To improve model performance, we refined the feature set by removing those with negligible importance, such as *is_weekend*', which consistently show zero importance across all buildings. This simplification can lead to a more efficient model without compromising accuracy, by focusing on the most impactful predictors for energy disaggregation across the portfolio. as in Table 2

Table 1. Selected building portfolio.

building_id	site_id	Primary_use	Square_feet
1242	14	Office	23,871
1251	14	Education	104,604
1260	14	Office	86,455
1287	14	Education	60,582
1296	14	Office	8,836

2.5. Portfolio disaggregation model validation and error calculation

To assess the performance of the energy disaggregation model, we employed two key evaluation metrics: the coefficient of determination R^2 and the Coefficient of Variation of the Root Mean Square Error (CV-RMSE). These metrics provide a comprehensive understanding of the model's accuracy and predictive capability.

The coefficient of determination, R^2, measures the proportion of variance in the observed data that is predictable from the model. It is defined as: $R^2 = 1 - \frac{\sum_{i=1}^{N}(y_i - \hat{y}_i)^2}{\sum_{i=1}^{N}(y_i - \bar{y}_i)^2}$ where y_i is the actual value, $\hat{y}_i$ is the predicted value, and $\bar{y}$ is the mean of the observed values. An R^2 value close to 1 indicates a high degree of correlation between the predicted and actual values. The CV-RMSE quantifies the ratio of the root mean square error to the mean of the observed values, providing a normalized measure of prediction error. It is calculated as: $\text{CV-RMSE} = \frac{\text{RMSE}}{\bar{y}} \times 100\%$ where $\text{RMSE} = \sqrt{\frac{1}{N}\sum_{i=1}^{N}(\hat{y}i - yi)^2}$ and $\bar{y}$ is the mean of the observed values. According to ASHRAE Guideline 14, a CV-RMSE value below 30% is considered acceptable for engineering applications. These metrics were selected for

their ability to provide insight into both the accuracy and reliability of the model's predictions, ensuring a robust evaluation of its performance across different scenarios.

3. RESULTS AND DISCUSSION

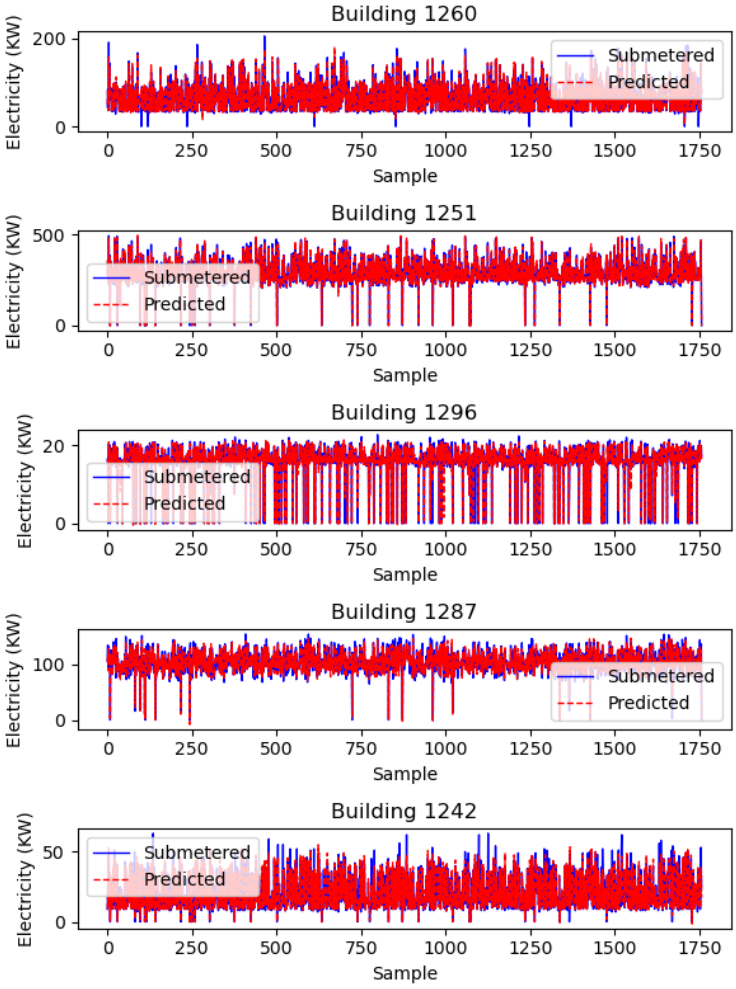

Figure 2. Comparison of submetered and predicted data by models trained with hourly data for electricity.

The XGBoost regressor models were developed and evaluated for five buildings using the features detailed in the methodology section. The performance was assessed using the coefficient of determination R^2 and the Coefficient of Variation of the Root Mean Square Error $CV-RMSE$. These metrics provide a comprehensive evaluation of model accuracy and reliability, consistent with ASHRAE Guideline 14 standards (Guideline, 2014). For Building 1260, the model achieved an impressive $R^2 = 0.94$, indicating a strong ability to capture the variability in electricity consumption. The $CV-RMSE$ was 0.11, well below the ASHRAE threshold, demonstrating excellent predictive accuracy. Feature importance analysis revealed that '$total_Elec$' was the most influential feature, followed by '$week_of_year$' and '$month$'.

In Building 1251, the model showed exceptional predictive capability with an $R^2 = 0.98$. A CV-

Table 2. Performance of the proposed regression models for electricity demand in hourly resolution.

building_id	CV-RMSE	R^2
1242	0.18	0.90
1251	0.03	0.98
1260	0.11	0.94
1287	0.07	0.88
1296	0.09	0.93

RMSE of 0.03 indicates the model's predictions are highly reliable. The model's performance was primarily driven by '$total_Elec$' and '$dew_temperature$', reflecting the impact of both historical consumption and weather conditions on energy use. For Building 1296, the $R^2 = 0.93$ suggests a robust model fit. The CV-RMSE at 0.09 confirms the model's practical applicability. The dominance of '$week_of_year$' highlights temporal patterns as key predictors, with 'day_of_month' and '$total_Elec$' also contributing significantly. The model for Building 1287 showed good performance with an $R^2 = 0.88$ and a CV-RMSE of 0.07, underscoring its accuracy. Here, '$total_Elec$' and '*hour*' were the most significant features, emphasizing the importance of both historical and daily patterns in predicting energy consumption. In Building 1242, the $R^2 = 0.90$ indicates a strong correlation between predicted and actual values. A CV-RMSE of 0.18, although within acceptable limits, suggests potential for further model enhancement. '*hour*' emerged as the predominant feature, signifying the critical role of time-of-day in energy usage predictions.

4. CONCLUSION AND FUTURE WORK

This research represents an improvement in addressing the complexities of energy disaggregation within building portfolios, which often suffer from a lack of comprehensive submetering systems. By utilizing XGBRegressor and the metadata and weather features from the ASHRAE Kaggle dataset, we have developed a model that effectively uses bulk meter data to provide detailed insights into electricity consumption across a portfolio of five buildings. A key achievement of this study is the creation of a robust tool that empowers energy managers with the capacity to identify inefficiencies and make informed decisions, even when granular sub-meter data is lacking. This model bridges a crucial knowledge gap in large-scale energy management and supports the broader goal of sustainability within the built environment. The availability of disaggregated energy data opens up numerous avenues for further analysis. This breakdown allows for enhanced applications such as fault detection and energy anomaly detection using Building Automation Systems (BAS) data. It also facilitates the identification of energy flow disaggregation for each end-use within buildings, providing a foundation for more targeted energy management strategies. Looking ahead, our future work will focus on expanding the model's application to scenarios where sub-meter data is either unavailable or inconsistently available across different portfolios of buildings. We plan to explore the integration of unsupervised learning techniques to further refine the model's ability to disaggregate energy usage at the individual building level. This will enhance the model's flexibility and scalability, making it a valuable asset in diverse energy management contexts. Through these efforts, we aim to not only improve the model's performance but also broaden its utility, contributing to more sustainable and efficient energy management strategies across various building portfolios.

ACKNOWLEDGMENTS

This research is supported by research funding provided by National Research Council Canada.

REFERENCES

Adabi A., Mantey P., Holmegaard E., and Kjaergaard M. B., 2015. Status and challenges of residential and industrial non-intrusive load monitoring. 2015 IEEE Conference on Technologies for Sustainability, SusTech 2015, 181–188.

Brucke K., Arens S., Telle J.-S., Hanke B., Maydell K. von, Agert C., et al., 2020. Particle swarm optimization for energy disaggregation in industrial and commercial buildings. arXiv preprint arXiv:2006.12940.

Calvo V. L. V., Giner-Santonja G., Alonso-Fariñas B., and Aguado J. M., 2021. The effect of the European Industrial Emissions Directive on the air emission limit values set by competent authorities in the permitting procedure: The case of the Spanish cement industry. Science of The Total Environment 773, 145491.

García D., Díaz I., Pérez D., Cuadrado A. A., Domínguez M., and Morán A., 2018. Interactive visualization for NILM in large buildings using non-negative matrix factorization. Energy and Buildings 176, 95–108.

Guideline A., 2014. Guideline 14-2014., 2014, Measurement of Energy and Demand Savings. American Society of Heating Refrigerating and Air-Conditioning Engineers Inc, Atlanta.

Meyers S., Mills E., Chen A., and Demsetz L., June 1996. Building data visualization for diagnostics. ASHRAE Journal 38, 8pp.

Miller C., Arjunan P., Kathirgamanathan A., Fu C., Roth J., Park J. Y., Balbach C., Gowri K., Nagy Z., Fontanini A. D., and Haberl J., 2020. The ASHRAE Great Energy Predictor III competition: Overview and results. Science and Technology for the Built Environment 26, 1427–1447.

Narges Zaeri Esfahani Burak Gunay A. A. and Rizvi F., 2023. An inquiry into the effect of thermal energy meter density and configuration on load disaggregation accuracy. Science and Technology for the Built Environment 29, 424–441.

Narges Zaeri Esfahani Araz Ashouri H. B. G. and Bahiraei F., 2024. Energy consumption disaggregation in commercial buildings: a time series decomposition approach. Science and Technology for the Built Environment 30, 660–674.

Yaniv A. and Beck Y., 2025. Advances in non-intrusive load monitoring for the industrial domain: Challenges, insights, and path forward. Renewable and Sustainable Energy Reviews 210, 115136.

Zaeri N., Ashouri A., Gunay H. B., and Abuimara T., 2022. Disaggregation of electricity and heating consumption in commercial buildings with building automation system data. Energy and Buildings 258, 111791.

Zaeri N., Gunay B., and Ashouri A., 2022. Effect of Thermal Energy Meter Density and Configuration on Disaggregation Accuracy. 5th International Conference on Building Energy and Environment (COBEE 2022)At: Montreal, Canada, 110867.

6th International Conference on Building Energy and Environment
Eindhoven University of Technology, The Netherlands
6 - 10 July 2025

Extraction of carbon emission factors for buildings at meso-scale

Yuanyuan Liu [1], Yan Wu [1,*], Bingyang Zhang [1], Tianle Chen [1]

[1] *Tongji University, Shanghai, China, 2430419@tongji.edu.cn*

SUMMARY
Localized carbon emission factors are crucial for the accurate formulation of carbon emission reduction policies. Aiming at the lack of building carbon emission factors at meso-scale in China, this paper proposes a method for extracting and calibrating the carbon emission factors of building materials and operation applicable to urban meso-scale and building micro-scale, and calculates them with case data. The results of the study show that: (1) the distribution of carbon emission factors of building materials in Chinese provinces and cities is concentrated in the range of 649.56-1317.48 $kgCO_2/m^2$ (2011-2020); (2) electricity consumption (indirect emission) accounts for the highest proportion of carbon emission in operation, and there is a significant difference in the regional differences, e.g., the intensity of indirect carbon emission of healthcare buildings spans from 5.52 to 163.71 $kgCO_2/m^2$; (3) economic level, energy structure and urbanization rate are the main drivers of building carbon emissions.

Keywords: *Carbon emission factor, Meso-scale, Building*.

1. INTRODUCTION

Buildings are an essential component of human social production and life, and are also major consumers of natural resources and contributors to environmental pollution. As the largest construction market in the world, China's carbon emissions from the construction industry account for more than a third of the country's total carbon emissions (Wang et al., 2024; Luo et al., 2016). Carbon emission factor unit of greenhouse gas emissions released by the use of a certain emission source, the extraction of building carbon emission factors can provide scientific support for energy saving and carbon reduction policymaking. Defining the boundary of carbon emission accounting is the first step to start the extraction of carbon emission factors. Currently, scholars have different definitions of the measurement scope for carbon emissions. Zhang and Wang divide the building lifecycle into three phases: materialization, operation, and demolition (Zhang & Wang, 2015). Some researchers split the materialization phase into two stages — production and construction (Cho et al., 2016). Additionally, some studies include the design phase of buildings in the calculation scope (Cui et al., 2019; Shen et al., 2018). In building carbon emission calculations, most researchers focus on measuring the carbon emissions of individual or multiple buildings to identify their main influencing factors (Chastas et al., 2018) or calculate carbon emission factors for building materials (Wang et al., 2024). However, research on carbon emission factors at scales larger than the micro-scale is relatively scarce. Studies have shown that carbon emission factors with localized and regional characteristics are more reflective of a region's carbon emission levels and are more suitable for national contexts. This study divides building carbon emission accounting into building materials, construction, and operation. Given that the carbon emissions during the construction process account for only about 1% (CABEE & Chongqing University, 2023), this study primarily focuses on the carbon emissions from building materials and operations. Based on existing research results, this study proposes a

method for calculating the carbon emission factors of building materials and operations applicable to the urban meso-scale and building micro-scale. It calculates carbon emission factors for building materials and operations that are more localized characteristic, using available data. The composition and distribution characteristics are analyzed to identify the causes of the emissions and to summarize the influencing factors.

2. METHOD

2.1 Carbon Emission Factors for Building Materials

Considering that the current carbon emission factors for building materials are generally micro-product level building materials factors that cannot measure the carbon emissions generated by the production and transport of building materials in a region, this study proposes a method for calculating the building materials factors at the city level, which is also applicable to the micro-architectural level.

The carbon emissions from building materials should include the production and transportation stages. The carbon emission factor calculation formula is shown in Eq. (1).

$$C_{jc} = \frac{\sum_{i=1}^{n} (EF_{i,m} M_i + M_i D_i T_i)}{A} \quad (1)$$

Here, C_{jc} represents the carbon emission factor of the building material; $EF_{i,m}$ represents the carbon emission factor of the i-th material; M_i represents the quantity of the i-th material; Di represents the average transportation distance of the i-th material; Ti represents the carbon emission factor for transportation per unit weight of the i-th material; A represents the building area; i represents the material type.

In light of the difficulty in obtaining meso-scale city-level statistics on construction material transport distances and conveyance modes, this study draws on standard documents, industry reports, and carbon-emission data from multiple engineering case studies to determine the proportional relationship between material production and transport emissions. The resulting ratios generally fall between 2 % and 7 %. Consequently, when transport data are unavailable, the transport-stage emissions may be estimated by applying a coefficient of 2 %–7 % of the production-stage material carbon emissions.

2.2 Operational Carbon Emission Factor

When calculating the carbon emission factor of building operations, this paper introduces the concept of "carbon emission intensity." The carbon emissions from building operations are divided into direct and indirect emissions, and the concept of "comprehensive carbon emission intensity" is introduced to better measure urban carbon emission levels. Direct carbon emissions are caused by energy consumption, such as natural gas, coal, etc.; indirect carbon emissions are caused by purchased electricity, heat, and cooling.

2.2.1. Comprehensive carbon emission intensity

The formula for calculating the comprehensive carbon emission intensity of building operations is constructed according to Eq. (2).

$$C_Z = \frac{C_M}{A} = C_d + C_{id} \quad (2)$$

Where C_Z represents the comprehensive carbon emission intensity of building operations; C_M represents the annual carbon emissions from building operations; C_d represents the direct carbon emission intensity from building operations; C_{id} represents the indirect carbon emission intensity from building operations.

2.2.2. Direct carbon emission intensity

The formula for calculating the direct carbon emission intensity of building operations is shown in Eq. (3) and Eq. (4).

$$C_d = \frac{\sum_{i=1}^{n}(EF_{i,e}E_i)}{A_h} \quad (3)$$

$$A_h = A_a \cdot m \quad (4)$$

Where $EF_{i,e}$ represents the carbon emission factor for the i-th energy type; E_i represents the quantity of the i-th non-renewable energy used in building operations, excluding electricity; A_h represents the residential building area; A_a represents the per capita residential building area; m represents the population number.

2.2.3. Indirect carbon emission intensity

The formula for calculating the direct carbon emission intensity of building operations is shown in Eq. (5).

$$C_{id} = EUI \cdot EF \quad (5)$$

Where *EUI* represents the annual electricity consumption intensity of the building; *EF* represents the electricity carbon emission factor of the region where the building is located.

2.3 Data Priority Levels

This study focuses on the extraction of meso-scale building carbon emission factors. Here, "meso-scale" is defined as the level of an individual city, a province, or an urban agglomeration composed of adjacent cities, rather than a sub-city district or a building complex. Accordingly, data published by authoritative national agencies are accorded the highest priority in the accounting process; secondary priority is assigned to limit values specified in relevant standards (for material accounting) or to operational data from energy-monitoring platforms (for operational accounting).

3. RESULTS AND DISCUSSION

3.1 Carbon Emission Factors for Building Materials

This study selects building material consumption data from 31 provinces and cities in China between 2011 and 2020 as the research sample. The data comes from the "China Building Industry Statistical Yearbook." Given the diversity of building materials and the incomplete building material factor database, this study, after considering the availability of data, selects the main carbon emission sources from building materials: steel, wood, aluminum, cement, and glass. The carbon emission factors for these materials are listed in Table 1.

Table 1. Carbon emission factors of building materials

	Steel (tCO_2/t)	Wood (tCO_2/m^3)	Cement (tCO_2/t)	Glass (tCO_2/m^2)	Aluminum (tCO_2/t)
Carbon emission factor	1.789	-0.843	0.822	0.047	2.600

Fig.1 shows the distribution of building material carbon emission factors across China's provinces and cities from 2011 to 2020. As observed in Fig.1, the majority of building material emission factors in Chinese provinces and cities range from 649.56 to 1317.48 $kgCO_2/m^2$.

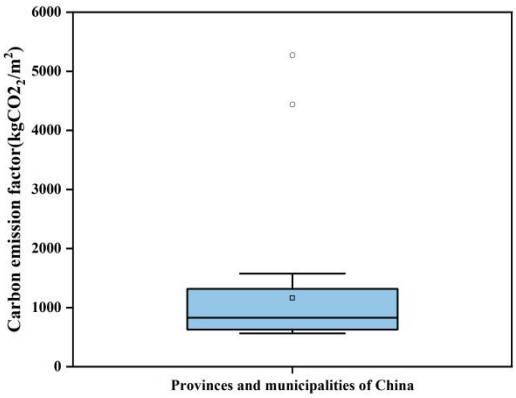

Figure 1. Distribution of building material emission factors across provinces and cities in China.

Fig.2 illustrates the composition of total building material carbon emissions in different provinces and cities of China in 2020. From Fig.2, it is evident that steel and cement are the main sources of carbon emissions among the five types of building materials. Moreover, it is clear that high-carbon-emission areas are clustered in the eastern provinces (e.g., Jiangsu, Zhejiang, Fujian), where economic development, technological capacity, and urbanization rates are generally higher. By contrast, low-carbon-emission regions are predominantly in the west (e.g., Qinghai, Ningxia, Tibet), where mountainous and plateau terrain has historically constrained early urban growth.This suggests that natural resources, geographical location, and climate conditions are also significant factors affecting building carbon emissions.

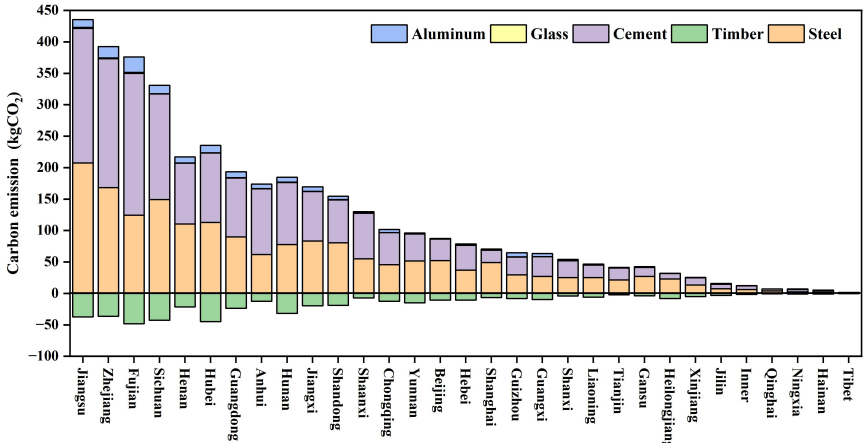

Figure 2. Composition of Building Material Carbon Emissions in Provinces and Cities of China (2020).

The year-on-year trend of carbon emission factors of building materials at the macro-country level tends to reflect the trend of policy orientation and market demand, and the driving factors behind them often significantly affect the change of meso-factors, so analysing the trend of their change can provide important references and bases for the study of meso-factors.

Fig.3 reflects the trends in China's building material carbon emissions and carbon emission factors from 2011 to 2020. Fig.4 shows the annual changes in China's building construction area from 2011 to 2020. From Fig.3, it can be observed that the carbon emission factors for building materials in China follow a similar trend to that of carbon emissions, with the highest carbon emission factor recorded in 2013 at 1286.18 $kgCO_2/m^2$. From 2015 to 2029, the carbon emission factors for building materials showed a gradually increasing trend, albeit at a slower rate. Notably, from 2012 to 2013, the building material carbon emission factor decreased significantly, despite an increase in the construction area (Fig.4). This is likely due to the implementation of policies promoting the use of green materials. Combining Fig.3 and Fig.4, from 2016 to 2029, the construction area and carbon emissions were inversely proportional, likely related to changes in the structure of its consumption of building materials.

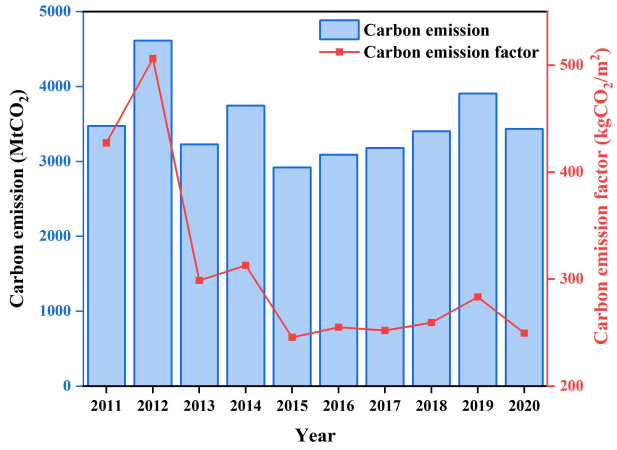

Figure 3. Carbon Emission Factors (2011-2020).

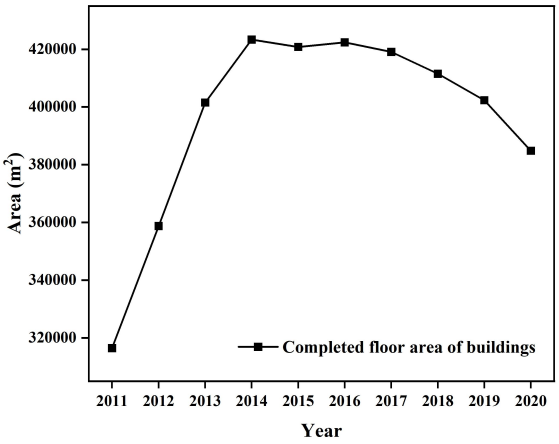

Figure 4. Changes in Construction Area (2011-2020).

3.2 Operational Carbon Emission Factor

Quantifying the carbon intensity of building operations in first-tier cities, which are highly concentrated in terms of economic and population density, and second- and third-tier cities, which are more densely distributed in China, can reveal the characteristics of carbon emissions at different stages of development in China. Considering the availability of data, Beijing, Shanghai, Shenzhen and Bozhou are selected as typical cities for this study.

3.2.1. Comprehensive carbon emission intensity

This study calculates the direct carbon emission intensity, indirect carbon emission intensity, and comprehensive carbon emission intensity of building operations in Shanghai for the years 2022 and 2023, using data from the Shanghai energy consumption monitoring report. The calculation results are shown in Table.2. From Table.2, it is clear that indirect carbon emissions, primarily

resulting from electricity consumption, make up the largest portion of building operational carbon emissions..

Table 2. Calculation results comprehensive carbon emission intensity

Year	direct carbon emission intensity ($kgCO_2/m^2$)	indirect carbon emission intensity ($kgCO_2/m^2$)	comprehensive carbon emission intensity ($kgCO_2/m^2$)
2022	5.2	35.4	40.6
2023	6.7	41.4	48.1

3.2.2. Direct carbon emission intensity

This study analyzes the direct carbon emission intensity of energy consumption from residential buildings in Bozhou, China, from 2019 to 2022. The data comes from the "Bozhou Statistical Yearbook." The energy consumption mainly considers natural gas and liquefied petroleum gas. The carbon emission factors for natural gas and liquefied petroleum gas are taken from "Building Carbon Emission Calculation Standard," which are 1.566 tCO_2/t standard coal and 3.1013 $kgCO_2/kg$, respectively.

Table.3 shows the calculation results of direct carbon emission intensity in Bozhou from 2019 to 2022. From the table, it can be seen that the direct carbon emission intensity in Bozhou has been increasing year by year, primarily due to the increase in urbanization rate, which leads to a higher population and thus an increase in energy consumption. Comparing the results of this calculation with the direct carbon emission intensity of Shanghai in Table 2, it is easy to find that Shanghai is significantly higher than Bozhou, which shows that the economic level significantly affects urban carbon emissions.

Table 3. Calculation results of direct carbon emission intensity

Year	Carbon emissions (10000 $kgCO_2$)		Per capita housing area (m^2)	Population (10000)	Housing area (m^2)	Direct carbon emission intensity ($kgCO_2/m^2$)
	Natural gas	LPG				
2019	5433.49	948.72	51	207.40	10577.40	0.603
2020	6789.25	925.93	57	212.40	12106.80	0.637
2021	7810.77	940.17	57	215.40	12277.53	0.713
2022	8525.21	1806.84	54.3	218.50	11864.55	0.871

3.2.3. Indirect carbon emission intensity

Residential buildings are a significant component of social production and life, and studying the indirect carbon emission intensity of residential building operations is of great importance. This study calculates the indirect carbon emission intensity of residential buildings across 30 provinces and cities in China, using energy consumption data as the sample. The data covers the years 2014 to 2024.

Fig.5 shows the distribution of indirect carbon emission intensities for various types of buildings, classified by function. It can be seen that the data for hotel buildings shows the least fluctuation among the various building types, with indirect carbon emission intensity remaining relatively stable across different regions. On the other hand, the indirect carbon emission intensity for many other buildings, such as healthcare buildings, shows a wide fluctuation range, with intensities varying from 5.52 $kgCO_2/m^2$ to 163.71 $kgCO_2/m^2$. This indicates that there are

significant regional differences in the indirect carbon emission intensity of building operations, primarily due to variations in regional economic scale, industrial structure, energy structure, and urbanization rate. This underscores the importance of localized, region-specific carbon emission factors.

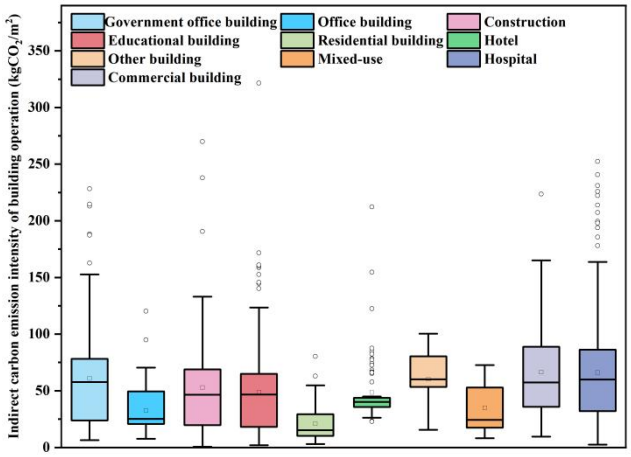

Figure 5. Distribution of indirect carbon emission intensity for various building types.

In order to examine more broadly the differences in the indirect carbon intensity of building operations in different regions, typical cities in the south, east, and north, namely Shenzhen, Shanghai, and Beijing, were selected for comparison. Fig.6 compares the indirect carbon emission intensities of different types of buildings in the cities of Beijing, Shanghai, and Shenzhen for 2023.

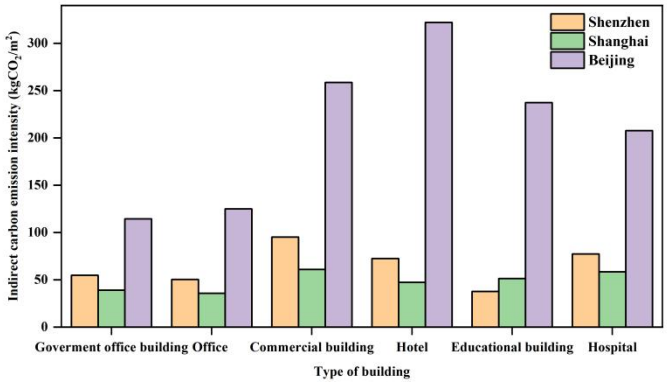

Figure 6. Indirect carbon emission intensity for various building types in first-tier cities.

As shown in Fig.6, the differences in indirect carbon emission intensity between Shanghai and Shenzhen are minimal, while Beijing's building operational indirect carbon emission intensity is significantly higher than the other two cities, mainly due to the heating energy consumption in Beijing. This also highlights the urgency of optimizing the regional energy mix.

4. Conclusions

Buildings are one of the main sources of urban carbon emissions, and the study of localised building carbon emission factors can provide a scientific basis for the formulation of efficient energy-saving and carbon reduction policies. In this paper, we propose a method for extracting building carbon emission factors applicable to urban mesoscale and building microscale, and calculate them with corresponding case data, and the conclusions are as follows:

The carbon emissions from building materials are primarily derived from steel and cement. From 2011 to 2020, China's macro building material carbon emission factors fluctuated, but the fluctuations became slower after 2016. Due to various factors such as policies and resource endowment, the building material consumption structure in different provinces and cities varies. The building material emission factors are mainly distributed between 649.56 $kgCO_2/m^2$ and 1317.48 $kgCO_2/m^2$.

Indirect carbon emissions are the primary component of building operational carbon emissions. The indirect carbon emission intensity for different types of buildings varies greatly across regions. For example, the indirect carbon emission intensity for healthcare buildings ranges from 5.52 $kgCO_2/m^2$ to 163.71 $kgCO_2/m^2$. Building operational carbon emission intensity is influenced by multiple factors, such as GDP, urbanization rate, and energy structure. This highlights the importance of considering regional and localized building carbon emission factors in order to accurately reflect the carbon emission levels of different regions.

ACKNOWLEDGEMENT

This work is supported by the National Key R&D Program of China (2023YFC3807700).

REFERENCES

Wang Z., Yang X., Zhan Z., Huang Z., 2024. Carbon emission measurement and evaluation of large public buildings in the materialization stage. Energy and Buildings 324, 114840.

Luo Z., Yang L., Liu J., 2016. Embodied carbon emissions of office building: A case study of China's 78 office buildings. Building and Environment 95, 365-371.

Zhang X., Wang F., 2015. Life-cycle assessment and control measures for carbon emissions of typical buildings in China. Building and Environment 86, 89-97.

Cho S.H., Chae C.U., 2016. A study on life cycle CO_2 emissions of low-carbon building in South Korea. Sustainability 8 (6), 579.

Cui C., Wang Z., Bin G., 2019. Life-cycle CO_2 emissions and their driving factors in construction sector in China. Chinese Geographical Science 29, 293-305.

Shen J., Yin X., Zhou Q., 2018. Research on a Calculation Model and Control Measures for Carbon Emission of Buildings. International Conference on Construction and Real Estate Management 2018.

Chastas P., Theodosiou T., Kontoleon K.J., Bikas D., 2018. Normalizing and assessing carbon emissions in the building sector: A review on the embodied CO_2 emissions of residential buildings. Building and Environment 130, 212-226.

Wang J., Pan K., Sha C., Wang Z., Sun Y., Kang Y., 2024. Carbon emission calculation and uncertainty analysis of asphalt concrete during the production stage. Construction and Building Materials 447, 138007.

CABEE & Chongqing University., 2023. China Building and Urban Infrastructure Carbon Emissions Research Report.

6th International Conference on Building Energy and Environment
Eindhoven University of Technology, The Netherlands
6 - 10 July 2025

A knowledge-augmented GPT for efficient data collection in home energy audits

Shih-Chi Liu [1], Kay Han [2], Ali Lesani [3], Chul Min Yeum [4], Graham Watt [5], Seungjae Lee [6]

[1]*Department of Civil & Mineral Engineering, University of Toronto, Toronto, Canada, shihchi.liu@mail.utoronto.ca*
[2]*Department of Civil and Environmental Engineering, University of Waterloo, Waterloo, Canada, k5han@uwaterloo.ca*
[3]*Department of Civil and Environmental Engineering, University of Waterloo, Waterloo, Canada, alesanis@uwaterloo.ca*
[4]*Department of Civil and Environmental Engineering, University of Waterloo, Waterloo, Canada, cmyeum@uwaterloo.ca*
[5]*Climate Tech Strategy & Innovation, Royal Bank of Canada, Toronto, Canada, graham.watt@rbc.com*
[6]*Department of Civil & Mineral Engineering, University of Toronto, Toronto, Canada, sjae.lee@utoronto.ca*

SUMMARY
This study explores the potential of large language models (LLMs) for facilitating data collection in home energy audits by comparing a baseline GPT-4 with a knowledge-augmented GPT that integrates multimodal retrieval-augmented generation (RAG) and prompt engineering. Using a ceiling insulation case study, we evaluate performance across task definition, execution instructions, insulation identification, and R-value estimation. Preliminary findings suggest that the knowledge-augmented GPT may offer more focused, reference-aligned guidance, potentially reducing user confusion and mitigating safety risks. Future work includes integrating multi-agent oversight to strengthen reliability and broaden applicability. By leveraging advanced LLM capabilities, the knowledge-augmented GPT demonstrates a promising pathway toward cost-effective, user-friendly, and widely accessible energy audits.

Keywords: home energy audit, language models, retrieval-augmented generation, prompt engineering

1. INTRODUCTION

Buildings are major contributors to global greenhouse gas emissions, with the residential sector alone accounting for approximately 11% (World Resources Institute, 2024). Previous studies suggest retrofitting existing residential stock is crucial for mitigating climate change (Haley & Torrie, 2021). The first step in a residential retrofit is a home energy audit, which involves the evaluation of home energy performance. However, the limited availability of experienced energy auditors, along with the high costs and lengthy evaluation times, have been bottlenecks. While automated approaches for home energy audits have been developed (Alanezi et al., 2021), gathering and inputting data remain challenging.

Large language models (LLMs), such as GPT-4 (OpenAI et al., 2023), have shown promise in bridging knowledge and resource gaps in fields traditionally reliant on professional expertise, partially through advanced conversational interaction, context-based referencing, and multimodal comprehension (Chu et al., 2024). Building on these LLM capabilities, our long-term goal is to develop an AI agent that can assist homeowners and energy auditors in conducting home energy

audits. The agent aims to make home energy audits more user-tailored, reliable, and accessible, ultimately encouraging broader adoption of home energy retrofits.

In this exploratory work, we investigate the potential of LLMs in facilitating efficient data collection in home energy audits—one of the key challenges impeding broader retrofitting efforts. Specifically, we compare the performance of the baseline GPT-4 against a knowledge-augmented GPT that incorporates multimodal retrieval-augmented generation (RAG) and prompt engineering.

2. METHODOLOGY

2.1. Native GPT-4: OpenAI Playground

As a baseline, we employ GPT-4 natively via the OpenAI Playground. The GPT-4 model is configured with a temperature of 0 for deterministic outputs, while all other settings remain at their defaults. We then provide the model with a series of queries simulating a homeowner's perspective—aligned with our case study's scenario—to evaluate its capabilities.

2.2. Knowledge-augmented GPT with Multimodal RAG and Prompt Engineering

We build a knowledge-augmented GPT based on GPT-4 (Fig. 1). Specifically, it leverages multimodal RAG (Zhao et al., 2023) to incorporate relevant references. To preserve context, references are loaded and partitioned by modality and section into "chunks"—representing original documents—which are then saved in a document store. To facilitate optimal semantic retrieval, GPT-4 generates text-based summaries of these original documents, which are stored in a paired vector database. Together, these interconnected databases form a multi-vector retriever. Upon receiving a homeowner's query, the retrieval system identifies the most relevant text-based summaries and then retrieves the corresponding original document chunks across various modalities, enabling reference-grounded responses.

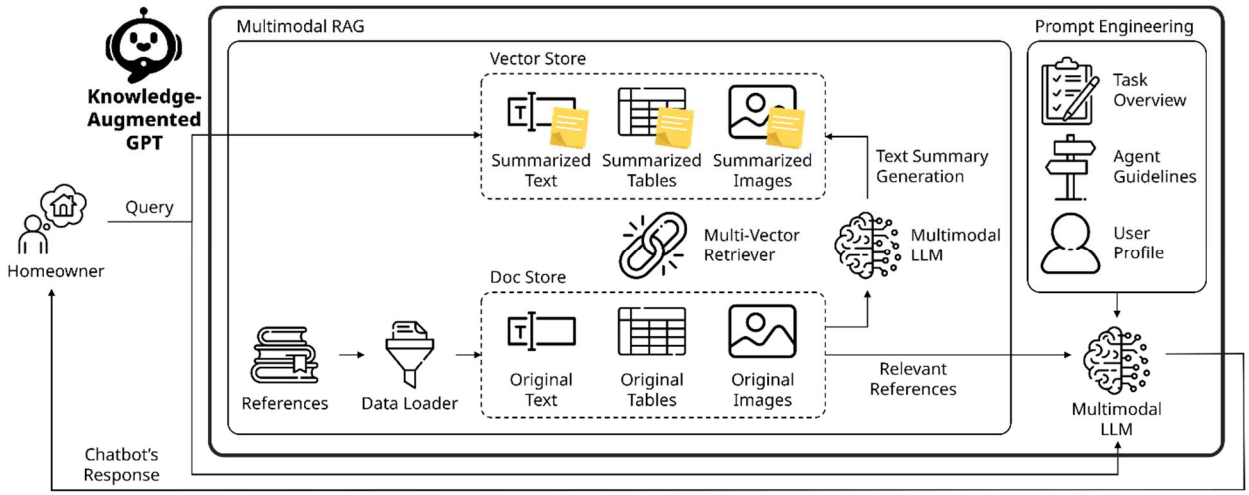

Figure 1. Knowledge-augmented GPT integrating multimodal RAG and prompt engineering.

Additionally, the knowledge-augmented GPT employs prompt engineering (Sahoo et al., 2024) to incorporate contextual information across three sections: (1) Task Overview, defining the role and responsibilities of the knowledge-augmented GPT; (2) Agent Guidelines, requiring consultation of relevant references before resorting to general knowledge, while providing proactive, concise

guidance and supporting image interpretation in a friendly tone; and (3) User Profile, reflecting the homeowner's limited background and preference for plain language. This structured approach fosters context-aware interactions. The knowledge-augmented GPT is then presented with the same series of queries as the native GPT-4, enabling a direct comparison.

3. RESULTS AND DISCUSSION

3.1. Case Study: Ceiling Insulation Data Collection

Ceiling insulation data collection is selected as the representative task. In this case study, we examine whether our knowledge-augmented GPT can provide the necessary guidance—referencing the EnerGuide Rating System (ERS) (Natural Resources Canada, 2023)—to help homeowners gather key information, such as insulation type and R-value. We assume a typical scenario where the homeowner has basic household tools (e.g., ladder, tape measure) but limited ERS familiarity, and a detached home with an accessible attic lacking a finished floor, leaving the joists and insulation in between them exposed for inspection.

3.2. Response Comparison: Native GPT-4 versus Knowledge-Augmented GPT

For task definition and execution instructions (Fig. 2), the native GPT-4 showed unwarranted generalities—such as advising homeowners to step only on joists—which might initially seem acceptable but conflicted with ERS's explicit warning against stepping off the ladder into the attic, posing potential safety risks. In contrast, the knowledge-augmented GPT—using multimodal RAG—generally appeared more aligned with ERS guidance. Its steps and details were more focused and actionable, and prompt engineering further refined these instructions to be more concise yet engaging (e.g., interpreting images).

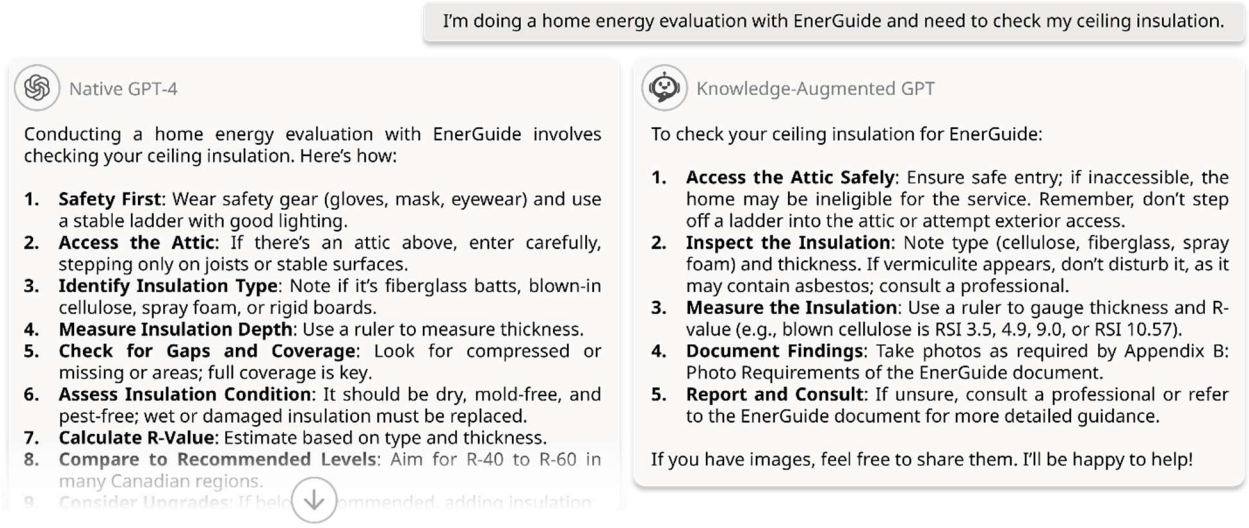

Figure 2. Native GPT-4 versus knowledge-augmented GPT: Task definition and execution instructions.

In the subsequent conversation about insulation identification and R-value estimation (Fig. 3), the native GPT-4 provided a range-based estimate that, while reasonable, could introduce unnecessary cognitive burden. In contrast, the knowledge-augmented GPT first presented a more deterministic, table-referenced R-value, potentially reducing guesswork. It also offered predefined response options aligned with the identified ceiling insulation, which may support more informed decision-

making. The knowledge-augmented GPT remained encouraging, guided by prompt engineering.

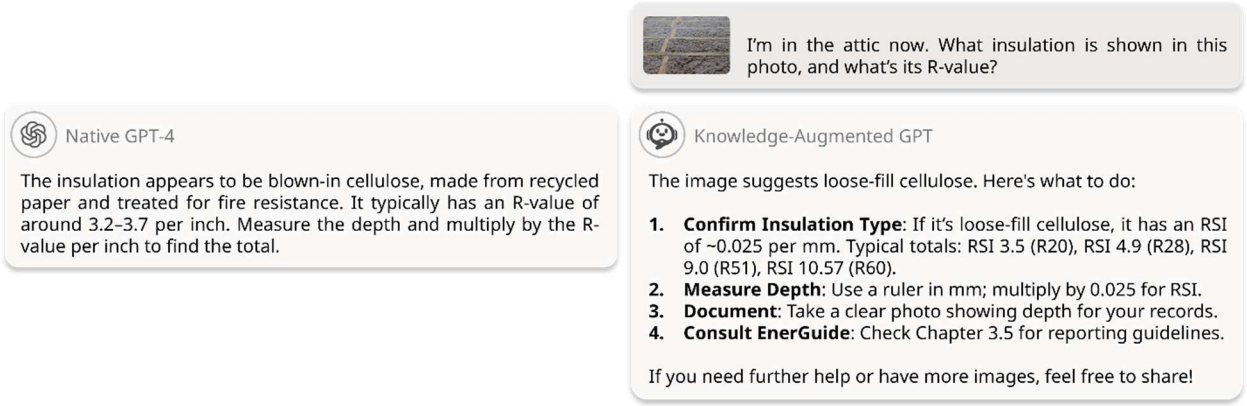

Figure 3. Native GPT-4 versus knowledge-augmented GPT: Insulation identification and R-value estimation.

While these initial findings appear promising, broad generalization remains challenging due to the volume and diversity of the required data and possible scenarios. Predefined workflows for complex tasks, supplemented by representative examples, could help improve the consistency of our knowledge-augmented GPT. Additionally, a multi-agent, LLM-based framework to oversee dialogue development may further enhance its robustness.

4. CONCLUSIONS

In this study, we explored LLMs for efficient data collection in home energy audits. Using a representative case, we compared native GPT-4 with a knowledge-augmented GPT integrating multimodal RAG and prompt engineering. Preliminary findings suggest that the knowledge-augmented GPT delivers more targeted, ERS-aligned guidance, highlighting a promising LLM-driven solution. Future work will extend into a multi-agent framework for broader applications.

ACKNOWLEDGEMENTS

This research was supported by the Natural Sciences and Engineering Research Council of Canada (Grant RGPIN-2022-04453).

REFERENCES

Alanezi, A., Hallinan, K. P., & Huang, K. (2021). *Automated residential energy audits using a smart WiFi thermostat-enabled data mining approach.* Energies, 14(9), 2500. MDPI.

Chu, Z., Wang, Y., Zhu, F., Yu, L., Li, L., & Gu, J. (2024). *Professional agents: Evolving large language models into autonomous experts with human-level competencies.* arXiv:2402.03628.

Haley, B., & Torrie, R. (2021). *Canada's Climate Retrofit Mission.* Ottawa: Efficiency Canada.

Natural Resources Canada. (2023). *EnerGuide Rating System—Standard—Version 15.12*. His Majesty the King in Right of Canada. Reproduced with the permission of the Department of Natural Resources, 2025.

OpenAI, Achiam, J., Adler, S., Agarwal, S., Ahmad, L., Akkaya, I., et al. (2023). *GPT-4 Technical Report.* arXiv:2303.08774.

Sahoo, P., Singh, A. K., Saha, S., Jain, V., Mondal, S., & Chadha, A. (2024). *A systematic survey of prompt engineering in large language models: Techniques and applications.* arXiv:2402.07927.

World Resources Institute. (2024). *World greenhouse gas emissions by sector 2021*. World Resources Institute.

Zhao, R., Chen, H., Wang, W., Jiao, F., Do, X. L., Qin, C., et al. (2023). *Retrieving multimodal information for augmented generation: A survey.* arXiv:2303.10868.

Wind Engineering & Aerodynamics (13:30-15:00 h)

6th International Conference on Building Energy and Environment
Eindhoven University of Technology, The Netherlands
6 - 10 July 2025

A hybrid approach for urban microclimate modeling for environmental and structural applications

Theodore Potsis[1], Shaoxiang Qin[2], Liangzhu (Leon) Wang[3], Ted Stathopoulos[4]

[1]*Department of Building, Civil and Environmental Engineering, Centre of Zero Energy Building Studies, Concordia University, Montreal, Canada, theodore.potsis@concordia.ca*
[2]*Department of Building, Civil and Environmental Engineering, Centre of Zero Energy Building Studies, Concordia University, Montreal, Canada, shaoxiang.qin@mail.mcgill.ca*
[3] *Department of Building, Civil and Environmental Engineering, Centre of Zero Energy Building Studies, Concordia University, Montreal, Canada, leon.wang@concordia.ca*
[4] *Department of Building, Civil and Environmental Engineering, Centre of Zero Energy Building Studies, Concordia University, Montreal, Canada, statho@bcee.concordia.ca*

SUMMARY
Climate change metrics have increased in recent years, and it is important for wind engineering to enhance the understanding of the complex interactions of wind in urban environments to mitigate the associated environmental and structural risks. Wind tunnel experiments can help to some limited extent due to the length restrictions and data availability. Computational fluid dynamics (CFD) has the potential to give valuable information regarding mean flow properties, but reliable fluctuating values are still an issue in the state-of-the-art. Research should work towards generalized tools that can give reliable data regarding mean and fluctuating properties of wind speed and temperature during extreme or regular wind events. In the present work, a hybrid approach is followed to overcome the current problems. This approach utilises CFD (LES-DT and CityFFD) and Localized Fourier Neural Operator (Local-FNO) to measure mean wind speed and turbulence properties in urban environment of Montreal. Practical applicability, efficiency and future targets of each method are highlighted.

Keywords: CityFFD, Large Eddy Simulation, Dynamic Terrain, urban microclimate, artificial neural networks, building energy, wind power, wind-induced loads

1. INTRODUCTION

Understanding the interaction of wind flow, temperature, humans and buildings in urban regions is vital for both environmental and structural applications. The former relates to climate change, pollutant dispersion, urban wind energy, while the latter deals with wind load estimation for safe and economical design. The complex nature of this interaction due to high turbulence in the lower atmospheric boundary layer, creates difficulties in the modelling techniques used in the state-of-the-art. This is especially the case for fluctuating properties such as turbulence.

This study utilises a hybrid approach in order to estimate the turbulence in a dense urban environment, based on Computational Fluid Dynamics (CFD) and data-driven based models. In the following section these methodologies are thoroughly discussed. In Section 3 aa case study is presented and, finally, in Section 4 the paper summarises and concludes.

2. METHODOLOGIES

CFD has been utilised for urban microclimate modelling extensively during the last decades, by means of RANS models that can capture mean properties. The need to expand the ability of these models to fluctuating properties as well, as to better understand and mitigate the risks of extreme weather conditions in urban settings, has evolved the research to LES modelling (Potsis et al., 2023, Tominaga et al., 2023). In the present study, two different LES approaches that have been recently developed by this working group are used.

First, a method based on CPU modelling, introducing fluctuations at the inflow wind based on the Dynamic Terrain approach (LES-DT). This methodology has proven capable of modelling fluctuating wind flow and structural loads (peaks) in urban environments (Potsis and Stathopoulos, 2024, Potsis et al., 2024). The other CFD method is based on GPU modelling and refers to the CityFFD approach that uses the semi Langrangian approach to model fluctuating wind flow and temperature properties in urban environments (Mortezazadeh and Wang, 2020, Mortezazadeh et al., 2022). It is highly efficient due to the GPU-based code and has been validated regarding mean wind flow and temperature metrics in urban configurations.

Data-driven methods have captured the attention of the wind engineering community recently, mainly due to the fast development of hardware and knowledge in similar engineering fields. In the present study, a Localized Fourier Neural operator (Local-FNO) method has been utilised. This approach has been applied recently in predicting accurately wind velocity and temperature in urban settings (Peng et al., 2024, Qin et al., 2025). Local-FNO is a localized variant of the Fourier Neural Operator designed to enhance data efficiency and deliver sharper prediction quality. The dataset consists of 30 3D CityFFD simulations, divided into 24 for training, 3 for validation, and 3 for testing. During training, each simulation is partitioned into small 3D patches via random sampling, effectively increasing the number of training samples. The model inputs include a building occupancy grid, the corresponding signed distance field (SDF), and a multi-directional distance feature that encodes geometry information beyond the scale of individual patches. The model is trained using the Root Mean Squared Error (RMSE) loss function. Early stopping is employed on the validation set to prevent overfitting.

3. CASE STUDY

In order to present each of the aforementioned methods applicability, efficiency and accuracy, a case study of downtown Montreal is selected. It consists of around 50 buildings, with various heights in an area of 985 m x 1204 m, as seen in Fig. 1(a). The reason that this particular cluster of buildings was selected is that both high rise buildings and mid-rise buildings are included. The two CFD approaches used are based on different settings, proven accurate through various validation studies (Mortezazadeh and Wang, 2020, Potsis et al., 2024). For example, CityFFD can utilise larger computatioonal domains and more finite volumes (23 million) as seen in Fig. 1(b), compared to LES-DT in Fig. 1(c) (7 million). CityFFD model has a length scale 1:1 (full-scale) and LES-DT 1:800.

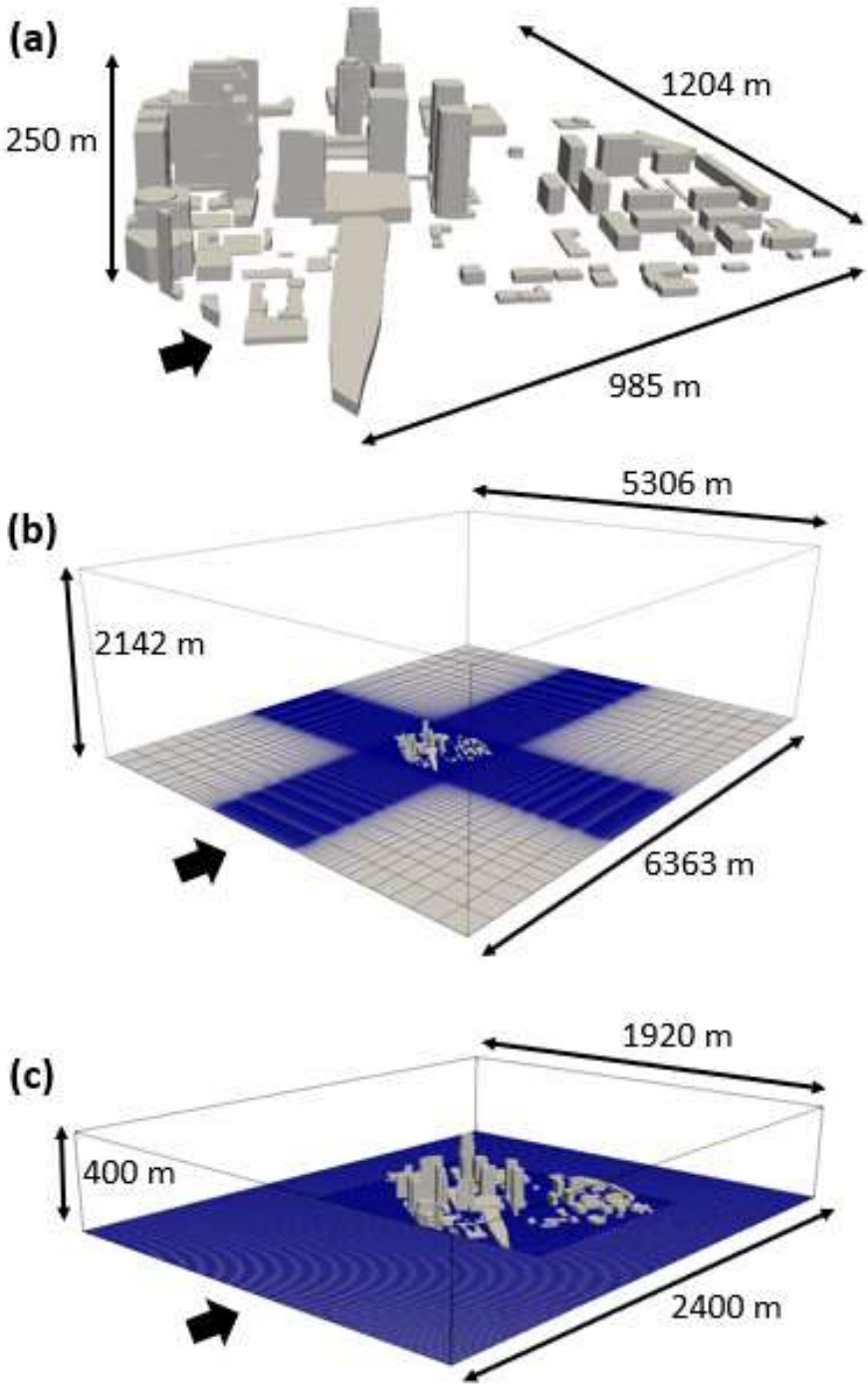

Figure 1. (a) Geometry of building clusters of case study, (b) computational domain setup in CityFFD, (c) computational domain setup in LES-DT.

3.1. Incident flow

A vital aspect as to understand the differences in the computational strategies and training procedure of the FNO, is an overview of the incident flow in the computational domain – that is the flow characteristic at the location exactly before the building cluster is placed. These profiles

are presented in Fig. 2 and extracted from analysis with empty computational domain. Fig. 1a presents the mean streamwise velocity normalized, based on the provisions of ASCE 49-21. As seen, the mean and longitudinal turbulence intensity profiles have good agreements with the experiments in Fig. 2a and Fig. 2b, where z_{ref} was selected as 10 m, based on provisions of ASCE 49-21. These profiles represent a suburban exposure B.

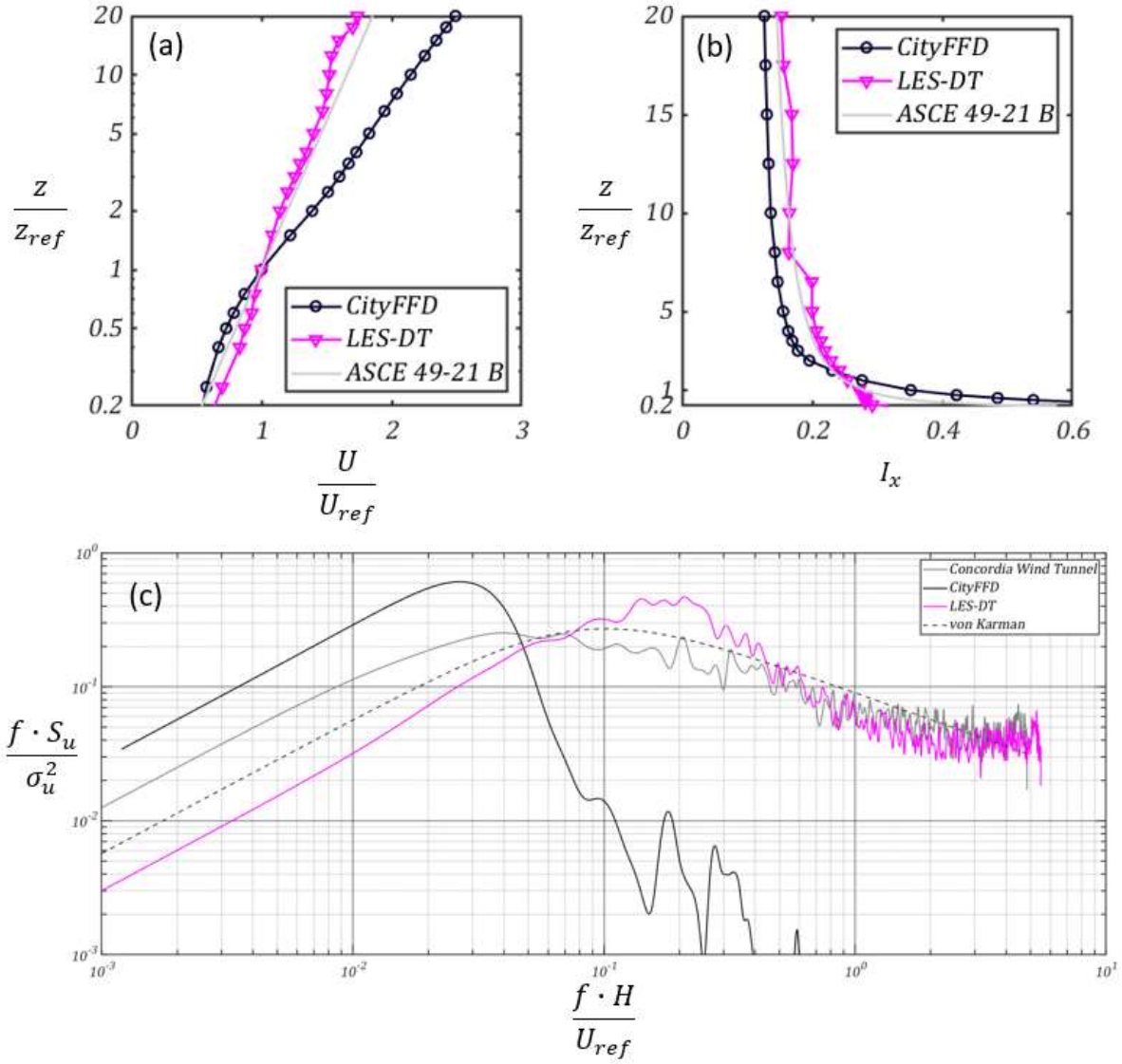

Figure 2. (a) Mean incident profile, (b) turbulence intensity incident profile, (c) spectrum at h = 64 m at incident location based on CityFFD, LES-DT, ASCE 49-21, Concordia Wind Tunnel and von Karman.

Another aspect that needs attention is also the spectrum of the longitudinal velocity at the incident location, that is presented for a height of 64 meters (full scale) in Fig. 2c. Similar results are achieved for other heights of the ABL. As discussed previously (Potsis and Stathopoulos, 2024 and Potsis et al., 2024), LES-DT is capable of reproducing the energy of these fluctuations with great accuracy, even after the cut-off frequency of LES. As shown, there is good correlation of

LES-DT with experimental results from Concordia Wind Tunnel and the theoretical von Karman Spectrum. Similar data from the CityFFD lack this capability, due to the combination of steady inflow properties and Fast Fluid Dynamics concept (Mortezazadeh and Wang, 2020), as also seen in Fig. 2c. Various techniques in the state-of-the-art reproduce similar results as the CityFFD regarding the spectrum (Potsis et al., 2023) – a limitation which is furhter explored in this work by comapring flow field metrics inside the urban canyons.

3.2. Flow field metrics inside urban canyons

Fig. 3 presents the normalized longitudinal mean wind flow at a plane of z = 30 m. Clearly, results by LES-DT and CityFFD have great similarity, except maybe the length of the detached eddies behind some of the buildings. As a next step this discrepancy will be further scrutinized and discussed in the conference presentation. The Local-FNO is able to reproduce the mean flow field with good accuracy, especially given the fact that the training was conducted in different cases resembling urban environments, and not the urban configuration presented in Fig. 1.

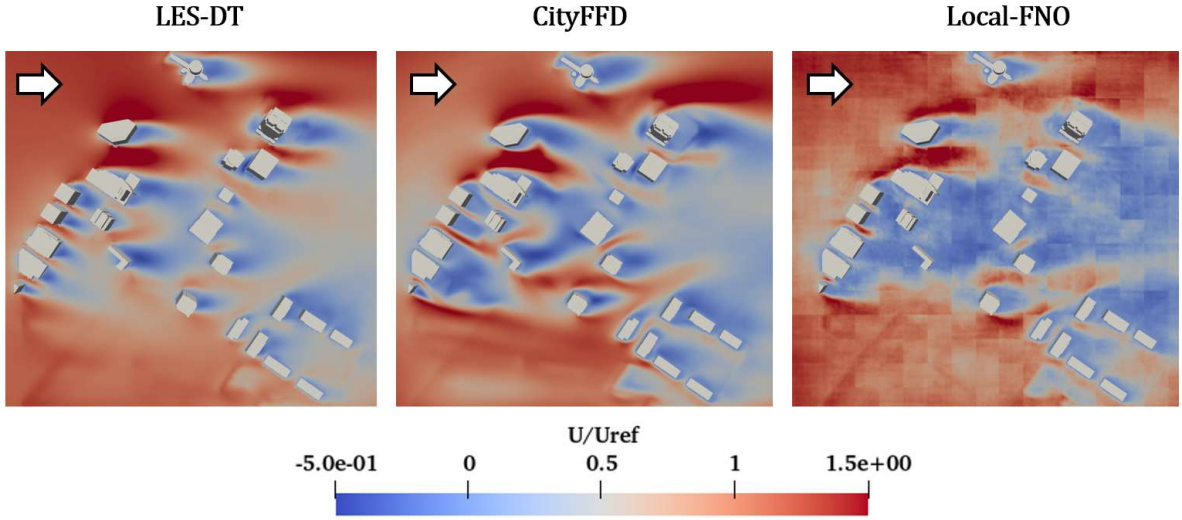

Figure 3. Mean normalised streamwise wind velocity at z = 30 m height form LES-DT (left), CityFFD (middle) and Local-FNO (right)

Furthermore, turbulence features in urban environments need to be modelled properly as to conduct meaningful environmental applications. These are also a prerequisite for structural applications, since these peak values relate closely with the gusts of the wind flow. In Figure 4, similar results are presented regarding the normalized time averaged turbulence kinetic energy distribution at the z = 30 m plane. As can be seen, LES-DT introduces more turbulence features in the computational domain, which has proven helpful for design applications resembling more gust winds for peak pressure estimation. CityFFD results agree to a great extent with LES-DT, although the turbulence kinetic energy near walls is not modelled very well. This is expected according to the modelling targets of this tool. Finally, Local-FNO captures the general character of the fluctuations, but more detailed comparisons are necessary to improve the training of the model.

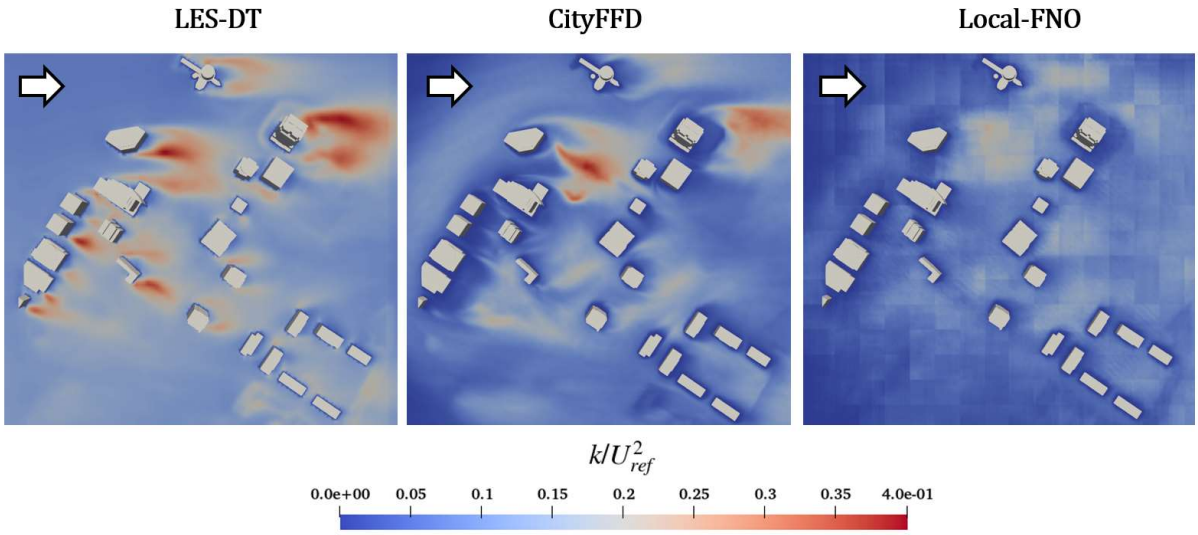

Figure 4. Time averaged turbulence kinetic energy of wind velocity at z = 30 m height form LES-DT (left), CityFFD (middle) and Local-FNO (right)

3.4. Efficiency and practical applicability

The target of this work is to discuss engineering-based solutions aiding various environmental or structural applications. For this purpose, Table 1 shows important aspects of each method. Environmental applications can be applied with each method at the moment, since they mainly refer to mean flow properties. Regarding environmental applications where turbulence features are needed LES-DT and CityFFD seem to be capable to predict turbulence features with similar accuracy. Aspects of further improvement of Local-FNO to capture fluctuating properties will be reported and discussed in detail in the conference presentation. Regarding structural applications, LES-DT is the only methodology tested capable of reproducing peak wind induced pressures as well. Additional results will be further communicated during the conference.

Table 1. Applicability and Efficiency of LES-DT, CityFFD and FNO

Method	Application		Efficiency
	Environmental	Structural	
CityFFD	X		23 million elements/6 hours on GPU
LES-DT	X	X	7 million elements/40 hours on 640 CPUs
Local-FNO	X		12 hours for training /1 minute for testing

4. SUMMARY - CONCLUSION

A hybrid approach based on two CFD methodologies (CPU-based and GPU-based) and Local-FNO have been utilised to model mean and turbulence wind flow in a dense urban environment in Montreal. Given the great potential in terms of calculation time of GPU-based tools (such as CityFFD), this work encompasses to create efficient engineering-based solutions for urban microclimate modelling. Details of the selected case study were presented and some results regarding the incident flow properties and flow field metrics inside urban canyons. Good accuracy is achieved between the three methods regarding mean flow properties, but some differences are highlighted for turbulence kinetic energy. The tremendous efficiency of Local-FNO constitutes it as an ideal tool for further development.

REFERENCES

Mortezazadeh, M., & Wang, L. (Leon). (2020). Solving city and building microclimates by fast fluid dynamics with large timesteps and coarse meshes. *Building and Environment*, *179*, 106955. https://doi.org/10.1016/J.BUILDENV.2020.106955

Mortezazadeh, M., Wang, L. L., Albettar, M., & Yang, S. (2022). CityFFD – City fast fluid dynamics for urban microclimate simulations on graphics processing units. *Urban Climate*, *41*, 101063. https://doi.org/https://doi.org/10.1016/j.uclim.2021.101063

Tominaga, Y., Wang, L. (Leon), Zhai, Z. (John), & Stathopoulos, T. (2023). Accuracy of CFD simulations in urban aerodynamics and microclimate: Progress and challenges. *Building and Environment*, *243*, 110723. https://doi.org/10.1016/J.BUILDENV.2023.110723

Peng, W., Qin, S., Yang, S., Wang, J., Liu, X., & Wang, L. (Leon). (2024). Fourier neural operator for real-time simulation of 3D dynamic urban microclimate. *Building and Environment*, *248*, 111063. https://doi.org/10.1016/J.BUILDENV.2023.111063

Potsis, T., & Stathopoulos, T. (2024). Wind induced peak pressures on low-rise building roofs via dynamic terrain computational methodology. *Journal of Wind Engineering and Industrial Aerodynamics*, *245*, 105630. https://doi.org/10.1016/J.JWEIA.2023.105630

Potsis, T., Ricci, A., & Stathopoulos, T. (2024). On the reliability of the dynamic terrain method to generate ABL winds for environmental applications. *Meccanica*. https://doi.org/10.1007/s11012-024-01810-5

Potsis, T., Tominaga, Y., & Stathopoulos, T. (2023). Computational wind engineering: 30 years of research progress in building structures and environment. *Journal of Wind Engineering and Industrial Aerodynamics*, *234*, 105346. https://doi.org/https://doi.org/10.1016/j.jweia.2023.105346

Qin, S., Zhan, D., Geng, D., Peng, W., Tian, G., Shi, Y., Gao, N., Liu, X., & Wang, L. (Leon). (2025). Modeling multivariable high-resolution 3D urban microclimate using localized fourier neural operator. *Building and Environment*, 112668. https://doi.org/10.1016/J.BUILDENV.2025.112668

6th International Conference on Building Energy and Environment
Eindhoven University of Technology, The Netherlands
6 - 10 July 2025

Pedestrian wind comfort assessment on the UTCB campus

Ioel Giger [1], Costin Ioan Coșoiu [2]

[1]*Aerodynamics and Wind Engineering Laboratory „Constantin Iamandi", Technical University of Civil Engineering of Bucharest, Bucharest, Romania, ioel.giger@student.utcb.ro*
[2]*Aerodynamics and Wind Engineering Laboratory „Constantin Iamandi", Technical University of Civil Engineering of Bucharest, Bucharest, Romania, costinioan.cosoiu@utcb.ro*

SUMMARY
The configuration of surrounding structures significantly affects pedestrian-level wind comfort in urban areas. This study assesses wind comfort on the UTCB campus using CFD simulations for ten relevant wind directions and respective meteorological data gathered from a nearby weather station. The building geometry was modeled by taking into account only critical features, while mesh generation used polygonal and hex-core cells. Simulations were performed using the Realizable k-ε turbulence model implemented in Ansys Fluent, with boundary velocity profiles adjusted for terrain roughness and exposure factors.
Dimensionless velocity fields were analyzed at 1.5 meters above ground, and site-specific data were used to calculate the probability of exceeding a 5 m/s wind speed. Results show that the campus meets the highest comfort class (Class A) year-round based on the Dutch Wind Nuisance Standard NEN 8100. This research validates the applicability of NEN 8100 for improving pedestrian wind conditions in complex urban environments.

Keywords: Pedestrian wind comfort, CFD simulation, building aerodynamics.

1. INTRODUCTION

Over the past decade, European cities have experienced a trend toward redensification, driven by population growth due to immigration and a decline in urban sprawl (Cortinovis et al., 2022). While Romania remains the European country with the highest rate of land occupation growth — primarily due to the conversion of agricultural land into urban functional areas (European Environment Agency, 2023) — the European Union set a "no-net-land-take" goal for 2050 in its Soil Strategy (2021). Consequently, further intensification of urban densification trends, including in Romania, is expected in the coming decades.

The past decade has brought numerous real estate developments, both residential and commercial, to Bucharest. These developments often feature high-rise buildings and increased density. Driven by a focus on maximizing profitability and sometimes possibly inadequate regulation enforcement, the new architectural landscapes are characterized by narrow spaces between buildings, which encourages the formation of air currents.

In this context, at the Technical University of Civil Engineering in Bucharest (UTCB), a method for evaluating pedestrian wind comfort is being developed, encompassing CFD (Computational Fluid Dynamics) simulations and wind tunnel experiments. Pedestrian comfort studies integrate meteorological data, aerodynamic information, and comfort and safety criteria (Blocken et al., 2007). Meteorological data can be obtained from weather stations near the study area and correlated with the site using terrain roughness, distance, and site type (Du et al., 2017).

Aerodynamic data can be acquired through experimental testing in boundary-layer wind tunnels and/or through CFD simulations (Blocken and Persoon, 2009), (Janssen et al., 2013), (Adamek et al., 2013), (Du et al., 2017). Although the Lawson (2001) and Davenport (Janssen et al., 2013) criteria are still commonly used regarding pedestrian comfort criteria, apart from the Dutch NEN 8100 standard (2006), there are currently no global regulations standardizing the evaluation of these parameters.

2. METEOROLOGICAL DATA

Velocity data was collected using an anemometer placed under standard conditions, specifically 10 meters above the ground near the meteorological station at Baloteşti, near OTP Airport, 15 km from the UCTB campus. Measurements were conducted over 5 years, from January 1, 2016, to March 5, 2020, with an hourly frequency. After filtering out irrelevant recordings, 42912 hours remained, providing a substantial dataset for statistical analysis. The highest recorded wind velocity was 20.6 m/s, while the calm period accounted for only 0.12% of the total duration. Figure 1 plots the wind rose at Baloteşti meteorological station.

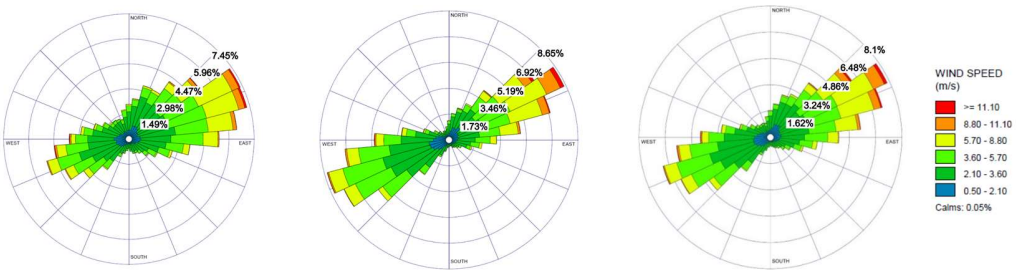

Figure 1. The wind rose at the Baloteşti meteorological site. Spring-summer (left), Autumn-Winter (middle), and whole period (right)

3. THE INVESTIGATED SITE

The UTCB campus was selected as a case study for a pedestrian wind comfort analysis. An extended area with a radius of approximately 350 meters was considered to quantify the influence of building geometry and other nearby obstacles. Figure 1 provides an overview of the entire area studied.

Figure 2. Satellite view of the area surrounding the modeled site (left) and Site sketch showing building footprint and layout details (right)

4. NUMERICAL INVESTIGATION METHOD

CFD isothermal simulations were carried out using Ansys Fluent 2023 for 10 wind directions, including cardinal, intercardinal, and 67.5° and 247.5°. A pressure-based solver was employed with the COUPLED algorithm to link pressure and velocity fields. Turbulence was modeled using the Realizable k-ε two-equation model, and all equations used second-order discretization schemes. The computational domain was cuboid-shaped, with the flow aligned to the longer side. A velocity profile was imposed at the inlet based on exposure factors, with 5 m/s at 10 m height. The outlet had a zero-gauge static pressure condition; the ground was modeled as a no-slip wall, while lateral surfaces were slip walls.

Each simulation used a different hybrid mesh with approximately 12.1 million cells, combining polygonal cells near boundaries and hex cells in the core flow. The minimum cell size near buildings was 0.5 m, while the largest cells reached 10 m at the outer edges. Size functions with a 10% growth rate were applied. Polyhedral cell layers were added between adjacent zones with different cell sizes to prevent abrupt transitions (greater than 1:8) in the hex-core regions.

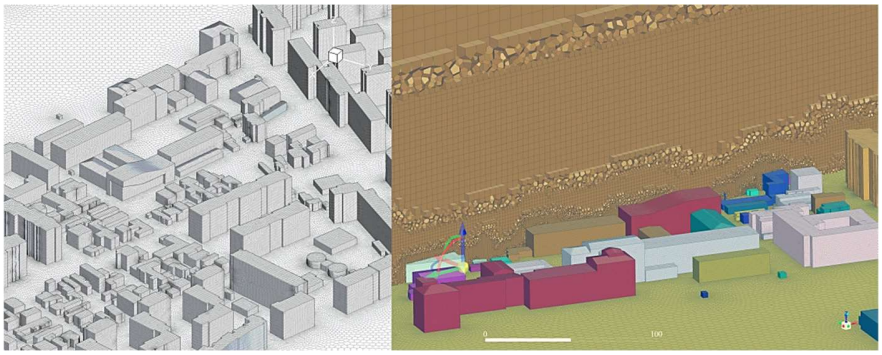

Figure 3. Detail of the fluid domain. Surface mesh (left) and volume mesh (right)

5. RESULTS

Dimensionless velocity fields U/U_{60} were evaluated in horizontal planes 1.5 meters above the ground, where U_{60} is the velocity at the blending height (60 m).

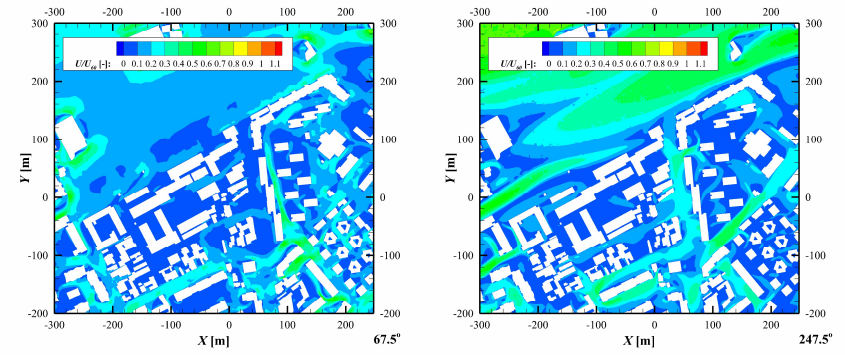

Figure 4. Nondimensional velocity contours U/U_{60} in a horizontal plane placed at 1.5 m above the ground. Wind direction 67.5° and 247.5°

Site-specific wind data were then used to calculate the probability of exceeding a wind speed threshold of 5 m/s at this height. This serves as the reference for determining pedestrian comfort class following the Dutch Wind Nuisance Standard NEN 8100. The results indicate that the entire UTCB campus meets the requirements for the highest comfort class (Class A) under both summer and winter conditions. This classification is achieved through a comprehensive analysis of the interaction between the wind and the built environment, factoring in site-specific contributions to wind speed variations.

5. CONCLUSIONS

Wind comfort at the pedestrian level in urban areas is greatly influenced by buildings' shape, size, placement, and orientation. Wind comfort criteria outlined by the Dutch Wind Nuisance Standard NEN 8100 were applied to the UTCB campus site. The combination of CFD simulation results for ten wind directions and statistical meteorological data indicates good wind quality for the campus area, meeting the requirements for comfort class A for pedestrian wind comfort.

ACKNOWLEDGEMENTS

The authors would like to thank the financial support from the GNaC2024 ARUST - UTCB grant - Numerical investigation method for determining pedestrian comfort parameters in urban areas (MORPHEUS)

REFERENCES

Adamek, K., Vasan, N., Elshaer, A., English, E., & Bitsuamlak, G. 2013. Pedestrian level wind assessment through city development: A study of the financial district in Toronto. Sustainable Cities and Society, 35, 178–190.

ANSYS Inc. 2023. Ansys Fluent 2023 Theory Guide.

Azcarate I., Acero J.A., Garmendia L., Rojí E., 2021, Tree layout methodology for shading pedestrian zones: Thermal comfort study in Bilbao (Northern Iberian Peninsula), Sustainable Cities and Society, Volume 72, 102996.

Blocken, B., Persoon, J. 2009. Pedestrian wind comfort around a large football stadium in an urban environment: CFD simulation, validation and application of the new Dutch wind nuisance standard. Journal of Wind Engineering and Industrial Aerodynamics, 97(5–6), 255–270.

Blocken B., Stathopoulos T., Carmeliet J. 2007. CFD simulation of the atmospheric boundary layer: wall function problems, Atmospheric Environment, Volume 41, Issue 2, Pages 238-252.

Cortinovis, C., Geneletti, D., & Haase, D. 2022. Higher immigration and lower land take rates are driving a new densification wave in European cities. Npj Urban Sustainability, 2(1).

Du Y., Mak C.M., Kwok K., Tse K.T., Lee T.C., Ai Z., Liu J., Niu J., 2017. New criteria for assessing low wind environment at pedestrian level in Hong Kong, Building and Environment, Volume 123, Pages 23-36,

European Environment Agency, 8th Environment Action Programme. 2023. Land take: net land take in cities and commuting zones in Europe.

Eslamirad N., De Luca F., Lylykangas K.S., Yahia S.B., 2023. Data generative machine learning model for the assessment of outdoor thermal and wind comfort in a northern urban environment, Frontiers of Architectural Research, Volume 12, Issue 3, pages 541-555.

Janssen W.D., Blocken B., van Hooff T. 2013. Pedestrian wind comfort around buildings: Comparison of wind comfort criteria based on whole-flow field data for a complex case study, Building and Environment, Volume 59, Pages 547-562.

Franke J., Hellsten A., Schlünzen H., Carissimo B.. 2007. Best Practice Guideline for the CFD Simulation of Flows in the Urban Environment.

Lawson T., Building Aerodynamics, World Scientific Publishing, 2001.

Liu P., Zhao T., Luo J., Lei B., Frei M., Miller C., Biljecki F. 2023. Towards Human-centric Digital Twins: Leveraging Computer Vision and Graph Models to Predict Outdoor Comfort, Sustainable Cities and Society, Volume 93, 2023, 104480,

NEN 8100:2006 Nl - Wind Comfort En Wind Danger in the Built Environment, 2006.

Verkaik, J. W. 2006. On Wind and Roughness over Land, Wageningen University and Research ProQuest Dissertations & Theses, 28238992.

Willemsen, E., Wisse, J. A. 2007. Design for wind comfort in The Netherlands: Procedures, criteria and open research issues. Journal of Wind Engineering and Industrial Aerodynamics, 95(9–11), 1541–1550.

COBEE

6th International Conference on Building Energy and Environment
Eindhoven University of Technology, The Netherlands
6 - 10 July 2025

Data-efficient rapid prediction of urban airflow and temperature fields for complex building geometries

Shaoxiang Qin[1,2], Dongxue Zhan[1], Ahmed Marey[1], Dingyang Geng[1], Theodore Potsis[1], Liangzhu (Leon) Wang[1]

[1] *Centre for Zero Energy Building Studies, Department of Building, Civil and Environmental Engineering, Concordia University, Montreal, Canada leon.wang@concordia.ca*
[2] *School of Computer Science, McGill University, Montreal, Canada shaoxiang.qin@mail.mcgill.ca*

SUMMARY

Predicting wind fields in urban environments requires capturing complex interactions between buildings and airflow, particularly long-range wake effects influenced by directional geometry. Traditional methods relying on computational fluid dynamics (CFD) are prohibitively expensive for large-scale simulations, while data-driven approaches struggle with limited training data and the need to model both local and far-field dependencies. In response, we propose a novel framework that leverages a multi-directional distance feature (MDDF) combined with localized training to achieve effective wind field predictions with minimal CFD data. By reducing the problem's dimensionality, localized training effectively increases the number of training samples, while MDDF encodes the surrounding geometric information to accurately model wake dynamics and flow redirection. Trained on only 24 CFD simulations, our localized Fourier neural operator (Local-FNO) model generates full 3D wind velocity and temperature predictions in under one minute, yielding a 500-fold speedup over conventional CFD methods. With mean absolute errors of 0.3 m/s for wind speed and 0.3 °C for temperature on unseen urban configurations, our method demonstrates strong generalization capabilities and significant potential for practical urban applications.

Keywords: Urban microclimate, wind engineering, deep learning, neural networks

1. INTRODUCTION

Modern urban planning demands a comprehensive analysis of the interplay between urban design and local environmental conditions (Yahia et al., 2018). Urban areas exhibit complex microclimates that are shaped by variations in building density, geometry, and the configuration of open spaces. These microclimatic variations can affect energy consumption for heating and cooling, the distribution of pollutants, and the overall comfort of residents. In this context, efficient and accurate predictive modeling provides urban planners with the necessary insights to design cities that optimize natural ventilation and thermal regulation. By capturing the intricate dynamics of airflow and temperature distribution, planners can better position buildings, tailor materials selection, and design public spaces that foster energy efficiency while enhancing human comfort and well-being.

Conventional CFD methods are highly detailed and accurate but come with substantial computational burdens that restrict their practical application in fast-paced urban planning contexts. These traditional simulations demand extensive processing time to capture the complex interactions of wind and temperature around intricate building configurations. The requirement for high-resolution meshes and long simulation runtimes makes it nearly impossible to perform real-time assessments or iterative design modifications. As a result, while CFD offers valuable insights into urban microclimate, its slow performance makes it impractical for the responsive and flexible analysis needed in modern urban development.

Recent advances in deep learning have shown significant promise in directly approximating CFD solutions from boundary conditions (Hao et al., 2023; Z. Li, N. Kovachki, et al., 2023). Once trained, models such as convolution neural networks, neural operators, and transformers can deliver orders-of-magnitude speedups compared to traditional, fine-grained CFD solvers, enabling real-time simulation of urban microclimate. This computational efficiency is pivotal for dynamic urban planning and design. However, these models require extensive, high-quality CFD simulation data to generalize effectively across diverse and complex urban geometries. It often necessitates no fewer than thousands of cases, even for relatively simple scenarios (Wang et al., 2025). This substantial training data requirement remains one of the key challenges in scaling these techniques for broader applications.

In this work, our proposed method leverages localized training combined with a novel geometry encoding scheme to achieve efficient and scalable urban wind field predictions with a remarkably small CFD dataset with only 24 simulations. The approach is based on the assumption that the wind behavior in a complex urban setting is largely dictated by the local building geometries, with distant influences playing a secondary role. By partitioning the overall simulation domain into smaller 3D patches, we effectively reduce the problem's dimensionality and augment the available training data. Within each patch, surrounding geometric information is encoded using a multi-directional distance feature (MDDF), providing detailed context about the nearby urban structures. Our strategy not only enhances the model's ability to predict localized wind phenomena but also benefits from parallel computations, ensuring scalability to large CFD domains with constrained computational resources.

Our experimental results reveal a significant advancement in generalizable urban wind field prediction. By training the localized Fourier neural operator (Local-FNO) model (Qin et al., 2025) on just 24 CFD simulations, with each covering a 1.2 km urban area with a 14.4-million-cell grid at a 4 m horizontal resolution, the model can generate full 3D predictions, including three-dimensional wind velocity and temperature fields, in under one minute. This constitutes an approximate 500-fold speedup over traditional CFD methods that typically require around eight hours for a similar simulation. The model achieves a wind speed mean absolute error (MAE) of 0.3 m/s and a temperature MAE of 0.3 °C, with correlation coefficients reaching 0.98 for both variables. These results highlight the potential of localized training for efficiently modeling wind field under complex urban boundary conditions. Furthermore, as a data-efficient approach, it stands to benefit further from additional training data, promising even more accurate predictions in the future.

2. METHODOLOGY

2.1. Urban Location Selection

We selected 30 urban locations to serve as the training, validation, and testing sets for our deep learning model, focusing on environments with high-rise buildings and complex layouts, the most challenging scenarios for urban wind field prediction. The selection process was based on comprehensive urban morphology indicators. Using the GBMI Tool (Biljecki and Chow, 2022), we extracted key three-dimensional morphological features such as building footprint area, height, and volume, as well as shape complexity metrics (e.g., compactness, equivalent rectangular index) and spatial configuration parameters. These indicators were chosen for their ability to capture the physical attributes and spatial arrangements that significantly influence urban microclimate, wind flow patterns, and energy performance, as demonstrated in prior studies (Hu et al., 2024; Kaseb et al., 2020). Through Euclidean distance analysis of standardized indicators, considering their mean, median, and standard deviation, we identified an initial pool of candidate locations from our database. It should be noted that the final selection of the 30 cities from this pool was not entirely based on these rules. Rather, they were manually chosen by referencing these rules to ensure their suitability for CFD simulation. Figure 1 illustrates the height maps for several selected sites. The dataset was then partitioned into 24 locations for model training, 3 for validation, and 3 for testing.

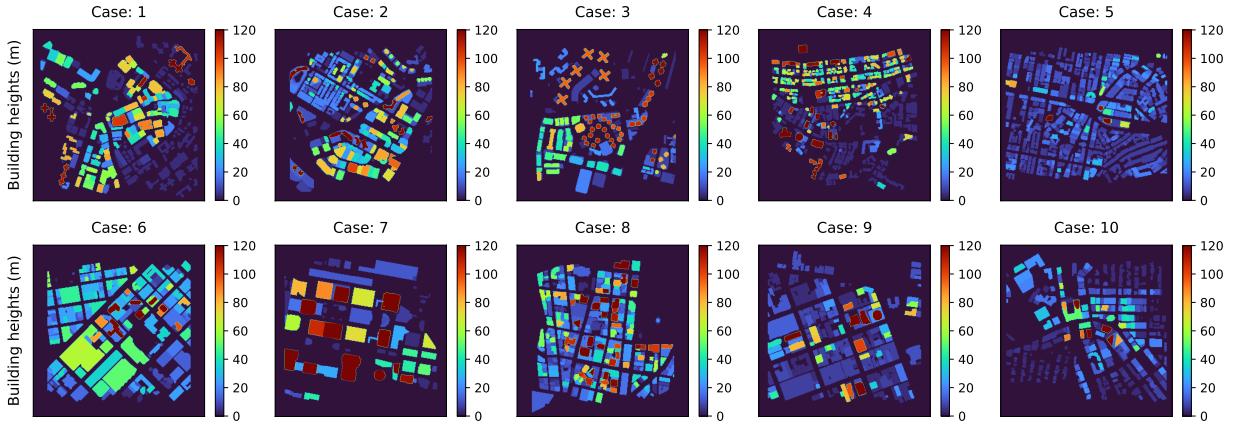

Figure 1. Building height maps for 10 cases in the dataset, covering a 1.2 km $\times$ 1.2 km domain.

2.2. Localized Fourier Neural Operator

The Fourier neural operator (FNO) has garnered attention in solving partial differential equations (PDEs) for its capacity to learn resolution-invariant mappings (Z. Li, N. B. Kovachki, et al., 2021). By operating predominantly in the Fourier domain, FNO efficiently extracts low-frequency global features, which are particularly useful in capturing the overall dynamics of fluid flow. FNO has been successfully applied to predict time-dependent urban wind velocity fields (Peng et al., 2024). However, FNO faces challenges in more complex, high-resolution scenarios, often producing blurry outputs, demanding high GPU memory, and requiring extensive data. The localized Fourier neural operator (Local-FNO) has been introduced to address these issues (Qin et al., 2025). Local-FNO enhances the traditional FNO framework by integrating local training strategies and patch

overlapping techniques, improving prediction quality and data efficiency and boosting generalization for multiscale turbulent flows.

Previous studies on FNO and Local-FNO for microclimate prediction have primarily focused on time-dependent forecasting, where the model takes an instantaneous flow field as input and predicts its future state. This requirement poses a limitation, as it restricts the model's use to scenarios where such input data are readily available. In our work, we extend the capabilities of Local-FNO by directly predicting the time-averaged flow field solely from building geometry. This method is inherently more challenging due to the lack of an input flow field for reference, yet it offers enhanced versatility and applicability, particularly in urban design and planning contexts where only the structural layout is available.

2.3. Multi-directional Distance Feature

The Multi-directional Distance Feature (MDDF) is a novel approach for encoding building geometry, designed to overcome the limitations of traditional signed distance functions (SDF) when applied to small local patches. SDF provides overall distance measurements but lacks the capacity to pinpoint the direction of obstacles within small, local patches, which is a critical shortcoming when predicting complex wind behaviors like the wake effect behind buildings. MDDF overcomes this limitation by calculating the distance to buildings at multiple fixed angles. In the horizontal plane, this is achieved by sampling distances at densely distributed angles over 360°, thereby furnishing every local patch with detailed directional information. For the vertical dimension, the MDDF is limited to a 180° span since the upward distance typically trends toward infinity and offers limited value. Moreover, MDDF's computational complexity scales linearly with the region's side length, in contrast to the SDF, whose complexity is proportional to the total number of grid cells (growing quadratically in 2D). This makes MDDF an efficient choice for encoding detailed urban geometries.

While MDDF employs a dense set of angular samples to ensure accurate encoding of building geometry, each angle's calculation is independent, which allows for effective parallel processing and significant reductions in computational time. In addition, the dense output of MDDF can be efficiently compressed using a Fourier transform, keeping only the essential low-frequency components. This selective retention not only maintains, but often enhances, model performance by filtering out high-frequency discretization noise. It ensures that the feature dimensionality presented to the deep learning model remains relatively low.

2.4. CFD Data Preparation

The CFD airflow and temperature data for training deep learning models are simulated from City Fast Fluid Dynamics (CityFFD) (Mortezazadeh et al., 2022). CityFFD uses a semi-Lagrangian approach and fractional stepping method to enhance accuracy while reducing computational costs. The built-in large eddy simulation (LES) model captures turbulence in the atmospheric boundary layer. A fourth-order interpolation scheme minimizes numerical errors, even on coarse grids. Developed with CUDA-C++ for GPU processing, CityFFD predicts local microclimate conditions and models urban aerodynamics. It has been validated against wind tunnel and real-world data, demonstrating reliability in airflow and temperature predictions (Yang, 2024). Additionally, CityFFD can integrate with WRF and building energy models for comprehensive urban climate

analysis (Zhan et al., 2023).

The CityFFD model numerically solves the governing equations for fluid dynamics, which include continuity, momentum, and energy conservation laws in Equation 1:

$$\begin{aligned} \nabla \cdot \vec{U} &= 0 \\ \frac{\partial \vec{U}}{\partial t} + (\vec{U} \cdot \nabla)\vec{U} &= -\nabla p + \left(\frac{1}{Re} + \nu_t\right)\nabla^2 \vec{U} - \frac{Gr}{Re^2}\,\theta \\ \frac{\partial \theta}{\partial t} + (\vec{U} \cdot \nabla)\theta &= \left(\frac{1}{Re \cdot Pr} + \alpha_t\right)\nabla^2 \theta \ , \end{aligned} \tag{1}$$

where $\vec{U}$, θ, and p denote velocity, temperature, and pressure, while Re, Gr, and Pr represent the Reynolds, Grashof, and Prandtl numbers. ν_t and α_t correspond to turbulent viscosity and thermal diffusivity.

Each of the 20 selected building clusters spans a 1.2 km $\times$ 1.2 km area, containing 200 to 600 buildings. The total computational domain covers 6 km $\times$ 5 km with a height of 2 km, containing 24 million grids. Near buildings, the grid resolution is 4 m $\times$ 4 m horizontally and 1.5 m vertically. The domain's vertical boundaries act as inlets or outlets based on wind direction, while the ground is a no-slip wall and the top is a symmetry plane. Simulations use an air temperature of 30 °C, a west wind at 4 m/s, and a building surface temperature of 40 °C. The wind profile follows a power-law equation:

$$u(z) = u_{\text{ref}} \left(\frac{z}{z_{\text{ref}}}\right)^{\alpha}, \tag{2}$$

where $u(z)$ is wind speed at height z, with $\alpha = 0.15$, $z_{\text{ref}} = 10$ m, and $u_{\text{ref}} = 4$ m/s. A time step of 0.5 s ensures a CFL number (Courant et al., 1928) of 0.5, calculated as $\text{CFL} = u \times \frac{\Delta t}{h_{\text{cell}}}$, where u is the local velocity and h_{cell} is the local cell size. Each simulation utilizes a single GPU and requires approximately 8 hours to achieve statistical stability. The final dataset includes the time-averaged wind field after convergence.

2.5. Model Training

The training leveraged wind field data from 30 cities, with the dataset partitioned into 24 cases for training, 3 for validation, and 3 for testing. To effectively increase the number of samples, each training instance was augmented by mirroring while preserving wind direction. The input data, with dimensions of $300 \times 300 \times 160$, is processed during training by randomly sampling local patches of size $46 \times 46 \times 48$ from the entire domain. For testing, these patches are arranged in a grid with overlapping regions so that only the central, more reliable areas contribute to the final prediction, thereby mitigating higher errors near patch boundaries. The input features include global coordinates, SDF, and MDDF.

Model training was conducted on a single 32GB GPU using the AdamW optimizer combined with a step learning rate scheduler and early stopping based on validation performance. The training comprised 100 epochs, with each epoch taking approximately 10 minutes, totaling around 16 hours. After training, the model is capable of predicting a full 3D wind field in 10 seconds. In

practical applications, when building geometry is provided as input, additional computation time is required for calculating SDF and MDDF. Nevertheless, the overall prediction time remains within one minute.

3. RESULTS

We demonstrate the performance of Local-FNO with MDDF on an unseen test case. Figures 2 and 3 show horizontal and vertical slices of the wind field's u, v, and w components, as well as temperature. The model effectively captures the overall flow pattern. Notably, the u component, which is aligned with the prevailing wind direction, achieves an MAE of 0.26 m/s and a correlation coefficient of 0.98, while temperature predictions reach an MAE of 0.27 °C with the same high correlation of 0.98. The v and w components exhibit lower correlations at 0.82, reflecting the greater complexity and sensitivity of these directions to building geometries. Although Local-FNO does not replicate every intrinsic small-scale flow feature within complex urban settings, it delivers fast and acceptable predictions in under one minute, despite being trained on only 24 CFD simulations. This high data efficiency suggests that performance can be further enhanced with additional training data. While localized training and testing result in visible discontinuities at patch boundaries, these artifacts can be mitigated using post-processing techniques such as smoothing.

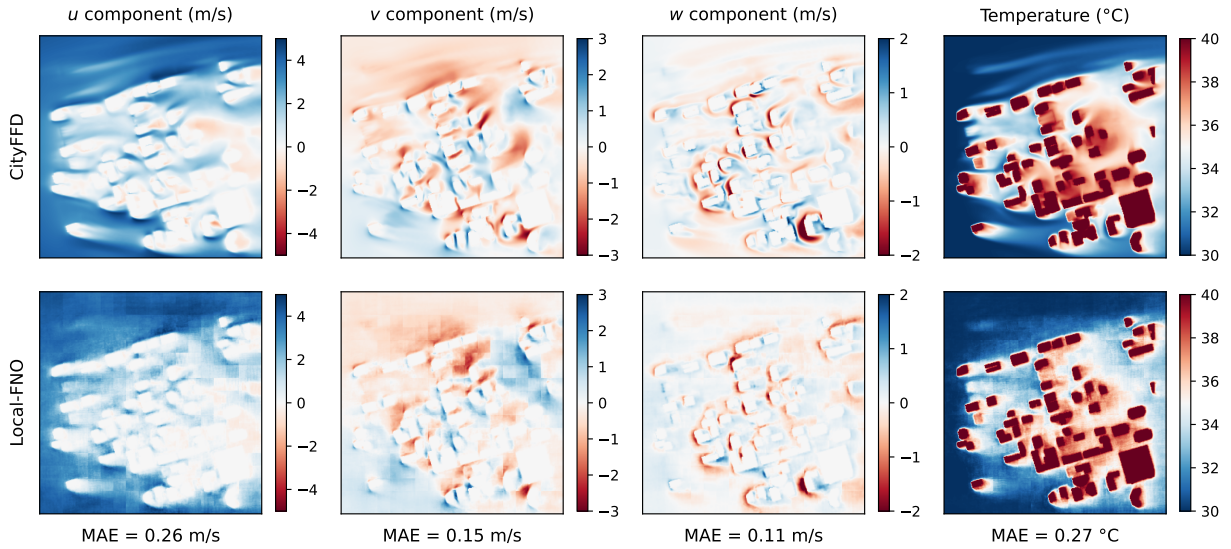

Figure 2. Visualization of wind speed and temperature for CityFFD and Local-FNO at a 30 m horizontal plane.

In Figure 4, we illustrate the flow stream as predicted by Local-FNO. The model effectively reproduces the general flow pattern, though discrepancies remain in the wake regions behind buildings relative to CityFFD.

4. CONCLUSIONS

This study presents a highly data-efficient deep learning framework that leverages localized training combined with a novel multi-directional distance feature encoding. Trained on just 24 CFD

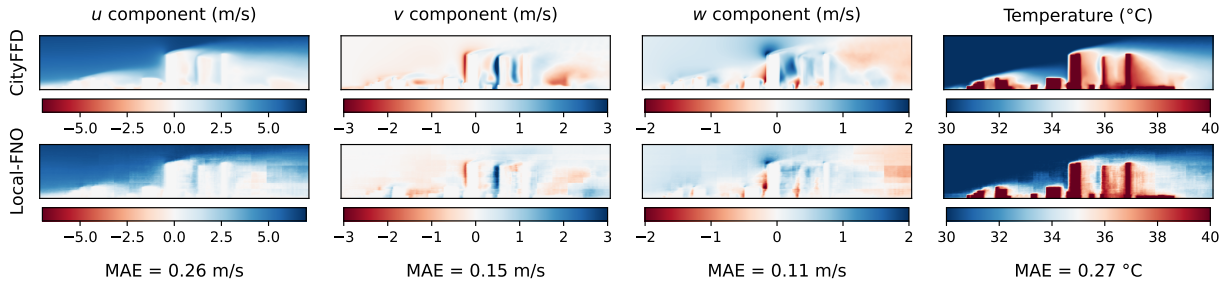

Figure 3. Visualization of wind speed and temperature for CityFFD and Local-FNO at a vertical plane.

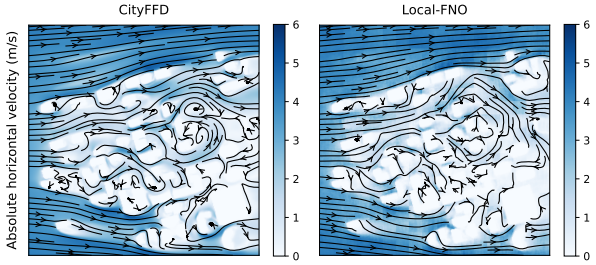

Figure 4. Visualization of flow stream for CityFFD and Local-FNO at a 30 m horizontal plane.

simulations, our approach successfully generalizes to new and complex urban geometries, delivering full 3D wind field predictions in under one minute. By directly leveraging building geometry to predict airflow and temperature, our approach holds substantial promise for enhancing applications in urban design and planning. Future work will focus on incorporating additional training data to further improve accuracy, refining post-processing techniques to smooth patch discontinuities, and exploring alternative model architectures beyond neural operators. These initiatives aim to further strengthen the accuracy and scalability of our framework for broader urban applications.

REFERENCES

Biljecki F. and Chow Y. S., 2022. Global Building Morphology Indicators. Computers, Environment and Urban Systems 95, 101809.

Courant R., Friedrichs K., and Lewy H., 1928. Über die partiellen Differenzengleichungen der mathematischen Physik. Mathematische annalen 100, 32–74.

Hao Z., Wang Z., Su H., Ying C., Dong Y., Liu S., Cheng Z., Song J., and Zhu J., 2023. Gnot: A general neural operator transformer for operator learning. Proceedings of International Conference on Machine Learning. PMLR, 12556–12569.

Hu J., Fan T., Tang X., Yang Z., and Ren Y., 2024. Nonlinear relations of urban morphology to thermal anomalies: A cross-time comparative study based on Grad-CAM and SHAP. Ecological Indicators 162, 112024.

Kaseb Z., Hafezi M., Tahbaz M., and Delfani S., 2020. A framework for pedestrian-level wind conditions improvement in urban areas: CFD simulation and optimization. Building and Environment 184, 107191.

Li Z., Kovachki N., Choy C., Li B., Kossaifi J., Otta S., Nabian M. A., Stadler M., Hundt C., Azizzadenesheli K., et al., 2023. Geometry-informed neural operator for large-scale 3d pdes. Advances in Neural Information Processing Systems 36, 35836–35854.

Li Z., Kovachki N. B., Azizzadenesheli K., Liu B., Bhattacharya K., Stuart A. M., and Anandkumar A., 2021. Fourier Neural Operator for Parametric Partial Differential Equations. Proceedings of 9th International Conference on Learning Representations, ICLR 2021, Virtual Event, Austria, May 3-7, 2021. OpenReview.net.

Mortezazadeh M., Wang L. L., Albettar M., and Yang S., 2022. CityFFD – City fast fluid dynamics for urban microclimate simulations on graphics processing units. Urban Climate 41, 101063.

Peng W., Qin S., Yang S., Wang J., Liu X., and Wang L. L., 2024. Fourier neural operator for real-time simulation of 3D dynamic urban microclimate. Building and Environment 248, 111063.

Qin S., Zhan D., Geng D., Peng W., Tian G., Shi Y., Gao N., Liu X., and Wang L. L., 2025. Modeling multivariable high-resolution 3D urban microclimate using localized fourier neural operator. Building and Environment, 112668.

Wang H., Ma W., Niu J., and You R., 2025. Evaluating a deep learning-based surrogate model for predicting wind distribution in urban microclimate design. Building and Environment 269, 112426.

Yahia M. W., Johansson E., Thorsson S., Lindberg F., and Rasmussen M. I., 2018. Effect of urban design on microclimate and thermal comfort outdoors in warm-humid Dar es Salaam, Tanzania. International journal of biometeorology 62, 373–385.

Yang S., 2024. Assessment of Urban Microclimate and Its Impact on Outdoor Thermal Comfort and Building Energy Performance. phdthesis, Concordia University.

Zhan D., Sezer N., Hou D., Wang L., and Hassan I. G., 2023. Integrating urban heat island impact into building energy assessment in a hot-arid city. Buildings 13, 1818.

6th International Conference on Building Energy and Environment
Eindhoven University of Technology, The Netherlands
6 - 10 July 2025

Grid impact of large eddy simulation on local gust wind prediction for a single isolated building

Usman Shaukat [1], Naoki Ikegaya [2], Knut Erik Teigen Giljarhus [1]

[1]*Department of Mechanical and Structural Engineering and Materials Science, University of Stavanger, Stavanger, Rogaland, Norway, usman.shaukat@uis.no*
[2]*Interdisciplinary Graduate School of Engineering Sciences, Kyushu University, Fukuoka, Kyushu, Japan, ikegaya.naoki@kyudai.jp*

SUMMARY
The study examines the influence of grid resolution in large-eddy simulations (LES) on predicting low-occurring wind gust events around a single isolated building (1:1:2) at a pedestrian height. Four grid size configurations (H/30, H/40, H/60, H/80) were evaluated by comparing LES predictions of wind speed with wind tunnel experiment (WTE) data. The accuracy of LES in capturing low-occurring peak wind speeds was assessed using power spectral density and peak factor analysis. The peak factors were calculated at 5%, 1%, and 0.1% exceedance probability values. While finer grids improved predictions, this came at a significantly higher computational cost. Among the tested configurations, the H/60 grid achieved normalized mean square error convergence, capturing almost 80% of peak factor measurements within 20% deviation from WTE results at 0.1% exceedance probability. However, the H/40 grid offered the optimal balance between accuracy and cost.

Keywords: Low-occurring high wind speed, LES, Pedestrian wind, wind gust

1. INTRODUCTION

In computational wind engineering, pedestrian-level wind environments have traditionally been evaluated using Reynolds-averaged Navier-Stokes (RANS) equations due to their ability to predict high mean wind speed regions with reasonable accuracy (Tominaga et al., 2023). However, RANS simulations often underestimate turbulent kinetic energy (TKE), leading to poor predictions for high-speed wind events such as wind gusts (Shirzadi and Tominaga, 2022). Although the coefficient in RANS can be tuned for TKE prediction, with advancements in computational power, large eddy simulation (LES) has gained some popularity as it offers higher accuracy than RANS in predicting mean wind speed and turbulent intensity (Zhong et al., 2022). Nevertheless, a key advantage of LES is its generation of ample time-series data, enabling detailed studies of gusts and peak wind events. Such analyses are important for ensuring pedestrian and cyclist safety for ground-level wind, facilitating safe drone operations, and identifying suitable locations for rooftop wind turbines.

The accuracy of LES and the amount of turbulence fluctuation that LES captures depends on the filter width conceptually applied to the governing equations, usually based on the grid size. While larger turbulent scales are resolved, smaller scales are modeled, making grid resolution a critical parameter. Given the computational expense of LES, simulation must be conducted with best practices to save time and cost and utilize its benefits for evaluating details of flow fields (Tominaga, 2024). Therefore, to establish good practices for LES for pedestrian-level wind

environments, researchers have focused on the benchmark case of a single isolated building. Various sensitivity analyses have been conducted, including blending first-order and second-order schemes (Ikegaya et al., 2018), timestep discretization (Liu and Niu, 2016), subgrid-scale (SGS) modeling, convergence criteria, and grid sensitivity using orthogonal meshes (Okaze et al., 2021). For a single isolated building, dividing the width and height into 20 and 40 equal parts, respectively, has been shown to provide sufficient resolution to predict mean flow and second-order turbulent statistics.

While these studies on LES suggested a minimum grid size of H-40, where H represents the building height, they do not address the sensitivity of grid sizes to low-occurring peak wind predictions. Unresolved part of turbulence in LES can cause peak wind events at pedestrian levels, such as gusts, one of the concerns for elderly pedestrian and cyclist safety. This study aims to fill this research gap by investigating the influence of grid resolution on the accuracy of LES in capturing low-occurring peak wind events at the pedestrian level. By analyzing the grid sensitivity for predicting rare gust occurrences, this research seeks to suggest and find an optimal trade-off between computational cost and accuracy.

2. METHODOLOGY

The wind tunnel experiment (WTE) was conducted at Tokyo Polytechnic University, Japan, using an open-circuit wind tunnel and a 1:1:2 (length, width, and height) single isolated building block model (Okaze et al., 2021). The Reynolds number, based on the building height H (0.2 m) and mean wind speed, was approximately 4.3×10^4. The measurements were taken at a sampling frequency of 1000 Hz for 60 seconds. Fig. 1 illustrates the locations of 383 sampling points at pedestrian height ($z = \mathrm{H}/16$). Complete details of the WTE setup and dataset are available in the referenced literature (AIJ, 2020) case-H.

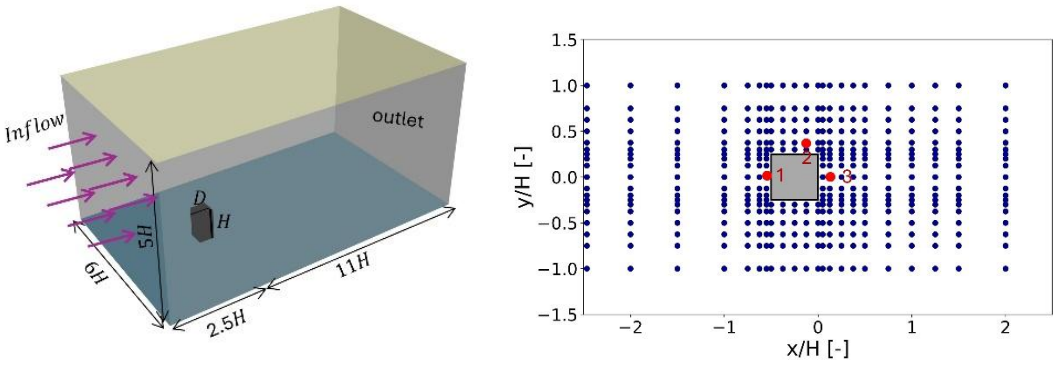

Figure 1. Shows the schematic of the WTE (left) and the location of points sampled on the pedestrian plane.

LES is performed on the same block model in OpenFOAM-v2206, replicating the WTE conditions. The computational domain extends 11 H(x) × 6 H(y) × 5 H(z) (streamwise, lateral, and vertical) following the computational wind engineering guidelines (Franke et al., 2011). The blockage ratio is about 1.67%. Fig. 1 presents a schematic of the LES domain setup, while Table 1 outlines the numerical conditions of the LES.

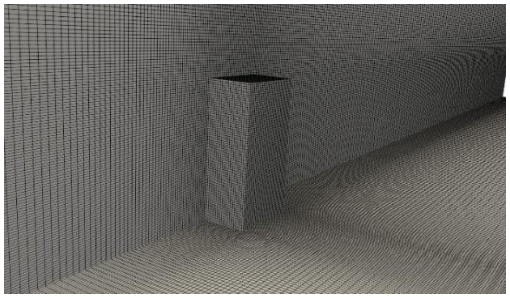

Figure 2. Grid illustration for grid cases. This figure represents the H-80 case.

For peak wind analysis, it is important to extract the simulation time-series data at the same sampling rate as the WTE. Accordingly, LES time-series velocities are sampled at a frequency of 1000 Hz for a duration of 40 s. All the analyses are non-dimensionalized using the building H and mean inlet velocity at the building height ($U_{\mathrm{H}} = 4.69\ m/s$).

Table 1. LES parameters setup

Settings	Details
Inflow	Precursor turbulence inflow data set obtained from the additional LES applied as time-varying mapped fixed boundary condition.
Wall B.C (top, building, sides and bottom)	Spalding wall function
Spatial discretization	Advection Filtered Linear 2V, and 2nd order central difference for remaining
Time step	1×10^{-4} s. maximum Courant number < 1
Time discretization	2nd order backward
Pressure-velocity coupling	PISO

2.1. Computational Grid

To investigate the impact of grid resolution on peak wind predictions, four grid configurations consisting entirely of hexahedral cells with building refinements (H/30, H/40, H/60, and H/80) are analyzed for sensitivity analysis. The cells near the building maintain an aspect ratio of one and are gradually stretched away from the building (stretching factor less than 1.04), as illustrated in Fig. 2. The time step was kept consistent across all grid refinement cases to ensure that any inaccuracies in wind predictions were solely attributed to grid resolution, thereby providing a clear evaluation of grid sensitivity on LES accuracy. The maximum Courant number was maintained below 0.7 for the finest grid case, resulting in even lower numbers for the coarser grid cases. The finest H-80 grid required 24 times more computational power than the coarse H-30 grid. Details of the refinement configurations are summarized in Table 2.

Table 2. Cases for grid sensitivity analysis.

Cases	Cell size building height	No of Cells (Millions)	Number of cells from ground to the pedestrian height	Average y^+ building block	Duration on 20 CPU (Wall clock hrs.)
H-30	H/30	0.65	1.9	58.98	34.6
H-40	H/40	1.49	2.5	46.97	68.4
H-60	H/60	4.3	3.75	31.58	162
H-80	H/80	9.7	5	23.82	824

2.2. Gust wind analysis

Accurately capturing peak gust wind velocities is crucial when assessing the safety of pedestrian wind environments (Hunt et al., 1975). Wind gust values are commonly evaluated in terms of mean μ_s and standard deviation (σ_s) at any exceedance probability as:

$$U_g = \mu_s + K(\sigma_s) \quad (1)$$

Where, K is the peak factor that quantifies the extremeness of gust wind speeds relative to the turbulence, expressed in terms of standard deviation. Low-fidelity models often assume a constant value of peak factor K, which can range between 0-3.5. However, there is no universal consensus on the appropriate value for pedestrian distress criteria (Vita et al., 2020). In this study, we calculated the peak factor (K_q) to better represent, low-occurring high wind speed events. The K_q is defined in terms of the probability of exceedance of the wind speed (s_q) as:

$$K_q = \frac{s_q - \mu_s}{\sigma_s} \quad (2)$$

Here, μ and σ are the mean and standard deviation of the wind speed s. Exceedance probabilities of 0.1%, 1%, and 5% indicate low-occurring high wind speed events at the pedestrian level. For example, a 0.1% exceedance probability corresponds to the 99.9th percentile wind speed, meaning only 0.1% of recorded samples surpass this threshold. With 40,000 samples collected over 40 s (1000 Hz sampling), this equates to 40 exceedances (0.04s). When scaled to the full 1.78-hour dataset, total exceedance reaches approximately 6.4 seconds.

3. RESULTS AND DISCUSSION

The results are presented in two parts: first, comparing LES wind speed spectra with WTE spectra and analyzing resolved TKE across grids; second, calculating and comparing the peak factor from Eq. (2) for LES and experiment.

3.1. Power spectra density and turbulence

Fig. 3 compares the power spectral density (PSD) of wind speed obtained from the WTE and LES across four grid refinements. This analysis is conducted for three probe points located at pedestrian height, z/H=1/16 (corresponding to 2 m in full scale). The probe locations are defined as follows: upstream of the building block where the horseshoe vortex forms (x/H = -0.55, y/H = 0), on the side of the building (x/H = -0.125, y/H=0.375), and downstream of the building (x/H= 0.125, y/H=0). These locations are marked in red in Fig. 1. Spectra are normalized with frequency and variance.

At point 1 (Fig. 3a), the spectral cutoff is observed at $f\mathrm{H}/U_{\mathrm{H}}$ = 1 for the H-30 grid, highlighting its limited resolution in capturing high-frequency turbulence in the inertial subrange, as indicated by the deviation from the −2/3 slope. With progressive grid refinement, the resolution of TKE improves, enabling the PSD to capture smaller-scale structures in the inertial subrange, with the normalized cutoff frequency extending to approximately 3-6 for the H-80 grid. At point 2 (Fig. 3b), the finest H-80 grid sustained the PSD at higher frequencies with more PSD spikes in the inertial subrange than observed in the experiment. This can be due to the numerical oscillation due to the 2nd-order central differencing scheme. At point 3 (Fig. 3c), all grid sizes adequately capture

the PSD peak. However, the downstream location is less susceptible to the numerical oscillation observed near sharp gradients or corners.

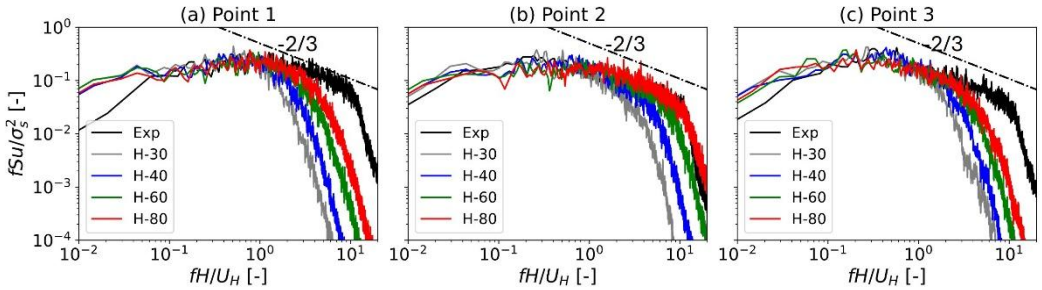

Figure 3. Wind speed power spectra density at three different locations of the pedestrian plane. Labels represent the grid refinement cases.

Fig. 4 illustrates iso-contours of the Q-criterion, highlighting vortical structures across four grid cases. As grid resolution increases (Fig. 4a–d), more flow structures are directly resolved by LES. While larger turbulence structures are captured on coarser grids, finer grids resolve smaller eddies, reducing subgrid-scale modeling. Notably, Fig. 4c and 4d show increased small-scale turbulence at pedestrian height, extending energy density spectra to higher frequencies (Fig. 3).

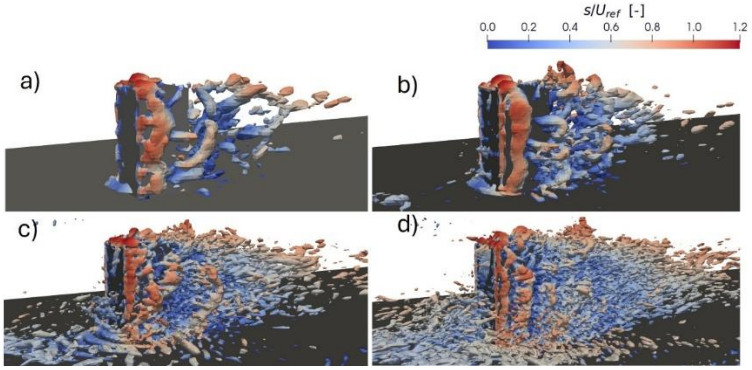

Figure 4. Comparison of iso-contours of the Q-criterion at $Q = 10000\ s^{-2}$ for four grid resolutions: a) H-30, b) H-40, c) H-60, and d) H-80.

The LES quality index proposed by (Celik et al., 2005) quantifies the ratio of resolved TKE to total TKE, which is defined as:

$$\mathrm{LES_{IQ}} = \frac{k_{res}}{k_{res}+k_{sgs}} = \frac{k_{res}}{k_{res}+a_k\Delta^p} \quad ,where\ k_{res} = \frac{1}{2}(\overline{u'u'} + \overline{v'v'} + \overline{w'w'}) \tag{3}$$

$$a_k\Delta^p = \frac{k_{res2}-k_{res1}}{\alpha^p-1} \quad ,where\ \alpha = \frac{\Delta_1}{\Delta_2} > 1 \tag{4}$$

Here, k_{res} is the resolved turbulent kinetic energy, Δ is the grid size, and $p = 2$ is the order of numerical accuracy. Fig. 5 presents a scatter plot illustrating the distribution of resolved TKE across different grids. The finer grid cases (H-40 and beyond) resolve more than 80% of the TKE, whereas the H-30 case resolves less than 80% of the TKE at pedestrian-level height, indicating a lower LES resolution in that region.

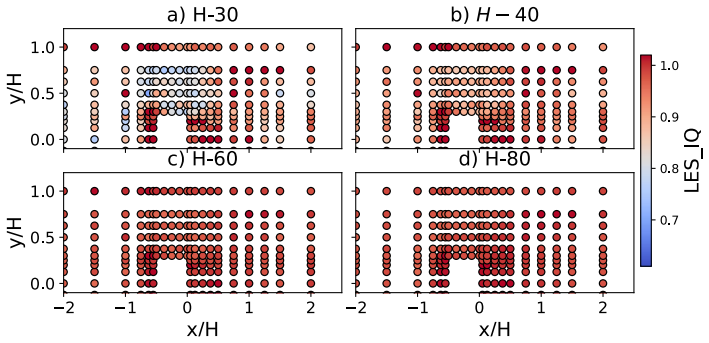

Figure 5. Scatter plot at pedestrian height colored by LES quality index for four grid refinement cases: a) H-30, b) H-40, c) H-60, and d) H-80.

3.2. Peak Factor

Fig. 6 presents a scatter plot comparing the peak factor at probabilities of exceedance of 5%, 1%, and 0.1%, representing high wind speed events of varying rarity, for four grid refinement cases in LES against WTE data. Two dotted lines indicate a ±20% deviation.

For the 5% exceedance probability (Fig. 6a), the peak factor values range from 1.5 to 2.3, with approximately 99% of the data points for all grid refinement cases falling within the ±20% deviation. At the 1% exceedance probability (Fig. 6b), which corresponds to rarer high-speed wind events, peak factor values range from 2 to 3.5. The data exhibits greater scatter compared to the 5% exceedance probability, though most points still lie within the ±20% accuracy range.

At the 0.1% exceedance probability (Fig. 6c), representing extremely rare high wind speeds, the peak factor values span from 3 to 5.5 across various locations. The scatter decreases progressively with finer grid refinement, indicating improved accuracy in predicting extreme wind phenomena. Overall, across all exceedance probabilities, LES predictions show a consistent overprediction of the peak factor compared to the WTE results.

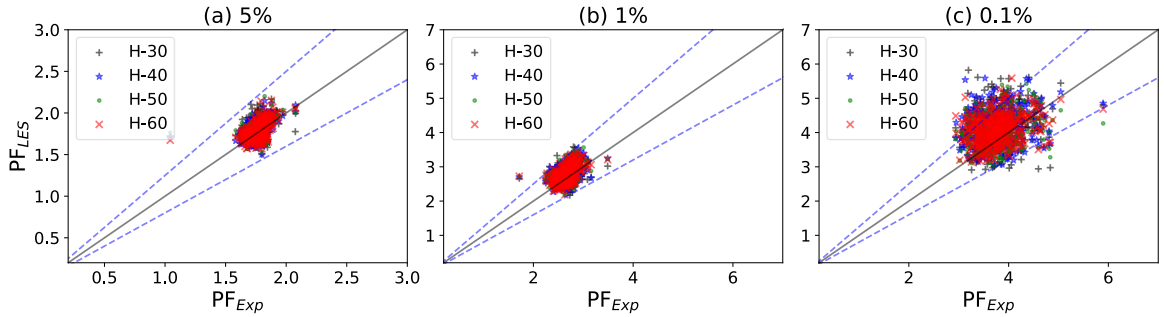

Figure 6. Scatter plot comparing peak factor values for 4 grid refinement cases with the experiment at 5%, 1%, and 0.1% probability of exceedance value. The blue line shows the 20% deviation.

The error metric for peak factor prediction is quantified in terms of normalized mean square error (NMSE), which represents the measure of scatter and, therefore, accounts for both systematic and random errors. It is defined as:

$$\text{NMSE} = \frac{\langle (O-P)^2 \rangle}{\langle O \rangle \langle P \rangle} \quad (5)$$

Here O is the observed peak factor and P is the predicted peak factor. For an ideal prediction, NMSE=0. The NMSE results, shown in Fig. 7a, are presented for the exceedance probability of 5%, 1%, and 0.1%. However, the NMSE results in Fig. 7b show the convergence of the grid as the O value in the NMSE equation is taken for the H-80 grid. Overall, the NMSE value increases as the exceedance probability decreases, indicating higher errors for lower-occurring high wind speed events. With successive grid refinements, the predictions improve as more high-frequency turbulence is resolved rather than modeled.

Although H-40 grid resolution resolves 80% of the turbulent kinetic energy at a 0.1% exceedance probability, the NMSE only converged for the H-60 (Fig. 7a) when compared to the experiment. However, in practicality, H-40 is an adequate resolution for sufficiently predicting very low-frequency extreme wind events. This grid resolution corresponds to the number of cells near 3 between ground and pedestrian height of 2 m, ensuring sufficient resolution for vortices resolution and reliable predictions.

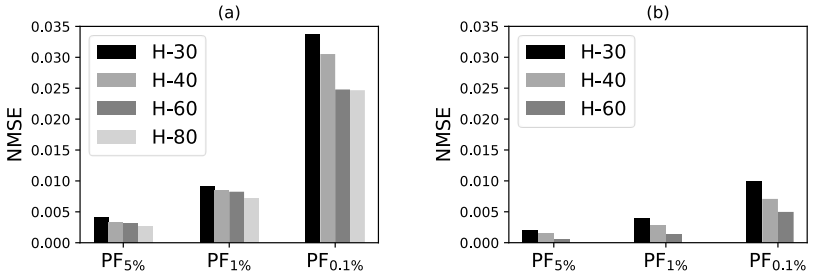

Figure 7. a) Bar graphs illustrate NMSE for four grid refinement cases at 5%, 1%, and 0.1% exceedance probabilities, comparing them with experimental data. b) shows the NMSE error of the coarser grid compared to the fine grid case. The bar color distinguishes grid refinement cases with each successive refinement.

CONCLUSION

This study examined the influence of grid resolution on low-occurring peak wind speed events at the pedestrian level, using a single isolated building block (1:1:2) as a benchmark case. Four grid resolutions (H/30, H/40, H/60, and H/80) were compared against WTE results. The findings demonstrated good overall predictions for peak factors for all the grid cases, with deviations within 20% for exceedance probabilities between 5% and 1%, representing high wind speed events. However, for a 0.1% exceedance probability, representing very rare high wind speed peaks, the grid resolution of H-60 achieved convergence for reliable prediction. This resolution included three cells from ground to pedestrian height and discretization of the building into 30 cells for width and 60 cells for height, resulting in nearly 80% of pedestrian regions being predicted within 20% deviation for 0.1% exceedance probability events. While grid refinement enhanced the accuracy of peak factor predictions, it came at an exponentially higher computational cost. Moreover, the grid resolution of H-40 and above was sufficient to resolve 80% of the TKE. Considering that H-60 grid resolution costs almost 3 times more computational power, the H-40 grid can still be used with reasonable accuracy for practical purposes.

Since this study is on a simplified benchmark case of a 1:1:2 building block with an impact on the surrounding flow at the pedestrian level, in real-world scenarios, the flow can be far more complex, with turbulence generated by smaller structures that can contribute to extreme peaks of wind speed. Therefore, further research efforts are needed to develop more complex benchmark cases that provide sufficient temporal resolution of velocity measurements for studying peak wind events and enabling meaningful comparison with the LES predictions.

ACKNOWLEDGEMENTS

his research is part of a Future Energy Hub Project funded by The Norwegian Research Council (project no.: 280458), the University of Stavanger, and local industry partners.

REFERENCES

AIJ (Architectural Institute of Japan), 2020. Guidebook for Practical Applications of CFD to Pedestrian Wind Environment Around Buildings. Architectural Institute of Japan. Available at: https://www.aij.or.jp/jpn/publish/cfdguide/index_e.htm.

Celik I.B., Cehreli Z.N., Yavuz I., 2005. Index of resolution quality for Large Eddy Simulations. Journal of Fluids Engineering 127(5), 949-958.

Franke J., Hellsten A., Schlunzen K.H., Carissimo B., 2011. The COST 732 Best Practice Guideline for CFD simulation of flows in the urban environment: A summary. International Journal of Environment and Pollution 44(1-4), 419-427.

Gousseau P., Blocken B., van Heijst G.J.F., 2013. Quality assessment of Large-Eddy Simulation of wind flow around a high-rise building: Validation and solution verification. Computers & Fluids 79, 120-133.

Hunt J.C.R., Poulton E.C., Mumford J.C., 1976. The effects of wind on people: New criteria based on wind tunnel experiments. Building and Environment 11, 15-28.

Ikegaya N., Okaze T., Kikumoto H., Imano M., Ono H., Tominaga Y., 2019. Effect of the numerical viscosity on reproduction of mean and turbulent flow fields in the case of a 1:1:2 single block model. Journal of Wind Engineering and Industrial Aerodynamics 191, 279-296.

Liu J., Niu J., 2016. CFD simulation of the wind environment around an isolated high-rise building: An evaluation of SRANS, LES, and DES models. Building and Environment 96, 91-106.

Okaze T., Kikumoto H., Ono H., Imano M., Ikegaya N., Hasama T., Nakao K., Kishida T., Tabata Y., Nakajima K., Yoshie R., Tominaga Y., 2021. Large-eddy simulation of flow around an isolated building: A step-by-step analysis of influencing factors on turbulent statistics. Building and Environment 202, 108021

Shirzadi M., Tominaga Y., 2022. CFD evaluation of mean and turbulent wind characteristics around a high-rise building affected by its surroundings. Building and Environment 225, 109637.

Tominaga Y., Wang L., Zhai Z., Stathopoulos T., 2023. Accuracy of CFD simulations in urban aerodynamics and microclimate: Progress and challenges. Building and Environment 243, 110723.

Vita G., Shu Z., Jesson M., Quinn A., Hemida H., Sterling M., Baker C., 2020. On the assessment of pedestrian distress in urban winds. Journal of Wind Engineering and Industrial Aerodynamics 203, 104200.

Zhong J., Liu J., Zhao Y., 2022. Recent advances in modeling turbulent wind flow at pedestrian-level in the built environment. ARIN 1, 5.

6th International Conference on Building Energy and Environment
Eindhoven University of Technology, The Netherlands
6 - 10 July 2025

CFD validation of thunderstorm outflow dynamics in street canyons using wind tunnel data

Mohammad Hadavi [1], Djordje Romanic [1]

[1] *Department of Atmospheric and Oceanic Sciences, Faculty of Science, McGill University, Montreal, Canada*
mohammad.hadavi@mail.mcgill.ca, djordje.romanic@mcgill.ca

SUMMARY
Thunderstorm outflows generate intense near-ground winds that can threaten urban safety. Previous studies have primarily focused on isolated outflows. As a result, the interaction between thunderstorm outflows, atmospheric boundary layer (ABL) winds, and urban geometries remains relatively underexplored. This study uses Computational Fluid Dynamics (CFD) to simulate outflow propagation within a street canyon in the presence of a background ABL wind. The CFD simulations closely reproduce wind tunnel measurements, highlighting the CFD's ability to complement experiments and provide detailed insights into urban wind dynamics. The low-Reynolds $k-\varepsilon$ turbulence model, with fine grids and low y^+ values, effectively resolves near-wall flow dynamics. The results show that street canyons amplify and sustain higher wind speeds, particularly at the pedestrian level, compared to open areas. This increases aerodynamic loads and makes urban infrastructure more vulnerable to wind damage, which highlights the critical role of urban geometry in determining outflow impacts.

Keywords: Thunderstorm outflow, CFD, Experiment, Street canyon.

1. INTRODUCTION

Thunderstorm outflows are characterized by intense winds near the ground and transient, localized flow conditions (Hjelmfelt, 1988), which differentiate them from typical atmospheric boundary layer (ABL) winds. These extreme wind events pose significant threats to urban infrastructure and public safety (Bélair et al., 2025; Solari et al., 2020). Research indicates that maximum radial outflow velocities typically occur between 50 and 120 m above ground level (Hjelmfelt, 1988) and cause substantial aerodynamic loads on structures (Solari, 2014).

The highly non-stationary and localized nature of thunderstorm outflows makes it difficult to capture these events with adequate spatiotemporal resolution, leading to limited full-scale data. Moreover, physical simulations in controlled facilities (i.e., wind tunnels) are costly (Hangan et al., 2017) and face limitations in rendering different configurations and scenarios. Computational Fluid Dynamics (CFD) is an effective approach to complement experiments by providing detailed insights into full-field flow characteristics. It also helps in interpreting complex flow dynamics that are often challenging to achieve through physical measurements alone.

Several techniques exist to simulate a thunderstorm outflow. One common approach is the impinging jet: a turbulent, axisymmetric air jet that impinges the ground perpendicularly and spreads radially. This method is widely acknowledged in wind engineering for its ability to replicate key dynamical features of an outflow, such as the primary and secondary vortices. The present research adopted the impinging jet approach.

Previous studies have thoroughly investigated the effects of ABL winds in urban environments (Blocken, 2014; Hadavi and Pasdarshahri, 2020). Similarly, the dynamics of an isolated thunderstorm outflow in an empty chamber is well-documented (Romanic et al., 2020a, Žužul et al., 2023). However, the interaction between thunderstorm outflows, background ABL winds, and urban geometries remains relatively underexplored—a critical gap given the projected increase in frequency and intensity of thunderstorms (Rädler et al., 2019). To address this research question, the present study numerically simulates the propagation of a thunderstorm outflow within a well-known urban configuration—a street canyon—in the presence of a background ABL flow.

2. METHODOLOGY

This research utilizes CFD to replicate the wind tunnel experiments conducted by Richter et al. (2018). They physically simulated a negatively buoyant gust using a jet impinging on a street canyon under the influence of a background ABL wind. Velocity fields within the canyon were measured using a two-dimensional Time-Resolved Particle Image Velocimetry system.

2.1. Scales

Figure 1 shows the computational domain and boundaries, with dimensions based on the experimental setup. The jet flow is ejected from a 10 mm diameter tube connected to pressurized air. The jet outlet is positioned 310 mm above the surface.

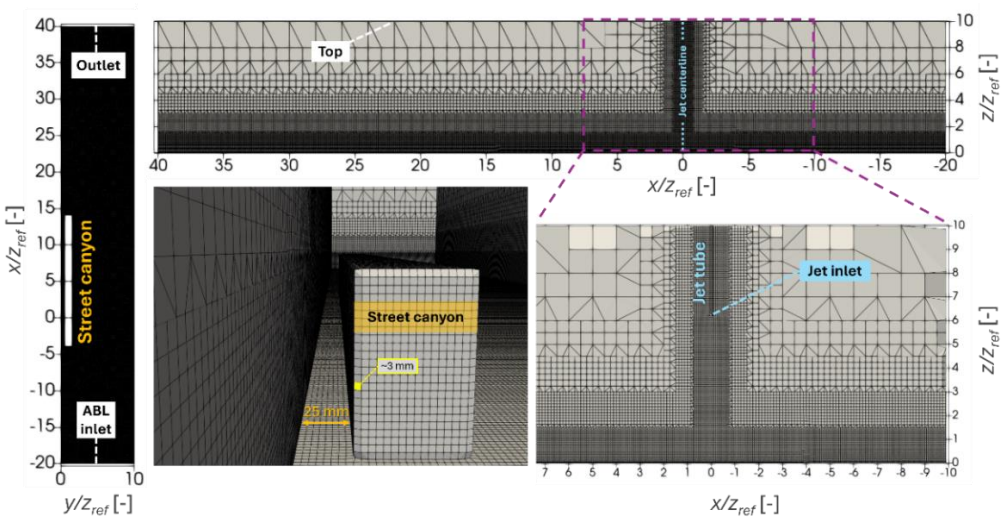

Figure 1. Computational domain with grid details and boundaries indications.

The street canyon model has dimensions of 75 mm in height, 50 mm in width, and 900 mm in length (Fig. 1). At a 1:200 scale, this represents a road width of 10 m and a low-rise building height of 15 m in reality. In addition to the original street canyon from Richter et al. (2018), the present study investigated a high-rise canyon with a height of 250 mm (equivalent to 50 m in reality), while maintaining the same width and length. For normalization, a reference height of 50 mm was selected, along with $U_{ref} = U(z_{ref})$, where U_{ref} represents the velocity of the background ABL flow in open terrain (i.e., without the canyon model).

2.2. CFD simulations

The steady-state and isothermal CFD simulations were performed using the simpleFoam solver from the OpenFOAM v2306 open-source CFD library. This solver employs the Semi-Implicit Method for Pressure-Linked Equations (SIMPLE) algorithm to solve the coupling between velocity and pressure in the Navier-Stokes equations. To save computational resources, half of the experimental setup was modeled (Fig. 1), assuming axisymmetric behavior. This approach is commonly used in CFD literature on flows that are symmetric along a plane (e.g., Žužul et al., 2023; Kim and Hangan, 2007). At the jet outlet face, a velocity of 45 m s^{-1} was prescribed, with the downward flow being perpendicular to the ABL flow. The developed ABL profile from an empty chamber was imposed to represent the background ABL flow. A zero-gauge pressure condition was applied at the outlet face. The near-wall flow was modeled using the atmWallFunction class for smooth surfaces.

The snappyHexMesh utility was used to generate a hexahedron-based unstructured mesh from a background grid created using the blockMesh tool. As shown in Fig. 1, the grid was significantly refined in critical regions, including the downdraft zone and the area where the outflow interacts with the street canyon. The grid sensitivity analysis was conducted by constructing three computational grids. The grid refinement factor is approximately 3.3 between the coarse (1.5 million cells) and medium (5 million cells) grids, and 1.9 between the medium and fine (9.4 million cells) grids. To quantify the error of the medium mesh compared to the fine mesh, the Grid Convergence Index (GCI) method is employed (Roache, 1994):

$$GCI = \frac{F_s|\epsilon|}{r^p - 1} \tag{1}$$

where F_s is the safety factor equals to 1.25, ϵ is the velocity relative error between the medium and fine mesh, r is the grid refinement factor, and p is the order of accuracy of the computation.

The first cell layer near the bottom surface was refined to 3 mm, yielding about 25 cells across the canyon height. Additionally, five cell layers with a growth ratio of 1.25 were added to the solid surfaces of the ground and canyon to maintain y^+ values within the desired range while minimizing computational cost.

The Reynolds-Averaged Navier-Stokes (RANS) approach was adopted to model turbulence. Four $k-\varepsilon$ and two $k-\omega$ turbulence models were tested: the standard $k-\varepsilon$, the realizable $k-\varepsilon$, the re-normalized group (RNG) $k-\varepsilon$, Launder and Sharma low-Reynolds $k-\varepsilon$, the standard $k-\omega$, and the shear stress transport (SST) $k-\omega$. Here, k is the turbulent kinetic energy, ε is the turbulent kinetic energy dissipation rate, and ω is the specific dissipation rate.

3. RESULTS

The comparison of turbulence models demonstrates the superior performance of the low-Reynolds $k-\varepsilon$ model, particularly when the canyon is present (not shown here due to the space limitation). For the case of open terrain (ABL+Jet), the performance of the standard $k-\varepsilon$ model is nearly equivalent to that of the low-Reynolds $k-\varepsilon$ model. The low-Reynolds $k-\varepsilon$ model is particularly effective in capturing near-wall flow characteristics. It resolves flow through the

viscous sublayer by utilizing thin cell layers with low y^+ values. Table 1 presents the y^+ values for each of the three simulated scenarios. The low y^+ values highlight the effective near-wall resolution achieved in this study. Table 1 also includes the GCI values for the medium-to-fine grid comparison. Given the low values of GCI on the two considered lines, it can be concluded that the medium grid successfully provides grid-independent results.

Table 1. y^+ values for each scenario in the form of [minimum, average, maximum]. GCI values for the medium-to-fine grid comparison are also reported; GCI_X: along a horizontal line (-6 < x/z_{ref} < 20) at y=0 and z=z_{ref}; GCI_Z: along a vertical line (0 < z/z_{ref} < 1.2) at y=0 and x/z_{ref}=5.7.

Scenario	y^+ Ground	y^+ Canyon	GCI_X $_{medium/fine}$	GCI_Z $_{medium/fine}$
ABL + Canyon	[2.2, 2.7, 3.0]	[0.1, 2.2, 4.2]	0.32%	0.16%
ABL + Jet	[1.1, 3.1, 5.9]	NA	1.11%	0.78%
ABL + Jet + Canyon	[2.1, 2.7, 3.1]	[0.2, 3.2, 8.8]	1.65%	1.06%

Figure 2 compares CFD and wind tunnel measurements for open terrain and street canyon scenarios via vertical profiles of horizontal velocity. To ensure consistency with the experimental study, the background ABL profile is subtracted. Overall, the CFD simulations accurately replicate the physical experiments, as evidenced by the Root Mean Square Error (RMSE) values (Fig. 2). The peak velocity reproduced in the CFD results cannot be fully confirmed due to absence of measurement data near the bottom surface, thereby highlighting the supplementary nature of CFD simulations to physical experiments. There is a trend of increasing error downstream from the downdraft, particularly in the canyon case. The CFD simulations become less accurate as the flow develops within the canyon after impingement, likely due to the turbulent eddies being modelled rather than resolved in the RANS turbulence models. Additionally, Fig. 2 shows that the horizontal velocity within the street canyon is higher at all heights compared to the open terrain case.

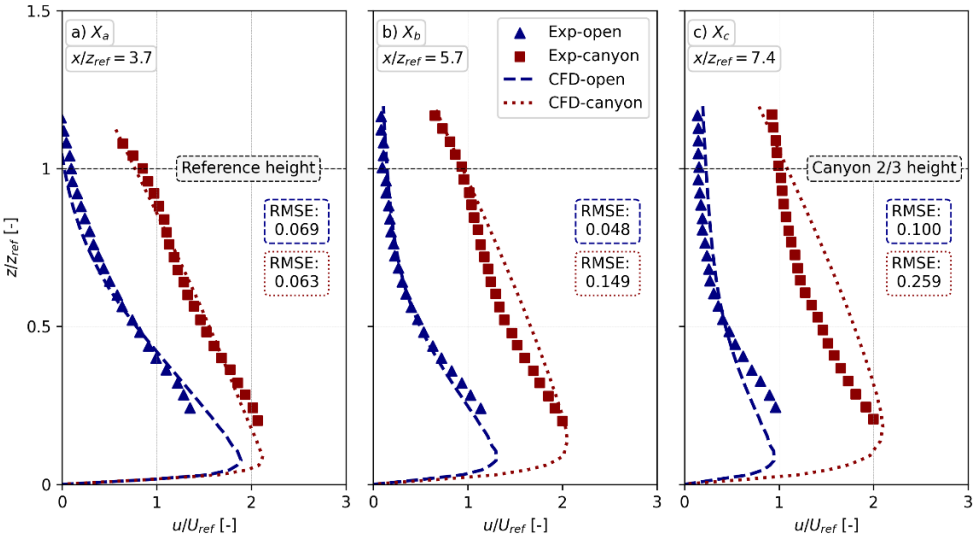

Figure 2. (a-c) Vertical profiles of normalized horizontal velocity at three streamwise positions downstream of the jet with y=0, comparing thunderstorm outflow propagation in open terrain and within a street canyon. The background ABL profile is subtracted. RMSE values quantify the difference between CFD and physical measurements in each case.

Figure 3 illustrates the development of horizontal wind along a horizontal line at z/z_{ref}=0.5, 1, 1.5, 2. This figure compares three background ABL velocities of ~2.3, 4.5, and 9.0 m s^{-1} at canyon height, corresponding to U_{Jet}/U_{ABL} ratios of 20, 10, and 5, respectively. The jet flow is entirely dissipated at the highest ABL velocity, with no peak observed. A slight velocity increase is noted for U_{Jet}/U_{ABL}=10 at x/z_{ref} ≅10, indicating that the touchdown point is advected downstream compared to U_{Jet}/U_{ABL}=20. Interestingly, near the ground in the canyon scenario (Fig. 3h), the lowest ABL case shows a velocity peak exceeding the other two cases. This demonstrates the nonlinear interaction between ABL and outflow winds. The combined flow is influenced by complex flow dynamics, such as turbulence, shear, and mixing, which prevent the velocities from simply adding up. This result aligns with Moeini and Romanic (2023), who proposed an analytical solution of the interaction between the ABL wind and isolated outflow.

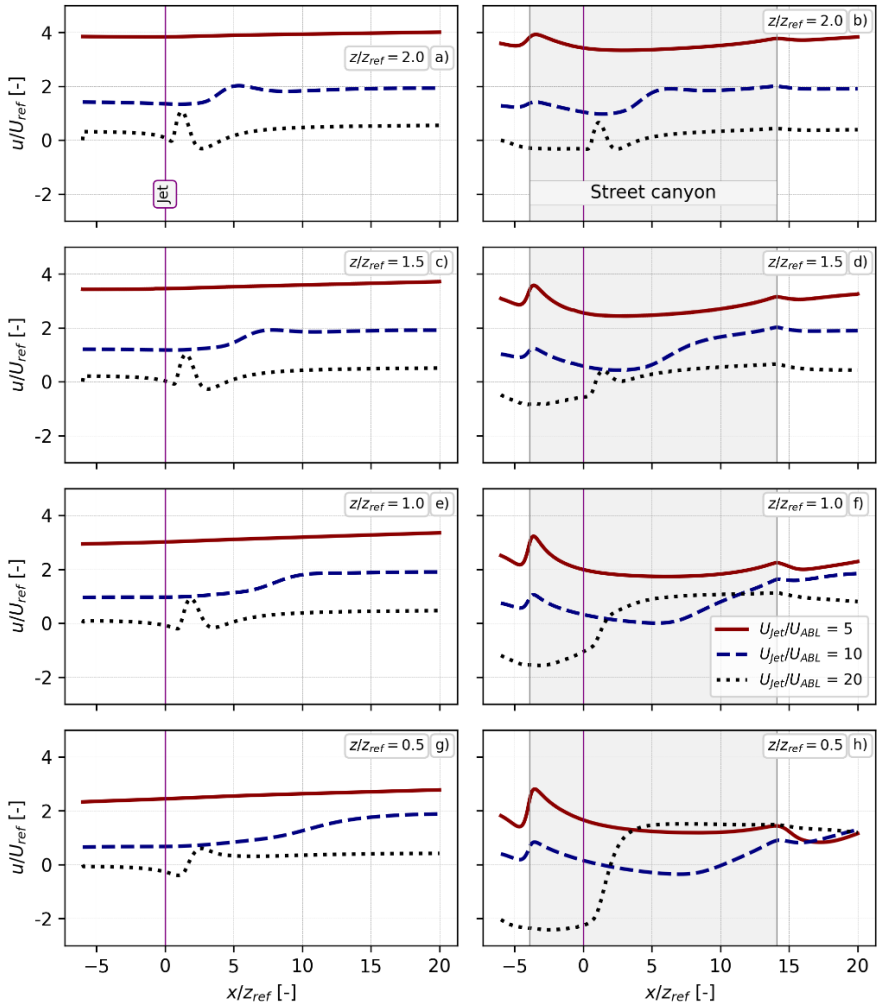

Figure 3. Horizontal wind speed development along the canyon centerline (y=0) at four different heights: (a-b) z/z_{ref}=2; (c-d) z/z_{ref}=1.5; (e-f) z/z_{ref}=1; (g-h) z/z_{ref}=0.5. The left column represents the open terrain scenario (ABL + Jet), while the right column shows the street canyon scenario (ABL + Jet + Canyon), with the canyon location shaded. The jet centerline is marked by a purple line at x=0 in all panels. Results are presented for U_{Jet}/U_{ABL} ratios of 20, 10, and 5, corresponding to three different background ABL velocities.

When the ABL is weak (i.e., U_{Jet}/U_{ABL}=20), the high velocities at approximately $x/z_{ref} = 2.5$ in the open terrain start to decrease soon after the downdraft region (Fig. 3a, c, e, g), which is a narrow region due to the small jet diameter. In contrast, velocity decay is less pronounced within the street canyon. As shown in the velocity contours (Fig. 4), the background ABL wind quickly weakens the jet in the open terrain, whereas the street canyon retains higher velocities after jet impingement by restricting the flow from spreading out. This flow dynamics results in maintaining the high wind intensity throughout the canyon (Fig. 4b). Noticeably, the canyon intensifies the negative impact of the outflow on the built environment. With the increased vertical distance from the canyon, the flow becomes similar to the open terrain (Fig. 3a-b and Fig. 4a-b).

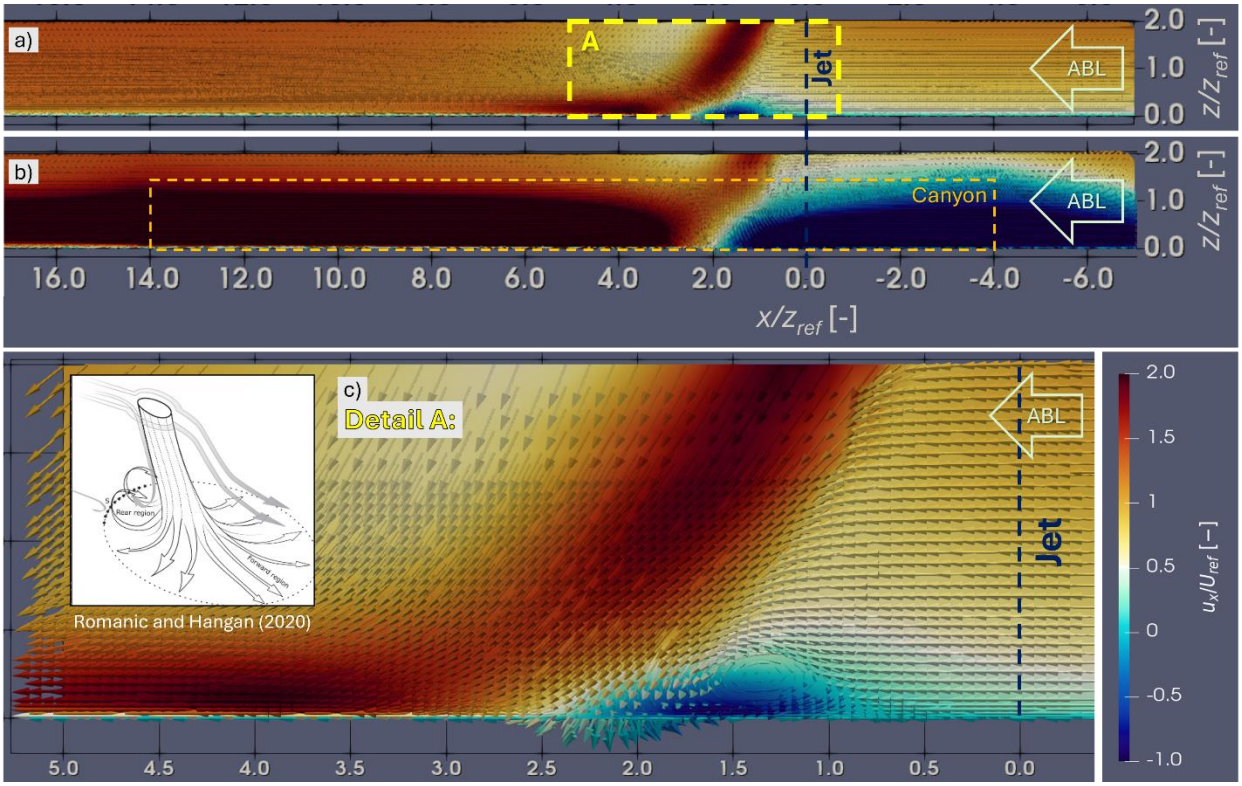

Figure 4. Sideview of the velocity contours and arrows of normalized horizontal velocity at y=0 for the scenarios of a) open terrain and b) street canyon. c) A zoom-in view of the touchdown area in the open terrain case, demonstrating agreement with the model proposed by Romanic and Hangan (2020b).

If we zoom in on the touchdown area in the open terrain scenario (Fig. 4c), a recirculation area can be observed just behind the stagnation point. The interaction between the radial outflow and opposing ABL wind generates a strong shear and convergence upwind of the impingement. This flow interaction forms a quasi-stationary recirculating vortex near the surface. In contrast, in the downwind region, the background wind aligns with and reinforces the radial outflow, flattening the outflow propagation. This observation is consistent with the conceptual model proposed by Romanic and Hangan (2020b) for outflow and ABL interaction.

Finally, Fig. 5 compares the results of the original canyon with those of a high-rise one. In the high-rise street canyon, the peak velocity is ~30% higher and conserved over a larger radial

distance. The peak velocity occurs at a slightly higher elevation in the high-rise canyon. Interestingly, despite the low-rise and high-rise canyons having heights of $1.5z_{ref}$ and $5z_{ref}$, respectively, the main difference in velocity magnitude remains confined to the pedestrian level below $0.5z_{ref}$. The velocity magnitudes between the two canyon cases approach each other above z_{ref}, particularly farther downstream from the jet impingement (Fig. 5c-d).

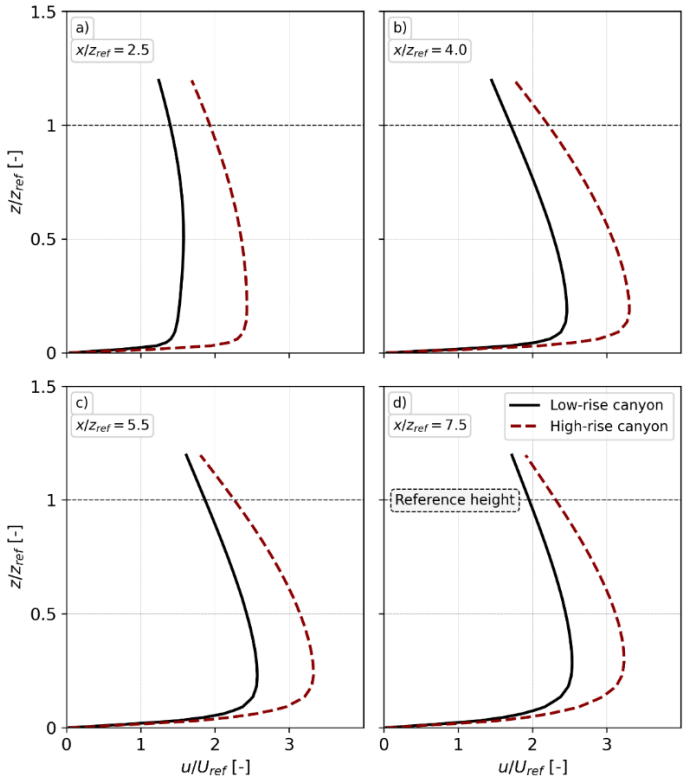

Figure 5. (a-d) Vertical profiles of normalized horizontal velocity at four streamwise positions downstream of the jet with y=0, comparing thunderstorm outflow propagation within a low-rise ($1.5z_{ref}$) and a high-rise ($5z_{ref}$) street canyon.

4. CONCLUSION

Thunderstorm outflows generate intense near-ground winds that pose significant risks to urban structures. This study addresses a gap in understanding the interaction between thunderstorm outflows, background atmospheric boundary layer (ABL) winds, and urban street canyons. Computational Fluid Dynamics (CFD) is used to reproduce wind tunnel measurements performed by Richter et al. (2018).

The study has two main objectives: 1) to evaluate CFD's ability in providing accurate insights into urban wind dynamics during outflow propagation, and 2) to investigate the influences of urban geometries, such as a street canyon, on outflow behaviour.

The results demonstrate that a low-Reynolds $k-\varepsilon$ turbulence model, combined with a highly refined mesh (y^+ primarily below 5), effectively resolves near-wall flow dynamics and acceptably

replicates wind tunnel measurements. This highlights CFD's value in complementing experiments and enhancing future experimental designs.

Findings also reveal that street canyons confine outflow propagation, amplify high wind velocities, and retain them over larger radial and vertical distances compared to open terrain. This escalates aerodynamic loads and the vulnerability of urban infrastructure, underscoring the significant influence of urban geometry on outflow behaviour.

ACKNOWLEDGEMENTS

The authors thank the Digital Research Alliance of Canada for providing access to supercomputer clusters used for running the CFD simulations. We acknowledge the financial support of the Natural Sciences and Engineering Research Council of Canada (NSERC) through Discovery Grant RGPIN-2021-02651. We appreciate the funding provided by the Fonds de recherche du Québec – Nature et technologies (FRQNT) through a Doctoral Research Scholarship. We also extend our gratitude to McGill University for their support through a Lorne Trottier Science Accelerator Fellowship.

REFERENCES

Bélair, F., Dyer-Hawes, Q. and Romanic, D., 2025. The dynamics of the urban boundary layer before and during a severe thunderstorm outflow over downtown Montréal. Boundary-Layer Meteorology, 191(1), p.6.

Blocken, B., 2014. 50 years of computational wind engineering: past, present and future. Journal of Wind Engineering and Industrial Aerodynamics 129, pp. 69-102.

Hadavi, M. and Pasdarshahri, H., 2020. Quantifying impacts of wind speed and urban neighborhood layout on the infiltration rate of residential buildings. Sustainable Cities and Society 53, 101887.

Hangan, H., Refan, M., Jubayer, C., Romanic, D., Parvu, D., LoTufo, J. and Costache, A., 2017. Novel techniques in wind engineering. Journal of Wind Engineering and Industrial Aerodynamics 171, pp. 12-33.

Hjelmfelt, M.R., 1988. Structure and life cycle of microburst outflows observed in Colorado. Journal of Applied Meteorology and Climatology, 27(8), pp. 900-927.

Kim, J. and Hangan, H., 2007. Numerical simulations of impinging jets with application to downbursts. Journal of wind engineering and industrial aerodynamics, 95(4), pp. 279-298.

Moeini, M. and Romanic, D., 2023. An analytical solution to the perturbation analysis of the interaction between downburst outflows and atmospheric boundary layer winds. Journal of the Atmospheric Sciences, 80(1), pp. 301-319.

Rädler, A.T., Groenemeijer, P.H., Faust, E., Sausen, R. and Púčik, T., 2019. Frequency of severe thunderstorms across Europe expected to increase in the 21st century due to rising instability. npj Climate and Atmospheric Science, 2(1), p.30.

Richter, A., Ruck, B., Mohr, S. and Kunz, M., 2018. Interaction of severe convective gusts with a street canyon. Urban Climate 23, pp. 71-90.

Roache, P.J., 1994. Perspective: a method for uniform reporting of grid refinement studies. Journal of Fluids Engineering 116, pp. 405-413.

Romanic, D., Nicolini, E., Hangan, H., Burlando, M. and Solari, G., 2020a. A novel approach to scaling experimentally produced downburst-like impinging jet outflows. Journal of Wind Engineering and Industrial Aerodynamics 196, 104025.

Romanic, D. and Hangan, H., 2020b. Experimental investigation of the interaction between near-surface atmospheric boundary layer winds and downburst outflows. Journal of Wind Engineering and Industrial Aerodynamics, 205, p.104323.

Solari, G., 2014. Emerging issues and new frameworks for wind loading on structures in mixed climates. Wind Struct, 19(3), pp. 295-320.

Solari, G., Burlando, M. and Repetto, M.P., 2020. Detection, simulation, modelling and loading of thunderstorm outflows to design wind-safer and cost-efficient structures. Journal of Wind Engineering and Industrial Aerodynamics 200, 104142.

Žužul, J., Ricci, A., Burlando, M., Blocken, B. and Solari, G., 2023. CFD analysis of the WindEEE dome produced downburst-like winds. Journal of Wind Engineering and Industrial Aerodynamics 232, 105268.

Health and Indoor Air Quality, Ventilation (13:30-15:00 h)

6th International Conference on Building Energy and Environment
Eindhoven University of Technology, The Netherlands
6 - 10 July 2025

Local and whole-body PBPK model to investigate the organ disposition concentration of di (2-Ethyhexyl) phthalate (DEHP) following inhalation exposure

Nguyen Dang Khoa [1], Kazuki Kuga [2], Kazuhide Ito [3]

[1]*Kyushu University, Fukuoka, Japan, ndkhoa@kyudai.jp*
[2]*Kyushu University, Fukuoka, Japan, kuga@kyudai.jp*
[3]*Kyushu University, Fukuoka, Japan, ito@kyudai.jp*

SUMMARY
This study employed a hybrid model of Computational fluid dynamics (CFD) and Whole-body physiologically-based pharmacokinetics (PBPK) to elucidate the systematic disposition of DEHP and its metabolites in human organs via inhalation exposure. The reliability of this hybrid approach was validated through the use of experimental data. The local diffusive absorption of DEHP was found to be dependent on the airway compartment. In light of these findings, the results obtained from the whole-body PBPK indicate varied time-course concentrations in different organs based on the effects of physiological and biochemical parameters. The results are expected to consolidate the current technique as a reliable tool to link indoor contaminant exposure to organ concentration.

Keywords: Computational Fluid Dynamics, Whole-body PBPK, Inhalation exposure, DEHP

1. INTRODUCTION

Di (2-Ethyhexyl) phthalate (DEHP) is the most pervasive phthalate in the environment, and it can be detected in various furniture, building materials, cosmetics, and food packaging products. Furthermore, its presence has been confirmed in soil, water, and ambient air (Rowdhwal & Chen, 2018). The respiratory system is recognized as an intermediary conduit, which acts as the pathway for indoor DEHP to enter the body. It has been demonstrated that DEHP can act as an endocrine disrupter, which has the potential to induce disorders in multiple internal tissues, including the testis, renal system, liver, heart, and brain (Wang et al., 2024). In this context, an advanced numerical approach has been employed to elucidate the systematic disposition of DEHP so-called whole-body PBPK model (Li et al., 2022). Nevertheless, this model is less comprehensive in linking indoor contaminant exposure and the health effects of breathing activities. Therefore, the present study aims to quantitatively reveal DEHP behaviors in the internal organs using the CFD and whole-body PBPK hybrid technique.

2. METHODOLOGY

2.1. Numerical domain and grid design

A human respiratory tract down to the 16th generation was integrated with a computer-simulated person (CSP) placed in an indoor space with dimensions of 3×3×3 m^3. The numerical domain was discretized using poly-hex core elements with 10 prism layers adjacent to the respiratory wall. The total cell count reached nearly 25 million.

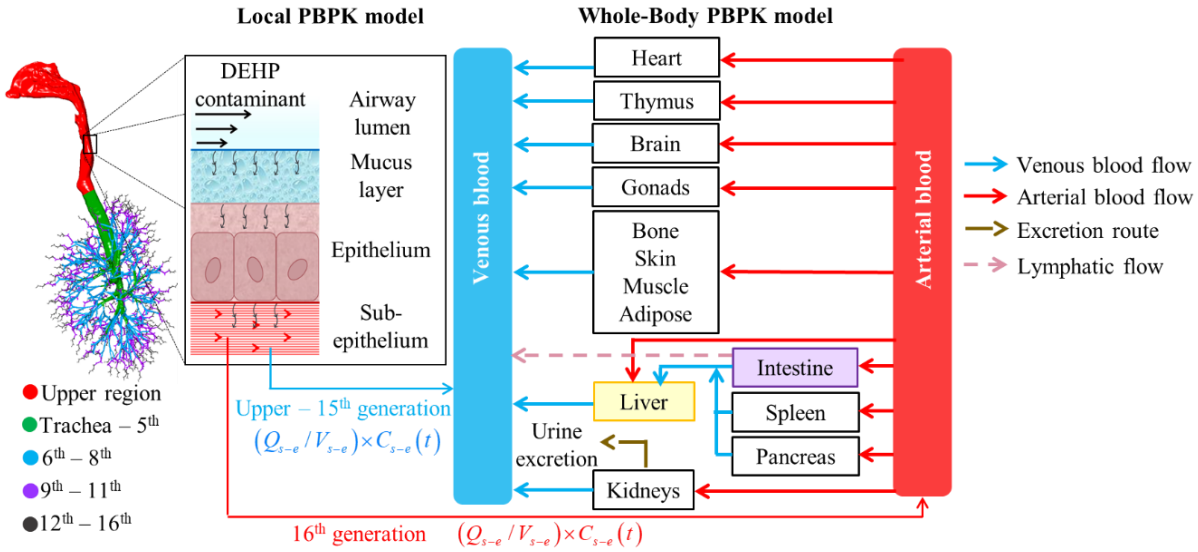

Figure 1. Diagram of the local and whole-body PBPK

2.2. Computational fluid dynamics method for airflow patterns and local PBPK

Incompressible, isothermal, and transient fluid flow was simulated by solving the Reynolds-averaged Navier-Stokes equations. The Low Reynolds type *k-ε* (Abe-Kondoh-Nagano) turbulent model was selected. This analysis applied the transient breathing flow profile retrieved from the experiment (Gupta et al., 2010). Six breathing cycles were simulated with a time step size of 0.005 s. Diffusion and transportation terms of DEHP in the respiratory tract were predicted using the scalar transport equation (Eq. (1)). For local PBPK, the absorption, diffusion, metabolic clearance, and blood perfusion occurred inside the respiratory tissue (Fig. 1) were simulated by Eq. (2) – (4).

$$\frac{\partial \overline{C_a}}{\partial t}+\frac{\partial \overline{U_i C_a}}{\partial x_i}=\frac{\partial}{\partial x_i}\left[\left(D_a+\frac{\nu_T}{\sigma}\right)\frac{\partial \overline{C_a}}{\partial x_i}\right] \tag{1}$$

$$\frac{\partial C_m(x,t)}{\partial t}=D_m\frac{\partial^2 C_m(x,t)}{\partial x^2} \tag{2}$$

$$\frac{\partial C_e(x,t)}{\partial t}=D_e\frac{\partial^2 C_e(x,t)}{\partial x^2} \tag{3}$$

$$\frac{\partial C_{s-e}(x,t)}{\partial t}=D_{s-e}\frac{\partial^2 C_{s-e}(x,t)}{\partial x^2}-\frac{Q_{s-e}}{V_{s-e}}C_{s-e}(x,t) \tag{4}$$

where U_i is the mean flow velocity, C_a is the ensemble mean contaminant concentration, D_a is the diffusion coefficient of DEHP in air, and σ is the turbulent Schmidt number. C_m, C_e, C_{s-e} and D_m, D_e, D_{s-e} are the contaminant concentrations and the diffusion coefficient in mucus, epithelium, and sub-epithelium, respectively. Q_{s-e} and V_{s-e} indicate the plasma flow rate and the volume in the sub-epithelium layer, respectively. The local PBPK model was simultaneously enabled with the transient breathing to predict the time-course concentration. During exhalation, airway outlets were set to zero concentration, assuming all DEHP absorption beyond the outlets. An exposure condition of 100 μg/m^3 in 3 hours were used following the experiment (Andersen et al., 2018).

2.3. Whole-body PBPK

After the local PBPK simulation, the uptake DEHP amount via the upper – 15th generation was administrated to venous blood and that of 16th generation was specified as arterial blood dose (Fig.1). In liver and gut, DEHP is primarily metabolized into byproducts including the mono(2-ethylhexyl) phthalate (MEHP), mono(2-ethyl-5-oxohexyl) phthalate, mono(2-ethyl-5-hydroxyhexyl) phthalate, and mono(2-ethyl-5-carbo) phthalate. The systematic distribution, metabolism, and clearance of DEHP and its metabolites are described by a set of ordinary differential equations involving the physiological and biomedical parameters.

3. RESULTS AND DISCUSSIONS

The local PBPK results indicate the discrete DEHP absorption percentage along the airway. Absorption was highest in the upper (~34%, Fig. 2a) and dropped close to 20% in the trachea – 5th generation and the 6th – 8th generation. For the 9th – 11th generation, the absorption percentage quickly declined to approximately 10% and even less than 1% in the 12th – 16th generation. Approximately 77% of inhaled DEHP was absorbed into the respiratory wall during one breathing cycle. These phenomena can be attributed to the employed parameters, such as the diffusion and partition coefficients, and the lack of geometry in the 8th – 16th generation. Then, DEHP was continuously diffused through airway tissue (Fig. 2b). Precisely, mucus concentration developed during inhalation – I and reached nearly zero during exhalation – E across all airway compartments. Similar fluctuations occurred in the epithelium and sub-epithelium, though an increment is observed, especially in the upper – 8th generation. Besides, the mucus concentration profiles remained lower value (around 3.6–5.0×10^3 μg/m^3) compared to the epithelium (roughly 45–1.2×10^5 μg/m^3) and sub-epithelium (about 10–2.8×10^4 μg/m^3) due to the partition coefficients.

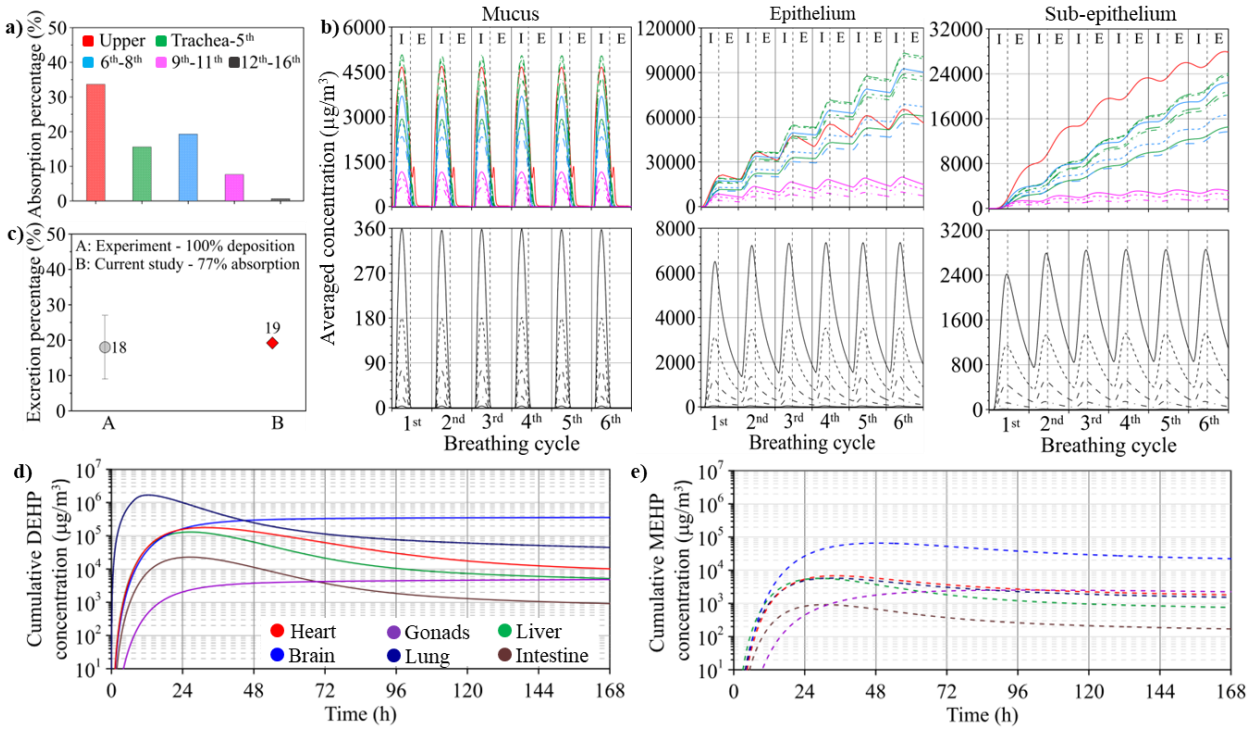

Figure 2. (a) DEHP absorption percentage onto the airway wall. (b) Averaged DEHP concentration in airway tissue. (c) Validation works against the experimental data. (d) DEHP and (e) MEHP transient concentration in organs.

Upon the local PBPK results, the venous and arterial blood doses up to 2,667 breathing cycles (corresponding to 3-hour exposure) were estimated based on the six breathing cycles using the logarithmic regression. Then, the whole-body PBPK simulation was launched to record DEHP's metabolites' total cumulative urine mass. The credibility of the hybrid model was verified based on the excretion factor, calculated by normalizing the total cumulative mass with the total absorption percentage and total DEHP inhaled amount. Notably, our simulation underpredicted the excretion factor (Fig. 2c); however, it is inevitable due to the foreseen uncertainties related to the biochemical and physiological parameters.

The time-course concentration in the organs was obtained via an 8-hour exposure case study (0 denoting the start of exposure) with an examined duration of 168 hours (7 days). As a result, the time-dependent of DEHP and MEHP significantly varied between organs (Figs. 2d and 2e). Specifically, DEHP concentration in the lung continuously progressed and reached its apex at 8 hours with a value of around 1.9×10^{6} μg/m^3, followed by a stiff decrement to around 5.0×10^{4} μg/m^3 at 168 hours (Fig. 2d). This evolutionary trend is also observed in the heart, liver, and intestine with different peak concentration time and value. Meanwhile, DEHP concentrations in the brain and gonads still continuously remained with the value of around 3.0×10^{5} μg/m^3 and 5.0×10^{3} μg/m^3, respectively, and required more time to be cleared. For MEHP (Fig. 2e), the time-course concentration in all organs experienced a downward trend after 48 hours, except for gonads, which delayed up to 120 hours. The peak concentration was found in the brain at approximately 7.0×10^{4} μg/m^3, and the lowest concentration of 9.0×10^{2} μg/m^3 occurred in the intestine. For other organs, the peak concentration ranged from 6.0×10^{3} to 7.0×10^{3} μg/m^3.

4. CONCLUSIONS

Development of the current whole-body PBPK coupling with the CFD analysis (local PBPK) offered a potential forecasting tool to monitor the time-dependent effects of exposure to DEHP. To precisely simulate the systematic disposition of DEHP and MEHP in the human body, it is essential to utilize the appropriate biochemical and physiological parameters. However, limitations include subject variability, parameter sensitivity, and limited validation data should be noted.

ACKNOWLEDGEMENTS

This study was partially funded by the FOREST program from JST, Japan (JPMJFR225R), JSPS KAKENHI (JP 25H00409, JP 22K18300, JP 25K21392, JP 25K17736), Health, Labour and Welfare Policy Research Grants (JP 24KD2001) and MEXT as "Program for Promoting Researches on the Supercomputer Fugaku" (JPMXP1020210316).

REFERENCES

Andersen, C., Krais, A. M., Eriksson, A. C., Jakobsson, J., Löndahl, J., Nielsen, J., Lindh, C. H., Pagels, J., Gudmundsson, A., & Wierzbicka, A. (2018). Inhalation and Dermal Uptake of Particle and Gas-Phase Phthalates—A Human Exposure Study. *Environmental Science & Technology*, *52*(21), 12792–12800.

Gupta, J. K., Lin, C.-H., & Chen, Q. (2010). Characterizing exhaled airflow from breathing and talking. *Indoor Air*, *20*(1), 31–39.

Li, A., Kang, L., Li, R., Wu, S., Liu, K., & Wang, X. (2022). Modeling di (2-ethylhexyl) Phthalate (DEHP) and Its Metabolism in a Body's Organs and Tissues through Different Intake Pathways into Human Body. *International Journal of Environmental Research and Public Health*, *19*(9), 5742.

Rowdhwal, S. S. S., & Chen, J. (2018). Toxic Effects of Di-2-ethylhexyl Phthalate: An Overview. *BioMed Research International*, *2018*, 1–10.

Wang, J., Liu, H., Kou, X., Zhang, Y., Wang, Y., Chen, C., Xiang, Z., Wang, X., Su, C., & Liu, Y. (2024). Toxic effects of DEHP and MEHP on gut-liver axis in rats via intestinal flora and metabolomics. *iScience*, *27*(11), 111135.

6th International Conference on Building Energy and Environment
Eindhoven University of Technology, The Netherlands
6 - 10 July 2025

A Study on the Automated Assessment of Workers' Health Impacts from Construction Noise using GPT

Juyeon Park [1], Kyungseok Oh [2], Yewon Hwang [3], Hyeonggyun Kim [4], Kwangbok Jeong [5*]

[1]Graduate Research Assistant, Deep Learning Architecture Research Center, Department of Architectural Engineering, Sejong University, Seoul, 05006, Republic of Korea, jupark0726@sju.ac.kr
[2]Graduate Research Assistant, Deep Learning Architecture Research Center, Department of Architectural Engineering, Sejong University, Seoul, 05006, Republic of Korea, ogs8608@sju.ac.kr
[3]Graduate Research Assistant, Deep Learning Architecture Research Center, Department of Architectural Engineering, Sejong University, Seoul, 05006, Republic of Korea, hyw1123@sju.ac.kr
[4]Graduate Research Assistant, Deep Learning Architecture Research Center, Department of Architectural Engineering, Sejong University, Seoul, 05006, Republic of Korea, hgkim@sju.ac.kr
*[5]Associate Professor, Deep Learning Architecture Research Center, Department of Architectural Engineering, Sejong University, Seoul, 05006, Republic of Korea, kbjeong7@sejong.ac.kr (*CORRESPONDING AUTHOR)*

SUMMARY
In general, the range of construction noise is from 80 dBA to 120 dBA, which causes construction workers to have health problems such as noise-induced hearing loss (NIHL). This study proposes a framework capable of assessing construction noise using a generative pre-trained transformer (GPT) model and supporting field managers' decision-making. This framework is intended to evaluate whether to exceed the standard of a time-weighted average (TWA) and assess the human health impact of noise-induced hearing loss (HHIN). The case study confirms that the proposed framework can be used to calculate the TWA level and HHIN of occupational noise in construction, based on which an occupational noise assessment report can be generated. The results of this study are expected to support field managers' decision-making, manage workers' safety on construction sites, and contribute to reducing the incidence of NIHL.

Keywords: Construction worker, Occupational noise exposure, Noise-induced hearing loss, Generative pre-trained transformer

1. INTRODUCTION

Construction noise levels range from 80 dBA to 120 dBA, which are higher on average than the occupational noise exposure standard (i.e., 90dBA) according to the Occupational Safety and Health Administration (OSHA) (Lee et al., 2019). When workers are continually exposed to noise above the occupational noise exposure standard, they are at risk of developing noise-induced hearing loss (NIHL) (Burella et al., 2021). NIHL is a hearing impairment that occurs due to continuous exposure to sources of loud noise. In 2022, workers' health examinations were conducted in South Korea, and the results showed that NIHL accounted for 98.2% of occupational diseases (Ministry of Employment and Labor, 2022). Moreover, since NIHL causes permanent hearing loss, precautionary measures need to be taken. However, most previous studies on construction noise focused on noise assessments and analyses of noise impacts on workers (Hong et al., 2022; Hong et al., 2023). Therefore, study is needed to reduce workers' health impacts through the practical management of construction sites.

Recently, various studies using a generative pre-trained transformer (GPT) model developed by OpenAI have been conducted in the construction industry. Saka et al.(2024) suggested that the GPT model be used to evaluate compliance with construction-related regulations (i.e., safety procedure, design guidelines) and generate a report from the results to simplify field managers' decision-making process. In this regard, this study seeks to propose a framework for assessing construction noise using the GPT model and supporting field managers' decision-making based on the assessment results.

2. GPT-BASED OCCUPATIONAL NOISE ASSESSMENT MODEL DEVELOPMENT

The GPT-based model proposed in this study is designed to analyze noise at a construction site and assess compliance with legal regulations and workers' health impacts. Accordingly, it aims to automatically perform the following tasks: (i) assessment of whether to exceed the time-weighted average (TWA) standard; and (ii) human health impacts of noise-induced hearing loss (HHIN) assessments. Finally, an assessment report, which includes measures to reduce workers' health impacts, can be automatically generated based on the derived TWA level and HHIN results.

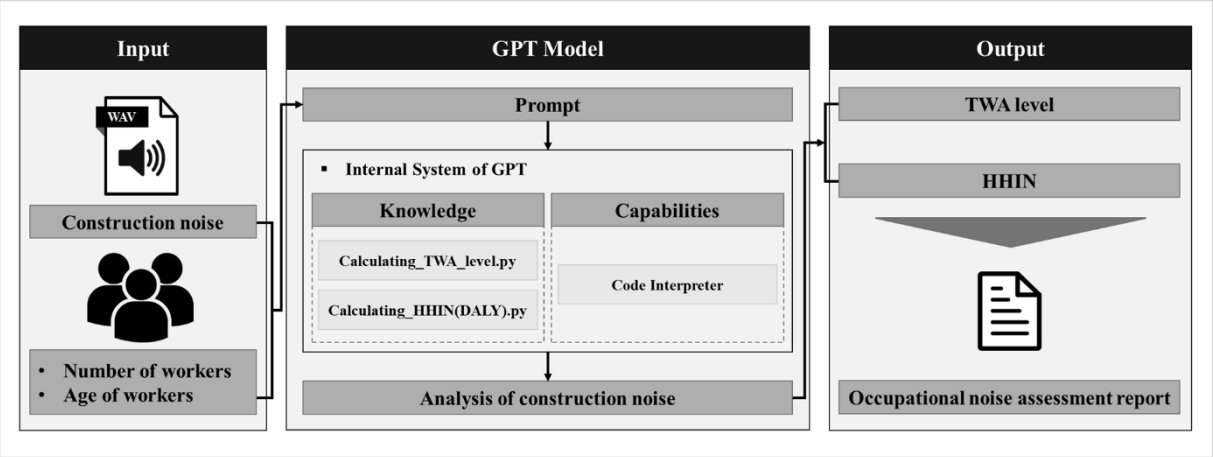

Figure 1. Framework for automated assessment of construction noise using GPT model

2.1. TWA level assessment method

Occupational noise exposure can be assessed using the TWA metric. TWA represents the value obtained by multiplying the noise measurement value by the occurrence time and then dividing that by 8 hours for a 8-hour workday. In this study, a standard for assessing workers' TWA levels was selected based on the *Exposure Standards for Chemical Substances and Physical Agents* of the Ministry of Employment and Labor. The standard requires that the TWA level not exceed 90 dBA for 8 hours, and applies a 5 dBA exchange rate. The TWA level can be calculated using Eq. (1). Here, *Dose* is the cumulative noise exposure level calculated by comparing the noise exposure level of workers with the acceptable noise exposure level.

$$TWA = 16.61 \log_{10}\left(\frac{Dose}{100}\right) + 90 \quad (1)$$

When the TWA level exceeds 90 dBA, the allowable noise exposure time (T_{allow}) for continuous exposure to noise above the standard is calculated using Eq. (2). Here, *L* is the noise level in the noise exposure section, and *ER* can be applied with 5 dBA in accordance with the standards of South Korea.

$$T_{allow} = \frac{8}{2^{(\frac{L-90}{ER})}} \quad (2)$$

2.2. HHIN assessment method

The workers' HHIN is calculated using the Disability-Adjusted Life Year (DALY) index. DALY is a value that considers both health loss due to disability and life loss due to premature mortality and can be calculated using Eq. (3) (Hofstetter et al., 2005). Here, *DALY* is HHIN, N_i is the number of workers in age group *i*, ER_i is the estimated excess risk of age group *i*, and *DW* is the disability weight. The *DW* value is applied with 0.192, which is the disability weight of NIHL based on the Korean standard (Mathers et al., 2003).

$$DALY = \sum_i (N_i \times ER_i \times DW) \quad (3)$$

ER represents the percentage value of additional risk caused by noise exposure in a specific age group. *ER* can be estimated based on the A-weighted noise exposure level normalized to an 8-hour working day ($L_{EX,8h}$). The estimated excess risk is defined differently depending on the noise exposure level and increases as the age group increases (Li et al., 2016). However, when $L_{EX,8h}$ is less than 85 dBA, the estimated excess risk of all age groups is calculated at 0. In other words, when $L_{EX,8h}$ is less than 85 dBA, HHIN does not occur.

3. CASE STUDY

A case study was carried out to verify the performance of the GPT model. To do this, construction noise was measured in three areas (i.e., zone A, B, and C) on the construction site, and information on the number of workers and age groups was obtained from daily construction logs.

The case study results are as follows. First, the TWA level was the lowest at 82.13 dBA in zone A and did not exceed the TWA standard (i.e., 90 dBA). On the other hand, the TWA levels of zones B and C were 97.23 dBA and 95.74 dBA, respectively, which exceeded the TWA standard. Second, the HHIN of workers were 0.1247 DALY and 0.1559 DALY, respectively, in zones B and C. However, it was 0 in zone A, where the TWA level of workers was below the standard (i.e., 90 dBA) (refer to Table 1). Therefore, HHIN did not occur in areas where the TWA level did not exceed the standard, but HHIN occurred in areas where the TWA level exceeded the standard. Third, an occupational noise assessment report was generated based on the construction noise assessment results. The report includes measures for regulatory compliance in areas where the TWA level is exceeded. For example, when continuous exposure to noise above the legal regulatory standard (i.e., 90 dBA) occurs in zones B and C, T_{allow} shall not exceed 2.9 hours (i.e., zone B) and 3.6 hours (i.e., zone C), respectively. This allows field managers to identify areas where the TWA standard is exceeded based on the occupational noise assessment report and take measures for regulatory compliance.

Table 1. GPT model-based construction noise assessment results

Zone	TWA level (dBA)	HHIN (DALY)	T_{allow} (hr)
A	82.13	-	-
B	97.23	0.1247	2.9
C	95.74	0.1559	3.6

Note. HHIN is the human health impact of noise-induced hearing loss; and T_{allow} is the allowable noise exposure time.

The GPT-based model helped assess occupational noise to calculate workers' TWA level and HHIN and generate an occupational noise assessment report that includes measures to reduce impacts on workers' health. This confirms the potential of the GPT model as an initial model for automated assessment of workers' health impacts from construction noise.

3. CONCLUSION

To reduce workers' health impacts from construction noise, this study proposed a framework for assessing and managing occupational noise based on a GPT model. To verify the performance of the model, a case study was carried out using actual construction noise. The results confirmed that the GPT model is capable of calculating the TWA level and HHIN of occupational noise, based on which an occupational noise assessment report can be generated. It is expected that the results of this study can be used as basic data for monitoring construction noise regulations and automating noise management.

ACKNOWLEDGEMENTS

This research was supported by the National Research Foundation of Korea (NRF) funded by the Ministry of Science and ICT (No. RS-2024-00336441).

REFERENCES

Burella, G., & Moro, L. (2021). A comparative study of the methods to assess occupational noise exposures of fish harvesters. Safety and health at work, 12(2), 230-237.

Ministry of Employment and Labor. (2022). Results of 2022 Workers' Health Examination. Public of Korea: Ministry of Employment and Labor.

Ministry of Employment and Labor (MOEL). Exposure limits for chemical substances and physical agents (MoEL Public Notice No. 2020-48).

Hofstetter, P., & Müller-Wenk, R. (2005). Monetization 18of health damages from road noise with implications for monetizing health impacts in life cycle assessment. Journal of Cleaner Production, 13(13–14), 1235–1245.

Hong, J. Y., Lam, B., Ong, Z. T., Ooi, K., Gan, W. S., & Lee, S. (2022). A multidimensional assessment of construction machinery noises based on perceptual attributes and psychoacoustic parameters. Automation in Construction, 140, 104295.

Hong, J., Choi, J., Lee, J., Cho, S., Hong, T., Han, S., ... & Lee, D. E. (2023). Virtual reality-based analysis of the effect of construction noise exposure on masonry work productivity. Automation in Construction, 150, 104844.

Lee, S. C., Kim, J. H., & Hong, J. Y. (2019). Characterizing perceived aspects of adverse impact of noise on construction managers on construction sites. Building and Environment, 152, 17-27.

Li, X., Song, Z., Wang, T., Zheng, Y., & Ning, X. (2016). Health impacts of construction noise on workers: A quantitative assessment model based on exposure measurement. Journal of Cleaner Production, 135, 721-731.

Mathers, C. D., Bernard, C., Iburg, K. M., Inoue, M., Fat, D. M., Shibuya, K., Stein, C., Tomijima, N., & Xu, H. (2003). Global Burden of Disease in 2002: data sources, methods and results.

Saka, A., Taiwo, R., Saka, N., Salami, B. A., Ajayi, S., Akande, K., & Kazemi, H. (2024). GPT models in construction industry: Opportunities, limitations, and a use case validation. Developments in the Built Environment, 17, 100300.

6th International Conference on Building Energy and Environment
Eindhoven University of Technology, The Netherlands
6 - 10 July 2025

Measurement of emitted liquid aerosols from an evaporative humidifier

Jianbo Yang [1], Feng Wang[2], Tengfei (Tim) Zhang [1,3,*]

[1]*Tianjin University, Tianjin, China, jianboyang@tju.edu.cn*
[2]*The Hong Kong Polytechnic University, Hong Kong, China, f.wang@polyu.edu.hk*
[3]*Dalian University of Technology, Dalian, China, timzhang@tju.edu.cn*

SUMMARY
Evaporative humidifiers are widely used to humidify the mechanically ventilated air. To minimize the probable contamination, an evaporative humidifier shall have the emitted liquid aerosols as few as possible. However, the liquid aerosol emissions from an evaporative humidifier are unclear so far. This investigation measured the liquid aerosol concentrations, inferred the particle/droplet emission rates, and examined the particle size spectrum. The particle emission rates in the humidifier above the packing, inside the packing, and below the packing, respectively, were quantified. Impacts of some operating parameters on the particle emissions were evaluated. The results revealed that most of the emitted liquid aerosols were from below the packing, and only a few from above the packing and few from the packing inside. A higher water circulation rate or a higher water dripping height results in increase of the particle emission rate and a higher percentage of the particles larger than 0.5 μm.

Keywords: evaporative humidifier, droplet emission, liquid aerosols, particle size spectrum, measurement

1. INTRODUCTION

Low-humidity indoor air may induce eye irritation, nasal allergy, dry throat and other non-specific syndrome symptoms (Wolkoff, 2018; Byber et al., 2021). Evaporative humidifiers are widely used to humidify the mechanically ventilated air for their simplicity, low cost, and ease for use. An evaporative humidifier comprises components of water distributor, packing, reservoir, and pump for water circulation. The air for humidification passes through the packing of the humidifier, which evaporates water into vapor. The dripped water from water distributors colliding with the packing, the air blowing the wet packing, and the water dripping into the reservoir, may generate droplets and their nuclei. In case the water for humidification is contaminated, the emitted droplets and their nuclei may contain pathogens (Strindehag et al., 1991; Lee et al., 2012; Hamilton and Iii, 2018). Consequently, an evaporative humidifier shall have the emitted droplets as few as possible, while maintaining humidification of the air majorly from evaporation of the water film inside the packing. However, the emitted liquid aerosol numbers and the particle size spectrum of an evaporative humidifier remain unclear so far. The exact emission of the droplets in different components/regions of the humidifier and impacts of the operating parameters to the emitted droplets are unknown either.

2. METHODS

2.1 Experimental test mockup and measurement instruments

This investigation conducted tests to measure the droplet or droplet nuclei emission rates and size spectrum and visualize the droplet emissions. Fig. 1 presents an evaporative humidifier for study. The multiple water distribution heads spray water to the packing below. The water inside the packing streams down and forms the water film, which is swept by the horizontal airflow from the ventilating duct. The unevaporated water drips down to the reservoir and subsequently is pumped to the water distribution heads for next evaporation cycle.

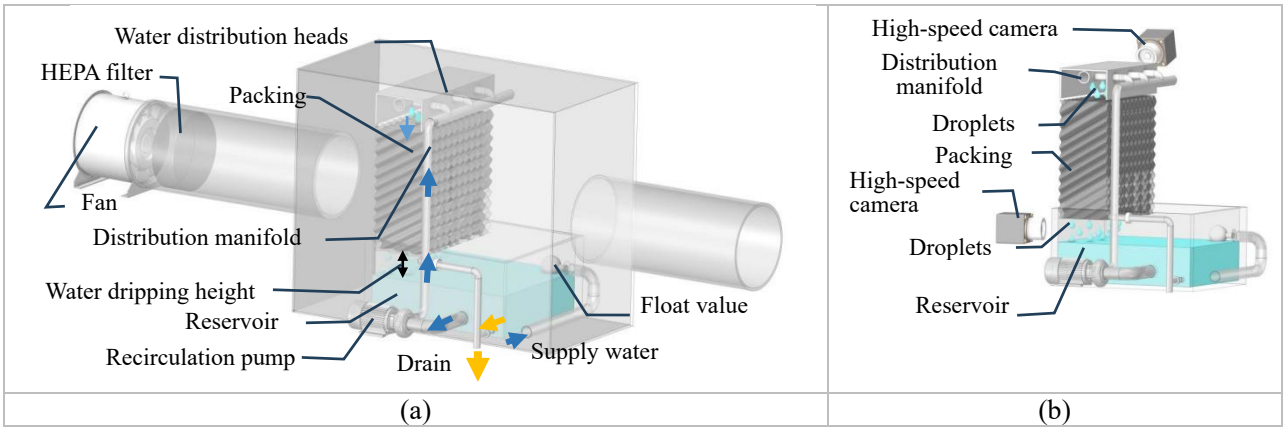

Figure 1. Schematic diagram of an evaporative humidifier for study: (a) overview of the test mockup and each individual component, (b) positioning of a high-speed camera for photographing the droplet emissions.

The tested humidifier has dimensions of 55 × 25 × 45 cm. The humidifier adopts the CELdek cellulose as the evaporation medium of the packing. The sizes of the packing are 25 × 10 × 25 cm, with 3 cm between the water distribution heads and the packing's upper rim. The humidifier is connected to circular ducts with a diameter of 11 cm. An axial fan with adjustable frequency mobilizes the ventilated air passing through the humidifier. To mitigate inference of the ambient aerosols to the tests, a high-efficiency particulate air (HEPA) filter is incorporated in upstream of the fan, thereby ensuring that the drawn air into the test humidifier are nearly ambient-particle free.

The number concentrations of the liquid aerosols were measured in downstream of the humidifier inside the duct. An optical particle sizer (type: 3330; TSI, USA) was adopted for measuring the particle concentrations and examining the size spectrum. The particle sizer counted particles in 16 bins with the particle size ranging from 0.3 to 10 μm. A high-speed camera (type: acA2000–340 km; Basler, Germany) was adopted to observe the splashed water and the generated droplets above the packing, the sprayed water streaming into the packing, and dripping of the water from the bottom packing to the reservoir, as shown in Fig. 1(b). Hence, the camera was positioned either slightly above the water distribution manifold or below the packing but higher than the water surface. During tests, the ventilation volumetric rate was measured by an anemometer (type: 425; TESTO, Germany). The ventilated air temperature and humidity were monitored by a temperature and humidity datalogger (type: 174H; TESTO, Germany).

2.2 Inference of the droplet nuclei emission rates and overview of the measurement cases

With the measured particle concentrations, the particle emission rates can be inferred. The governing equation of the particle concentrations in downstream of the humidifier can be cast as:

$$\frac{dC}{dt} = \frac{E}{V} + P \cdot \alpha \cdot C_{out} - (\alpha + k)C \quad (1)$$

where C is the temporal particle concentration in downstream of the humidifier, #/cm^3; t is time, s; E is the particle emission rate, #/s; V is the void volume of the humidifier, m^3; P is the particle penetration rate from the outside to the humidifier; α is the air exchange rate of the humidifier, s^{-1}; k is the particle deposition loss rate, s^{-1}. The particle emission rate, E, can be obtained by integrating Eq. (1) over time.

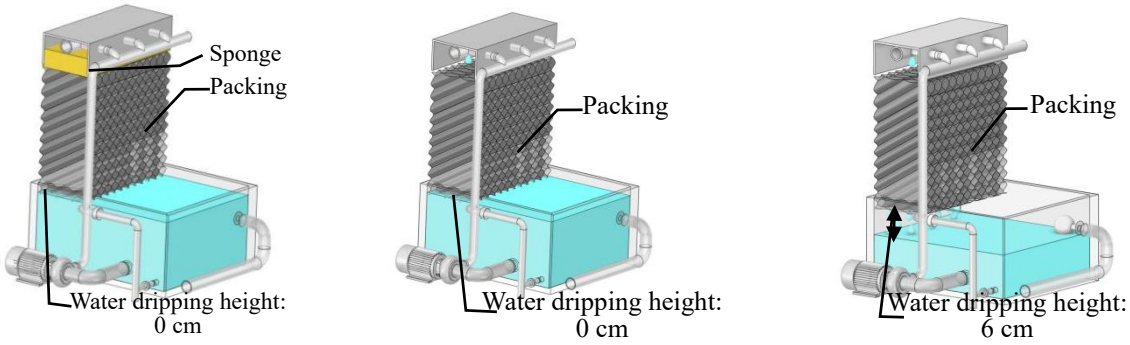

(a) Case 1 (b) Case 2 (c) Case 3

Figure 2. Schematic diagram of measurement scenarios for inferring the particle emission rates in different regions of the humidifier: (a) from only the packing inside in Case 1, (b) from both above and inside the packing in Case 2, (c) from above, inside, and below the packing in Case 3.

Table 1 Operating parameters of the evaporative humidifier for inferring the particle emission rates from different regions of the humidifier

Case with particle emission in different regions	Water circulation rate (L/h)	Water dripping height (cm)	Ventilated air velocity (m/s)
Case 1: inside the packing (with sponge filled above the packing), as shown in Fig. 2(a)	60	0	1.0
Case 2: above and inside the packing, as shown in Fig. 2(b)	60	0	1.0
Case 3: above, inside and below the packing, as shown in Fig. 2 (c)	60	6	1.0

In principle, droplets can be emitted from different regions of the humidifier, i.e., above the packing, inside the packing, and below the packing. Fig. 2 presents the schematics to illustrate the particle emissions from different regions of the humidifier in three cases. Table 1 presents detailed operating parameters of the three cases. All of the three operating cases were maintained with the same ventilating velocity of 1 m/s inside the ventilating duct and the same water circulation rate of 60 L/h. In Cases 1 and 2, the packing bottom was immersed into the reservoir, so that the water dripping height was zero. Note that there was nearly no water splashing above the packing in Case 1 due to the buffering by the filled sponge layer. Case 3 corresponded to the ordinary operation of an evaporative humidifier with the water dripping height of 6 cm. Assume that the particle emissions in different regions of the humidifier are repeatable and do not vary with the adjusted conditions in other regions. Then the particle emission rates inside the packing can be obtained from Case 1, the emission rates above the packing can be obtained by subtracting Case 1 from Case 2, and below the packing by subtracting Case 2 from Case 3.

It is intuitive that different water circulation rates, water dripping heights, and ventilated air velocities may affect the droplet emission rates. To evaluate impact of each individual parameter on the droplet emissions, only one parameter was varied while maintaining the other two operating parameters unchanged, as shown in Table 2. The water circulation rate was varied from 10 to 60 L/h with an increasing interval of 10 L/h, the water dripping height from 0 to 6 cm with an increasing interval of 1 cm, and the ventilated air velocity from 0.4 to 2 m/s with an interval of 0.4 m/s. In these test cases, both the particle emission rates and the particle size spectrum were examined.

Table 2 Variations of some operating parameters of the evaporative humidifier for evaluating their impacts on the droplet emission rates

Variable	Water circulation rate (L/h)	Water dripping height (cm)	Ventilating air velocity (m/s)
Water circulation rate	10-60	6	0.4
Water dripping height	60	0-6	0.4
Ventilating air velocity	60	6	0.4-2.0

3. RESULTS AND DISCUSSION

This section presents the measured temporal particle concentrations and the inferred droplet emission rates in a typical case. Then the inferred droplet emission rates in different regions of the humidifier are presented. Finally, impacts of some operating parameters of the humidifier to the droplet emissions are addressed.

3.1 Temporal particle concentrations and droplet emission rates in a typical case

A representative operating case with the water circulation rate of 60 L/h, the water dripping height of 5 cm above the reservoir, and the ventilating velocity of 1 m/s, was selected to analyze the measured particle concentrations and the inferred droplet emission rates. This case was quite similar to Case 3 in Table 1 but with a slightly lower water dripping height.

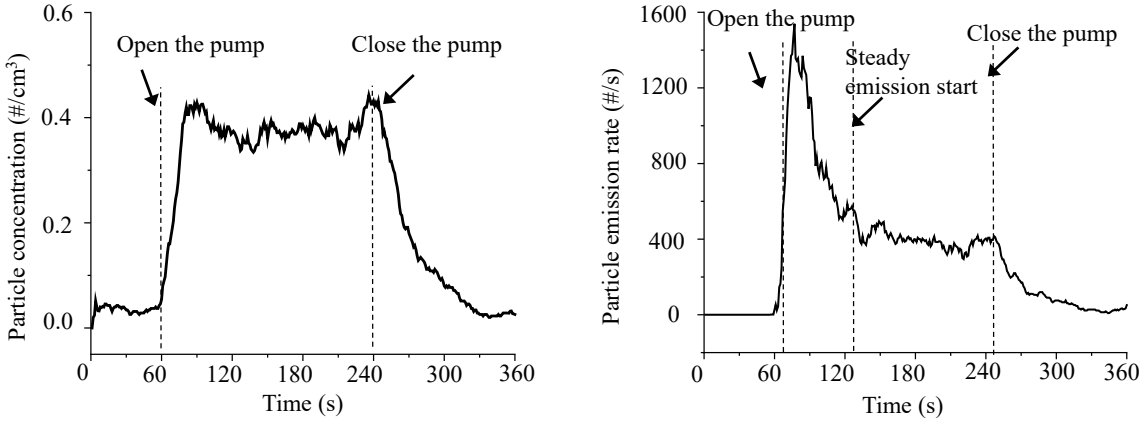

(a) Particle concentration (b) Particle emission rate

Figure 3. Measured particle concentrations and inferred particle emission rates in a typical case with the water circulation rate of 60 L/h, the water dripping height of 5 cm above the reservoir, and the ventilating velocity of 1 m/s.

Fig. 3(a) presents the measured temporal particle concentrations in downstream of the humidifier. The pump for water circulation was switched on at t = 60 s and switched off at t = 240 s. Before the pump was switched on, the average particle concentration was approximately 0.037 #/cm^3, which implies there were some of the leaked particles from the HEPA filter or some of the respuspended particles from the duct's inner surfaces or the humidifier. Once the pump was switched on at t = 60 s, the water was started for circulation. It took approximately 5 s for the water in the reservoir to be pumped to the water distributor. Then the water was sprayed from the multiple distribution heads to the packing and some of the water was splashed but finally streamed into the packing. The water started to drip down to the reservoir at t = 75s and then the full water circulation cycle was established. The recorded particle concentration was rapidly increased from 0.037 #/cm^3 at t = 60 s to 0.43 #/cm^3 at t = 80 s. After t = 120 s the concentrations fluctuated slightly in surrounding to the average value of 0.35 #/cm^3. At t = 240 s, the pump was shut off and the concentration started to decrease gradually to the slightly over the background particle concentration.

Fig 3(b) presents the inferred temporal droplet emission rates from Eq. (1). The emission rate was zero until t = 65 s. The particle emission rate was sharply increased to the peak emission rate of 1530 #/s at t = 65 s. Then the emission rate dropped gradually to approximately 560 #/s at t = 120 s. The sudden increase of the droplet emission rate might be due to the splashing of the water in the initially dry packing, which contained nearly no particle inside and thus promoted the particle emission. Once the water circulation was established, the dropping droplets and the formed water film inside the packing might capture some of the airborne particles to the circulated water, which refrained the particle emission somehow. The particle emission rates tended to be stabilized since t=120 s. The averaged particle emission rate was approximately 410 #/s, which can be deemed as the relatively steady particle emission rate in this case.

3.2 Emitted droplets in different regions of the humidifier

Similar to the measurements and data operations as in Section 3.1 above, the average particle emission rates were obtained for all three cases shown in Fig. 2 and Table 1. Fig. 4(a) presents the droplet emission rates in different regions of the humidifier. The droplet emission rate inside the packing was close to 25 #/s, which was nearly negligible. This was because the ventilated air swept the water film inside the packing gently. The quite few generated droplets were mainly from the occasionally formed water drips in some intersections of water flow channels inside the packing. The droplet emission rate above the packing was inferred to 70 #/s, due to the sprayed water from the water distribution heads which was splashed once colliding with the upper rims of the packing. In contrast, the droplet emission below the packing was closed to 330 #/s. The huge number of emitted droplets below the packing was due to interaction of the dripping water from the packing with the water surface inside the reservoir.

Fig. 5 presents interaction of dripped water from the packing with the water inside the reservoir. The falling water from the packing formed water drips in different sizes due to the surface tension at t=1 ms. The large water drip hit the water surface and formed a hemispherical cavity in the water and some of the water was splashed at t = 4 ms. The cavity was contracted and broken, resulting in upward ejection of a sharp water jet at t = 12 ms. The upper section of the up-moving water jet

was broken and several secondary droplets were ejected at t = 16 ms. The jet lost momentum and was broken into more secondary droplets at t = 20 ms. The falling water drips also collided with the secondary droplets. The hitting, splashing, bubble breaking, jet breaking, collision, impacting, etc., were responsible for emission of water droplets, some of which were later evaporated into the droplet nuclei for airborne transmission.

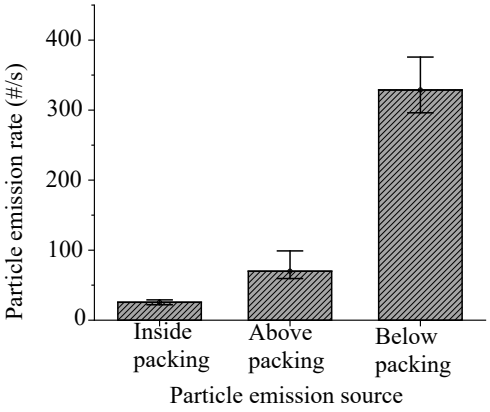

(a) Particle emission rates in different regions

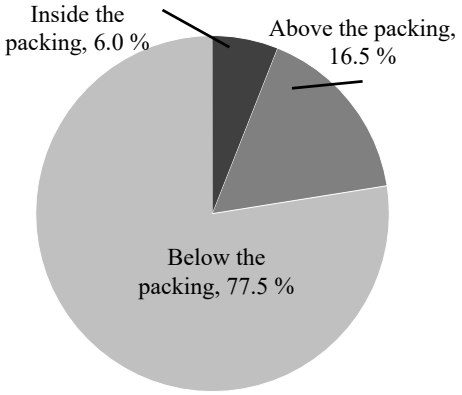

(b) Proportion of particle emission in different regions

Figure 4. Particle emission rates in different regions of the humidifier under the operating conditions with the water circulation rate of 60 L/h, the water dripping height of 6 cm above the reservoir, and the ventilating velocity of 1 m/s.

Fig 4(b) shows the emitted droplet nuclei below the packing possessed 77.5% of the total emission, which was the most contributor of the particle (droplet nuclei) source. Above the packing, the emitted particles possessed 16.5%. The emitted particles from the packing inside were quite few, possessing only 6.0 %.

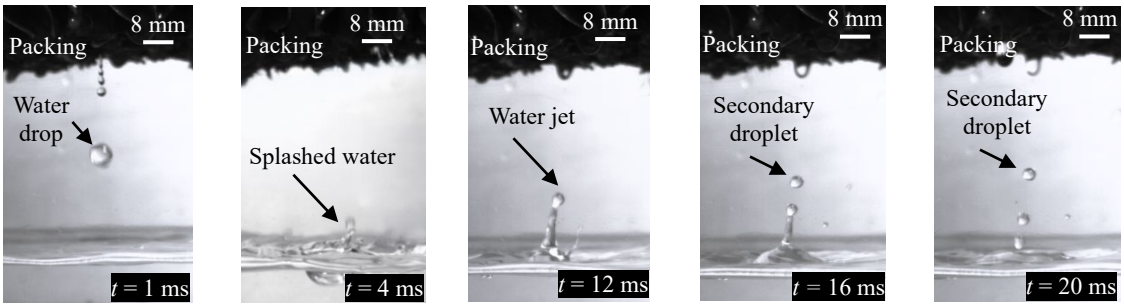

Figure 5. Images of interaction of the dripped water from the packing with the water in the reservoir at different time.

3.3 Impacts of operating parameters to the droplet emission rates

Fig. 6 presents variation of the particle emissions with the water circulation rate. With increase of the water circulation rate, the particle emission rate steadily increased, as shown in Fig. 6(a). The humidifier produced 130 #/s at the water circulation rate of 10 L/h, whereas the humidifier at 60 L/h produced 600 #/s, which was 4.62 times that of 10 L/h. Fig. 6(b) shows with increase of the water circulation rate, the percentages of both supermicron particles and the particles between 0.5 to 1 μm steadily increased, while the percentage of the particles between 0.3 to 0.5 μm steadily

decreased. With an increasing water circulation rate, impact/collision of the dripping water with the water inside the reservoir also steadily increased, as shown in Fig. 6(c). The dripping water's impact/collision with the water surface resulted in a thick jet and emission of single secondary droplets regardless of the water circulation rate. The increased water circulation rate also led an increase of the proportion of particles in sizes between 0.5-2.0 μm.

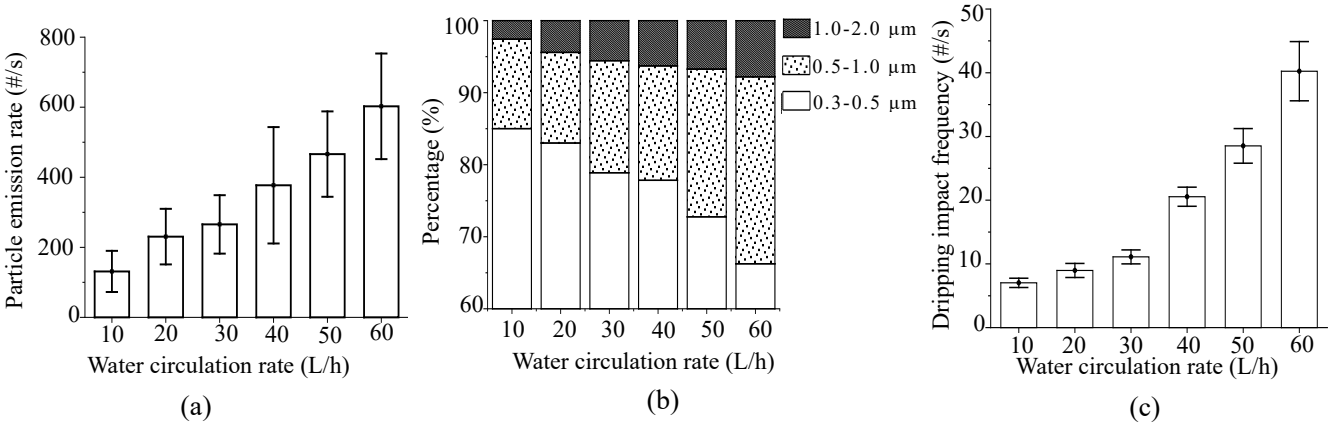

Figure 6. Variation of the particle emissions with the water circulation rates from 10 to 60 L/h under the fixed water dripping height of 6 cm and the fixed ventilating air velocity of 0.4 m/s: (a) particle emission rates, (b) particle spectrum, (c) impact/collision frequency of the dripping water from the packing with the water inside the reservoir.

Fig. 7 presents variation of the particle emission rate with increase of the water dripping height. Impacts of the water dripping height to both the particle emission rates and the particle spectrum resemble those of the water circulation rate. The particle emission rates and the particle percentages for both the supermicron particles and the particles between 0.5 to 1 μm steadily increased with the water dripping height. This was because with increase of the water dripping height, the water drips had higher energy and inertia to impact with the water inside the reservoir, which created stronger water jets and more secondary droplets in larger sizes. Notably, at the water dripping height of zero, only the submicron particles were emitted.

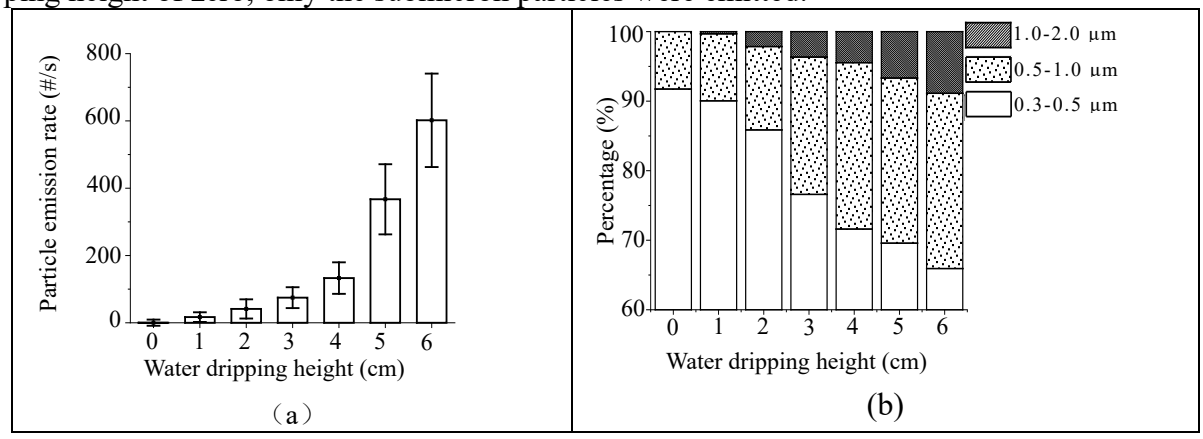

Figure 7. Variation of the particle emissions with the water dripping height of 0-6 cm under the fixed water circulation rate of 60 L/h and the fixed ventilating air velocity of 0.4 m/s: (a) particle emission rates, (b) particle spectrum

Fig. 8 presents variation of the particle emissions with the ventilated air velocity. Both the particle emission rates and the size spectrum were nearly independent on the tested ventilated air velocity.

This was because the tested velocity was no higher than 2 m/s, which was quite gentle to shear the water film inside the packing to form droplets for particle emissions. Note that the air velocity inside the packing was much lower than inside the ventilating duct.

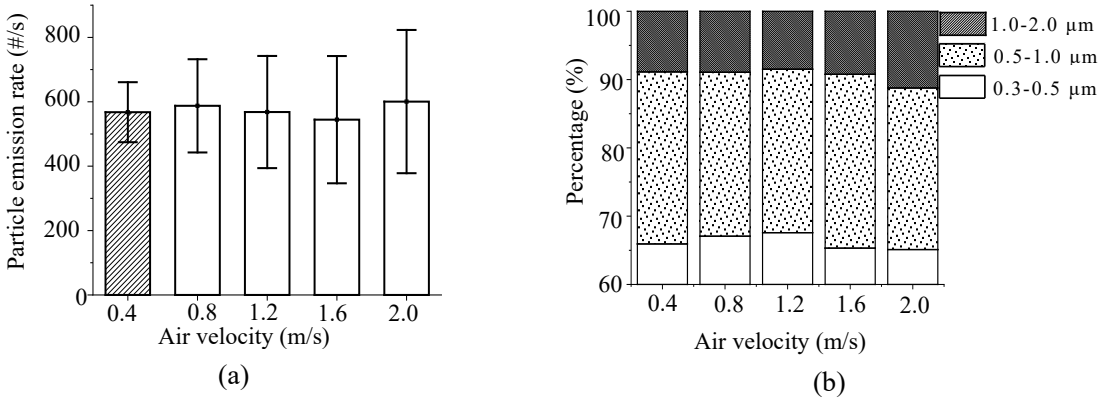

Figure 8. Variation of the particle emissions with the ventilated air velocity from 0.4 to 2 m/s under the fixed water circulation rate of 60 L/h and the fixed water dripping height of 6 cm: (a) particle emission rates, (b) particle spectrum.

4. CONCLUSIONS

This investigation measured the liquid aerosol concentrations, inferred the particle/droplet emission rates, and examined the particle size spectrum. The particle emission rates in the humidifier above the packing, inside the packing, and below the packing, respectively, were quantified. Impacts of some operating parameters of the humidifier on the particle emissions were evaluated. Based on the obtained results, the following conclusions can be drawn:

1. Most of the emitted liquid aerosols were from below the packing, and only a few from above the packing and few from inside the packing. The dripped water from the packing impacted with the water inside the reservoir, which generated secondary droplets in smaller sizes that may be transmitted in air after evaporation.
2. Both the water circulation rate and the water dripping height affected the particle emission rate and particle size spectrum in similar trends. A higher water circulation rate or a higher water dripping height resulted in increase of both the particle emission rate and the percentage of the particles larger than 0.5 μm.

REFERENCES

Byber, K., T. Radtke, D. Norbäck, C. Hitzke, D. Imo, M. Schwenkglenks, M. A. Puhan, H. Dressel, and M. Mutsch, 2021, Humidification of indoor air for preventing or reducing dryness symptoms or upper respiratory infections in educational settings and at the workplace: Cochrane Database of Systematic Reviews, v. 2021, no. 12, .

Hamilton, L. A., and J. O. F. Iii, 2018, Aerosolization of Mycobacterium avium and Mycobacterium abscessus from a household ultrasonic humidifier: Journal of Medical Microbiology, v. 67, no. 10, p. 1491–1495.

Lee, J. H., K. H. Ahn, and I. J. Yu, 2012, Outbreak of Bioaerosols with Continuous Use of Humidifier in Apartment Room: Toxicological Research, v. 28, no. 2, p. 103–106.

Strindehag, O., I. Josefsson, and E. Henningson, 1991, Emission of bacteria from air humidifiers: Environment International, v. 17, no. 4, p. 235–241.

Wolkoff, P., 2018, Indoor air humidity, air quality, and health – An overview: International Journal of Hygiene and Environmental Health, v. 221, no. 3, p. 376–390.

6th International Conference on Building Energy and Environment
Eindhoven University of Technology, The Netherlands
6 - 10 July 2025

Airflow diffusion characteristics and exhaust solutions for smoke discharged from kitchen into corridor in old residences in Shanghai

Zhuang Zhi[1], Gu Wen[2], Chen Yuming[3], Chang Tianxin[4], Ye Hai[5]

[1] *Tongji University, Shanghai, China, zhuangzhi@tongji.edu.cn*
[2] *Tongji Architectural Design Group Co., Ltd, Shanghai, China, 740512658@qq.com*
[3] *Tongji University, Shanghai, China, 2252478@tongji.edu.cn*
[4] *Tongji University, Shanghai, China, 19117172667@163.com*
[5] *Tongji University, Shanghai, China, yehai@tongji.edu.cn, corresponding author*

SUMMARY
Kitchen smoke is often directly exhausted into internal corridor for many typical old residential buildings in Shanghai China, which severely pollutes air quality and directly affects residents' daily lives. While prior studies and field measurements have identified the problem, existing approaches fail to address dynamic factors like seasonal thermal effects and vertical pollutant diffusion patterns. This study utilizes CFD simulations to analyse smoke behaviours, revealing that discharged smoke accumulates in upper corridor sections and stairwells, with lower-floor emissions disproportionately impacting higher floors. Winter's thermal stack effect accelerates upward diffusion, whereas summer conditions result in slower dispersion but higher average corridor pollutant concentrations. To deal with these issues, the retrofit by adding intake draft fans in the internal corridor is proposed and verified by simulation. This study will provide references for future kitchen smoke exhaust renovations in other old residential buildings in China.

Keywords: old residential buildings, cooking smoke pollution, kitchen smoke exhaust retrofit.

1. INTRODUCTION

The 19th National Congress of the Communist Party of China emphasized the importance of improving people's livelihoods and enhancing the living conditions and quality of life for residents in old residential areas. This is a crucial measure to ensure that people live and work in peace and share the fruits of reform and development (Luo, 2019). The renovation of old urban residential areas has evolved from local initiatives to a major national-level livelihood project. According to the Shanghai Statistical Yearbook, the total area of residential buildings in Shanghai was 699.91 million square meters by the end of 2019, with buildings over 30 years old accounting for about 29.8% of the total residential building area. Nearly 30% of residential buildings require renovation or updating (Shanghai Municipal Statistics Bureau, 2021). The kitchen smoke exhaust methods in old residential areas in Shanghai mainly have two categories: 1) direct exhaust through external wall openings, and 2) exhaust into internal corridor through external wall openings. Field measurements have shown that the second method, which discharges smoke directly into internal corridor, significantly increases the PM2.5 concentration in the corridors during cooking periods. In some cases, the peak concentration exceeds the national standard (GB3095-2012) by more than eight times, reaching severe pollution levels (Gu, 2021). So there is an urgent requirement to deal with this issue by taking retrofit measures. Due to the limited height of corridor in old residential buildings, installing exhaust ducts would further reduce the net height of corridor and also increase

flow resistance, making it difficult for smoke to be effectively exhausted. Therefore, this study proposes in-stalling intake/exhaust draft fans at the external windows of the internal corridor used for diluting or exhausting kitchen smoke. How to effectively carry out the retrofit design of the draft fan, it is necessary to investigate to better understand the airflow characteristics of smoke in corridor of residential buildings, and its impact on indoor air quality, which help to find the optimal retrofit proposal to minimize exposure risk.

Existing research mainly adopts the method combining numerical simulation and experimental verification, focusing on aspects such as the smoke diffusion mechanism, pollutant distribution characteristics, and ventilation optimization strategies. He et al. (2021) proposed a kitchen air quality evaluation method based on air age and ventilation efficiency, providing a theoretical framework for quantitatively evaluating ventilation performance. Regarding the smoke diffusion law, Guo et al. (2025) systematically revealed the dynamic diffusion patterns of particles under different cooking scenarios through the collaborative analysis of orthogonal experiments and CFD simulations, and optimized the ventilation system de-sign based on the window opening and closing conditions. Xu et al.(2024), through experimental research and orthogonal experimental design, explored the coupled action mechanism of ventilation modes and cooking methods on the PM2.5 con-centration distribution in the kitchen and adjacent rooms, and further quantified the human exposure risk. In addition, Chen et al. (2025) deeply explored the pollutant removal efficiency of kitchen hoods and natural ventilation openings under different seasonal conditions through CFD simulations, revealing the differential impacts of winter and summer ventilation strategies on the air flow organization and pollutant distribution. Although scholars have conducted a large amount of research on the problem of kitchen smoke diffusion, existing studies have rarely investigated the conditions when the smoke is exhausted into corridor in old residential buildings. Moreover, how to reasonably select the fan type, choose the fan installation location, and determine the fan control strategy are the issues that need to be determined.

Therefore, this paper utilizes computational fluid dynamics tool to simulate airflow distribution to further analyze the diffusion patterns and characteristics of cooking smoke in internal corridor under different cases, providing references and suggestions for retrofit proposal.

2. METHODOLOGY

2.1 Model Setup

Computational Fluid Dynamics (CFD) is a widely used tool for simulating various airflow-related scenarios such as optimization of kitchen ventilation. Its ad-vantages include the ability to simulate results for different settings by adjusting conditions. Researchers have used CFD to assess airflow in kitchens to support the exhaust system effectively during cooking while minimizing undesirable air-flow patterns and smoke dispersion (Zhou, 2016). Therefore, the simulation analysis in this study was conducted using Airpak 3.0 software, with the primary goal of investigating the impact of residential kitchen smoke on the air quality in corridor. A typical five-story residential building in an old residential area in Shanghai was selected for modeling. The building has a floor height of 3 meters, with the corridor located on the north side. The corridor was set as the computational domain, with all apartment doors assumed to be closed and windows facing the outdoor area open. Figure 1 shows the 3D model of the residential building.

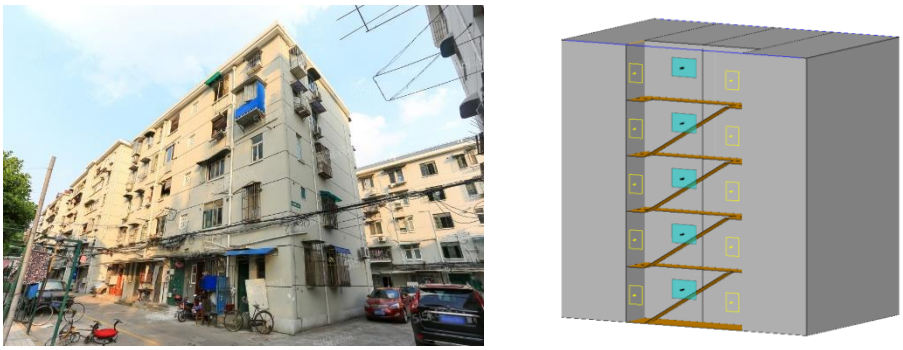

(a) (b)

Figure 1. 3D model of the residential building.

2.2 Model settings and case design

2.2.1. Current Scenario

There are two exhaust vents for two families on each floor. Based on market survey, the airflow rate of kitchen hoods currently sold on the market ranges from 16 m³/min to 21 m³/min. For this study, the airflow rate was set at 18 m³/min, with an exhaust vent area of 0.04 m², resulting in an exhaust velocity of 7.5 m/s. The temperature of the exhaust smoke was set at 30°C and the CO_2 was used as a representative pollutant due to its high relationship with smoke concentration(as shown in Figure 2) to analyze the airflow diffusion of pollutants based on field test (Gu, 2021). The outdoor CO_2 concentration was set at 400 ppm. The CO_2 concentration at the exhaust vent was set at 2000 ppm by field test, and the outlet was set as the windows on the outer side of each floor's corridor, with free outflow conditions. The effect of outdoor wind is not considered in this study. To study the impact of kitchen smoke exhaust on the corridor and the interaction between different floors, six simulation cases were set up, as shown in Table 1. The simulations were conducted for both winter and summer cases. The average outdoor temperature for winter was set at 4.2°C, and for summer, it was set at 31.2°C, based on Shanghai's typical outdoor temperatures.

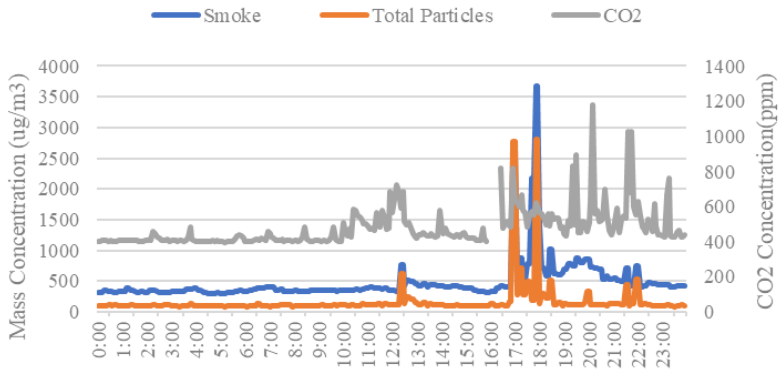

Figure 2. Pollutant concentrations relationships among somke, particles and CO_2 (Gu, 2021)

Table 1. Simulation cases for airflow distribution of current scenario.

Case No.	Definitions
C1	First-floor exhaust vents work
C2	Second-floor exhaust vents work
C3	Third-floor exhaust vents work
C4	Fourth-floor exhaust vents work

C5	Fifth-floor exhaust vents work
C6	All exhaust vents work on all five floors

2.2.2. Retrofit scenario

In order to effectively carry out the retrofit design of the draft fan, it is necessary to investigate factors such as the layout position, quantity, fan type and airflow capacity of the draft fan. Based on the above simulation results, smoke tends to accumulate in the area near the entrance stairwell and is difficult to diffuse out-ward due to the floor slab obstruction in winter. In summer, smoke diffusion is more uniform on both sides of the corridor. The draft fans can be installed at the external windows on east or west side or both sides of the corridor. It's better to use less fans. The airflow capacity of the fans can be referenced from the kitchen ventilation design standards, with air change rates between 40-60 times per hour, and the base airflow capacity is set at 0.5 m³/s. The worst smoke exhaust condition is selected for study, i.e. all the smoke exhaust vents work on all five floors. Therefore, the following cases are designed for simulation (as shown in Table 2), and the final solution can be determined by comparing the effectiveness of draft fans in different cases.

Table 2. Simulation cases for airflow distribution of retrofit scenario.

Case No.	Definitions
RP1	One intake fan at east side, fan airflow capacity 0.5000 m^3/s
RP2	One exhaust fan at east side, fan airflow capacity 0.5000 m^3/s
RP3	One intake fan at west side, fan airflow capacity 0.5000 m^3/s
RP4	One exhaust fan at west side, fan airflow capacity 0.5000 m^3/s
RP5	One intake fan at east side, one intake fan at west side, fan airflow capacity 0.5 m^3/s
RP6	One intake fan at east side, one exhaust fan at west side, fan airflow capacity 0.5 m^3/s
RP7	One exhaust fan at east side, one intake fan at west side, fan airflow capacity 0.5 m^3/s
RP8	One exhaust fan at east side, one exhaust fan at west side, fan airflow capacity 0.5 m^3/s
RC1	The best RP case with fan airflow capacity 0.125 m^3/s
RC2	The best RP case with fan airflow capacity 0.250 m^3/s
RC3	The best RP case with fan airflow capacity 0.500 m^3/s
RC4	The best RP case with fan airflow capacity 1.000 m^3/s

3. RESULTS AND DISCUSSIONS

3.1 Current scenario

3.1.1. Winter results

Figure 3 shows the pollutant concentrations on each floor at a height of 1.5 meters above the pedestrian area under different cases in winter. It is evident that the emission of pollutants on the current floor has a direct impact on the pollutant concentration of the floor above. When all five floors are operational, the fifth floor exhibits the highest concentration of pollutants, followed by the third, second, fourth, and first floors, in descending order. The analysis reveals that while pollutants increase progressively with each floor, the diffusion to the fourth floor is unique. The absence of a staircase on the fifth floor allows the smoke from the left side of the fourth floor to ascend rapidly to the fifth floor without lingering or accumulating on the fourth floor, resulting in a significantly higher concentration of pollutants on the fifth floor compared to the others. Both the second and third floors are subject to the obstruction of staircases, which causes pollutants to linger, leading to slightly higher concentrations than on the unobstructed fourth floor.

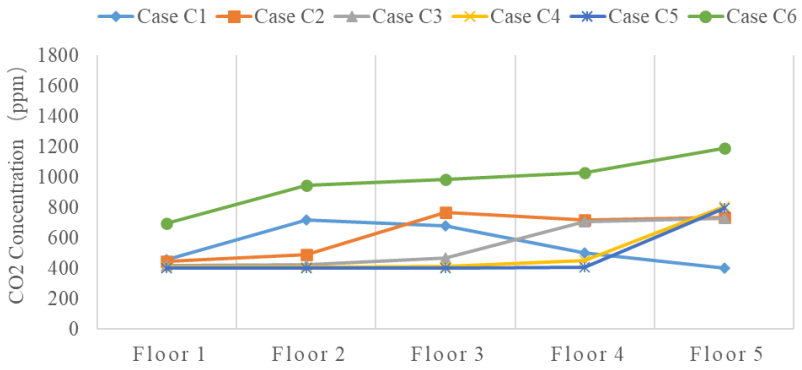

Figure 3. Pollutant concentrations at 1.5m above pedestrian area in winter

Figure 4 shows the pollutant concentration distribution in the corridor under these cases. The results indicate that kitchen smoke exhaust on the current floor affects the upper floors, with the most significant impact on the adjacent upper floor. The effect gradually weakens as the floor level increases. Due to the thermal stack effect, pollutants rise along the stairwell, with higher concentrations on the right side due to the stairwell's structure. The more exhaust vents are open on lower floors, the higher the pollutant concentration on upper floors. When all five floors' exhaust vents are open, the pollutant concentration on the fifth floor is 3.6 times higher than when only the current floor's vents are open.

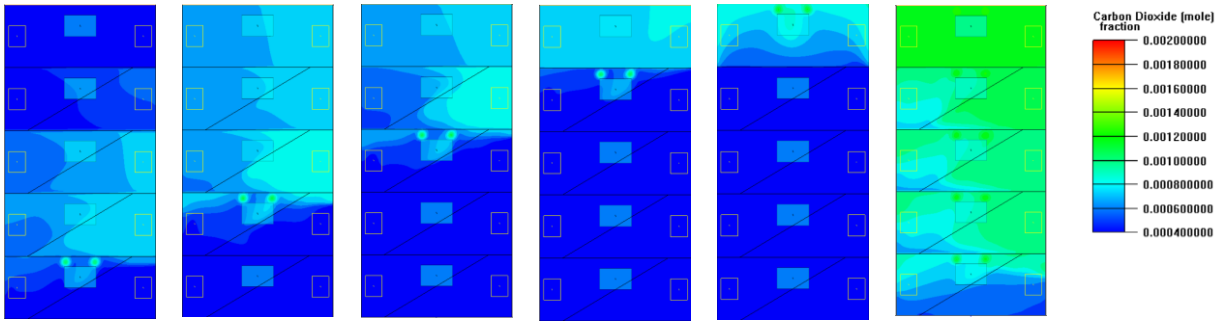

(a) Case C1 (b) Case C2 (c) Case C3 (d) Case C4 (e) Case C5 (f) Case C6

Figure 4. Pollutant concentration distribution in the corridor section in winter

3.1.2. Summer results

Figure 5 shows the pollutant concentrations on each floor at a height of 1.5 meters above the pedestrian area under different cases in summer. It can be seen that the emission of pollutants on the current floor exerts a direct influence on the pollutant concentration of the floor immediately above. The concentration of pollutants on the same floor exhibits a significant increase compared to that in the winter conditions. The main reason is attributed to the big temperature difference between the corridor and the outdoor environment during winter, which facilitates the diffusion and dilution of smoke due to the stack effect. Conversely, the temperature difference between the corridor and the outdoor environment is relatively small during summer, which reduce the dispersion of pollutants, leading to their accumulation and higher concentration levels within the building's interior spaces. From Figure 6, it can be observed that kitchen smoke exhaust on a given floor primarily affects the current floor and the floor above, with less noticeable thermal stack effects. The pollutant distribution across floors is more uniform in summer. The average pollutant

concentration across all floors is significantly higher in summer than in winter.

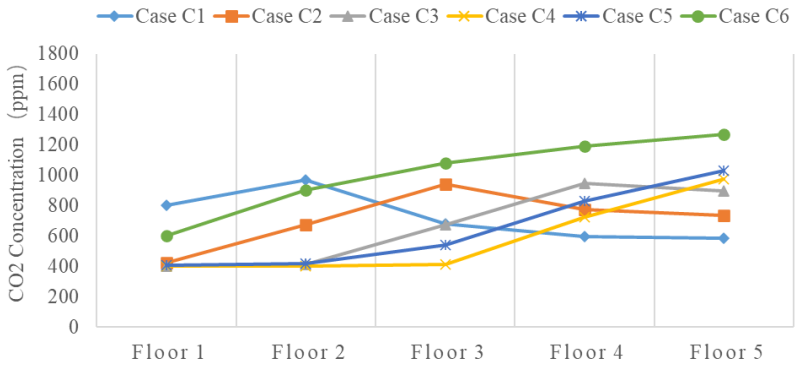

Figure 5. Pollutant concentrations at 1.5m above pedestrian area in summer

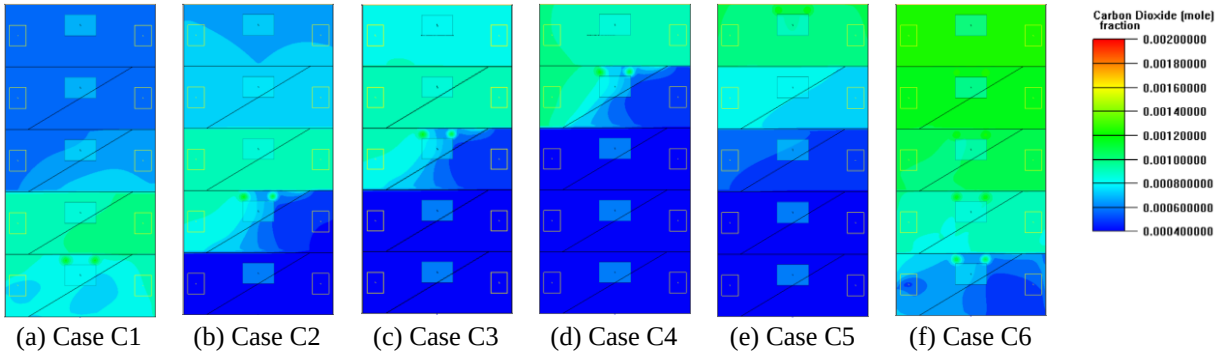

(a) Case C1 (b) Case C2 (c) Case C3 (d) Case C4 (e) Case C5 (f) Case C6

Figure 6. Pollutant concentration distribution in the corridor section in summer

3.2 Retrofit scenario

3.2.1. Effect of fan retrofit design

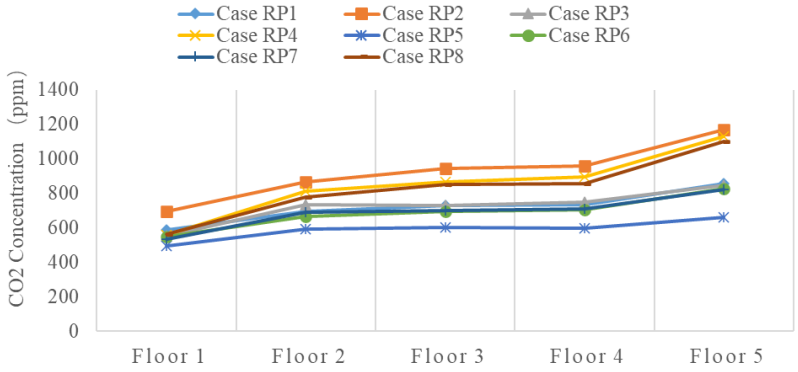

Figure 7. Pollutant concentration comparisons under different retrofit cases

Figure 7 compares the simulation results of pollutant concentrations under various cases, considering different fan positions, types, and quantities. From this figure, it can be observed that when only one fan is installed (cases RP1-RP4), the position of the fan has a small impact on the dilution of pollutants. Supply fans exhibit better pollutant dilution performance compared to exhaust fans, primarily because the fans are positioned in the middle of open windows, which

limits their ability to create effective suction. Comparing cases RP5-RP8, where two fans are installed, the best pollutant dilution effect is achieved when both fans are supply fans (Case RP5), showing a significant improvement over a single supply fan. However, when one of the fans is an exhaust fan, increasing the number of fans provides very little improvement in pollutant dilution. Therefore, the optimal retrofit solution (Case RP5) is to install supply fans on both sides of the corridor, as illustrated in Figure 8. This configuration introduces fresh outdoor air into the corridor, effectively diluting kitchen fumes, which are expelled through the central opening of the corridor.

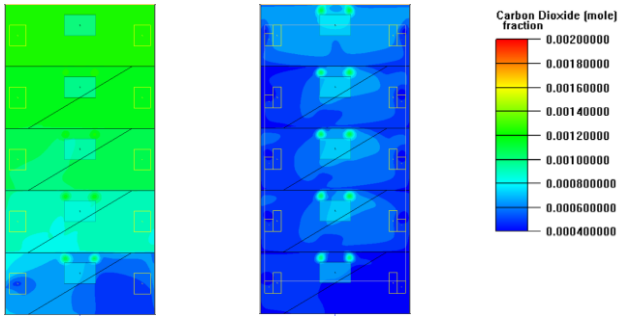

(a) Before retrofit (b) After retrofit

Figure 8. Pollutant concentration distribution in the corridor section for Case RP5

3.2.2. Effect of fan airflow capacity

The airflow rate of the fans affects pollutant dilution efficiency, fan energy con-sumption, and operational noise. Therefore, the pollutant removal efficiency under different airflow rates was compared. Figure 9 shows the simulation results of pollutant concentrations under various airflow rates. As the airflow rate increases, the steady-state pollutant concentration in the corridor significantly decreases, indicating that higher airflow rates improve dilution. However, this also leads to higher energy consumption and noise levels. Given that pollutant emissions in the corridor occur intermittently during cooking, the recommended airflow rate for the fans should not exceed 0.5 m³/s based on the calculation results.

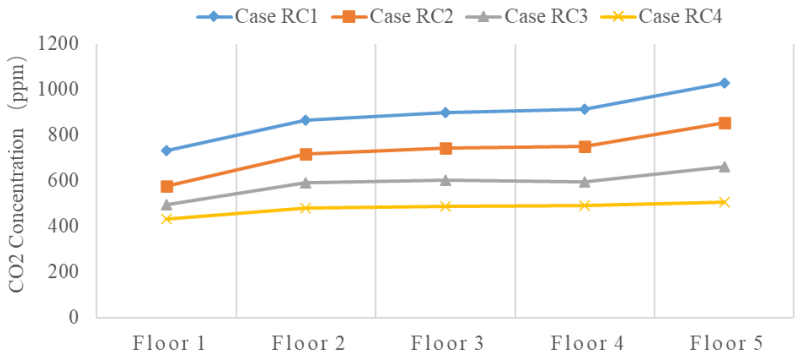

Figure 9. Pollutant concentrations on each floor after renovation under summer cases

Additionally, to further reduce energy consumption, considering the vertical distribution of pollutant concentrations, which increase with height, it is practical to install low-capacity fans on lower floors and high-capacity fans on upper floors. Furthermore, fan operation can be synchronized with the user-side kitchen hood or controlled using sensors for more efficient operation. PM2.5 or smoke sensors can be installed in the internal corridor. When the smoke

concentration exceeds a set threshold, the induced draft fans on the corresponding floor are activated. When the concentration falls below the threshold, the fans will be shut down.

5. CONCLUSIONS

This study investigates the real issue of direct kitchen exhaust emissions into the corridors of old residential buildings in Shanghai, which significantly impacts residents' quality of life and health. Therefore, this study uses simulations to analyze the dispersion patterns of pollutants within the corridors during both winter and summer seasons. Based on these findings, the retrofit proposal is given and verified. The main conclusions are as follows:The simulation results show that after being discharged into the internal corridor, kitchen smoke tends to linger in the upper part of the local floor and diffuse up-ward along the stairwell, with the most severe pollution occurring in the adjacent upper corridor. The more smoke exhaust on the lower floors, the greater the im-pact on the higher floors. In winter, due to the thermal stack effect, pollutants diffuse rapidly to the upper floors, while in summer, the diffusion is slower. However, the average pollutant concentration in the corridor is higher in summer than that in winter. To deal with these issues, the optimal retrofit solution by installing intake fans on both sides of the corridor is prosed and verified by simulation. This configuration introduces fresh outdoor air into the corridor, effectively diluting kitchen fumes, which are then expelled through the central opening of the corridor. The intake draft fans can be independently controlled based on the smoke concentration on each floor or linked to the kitchen hoods to ensure that the smoke con-centration remains low and does not adversely affect residents' lives. It is hoped that this study will provide references for future kitchen smoke exhaust renovations in old residential areas in Shanghai. The limitation of this study is that the simulation and analysis without considering the influence of the change of wind speed in the vertical direction of high-rise buildings on the effect of air flow distribution, which will be included in the future.

ACKNOWLEDGEMENTS

This work is supported by the Research Project of Shanghai Housing and Urban-Rural Development Commission: Study on renovation technology for direct exhaust of kitchen smoke in corridor of old residential buildings in Shanghai (No. 2024-005-005).

REFERENCES

Chen S.W., Chang C.Y., Chan Y.C., 2025. Assessing the impact of kitchen hoods and ventilation openings on indoor air quality post-cooking. Journal of Building Engineering 100, 111721.

Gu W., Wang Z., Zhuang Z.,2021. Investigation and field measurement of kitchen smoke exhaust in old residential areas in Shanghai. Residential Science and Technology 10, 53-57.

Guo Z., Li H., Feng G., et al., 2025. Investigation on inherent angle ventilation control of residential kitchen range hoods. Energy and Built Environment 6(3),432-447.

He H., Chen Z., Lv X., et al., 2020. Impact of the range hood fresh air system on the air quality in residential kitchens. Journal of Ningbo University 33(1), 110-115.

Luo C., Zheng X., Wang J.,2019. Research report on comprehensive improvement of old residential areas in Shanghai. Industry Orientation 12, 43-44.

Shanghai Municipal Statistics Bureau. Shanghai Statistical Yearbook 2021. China Statistics Press, 2021.

Xu X., Hu K., Zhang Y., et al.,2024. Experimental evaluation of the impact of ventilation on cooking-generated fine particulate matter in a Chinese apartment kitchen and adjacent room. Environmental Pollution 348, 123821.

Zhou B., Chen F., Dong Z.B., et al., 2016. Study on pollution control in residential kitchen based on the push-pull ventilation system. Building and Environment 107, 99-112.

6th International Conference on Building Energy and Environment
Eindhoven University of Technology, The Netherlands
6 - 10 July 2025

Evaluating indoor environment and electricity consumption of UK homes retrofitted with air source heat pumps

Rajat Gupta [1], Sahar Zahiri[1]

[1]*Low Carbon Building Research Group, School of Architecture, Oxford Brookes University, Oxford OX3 0BP, rgupta@brookes.ac.uk*

SUMMARY
Heat pumps are integral to the UK's Net Zero strategy. This study investigates the impact of air source heat pumps (ASHPs) on indoor environmental conditions and electricity use in nine retrofitted homes in Oxford during winter 2023–2024. Adopting a mixed-methods approach, indoor and outdoor temperatures, relative humidity, and CO_2 levels were monitored, alongside Energy Performance Certificate data and household surveys. Most homes maintained indoor temperatures above the WHO-recommended 18°C, though some fell below 20°C, which may be inadequate for vulnerable occupants. Smart meter data from four homes showed daily electricity use ranging from 9.4 to 23.2 kWh, with peak demand typically outside the 4–7 p.m. window. Variability of electricity use was strongly influenced by occupant behaviour. Findings highlight the potential for time-of-use tariffs to encourage off-peak heating and the need for tailored retrofit approaches that consider user practices. Optimising heat pump use requires balancing comfort, cost, and system efficiency through user engagement and adaptive control.

Keywords: Heat pump, electricity use, environmental monitoring, occupant behaviour

1. INTRODUCTION AND BACKGROUND

To meet its legally binding Net Zero emissions target by 2050, the UK Government aims to install 600,000 low-carbon heat pumps annually by 2028 (HM Government, 2020), accelerating the phase-out of gas boilers, which currently account for approximately 30% of national energy demand (BEIS, 2022; DESNZ, 2023). Within this ambition, an estimated 5 million heat pumps are expected to be deployed by 2030, rising to 19 million by 2050. The widespread adoption of heat pumps could place considerable strain on the electricity network, potentially exceeding the UK power system's current peak load capacity of 60 GW (Watson et al., 2021). This presents an urgent need for demand-side management strategies to ensure system stability and cost-effectiveness.

Smart control technologies have emerged as key enablers for managing peak loads and enhancing grid flexibility. Evidence suggests that smart systems can reduce energy use by up to 39% and shift demand away from peak periods, alleviating network stress (Pallonetto et al., 2021; Carbon Trust, 2020). Time-of-Use (TOU) tariffs, when combined with automated controls, allow households to shift electricity use to off-peak hours, reducing operational costs and peak demand (Rosenow & Lowes, 2020). For example, a Carbon Trust (2020) study found that integrating TOU tariffs in 15 London homes led to a 25% reduction in energy costs. Yet, such interventions are often undermined by behavioural and cultural dynamics, including fixed daily routines, concerns over comfort, and mistrust in automated systems (Dimitrokali et al., 2015; Powells et al., 2014).

Empirical studies have demonstrated that user operation mode is a critical determinant of heat pump performance. In a study of 50 social housing dwellings in Oxford, Gupta and Zahiri (2023) found that residents' preference for manual operation significantly increased electricity use compared to timer-based operation, which adapts to weather conditions. Similarly, thermal

performance of the building fabric plays a key role in determining heat pump efficiency. Research by Stafford and Bell (2009) and Sarbu and Sebarchievici (2015) emphasises that low-temperature heating systems perform best when combined with adequate insulation and airtightness.

Despite the growing deployment of air source heat pumps (ASHPs) across the UK, there remains limited evidence on their impact on indoor environmental quality, electricity use, and occupant behaviour - particularly across diverse household types and in real-world settings. Existing research often overlooks the dynamic interactions between residents, building performance, and heating technologies, as well as the broader implications for equity and system flexibility.

In this context, the present study investigates the effects of ASHP retrofits on indoor environmental conditions and electricity consumption in nine nearly identical dwellings in Oxford (UK) during the winter of 2023–2024. Using a mixed-methods approach, the study monitors indoor temperature, relative humidity, CO_2 concentrations, and electricity use via smart meters, supplemented by pre-heat pump household surveys and Energy Performance Certificate (EPC) data. This research aims to fill a critical gap in understanding how heat pump operation affects household energy demand, thermal comfort, and the potential for alignment with TOU tariffs during peak periods (4–7 p.m.). The findings provide empirical insights for policymakers, energy providers, and retrofit practitioners aiming to optimise heat pump performance while maintaining occupant comfort and reducing peak electricity loads.

2. METHODOLOGY

This study adopted a mixed-methods approach to investigate the impact of air source heat pump (ASHP) installations on indoor environmental quality and electricity consumption across nine residential dwellings (D01–D09) located in Oxford, UK. The approach combined quantitative monitoring of environmental parameters and electricity use with qualitative survey data to contextualise occupant experience. Environmental monitoring was conducted in bedrooms and living rooms, alongside outdoor measurements, from 21 December 2023 to 28 February 2024, a period characterised by peak seasonal heating demand. Indoor temperature, relative humidity, and CO_2 concentration were recorded at 15-minute intervals using Bluetooth-enabled HOBO data loggers. Outdoor temperature and humidity were also monitored. Smart meter data were extracted from four dwellings (D01–D03 and D07) using Ivie-Bud meters, allowing analysis of hourly electricity consumption, including time-of-use patterns and cost variability across tariff bands. To assess the change in energy consumption due to heat pump installation, post-installation electricity use (February 2024) was compared to pre-installation use during the same period in 2023. The specifications of the monitoring devices and smart meters are detailed in Table 1.

Table 1. Specification of the environmental monitoring devices, and smart meter

Monitoring devices		Location	Parameter	Range	Accuracy	Resolution
	HOBO MX2301	Garden	Outdoor temperature (°C)	-40-70	±0.2	0.036
			Outdoor relative humidity (%)	0-100	±2.5-3.5 (10% to 90%); ±5 (below 10% and above 90%)	0.01
	HOBO MX1101	Principal bedroom	Indoor temperature (°C)	-20-70	±0.2	0.024
			Indoor relative humidity (%)	1-90	±2 (20% to 80%) ±6 (below 20% and above 80%)	0.01
	HOBO MX 1102	Living room	Indoor temperature (°C)	0-50	±0.2	0.024
			Indoor relative humidity (%)	1-90	±2 (20% to 80%); ±6 (below 20% and above 80%)	0.01
			CO_2 (ppm)	0-5000	±50 ppm ±5% of reading at 25°C, less than 90% RH non-condensing and 1,013 mbar	N/A
	Ivie-Bud smart meter	Living room	Readings and Powers (Watt) Time period and segments Electricity cost (per hour) Ambient (amber, green, red)	N/A	N/A	N/A

In addition to monitoring, pre-installation Energy Performance Certificate (EPC) data were used to extract information on dwelling characteristics, including floor area, thermal fabric, energy efficiency rating, and annual space heating demand. This was complemented by in-person, questionnaire-based household surveys, which gathered information on thermostat settings, energy tariffs, satisfaction with heating systems, and attitudes towards energy use. The surveys incorporated scalar, nominal, and ordinal variables, including Likert-scale responses (1 = strongly disagree to 5 = strongly agree) and were carried out before installation of heat pumps. Socio-demographic and lifestyle segmentation was further informed by Acorn and Mosaic classifications to explore the influence of household characteristics on heating behaviours.

3. OVERVIEW OF THE CASE STUDY DWELLINGS AND HOUSEHOLDS

The nine case study dwellings, all retrofitted with ASHPs between April and November 2023, are located in the Iffley and Rose Hill areas of Oxford (UK). The sample included five end-terrace, three semi-detached, and one mid-terrace house, reflecting a range of typical UK housing typologies. Despite their similar construction age and external conditions, the dwellings varied significantly in floor area (62–128 m²), energy performance, and heating demand. Energy Performance Certificates (EPCs) revealed a broad range of pre-installation energy efficiency ratings, from B (very efficient) in dwelling D01 to E (least efficient) in D09. Annual space heating demands ranged from 6,804 kWh to 12,870 kWh, depending on insulation, building form, and glazing type. All homes were naturally ventilated and predominantly double-glazed, with varying levels of wall and loft insulation. Detailed dwelling characteristics are presented in Table 2.

Table 2. Dwelling characteristics extracted from energy performance certificates (EPCs)

Dwelling ID	Dwelling type	Floor area m²	No of bedroom	Energy efficiency rating	Heating demand kWh/year		Wall type	Roof type	Glazing type
					Space	Hot water			
D01	End-terrace house	92	3	91 B	6,804	1,934	Filled cavity wall with external insulation	Pitched, 270 mm and 350 mm loft insulation	Mostly double glazed
D02	End-terrace house	62	2	63 D	8,759	1,888	Cavity wall with and without insulation	Pitched, 270 mm loft insulation	Double glazed
D03	Semi-detached house	75	2	77 C	8,592	2,619	Filled cavity wall, with filled insulation	Pitched and dwelling with 100 mm loft insulation	Double glazed
D04	End-terraced house	117	3	57 D	12,870	2,958	Cavity wall, and solid brick with insulation	Pitched roof with 270 mm loft insulation	Double glazed
D05	Mid-terrace house	74	2	61 D	7,063	2,760	Filled cavity wall and solid brick	Pitched, 200 mm loft insulation	Double glazed
D06	Semi-detached house	128	3	68 D	12,078	2,303	Filled cavity wall insulation	Dwelling roof insulation	Mostly double glazed
D07	End-terrace house	77	3	64 D	8,475	2,076	Filled cavity wall, and solid brick	Pitched and dwelling roof, 150 mm loft insulation	Mostly double glazed
D08	End-terrace house	93	2	72 C	8,920	1,953	Filled cavity wall insulation	Pitched and dwelling roof, 100 mm lost insulation	Double glazed
D09	Semi-detached house	76	3	41 E	8,669	3,386	Filled cavity wall insulation	Pitched, 270 mm loft insulation	Double glazed

The socio-economic composition of the households was diverse in terms of tenure, income, age, and household structure. Six dwellings were owner-occupied, with residents having lived in the homes for between four and eleven years. The majority of respondents fell within the 36–55 age band, and household incomes ranged from £15,000–£19,999 (e.g. D02) to £50,000–£64,999 (e.g. D07), indicating a range of economic conditions. Lifestyle classifications indicated a mix of household types, including “mature families,” “elderly households,” and “mature singles.” One household (D06) included young children, while another (D05) comprised a family of five. Pre-installation survey results showed that one-third of respondents were on a standard tariff, and most set their main thermostat to 20°C. Heating usage was typically seasonal, operating between

October and March, with reported differences in thermal comfort preferences between occupants. Although two-thirds of participants indicated a reluctance to compromise on comfort to reduce energy bills, most expressed a willingness to adjust their energy use to reduce costs - highlighting the potential for behavioural flexibility. These contextual insights are essential to interpreting the monitored performance data in light of real-world user behaviour and preferences.

4. FINDINGS

4.1. Indoor temperature and relative humidity

Descriptive statistics and distributions of indoor temperature and relative humidity (RH) levels, presented in Figure 1, demonstrate spatial and temporal variability across bedrooms and living rooms in the nine case study dwellings between 21 December 2023 and 29 February 2024. Excluding the largely unoccupied dwelling D04, bedroom temperatures ranged from 15.5°C in end-terrace dwelling D02 to 21.5°C in semi-detached dwelling D03. Living room temperatures varied more widely, from 16.1°C (D02) to 21.5°C (D06). While bedroom temperatures largely conformed to the CIBSE Guide A comfort range of 17–19°C (CIBSE, 2021), most living rooms failed to achieve the recommended comfort range of 22–23°C, possibly due to the lower output temperatures of ASHPs and resident control preferences. Variations in indoor temperature closely correlated with RH levels, which ranged from 45% (D03, D05) to 75% (D08) in bedrooms, and from 49% (D06) to 71% (D08) in living rooms.

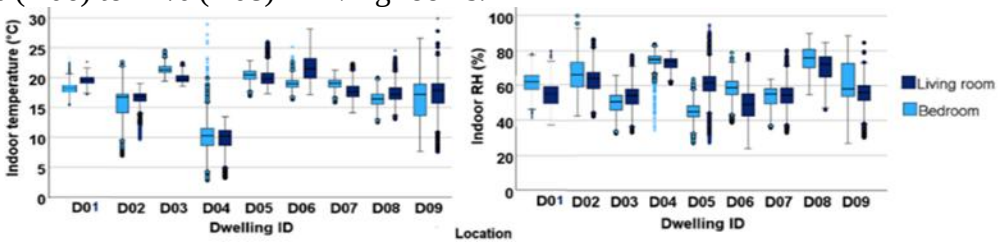

Figure 1. Distribution of indoor temperature and relative humidity between 21st December 2023 and 29th February 2024 in the bedrooms and the living rooms of the nine dwellings

As shown in Figure 2, daily temperature profiles remained relatively stable throughout the monitoring period, with most peaks occurring outside the national electricity peak demand window (4–7 p.m.). This suggests that ASHP operation in these homes may have been strategically or habitually aligned with off-peak periods.

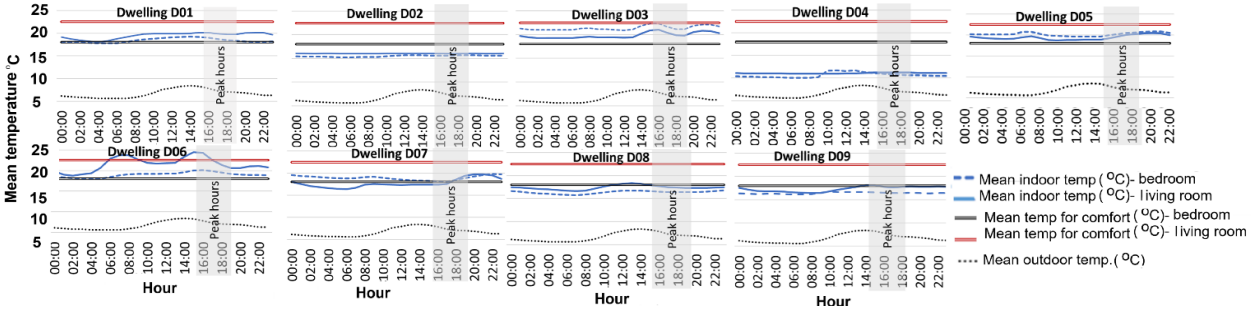

Figure 2. Mean daily indoor temperature profiles between 21st December 2023 and 29th February 2024 across the bedrooms and living rooms of nine dwellings

Indoor temperatures consistently exceeded the WHO-recommended minimum of 18°C in dwellings D01, D03, and D05–D07, with the highest recorded temperatures - up to 24.8°C - occurring at 8:00 a.m. and 3:00 p.m. in D06, a family home with young children. However, most

living room temperatures remained below the recommended 22–23°C comfort range, as well as the 20°C threshold for vulnerable groups set by WHO guidelines.

4.2 Indoor CO_2 concentration

The distribution and daily profiles of CO_2 concentrations, summarised in Figure 3, showed notable variation across living rooms in the nine dwellings. The highest recorded value- over 3000 ppm - occurred in D05, a mid-terrace home occupied by a family of five, where the mean daily CO_2 concentration reached 890 ppm. In contrast, the lowest mean concentration (427 ppm) was recorded in D04, which had limited occupancy. Despite some exceedances, the majority of daily mean concentrations remained within the 800–900 ppm threshold recommended for good indoor air quality. Temporal alignment between CO_2 and temperature peaks suggests that increased occupancy levels may have led to more frequent heat pump operation to maintain comfort, indicating behavioural coupling between environmental control and indoor air quality.

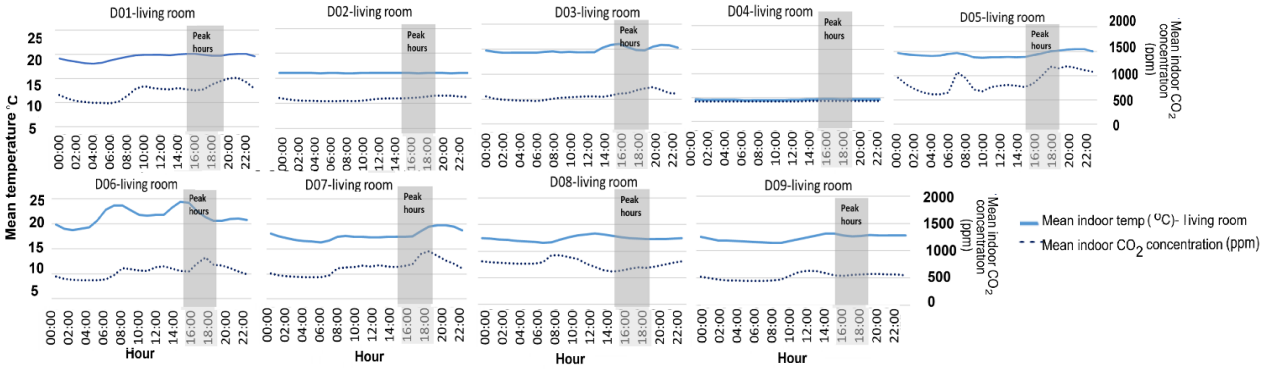

Figure 3. Distribution and mean daily indoor CO_2 concentration profiles between 21st December 2023 and 29th February 2024 across the living rooms of nine dwellings

4.3 Electricity use in a subset of four dwellings

Smart meter data from four dwellings (D01–D03 and D07) were analysed to examine patterns in electricity use following heat pump installation. Descriptive statistics for daily electricity use are presented in Table 3. Mean daily usage ranged from 9.4 kWh in D02 to 23.2 kWh in D07 - both dwellings with similar energy efficiency ratings (D) but differing significantly in household income and occupancy, suggesting socio-behavioural factors strongly influenced energy demand.

Table 3. Descriptive statistics and distribution of daily electricity use between 21st December 2023 and 29th February 2024 in four dwellings

Descriptive Statistics- Daily electricity use (kWh)				
Dwelling ID	Min	Max	Mean	Std. Deviation
D01	.1	46.9	20.3	9.7
D02	.1	33.3	9.4	6.7
D03	.2	45.1	19.9	8.6
D07	.9	46.6	23.2	9.2

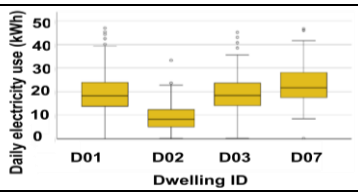

As illustrated in Figure 4, daily electricity use patterns mirrored fluctuations in outdoor temperatures, indicating that heating demand was the principal driver of energy consumption. While peak consumption generally occurred outside the 4–7 p.m. window - often around 6:00 a.m. - the highest recorded peak (1.25 kWh at 6:00 p.m.) was observed in D07, likely reflecting evening occupancy patterns and concurrent appliance use.

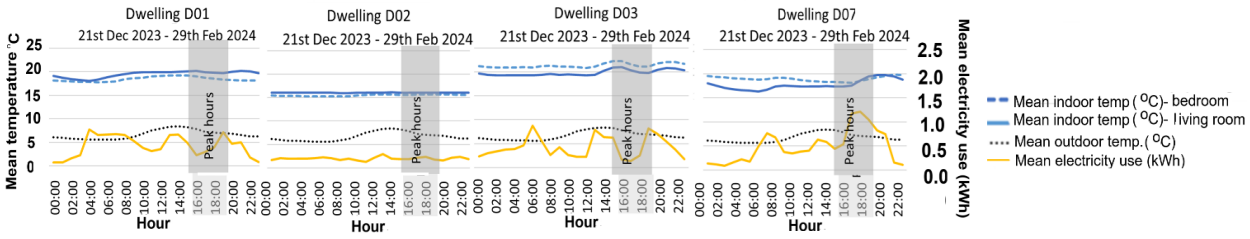

Figure 4. Daily electricity use and mean indoor and outdoor temperature profiles in four dwellings between 21st December 2023 and 29th February 2024

4.3.1 Electricity use before and after heat pump installation

Electricity consumption was compared across two matched timeframes: pre-installation (18–28 Feb 2023) and post-installation (18–28 Feb 2024). As shown in Figure 5, mean daily use increased significantly in all four dwellings post-installation, with D02 rising from 2.8 kWh to 9.7 kWh and D07 from 12.5 kWh to 21.8 kWh. These increases align with the added heating load of the ASHPs in winter. While total electricity use increased, peak demand remained largely outside the 4-7 p.m. period in most cases. Exceptions included D07, where a peak of 2.4 kWh was recorded at 6:00 p.m., again suggesting behavioural patterns may override economic incentives for off-peak usage. Interestingly, electricity use patterns remained consistent in terms of timing, suggesting limited behavioural adaptation following heat pump installation. This indicates that while ASHPs can operate efficiently during off-peak hours, achieving demand-side response (DSR) benefits may require more proactive control strategies or greater user engagement.

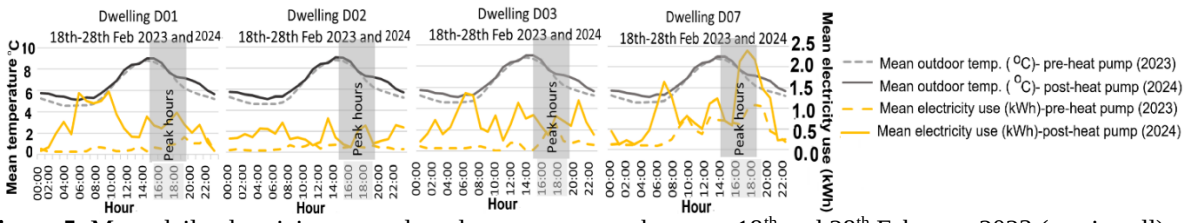

Figure 5. Mean daily electricity use and outdoor temperature between 18th and 28th February 2023 (pre-install) and 2024 (post-install) across four dwellings

5. DISCUSSION

The pre-heat pump installation household surveys revealed that most occupants maintained their heating systems from October through March, with thermostat settings typically around 20°C. This indicates a strong preference for thermal comfort, suggesting that resident training on the operation of low-flow continuously operating heat pumps could enhance performance. Encouraging adaptive thermal behaviours, supported by smart heating controls, may optimise energy use by enabling more efficient setpoint schedules while maintaining comfort. Although two-thirds of respondents were reluctant to compromise comfort to reduce energy bills, a majority expressed willingness to modify electricity use patterns to save on energy costs. This reinforces the potential of time-of-use (TOU) tariffs to encourage off-peak heating behaviours, particularly given the financial pressures on lower-income households in the current energy pricing landscape (Gupta & Zahiri, 2024).

Temperature data collected during the monitoring period demonstrated that while mean daily bedroom temperatures largely aligned with the CIBSE Guide A comfort range (17–19°C), mean living room temperatures averaged only 17.6°C-below both the CIBSE-recommended range (22–23°C) and the WHO's minimum of 20°C for vulnerable residents. These findings highlight the importance of personalised temperature control and the need to better align heat pump operation

with occupant comfort requirements. Although indoor temperature variations were primarily influenced by occupant behaviour, the role of building fabric performance was also evident, supporting existing literature on the importance of fabric upgrades prior to low-temperature heating system retrofits (Sarbu & Sebarchievici, 2015; Stafford & Bell, 2009).

Smart meter data from four dwellings indicated that electricity consumption increased significantly following heat pump installation, with mean daily use ranging from 9.4 kWh (D02) to 23.2 kWh (D07), despite similar dwelling types and energy ratings. These discrepancies are likely attributable to socio-economic differences and household size. For instance, D02-a low-income, single-occupant household-recorded the lowest energy consumption and indoor temperatures, likely due to cost constraints. In contrast, D07-occupied by a higher-income family-demonstrated greater electricity use and warmer indoor conditions, particularly during colder periods. These patterns confirm that occupant behaviour, influenced by income and household structure, is a key determinant of heat pump energy use. Interestingly, peak electricity consumption occurred predominantly outside the 4–7 p.m. peak demand window, supporting the potential role of ASHPs in reducing network stress when supported by appropriate behavioural or automated control strategies. However, in some cases (e.g., D07), peaks aligned with evening activity, suggesting that behavioural factors may limit flexibility unless incentivised through pricing or automation.

Indoor air quality was generally within acceptable limits, with most dwellings maintaining mean daily CO_2 concentrations below the 800–900 ppm threshold. While dwelling D05 exceeded 3000 ppm during periods of high occupancy, this was an exception. These findings suggest that natural ventilation was largely sufficient, though occupancy-related variation reinforces the importance of tailored ventilation strategies to support both energy efficiency and indoor environmental quality.

Although this study was limited to a single winter season, early findings suggest strong interdependencies between occupant behaviour, socio-economic context, building performance, and heat pump operation. Future longitudinal studies across multiple seasons can capture changes in household practices over time, understand behavioural adaptation, and optimise post-retrofit performance in diverse household types.

6. CONCLUSION

This study evaluated the impact of air source heat pumps (ASHPs) on indoor environmental quality and electricity consumption in nine retrofitted dwellings in Oxford (UK) during the winter of 2023–2024. Using a mixed-methods approach, the research combined high-resolution monitoring of temperature, relative humidity, CO_2 levels, and electricity use, alongside household surveys and Energy Performance Certificate data.

Findings showed that most dwellings maintained indoor temperatures above the WHO minimum threshold of 18°C during the heating season. However, mean living room temperatures remained below recommended comfort levels, particularly for vulnerable populations, emphasising the need for tailored thermal comfort strategies and greater occupant awareness of heat pump operation. While electricity consumption increased following ASHP installation, smart meter data revealed off-peak usage patterns in most households, suggesting compatibility with TOU tariffs and demand-side response schemes. Socio-economic variation and household composition significantly influenced heating behaviours and energy consumption. Lower-income households

appeared to restrict energy use due to affordability, while higher-income households tended to maintain greater thermal comfort. These findings underscore the importance of personalised retrofit strategies that address both building performance and behavioural factors.

To encourage broader adoption of heat pumps and ensure optimal performance, policymakers should support residents with tailored energy tariffs, user-centred controls, and targeted communication strategies. Financial and technical support for low-income households is especially important to ensure equitable outcomes. Furthermore, future policies should promote longitudinal evaluation of heat pump use to better understand behavioural adaptation and system performance over time. Aligning these strategies with broader decarbonisation goals will be critical to supporting a just and efficient transition to low-carbon residential heating in the UK.

ACKNOWLEDGEMENT

This study has been undertaken as part of the Clean Heat Streets research project (Ref: PRJ 884) funded under the Heat Pump Ready innovation programme sponsored by the UK Department for Energy Security and Net Zero (DESNZ). We are grateful to the residents of the case study dwellings.

REFERENCES

Arabkoohsar, A. & Alsagri, A.S., 2020. A new generation of district heating system with neighborhood-scale heat pumps and advanced pipes, a solution for future renewable-based energy systems. Energy, 193.

BEIS, 2022. Decarbonising heat in homes- Seventh report of session 2021-22. Business, Energy and Industrial Strategy Committee, House of Commons: London.

Carbon Trust, 2020. Heat Pump Retrofit in London. Carbon Trust.

CIBSE, 2021. CIBSE Guide A. Environmental design. Chartered Institution of Building Services Engineers: London.

DESNZ, 2023. Digest of UK Energy Statistics (DUKES), Annual data for UK. Department for Energy Security & Net Zero: London, UK.

Dimitrokali, E., Mackrill, J., Jennings, P., Khanna, S., Harris, V. & Cain, R., 2015. Exploring homeowners' perception and experiences in using a domestic smart home heating controller. Indoor and Built Environment, 24(7).

HM Government, 2020. The Ten Point Plan for a Green Industrial Revolution. HM Government.

Gupta, R. & Zahiri, S., 2024. Impact of energy price rise on electricity use and indoor temperatures in UK dwellings retrofitted with heat pumps. The European Council for an Energy Efficient Economy (ECEEE) 2024 Summer Study on Energy Efficiency, 10-15 June 2024, Center Parcs Lac d'Ailette, France. Conference paper.

Gupta, R. & Zahiri, S., 2023, November. Field study of energy and environmental performance of ground source heat pumps retrofitted in a cluster of UK social housing dwellings. In Journal of Physics: Conference Series (Vol. 2600, No. 6, p. 062004). IOP Publishing.

Lowes, R., Rosenow, J., Qadrdan, M. & Wu, J., 2020. Hot stuff: Research and policy principles for heat decarbonisation through smart electrification. Energy research & social science, 70, p. 101735.

Pallonetto, F., De Rosa, M., & Finn, D.P., 2021. Impact of intelligent control algorithms on demand response flexibility and thermal comfort in a smart grid ready residential building. Smart Energy, 2.

Powells, G., Bulkeley, H., Bell, S. & Judson, E., 2014. Peak electricity demand and the flexibility of everyday life. Geoforum, 55, pp. 43-52.

Rosenow, J. & Lows, R., 2020. Heating Without the Hot Air: Principles for Smart Heat Electrification. Regulatory Assistance Project (RAP): Brussels, Belgium.

Stafford, A. & Bell, M., 2009. Evaluation of Heat Pump Installations: Extracting Meaning from Existing Datasets. Leeds Beckett University: Leeds, UK.

Sarbu, I. & Sebarchievici, C., 2015. A study of the performances of low-temperature heating systems. Energy Efficiency, 8(3), pp. 609-627.

Watson, S.D., Lomas, K.J. & Buswell, R.A., 2021. How will heat pumps alter national half-hourly heat demands? Empirical modelling based on GB field trials. Energy and buildings, 238, p. 110777.

6th International Conference on Building Energy and Environment
Eindhoven University of Technology, The Netherlands
6 - 10 July 2025

Spatiotemporal concentration distribution profile of odorants from the indoor environmental scale to the airway microstructure

Islam M. S. Abouelhamd[1], Kazuki Kuga[2], Kazuhide Ito[3]

[1] *Interdisciplinary Graduate School of Engineering Sciences, Kyushu University, abouelhamd@kyudai.jp*
[2] *Faculty of Engineering Sciences, Kyushu University, Kasuga-koen, Kasuga, kuga@eee.kyushu-u.ac.jp*
[3] *Faculty of Engineering Sciences, Kyushu University, Kasuga-koen, Kasuga, ito@kyudai.jp*

SUMMARY
The transport of the odorants from the indoor environment to the human respiratory tract is still poorly understood. This study used the computational fluid dynamics and physiologically based pharmacokinetic models (CFD-PBPK) to investigate the spatiotemporal transport patterns of acetaldehyde (released from a yogurt vessel as the source of the odorants) within different measuring spots, namely the indoor domain, breathing zone, the source of the released odorant, the nostrils, the fluid region of the airway, and the mucus-to-tissue layers of the airway microstructure. The results indicate that the nostrils and olfactory regions can capture a reasonable odorous concentration of the chemicals that correctly reflects the perceived intensity in the logarithmic correlations. However, the quantified volume-average concentration in the breathing zone or the room scale reflected unreasonable or odourless concentrations. Emphasizes the importance of the airway microstructure scale for assessment of indoor air quality by using the *in-silico* models, particularly for the harmful contaminants.

Keywords: Indoor Environment, Odorants, Air Quality, Airway Microstructure.

1. INTRODUCTION

Olfaction is a central function in assessing the acceptability and quality of the indoor environment, influencing communication, behavior, and food preferences (Dan et al., 2021; Hsieh et al., 2017). The transport dynamics of the odorants from the indoor environment to the respiratory tract remain poorly understood, with challenges induced by ethical considerations, *in-vivo* quantification complexities, and individual variability. Literature has highlighted the relationship between indoor air quality and acetone concentration (Bluyssen and Fanger, 1991), prompting studies aimed at enhancing odor perception and supporting healthy building principles. However, traditional odor intensity assessments relying on trained panelists are often inconsistent. While recent findings suggest a logarithmic correlation between odor intensity and concentration (David et al., 2024), these studies frequently overlook the complex interactions within the human airway domain, neglecting the microstructural complexities of the olfactory region. The literature lack empirical data of the relationship between odor intensity and concentration in each environmental scale, particularly the perceived intensity by human in the olfactory region. By integrating computational modeling and previous experimental data, this study aims to bridge these gaps, offering insights into odorants transport and interaction mechanisms at the receptor level, enhancing predictions of olfactory perception, and advancing indoor air quality research.

2. METHODOLOGY

This study used a coupled computational fluid dynamic (CFD) and physiologically based pharmacokinetic (PBPK) models to simulate odorant dynamics. The validated respiratory tract model incorporated a multi-layer air-mucus-tissue-blood (AMTB) model for odorant absorption analysis, as proposed by Tian and Longest (2010). The surface concentration was calculated at the air-mucus boundary using the absorption equilibrium and diffusion flux conservation equations for the low-viscosity layer. Odorant concentrations in the yogurt vessel were replicated from the experimental data to ensure consistent initial conditions and comparability to the parameters concluded from the odor sensory tests (OSTs). The acetaldehyde was used as a key odorant of the yogurt, as it includes guideline substances for assessing indoor air quality. The computational domain consisted of a CT-scanned seated computer-simulated person (CSP) combined with an airway model and placed in the center of a mixed-ventilated room (Fig. 1). The respiratory tract consists of seven main sections, while the olfactory surface region was divided into four segments to detect the spatial olfaction dynamics (Kuga et al., 2024; Kuga et al., 2023). Three breathing profiles were tested: normal breathing with two different airflow rates of 38 L/min and 24 L/min, and a sniffing cycle. The validation and verification of the computational domain were applied according to the prior studies (Yoo and Ito, 2022; Ito, 2016). The CFD boundary conditions and solving methods are summarized in Table 1.

Table. 1. Boundary conditions and solving methods for the CFD-PBPK numerical model.

Domain/	**Boundary Conditions**
Indoor Inlet Boundary	Velocity inlet = U_{in} = 0.51 m/s - Relative Humidity: RH_{in} =50 % RH
	Ambient air temperature: T_{in} = 25 °C (fixed value)
Indoor Outlet Boundary	Gradient zero conditions
Wall Treatment (room)	Temperature: adiabatic condition - Humidity: gradient zero
Airway Inlet Boundary	Velocity inlet, transient profile, 20 seconds durations
Wall treatment (airway)	Local PBPK integrated model - Wall Temperature = $T_{surface}$ = 36 °C
Wall Treatment (CSP)	No-slip wall, Fanger's model for heat generation.
Wall Treatment (Yogurt Vessel)	Temperature: adiabatic condition - Exterior walls: No Slip walls
Grid Design	Polyhedral Meshing. Total number of cells = 9.5 million.
Turbulence Model	SST k-ω model
Scheme/Algorithm	SIMPLE for Pressure-velocity coupling
Radiation Model	Surface-to-surface (S2S) model using "view factors"

3. RESULTS & DISCUSSION

In terms of concentration profiles across different measurement spots, fluctuation of odor concentration in the nostrils and the source of the odorants (the yogurt headspace) was associated with the breathing airflow jet during the inhalation and exhalation stages and the continued release of the chemicals from the yogurt vessel. The indoor domain showed negligible and highly mixed time-average concentration, reflecting the vast gap between the source of odorants and the surroundings. Fig 1A illustrates the correlations between the perceived odor intensity as a function of time-averaged equilibrium concentration measured in the indoor domain (Spot A), the headspace of the yogurt (Spot B), breathing zone (Spot C), nostrils (Spot D), and mucus layer in the olfactory wall (Spot E). The correlation coefficient R^2 indicates that nostrils and olfactory regions are good indicators as measuring spots, reflecting acceptable logarithmic approximation of the perceived odor intensity. The assessments of odorant concentration in the indoor domain or

the breathing zone can significantly overestimate or underestimate the odor intensity.

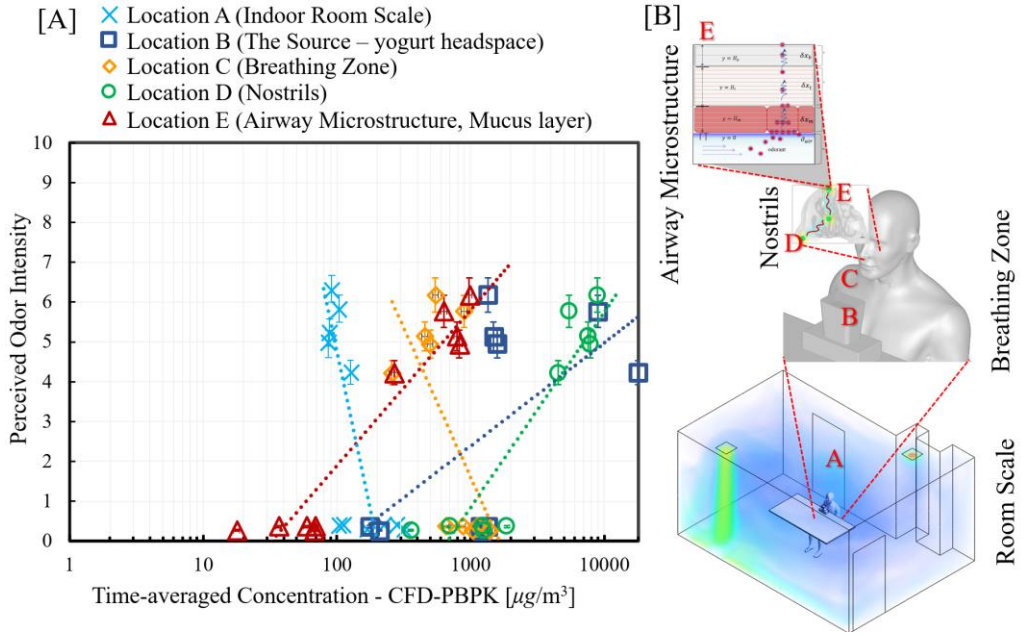

Figure 1. Panel [A] shows the correlation between perceived odor intensity and time-average concentration of the acetaldehyde in different physical scale. Panel [B] identifies these scales, which represented in the room scale, breathing zone, the source, nostrils, and the airway wall microstructure.

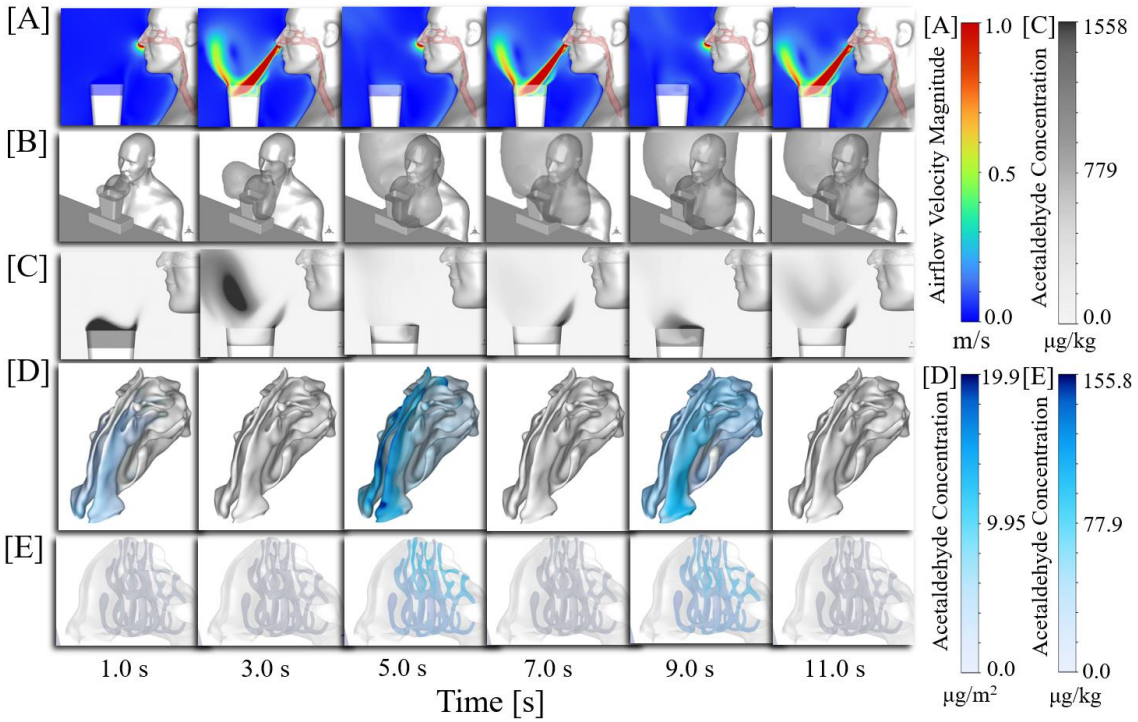

Figure 2. Visualizations of the spatial distribution of acetaldehyde concentration in the different regions. Figures in panel [A], [B], [C], [D], and [E] illustrates the velocity magnitude, scalar iso-surface, scalar concentration in the breathing zone, odor concentration in the nasal cavity wall, and inside the nasal passages, respectively.

The visualizations through the CFD-PBPK track can enrich our understanding of the transport of odorants in the room domain and the small passages of the olfactory recess. That reflects the

olfaction dynamics and transport between the indoor environment and microstructure of the airway wall (Fig. 2). Once the simulation was initialized with the first inhalation phase in parallel with the opening of the yogurt vessel, the acetaldehyde was released from the headspace with a dispersion route directed toward the nose. However, due to the distance between the vessel and the olfactory region with a short duration of inhalation, a low concentration of acetaldehyde reached the tissue layers. At 3.0 seconds, the peak of the exhalation phase, the puff from the nostrils caused extensive scattering of acetaldehyde into the outer regions. Correspondingly, low concentration was observed in the airway domain induced by the clearance. Furthermore, the yogurt lost its condensed odorant concentration in the headspace, which was reflected in the low concentration trend of the first cycle. During the second breathing cycle (around 5.0 seconds), the CSP inhaled the diffused odorants near the breathing zone, which occurred in the prior exhalation phase. Therefore, the second cycle showed higher concentration distribution in the airway domain compared to the first cycle. After the third cycle and subsequent cycles, the concentration started to be almost constant or with a slight increase.

4. CONCLUSION

This study has concluded that the perceived odor intensity from OSTs can be predicted logarithmically in correlation with the odorant concentration in the olfactory mucus layer. This offers a reliable *in-silico* prediction model for odor sensation based on numerically quantifiable parameters. Neglecting the human respiratory domain or the airway microstructure leads to underestimation of the olfaction phenomena and indoor air quality assessments, as the study proved that such domains could properly reflect the intensity of the odorants, unlike the wide room domain. This model offers potential implications for electric noses, food assessments, fragrance development, and indoor air sensor applications, particularly for long-term exposure in industries that emit odorous and harmful compounds.

ACKNOWLEDGEMENTS

This study was partially funded by the JSPS KAKENHI (JP 22H00237, JP 22K18300, JP 22K14371, JP 24KK0094), the MEXT as a “Program for Promoting Research on the Supercomputer Fugaku” (JPMXP1020210316), and JST, FOREST program (JPMJFR225R), and Health, Labour and Welfare Policy Research Grants (JP 24KD2001).

REFERENCES

Bluyssen P.M., Fanger P.O., 1991. Addition of olfs from different pollution sources, determined by a trained panel. *Indoor Air* 1, 414–421.

Dan X., Wechter N., Gray S., Mohanty J.G., Croteau D.L., Bohr V.A., 2021. Olfactory dysfunction in aging and neurodegenerative diseases. *Ageing Research Review* 70, 101416.

David M., Sucker K., Hameister J., Gerull F., Grams H., Röhl C., et al., 2024. The German approach to evaluate complaints about odour annoyance in indoor environments. *Indoor Environment* 1, 100020.

Hsieh J.W., Keller A., Wong M., Jiang R.-S., Vosshall L.B., 2017. SMELL-S and SMELL-R: Olfactory tests not influenced by odor-specific insensitivity or prior olfactory experience. *PNAS USA* 114, 11275–11284.

Ito K., 2016. Toward the development of an in silico human model for indoor environmental design. *Proc Jpn Acad Ser B* 92, 185–203.

Kuga K., Hoshiyama S., Wargocki P., Ito K., 2023. A pilot numerical study of odorant transport to the olfactory region during sensory evaluations following ISO 16000-28. *Building and Environment* 110868.

Kuga K., Kizuka R., Abouelhamd I.M.S., Ito K., 2024. Aspiration efficiency and respiratory tract deposition of indoor suspended micro-particles during steady and transient breathings. *Building and Environment* 249, 111114.

Tian G., Longest P.W., 2010. Development of a CFD boundary condition to model transient vapor absorption in the respiratory airways. *J Biomechanical Engineering* 132, 5.

Yoo S.-J., Ito K., 2022. Validation, verification, and quality control of computational fluid dynamics analysis for indoor environments using a computer-simulated person with respiratory tract. *Japan Architectural Review* 5, 714–727.

Thermal Storages (13:30-15:00 h)

6th International Conference on Building Energy and Environment
Eindhoven University of Technology, The Netherlands
6 - 10 July 2025

Energy Performance of Phase Change Materials-Embedded Wall Systems in Residential Buildings in Hot Climates

Saleh Al-Saadi[1,2], Said Al-Harthi[3], Hayder Khan[4], Khalifa Al-Jabri[5]

[1]*Sustainable Energy Research Center (SERC), Sultan Qaboos University, Muscat, Sultanate of Oman*
[2]*Department of Civil and Architectural Engineering, College of Engineering, Sultan Qaboos University, Muscat, Sultanate of Oman, salsaadi@squ.edu.om*
[3]*Department of Civil and Architectural Engineering, College of Engineering, Sultan Qaboos University, Muscat, Sultanate of Oman, s55749@student.squ.edu.om*
[4]*Department of Civil and Architectural Engineering, College of Engineering, Sultan Qaboos University, Muscat, Sultanate of Oman, khan@squ.edu.om*
[5]*Department of Civil and Architectural Engineering, College of Engineering, Sultan Qaboos University, Muscat, Sultanate of Oman, aljabri@squ.edu.om*

SUMMARY
This study examines the feasibility of incorporating Phase Change Materials (PCMs) into residential building walls across three Omani climates (i.e., hot, moderate, and high-altitude) to reduce energy consumption, particularly for cooling energy. Using DesignBuilder software, a typical villa was simulated where various PCMs thermal properties such as melting temperature, latent heat, and thickness were explored. PCM layers performed best when placed on the inner wall side in hot climates and the outer side in high-altitude climates, with 25 mm thickness offering the greatest energy reduction. The optimal melting temperature was found close to the indoor setpoint (~24-25°C) for the hot climates but lower (19°C) for the high-altitude climate. The results indicated that energy consumption can be reduced by as much as 3.93% in a high-altitude climate, 3.65% in a hot climate, and 2% in a moderate climate for 25 mm PCM thickness. Several heat transfer enhancement techniques, such as adding Ferrochrome slag and thermal insulation were explored but did not yield better results than pure PCM. In conclusion, the study found that the PCMs behaved as a thermal insulation and therefore any thermal conductivity enhancement technique may reduce its thermal performance.

Keywords: Annual Energy Consumption, Hot climates, Phase change Materials (PCMs)

1. INTRODUCTION

The building sector contributes significantly to global energy consumption and greenhouse gas (GHG) emissions, accounting for approximately 41% of energy use and 30% of annual GHG emissions (Ahmed and Asif, 2021). This trend is driven by increasing comfort demands and the absence of energy-efficient standards, particularly in developing countries. In Oman for example, residential and commercial buildings consumed about 83% of electrical energy in 2020, according to the Authority for Public Services Regulation (APSR) report (APSR, 2020). More than 70% of this energy is attributed to the use of air conditioning systems (JICA and TEPCO, 2013). To

address these challenges, Phase Change Materials (PCMs) have emerged as a promising solution for reducing energy consumption in buildings by enhancing thermal energy storage.

PCMs store and release heat during phase transitions, providing higher energy storage capacity than conventional materials (Frigione et al., 2019). Most applications in building structures consist of PCM panels or the incorporation of a PCM into a concrete, mortar mix, or plaster. There is a good potential for reducing energy using PCMs in the envelope for residential buildings in hot climates. For example, fixing a PCM layer with a thickness of 20 mm reduced the heat gain by 15.4% and 13.8% through the roof and walls, respectively, in a Kuwait City residential building (Al-Rashed et al., 2021). In a study conducted in six Australian climates, the results indicated a reduction in annual energy of 17-23% (Alam et al., 2014). A study by Panayiotou et al. (2016) under the Cyprus climate (Mediterranean climate) concluded that combining PCM with thermal insulation may achieve a 67.6% reduction in energy consumption. Integrating conventional PCM wall panels (paraffin wax and ethylene-based polymer) in the envelope of a house in a Saharan climate (i.e., Ghardaia, Algeria) could reduce energy consumption by 36.4% when using PCMs (Hamdani et al., 2021). The literature indicated the potential of using the PCM in hot climates and its effect in reducing energy consumption or indoor peak temperature. Numerical results by Jin et al. (2016) concluded that many factors could affect the selection of the optimal PCM in a wall. These factors are layer thickness, latent heat capacity, interior wall surface temperature, and melting temperature. In order to optimize the PCM selection, these parameters should be studied for the climate under consideration. Therefore, the objective of this study is to explore the potential of PCMs in reducing energy consumption in extreme climates and select the optimal thermal properties for the proper deployment of this technology.

2. METHODOLOGY

2.1 Climate context

Based on Al-Saadi et al. (2023), the Omani climate is classified into a hot-dry climate, a hot-humid climate, a warm-humid climate, and a high-altitude climate, as illustrated in **Figure 1**. The high-altitude climate is mainly in Al Jabal Al Akhdar, where both heating and cooling are required. The warm-humid climate exists in southern Oman due to the monsoon season (i.e., represented by Salalah City), while the hot-humid climate is found in the seaside areas of the Sea of Oman (i.e., represented by Muscat City). According to this study, the rest regions of Oman are mainly desert with a hot and dry climate (i.e., represented by Nizwa).

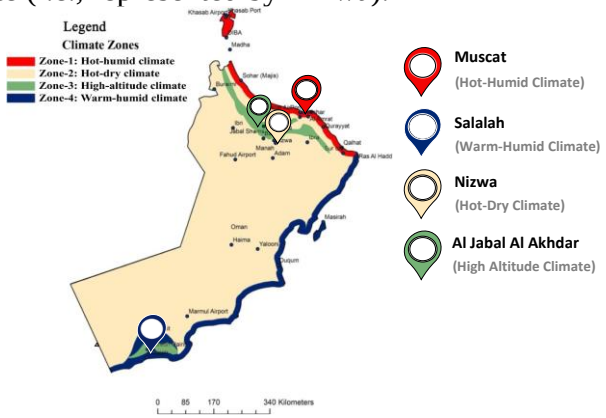

Figure 1. Climate Classifications in Oman (S. Al-Saadi et al., 2023).

2.2 Case study, model, and calibration

The base case for this study is a conventional Omani villa suggested by (S. N. Al-Saadi & Al-Jabri, 2020; Al Shamsi, 2017), as illustrated in **Figure 2**. The simulation tool used is the DesignBuilder software, a graphical user interface (GUI) of EnergyPlus. The model results were then compared to the actual utility bills using the Normalized Mean bias error (NMBE) and Coefficient of Variance (Root-mean-square error) (CV(RMSE)). The NMBE and CV (RMSE) were -1.03% and 7%, respectively, which were found to be within ± 5% and + 15% as per the acceptable range specified in ASHRAE guideline 14 (ASHRAE, 2014).

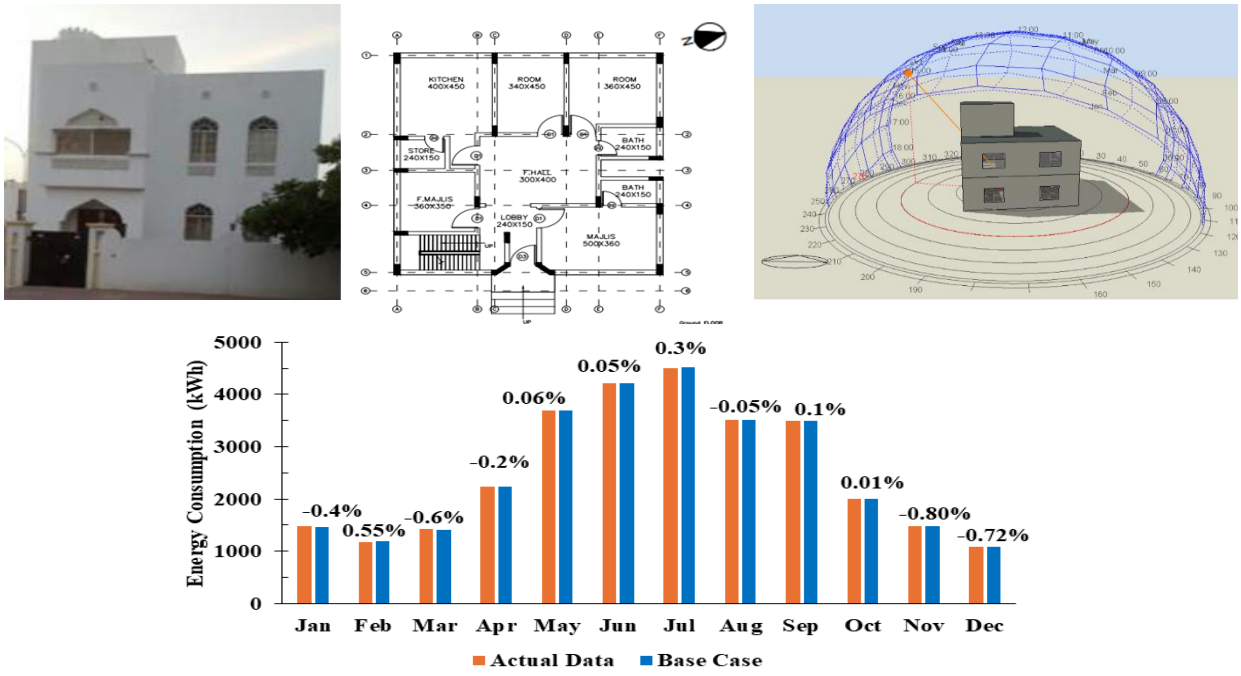

Figure 2. Building image, typical floor plan, 3D model in DesignBuilder, and model calibration.

2.3 Numerical modeling of PCMs in EnergyPlus

DesignBuilder uses EnergyPlus engine to calculate the building energy. This engine uses a Conduction Finite Difference (CondFD) algorithm to model PCMs. The (CondFD) algorithm approximates the wall layers into nodes and mathematically solves the heat transfer equations using a finite difference method (FDM) (EnergyPlus Engineering Reference, 2021). This study chooses the fully implicit scheme combined with the enthalpy-temperature function for PCM. Several studies found a good agreement between the simulation of the PCM in EnergyPlus and the experimental studies (Sarri et al., 2021).

2.4 PCM-embedded wall designs

The work investigates the impact of using PCM when embedded in wall systems in four different climates of Oman. The PCM used for each climate could differ according to the thermal properties (i.e., melting temperature, melting range, latent heat of fusion), thickness, and location. In addition, other parameters may also have an impact on the thermal performance such as the availability of

thermal insulation or other materials that may influence the thermal conductivity. The parameters that have been considered in this study are listed in **Table 1**.

Table 1. PCM thermal and physical characteristics for different wall designs.

Melting Temperature (°C**),** (Inside and outside)	18	19	20	21	22
	23	24	25	26	
Latent Heat (kJ/kG), (Inside and outside)	50	100	150	200	250
	300	350	400		
Melting Range (°C)	0.05	0.1	0.5	1	2
	3	4	5		
PCM Thickness (mm)	10	25	50	100	150
Insulation Thickness (mm), (Inside and outside)	10	25	50	100	150
Cement-PCM-Ferrochrome Slag-Mixture Plaster	Several cement-PCM-Ferrochrome mixes where the thermal conductivity varies between 0.38 to 0.86 W/m.K (Both sides, inside and outside)				

3. RESULTS

3.1 Impact of Thermal Properties

The impact of thermal properties of a 10 mm PCM layer was investigated for the four climates. Selected results for one climate are discussed and a summary of results for other climates is afterwards presented. **Figure 3** illustrates the percentage reduction in the annual energy consumption (and annual cost) for the different cases under Muscat climate. In this figure, the T23H200 case represents PCM with a melting temperature of 23 ºC and latent heat of 200 kJ/kg, and as such all cases are designated in this manner. As clear from the figure, when the PCM layer is located indoors, the reduction in energy consumption is higher than when it is located outdoors. The optimal melting temperature is when it is close to the setpoint temperature (i.e., 24°C). It is also interesting to note that as the latent heat of fusion increases beyond 250 kJ/kg, the benefits are reduced. The maximum savings in annual energy consumption is 1.45% and the corresponding reduction in annual energy cost is 1.56%, as represented by the red bar in **Figure 3**. **Table 2** summarizes the results for the four climates. It is observed that the PCM performs better (~2%) in high-altitude climates (i.e., Jabal Al Akhdar) with a higher latent heat of fusion when PCM is located on the exterior side compared to other climates. The optimal melting temperature is 19°C.

3.2 Impact of PCM thickness

In addition to the PCM base case thickness (i.e., 10 mm), four different thicknesses were evaluated: 25 mm, 50 mm, 100 mm, and 150 mm. The optimal thermal properties of the PCM layer from the previous section were assumed. For comparison purposes, the PCM layer was replaced with an Expanded Polystyrene (EPS) thermal insulation layer that has identical thermophysical properties to the PCM layer but no latent heat. As clear from **Figure 4**, the PCM layer acts as an insulation layer. This means that the PCM layer is in a liquid form most of the time of the year or the diurnal temperature is limited in this climate which hinders the charging and discharging process of the PCM layer. Likewise, the performance of the PCM is similar in other climates with a slightly improved performance in the high-altitude climate (3.93%) and lower performance in the warm-humid climate (2%) for the case when the PCM thickness was 25 mm.

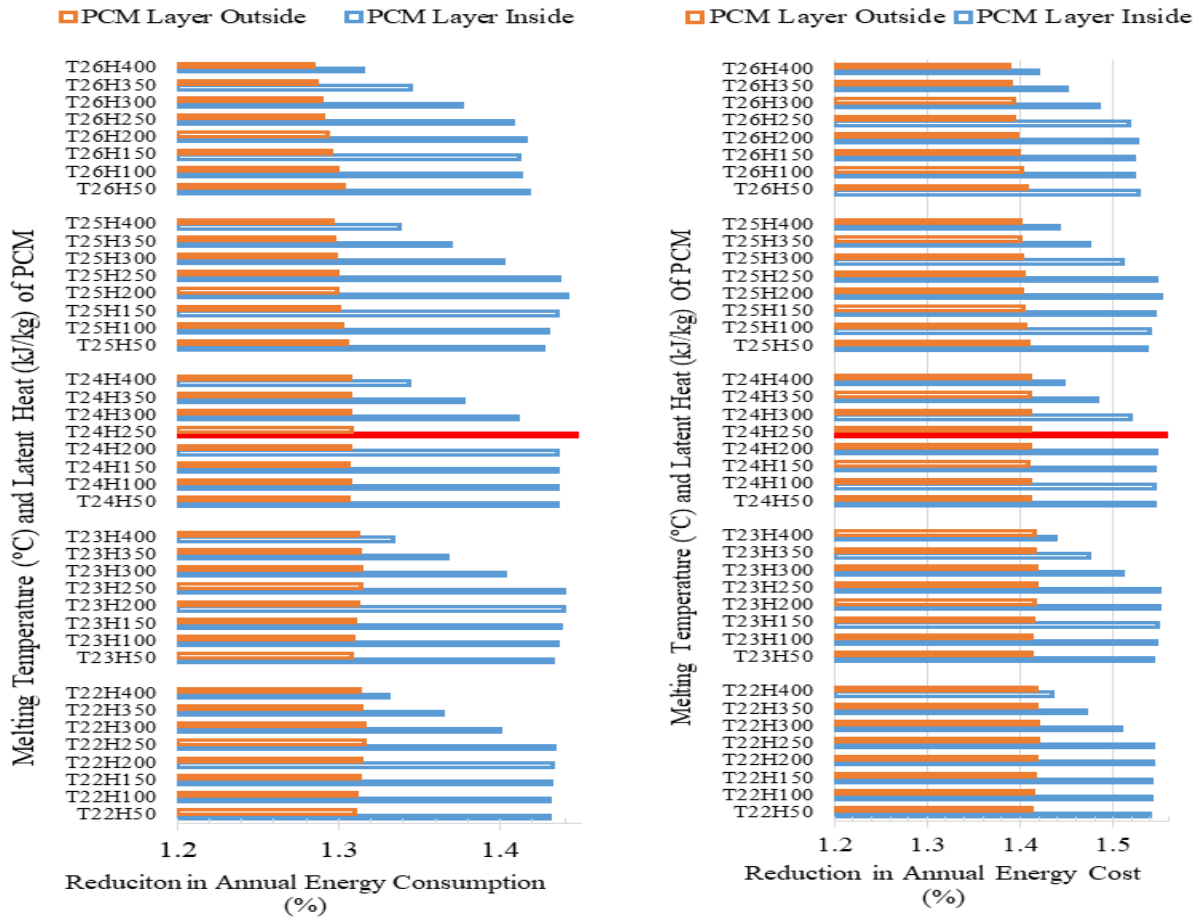

Figure 3. Impact of different PCM's melting temperature and latent heat under Muscat climate on annual energy consumption and cost.

Table 2. Optimal Cases of Melting Temperature, Latent Heat, and PCM Location.

Climate	Melting Temp. (°C)	Latent Heat (kJ/kg)	PCM Layer Location	Reduction in Energy Usage	Reduction in Energy Cost
Muscat (Hot-Humid)	24	250	Inside	1.45%	1.56%
Salalah (Warm-Humid)	24	250	Inside	0.79%	0.79%
Nizwa (Hot-Dry)	25	200	Inside	1.56%	1.63%
Al Jabal Al Akhdar (High-altitude)	19	400	Outside	1.99%	1.99%

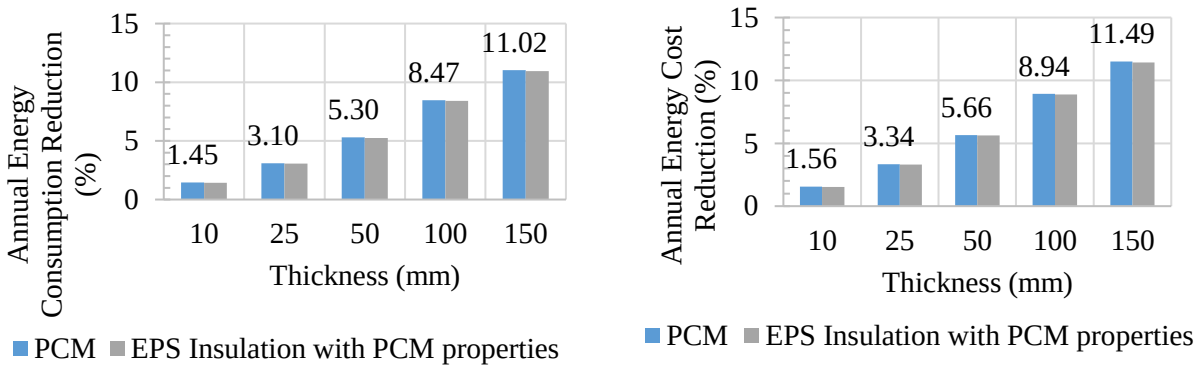

Figure 4. Impact of different PCM's thicknesses under Muscat climate on annual energy consumption and energy cost.

3.3 Impact of thermal insulation when integrated with PCM layer

In order to enhance the PCM's energy performance, a thermal insulation layer was added to the interior and exterior sides. The thickness of the thermal insulation was varied at 1 cm, 2.5 cm, 5 cm, 10 cm, and 15 cm, as shown in **Figure 5**. For all the cases, PCM thickness was fixed at 1 cm for the analysis in this section. The first observation from the figure is that the thermal insulation performs better when located on the interior side. However, its performance is slightly lowered when the PCM is combined. When the PCM is combined with exterior insulation, the performance of the system is better when compared to the insulation case only. **Table 3** summarizes the results for other climates when PCM is combined with 1 cm thermal insulation. In all cases, the thermal insulation provides better savings due to its higher thermal properties. The thermal insulation thickness of 1 cm was selected due to the effect of diminishing returns when increasing the thermal insulation thickness, making it appropriate to combine 1 cm of PCM with a similar thickness of insulation.

Table 3. Reduction of the annual energy consumption for the PCM when integrated with insulation layer for other climates.

Climate	1 cm PCM only	1 cm Insulation only	Combined
Muscat (Hot-Humid)	1.45% (inside)	4.98% (inside)	5.4%
Salalah (Warm-Humid)	0.79% (inside)	2.78% (inside)	3%
Nizwa (Hot-Dry)	1.56% (inside)	5.7% (inside)	6.2%
Al Jabal Al Akhdar (High-altitude)	1.99% (outside)	4.9% (inside)	6.1%

3.4 Enhancing the thermal conductivity of the PCM with ferrochrome slag (FeCR)

In this section, a mixture of PCM, ferrochrome slag (FeCr), and cement was used as a partial replacement for regular indoor/outdoor cement plasters. With the addition of ferrochrome slag (FeCR) slag, the thermal conductivity was increased. Despite the fact that increasing the thermal conductivity for the PCM is advantageous to enhance the charging the discharging process. In this case, it became a disadvantage because the PCM lost its thermal resistance capability.

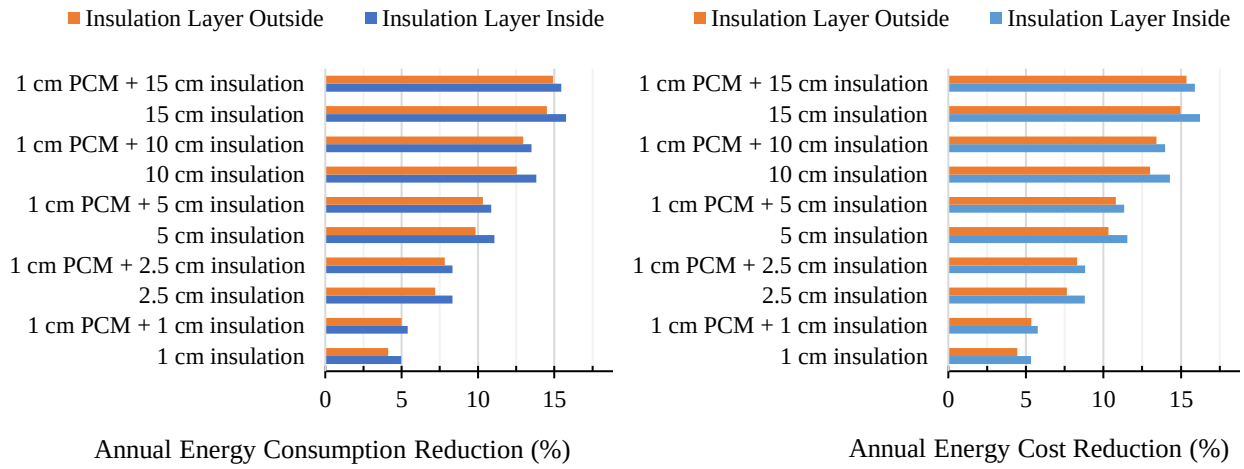

Figure 5. Impact of thermal insulation when combined with PCM layer under Muscat climate on annual energy consumption and energy cost.

4. CONCLUSIONS

In this work, PCMs were evaluated when integrated into wall systems in residential buildings in extreme climates. The following can be concluded:

1) The results indicate that the PCMs provided an equivalent energy performance as thermal insulation across climates in Oman.
2) For hot climates, the best location for the PCM is indoors whereas for the high-altitude climate is outdoors.
3) For hot climates, the optimal melting temperature was found close to the indoor setpoint between 24°C to 25°C, but for high-altitude climates, it was found 19°C.
4) A maximum of 250 kJ/kg is found appropriate for hot climates but as high as 400 kJ/kg is appropriate for high altitude climates.
5) An optimal thickness of 25 mm of PCM layer can be considered which provided between 2 and 3.93% of annual energy and cost savings.
6) Enhancement with thermal insulation materials was not significant.
7) When PCM was mixed with cement plaster, the thermal resistance was improved providing extra heat resistance. However, when Ferrochrome slag was added, the energy performance was reduced.

5. REFERENCES

Ahmed, W., & Asif, M. (2021). A critical review of energy retrofitting trends in residential buildings with particular focus on the GCC countries. *Renewable and Sustainable Energy Reviews*, *144*(June 2020), 111000. https://doi.org/10.1016/j.rser.2021.111000

Al-Rashed, A. A. A. A., Alnaqi, A. A., & Alsarraf, J. (2021). Energy-saving of building envelope using passive PCM technique: A case study of Kuwait City climate conditions. *Sustainable Energy Technologies and Assessments*, *46*(January), 101254. https://doi.org/10.1016/j.seta.2021.101254

Al-Saadi, S., Al-Rawas, G., Gunawardhana, L., Al-Farsi, N., & Al-Kalbani, H. (2023). Developing Climate Classification for Oman Using Degree-Days Method. *Arabian Journal for Science and Engineering*, *48*(9), 11391–11405. https://doi.org/10.1007/s13369-022-07463-4

Al-Saadi, S. N., & Al-Jabri, K. S. (2020). Optimization of envelope design for housing in hot climates using a genetic algorithm (GA) computational approach. *Journal of Building Engineering*.

https://doi.org/10.1016/j.jobe.2020.101712
Al Shamsi, Y. (2017). *Passive and renewable low carbon strategies for residential buildings in hot humid climates* [University of Bath]. https://researchportal.bath.ac.uk/files/191657043/Yahya_thesis_Redacted.pdf
Alam, M., Jamil, H., Sanjayan, J., & Wilson, J. (2014). Energy saving potential of phase change materials in major Australian cities. *Energy and Buildings*, *78*, 192–201. https://doi.org/10.1016/j.enbuild.2014.04.027
APSR. (2020). *Annual report of the Authority for Public Services regulation 2020*. Authority for Public Services Regulation.
ASHRAE. (2014). ASHRAE Guideline 14-2014: Measurement of Energy, Demand, and Water Savings. In *ASHRAE Guideline 14-2014* (Vol. 4).
Berkeley, L., Ridge, O. A. K., Ut-battelle, M. B. Y., For, A., Energy, S., Or, D., In, T., Form, A. N. Y., By, O. R., Means, A. N. Y., & The, W. (2018). *Engineering Reference*.
Frigione, M., Lettieri, M., & Sarcinella, A. (2019). Phase change materials for energy efficiency in buildings and their use in mortars. *Materials*, *12*(8). https://doi.org/10.3390/ma12081260
Hamdani, M., Bekkouche, S. M. E. A., Al-Saadi, S., Cherier, M. K., Djeffal, R., & Zaiani, M. (2021). Judicious method of integrating phase change materials into a building envelope under Saharan climate. *International Journal of Energy Research*. https://doi.org/10.1002/er.6951
JICA, & TEPCO. (2013). *Project for Energy Conservation Master Plan in the Power Sector in the Sultanate of Oman - Final Report* (Issue February).
Jin, X., Medina, M. A., & Zhang, X. (2016). Numerical analysis for the optimal location of a thin PCM layer in frame walls. *Applied Thermal Engineering*, *103*, 1057–1063. https://doi.org/10.1016/j.applthermaleng.2016.04.056
Panayiotou, G. P., Kalogirou, S. A., & Tassou, S. A. (2016). Evaluation of the application of Phase Change Materials (PCM) on the envelope of a typical dwelling in the Mediterranean region. *Renewable Energy*, *97*, 24–32. https://doi.org/10.1016/j.renene.2016.05.043
Sarri, A., Bechki, D., Bouguettaia, H., Al-Saadi, S. N., Boughali, S., & Farid, M. M. (2021). Effect of using PCMs and shading devices on the thermal performance of buildings in different Algerian climates. A simulation-based optimization. *Solar Energy*, *217*, 375–389. https://doi.org/https://doi.org/10.1016/j.solener.2021.02.024

6th International Conference on Building Energy and Environment
Eindhoven University of Technology, The Netherlands
6 - 10 July 2025

Numerical and experimental investigation of the thermal performance of an Earth-Air Heat Exchanger (EAHE) for greenhouse applications

Amir Imanloozadeh [1], William David Lubitz [2, *]

[1] *Graduate Research Assistant, School of Engineering, University of Guelph, 50 Stone Rd. E., Guelph, Ontario, Canada N1G 2W1, aimanloo@uoguelph.ca*
[2] *Associate Professor, School of Engineering, University of Guelph, 50 Stone Rd. E., Guelph, Ontario, Canada N1G 2W1, wlubitz@uoguelph.ca*

SUMMARY
This study investigates the thermal performance of a single-pipe horizontal Earth-Air Heat Exchanger (EAHE). The laboratory experiment utilized a 0.0254 m (1 inch) copper pipe embedded in a cylindrical soil volume. Air is passed through the pipe at controlled inlet temperature and volume flow rate. Temperature variations were captured using 20 thermocouples positioned at the air inlet, air outlet, and throughout the soil. Soil properties were directly measured, including density (905 kg/m3), moisture content (50.62%), thermal conductivity (0.339 W/m·K), and specific heat capacity (2109 J/kg·K). A transient numerical model of the laboratory experiment was developed in COMSOL and validated with the experimental data. Simulations showed strong agreement with experimental data, confirming the model's accuracy. Minor discrepancies arose due to soil heterogeneity affecting thermal properties and slight inlet air temperature fluctuations. This validated energy model provides a foundation for simulation studies to optimize EAHE design and operation.

Keywords: Earth-Air Heat Exchanger, Greenhouse Energy System, Energy Modelling and Optimization.

1. INTRODUCTION

Building energy systems encompass various power generation and energy storage technologies designed to meet heating and cooling demands. One of these technologies is the Earth-to-Air Heat Exchanger (EAHE). EAHE systems consist of pipes buried in soil, often under or adjacent to a building, through which air is moved by a fan or blower. The air source can be either inside or outside the building, depending on the EAHE implementation, while the air exiting the EAHE is typically supplied to the building interior. EAHE systems utilize sensible heat transfer between the air and soil to store thermal energy in the soil surrounding the pipes to regulate indoor temperatures across diverse building applications with varying energy demands (Guezgouz et al., 2019). The primary function of EAHEs, like other heat exchangers, is to reduce the heating and cooling loads of conventional energy systems, thereby lowering operational costs and improving overall system efficiency (Pintaldi et al., 2015). Researchers have also explored the integration of EAHEs with auxiliary energy systems such as combined heat and power (CHP) units and heat pumps to enhance performance efficiency (Tian and Zhao, 2013)).

The performance of an EAHE will depend on the interior climate needs of the building, and the weather and climate of the building surroundings. There remains a significant research gap in the energy modeling and optimization of EAHEs (Aresti et al., 2018; Bordoloi et al., 2018). Accurate energy models of EAHEs would support design and optimization to maximize the benefit of an

EAHE in a building system. Some researchers have developed custom heat transfer and energy models tailored to EAHEs and their surrounding systems, while others have utilized specialized simulation tools such as ANSYS Fluent and COMSOL for fluid flow and heat transfer analysis (Al-abidi et al., 2013). Existing studies on EAHEs and building energy simulations can be broadly classified into time-dependent (transient) and steady-state models. While steady-state models are the most prevalent in the literature due to their lower computational demands and simpler calculations (Fazlikhani et al., 2017), transient models provide deeper insights into EAHE operation, and are needed to optimize an EAHE installation. Transient energy models vary in dimensional complexity, ranging from one-dimensional to three-dimensional representations. Most studies have employed one-dimensional models (Belloufi et al., 2022). These models are typically implemented using MATLAB (Belatrache et al., 2017) or Python (Misra et al., 2018), consider heat transfer only in the radial direction, omitting axial heat transfer along the pipes and surrounding soil (Benzaama et al., 2019). Two-dimensional models, which account for both radial and axial heat transfer, offer improved accuracy but require more complex calculations (Bady and Ouzzane, 2024). Three-dimensional models are generally reserved for specialized EAHE designs, often when more than one pipe is used. While COMSOL and ANSYS Fluent are the most widely used tools for EAHE energy simulations (Agrawal et al., 2018), some studies have used TRNSYS for building energy modeling, incorporating EAHEs as heat storage systems (Qi et al., 2022).

Despite the breadth of existing EAHE energy models, several challenges persist. Most studies are specific case studies of a particular EAHE installation in a particular climate, and results are often not generalizable or transferable. One major limitation of existing experimental studies is the scarcity of comprehensive datasets that cover a wide range of operational parameters. Some studies present limited experimental results, which may not be sufficient for validating detailed numerical models. Another challenge lies in accessing experimental studies that report all essential data, including air temperature at different locations, moisture content, latent heat effects, soil temperature variations, and long-term experimental results under different environmental conditions. Most numerical studies validate their models using experimental data obtained from prior research (Heyat Jilani et al., 2023). While not all studies require such extensive datasets, some investigations necessitate more data than what is typically available (Sakhri et al., 2020). Moreover, most experimental EAHE studies are conducted in outdoor settings rather than controlled environments. As a result, fluctuating parameters such as air temperature, wind speed, and solar radiation can introduce variability in test results (Ahmed et al., 2015). While some useful studies exist for model validation (e.g. (Misra et al., 2018)), there is a need for more validation datasets with complete sets of reported and measured variables.

This study aims to develop an accurate transient energy model for a horizontal EAHE that can be utilized for system optimization. Additionally, an experimental setup of a horizontal EAHE has been constructed in a controlled laboratory environment, allowing characterization of operating parameters while minimizing environmental parameter fluctuations and maintaining a fixed inlet airflow. This experiment in controlled conditions will enable validation of simulation models.

2. EXPERIMENTAL STUDY

A laboratory-scale horizontal closed-loop EAHE was designed and built for this study. A 2.54 cm (1 inch) interior diameter straight copper pipe was centered in a cylindrical container filled with

soil and insulated at both ends. The soil volume is 112 cm long and has a radial thickness of 15 cm outward from the pipe wall. A blower at the inlet of the air pipe ran continually during the experiment and producing a consistent measured mean air velocity of 10.0 m/s. The air pipe upstream of the soil was wrapped in electric heater tape and connected to a PID controller that maintained a consistent inlet air temperature of 44.75 °C in the pipe measured at the location where it enters the soil volume. Twenty thermocouples installed in the system recording inlet, outlet, before the heater, and ambient air temperatures. Thermocouples are evenly distributed inside the soil volume (3 on the outer pipe wall and 12 in the soil), measuring temperature; therefore, we record the data for 3 longitudinal segments and 5 radial layers (Fig. 1). A Keysight data logger continuously recorded data from all thermocouples during experiments.

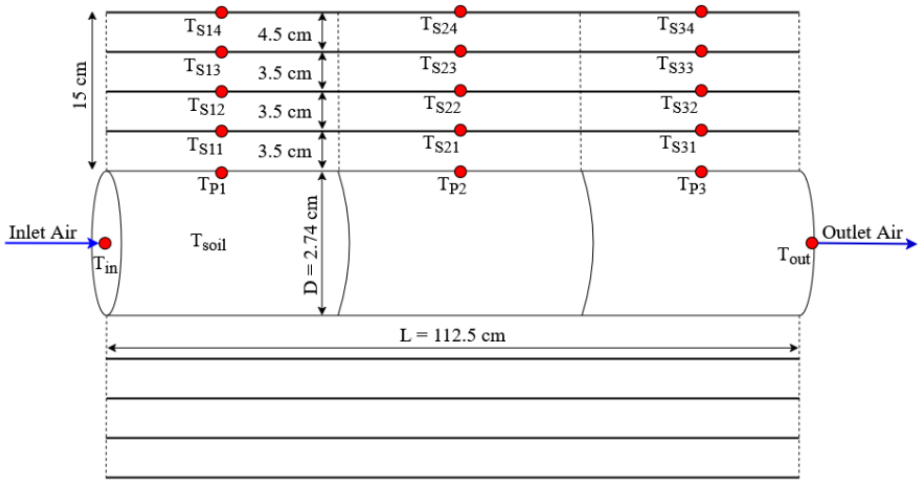

Fig. 1. Thermocouple placement in the EAHE lab experiment

Fig. 2 shows an example of experimental data collected over a 29 hour run. The experiment commenced with the activation of the fan; the heating system was started and inlet air temperature maintained at 44.75 °C beginning 40 minutes after experiment start. The several-degree increase in air temperatures during the first 40 minutes in Fig. 2 is due to waste heat from the blower motor unavoidably warming the inlet air before the heating system was engaged. Soil temperatures show an asymptotic exponential response that would be expected following a step change in inlet air temperature, with the soil closest to the pipe warming fastest and reduced rates of temperatures increase at greater radial distances from the pipe.

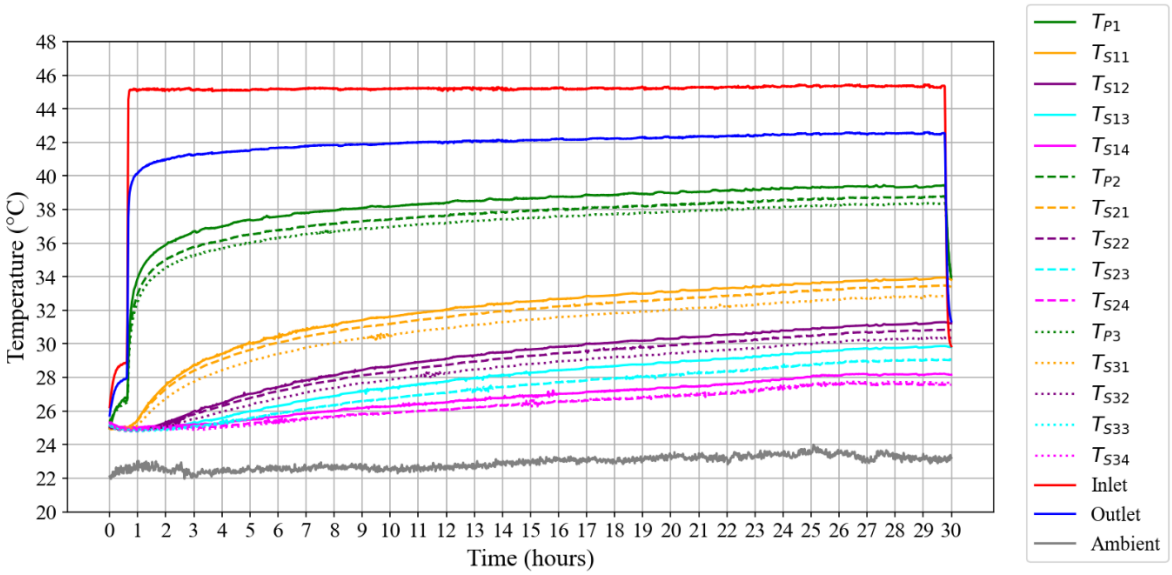

Fig. 2. Experimental results of EAHE

The soil used in the experiment was garden topsoil (Green Horizons Sod Farms, Breslau, ON, Canada). Soil density was calculated from the system mass difference before and after filling, divided by measured soil-occupied volume. Soil thermal conductivity and specific heat capacity were measured by transient line heat source method using a Decagon KD2 Pro Thermal Properties Analyser (SH1 – 04837 11323 – 04 03/31/17 with SH-1 probe) with tests conducted on multiple samples at different times and ambient. Soil moisture content was measured by oven drying. Table 1 shows the resulting measured soil parameters used in the simulations.

Table 1. Measured soil properties.

Property/Value	**Variable**	**Mean value**	**Number of tests**	**Standard deviation**
Soil thermal conductivity	k_{soil}	0.339 (W/m·K)	12	0.005 (W/m·K)
Soil heat capacity	cp_{soil}	2102 (J/kg·K)	12	29.17 (J/kg·K)
Soil density	ρ_{soil}	905 (kg/m^3)	1	-
Moisture percentage		50.62%	5	5.512%

3. NUMERICAL MODEL

A transient numerical model of the laboratory EAHE was developed in COMSOL v.6.3 using the presented experimental results to represent the lab setup. Table 2 shows the details of the parameters used in the simulation. The energy model was developed in COMSOL using the conjugate heat transfer and heat transfer in solids and fluids modules. The inlet airflow was set to a constant 44.5 °C with a 10 m/s velocity resulting in a Reynolds number based on pipe diameter of 16,000. Table 2 shows simulation parameters. Inflow and outflow boundaries were used at the pipe inlet and outlet. Heat transfer mechanisms applied include convective heat transfer between the fluid flow and the pipe wall, and conductive heat transfer between the pipe wall and the surrounding soil layers. The outer surface of the cylindrical soil volume and the soil ends were adiabatic. Simulation time period was 10 hours. Normal meshing settings were used with additional mesh refinement at the boundaries.

Table 2. COMSOL simulation parameters.

Parameter	Value	Description
T_{amb}	23 °C	Ambient air temperature
T_{in}	44.75 °C	Inlet air temperature
T_{i_pipe}	25.3 °C	Initial pipe temperature
T_{i_soil}	24.3 °C	Initial soil temperature
cp_{pipe}	385 J/kg·K	Pipe specific heat capacity
cp_{soil}	2102 ± 29.17 J/kg·K	Soil specific heat capacity
d	2.54 cm	Pipe inner diameter
D	2.74 cm	Pipe outer diameter

Parameter	Value	Description
d_{soil}	0.15 m	Soil thickness around the pipe
k_{pipe}	400 W/m·K	Pipe thermal conductivity
k_{soil}	0.339 ± 0.005 W/m·K	Soil thermal conductivity
L	1.125 m	Pipe length within soil
v_{air}	10.0 m/s	Inlet air velocity
ρ_{pipe}	8700 kg/m³	Pipe density
ρ_{soil}	905 kg/m³	Soil density
ρ_{air}	1.225 kg/m³	Air density

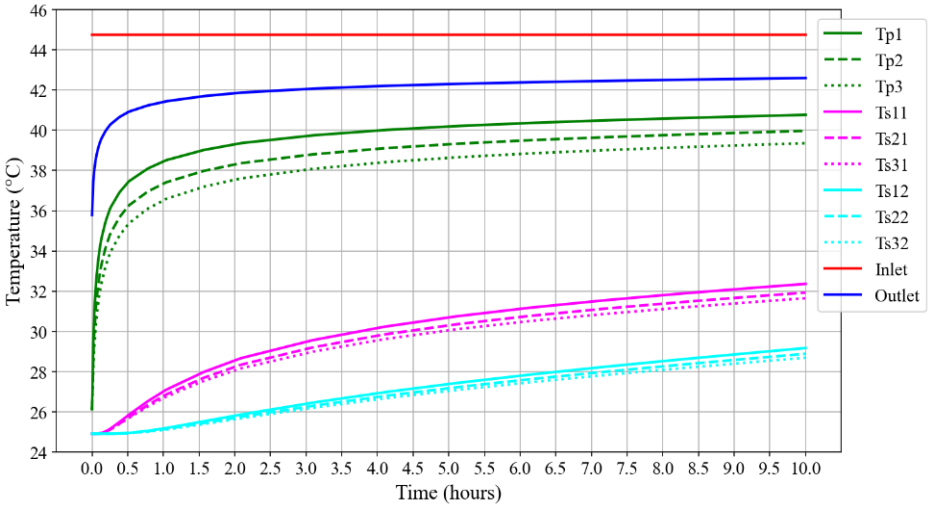

(a)

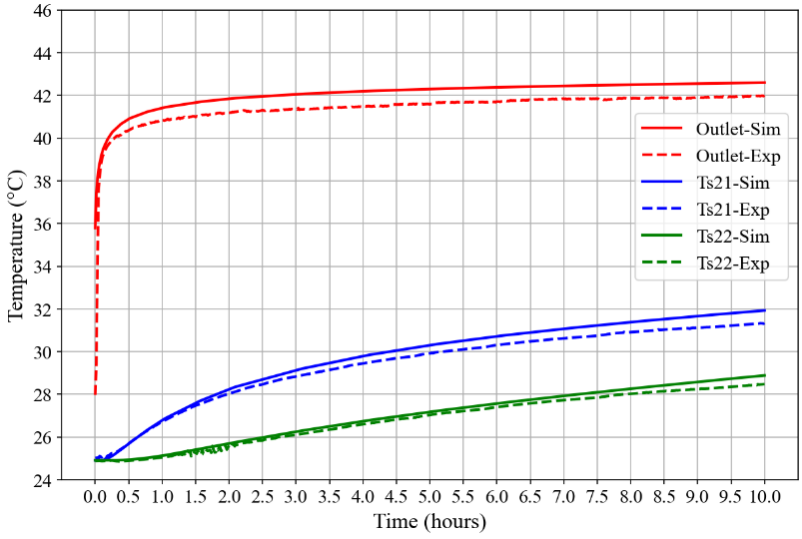

(b)

Fig. 3. (a) EAHE simulation results and (b) comparison with experimental data.

Fig. 3a shows resulting simulated and experimental data, particularly in terms of temperature variation trends over time. Fig. 3b compares simulated temperature at example soil locations to corresponding experimental data. Fig. 3 suggests good agreement between the simulations and experiment. Root mean square error (RMSE) and mean absolute error (MAE) for the TS21 node temperature comparison were 0.58 °C for RMSE and 0.35 °C for MAE. However, there are differences between the simulation and experiment. Potential sources of these differences include variation in soil properties. Even though soil density, thermal conductivity and specific heat capacity were measured, potential error remains due to probe accuracy and potential nonhomogeneity of the soil. Unavoidable variations in compaction, air, and moisture content within the soil volume could lead to variation in conductivity and heat capacity, as moisture and latent heat transfer significantly influence heat transfer. Additionally, although less impactful, the model assumes adiabatic condition at the outer soil radius, which may slightly affect results. Finally, the initial soil temperature was approximated by averaging values from different axial and radial measurement positions, introducing further potential deviation from the actual case.

The rate at which heat can be transferred into or out of storage in the soil is an important aspect of EAHE performance. Heat storage was calculated based on the temperature difference between inlet and outlet air, assuming all heat loss from the air was transferred to the soil. A sensitivity analysis was conducted to examine the impact of inlet air velocity on heat storage rates in the EAHE. Air velocities of 0.5, 1, 2, 4, 6, 8, and 10 m/s were simulated using the model. The resulting heat storage rates were then analyzed and compared with the experimental test results (Fig. 4).

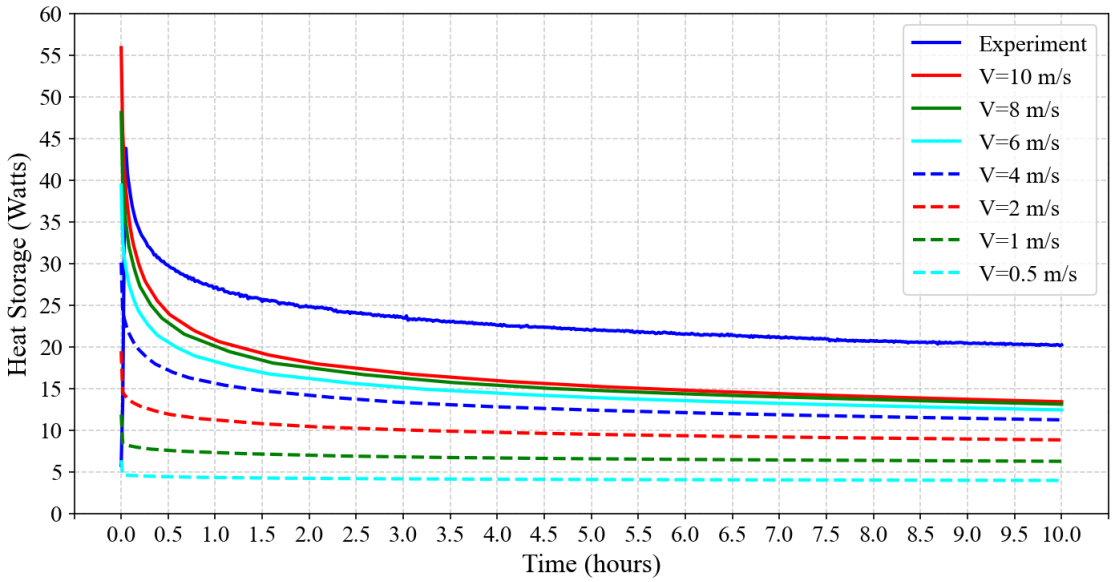

Fig. 4. Heat storage rate in EAHE for simulated and experiment models

The calculated results show an average heat storage rate of 17 W for the numerical model and 23 W for the experimental test over 10 hours of heater operation (Fig. 4). As expected, the storage rate decreases as the gradient diminishes over time. Lower air velocities result in lower outlet temperatures, as air remains in contact with the pipe and soil longer, enhancing heat absorption. A lower outlet temperature, relative to a fixed inlet, indicates greater heat transfer. Initially, heat

transfer is high near the pipe inlet due to the larger temperature difference. As air travels and its temperature nears that of the pipe and soil, especially at low velocities, heat transfer decreases. Higher velocities shorten residence time, preserve the temperature gradient and sustain a higher heat transfer rate. Higher velocities correspond to a higher mass flow rate, which increases total heat transfer into the soil, but decreases the efficiency of heat transfer from the air to the soil. (Since the air exits the EAHE at higher temperature, smaller fraction of the available thermal energy in the air is transferred to the soil.) Sensitivity analysis of inflow velocity on heat transfer rate confirms that higher velocities enhance heat transfer in the EAHE system. After prolonged operation, changes in heat transfer rate reduce as temperature gradients in the soil stabilize, reducing temperature variations at the outlet. When designing an EAHE system, factors such as achievable inlet air velocity, pressure drop and cost must be considered to find an optimal value of the inlet air velocity that satisfies different objectives.

4. CONCLUSION

This study examined a laboratory-scale earth-to-air heat exchanger (EAHE) in a controlled laboratory environment, which was then used to validate simulations of the EAHE in COMSOL software. Temperatures were measured throughout the soil volume, and soil properties including moisture content, thermal conductivity and specific heat capacity were experimentally measured to reduce uncertainties in heat transfer calculations. There was good agreement between the numerical model and experimental results, with RMSE and MAE values of 0.58 °C and 0.35 °C, respectively. A sensitivity analysis showed that higher air velocities enhance heat transfer due to increased mass flow and sustained temperature differences. This study has provided a foundation for future research on EAHE performance and optimization. The developed simulation tools will next be used to analyze various influencing parameters and explore optimal design and operational strategies for EAHEs in building thermal storage applications.

ACKNOWLEDGEMENTS

This study was part of a larger project on improving greenhouse energy efficiency funded by the Ontario Ministry of Agriculture, Food and Agribusiness (OMAFA) grant UG-T1-2022-101719.

REFERENCES

Agrawal K.K. et al., 2018. Optimization of operating parameters of earth air tunnel heat exchanger for space cooling: Taguchi method approach. Geothermal Energy 6(1), 10.

Ahmed S.F. et al., 2015. Performance assessment of earth pipe cooling system for low energy buildings in a subtropical climate, Energy Conversion and Management 106, 815–825.

Al-abidi A.A. et al., 2013. CFD applications for latent heat thermal energy storage: a review', Renewable and Sustainable Energy Reviews 20, 353–363.

Aresti L. et al., 2018. A review of the design aspects of ground heat exchangers. Renewable and Sustainable Energy Reviews 92, 757–773.

Bady, M., Ouzzane, M., 2024. Efficient operation of earth–air heat exchanger system for air cooling in a hot climate based on a new control strategy. Applied Thermal Engineering 244, 122782.

Belatrache, D et al., 2017. Numerical analysis of earth air heat exchangers at operating conditions in arid climates. International Journal of Hydrogen Energy 42(13), 8898–8904.

Belloufi, Y. et al., 2022. Transient assessment of an earth air heat exchanger in warm climatic conditions. Geothermics 104, 102442.

Benzaama, M.H. et al., 2019. Experimental and numerical analysis of the energy performance of a water/soil exchanger coupled to a cooling floor for North Africa. Geothermics 80, 8–19.

Bordoloi, N. et al., 2018. An intense review on the latest advancements of Earth Air Heat Exchangers. Renewable and Sustainable Energy Reviews 89, 261–280.

Fazlikhani, F. et al., 2017. Numerical analysis of the efficiency of earth to air heat exchange systems in cold and hot-arid climates. Energy Conversion and Management 148, 78–89.

Guezgouz, M. et al., 2019. Optimal hybrid pumped hydro-battery storage scheme for off-grid renewable energy systems. Energy Conversion and Management 199, 112046.

Heyat Jilani, Md.N. et al., 2023. Design and performance evaluation of a greenhouse integrated thin-film photovoltaic system and an earth air heat exchanger. Applied Thermal Engineering 231, 120856.

Misra, R. et al., 2018. Field investigations to determine the thermal performance of earth air tunnel heat exchanger with dry and wet soil: energy and exergetic analysis. Energy and Buildings, 171, 107-115.

Pintaldi, S. et al., 2015. A review of thermal energy storage technologies and control approaches for solar cooling. Renewable and Sustainable Energy Reviews 41, 975–995.

Qi, D. et al., 2022. Structural optimization of multi-pipe earth to air heat exchanger in greenhouse. Geothermics 98, 102288.

Sakhri, N. et al., 2020. Experimental investigation of the performance of earth-to-air heat exchangers in arid environments. Journal of Arid Environments 180, 104215.

Tian, Y., Zhao, C.Y., 2013. A review of solar collectors and thermal energy storage in solar thermal applications. Applied Energy 104, 538–553.

6th International Conference on Building Energy and Environment
Eindhoven University of Technology, The Netherlands
6 - 10 July 2025

Evaluation on the Photothermal Performance of a Semi-Transparent Phase Change Material Blind in a Double Skin Façade System

Yilin Li [1,2,3], Aiwei Luo [1], Lulu Zhu[1], Wanting Tao [1], Yuke Peng [1]

[1] *University of Shanghai for Science and Technology, Shanghai, China, yilin.li@usst.edu.cn*
[2] Jiangsu Province Engineering Research Center of *Construction* Carbon Neutral Technology, Suzhou University of *Science* and Technology, Suzhou, *China*
[3] *Key Laboratory of Ecology and Energy Saving Study of Dense Habitat, Ministry of Education, China*

ABSTRACT
Double skin facades (DSFs) are widely used in modern buildings as a sustainable design element. However, its cavity overheating or overcooling problem often leads to high energy consumption, room temperature fluctuation, and poor thermal environment. Although integrating phase change materials (PCMs) into the shading devices can improve the thermal performance of the system, most of the current systems adopted opaque metal shell blinds, which affects the light transmittance of the facade. In this paper, a PCM blind with a transparent shell was proposed for integration into DSF system. Experimental study on the proposed system was carried out during both high and low-temperature seasons. A comparison of the photothermal performance was conducted on the PCM-DSF system and DSF with traditional aluminium blind. The results show that during the high temperature season, the maximum blind surface temperature was about 52°C, which was 5.2°C lower than the aluminium blind. The cavity air temperature was stable for the PCM-DSF system and the maximum cavity air temperature was about 47°C. In addition, the 45°blind tilt angle provided a stabilized state of scattered radiation with a maximum value of about 200 W/m² for two hours. During the low temperature season, the PCM blind surface temperature with tilt angle of 45° was 17.5~21.8°C, and the thermal stability effect can last 7 hours. The PCM blind with 45° tilt angle can provide smooth scatter radiation and remains stability after a peak of 271 W/m². Therefore, the PCM blind with 45° tilt angle was able to maintain a comfortable indoor thermal environment, and stable indoor scattered radiation which helps to create a preferable indoor light environment.

Keywords: double skin façade, phase change material, photothermal performance, blind system.

1 INTRODUCTION

As urbanization accelerates, global building energy consumption continues to grow at an average annual rate of 1.5 %(Araji M T et al., 2024). Building energy consumption is the main type of energy consumption, accounting for 33 % of total energy consumption in China, and up to 40 % in the United States (Liu X J et al., 2023). As a major component of the building envelope, curtain wall play an important role in maintaining comfortable thermal and optical indoor environment. However, traditional single-layer glass curtain walls often suffer from poor natural ventilation, poor thermal comfort, susceptibility to glare, and excessive energy consumption (Shameri M A et al.,2011)(Zhou J,2010)(Blanco J M et al.,2014). As a promising passive building technology, double skin facade (DSF) shows significant potential for improving energy efficiency and indoor thermal comfort (Zhao M et al.,2022).

DSF refers to one or more layers of curtain wall structures covering a building façade, often

separated by air cavities and equipped with controlled shading systems. It can act as thermal barriers against adverse climatic influences with natural or mechanically-assisted ventilation, reduce heat loss from the building in winter. The DSF can also reduce lighting energy consumption, not only by taking into account the position and orientation of the building and interior spaces, but also by introducing internal sunshade louvers to ensure that daylight does not adversely affect the occupants (Hien W N et al., 2005).However, in the summertime, the DSF often suffer from overheating effect which increases the building's cooling energy consumption (Gratia E, 2007). The DSF overheating problem is often mitigated by ventilation or the addition of solar shading louvers, but the effect is limited.

Phase Change Materials (PCM) have attracted much attention for their applications in thermal storage and temperature regulation systems (Ahmed M M S et al.,2021)(Koželj R et al.,2021)(Meng Q et al.,2022). Integrating PCM into DSF can effectively alleviate the problem of cavity overheating in summer and reduce the cooling load; in winter, it could also release the heat stored during the day through the phase change process and reduce the heating load (Huang Y et al.,2021) (Zhang Z et al.,2023) (Zhang S et al.,2022). However, most of previous PCM integrated DSF systems are encapsulated in opaque shell, which may hinder the transparent feature of the DSF system and reduce the natural light into the building (Berardi U, 2014). Compared with conventional aluminum shell, transparent shell has good light transmission, low cost, and moisture and fire resistance, suitable for large-scale applications.

So far, there is still a relative lack of research on semi-transparent PCM blind system for DSFs, and the existing research seldom consider the impact of PCM blind systems integrated DSF on the coupling effect of indoor thermal and optical environments in buildings. Therefore, it is necessary to develop a semi-transparent PCM blind system and to evaluate the photothermal performance of the system in a DSF to comprehensively understand its influence on the indoor thermal and optical environment.

2 METHODS

2.1 Development of the PCM blind in DSF system

Figure 1(a) demonstrates the schematic diagram of the PCM blind in DSF system with transparent polycarbonate encapsulated paraffin PCM to optimize the DSF photothermal performance. As shown in Figure 1(b), the integrated system is with a size of 940 mm × 790 mm and an air cavity of 180 mm. The blind tilt angle can be adjusted to adapt to different seasons and sunlight; The PCM was encapsulated with a transparent polycarbonate shell to ensure light transmittance and to support the PCM to maintain light transmittance in the process of heat absorption and heat release.

The experimental test rig was located on the roof of an office building in University of Shanghai for Science and Technology, facing 30° southeast. The experiments were conducted from July 1st to August 31st, 2022 during the high-temperature season, and from January 1st to January 8th, 2022 during the low-temperature season. Data collection was conducted, including measurements of blind surface temperature, cavity temperature, indoor temperature, solar radiation, and wind speed. The distribution of the experimental measurement points is shown schematically in Figure 1(c).

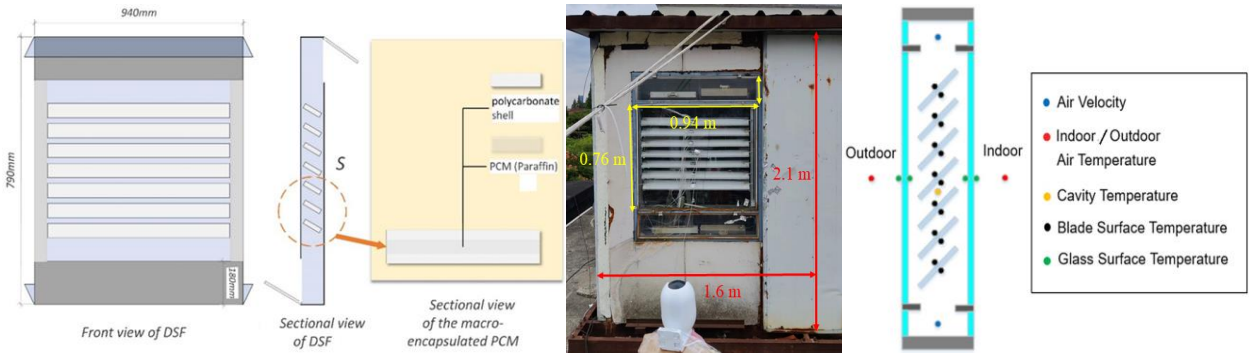

(a) (b) (c)

Figure 1 (a). Schematic diagram of DSF integrated with the PCM blind. **(b).** Experimental platform of the PCM-DSF system. (**c).** Schematic diagram of experimental measurement points

2.2 Characterization of optical properties of PCM

The spectral properties are directly related to the absorption and reflection ability of the PCM , thus the transmission spectra properties of the PCM were measured and analysed. The transmission spectra tests were conducted by using a ultraviolet(UV)-3600 plus dual-beam UV-visible spectrophotometer manufactured by Shimadzu, and the principle of the UV-3600 plus dual-beam UV-visible spectrophotometer is shown in Figure 2. In order to determine the optical constants of PCM in the high temperature and low-temperature seasons, the transmission spectra of two PCMs before and after the phase transition were examined at different optical ranges. The temperature was kept constant during the experiment, and the transmission spectra of selected paraffin waxes with melting points of 40 ℃ and 20 ℃ were measured before and after the phase transition at optical ranges of 5 mm and 10 mm, respectively. In addition, the transmission spectra of 40 ℃ paraffin wax were measured at 65 ℃ and 20 ℃ paraffin wax at 35 ℃.

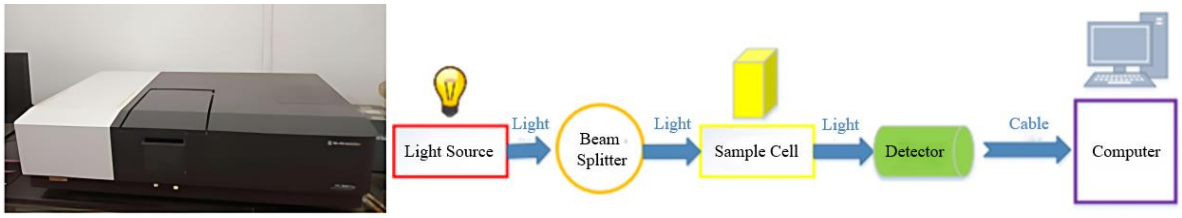

Figure 2 UV-3600plus Dual-beam UV-Vis Spectrophotometer and its main components diagram

2.3 Coordination index of the system photothermal performance

A coordination index was proposed for evaluating the photothermal performance of the PCM-DSF system, which encompasses two proportion: indoor heat gain and natural lighting. The indoor heat gain index mainly considers the radiant heat transferred through the DSF and the heat absorbed by the PCM blind. Meanwhile, natural lighting is represented by the average daylighting factor (ADF), where a higher ADF value corresponds to better lighting quality. A coupling coordination index was applied to achieve a balance between lighting and thermal performance, and an entropy weighting method was used to calculate the weights of the index. The coupling degree (C) measures the interaction between the subsystems; the comprehensive coordination index (T) indicates the overall coordination effect; and the coupling coordination degree (D) reflects the overall coordination quality, with a larger D value signifying better coordination. These indices enable an assessment of the photothermal performance and coordination of the PCM-DSF system under various operating conditions. The coupling coordination degree is calculated as follows:

$$C = \frac{(\prod_{i=1}^{n} U_i)^{\frac{1}{n}}}{\frac{1}{n}\sum_{i=1}^{n} U_i} \quad (1)$$

$$T = \sum_{i=1}^{n} \omega_i U_i \quad (2)$$

$$D = \sqrt{CT} \quad (3)$$

Table 1. Classification of coupling coordination relationships

Type of coupled coordination	Degree of coupling coordination	Coupling Harmonization Level
Dysfunctional Decline Type	[0.0,0.1)	Extreme Dissonance
	[0.1,0.2)	Severe Dissonance
	[0.2,0.3)	Moderate Dissonance
	[0.3,0.4)	Mildly dysfunctional
Coordinated Transitional	[0.4,0.5)	Nearly dysfunctional
	[0.5,0.6)	Barely coordinated
Coordinated Developmental	[0.6,0.7)	Elementary coordination
	[0.7,0.8)	Intermediate coordination
	[0.8,0.9)	Good coordination
	[0.9,1.0]	Quality coordination

3 RESULTS AND DISCUSSION

3.1 Analysis of PCM transmissivity

Figure 3(a) refers to the transmission spectrum of paraffin wax at 40 ℃ for different light ranges. Decreasing the optical range increased the transparency of paraffin waxes in the UV and visible wavelengths to about 58.06 % at a range of 10 mm. The lowest transmittance of paraffin waxes in the visible wavelengths was about 62.74 % at a range of 5 mm. In the near- ultraviolet(NUV) band from 200 to 400 nm, the optical range decreases, and the difference in the transmittance of paraffin wax rises rapidly with the wavelength, with a maximum of 11.28 percent in the UV band of 377 nm, while the growth rate of the transmittance of paraffin waxes in the visible band from 400 to 900 nm decreases gradually.

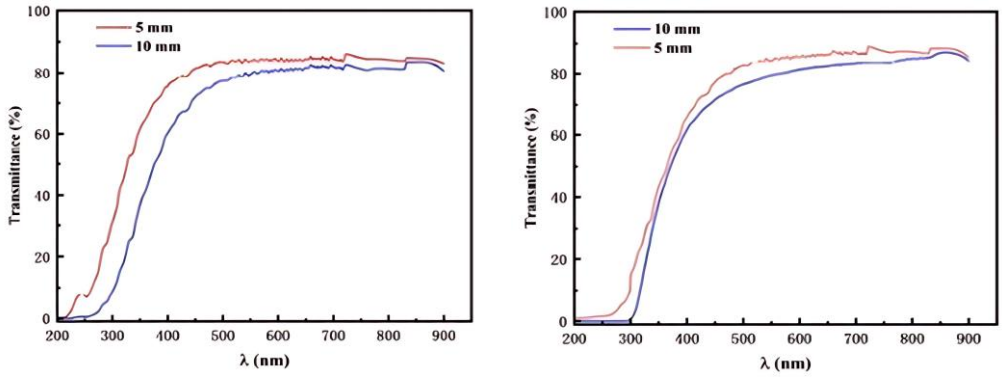

(a) (b)

Figure 3 Transmission spectra of paraffin waxes at different temperatures with different optical intervals (a)at the 40 ℃ (b) at the 20 ℃

Figure 3(b) shows that the maximum difference in the transmittance of 20 °C paraffin at 35 °C for different optical ranges was about 27.41 % in the NUV band. In the visible band, the effect of optical range on transmittance gradually decreases and finally reaches a steady state, and the maximum difference in transmittance is about 15.25 %. The lowest transmittance of paraffin wax in the visible band was about 60.54 % for the 5 mm optical range, and the lowest visible transmittance of paraffin wax in the visible band was about 75.77 % for the 10 mm optical range. The transmittance difference of paraffin waxes increased rapidly with the wavelength as the light range decreased in the near-ultraviolet band, and the transmittance difference reached a peak value of 27.41 % at 330 nm.

3.2 System performance during high temperature season

As shown in Figure 4(a), the PCM blind maintains the cavity temperature at 44~46.2 ℃ during peak hours (10:00-13:30), lowering the peak temperature by 3.1 ℃ and the average temperature by 2.6 ℃ compared to the aluminum blind. At night, their heat release slows the cooling process, demonstrating optimal thermal storage. Overall, the PCM blind reduces the minimum temperature to 20 ℃, outperforming aluminum blind (29 ℃), effectively enhancing building thermal comfort and energy efficiency.

Figure 4(b) shows that as the blind tilt angle increases, indoor heat gain decreases due to increased shading. On sunny days, external circulation ventilation is more effective than the fully enclosed mode in reducing heat gain between 0° and 60°, enhancing heat dissipation. Beyond 60°, both modes converge, indicating that a large tilt angle reduces the effectiveness of external ventilation. On cloudy days, with weaker solar radiation, the difference between the two modes is smaller, but external circulation still slightly reduces heat gain in the 0°–60° range, with the difference diminishing as the tilt angle increases.

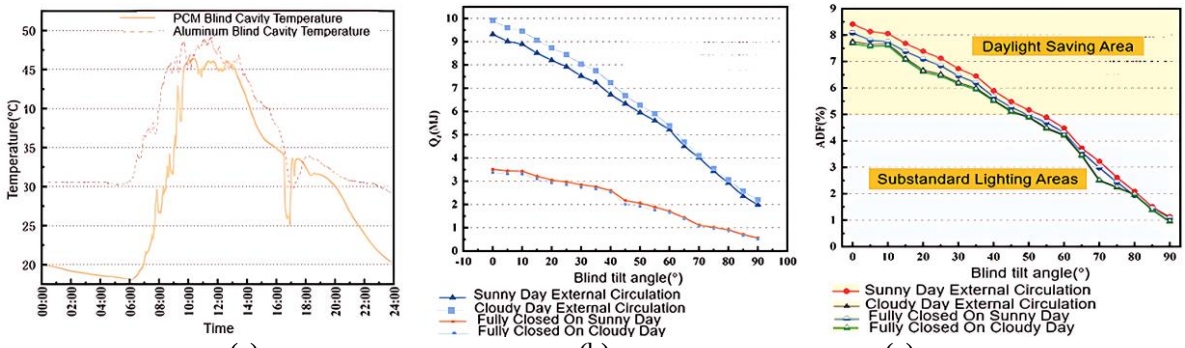

(a) (b) (c)

Figure 4. (a) Comparison of cavity temperatures between aluminum blind and PCM blind systems on a typical day. **(b)** Indoor heat gain under different conditions on a typical day. **(c)** Average indoor lighting coefficients under different working conditions on a typical day.

Figure 4(c) shows that the ADF is higher for external circulation than for the fully enclosed condition on both sunny and cloudy days. On sunny days, the ADF for external circulation is 0.2%–0.5% higher than for the fully enclosed condition at tilt angles between 0° and 60°, with the difference decreasing as the angle increases. On cloudy days, the ADF difference is minimal. Overall, ADF decreases with higher tilt angles, following similar trends for both conditions. On sunny days, external circulation achieves an ADF greater than 5% in the 0°–50° range, meeting lighting requirements and improving indoor lighting. Under cloudy conditions, the impact on

daylighting is minimal due to the small ADF difference.

3.3 System performance during low temperature season

As shown in Figure 5(a), the PCM blind excels in regulating cavity temperature. During the day (10:01-13:15), its PCM absorbs heat, reducing the peak temperature by 12.3 °C and delaying it by 36 minutes. In the evening (15:30-18:28), heat release slows cooling, extending the effect for about 3 hours. Overall, the PCM blind stabilizes temperature throughout the day, enhancing building thermal comfort and energy efficiency.

Figure 5(b) shows that as the blind tilt angle increases, radiative heat gain in the PCM-DSF system decreases under both sunny and cloudy conditions, primarily due to increased solar shading. On sunny days, internal circulation ventilation results in higher heat gain than the fully enclosed mode at tilt angles between 0° and 90° because it utilizes solar radiation more efficiently. However, as the tilt angle increases, the difference between the two modes decreases. On cloudy days, weaker solar radiation reduces heat gain for both modes, with minimal differences, indicating that ventilation mode has little impact on heat gain.

Figure 5(c) shows that indoor heat gain in the PCM-DSF system decreases with higher blind tilt angles on both sunny and cloudy days. On sunny days, heat gain decreases at 0°–55° due to shading, increases slightly at 55°–60° from direct radiation, and decreases again at 60°–90° as shading increases. On cloudy days, heat gain decreases at 0°–40° with shading, increases slightly at 40°–45° from radiation absorption, and declines at 45°–90°. Overall, heat gain decreases with higher tilt angles, showing similar trends for both conditions. On sunny days, internal circulation ventilation leads to higher heat gain than the fully enclosed mode at 0°–55°, with the difference reducing as the angle increases. On cloudy days, the difference is greater at 0°–40° but diminishes with higher angles, weakening the impact of ventilation mode.

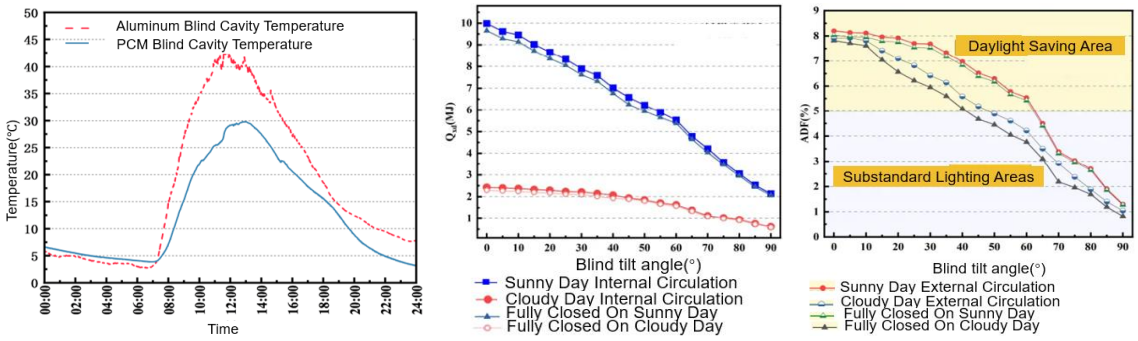

(a) (b) (c)

Figure 5. **(a)** Comparison of cavity temperatures between aluminum blind and PCM blind systems on a typical day. **(b)** Indoor heat gain under different conditions on a typical day. **(c)** Average indoor lighting coefficients under different working conditions on a typical day.

3.4 Optimal operation modes of the system under different seasons

Based on the coupling coordination model, the coupling coordination degree D value of the PCM-DSF system is analyzed in different climates with different tilting angles of blinds, and the corresponding control strategies for the tilting angle of blinds and ventilation mode are proposed. On a sunny day in the high-temperature season, the maximum coordination D is 0.73 when the external circulation ventilation mode is adopted and the tilt angle of blinds is 60°, which indicates

that the heat absorption and storage effect is good and the indoor temperature can be reduced effectively. On cloudy days, the maximum coordination D is 0.747, indicating the best performance. During the low-temperature season, the internal circulation ventilation mode has the highest D value with parallel blinds, which helps heat release and increases the room temperature. On cloudy days, a 10° inclination angle achieves the best performance. Meanwhile, the inclination range can be adjusted according to the D-value, which makes the system optimally coordinated in terms of natural lighting and comfort. The differences between model predictions and experimental data were 8.2% and 5.3%, respectively, confirming the model's accuracy and supporting its optimal design.

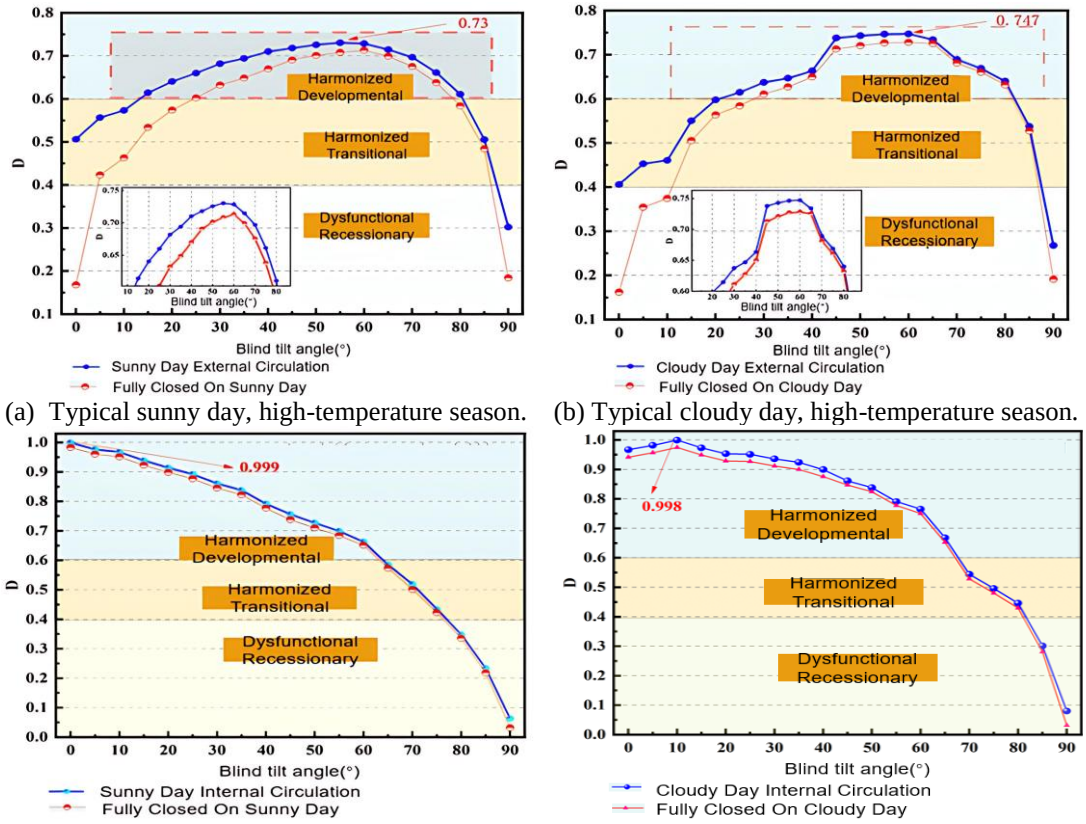

(a) Typical sunny day, high-temperature season. (b) Typical cloudy day, high-temperature season.

(c) Typical sunny day, low-temperature season. (d) Typical cloudy day, low-temperature season.

Figure 6. (a) Harmonization of photo-thermal indexes for PCM-DSF under different climatic conditions

4 CONCLUSION

This research paper centers on the PCM-DSF system to analyze its photothermal regulation performance. The experimental results show that liquid paraffin improves the lighting effect due to the low extinction coefficient in the visible light band, while solid paraffin reduces the heat gain from solar radiation through the high extinction coefficient. The comprehensive indoor heat gain index was established by considering the effects of louver inclination angle on transmitted radiation, long-wave radiation, and convective heat transfer. Meanwhile, based on the influence of the blind inclination angle on the uniformity of indoor natural lighting, the average lighting coefficient index is established. Combined with the coupled coordination model, the PCM-DSF photothermal performance evaluation system is constructed. For sunny days in the high-temperature season, the external circulation ventilation mode is recommended, and the louver

inclination angle is 60°, while the 60° inclination angle is optimal for cloudy days. On sunny days in low-temperature seasons, it is recommended to use the internal circulation ventilation mode with an inclination angle of 0°. In the range of 0~25° inclination angle, the system can maintain an excellent coordination level. When the blind inclination angle is set to 10° inclination angle on cloudy days in the low-temperature season, the performance is optimal.

To conclude, the PCM blind can provide satisfactory thermal and optical performance as compared with conventional aluminum blinds. Future studies can optimize PCM-DSF control strategies with intelligent technology for energy management and environmental monitoring.

Acknowledgment

This research was supported by Jiangsu Province Engineering Research Centre of Construction Carbon Neutral Technology (Grant No. JZTZH2023-0201), Key Laboratory of Ecology and Energy Saving Study of Dense Habitat, Ministry of Education (Grant No. 20230102), National Natural Science Foundation of China (Grant No. 52008245), Shanghai Sailing Program (Grant No. 20YF1432000).

References

Araji M T,Elmalky A M,Yao M G.,2024.Experimental validation of ventilated double skin facades aided by neural networks and thermal modelling for heating demand reduction.Building and Environment 256,111500.

Liu X J, Shen C, Wang J L, et al.,2023. Static and dynamic regulations of photovoltaic double skin facades towards building sustainability: A review. Renewable & Sustainable Energy Reviews 183.

Shameri M A, Alghoul M A, Sopian K, et al. ,2011.Perspectives of double skin façade systems in buildings and energy saving. Renewable and Sustainable Energy Reviews15(3): 1468-75.

Zhou J, Chen Y.,2010. A review on applying ventilated double-skin facade to buildings in hot-summer and cold-winter zone in China. Renewable and Sustainable Energy Reviews 14(4): 1321-8.

Blanco J M, Arriaga P, Rojí E, Cuadrado J.,2014. Investigating the thermal behavior of double-skin perforated sheet façades: Part A: Model characterization and validation procedure. Building and Environment 82: 50-62.

Zhao M, Mehra S-R, Künzel H M.,2022. Energy-saving potential of deeply retrofitting building enclosures of traditional courtyard houses – A case study in the Chinese Hot Summer-Cold-Winter zone. Building and Environment 217: 109106.

Gratia E, De Herde A.,2007. Are energy consumptions decreased with the addition of a double-skin?. Energy and Buildings 39(5): 605-19.

Ahmed M M S, Radwan A, Serageldin A A, et al.,2021. The thermal potential of a new multifunctional sliding window . Solar Energy 226: 389-407.

Koželj R, Mlakar U, Zavrl E, et al.,2021. An experimental and numerical analysis of an improved thermal storage tank with encapsulated PCM for use in retrofitted buildings for heating. Energy and Buildings, 2021, 248: 111196.

Meng Q , Xi Y , Ren X, et al.,2022. Thermal Energy Storage Air-conditioning Demand Response Control Using Elman Neural Network Prediction Model. Sustainable Cities and Society 76: 103480.

Huang Y, El Mankibi M, Cantin R, Coillot M.,2021. Application of fluids and promising materials as advanced inter-pane media in multi-glazing windows for thermal and energy performance improvement: A review. Energy and Buildings 253: 111458.

Zhang Z, Zhang N, Yuan Y, et al.,2023.Thermal performance analysis of an existing building heating based on a novel active phase change heater. Energy and Buildings 278: 112646.

Zhang S, Pu L, Mancin S, et al.,2022. Experimental study on heat transfer characteristics of metal foam/paraffin composite PCMs in large cavities: Effects of material types and heating configurations. Applied Energy 325: 119790.

Berardi U, Wang T., 2014. Daylighting in an atrium-type high performance house. Building and Environment 76: 92-104.

Hien W N, Liping W, Chandra A N, et al.,2005. Effects of double glazed facade on energy consumption, thermal comfort and condensation for a typical office building in Singapore. Energy and Buildings 37(6): 563-72.

6th International Conference on Building Energy and Environment
Eindhoven University of Technology, The Netherlands
6 - 10 July 2025

Performance and optimization study of a novel biomimetic bamboo-joint latent heat thermal energy storage system

Senlin Chen [1], Weilan Wu [2], Huating Zhang [3], Tiecheng Zhou [4], Yimin Xiao [5*]

[1]*College of Civil Engineering, Chongqing University, China, 754761808@qq.com*
[2]*CMCU Engineering Co., Ltd, China, wwl1971123@126.com*
[3]*CMCU Engineering Co., Ltd, China, 20231601115G@stu.cqu.edu.cn*
[4]*CMCU Engineering Co., Ltd, China, ztc18875207580@126.com*
[5]*College of Civil Engineering, Chongqing University, China, xiaoyimin@cqu.edu.cn (Corresponding author)*

SUMMARY
To enhance the efficiency of energy storage systems, this study proposed a novel biomimetic bamboo-joint latent heat thermal energy storage system (BBJ-LHTES), inspired by the structural characteristics of natural bamboo joints. A numerical model of the BBJ-LHTES system was developed using computational fluid dynamics (CFD), and the PCM melting process was compared, validated, and analyzed across three cases to evaluate system performance. The results indicated that the biomimetic bamboo-joint structure expanded the heat transfer area and significantly enhanced the PCM melting rate. When the biomimetic structure was positioned in the lower section of the energy storage system, the melting process was accelerated, the complete melting time of the PCM was reduced by 40 %, and the heat storage rate of the system was increased by up to 29.5 %. Additionally, the biomimetic structure facilitated vortex formation and intensified fluid disturbances within the system, thereby promoting heat transfer.

Keywords: Biomimetic bamboo-joint structure, Enhanced heat transfer, Latent heat storage, Phase change material

1. INTRODUCTION

With the global emphasis on achieving the "dual-carbon" targets and the increasing energy demand, phase change energy storage technology has garnered significant attention from the academic community. However, the large-scale application of phase change energy storage technology has been hindered by challenges related to heat transfer enhancement (Zheng et al., 2018). In recent years, fins have been widely employed by researchers to improve the heat transfer performance of shell-and-tube latent heat thermal energy storage (LHTES) systems, owing to their simple structure, low cost, and high efficiency.

In studying the effects of different fin shapes on the thermal performance of LHTES systems, Low et al. (Low et al., 2024) reviewed the geometric configurations of fins in various systems and classified them into longitudinal, annular, stepped, pin-shaped, and plate-type fins, thereby providing theoretical and technical guidance for system design. Dekhil et al. (Dekhil et al., 2021) analyzed the effect of longitudinal fins on LHTES systems and found that the melting rate increased by 27 % compared to that of systems without fins. Yang et al. (Yang et al., 2020) proposed a design employing non-uniformly distributed annular fins to address the uneven distribution of liquid fraction during PCM melting. The results showed that the PCM melting time and the average temperature difference were reduced by 62.8 % and 34.4 %, respectively. Baby and Balaji (Baby and Balaji, 2013) experimentally investigated PCM melting using aluminum pin fins in quantities of 33, 72, and 120. They found that the configuration with 72 fins exhibited the highest liquid fraction. Although the aforementioned fin designs effectively

enhanced heat transfer, the low thermal conductivity of PCM continued to hinder the optimization of LHTES system performance. This highlights the urgent need for new strategies to improve the performance of LHTES systems. Among these, innovative fin shapes represent a promising approach for improving system performance (Tian et al., 2021).

Nature has provided inspiration for addressing many challenges in heat transfer enhancement. Biomimetic design methods have recently attracted significant attention due to their potential to enhance thermal performance in energy storage systems by leveraging the principles of thermodynamics and fluid dynamics, and have been applied in optimizing LHTES systems (Rashid et al., 2025). Diaz and Yaconi (Diaz and Yaconi, 2023) numerically investigated PCM charging and discharging behavior in an annular LHS system equipped with tree-like and straight fins. The results indicated that tree-like fins outperformed straight fins in terms of thermal performance. Moreover, reducing the length of fin branches relative to the maximum fin length increased thermal contact between fins and PCM, thereby enhancing thermal performance. Sheikholeslami et al. (Sheikholeslami et al., 2016) proposed a novel fin geometry inspired by the crystalline structure of snowflakes. The branching pattern of the snowflake-shaped fins led to a more uniform temperature distribution across the fin surface, which enhanced effective thermal conductivity and significantly improved heat storage performance. Ren et al. (Ren et al., 2022) designed a vertical LHTES system incorporating an optimized spider web-shaped fin structure using response surface methodology. The study revealed that optimizing parameters such as spider web fin spacing, main fin thickness, and branching fin thickness shortened PCM solidification time and enhanced heat dissipation in the LHTES system. Specifically, reduced fin spacing improved heat transfer, increased main fin thickness decreased thermal resistance, and thicker branching fins led to a reduction in PCM volume. Redoine et al. (Redoine et al., 2024) introduced a novel approach by incorporating hexagonal honeycomb-shaped annular fins into the LHTES system. The results demonstrated that the inclusion of honeycomb fins significantly enhanced heat transfer, reducing PCM melting time from 840 to 216 seconds due to the increased heat transfer surface area. These studies collectively demonstrated that biomimetic structural designs significantly improved the energy storage efficiency of LHTES systems. Additionally, Gao et al. (Gao et al., 2024) inspired by the internal air channel distribution of lotus roots, proposed a new heat transfer enhancement technique and evaluated its thermal storage performance through numerical simulations. The results indicated that, compared to conventional LHTES systems, the bionic lotus root-inspired design reduced total PCM melting time by 89.1 %. This study offers valuable insights into improving LHTES system performance through biomimetic optimization of internal flow channel structures.

The literature review reveals that current strategies for optimizing LHTES system performance primarily involve structural modifications such as adding fins to increase heat transfer area or employing biomimetic structures to optimize internal flow channels. Accordingly, this study proposes a biomimetic bamboo-joint latent heat thermal energy storage system (BBJ-LHTES), inspired by the structural morphology of bamboo joints. The bamboo-joint structure extends outward from the heat exchange tube, simultaneously influencing heat transfer processes both inside and outside the tube. This design not only enlarges the heat transfer surface area but also induces flow disturbances within internal channels, thereby enhancing heat transfer and improving the system's energy storage efficiency. Initially, a transient numerical model was developed to simulate the melting heat transfer process. Based on the validated model, the

optimized OBBJ-LHTES system was compared with both the conventional shell-and-tube LHTES system and the original BBJ-LHTES design. The thermal performance of different biomimetic configurations was evaluated in terms of liquid fraction, temperature distribution, and flow field characteristics. This study is an extension of biomimetic design research for LHTES systems.

2. PHYSICAL AND MATHEMATICAL MODELS

2.1. Physical model

Fig. 1 illustrates the schematic of the BBJ-LHTES system, which consists of two concentric cylinders. The outer pipe has an inner diameter of 62 mm, while the bamboo-joint-shaped steel inner pipe features an inner diameter of 22 mm and a total length of 200 mm. The inner pipe serves as the fluid domain, and the annular space between the inner and outer pipes is filled with PCM. A high-temperature heat transfer fluid (HTF) flows through the inner pipe, transfers heat to the PCM, and then exits the system. Due to the symmetrical distribution and rotational symmetry of the system, the heat transfer characteristics remain consistent in the radial direction. To improve computational efficiency, the domain was simplified to a two-dimensional (2D) model, as shown in Fig. 1(c), while Fig. 1(b) presents the three-dimensional (3D) schematic. The bamboo-joint structures surrounding the inner pipe are defined by the joint spacing (l), the side length of the protruding triangle (h), and the interior angle (θ).

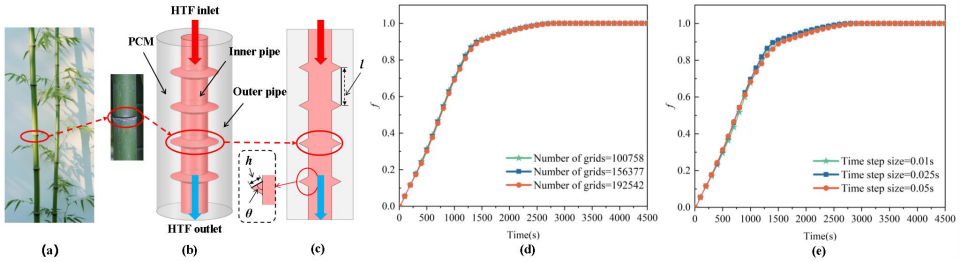

Figure 1. (a) Natural bamboo-joint structure; (b) 3D structure of the BBJ-LHTES system; (c) Simplified 2D model; (d) Grids independence; (e) Time steps independence

2.2. Mathematical model

Accurately tracking the phase change interface is a critical challenge in numerical simulations. The enthalpy-porosity method is considered the most appropriate approach, as it eliminates the need for explicitly defining the phase change interface. To ensure accurate simulation results, the following assumptions were adopted in the mathematical model (Shademan and Hossein Nezhad, 2021): (1) the liquid phase of the PCM is considered to be an incompressible laminar flow state; (2) the PCM density uses Boussinesq assumptions; (3) the contact thermal resistance between the PCM and the inner pipe, as well as the bionic structure surface, is neglected; and (4) the viscous dissipation effects are neglected. Based on these assumptions, the governing equations are simplified as follows.

Continuity equation :

$$\frac{\partial u}{\partial x}+\frac{\partial v}{\partial y}=0 \tag{1}$$

Where u, v represent the velocity components of the fluid in the x and y directions, respectively.
Momentum equation:

$$\frac{\partial V}{\partial t} + \vec{V} \bullet \nabla \vec{V} = \frac{1}{\rho}\left(-\nabla P + \mu \nabla^2 \vec{V} + \rho \vec{g} \beta \left(T - T_{ref}\right)\right) + \vec{S} \quad (2)$$

Where v represents the fluid velocity; ρ is the density of the phase change material; P denotes pressure; μ is the dynamic viscosity of the fluid; g is the gravitational acceleration; T is the temperature, T_{ref} is the reference temperature; β is the thermal expansion coefficient, and S is the source term.
The porosity method treats the mushy zone as a porous medium, where porosity is the liquid fraction of the unit. When the unit is a solid, the porosity is zero, and the source term is zero. When considering the phase change induced by natural convection, Darcy's law damping term is added to the momentum equation as a source term, which is defined as follows:

$$S = - C \frac{(1-f)^2}{f^3 + \varepsilon} \quad (3)$$

Where C is a constant for the mushy zone with a range of 10^5 to 10^8 and was assumed to be 10^5 in this study. ε is a small number (0.001), used here to prevent mathematical singularities. f represents the liquid fraction in the computational domain, varying between zero (solid phase) and one (liquid phase), and is defined as follows:

$$f = \begin{cases} 0, & T < T_s \\ \frac{T - T_s}{T_l - T_s}, & T_s \le T \le T_l \\ 1, & T > T_l \end{cases} \quad (4)$$

Where T is the temperature of the phase change material.
Energy equation:

$$\frac{\partial(\rho H)}{\partial t} + \nabla \cdot \left(\rho \vec{V} H\right) = \nabla \cdot (k \nabla T) \quad (5)$$

Where k is the thermal conductivity of the phase change material, H is the enthalpy, defined as the sum of the sensible heat enthalpy H_{sens} and the latent heat enthalpy H_{lat}, defined as follows:

$$H = H_{sens} + H_{lat} = H_{ref} + \int_{T_{ref}}^{T} C_p \, dT + fL \quad (6)$$

Where C_p is the specific heat capacity of the phase change material and H_{ref} is the reference enthalpy at the reference temperature T_{ref}.

In practical applications, significant temperature differences between the LHTES system and its surroundings necessitate the consideration of heat loss. In this study, an empirical correlation for natural convection in infinite space was used to calculate the heat transfer coefficient h, which characterizes the heat exchange between the system and the environment (Al-Urabi and Salman, 1980):

$$Nu = \frac{hD}{\lambda} = 0.59(GrPr)_m^{1/4} \quad (7)$$

Where λ represents the thermal conductivity of air, D is the characteristic length of LHTES unit. To quantitatively compare and analyze the performance of thermal storage units with different bionic structures, the following parameters were used in this study.The heat storage rate at which the PCM melts when absorbing heat can be expressed as:

$$\eta_v = \frac{Q_{pcm}=mc_p(T_c-T_i)+mfL}{t} \quad (8)$$

Where the total thermal energy storage Q_{pcm} is divided into latent and sensible heat when they absorb heat and melt, Tc is the current temperature and Ti is the initial temperature. In addition, L is the latent heat value and C_p is the specific heat capacity.

3. NUMERICAL METHODS AND INITIAL CONDITIONS

3.1. Numerical calculation methods

In this study, specialized software was utilized for mesh generation and for solving the governing equations, ensuring both computational accuracy and efficiency. The mesh was generated using Mesh software, while Fluent 2021 R1 with the solidification/melting model was utilized to solve the governing equations. The SIMPLE algorithm was adopted for pressure-velocity coupling, while second-order upwind schemes were used for the discretization of the energy and momentum equations, and the PRESTO! scheme was applied for pressure discretization (Kalapala and Devanuri, 2021). A time step of 0.025 s and a mesh with 156,377 cells were selected based on a mesh independence analysis to balance computational efficiency and accuracy (Fig. 1). As shown in Fig. 2(a), the numerical model was validated against experimental data from Liu et al. (2023), exhibiting good agreement, with a maximum average absolute error of 4.61 ℃ and a relative error of 8.19%, thereby confirming the model's reliability for further analysis.

3.2. Initial conditions

The inlet temperature and velocity of the HTF were set to 350 K and 0.01 m/s, respectively, while the initial temperature of the system was 295 K. Coupled boundaries were defined at the interfaces between the biomimetic structure, the PCM, and the HTF. As shown in Table 1, the thermophysical properties of the PCM are provided in reference (Liu et al., 2023). Numerical simulations were conducted to compare three configurations: Case A (shell-and-tube LHTES), Case B (BBJ-LHTES), and Case C (optimized BBJ-LHTES with the biomimetic bamboo-joint structure positioned in the lower section). The raised triangular section in Cases B and C occupied 2.95 % of the PCM-filled volume, as illustrated in Fig. 2(b).

Table 1. Thermophysical values of paraffin wax

Thermophysical properties	Density (kg/m^3)	C_p ($J/(kg \cdot K)$)	Thermal conductivity ($W/(m \cdot K)$)	Dynamic viscosity ($kg/(m \cdot s)$)	Thermal expansion coefficient (K^{-1})	Latent heat of fusion (J/kg)	T_m (K)
Numerical value	880 (s)/ 760 (*l*)	2000	0.2	0.005302	0.001	160000	316-322

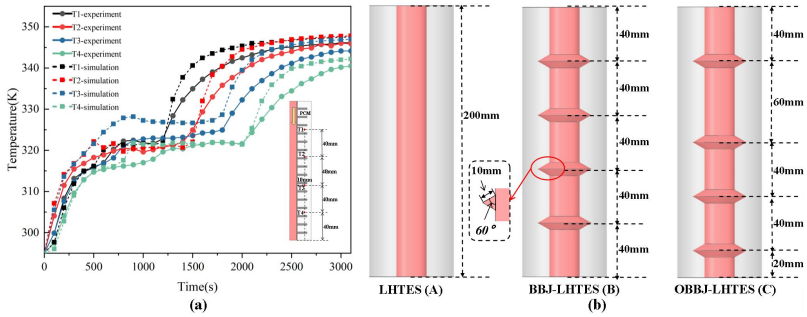

Figure 2. (a) Comparison between experimental data and simulation results; (b) Simulation cases A, B, C

4. RESULTS AND DISCUSSION

4.1. Analysis of PCM melting situation

Fig. 3(a) illustrates the variation of the liquid fraction of the PCM over time for different cases. The BBJ-LHTES (Case B) and OBBJ-LHTES (Case C) systems, both incorporating the biomimetic bamboo-joint structure, exhibited significantly higher PCM melting rates compared to the conventional shell-and-tube LHTES system (Case A). As shown in Fig. 3(b), the complete melting times for Cases A, B, and C were 4000 s, 2800 s, and 2400 s, respectively. This result indicates that Case C, which features the biomimetic structure in the lower section of the system, achieved the fastest melting rate, reducing the complete melting time by up to 40 %. Furthermore, at 800 s, the heat storage rate of the system increased by up to 29.5 %.

Fig. 4(a) illustrates the liquid fraction and temperature distributions during the PCM melting process for different cases, with the left side showing the liquid fraction distribution. As shown in Fig. 4(a), the solid–liquid interface initially formed near the heat exchanger tube, and the PCM near the system inlet melted first. This phenomenon occurred because heat was transferred sequentially from the heat transfer fluid to the heat exchanger tube, and subsequently to the PCM. The temperature near the heat exchanger tube was higher than in other regions of the system, resulting in its earlier melting. The PCM around the raised bamboo-joint structures in Cases B and C melted earlier than that in Case A. Subsequently, the molten PCM, which had a higher temperature, overcame gravity and moved upward due to the density difference, while the solid PCM, with a lower temperature, accumulated at the bottom.

As shown in Fig. 4(a), the PCM melting process after 800 s revealed that the system incorporating the bamboo-joint structure exhibited a progressively higher melting rate. This enhancement was primarily attributed to the bamboo-joint structure, which increased the heat transfer area and expanded the thermally affected region, thereby accelerating the PCM melting process. Notably, in conjunction with Fig. 3(b), it can be observed that at 800 s, the targeted placement of the bamboo-joint structure in the lower section of the system in Case C resulted in slower PCM melting in the upper region during the early stage. As a result, the early-stage heat storage rate of Case C (71.48 J/s) was slightly lower than that of Case B (72.03 J/s). However, the overall melting performance indicated that Case C achieved the fastest PCM melting rate. For instance, by 2500 s in the late melting stage, Case C had fully melted, whereas residual PCM was still present at the bottom of Case B. This finding suggests that placing the bamboo-joint structure in the lower section effectively enhanced the PCM melting rate in a vertically oriented

LHTES system. These results confirm that the incorporation and strategic placement of bamboo-joint structures significantly improve the melting performance of vertically oriented LHTES systems.

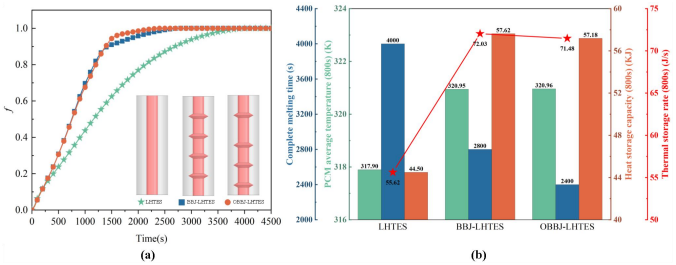

Figure 3. (a) Liquid fraction curves of PCM melting under different cases; (b) Thermodynamic performance analysis under different cases

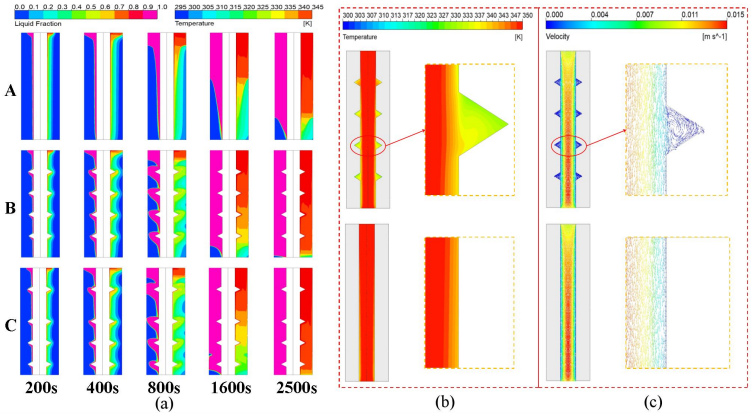

Figure 4. (a) Liquid fraction and temperature distribution of PCM melting under different cases; (b) Temperature distribution in the heat exchanger tube; (c) Velocity vector in the heat exchanger tube

4.2. Analysis of flow field in heat exchanger tube

To examine the influence of the biomimetic bamboo-joint structure on flow characteristics, Fig. 4(b) presents the temperature distribution within the heat exchanger tubes of both the LHTES and BBJ-LHTES systems, whereas Fig. 4(c) shows the corresponding velocity vectors. Fig. 4(b) clearly shows that the incorporation of the biomimetic structure resulted in a more pronounced variation in the temperature distribution within the heat exchanger tube. This phenomenon can be attributed to the vortex generation at the bamboo-joint structures, as shown in Fig. 4(c), where the induced vortices continuously sweep the tube walls, thereby disrupting the velocity and thermal boundary layers. Therefore, the incorporation of the biomimetic structure significantly influenced the internal flow characteristics, promoting vortex formation and development, and consequently enhancing the heat transfer performance within the heat exchanger tube.

5. CONCLUSIONS

In this study, a numerical model of the system was developed based on CFD, validated, and analyzed for performance. The conclusions of this study are as follows:

(1) The incorporation of the biomimetic bamboo-joint structure enhanced the heat transfer area

and significantly increased the PCM melting rate, reducing the total melting time by up to 40 %. Moreover, the early-stage heat storage rate of the system increased by up to 29.5 %.

(2) Placing the biomimetic structure in the lower section of the system accelerated the PCM melting process.

(3) The bamboo-joint structure facilitated vortex formation, disrupting the velocity and thermal boundary layers near the tube wall, thereby enhancing the system's heat exchange performance.

ACKNOWLEDGEMENTS

This work was supported by Graduate Research and Innovation Foundation of Chongqing, China (No. CYB240037).

REFERENCES

Al-Urabi, M., Salman, Y.K., 1980. Laminar natural convection heat transfer from an inclined cylinder. International Journal of Heat and Mass Transfer 23, 45–51.

Baby, R., Balaji, C., 2013. Thermal optimization of PCM based pin fin heat sinks: An experimental study. Applied Thermal Engineering 54, 65–77.

Dekhil, M.A., Simo Tala, J.V., Bulliard-Sauret, O., Bougeard, D., 2021. Numerical analysis of the performance enhancement of a latent heat storage shell and tube unit using finned tubes during melting and solidification. Applied Thermal Engineering 192, 116866.

Diaz, A.J., Yaconi, V., 2023. Exploring tree-like fins for enhanced latent heat storage performance. Energy Storage 5, e478.

Gao, L., Deng, Y., Liu, S., Ren, F., Wan, M.P., Yang, L., 2024. Design and optimization of a bionic-lotus root inspired shell-and-tube latent heat thermal energy storage unit. International Journal of Heat and Mass Transfer 226, 125437.

Kalapala, L., Devanuri, J.K., 2021. Effect of orientation on thermal performance of a latent heat storage system equipped with annular fins − An experimental and numerical investigation. Applied Thermal Engineering 183, 116244.

Liu, X., Qin, X., Tian, Y., Luo, Q., Yao, H., Wang, J., Dang, C., Xu, Q., Lv, S., Xuan, Y., 2023. Biomimetic optimized vertically aligned annular fins for fast latent heat thermal energy storage. Applied Energy 347, 121435.

Low, Z.H., Qin, Z., Duan, F., 2024. A review of fin application for latent heat thermal energy storage enhancement. Journal of Energy Storage 85, 111157.

Rashid, F.L., Dhaidan, N.S., Mahdi, A.J., Kadhim, S.A., Hammoodi, K.A., Al-Obaidi, M.A., Mohammed, H.I., Ahmad, S., Salahshour, S., Agyekum, E.B., 2025. Heat transfer enhancement of phase change materials using tree shaped fins: A comprehensive review. International Communications in Heat and Mass Transfer 162, 108573.

Redoine, F., Belouaggadia, N., Lbibb, R., Sebaibi, N., 2024. Improving thermal energy storage system performance with innovative honeycomb fins. Thermal Science and Engineering Progress 55, 102988.

Ren, F., Du, J., Cai, Y., 2022. Solidification performance analysis of bionic spider web vertical latent heat system based on response surface method optimization. Journal of Energy Storage 55, 105519.

Shademan, M., Hossein Nezhad, A., 2021. Numerical investigation of a vertical finned-tube and shell energy storage system using coupled boundary condition. Journal of Energy Storage 41, 102831.

Sheikholeslami, M., Lohrasbi, S., Ganji, D.D., 2016. Numerical analysis of discharging process acceleration in LHTESS by immersing innovative fin configuration using finite element method. Applied Thermal Engineering 107, 154–166.

Tian, Y., Liu, X., Xu, Q., Luo, Q., Zheng, H., Song, C., Zhu, Z., Gao, K., Dang, C., Wang, H., Xuan, Y., 2021. Bionic topology optimization of fins for rapid latent heat thermal energy storage. Applied Thermal Engineering 194, 117104.

Yang, X., Guo, J., Yang, B., Cheng, H., Wei, P., He, Y.-L., 2020. Design of non-uniformly distributed annular fins for a shell-and-tube thermal energy storage unit. Applied Energy 279, 115772.

Zheng, Z.-J., Xu, Y., Li, M.-J., 2018. Eccentricity optimization of a horizontal shell-and-tube latent-heat thermal energy storage unit based on melting and melting-solidifying performance. Applied Energy 220, 447–454.

6th International Conference on Building Energy and Environment
Eindhoven University of Technology, The Netherlands
6 - 10 July 2025

Innovative solutions for energy-efficient building retrofitting: phase change materials and passive ventilation strategies

Rossella Cottone[1,2], Miroslav Čekon[1,3], Stefano Fantucci[4], Christ Glorieux[5], Monika Rychtáriková[1,2]

[1]*Slovak University of Technology, Faculty of Civil Engineering, Department of Materials Engineering and Physics, Radlinského 2766/11, 810 05 Bratislava, Slovakia, rossella.cottone@stuba.sk, miroslav.cekon@stuba.sk*
[2]*KU Leuven, Department of Architecture, Campus Brussels and Ghent, Paleizenstraat 65, 1030 Brussels, Belgium, rossella.cottone@kuleuven.be, monika.rychtarikova@kuleuven.be*
[3]*Slovak Academy of Sciences, ICA, Dúbravská cesta 9, 845 03 Bratislava, Slovakia, miroslav.cekon@savba.sk*
[4]*Department of Energy, Politecnico di Torino, Corso Duca degli Abruzzi 24, 10129 Torino, Italy, stefano.fantucci@polito.it*
[5]*KU Leuven, Department of Physics and Astronomy, Laboratory of Soft Matter and Biophysics, Celestijnenlaan 200D, 3000 Leuven, Belgium, christ.glorieux@kuleuven.be*

SUMMARY
Building rehabilitation represents a significant opportunity to improve energy efficiency and reduce the environmental impact of the building sector. Integrating phase change materials (PCM) within building components offers a promising approach for enhancing thermal regulation and efficiency in building retrofitting. This study focuses on evaluating the summer performance of an innovative latent thermal energy storage system (LTES) using a high PCM content embedded in a highly porous panel, combined with passive cooling strategies. Thermal analysis and computational simulations were used to evaluate the effectiveness of the composite PCM in moderating temperature fluctuations, highlighting the material and design efficiencies made possible by LTES systems. The results underline the potential of innovative LTES systems as a sustainable solution for retrofitting existing buildings, demonstrating improvements in thermal comfort.

Keywords: PCM-impregnated board, building simulation, night ventilation, occupant thermal comfort.

1. INTRODUCTION

In Europe buildings account for 40% of total energy consumption and 36% of greenhouse gas emissions, and 75% of EU buildings currently operating inefficiently (Recovery and Resilience Scoreboard, Thematic Analysis, Energy Efficiency in Buildings, 2023). In this context, the shift towards sustainable development is crucial, as is the retrofitting of buildings as an opportunity to improve energy efficiency and reduce the building sector's environmental footprint. The integration of Phase Change Materials (PCMs) into building components has gained significant attention as a promising solution to enhance thermal performance and reduce energy consumption in buildings (Cunha et al., 2016). By exploiting their latent thermal energy storage (LTES) capabilities, passive design strategies with PCMs can contribute to thermal comfort, reduced indoor temperature and lower HVAC energy consumption and sizes (Pielichowska & Pielichowski, 2014). However, to maximize their effectiveness, PCMs must undergo complete thermal charging and discharging cycles within a 24-hour period to efficiently absorb and release

heat energy (Ahmad & Memon, 2024). In this context, the integration of ventilation strategies has been identified as a key approach to optimizing PCM performance by enhancing the thermal charging and discharging process (Piselli et al., 2020). A review of the literature highlights a research gap in optimizing building envelope performance through the combined use of PCMs and ventilation (Salihi et al., 2024).

This study aims to investigate the potential of LTES coupled with different night ventilation configurations, analysing their impact on adaptive thermal comfort during the summer season. The analysis focuses on a recently developed innovative leak-proof porous calcium silicate panel impregnated with PCM (Cottone et al., 2025) assessing the potential application in building. Dynamic simulations, performed using Energy Plus software and a validated model on a sloping roof of a test room, assess the extent to which PCMs can optimise latent heat storage and release in conjunction with controlled night ventilation strategies. The primary objective is to improve thermal comfort by effectively utilizing the PCM's phase transition to moderate indoor temperatures. Roof structures play a critical role in heat transfer dynamics, as they are the area most exposed to solar radiation, making the attic particularly vulnerable to high summer heat loads and the risk of overheating (Liu et al., 2023). By incorporating PCMs into the roof structure, a significant portion of incoming solar radiation and ambient heat energy can be absorbed and later dissipated. This not only mitigates temperature peaks, but also helps stabilise internal temperatures, reducing fluctuations, and improving overall thermal comfort in the space below. Additionally, this study examines the effects of thermal hysteresis of the material on the PCM's charging and discharging behavior, which can influence its effectiveness in real-world applications. The findings provide key insights into the optimisation of PCM integration, offering valuable contributions to the field of energy-efficient building renovation and the development of resilient passive cooling solutions.

2. MATERIALS AND METHODS

The present study analyses a calcium silicate panel impregnated with 72 wt.% of paraffinic PCM Rubitherm RT27 (PCM-B-CRT27), characterised by a latent heat of fusion of 119 kJ/kg with melting temperature peak at 28°C, and a latent heat of solidification of 115 kJ/kg with a solidification peak at 26°C. An energy model of a Test Roofing Innovative System (TRIS), an experimental apparatus designed for the thermal analysis of advanced roofing components (Fantucci et al., 2022), was used to evaluate the summer performance of the developed system. The TRIS test cell, with a volume of approximately 2 m^3, is located in the attic of a residential building in the metropolitan area of Turin, Italy.

1.1 Energy model validation

For the validation of the energy model, the test cell without the PCM layer was modelled in EnergyPlus, and the model was calibrated using experimental data obtained during a monitoring campaign. Figure 1 shows a section of the TRIS cell with the roof stratigraphy and sensor layout, while Table 1 shows the input data for the roof materials. Different algorithms were considered for the determination of the convective transfer coefficients. The comparison between the simulated and experimental data showed a high correspondence using the TARP (Thermal Analysis Research Program) algorithm for the external surface, which considers both forced and natural convection, and the ASTM C1340 method for the internal surface, which takes into account the direction of heat flow. In addition, a variable flow rate as a function of wind speed was adopted for the air gap, which significantly reduced the uncertainty compared to the assumptions of

constant flow rate or still air. Figure 2 shows the comparison between the simulated and measured heat flow of a typical day, exchanged between the inner layer of the roof and the air in the cell, considering both conduction and convection. The simulated profile is comparabale to the experimental one, confirming the validity of the developed energy model.

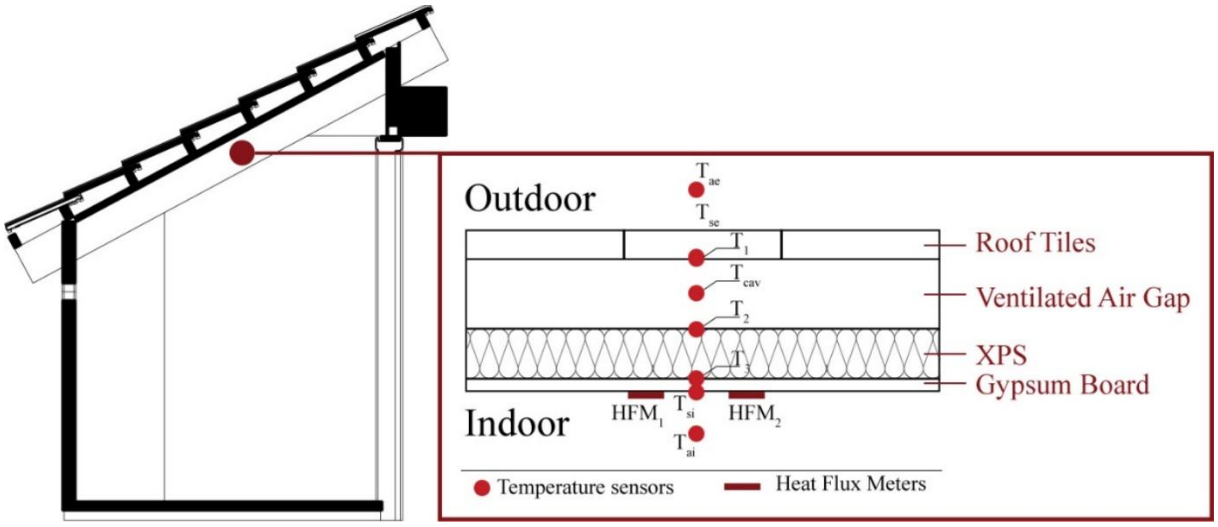

Figure 1. Section of TRIS cell and roof stratigraphy for model validation

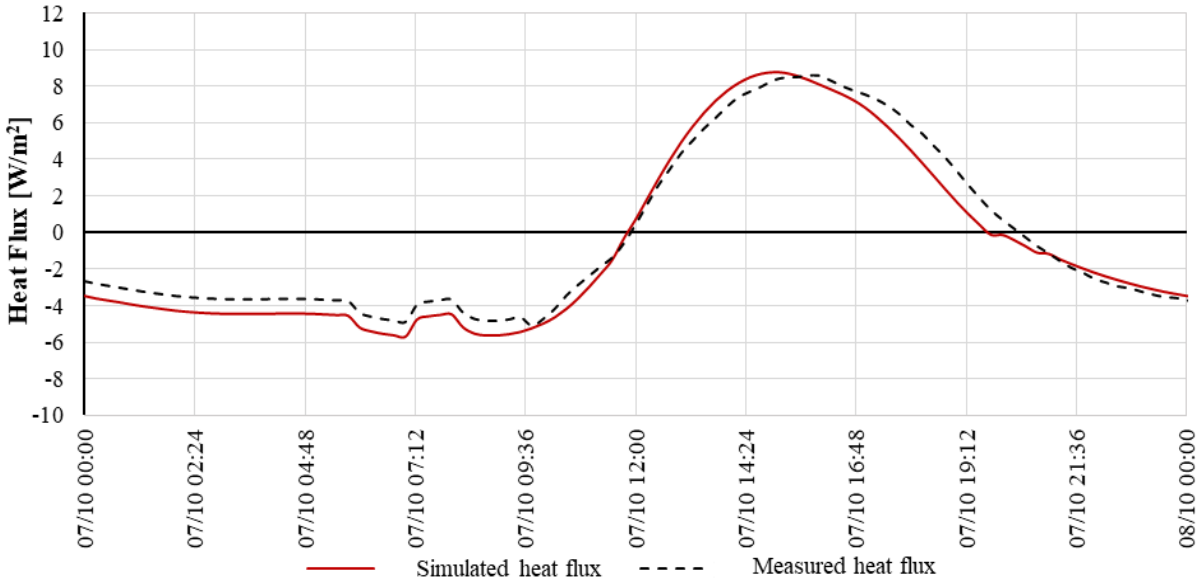

Figure 2. Comparison of measured and simulated heat flow

1.2 Evaluation of summer performance of the innovative system with PCM

The aim of this work is to employ the validated model to simulate the performance of the innovative panel system with embedded PCM (Figure 3). In particular, the conduction finite difference method (CondFD) was implemented for modelling the hysteresis of the PCM. Table 1 shows the stratigraphy of the roof together with the characteristics of the materials, highlighting in red the PCM-B-CRT27 layer with a thickness of 30 mm, placed close to the inner side of the room.

Table 1. Roofing stratigraphy.

Layers from outside	Thickness [mm]	Thermal conductivity [W/mK]	Specific heat [J/kgK]	Density [kg/m^3]	
Roof Tiles	30	0.700	840	1700	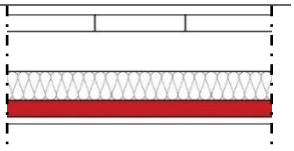
Ventilated Air Gap	70	-	-	-	
XPS	50	0.038	1500	33	
PCM-B-CRT27	30	0.190	2400	909	
Gypsum Board	12.5	0.250	1000	900	

As shown in the methodology workflow (Figure 3), a free cooling system based on night ventilation (NV), from 00:00 to 08:00, was implemented to allow the discharge of the PCM and maintain the internal temperature in the comfort zone during the day. The temperature in the middle node of the PCM layer was evaluated for the entire summer period, thus considering June, July and August. This approach allows the calculation of a performance indicator to identify the exploitation capability of the PCM in percentage terms through the following equation:

$$PCM\ exploitation\ (\%) = \frac{n°\ of\ hours\ in\ the\ latent\ phase}{n°\ of\ total\ hours\ in\ the\ considered\ period} \cdot 100 \quad (1)$$

In parallel, the adaptive thermal comfort was evaluated according to the ASHRAE 55 standard (ASHRAE, 2021), which defines threshold values of the indoor operating temperature as a function of the prevailing mean outdoor temperature. In particular, two scenarios were considered. The first assumed the absence of NV with only natural infiltration at 0.4 air changes per hour (ACH), while the second include NV at 5 ACH, in order to quanify how strategic implementation of NV maximises the utilisation of PCM-B-CRT27 without compromising thermal comfort.

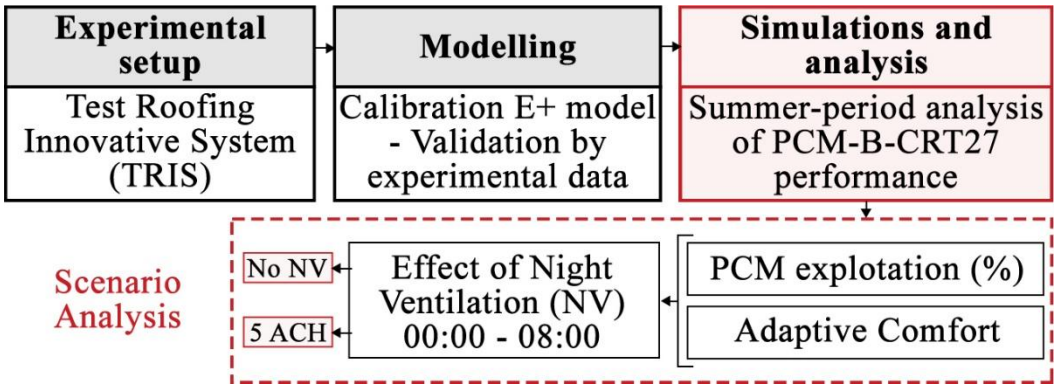

Figure 3. Methodology workflow

3. RESULTS

3.1 Phase Change Materials exploitation

Figure 4 shows the temperature trend in the inner node of the PCM-B-CRT27 layer as a function of the different simulated ACHs and the range of the latent phase, which is between 24 and 29 °C. It turns out that night ventilation is not necessary during the month of June, where the exploitation

of the PCM is already maximised up to 99% (see Figure 5). In addition, fixed ventilation rates of 5 ACH lead to temperatures out of the latent range of the PCM-B-CRT27 on the mildest days of June, which could generate indoor thermal discomfort. On the other hand, the analysis of July and August shows how the absence of NV is not sufficient to maximise the exploitation of the system and recharge the PCM-B-CRT27. Indeed, in July the exploitation is between 40% in the absence of NV, but with 5 ACH this increases to 100%, in fact the temperature profile of the PCM node falls completely within the latent phase marked by the green area. Similarly in August, an exploitation of 34% is reached in the absence of NV and 89% with 5 ACH, in fact, especially in the first ten days of the month a higher temperature occurs. It can therefore be concluded that to maximise the latent phase of the material studied, the implementation of NV is necessary.

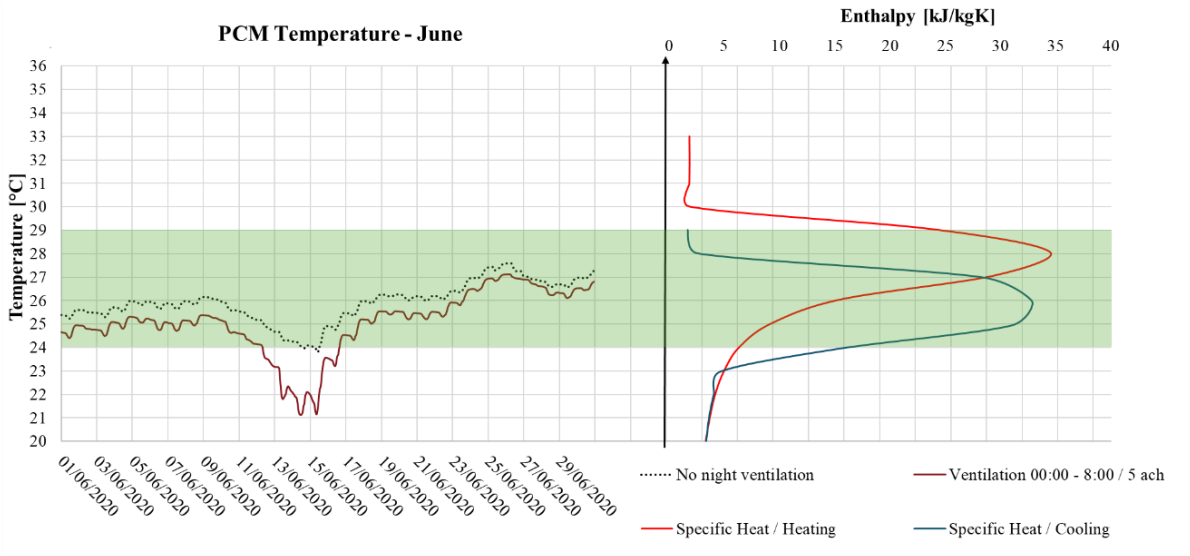

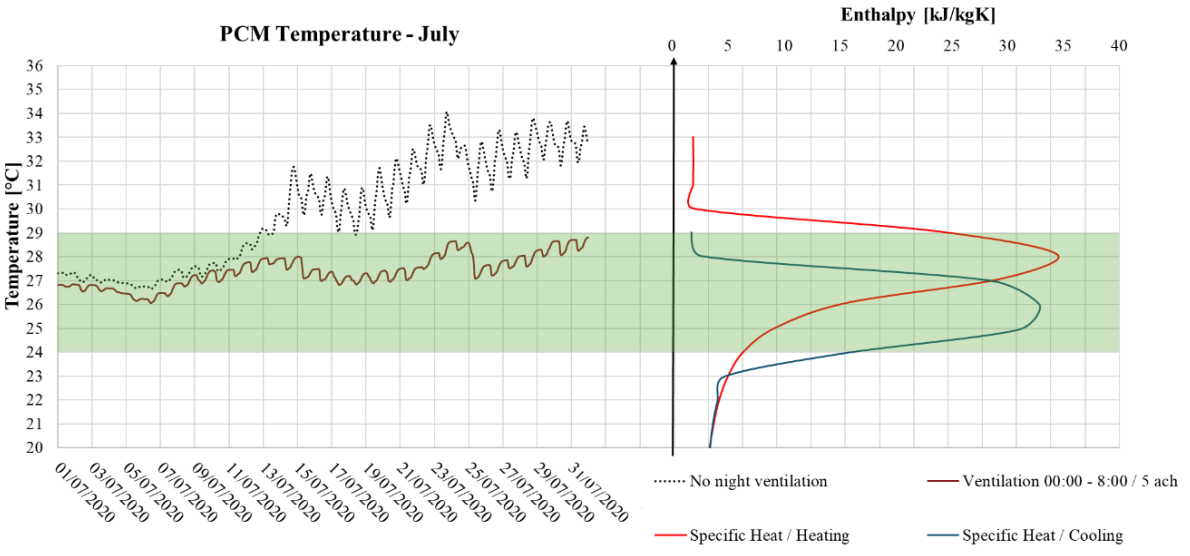

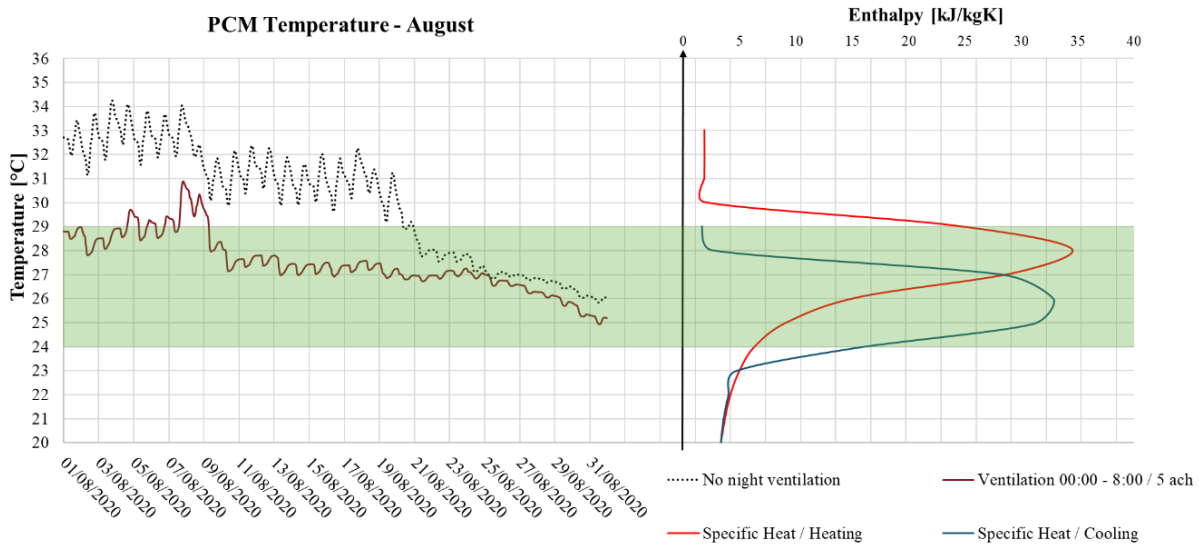

Figure 4. Temperature trend in the inner node of the PCM during the months considered: absence of night ventilation and different 5 air change per hour

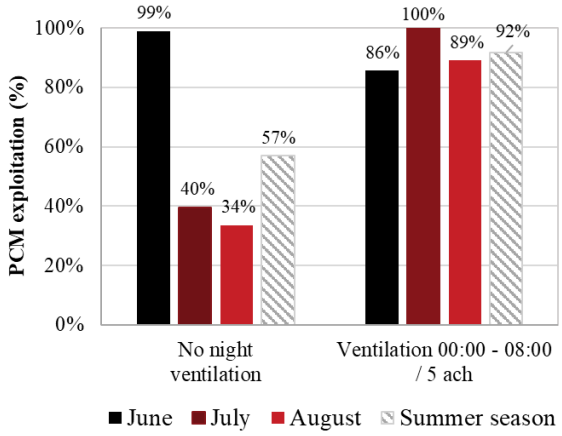

Figure 5. PCM exploitation with the absence of night ventilation and 5 ACH.

3.2 Indoor thermal comfort improvement

Figure 6 shows the number of hours above the upper limits of acceptability defined by the ASHRAE-55 standard for the assessment of adaptive thermal comfort, considering scenarios with and without the application of a PCM layer to evaluate the effectiveness of the material in the thermal regulation of indoor spaces. The results show that the application of night ventilation leads to a significant reduction in the number of hours when indoor conditions exceed acceptable limits. This trend can be observed in both scenarios with and without PCM. However, the combined effect of PCM and adequate night ventilation proves to be particularly effective in optimising thermal comfort. The application of a PCM layer amplifies the reduction of out-of-comfort hours as the ACH increases, demonstrating how NV is able to discharge the PCM and prepare it for heat flow reduction during the following day. These observations highlight two key aspects: 1) an air exchange rate (≥5 ACH) is essential to maximise the potential of PCM, ensuring its thermal discharge during the night; 2) the addition of a PCM layer offers significant added value, allowing

higher thermal attenuation during daytime hours, even with moderate natural ventilation strategies.

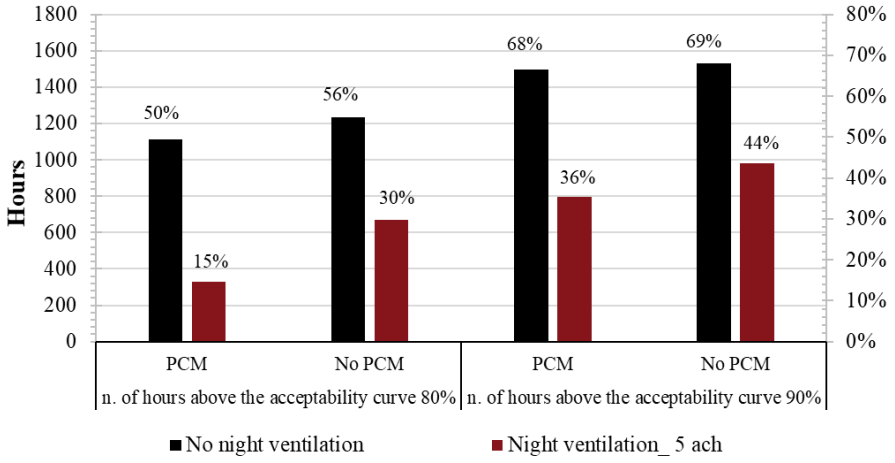

Figure 6. Hours above the upper acceptability limits 80% and 90% following the standard ASHRAE 55-2020.

Figure 7 compares the scatter plot of the adaptive comfort of the two scenarios with PCM, without NV and with 5 ACH. The comfort zone, highlighted in red, represents the range of acceptable conditions according to the ASHRAE 55 standard. Analysis of the results clearly shows that in the absence of night ventilation most of the data is distributed outside the comfort zone, indicating a prevalence of unfavourable thermal conditions. On the contrary, at 5 ACH, a significantly higher proportion of hours fall within the comfort limits due to the nightly PCM unloading and the reduction of thermal fluctuations that maintain more stable indoor temperatures. This demonstrates that an adequate ventilation rate not only exploits the potential of the PCM, but also ensures more stable and prolonged thermal comfort.

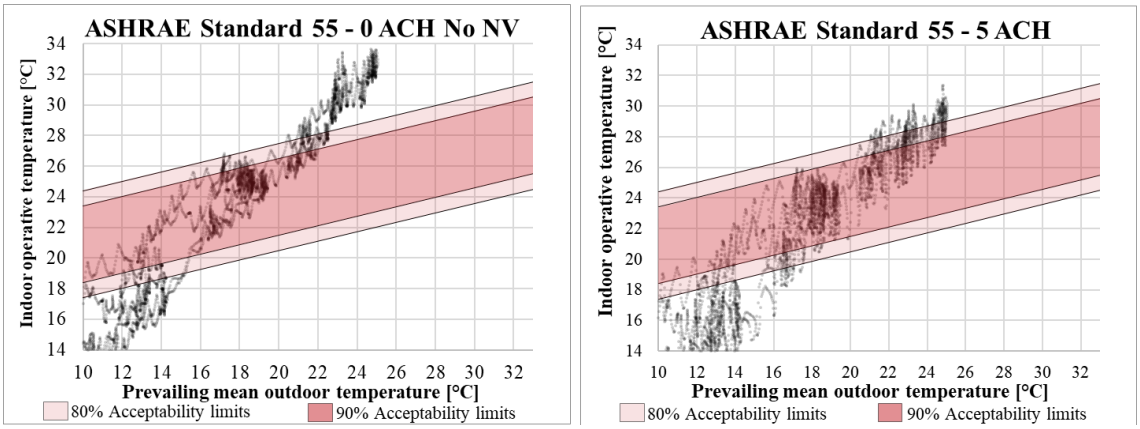

Figure 7. Operating temperature scatter plot as a function of prevailing mean outdoor temperature.

4. CONCLUSIONS

The integration of a PCM-impregnated system in building retrofitting offers significant improvements in thermal comfort and energy efficiency, especially when combined with effective

night ventilation strategies. The study shows that night ventilation, with air exchange rate of 5 ACH, optimises the performance of PCM, ensuring maximum utilisation of its latent heat storage capacity, with exploitation rates reaching 92% during the summer season. Although night ventilation is not necessary in June leading to 99% PCM utilisation, its absence throughout all summer period results in high levels of discomfort. The combination of LTES and night ventilation reduces the number of hours above the upper acceptable limits for indoor temperatures by up to 35% compared to the scenarios without PCM or ventilation, thus improving occupants' thermal comfort. This underlines the remarkable efficiency of PCM systems in reducing the need for excessive insulation during retrofitting processes. These results highlight the potential of PCM-based LTES systems as a sustainable and efficient solution especially for retrofitting existing buildings, but also for new constuctions, contributing to both energy savings and improved occupant comfort.

The developed model will be calibrated and validated by an experimental campaign with a scenario including a PCM layer. Future research will evaluate incremental NV (ACH) values to identify the optimal value that maximises the exploitation of the PCM-B-CRT27 without compromising thermal comfort. Additionally, the study will explore the implementation of ventilation control strategies based on the PCM's thermal response and outdoor temperature. The research will also assess the performance of PCM-B-CRT27 during the winter season by coupling it with an integrated heating system, aiming to enhance energy efficiency while potentially reducing the required insulation thickness.

ACKNOWLEDGEMENTS

This project has received funding from the European Union's Horizon Europe research & innovation programme under the HORIZON-MSCA-2021-DN-01 grant agreement No. 101072598 – "ActaReBuild, and VEGA 2/0145/24. The authors would like to thank E. Fenoglio and G. Peano for contributing to the validation of the energy model.

REFERENCES

Ahmad, A., & Memon, S. A. (2024). A novel method to evaluate phase change materials' impact on buildings' energy, economic, and environmental performance via controlled natural ventilation. Applied Energy, 353, 122033.

Cottone, R., Čekon, M., Glorieux, C., Fantucci, S., Čurpek, J., Slávik, R., & Rychtáriková, M. (2025). Investigation of Phase Change Material Impregnation in a Highly Porous Structure. In U. Berardi (Ed.), Multiphysics and Multiscale Building Physics (pp. 455–460). Springer Nature Singapore.

Cunha, S., Lima, M., & Aguiar, J. B. (2016). Influence of adding phase change materials on the physical and mechanical properties of cement mortars. Construction and Building Materials, 127, 1–10.

Fantucci, S., Autretto, G., Fenoglio, E., Sassaroli, E., & Perino, M. (2022). Laboratory Assessment and In-Field Monitoring of Macro-Encapsulated Phase Change Materials for Building Envelope Applications. Applied Sciences, 12(4), 2054.

Pielichowska, K., & Pielichowski, K. (2014). Phase change materials for thermal energy storage. Progress in Materials Science, 65, 67–123.

Piselli, C., Prabhakar, M., De Gracia, A., Saffari, M., Pisello, A. L., & Cabeza, L. F. (2020). Optimal control of natural ventilation as passive cooling strategy for improving the energy performance of building envelope with PCM integration. Renewable Energy, 162, 171–181.

Recovery and resilience scoreboard, Thematic analysis, Energy efficiency in buildings. (2023). European Commission. https://ec.europa.eu/economy_finance/recovery-and-resilience-scoreboard/assets/thematic_analysis/scoreboard_thematic_analysis_efficiency.pdf

Salihi, M., Chhiti, Y., El Fiti, M., Harmen, Y., Chebak, A., & Jama, C. (2024). Enhancement of buildings energy efficiency using passive PCM coupled with natural ventilation in the Moroccan climate zones. Energy and Buildings, 315, 114322.

6th International Conference on Building Energy and Environment
Eindhoven University of Technology, The Netherlands
6 - 10 July 2025

Assessing the Impact of Urban Morphology on BIPV Potential in High-density Urban Area: A Case Study in Shanghai

Xinyu Li [1], Jie Shi [1, *], Yucheng Guo [2,*], Sixing Lin [1], Xinman Niu [1], Hui Yang [1], Zhikai Peng [3], Lingqi Su [1, *]

[1] *Sino-German College of Applied Sciences, Tongji University, Shanghai, China, shijie@tongji.edu.cn; lingqi_su@tongji.edu.cn*

[2] *College of Architecture and Urban Planning, Tongji University, Shanghai, China, 2230059@tongji.edu.cn*

[3] *Delft University of Technology, Delft, Netherlands, z.p.peng@tudelft.nl*

SUMMARY

The building sector is a major contributor to global carbon emissions and energy consumption. A promising solution to mitigate this impact is the utilization of renewable energy, especially solar energy. However, in a high-density built environment, the application of photovoltaic (PV), especially on the building facades, is often hindered by shading from surrounding structures. To optimize solar energy use in urban area, it is important to understand the influence of key urban morphological parameters on solar energy utilization in densely built environment. This study aims to explore the relationship between urban morphology and building-integrated photovoltaic (BIPV) performance with a typological approach, while ensuring life cycle economic and environmental benefits. The findings are expected to inform design and planning strategies for effectively integrating solar energy into urban environments, thereby promoting more sustainable and energy-efficient cities and supporting long-term carbon neutrality objectives.

Keywords: High-density Urban Morphology, Solar Potential, Block Prototypes, Life Cycle Assessment

1. INTRODUCTION

1.1 Background

As one of the largest contributors to global energy consumption and greenhouse gas emission, cities should play a leading role in the process of energy transition. Thus, Solar energy is now widely used in built environments. Building-integrated photovoltaic (BIPV) integrates photovoltaic (PV) modules into building structures, providing the benefits of both clean energy production and enhanced building performance. However, the widespread application of BIPV faces several challenges. Besides economic barriers, a significant issue lies in the inflexibility of implementation, since the positioning of PV modules is often fixed during the construction phase. In the implementation of BIPV in high-density urban environments, the drawback of fixed-position installation of PV modules is further aggravated, where shading from surrounding structures can significantly decrease the PV performance. Therefore, meticulous planning and evaluation are crucial for the successful deployment and promotion of BIPV systems.

To provide a theoretical foundation for the planning of BIPV, this paper aims to investigate the impact of urban morphology on the potential of BIPV. Focusing on Shanghai as a representative high-density metropolis, this study explored the influence of key urban morphology on the BIPV energy potential at meso scale with the prototypes identified through clustering algorithm. The

findings of this study aim to offer valuable insights for optimizing BIPV integration in urban planning, thereby supporting the development of more sustainable and energy-efficient cities.

1.2 Literature Review

Strategic urban morphology planning has been recognized as a critical factor in maximizing solar energy utilization (Amado et al., 2012). Recent studies have adopted an established methodology that integrates quantitative urban morphology analysis with prototype selection, systematically examining parameter variations and their combinatorial effects on solar performance (Schirmer et al., 2016). One crucial step in this research lies in the identification of appropriate morphological parameters, which directly determines the representativeness of extracted urban block prototypes. The definitions of common parameters and their related literature can be found in Table 1.

Table 1. Morphological parameters commonly used in studies related to solar potential

Parameter	Description	Related Literature
Density / Building Coverage Ratio	Building Footprint Area / Site Area	Basic parameters adopted for the most research
Floor Area Ratio / Plot Ratio	Building Floor Area / Site Area	
Average Building Floor	Building Floor Area / Building Footprint Area	
Average Building Height	Average Building Height × Floor Height	
Sky View Factor	Upper hemisphere visible sky percentage	(Liu et al., 2023) (Poon et al., 2020)
Orientation	Orientation of the main façade of the building	(Mahaya et al., 2022) (Yang et al., 2024)
Open Space Ratio	1/ Floor Area Ratio – 1 / Average Building Floor	(Zhu et al., 2020) (Zhang et al., 2019)
The Form of Single Buildings	Single building form, including slab, tower, courtyard, etc.	(Tian er al., 2021)

The selection of research cases generally follows two approaches: analysis of existing urban configurations (Jareemit et al., 2025) or generation of sample library with different morphological parameters combination (Du et al., 2024). The difficulty with the former is how to select a representative prototype in a number of cases. Limitations of the latter approach in capturing real-world complexity have been shown in previous research. To over this bridge, this study employs real-world urban blocks in Shanghai as research prototypes with a clustering approach, the potential for solar potential will be compared to analyze the impact of morphology on it.

2. METHODOLOGY

This research consists of the following four stages, as shown in Figure 1.

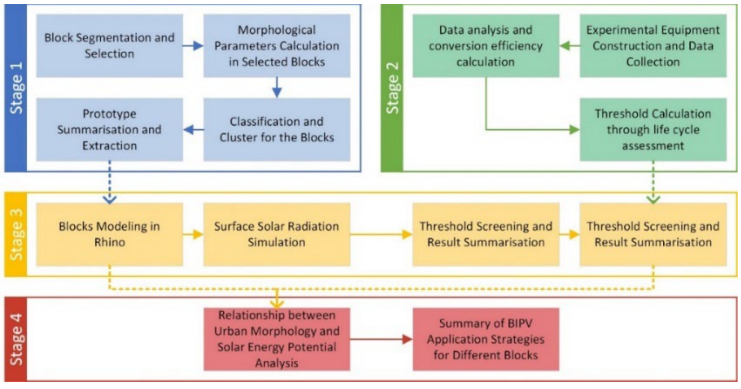

Figure 1. The Framework of this research

From the review of the related research in Section 1.2, 7 key parameters are selected for analyzing urban morphology, as shown in Table 2. Following the Chinese standard GB 50352-2019, we classified buildings into three categories: low-rise (1-3 floors), multi-rise (4-9 floors) and high-rise (≥10 floors). The prototype extraction process was implemented in two sequential stages. First, urban blocks were classified with density and average number of floors. Then, block types were clustered with the percentage of floor area of each building height category as the primary criterion.

Table 2. Selected morphological indicators

Parameter	Unit	Description
Block Area *A*	m^2	The site area of the research block
Building Footprint Area *F*	m^2	The footprint area of buildings in the research block
Building Floor Area *B*	m^2	The total building area in the research block
Density of Block *D*	-	F / B
Floor Area Ratio *FAR*	-	B / A
Average Building Floor N_{Floor}	-	B / F_t
Percentage of Floor Area of Different Type Building Height n_i	%	$S_{Building,\ i} / S_{Building}$

For BIPV performance evaluation, modules were constructed in building surface to evaluate conversion efficiency under real-world conditions. The experimental equipment is listed in Table 3. The radiation threshold is important for the selection of the usable building surfaces, ensuring both environmental and economic benefits. These benefits, noted as $R_{T,en}$ for environmental and $R_{T,ec}$ for economic benefits, can be calculated through Equations (1) and (2) , respectively. Table 4 details the values for each parameter in this study.

Table 3. Experiment devices

Equipment		Function	Sampling Rate
PV panels		Converting solar energy into electricity	-
Kipp & Zonen CMP11		Measuring solar radiation on the ground	-
Kipp & Zonen LOGBOX SE		Record the test data transmitted by CMA11	1 min
DAM3053DC		Measure the actual output power of the PV panel	1 min

$$R_{T,en} = \frac{\sum_{t=0}^{n} \frac{C_t}{(1+d)^t}}{\sum_{t=1}^{n} \frac{LCOE_t \times \eta_t}{(1+d)^t}} \tag{1}$$

$$R_{T,ec} = \frac{\sum_{t=0}^{n} EF_{PV,t}}{\sum_{t=1}^{n} EF_E \times \eta_t} \tag{2}$$

Table 4. Required Parameters for the performance evaluation

Parameter	Values
Life Cycle *n*	25a
Levelized Cost of Energy *LCOE*	0.737 RMB/kWh

Initial Investment C_0	3.0 RMB/W
Subsequent Investment C_t (t is from 1 to 25)	3% of the initial investment
Conversion Efficiency of PV η_t	Calculations based on experiment data. Annual degradation rate: 2.5%/a in the first year and 0.7 %/a thereafter
Discount Rate n	8%/a
Electricity Carbon Emission Factor EF_E	0.581kg/kWh
PV Carbon Emission Factor $EF_{PV,\,t}$	Only the carbon emission during production process is considered with the Report by Deloitte and Envision Group (Deloitee et al., 2024), 1.22 kgCO2/Wc

The block prototypes will be extracted through a clustering approach, then the geometry data of the selected cases are exported from ArcGIS and reconstructed into 3D models with Rhino. The simulation of the solar radiation on the building surfaces was performed with the Ladybug plug-in, enabling the identification of surfaces meeting the predefined application thresholds. Based on these results, a comparative analysis of BIPV application potential was conducted across different block types.

3. CASE STUDY

3.1 Block Prototype Extraction

Urban blocks serve as fundamental elements of urban fabric, enabling the analysis of building interactions and providing insights for larger-scale urban planning and design. This study adopts the three-tier living circle system as the scale of block extraction: 5-minute, 10-minute, and 15-minute walking distances. Given that a 5-minute walk for adults is approximately 400 meters, the block scales within the range of 400 m × 400 m to 1200 m × 1200 m, corresponding to an block area between 0.16 km^2 and 1.44 km^2. Block parcels were generated from urban data by first establishing road buffer zones. Road widths were set at 40 m, 30 m, 25 m, and 12 m, following Technical Standard of Highway Engineering (JTG B01-2014), resulting in 1,515 parcels. These parcels were further categorized into nine groups based on their density and their number of floors. Density classification was performed using the K-means algorithm (K=3), yielding three density clusters: low-density (< 0.18), middle-density (0.18–0.27), and high-density (> 0.27). The distribution of the nine block types is shown in Figure 2.

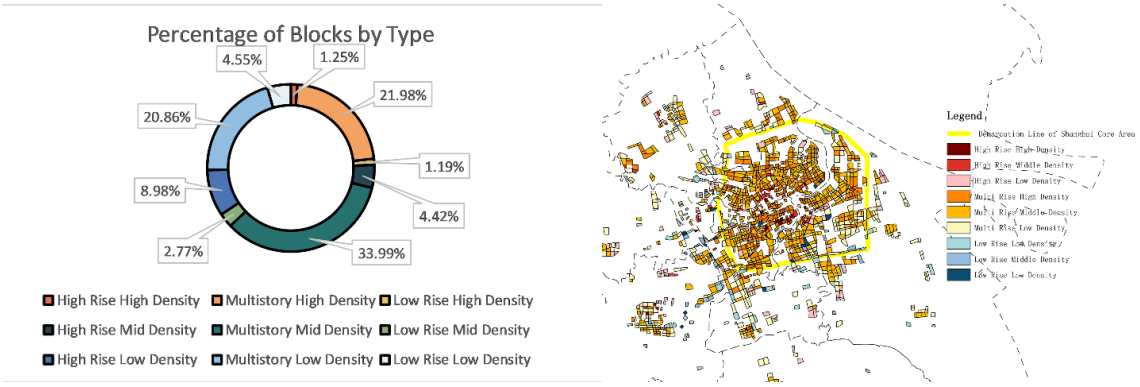

Figure 2. Percentage and Distribution of Blocks by Type (Urban Data Source: Baidu Map, OpenStreetMap)

High-rise high-density (HH), multi-rise high-density (MH), high-rise middle-density (HM) and

multi-rise middle-density (MM) blocks were identified as the dominant types in Shanghai center. Further analysis focused on the mixing ratios of high-rise, multi-rise, and low-rise floor areas within MH and MM blocks. The Affinity Propagation (AP) algorithm was employed to cluster blocks within each type. The MH blocks were further divided into four clusters: multi-rise dominated (MH-A), multi-rise low-rise hybrid (MH-B), multi-rise dominated multi-rise high-rise hybrid (MH-C), and high-rise dominated multi-rise high-rise hybrid (MH-D). Similarly, the MM blocks were classified into five clusters: multi-rise low-rise hybrid (MM-A), multi-rise dominated (MM-B), high-rise dominant mixed (MM-C), multi-rise intercourse mixed (MM-D) and high-rise multi-rise mixed (MM-E). The plot scales were further divided into three intervals of $0.16km^2$~$0.64km^2$ (small plot), $0.64km^2$~$1.00km^2$ (middle plot), and $1.00km^2$~$1.44km^2$ (huge plot).

Table 5. Prototypes used for research

Type	Small Plot (SP)	Middle Plot (MP)	Huge Plot (HP)
High-rise High-density (HH)	√		
Middle-rise High-density A (MH-A)	√	√	√
Middle-rise High-density B (MH-B)	√	√	√
Middle-rise High-density C (MH-C)	√	√	√
Middle-rise High-density D (MH-D)	√	√	
High-rise Middle-density (HM)	√	√	
Middle-rise Middle-density A (MM-A)	√	√	√
Middle-rise Middle-density B (MM-B)	√	√	√
Middle-rise Middle-density C (MM-C)	√	√	√
Middle-rise Middle-density D (MM-D)	√	√	√
Middle-riseMiddle-density E (MM-E)	√	√	√

3.2 Radiation Threshold for BIPV Application

For the performance evaluation, the nominal conversion efficiency of PV panels was assumed to be 17.36% in this study. Our experimental results indicated an average conversion efficiency found of 16.61%. Based on the calculation method described in Section 2.2, the radiation threshold for PV application can be calculated as $404.5kWh/m^2$ because of the economic factors considering the PV feed-in subsidy. This threshold can be reduced to $392.14kWh/m^2$ if carbon quota trading was incorporated into the analysis. For environmental benefits the threshold value is 91.46 kWh/m^2 to meet PV application requirements. Consequently, the threshold of 400 kWh/m^2 for PV application was selected in this study.

3.3 Building Solar Radiation Potential Analysis

Solar radiation analysis was conducted using the Ladybug tool within the Grasshopper plugin. A computational framework was established, as shown in Figure 3, which determines the solar radiation on building surfaces and identifies the areas meeting the specified radiation threshold. Simulations were performed for both roofs and façades across 29 selected urban blocks in Shanghai. The results of these calculations are summarized in Table 6.

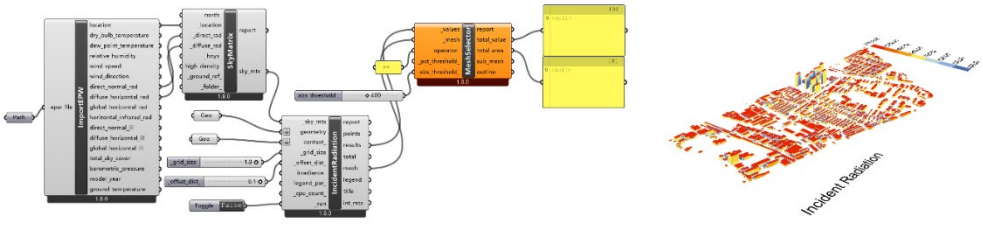

Figure 3. Grasshopper-LB-HB components for BIPV simulations and example of simulation results

Table 6-a. Simulation results (High Density)

Study Case	Radiation per unit area of the roof kWh/m^2	Radiation per unit area of the facade kWh/m^2	Radiation per unit area of all building surfaces kWh/m^2	Proportion of usable building surface area
HH SP	1039.14	563.75	730.40	28.62%
MH-A SP	1146.41	604.29	880.60	40.44%
MH-A MP	1159.95	658.94	988.84	49.38%
MH-A HP	1157.95	575.80	834.72	60.48%
MH-B SP	1166.04	571.43	904.53	59.91%
MH-B MP	1132.30	599.67	866.69	66.25%
MH-B HP	1152.92	603.12	819.99	60.29%
MH-C SP	1131.72	578.39	814.07	46.90%
MH-C MP	1134.20	591.54	844.84	44.60%
MH-C HP	1156.26	604.05	859.89	47.24%
MH-D SP	1091.25	598.10	812.55	49.94%
MH-D MP	1167.07	590.85	926.42	51.23%

Table 6-a. Simulation results (Middle Density)

Study Case	Radiation per unit area of the roof kWh/m^2	Radiation per unit area of the facade kWh/m^2	Radiation per unit area of all building surfaces kWh/m^2	Proportion of usable building surface area
HM SP	1190.55	588.22	808.59	38.68%
HM MP	1024.34	573.57	706.62	46.93%
MM-A SP	1172.92	652.21	937.50	58.63%
MM-A MP	1146.74	592.35	791.76	53.59%
MM-A HP	1117.65	597.60	804.57	42.96%
MM-B SP	1184.70	628.37	896.98	50.64%
MM-B MP	1162.40	590.76	810.57	42.10%
MM-B HP	1197.37	565.78	945.76	65.37%
MM-C SP	1088.40	583.27	796.80	37.23%
MM-C MP	1117.07	581.21	790.01	35.71%
MM-C HP	1150.87	620.31	866.88	32.65%
MM-D SP	1153.49	563.90	789.24	41.18%
MM-D MP	1163.77	601.10	877.67	46.39%
MM-D HP	1130.74	585.80	787.21	41.57%
MM-E SP	1141.93	609.69	836.52	46.45%
MM-E MP	1147.80	587.00	752.62	45.63%
MM-E HP	1127.02	606.94	826.61	36.56%

4. DISSCUSSION

These block types exhibit significant vertical development intensity, especially for MH-A MP, MM-B SP resulting in façade areas substantially larger than roof areas. This morphological feature highlights the considerable potential for façade-integrated BIPV applications. The analysis of BIPV potential can be categorized into two aspects: irradiation per unit area and the proportion of usable area, which determine the quality and quantity of BIPV deployment.

The solar energy potential of roofs is found to be relatively consistent across 29 study examples and less affected by morphological variations, with the irradiation levels exceeding 1000 kWh/m^2. In contrast, the solar potential of façades is significantly influenced by morphology. Despite the threshold of 400 kWh/m^2, the average radiation intensity on qualifying façade surfaces exceeded 550 kWh/m^2, ensuring both economic viability and substantial coverage of building surfaces. Meanwhile, building height emerged as a critical factor of the overall solar potential, as seen in both HH and HM cases ranking at the bottom in BIPV performance (Table 6-a, 6-b).

Among MH blocks, the MH-A type performed well across all three scales, while MH-B demonstrates the highest radiant intensity. MH-C exhibits optimal performance in compact plots, while MH-D demonstrates better performance only in medium plots. Within MM blocks, MM-B shows consistent suitability across multiple scales. These results suggest that multi-rise-dominated or multi-rise-low-rise hybrid configurations are most suitable for both MM and MH blocks.

In terms of the proportion of usable surfaces, HH blocks consistently showed the lowest values. Among MH blocks, MH-B has the highest proportion of usable surfaces, while MH-C has the lowest. Within MM blocks, MM-A and MM-B achieved the largest proportions of usable surfaces, with MM-D and MM-E demonstrating similar performance with over 40% of usable area. Conversely, MM-C shows the lowest proportion of usable area.

These results reveal that multi-rise-dominated or multi-rise and low-rise mixed-type blocks generally outperform high-rise blocks in solar energy potential within Shanghai's high-density urban context.This suggests that urban planners could prioritize mid-rise developments in area with high solar resources, while reserving high-rise typologies for areas where vertical density provides critical benefits. Such approach would balance the energy efficiency objectives with broader urban development goals.

5. CONCLUSION

This study investigated the impact of urban morphology on building-integrated photovoltaic (BIPV) potential in high-density urban environments, using Shanghai as a case study. With a clustering approach, urban blocks were classified into nine types, with four dominant types identified in the city's core: high-rise high-density (HH), multi-rise high-density (MH), high-rise medium-density (HM), and multi-rise medium-density (MM). These blocks were further subdivided into 29 clusters based on the plot scale and the mixing of various building height types. The solar radiation threshold was determined with a PV life cycle analysis framework. The solar radiation simulations were conducted for 29 selected block samples, and surfaces meeting the threshold were identified and analyzed. The results revealed significant variations in solar potential across different morphological block types, with multi-rise-dominated and multi-rise-low-rise hybrid configurations demonstrating the highest potential for BIPV applications. These insights shall provide valuable guidance for urban planners and policymakers aiming to integrate BIPV systems into high-density urban environments, ultimately supporting the development of more sustainable and energy-efficient cities.

However, this study has several limitations. First, the sample size was insufficient for rigorous quantitative analysis of the relationship between morphology parameters and solar energy

potential. Second, the abstraction process of quantifying the urban morphology was only limited to several parameters, which may not fully capture the complexity of morphology's influence on solar energy potential.

These limitations will be addressed in our future research, by incorporating interpretable machine learning methods based on the expanded sample size to enhance the robustness and generalizability of the findings and so that a quantitative relationship can be addressed for decision-making in the design and urban planning process. The external factors such as air pollution and season will be also considered in a more detailed experimental design to calculate the conversion efficiency to increase the credibility of the results. Furthermore, the spatial-temporal transportability of the results is also significant which determines the value of the application. Migration studies within and across climate zones will be further developed to confirm the validity of the method.

ACKNOWLEDGEMENTS

This work is supported by Student Innovation Training Program (No. X2024353), we would like to express our gratitude to this funding, also for the reviewers for their invaluable suggestions.

REFERENCES

Schirmer, P. M., & Axhausen, K. W. (2016). A multiscale classification of urban morphology. Journal of Transport and Land Use, 9(1), 101-130.

Amado, M., & Poggi, F. (2012). Towards Solar Urban Planning: A New Step for Better Energy Performance. Energy Procedia, 30, 1261-1273. https://doi.org/https://doi.org/10.1016/j.egypro.2012.11.139

Zhu, D., Song, D., Shi, J., Fang, J., & Zhou, Y. (2020). The Effect of Morphology on Solar Potential of High-Density Residential Area: A Case Study of Shanghai. Energies, 13(9). https://doi.org/10.3390/en13092215

Liu, K., Xu, X., Zhang, R., Kong, L., Wang, W., & Deng, W. (2023). Impact of urban form on building energy consumption and solar energy potential: A case study of residential blocks in Jianhu, China. Energy and Buildings, 280, 112727. https://doi.org/https://doi.org/10.1016/j.enbuild.2022.112727

Tian, J., & Xu, S. (2021). A morphology-based evaluation on block-scale solar potential for residential area in central China. Solar Energy, 221, 332-347. https://doi.org/https://doi.org/10.1016/j.solener.2021.02.049

Li, D., Cui, X., Shi, L., & Li, Y. (2024). An overview of the research on the correlation between solar energy utilization potential and spatial morphology. Results in Engineering, 24, 103444. https://doi.org/https://doi.org/10.1016/j.rineng.2024.103444

Poon, K. H., Kämpf, J. H., Tay, S. E. R., Wong, N. H., & Reindl, T. G. (2020). Parametric study of URBAN morphology on building solar energy potential in Singapore context. Urban Climate, 33, 100624. https://doi.org/https://doi.org/10.1016/j.uclim.2020.100624

Mahaya, C., Zemmouri, N., Benharra, H., & Elnokaly, A. (2022). Solar Access Assessment in Semi-Arid Urban Context: An Application Study for Ten Urban Forms of Existing Apartment Buildings Districts in Batna City, Algeria. Sustainable Cities and Society, 83, Article 103909. https://doi.org/10.1016/j.scs.2022.103909

Yang, C., Cai, S., & Gou, Z. (2024). Unlocking solar potential in high-latitude urban areas: A study of morphological indicators and zero energy potential of Glasgow. Solar Energy, 283, 113023. https://doi.org/https://doi.org/10.1016/j.solener.2024.113023

Zhang, J., Xu, L., Shabunko, V., Tay, S. E. R., Sun, H., Lau, S. S. Y., & Reindl, T. (2019). Impact of urban block typology on building solar potential and energy use efficiency in tropical high-density city. Applied Energy, 240, 513-533. https://doi.org/10.1016/j.apenergy.2019.02.033

Du, S., Kuang, X., Chen, J., Ye, Y., Li, P., & Shi, X. (2024). Development of an expanded local climate zone scheme to accommodate diversified urban morphological evolution: A case study of Shanghai, China. Urban Climate, 56, 102009. https://doi.org/https://doi.org/10.1016/j.uclim.2024.102009

Jareemit, D., Srivanit, M., Tanapant, S., & Limeechokchai, B. (2025). Role of urban morphology integrated building envelope materials in achieving zero emissions: A simulation-based study in complex-shaped urban blocks. Energy Reports, 13, 27-39. https://doi.org/https://doi.org/10.1016/j.egyr.2024.11.088

Deloitte, Envision Group (2024). Photovoltaic Modules - Carbon Footprint and Low Carbon Development Report. https://www2.deloitte.com/content/dam/Deloitte/cn/Documents/climate-sustainability/deloitte-cn-sustainability-photovoltaic-modules-report-zh-240425.pdf

6th International Conference on Building Energy and Environment
Eindhoven University of Technology, The Netherlands
6 - 10 July 2025

Thermal performance and energy efficiency evaluation of two typical air cooling systems in data centers

Jinkyun Cho [1], Joo Hyun Moon [2]

[1]*Hanbat National University, Daejeon, Republic of Korea, jinkyun.cho@hanbat.ac.kr*
[2]*Hanbat National University, Daejeon, Republic of Korea, jhmoon9@hanbat.ac.kr*

SUMMARY
This study evaluates the thermal performance and energy efficiency of two widely used cooling systems in data centers: ALT-1 (Fan Wall Unit-based Slab Floor) and ALT-2 (CRAH-based Raised Floor). Using CFD simulations, airflow distribution, temperature compliance, and cooling capacity were analyzed under varying supply air temperature (SAT) conditions. ALT-1 demonstrated superior airflow uniformity, stable temperature distribution, and minimal bypass and recirculation, consistently maintaining IT inlet temperatures within ASHRAE's recommended range of 18°C–27°C. In contrast, ALT-2 exhibited greater temperature and airflow variability, leading to localized hotspots and higher cooling capacity deviations. While both systems achieved comparable average net cooling power, ALT-1 proved more reliable and energy-efficient due to its consistent performance. These findings highlight the advantages of FWU-based slab floor configurations for high-density data centers, providing improved thermal management and operational efficiency. Future research could explore optimizing FWU designs for further energy savings and performance enhancement.

Keywords: data center, cooling system, thermal performance, energy efficiency

1. INTRODUCTION

The cooling method of data centers has been a critical topic in the IT industry, particularly regarding the efficiency of different air distribution strategies (Cho et al., 2014). Traditional approaches involve the use of raised floors to supply air through computer room air handling units (CRAH) or the deployment of fan wall units (FWU) to manage airflow within slab floor configurations (Xiong et al., 2021; Wu et al., 2024). This study aims to analyze the performance of these two widely adopted cooling methods in air-cooled data centers by evaluating their airflow distribution, cooling efficiency, and impact on IT equipment inlet temperature.

Energy efficiency and temperature control are essential for maintaining optimal data center operations. The study specifically investigates the differences in supply air distribution between under-floor air distribution (UFAD) with CRAH and slab floor air distribution (SFAD) with FWU. By gradually increasing the supply air temperature from 16°C to 24°C, the effect on IT equipment inlet temperatures is analyzed. A smaller difference between the supply air temperature and the IT inlet temperature signifies improved air distribution efficiency, minimizing bypass and re-circulation. If the IT equipment inlet temperature remains within ASHRAE's recommended range (ASHRAE, 2021), energy efficiency can be enhanced through better system coefficient of performance (COP) and increased economizer operation.

2. METHODOLOGY

To quantitatively assess the cooling performance of these two systems, a computational fluid dynamics (CFD) simulation was conducted using Cadence Reality DC Design.

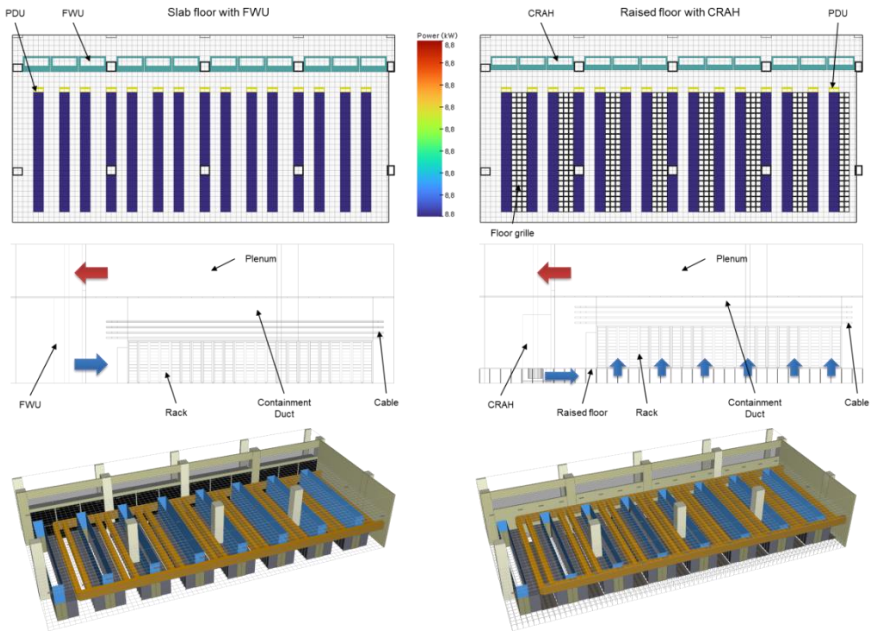

Figure 1. Cooling configurations: raised floor (ALT-2) vs. slab floor (ALT-1).

Table 1. Comparison of cooling strategies: raised floor (ALT-2) vs. slab floor (ALT-1).

Category	Raised Floor (ALT-2)	Slab Floor (ALT-1)
Cooling method	CRAH unit supplying air under a raised floor	FWU supplying air through the walls
Floor structure	Raised floor with 800mm height	Standard slab floor
Airflow pattern	Air supplied through floor grilles	Air supplied through wall-mounted FWU
Containment	Hot aisle containment	Hot aisle Containment
Air return	RA recovery through false ceiling	RA recovery through false ceiling

The study focuses on an IT Hall comprising 339 racks with a total IT load of 2983.2 kW (8.8 kW × 339EA). The comparison is based on key factors such as airflow distribution, temperature uniformity, and cooling performance. The CFD Solver is k-Epsilon turbulence model.

As shown in Figure 1, raised floor and slab floor cooling strategies differ primarily in air supply methodology. The raised floor system uses CRAH units to supply air under an 800 mm high raised floor, distributing it through floor grilles into the white space. In contrast, the slab floor system employs FWUs to supply conditioned air directly through the walls, eliminating the need for raised floors. Both methods implement hot aisle containment and return air collection through false ceilings. The comparison of these two methods is summarized in Table 1.

To ensure accuracy, an unstructured Cartesian grid was used, with ALT-1 containing 5,671,331 cells and ALT-2 containing 8,280,376 cells. The grid size ranged from a maximum of 250mm to a minimum of 25mm. Boundary conditions included an inlet supply air temperature of 16°C to 24°C, a pressure-based outlet discharge condition, and adiabatic walls. The key evaluation metrics were temperature distribution, airflow patterns, and cooling performance, focusing on IT equipment inlet temperature stability within ASHRAE's recommended range.

3. NUMERICAL RESULTS

This section analyzes the simulation results of the cooling strategies for ALT-1 (FWU-based slab floor) and ALT-2 (CRAH-based raised floor), focusing on airflow distribution, temperature compliance, and cooling performance. Key evaluation metrics include ASHRAE temperature compliance, rack mean inlet temperature, airflow distribution, and cooling capacity (Figure 2).

3.1 ASHRAE Temperature Compliance

Compliance with ASHRAE's recommended temperature range (18–27°C) was evaluated for each SAT (Supply Air Temperature) condition (16–24°C). ALT-1 consistently maintained rack inlet temperatures within the recommended range across all SAT conditions, with minimal temperature variation. This highlights the effectiveness of the FWU system in delivering uniform airflow. In contrast, ALT-2 exhibited increased inlet temperatures in racks located farther from the CRAH units, indicating uneven airflow distribution in the raised floor configuration.

3.2 Rack Mean Max Inlet Temperature

The analysis of rack mean inlet temperatures for each SAT condition showed that ALT-1 maintained a consistent temperature range across all racks, demonstrating uniform airflow. ALT-2 exhibited greater temperature variation due to uneven airflow distribution within the raised floor plenum, particularly in racks located farther from the CRAH units (Table 2).

3.3 Airflow Distribution

ALT-1's FWU-based approach effectively separated the cold and hot aisles, minimizing re-circulation while delivering uniform airflow. ALT-2, on the other hand, exhibited uneven velocity distribution in the raised floor plenum, leading to non-uniform air delivery through floor grilles. This was identified as a primary cause of increased temperatures in racks farther from the CRAH units.

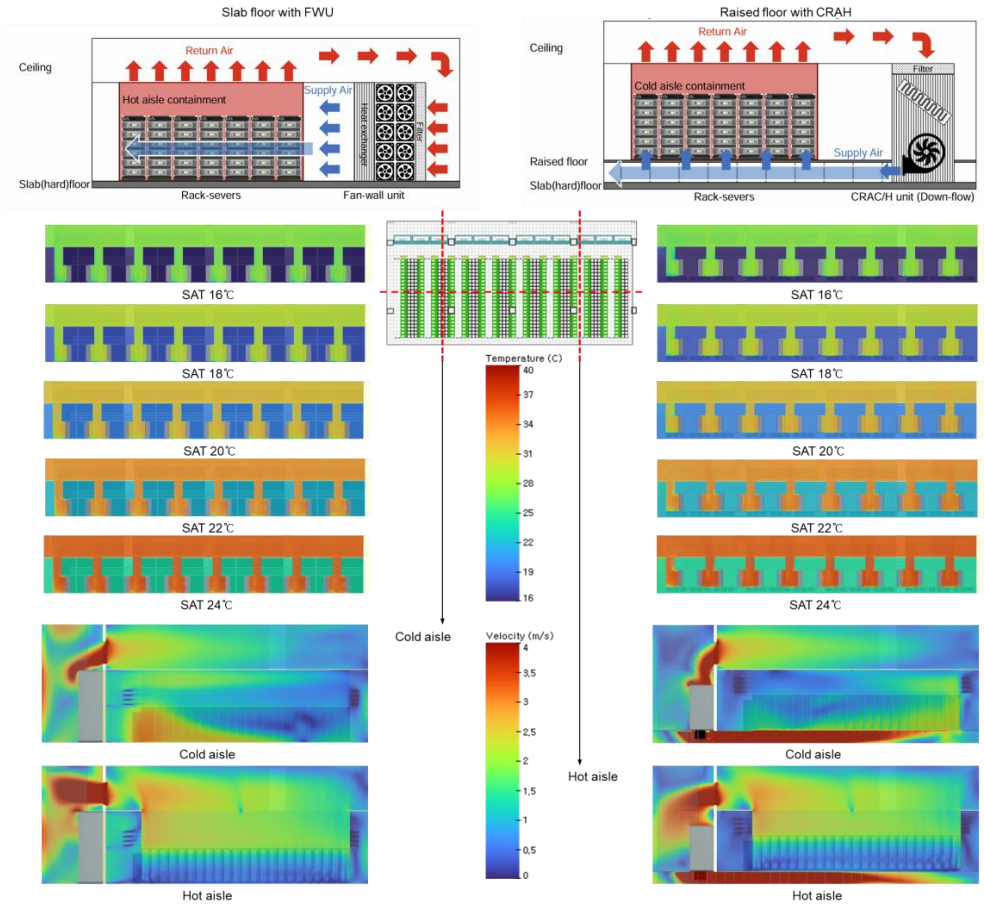

Figure 2. CFD results: ALT-1 vs. ALT-2 temperature and airflow distribution.

Table 2. Mean maximum inlet temperatures for ALT-1 and ALT-2 at different SATs.

SAT (°C)	ALT-1 mean max inlet temp (°C)	ALT-2 mean max inlet temp (°C)
16	16.07985 (+0.50%)	16.18428 (+1.15%)
18	18.07985 (+0.44%)	18.18448 (+1.02%)
20	20.07988 (+0.40%)	20.18469 (+0.92%)
22	22.07988 (+0.36%)	22.18475 (+0.84%)
24	24.07982 (+0.33%)	24.18478 (+0.77%)

3.4 Temperature Distribution by Rack Height

Temperature was measured at three rack height levels: base (0.1m), middle (1.0m), and top (1.8m). ALT-1 maintained consistent temperature profiles across all heights, with minimal variation between racks. In contrast, ALT-2 showed greater temperature differences at the base level due to uneven airflow, although the middle and top levels exhibited improved uniformity.

3.5 Cooling Capacity Analysis

Under identical load conditions, the net cooling power of ALT-1 and ALT-2 was similar on average. However, ALT-2 exhibited greater variation in cooling capacity among units due to differences in airflow distribution. ALT-1 maintained smaller capacity variations thanks to the uniform air distribution achieved by the FWU system (Table 3).

Table 3. Net cooling power comparison between ALT-1 and ALT-2.

Cooling metric	ALT-1	ALT-2
Net cooling power	248.68 kW	248.65 kW
Standard deviation	±2.12%	±4.15%

4. DISCUSSION

This study compared the performance of ALT-1 (Fan Wall Unit-based Slab Floor) and ALT-2 (CRAH-based Raised Floor) in data centers. CFD simulations revealed that ALT-1 maintained uniform airflow and stable temperature distribution, consistently meeting ASHRAE's recommended temperature range. While ALT-2 showed similar average cooling performance, it exhibited greater variability, leading to localized inefficiencies. Thus, the FWU-based slab floor configuration proves to be a more reliable and energy-efficient solution for high-density data centers.

ACKNOWLEDGEMENTS

This work was supported by the National Research Foundation of Korea (NRF) grant funded by the Ministry of Science and ICT (MSIT) of the Republic of Korea (No. RS-2025-00560224).

REFERENCES

Cho J., Yang J., Park W., 2014. Evaluation of air distribution system's airflow performance for cooling energy savings in high-density data centers. Energy and Buildings,68(Part A), pp. 270-279.

Xiong X., Fulpagare Y., Lee P.S., 2021. A numerical investigation of fan wall cooling system for modular air-cooled data center. Building and Environment 205, 108287.

Wu L., Mao R., Zhang J., Li C., Gan J., Zhou J., Zhang Z., 2024. An experimental study on improving the thermal environment of data centers by optimizing fan wall arrangement. Journal of Building Engineering 96, 110421.

ASHRAE, Thermal Guidelines for Data Processing Environments, fifth ed. American Society of Heating, Refrigerating and Air-Conditioning Engineers (ASHRAE), 2021.

6th International Conference on Building Energy and Environment
Eindhoven University of Technology, The Netherlands
6 - 10 July 2025

Evaluating Thermal Comfort in Buildings with Different PCM Configurations- A Simulation-Based Approach

C.K.Oluah[1], K. Schollbach[2], S. Gaastra-Nedea[1], H.A. Zondag[1,3]

[1] *Department of Mechanical Engineering, Eindhoven University of Technology, Eindhoven, The Netherlands, c.k.oluah@tue.nl*

[2] *Department of the Built Environment, Eindhoven University of Technology, Eindhoven, The Netherlands, k.schollbach@tue.nl*

[1] *Department of Mechanical Engineering, Eindhoven University of Technology, Eindhoven, The Netherlands, s.v.nedea@tue.nl*

[1,3] *Department Energy Transition TNO, Petten, The Netherlands, h.a.zondag@tue.nl*

ABSTRACT

This study explores the potential of Phase Change Materials (PCMs) in improving both thermal comfort and energy efficiency in buildings. Nine PCM configurations (S1-S9), varied by melting temperature, thickness, and location (wall, roof, floor), were evaluated using EnergyPlus simulations. Thermal comfort was assessed with the Predicted Mean Vote (PMV) and Percentage of People Dissatisfied (PPD) indices, following ASHRAE Standard 55. The PCM melting temperatures were 18°C, 21°C, and 23°C, representing variations in their thermal behavior under different seasonal conditions. The results of the simulations showed that the integration of PCM in the building envelope reduced energy demand while maintaining thermal comfort. The floor configurations (S3, S5, S7) demonstrated the lowest heating energy demand while achieving acceptable comfort levels. These findings suggest that strategic placement of PCMs in building floors is an effective solution for optimizing energy consumption without compromising occupant comfort. .

Keywords: Phase change materials, whole building simulation, thermal comfort assessment,

1. INTRODUCTION

Building energy efficiency has become a central focus in addressing global energy consumption and reducing greenhouse gas emissions. Buildings account for a significant portion of global energy use, primarily due to the demand for heating and cooling to maintain indoor comfort. According to the International Energy Agency (IEA), buildings contribute to nearly one-third of global energy use and carbon emissions, emphasizing the urgent need for sustainable solutions in buildings (Agency, 2020). The integration of innovative materials, such as Phase Change Materials (PCMs), offers promising solutions to improve thermal performance and reduce energy consumption in buildings. PCMs are materials that absorb or release heat during phase transitions, making them particularly useful in regulating indoor temperatures by storing excess heat during peak periods and releasing it during temperature drops (Sharma et al., 2009).

Thermal comfort in buildings is a crucial factor for occupant well-being and energy efficiency. The design and operation of buildings must balance these two aspects, ensuring that thermal conditions fall within acceptable limits for occupants while minimizing energy demand. Standards such as ASHRAE Standard 55 provide a framework for assessing indoor environmental quality, using indices like the Predicted Mean Vote (PMV) and Percentage of People Dissatisfied (PPD) to quantify comfort levels (ASHRAE, 2017).

In recent years, PCM integration has gained attention as a viable solution to address both energy demand and thermal comfort. Strategically incorporating PCMs in building envelopes (walls, roofs, and floors), has shown great possibilities in shifting the thermal response of the building, reducing the need for mechanical heating and cooling systems. Previous studies have investigated PCM performance under different climate conditions, highlighting the potential of the material to reduce energy consumption during peak cooling and heating periods (Cabeza et al., 2010; Kalogirou, 2009). However, the application of PCMs in buildings remains complex, as the performance is highly dependent on several factors, including the PCM's melting temperature, thickness, and placement within the building structure (Zhang and Liu, 2015).

Thermal comfort in buildings is also influenced by the dynamic interaction between building design, indoor climate, and external environmental factors. While PCM integration has been studied for its energy-saving potential, its effect on indoor comfort remains an area of active research, with results varying based on building type and local climate conditions (Yang et al., 2016). Understanding how to optimize PCM configuration in buildings is critical to maximize both energy savings and occupant satisfaction.

While previous studies have primarily focused on PCM energy-saving potential, this study uniquely examines multiple PCM variables and their effect on both thermal comfort and energy demand. This study employs a Taguchi L9 orthogonal array to systematically evaluate nine configurations combining three melting temperatures (18°C, 21°C, and 23°C), thicknesses (0.06m, 0.04m, and 0.02m), and locations (wall, roof, and floor). We further assessed both thermal comfort, using the ASHARAE-55 standard and energy demand pattern, providing insights on optimal configuration for PCM integration in buildings.

2. METHOD

This section provides an overview of the simulation setup used to evaluate the impact of various PCM configurations on energy consumption and thermal comfort in buildings. The building was designed in DesingBuilder with simulations run on Energyplus Engine to evaluate the building's thermal performance with different PCM con- figurations. The results of these simulations were then fed into a thermal comfort tool to assess the thermal comfort levels for the various configurations. Figure 1 below summarizes our work process, the key simulation parameters, and the tools used in the study.

2.1. Simulation Setup

The simulation process involved using DesignBuilder and EnergyPlus to model the energy performance of the building. These tools provided the platform for simulating the building and evaluating the effects of different PCM configurations on thermal behavior and energy demand. Simulations were conducted for a full year (January 1 to December 31) 2002, using EnergyPlus weather data of Eindhoven's climate sourced from the EnergyPlus database for accurate representation of local conditions.

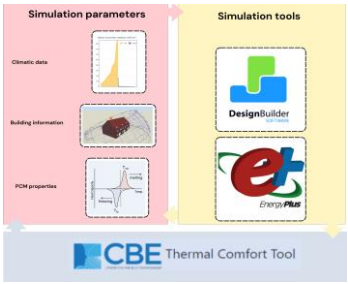

Figure 1. Simulation study.

2.1.1. Simulation tool

EnergyPlus has proven to be particularly effective for modeling buildings with PCMs, as it enables precise calibration and validation of PCM models. The tool allows for detailed simulations of PCM's ability to absorb and release heat, using a one-dimensional conduction finite difference (CondFD) algorithm that accounts for the thermal transfer and storage processes of PCMs (see equation 1). This capability is critical for evaluating the energy-saving potential of PCMs, as the software can dynamically update temperature-dependent properties, such as specific heat, based on phase change energy. These features make EnergyPlus an invaluable tool for simulating PCM integration in buildings. (Feng et al., 2022; Tabares-Velasco et al., 2012).

$$c_p \rho \Delta x \frac{T_i^{j+1} - T_i^j}{\Delta t} = \frac{1}{2}\left(k_W \frac{T_{i+1}^{j+1} - T_i^{j+1}}{\Delta x} + k_E \frac{T_{i-1}^{j+1} - T_i^{j+1}}{\Delta x} + k_W \frac{T_{i+1}^{j} - T_i^{j}}{\Delta x} + k_E \frac{T_{i-1}^{j} - T_i^{j}}{\Delta x}\right) \quad (1)$$

Where:

T = node temperature, Δx = calculation time step, Δx = finite difference layer thickness, C_p = specific heat of material, k_W = thermal conductivity for interface between node i and node $i+1$, k_E = thermal conductivity for interface between node i and node $i-1$, ρ = density of material.

with superscripts and subscripts: i = node being modeled, $i+1$ = adjacent node to the interior of the construction, $i-1$ = adjacent node to the exterior of construction, $j+1$ = new time step, i = previous time step.

2.1.2. Building Model

To evaluate the impact of various PCM configurations on the building, a detailed residential building model was developed using DesignBuilder software (see Fig. 2). The study specifically focuses on terrace buildings constructed between 1940 and 1980, which represent a significant portion of

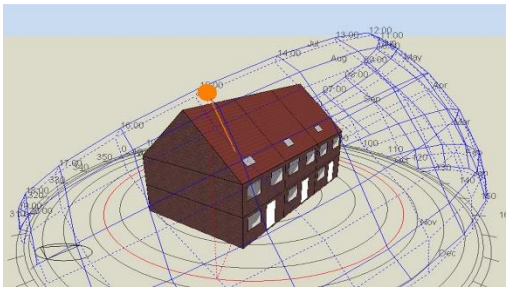

Figure 2. Building model.

the building stock in Eindhoven. The building dimensions, material properties, and other relevant details are based on standardized references (Ondernemend Nederland (RVO), 2017). These properties were used to simulate the thermal behavior of the building and assess the performance of PCM integration in the envelope. The Infinte PCM used for the simulation was sourced from Insolcorp LLC, 2023 with different melting temperatures as described in Section 1.

2.1.3. PCM Configurations

Nine PCM configurations (S1-S9) were designed using a Taguchi L9 orthogonal array, a standardized experimental design method that efficiently evaluates multiple factors and their interactions with a minimal number of runs (Liu et al, 2019). Three factors were considered: melting temperature (18°C, 21°C, 23°C), PCM thickness (0.02m, 0.04m, 0.06m), and location (wall, roof, floor), each at three levels. The matrix of variables (σ) shown in eqn (2), was used to generate the Taguchi L9 array in Table 1. Taguchi systematically combines these factors to assess their combined and relative effects on thermal comfort and energy demand.

$$\sigma = \begin{bmatrix} T_1 & T_2 & T_3 \\ x_1 & x_2 & x_3 \\ c_1 & c_2 & c_3 \end{bmatrix} \qquad (2)$$

where T_1 is the melting temperature =18°C, which is T_2 is the melting temperature =21°C, and T_3 is the melting temperature of =23°C.

while x_1 = 0.06, x_2 = 0.04, x_3 = 0.02. and c_1, c_2 and c_3, corresponds to wall roof and floor respectively. Each configuration was integrated into the EnergyPlus model, allowing the simulation of the building's thermal response to different PCM configurations across a full year.

2.2. Thermal Comfort Assessment

According to ANSI/AHSRAE Standard 55, thermal comfort is defined as the mental state reflecting an individual's satisfaction with the thermal environment, typically assessed through subjective evaluation (Kim et al., 2019). Since thermal comfort varies by individual, creating a universally satisfying thermal environment is challenging. What is comfortable for one group may be uncomfortable for another (Su et al., 2024). Thermal comfort was assessed using the PMV and PPD indices, as outlined in ASHRAE Standard 55. The PMV ranges from -3 (cold) to +3 (hot), with a neutral comfort value of 0. However, ASHRAE 55 makes it clear that it considers the acceptable comfort range to be a PMV score in the range of -0.5 to +0.5. The PPD index estimates dissatisfaction, with values under 10% deemed acceptable for comfort. EnergyPlus simulations provided hourly data, which was used to calculate PMV and PPD, considering factors like air temperature, mean radiant temperature, air velocity, relative humidity, clothing insulation and metabolic rate. The CBE Thermal Comfort Tool was employed to calculate these indices, essential for evaluating occupant satisfaction with indoor conditions (Tartarini et al., 2020).

2.3. Assumptions

For this simulation, we modeled a residential building with gas heating, mechanical ventilation, and natural ventilation for winter heating and summer cooling. Metabolic rates were set at 1.0 for men, 0.85 for women, and 0.75 for children and a clo of 0.5 (Ioannou and Itard, 2015; Ioannou, Itard, and Agarwal, 2018). The heating system is activated when the room temperature drops below 18°C, and cooling begins at 25°C, with a setback temperature of 30°C. The building uses both gas heating and mechanical ventilation, complemented by natural convection. It was also assumed that the building had four occupants: two adults and two teenagers.

3. RESULTS

In this section, we present the results of the thermal comfort assessment and heating energy demand for the different PCM integration configurations in the building. The simulations were conducted with various configurations, each characterized by distinct melting temperatures, PCM thicknesses, and locations within the building. These configurations were evaluated to assess their effectiveness in improving thermal comfort and reducing heating energy demand. Table 1 below summarizes the different simulation runs, providing a detailed overview of the configurations tested.

Table 1. Summary of building simulation runs.

Simulation run	Temperature (T)	Thickness	Configuration (c)
S1	T_1	x_1	c_1
S2	T_1	x_2	c_2
S3	T_1	x_3	c_3
S4	T_2	x_1	c_2
S5	T_2	x_2	c_3
S6	T_2	x_3	c_1
S7	T_3	x_1	c_3
S8	T_3	x_2	c_1
S9	T_3	x_3	c_2

The simulation runs can be categorized into three groups based on the PCM location within the building: wall configurations (S1, S6, S8), roof configurations (S2, S4, S9), and floor configurations (S3, S5, S7). Each category represents distinct placements of PCM in the building's envelope, and the performance results for each category will be discussed in the subsequent subsections.

3.1. Wall Configuration

The thermal comfort assessment for the wall configurations (S1, S6, and S8) shows that all configurations comply with the ASHRAE 55-2023 standard as shown in Fig. 3. The Predicted Mean Vote (PMV) values for the three configurations are -0.28, -0.09, and 0.25, respectively, all indicating a neutral thermal sensation. Similarly, the Percentage of People Dissatisfied (PPD) values for the wall configurations are within the acceptable range of 5-7%, with S1 showing the highest PPD at 7%. The Set Effective Temperature (SET) for each configuration varies slightly, with S1 having a

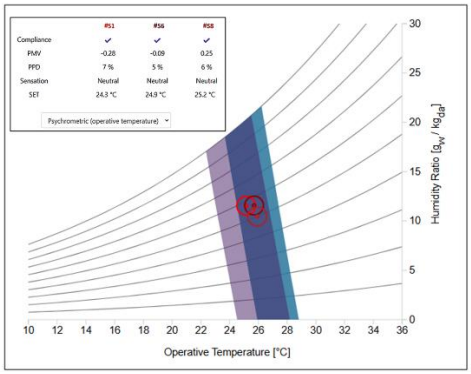

Figure 3. Thermal comfort assessment for wall configurations

SET of 24.3°C, S6 at 24.9°C, and S8 at 25.2°C, all remaining within the range of comfort. These results suggest that the wall configurations, despite differences in PCM mass and location, provide a neutral thermal environment for occupants, aligning well with ASHRAE 55 standards.

3.2. Roof Configuration

The thermal comfort assessment for the roof configurations (S2, S4, and S9) shows varying levels of compliance with ASHRAE 55-2023 standards shown in Fig. 4. S2 complies with the standard, showing a PMV of 0.28, PPD of 7%, and a neutral sensation. The SET is 26.0°C, indicating

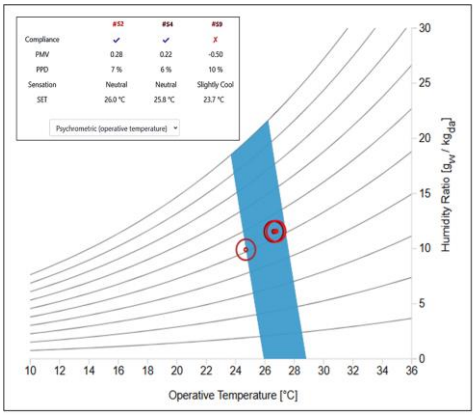

Figure 4. Thermal comfort assessment for roof configurations

a comfortable thermal environment for occupants. Similarly, S4 also complies with ASHRAE 55, with a PMV of 0.22, PPD of 6%, and a neutral sensation. The SET for S4 is 25.8°C, indicating a comfortable indoor temperature. However, S9 does not fully comply with the standard, as it shows a PMV of -0.50 and PPD of 10%, indicating a slightly cool sensation and a higher level of dissatisfaction. The SET for S9 is 23.7°C, which is below the ideal comfort range.

3.3. Floor Configuration

The thermal comfort assessment for the floor configurations (S3, S5, and S7) presented in Fig. 5 shows that all configurations comply with ASHRAE 55-2023 standards. S3 shows a PMV of 0.36, PPD of 8%, and a neutral sensation with a SET of 26.2°C. S5 shows a PMV of -0.17, PPD of 6%, and a neutral sensation, with a SET of 24.7°C. Similarly, S7 also complies with the standard, with a PMV of 0.05, PPD of 5%, and a neutral sensation. The SET for S7 is 25.3°C.

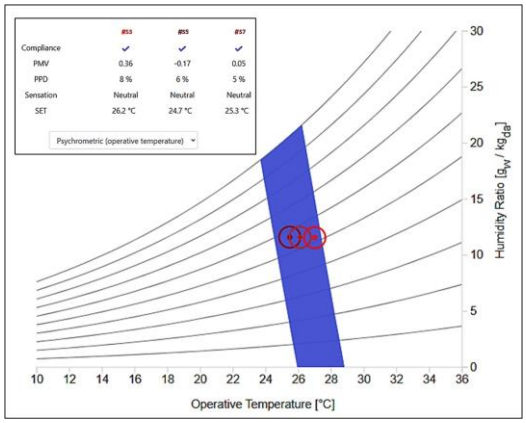

Figure 5. Thermal comfort assessment for floor configurations.

3.4. Heating Energy Demand Across Simulation Runs

Figure 6 presents the mean heating energy demand across the different simulation runs, with each configuration representing different placements of PCM in the building. This plot is critical in illustrating the energy trade-offs associated with maintaining thermal comfort. As the results show, although some configurations met the ASHRAE 55-2023 thermal comfort standards, they were more energy-efficient than others.

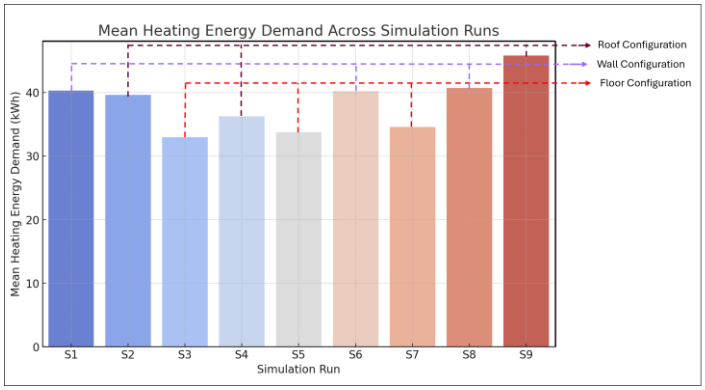

Figure 6. Heating energy demand across simulation runs for different PCM configurations.

For example, while configurations such as S1, S6 and S8 complied with thermal comfort standards, their heating energy demands were relatively high compared to others. Also evident from the result is that S9 does not meet the thermal comfort standards; this is because it has the least PCM density, is located on the roof, and has the highest energy demand, indicating that this configuration is the least suitable for the building with a net heat loss to the ambient. The graph also shows that the floor configurations maintained thermal comfort with lower energy demand, providing information on the energy-efficient benefits of strategic PCM integration.

4. DISCUSSION

PCM integration offers energy and comfort benefits but faces challenges like high initial costs, especially for retrofits, degradation over time, and maintenance needs, potentially limiting adoption. The Taguchi L9 design reveals that lower melting temperatures (e.g., 18°C in S3) enhance thermal storage, improving PMV (0.36) and reducing energy demand, while thicker layers (0.06m in S3, S7) and floor placement minimize heat loss, explaining why floor configurations outperform roof (e.g., S9: 0.02m, 23°C, highest demand) and wall setups. However, further research is needed on wall orientation and PCM-to-surface ratio effects. Statistical methods like ANOVA can isolate individual parameter effects for sensitivity analysis.

5. CONCLUSION

This study shows that PCM configurations significantly impact thermal comfort and heating energy demand, with floor configurations (S3, S5, S7) achieving the lowest energy demand while maintaining ASHRAE 55-2023-compliant comfort. S3 (18°C, 0.06m) performed best, due to minimal ambient heat loss, enhanced thermal storage from lower melting temperatures, and better heat retention with thicker layers. These findings highlight floor PCM integration as an efficient solution for reducing energy consumption without compromising comfort. Future research should explore wall orientation effects and use statistical methods like ANOVA to isolate parameter impacts.

REFERENCES

Agency I. E., 2020. *World Energy Outlook 2020*. https://www.iea.org/reports/world-energy-outlook- 2020. Accessed: 2025-01-13.

ASHRAE, 2017. ASHRAE Standard 55-2017: Thermal Environmental Conditions for Human Occupancy. American Society of Heating, Refrigerating and Air-Conditioning Engineers.

Cabeza L. F., Gracia L. F. de, Castell A., Barreneche A., Rodríguez M. M., Valverde I., Fuente A. L. de la, Fernández A., and Bovea E. G., 2010. Thermal energy storage materials—A review. Renewable and Sustainable Energy Reviews 14, 935–948.

Feng F., Fu Y., Yang Z., and O'Neill Z., 2022. Enhancement of phase change material hysteresis model: A case study of modeling building envelope in EnergyPlus. Energy and Buildings 276, 112511.

Insolcorp LLC, 2023. *InfiniteR Mat 18C 65F Data Sheet*. https://infiniterpcm.com/data-sheets. Accessed: September 26, 2024.

Ioannou A. and Itard L., 2015. Energy performance and comfort in residential buildings: Sensitivity for building parameters and occupancy. Energy and Buildings 92, 216–233.

Ioannou A., Itard L., and Agarwal T., 2018. In-situ real time measurements of thermal comfort and comparison with the adaptive comfort theory in Dutch residential dwellings. Energy & Buildings 170. This is an open access article under the CC BY license, 229–241.

Kalogirou S. A., 2009. Solar energy applications in buildings. Progress in Energy and Combustion Science 35, 231–249.

Kim J., Bauman F., Raftery P., Arens E., Zhang H., Fierro G., Andersen M., and Culler D., Jan. 2019. Occupant comfort and behavior: High-resolution data from a 6-month field study of personal comfort systems with 37 real office workers. Building and Environment 148, 348–360.

Liu, X., Zhou, Y., Li, C.-Q., Lin, Y., Yang, W., & Zhang, G. (2019). "Optimization of a New Phase Change Material Integrated Photovoltaic/Thermal Panel with the Active Cooling Technique Using Taguchi Method." Energies 12 (6): 1022. https://doi.org/10.3390/en12061022

Ondernemend Nederland (RVO) R. voor, 2017. *Referentiegebouwen BENG*. Accessed: 2024-11-06.

Sharma A., Tyagi V. V., Chen C. R., and Buddhi D., 2009. Review on thermal energy storage with phase change materials and applications. Renewable and Sustainable Energy Reviews 13, 318–345.

Su X., Yuan Y., Wang Z., Liu W., Lan L., and Lian Z., Dec. 2024. Human thermal comfort in non-uniform thermal environments: A review. Energy and Built Environment 5, 853–862.

Tabares-Velasco P., Christensen C., and Bianchi M., 2012. Verification and validation of EnergyPlus phase change material model for opaque wall assemblies. Building and Environment 54, 186–196.

Tartarini F., Schiavon S., Cheung T., and Hoyt T., 2020. CBE Thermal Comfort Tool: Online tool for thermal comfort calculations and visualizations. SoftwareX 12. This is an open access article under the CC BY license, 100563.

Yang X., He J., Wang J., Li Z., and Zhang Z., 2016. Thermal performance and energy saving potential of PCM-based building materials: A review. Renewable and Sustainable Energy Reviews 59, 1216–1227.

Zhang H. and Liu G., 2015. A review on the thermal performance of phase change materials integrated into building envelopes. Renewable and Sustainable Energy Reviews 44, 187–202.

6th International Conference on Building Energy and Environment
Eindhoven University of Technology, The Netherlands
6 - 10 July 2025

Interface characteristics of PVDF membrane used for dehumidification by liquid desiccant

Tingting Chen [1], Zhimin Chang [1], Yang Li[2]

[1]*China University of Mining and Technology, Xuzhou, China, chenttmail@cumt.edu.cn*
[2]*Suzhou Zhonghuiyun Engineering Technology Limited Company, Suzhou, China, 1312837151@qq.com*

SUMMARY
Polyvinylidene fluoride (PVDF) membrane is used to separate the liquid desiccant and air for avoiding corrosion during dehumidification. The contact angle of the liquid droplet on the PVDF membrane was simulated by taking lithium bromide (LiBr) aqueous solution as the liquid desiccant. Interface characteristics of liquid-PVDF-gas systems were simulated using molecular dynamics. Interface thickness and hydrogen bond distribution of liquid-PVDF-gas systems were further analyzed and compared. Results show that the cube droplet on the PVDF membrane firstly transforms into a spherical shape rapidly and then spreads along the PVDF surface slowly. The simulated contact angle of LiBr solution on the PVDF membrane is about 93° when the concentration is 50%. It is found that the thickness of the interface between the LiBr solution and PVDF membrane is much larger than that of the interface between the LiBr solution and air especially for conditions with high solution concentration. Hydrogen bonds are formed between PVDF and water in the interface zone and PVDF tends to be the acceptor.

Keywords: dehumidification, contact angle, interface thickness, hydrogen bonds.

1. GENERAL INSTRUCTIONS

Liquid desiccant dehumidification has attracted much attention to realize thermal comfort with low energy consumption in the past decades (Yin et al., 2014; Gurubalan et al., 2021). However, the application of the liquid desiccant dehumidification is limited in some situations due to the corrosion which occurs inevitably when the liquid desiccant absorbs water in air by direct contact.

Membrane based dehumidification using liquid desiccant is proposed to solve aforementioned problems by applying membranes to separate the liquid desiccant and air (Liu et al., 2019). But the use of membranes increases mass transfer resistance simultaneously. PVDF (polyvinylidene fluoride) is a commonly used membrane material but usually suffers from problems of fouling and solution leakage. All drawbacks depend on the interface characteristics between phases to some degree regardless of mass transfer, fouling or solution leakage. Promoting membrane performance plays an important role in enhancing dehumidification, bringing about the energy conservation and emission reduction. Investigation from the microscopic level helps develop and propose superior membrane because some crucial details cannot be achieved from the macroscopic level. With the rapid development of computers, molecular simulation has been widely used to study gas-liquid interface characteristics and reveal the microscopic mechanism of chemical processes (Nagata et al., 2015; Weng et al., 2016). Björneholm et al. discussed the density profile and h-bond distribution of the gas-liquid interface for pure water (Björneholm et al., 2016). The mixed matrix membrane using PVDF as the matrix was investigated by molecular dynamics simulation. It was verified that the addition of zwitterion and TiO_2 improved the hydrophilicity and oil resistance of

the membrane (Bui et al., 2021). Relevant researchers also used molecular dynamics and Monte Carlo simulation to obtain the density, free volume fraction, diffusion, permeability and selectivity of PVA-PVDF membranes (Liu et al., 2022).

Membrane based dehumidification using liquid desiccant is related with the mass transport through the gas-solid interface, the membrane and the liquid-solid interface. Studying the interface and interactions of the liquid-PVDF-gas system at the microscopic level is beneficial for developing novel membrane materials and enhancing dehumidification process essentially. The contact angle has obvious effects on dehumidification and fouling (Wen et al., 2018) and hydrogen bonds are often non-negligible as to interactions. So in this paper, the interface characteristics of liquid-membrane-gas systems were analyzed by molecular dynamics simulation. The lithium bromide (LiBr) aqueous solution was taken as the liquid desiccant and PVDF was taken as the membrane to separate the liquid desiccant and air here. The contact angle of LiBr solution on the PVDF membrane was simulated and calculated. The distributions of density and hydrogen bonds for liquid-PVDF-air systems were also obtained. Liquid-gas interfaces and liquid-solid interfaces were further compared. This study sets foundation for further disclosing the mechanism of membrane based dehumidification by molecular dynamics.

2. METHOD

All simulations were performed based on GROMACS 5.1.1 software and periodic conditions were applied in three directions. SPC/E water model was used and OPLS-AA force field was adopted for PVDF considering precision and compatibility. Parameters of force fields for ions were listed in Table 1, which were validated with good performance in our previous work (Chen et al., 2019). All atoms or ions were considered as Lennard-Jones (LJ) particles with charges. The intermolecular potentials were the summation of LJ potentials and Coulombic potentials. LJ interactions between different kinds of atoms were produced by Lorentz-Berthelot combining rules. The cutoff distance was set as 1.2 nm for Lennard-Jones potential and short-range electrostatic interactions. Potentials switched smoothly to 0 between 1.0 nm and 1.2 nm and PME solver was applied to calculate long-range electrostatic interactions. Water molecules were constrained by SETTLE algorithm and all bonds of PVDF were constrained by LINCS algorithm. Center of mass translation was removed every 500 time steps. Newtonian equations of motion were solved by the leap-frog algorithm with the timestep of 1 fs.

Table 1. Parameters of force fields for ions

Ions	ε (kJ/mol)	σ (Å)	q (e)
Li^+	0.6904	1.505	1
Br^-	0.4184	4.539	-1

2.1. Simulation of Contact Angle

The simulation system for computing contact angle is shown in Fig. 1. The simulation box was 10 nm in length, 10 nm in width and 12 nm in height. As shown in Fig. 1, the simulated system mainly consisted of three parts including the fixed layer on the bottom, the PVDF layer in the middle and the square droplet of LiBr aqueous solution. Before constructing the system, an annealing simulation of 6 ns was conducted for the PVDF layer with the temperature between 300 K and 500 K. The size of the droplet was 4 nm in all directions and the initial density was set corresponding to one atmosphere. The system was run in the NVT ensemble for 20 ns with the output interval of

2 ps after energy minimization. 2D number-density maps were derived from GROMACS when reaching equilibrium. The density contour was further fitted by equation of a circle and the contact angle was calculated finally (Kitabata et al., 2018).

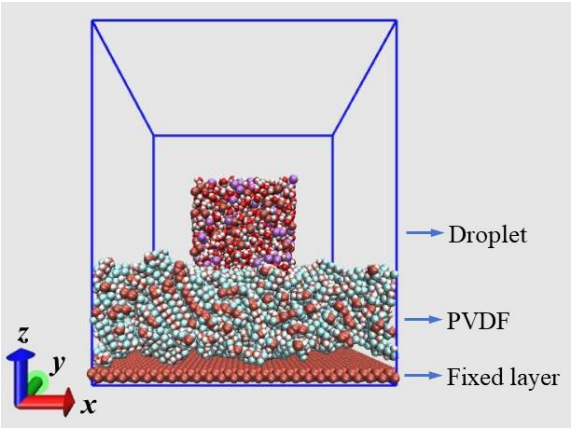

Figure 1. System for simulating contact angle

2.2. Simulation of Density Profiles and Interface Thickness

Fig. 2 illustrates the liquid-PVDF-air system using LiBr solution as the liquid desiccant. The simulation box was 5 nm in width, 5 nm in length and 15 nm in height. PVDF was formed by 19 single chains with the polymerization degree of 50. Solid-liquid interface and liquid-gas were produced simultaneously due to periodic conditions. LiBr aqueous solution had 2000 water molecules and corresponding ions according to the concentration. Air is represented by empty zone for simplification. All initial configurations were provided by Packmol software. After an equilibration run of 1000 ps under NVT ensemble of 300 K, thermodynamics data and trajectories of atoms were output every picosecond during the production run of 500 ps.

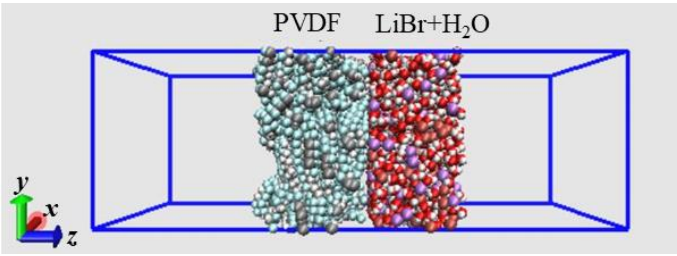

Figure 2. Liquid-PVDF-gas systems

The simulation system was divided into slices with the thickness of 0.1 nm along *z* direction and the density for every slice could be computed using the built-in programs of GROMACS software. The interface thickness could be achieved after correlating the density profiles using hyperbolic tangent functions.

2.3. Analysis of Hydrogen Bond

The number of hydrogen bonds were analyzed based on VMD software and Python codes. Trajectories from GROMACS were input in VMD software and data of hydrogen bonds were output. The distance between acceptors and donors was set as 0.35 nm. The number of hydrogen

bonds for every slice was half of the summation of the donor number and the acceptor number. The final result adopted the average value of the production run.

3. RESULTS AND DISCUSSION

3.1. Contact Angle of LiBr Solution on PVDF membrane

The concentration of the LiBr aqueous solution was 50% here and the contact angle of the aforementioned solution on the PVDF membrane was simulated. Fig. 3 gives the root mean square deviation (RMSD) by comparing two structures at different times. This indicates that at least 12 ns is needed for system equilibration and the followed data is used to calculate the contact angle accurately.

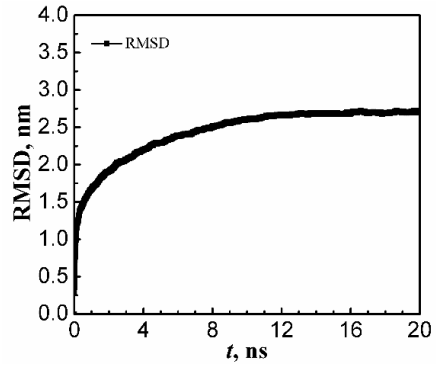

Figure 3. RMSD of simulation

Fig. 4 illustrates the droplet change as the simulation goes on. It seems that the droplet change can be divided into two periods. The droplet changes from the cube shape to the spherical shape rapidly due to the effects of interactions during the first period. The contact area between the droplet and the PVDF membrane as well as the height of the droplet almost keeps unchanged. Compared with the first period before 500 ps, the second period proceeds more slowly. The droplet of LiBr solution spreads along the PVDF surface during the second period. The contact area between the droplet and the PVDF membrane increases gradually and the height of the droplet decreases till equilibration.

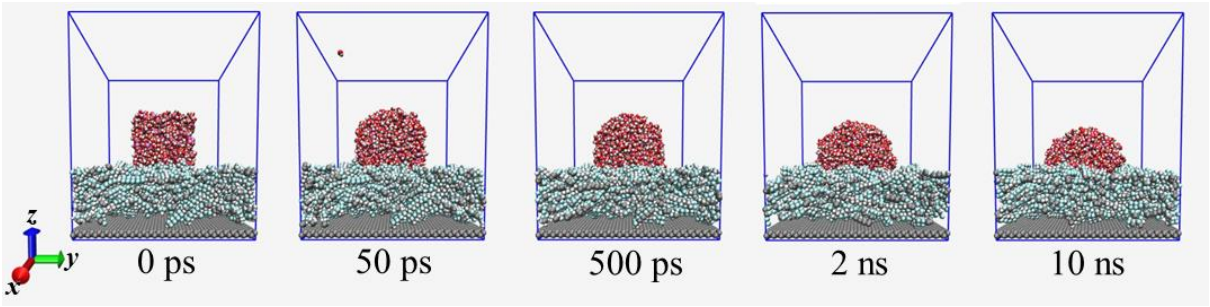

Figure 4. Droplet variation with time

The number density map of *yz* plane is shown in Fig. 5. Fig. 5(a) presents different density contours.

The data set in Fig .5(a) with the density of 5 nm^{-2} is extracted and is further fitted using the equation of a circle. The contact angle can be calculated according to the circle parameters and the position of the liquid-solid interface. The final result is the average value of *yz* plane and *xz* plane. The contact angle of the LiBr solution on the PVDF membrane is about 93^o by simulation calculation here, which agrees well with the experimental results. This means the molecular dynamics and the used force field could investigate phenomena involving liquid-PVDF-gas systems with satisfied accuracy. Further, molecular dynamics can be relied on to verify whether the novel membranes can enhance dehumidification and anti-fouling or not.

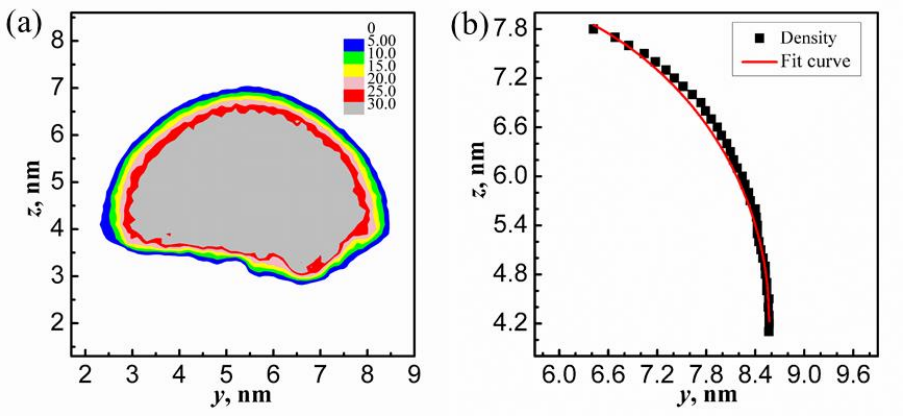

Figure 5. Density map: (a) 2D density contour; (b) circle fitting

3.2. Density Profiles and Interface Thickness of Liquid-membrane-gas Systems

The mass density profile of liquid-PVDF-air system for pure water is shown in Fig. 6. Two different interfaces can be seen from Fig. 6(a) where the left shadow area is the solid-liquid interface and the right shadow area is the liquid-gas interface. The PVDF density reduces from 1555 kg/m^3 to 0 along the interface normal direction in the zone of the solid-liquid interface. The water density rises from nearly 0 to 993 kg/m^3 in the zone of the solid-liquid interface while drops from nearly 993 kg/m^3 to 0 in the zone of the liquid-gas interface. The thickness of interfaces is calculated by fitting density profiles of water (Fig. 6(b)). The thickness of PVDF-water interface is about 0.455 nm. The thickness of water-air interface is about 0.392 nm, reduced by 16% compared with the PVDF-water interface.

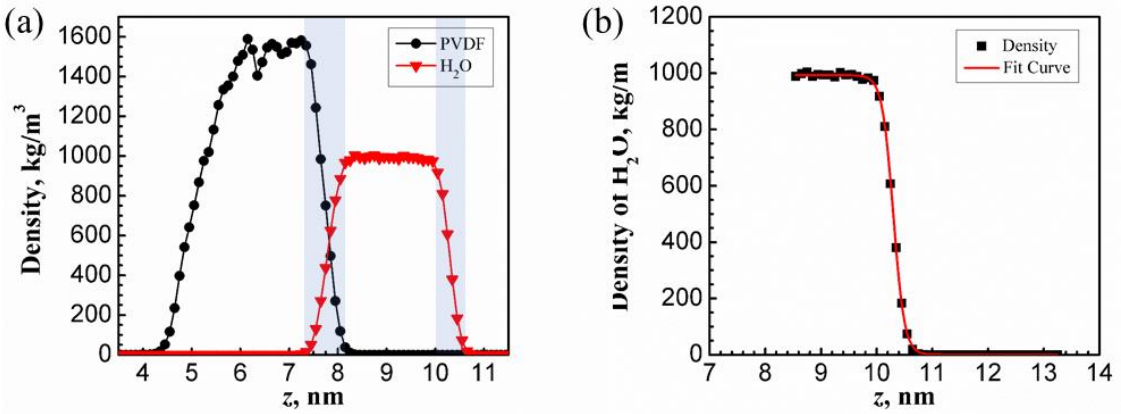

Figure 6. Density profiles of water-PVDF-air system: (a) mass density; (b) hyperbolic tangent fitting

Density profiles of liquid-PVDF-air system for LiBr aqueous solution are shown in Fig. 7. With an increase in concentration, the water density decreases while the ion density increases (Fig. 7(a) and Fig. 7(b)). Compared with the system using pure water, the density profile of LiBr aqueous solution fluctuates more significantly because of the ion accumulation position.

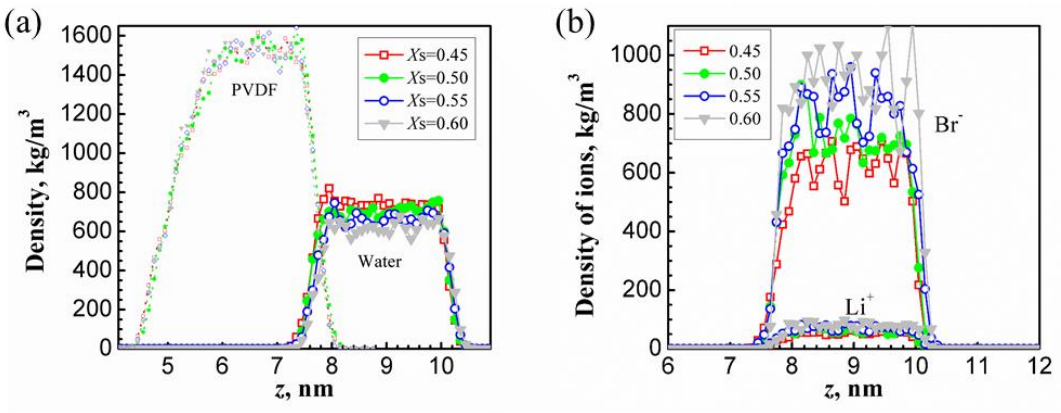

Figure 7. Density profiles of solution-PVDF-air systems: (a) PVDF and water; (b) ions

The thickness comparison between the liquid-solid interface and liquid-gas interface using LiBr aqueous solution is shown in Fig. 8. The thickness of the liquid-air interface declines from 0.345 nm to 0.260 nm with an increase in the concentration of LiBr solution. The stronger interactions from the liquid phase can account for the shrink of interface. But for the thickness of the solid-liquid interface, it seems a minimum value of 0.382 nm emerges with the solution concentration of 50%. This may be because different interactions predominate within different concentration ranges.

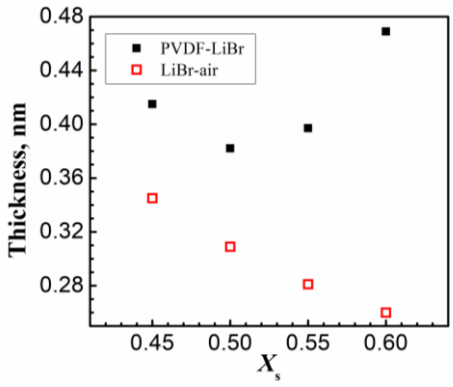

Figure 8. Thickness of liquid-solid interface and liquid-gas interface

As a result, the thickness of liquid-solid interface is much higher than that of liquid-air interface especially for LiBr solution with the concentration larger than 50%. The extension of liquid-PVDF interface may be attributed to larger interactions from PVDF than gas. When the concentration of LiBr solution is 55% and 60%, the PVDF-liquid interface is 41% and 80% thicker than the liquid-air interface respectively. This implies that using PVDF to separate air and LiBr solution produces higher resistance for transport prominently even without considering membrane resistance. This is

because the membrane based dehumidification is related with the solid-liquid interface while the conventional liquid desiccant dehumidification is related with the liquid-air interface. Develop novel membrane materials for dehumidification could resort to reducing the thickness of solid-liquid interface.

3.3. Hydrogen Bond of Liquid-membrane-gas Systems

Fig. 9 describes the distribution of hydrogen bonds for liquid-PVDF-air systems. Fig. 9(a) is the system adopted pure water of 300 K and Fig. 9(b) is the system adopted LiBr aqueous solution with the concentration of 60%. As depicted in Fig. 9(a), the hydrogen bonds in the zone of PVDF-water interface consist of three parts. Hydrogen bonds can be formed between PVDF and PVDF, between PVDF and water, and between water and water respectively. Hydrogen bonds formed between PVDF and water can also include two types in terms of water as the acceptor or donor. In the zone of PVDF-water interface, the number of hydrogen bonds formed between PVDF and PVDF becomes less and less along *z* direction. The number of hydrogen bonds formed between water and water increases sharply. This is consistent with the density distribution of each component in the interface zone. Moreover, almost all hydrogen bonds formed between PVDF and water are types of water as the donor and PVDF as the acceptor. The number of hydrogen bonds formed between PVDF and water firstly reaches the maximum and then decreases in the interface region. Compared with the liquid-PVDF-air system using water, the total number of hydrogen bonds for systems using LiBr aqueous solution decreases by more than half according to Fig. 9(b). However, it must be mentioned that the number of hydrogen bonds formed between PVDF and water is nearly the same in the interface zone regardless of liquid types. This may be due to the fact that the number of hydrogen bonds formed between PVDF and water is dominated by the number of available acceptors.

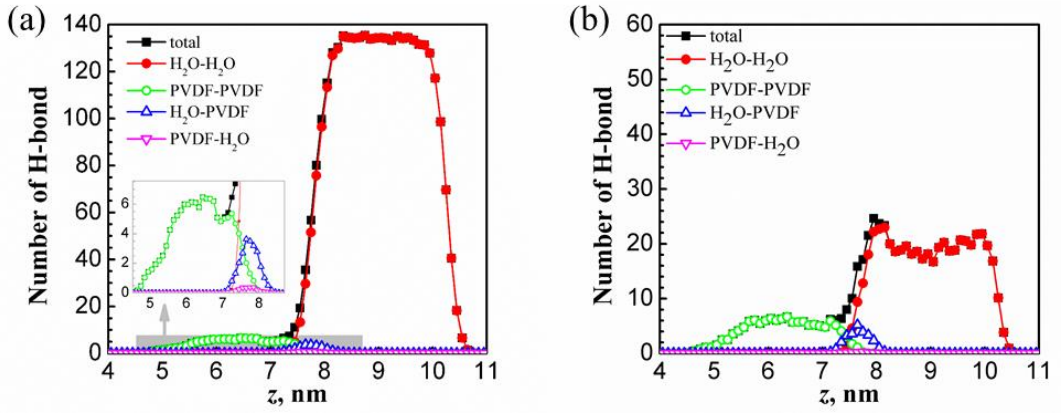

Figure 9. H-bond profiles of liquid-PVDF-air systems: (a) water; (b) 60% LiBr solution

In addition, the total number of hydrogen bonds in the zone of PVDF-liquid interface is higher than that in the zone of liquid-air interface. This can be attributed to the contribution of PVDF membrane, which participates in the formation of additional hydrogen bonds. The water transport through PVDF membrane and PVDF-liquid interface deserves further study from aspects of the formation and destruction of hydrogen bonds.

4. CONCLUSIONS

Interface characteristics of liquid-solid-gas systems were obtained using molecular dynamics by taking PVDF as the membrane to separate the LiBr aqueous solution and air. This study sets foundation for developing novel membrane materials with excellent performance and enhancing dehumidification process essentially. Main findings are summarized below:

(1) The cube droplet of LiBr solution on the surface of PVDF membrane was simulated by molecular dynamics. The change of droplet can be divided into two periods. The former is the rapid period of spherize while the latter is the slow period of spread on the surface. The simulated contact angle of LiBr solution on the PVDF membrane is about 93^{o}.
(2) Density profiles of liquid-PVDF-air systems were compared and interface thicknesses were further obtained. In general, the thickness of liquid-PVDF interface was much higher than that of liquid-air interface especially using LiBr aqueous solution with high concentration. The thickness of PVDF-liquid interface could increase by more than half compared with the liquid-air interface when the concentration of LiBr aqueous solution is over 0.55. This indicated higher interface resistance of the membrane based dehumidification.
(3) Hydrogen bond distribution of liquid-PVDF-air systems were discussed and the composition of hydrogen bonds in the interface zone was analyzed. Hydrogen bonds can be formed between PVDF and water for liquid-solid interfaces between LiBr solution and PVDF membrane. PVDF usually acted as the hydrogen bond acceptor in the interface zone, which meant PVDF had important effects on molecular transport through the interface.

ACKNOWLEDGEMENTS
This work was supported by the Natural Science Foundation of China (52308124).

REFERENCES

Björneholm O., Hansen M., Hodgson A., et al., 2016. Water at Interface. Chemical Reviews 116, 7698–726.
Bui W., Abdelrasoul A., McMartin D., 2021. Investigation on the stability and antifouling properties of Polyvinylidene Fluoride (PVDF)-Zwitterion mixed matrix membranes (MMMs) using molecular dynamics simulation (MDS). Computational Materials Science 187, 110079.
Chen T., Yin Y., Zhang Y., et al., 2019. Model evaluation of lithium bromide aqueous solution and characteristics of water transport behaviors in liquid–vapor systems by molecular dynamics. International Journal of Refrigeration, 107, 165-73.
Gurubalan A., Simonson C., 2021. A comprehensive review of dehumidifiers and regenerators for liquid desiccant air conditioning system. Energy Conversion and Management 240, 114234.
Kitabata M., Taddese T., Okazaki S., 2018. Molecular dynamics study on wettability of poly(vinylidene fluoride) crystalline and amorphous surfaces. Langmuir 34, 12214−23.
Liu X., Qu M., Liu X., et al., 2019. Membrane-based liquid desiccant air dehumidification: A comprehensive review on materials, components, systems and performances. Renewable and Sustainable Energy Reviews 110, 444–66.
Liu Y., Cui X., Yan W., et al., 2022. A molecular level based parametric study of transport behavior in different polymer composite membranes for water vapor separation. Applied Energy 326, 120007.
Nagata Y., Usui K., Bonn M., 2015. Molecular mechanism of water evaporation. Physical Review Letters 26, 1–5.
Weng L., Song W., Jacobs D., et al., 2016. molecular insights into water vapor absorption by aqueous lithium bromide and lithium bromide / sodium formate solutions. Applied Thermal Engineering 102, 125–33.
Wen T., Lu L., Dong C., 2018. Enhancing the dehumidification performance of licl solution with surfactant pvp-k30. Energy and Buildings 171, 183-195.
Yin Y., Qian J., Zhang X., 2014. Recent advancements in liquid desiccant dehumidification technology. Renewable and Sustainable Energy Reviews 31, 38–52.

6th International Conference on Building Energy and Environment
Eindhoven University of Technology, The Netherlands
6 - 10 July 2025

Computational Fluid Dynamics Analysis of Airflow and Thermal Comfort in Large Exhibition Spaces

Yu-Lieh Wu [1], Ting-Syuan Wu [2], Jia-Wei Zheng [3]

[1] *Department of Refrigeration, Air Conditioning, and Energy Engineering, National Chin-Yi University of Technology, Taichung 411, Taiwan, wuyl@ncut.edu.tw*
[2] *Department of Refrigeration, Air Conditioning, and Energy Engineering, National Chin-Yi University of Technology, Taichung 411, Taiwan, shelly10504@gmail.com*
[3] *Graduate Institute of Precision Manufacturing, National Chin-Yi University of Technology, Taichung 411, Taiwan, trytofigureout710@gmail.com*

SUMMARY
Reducing building energy consumption is crucial due to growing concerns about global warming. Architecture and urban planning actively embrace sustainable development, with policies promoting energy efficient spaces. However, unique structures such as large convention spaces pose HVAC design challenges. Achieving a balance between healthy air, thermal comfort, and energy efficiency requires a multifaceted approach. This study focuses on an 1804 m² two story convention space that has been certified by the Ecology, Energy Saving, Waste Reduction, and Health (EEWH) the Taiwan green building evaluation system. We used ANSYS FLUENT to conduct a detailed analysis of thermal comfort standards and energy optimization. We realistically simulated temperature and airflow under varying loads and assessed occupant perception and acceptance through thermal comfort evaluations (Predicted Mean Vote, PMV). We also simulated thermal comfort to evaluate potential improvements, including air conditioning optimization and energy saving strategies. Key findings: (1) The numerical technique used accurately predicted the airflow and temperature distribution in high rise air conditioned spaces. (2) The study found that supply air velocity and temperature, diffuser count, and space height significantly impact thermal comfort. (3) Case2, which had optimal supply air velocity and diffuser configurations, achieved the best system performance and thermal comfort. These results provide valuable operational and design guidelines for large convention spaces, enabling a win-win scenario of enhanced thermal comfort alongside energy savings. This contributes to sustainable development and provides insights for managing the thermal environment of similar venues.

Keywords: Thermal comfort, Energy saving, CFD, Large Exhibition spaces, Air conditioning.

1. INTRODUCTION

In contemporary society, expansive exhibition spaces are essential not only for cultural exchange but also for commercial activities and art exhibitions. With the continuous development of modern building technology, people's living environments are increasingly evolving towards larger spaces and higher ceilings. Simultaneously, architectural structures are also incorporating more innovative artistic design elements. People spend more than 90% of their time indoors, making indoor thermal environment and thermal comfort crucial(Cheng et al., 2012). This is particularly important for large exhibition spaces, such as venues, where the air conditioning system load, heat transfer properties, airflow organization, and indoor air quality control face significant challenges. Large exhibition spaces pose unique challenges for controlling the internal environment due to frequent entry and exit of unspecified individuals, uncertain retention times, and drastic changes in peak loads. Therefore, it is crucial to have a flexible air conditioning system and prioritize energy efficiency. Therefore, achieving appropriate airflow organization in large exhibition spaces

to ensure that the indoor environment meets the needs of users has become an important research topic for contemporary designers(Tu et al., 2023).

The fear from cold draft formation leading to unaccepted indoor conditions, and pose significant challenges for indoor air quality control due to the air conditioning system load, heat transfer properties, and airflow organization(Youssef et al., 2018). It is important to address these challenges to ensure optimal indoor air quality. Additionally, the frequent entry and exit of unspecified individuals and the uncertainty of crowd retention time contribute to more drastic changes in peak loads. The internal environment of a building can be difficult to control due to its complex characteristics(Kwon, 2016). Therefore, it is important to focus on flexible operation of the air conditioning system and energy saving measures. Contemporary designers must research how to achieve appropriate air flow organization in large exhibition spaces to ensure that the indoor environment meets the needs of users.

2 MODELING

To accurately simulate the thermal comfort environment, the following basic assumptions are used:

1. Steady, incompressible turbulent flow
2. Ignore radiation effects
3. Gravitational forces
4. Pressure-based solver, and the k-ε RNG model
5. The design and location of the air conditioning system. For example, the direction and volume of air supply will have a direct impact on airflow and comfort.

Environmental thermal comfort can be modelled and predicted based on these factors, and the model can be used to determine appropriate strategies for optimizing comfort. The functional design of the ground floor and the simulation model is shown in Figure 1.

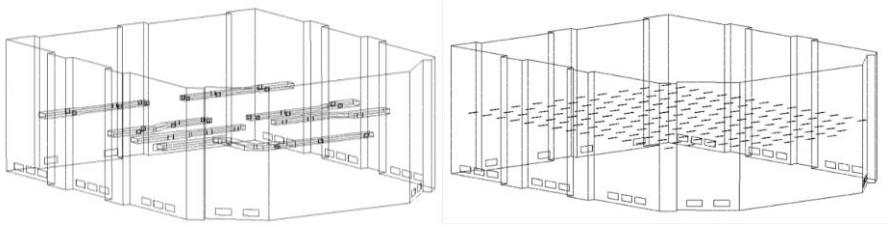

(a) (b)

Figure 1. Various air duct designs (a) Side blow systems (Case1) (b) Downdraft System (Case2).

2.1 Model boundary conditions

This study focuses on a large convention space with three as the research subject. Case1 employs the originally designed side blow system, while Case2 uses a downdraft system. Both cases are supplied by seven on site air conditioning units, with three units providing an air volume of 25,200 cubic meters per hour (CMH), three units providing 31,500 CMH, and one unit providing 15,800 CMH. As the space is located in the center of the building and serves as the main activity area, it is surrounded on all sides by lobby corridors or adjacent office spaces. Therefore, the walls are

defined as adiabatic in the simulation. The boundary conditions are shown in Table 1. The ISO 14505-4:2021 standard (International Organization for Standardization, 2021) proposes three conditioning principles for thermal human models, including a constant skin surface model, a constant heat flux model and a comfort equation model. In these models, the human body boundary conditions of Cheng et al.(Cheng et al., 2012) will be utilized in this study, with detailed settings including a constant skin temperature of 34°C. The detailed settings are shown in Table 2 and Figure 2.

Table 1. The boundary conditions of CFD simulations.

Type	CFD simulation
Dimension	1804m^2 × 15.21m
Occupants	0.4m × 0.4m× 1.7m
Supply air duct	6.7m above the floor
Exhaust air duct	2m×0.8m / 0.5m above the floor
Walls / Ceiling / Floor	Adiabatic

Table 2. Case2 air volume design.

Supply air duct	Inlet 1	Inlet 2	Inlet 3
Air volume (m^3/h)	1008	1260	988
Supply air duct size (m^2)	1.5m×0.15m		
Air velocity (m/s)	1.24	1.5	1.22

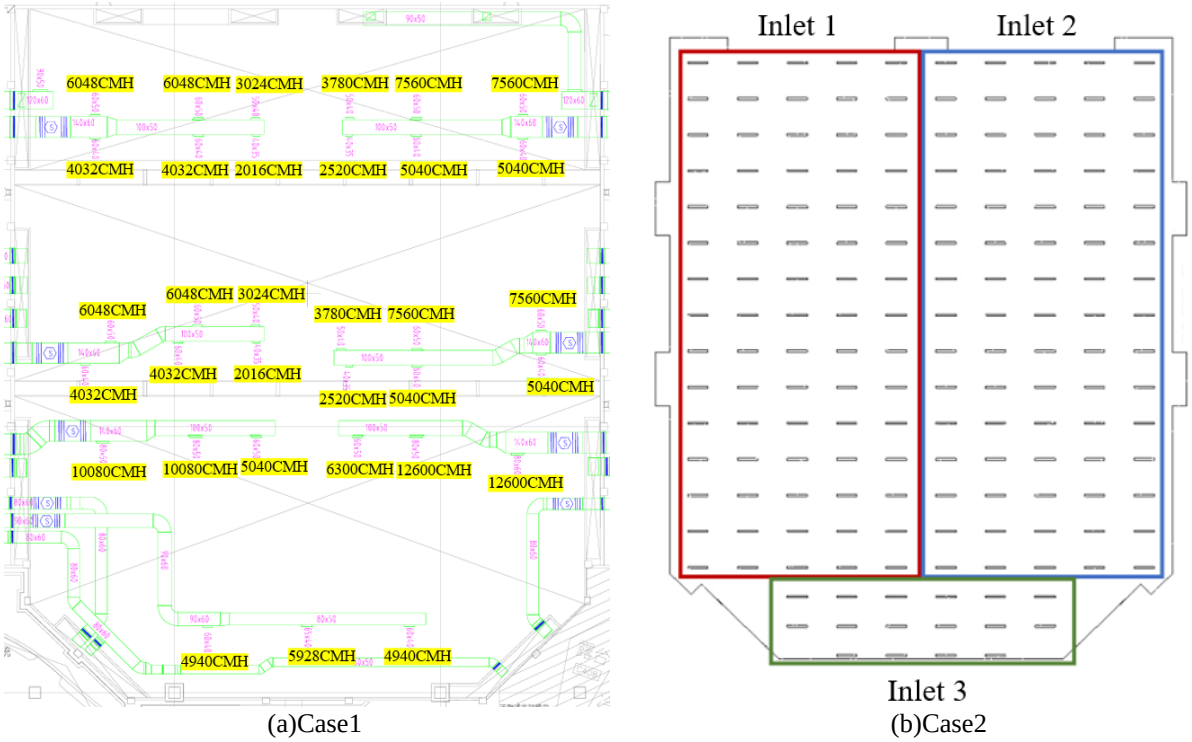

(a)Case1 (b)Case2

Figure 2. Supply air duct design.

In this study, the mass, momentum, and energy conservation equations are considered along with the time averaged equations for the incompressible flow can be expressed in a general form including four terms, transient, convective, diffusive and source terms, denoted as Eq (1):

$$\frac{\partial}{\partial t}\int_{v} \rho\phi \, dV + \oint_{A} \rho\phi V \cdot dA = \oint_{A} \Gamma_{\phi} \nabla\phi \cdot dA + \int_{V} S_{\phi} dV \quad (1)$$

Where ρ is the fluid density $\emptyset$ represents the dependent variable, which could represent either a velocity component, $\vec{V}$ denotes the velocity vector, Γ represents the diffusion coefficient, and $S_{\emptyset}$ stands for the source term.

Solving the Reynolds-averaged Navier-Stokes (RANS) equations requires the use of turbulent models. Studies comparing these models (Cheng et al., 2012) have shown that the RNG k-ε turbulent model performs the best in predicting indoor airflow properties. This is because it can handle both low velocity and high velocity airflow effectively.

2.2 Air Diffusion Performance Index

The Air Distribution Properties Index (ADPI) is a formula developed in accordance with ANSI/ASHRAE Standard 113(ANSI/ASHRAE Standard 113-2013, 2013), as defined in Eqs.(2) and (3). It is primarily used to evaluate air diffusion performance and quantify the cooling system's impact on thermal comfort. ADPI is the percentage of eligible Effective Draft Temperature (EDT) divided by the number of test points, where the EDT is calculated from the air temperature and air velocity. ASHRAE recommends higher ADPI values to indicate better air distribution performance. Generally, an ADPI value of 80% or higher is considered acceptable. This ensures efficient and even distribution of air throughout the interior space, providing good thermal comfort. A high ADPI value indicates even air movement, reducing temperature variations and improving overall indoor air quality.

$$\boldsymbol{ADPI = \frac{N_{EDT}}{N} \times 100\%} \quad (2)$$

$$\boldsymbol{EDT(\theta) = (T_X - T_I) - 8(V_X - 0.15)} \quad (3)$$

Where EDT(θ) is between -1.7 °C < EDT < 1.1 °C, which is comfortable for most people; N_{EDT} is the number of test points when the EDT is between -1.7 °C < EDT < 1.1 °C; N is the total number of test points; T_X is the temperature at the test point (°C); T_I is the average indoor temperature (°C); and V_X is the Air velocity at a point in the working area (m/s).

2.3 Concept of Grid Independence

Grid independence refers to the state in which the results of a numerical simulation do not change significantly as the mesh is refined. When the mesh is sufficiently fine, the solution stabilizes, and further mesh refinement leads to negligible changes in the results. The goal of a grid independence study is to identify this threshold at which the mesh provides a sufficiently accurate representation

of the physical system, while avoiding unnecessary computational effort.

The grid division in this study can be roughly categorized into four parts: the large space, personnel, supply air vents, and return air vents, each assigned different grid sizes. The analysis was conducted by proportionally reducing the grid sizes, as shown in Figure 3. Ultimately, a grid count of 8.3 million was used for simulation, where all test points maintained an error below 5%, compared to a reference grid count of 10.6 million.

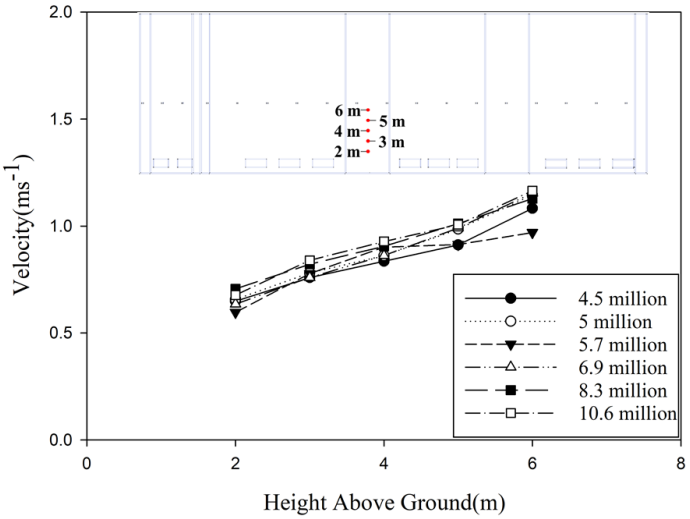

Figure 3. Grid Independence Test.

3 RESULTS AND DISCUSSION

Upon further analysis, it was discovered that in the Case1 design, the supply air duct was arranged horizontally with the floor. As a result, the simulated air velocity data for work points located at the lower bottom of the large space was low. This low air velocity reduces the effective ventilation of the air to the human body and increases the likelihood of localized air stagnation, which affects the EDT values, are shown in Figure 4. In contrast, Case2 utilizes a downdraft design, which is more effective at improving airflow, particularly in the bottom areas of large spaces. This improves ventilation and reduces discomfort and air quality issues.

Additionally, the velocity of inlet 1 in Case2 is slightly lower than that of inlet 2, resulting in EDT results slightly below the comfort range (-1.7~1.1) for the area directly below the inlet 1 air inlet in Case2. The ADPI's overall performance is slightly reduced in this situation. Although the EDT value is lower below the inlet 1 air duct in Case2, the overall ADPI value still exceeds the standard requirement, indicating a comfort advantage.

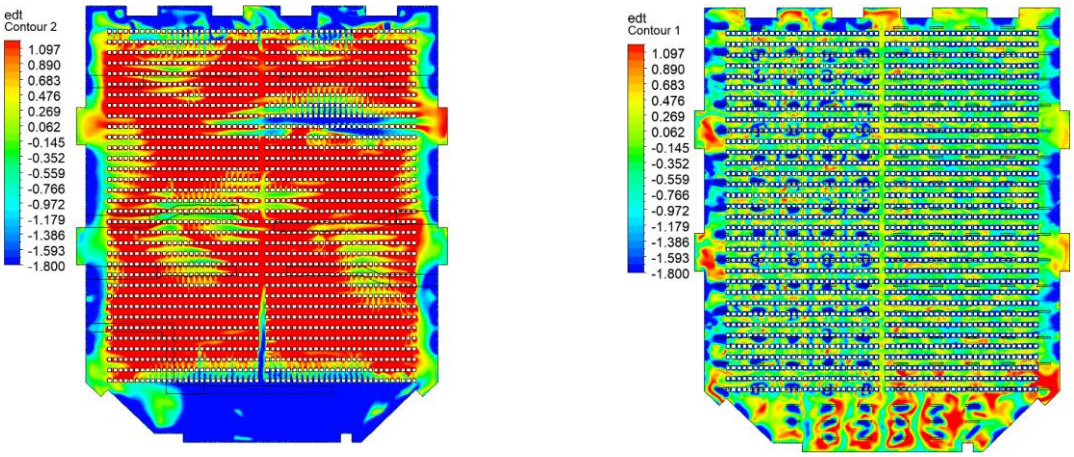

(a)Case1 (b)Case2

Figure 4. EDT on 1.4m plane.

4 CONCLUSIONS

Based on the data extracted from 86 working points on the plane from Figure 4, the following conclusions were calculated:

1. In Case1, the supply air duct was arranged horizontally, resulting in low air velocity at lower areas of the space. This reduced ventilation and increased air stagnation, leading to an ADPI value of 45.35%, far below the 80% recommended by ANSI/ASHRAE Standard 113. Personnel may feel discomfort due to poor air quality and low comfort levels.
2. The ADPI value for Case2 is 87.21%, which complies with the recommendations of ANSI/ASHRAE Standard 113. The study indicates that utilizing a downdraft design is more effective in improving airflow, particularly in the lower regions of large spaces. As a result, personnel are typically comfortable in Case2 environments due to the high level of air quality and comfort.

In conclusion, the results highlight the importance of proper airflow design in large spaces to ensure air quality and comfort. Effective ventilation and air conditioning measures are essential to enhance air circulation, reduce discomfort, and promote the health and wellbeing of personnel.

ACKNOWLEDGEMENTS

The authors thank the National Science and Technology Council of Taiwan (112-2221-E-167-009 and 113-2218-E-167-002) for financially supporting this study.

REFERENCES

Cheng, Y., Niu, J., Gao, N., 2012. Stratified air distribution systems in a large lecture theatre: A numerical method to optimize thermal comfort and maximize energy saving. Energy Build 55, 515–525.

Hussain, S., Oosthuizen, P.H., Kalendar, A., 2012. Evaluation of various turbulence models for the prediction of the airflow and temperature distributions in atria. Energy Build 48, 18–28.

International Organization for Standardization, 2021. ISO 14505-4:2021 Ergonomics of the thermal environment – Evaluation of thermal environments in vehicles – Part 4: Method for the assessment of the thermal environment using a numerical manikin. Geneva, Switzerland.

Kwon, Y.-I., 2016. A Study on the Improvement of ADPI and Ventilation Effectiveness in a Small Theater. International Journal of Air-Conditioning and Refrigeration 24, 1650019.

Method of Testing for Room Air Diffusion, American Society of Heating, Refrigerating and Air-Conditioning Engineers, 2013. . ANSI/ASHRAE Standard 113-2013, Atlanta, GA, USA.

Tu, D., Tang, J., Zhang, Z., Sun, H., 2023. Thermal environment optimization in a large space building for energy-saving. Case Studies in Thermal Engineering 51, 103649.

Youssef, A.A., Mina, E.M., ElBaz, A.R., AbdelMessih, R.N., 2018. Studying comfort in a room with cold air system using computational fluid dynamics. Ain Shams Engineering Journal 9, 1753–1762.

NudgeFlow – the next generation of residential ventilation (13:30-15:00 h)

6th International Conference on Building Energy and Environment
Eindhoven University of Technology, The Netherlands
6 - 10 July 2025

A distributed control framework for residential ventilation system: "NudgeFlow"

Douaa Al-Assaad[1,2], Hilde Breesch[1]
[1]KU Leuven, Gent, Belgium, douaa.al-assaad@kuleuven.be, [2]TU Eindhoven, Eindhoven, the Netherlands

SUMMARY

The COVID-19 pandemic exposed serious shortcomings in existing residential ventilation systems, which struggled to meet new demands for higher airflow to prevent virus spread. This was soon followed by an energy crisis, requiring these systems to also become more energy-efficient—creating conflicting demands. Most current systems lack true "smart" capabilities, as defined by the Air Infiltration and Ventilation Centre (AIVC). Meanwhile, the market is shifting toward performance-based, robust, and distributed ventilation solutions. New room-based systems have emerged, but they often fall short in controlling airflow throughout an entire building. In the framework of the Flemish VLAIO Flux50 project, we propose a smart novel decentralized residential ventilation system consisting of low pressure drop components connecting zones directly to each other and to the outdoors. This system coined as "NudgeFlow" would adjust airflow dynamically based on room conditions, user needs, and environmental factors, serving as a potential breakthrough for the Flemish ventilation industry and making it an adequate renovation solution. The following paper discusses a potential distributed control framework for such a system.

Keywords: NudgeFlow system, residential ventilation, passive components, distributed control architecture

1. INTRODUCTION

1.1 Challenges facing residential ventilation

The residential ventilation market is continuously evolving due to shifting performance demands. The SARS-CoV-2 pandemic emphasized the importance of indoor air quality (IAQ), prompting systems to prioritize airflow and responsiveness. This was quickly followed by an energy crisis, challenging systems to maintain IAQ while reducing energy consumption. Simultaneously, the EU's "Renovation Wave" initiative is pushing the market from traditional, prescriptive standards toward performance-based design approaches. Renovation constraints, such as limited space for ducts and a focus on sustainable, circular solutions, have renewed interest in decentralized ventilation systems. These must be user- and context-aware, with some incorporating local heat recovery via compact units like push-pull systems and rotary exchangers.

1.2 NudgeFlow system: A potential solution

The previous VLAIO Flux50 cluster for energy project "SmartVent" (Breesch et al., 2022) introduced a holistic, performance-based framework that allows for more flexible and robust ventilation designs. This approach avoids the single points of failure found in systems like MEV and MVHR, paving the way for more distributed solutions. In this context, the NudgeFlow system is proposed as the next generation of residential ventilation: decentralized, intelligent, and minimally invasive—ideal for renovation. It ensures high IAQ and low energy use by smartly guiding natural airflow through a dwelling. Using local, low-pressure components and adaptive control, the system responds to changing conditions and user needs, offering a resilient and future-ready solution. **Figure 1** illustrates the difference between a typical residential ventilation system and a NudgeFlow system for a typical Belgian dwelling. The typical system is equipped with exhaust fans in wet polluted areas (bathroom, WC, kitchen). When operated, this drives outdoor

airflow to infiltrate through the building envelope (cracks, unintended window opening). The airflow can subsequently circulate in the house in between zones driven by pressure and temperature differences. Such airflows are often left unguided and may result in increased cooling or heating loads (e.g., unintentional flow of cool outdoor air to an unoccupied living room increasing heating energy demand) or an untapped ventilation and energy saving potential (e.g., a flow of fresh air from the hallway to the bedroom is not taken advantage of if door remains closed). On the other hand, the impact of occupant disturbances (opening of windows or leaving doors half open) and outdoor weather fluctuations on system performance is often left unchecked. On the contrary, NudgeFlow is a context aware intentional system that taps into the potential of interzonal airflows and guides and distributes airflows throughout the dwelling where it is needed through bidirectional fans with adjustable flow rates and intentional window and door opening and by taking advantage of occupant behaviors in its control loop. For example, a NudgeFlow system would redirect flow from unintentional opening of window from an unoccupied room to a room where it is needed or it would open the door between the hallway and bedroom for energy efficient ventilation. **Table 1** shows sample scenarios comparing both system behaviors applied to the dwelling in **Figure 1**.

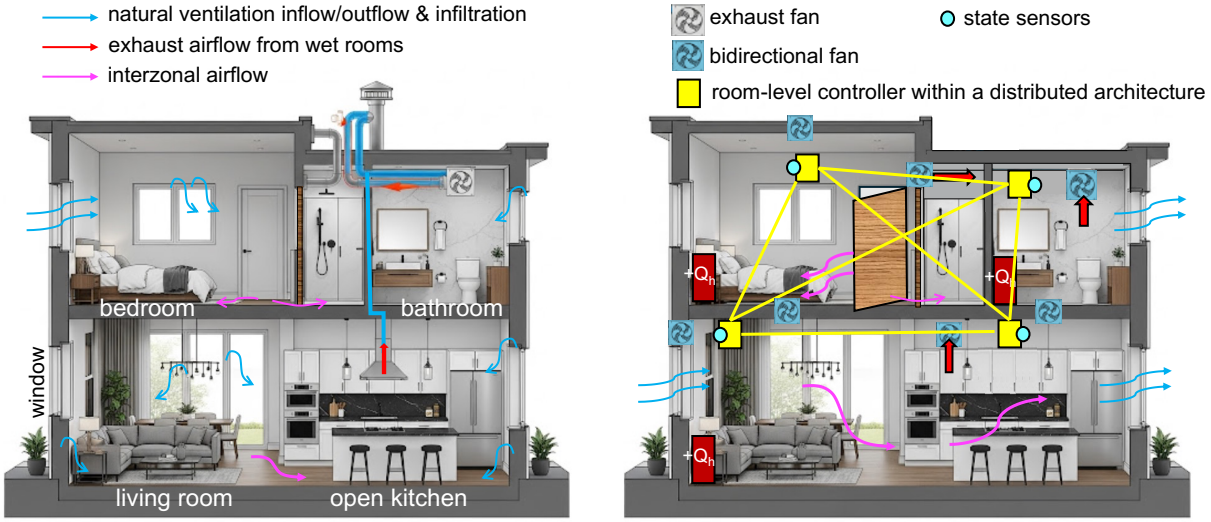

(a) typical mechanical ventilation system: Exhaust from wet polluted areas and infiltration through building envelope/intentional openings and fixed interzonal airflow path with outdoor and occupant disturbances not considered.

(b) NudgeFlow system: Controlled zonal and interzonal airflows and airflow paths through intentional opening of windows and considering outdoor dynamic disturbances and uncontrolled leakages

Figure 1. Illustration of a reference Belgian dwelling equipped with (a) a typical mechanical ventilation system and (b) the novel NudgeFlow system

Table 1. Scenarios showing differences between typical and NudgeFlow system response & performance

Scenario	Typical system	NudgeFlow system
Occupants are away. Cold wind is blowing on the façade of the unoccupied dwelling and infiltrates to a room through a trickle vent	No response. Increased heating energy demand. Situation is worse if occupants leave internal doors open. Potential thermal discomfort during occupancy	System will close trickle vents to minimize ventilation losses. Potential discomfort reduced

Occupants sleeping in the bedroom with internal doors closed during winter. Increased CO_2 levels.	Cold air comes in through trickle vents due to activation of bathroom exhaust fan. Increased heating energy demand	Activates inter room fan from hallway where the air is clean but warmer than the outdoors. Energy saving potential
Occupant cooking in the kitchen with internal door to living room open	Extracts from the kitchen but may let odors spread if airflow paths are imbalanced	Senses pressure/CO_2/temp rise in the kitchen and actively redirects flow to the hallway or adjacent room to contain and evacuate the air more quickly
Occupant taking a shower increasing humidity levels after use and left their damp clothing in the bathroom	Extracts moist air but water vapor can still spread in the house if humidity is too high	Detects high humidity and boosts airflow temporarily, using interzonal fans or windows to rapidly dry the space, then scales back to save energy.

1.3 A promising control approach for NudgeFlow

Centralized controllers are impractical for multi-zone dwellings with dynamic conditions, especially in systems like NudgeFlow. Central control requires complete system data and assigns actions to each component, making data collection costly and fault detection difficult (Ygge et al. 1999). A single component failure can disrupt the entire system and require manual intervention. NudgeFlow systems add complexity due to their spatial and temporal dynamics and inter-zone connectivity, making centralized control even less viable. Carbonare et al. (2021) demonstrated an occupant-centric, self-learning controller with decentralized micro-controllers for room-specific fan control based on discomfort models. However, their system did not manage airflow across the entire dwelling, and they reported significant issues with central-to-local communication—issues likely worsened in NudgeFlow setups. Advancements in IoT sensing and open building automation now make distributed control a feasible solution for NudgeFlow. Distributed, model-based controllers—like those proposed by Walker et al. (2017) and Li and Wang (2022) —have shown robust performance and efficiency in HVAC applications. Zhao et al. (2018) introduced the Insect Intelligent Building (I^2B) architecture, where each node is autonomous, sensing, communicating, and making decisions locally. Studies confirm this approach outperforms centralized control in flexibility and energy efficiency, making it ideal for NudgeFlow.

2. PROBLEM SETUP & FORMULATION

In a distributed control architecture, subsystems include the room controllers (each room has a controller solving locally for its own objectives), the coordinating agent which has its own global objective which is to find consensus between the zones since they share components (fans, doors). Each room $i \in \mathcal{R}$ is characterized by complex thermal, acoustics and air quality dynamics (temperature $T_i(t)$, species' concentrations $C_{s,i}(t)$, noise level $A_i(t)$) resulting from the presence of heaters and bi-directional fans, operable windows (both controlled and occupant-driven), solar gains through the envelope, and internal acoustic sources (appliances, voices, fans). **Table 2** presents the different variables and parameters involved in a NudgeFlow system and **Figure 2** presents a graphic representation of the physical problem for the first floor of the dwelling. Each room is represented by one node assuming fully mixed conditions. It is connected (edge

representation) to the outdoor node and adjacent indoor nodes (other rooms) via thermal and mass couplings. The coupling with the outdoors is due to the external walls and controlled or occupant-driven window openings while the coupling with the indoors is due to the internal walls, bidirectional fans operation and uncontrolled leakages through doors.

Table 2. The different types of variables and parameters in a NudgeFlow system.

State variables (quantities describing current state of each room and its evolution over time and measurable via sensors)	$T_i(t)$: indoor temperature (°C) $C_{s,i}(t)$: indoor pollutant concentration (ppm) $\omega_i(t)$: indoor water vapor content (g/kg) $A_i(t)$: indoor sound pressure level (dB)
Control variables (actuator inputs that can be directly manipulated to influence system performance)	$Q_{i,h}$: heater power (W) $\dot{m}_{ij,fan}(t)$: fan airflow between rooms (kg/s) $W_i(t)$: window opening fraction (0 to 1)
Disturbance inputs (external or occupant driven influences not directly controlled that can be measured)	$W_{i,occ}(t)$: occupant-induced window state (0 to 1) $D_{i,occ}(t)$: occupant-induced door state (0 to 1) $T_{out}(t)$: outdoor temperature (°C) $C_{s,out}(t)$: outdoor pollutant concentration (ppm) $\omega_{out}(t)$: outdoor water vapor content (g/kg) $A_{out}(t)$: outdoor sound pressure level (dB) $a_{int}(t)$: internally generated noise (dB)

In a distributed controller, each room solves its own objective function real-time. The objective function per room is shown in equation (1):

$$\min J_i = \omega_1\left(\max(0, \left|T_i - T_i^{comf}\right| - \delta)^2 + \max(0, \left|DR_i - DR_i^{comf}\right|)^2\right) + \omega_2 \max(0, C_{s,i} - C_{s,i,th})^2 + \omega_3 \max(0, A_i - A_{i,th})^2 + \omega_4 \left(Q_{i,h} + \sum_j \left|\frac{\dot{m}_{ij,fan}\Delta P}{\eta}\right|\right) \quad (1)$$

The first term in equation (1) is a penalizing deviation from an adaptive thermal comfort range as defined in EN 15251. The adaptive comfort model defines a comfort band that depends on the outdoor temperature T_{out}. δ is the half-width of acceptable comfort range (e.g., ± 2.5°C). The second term is the penalizing deviation from the draft risk according to ISO 7730 that depends on the air velocity and turbulence. The second term is the penalizing deviation from the threshold concentration of pollutants *s* of interest in the dwelling. The third term is the deviation from acoustic thresholds, and the final term is the energy consumption due to fans and heaters. Different rooms can have different thresholds of comfort, air quality and acoustics depending on their usage. The objective function in equation (1) is subject to following hard and soft constraints:

- Hard (enforced via inequality constraints): (a) components' control bounds within physical limits (heater, fan speeds, window and door positions) (b) bi-directional shared fan between zones flow conservation ($\dot{m}_{ij,fan}(t) = \dot{m}_{ji,fan}(t)$) , (c) connectivity constraints: preventing opposing shared fan, window and door states, (d) acoustic resistance defines hard constraints to limit sound transfer during fan operation or select airflow paths that balance ventilation without exceeding noise thresholds.
- Soft (imposed objective penalties via quadratic functions): (a) thermal comfort according to the adaptive comfort band and draft discomfort, (b) IAQ,

The weighting factors multiplying the different terms in equation (1) should be adequately tuned per room and time depending on its requirements at the current state (e.g., prioritizing IAQ during cooking events in the kitchen) or even user preferences. This is expected to be the most challenging task in minimizing the objective function.

The state variables in equation (1) can be solved iteratively and dynamically using an adequate state space model of the dwelling and an adequate solver. Temperature and concentration dynamics are described in equations (2) and (3):

$$T_i(t+1) = T_i(t) + \frac{\Delta t}{C_i}.\left[Q_{h,i}(t) + Q_{envelope} + Q_{Internal\ gains} + Q_{leakage+ventilation\ losses}\right] \quad (2)$$

$$C_i(t+1) = C_i(t) + \Delta t.\left[\frac{1}{V_i}\left(\sum_{j=1}^{N}(d_{ji}^{leak}(t) + \dot{m}_{fan,ji}(t))C_j(t) - \sum_{j=1}^{M}(d_{ij}^{leak}(t) + \dot{m}_{fan,ij}(t))C_i(t) + \dot{m}_i^{window}(t).C_{out,t}\right) + G_i(t)\right] \quad (3)$$

$G_i(t)$ is the generation rate of pollutant in question (e.g., CO_2 from people or VOCs from cooking, etc.). d_{ij}^{leak} is the inherent leakage through passive components between room i and j (door slits, cracks). They are expressed in equation (4) where k_{ij} is the leakage conductance function of the geometry and door opening fraction.

$$d_{ij}^{leak}(t) = k_{ij}^{leak}\Delta P_{ij}(t) \quad (4)$$

The model should be able to capture all relevant physics influenced from control actions and uncontrolled disturbances (**Table 2**). This includes handling inter-room couplings; arising nonlinearities and discretizing the continuous dynamics with an appropriate sampling time matching the system dynamics and eventually control hardware capabilities to support real-time operation. Literature has shown that tools such as Modelica can be promising as it supports detailed modelling of pressure and buoyancy-driven airflows in multi-zone buildings connected by doors, cracks, leaks, windows and vents. Moreover, it allows a direct coupled thermal and airflow simulations in addition to possibility of coupling with control algorithms. However, limitations exist in its assumption of lumped parameters, simplifications of 3D geometries (i.e., openings are represented as ports or flow resistances), calibration requirements of flow coefficients (i.e., leakages, discharge coefficients). Consequently, thorough testing of this tool and its solvers is needed.

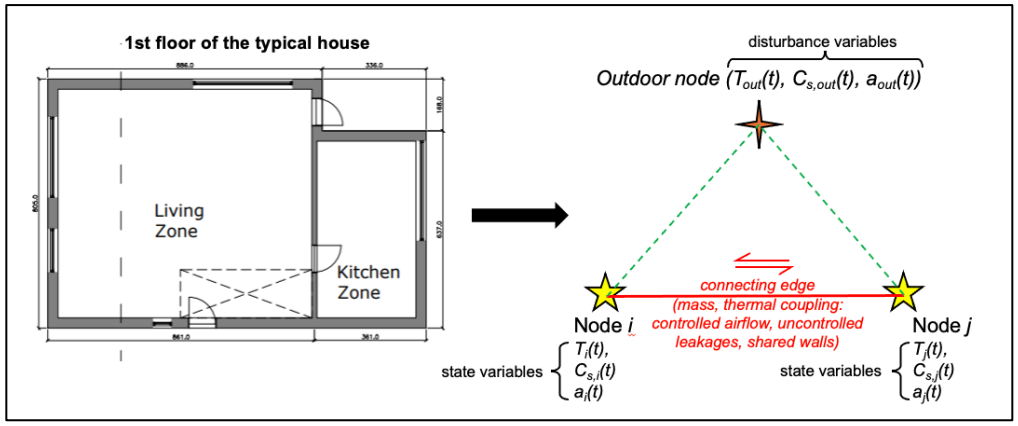

Figure 2. Graphical representation of the NudgeFlow equipped dwelling

3. CHALLENGES OF A DISTRIBUTED CONTROL

To coordinate control across zones in real time without relying on a fully centralized controller, an effective distributed optimization approach needs to be defined. The framework decomposes the global control problem into smaller local problems for each zone, enabling independent optimization with local states and controls, while enforcing consensus constraints on shared coupling variables through a coordinator. The risk remains that a consensus would be difficult to

reach between rooms on shared variables. In this case, the coordinator can still change its function encouraging cooperation between zones rather than finding a single consensus. Cooperation can include prioritizing zones over others over time depending on the context. Thus, year-round performance can still be achieved. For example, the bedroom and bathroom are both occupied, and a bidirectional fan is shared between them. The bedroom wants to operate the fan to discharge pollutants into the bathroom, but the bathroom controller wants to operate the ceiling fan only and prevent additional pollutants from being discharged into the bathroom to reach its IAQ objectives as the ceiling fan cannot further increase flow rates. A cooperation between zones means prioritizing the bedroom due to its longer occupancy periods and compromising the bathroom IAQ for the short duration of time during which the shower is in use.
Other functions that the coordinator can take is a supervisory role setting hard constraints over certain airflow path or variables (power use, comfort, acoustics) which can facilitate the cooperation between rooms by eliminating certain control actions. For example, if both bedroom and bathroom are occupied, the coordinator can set a hard rule prohibiting local agents from operating the bidirectional fan. In this case, the agents must use other NudgeFlow components (e.g., windows) to reach their local objectives.

ACKNOWLEDGEMENTS
This work has been supported by the Flemish Agency for Innovation and Entrepreneurship (VLAIO) Flux50 cSBO project 'NudgeFlow' (HBC.2023.0488)

REFERENCES

Breesch, H., Al-Assaad, D., Laverge, J., Verhaert, I., Van Hooff, T., De Geetere, L., & Van Gaever, R. (2022). "Towards Smart Ventilation" in Mid-sized buildings: Project content, objectives and structure, organization and work plan.

Carbonare N. (2021), Occupant-centered control strategies for decentralized residential ventilation, PhD thesis, Karlsruhe Institute for Technology, Germany, https://doi.org/10.5445/IR/1000135407

Li, W., & Wang, S. (2022). A fully distributed optimal control approach for multi-zone dedicated outdoor air systems to be implemented in IoT-enabled building automation networks. *Applied Energy*, *308*, 118408.

Walker, S. S., Lombardi, W., Lesecq, S., & Roshany-Yamchi, S. (2017). Application of distributed model predictive approaches to temperature and CO2 concentration control in buildings. *IFAC-PapersOnLine*, *50*(1), 2589-2594.

Ygge, F., & Akkermans, H. (1999). Decentralized markets versus central control: A comparative study. *Journal of artificial intelligence research*, *11*, 301-333.

Zhao, Q., & Jiang, Z. (2019). Insect Intelligent Building (I 2 B): a new architecture of building control systems based on Internet of Things (IoT). In *Advancements in Smart City and Intelligent Building: Proceedings of the International Conference on Smart City and Intelligent Building (ICSCIB 2018)* (pp. 457-466). Springer Singapore.

Urban microclimate & Pollutant dispersion (15:30-17:00 h)

6th International Conference on Building Energy and Environment
Eindhoven University of Technology, The Netherlands
6 - 10 July 2025

Microclimate simulation of the cooling effect of vegetation during heatwaves for Montreal (continental), Singapore (tropical), and Morocco (arid climate)

Clément Nevers [1], Aytac Kubilay [2], Jan Carmeliet[2], Dominique Derome [1]

[1]*Université de Sherbrooke, Sherbrooke, Canada, Dominique.Derome@usherbrooke.ca*
[2]*ETH Zurich, Zurich, Switzerland, Cajan@ethz.ch*

SUMMARY
The impact of vegetation, more specifically trees, is analyzed across three different climates: continental climate in Montreal, Canada, tropical climate in Singapore, and arid climate in Morocco. Based on the pedestrian thermal comfort assessed by the Universal Thermal Climate Index (UTCI), two new heat indices are proposed: heat exposure and cooling efficiency by mitigation measures. Trees yield local improvements in all three cases. In tropical climate, air cooling by vegetation is largely canceled out by an increase in relative humidity, resulting in a reduced thermal comfort impact. The primary factor of trees contributing to improvement in pedestrian thermal comfort in all climates is shading. However, apart from local cooling, trees show a nonlocal heating effect due to blocking of wind and an increase in relative humidity due transpiration from leaves.

Keywords: Urban microclimate model, Vegetation, Heat exposure, Cooling efficiency

1. METHODOLOGY

The urban microclimate is modeled using the high-fidelity open-source model urbanMicroclimateFoam (2024), developed by the authors based on OpenFOAM. It solves for turbulent and buoyant flow in the air domain, coupled heat and moisture transport in porous urban materials, and solar and longwave radiation between the urban surfaces and the sky (Kubilay et al. 2020). The different models have been validated separately and the urban micromodel for the case of a patio with and without trees. Environmental boundary conditions are downscaled from the mesoscale meteorological model WRF (Weather Research and Forecasting) for a typical heatwave. Vegetation is modeled as porous zones characterized by a leaf area density introducing source/sink terms for momentum, heat, moisture, producing shadowing and evaporative cooling. Leaf heat balance is based on the sensible, radiative and latent heat fluxes. Impact of vegetation is analyzed for three different climates: continental climate in Montreal, Canada (Nevers et al., 2025), tropical climate in Singapore, and arid climate in Oujda, Morocco. Thermal comfort is assessed using the Universal Thermal Climate Index (UTCI), which represents the human thermal sensation with an equivalent temperature, accounting for long-wave radiation from surfaces, solar radiation, humidity, air speed, and air temperature. To provide a metric of the cumulative heat stress an individual might experience, we introduce the heat exposure index, defined as the integral of UTCI exceeding a specified threshold over a given time period. This metric incorporates a weighting factor based on the dynamic thermal sensation to take into account the higher impact of extreme heat stress on a person. Heat exposure is expressed in UTCI_degree_hours (UTCI_DH). Additionally, the cooling efficiency (CE) by vegetation is defined as the relative

improvement/deterioration in terms of the heat exposure index achieved by vegetation compared to a mineral case without vegetation. The simulations are conducted on a high-performance computing cluster and took around 30 hours.

2. LOCAL HEAT EXPOSURE AND COOLING EFFECT OF VEGETATION DURING HEATWAVE IN MONTREAL (CANADA), SINGAPORE AND OUJDA (MOROCCO)

In Montreal (continental climate), a typical neighborhood of Plateau-Mont-Royal, a late 19th-century working-class area, is studied. The simplified urban layout consists of six urban lots each with four buildings of 10 m height arranged around an inner courtyard (Figure 1a). Trees in streets are medium-aged, evenly distributed, with foliage 6 m high and wide at 3 m from ground, while backyard trees are taller, more mature, with foliage of 8 m high and wide at 4 m, reaching above the buildings. To study the urban microclimate in a tropical climate, we focus on Sun Plaza Park and its neighboring 12-story apartment buildings, some with open ground floors, in Tampines neighborhood in Singapore, a densely populated residential area (Figure 1b). The girth size, location, species of trees in the park are extracted from the National Parks Service of Singapore database, while foliage height and diameter are determined using allometric equations. Trees between buildings have a height of 8 m and crown diameter of 5.5 m at 12 m spacing. For the arid climate we focus on the El Qods neighborhood in Oujda (Figure 1c), a border city in the north-east of Morocco. In the area of interest, trees are only present in the local park and around the school courtyard. Foliage height and crown diameter are classified into four categories: 2m, 3.5m, 5m and 7m, with the majority of trees falling within the first two categories. The built environment mostly consists of two-story buildings with a height of 7m.

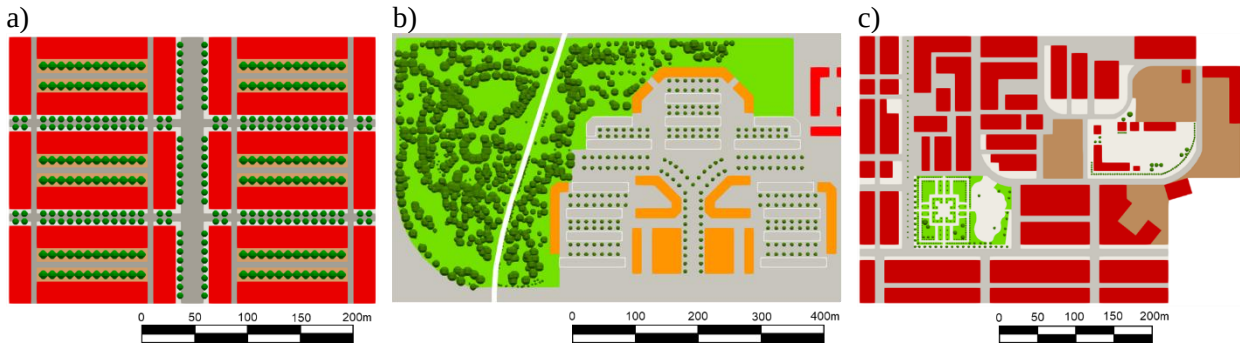

Figure 1. Layout of the neighborhoods (a) in Montreal (Canada) with trees in streets and courtyards, (b) in Singapore with an urban park and adjacent buildings, (c) in Oujda (Morocco) in a residential area with park.

Figure 2 shows the map of heat exposure expressed in UTCI Degree Hours (UTCI_DH with units °C·h) for present situation with existing vegetation. We remark that the UTCI_DH ranges differ for different climates with lower values between 200 – 500°C·h for Montreal case study, higher values between 300 – 700°C·h for Singapore case study and extreme values between 550 – 850°C·h for Oujda case study, as expected for continental, tropical and arid climates, respectively. In all the three climates, we observe lower heat exposure locally around and under trees due to shadowing effect of trees. The highest heat exposure is observed in unshaded zones in the park, courtyards and streets not shaded by trees. For Montreal case study (Figure 2a) wind flowing from south cools the main boulevard which is along the wind direction (250 – 300°C·h), while the unshaded parts in the courtyards and small streets exposed to low winds experience higher heat

exposure (~350°C·h). For Singapore case study (Figure 2b), the part shaded by trees experiences less heat exposure (~400°C·h) compared to unshaded parts in park and in between the buildings (600 – 650°C·h). For Oujda case study (Figure 2c) extreme heat exposure is observed in streets in densely built areas (~800°C·h), while lower heat exposure values are attained in zones open to wind flow and shaded by trees (550 – 700°C·h).

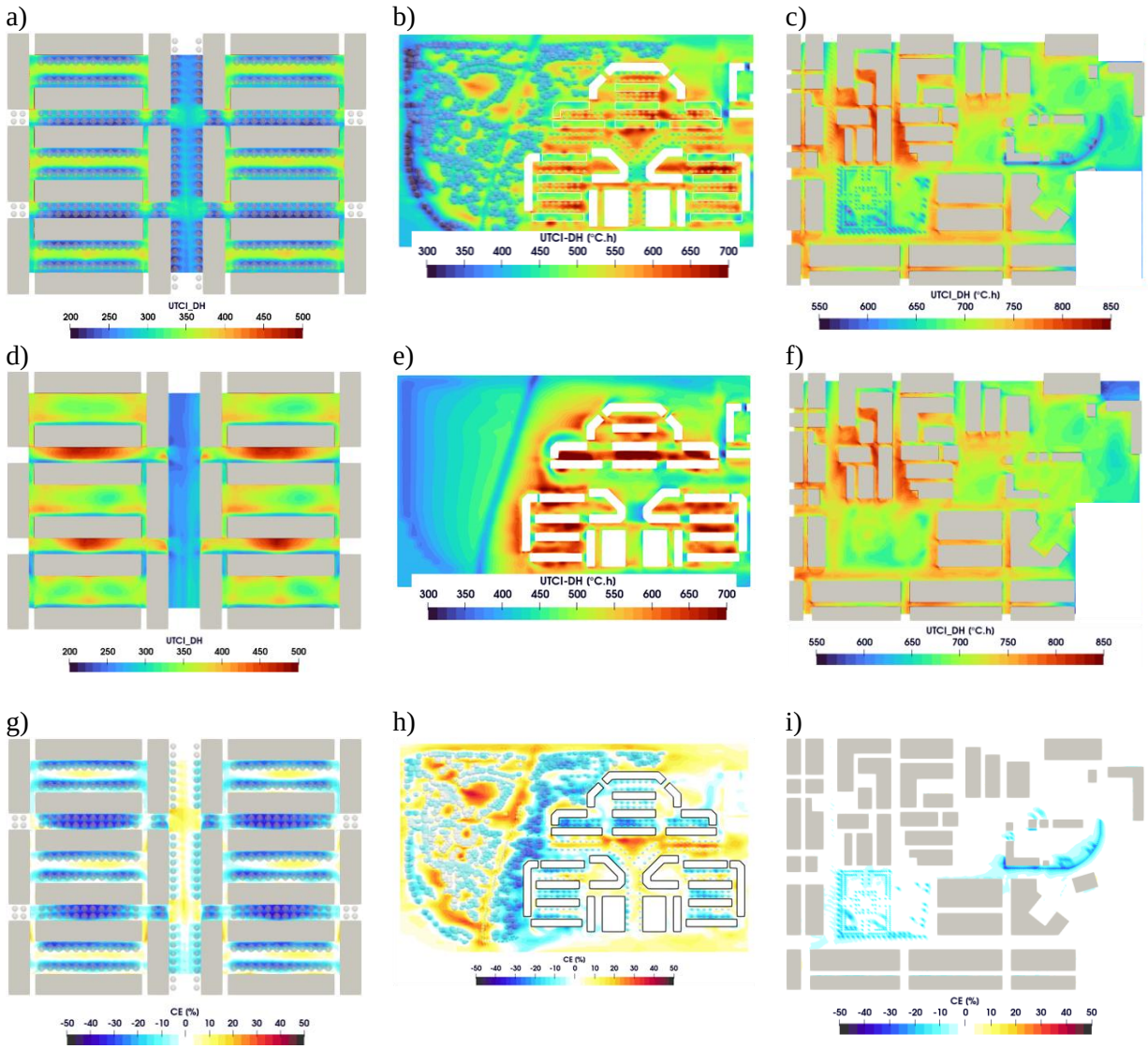

Figure 2. Heat exposure map expressed in UTCI_ DH for existing situation with vegetation in (a) Montreal, (b) Singapore, (c) Oujda. Heat exposure map for mineral case without vegetation in (d) Montreal, (e) Singapore, (f) Oujda. Map of Cooling Efficiency (CE) in (g) Montreal, (h) Singapore, (i) Oujda.

Figures 2d-f show the heat exposure map for the mineral cases without trees. We observe in general that heat exposure increases in zones where trees are removed. For Montreal case study (Figure 2d), this occurs mainly in transverse streets reaching ~450°C·h and to a lesser degree in courtyards (350 – 400°Ch). For Singapore case study (Figure 2e), heat exposure in the park increases along the wind direction coming from west, starting at approximately 350°C·h and reaching up to 650°C·h nearing the building blocks. The space between building blocks experiences very high

heat exposure, with values exceeding 700°C·h. For Oujda case study (Figure 2f), we see only local increases in heat exposure where trees are removed, i.e. in the park and along the school yard (up to 700°C·.h).

Comparing the situation with and without trees in Montreal and Singapore case studies, some hotter zones appear in the existing case with vegetation compared to the mineral case. To understand the cause of these hotter zones and to quantify the cooling and heating effects by trees, the cooling efficiency is determined as shown in Figures 2g-i. For Montreal case study, we see cooling effects by trees especially in the transverse streets with a reduction of -40% and in the courtyards under the trees of -25% indicating the positive effect of trees by shadowing and air cooling by transpiration. However, we also observe heating effects reaching +15% in some areas, referred to as nonlocal heating. This nonlocal heating is mainly caused by the blocking of wind due to the presence of trees in areas not shaded by trees, and to a lesser extent by increase in relative humidity by transpiration from leaves, which deteriorate the thermal comfort. For Singapore case study (Figure 2h) we see local cooling effects of trees in the park ranging from -15% in the west side of the park to -40% in the transition zone between the park and the building blocks. The lower CE in the west side of the park is due to the reduction of incoming wind speeds and increase in relative humidity due transpiration by trees, while in the transition wind hits the higher buildings and is guided down. We also observe strong non-local heating effects of +10% to +25% in unshaded zones within the park and between the building blocks. These high nonlocal effects are due to blocking of wind and, especially, due to the increase in relative humidity by transpiration from trees. The baseline relative humidity in Singapore is already high reaching ~70%RH, which further increases to almost 90%RH when passing through the park due to transpiration from leaves, which significantly deteriorates the thermal comfort. For Oujda case study, cooling effects by trees are relatively lower with values between -10% to -25%, which is mainly due to shadowing effects and transpiration cooling. Unlike in tropical climates, in arid context, where the baseline relative humidity is ~10%, a moderate increase in humidity is beneficial for thermal comfort. The lower CE values are attributed to the low numberof sparsely placed trees with also small foliage volume, resulting in a smaller impact on both air cooling by transpiration and shading.

In conclusion, our findings demonstrate the dual nature of trees providing both positive and negative benefits on thermal comfort. While trees provide local cooling through shading, they can also deteriorate thermal comfort non-locally by increasing relative humidity and blocking wind. Trees significantly cool in Montreal via shading and evapotranspiration. In Singapore, high humidity and low wind reduce their impact by 50%. In Morocco, trees enhance comfort through shading, though soil moisture is a limiting factor.

ACKNOWLEDGEMENTS

The authors would like to express their gratitude to the NSERC/Hydro-Québec research Chair on tree growth (C Messier, NSERC grant number ALLRP-570649-2021), the Natural Sciences and Engineering Research Council of Canada (NSERC) (NSERC Discovery Grant RGPIN-2021-03686), the Canada Research Chair (CRC) tier 1 on Multiscale Building Physics, Digital Research Alliance of Canada (Allocation RGR #4645 and Default Resource Allocation Project), and the Ministry of International Relations and Francophonie of Quebec through the Quebec-Singapore Cooperation program.

REFERENCES

Kubilay, A., Allegrini, J., Strebel, D., Zhao, Y., Derome, D., Carmeliet, J., 2020. Advancement in Urban Climate Modelling at Local Scale: Urban Heat Island Mitigation and Building Cooling Demand. Atmosphere 11, 1313.

urbanMicroclimateFoam - An open-source solver for coupled physical processes modeling urban microclimate based on OpenFOAM, 2024. URL https://gitlab.ethz.ch/openfoam-cbp/solvers/urbanmicroclimatefoam

Nevers, C., Carmeliet, J., Strebel, D., Wood, S., Kubilay, A., Derome, D., 2025. Understanding Cooling Potential of Urban Trees in a Typical North America Neighborhood. https://doi.org/10.2139/ssrn.5122739

6th International Conference on Building Energy and Environment
Eindhoven University of Technology, The Netherlands
6 - 10 July 2025

urbanMicroclimateFoam for assessing wind-driven rain, wind and thermal comfort in complex urban environments

Aytac Kubilay[1], Andreas Rubin[1], Dominique Derome[2], Jan Carmeliet[1]

[1]*ETH Zurich, Zurich, Switzerland, Cajan@ethz.ch*
[2]*Université de Sherbrooke, Sherbrooke, Canada, Dominique.Derome@usherbrooke.ca*

SUMMARY
In this paper we use the urban microclimate model 'urbanMicroclimateFoam' developed by the authors to compare the thermal comfort during a heatwave in three neighborhoods in Switzerland, two in Geneva and one in Fribourg, with different topography, urban form and green cover. The local thermal comfort is found mainly to depend on the interaction of shadowing by buildings, vegetation and wind flow. In a second study, the impact of high-rise buildings on the wind and thermal comfort in a square is analyzed, showing that zones with higher wind speeds are more susceptible to wind discomfort, while offering higher thermal comfort during heatwaves.

Keywords: Urban microclimate model, thermal comfort, wind comfort, wind driven rain

1. DESCRIPTION OF THE MODEL

A multiscale numerical approach is developed to model the urban climate with one-way coupling between the scales (Kubilay et al., 2020). At mesoscale, the climate is predicted by a nested meteorological weather prediction model, such as WRF (Weather Research and Forecast Model), for cities and their surroundings with a domain size around 50 km (Strebel et al., 2024). At microscale, the climate is predicted for urban neighborhoods with a domain size around 1-2 km using a solver developed by the authors, urbanMicroclimateFoam (2024), which is based on OpenFOAM libraries. The solver employs consecutive calculations of air flow with steady Reynolds-averaged Navier-Stokes (RANS), coupled with an unsteady heat and moisture (HAM) transport model for urban materials considering dynamic heat and moisture storage. Direct solar irradiation is modeled with ray casting to capture shading. The long-wave and the reflected short-wave radiative exchanges are calculated with view factors using a radiosity approach with multiple reflections. Foliage of trees is modeled as porous zones with leaf area density (LAD), introducing source/sink terms for momentum, heat, moisture and shadowing. Leaf heat balance is based on the sensible, radiative and latent heat fluxes. In a postprocessing step, the outdoor thermal comfort is assessed using the Universal Thermal Climate Index (UTCI) which represents the human thermal sensation with an equivalent temperature considering long-wave radiation from surfaces, solar radiation, air relative humidity and air speed in addition to the air temperature.

2. THERMAL COMFORT DURING A HEATWAVE

In this case study we simulate the outdoor thermal comfort during a heatwave in three neighborhoods in two Swiss cities, two neighborhoods in Geneva and one in Fribourg. The neighborhoods differ in topography, urban form, and green cover (Figure 1a-c). *Jonction* is a neighborhood in Geneva that sits near the confluence of the Rhône and Arve rivers and has a mix of residential, industrial, and green spaces, with a building footprint ratio of 33%, a grass area ratio

of 9%, a tree cover ratio of 10% and impervious area ratio of 48%. *Carouge* is a neighborhood south of the historic center known for its 18th-century buildings, with a building footprint ratio of 32%, a grass area ratio of 18%, a tree cover ratio of 19%, and an impervious area ratio of 50%. *Schoenberg* is a residential neighborhood, located at the eastern side of the river on a plateau outside the city of Fribourg characterized by a mix of modern and older buildings, with a building footprint ratio of 15%, a grass area ratio of 35%, a tree cover ratio of 16% and an impervious area ratio of 50%.

We examine the meteorological conditions associated with the heatwave that occurred from June 24-26, 2019, as simulated by the mesoscale Weather Research and Forecasting (WRF) model. Figures 1d-f show the maps of the UTCI at a height of 2m at 4 pm on June 24, 2019, in the core of three domains. All three neighborhoods show zones with moderate, strong and very strong heat stress. Zones shadowed by trees and buildings, and ventilated streets show moderate heat stress. In Jonction and Carouge, courtyards and streets without shadowing from trees and buildings and with low wind speed show very strong heat stress. Interestingly, Schoenberg, characterized by a lower building density compared to Carouge and Jonction, shows larger zones of strong and very strong heat stress. Built areas and streets without trees experience the highest heat stress when they are also less ventilated by wind. This means that the cooling effect by trees and wind depends on the complex interaction of factors such as street orientation, wind patterns, building morphology and tree planting patterns.

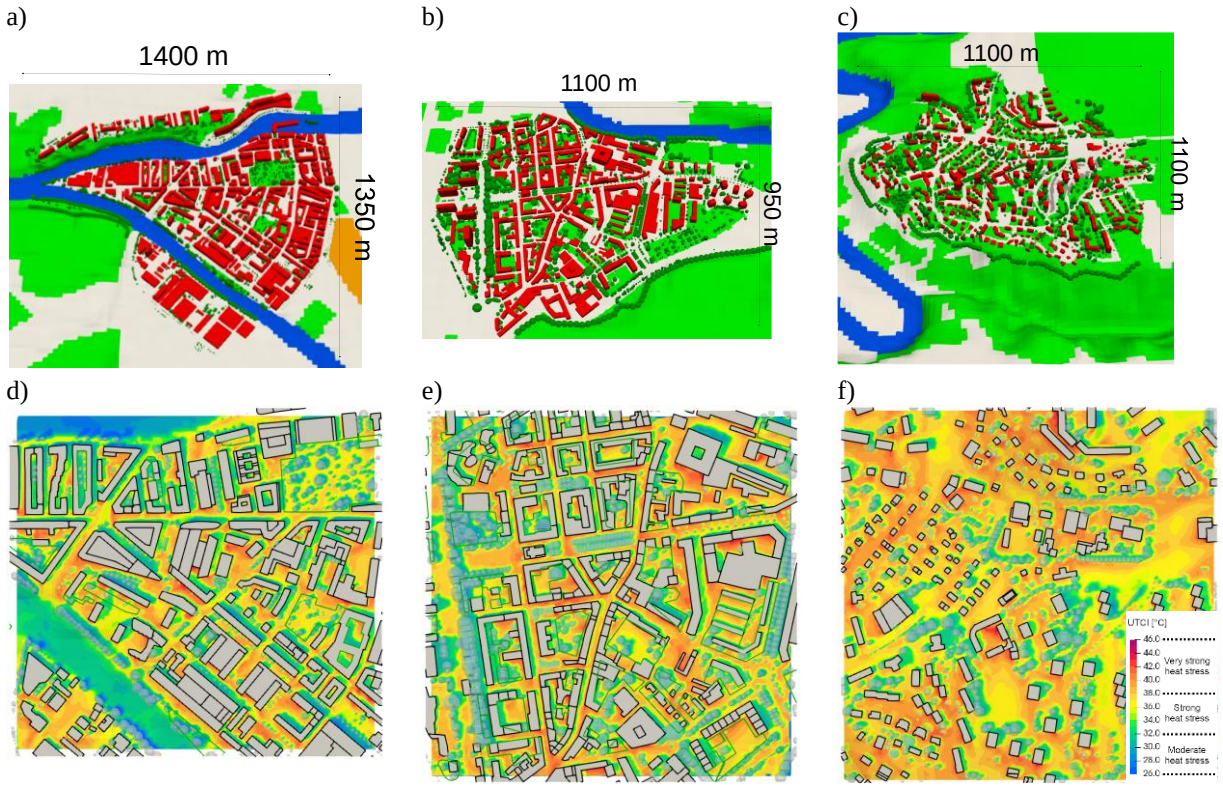

Figure 1. a) Neighborhood Jonction in Geneva. b) Neighborhood Carouge in Geneva. c) Neighborhood Schönberg in Fribourg. d-f) UTCI map at 2m height at 4 pm on 24 June 2019

2. WIND AND THERMAL COMFORT BETWEEN HIGH-RISE BUILDINGS

In a second study, the wind and thermal comfort in and around an urban square, Place Étoile near the neighborhood Carouge, Geneva, is assessed. The city of Carouge is planning to transform the industrial area La Praille-Acacias into a new urban area, with Place de l'Etoile in the heart of the new development surrounded by some high-rise buildings (Figure 2a). To support an architectural competition, wind and thermal comfort are assessed to identify mitigation measures.

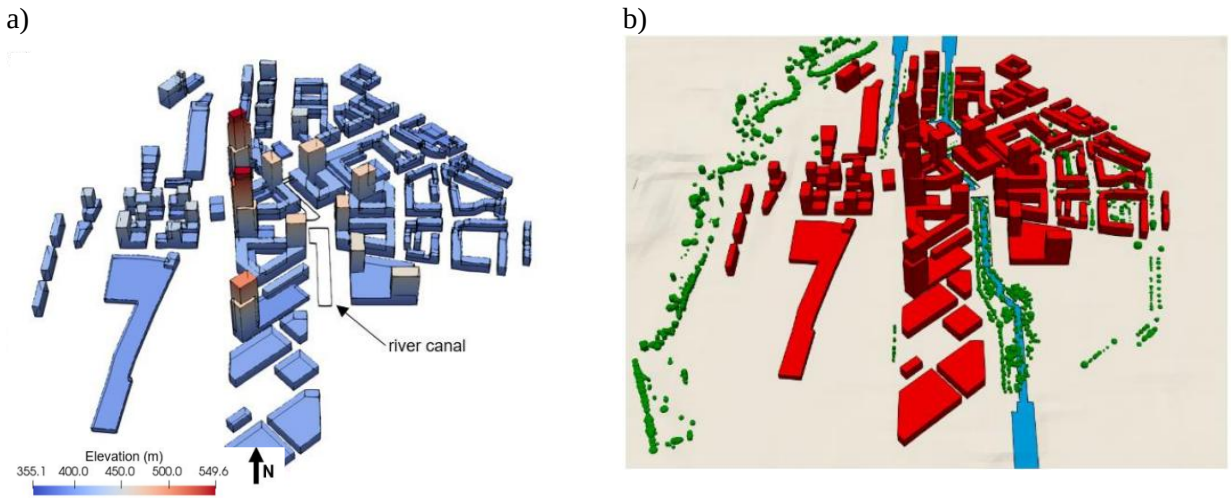

Figure 2. a) Place Etoile and surrounding buildings with elevation for wind comfort study. b) Domain for thermal comfort study with trees and water.

The assessment of wind comfort around buildings is based on aerodynamic information, statistical meteorological data and wind comfort criteria (Blocken et al., 2004). The wind comfort criteria according to Isyumov and Davenport (1975) and grades ranked from A to E are used to distinct for different activities, such as traversing, strolling and sitting. Figure 3a shows the wind rose data, with the most frequent wind directions and highest wind speeds from southwest and northeast. Figure 3b shows the local wind-amplification factor at pedestrian height, i.e. the ratio between wind speed at pedestrian height around buildings and a reference wind speed without presence of buildings. We observe that flow separation with accelerated wind speeds occurs at the upstream corners of the buildings, low wind speed regions in the wake of buildings, downflow due to the high-rise buildings around the plaza leading to corner streams with high wind speed, and channeling flows between the buildings oriented southwest-northeast.

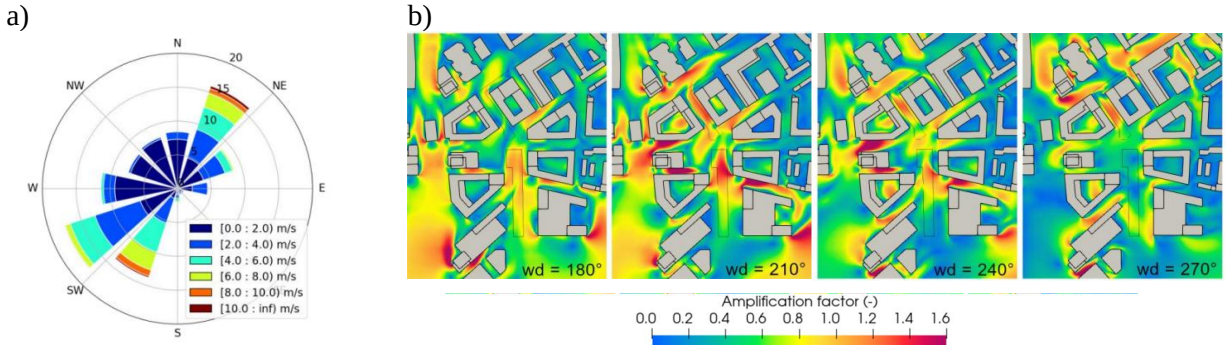

Figure 3. a) Wind rose obtained from MeteoSwiss weather station Genève / Cointrin. b) Wind-amplification factor at 2m for winds from south (180°), west (270°) and two in-between directions.

Based on the amplification factor calculation for 12 wind directions and statistical meteorological data, a map with wind comfort grades is determined (Figure 4a), where A being the most comfortable. Some regions with higher wind discomfort (grade C) can be distinguished especially around high-rise buildings in the west center of the plaza, along the river canal and at the southeast of the plaza. Figure 4b shows the thermal comfort levels at 2 m based on UTCI on June 24, 2019, at 4 pm. The highest values are observed in courtyards and near facades facing south indicating higher thermal stress. Figure 4c combines the regions showing wind discomfort (grade B and higher, in lavender), thermal discomfort (UTCI threshold of 32°C, in pink) and overlapping wind and thermal discomfort (in purple). Zones with higher wind speeds are clearly more susceptible to wind discomfort, while zones with lower wind speeds are characterized by lower thermal comfort. During heatwaves, high-rise buildings provide shade and downflow bringing cooler air to street level, enhancing thermal comfort. **In conclusion**, wind is found to be a complex phenomenon that significantly influences wind and thermal comfort, and to the best of our knowledge, no research has combined them in a comprehensive way as in this study. At the conference we will also present wind drive rain results showing that high-rise buildings increase wind exposure and rain at pedestrian level,

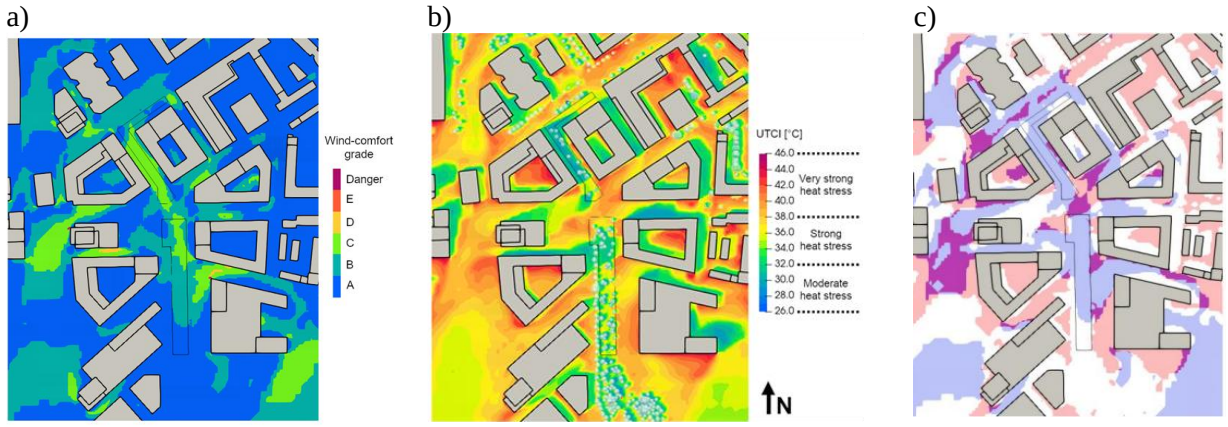

Figure 4. a) Wind-comfort grades. b) UTCI map at 2 m on June 24, 2019, at 4 pm. c) map of wind discomfort (grade B and higher, in lavender), thermal discomfort (UTCI threshold of 32°C, in pink) and overlapping wind and thermal discomfort (in purple).

ACKNOWLEDGEMENTS

The authors would like to thank the financial support of project SWICE (Sustainable Wellbeing for the Individual and the Collectivity in the Energy Transition) within the funding program SWEET of the Swiss Federal Office of Energy. We also acknowledge the Canton of Geneva and the City of Carouge for requesting the study.

REFERENCES

Kubilay, A., Allegrini, J., Strebel, D., Zhao, Y., Derome, D., Carmeliet, J., 2020. Advancement in Urban Climate Modelling at Local Scale: Urban Heat Island Mitigation and Building Cooling Demand. Atmosphere 11, 1313.

Strebel, D., Derome, D., Kubilay, A., Carmeliet, J., 2024. Improved mesoscopic meteorological modeling of the urban climate for building physics applications. J. Build. Phys. 17442591241266553.

urbanMicroclimateFoam - An open-source solver for coupled physical processes modeling urban microclimate based on OpenFOAM 2024. URL https://gitlab.ethz.ch/openfoam-cbp/solvers/urbanmicroclimatefoam

Blocken, B., Roels, S., Carmeliet, J., 2004. Modification of pedestrian wind comfort in the Silvertop Tower passages by an automatic control system. J. Wind Eng. Ind. Aerodyn. 92, 849–873. https://doi.org/10.1016/j.jweia.2004.04.004

Isyumov, N., Davenport, A.G., 1975. The ground level wind environment in built-up areas, in: Proceedings of the 4th International Conference on Wind Effects on Buildings and Structures,(Heathrow 1975). pp. 403–422

6th International Conference on Building Energy and Environment
Eindhoven University of Technology, The Netherlands
6 - 10 July 2025

Development of surrogate model for predicting outdoor airflow and pollutant dispersion under varying wind conditions

Ting Dai [1], Sumei Liu [2], Junjie Liu [3], Nan Jiang [4], Qingyan Chen [5]

[1] *Department of Building Environment and Energy Engineering, The Hong Kong Polytechnic University, Kowloon 999077, Hong Kong SAR, China, ting.dai@polyu.edu.hk*
[2] *Tianjin Key Laboratory of Indoor Air Environmental Quality Control, School of Environmental Science and Engineering, Tianjin University, Tianjin 300072, China, smliu@tju.edu.cn*
[3] *Tianjin Key Laboratory of Indoor Air Environmental Quality Control, School of Environmental Science and Engineering, Tianjin University, Tianjin 300072, China, jjliu@tju.edu.cn*
[4] *School of Mechanical Engineering, Tianjin University, Tianjin 300072, China, nanj@tju.edu.cn*
[5] *Department of Building Environment and Energy Engineering, The Hong Kong Polytechnic University, Kowloon 999077, Hong Kong SAR, China, qingyan.chen@polyu.edu.hk*

SUMMARY
Investigating outdoor airflow and pollutant dispersion in building areas is crucial for protecting public health. The inherent variability of wind conditions introduces significant uncertainty into airflow and pollutant dispersion around buildings. Previous studies addressed this variability by performing multiple simulations under different wind conditions, which substantially increases computational time. To address this challenge, this study employs the Polynomial Chaos Expansion (PCE) method to develop surrogate model for predicting outdoor airflow velocity and pollutant concentration under varying wind conditions. The surrogate model approximates velocity and concentration by expanding orthogonal polynomials, with wind direction and wind speed as input variables. The correlation coefficient between the surrogate model and the original simulation results ranges from 0.95 to 0.98, verifying the model's accuracy. This surrogate model enables rapid calculations of airflow velocity and pollutant concentration, establishing the response surface of these variables with respect to wind conditions. By avoiding the necessity for repeated, computationally demanding simulations, this method facilitates direct and efficient predictions of outdoor environments. Consequently, it provides a fast, comprehensive, and accurate tool for predicting airflow and pollutant dispersion in urban environments.
Keywords: Urban airflow and pollutant, Varying wind conditions, Surrogate model.

1. INTRODUCTION

With the advancement of industrialization, emissions of pollutants such as CO, SO_2, and NO_x have significantly increased (Li et al., 2018). These pollutants disperse into the surrounding environment, infiltrating buildings and degrading air quality (Li et al., 2020). Research indicates that air pollution can irritate the respiratory system, contributing to chronic diseases, and premature mortality (Saleh et al., 2020). According to a 2016 report by the World Health Organization, air pollution is responsible for approximately 4.2 million deaths annually, ranking it as the sixth leading cause of death worldwide (WHO, 2016). Therefore, investigating pollutant dispersion in urban areas is essential for mitigating health risks and enhancing living conditions.

Computational fluid dynamics (CFD) is widely recognized as an efficient method for simulating airflow and pollutant dispersion in outdoor environments (Liu et al., 2022; Dai et al., 2022, 2023). Studies have simulated airflow and pollutant dispersion around buildings under various scenarios

(Oaks et al., 2021). Previous simulations often rely on prevailing wind direction and speed. However, actual wind conditions are dynamic and frequently fluctuate, introducing uncertainty into outdoor wind environments (Yassin et al., 2005). Simulations based on prevailing wind conditions may provide probable outcomes but fail to capture the impact of wind variability. Thus, investigating airflow and pollutant dispersion under varying wind conditions is essential.

Methods for investigating outdoor environment under varying wind conditions include the local expansion method, sampling methods, and surrogate models (Paudel et al., 2022; Wang et al., 2021). The local expansion method linearizes responses near a reference point using a Taylor series, providing statistical insights into the results (Paudel et al., 2022). However, it tends to amplify uncertainties, limiting its applicability to scenarios with high nonlinearity (Wilson et al., 2013). Its accuracy declines under strong nonlinear variations, such as those induced by fluctuating wind conditions. Sampling methods are approaches which conduct simulation under various wind conditions and evaluate the corresponding result (Wang et al., 2021). A study uses simulations under varying wind directions to analyze pollutant dispersion distribution (Jon et al., 2023). However, these studies are often constrained by limited sample sizes, leading to predominantly qualitative conclusions. Additionally, re-simulations for new conditions are required, which are computationally inefficient in large-scale outdoor environments. In contrast, surrogate models are efficient method for studying airflow and pollutant dispersion under varying wind conditions. Common surrogate models include Kriging, neural networks, and Polynomial Chaos Expansion (PCE), with PCE distinguished by its lower computational demands and physical interpretability, making it widely adopted in built environment research (Wiener, 1938; Mohamed, 2025).

Surrogate models based on polynomial chaos expansion have been increasingly applied to predict building environments (Sun et al., 2017). It establishes relationships between outdoor velocity, pollutant concentration, and wind conditions to quantify the impact of wind variability. For instance, it was employed to compare numerical simulations with field experiments conducted in downtown Oklahoma City under uncertain inflow conditions and to evaluate the impact of inflow variability on airflow within urban canopies (Garcia-Sanchez et al., 2014, 2017). However, these studies demanded numerous simulation results, leading to significant computational costs Therefore, further optimization of this method is necessary to improve prediction efficiency.

In conclusion, prior research on airflow and pollutant dispersion under varying wind conditions has predominantly relied on extensive and repetitive simulations, which limits its applicability to real-world scenarios. This study aimed to apply surrogate models based on polynomial chaos expansion to enhance efficiency and broaden practical applications. Significant advancements were achieved through the implementation of an innovative truncation scheme, which effectively reduced simulation times. The validity of this method was demonstrated using two benchmark building cases different degrees of building geometric complexity. This approach enables direct and rapid predictions of air velocity and pollutant concentration while avoiding repeated simulations under varying wind conditions, thereby significantly enhancing computational efficiency. Consequently, this method offers more comprehensive insights into airflow and pollutant dispersion in outdoor building environments.

2. METHOD

The surrogate model based on polynomial chaos expansion is an effective tool for evaluating air velocity and pollutant concentration under varying wind conditions. This section introduces the method, emphasizing its four key components: the determination of orthogonal polynomials, hyperbolic truncation, coefficient calculation, and practical application. In this approach, velocity and concentration are represented as polynomial expansions of wind direction and speed (Wiener, 1938; Cameron et al., 1945):

$$R = F(x) = c_0\Phi_0 + \sum_{i_1=1}^{\infty} c_{i_1}\Phi_{i_1}(x_1) + \sum_{i_2=1}^{\infty} c_{i_2}\Phi_{i_2}(x_2) + \sum_{i_1=1}^{\infty}\sum_{i_2=1}^{i_1} c_{i_1 i_2}\Phi_{i_1 i_2}(x_1, x_2) \quad (1)$$

where R are the velocity and concentration results; x_1 and x_2 represent the variables of wind direction and speed, respectively; $\Phi_{i_1}(x_1)$ and $\Phi_{i_2}(x_2)$ represent the two orthogonal polynomials corresponding to the wind direction and speed, respectively. Here $\Phi_{i_1 i_2}(x_1, x_2)$ is the product combination of these two orthogonal polynomials of order i_1 and i_2, which are determined through a hyperbolic truncation scheme. c are the coefficients calculated with regression method.

2.1. Determination of Orthogonal Polynomial

The determination of orthogonal polynomials is a crucial step in polynomial chaos expansion. Various types of orthogonal polynomials are available, and their selection depends on matching the weight function with the probability density distribution of the variables (Xiu et al., 2002). For cases where wind direction and speed follow ideal distributions, previous studies have identified their corresponding orthogonal polynomials, as summarized in Table 1 (Xiu, 2010).

Table 1. Summary of orthogonal polynomials corresponding to ideal distributions

Distribution type	Normal distribution	Uniform distribution	Beta distribution	Index distribution
Corresponding orthogonal polynomial	Hermite $H_i(x)$	Legendre $P_i(x)$	Jacobi $J_i(x)$	Laguerre $L_i(x)$

For non-ideal distributions, the λ-PDF distribution (Ma et al., 2004) is a general framework for probability density functions that are unimodal, bounded, and symmetric within the interval [-1,1]. Its formulation, along with the corresponding Gegenbauer orthogonal polynomial (Fang et al., 2004), are defined as follows:

$$f_\xi^\lambda(\xi) = \begin{cases} k_\lambda(1-\xi^2)^{\lambda-1/2}, & |\xi| \le 1 \\ 0, & |\xi| > 1 \end{cases} \quad (2)$$

$$G_i^\lambda(\xi) = \sum_{d=0}^{i} \frac{1}{d!(i-d)!} \frac{(2\lambda)_i (2\lambda+i)_d}{(\lambda+1/2)_d} \left(\frac{\xi-1}{2}\right)^d, \quad i = 0,1,2,\ldots \quad (3)$$

2.2. Hyperbolic Truncation Scheme

The expanded polynomial for velocity and concentration initially comprises an infinite number of terms with varying degrees of influence. While increasing the number of terms improves accuracy, it also requires a larger number of samples. To address this, a hyperbolic truncation scheme (Montgomery, 2004) is applied to reduce the expansion to a finite set of terms by retaining influential low-order terms while eliminating less significant high-order ones, thereby achieving a balance between accuracy and computational efficiency. In this scheme, the q-norm of the variable order vector is constrained to remain below the overall truncation order (Blatman, 2009):

$$||i||_q = (i_1^q + i_2^q)^{\frac{1}{q}} \le d \quad (4)$$

where d is the overall truncation order, $i = (i_1, i_2)$ the order vector of the orthogonal polynomial corresponding to wind direction and speed, and q the truncation norm, in the range of [0, 1]. The orthogonal polynomials, whose orders satisfy the aforementioned relationship, are substituted into Expression (1), thereby completing the fundamental structure of the truncated polynomial.

2.3. Coefficient Determination

The above procedures establish a formula relating velocity, concentration, and wind conditions with undetermined coefficients. By substituting wind conditions and their corresponding

simulation results into the formula, a system of equations is obtained. These coefficients are determined by solving this system through regression method, minimizing the residual mean squared error between the simulated and predicted results. (N$\ddot{a}$ther, 2010):

$$c = argminE[\varepsilon^2] = argmin\frac{1}{N}\sum_{i=0}^{N}[(Y - \sum_{i=0}^{N} c_i\Phi_i)^2] = (\Phi^T\Phi)^{-1}\Phi^T\mathrm{Y} \quad (5)$$

where ε^2 represents the squared residuals; Y the simulation result; Φ the orthogonal polynomial corresponding to the wind variables; and N the number of simulations. The simulations are performed using FFD with the ANN dynamic Smagorinsky model (Dai et al., 2023) in OpenFOAM (Weller et al., 1998).

2.4. Application of the Method

By substituting the determined coefficients into the expression, surrogate models are constructed to represent velocity and concentration as functions of wind conditions. These models enable the rapid prediction of velocity and concentration under varying wind scenarios. Their accuracy is validated through comparisons with experimental and simulation data. Overall, this approach offers an efficient and comprehensive framework for investigating airflow and pollutant dispersion in outdoor environments.

3. RESULT

This section evaluates the performance of the surrogate model based on polynomial chaos expansion under varying wind conditions in both single-building and three-building scenarios.

3.1. Single Building Case

The single-building case, shown in Fig. 1(a), is a classic benchmark for outdoor environment studies (Tanaka et al., 2006). The airflow follows a power-law profile with an exponent of α = 1/4. To analyze airflow and pollutant dispersion under varying wind conditions in this case, wind speed and the sine of the wind direction are assumed to follow a normal distribution, as shown in Fig. 1(b, c).

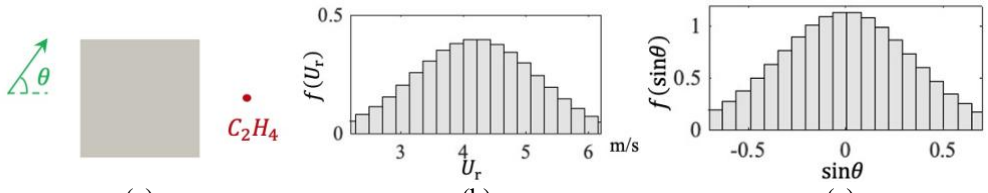

(a) (b) (c)

Figure 1. (a) Geometric configuration and probability density distributions of the (b) wind speed and (c) sine value of the wind direction in the single-building case.

Figure 2 presents the correlation analysis between surrogate model and simulation results for the three velocity components and concentration at sampling points 1–9 (Fig. 2c). The inflow wind velocity was 4.74 m/s, with a wind direction angle θ = -21.1°. The figure demonstrates a strong correlation between the surrogate model and simulation results, with correlation coefficients for velocity and concentration exceeding 0.98 for velocity and 0.97 for concentration. In the wind tunnel experiment, the wind speed was 4.2 m/s, and the wind direction angle was 0°. A comparison between the experimental and surrogate model results under this condition showed errors of 5.1% and 8.4% for velocity and concentration, respectively. These results validate the surrogate model's high accuracy and reliability.

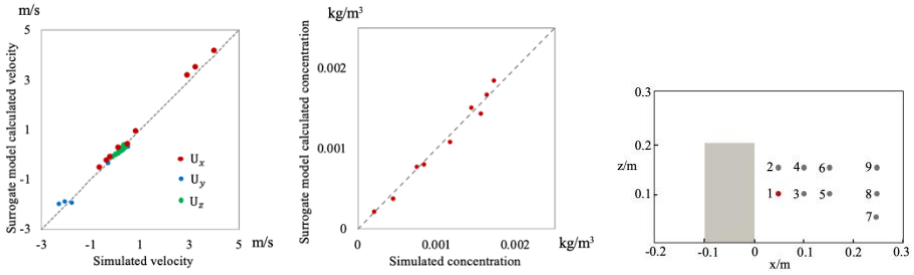

(a) (b) (c)

Figure 2. Correlation analysis between surrogate model calculated results and simulation results for (a) velocity components in three directions, (b) concentration at 9 sampling points, and (c) locations of the sampling points.

After deriving accurate surrogate model, the distributions of velocity components and concentration with respect to wind speed and direction were analyzed. Taking point 1 (0.1, 0, 0.1) as an example, Fig. 9 illustrates the distribution of its velocity and concentration, with the two horizontal axes representing wind speed and the sine of the wind direction. Since point 1 is located on the center plane of the recirculation zone behind the building and the wind direction varies within the range of [-45°, 45°], U_x remains negative and symmetric about the 0° wind direction plane. The reverse velocity decreases with increasing direction angle but increases with higher wind speed. For U_y, its absolute value increases with both wind speed and wind-direction angle. U_z increases with wind speed and remains positive, as this point is situated in the upwelling airflow region near the building's leeward side. The concentration decreases as wind speed and direction angle increase. At low wind speeds and small wind-direction angles, pollutants accumulate in the recirculation zone behind the building. In contrast, as wind speed and direction angle increase, pollutant dispersion intensifies, reducing concentration at this location.

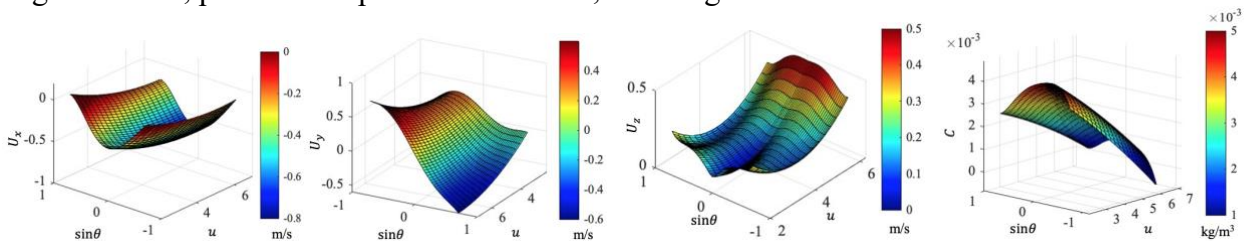

(a) (b) (c) (d)

Figure 3. Distributions of (a)U_x, (b)U_y, (c)U_z, and (d) concentration with respect to wind speed and direction.

3.2. Three-building Case

The geometry of the three-building case (Chavez et al., 2011) is shown in Fig. 4(a). The geometry is more complex, considering interactions between buildings, making it closer to real urban environments. The airflow followed a power-law profile with α = 1/3. To analyze the airflow and pollutant dispersion under varying wind conditions in this case, wind speed and the sine of wind direction were assumed to follow a normal distribution, as illustrated in Fig. 4(b, c). Compared to the single-building case, the three-building case demonstrated a wider range of wind speeds and directions, allowing for evaluation of the surrogate model under more diverse conditions.

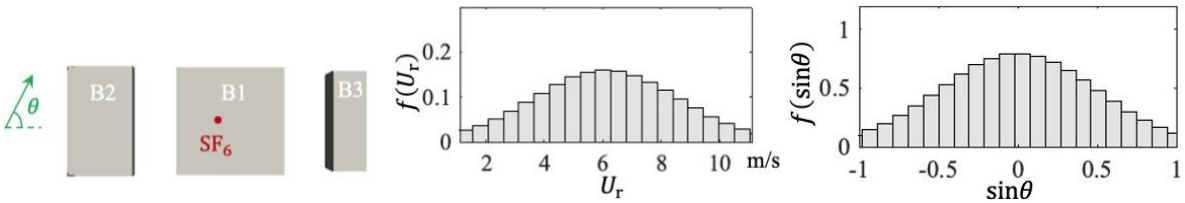

(a) (b) (c)

Figure 4. (a) Geometric configuration and probability density distributions of the (b) wind speed and (c) sine value of the wind direction in the three-building case.

Fig. 5 presents a correlation analysis between the surrogate model predictions and simulation results. The analysis includes the three velocity components and concentration at the red sampling points shown in Fig. 5(e) under three different wind conditions. In these validation cases, wind speeds range from 4.8 m/s to 8.7 m/s, while wind direction angles vary between -14° and 8°. As illustrated in the figure, the velocity and concentration values predicted by the surrogate model show a strong correlation with the simulation results, with correlation coefficients exceeding 0.95, thereby confirming the model's accuracy. Since the wind-tunnel experiments measured concentration values at only a few wall points, which were not representative, no comparison with the surrogate model predictions was conducted.

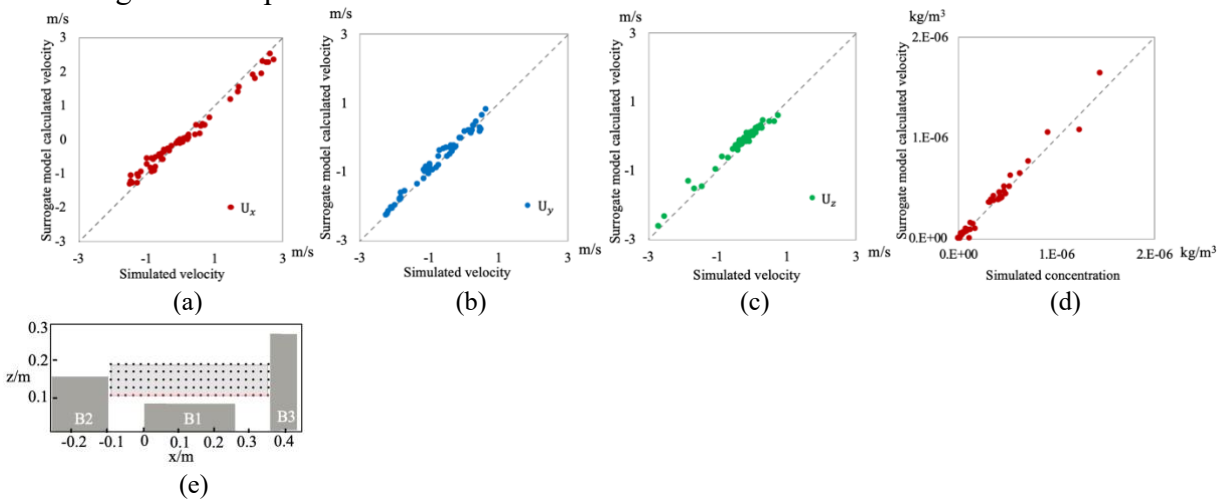

Figure 5. Correlation analysis between surrogate model calculated results and simulation results for(a) U_x, (b) U_y, (c) U_z, and (d) concentration under three different wind conditions, and (e) the locations of the sampling points.

Figure 6 illustrates the velocity and concentration contours obtained from surrogate model calculations and simulations within the shaded region of Fig. 5(e). The surrogate model contours were generated based on the results of sampling points. The wind condition was a velocity of 6.77 m/s and direction angle θ of -3.4°. A recirculation zone formed in this case due to the influence of the B2 building. In the U_x contour, the flow transitioned from forward to reverse as altitude decreased, with smaller values observed in the rear due to obstruction by the B3 building. In the U_y contour, the negative direction angle produced negative values in the rear, while recirculation flow generated small positive values in the front. For U_z, the recirculation created downward velocities in the rear and upward velocities in the front, with higher vertical velocities near the chimney due to its high release velocity. In the concentration contour, pollutants spread forward with the reverse airflow and dispersed along the recirculation zone, as the chimney was located at the bottom of this zone. These results demonstrate that the surrogate model accurately captures airflow and pollutant dispersion, confirming its accuracy.

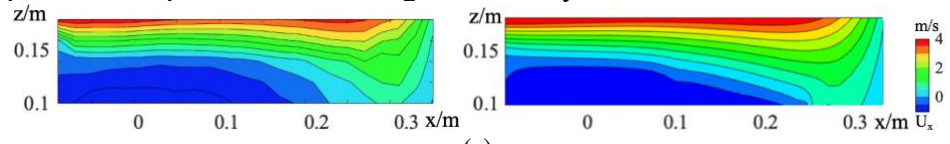

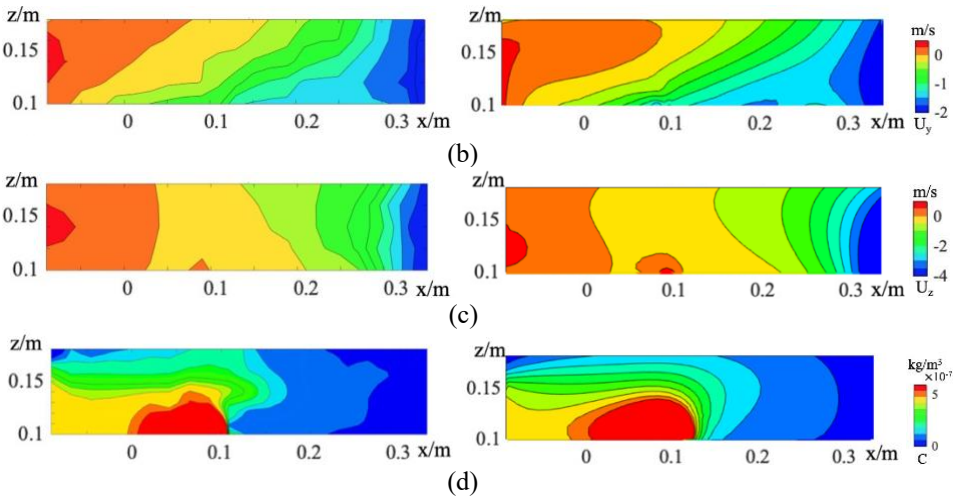

Figure 6. Contours for (a) U_x, (b) U_y and (c) U_z, and (d) the concentration obtained from surrogate model calculation (left) and simulation (right).

4. CONCLUSION

This study utilized surrogate model based on polynomial chaos expansion to investigate the effects of varying wind conditions on air velocity and pollutant concentration. The surrogate model was constructed to represent air velocity and pollutant concentration as functions of wind conditions. Correlation coefficients between the surrogate model and simulation results, ranging from 0.95 to 0.98, demonstrate the model's high accuracy. This approach enables rapid predictions and facilitates uncertainty analysis of airflow and pollutant concentration in outdoor environments under varying wind scenarios.

Due to space limitations, this study focused on validating the model using idealized cases with specific wind distributions. Future work can extend the model's application to more complex real-world building scenarios under actual wind conditions, incorporating measurements and case studies for further validation.

In conclusion, this method allows for direct and efficient predictions of outdoor airflow and pollutant dispersion, eliminating the need for repeated simulations under varying wind conditions and significantly improving computational efficiency. In summary, it provides comprehensive insights into airflow and pollution dispersion in urban environments.

ACKNOWLEDGEMENTS

The authors would like to acknowledge the support by the National Key R&D Program of the Ministry of Science and Technology, China, on "National Quality Infrastructure (NQI)" through Grant No. 2023YFF0613101, by the National Natural Science Foundation of China (NSFC) through grant No. 52108084, and by the Global STEM Professorship from the Hong Kong government received by Qingyan Chen.

REFERENCES

Blatman, G. (2009). Adaptive sparse polynomial chaos expansions for uncertainty propagation and sensitivity analysis. PhD thesis, Universit´e Blaise Pascal, Clermont-Ferrand.

Cameron, R., & Martin, W. (1945). Transformations of Wiener integrals under a general class of linear transformations. Transactions of the American Mathematical Society. 58 (2), 184–219.

Chavez, M., Hajra, B., Stathopoulos, T., & Bahloul, A. (2011). Near-field pollutant dispersion in the built environment by CFD and wind tunnel simulations. Journal of Wind Engineering and Industrial Aerodynamics, 99(4), 330-339.

Dai, T., Liu, S. M., Liu, J. J., Jiang, N., & Chen, Q. (2022). Evaluation of fast fluid dynamics with different turbulence models for predicting outdoor airflow and pollutant dispersion. Sustainable Cities and Society, 77, 103583.

Dai, T., Liu, S. M., Liu, J. J., Jiang, N., & Chen, Q. (2023). Development of a new dynamic Smagorinsky model by an artificial neural network for prediction of outdoor airflow and pollutant dispersion. Building and Environment, 243(10), 110624.

Fang, T., Leng, X.L., Ma, X.P., & Meng, G. (2004). λ-PDF and Gegenbauer polynomial approximation for dynamic response problems of random structures. Acta Mechanica Sinica, 20, 292-298.

Garcia-Sanchez, C., Philips, D.-A., & Gorle, C. (2014). Quantifying inflow uncertainties for cfd simulations of the flow in downtown Oklahoma City. Building and Environment, 78, 118-129.

Garcia-Sanchez, C., Van Tendeloo, G., & Gorle, C. (2017). Quantifying inflow uncertainties in rans simulations of urban pollutant dispersion. Atmospheric Environment, 161, 263-273.

Jon, K. S., Sin, C. H., Luo, Y., Cui, P. Y., Huang, Y. D., & Tokgo, J. (2023). Impacts of wind direction on the ventilation and pollutant dispersion of 3d street canyon with balconies. Building and Environment, 230, 110034.

Li, H., Lu, J., & Li, B. (2020). Does pollution-intensive industrial agglomeration increase residents' health expenditure?. Sustainable Cities and Society, 56, 102092.

Li, M., Li, C., & Zhang, M. (2018). Exploring the spatial spillover effects of industrialization and urbanization factors on pollutants emissions in China's Huang-Huai-Hai region, Journal of Cleaner Production, 195, 154-162.

Liu, W., Sun, H. W., Lai, D. Y., Xue, Y., Kabanshi, A., & Hu, Simon. (2022). Performance of fast fluid dynamics with a semi-Lagrangian scheme and an implicit upwind scheme in simulating indoor/outdoor airflow. Building and Environment, 207, 108477.

Ma, X.P., Leng, X.L., Meng, G., & Fang, T. (2004). Evolutionary earthquake response of structure with bounded random parameters. Probabilistic Engineering Mechanics, 19(3), 239-246.

Mohamed, H., Schöner, C., & Jekel, D. (2025). Sampling-efficient surrogate modeling for sensitivity analysis of brake squeal using polynomial chaos expansion. Results in Engineering, 26, 104649.

Montgomery, D.C. (2004). Design and analysis of experiments. John Wiley and Sons, New York.

Na¨ther W. (2010). Optimum experimental designs. Publications of the American Statistical Association, 103(483), 13 27-1328.

Oaks, W. R., Flora, K., & Khosronejad, A. (2021). Eulerian numerical modeling of contaminant transport in lower manhattan, new york city, from a point-source release under the dominant wind condition: Insights gained via les. Atmospheric Environment, 262(1), 118621.

Paudel, A., Gupta, S., Thapa, M., Mulani, S. B., Walters, R. W. (2022). Higher-order Taylor series expansion for uncertainty quantification with efficient local sensitivity. Aerospace Science and Technology, 126(7), 107574.

Saleh, S., Shepherd, W., Jewell, C., Lam, N., Balmes, J., Bates, M., et al. (2020). Air pollution interventions and respiratory health: a systematic review. The International Journal of Tuberculosis and Lung Disease, 24, 150-64.

Sun, X., Park, J., Choi, J. I., & Rhee, G. H. (2017). Uncertainty quantification of upstream wind effects on single-sided ventilation in a building using generalized polynomial chaos method. Building and Environment, 125, 153-167.

[dataset] Tanaka, H., Yoshie, R., & Cheng, H.-H. (2006). Tokyo Polytechnic University, Database on Indoor/Outdoor Air Pollution. http://www.wind.arch.t-kougei.ac.jp/info_center/pollution/pollution. html.

Wang, H. H., & Ngan, K. (2021). Effects of inhomogeneous ground-level pollutant sources under different wind directions. Environmental Pollution, 289, 117903.

Weller, H.G., Tabor, G., Jasak, H., & Fureby, C. (1998). A tensorial approach to computational continuum mechanics using object-oriented techniques. Computers in Physics, 12(6), 620-631.

WHO (World Health Organization). (2016). Ambient air pollution: a global assessment of exposure and burden of disease. https://apps.who.int/iris/handle/10665/ 250141. [accessed 22 May 2024].

Wiener N. (1938). The homogeneous chaos. American Journal of Mathematics, 60(4), 897–936.

Wilson, B. M., Smith, B. L. (2013). Taylor-series and Monte-Carlo-method uncertainty estimation of the width of a probability distribution based on varying bias and random error. Measurement Science and Technology, 24(3), 35301 -35311.

Xiu D. B. (2010). Numerical methods for stochastic computations: a spectral method approach. Princeton University Press.

Xiu, D. B., & Karniadakis, G.E. (2002b). Modeling uncertainty in steady state diffusion problems via generalized polynomial chaos. Computer Methods in Applied Mechanics and Engineering, 191(43),4927–4948.

Yassin, M. F., Kato, S., Ooka, R., Takahashi, T., & Kouno, R. (2005). Field and wind-tunnel study of pollutant dispersion in a built-up area under various meteorological conditions. Journal of Wind Engineering and Industrial Aerodynamics, 93(5), 361-382.

6th International Conference on Building Energy and Environment
Eindhoven University of Technology, The Netherlands
6 - 10 July 2025

Influence of modelled urban features in CFD simulations for wind microclimate assessments

N.J.V. Vlaun [1], R.P.W. Maas [1], T.C. Fahner [1]

[1] *Actiflow B.V., Breda, The Netherlands, contact@actiflow.com*

SUMMARY
This investigation compares several CFD simulations of a given urban high-rise context (downtown Rotterdam), where the environment is represented differently in each model variant. An assessment region is defined that includes building geometries, while the surroundings within the computational domain are described by roughness parameters. The dimensions of the domain and assessment region are changed in each variant to assess the influence of modelled urban features on the simulated flow fields. The results of this study show that models set up according to known guidelines, where the assessment region is typically limited to a few hundred metres across, significantly overestimate both the wind speeds and exceedance probabilities, compared to a model in which the entire city district is reconstructed. This research serves to expand on procedures and guidelines for urban wind microclimate assessments.

Keywords: urban microclimate, pedestrian wind comfort, computational fluid dynamics (CFD), 3D city modelling.

1. INTRODUCTION

With increasing attention to urban microclimate, driven in part by continuous urbanization and the subsequent densification of major cities, wind microclimate assessment has become critical to urban planning and design. Especially high-rise buildings are known to cause high wind velocities at the pedestrian level frequently leading to uncomfortable and even dangerous wind conditions in urban areas (Hågbo & Giljarhus, 2024). Such wind microclimate assessments are generally performed on physical scale models through wind tunnel testing or full-scale digital models through computational fluid dynamics (CFD) of an urban configuration. The study area is typically limited to a few hundred meters (Blocken, 2015; Liu et al., 2018). Model dimensions vary based on the height of a given target building, the composition of its surroundings and the detail needed to capture local flow phenomena to adequately predict wind comfort or distress and, traditionally, size restrictions of an atmospheric boundary layer wind tunnel. As only a limited area is tested in a typical assessment, wind flow patterns on a district or city level are inherently not captured.

The use of CFD simulations has become the dominant approach in urban microclimate studies, due to advancements in high-performance computing, which makes CFD increasingly accessible and affordable (Abu-Zidan et al., 2021; Yang et al., 2023; Hågbo & Giljarhus, 2024). Its application is however not trivial and requires many choices to be made by the user – including but not limited to the geometrical implementation of the model, sizing the computational domain, and setting appropriate boundary conditions – all of which can have a large impact on the accuracy of the results (Blocken, 2015). For purposes of quality assurance, best practice guidelines for the application of CFD have been established in scientific literature, such as Franke et al. (2007), Tominaga et al. (2008) and Blocken (2015). The question arises whether these are fully applicable

to district-scale assessments when the size of the modelled area and the number of geometries considered are both drastically increased. In this investigation we thus focus on the size of the assessment region and how buildings within are represented. Existing guidelines mostly define a minimum area to be explicitly modelled around a given target building. Tominaga et al. (2008) suggests that all buildings within the region to be assessed should be clearly reproduced and that said assessment region typically has a radius of 1 to 2 times the height of the target building, plus one additional street block in each direction. Tong et al. (2016) defines the influence region as typically two or three layers of surrounding buildings to be modelled depending on urban configuration and wind direction. Liu et al. (2018) concludes that the region within a radius of at least 3 times the maximum dimension of the target building should be simulated with detailed building structures. The Dutch NEN 8100 (2006) standard for the classification of wind comfort, defines a 'sphere of influence' as the area with a radius 6 times the height of the target structure and mandates that the surrounding buildings within a radius of at least 250 m to 300 m be modelled. Maximum dimensions for neither the assessment region nor domain boundaries are given in literature as increasing either is generally considered to be laborious and computationally inefficient (Abu-Zidan et al., 2021; Pađen et al., 2022). The effects of urban features outside the assessment region are instead accounted for through prescribing aerodynamic roughness lengths (Blocken et al., 2007; Liu et al., 2018; Ricci et al., 2020).

In this study we investigate the influence of modelled urban features, such as surrounding buildings and terrain, on the simulated flow fields of a typical pedestrian wind comfort study. This is done by comparing several CFD models of the same location, each set up with different domain sizes and varying number of buildings (i.e. varying the size of the assessment region). As such, we aim to quantify this influence and assess the applicability of existing guidelines to wind microclimate assessments conducted in complex urban contexts at larger scales.

2. RESEARCH METHOD

2.1 Geometric model

A detailed geometric model of downtown Rotterdam, the Netherlands serves as our base model. This model, shown in Fig. 1, covers a total area of roughly 20 km² and includes several districts with distinct urban morphologies from low-rise residential and industrial zones to the city centre with high-rise buildings up to 215 m tall.

The computational model is a cylindrical domain with a height of 800 m and a radius of 4.0 km. In its centre, within a 5.5 km wide circular area, all buildings (3,200 in total) and trees are modelled explicitly. The input geometry is constructed from open geodata including topographical maps, aerial photos, LiDAR scans and building model databases. Structures were added manually where data was missing or resulted in overly complex geometries. In the remaining outer region, the built environment is represented by roughness lengths assigned to the bottom of the domain. This outer ring serves as upstream or downstream region depending on the wind direction. The assigned roughness lengths, shown in Fig. 2, are in accordance with Dutch guideline NPR 6097 (2006) and generally categorize subregions by building height, terrain typology and urban density.

Figure 1. Base model and mesh section for the wind assessment of downtown Rotterdam, the Netherlands.

For the purposes of this study, two more models were created from the base model in Fig. 2(a). In the variant shown in Fig. 2(b) the assessment region (AR) is decreased to a radius of 300 m while the size of the computational domain is unchanged. Buildings outside the assessment region are simplified into flat terrain with roughness lengths assigned. In the third variant, see Fig. 2(c), the domain is decreased to 3.0 km diameter, which is a typical setup for a pedestrian wind comfort study following the NEN 8100 standard, also adhering to best practice guidelines on domain sizing (Franke et al., 2007). Directly comparing these three cases provides insight into the effects of domain size and building geometries on the results of microclimate assessments.

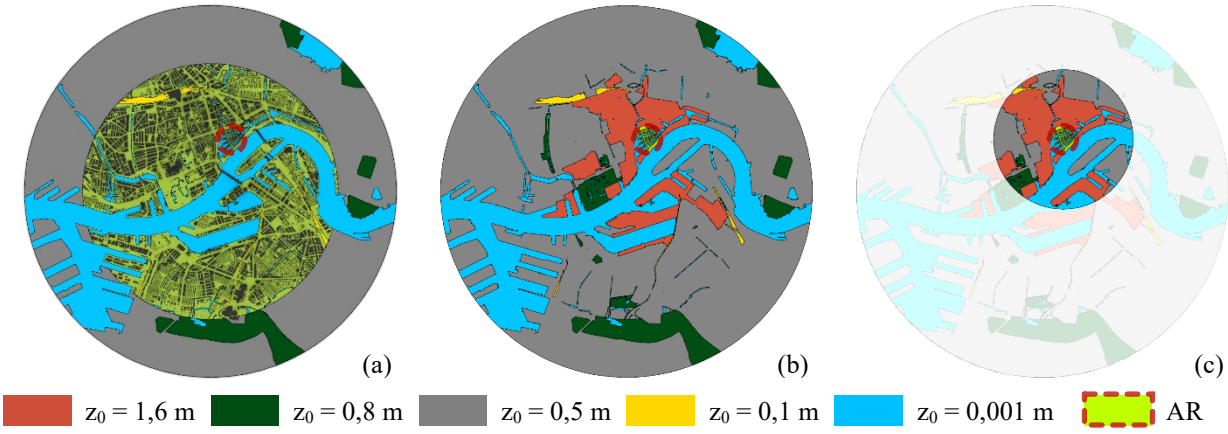

Figure 2. Roughness lengths assigned to the geometric models.

2.2 Computational mesh

The computational meshes for the CFD simulations of each case were generated using snappyHexMesh from OpenFOAM v2312. A conformal hexcore mesh with polyhedral cells between different levels of refinement is utilized in each model variant. The maximum grid size is 64 m near the domain perimeters, and the smallest surface cells have an edge length of 0.25 m to describe detailed features. Edge sizes on the bottom plane in the assessment region are 1 m to 2 m wide. Cell sizes on the buildings in the centre of the domain typically vary between 0.5 m to 4 m,

except for the small 0.25 m features mentioned above. Prismatic layers are added on all walls, of both terrain and buildings. Vegetation is modelled using porous zones that are created at the meshing stage, with cell sizes that vary between 0.5 m and 2 m. This resulted in a final mesh of 583 million cells for the base model. Using the same method, the mesh sizes for the models in Fig. 2(b) and Fig. 2(c) are 20.6 million and 18.6 million, respectively.

2.3 Boundary conditions

A neutral atmospheric boundary layer (ABL) profile is prescribed at the inflow boundary of the cylindrical domain, while the outflow boundary is prescribed as a pressure outlet. Turbulence profiles for the ABL are added at the inflow boundary, with a zero normal gradient outflow. Turbulence close to walls is modelled using wall functions. On the implicitly modelled areas, roughness was used to maintain the ABL up to the explicitly modelled assessment region. Turbulence is modelled using the k-ω SST model (Menter et al., 2003). Velocity profiles and turbulence quantities are set according to the following expressions (Richards & Hoxey, 1993; Yang et al., 2009):

$$U = \frac{u^*}{\kappa} \ln\left(\frac{z + z_0}{z_0}\right) \tag{1}$$

$$u^* = \frac{U_{ref}\,\kappa}{\ln\left(\frac{z_{ref} + z_0}{z_0}\right)} \tag{2}$$

$$k = \frac{(u^*)^2}{\sqrt{C_\mu}} \tag{3}$$

$$\omega = \frac{u^*}{\kappa\sqrt{C_\mu}} \frac{1}{z + z_0} \tag{4}$$

In the simulations, a reference wind speed U_{ref} of 5 m·s^{-1} is set at the domain boundary at a reference height z_{ref} of 60 m. Eq. 1 and Eq. 2 describe the velocity profile, where U is the horizontal wind speed, u^* is the friction velocity, z is the height from ground level, z_0 is the aerodynamic roughness length and κ is the "von Kármán" constant (= 0.41). The turbulent kinetic energy k and specific turbulent dissipation rate ω profiles at the inflow part of the domain are calculated using Eq. 3 and Eq. 4. C_μ is a turbulence model constant (= 0.09).

2.4 CFD model

The simulations are performed using the simpleFoam solver from OpenFOAM v2312. This is a steady-state solver for turbulent incompressible flows. For the base model, convergence is determined by monitoring the forces acting on the various bridge structures within the model. When the drag coefficient of these bridges varied by less than 1 count the solutions were considered converged. An additional 500 iterations were run and averaged to reach the presented results. Per model 24 (2×12) simulations are performed to account for all wind directions and different vegetation states. The simulations for the base model had a computational cost of around 7,300 core-hours each on Actiflow's cloud cluster using AWS parallelCluster technology. For models 2(b) and 2(c), the simulations ran on Actiflow's in-house HPC cluster, where each simulation had a cost of approximately 150 core-hours.

2.4.1. Numerical setup

The SIMPLEC algorithm was chosen for the pressure-momentum coupling, while the pressure equation was solved using the Geometric agglomerated algebraic multi-grid (GAMG) method with Gauss-Seidel smoothing. The momentum and turbulence equations were solved using the Preconditioned Bi-conjugate gradient stabilised solver using the Diagonal-based Incomplete Lower-Upper preconditioner.

2.4.2. Post-processing with historical wind data

To assess ground-level wind conditions each model variant is simulated from 12 wind directions, in increments of 30°, as outlined by the NEN 8100 standard. The simulated velocity fields are processed using statistical meteorological data for Rotterdam taken from two different datasets: the Dutch Offshore Wind Atlas (DOWA) time series files from 2008-2017 (Wijnant et al. 2019), and wind statistics from the NPR 6097 guideline covering the period of 1963-2002. The latter specifically takes land use into account and its use is mandated for pedestrian wind comfort studies in the Netherlands.

3. RESULTS

The simulation results are shown in Table 1 and Fig. 3 at a height of 1.75 m above ground level, for the same assessment region (r = 300 m) in each model variant. To clarify, the base model is thus the only variant in which surrounding buildings outside of this region are modelled explicitly. Models 2(b) and 2(c) show both a significantly higher average wind speed (increase of 18-32%) and a significantly higher exceedance probability for the 5 $m \cdot s^{-1}$ threshold wind speed (mean value increase of 81-113%) in the assessment region, compared to the base model.

Table 1. Simulation results: mean values within r = 300 m assessment region of the average local wind speed (U_{loc}) and exceedance probability of 5 $m \cdot s^{-1}$ threshold wind speed (p), at 1.75 m height.

		DOWA		NPR 6097	
	base model	model 2(b)	model 2(c)	model 2(b)	model 2(c)
Local wind speed U_{loc} $[m \cdot s^{-1}]$	1.64	2.16	2.15	1.93	1.93
Difference ΔU_{loc}	--	+ 0.52	+ 0.51	+ 0.29	+ 0.29
Exceedance probability p [%]	2.96	6.31	5.96	5.58	5.37
Difference Δp	--	+ 3.35	+ 3.00	+ 2.62	+ 2.41

The average wind speed across the assessment region is visualised in the first row of Fig. 3(a1-d1) with the second row, Fig. 3(b2-d2), showing the deviation of the results from the base model for each variant. In models 2(b) and 2(c) average wind speeds are overpredicted by up to 1.5 $m \cdot s^{-1}$ compared to the base model. The exception to this is the southeastern part of the assessment region, where the predicted wind speeds are less than those found in the base model simulation. A similar trend is found for the exceedance probability, which is visualised in the third row of Fig. 3(a3-d3). The final row, Fig. 3(b4-d4), displays the relative difference of the exceedance probabilities between the base and comparison models, showing a deviation up to 15 % in some areas.

The comparison indicates that explicit modelling of features outside the assessment region in the base model has a significantly higher influence on the approach flow than those cases where the surroundings are solely described by roughness. As models 2(b) and 2(c) only differ in the distance from the assessment region to the domain boundary, while both have a close match in their results, increasing the surrounding areas does not seem to notably alter the outcomes.

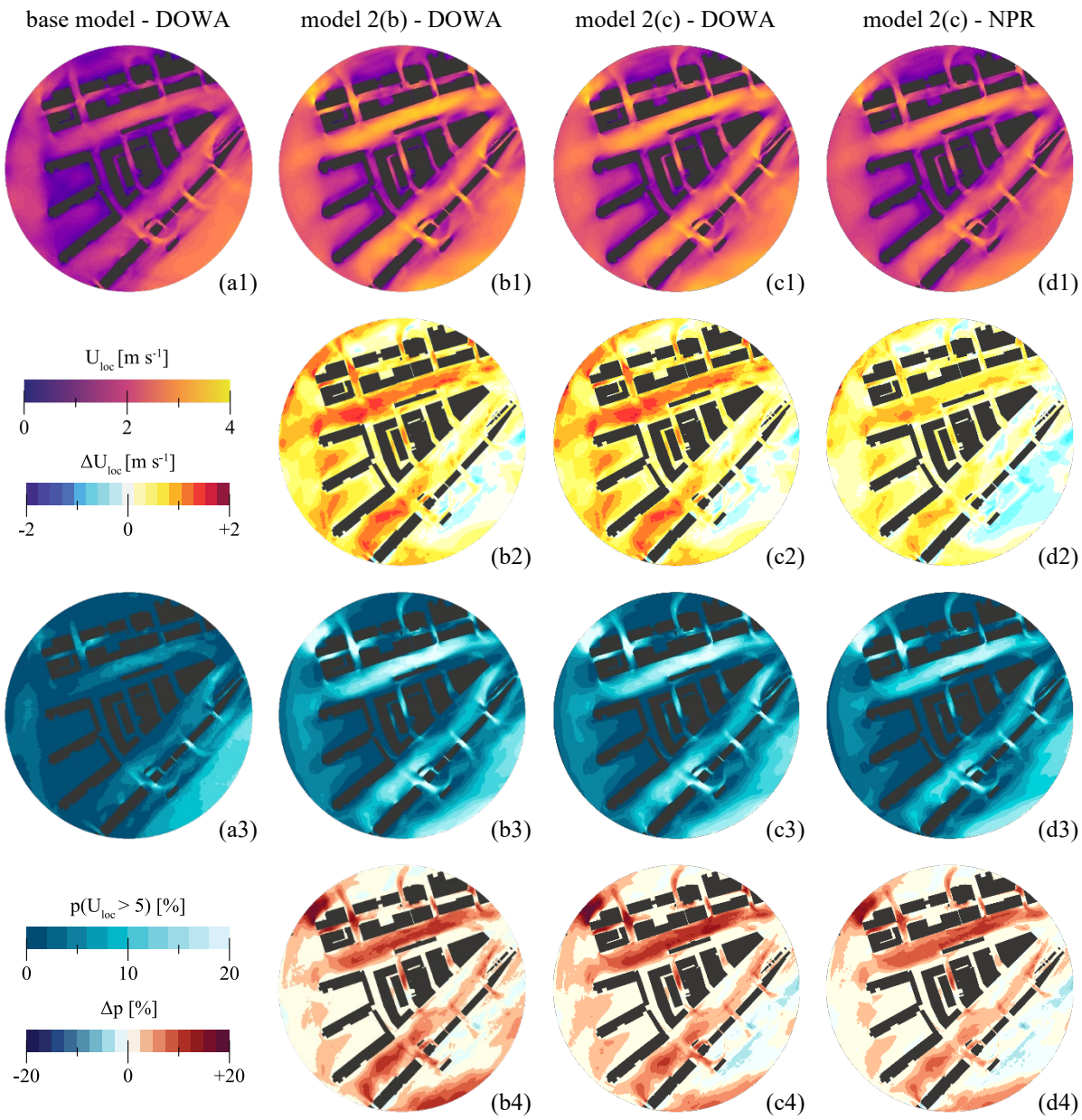

Figure 3. Simulation results for r = 300 m assessment region.

In Fig. 4, pedestrian wind comfort classification according to the Lawson LDDC and NEN 8100 criteria is projected onto the simulation results. These maps show a discrepancy between the models of up to 2 (Lawson LDDC) or 3 (NEN 8100) wind comfort classes.

4. DISCUSSION

As the results shown in Fig. 3(a1-c4) are processed from the same wind statistics, the differences between the variants are found in the calculated wind velocities. Care must also be taken when interpreting these results, as the relationship between local wind speed and exceedance probability

is not linear. The biggest differences in average wind speeds are found in street canyons with their axis aligned to the prevailing southwestern wind direction. The assessment region is relatively open when isolated from its surroundings. In reality, and as shown in the base model, this region is situated within a densely built-up urban centre, several kilometres wide, including multiple clusters of high-rise buildings. Shielding effects from buildings close or adjacent to the assessment region do not seem to be captured properly by parameterization into roughness lengths.

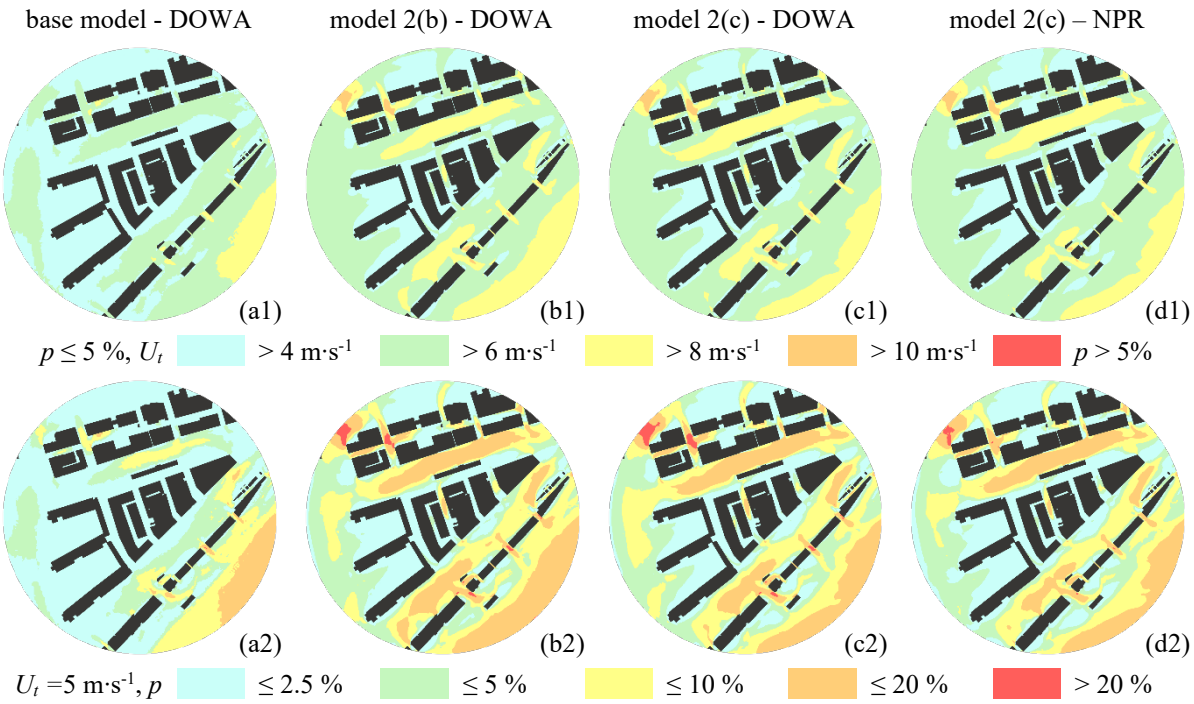

Figure 4. Pedestrian wind comfort maps based on Lawson LDDC (above) and NEN 8100 (below) comfort criteria.

The effect of the utilized wind statistics is also considered. The NPR 6097 guideline provides statistical wind data for any location in the Netherlands, based on a potential wind speed at a height of 60 m, accounting for land use. The variants processed with this data show improved agreement to the base model, as shown in the rightmost columns of Fig. 3(d1-d4) and Fig. 4(d1-d2), though the differences for both wind speed and exceedance probability remain significant. Since this study considers a single urban configuration, it remains an open question whether another configuration will yield similar trends and discrepancies. To further quantify the influence of modelled urban features (or lack thereof) in CFD studies, more configurations, different contexts, and varying model sizes should be considered.

5. CONCLUSION

This study compared CFD models of the same location, each set up with different domain sizes and varying number of buildings, to investigate the influence of modelled urban features on a typical pedestrian wind comfort assessment. It is found that typical models, in which building geometries outside of a small assessment region are excluded, significantly overestimate both the average wind speed and the exceedance probability, compared to a model of the same location in

which the entire city district is reconstructed. Part of this difference can be explained by consideration of wind statistics but is mainly due to the omission of (large) objects in the wider surroundings. In cases where no building geometries are added outside the assessment region and the surrounding areas are described purely through roughness parameters, increasing the domain size beyond standard practice has almost negligible effects on the results. For dense urban environments with many high-rise structures, a reconsideration of procedures for wind microclimate assessments may be appropriate. These findings should be justified by comparison with measurements or by examining a wider range of urban configurations and different cities.

ACKNOWLEDGEMENTS

The authors of this paper express their gratitude toward the municipality of Rotterdam who funded part of this research through the 'Kennis en Innovatiefonds'. More specifically we like to thank Simone Tax who was the driving force behind starting this research and who stands side by side with us to disseminate knowledge of wind as a key factor in urban climate to a broad audience.

REFERENCES

Abu-Zidan Y., Mendis P., Gunawardena T., 2021. Optimising the computational domain size in CFD simulations of tall buildings. Heliyon, Vol. 7(4), Article e06723.

Blocken B., Stathopoulos T., Carmeliet J., 2007. CFD simulation of the atmospheric boundary layer: wall function problems. Atmospheric Environment, Vol. 41(2), pp. 238-252.

Blocken B., 2015. Computational fluid dynamics for urban physics; Importance, scales, possibilities, limitations and ten tips and tricks toward accurate and reliable simulations. Building and Environment 91, pp. 219-245.

Franke J., Hellsten A., Schlünzen H., Carissimo B., 2007. Best practice guideline for the CFD simulation of flows in the urban environment. Brussels, Belgium. COST Office, 2007, ISBN 3-00-018312-4.

Hågbo T.-O., Giljarhus K.E.T., 2024. Sensitivity of urban morphology and the number of CFD simulated wind directions on pedestrian wind comfort and safety assessments. Building and Environment 253, Article 111310.

Liu S., Pan W., Zhao X., Hao Z., Cheng X., Long Z., Chen Q., 2018. Influence of surrounding buildings on wind flow around a building predicted by CFD simulations. Building and Environment 140, pp. 1-10.

Menter F.R., Kuntz M., Langtry R., 2003. Ten years of industrial experience with the SST turbulence model. Heat and Mass Transfer 4, pp. 625-632.

NEN, NEN 8100-Wind comfort and wind danger in the built environment. Delft, the Netherlands: Netherlands Standardization Institute (NEN), 2006.

NEN, NPR 6097-Application of the statistics of the mean wind speed for the Netherlands. Delft, the Netherlands: Netherlands Standardization Institute (NEN), 2006.

Pađen I., García-Sánchez C., Ledoux H., 2022. Towards automatic reconstruction of 3D city models tailored for urban flow simulations. Frontiers in Built Environment, Vol. 8.

Ricci A., Kalkman I., Blocken B., Burlando M., Repetto M.P., 2020. Impact of turbulence models and roughness height in 3D steady RANS simulations of wind flow in an urban environment. Building and Environment 171, Article 106617.

Richards P.J., Hoxey R.P., 1993. Appropriate boundary conditions for computational wind engineering models using the k-ε turbulence model, Journal of Wind Engineering and Industrial Aerodynamics, Vol. 46 & 47, pp. 145-153.

Tominaga Y., Mochida A., Yoshie R., Kataoka H., Nozu T., Yoshikawa M., Shirasawa S., 2008. AIJ guidelines for practical applications of CFD to pedestrian wind environment around buildings. Journal of Wind Engineering and Industrial Aerodynamics 96, pp. 1749–1761.

Tong Z., Chen Y., Malkawi A., 2016. Defining the Influence Region in neighborhood-scale CFD simulations for natural ventilation design. Applied Energy 182, pp. 625–633.

Wijnant I.L, van Ulft B., van Stratum B., Barkmeijer J., Onvlee J., de Valk C., Knoop S., Kok S., Marseille G.J., Klein Baltink H., Stepek A., 2019. The Dutch Offshore Wind Atlas (DOWA): description of the dataset. KNMI Technical Report, TR-380.

Yang S., Liangzhu L., Stathopoulos T., Marey A.M., 2023. Urban microclimate and its impact on built environment – A review. Building and Environment 238, Article 110334.

Yang Y., Gu M., Jin X., 2009. New inflow boundary conditions for modeling the neutral equilibrium atmospheric boundary layer in SST k-ω model. In: The Seventh Asia-Pacific Conference on Wind Engineering, Taipei, Taiwan.

6th International Conference on Building Energy and Environment
Eindhoven University of Technology, The Netherlands
6 - 10 July 2025

Evaluating the impact of blue and green infrastructure on urban microclimate under heatwave condition

Juui Kim[1], Seungkeun Yeom [2], Taehoon hong [3], Juwon Hong[4]

[1] *Department of Architecture & Architectural Engineering, Yonsei University, Seoul, Republic of Korea, caution0210@yonsei.ac.kr*
[2] *Department of Architecture & Architectural Engineering, Yonsei University, Seoul, Republic of Korea, kevinysk@yonsei.ac.kr*
[3] *Department of Architecture & Architectural Engineering, Yonsei University, Seoul, Republic of Korea, hong7@yonsei.ac.kr*
[4] *Department of Architecture & Architectural Engineering, Yonsei University, Seoul, Republic of Korea, juwonae@yonsei.ac.kr*

SUMMARY
Heat waves are growing more frequently and intensely worldwide, with urban areas especially vulnerable due to the urban heat island (UHI) effect. This study evaluated the cooling potential of various green and blue infrastructure configurations within a redevelopment zone in Seoul using ENVI-met simulations. The analysis compared multiple scenarios of park development, incorporating different vegetation types with and without water features. Results demonstrated that plane trees exhibited superior cooling performance to ginkgo and grass coverage. Integrating water bodies with vegetation significantly enhanced cooling effectiveness across all scenarios. These findings provide quantitative evidence for the importance of design and species selection for urban parks to mitigate extreme heat events.

Keywords: Heatwave, ENVI-met, Urban green and blue infrastructure

1. INTRODUCTION

Heat waves have intensified, becoming more frequent and prolonged across the world. For instance, in South Korea, the number of heatwave days in 2023 was 13.9—an increase of 3.6 days from the previous year. Consequently, 2,818 cases of heat-related illnesses were reported, including 32 fatalities (Korea Meteorological Administration, 2023).

The risk of heat waves is more critical in urban areas due to the urban heat island (UHI) effect (Luo et al., 2023; Xin et al., 2024). UHI is the phenomenon in which cities exhibit higher temperatures than surrounding rural areas (Oke et al., 1982). Hong et al., (2019) reported a UHI intensity of 2.5 ± 0.9°C during heatwaves, approximately 0.9°C higher than during non-heatwave periods. Park et al. (2023) analyzed 25-year (1997–2021) observations in Seoul and confirmed that such positive interactions between UHIs and heat waves have become frequent in recent years.

To reduce UHI intensity under heatwave events, urban green and blue infrastructure has emerged as a promising nature-based solution for heat mitigation. Vegetation provides cooling through transpiration and shading, whereas water bodies contribute via evaporation and thermal stratification (Budzik et al., 2025). Numerous studies have investigated the cooling effects of trees

and grasses in existing urban environments. However, there remains a significant research gap in comparing the performance of green and blue infrastructure in newly developed urban parks. To address this, the current study employed Computational Fluid Dynamics (CFD) methodology to quantify the cooling effects of various nature-based solutions. This research aimed to identify optimal combinations of vegetation types and water bodies for maximum cooling effectiveness.

2. METHODOLOGY

2.1. Site description

The study area is a densely populated, low-rise commercial district located in Seoul, South Korea (37.565°N 127.005°E). According to the Köppen-Geiger climate classification system, Seoul experiences a humid continental climate (Dwa), characterized by distinct seasonal variations in temperature and precipitation. The target area comprises 12,096.9m^2 within a larger 111,425m^2 redevelopment zone (refer to Fig. 1). This district has been identified as highly vulnerable to heatwaves based on thermal, demographic, and socioeconomic factors (Kim et al., 2021). Therefore, the area was selected for green space development to improve the thermal environment.

To measure the mitigation of UHI effects during heatwave events, a single-day simulation was performed using meteorological data from August 8, 2023—the hottest day recorded in Seoul that year. In South Korea, a heatwave warning is issued when the daily maximum apparent temperature is forecasted to remain at 33°C or higher for at least two consecutive days. On August 8, the highest temperature of the year was recorded at 35.8°C, and since the daily maximum temperature exceeded 33°C for 12 consecutive days, this period meets the criteria for classification as a heat wave. On this day, the minimum and maximum temperatures were 26.3℃ and 36.4℃, respectively, with relative humidity ranging from 40% to 66%. The daily average wind speed was 2.08 m/s, and the wind direction was 60.97° .

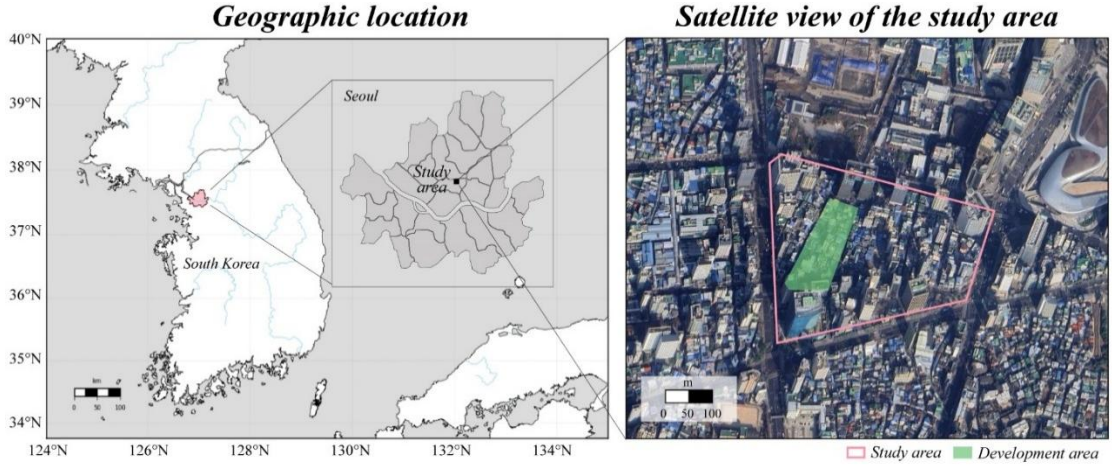

Figure 1. Study site

2.2. ENVI-met model development

A CFD simulation was conducted to evaluate outdoor thermal comfort resulting from the development of green spaces. ENVI-met V5.7.1 was employed as the simulation tool because it specializes in analyzing the cooling effects of vegetation (Liu et al., 2021). Specifically, a three-

dimensional plant tool 'Albero' simulates the physiological activities of plants using $A - g_s$ model, where A represents the photosynthetic rate and g_s denotes stomatal conductance (Bruse, 2004). The model replicates plant strategies involving water use and CO_2 assimilation. The relationship is expressed as in Eq. (1), where C_s and C_i are the CO_2 concentrations at the leaf surface and inside the leaf, respectively. Coefficient 1.6 accounts for the difference in diffusivity between CO_2 and H_2O in the air.

$$g_s = 1.6 \frac{A_n}{C_s - C_i} \quad (1)$$

The 3D model was developed using QGIS 3.40.1. The input data included building geometry surface information and vegetation shape. Detailed input parameters were based on previous research (Kim et al., 2024). The model used 3 m grid sizes in all dimensions, with a simulation domain of 185 × 146 × 25 grid cells and was further refined using the ENVI-met SPACES tool. Initial meteorological data, including air temperature, wind speed, and relative humidity, were obtained from the nearest automatic weather station (AWS). Table 1 details the simulation settings.

Table 1. Detailed settings of ENVI-met simulation

Category	Information
Software	ENVI-met V 5.7.1
Computation domain	555×439×482.2 m (171×135×25 grid cells)
Simulation site	Gwanghui-dong, Seoul, Korea
Simulation period	00:00-23:00 on 8th August, 2023
Meteorology method	Simple Forcing
Meteorological data	Temperature: 26.3℃-36.4℃ Humidity: 40%-66% Wind speed: 2.08 m/s Wind direction: 60.97°

2.3. ENVI-met model validation

The simulation results were validated by comparing the baseline scenario with outdoor sensor data. Environmental data, including temperature, humidity, wind speed, and wind direction, were obtained from Smart Seoul Data of Things (S-DoT) sensors (Bae et al., 2022; Hwang et al., 2023) on August 8, 2023.

To systematically compare the results, a 10 m × 10 m grid was generated in QGIS. Since no S-DoT measurement points were directly within the simulation domain, spatial interpolation was employed in QGIS to create a thermal map with 3 m resolution. Subsequently, ENVI-met results were imported to QGIS. The mean temperature values for each grid cell were extracted using zonal statistics, enabling hourly comparisons over 24 hours.

Statistical analysis of the validation results revealed that the root mean square error (RMSE) varied between 0.26℃ and 1.76℃ (median 1.15℃) (refer to Fig. 2). The mean absolute error (MAE) ranged from 0.17℃ to 1.70℃ (median of 0.92℃). These values align with previous ENVI-met validation studies. For instance, Yang et al. (2021) reported a median RMSE of 1.89°C and 0.86°C. Similarly, Tsoka et al. (2018) found a median RMSE of 1.51°C and a median MAE of 1.34°C.

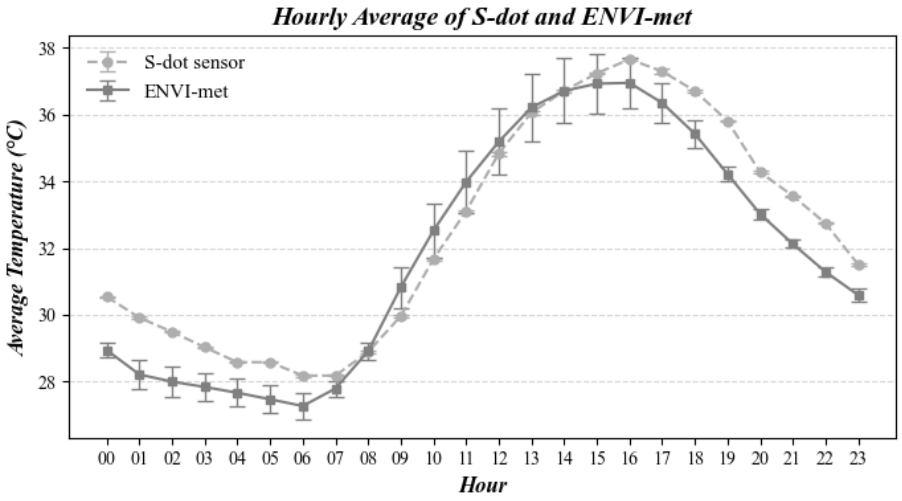

Figure 2. Validation of ENVI-met results against sensor data

2.4. Design strategies for cooling

The green and blue infrastructure development was evaluated through multiple ENVI-met simulation scenarios. A blank scenario was established for the baseline by removing existing structures from the study area. For the development of green and blue space scenarios, 7,974 m² of the target surface was converted to loamy soil to create a park area.

Three vegetation configurations were implemented for green space development: grass, ginkgo with grass, and plane tree with grass. Ginkgo and plane tree species were selected due to their prevalence in Seoul, representing 35% and 16% of urban tree populations, respectively. Table 2 specifies the properties of each vegetation type.

Table 2. Properties of simulated vegetation types

	Grass	Ginkgo	Plane tree
ENVI-met ID	Grass	Ginkgo / Fan Leave Tree (young)	London Plane Tree (young)
Leaf Type	Grass	Deciduous	Deciduous
Height (m)	0.25	8.45	10.55
Width (m)		4.56 × 4.65	5.10 × 5.12
Emissivity of Leaves	0.97	0.96	0.96
LAD	0.3	0.32	0.54

For the development of green space scenarios, grass coverage was implemented uniformly across the loamy soil substrate. In scenarios incorporating trees, 100 planting locations were algorithmically determined using random point generation in QGIS, with a minimum spacing of 6 meters to ensure appropriate canopy development. Previous studies indicated that tree-based green spaces and water features achieve optimal efficiency at approximately 0.30 hectares (Tan et al., 2021). Based on this threshold, water bodies of 3,000 m^2 were incorporated into various scenarios. Consequently, six distinct green and blue infrastructure scenarios (GR, GG, PG, GRW, GGW, PGW) were developed (refer to Fig. 3.)

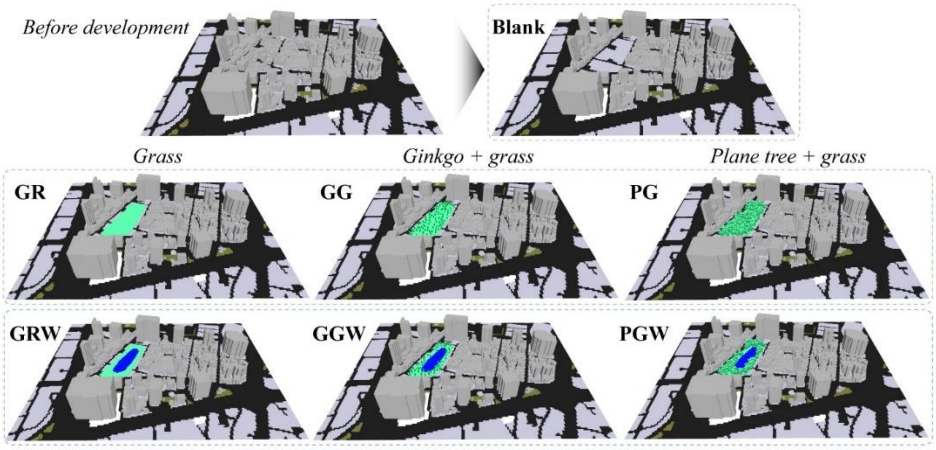

Figure 3. ENVI-met simulation scenarios
(GR(W): grass (and water), GG(W): ginkgo with grass (and water), PG(W): plane tree with grass (and water))

3. RESULTS AND DISCUSSION

The ENVI-met simulation results were pre-processed using the methodology from the validation study to derive the average temperature for each grid cell. To quantify the cooling performance of different scenarios, temperature differences relative to the blank scenario were calculated. These differences were then aggregated and multiplied by the grid area to determine the cumulated cooling effect (in °C×m^2). This analysis was conducted at hourly intervals from 6:00 to 21:00 hours (refer to Fig. 4).

Analysis revealed distinct patterns in cooling effectiveness across scenarios. The grass-only scenario (GR) consistently demonstrated the lowest cumulated cooling effect throughout the observation period, while the plane tree with grass and water body (PGW) exhibited the highest cooling performance. When comparing vegetation types, plane trees showed superior cooling than ginkgo. Generally, the partial replacement of vegetated areas with water bodies enhanced the overall cooling effect of all vegetation configurations. These findings support past studies claiming that water bodies exhibit greater cooling efficacy compared to vegetated areas (Mitra et al., 2024).

While air temperature reached a maximum between 15:00 and 16:00 during the simulation day, the cooling efficiency exhibited a notable decline from 12:00 to 15:00 across all scenarios. This was followed by a temporary recovery in cooling effectiveness until 17:00, after which cooling diminished in correlation with declining ambient temperatures. This temporal pattern can be attributed to the physiological response of stomatal resistance to temperature stress. Particularly, when average air temperatures peaked at 37°C at 15:00, the ENVI-met tree model simulated an increase in stomatal resistance, resulting in reduced transpiration rates and consequently diminished cooling capacity. Recent studies have also highlighted this limitation in vegetation-based cooling strategies under extreme temperature conditions (Gao et al., 2024).

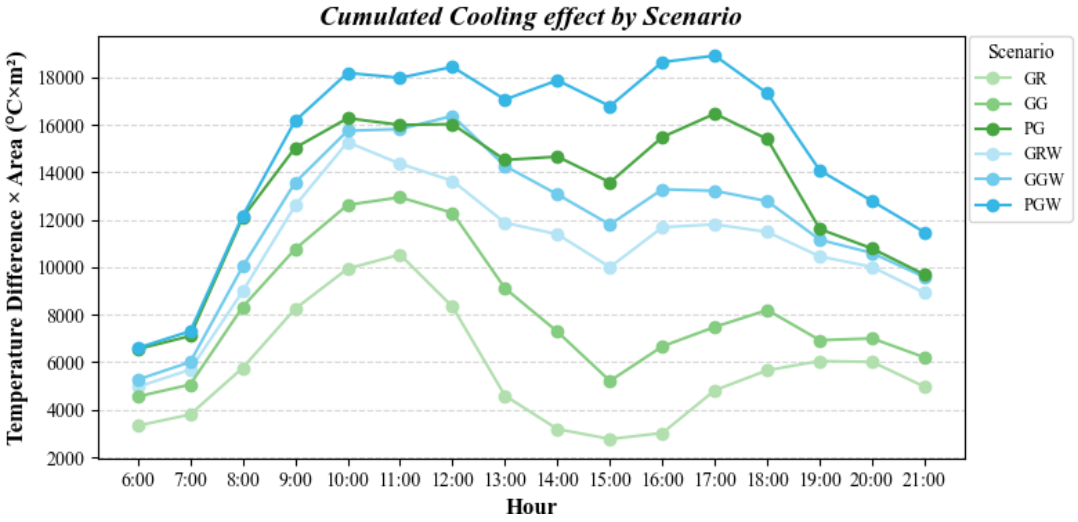

Figure 4. Hourly cumulated cooling effect by scenario

The spatial distribution of cooling effects was visualized at four temporal points (09:00, 12:00, 15:00, and 18:00), revealing distinct patterns across different scenarios (refer to Fig. 5). The grass-only scenario (GR) yielded relatively modest cooling effects. Contrarily, scenarios incorporating ginkgo (GG) and plane tree (PG) demonstrated progressively more intense and spatially extensive cooling patterns. Notably, in scenarios with water bodies, areas designated for water displayed concentrated cooling effects. These spatial patterns indicate the formation of localized "cool islands" by implementing integrated green and blue infrastructure.

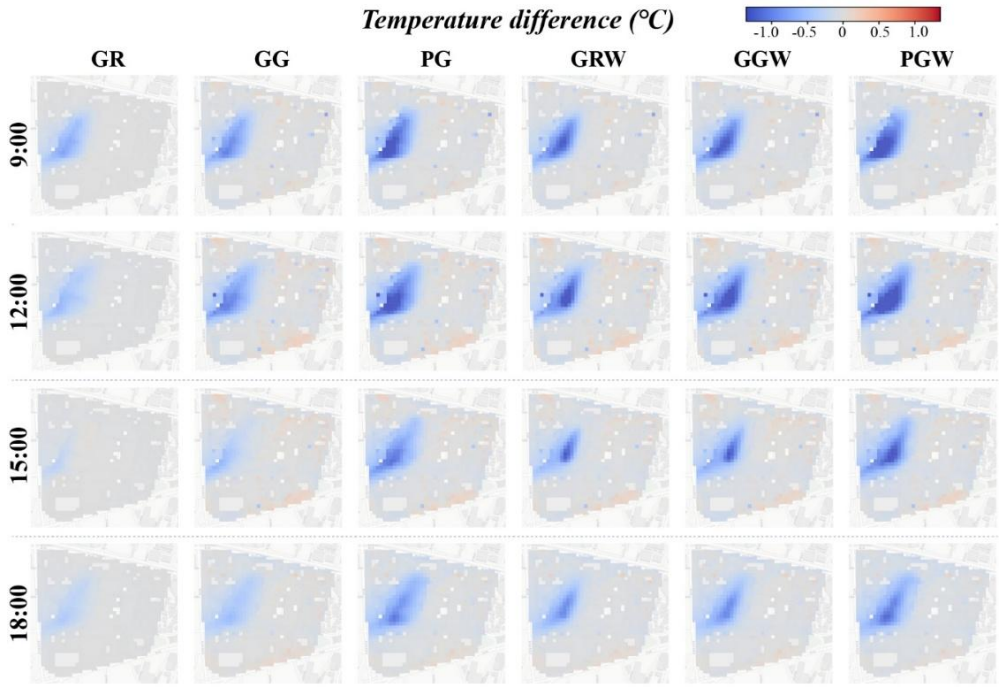

Figure 5. Visualization of cooling effect by scenario during daytime

The observed variations in cooling effectiveness among different vegetation types can be attributed to biophysical parameters. Previous research consistently demonstrates that trees outperform grass in improving the thermal environment (Koc et al., 2018). This superior cooling effect arises from two mechanisms: interception of incoming solar radiation and evaporative cooling through transpiration. The Leaf Area Index (LAI), defined as the total one-sided leaf area per unit ground area (Gao et al., 2023), has been identified as the dominant physical property influencing thermal comfort in urban vegetation (Zhang et al., 2018). In the developed tree scenarios, the plane tree has a high LAI of 5.70 compared to ginkgo's 2.70. The higher LAI values correspond to denser canopies that intercept and absorb a large proportion of incoming solar radiation. Moreover, the higher LAI values provide increased leaf surface area for transpiration, enhancing their potential for evaporative cooling of the environment.

4. CONCLUSION

This study employed ENVI-met simulations to evaluate multiple green and blue infrastructure scenarios in an urban redevelopment area. Implementing approximately 8,000m² of green space contributed to significant improvements in daytime thermal conditions. Among the vegetation configurations analyzed, the plane tree with grass presented superior cooling performance. Furthermore, the integration of a water patch into the vegetation enhanced the cooling effects, suggesting that blue-green infrastructure solutions may be more effective than vegetation-alone strategies during extreme heat events.

This study provides valuable insights into urban climate research and planning. First, it provides a framework to evaluate thermal environment for planned green spaces rather than existing vegetation. Second, the comparative analysis can help policymakers or decision makers to assess various vegetation types and water body configurations based on cooling effectiveness. Specifically, planners can use the results to decide whether to incorporate water bodies into green infrastructure, considering several factors, such as resource availability, budget, and desired uses of the space. As a result, this evidence-based approach is expected to support more strategic, targeted, and cost-effective urban design solutions to mitigate extreme heat.

However, some limitations of the study should be noted. For example, a limited number of tree species were analyzed, even though cooling efficacy varies with tree characteristics, such as crown architecture, stem morphology, and phenology (Li et al., 2024). Future research could benefit from incorporating a broader range of species and conducting more comprehensive parametric analysis. Additionally, integrating advanced methodological approaches, such as the combined CFD-machine learning framework could enhance the robust parametric investigations (Ahn et al., 2024). Finally, incorporating field measurements and advanced remote sensing data from UAVs and drones could provide more robust validation of cooling mechanisms associated with trees and water features.

ACKNOWLEDGEMENTS

This work was supported by the National Research Foundation of Korea (NRF) grant funded by the Korea government (MSIT; Ministry of Science and ICT) (NRF-2021R1A3B1076769).

REFERENCES

Ahn, J., Kim, J., & Kang, J. (2024). Development of an artificial intelligence model for CFD data augmentation and improvement of thermal environment in urban areas using nature-based solutions. *Urban Forestry & Urban Greening*, 128629.

Bae, W. K., & Kan, J. H. (2022). Analysis of CFD Simulation of Green Areas and Pilotis in Apartment Complexes during Heat Wave. *Journal of the Architectural Institute of Korea*. https://doi.org/10.5659/JAIK.2022.38.1.153

Bruse, M. (2004, February). ENVI-met implementation of the Jacobs A− gs Model to calculate the stomata conductance.

Budzik, G., Krajewski, P., Soszyńska, A., Lebiedzińska, M., & Kowalczyk, T. (2025). Factors influencing spatiotemporal cooling potential of blue–green infrastructure across diverse local climate zones—Case study of Wroclaw, Poland. *Building and Environment*, 267, 112162.

Gao, G., Qi, J., Lin, S., Hu, R., & Huang, H. (2023). Estimating plant area density of individual trees from discrete airborne laser scanning data using intensity information and path length distribution. *International Journal of Applied Earth Observation and Geoinformation*, 118, 103281.

Gao, K., Feng, J., & Santamouris, M. (2024). Are grand tree planting initiatives meeting expectations in mitigating urban overheating during heat waves?. *Sustainable Cities and Society*, 113, 105671.

Hong, J. W., Hong, J., Kwon, E. E., & Yoon, D. (2019). Temporal dynamics of urban heat island correlated with the socio-economic development over the past half-century in Seoul, Korea. *Environmental Pollution*, 254, 112934.

Hwang, M., & Kim, H. (2023). Changes in Microclimate and Thermal Comfort in Summer after Creating the New Gwanghwamun Square. *Journal of the Urban Design Institute of Korea Urban Design*. https://doi.org/10.38195/judik.2023.02.24.2.23

Kim, J., Yeom, S., & Hong, T. (2024). Analyzing the Cooling Effect, Thermal comfort, and Energy Consumption of Integrated Arrangement of High-Rise Buildings and Green Spaces on Urban Heat Island. *Sustainable Cities and Society*, 106105.

Kim, S. W., Park, J., Kim, T., & Chae, Y. (2021). Identification of heatwave hotspots in Seoul using high-resolution population mobility data. *Urban Climate*. https://doi.org/10.1016/j.uclim.2021.100771

Koc, C. B., Osmond, P., & Peters, A. (2018). Evaluating the cooling effects of green infrastructure: A systematic review of methods, indicators and data sources. *Solar Energy*, 166, 486-508.

Korea Meteorological Administration. (2023). *2023 Abnormal Climate Report (in Korean)*.

Li, H., Zhao, Y., Wang, C., Ürge-Vorsatz, D., Carmeliet, J., & Bardhan, R. (2024). Cooling efficacy of trees across cities is determined by background climate, urban morphology, and tree trait. *Communications Earth & Environment*, 5(1), 1-14.

Liu, Z., Cheng, W., Jim, C. Y., Morakinyo, T. E., Shi, Y., & Ng, E. (2021). Heat mitigation benefits of urban green and blue infrastructures: A systematic review of modeling techniques, validation and scenario simulation in ENVI-met V4. *Building and Environment*, 200, 107939.

Luo, F., Yang, Y., Zong, L., & Bi, X. (2023). The interactions between urban heat island and heat waves amplify urban warming in Guangzhou, China: Roles of urban ventilation and local climate zones. *Frontiers in Environmental Science*, 11, 1084473.

Mitra, S., Mondal, M., Biswas, M., Datta, S., & Roy, A. K. (2024). Managing urban heat islands in Rajarhat-Newtown, India, with the help of greenery and waterscapes. *Sustainable Cities and Society*, 106033.

Oke, T. R. (1982). The energetic basis of the urban heat island. *Quarterly Journal of the Royal Meteorological Society*, 108(455), 1-24.

Park, K., Jin, H. G., & Baik, J. J. (2023). Contrasting interactions between urban heat islands and heat waves in Seoul, South Korea, and their associations with synoptic patterns. *Urban Climate*, 49, 101524.

Tan, X., Sun, X., Huang, C., Yuan, Y., & Hou, D. (2021). Comparison of cooling effect between green space and water body. *Sustainable Cities and Society*, 67, 102711.

Tsoka, S., Tsikaloudaki, A., & Theodosiou, T. (2018). Analyzing the ENVI-met microclimate model's performance and assessing cool materials and urban vegetation applications–A review. *Sustainable Cities and Society*, 43, 55-76.

Xin, J., Zhang, Y., Bai, W., & Song, Z. (2024). Response of urban heat island effects within the planetary boundary layer to heat waves and impact of horizontal advection over Shanghai. *Atmospheric Research*, 311, 107721.

Yang, J., Hu, X., Feng, H., & Marvin, S. (2021). Verifying an ENVI-met simulation of the thermal environment of Yanzhong Square Park in Shanghai. *Urban Forestry & Urban Greening*, 66, 127384.

Zhang, L., Zhan, Q., & Lan, Y. (2018). Effects of the tree distribution and species on outdoor environment conditions in a hot summer and cold winter zone: A case study in Wuhan residential quarters. *Building and Environment*, 130, 27-39.

6th International Conference on Building Energy and Environment
Eindhoven University of Technology, The Netherlands
6 - 10 July 2025

Analysis of urban greenhouse gas emissions and dispersion using computational fluid dynamics

Quinn Dyer-Hawes [1], Djordje Romanic [1], Yi Huang [1], John R. Gyakum[1], Peter Douglas[2,3], Regina Gonzalez Moguel[1], Jacob Asomaning[2], John Stix[2], Gustavo Villarruel[2], Keyvan Ranjbar[4], Leonid Nichman[4], Felix Vogel[5]

[1]*Department of Atmospheric and Oceanic Sciences, McGill University, Montréal, Canada, quinn.dyer-hawes@mail.mcgill.ca*

[2]*Department of Earth and Planetary Sciences, McGill University, Montréal, Canada*

[3]*Geotop Research Centre, McGill University, Montréal, Canada*

[4]*National Research Council Canada, Ottawa, Canada*

[5]*Climate Research Division, Environment and Climate Change Canada, Toronto, Canada*

SUMMARY
Urban wind conditions and greenhouse gas dispersion dynamics in downtown Montréal are simulated using computational fluid dynamics. The numerical models are initialized and validated using data from a large-scale measurement campaign conducted on February 21, 2024. Different numerical solvers are tested to assess their impact on the simulated dynamics. In addition, a cylindrical domain with a rotated inlet and outlet is used to reproduce the observed shift in wind direction with height. When properly initialized, the simulations show good agreement with the observed profiles of wind speed and direction. The model is also able to properly reproduce turbulent dispersion of downtown emissions of carbon dioxide and methane. The distributions and vertical profiles of these greenhouse gases are compared with in-situ measurements and satellite data, and regions with unique dispersion phenomena are investigated.

Keywords: computational fluid dynamics, urban wind flow, greenhouse gas dispersion, measurement campaign.

1. INTRODUCTION

The emission of greenhouse gases (GHGs) into the atmosphere drastically affects the Earth's climate. Emissions from the burning of fossil fuel for energy production, vehicle exhausts, and other anthropogenic sources of GHGs have contributed to an extreme warming trend globally, with the decade from 2014 to 2023 being the warmest ever recorded (NOAA National Centers for Environmental Information, 2024). As temperatures continue to rise, more disastrous effects will begin to be felt across the world (Herring et al., 2018). Additional byproducts of fossil fuel usage include particulate matter, ozone, and other forms of air pollution, which are directly harmful to human health and are attributed to 3.61 million excess deaths per year (Lelieveld et al., 2019). The majority of GHGs and pollutants are emitted in urban areas (UN-Habitat, 2024), where over half of the world's population resides (Ritchie et al. 2024). The negative impacts of these emissions are magnified in these densely populated areas, necessitating thorough study of

the interaction between complex, urban built environments and the dispersion of GHGs and air pollution. Precise knowledge of the spatial and temporal variability of GHGs is also crucial for evaluating their effects on climate. Moreover, satellites measuring atmospheric concentrations of GHGs are able to quantify emissions through source inversion techniques but require their two-dimensional distribution (Jacob et al. 2016). Measure of their distribution is complicated by the morphology of city buildings, leading to strongly local dispersion characteristics. Study of these characteristics is paramount to improving the sustainability of cities and developing strategies to mitigate climate change.

Traditionally, study of air quality in cities has been conducted using in-situ measurements as well as wind tunnel testing. More recently, computational fluid dynamics (CFD) has emerged as a promising way to simulate urban wind flow and dispersion characteristics. The method by which CFD works is to apply simplifications to the Navier-Stokes equations for fluid flow, decreasing the computational expense to solve them and allowing for the investigation of more complex phenomena. Large eddy simulations (LES) provide time dependent solutions and resolve the larger scales of turbulence, while Reynolds-averaged Navier-Stoke (RANS) simulations solve only for steady-state flow and parameterize all scales of turbulence. CFD is uniquely advantaged in its ability to provide GHG concentrations at every location within an area of study, especially important in urban environments. It also provides full control over meteorological conditions and allows for the simulation and investigation of events before they occur. Previous studies have focused primarily on near-field dispersion phenomena, especially in regard to traffic emissions (Tominaga & Stathopoulos 2013; Zhong et al. 2016). Some literature exists simulating the dispersion of GHGs in urban environments, such as Toja-Silva (2017), which investigated the dispersion phenomena from an urban power plant and analyzed the influence of turbulent Schmidt number. The study presented here uses CFD in conjunction with an extensive field measurement campaign to simulate and investigate the distribution of GHGs in the downtown region of Montréal, Canada, for the day of February 21, 2024.

2. METHODOLOGY

Incompressible and compressible steady-state RANS simulations with the standard k-ε turbulence model were carried out using the open-source CFD software OpenFOAM to investigate the urban flow and the dispersion of GHGs across the city. This study also presents the results of an extensive measurement campaign conducted in Greater Montréal, Quebec, Canada, on the day of February 21, 2024, and coordinated in part with these simulations. The campaign's goal was to provide direct measurements of the spatiotemporal variability of GHGs emitted in Montréal, in particular carbon dioxide (CO_2) and methane (CH_4), as these are frequently emitted in cities. Data was taken across the morning and afternoon, both inside the city and off the island of Montréal, allowing for analysis of the differences across the day and to single out the contribution of urban emissions. Wind conditions inside the city were measured using a Halo Photonics StreamLine XR Doppler lidar, which provides vertical profiles of wind velocity. This instrument was positioned downtown on the roof of McGill University's Burnside Hall (45.5047°N, 73.5751°W), atop which was also a Picarro GasScouter for measuring the concentrations of CO_2 and CH_4. To capture the vertical distribution of these GHGs, drone flights were used, measuring the concentrations from 0–120 m above ground level (AGL). The simulated concentrations of GHGs at these locations are then compared directly to these

downtown measurements. Outside of the city, upper air soundings were launched from McGill University's Gault Nature Reserve, 40 km east of Montréal. The Earth Observation System laboratory at the nature reserve was also capable of measuring pertinent meteorological properties as well as concentrations of CO_2. Finally, two flight campaigns were conducted by the National Research Council Canada using its Convair 580 aircraft to record atmospheric properties over Montréal and its surrounding areas. These aircraft flights flew between Ottawa International Airport and the Montréal Metropolitan Airport, passing over the city and making multiple missed approaches while measuring variables such as temperature, wind velocity, and concentration of CO_2 and CH_4.

One aspect revealed by these measurements is a significant difference in the surface level and upper level wind directions. Aircraft measurements from a missed approach at Montréal Metropolitan Airport show northeast flow near the ground and southerly flow aloft, characteristic of veering winds. The Gault radiosonde measurements again show northeast flow near the surface with a west-southwest component higher up. Downtown, the lidar recorded a southeasterly wind shifting to the southwest within the first kilometer. The slight disagreement in surface level wind direction between the measurement sources makes the appropriate selection of inlet wind conditions challenging. However, it is the shift in wind direction with height which presents an even more significant challenge in terms of simulating the actual wind conditions. Traditionally, computational domains model wind direction as a fixed constant with height across a single inlet. With the dispersion and distribution of GHGs depending greatly on the prevailing wind direction, it is vital to be able to reproduce any differences in wind direction across height. Therefore, it was necessary to design the computational domain to facilitate multiple inlet directions, accomplished using a 36-sided cylinder. The cylinder faces were then split horizontally at different heights to correspond with the vertical changes in wind direction. In each resulting vertical section, individual faces were then defined as either inlet, side, or outlet to create a domain in which these faces rotate with height to take into account the shift in wind direction with height (Fig. 1a). Both the aircraft and radiosonde measurements also reveal the presence of a strong low-level jet. As such, the classical logarithmic wind speed profile would not be a suitable boundary condition, and instead, the inlet wind speed was taken directly from the sounding and aircraft data. Both sources of wind speed and direction were tested to assess which led to the best agreement with downstream measurements. For the compressible simulations, temperature and pressure profiles measured by the radiosonde were also used for initialization.

To model GHG emissions within the city, three separate sources were used. According to McGill University's Facilities Management and Ancillary Services, the university's power plant accounts for over 90% of its downtown emissions and burned an estimated 55,900 m^3 of natural gas on February 21, 2024. Emissions rates of CO_2 and CH_4 were calculated according to the National Inventory Report 1990–2022: Greenhouse Gas Sources and Sinks in Canada Annex 6 emission factors (Environment and Climate Change Canada, 2024). Additionally, the city of Montréal releases data on annual natural gas consumption of government buildings which are over 2000 m^2, four of which are included in the domain (Ville de Montréal 2021). The final source considered was emissions resulting from downtown vehicle traffic. Rates of traffic and vehicle type were then estimated from data from the city of Montréal, with different emission factors being used for each category of vehicle. Modified versions of the solvers including

turbulent diffusion were run to simulate the dispersion of the emitted GHGs after the converged wind field was found. In these simulations, the turbulent Schmidt number was set to 0.6, as this was found to most accurately reproduce turbulent dispersion in downtown Montréal (Dyer-Hawes et al., 2024).

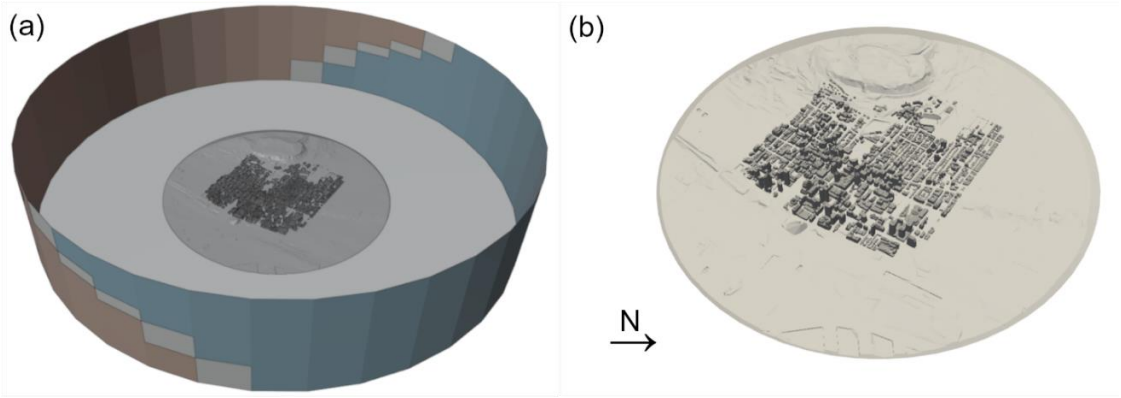

Figure 1. (a) Computational domain highlighting rotating inlet (red) and outlet (blue). (b) Enlarged view of inside of domain with explicitly modelled downtown buildings and topography.

3. RESULTS

Simulations testing the wind speed initialized with either the sounding or aircraft measurements were first conducted. It was found that the sounding wind speed provided the most accurate wind profile as compared to the lidar. These boundary conditions were therefore used for the compressible solver. The comparison between these three simulations and the lidar wind profile is shown in Fig. 2a. Moderate improvements in the prediction of wind speeds are found with the compressible solver. The sounding wind speed profile was also used to test the influence of the wind direction profile used, again comparing between the sounding and aircraft measured wind direction. Here too the sounding measurements provided the best agreement with the lidar measurements (Fig. 2a), and as such the wind speed and direction from the upper air sounding are used to initialize the compressible solver and simulations including GHG dispersion. Turbulence characteristics such as turbulence intensity are also analyzed across the models.

In analyzing the dispersion of GHGs, an initial test was run using the converged incompressible wind field and only including the transport of the background concentrations of CO_2 and CH_4 as measured by the aircraft. No emission sources inside the city were included, resulting in a CO_2 concentration of 403.3 ppm at the location of the downtown Picarro GasScouter. This instrument recorded an average CO_2 concentration of 475.0 ± 5.51 ppm at the time simulated, demonstrating a large discrepancy when emission sources are not modeled. With the downtown emission sources included in the dispersion simulation, the predicted concentration of CO_2 increases to 478.8 ppm, a close match to the observed value. This points to the urban emission sources modeled contributing significantly to local concentrations of GHGs near the GasScouter. With the compressible solver, the predicted concentration decreases to only 426.4 ppm. It is likely that the stable atmospheric conditions and temperature inversion on this day supress the upwards transport of traffic emissions in the compressible simulation. The predicted concentration distributions of CO_2 within the domain are shown in Fig. 3, which suggests that both the

compressible and incompressible solver predict similar distributions of CO_2. Close to streets, the contribution from traffic emissions is greatest. The power plant also significantly affects concentrations in the surrounding areas. Interesting gradients are also noted around the mountain of Mount Royal, suggesting even more local effects in this region. Future measurement campaigns could investigate this phenomenon to better identify the strength of these gradients. Further analysis into the distributions of GHGs can help in the placement of future GHG monitoring stations to properly assess representative concentrations.

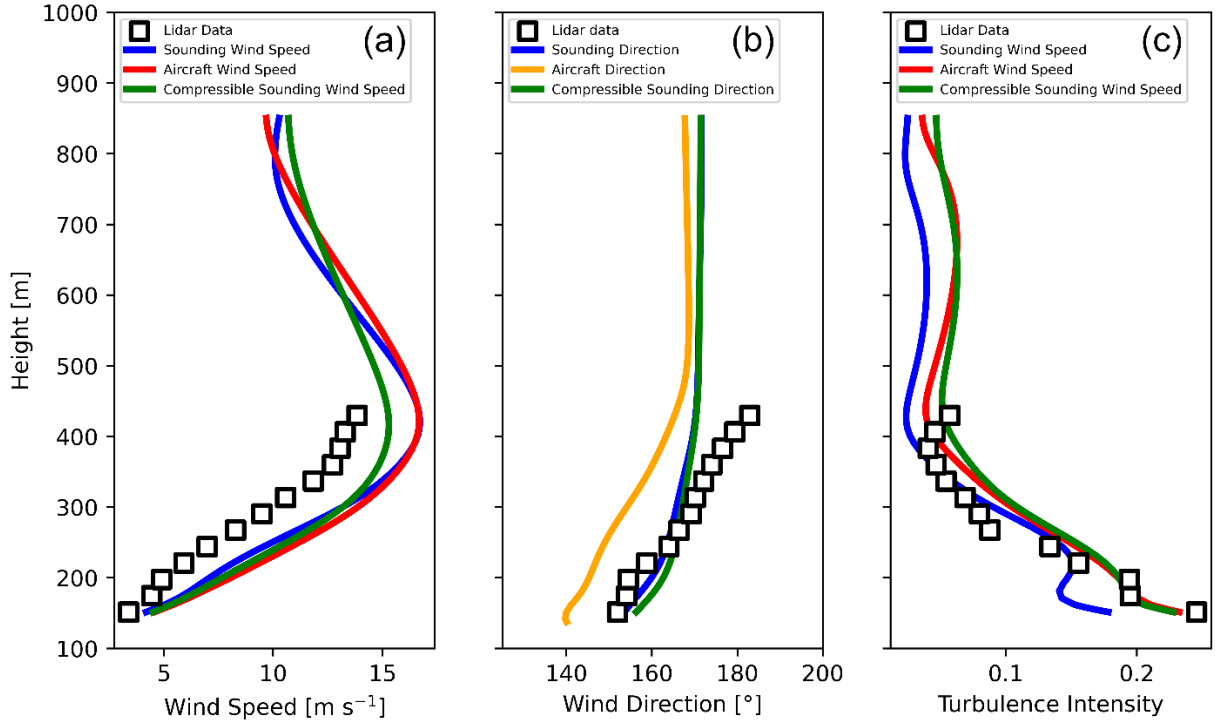

Figure 2. Predicted (a) wind speed, (b) direction, and (c) turbulence intensity by different model configurations compared with 20-min averaged lidar measured wind speed.

The simulated profiles of GHG concentrations are also compared with drone measurements up to a height of 120 m AGL (Fig. 4). While in the case of CO_2, the models properly predict a decrease in concentration with height, disagreement exists between the observed and simulated profiles. The discrepancy points to missing emission sources in the model near the location of the drone measurements. This model underestimation is even more present for CH_4 (Fig. 4b), and this is likely due to the omission of the primary sources of urban CH_4 emissions of natural gas distribution and storage and landfills (Zazzeri et al. 2015; Xueref-Remy et al. 2020). Finally, the results of the dispersion simulations are used as a comparison with satellite measurements of column-averaged CO_2 from the OCO-2 Satellite. This provides a way of validating both the CFD model and satellite measurements, as well as providing the two-dimensional distribution of GHGs needed for satellite source inversion techniques. Additional discussion of the vertical profile of CO_2 at various locations in the city and computational domain are also presented.

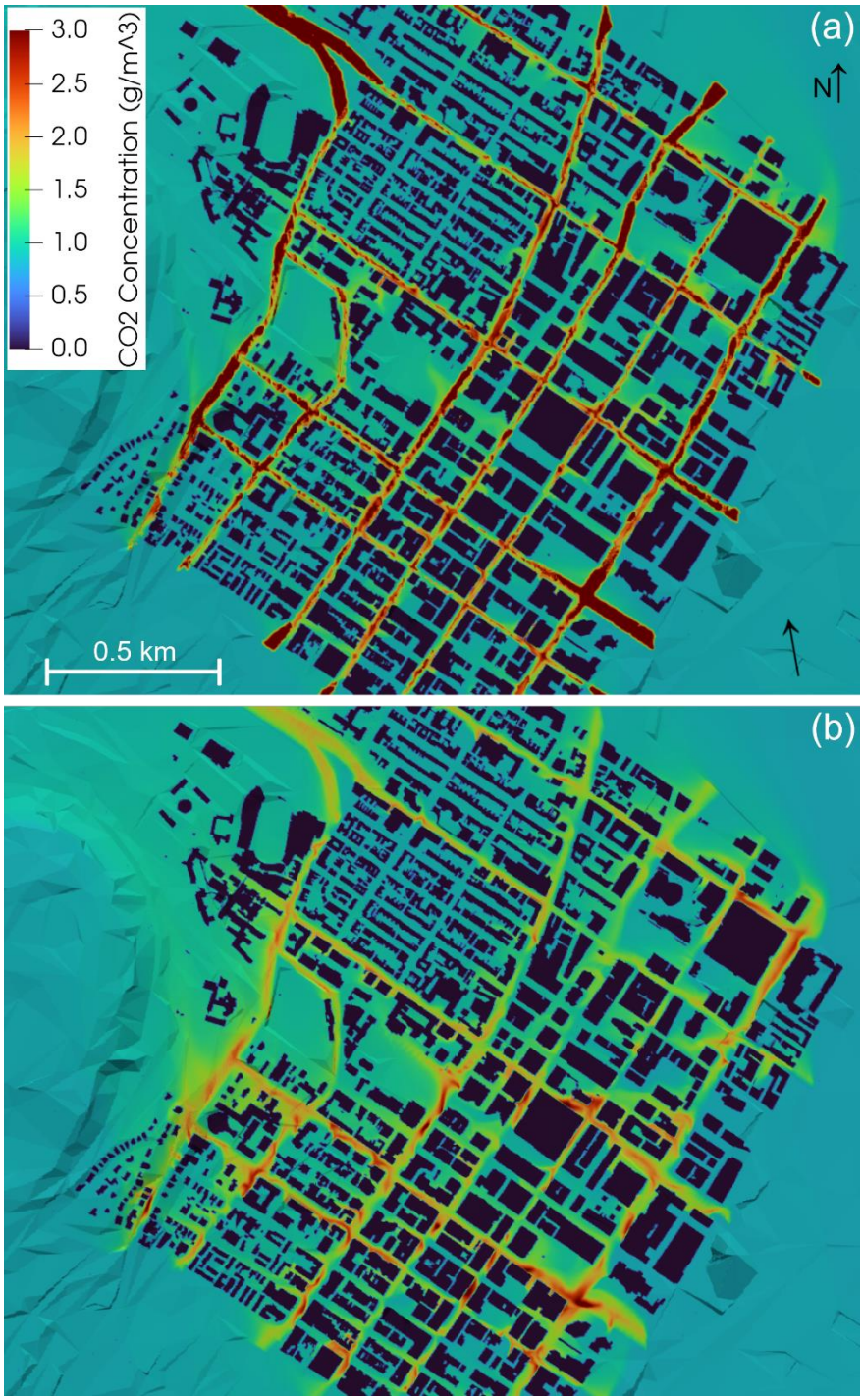

Figure 3. Concentration distribution of CO_2 predicted by (a) incompressible solver and (b) compressible solver. Black arrow in bottom right indicates mean flow direction.

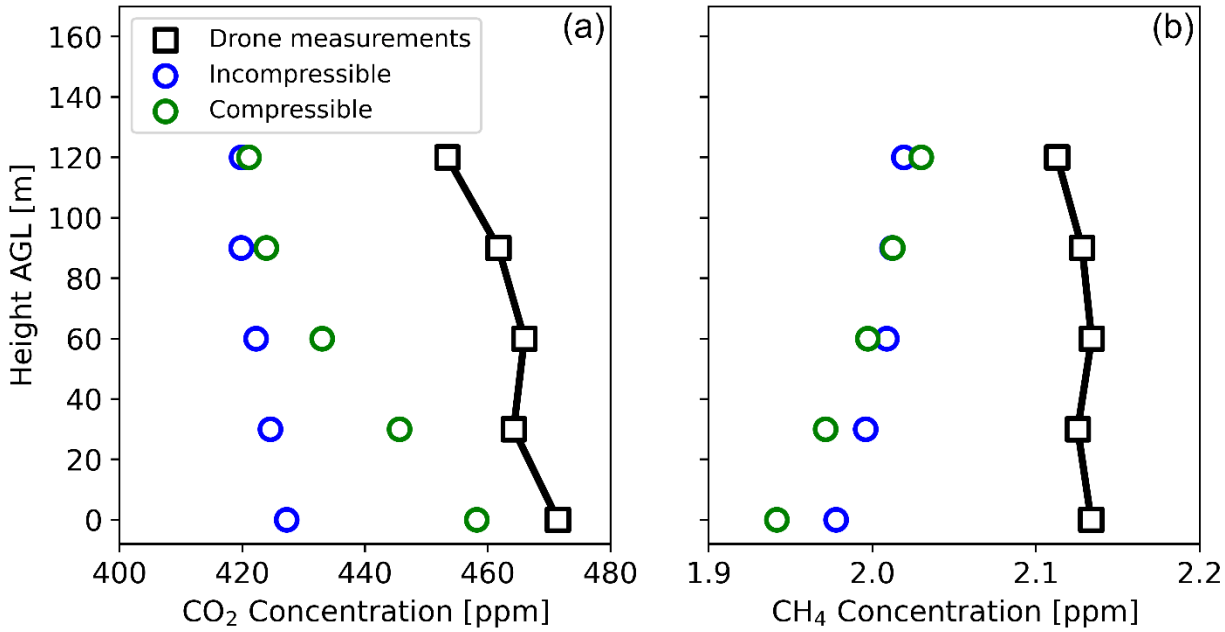

Figure 4. Comparison of model predictions and drone measurements of (a) CO_2 concentration and (b) CH_4 concentration.

4. CONCLUSIONS

This study, by combining computational fluid dynamics with a robust measurement campaign, has demonstrated the ability for numerical simulations to provide estimations of greenhouse gas (GHG) concentrations in complex urban environments such as Montréal. It also puts forward a novel way of designing computational domains to account for shifts in wind direction with height. With this adjustment, the numerical model using both compressible and incompressible Reynolds-average Navier-Stokes simulations accurately reproduced the complex wind conditions present in Montréal on the morning of February 21, 2024. The large variety of measurement campaign data sources allowed for the testing of multiple initial boundary conditions to assess their agreement with the wind velocity profile measured inside the domain by a Doppler lidar. The dispersion of carbon dioxide and methane emitted from buildings and traffic was also simulated, specifically accounting for turbulent diffusion. The resulting distributions were then analyzed investigating local dispersion characteristics in the urban environment. The predicted concentrations were validated against rooftop measurements in the center of downtown, drone measurements, and satellite data. With more emission sources included, future work could investigate the effect of different atmospheric stability conditions, as well as transient dispersion dynamics with large eddy simulations. Additionally, some areas with potential air quality issues were identified using the models. Due to health concerns around exposure to vehicle emissions and their relative importance in urban GHG concentrations, future studies could look to perform more detailed simulations of traffic dispersion dynamics in this downtown region.

ACKNOWLEDGEMENTS

This work was supported by the Government of Canada (Environment and Climate Change Canada Grant: EDF-CA-2021i022).

REFERENCES

Dyer-Hawes, Q., Romanic, D., Huang, Y., Gyakum, J. R., Douglas, P., 2024: Analysis of urban wind conditions and wildfire smoke dispersion for downtown Montréal using computational fluid dynamics. Building and Environment 266, 112103. https://doi.org/10.1016/j.buildenv.2024.112103.

Environment and Climate Change Canada, 2024: National Inventory Report 1990–2022: Greenhouse Gas Sources and Sinks in Canada. https://publications.gc.ca/site/eng/9.506002/publication.html.

Herring, S. C., Christidis, N., Hoell, A., Kossin, J. P., Schreck III, C. J., Stott, P. A., 2018. Explaining extreme events of 2016 from a climate perspective. Bulletin of the American Meteorological Society 99, S1-S157. https://doi.org/10.1175/BAMS-ExplainingExtremeEvents2016.1.

Jacob, D. J., Turner, A. J., Maasakkers, J. D., Sheng, J., Sun, K., Liu, X., Chance, K., Aben, I., McKeever, J., Frankenberg, C., 2016. Satellite observations of atmospheric methane and their value for quantifying methane emissions. Atmospheric Chemistry and Physics 16, 14371-14396. https://doi.org/10.5194/acp-16-14371-2016.

Lelieveld, J., Klingmüller, K., Pozzer, A., Burnett, R. T., Haines, A., Ramanathan, V., 2019. Effects of fossil fuel and total anthropogenic emission removal on public health and climate. Proceedings of the National Academy of Sciences of the United States of America 116, 7192-7197. https://doi.org/10.1073/pnas.1819989116.

NOAA National Centers for Environmental Information, 2024. Monthly Global Climate Report for Annual 2023. https://www.ncei.noaa.gov/access/monitoring/monthly-report/global/202313.

Ritchie, H., Samborska, V., Roser, M., 2024. Urbanization. https://ourworldindata.org/urbanization.

Toja-Silva, F., Chen, J., Hachinger, S., Hase, F., 2017. CFD simulation of CO_2 dispersion from urban thermal power plant: Analysis of turbulent Schmidt number and comparison with Gaussian plume model and measurements. Journal of Wind Engineering and Industrial Aerodynamics 169, 177-193. https://doi.org/10.1016/j.jweia.2017.07.015.

Tominaga, Y., Stathopoulos, T., 2013. CFD simulation of near-field pollutant dispersion in the urban environment: A review of current modeling techniques. Atmospheric Environment 79, 716-730. https://doi.org/10.1016/j.atmosenv.2013.07.028.

UN-Habitat, 2024. Annual Report 2023. https://unhabitat.org/sites/default/files/2024/05/annual_report_2023.pdf.

Ville de Montréal, 2021. Consommation d'énergie et émissions de gaz à effet de serre des bâtiments municipaux de 2000 m² et plus. Bureau de la transition écologique et de la résilience. https://donnees.montreal.ca/dataset/consommation-emissions-batiments-municipaux.

Xueref-Remy, I., Zazzeri, G., Bréon, F. M., Vogel, F., Ciais, P., Lowry, D., Nisbet, E. G., 2020: Anthropogenic methane plume detection from point sources in the Paris megacity area and characterization of their δ13C signature. Atmospheric Environment 222, 117055. https://doi.org/10.1016/j.atmosenv.2019.117055.

Zazzeri, G., Lowry, D., Fisher, E., France, J. L., Lanoisellé, M., Nisbet, E. G., 2015: Plume mapping and isotopic characterisation of anthropogenic methane sources. Atmospheric Environment 110, 151-162. https://doi.org/10.1016/j.atmosenv.2015.03.029

Zhong, J., Cai, X.-M., Bloss, W. J., 2016. Coupling dynamics and chemistry in the air pollution modelling of street canyons: A review. Environmental Pollution 214, 690-704. https://doi.org/10.1016/j.envpol.2016.04.052.

Advanced Modeling and Building Simulations (15:30-17:00 h)

6th International Conference on Building Energy and Environment
Eindhoven University of Technology, The Netherlands
6 - 10 July 2025

The impact of urban morphology on vehicular emissions: an assessment of urban air pollution dynamics in Italian cities

Chiara Metrangolo [1], Adelaide Dinoi [2], Antonio Esposito [1], Gianluca Pappaccogli [1], Antonio Donateo [2], Prashant Kumar [3], Jose Luis Santiago [4], Riccardo Buccolieri [1,2]

[1]University of Salento, Dipartimento di Scienze e Tecnologie Biologiche ed Ambientali, Laboratory of Micrometeorology, S.P.6 Lecce-Monteroni, 73100 Lecce, Italy, chiara.metrangolo@unisalento.it, antonio.esposito@unisalento.it, gianluca.pappaccogli@unisalento.it, riccardo.buccolieri@unisalento.it
[2]National Research Council of Italy, Institute of Atmospheric Sciences and Climate (CNR-ISAC), S.P.6 Lecce-Monteroni, 73100, Lecce, Italy, adelaide.dinoi@cnr.it, antonio.donateo@cnr.it
[3]Global Centre for Clean Air Research (GCARE), School of Sustainability, Civil and Environmental Engineering, Faculty of Engineering and Physical Sciences, University of Surrey, Guildford GU2 7XH, United Kingdom, p.kumar@surrey.ac.uk
[4]Atmospheric Modelling Unit, Environmental Department, CIEMAT, Madrid, Spain, jl.santiago@ciemat.es

SUMMARY
Urban air pollution, primarily caused by vehicular emissions, poses significant public health risks in densely populated cities. This research study investigates the relationship between urban morphology and vehicular pollutant dispersion in four Italian cities: Lecce, Bari, Milan, and Rome. Employing the high-resolution ADMS-Roads dispersion model integrated with urban morphological data, the study analyses pollutant concentrations of NO_2 and PM_{10} across different urban layouts. The results demonstrate how urban configurations influence pollutant dispersion, with compact urban forms exacerbating pollutant accumulation. Findings emphasise the urgent need for sustainable mobility policies and urban planning that mitigate pollution in high-density environments.

Keywords: urban air pollution, urban morphology, AMD-Roads, NO_2 and PM_{10} dispersion patterns.

1. INTRODUCTION

Urban air pollution poses a significant health risk in European cities, where citizens remain exposed to concentrations exceeding the WHO recommendations (Pascal et al., 2013). The spatial structure of urban areas, known as urban morphology, plays a crucial role in shaping pollutant dispersion. In particular, street canyons can act as traps for pollutants, leading to concentrations that exceed ambient levels due to restricted natural airflow (Vardoulakis et al., 2003).

While there has been extensive research on the relationship between urban morphology and pollutant dispersion in Northern European and Asian cities, there is a notable scarcity of studies focusing on Mediterranean urban areas. This gap is significant, as Southern European cities typically feature dense urban forms and experience warmer, drier climates. Combined with seasonal meteorological variability, these factors can uniquely influence pollution dispersion, making the Mediterranean region particularly vulnerable to air pollution (Lelieveld et al., 2002). Addressing this gap is essential, given the escalating concerns about air pollution in Mediterranean cities. It is vital to understand how urban morphology influences pollutant dispersion in these regions so that effective urban planning and environmental health policies can be developed,

considering their specific climatic and structural characteristics.

The present study aims to bridge this knowledge gap by providing a comprehensive analysis of pollutant dispersion using the dispersion model ADMS-Roads (www.cerc.co.uk), across varied urban forms in four Italian cities: Lecce, Bari, Milan, and Rome. A preliminary analysis was presented in Metrangolo et al. (2024). A key objective of this research is to integrate high-resolution dispersion modelling with urban morphological data to develop vehicular pollutant dispersion scenarios - focusing on NO_2 and PM_{10} - that can serve as a foundation for policymakers and urban planners in designing air pollution mitigation strategies for high-density urban environments.

2. METHODOLOGY

2.1. Study areas

The present study focuses on four Italian cities selected for their geographical and morphological diversity: Lecce, Bari, Milan, and Rome. Lecce has a compact historic centre with radial urban growth, while Bari, a coastal city, features both orthogonal grids and irregular layouts. Milan represents a densely populated metropolitan area with a radial and compact configuration, whereas Rome, characterized by a fragmented radial layout, includes extensive green spaces. Fig. 1 shows the geographical locations of the four cities, while Fig. 2 shows the study area configurations in each city.

Fig. 1 Aerial view of Italy with the locations of the four cities investigated in this work.

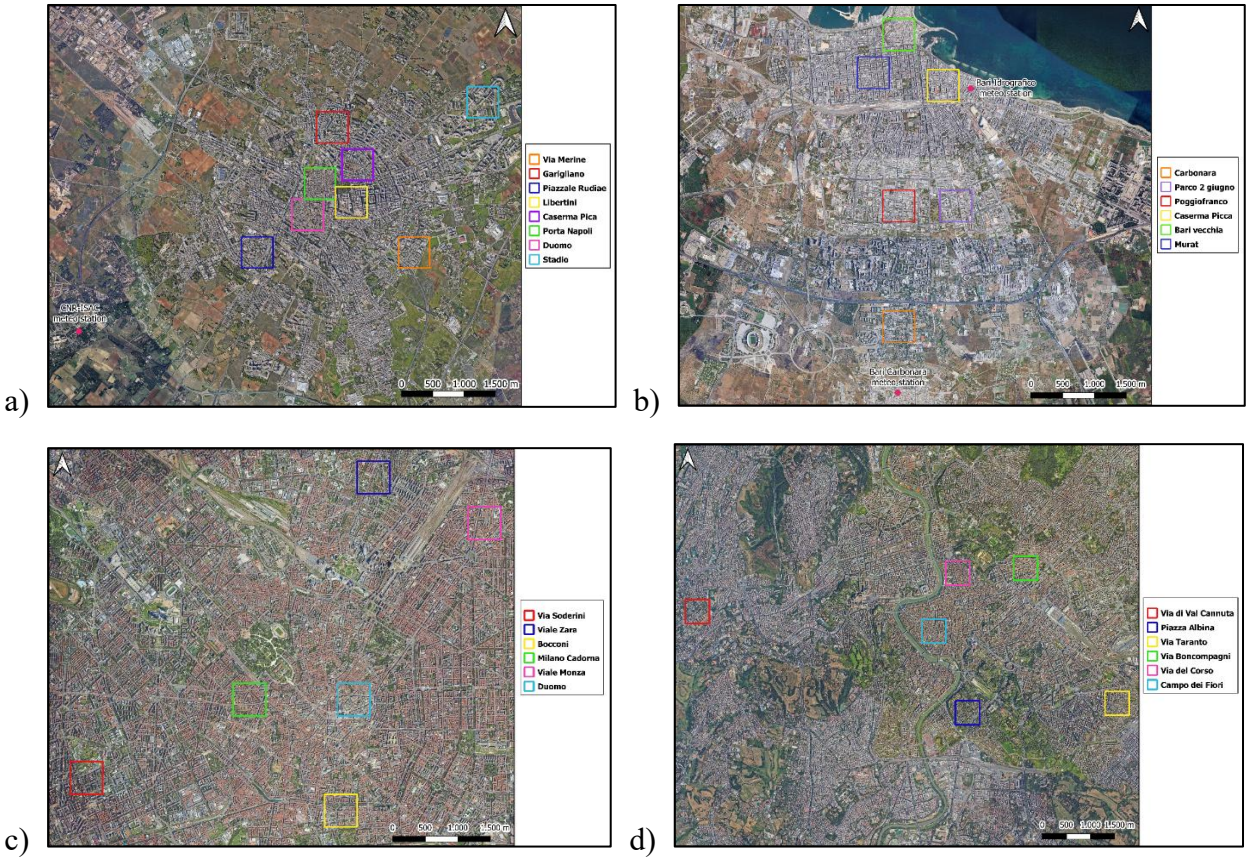

Fig. 2 Aerial view of a) the eight study areas in Lecce (the red point indicates the position of meteorological stations), b) the six study areas in Bari (including the positions of meteorological stations), c) the six study areas in Milan, and d) the six study areas in Rome.

2.2. Selection and characterization of the study areas using QGIS

The selection process of the study areas emphasised quantifiable morphological parameters, including the building plan area fraction (λ_p), the aspect ratio of street canyons (AR) and the mean building height (H). These parameters were computed in QGIS using a 0.1 × 0.1 km grid. Mean morphological values were used to compare urban areas within a consistent range of λ_p values. Four distinct morphological categories were considered: sparse canopy (low λ_p), intermediate canopy ($\lambda_p \approx 0.25$), compact canopy ($\lambda_p \approx 0.40$) and very compact canopy (high λ_p) (Buccolieri et al., 2010).

Initially, eight study sites were examined in Lecce, but this number was reduced to six in Bari, Milan, and Rome for validation purposes. The QGIS plugin "UMEP" was then used to calculate roughness length (z_0) for each grid cell, following the method outlined by Macdonald et al. (1998). The roughness values were integrated into ADMS-Roads to account for the effects of complex terrain.

2.3. Processing of meteorological parameters

Hourly meteorological data - including wind speed, wind direction, air temperature, relative humidity, precipitation and solar radiation - were collected for the period 2019 - 2021. As no

meteorological stations were located directly within the study areas, data from a single station were applied to all sites within each city. The collected data were processed in MATLAB to generate meteorological inputs for ADMS-Roads, which was used to simulate various emission scenarios. Four typical seasons were defined, each representing a three-month period within the 2019 - 2021 timeframe: autumn (September - November), winter (December - February), spring (March - May), and summer (June - August). Hourly averages were calculated for wind speed, air temperature, relative humidity, and solar radiation, while wind direction was determined based on prevailing patterns. These processed data were then used to generate four hourly meteorological files, which were entered into ADMS-Roads. The software's internal meteorological pre-processor further refined these inputs to enhance the characterization of local meteorology and atmospheric turbulence - both critical for accurately simulating pollutant dispersion.

In ADMS-Roads, the vertical wind profile is computed based on a flat-terrain assumption, using the Monin-Obukhov similarity theory within a spatially homogeneous boundary layer. The model allows for specification of different z_0 for the meteorological input site and for each modelled urban area. These z_0 values influence the wind and turbulence profiles, which are adjusted accordingly by the model. Although no complex terrain or building-resolved flow was simulated the change in surface roughness between the meteorological site and the urban modelling areas is accounted for internally by ADMS-Roads to better represent urban wind conditions. This allows for a realistic approximation of how urban morphology affects the local wind profile and, consequently, the dispersion of pollutants.

The mean wind speed, its standard deviation and the prevailing wind direction for the summer season in each city are summarised in Table 1 and graphically shown in Fig. 3.

Table 1. Average wind speed, σ wind speed and mode of wind direction for Lecce, Bari, Milan and Rome, for the "summer season".

City	Average wind speed (m/s)	σ wind speed	Mode of the wind direction
Lecce	2.0	1.1	350
Bari	3.5	1.2	321
Milan	1.3	0.6	121
Rome	2.3	1.3	174

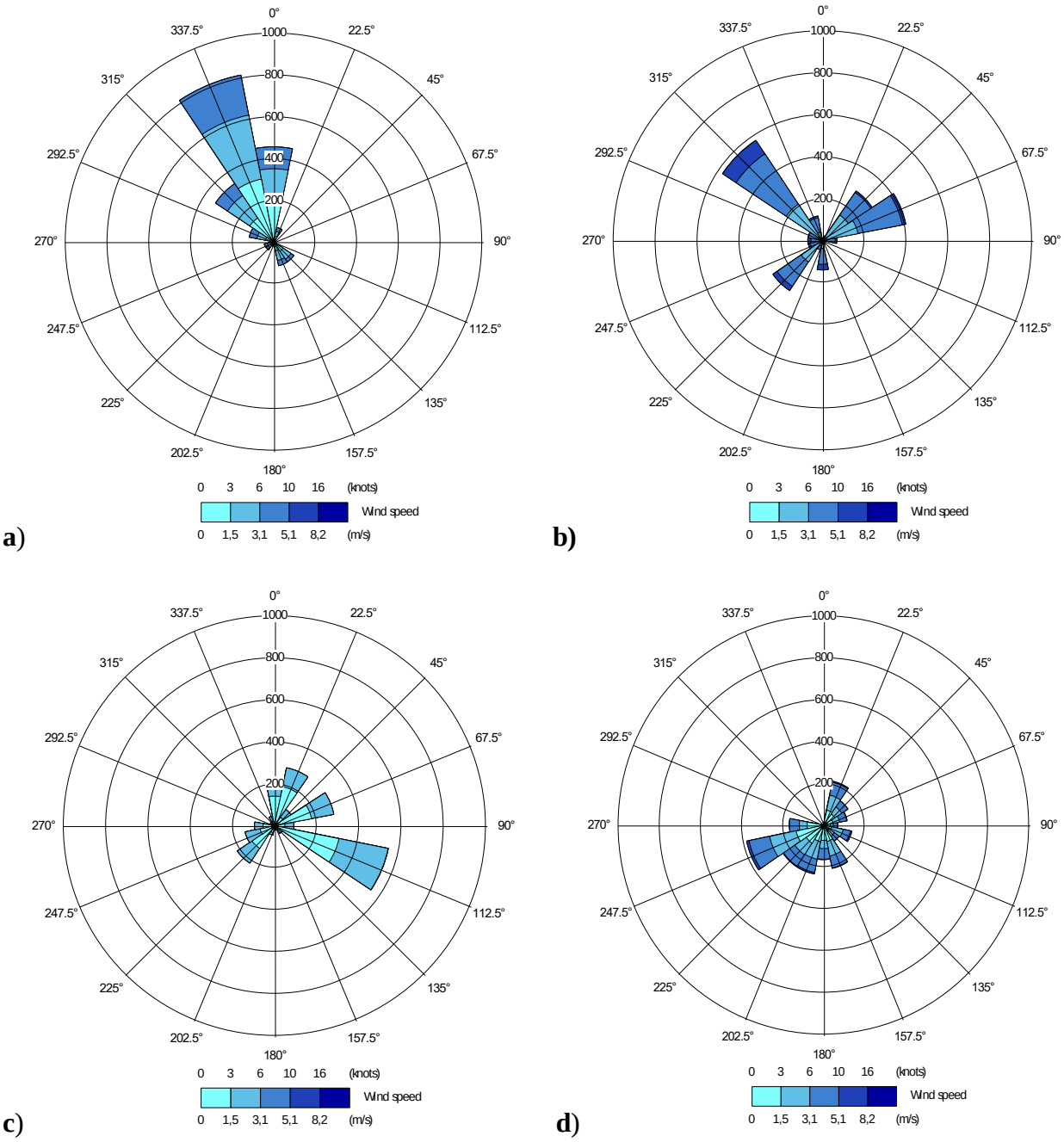

Fig. 3 Wind roses for the "summer season" for the cities of a) Lecce, b) Bari, c) Milan and d) Rome.

2.4. Road geometries and emission modelling

In ADMS-Roads, road geometries were digitised using QGIS, with key parameters such as road width, length and average road canyon height calculated and assigned to each modelled road segment. These parameters ensured an accurate representation of the road network, forming the basis for pollutant dispersion modelling. Additionally, numerical values were assigned to each road source, specifying vehicle types (light duty vehicles), vehicle counts, and average hourly speeds. A standardized capacity of 23,250 light vehicles per study area was assumed, travelling at an average speed of 30 km/h. These values, derived from an estimated daily average of 8,000

vehicles per road based on typical traffic patterns, were applied consistently across all study areas. Vehicle distribution among roads within each area was informed by traffic data from Google Traffic, with adjustments made for variations in traffic volumes across different times of the day and week. The "3DayDiurnal scheme," provided by ADMS-Roads, was used to capture the temporal dynamics of traffic emissions, reflecting increased emissions during weekdays and standard working hours. This methodological approach ensured a more nuanced representation of transport emissions in the model.

The internal ADMS-Roads dataset, designated 'UK EFT v9.0 (2VC)', was used to estimate road transport emissions, with 2022 set as the emission year and 'England (urban)' as the road type. The 2022 emission dataset was chosen to incorporate the most recent emission factors available in the software, aligning with the study's primary focus on the role of urban morphology in pollutant dispersion rather than on precise pollutant concentrations for specific years. The modelling accounted for road canyons and traffic-induced turbulence. The road canyon module, based on the Danish Operational Street Pollution Model (OSPM, Hertel and Berkowicz, 1990), provided an advanced framework for representing complex urban road geometries and their influence on pollutant dispersion. The consistent use of the 'UK EFT v9.0 (2VC)' dataset and the 'England (urban)' road type across all study areas facilitated robust comparisons of how urban morphology affects pollutant dispersion patterns.

The model outputs included pollutant concentrations for two primary vehicle emissions: the hourly average concentration of NO_2 ($\mu g/m^3$) and the daily average concentration of PM_{10} ($\mu g/m^3$). To capture detailed variations in pollutant distribution, each study area was divided into a 31x31 "source-oriented" grid. Additional grid points were strategically placed near road sources to enhance the representation of concentration profiles, ensuring a comprehensive analysis of both spatial and temporal variations in pollutant levels.

3. RESULTS & DISCUSSION

Although street aspect ratio and orientation are known to influence local-scale pollutant dispersion, in this study our aim is to explore broader correlations between overall urban morphology, expressed through the planar building density (λ_p) and simulated pollutant concentrations. The effect of individual street canyons is still accounted for in ADMS-Roads through the explicit input of canyon height and width for each road source, while the dispersion outside canyon zones is parameterized using the area's z_0. Therefore, the aspect ratio is indirectly considered within the modelling framework, even if not directly discussed in the results. Table 2 and Fig. 4 present the ground-level NO_2 and PM_{10} concentrations calculated during the summer months in the study areas of Lecce, Bari, Milan and Rome. Since emissions were homogenized across all study areas to allow for consistent comparison (see subsection 2.4), the results reveal clear distinctions influenced by variations in urban morphology (λ_p) and meteorological conditions.

Pollutants levels vary significantly between cities. Lecce exhibits moderate NO_2 and PM_{10} concentrations, with a decline at high λ_p values. This phenomenon is likely due to a combination of favourable meteorological conditions and specific urban configurations that promote enhanced dispersion of pollutants. Bari, benefiting from the highest average wind speeds among the four cities, shows a clear relationship between urban compactness and pollutant levels. The "Carbonara" area, with a greater proportion of open spaces, displays significantly lower concentrations, whereas the denser "Murat" area experiences higher levels due to pollutant

trapping. Milan records the highest NO_2 and PM_{10} concentrations, particularly in areas with low and intermediate λ_p values, likely due to its dense urban fabric and stagnant atmospheric conditions. In contrast, Rome exhibits a more consistent trend, with slightly lower concentrations in less compact areas, aligning with the presence of extensive open green spaces that facilitate pollutant dispersion.

Table 2. Average NO_2 and PM_{10} concentrations per study area for the city of Lecce, Bari, Milan and Rome, for the summer season, sorted by increasing λ_p value.

Lecce			
Study area	λ_p	NO_2	PM_{10}
Stadio	11.9	20.6	5.3
Via Merine	18.9	22.1	8.7
Garigliano	25.3	22.8	8.2
Piazzale Rudiae	27.1	23.7	9.1
Libertini	39.8	25.7	9.4
Caserma Pica	44.6	26.7	10.0
Porta Napoli	59.2	14.6	5.8
Duomo	60.9	19.1	7.2
Bari			
Study area	λ_p	NO_2	PM_{10}
Carbonara	17.9	14.8	6.1
Parco 2 Giugno	25.6	18.6	6.6
Poggiofranco	32.6	12.9	5.0
Caserma Picca	48.8	11.1	4.3
Bari vecchia	49.8	6.5	2.5
Murat	58.5	22.0	8.1
Milan			
Study area	λ_p	NO_2	PM_{10}
Via Soderini	16.4	34.6	12.7
Viale Zara	23.3	21.1	7.9
Bocconi	35.4	29.6	11.0
Milano Cadorna	46.0	25.2	9.5
Viale Monza	51.9	26.4	9.9
Duomo	59.5	18.4	6.9
Rome			
Study area	λ_p	NO_2	PM_{10}
Via di Val Cannuta	14.6	21.1	8.1
Piazza Albina	25	13.2	5
Via Taranto	35.4	14.6	5.3
Via Boncompagni	43.8	18.5	6.6
Via del Corso	57.9	18.7	6.9
Campo dei Fiori	65	12.2	4.5

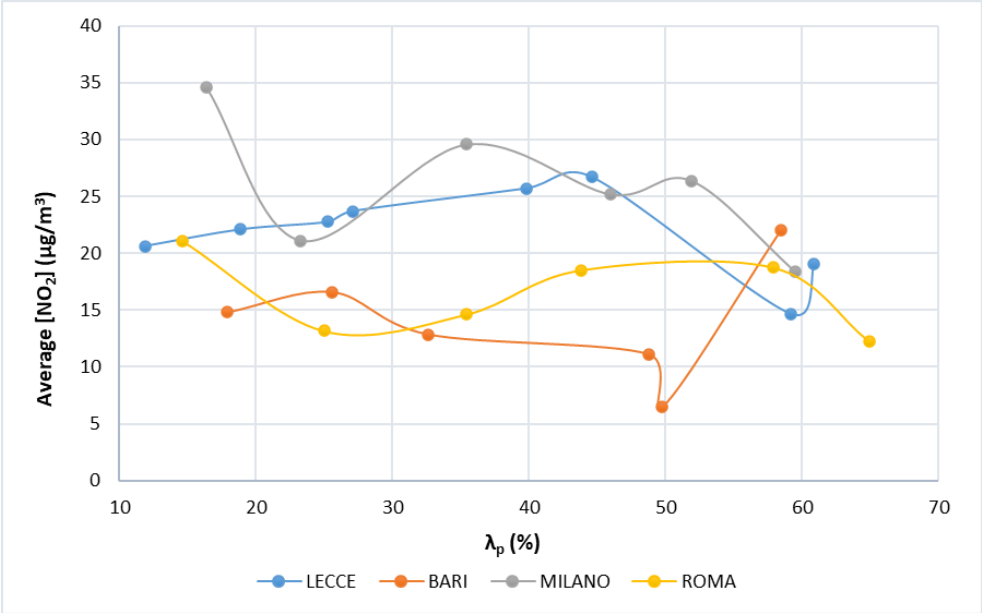

Fig. 4 Graph of the trend in hourly NO_2 concentrations for the "summer season" (averaged over the three years of simulation) for the cities of Lecce Bari, Milan and Rome vs. the spatially averaged λ_p of each study area.

As shown in Fig. 5, contour plots of the average NO_2 concentrations during the summer season are provided for the "Garigliano" area in Lecce, the "Parco 2 Giugno" area in Bari, the "Viale Zara" area in Milan and the "Piazza Albina" area in Rome. These plots generated using ADMS-Roads and refined in QGIS, focus on areas with intermediate λ_p values (around 25%), allowing for a meaningful comparison. As mentioned in subsections 2.3 and 2.4, ADMS-Roads model does not explicitly represent buildings in the domain; instead, it uses a parameterization approach based on z_0 to characterize the influence of urban morphology on dispersion. Consequently, pollutant concentration maps refer to concentrations calculated at ground-level and do not account for building volumes or rooftop height. The presence of pollutant values in correspondence with rooftops does not indicate actual rooftop exposure but reflects the ground-level concentrations projected over the entire map area. For street canyons, the model applies a specific parameterization to capture canyon effects within user-defined canyon zones, while outside these zones, dispersion is modelled based on open terrain characteristics. The plots indicate that pollutant dispersion is strongly influenced by wind direction, with NO_2 spreading predominantly in the direction opposite to the prevailing wind. In Lecce and Bari, this results in a broader dispersion area south of the road source, whereas in Milan and Rome, the dispersion extends further to the north or northwest. Additionally, the contour plots in Fig. 5 highlight that the highest NO_2 concentrations - also applicable to PM_{10} - are primarily found at road intersections, where vehicular flows from multiple directions converge. High concentrations are also observed along roads with heavy traffic volumes and in areas with pronounced street canyons, which further restrict pollutant dispersion.

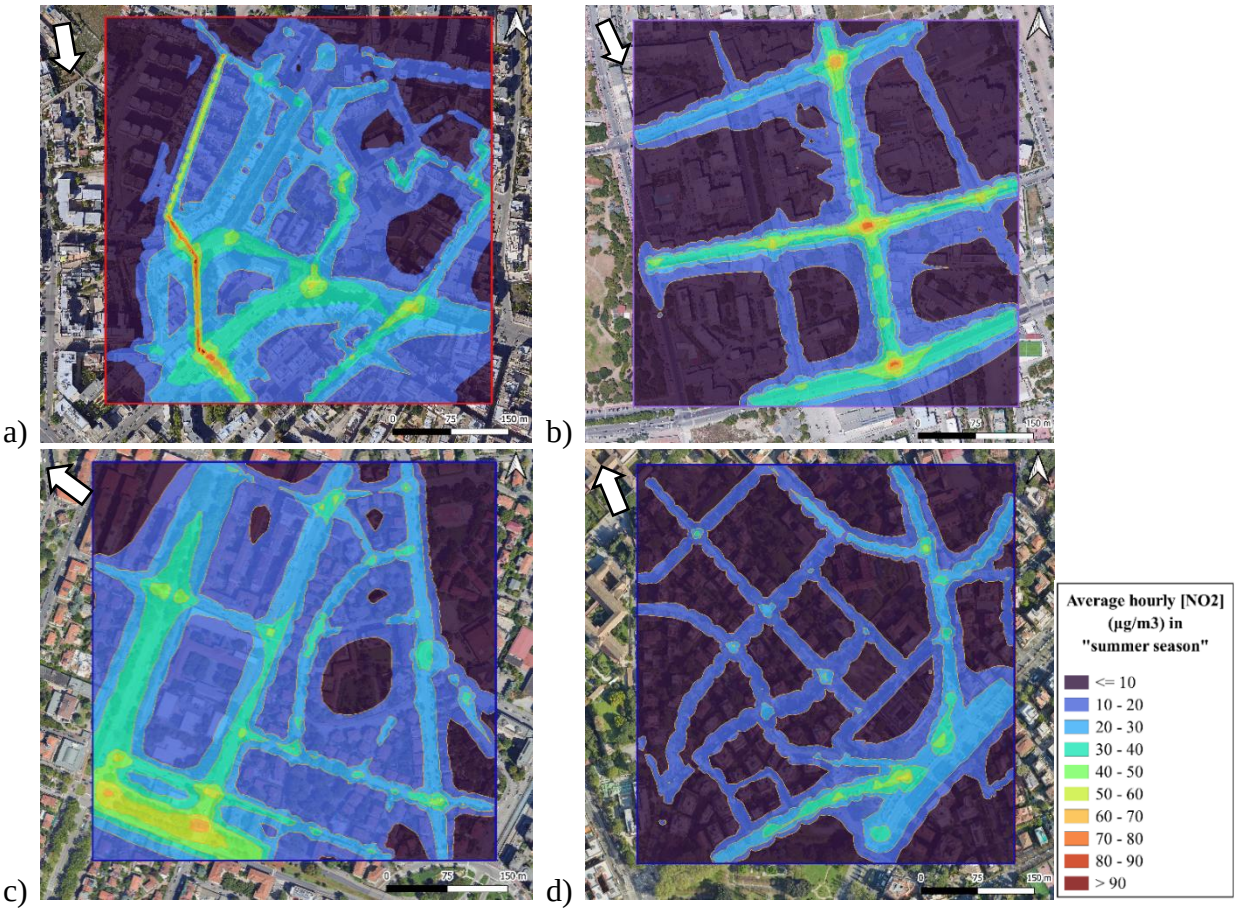

Fig. 5 Contour plot of the 3-year mean values of NO_2 concentration in "summer season" for (a) the "Garigliano" area in Lecce, (b) the "Parco 2 Giugno" area in Bari, (c) the "Viale Zara" area in Milan and (d) the "Piazza Albina" area in Rome. The white arrow on the left serves as an indicator of the wind direction mode.

4. CONCLUSIONS

This study provides quantitative evidence on how urban form influences the dispersion of traffic-related pollutants across four Italian cities with varying morphological and meteorological characteristics. We find that more compact areas (λ_p > 40%) are generally associated with higher pollutant concentrations. However, our results also show that high density does not universally correspond to poor air quality. In Lecce and Rome, some of the most compact areas exhibit lower concentrations than expected, likely due to favourable wind exposure or more ventilated street canyons. In Bari, the contrast is more pronounced: zones with λ_p > 50% show up to 70% higher NO_2 levels than surrounding areas, highlighting how local morphology can amplify pollutant accumulation. These insights demonstrate that morphology alone is not a sufficient predictor; rather, its interaction with local meteorology and emission sources determines the spatial distribution of air pollution. Future developments will focus on integrating more accurate emissions inventories and on validating model predictions with in-situ sensor data. This will strengthen the application of this method in supporting evidence-based urban and environmental policies.. Future research will focus on refining model inputs with more detailed data and integrating sensor measurements to improve accuracy, thus enabling a deeper understanding of urban air pollution dynamics and supporting targeted interventions within the PNRR National Centre for Sustainable Mobility (CN MOST) project. The objective is to develop possible future

pollutant dispersion scenarios, thereby furnishing policy makers and urban planners with useful information to implement effective pollution mitigation strategies. The research will be expanded to other urban areas and incorporate real-time data.

ACKNOWLEDGEMENTS

The ADMS-Roads software was kindly made available by CERC - Cambridge Environmental Research Consultants. The work has been funded by the European Union – Next Generation EU (however, the views and opinions expressed are solely those of the authors and do not necessarily reflect those of the European Union or the European Commission. Neither the European Union nor the European Commission can be held responsible for them) – PNRR - MISSIONE 4 - COMPONENTE 2 - INVESTIMENTO 1.4 - Project Sustainable Mobility Centre (Centro Nazionale per la Mobilità Sostenibile – CNMS) Spoke 7 - Code CN00000023, CUP: F83C22000720001.

REFERENCES

Buccolieri R., Sandberg M., Di Sabatino S., 2010. City breathability and its link to pollutant concentration distribution within urban-like geometries. Atmos Environ 44:1894–1903

Hertel O., Berkowicz R., 1990. Vurdering af spredningsmodellen i den Nordiske Beregningsmetode for Bilavgasser. Sammenfattende rapport (in Danish), DMU Luft A-136. 27p.

Lelieveld J., Berresheim H., Borrmann S., Crutzen P.J., Dentener F.J., Fischer H., Feichter J., Flatau P.J., Heland J., Holzinger R., Korrmann R., Lawrence M.G., Levin Z., Markowicz K.M., Mihalopoulos N., Minikin A., Ramanathan V., de Reus M., Roelofs G.J., Scheeren H.A., Sciare J., Schlager H., Schultz M., Siegmund P., Steil B., Stephanou E.G., Stier P., Traub M., Warneke C., Williams J., Ziereis H., 2002. Global Air Pollution Crossroads over the Mediterranean. Science 298, 794–799.

MacDonald R.W., Griffiths R.F., Hall D.J., 1998. An improved method for the estimation of surface roughness of obstacle arrays. Atmos Environ 32:1857–1864

Metrangolo C., Dinoi A., Esposito A., Pappaccogli G., Donateo A., Santiago J. L., Buccolieri R., 2024. Assessing urban air pollution dynamics: the impact of traffic emissions and urban morphology in Lecce and Bari, Italy. Bulletin of Atmospheric Science and Technology, 5(1), 13.

Pascal M., Corso M., Chanel O., Declercq C., Badaloni C., Cesaroni G., Henschel S., Meister K., Haluza D., Martin-Olmedo P., Medina S., 2013. Assessing the public health impacts of urban air pollution in 25 European cities: results of the Aphekom project. Science of the Total Environment, 449, 390-400.

Vardoulakis S., Fisher B. E., Pericleous K., Gonzalez-Flesca N., 2003. Modelling air quality in street canyons: a review. *Atmospheric environment*, *37*(2), 155-182.

6th International Conference on Building Energy and Environment
Eindhoven University of Technology, The Netherlands
6 - 10 July 2025

Evaluating the indoor thermal conditions in a room with a Trombe Wall system: A CFD study

Ceylin Şirin[1,2], Jamie Goggins[1,2,3], Magdalena Hajdukiewicz[1,2,3]

[1]School of Engineering, College of Science and Engineering, University of Galway, Galway, Ireland
[2]MaREI Centre and the Ryan Institute University of Galway, Galway, Ireland
[3]Construct Innovate, University of Galway, Galway, Ireland
email: c.sirin1@universityofgalway.ie, jamie.goggins@universityofgalway.ie, magdalena.hajdukiewicz@universityofgalway.ie

SUMMARY
Sustainable design and green construction practices are effective solutions to provide comfortable thermal conditions for occupants while decreasing the seasonal heating/cooling demand in buildings. Trombe walls (TWs) are building components that can be used to regulate indoor thermal environment. Utilising TWs as a passive heating and cooling method can help in providing desirable indoor comfort conditions while reducing the reliance on mechanical systems. This study evaluates the indoor thermal conditions in a model room with a TW system. This is done by analysing air temperature and velocity distribution under the defined heat flux values on a TW (200, 250, 300, and 350 W/m²) in both summer and winter conditions typical of Irish weather. Using the grid convergence index (GCI) method to optimize the computational fluid dynamics (CFD) model, the study examines how these heat flux values affect the room conditions in relation to thermal comfort standards.

Keywords: Trombe wall; Dwellings; Building performance; Indoor thermal comfort.

1. INTRODUCTION

Trombe walls (TWs) have become a popular passive solar heating system [1-3]. TWs can influence indoor temperature by utilising solar energy and thermal mass [5]. They are composed of a glass layer placed in front of a south-facing wall (for northern hemisphere) composed of a high thermal mass material, such as concrete or adobe [6]. Sunlight passing through the glass during the day heats the wall's surface and allows the TW to absorb thermal energy. The heat is conducted through the TW's structure and slowly released to the indoor environment, providing required indoor thermal conditions [7]. Natural convection and forced convection systems are the two primary varieties of TWs [8]. Natural convection TWs rely on warm air's buoyancy to flow through vents at the top and bottom of the TW structure. TWs with forced convection use fans or other mechanical systems to improve airflow, which can boost the heat transfer efficiency [8]. TWs have been utilised in a variety of settings and structures, including commercial and residential buildings [9]. However, using computational fluid dynamics (CFD) to optimise the design and performance of TWs is essential [10]. CFD models can assist designers in fine-tuning a variety of parameters, including vent size and location, TW thickness and glazing qualities, and simulating airflow and heat transfer within and around the TW [11].

Previous research comprehensively examined the impacts of mesh types and refinement methodology utilising the grid convergence index (GCI) [12] to ensure accurate and reliable results. Baker et al. [13] used the GCI approach to assess how the mesh resolution affected the accuracy of numerical results, i.e. indoor air velocities. Lee et al. [14] developed a method to determine the most suitable mesh for CFD simulations by reducing grid independence tests, focusing on optimal grid resolution, and validating the approach through case studies using GCI method. Hajdukiewicz et al. [15] utilised the GCI method in a 3D CFD model of an internal environment of a room. The GCI values were compared with the accuracy of physical

measurements in a demonstration building and a suitable mesh, as a compromise between the level of uncertainty and computational cost, was selected for further analysis.
The research presented here aims to investigate indoor conditions inside a model room by numerically assessing the effect, of varying heat flux values applied to a TW, on the indoor air temperatures and velocities.

2. METHODOLOGY

2.1. Model Description and boundary conditions

This research utilised a CFD (ANSYS Fluent [16]) model of a room with a natural convection TW system. Different heat flux values were applied on the TW surface, under the summer and winter conditions in Galway, Ireland, to evaluate their impact on indoor air temperature and velocity. The dimensions of the room and some boundary conditions were adopted from a previously published study [17]. The geometry of the investigated room is presented in Figure 1, with room dimensions of 3 m × 4 m × 4 m and the TW 2.4 m high and 0.3 m thicks, with a 0.3 m air gap between the TW and glazing. There were an inlet and outlet defined in the glazing (Figure 1, both 0.1 m wide) to enhance the airflow through the room.

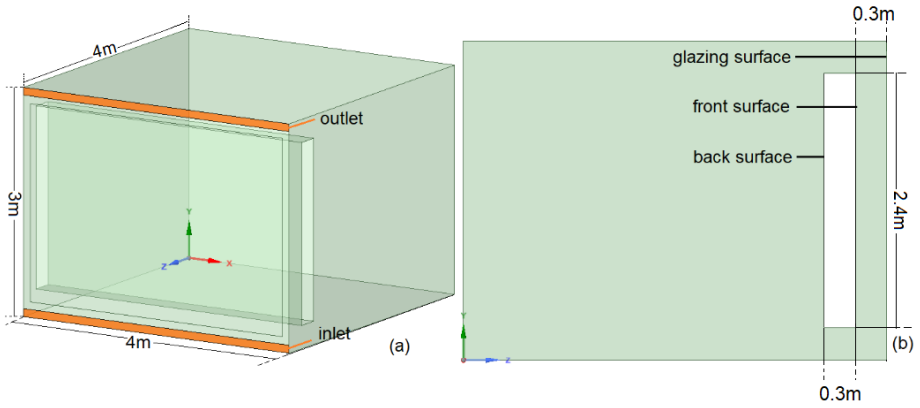

Figure 1. (a) Room geometry with inlet and outlet locations. (b) Cross-sectional view showing the glazing surface, TW front surface, and TW back surface.

Table 1 presents the boundary conditions for the CFD model. Four different heat flux values, including 200, 250, 300 and 350 W/m^2, were applied on the TW front surface to evaluate their impact on the thermal and flow behaviour inside the room. A fixed temperature was assigned to the TW back surface to simulate thermal behaviour. The heat flux values were based on typical solar heat flux values for Galway. The mean outdoor temperatures were assumed as 15.9 $^{\circ}$C for summer conditions (as the average measured [18] air temperature in Galway in August 2020), and 6.3 $^{\circ}$C for winter conditions (as the average measured [18] air temperature in Galway in December 2020). Ideal gas with fixed thermophysical properties was selected as a working fluid in the CFD model. The standard k-ε RNG turbulence model was used. The simulation did not employ a radiation model.

Table 1. Boundary conditions.

Element	Floor	Roof	Glazing surface	Glazing surface	Front surface	Back surface	Other walls	Inlet (summer)	Inlet (winter)	Outlet (summer & winter)
Parameters	T= 15°C	T=25°C & HTC= 90 W/m^2	T=15.9 °C (summer)	T=6.3 °C (winter)	HF: 200-350* W/m^2	T=25°C & HTC= 90 W/m^2	Adiabatic	V=0.1 m/s & Air T=15.9°C (T_{in})	V=0.1 m/s & Air T=6.3°C (T_{out})	1 atm gauge pressure (101,325 Pa)

**: from the surface of TW to the air cavity*

T: Temperature (°C), HF: heat flux (W/m^2), HTC: heat transfer coefficient (W/m^{2}K), V: Air velocity (m/s)

2.2. Grid convergence index method (GCI)

The Richardson Extrapolation approach [19], which requires consistency and uniformity in the mesh refinement, is an error estimator based on merging the discrete solution of two systematically refined meshes. Numerical errors are introduced through the discretisation procedure. Discretisation errors can be quantified with the GCI method. Figure 2 shows the main steps in the GCI method.

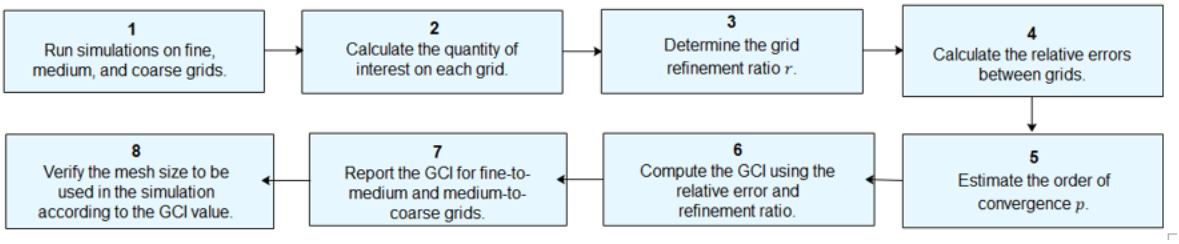

Figure 2. GCI calculation steps

Following the Richardson's extrapolation, the GCI was computed using the following equation [16]:

$$GCI = F_s \frac{\varepsilon}{r^p - 1} \quad (1)$$

Where, ε is the relative error of two grid conditions in the simulation, p is the order of convergence and F_s is the safety factor. When comparing three or more grids, F_s is calculated using a value of 1.25 [12].

2.3. Model Verification

The grid verification was carried out for the model with a heat flux value of 200 W/m^2, where the results of indoor air temperatures were analysed Table 2 presents the number of mesh elements and the grid refinement ratio (r) for those meshes. Using Richardson Extrapolation [19], r values greater than 1.3 (r_{32}=1.35, r_{21}=1.34) were achieved, meeting the recommended criteria [20].

Table 2. Grid parameters for three different mesh sizes.

	Coarse $\boldsymbol{\Delta_3}$	Medium $\boldsymbol{\Delta_2}$	Fine $\boldsymbol{\Delta_1}$	grid refinement ratio ($\boldsymbol{r}$)	
Number of elements	259770	638024	1531189	Coarse- Medium (r_{32})	Medium-Fine (r_{21})
Size of mesh elements	50 mm	20 mm	10 mm	1.35	1.34

The GCI was utilised to perform quantitative grid verification under conditions where monotonic convergence was observed. Table 3 shows the grid convergence error for the computed indoor air temperature on the assigned horizontal planes at head (1.7 m above the floor) and ankle (0.1 m above the floor) levels. The average convergence value (p= 2.3) was applied. The GCI values reduced with grid refinement, demonstrating improved accuracy, with the lowest error observed for the medium-fine grid comparisons (i.e. GCI = 1.5% at head level).

Table 3. Grid convergence error for indoor air temperatures.

	Grid No	Relative Error ($\boldsymbol{\varepsilon}$)	Average convergence value ($\boldsymbol{p}$)	GCI (%)
Head Level	Coarse-medium	0.026	2.3	*3.3*
Head Level	Medium-fine	0.011		*1.5*
Ankle Level	Coarse-medium	0.027		*3.5*
Ankle Level	Medium-fine	0.016		*2.1*

The ASME V&V 20 standard [21] suggests a GCI value below 5% for high-precision simulations, and some researchers even aim for values as low as 1-2%, depending on the study's sensitivity and accuracy requirements [22]. In this research, at the head and ankle levels, the air temperature results showed a GCI error of 1.5% and 2.1%, respectively, between the medium and fine meshes. The medium mesh ($\boldsymbol{\Delta_2}$= 638024) was selected for further calculations, with errors in the lower range of 1-2%, ensuring higher accuracy and reasonable computational resources. The closer to zero the GCI value is, the lower the discretisation error, but higher the computational resources.

3. RESULTS

In order to evaluate the effect of air cavity warming on indoor thermal conditions, the head (XZ plane I - Y = 1.7 m) and ankle (XZ plane II - Y = 0.1 m) levels of a standing occupant were selected as reference planes to analyse results. The air temperature and velocity profiles were simulated for all heat flux values under the summer and winter conditions. Figure 3 illustrates the air temperature distribution on plane I and plane II, for the heat flux of 250 W/m² for both summer and winter conditions. The head level in summer (Plane I) experienced the highest temperature gradients, likely due to hot air rising and accumulating at the upper levels of the room. The colder regions at the ankle level (Figure 3 b and d) resulted from fresh outdoor air entering the space below the TW and warming up due to interaction with the warm air coming from the air cavity between the glass and TW. Figure 4 shows the air velocity streamlines inside the room. The air entered the room through the inlet (at the bottom of the glazing) at velocity of 0.1 m/s, and after mixing with the stale air inside the room and inside the cavity between the TW and glazing, it exited through the outlet. The outlet was set to atmospheric pressure, assumed to be 1 atm, to ensure a consistent flow boundary condition.

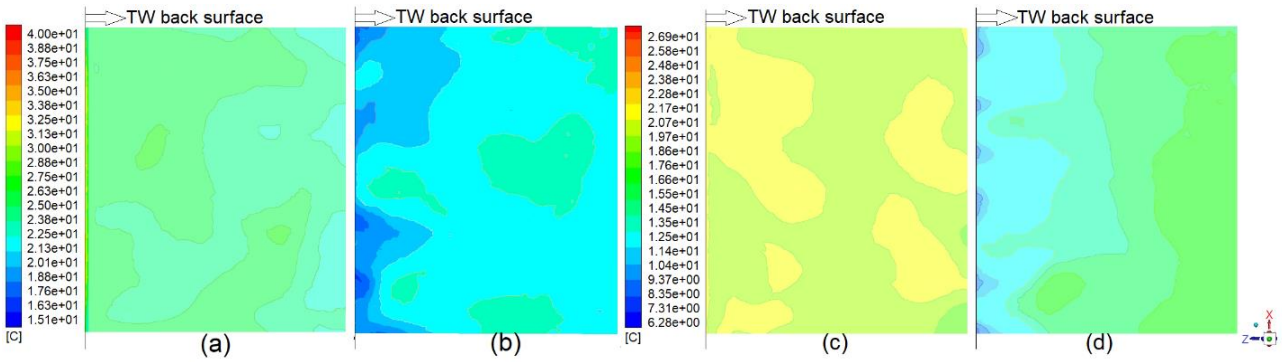

Figure 3. Air temperature distribution for a 250 W/m² heat flux value: (a) plane I (head level) summer, (b) plane II (ankle level) summer, (c) plane I winter, (d) plane II winter.

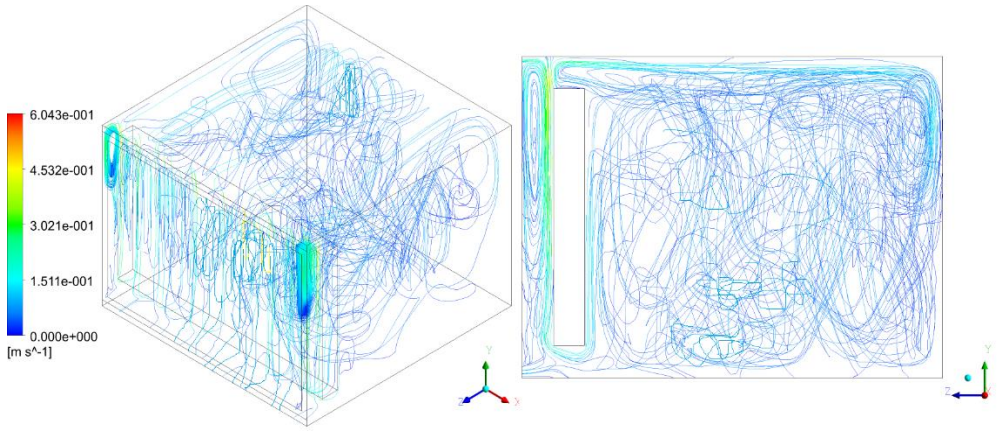

Figure 4. Air velocity distribution inside the room for 250 W/m² heat flux in summer conditions.

Tables 4 and 5 show air temperatures and velocities at the head and ankle levels for all simulated heat fluxes in the summer and winter conditions. At head level (Plane I), the average air temperature increased from 24.17°C to 30.43°C as the heat flux reached from 200 W/m² to 350 W/m². The range of air temperatures across all heat fluxes at head level was between 16.79°C - 32.37°C, showing a consistent rise with increasing heat flux in the summer. In addition, the average air temperature at the ankle level ranged from 20.67°C to 24.34°C, with a lower temperature rise compared to head level due to stronger impact of the inlet air conditions. Table 5 shows the average air temperatures in winter, ranging between 18.21–24.09°C at the head level, and 13.75–17.45°C at the ankle level. Indoor air velocities at head and ankle levels ranged between 0.03 and 0.05 m/s, for both summer and winter.

Table 4. Temperature and velocity results obtained on Plane I and Plane II (summer).

Heat flux (W/m^2)	Head level				Ankle Level			
	Temperature (°C)			Velocity (m/s)	Temperature (°C)			Velocity (m/s)
	Maximum	Minimum	Average	Average	Maximum	Minimum	Average	Average
200	25.69	16.79	24.17	0.04	22.76	17.00	20.67	0.03
250	28.02	17.73	26.02	0.03	24.52	18.14	21.94	0.03
300	30.08	18.71	28.39	0.04	25.65	17.27	23.05	0.04
350	32.37	19.76	30.43	0.04	27.38	18.51	24.34	0.05

Table 5. Temperature and velocity results obtained on Plane I and Plane II (winter).

Heat flux (W/m^2)	Head level				Ankle Level			
	Temperature (°C)			Velocity (m/s)	Temperature (°C)			Velocity (m/s)
	Maximum	Minimum	Average	Average	Maximum	Minimum	Average	Average
200	19.14	14.26	18.21	0.03	16.36	7.50	13.75	0.05
250	21.76	15.18	20.14	0.03	17.52	7.77	15.11	0.04
300	23.73	15.53	22.15	0.04	19.33	7.94	16.50	0.06
350	25.96	16.93	24.09	0.03	21.07	8.96	17.45	0.05

4. DISCUSSION

There are several standards and guidelines used to assess and ensure thermal comfort in buildings. These standards aim to define and regulate the key environmental factors, such as air temperature, humidity, and air movement, that contribute to occupant's comfort. Among the widely referenced organizations providing such frameworks are the Chartered Institution of Building Services Engineers (CIBSE) [24], the International Organization for Standardization (ISO) [25], and the American Society of Heating, Refrigerating, and Air-Conditioning Engineers (ASHRAE) [26], each offering guidelines on different aspects of thermal comfort and environmental performance. Thermal comfort refers to the state in which the building occupants feel neither too hot nor too cold. Table 6 shows the comparison of average room temperature and velocity values with standardized thermal comfort criteria under summer and winter scenarios.

Table 6. Comparison of average indoor air parameters of the room with thermal comfort standards under simulated heat flux scenarios.

Parameter	Thermal comfort bandwidth	HF=200W/m^2	HF=250W/m^2	HF=300W/m^2	HF=350W/m^2
Air Temperature	24-26°C [27], [28]	✓ (S)	✓ (S)	X	X
	25-28°C [29]	✓ (S)	✓ (S)	✓ (S)	X
	24-26°C summer, 25°C winter [30]	✓ (S)	✓ (S)	X	X
	20-23°C in the winter, 22-26°C in the summer [23]	✓ (S)	✓ (S), ✓ (W)	✓ (W)	✓ (W)
Air Velocity	< 0.1 m/s [31]	✓ (S), ✓ (W)	✓ (S), ✓ (W)	✓ (S), ✓ (W)	X
	0.5-1.0 m/s [23]	✓ (S), ✓ (W)	✓ (S), ✓ (W)	✓ (S), ✓ (W)	X

**S: Summer, W: Winter.*

For summer conditions, the average indoor air temperature aligned with the thermal comfort range (22–26°C) at lower heat fluxes (200 W/m² and 250 W/m²). However, at higher heat fluxes (300 W/m² and 350 W/m²), the average air temperature exceeded the comfort thresholds. In winter conditions, the comfortable average air temperatures were met at 250, 300 and 350 W/m², but not achieved at 200 W/m² due to insufficient heating. Air velocity in both seasons remained within acceptable limits (<0.1 m/s) at all heat flux vales. In addition, all scenarios were considered in the previous tables, the average temperatures at ankle level are notably lower compared to head level. This cooler temperature at the lower zone could lead to thermal discomfort, as occupants may experience a cold feet sensation, especially during winter conditions, due to insufficient heat distribution and stratification in the indoor environment. Low temperatures at ankle level may result from the inlet's position, directing fresh air toward the feet and causing discomfort. Adjusting the inlet/outlet configurations could improve heat distribution and enhance thermal comfort. These results suggested that while specific heat flux values could achieve compliance with thermal

comfort standards, the TW system might require further optimisation to reduce vertical temperature stratification and enhance overall performance.

5. CONCLUSION

This study evaluated the indoor thermal and airflow conditions inside a room with a TW system, under varying heat flux conditions in both summer and winter scenarios. The results demonstrated that while specific heat flux values could meet thermal comfort standards for indoor temperature and air velocity, vertical temperature stratification remained a challenge, exceeding recommended limits in some cases. Optimal heat flux values for maintaining comfort conditions were identified as 200 and 250 W/m² in summer and 250, 300 and 350 W/m² in winter with further optimisation and modelling techniques required for decreasing air temperature differences. This study has limitations; it focused on evaluating the indoor environment under the predefined boundary conditions. While the results provided valuable insights, the study did not account for detailed effect of heat transfer through the TW. Future research could explore modelling the TW as a solid structure to include heat conduction through its material and convection between its surfaces and the indoor air. Additionally, the TW could be modelled with integrated phase change materials (PCM) or enhanced with fin geometries to improve heat transfer performance. Such advancements would provide a deeper understanding of the TW system's thermal behavior and its potential applications in diverse building designs. While this study primarily focused on the effect of varying heat flux values on thermal comfort at different vertical levels, it is recognized that the design and placement of inlets and outlets can also significantly influence vertical temperature stratification. A sensitivity analysis on inlet/outlet configuration was not included in the current study but represents an important area for future investigation to better understand airflow dynamics and enhance overall comfort prediction accuracy. Furthermore, incorporating a detailed radiation model in future simulations would allow for a more realistic representation of solar heat transfer, leading to improved prediction of the TW system's thermal response and its impact on indoor comfort conditions.

ACKNOWLEDGEMENTS

The authors would like to acknowledge the financial support from Science Foundation Ireland (SFI) for the ERBE Centre for Doctoral Training (CDT) under grant agreement no. 18/EPSRC-CDT/3586 and the MaREI Centre under grant agreement no. 12/RC/2302_P2, as well as the Engineering and Physical Sciences Research Council under grant no. EP/S021671/1 for the ERBE CDT. The authors also acknowledge the financial support from the European Union's Horizon 2020 research and innovation programme under the METABUILDING LABS project (grant agreement no. 953193) and funding from Enterprise Ireland for Construct Innovate, Ireland's national research centre for construction technology and innovation, under grant agreement no. TC-2022-0033.

REFERENCES

[1] Hami, K., Draoui, B., Hami, O. (2012), 'The thermal performances of a solar wall', Energy, 39(1), 11-16.
[2] Duan, S., Jing, C., Zhao, Z. (2016), 'Energy and exergy analysis of different Trombe walls', Energy and Buildings, 126, 517-523.
[4] Sergei, K., Shen, C., Jiang, Y. (2020), 'A review of the current work potential of a Trombe wall', Renewable and Sustainable Energy Reviews, 130, 109947.
[5] Dabaieh, M., Elbably, A. (2015), 'Ventilated Trombe wall as a passive solar heating and cooling retrofitting approach; a low-tech design for off-grid settlements in semi-arid climates', Solar Energy, 122, 820-833.
[6] Wilson, A. (1979), 'Thermal storage wall design manual', New Mexico Solar Energy Association.
[7] Rabani, M., Kalantar, V., Dehghan, A. A., Faghih, A. K. (2015), 'Experimental study of the heating performance of a Trombe wall with a new design', Solar Energy, 118, 359-374.

[8] Ellis, P. G. (2003), 'Development and validation of the unvented Trombe wall model in EnergyPlus', (Doctoral dissertation, University of Illinois at Urbana-Champaign).
[9] Hu, Z., He, W., Ji, J., Zhang, S. (2017), 'A review on the application of Trombe wall system in buildings', Renewable and Sustainable Energy Reviews, 70, 976-987.
[10] Ali, M. H., Mawlood, M. K., Jalal, R. E. (2024), 'Minimizing energy losses and enhancing performance of Trombe wall systems through partial evacuation of the air gap', Energy and Buildings, 307, 113959.
[11] Zhu, N., Deng, R., Hu, P., Lei, F., Xu, L., Jiang, Z. (2021), 'Coupling optimization study of key influencing factors on PCM trombe wall for year thermal management', Energy, 236, 121470.
[12] P.J. Roache, QUANTIFICATION OF UNCERTAINTY IN COMPUTATIONAL FLUID DYNAMICS, Annu. Rev. Fluid Mech. 29 (1) (1997) 123–160.
[13] Baker, N., Kelly, G., O'Sullivan, P. D. (2020). A grid convergence index study of mesh style effect on the accuracy of the numerical results for an indoor airflow profile. International Journal of Ventilation, 19(4), 300-314.
[14] Lee, M., Park, G., Park, C., Kim, C. (2020). Improvement of grid independence test for computational fluid dynamics model of building based on grid resolution. Advances in Civil Engineering, 2020(1), 8827936.
[15] Hajdukiewicz, M., Geron, M., & Keane, M. M. (2013). Formal calibration methodology for CFD models of naturally ventilated indoor environments. Building and Environment, 59, 290-302. [16] Ansys® Academic Research Mechanical, Release 18.1, Help System, Coupled Field Analysis Guide, ANSYS, Inc.
[17] Dhahri, M., Khalilpoor, N., Aouinet, H., Issakhov, A., Sammouda, H., Emani, S. (2021). 'Numerical study on the thermal performance of trombe wall for passive solar building in semiarid climate', International Journal of Photoenergy, 2021, 1-12.
[18] Informatics Research Unit for Sustainable Engineering (IRUSE) Weather Data, https://weather.universityofgalway.ie, online.
[19] Roache, P. J. (1994). Perspective: A method for uniform reporting of grid refinement studies. Journal of Fluids Engineering, 116(3), 405–413
[20] Celik, I. B., Ghia, U., Roache, P. J., Freitas, C. J. (2008). Procedure for estimation and reporting of uncertainty due to discretization in CFD applications. Journal of fluids Engineering-Transactions of the ASME, 130(7).
[21] American Society of Mechanical Engineers (ASME). Standard for Verification and Validation in Computational Fluid Dynamics and Heat Transfer: ASME V&V 20-2009.
[22] Ali, M. S. M., Doolan, C. J., Wheatley, V. (2009, December). Grid convergence study for a two-dimensional simulation of flow around a square cylinder at a low Reynolds number. In Seventh International Conference on CFD in The Minerals and Process Industries (ed. PJ Witt & MP Schwarz) (pp. 1-6).
[23] ANSI/ASHRAE Standard 55-2017, Thermal Environmental Conditions for Human Occupancy
[24] Chartered Institution of Building Services Engineers (CIBSE), https://www.cibse.org, Accessed: 2024/10/14.
[25] ISO 7730 2005-11-15 Ergonomics of the Thermal Environment: Analytical Determination and Interpretation of Thermal Comfort Using Calculation of the PMV and PPD Indices and Local Thermal Comfort Criteria, 2005-2015.
[26] American Society of Heating, Refrigerating and Air-Conditioning Engineers. ASHRAE, https://www.ashrae.org/.
[27] International Organization for Standardization (ISO), Ergonomics of the thermal environment — Analytical determination and interpretation of thermal comfort using calculation of the PMV and PPD indices and local thermal comfort criteria, ISO 7730:2005.
[28] Chartered Institution of Building Services Engineers (CIBSE), Guide A: Environmental design (2015), (p.401), March 2015. ISBN: 9781906846541
[29] Chartered Institution of Building Services Engineers (CIBSE), Guide A: Environmental design (2006), (p.314), January 2006, ISBN: 1903287669.
[30] British Standards Institution (BSI), BS EN 15251:2007: Indoor environmental input parameters for design and assessment of energy performance of buildings addressing indoor air quality, thermal environment, lighting and acoustics, 2007, ISBN: 9780580553912.
[31] Chartered Institution of Building Services Engineers (CIBSE), TM52: The limits of thermal comfort: avoiding overheating, 2013, (p.24), October 2013, ISBN: 9781906846343

6th International Conference on Building Energy and Environment
Eindhoven University of Technology, The Netherlands
6 - 10 July 2025

A CFD-based Optimization of Airflow Mixing based on Taguchi, ANOVA, and GRA Methods

Ibrahim Reda [1], Dahai Qi [1], Liangzhu (Leon) Wang [2], Theodore Stathopoulos [2], Andreas Athienitis [2]

[1] *Department of Civil and Building Engineering, Université de Sherbrooke, 2500 boul. de l'Université, J1K 2R1, Sherbrooke, Québec, Canada, ibrahim.reda@usherbrooke.ca, dahai.qi@usherbrooke.ca*
[2] *Centre for Zero Energy Building Studies, Concordia University, 1515 St. Catherine W., H3G 2W1, Montreal, Québec, Canada, leon.wang@concordia.ca, theodore.stathopoulos@concordia.ca, andreask.athienitis@concordia.ca*

SUMMARY
Optimizing airflow mixing is critical for improving ventilation, especially in dense-intermittent occupied spaces such as classrooms. However, achieving optimal airflow mixing is challenging due to complex interactions between design parameters. This study explores a promising framework for optimizing airflow mixing in mixed-ventilated classrooms under realistic conditions. Computational Fluid Dynamics (CFD) simulations, combined with Taguchi, ANOVA, and Grey Relational Analysis (GRA), evaluated five parameters: placement and shape of diffusers, air change rate, inlet temperature, and source location. Discrepancies in factor rankings were observed due to variations in response metrics, for instance, source location was identified as both the most influential and least impactful depending on whether CO_2-air mixing or draft risk was prioritized. GRA was used to optimize the overall performance of these factors on airflow mixing and verified then using confirmation CFD runs. These findings provide insights for improving airflow mixing, enhancing air quality, and ensuring occupant comfort in classrooms.

Keywords: Airflow mixing, CFD, Taguchi, GRA.

1. INTRODUCTION

Airflow mixing is critical in building ventilation for improving thermal comfort and indoor air quality (Awbi, 1998). Effective air mixing systems reduce energy consumption and the carbon footprint of heating and cooling. This is particularly important in densely occupied spaces like classrooms, where air quality directly affects students' performance. Over the past fifty years, Computational Fluid Dynamics (CFD) has become a key tool for predicting airflow and ventilation performance in buildings. Providing detailed insights into airflow and pollutant dispersion, CFD enables cost-effective optimization of ventilation systems. It facilitates the evaluation of multiple scenarios, saving time and improving design efficiency. However, CFD is computationally intensive, sensitive to assumptions and mesh quality, and requires specialized expertise. Moreover, the large number of simulation parameters poses a challenge, particularly in parametric studies, where testing all possible cases is often impractical.

Coupling CFD with statistical methods addresses this limitation, showing success in solving problems in the ventilation field and other disciplines. Instead of evaluating all combinations of parameters, a method like Taguchi (Taguchi, 1986) employs orthogonal array techniques to design a simulation matrix with fewer CFD runs, covering the parametric space effectively. This allows

for reliable conclusions without sacrificing simulation outcomes. However, Taguchi's method, suited for single-response optimization, is limited in multi-response problems such as airflow mixing studies. To overcome this, Grey Relational Analysis (GRA) (Julong, 1989) is often integrated with the Taguchi method. Despite these advantages, studies applying Taguchi and GRA methods in building ventilation research often focus on specific applications, limiting generalizability. For instance, Ye et al. (Ye et al., 2021) optimized impinging jet ventilation (IJV) systems, offering insights into airflow and energy efficiency, but excluding other modes such as mixed ventilation. Similarly, Niu et al. (Niu et al., 2022) focused on data center cooling with under-floor air distribution, making their conclusions less relevant to other building types. Yuce et al. (Yuce et al., 2022) applied Taguchi, analysis of variance (ANOVA), and GRA to a two-dimensional benchmark case, but their simplified model lacks the complexity of real-world, three-dimensional environments. Therefore, this research aims to expand the applicability of this approach by testing it in a mixed-ventilated CFD classroom model under realistic conditions, aiming to generalize its use across various scenarios.

2. METHODOLOGY

This research integrates CFD simulations with Taguchi, ANOVA, and GRA methods to optimize five design parameters influencing airflow mixing in classrooms. A validated CFD model was developed with 25 different settings for air terminal layout, air change rates (ACH), inlet temperature (T_{in}), and exhaled CO_2 source location, resulting in 25 simulations based on an orthogonal array (Taguchi method). Four responses were predicted: uniformity index (U_i), zone distribution effectiveness (E_z), draft risk (DR), and temperature difference (ΔT) between head and ankle levels. A mono-assessment using Taguchi and ANOVA evaluated the impact of each factor, while a multi-assessment using Grey Relational Analysis (GRA) consolidated these responses into a single metric, Grey Relational Grade (GRG). Optimal and worst design combinations were identified, and two confirmation simulations validated the multi-response approach. Additionally, the U_i values for these settings are summarized to support the broader application of the Modified Decay Method (Reda et al., 2023), a novel method for measuring air change rates in non-uniformly mixed spaces.

The Taguchi method is a robust tool for identifying the best and worst combinations of factors for a given objective function, offering an efficient and systematic approach to optimizing design performance. By employing an orthogonal array, desired outcomes can be achieved with significantly fewer simulations. In this study, the Taguchi method was applied to design the CFD simulations using the L25 (5^5) orthogonal array, to study the effects of selected factors on airflow mixing at five levels, as summarized in Table 1. The levels and ranges of the factors were chosen after reviewing numerous classroom layouts and HVAC system designs from a relevant study (Reda et al., 2024) for the same building, aligned with recommended design considerations and operating conditions.

Table 1. Five-level factors were examined in the assessment of airflow mixing.

Level	Terminal Layout	Terminal shape	Air change rate [h^{-1}]	Inlet temperature [^oC]	Source location
1	Single	Square	3	12	5
2	Double	Round	6	18	11
3	Triple	Linear	9	24	21
4	Quadruple	Swirl	12	30	31
5	Quintuple	Perforated	15	36	41

The Taguchi method was used to rank factors and identify the best and worst combinations by calculating signal-to-noise ratios (S/N), determining the delta S/N (difference between the maximum and minimum values), and ranking the factors. The factor with the largest delta value is the most influential, while the one with the smallest delta value is the least effective. For U_i and Ez, the "larger-is-better" criterion Eq. (1) was applied to calculate S/N, and for DR and ΔT, the "smaller-is-better" criterion Eq. (2) was used. The ANOVA test quantified the contribution ratio of each factor, with significance accepted below 5%. Meanwhile, GRA was applied for multi-response analysis, converting U_i, E_z, DR, and ΔT into a single GRG. The GRA steps included normalizing each response, calculating the Grey Relational Coefficient (GRC), and determining the GRG based on weights assigned to each response. Various weighting methods, including averaged weight, Principal Component Analysis (PCA) (Qazi et al., 2020), and delta S/N, were tested, but only the averaged weight and PCA methods are presented due to their comparable results. For further details on these methods, readers are referred to previous studies (Ye et al., 2021; Yuce et al., 2022).

$$S/N = -10\,log\left(\frac{1}{n}\sum_{i=1}^{n}\frac{1}{{Y_i}^2}\right) \quad (1)$$

$$S/N = -10\,log\left(\frac{1}{n}\sum_{i=1}^{n}{Y_i}^2\right) \quad (2)$$

where n is the number of simulations and Y_i represents the resulting value for the ith performance characteristics.

A classroom model was developed based on the real dimensions of a classroom from a previous study (Reda et al., 2023). The computational domain included 25 different configurations, as illustrated in Figure 1. The classroom has a floor area of 78 m^2, a height of 3.4 m, and accommodates 40 students and one teacher. Air terminals were positioned on the ceiling for mixed ventilation. ANSYS Fluent software was used for mesh discretization, employing polyhedral meshes for better computational efficiency and accuracy (Chen et al., 2021). A mesh-independency study confirmed the selected resolution was optimal (0.05 m element size and 5,481,036 elements). Mesh quality was assessed using the U_i of CO_2, the root mean square error of CO_2 concentration logs (RMSEL), skewness, and orthogonal quality.

The boundary conditions used were derived from field-collected data in the same classroom (Reda et al., 2023). Supply inlets were defined as mass flow inlets with flow rates ranging from 0.3 to 1.3 kg/s, calculated based on the desired air change rate and diffuser area. The inlet temperature range was set between 12°C and 36°C. The exhaled CO_2 source was modeled as a mass flow inlet, releasing 0.0002 kg/s of air at 34°C with a CO_2 mole fraction of 0.04 (Georgescu et al., 2020). The classroom was maintained at 10% positive pressurization, as indicated by building automation system data. Consequently, the outlet was assigned a mass flow outlet equal to 90% of the inlet flow, with the remaining 10% exiting through the door gap. A no-slip condition was applied to all interior surfaces, and the walls were modeled as adiabatic due to negligible heat transfer compared to occupant heat gains. Seated students and the standing teacher were assumed to generate heat at a rate of 60 W/m^2 across their total body surface area, reflecting sedentary activity levels (ASHRAE, 2023).

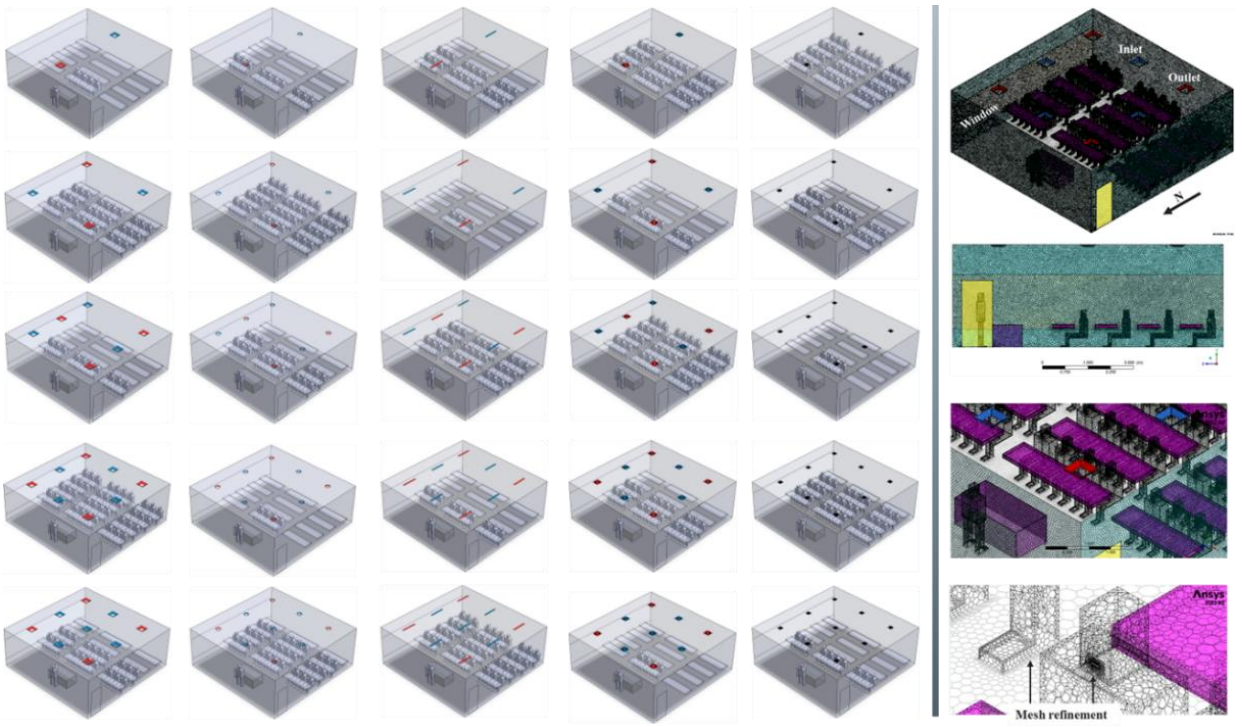

Figure 1. 3D views of the classroom model with air terminal types (square, round, linear, swirl, perforated) in columns and layout configurations (single to quintuple) in rows. Supply diffusers (blue) and return diffusers (red) are shown. The right panel illustrates polyhedral mesh generation for case 16, including refinement details.

Steady-state simulations were conducted governed by conservation equations for mass, momentum, energy, and species transport, with buoyancy effects accounted for by the Boussinesq approximation. The SST k-ω turbulence model (Menter, 1994) was employed with a pressure-based solver of a second-order upwind scheme. Convergence was achieved after 3000 iterations with criteria set to 10^{-4} for most equations and 10^{-6} for energy. The model was validated by comparing predicted CO_2 concentrations with measured data, showing a U_i of 0.74 and 0.76. The mesh with 5.5 million elements was sufficient, and further refinement did not significantly improve accuracy but increased computation time. Discrepancies near the source were attributed to proximity effects. The RMSEL for CO_2 was 12%, with a maximum skewness below 0.85 and a minimum orthogonal quality exceeding 0.1. A fine mesh was applied near occupants to resolve the laminar sublayer effectively.

Airflow mixing was quantified for each simulated case using exhaled-CO_2 tracer gas, employing the U_i (Reda et al., 2023) and E_z (ASHRAE, 2022). Maximizing the U_i and E_z values toward unity indicates a high level of airflow mixing; therefore, the "larger-is-better" criterion was applied in the Taguchi and GRA methods. Additionally, temperature and air velocity fields were analyzed to assess thermal sensation using the DR and ΔT between head and ankle levels. DR should be below 20% to ensure comfort (ASHRAE, 2023), with limitations to temperatures below 34°C and velocities above 0.05 m/s. For cases that included these limitations, DR was set to zero, and the ΔT metric was deemed more representative for assessing discomfort. A maximum ΔT threshold of 3°C between head and ankle levels is recommended (ASHRAE, 2023). The results are presented at the breathing level (1.1m from the floor level).

3. RESULTS AND DISCUSSION

Twenty-five CFD simulations were conducted to investigate the effects of air terminal layout and shape, air change rate, inlet temperature, and source location on airflow mixing at the breathing level (Figure 2). The five-response metrics (U_i, E_z, DR, ΔT, and GRG) along with their corresponding S/N ratios, are summarized in Table 2. This analysis was performed using a mono-assessment and multi-assessment approach. A comparison of these approaches is presented in the final section, along with a summary of the U_i values for all tested cases.

For the U_i (Figure 2.1), the source location emerges as the most influential factor with a p-value of 0.001, while the layout of air terminals has the least impact. The optimal configuration for achieving the highest U_i value is a setup with triple inlets and outlets using swirl diffusers, tested at a 3 h^{-1} ACH, 36°C inlet temperature, and 5-source locations (Tri-Swr-3-36-5). Conversely, the worst case for U_i is Quin-Perf-9-12-41. For the E_z (Figure 2.2), the ACH is the most significant factor with a p-value of 0.03, while the layout of air terminals again has the least impact. The optimal configuration for E_z is Quad-Sq-3-12-31, while the worst case is Quin-Perf-15-36-5. Notably, these optimal and worst scenarios were not part of the conducted simulations (Table 2), highlighting the strength of the Taguchi method in predicting extreme combinations without requiring all possible cases to be modeled.

For the DR (Figure 2.3), the inlet temperature is identified as the most influential factor (p-value = 0.04), while the source location has the least impact. The optimal combination of factors for minimizing DR is Sing-Sq-6-30-41. Conversely, the worst combination is Quin-Ro-15-12-21. For the ΔT (Figure 2.4), the shape of air terminals emerges as the most effective factor (p-value = 0.02), while the layout of air terminals has the least influence. The optimal combination for ΔT is Quin-Perf-15-30-5, while the worst combination is Doub-Sq-3-24-41. Like previous metrics, these optimal and worst combinations were not part of the conducted simulations. These findings were independently analyzed using the "larger-is-better" criterion for U_i and E_z, while DR and ΔT were examined with the "smaller-is-better" criterion. All least influence factors show a p-value exceeding 0.05.

The four latter metrics were analyzed dependently by transforming them into the GRG, applying the "larger-is-better" criterion. The GRA results are presented in Table 2, both with the average weight of responses and using the PCA. Figures 2.5 and 2.6 show the S/N ratios of the GRG based on both methods, respectively. Using the average weight of responses, the source location is identified as the most influential factor (p-value = 0.03), while the layout of air terminals has the least impact. The best and worst combinations are Tri-Sq-15-12-5 and Quad-Swr-3-30-41. Similarly, applying the PCA method confirms that the source location remains the most effective factor (p-value = 0.01), with the layout again being the least effective. The best and worst combinations are comparable with the average method, being Tri-Ro-15-12-5 and Quad-Swr-3-30-41, respectively. It is also observed that the air change rate and inlet temperature interchangeably rank as the second and third most significant factors affecting airflow mixing. None of these combinations were included in the conducted simulations. Verifying the GRG-PCA optimization, Figures 2.7-2.12 present two confirmation cases i.e., the optimal case (Tri-Ro-15-12-5) and the worst case (Quad-Swr-3-30-41). The average values of the U_i, E_z, DR, and ΔT at the breathing level equal 0.97, 0.18, 14%, and 0.3 ^oC for the optimal case, which become 0.53, 0.73, 2%, and 3.8 ^oC for the worse case.

Table 2. Inputs and outputs of the L25 Taguchi orthogonal array for airflow mixing analysis.

	Factors (inputs)					Mono-assessment responses								Multi-assessment responses			
Case	Layout	Shape	ACH [h^{-1}]	T_{in} [°C]	Source #	U_i	S/N [dB]	E_z	S/N [dB]	DR	S/N [dB]	ΔT [°C]	S/N [dB]	GRG (Ave)	Rank	GRG (PCA)	Rank
1	Sing	Sq	3	12	5	0.77	-2.3	0.98	-0.1	5.11	-14.2	0.80	1.9	0.79	1	0.72	9
2	Sing	Ro	6	18	11	0.67	-3.5	0.56	-5.0	9.23	-19.3	0.64	3.9	0.62	10	0.69	11
3	Sing	Lin	9	24	21	0.50	-6.1	0.42	-7.5	4.89	-13.8	0.51	5.8	0.56	15	0.63	13
4	Sing	Swr	12	30	31	0.60	-4.5	0.49	-6.2	0.86	1.4	0.12	18.4	0.52	19	0.58	16
5	Sing	Perf	15	36	41	0.48	-6.4	0.33	-9.8	4.27	-12.6	0.14	17.1	0.49	22	0.57	17
6	Doub	Sq	6	24	31	0.47	-6.6	0.69	-3.2	0.94	0.5	3.09	-9.8	0.49	21	0.49	23
7	Doub	Ro	9	30	41	0.39	-8.1	0.53	-5.4	3.28	-10.3	1.53	-3.7	0.48	23	0.51	21
8	Doub	Lin	12	36	5	0.80	-1.9	0.28	-10.9	3.15	-10.0	0.15	16.5	0.64	8	0.79	4
9	Doub	Swr	15	12	11	0.70	-3.1	0.34	-9.4	28.25	-29.0	0.23	12.8	0.75	2	0.91	1
10	Doub	Perf	3	18	21	0.61	-4.3	0.69	-3.2	11.25	-21.0	0.20	14.0	0.53	16	0.55	19
11	Trip	Sq	9	36	11	0.68	-3.3	0.52	-5.8	2.37	-7.5	0.45	6.9	0.69	5	0.71	10
12	Trip	Ro	12	12	21	0.58	-4.7	0.52	-5.8	16.61	-24.4	0.73	2.7	0.72	3	0.76	5
13	Trip	Lin	15	18	31	0.54	-5.3	0.48	-6.5	13.05	-22.3	0.56	5.0	0.68	6	0.73	8
14	Trip	Swr	3	24	41	0.55	-5.1	0.77	-2.2	1.71	-4.7	1.72	-4.7	0.39	25	0.37	25
15	Trip	Perf	6	30	5	0.74	-2.6	0.39	-8.2	2.10	-6.4	0.03	30.5	0.63	9	0.73	7
16	Quad	Sq	12	18	41	0.44	-7.2	0.50	-6.0	8.28	-18.4	1.30	-2.3	0.59	12	0.62	15
17	Quad	Ro	15	24	5	0.88	-1.1	0.37	-8.6	7.98	-18.0	0.10	20.0	0.66	7	0.84	2
18	Quad	Lin	3	30	11	0.74	-2.6	0.74	-2.6	0.52	5.6	0.52	5.7	0.46	24	0.49	24
19	Quad	Swr	6	36	21	0.63	-4.0	0.66	-3.7	3.81	-11.6	0.48	6.4	0.53	17	0.56	18
20	Quad	Perf	9	12	31	0.38	-8.3	0.47	-6.6	17.81	-25.0	0.18	14.9	0.57	14	0.62	14
21	Quint	Sq	15	30	21	0.56	-5.1	0.33	-9.6	0.92	0.7	0.43	7.3	0.58	13	0.65	12
22	Quint	Ro	3	36	31	0.53	-5.5	0.75	-2.5	11.01	-20.8	1.78	-5.0	0.49	20	0.49	22
23	Quin	Lin	6	12	41	0.39	-8.1	0.66	-3.6	7.97	-18.0	0.86	1.3	0.52	18	0.53	20
24	Quint	Swr	9	18	5	0.78	-2.2	0.36	-8.9	10.57	-20.5	0.05	26.0	0.70	4	0.84	3
25	Quint	Perf	12	24	11	0.66	-3.6	0.38	-8.3	9.87	-19.9	0.08	21.9	0.62	11	0.74	6

Layout: Sing is single, Doub is double, Trip is triple, Quad is quadruple, and Quint is quintuple.
Shape: Sq is square, Ro is round, Lin is linear, Swr is swirl, and Perf is perforated.
ACH is the air change rate [h^{-1}], T_{in} is the inlet temperature [°C], and source # is the number of locations of exhaled-CO_2 from nostrils. U_i is the uniformity index, S/N is the signal-to-noise ratio [dB], E_z is the zone distribution effectiveness, DR is the draft risk, and ΔT is the temperature difference between head and ankle levels [°C].
GRG is the grey relational grade, Ave is the averaged value of responses, and PCA is the principal components analysis.

The comparison of mono-assessment and multi-assessment approaches reveals significant differences in factor rankings. Source location and air change rate are identified as key factors affecting CO_2-air mixing in the classroom, aligned with prior findings (Niu et al., 2022; Ye et al., 2021; Yuce et al., 2022), highlighting the importance of supply inlet height, velocity, nozzle positioning, and inlet dimensions for optimizing ventilation and comfort. Inlet temperature and air terminal shape also strongly influence draft risk and temperature discomfort, with latter studies confirming their role in thermal comfort and energy efficiency. Discrepancies in factor rankings, such as the varying impact of source location on U_i and DR, reflect context-dependent responses. When using a single metric (GRG) to evaluate overall system performance, four dominant factors source location, air change rate, inlet temperature, and air terminal shape emerge. The diffuser layout shows minimal impact on airflow mixing, explaining its limited focus in past research compared to other factors.

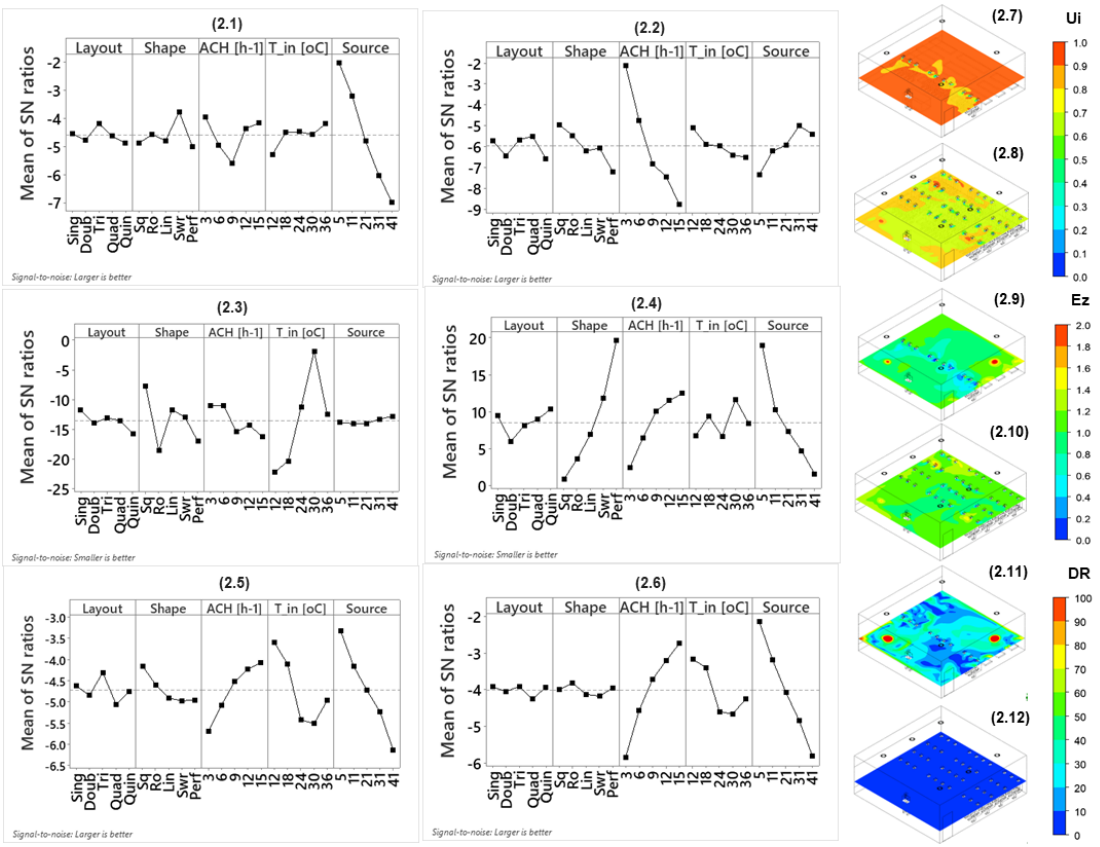

Figure 2. Left: Signal-to-noise (S/N) ratio plots for layout, air terminal shape, ACH, inlet temperature, and source location. Mono assessment: (2.1) Ui, (2.2) Ez, (2.3) DR, (2.4) ΔT. Multi assessment: (2.5) GRG (average weights), (2.6) GRG (PCA). Right: Contour plots for optimal (Tri-Ro-15-12-5) and worst (Quad-Swr-3-30-41) cases, showing Ui (2.7, 2.8), Ez (2.9, 2.10), and DR (2.11, 2.12) at the breathing level.

The previous analysis examines how the studied factors influence airflow mixing in classrooms, quantified using the U_i. Recently, U_i has proven effective in improving the accuracy of the decay method, which tends to underestimate air change rates by 20-25% due to the well-mixed air assumption. Therefore, a modified decay method (Reda et al., 2023) was developed and validated in a real classroom using field testing, wherein the U_i value was experimentally calculated at the breathing level. The U_i values for various mixed ventilation settings tested here can further enhance the applicability of the modified decay method. Across the tested scenarios, the U_i values range from 0.38 to 0.88, with an average of 0.60 ± 0.13, highlighting variability in airflow distribution.

4. CONCLUSIONS

This study tested a systematic framework to optimize airflow mixing in classrooms with mixed ventilation, considering the interactions among design factors in real-world settings. Using CFD simulations combined with the Taguchi method, ANOVA, and Grey Relational Analysis (GRA), five key parameters were analyzed: air terminal layout and shape, air change rate (ACH), inlet temperature, and exhaled CO_2 source placement. The Taguchi and ANOVA methods were initially applied (Mono assessment) to assess the impact of each factor on uniformity index (U_i), zone distribution effectiveness (E_z), draft risk (DR), and temperature difference (ΔT) between head and ankle levels. Followed by a multi-assessment approach using GRA to consolidate these responses into a single metric, Grey Relational Grade (GRG), for a comprehensive evaluation of airflow

mixing. Key findings revealed that source location and ACH significantly affect airflow mixing. The optimal configurations, involving Tri-Sq-15-12-5 and Tri-Ro-15-12-5 setups with triple square and round diffusers, respectively, with an ACH of 15 h^{-1}, an inlet temperature of 12°C, and 5 source locations, achieved high uniformity and distribution effectiveness. In contrast, poor configurations, such as Quad-Swr-3-30-41 and Trip-Swr-3-24-41, with lower ACHs and higher inlet temperatures, led to poor mixing. Discrepancies in rankings between mono-assessment and multi-assessment approaches showed varying impacts depending on the metric, with source location being crucial for U_i but less influential for DR. These results highlight the complex interactions in ventilation design and the need for tailored solutions. Future research should expand simulation sets, incorporate different geometries with dynamic occupancy, and integrate real-world data to enhance model accuracy and adaptability in educational environments.

ACKNOWLEDGEMENTS

This work was supported by the Fonds Québécois de la Recherche sur la Nature et les Technologies – Team Research Project [under grant no. 2022-PR-299939] and Discovery Grants of Natural Sciences and Engineering Research Council of Canada (NSERC) [grant No. RGPIN-2019-05824]. We sincerely appreciate Dr. Huizhong Lu's assistance in setting up the CFD part in the cluster on behalf of Compute Canada - Mammoth-Mp2b - Université de Sherbrooke.

REFERENCES

ASHRAE. (2022). American Society of Heating Refrigerating and Air-Conditioning Engineers , ANSI/ASHRAE Standard 62.1-2022, Ventilation and Acceptable Indoor Air Quality. In. Atlanta, GA: ASHRAE.

ASHRAE, A. S. o. H. R. a. A.-C. E. (2023). ANSI/ASHRAE Standard 55-2023: Thermal Environmental Conditions for Human Occupancy. In. Atlanta, GA: ASHRAE.

Awbi, H. B. (1998). Energy efficient room air distribution. *Renewable Energy*, *15*(1), 293-299. https://doi.org/https://doi.org/10.1016/S0960-1481(98)00176-1

Chen, H., Zhou, X., Feng, Z., & Cao, S.-J. (2021). Application of polyhedral meshing strategy in indoor environment simulation: Model accuracy and computing time. *Indoor and Built Environment*, *31*(3), 719-731. https://doi.org/10.1177/1420326X211027620

Georgescu, M. R., Meslem, A., & Nastase, I. (2020). Accumulation and spatial distribution of CO2 in the astronaut's crew quarters on the International Space Station. *Building and Environment*, *185*, 107278. https://doi.org/https://doi.org/10.1016/j.buildenv.2020.107278

Julong, D. T. J. o. g. s. (1989). Introduction to grey system theory. *1*(1), 1-24.

Menter, F. R. (1994). Two-equation eddy-viscosity turbulence models for engineering applications. *AIAA Journal*, *32*, 1598-1605.

Niu, B., Shi, M., Zhang, Z., Li, Y., Cao, Y., & Pan, S. (2022). Multi-objective optimization of supply air jet enhancing airflow uniformity in data center with Taguchi-based grey relational analysis. *Building and Environment*, *208*, 108606. https://doi.org/https://doi.org/10.1016/j.buildenv.2021.108606

Qazi, M. I., Akhtar, R., Abas, M., Khalid, Q. S., Babar, A. R., & Pruncu, C. I. (2020). An Integrated Approach of GRA Coupled with Principal Component Analysis for Multi-Optimization of Shielded Metal Arc Welding (SMAW) Process. *Materials*, *13*(16).

Reda, I., Ali, E., Berquist, J., Shu, C., Zhang, X., Aram, M.,…Athienitis, A. (2024). Exploring high-rise preventive ventilation: Experimental investigation of inter-zone air pressurization with tracer gas analysis. *Building and Environment*, *258*, 111566. https://doi.org/https://doi.org/10.1016/j.buildenv.2024.111566

Reda, I., Ali, E., Qi, D., Wang, L., Stathopoulos, T., & Athienitis, A. (2023). A modified decay method based on a proposed uniformity index for measuring air change rates in non-uniform air mixed spaces. *Building and Environment*, *245*, 110941. https://doi.org/https://doi.org/10.1016/j.buildenv.2023.110941

Taguchi, G. (1986). *Introduction to quality engineering: designing quality into products and processes*.

Ye, X., Kang, Y., Chen, B., Deng, S., Yan, Z., & Zhong, K. (2021). Study of multi-objective optimization of overall ventilation performance for an impinging jet ventilation system using Taguchi-based grey relational analysis. *Building and Environment*, *188*, 107431. https://doi.org/https://doi.org/10.1016/j.buildenv.2020.107431

Yuce, B. E., Nielsen, P. V., & Wargocki, P. (2022). The use of Taguchi, ANOVA, and GRA methods to optimize CFD analyses of ventilation performance in buildings. *Building and Environment*, *225*, 109587. https://doi.org/https://doi.org/10.1016/j.buildenv.2022.109587

Climate Change and multi hazard risk assessment (15:30-17:00 h)

6th International Conference on Building Energy and Environment
Eindhoven University of Technology, The Netherlands
6 - 10 July 2025

Informal shading: Supplementary approach for countering heat waves in high-density old urban neighbourhoods

Qiu Jin [a], Wenjian Pan [b,*]

[a] *School of Architecture and Urban Planning, Huazhong University of Science and Technology, Wuhan, China, Email address: m202478089@hust.edu.cn*
[b] *School of Architecture and Urban Planning, Huazhong University of Science and Technology, Wuhan, China, Email address: blueice3@163.com; wenjian-pan@connect.hku.hk*

SUMMARY
Old urban neighbourhoods usually possess diverse morphological patterns while fostering many intellectual and adaptive strategies to cope with heat waves. Shading, an approach of establishing thermally comfortable outdoor environments and a medium of place-making in high-density old urban neighbourhoods, can be traced and learned for climatic adaptive rehabilitation and urban governance. This study takes *Chang'an Neighbourhood* as a case study site, representing a typical traditional and old neighbourhood with high-density morphological characteristics in Wuhan, China. The study adopted Christopher Alexander's *Pattern Language* theory and methodology for field survey to systematically investigate the typical forms of informal shadings to be employed by occupants in the site. It then conducted computational simulations with the ENVI-met platform to test the cooling effect of these soft and micro-scale shading strategies during peak hours in summer daytime. The paper also preliminarily discusses how the informal shading strategies can be applied in old urban neighbourhoods to alleviate urban heat island effects during urban design and planning. Findings of the study provides insights of informality into urban renewal that aim to achieve ecologically resilient and healthy development.

Keywords: Shading forms, Cooling effect, Computational simulations, Urban informality

1. INTRODUCTION

With the increase of global warming and rapid urban transformation, thermal environments in urban spaces are gradually deteriorating in recent years, with increasingly frequent heat wave events posing significant threat to human health and well-being. People urgently need to seek more effective and adaptive approaches to counter such tricky situations, particularly, in cities located within high temperature and humid climate zones. The effects and beneficials of shading in urban outdoor spaces have been widely investigated and demonstrated. Watanabe et al. (2014) conducted an on-site study to examine the performance of shadows of several shading forms. Their test results illustrated that the cooling effect from buildings' shadows outperformed the pergola shadows. Focusing on the impact of shading forms on campus thermal environments, Xiong et al. (2024) carried out field measurements and found that shading could effectively block solar radiation during hot summer days. Specifically, pavilion and awning shadings offered better thermal comfort conditions compared to the shadings by tree canopies. They concluded that distinct spatial morphological elements affected outdoor spaces' micro-climate conditions, with varying shadows exhibiting different levels of cooling effects. Using ladybug tools, Nicholson et al. (2024) tested multiple thermal effects of shadings in urban street spaces and developed a workflow for effective shading design. In addition, Al Tahir et al. (2025)'s experiments further verified the cooling performances of artificial shadings, which were affected by structural and material characteristics.

Buildings, structures, and plants are prevalent sources of shadows in urban built-up areas. In high-density old urban neighbourhoods, residents always improvise soft and adaptive approaches to enable shadings, so as to ameliorate their outdoor living environments, characterized by their ease of construction, and thus highlighting their flexibility and adaptability to diverse spatial patterns. Lin et al. (2010) pointed out that low rate of shadows in outdoor spaces are discomfort for people during hot summer, while outdoor environments with a high rate of shadows are not comfortable for outdoor activities in cold winter. People seek shaded areas to shield themselves from the sun's beams in summer, whereas in winter, they need sufficient sunlight to increase air temperature and illumination of their houses and outdoor spaces. In this regards, informal shading can be adopted to adapt to various local climatic conditions, so as to enhance thermal resistance of outdoor spaces within the neighbourhoods. This study aims to examine the cooling effect of informal shadings in high-density old urban neighbourhoods. Taking Wuhan's *Chang'an Neighbourhood* as a case site, the study adopted Christopher Alexander's *Pattern Language* for field survey to systematically investigate the typical forms of informal shading to be employed by occupants in the site. It then conducts computational simulations with the ENVI-met platform to measure the cooling effects of these soft and micro-scale shading strategies during peak hours of summer daytime. The paper also discusses how the informal shading strategies can be integrated into the processes of urban planning and design to alleviate urban heat islands. Findings of the study provide insights of informality into urban renewal that aim to achieve ecologically resilient and healthy development.

2. MATERIALS AND METHODS

2.1. Case Study Site

Wuhan, which is a metropolis located on the eastern Jianghan Plain in central China, features a subtropical mild monsoon climate characterized by hot-humid and abundant rainfall. The city of Wuhan has a long summer season that starts in early May and lasts until late September, with air temperatures frequently reaching among the range of 37~39 ℃. Meanwhile, there are thousands of lakes and rivers in this city, which significantly contribute to the forming of stuffy and thermally uncomfortable feeling in the summer (Wang et al., 2013).

Old urban neighbourhoods (*lao-jie-qu*), specifically those *Lifen* neighbourhoods within the core area of Wuhan's concessions, still co-exist and co-develop with modern residential areas in the city (Pan, 2023; Xi et al., 2024). The traditional buildings with old masonry structural systems and poor infrastructure have hindered residents' quality of life and social well-being in the contemporary era, particularly, when confronting the threatening of climate change and the shock of radical urban transformations. A field survey by Yuan et al. (2014) have identified that there are several issues of liveability in Wuhan's French Concession, including deteriorating living conditions and environmental qualities, as well as lack of sufficient amenities and aging facilities. The street spaces in these typical old neighbourhoods, including those narrow and heterogeneous alleys, usually serve multiple habitation functions, ranging from playing, chatting, planting, cooking, cleaning, to drying vegetables and fruits, etc. Thus, this study specifically evaluates the impact of informal shading forms on thermal comfort conditions in street spaces of high-density old urban neighbourhoods as residents often adjust their outdoor living spaces by adopting and integrating informal and intellectual shading strategies. The *Chang'an Neighbourhood*, which is a typical *Lifen* neighbourhood situated in the French Concession, was chosen for case study (Fig. 1).

Fig. 1. Location and urban contexts of the case study site (source: drawn by authors based on Baidu Satellite Map)

2.2 Forms of Informal Shading

The theory and methodology of *Pattern Language* was initially established by Christopher Alexander for systematically capturing material, social and humanistic attributes of architectures and spaces in cities (Alexander, 1977). The *Pattern Language* provides a clear logic and working framework for identifying both physical elements and social features that constitute architectural and urban spaces, which can further be utilized to examine their individual roles and interactive functions and thereby facilitating effective place-making in urban planning and design. Two typical types of informal shading forms in *Chang'an Neighbourhood* have been surveyed and analysed in this study, namely, Climbing Plants (Type A) and Canvas Roofs (Type B) (Table 1).

Table 1. Examined forms of informal shading based on *Pattern Language* (source: surveyed by authors)

Type A	**Climbing Plants**		
Hypothesis	Climbing plants can fill up the gaps in leaves and provide soft and biophilic shading in high-density neighbourhoods.		
Problems it tackles	From an environmental standpoint, it enhances the beauty of the surroundings; from an architectural standpoint, it offers sections of shade during the sweltering summer days and lessen the amount of heat radiation that buildings absorb. Its biophilic design well fits with the scorching summers and chilly winters found in cities located in hot and humid climate zones.		
Practical implications	Regular pruning is required, which makes upkeep inconvenient and expensive. With the plants grow and spread, they put more strain on the building roofs and facades, which need to be care about the issue of safety and fire risks.	*Related to other patterns*	- Housing clusters - Small path shape - Entrance transition
Type B	**Canvas Roofs**		
Hypothesis	There are common usage forms of canvas roofs in high-density traditional and old urban neighbourhoods across Chinese cities.		
Problems it tackles	Increase the lifespan of ground items, diversify, and customize the shapes, colours, and materials; lessen the glare issue brought on by the west sun; and lessen the erosion of rain on building components that are more susceptible to damage, such the gate.		
Practical implications	Beyond generation of some safety issues such as structural damage in events of heavy rain or snowfall, when confronting strong wind, canvas roofs can also contribute to noise pollution.	*Related to other patterns*	- Edge of Buildings - Entrance transition - Small path shape

2.2 Data Source and Protocol of Computational Simulations

Computational fluid dynamics (CFD) is an evaluation technique that employs computer algorithms and mathematical models to predict fluid flow behaviors. ENVI-met, a prevailing microclimate numerical modeling software, enables effective simulation of the impact of buildings, vegetation, and surface materials on urban environmental performances, and has been extensively applied to assess the effectiveness of various strategies in mitigation of urban heat islands and enhancement of outdoor thermal comfort conditions. In this study, the meteorological data to be used to set the background climatic and initial environmental conditions for CFD simulations was obtained from the platform of Meteorological Station Data (https://www.ladybug.tools/epwmap/), including the data of dry bulb temperature, relative humidity, wind speed and wind direction, etc. In addition, the modelling base maps were adapted from Google Earth, and information of building heights and spatial geometries of the site were collected from field measurement by employing a laser rangefinder. Meanwhile, this study established 3D models for simulations in ENVI-met V5.7.1, with a modelling area size of 108m×80m×30m and a unit grid size of 4.00m×4.00m×1.00m. Taking 31 July as a peak summer day in Wuhan City, all the simulations were set to run from 08:00 am to 18:00 pm (10 hours, covering the hottest period of 10:00 am~16:00 pm). The observation height was set at a pedestrian level (1.5 meters high). Details of the initial settings for the simulations as well as the 24-hour cycle of the air temperature (Ta) and relative humidity (RH) were shown in Table 2 and Table 3, respectively. Finally, the thermal comfort conditions of the *Original* (Scenario 1: without shadings), *Type A* (Scenario 2: with shadings of climbing plants), and *Type B* (Scenario 3: with shadings of canvas roofs) were simulated and compared.

Table 2. Initial settings of environmental parameters for the CFD simulations

Environmental Parameters	Settings/ Assigned Values	
Location of the tested sites	Wuhan City, China	
Climate type	Subtropical climate	
Model dimension	x-Grids: 27, y-Grids: 20, z-Grids: 20	
Size of grid cell	dx=4.00m, dy=4.00m, dz=1.00m	
Simulation date	31 July	
Start simulation time	08:00:00 am	
Total simulation time in hours	10 hours (08:00 am~18:00 pm)	
Wind speed at 10 meters high	1.5 m/s	
Wind direction at 10 meters high	164°	
Roughness length	0.1	
Specific humidity in 2500 m	8.00 g/kg	
Buildings	Default Wall	
	Roofing: Tile	
Vegetation	CO_2 fixation type: C3-plant	Leaf type: Deciduous Leaf
	Foliage shortwave Albedo: 0.23	Foliage shortwave Transmittance: 0.1
	Isoprene Capacity: 3.0	Leaf Weight: 137.5g/m^2
Soil and surface	Basalt Brick Road	
	Concrete Pavement Gray	
Canvas roofs construction	Thickness of layers: 0.001, 0.001, 0.001	
	Roughness length: 0.02	
Personal parameters	Male (35 y), Outdoor: 0.90 clo, pref. Speed: 1.34 m/s	

Scenario 1: *Original* (without any shading strategies)	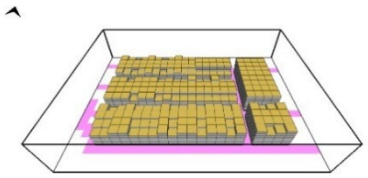	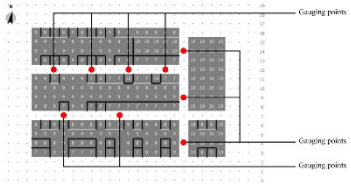
Scenario 2: *Type A* (with shadings of climbing plants)	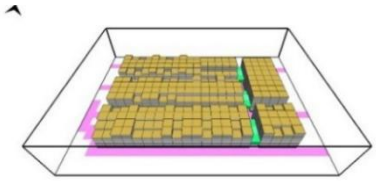	
Scenario 3: *Type B* (with shadings of canvas roofs)	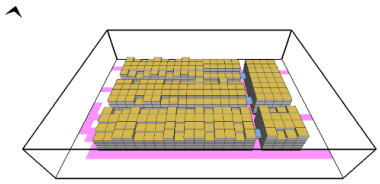	

Table 3. Background meteorological parameters (source: obtained from Meteorological Station Data)

Time	00:00	01:00	02:00	03:00	04:00	05:00	06:00	07:00	08:00	09:00	10:00	11:00
Ta (℃)	34.46	34.04	33.40	32.54	31.75	31.40	31.76	32.63	33.70	34.70	35.59	36.38
RH (%)	84	84	84	84	84	84	84	84	84	85	78	78
Time	12:00	13:00	14:00	15:00	16:00	17:00	18:00	19:00	20:00	21:00	22:00	23:00
Ta (℃)	37.07	37.68	38.20	38.62	38.80	38.51	37.77	36.74	35.60	34.49	33.41	32.36
RH (%)	72	72	72	72	72	78	78	85	85	84	84	84

This study measured air temperature (T_a), mean radiant temperature (MRT), predicted mean vote (PMV), and operative temperature (T_{op}) under different informal shading forms. For each scenario, all the simulated environmental parameters of the nine tested points were averaged for further analysis and comparison (Table 2). The index of T_{op}, which combines both effects of T_a and MRT, was calculated using Eq. 1, where the wind speed (v) was measured at the same height as the observation height of the study (Tymkow et al., 2013). The values of T_{op} (ºC) were calculated based on Eq. 1, while the values of MRT (ºC) and PMV (-3 ~ +3) could be directly computed and outputted by ENVI-met simulations Notably, this study looked at relative values of environmental indices to quantify the extent of change of thermal conditions by comparing informal shading and the original situations, including $\triangle$PMV (Eq. 2) and $\triangle T_{op}$ (Eq. 3).

$$T_{op} = \frac{\mathrm{MRT} + (\mathrm{Ta} \times \sqrt{10v})}{1 + \sqrt{10v}} \qquad \text{(Eq.1)}$$

$$\triangle \mathrm{PMV} = \left| \mathrm{PMV} - \mathrm{PMV}_{original} \right| \quad \text{(Eq.2)} \qquad \triangle T_{op} = \left| T_{op} - T_{op_original} \right| \quad \text{(Eq.3)}$$

3. RESULTS AND DISCUSSION

3.1 Variations and Trends of Cooling Performances

Test results illustrated that the informal shadings Type A and Type B's average values in T_a, MRT, PMV and T_{op} were all lower than the *Original* situation hour by hour during 10:00 am~16:00 pm. Thus, the $\triangle$ PMV and $\triangle T_{op}$ values theoretically reflected the informal shadings' degrees of

amelioration in outdoor thermal comfort conditions. T_a and MRT closely correlates with the angle of solar altitude. Specifically, the three scenarios' T_a and MRT was observed to be above 40°C and 45°C respectively during 13:00 pm~16:00 pm, reflecting extremely hot conditions. The hourly average PMV and T_{op} in Type A and Type B were all lower than the original situation during 13:00 pm~16:00 pm. Among Type A and Type B, their hourly $\triangle$PMV and hourly $\triangle T_{op}$ varied by ranges of 0.24~1.69 and 1.62 °C~9.73°C, respectively. The maximum difference of $\triangle$PMV and $\triangle T_{op}$ among the three scenarios both occurred at 13:00 pm (Fig. 2). These preliminarily reveal that adding informal shading elements could ameliorate outdoor spaces' thermal comfort conditions while maintaining the original building layouts and spatial forms of the old neighbourhoods.

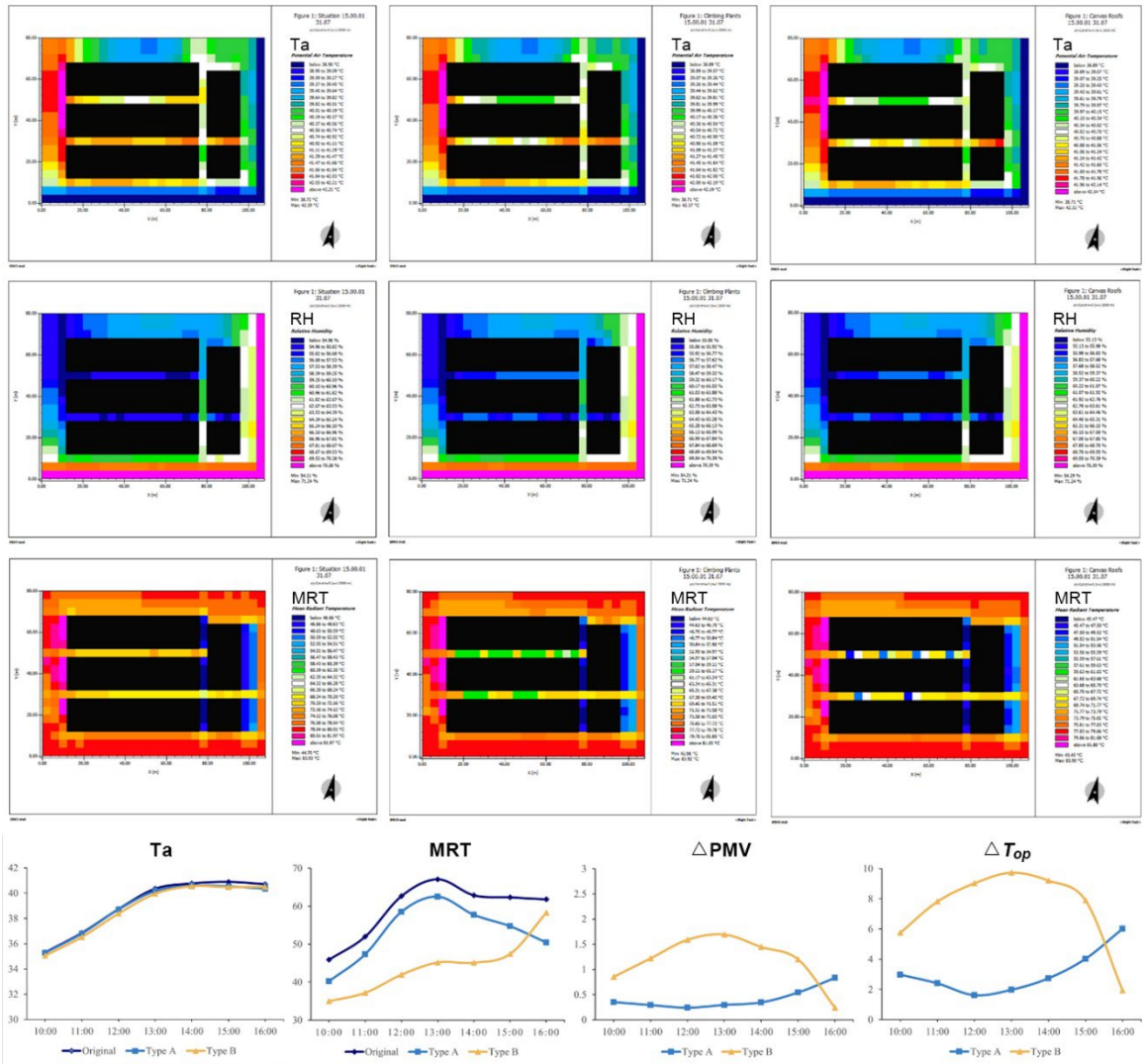

Fig. 2. Results of simulations (Ta, RH, MRT at 15:00 pm, Original, Type A, and Type B, respectively) and change trend of Ta (°C), MRT (°C), $\triangle$PMV and $\triangle T_{op}$ (°C) during peak hours (10:00 am~16:00 pm)

On the other hand, Type B exhibited greater cooling effect than Type A during 10:00 am~15:00 pm. However, the situation reversed during 15:00 pm~16:00 pm. Type B's $\triangle$PMV started to present a decreasing trend at 12:00 pm, and its $\triangle T_{op}$ declined beginning at 13:00 pm as well. In

comparison, both $\triangle$PMV and $\triangle T_{op}$ in Type A experienced decrease during 10:00 am~13:00 pm while went up stably from 13:00 pm to 16:00 pm. This indicates that Type A's cooling effect strengthened hour by hour after the noon. It is worthy noted that the $\triangle$PMV and $\triangle T_{op}$ in Type A was observed to be higher than that in Type B at 16:00 pm, indicating that Type B's cooling effect is degrading hour by hour starting from 16:00 pm (Fig 2). This could be due to the climbing plants' transpiration in Type A. The cooling effect to be generated from transpiration continues to work even though the sun's angle shifts and the level of solar radiation declines in late afternoon.

The thermal environments in alley spaces are greatly influenced by the ratio of shaded areas during daytime. The average T_a and MRT of all tested points in Type B presented an increasing trend starting from 15:00 pm, while MRT in nearby unshaded areas within the site exhibited a decreasing trend (Fig. 2). This resulted from the significant change of shadow areas' locations as the solar altitude angle shifts throughout the day and significantly affects the shading effect in narrow alleys. Notably, considerable difference in spaces with North-South orientation was observed since all tested points in these spaces were blocked by building shadows in the daytime. By contrast, shadow areas in East-West alleys were not fixed, instead, keep gradually changing along with the shifting of solar angle in the sky (Fig. 3). Consequently, the climbing plants in Type A could still absorb heat and energies via transpiration mechanism while reflecting sunlight by the leaves. In summary, this study has captured obvious cooling effects in informal shadings Type A and Type B. Type A exhibited stronger cooling effect after 16:00 pm, while Type B performed better before to that time. These findings also generally consistent with existing studies, e.g., Xiong et al., 2024.

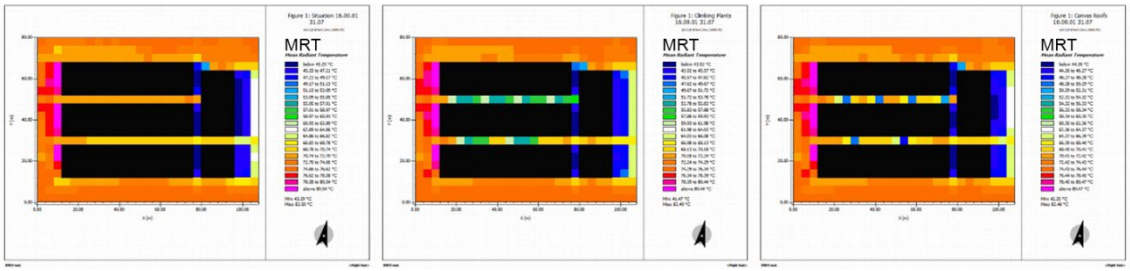

Fig. 3. The MRT (°C) variations at 16:00 pm in scenarios of Original, Type A, and Type B, respectively

3.2 Functions and Roles of Informal Shading in High-density Dwellings

Street spaces, particularly those narrow alleys in high-density old urban neighbourhoods, serve as important "outdoor living rooms", covering regular daily activities, recreation, and transportation functions (Pan, 2023). Shading is crucial for residents during hot summer as it generates shadows for ameliorating outdoor thermal comfort conditions, enabling people to conduct diverse everyday life activities, and as a result, maintaining urban dynamics and developing community social capital (Pan, 2024). High-density old urban neighbourhoods, like *Lifen* in Wuhan, usually possess narrow alleys with high aspect ratio (H/W) and diverse forms of small-scale public spaces. This study has demonstrated that the absence of shadows in compact old urban neighbourhoods can be compensated by introducing informal shading elements and then enable enhancement of outdoor thermal comfort conditions. However, there are much less green areas in high-density old urban neighbourhoods. The informal shading form of Type A (Climbing Plants) could be utilized to supplement the amount of greenery for the neighbourhoods while functioning as efficient way to establishing both thermally and visually comfortable spaces for residents. Meanwhile, growing specific climbing plants (e.g., grapes, loofah, and gourds) can be combined with the purposes of

urban framing and food production. For Type B (Canvas Roofs), by obstructing direct sunlight, it could effectively improve outdoor spaces' thermal environments as well. Additionally, those traditional old neighbourhoods located in central urban areas keep transforming with the city (re)development. Therefore, the added shading elements need to be adaptive to the emerging situations to promote urban resilience. While employing canvas roofs with diverse shapes, hues, and materials could foster soft habitation environments and new neighbourhood cultures.

4. CONCLUSION

This study has examined the cooling effect of two typical informal shading forms in Wuhan's old urban neighbourhood through computational simulations. The results illustrated that these two informal shading forms functioned to enhancing outdoor thermal comfort conditions. Canvas roofs generally presented greater cooling effect than climbing plants before late afternoon. The $\triangle$PMV difference reached the greatest at noon, and canvas roofs exhibited lower $\triangle$PMV than climbing plants in late afternoon. Meanwhile, the changing solar angle had significant impact on the cooling performance of canvas roof. Overall, informal shading, containing multiple daily functions and fostering community place-making, enables residents' continuing outdoor living in old urban neighbourhoods. Since the study was initiated in the autumn of 2024, our field measurement data did not reflect summer conditions in Wuhan. Thus, this pilot study relied on open-source data for CFD simulations. Future study should investigate more detailed spatial characteristics of informal shadings and collect more accurate environmental data for detailed and more efficient simulations.

FUNDING

This study was funded by the Huazhong University of Science and Technology (HUST) Initial Scientific Research Fund for Youth Faculty (Ref. No. 3034220113).

REFERENCES

Al Tahir I., Fattah A., Mohammed M., Asif M., Almahdy O. 2025. Evaluating the performance of outdoor shading devices on human thermal comfort in hot humid climates: A case study of Dhadran. *Building and Environment*, *271*, 112625.

Alexander C. 1977. *A Pattern Language: Towns, Buildings, Construction*. Oxford: Oxford University Press.

Lin T.-P., Matzarakis A., & Hwang R.-L. 2010. Shading effect on long-term outdoor thermal comfort. *Building and Environment*, *45*, 213-221.

Nicholson S., et al. 2024. Data driven design for urban street shading: Validataion and application of ladybug tools as a design tool for outdoor thermal comfort. *Urban Climate*, *56*, 102041.

Pan W. 2023. Self-adaptive hybrid urban morphologies community (HUMC): Its shared environment and soft intervention for sustainable urban governance. *Building and Environment*, *236*, 110251.

Pan W. 2024. From "Human-centered" to "System-oriented": Eco-Cultural Legacy of Feng Shui and Scientific Principles for Establishing Modern Resilient Cities. *Blue-Green Infrastructure for Sustainable Urban Settlements: Implications for Developing Countries Under Climate Change*, Springer, Cham, 167-191.

Tymkow P., Tassou S., Kolokotroni M., Jouhara H. 2013. *Building Services Design for Energy Efficient Buildings*. London, Routledge.

Wang S., Tong J., Liu C., Zeng K. 2013. Correlation analysis between intra-annual variation of climatic comfort and tourist online attention in Wuhan. *Journal of Subtropical Resources and Environment*, *8*, 24-28.

Watanabe, S., Nagano, K., Ishii, J., & Horikoshi, T. 2014. Evaluation of outdoor thermal comfort in sunlight, building shade, and pergola shade during summer in a humid subtropical region. *Building and Environment*, *82*, 556-565.

Xi H., Wang B., Hou W. 2024. Machine learning-based prediction of indoor thermal comfort in traditional Chinese dwellings: A case study of Hankou Lifen. *Case Studies in Thermal Engineering*, *61*, 105048.

Xiong K., Zhang Y., & He B. 2024. Impact of shading form on campus thermal environment in humid and hot areas. *Journal of Human Settlements in West China*, *39*, 149-156.

Yuan X., Li Y., Wang S. 2014. Analysis on the characteristics of interstices based on the residential buildings in Wuhan. *Art Education Research*, 166-167.

6th International Conference on Building Energy and Environment
Eindhoven University of Technology, The Netherlands
6 - 10 July 2025

Performance Investigation of Localised Outdoor Cooling Hubs using Radiant Cooling Solution

K. Dharmasastha[1], Liang Yan[1,2], Junran Yang[1,3], Jianlei Niu[1]

[1] *Department of Building Environment and Energy Engineering, The Hong Kong Polytechnic University, Hung Hom, Hong Kong*
[2] *Swiss Federal Laboratories for Materials Science and Technology Empa, Laboratory for Biomimetic Membranes and Textiles, Lerchenfeldstrasse 5, 9014, St. Gallen, Switzerland*
[3] *KU Leuven, Department of Civil Engineering, Building Physics and Sustainable Buildings, Ghent and Aalst Technology Campuses, Gebroeders De Smetstraat 1, 9000, Gent, Belgium*

SUMMARY
Urban heat waves and rising temperatures pose significant threats to human health, leading to increased mortality in many urban areas. Bus commuters, outdoor workers, the elderly, and socially vulnerable populations, including the homeless, are particularly at-risk during heat waves. While outdoor cooling spots can provide relief, existing solutions such as conventional air conditioning and evaporative cooling systems are often expensive or ineffective in humid climates. This study proposes a membrane-assisted radiant cooling system for outdoor applications that directly cools nearby individuals through radiative heat transfer, minimizing convective heat loss to the ambient environment. The thermal performance and human thermal sensation of this cooling hub were analyzed using Computational Fluid Dynamics (CFD) techniques and the CFD-CTM-JOS3 coupling method, considering factors such as solar radiation, asymmetric long-wave radiation, and other environmental conditions. On a typical summer day in Hong Kong, the proposed system's maximum heat extraction rate is 280.5 W/m² at 13:00 hr (air temperature: 31.6°C, relative humidity: 60%) for the street canyon configuration. Individuals under the cooling hub experienced a thermal sensation vote of -1 (indicating slightly cool), while those at the conventional bus stop had a vote of 3.57 (indicating hot). The current design has a radiative heat transfer efficiency of 8%, indicating significant potential for energy savings. Future research will focus on optimizing the structural design to enhance cooling efficiency and maximize this potential.

Keywords: membrane-assisted radiant cooling system, outdoor cooling, human thermal sensation, cooling shelter.

1 RESEARCH BACKGROUND

Urban heat waves and urban heat island effects are pressing issues that need urgent solutions, especially in outdoor environments. The vulnerable populations affected by these heat issues include children, the elderly, and those who spend considerable time outdoors. Many cities are inadequately designed and prepared to handle extreme heat events, resulting in increased heat-related mortality and morbidity rates worldwide (Campbell, Remenyi, White, & Johnston, 2018). Climate injustice directly impacts low-income communities, particularly those who work outdoors or wait for public transport in the scorching sun. Individuals in these situations require not just shelters but also cooling strategies that can protect them from intense heat stress.

Outdoor cooling strategies such as shading, park cooling, induced wind movement through surrounding building designs, green cover, and reflective coatings on road surfaces can help reduce temperatures. However, their effectiveness in improving outdoor comfort during extreme heat

events is often questionable. Techniques like mist cooling and evaporative cooling offer localized cooling options but tend to consume a lot of water and may not be effective in humid climates (Kyogoku & Takebayashi, 2023). In addition to existing urban cooling techniques, providing localized outdoor cooling hubs is an effective way to safeguard people from heat waves. These challenges highlight the need for alternative outdoor cooling solutions.

One such alternative cooling technique is to cool individuals directly, rather than the air. The membrane-assisted radiant cooling technique is a proven method for semi-outdoor and outdoor spaces, as it radiatively cools the occupants (Teitelbaum, Chen, et al., 2019; Yang et al., 2024). The schematic of the membrane-assisted radiant cooling panels in the localised outdoor cooling hub (LOCH) is shown in Figure 1 (Dharmasastha, Zhong, Niu, & Liang, 2024). The concept of membrane-assisted radiant cooling system was proposed by Morse in 1963, and recently revived by Teitelbaum in 2019 ((Morse, 1963; Teitelbaum, Rysanek, et al., 2019). An infrared transparent (IRT) film is used to isolate the radiant panel from the humid ambient environment, and the air gap design between the panel and membrane ensures the lowest convective heat transfer and reduces the risk of condensation. The IRT membrane allows infrared radiation to pass through, enabling the cooling panel to absorb radiation from both human bodies and surrounding heat sources. This makes it suitable for humid outdoor conditions, and experimental studies have demonstrated promising thermal comfort results in semi-outdoor and outdoor settings (Teitelbaum, Chen, et al., 2019; Yang et al., 2024). However, despite these promising results, there is a scarcity of numerical studies investigating the thermal comfort performance of membrane-assisted radiant cooling in outdoor applications, particularly within street canyon environments. This study addresses this gap by developing a numerical model of a LOCH equipped with a membrane-assisted radiant cooling system within a street canyon setting. This model incorporates all relevant outdoor ambient factors and replicates a typical Hong Kong bus stop structure. The heat transfer components of the cooling system in the outdoor is shown in Figure 1b. The system's cooling performance is analyzed for a typical summer day in Hong Kong (July 21st) and compared to a conventional bus stop.

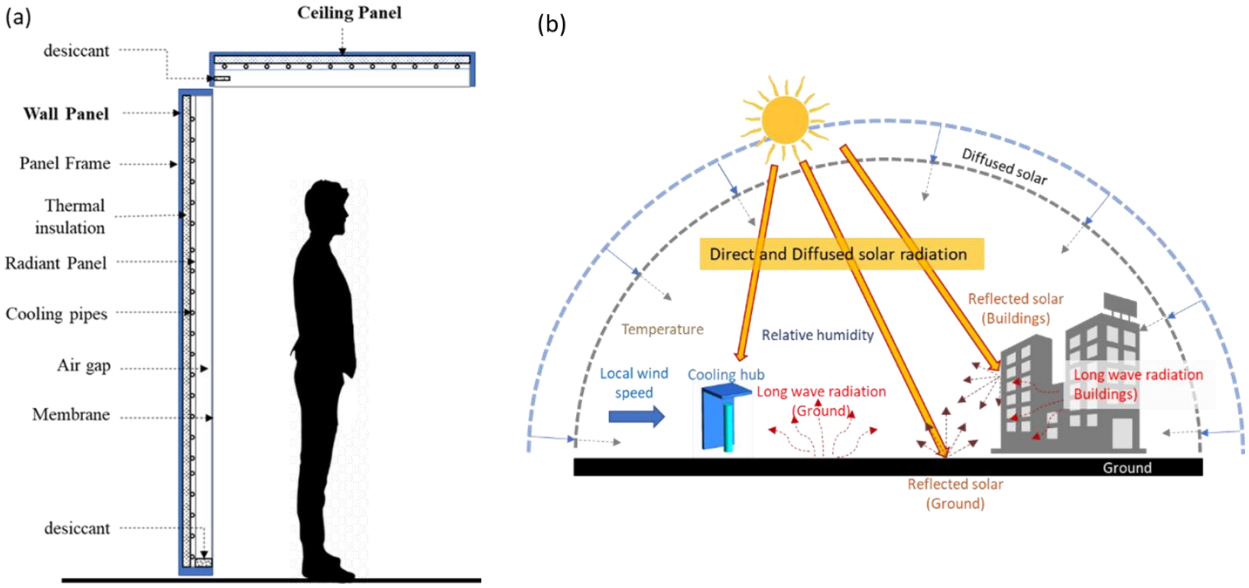

Figure 1 (a) Schematic of LOCH (b) Heat transfer components of the membrane-assisted RCS in the outdoor environment (Roshan, Moghbel, & Attia, 2020)

2 METHODOLOGY

A steady-state 3D CFD model of the localized cooling hub (LOCH) with a standing female computational thermal manikin (CTM) in the outdoor environment has been developed using ANSYS Fluent. The thermal sensation under the cooling hub is assessed by coupling the CFD simulation with the human thermoregulation model (CFD-CTM-JOS3 coupling method), along with the CBE comfort model (K Dharmasastha et al., 2024).

The framework of the methodology utilized in the study is shown in Figure 2. Initially, energy and radiation modelling using Rhino-Grasshopper is employed to simulate the building and ground surface temperatures for the street canyon configurations. Key inputs to this modelling include local weather data, street canyon geometry, and material properties. The resulting ground and building surface temperatures were then used as boundary conditions for the subsequent CFD simulations. Since the one-way coupling method (CFD-CTM-JOS-3 coupling) is suitable for the outdoor environment (K Dharmasastha et al., 2024), the ambient parameters and heat transfer coefficients acquired in the CFD simulation were directly input into the JOS-3 model (Takahashi et al., 2021) to simulate skin temperature. Finally, the obtained skin temperature data will be post-processed for thermal sensation assessment using the updated CBE comfort model (Xie et al., 2018; Xie et al., 2020).

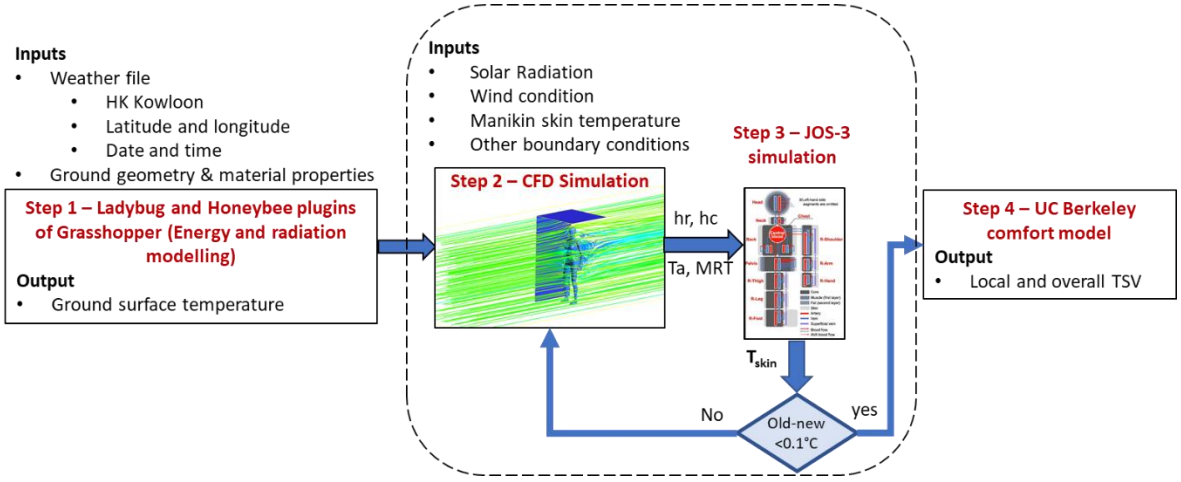

Figure 2 Framework of the methodology to assess the heat extraction rate and thermal sensation

The CFD model was validated against chamber test results, and the coupling method was compared with thermal comfort survey results (Yang et al., 2024). Thermal and comfort performance, in terms of cooling capacity and thermal sensation vote (TSV), were analyzed at 9:00, 11:00, 13:00, and 15:00 on a typical Hong Kong summer day (July 21st).

3 RESULTS AND DISCUSSIONS

3.1 Cooling performance analysis

Figure 3 shows the total heat extraction rate (Q_t), radiative heat flux (Q_r), convective heat flux (Q_c) and solar heat flux (Q_s) handled by the radiant cooling panels at different times of the day. A maximum heat extraction rate of 280.50 W/m² was observed at 13:00 hr. This study utilized a mid-infrared (MIR)-selective membrane, which reflects direct solar radiation. Consequently, even with

direct solar exposure at 9:00 hr, excessive heat extraction load was controlled. Building heights and street widths contribute to shading sidewalks during morning and evening hours. The observed maximum solar heat flux was 21% of the total heat extraction rate. Absorption of direct solar radiation by surrounding surfaces increases their temperature, leading to increased long wave radiative heat loads on the panel. Radiative heat load contributes 56-63% of the total heat extraction rate during the analyzed times. The radiative heat transfer efficiency was estimated for the current design is 8%. This suggests significant energy-saving potential, as the majority of the heat load originates from the surroundings, not occupants. This can be mitigated by shelter designs that maximize the view factor between the panels and occupants while minimizing the view factor between the panels and the surroundings. Alternatively, using a sky-window selective coating or membrane can control radiative heat load within the 8-13µm wavelength band, where human radiation emission is concentrated.

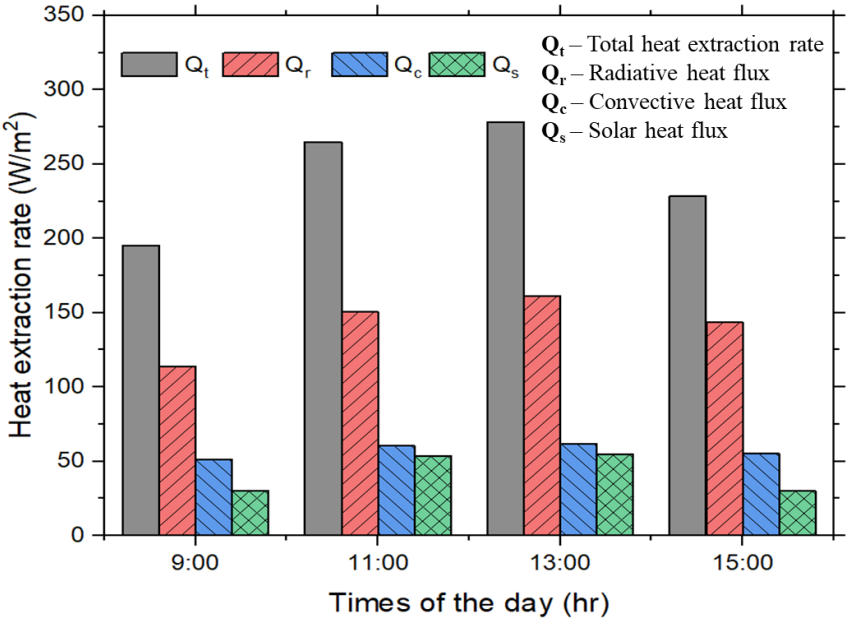

Figure 3 Comparison of heat load components for different times of the day

3.2 Comfort performance analysis

Solar radiation, particularly direct exposure and inhomogeneous exposure, significantly influences thermal sensation. Figure 4 illustrates the solar heat flux contour on the CTM body parts at different times. At 13:00 hr, the entire CTM body is shaded, while at other times, partial exposure to solar radiation creates inhomogeneous thermal condition, influencing local thermal sensation and skin temperature, affecting overall sensation. Figure 5 presents skin temperature and thermal sensation under the LOCH. At 09:00, direct solar radiation on the front of the body creates an uncomfortable and inhomogeneous thermal situation. This localized heating is evident in the predicted skin temperature and local thermal sensation of the chest, rated 3.4 (hot). However, the LOCH cools the back surface, positively influencing overall thermal sensation. Despite the front body's exposure to solar radiation, the strong cool sensation on the back (TSV_back: -1.8) improves the overall thermal sensation (TSV_overall: -1.8). This is because, according to the CBE comfort model, local thermal sensations below -1 on dominant body parts (forehead, chest,

abdomen, back, and pelvis) strongly influence the overall thermal sensation. At 11:00, the lower body (legs, thighs, and feet) is exposed to solar radiation, again creating inhomogeneous exposure and localized discomfort. By 13:00 hr, the entire body is shaded, but local thermal sensation on most body parts (excluding the back) is warmer than at other times. Consequently, the overall thermal sensation is warmer at 13:00 hr (TSV: -0.99, slightly cool) than at other times. Despite peak summer conditions (31.6°C and 60% relative humidity), the LOCH provides a comfortable, slightly cool sensation. At 15:00, the building behind the LOCH provides partial shade, improving local thermal sensation for most body parts compared to 11:00 and 13:00. The overall thermal sensations at 09:00, 11:00, 13:00, and 15:00 are -1.8, -1.3, -0.99, and -0.17, respectively.

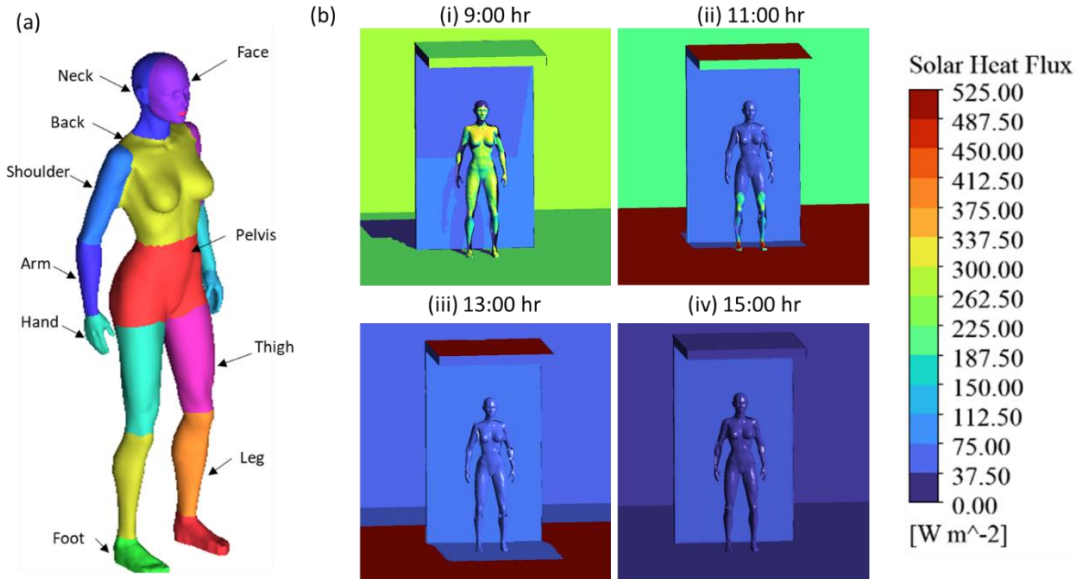

Figure 4 (a) Body parts of CTM (b) Solar heat flux contour of CTM and radiant cooling panel

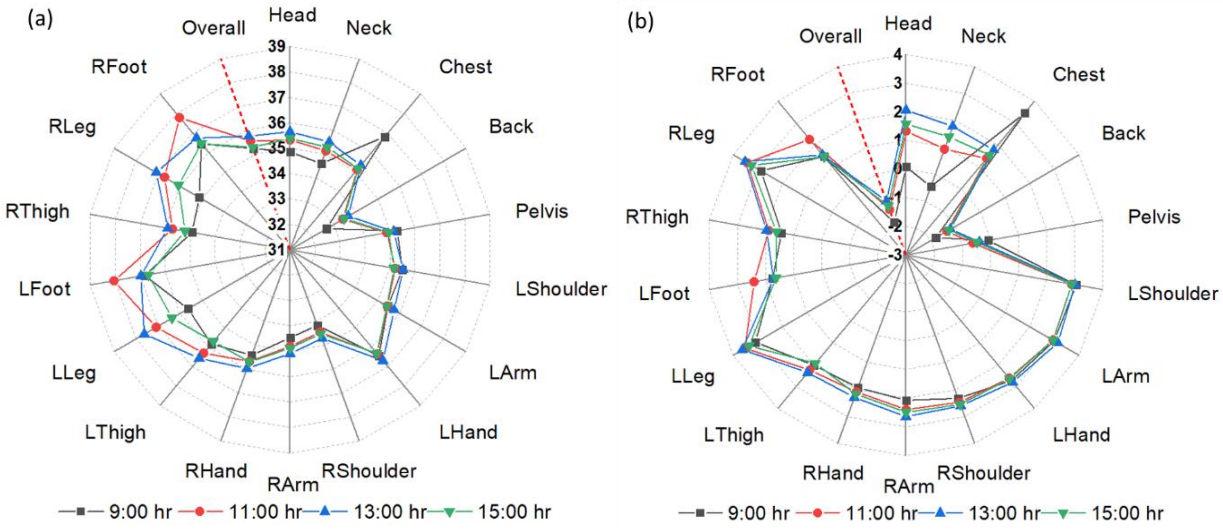

Figure 5 Local and overall (a) skin temperature and (b) thermal sensation in the LOCH

3.3 Comfort performance comparison with conventional bus stop

This section compares and analyzes the comfort performance of the LOCH against a conventional bus stop. Figure 6 shows the skin temperature and TSV comparison at 13:00 hr. A 1.7°C temperature difference is observed between the LOCH and the conventional bus stop on the back surface of the body, while other body parts show differences of less than 0.5°C. The proposed cooling system predominantly influences the back, head, and Neck. Regarding local thermal sensation on the back, a marginal difference exists between the LOCH and the conventional bus stop. This is because the predicted back skin temperature falls within the acceptable range i.e., within the null zone range (Xie et al., 2020). However, the LOCH induces a strong cooling thermal sensation on the back (TSV < -1), in turn, the overall thermal sensation within the LOCH is slightly cool (TSV: -0.99). Small skin temperature differences on the head and neck, i.e., 0.4°C and 0.5°C, respectively, between the conventional bus stop and the LOCH result in significant differences in local TSV i.e., 0.7 and 1.0, respectively. The dominant local discomfort on the head and neck in the conventional bus stop case (TSV of 2.8 and 2.7, respectively) leads to a hot overall TSV of 3.57, compared to a slightly cool -0.99 within the LOCH.

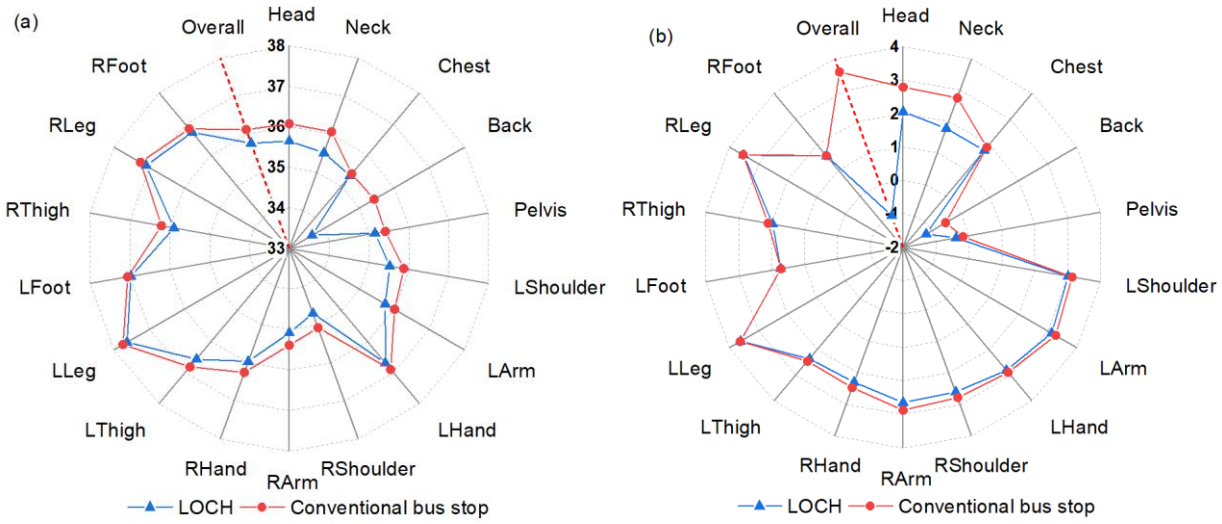

Figure 6 Comparison of (a) skin temperature and (b) TSV between LOCH and conventional bus stop at 13:00 hr

3.4 Discussions

The proposed cooling system design provides a cool thermal sensation during a typical Hong Kong summer day. However, exposed body parts experience hot local thermal sensations. The current prototype accommodates a single person, but a practical design should accommodate 3-5 people. This study is limited to a North-South orientation of street canyon. In this case, occupants may experience sun exposure during either morning or evening, depending on the LOCH's facing direction, especially if the opposite building is not sufficiently tall. In West-East oriented canyons, individuals standing at the edges will be exposed to solar radiation during morning and evening, leading to local discomfort, while those within the cooling hub should experience a comparatively better thermal sensation. Therefore, the primary modification needed is to maximize shading throughout the day. Even with full shade at noon, high diffuse solar radiation can cause occupants to feel warm or hot. The current design's large view factor between occupants and the surroundings increases radiative heat transfer, contributing to discomfort. Modifying the design to maximize the

view factor between occupants and the cooling panel, while minimizing the view factor with the surroundings, can address this issue. This strategy enhances both comfort and energy efficiency.

4. CONCLUSION

This study investigated the thermal and comfort performance of LOCH within a street canyon configuration at various times during a typical Hong Kong summer day. Comfort performance was analyzed using skin temperature and Thermal Sensation Vote (TSV) derived from coupling CFD and the JOS-3 human thermoregulation model along with an updated CBE comfort model. For the panel temperature of 10°C, a maximum heat extraction rate of 280.50 W/m² was observed at 13:00 hr. The radiative heat load contributes 56-63% of total heat extraction rate, and only around 8% of radiative heat transfer is from occupant, and remaining from the surrounding surfaces.

Solar heat flux significantly influences thermal sensation, and the cooling system effectively reduces back skin temperature, improving local and overall thermal sensation. Due to the ineffective structure design of LOCH which is replication of conventional bus stop, during morning and evening hours, solar exposure on certain body parts causes significant local discomfort. At 13:00 hr, while the LOCH design provides shade, diffuse and longwave radiation still contribute to a warmer sensation; however, a slightly cool overall thermal sensation (TSV: -0.99) is achieved even during peak Hong Kong summer conditions (Ta: 31.6°C, RH: 60%). A conventional bus stop failed to provide comfort at 13:00 hr, with occupants experiencing a hot thermal sensation, in contrast to the LOCH's slightly cool sensation. A limitation of this study is the exclusion of clothing insulation in the JOS-3 model, which will be addressed in future work. Further research will also optimize the design to maximize the view factor between occupants and the cooling panel while minimizing it with the surroundings, enhancing both efficiency and comfort. The performance of membrane-assisted radiant cooling in high-temperature locations, design improvements for extreme conditions and mitigating longwave radiation effects, and integration with low-grade energy sources will also be explored.

ACKNOWLEDGEMENTS

This work was fully supported by the General Research Funding of the Research Grant Council of the Hong Kong SAR, China (Project No. 15209621).

REFERENCES

Campbell, S., Remenyi, T. A., White, C. J., & Johnston, F. H. (2018). Heatwave and health impact research: A global review. Health & Place, 53, 210-218. doi:https://doi.org/10.1016/j.healthplace.2018.08.017

Dharmasastha, K., Liang, H., Lin, J., Xie, Y., Yu, Y., & Niu, J.-l. (2024). Evaluating thermal sensation in outdoor environments - Different methods of coupling CFD and radiation modelling with a human body thermoregulation model. Building and Environment, 266, 112081. doi:https://doi.org/10.1016/j.buildenv.2024.112081

Dharmasastha, K., Zhong, Z., Niu, J., & Liang, H. (2024). Thermal performance investigation of membrane-assisted radiant cooling system for localised outdoor cooling hub. Sustainable Cities and Society, 101. doi:10.1016/j.scs.2024.105173

Kyogoku, S., & Takebayashi, H. (2023). Experimental Verification of Mist Cooling Effect in Front of Air-Conditioning Condenser Unit, Open Space, and Bus Stop. Atmosphere, 14(1). doi:10.3390/atmos14010177

Morse, R. N. (1963). Radiant Cooling. Architectural Science Review, 6(2), 50-53. doi:10.1080/00038628.1963.9696068

Roshan, G., Moghbel, M., & Attia, S. (2020). Evaluating the wind cooling potential on outdoor thermal comfort in selected Iranian climate types. Journal of Thermal Biology, 92, 102660. doi:https://doi.org/10.1016/j.jtherbio.2020.102660

Takahashi, Y., Nomoto, A., Yoda, S., Hisayama, R., Ogata, M., Ozeki, Y., & Tanabe, S.-i. (2021). Thermoregulation model JOS-3 with new open source code. Energy and Buildings, 231. doi:10.1016/j.enbuild.2020.110575

Teitelbaum, E., Chen, K. W., Meggers, F., Pantelic, J., Aviv, D., & Rysanek, A. (2019). The Cold Tube: Membrane assisted radiant cooling for condensation-free outdoor comfort in the tropics. Journal of Physics: Conference Series, 1343(1). doi:10.1088/1742-6596/1343/1/012080

Teitelbaum, E., Rysanek, A., Pantelic, J., Aviv, D., Obelz, S., Buff, A., . . . Meggers, F. (2019). Revisiting radiant cooling: condensation-free heat rejection using infrared-transparent enclosures of chilled panels. Architectural Science Review, 62(2), 152-159. doi:10.1080/00038628.2019.1566112

Xie, Y., Huang, T., Li, J., Liu, J., Niu, J., Mak, C. M., & Lin, Z. (2018). Evaluation of a multi-nodal thermal regulation model for assessment of outdoor thermal comfort: Sensitivity to wind speed and solar radiation. Building and Environment, 132, 45-56. doi:10.1016/j.buildenv.2018.01.025

Xie, Y., Niu, J., Zhang, H., Liu, S., Liu, J., Huang, T., . . . Mak, C. M. (2020). Development of a multi-nodal thermal regulation and comfort model for the outdoor environment assessment. Building and Environment, 176. doi:10.1016/j.buildenv.2020.106809

Yang, J., Liang, Y., Zhong, Z., Dharmasastha, K., Xie, Y., & Niu, J.-L. (2024). Thermal Comfort Investigation of Membrane-assisted Radiant Cooling in Outdoor Settings. Sustainable Cities and Society, 105634. doi:https://doi.org/10.1016/j.scs.2024.105634

6th International Conference on Building Energy and Environment
Eindhoven University of Technology, The Netherlands
6 - 10 July 2025

Bridging the Climate Divide: Oman's Blueprint for Resilient Infrastructure

Abdullah Ansari[1], Khalifa Al-Jabri[2], Mubarak Al-Alawi[2]

[1]Earthquake Monitoring Center, Sultan Qaboos University, Muscat, PC: 123 Al Khoudh, Oman
[2]Department of Civil and Architectural Engineering, Sultan Qaboos University, Muscat, PC: 123 Al Khoudh, Muscat, Oman

SUMMARY
Oman, located in a climatically sensitive region, faces escalating challenges to its infrastructure from climate change impacts, notably extreme temperatures, cyclones, and floods. This study offers a technical evaluation of climate change's direct impacts on critical infrastructure systems in Oman, analyzing the economic and operational disruptions. Recent events, such as cyclones and flooding, have intensified economic losses, severely affecting transportation networks, urban infrastructure, and energy projects. Key infrastructure projects, including coastal developments and major roadways, serve as case studies to underscore the vulnerability of Oman's infrastructure to climatic hazards. The paper systematically reviews adaptation strategies initiated by the government, assessing their effectiveness in reducing infrastructure vulnerability and promoting resilience, especially in high-risk coastal regions. Despite ongoing efforts, significant challenges persist, such as funding limitations, coordination gaps among agencies, and inadequate long-term planning frameworks. The study presents a detailed technical assessment of adaptation measures, highlighting both successful initiatives and areas requiring enhanced focus. The analysis links findings to Vision Oman 2040, emphasizing the alignment between sustainable infrastructure development and climate resilience goals. By offering a comprehensive review of climate impacts and adaptive responses, the study guides policymakers on integrating climate risk assessments into infrastructure projects, encouraging more robust planning mechanisms, and fostering community engagement. This paper contributes to the global dialogue on climate adaptation and resilience, providing valuable insights for other nations with similar environmental vulnerabilities.

Keywords: climate change, infrastructure resilience, cyclones, flooding, sustainable development, vision Oman 2040

1. INTRODUCTION

Oman, located on the southeastern coast of the Arabian Peninsula, is characterized by diverse geographical features, including mountainous regions, deserts, and a long coastline along the Arabian Sea. Its strategic location makes it susceptible to various climate-related hazards, such as cyclones, floods, and extreme temperatures (Mansour et al. 2021). For instance, Cyclone Gonu in 2007 caused damages estimated at over $4 billion, while flash floods in 2010 led to losses exceeding $1 billion. Such events highlight the urgent need for effective climate change adaptation strategies to safeguard Oman's infrastructure and economy (Fritz et al. 2010). In the last decade, Oman, alongside its neighboring countries in the Gulf Cooperation Council (GCC), has faced numerous climate challenges, as illustrated in the table below (CAA 2020).

The present study focuses on the impact of climate change on infrastructure projects in Oman, examining the specific hazards posed by cyclones, floods, and rising temperatures. It aims to assess the resilience of current infrastructure and explore adaptation strategies that align with national development goals. Vision Oman 2040 (2021) emphasizes the importance of sustainable development and resilience in the face of climate challenges. By addressing climate vulnerabilities and promoting sustainable practices, the present study aligns with Vision Oman 2040 (2021)

objectives of fostering a robust and adaptive economy while ensuring the safety and welfare of its citizens.

2. IMPACT OF CLIMATE CHANGE ON INFRASTRUCTURE

2.1. Cyclones and Floods

Cyclones and floods have severely impacted Oman's infrastructure, particularly in coastal and low-lying regions. Both types of events have caused extensive damage to roads, bridges, and other critical infrastructure, leading to significant disruptions and economic losses. Table ` highlights key infrastructure projects affected by cyclones and major flood events.

Table 1. Notable climate events, economic impacts, and vulnerabilities in GCC countries (Waha et al. 2017).

Country	Notable Climate Events (Last 10 Years)	Economic Impact	Climate Vulnerabilities
Oman	Cyclone Mekunu (2018), Cyclone Shaheen (2021), floods in 2010, 2022 and 2024	$5 billion	Coastal erosion, flooding, heatwaves
Qatar	Extreme heat events (2015, 2019), flash floods (2018)	$600 million	Heat stress, water scarcity
UAE	Extreme heatwaves (2017, 2020), heavy rains and flooding (2021)	$800 million	Coastal flooding, water scarcity
Saudi Arabia	Dust storms, extreme heatwaves (2016-2022), flooding in Jeddah (2020)	$2 billion	Heat stress, desertification, flooding
Bahrain	Extreme heat events, flooding (2017), rising sea levels	$400 million	Coastal flooding, water scarcity

These events highlight the vulnerabilities in Oman's infrastructure, especially in flood-prone areas (Al Rasbi 2019). Cyclones and floods have had profound effects on transportation routes, drainage systems, and accessibility, emphasizing the necessity for improved resilience measures in the design and management of infrastructure. Figure. 1 shows the impact of climate events on the infrastructure and urbans areas in Oman.

2.2. Extreme Temperatures

Rising temperatures are another pressing challenge, affecting the longevity and functionality of Oman's infrastructure. Table 2 shows key projects impacted by prolonged periods of extreme heat:

Table 2. Thermal impacts on infrastructure projects highlighting maintenance challenges (Coll 2015).

Project	Year(s)	Impact
Sultan Qaboos Grand Mosque Complex	Ongoing (since 2015)	Thermal expansion has caused cracks in stone surfaces and pavement damage, requiring regular maintenance.
Muscat International Airport	Ongoing (since 2010)	Extreme heat has accelerated runway surface degradation, increasing resurfacing needs.
Oil and Gas Pipelines in Desert	Ongoing	Prolonged high temperatures have caused material fatigue, raising the risk of leaks and increasing cooling demands at pumping stations.

These impacts highlight the need for adaptive strategies, such as the use of heat-resistant materials, to mitigate long-term damage and operational disruptions in key sectors like aviation and energy.

(a) Infrastructure

(b) Urban Areas

Figure 1. The impact of climate events on the infrastructure and urbans areas in Oman.

3. VULNERABILITY AND RISK MANAGEMENT

Vulnerability and risk assessments are vital for understanding the susceptibility of infrastructure to climate-induced risks. These assessments inform the design and implementation of resilience measures across various sectors, including transportation, urban development, and energy infrastructure in Oman.

3.1 Transportation Infrastructure Vulnerability

Oman's transportation networks face significant risks from extreme weather, particularly cyclones and floods. Table 3 is summarizing the vulnerability of critical transportation infrastructure to climate change-related events. It shows how critical transportation projects such as the Batinah Coastal Road and Al Sharqiyah Expressway are exposed to various climate-related risks. Upgrading drainage capacity and constructing protective barriers are some of the key adaptation strategies identified.

3.2 Urban Development

Urban areas in Oman, particularly Muscat and Salalah, are at high risk of flooding. The vulnerability of key urban infrastructure projects and proposed adaptation measures as shown in Table 4. Table 4 shows that urban flood management is critical in cities like Muscat and Salalah. Adaptation strategies involve enhancing drainage systems and integrating green infrastructure solutions to reduce the impact of future floods.

Table 3. Transportation infrastructure projects with climate risks, impacts, and adaptation measures (Al-Awadhi et al. 2019; Ansari et al. 2024).

Project Name	Infrastructure Type	Climate Risk	Impact	Proposed Adaptation
Batinah Coastal Road	Coastal Highway	Cyclones, Storm Surges	Road blockages, structural damage	Upgrade drainage systems, build flood barriers
Al Sharqiyah Expressway	Inland Highway	Flash Floods	Road washouts, erosion	Enhance drainage capacity, adjust elevation of vulnerable sections
Al-Sharqiyah Expressway Tunnel-2 (AST2)	Tunnel	Flooding, Seismic Events	Tunnel closure, water ingress, collapse	Reinforce lining, improve drainage systems

Table 4. Urban development projects with climate risks, impacts, and adaptation measures (Al Shueili 2015).

Project Name	Infrastructure Type	Climate Risk	Impact	Proposed Adaptation
Muscat Urban Infrastructure	Muscat	Flash Floods, Cyclones	Submerged roads, damage to buildings	Upgrade drainage systems, build retention basins
Salalah Flood Mitigation Project	Salalah	Intense Rainfall, Floods	Road closures, residential area flooding	Expand drainage channels, construct retention ponds

4. CLIMATE RESILIENT INFRASTRUCTURE

Adaptation strategies are crucial for mitigating the impacts of climate change on oman's infrastructure. This section delves into specific projects and the adaptation measures implemented to enhance resilience, focusing on transportation networks, urban development, and energy infrastructure. Below is a detailed explanation of the ongoing and planned adaptation strategies, supported by actual project details presented in Table 5.

4.1 Transportation Sector Adaptation

Oman’s transportation network, particularly coastal highways and tunnels, is highly susceptible to extreme weather events like cyclones, flooding, and high temperatures. To address these vulnerabilities, key projects have been designed or upgraded to withstand climate-related hazards.

In the transportation sector, projects like the Batinah Coastal Road and Al-Sharqiyah Expressway Tunnel-2 highlight key adaptation strategies such as road elevation, slope stabilization, and advanced drainage systems. The Bausher-Al Amerat Tunnel, once completed, will replace a frequently flooded mountain road, providing a more resilient transport link between Muscat and Al Amerat cities.

4.2 Urban Development Adaptation (NCSI 2023)

Urban areas in Oman, particularly Muscat and Salalah, are prone to flooding during heavy rainfall and cyclones. To mitigate these risks, urban development projects (Table 6) have focused on

enhancing flood management through the construction of stormwater drainage systems, retention basins, and the integration of green infrastructure solutions.

Table 5. Current status of transportation infrastructure projects (TMST 2023).

Project Name	Location	Climate Risk	Adaptation Strategy	Project Status
Batinah Coastal Road	Northern Oman	Cyclones, Storm Surges	Elevated road sections, drainage upgrades, flood barriers	Ongoing (Phase 2 construction)
Al-Sharqiyah Expressway	Eastern Oman	Flash Floods	Advanced drainage systems, slope stabilization	Completed (2023)
Al-Sharqiyah Expressway Tunnel-2	Al-Sharqiyah Region	Flooding, Landslides, Seismic Risks	Lining reinforcement, enhanced drainage, flood-resistant design	Ongoing (expected completion 2025)
Bausher-Al Amerat Tunnel Project	Muscat	Heavy Rain, Flash Floods	Tunnel construction to replace vulnerable mountain road	Planned (proposal stage)

Table 6. Current status of urban development projects.

Project Name	City	Climate Risk	Adaptation Strategy	Project Status
Muscat Drainage Improvement Plan	Muscat	Flash Floods, Cyclones	Expansion of drainage systems, retention basins, green spaces, protection dams	Planned (to begin in 2024)
Salalah Flood Mitigation Project	Salalah	Intense Rainfall, Cyclones	Upgraded drainage channels, flood retention ponds, protection dams	Completed (2022)
Duqm Smart City Project	Duqm	Rising Sea Levels, Storm Surges	Coastal flood defenses, permeable pavements, green infrastructure	Ongoing (Phase 1 completion in 2025)
Sohar Industrial City Flood Management	Sohar	Flash Floods	Industrial drainage systems, flood-resistant design	Planned (early stages)

In Muscat and Salalah, urban drainage improvement projects and flood mitigation efforts have been prioritized, with Muscat planning to expand its stormwater drainage systems. The Duqm Smart City project, a major urban development, integrates climate-resilient infrastructure with coastal defenses and green infrastructure. Figure 2 shows, as an example, the flood route of Wadi Al-Khoudh in Muscat and the proposed flood mitigation's solution.

Figure 2. The flood's route of Wadi Al-Khoudh in Muscat and the proposed route

4.3 Water Management and Agriculture Adaptation

Oman's water management and agricultural sectors are increasingly affected by reduced rainfall, flash floods, and rising temperatures. Various projects have been initiated to improve water security, including desalination plants and modern irrigation techniques to adapt to changing climate conditions. Table 7 presents the current status of water management and agriculture related projects

Table 7. Current status of water management and agriculture related projects **(**Shammas 2007; Muscat Municipality 2024).

Project Name	Location	Climate Risk	Adaptation Strategy	Project Status
Barka Desalination Plant Expansion	Barka	Drought, Water Scarcity	Increased desalination capacity, water storage infrastructure	Ongoing (Phase 3)
Wadi Dayqah Dam Irrigation Project	Al Sharqiyah Region	Drought, Flash Floods	Efficient irrigation systems, water storage management	Completed (2021)
Nizwa Aquifer Recharge Project	Nizwa	Water Scarcity, Overuse	Managed aquifer recharge, sustainable water extraction	Planned (design stage)

In the water management sector, the Barka Desalination Plant and the Nizwa Aquifer Recharge Project are two key projects aimed at securing water resources for Oman’s growing population. Modern irrigation techniques such as drip irrigation and rainwater harvesting are being implemented to enhance the resilience of the agricultural sector.

5. CHALLENGES IN IMPLEMENTATION

5.1 Technical expertise and capacity building

Oman faces challenges related to the technical expertise required for designing and implementing climate-resilient infrastructure (MOF 2024). Although international collaboration is helping bridge this gap, the local workforce may still lack the specialized knowledge necessary to design solutions for complex climate scenarios, particularly for large-scale projects like tunnels and coastal defenses (Shammas 2007; McBean and Rodgers 2010). To enhance scientific robustness, integrate quantitative analyses such as cost-benefit assessments, climate vulnerability indices, or scenario modeling to evaluate the long-term effectiveness and feasibility of adaptation strategies across diverse climatic contexts.

5.2 Public and community engagement

Engaging the public and local communities is critical for the success of adaptation projects. However, in Oman, public awareness of climate risks and the benefits of climate-resilient infrastructure is still developing (Hafidh et al. 2017; UNDP 2020). In regions of Oman, particularly coastal areas such as Qurayyat, community involvement in climate-resilient design has been effective, as local feedback has influenced flood mitigation strategies. Nevertheless, challenges like a lack of technical knowledge and minimal engagement in rural interior regions obstruct wider implementation, highlighting the necessity for comprehensive education and outreach initiatives. Without adequate community participation, especially in urban planning or water management projects, adaptation efforts may face resistance or fail to address local needs

effectively. Adaptation strategies need to include engineering standards like raised road embankments capable of enduring flooding that occurs once every century, sturdy concrete culverts for efficient drainage, and roofing systems that resist high winds in accordance with cyclonic load criteria. These measures are informed by revised construction regulations specific to local geoclimatic hazards. Table 8 summarizes examples of challenges in climate change adaptation projects in Oman, focusing on project success rates and economic aspects:

Table 8. Project challenges and economic impact (Vision Oman 2040 (2021))

Project Name	Key Challenges	Project Success Rate	Economic Aspects
Al-Sharqiyah Expressway Tunnel-2	Delays due to inter-ministerial approvals	Moderate	Increased costs due to delays; potential for improved trade and transport efficiency once completed.
Duqm Smart City Project	Limited local technical expertise	Moderate	High initial investment required; potential for long-term economic benefits through sustainable urban development.
Muscat Drainage Improvement Plan	Public resistance and lack of community engagement	Moderate	Project funding impacted by community opposition; successful implementation could reduce economic losses from flooding.

6. CONCLUSIONS

The pressing challenges posed by climate change necessitate immediate and coordinated responses to safeguard infrastructure in Oman. This research underscores the profound vulnerabilities inherent in Oman's geographical location, making it susceptible to a range of climate hazards, including cyclones, floods, and extreme temperatures. Significant events, such as Cyclone Mekunu and Cyclone Shaheen, have not only inflicted substantial economic losses but have also disrupted essential services and infrastructure, underscoring the urgent need for effective adaptation strategies. The findings illustrate that while some infrastructure projects, such as the Al-Sharqiyah Expressway Tunnel-2 and the Batinah Coastal Road, have begun to incorporate resilience measures, many others remain at risk due to inadequate planning and resource allocation. The paper highlights the necessity for innovative approaches that integrate climate adaptation into all stages of project development, ensuring that infrastructure can withstand the increasing frequency and intensity of climate events.

A comprehensive perspective on the sustainability of Oman’s climate-resilient infrastructure design stresses the importance of incorporating adaptive strategies like raised roadways, strong drainage systems, and structures designed to withstand cyclones. These measures, in harmony with green technologies and local risk evaluations, guarantee longevity, reduce maintenance expenses, and enhance the objectives of Vision Oman 2040 for sustainable urban progress. Moreover, the alignment of these adaptation strategies with Vision Oman 2040 presents a unique opportunity to promote sustainable development while enhancing national resilience. Emphasizing the importance of collaboration among government, private sector, and communities will be crucial for developing effective policies and investment strategies that prioritize climate resilience.

REFERENCES

Mansour, S., Darby, S., Leyland, J., & Atkinson, P. M. (2021). Geospatial modelling of tropical cyclone risk along the northeast coast of Oman: Marine hazard mitigation and management policies. Marine Policy, 129, 104544.

Fritz, H. M., Blount, C. D., Albusaidi, F. B., & Al-Harthy, A. H. M. (2010). Cyclone Gonu storm surge in Oman. Estuarine, Coastal and Shelf Science, 86(1), 102-106.

Waha, K., Krummenauer, L., Adams, S., Aich, V., Baarsch, F., Coumou, D., ... & Schleussner, C. F. (2017). Climate change impacts in the Middle East and Northern Africa (MENA) region and their implications for vulnerable population groups. Regional Environmental Change, 17, 1623-1638.

Al Rasbi, T. S. S. (2019). Social vulnerability to tropical cyclones: A case study in Muscat Governorate, Oman (Doctoral dissertation, University of Leeds).

Coll, J. (2015). Recent trends in temperature and precipitation in Al Jabal Al Akhdar, Sultanate of Oman, and the implications for future climate change. Journal of Earth Science and Climate Change, 6(8).

Al-Awadhi, T., Charabi, Y., & Choudri, B. S. (2019). Pathways for building urban resilience to climate change in Oman. Development in Practice, 29(5), 594-605.

Ansari, A., El-Hussain, I., Deif, A., Mohamed, A. M., Al-Shijbi, Y., Al-Jabri, K., & Huang, Z. (2024). Seismic vulnerability assessment and fragility analysis of tunnels in Oman: Development of risk matrices and functionality guidelines. Structures (Vol. 69, p. 107428).

Al Shueili, K. (2015). Towards a sustainable urban future in Oman: Problem and process analysis (Muscat as a case study) (Doctoral dissertation, The Glasgow School of Art).

Tourism Strategy (TMST). (2023). Tourism Development Plan. The Sultanate of Oman.

National Center for Statistics and Information (NCSI). (2023). Statistical Book 2023.

Muscat Municipality. (2024). Flood Risks Prevention Projects and Rainwater Accumulations Treatment, Muscat.

Shammas, M.I. (2007). Sustainable management of the Salalah coastal aquifer in Oman using an integrated approach. Doctoral dissertation, KTH Royal Institute of Technology, Sweden.

Ministry of Finance (MOF). (2024). A Guide to the State's General Budget for the Fiscal Year 2024. https://www.mof.gov.om/UploadsAll/YearlyBudget/1704186746126Budget%202024.pdf

McBean, G., & Rodgers, C. (2010). Climate hazards and disasters: the need for capacity building. Wiley Interdisciplinary Reviews: Climate Change, 1(6), 871-884.

Hafidh, A., Noel, S., Ahmad, M. R., & Jafar, J. (2017). Evaluating ecotourism challenges in Oman. In International Tourism Development and The Gulf Cooperation Council States, pp. 156-168, Routledge.

United Nations Development Programme (UNDP). (2020). Toolkit for value chain analysis and market development integrating climate resilience and gender responsiveness. Integrating agriculture in National Adaptation Plans (NAP-Ag) Programme.

Vision Oman 2040, Implementation Follow-up Unit, Annual Report 2021 Citizen Version. (2021). Sultanate of Oman.

Ministry of Environment and Climate Affairs (MECA). (2019). Initial National Communication under The United Nations Framework Convention on Climate Change. https://unfccc.int/resource/docs/natc/omnnc1.pdf

Civil Aviation Authority (CAA). (2020). National Strategy for Adaptation and Mitigation to Climate Change for the Sultanate of Oman (2020-2040).

Building Mechanical System and Controls (15:30-17:00 h)

6th International Conference on Building Energy and Environment
Eindhoven University of Technology, The Netherlands
6 - 10 July 2025

Natural ventilation effects on a residential building sensible and latent energy loads in Toronto

Amir A. Aliabadi[1]

[1] *School of Engineering, University of Guelph, Guelph, Ontario, Canada, aaliabad@uoguelph.ca*

ABSTRACT

Natural Ventilation (NV) is a passive approach to reduce the building energy demand in suitable climate zones. However, most studies considering NV models or experiments only focus on the sensible load (cooling) reduction of buildings, while they do not investigate the implications of NV in latent load (humidification and dehumidification) changes in buildings. This study uses an urban physics model, the Vertical City Weather Generator (VCWG v1.4.7) software, to address this research gap. Simulations are executed for the climate of Toronto (zone 5) in 2020 to analyze the NV potential for single-detached two-story residential homes. A rule-based controller is implemented to make decisions on opening/closing windows based on indoor/outdoor temperatures, humidities, and sensible cooling/heating loads, while targeting temperature and humidity setpoints. The base case building of interest exhibits features (envelop thermal resistance, infiltration rate, ventilation rate, glazing ratio, and solar heat gain coefficient) according to common codes and standards in the region. Some sensitivity tests are performed to understand the effects of building envelop infiltration and thermal resistance in the performance of the NV system. Additional cases exhibit air tight buildings, high insulation buildings, and air tight/high insulation buildings associated with the Passive House standard. Using NV, annual energy savings around ~ 10 kW-hr m^{-2} are possible for combined sensible and latent loads. The implications of latent load, envelop infiltration, and envelop thermal resistance are discussed.

Keywords: building energy modeling, natural ventilation, sensible and latent loads.

INTRODUCTION

To moderate the impact of buildings on climate change [9], Natural Ventilation (NV) is a suitable technique to lower the sensible cooling demand of buildings in favorable climates. However, most typically, NV is only analyzed by considering the sensible cooling demand of buildings, while ignoring the implications on the latent demand. For instance, by opening windows, the sensible cooling demand of a building may be reduced, but air that is either too moist or too dry can enter the building and increase the latent demand, i.e. by dehumidification or humidification demands, respectively [7, 8, 16, 15]. In this study, an urban physics model is used to consider the implications of both sensible and latent demands when using NV for the climate of Toronto. Simulations are conducted for a full year in 2020. A rule-based controller is developed and implemented to decide when windows shall be opened to enhance NV ventilation based on environmental and building performance variables.

METHODS

Model Description

The Vertical City Weather Generator (VCWG v1.4.7) is a microscale and multiphysics urban physics model that predicts the urban environmental and building performance variables. As shown in Figure 1, it integrates various submodels to account for exchanges of momentum, heat, humidity, and water through soil, urban surfaces, and the atmosphere. The modelling paradigms employed are the Resistance Capacitance (RC) thermal network, Navier-Stokes transport in the vertical direction, Monin-Obukhov Similarity Theory (MOST), and lump energy modeling [1]. Full descriptions of the model are provided in prior literature [4, 10, 11, 2, 15, 14]. VCWG is forced with weather data generated by another software titled the Vatic Weather File Generator (VWFG v1.0.0), which uses the ERA5 dataset from the European Centre for Medium-Range Weather Forecasts (ECMWF) and prepares data in the EnergyPlus Weather (EPW) file format at hourly resolution [3]. The rule-based controller for NV is discussed in our previous study [15]. Briefly, NV is considered under cooling mode. If $T_{\text{out}} < T_{\text{in}}$ & $T_{\text{set}} < T_{\text{in}}$ [K] then a specific humidity condition is checked to trigger NV. For this condition either of the following criteria must be met: $q_{\text{in}} > q_{\text{set}}$ & $q_{\text{out}} < q_{\text{in}}$ or $q_{\text{in}} < q_{\text{set}}$ & $q_{\text{out}} > q_{\text{in}}$ [kgv kga^{-1}]. To trigger NV, windows are opened and a new air exchange rate is calculated due to ventilation, infiltration, and NV.

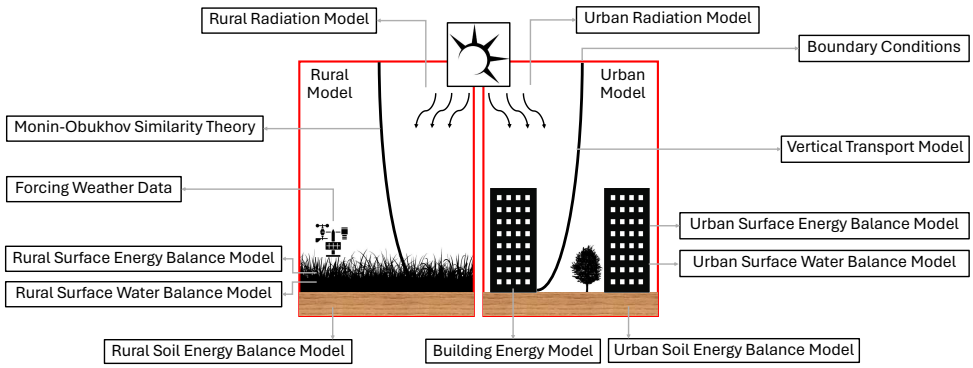

Figure 1. Schematic of the Vertical City Weather Generator (VCWG v1.4.7).

Simulation Cases

Two sets of simulations are conducted with and without NV. Four buildings are considered according to Table 1. The base building is associated with relevant codes and standards [12, 6, 5]. The air tight or high insulation buildings exhibit a low infiltration rate or a high envelop thermal resistance. The Passive House building exhibits both a low infiltration rate and a high envelop thermal resistance [13]. It is primarily intended to conduct the simulations for the year 2020, although some months (February, March, April) have been substituded in prior years (2018 and 2019), for which the forcing weather data have not been reliable in 2020.

Building Energy Loads

NV is formulated in the context of the building sensible and latent load calculation. The sensible load, $\pm[Q_{\text{vent}} + Q_{\text{inf}} + Q_{\text{int}} + Q_{\text{mass}} + Q_{\text{wall}} + Q_{\text{ceil}} + Q_{\text{win}} + Q_{\text{tran}}]$, involves ventilation load Q_{vent}, infiltration load Q_{inf}, internal heat from occupants and equipment Q_{int}, heat from the building's mass Q_{mass}, heat from walls Q_{wall}, heat from ceilings Q_{ceil}, heat conduction through windows

Table 1. Building features for Toronto (zone 5) based on codes and standards.

Parameter	Base	Air Tight	High Insulation	Passive House
Roof Resistance [m^2 K W^{-1}]	6.41	6.41	11.5	11.5
Wall Resistance [m^2 K W^{-1}]	3.6	3.6	7.0	7.0
Window U-value [W m^{-2} K^{-1}]	1.9	1.9	1.9	1.9
Infiltration Rate [ACH]	3.0	0.6	3.0	0.6
Ventilation Rate [L s^{-1} m^{-2}]	0.3	0.3	0.3	0.3
Glazing Ratio [-]	0.4	0.4	0.4	0.4
Solar Heat Gain Coefficient [-]	0.4	0.4	0.4	0.4

Q_{win}, and radiant heat passing through windows Q_{tran} [W]. In this formulation, the positive sign (+) will be used to calcaulte the sensible cooling demand, and the negative sign (−) will be used to calculate the sensible heating demand. Except for Q_{int}, which is scheduled in VCWG, the other terms are parameterized using the heat balance method:

$$
\begin{aligned}
Q_{\text{vent}} &= V_{\text{vent}} \rho_a c_{pa} (T_{\text{out}} - T_{\text{set}}) \\
Q_{\text{inf}} &= V_{\text{inf}} \rho_a c_{pa} (T_{\text{out}} - T_{\text{set}}) \\
Q_{\text{mass}} &= A_{\text{bui}} h_m (T_{\text{mass}} - T_{\text{set}}) \\
Q_{\text{wall}} &= A_{\text{wall}} h_w (T_{\text{wall}} - T_{\text{set}}) \\
Q_{\text{ceil}} &= A_{\text{bui}} h_c (T_{\text{ceil}} - T_{\text{set}}) \\
Q_{\text{win}} &= A_{\text{win}} U_w (T_{\text{out}} - T_{\text{set}}) \\
Q_{\text{tran}} &= A_{\text{win}} S \times SHGC,
\end{aligned}
\tag{1}
$$

where V_{vent} and V_{inf} [m^3 s^{-1}] are ventilation and infiltration air flow rates, ρ_a [kg m^{-3}] is density of air, c_{pa} [J kg^{-1} $^\circ C^{-1}$] is heat capacity of air, A_{bui} [m^2] is building footprint area, T_{mass}, T_{wall}, T_{ceil}, T_{set}, and T_{out} [$^\circ$C] are mass, wall, ceiling, set-point, and outdoor temperatures, A_{bui}, A_{wall}, and A_{win} [m^2] are building footprint, wall, and window areas, h_m, h_w, and h_c [W m^{-2} $^\circ C^{-1}$] are convective heat transfer coefficients, U_w [W m^{-2} $^\circ C^{-1}$] is the window U-value, S [W m^{-2}] is the shortwave radiation flux through the window, and $SHGC$ [-] is the solar heat gain coefficient for the window. The sensible load is met by the building's sensible cooling/heating equipment. The latent load, $\pm[Q_{\text{latvent}} + Q_{\text{latinf}} + Q_{\text{latint}}]$, involves latent heat from ventilation Q_{latvent}, latent heat from infiltration Q_{latinf}, and latent heat from internal heat from occupants and equipment Q_{latint} [W]. In this formulation, the positive sign (+) will be used to calcaulte the dehumidification demand, and the negative sign (−) will be used to calculate the humidification demand. These loads are met by the building's humidification/dehumidification equipment. Except for Q_{latint}, which is scheduled in VCWG as a fraction of sensible heat from occupants and equipment Q_{int}, the other terms are parameterized using the humidity balance method:

$$
\begin{aligned}
Q_{\text{latvent}} &= V_{\text{vent}} \rho_a L_v (q_{\text{out}} - q_{\text{set}}) \\
Q_{\text{latinf}} &= V_{\text{inf}} \rho_a L_v (q_{\text{out}} - q_{\text{set}}),
\end{aligned}
$$

where L_v [J kg_v^{-1}] is latent heat of vaporization for water, and q_{out} and q_{set} [kgv kga^{-1}] are outdoor and set-point specific humidities, respectively. When NV is deployed, the model enhances the infiltration rate V_{inf} [m^3 s^{-1}] and thus captures the physics properly. In this version of VCWG,

latent load is only computed if the building is cooled or heated, regardless of building sensible (cooling or heating) demands. The cooling is triggered when the sensible cooling load is positive and canyon air temperature is greater than 288 K. The heating is triggered when the sensible heating load is positive and canyon air temperature is less than 288 K. The buildings are arranged in rows with a separation of 30 m maintained in each horizontal direction (x and y). Temperature, specific humidity, and wind (the x and y components) data within the urban roughness sub-layer were extracted along the vertical direction (z) from VCWG. The buildings are low-rise residential units designed with dimensions of 13.8 m $\times$ 13.8 m $\times$ 6 m. Each story features two windows on each side, with an equivalent area of 26.4 m^2 per facade. The NV system model assumes a single equivalent window on each building side and is based on the ASHRAE Fundamentals handbook. The calculation of the NV system air flow rate is performed by $Q_{NV} = CAU$, where Q_{NV} [m^3 s^{-1}] is flow rate, $C = 0.5$ [-] is a coefficient describing the effectiveness of windows (it can be assumed to be 0.5 to 0.6 for normal winds and 0.25 to 0.35 for diagonal winds), A [m^2] is the free area of inlet openings, and U [m s^{-1}] is the wind speed normal to the facade. Once Q_{NV} is known, it can be added to the base infiltration rate V_{inf} [m^3 s^{-1}] in the VCWG model.

Diagnostic Equations for Indoor Temperature and Specific Humidity

Following the sign conventions discussed above, the heat balance equation can be rewritten in the following form, which separates terms including or excluding the unknown indoor temperature

$$\underbrace{\text{Cooling Load} - \text{Heating Load} - Q_{\text{tran}} - Q_{\text{int}}}_{Q} = Q_{\text{vent}} + Q_{\text{inf}} + Q_{\text{mass}} + Q_{\text{wall}} + Q_{\text{ceil}} + Q_{\text{win}} \tag{2}$$

$$\begin{aligned} Q = {} & \underbrace{V_{\text{vent}}\rho_a c_{pa} T_{\text{out}} + V_{\text{inf}}\rho_a c_{pa} T_{\text{out}} + A_{\text{bui}} h_m T_{\text{mass}} + A_{\text{wall}} h_w T_{\text{wall}} + A_{\text{bui}} h_c T_{\text{ceil}} + A_{\text{win}} U_w T_{\text{out}}}_{H1} \\ & - [\underbrace{V_{\text{vent}}\rho_a c_{pa} + V_{\text{inf}}\rho_a c_{pa} + A_{\text{bui}} h_m + A_{\text{wall}} h_w + A_{\text{bui}} h_c + A_{\text{win}} U_w}_{H2}] T_{\text{in}} \end{aligned} \tag{3}$$

Likewise the specific humidity balance equation can be rewritten as the following form, which separates terms including or excluding the unknown indoor specific humidity

$$\underbrace{\text{Dehumidification Load} - \text{Humidification Load} - Q_{\text{latint}}}_{QL} = Q_{\text{latvent}} + Q_{\text{latinf}} \tag{4}$$

$$QL = \underbrace{V_{\text{vent}}\rho_a L_v q_{\text{out}} + V_{\text{inf}}\rho_a L_v q_{\text{out}}}_{HL1} - \underbrace{[V_{\text{vent}}\rho_a L_v + V_{\text{inf}}\rho_a L_v]}_{HL2} q_{\text{in}} \tag{5}$$

In VCWG v1.4.7, the resulting two equations $T_{\text{in}} = (H1 - Q)/H2$ and $q_{\text{in}} = (HL1 - QL)/HL2$ are re-evaluated in each timestep to give the indoor temperature and specific humidity.

Waste Heat Rejection into the Urban Environment

Under cooling mode, we assume that both sensible cooling and dehumidification demands are met by a refrigeration cycle with a known Coefficient Of Performance (COP). Using the first law of thermodynamics, the waste heat rejected to the environment will be given by,

$$\text{Waste Heat} = (\text{Sensible Demand} + \text{Dehumidification Demand}) \left(1 + \frac{1}{COP}\right). \tag{6}$$

Under heating mode, we assume that both sensible heating and humidification demands are met by a furnace with a known thermal efficiency (η). Using the first law of thermodynamics, the waste heat rejected to the environment will be given by,

$$\text{Waste Heat} = (\text{Sensible Demand} + \text{Humidification Demand}) \left(\frac{1}{\eta} - 1 \right). \quad (7)$$

What if the building has a humidification demand under cooling mode, or dehumidification demand under heating mode? In this case, latent demand is properly logged, but its associated waste heat is not considered by the model. In another word, the waste heat for latent demand in our model is formulated for dry climates under heating mode and humid climates under cooling mode.

RESULTS AND DISCUSSION

Figure 2 shows the monthly energy demands for the base and Passive House cases with and without using NV. Compared to the base case, the Passive House exhibits lower heating, dehumidification, and humidification demands, but it exhibits greater cooling demand. Under cooling mode, the energy savings using NV is greater for the Passive House than the base case. However, NV causes greater dehumidification demand for the Passive House compared to the change in dehumidification demand for the base case. Reasons for these findings are justified in our previous study [15]. Figure 3 shows the hourly results for temperatures, specific humidities, sensible energy demands, latent energy demands, and window state for the greater part of the month of May. This month, in shoulder season, is suitable to assess the effectiveness of NV because the building can be under sensible cooling, sensible heating, or neither. The indoor temperature is maintained strictly between the cooling set point (297.05 K) and heating set point (291.15 K). On the other hand, although mostly maintained within the corresponding cooling relative humidity (60 %) and heating relative humidity (40 %), the specific humidity can deviate outside this range. This is due to the fact that humidification and dehumidification only occur when there is sensible cooling or heating. When there is no sensible cooling or heating, the indoor specific humidity approaches that of the outdoor specific humidity. The window state time series show that windows are only opened when indoor/outdoor temperature and specific humidities are favorable for NV. For example, for the last third of the month (>600 hr), the windows actively open when the building has sensible cooling demand and indoor/outdoor temperature and specific humidity meet the conditions of the NV controller. Table 2 shows the annual energy savings by using NV. Since the rule-based control algorithm primarily attempts to save the sensible energy demand, we can note that the greatest energy saving is associated with the sensible cooling demand. Under heating mode, the indoor and outdoor conditions are seldom met for NV, so no savings are possible for the sensible heating demand. The saving in sensible cooling demand is notably more for air tight buildings. Further, increasing thermal insulation of the building envelop does not impact the building energy loads as far as NV is concerned. It can be seen that NV implicates the latent loads, but since the control is designed to operate windows considering indoor and outdoor humidities, the changes in latent loads are an order of magnitude less than those of the sensible cooling loads as a result of triggering NV.

CONCLUSIONS

Our study shows that consideration of both sensible and latent energy demands are possible when using Natural Ventilation (NV). Using the simulations for Toronto in 2020, we find that up to 10

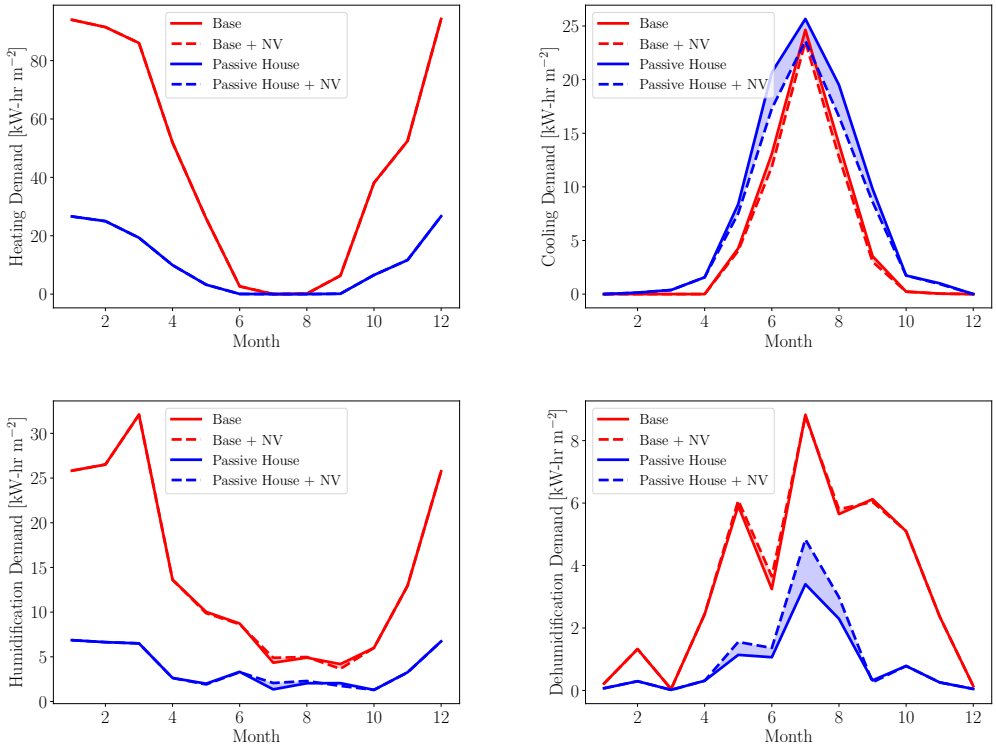

Figure 2. Monthly building energy demands for the base and Passive House cases; the difference between employing no Natural Ventilation (NV) and employing NV is shown with shaded color.

Table 2. Annual energy savings (+) and losses (−) due to using Natural Ventilation (NV).

Building Energy Demand	Base	Air Tight	High Insulation	Passive House
Sensible Heating [kW-hr m^{-2}]	−0.10	−0.08	−0.11	−0.07
Sensible Cooling [kW-hr m^{-2}]	+4.28	+10.86	+4.13	+10.51
Dehumidification [kW-hr m^{-2}]	−0.59	−0.90	−1.8	−2.78
Humidification [kW-hr m^{-2}]	+0.12	−0.68	+0.33	−0.51

kW-hr m^{-2} of sensible cooling energy can be saved per year by employing NV, with implications on latent demand being less than one order of magnitude compared to the sensible cooling demand. We also find that the effectiveness of NV is most sensitive to the building's air tightness, as opposed to the envelop's thermal resistance. Air tight buildings exhibit greater potential for energy savings using NV. Our findings suggest that NV has a potential to reduce building energy loads under cooling conditions. These simulation findings are yet to be corroborated by field experiments.

REFERENCES

[1] A. A. Aliabadi. *Turbulence: A Fundamental Approach for Scientists and Engineers*. Springer, Cham, 2022.

[2] Amir A. Aliabadi, Xuan Chen, Jiachuan Yang, Ali Madadizadeh, and Kamran Siddiqui. Retrofit optimization of building systems for future climates using an urban physics model. *Building and Environment*, 243:110655, 2023.

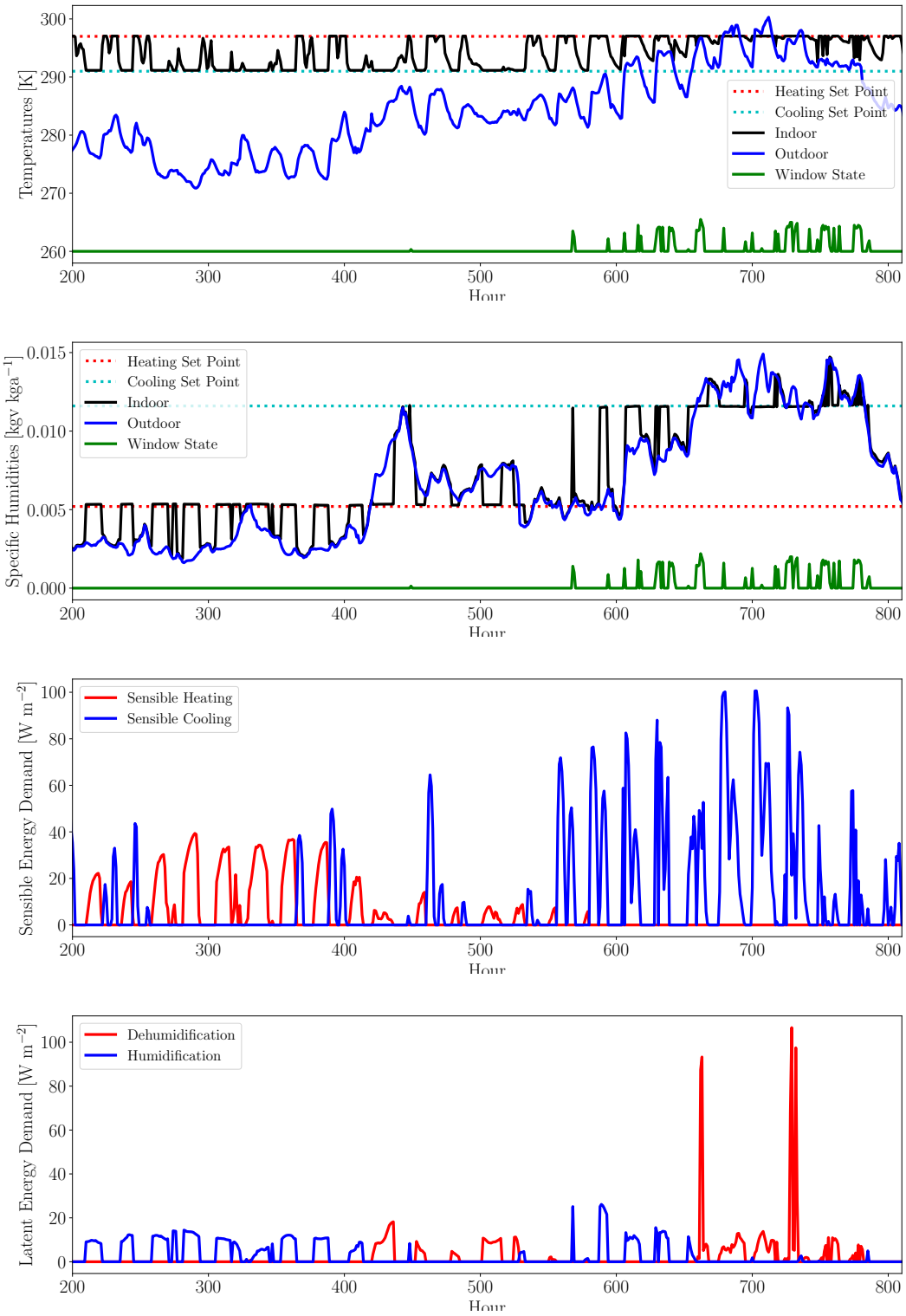

Figure 3. Hourly time series for temperatures, specific humidities, sensible building energy demands, and latent building energy demands; Passive House with Natural Ventilation (NV); selected hours in the month of May; window state shown at the bottom of temperature and specific humidity plots.

[3] Amir A. Aliabadi and Rachel M. McLeod. The Vatic Weather File Generator (VWFG v1.0.0). *Journal of Building Engineering*, 67:105966, 2023.

[4] Amir A. Aliabadi, Mohsen Moradi, Rachel M. McLeod, David Calder, and Robert Dernovsek. How Much Building Renewable Energy Is Enough? The Vertical City Weather Generator (VCWG v1.4.4). *Atmosphere*, 12(7):882, 2021.

[5] ASHRAE. Standard 90.2: Energy-Efficient Design of Low-Rise Residential Buildings. Technical report, American Society for Heating Refrigeration and Airconditioning Engineers, Peachtree Corners, 2018.

[6] ASHRAE. Standard 62.2: Ventilation and Acceptable Indoor Air Quality in Residential Buildings. Technical report, American Society for Heating Refrigeration and Airconditioning Engineers, Peachtree Corners, 2022.

[7] Jun Cheng, Dahai Qi, Ali Katal, Liangzhu Leon Wang, and Ted Stathopoulos. Evaluating wind-driven natural ventilation potential for early building design. *Journal of Wind Engineering and Industrial Aerodynamics*, 182:160–169, 2018.

[8] Benjamin Dyer, Mohammad Biglarbegian, and Amir A. Aliabadi. The autonomous robotic environmental sensor (ARES). *Science and Technology for the Built Environment*, 27(10):1461–1472, 2021.

[9] Ali Madadizadeh, Kamran Siddiqui, and Amir A. Aliabadi. Review: The Economics Landscape for Building Decarbonization. *Sustainability*, 16(14):6214, 2024.

[10] M. Moradi, B. Dyer, A. Nazem, M. K. Nambiar, M. R. Nahian, B. Bueno, C. Mackey, S. Vasanthakumar, N. Nazarian, E. S. Krayenhoff, L. K. Norford, and A. A. Aliabadi. The Vertical City Weather Generator (VCWG v1.3.2). *Geosci. Model Dev.*, 14(2):961–984, 2021.

[11] Mohsen Moradi, E. Scott Krayenhoff, and Amir A. Aliabadi. A comprehensive indoor–outdoor urban climate model with hydrology: The Vertical City Weather Generator (VCWG v2.0.0). *Building and Environment*, 207:108406, 2022.

[12] NRCan. National Energy Code of Canada. Technical report, Office of Energy Efficiency, Natural Resources Canada, Gatineau, QC, 2017.

[13] Passive-House-Institute. Criteria for the Passive House EnerPHit and PHI Low Energy Building Standard. Technical report, Passive House Institute, Darmstadt, 2015.

[14] Mojtaba Safdari, Mohammad Al Janaideh, Kamran Siddiqui, and Amir A. Aliabadi. Weather-adaptive fuzzy control of setpoints for energy-efficient hvac in urban buildings. *Journal of Building Engineering*, 104:112317, 2025.

[15] Mojtaba Safdari, Kadeem Dennis, Bahram Gharabaghi, Kamran Siddiqui, and Amir A. Aliabadi. Implications of latent and sensible building energy loads using natural ventilation. *Journal of Building Engineering*, 96:110447, 2024.

[16] Haihua Zhang, Dong Yang, Vivian WY Tam, Yao Tao, Guomin Zhang, Sujeeva Setunge, and Long Shi. A critical review of combined natural ventilation techniques in sustainable buildings. *Renewable and Sustainable Energy Reviews*, 141:110795, 2021.

6th International Conference on Building Energy and Environment
Eindhoven University of Technology, The Netherlands
6 - 10 July 2025

Development of a evaluation system for the low-carbon renewal of bungalow courtyards in Beijing

Jiyun Miao [1], Xiujiao Song [2], Yue Zhang[3], Xudong Yang[4]

[1]*Tsinghua University, Beijing, China, miaojy23@mails.tsinghua.edu.cn*
[2]*Tsinghua University, Beijing, China, sxj19@tsinghua.org.cn*
[3]*Tsinghua University, Beijing, China, yuezhang@tsinghua.edu.cn*
[4]*Tsinghua University, Beijing, China, xyang@mail.tsinghua.edu.cn*

SUMMARY
The low-carbon renewal of traditional buildings is crucial for achieving global climate targets. However, current evaluation standards fail to adequately address the characteristics and preservation needs of traditional buildings, leading to ineffective guidance for their sustainable renewal. This study focuses on the applicability of China's current standard "Assessment standard for green building" GB/T50378-2019 in the low-carbon retrofit of bungalow courtyards in the Old City of Beijing through the methods including field surveys, expert ratings, and analytic hierarchy process(AHP). Ultimately, 13 mandatory control indicators such as the use of underground space and adjustable sun shading are removed, and 4 flexible scoring indicators are added, including the inheritance of courtyard spatial patterns, coordination of facade styles, prolongation and utilization of brick-wood structures, and enhancement of functional suitability. The new evaluation index system conforms to the low-carbon renewal of bungalow courtyards in the Old City of Beijing which includes six aspects: durability, comfort, environment, energy, management, and value sustainability, with 47 scoring indicators are assigned weights.

Keywords: bungalow courtyards, evaluation system, low-carbon renewal

1. INTRODUCTION

In response to global climate change, carbon and emission reduction have emerged as significant international concerns in recent years(Zhang et al., 2021).The China Construction Carbon Emissions Report shows that in 2020 the total carbon emissions from the entire construction process constituted 50.9% of the national carbon emissions. Green retrofitting of existing buildings is a crucial approach to reducing these emissions(Villalba et al., 2024), particularly for historic buildings, which often have low energy efficiency and significant potential for low-carbon renovation(Arumägi & Kalamees, 2014; Qian et al., 2024).The green renovation of traditional buildings not only needs to follow the requirements of environmental comfort and energy saving, but also the heritage conservation(Gremmelspacher et al., 2021).However, there is a conflict between the need to conserve historical features and the carbon reduction measures typically applied to new construction(Franco & Mauri, 2024; Serrano et al., 2022).Currently, China’s Building Evaluation Standard for Green Retrofit of Existing Buildings does not adequately address the unique characteristics and preservation requirements of traditional buildings, rendering it ineffective for guiding their sustainable renovation.

The bungalow courtyards in Beijing represent one of the important typologies Chinese traditional dwellings. The old city of Beijing contains nearly 7 million square metres of brick-and-wood

structured bungalow courtyards, which offer substantial potential for low-carbon renovation. Therefore, it is necessary to develop a green building evaluation system that is more suitable for the renovation of traditional courtyards in Beijing by modifying the indicators and adjusting the weights.

2. LITERATURE REVIEW

2.1. Existing evaluation for green retrofit of existing buildings worldwide

Several countries have developed evaluation systems for the green renovation of existing buildings, such as BREEAM, LEED, DGNB, and CASBEE(Ferrari et al., 2022). The evaluation systems adjust indicators and their weights to suit the characteristics of retrofitting. For example, BREEAM Domestic Refurbishment, a standard for residential renovations, removing those like “ecology” and “runoff,” which are relevant only to new builds. DGNB, meanwhile, assigns zero weighting to site quality, as it cannot be determined in renovation projects.

A comparison of green renovation evaluation systems for existing buildings across countries shows that resource conservation is a core focus. China’s 2021 Green Renovation Standard covers six areas: safety and durability, health and comfort, convenience, resource conservation, environmental livability, and innovation. "Resource conservation" is assigned a maximum score of 200 points, while the others each have a maximum of 100 points. Some systems include qualitative requirements for heritage-protected traditional buildings. For example, BREEAM allows special consideration for historically or architecturally significant buildings if energy efficiency measures would compromise their appearance. DGNB evaluates functionality and aesthetic quality, focusing on enhancing adaptability while preserving original form. For heritage buildings, DGNB suggests qualitative assessment methods. China’s system aligns poorly with traditional building renovations, with only 2.9% of the total score related to cultural value. Scholars propose adjusting indicators and emphasising those reflecting cultural value(Zuo & Gao, 2017).

2.2. Research on evaluation for green retrofit of existing buildings

Current research focuses on green renovation evaluation systems tailored to different climate characteristics or building types. Some studies have developed systems specifically for industrial or public building renovations(Guo et al., 2022). Historical buildings, particularly traditional residential buildings, have attracted considerable scholarly attention(Fiore et al., 2020; Gravagnuolo et al., 2020; Martínez-Molina et al., 2016). While energy consumption and conservation are primary criteria in the renovation of historical buildings, other factors, such as sustainability, economic considerations and cultural value are also important(Webb, 2017). Roberti et al. used the Analytic Hierarchy Process (AHP) to assess the relative importance of various building components in visual, spatial and physical terms based on expert ratings(Roberti et al., 2017). Additionally, some studies have adjusted indicator weights based on climate characteristics(Ma et al., 2021), such as Ma et al.’s modification of indicator weightings for residential buildings in cold regions(Cao et al., 2024). Furthermore, some research has enhanced green building evaluation systems from a lifecycle perspective, emphasising low-carbon energy conservation in renovations throughout a building's entire life-cycle(Song et al., 2024).

The adjustment of evaluation system weights includes both objective and subjective weighting methods, such as the grey comprehensive evaluation method, fuzzy comprehensive evaluation method, data envelopment analysis (DEA) method, artificial neural network (ANN) method, and

the TOPSIS method(Villalba et al., 2024). The Analytic Hierarchy Process (AHP), proposed by Saaty, is one of the most widely used subjective weighting methods(Saaty, 1980).AHP simulates human reasoning in the decision-making process to handle uncertainty, making it suitable for determining the weights of qualitative indicators that are difficult to quantify(Lallam et al., 2023). AHP has been successfully applied by many scholars in decision-making for weight adjustments(Abadi & Moore, 2022; Mayhoub et al., 2021).

2.3. Low-carbon retrofit of bungalow courtyards

Research shows that the uniqueness of green renovation for traditional buildings lies in their physical characteristics and preservation principles(Webb, 2017). The physical characteristics of Beijing's traditional courtyard houses include: 1) courtyard layout with limited space; 2) brick-wooden structure with pitched roof; 3) small proportion of exterior windows; 4)wooden doors and tiled roofs, leading to poor airtightness. Regarding preservation principles, the retrofitting of traditional courtyards must adhere to the Technical Guidelines for the Protection and Repair of the Old City of Beijing (2019), which impose stringent controls on the structure, proportions, scale, colour, materials, and detailing. Certain green renovation measures, such as external wall insulation, shading devices, and renewable energy systems, may impact the traditional façade. As a result, the green renovation of courtyard houses within the core functional area of the capital is constrained by façade protection regulations.

3. METHOD

3.1. Construction of evaluation index system

The construction of the indicator system is based on the current Green Building Evaluation Standard for Existing Buildings, incorporating multi-objective decision-making on energy consumption, thermal comfort, and the preservation of traditional architectural façades. This process ensures the systematic and comprehensive nature of the system by determining the reduction and adjustment of indicators. Through field research and the Delphi method(Fathullah et al., 2023), interviews were conducted with 10 industry experts, followed by feedback processing, expert consultation, and further rounds of opinion solicitation. This iterative process was repeated twice to analyse the compatibility of various items with the courtyard houses in the core functional area of the capital. Based on the existing evaluation system, the new set of indicators will be adjusted to address the material spatial characteristics and cultural significance of existing residential building renovations and the traditional courtyard houses in the core functional area of the capital.

3.2. Determination of the weight of evaluation index

To ensure the objectivity of the weight construction process, this study will employ expert scoring and the Analytic Hierarchy Process (AHP) to establish a weighting system for the new set of indicators. The construction of the evaluation system involves six experts with extensive experience in the green building industry, who will assess the appropriateness and significance of each indicator in the context of renovation projects for this type of building. The experts include three practitioners involved in building projects and three academic researchers. Scoring results from the professionals will be collected through a survey questionnaire, followed by the creation of a judgement matrix and consistency testing of the matrix.

4. RESULT

4.1. Evaluation index system

After adjustment, the system consists of 6 top-level indicators, 13 middle-level indicators, and 47 bottom-level indicators, as shown in Fig.1. The goal layer includes safety and durability, health and comfort, convenience, resource conservation, environmental livability, and value sustainability. In alignment with the characteristics of the old city courtyard houses, the original additional item "Enhancement and Innovation" has been specified as "Value Sustainability," as shown in the table. Compared to the current Green Building Evaluation Standard, the green evaluation system for the courtyard houses in the core functional area of the capital has undergone two types of changes: deletions and additions.

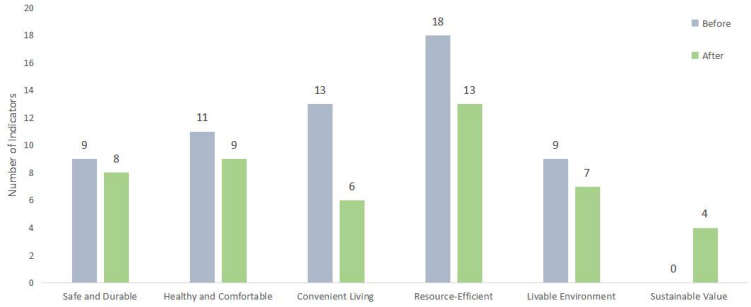

Figure 1. Comparison of the number of indicators before and after adjustment.

A total of 17 indicators have been removed from the system. The exclusion of these indicators is based on an analysis of their compatibility with the renovation process of courtyard houses. The 17 removed indicators primarily fall into two categories: 1) scoring items that cannot be achieved due to the inherent characteristics of courtyard houses, such as sunlight exposure and evacuation distance; and 2) scoring items that do not apply to the scale of courtyard house renovations, such as those related to underground spaces and community-scale issues. The reasons for the removal of each indicator are outlined in Table 1.

Table 1. Deleted indicators and reasons.

top-level indicators	bottom-level indicators	Deleted reasons
A Safety and Durability	Pedestrian and Vehicle Separation	More than 50% of the roads are between 3-5 meters, making it difficult for most roads to meet pedestrian and vehicle separation requirements.
B Health and Comfort	Water Storage Facilities	Water storage facilities are required for buildings over six stories that require secondary water supply; however, most courtyard houses in the old city are single-story and do not need water storage facilities.
	Sunshade Facilities	Traditional bungalow courtyards in Beijing, situated in a severe cold climate zone, have small windows for winter insulation, with protruding eaves providing natural shading. Installing external sunshades would compromise architectural style protection.
C Safety and Convenience	Public Transport Accessibility	Not applicable for existing building renovations where site selection cannot be changed.
	Urban Public Space Walkability	
	Provision of Public Services	Not suitable for courtyard renovation projects with limited space.
	Fitness Area Setup	
	Energy Monitoring	Courtyard houses are multi-family residences with complex ownership issues, making it difficult to install monitoring equipment due to property rights conflicts.
	Air Quality Monitoring	
	Property Management and Implementation	Traditional courtyards do not have property management.

D Resource Efficiency	Land Conservation	Courtyard renovations do not involve land changes.
	Underground Space Development	Traditional blocks do not allow underground development.
	Parking	Courtyard renovations do not involve parking issues.
	Outdoor Scenic Water Bodies	Courtyard spaces are limited and do not have scenic water bodies.
	Use of Non-traditional Water Sources	Courtyard updates cannot renovate water sources; this indicator only applies to concentrated renovations or new construction projects.
E Environmentally Livable	Protection of Site Natural Ecology	This evaluation criterion is for large-scale new construction or reconstruction projects; courtyard renovations do not involve damaging site ecology.
	Site Noise	Renovations of flat courtyard houses do not affect site noise environment.

A total of four new indicators have been added to the indicator layer. In response to the unique challenge of cultural heritage preservation in the renovation of Beijing's traditional bungalow courtyard,a new goal layer, "Value Sustainability," has been introduced.This layer incorporates both cultural heritage and building renovation aspects, including four indicators: preservation of courtyard spatial layout, façade harmony, extended lifespan of brick-wooden structures, and enhancement of functional suitability. From a life-cycle perspective, the retrofitting addresses the needs of green low-carbon and sustainable development by reusing structure and materials, while updating the functionality to meet modern requirements.

4.2. Weight of the evaluation index

The determination of weights is based on a judgment matrix derived from the Analytic Hierarchy Process, using the modified Saaty's 1–9 scale to obtain the ratings of six experts for the indicator weights, followed by consistency testing. Taking the first expert as an example, the judgment matrix for the goal layer is shown in Table 2. The final weights for each level of the indicators are derived by aggregating the experience-based weight sequences provided by the six experts.

Table 2. Empirical judgment matrix for the weight of the criteria layer index of the first expert.

	Safe and Durable	Healthy and Comfortable	Convenient Living	Resource-Efficient	Livable Environment	Sustainable Value	Weight
Safe and Durable	1	1	2	1/2	1	1/2	0.134
Healthy and Comfortable	1	1	2	1/2	1	1/2	0.134
Convenient Living	1/2	1/2	1	1/4	1	1/4	0.077
Resource-Efficient	2	2	4	1	2	1	0.267
Livable Environment	1	1	1	1/2	1	1/2	0.121
Sustainable Value	2	2	4	1	2	1	0.267

λ max=6.0546，CR=0.0087

Table 3. Empirical judgment values of top-level index weight by experts.

Top-level indicators	**Experts**					
	1	2	3	4	5	6
Safe and Durable	0.152	0.211	0.111	0.195	0.056	0.250
Healthy and Comfortable	0.174	0.158	0.148	0.171	0.111	0.139
Convenient Living	0.130	0.105	0.111	0.171	0.056	0.111
Resource-Efficient	0.196	0.211	0.074	0.073	0.500	0.194
Livable Environment	0.152	0.158	0.259	0.171	0.167	0.111
Sustainable Value	0.196	0.158	0.296	0.220	0.111	0.194

5. DISCUSSION

Compared to the initial weights, the weights of the Top-level indicators "Resource Conservation", "Convenient Living" and "Health and Comfort" have relatively decreased, while the remaining indicators have seen an increase, as shown in Table 4. Notably, the weight of "Value Sustainability" has risen by 14.5%. Given the cultural significance of courtyard houses in the core functional area of the capital, the importance of value continuity and façade preservation is extremely high, resulting in a substantial increase in its weight in the green evaluation. "Resource Conservation" still holds the highest weight, while the reduction in the weight of "Convenient Living" is primarily due to the smaller number of indicators in this category after the reconfiguration. During the expert scoring process, the influence of the reduced number of indicators led to a corresponding decrease in its weight.

After removing indicators that are not applicable to the bungalow courtyard in the core functional area of the capital, over 70% of the indicators in the system have seen an increase in their weight. This adjustment provides more effective guidance for the selection of strategies in the renovation projects. A few indicators have experienced a decrease in weight, mainly those that are of lower importance or difficult to implement in the context of courtyard house renovations, such as "Safety Protection Design," which is relatively less critical for courtyard houses, and "Renewable Energy," which conflicts with façade preservation(López & Frontini, 2014).

Table 4. Initial and adjusted weights of the bottom-level indicators.

top-level indicators	Initial Weight	Adjusted Weight	bottom-level indicators	Initial Weight	Adjusted Weight
A Safety and Durability	0.157	0.159	Enhanced Earthquake Resistance	1.4%	2.7%
			Safety Protection Design	2.1%	1.8%
			Safety Protection Products	1.4%	1.9%
			Pavement Anti-Slip Measures	1.4%	2.3%
			Improved Flexibility	2.6%	1.7%
			Durability of Components and Parts	1.4%	1.9%
			Durability of Structural Materials	1.4%	2.0%
			Durability of Finishing Materials	1.3%	1.7%
B Healthy and Comfortable	0.157	0.143	Air Pollutant Concentration	1.7%	1.6%
			Healthy Interior Decoration Materials	1.1%	1.7%
			Water Quality Requirements	1.1%	1.6%
			Drainage facility signage	1.1%	1.5%
			Indoor Noise Control	1.1%	1.0%
			Room Sound Insulation	1.4%	1.3%
			Natural Daylighting	1.7%	1.4%
			Thermal and Humid Environment	1.1%	2.2%
			Natural Ventilation	1.1%	2.0%
C Safety and Convenience	0.157	0.105	Age-Inclusive Accessibility	1.1%	2.2%
			Water Usage Monitoring	1.0%	1.7%
			Intelligent Service System	1.3%	1.9%
			Average Water Consumption	0.7%	1.6%
			Operational Assessment	0.7%	1.7%
			Green Education	1.7%	1.5%
D Resource-Efficient	0.313	0.220	Thermal Performance of Building Envelope	2.1%	2.3%
			Energy Efficiency of Cooling and Heating Systems	1.4%	1.7%
			Reduced energy consumption for air conditioning	0.7%	1.1%
			Energy-Saving Electrical Equipment	1.4%	1.4%
			Building Energy Consumption	1.4%	1.7%
			Renewable Energy	1.4%	1.0%

			Water Efficiency of Sanitary Appliances	2.1%	3.7%
			Water-Saving Equipment and Technology	1.7%	2.1%
			Integration of Civil Engineering and Decoration	1.1%	1.2%
			Structural Materials and Elements	1.4%	1.3%
			Selection of Decoration Items	1.1%	1.3%
			Recyclable Materials	1.7%	1.5%
			Green Building Materials	1.7%	1.6%
E Livable Environment	0.157	0.164	Control of stormwater runoff	1.4%	2.0%
			Outdoor Smoking Area	2.1%	1.2%
			Outdoor Green Space	1.1%	2.7%
			Green Rainwater Management Facilities	1.4%	2.6%
			Light Pollution	1.4%	2.5%
			Site Wind Environment	1.4%	3.0%
			Reduction of Urban Heat Island	1.7%	2.3%
F Sustainable Value	0.063	0.208	Preservation of Courtyard Layout	1.4%	5.6%
			Facade Aesthetics Harmonization	1.4%	5.8%
			Lifespan Extension of Brick and Timber Structures	1.4%	4.1%
			Enhancement of Functional Suitability	1.4%	5.2%

6. CONCLUSION

This study addresses the challenges of retrofitting bungalow courtyards in Beijing's old city, focusing on difficulties in achieving high green building ratings and supporting dual carbon goals. Each of the 60 items in the Green Building Evaluation Standard is assessed for compatibility with these courtyard houses, using expert interviews, field research, and the Analytic Hierarchy Process (AHP) with the Delphi method.

In terms of the indicators,17 indicators that do not align with the renovation of the old city courtyard houses are removed, while four new indicators reflecting the unique characteristics are added,including the inheritance of courtyard spatial patterns, coordination of facade styles, prolongation and utilization of brick-wood structures, and enhancement of functional suitability. The new evaluation index system conforms to the low-carbon renewal of bungalow courtyards in the Old City of Beijing which includes six aspects: durability, comfort, environment, energy, management, and value sustainability, with 47 scoring indicators.

In terms of weights, the adjusted weight reflects the comprehensive consideration of low-carbon and heritage conservation. "Resource Conservation" retains the highest weight, while "Value Sustainability" has increased by 14.5%. Over 70% of the bottom-level indicators have seen weight increases, the weight of the indicators that are less important or difficult to implement in the retrofit of the bungalow courtyard has been reduced, leading to more effective guidance for the sustainable renewal.

ACKNOWLEDGEMENTS

Gratitude is extended to the professors and colleagues for their collective efforts, and to the experts for their support in the data collection for the new evaluation system. Writing assistance were provided by National Key R&D Program of China (2022YFC3803801 in 2022YFC3803800).

REFERENCES

Abadi, M., & Moore, D. R., 2022. Selection of circular proposals in building projects: an MCDM model for lifecycle circularity assessments using AHP. Buildings, 12(8), 1110.

Arumägi, E., & Kalamees, T., 2014. Analysis of energy economic renovation for historic wooden apartment buildings in cold climates. Applied Energy, 115, 540-548.

Cao, H., Liu, X., Feng, G., Wang, C., Huang, K., Hou, X., & Chen, J., 2024. Research on the evaluation of the renovation effect of existing energy-inefficient residential buildings in a severe cold region of China. Energy and Buildings, 312, 114184.

Fathullah, M. A., Subbarao, A., & Muthaiyah, S., 2023. Methodological investigation: traditional and systematic reviews as preliminary findings for Delphi technique. International Journal of Qualitative Methods, 22, 16094069231190747.

Ferrari, S., Zoghi, M., Blázquez, T., & Dall'O, G., 2022. New Level (s) framework: Assessing the affinity between the main international Green Building Rating Systems and the european scheme. Renewable and Sustainable Energy Reviews, 155, 111924.

Fiore, P., Sicignano, E., & Donnarumma, G., 2020. An AHP-based methodology for the evaluation and choice of integrated interventions on historic buildings. Sustainability, 12(14), 5795.

Franco, G., & Mauri, S., 2024. Reconciling Heritage Buildings' Preservation with Energy Transition Goals: Insights from an Italian Case Study. Sustainability, 16(2), 712.

Gravagnuolo, A., Angrisano, M., & Nativo, M., 2020. Evaluation of environmental impacts of historic buildings conservation through Life Cycle Assessment in a circular economy perspective. Aestimum, 241-272.

Gremmelspacher, J. M., Pizarro, R. C., van Jaarsveld, M., Davidsson, H., & Johansson, D., 2021. Historical building renovation and PV optimisation towards NetZEB in Sweden. Solar Energy, 223, 248-260.

Guo, C., Bian, C., Liu, Q., You, Y., Li, S., & Wang, L., 2022. A new method of evaluating energy efficiency of public buildings in China. Journal of Building Engineering, 46, 103776.

Lallam, M., Djebli, A., & Mammeri, A., 2023. Fuzzy analytical hierarchy process for assessing damage in old masonry buildings: A case study. International Journal of Architectural Heritage, 1-20.

López, C. S. P., & Frontini, F., 2014. Energy efficiency and renewable solar energy integration in heritage historic buildings. Energy Procedia, 48, 1493-1502.

Ma, G., Liu, T., & Shang, S., 2021. Improving the climate adaptability of building green retrofitting in different regions: A weight correction system for Chinese national standard. Sustainable Cities and Society, 69, 102843.

Martínez-Molina, A., Tort-Ausina, I., Cho, S., & Vivancos, J.-L., 2016. Energy efficiency and thermal comfort in historic buildings: A review. Renewable and Sustainable Energy Reviews, 61, 70-85.

Mayhoub, M. M. G., El Sayad, Z. M. T., Ali, A. A. M., & Ibrahim, M. G., 2021. Assessment of green building materials' attributes to achieve sustainable building façades using AHP. Buildings, 11(10), 474.

Qian, Y., Leng, J., Wang, H., & Liu, K., 2024. Evaluating carbon emissions from the operation of historic dwellings in cities based on an intelligent management platform. Sustainable Cities and Society, 100, 105025.

Roberti, F., Oberegger, U. F., Lucchi, E., & Troi, A., 2017. Energy retrofit and conservation of a historic building using multi-objective optimization and an analytic hierarchy process. Energy and Buildings, 138, 1-10.

Saaty, T. L., 1980. The analytic hierarchy process (AHP). The Journal of the Operational Research Society, 41(11), 1073-1076.

Serrano, T., Kampmann, T., & Ryberg, M. W., 2022. Comparative Life-Cycle Assessment of restoration and renovation of a traditional Danish farmer house. Building and Environment, 219, 109174.

Song, P., Wu, L., Zhao, W., Ma, W., & Hao, J., 2024. Life Cycle Sustainability Assessment: An Index System for Building Energy Retrofit Projects. Buildings, 14(9), 2817.

Villalba, P., Sánchez-Garrido, A. J., & Yepes, V., 2024. A review of multi-criteria decision-making methods for building assessment, selection, and retrofit. Journal of Civil Engineering and Management, 30(5), 465–480-465–480.

Webb, A. L., 2017. Energy retrofits in historic and traditional buildings: A review of problems and methods. Renewable and Sustainable Energy Reviews, 77, 748-759.

Zhang, Y., Luo, A., & Wang, C., 2021. Analysis of international trends in carbon neutral actions. Adv Clim Chang Res, 17(01), 88-97.

Zuo, Y., & Gao, Y., 2017. Research on Energy Evaluation Methods for the Protection and Reuse of Historic Buildings. New Building, 35(1), 130-133.

6th International Conference on Building Energy and Environment
Eindhoven University of Technology, The Netherlands
6 - 10 July 2025

Thermal environment analysis of radiant floor and floor-supplied air-conditioning systems: an empirical study with BES-CFD simulation

Xianzhe Yang [1], Akihito Ozaki [2], Seonghwan Yoon [3], Sung-Jun Yoo [4], Younhee Choi [5], Yusuke Arima [6]

[1]*Graduate School of Human-Environment Studies, Kyushu University, Fukuoka, Japan, yang.xianzhe.746@s.kyushu-u.ac.jp*
[2]*Faculty of Human-Environment Studies, Kyushu University, Fukuoka, Japan, ozaki@arch.kyushu-u.ac.jp*
[3]*Department of Architecture, Pusan National University, Busan, South Korea, yoon@pusan.ac.kr*
[4]*Platform of Inter-/Transdisciplinary Energy Research, Kyushu University, Fukuoka, Japan, yoo@kyudai.jp*
[5]*Faculty of Human-Environment Studies, Kyushu University, Fukuoka, Japan, yunichoi@arch.kyushu-u.ac.jp*
[6]*Faculty of Human-Environment Studies, Kyushu University, Fukuoka, Japan, arima@arch.kyushu-u.ac.jp*

SUMMARY
This study focuses on clarifying the thermal environment created by different air-conditioning (AC) systems and developing a simulation method to analyze the coupled heat transfer and airflow processes. Field measurements were conducted to evaluate the performance of radiant floor, floor-supplied, and ceiling-supplied AC systems, providing insights into the temperature control efficiency and distribution characteristics of different AC systems. Furthermore, a coupling simulation method combining building energy simulation (BES) and computational fluid dynamics (CFD) was established to accurately reproduce the thermal and airflow dynamics. Validation through transitional, cooling, and heating seasons showed strong agreement between the simulated and measured data. This approach enables detailed predictions and assessments of thermal comfort and energy efficiency. These findings will contribute to the development of efficient AC system designs, support energy-saving strategies, and enhance the thermal comfort in large-scale buildings.

Keywords: large space building, air-conditioning systems, thermal environment, coupling simulation

1. INTRODUCTION

In Japan, achieving carbon neutrality by 2050 has become a national priority. The building sector accounts for approximately 40% of the total primary energy use and 38% of energy-related CO_2 emissions (Wang and Hong, 2020). Among these, large-scale buildings (over 10,000 m²) constitute only 1% of the building stock but consume 36% of the total energy. Addressing this imbalance is critical, and the adoption of high-efficiency equipment in such buildings is expected to significantly advance the transition to a decarbonized society.

Stratified air conditioning has become a widely used technique to promote energy efficiency in large-scale buildings because of its advantages in reducing energy consumption and improving indoor air quality. Radiant floor cooling and floor-supplied air conditioning (AC) systems are commonly employed to achieve stratified AC. A key feature of these systems is the vertical temperature distribution, which is essential for optimizing energy efficiency and ensuring thermal comfort. However, the accurate prediction of the thermal environment and energy-saving

performance of stratified AC systems during the design phase remains challenging.

In this study, we analyzed the thermal environment of a large-scale building certified to achieve at least 50% reduction in primary energy consumption compared to the reference value during the design phase. The building features a high-efficiency AC system that combines radiant floor, floor-supplied, and ceiling-supplied AC systems, designed to ensure thermal comfort while reducing energy use.

The primary objectives of this study were to clarify the thermal environment and verify the performance of the AC systems. This research is structured around two main components: (1) field measurements to capture the actual thermal conditions in the target building and (2) the development of a coupling simulation method for further assessment of the complex AC system. Numerical simulations that consider coupled heat transfer and airflow processes were conducted using the BES-CFD coupling method. This method leverages the advantages of building energy simulations (BES) and computational fluid dynamics (CFD). As an initial step, this study verifies the effectiveness and predictive accuracy of the method, laying the groundwork for future design applications and assessments.

2. TARGET BUILDING

Fig. 1 shows photographs of the target building located in Fukuoka, Japan. Designed as a public administration building, it has a total floor area of 11,716 m² and is constructed to achieve significant energy savings through a highly insulated exterior envelope and highly efficient equipment. In addition to its thermal insulation performance, the facade design incorporates strategies to reduce external skin loads while maximizing the use of natural light.

Fig. 2 shows the AC zoning diagrams for each floor, illustrating the use of different AC systems according to the purpose and scale of each area. Notably, on the first floor, the zoning diagram shows a combination of radiant floor AC (Fig. 2(a)) and floor-supplied AC systems (Fig. 2(b)) in the entrance lobby area, while the office area was equipped with a ceiling-supplied AC system. The lobby and office areas were integrated into a connected large open space. Consequently, three types of AC systems—radiant floor AC, floor-supplied AC, and ceiling-supplied AC—operate simultaneously in this large-scale space, potentially creating complex temperature and airflow distributions. Notably, an outdoor air handling unit was integrated into the ventilation system.

(a). Exterior view.

(b). Entrance lobby.

Figure 1. Photos of target building.

(a). Radiant floor AC.

(b). Floor-supplied inlet.

Figure 2. Photos of radiant floor and floor-supplied inlet.

3. METHODOLOGY

3.1. Field Measurement

In the first stage, field measurements were conducted in a target building. The measurements included air temperature, humidity, and floor surface temperature. As shown in Fig. 3, the measurement locations were established on the first and third floors. The measured areas comprised areas with a combination of floor-supplied AC and radiant floor AC (Locations 1 and 2), an area with ceiling-supplied AC (Location 3), and an area with only a floor-supplied AC system (Location 4). Furthermore, measurement points were set up at different heights at each location to capture the vertical temperature stratification. The measurements began in the summer of 2024, with data collected at 10-minute intervals, providing a comprehensive dataset for evaluating the thermal environment under typical operational conditions.

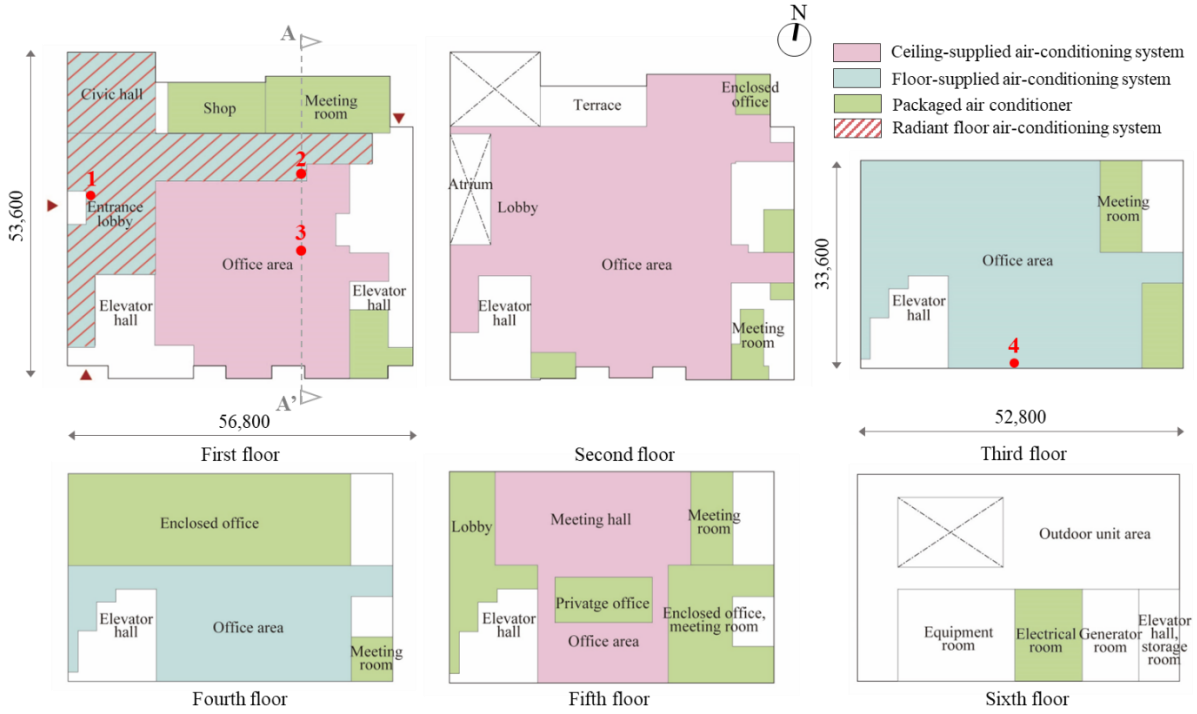

Figure 3. Air conditioning zoning plan.

3.2. Numerical Simulation

In this study, we employed the BES tool THERB for HAM to simulate the thermal environment (Ozaki and Tsujimaru, 2006). THERB for HAM models each room as a node and calculates the spatial temperature, humidity, and heat load over time and periods, strictly concerning conduction, convection, and radiation. The software was validated through standardized Japanese tests and officially approved by the Japanese government. Numerous studies have demonstrated the predictive accuracy of THERB for HAM across buildings of varying scales (Lee et al., 2019; Ozaki and Tsujimaru, 2006.; Yang et al., 2024).

The accurate prediction of the thermal environment of a target building requires the reproduction of coupled heat transfer and airflow processes. THERB for HAM effectively predicts environments dominated by natural convection but struggles in spaces with forced convection,

such as those with an operating AC system, owing to its inability to account for airflow. Conversely, although CFD provides detailed insights into the airflow and temperature distribution, it relies on simplified thermal boundary conditions, limiting its accuracy in accounting for thermal storage and external influences.

Thus, to precisely predict the temperature and airflow distribution in the large space of a target building, we employed a static coupling strategy using a one-step approach (Zhai et al., 2002). To address the limitations of CFD, surface temperature data from THERB for HAM were provided as the thermal boundary conditions to CFD (Zhai and Chen, 2003). This coupling method enhanced the reliability of predictions regarding heat transfer and airflow dynamics, enabling a detailed assessment of the thermal environment created by various AC systems.

In this study, we focused on developing a coupling simulation method to accurately reproduce the thermal environment of a complex AC system and validate its accuracy. The accuracy of the method was assessed in two steps: (1) by comparing THERB for HAM-simulated results with measured data during the transitional season when the AC system was off and (2) by comparing THERB for HAM-CFD-simulated results with measured data during the cooling and heating seasons to validate the reproduction of coupled heat transfer and airflow processes. The simulation conditions are listed in Tables 1 and 2.

Table 1. Simulation conditions for THERB for HAM

Weather data	Maebaru, Fukuoka, Japan (2024)
Calculation time interval	600s
HVAC system	Transitional season: ventilation 0.5ACH Cooling season: air temperature 25.5 °C (9:00-17:00); ventilation 0.5ACH Heating season: air temperature 22 °C (9:00-17:00); ventilation 0.5ACH
Internal heat gain (sensible heat)	Occupants: 21W/m² Equipment, lighting: 30W/m² (ASHRAE, 2019)

Table 2. Numerical and boundary conditions for the CFD analysis.

Algorithm	SIMPLEC
Time	Steady
Mesh	1.2 million tetrahedral meshes
Turbulence model	High Reynolds number k–ε turbulence model
Inflow boundary	Velocity inlet
Outflow boundary	Velocity outlet
Solver settings	2nd-order upwind scheme for convection

4. RESULTS OF FIELD MEASUREMENT

4.1. Cooling season

Fig. 4 presents a comparison of the temperature variations over time at different locations during the cooling season. For the first-floor locations (Locations 1–3), the observation period spanned three days, from September 17 to 19, 2024, whereas for the third-floor location (Location 4), it spanned from October 8 to 10, 2024. Fig. 4(b) and 4(c) clearly demonstrate the vertical temperature stratification at Locations 1 and 2, where floor-supplied AC and radiant floor AC systems were applied. The temperature variation over time indicated that the temperature began to decrease at approximately 9:00, when the AC system started, and continued to drop until 17:00, when the

system was turned off. This trend is likely influenced by the thermal storage effect of the floor. However, at Location 3, which used a ceiling-supplied AC system, the temperature decreased sharply after the start of cooling and remained relatively stable until cooling was stopped. As shown in Fig. 4(f), at Location 4, where a floor-supplied AC system was applied, the vertical temperature stratification was the most significant. The temperature at a height of 1000 mm drops markedly when the AC system starts operating, showing a difference of approximately 2 °C compared to the temperature at 2000 mm. This indicates that the floor-supplied AC system efficiently conditions the occupied zone in the workspace, effectively providing localized cooling where it is most required. While such stratification can enhance energy efficiency by targeting cooling to where it's needed, it may also suppress vertical mixing under strong inversion conditions, potentially reducing convective cooling effectiveness. Airflow dynamics should therefore be considered to ensure both thermal comfort and energy performance.

Fig. 5 shows the humidity measured at a consistent height of 1000 mm across all locations. The results showed that while the AC system was operating, the relative humidity differences among the locations were minimal. Additionally, the relative humidity consistently remained within the range of 40–60% at all locations, ensuring a comfortable indoor humidity environment.

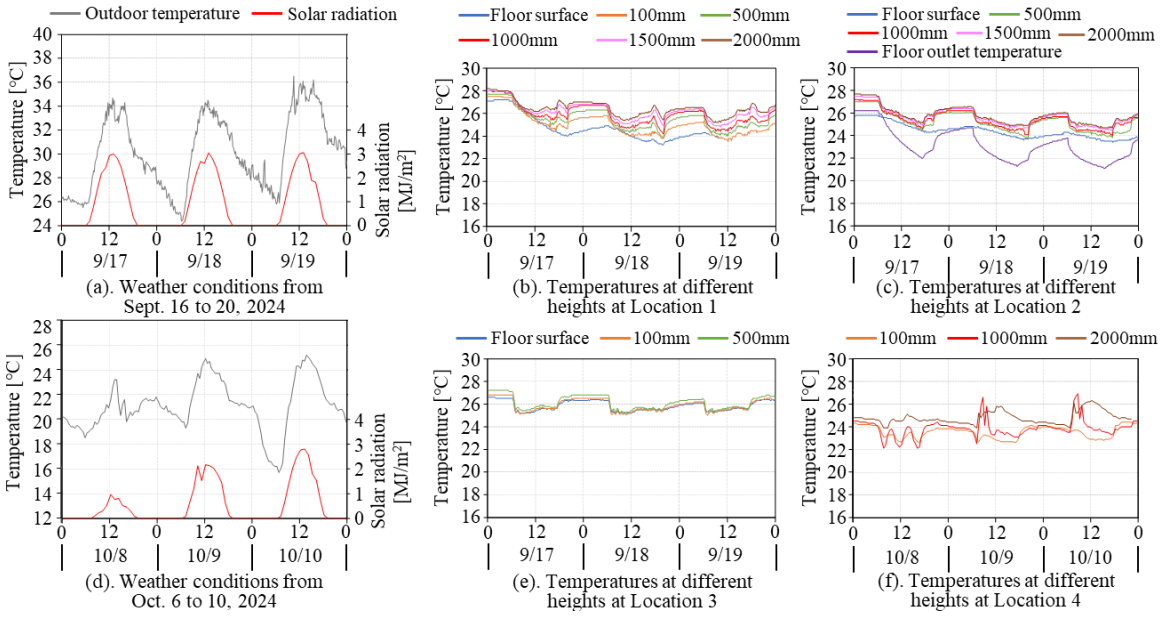

Figure 4. Measured temperatures at different locations alongside outdoor conditions during the summer season.

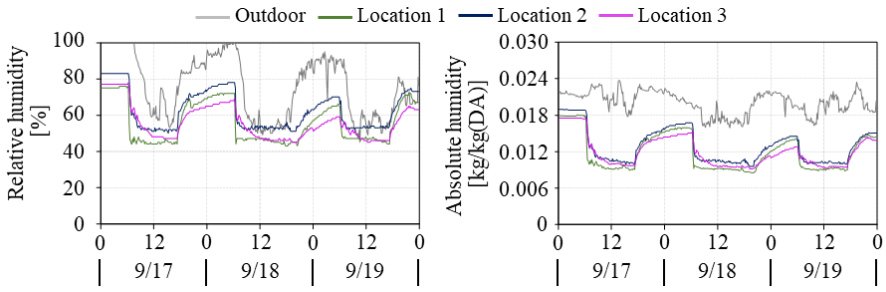

Figure 5. Measured humidity at different locations alongside outdoor conditions during the summer season.

4.2. Heating season

Fig. 6 compares the temperature variations at different locations during the heating season based on data measured from December 24 to 26, 2024. As presented in Fig. 6(b) and 6(c), the vertical temperature differences at the same locations were relatively small during the heating season at Locations 1 and 2, where floor-supplied AC and radiant floor AC systems were used. Temperatures in these locations increased gradually after the AC system started and continued to rise until it stopped, with the effect being particularly notable in Location 1, which was situated in the entrance lobby, an area prone to significant heat loss. At Location 3 (Fig. 6(d)), which used a ceiling-supplied AC system, the temperatures increased sharply after heating began and remained relatively stable throughout the operation. At Location 4 (Fig. 6(e)), where a floor-supplied AC system was applied, the temperatures increased significantly within approximately three hours of heating. Notably, Location 2, despite being in the interior zone like Location 3, exhibited about 1°C higher temperatures attributed to the use of floor-supplied and radiant floor AC systems.

Regarding the humidity environment, Fig. 7 demonstrates that, similar to the findings during the cooling season, there was a minimal difference in the humidity levels between the various air-conditioning systems across different locations.

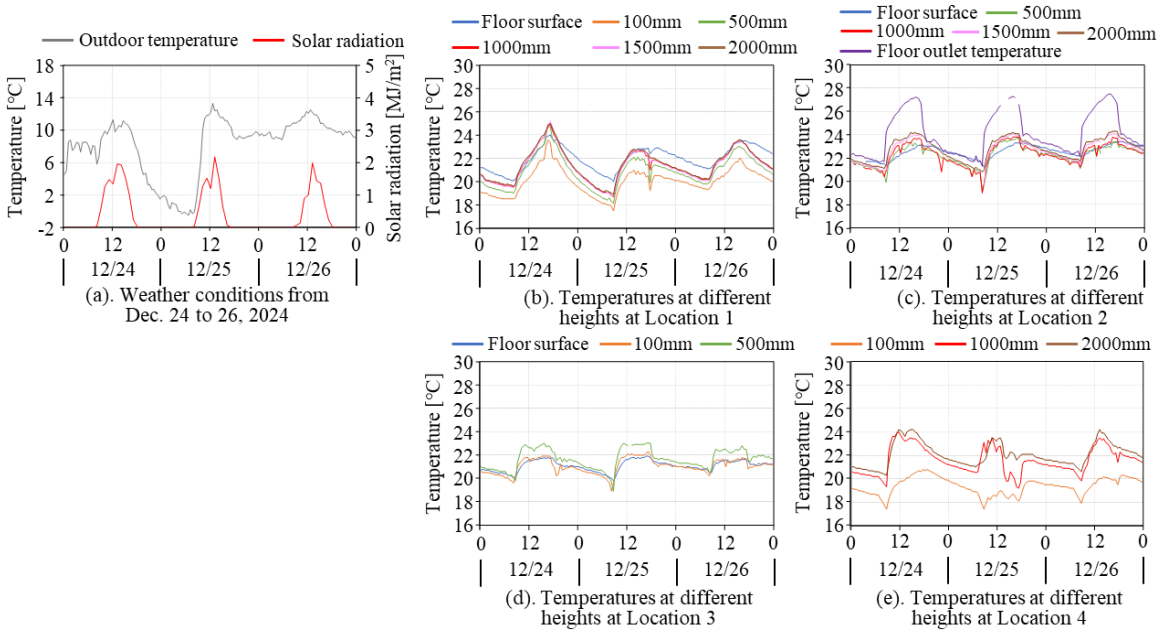

Figure 6. Measured temperatures at different locations alongside outdoor conditions during the winter season.

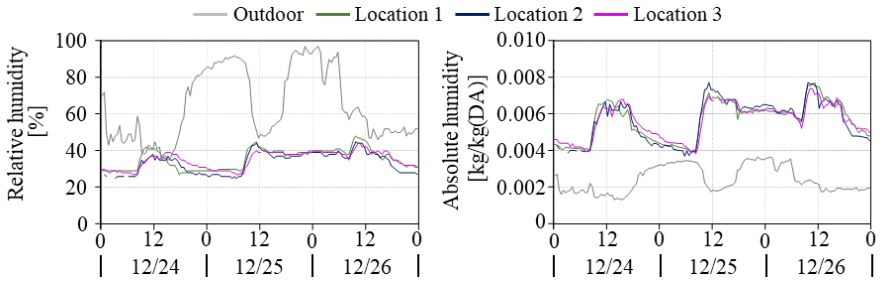

Figure 7. Measured humidity at different locations alongside outdoor conditions during the summer season.

5. RESULTS OF SIMULATION

Fig. 8 compares the air and floor surface temperatures at Locations 2 and 3 simulated using THERB for HAM with the measured data obtained during the transitional season when the AC system was off. The results show a strong agreement between the simulated and measured data, validating capability of THERB for HAM to accurately predict the thermal environment in indoor spaces dominated by natural convection.

To predict the heat transfer and airflow dynamics in the target space during the cooling season, an unsteady simulation using THERB for HAM was conducted on September 18, 2024. The surface temperatures calculated at 12:00 were extracted and set as the boundary conditions for CFD. Fig. 9 shows the THERB for the HAM-CFD-simulated temperature distribution under these conditions. Vertical temperature stratification was particularly pronounced at Location 2, which is consistent with the field measurement findings. A comparison of the simulated and measured temperatures at various heights at Locations 2 and 3 further demonstrated strong agreement.

Similarly, during the heating season, the surface temperatures at 12:00, simulated by THERB for the HAM on December 27, 2024, were provided to the CFD. Fig. 10 shows the THERB for the HAM-CFD-simulated temperature distribution under these conditions, which aligns closely with the measured data at Locations 2 and 3. Moreover, the vertical temperature stratification throughout the space during the heating season was more pronounced than that during the cooling season, as illustrated in the distribution figure.

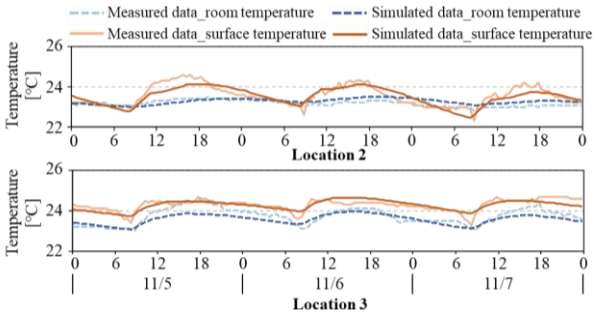

Figure 8. Comparison of temperature between measured and simulated data in transitional season.

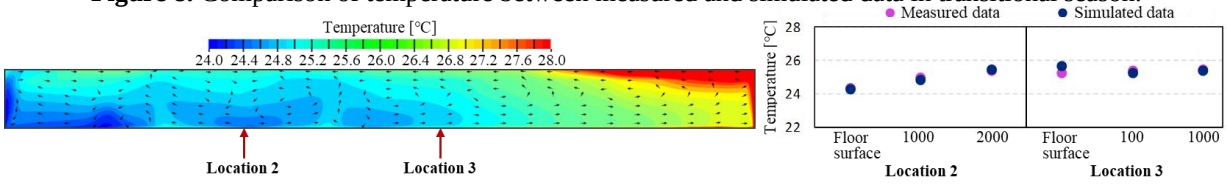

Figure 9. Temperature distribution predicted by THERB for HAM-CFD and comparison with measured data in cooling season.

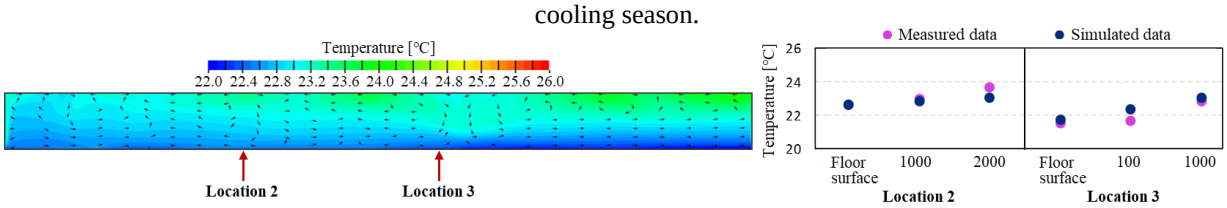

Figure 10. Temperature distribution predicted by THERB for HAM-CFD and comparison with measured data in heating season.

6. CONCLUSIONS

This study aimed to analyze the thermal environment of a space equipped with a combined AC system that integrates radiant floor AC, floor-supplied AC, and ceiling-supplied AC systems. Field measurements were conducted to capture the thermal characteristics generated by the different AC systems. Additionally, a simulation method accounting for coupled heat transfer and airflow processes was developed, and its predictive accuracy was validated.

Field measurements highlighted the unique thermal behaviors of each AC system. The combination of radiant floor and floor-supplied AC resulted in a gradual temperature rise after activation, demonstrating the floor's thermal storage capacity—an aspect that can be leveraged for energy-efficient heating/cooling strategies. The ceiling-supplied AC system maintained a stable and uniform temperature, making it suitable for spaces requiring consistent thermal conditions. Meanwhile, the floor-supplied AC system effectively regulated the temperature in occupied zones, suggesting its potential for improving occupant comfort with localized control. Across all systems, humidity distribution remained relatively uniform, reinforcing the overall stability of indoor air conditions.

A coupled simulation method was established and shown to effectively reproduce the heat transfer and airflow dynamics during AC operation. Future studies will focus on analyzing the characteristics of different AC systems and their efficiencies in terms of both thermal comfort and energy consumption through parameter sensitivity analyses. This study can serve as a reference for future AC system design applications.

ACKNOWLEDGEMENTS

This work was supported by JST SPRING, Japan Grant Number JPMJSP2136.

REFERENCES

ASHRAE, ANSI/ASHRAE/IES Standard 90.1-2019: Energy Standard for Buildings Except Low-Rise Residential Buildings, 2019.

Lee H., Ozaki A., Lee M., Cho W., 2019. A fundamental study of intelligent building envelope systems capable of passive dehumidification and solar heat collection utilizing renewable energy, Energy and Buildings 195, pp. 139–148. https://doi.org/10.1016/j.enbuild.2019.04.039

Ozaki A., Tsujimaru T., 2006. Prediction of hygrothermal environment of buildings based upon combined simulation of heat and moisture transfer and airflow. Journal of the International Building Performance Simulation Association 16, pp. 30–37.

Wang Z., Hong T., 2020. Reinforcement learning for building controls: The opportunities and challenges. Applied Energy 269. https://doi.org/10.1016/j.apenergy.2020.115036

Yang X., Ozaki A., Arima Y., Choi Y., Yoo S.-J., 2024. Numerical modeling of biophilic design incorporating large-scale waterfall into a public building: Combined simulation of heat, air, and water transfer. Building and Environment 266, 112104. https://doi.org/10.1016/j.buildenv.2024.112104

Zhai Z., Chen Q., 2003. Solution characters of iterative coupling between energy simulation and CFD programs. Energy and Buildings 35, pp. 493–505.

Zhai Z., Chen Q., Haves P., Klems J.H., 2002. On approaches to couple energy simulation and computational fluid dynamics programs. Building and Environment 37, pp. 857–864. https://doi.org/10.1016/S0360-1323(02)00054-9

6th International Conference on Building Energy and Environment
Eindhoven University of Technology, The Netherlands
6 - 10 July 2025

Experimental study of a combined heat recovery ventilator and building integrated photovoltaic system in cold climate

Jing Li , Kai Ye, Daniel Baril, Hua Ge, Radu Zmeureanu, Andreas K. Anthienitis

Centre for Zero Energy Building Studies, Department of Building, Civil and Environmental Engineering, Gina Cody School of Engineering and Computer Science, Concordia University, Montreal, Qc, Canada,
j_li201@live.concordia.ca

ABSTRACT

This paper presents the experimental results of a heat recovery ventilator (HRV) preheated by a building integrated photovoltaic thermal (BIPV/T) system, carried out during the winter in a test cell of the Future Buildings Laboratory (FBL) at Concordia University in Montreal, Canada. First, the influence of the various airflow rates on the operation and performance of the integrated BIPV/T and HRV system is investigated, for the fault-free case, including 1) supply air temperature from HRV, 2) HRV fans power input, and 3) sensible heat transfer effectiveness of HRV. Second, the HRV filters clogging is introduced through the manual blockage with aluminium adhesive tape and its impact on the thermal efficiency of HRV is evaluated. The following physical variables are measured: the air temperature, relative humidity, and airflow rate at the inlets and outlets of HRV, and the electric power input to HRV fans. The derived variables are sensible heat transfer effectiveness of HRV and heat recovery rate of HRV. The variation of the measured and derived variables is presented with respect to various airflow rates and severity of filters clogging. The results show that the increase of airflow rate increases the heat recovery rate of HRV at the cost of the increased energy consumptions of fans and reduced sensible heat transfer effectiveness of HRV. Moreover, compared with fault-free HRV operation, HRV filters clogging reduces the energy consumptions of HRV fans and required to reheat the supply air.

Keywords: Heat recovery ventilator, Building integrated photovoltaics/thermal, Faults, Various airflow rates.

1. INTRODUCTION

Heat recovery ventilators (HRVs) are increasingly being used in cold climate housing to deliver fresh air to occupied spaces while simultaneously recovering heat from the exhaust air.
The proper ventilation rate is required by the standard. The inadequate ventilation rate leads to the potential health risk to the occupants and deteriorates the indoor air quality (IAQ). Hereby, a number of publications have investigated the impact of various airflow rates on the HRV operation. HRVs enhanced ventilation and decreased the risk of wheezing and rhinitis in this population (Kovesi et al., 2009). A recent systematic review revealed that reduced ventilation results in an increased risk of respiratory infection with several infectious agents, including influenza virus (Li et al., 2007).

A simulation study of the HRV preheated by BIPV/T systems operating in the low Arctic climate of Nunavik reveals that higher flow rates result in lower supply air temperatures, while lower flow rates lead to higher supply air temperatures(Baril et al., 2021). The performance of three types of heat pipe ~~heat~~ recovery unit were tested (Riffat and Gan, 1998). It can be noted that the effectiveness decreases with the increase of air velocity. Similar findings were found by (Kim., 2022): the heat transfer effectiveness decreases with the increase of the airflow rate. Moreover,

the pressure drops and heat transfer rate of HRV increased with the increased airflow rate (Kim., 2022; Akbari and Oman. 2013)

A simulation study, conducted at three cities: Winnipeg, Seattle and Lake Charles at the house developed based on the Canada Mortgage and Housing Cooperation, showed that the energy savings varied from 3300 to 12,000 kWh per year for ventilation rates ranging 20–70 L/s, and the annual saving was approximately $165 to $600 (Barringer and McGugan, 1989). The increase of the airflow rate can significantly reduce the level of the radon (Akbari and Oman. 2013) Moreover, the fans power drop as the reduction of the airflow rate. Ventilation heat lossesare increasing due to the new indoor air quality standards and the focus on reducing indoor radon concentration in cold climates. The ventilation losses increase with the increased airflow rate of HRV (Akbari and Oman. 2013).

A regular replacement of the air filters should be undertaken to prevent the filter clogging. The resistance increases when the filter is fouled and causes higher energy consumption (Liu et al, 2017). A clogged HRV filter increased the allergen exposure, reduced its ability to remove stale air and pollutants, leading to stagnant air and higher concentrations of indoor air contaminants (Penney, M. 2024). However, to our knowledge, there hasn't been studies investigating the thermal and energy impact of the HRV air filter clogging.

Building upon these findings, this study first investigates the influence of the various airflow rates on the operation and performance of the integrated BIPV/T and HRV system in cold climate under the fault-free conditions. the analysis includes 1) supply air temperature from HRV to the building, 2) HRV fans power input, and 3) sensible heat transfer effectiveness of HRV. Second, the HRV filters clogging is introduced through the manual blockage with aluminums adhesive tape and its impact on the thermal efficiency of HRV is evaluated.

2. METHODS AND MATERIALS

2.1. Test setup and materials

The testing of the HRV preheated by the BIPV/T system is carried out in a test cell located at the Future Building Lab (FBL) at Concordia University, Montreal, Canada. The HRV test setup, illustrated in Fig.1, consists of one HRV unit, three flexible ducts, and a test-duct station installed on each duct. Before entering the HRV, the outside air passes through the cavity of the BIPV/T system.

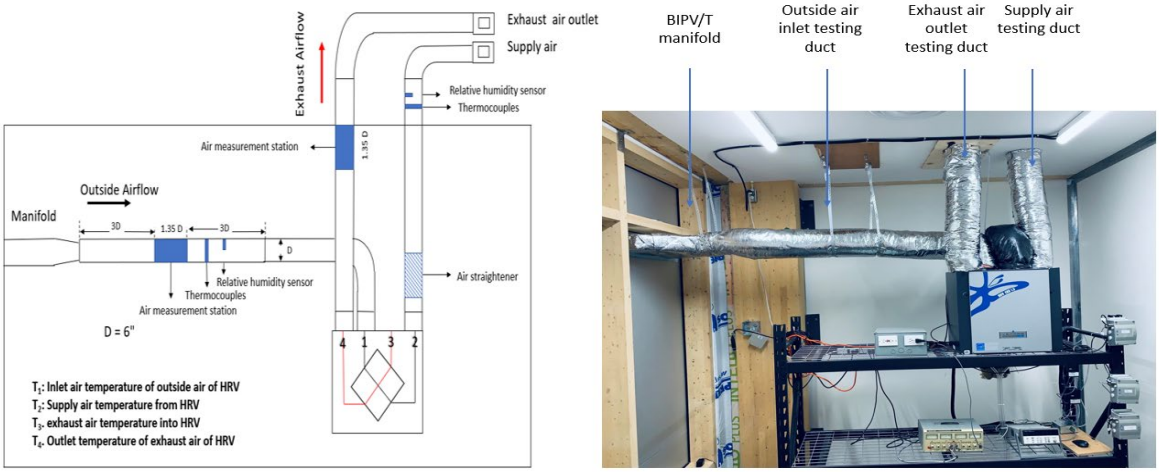

Figure 1: The schematics of the HRV test setup

This study utilizes the Venmar AVS EKO 1.5 heat exchanger, a cross-flow heat exchanger with an apparent sensible heat recovery effectiveness ranging from 72% to 89%, depending on the outdoor air temperature and airflow rate. The HRV unit includes four airstream ports: outside air inlet, supply airflow, exhaust airflow, and exhaust air outlet. Additionally, it operates under the high/medium high/medium low/low fans speed modes. In each fans speed mode, the HRV fans can be set at maximum or minimum fans speed mode.

The details of the BIPV/T panels were presented in detail in the previous publication (Li et al., 2023). A test-duct setup, designed based on ASHRAE standard (ASHRAE Stand. 41.2, 1987) and recommendation from the manual of the Dwyer air measurement station (Dwyer Instruments, n.d), is used for the measurements of air temperature (T), relative humidity (RH), and airflow rate ($\dot{m}$). The test duct is 152.4 mm in diameter (D) and constructed of galvanized steel. The test-ducts are wrapped with mineral wool insulation and vapour barrier in order to reduce the heat loss/gains from the ambient air in the laboratory and reduce the potential for condensation on the ducts. There are three testing duct setups: (a) one for the outside air inlet (Fig. 2 (a)), (b) one for the supply airflow (Fig. 2 (b)), and (c) one for the exhaust air outlet (Fig. 2 (c)). The relative humidity and temperature in the exhaust air inlet is obtained by measuring the room air temperature and relative humidity. All the specifications of sensors used are presented in the previous publication (Li et al., 2023)

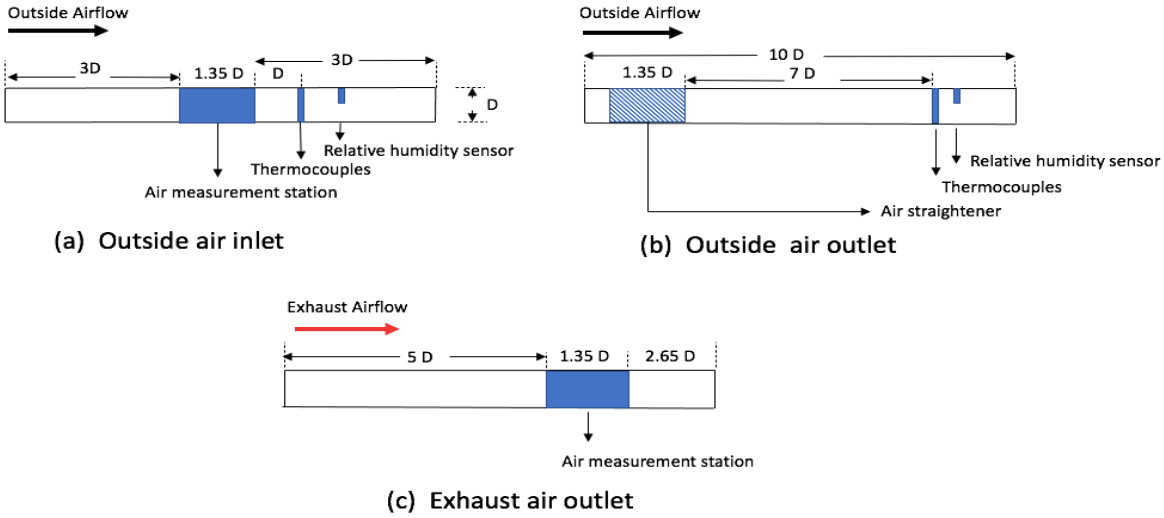

Figure 2: The testing duct configurations for the outside air inlet, outside air outlet and exhaust air outlet.

The HRV tests are carried out at four fan speeds: 1) low speed (minimum), 2) medium low (maximum), 3) medium high (maximum) and high (maximum). Then the supply airflow filter is blocked by the Aluminium foil thermal insulation by 25%, 50% and 75% to simulate the minimum, medium and serious filter clogging. After the HRV reached steady-state, measurements were taken for 30 min at each airflow setting and each supply airflow clogging level.

2.3. Performance monitoring

The sensible heat recovery effectiveness $\in_{sens}$, and heat recovery rate, Q_{hrv} are used as performance indicators to evaluate the thermal performance of HRV using measurements taken on a minute-by-minute basis.

The sensible heat recovery effectiveness (**Equation 1**).

$$\in_{sens} = \frac{\dot{m}_1 \cdot Cp \cdot (T_2 - T_1)}{\dot{m}_{min} \cdot Cp \cdot (T_3 - T_1)} \quad (1)$$

Where T_1 is the outside air inlet temperature leaving the BIPVT and entering the HRV; T_2 is the supply air temperature of the HRV; and T_3 is the room temperature; $\dot{m}_1$ is the outside air mass flow rate, kg/s; $\dot{m}_{min}$ is the lowest of the mass flow rate of $\dot{m}_1$ and $\dot{m}_4$, kg/s and Cp is the specific heat capacity of air at average temperature, J/kg K. $\dot{m}_1 \cdot Cp \cdot (T_2 - T_1)$ represent the heat recovery rate of HRV.

3. RESULTS

The performance of the HRV at various airflow rates at "fault-free" and supply air filter clogging operation conditions are monitored from November 15th, 2024 to January 10th, 2025. The test cell is conditioned by an air handling unit located in the FBL building, maintaining a room setpoint temperature of 20°C and a relative humidity of 35%. All measurements are recorded at 1-minute intervals using an Agilent 34970A data logger.

The measurements at the time of non-solar irradiance are used for the HRV thermal performance analysis to prevent the impact of the BIPV/T preheating. The comparison of the HRV at various airflow rates and supply air filter clogging is presented here (Fig. 3 and Fig. 4) at 6℃ and -7℃ of outdoor temperature respectively.

The parameters compared include the sensible heat recovery effectiveness, $\in_{sens}$, supply air temperature, T_2, outside air flow rate, $\dot{m}_1$ and exhaust air flow rate, $\dot{m}_4$ as well as the heat recovery rate of HRV averaged over the entire period at each outdoor temperature.

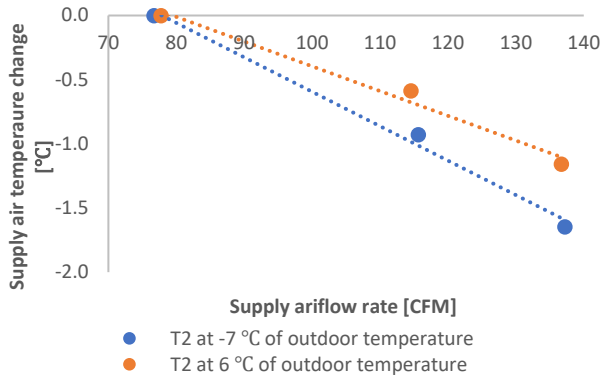

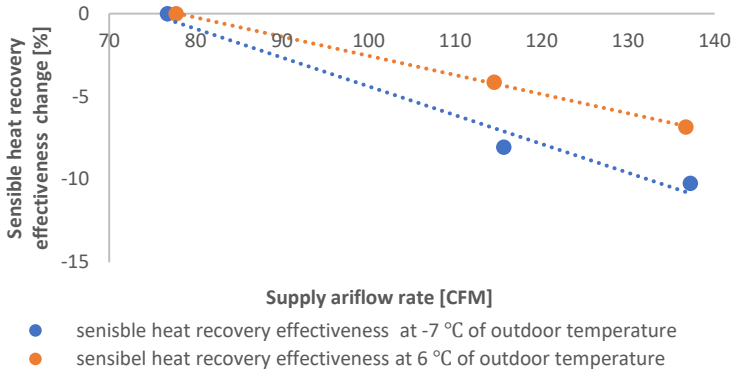

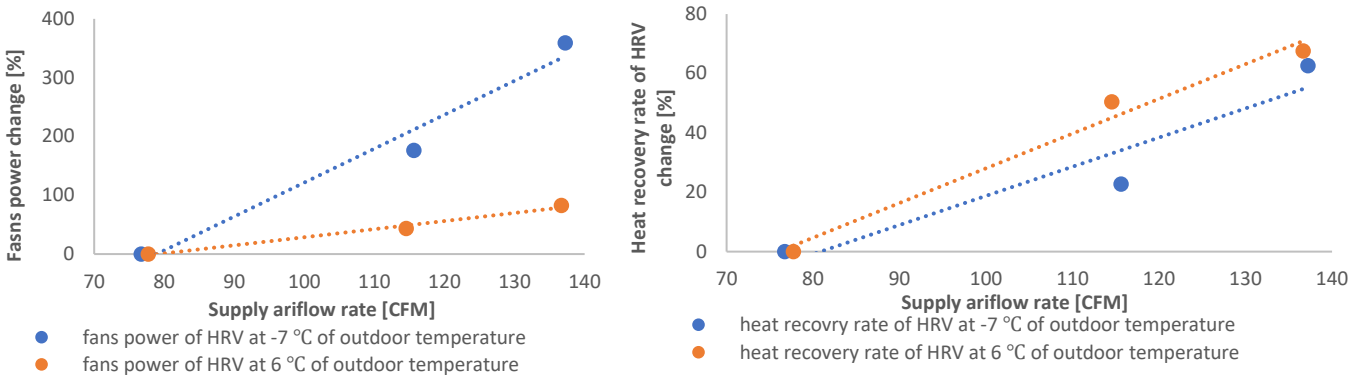

Monitored parameters	Correlation-based models	R_2
-7 ℃ of outdoor temperature		
Supply air temperature T_2	y = -0.027x+2.09	0.99
Sensible heat recovery effectiveness of HRV, $\in_{sens}$	y = -0.17x+12.98	0.98
Fans power of HRV	y = 5.77x-455.16	0.97
Heat recovery rate of HRV	y = 0.98x-79.39	0.90
6 ℃ of outdoor temperature		
Supply air temperature T_2	y = -0.02x+1.53	0.98
Sensible heat recovery effectiveness of HRV, $\in_{sens}$	y = -0.12x+9.01	0.99
Fans power of HRV	y = 1.38x-108.95	0.99
Heat recovery rate of HRV	y = 1.17x-88.89	0.98

Figure 3: Comparison of sensible heat recovery effectiveness $\in_{sens}$, supply air temperature, T_2, airflow rate and heat recovery rate of HRV at different HRV fans speed setting at 6 ℃ and -7℃ outdoor air temperatures at "fault-free" operation condition.

As shown in Fig. 3, the supply air temperature T_2 reduces with the increase of airflow rate of HRV by a maximum of -1.2℃ and -1.9℃ at 6℃ and -7℃ of outdoor temperature, respectively . The sensible heat recovery effectiveness decreases with the increase of airflow rate by a maximum of -6.8% and -10.2% at high fan speed (maximum) at 6℃ and -7℃ of outdoor temperature, respectively.

Due to the increased airflow rate, a maximum increase of the fans power of HRV is by 359% and 39% (Fig. 3) at 6◦C and -7℃ of outdoor temperature, respectively. Although the sensible heat recovery effectiveness drops, the increased supply airflow rate results in the greater heat recovery rate at higher airflow rate, a maximum increase by 67% and 62% at 6℃ and -7℃ of outdoor temperature.

Moreover, the above-mentioned thermal performance variation due to the airflow rate change is associated with the outdoor temperature. For example, both the supply air temperature and

sensible heat recovery effectiveness experience the greater reduction at -7°C of outdoor temperature than that at 6°C of outdoor temperature. Fan power of HRV increases more significantly at -7°C of outdoor temperature than that of 6°C of outdoor temperature due to the increased static pressure of HRV at colder outdoor temperature.

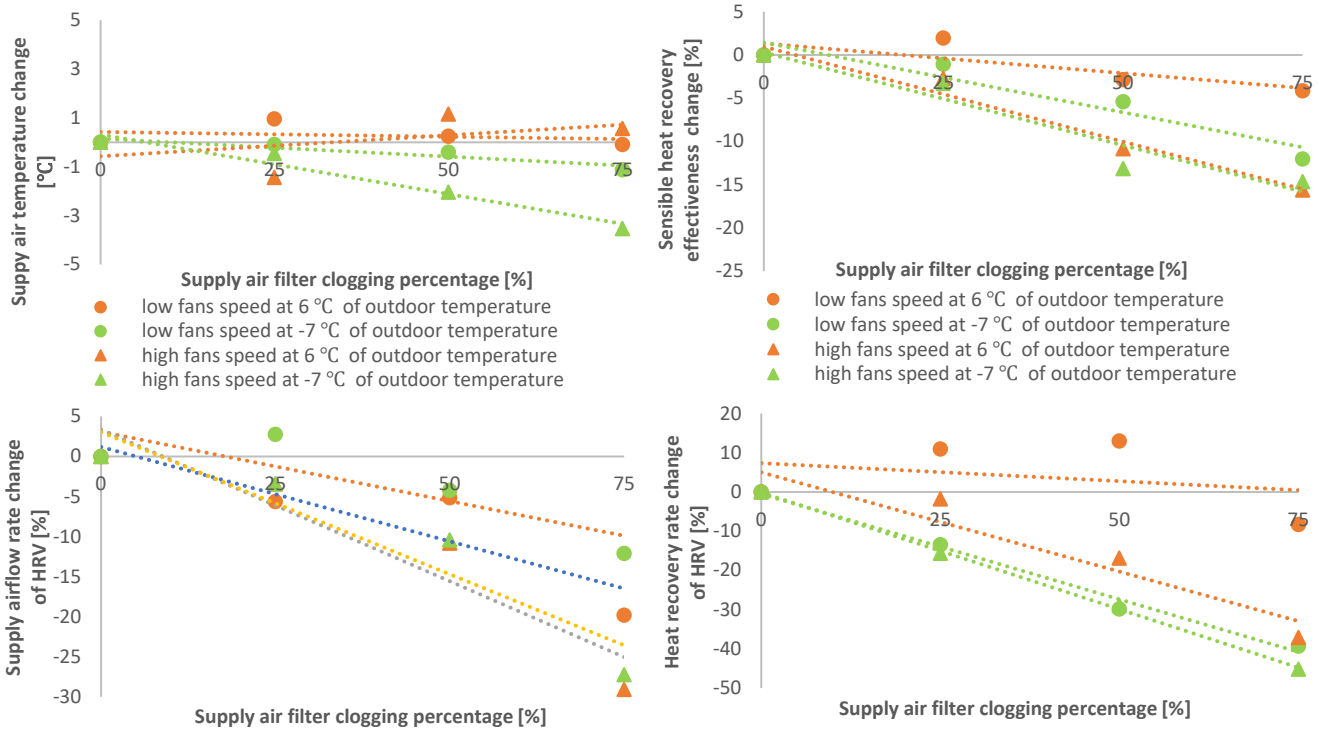

Figure 4: The comparison of sensible heat recovery effectiveness $\in_{sens}$, supply air temperature, T_2, airflow rate of HRV and heat recovery rate of HRV at different severity of HRV supply filter clogging at 6°C and -7°C of different outdoor air temperatures

Compared to the "fault free" HRV operation, the supply air temperature (T_2) decreases with the increase of supply air filter clogging at high fans speed mode by a maximum of -1°C and -3.5°C at 6°C and -7°C of outdoor temperature, respectively. The sensible heat recovery effectiveness drops with the increase of the supply air filter clogging at high fans speed mode of HRV by a maximum of -20.8% and -17.7% at 6°C and -7°C of outdoor temperature.

Supply air filter clogging leads to significant reduction of the supply airflow rate for both high and low fans speed setting, a maximum of -27.2% and -29.1% at 6°C and -7°C of outdoor temperature, respectively. The exhaust airflow and fans power of HRV remains constant for different severity of the supply filter clogging. Furthermore, due to the significant reduction of the supply air flow rate, the heat recovery rate of the HRV reduces greatly with the increased supply filter clogging at high fans speed mode of HRV by a maximum of 37.2% and 45.2% at 6°C and -7°C of outdoor temperature.

Moreover, the above-mentioned thermal performance variation due to the supply filer clogging is associated with the fans speed of HRV. For example, the supply air temperature, sensible heat recovery effectiveness and heat recovery rate are influenced more significantly at high fans

speed mode, compared with low (min) fan speed mode. The change of the thermal performance due to the supply filer clogging is not influenced by the outdoor temperature.

4. CONCLUSIONS

The aim of this study is to investigate the influence of the various airflow rates on the operation and performance of the integrated BIPV/T and HRV system in cold climate, and thermal efficiency of HRV with the filter clogging issue. The HRV preheated by the BIPV/T system is tested in the Future Buildings Lab (FBL) at Concordia University, Montreal during the winter period from November 15th, 2024 to January 10th, 2025. The experimental setup of the HRV and BIPV/T system is first presented. Then, the key performance indicators and parameter measured are presented, including the sensible heat recovery effectiveness $\in_{sens}$, supply air temperature T_2 and outside air flow rate, $\dot{m}_1$ and exhaust air flow rate $\dot{m}_4$ and heat recovery rate of HRV.

For the "fault-free" case, the increased fans speed of the HRV can lead to the increased supply and exhaust airflow rateat the cost of the significant increase of the fans power. In the meantime, compared with the low airflow rate of HRV, the supply air temperature (T_2) and sensible heat recovery effectiveness reduce with the increased airflow rate of HRV at 6◦C and -7◦C of outdoor temperature. Furthermore, the increased supply airflow rate results in the greater heat recovery rate at higher airflow rate, a maximum increase by 67% and 62% at 6℃ and -7℃ of outdoor temperature. The thermal performance variation due to the airflow rate change is associated with the outdoor temperature, the lower outdoor temperature, the greater influence on the thermal performance by varying the airflow flow rate.

For the faulty HRV operation of supply filter clogging, compared to the "fault-free" HRV operation, supply air filter clogging leads to the great reduction of supply air temperature by -3.5℃, the supply airflow rate by a maximum of -29.1%, and sensible heat recovery effectiveness of HRV by -20.8% as well as the heat recovery rate of HRV by -45.2%. Moreover, the above-mentioned thermal performance variation due to the supply filer clogging is associated with the fans speed of HRV, the higher fans speed of HRV, the greater impact on the thermal performance of HRV. The change of the thermal performance due to the supply filer clogging has nothing to do with the outdoor temperature.

The monitoring of the experimental setup of HRV preheated by the BIPV/T will continue throughout winter 2026. This further monitoring data will be used to analyse the defrosting hours, post-heater energy consumption and potentially the electricity generation efficiency impact of BIPV/T by preheating the HRV at different air flow rates

REFERENCE

ANSI/ASHRAE Stand. 41.2 Standard Methods for Laboratory Air-flow Measurement, USA: American Society of Heating, Refrigerating and Air-Conditioning Engineers (ASHRAE), 1987.

ANSI/ASHRAE Stand. 41.1 Standard Method for Temperature Measurement, USA: American Society of Heating, Refrigerating and Air-Conditioning Engineers (ASHRAE), 2013.

Akbari K., Oman R., 2013. Impacts of heat recovery ventilators on energy savings and indoor radon in a Swedish detached house. WSEAS Trans. Environ. Dev 1(9): 24-34.

Baril, D., Athienitis A and Ge H., 2021. BIPV/T for Arctic Residential Applications. In: 8th International Building Physics Conference, Vol. 2069, 012227

Barringer CG., McGugan CA, 1989. Effect of residential air-to-air heat and moisture exchangers on indoor humidity. ASHRAE Transactions 2: 461–474.

Kim W.S., 2022, Design optimization of cross-counter flow compact heat exchanger for energy recovery ventilator, International Journal of Air-Conditioning and Refrigeration 30.1: 16.

Kovesi T., Zaloum C., Stocco C., Fugler D., Dales R. E., Ni A., Barrowman N., Gilbert N. L., & Miller J. D., 2009. Heat recovery ventilators prevent respiratory disorders in Inuit children. Indoor Air 19(6): 489–499.

Li J., Ye K., Baril D., Ge H., Zmeureanu R., Athienitis A. K., 2023. Experimental study of a heat recovery ventilator preheated by a Building Integrated Photovoltaic system in a cold climate. In: Journal of Physics: Conference Series, 13th Nordic Symposium on Building Physics, Alborge, Danmark, Vol. 2654(1), 012103.

Li, Y., Leung, M., Tang, J. W., Yang, X., Chao, C. Y. H., Lin, J. Z., ... & Yuen, P. L. (2007). Role of ventilation in airborne transmission of infectious agents in the built environment–a multidisciplinary systematic review. Indoor air, 17(1).

Liu G., Xiao M., Zhang X., Gal C., Chen X., Liu L., Pan S., Wu J., Tang L., Clements-Croome D., 2017. A review of air filtration technologies for sustainable and healthy building ventilation, Sustainable Cities and Society 32: 375–396.

Penney M., 2024. HRV/Air Exchanger Cleaning for Allergy and Asthma Sufferers. DeepClean NL Ltd. | Cleaning & Maintenance Services in NL. https://deepcleannl.com/hrv-air-exchanger-cleaning-for-allergy-and-asthma-sufferers/

Riffat SB, Gan G., 1998. Determination of effectiveness of heat-pipe heat recovery for naturally-ventilated buildings. Applied Thermal Engineering 18:121–30.

Series STRA | Duct Mounted Airflow Measurement Station Is Easy to Install and Utilizes an Airflow Averaging Element. | Dwyer Instruments, n.d.

6th International Conference on Building Energy and Environment
Eindhoven University of Technology, The Netherlands
6 - 10 July 2025

Towards a Framework for low carbon Retrofits on Community Scale

Heike Schreiber, Travis Moore, Hadia Awad

National Research Council (NRC) Canada, Ottawa, Canada,
heike.schreiber@nrc-cnrc.gc.ca
travis.moore@nrc-crnc.gc.ca
hadia.awad@nrc-cnrc.gc.ca

SUMMARY
The paper outlines a framework for community-scale building retrofits aimed at reducing greenhouse gas emissions. Retrofitting existing buildings is a key strategy to meet Canada's 2030 and 2050 emissions reduction targets. The framework involves: assessing the current status of community buildings, identifying potential retrofit measures, analysing the measures for retrofit performance, recommending retrofit scenarios, implementing and verifying the retrofits, and engaging the community throughout the process. The approach integrates grid interaction and emphasises the importance of incorporating innovative technologies and life cycle cost assessment. The paper highlights research gaps, including the need for standardised emissions baselines and methods to account for microclimate effects and cross-sector decarbonisation strategies. It calls for tools to optimise energy, affordability, and resiliency in retrofit models, aiming for a holistic guideline for community-scale retrofits.

Keywords: community retrofit, emissions reduction plans, grid integrated buildings.

1. INTRODUCTION

In Canada's Emissions Reduction Plan, the government of Canada has committed to reducing greenhouse gas (GHG) emissions by 40-45% from 2005 levels by 2030, with a goal of achieving net-zero emissions by 2050. Large portions of Canada's existing emissions stem from energy use in residential, commercial, and institutional buildings [Statistics Canada 2023]. Since a majority of buildings in Canada that will be in use until 2050 are already built, and new buildings are being built to higher standards, the focus for emissions reductions needs to be on retrofits. Retrofitting buildings can generally be defined as "modification of existing equipment, systems, or buildings to improve performance, update operation, improve energy performance, or all three" [ASHRAE 2024]. In the context of this work, the goal is to ensure that modifications lead to lowest life cycle GHG emissions, minimised over the life cycle of the buildings, and that ideally includes emissions associated with raw materials extraction, manufacturing or processing, transportation, building use, and end-of-life management of buildings and all their individual components. Given that for existing buildings, the energy consumption during their use phase makes up a large portion of those emissions, it becomes clear that the energy supply to the buildings plays a pivotal role in minimising emissions, which can be achieved either by reducing energy use or by reducing emissions from the energy source.

The energy source that has the highest potential for emissions reduction is electricity, since it can be generated from renewable energy sources. However, there are limits to harvesting renewable

energy, like the intermittence of availability, geographical access limitations and finite resources for the production of renewable electricity generators. Although many Canadian provinces have the advantage of large resources of hydro power, a renewable energy source that allows for dispatchable electricity supply, even in regions with on average low-emission intensity electricity supply, peak electricity load may come from non-renewable, high emitting sources [Ghobadi 2023]. Further, as demand increases due to electrification of heating, transport and industrial processes, the frequency of hours of high peak demand on the grid will increase further and peak load will shift from summer to winter. Also, existing load profiles are expected to change. As an integral part of the Emissions Reduction Plan, the government of Canada is developing Clean Electricity Regulations to help achieve decarbonisation targets and progress towards clean electricity grids in all Canadian provinces, with a target to be Net-Zero by 2050 [GoC2025]. In this landscape, buildings as main users of electricity from the grid can actively support those decarbonisation targets by shaping the electricity demand profiles in coordination with the grid's clean electricity supply potential [ASHRAE 2023]. To assess the interactions between buildings and the electricity grid, the scope of a retrofit study should encompass several buildings of various use types and sizes in a mix that is representative of consumers of the electricity supplied by the grid. It is on the aggregate level that the buildings' electricity use profile will have an impact on the electricity supply and the variability in use profiles of various buildings can further help reduce the stress on the electricity grid. Hence does the proposed framework follow a community scale approach for retrofit planning.

The goal is to develop optimised pathways of community retrofits for lowest GHG emissions. This paper will outline the required steps, and discuss existing gaps in the framework for low carbon building and energy retrofits on community scale.

2. WORK FLOW FOR RETROFITS – A COMMUNITY SCALE APPROACH

For the development of a retrofit pathway buildings in a community we propose the outlined workflow shown in Fig. 1: (1) assessment of status quo of the community and buildings within; (2) identification of retrofit measures; (3) analysis of the identified measures; (4) developing recommendations of retrofit scenarios; and finally, (5) plan implementation and verification of the retrofit packages and their actual performance. Each step has to be performed in close consultation with the community, property owners and occupants (6) in order to: (a) understand

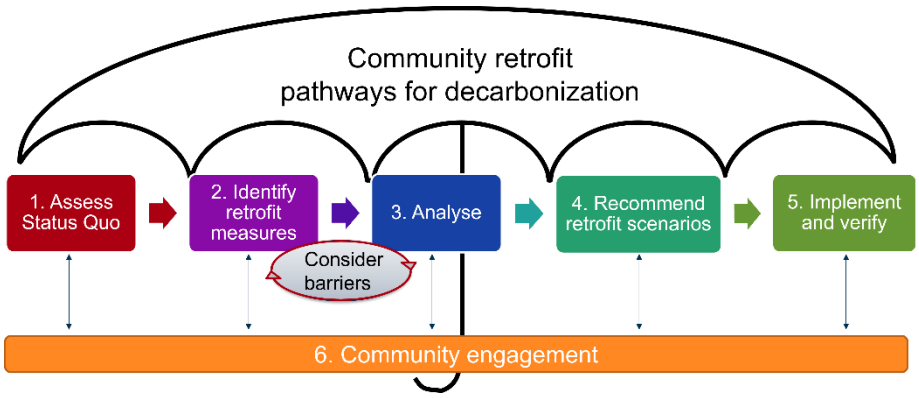

Figure 1. Work flow for community retrofits

their requirements and constraints; (b) ensure buy in for the proposed solutions and the necessary engagement to implement; (c) maintain the benefits of any form of retrofit over the long term; and (d) ensure that the proposed solutions optimally satisfy both low embodied carbon and low operational carbon. Steps (1)-(6) are detailed further in the following subsections.

2.1. Assessment of the status quo

The assessment of the status quo of the community aims to identify the condition and energy performance of the buildings to understand retrofit needs and technical constraints. The performance assessment identifies the current emissions profile of the buildings in the community (baseline emissions), by assessing the current demand profiles for heating, cooling, domestic hot water, and the associated energy sources/energy supply structure, as well as the electricity demand profile and the current electricity grid source energy characteristics. The first comprehensive standard to measure, manage and report GHG emissions on a community level was published by World Resources Institute [Fong 2021]. Relevant to this framework is the guidance on how to calculate the emissions from residential, commercial and institutional buildings and facilities. The data required can come from various sources, such as energy use data from utility bills, survey data, home rating data and energy audits. Establishing retrofit recommendations for the buildings in the community requires knowledge of building attributes which may or may not be available in these datasets. Accordingly, there is a need for advanced methods to complete building specific auditing using cost effective, non-intrusive, rapid, sensing techniques and remote auditing tools. These methods are relatively novel to the market, but have great potential for scalability. Some examples include use of infrared cameras and unmanned aerial vehicles to identify thermal losses from building envelopes and use of smart thermostat data (indoor air temperature, temperature set point, and heating/cooling scheduling) to characterise a buildings thermal performance [Doma and Ouf 2023]. These methods still require research like validation through traditional building auditing techniques, such as submetering, envelope instrumentation (e.g., blower door tests), occupant surveys, utility bills, etc., to demonstrate the ability to derive quantitative assessment data. Once building specific data has been derived, methods to generate community specific archetypes, such as those commonly used in building energy modelling tools, need to be developed.

The assessment leads to building and site condition reports that define status quo of the existing building envelope (thermally and structurally), mechanical systems, indoor environmental quality, energy demand and supply structure and renewables potential within the community.

2.2. Identification of retrofit measures

The initial assessment defines the baseline for the retrofit pathways: Modifications of the status quo should lead to improvements that can be assessed in comparison to this baseline and improvement targets can be set accordingly. Those targets depend on the purpose of the retrofit. Typically, the incentive for a community to undergo retrofit would be to increase the resilience of buildings and occupants to withstand disaster and changes in climate, enhance the durability of built assets and reduce the cost of operating the buildings. The additional goal for a low carbon retrofit is to achieve these upgrades while reducing emissions. Utilities can also benefit from community retrofits in terms of grid side management. Demand reduction, especially during critical peaks will reduce the stress on the grid, leading to a more resilient, self-sufficient utility grid. Furthermore, it will reduce the utility’s operational costs. Self-sufficiency means

reduced costs of importing electricity from nearby jurisdictions. Since resilience upgrades and energy efficiency measures have the potential to lead to GHG emissions reductions over the life of the community, those solutions should be preferred.

Based on the initial assessment of the community and its buildings, location and energy supply structure, suitable retrofit measures need to be identified. Retrofit measures would include upgrades to enhance resilience, energy efficiency, environmental quality and energy supply on both individual building and community level: Examples of typical building retrofit measures include: i. Structural upgrades (as needed); ii. Building envelope upgrades to reduce energy use and increase resiliency; iii. Resilient HVAC solutions to increase efficiency of heating and cooling; and, iv. Smart technologies such as smart thermostats and smart meters. However, there is a need to move beyond these traditional technologies, and include technologies which provide: adaptive building operations, smart controls and demand side management including dispatchable loads that enable micro-grid and community energy systems strategies through integration of distributed energy resources (DER) including renewables and energy storage.

To effectively make recommendations for low carbon and resilient retrofit measures, data is needed that specifies: technological specifications and performance, costing data, supply availabilities, timelines of implementation and service life, potential interactions and symbiosis between measures for all retrofit technologies being considered.

2.3. Analysis

Once the baseline of community performance and condition is established, and potential retrofit measures have been identified, analyses will take place to estimate the improvement that can be achieved through retrofitting the community. The analysis of retrofit scenarios currently focuses on energy savings and cost. For the energy analysis, (urban) building energy modelling tools can be used, which mostly are based on physics-based modelling with a bottom-up approach [Reinhart 2016]. Further to data from the initial assessment, the analysis will consider climate data, ideally future weather data, to ensure retrofit measures meet resiliency requirements.

For low carbon retrofits, the analysis should expand, at minimum to include GHG emissions associated with the energy use in the buildings. To calculate emissions from building energy use and consider integration with the electricity grid, it is essential to have grid carbon intensity data and, importantly, forecasts of this intensity. The grid carbon intensity refers to GHG emissions produced per unit of electricity generated and supplied to the power grid, and is also called grid emissions factor. Accurate emissions factors are a foundational input to emissions reduction pathways since they are used to calculate the changes in emissions caused by retrofit measures that affect electricity use [Sotes 2021]. To calculate future emissions factors, predictions of the future electricity supply structure are needed. Hence, the development of a retrofit pathway for buildings in a community should incorporate the emissions reduction plan of the local utility.

Ideally, the goal is to optimise the solutions space for lowest life cycle carbon, which would include so called embodied emissions associated with the materials and systems that are added and construction practices that are involved in the retrofit process. Practically, considering locally sourced, low embodied carbon retrofit materials, minimal transportation of materials, as well as efficient construction operations, can potentially reduce embodied GHG emissions.

To achieve the scale of low carbon retrofit that is needed for Canada's emissions reduction targets, the proposed retrofit solutions should ideally have an economic incentive for the building owners and/or occupants. Considerations of the economic viability of the retrofit via life cycle costing (LCC) tools should thus be integrated with life cycle assessment (LCA) in life cycle cost assessment (LCCA) [Prabatha 2020]. LCA is needed to comprehensively examine the environmental impacts over the life span of buildings and communities. LCA is standardised in ISO 14040 [ISO 2006a] and ISO 14044 [ISO 2006b] from the International Organisation for Standardisation, which provide guidelines how to conduct LCA and define the scope for LCA, i.e. the stages in the life cycle to be assessed and the impact categories to use in the assessment.

Optimisation tools, like MANGOret [Petkov 2022] or python-based frameworks [Zhang 2021], have become popular in LCA studies [Toosi 2020]; and could be used to identify optimal retrofit pathways. The defined targets from section 2.2 are the objective function for this optimisation, which also needs to consider technical constraints and barriers that may limit the solutions space. Besides technical constraints of the given properties, the community may face other constraints that need to be taken into consideration when analysing retrofit options, such as i. Consideration of practical and budgetary barriers; ii. Access to occupied buildings; iii. Heritage, cultural, or historical significance of the asset; iv. Supply chain issues; v. Skilled trades shortage. Richarz [2023] et al suggest a method to incorporate skilled trades shortages into optimising retrofit roadmaps. Similar approaches could be taken to account for supply chain issues. With consideration of cost and technical constraints and other barriers, iterations may be required between step 2, identification of measures, and 3, analysis. To mitigate the impacts of retrofit site work on tenants, faster and less intrusive construction practices should be enhanced. For example, the use of 3D scanning technology to scan damaged building envelopes, and construction of replacements through off-site methods could increase production and reliability.

2.4. Recommendation of retrofit scenarios

Through the analysis and optimisation described in the last section, pareto optimal solutions sets for least cost and emissions pathways can be provided [Prabatha 2024]. From this solution space, an implementation plan for the retrofits in the community can be developed. Depending on cost and financing constraints, this plan can entail a staged approach to retrofitting portions of buildings in the community at a time. Again, the local utility should be included in the planning of retrofits since the measures will impact its operations.

2.5. Implementation and verification

The last step in the framework is to plan for implementation and verification of the retrofit packages and their performance. The retrofit implementation or construction phase should be minimally disruptive to building occupants. While this may drive up costs of the retrofit measures, it could be crucial to acceptance of the implementation plan by occupants. Innovative construction practices, such as panelised construction methods and robotics and automation, may speed up the retrofit process and minimise the disruptions affecting the occupants.

In order to verify the emissions savings that are achieved through the retrofit, post measurements will be required. The results from the post assessment can provide valuable insights for future retrofits and lessons learned can be shared, in particular if a staged approach has been chosen for retrofit implementation while similar measures are being planned for similar groups of buildings.

2.6. Community engagement

The base for a successful community retrofit pathway is engagement with the community stakeholders, which include, broadly speaking, building owners, occupants, building operators, local authorities, community associations, utility providers and business owners and operators. This engagement is required from the very first step to ensure community buy-in and sustained involvement throughout the retrofit process [Shwashreh 2024]. While required at all times, engagement is crucial during the initial stages when the potential solution space is being defined. For highest chance of success, the retrofit measures need to be those that are readily adoptable by the community, which may not necessarily be the optimal scenarios. This highlights the need to increase retrofit literacy in the community previous to providing final recommendations.

3. DISCUSSION OF RESEARCH GAPS

Presently in Canada, there is a considerable number of publications for guidance on energy retrofit strategies in buildings, including not limited to: NRCan's Major Energy Retrofit Guidelines [NRCan 2024], derived from a similar publication by the US Office of Energy, retrofit guidelines for developers, builders and operators by Sustainable Buildings Canada, a not-for-profit organisation [SBC 2025], and resources for homeowners [DER 2025, BDC 2025]. These documents help identify retrofit strategies for singular building types; however, guidance on methods to complete this in an optimised fashion at the community scale for the purposes of energy, decarbonisation and resiliency are lacking. This is especially true when considering the impacts of building retrofits on other sectors, such as the electricity generation sector. This necessitates a holistic framework to be developed, which can leverage and build on, the methods described previously in this paper. To enable the development of a holistic guideline that can be used to encourage resilient and low carbon retrofits at scale, i.e., move beyond the one size fits all approach, there is a need to develop tools and methods to address many barriers. Presently the following barriers are the focus of research at NRC Construction Research Centre in Canada:

3.1 Establishing pre- and post-retrofit performance

A major barrier to rapid deployment of retrofit strategies is establishing the condition and performance of the initial building, as this dictates the options for retrofit. This is needed to move from our current state of one-size fits all recommendations for retrofits, to a tailored approach that can accelerate optimised retrofit decision making. Additionally, post-retrofit performance is rarely documented. There is a need to increase data gathering to determine the accuracy of modelling and planning methods that currently exist, to understand their validity in retrofit planning and identify areas of improvement or gaps.

3.2 Establishing the impact of microclimate and resiliency requirements

Microclimate effects can result in different adaptation strategies on individual buildings, even within the same city. A prime example is urban heat island effect, where the overheating risk in buildings could be significantly different, even for two buildings of the same construction type and occupants, based on surrounding topography, greenery and exposure to water bodies. The same differences in microclimate that effect adaptation considerations would also affect the energy use to heat and cool buildings. Thus, scientific based methods to generate, and incorporate microclimate effects into retrofit planning are needed.

Resiliency can be achieved through exhaust heat exchange between proximity buildings and water bodies within a community. For example, data centres or buildings with large boilers, such as sports facilities and hotels: Exhaust heat can be captured and utilised, in order to reduce heating demands in target buildings.

3.3 Establish standard methods to determine baseline emissions at the community scale

There are standards for determining GHG emissions for different community processes [Fong, 2021], but limited guidance on what to count and how to reach Net Zero emission goals. Guidance on a consistent, and standardised metric needs to be determined. To understand the effect of building retrofits on a community scale, knowledge of the temporal variance in emissions due to electricity use, now and in the future, is needed [Bontekoe 2024]. Presently, in Canada, this is only possible in Ontario and Alberta due to open electricity markets. However – other provinces could enable this through better data sharing requirements.

3.4 Optimisation for affordability, resiliency and energy use of buildings and LCA analysis

While guidance may exist to complete each of these analyses separately, little guidance is provided on how to optimise for these design requirements in practice. Further case studies are needed to derive best practices.

Reviews for LCA studies specific to building retrofits have shown that in practice, the applied LCA scope varies from study to study, making the results incomparable [Fahlstedt 2024]. This emphasises the need to standardise the LCA methods and scope [Fahlstedt 2024], which has huge impact on the outcomes and comparability of building retrofit studies. For example, the assumption of the building lifespan significantly changes the results [Leichter 2024]. In the same sense, the actual service life of building components is necessary for accurate LCA results [Fahlstedt 2024], so there is the need to establish and standardise test methods to predict (remaining) service life and durability of building components under the changing climate.

3.5 Cross Sector data considerations

The community decarbonisation lens extends beyond buildings and the electricity sector. Electrification of other sectors, such as transport (road and marine) may necessitate a more holistic view of community decarbonisation strategies. Therefore, decarbonisation studies of buildings need to consider how the data and conclusions are gathered and presented, such that they can be fed up to a broader model, which considers all cross-sector decarbonisation potential.

4. CONCLUSION

This paper proposes a framework for guidance on developing optimised pathways to retrofit buildings in a community to achieve resiliency and low GHG emissions. The framework consists of (1) Assessing status quo; (2) Identifying retrofit measures; (3) Analysing identified measures; (4) Recommending retrofit scenarios; and finally, (5) Implementing and verifying retrofit packages and their actual performance. Each step has to be performed in close consultation with the community, property owners and occupants (6). Further, research areas to enable resilient low carbon retrofits of buildings at the community scale were identified, with some examples provided. Ultimately, the purpose of this paper is to present the framework and solicit feedback and guidance on missing areas, tools or considerations as this research project progresses.

ACKNOWLEDGEMENTS
The authors would like to acknowledge financial support by Natural Resources Canada, Office of Energy Research and Development under the Program of Energy Research and Development (PERD).

REFERENCES
ASHRAE Terminology, 2024.
Statistics Canada, Report on Energy Supply and Demand in Canada, 2000-2021, Ottawa, 2023.
Ghobadi, M., D. Heidari, and M. Bartko. 2024. How much retrofit is enough? ASHRAE Proceedings of the International Buildings Decarbonization Conference 2024.
Government of Canada (GoC). 2025. Clean Electricity Regulations: maintaining reliability. Retrieved Jan 2025 from https://www.canada.ca/en/services/environment/weather/climatechange/climate-plan/clean-electricity/regulations-reliability.html
ASHRAE Task Force for Building Decarbonization, Grid-Interactive Buildings for Decarbonization: Design and Operation Resource Guide, 2023.
Fong, W.K., Sotos, M., Doust, M., Schultz, S., Marques, A., Deng-Beck, C.. Global Protocol for Community-Scale Greenhouse Gas Inventories. Greenhouse Gas Protocol, World Resources Institute, 2021.
Doma, A. and Ouf, M., 2023. Data-driven approach to prioritize residential buildings' retrofits in cold climates using smart thermostat data. Architechtual Science Review, 66 (3), 172–186
Reinhart, C.F., Davila, C.C.. Urban building energy modeling – A review of a nascent field, 2016. Building and Environment, 97, pp. 196-202
Prabatha, T., Hewage, K., Karunathilake, H., Sadiq, R. 2020. To retrofit or not? Making energy retrofit decisions through life cycle thinking for Canadian residences, Energy and Buildings, 226, 110393
Sotes, J. A Clearer View of Ontario's Emissions, The Atmospheric Fund, 2021.
International Organization for Standardization (ISO), Environmental management - Life cycle assessment – Principles and framework (ISO 14040:2006). 2006.
International Organization for Standardization (ISO), Environmental management - Life cycle assessment – Requiremetns and Guidelines (ISO 14044:2006). 2006.
Fahlstedt, O., Rasmussen, F. N., Temeljotov-Salaj, A., Huang, L., Bohne, R. A., 2024. Building renovations and life cycle assessment - A scoping literature review, Renewable and Sustainable Energy Reviews, 203, 114774.
Leichter, M., Piccardo, C., 2024. Assessing life cycle sustainability of building renovation and reconstruction: A comprehensive review of case studies and methods, Building and Environment, 262, 111817.
Petkov, I., Mavromatidis, G., Knoeri, Ch., Allan, J., Hoffmann, V. H., 2022. MANGOret: An optimization framework for the long-term investment planning of building multi-energy system and envelope retrofits, Applied Energy, 314, 118901.
Zhang, H., Hewage, K., Prabatha, T., Sadiq, R.. 2021. Life cycle thinking-based energy retrofits evaluation framework for Canadian residences: A Pareto optimization approach. Building and Environment, 204, 108115.
Toosi, H. A., Lavagna, M., Leonforte, F., Del Pero, C., Aste, N., 2020. Life Cycle Sustainability Assessment in Building Energy Retrofitting; A Review, Sustainable Cities and Society, 60, 102248.
Richarz, J., Fuchs, N., Hering, D., Mueller, D., 2023. Modernization Roadmaps for Existing Buildings under Limited Energy Resources and Craftwork Capacities. Energies, 16, 4822.
Shwashreh, L., Taki, A., Kagioglou, M. 2024. Retrofit Strategies for Alleviating Fuel Poverty and Improving SubjectiveWell-Being in the UK's Social Housing. Buildings, 14, 316.
Natural Resources Canada (NRCan). Retrofit Hub - guides. 2024. Retrieved Jan 2025 from https://natural-resources.canada.ca/retrofit-hub-guides/26034
Sustainable Buildings Canada (SBC). Guides. Retrieved Jan 2025 from https://sbcanada.org/guides/
Deep Energy Retrofits Canada (DERC). Last visited Jan 2025 https://deepenergyretrofits.ca/
Business Development Bank of Canada (BDC): A practical guide to retrofitting your building for energy efficiency. Last visited Jan 2025 https://www.bdc.ca/en/articles-tools/sustainability/climate-action-centre/articles/practical-guide-retrofitting-building-energy-efficiency
Bontekoe, E., Schade, J., Erikkso, L., Tsarchopoulos, P., Lampropoulos, I., van Sark, W., 2024. On the discrepancy of using annual or hourly emission factors for power generation to estimate CO2 reduction of building retrofitting. Energy and Buildings, 319, 114499.

COBEE 2025 – Proceedings

TUESDAY

Advanced Modeling and Building Simulations (11:00-12:30 h)

6th International Conference on Building Energy and Environment
Eindhoven University of Technology, The Netherlands
6 - 10 July 2025

A novel air distribution system to humidify an aircraft cabin while minimizing water vapor condensation on cabin walls

Tengfei (Tim) Zhang[1], Xiang Guo[2], Feng Wang[3,*]

[1]*Dalian University of Technology, Dalian, China, tzhang@dlut.edu.cn*
[2]*Dalian University of Technology, Dalian, China, 32206124@mail.dlut.edu.cn*
[3]*The Hong Kong Polytechnic University, Hong Kong, China, f.wang@polyu.edu.hk*

SUMMARY
Commercial aircraft cabins have long been criticized for the air dryness inside. On the one hand, aircraft cabin requires humidification to improve the comfort feeling. But on the other hand, the aircraft cabin walls must be maintained in a relatively dry status to refrain water vapor condensation. To resolve the above paradox, this investigation proposed a new air system by suppling the humidified, outboard conditioned air into the interior passenger zone, while circulating the relatively warm, dry air along the cabin walls. The validated CFD was adopted to solve the airflow, temperature, and relative humidity distribution. The results revealed that the new air system is able to enhance the relative humidity of the interior passenger zone from the existent 6-8% on inter-continent flights to approximately 22%. Meanwhile, the water vapor content near the cabin walls is maintained 3 g/m^3 lower than the interior passenger zone.

Keywords: Aircraft cabin, Air distribution, Humidification, Moisture condensation, Draught risk

1. INTRODUCTION

Commercial aircraft cabins have long been criticized for the air dryness inside. Low moisture content may induce the headache, skin itching, nose dryness or stuffiness, eye irritation, tiredness and many other non-specific symptoms (Derby et al. 2017). Consequently, scholars strongly recommend increasing the relative humidity in aircraft cabins by 5% to 10% to alleviate the discomfort associated with the air dryness (Nagda et al. 2001). However, even without carrying out humidification, a twin-engine aircraft was claimed having increased its weight by 680 kg due to condensation of water vapor on the internal fuselage skins (Specht et al. 1999). The enhanced humidity inside the cabin will inevitably lead more condensation of water vapor on the fuselage skins. An air distribution system by delivering the humid air into the passenger zone while circulating the relatively dry air along the cabin walls seems a good strategy to resolve the paradox (Zhang et al. 2010). However, such air system was proposed only based on the displacement ventilation (Zhang et al. 2010), which has not been put to practical use yet. There is still a pressing need of a novel air distribution system that can resolve the paradox of the water vapor in aircraft cabin based on the widely used mixing ventilation system. This investigation presents our efforts to address the challenges.

2. METHODS

The new system consists of five slot vents (as labeled by Inlet-1 to Inlet-5) and three gaspers (as labelled by Inlet-6) in half a cabin of a wide-body aircraft as shown in Fig. 1. Inlet-1, Inlet-3, and Inlet-5 supply only the conditioned outboard dry air, with the former two discharging air nearly horizontally and the last discharging air nearly vertically. Inlet-2 and Inlet-4 supply the recirculated, humid air slightly downward to the cabin. The gaspers are located at relatively lower

positions, as highlighted by Inlet-6. These gaspers deliver the humidified, outboard air at a relatively high speed but with a very small volumetric rate to the breathing zones, and the air jets are directed to the both passengers seated close to the aisle and the middle passenger seated in the side. No gasper is toward the passenger seated near window and the central passenger of the cabin.

The total ventilation rates of Inlet-1 to Inlet-5 are 10 L/s per passenger, as shown in Table 1. In the total ventilation rate, a half is from the outboard air and the other half from the recirculated air. The CO_2 concentration of the outboard air is fixed to 350 ppm, while the recirculated air is 1350 ppm. Because Inlet-2 and Inlet-4 discharge the fully recirculated air, the supplied air has a relative humidity of 30.7%. The supplied air from Inlet-6 has a relative humidity of 81.3%, which corresponds to a humidification rate of 40 g/h per passenger. Regarding to temperature, Inlet-5 supplies the warm air at 32 ℃ to heat the cold sidewall and window panels. Inlet-6 (gaspers) discharges air at 24 ℃, while the remaining inlets deliver air at 19 ℃. More details of the design parameters can be found in Table 1.

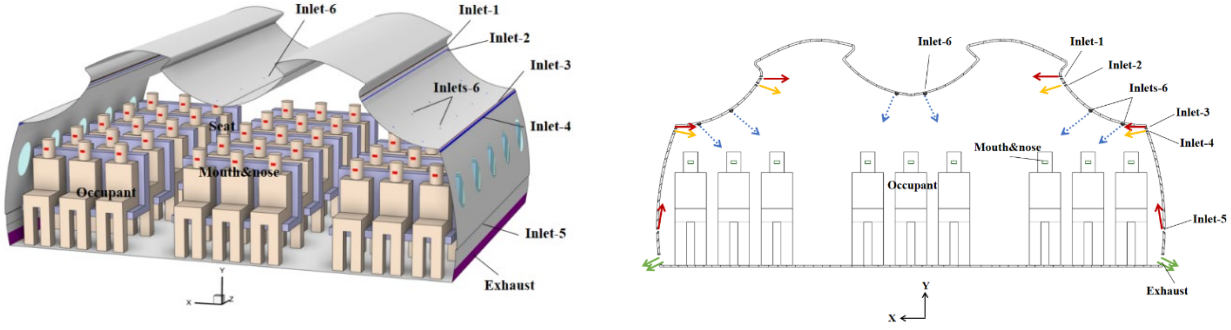

Figure 1. Novel air distribution system in a wide-body aircraft: (a) overview of the geometry and multiple air-supply inlets, (b) sectional view of the aircraft cabin and the air-supply directions form different inlets.

Table 1. Major design parameters of the multiple air supply inlets

Item	Inlet-1	Inlet-2	Inlet-3	Inlet-4	Inlet-5	Inlet-6
Supply air rate per person (l/s)	2.25	2	1.25	3	1.5	0.615
Supply air velocity (m/s)	1.985	1.323	1.324	0.793	1.324	3.059
Supply air temperature (℃)	19	19	19	19	32	24
Supply CO_2 concentration (ppm)	350	1350	350	1350	350	350
Supply air RH	0	30.7%	0	30.7%	0	81.3%

The new air system in a section of a wide-body aircraft with five rows was modelled by the validated computational fluid dynamics (CFD) program. All of the seats were seated by a thermal manikin with the skin temperature of 30.3 ℃. Each passenger was assumed to release the water vapor at a rate of 50 g/h and CO_2 at 18 L/h. The ceiling temperature was set to 23 ℃, the sidewall 18 ℃, and the floor near 24 ℃. All of the seats were treated as adiabatic. The front and rear cross sections were assumed to be periodic.

The RNG k-ε model with the enhanced wall function was adopted to resolve the turbulence. The thermal buoyancy was represented by the Boussinesq approximation. All of the physical variables were discretized by the second-order upwind scheme. The pressure and velocity were solved by the SIMPLE algorithm. The space claim direct modeler (SCDM) software was used to create the

geometric model and generation of the unstructured grid meshes with the "polyhedra" scheme. The mesh size at the air supply inlets was 0.2 cm, around the passenger skins was 2.5 cm, and at the passenger's mouth and nose was 0.5 cm. The maximum mesh size in space did not exceed 6 cm. Because the enhanced wall function was adopted to resolve the wall effect, in order to achieve $y+$ less than 5, three boundary layers were added near the walls. The type of the boundary layer was the smooth-transition, with the transition ratio of 0.272 and the growth rate of 1.15. The total grid cell number was 4,321,034. Once the relative residual of the energy was less than 1.0e-6, the concentration of water vapor and CO_2 was less than 1.0e-3, and the ratio of the sum of mass gain and loss on all boundaries to the total mass gain in the cabin was less than 1.0e-6, the solutions were judged having reached numerical convergence.

The CFD model was first validated with the experimental data obtained in a wide-body aircraft cabin mockup. More details of the model validation can be found in the appendix. Then the distribution of airflow, temperature, CO_2 concentration, and relative humidity were solved. The draught risk (ASHRAE 2021) to the passengers was also evaluated.

$$PD = (34 - t_a) \cdot (V - 0.05)^{0.62} \cdot (0.37 \cdot V \cdot Tu + 3.14)$$

where t_a--- local air temperature, °C
V--- local mean air velocity, m/s
Tu--- local turbulence intensity, %

For V< 0.05 m/s, force V= 0.05 m/s; and for PD > 100%, force PD =100%.

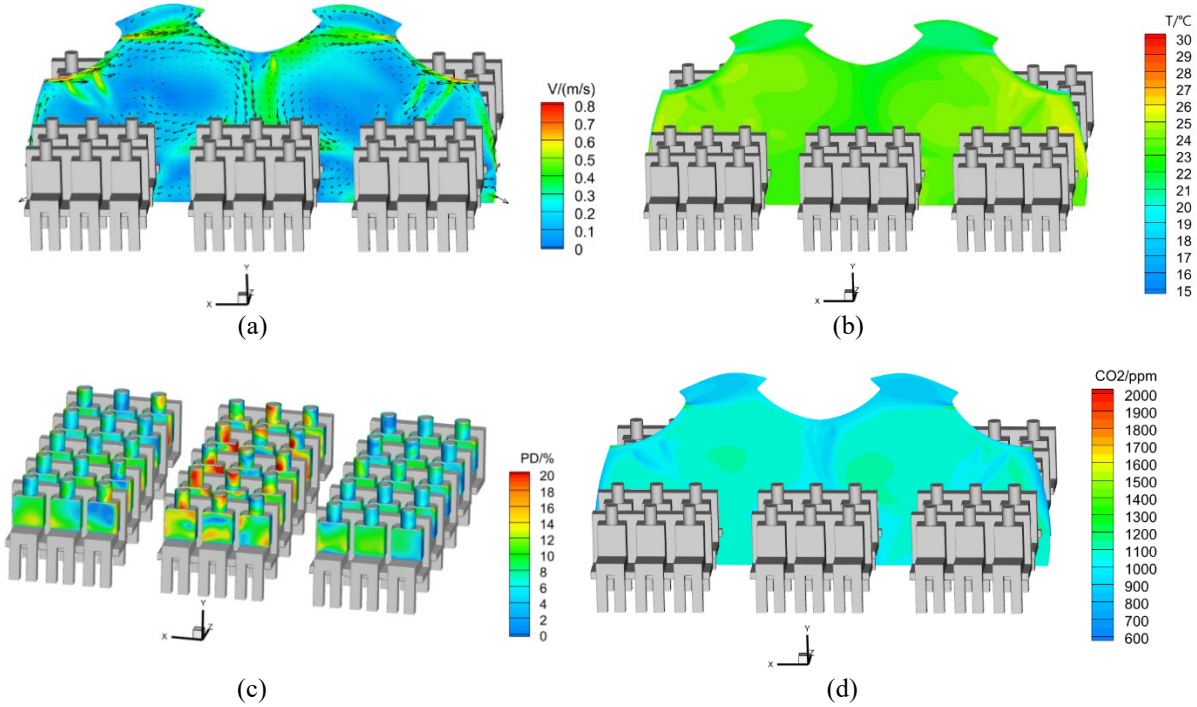

Figure 2. Thermal environment and CO_2 concentration distribution inside the aircraft cabin with the new air system: (a) airflow distribution, (b) air temperature, (c) percentage of dissatisfied (PD), (d) CO_2 concentration.

3. RESULTS

Fig. 2(a) presents the airflow distribution in a cross section across the third row. The supplied air into the aircraft cabin formed two big vortices in both sides. The high speed airflow from the gaspers to the side passengers, across the upper aisle region, and in the central region above the middle passengers can be viewed. Fig. 2(b) presents the air temperature distribution, in which the temperature is relatively uniform. However, the slightly high temperature (approximately 26 °C) near the cabin sidewalls and in the region above the side passengers can also be observed. Fig. 2(c) shows distribution of the percentage of dissatisfied (PD) on the upper body surfaces of each passenger. The local PD on the faces of the middle seated passengers is slightly higher, approaching nearly 20%. However, the PD on the faces of the side-seated passengers are less than 15%. Fig. 2(d) shows the CO_2 concentration is generally lower than 1200 ppm. The slightly lower CO_2 concentration due to the downward jets can also be seen.

Fig. 3(a) presents the relative humidity distribution in the cross section across the third row. The relative humidity in the interior passenger zone is much higher, especially in the region with the downward jets from the gaspers. The average humidity inside the internal passenger zone is approximately 22%. In contrast, the low relative humidity (around 15% RH) along the cabin walls can be clearly seen. If converting the relative humidity into the water vapor content, the water vapor content near the cabin walls is 3 g/m^3 lower than that in the interior zone. This shows the good capability of the new air system in minimizing condensation of the water vapor along the cabin walls. Fig. 3(d) presents the relative humidity in the breathing zone of each passenger. The breathing zone is represented by a sphere with a diameter of 0.26 m attached to the face of each passenger. The relative humidities inside the breathing zone of each passenger are not identical, with the relative humidities ranging from 18% to 30%. Note that the relative humidity on the surveyed inter-continent flights is approximately 6-8% (Water et al., 2002).

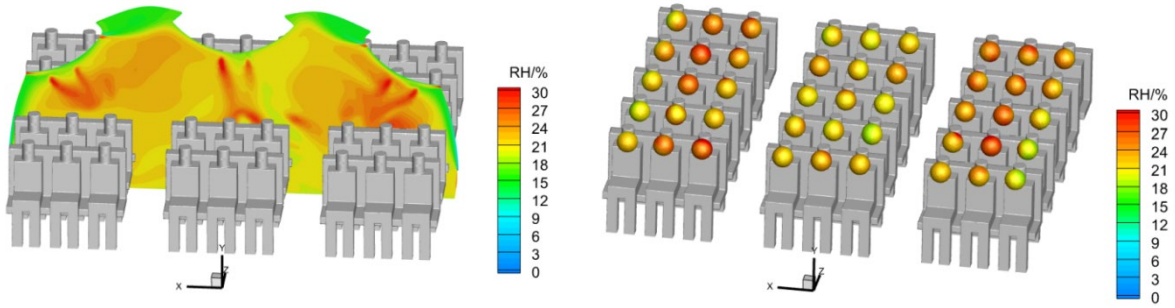

(a) (b)

Figure 3. Relative humidity distribution inside the aircraft cabin with the new air system: (a) relative humidity in a cross section across the third row, (b) relative humidity in the breathing zone of each passenger.

4. CONCLUSIONS

This investigation adopted the validated CFD modeling to evaluate performance of a newly proposed air distribution system. The system supplies the humidified, outboard conditioned air into the interior passenger zone, while circulating the relatively warm, dry air along the cabin walls. The new air system is found being able to enhance the relative humidity of the interior passenger zone from the existent 6-8% to approximately 22%. Meanwhile, the water vapor content near the cabin walls is maintained 3 g/m^3 lower than the interior passenger zone. The water consumption rate for humidification is 40 g/h per passenger. These justify the good performance of the proposed air system to enhance the relative humidity around passengers while minimizing the water

condensation risk along the cabin walls.

REFERENCES

Ashrae. Ashrae handbook fundamentals. Atlanta: American Society of Heating, Refrigerating and Air-Conditioning Engineers; 2021.

Derby M.M., Hamehkasi M., Eckels S., Hwang G.M., Shulan D., 2017. Update of the scientific evidence for specifying lower limit relative humidity levels for comfort, health, and indoor environmental quality in occupied spaces (rp-1630). Science and Technology for the Built Environment, 23(1): 30-45.

Nagda N.L., Hodgson M., 2001. Low relative humidity and aircraft cabin air quality. Indoor Air, 11(3) : 200-214.

Specht P.R., Asfia J.F., Buzza T.G., Flotow A.V., 1999. Air curtain insulating system for aircraft cabin. US, US05897079A.

Waters M, Bloom T, Grajewski B. Measurements of indoor air quality on commercial transport aircraft. In: Proceedings of Indoor Air 2002, p. 782–787.

Zhang T., Yin S., Wang S., 2010. An under-aisle air distribution system facilitating humidification of commercial aircraft cabins. Building and Environment, 45(4): 907-915.

APPENDIX (Validation of CFD modeling)

To assure the CFD modeling accuracy, validation of the CFD modeling for numerically solving spatial distribution of the airflow, relative humidity, and air temperature in a wide-body aircraft cabin, as shown in Fig. A.1, was carried out. In addition to the same geometric settings as the B767 aircraft, two gaspers were adopted to deliver the humid air to the both passengers seated near the side. The ultrasonic anemometer (type: DA-650&TR-92T; Kaijo Sonic, Japan) was adopted to measure the 3-D velocity distribution and air temperature. The relative humidity was measured by a high precision humidity sensor (type: HMT333; Vaisala, Finland). The relative humidity inside the cabin without carrying out humidification was 10.7% RH. The humidification rate to each of the both passengers was 76.2 g/h.

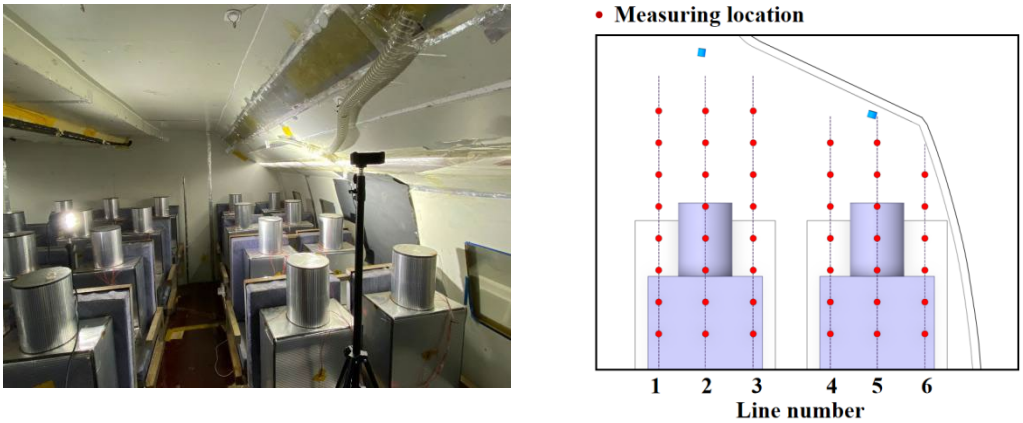

(a) (b)

Figure A.1 Measurement test in a wide-body aircraft cabin similar to B767 for validation of the CFD modeling: (a) picture of the cabin mockup, (b) points for measuring velocity, air temperature, and relative humidity

Fig. A.2(a) compares the CFD solved airflow with the measurement data in a cross section across the third row and in front of the two side passengers. The big vortex of the flow was well resolved by both methods, with a very minimal difference between each other. Fig. A.2(b) presents the relative humidity along line 2, as shown in Fig. A.1(b). The relative humidity increases with the

height, since the humidified air was supplied from the gaspers on ceiling. The CFD provided the relative humidity profile more or less similar to the measurement. Fig. A.2(c) compares the air temperature also along line 2, where the temperature was quite uniform. The CFD provided air temperatures in excellent agreement with the measurement. The above comparison between both methods validated the CFD modeling performing well and having good accuracy in this investigation.

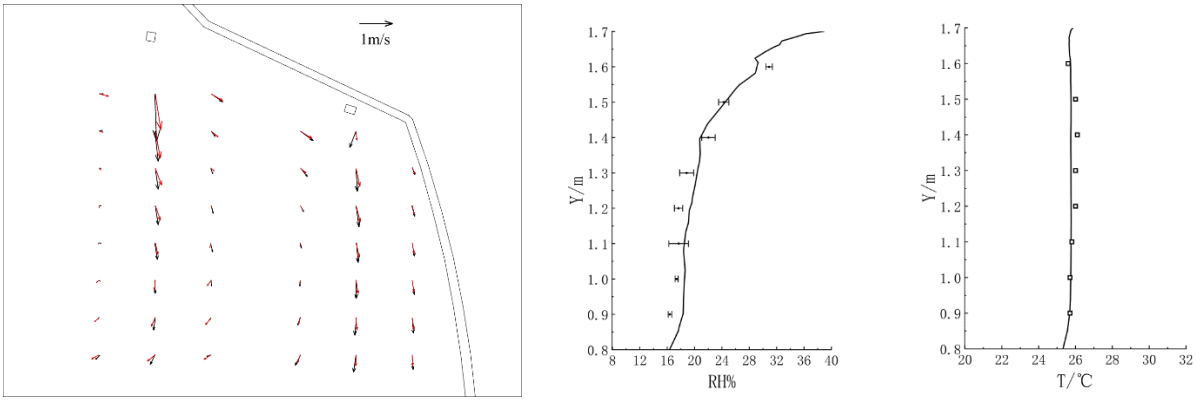

(a) (b) (c)

Figure A.2 Comparison of the CFD solved results with the measurement data: (a) airflow distribution in the section of the third row, red arrows for measurement and black arrows for CFD, (b) relative humidity along line 2, line for CFD and symbols for measurement, (c) air temperature at line 2.

6th International Conference on Building Energy and Environment
Eindhoven University of Technology, The Netherlands
6 - 10 July 2025

Novel regression-based climatic stress curves to predict building heating demand

Rosa Francesca De Masi[1], Gerardo Maria Mauro[2], Alessia Pedace[3], Francesca Villano[4]

[1]*Department of Engineering, Università degli Studi del Sannio, Benevento, Italy, rfdemasi@unisannio.it*
[2]*Department of Architecture, Università degli Studi di Napoli Federico II, Naples, gerardomaria.mauro@unina.it*
[3]*SENEA SRL, via John Fitzgerald Kennedy 365, 80125 Napoli, Italy, apedace@senea.it*
[4]*Department of Engineering, Università degli Studi del Sannio, Benevento, Italy, f.villano2@studenti.unisannio.it*

SUMMARY
Forecasting residential building energy demand is crucial due to its impact on energy use and emissions. This study proposes a method to predict thermal energy demand for heating (TED_h) using building envelope characteristics and the heating stress index (*HSI*). A 200-building stock made up by multi-family and apartment block typologies is simulated in 63 Italian climatic locations with EnergyPlus. The two-step method involves: (1) developing a polynomial TED_h - *HSI* regression and (2) a first order double regression linking the polynomial coefficient to building features like dispersing surface/conditioned volume ratio, inter-floor height and global heat exchange coefficient. With an average coefficient of determination of 0.97 and coefficient of variance of root mean square error of 9.32%, the method achieves high accuracy, adhering to ASHRAE Guidelines 14-2002 standards. This approach provides climatic stress curves with TED_h predictions based on climatic conditions and building geometric/thermophysical characteristics.

Keywords*: climatic stress indices, energy demand forecasting, residential building stock, space heating.*

1. INTRODUCTION

Buildings play a crucial role in global energy consumption and carbon emissions. Around 40% of European final energy consumption and 36% of global energy-related CO_2 emissions are attributed to building operations, and these values are expected to rise in the coming years (Directive (EU) 2024/1275, 2024). Given the pressing challenges of global warming and non-renewable resources depletion, improving building energy performance is essential to mitigating the construction sector environmental impact. In response to these challenges, significant efforts have been made to enhance energy efficiency. Over recent years, European policies have increasingly prioritized sustainability to promote renewable energy use, reduce pollution, and lower energy costs (Recast, E. P. B. D., 2010; Directive (EU) 2024/1275, 2024). In Italy, national legislative incentives, e.g., Ecobonus and Superbonus 110%, have been introduced to support energy retrofit costs (Magnani et al., 2020), thus encouraging large-scale renovation, particularly in older buildings (dating back to before 1970s), which dominate the Italian residential sector. Notably, targeted interventions can achieve energy savings of up to 30% in the residential sector and 27% in commercial buildings (de Haan et al., 2007; Sorrell & Dimitropoulos, 2008). Given that the civil sector accounts for 41.6% of Italy's final energy consumption (Annual Energy Efficiency Report, 2023), improving energy efficiency remains a national priority. To maximize the impact of these policies and ensure that retrofit strategies are data-driven and effective, it is essential to develop accurate methods for predicting building thermal energy demand (*TED*). Building energy performance prediction is

fundamental to designing effective global retrofit strategies, ensuring that interventions yield maximum efficiency gains. The Green Houses Directive (Directive (EU) 2024/1275, 2024) highlights the role of intelligent technologies, e.g., automated heating/cooling, in optimizing energy use. As regulatory frameworks increasingly mandate energy efficiency improvements, the ability to accurately forecast *TED* becomes essential to support effective decision-making. However, *TED* forecasting remains a complex challenge due to multiple influencing factors as weather conditions, building characteristics, occupancy patterns, and HVAC system schedules (Zhao & Magoulès, 2012). To address these challenges, there are three commonly used *TED* prediction approaches, i.e., engineering methods, regression-based models, and artificial intelligence techniques. The first rely on physical principles to assess building energy performance in dynamic simulation tools such as EnergyPlus (US Department of Energy. EnergyPlus (Version 8.4)., n.d.), TRNSYS (Transient System Simulation Program, University of Wisconsin., n.d.), ESP-r (*ESP-r.*, n.d.), and IDA ICE (*IDA-ICE, IDA Indoor Climate and Energy.*, n.d.) providing high accuracy but greater computational complexity. Regression-based models, on the other hand, uses historical data, for weather too, to predict energy consumption trends, making them useful for evaluating climate change impacts. Finally, artificial intelligence techniques, i.e., machine/deep learning approaches, can autonomously develop analytical models by learning directly from data. By integrating predictive models with policy-driven incentives, building energy efficiency is enhanced. Accurate energy consumption forecasts can lead policymakers, designers, and stakeholders to more cost-effective energy strategies.

1.1 Literary review

Regression-based methods are frequently used for predicting building energy performance/consumption. *TED* forecasting can help energy efficiency/sustainability, especially if related to thermal and geometric parameters as well as climatic indices. This review explores the state-of-the-art approaches for *TED* prediction, focusing on the application of regression-based methods, which range from simple linear models to more complex ones, to capture the complex interplay between building characteristics and external climatic factors. The integration of climatic stress indices that account for the current rise in temperatures is crucial for improving *TED* prediction accuracy, as conventional regulatory climatic indices do not incorporate this aspect (Mazzaferro et al., 2020). There are various studies that define new climatic indices, such as that of Ascione et al. (2021) and De Masi et al. (2023), focused on novel climatic stress indices and curves, or Salmeron et al. (2013) that proposed a climatic severity index for *TED* for heating forecasting. A comparable approach was adopted by De Rosa et al. (2014), who performed a regression analysis between energy consumption (dependent variable) and degree days (independent variable), incorporating adjustments to account for additional influencing factors such as solar irradiation and thermal inertia. The correlation between *TED* and building characteristics is more complex than the correlation with external climatic conditions since it requires an analysis of building features that can substantially influence the output. Multiple linear regression can establish relationships between building *TED* and the most influencing building variables, as done in the research by Ciulla et al. (2019), with promising results, i.e., a coefficient of determination up to 0.9. Linear regression is one of the most common methods used to model the energy demand in buildings, since it combines the speed of a simple method and the precision of a dynamic thermal simulation. Building *TED* can be combined with key design and operational parameters, e.g., insulation, glazing type, how the building is positioned with respect to the sun, occupant schedules (Amiri et al., 2015). Bayesian regression, offering improved accuracy, can also

be employed for *TED* forecasting by integrating historical energy consumptions and temperature data (Su et al., 2024). A more specialized form of regression analysis is lasso regression (Khosravi et al., 2023), which applies a penalty to linear regression models to reduce complexity and eliminate irrelevant variables, making it useful for energy consumption prediction only considering the most influential building characteristics. A novel contribution of the proposed approach lies in the application of a double-step polynomial regression approach to derive specific climatic stress curves for each building, tailored to its envelope characteristics. This method correlates thermal energy demand for heating (TED_h) with a new heating stress index (*HSI*) and some building parameters. The resulting curves will offer TED_h predictions for any location based on the corresponding *HSI*.

2. MATERIALS AND METHODS

The study examines multi-family building (a) and apartment block (b) constructed in 1961-1975. They have a structural frame in reinforced concrete, walls in hollow bricks with air cavities and a horizontal envelope in mixed brick-reinforced concrete. The main geometric/thermos-physical characteristics are taken from TABULA project (Corrado et al., 2012) and are summarized in Figure 1. The heating system is a centralized natural gas boiler connected to hot water radiators while cooling is provided by electric air-source split air conditioners. The heating setpoint temperature is set equal to 20°C.

Figure 1. Reference buildings of TABULA

This research is based on a previous one by the authors, where building energy demand was predicted using new climatic stress indices (De Masi et al., 2023). It was founded on the SLABE (simulation-based large-scale uncertainty/sensitivity analysis of building energy performance) methodology (Mauro et al., 2015) designed to conduct sensitivity and uncertainty analyses on building stocks energy performance. A climatic stress index investigated was the heating stress index (*HSI*) in Eq. (1), to fit building's thermal energy demand for heating (TED_h). Its calculation followed the normative methodology for heating degree days but the outdoor air temperature is replaced by the sol-air temperature ($T_{sol\text{-}air}$) in Eq. (2), to consider the effects of solar radiation too.

$$HSI = \sum_{heating\ period}(T_b - T_{sol-air})^+ \quad (1)$$

$$T_{sol-air} = T_{out} + G \cdot \frac{\alpha_{sol}}{h_e} \quad (2)$$

Where T_b was the base temperature that assures thermal comfort with plant off, T_{out} was the outdoor temperature, G was the solar irradiance, the solar radiation absorption coefficient α_{sol} was set equal to 0.5 (typical mean value for the external opaque envelope) while the external liminal conductance h_{ext} was set equal to 25 W/m^{2}K, as recommended by Italian standards.

By varying several building parameters within suitable ranges, the random sampling building (RBS-a) dataset is generated, which consists of 100 buildings. A similar methodology is applied to the RBS-b. The combination of the two RBS from the initial buildings consists in a total of 200 buildings. After the RBS creation, energy performance simulations are conducted by integrating MATLAB® (MathWorks, MATLAB – (Version 2022)., n.d.) with EnergyPlus for 63 climatic locations to cover all typical Italian climatic conditions. Figure 2 shows the input parameters for the RBS generation, divided into two groups related to geometry ($v_1 – v_6$) and envelope ($v_7 – v_{19}$), as well as the 63 cities for the energy simulations and a schematic flowchart of the RBS creation. The main aim is to establish a correlation between current TED_h and the following geometric/thermo-physical characteristics of individual buildings in the stock:

- S/V [m^{-1}], ratio between the dispersing surface area (S [m^2]) and the gross volume (V [m^3]);
- h [m], inter-floor building height, i.e., the ratio between the air-conditioned volume (V_c [m^3]) and the air-conditioned area (A_c [m^2]);
- H_{ts} [$W \cdot K^{-1} \cdot m^{-2}$], global heat transfer coefficient specific to A_c, sum of heat transfer coefficient of the building transparent (H_{tr}) and opaque (H_{op}) envelope, as in Eq. (3). It depends on the thermal transmittance (U [W/m^2K]) and the surface areas (S [m^2]) of opaque (subscript "*op*") and transparent (subscript "*tr*") envelope elements.

$$H_{ts} = \frac{\sum(U \cdot S)_{tr} + \sum(U \cdot S)_{op}}{A_c} \quad (3)$$

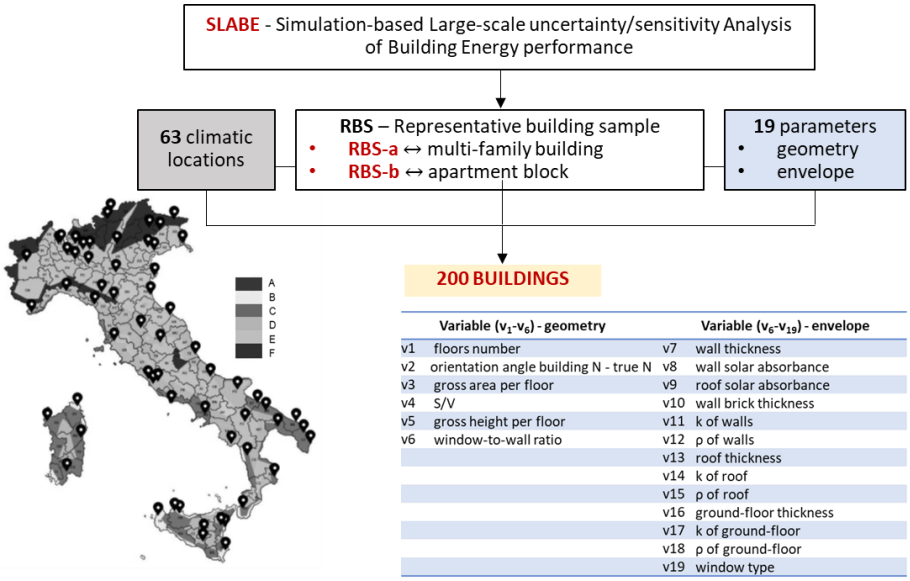

Figure 2. 200 buildings creation flowchart, 63 climatic locations and input parameters for RBS creation

The methodology follows a two-step regression process. First, a polynomial regression is performed to establish the relationship between TED_h and the *HSI* climatic index. Once this relationship is determined, the second step refines the prediction by correlating the polynomial coefficients obtained in the first step with key building envelope characteristics. To relate TED_h and *HSI*, a polynomial regression is done, i.e., a comparison is made among first, second and third order polynomial regressions. Since *HSI* equal to zero means the absence of heating need, the polynomial regression curves are forced to pass through zero. This facilitates the analysis too,

deleting one polynomial term. Figure 3 shows the 3 polynomial regression orders for 4 random buildings in the RBS, i.e., buildings number 21 and 99 for the RBS-a and buildings number 107 and 174 for the RBS-b.

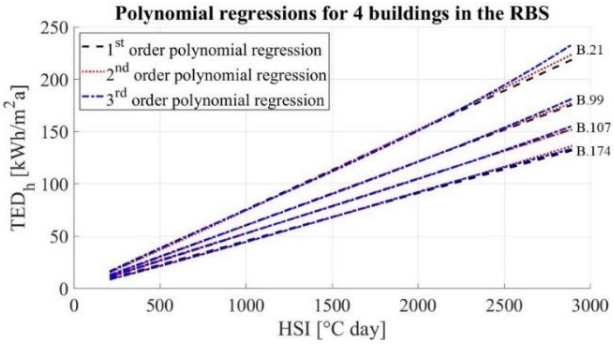

Figure 3. First, second and third order polynomial regressions: TED_h vs *HSI*

In the second step, the focus shifts to understanding how building envelope characteristics (*S/V*, *h*, and H_{ts}) influence TED_h. To achieve this, a multiple linear regression is conducted between the polynomial coefficients obtained in the first step and these geometric and thermo-physical parameters. This step refines the model, ensuring that TED_h predictions account for both climatic influences and building-specific properties. Finally, a climatic stress curve is obtained for each RBS building to predict TED_h as a function of *HSI*.

3. RESULTS AND DISCUSSION

The first order regression provides correlation comparable to the second and third order ones, as shown in the figures below, where the curves for the three regressions are almost coincident. Two error indices have been evaluated: the correlation coefficient (R^2) and the coefficient of variation of the root mean square error (*CV(RMSE)*) – see Eq. (4). In particular, Figure 4 shows the trend in the values of R^2 and *CV(RMSE)* for the three polynomial regressions related to the 200 buildings of the RBS. Since error indices for the three considered regressions are very similar, it is possible to proceed with a first order regression, i.e., $TED_h = p_1 \cdot HSI$, where the TED_h is a function of *HSI* via the only polynomial coefficient p_1. The first order regression TED_h - *HSI* thus provides a climatic stress curve for each building in the RBS. From the first order polynomial regression to correlate TED_h and *HSI*, minimum and maximum R^2 values are 0.963 (in correspondence of the building number 25) and 0.994 (in correspondence of the building number 126) respectively while the average R^2 is equal to 0.986 for the RBS sample. High R^2 values indicate a strong correlation TED_h - *HSI* across the entire sample. In addition, *CV(RMSE)* minimum and maximum values are 4.22% and 12.6% while its average is 6.73%. These values are in accordance with the ASHRAE Guideline 14-2002, for which regressions with *CV(RMSE)* values less than 15% are acceptable (ASHRAE Guideline 14, Measurement of Energy and Demand Savings, 2002).

$$R^2 = 1 - \frac{\sum_N (x_i - y_i)^2}{\sum_N (x_i - \bar{x})^2}; CV(RMSE) = \frac{1}{\bar{x}} \cdot \sqrt{\frac{1}{N} \cdot \sum_N (x_i - y_i)^2} \quad (4)$$

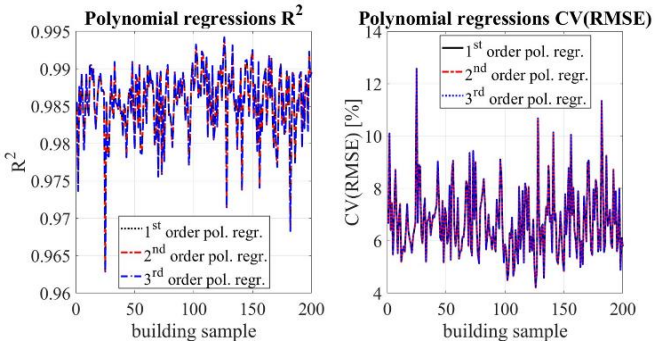

Regression order	R^2 min	R^2 max	R^2 mean
I	0.963	0.994	0.986
II	0.979	0.995	0.989
III	0.982	0.995	0.990

Regression order	CV(RMSE) min	CV(RMSE) max	CV(RMSE) mean
I	4.21 %	12.56 %	6.73 %
II	4.04 %	8.89 %	5.85 %
III	4.02 %	8.11 %	5.64 %

Figure 4. Polynomial regressions: R^2 and *CV(RMSE)*

From the second step, the only polynomial coefficient p_1 of the first order regression is related to building geometric/thermo-physical features, i.e., *S/V*, *h* and H_{ts}. The double regression reports the trends in Figure 5 for R^2 and *CV(RMSE)* in comparison with the trends from the first order polynomial regression. R^2 is still high, with minimum, maximum and average values equal to 0.846, 0.992 and 0.970 respectively. Similarly, *CV(RMSE)* values are still acceptable, with an average value equal to 9.32%. The proposed method shows that these curves have good reliability in terms of R^2 and *CV(RMSE)*. Figure 6 shows the first order double regression for the 4 test buildings. The curves proposed in this paper have the expression in Eq. (5).

$$TED_h = \left(0.0819 \cdot \frac{S}{V} + 0.0177 \cdot h + 0.003 \cdot H_{ts} - 0.042\right) * HSI \quad (5)$$

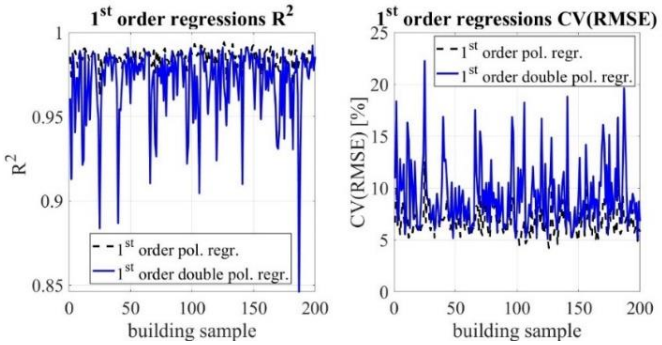

Figure 5. First order regression: R^2 and CV(RMSE)

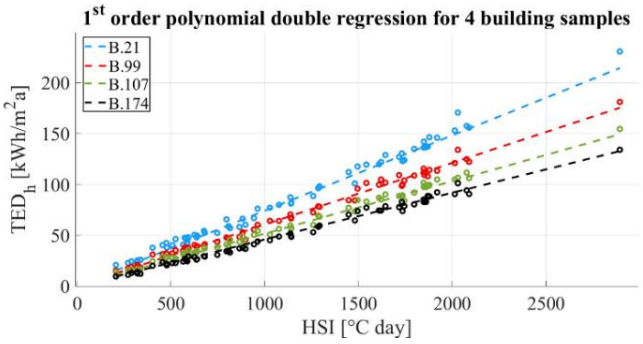

Figure 6. First order polynomial double regression for 4 random buildings in the RBS dataset

The proposed curves can be a user-friendly tool to forecast the building thermal energy demand for heating as a function of the climatic stress. This approach can be adapted to the climate change by updating the *HSI* value can with the novel outdoor temperature and the solar irradiance.

4. CONCLUSIONS

The proposed method, based on the SLABE methodology from previous research, enables the creation of a representative building sample (RBS) using two typologies, i.e., multi-family buildings and apartment blocks, whose characteristics are derived from the TABULA project. The RBS consists of 200 buildings, with energy simulations conducted for 63 Italian locations across all national climatic zones. The approach involves two regression steps: 1) a polynomial regression correlates thermal energy demand for heating (TED_h) with the novel heating stress index (*HSI*); 2) a multiple regression links the polynomial coefficients to building envelope characteristics (*S/V*, inter-floor height, and thermal exchange coefficient). The first-order polynomial regression achieves high accuracy (R^2 = 0.963–0.994, average 0.986; CV(RMSE) = 4.22%–12.6%, average 6.73%), within ASHRAE Guideline 14-2002 limits (15%). The second step further refines predictions (R^2 = 0.846–0.992), ensuring robustness across the RBS. This method is adaptable to evolving climatic conditions by updating HSI with new temperature and solar irradiance values, making it a practical tool for TED_h forecasting. It can assist both private users, by accurately predicting TED_h and assessing retrofit impacts, and policymakers, by informing large-scale energy strategies. Future research should validate the method in different climatic contexts to enhance its global applicability. Additionally, further investigation is needed to assess the link between the simplification to a first-order polynomial and predictive accuracy in extreme climatic conditions. Expanding to cooling energy demand and energy retrofit scenarios could make the proposed approach a more comprehensive method.

ACKNOWLEDGEMENTS

This work was supported by the Italian Government MUR PNRR ("*Piano Nazionale di Ripresa e Resilienza*").

REFERENCES

Amiri, S. S., Mottahedi, M., & Asadi, S. (2015). Using multiple regression analysis to develop energy consumption indicators for commercial buildings in the U.S. *Energy and Buildings*, *109*, 209–216. https://doi.org/10.1016/J.ENBUILD.2015.09.073

Annual Energy Efficiency Report. (2023). https://www.efficienzaenergetica.enea.it/component/jdownloads/?task=download.send&id=616&catid=9&Itemid=101

Ascione, F., Bianco, N., Mauro, G. M., Napolitano, D. F., & Vanoli, G. P. (2021). Building heating demand vs climate: Deep insights to achieve a novel heating stress index and climatic stress curves. *Journal of Cleaner Production*, *296*, 126616. https://doi.org/10.1016/J.JCLEPRO.2021.126616

ASHRAE Guideline 14, Measurement of Energy and Demand Savings (2002).

Ciulla, G., & D'Amico, A. (2019). Building energy performance forecasting: A multiple linear regression approach. *Applied Energy*, *253*, 113500. https://doi.org/10.1016/J.APENERGY.2019.113500

Corrado, V., Ballarini, I., & Corgnati, S. P. (2012). *National scientific report on the TABULA activities in Italy.*

de Haan, P., Peters, A., & Scholz, R. W. (2007). Reducing energy consumption in road transport through hybrid vehicles: investigation of rebound effects, and possible effects of tax rebates. *Journal of Cleaner Production*, *15*(11–12). https://doi.org/10.1016/j.jclepro.2006.05.025

De Masi, R. F., Mauro, G. M., Ruggiero, S., & Villano, F. (2023). Predicting Building Energy Demand and Retrofit Potentials Using New Climatic Stress Indices and Curves. *Energies*, *16*(16). https://doi.org/10.3390/en16165861

De Rosa, M., Bianco, V., Scarpa, F., & Tagliafico, L. A. (2014). Heating and cooling building energy demand evaluation; a simplified model and a modified degree days approach. *Applied Energy*, *128*, 217–229. https://doi.org/10.1016/J.APENERGY.2014.04.067

DIRECTIVE (EU) 2024/1275 OF THE EUROPEAN PARLIAMENT AND OF THE COUNCIL (2024). https://eur-lex.europa.eu/legal-content/IT/TXT/PDF/?uri=OJ:L_202401275

ESP-r. (n.d.). Retrieved May 22, 2024, from http://www.esru.strath.ac.uk/Programs/ESP-r.htm

IDA-ICE, IDA Indoor Climate and Energy. (n.d.). Retrieved May 22, 2024, from http://www.equa.se/ice/intro.html

Khosravi, H., Sahebi, H., Khanizad, R., & Ahmed, I. (2023). Building Energy Efficiency through Advanced Regression Models and Metaheuristic Techniques for Sustainable Management. *ArXiv Preprint ArXiv:2305.08886*.

Magnani, N., Carrosio, G., & Osti, G. (2020). Energy retrofitting of urban buildings: A socio-spatial analysis of three mid-sized Italian cities. *Energy Policy*, *139*. https://doi.org/10.1016/j.enpol.2020.111341

MathWorks, MATLAB – MATrixLABoratory (version 2022). (n.d.). Retrieved May 22, 2022, from https://it.mathworks.com/products/matlab.html

Mauro, G. M., Hamdy, M., Vanoli, G. P., Bianco, N., & Hensen, J. L. M. (2015). A new methodology for investigating the cost-optimality of energy retrofitting a building category. *Energy and Buildings*, *107*. https://doi.org/10.1016/j.enbuild.2015.08.044

Mazzaferro, L., Machado, R. M. S., Melo, A. P., & Lamberts, R. (2020). Do we need building performance data to propose a climatic zoning for building energy efficiency regulations? *Energy and Buildings*, *225*, 110303. https://doi.org/10.1016/J.ENBUILD.2020.110303

Recast, E. P. B. D. (2010). Directive 2010/31/EU of the European Parliament and of the Council of 19 May 2010 on the Energy Performance of Buildings (Recast). Official Journal of the European Union, 18(06) (2010).

Salmerón, J. M., Álvarez, S., Molina, J. L., Ruiz, A., & Sánchez, F. J. (2013). Tightening the energy consumptions of buildings depending on their typology and on Climate Severity Indexes. *Energy and Buildings*, *58*, 372–377. https://doi.org/10.1016/J.ENBUILD.2012.09.039

Sorrell, S., & Dimitropoulos, J. (2008). The rebound effect: Microeconomic definitions, limitations and extensions. *Ecological Economics*, *65*(3). https://doi.org/10.1016/j.ecolecon.2007.08.013

Su, H., Duan, M., Zhuang, Z., & Bai, Y. (2024). Building energy consumption prediction method based on Bayesian regression and thermal inertia correction. *International Journal of Renewable Energy Development*, *13*(1). https://doi.org/10.14710/ijred.2024.58012

TRNSYS®, Transient System Simulation Program, University of Wisconsin. (n.d.). Retrieved May 22, 2024, from https://trnsys.org/

US Department of Energy. Energy Efficiency and Renewable Energy Office, Building Technology Program, EnergyPlus (version 8.4). (n.d.). Retrieved May 22, 2024, from https://energyplus.net/

Zhao, H. X., & Magoulès, F. (2012). A review on the prediction of building energy consumption. In *Renewable and Sustainable Energy Reviews* (Vol. 16, Issue 6). https://doi.org/10.1016/j.rser.2012.02.049

6th International Conference on Building Energy and Environment
Eindhoven University of Technology, The Netherlands
6 - 10 July 2025

Assessing the impact of climate change on a Canadian commercial building that has undergone a panelized retrofit

Isaac Rudnicki [1], Cynthia A. Cruickshank [2], Daniel Chung [3]

[1]*Carleton University, Ottawa, Canada, isaacrudnicki@cmail.carleton.ca*
[2]*Carleton University, Ottawa, Canada, cynthiacruickshank@cunet.carleton.ca*
[3]*University of Toronto, Toronto, Canada, danielh.chung@daniels.utoronto.ca*

SUMMARY
The Energiesprong method of installing prefabricated highly insulated and airtight exterior panels onto existing buildings has been shown to be effective at delivering net zero energy retrofits around the world. These retrofits dramatically reduce the energy consumption of a building once deployed. As the global climate continues to change, extreme weather events are becoming more common. This paper aims to investigate the impact of future climate scenarios on the performance of a building that has undergone a panelized retrofit. A calibrated building energy model is created in TRNSYS to compare the thermal energy consumption, and thermal comfort of the building occupants before and after it has undergone a panelized retrofit in various future climate scenarios. It was found that there was a 7.3% decrease in energy savings and a decrease in thermally comfortable hours from the retrofit in the most extreme climate scenario when compared to the historical scenario.

Keywords: TRNSYS, Panelized retrofit, Thermal resilience, Energy modelling

1. INTRODUCTION & BACKGROUND

Buildings account for nearly 30% of consumed energy in Canada. Energy consumption from commercial and institutional buildings equated to almost 1258 PJ of energy in 2019 alone (Environment and Climate Change Canada, 2022). More stringent energy efficiency codes and technologies are being adopted in new construction, however since about 64% of the current commercial and institutional building stock in Canada was built before the national energy building code was developed in 1997, many existing buildings will need to be retrofitted to achieve a significant reduction in building sector energy consumption.

To meet Canada's emission reduction and climate goals for 2050, the rate at which buildings are being retrofitted needs to accelerate. Currently only 1.4% of commercial building floor area is being retrofitted per year in Canada, which at that pace, is not sufficient to meet Canada's 2050 emission targets for the buildings sector (Efficiency Canada, 2021). The Energiesprong method, developed in the Netherlands, offers a scalable solution to delivering net zero energy retrofits to buildings by using off-site construction that results in a fast project delivery. The Energiesprong method uses prefabricated exterior insulated retrofit panels that drastically increase the thermal insulation and airtightness of the building. Combined with mechanical upgrades, these retrofits can result in a reduction of up to 80% of heating and cooling energy consumption (Biega & Krarti, 2024). The Energiesprong method, and by extension, panelized retrofits offer great potential in reducing energy consumption in the existing building stock. However, the impact of climate change on retrofit analysis is significant (Shen et al., 2019) and so this paper will use a

calibrated TRNSYS energy model of a community centre in Quebec, Canada to model the effects of future climate scenarios on building energy usage and thermal comfort before and after a panelized retrofit. This study advances research by creating a calibrated energy model of a real-world building that is a candidate for a panelized retrofit and investigating the impacts of future climate scenarios. This study offers a unique opportunity for future research to compare the calibrated simulation results of this study with real post-retrofit monitored data once the planned panelized retrofit is complete.

2. METHODOLOGY

Transient System Simulation Software, commonly referred to as TRNSYS is a tool developed by the University of Wisconsin that can simulate the behaviour of transient systems such as multizone buildings (Solar Energy Laboratory, University of Wisconsin-Madison, 1975). This study uses TRNSYS to create a calibrated building energy model of a community centre located in Île Bizard, in the jurisdiction of Montreal. The community centre was chosen as a candidate for a panelized deep energy retrofit due to its simple architectural form, high existing EUI, and available space to stage a panelized construction project. The Île Bizard community centre (hereafter: IBCC) consists of a general assembly space, and offices that serve as working space for employees and other community groups. Fig. 1a shows a satellite derived image of the IBCC. The literature relating to calibrating building energy model simulations in the context of retrofits is well established (Coakley et al., 2014; Sharma et al., 2022), as well as the methods for using future climate data in building energy models (Moazami et al., 2019).

2.1 Base case energy model

An energy model was created to represent the pre retrofit case of the IBCC. This model was then calibrated using sub metered energy usage and monthly utility bills from 2023 and 2024. The model's geometry was based off as-built drawings and has 11 thermal zones and a window-to-wall ratio (WWR) of 6.6%. Fig. 1b and 1c shows the IBCC wall assembly, and a 3D representation of the energy model as constructed in TRNSYS respectively.

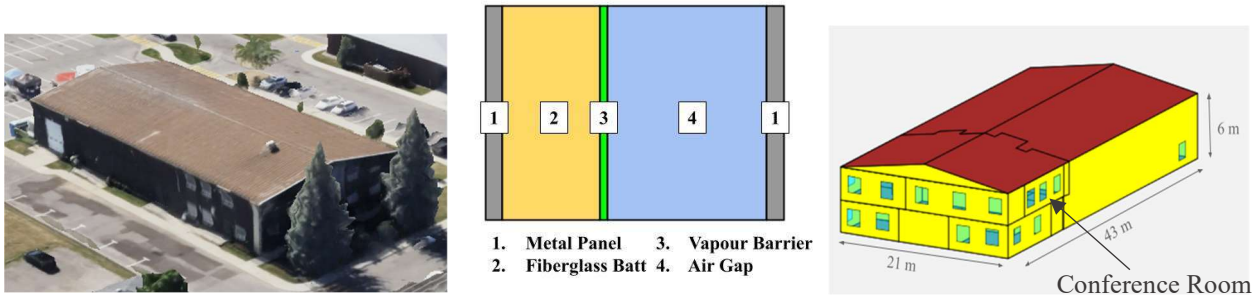

(a) (b) (c)

Figure 1. (a) IBCC (Google Earth, 2025) (b) IBCC wall assembly and (c) TRNSYS model of the IBCC.

2.1.1 Existing building

The IBCC was constructed in 1978 at a time when energy codes were in their infancy in North America. The structure is steel framed with corrugated metal panels covering the exterior walls and roof. The building envelope assembly consists of a 140 mm layer of fiberglass insulation, a vapour barrier, and an air gap which ranges between 114 mm and 216 mm throughout the

building (Dalkowski, 2024). 21 double glazed windows are located primarily in the office section of the building. The HVAC systems in the building include a single AHU that provides conditioning and ventilation and is complimented with auxiliary wall-mounted space heaters that meet additional heating demand that the AHU cannot meet on its own. The offices are conditioned with two centrally ducted AC units and electric baseboard heaters.

2.1.2 Building survey

A building survey was conducted to inspect the buildings condition and interview building occupants to better ascertain building operation, systems, setpoints, and occupancy trends. The survey was a critical step in verifying the information received from the building drawings and developing occupancy schedules for the energy model.

2.1.3 Energy modelling inputs

The previously mentioned wall composition was determined from investigations during site visits. Typical thermophysical values for conductivity, density, and specific heat for the relevant materials, were obtained from the ASHRAE handbook of fundamentals (The American Society of Heating, Refrigerating, and Air-Conditioning Engineers, 2021). This process was repeated for the concrete slab floor and roof. Because the slab floor and roof composition were not known, typical constructions were assumed for those assemblies. Additionally, as outlined by Amiri et al., thermal imaging and in-situ heat flux sensors were used to estimate the RSI of the walls using a spatial averaging method (Amiri et al., 2022). The insulation thickness of the walls was then modified in the model to match the calculated RSI obtained from the spatially averaged method. Table 1 below shows the RSI values of each envelope component.

Table 1. RSI value of envelope components

Envelope component	RSI ($m^2 \cdot K/W$)	Method
177 mm Wall	1.30	Thermal imaging and in-situ sensors
330 mm Wall	2.35	Thermal imaging and in-situ sensors
Ground Floor	1.78	ASHRAE area weighted method
Roof	2.82	ASHRAE area weighted method

The community centre hosts groups such as summer camps, badminton players, daycares, and staff. The IBCC is also known to host large events with a capacity of 450 people. Based off interviews with occupants, occupancy schedules were developed for the staff, daycare, and badminton players. Typical occupant, lighting, and equipment heat gains were obtained from the 2021 ASHRAE handbook. A blower door test was completed to determine the airtightness of the building and the results of the test showed that the building has an air change rate of 3.27 ACH50 with a unit leakage area of 2.3 cm^2/m^2. The Sherman Grimsrud infiltration model – an empirically derived method that accounts for wind speed and temperature difference – was used in the TRNSYS energy model. However, during the discussion with the occupants, it was revealed that the occupants commonly open doors or windows to allow for increased natural ventilation during both the summer and winter months to avoid overheating. Finally, ideal heating and cooling was added to the energy model with set points of 21°C and 23°C based off site visit information.

2.1.4 Energy model calibration

To improve the accuracy of the model, measured data was used to calibrate the model following

the ASHRAE 14 guideline (The American Society of Heating, Refrigerating, and Air-Conditioning Engineers, 2014). Real time sub metered data for the building heating systems was monitored and recorded. This included the power consumption of the AHU, as well as the electric resistance heaters in the gym and offices. The measured cooling data was derived via a regression analysis that used the relationship between recorded outdoor temperature and power consumption obtained from the monthly utility bills. As per the guideline, two metrics were used for calibrating the heating and cooling loads of the IBCC. The net mean bias error (NMBE) and the coefficient of the variation of the root mean square error (CVRMSE). To meet the calibration standards the NMBE and CVRMSE between the simulated and measured data was required to be less than 5% and 15% respectively.

The calibration procedure was to run the simulation, check if the calibration requirements were satisfied, and if not, adjust the calibration parameters. This iteration was continued until the calibration threshold was achieved. Calibration parameters were chosen based off their uncertainty and impact on energy use. These included the natural ventilation rate and the number of occupants in the building. The natural ventilation rate was included due to the previously mentioned unpredictability of the occupants opening and closing windows and doors, whereas the occupant number was chosen based off the uncertainty associated with the occupant schedule. The monthly adjustments made to each calibration parameter is summarized in Table 2. The simulated heating and cooling demand of the calibrated model is compared to the measured data on Fig. 2. The calibration procedure yielded a NMBE of -4% and 15% for heating load and a CVRMSE of 4% and 14% for cooling load.

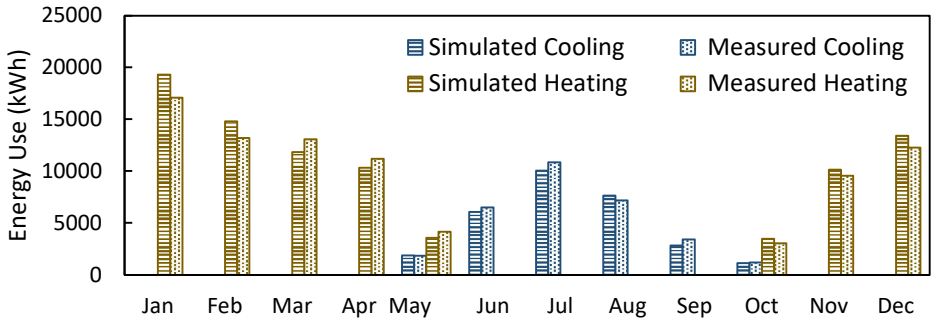

Figure 2. Comparison of simulated and measured heating and cooling energy use of calibrated model.

2.2 Post retrofit energy model

The proposed exterior panels that are to be installed over the existing envelope consist of an additional layer of mineral wool batt insulation, as well as an air and moisture resistive barrier. The addition of these highly insulated exterior panels will result in an improvement in the thermal insulation of the building. The new overall thermal resistance values for the envelope components are listed in Table 3. A THERM model was created to estimate the overall post retrofit RSI of the wall assemblies (Amiri et al., 2022). The post retrofit RSI of the roof was estimated based off the proposed roof assembly. Finally, since airtightness of the building after the panelized retrofit is unknown, the post retrofit airtightness was assumed to be the same as the pre-retrofit scenario as measured by the blower door test.

Table 2. Calibration parameter adjustments

Month	Pre-Calibration Occupancy	Post-Calibration Occupancy	Post-Calibration Infiltration Adjustments
January	65 building occupants	110 building occupants	No changes
February	65 building occupants	110 building occupants	No changes
March	65 building occupants	65 building occupants	No changes
April	65 building occupants	65 building occupants	+150% infiltration in whole building
May	65 building occupants	65 building occupants	+200% infiltration in gym, front office, and side office zones
June	65 building occupants	110 building occupants	No changes
July	118 building occupants	163 building occupants	No changes
August	118 building occupants	143 building occupants	No changes
September	65 building occupants	65 building occupants	+100% infiltration in gym zone
October	65 building occupants	90 building occupants	No changes
November	65 building occupants	90 building occupants	No changes
December	65 building occupants	90 building occupants	No changes

Table 3. Post retrofit parameters

Parameter	Value	Method
177mm Wall post retrofit RSI	4.95 m^2·K/W	THERM model
330mm Wall post retrofit RSI	5.35 m^2·K/W	THERM model
Roof post retrofit RSI	13.2 m2·K/W	ASHRAE area weighted method

2.1 Weather files

To assess the vulnerability of the IBCC before and after the panelized retrofit, six Montreal weather files were used with the TRNSYS energy model to investigate the behaviour of the building under different climate scenarios. Future climate weather files developed by Gaur and Lacasse were used for the purpose of this study (Gaur & Lacasse, 2022). These scenarios included typical meteorological year (TMY) weather files that represent an increase of 1.5 °C, 2.5 °C, and 3.5 °C in global temperatures. An extreme warm year (EWY) for the 3.5 °C scenario was also included in the analysis. A historical TMY file representing the years 1991 – 2021 and the actual meteorological year (AMY) weather file used for the model calibration was also included. The AMY file is referred to as the 'baseline' scenario hereafter. The TMY future climate weather files were created from climate simulations from a group of Canadian Regional Climate Models by dynamically downscaling Canadian Earth System model large ensemble simulations. The six weather files were run in both pre and post retrofit scenarios for a total of twelve simulations.

3. RESULTS

Thermal energy consumption and thermal comfort were both analyzed in each simulation scenario to investigate how the behaviour of the building changed both before and after the panelized retrofit, and in different future climate scenarios. The metric that was used to quantify thermal comfort is the predicted mean vote (PMV). Developed by P.O. Fanger, PMV is a measure of a humans thermal comfort that takes into account their metabolic rate (met), clothing insulation (clo), air speed, and ambient conditions (Fanger, 1988). The PMV is a scale that ranges from -3 to +3. -3 indicates that the occupant is cold, whereas +3 indicates that the occupant is hot. A value of 0 indicates the occupant is thermally comfortable. ASHRAE 55 recommends a PMV between -0.5 and 0.5, although these recommendations vary depending on

the standard. In the TRNSYS energy model, occupants were assumed to have a 0.61 clo and 1.1 met to match the typical values of an office occupant as listed in ASHRAE standard 55. The airspeed was set to a typical value for office zones of 0.1 *m/s*. The PMV TRNSYS output was measured from the 'conference room' zone as this zone had multiple windows, and is adjacent to outdoor conditions, conditioned, and non-conditioned zones.

3.1 Thermal Energy Consumption

Fig. 3 shows the TRNSYS simulation results for the thermal energy consumption for all climate scenarios before and after the proposed panelized retrofit. In both retrofit scenarios, as the global warming scenarios intensify, the heating load decreases, and the cooling load increases. This is consistent with many studies on the effect of a warming climate on thermal energy consumption in cold climates (Chidiac et al., 2022), (Li et al., 2012). As key climate parameters such as temperature increase due to climate change, traditionally heating dominated cities like Montreal will see less heating and more cooling demand required. Since panelized retrofits typically yield the greatest energy savings in heating, the projected reduction in heating demand under future climate scenarios may diminish the panelized retrofits overall energy-saving potential. This is apparent when comparing the percent reduction in total thermal energy use due to the retrofit for different climate scenarios. The total thermal energy savings from the retrofit is 29.9% for the historical climate scenario compared to only 22.6% for the 3.5 °C EWY scenario, yielding a 7.3% drop in estimated energy savings. This loss in energy savings equates to roughly 13,170 kWh.

3.2 Thermal comfort

The thermal comfort measured in PMV was simulated for an occupant in the conference room zone. Annual simulations were conducted for each climate scenario before and after the panelized retrofit. A heat map is shown in Fig. 4 which displays a visualization of the average PMV at any given hour of the day in all simulations. Blue, green, and red indicate low, neutral, and high PMV values respectively. The retrofit measure in the historical scenario results in an additional 1418 hours of acceptable comfort hours (-0.5 < PMV < 0.5), whereas the retrofit in the 3.5 °C EWY scenario decreases the number of comfortable hours in the year by 7 hours.

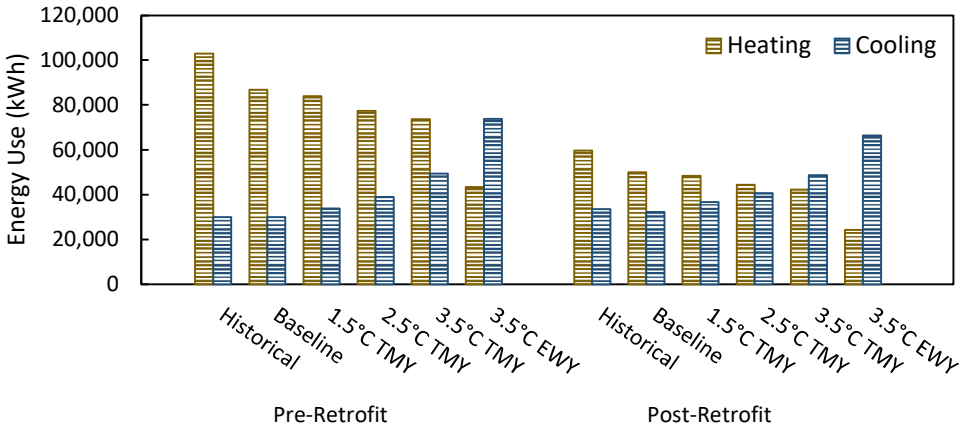

Figure 3. TRNSYS simulation results of thermal energy use in all simulated scenarios.

	Time of Day	12:00 AM	1:00 AM	2:00 AM	3:00 AM	4:00 AM	5:00 AM	6:00 AM	7:00 AM	8:00 AM	9:00 AM	10:00 AM	11:00 AM	12:00 PM	1:00 PM	2:00 PM	3:00 PM	4:00 PM	5:00 PM	6:00 PM	7:00 PM	8:00 PM	9:00 PM	10:00 PM	11:00 PM
Pre-Retrofit	Historical	-1.2	-1.2	-1.3	-1.3	-1.3	-1.3	-1.3	-1.2	-1.0	-0.9	-0.8	-0.8	-0.7	-0.7	-0.7	-0.7	-0.7	-0.7	-0.9	-1.0	-1.0	-1.1	-1.1	-1.2
	Baseline	-1.2	-1.2	-1.2	-1.3	-1.3	-1.3	-1.3	-1.3	-1.0	-0.8	-0.8	-0.7	-0.7	-0.6	-0.6	-0.6	-0.7	-0.7	-0.9	-1.0	-1.0	-1.0	-1.1	-1.1
	1.5°C TMY	-1.1	-1.2	-1.2	-1.2	-1.3	-1.2	-1.2	-1.1	-0.9	-0.8	-0.7	-0.7	-0.6	-0.6	-0.6	-0.6	-0.6	-0.6	-0.8	-1.0	-1.0	-1.0	-1.1	-1.1
	2.5°C TMY	-1.1	-1.1	-1.2	-1.2	-1.2	-1.2	-1.2	-1.1	-0.9	-0.7	-0.7	-0.6	-0.5	-0.5	-0.5	-0.5	-0.5	-0.6	-0.8	-0.9	-0.9	-0.9	-1.0	-1.0
	3.5°C TMY	-1.0	-1.1	-1.1	-1.1	-1.1	-1.1	-1.1	-1.0	-0.8	-0.7	-0.6	-0.6	-0.5	-0.5	-0.5	-0.5	-0.5	-0.5	-0.8	-0.9	-0.8	-0.9	-0.9	-1.0
	3.5°C EWY	-0.7	-0.7	-0.8	-0.8	-0.8	-0.8	-0.8	-0.8	-0.5	-0.3	-0.3	-0.2	-0.1	-0.1	0.0	0.0	0.0	-0.1	-0.4	-0.5	-0.5	-0.5	-0.6	-0.6
Post-Retrofit	Historical	-0.6	-0.7	-0.7	-0.8	-0.8	-0.8	-0.8	-0.8	-0.4	-0.2	-0.1	0.0	0.0	0.1	0.1	0.1	0.1	0.0	-0.3	-0.5	-0.3	-0.3	-0.5	-0.5
	Baseline	-0.5	-0.6	-0.6	-0.7	-0.7	-0.8	-0.9	-0.9	-0.4	-0.1	0.0	0.1	0.1	0.2	0.2	0.2	0.1	0.0	-0.2	-0.4	-0.2	-0.2	-0.4	-0.4
	1.5°C TMY	-0.4	-0.5	-0.5	-0.6	-0.6	-0.7	-0.7	-0.7	-0.2	0.0	0.1	0.2	0.2	0.3	0.3	0.3	0.3	0.3	-0.1	-0.3	-0.1	-0.1	-0.2	-0.3
	2.5°C TMY	-0.3	-0.4	-0.4	-0.5	-0.6	-0.6	-0.6	-0.6	-0.1	0.1	0.2	0.2	0.3	0.3	0.4	0.4	0.4	0.3	0.0	-0.2	0.0	0.0	-0.2	-0.2
	3.5°C TMY	-0.3	-0.3	-0.4	-0.5	-0.5	-0.5	-0.6	-0.6	-0.1	0.1	0.2	0.2	0.3	0.4	0.4	0.4	0.4	0.3	0.0	-0.2	0.0	0.0	-0.1	-0.2
	3.5°C EWY	0.3	0.2	0.1	0.1	0.0	0.0	-0.1	-0.1	0.4	0.6	0.7	0.8	0.8	0.9	0.9	0.9	1.0	0.9	0.5	0.4	0.5	0.6	0.4	0.3

Figure 4. Average simulated daily PMV for office occupant in conference room zone.

4. DISCUSSION

Panelized retrofits are a promising emerging retrofit solution that can reduce energy consumption of existing buildings. However, as global temperatures continue to rise, it is important to study how buildings that have undergone these panelized retrofits will behave in future climate scenarios. While panelized retrofits result in reduced thermal energy demand, the total thermal energy savings are diminished as global warming scenarios intensify due to a lower overall heating demand. However, significant reductions in energy were still achieved in the worst climate scenario simulated. Simulated PMV values indicate that after the panelized retrofit, the building occupants are more vulnerable to feeling the effects of extreme weather compared to occupants in the pre-retrofit building. These findings suggest that buildings that undergo panelized retrofits must be equipped with sufficient, low-energy, cooling and ventilation systems that can satisfy increased energy and comfort demand due to climate change induced warming. These findings also suggest that the lifetime energy savings from these retrofits should account for the variability of future climate scenarios and extreme weather events.

5. CONCLUSIONS

This paper studied how a panelized retrofit would affect the heating, cooling, and thermal comfort of the building occupants in a community centre during future climate scenarios. A building in Montreal was modelled and calibrated in TRNSYS and a set of simulations were run using future climate and historical weather files to investigate how different climate scenarios impact the behaviour of the building. It was found that energy savings from a panelized retrofit could have diminishing returns as the building becomes less heating dominated due to climate change. The PMV, which represents the thermal comfort of the occupants also risks increasing past the comfort threshold during extreme heat wave events. Future research should further explore this avenue by testing more extreme future climate scenarios and testing various levels of insulation on the post-retrofit model to further understand the behaviour of these retrofitted buildings in the context of future climate scenarios. Additional research could also compare the results of these simulations with measured data upon the completion of the IBCC panelized retrofit.

ACKNOWLEDGEMENTS
The authors would like to acknowledge the support of Natural Sciences and Engineering Research Council of Canada, the Reconstruct Initiative and the Centre for Advanced Building Envelope to conduct the research.

REFERENCES

1. Amiri, A. S., Jemtrud, M., Lavigne, K., & Chung, D. (2022). *Comparing simulations of deep energy retrofits for a community center using past and future weather scenarios*. *13*, 0–0. https://publications.ibpsa.org/conference/paper/?id=esim2024_158
2. Biega, K., & Krarti, M. (2024). Evaluation of exterior insulated panels for residential deep energy retrofits. *Energies*, *17*(16), Article 16. https://doi.org/10.3390/en17163988
3. Chidiac, S. E., Yao, L., & Liu, P. (2022). Climate change effects on heating and cooling demands of buildings in Canada. *CivilEng*, *3*(2), Article 2. https://doi.org/10.3390/civileng3020017
4. Coakley, D., Raftery, P., & Keane, M. (2014). A review of methods to match building energy simulation models to measured data. *Renewable and Sustainable Energy Reviews*, *37*, 123–141. https://doi.org/10.1016/j.rser.2014.05.007
5. Dalkowski, T. M. (2024, September 12). *Development of panelized exterior retrofit solutions for commercial and institutional buildings*. Carleton University.
6. Efficiency Canada. (2021). *Canada's climate retrofit mission: Why the climate emergency demands an innovation-oriented policy for building retrofits*. https://www.efficiencycanada.org/retrofit-mission/
7. Environment and Climate Change Canada. (2022, June 22). *Canada's 2030 emissions reduction plan*. https://www.canada.ca/en/services/environment/weather/climatechange/climate-plan/climate-plan-overview/emissions-reduction-2030/plan.html
8. Fanger, P. O. (1988). Fundamentals of thermal comfort. In W. H. Bloss & F. Pfisterer (Eds.), *Advances In Solar Energy Technology* (pp. 3056–3061). Pergamon. https://doi.org/10.1016/B978-0-08-034315-0.50562-0
9. Gaur, A., & Lacasse, M. (2022). Climate data to support the adaptation of buildings to climate change in Canada. *Data*, *7*(4), Article 4. https://doi.org/10.3390/data7040042
10. Google Earth. (2025). *Map showing la centre socioculturel de L'Ile Bizard*. https://earth.google.com/web/
11. Li, D. H. W., Yang, L., & Lam, J. C. (2012). Impact of climate change on energy use in the built environment in different climate zones – A review. *Energy*, *42*(1), 103–112. https://doi.org/10.1016/j.energy.2012.03.044
12. Moazami, A., Nik, V. M., Carlucci, S., & Geving, S. (2019). Impacts of future weather data typology on building energy performance – Investigating long-term patterns of climate change and extreme weather conditions. *Applied Energy*, *238*, 696–720. https://doi.org/10.1016/j.apenergy.2019.01.085
13. Sharma, S. K., Mohapatra, S., Sharma, R. C., Alturjman, S., Altrjman, C., Mostarda, L., & Stephan, T. (2022). Retrofitting Existing Buildings to Improve Energy Performance. *Sustainability*, *14*(2), Article 2. https://doi.org/10.3390/su14020666
14. Shen, P., Braham, W., & Yi, Y. (2019). The feasibility and importance of considering climate change impacts in building retrofit analysis. *Applied Energy*, *233–234*, 254–270. https://doi.org/10.1016/j.apenergy.2018.10.041
15. Solar Energy Laboratory, University of Wisconsin-Madison. (1975). *TRNSYS, a transient simulation program*. Madison, Wis.: The Laboratory.
16. The American Society of Heating, Refrigerating, and Air-Conditioning Engineers. (2014). *ASHRAE Guideline 14: Measurement of Energy, Demand, and Water Savings*. https://webstore.ansi.org/standards/ashrae/ashraeguideline142014?srsltid=AfmBOopOpJsUSEL36h8i_kA0H-2oWaZQ5HUbDJ5Uc0I7W2vr7pc0m930
17. The American Society of Heating, Refrigerating, and Air-Conditioning Engineers, R. and A.-C. E. (2021). *2021 ASHRAE handbook: Fundamentals* (Inch-pound edition.). American Society of Heating Refrigerating and Air-Conditioning Engineers Inc. ASHRAE.

6th International Conference on Building Energy and Environment
Eindhoven University of Technology, The Netherlands
6 - 10 July 2025

Case study assessment of the energy performance of emission control strategies in office buildings

Lukas Vandenbogaerde [1,*], Jasmine Meysman [1], Amaryllis Audenaert[1], Stijn Verbeke [1,2]

[1]*University of Antwerp – Faculty of Applied Engineering, Antwerp, Belgium*
[2]*Unit Water and Energy Transition – VITO/EnergyVille, Mol, Belgium*
[*]*Corresponding Author: Lukas.vandenbogaerde@uantwerpen.be*

SUMMARY
The built environment plays a major role in global energy consumption and carbon emissions, with Building Automation and Control Systems (BACS) offering significant potential for improving energy efficiency. These systems include the control of HVAC, lighting, and shading, yet reliable data on their energy-saving potential remains scarce. Standard EN 52120-1 provides generic BACS efficiency factors but overlooks building-specific factors affecting performance. This study uses EnergyPlus simulations to assess energy savings across 1,944 variants of an case study office building, incorporating stochastic occupancy behavior. Results show that the BAC-factor method fails to accurately estimate heating and cooling savings, as it ignores building characteristics. Heating savings of around 20% to 30% were observed for individual room thermostats with time setback, and up to 40% for occupancy setback. Cooling savings were up to 20% in buildings with high initial cooling demand but were less significant in those with lower initial consumption.

Keywords: BACS, BEPS, Emission control

1. INTRODUCTION

The operation of buildings is accountable for 30% of the global final energy consumption which empathizes the need for an increased retrofitting rate (Delmastro et al., 2023). Beyond conventional measures, i.e. lowering thermal transmittance of envelope constructions or increasing the efficiency of technical installations, novel polices, notably the European Energy performance of Buildings Directive (EPBD), also include provisions on BACS (European Commission, 2024).

BACS are an asset for buildings to monito and automatically adjust energy using technologies (eu.bac, n.d.). EN 52120-1, part of the EPBD series of standards, divides the functionalities of BACS into heating, hot water, cooling, ventilation/air conditioning, lighting, blinds and technical home and building management (European Committee for Standardization, 2022). For each control domain, multiple functionalities are listed which are subdivided into automation functions and classes ranging from class D to class A. Class D represents non energy efficient BAC systems, class C standard BACS, class B advanced BACS and class A high-energy performance BACS. EN52120-1 provides saving factors for space heating and cooling ($f_{BAC,H}$ & $f_{BAC,C}$), domestic hot water generation ($f_{BAC,DHW}$) and electric energy for ventilation, lighting and auxiliary devices ($f_{BAC,el}$). These factors allow to easily assess the energy performance of BACS implementation compared to the reference scenario.

Table 1: BAC-factors for office buildings from EN52120-1

	Class D	Class C	Class B	Class A
Thermal	1.51	1	0.80	0.70
Electric	1.10	1	0.93	0.87
$f_{BAC,H}$	1.44	1	0.79	0.70
$f_{BAC,C}$	1.57	1	0.80	0.57
$f_{BAC,DHW}$	1.11	1	0.90	0.80
$f_{BAC,,el,L}$	1.10	1	0.85	0.72
$f_{BAC,,el,aux}$	1.15	1	0.86	0.72

These factors enable facility managers, building owners, and portfolio managers to easily evaluate the potential of integrating (advanced) BACS. However, as these factors have originally been derived from single-zone simulations without accounting for additional boundary conditions, they represent only a rough estimate which might not be applicable to all buildings and contexts. This study will explore emission control strategies for heating and cooling into a case study office building.

2. METHODOLOGY

The case study analysed in this paper is a single floor office, part of a mixed-use building. The floor is showed in figure 1 below, the boundary condition of the roof is adiabatic, as are the two sidewalls. The floor area of this case study is 382.5 m², of which 81.4 m² is a corridor, 85.1 m² are auxiliary rooms, 99.0 m² is assigned to meeting rooms and 117.0 m² are office spaces. The heating and cooling demand is met using an 'ideal load air system' with unlimited heat and cold supply capacity, ensuring that the heating and cooling requirements corresponding to different automation functions are precisely satisfied.

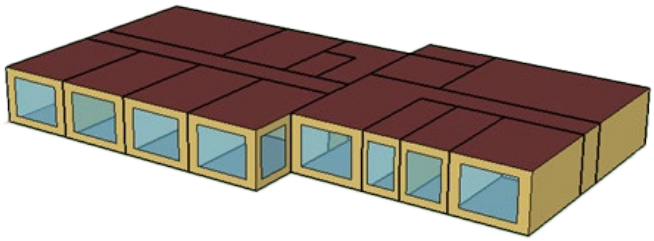

Figure 1: Geometry of the case study typology

A fixed occupancy schedule is used throughout the variations, generated by the LBNL stochastic occupancy generator (Chen et al., 2018). In the office zones, an occupancy assumption of 10 m² per person is applied in the office spaces, resulting in a maximum of 10 occupants in this case study building. The figure below illustrates occupancy on the first three days.

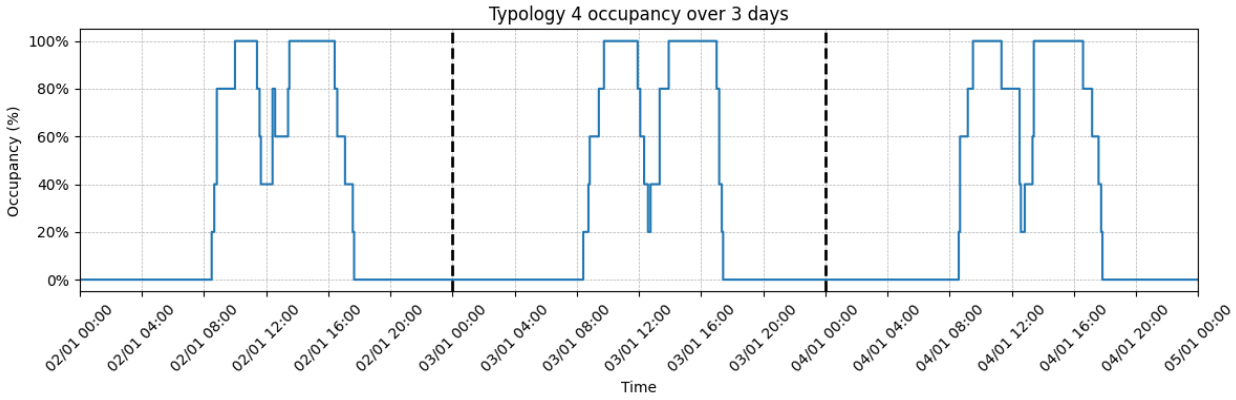

Figure 2: Extract of the occupancy profile generated with the LBNL occupancy simulator.

EnergyPlus[1] is utilized as the simulation engine to evaluate energy consumption in a case study building under various BACS functions. The study explores variations in the window-to-wall ratio (WWR), envelope characteristics (U-values and infiltration rates), and equipment and lighting power.

- Window-to-wall ratio: variations of 20%, 50%, and 80% are considered.
- Envelope characteristics: three categories are evaluated: pre-EPB (1970s properties), EPB-compliant (2006 standards), and passive house standards (Flemish Energy Decree: Annex VII, 2006; Gevorgian et al., 2021; Hines, 2015). The following table summarizes the corresponding U-values and infiltration rates:

Table 2: Thermal characteristics for the different envelope scenarios

	Pre-EPB	**EPB (2006)**	**Passive**
U-Value floor & roof	2.2 W/m².K	0.4 W/m².K	0.1 W/m².K
U-Value wall	1.75 W/m².K	0.6 W/m².K	0.1 W/m².K
U-Value window	4.2 W/m².K	1.6 W/m².K	0.8 W/m².K
Infiltration rate	0.00027 m³/s.m²	0.00013 m³/s.m²	0.08 ACH

- Equipment and lighting power: high-power scenarios are based on the lighting power density outlined in ASHRAE 90.1-2022 (ASHRAE, 2022). Low-power scenarios use half this value. Additionally, equipment power settings are defined as 5.83 W/m² for 100% desktop use and 3.67 W/m² for laptop use with docking stations, assuming 15.5 m²/person (ASHRAE, 2021).

The functionalities assessed include emission control for heating and cooling, shading control, ventilation flow control, and lighting control. In combination with the boundary condition variations, this results in 1,944 unique simulation scenarios. This paper specifically examines the emission control strategies for heating and cooling as in function 1.1 and 3.1 as described in EN52120-1. Three control scenarios are analysed:

[1] https://energyplus.net/

Table 3: details of the thermostat control scenarios in this research

Control strategy	Controlled zones	Heating activation	Cooling activation	Comments
Central thermostat (Class D)	Single zone (kitchenette, central control)	Below 20.5°C (in central zone)	Above 24.5°C (in central zone)	Heating Setpoint: 22°C Cooling Setpoint: 23°C (hysteresis buffer between 21°C and 24°C in central zone)
Individual room thermostat with time setback (Class B)	Individual room control (except corridor & auxiliary rooms)	7AM–5PM: 21°C 5PM–7AM: 16°C Weekends: 16°C	7AM–5PM: 24°C 5PM–7AM: 28°C Weekends: 28°C	
Individual room thermostat with occupancy setback (Class A)	Individual room control (except corridor & auxiliary rooms)	Occupied: 21°C Unoccupied: 18°C Weekends: 16°C	Occupied: 24°C Unoccupied: 26°C Weekends: 28°C	

Infiltration rates are based on BLAST values, producing a rate of x1 for a ΔT (inside-outside) of 0 °C and wind speed of 3.35 m/s (Gowri et al., 2009). The ventilation flow rate is set to 22 m^3/h per person for occupied rooms and 1.3 $m^3/h \cdot m^2$ for restrooms, in line with Flemish design requirements for non-residential buildings (European Committee for Standardization, 2004).

The weather data used in this study is derived from a typical meteorological year (TMY) for Uccle, (Brussels, Belgium). Manual control of lighting, shading, and windows is modeled using established occupancy behavior models, specifically those developed by Reinhart and Haldi & Robinson. These models predict user interactions based on various environmental conditions.

- Lighting control follows Reinhart's model, where switching behaviour is influenced by workplane illuminance and occupancy events, such as arrival, intermediate presence, and departure (Reinhart, 2004).
- Window operation is modelled using Haldi & Robinson's approach, where opening and closing probabilities depend on indoor and outdoor temperatures, with additional influence from rain in certain cases (Haldi & Robinson, 2009).
- Shading control is based on a combination of Reinhart and Haldi & Robinson, where shading adjustments are triggered by outdoor temperature and occupant presence (Haldi & Robinson, 2008; Reinhart, 2004).

3. RESULTS

First of all, the savings of individual room thermostat control with time setback and occupancy setback are compared to a central thermostat. The graph below shows the consumption of both scenarios in $kWh/y.m^2$ and the scale factors. The data is categorized by envelope characteristic and ventilation automation type as these parameters seem to have the greatest influence on the initial heating consumption and savings.

Figure 3a

Figure 3b

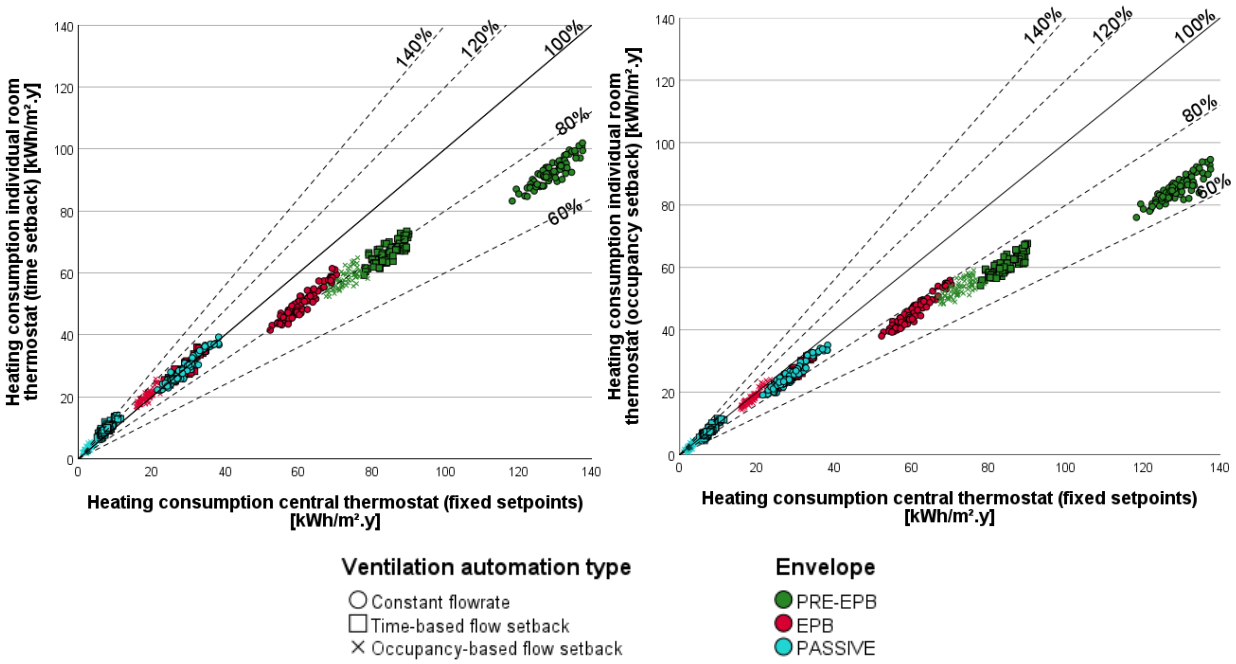

Figure 3: (a) heating consumption of a central thermostat compared to individual room control with time setback. (b) heating consumption of a central thermostat compared to individual room control with occupancy setback.

The results indicate that initial heating energy consumption, categorized by thermal transmission of the envelope and ventilation automation strategies, significantly impacts the achievable energy savings. In buildings with minimal heating demand, i.e. those with passive envelopes and advanced ventilation control, individual room control with temperature setbacks has a negligible effect in absolute terms.

On average, buildings with pre-EPB envelope characteristics achieve energy savings of 22.8%, whereas buildings with EPB-compliant envelopes exhibit a significantly lower savings potential of only 2.8%. The results further reveal a clear trend in savings relative to initial consumption: cases with heating demands exceeding 100 kWh/m²·y achieve savings of approximately 30%, while cases with initial consumption between 50 and 100 kWh/m²·y show savings around 20%. In contrast, buildings with an initial consumption below 50 kWh/m²·y exhibit negligible savings, fluctuating around 0%.

The time based and occupancy based temperature setback also affect the cooling demand. The cooling consumption data is categorized according to envelope characteristics and window-to-wall ratio.

Figure 4a

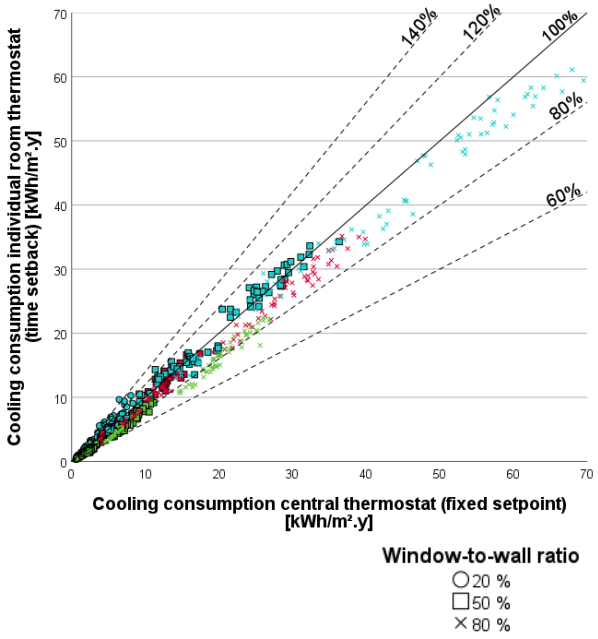

Figure 4b

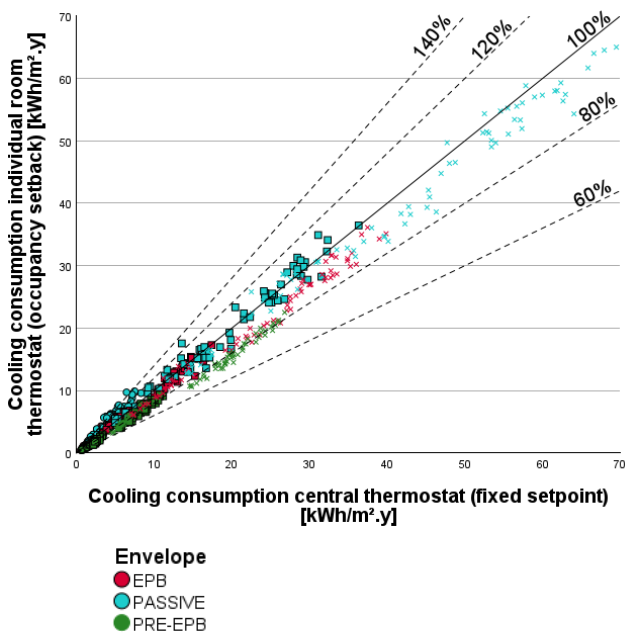

Figure 4: (a) cooling consumption of a central thermostat compared to individual room control with time setback. (b) cooling consumption of a central thermostat compared to individual room control with occupancy setback.

It is evident that buildings with a high WWR exhibit higher initial cooling loads. In these cases, the implementation of a time-based temperature setback generally results in energy savings between 0% and 20%. Buildings with a pre-EPB envelope, despite having relatively low initial cooling consumption, achieve relative savings of up to 40%. In contrast, cases with passive envelopes and a WWR of 20% or 50% are predominantly positioned around the 100% scaling factor, indicating negligible energy savings. A similar trend is observed when comparing a central thermostat with individual room control incorporating occupancy-based temperature setback; however, in this case, most scenarios demonstrate positive energy savings. In the case of heating consumption, the cases with the highest initial consumption could achieve high savings by thermostat controls, i.e., between 20% and 40%. This effect is less pronounced for cooling energy, where cases with the highest cooling demand demonstrate a savings potential of only 0% to 20%.

4. DISCUSSION

A direct comparison between the case study results and the BAC factors from the EN 52120-1 standard cannot be made in its entirety, as this paper focuses solely on functions 1.1 and 3.1 described in EN 52120-1 , which pertain specifically to 'emission control' for heating and cooling systems. The standard presents various functions within each domain to evaluate BACS performance. To be able to compare with the BAC-factor for, e.g., heating control, other functions to consider are control of hot water temperature, control of pumps, hydronic balancing, intermittent control of emission and/or distribution and heat generator control.

Therefore, it is a logic result that the savings obtained in this research is less profound than what

the BAC-factor estimates, as shown in table 3 below. Though these scaling factors provide generalized energy saving estimates but do not take into account variations in specific building characteristics, i.e. the building envelope, HVAC-system configuration, efficiency of lighting and appliances, or occupant behavior. As this research shows the impact of these various parameters on the results, the BAC-factors are limited in only providing a single scaling factor.

Table 4: The BAC-factors for yearly heating and cooling energy consumption savings.

	Class D	**Class B**	**Class A**
$\mathbf{f_{BAC,H}}$	1.44	0.79	0.70
Heating energy savings compared to non-energy efficiency BACS (class D) [%]	0.0%	45.1%	51.4%
$\mathbf{f_{BAC,C}}$	1.57	0.80	0.57
Heating energy savings compared to non-energy efficiency BACS (class D) [%]	0.0%	49.0%	63.7%

In cases with low heating or cooling demand, the scaling factors from the BAC guidelines may be particularly confusing. This is because the absolute energy savings are minimal, and even small variations in building characteristics, occupancy patterns, or control strategies can lead to relatively large relative changes. In such cases, the BAC factors may suggest a more significant impact than what is realistically achievable, given the low absolute baseline consumption.

It is noteworthy that the BAC factors suggest higher cooling energy savings than heating energy savings, with figures up to 63.7% for cooling, compared to 51.4% for heating. In contrast, the results from this study indicate a reversed trend, with higher savings observed in heating energy consumption than in cooling.

This research only focuses on 1 specific case study typology, a small office building with only 5 office spaces and 2 meeting rooms. As the geometry, amount of offices and meeting rooms and office space types (private office or open-plan office) could affect the saving potential, it is an important parameter to vary in further research endeavours. In addition, other parameters could affect the saving potential, e.g. climate, HVAC-configuration (no ideal heating or cooling conditions as in this research), occupancy patterns and thermal mass. A detailed statistical analysis can reveal which parameters have major influence on the saving potential and should be taken into account into assessment methodologies.

5. CONCLUSION

This study evaluated the impact of different emission control strategies for heating and cooling in a case study office building, comparing a central thermostat (Class D), individual room thermostats with time-based setback (Class B), and occupancy-based setback control (Class A). The extent of savings is highly dependent on various building characteristics, i.e. envelope characteristics, ventilation strategies, and window-to-wall ratio. Although the results of this research could not be directly compared to the BAC-factors of EN 52120-1, it is clear that variating building characteristics have an effect on the saving potential which is disregarded in the single number BAC-factors.

The case study of a single-floor office building demonstrates that individual room thermostat control with time or occupancy-based setbacks can lead to notable energy savings, particularly in buildings with high initial heating demands. However, the savings are less pronounced in buildings with low heating or cooling demands, highlighting the limitations of generalized BAC factors. The study also reveals that while BAC factors suggest higher cooling energy savings, the actual results indicate greater savings in heating energy consumption.

Future research should consider varying building geometries, HVAC configurations, occupancy patterns, and climates to better understand the potential energy savings of BACS. A detailed statistical analysis could identify the most influential parameters, leading to more accurate assessment methodologies.

6. REFERENCES

2021 ASHRAE handbook: Fundamentals (2021).

ASHRAE. (2022). *Standard 90.1-2022—Energy Standard for Sites and Buildings Except Low-Rise Residential Buildings*. https://www.ashrae.org/technical-resources/bookstore/standard-90-1

European Committee for Standardization. (2022). *EN 52120-1 Energy performance of buildings - Contribution of building automation, controls and building management - Part 1: General framework and procedures*. https://edu.mynbn.be/nbnframework/index.php/pdfMeta/RO/589148?l=E

Chen, Y., Hong, T., & Luo, X. (2018). An agent-based stochastic Occupancy Simulator. *Building Simulation*, *11*(1), 37–49. https://doi.org/10.1007/S12273-017-0379-7/METRICS

Delmastro, C., De Bienassis, T., Goodson, T., Lane, K., Le Marois, J.-B., Martinez-Gordon, R., & Husek, M. (2023). *Buildings – Analysis*. https://www.iea.org/reports/buildings

European Commission. (2024). *Directive (EU) 2024/1275 of the European Parliament and of the Council of 24 April 2024 on the energy performance of buildings (recast)*. https://eur-lex.europa.eu/legal-content/EN/TXT/HTML/?uri=OJ:L_202401275

European Committee for Standardization. (2004). *EN 13779 Ventilation for non-residential buildings*. https://edu.nbn.be/data/r/platform/eduportal/edu-collection?clear=20,0&session=16110523041487

Flemish Energy decree: Annex VII. (2006).

Gevorgian, A., Pezzutto, S., Zambotti, S., Croce, S., Filippi Oberegger, U., Lollini, R., & Müller, A. (2021). *European Building Stock Analysis A country by country descriptive and comparative analysis of the energy performance of buildings*.

Gowri, K., Winiarski, D., & Jarnagin, R. (2009). *Infiltration Modeling Guidelines for Commercial Building Energy Analysis*.

Haldi, F., & Robinson, D. (2008). On the behaviour and adaptation of office occupants. *Building and Environment*, *43*(12), 2163–2177. https://doi.org/10.1016/J.BUILDENV.2008.01.003

Haldi, F., & Robinson, D. (2009). Interactions with window openings by office occupants. *Building and Environment*, *44*(12), 2378–2395. https://doi.org/10.1016/J.BUILDENV.2009.03.025

Hines, J. (2015). *How to build a Passivhaus: Rules of thumb*. www.passivhaustrust.org.uk

Reinhart, C. F. (2004). *Lightswitch-2002: a model for manual and automated control of electric lighting and blinds*. https://doi.org/10.1016/j.solener.2004.04.003

What are BACS? (2021) *EUBAC*. Available at: https://eubac.org/about/what-are-bacs/ (Accessed: October 1, 2025).

6th International Conference on Building Energy and Environment
Eindhoven University of Technology, The Netherlands
6 - 10 July 2025

Rules of thumb and design metrics for evaluating daylighting performance

Shuyang LI [1], Emmanuel I. AGHIMIEN [2], Ernest K.W. TSANG [3], Danny H.W. LI [4]

[1] *Department of Construction and Quality Management, Hong Kong Metropolitan University, Kowloon, Hong Kong SAR, shyali@hkmu.edu.hk*
[2] *School of Architecture, The University of Utah, Utah, USA, emmanuel.aghimien@utah.edu*
[3] *Department of Construction and Quality Management, Hong Kong Metropolitan University, Kowloon, Hong Kong SAR, ekwtsang@hkmu.edu.hk*
[4] *Department of Architecture and Civil Engineering, City University of Hong Kong, Kowloon, Hong Kong SAR,*

SUMMARY
Daylighting is an effective and sustainable development strategy to alleviate problems in energy and the environment. It is also useful for enhancing visual comfort and health. Climate-based daylight metrics (CBDMs) have recently been adopted for providing additional information by considering the hours of real situations and actual weather conditions for a given location. Thus, the use of CBDMs offers a substantial functional account of true daylighting environments for a building in a certain location. However, CBDMs are typically determined in full-scale computer simulations using sophisticated software, which are laborious and require technical skills. Traditionally, daylight factor (DF) only represents the daylight condition under the overcast sky. Until recently, DF calculations have been extended for all sky conditions. It means that the daylight factor-based metric (DFBM) can also be another dynamic metric and it can take into account the building directions, solar positions and the effects of direct and reflected sunlight. Indoor daylight illuminance is the product of a (DFM) and a horizontal sky-diffuse component, which means that the absolute indoor daylight illuminance can be predicted from the DFMs. This paper reviews the existing daylight metrics and proposes further studies to correlate CBDMs and DFMs for buildings facing various directions. The findings and recommendations could be useful for architects and practitioners involved in architectural and daylighting design and evaluations. It will also significantly contribute to the educational landscape by enriching the curriculum for students.

Keywords: Daylight performance, climate daylight factor metrics, visual comfort

1. INSTRUCTIONS

Daylighting is recognized as a useful sustainable strategy, green building development (Kwong, 2020), visual comfort enhancement (Xue et al., 2014) and energy-efficient building designs (Mavromatidis et al., 2014). Natural lighting is an essential aspect that requires examination in depth during the early stages of building designs (Freewan, 2015; Petersen et al., 2014). Various rules of thumb and design metrics are commonly used by architects and architectural engineers for predicting and assessing daylighting capability.

Recently, climate-based daylight metrics (CBDMs) have gained traction as valuable tools for assessing diverse daylight conditions over the course of a year. These metrics specifically focus on the actual working hours and prevailing weather conditions of a specific location, enabling a comprehensive evaluation of authentic daylighting environments.

Daylight factor metrics (DFMs) have been adopted in assessing the indoor daylighting designs.

Due to its simplicity, DF can be determined by simple equations, tables or calculation steps, which is particularly useful in the early design stage. This paper reviews the strengths and weaknesses of DFMs and CBDMs and proposes appropriate schemes to link up these two essential metrics for architectural and daylighting designs and evaluations.

2. DAYLIGHT METRICS

In general, the DFMs include point daylight factor (PDF), average daylight factor (ADF) and vertical daylight factor (VDF). The CBDMs contain daylight autonomy (DA), continuous daylight autonomy (cDA), spatial daylight autonomy (sDA), annual sunlight exposure (ASE) and useful daylight illuminance (UDI). The major characteristics, strengths and limitations are elaborated as follows.

2.1. Daylight factor metrics

The PDF is the ratio of illuminance due to daylight at a point without direct sunlight on an indoor working plane to the simultaneous outdoor illuminance on a horizontal surface (E_{HD}) from an unobstructed hemisphere of the International Commission on Illumination (CIE) overcast sky. The PDF can be used to predict the reduction in electrical lighting achievable from the use of daylighting controls (Mattoni et al., 2018). An ADF indicates the visual adequacy for an interior area rather than any specific point within the area (Longmore, 1975). As an ADF directly relates to window openings and requires input data less detailed than those required by the PDF, the ADF is useful in developing building envelope schemes during a preliminary design phase (Lynes & Littlefair, 1990). The VDF accounts for light from the sky and daylight reflected from the surrounding buildings and ground onto a vertical plane and is applied to compact city regions with vast external obstructions.

DFM has been employed by different design manuals for providing criteria which are widely adopted in many places (Hraska, 2011). In Norway, for example, a DF of 2% is taken as the criterion in sizing windows in architectural design practice (Moscoso et al., 2020). In Iran, the ratio of the window area to floor area is taken as the criterion in assessing the DF (Vaisi & Kharvari, 2019). In 2018, European standard EN17037 (Daylight in Building) was established and its criteria were expressed as DFs (European Committee for (Standardization, 2018). In Hong Kong, VDFs are used to quantify the daylighting performance of buildings (Buildings & Department, 2015). Currently, ADFs, VDFs and PDFs remain in use for daylighting schemes.

However, DFMs, despite their valuable contributions, exhibit limited adaptability in accurately forecasting variations in daylight conditions caused by the sun's movement during non-overcast periods. It can lead to overglazed buildings under clear sky conditions (Mardaljevic et al., 2009). Therefore, although high values of DFMs indicate well-daylit spaces with low demands for artificial lighting, DFMs cannot be used to identify spaces of visual discomfort, such as daylight glare.

2.2. Climate based daylight metrics

CBDMs have been developed and adopted to assess the daylighting performance on annual and seasonal bases. CBDMs mainly contain DA, cDA, sDA, ASE and UDI. The DA is the percentage of daylight hours on an annual basis during which the daylight illuminance at a given interior point

(E_{DL}) exceeds a specified minimum illuminance (E_{SMI}). It can be used to predict artificial-lighting energy savings under standard daylighting controls. Mathematically, it can be expressed as Eq. (1) (Carlucci et al., 2015):

$$DA = \frac{\sum_i (wf_i \times t_i)}{\sum_i t_i} \in [0,1] \quad (1)$$
$$with\ wf_i = \begin{cases} 1\ if\ E_{DL} \geq E_{SMI} \\ 0\ if\ E_{DL} < E_{SMI} \end{cases}$$

where t_i is every occupied hour in a year; wf_i is a weighting factor depending on values of E_{DL} and E_{SMI}.

The cDA is a modification of the DA that awards partial credit for daylight levels below a user-defined threshold in a linear fraction as shown in Eq. (2) (Carlucci et al., 2015). It is useful for computing the energy savings for top-up or multi-level on–off controls.

$$cDA = \frac{\sum_i (wf_i \times t_i)}{\sum_i t_i} \in [0,1] \quad (2)$$
$$with\ wf_i = \begin{cases} 1\ if\ E_{DL} \geq E_{SMI} \\ \dfrac{E_{DL}}{E_{SMI}}\ if\ E_{DL} < E_{SMI} \end{cases}$$

The sDA expresses the percentage of floor area that exceeds a given illuminance level (e.g., 300 lux) for a norm percentage (e.g., 75%) of the annual occupied daily hours (e.g., 8 am to 6 pm) of a space. The Illuminating Engineering Society guidelines recommend the use of two different sDAs: (1) the preferred daylight sufficiency, which is when at least 75% of an analysis area meets the standards, and (2) the nominally accepted daylight sufficiency, which is when 55% of an analysis area meets the standards (IES, 2012). The ASE is the sum of sunlight (≥1000 lux) incident on a given point over the course of a year (recorded in lux hours) and indicates the fraction of a space that is exposed to too much glare-generating direct sunlight. A credit offered by the Leadership in Energy and Environmental Design (LEED) rating system (USGBC, 2018) requires that the ASE not be exceeded for more than 250 hours a year for more than 10% of a space.

The UDI indicates the daylight levels that are useful for an occupant and is described by a set of three metrics for every point in a space, namely the percentage of times that a point is below the minimum threshold (<100 lux), within the useful range (100–2000 lux), and above the maximum threshold (>2000 lux). Eq. (3) presents its formulation (Carlucci et al., 2015):

$$UDI = \frac{\sum_i (wf_i \times t_i)}{\sum_i t_i} \in [0,1] \quad (3)$$
$$with\ wf_i = \begin{cases} 1\ if\ E_{Ut} \geq E_{DL} \geq E_{Lt} \\ 0\ if\ E_{Ut} > E_{DL}\ or\ E_{Lt} < E_{DL} \end{cases}$$

The lower threshold (E_{Lt}) is useful for determining the perception of the visual environment whereas the upper threshold (E_{Ut}) indicates the times when there is a daylight oversupply that may cause glare.

CBDMs reflect real daytime conditions and are determined using weather databases for a given location, which means that they represent actual daylight surroundings and are appropriate for determining luminous comfort, daylight glare and settings for daylighting controls. In order to achieve results that closely resemble real-life daylight conditions, the appropriate approach is to employ lighting simulations (Navvab, 2014). However, conducting a comprehensive hour-by-hour computer simulation for an entire year is a time-consuming and costly, as it involves modelling the building's geometry over an extended simulation period and extensive input and post-processing procedures. The LEED rating system recommends three options for daylighting based on CBDMs (USGBC, 2018). Option 1 is to determine sDA and the annual ASE using calculation cells of not more than 600 mm. However, the application of such cells in an hourly time-step parametric analysis using typical weather-year data and a sophisticated simulation package would take an enormous amount of time. In addition, CBDMs are simulated using representative annual daylight data, which may not be readily obtainable for many locations or may not reflect current daylighting criteria and situations at a location (Li et al., 2017). In recent years, there has been a development of user-friendly design tools that aim to simplify the complex process of designing buildings. These tools, including simplified geometry maps, regression equations, and charts, have been created through extensive examinations utilizing advanced simulation techniques (Kleindienst et al., 2008; Petersen et al., 2014; Šprah & Košir, 2019). They are intended to be utilized during the initial planning phase of a project, providing architects, engineers, and students with fundamental and concise insights into the interconnectedness of various daylight parameters. Once a preliminary design has been established, more detailed information is sought through full-scale building simulations. Previous studies have attempted to establish links between DA and sDA metrics with DFs (Acosta et al., 2019; Asfour, 2020). However, no straightforward formulas have been recommended. Lo Verso et al. (Lo Verso et al., 2017) have developed mathematical models that estimate various daylight autonomy and energy demands for lighting during the early stages of building design. However, these models require a substantial number of input variables, such as architectural features, leading to the generation of complex mathematical expressions and associated uncertainties.

3. WORKS FOR AMELIORATING DAYLIGHT METRICS

In view of the features of CBDMs and DFMs, it is necessary to take advantage of the merits of DFMs to overcome the shortcomings of the approaches usually adopted to determine CBDMs. The determination of the absolute daylight illuminance at various reference points, simulations could be conducted, and DFMs could be calculated by dividing the modelled daylight illuminance by the corresponding E_{HD} under CIE Sky 1 condition (CIE, 2003; Kittler et al., 1998). The VDFs could be calculated at the centre point of the window, while the PDFs could be represented by the values of individual interior grid points. The ADF could be determined as the mean value of the PDFs across all grid points. By simulating the year-round indoor daylight illuminance, the DA and UDI could be obtained. Since DFMs remain constant regardless of solar position and orientation under overcast-sky conditions, their correlation with UDI and DA values should reflect their correlation with CIE Sky 1. Consequently, the required DFMs would only need to be simulated once for a specific E_{HD}, resulting in significantly reduced simulation time. Furthermore, all data could be generated using the same simulation programs and techniques. Alternatively, DFMs under Sky 1 can also be calculated from room parameter inputs using simple formulas, diagrams, or calculation aids (Hopkinson et al., 1966). Figures 1 to 3 display the correlations between

CBDMs and DFMs for rooms located in Hong Kong facing different cardinal orientations (Li et al., 2023). As shown in the figures, the CBDMs and DFMs are strongly correlated.

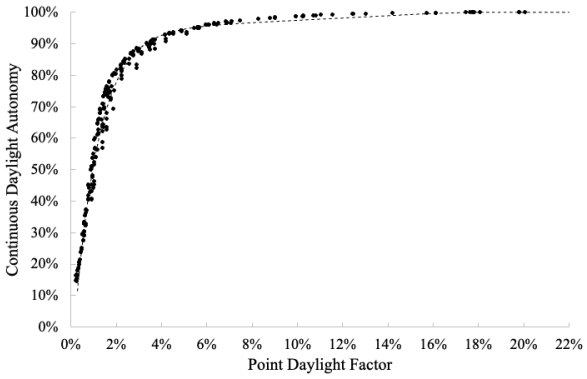

Figure 1. Example of figure.

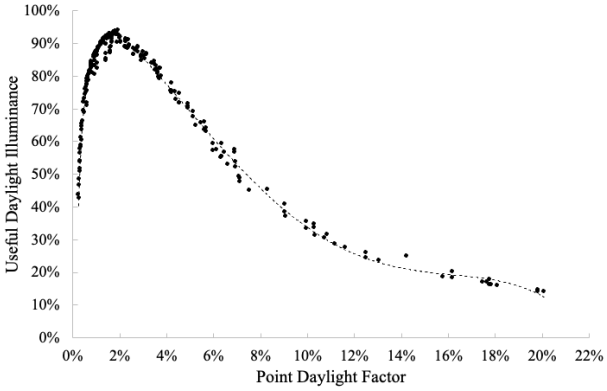

Figure 2. Correlation between PDF and UDI facing south.

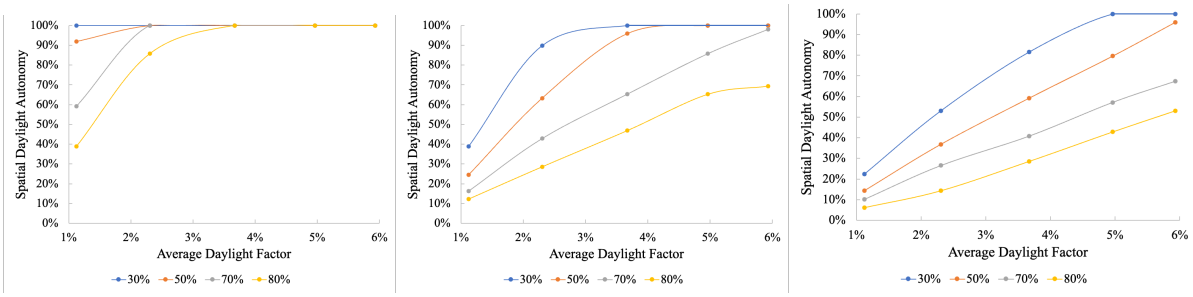

(a) 100 lux (b) 300 lux (c) 500 lux

Figure 3. Correlation between ADF and sDA facing south with three illuminance thresholds (a) 100 lux; (b) 300 lux; (c) 500 lux.

It has been reported that the CIE Overcast Sky offers the best performance among many models applied worldwide for various climates under overcast conditions (Enarun & Littlefair, 1995; Li et al., 2001). The outdoor illuminance of a particular location is mainly determined by the solar position and local sky conditions. Sensitivity analyses should be applied to all inputs to account for the fact that various locations have different sky-diffuse and direct sunlight datasets. Importantly, as the proposed method using DFMs under CIE Sky 1 could afford suitable architectural and daylighting designs based on inputs from ADFs, it would be possible to accurately predict CBDMs for a given location. Contrarily, individual room parameters in a simple general CBDMs mathematical model may not be mutually exclusive (Lo Verso et al., 2017). To enhance the generalisability and representative, places of miscellaneous latitudes containing typical weather files with diffuse and direct sunlight data should be dealt with. Reference should be made to guidebooks and research publications in adopting the usual ranges of these parameters.

Shading devices such as overhangs, side-fins and recessed windows should be studied for topmost floor of high-rise blocks facing unobstructed skies. The VDFs for various overhang projection factors, side-fins projection factors, and recessed window depths would be simulated and

correlated with the scattering angle (χ), which is the shortest distance between the sun and the sky element that the window is facing normally, under the 15 CIE standard skies (15 CIESS). The corresponding ADFs and PDFs would be computed for subsequent analysis. This would allow building and daylighting design implications to be investigated and clarified. Shading by surrounding buildings can substantially decrease light coming from the sky into a building interior, particularly into rooms on the lower floors of a building. In contrast, under obstructed skies, the externally reflected component (ERC) of daylight can be relatively large. The magnitude of the ERC is dependent on how well surrounding buildings' surfaces are illuminated and on these surfaces' reflectance. The layout affecting the ERC in terms of the upper obstruction angle of a target window (α_U), the lower obstruction angle of the window (α_L) and the obstruction angle of the reference building (α_B) should be described. Figure 4 presents such angles. The correlations between DFMs could also aid multi-point internal daylight illuminance measurements as proposed by the LEED rating system Option 3 (USGBC, 2018), as they will allow the minimum number of illuminance meters to be reduced. Daylight illuminance is the product of DF and the horizontal sky-diffuse component, and the total daylight illuminance in a room is the sum of sky-diffuse illuminance and the direct sunlight, if any. Accordingly, the DFMs obtained, and the simple equations devised by Tregenza (Tregenza, 1995) could be used to compute direct sunlight and thereby determine interior daylight. This will constitute a non-simulation approach to calculating the absolute daylight illuminance, thereby allowing CBDMs to be obtained from DFMs.

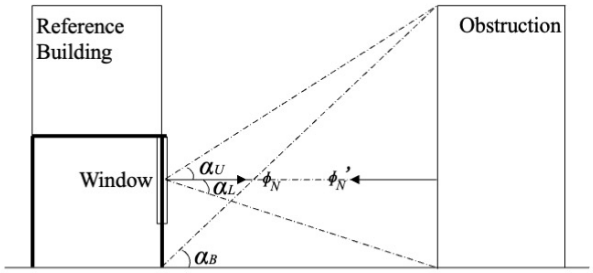

Figure 4. The angles for the centre point of the whole vertical window.

4. CONCLUSIONS

A review of DFMs and CBDMs in terms of their characteristics, advantages and drawbacks was conducted. The findings indicated that CBDMs could be linked with DFMs to eliminate their shortcomings and reinforce their strengths. Through the mathematical models, CBDMs could properly be estimated from DFMs of appropriate room parameters which are simple and fast calculation tools, attaining appropriate architectural and daylighting designs. It would be particularly useful for meeting the LEED Option-1. The strong correlations between PDF, VDF and ADF show that interior daylight illuminance can be calculated once the corresponding horizontal sky-diffuse illuminance and sky conditions have been determined. As direct sunlight can also be computed based on simple solar geometry, this will constitute a non-simulation method of calculating the absolute daylight illuminance, thereby allowing CBDMs to be obtained from DFMs. Such a study would also be advantageous to the actual measurement in LEED Option -3. For representative annual daylight data, it has been proposed to use 15 CIE Standard Skies and the three Representative Skies. It would be more appropriate for places without measured outdoor illuminance records for conducting daylight simulation in LEED Option-2. Visual comfort

variables such as glare and uniformity are important to daylighting design and evaluation and thus to establishing criteria for CBDMs. It is suggested that correlations between CBDMs and visual comfort factors should be made. To have a comprehensive daylighting design, building energy issues in terms of daylight-linked lighting controls are required. Further open- and closed-loops for daylighting switching and dimming controls using DA, cDA, VDF and PDF should be investigated. Besides having academic merit, the findings will have practical value in terms of developing architectural and daylighting schemes that are useful in the early design stage when various conceptual building façade plans are being considered. The tools developed will be of interest to local and overseas researchers and building professionals and particularly appropriate to novice students.

ACKNOWLEDGEMENTS

Work described was fully supported by a Faculty Development Scheme from the Research Grant Council of HKSAR [Project no. UGC/FDS16/E07/23] and Research Matching Grant Scheme from the Research Grant Council of HKSAR [Ref. no. 2021/3006]. The late Prof. Danny Li passed away during the conduct of research project. All the author would like to recongnize his contribution in the research work.

REFERENCES

Acosta, I., Campano, M. Á., Domínguez, S., & Fernández-Agüera, J. (2019). Minimum Daylight Autonomy: A New Concept to Link Daylight Dynamic Metrics with Daylight Factors. *Leukos, 15*(4), 251-269. doi:10.1080/15502724.2018.1564673

Asfour, O. S. (2020). A comparison between the daylighting and energy performance of courtyard and atrium buildings considering the hot climate of Saudi Arabia. *Journal of Building Engineering, 30*. doi:10.1016/j.jobe.2020.101299

Buildings, & Department. (2015). *Practice Note for Authorized Persons, Registered Structural Engineers and Registered Geotechnical Engineers APP-130, Lighting and Ventilation Requirements-Performance-based Approach.* .

Carlucci, S., Causone, F., Rosa, F. D., & Pagliano, L. (2015). A review of indices for assessing visual comfort with a view to their use in optimization processes to support building integrated design. *Renewable and Sustainable Energy Reviews, 47*, 1016-1033.

CIE. (2003). Spatial Distribution of Daylight-CIE Standard General Sky. In (Vol. S 011/E:2003/ISO 15469:2003 (E)). Vienna, Austria: CIE General Bureau.

Enarun, D., & Littlefair, P. (1995). Luminance models for overcast skies: assessment using measured data. *Lighting Research & Technology, 27*(1), 53-58.

Freewan, A. A. Y. (2015). Developing daylight devices matrix with special integration with building design process. *Sustainable Cities and Society, 15*, 144-152. doi:10.1016/j.scs.2014.11.003

Hopkinson, R. G., Petherbridge, P., & Longmore, J. (1966). *Daylighting*. London: UK: Heinemann.

Hraska, J. (2011). *Criteria of daylighting and sunlight access in sustainable construction evaluation systems*. Paper presented at the Proceedings of the 5th International Conference on Solar Radiation and Daylighting, Brno University of Technology, Czech Republic.

IES. (2012). Approved Method: Spatial Daylight Autonomy and Annual Sunlight Exposure. In. USA: IES LM-83-12.

Kittler, R., Darula, S., & Perez, R. (1998). *A set of standard skies*: Bratislava: Ploygrafia

Kleindienst, S., Bodart, M., & Andersen, M. (2008). Graphical Representation of Climate-Based Daylight Performance to Support Architectural Design. *Leukos, 5*(1), 39-61. doi:10.1080/15502724.2008.10747628

Kwong, Q. J. (2020). Light level, visual comfort and lighting energy savings potential in a green-certified high-rise building. *Journal of Building Engineering, 29*. doi:10.1016/j.jobe.2020.101198

Li, D. H. W., Lau, C. C. S., & Lam, J. C. (2001). Evaluation of overcast-sky luminance models against measured Hong Kong data. *Applied Energy, 70*, 321-331.

Li, D. H. W., Lou, S. W., Ghaffarianhoseini, A., Alshaibani, K. A., & Lam, J. C. (2017). A review of calculating procedures on daylight factor based metrics under various CIE Standard Skies and obstructed environments. *Building and Environment, 112*, 29-44. doi:10.1016/j.buildenv.2016.11.019

Li, S., Li, D. H. W., Chen, W., Lou, S., & Tsang, E. K. W. (2023). Simple mathematical models to link climate-based daylight metrics with daylight factor metrics and daylighting design implications. *Heliyon, 9*(5). doi:10.1016/j.heliyon.2023.e15786

Lo Verso, V. R. M., Mihaylov, G., Pellegrino, A., & Pellerey, F. (2017). Estimation of the daylight amount and the energy demand for lighting for the early design stages: Definition of a set of mathematical models. *Energy and Buildings, 155*, 151-165. doi:10.1016/j.enbuild.2017.09.014

Longmore, J. (1975). Daylighting: a current view. *Light and Lighting, 68*, 113-119.

Lynes, J. A., & Littlefair, P. J. (1990). Lighting energy savings from daylight: Estimation at the sketch design stage. *Lighting Research & Technology, 22*(3), 129-137.

Mardaljevic, J., Heschong, L., & Lee, E. (2009). Daylight metrics and energy savings. *Lighting Research & Technology, 49*(3), 261-283.

Mattoni, B., Bisegna, F., Mangione, A., Rizzo, G., Scaccianoce, G., & Zinzi, M. (2018). Towards a More Sustainable City: The Role of the Daylight Factor in Evaluating the Energy Requirements of Buildings. *International Journal of Structural and Civil Engineering Research*, 390-394. doi:10.18178/ijscer.7.4.390-394

Mavromatidis, L. E., Marsault, X., & Lequay, H. (2014). Daylight factor estimation at an early design stage to reduce buildings' energy consumption due to artificial lighting: A numerical approach based on Doehlert and Box–Behnken designs. *Energy, 65*, 488-502. doi:10.1016/j.energy.2013.12.028

Moscoso, C., Chamilothori, K., Wienold, J., Andersen, M., & Matusiak, B. (2020). Window Size Effects on Subjective Impressions of Daylit Spaces: Indoor Studies at High Latitudes Using Virtual Reality. *Leukos*, 1-23. doi:10.1080/15502724.2020.1726183

Navvab, M. (2014). Opinion: Simulation in lighting design and research. *Lighting Research & Technology, 46*(2), 92-92. doi:10.1177/1477153514525893

Petersen, S., Momme, A. J., & Hviid, C. A. (2014). A simple tool to evaluate the effect of the urban canyon on daylight level and energy demand in the early stages of building design. *Solar Energy, 108*, 61-68. doi:10.1016/j.solener.2014.06.026

Šprah, N., & Košir, M. (2019). Daylight Provision Requirements According to EN 17037 as a Restriction for Sustainable Urban Planning of Residential Developments. *Sustainability, 12*(1). doi:10.3390/su12010315

Standardization, E. C. f. (2018). EN 17037:2018 - Daylight in Buildings. In.

Tregenza, P. R. (1995). Mean daylight illuminance in rooms facing sunlit streets. *Building and Environment, 30*(1), 83-89.

USGBC. (2018). LEED reference guide for building design and construction v4. In. Washington D.C.: U.S. Green Building Council.

Vaisi, S., & Kharvari, F. (2019). Evaluation of Daylight regulations in buildings using daylight factor analysis method by radiance. *Energy for Sustainable Development, 49*, 100-108. doi:10.1016/j.esd.2019.02.002

Xue, P., Mak, C. M., & Cheung, H. D. (2014). The effects of daylighting and human behavior on luminous comfort in residential buildings: A questionnaire survey. *Building and Environment, 81*, 51-59. doi:10.1016/j.buildenv.2014.06.011

Building Codes and Standards (11:00-12:30 h)

6th International Conference on Building Energy and Environment
Eindhoven University of Technology, The Netherlands
6 - 10 July 2025

Size-Dependent Removal Efficiency of Clean Air from Various Origins: Concerning Particles from 0.001 to 10 μm

Yiqun Li[1], Mingqi Liu[1], Yuan Wei[1], Bin Xu[2], Yuanchen Wang[3], Wei Ye[1,4,*]

[1] *School of Mechanical Engineering, Tongji University, Shanghai 201804, P. R. China*
[2] *State Key Laboratory of Pollution Control and Resource Reuse, College of Environmental Science and Engineering, Tongji University, Shanghai 200092, P. R. China*
[3] *Institute for Building Energetics, Thermotechnology and Energy Storage (IGTE), University of Stuttgart, Stuttgart, Germany*
[4] *Key Laboratory of Engineering Structure Performance Evolution and Control, Ministry of Education, Tongji University, Shanghai 200092, P. R. China*

** Corresponding email: weiye@tongji.edu.cn*

SUMMARY
Enhancing clean air systems to achieve improved indoor air quality and environmental sustainability is crucial. The COVID-19 pandemic has underscored the importance of portable air cleaners (PACs) and broadened the scope of clean air classification by integrating indoor and outdoor sources with purification technologies. This study examines particulate matter from 0.001 μm to 10 μm across three common clean air systems: mechanical ventilation and PACs. Natural ventilation was also included for comparison. A theoretical framework, validated by literature and experiments, alongside computational fluid dynamics, was developed to analyze the benefits and risks. Results indicated that over 70% of purification benefits were due to air changes per hour, with evident variation in deposition across particle sizes, affected by different indoor airflow diffusion designs. Infiltration was dual, while differences in the coagulation term were negligible. Additionally, penetration, deposition, and coagulation variations were significantly affected by building types and occupant behaviors.

Keywords: Clean air, mechanical ventilation, portable air cleaners, particles.

1. INTRODUCTION

Clean air is increasingly recognized as a fundamental human right, with the UN General Assembly declaring access to a clean, healthy, and sustainable environment a universal right in 2022. While significant efforts focus on managing outdoor air quality, equal attention is needed for indoor air, as people spend most of their time indoors (Wargocki, 2021). Ventilation is key to ensuring clean indoor air, essential for human cognitive ability and well-being (Carrer et al., 2018). Outdoor air, often deemed "fresh," can be introduced indoors through natural ventilation (NV) or mechanical ventilation (MV), with MV systems playing a crucial role in modern buildings. Despite established air change rates (ACHs) in building codes, the actual effectiveness of MV in delivering clean air can also face challenges as increasing ventilation needs and heavy energy burdens appear. Sometimes, the quality of the incoming air can also introduce health risks (Riederer et al., 2021), underscoring the need for a greater focus on the quality of air supplied indoors.

Among the various methods for providing clean air, i.e., MV, NV, and purified indoor air by

portable air cleaners (PACs), each adopts distinct principles and relies on different sources. These differences can result in variations in indoor air pollutants (IAPs) and energy consumption. Although integrating different clean air systems is becoming increasingly common, most efforts focus on simple combinations rather than evaluating their collective cleaning efficiency and corresponding air change per hour (ACH) (Li et al., 2024). An investigation into optimizing the integration is crucial to improve indoor air quality (IAQ) while maintaining energy efficiency.

In this study, theoretical methods validated through experiments and literature were employed to compare the cleaning efficiencies of MV, NV, and PAC(s) concerning particulate matter (PM), which is a well-recognized IAP with significant health risks.

2. METHODS

Eq. (1) was established to quantify the differences between the composition of clean air provided by MV, NV, or PACs. The first term on the right side of the equation represents the cleaning efficiency, which is fixed once the cleaning air systems and their corresponding filter classifications are determined. The second term accounts for the penetration rate (P), calculated using the method described by Ref (Alvin C. K. Lai and Nazaroff, 2000). Deposition and coagulation terms can be estimated based on the corresponding rates (h^{-1}), as detailed in Eq. (2) (Lv and Zhao, 2022) and Eq. (3) (Jeong et al., 2021). Secondary organic aerosol (SOA) and source terms are associated with gaseous pollutants, such as ozone, and typical occupant activities. These are models using $S_{\mathrm{SOA}}(i,t)$, as shown in Eq. (4) (Weschler and Nazaroff, 2023)), and $S(i,t)$.

$$\frac{\mathrm{d}C_{\mathrm{in}}(d_{\mathrm{p}},t)}{\mathrm{d}t} = \sum_{j=1}^{3}\{[(1-\eta_{\mathrm{PM,out},j})\cdot C_{\mathrm{out}}(d_{\mathrm{p}},t) - \eta_{\mathrm{PM,in},j}\cdot C_{\mathrm{in}}(d_{\mathrm{p}},t)]\cdot n_j\} + n_{\mathrm{s}}\cdot(P_{\mathrm{PM}} \cdot C_{\mathrm{out}}(d_{\mathrm{p}},t) - C_{\mathrm{in}}(d_{\mathrm{p}},t)) - (k_{\mathrm{d}}+k_{\mathrm{c}})\cdot C_{\mathrm{in}}(d_{\mathrm{p}},t) + \frac{S_{\mathrm{SOA}}(d_{\mathrm{p}},t)+S(d_{\mathrm{p}},t)}{V} \quad (1)$$

$$k_{\mathrm{d}} = \frac{v_{\mathrm{d,v}}\cdot A_{\mathrm{v}} + v_{\mathrm{d,u}}\cdot A_{\mathrm{u}} + v_{\mathrm{d,b}}\cdot A_{\mathrm{b}}}{V} \quad (2)$$

$$k_{\mathrm{c}}(d_{\mathrm{p}},t) = \frac{1}{C_{\mathrm{in}}(d_{\mathrm{p}},t)}[\frac{1}{2}\cdot\int_0^{d_{\mathrm{p}}}[\beta(d_{\mathrm{p}}-\overline{d_{\mathrm{p}}},\overline{d_{\mathrm{p}}})\cdot C_{\mathrm{in}}(d_{\mathrm{p}}-\overline{d_{\mathrm{p}}},t)\cdot C_{\mathrm{in}}(\overline{d_{\mathrm{p}}},t)]\mathrm{d}\overline{d_{\mathrm{p}}} - C_{\mathrm{in}}(d_{\mathrm{p}},t) \cdot\int_0^{\infty}[\beta(\overline{d_{\mathrm{p}}},d_{\mathrm{p}})\cdot C_{\mathrm{in}}(\overline{d_{\mathrm{p}}},t)]\mathrm{d}\overline{d_{\mathrm{p}}}] \quad (3)$$

$$C_{\mathrm{SOA}} \approx \xi \times C_{\mathrm{O_3,loss}} = \xi\times(C_{\mathrm{O_3,out}} - C_{\mathrm{O_3,in}}) \quad (4)$$

where $C_{\mathrm{in}}(d_{\mathrm{p}},t)$ and $C_{\mathrm{out}}(d_{\mathrm{p}},t)$ are the indoor and outdoor concentrations (#/m^3 or μg/m^3); $\eta_{\mathrm{out},j}$ and $\eta_{\mathrm{in},j}$ are the cleaning efficiencies of the j-th type of clean air for the inflow and outflow of the room; n_j is the ACH of the j-th clean air (h^{-1}); and n_{s} is the infiltration rate (h^{-1}), varied by different systems.

Computational fluid dynamics (CFD) simulations were conducted using a standardized room to analyze various clean air systems further. The dimensions of the model were based on an actual test cabin, as shown in Fig. 1. The renormalization group (RNG) $\boldsymbol{k-\varepsilon}$ turbulence model was used to obtain the friction velocity. Dimensionless factors were introduced to quantify the benefits and risks associated with each parameter per ACH of clean air, as outlined in Table 1.

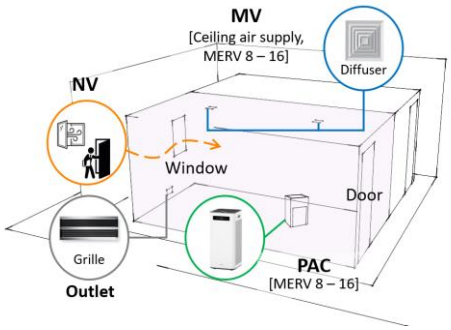

Figure 1. Schematic diagram of the room.

Table 1. Dimensionless factors

Terms	Gain Coefficient ($GC_{x,j}$)	Risk Coefficient ($RC_{x,j}$)
Clean air term	$-\eta_{\mathrm{PM,in},j}$	$(1-\eta_{\mathrm{PM,out},j})$
Penetration term	$-n_{\mathrm{s},j}/n_j$	$P_j \cdot n_{\mathrm{s},j}/n_j$
Deposition term	$k_{\mathrm{d},j}/n_j$	–
Coagulation term	$k_{\mathrm{c},j}/n_j$	–

3. RESULTS

3.1 Characterization of key factors in clean air systems

$GC_{x,j}$ and $RC_{x,j}$ across different bin sizes are shown in Fig. 2. Implementing equipped filters and improved classification systems significantly reduced the risks associated with outdoor air introduction. They enhanced the cleaning efficiency of PAC, which relied on internal recirculation. $RC_{P,MV}$ can be reduced by narrowing pressure differences, which may also diminish the dilution effects. The variation in $GC_{d,j}$ was evident across particle sizes and was affected by different air distributions. However, no significant differences were observed in $GC_{c,j}$.

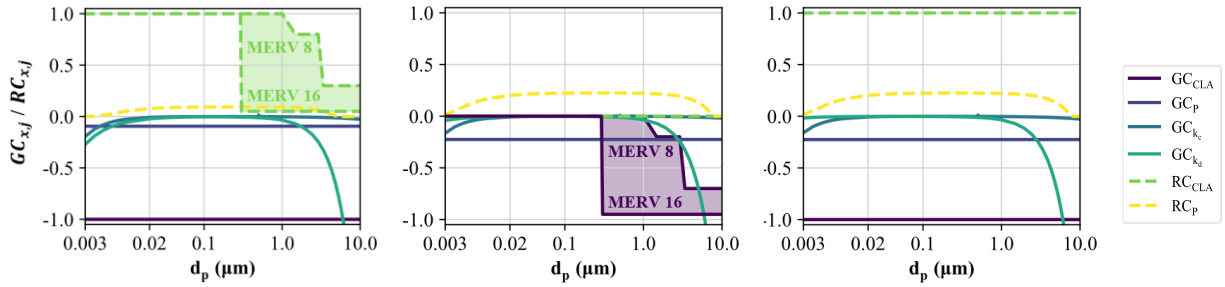

(a) MV (b) PAC (c) NV

Figure 2. $GC_{x,j}$ and $RC_{x,j}$ for clean air systems.

3.2 Comparison of concentration variations

The removal quantities were compared based on the combination of $GC_{x,j}$, $RC_{x,j}$ and I/O ratios derived from Eq. (1), illustrated in Fig. 3. A consistent trend was observed across clean air systems despite key factors varying with particle size bins. Compared to other factors, the clean air term had the most significant impact on IAQ, contributing to 69% and 79% improvements for NV and MV on average, respectively. Although infiltration can be managed under MV, this often reduces dilution effects. Due to relatively high velocities within the room, the deposition term under MV also played a crucial role. Additionally, NV posed the highest introduction risks, whereas PAC presented the least risk, though its cleaning efficiency was limited by the filter classes used. Once the building scenarios (including occupant patterns and weather conditions) and clean air systems were established, the concentration patterns were similar across the systems.

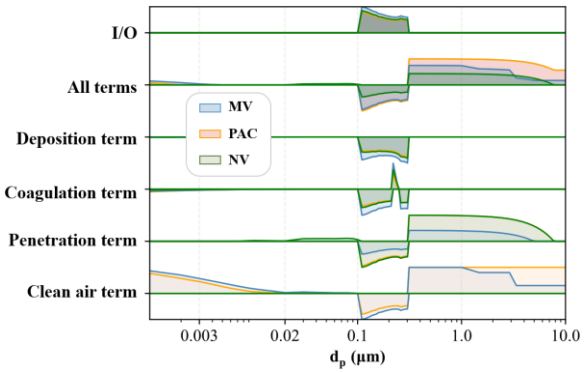

Figure 3. Variations in PM concentrations. (Positive values above the axis indicate beneficial effects).

4. CONCLUSIONS

This study employed a theoretical method to compare the cleaning efficiencies of MV, NV, and PAC concerning PM. Benefits and risk factors were evaluated, and the amounts of PM removed were calculated. The key conclusions are: 1) In the proposed model to quantify indoor air compositions, the clean air term was the most significant contributor to cleaning efficiencies, accounting for over 70% of MERV8 filters. However, the associated risks and benefits were closely linked to the classification of filters used, particularly for smaller particle size bins; 2) The performance of clean air systems was significantly affected by building types, outdoor environments, and occupant behaviors. Therefore, systems should be customized to the specific regional and building characteristics to optimize cleaning efficiency and energy consumption.

ACKNOWLEDGEMENTS

This research has been supported by the Fundamental Research Funds for the Central Universities (at Tongji University) through No. 2023-3-YB-03 and the Shanghai Professional Technical Service Platform of Smart and Low-Carbon Controlled Built Environment through No. 23DZ2290100.

REFERENCES

Alvin C. K. Lai and Nazaroff WW (2000) Modeling indoor particle deposition from turbulent flow onto smooth surfaces. *Journal of Aerosol Science*.

Carrer P, de Oliveira Fernandes E, Santos H, et al. (2018) On the Development of Health-Based Ventilation Guidelines: Principles and Framework. *Int J Environ Res Public Health* 15(7).

Jeong SG, Wallace L and Rim D (2021) Contributions of Coagulation, Deposition, and Ventilation to the Removal of Airborne Nanoparticles in Indoor Environments. *Environmental Science & Technology* 55(14): 9730-9739.

Li Y, Fan Y, Wei Y, et al. (2024) Can portable air cleaners reconcile conflicting needs for open-door/window autonomy and indoor air quality for occupants in densely populated offices? *Applied Energy* 358.

Lv L and Zhao B (2022) Deposition of non-spherical particles on indoor surfaces: Modification of diffusion coefficient. *Aerosol Science and Technology* 56(12): 1190-1200.

Riederer AM, Krenz JE, Tchong-French MI, et al. (2021) Effectiveness of portable HEPA air cleaners on reducing indoor PM2.5 and NH3 in an agricultural cohort of children with asthma: A randomized intervention trial. *Indoor Air* 31(2): 454-466.

Wargocki P (2021) What we know and should know about ventilation. *REHVA Journal* 58(2): 5-13.

Weschler CJ and Nazaroff WW (2023) Ozone Loss: A Surrogate for the Indoor Concentration of Ozone-Derived Products. *Environmental Science & Technology*. DOI: 10.1021/acs.est.3c03968.

6th International Conference on Building Energy and Environment
Eindhoven University of Technology, The Netherlands
6 - 10 July 2025

Flood resilience for Australian houses: The case for biomimetic wet-proofing to encourage building retention after flooding

Christopher Jensen [1], Jane Toner [2]

[1]*Melbourne School of Design, University of Melbourne, Melbourne, Australia, cjensen@unimelb.edu.au*

[2]*Griffith University, Brisbane, Australia, jane.toner@griffithuni.edu.au*

SUMMARY
Australian homes are increasingly vulnerable to flooding, often leading to demolition or costly repairs. Climate change is driving more frequent and severe flooding, and the impacts are compounded by poor land use planning and limited adoption of flood resilient construction practices. Despite the escalating risks, Australian building regulations are relatively simplistic and lag behind best practice for flood resilience. Biomimicry – the practice of emulating adaptive strategies from living systems – offers promising opportunities to enhance flood resilience in the built environment. By learning from nature's adaptations for managing water, biomimetic design can contribute to reducing the social, economic and environmental impacts of flooding in the built environment. This research investigates how biomimetic solutions could be integrated into the design, construction and operation of Australian residential construction to improve flood resilience within the constraints of the existing building code.

Keywords: flood, resilience, biomimicry, built environment, housing

1. INTRODUCTION

1.1 Flood Risk in Australia

Flood events are already causing significant damage across urban and regional areas of Australia (De Wilde, 2014), with climate models providing medium to high levels of confidence that climate change will further intensify extreme weather events (The Climate Council, 2017). In Australia, floods cause more damage on average than any other natural disaster. From 1967 to 1999, the total cost of floods is estimated at $10.4 billion or 29% of the average proportional annual cost of natural disasters. More recently in 2021 and 2022, flood events in Queensland and New South Wales caused $6.3 billion in damages making them Australia's most expensive natural disaster, much of which is due to unrecoverable building damage (Insurance Council of Australia, 2024). Between 2005 and 2022, the Australia government spent $24.5b on natural disasters, most of this ($23.99b) was for post disaster relief programs, while only $0.51b was for initiatives focused on building resilience (The McKell Institute, 2022). This reactive approach suggests a limited understanding of the opportunities available to reduce post-disaster relief costs by supporting resilient design. A recent report, 'Resilience, Durability in the National Construction Code (NCC)', highlights that the current Australian Building Codes Board (ABCB) flood standard " ...is designed to reflect the current NCC objectives of health, safety, amenity and sustainability, so it primarily focuses on structural safety and life safety, rather than building resilience" (The Centre for International Economics, 2023). This narrow focus overlooks the unsustainable impacts of post-flood building rectification, demolition and reconstruction.

1.2 Current Building Regulations in Australia

Flood mitigation in Australia typically focuses on urban-scale interventions. However, strategies at the building-scale, including material specifications are also critical for reducing flood damage. Flood resilience for new housing is currently addressed by two consecutive mechanisms (Victorian Building Authority, 2023). First, local planning provisions designate flood-prone zones developed in consultation with floodplain management authorities. Estimated flood heights are usually based on the 100-year average recurrence interval (ARI) derived from historical flood data. Second, the National Construction Code (NCC) specifies minimum floor heights and freeboard requirements for new construction. From an architectural perspective, compliance can be achieved by raising the habitable floor level above the minimum freeboard, as shown in Figure 1.

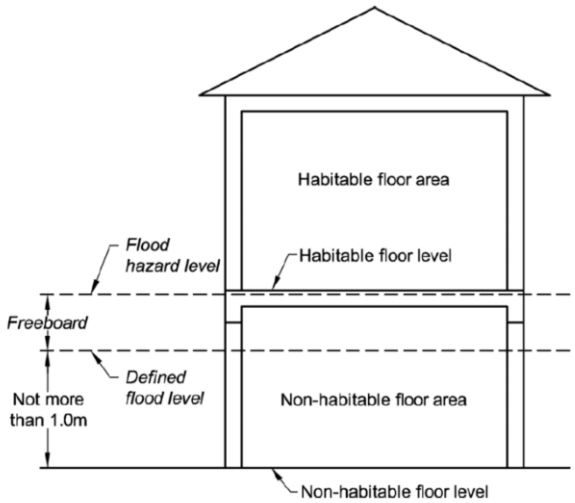

Figure 1: Current Australian building regulations define habitable floor levels based on historical flood data

This raises two key challenges: 1) current building regulations fail to address the increasing flood risks associated with climate change, and 2) they do not encourage or allow innovative alternative solutions. These limitations are compounded by standard construction practices in Australia, which rely on materials and methods poorly suited to flood resilience. Typical construction methods include concrete slab-on-ground floors, and materials vulnerable to water damage such as plasterboard, timber framing and low-lying electrical wiring. As a result, even minor flooding can lead to costly rectification works or demolition.

2. LITERATURE REVIEW

1.3 Existing Knowledge of Flood Resilience

Flood mitigation research has largely focused on ‘hard’ infrastructure solutions at the urban scale (Bignami et al., 2019), such as dykes and embankments in the Netherlands (Vis et al., 2003) and dams in Australia (Cook, 2023). More recently, attention has shifted towards exploring ‘soft’ green infrastructure alternatives, such as water sensitive urban design (DFAT AWP, 2022) and green roofs (Cook et al., 2019). China’s ‘sponge city’ concept, for example, is designed to detain and slow water flow by absorbing and storing rainwater, mitigating the effects of urban flooding, with a goal of enabling 80% of urban areas to harvest and reuse 70% of rainwater (Griffiths et al., 2020). While these strategies are proving effective at catchment scale, less attention has been given to improving flood resilience at property or building scale. Building scale mitigation strategies can be grouped in three categories: 1) elevation - raising buildings above a fixed flood level or by

allowing it to float, 2) dry-proofing to prevent water entry, and 3) wet-proofing - allowing controlled water entry while minimising damage through materials and design choices that optimise recoverability (Ameh et al., 2024). Each strategy presents design challenges for architects, including planning and site constraints, limited material options, and resistance to innovation within the construction industry.

From a design perspective, *elevation* above a defined flood level can be achieved with either a fixed elevated structural platform, or by allowing dynamic elevation (flotation) - a more complex solution. Elevation is the primary strategy for flood resilience defined in the National Construction Code (NCC) (ABCB, 2019), however, this creates limitations in design, such as maximum height limits to prevent overshadowing of neighbouring properties. The NCC currently has no provisions for floating structures, instead requiring footing systems to resist flotation or significant permanent movement. *Dry-proofing* involves sealing a building (or enclosures within it) to prevent water entry. Dry-proofing relies on resisting hydrostatic forces (the pressure from standing or slow-moving water) by sealing openings such as windows and doors; ensuring water-tight construction systems (especially at floor-to-wall junctions); applying waterproofing sealant to walls and floors to reduce seepage, and installing floor drains and sump pumps to manage residual water (USACE, 1995). However, typical Australian construction methods make dry-proofing hard to achieve, as the comprehensive sealing required often conflicts with other regulatory requirements, such as cavity ventilation and managing hydrostatic pressure. *Wet-proofing* offers a viable solution when flood is infrequent and of short duration (De Graaf et al., 2012). Key strategies include: installing flood openings to automatically equalize hydrostatic forces on exterior walls; anchoring buildings to resist flotation, collapse, and lateral movement; using water-resistant materials below the base flood elevation; and elevating mechanical and utility equipment or by configuring components to minimize damage (FEMA, 2022). While wet-proofing is widely used in flood prone regions globally, it is rarely adopted in Australian buildings.

1.4 Lessons from Nature

Guided by the overarching philosophy that ‘life creates conditions conducive to life’ (Benyus & Morrow, 1998), biomimicry is an innovative discipline that looks to the natural world for sustainable design solutions (Baumeister & Tocke, 2014). Biomimetic strategies are considered at three nested levels: organism, behaviour and ecosystem (Zari, 2018). Over deep time, nature has evolved materials, forms, processes and networked systems to meet complex dynamic challenges imposed by the environment, from macro to nanoscale (Bhushan, 2009). As living systems are dependent on water for survival, nature has adapted and evolved numerous functional strategies to manage it, such as harvesting, storing, distributing, absorbing and filtering. These natural strategies offer a wide range of innovative solutions that can be applied by biomimicry design thinking to address challenges in the built environment. In this paper, biomimicry is presented as a method for developing alternative solutions to enhance the flood resilience of buildings by emulating nature’s efficient and resilient strategies.

1.5 Knowledge Gap

Current building practices and regulations limit the adoption of alternate solutions for flood resilience in Australian housing. Biomimicry - innovation inspired by nature - offers significant potential to overcome these challenges, with a growing body of research and practical applications for responding to rising water levels at ecosystem scale. However, research on biomimetic

solutions specifically aimed at enhancing flood resilience at the building scale remains limited.

3. METHODOLOGY

This paper addresses the knowledge gap identified by exploring a biomimetic approach to translate nature's solutions for managing water into architectural design solutions. The aim is to apply biomimicry tools developed by Biomimicry 3.8, pioneers of the interdisciplinary process of translating nature's strategies into design principles for technological innovation (Vincent et al., 2006). 'Biomimicry Thinking' is an adaptive framework for integrating biomimicry into the design process across disciplines and scales (Biomimicry 3.8, 2015). The process is flexible, can begin at any stage, and iteration is encouraged to refine and optimise design solutions. In this study, the Biomimicry Thinking Challenge to Biology (Figure 2) is used to address the specific challenge of improving flood resilience in the built environment.

Figure 2: Biomimicry DesignLens. At left, Biomimicry Thinking - Challenge to Biology. At right, Life's Principles (2015 Biomimicry 3.8 CC-BY-NC-ND)

'Life's Principles' are overarching patterns that all living systems follows to survive and thrive (Biomimicry 3.8, 2015). They serve both as a guide and evaluation tool within the design process, encouraging alignment with living systems (Ilieva et al., 2022). For example, "cultivating cooperative relationships", encourages designers to adopt practices that encourage mutually beneficial relationships, much like those found in flourishing ecosystems (Stevens et al., 2022). Applying Life's Principles as evaluation criteria can reveal limitations in current practices and identify opportunities for more sustainable outcomes. For instance, the principle of 'recycling all materials', challenges the widespread use of building materials that end up in landfill after flood damage, indicating the need for new, regenerative material systems. This research applies the four main stages of the Biomimicry Thinking - Challenge to Biology process as outlined in Table 1.

Table 1: Biomimicry Thinking process and how it has been addressed at each design stage

Design Stage and Steps	**How this has been addressed**	**Structure of this research**
SCOPING: Define context. Identify functions needed to 'solve the challenge'.	Literature review established context and identified relevant functions	Literature review
DISCOVERING: Discover natural models (forms, processes, systems) that embody required functions. Abstract design principles from strategies.	Conducted 'biological brainstorm' to identify natural models addressing required functions. Generated abstracted design principles.	Results (See Table 2)

CREATING: Develop bio-inspired ideas from design principles. Design solutions that integrate abstracted design principles.	Explored human solutions like those identified in nature to identify gaps and opportunities for further research.	Discussion
EVALUATING: Apply Life's Principles to assess solutions and identify where they can be refined.	To be addressed in future research.	Future research

4. RESULTS

In the *Discovering* stage, a 'biological brainstorm' was conducted to identify organisms, processes and systems in nature that demonstrate effective flood resilience strategies. This involved reviewing relevant literature, consulting the AskNature database, and drawing on our own experience. The results are summarized in Table 2 under the three categories of flood resilient design: avoiding flood, dry-proofing and wet-proofing - with each functional strategy framed as a question for nature, such as, "How does nature anchor structures in water?"

Table 2: Biomimetic flood resilience strategies identified in the literature

Functional strategy	**Biological Inspiration (ref)**	**Abstracted design principles (biological references removed from description)**	**Similar Human Design Solution/s**
Avoiding Flood water			
Physically Avoid	Wombats (Triggs, 2009)	Leave accommodation during flooding and return when waters recede.	Behavioral - Occupants leave house
Physically avoid / Anchor	Mangrove dwelling ants (Nielsen, 1997)	Elevate critical openings above anticipated flood levels. Incorporate self-sealing and air-trapping mechanisms to adapt to flooding.	Elevate floor levels. Adaptive sealing systems.
Divert flow	Ground squirrels (Shuker, 2001)	Use raised circular barriers around openings to divert water away and prevent water ingress.	Hard structures (dykes). Make-shift structures (sandbags)
Anchor / Float	Peatland Plants (Rydin et al., 2013)	Platforms with adjustable buoyancy, interconnected anchoring systems that allow vertical movement while remaining in place	Amphibious Architecture
Dry-proofing			
Prevent water penetration	Platypus & Sea Otter fur	Dual layer, high-density, textured materials that combine water repellency with air-trapping insulation.	Closed cell foam insulation
Repel water	Lotus effect (Nature's Raincoats, 2025)	Micro- and nano-scale textures enhance water resistance of surfaces and promote self-cleaning.	Super-Hydrophobic, self-cleaning materials (Hsu & Sigmund, 2010)
Wet-proofing			
Anchor	Mangroves (Méndez-Alonzo et al., 2015)	Flexible interconnected structural elements and anchoring systems within permeable barriers to stabilise structures and moderate water flow.	Flexible anchors. Sediment traps that mitigate coastal erosion.
Prevent fungus / bacteria	Plasterer Bees (Ask Nature, 2025)	Apply bio-inspired, water tolerant surface coatings that inhibit microbial growth using life-friendly chemistry.	Bio-plastics. Water resistant wall assemblies.
Protect from microbes / fouling	Long-finned Pilot Whale (Baum et al., 2002)	Use textured, enzyme active surfaces to reduce bio-fouling and maintain surface performance during prolonged water exposure.	Anti bio-fouling surfaces

This rapid bio-brainstorm reveals a range of strategies nature has evolved to manage water inundation. While these strategies have been grouped as flood resilient design responses, in

practice nature rarely relies on a single approach. Instead, organisms combine multiple strategies depending on context, creating redundancy and enhancing resilience. For example, some species elevate themselves and use water-resistant materials. This suggests that buildings may achieve greater adaptive resilience by integrating a combination of flood-resilient strategies.

5. DISCUSSION - FLOOD RESILIENCE STRATEGIES

At the behavioural level, animals relocate to higher ground during floods (elevation), a strategy also used by humans. However, like plants buildings are 'rooted in place' and must rely on structural solutions. Fixed elevation above flood levels using structural supports is a relatively straightforward concept that forms the primary strategy prescribed by Australian regulations. Plants such as mangroves and floodplain trees offer inspiration for lightweight, flexible, and adaptive anchored structures responsive to the dynamics of floodwaters. Another elevation strategy is flotation, achieved through internal air spaces that provide buoyancy, such as the air-filled structures of waterlily pads. In the built environment, this is reflected in the concept of amphibious architecture – floating buildings designed to respond dynamically to fluctuating flood levels (Ameh et al., 2024). While a promising solution, amphibious architecture has practical challenges, including planning restrictions, structural complexity and cost barriers.

In nature, adaptability is more common than total exclusion (dry-proofing), yet some organisms have evolved highly effective strategies to remain dry through surface design and material properties. Notable examples include the superhydrophobic 'lotus effect' and the water shedding properties of cicada wings – both achieved by nano-scale surface architecture. While these principles have informed the development of water repellent coatings, at this time their application to buildings remains limited, particularly at the scale and durability required for flood resilience. Biomimetic waterproof sealants, inspired by organisms such as mussels and sandcastle worms, offer promising solutions for dry-proofing by enabling strong durable adhesion in wet conditions where conventional materials might fail. Dry-proofing a building requires comprehensive sealing of all potential water entry points, such as doors, structural vents and air ventilation openings, similar to how a boat is treated. In Australia, achieving this level of dry-proofing is challenging with typical construction techniques and would require a complete rethink of the building design and construction methods. Avoiding flooding by employing ecosystem level strategies such as levies and dykes, and water sensitive urban design are more practical dry-proofing solutions to protect buildings, neighbourhoods and cities at risk from elevated water levels.

Wet-proofing tolerates occasional inundation while minimising damage, emulating how natural ecosystem adapt to periodic inundation flooding. This strategy deliberately allows water to flow through a building, reducing structural stress. For example, passive flood vents could be designed to activate in response to rising water levels, similar to how pinecones open and close using passive material movements that respond to moisture. Australian regulations restrict the use of wet-proofing to non-habitable spaces, significantly limiting its application and creating dependence on other strategies. Many plants adapt to flooding by layering hydrophobic materials to protect their core from water – a principle that could inform the specification of flood tolerant finishes and materials for habitable areas. True hydrophobic materials are rare, but some common building materials, like masonry, can absorb and release water without lasting damage. Crucially, it is not just individual materials but complete construction systems that must withstand flooding without causing long-term damage or mould growth. Vulnerable elements, such as electrical systems will

still require elevation or dry-proofing in small areas. While elevation and dry-proofing strategies are found in nature, natural systems often utilise wet-proofing to accommodate temporary flooding. For buildings, this is a valuable insight, as immoveable structures will inevitably experience water ingress during flood events.

6. CONCLUSIONS

In line with climate change projections, Australian houses are increasingly vulnerable to flooding, which now causes more damage than any other disaster. At the building scale, current Australian building regulations remain simplistic and limit the adoption of innovative flood resilience solutions. Nature offers inspiring strategies to inform biomimetic solutions for flooding. Among these, plant-inspired strategies offer valuable insights for buildings, which like plants are fixed in place during floods. Strategies such as anchored flotation, structural resistance to hydrostatic forces, and the use of hydrophobic materials suggest how buildings might better withstand temporary inundation and recovery without lasting damage. These approaches remain under-utilized in Australian housing due to regulatory barriers. However, modest adaptations of the regulations such as permitting wet-proofing in habitable spaces, specifying water-resistant materials, incorporating openings to manage water flow, and elevating services, could enable the practical application of these biomimetic strategies and encourage further innovation. Further research is needed to explore international examples of wet-proofing and to test their suitability for the Australian context.

7. REFERENCES

ABCB. (2019). Construction of buildings in flood hazard areas-ABCB Standard 2012.3.

Ameh, H., Badarnah, L., & Lamond, J. (2024). Amphibious Architecture: A Biomimetic Design Approach to Flood Resilience. *Sustainability*, *16*(3), 1069.

Ask Nature. (2025). *Secretion Waterproofs Nest*. Retrieved 25/01/2025 from https://asknature.org/strategy/secretion-waterproofs-nest/

Baum, C., Meyer, W., Stelzer, R., Fleischer, L.-G., & Siebers, D. (2002). Average nanorough skin surface of the pilot whale (Globicephala melas, Delphinidae): considerations on the self-cleaning abilities based on nanoroughness. *Marine Biology*, *140*, 653-657.

Baumeister, D., & Tocke, R. (2014). Biomimicry resource handbook: a seed bank of best practices. Biomimicry 3.8.

Benyus, J. M., & Morrow, W. (1998). Biomimicry: innovation inspired by nature. In: Harper Collins.

Bhushan, B. (2009). Biomimetics: lessons from nature–an overview. Philosophical Transactions of the Royal Society A: Mathematical, Physical and Engineering Sciences, 367(1893), 1445-1486.

Bignami, D. F., Rosso, R., & Sanfilippo, U. (2019). *Flood proofing in urban areas*. Springer.

Biomimicry 3.8. (2015). Biomimicry Design Lens: a visual guide.

Cook, M. (2023). A River with a City Problem: A History of Brisbane Floods University of Queensland Press.

Cook, S., van Roon, M., Ehrenfried, L., LaGro Jr, J., & Yu, Q. (2019). WSUD "best in class"—case studies from Australia, New Zealand, United States, Europe, and Asia. In *Approaches to water sensitive urban design* (pp. 561-585). Elsevier.

De Graaf, R., Roeffen, B., Czapiewska, K., Dal Bo Zanon, B., Lindemans, W., Escarameia, M., Walliman, N., & Zevenbergen, C. (2012). The effectiveness of flood proofing vulnerable hotspots to improve urban flood resilience. *Comprehensive flood risk management*, 1351-1358.

De Wilde, P. (2014). The gap between predicted and measured energy performance of buildings: A framework for investigation. *Automation in Construction*, *41*, 40-49.

DFAT AWP. (2022). The Sukhumvit Green Triangle Case Study Report. Valuing the Benefits of Nature-based Solutions for Integrated Urban Flood Management in the Greater Mekong Region.

Dundar Arisoy, F., Kolewe, K. W., Homyak, B., Kurtz, I. S., Schiffman, J. D., & Watkins, J. J. (2018). Bioinspired photocatalytic shark-skin surfaces with antibacterial and antifouling activity via nanoimprint lithography. *ACS applied materials & interfaces*, *10*(23), 20055-20063.

FEMA. (2022). *Wet Floodproofing Requirements and Limitations*. https://www.fema.gov/sites/default/files/documents/fema_nfip-technical-bulletin-7-wet-floodproofing-guidance.pdf
Fernandes, M. C., Aizenberg, J., Weaver, J. C., & Bertoldi, K. (2021). Mechanically robust lattices inspired by deep-sea glass sponges. *Nature Materials*, *20*(2), 237-241. https://doi.org/10.1038/s41563-020-0798-1
Gandyra, D., Walheim, S., Gorb, S., Ditsche, P., Barthlott, W., & Schimmel, T. (2020). Air retention under water by the floating fern Salvinia: The crucial role of a trapped air layer as a pneumatic spring. *Small*, *16*(42), 2003425.
Griffiths, J., Chan, F. K. S., Shao, M., Zhu, F., & Higgitt, D. L. (2020). Interpretation and application of Sponge City guidelines in China. *Philosophical Transactions of the Royal Society A*, *378*(2168), 20190222.
Hsu, S.-H., & Sigmund, W. M. (2010). Artificial Hairy Surfaces with a Nearly Perfect Hydrophobic Response. *Langmuir*, *26*(3), 1504-1506. https://doi.org/10.1021/la903813g
Ilieva, L., Ursano, I., Traista, L., Hoffmann, B., & Dahy, H. (2022). Biomimicry as a sustainable design methodology—Introducing the 'Biomimicry for Sustainability' framework. *Biomimetics*, *7*(2), 37.
Insurance Council of Australia. (2024). *Insurers welcome Parliamentary report into 2022 flood response* https://insurancecouncil.com.au/resource/insurers-welcome-parliamentary-report-into-2022-flood-response/
Méndez-Alonzo, R., Moctezuma, C., Ordoñez, V. R., Angeles, G., Martínez, A. J., & López-Portillo, J. (2015). Root biomechanics in Rhizophora mangle: anatomy, morphology and ecology of mangrove's flying buttresses. *Annals of Botany*, *115*(5), 833-840.
Nature's Raincoats. (2025). *Adaptation of plants to water*. Retrieved 24/01/2025 from https://naturesraincoats.com/adaptation-of-plants-to-water/
Nielsen, M. (1997). Nesting biology of the mangrove mud-nesting ant Polyrhachis sokolova Forel (Hymenoptera, Formicidae) in northern Australia. *Insectes Sociaux*, *44*, 15-21.
Rydin, H., Jeglum, J. K., & Bennett, K. D. (2013). *The biology of peatlands, 2e*. OUP Oxford.
Shuker, K. (2001). The hidden powers of animals: uncovering the secrets of nature. Reader's Digest Association.
Stevens, L. L., Whitehead, C., & Singhal, A. (2022). Cultivating cooperative relationships: Identifying learning gaps when teaching students systems thinking biomimicry. *Biomimetics*, *7*(4), 184.
The Centre for International Economics. (2023). *Resilience, Durability and the National Construciton Code*. https://www.thecie.com.au/publications-archive/resilience-durability-and-the-national-construction-code
The Climate Council. (2017). Critical Decade 2017: Accelerating Climate Action. https://www.climatecouncil.org.au/uploads/6d762163fc81535d1813585d8ad43854.pdf
The Climate Council. (2022). Uninsurable Nation: Australia's most climate vulnerable places. https://www.climatecouncil.org.au/wp-content/uploads/2022/05/CC_Report-Uninsurable-Nation_V5-FA_Low_Res_Single.pdf
The McKell Institute. (2022). *The Cost of Extreme Weather*. https://insurancecouncil.com.au/wp-content/uploads/2022/09/McKell_Cost-of-Natural-Disasters_SINGLES_WEB.pdf
Triggs, B. (2009). *Wombats*. CSIRO PUBLISHING.
Turner, C., Frankel, M., & Council, U. G. B. (2008). *Energy performance of LEED for new construction buildings*. New Buildings Institute Washington, DC.
USACE. (1995). *Flood Proofing Regulations* (U. S. A. C. o. Engineers, Ed.).
Victorian Building Authority. (2023). Flood Hazard FH 01 | Building in flood hazard areas.
Vincent, J. F., Bogatyreva, O. A., Bogatyrev, N. R., Bowyer, A., & Pahl, A.-K. (2006). Biomimetics: its practice and theory. *Journal of the Royal Society Interface*, *3*(9), 471-482.
Vis, M., Klijn, F., De Bruijn, K., & Van Buuren, M. (2003). Resilience strategies for flood risk management in the Netherlands. *International journal of river basin management*, *1*(1), 33-40.
Whittlesey, R. W., Liska, S., & Dabiri, J. O. (2010). Fish schooling as a basis for vertical axis wind turbine farm design. *Bioinspiration & biomimetics*, *5*(3), 035005.
Zari, M. P. (2018). Regenerative urban design and ecosystem biomimicry. Routledge.
Zari, M. P., Connolly, P., & Southcombe, M. (2020). Ecologies design: Transforming architecture, landscape, and urbanism. Routledge.

6th International Conference on Building Energy and Environment
Eindhoven University of Technology, The Netherlands
6 - 10 July 2025

Overheating investigation and mitigation in Canadian social housing dwellings: an empirical study

Farid Bahiraei [1], Zahra Jandaghian [1], Marzieh Riahinezhad [1]

[1] *National Research Council Canada, Ottawa, ON K1A 0R6, Canada*
Farid.Bahiraei@nrc-cnrc.gc.ca, Zahra.Jandaghian@nrc-cnrc.gc.ca, Marzieh.Riahinezhad@nrc-cnrc.gc.ca

SUMMARY
As the impacts of climate change become more evident, maintaining healthy indoor air quality (IAQ) and preventing overheating are becoming increasingly critical. Canadian buildings, traditionally designed to retain heat, now face challenges due to more frequent and intense heatwaves. Older social housing stock, in particular, lacks adequate IAQ monitoring and management with insufficient data on indoor conditions. This study examines indoor conditions in selected social housing units in Western Canada. Using Internet of Things (IoT) sensors, we monitored IAQ in 20 social housing dwellings. Findings indicate a tendency for these units to overheat, often exceeding comfort thresholds, even with moderate outdoor temperatures. It was shown that sole reliance on weather observations and forecasts can misclassify indoor overheating and its effects. To address this, an automated predictive model was developed to forecast indoor temperatures 24 hours in advance, acting as an early warning system for building managers to efficiently respond to potential overheating events.

Keywords: Indoor overheating, social housing, mitigation strategy, predictive modeling

1. INTRODUCTION

Overheating and prolonged periods of hot weather can have a significant impact on increasing mortality and morbidity. Studies have demonstrated a significant increase in mortality due to heat stress in various Canadian cities (Jandaghian and Akbari 2018, Boudreault *et al.* 2024). Occupants of social housing dwellings are among the most vulnerable to extreme heat (Morey *et al.* 2020). However, there has been limited research on these buildings within the Canadian context. (Laouadi *et al.* 2023) developed an approach that combines the building simulation and bioheat models to generate health-based limit criteria for overheating in long-term care homes. They calibrated their building simulation models using indoor temperature and humidity measurements, allowing the method to predict overheating risks consistent with overall thermal comfort during extreme heat events, in contrast to the comfort-based methods. (Wang et al. 2020) conducted a series of field measurements and simulation studies to assess the overheating risks in vulnerable buildings in Montreal, Canada.

Despite the limited research on social houses, several studies have shown that the impacts of heatwaves in Canada are profound and far-reaching and they are linked to excess mortality and illness caused by elevated indoor temperatures (Khan et al. 2024). Therefore, it is crucial to better understand the indoor conditions in the vulnerable Canadian built environment. Understanding how indoor conditions vary during heatwaves is essential for mitigating the potential impacts of overheating on occupants' wellbeing. Regardless of the overheating mitigation strategy, advanced warning of impending indoor heat exposure risks is critical to minimize future heat-related health risks (Gustin et al. 2020). An early warning of high indoor temperatures can help ensure that healthcare staff and resources are fully prepared for hot weather periods that might impact health. This is particularly relevant for large portfolios of social housing, where prioritizing resources is essential during heatwaves. Therefore, the main focus of this work is to examine the variability of indoor heat exposure in selected vulnerable buildings located in Western Canada and develop an indoor temperature forecasting platform to mitigate the effects of indoor overheating on social housing occupants.

2. METHODOLOGY

2.1. DATASET

We measured indoor conditions in 20 dwellings across three different buildings, all serving as social housing and constructed around the 1970s. Unlike newly built social housing units, these older buildings have demonstrated vulnerability to recent extreme heat events in Western Canada and therefore, were selected for this study. The details of the monitored buildings and dwellings are provided in Table 1. The data collection began in June 2024 and contained until September 15, 2024. All monitored dwellings are studio units, consisting of a single living area used both during the day and at night. None of the units are equipped with a mechanical cooling system. We installed sensors at the thermostat height in locations shielded from direct solar radiation. These sensors recorded indoor temperature and relative humidity at 30-minute intervals. Data was transferred via LoRaWAN technology, to allow for near real-time uploads to a central cloud database. Additionally, hourly weather forecast data was retrieved from the nearest weather station using the Environment and Climate Change Canada (Government of Canada 2024) portal.

Table 1. Characteristics of the monitored buildings

Building	Number of dwellings in building	Monitored dwellings floor	Orientation
A	4	2	North-South
B	8	2 and 5	East-West
C	8	2 and 7	East-West

2.2. INDOOR OVERHEATING ASSESSMENT CRITERIA

The critical review by (Rahif et al. 2021) analyzed the overheating evaluation methods for residential buildings and examined five European national building codes. They found that most standards recommend static comfort models for air-conditioned buildings and adaptive comfort models for non-air-conditioned ones. In Canada, there is a growing focus on addressing indoor overheating in both national and provincial building codes. Notably, the British Columbia Building Code recently introduced a new provision to minimizing the risks to health and safety due to overheating in dwelling units (BC Government 2024). This provision advises that each dwelling unit should have a living space capable of maintaining an indoor design temperature of no more than 26°C. Although more comprehensive overheating criteria can provide valuable insights into the effects of indoor conditions on the occupants, in this work, we adopted the British Columbia Building Code's overheating provision. While this provision is primarily recommended for newly constructed dwellings, it is formulated to mitigate the dangers of indoor overheating and, therefore, may be employed to evaluate heat exposure risks in existing buildings. Comparing indoor conditions in existing buildings against this provision offers insights into the performance of the current social housing units and helps identifying required retrofit measures to achieve the recommended safe indoor conditions. Furthermore, using this criterion ensures the results are comparable to other studies and can be easily reproduced.

3. RESULTS AND DISCUSSION

3.1. INDOOR CONDITIONS VARIATION WITH BUILDING CHARACTERISTICS

The investigated dwellings in each building are located on different floor levels with various orientations (see Table 1), but are equal in size, floor plan and window to wall ratio. Consequently, this section focuses on analyzing the building characteristics related to floor level and orientation.

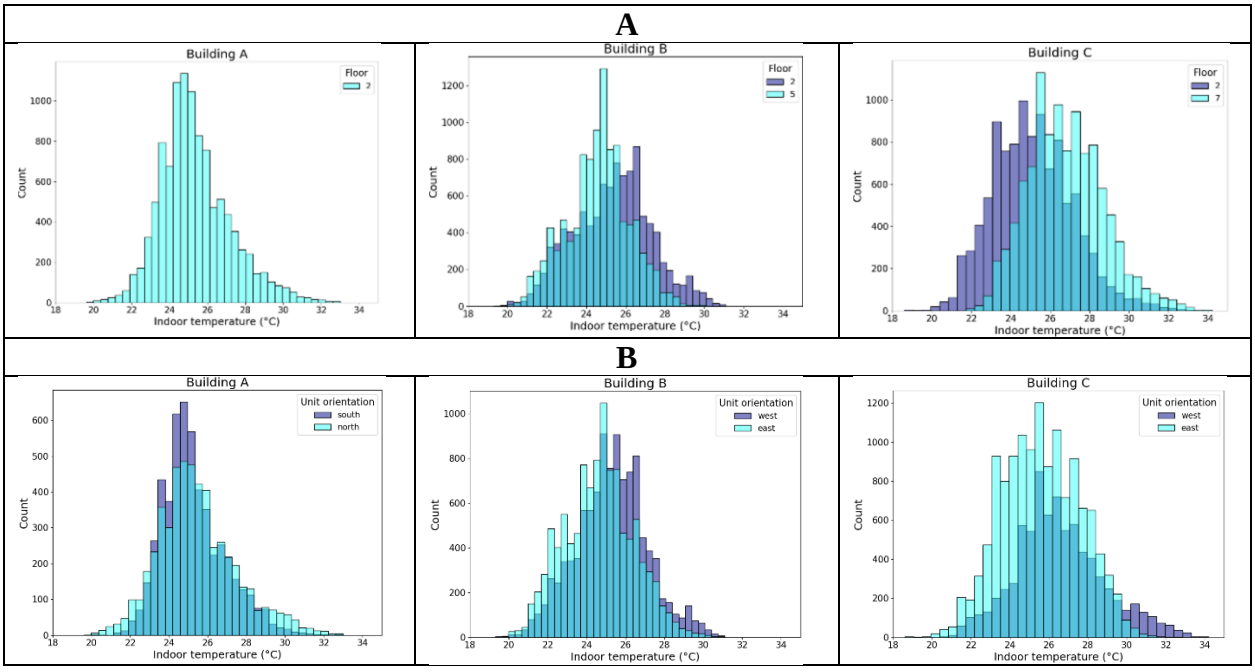

Figure 1. Distribution of hourly indoor temperature measurements with floor level

We aim to investigate whether a basic characteristic, such as orientation, can help pre-determine potentially more vulnerable dwellings within a building. Figure 1A shows the distribution of the indoor temperature for dwellings on different floor levels. The indoor temperatures on the upper floor tend to be higher in Building C, however, this pattern is not observed in Building B. As shown in Figure 1B, west-facing dwellings in Buildings B and C experienced a higher indoor temperature, likely due to increased solar gain in west facing dwellings. In contrast, Building A showed no significant difference in indoor temperatures between north- and south-facing dwellings. Overall, basic dwelling characteristics, such as the floor level or orientation, influence indoor temperature inconsistently. Similar patterns were reported by (Walikewitz *et al.* 2018), suggesting that indoor temperatures are strongly affected by other factors, such as occupant behaviour and outdoor conditions.

3.2. INDOOR TEMPERATURE VARIATION WITH OUTDOOR CONDITIONS

Heat exposure of a population is often estimated using outdoor temperature values. In this section, we examine whether outdoor conditions can reliably indicate the risk of indoor overheating in buildings housing vulnerable occupants. In Canada, humidex rating is used to inform the public about uncomfortable heat and humidity conditions (CCOHS 2024).

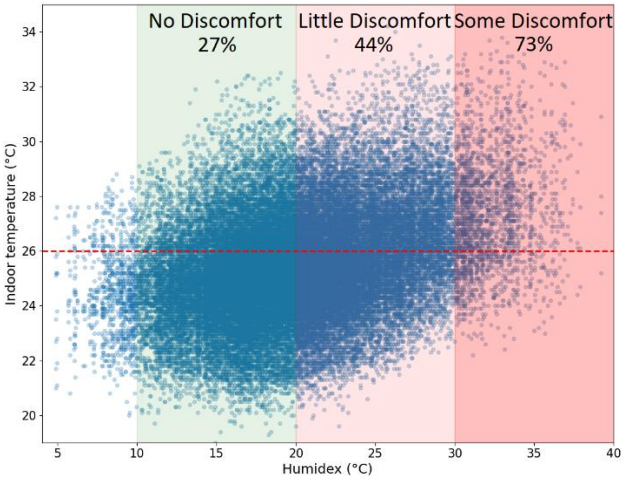

Figure 2. Variation of indoor temperature with outdoor humidex values. Outdoor humidex range descriptions used by Environment Canada are shown. In contrast, percentage values show the fraction of hourly indoor temperatures above 26^{o}C in each range.

Humidex combines temperature and humidity, measured at weather stations, to reflect the perceived temperature. Figure 2 shows the variation in measured indoor temperatures across all dwellings relative to outdoor humidex values. The humidex threshold values are sourced from (CCOHS 2024), and the 26^{o}C indoor temperature threshold from BC Building Code is also displayed. Although, as expected, there is a correlation between indoor and outdoor humidex values, elevated indoor temperatures (i.e., above 26°C) can frequently happen even when outdoor conditions are classified as “no discomfort” or “little discomfort”. This finding underscores the limitations of using outdoor conditions alone to assess the risk of indoor overheating. To better

understand indoor conditions in the studied dwellings, Figure 3 shows the percentage of time during which the indoor temperature exceeded the maximum temperature limit recommended by the BC Building Code. This figure highlights significance discrepancies between dwelling units, even within the same building. As Figure 1 suggests, this variance may primarily be attributed to occupants' behavior and unmeasured mitigation strategies, such as using blinds or opening windows.

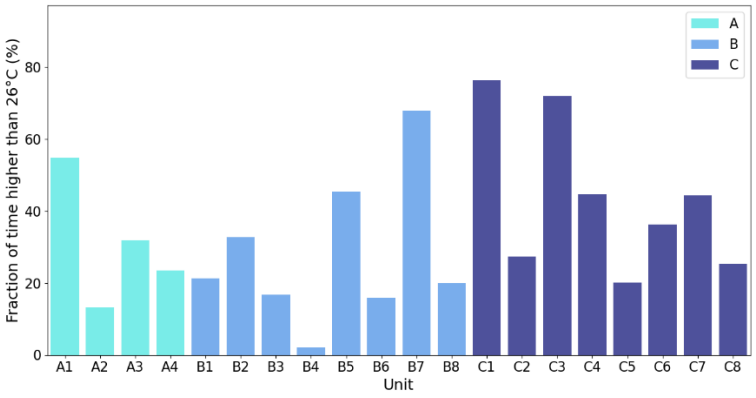

Figure 3. Fraction of time with indoor temperature higher than 26°C for each dwelling

Furthermore, the high indoor temperatures may occur even during relatively mild outdoor conditions, as shown in Figure 2. This emphasizes the need for both short-term and long-term mitigation strategies that prioritize indoor conditions rather than relying solely on weather forecasts.

4. INDOOR TEMPERATURE FORECASTING

An early warning of high indoor temperatures, powered by a forecasting model, may serve as a short-term mitigation strategy. It can help ensure that healthcare staff and resources are prepared for hot weather periods. The development of dwelling-specific forecasting models offers an opportunity to tailor results to the behavioural patterns and vulnerability of the occupants. A practical real-time forecasting framework should leverage low-cost sensors, easily obtainable exogenous data and automated predictive procedures, while generating reasonably accurate results.

4.1. MODEL PARAMETERS

In this work, we used battery-operated IoT sensors to minimize the intrusiveness of the system. All dwelling sensors in a building were connected to a single gateway, which utilized a cellular connection to transfer the measured data to a cloud platform in near real-time. Our ultimate objective is to extend the forecasting framework to a large portfolio of social housing settings. Due to cost constraints, onsite measurement of outdoor conditions is not feasible. Instead, we obtained

hourly temperature and humidity forecasts from Environment Canada (Government of Canada 2024). Solar radiation and wind speed forecasts are not reported at many weather stations. Although these are available from other sources, using the minimum amount of exogenous data can help to cost-effectively scale up the framework across geographically dispersed buildings portfolios. Therefore, we explored the possibility of developing the forecast models using only one exogenous datapoint, namely outdoor temperature obtained from the nearest weather station.

Prediction errors typically increase as the forecasting horizon lengthens. However, a longer forecast horizon is advantageous as it allows for better planning for forecasted indoor heat exposure events. After consulting with the portfolio managers, we determined that a 24-hour forecast horizon may provide a trade-off between maintaining reasonable accuracy and ensuring adequate response time to potential indoor overheating risk.

For large-scale implementation, the models should be designed to be both building- and dwelling-agnostic, incorporating an automated, near-optimal model selection procedure for each dwelling. To this end, we used a sliding window autoregressive model with exogenous parameters, varying lags and training lengths. The procedure for near-optimal model selection and the associated parameters are presented in Figure 4.

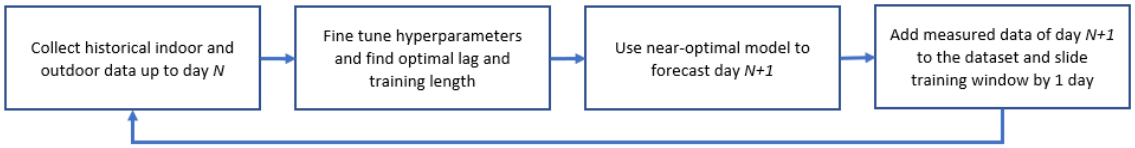

Figure 4. Model development procedure

To forecast indoor temperature for day *N+1*, namely the forecast day, the model was trained and optimized using the data from the hourly historical dataset up to day *N*. We used combinations of model hyperparameters, lags and training lengths to identify the optimized model. We used hour of day, day of week, and hourly outdoor temperature as features. We tested four different training lengths, i.e., 168, 336, 504 and 672 hours to find the optimized model. The combination that leads to the minimum mean absolute error (MAE) was selected to forecast the indoor temperature for day *N+1*. We used a recursive prediction method where an hourly forecasted temperature was fed forward to the next timestep. Training the models every 24 hours with varying training lengths and lags enabled a more flexible framework. This flexibility helps the model to better respond to gradual changes in outdoor conditions and occupants' behaviour patterns within each dwelling. We used XGBoost (Chen and Guestrin 2016) as the base model and implemented the fine-tuning process with Optuna (Akiba et al. 2019). XGBoost, as a decision tree-based method, provides a non-linear regression capability similar to neural networks while being easier to train and less prone to overfitting (McElfresh et al. 2023). The procedure was implemented in Python.

We evaluated the performance of the forecasting approaches using five randomly selected days, referred to as test days. The test days were consistent across all 20 dwellings. For each test day, the near-optimal model was found and then used to forecast the indoor temperature starting at 12

am. Figure 5 shows the MAE for each dwelling, comparing the same-day (day *N*) and test day (day *N+1*) prediction results. As expected, the same-day errors are lower with an average MAE of 0.4°C. The average next-day MAE is consistently below 0.7°C for all dwellings. While this level of accuracy may not suffice for applications such as predictive control, it offers valuable insights into overheating risks. This is particularly noteworthy given the minimal requirement for exogenous data and the dwelling-agnostic nature of the forecasting approach.

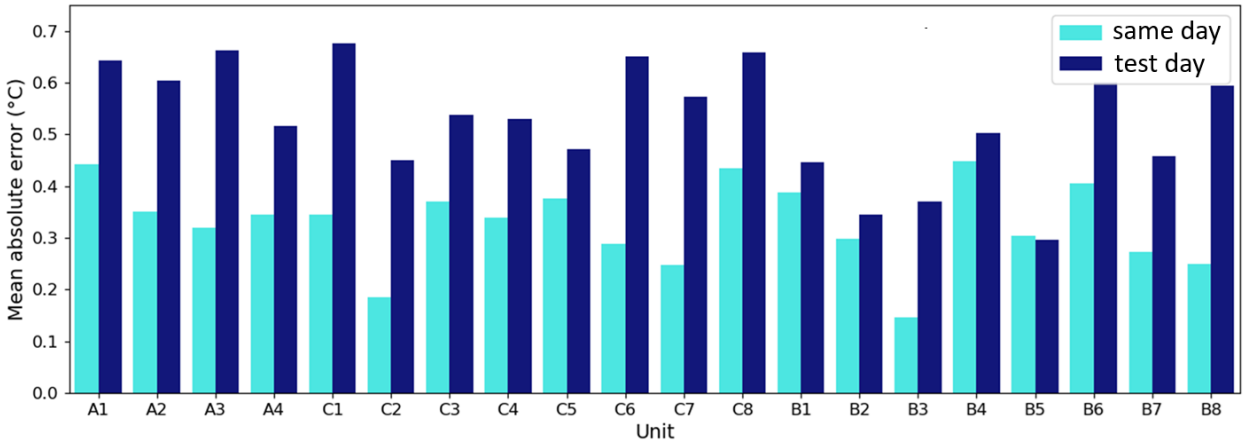

Figure 5. Prediction error for each dwelling

5. CONCLUSIONS

Measurements from 20 social housing dwellings in Western Canada confirm that outdoor conditions are an unreliable indicator of excessive heat exposure risks in occupied homes. Currently, heat alerts rely solely on weather forecasts. However, our assessment indicates that elevated indoor temperatures can occur even during relatively mild outdoor conditions. These findings and similar findings from previous studies underscore a flaw in the existing public weather alerts. This issue is particularly important in the context of social housing due to the potential vulnerability of both the buildings and their occupants. As a short-term mitigation strategy, we developed an automated indoor temperature forecasting framework that uses only publicly available weather forecast data. This framework identifies where, when, and to what extent occupants of individual dwellings might experience overheating. It provides portfolio managers with actionable insights and enables them to effectively prioritize resources during overheating events.

Overall, this work demonstrates that the current heat alerts are not sufficient in responding to the increasing risk of indoor overheating in Canada. The proposed forecasting platform can facilitate the development of a cost-effective and computationally efficient heat alert system. Such systems would inform social housing management about impending heat-related health risks, allowing for timely and individually targeted mitigations. This approach could reduce the heat-related morbidity and mortality among vulnerable occupants and support a coordinated response during extreme heat events.

Acknowledgements

BC Housing develops, manages, and administers a wide range social housing across the province of British Columbia. In all new buildings, BC Housing requires active cooling systems and air filtration systems be installed. However, many buildings in our portfolio are decades old and were built for a cooler climate than what British Columbians are more recently experiencing due to climate change. BC Housing is taking steps to address these challenges through retrofit measures, and installing portable air conditioning units, where possible. BC Housing also provides emergency cooling and clean air items that are distributed to housing operators as needed, during periods of extreme heat. In 2023/24, BC Housing updated our Extreme Heat and Wildfire Smoke Action Plan. This document provides an overview of key priority areas, short and long-term actions, and timelines to ensure that BC Housing, as an organization, is prepared to support people living in social housing and our partners during extreme heat and wildfire smoke events.

This paper is being carried out as a part of the R&D project at the National Research Council of Canada (NRC) under the Climate Resilient Build Environment (CRBE) Initiative.

6. REFERENCES

Akiba, T., Sano, S., Yanase, T., Ohta, T., and Koyama, M., 2019. Optuna: A Next-generation Hyperparameter Optimization Framework. *Proceedings of the ACM SIGKDD International Conference on Knowledge Discovery and Data Mining*, 2623–2631.

BC Government, 2024. *Protection from Overheating in Dwelling Units*.

Boudreault, J., Lavigne, É., Campagna, C., and Chebana, F., 2024. Estimating the heat-related mortality and morbidity burden in the province of Quebec, Canada. *Environmental Research*, 257 (May).

CCOHS, 2024. Humidex Rating [online]. Available from: https://www.ccohs.ca/oshanswers/phys_agents/humidex.html [Accessed 20 Dec 2024].

Chen, T. and Guestrin, C., 2016. XGBoost: A scalable tree boosting system. *Proceedings of the ACM SIGKDD International Conference on Knowledge Discovery and Data Mining*, 13-17-August-2016, 785–794.

Government of Canada, 2024. Canadian Weather - Environment Canada [online]. Available from: https://climate.weather.gc.ca/ [Accessed 23 Dec 2024].

Gustin, M., McLeod, R.S., Lomas, K.J., Petrou, G., and Mavrogianni, A., 2020. A high-resolution indoor heat-health warning system for dwellings. *Building and Environment*, 168, 106519.

Jandaghian, Z. and Akbari, H., 2018. The effects of increasing surface reflectivity on heat-related mortality in Greater Montreal Area, Canada. *Urban Climate*, 25 (June), 135–151.

Khan, L., Kawano, T., Hutton, J., Asamoah-Boaheng, M., Scheuermeyer, F.X., Christian, M., Baranowski, L., Barbic, D., Christenson, J., and Grunau, B., 2024. The association of extreme environmental heat with incidence and outcomes of out-of-hospital cardiac arrest in British Columbia: A time series analysis. *Resuscitation Plus*, 17 (November 2023), 100560.

Laouadi, A., Ji, L., Shu, C., Wang, L., and Lacasse, M.A., 2023. Overheating Risk Analysis in Long-Term Care Homes—Development of Overheating Limit Criteria. *Buildings*, 13 (2).

Liangzhu (Leon) Wang, Chang Shu, Hua Ge, Radu Zmeureanu, M.L., 2020. Assessment of summertime overheating conditions in vulnerable buildings in Montréal. *In*: *2nd International Conference on New Horizons in Green Civil Engineering (NHICE-02)*. Victoria, BC, Canada.

McElfresh, D., Khandagale, S., Valverde, J., Prasad, V.C., Ramakrishnan, G., Goldblum, M., and White, C., 2023. When Do Neural Nets Outperform Boosted Trees on Tabular Data? *Advances in Neural Information Processing Systems*, 36 (NeurIPS), 1–39.

Morey, J., Beizaee, A., and Wright, A., 2020. An investigation into overheating in social housing dwellings in central England. *Building and Environment*, 176 (February), 106814.

Rahif, R., Amaripadath, D., and Attia, S., 2021. Review on Time-Integrated Overheating Evaluation Methods for Residential Buildings in Temperate Climates of Europe. *Energy and Buildings*, 252, 111463.

Walikewitz, N., Jänicke, B., Langner, M., and Endlicher, W., 2018. Assessment of indoor heat stress variability in summer and during heat warnings: a case study using the UTCI in Berlin, Germany. *International Journal of Biometeorology*, 62 (1), 29–42.

6th International Conference on Building Energy and Environment
Eindhoven University of Technology, The Netherlands
6 - 10 July 2025

A comparison of energy use among modular and site-built multifamily buildings in the U.S.

K.R. Grosskopf, Ph.D. [1]

[1]*University of Nebraska, Lincoln, USA, kevin.grosskopf@unl.edu*

SUMMARY
Prefabrication in a controlled, factory setting may improve the energy performance of modular buildings compared to traditional site-built buildings. This research provides energy performance data on 48 modular and 158 site-built multifamily buildings in the U.S. Results suggest that the performance of energy measures in modular multifamily construction meets or exceeds the performance of energy measures in site-built construction. Although few differences were observed between the types of materials and equipment used in either modular or site-built multifamily construction, the installation quality of energy measures in modular multifamily construction appeared to be better when compared to site-built construction. Findings also suggest that the post-occupancy energy use of modular multifamily buildings (113.6kWh/m^2/yr) was comparable to site-built buildings (112.9kWh/m^2/yr). However, since two-thirds of the modular projects studied were affordable housing, dwelling units were smaller (51.9m^2) compared to market rate site-built units (76.9m^2). When normalized for ~30% higher occupant density, modular buildings had significantly better energy efficiency compared to site-built buildings.

Keywords: buildings, energy, modular, multifamily.

1. INTRODUCTION

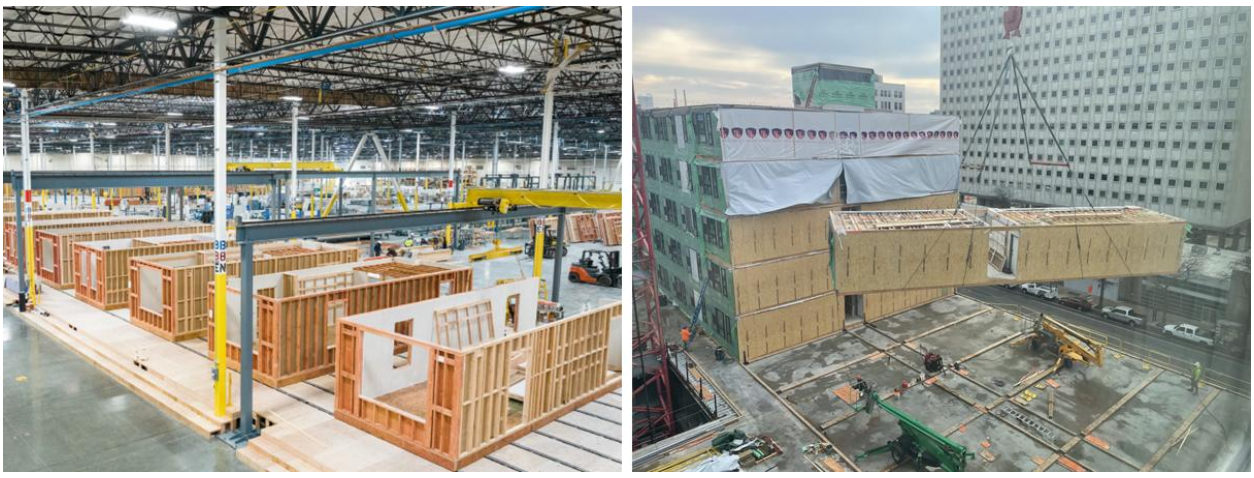

Figure 1. Modular factory (left) and work site (right)**.**

Modular construction consists of building components prefabricated offsite in a manufacturing facility. These components are then transported and assembled onsite (Figure 1). Since both offsite and onsite work occur simultaneously, opportunities exist to shorten construction schedules and speed income generation, particularly for projects with repetitive building units such as apartments and hotels. Modular construction may also reduce costs while improving building performance.

2. METHODS

Multifamily buildings selected for this study were located in four urban areas of the U.S. (Los Angeles, San Francisco, Philadelphia and Seattle) representing two temperate climate zones. Buildings averaged 6 stories, 13,000m^2 and 144 units each. Data was first collected on energy-related material and equipment systems for a total of 25 modular and 30 site-built multifamily buildings under construction. Data collection for each building began with a design document review followed by factory and construction site inspections. In addition, post-occupancy energy use data was collected on another 23 modular and 128 site-built multifamily buildings completed between 2013-2022 in the same urban areas.

3. RESULTS AND DISCUSSION

3.1. Energy Systems

In climate zone 3 (Los Angeles and San Francisco), the average energy efficiency of modular material and equipment systems exceeded most energy code requirements (Figure 2). The exception was thermal transmittance (U) for exterior walls. Similarly, the energy efficiency of modular material and equipment systems exceed the energy efficiency of site-built systems in CZ3 except window solar heat gain coefficient (SHGC).

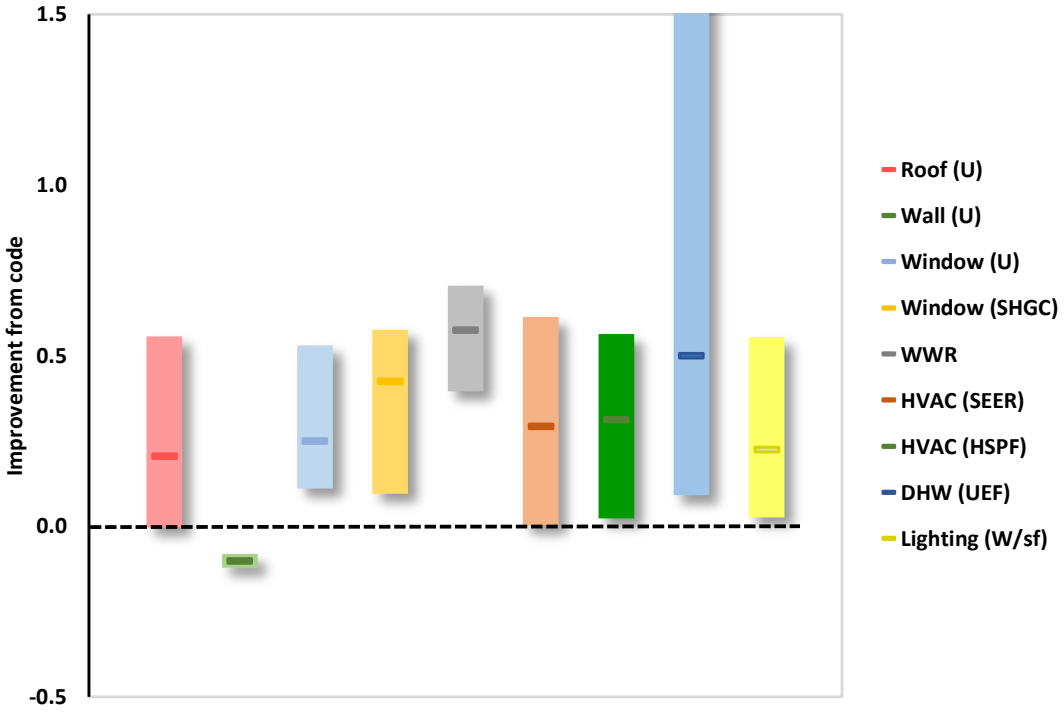

Figure 2. Design improvement from code, U.S. climate zone 3 (Los Angeles and San Francisco).

In climate zone 4 (Philadelphia and Seattle), the average energy efficiency of modular material and equipment systems exceeded all energy code requirements (Figure 3). One modular building failed to meet code requirements for maximum window-to-wall ratio (WWR). The energy efficiency of modular material and equipment systems, however, did *not* exceed the energy efficiency of site-built systems in CZ4 except thermal transmittance for roofs and exterior walls.

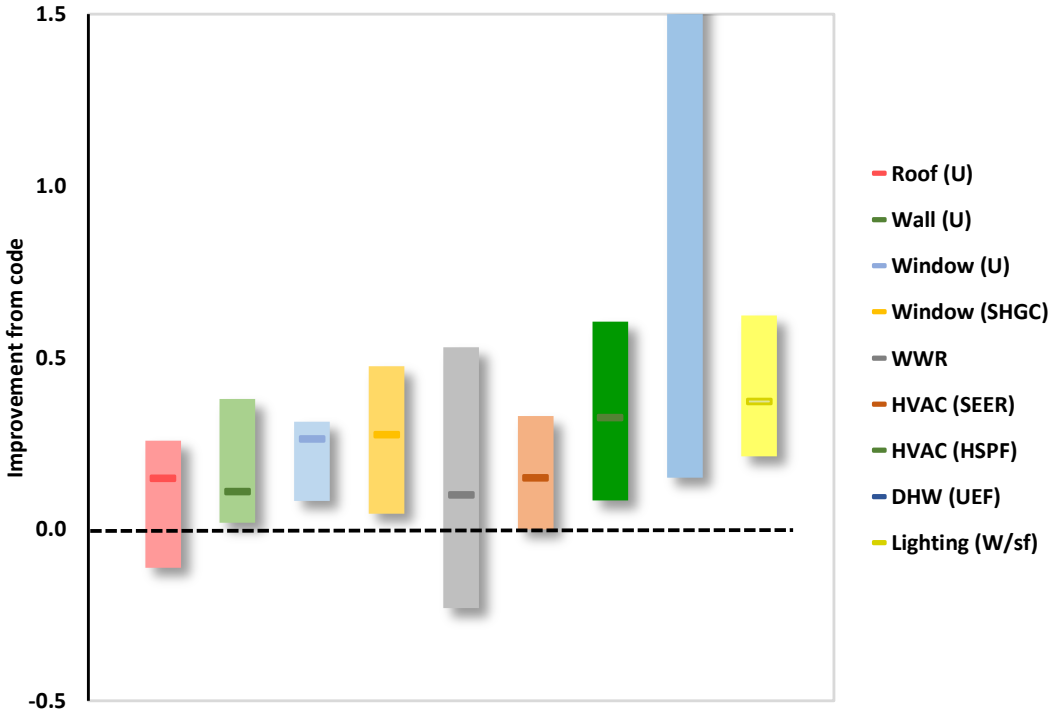

Figure 3. Design improvement from code, U.S. climate zone 4 (Philadelphia and Seattle).

Overall, few differences were observed between the types of materials and equipment used in either modular or site-built multifamily construction. However, the installation quality of insulation, air barrier and other building envelope measures in modular multifamily construction appeared to be better when compared to site-built construction.

3.2. Energy Use

For buildings with at least 1-year of post-occupancy energy use data, the energy use intensity (EUI) of modular multifamily buildings (113.6kWh/m^2/yr) was comparable to site-built buildings (112.9kWh/m^2/yr). However, since two-thirds of the modular projects studied were affordable housing, dwelling units were smaller (51.9m^2) on average compared to market rate site-built units (76.9m^2). When normalized for ~30% higher occupant density and other factors, modular multifamily buildings had higher U.S. Department of Energy (DOE) *Energy Star* scores compared to site-built buildings. The *Energy Star* score represents the energy efficiency percentile of a building in relation to similar buildings in the U.S.

Table 1. Post-occupancy energy performance of modular and site-built multifamily buildings.

	Modular			Site-Built		
Location	Number of Buildings	EUI (kWh/m^2/yr)	Energy Star Score	Number of Buildings	EUI (kWh/m^2/yr)	Energy Star Score
Los Angeles	6	122.7	58	25	112.0	76
San Francisco	9	122.4	91	64	104.1	86
Philadelphia	3	111.7	87	19	146.1	63
Seattle	5	88.3	98	20	100.9	93
Total	23	113.6	86	128	112.9	81

4. CONCLUSIONS

Unlike site-built construction, modular construction relies on a permanent factory workforce under a central point of control. As a result, modular construction may be able to maintain higher levels of quality control when compared to site-built construction. This may explain why modular multifamily construction, when normalized for higher occupant density and other factors, appears to have better energy efficiency compared to site-built construction despite using similar materials and equipment.

Modular projects in this study were completed 30% faster on average when compared to site-built construction. Due to shorter construction schedules, modular projects achieved an average 5% cost savings. Growth for modular multifamily construction in the U.S. is being realized in the Northeast and along the West Coast where roughly one-third of the population lives in multifamily housing as a result of the ongoing housing affordability crisis.

ACKNOWLEDGEMENTS

This material is based upon work supported by the U.S. Department of Energy's Office of Energy Efficiency and Renewable Energy (EERE) under Building Technologies Office award number DE-EE0009082. A full copy of this report can be downloaded at the USDOE Office of Scientific and Technical Information (OSTI) https://www.osti.gov or https://doi.org/10.2172/2229244.

REFERENCES

Grosskopf, K.R. 2023. Modular multifamily construction: a field study of energy code compliance and performance through offsite prefabrication. Final Report to the Office of Energy Efficiency and Renewable Energy (EERE). U.S. Department of Energy (DOE).

6th International Conference on Building Energy and Environment
Eindhoven University of Technology, The Netherlands
6 - 10 July 2025

Optimizing Glazing Visible Transmittance in Multi-Sectional Curtain Wall Facades to Improve Indoor Daylighting

Elham Shokri [1], Mohammad Reza Razavi [2], Payam Rahnamayiezekavat [3], Keivan Bamdad[4],

1 School of engineering, design, and built environment, Western Sydney University, Sydney, Australia, e.shokri@westernsydney.edu.au
2 School of engineering, design, and built environment, Western Sydney University, Sydney, Australia, R.Razavi@westernsydney.edu.au
3 School of engineering, design, and built environment, Western Sydney University, Sydney, Australia, p.zekavat@westernsydney.edu.au
4 School of engineering, design, and built environment, Western Sydney University, Sydney, Australia, K.Bamdad@westernsydney.edu.au

SUMMARY
This research aims to maximize acceptable indoor daylighting levels by optimizing glazing Visible Transmittance (VT) parameter across multi-sectional curtain wall facades. A north-facing, side-lit office in Sydney, Australia, serves as the case study, where optimization is performed using the Brute Force algorithm via Grasshopper's Colibri plugin. Daylight performance is assessed with Ladybug Tools and the Radiance engine based on the well-lit area (D_L) metric where it is between 320 to 800 lux for three visible transmittance values in daylight, view, and spandrel sections (VT_D, VT_V, VT_S). The proposed multi-sectional optimization $(VT_{MSO}, Scenario\ A)$ achieves a 21% improvement in the well-lit area (D_L), outperforming alternative approaches with 8%, 13%, 14.5%, and 16% enhancement for spandrel $(VT_{SSO}, Scenario\ D)$, daylight $(VT_{DSO}, Scenario\ B)$, view $(VT_{VSO}, Scenario\ C)$, and uniformly optimized VT $(VT_{UO}, Scenario\ E)$, respectively, with specific VT values in each section and provided well-lit area (D_L), offering design guidelines for sustainable daylighting practices.

Keywords: Indoor daylighting, Multi-Sectional curtain wall facades, Glazing visible transmittance (VT), Brute force optimization.

1. INTRODUCTION

Daylight is a crucial factor in enhancing occupant well-being by supporting circadian rhythm regulation(Lockley, 2010), productivity, and satisfaction in workspaces(Haynes, 2008), fostering healing process in medical environments(Joarder, 2011), boosting academic performance and contributing to better learning outcomes(Irnawaty et al., 2019), reducing lighting energy consumption in buildings (Bodart & De Herde, 2002). However, high-rise buildings with curtain wall facades, a common construction type in today's world, often face challenges with uneven indoor daylight distribution, particularly in deep side-lit spaces where facade daylight performance is critical and constitutes a substantial portion of the design layout (Government, 2022). In such space, near glazed facades, excessive daylight creates high-intensity illuminance (lux) (over-lit zones), while the back of rooms experiences insufficient daylight illuminance (lux), as daylight typically extends only up to twice the window height (Beltrán, 2020). To address the challenge of

difficulty in balancing indoor daylight penetration and uniformity in such space, a key primarily parameter in effective daylight design and solutions for curtain wall facades is glazing Visible Transmittance (VT) which controls daylight transmission through glazing (Chen et al., 2019; Gündoğdu & Kunduraci, 2019).

1. 1 Literature Gap and Aim

Previous research highlight the critical role of VT, in optimizing indoor daylight illuminance in such space (Hosseini et al., 2018; Singh et al., 2022; Singh et al., 2016). However, applying a single daylight solution or VT value across the entire facade does not ensure uniform distribution across the entire space, highlighting the importance of using specific daylight controls for the daylighting and view sections of the facade, as each section serves a distinct role in optimizing indoor lighting (Aiziewood, 1993; Lim et al., 2012; Tan et al., 2023). Daylighting section typically refers to windows above 2 meters, though this can vary based on room size and facade design but should not be less than 0.75 meters, enhancing light levels in deeper spaces. View section typically refers to window between task area and daylighting glazing, balancing daylight, shading, and outdoor views near task areas, if appropriate daylight controls are utilized(Elkhatieb, 2017). The significance of both glazing Visible Transmittance (VT) and the separation strategy in improving indoor daylight illuminance levels inspired the concept behind this research, which remains to be relatively unexplored in the existing literature. A purpose-driven method to evaluate different VT values in the daylight (upper(D)), view (middle(V)), and spandrel (lower(S)) sections to ensure optimal indoor daylight distribution, is rarely addressed in current studies. Existing approaches typically focus on daylight penetration or glare reduction but often neglect uniformity and the optimal distribution of light across the entire space, relying on simplistic applications such as clear glass above and tinted or shaded glass below without robust optimization tools (Aiziewood, 1993; Hashemi, 2014; Lim et al., 2012; Tan et al., 2023). Therefore, this research is going to address the gap and:

- Proposing a new three-variable optimization method to maximize the acceptable indoor daylight level (well-lit area) in side-lit spaces. The optimization simultaneously focuses on Visible Transmittance (VT) values across the three horizontal sections—daylight (VT_D), view (VT_V), and spandrel (VT_S) —of multi-sectional curtain wall facade (VT_{MSO}).
- Comparing the effectiveness of the proposed approach with other four alternative approaches: daylight (VT_{DSO}), view (VT_{VSO}), spandrel (VT_{SSO}), and uniformly optimized section Visible Transmittance (VT_{UO}).
- Bridging the research gap by providing new insights into optimizing indoor daylight distribution, contributing to both academic knowledge and practical daylighting design, and offering to improve building design and indoor daylighting level.

2. METHODOLOGY

This research outlines the simulation and optimization process, as shown in Figure 1. Following a review of existing gaps and literature, a simulation-based optimization approach is employed using Rhinoceros, Grasshopper, Ladybug, and Honeybee plugins. Rhinoceros is a CAD tool enabling precise 2D and 3D modeling, while Grasshopper facilitates parametric evaluations and algorithm development(Talaei et al., 2021). Ladybug imports Sydney-CBD specific meteorological data based on the Energy Plus weather dataset (EPW format). Meanwhile, the Honeybee plugin connects to Radiance**,** a validated lighting simulation engine employing backward ray tracing for daylight analysis (Reinhart, 2019). Validation studies confirm their precision within ±10%

compared to CIE Test Cases (Reinhart, 2019). Also, a single brute force optimization algorithm using the Colibri plugin in Grasshopper is perform, systematically evaluating all possible VT combinations for the three horizontal curtain wall sections. The analysis focuses on a grid-based daylight illuminance simulation for north-facing glazing on December 21 at 12:00 noon—representing the highest sun altitude and daylight level in the Southern Hemisphere during the summer solstice. The average solar radiation in this month is around 6000 lux, the highest compared to other months of the year. During daytime hours (9 AM to 4 PM), the highest average daylight illuminance is recorded at 8501 lux on December 21st, with a peak at 12 PM. At this peak, direct sunlight contributes 992 lux, while diffuse skylight accounts for 119 lux. Given the time and location, the sky condition in Sydney at 12:00 PM on December 21 is likely to correspond to the "CIE Standard Clear Sky" model. Therefore, for precise modeling or simulation purposes, the ε (epsilon) and δ (delta) values—based on the ISO 15469 standard—are approximately 0.351 and 0.161, respectively. This is ideal for assessing indoor daylight performance under challenging conditions, representing the peak risk of uneven indoor daylight distribution and highest daylight level. According to Eq.1, current research aims to maximize the percentage of the area achieving illuminance between 320 lux and 800 lux ($\text{Well} - \text{lit Area}$), referred to as the D_L metric, by optimizing three VT variables VT_D, VT_V, VT_S through five optimization approaches, as outlined in Figure 1. Where $l \leq VT_D, VT_V, VT_S \leq u$ with $l \; and \; u$ are the lower and upper bounds of the variables ([0.20,0.90] with 0.10 increments).

$$\max\ (\text{Well} - \text{lit Area}) = \max\ (F(VT_D, VT_V, VT_S)) \qquad \text{Eq.1}$$

The case study depicted in Figure 2 examines deep side-lit office layouts, which are common in modern design practices and widely used in high-rise buildings, particularly in Australia. Given the significance of visual comfort, productivity, and health for employees (Government, 2022), there is a strong need for targeted solutions to enhance daylight performance in such environments. Due to the emphasis on daylighting in Australian sustainability policies and rating tools such as NABERS and Green Star, Australia is considered as case study location (Diesendorf & Diesendorf, 2007; Hall, 2010). Among Australia's diverse climate zones, Sydney falls within Climate Zone 5 (Humid Subtropical, Cfa), which represents a significant portion of high-rise buildings across the country, making it a relevant choice for assessing daylight performance under typical climate conditions. Moreover, despite the benefits of ample sunlight and typical CBD office designs in Sydney, current Australian building codes provide limited guidance specific guidance on optimizing VT values for indoor daylight distribution in offices (Board, 2022). While the Australian Glass and Window Association (AGWA) and the Australian Building Codes Board's facade performance calculator offer energy efficiency guidance, they provide less attention to indoor daylight uniformity through appropriate VT. The case study is a large rectangular side-lit office space with an indoor area of 50 m², representative of multi-user offices in large Australian commercial buildings with a window-to-wall ratio (WWR) of 95% on the north-facing wall (5 m × 3 m). The space has a length of 10 m, chosen to align with typical daylighting needs in open-plan offices. Additionally, this configuration represents a perimeter-occupied zone within a large-plate (>30 m) multistory office building, a common layout in contemporary commercial architecture. Moreover, Australian standards (Standard Australia: Sydney, 2006) for office interiors tasks are applied, setting the work plane height at 0.70 m for daylight grids and using the illuminance thresholds including 320 lux- routing office tasks, reading, writing, typing, and inquiry desks and 800 lux-very difficult tasks with very small details and threshold for quality of daylight.

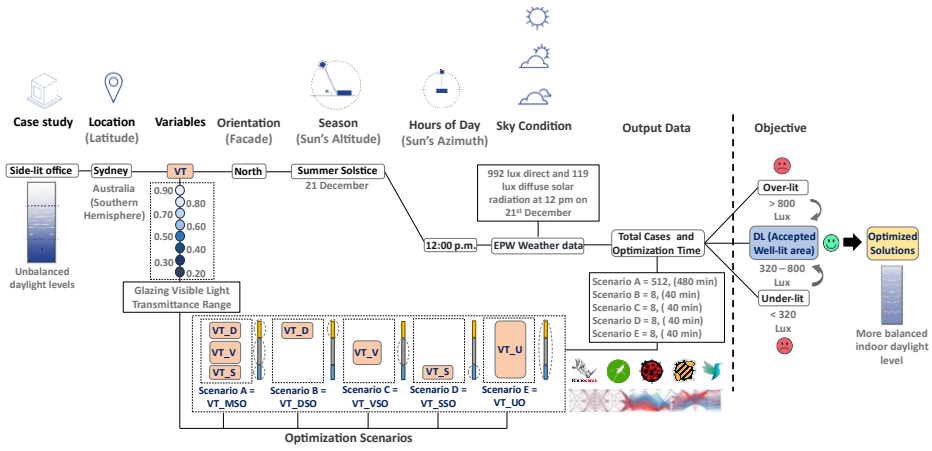

Figure 1. The overall research methodology framework.

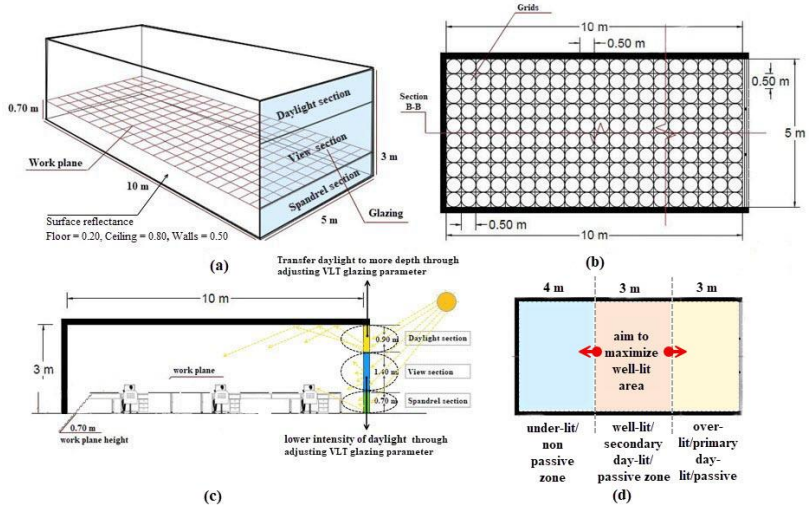

Figure 2. a) 3D view of the case study and details, b) plan view of Illuminance grid points and dimensions of the case study in grid-based daylight analysis, c) section B-B of the case study detail, and performance of the multi sectional glazing facade, d) visualization of daylight zones in the case study**.**

3. RESULTS AND DISCUSSION

According to Figure 3 for Scenario A, Multi-Sectional Optimization of Visible Transmittance (VT_{MSO}), the top graph uses a parallel coordinates plot to visualize the range of design solutions and the relationships between visible transmittance values (VT_D, VT_V, VT_S) and the well-lit area (D_L) metric. Where $l \leq VT_D, VT_V, VT_S \leq u$ with $l \; and \; u$ are the lower and upper bounds of the variables ([0.20,0.90] with 0.10 increments). Red lines indicate lower-performing solutions, while blue lines represent higher-performing ones, with a gradient illustrating the optimization quality. This visualization reveals how variations in visible transmittance values influence daylight performance and highlights interdependencies among the sections. The bottom graph shows the progression of well-lit area as a function of the 512 visible transmittance (VT) combinations explored. The well-lit area (D_L) ranges from approximately 22% to a maximum of 46%, demonstrating the algorithm's ability to incrementally enhance daylight performance. The "Base

Case," achieving a well-lit area of 38%, serves as a benchmark. Optimized solutions surpass this benchmark, achieving well-lit area values between 40% and 46%, representing improvements of 2% to 21%. Notably, 155 solutions outperform the Base Case, with 23 solutions achieving the highest well-lit area values (44.5% to 46%). These top-performing solutions, highlighted in the right graph, form clusters that exhibit consistent performance and reflect a 17% to 21% improvement over the Base Case, emphasizing the robustness of the optimization process. The highest-performing designs include configurations reflects 21% improvement in well-lit area (D_L) metric with visible transmittance combinations for daylight, view, and spandrel sections, including VT_D.0.60, VT_V.0.80, VT_S.0.50, and VT_D.0.60, VT_V.0.90, VT_S.0.20. These solutions. The results indicate that the optimization approach effectively identifies design solutions that enhance indoor daylight performance. The horizontal bands in the right graph underscore the consistency of top-performing designs, suggesting flexibility in achieving optimal outcomes. To assess practical application, these results are compared with other scenarios, highlighting the advantages of simultaneous multi-sectional optimization.

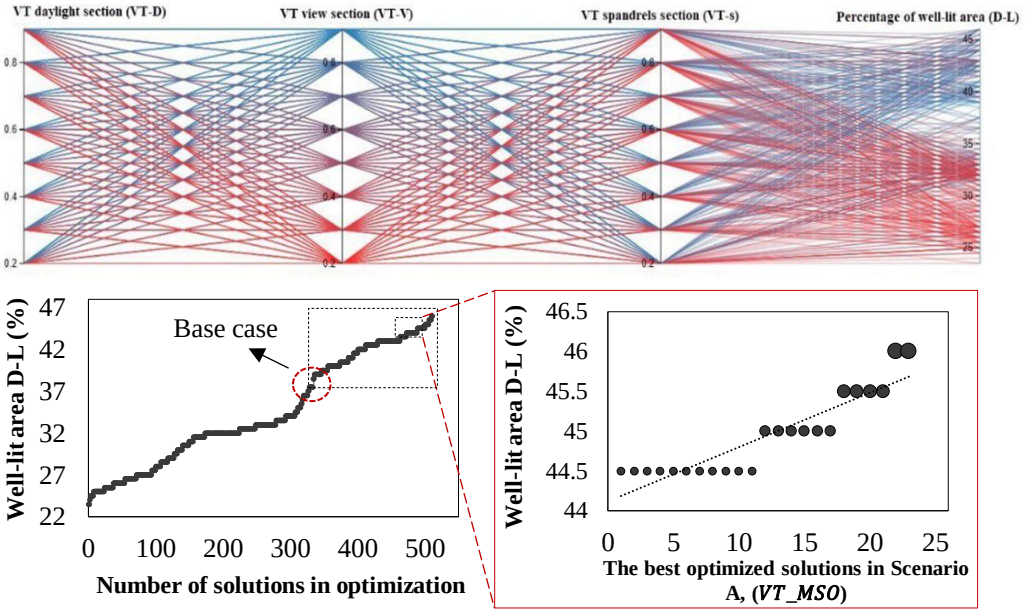

Figure 3. All possible solutions and the best optimized ones in multi sectional optimization (Scenario A, (VT_{MSO})) and provided well-lit area (%) (D_L).

Based to Figure 4, in Scenario B, Daylight Section-Optimized Visible Transmittance (VT_DSO), optimization results show a 13% improvement in the well-lit area (D_L) metric. Well-lit areas increase from 38% (base case) to 43%, with the optimal visible transmittance for daylight section (VT_D) being 0.20. Where $l \leq VT_D \leq u$ with $l\ and\ u$ are the lower and upper bounds of the variables ([0.20,0.90] with 0.10 increments) and $VT_V, VT_S\ are\ fixed\ at$ 0.90. The results indicate that reducing visible transmittance in the daylight section enhances indoor daylight uniformity. The steady increase in Well-lit areas, without significant fluctuations, underscores the critical role of the daylight section in achieving balanced daylight distribution. In Scenario D, Spandrel Section-Optimized Visible Transmittance (VT_SSO), Where $l \leq VT_S \leq u$ with $l\ and\ u$ are the lower and upper bounds of the variables ([0.20,0.90] with 0.10 increments) and $VT_D, VT_V\ are\ fixed\ at$ 0.90, the improvement in Well-lit areas is more modest at 8%, with well-

lit areas ranging from 38% to 41%. The optimal visible transmittance for daylight section (VT_S) is 0.20, indicating that reducing spandrel visible transmittance (VT) improves daylight distribution but to a lesser extent than Scenario B. Scenario C, View Section-Optimized Visible Transmittance (VT_VSO), shows the most significant improvement among single-section scenarios. Where $l \leq VT_V \leq u$ with $l\ and\ u$ are the lower and upper bounds of the variables ([0.20,0.90] with 0.10 increments) and $VT_D, VT_S\ are\ fixed\ at$ 0.90. Well-lit areas increase from 32% to 43.50%, representing a 14.5% improvement. This metric peaks at 43.5% with a visible transmittance for the view section (VT_V) of 0.50 but declines as visible transmittance (VT) decreases further to 0.20. This suggests that mid-range visible transmittance (VT) values for the view section result in optimal daylight performance, while overly low VT reduces its effectiveness. Scenario E, Uniformly Optimized Visible Transmittance (VT_UO) that applies a single, uniform VT value across all sections to ensure consistency in light transmission, Where $l \leq VT_D + VT_V + VT_S \leq u$ with $l\ and\ u$ are the lower and upper bounds of the variables ([0.20,0.90] with 0.10 increments), achieves well-lit areas ranging from 25% to 44%, with a 16% improvement at a uniform visible transmittance of 0.70.

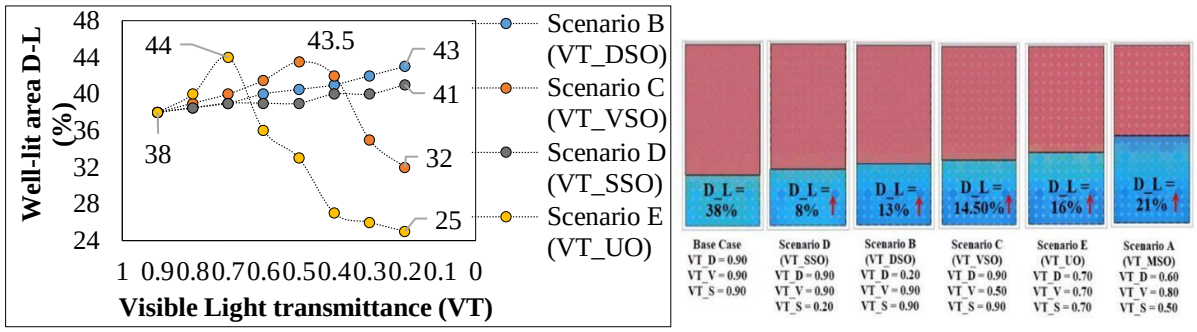

Figure 4. Comparison of five optimized solutions for providing the well-lit area in the north-facing facade on December 21 at 12 p.m.

Although performance fluctuates similarly to Scenario C, Scenario E spans a wider Well-lit area (D_L) range (25% to 44%) compared to Scenario C (32% to 43.5%). The results reveal a nonlinear relationship between visible transmittance (VT) and well-lit area (D_L), with diminishing returns or declines in performance at higher visible transmittance (VT) values in some scenarios. Notably, Scenario A (VT_{MSO}), which simultaneously optimizes all three visible transmittance variables, achieves the highest and most consistent $\text{Well} - \text{lit area}\ (D_L)$ outcomes. This highlights the effectiveness of multi-sectional optimization in balancing visible light transmittance across the daylight, view, and spandrel sections to improve indoor daylight distribution. The figure 4 further illustrates the comparative improvement in daylight performance across all optimization scenarios relative to the base case, with Scenario A emerging as the most robust solution for achieving uniform and well-lit indoor environments. In addition, the figure demonstrates design configurations that yield less favorable outcomes based on the selected performance metric are Lower-performing solutions based on their well-lit area **(**D_L), which is the metric visualized in the color bar. Solutions with lower D_L values achieve less daylight coverage across the space, indicating reduced daylight performance. The figure also, presents the distribution of daylight within the case study, with well-lit areas shown in blue and inadequately lit areas in red in all five optimization scenarios.

4. CONCLUSION

This research introduces a new optimization method for Visible Light Transmittance (VT) across three distinct horizontal sections of multi-sectional curtain wall facades. Using advance simulation tools— a Brute Force optimization algorithm through Grasshopper's Colibri plugin, supported by Ladybug Tools (LBTs) and the Radiance engine— this research addresses the challenge of achieving uniform indoor daylight distribution in side-lit spaces—common in high-rise buildings. A north-facing office in Sydney, Australia, serves as the case study, exploring an issue not thoroughly investigated in previous studies. The research evaluates the concept of assigning distinct VT values to each horizontal section —daylight (VT_D) , view (VT_V), and spandrel (VT_S) – as three variables within a VT range of 0.20 to 0.90. The evaluation focuses on the well-lit area percentage, defined by the D_L metric, for a case study conducted on 21 December at 12 noon. It also compares the effectiveness of the proposed multi-sectional optimization approach ($VT_{MSO}, Scenario\ A$) with alternatives including daylight section optimized ($VT_{DSO}, Secnario\ B$), view section optimized ($VT_{VSO}, Scenario\ C$), spandrel section optimized ($VT_{SSO}, Scenario\ D$), and uniformly optimized VT ($VT_{UO}, Scenario\ E$). Although, the research has some limitations that open directions for future work, such as adapting the methodology to different climates, facade geometries, types, orientations, and building categories. Future studies could also extend the analysis to additional hours and days throughout the year and integrate dynamic facade systems or smart technologies. Moreover, employing more advanced optimization methods, such as multi-objective optimization, and incorporating additional metrics for glare, thermal, or energy performance—along with real-world case studies or sensitivity analyses—could enhance the robustness and credibility of the findings. Overall, key findings reveal that:

- The proposed multi-sectional optimization (VT_{DSO} , Scenario A) achieved up to a 21% improvement in well-lit area (D_L metric) with VT combinations including VT_U = 0.60, VT_V = 0.80, VT_S = 0.50, and VT_U = 0.60, VT_V = 0.90, VT_S = 0.20, compared to the base case (D_L= 0.38%), highlighting the effectiveness of sectional optimization and adjusting VT values for individual sections in enhancing daylight penetration and uniformity.
- Optimizing VT for individual sections shows that spandrel section optimized ($VT_{SSO}, Scenario\ D$), daylight section optimized ($VT_{DSO}, Scenario\ B$), view section optimized ($VT_{VSO}, Scenario\ C$) , and uniformly optimized VT ($VT_{UO}, Scenario\ E$), achieve improvement of 8%, 13%, 14.5%, and 16% , respectively, in well-lit area (D_L metric), placing them in the subsequent choices.
- Considering VT_S = 0.20 in Scenario D, VT_D = 0.20 in Scenario B , VT_V = 0.50 in Scenario C, and VT_U = 0.70 in Scenario E, with the other two VT values kept at 0.90, represent the best optimized solutions, leading to the highest D_L value.
- The extension of this research has the potential to provide architectural design guidelines for related areas of building design and codes, optimizing VT values for enhanced daylight performance and aligning with sustainability rating tools such as NABERS and GREEN STAR.

ACKNOWLEDGEMENTS

Special thanks to all those who provided guidance and unwavering support throughout the course of this research. The author also acknowledges the resources and support provided by Western Sydney University, which were essential for the completion of this work.

REFERENCES

Aiziewood, M. (1993). Innovative daylighting systems: An experimental evaluation. International Journal of Lighting Research and Technology, 25(4), 141-152.

Beltrán, L. O. (2020). Assessing the Lighting Performance of an Innovative Core Sunlighting System. Smart and Sustainable Cities and Buildings, 631-641.

Board, A. (2022). National Construction Code: Building Code of Australia', Australian Building Codes Board, Canberra. In.

Bodart, M., & De Herde, A. (2002). Global energy savings in offices buildings by the use of daylighting. Energy and Buildings, 34(5), 421-429.

Chen, X., Zhang, X., & Du, J. (2019). Glazing type (colour and transmittance), daylighting, and human performances at a workspace: A full-scale experiment in Beijing. Building and environment, 153, 168-185.

Diesendorf, M., & Diesendorf, M. (2007). Greenhouse solutions with sustainable energy (Vol. 20). University of New South Wales Press Sydney, Australia:.

Elkhatieb, M. A. (2017). A Performance-Driven Design Model of Territorial Adaptive Building Skin (TABS) for Daylighting Performance Optimisation in Office Buildings in Egypt. The University of Liverpool (United Kingdom).

Government, A. (2022). Energy efficiency in commercial buildings. (Australian Government Department of Industry, Science, EnergyDepartment of Industry, Science, Energy

and Resources through the Climate Solutions Package).

Gündoğdu, E., & Kunduraci, A. C. (2019). Effect of window glazings' visible transmittance to daylight factor and energy efficiency in an architecture studio. Journal of Emerging Trends in Engineering and Applied Sciences, 10(4), 171-178.

Hall, S. (2010). Assessment of the performance of green commercial buildings: A sustainable built environment national research centre literature review. On: Curtin University and Queensland University of Technology.

Hashemi, A. (2014). Daylighting and solar shading performances of an innovative automated reflective louvre system. Energy and Buildings, 82, 607-620.

Haynes, B. P. (2008). An evaluation of the impact of the office environment on productivity. Facilities, 26(5/6), 178-195.

Hosseini, S. M., Mohammadi, M., Rosemann, A., & Schröder, T. (2018). Quantitative investigation through climate-based daylight metrics of visual comfort due to colorful glass and orosi windows in Iranian architecture. Journal of Daylighting, 5(2), 21-33.

Irnawaty, I., Rahim, M. R., Hamzah, B., & Jamala, N. (2019). Daylight intensity analysis of secondary school buildings for environmental development. IOP Conference Series: Earth and Environmental Science,

Joarder, A. R. (2011). Incorporation of therapeutic effect of daylight in the architectural design of in-patient rooms to reduce patient length of stay (LoS) in hospitals.

Lim, Y.-W., Kandar, M. Z., Ahmad, M. H., Ossen, D. R., & Abdullah, A. M. (2012). Building façade design for daylighting quality in typical government office building. Building and environment, 57, 194-204.

Lockley, S. W. (2010). Circadian rhythms: Influence of light in humans. In Encyclopedia of neuroscience (pp. 971-988). Elsevier.

Reinhart, C. (2019). Daylight performance predictions. In Building performance simulation for design and operation (pp. 221-269). Routledge.

Singh, R., Buddhi, D., Thapa, S., Prakash, C., Singh, R., Sharma, A., Sheoran, S., & Saxena, K. K. (2022). Sensitivity Analysis for Decisive Design Parameters for Energy and Indoor Visual Performances of a Glazed Façade Office Building. Sustainability, 14(21), 14163.

Singh, R., Lazarus, I. J., & Kishore, V. (2016). Uncertainty and sensitivity analyses of energy and visual performances of office building with external venetian blind shading in hot-dry climate. Applied Energy, 184, 155-170.

Standard Australia: Sydney, A. (2006). Standard Australia. AS/NZS 1680.1. Interior and Workplace Lighting. . In Part 1: General Principles and Recommendations; .

Talaei, M., Mahdavinejad, M., Azari, R., Prieto, A., & Sangin, H. (2021). Multi-objective optimization of building-integrated microalgae photobioreactors for energy and daylighting performance. Journal of Building Engineering, 42, 102832.

Tan, Y., Peng, J., Luo, Z., Luo, Y., Ma, T., Ji, J., Yang, H., Wang, F., & Zhu, M. (2023). Multi-function partitioned design method for photovoltaic curtain wall integrated with vacuum glazing towards zero-energy buildings. Renewable Energy, 218, 119257.

Urban Green Infrastructure (11:00-12:30 h)

6th International Conference on Building Energy and Environment
Eindhoven University of Technology, The Netherlands
6 - 10 July 2025

Enhancing Building Performance with Moss-Based Vertical Greening: Energy Efficiency and Thermal Comfort in Canadian Climates

Bahador Ziaeemehr [1], Hua Ge[2], and Michael Lacasse [3]

[1]*Concordia University, Montreal, Canada, Bahador.Ziaeemehr@concordia.ca*
[2]*Concordia University, Montreal, Canada, Hua.Ge@Concordia.ca*
[3]*National Research Council, Ottawa, Canada, Michael.Lacasse@nrc-cnrc.gc.ca*

ABSTRACT

Evaluating the potential benefits of moss-based vertical greening systems on the Indoor Thermal Autonomy and Energy demand of residential buildings located in various Canadian cities of differing climate was the intent of this study. Moss is considered as a useful nature-based solution given its low maintenance requirements, high resilience, and potential as a sustainable alternative to conventional green facades and "living walls". Simulations were conducted using typical residential archetypes derived from databases available from Natural Resources Canada (NRCan) and the American Society of Heating, Refrigerating, and Air-Conditioning Engineers (ASHRAE). These archetypes represent buildings constructed in 1980 and 2020 and are modeled for three Canadian cities: Montreal, Toronto, and Vancouver. Building geometries were developed in Rhino3D-Grasshopper®, and the analysis incorporated both historical and future projected weather data to assess the impacts of the integration of moss on building energy consumption and thermal comfort under current and future climate scenarios. The results indicate that moss provides insulation benefits, reducing heating energy consumption; however, it also retains heat in summer, slightly increasing cooling demand. Energy savings are more noticeable in older buildings and colder climates, such as Toronto and Montreal, but become negligible in newer buildings and milder climates like Vancouver, especially under future weather conditions. Additionally, moss-based systems have a minimal effect on indoor overheating. Therefore, their effectiveness depends on climate-specific applications, and they may be best utilized alongside other passive design strategies.

Keywords: Vegetation, Energy, Thermal comfort.

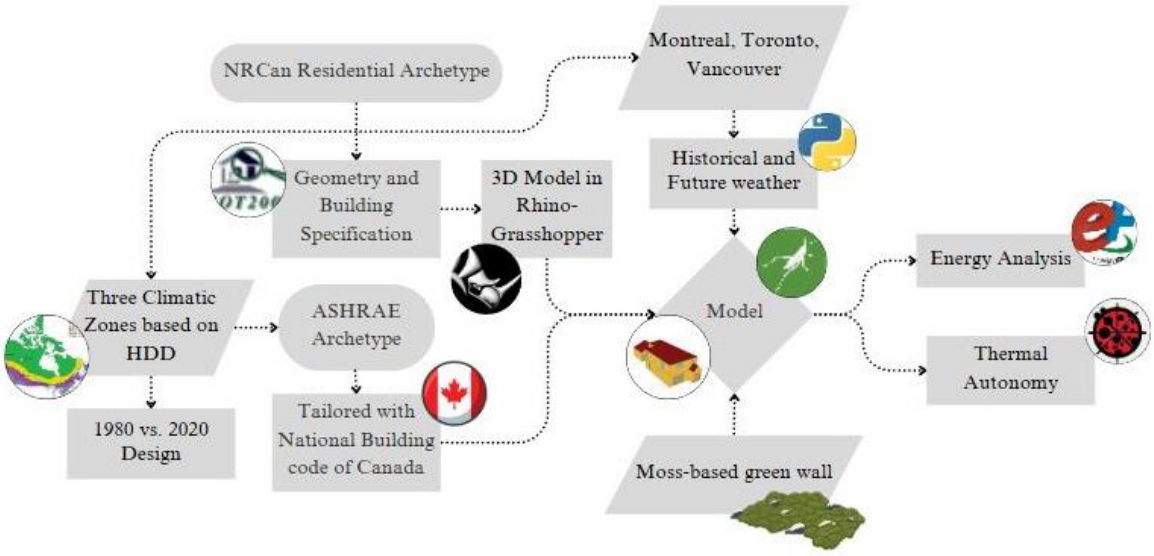

Figure 1. Graphical Abstract

1. Introduction

his study explores the use of moss-covered vertical surfaces as a sustainable design strategy to improve energy efficiency and thermal comfort in residential buildings. Moss is highlighted for its resilience, low maintenance, and adaptability, making it suitable for urban sustainability efforts. The research models moss application on NRCAN archetype buildings in three Canadian cities, comparing 1980 and 2020 construction standards. It includes a literature review on green walls and moss species, outlines the modeling methodology, and analyzes energy use and Indoor Thermal Autonomy (ITA). The findings aim to guide sustainable building practices in Canada.

2. Literature Review

Vegetation on building façades has been demonstrated to significantly reduce energy demand for heating and cooling, while also offering additional benefits such as improved air quality and urban biodiversity [1]. Using simulation and experimental mix research, *Moore et al.* showed that a green wall can provide thermal resistance comparable to a 2.5 cm layer of expanded polystyrene insulation. This highlights the potential of green walls as an insulating solution that contributes to energy efficiency in building design [2]. Also, Green walls can contribute to Urban Heat Island (UHI) Mitigation [3]. *Iaria et al.* found that increasing the coverage and leaf area index (LAI) of green roofs, living walls, and green façades significantly boosts their Urban Heat Island (UHI) mitigation potential. LAI increases from 1.5 to 3 greatly enhanced UHI reduction—by 70% for green roofs and 90% for living walls. Green roofs' effectiveness declines with taller buildings, becoming negligible above 40 m, while living walls and façades perform better up to 20 m. The study highlights the need to optimize coverage, LAI, and consider building height for effective UHI mitigation [4]. Green walls, also known as living walls or vertical gardens, are created using a variety of plant species that are suited to vertical growth, thrive in low-maintenance settings, and contribute to aesthetic and environmental benefits like insulation, air purification, and biodiversity support. Table 1 presents the thermal properties of each type of vegetation that can be incorporated into a thermal model. Common vegetation types used for green walls include (Figure 2):

1) Ivy is a popular green wall plant for its fast growth, surface adhesion, and adaptability to light, providing year-round greenery in mild climates. In colder regions, it may lose leaves or suffer winter damage. Ivy also improves air quality by capturing dust and pollutants, acting as a "particle sink," especially in high-traffic urban areas [5]. Additionally, Ivy canopies help regulate wall surface microclimates, reducing risks of frost and salt damage, which aids in preserving building materials in five sites across a range of climatic settings within England [6]. Studies in Manchester show that ivy-covered walls can raise external temperatures in late winter, reducing energy loss by 8%. Nighttime temperatures increase by 1.4°C, while daytime temperatures drop by 1.7°C due to shading. However, on warmer days, ivy may slightly reduce passive solar heat gain. Overall, evergreen walls like ivy can enhance energy efficiency and lower heating costs [7].

2) Virginia Creeper is valued for its fast growth and vibrant appearance, offering extensive facade coverage. As a deciduous plant, it provides summer shading that reduces cooling demand and allows winter solar gain to lower heating needs. This dual seasonal benefit makes it especially effective for thermally retrofitting poorly insulated buildings [8]. A comparative analysis of its thermal performance relative to English Ivy was conducted under controlled laboratory conditions, with experimental results validating its efficacy [9].

Figure 2. English Ivy (left) [8], Virginia Creeper (middle) [9], and Wisteria frutescens (right) [10].

3) Rosa setigera and Wisteria frutescens are ideal for green façades due to their lush growth and ability to reduce solar heat gain. While studies on climbing roses are limited, Wisteria performs well on sunlit west or south walls, improving thermal comfort. It can lower wall surface temperatures by up to 9°C and reduce heat flux by 22.3 W/m² in summer and 8 W/m² in winter, making it an effective, low-cost option for enhancing thermal performance in affordable housing [10].

2.1. Mosses

Bryophytes are a group of non-vascular plants that include mosses, liverworts, and hornworts. They are characterized by their simple structures and lack of true vascular tissues, which are typically found in higher plants. This means they rely on diffusion and osmosis to transport water and nutrients, limiting their size and growth to moist environments [11]. osses have existed for over 450 million years and are often overlooked due to their simple structure. Sphagnum, a genus of about 380 species, is a key ecological engineer and one of the oldest moss clades. Found in peatlands, which cover 3% of Earth's surface, Sphagnum stores about 30% of global soil carbon—twice as much as all forests—making it vital for carbon cycling and climate regulation [12].

2.1.1. Sphagnum moss

Sphagnum Palustre is commonly used in green walls for its excellent moisture retention and adaptability to humidity, supporting other plant growth and thriving in shaded, indoor settings. However, it is less suitable for sunny exterior walls and may negatively affect wall durability and moisture performance [11].

Figure 3. Sphagnum Fallax (Left) is typically found in moist, acidic environments such as bogs, fens, and wet heathlands. Sphagnum Palustre (right), also known as marsh moss, is commonly found in wetter environments, particularly in marshes, swamps, and around the edges of ponds [12]**.**

2.1.2. Hypnum Moss (Hypnum Cupressiforme)

Known for its ability to grow on a variety of surfaces, including stone and wood, this moss is suitable for vertical gardens (Figure 4). It can tolerate partial shade and does well in moist environments, making it a low-maintenance option for urban green walls[11].

Figure 4. Hypnum Moss (Hypnum Cupressiforme) Photo by Claire Halpin [11].

2.1.3. Sheet Moss (Hypnum imponens)

It forms a dense carpet of green that is highly effective for vertical surfaces. Sheet moss is often used in moss walls and vertical gardens for its aesthetic appeal and ability to cover large areas uniformly. Sheet Moss (Hypnum imponens): Often used for vertical green walls due to its lush, uniform appearance and ability to grow on various substrates [11].

Figure 5. Hypnum imponens, Photo by Sharon Pilington [11].

Figure 6 shows a real case for the Moss-based vertical wall The polyurethane sheet is securely attached to the building's wall, maintaining a gap that allows for monitoring the irrigation and fertilization system, which is divided into zones at different heights. This system consists of a layered network of pipes with emitters, supplied by a pump. Irrigation occurs vertically in multiple layers, using gravity to moisten the wool and distribute water to the plants, with the entire process being automated. To prevent moisture-related issues, proper ventilation and drainage must be ensured within the gap.

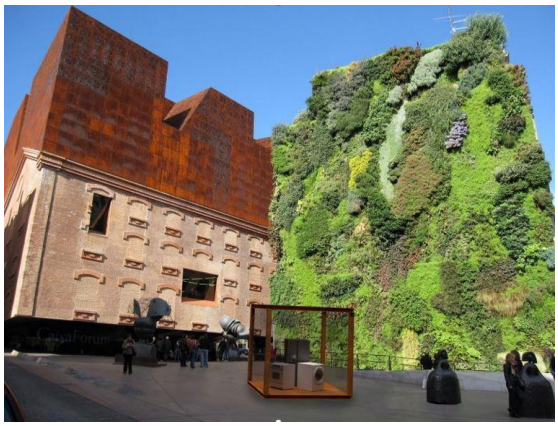

Figure 6. Caixa Forum Madrid, Patrick Blanc's Le Mur Vegetal System [13].

3. Methodology

Archetype data on geometry and thermal features is crucial for quick energy modeling of homes, covering dimensions, envelope, systems, and ventilation. Metered energy use offers a baseline, while age and climate-specific defaults aid thermal predictions. NRCan's "11 archetypes" were developed from 6,000 Energy Guide records using averaging techniques [14]. These archetypes, representing attached and detached residential buildings, are used for modeling and analyzing the feasibility and impact of building codes. In this study, Archetype 7, with the total gross floor area of 375 m^2—representing a two-story detached house without a basement—is modeled (Figure 7) [15]. The minimum insulation requirements, aligned with the Canadian climate, are evaluated for two construction years, 1980 and 2020, reflecting the National Building Code of Canada versions 7 and 15, respectively. The analysis is conducted for three cities—Montreal, Toronto, and Vancouver—each representing distinct climate zones in Canada. By analyzing the modeled archetype under different insulation standards and climate zones, the study can also assess the impact of vertical moss-based walls, on energy efficiency and thermal behavior. This evaluation helps determine the potential benefits of integrating sustainable and nature-based solutions into

modern building designs, particularly in the context of evolving building codes and climate-specific requirements.

Figure 7. NRCan Archetype 7, representing a two-story detached house without a basement.

The analysis was conducted using the Rhino Grasshopper simulation tool, which utilized the EnergyPlus module for energy analysis and the Ladybug plugin for thermal comfort evaluation [16]. The study incorporated National Building code of Canada insulation requirements and the characteristics of a vertical moss-based wall, modeled as an external additional layer to the wall assembly. Detailed specifications for the insulation requirements and the moss-based wall are provided in Table 1 and Table 2, respectively. The moss-based wall was modeled as an external layer added to the default building envelope. A stomatal resistance of 300 s/m was assumed, and the soil reflectivity and emissivity were set at 0.3 and 0.9, respectively.

Table 1. Minimum Insulation Requirements (NBC).

No.	Code	Year	Zone 4		Zone 5		Zone 6		Description
			Heating Degree Days (HDD)<3000		3000<HDD<4000		4000<HDD<5000		
			Vancouver (HDD=2825)		Toronto (HDD=3520)		Montreal (HDD=4200)		
			Minimum R SI (m^2K/W)		Minimum R SI (m^2K/W)		Minimum R SI (m^2K/W)		
			Wall	Roof	Wall	Roof	Wall	Roof	
1	NBC (7th Edition)	1977	1.47	1.43	1.60	1.57	1.73	1.71	Refers to The ACNBC Residential Standards 1977 (based on economic considerations)
2	NBC (15th Edition)	2020	2.78	4.67	3.08	4.67	3.08	4.67	Buildings without Heat-Recovery Ventilator

Table 2. The properties of green wall vegetation that are assumed for moss-based wall model.

Thickness (mm)	Leaf emissivity	Leaf Reflectivity	Plant Height (mm)	Leaf Area Index	Specific Heat (J/kg·K)	Thermal Conductivity (W/m·K)	References
50	0.95	0.2	20	0.5	1500	0.06	[17], [18], [19], [20]

Historical and projected future weather files for energy analysis were used in this study. Historical data is sourced from the Canadian Weather Year for Energy Calculation (CWEC) dataset, created by the Meteorological Service of Canada (MSC). The CWEC dataset uses the Typical Meteorological Year (TMY), selecting twelve representative months from 15 to 30 years of hourly data to form a synthetic year reflecting average weather conditions [21]. These files are widely used in building performance evaluations and align with the National Building Code of Canada. For future projections, this study uses the Representative Concentration Pathway (RCP) 8.5 scenario, which predicts a 3.5°C temperature rise due to high greenhouse gas emissions. RCP 8.5 assumes high population growth, slow income growth, and limited technological advancements, leading to increased energy demand and GHG emissions without climate policies [21]. [22]

4. Results and Discussion

4.1. Energy demand

Table 3 show the heating and cooling demand for different scenarios.Table 3. Cooling and Heating demand for the different scenarios.

Construction Year	Weather file (TMY)	Building envelope	Energy Demand KWh/m^2	Montreal	Toronto	Vancouver
1980	Historical	Default	Heating	339.0	323.4	195.1
			Cooling	13.7	13.7	3.0
1980	Historical	Moss Wall	Heating	323.6	305.6	183.3
			Cooling	13.5	13.4	3.0
1980	Future RCP 8.5	Default	Heating	231.5	192.3	104.9
			Cooling	58.3	58.3	14.1
1980	Future RCP 8.6	Moss Wall	Heating	220.8	181.3	99.1
			Cooling	60.2	59.1	14.7
2020	Historical	Default	Heating	264.5	251.2	154.4
			Cooling	8.9	8.6	1.3
2020	Historical	Moss Wall	Heating	257.7	243.4	148.7
			Cooling	8.9	8.6	1.3
2020	Future RCP 8.5	Default	Heating	178.8	147.7	80.7
			Cooling	47.0	47.3	11.6
2020	Future RCP 8.5	Moss Wall	Heating	174.1	142.9	78.1
			Cooling	48.3	48.1	12.0

Buildings constructed in 2020 consistently consume less energy for both heating and cooling compared to those built in 1980 as the newer buildings are more energy-efficient, likely due to improved insulation, better construction materials. Also, Future weather files predict higher cooling energy consumption and lower heating energy consumption compared to historical data. This aligns with climate change projections, where warmer temperatures reduce heating demand but increase cooling demand. Montreal has the highest heating energy consumption due to cold winters. Cooling energy consumption is relatively low, Toronto has the moderate heating and

cooling energy consumption, and Vancouver has the Lowest heating and cooling energy consumption due to its mild climate.

Moss walls improve building energy efficiency by reducing heating demand, especially in colder climates, while having minimal impact on cooling. For 1980 buildings, heating demand drops by up to 6% under historical weather and up to 5.7% under future RCP 8.5 scenarios. Cooling demand remains largely unchanged or slightly increases. For 2020 constructions, heating reductions are smaller (2.6–3.7%), with no significant cooling effect. Overall, moss walls are most effective for enhancing heating performance in older, less insulated buildings.

4.2. **Indoor Thermal Autonomy**

To further evaluate the benefits of moss-based vegetation, its impact on thermal autonomy was analyzed for a 1980-built structure in Montreal under RCP 8.5 future weather conditions, representing a 3.5°C temperature increase due to global warming. The operative temperature data in the southwest room, which receives the most sunlight and is considered the hottest space, is used for the analysis (Figure 8). Indoor Thermal autonomy (ITA) measures the proportion of hours throughout the year during which indoor operative temperatures (equation 1) fall within a comfortable range, typically defined between 18°C (64.4°F) and 25°C (77°F) [22]. Operative temperature averages air and mean radiant temperatures to accurately reflect how building elements impact thermal comfort. For Indoor Thermal Autonomy (ITA) evaluation, buildings are simulated in "free running" mode without active systems or occupancy, assessing how many hours annually (out of 8,760) the indoor operative temperature stays within a comfort range [23].

$$t_o = \frac{(h_r t_{mr} + h_c t_{a)}}{h_r + h_c} \qquad (1)$$

t_o = operative temperature (°C)

h_c = convective heat transfer coefficient (W/m²·K)

h_r = linear radiative heat transfer coefficient (W/m²·K)

t_a= air temperature (°C)

t_{mr}= mean radiant temperature (°C)

Overly hot conditions increased from 31.9% to 32.0% of the year (+0.1%), thermal autonomy decreased from 17.7% to 17.6% (-0.1%), and overly cold conditions decreased from 50.4% to 50.3% (-0.1%) (Table 4). These results indicate that the moss-based wall has a negligible impact on ITA, with a slight trade-off between increased heat retention in warmer periods and improved insulation in colder conditions.

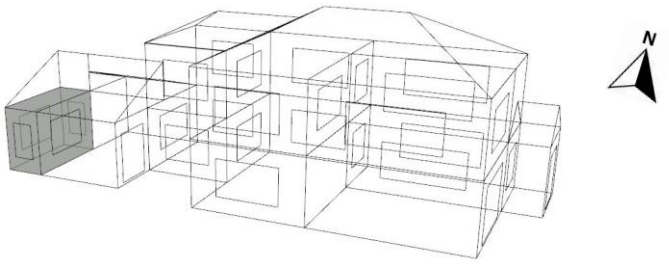

Figure 8. The operative temperature data were recorded from an indoor sensor located in the southwest room, which receives the most sunlight and is considered the hottest space, ensuring the maximum potential impact is captured.

Table 4. Indoor Thermal Autonomy status for a house located in Montreal in Future climate with default and Moss-based green wall.

Condition	Default Envelope	Moss-Based wall
Overly Hot (Temp>25 °C)	31.9%	32.0%
Thermal Autonomy (18<Temp<25 °C)	17.7%	17.6%
Overly Cold (Temp<18 °C)	50.4%	50.3%
Total Hour of the year (8760)	100%	100%

5. Conclusions

The findings suggest that while moss walls offer some insulation benefits by reducing heating energy consumption, their tendency to retain heat in summer leads to a slight increase in cooling demand. Energy savings are more pronounced in older buildings and colder climates, such as Toronto and Montreal, but become negligible in newer buildings and milder climates like Vancouver, particularly under future weather conditions. As global temperatures rise, the reduced heating demand and increased cooling needs may limit the effectiveness of moss walls as a passive energy-saving strategy.

One of the key benefits of green walls (including moss walls) is their ability to reduce cooling loads through shading and evaporative cooling. With minimal shading, the moss wall's ability to lower indoor temperatures during summer would be limited, potentially resulting in higher indoor operative temperatures. Future studies should explore strategies to reduce moss walls' slight summer cooling drawbacks, address real-world challenges like maintenance and regulatory integration, and clarify moss's advantages over conventional green walls in Canada. Additionally, assessing whether the modest energy savings justify the investment compared to other passive measures and examining policy and design implications for moss wall adoption in Canadian buildings is recommended.

6. References

[1] Z. Al-Shatnawi, C. Hachem-Vermette, M. Lacasse, and B. Ziaeemehr, 'Advances in Cold-Climate-Responsive Building Envelope Design: A Comprehensive Review', *Buildings*, vol. 14, no. 11, p. 3486, Oct. 2024, doi: 10.3390/buildings14113486.

[2] O. Moore, L. Blackburne, K. Gharehbaghi, and N. Hurst, 'Lessening the energy usage of buildings: an exploration into green walls' practicalities', *Proceedings of the Institution of Civil Engineers - Municipal Engineer*, pp. 1–17, Sep. 2024, doi: 10.1680/jmuen.24.00015.

[3] B. Ziaeemehr, Z. Jandaghian, H. Ge, M. Lacasse, and T. Moore, 'Increasing Solar Reflectivity of Building Envelope Materials to Mitigate Urban Heat Islands: State-of-the-Art Review', *Buildings*, vol. 13, no. 11, p. 2868, Nov. 2023, doi: 10.3390/buildings13112868.

[4] J. Iaria and T. Susca, 'Analytic Hierarchy Processes (AHP) evaluation of green roof- and green wall- based UHI mitigation strategies via ENVI-met simulations', *Urban Clim*, vol. 46, p. 101293, Dec. 2022, doi: 10.1016/j.uclim.2022.101293.

[5] T. Sternberg, H. Viles, A. Cathersides, and M. Edwards, 'Dust particulate absorption by ivy (Hedera helix L) on historic walls in urban environments', *Science of The Total Environment*, vol. 409, no. 1, pp. 162–168, Dec. 2010, doi: 10.1016/j.scitotenv.2010.09.022.

[6] T. Sternberg, H. Viles, and A. Cathersides, ‘Evaluating the role of ivy (Hedera helix) in moderating wall surface microclimates and contributing to the bioprotection of historic buildings’, *Build Environ*, vol. 46, no. 2, pp. 293–297, Feb. 2011, doi: 10.1016/j.buildenv.2010.07.017.
[7] C. Bolton, M. A. Rahman, D. Armson, and A. R. Ennos, ‘Effectiveness of an ivy covering at insulating a building against the cold in Manchester, U.K: A preliminary investigation’, *Build Environ*, vol. 80, pp. 32–35, Oct. 2014, doi: 10.1016/j.buildenv.2014.05.020.
[8] M.-A. Kenai, L. Libessart, S. Lassue, and D. Defer, ‘Impact of green walls occultation on energy balance: Development of a TRNSYS model on a brick masonry house’, *Journal of Building Engineering*, vol. 44, p. 102634, Dec. 2021, doi: 10.1016/j.jobe.2021.102634.
[9] M.-A. Kenai, L. Libessart, S. Lassue, and D. Defer, ‘Impact of plants obscuration on energy balance: Theoretical and numerical study’, *Journal of Building Engineering*, vol. 29, p. 101112, May 2020, doi: 10.1016/j.jobe.2019.101112.
[10] P. Fensterseifer, E. Gabriel, R. Tassi, D. G. A. Piccilli, and B. Minetto, ‘A year-assessment of the suitability of a green façade to improve thermal performance of an affordable housing’, *Ecol Eng*, vol. 185, p. 106810, Dec. 2022, doi: 10.1016/j.ecoleng.2022.106810.
[11] https://www.britishbryologicalsociety.org.uk/, ‘The British Bryological Society’.
[12] V. M. Lueth and R. Reski, ‘Mosses’, *Current Biology*, vol. 33, no. 22, pp. R1175–R1181, Nov. 2023, doi: 10.1016/j.cub.2023.09.042.
[13] https://www.verticalgardenpatrickblanc.com/realisations/madrid/caixa-forum-madrid, ‘Vertical Garden Patrick Blanc’.
[14] Anil Parekh, ‘Development of archetypes of building characteristics Libraries for simplified energy use evaluation of houses’, in *Ninth International IBPSA Conference*, Montreal, Canada, 2005.
[15] R. Asaee, A. Ferguson, and A. Wills, ‘Application of A Housing Technology Assessment Simulation Platform in Regulation R&D’, 2019, pp. 3940–3947. doi: 10.26868/25222708.2019.210805.
[16] Robert McNeel & Associates, ‘Rhino 3D’, 2024, *Seattle*: 8.
[17] M. Sharbafian, M. Yeganeh, and M. Baradaran Motie, ‘Evaluation of Shading of Green Facades on Visual Comfort and Thermal load of the Buildings’, *Energy Build*, vol. 317, p. 114303, Aug. 2024, doi: 10.1016/j.enbuild.2024.114303.
[18] C. J. Moore and G. Fisch, ‘Estimating heat storage in Amazonian tropical forest’, *Agric For Meteorol*, vol. 38, no. 1–3, pp. 147–168, Oct. 1986, doi: 10.1016/0168-1923(86)90055-9.
[19] E. Erell, D. Pearlmutter, and T. Williamson, *Urban Microclimate*. Routledge, 2012. doi: 10.4324/9781849775397.
[20] L. Libessart and M. A. Kenai, ‘Measuring thermal conductivity of green-walls components in controlled conditions’, *Journal of Building Engineering*, vol. 19, pp. 258–265, Sep. 2018, doi: 10.1016/j.jobe.2018.05.016.
[21] https://climate.weather.gc.ca/prods_servs/engineering_e.html, ‘Engineering Climate Datasets’.
[22] B. Levitt, S. Ubbelohde, G. Loisos, and N. Brown, ‘Thermal Autonomy’, 2013.
[23] T. Kesik, O. Liam, A. Ozkan, and A. Chong, ‘Thermal Resilience Design Guide’, Toronto, 2019.

6th International Conference on Building Energy and Environment
Eindhoven University of Technology, The Netherlands
6 - 10 July 2025

Resilient Urban Rooftops for Brussels: A simulation-based investigation into the effectiveness of cool and green roofs under current and future climate scenarios.

Ferre Maes [1], Sanae Chaga [2], Bert Belmans [3,4]

[1]*Vrije Universiteit Brussel, Brussels, Belgium, ferre.maes@vub.be*
[2]*Vrije Universiteit Brussel, Brussels, Belgium, sanae.chaga@vub.be*
[3]*Vrije Universiteit Brussel, Brussels, Belgium, bert.belmans@vub.be*
[4]*Universiteit Antwerpen, Antwerp, Belgium, bert.belmans@uantwerpen.be*

SUMMARY
This study evaluates the effectiveness of cool roofs and green roofs as climate adaptative summer comfort control strategies for a case study building in Brussels and Madrid under current and future climate scenarios. Using EnergyPlus simulations, the study compares these strategies with standard roofs in terms of thermal comfort and operative temperature. Key findings show that both cool and green roofs can significantly improve thermal comfort in the case study building compared to the traditional roof covering, both in terms of the number of unmet hours and the extent to which comfort limits are exceeded. The cool roof option finish is shown to generally perform better in Brussels, while green roofs show greater adaptability to higher temperatures, excelling in the Madrid climate. In both locations, both strategies significantly reduce unmet comfort hours during the current summer, with a slight decrease in effectiveness projected for future summers. Their benefits are most notable during temperature peaks and heat waves. However, these strategies come with certain limitations, such as a potential winter penalty. As climates continue to shift and winters grow milder, adapting rooftop mitigation strategies to these evolving conditions offers the potential for more balanced and optimal performance year-round.

Keywords: rooftops, thermal comfort, climate

1. INTRODUCTION

In the context of climate change, regions traditionally associated with heating requirements, such as Belgium, are increasingly encountering the challenge of cooling during the summer months and frequent heatwaves. This transition is particularly evident in urban areas, which are more susceptible to global warming and extreme temperatures due to the urban heat island effect (Wouters et al., 2017). Roofs, as the most exposed building surfaces, play a crucial role in mitigating climate extremes and improving thermal performance. Recent research has underscored the importance of adaptive roof strategies (D'Agostino et al., 2024), particularly for cool and green roofs, as promising solutions. Cool roofs reflect more sunlight and absorb less heat than traditional roofs owing to their high solar reflectance and thermal emittance. Green roofs can be either extensive or intensive, with extensive roofs being lightweight and low maintenance, whereas intensive roofs support diverse plants and recreational use. Despite extensive research on these individual rooftop mitigation strategies (Zinzi and Agnoli 2012; Bozonnet, Doya, and Allard 2011; Li and Yeung 2014; Cirrincione, Marvuglia, and Scaccianoce 2021), research gaps remain, particularly regarding long-term performance under future climate scenarios and limited data on cool and green roofs in moderate climates, such as Belgium.

The main aims of this study were threefold: First, it sought to address the knowledge gap through simulation-based assessments of green and cool roofs in current and future climate scenarios. Second, the study aims to provide a direct comparison of different rooftop mitigation strategies. Finally, it intends to offer comprehensive guidance to support informed decision making for future renovation projects in moderate climates in Western Europe.

3. METHODOLOGY

3.1 Research design

A case study building in Brussels, "Co-working office La Lustrerie," was selected to compare the current rooftop configuration with cool roof (CR) and green roof (GR) strategies. A post-occupancy survey evaluated summer comfort in the existing condition, featuring a traditional black bitumen roof, revealing severe overheating often described as "unbearable." To analyse these problems, a digital twin of the building was created using actual usage data, consumption profiles, material specifications, and details from building plans and site visits. This model was enriched with insights from user surveys and effectively replicated overheating problems, thereby reinforcing its relevance. Using the EcoRoof model and roof surface absorption properties in EnergyPlus, this study simulates and compares green, cool, and traditional roof finishes for summertime thermal comfort. The comparison spans 2024, 2050, and 2080 for Belgium and Madrid, reflecting the shifting climate zones. Lessons from Madrid's strategies can inform solutions for Brussels while assessing the future effectiveness of these approaches in Madrid.

3.2 Roofing strategies

3.2.1 Standard roofing

Reference scenarios were needed to evaluate and compare the performance of the cool and green roofs. A flat roof with a traditional construction setup was used consisting of a black bituminous roof membrane, an insulation layer with variable thickness - (0.0001 cm), 5 cm, 10 cm and 15 cm - and a roof slab in light-weight concrete. Both mitigation strategies are implemented on this roofing typology.

3.2.2 Cool roofs

For the implementation of the cool roof, the black bituminous roofing membrane is changed to a cool roof layer. This layer is made of a highly reflective coating designed to minimize solar absorption and maximize thermal emittance. Below this layer, the conventional roof layers follow as before. Properties of the standard roof and the changed cool roof layer are given in Table 1.

Table 1. Layers and used parameters of conventional flat and pitched roof

Layers	Thickness (m)	Density (kg/m³)	Conductivity (W/mK)	Specific heat (J/kgK)	Thermal absorptance (-)	Solar absorptance (-)	Visible absorptance (-)
Cool roof / Roofing membrane	0.01	40	0.1	1400	0.95	0.15	0.15
	0.01	1120	0.16	1460	0.9	0.65	0.65
Insulation	~	43	0.03	1210	0.9	0.7	0.7
Light-weight concrete	0.15	1280	0.53	840	0.9	0.8	0.8

3.2.3 Green roofs

To implement the green roof, an additional green roof layer is added to the standard roof. The

parameters are divided into two parts: vegetation (Table 2) and soil (Table 3). The minimum stomatal resistance indicates the evapotranspiration rate of the plants. Soil parameters include saturation content (moisture at full saturation), residual content (dry matter) and initial moisture content at the start of the simulation.

Table 2. Used parameters for the green roof vegetation layer

Layer	Height of plants (m)	Leaf Area Index (-)	Leaf reflectivity (-)	Leaf emissivity (-)	Minimum stomatal resistance (m/s)
Vegetation	0.05	5	0.25	0.95	180

Table 3. Used parameters for the green roof soil layer

Layer	Thickness (m)	Density of dry soil (kg/m³)	Conductivity of dry soil (W/mK)	Specific heat of dry soil (J/kgK)	Saturation content (-)	Residual content (-)	Initial content (-)
Soil	0.10	1100	0.35	1200	0.5	0.1	0.5

3.3 Adaptive comfort model

To assess thermal comfort, an adaptive comfort model is used, which is based on the principle that individuals adapt to their environment. An adaptive model is used because the idea around "comfort" will change in the future, in extreme situations we will need to adapt more than in other situations. As a result, the indoor comfort temperature is not fixed but varies depending on the running average of the outdoor air temperature. The model (CEN 15251) is divided into three categories: Category I represents a high comfort level for sensitive occupants, such as those in hospitals, elderly care facilities, and nurseries; Category II reflects normal comfort expectations for most buildings, including offices and homes; and Category III applies to moderate comfort expectations, typically for existing buildings or less demanding environments. Since the building in question is an office, Category II is selected. The adaptive comfort model in CEN Standard EN15251 has been shown to be an effective approach for evaluating thermal comfort in naturally ventilated buildings across various climates and regions (Sánchez-García et al., 2018).

3.4 Climate scenarios

This study examines two types of climate: Belgium's moderate maritime climate and the more extreme Mediterranean climate, using Brussels and Madrid as reference cities. Belgium has an average annual temperature of 10°C, while Brussels ranges from ~0°C in January to 22°C in July (Climatestotavel.com, 2024a). Madrid's climate is characterized by mild winters (6.3°C in January) and hot summers (26°C on average, peaking at 40°C) (Climatestotavel.com, 2024b). Simulations use EnergyPlus Weather (EPW) files for typical years, derived from 18 years of hourly data. Future scenarios for 2050 and 2080 use IPCC-based climate-adjusted EPW files (Jentsch et al., 2012).

4. RESULTS

4.1 Thermal comfort summer

4.1.1 Unmet hours

Unmet hours were calculated for the summer period from June 21 to September 21. As explained in Chapter 3.3, for comfort class II these occur when the operative temperature exceeds the comfort

temperature by ±3°C. Hours are only counted when people are present in the building —, this corresponds to full days during working hours on weekdays and partial occupancy on Saturdays. The 93-day period leads to 1042 hours. Figure 1 shows results for the current climate, 2050, and 2080. Standard roofs show the highest number of unmet hours, with a significant increase by 2080. Both rooftop mitigation strategies demonstrate fewer unmet hours compared to the standard roof. However, this still results in uncomfortable summer indoor conditions for approximately 40% of the time. The simulation assumes no active air conditioning and closed windows. On a yearly basis, the percentage would decrease with winter comfort controls, but additional measures like the planned renovation as explained before are needed to keep the building comfortable.

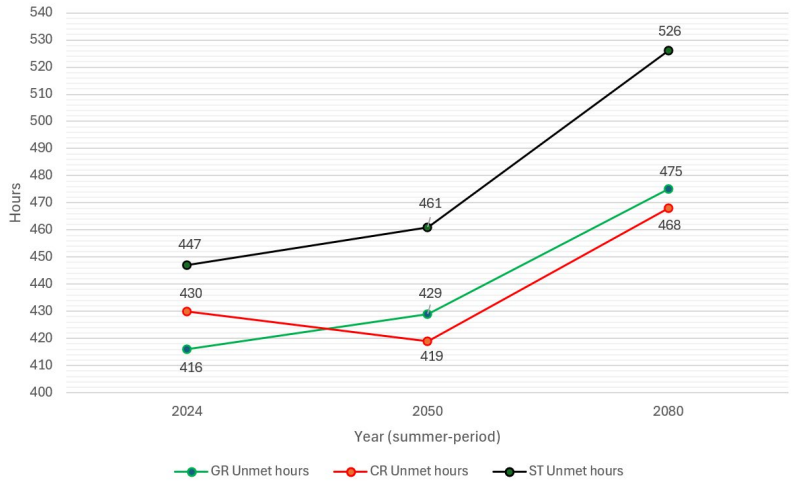

Figure 1. Unmet hours for summer season.

4.1.2 Temperature balance July

To thoroughly examine thermal performance strategies during hot spells, simulated temperatures were assessed throughout July. These included the external dry bulb temperature, the internal radiant surface temperature of the roof, the external surface temperature of the roof, the mean operative temperature of the space, and the mean air temperature (dry bulb) of the space. These simulation results were requested for the case study building in both Brussels and Madrid for the years 2024, 2050, and 2080. Figures 2 and 3 display these findings, although only 2024 and 2080 are shown since 2050 was very similar to 2080, but with smaller variations. The results presented all pertain to the scenario with an insulation thickness of 5 cm. While the operative temperature alone would suffice to compare the different strategies, the additional temperatures reported provide a deeper insight into the thermal response of each strategy. Trend lines are employed to facilitate a more straightforward evaluation of the hourly temperatures, making it easier to compare the strategies.

Overall, the results for cool roofs and green roofs are quite similar. Green roofs lower indoor air temperatures by just over 0.5°C compared to standard roofs, while cool roofs achieve a reduction of nearly 1°C. The differences are more noticeable during high temperature peaks than during cooler periods. Specifically, the internal radiant temperature of the cool roof in the case study is almost 2°C lower than that of the standard roof. Similar findings were reported by (Xing and Jones,

2019) , where a green roof reduced indoor air temperatures by 2.5°C compared to a bare aluminum roof during a heatwave event in the UK. Other research from Italy found that during the summer, cool roofs can decrease the indoor operative air temperature by more than 3°C (Pisello, Cotana, and Rossi, 2014). The external surface temperature offers additional insights, showing the consistency of these mitigation strategies. It rises steadily with outdoor air temperature but does not exhibit significant fluctuations. For conventional roofs, the external surface temperature surpasses 40°C during peak times (with a trend line around 33°C) and falls below the operative temperature during cooler periods. This pattern suggests strong solar radiation during peak times and limited sunlight during cooler periods. The external surface temperature of the mitigation strategies also underscores their effectiveness, remaining below the operative temperature and demonstrating the cooling effect of evapotranspiration in green roofs and the material properties of cool roofs. Similar findings were reported by Pisello et al., where cool roofs reduced the average external roof surface temperature by more than 10°C (Pisello, Cotana, and Rossi, 2014).

The elevated operative temperature is not due to a hot external roof surface but rather higher internal air temperatures, likely caused by the building's large windows, which allow significant solar gain. In the simulations, the windows remain closed, but opening them in reality could help cool the indoor air while the mitigation strategies manage the roof's thermal performance. In future climate scenarios, these effects are observed but amplified, with larger differences. Green roofs become more effective as their external surface temperature aligns more closely with the outdoor air temperature, while that of cool roofs increases. This is because cool roofs reflect solar radiation, which remains unchanged in future scenarios, while the general outdoor temperature and ambient heat rise. Green roofs better mitigate these effects. In Madrid, where temperatures are generally higher, green roofs outperform cool roofs even in the 2024 climate. Green roofs slightly lower the operative temperature and significantly reduce the external surface temperature compared to cool roofs, highlighting their advantage in hotter conditions. This advantage assumes a permanently active irrigation system for the green roof, as it is a fixed parameter in the simulations.

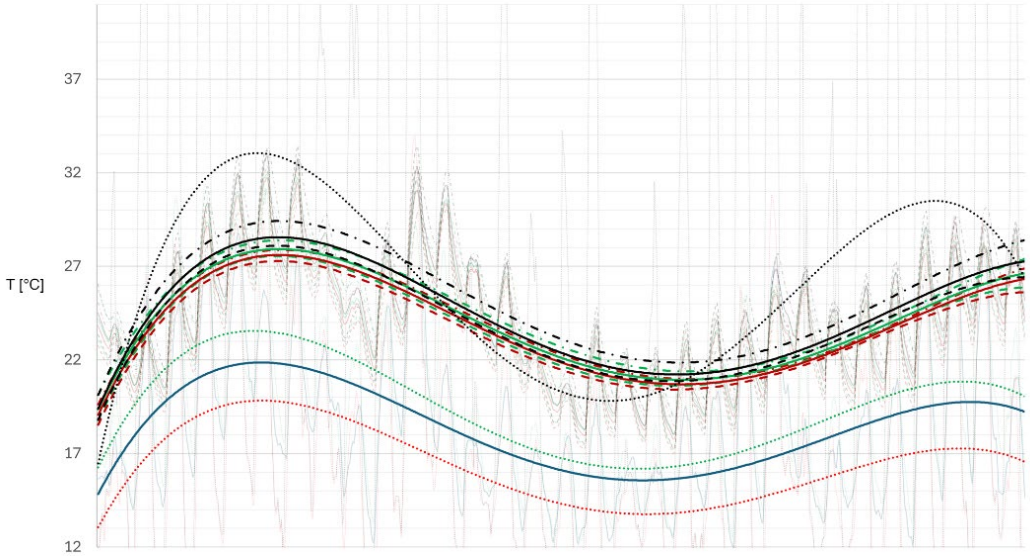

Figure 2. Thermal performance July, Brussels 2024.

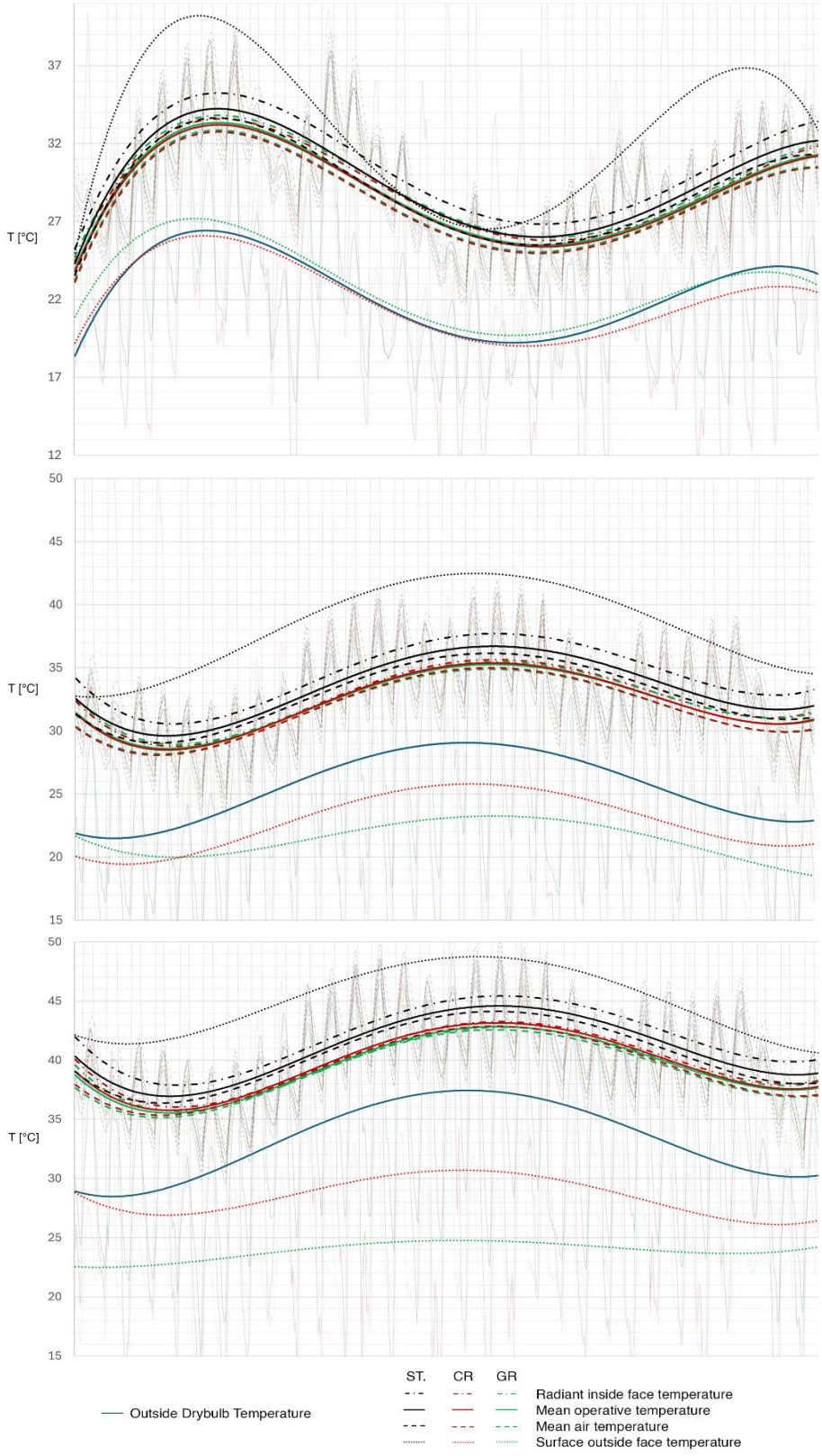

Figure 3. Thermal performance July. Top: Brussels 2080, middle: Madrid 2024, bottom: Madrid 2080.

4.5 Heatwave performance

In this study, a heatwave is defined as at least five consecutive days with maximum temperatures of 25°C or more, including three days over 30°C. This period was analysed to understand daily temperature trends. Figure 4 shows temperature peaks around 2 pm over five days. Similar to the monthly chart, nighttime outdoor temperatures drop, but rooftop mitigation strategies show a smaller decrease. Standard roof radiant temperatures vary more during the day, the mitigation strategies show more equilibrium between radiant and operative temperatures. At noon, operative temperatures exceed radiant ones, but the reverse occurs at night, suggesting high operative temperatures are influenced by elements like windows, while roof temperatures remain stable. Data from the standard roof supports this, as operative temperatures never exceed radiant ones, highlighting the effect of traditional roofing materials during peaks. These conclusions are backed by the research of (Di Giuseppe and D'Orazio, 2014) on green and cool roofs in a Nearly Zero Energy Building. Findings confirm that high albedo materials with a low U-value have limited internal comfort effectiveness, suggesting the building's U-value in this study is not low, as the cool roof outperforms the green roof during heatwaves.

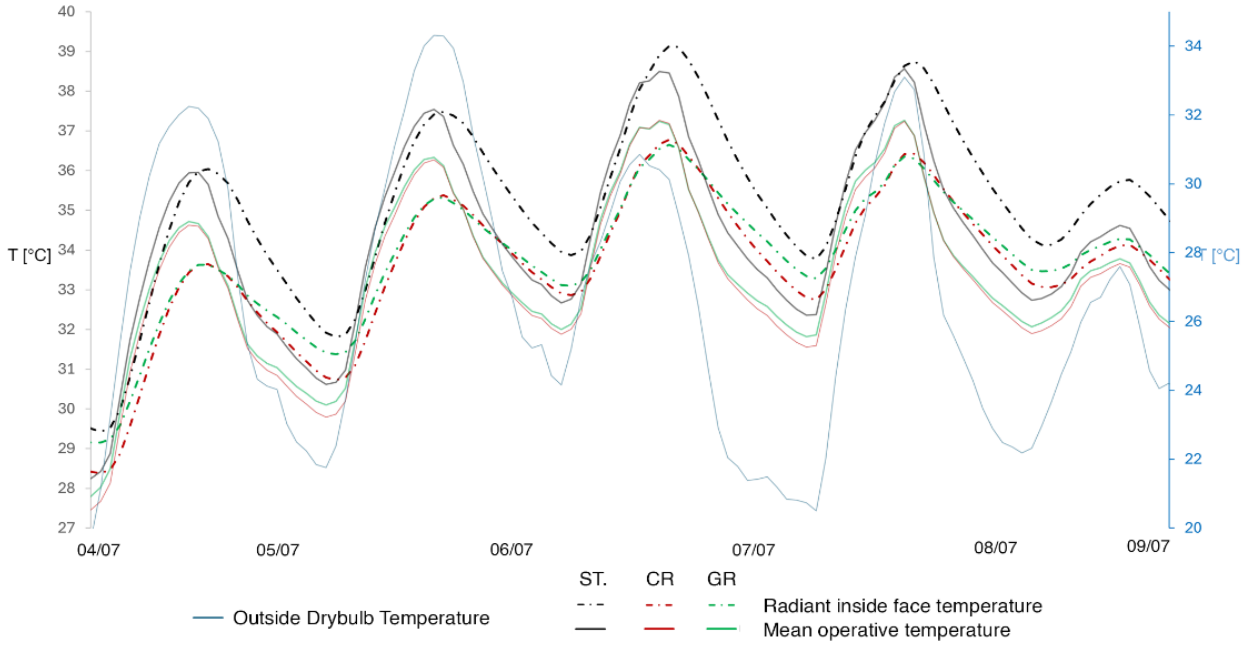

Figure 4. Heatwave performance

5. CONCLUSION

This research highlighted the effectiveness of cool and green roofs in Brussels and Madrid under current and future climate scenarios. Both roof types enhanced thermal performance compared to standard roofs, with cool roofs proving most effective in Brussels, while green roofs excel in hotter climates like Madrid. In future climate scenarios, as temperatures shift northward, green roofs were projected to offer better thermal comfort in Brussels. However, it is important to note that the case study building used in this research did not represent a typical structure for Madrid's hotter climate, given its large windows and lack of external shading. In such cases, mitigation strategies alone are insufficient to maintain comfort during extreme heat. Simple measures, such as adding daytime

shading and utilizing natural night ventilation, could significantly improve thermal comfort. Further studies are needed to assess the thermal performance of these mitigation strategies in buildings with diverse typologies in both climates. Additionally, research should investigate other factors, including cost, energy performance, stormwater management, and environmental impacts such as biodiversity. Finally, future studies should explore the potential of combining multiple strategies across various roof types to reduce the urban heat island effect and enhance both building and environmental comfort.

ACKNOWLEDGEMENTS

This work builds on the Master's thesis conducted by Sanae Chaga at the Vrije Universiteit Brussel. The case study and parts of the methodology - including the use of an EnergyPlus script and material parameter specifications - have been adopted from the original research.

REFERENCES

Bozonnet, E., M. Doya, and F. Allard. 2011. 'Cool Roofs Impact on Building Thermal Response: A French Case Study'. *Energy and Buildings* 43 (11): 3006–12. https://doi.org/10.1016/j.enbuild.2011.07.017.

Cirrincione, Laura, Antonino Marvuglia, and Gianluca Scaccianoce. 2021. 'Assessing the Effectiveness of Green Roofs in Enhancing the Energy and Indoor Comfort Resilience of Urban Buildings to Climate Change: Methodology Proposal and Application'. *Building and Environment* 205 (November):108198. https://doi.org/10.1016/j.buildenv.2021.108198.

Climatestotavel.com. 2024a. 'Climate in Belgium'. 2024. https://www.climatestotravel.com/climate/belgium.

———. 2024b. 'Climate in Madrid (Spain)'. 2024. https://www.climatestotravel.com/climate/spain/madrid.

D'Agostino, Delia, Paolo Maria Congedo, Paola Maria Albanese, Alessandro Rubino, and Cristina Baglivo. 2024. 'Impact of Climate Change on the Energy Performance of Building Envelopes and Implications on Energy Regulations across Europe'. *Energy* 288 (February):129886. https://doi.org/10.1016/j.energy.2023.129886.

Di Giuseppe, Elisa, and Marco D'Orazio. 2014. 'Assessment of the Effectiveness of Cool and Green Roofs for the Mitigation of the Heat Island Effect and for the Improvement of Thermal Comfort in Nearly Zero Energy Building'. *Architectural Science Review* 58 (November). https://doi.org/10.1080/00038628.2014.966050.

Jentsch, Mark, Patrick James, Leonidas Bourikas, and AbuBakr Bahaj. 2012. 'CCWorldWeatherGen'. https://energy.soton.ac.uk/climate-change-world-weather-file-generator-for-world-wide-weather-data-ccworldweathergen/.

Li, W.C., and K.K.A. Yeung. 2014. 'A Comprehensive Study of Green Roof Performance from Environmental Perspective'. *International Journal of Sustainable Built Environment* 3 (1): 127–34. https://doi.org/10.1016/j.ijsbe.2014.05.001.

Pisello, Anna, Franco Cotana, and Federico Rossi. 2014. 'Summer and Winter Effect of Innovative Cool Roof Tiles on the Dynamic Thermal Behavior of Buildings'. *Energies* 7 (April). https://doi.org/10.3390/en7042343.

Sánchez-García, Daniel, Jacinto Canivell, Fco Javier Guevara-García, Jesús A Pulido-Arcas, and Carlos Rubio-Bellido. 2018. 'Adaptive Comfort Models Applied to Existing Dwellings in Mediterranean Climate Considering Global Warming'. *Sustainability* 10 (September). https://doi.org/10.3390/su10103507.

Wouters, Hendrik, Koen De Ridder, Lien Poelmans, Patrick Willems, Johan Brouwers, Parisa Hosseinzadehtalaei, Hossein Tabari, Sam Vanden Broucke, Nicole P. M. van Lipzig, and Matthias Demuzere. 2017. 'Heat Stress Increase under Climate Change Twice as Large in Cities as in Rural Areas: A Study for a Densely Populated Midlatitude Maritime Region'. *Geophysical Research Letters* 44 (17): 8997–9007. https://doi.org/10.1002/2017GL074889.

Xing, Yangang, and Phil Jones. 2019. 'In-Situ Monitoring of Energetic and Hydrological Performance of a Semi-Intensive Green Roof and a White Roof during a Heatwave Event in the UK'. *Indoor and Built Environment* 30 (November). https://doi.org/10.1177/1420326x19887218.

Zinzi, M., and S. Agnoli. 2012. 'Cool and Green Roofs. An Energy and Comfort Comparison between Passive Cooling and Mitigation Urban Heat Island Techniques for Residential Buildings in the Mediterranean Region'. *Energy and Buildings* 55 (December):66–76. https://doi.org/10.1016/j.enbuild.2011.09.024.

6th International Conference on Building Energy and Environment
Eindhoven University of Technology, The Netherlands
6 - 10 July 2025

Impacts of Potted Tree Configurations on $PM_{2.5}$ Concentration in the Field Lab Haarlemmermeer near Schiphol Airport

Tingxiao Li [1], Gustaf Wuite[2,3], Martijn Lugten[1,2], Benthe Thielen[3], Hailin Zheng[4], Zhikai Peng[1,2]

[1]*Amsterdam Institute for Advanced Metropolitan Solutions, The Netherlands, tingxiao.li@ams-institute.org*
[2]*Delft University of Technology, The Netherlands, z.p.peng@tudelft.nl*
[3]*Wageningen University & Research, The Netherlands, benthe.thielen@wur.nl*
[4]*Eindhoven University of Technology, The Netherlands, h.zheng1@tue.nl*

SUMMARY
This study examines the impact of potted tree configurations on $PM_{2.5}$ concentrations from air traffic emissions near Schiphol Airport. Air quality sensors collected data between 2022 and 2024 at a field lab 5 km from the Kaagbaan runway. ENVI-met simulations were first validated and calibrated using ground-truth measurements under stable meteorological conditions, followed by simulations of $PM_{2.5}$ concentrations across six tree configurations in the field lab. The *'V7_End_Dense'* configuration achieved the greatest $PM_{2.5}$ reduction, while *'V2_Dispersed'* and *'V3_Double_Row'* showed moderate effects. In contrast, *'V4_Exposed,' 'V5_Exposed_Dense,'* and *'V6_Gate_Dense'* unexpectedly hindered reduction, highlighting the complex interactions between wind corridors, tree layouts, and built environments. The findings emphasise the need for long-term ENVI-met validation against real measurements, as seasonal variations were not captured in short-term analyses. Despite limitations, the study provides practical guidance for urban designers, highlighting the nuanced role of green infrastructure in mitigating aircraft-induced air pollution and emphasising the complexity of wind and pollution dynamics in urban environments.

Keywords: $PM_{2.5}$, aircraft emission, urban morphology, urban green infrastructure, tree configuration

1. INTRODUCTION

Particulate matter ($PM_{2.5}$) is widely recognised as a major contributor to illnesses such as heart disease, respiratory infections, and chronic lung disease, causing approximately 4 million deaths worldwide (Thangavel et al., 2022). Schiphol Airport, one of the busiest airports in the country, exposes nearby residents to elevated pollutant concentrations from air traffic, increasing health risks (RIVM, 2019). Research shows that linear green infrastructure positively impacts $PM_{2.5}$ concentrations (Jeong et al., 2023a); However, studies on the effects of different tree configurations on air pollution, especially $PM_{2.5}$, remain insufficient compared to research in other domains such as urban heat, noise, and glare pollution (Lugten et al, 2024, Wuite et al, 2023). From a planning perspective, it is crucial to explore how trees mitigate air traffic-related pollution and identify the most effective tree configurations for filtering $PM_{2.5}$, benefiting residents exposed to air traffic pollution. To address this, the Urban Comfort Lab (UCLab) at AMS Institute established a field lab in Hoofddorp, located less than 1 km from Schiphol Airport's Kaagbaan runway. Between 2022 and 2024, the lab collected empirical data on sound pressure levels, air quality, meteorological conditions, and flight activity. These data form the foundation for ongoing and future research in a semi-controlled lab environment, aimed at evaluating the pollution mitigation effects of urban greenery. The lab findings are intended to address real-world challenges related to climate and built environments.

According to Dellaert and Hulskotte (2017), air pollutant emissions from civil aviation including PM have increased significantly in recent years in the Netherlands. Green infrastructure, such as trees, can help reduce urban $PM_{2.5}$ concentrations (Isaifan & Baldauf, 2019b). Jeong et al. (2023b) examined the impact of urban street trees on $PM_{2.5}$ concentrations and found that reductions depend on tree presence and planting structure. Notably, areas with multi-layered planting structures (e.g., shrubs, arbours) experienced greater reductions. Similarly, Wu et al. (2021) assessed three road green belt configurations and found that combinations of arbour and shrub species performed best in reducing PM concentrations from road traffic.

Although studies on tree impacts on air pollution and $PM_{2.5}$ are limited, existing research suggests trees can mitigate pollutant concentrations by capturing particles or reducing secondary pollutant formation (Isaifan & Baldauf, 2019a). Chen et al. (2017) investigated different abilities of tree species to capture $PM_{2.5}$ after rainfall and identified species with high PM-capturing potential in urban areas. Liu et al. (2022) used ENVI-met (a numerical modelling tool) to analyse how tree height influences $PM_{2.5}$ concentrations near roads and found that the optimal height depends on street canyon openness. Traffic-related PM emissions can also be affected by trees, evidenced by Popek et al. (2022) who studied PM accumulation in urban forests and identified key influencing factors, including crown width, leaf area density, and seasonality.

While existing studies explore tree characteristics (e.g., height, crown width) and their effects on PM emissions from road traffic, very rare research has examined PM emissions from air traffic or their correlation with tree configurations (e.g., tree layout). This gap is likely due to the lack of long-term aircraft pollution measurements beneath tree canopies at street level, as well as the confounding effects of urban heat islands (UHI) from diverse anthropogenic activities. This paper examines aircraft emissions and three key factors influencing simulation accuracy: area geometry (e.g., courtyards, tree configurations), pollutant sources (e.g., air traffic volume, emission position), and meteorological conditions affecting dispersion.

2. MATERIALS & METHODS

2.1 Data

ENVI-met is a 3D modeling software for microclimates and pollutant dispersion, but its accuracy in simulating particulate matter (PM) remains uncertain. Despite significant model limitations, some studies suggest it performs well in modeling PM10 dispersion in urban street canyons (Hofman & Samson, 2014; Paas & Schneider, 2016). Therefore, we assess the validity of ENVI-met in simulating $PM_{2.5}$ concentrations before evaluating intervention strategies.

Figure 2. ENVI-met model (left); Courtyard 2 double-row tree (middle); Courtyard 1 without vegetation (right)

The raw weather files were retrieved from the KNMI weather services and morphed with UHI effects to force the boundary conditions of the ENVI-met model. The simulation period was set to September 2023 to ensure a comprehensive comparison with measured $PM_{2.5}$ concentrations, as this month had the highest recorded levels and the most complete dataset for the double-row tree configuration. Double row in courtyard 2 was chosen to be the tree configuration for validation and courtyard 1 was kept bare comprising a geometry with a slanted roof during simulation period. The layout of courtyards and double row tree configuration are shown in Figure 2.

Historical meteorological data for September 2023 was retrieved from the KNMI database and linked to a weather mast at Schiphol Airport. The dataset includes cloud cover, wind direction, wind speed, air temperature, relative humidity, and precipitation. Meteorological conditions from 6am on 14 Sep 2023 to the same hour on 17 Sep 2023 were extracted to adjust boundary conditions for validation, calibration, and simulation in ENVI-met. Using measured hourly flight data, hourly $PM_{2.5}$ emissions from air traffic at Kaagbaan were calculated and implemented as a line source emission in ENVI-met, following the equation (1) by Smulders (2022).

$$Line\ source\ \left[\frac{\mu g}{m*s}\right] = \frac{N*E*1000[\frac{\mu g}{mg}]}{d} \quad (1)$$

Where

N: number of hourly flights
E: PM emissions (mg/s) per flight
d: average distance between fights (m), 4167m

2.2 Simulation constraints

Over the past three years (2021–2024), the UCLab collected air pollution and meteorological data at a high temporal resolution (10-minute intervals). To ensure representative longitudinal analysis, specific criteria were applied: periods with relatively high $PM_{2.5}$ concentrations were selected for simulation validation. Precipitation-free conditions were prioritized to avoid biases from wetting losses and splashing effects, as the Nanenos partector 2 (<30% error), BC Carbon (<25% error), and NodeMCU sensors V3 (<10% voltage-dependent error) have limited correction capabilities (Bezantakos et al, 2024; Naneos Particle Solutions GmbH, 2022). Wind direction was restricted to northeast–southwest, aligning with in-situ measurements identifying Kaagbaan runway as the primary pollution source, with emissions dispersing southwest (Thielen et al., 2024a). Wind speeds at roof level (10m) were kept below 3 m/s, as higher speeds negatively correlate with $PM_{2.5}$ concentrations (Wang & Ogawa, 2015; Thielen et al., 2024b). Relative humidity was capped at 85% to maintain sensor accuracy and avoid misreading water particles as PM (Casari & Po, 2023). Finally, ENVI-met simulations were extended to 72 hours to ensure model convergence.

2.3 Validation and calibration protocols

ENVI-met validations and calibrations were iteratively conducted to assess atmospheric stability, verifying pollutant source presence, wind conditions, and courtyard materials. Validation was performed at a single point in the courtyard due to limited apparatus availability, selected based on PM sensor locations (Figure 3). Two citizen sensors were positioned at (29, 36) in Courtyard 1 and (29, 44) in Courtyard 2, both 1.5m above ground. Measured and simulated $PM_{2.5}$ concentrations were compared across multiple calibration rounds, with results presented as time series data and discrepancies quantified using Root Mean Square Error (RMSE). Due to instability,

a constant wind direction (averaged over 72 hours) was maintained to approximate real-world conditions. Sensitivity tests included pollution source height (1-18m), configuration (line vs. surface source), and emission intensity normalization (divided by number of different heights, in this paper they are 18 for the wide surface or 36 for the narrow one) when transitioning from line to tilted surface sources. Once the calibrated scenario best aligned with measurements, it was applied as the boundary condition in ENVI-met for the follow-up simulations with different trees interventions.

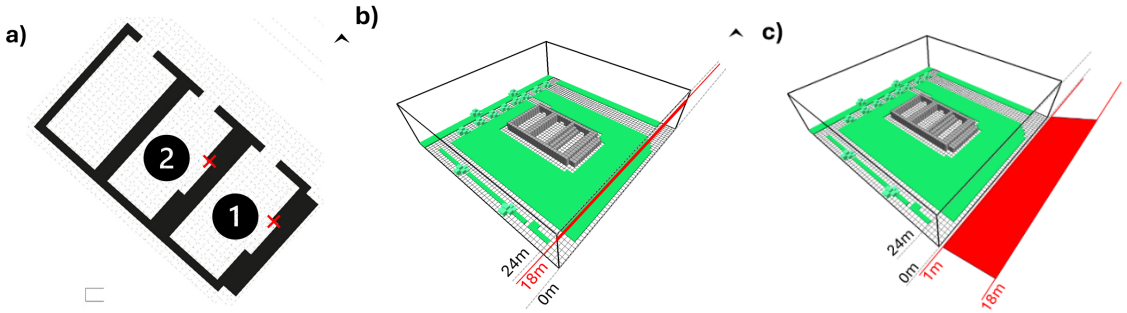

Figure 3. a) Positions of citizen sensors (red crosses) in Courtyard 1 and 2, b) Pollutant source as a line at 18m, and c) Pollutant source as a tilted plane, consisting of 18-line sources ranging from the height of 1m to 18m

2.4 Tree configuration

All seven configurations, including the baseline 'Bare' scenario (no vegetation) were selected from the tree configuration log (Figure 4) and tested in ENVI-met to assess their impact on air pollution.

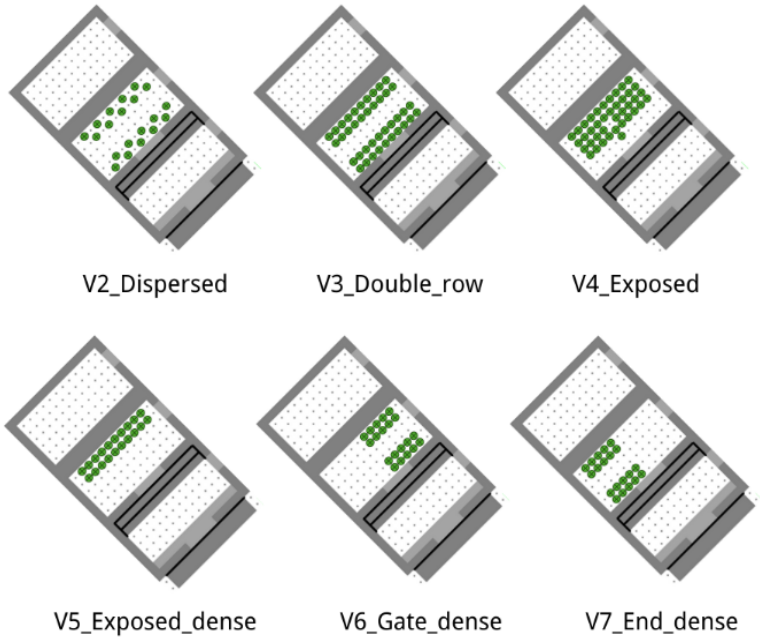

Figure 4. Tree configuration log in Courtyard 2, UCLab, from 2023 to 2024. V3 was used for validation.

3. RESULTS

3.1. Validation and calibrations

The RMSE results indicate that the modified pollution source aligns most closely with the measured data (Figure 5). Figure 6 illustrates PM diffusion in the Y-Z section under the modified pollution source, featuring a line-to-surface source with 18 steps at uniformly spaced heights.

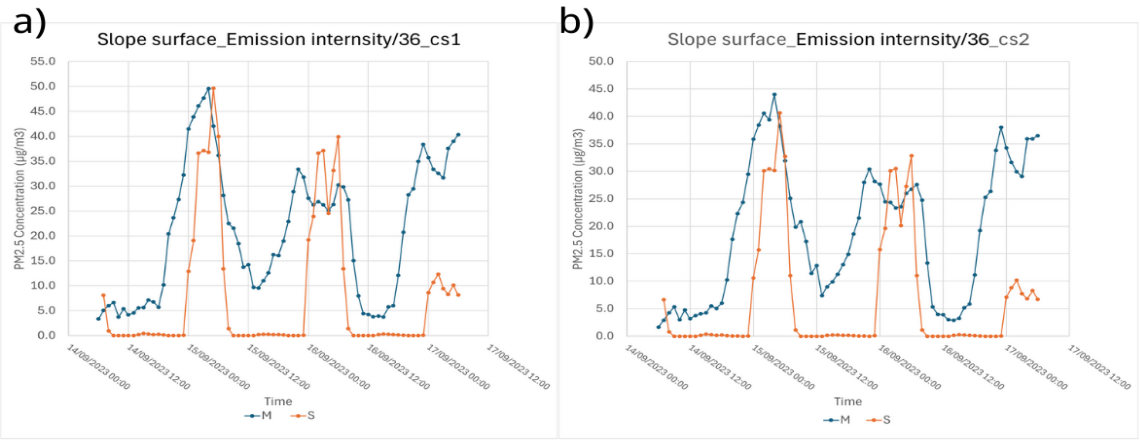

Figure 5. Temporal validations comparing simulated $PM_{2.5}$ concentrations with measured data in a) Courtyard 1 and b) Courtyard 2 (blue line: measurements, orange line: simulation).

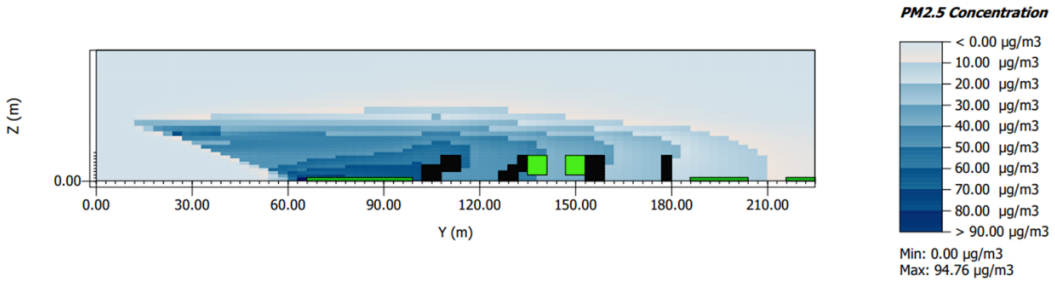

Figure 6. Y-Z section of PM concentration with Pollutant source as a tilted plane

3.2. $PM_{2.5}$ patterns with different tree configurations

Courtyard 2 (trees courtyard) was meshed and divided into 78 grids, and the absolute PM concentration difference for each grid was calculated. Figure 7 illustrates the intra-courtyard $PM_{2.5}$ concentration at 6am and the difference with other five tree variants. The *V7 End Dense* and *V3 Double Row* configurations demonstrated the most significant $PM_{2.5}$ reductions compared to other layouts. The largest reductions occurred at the end side and upper left side of Courtyard 2, while $PM_{2.5}$ concentrations increased near the gate side.

Figure 8 presents the descriptive statistics of absolute PM concentration differences for each tree configuration, supported by a Kruskal-Wallis test. The negative average absolute difference in PM

concentration between *V3 Double Row* and *B1 Bare Ground* indicates that the double-row configuration effectively reduces $PM_{2.5}$ concentrations in Courtyard 2. In contrast, the positive average absolute difference for *V4 Exposed* suggests an increase in PM concentration compared to the baseline. Among configurations with 20 trees, *V2 Dispersed* and *V7 End Dense* contributed to PM reduction, with the greatest decrease under *V7 End Dense*. Conversely, *V5 Exposed Dense* and *V6 Gate Dense* led to increased PM concentrations in Courtyard 2.

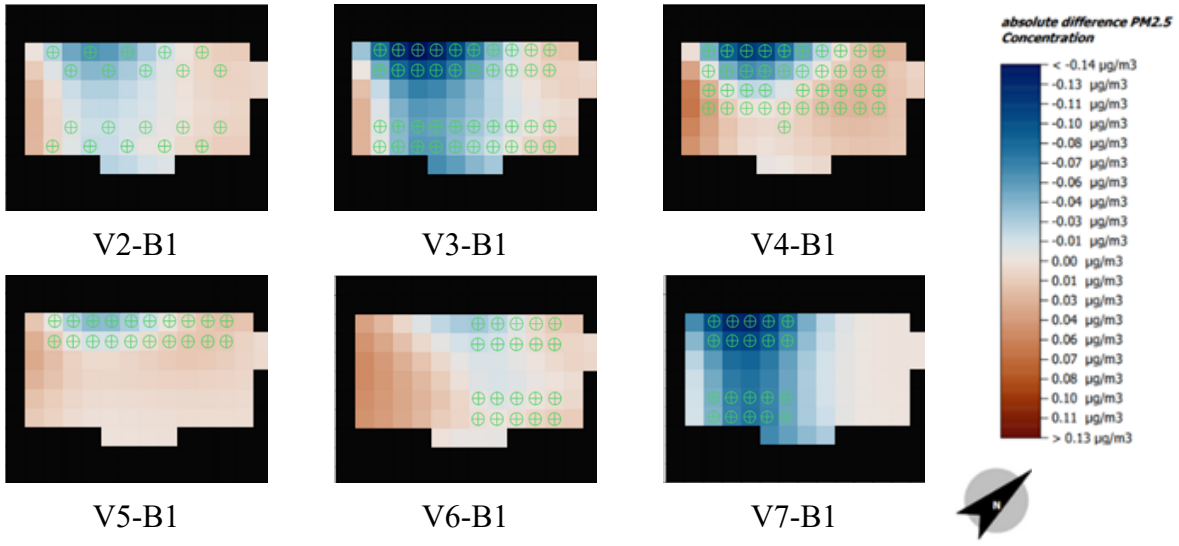

Figure 7. Absolute difference of PM concentration in grids of courtyard 2 (tree courtyard) at 6am.

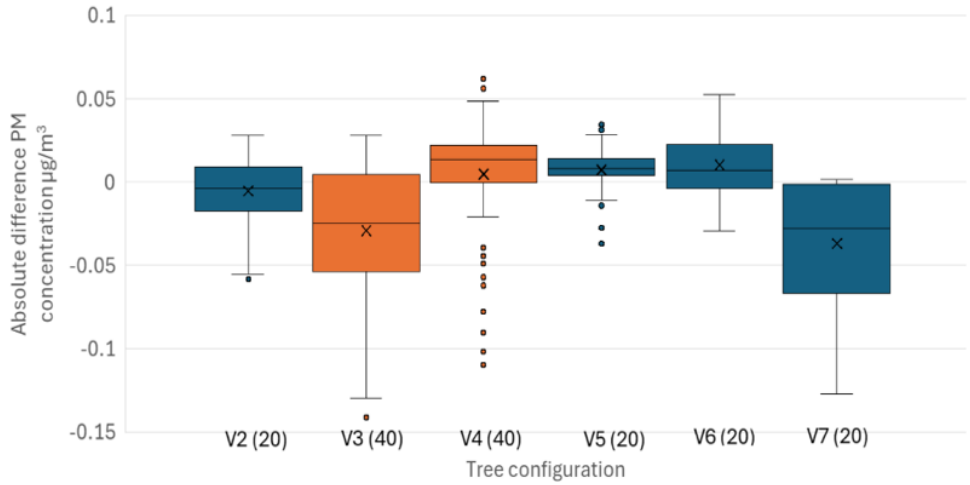

	V2_B1	V3_B1	V4_B1	V5_B1	V6_B1	V7_B1
Mean	-0.00548	-0.02913	0.004863	0.007234	0.010225	-0.03678
STD	0.018442	0.038209	0.033129	0.012244	0.019581	0.03509

Figure 8. Descriptive statistics of the absolute PM concentration difference at 6:00 AM for each tree variant (V) compared to the baseline (B). Orange represents variants with 40 trees, and blue denotes those with 20 trees.

4. DISCUSSIONS & CONCLUSIONS

This study demonstrates that under controlled conditions—constant wind direction (averaged over the simulation period), a pollutant source modelled as a tilted plane (1 m to 18 m high), and emission intensity scaled to 1/36 of the initial value—ENVI-met performs well in simulating $PM_{2.5}$ over a 72-hour period in September compared to real measurements. Among the six configurations tested, the *End-Dense* layout had the most significant impact in reducing $PM_{2.5}$ concentrations in courtyard spaces affected by air traffic pollution. For urban planners, these findings highlight the importance of considering both pollutant dispersion patterns and site-specific wind conditions when designing tree layouts. Dense tree clusters in strategic locations, such as pollutant accumulation zones, can effectively reduce $PM_{2.5}$ concentrations, while uniform tree distribution may help prevent wind corridors that allow unfiltered pollutant flow. We recommend that tree configurations should balance air pollution mitigation with acoustic and thermal effects, adopting a multidimensional approach to enhance overall urban comfort. Future research should incorporate additional pollutant sources, particle size interactions, and long-term simulations to improve the accuracy and applicability of $PM_{2.5}$ reduction strategies in diverse urban environments.

ACKNOWLEDGEMENTS

The research is funded by the municipality of Haarlemmermeer, the Dutch ministry for infrastructure and water management, the Dutch ministry for housing and domestic affairs, Stichting leefomgeving Schiphol, and the AMS institute for advanced metropolitan solutions. T. Li would like to express his gratitude to the Urban Comfort Lab team for their support. Special thanks to M. Lugten for organising weekly meetings and providing feedback, Z. Peng for guidance on ENVI-met modelling and proofreading, G. Wuite for support on data analysis, and H. Zheng for expertise on air quality. He also extends his appreciation to B. Thielen for onboarding assistance and valuable suggestions on the research topic on urban air quality.

REFERENCES

Bezantakos, S., Varnava, C. K., Papaconstantinou, R., & Biskos, G. (2024). Performance of the Naneos partector 2 multi-metric nanoparticle detector at reduced temperature and pressure conditions. Aerosol Science and Technology, 58(5), 584-593.

Bruse, M. (2007). ENVI-met implementation of the gas / particle dispersion and deposition model PDDM. 1–7.

Casari, M., & Po, L. (2023). Mitigating the Impact of Humidity on Low-Cost PM Sensors. CEUR Workshop Proceedings, 3486, 599–604.

Chen, L., Liu, C., Zhang, L., Zou, R., & Zhang, Z. (2017). Variation in Tree Species Ability to Capture and Retain Airborne Fine Particulate Matter ($PM_{2.5}$). Scientific Reports, 7(1), 1–11. https://doi.org/10.1038/s41598-017-03360-1

Cholianawati, N., Sinatra, T., Nugroho, G. A., Permadi, D. A., Indrawati, A., Halimurrahman, Kallista, M., Romadhon, M. S., Ma'ruf, I. F., Yudhatama, D., Madethen, T. A. P., & Awaludin, A. (2024). Diurnal and Daily Variations of $PM_{2.5}$ and its Multiple-Wavelet Coherence with Meteorological Variables in Indonesia. Aerosol and Air Quality Research, 24(3), 1–18. https://doi.org/10.4209/aaqr.230158

Dellaert, S. N. C., & Hulskotte, Ir. J. H. J. (2017). Emissions of air pollutants from civil aviation in the Netherlands. TNO, 22.

Hofman, J., & Samson, R. (2014). Biomagnetic monitoring as a validation tool for local air quality models: A case study for an urban street canyon. Environment International, 70(2014), 50–61. https://doi.org/10.1016/j.envint.2014.05.007

Isaifan, R. J., & Baldauf, R. W. (2019). Estimating economic and environmental benefits of urban trees in desert regions. Advances in Ecological Research, 60, 1–24. https://doi.org/10.3389/fevo.2020.00016.Submit

Jeong, N. R., Han, S. W., & Ko, B. (2023). Effects of Green Network Management of Urban Street Trees on Airborne Particulate Matter ($PM_{2.5}$) Concentration. International Journal of Environmental Research and Public Health, 20(3). https://doi.org/10.3390/ijerph20032507

Kong, D., Ning, G., Wang, S., Cong, J., Luo, M., Ni, X., & Ma, M. (2021). Clustering diurnal cycles of day-to-day temperature change to understand their impacts on air quality forecasting in mountain-basin areas. Atmospheric Chemistry and Physics, 21(19), 14493–14505. https://doi.org/10.5194/acp-21-14493-2021

Liu, J., Zheng, B., Xiang, Y., & Fan, J. (2022). The Impact of Street Tree Height on $PM_{2.5}$ Concentration in Street Canyons: A Simulation Study. Sustainability (Switzerland), 14(19). https://doi.org/10.3390/su141912378

Lugten, M., Wuite, G., Peng, Z., & Tenpierik, M. (2024). Assessing the influence of street canyon shape on aircraft noise: Results from measurements in courtyards near Amsterdam Schiphol Airport. *Building and Environment*, *255*, 111400.

Masiol, M., & Harrison, R. M. (2014). Aircraft engine exhaust emissions and other airport-related contributions to ambient air pollution: A review. Atmospheric Environment, 95, 409–455. https://doi.org/10.1016/j.atmosenv.2014.05.070

Naneos Particle Solutions GmbH. (2022). Partector 2 [PDF]. naneos.ch/pdf/naneos_partector2_operation_manual.pdf

Olivares, I., Langner, J., Soto, C., Monroy-Sahade, E. A., Espinosa-Calderón, A., Pérez, P., Rubio, M. A., Arellano, A., & Gramsch, E. (2023). Vertical distribution of $PM_{2.5}$ in Santiago de Chile studied with an unmanned aerial vehicle and dispersion modelling. Atmospheric Environment, 310(92). https://doi.org/10.1016/j.atmosenv.2023.119947

Paas, B., & Schneider, C. (2016). A comparison of model performance between ENVI-met and Austal2000 for particulate matter. Atmospheric Environment, 145, 392–404. https://doi.org/10.1016/j.atmosenv.2016.09.031

Popek, R., Fornal-Pieniak, B., Chyliński, F., Pawełkowicz, M., Bobrowicz, J., Chrzanowska, D., Piechota, N., & Przybysz, A. (2022). Not Only Trees Matter—Traffic-Related PM Accumulation by Vegetation of Urban Forests. Sustainability (Switzerland), 14(5). https://doi.org/10.3390/su14052973

RIVM. (2019). Ultrafine particles in the vicinity of Schiphol Airport affect health. Retrieved August 14, 2024, from https://www.rivm.nl/en/news/ultrafine-particles-in-vicinity-of-schiphol-airport-affect-health

Smulders, B. (2022). Simulating the air quality side effects of noise adaptive green structures Thesis report.

Thangavel, P., Park, D., & Lee, Y. C. (2022). Recent Insights into Particulate Matter ($PM_{2.5}$)-Mediated Toxicity in Humans: An Overview. International Journal of Environmental Research and Public Health, 19(12). https://doi.org/10.3390/ijerph19127511

Thielen, B., Fry, J., & Lugten, M. (2024). Assessing the Influence of Tree Arrangements on PM Concentration and Meteorological Variables: A Case Study of Hoofddorp, Netherlands. AMS Conference 2024.

Wang, J., & Ogawa, S. (2015). Effects of meteorological conditions on $PM_{2.5}$ concentrations in Nagasaki, Japan. International Journal of Environmental Research and Public Health, 12(8), 9089–9101. https://doi.org/10.3390/ijerph120809089

Wu, J., Luo, K., Wang, Y., & Wang, Z. (2021). Urban road greenbelt configuration: The perspective of $PM_{2.5}$ removal and air quality regulation. Environment International, 157, 106786. https://doi.org/10.1016/j.envint.2021.106786

Wuite, F. G. E., Peng, Z., Kim, K. J., Lugten, M. C., & Tenpierik, M. J. (2024). Integrating simulation and measurement techniques to model outdoor noise and heat in airport neighbourhoods with varying urban geometries. *Proceedings of Building Simulation 2023*.

Zhao, X., Zhang, X., Xu, X., Xu, J., Meng, W., & Pu, W. (2009). Seasonal and diurnal variations of ambient $PM_{2.5}$ concentration in urban and rural environments in Beijing. Atmospheric Environment, 43(18), 2893–2900. https://doi.org/10.1016/j.atmosenv.2009.03.009

6th International Conference on Building Energy and Environment
Eindhoven University of Technology, The Netherlands
6 - 10 July 2025

A design approach for ecological building envelopes: the ECOLOPES project

Katia Perini[1], Francesca Mosca[1], Maria Canepa[1], Sissy Xi Chen[2], Yasha J. Grobman[3], Michael Hensel[4], Surayyn Uthaya Selvan[3], Albin Ahmeti[4], Shany Barath[3], Thomas E. Hauck[5], Ferdinand Ludwig[2], Defne Sunguroglu Hensel[4], Jakub Tyc[4], Wolfgang Weisser[2]

[1]University of Genoa, Italy, katia.perini@unige.it; [2]Technical University of Munich, Germany;[3]Technion - Israel Institute of Technology, Israel; [4]Vienna University of Technology, Austria; [5]Animal-Aided Design, Germany

SUMMARY
Urbanization leads to the loss of green spaces, which results in ecosystem degradation and diminishes the quality of life for residents. Consequently, urban areas are facing significant challenges related to human well-being and ecosystem health. Incorporating ecological principles into the design process at various scales (from buildings to the urban scale) can greatly improve ecological sustainability, reducing environmental degradation, and enhancing comfort and livability conditions for humans. The ECOLOPES project developed an innovative design approach, along with related methods and tools, to incorporate ecological processes and objectives into the design of building envelopes. This contribution presents the interdisciplinary design process and some of the computational components developed, outlining the implications and future perspectives.

Keywords: Urban greenery, ecology, optimization, microclimate

EXTENDED ABSTRACT

Urbanization is regarded as one of the most transformative processes, significantly altering ecosystems' biotic and abiotic characteristics and substantially impacting biodiversity and ecosystem services. Several studies highlight the crucial role of green spaces within cities in supporting biodiversity and enhancing human well-being, thanks to ecosystem services provision (Sadler et al. 2010). Conversely, evidence indicates that higher population density facilitates the development of compact, low-carbon cities, which help preserve habitats at the edges of expanding urban areas while promoting walkable and more livable environments (McDonald et al., 2023).

The ECOLOPES design approach aims at introducing ecological knowledge and related data into the architectural design process (Weisser et al. 2023). To do this, we integrate the ecological requirements and ecological consequences into the architectural design process. This was achieved by modifying the standard architectural design process (Figure 1). Importantly, the general workflow of building design is not changed, but enriched to include the requirements of plants, animals and other living organisms, i.e. non-human inhabitants, as highlighted in Figure 1. One important advance in the ECOLOPES project is that the use of Key Performance Indicators (KPIs) that address the needs of human, and of other species, aligning design development with the dual objectives of designing for humans as well as for other inhabitants such as plants (Selvan et al. 2023). The selection and assessment of appropriate KPIs have proven effective in aligning design development with the dual objectives, which depend largely on the ecological knowledge and data

that designers acquire at the outset.

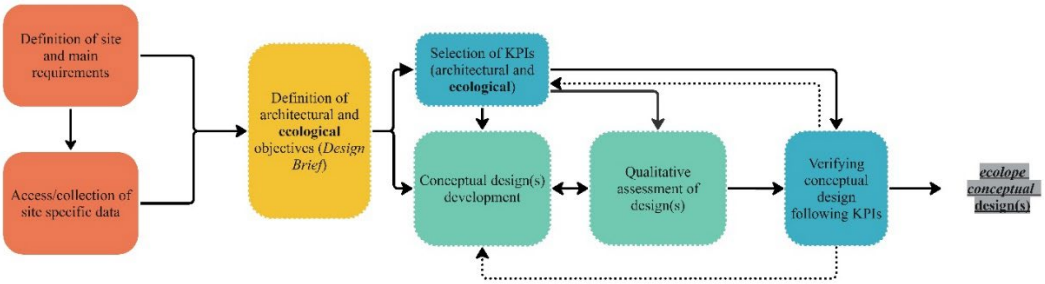

Figure 1. ECOLOPES simplified design workflow (based on Weisser et al., 2023).

The design workflow was tested by master students at the Technical University of Munich, in order to identify the potential and the limitations of the ECOLOPES approach. We will now briefly describe some of the components developed within the ECOLOPES project to support the design process. A case study in the city of Munich (Neuperlach district, in the South-East area of the city) is finally presented to show how a design proposal can be developed following the envisioned design process.

To address the needs of the plants and animals, it became clear that it would be necessary to integrate into the design workflow the interactions between the building, humans, and the other inhabitants (Grobman et al. 2023). This is because the way a building is designed will affect where plants and animals can live. Conversely, plants and animals will modify the building (environmental) conditions, through processes such as colonization, extinction and succession. In this context, interactions and the further development of the site are highly relevant. For this reason, ECOLOPES has started to develop a **plant-animal-soil model** that can simulate the development of the plant and animal community based on soil conditions, and the mutual feedback between the building, plants and animals. In order to deal with the enormous variety of organisms, the project chose to summarize plant and animal species in plant and animal functional groups (Weisser et al. 2023). The model will evolve in complexity over time. At present, buildings affect plants mainly by the shading they exert on plants, and by the depth of soil on various surfaces. The geometry of the building affects the locomotion of animals and the number of resources, for example, the amount of plant biomass, affects what animals can occur on or next to the building, and what their home range is.

Another component is the **optimization** and evaluation of *ecolopes* design alternatives, based on a hybrid multi-criteria decision-making (MCDM) (Selvan et al. 2023). In particular, a model was developed to facilitate the refinement of multispecies distribution on an *ecolope* based on inhabitants' objective priorities. The model sequentially employs multi-objective (MODM) and multi-attribute decision-making (MADM) to streamline the computation of key performance indicators, such as Soil volume, Solar Radiation, Local PFGs richness, Structural Connectivity, informed by ecological knowledge for architectural design decision-making. The resulting ranked alternatives can be represented geometrically, through a catalogue format, and numerically, through dataframes describing the overall performances of the alternative pool and the abiotic and biotic metadata of each cell per alternative.

The assessment of ecological building envelopes' **impact on microclimate** can then be implemented through the integration of Plant Functional Groups (PFGs) features into a computational-fluid-dynamics (CFD) simulation approach, allowing a stronger connection between ecological and environmental performances. Based on geometrical features of PFGs, such as crown diameter and plant height, the group of plants can be modelled in the 3D CAD

environment and their capacity to provide shading calculated. The integration of this component into the design process serves as a starting point for including the quantification of the environmental performance of the envelope, in addition to ecological performance, with the aim of supporting the ecosystem while also enhancing livability in urban areas (Mosca et al., 2025). Eventually, the interactions between the building and the inhabitants will be encapsulated in an ontology. The **Ontologies** provide knowledge representation for reasoning and can be queried by the designer and aid rule-based processes (Pruski & Hensel, 2022). The initial design consists of (1) the *translational* process and (2) the *generative* process. In the former the designer analyses, correlates, and spatially locates architectural and ecological requirements contained in a design brief, taking into consideration relevant constraints. This process involves a knowledge graph that is queried by the designer to support decision making concerning spatially locating architectural and ecological elements in the CAD environment. The spatially located elements in the CAD environment and datasets in the ECOLOPES Voxel Model, are input for the *generative* design process in which rule-based generative processes are aided by ontologies, resulting in variations of spatial organization and surface geometry in urban and building scales. Design outputs of the initial design stage are 3D geometry in Rhinoceros 3D, datasets in the ECOLOPES Voxel Model, and ontological output.

Case study: The proposed approach has been applied by an interdisciplinary team of architects and landscape architects, supported by ecological experts, to renovate building façades in Munich as a case study. The project focused on the 3D transitional space beyond the building envelope proposing refurbishment strategies to address two key challenges: wildlife damage to the building envelope and excessive heat on the south-facing balconies. Computational tools optimized soil distribution in the gabion walls and balcony sizes, while plant selection for the southern façade was based on sun exposure analysis. Vegetation will completely envelop the structure, improving air quality, reducing the urban heat island effect, and serving as a model for sustainable urban architecture. Figure 2 shows the application of the design workflow on the real case study described and the proposed design outcomes.

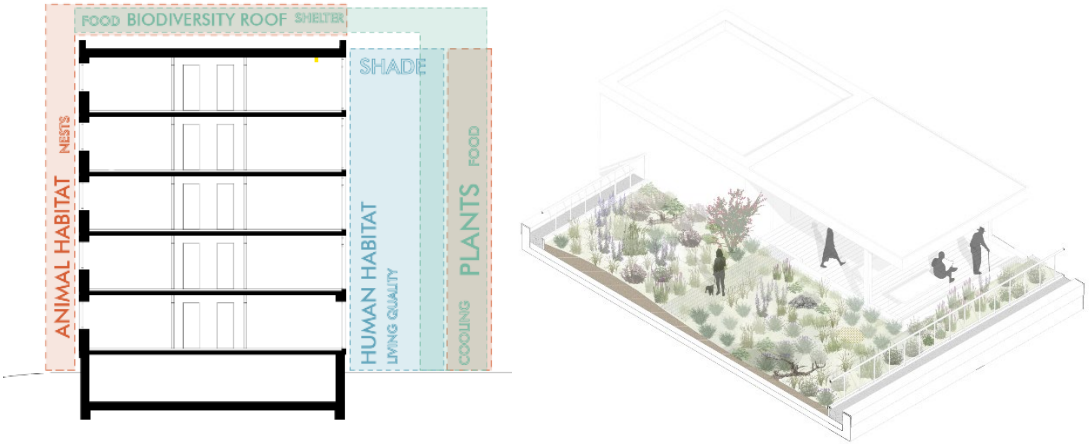

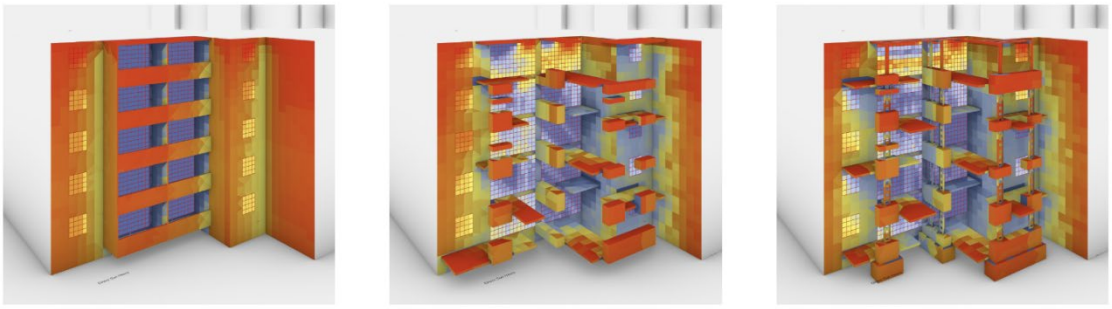

Figure 2. ECOLOPES case study concept and visualization. Top: concept and floor plan; bottom: façade surface temperatures from current state to design project, high (red) to low (blue) (credit: Lukas Meisner, Nairi Koulakezian, Nicklas Neubauer, Lewin Schmid).

Summary and future perspectives: The ECOLOPES approach can lead to integrating the interactions between the building, humans, and the other inhabitants in the design process. This establishes foundational frameworks for future advancements at multiple scales, such as environmental integration within urban infrastructure and architectural elements for the building envelope, multispecies components for animals and plants. Furthermore, considerations arise regarding the maintenance needs of multispecies habitats and their integration into existing building maintenance protocols. Additionally, the interplay between humans, animals, and plants—particularly human responses to the introduction of animals into urban environments—requires careful consideration and understanding of its broader implications.

ACKNOWLEDGEMENTS

The presented work summarizes part of the results achieved within the ECOLOPES research project, funded within the EU H2020 FET-OPEN program (grant agreement number 964414, https://ecolopes.org/). All the ECOLOPES partners and members are thanked for their fundamental contribution.

REFERENCES

McDonald, R. I., Aronson, M. F. J., Beatley, T., Beller, E., Bazo, M., Grossinger, R., Jessup, K., Mansur, A. V., Puppim De Oliveira, J. A., Panlasigui, S., Burg, J., Pevzner, N., Shanahan, D., Stoneburner, L., Rudd, A., & Spotswood, E. (2023). Denser and greener cities: Green interventions to achieve both urban density and nature. People and Nature, 5(1), 84–102.

Mosca, F., Calbi, M., Roccotiello, E., & Perini, K. (2025). A computational approach to assess the effects of ecological building envelopes on outdoor thermal comfort. Sustainable Cities and Society, 106170. https://doi.org/10.1016/j.scs.2025.106170.

Pruski, C., & Hensel, D. S. (2022). The Role of Information Modelling and Computational Ontologies to Support the Design, Planning and Management of Urban Environments: Current Status and Future Challenges. In A. Chokhachian, M. U. Hensel, & K. Perini (Eds.), Informed Urban Environments: Data-Integrated Design for Human and Ecology-Centred Perspectives (pp. 51–70). Springer International Publishing.

Sadler, J., Bates, A., Hale, J., & James, P. (2010). Bringing cities alive: the importance of urban green spaces for people and biodiversity. Urban ecology, 230-260.

Selvan, S.U., Saroglou, S.T., Mosca, F., Tyc, J., Joschinkski, J., Calbi, M., Vogler, V., Weisser, W. W., Grobman, Y. J. and Barath, S. (2023). Multi-species building envelopes: Developing a multi-criteria decision-making methodology for cohabitation. in Proceedings of the 28th International Conference of the Association for Computer-aided Architectural Design Research in Asia.

Weisser, W. W., Hensel, M., Barath, S., Culshaw, V., Grobman, Y. J., Hauck, T. E., Joschinski, J., Ludwig, F., Mimet, A., Perini, K., Roccotiello, E., Schloter, M., Shwartz, A., Hensel, D. S., & Vogler, V. (2023). Creating ecologically sound buildings by integrating ecology, architecture and computational design. People and Nature, 5(1), 4–20. https://doi.org/10.1002/pan3.10411

Low / Zero Carbon Emission Buildings and Communities Grid (11:00-12:30 h)

6th International Conference on Building Energy and Environment
Eindhoven University of Technology, The Netherlands
6 - 10 July 2025

Modelling control schemes of a desalination battery for electrolysis and trigeneration designed for ships at seaports

Himanshu Dehra

Monarchy of Concordia, Wellstar Beacon Labs, Faridabad, India, anshu_dehra@hotmail.com

ABSTRACT

The objective of this study is to present a generalized scheme for simultaneously achieving: i) desalination with a rechargeable seawater battery using Na metal redox flow cell system; ii) electrolysis of water for hydrogen production in a separate electrochemical cell; iii) trigeneration for heat, cooling and electric power using direct-current generator's engine utilizing hydrogen blend as fuel. Sodium metal-based battery systems have recently attracted increasing research interest due to the abundant resources of the raw materials with use of seawater and sodium related compounds as the positive and negative electrodes. The extra stream of freshwater is utilized in the electrolysers for generation of hydrogen as a blended fuel for marine engines. Considering the thermal processes with the utilization of heat recovery, this study proposes a novel auxiliary trigeneration system for ships based on the waste heat of its engine to produce electricity, cooling, and freshwater. The system consists of a regenerative organic Rankine cycle with R600 working fluid, a lithium-bromide/water single-effect absorption chiller, and a sodium metal-based desalination battery unit. The integrated control scheme of the full system configuration with a redox flow battery is summarized both from the ship's micro grid and energy storage sides. The control technology of the redox flow sodium metal seawater battery energy storage system is also briefly outlined.

Keywords: Desalination Battery, Electrochemical Cell, HVAC.

1.0 INTRODUCTION

An electrochemical reactor or cell is a device that can generate electrical energy from the chemical reactions occurring in it, or use the electrical energy supplied to it to facilitate chemical reactions in it (Haverkort, 2024). These devices can convert chemical energy into electrical energy, or vice versa. In the electrochemical flow reactor, there are combined features for processes of electrochemistry and flow chemistry, example is a parallel-plate industrial electrolyser for generation of hydrogen from electrolysis of water (Rajora et al., 2022). Figure 1 presents a simple tank cell based electrochemical flow reactor.

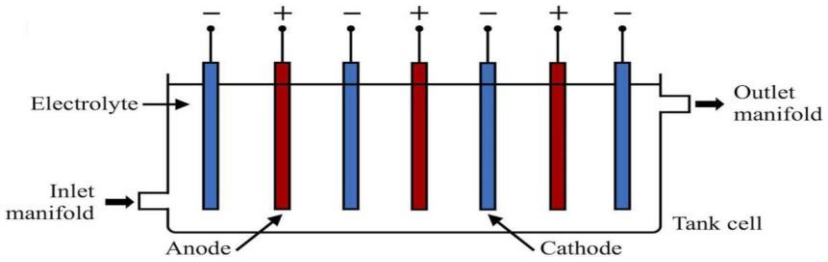

Figure 1. Electrochemical flow reactor

The Seawater battery with desalination (SWB-D) process, which is an electrochemical redox flow reactor, has been experimentally tested only in a steady-state (or batch) at the laboratory scale mode so far, so there was not much consideration for limiting factors such as the diffusion of ions and conductivity of influent solution. In the current scenario, the continuous flow cell of SWB-D process is tested at the laboratory scale in South Korea and Italy (see Figure 2) (Son, et al, 2022; Barelli et al, 2023). To compare SWB-D technology with other seawater desalination technologies, the development of a continuous process such as a flow-cell, which is exclusively designed for ships to eventually fully commercialize the technology must be investigated. The schematic of a generalized redox flow battery is presented in Figure 3, whilst the generalized design parameters for the electrochemical flow reactor are presented in Figure 4.

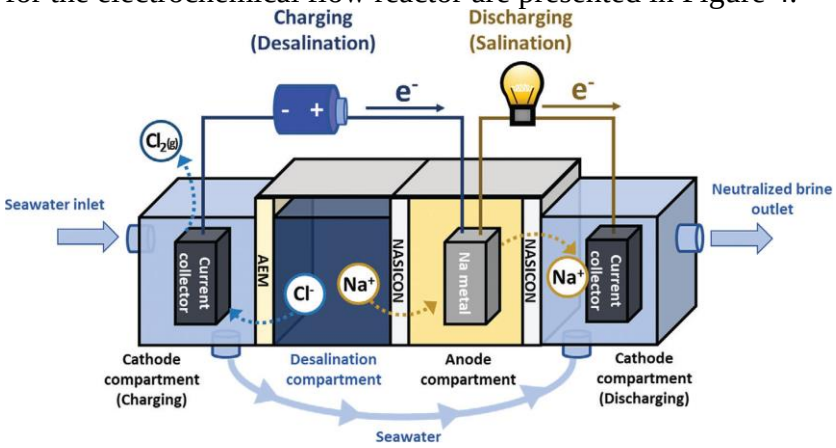

Figure 2. Schematic illustration of the SWB-D system (Son, et al, 2022)

2.0 PERFORMANCE INDICATORS

Performance indicators of a good electrochemical flow reactor include (see Figure 4):
m, Mass transfer coefficient for 2D electrode;
k_mA_e, Volumetric Mass transfer coefficient for 3D electrode;
X_A, Fractional conversion of reactant;
STY, The space time yield of an electrosynthesis cell;
NSV, The normalized space velocity of environmental treatment cell.

Hydraulics parameters include:
Q, Volumetric flow rate of electrolyte, cm3/s; v, Mean linear flow velocity past the electrode surface, cm/s; P, Pressure, Pa; Re, Renard's number

Requirements of good flow cell:
- High productivity
- Good mass transport
- Good temperature control
- Low electrical resistance
- Ease of operation
- Safety in operation
- Ability to deal with gaseous products and reactants
- Minimum cost

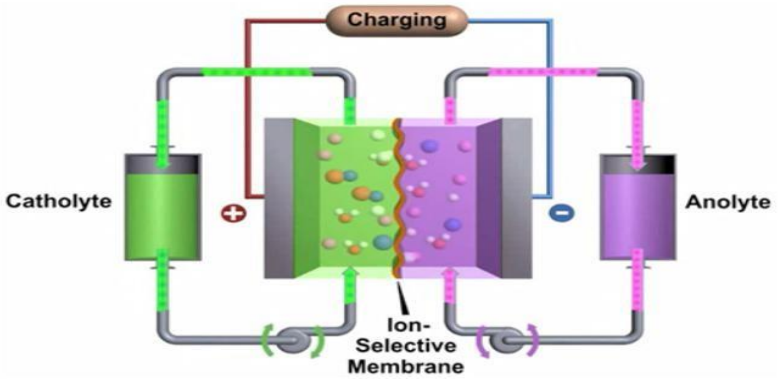

Figure 3. Schematic of a Redox Flow Battery

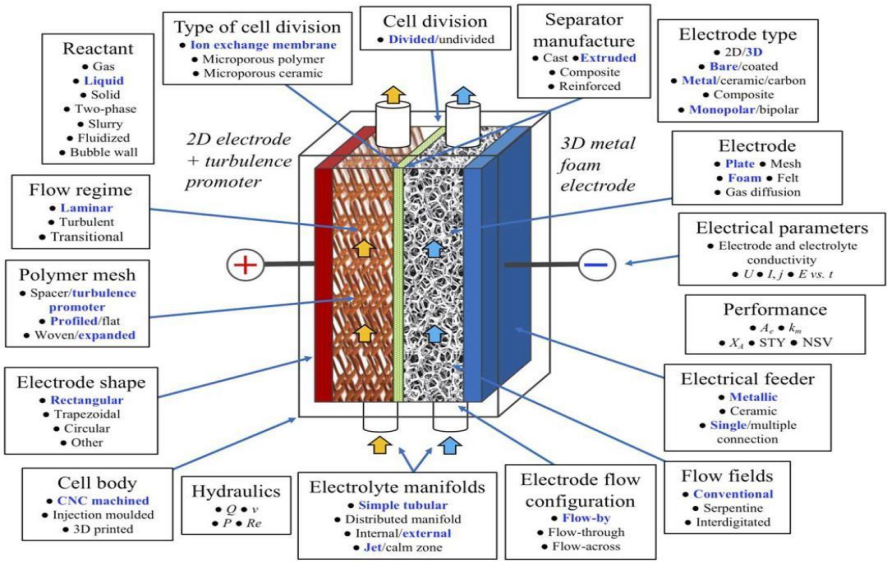

Figure 4. Design Parameters in Electrochemical Flow Reactors

3.0 OBJECTIVES AND PROCESS FLOW DESCRIPTION

The objectives of this study are summarized as follows:

a) The objective of this study is to present integrated process flow scheme for simultaneously achieving (Dehra, 2024) (see Figure 5): i) desalination with a rechargeable seawater battery using Na metal redox cell system; ii) electrolysis of water for hydrogen production in a separate electrochemical cell; iii) trigeneration for heat, cooling and electric power using direct-current generator's engine utilizing hydrogen blend as fuel. The integrated control scheme of the full system configuration with a redox flow battery is summarized both from the ship's micro grid and energy storage sides.

b) The control technology of the redox flow battery energy storage system is also briefly outlined.

Once this energy technology is developed, it will be utilized in the ship's power plant for improving its energy efficiency. Sodium metal-based battery systems have recently attracted increasing research interest due to the abundant resources of the raw materials with use of seawater and sodium related compounds as the positive and negative electrodes. Upon charge, Na+ ions are reduced in the anodic compartment, which needs to be closed, (i.e., isolated from seawater via a solid electrolyte layer enabling the flow of Na+ ions only) while several oxidation reactions can

take place at the positive electrode, such as the oxidation of hydroxide anions (OH-) resulting in the oxygen evolution reaction and that of chloride ions (Cl-) resulting in the formation of chlorine. Herein, the sodium seawater battery technology considered employs sodium-biphenyl (Na-BP) as the anolyte (Kim et al., 2022). Seawater battery cells utilizing biphenyl have demonstrated high energy efficiency, exceeding 80%, which is higher than lead-acid batteries and vanadium redox flow batteries. The use of sodium metal seawater system as large-scale, stationary, rechargeable batteries, these cells can also be utilized for production of sodium metal from seawater via the extraction of sodium produced at the negative electrode. An important by-product of the sodium metal production (i.e., the charging phase) via seawater cells is chlorine (Cl2). This is a precious reactant chemical heavily used by the chemical industry, which commercializes many chlorine-containing compounds. The potential use of sodium production via seawater cells is desalination, by a modification of this system for producing freshwater. The extra stream of freshwater is utilized in the electrolysers for generation of hydrogen as a blended fuel for marine engines.

Considering the thermal processes with the utilization of heat recovery, this study proposes a novel auxiliary trigeneration system for ships based on the waste heat of its engine to produce electricity, cooling, and freshwater. The system consists of a regenerative organic Rankine cycle with R600 working fluid, a lithium-bromide/water single-effect absorption chiller, and a sodium metal-based desalination battery unit. A multi-heat recovery technique is implemented in this conceptual design framework, having a well-organized waste recovery system with three subsystems (Cao et al, 2022).

Firstly, using the heat-based energy of the hot exhaust gases of the ship's engine, the Rankine cycle is inducted via a high recovery vapor generator. By conveying heat, the combustion gases are purged out of the system. The Rankine cycle uses the R600 organic working fluid (Jiménez-García et al., 2023). The R600 organic working fluid enters pump in the form of saturated liquid and is directed towards the vapor generator and receives heat from the combustion gases leaving the ship's engine. Thereafter, it enters the turbine where it is expanded, and a share is drawn out of it and sent back to the open feed heater. After producing mechanical work energy which is converted to electrical power by a direct-current (DC) electrical generator. The rest of the stream is conveyed to a generator of single-effect absorption refrigeration cycle. By transfer action, the heat enters a condenser to turn into saturated liquid and is then sent to the feed heater via another pump, together with the turbine's exit, and this cycle is repeated. In the absorption refrigeration cycle that utilizes water (H2O) as the refrigerant and lithium bromide (LiBr) as the absorbent, the weak solution leaves the absorber and is pumped to the heat exchanger. The preheated weak solution enters the refrigeration cycle's generator.

The Direct-Current (DC) generator distribution system has been proposed in this research, as a replacement for the alternating-current (AC) power distribution system for ships with electric propulsion. The biggest potential with DC generator for fuel savings lies in the ease with which energy storage devices, such as batteries or super capacitors, can be easily added to the DC system. Energy storage will help the marine engines level out load variations from the thrusters and other large loads. DC distribution system allows for new ways of thinking regarding operational optimization. The system is flexible and can combine different energy sources such as engines, turbines, and fuel cells. This means that there is the potential to implement an energy management system that considers varying fuel prices and the availability of different fuels (ABB, 2011).

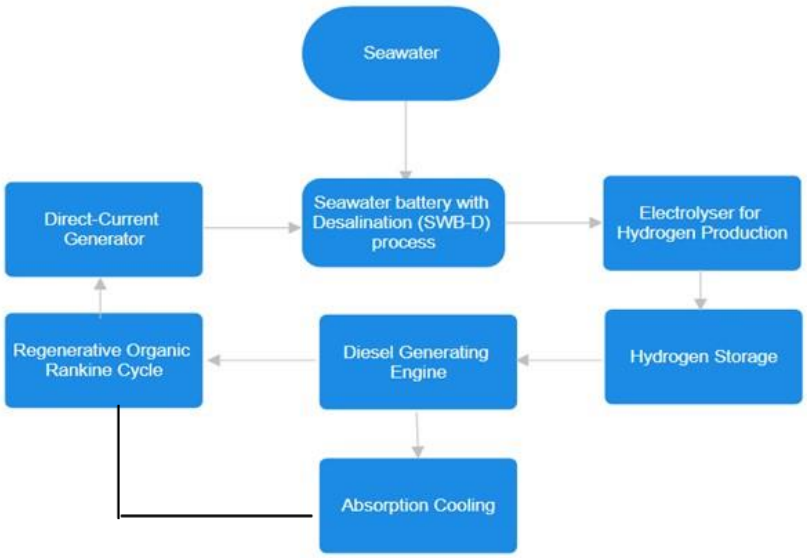

Figure 5: Process Flow Diagram of a Desalination Battery for Electrolysis and Trigeneration

3.1 On the Advantages of Sodium Metal Batteries

Sodium ion batteries have advantages of rich resources, low-cost, high-energy conversion efficiency, long cycle life, and low maintenance cost, which have been regarded as a promising energy storage technology. But due to their relatively low energy density compared with the commercialized lithium–ion batteries still impede their application for power systems. Anode–free rechargeable sodium–metal batteries (AFSMBs) pose a solution to boost energy density and tackle the safety problems of metal batteries. Combination of electrolyte, interface, and current collector strategies will eventually bring the AFSMBs closer to high energy and long–life AFSMBs for energy storage systems or power batteries. The strategies such as electrolyte optimization, interfacial chemistry engineering, and current collector modification, are also expected to be utilized for better understanding of anode-free rechargeable sodium-metal batteries (Ni et al., 2022). Sodium batteries demonstrate exceptional performance stability and capacity retention across a wide temperature spectrum. This unique characteristic positions them as a highly promising technology for various applications in extreme environments. As research progresses and costs continue to decline, sodium batteries are poised to play a transformative role in the future of electric vehicles, energy storage systems, and renewable energy integration.

3.2 Quantifying Performance: Capacity Retention Rate

The capacity retention rate is a vital indicator of how well a battery holds its original capacity under varying temperatures. Sodium batteries shine in this aspect too, exhibiting remarkable stability across a wide range of -40°C to 80°C.

- **Low-Temperature Capacity Retention:** Even at -40°C, sodium batteries can retain over 70% of their capacity. This is a testament to their optimized design and the use of low-temperature-friendly electrolytes. These features allow sodium batteries to deliver high energy output and efficient charge-discharge cycles even in extreme cold.
- **High-Temperature Capacity Retention:** Similarly, under scorching temperatures of 80°C, sodium batteries retain over 80% of their capacity. This impressive feat is a result of their inherent high-temperature stability and the effectiveness of their thermal management systems. By keeping the internal temperature low despite the external heat, these systems

ensure continued performance stability.

3.3 Modelling Control Schemes

Here are some important pointers to consider when modelling and controlling a sodium metal based redox flow battery (RFB):

- **Electrolyte**: The electrolyte concentration and capacity can be changed to alter the energy storage capacity of the battery.
- **Reactor size**: The output power of the battery can be changed by adjusting the size of the reactor.
- **Charging and discharging**: The charging and discharging efficiencies of the RFB increase as the power increases.
- **Pump loss**: The pump loss is relatively constant, so the charging and discharging efficiencies of a RFB increase as the power increases.
- **Charging power**: When the charging power is less than 9% of the rated power, the charging efficiency is considered zero. This is because the charging power is not enough to start the pump operation.
- **State of charge**: There are techniques to estimate the state of charge of a RFB.
- **Control strategies**: There are main control strategies for RFB systems.

A RFB system consists of three main components: the electrolyte, the cell stack, and the balance of plant (BOP). A Power Conversion System (PCS) is a device for bidirectional conversion of electrical energy connected between the battery system and the grid and/or load. This device should have charge and discharge functions, active and reactive power control functions and off-line switching functions. The PCS device enables the grid to work in both types of ships whether it is Direct-Current or Alternating-Current based electrical distribution system.

A "PCS Parallel System" refers to a system where multiple Power Conversion Systems (PCS) operate in parallel, meaning they are connected to share the load and work simultaneously, typically used in large-scale energy storage applications to efficiently manage the flow of electricity between the grid and battery storage units by combining the power output from several PCS units (Liu et al. 2023).

3.3.1 Key points about PCS Parallel Systems:

- **Function:** Each PCS acts as a converter, transforming DC power from the battery bank into AC power for the grid, and vice versa, allowing for bidirectional energy flow. In case the ship distribution system is based on DC power the PCS parallel system is based on DC-DC converter.
- **Redundancy:** By having multiple PCS units operating in parallel, the system can maintain power output even if one PCS fails, enhancing reliability.
- **Scalability:** This design allows for easy expansion of the energy storage capacity by simply adding more PCS units as needed.
- **Load Balancing:** The control system within the parallel PCS network can distribute the load evenly across all operating units, optimizing performance and extending lifespan.

3.3.2 Applications of PCS Parallel Power Systems:

- **Renewable Energy Integration:** To manage fluctuations in power generation from solar or wind farms at seaports coastal zones by storing excess energy in batteries and feeding it back to the grid when needed.

- **Microgrids:** To provide reliable power supply to the ship's localized area by combining distributed generation sources with Na metal seawater battery redox cell storage.

3.3.2 Important Design Considerations for PCS Parallel Systems

- **Synchronization:** Ensuring all PCS units are precisely synchronized to maintain stable power quality and avoid grid disturbances.
- **Control System Design:** Developing a robust control system to manage power sharing, fault detection, and protection mechanisms across the parallel PCS units. In a DC microgrid, such as in the ship "droop control" is a decentralized control strategy that enables multiple distributed power sources (like batteries or solar inverters) to automatically share load based on their available power. This is achieved by adjusting their output voltage slightly according to their current output, effectively acting like a virtual resistance to achieve balanced current sharing without the need for complex communication between devices. Essentially, the more current a source is supplying, the slightly lower its output voltage becomes, encouraging other sources to contribute more power to the grid. A droop control mode considering power cost, discusses the real-time relationship between the operation efficiency and control parameters by introducing bus voltage reference value, and realizes real time adjustment of droop coefficient of electric-hydrogen hybrid energy storage system (see Figure 6).

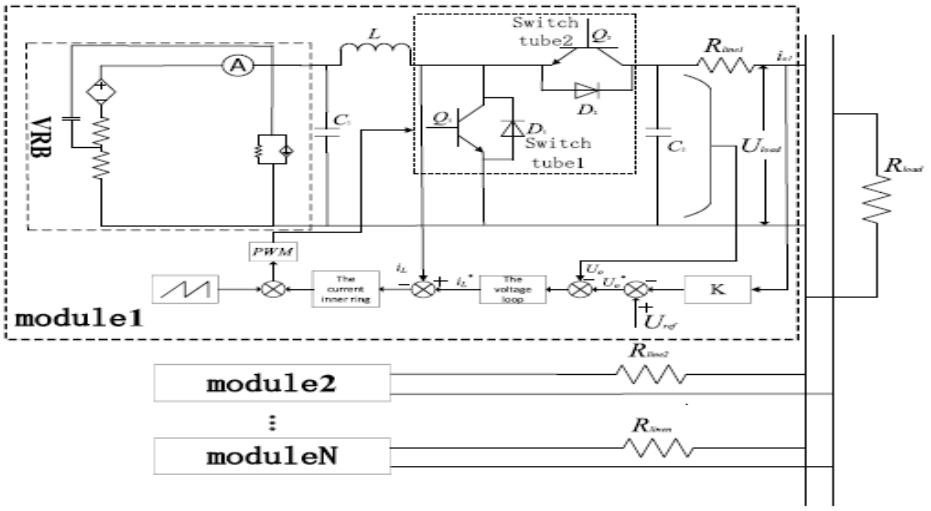

Figure 6. Droop Control Topology (Liu et al. 2023)

4. CONCLUSION AND FUTURE RECOMMENDATIONS

The paper presented a brief description of Seawater Battery with Desalination (SWB-D) system for electrolysis and trigeneration designed for ships at seaports. Currently, the shipping industry is facing many challenges for improving the fuel's energy efficiency. The ship power plant's energy efficiency can be improved and many strategies for decarbonization can be utilized (Barone et al., 2023). The proposed research is aiming at developing tools in COMSOL software and developing a Python code and linking it to the Arduino Cloud (for Python) (Rajora et al., 2022; Zheng 2023). These tools will be useful for modelling, simulation, and real-time control (for MIMO Control System problems such as Model-Predictive Control).

The modelling phase of this project comprises of the following i) model for Sodium Metal based

Redox Flow Desalination Battery; ii) model for the Electrolyser; iii) model for DC Electric Power from DG Engines/Gas Turbine Sets with hydrogen blend as fuel; iv) model for Absorption Cooling based on heat recovery from engine exhaust; vi) overall Mass & Energy Balance Model for calculating the energy-efficiency.

In general, the outcome of the study will be useful in: i) optimum utilization of earth's natural resources and switching from carbon economy to hydrogen economy; ii) modelling of systems through observer design with tipping point for GHG emissions and setpoint air temperature for multiple inputs and multiple outputs approach and considering the nature's abundant wealth of natural resources with transitioning through electrochemical energy conversion and storage through sodium batteries while switching from carbon economy to hydrogen economy.

The potential challenges related to practical shipboard implementation such as spatial constraints, system scalability, integration complexities, and maintenance requirements would be tested with complete full-scale experimental prototype exclusively designed with integrated control scheme for ships so as to guide future research for real-world applications.

REFERENCES

ABB, "DC distribution system - A significant step forward in electric propulsion increasing vessel efficiency up to 20%"(https://web.archive.org/web/20111009175011/http://www05.abb.com/global/scot/scot293.nsf/veritydisplay/9aef0fff204391adc12578ab001a3dd6/%24file/abb%20onboard%20dc%20grid_flyer_2011.pdf), 2011.

Barelli, l., Pelosi, D., Bidini, G., Di Donato, G., Navarra, M. A., Passerini, S. Na-seawater battery technology integration with renewable energies: The case study of Sardinia Island, Renewable and Sustainable Energy Reviews 187 (2023) 113701.

Barone, G., Buonomano, A., Papa, G. D., Forzanoa, C., Giuzio, G. F., Maka, R., Palombo, A., Russo G., and Vanoli, R., Improving the Energy Efficiency of Ships: Modelling, Simulation, and Optimization of Cost-effective Technologies, 4TH INTERNATIONAL CONFERENCE ON MODELLING AND OPTIMISATION OF SHIP ENERGY SYSTEMS 26-27 OCTOBER, 2023 DELFT, NETHERLANDS, DOI: https://doi.org/10.59490/moses.2023.665

Cao, Y., Delpisheh, M., Yousefiasl, S., Athari, H., El-Shorbagy, M. A., Jarad, F., Dahari, M., Wae-hayee, M., Examination and optimization of a novel auxiliary trigeneration system for a ship through waste-to-energy from its engine, Case Studies in Thermal Engineering 31 (2022) 101860

Dehra, H., Sodium Metal Based Desalination Battery for Electrolysis and Trigeneration using Direct-Current Generator, abstract presentation in the 75th Annual Meeting of the International Society of Electrochemistry, Montréal, Canada from 18 to 23 August 2024, (Symposia 11: Energy Electrochemical Technology/Electrosynthesis and Industrial Processes) (https://annual75.ise-online.org/index.php).

Haverkort, J.W., "Electrolysers, Fuel Cells and Batteries: Analytical Modelling", 2024, **DOI:** https://doi.org/10.59490/tb.93, ISBN: 9789463668538, Publisher: TU Delft OPEN Publishing.

Jiménez-García, J.C.; Ruiz, A.; Pacheco-Reyes, A.; Rivera,W. A Comprehensive Review of Organic Rankine Cycles. Processes 2023, 11, 1982. https://doi.org/10.3390/pr11071982

Kim, Y., Jung, J., Yu, H., Kim, G-T., Jeong, D., Bresser, D., Kang, S. J., Kim, Y., and Passerini, S., Sodium Biphenyl as Anolyte for Sodium–Seawater Batteries, Adv. Funct. Mater. 2020, 30, 2001249, DOI: 10.1002/adfm.202001249

Liu, Y., Wang, Y., Bai, X., Li, X., Ning, Y., Song, Y., Li, X., Mu, D., Review on modeling and control of megawatt liquid flow energy storage system, Energy Reports 9 (2023) 113–123, https://doi.org/10.1016/j.egyr.2023.02.060

Ni, Q.; Yang, Y.; Du, H.; Deng, H.; Lin, J.; Lin, L.; Yuan, M.; Sun, Z.; Sun, G. Anode-Free Rechargeable Sodium-Metal Batteries. Batteries 2022, 8, 272. https://doi.org/10.3390/batteries8120272

Rajora, A., Haverkort, J. W., An analytical multiphase flow model for parallel plate electrolyzers, Chemical Engineering Science 260 (2022) 117823, https://doi.org/10.1016/j.ces.2022.117823

Son, M., Park, S., Kim, N., Angeles, N. T., Kim, Y., and Cho, K. H., Simultaneous Energy Storage and Seawater Desalination using Rechargeable Seawater Battery: Feasibility and Future Directions, Adv. Sci. 2021, 8, 2101289, DOI: 10.1002/advs.202101289

Zheng W., (2023), Python for Electrochemistry: A Free and All-In-One Toolset, ECS Adv. 2 040502, **DOI** 10.1149/2754-2734/acff0b

6th International Conference on Building Energy and Environment
Eindhoven University of Technology, The Netherlands
6 - 10 July 2025

Life cycle-based optimization of building energy retrofits for net zero energy goals: A systematic review

Farzad Mostafazadeh [1,2], Yasaman Dadras [1,2], Mehdi Ghobadi [2], Miroslava Kavgic [1]

[1] *Department of Civil Engineering, University of Ottawa, 161 Louis-Pasteur Private, Ottawa, K1N 6N5, Ontario, Canada, farzad.mostafazadeh@uottawa.ca*
[2] *Construction Research Center, National Research Council of Canada, 1200 Montreal Road, Ottawa, K1A 0R6, Ontario, Canada,*

SUMMARY
Canada's Pan-Canadian Framework aims to reduce GHG emissions by 40-45% by 2030 and achieve net zero emissions by 2050, with retrofitting existing buildings for energy efficiency being crucial to meet these targets. While prior literature reviews address energy efficiency optimization or Life Cycle Assessment (LCA) in isolation, the systematic decoupling of these domains has led to fragmented frameworks that fail to resolve the inherent tension between short-term energy savings and long-term lifecycle consequences. This study presents a systematic literature review on building energy retrofit optimization, focusing on integrating LCA for net-zero energy buildings. It explores optimization models, algorithms, tools, simulation software, and lifecycle considerations, highlighting gaps for future research. These gaps include uncertainties in simulation inputs, underrepresentation of non-residential buildings, neglect of social aspects, limited post-intervention monitoring, neglect of embodied energy, underutilization of LCA tools, lack of comprehensive life cycle inventory databases, exclusion of full life cycle phases, and the need for integrated approaches at the district scale.

Keywords: Building energy retrofit, Optimization, Life cycle assessment (LCA), Net zero energy buildings (NZBE)

1. INTRODUCTION

Buildings account for about 30% of worldwide energy use and greenhouse gas emissions (“World Energy Outlook 2024 – Analysis - IEA,” n.d.). In Canada, this challenge is amplified by an aging building stock: over 50% of residential buildings are older than 30 years, with 20% exceeding 50 years (“Residential Housing Stock and Floor Space | Natural Resources Canada,” n.d.). These aging structures often lack modern energy efficiency measures, contributing disproportionately to the sector’s carbon footprint. To address this, Canada has committed to an 80% reduction in carbon emissions by 2050 compared to 2005 levels, a target demanding urgent, scalable retrofitting strategies (“Government of Canada sets ambitious GHG reduction targets for federal operations - Canada.ca,” n.d.). While conventional retrofits focus on operational energy savings, achieving life-cycle net-zero energy (NZBE) requires a paradigm shift. As defined by the U.K. Green Building Council, true NZBE necessitates balancing both operational and embodied energy impacts over a building’s lifespan, ensuring net-zero emissions across all lifecycle phases (“2019: Net Zero Carbon Buildings: A Framework Definition | UKGBC,” n.d.). Additionally, retrofits inherently involve balancing upfront investments against long-term environmental, economic, and social benefits (Mostafazadeh et al., 2023). These interdependencies necessitate robust optimization frameworks to systematically evaluate trade-offs and identify Pareto-optimal solutions.

While existing literature reviews have investigated optimization methods for retrofitting existing buildings (Hashempour et al., 2020), genetic algorithm-based retrofit optimization approaches (Costa-Carrapiço et al., 2020), optimization of low-energy buildings (Longo et al., 2019), and building envelope optimization (Kheiri, 2018) and life cycle assessment (LCA) in buildings (Amini Toosi et al., 2020; Dahiya and Laishram, 2024; Li et al., 2020), a critical disconnect persists between energy optimization and LCA frameworks. This fragmentation has led to retrofit strategies prioritize short-term operational efficiency while neglecting embodied carbon impacts. Most existing frameworks fail to holistically integrate energy retrofit optimization with LCA methodologies, resulting in suboptimal solutions that hinder progress toward Net-Zero Energy Buildings (NZEB). This oversight underscores a pressing need for a unified approach that bridges energy performance optimization with lifecycle sustainability.

This study provides the first systematic synthesis of energy retrofit optimization and LCA studies to bridge this foundational gap to achieve NZBE. Unlike previous fragmented reviews, this work:

- Synthesizes critical components, objective functions, optimization models, algorithms, and tools, while explicitly linking them to lifecycle considerations.
- Identifies key synergies and trade-offs between operational energy savings and embodied carbon impacts, enabling more robust, future-proof retrofit strategies.
- Proposes a novel research agenda to advance integrated optimization-LCA frameworks, offering actionable insights for policymakers, engineers, and sustainability practitioners.

By harmonizing these currently siloed domains, this study not only fills a major methodological gap but also its findings are poised to reshape retrofit practices by ensuring that energy efficiency gains do not come at the expense of long-term environmental burdens.

2. METHODOLOGY

This systematic literature review follows the PRISMA (Preferred Reporting Items for Systematic Reviews and Meta-Analyses) guidelines to ensure methodological rigor and transparency (Moher et al., 2009). The search strategy was executed on the Scopus database on 9th January 2025. Titles, abstracts, and keywords were searched using the following query, which yielded 47 results:
(building* AND energy AND (retrofit* OR refurbishment OR rehabilitation OR renovation OR "existing building*") AND optimi* AND (lca OR "life cycle" OR life-cycle OR lifecycle OR embodied) AND (nzeb OR zeb OR "net-zero energy" OR "zero energy" OR "nearly zero energy"))

The screening process followed a sequential three-step approach to refine the results. First, 13 records were excluded during the initial screening phase due to non-English language, review articles, book chapters, or ineligible document types. Subsequently, title and abstract screening assessed relevance to the integration of optimization, retrofits, LCA, and NZBE principles, excluding 9 studies with insufficient focus on these themes. Finally, a full-text review evaluated methodological alignment with the study's scope, eliminating 6 articles. This process resulted in a final set of 19 articles for in-depth analysis.

3. RESULTS AND DISCUSSION

Table 1 presents a detailed summary of key aspects evaluated and discussed in the final screened papers.

Table 1. Summary of investigated studies.

Res: Residential, His: Historic, Off: Office, Edu: Educational, Envi: Environmental, Eco: Economic, Soci: Social, EUI: Energy Use Intensity, HD: Heating demand, CD: Cooling Demand, EC: Energy Consumption, PEC: Primary Energy Consumption, RCP: Indicator for Environmental Damage, EB: Energy Balance, EE: Embodied Energy, ED: Energy Demand, ES: Energy Supply, HC: Heating Cost, CC: Cooling Cost, PP: Payback Period, TGC: Total Global Cost, ThComf: Thermal Comfort, HS: HVAC System, LS: Lighting System, DHW: Domestic Hot Water, SC: Solar Collector, PV: Photovoltaic, PVT: Photovoltaic Thermal, LC: Lighting Control, SetC: Setpoint Control, EI: Envelope Insulation, WR: Window Replacement, AoI: Airtightness of Infiltration, NL: Natural Lighting, SH: Shading Device, WWR: Window to Wall Ratio, VAF: Ventilation Air Flow, Simub: Simulation-based, Simu: Simulation software

Authors	Case study location	Case study type, construction year	Objective functions	Optimization model (OptM), Algorithm (OptA)	Software	Energy retrofit measures	Database	Service lifespan
(Munguba et al., 2024)	Brazil	Edu, 1990	Envi: EUI Eco: LCC (NPV) Soci: -	OptM: Simub OptA: Tabu search	Opt: Python Simu: Proarcondicionado	Active: HS, LS Passive: EI, WR, White tile on Facade Renewable: PV	Brazilian suppliers, SINAPI, INMETRO	25
(Las-Heras-Casas et al., 2021)	Spain	Res, -	Envi: HD, CD Eco: HC, CC, PP Soci: -	OptM: Simub OptA: P1-P2	Opt: - Simu: HULC	Active: HS Passive: EI, WR Renewable: -	Literature	-
(Abdou et al., 2021)	Morocco	Res, -	Envi:EC Eco: LCC (NPV) Soci: ThComf	OptM: Simub OptA: NSGA-II	Opt: MOBO Simu: TRNSYS	Active: - Passive: EI, WR, AoI, WWR, BO Renewable: PV, SC	-	25
(Ruparathna et al., 2017)	Canada	Recreational, -	Envi: GHGe, EC Eco: LCC (NPV) Soci: -	OptM: Simub OptA: Rank (weighted sum)	Opt: Excel Simu: DesignBuilder	Active: HS, LS Passive: EI, WR Renewable: PV, SC, GPHC	-	-
(Lohse et al., 2016)	Austria, Germany	Res and Off, 1960	Envi: PEC Eco: LCC (NPV) Soci: -	OptM: Simub OptA: Estimative	Opt: - Simu: PHPT	Active: HS, LS, DHW Passive: EI, WR, AoI, NL, SH Renewable: -	-	40, 33
(Niemelä et al., 2017a)	Finland	Res, 1960	Envi: PEC Eco: LCC (NPV) Soci: -	OptM: Simub OptA: Pareto-Archive NSGA-II	Opt: MOBO Simu: IDA-ICE	Active: HS Passive: EI, WR Renewable: PV, SC	Literature, manufacturers, consultants	25
(Ismaeil and Sobaih, 2023)	Saudi Arabia	Res, -	Envi: EC Eco: - Soci: -	OptM: Simub OptA: Heuristic	Opt: - Simu: HAP, PVsyst	Active: HS Passive: - Renewable: PVT	Manufacturers, specialist designers	-
(Naves et al., 2021)	Brazil	Res, -	Envi: EC Eco: LCC (NPV) Soci: -	OptM: Simub OptA: -	Opt: GenOpt Simu: TRNSYS	Active: HS, TES Passive: - Renewable: PV	-	20
(Zuhaib and Goggins, 2019)	Ireland	Edu, 1975	Envi: PEC Eco: LCC (NPV) Soci: ThComf	OptM: Simub OptA: NSGA-II	Opt: jEPlus Simu: EnergyPlus	Active: HS, LS Passive: EI, WR, AoI Renewable: PV Other:LC, SC	Literature	30
(Rabani et al., 2020)	Norway	Off, 1980	Envi: EC Eco: LCC Soci: -	OptM: Simub OptA: PSO	Opt: GenOpt Simu: IDA-ICE	Active: HS Passive: WR, EI, SH, VAF, ST Renewable: -	-	60
(Abokersh et al., 2021)	Netherlands	Res, -	Envi: RCP Eco: LCC (NPC) Soci: -	OptM: Meta OptA: Genetic	Opt: MATLAB Simu: TRNSYS	Active: HS, DHW Passive: EI Renewable: PV, SC	-	40
(Wu et al., 2021)	China	Res, -	Envi: EB Eco: CR Soci: -	OptM: Simub OptA: NSGA-II	Opt: - Simu: -	Active: - Passive: - Renewable: -	-	-
(Amani and Kiaee, 2020)	Iran	Res, -	Envi: EC, CO2e Eco: - Soci: -	OptM: Simub OptA: -	Opt: - Simu: DesignBuilder	Active: - Passive: EI Renewable: -	EPBD CA	100
(Niemelä et al., 2017b)	Finland	Res, Late 1960s to mid 1970s	Envi: PEC, CO2e Eco: LCC (NPV) Soci: -	OptM: Simub OptA: NSGA-II	Opt: MOBO Simu: IDA-ICE	Active: HS Passive: EI, WR Renewable: PV	360Optimi, ICE and EPBD	30
(Shadram et al., 2020)	Sweden	Res, 1980	Envi: EE, EC Eco: - Soci: -	OptM: Simub OptA: Genetic	Opt: Octopus Simu: Honeybee	Active: HS Passive: EI, WR Renewable: -	EPD and ICE	30
(Gremmelspacher et al., 2021)	Sweden	His, 1966	Envi: - Eco: LCC (NPV) Soci: -	OptM: Simub OptA: -	Opt: TT Toolbox Simu: Honeybee	Active: HS, LS Passive: EI, WR, AoI Renewable: PV	-	Building: 50 PV: 25
(Ferrara et al., 2019)	Italy	Res, 2014	Envi: ED, ES Eco: TGC Soci: -	OptM: Simub OptA: PSO	Opt: GenOpt Simu: TRNSYS	Active: HS Passive: EI, WR Renewable: PV, SC	-	30
(Lorenzati et al., 2019)	Italy	Res, -	Envi: EP Eco: TGC Soci: -	OptM: Simub OptA: NSGA-II	Opt: - Simu: EnergyPlus	Active: HS Passive: EI, WR Renewable: PV, SC	-	Building: 20 systems: 15-20
(Krarti and Dubey, 2018)	Bahrain	Res, -	Envi: ESa Eco: LCC Soci: -	OptM: Simub OptA: Sequential search	Opt: - Simu: EnergyPlus	Active: HS, LS Passive:EI, WR, AoI Renewable: PV	-	30

3.1. Typology and building function

Studies on energy retrofit optimization are broadly categorized by building type: residential and non-residential (commercial, educational, industrial, office, and special-function buildings like

hospitals or hotels). Residential buildings dominate the literature, reflecting their substantial share (~70%) of global building energy consumption ("World Energy Outlook 2024 – Analysis - IEA," n.d.). Non-residential retrofits, crucial for sectoral decarbonization, are underrepresented in research (~30% of studies), likely due to operational complexity, and challenges in minimizing retrofit disruptions (Dadras and Kavgic, 2022; Munguba et al., 2024; Rabani et al., 2020).

3.2. Objective functions

Objective functions define the goals of optimization models and are critical for identifying optimal retrofit strategies. In building energy retrofit studies, objective functions are typically categorized into three domains: environmental, economic, and social, each reflecting distinct and often conflicting priorities in decision-making (Citadini de Oliveira et al., 2024).

Environmental objectives focus on reducing the environmental impact of buildings, primarily by minimizing energy consumption and greenhouse gas emissions. These objectives are critical for aligning retrofit projects with global sustainability goals, such as achieving net-zero energy buildings or meeting climate targets. The most frequently employed environmental objective functions, used in about 90% of studies, focus on minimizing energy consumption metrics such as primary energy consumption, total energy demand, and heating or cooling demand (Ismaeil and Sobaih, 2023; Las-Heras-Casas et al., 2021). As shown in Table 1, only 16% of studies quantified GHG emissions as core optimization targets (Amani and Kiaee, 2020; Niemelä et al., 2017a; Ruparathna et al., 2017) despite the fact that it is a necessity to achieve true NZBE.

Economic objectives aim to optimize the financial performance of retrofit projects, ensuring cost-effectiveness and maximizing return on investment. By focusing on economic objectives, optimization models can identify retrofit strategies that balance upfront costs with long-term savings, ensuring that projects deliver measurable financial benefits. The most frequently employed economic objective function, used in 63% of studies, is minimizing lifecycle costs using the net present value method (Gremmelspacher et al., 2021; Niemelä et al., 2017b). Additional financial metrics, including initial investment or payback period, are occasionally calculated as auxiliary metrics (Lohse et al., 2016; Naves et al., 2021; Wu et al., 2021).

Social objectives, such as thermal comfort, visual comfort, and indoor air quality, address occupant well-being and societal benefits. However, only 10% of the reviewed studies have addressed social objectives, with a sole focus on thermal comfort (Seghier et al., 2022; Zuhaib and Goggins, 2019). For the widespread adoption of NZEBs, it is essential to ensure occupant comfort, as it is a key factor in securing stakeholder support.

3.3. Optimization models and frameworks

Optimization algorithms are essential for solving building energy retrofit problems, with metaheuristic algorithms such as GA and PSO being the most widely adopted, used in 53% of studies, due to their ability to handle complex, non-linear, and multi-modal problems (Ferrara et al., 2019; Lorenzati et al., 2019). Simulation-based optimization integrates building energy simulation tools with optimization algorithms to identify optimal retrofit strategies. This approach leverages detailed building performance simulations to evaluate the impact of different retrofit measures. Building energy simulation tools are used to model the building's energy performance. Optimization algorithms iteratively explore the solution space by running simulations for different

retrofit scenarios. The algorithm identifies the combination of retrofit measures that best meet the defined objectives. One of the key advantages of simulation-based optimization is high fidelity in predicting actual building performance, as it relies on detailed physics-based models (Mirzaei et al., 2020; Shadram et al., 2020; Tavakolan et al., 2022). It is also capable of handling complex, non-linear relationships between variables, making it suitable for evaluating a wide range of retrofit measures. While simulation-based optimization is effective for individual buildings or small portfolios, its reliance on numerous iterative simulations makes it computationally expensive and time-consuming for large-scale or complex problems. Additionally, achieving true NZEBs requires simultaneous optimization of both operational and embodied energy, further increasing computational demands due to the need for separate software tools for each assessment.

Metamodel-based optimization, also known as surrogate model-based optimization, addresses the computational challenges of simulation-based optimization by replacing the detailed simulation model with a simplified, data-driven approximation. In this approach, a metamodel is trained using input-output data generated from a limited number of building energy simulations (Abokersh et al., 2021). The trained metamodel is then used as a surrogate for the simulation tool during the optimization process. The primary advantage of metamodel-based optimization is its computational efficiency, making it faster than simulation-based optimization and suitable for more complex or large-scale problems or when multiple optimization runs are required (Batres et al., 2023; Mostafazadeh et al., 2025). However, as shown in Table 1, only one study (Abokersh et al., 2021) has utilized metamodels, highlighting a critical research gap that needs to be addressed.

3.4. Optimization tools and software

Optimization tools provide the computational framework necessary to integrate building energy simulations, optimization algorithms, and data analysis by automating the iterative process of evaluating multiple retrofit scenarios. These tools can be broadly classified into programming languages and specialized optimization software. Programming languages, such as MATLAB and Python, offer flexibility and customization, enabling users to implement a wide range of optimization algorithms tailored to specific needs (Munguba et al., 2024). On the other hand, specialized optimization tools like GenOpt and jEplus are designed specifically for building energy optimization. They provide user-friendly interfaces and seamless integration with building energy simulation software, making them accessible without extensive programming expertise (Rabani et al., 2020); however, they are less flexible than programming languages. EnergyPlus is the most widely used simulation software for calculating operational energy demand due to its reliability, open-source nature, and text-based framework. However, there is a lack of integration of LCA tools in retrofit optimization frameworks, which are essential for evaluating embodied energy.

3.5. Energy retrofit measures (decision variables)

Energy retrofit measures, serving as decision variables in optimization frameworks, are broadly categorized into passive, active, renewable energy systems, user behavior, and smart building controls (Citadini de Oliveira et al., 2024). Passive measures such as upgrading insulation materials and window glazing properties mainly focus on improving the building envelope to reduce energy demand. These measures minimize heat transfer and air infiltration, thereby lowering heating and cooling loads without reliance on mechanical systems (Rabani et al., 2020). Active measures such as replacing conventional HVAC systems with efficient alternatives and installing advanced lighting controls involve upgrading or retrofitting mechanical and electrical

systems to improve operational efficiency. Such measures optimize energy use dynamically, responding to real-time occupancy patterns and environmental conditions (Lohse et al., 2016). Renewable measures often interact synergistically with passive and active strategies. Renewable energy systems address energy supply by integrating on-site generation technologies to offset non-renewable energy use. As shown in Table 1, solar-based renewable energies, including photovoltaic (PV) panels and solar thermal collectors (SC), are used in 70% of the studies (Ferrara et al., 2019; Lorenzati et al., 2019). Achieving NZBE requires a holistic integration of passive, active, and renewable energy retrofit measures. There is a widely acceptable rationale to build nearly zero energy buildings to reduce the energy demand first and then supply energy from renewable sources ("World Energy Outlook 2024 – Analysis - IEA," n.d.).

3.6. Life cycle assessment

LCA is a critical methodology for evaluating the environmental and economic impacts of building energy retrofits across their entire lifecycle. According to the EN 15978 standard (BS EN 15978, 2011) the life cycle of a building is divided into product stage (material extraction and manufacturing), construction stage, use stage (operational energy and maintenance), and end-of-life stage (demolition and disposal). The most commonly considered system boundary in retrofit studies is operational stage excluding product and end-of-life stages due to data limitations or lower relative impact. Investigated studies relied on Environmental Product Declarations (EPDs) or existing literature to estimate embodied carbon and energy, as conducting full-scale LCAs can be resource-intensive with high levels of uncertainty. The service life span considered in retrofit studies typically ranges from 20 to 30 years, reflecting the expected lifespan of retrofit measures.

The connection between LCA and NZBE is particularly significant, as achieving NZBE requires balancing operational energy reductions with embodied energy impacts. While operational energy dominates traditional building energy use, embodied energy from materials and construction processes becomes increasingly important as operational energy decreases. However, investigated studies focus solely on life cycle cost (LCC) and operational energy, neglecting embodied energy and comprehensive environmental LCA analysis. This oversight can lead to suboptimal retrofit strategies that minimize operational impacts but inadvertently increase embodied carbon, undermining overall sustainability goals. Integrating both operational and embodied energy assessments into retrofit optimization is essential for achieving true NZBE and ensuring that environmental benefits are not offset by upstream impacts.

4. CONCLUSION

This paper systematically reviewed the methodologies and tools for optimizing building energy retrofits, focusing on their role in advancing NZBE objectives. Our analysis explored optimization models, algorithms, and tools that enable the integration of energy performance simulations with retrofit decision-making. We examined energy retrofit measures as critical decision variables and emphasized the importance of LCA in evaluating environmental and economic impacts. The following gaps have been identified in the reviewed studies:

- High uncertainty in simulation model inputs (e.g., retrofit costs, energy prices, emissions, material variability, grid carbon intensity, and model assumptions) remains unresolved.
- Overlooked uncertainties in occupant behavior, maintenance, and replacement scenarios limit real-world applicability.

- Inadequate consideration of future climate projections, energy price fluctuations, system degradation, and evolving energy mixes.
- Limited pre- and post-intervention monitoring undermines confidence in retrofit outcomes, hindering robust conclusions.
- Prioritizing operational energy reduction while neglecting embodied energy and environmental impacts of materials.
- Underutilization of LCA tools, insufficient documentation, and lack of comprehensive life cycle inventory (LCI) databases hinder accurate embodied energy assessment.
- Lack of integration of LCA tools in retrofit optimization frameworks, which are essential for evaluating embodied energy.
- Ignoring end-of-life impacts, and circular economy principles in retrofit optimization.
- Focusing on environmental (LCA) or economic (LCC) dimensions while neglecting social aspects of sustainability.
- Non-residential buildings are underrepresented despite their complex retrofit challenges.
- Scarcity of research on integrated retrofit solutions at the neighborhood or district scale.

6. REFERENCES

2019: Net Zero Carbon Buildings: A Framework Definition | UKGBC [WWW Document], n.d. URL https://ukgbc.org/resources/net-zero-carbon-buildings-a-framework-definition/ (accessed 2.2.25).

Abdou, N., EL Mghouchi, Y., Hamdaoui, S., EL Asri, N., Mouqallid, M., 2021. Multi-objective optimization of passive energy efficiency measures for net-zero energy building in Morocco. Build. Environ. 204, 108141.

Abokersh, M.H., Gangwar, S., Spiekman, M., Vallès, M., Jiménez, L., Boer, D., 2021. Sustainability insights on emerging solar district heating technologies to boost the nearly zero energy building concept. Renew. Energy.

Amani, N., Kiaee, E., 2020. Developing a two-criteria framework to rank thermal insulation materials in nearly zero energy buildings using multi-objective optimization approach. J. Clean. Prod. 276, 122592.

Amini Toosi, H., Lavagna, M., Leonforte, F., Del Pero, C., Aste, N., 2020. Life Cycle Sustainability Assessment in Building Energy Retrofitting; A Review. Sustain. Cities Soc, 102248.

Batres, R., Dadras, Y., Mostafazadeh, F., Kavgic, M., 2023. MEVO: A Metamodel-Based Evolutionary Optimizer for Building Energy Optimization. Energies 16.

BS EN 15978, 2011. BS EN 15978:2011 Sustainability of construction works — Sustainability assessment of buildings - Part 1: Calculation method. Br. Stand. Publ. 64.

Citadini de Oliveira, C., Catão Martins Vaz, I., Ghisi, E., 2024. Retrofit strategies to improve energy efficiency in buildings: An integrative review. Energy Build. 321, 114624.

Costa-Carrapiço, I., Raslan, R., González, J.N., 2020. A systematic review of genetic algorithm-based multi-objective optimisation for building retrofitting strategies towards energy efficiency. Energy Build. 210, 109690.

Dadras, Y., Kavgic, M., 2022. The applicability of simplified whole-building energy model for energy-efficiency retrofit analysis.

Dahiya, D., Laishram, B., 2024. Life cycle energy analysis of buildings: A systematic review. Build. Environ. 252.

Ferrara, M., Rolfo, A., Prunotto, F., Fabrizio, E., 2019. EDeSSOpt – Energy Demand and Supply Simultaneous Optimization for cost-optimized design: Application to a multi-family building. Appl. Energy 236, 1231–1248.

Government of Canada sets ambitious GHG reduction targets for federal operations - Canada.ca [WWW Document], n.d. URL https://www.canada.ca/en/treasury-board-secretariat/news/2017/12/government_of_canadasetsambitiousghgreductiontargetsforfederalop.html (accessed 2.2.25).

Gremmelspacher, J.M., Campamà Pizarro, R., van Jaarsveld, M., Davidsson, H., Johansson, D., 2021. Historical building renovation and PV optimisation towards NetZEB in Sweden. Sol. Energy 223, 248–260, 02.067.

Hashempour, N., Taherkhani, R., Mahdikhani, M., 2020. Energy performance optimization of existing buildings: A literature review. Sustain. Cities Soc. 54, 101967. https://doi.org/10.1016/j.scs.2019.101967

Ismaeil, E.M.H., Sobaih, A.E.E., 2023. Heuristic Approach for Net-Zero Energy Residential Buildings in Arid Region Using Dual Renewable Energy Sources. Buildings 13.

Kheiri, F., 2018. A review on optimization methods applied in energy-efficient building geometry and envelope design. Renew. Sustain. Energy Rev. 92, 897–920, 04.080.

Krarti, M., Dubey, K., 2018. Benefits of energy efficiency programs for residential buildings in Bahrain. J. Build. Eng. 18, 40–50, 02.018.
Las-Heras-Casas, J., López-Ochoa, L.M., López-González, L.M., Olasolo-Alonso, P., 2021. Energy Renovation of Residential Buildings in Hot and Temperate Mediterranean Zones Using Optimized Thermal Envelope Insulation Thicknesses: The Case of Spain. Appl. Sci. 11, 1–30.
Li, C.Z., Lai, X., Xiao, B., Tam, V.W.Y., Guo, S., Zhao, Y., 2020. A holistic review on life cycle energy of buildings: An analysis from 2009 to 2019. Renew. Sustain. Energy Rev. 134, 110372.
Lohse, R., Staller, H., Riel, M., 2016. The economic challenges of deep energy renovation - Differences, similarities, and possible solutions in central Europe: Austria and Germany. ASHRAE Conf. 122, 69–87.
Longo, S., Montana, F., Riva Sanseverino, E., 2019. A review on optimization and cost-optimal methodologies in low-energy buildings design and environmental considerations. Sustain. Cities Soc. 45, 87–104, 11.027.
Lorenzati, A., Ballarini, I., De Luca, G., Corrado, V., 2019. Social housing in Italy: Energy audit and dynamic simulation towards a nZEB policy. Build. Simul. Conf. Proc. 7, 4990–4997, 210428.
Mirzaei, K., Safari, A., Jalilzadeh, S., Mostafazadeh, F., Tavakolan, M., Safari, M., 2020. Environmental, Social, and Economic Benefits of Buildings Energy Retrofit Projects: A Case Study in Iran's Construction Industry, in: Construction Research Congress 2020. American Society of Civil Engineers, Reston, VA, pp. 693–701.
Moher, D., Liberati, A., Tetzlaff, J., Altman, D.G., Antes, G., Atkins, D., Barbour, V., Barrowman, N., Berlin, J.A., Clark, J., Clarke, M., Cook, D., D'Amico, R., Deeks, J.J., Devereaux, P.J., Dickersin, K., Egger, M., Ernst, E., Gøtzsche, P.C., Grimshaw, J., Guyatt, G., Higgins, J., Ioannidis, J.P.A., Kleijnen, J., Lang, T., Magrini, N., McNamee, D., Moja, L., Mulrow, C., Napoli, M., Oxman, A., Pham, B., Rennie, D., Sampson, M., Schulz, K.F., Shekelle, P.G., Tovey, D., Tugwell, P., 2009. Preferred reporting items for systematic reviews and meta-analyses: The PRISMA statement. Ann. Intern. Med. 151, 264–269.
Mostafazadeh, F., Dadras, Y., Kavgic, M., Batres, R., 2025. Application of Metamodel-Based Evolutionary Optimizer (MEVO) to Improve Energy Efficiency of a Dormitory Building in Canada, Lecture Notes in Civil Engineering. Springer Nature Singapore.
Mostafazadeh, F., Eirdmousa, S.J., Tavakolan, M., 2023. Energy, economic and comfort optimization of building retrofits considering climate change: A simulation-based NSGA-III approach. Energy Build. 280, 112721.
Munguba, C.F.L., Leite, G.N.P., Ochoa, A.A.V., Michima, P.S.A., Silva, H.C.N., Vilela, O.C., Kraj, A., 2024. Enhancing cost-efficiency in achieving near-zero energy performance through integrated photovoltaic retrofit solutions. Appl. Energy 367, 123307.
Naves, A.X., Jim, L., Haddad, A.N., 2021. Sustainability-13-12831-V2.Pdf 1–29.
Niemelä, T., Kosonen, R., Jokisalo, J., 2017a. Cost-effectiveness of energy performance renovation measures in Finnish brick apartment buildings. Energy Build. 137, 60–75, 12.031.
Niemelä, T., Kosonen, R., Jokisalo, J., 2017b. Energy performance and environmental impact analysis of cost-optimal renovation solutions of large panel apartment buildings in Finland. Sustain. Cities Soc. 32, 9–30, 02.017.
Rabani, M., Bayera Madessa, H., Mohseni, O., Nord, N., 2020. Minimizing delivered energy and life cycle cost using Graphical script: An office building retrofitting case. Appl. Energy 268, 114929.
Residential Housing Stock and Floor Space | Natural Resources Canada [WWW Document], n.d. URL https://oee.nrcan.gc.ca/corporate/statistics/neud/dpa/showTable.cfm?type=HB&sector=res&juris=00&rn=11&year=2020&page=4 (accessed 2.2.25).
Ruparathna, R., Hewage, K., Sadiq, R., 2017. Rethinking investment planning and optimizing net zero emission buildings. Clean Technol. Environ. Policy 19, 1711–1724.
Seghier, T.E., Lim, Y.W., Harun, M.F., Ahmad, M.H., Samah, A.A., Majid, H.A., 2022. BIM-based retrofit method (RBIM) for building envelope thermal performance optimization. Energy Build. 256, 111693.
Shadram, F., Bhattacharjee, S., Lidelöw, S., Mukkavaara, J., Olofsson, T., 2020. Exploring the trade-off in life cycle energy of building retrofit through optimization. Appl. Energy 269, 115083.
Tavakolan, M., Mostafazadeh, F., Jalilzadeh Eirdmousa, S., Safari, A., Mirzaei, K., 2022. A parallel computing simulation-based multi-objective optimization framework for economic analysis of building energy retrofit: A case study in Iran. J. Build. Eng. 45, 103485.
World Energy Outlook 2024 – Analysis - IEA [WWW Document], n.d. URL https://www.iea.org/reports/world-energy-outlook-2024 (accessed 2.2.25).
Wu, W., Meng, Q., Lv, Y., Li, X., Hou, H., Gao, Y., Cao, W., 2021. An optimization and evaluation method construction of zero-energy residential building renovation. IOP Conf. Ser. Earth Environ. Sci. 675.
Zuhaib, S., Goggins, J., 2019. Assessing evidence-based single-step and staged deep retrofit towards nearly zero-energy buildings (nZEB) using multi-objective optimisation. Energy Effic. 12, 1891–1920.

6th International Conference on Building Energy and Environment
Eindhoven University of Technology, The Netherlands
6 - 10 July 2025

Ensuring building energy efficiency leads to decarbonization

Mehdi Ghobadi [1], Travis Moore[2]

[1]*National Research Council Canada, Ottawa, Ontario, Canada, Mehdi.Ghobadi@nrc-cnrc.gc.ca*
[2]*National Research Council Canada, Ottawa, Ontario, Canada, Travis.Moore@nrc-cnrc.gc.ca*

SUMMARY
Improving building energy performance is central to reducing energy bills, reducing electricity demand, increasing resiliency and enhancing the health and comfort of building occupants within their communities. In 2025, it is expected that the National Model Building Code of Canada will set operational carbon limits for buildings located in every province using annually averaged emission factors for the electrical grid and natural gas which assumes that the carbon intensity of electrical usage remains constant during the year and is not affected by seasonal and daily variations. Whereas, in reality, emission factors vary during the year, especially in an electrical utility where both fossil fuel and renewable generation assets are used. In this paper, we will compare how the energy demand and operational carbon calculation is affected using annually averaged data versus hourly data for the grid carbon emission factors in an example of an electrified heating dominated mixed-source grid, during a winter peak event.

Keywords: building decarbonization, energy efficiency, grid carbon intensity

2. INTRODUCTION

The recent Pan-Canadian Framework on clean growth and climate change, as developed by the Canadian Government, has set the goal to reduce GHG emissions from 40 to 45% by 2030, as compared to the amount emitted in 2005, and as well, has legislated a commitment to reach net zero emissions by 2050. Globally, operational and embodied emissions of buildings account for 28 and 11 percent of the global emissions (IEA, 2023). Two main components that can transform the construction sector to achieve its environmental targets are energy efficiency and building decarbonization. Although these two terms are often used interchangeably, and are interconnected approaches for achieving sustainability in buildings, there can be distinct and critical differences between them. Achieving energy efficiency in buildings typically involves the implementation of the following measures:

- High performance building envelope: Building envelopes include the exterior walls, foundations, roofs, windows, and doors. Improving the insulation and air sealing of the building envelope can reduce heat losses and the need for heating and cooling of the building.
- High-efficiency equipment: Energy efficient HVAC systems and appliances can directly reduce the energy demand for the same level of service.
- Smart building controls: Advanced control systems that can use the real time and forecasted data to minimize energy demand.
- Lighting design: Maximizing the use of natural light within buildings, and the use of energy efficient fixtures, such as LED lighting and automatic sensors, can reduce the energy demand for lighting.
- Building occupant behaviour: Building occupants can play a very important role by

employing energy saving practices whereby energy is used responsibly. Includes measures such as changing thermostat set point to reduce cooling and heating loads, using a drying line instead of mechanical dryers, and participating in demand response programs with the utility.

Energy efficiency measures have the potential to reduce emissions, contribute to energy security, reduce the operational energy costs and improve the thermal comfort within buildings, and the health of building occupants [IEA, 2023]. Energy efficiency is the key element of plans by the Canadian Government to reduce emissions by up to 45 percent by 2030, and achieve a carbon neutral economy by 2050. Hence, the main approach, as adopted by the relevant committees of the National Building Code of Canada, has focused on energy efficiency, for which five energy tiers have been introduced that represent a reduction in energy use in buildings and residential houses, with an anticipated correlation to operational carbon emissions (Magwood et al., 2020). There is a widely accepted rationale to implementing these changes by first constructing nearly zero-energy buildings to reduce the energy demand, and thereafter, provide energy to these buildings from renewable sources (IEA, 2023).

Decarbonization mainly focuses on reducing or eliminating carbon emissions associated with the construction, maintenance, and operations of a building. In respect to operational carbon emissions, decarbonization focuses on shifting from fossil fuel-based energy sources to cleaner, renewable alternatives. The key pillars of building decarbonization according to the ASHRAE Centre of Excellence for Building Decarbonization are:

- Efficiency measures and building electrification
- Operations and maintenance
- Refrigerants: Low-GWP, minimizing volume, and improving management
- Renewable energy sources (on and off-site) and energy storage
- Building-grid integration and real-time carbon signals
- Embodied carbon
- Decarbonized electrical grid

In addition to these pillars, carbon offsetting technologies have been used to offset the released emissions. Some other energy storage solutions such as batteries and thermal mass storage solutions are also being explored; however, the primary barriers to the uptake of these solutions are their high initial costs and associated embodied carbon [ASHRAE 228, 2023].

Electrification is often used as a decarbonization strategy, especially in Canada where until recently, the electricity grids had a target of net-zero emissions by 2035. This was also coupled with a federal policy push to increase electrification of heating, not necessarily focused on reduction in demand. Additionally, decarbonization potential of electrification is typically determined using annual average emissions factors, with limited studies being completed on the potential effects of sub-annual emissions factors impact on decarbonization potential due to a lack of published data. Lou et al. investigated the potential of five different retrofit energy conservation measures to reduce emissions through modelling of an archetype mid-sized office building using dynamic hourly emission rates for five different climate locations across the U.S. (having correspondingly different grid-mixes and renewable adoption rates). In this paper it was

demonstrated that the impact of different retrofit measures for medium office buildings can vary depending on the climate and grid-mix, with warmer climates more likely to benefit from equipment efficiency and lighting upgrades, whereas, in colder climates, the benefits of retrofitting the building envelope has increasing potential for reducing emissions. St. Jacques et al. (2023) provided an important contribution to understanding the impacts of using hourly emission factors compared to annual emission factors to account for the GHG emissions of several buildings in a number of different cities in Ontario using whole building energy modelling. The authors additionally investigated the impact on building operational GHG emissions if fuel switching, from natural gas heating to a ground source heat pump, was completed. The results of the study demonstrated the importance of accounting for the hourly energy usage (i.e., consumption based hourly emission factors) when calculating emissions for different grid-mixes. It was estimated that, for most locations, the switch to electrified heating would significantly reduce building operational GHG emissions, however limitations in the scale up of electrified heating, that necessitated utility capacity increases, were not considered.

In this paper, focus is on how electrification can be employed as a decarbonization strategy and how reductions of building operational emissions can be leveraged to optimize cross sector emissions in the electricity grid, especially considering the push in Canada towards electrification of heating sources. Electricity sources and emissions factors in different provinces are discussed, as well as how the electricity supply has evolved over the last 30 years, and how energy efficiency measures correlate with carbon reductions. As an example, the importance of using hourly emissions in New Brunswick, Canada, is demonstrated for a province having predominantly electrified heating and a mixed-emission source electricity grid.

2. CANADIAN ELECTRICITY MIXES AND ELECTRIFICATION

According to the IEA buildings NetZero plans, energy efficiency measures and electrification will need to account for roughly 30% and 40% of global direct emissions reductions by 2050, respectively. According to the Canadian Energy Regulator (CER), in 2021, Canada produced 625.7 terawatt-hours (TWh) of electricity. More than half (60%) was generated from hydroelectricity. The remainder was produced from other sources that included nuclear, natural gas, wind, coal, biomass, solar, and petroleum. Canada is also a net exporter of electricity (27.6 TWh in 2023). According to IEA, 2023 report, electricity production has only increased by 3% between 2000-2023, whereas, electricity consumption (demand) per capita has decreased by 16% within the same time. Electricity in buildings is primarily used for heating, cooling, lighting, cooking, and to power devices. Further electrification of end-uses, especially transportation, in conjunction with the decarbonization of electricity generation, is an important pillar of clean energy transitions. The industry sector is the largest consuming sector of electricity (35%) followed closely by residential buildings (33%). It is also worth mentioning that currently, 47% of the residential energy demand is provided by electricity and 44% is from natural gas. Energy efficiency measures recommended by the National Building Code of Canada (NBC) have resulted in an overall 28% decrease in the energy intensity of residential buildings between 2000-2023 [CER, 2023], and they have been proven to be effective despite the increased population and the total square footage of the built environment.

Canada’s electricity grid is regulated at the provincial and territorial levels. There is also a significant variation between the sources of generation and grid type. For all provincial electrical

utilities, the historical electricity use emission factors are available as annual averages from the National GHG Inventory datasets, published on the CER website, as presented in Figure 1. Only two provinces (Ontario and Alberta) have the potential for historical hourly emissions factors to be calculated with public data as they have open electricity markets. Although annualized average emissions are useful to link the energy demand and the associated GHG emission, for mixed grids, that contain high and low carbon generation sources, the uncertainties associated with using them to assess the potential for retrofits to reduce emissions can be significant.

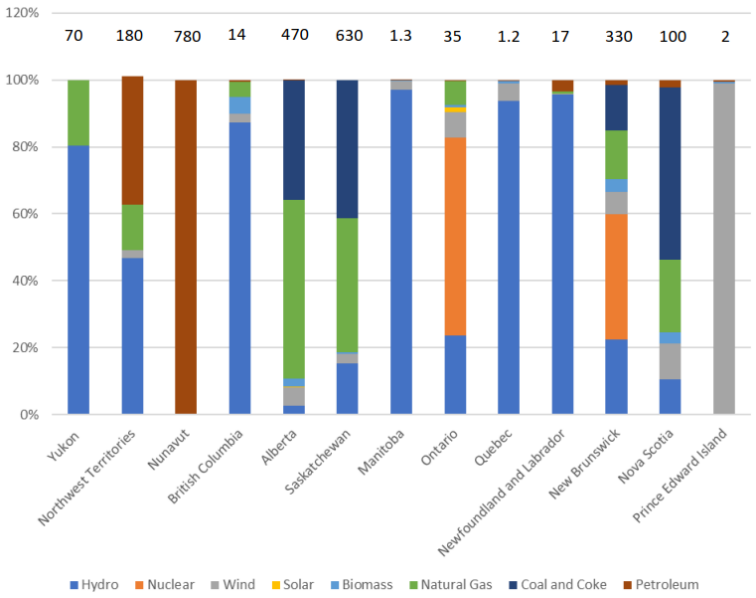

Figure 1. Annual distribution of generation sources per provincial grid and emissions factors (gCO_{2e}/kWh), (CER, 2022)

3. RESULTS AND DISCUSSION FOR THE NEW BRUNSWICK ELECTRICITY

Energy demand in Canada (IEA, Canada 2022), is dominated by space heating and accordingly the heating source and the grid mix play very important roles in the GHG emissions of the building sector. As can be seen in Figure 1, the present Canadian energy mix varies across all provinces. Additionally, the source fuel for heating in buildings varies across provinces, with high use of natural gas for heating fuel in provinces like Alberta, Ontario and BC, and high use of electrified heating in Quebec and the Atlantic provinces (NRCan, 2019). In the Atlantic provinces, New Brunswick (NB) provides a unique opportunity to investigate the effects of electrified heating on utility emissions, given NB grid contains a mix of high and low-intensity carbon generation sources (Figure 1) and is predominantly electrified residential heating, with a high penetration of heat pumps. The mix of renewables with fossil fuels and high penetration of electrified heating is representative of the challenges many other utilities will face in the future as electrified heating increases.

Figure 2 (NB Power, 2023) shows an example of how daily energy demand is met with different generation sources for a system peak day in winter. For this example day, two peak demand periods are also shown at 6 to 9 a.m. and 4 to 8 p.m., and are attributed to increased demand from the residential sector (NB Power, 2023). It is important to note this is a representative example and

that the actual allocations of electricity generation and amounts are dependent upon many factors including weather, demand, availability, and market prices and conditions. However, this example figure demonstrates that in a mixed-energy source utility, emissions factors are likely to vary during the day, dependant on which assets are used to meet demand, meaning that there are times during the year where the annual average emission factor is likely to deviate significantly from the hourly factor.

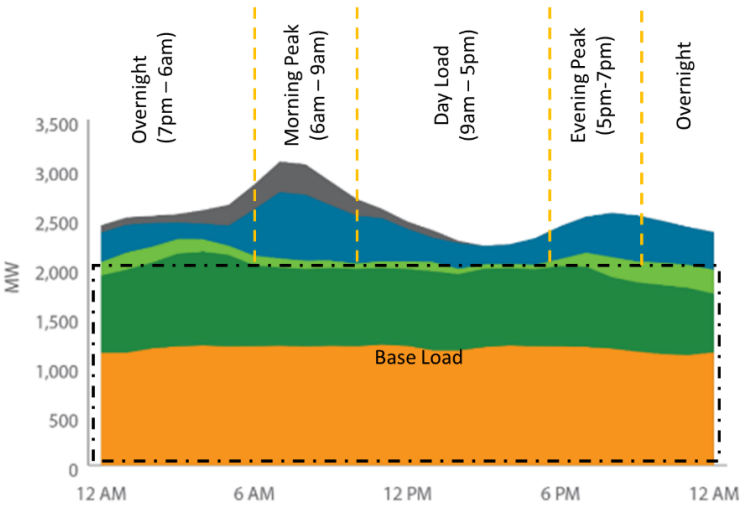

Base Load

1. Wind up to wind capacity factor, then
2. Up to 100% Nuclear, then
3. Up to 30% Coal, then
4. Up to 100% Natural Gas, then
5. Up 70% Coal, then
6. Up to 100% Fuel Oil Reserve

Morning Peak

7. Base Load, then
8. Up to 100% Peaking Hydro, then
9. Up to 100% Peaking Diesel

Day load

7. Base Load, then
8. Up to 50% of Peaking Hydro, then
9. Up to 100% Diesel

Evening Peak

7. Base Load, then
8. Up to 80% of Peaking Hydro, then
9. Up to 100% Diesel

Overnight

7. Base Load, then
8. Up to 30% of Peaking Hydro, then
9. Up to 100% Diesel

Figure 2. NB power winter dispatch example, exhibiting the NB two-peak challenge (NB Power, 2023) and the dispatch category

To compare the potential difference in emissions between hourly and annual factors, one would need the hourly energy source mix, which is not typically publicly available for Canadian utilities. However, the total hourly demand for the NB grid is published. Therefore, for the purposes of demonstrating the comparison between emissions factors in this paper, a winter dispatch sequence was derived from Figure 2, and applied to the published historical total hourly NB demand. In this case, a dispatch sequence consists of determining the order in which power generation assets are used to meet a given demand. With the total demand and dispatch sequence, the total power produced by each asset in a given hour to meet the total demand can be calculated. Thereafter the hourly emissions can be determined by multiplying the power generated in a given hour by a given generator by that generator emissions factor. The electricity emission factor is then determined as the total emissions due to generation in an hour, divided by the total demand in the hour. This is shown in (**1**.

$$GHG_{perMWh_h} = \sum_{i}^{n} \frac{Gen_i EF * MWh_{Gen_i}}{Total\ Demand + Transfers} \quad (1)$$

Where:

GHG_{perMWh_h}	is the hourly emission factor in kg CO_{2eq}/ MWh
Gen_iEF	is the emissions factor for generator 'i' to produce a MWh
MWh_{Gen_i}	is the amount of power produced by Generator i
$Total\ Demand + Transfers$	Total demand in NB, net transfers between other adjacent utility grids.
i	Each generator
n	Number of generation stations used in the given hour

The NB Power generation assets, and corresponding emissions factor associated with each asset to calculate the hourly emissions factor, are provided in Table 1. The emission factors for each asset were calculated from the National GHG Emission Inventory Dataset (ECCC, 2023) for New Brunswick.

Table 1. NB Power grid generation capacity

NB Power Grid Generating Capacity (Total, MW)		**MW**	**Emissions factor (gCO2e/kWh)**
Base Load	**Nuclear Generation**	663	0
	Coal	467	965
	Natural Gas	284	582
	Fuel Oil Reserve	972	1138
Peaking Hydro		668	0
Wind		355	0
Peaking Diesel		525	1138

To determine the power produced by each asset in a given hour, the total demand for each hour was divided into five dispatch sequence categories, depending on time of day, consisting of: base load, morning peak, day load, evening peak, and overnight. The base load was determined as the lowest load during each respective day, and was used to calculate how much each base load. The dispatch sequence for each category is provided in Figure 2**Error! Reference source not found.**.

In addition to the assumptions made for the categories shown in Figure 2**Error! Reference source not found.**, a method to calculate the potential wind generation for each hour was needed. The hourly wind power potential was calculated by multiplying the hourly average windspeed, measured at the closest weather station (scaled to the hub height), by the corresponding turbine power output curve (Wind Power, 2024) for each turbine location and corresponding turbine type (Government of Canada, 2024) in NB. It to supplement fossil fuel generation of the base load. Given the assumptions to incorporate wind power, two utilization factors were used to see the effect of wind on hourly emissions: i. 30% of the available wind power generation; and, ii. 100% of available wind generation. The 30% value was estimated based on the utilization factor quoted in the NB Power Integrated Resource plan (NB Power, 2023). It is important to note that the model results presented in this paper are completely hypothetical, as many assumptions needed to be made to create the dispatch sequence from Figure 2. Hence, the model values should not be taken as accurate for NB Power generation hourly emissions, rather that the intent of the model is to provide an example of considerations needed when estimating the effectiveness of building retrofit scenarios to achieve decarbonization in a province where building heating is predominantly electrified.

Using the dispatch model, the hourly emission factors for each hour in the winter of 2022

(December, January and February) were calculated. The results were then averaged to represent a typical 24-hour day over this period. The results, compared with the published annual emission factor for the NB Grid in 2022 from the CER website, of 330 g CO2eq/kWh, are depicted in **Figure 3**. Winter months are selected due to the higher seasonal electricity demand; one can anticipate that the hourly emissions would be higher that the annually averaged emissions factor. It can be seen that during the high demand times, the annual averaged data underestimates the emissions in comparison to the hourly emissions scenarios. The results show that the energy efficiency measure are more important than one can assume using the annually averaged emissions factors. First, the energy demand reduction can lead into a higher absolute emissions reduction, and second, if they are employed across all the existing buildings through retrofit and new buildings through the National Model Codes, one can anticipate that the hourly emissions factor can also be decreased. It is still recommended that analysis should be done on a case-by-case basis, to ensure that the energy efficiency measures result in decarbonization for other electricity grids.

due the anticipated higher electricity demand and hourly emission factors (). The results were then averaged to represent a typical 24-hour day over this period. The results, compared with the published annual emission factor for the NB Grid in 2022 from the CER website, of 330 g CO2eq/kWh, are shown in **Figure 3**. One can conclude that energy efficiency measures are more important than what one could assume using the annually averaged data only. First since
As one can see the electricity demand is the highest during winter and the absolute value of emissions are expected to be at the highest.

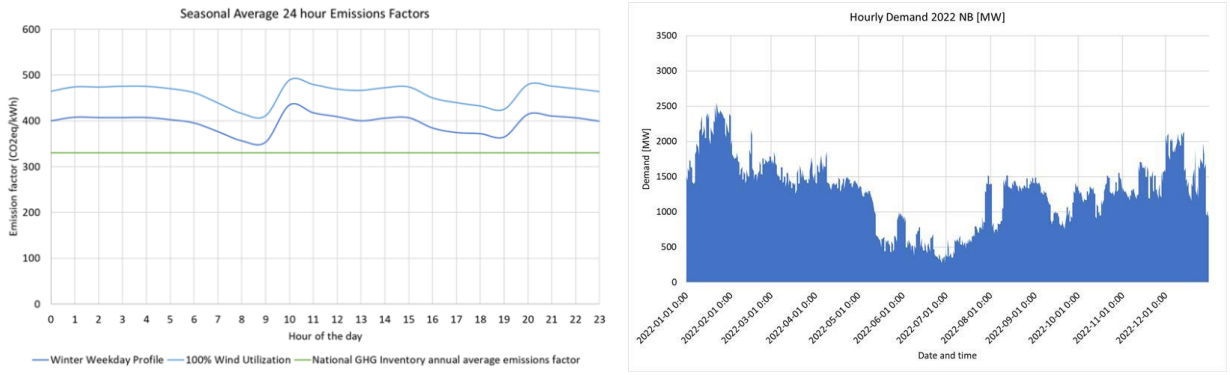

Figure 3: Hourly emission factor for winter compared to annual average (left), hourly demand in 2022 (right)

7. CONCLUSIONS

It has been shown that increasing the energy efficiency of buildings has the potential to lead to several benefits including the reduction of GHG emissions. Although there are many overlaps between energy efficiency and decarbonization, these two concepts do not always represent the same outcome. It is very important to understand their differences and how reductions in operational energy can be translated into building decarbonization. In this paper, the following points were discussed:

- The key differences between energy efficiency in buildings and building decarbonization.
- How the electricity supply has evolved in Canada in the last 33 years.
- The viability of relying on electrification as the main mode of decarbonization considering the capacity issues and electrification in other sectors.

- The importance of using hourly emissions factors versus the annualized average emissions factors when considering energy efficiency measures in buildings.

This paper unfolds new research topics to be explored in the future. It has been shown that a comprehensive study on the electricity supply is needed to further understand plans to meet the increasing electricity demands before suggesting electrification as the primary method for decarbonization. For future work, the balance between the energy demand and supply in different locations in Canada will be assessed and the best path forward to decarbonize the construction sector will be considered in relation to the demand and supply of electricity in the respective provinces.

ACKNOWLEDGEMENTS

The authors acknowledge the support of NB Power in providing technical comment on this publication.

REFERENCES

2023 Integrated Resource Plan, Pathway to a Net-Zero Lectricity System, New Brunswick Power Corporation, 2023. https://www.nbpower.com/media/1492472/2023-integrated-resource-plan-en.pdf

https://www.canada.ca/en/environment-climate-change/news/2021/07/government-of-canada-confirms-ambitious-new-greenhouse-gas-emissions-reduction-target.html

ANSI/ASHRAE Standard 228, Standard Method of Evaluating Zero Net Energy and Zero Net Carbon Building Performance.

Canada's Energy Future 2023: Energy Supply and Demand Projections to 2050 – Data Supplement- CER – Canada's Energy Future 2023: Energy Supply and Demand Projections to 2050 – Data Supplement

International Energy Agency, Capturing the Multiple Benefits of Energy Efficiency Executive Summary: "Energy efficiency retrofits in buildings" [Online] Available from: https://www.iea.org/reports/capturing-the-multiple-benefits-of-energy-efficiency.

International Energy Agency, Canada 2022 Energy policy review, [Online] Available from: https://www.iea.org/reports/canada-2022

IEA. 2022. "Global CO2 Emissions from Buildings, Including Embodied Emissions from New Construction." Retrieved August 7, 2023 (https://www.iea.org/data-and-statistics/charts/global-co2-emissions-from-buildings-including-embodied-emissions-from-new-construction-2022).

Magwood, C., Ahmed, J., Bowden, E., Racusin, J., 2021. Achieving real net-zero emission homes: Embodied carbon scenario analysis of the upper tiers of performance in the 2020 Canadian National Building Code.

St-Jacques, M., Bucking, S., O'Brien, W., & Macdonald, I., 2023. Spatio-temporal electrical grid emission factors effects on calculated GHG emissions of buildings in mixed-grid environments. Science and Technology for the Built Environment, 30(1), 37–50. https://doi.org/10.1080/23744731.2023.2276012

Yingli L., Yunyang Y., Yizhi Y., Wangda Z., 2022. Long-term carbon emission reduction potential of building retrofits with dynamically changing electricity emission factors, Building and Environment,Vol. 210, 108683, ISSN 0360-1323, https://doi.org/10.1016/j.buildenv.2021.108683

Energie NB Power (2024). System Information Archive. System Information Archive. Energie NB Power. Accessed January 2025.

Environment and Climate Change Canada (ECCC), "National Inventory Report 1990-2021: Greenhouse Gas Sources and Sinks in Canada Part 3," Environment and Climate Change Canada, Gatineau, QC, 2023.

NRCan CANMET (2024). Canadian Wind Turbine Database.Government of Canada. Accessed January 2025. https://open.canada.ca/data/en/dataset/79fdad93-9025-49ad-ba16-c26d718cc070/resource/4d86e84b-0cc8-45a3-9274-119f8313907b

The Wind Power (2024) the Wind Power. Accessed January 2025. https://www.thewindpower.net/index.php

Natural Resources Canada (2019). Survey of Household Energy Use (SHEU-2019) Data Tables," Government of Canada, [Online]. Available: https://oee.rncan-nrcan.gc.ca/corporate/statistics/neud/dpa/showTable.cfm?type=SH&sector=aaa&juris=ca&year=2019&rn=41&page=1. [Accessed 20 02 2024].

6th International Conference on Building Energy and Environment
Eindhoven University of Technology, The Netherlands
6 - 10 July 2025

Research Progress on Carbon Emission of Bamboo-Structured Architecture

Ao Li [1], Jingfeng Xu [2]

[1]*School of Architecture and Urban Planning Chongqing University, Chongqing, China, 1029312880@qq.com*
[2]*School of Architecture and Urban Planning Chongqing University, Chongqing, China, 151431437@qq.com*

SUMMARY
Carbon emissions in the construction industry are significant, and bamboo is recognized as an eco-friendly building material. It plays an important role in achieving sustainable development in the construction sector and the carbon peak and carbon neutrality goals. This paper reviews domestic and international research on carbon emissions from bamboo structures, covering three aspects: bamboo carbon emission factors, life-cycle carbon emission calculations, and carbon emission comparisons with other building structures, as well as carbon reduction strategies. It highlights existing issues such as insufficient fundamental data research, inconsistent calculation methods, and insufficient in-depth research on carbon reduction strategies. Future efforts should focus on strengthening fundamental data research, constructing a unified and comprehensive bamboo carbon emission factor database, establishing standards and guidelines, developing carbon emission calculation methods specifically for bamboo structures, and enhancing research on carbon reduction strategies.

Keywords: Bamboo construction, Carbon emission, Life cycle.

1. INTRODUCTION

The global climate crisis is becoming increasingly severe, and high carbon emissions in the construction industry are one of the key contributors to exacerbating this problem. In response to this challenge, China has actively advocated for a green transformation of production and lifestyle in the 14th Five-Year Plan period. The construction sector urgently needs to embrace a green transformation to move towards sustainable development. Bamboo has unique advantages in China: it is abundant, grows rapidly, and its annual output value far exceeds that of wood (Abrahams et al., 2003). Bamboo also has strong carbon sequestration capabilities (Li et al., 2015) and is widely recognized as an eco-friendly building material. Known as "plant steel," bamboo exhibits excellent properties such as light weight, high strength, and high bending flexibility. Its tensile strength is almost equal to that of steel, and its compressive strength is twice that of concrete (Yadav and Mathur, 2021).

Today, more and more scholars are recognizing the tremendous potential of bamboo in fields such as architecture and furniture, believing that it holds significant value for widespread application. As research on bamboo structures continues to deepen, studies on carbon emissions have increasingly captured scholars' attention. However, existing research is relatively fragmented. This paper aims to review the current research progress, providing valuable insights for carbon emission research in the construction industry.

2. RESEARCH METHODS

This study strictly follows the PRISMA guidelines for systematic reviews, clearly defining the search strategy, literature screening process, and inclusion criteria. The search keywords center around *bamboo building, bamboo structures, bamboo materials, carbon emissions, and life cycle,* and are expanded to include related concepts such as *carbon sink* and *low-carbon bamboo architecture* to enhance the comprehensiveness of the literature coverage. Three authoritative databases—Web of Science (Core Collection), China National Knowledge Infrastructure (CNKI), and Wanfang Data—were selected as the primary sources for the literature search.

The inclusion criteria are as follows: the content must focus on carbon emissions in bamboo-structured architecture, covering key themes such as the determination of carbon emission factors, life cycle carbon calculation models, comparative analyses with traditional building materials, and carbon reduction strategies for bamboo structures. Priority is given to literature published within the past ten years (2014 to 2024), although classic theories and key data are considered with some flexibility. Only core journal articles, international conference papers, and authoritative research reports are included; a small number of high-quality dissertations were also included after full-text screening.

The specific literature screening process is as follows: an initial search yielded 769 documents. After a preliminary screening based on titles and abstracts, 141 duplicates were removed, leaving 628 documents. Following a full-text evaluation, 53 documents met the inclusion criteria, and ultimately, 17 highly relevant studies were included in the review.

3. RESEARCH PROGRESS ON CARBON EMISSIONS IN BAMBOO STRUCTURES

Bamboo has a long history of application in the construction industry, and research on its carbon emissions primarily focuses on its carbon sequestration capacity, the environmental friendliness of engineered bamboo, and the carbon footprint of bamboo products. At present, carbon emissions research on bamboo-structured buildings is still in its early stages. Existing studies have made some progress in areas such as bamboo carbon emission factors, life-cycle carbon emissions calculations, and carbon reduction strategies. Many studies compare bamboo-structured buildings with traditional reinforced concrete, steel, and timber structures to demonstrate their advantages in terms of carbon emissions.

3.1. Research on Bamboo Carbon Emission Factors

The bamboo carbon emission factor is a fundamental basis for carbon emission calculations and is crucial for accurately assessing the environmental impact of bamboo-structured buildings. Currently, scholars primarily conduct field investigations of the bamboo production process, considering carbon emissions from various aspects, such as materials and energy consumption, and integrating these factors with bamboo's carbon sequestration characteristics to calculate its carbon emission factor. Zhang et al., (2021) based on an investigation of the bamboo particleboard production process, analyzed the materials and energy inputs involved in manufacturing pretreated bamboo and bamboo particleboard, and, in turn, assessed the carbon emission factors for these materials. Zhang et al., (2023) using the 'Fish Leisure Bamboo Pavilion' at the Yangzhou World Horticultural Expo as a case study, conducted factory surveys to gather data and proposed a calculation method for the carbon emission factor of round bamboo building materials. They

derived the carbon emission factor for round bamboo and pointed out that carbon emissions from the cooking and degumming processes, as well as the hot bending and straightening stages, were particularly high. They suggested that improving energy usage strategies during the production stages could reduce overall emissions.

3.2. Research on Carbon Emission Calculations for Bamboo-Structured Buildings

With the deepening research into life cycle assessment (LCA) theory, researchers have applied it to the carbon emission calculations of different types of bamboo materials or bamboo-structured buildings to comprehensively assess the environmental impact of bamboo structures throughout their entire life cycle. Early studies focused primarily on bamboo building materials or bamboo products. For example, Liu et al., (2024) conducted a life cycle assessment (LCA) on structural glued laminated bamboo (SGLB), focusing on its carbon emissions from raw material extraction to the production stage. They emphasized the advantages of using renewable energy to reduce carbon emission. These studies laid the foundation for the broader application of bamboo materials in construction and provided significant theoretical support and practical references for subsequent environmental impact assessments of bamboo-structured buildings.

In recent years, research on the carbon emissions of various types of bamboo-structured buildings has gained momentum. Chen et al., (2015) divided the entire life cycle of bamboo frame houses in Zizhuyuan Park into stages: raw material acquisition, transportation of building materials, production of building components, and construction. Their analysis revealed that bamboo-structured houses maintain a negative carbon state throughout their life cycle, classifying them as green housing. Zhang et al., (2023), following the "Building Carbon Emission Calculation Standard" (GB/T 51366-2019), divided the life cycle of round bamboo landscape buildings into stages: material production and transportation, operation, construction, and demolition. Using the "Fish Leisure Bamboo Pavilion" at the Yangzhou World Horticultural Expo as a case study, they performed a life cycle carbon emission calculation. Their results showed that carbon emissions during the material production stage accounted for the highest proportion (66.70%) of total emissions. Due to bamboo's carbon sequestration characteristics, total emissions during this stage were negative, achieving a negative carbon design. Zhu et al., (2024) divided the life cycle of bamboo-wood hybrid structures into three phases: materialization, operation, and demolition, and conducted a life cycle carbon emission analysis of a bamboo residential building at Nanjing Forestry University. They found that emissions during the operation phase were the highest, accounting for approximately 89.8% of total life cycle emissions, while bamboo's carbon storage accounted for 8.8%. The results indicated that the materialization phase, particularly the material production stage, was the primary source of carbon emissions. Huang et al., (2024) proposed a carbon emission measurement model for bamboo ribbed houses, dividing the life cycle into five stages: material production, transportation, construction, operation, and demolition. Their case analysis concluded that the operation phase contributed the largest share of carbon emissions, while the material production stage within the materialization phase had the highest proportion.

3.3. Comparative Research on Carbon Emissions of Bamboo-Structured Buildings

Researchers have quantified the carbon emissions of bamboo-structured buildings throughout their life cycles to identify their carbon emission characteristics. By comparing bamboo structures with other types of buildings, they assess the carbon reduction potential of bamboo structures and their advantages in reducing carbon emissions.

Zhu et al., (2024) compared the life cycle carbon emissions of bamboo structures with those of timber, steel, and hybrid bamboo-wood residential buildings. Their results showed that the carbon emissions during the operation phase were the highest for bamboo-structured houses, but the net carbon emissions of different bamboo-wood structures were similar. In contrast, the carbon emissions of steel structures were approximately 89.9% higher than the average carbon emissions of bamboo-wood structures, demonstrating that bamboo-structured buildings have significant energy-saving potential during the operation phase and offer advantages in overall life cycle carbon emissions. Liu et al., (2023) compared the life cycle carbon emissions of rural glued bamboo residential buildings in Ningbo, Zhejiang, with those of reinforced concrete buildings. They found that the life cycle carbon emissions of bamboo-structured buildings were 30.4% lower than those of reinforced concrete buildings, with significant carbon reduction potential in the production and transportation stages. Yu et al., (2011) compared the energy consumption and carbon emissions of bamboo structures with those of brick-concrete buildings. Their findings indicated that bamboo-structured buildings consumed less energy and emitted fewer carbon emissions while meeting the same functional requirements. Bamboo structures also had better thermal insulation properties. Additionally, through scientific management and technological applications, bamboo structures can more effectively facilitate resource recycling and reduce the environmental burden over the building's life cycle, particularly in terms of the use of recycled materials and construction waste recovery. Zhao et al., (2023) quantified the energy-saving and carbon reduction potential of bamboo in residential buildings in cold and extremely cold regions of China. By comparing the carbon emissions of bamboo laminated board (LBL) buildings in different cities, they demonstrated the carbon reduction effects of bamboo structures under various geographical and environmental conditions. Bundi et al., (2024) compared bamboo-structured buildings in the Philippines with concrete brick buildings and found that bamboo construction could reduce carbon emissions by 70%. Zea Escamilla et al., (2018) compared four types of building materials (round bamboo, brick, concrete hollow blocks, and engineered bamboo) in the Colombian region, analyzing the environmental impacts over their entire life cycle. They considered factors such as transportation and material production efficiency and found that bamboo structures had an environmental advantage due to their lightweight and low-density properties. Even with longer transportation distances, bamboo structures still resulted in lower environmental impacts. Rincón et al., (2023) compared the environmental impacts of traditional clay brick houses (CSB) in Colombia with those of light cement bamboo frame (LCBF) houses built using locally improved Guadua bamboo. The results showed that the carbon footprint of bamboo houses was approximately 36% of that of traditional brick houses.

Existing studies have demonstrated that bamboo-structured buildings offer clear advantages in terms of carbon emissions, positioning bamboo as a key driver in the construction industry's transition toward low-carbon solutions.

3.4. Carbon Reduction Strategies for Bamboo-Structured Buildings

Building upon research into the carbon emissions of bamboo-structured buildings, scholars have conducted a series of studies on carbon reduction strategies. Zea Escamilla and Habert, (2014) performed a life cycle assessment (LCA) on five types of bamboo-based construction materials and found that bamboo species and harvesting methods did not significantly contribute to the overall environmental impact, providing evidence for the environmental friendliness of bamboo.

The study also highlighted that as industrialization increases, so does the environmental impact, with electricity consumption emerging as a major influencing factor. They suggested changing the energy mix (e.g., reducing the proportion of coal-based electricity), as this would be more effective in reducing environmental impact than merely improving production efficiency. Additionally, since bamboo-based materials are lightweight and have relatively short transportation distances, the environmental impact from local transportation is limited. Therefore, the study recommended focusing bamboo cultivation in regions where production is concentrated and processing in areas with diversified or abundant renewable energy sources to further enhance the environmental performance of bamboo-based materials. Chang et al., (2018) applied the LCA method to the production of bamboo plywood from Moso bamboo in Taiwan, examining the environmental impacts of the production process and comparing them with other materials. They proposed a series of recommendations, including optimizing the processing steps, improving chemical treatments, enhancing energy structures, and increasing production efficiency to reduce the environmental impact of bamboo material processing. Zhang et al., (2021) compared the life cycle carbon emissions of a steel-bamboo composite frame (SBF) structure with a traditional reinforced concrete frame (RCF) structure. They found that the SBF solution showed carbon reduction potential at most stages of its life cycle, especially during the construction and material production stages. The study suggested focusing on the carbon emissions from the production of materials like steel plates and bamboo to further enhance the reduction effect.

These studies collectively emphasize the importance of strategic approaches to reducing carbon emissions associated with bamboo-structured buildings, including optimizing production processes, shifting to cleaner energy sources, and improving material efficiency throughout the supply chain.

4. EXISTING PROBLEMS

Accurate data support is crucial for carbon emission research on bamboo-structured buildings. However, there is currently a lack of authoritative bamboo carbon emission factor databases both domestically and internationally, which hinders the progress of related studies. In determining the carbon emission factors and resource consumption data for bamboo-structured buildings, some studies rely on limited surveys or literature data, which fail to accurately reflect the actual conditions across different regions and production processes. The application of bamboo materials is still in its early stages, with many bamboo processing enterprises being small and medium-sized businesses with relatively low market shares. As a result, obtaining accurate data on material consumption and energy use remains challenging. Furthermore, the diversity in bamboo production processes, differences in technical levels, energy consumption uncertainties, and regional disparities further complicate data collection and hinder the standardization of carbon emission calculations.

When calculating carbon emissions for bamboo-structured buildings, researchers often use life cycle assessment (LCA) theory, which covers all stages from raw material acquisition to building demolition. While research on bamboo structures and bamboo building materials has made progress, bamboo-structured residential buildings have not yet been widely adopted, and there is no authoritative carbon emission calculation standard specifically for bamboo structures. The existing methods for calculating carbon emissions in bamboo structures suffer from issues such as insufficient accuracy and inconsistency. In particular, research on the disposal phase of bamboo

structures lacks case studies, which results in an incomplete evaluation of carbon reduction across the entire life cycle of bamboo structures. This limitation makes it difficult to effectively compare results and hinders the application of research findings in guiding architectural design and construction.

Current research on carbon reduction strategies for bamboo-structured buildings tends to focus on increasing the use of bamboo-wood materials, which offer advantages in carbon sequestration and low carbon emissions, to replace traditional high-carbon building materials. Additionally, there is strong advocacy for the use of clean energy, such as solar and wind power, throughout the life cycle of bamboo-structured buildings to reduce dependence on fossil fuels and optimize the energy mix. Many researchers emphasize the importance of optimizing processes in each phase of the life cycle, recommending that studies cover production, transportation, construction, and demolition stages. Specific measures include optimizing transportation routes and increasing material recycling rates to reduce resource consumption and carbon emissions. However, most research currently focuses only on carbon emission calculations and basic comparisons. There is a lack of in-depth analysis of key carbon reduction areas and potential influencing factors. Although the carbon sources and carbon sinks at each stage are well-defined, there is still a lack of specific technical support and strategic guidance for effectively addressing high carbon emissions in the production phase. As a result, developing a comprehensive and actionable carbon reduction plan remains challenging.

5. SSUMMARY AND OUTLOOK

Public understanding of bamboo-structured buildings remains limited, yet their development plays a crucial role in the sustainable growth of the construction industry and the achievement of China's "dual carbon" goals. At present, research on bamboo-structured buildings faces several challenges, particularly in areas such as basic data, carbon emission calculation methods, and carbon reduction strategies.

To advance research on carbon emissions from bamboo-structured buildings and promote their wider adoption, future studies should focus on enhancing the understanding of bamboo carbon emission factors and other fundamental data. This involves considering regional differences and variations in processing methods, which will contribute to the development of a more robust and reliable database to ensure data accuracy and consistency. Establishing regulations and standards specific to bamboo materials and structures is also crucial. These standards should define appropriate carbon emission calculation models, tailored to the unique characteristics of bamboo structures, and provide precise carbon emission assessments for each stage of the building's life cycle. This would provide stronger theoretical support for the broader adoption of bamboo structures in construction.

Building on this foundation, researchers should focus on exploring carbon reduction strategies for bamboo-structured buildings, including quantifying the carbon reduction effects and further minimizing emissions during the production phase. The goal is to develop a comprehensive set of guidelines for low-carbon bamboo structure design, providing scientific evidence for architectural planning. Additionally, creating an accurate assessment methodology for carbon emissions in bamboo-structured buildings will help promote their use in the low-carbon building sector, advancing sustainable construction practices.

In the future, these efforts will not only promote bamboo-structured buildings as a sustainable construction solution but also contribute to global carbon neutrality goals by integrating them into mainstream building practices.

ACKNOWLEDGEMENTS

First, I would like to express my sincere gratitude to my supervisor and all the experts and scholars who have provided invaluable assistance throughout this research. Your guidance on the research direction, support in data analysis, and insightful feedback have been essential to the successful completion of this thesis. Secondly, I am deeply grateful to my family and friends for their constant encouragement and companionship, which have given me the perseverance to keep moving forward. Finally, I would like to thank all the institutions and organizations that have contributed to this research. Your support has been instrumental in my growth throughout this academic journey.

REFERENCES

Abrahams, Van Den Dobbelsteen, Van Der Lugt, 2003. Bamboo as a building material alternative for Western Europe? A study of the environmental performance, costs and bottlenecks of the use of bamboo (products) in Western Europe. Journal of Bamboo and Rattan 2, 205–223.

Bundi, T., Lopez, L.F., Habert, G., Zea Escamilla, E., 2024. Bridging Housing and Climate Needs: Bamboo Construction in the Philippines. Sustainability 16, 498.

Chang, F.-C., Chen, K.-S., Yang, P.-Y., Ko, C.-H., 2018. Environmental benefit of utilizing bamboo material based on life cycle assessment. Journal of Cleaner Production 204, 60–69.

Huang, Y., Song, Z., Wang, C., 2024. Whole Life Cycle Carbon Emission Research of Original Bamboo Keel House. Construction Technology 53, 80-85+109.

Li, P., Zhou, G., Du, H., Lu, D., Mo, L., Xu, X., Shi, Y., Zhou, Y., 2015. Current and potential carbon stocks in Moso bamboo forests in China. Journal of Environmental Management 156, 89–96.

Liu, K., Jayaraman, D., Shi, Y., Xiong, Z., Yang, J., Symeonidis, A., Escamilla, E.Z., 2024. Life cycle assessment (LCA) of the industrial production of structural glued laminated bamboo. Journal of Cleaner Production 485,

Liu, Y., Zhang, J., Xu, J., Wang, Y., Li, B., Zhang, S., 2023. Carbon emission-based life cycle assessment of rural residential buildings constructed with engineering bamboo: A case study in China. Journal of Building Engineering 76, 107182.

Rincón, C.E., Montoya, J.A., Archila, H.F., 2023. Bamboo Construction Inspired by Vernacular Techniques for Reducing Carbon Footprint: A Life Cycle Assessment (LCA). Sustainability 15, 16893.

Yadav, M., Mathur, A., 2021. Bamboo as a sustainable material in the construction industry: An overview. Materials Today: Proceedings, CRMSC-2021 43, 2872–2876.

Yu, D., Tan, H., Ruan, Y., 2011. A future bamboo-structure residential building prototype in China: Life cycle assessment of energy use and carbon emission. Energy and Buildings 43, 2638–2646.

Zea Escamilla, E., Habert, G., 2014. Environmental impacts of bamboo-based construction materials representing global production diversity. Journal of Cleaner Production 69, 117–127.

Zea Escamilla, E., Habert, G., Correal Daza, J.F., Archilla, H.F., Echeverry Fernández, J.S., Trujillo, D., 2018. Industrial or Traditional Bamboo Construction? Comparative Life Cycle Assessment (LCA) of Bamboo-Based Buildings. Sustainability 10, 3096.

Zhang, Xiaocun, Xu, J., Zhang, Xueqi, Li, Y., 2021. Life cycle carbon emission reduction potential of a new steel-bamboo composite frame structure for residential houses. Journal of Building Engineering 39, 102295.

Zhang, Z., Li, Y., Meng, X., Liu, K., Gao, Y., Wang, J., 2023. Analysis on life cycle assessment for carbon emission of round bamboo structure landscape architecture. Building Structure 53, 24-29+13.

Zhao, B., Yu, Y., Xu, Y., Guo, H., 2023. Bamboo as a sustainable construction material for residential buildings in the cold and severe cold regions of China. Architectural Engineering and Design Management 1–18.

Chen, G., Xiao, Y., 2015. Life cycle of bamboo frame construction in purple bamboo park. Journal of Guangxi University(Natural Science Edition) 40, 81–86.

Zhu, F., Yu, R., Zheng, W., Gong, Y., Tao, P., Gao, Y., 2024. Life-Cycle Carbon Emission Assessment of Bamboo House. Chinese Journal of Wood Science and Technology 38, 43–50.

6th International Conference on Building Energy and Environment
Eindhoven University of Technology, The Netherlands
6 - 10 July 2025

Alternative Approach to Simplified Energy Disaggregation: Heating Energy Estimation Considering Monthly Hot Water Energy Consumption in District Heating

Hyery Shin [1], Yumin Kim[2,]

[1] *Department of Building Energy Research, Korea Institute of Civil Engineering and Building Technology, Goyang-si, South Korea, hyeryshin@kict.re.kr*
[2] *Department of Building Energy Research, Korea Institute of Civil Engineering and Building Technology, Goyang-si, South Korea, ymkim@kict.re.kr*

SUMMARY
Buildings consume energy for various purposes, including heating, cooling, hot water supply, and cooking. While reducing energy consumption requires targeted measures for each purpose, direct monitoring is costly. The Simplified Energy Disaggregation (SED) methodology can separate heating, cooling, and baseload energy, but has limitations in reflecting changes in baseload energy. This study analyzed monthly variations in hot water energy consumption in district heating-supplied apartment complexes and evaluated the error rate compared to heating energy estimated by SED. Analysis of 142 apartment complexes showed that SED overestimated heating energy by 28% and underestimated hot water energy by 44%. As building insulation regulations become more stringent and heating energy proportion decreases, the possibility of larger estimation errors in SED's calculations increases, necessitating a new methodology for estimating hot water energy consumption.

Keywords: Apartment Buildings, Simplified Energy Disaggregation, Heating Energy Consumption, Hot Water Energy Consumption

1. INTRODUCTION

The Korean government has committed to achieve a reduction in greenhouse gas emissions in the building sector by 88.1% by 2050 compared to 2018 levels as part of its carbon neutrality goals (Korean government, 2021). To achieve this reduction target, detailed implementation measures are necessary, which requires distinguishing energy consumption by purpose for different energy sources used in buildings. Given Korea's climate conditions, heating energy shows the highest Energy Use Intensity(EUI)(Jin et al., 2020), necessitating the estimation of heating energy consumption and the development of specific implementation measures based on these estimates.

When disaggregating energy consumption data using methodologies such as Simplified Energy Disaggregation (SED), energy consumption is typically disaggregated into heating, cooling, and baseload energy consumption, with the baseload assumed to include purposes such as hot water supply and cooking (Meng et al., 2017). This study proposes a methodology to separately identify hot water energy consumption as an alternative approach to the existing SED methodology. Through this methodology, we aimed to improve the accuracy of heating energy consumption estimates.

2. SCOPE AND LIMITATIONS

As of 2023, the building sector in South Korea consumes approximately 56.6% of energy in the residential sector and 43.4% in the non-residential sector (Korea Real Estate Board). This study focused on analyzing the residential sector, which accounts for more than half of the total energy consumption. Specifically, we examined apartment buildings, which represent 73.4% of residential buildings and constitute the largest proportion of housing types in South Korea (MOLIT, 2024).

The heating energy sources in apartment buildings are mainly divided into city gas and district heating. While city gas is used for heating, hot water supply, and cooking, district heating is used exclusively for heating and hot water supply (Kim et al., 2024). Since this study aimed to estimate heating energy consumption more accurately by separating hot water energy consumption, we examined energy consumption data from apartment complexes using district heating, which consists solely of heating and hot water consumption.

The analysis was performed using data from 171 apartment complexes using district heating in the Seoul region, emphasizing the study of their energy consumption patterns and characteristics. In particular, we utilized the distinct feature of district heating systems that clearly separates heating and hot water energy consumption as an alternative approach to the existing SED methodology and attempt more accurate energy consumption estimates.

3. METHODOLOGY

3.1 Data Collection and Description

The Korea Real Estate Board has developed and maintained the National Building Energy Integrated Database (NBEIDB), combining building registration information and energy consumption billing data from the past decade (Ji et al., 2020; Seok et al., 2017). NBEIDB provides energy consumption information linked to nationwide building data, comprising approximately 6.25 billion electricity, gas, and district heating consumption records collected from about 50 million individual meters connected to approximately 7.3 million buildings across South Korea. Management costs for apartment complexes with 100 or more households are disclosed through the national Apartment Management Information System (K-apt), with billing costs for heating and hot water energy consumption separately reported for each complex.

In this study, we examined district heating consumption data from Seoul apartment complexes for 2023, the most recent year with complete 12-month data available. Furthermore, we obtained data on billing costs for heating and hot water energy consumption from 171 apartment complexes with 100 or more households through K-apt.

3.2 Data Preprocessing

The monthly energy consumption data from 171 apartment complexes using district heating was analyzed following disaggregating heating and hot water energy consumption and removing data outliers. Cases were excluded where monthly energy consumption data showed negative values, zero heating or hot water energy consumption over 12 months, and zero heating or hot water energy consumption during winter months (Jan.-Feb., Nov.-Dec.). The final analysis was performed

using data from 142 complexes.

3.3 Energy Disaggregation Method

The Simplified Energy Disaggregation (SED) methodology assumes that the energy consumption of the month with lowest energy consumption represents baseload energy consumption, with the remaining energy consumption classified as heating and cooling. For apartment complexes using district heating as their energy source in this study, since district heating is used only for heating and hot water supply, the baseload energy becomes hot water energy, and the remaining energy consumption is estimated as heating energy. Under the SED methodology, hot water energy consumption is assumed to remain constant over the 12-month period.

To disaggregate hot water energy consumption more realistically, this study utilized heating and hot water energy cost data from K-apt. We calculated the ratio of billing costs for heating energy consumption to the total sum of billing costs for heating and hot water energy consumption for 171 Seoul apartment complexes, and applied this ratio to district heating energy consumption to derive heating and hot water energy consumption.

4. DATA ANALYSIS

Heating energy consumption estimates using the existing SED methodology's baseload separation were on average 28% higher, and hot water energy consumption estimates were 44% lower compared to heating energy consumption derived from separating heating and hot water energy. Furthermore, when comparing the proportion of hot water energy consumption during winter months (Jan.-Feb., Nov.-Dec.), differences reaching 300% were observed (Table 1).

Table 1. Ratio of hot water energy consumption to total district heating energy consumption

Methodology \ Month	1	2	3	4	5	6	7	8	9	10	11	12
SED	7%	10%	15%	25%	41%	68%	77%	100%	84%	35%	13%	8%
Actual Consumption	21%	27%	38%	53%	70%	76%	75%	73%	74%	57%	31%	24%

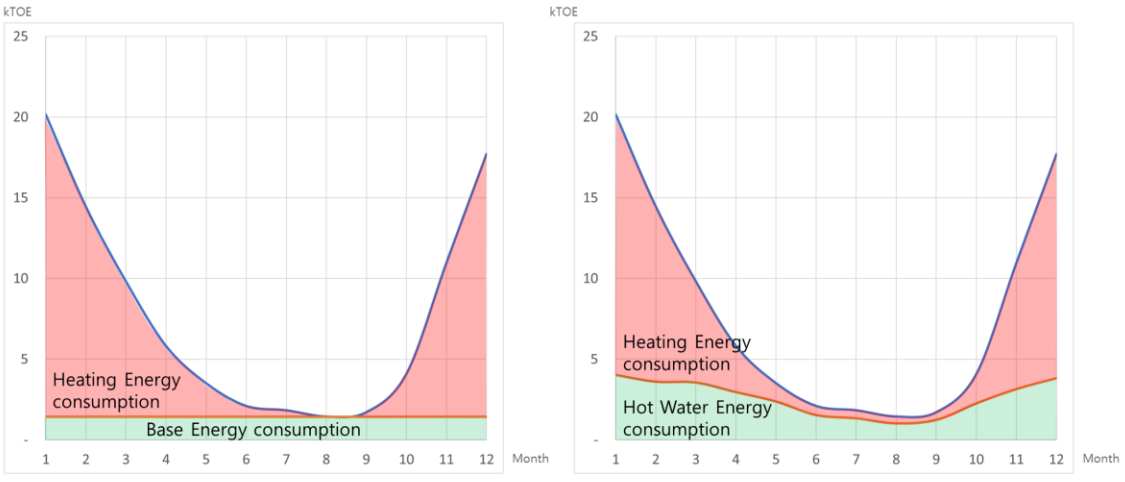

Figure 1. Monthly Heating and Hot Water Energy Consumption Patterns: SED vs. Actual Consumption

As shown in Figure 1, while the existing SED methodology assumes constant baseload energy (hot water energy) consumption throughout the 12-month period, our proposed methodology demonstrates variations in monthly hot water energy consumption. The results reveal that hot water energy consumption tends to increase during winter months, demonstrating that hot water energy consumption is also influenced by seasonal changes.

5. DISCUSSION AND CONCLUSION

This study aimed to improve the accuracy of heating energy consumption estimates by separating hot water energy consumption, considering the limitations of the existing SED methodology. Analysis of data from 142 apartment complexes using district heating in the Seoul region revealed that, compared to the method proposed in this study, the existing SED method overestimated heating energy by 28% and underestimated hot water energy by 44%. This indicates that the conventional method may tend to overestimate heating energy consumption. Considering seasonal variations in hot water energy use could enable more precise disaggregation of energy purposes, and this refinement is expected to serve as a more detailed policy reference when implementing carbon neutrality-related measures in the future.

As building insulation regulations continue to become more stringent, the proportion of heating energy is expected to decrease relative to hot water energy consumption in the future. This suggests that the estimation errors in heating energy using the SED methodology may become even larger, highlighting the need for a methodology to estimate hot water energy consumption. City gas is used as a heat source in many buildings, while electricity is used for cooling and various appliances. A detailed base load analysis is also necessary for these energy sources.

ACKNOWLEDGEMENTS

This work is supported by the Korea Agency for Infrastructure Technology Advancement (KAIA) grant funded by the Ministry of Land, Infrastructure and Transport (Grant RS-2023-00244769).

REFERENCES

Ji, C.Y., Choi, M.S., Gwon, O.I., Jung, H.R., Shin, S.E. (2020). Greenhouse Gas Emissions from Building Sector based on National Building Energy Database. Journal of the Architectural Institute of Korea Structure & Construction, 36(4), 143-152.

Jin, H.S., Lee, S.J., Kim, Y.J., Ha, S.Y., Kim, S.I., Song, S.Y. (2020). Estimation of energy use and CO2 emission intensities by end use in South Korean apartment units based in situ measurements. Energy and Buildings, 207, 109603.

Kim, Y.M., Shin, H.R. (2024). Estimation of Petroleum Energy Consumption in Non-residential Buildings to Determine the Status of Fossil Fuel Use in the Building Sector. Journal of Energy & Climate Change, 19(2), 302-315.

Korea Real Estate Board (2025). Green Building Statistics. Available at: https://www.greentogether.go.kr (accessed 6 February 2025).

Korean Government (2021). 2050 Carbon Neutrality Scenario.

Meng, Q., Mourshed, M. (2017). Degree-day based non-domestic building energy analytics and modelling should use building and type specific base temperatures. Energy and Buildings, 155, 260-268.

Ministry of Land, Infrastructure and Transport (2024). 2023 Building Status Statistics.

Ministry of Land, Infrastructure and Transport, Korea Real Estate Board (2025). K-apt. Available at: https://www.k-apt.go.kr (accessed 6 February 2025).

Multi-Family Housing Management Act (2023). Act No.19764.

Seok, C., Min, O., Seung, Y., Ji, C., Lee, D.Y. (2017). An Analysis of Residential Building Energy Consumption Using Building Energy Integrated Database - Focused on Building Uses, Regions, Scale and the Year of Construction Completion. Journal of Real Estate Analysis, 3(1), 101-118.

6th International Conference on Building Energy and Environment
Eindhoven University of Technology, The Netherlands
6 - 10 July 2025

Use numerical analysis to study the impact of energy recovery ventilators on cabin indoor air quality and air conditioning energy consumption

Tong-Bou Chang [1], Yu-Chun Chang [2], Jhong-Wei Huang [3]

[1]*Department of Mechanical and Energy Engineering, National Chiayi University, Chiayi, Taiwan, tbchang@mail.ncyu.edu.tw*
[2] *Department of Mechanical and Energy Engineering, National Chiayi University, Chiayi, Taiwan, jim2520080000@gmail.com*
[3] *Department of Mechanical and Energy Engineering, National Chiayi University, Chiayi, Taiwan, m991a106@gmail.com*

SUMMARY
Excessive CO_2 concentration in the car will affect the driver's mental state and driving safety. The CO_2 concentration in the cabin can be reduced by using fresh air mode. However, PM pollutants from outside will also be introduced into the cabin, and the high-temperature outside air will increase the air conditioner's energy consumption. This study recommends using energy recovery ventilators (ERVs) to improve cabin air quality and reduce air conditioning energy consumption. Furthermore, this study uses numerical analysis to investigate the performance of ERVs. The results showed that when the ERV was running at high-speed for 30 minutes, the CO_2 concentration of the five passengers dropped from 7557ppm when the ERV was not turned on to about 2418ppm. The number of suspended particles will also drop from 1089 particles/cm^3 when ERV is not turned on to approximately 530 particles/cm^3. The net energy savings for high-speed operation is 110.3W. Using ERV can simultaneously reduce cabin CO_2 and PM concentrations, achieve higher indoor air quality, and reduce energy consumption.

Keywords: numerical analysis, energy recovery ventilator, IAQ.

1. GENERAL INSTRUCTIONS/ INTRODUCTION

According to statistics released by Taiwan's Ministry of Transportation, traffic accidents increased from approximately 300,000 in 2014 to 400,000 in 2023 (Official Website, 2024). Although the reasons for these accidents were not reported, driver fatigue is known to be one of the leading causes of traffic accidents (Jaydarifard et al., 2024). Fatigue worsens through prolonged use of the recirculation air mode (RC mode), with the windows kept closed since this slows the exchange of air between the cabin and the outdoors and thus leads to a higher CO_2 concentration. Consequently, the development of engineering solutions that enhance cabin indoor air quality (IAQ) and maintain driver alertness has become a key focus of automotive researchers and road safety specialists.

To maintain the concentration of CO_2 in the cabin below the 1000 ppm threshold specified in the ASHRAE standard (ASHRAE, 2013), an increase in the flow rate of outdoor air is required. One of the most effective ways of achieving this is to increase the vehicle's speed, thereby increasing the leakage air flow rate (Chang et al., 2017). However, this is impractical in real-world driving conditions. Hence, most proposed methods involve opening the windows regularly or switching the ventilation system to the FA mode (Chang et al., 2023; Hudda and Fruin, 2018; Jung et al., 2017). However, both methods increase the level of PM pollutants within the cabin. Furthermore,

although this problem can be mitigated using a high-efficiency in-cabin filter, the introduction of outside fresh air makes it more challenging to maintain the cabin's thermal comfort, thereby increasing the cooling load on the air-conditioner.
Accordingly, the present study proposes using an Energy Recovery Ventilator (ERV) to perform heat exchange between the outgoing cabin air and the incoming fresh air, thereby enabling cold energy recovery. In this way, the ERV not only improves the cabin IAQ by facilitating the discharge of accumulated CO_2 but also reduces the energy consumption of the air-conditioner. In addition, the ERV incorporates a high-efficiency filter that effectively removes suspended particles from the incoming fresh air, further improving the IAQ in the cabin. The performance of the proposed ERV system is evaluated by performing numerical analysis to examine the concentrations of CO_2 and suspended particles given different numbers of occupants in the cabin and operating speeds of the ERV. Overall, the results confirm that the ERV improves the cabin IAQ and reduces the energy cost of the vehicle air-conditioner.

2. RESEARCH METHODS

Numerical analysis studies using approximate value algorithms in mathematical analysis problems. Numerical analysis often cannot obtain precise values in many issues, but it can obtain approximate solutions to a specific error. In the early days, numerical analysis usually used manual calculations, which took a long time and carried the risk of calculation errors. However, many programming language software have emerged to replace manual calculations with fast and accurate features.
In a ventilated cabin, carbon dioxide enters the cabin along with outdoor air, so the concentration of carbon dioxide in the cabin is related to the ambient concentration. However, carbon dioxide is also emitted naturally as part of the respiratory cycle. Hence, the concentration of carbon dioxide also changes with the number of passengers in the cabin and their activity levels, so the concentration of carbon dioxide in the cabin inevitably exceeds the outdoor concentration. Assuming the indoor air is thoroughly mixed, and the cabin is used as the control volume, Figure 1 shows the corresponding CO_2 transient mass balance diagram.

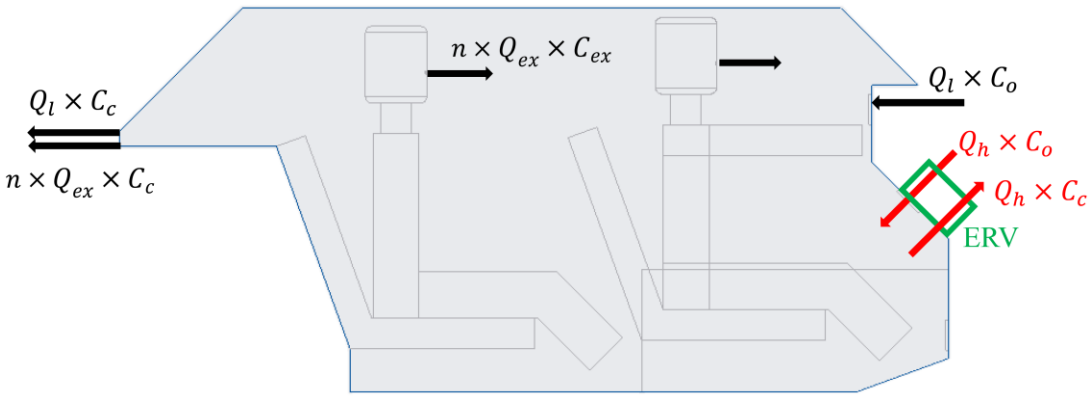

Figure 1. Transient mass balance diagram of CO_2 using cabin as control volume.

As shown in Figure 1, the CO_2 concentration is increased by the breathing of the passengers and reduced by the introduction of outdoor air with a volumetric flow rate Q and the exhaust of indoor air with a volumetric flow rate Q into the environment. Changes in the amount of CO_2 in the cabin. In other words, the change in CO_2 in the cabin over time equals the amount of CO_2 produced by

passengers minus the amount of CO_2 removed by ventilation. That is,

$$V_c \times \frac{dC_c}{dt} = n \times Q_{ex} \times C_{ex} + Q_l \times C_o + Q_h \times C_c - Q_l \times C_c - n \times Q_{ex} \times C_c - Q_h \times C_o \quad (1)$$

where n is the number of occupants within the cabin, Q_{ex} is the breath volume flow rate of each occupant, C_{ex} is the CO_2 concentration of each exhaled breath, C_c is the CO_2 concentration within the cabin, C_o is the CO_2 concentration in the outdoor environment, Q_l is the leakage ventilation volume flow rate, Q_h is the ventilation volume flow rate of ERV and V_c is the volume of the cabin. The present simulations evaluate the CO_2 concentration in the cabin under different conditions using the following finite difference equation derived from Eq. (1):

$$C_{c,k+1} = C_{c,k} + \frac{dt}{V_c} \times \{n \times C_{ex} \times Q_{ex} + (Q_l + Q_h) \times [C_o - C_{c,k}] - n \times Q_{ex} \times C_{c,k}\} \quad (2)$$

where dt is the time interval, and k is the time step.

Figure 2 is a schematic diagram of PM's transient mass balance diagram using the cabin as the control volume. Unlike the concentration of carbon dioxide, the vehicle's air conditioning system has a filter that can filter the suspended particles in the vehicle. In addition, the ERV proposed in this study also has a filter. Therefore, the filtration efficiency of the filter needs to be considered when calculating. Also, passengers' breathing does not cause an increase or decrease in suspended particles, so human exhalation is ignored when calculating the equation for suspended particles.

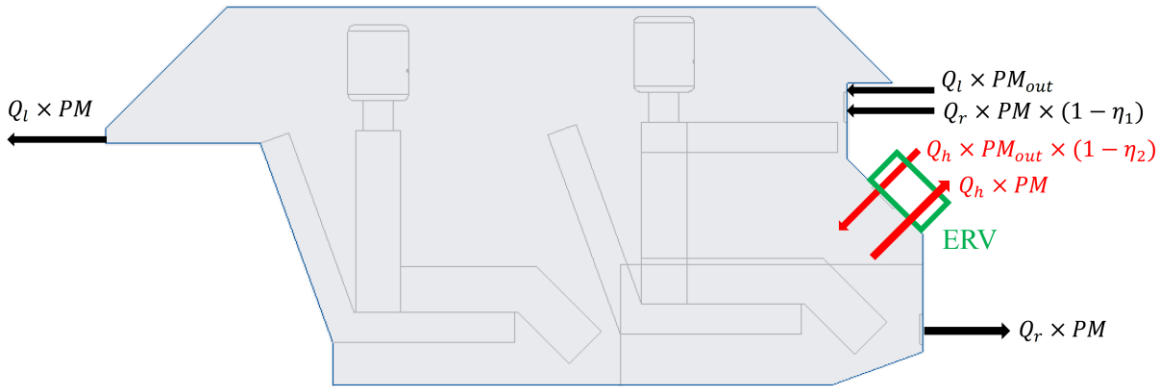

Figure 2. Transient mass balance diagram of PM using the cabin as control volume.

As shown in Figure 2, $Q_l \times PM_{out}$ is the outside suspended particulate matter that flows into the cabin through leakage ventilation, and $Q_l \times PM$ is the suspended particulates that flow out of the cabin due to leakage ventilation. When the air conditioner is in recirculation air mode, the suspended particles flow into the air conditioner is $Q_r \times PM$ and the suspended particles sent back into the cabin through the air conditioner filter is $Q_r \times PM \times (1-\eta_1)$. The suspended particles flow into the cabin through the ERV filter is $Q_h \times PM_{out} \times (1-\eta_2)$, and the suspended particles flow out of the cabin through the ERV is $Q_h \times PM$. Using the concept of control volume, the above PM inflow and outflow can be expressed as the suspended particulate mass balance equation:

$$V_c \times \frac{dPM}{dt} = Q_l \times PM_{out} + Q_r \times PM \times (1-\eta_1) + Q_h \times PM_{out} \times (1-\eta_2) - Q_l \times PM - Q_r \times PM - Q_h \times PM \quad (3)$$

where PM is the suspended particles concentration within the cabin, PM_{out} is the suspended

particles concentration in the outdoor environment, Q_r is recirculation air flow rate, η_1 is the filtration efficiency of in-car filter, η_2 is the filtration efficiency of ERV filter. The present simulations evaluate the suspended particle concentration in the cabin under different conditions using the following finite difference equation derived from Eq. (3):

$$PM_{k+1} = PM_k + \frac{dt}{V_c} \times \{Q_l \times [PM_{out} - PM_k] + Q_h \times [PM_{out} \times (1-\eta_2) - PM_k] - Q_r \times \eta_1 \times PM_k\} \quad (4)$$

Table 1 Parameters used in analysis.

number of occupants：n	1~5
The volume of the cabin：V_c (m^3)	3.821
The CO_2 concentration of each exhaled breath：C_{ex} (ppm)	40,000
The breath volume flow rate of each occupant：Q_{ex} (m^3/s)	0.0001145
The initial value of the CO_2 concentration in the cabin：$C_{c,k=1}$ (ppm)	420
The outdoor CO_2 concentration：C_o (ppm)	420
Time interval: dt (s)	1
The outdoor suspended particles concentration：PM_{out} (particles/cm^3)	8,000
The initial value of the suspended particles concentration in the cabin：$PM_{k=1}$ (particles/cm^3)	8,000
In-car filter filtration efficiency/ ERV filter filtration efficiency：η_1 /η_2	0.25 / 0.999
The ventilation flow rates when ERV operate at low speed/ high speed： Q_{hl} / Q_{hh} (m^3/s)	0.00675 / 0.00944
Leakage ventilation flow rate of cabin：Q_l (m^3/s)	0.00127
Recirculation air flow rate：Q_r (m^3/s)	0.03461

3. RESULTS AND DISCUSSION

3.1 Verification of CFD model

The validity of the numerical model was confirmed by comparing the simulation results for the CO_2 and PM concentrations in the cabin with the experimental results presented by Jung et al., 2017. For both sets of results, the ventilation system was set to the recirculation air mode for the first 23 minutes and was then switched to the fresh air mode for the next 15 minutes. The average CO_2 and PM concentrations were recorded every minute, as shown in Figs. 3(a) and 3(b), respectively. It is seen that the simulation results are in good agreement with the experimental data for both the CO_2 concentration and the PM concentration. Consequently, the feasibility of the proposed model is confirmed. The minor discrepancy between the two sets of results is most likely due to slight variations in the outdoor environment during the experimental measurement process, which are unknown and thus cannot be replicated in the simulations.

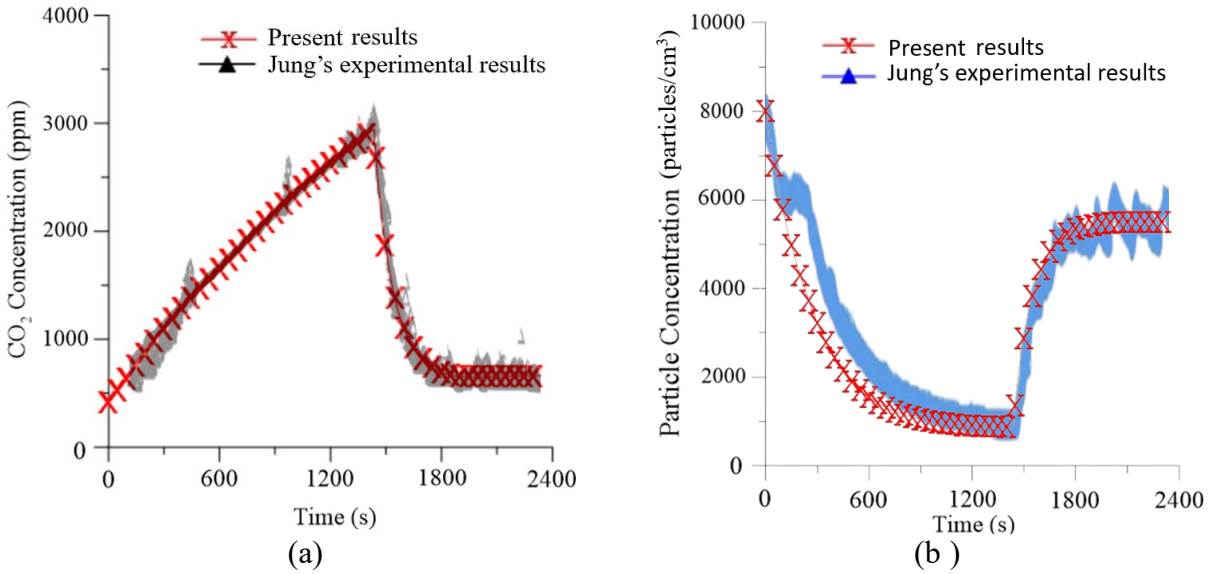

Figure 3 Comparison of simulation results and experimental values reported by Jung et al., 2017 for (a) CO2 concentration and (b) suspended particulate concentration.

3.2 Simulation results under different ERV operating conditions

3.2.1 Simulation results for IAQ when ERV is turned off

Figure 4 shows the variation in the CO_2 concentration over time for different numbers of occupants within the cabin when the ERV is not turned on. When using the recirculation air mode, the only fresh air entering the cabin ingresses through leakage ventilation. Consequently, the CO_2 concentration increases rapidly over time. For a single occupant, the CO_2 concentration reaches 1000 ppm after 539 seconds and 1989 ppm after 30 minutes. Moreover, the CO_2 concentration scales proportionally with the number of occupants. Thus, for five people in the cabin, the CO_2 concentration reaches 1000 ppm after only 101 seconds and climbs to 7557 ppm after 30 minutes.

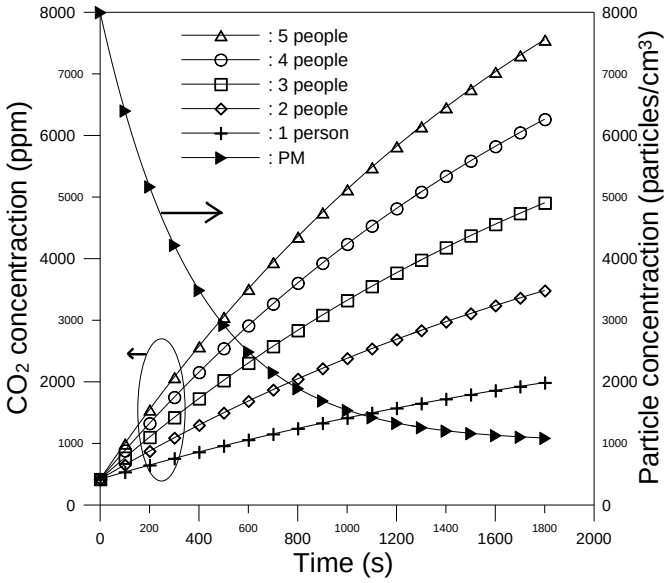

Figure 4 The variations in the CO_2 and PM concentrations over time for different numbers of occupants within the cabin when the ERV is not turned on

Figure 4 also shows the change in the average concentration of the suspended particles in the cabin

over time for 1–5 occupants when the ERV is not turned on. It can be seen that PM concentration is independent of the number of people from Equation (3). Moreover, since the air-conditioning system is set to the recirculation air mode, very little outside air enters the cabin. Consequently, the number of suspended particles reduces over time owing to the effects of the filter system in the air-conditioning unit. The suspended particle concentration decreases from the initial value of 8000 particles/cm^3 (see Table 1) to 1089 particles/cm^3 after 30 minutes.

3.2.2 Simulation results for IAQ when ERV operates at low speed

Figure 5 shows the variation in the CO_2 concentration over time for different numbers of occupants in the cabin when the ERV operates at a low speed (0.00675 m^3/s). Compared with the case when the ERV is not turned on, the overall concentration of CO_2 is reduced. Moreover, the rate of increase in the CO_2 concentration saturates after approximately 12 minutes, rather than increasing continuously, as shown in Fig. 4. Thus, after 30 minutes, the concentration of CO_2 is still lower than 1000 ppm for a single occupant in the cabin. Moreover, for the maximum occupancy case, the CO_2 concentration is approximately 3011 ppm, compared to 7557 ppm in Fig. 4. Figure 5 also shows the change in the average concentration of the suspended particles within the cabin. Compared to the case where the ERV is turned off (Fig. 4), both concentration values are significantly lower than those shown in Fig. 4 for the case where the ERV is not turned on. The ERV increases the AER between the inside and outside of the cabin, consequently, the CO_2 concentration decreases. Moreover, since the ERV incorporates a high-efficiency filter (99.9%), the particulate concentration also reduces. A comparison of Figs. 4 and 5 shows that using the ERV reduces the particulate concentration by almost half (~615 particles/cm^3) compared to the case where the ERV is not used (1089 particles/cm^3).

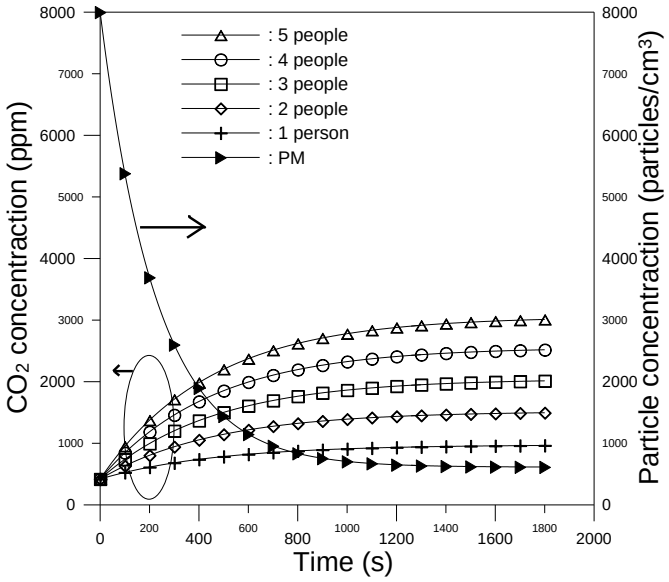

Figure 5 The variations in the CO_2 and PM concentrations over time for different numbers of occupants within the cabin when the ERV operates at a low speed

3.2.3 Simulation results for IAQ when ERV operates at high speed

Figure 6 shows the variation in the CO_2 concentration over time for different numbers of people in the cabin when the ERV operates at a high speed (0.00944 m^3/s). Compared with the case where the ERV is not turned on or is operated in the low-speed mode, the high-speed mode results in a

lower CO_2 concentration level and stabilizes the concentration more quickly. For a single occupant in the cabin, the CO_2 concentration stabilizes within around 10 minutes. Even with five occupants in the cabin, the CO_2 concentration approaches a constant value after approximately the same time. After 30 minutes, the CO_2 concentration for a single occupant is just 836 ppm, while that for five occupants is around 2419 ppm, which is about 20% lower than when the ERV is operated at a low speed. Figure 6 also shows the average concentration of suspended particles in the cabin for 1–5 occupants and the ERV operating at a high speed. As for the low-speed ERV mode, the suspended particulate concentration drops very quickly as soon as the ERV is turned on and stabilizes within approximately ten minutes (~530 particles/cm^3).

Comparing Figs. 4-6, it can be seen that the improved IAQ can be attributed to the greater AER under high-speed ERV operating conditions. For 2–5 occupants, the CO_2 concentration exceeds the ASHRAE standard of 1000 ppm. In fact, for 4 and 5 occupants, the CO_2 concentration is more than double the standard (2035 ppm and 2418 ppm, respectively). Nonetheless, as reported by Chang et al., 2023, cognitive function is not impaired even at CO_2 concentrations of around 2000 ppm, provided that the average driving time does not exceed 8 hours.

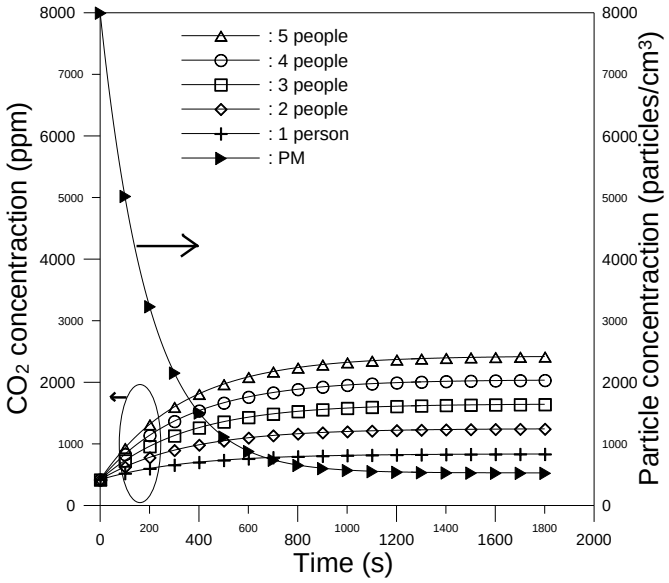

Figure 6 The variations in the CO_2 and PM concentrations over time for different numbers of occupants within the cabin when the ERV operates at a high speed

3.3 Estimated ERV energy savings

To estimate the energy savings of the ERV, the outdoor temperature and relative humidity were set to 35℃ and 80%, respectively (that is, the enthalpy value h_{out} was equal to 109.42 kJ/kg). The cabin temperature and relative humidity were set at 25℃ and 60%, respectively (h_{in}=55.45 kJ/kg). The enthalpy difference between outdoor and indoor air was thus 53.97 kJ/kg. By Cho et al., 2023, the enthalpy recovery efficiency was set as 60%. Consequently, the enthalpy recovery amount per unit mass of air exchanged was 53.97×0.6 = 32.38 kJ/kg. According to Chang et al.,2021, the coefficient of performance (COP) of electric vehicles in the air conditioning mode is around 3.18. The total amount of enthalpy recovery divided by the COP gives the energy consumption of the air conditioner saved. Subtracting the power consumption of the ERV (low-speed consumption: 1.9 W, high-speed consumption: 2.7 W) then gives the net energy savings provided by the ERV. As shown in Table 2, the ERV system considered in the present study achieved net energy savings

of 79.6 W and 110.3 W in low-speed and high-speed running conditions, respectively.

Table 2 Enthalpy recovery amount and net energy saving of ERV under low-speed and high-speed running conditions

	Air mass flow rate (kg/s) A	Total enthalpy recovery (W) B=A×32.38×1000	Air conditioning power reduction (W) C=B/3.18	ERV power consumption (W) D	Net energy savings (W) E=C-D
Low speed	0.008	259.1	81.5	1.9	79.6
High speed	0.0111	359.4	113	2.7	110.3

4. CONCLUSION

This study has proposed using an ERV to improve the IAQ of vehicle cabins and recover the cooling enthalpy to reduce the energy consumption of air conditioners. CFD simulations have been conducted to investigate the performance of the ERV in regulating the CO_2 and suspended particulate concentrations within the cabin at different numbers of occupants and ERV operating conditions (low and high speed). Overall, the results confirm that the ERV system not only improves the IAQ in the vehicle cabin but also reduces the air conditioning load and therefore lowers the energy consumption.

5. ACKNOWLEDGEMENTS

The authors gratefully acknowledge the financial support provided to this study by the National Science and Technology Council (NSTC) of Taiwan under Grant numbers NSTC 112-2221-E-415-007 and NSTC 113-2221-E-415 -014 –MY3.

6. REFERENCES

ASHRAE, ANSI/ASHRAE 62.1- Ventilation for Acceptable Indoor Air Quality. Atlanta, GA, USA: American Society of Heating, Refrigerating and Air-Conditioning Engineers (ASHRAE), 2013.

Chang T.B., Lin Y.S., Hsu Y.T., 2023. CFD simulations of effects of recirculation mode and fresh air mode on vehicle cabin indoor air quality. Atmospheric Environment 293, 119473.

Chang T.B., Sheu J.J., Huang J.W., 2017. Vehicle air leakage ventilation and its effect on cabin indoor air quality. Proceedings of the Institution of Mechanical Engineers, Part E: Journal of Process Mechanical Engineering 231, 1226–34.

Chang T.B. , Sheu J.J., Huang J.W., 2021. High-Efficiency HVAC System with Defog/Dehumidification Function for Electric Vehicles. Energies 14(1), 46.

Cho H.J., Cheon S.Y., Jeong J.W., 2023. Experimental analysis on energy recovery ventilator with latent heat exchanger using hollow fiber membrane. Energy Conversion and Management 278, 116706.

Hudda N., Fruin S.A., 2018. Carbon dioxide accumulation inside vehicles: The effect of ventilation and driving conditions. Science of The Total Environment 610–611, 1448-56.

Jaydarifard S., Behara K., Baker D., Paz A., 2024. Driver fatigue in taxi, ride-hailing, and ridesharing services: a systematic review. Transport Reviews 44, 572–90.

Jung H.S., Grady M.L., Victoroff T., Miller A.L., 2017. Simultaneously reducing CO2 and particulate exposures via fractional recirculation of vehicle cabin air. Atmospheric Environment 160, 77-88.

Official Website of the Ministry of Transportation and Communications of Taiwan, Available online, https://stat.motc.gov.tw/mocdb/stmain.jsp?sys=100,2024(accessed on 22 September 2024).

6th International Conference on Building Energy and Environment
Eindhoven University of Technology, The Netherlands
6 - 10 July 2025

Comprehensive Assessment Framework for Policy Guidelines toward Carbon Neutral Existing Public Building on South Korea

Se-Min, Oh [1], Seung-Hee, Kim [2], Hwaseok, Shin [3], Changyoon, Ji [4], Cheol-min Choi [5]

[1]*Green-Remodeling Support Department of Korea Authority of Land & Infrastructure Safety, seminoh@kalis.or.kr*
[2]*Green-Remodeling Support Department of Korea Authority of Land & Infrastructure Safety, seunghkim@kalis.or.kr*
[3]*Green-Remodeling Support Department of Korea Real Estate Board, k25561@reb.or.kr*
[4]*Green-Remodeling Support Department of Korea Real Estate Board, k25960@reb.or.kr*
[5]*Department of Green-Building of Ministry of Land, Infrastructure and Transport, kop511@korea.kr*

SUMMARY
This paper offers a detailed analysis of the South Korean government's green remodeling initiatives for public buildings. It explores the critical challenges and strategies associated with the mandatory implementation of green remodeling for public buildings, set to begin in 2025. The paper further investigates potential solutions, focusing on the development of a strategic roadmap, evaluation methodologies, and effective policy implementation, underpinned by technical and research methodologies designed to support South Korea's carbon neutrality goals.

Keywords: Green-Remodeling, Building Energy, Mandatory Green-Remodeling for Public Buildings

1. GENERAL INSTRUCTIONS

South Korea has committed to carbon neutrality by 2050, with substantial efforts across various sectors, including industry, transport, and buildings. The building sector, accounting for 24.6% of national greenhouse gas emissions in 2018, faces a target of a 32.8% reduction by 2030. Achieving this reduction remains a significant challenge(South Korea’s 2030 Nationally Determined Contributions (NDC)). To this end, the Green Buildings Construction Support Act (2012) encourages Zero Energy Buildings (ZEB) for new constructions and Green Remodeling (GR) for existing buildings. Green remodeling is considered a pivotal strategy, especially for public buildings, with mandatory green remodeling set to begin in 2025. This paper analyzes the current policies, identifies issues in the implementation of green remodeling for public buildings, and proposes solutions within the domains of policy, technology, and evaluation frameworks.

2. KOREAN GOVERNMENT POLICY : GREEN-REMODELING OF PUBLIC BUILDING

2.1. What is green-remodeling?

Green remodeling can be defined as the process of improving the performance of insulation, facilities, and other building systems in aging buildings to enhance energy efficiency, thereby reducing heating and cooling costs, lowering greenhouse gas emissions, and creating a more comfortable living environment. Nationally Determined Contribution(NDC) for the building sector in South Korea and the specific implementation measures are presented in Figure 1.

Building sector
Nationally Determined Contribution

2030 Nationally Determined Contribution
(an upward plan, '21.10)

▼

The 8th government
Selection of 120 national tasks (`22.7)

▼

The First national carbon neutrality and
green growth master plan ('23.4)

Division	Key tool	Means of implementation	
New building	Zero Energy Buildings	Public	• Mandatory zero energy building certification
		Private	• Strengthening design standards • Incentive
Existing building	Green Remodeling	Public	• Support project • Mandatory project
		Private	• Interest support • Accredited Accreditation System, etc.

Figure 1. Overview of South Korea's Carbon Neutrality Policy and Achieving Measures in the Building Sector

2.2. Green-remodeling…How is it promoted?

The South Korean government's strategy for green remodeling presents the vision of "leading the transformation of aging public buildings into green buildings and expanding this approach to private buildings." The green remodeling initiatives in the public sector can be divided into four stages, as outlined below.

- Initiation Phase (2013-2019) : Pilot projects, providing partial funding for 15 sites annually.
- Adaptation Phase (2020-2024) : Financial support for approximately 200 billion KRW allocated annually to 700 public buildings, preparing for the mandatory phase.
- Stabilization Phase (2025-2029) : Large-scale funding for both "Support Projects" (phased out) and "Mandatory Projects" (phased in).
- Expansion Phase (2030 onward) : Widening the scope to include private buildings.

2.3. Green-remodeling for public buildings…what's next?

As a detailed measure within the medium- and long-term reduction strategies for the building sector outlined in the "First National Carbon Neutrality & Green Growth Master Plan (April 2023)," the Korean government has emphasized the promotion of green remodeling for existing buildings. In the public sector, these efforts are primarily categorized into two main initiatives: the "Support Projects" and the "Mandatory Projects" (Figure 2).

The First national carbon neutrality and green growth master plan (sector) promotion work

Transition	Industry	Building	Transport	Agricultural, livestock and fisheries
- Reducing coal power generation - Nuclear power plant + renewable energy ↑ - Demand efficiency	- Core technology secure - Company support - Advanced emissions reduction	- Expanding zero-energy buildings - Green remodeling	- Supply zero-emission vehicle - Low-carbonization or railways, ports and shipping	- Transition to a low-carbon agricultural structure - low-carbonization of fishing vessels and facilities

- **Green remodeling of existing buildings** (※ Detailed tasks for mid to long-term reduction measures by sector)

○ **Expanding the support target and making it mandatory for green remodeling projects for public buildings**
(Ministry of Land, Infrastructure, and Transport)

· **Expanding the support target to include energy-intensive facilities, a large quantity facilities, etc., and discovering business models to activate remodeling**

· To expand green remodeling of old public buildings, phased application of mandatory green remodeling of old public buildings ('25~, 'The green buildings construction support act' revision promotion)

Figure 2. First National Carbon Neutrality & Green Growth Master Plan on South Korea

2.3.1. Green-remodeling 'support project' for public buildings

The Green Remodeling Support Program for Public Buildings was launched by the public sector in 2020 to lead the widespread adoption of green remodeling. This initiative began with hospitals, health centers, and daycare centers, and is a nationwide project that will invest approximately 900 billion KRW into around 3,400 public buildings by 2024. An analysis of the 2,908 buildings targeted from 2020 to 2023 shows an estimated reduction of 118,363 tons of greenhouse gas emissions and an energy cost savings of approximately 9 million KRW per building. This contributes to the achievement of national greenhouse gas reduction goals and is regarded as a successful integration of Korea's green remodeling industry and market (Source: 2024 Green Building Conference, Oh Se-min, "Strategies for the Implementation of Mandatory Green Remodeling of Public Buildings," partially cited, Table 1).

Table 1. Progress of the Public Building Green Remodeling Support Program (As of December 2024)

Division	(unit : billion KRW)			(unit : number of buildings)					
	Total	**Governmental expenses**	**Local governmental expenses**	**Total**	**Daycare center**	**Health center**	**Hospital**	**Senior citizen center**	**Library**
2020	**3,260**	2,180	1,080	**821**	411	369	41	-	-
2021	**3,197**	2,141	1,056	**895**	443	395	57	-	-
2022	**2,806**	1,836	970	**575**	271	276	28	-	-
2023	**2,545**	1,709	836	**617**	72	127	4	376	38
2024	**1,520**	1,031	489	**562**	58	163	1	340	-
Total	**13,334**	8,901	4,433	**3,470**	1,255	1,330	131	716	38

Considering the limited national resources, the achievement of the 2030 NDC targets, and the various types and sizes of public buildings, a scenario for the 'Support Program' has been proposed as follows. The aim is to maximize the expected benefits of large-scale national financial investments in the 'Support Program' while gradually transitioning to the 'Mandatory Program' in 2025. The transition will begin with the most common building types in 2025-2026 and gradually reduce the scope over time (Table 2).

- Implementation Strategy : (Priority 1) : Buildings primarily used by vulnerable groups (e.g., health centers, hospitals, daycare centers, etc., until 2023), (Priority 2) : Energy-intensive buildings (e.g., educational and research facilities, neighborhood service facilities, public facilities, etc., until 2027), (Priority 3) : Public buildings with a large variety of functions (e.g., other public facilities, museums, fire stations, etc., until 2029).

Table 2. Proposed Implementation Strategy for Public Building Green Remodeling 'Support Program'

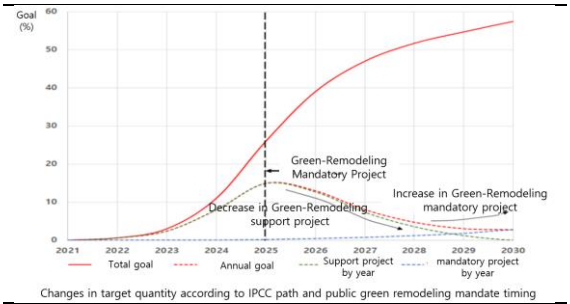

Changes in target quantity according to IPCC path and public green remodeling mandate timing

Status of priority setting by building uses		
Division	Building uses	note
1st	health centers, hospitals, daycare centers, etc.	vulnerable groups
2nd	library, welfare facilities for senior citizens, etc.	energy- intensive facilities
3rd	educational facilities, other educational research facilities, etc.	
4th	other public facilities, social welfare facilities, etc.	a large quantity facilities
5th	museum, fire station, etc.	

Number of green remodelling support purposes by year (target)									
2020	2021	2022	2023	2024	2025	2026	2027	2028	2029
3 types	3 types	3 types	5 types	4 types	9 types	10 types	9 types	7 types	3 types

2.3.2. Green-remodeling 'mandatory project' for public buildings

The Korean government aims to prioritize the mandatory implementation of green remodeling for public buildings, while simultaneously encouraging its expansion to the private sector. To achieve this, the government seeks to establish a detailed policy framework for the mandatory green remodeling of public buildings and present a leading model to ensure the private sector's acceptance. The details of these efforts are summarized in Figure 3, which outlines the 'Support Program' and 'Mandatory Program' for public building green remodeling.

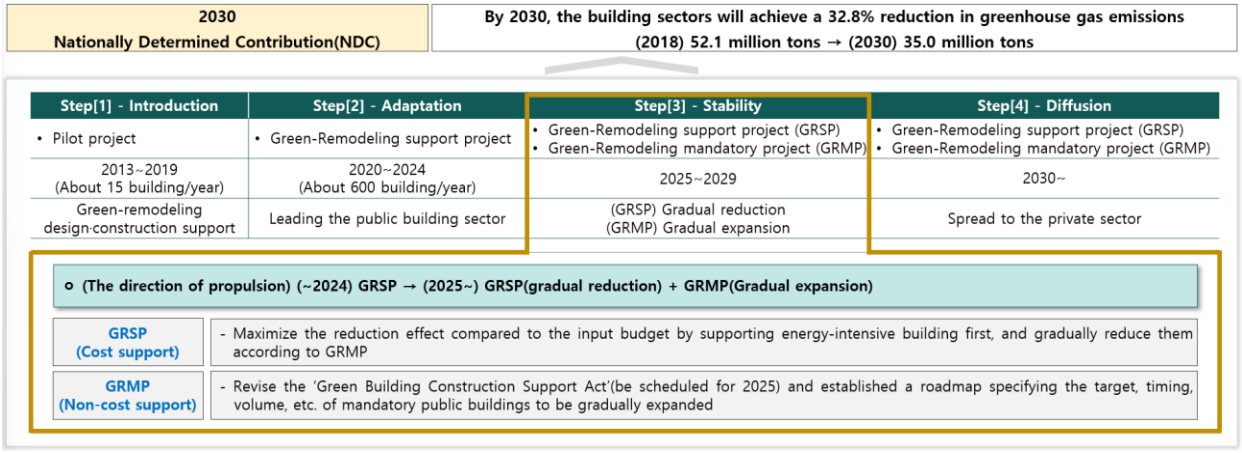

Figure 3. South Korea's National Strategy for Green-Remodeling

3. VARIOUS ISSUES AND RESPONSE STATUS OF GREEN-REMODELING PROJECT FOR PUBLIC BUILDING

3.1 Issues in green-remodeling of public building on south korea

In order to gradually promote the green remodeling mandatory project for public buildings, related standards and grounds must be established. In order to establish a plan to promote mandatory green remodeling of public buildings, it is necessary to clearly define public buildings and organize data on public buildings suitable for mandatory green remodeling of public buildings. Based on this, a promotion system that includes criteria for selecting mandatory targets to achieve reduction goals, promotion procedures, participating organizations, and roles must be established. In addition, in order to evaluate the performance improvement effect of buildings subject to mandatory green remodeling, evaluation methods and tools suitable for green remodeling should be developed.

In order to systematically promote the mandatory project, we are carrying out various tasks in stages, such as preparing public building data, developing evaluation methods and tools, and the current status is as shown in Section 3.2.

3.2. Development of roadmap for mandatory green-remodeling of public buildings

3.2.1. Preparing public building data-sets

In order to establish a medium- and long-term roadmap for the mandatory green remodeling of public buildings, it is essential to first understand the current state of public buildings. This study utilizes the National Building Energy Integrated Database (NBEID) operated by the South Korean government (Ministry of Land, Infrastructure and Transport) to construct a dataset for public buildings. The dataset is based on the reference year 2018, which aligns with South Korea's 2030 Nationally Determined Contributions (NDC), and considers the target years of 2030 and 2050. The

procedure for constructing the dataset is outlined below, and further details can be found in the research report titled "Establishing the Implementation Plan for the Mandatory Green Remodeling of Public Buildings."

- Identification of Public Building Targets : Extract public buildings owned by the public sector from South Kores's 7.45 million buildings using the 2018 and 2023 building registry data
- Ownership Proportions of Public Buildings : Detemine the public-private ownership proportions in buildings with partial ownership
- Identification of Ownership Types of Public Buildings : Idenitify public buildings for mandatory green-remodeling by examining ownership status and defining those 100% owned by a single public entity
- Construction of Public Building Dataset : Create a data-set to track public building current status and support the development of a roadmap for mandatory green-remodeling

As of 2023, the total number of public buildings in South Korea is identified as 417,066, with 232,657 buildings being fully owned by the public sector. Considering the feasibility and ease of implementing the mandatory green remodeling of public buildings starting in 2025, the scope for mandatory green remodeling will be defined by excluding certain building types (e.g., small-scale buildings under 100m², military facilities, etc.). This target group is responsible for 45.8% (6,042,000 tCO_2eq) of the total greenhouse gas emissions from public buildings, with 39.9% (793,000 tCO_2eq) from direct emissions and 46.9% (5,249,000 tCO_2eq) from indirect emissions (Table 3).

Table 3. Dataset Construction (Partial) and Proposed Scope for Mandatory Green Remodeling of Public Buildings

Criteria for Distinction				No. of Buildings	GFA (m^2)	Energy Consumption (toe)	GHG emissions ($tCO_2eq.$)
Included building uses	100% public ownership	Sole ownership	Individual	37,272 (8.94%)	111,869K (33.52%)	952.9K (31.20%)	4,277K (32.40%)
			Multi-unit	131 (0.03%)	768K (0.23%)	5.2K (0.17%)	22K (0.17%)
		Fractional ownership	Individual	26,348 (6.32%)	45,016K (13.49%)	386.9K (12.67%)	1,731K (13.12%)
			Multi-unit	45 (0.01%)	324K (0.10%)	3.1K (0.10%)	12K (0.09%)
		Fractional ownership	Individual	36,805 (8.82%)	46,852K (14.04%)	506.1K (16.57%)	2,244K (17.00%)
			Multi-unit	1,635 (0.39%)	1,981K (0.57%)	24.4K (0.80%)	106K (0.80%)
Excluded building uses	100% public ownership	Sole ownership	Individual	132,738 (31.83%)	43,259K (12.96%)	321.6K (10.53%)	1,444K (10.94%)
			Multi-unit	8,538 (2.05%)	15,776K (4.73%)	120.6K (3.95%)	415K (3.14%)
		Fractional ownership	Individual	27,084 (6.49%)	14,290K (4.28%)	110.2K (3.61%)	472K (3.58%)
			Multi-unit	501 (0.12%)	2,090K (0.63%)	19.6K (0.64%)	76K (0.57%)
		Fractional ownership	Individual	47,035 (11.28%)	11,696K (3.50%)	222.3K (7.28%)	1,036K (7.85%)
			Multi-unit	98,934 (23.27%)	39,885K (11.95%)	381.0K (12.48%)	1,364K (10.34%)
Total				417,066 (100%)	333,760K (100%)	3,054K (100%)	13,199K (100%)

3.2.2. Development of roadmap for mandatory green-remodeling of public buildings

Based on the previously constructed dataset of public buildings, this paper aims to propose a roadmap for the implementation of mandatory green remodeling in public buildings. Considering the direct emission reduction targets for the building sector outlined in South Korea's 2030 Nationally Determined Contributions (NDC) and 2050 carbon neutrality scenarios, it is deemed essential to establish the roadmap based on direct emissions. It is also necessary to plan a phased expansion, taking into account factors such as building usage, scale, age, and ownership type.

- Phase 1 (2025-2030) : (Scale) floor area of 3,000 m² or more, (Usage) 6 building types, (Ownership) Public sector ownership only (general buildings).
- Phase 2 (2031-2035) : (Scale) floor area of 500 m² or more, (Usage) 6 building types, (Ownership)

Public sector ownership only (general buildings).

- Phase 3 (2036-2040) : (Scale) floor area of 3,000 m² or more, (Usage) 10 building types, (Ownership) Public sector ownership only (general buildings).
- Phase 4 (2041-2045) : (Scale) floor area of 500 m² or more, (Usage) 16 building types, (Ownership) Public sector ownership only (general buildings).
- Phase 5 (2046-2050) : (Scale) floor area of 500 m² or more, (Usage) 16 building types, (Ownership) Public sector multiple ownership (general buildings).

3.3. Development of green-remodeling evaluation method

Given the heterogeneity of existing buildings, a dual evaluation approach Asset Rating (AR) and Operational Rating (OR) is proposed. AR assesses energy performance based on simulation models, while OR evaluates post-retrofit energy savings through actual usage data.

3.3.1. Development of simulator for setting energy performance improvement targets in the pre-construction phase of green-remodeling

The dynamic energy analysis of buildings based on EnergyPlus allows for the interpretation of thermal behavior within a building when applying interconnected green remodeling technologies. Unlike new buildings, which have relatively uniform operation conditions, existing buildings exhibit diverse operational conditions and usage patterns. Therefore, we aim to develop a dynamic evaluation program that reflects these characteristics and incorporates such diversity.

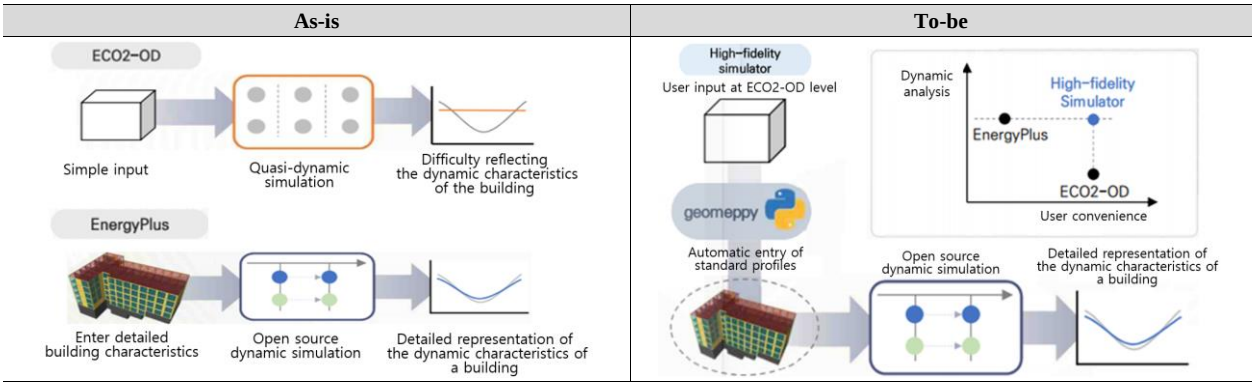

Figure 4. Approach for development of green-remodeling simulator
(Dong-A Univ., Seoul National Univ., 2024, Development of a prototype energy and greenhouse gas simulator for existing buildings, Progress report presentation material)

3.3.2. Development of evaluation method based on actual energy use post-construction phase of green-remodeling

The effectiveness of green remodeling can be assessed through various approaches. The first is relative evaluation, which compares the target building with a group of similar buildings to assess the change in energy performance. The second is absolute evaluation, which quantifies energy savings or greenhouse gas reductions by comparing the energy consumption or emissions of the building before and after green remodeling. The third is change point method (CPM), which is a methodology to analyze the energy consumption pattern of a building based on the relationship between monthly energy usage and average outdoor temperature. Each of these evaluation methods has its own strengths and limitations. In order to increase the robustness of green remodeling performance evaluation, we are developing an evaluation model that integrates the

results of relative evaluation, absolute evaluation, and CPM analysis to ensure a more comprehensive and accurate evaluation of energy savings and greenhouse gas reductions (Figure 5).

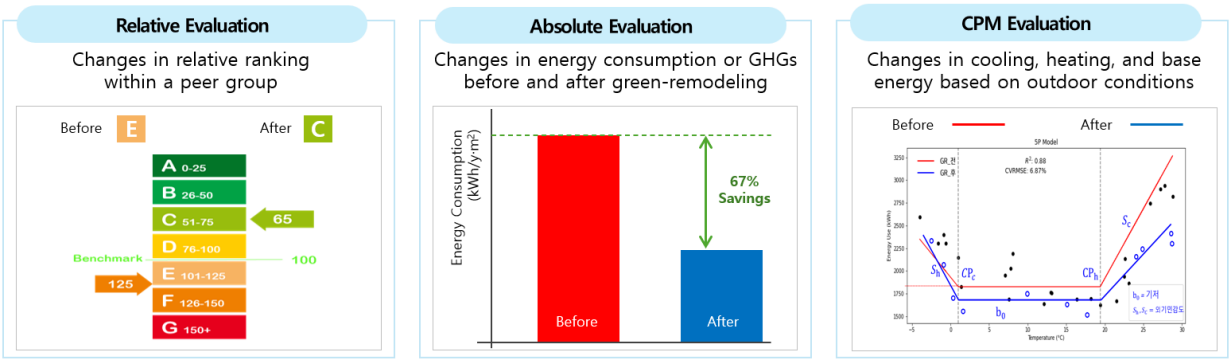

Figure 5. Framework of the comprehensive evaluation model for green remodeling

3.4. Calculation of greenhouse gas emission reduction factors through green-remodeling

The greenhouse gas emissions of individual buildings through green remodeling are calculated based on actual energy usage data. However, there are various alternatives that can apply green remodeling technology in the planning stage before actual construction. Reviewing these alternatives requires a lot of manpower, time, and resources. To solve this problem, we developed a "green remodeling greenhouse gas emission reduction factor(Table 4)" using dynamic simulation, deep learning techniques, etc. (Figure 6). This factor serves as a threshold for quickly and easily evaluating the greenhouse gas reduction amount through green remodeling in the early planning stage, and the factor may change if the building use, etc. are subdivided in the future.

Table 4. Green Remodeling Greenhouse Gas Emission Reduction Factor

Building Use	Reduction Coefficient ($kgCO_{2,eq}/m^2$)	Building Use	Reduction Coefficient ($kgCO_{2,eq}/m^2$)
① Detached house	31.2	⑪ Children's facilities	4.3
② Business facility	5.0	⑫ Elementary/Middle/High school	4.6
③ Police substation	14.7	⑬ University	3.4
④ Fire station	10.4	⑭ Research institute	4.4
⑤ Post office/Telephone office	7.2	⑮ Training facility	10.6
⑥ Performance facilities	6.2	⑯ Sportsfacilities	12.8
⑦ Exhibition hall	5.9	⑰ Small apartment types	12.1
⑧ Passenger facilities	6.3	⑱ Apartment types	8.8
⑨ Railway/Airport	6.3	⑲ Business support facility types	10.7
⑩ Haspital	10.0	⑳ Library types	7.1

4. CONCLUSION

This paper analyzes the green remodeling policies and initiatives for public buildings currently being promoted by the South Korean government. It also discusses the key issues and corresponding solutions for the mandatory implementation of green remodeling in public buildings, set to begin in 2025. Various technological and research methodologies have been explored to provide solutions to these key issues.

In South Korea, public building green remodeling is being pursued through two distinct approaches: the "Support Program" and the "Mandatory Program." The Support Program will gradually scale down, while the Mandatory Program will gradually expand, as part of the strategy to achieve the 2030 NDC and 2050 carbon neutrality goals. To facilitate this, a dataset for public buildings (totalling 417,066 buildings) has been established, and a roadmap for the mandatory implementation

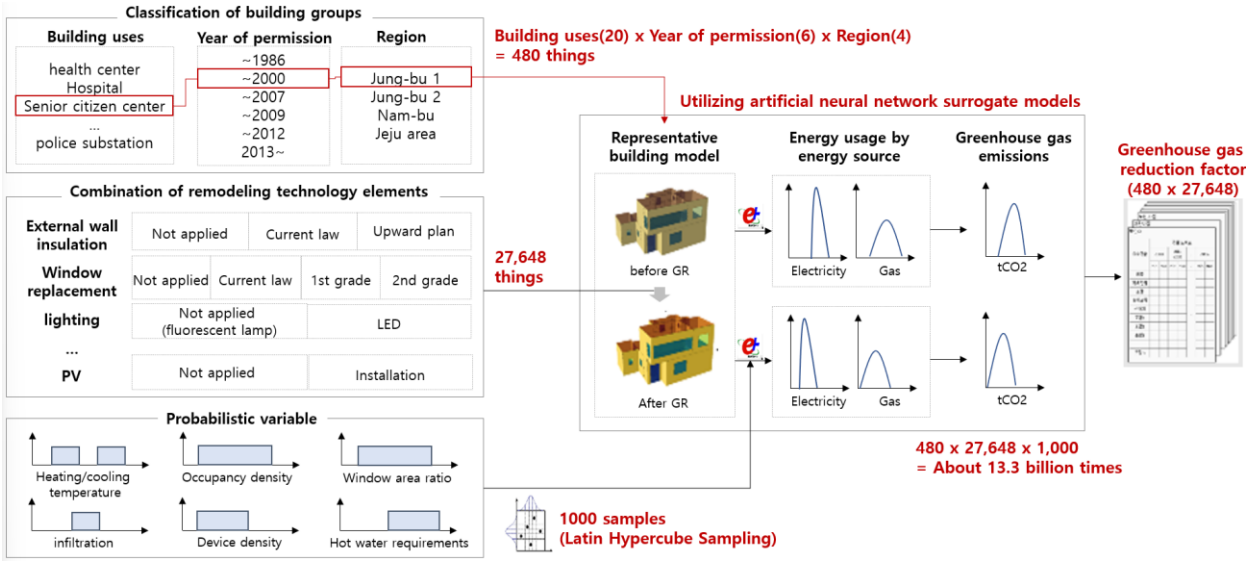

Figure 6. Overall process of deriving greenhouse gas emission reduction factors through green-remodeling
(Dong-A Univ., Seoul National Univ., 2024, Development of a prototype energy and greenhouse gas simulator for existing buildings, Progress report presentation material)

of green remodeling has been outlined, spanning through to 2050. Additionally, two evaluation methodologies, Asset Rating (AR) and Operational Rating (OR), have been proposed for green remodeling, and a greenhouse gas emission reduction coefficient through green remodeling is currently being developed. The results presented in this paper from the policy, technical, and research perspectives are expected to serve as valuable tools for future government policies and regulations and contribute to achieving national greenhouse gas reduction targets.

ACKNOWLEDGEMENTS

This research was funded by the South Korean government's “Green Remodeling Program for Public Buildings”.

REFERENCES

Dong-A Univ. and Seoul National Univ., 2024, Development of a prototype energy and greenhouse gas simulator for existing buildings, Progress report presentation material.

EPA, 2021, ENERGY STAR buildings and plants: Program overview, Environmental Protection Agency.

EPA, 2023, Portfolio Manager Technical Reference: Source Energy, Environmental Protection Agency.

Jin-Ha Yoon, et al., 2017, Classification of Energy Consumption Patterns in University Buildings Using Change Point Model and Analysis According to Energy Impact Factors, Journal of the Architectural Institute of Korea Structure & Construction Vol.33, No.11.

Lee, Seung-Ju·Jo, et al., 2024, Issue and Recommendation for Quasi Steady-State Building Energy Analysis : Focusing on a Domestic Building Energy Efficiency Rating Program(ECO2), Journal of the Architectural Institute of Korea, Vol.40, No.1, pp.169-176.

Oh Se-min, 2024, Strategies for the Implementation of Mandatory Green Remodeling of Public Buildings, 2024 Green Building Conference.

UK, 2016, The Energy Performance of Buildings (England and Wales) Regulations (S.I. 2016/284).

UK, 2015, Improving the energy efficiency of our buildings: a guide to display energy certificates and advisory reports for public buildings, Department for Communities and Local Government.

Yeonsook Heo, et al., 2012, Gaussian process modeling for measurement and verification of building energy savings, Energy and buildings, Vol.53, pp.7-18.

2030 NDC(Nationally Determined Contribution), Presidential Commission on Carbon Neutrality and Green Growth.

3rd Master Plans for Green Buildings (2024), Ministry of Land, Infrastructure and Transport.

6th International Conference on Building Energy and Environment
Eindhoven University of Technology, The Netherlands
6 - 10 July 2025

Analysis of weather normalization in building energy consumption using Two One-Sided Test (TOST)

Hye-Gi Kim[1], Young-Seo Yoo[2], Han-Gyeong Chu[3], Deuk-Woo Kim[4*]

[1]*Korea Institute of Civil Engineering and Building Technology, Goyang-si, South Korea, kimhyegi@kict.re.kr*
[2]*Seoul National University, Seoul, South Korea, youngseo.yoo@snu.ac.kr*
[3]*Korea Institute of Civil Engineering and Building Technology, Goyang-si, South Korea, hankyon0122@kict.re.kr*
[4]*Korea Institute of Civil Engineering and Building Technology, Goyang-si, South Korea, deukwookim@kict.re.kr (*corresponding author)*

SUMMARY
This study introduces an application of Two One-Sided Test (TOST) to validate weather normalization in building energy consumption analysis. Unlike traditional hypothesis testing which focuses on detecting differences, TOST directly tests for practical equivalence by defining acceptable bounds of similarity. Heating energy use intensity (EUI) data from 30,894 buildings was analyzed across three years (2018-2020), with weather normalization applied to adjust for climate variations. Buildings were stratified by regions and building types, and both paired TOST and Wilcoxon Signed-Rank based TOST were employed depending on data normality to verify the statistical equivalence of normalized energy consumption between years within each stratum. The effectiveness of this approach was validated using multi-year energy consumption data, with 2018 as the baseline year, offering a rigorous framework for building energy analysis while considering building characteristics and regional factors.

Keywords: equivalence testing, weather normalization, building energy consumption, Two One-Sided Test (TOST)

1. INTRODUCTION

The importance of weather normalization in analyzing building energy consumption has been widely recognized (Hong et al., 2016). Numerous studies have implemented weather normalization techniques to account for the significant impact of weather variations on heating and cooling energy use (Yu et al., 2011). This normalization process is crucial for accurately assessing energy performance improvements over time, independent of climatic fluctuations.

While the application of weather normalization is prevalent, the methods used to validate its effectiveness have been limited in their approach. The majority of existing studies rely on quantitative analyses such as variance reduction, t-tests, or ANOVA to demonstrate the absence of significant differences post-normalization. These methods typically focus on proving that weather-normalized data sets do not differ significantly.

However, these conventional statistical approaches may not be sufficient to fully validate the effectiveness of weather normalization. The absence of a significant difference does not necessarily equate to equivalence, which is the true goal of weather normalization. This study proposes a novel approach to address this gap in the current methodology.

In this study, the Two One-Sided Test (TOST) procedure is applied to validate weather

normalization. Unlike traditional difference-based tests, TOST is specifically designed to establish statistical equivalence (Schuirmann, 1987; Rogers et al., 1993; Wellek, 2010). This method allows for a more rigorous and appropriate validation of weather normalization by demonstrating that normalized data sets are equivalent within a predefined range of practical insignificance.

In this research, a multi-year energy consumption dataset from 30,894 buildings is analyzed. Weather normalization is performed using 2018 as the baseline year. The effectiveness of this normalization is then validated using TOST, providing a statistical confirmation of equivalence that has not been achieved in previous studies.

This novel application of TOST in weather normalization validation addresses a critical gap in current research methodologies. The findings underscore the importance of appropriate statistical techniques in energy analysis and pave the way for more accurate and reliable long-term evaluations of building energy efficiency.

2. THEORETICAL BACKGROUND OF EQUIVALENCE TESTING

The limitations of traditional hypothesis testing methods in demonstrating equivalence have been well documented in statistical literature. In conventional t-tests, the null hypothesis of no difference (H_0: $\mu_1 - \mu_2 = 0$) is tested against an alternative hypothesis of difference existence (H_1: $\mu_1 - \mu_2 \neq 0$). However, a failure to reject this null hypothesis cannot be interpreted as proof of equivalence; rather, it merely indicates insufficient evidence for difference detection. This limitation is particularly pronounced in weather normalization validation, where equivalence demonstration between normalized energy consumption values across years is sought. The Two One-Sided Test (TOST) methodology has been developed to address this statistical constraint through a reversed hypothesis structure. In TOST, the null hypothesis is formulated to assume differences beyond specified bounds (H_0: $|\mu_1 - \mu_2| \geq \theta$), while equivalence within these bounds is directly tested through the alternative hypothesis (H_1: $-\theta < \mu_1 - \mu_2 < \theta$), where θ represents the predetermined equivalence bound. Through this reformulation, a more rigorous statistical framework is established, wherein practical equivalence in building energy consumption can be demonstrated with statistical validity.

3. METHODS

3.1 Development of weather normalization coefficient

Weather normalization coefficients were developed to standardize building energy consumption across different climate conditions. The degree-days method was employed using hourly outdoor temperature data. Heating degree days (HDD) were calculated using a base temperature of 18°C, which represents the outdoor temperature threshold below which heating is typically required. The calculation was performed according to Eq. (1), as formulated by ASHRAE (2013):

$$\mathrm{HDD} = \sum_{d=1}^{365}\left[\frac{\sum_{i=1}^{24}\left(T_{base}-T_{o_i}\right)^{+}}{24}\right] \quad (1)$$

Where T_{base} is the balance point temperature (18 ℃), and T_{o_i} is the hourly outside air temperature (℃). Seoul was designated as the standard region for normalization based on its central geographical location and representative climate conditions for the country. The weather normalization coefficient (location) for each region was determined as the ratio of local HDD to

the standard region's HDD, as shown in Eq. (2):

$$C_{location\#} = \frac{HDD_{location\#}}{HDD_{standard}} \quad (2)$$

The normalized energy use intensity ($EUI_{normalized}$) was then calculated by applying this coefficient to the original EUI value, as shown in Eq. (3):

$$EUI_{normalized} = \text{EUI} \times \frac{1}{C_{location}} \quad (3)$$

The normalization coefficient functions as a scaling factor that adjusts the energy consumption values to account for regional climate differences. Regions with higher HDD values (colder climates) will have normalization coefficients greater than 1, resulting in lower normalized EUI values. Conversely, regions with lower HDD values (warmer climates) will have coefficients less than 1, resulting in higher normalized EUI values. This approach effectively standardizes energy consumption as if all buildings were operating under the climate conditions of the reference region (Seoul), enabling more accurate comparisons across different geographic locations.

3.2 Data collection and processing

Data for this study was obtained from the National Integrated Building Energy Database (NBED) (Ji et al., 2017; Cho and Le, 2017; Ji et al., 2020), focusing on public buildings to address privacy concerns. The initial dataset contained 136,254 public buildings across South Korea. A systematic data cleaning process was implemented to ensure data quality and reliability. Buildings with invalid identification codes, missing electricity meters, and incomplete floor area information were excluded in the primary validation phase. Technical validation was performed to eliminate cases with anomalous meter usage periods and insufficient energy usage pattern correlations (R^2). Buildings exhibiting heating energy consumption below 0.1 kWh/m² or lacking weather normalization coefficients were removed from the dataset. Outliers were identified and excluded using the interquartile range (IQR) method with a threshold of three times the IQR, following established statistical practices (Tukey, 1977; Hoaglin et al., 1986). To ensure statistical significance, only buildings with floor areas between 100m² and 30,000m² were included, and a minimum sample size of 10 buildings per building type and region was established. Through this comprehensive filtering process, the final dataset was reduced to 30,894 buildings. The weather normalization coefficients were then applied to standardize the energy consumption data across different climate conditions, with Seoul serving as the reference region.

3.3 Equivalence Testing

The equivalence testing process was conducted through a two-phase approach based on data normality. Since the analysis involved repeated measurements of the same buildings across different years, paired testing methods were employed. The Shapiro-Wilk test was performed on the year-to-year differences in energy consumption, with paired TOST applied for normal distributions ($p > 0.05$) and Wilcoxon Signed-Rank based TOST for non-normal distributions. The Shapiro-Wilk test was selected due to its superior power for detecting departures from normality compared to alternative tests such as Kolmogorov-Smirnov, particularly for the sample sizes encountered in this study (Razali and Wah, 2011; Ghasemi and Zahediasl, 2012). For non-normal distributions, the Wilcoxon Signed-Rank test was chosen as it makes no assumptions about the

underlying distribution and is robust against outliers (Kitchen, 2009; Derrick & White, 2017). This non-parametric approach is particularly suitable for building energy data, which often exhibits skewed distributions (Kim et al., 2020).

The equivalence bounds framework was initially designed to vary with the coefficient of variation (CV), with proposed thresholds of ±3% for stable energy consumption patterns (CV < 30%), ±5% for moderate variability (30% ≤ CV < 50%), and ±10% for high variability (CV ≥ 50%). This adaptive approach accounts for the inherent variability differences across building types, providing more appropriate equivalence criteria for each category.

Pairwise comparisons were conducted between years (2018-2019, 2019-2020, and 2018-2020). For normal distributions, the test evaluated mean differences between paired observations, while median differences were used for non-normal distributions. The maximum p-value among these comparisons was adopted for conservative interpretation, with statistical equivalence concluded at $\alpha = 0.05$.

4. RESULTS AND DISCUSSION

From the total dataset of 30,894 buildings analyzed in this study, the equivalence testing plots shown in Figure 1 represent a sample case of Class 1 neighborhood living facilities in Seoul (N=891). This sample was selected as a representative case to demonstrate the detailed results of the equivalence testing methodology. The analysis reveals significant improvements in energy use consistency after weather normalization.

Before normalization (Group 0), the median difference was 5.919, showing considerable deviation from zero. However, after weather normalization (Group 1), the median difference substantially decreased to 0.88, demonstrating a clear convergence toward zero. This convergence indicates that the weather normalization effectively reduced the variations in energy use intensity.
Moreover, the equivalence test results show that while the 90% confidence interval before normalization fell outside the equivalence bounds, it satisfied the equivalence criteria after normalization, falling within the bounds of -6.47 to 6.47. This improvement in the equivalence test results provides statistical evidence that weather normalization successfully enhanced the consistency and comparability of energy use intensities across different time periods.

The advantages of TOST over traditional hypothesis testing are clearly demonstrated in Figure 1. The plot shows both 95% confidence intervals (CI) for traditional hypothesis testing(t-test) and 90% CI for TOST, along with the predefined equivalence bounds. Although traditional hypothesis testing can show that two groups are not significantly different when the 95% CI includes zero, this does not necessarily mean the groups are equivalent. In contrast, TOST provides direct evidence of equivalence by showing that the 90% CI falls completely within the equivalence bounds after normalization. This illustrates how TOST not only detects the absence of significant differences but positively confirms practical equivalence within specified bounds, providing a more rigorous validation of weather normalization effectiveness.

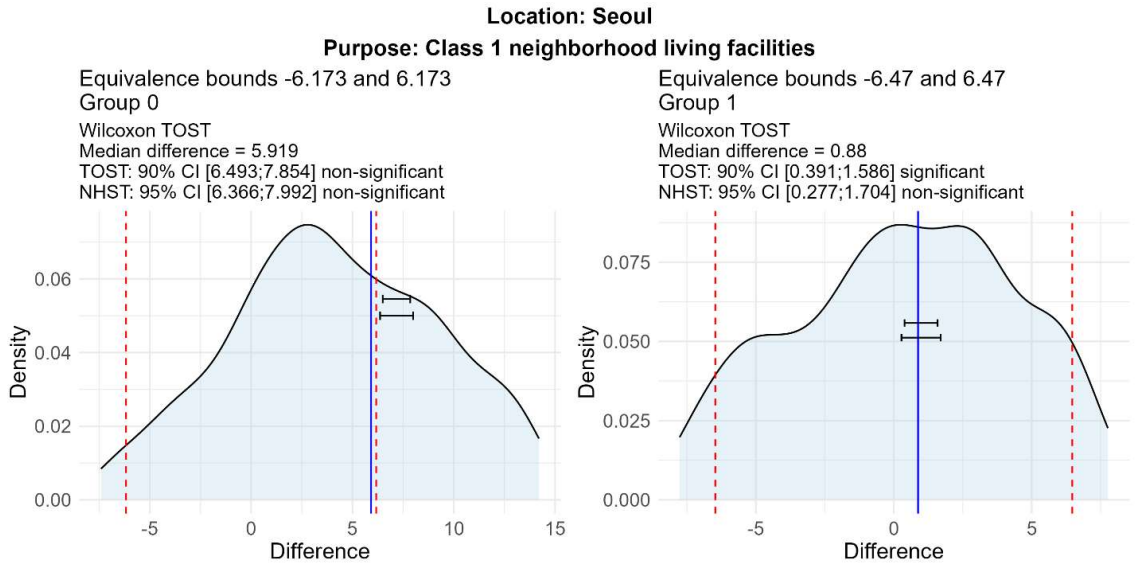

Figure 1. Equivalence test results for a sample case of Class 1 neighborhood living facilities in Seoul

This study primarily focused on public buildings that serve various community functions. The buildings in the dataset are predominantly operated for public service purposes, ranging from educational facilities to administrative buildings and community centers.

The effectiveness of weather normalization varied significantly across building types, which can be attributed to the diversity of specific uses within each building category.

Despite this inherent complexity in building operations and uses, the success rates of weather normalization showed an overall increasing trend across most building types as shown in Figure 2, although religious facilities exhibited lower improvement in normalized results. This suggests that weather normalization can be effective in standardizing energy consumption patterns across different time periods, while acknowledging that the effectiveness may vary depending on specific building characteristics and operational patterns.

The analysis revealed that some building types, particularly educational facilities and business facilities, exhibited substantial improvement after weather normalization. This can be attributed to their relatively consistent operational schedules and standardized usage patterns. Educational facilities typically operate on fixed academic calendars with predictable occupancy patterns, while business facilities generally maintain regular working hours and stable internal loads.
In contrast, religious facilities showed decreased success rates after normalization, likely due to several factors: inconsistent usage patterns (varying attendance at services), diverse architectural characteristics (often including large, high-ceiling spaces that are challenging to heat uniformly), and variable operational schedules (intermittent usage with periods of full occupancy followed by minimal activity).

Cultural and assembly facilities demonstrated slightly improvement. Their energy consumption patterns are influenced by operation-based usage, which introduces variability that weather normalization alone cannot fully address.

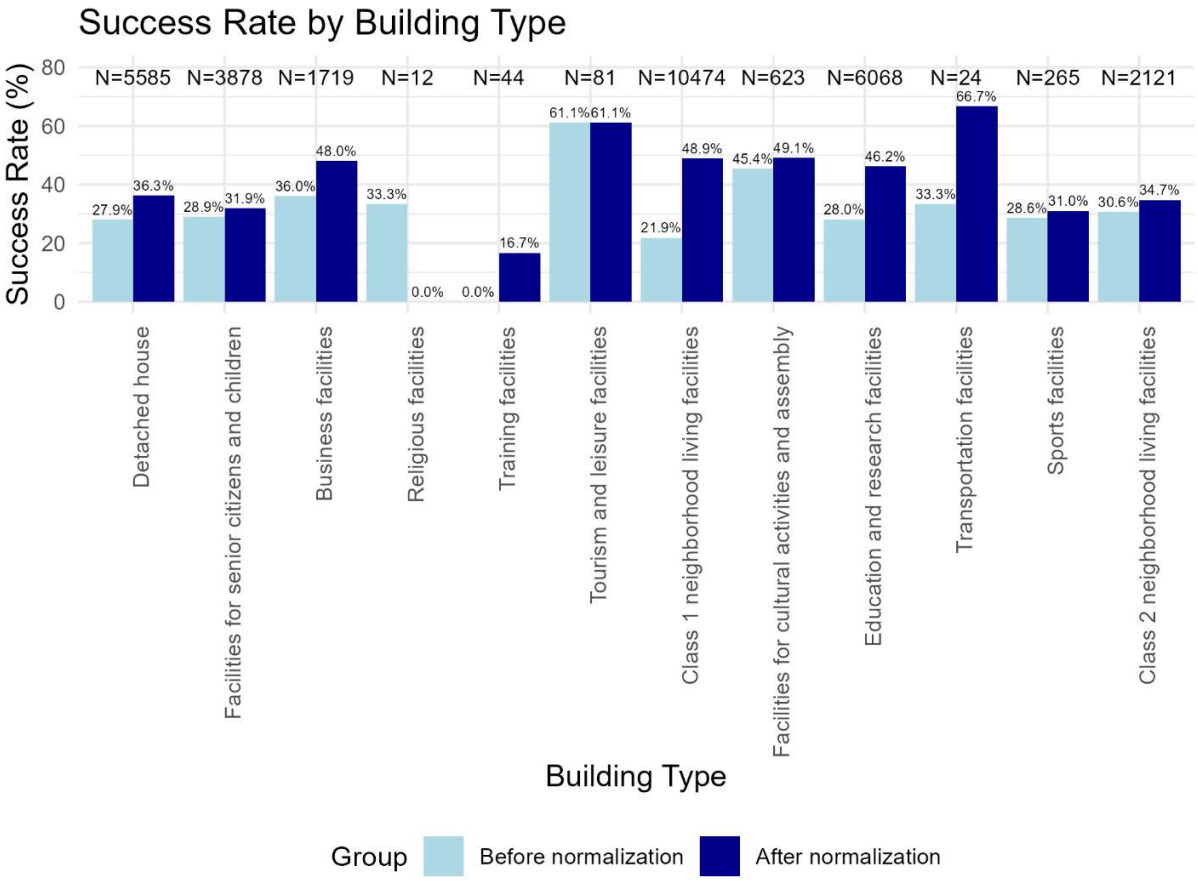

Figure 2. Success rate by building type (p-value < 0.05)

5. CONCLUSION

This study introduces a novel application of Two One-Sided Test (TOST) for validating weather normalization in building energy consumption analysis, addressing a significant methodological gap in the field. Through the analysis of 30,894 public buildings across South Korea over a three-year period (2018-2020), several key findings emerge:

First, the study demonstrates that TOST provides a more rigorous and appropriate framework for validating weather normalization compared to traditional hypothesis testing methods. By directly testing for practical equivalence rather than merely the absence of significant differences, TOST offers a more reliable approach to confirming the effectiveness of weather normalization procedures.

Second, the implementation of adaptive equivalence bounds based on coefficient of variation (CV) proves effective in accounting for different building types' inherent variability in energy consumption patterns. This flexible approach allows for more meaningful comparisons across diverse building categories while maintaining statistical rigor. However, the selection of appropriate equivalence bounds remains challenging and context-dependent, representing a limitation of the TOST approach that requires careful consideration in future applications. The

choice of equivalence bounds significantly affects the success rate of equivalence testing. The adaptive bounds approach used in this study accounts for the inherent variability of different building types, but it has limitations. Too narrow bounds might reject practical equivalence when it exists, while too wide bounds might accept equivalence when meaningful differences persist.

Third, the results show improvements in energy use consistency after weather normalization, as evidenced by the convergence of normalized data within established equivalence bounds. This improvement was particularly notable in certain building types, suggesting that the effectiveness of weather normalization varies with building characteristics and operational patterns.
Educational and business facilities showed the most significant improvements, while religious facilities demonstrated limited benefit from weather normalization alone. These findings highlight the importance of considering building-specific characteristics when applying weather normalization techniques. While weather normalization successfully improves energy consumption comparability across years for most building types, its effectiveness is moderated by factors such as operational schedules, occupancy patterns, and architectural features.
The varying effectiveness of normalization across building types suggests that complementary approaches may be necessary for buildings with highly variable usage patterns. For instance, religious facilities might benefit from additional normalization factors that account for occupancy patterns and usage intensity, beyond simple weather adjustments. This indicates that a one-size-fits-all approach to weather normalization may not be appropriate for all building categories.

These findings have important implications for building energy analysis and policy development. The methodological framework presented here provides a more robust foundation for comparing building energy performance across different climate conditions and time periods. This enhanced analytical approach can support more accurate energy efficiency assessments and better-informed decision-making in building energy management. Future research directions include exploring complementary normalization approaches for buildings with high variability, investigating the optimal selection of equivalence bounds for different building categories, and extending the TOST methodology to other aspects of building performance assessment.

ACKNOWLEDGEMENTS
This work is supported by the Korea Agency for Infrastructure Technology Advancement (KAIA) grant funded by the Ministry of Land, Infrastructure and Transport (Grant RS-2023-00244769, Development of a data framework for integrating building energy datasets and applications to accelerate carbon neutrality in the building sector).

REFERENCES

American Society of Heating, Refrigerating and Air-Conditioning Engineers (ASHRE). (2013). 2013 ASHRAE Handbook: Fundamentals. ASHRAE.

Cho, M. S., Le, D. Y. (2017). An analysis of residential building energy consumption using building energy integrated database-focused on building uses, regions, scale and the year of construction completion. Journal of Real Estate Analysis, 3(1), 101-118.

Derrick, B., & White, P. (2017). Comparing two samples from an individual Likert question. International Journal of Mathematics and Statistics, 18(3), 1-13.

Hoaglin, D. C., Iglewicz, B., & Tukey, J. W. (1986). Performance of some resistant rules for outlier labeling. Journal of the American Statistical Association, 81(396), 991-999.

Hong, T., Chen, Y., Lee, S.H., Piette, M.A., 2016. CityBES: A web-based platform to support city-scale building energy efficiency. Urban Computing 2016, 1-19.

Ji, C. Y., Choi, M. S., Shin, S. E., Oh, S. Y. (2017). The Development and Application of Method for Validating the Data Reliability of National Building Energy Integrated Database. Journal of Real Estate Analysis, 3(2), 57-76.

Ji, C. Y., Choi, M. S., Gwon, O. I., Jung, H. R., Shin, S. E. (2020). Greenhouse gas emissions from building sector based on national building energy database. Journal of the Architectural Institute of Korea Structure & Construction, 36(4), 143-152.

Kim, D., Cox, S., Cho, H., & Im, P. (2020). Evaluation of energy savings potential of variable refrigerant flow systems in hot and humid climates using occupancy-based predictive controls. Energy and Buildings, 214, 109834.

Kitchen, C. M. (2009). Nonparametric versus parametric tests of location in biomedical research. American Journal of Ophthalmology, 147(4), 571-572.

Razali, N. M., & Wah, Y. B. (2011). Power comparisons of Shapiro-Wilk, Kolmogorov-Smirnov, Lilliefors and Anderson-Darling tests. Journal of Statistical Modeling and Analytics, 2(1), 21-33.

Rogers, J. L., Howard, K. I., & Vessey, J. T. (1993). Using significance tests to evaluate equivalence between two experimental groups. Psychological Bulletin, 113, 553-562.

Tukey, J. W. (1977). Exploratory Data Analysis. Addison-Wesley.

Schuirmann, D. J. (1987). A comparison of the two one-sided tests procedure and the power approach for assessing the equivalence of average bioavailability. Journal of Pharmacokinetics and Biopharmaceutics, 15, 657-680.

Wellek, S. (2010). Testing statistical hypotheses of equivalence and noninferiority (2nd ed.). Boca Raton, FL: CRC Press.

Yu, Z., Haghighat, F., Fung, B.C., Yoshino, H., 2011. A systematic procedure to study the influence of occupant behavior on building energy consumption. Energy and Buildings 43(6), 1409-1417.

6th International Conference on Building Energy and Environment

Eindhoven University of Technology, The Netherlands

6 - 10 July 2025

Cluster Analysis of Hospital Building Stock Energy Consumption Using Public Data

Jihyun Oh[1], Yeonjin Kim[1], Seongyun Kang[1], Hye-Jin Kim[2], In-Ho Yang[2], Sunsook Kim[3]

[1] *Department of Smart Convergence Architecture, Ajou University, Suwon, South Korea*
[2] *Division of Architectural Engineering, Dongguk University, Seoul, South Korea*
[3] *Department of Architecture, Ajou University, Suwon, South Korea, kss@ajou.ac.kr*

SUMMARY
This study proposed a cluster analysis-based benchmarking approach using public data to address data acquisition limitations and better reflect energy consumption characteristics. The approach was applied to hospital building stock in South Korea, employing k-means clustering to classify peer groups and develop benchmarks. Two energy consumption indicators and four feature combinations were tested, with clustering results validated using the elbow method, silhouette index, Davies-Bouldin index, and ANOVA. As a result, five clusters were identified, and thirteen features were selected, including total floor area, annual energy consumption, cooling/heating/mid-season energy ratios, number of elevators, doctors, and beds, along with five dummy variables representing hospital types. The clustering results were analyzed based on the two energy consumption indicators. This approach demonstrated a practical method for analyzing building stock without additional data collection. It provides a valuable tool for researchers and policymakers to understand and manage energy consumption using public data.

Keywords: Building energy benchmark, Clustering analysis, Hospital

1. INTRODUCTION

Defining appropriate peer groups and benchmarks is essential for fair and effective energy benchmarking. The most common approach normalizes values within peer groups classified by building use, floor area, and region (Oh et al., 2023). While widely used, this method overlooks variations in energy consumption. Alternative approaches, such as regression models and machine learning techniques have been introduced to improve benchmarking accuracy (Capozzoli et al., 2016; Kim et al., 2023; Oh et al., 2023; Wu et al., 2023). However, these require extensive data collection such as national-level surveys or detailed building audits, often limiting analysis to subsets of buildings. Furthermore, benchmarking results may vary depending on the selected indicators, necessitating a comprehensive review of multiple indicators (Capozzoli et al., 2016). This study addresses these challenges by introducing a clustering-based approach using public data, focusing on hospital buildings, which account for significant energy consumption in the building sector. In South Korea, hospitals rank third in energy use per building, following retail and office building (KOSIS, 2024).

2. METHODS

This study utilizes two major databases: the National Building Energy Integrated Database (NBEID) and the Health Insurance Review and Assessment Service Database (HIRAD). NBEID contains building registration and monthly utility billing data (Kim et al., 2024), while HIRAD provides information on status of hospitals and pharmacies facility nationwide (HIRA, 2024). In this study, the building and monthly energy data from January to December 2022 were analyzed. To ensure that building characteristics were not diluted by mixed-use facilities, the analysis was restricted to buildings that contained only a single building and hospital on a given lot (Kim et al., 2024) Among various types of medical facilities, this study focuses on hospital-level buildings that provide inpatient care and have designated bed capacities. Facilities without inpatient services and tertiary hospitals were excluded. After the data cleansing procedure, a total of 933 buildings were included in the analysis, comprising 426 convalescent hospitals, 309 hospitals, 72 general hospitals, 62 oriental medicine hospitals, 47 psychiatric hospitals, and 17 dental hospitals.

Table 1. Feature combinations for clustering analysis.

id	Features	Source	Type	Set1	Set2	Set3	Set4
X1	TFA	NBEID	Float	●	●	●	●
X2-13	12-month energy consumption	NBEID	Float	●	●	●	
X14	Annual energy consumption	NBEID	Float				●
X15-X17	Heating, cooling, and mid-season energy consumption ratio	Calculated from X2-13	Float	●	●	●	●
X18	Number of elevators	NBEID	Int		●	●	●
X19	Number of doctors	HIRAD	Int		●	●	●
X20	Number of beds	HIRAD	Int		●	●	●
X21-X25	Dummy variables for six hospital types	HIRAD	Binary			●	●

Despite being categorized under the same medical facility type, variations exist in building use, scale, region, and operations. To account for this, k-means clustering was used, with all features normalized using a min-max scaler. Clustering results were validated using the elbow method and cluster Validity Indices (VIs), including the Silhouette Index ($Si_{Avg.}$) and Davies-Bouldin Index (DBI) (Bourdeau et al., 2021). ANalysis Of VAriance (ANOVA) tested statistical significance of clustering results. This study considered two key energy consumption indicators. Total Energy Consumption (TEC) represents absolute energy use, while Energy Use Intensity (EUI) normalizes consumption by Total Floor Area (TFA) for comparative analysis. Four feature sets were tested, summarized in Table 1, selected based on prior research (Oh et al., 2023) and correlation analysis of available data from NBEID and HIRAD.

3. RESULTS AND DISCUSSION

The elbow method showed a sharp decline in error when the number of cluster (k) ranged from 2 to 6. Clustering was conducted for these values, and results were evaluated using $Si_{Avg.}$ and DBI, as summarized in Fig. 1. For k = 2, feature sets 1 and 2 performed best ($Si_{Avg.} \approx 0.8$, DBI ≈ 0.5), but the mid-season energy ratio (X17) was found to be statistically insignificant based on the one-way ANOVA test. Excluding these cases, feature set 4 achieved the best performance across all evaluations. Specifically, for k = 5 and k = 6, feature set 4 yielded the highest $Si_{Avg.}$ and the lowest

DBI for both energy consumption indicators. As indicated in Fig. 1, TEC-based clustering achieved 5% higher $Si_{Avg.}$ and 11% lower DBI than EUI-based clustering. While clustering with k = 6 successfully distinguished six hospital types, the small sample size of dental hospitals (n = 17) led to the final selection of k = 5. With k = 5, clusters remained classified by hospital types, grouping dental hospitals with hospitals.

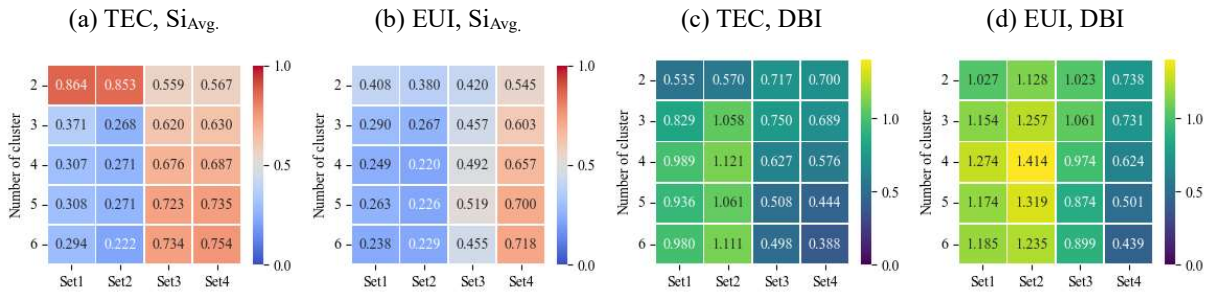

Figure 1. $Si_{Avg.}$ and DBI results by indicators, feature sets, and the number of k.

The clustering results showed that feature set 4 with k = 5 achieved the best VIs for both TEC and EUI. Based on these findings, the results of these two indicators were compared and discussed. To establish meaningful benchmarks, it is essential to verify whether energy consumption differences among clusters are statistically significant. The normality of energy consumption distributions was tested using the Kolmogorov-Smirnov test, where the null hypothesis ($\boldsymbol{H_0}$) states that the data follows a normal distribution. The results indicated that some clusters did not follow a normal distribution ($p<0.05$, $\boldsymbol{H_0}$ rejected). Consequently, both one-way ANOVA and the Kruskal-Wallis test were conducted, with the latter supplementing ANOVA due to its sensitivity to non-normality. As a result, the statistical tests confirmed significant differences in energy consumption values among indicators and clusters.

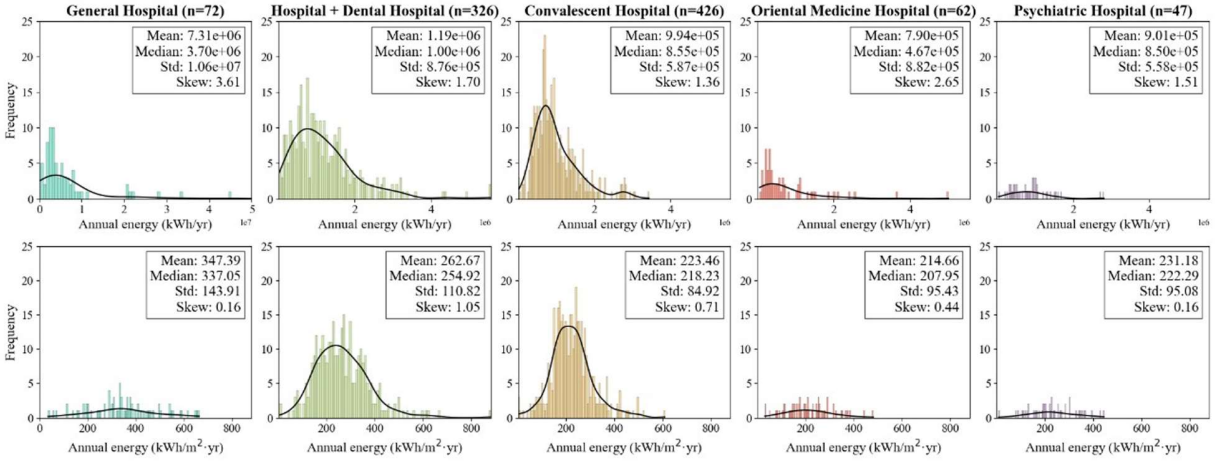

Figure 2. Distribution of annual energy consumption by indicators and clusters with feature set4 and k=5.

Fig. 2 illustrates annual energy consumption distributions for TEC and EUI with feature set 4 and k = 5. All clusters exhibited positive skewness, but EUI clusters normalized by TFA had skewness values below 1.0, making EUI a more balanced benchmarking metric. The largest skewness

difference (3.45) was found in general hospitals, followed by oriental medicine hospitals (2.21) and psychiatric hospitals (1.35). These findings suggest that TEC-based clustering should incorporate additional segmentation based on TFA to improve balance. This is particularly relevant for general hospitals, where large facilities introduce variability in energy consumption. Further preprocessing, such as refining cluster segmentation, is recommended. The results of the statistical tests support prioritizing median values over mean values to ensure more robust benchmarks.

4. CONCLUSION

This study proposed a cluster analysis-based benchmarking approach using public data to address data acquisition limitations while incorporating energy consumption characteristics. The results demonstrated that this approach effectively classifies peer groups and develops benchmarks without requiring additional data collection. Although applied to hospital building stock in South Korea, this approach can be extended to other countries or building types if relevant data is available. The findings highlight that TEC-based clustering and EUI-based clustering yield different peer groups, emphasizing the importance of selecting appropriate indicators for benchmarking. This approach provides a robust framework for researchers and policymakers, enabling data-driven energy benchmarking and more effective building energy management using publicly available data. Hospital administrators and policymakers can use the resulting peer group benchmarks to identify inefficiencies and set realistic energy conservation targets based on comparable facilities.

ACKNOWLEDGEMENTS

This work was supported by the Korea Agency for Infrastructure Technology Advancement (KAIA) grant funded by the Ministry of Land, Infrastructure and Transport (Grant RS-2023-00244769) and by the Basic Science Research Program through the National Research Foundation of Korea (NRF) grant funded by the Ministry of Science, ICT (Grant RS-2025-00556638).

REFERENCES

Bourdeau, M., Basset, P., Beauchêne, S., Da Silva, D., Guiot, T., Werner, D., Nefzaoui, E., 2021. Classification of daily electric load profiles of non-residential buildings. Energy and Buildings 233, 110670.

KOSIS, 2024. Building energy consumption by uses. Available from https://kosis.kr/statHtml/statHtml.do?sso=ok&returnurl=https%3A%2F%2Fkosis.kr%3A443%2FstatHtml%2FstatHtml.do%3Fconn_path%3DI3%26tblId%3DDT_408003_A000_0%26orgId%3D408%26.

Capozzoli, A., Piscitelli, M. S., Neri, F., Grassi, D., Serale, G., 2016. A novel methodology for energy performance benchmarking of buildings by means of Linear Mixed Effect Model: The case of space and DHW heating of out-patient Healthcare Centres. Applied Energy 171, 592–607.

Kim, H. G., Jeong, D. W., Kwon, S. J., Kim, S. S., 2023. Development of building energy performance benchmark for hospitals. Buildings 13(1).

Kim, H. G., Kim, S. S., & Ahn, H., 2024. Data-driven analysis of heating and cooling base temperatures for buildings: Case studies in South Korea. Energy and Buildings 322, 114709.

Oh, J. H., Kim, H. G., & Kim, S. S., 2023. Cluster analysis-based energy performance assessment for office building stock. Journal of Physics: Conference Series 2600(8), 082025.

HIRA, 2024. The status of hospitals and pharmacies nationwide. Available from https://opendata.hira.or.kr/op/opc/selectOpenData.do?sno=11925.

Wu, T., Wang, B., Zhang, D., Zhao, Z., & Zhu, H., 2023. Benchmarking evaluation of building energy consumption based on data mining. Sustainability 15(6), Article 6.

Thermal Comfort (13:30-15:00 h)

6th International Conference on Building Energy and Environment
Eindhoven University of Technology, The Netherlands
6 - 10 July 2025

Harnessing infrared thermography and motion cameras to explore outdoor thermal adaptive behaviors - insights from an urban park investigation

Xiling Lu, Jiading Zhong, Shaowen Wang, Yang He, Jianlin Liu*

College of Environmental Science and Engineering, Donghua University, Shanghai 201620, China, jianlin.liu@dhu.edu.cn

SUMMARY
Frequent extreme high temperatures and the urban heat island effect worsen outdoor thermal environments, driving people to adopt adaptive behaviors for thermal comfort. This study in an urban park during summer monitored thermal conditions at four sites, recorded pedestrian behaviors and skin temperatures with the motion camera and infrared thermography. Results identified seven thermal adaptive behaviors, with the four most common ones (using sunshades, seeking tree shade, drinking cold water, seeking building shade) accounting for 30.4%, 25.9%, 16.5%, and 8.6% respectively. Meanwhile, quantitative analysis was performed in combining physiological equivalent temperature (PET) to examine the relationship between skin temperatures of various behaviors and outdoor thermal comfort. When PET is below 35°C, skin temperature cannot predict people's thermal comfort with thermal adaptive behaviors. This research summarizes multiple human thermal adaptive behaviors, fueling urban park design, and the exploration of the potential applications of infrared thermography technology in predicting outdoor thermal comfort.

Keywords: outdoor thermal comfort, infrared thermography, thermal adaptation, skin temperature.

1. INTRODUCTION

Global warming is giving rise to extreme climate events. The continuously increasing extreme high - temperature weather leads to frequent and severe heat stress Ebi et al. (2021); (Jay et al. 2021), which in turn affects the thermal comfort of outdoor residents in cities. Outdoor environments are more diverse than indoors, with pedestrians being directly exposed to an unsteady environment with dynamic wind speeds and solar radiation (Gehl 2001; Niu et al. 2015). Consideration of human initiative and thermal adaptive behavior is critical to understanding the relationship between the outdoor thermal setting and thermal comfort. The types of outdoor activities and their intensities can affect the human body's heat production and dissipation capabilities, thus influencing human thermal comfort. Peng et al. (2019) investigated the thermal comfort of outdoor activities like sitting, standing, strolling, and walking in squares, and found that people prefer shaded areas, confirming the correlation between thermal comfort and behavior. People tend to maintain body temperature stability through behavioral regulation. Nakano and Tanabe (2020) discovered that in the semi-outdoor environment of Tokyo, clothing adjustment is the primary form of behavioral adaptation, and the daily average outdoor temperature is the main factor influencing clothing adjustment.

Research methods for outdoor thermal comfort mainly include horizontal investigations and longitudinal trials. Outdoor thermal comfort studies often combine subjective questionnaires with objective measurements to obtain comprehensive and accurate data, but the questionnaire survey

has issues such as subjective authenticity, subjective authenticity. The application of non-contact technology compensates for the limitations of traditional subjective questionnaires. Non-contact measurement can capture the human body's physiological responses to changes in the outdoor thermal environment, such as skin temperature. Liu et al. (2020) used local skin temperature and heat load as inputs and observed that monitoring the skin temperature of two local body parts can effectively understand the body's outdoor thermal state. Speak et al. (2021) used infrared thermography to measure the forehead temperature of subjects to evaluate outdoor thermal comfort. The results showed that tree shade can significantly reduce heat stress and improve comfort, indicating that this technology is an effective tool for assessing human thermal sensation. Non-contact technology can also identify the human behavior outdoors (Kim and Brown 2022). Nevertheless, the current non-contact technologies are relatively limited in outdoor applications and have not yet combined thermal environmental parameters, human thermophysiological and crowd behavior recognition.

This study adopts the infrared thermography and the motion camera to record people's thermal adaptive behaviors as well as their physiological parameters, and analyses outdoor thermal comfort of thermal behaviors by the physiological equivalent temperature (PET). The main objectives were to: 1) determining human skin temperature and PET values with various thermal behaviors; 2) exploring the relationship between human behavior and outdoor thermal comfort; 3) providing references for urban design to enhance outdoor comfort.

2. METHODS

2.1. Research sites

The panel experiment was conducted in an urban park of approximately 200,000 square meters at the central area of Shanghai. Considering the diversity of human behavior, we chose four high-traffic sites in the park to carry out our research: the Milan Square, the Atrium Pergola, the Leisure Plaza, the Tree-lined Runway, respectively. Fig. 1 presents their environmental characteristics. The Milan Square (MS) contained a large area for recreation, surrounded by greenery; the Atrium Pergola (AP) was a corridor-like structure that provided artificial shade; the Leisure Plaza (LP) had stone piers for resting under the trees; the Tree-lined Runway (TR) was mainly for walking and connecting the par's attractions. These measurement locations involved various usage situation and nature-artificial shade, with multiple pedestrian thermal behaviors. Incidentally, subsequent references to the above study sites are abbreviated.

Figure 1. The field measurements were taken in the city parks: (1) the Milan Square (MS), (2) the Atrium Pergola

(AP), (3) the Leisure Plaza (LP), (4) the Tree-lined Runway (TR).

2.2 . Field experiments

Outdoor pedestrians had relatively low clothing thermal insulation, and the skin surface area directly exposed to the outdoors was the largest, thus it's easily to observe and record the individuals' physiological responses. The researchers utilized a handheld infrared thermography (IRT) to obtain human thermal infrared image, which analyzed their skin temperature. To capture timely pedestrian thermal condition when they developed thermal behaviors, a portable backpack with the meteorological monitoring sensors (the backpack weather station, BWS) was wore by the investigators to record climate parameters where people stayed, containing outdoor air temperature (T_a), relative humidity (RH), wind speeds (v), and the global solar radiation (G_r). And a sports camera on the shoulder belt of the backpack to shoot and document some information of pedestrians, including personal basic information, clothing, types of activities, and thermal adaptive behaviors. The survey took place on 15 rain-free days of the period July 27 to August 25, 2023, with each measured site being visited once or twice a day for a sustained period of 30 minutes between 11:00 and 15:00. The experimental equipment used for the study are shown in Fig. 2 and listed in Table 1–2 with their detailed specifications, which were calibrated prior to the investigation and fulfilled the standard ISO (2001).

Figure 2. Experimental instruments in this survey: (a) backpack weather station (BWS), (b) infrared thermography (IRT), (c) sports camera.

Table 1. Specifications of the backpack weather station on outdoor meteorological parameters.

Parameter	Type	Measuring range	Deviation
Air temperature（T_a）	S-THB-M002	−40℃ ~ 75℃	± 0.21℃（0℃~50℃）
The relative humidity（RH）	S-THB-M002	0 ~ 100%	± 2.5%（10%~90%）
The global solar radiation（G_r）	S-LIB-M003	0 ~ 1280 W/m^2	± 10 W/m^2（±5%）
Wind speed（v）	S-WSB-M003	0 ~ 75 m/s	± 1.1 m/s（±4%）
The skin temperature（T_{sk}）	Testo 865	-20 ~ 280℃	± 2℃

Table 2. The type and general parameters of the sports camera.

Type	Angle of view	Resolution	Range of focus	Operating temperature (℃)
Osmo Action 3	155°	4096 × 3072 (60fps)	0.3 m ~ ∞	-20 ~ 45℃

2.3. Data analysis and processing

Using the Testo software IRSoft to draw measurement boxes on images to obtain people's skin temperatures of the forehead (T_{face}) and forearms (T_{arm}), with an emissivity setting of 0.98 (Clark et al. 1977) and a reflected temperature set to air temperature. After aligning the time codes of the infrared camera and the motion camera, comparing the thermal images of the same individual with corresponding video frame snapshots, recording basic information such as gender, age group, clothing, activity types, and thermal adaptive behavior. The physiological equivalent temperature (PET) was chosen to assess outdoor human thermal comfort (Höppe 1999), and its calculations were performed by RaymanPro software (Lee and Mayer 2016) with input parameters including thermal environment parameters, geographic location information, and basic information about outdoor pedestrians (gender, age, height, weight, activity level, metabolic rate, and overall clothing thermal insulation).

3. RESULUTS AND DISCUSSION

3.1. Demographic parameters

Fig. 3 shows the gender and age distribution of the research subjects. A total valid sample size of 720 are acquired, involving 56.9% of males and 43.1% of females. And four age groups are covered, with 4.3% of adolescents (< 18 years old), 36.4% of young person (18 – 39 years old), 43.8% of middle-aged person (40 – 59 years old), and 15.5% of the elderly (> 59 years old).

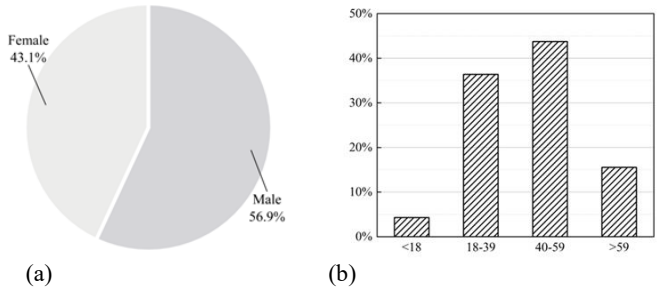

Figure 3. The distribution of subjects: (a) gender, (b) age.

Table 3. The survey participants' garment thermal insulation and metabolic rate values.

Variable	Location	Mean	Max	Min	Standard deviation
Clothing insulation, I_{cl} (clo)	MS	0.34	0.38	0.24	0.05
	AP	0.35	0.63	0.14	0.07
	LP	0.34	0.63	0.12	0.07
	TR	0.33	0.63	0.12	0.06
Metabolic rate, M (met)	MS	2.3	3.8	1.0	1.1
	AP	1.3	2.6	1.0	0.4
	LP	1.2	3.8	1.0	0.5
	TR	2.1	3.8	1.0	0.4

The clothing thermal insulation (I_{cl}) and metabolic rates (M) shown in Table 3 against the standard values in the ASHRAE (2023). The mean values of clothing insulation and metabolic rate for people at the four sites range from 0.33-0.35 clo and 1.2–2.3 met, respectively. At the MS, the

respondents have the less variation in clothing thermal resistance, a maximum o–f only 0.38 clo, while the average metabolic rate reaches 2.3 met. Compared to the other sites, site AP has the highest mean clothing thermal insulation of 0.35 clo, yet the mean metabolic rate is low at 1.3 met. The above human factors parameters of site LP are similar to the site AP. Folks at the TR walk slowly, and their metabolic rate is 2.1 met, second to the measured site MS.

3.2. Meteorological parameters of measured sites

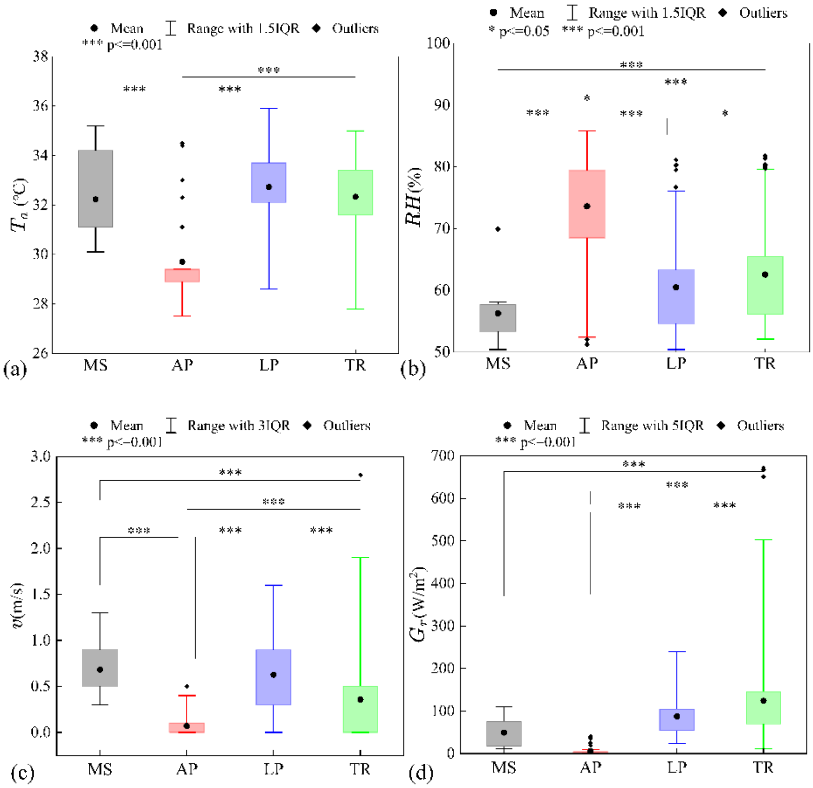

Figure 4. Distribution of different environmental parameters at four measured locations: (a) the T_a, (b) the *RH*, (c) the *v*, (d) the G_r. (* p<=0.05, *** p<=0.001)

Four scenarios' climatic conditions are shown in the Fig. 4. Site AP has the lowest average air temperature of 29.7°C, which is 2–3°C lower than the site MS (32.2°C), LP (32.8°C), and TR (32.5° C). And this urban park has an ornamental lake and high ambient humidity. The most elevated average relative humidity value of 73.6 % is found at the AP compared to the other three survey locations. The monitored place AP is primarily located in a shaded area and is closer to the lake. Significant differences ($p < 0.001$) in the T_a and *RH* values of the AP with respect to the others can be noted from Fig. 4 (a–b). The mean of *v* at the MS, AP, LP, TR are 0.7 m/s, 0.1 m/s, 0.6 m/s and 0.4 m/s, respectively. Due to the large amount of vegetation in the park, it is primarily in low winds. The *v* of the AP and TR differ prominently ($p < 0.001$) compared to the other locations. As observed for the AP (Fig. 4(c)), the wind speeds are lower with less variation, whereas the site TR experiences relatively higher wind speeds with a wider range of fluctuations. The global solar radiation values of the MS and AP areas are considerably smaller than that of the LP and TR areas, with the site AP having the lowest average G_r (5.9 W/m^2). The results on the one hand are attributed to the shading of trees and building galleries at the tested site, and on the other hand to the human

recreational time. The older people, for example, always gather in the Milan Square (MS) in the afternoon to exercise, during which time the intensity of the solar radiation is on a weakening trend. In addition, the G_r values of tested location TR are quite variable and markedly distinct from the rest of other three research places ($p<0.001$). Since the tree-lined runway (TR) is a necessary access to other parts of the park where the folks pass through at various times during the survey period, they will be exposed to broader values of solar radiation intensity here.

3.3. Thermal adaptive behavior

3.3.1. Classification of human various thermal behaviors

Thermal adaptive behaviors of pedestrians at different measured locations in the urban park were recorded by a motion camera during the field survey, and the IRT was used to capture people's thermographic images when performing these behaviors, thereby acquiring their physiological parameters in real time. Fig. 5 shows the proportion of thermal adaptive behaviors at different locations in the park. In this study, seven heat adaptive behaviors are identified, including moving to building or tree shade, using sunshade devices, drinking cold beverages, fanning, undressing, and wiping sweat. It can be found that the thermal adaptation behaviors mainly appear at TR and LP sites, which account for 48.8% and 33.1%, respectively, while MS and AP sites collectively make up 18.1% of the total. At the three locations—the MS, AP, and LP—occupants predominantly resort to the thermal adaptation strategy of relocating to areas shaded by buildings or trees. Specifically, the prevalence of such behavior is 4.4% at the MS, 8.6% at the AP, and 20.7% at the LP. Notably, a different phenomenon is observed at the TR. Here, a substantial 48.1% of the individuals choose to regulate their physiological states (the blue color block in Fig. 5) as their primary means of adapting to the thermal environment. This is because the individuals observed at location TR are mostly those making brief stops, such as commuters. And people spend extended periods at the other three locations, engaging in activities like resting or physical exercise. This significant disparity indicates that when people adopt thermal adaptation behaviors, they are influenced not only by the current thermal environment but also by the functional uses they assign to different places.

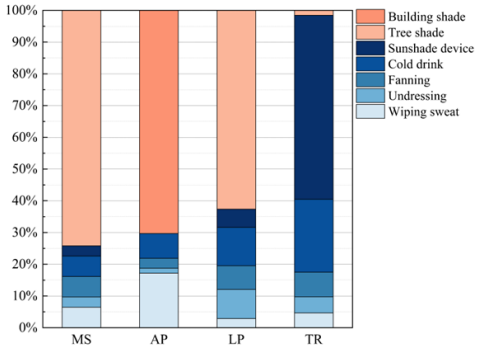

Figure 5. The percentage of human outdoor thermal adaptive behaviors during the investigation with various measured sites.

3.3.2. Evaluation of outdoor thermal comfort by PET

Fig. 6 present the relationship between skin temperature of forehead and forearm and PET for populations with different thermal adaptation behaviors, respectively. For pedestrians with thermal adaptation behaviors such as moving to building shade, tree shade, drinking cold beverages, fanning, undressing, wiping sweat, as well as those without thermal adaptation behaviors, there is

a positive linear correlation between the skin temperature and PET values. While a positive correlation exists between the skin temperature and PET for individuals engaging in other thermal adaptation behaviors as well as those without thermal behaviors. For people with using sunshade devices, the T_{sk} of they have an exponential positive correlation with PET values. Based on the magnitudes of the slopes of T_{sk} with respect to PET, we can rank the thermal sensitivities of people with different thermal adaptation behaviors as follows: undressing > wiping sweat > fanning > drinking cold drinks > moving to building shade > moving to tree shade. The group using sunshade equipment is rather special, as its thermal sensitivity weakens as PET increases. Furthermore, the order of the cooling effects of these thermal adaptation behaviors on skin temperature, from strongest to weakest, is opposite to the order of thermal sensitivity in these behaviors. Moreover, it can be observed that when PET < 35°C, as PET decreases, the skin temperatures of the surveyed individuals engage in thermal behaviors begin to gradually drop below that of those without thermal behaviors. This indicates that when PET values are less than 35°C, the T_{sk} cannot serve as a direct indicator for predicting the human thermal comfort with adopting thermal adaptative behaviors in the park. However, when PET < 33°C or PET > 39°C, the skin temperature cannot be directly used as an indicator to judge the thermal comfort of people when they adopt the thermal adaptation behavior of using sunshade devices.

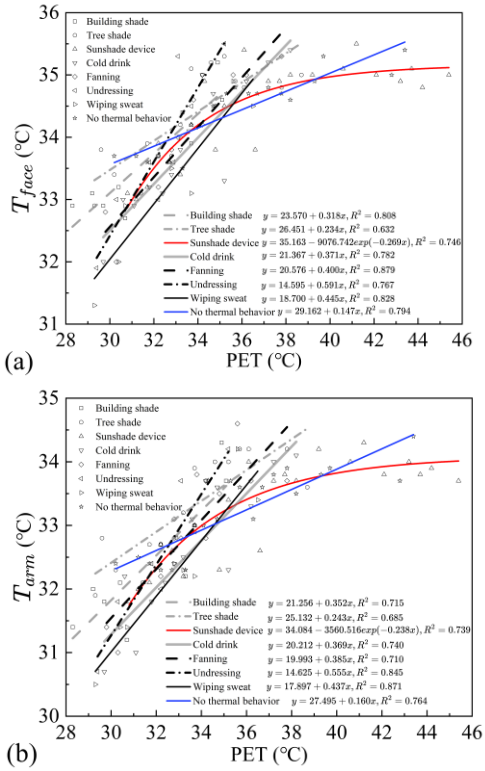

Figure 6. The relationship between human skin temperature and PET with different thermal adaptive behaviors: (a) T_{face}, (b) T_{arm}.

4. CONCLUSIONS

In this research, a motion camera was utilized to capture the human thermal adaptative behaviors in the park, while their skin temperatures were monitored in real time using an IRT. Aiming to explore the differences in outdoor thermal comfort with various thermal adaptation behaviors. The

principal findings are as follows: 1) the four common thermal adaptation behaviors in the park are using sunshade devices, seeking tree shade, drinking cold beverages, and staying in building shade, accounting for 30.4%, 25.9%, 16.5%, and 8.6% respectively; 2) people choose thermal adaptive behaviors with the following priorities in descending order: seeking tree shade, staying in building shade, drinking cold drinks, fanning, wiping sweat, and undressing, and when the PET values exceed 40°C, usage of sunshade devices become the preferred choice; 3) each type of thermal adaptation behavior has its specific critical PET value, when PET exceeds this value, the Tsk can be regarded as a direct indicator for predicting human thermal comfort with particular thermal adaptation behavior.

ACKNOWLEDGEMENT

The work described in this paper was supported by the National Natural Science Foundation of China (52278094, 52008079) and the Fundamental Research Funds for the Central Universities and Graduate Student Innovation Fund of Donghua University (CUSF-DH-D-2024028).

REFERENCES

ASHRAE, ANSI/ASHRAE 55-Thermal Environmental Conditions for Human Occupancy. Atlanta, GA, USA: American Society of Heating, Refrigerating and Air-Conditioning Engineers (ASHRAE), 2023.

Clark RP, Mullan BJ, Pugh LG, 1977. Skin temperature during running--a study using infra-red colour thermography. The Journal of physiology 267, 53-62.

Ebi KL, Capon A, Berry P, et al., 2021. Hot weather and heat extremes: health risks. The Lancet 398, 698-708.

Gehl J *Life between buildings: using public space.* Copenhagen. The Danish Architectural Press, 2001.

Höppe P, 1999. The physiological equivalent temperature -: a universal index for the biometeorological assessment of the thermal environment. International Journal of Biometeorology 43, 71-75.

ISO, ISO 7726-Ergonomics of the thermal environment-Instruments for measuring physical quantities. Geneva: International Organization for Standardization, 2001.

Jay O, Capon A, Berry P, et al., 2021. Reducing the health effects of hot weather and heat extremes: from personal cooling strategies to green cities. Lancet 398, 709-724.

Kim SW, Brown RD, 2022. Pedestrians' behavior based on outdoor thermal comfort and micro-scale thermal environments, Austin, TX. Science of The Total Environment 808, 152143.

Lee H, Mayer H, 2016. Validation of the mean radiant temperature simulated by the RayMan software in urban environments. International Journal of Biometeorology 60, 1775-1785.

Liu K, Nie T, Liu W, et al., 2020. A machine learning approach to predict outdoor thermal comfort using local skin temperatures. Sustainable Cities and Society 59, 102216.

Nakano J, Tanabe S-i, 2020. Thermal Adaptation and Comfort Zones in Urban Semi-Outdoor Environments. Frontiers in Built Environment 6,

Niu J, Liu J, Lee T-c, et al., 2015. A new method to assess spatial variations of outdoor thermal comfort: Onsite monitoring results and implications for precinct planning. Building and Environment 91, 263-270.

Peng Z, Wang Y, Li L, 2019. Correlational study on thermal comfort and outdoor activities. Journal of Physics: Conference Series 1343, 012025.

Speak A, Montagnani L, Wellstein C, et al., 2021. Forehead temperatures as an indicator of outdoor thermal comfort and the influence of tree shade. Urban Climate 39, 100965.

6th International Conference on Building Energy and Environment

Eindhoven University of Technology, The Netherlands

6 - 10 July 2025

Experimental data-informed modelling of the thermal characteristics of a point connection with and without structural thermal breaks

Hamid Narei[1], Richard Fitton[2], William Swan[3], Chris Lister[4]

[1] Energy House Laboratories, School of Science, Engineering and Environment, University of Salford, Manchester, United Kingdom, h.narei@salford.ac.uk

[2] Energy House Laboratories, School of Science, Engineering and Environment, University of Salford, Manchester, United Kingdom, r.fitton@salford.ac.uk

[3] Energy House Laboratories, School of Science, Engineering and Environment, University of Salford, Manchester, United Kingdom, w.c.swan@salford.ac.uk

[4] Farrat IsoLevel LTD, Altrincham, Manchester, United Kingdom, chris.lister@farrat.com

SUMMARY

This study aimed to develop a reliable in-situ evaluation method to capture parameters needed for thermal modelling of the point thermal transmittance and use them to calibrate the finite element thermal simulation. Farrat's structural thermal breaks were used to thermally break the heat transfer from the point thermal bridge connection created at the Energy House (EH) at the University of Salford. The numerical modelling was conducted in ABAQUS and calibrated using the experimental data. The findings revealed that using STBs reduced the χ-value of the bare wall by 6.73% and that of the externally insulated wall by 15.43%. These results highlight two key points: firstly, the significance of employing STBs to mitigate heat transfer through point TBs, achieving at least a 6.73% reduction; and secondly, the more pronounced impact of STBs in well-insulated structures. Furthermore, this research established a dependable in-situ method to gather the necessary parameters for evaluating thermal bridges.

Keywords: Thermal Bridging, Experimental measurement, Calibrated numerical modelling

1 INTRODUCTION

Point Thermal Bridges (TBs) are localised thermal anomalies that significantly impact the thermal performance of building envelopes. These TBs are characterised by their point-thermal transmittance, commonly called the chi-value ('χ-value'). The complex 3D heat flux associated with point TBs poses a significant challenge for accurate measurement and evaluation (Pemberton, 2024). Currently, no standardised measurement method exists for point TBs, leading to a reliance

on numerical calculations guided by standardised protocols (ISO, 2017b). This reliance introduces potential performance gaps due to the assumptions required for sensitive parameters such as surface resistance (Fitton, 2016).

In this study, we aim to address this challenge by integrating experimental data into the numerical modelling of the thermal characteristics of point connections, both with and without structural thermal breaks (STBs). STBs are designed to interrupt the thermal path and reduce heat transfer, thereby improving the overall thermal performance of the building envelope. By incorporating experimental measurements, we seek to enhance the accuracy of numerical models and provide a more reliable assessment of point TBs. The experimental setup involved measuring the U-value of the wall, as well as internal and external temperatures and surface resistances. These measurements were then incorporated into a numerical thermal model to simulate the thermal behaviour of point connections. The primary objective was to calibrate the parameters within a 3D finite element (FE) model, which is essential for quantifying point-TB transmittance accurately.

2 METHODOLOGY

2.1 Experiment

The experimental design was developed at EH, a climatic-controlled test facility at the University of Salford. A 0.5 m long steel-beam cantilever was bolted to the external wall, representing a single cantilever support (Fig. 1, left). This setup created a point penetration in the thermal envelope, enabling measurement of the 3D heat transfer through this TB both with and without STBs. We used Farrat's Struktra^{TM} STBs (Fig. 1, middle), which have a compressive strength comparable to steel and a thermal conductivity akin to wood (Table 1).

Table 1: Material properties of Farrat TBK material (Farrat, 2025)

Property	Farrat TBK	Property	Farrat TBK
Characteristic {Design} compressive strength [MPa]	312 {250}	**Density [kg/m^3]**	1465
Elastic modulus [MPa]	5178	**Water Absorption**	0.14%
Thermal conductivity [W/mK]	0.187	**Long term creep**	20%

Four test phases were conducted to understand the impact of the STB, with one factor changed at a time. Unquestionably, this approach could determine how altering a variable affects a given output, which resonates well with the current study. These phases were as follows:

- Phase 1 – Bare wall, steel only
- Phase 2 – Bare wall, steel thermally broken with STB
- Phase 3 – EWI wall, steel only
- Phase 4 – EWI wall, steel thermally broken with STB

Since this setup does not represent typical STB product utilisation, attempts were made to exacerbate the thermal bridging effect by retrofitting external wall insulation (EWI) to the wall in phases 3 and 4. The hypothesis was that the beam itself bridges more insulation, increasing the relative effects of bridging. Hence, a greater reduction can be measured when applying the STB solution. The EWI layers comprised soft mineral wool glued to EPS on plasterboard, chosen so that when retrofitted to the wall, the soft mineral wool would close the air gaps caused by the rough wall surface (see Fig. 1, right).

Fig. 1: The experiment set-up at EH (left), Farrat 25mm TBK STB (middle), and the external wall insulation retrofitted to the brick (right).

2.1.1 *Sensor Array:*

Internally, a T-type Thermocouple (TC) array ran parallel to the high-ε tape, linking the unaffected to the affected zone using vertical and horizontal lengths intersecting at the cold spot. Two heat flux meters (Hukseflux) were installed in the unaffected zones, all located with qualitative IR. T-type TCs monitored internal and external air temperatures, which were used to set up the simulation and U-value calculation (with heat flux), considering proper error propagation in the uncertainty analysis. Four 'FluxTeq' thin-film flux sensors (measuring flux and temperature) were embedded within the connection on either side of the break to measure the heat flux through the break itself. Measurements were compared with the model's probed responses for re-calibration. Table **2** lists the sensors used in the experiments and their absolute and relative uncertainties. The data logger also introduces a systematic error that applies to all detected signals, assumed to be 0.1% as per the manufacturer's specification.

Table 2: Absolute and relative uncertainties of sensors used in this experiment.

Sensor/Equipment	Measurement	Unit	Absolute Uncertainty	Relative Uncertainty
FluxTeq HFM	Heat Flux	W/m^2	±0.03 [W/m^2]	± 5%
T-type TC	Temperature	°C	± 1°C	± 1%
PT100 TC	Temperature	°C	± 1 °C	± 0.5%
Hukseflux HFM	Heat Flux	W/m^2	specific to individual sensors	± 6%

2.2 **Calculation:**

Due to the exciting internal airflow, it was deemed necessary to understand the internal surface-fluid HTC [W/m²K]. Therefore, measurements (fluid/surface heat flux along with local air and surface temperatures) were captured on each surface exposed to the internal and external environments. SR can be calculated using (1 – encapsulating both the convective and radiative terms in one expression (CIBSE, 2015):

$$\mathrm{SR} = \frac{1}{\frac{Q}{Ta - Ts}} \tag{1}$$

where 'SR' is the SR [m²K/W], 'Q' is the heat flux [W/m²], 'Ta' is the air temperature [K], and 'Ts' is the surface temperature [K]. Input parameters can be adjusted within their confident uncertainty intervals to calibrate the model. The sensitivities of 'dT' and the 'flux' estimates to the calculated measurand were calculated and then multiplied with the combined standard uncertainty for the respective estimate. These were then combined in quadrature (RSS–squared and summed) before the square-root. We avoided getting into details of uncertainty due to limited space here.

The U-value of the wall can be calculated using (2):

$$\mathrm{U} = \frac{\mathrm{Q}}{Tai - Tao} \tag{2}$$

where 'U' is the thermal transmittance [W/K], 'Q' is the heat flux [W/m²], 'Tai' is the inside air temperature [K], and 'Tao' is the outside air temperature [K].

The chi-value (χ-value) of point thermal bridging can be calculated using Eq. 3 ((ISO, 2017b; Ward et al., 2016):

$$\chi = L_{3D} - \sum_{i=1}^{N_i} U_i \,.\, A_i - \sum_{j=1}^{N_j} \psi_j . l_j \tag{3}$$

where 'χ' is the point-thermal transmittance or chi-value [W/K], 'L_{3D}' is the 3D coupling coefficient [W/K] (total energetic loss divided by the applied temperature differential), 'U_i' is the 1D U-value [W/m^{2}K], 'A_i' is the area the 1D U-value is effective over [m^2], 'ψ_j' is the psi-value (ψ-value) [W/mK], 'l_j' is the length over which the psi value exists [m] (ISO, 2017b). In this 3D experiment, there was no linear transmittance, therefore, this part of the equation can be ignored.

2.3 **Simulation**

The steady-state heat transfer finite element (FE) analysis in ABAQUS calculates the conduction through the investigated construction detail. Convective and radiative transfers are represented as SRs (prescribed as surface-fluid HTCs) in the models at surface boundaries exposed to environmental conditions (BSI, 2017c) and temperature. After creating the 3D model of the set-up, it is meshed by dividing the geometry into numerous elements each with four nodes. The

conduction equation and energy conservation laws are then applied to these nodes, forming a system of equations as a function of temperature. Through direct or iterative solutions, a temperature distribution field is determined, and interpolation is used to calculate the heat flows (BSI, 2017b).

3 RESULTS AND DISCUSSION

3.1 Experiment

Table 3 presents the measured values for surface-fluid HTC, the reciprocal of the SR.

Table 3: Measured values for surface-fluid HTC [W/m^{2}K], the reciprocal of the SR [m^{2}K/W].

	Phase1 [W/m^{2}K]	**Phase2 [W/m^{2}K]**	**Phase3 [W/m^{2}K]**	**Phase4 [W/m^{2}K]**
External	4.64 ± 0.21	4.64 ± 0.21	4.64 ± 0.21	4.64 ± 0.21
Internal	22.87 ± 11.42	22.87 ± 11.42	22.87 ± 11.42	22.87 ± 11.42

Contrary to the standardised assumptions of 25 and 7.7 W/m²K for surface-fluid HTC, externally and internally respectively, as outlined in BS EN ISO 6946 (ISO, 2017a), the measured surface-fluid HTC values averaged 22.87 ± 11.42 [W/m²K] (±50%) internally and 4.64 ± 0.21 [W/m²K] (±5%) externally. Compared to the standardised values, the increase in internal surface-fluid HTC was significantly impacted by eliminating internal stratification through air excitation with a fan. Additionally, the decrease in external surface-fluid HTC was attributed to the absence of weather conditions (solar, wind, rain) as the tests were conducted in a controlled chamber.

Table 4 presents each U-value and its uncertainty at a 95% (k=2) level of confidence.

Table 4: Average U value and their uncertainty at a 95% (k=2) level of confidence.

Phase	**U= $\bar{U} \pm \delta_U$**
Phase 1 (Bare brick)	$U_1 = 1.67 \pm 0.14$ $(\pm 8.5\%)$
Phase 2 (Bare brick)	$U_2 = 1.67 \pm 0.15$ $(\pm 9.1\%)$
Phase 3 (EWI)	$U_3 = 0.58 \pm 0.06$ $(\pm 11.0\%)$
Phase 4 (EWI)	$U_4 = 0.69 \pm 0.05$ $(\pm 7.4\%)$

Retrofitting EWI improved the U-value, achieving between 0.58 ± 0.06 and 0.69 ± 0.05 [W/m²K], compared to the pre-retrofit U-value of 1.67 ± 0.2 [W/m²K].

The measured averages of external and internal air temperatures and maximum and minimum internal surface temperatures can be seen in Table 5.

Table 5: Experimental measurement results averaged over a 12hr period.

Measurements	Ext Air Temp [°C]	Int Air Temp [°C]	Ext Surf Temp [°C]	Int Surf Temp [°C]
Phase1	5.88 ±1°C	23.39 ±1°C	20.04 ±1°C	22.47 ±1°C
Phase2	6.10 ±1°C	23.35 ±1°C	20.14 ±1°C	22.52 ±1°C
Phase3	5.61 ±1°C	23.35 ±1°C	21.35 ±1°C	22.97 ±1°C
Phase4	5.69 ±1°C	28.95 ±1°C	25.89 ±1°C	28.31 ±1°C

The measured averages of the embedded flux are seen in Table 6 below.

Table 6: The experimental measurement average and uncertainty of embedded flux over a 12-hour period.

Measurements	HF1 [W/m^2]	HF2 [W/m^2]	HF3[W/m^2]	HF4 [W/m^2]
Phase1	51.16 ± 2.76	40.98 ± 2.21	55.71 ± 3.00	50.32 ± 2.71
Phase2	29.99 ± 1.62	16.71 ± 0.9	24.44 ± 1.32	16.96 ± 0.91
Phase3	34.86 ± 1.88	38.58 ± 2.08	31.73 ± 1.71	38.07 ± 2.05
Phase4	201.77± 10.87	103.17 ± 5.56	140 ± 7.54	74.04 ± 3.99

3.2 **Simulation**

For all phases, the model geometry and material properties were adjusted to reproduce the measured U-value (as shown in Table 4). The tolerance of their adjustable range is dictated by the uncertainty analysis. We used the calculated U-value instead of measured temperatures and heat fluxes so that only one parameter is needed to be reproduced while adjusting the model geometry and material properties. The final calibrated model parameters are presented below in Table 7.

Table 7: Calibrated thermophysical properties: final parameters.

	Phase 1+2 Conditions		**Phase 3+4 Conditions**	
Material	Thickness [m]	Conductivity [W/mK]	Thickness [m]	Conductivity [W/mK]
Brick	0.225	0.7	0.225	0.7
Plaster	0.013	0.2	0.013	0.2
Skim	0.005	0.2	0.005	0.2
TBK	0.025	0.187	0.025	0.187
EWI	~	~	0.05	0.05
Internal Temperature [°C]		23°C	Internal [°C]	P3(23°C), P4(29°C)
Internal Surface-Fluid HTC		25[W/m^{2}K]	Internal	25[W/m^{2}K]
External Temperature [°C]		6°C	External [°C]	6°C

External Surface-Fluid HTC	4.85[W/m^{2}K]	External	4.85[W/m^{2}K]

Analytically, the U-value depends on properties contributing to the total thermal resistance of the wall: SRs, material thickness, and their conductivities. The measured SRs, as shown in Table 3, are 22.87 ± 11.42 W/m²K (±50%) and 4.64 ± 0.21 W/m²K (±5%) for the internal and external surfaces, respectively. These values were applied to the models.

The following images examine temperature isotherms of cross-sections through the centre of the TB, allowing visual comparison in bare wall phases and retrofitted ones (Figure 2). In the top images, the limits to the temperature scale were not adjusted, whereas in the bottom images, the temperature scale limits were adjusted, illustrating isotherm deflection. The maximum and minimum were set, focusing on the temperature gradient through the TB break junction. Because the measured internal temperature conditions for phases 3 & 4 were different (23°C and 29°C, respectively), the illustrated example considered identical conditions, i.e. 23°C and 6°C, for internal and external temperatures in each simulation – producing a fair visual comparison between phases.

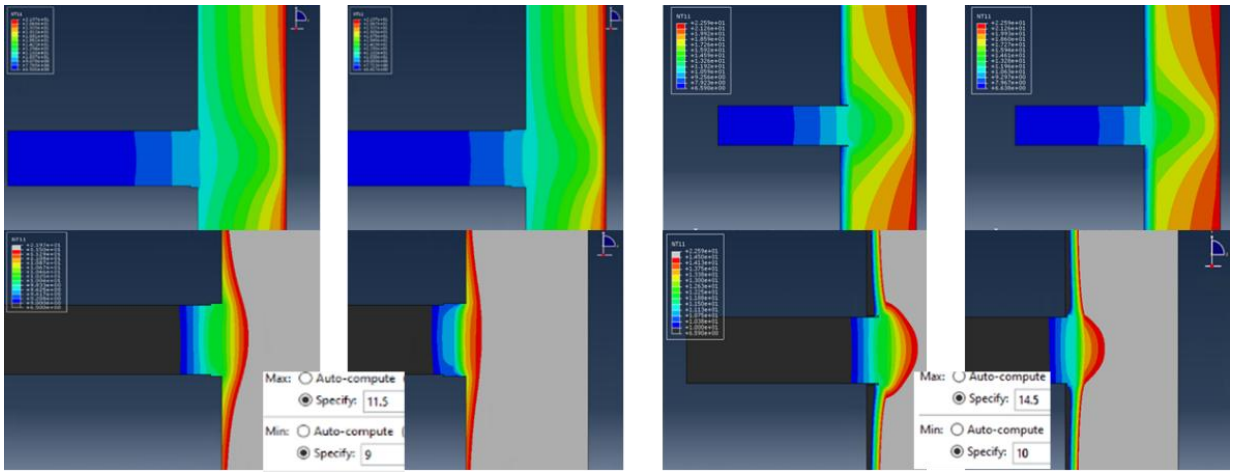

Figure 2: Left to Right: Phase 1 to 4, respectively. Temperature is scaled between 9°C and 11.5°C for phases 1 & 2 and between 10°C and 14.5°C for phases 3 & 4 in the bottom images.

Table 8 presents the calculated chi-value (following the standardised BRE methods) for each phase and the corresponding reduction when the STB solution is applied. A 6.73% reduction in TB-transmittance is observed between phases 1 and 2 (where no external wall insulation is present), raising the minimum internal temperature by a modest 0.1°C. In contrast, a 15.43% reduction in TB-transmittance is noted between phases 3 and 4 (when external wall insulation is retrofitted to exacerbate bridging), raising the minimum internal temperature by 4-5°C. This demonstrates an increase in overall TB-transmittance when EWI is retrofitted, confirming that the higher the resistance of the wall, the greater the benefit from STB solutions.

Table 8: Chi-value results of each phase and % reduction when STB used

	Phase1	**Phase2**	**Phase3**	**Phase4**

Chi-Value [W/K]	0.104	0.097	0.1814	0.2145
% Reduction	6.73%		15.43%	

4 CONCLUSION AND FUTURE WORKS

This study successfully developed a reliable in-situ evaluation method to capture the parameters necessary for thermal modelling of point thermal transmittance. By using Farrat's STBs at the EH at the University of Salford, we were able to thermally break the heat transfer from the point thermal bridge connection. The numerical modelling, conducted in ABAQUS and calibrated with experimental data, demonstrated that STBs significantly reduce the χ-value of point thermal bridges. Specifically, the χ-value of the bare wall was reduced by 6.73%, and the externally insulated wall saw a reduction of 15.43%. These findings underscore two critical insights: the importance of employing STBs to mitigate heat transfer through point TBs, achieving at least a 6.73% reduction, and the more pronounced impact of STBs in well-insulated structures. This research not only highlights the effectiveness of STBs but also establishes a dependable in-situ method for gathering the necessary parameters to evaluate thermal bridges accurately. In conclusion, the integration of experimental data into numerical models has proven to be a significant advancement in the accurate assessment of point TBs. This approach enhances the understanding of thermal characteristics in building envelopes and supports the design of more energy-efficient structures. The results of this study provide a robust framework for future research and practical applications in the field of thermal performance evaluation and provide the framework to test the thermal performance of connections in projects outside the controlled conditions.

Acknowledgement

The team at Farrat and the University of Salford would like to acknowledge the work of the late Dr. Joe Pemberton, whose work has been extended in this paper

References:

CIBSE. (2015). Environmental Design: CIBSE Guide A (K. Butcher & B. Craig, Eds.). Chartered Institution of Building Services Engineers. https://books.google.co.uk/books?id=EwPesgEACAAJ

Farrat. (2025). https://farrat.com/product/struktra-tbk/.

Fitton, R. (2016). The thermal energy performance of domestic dwellings in the UK. University of Salford.

ISO. (2017a). Building components and building elements - Thermal resistance and thermal transmittance - Calculation methods. BSI British Standards.

ISO. (2017b). Thermal bridges in building construction. Heat flows and surface temperatures. Detailed calculations. BSI British Standards. https://doi.org/10.3403/30313350

Pemberton, J. (2024). An exploration of the measured and modelled thermal characteristics of structural thermal breaks in UK buildings. University of Salford.

Ward, T., Hannah, G., & Sanders, C. (2016). Conventions for Calculating Linear Thermal Transmittance and Temperature Factors: (br 497). IHS BRE Press.

6th International Conference on Building Energy and Environment
Eindhoven University of Technology, The Netherlands
6 - 10 July 2025

Resilient Cooling Strategies for Mitigating Indoor Overheating in Mixed-Use Neighborhood: A UBEM-Based Retrofit Approach Considering Climate Change

Dican Deniz Kose[1], Ilkim Canli [1,4], Fatma Ece Gursoy [1], Sinan Kalkan [2,5], Aysen Erdincler [3], Rasit Turan [4], Ipek Gursel Dino [1,6]

[1]Middle East Technical University, Dept of Architecture, Ankara, Turkiye, dican.kose@metu.edu.tr, ilkim.canli@metu.edu.tr, *gursoy.ece@metu.edu.tr*, *ipekg@metu.edu.tr*
[2]*Middle East Technical University, Dept.of Computer Engineering, Ankara, Turkiye, skalkan@metu.edu.tr*
[3]*Boğaziçi University, Institute of Environmental Sciences, Istanbul, Turkiye, erdincle@bogazici.edu.tr*
[4]*METU GÜNAM, Center for Solar Energy Research and Application Center, Ankara, Turkiye, ilkim.canli@odtugunam.org, rasit.turan@odtugunam.org*
[5]*METU-ROMER, Center for Robotics and Artificial Intelligence, Ankara, Turkiye*
[6]*METUCLIMATE, Climate Change and Sustainable Development Application and Research Center, Ankara, Turkiye*

SUMMARY
Rising temperatures due to climate change increasingly compromise thermal comfort and pose health risks in naturally ventilated buildings. Passive cooling strategies offer sustainable solutions to maintain indoor comfort while reducing energy use. While extensively studied for individual buildings, passive strategies at the neighborhood scale under future climate scenarios remain underexplored. This study assesses overheating risks in a mixed-use neighborhood in Kadıköy, Istanbul, with 2,455 buildings, 5999 zones, using a calibrated Urban Building Energy Model under the Chartered Institution of Building Services Engineers Technical Memorandum 52 and 59 criteria. Long-term overheating risks were calculated under the Shared Socioeconomic Pathway 5-8.5 extreme scenario, for residential and non-residential zones, separately until 2080. Retrofit scenarios incorporating cool envelope materials and glazing with low solar heat gain coefficient were investigated to mitigate overheating. Results showed that passive strategies can reduce overheating risks up to 36%, delaying the need for mechanical cooling to 12.19 years on average. The developed method can inform long-term retrofit processes and provide well-informed decision-making.

Keywords: indoor overheating risk, passive cooling, urban building energy modeling, climate change

1. INTRODUCTION

In urban areas, climate change increasingly harms public health and the built environment. Intensifying hot extremes disrupt sanitation, energy services, and overall human well-being (IPCC, 2023). Climate change, therefore, poses serious threats to the built environment, emphasizing the need for effective heat mitigation and adaptation strategies to protect vulnerable populations in urban areas (Ballester et al., 2023). The growing vulnerability of buildings under extreme heat conditions has prompted increased interest in energy retrofit (ER) strategies. Most ER strategies focus on energy use and decarbonization while often overlooking overheating in buildings without mechanical cooling. As temperatures rise, indoor overheating is becoming a critical performance metric due to its impact on occupant health and comfort. Consequently, addressing overheating in both existing and newly designed buildings is becoming an increasingly urgent priority for policymakers, researchers, and practitioners alike. In response, passive cooling strategies represent

a critical avenue for mitigating the effects of overheating in buildings and enhancing thermal resilience in the coming years.

Studies on building thermal resilience and cooling strategies largely fall into two main areas: (1) reviewing definitions of thermal resilience, comfort, energy performance, and mitigation strategies, and (2) assessing thermal resilience through simulations or real-time data. The first category focuses on defining key performance indicators related to thermal comfort, heat stress and energy performance (Hong et al., 2023; Holzer et al., 2024). Other studies in this category involve the evaluation of cooling strategies, particularly in extreme heat conditions or power outages (Elnagar et al., 2023). In the second category, several studies assess resilient cooling alternatives in retrofit scenarios using Building Performance Simulations (BPS), focusing on indoor overheating in individual buildings (Mehmood et al., 2023). Other studies focus on the prediction of future conditions (Abbas et al., 2024), and the examination of thermal resilience without retrofit scenarios through simulations and real-time data (Palma et al., 2024), typically by relying on existing metrics. At the district scale, studies often focus on residential zones (Morales et al., 2025). A study investigated the performance of combined heating and cooling systems in mixed-use buildings within a synthetic district (Gautier et al., 2022). Despite these, there remains a significant gap in research regarding the assessment of overheating risks and passive cooling retrofit strategies for the urban-scale, long-term continuous assessment of buildings.

This study aims to fill this gap by presenting a methodology for assessing the long-term overheating risk using adaptive comfort standards (CIBSE TM52 and TM59) and calculating the impact of passive cooling strategies in naturally ventilated homes and offices in mixed-use neighborhood in Istanbul, Turkiye. For buildings where passive strategies remain insufficient, this study also forecasts the future year that the indoor discomfort would require air conditioning. The methodology can help decision-makers in long-term planning of ER actions while indoor overheating.

2. METHODOLOGY

This study presents a methodology for the long-term assessment of the effect of resilient cooling strategies on indoor overheating considering future climate change impacts.

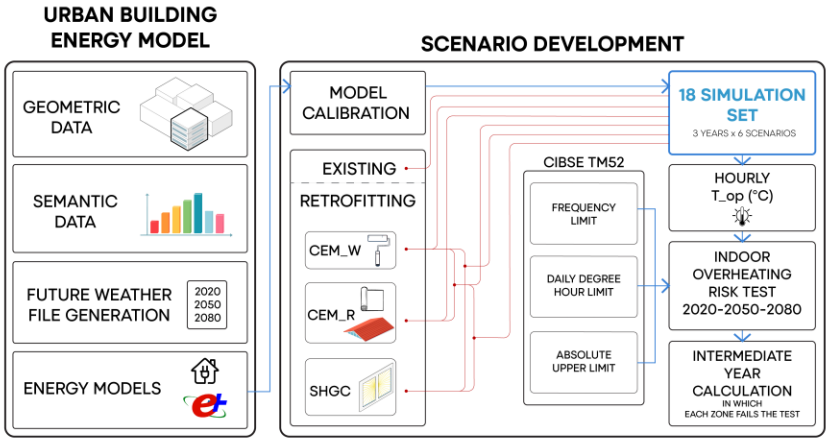

Figure 1. The overall workflow of the study.

To this end, a zone-level Urban Building Energy Modelling (UBEM) of a mixed-use neighborhood in Istanbul, Türkiye is developed, consisting of 2,455 buildings with a total number of 12016 zones. The method is developed based on three main steps (Fig. 1): (i) UBEM Development and Simulations, (ii) Retrofit Scenario Development, and (iii) Indoor Overheating Risk Assessment.

2.1. UBEM Development and Simulations

The development of the analysis dataset involves four steps: (i) Urban Building Energy Modelling (UBEM), (ii) Future Weather File Generation, (iii) Model Calibration, and (iv) Simulation-based Data Generation.

2.1.1. Urban building energy modeling

In the study, 2,455 mixed-use (residential + office) buildings, containing 12,016 zones in Istanbul, Kadikoy neighborhood (Fig. 2.), are modeled and simulated. This neighborhood represents diverse building thermal characteristics due to the various construction years (1960s to now). For the development of UBEM, two main types of data (i) geometric and (ii) semantic data are required. For 3D building geometries and their programs, a city GIS database is used. In each building, each floor is modeled as a single thermal zone. Grasshopper Ladybug V0.0.69 and Honeybee V0.0.66 plugins (Sadeghipour Roudsari et al., 2013) are used to create a basic EnergyPlus model for each building, ensuring uniform assignment of key parameters such as schedules, mechanical and natural ventilation setups. Out of the total number of 12,016 zones, 5,088 residential zones and 911 office zones are solely naturally ventilated without mechanical cooling. For heating, natural gas boilers with different efficiencies are used. All zones are naturally ventilated when the T_{indoor}>24.5°C and $T_{indoor}>T_{outdoor}$. The ANSI/ASHRAE/IES Standard 90.1 (2022) is used for the occupancy, equipment, and lighting schedules of the prototype midrise apartment building (midrise apartment apartment and midrise apartment office). Additionally, each building is considered as context shading to other buildings in simulations).

Following, using eppy, a Python library that can parse and edit EnergyPlus files (Santosh, 2014), all building-level and zone-level semantic data are assigned. Building-level semantic data includes characteristics of envelope materials (u_{Roof}, u_{Wall}, u_{Window}, u_{Ground}), infiltration rate, solar heat gain coefficient (SHGC), and boiler efficiency (η_{boiler}). For zones, lighting power density (LPD), equipment power density (EPD), people density (PPD), and heating set point ($T_{Heating}$) are assigned. U-values are assigned to buildings with an Energy Performance Certificate (EPC) (120 buildings), while for buildings without an EPC (2,291 buildings), U-values are generated using Kernel Density Estimation (KDE) based on the existing data. Except for U-values, all other data has 100% missingness; therefore, values obtained from the literature are used to generate a uniform distribution and assigned to buildings and zones accordingly (detailed modeling information can be found in our previous work (Canlı et al., 2024)).

Finally, simulations are performed to calculate zones' annual indoor operative temperature (T_{op}). In simulations, city's typical meteorological year EPW and future weather files (Section 2.1.2) is used.

Figure 2. A satellite image of the neighborhood (left) and a street view image of an example building (right) are considered in the paper.

2.1.2. Future weather file generation

A typical meteorological year (TMY) file of Istanbul obtained from the years 2007-2021 is used for simulations to represent current weather conditions. Future weather files for 2050 and 2080 are generated using the "Future Weather Generator" tool (Rodrigues et al., 2023), which converts current EPW data into 8760-hour future scenarios. The tool considers four SSPs (SSP1-2.6, SSP2-4.5, SSP3-7.0, and SSP5-8.5); this study uses SSP5-8.5 (the worst-case scenario) to ensure buildings are prepared for extreme conditions. Both the existing and generated weather files are used in the simulations.

2.1.3. Model calibration

The UBEM is developed using data from EPCs. U-values of building components and LPD values are sourced from EPCs. Infiltration rate, $T_{Heating}$, and EPD are the three parameters used to calibrate energy models for 120 buildings, selected based on available EPCs and annual consumptions acquired from the natural gas distribution company. The calibration of 120 buildings resulted in a 2.42% MAPE for heating energy demand.

2.1.4. Simulation-based data generation

CIBSE TM52 and TM59 standards are selected to quantify overheating because (i) they distinguish zones based on their function, (ii) they use adaptive comfort limits, and (iii) they extensively can evaluate zones using multiple criteria such as frequency of overheating hours, daily degree hours and absolute upper limit. Analyses were conducted between May 1st and September 30th. Only zones that use natural ventilation for cooling are tested, which are 5,999 zones out of 12,016. Both residential and non-residential zones are assessed, but using different criteria defined by CIBSE standards. To calculate a zone's risk of overheating, the hourly T_{op} and the maximum operative temperature the zone can experience according to adaptive comfort limits (T_{max}) were compared. CIBSE TM52 defines three criteria that require at least two of them to be met for the office zones to be not at risk of overheating, and only the first criterion to be met by the residential zones. First is the Frequency Limit (FL), where the indoor operative temperature cannot exceed T_{max}+1 more than 3% of the occupied hours (Eq. (1)). Second is the Daily Degree Hours Limit (DDHL), where the daily degree-hours should not exceed 6°C, (Eq. (2)). The third is the Absolute Upper Limit

(AUL), where the T_{max} should never be exceeded by the T_{op} by more than 4°C (Eq. (3)).

$$\frac{\sum_{h\in H} 1[T_{op}(h)>T_{max}+1]}{|H|} \leq \frac{3}{100} \quad (1)$$

$$\forall d \in D, \left(\sum_{h\in d} \max\left(T_{op}(h) - T_{max}(h), 0\right)\right) \leq 6 \quad (2)$$

$$\forall h \in H, \; T_{op}(h) - T_{max}(h) \leq 4 \quad (3)$$

Where $T_{op}(h)$ is the operative temperature (°C) at hour at h, $T_{max}(h)$ is the maximum comfort temperature (°C) at hour at *h*, the set *D* is the days of interest (May–September), the set *H* be the occupied hours of interest (May–September). T_{max} is calculated according to BS N 15251 (Eq. (4)), for category 2, which is recommended for renovations. The running mean temperature (T_{rm}) is calculated using Eq. (5), using the outdoor temperature of the previous day (T_{od-1}).

$$T_{max} = 0.33 \times T_{rm} + 18.8 + 3 \quad (4)$$

$$T_{rm} = (1 - 0{,}8) \times \{T_{od-1} + 0.8 \times T_{od-2} + 0.64 \times T_{od-3} + \cdots\} \quad (5)$$

2.2. Scenario Development

Overheating risk calculation is conducted for three years (2020, 2050, and 2080) and six (existing and five retrofit) scenarios. The scenarios are developed based on two main passive cooling strategies; (i) installation of window glazings with SHGC=0.3 and (ii) application of cool envelope materials (CEM) to the building exterior surfaces (Table 1).

Table 1. Passive cooling retrofit scenario parameters related to building components.

	CEM_W	CEM_W_R	SHGC	CEM_W + SHGC	CEM_W_R + SHGC
Exterior Wall Solar Absorbtion	0.32	0.32	Existing Distribution	0.32	0.32
Exterior Wall Visible Absorption	0.39	0.39	Existing Distribution	0.39	0.39
Roof Solar Absorption	Existing Distribution	0.32	Existing Distribution	Existing Distribution	0.32
Roof Visible Absorption	Existing Distribution	0.39	Existing Distribution	Existing Distribution	0.39
Window Glazing Solar Heat Gain Coefficient	Existing Distribution	Existing Distribution	0.3	0.3	123

2.3. Indoor Overheating Risk Test

Hourly $\Delta T_{comfort}$ ($T_{op} - T_{max}$) values for both existing and retrofit scenarios are computed from EnergyPlus simulations for 2020, 2050, and 2080. Spline interpolation is applied between 2020–2050 and 2050–2080 to achieve a continuous approximation over limited data points. This method enables annual testing of each zone against CIBSE overheating criteria to the specific year when a zone exceeds the threshold and would require active cooling.

3. RESULTS AND DISCUSSION

The gap between operative (T_{op}) and maximum indoor (T_{max}) temperatures widens over time, with passive cooling strategies only partially mitigating this trend by delaying the increase in $\Delta T_{comfort}$ (Fig. 3). Notably, the combined strategies in Scenarios E and F reduce overheating risks effectively in 2020 and 2050 By 2080, passive strategies help mitigate overheating but cannot fully eliminate risks, emphasizing their role in *delaying* rather than *entirely preventing* the need for mechanical cooling. Without passive cooling, overheating risks affect 35.92% of residential and 79.68% of office zones in 2020, rising to 75.84% and 93.02% by 2050, and 89.2% and 95.94% by 2080. In contrast, with measures such as CEM and low-SHGC glazings, the overheating risk in residential zones is reduced to 4.6%, 51.2%, and 78.8% for 2020, 2050, and 2080 respectively (Fig. 3).

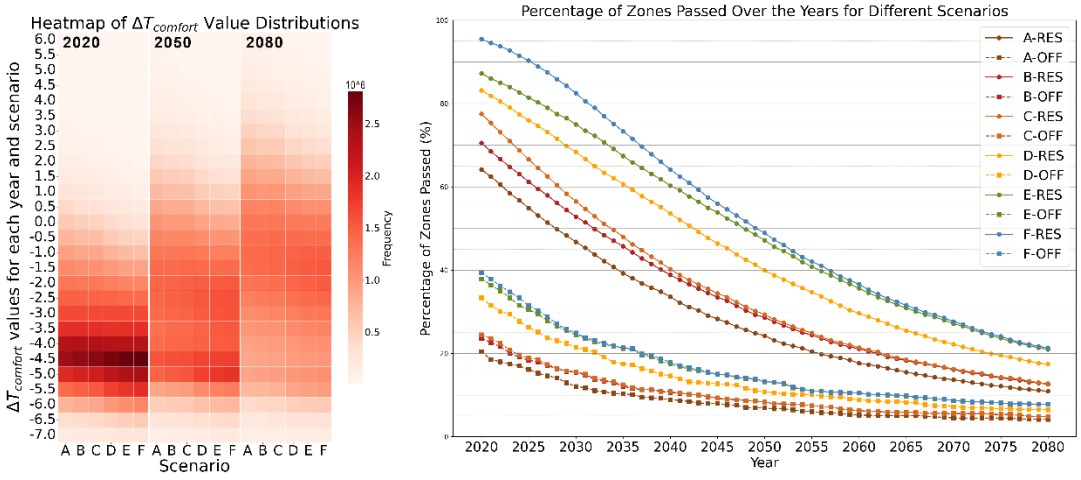

Figure 3. Heatmap of $\Delta T_{comfort}$ values of the zones in different scenarios and years (left), and percentage of zones that failed each criterion through the years (right) for each scenario: Exiting (A), CEM_W (B), CEM_W_R (C), SHGC (D), CEM_W + SHGC (E), CEM_W_R + SHGC (F).

A steep decline in the percentage of zones passing the CIBSE criteria is observed, indicating a significant increase in overheating risks over time without intervention. By 2080, less than 20% of zones meet the criteria. Residential zones generally exhibit higher compliance compared to office zones across all scenarios, highlighting differences in internal thermal loads. Another reason is that the offices are exposed to higher outdoor temperatures and higher solar heat gains during their operational hours (07:00-23:00). In contrast, residential zones are used throughout the day, and benefit from lower outdoor temperatures during nighttime hours, leading to lower overheating percentages. Due to these differences of occupancy hours and the dependent calculation routines, the overheating risk assessment do no serve to compare two zone groups of different functions.

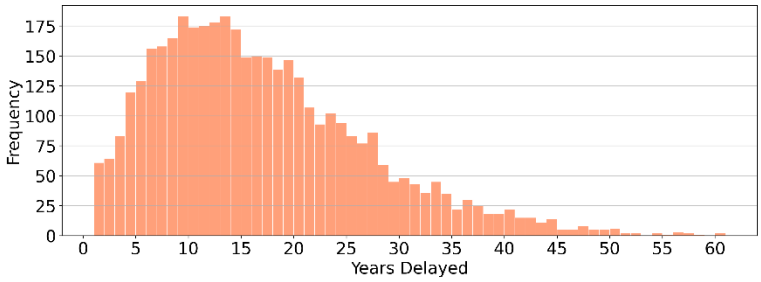

Figure 4. Distribution of Years of Overheating Delayed

Out of the 5999 zones, the predicted failure of 4842 falls within our analysis range. For those, on average, the combination of the application of CEM and low-SHGC glazing can delay the year in which the zone will need mechanical cooling for 12.19 years. This delay can go up to 60 years in residential zones and 56 years in office zones. The delay of overheating risk is 0 years for 783 zones. The distribution of 4059 non-zero years delayed can be seen in Fig 4.

4. CONCLUSION AND FUTURE WORK

While forecasting overheating risks until 2080, 1,157 zones did not fail within our analysis period, leaving the delay effect of passive strategies unclear. Future work could extend the analysis to cover all zones. Although passive strategies mitigate overheating risks, findings highlight the future need for active cooling systems. Further research should explore active systems (e.g., air conditioning, heat pumps) and provide a detailed analysis of various other environmental and financial parameters such as energy use, cost, and carbon emissions on an urban scale. The urban building layout and the corresponding resolution is too high to accommodate the functional differences in a residential unit due to the high number of buildings comprised in this UBEM. Future work can increase zonal resolution of buildings and apply CIBSE criteria separately to assess different functional zones, i.e., bedroom and living room. However, the additional modeling and computational burden should be considered accordingly.

The forecast of the year in which each zone will fail CIBSE overheating risk criteria can lead to the impact assessment in terms of the reduction of carbon footprint that passive cooling strategies can promise, and therefore, inform the urban-scale policymaking.

ACKNOWLEDGEMENTS

This study is funded by the Horizon Europe under grant number 101096405 and the Scientific and Technological Research Council of Turkey (TUBITAK) under grant number 22AG019.

REFERENCES

ANSI/ASHRAE/IES Standard 90.1. (2022). ANSI/ASHRAE/IES Standard 90.1 [Online]. Retrieved January 26, 2025, from https://www.energycodes.gov/prototype-building-models#ASHRAE

Abbas, G. M., Meral Akgül, Ç., & Dino, I. G. (2024). Resilient cooling of the Mediterranean office spaces under climate change. Architectural Engineering and Design Management, 1–22. https://doi.org/10.1080/17452007.2024.2400577

Ballester, J., Quijal-Zamorano, M., Méndez Turrubiates, R. F., Pegenaute, F., Herrmann, F. R., Robine, J. M., Basagaña, X., Tonne, C., Antó, J. M., & Achebak, H. (2023). Heat-related mortality in Europe during the summer of 2022. Nature Medicine, 29(7), 1857–1866. https://doi.org/10.1038/s41591-023-02419-z

Canli, I., UÇAR, Ş., Gursoy, F. E., Halacli, E. G., Iseri, O. K., YAVUZ, F., ... GÜRSEL DİNO, İ.(2024). Transfer Learning-Based Prediction of Heating Energy Consumption Using Urban Building Energy Models (UBEM) . 31st International Workshop on Intelligent Computing in Engineering, EG-ICE 2024 (pp.580-589). Vigo, Spain

Chartered Institution of Building Services Engineers (CIBSE). (2013). CIBSE TM52: The limits of thermal comfort: Avoiding overheating in European buildings. London: CIBSE.

Chartered Institution of Building Services Engineers (CIBSE). (2017). CIBSE TM59: Design methodology for the assessment of overheating risk in homes. London: CIBSE.

"Eppy: Python library for EnergyPlus," 2014. Accessed: Jan. 26, 2025. [Online]. Available: https://eppy.readthedocs.io.

Elnagar, E., Zeoli, A., Rahif, R., Attia, S., & Lemort, V. (2023). A qualitative assessment of integrated active cooling systems: A review with a focus on system flexibility and Climate Resilience. Renewable and Sustainable Energy Reviews, 175, 113179. https://doi.org/10.1016/j.rser.2023.113179

Gautier, A., Wetter, M., & Sulzer, M. (2022). Resilient cooling through Geothermal District Energy System. Applied Energy, 325, 119880. https://doi.org/10.1016/j.apenergy.2022.119880

Holzer, P., Abhishek, G., Arens, E., Attia, S., Corrado, V., Gupta, R., Hamdy, M., Homaei, S., Laouadi, A., Levinson, R., Selkowitz, S., Sengupta, A., Sodagar, B., Wang, L. (Leon), & Zinzi, M. (2024). International Energy Agency - Resilient Cooling of Buildings - Key Performance Indicators Report (Annex 80). https://doi.org/10.52776/rhet5776

Hong, T., Malik, J., Krelling, A., O'Brien, W., Sun, K., Lamberts, R., & Wei, M. (2023). Ten questions concerning thermal resilience of buildings and occupants for climate adaptation. Building and Environment, 244, 110806. https://doi.org/10.1016/j.buildenv.2023.110806

Intergovernmental Panel on Climate Change (IPCC). (2023). Summary for policymakers. In H.-O. Pörtner, D. C. Roberts, M. Tignor, et al. (Eds.), Climate Change 2023: Synthesis Report. IPCC. Retrieved from https://www.ipcc.ch/report/synthesis-report/ar6

Mehmood, S., Lizana, J., & Friedrich, D. (2023). Low-energy resilient cooling through geothermal heat dissipation and latent heat storage. Journal of Energy Storage, 72, 108377. https://doi.org/10.1016/j.est.2023.108377

Monge Palma, R., Castro Medina, D., Guerrero Delgado, Mc., Sánchez Ramos, J., Montero-Gutiérrez, P., & Álvarez Domínguez, S. (2024). Enhancing the building resilience in a changing climate through a passive cooling roof: A case study in Camas (Seville, Spain). Energy and Buildings, 321, 114680. https://doi.org/10.1016/j.enbuild.2024.114680

Morales, R. D., Audenaert, A., & Verbeke, S. (2025). Thermal comfort and indoor overheating risks of Urban Building Stock - a review of modelling methods and future climate challenges. Building and Environment, 269, 112363. https://doi.org/10.1016/j.buildenv.2024.112363

Rodrigues, E., Fernandes, M. S., & Carvalho, D. (2023). Future Weather Generator for building performance research: An open-source morphing tool and an application. Building and Environment, 233, 110104. https://doi.org/10.1016/j.buildenv.2023.110104

Sadeghipour roudsari, M., Pak, M., & Viola, A. (2013). Ladybug: A parametric environmental plugin for grasshopper to help designers create an environmentally-conscious design. Building Simulation Conference Proceedings. https://doi.org/10.26868/25222708.2013.2499

Santosh, R. (2014). Eppy: scripting language for EnergyPlus IDF files. GitHub. Retrieved from https://github.com/santoshphilip/eppy

6th International Conference on Building Energy and Environment
Eindhoven University of Technology, The Netherlands
6 - 10 July 2025

Evaluating the impact of bio/geobased building materials on summer thermal comfort

Thibaut COLINART[1], Chi-Kien NGUYEN[2]

[1]*Univ. Bretagne Sud, UMR CNRS 6027, IRDL, F-56100 Lorient, France, thibaut.colinart@univ-ubs.fr*
[2]*Saint-Gobain Recherche Paris, F-93300 Aubervilliers, France, Chi-Kien.Nguyen@saint-gobain.com*

SUMMARY
This study aims to quantify the impact of bio/geobased materials, through their hygrothermal properties, on comfort at building scale, compared with other materials. To this end, dynamic hygrothermal simulations are carried out at the scale of a model building (Bestest type), considering coupled heat and moisture transfers in the envelopes, using WUFI Plus software. Several wall typologies are tested for residential or tertiary building subjected to different climates in France (Brest, Nancy, Marseille). Various thermal comfort metrics are analysed over the summer period. The impact of wall designs on summer thermal comfort is compared with conventional summer thermal comfort measures, such as night-time over-ventilation or solar gain management. Results shows that actions to limit and manage solar gain have more influence on thermal comfort than wall design including or not bio/geobased materials.

Keywords: hygrothermal behaviour, thermal comfort, biobased materials

1. INTRODUCTION

Maintaining the hygrothermal comfort of a building's occupants at a minimum energy cost is a key concern for thermal engineers. However, several challenges lie behind this simple objective. Firstly, although a generic definition is proposed in ASHRAE Standard 55, assessing thermal comfort remains complex. It depends on numerous variables such as temperature, humidity, and air speed, which are influenced by factors related to the building, external conditions, human activities, and physiological and psychosociological factors (Rupp et al., 2015). Secondly, numerous thermal comfort indicators have been developed over the last few decades, each with its own well-defined construction logic. For instance, Attia et al. (2023) list various overheating indicators used in Europe and note that the *DH* indicator proposed in the latest French thermal regulation, *RE 2020*, is one of the most advanced and relevant indicators for assessing summer thermal comfort. These indicators are frequently evaluated through building thermal simulations carried out with dedicated software, which have their own limitations. These tools offer great flexibility for assessing the impact of envelope design (level of insulation and thermal inertia, glazing and solar protection, etc.) and/or building operation (ventilation scenarios, shading, etc.) on thermal comfort (Alrasheed and Mourshed, 2023; Verbeke and Audenaert, 2018; Guo et al., 2019; Evola et al., 2013). In the case of summer thermal comfort, these studies confirm the importance of limiting heat gains and managing these gains over time. Recently, bio/geosourced materials have been increasingly used in the building sector, both for new construction and renovation, due to their low environmental impact and their potential benefits for summer thermal comfort, which are related to notions of inertia and hygrothermal transfers. However, studies on summer thermal comfort in buildings containing bio/geosourced materials in the envelope are scarce and sometimes imprecise or unrealistic (Barclay et al., 2019; Hema et al., 2020; Ben-Alon

and Rempel, 2023). This study therefore aims to clarify the impact of bio/geosourced materials on summer thermal comfort compared with more conventional solutions, using a geometrically simple building as a case study.

2. CASE STUDY

The case study concerns a BESTEST building with a simple geometry (6 m long, 8 m wide and 2.7 m high). The floor and ceiling (composed of very closed vapour barriers, 10 cm concrete and external insulation) have thermal resistances of 3.8 and 6.3 $m^2.K.W^{-1}$ respectively. Three representative types of opaque side walls (R = 5 $m^2.K.W^{-1}$) are studied:

- ITICS (Internal Thermal Insulation Composite System): rendered concrete walls are insulated from the inside either with insulation (glass wool GW or wood fibre WFI) under vapour barrier (Sd = 1 m), cavity and gypsum board, or with light-earth (LE) covered with a straw-earth render.
- ETICS (Internal Thermal Insulation Composite System): exterior insulation under cladding is applied to two walls: concrete combined with cavity and gypsum board or uncovered compressed earth bricks (CEB) to potentially maximize moisture exchange with indoor room.
- WFW (wood-framed walls): it comprises cladding, ventilated cavity, rainscreen, OSB board, insulation (GW or WFI) under a vapour barrier (Sd = 1 m), cavity and gypsum board.

Fig. 1 illustrates the wall designs, insulation thicknesses, and main hygrothermal characteristics, including the damping factor and phase shift calculated according to ISO 13786. Due to the higher thermal conductivity of LE, the ITICS LE wall is the thickest. Although the thermal mass per unit area of the heavy walls (ITICS/ETICS) is approximately two times greater than that of the ceiling and floor, the vertical and horizontal walls contribute equally to the building's inertia when considering their respective surface areas. Phase shift and damping are closely correlated with thermal mass: the greater the mass, the lower the damping factor and the greater the phase shift. Additionally, all walls containing concrete are more resistant to vapor transfer compared to other walls. In accordance with the design of Bestest buildings, two 6 m² double-glazed windows (g = 0.6, Uw = 2.7 W/m²K) are integrated into the south façade. By default, these windows have no solar shading or overhangs to limit solar gain in the summer.

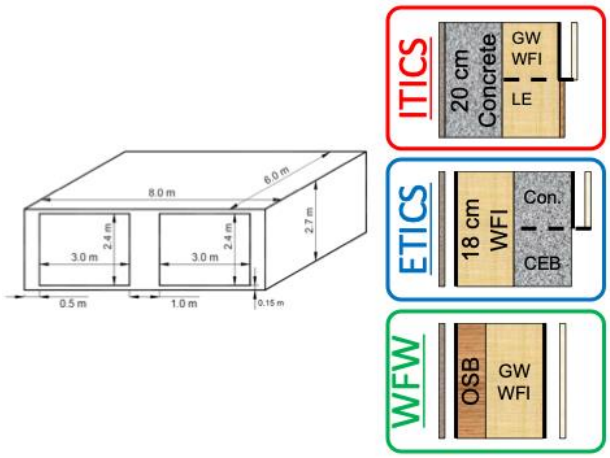

Wall	Insul. th. [cm]	C [kJ.m^{-2}.K^{-1}]	*f* [-]	φ [h]	Sd [m]
Ceiling	25	208	0.36	8.4	28.5
Floor	15	203	0.42	6.2	28.4
ITICS GW	14.9	432	0.16	8.8	36.5
ITICS WFI	19.5	470	0.07	15.5	37.0
ITICS LE	38.3	552	0.03	21.4	37.6
ETICS Con	18.6	460	0.06	15.9	37.2
ETICS CEB	18.9	388	0.13	15.8	3.2
WFW GW	14.3	35	0.93	2.7	2.4
WFW WFI	18.8	72	0.4	9.5	2.8

Figure 1. Overview of the building and opaque walls considered in the case study.

Residential (single-family home) and tertiary occupancy scenarios are defined for two people, in accordance with current French thermal regulations (with no other internal thermal loads). Air renewal is provided by infiltration (calculated for a permeability of 0.6 $m^3.h^{-1}.m^{-2}$) and by a mechanical ventilation system (with a default flow rate of 50 $m^3.h^{-1}$, i.e., 0.38 volumes per hour). An ideal, high-powered heating system maintains a minimum temperature of 20 °C in the building. However, there are no restrictions on maximum temperature or relative humidity.

Building simulations are carried out using WUFI Plus (v3.3). This building thermal simulation software has the particular capability of solving hygrothermal transfer equations in walls. The hygrothermal properties of materials are either measured in the laboratory (Colinart et al., 2020) or taken from the WUFI database. To eliminate the effect of initial conditions, simulations are carried out over five consecutive years. The building's hygrothermal behavior is evaluated for three climates in France: Brest (oceanic climate, Köppen climate zone Cfb), Nancy (semi-continental climate, Köppen climate zones Cfb to Dfb), and Marseille (Mediterranean climate, Köppen climate zone Csa). The TMY weather files available by default in the software and used for the simulations do not include any heatwave periods, notably due to their age (Nancy: 1996; Marseille: 1999). The simulated operative temperature, defined as mean of indoor temperature and mean indoor surface temperature, is used to evaluate four thermal comfort indicators in occupancy (Lauzet et al., 2021):

- The cumulative number of hours when the operating temperature is above 28 °C. This criterion is used in design programs or in CIBSE's "Guide A: Environmental design".
- Cumulative hours spent outside a Givoni comfort zone defined on the psychrometric diagram for still air (corresponding to a maximum temperature of 27 °C).
- Cumulative hours spent outside an adaptive comfort zone defined in accordance with EN 16798-1 (category II building). This indicator allows to consider the adaptability of users when assessing comfort.
- Cumulative hours spent outside an adaptive comfort zone defined in the French thermal regulation *RE 2020* and the number of *DH* degree-hours.

These thermal comfort indicators are evaluated over an entire year or over the summer period (June 1 to September 30), as well as over the hours of occupancy of an entire day or night (10 pm to 6 am). Note that these indicators do not require information on human clothing or metabolic rate.

3. RESULTS AND DISCUSSIONS

3.1. Analysis of a non-optimized reference case in terms of summer comfort

The case of a building with walls insulated on the inside with light earth (ITICS LE) in the climate of Nancy is presented in detail. Indoor temperature and relative humidity vary between 20 °C and 32 °C and 20 %rh and 58 %rh respectively, while exterior values vary between -13 °C and 32 °C and 15 %rh and 100 %rh respectively. These indoor data are analyzed using the summer thermal comfort indicators shown in Figure 2. Several observations can be made:

- Comfort indicators vary by a few hours from one year to the next, given the shift in days over the years (Year 1 starts on a Monday, Year 5 on a Saturday). For the remainder of the study, the results for Year 5 are analyzed. Moreover, discomfort occurs almost exclusively during the summer period (June 1 to September 30).
- The different indicators inevitably lead to varying levels of discomfort, due to their construction. They range from 557h to 806h over the entire summer period and from 159h

to 426h over the night periods. For the latter, the following order is observed: *RE 2020* (426h) > *Givoni* (302h) > *Adaptive* (159h), due to nighttime temperature thresholds of 26 °C, 27 °C and 28 °C, respectively.

- In relation to annual occupancy hours, discomfort ranges from 5% to 15%. On the other hand, since discomfort occurs only during the summer period, it should be considered in relation to the number of hours the dwelling is occupied during this period. In this case, discomfort range from 24% (*Adaptive*) to 35% (*Givoni*) over the entire day and from 16% (*Adaptive*) to 44% (*RE 2020*) during nighttime only. Ultimately, discomfort occurs between 23% and 54% of the time at night. The *RE 2020* indicator shows a high level of discomfort at night, due to a lower threshold temperature than during the day (26 °C vs. adaptive temperature). This leads to a high *DH* of 1240 °C.h.

These periods of discomfort do not necessarily occur simultaneously. However, discomfort is predicted by all indicators for 490h (i.e. 21% of summer occupancy), including 155h during the night (i.e. 16% of summer night occupancy). These periods of discomfort occur over a few days in June and especially in July and August, mainly at the end of the day and into the early hours of the night. With rare exceptions, discomfort is not continuous throughout the day.

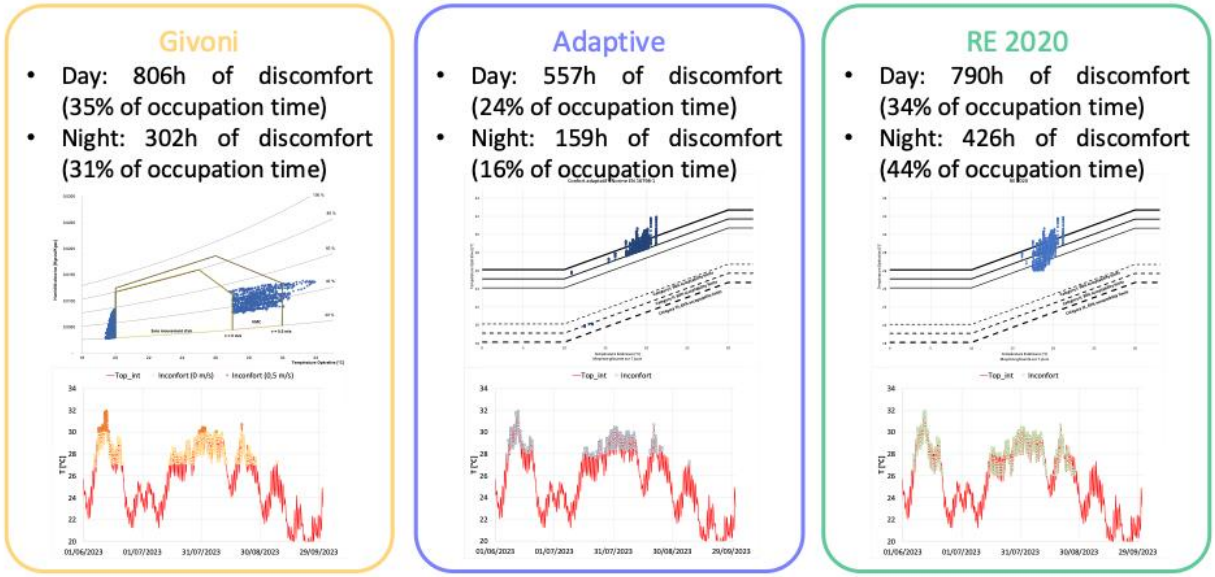

Figure 2. Analysis of summer thermal discomfort periods in a building internally insulated with light earth in a Nancy climate.

These discomfort levels are well in excess of frequently defined or tolerated thresholds. Therefore, additional simulations (noted as *V1*) are therefore carried out using conventional summer comfort control measures, specially 40% shading of windows from 2 to 7 p.m. and night ventilation of 150 $m^3.h^{-1}$ from 10 p.m. to 7 a.m. during the summer period. As shown in Fig. 3, these two measures lead to a drastic reduction in summer thermal discomfort, both during the day and at night, compared to the original simulation (noted as *V0*). Consequently, the *DH* indicator reaches a value of 216 °C.h, which is in line with the thresholds recommended by the French thermal regulation. These measures are retained for the remainder of the study.

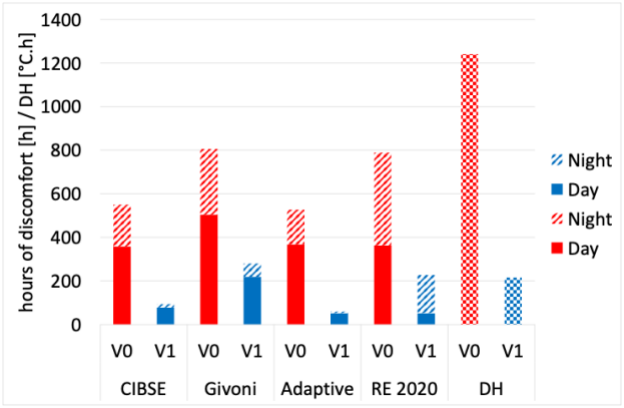

Figure 3. Number of hours of summer thermal discomfort and *DH* before (red-V0) and after (blue-V1) improvement in a building internally insulated with light earth in Nancy climate.

3.2. Influence of wall's type

Summer thermal discomfort indicators have been evaluated for various buildings made with the walls shown in Fig. 1. The *Adaptive* and *DH* indicators are presented in Fig. 4. Several observations can be made:

- For ITICS walls, replacing light thermal insulation (GW, WFI) with more inertial insulation (LE) results in a decrease of approximately 1 °C in interior temperature variations. This is due to latent effects associated with moisture exchanges: moisture flows from the wall to the zone, and this desorption at the surface is accompanied by a drop in surface temperature, and consequently, in operative temperature. As a result, discomfort is reduced by a maximum of 26h (i.e. a difference in occupancy of around 1%) and *DH* by 38 °C.h. Alternatively, reducing the light earth thickness to 20 cm (note as LE20), in line with current craftsman practices (i.e. a reduction of approximately 50% in the wall's thermal resistance) improves comfort. Since the indoor temperature is predominantly higher than the outdoor temperature in summer, losses through this wall are higher, allowing the building to cool down during both day and night. The reduction in discomfort ranges between 27 and 40%.
- Insulating walls from the outside reduces discomfort by approximately 50h during the day and 10h at night (i.e. a difference in occupancy of around 2.5%) and significantly reduces *DH* compared to ITICS WFI. Bringing inertia indoors dampens the temperature load, but heat accumulated in the envelope also requires longer periods to be removed during summer. Comparatively, a concrete wall provides more comfort than CEB masonry, due to its higher thermal effusivity, which allows the envelope to be unloaded at night. On the other hand, although humidity responses are slightly different, their impact on comfort indicators is minimal.
- Lightweight WFW results in discomfort levels equivalent to those observed for internally insulated walls. The GW wall exhibits higher discomfort level than the WFI wall due to its lower thermal inertia, which leads to greater interior temperature variations (of 0.5 °C on average) and more frequent threshold overshoots. Integrated over time, these overshoots balance out, resulting in equivalent *DH* levels between the two walls. A variant (walls marked *) involves incorporating a 15 cm internal partition made of CEB to provide additional internal thermal inertia (thermal mass = 246 $kJ.m^{-2}.K^{-1}$). The modification is beneficial for comfort, although it slightly reduces the room's air volume (by 2.43 m^3) and

thus its thermal inertia and infiltration rates, making the analysis of this variant more complex from a computational point of view. Finally, an additional simulation with light earth (with the same insulation thickness as WFI) also results in lower discomfort levels due to reduced thermal resistance (similar to the variant with the ITICS LE wall).

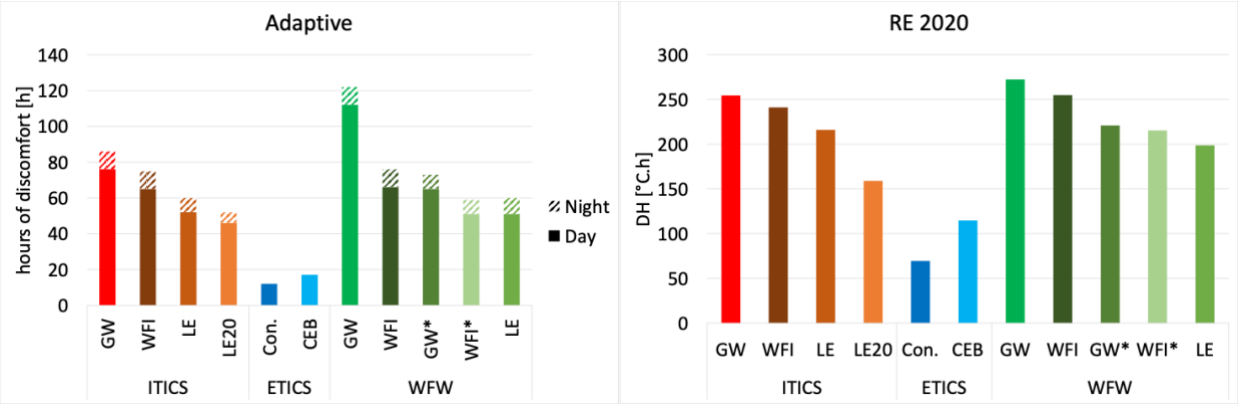

Figure 4. Influence of wall type on the number of hours of summer thermal discomfort (left) and on *DH* indicator (right) in a residential building in Nancy climate.

3.3. Influence of climate and occupancy

These analyses are reproduced for the oceanic climate of Brest and the mediterranean climate of Marseille. For Brest, there is no thermal discomfort in summer due to moderate outdoor temperatures. In contrast, for Marseille, discomfort frequently exceeds 1000h and *DH* exceeds 5000 °C.h due to high outdoor temperatures. This indicates that the summer thermal comfort improvement measures proposed for a semi-continental climate are insufficient for a mediterranean climate. Despite this observation, a relative discomfort analysis is carried out for four wall typologies, including wood fiber as thermal insulation. For each indicator, the relative discomfort presented in Fig. 5 is calculated in relation to the most unfavorable wall in terms of comfort. For example, for the climate of Nancy and the adaptive indicator, the WFW wall is the most unfavorable (relative discomfort = 100%), followed by the ITICS, WFW + CEB and ETICS walls. This beneficial effect of thermal inertia is observed for all indicators for a building optimized for summer thermal comfort in Nancy's climate. In contrast, inertia plays a lesser role for a building in Marseille's climate. Therefore, it is advisable to first optimize measures to improve summer comfort, such as shading of transparent walls and managing ventilation before addressing the level and location of thermal inertia.

These initial observations were made for residential buildings. The analysis is extended for tertiary buildings, with results shown in Fig. 6. Firstly, the number of hours of discomfort is greater for tertiary buildings due to higher occupancy (and therefore higher internal loads) during the day and zero at night. In relation to the number of hours of occupancy (792h), discomfort can exceed 20%. Secondly, the benefits of interior thermal inertia are confirmed.

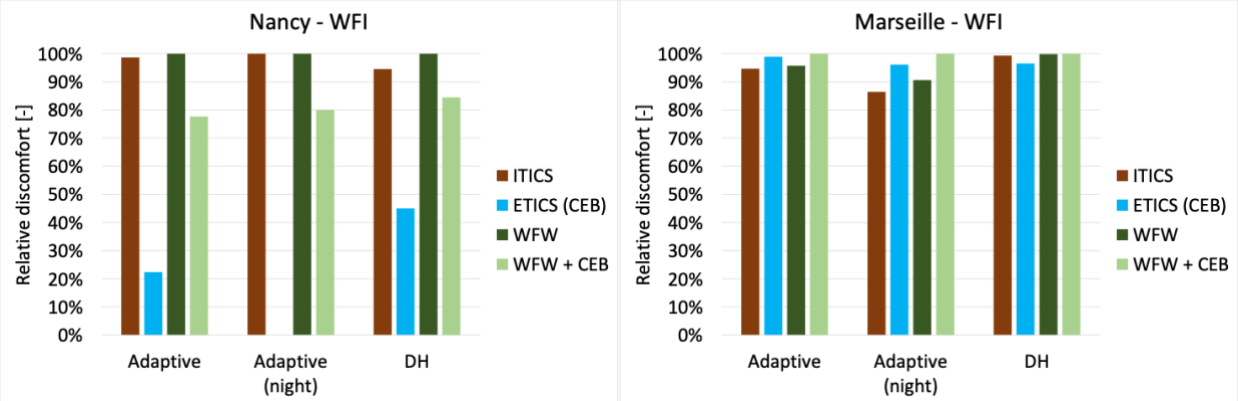

Figure 5. Influence of thermal inertia on the number of hours of summer thermal discomfort in a residential building in the climates of Nancy and Marseille.

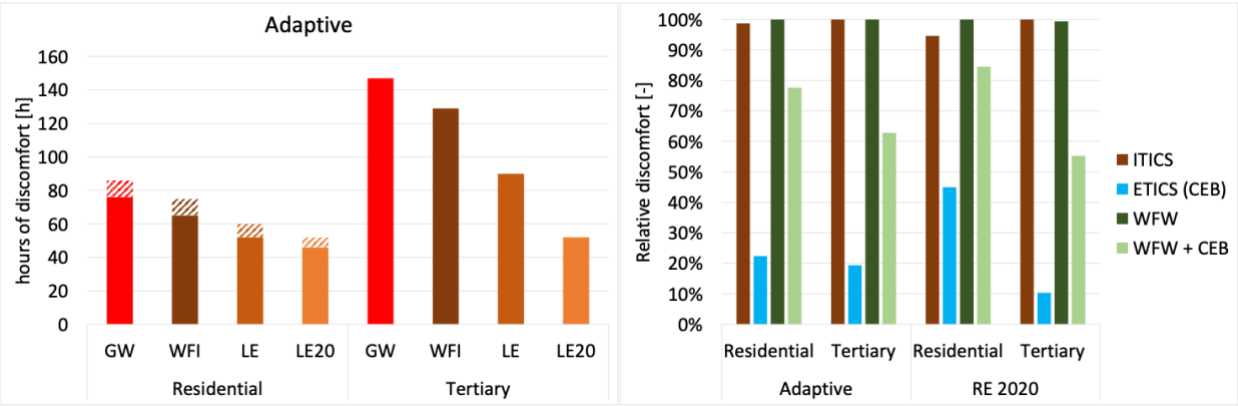

Figure 6. Influence of occupancy type on the number of hours of summer thermal discomfort in a tertiary building in a Nancy climate.

4. CONCLUSIONS AND OUTLOOK

Using Wufi Plus software, this study assessed summer thermal comfort in a model building that could incorporate bio/geosourced materials in its envelope. The results indicate that the most significant factors in predicting summer thermal comfort are actions to limit and manage solar gain, such as shading of glazed surfaces and implementing night-time over-ventilation. Additionally, wall design also plays an important role: adding thermal inertia inside the building (ETICS, WFW + CEB) is more beneficial for summer thermal comfort, provided that the building is already "optimized" (otherwise discomfort may be accentuated). Finally, walls incorporating bio/geosourced insulating materials, which generally offer greater thermal inertia, are less beneficial in terms of summer comfort than conventional walls.

This initial study should be continued to expand the scope of these preliminary conclusions. While retaining the simplicity of the Bestest building, other variants can first be tested to assess the influence of building design (orientation/size of glazing, floor/ceiling inertia, etc.), climate (current/future) or materials (formulation of lightened earth and coatings, wall design, etc.). The goal is to identify and classify the various parameters affecting summer thermal comfort, particularly the effects of water transfers and associated latent transfers on daily or seasonal heat

balances, as well as on comfort indicators. However, to meet the industry expectations, these results need to be confirmed for more realistic building types (e.g., detached houses, apartment blocks, etc.) and should be ideally experimentally validated.

REFERENCES

Alrasheed M., Mourshed M., 2023. Domestic overheating risks and mitigation strategies: The state-of-the-art and directions for future research. Indoor and Built Environment 32(6), 1057.

Attia S., Benzidane C., Rahif R., Amaripadath D., Hamdy M., Holzer P. et al., 2023. Overheating calculation methods, criteria, and indicators in European regulation for residential buildings. Energy and Buildings 292, 113170.

Barclay, M., Holcroft N., Shea A.D., 2014. Methods to determine whole building hygrothermal performance of hemp–lime buildings. Building and Environment 80, 204.

Ben-Alon L., Rempel A.R., 2023. Thermal comfort and passive survivability in earthen buildings. Building and Environment 238, 110339.

Colinart T., Vinceslas T., Lenormand H., Hellouin De Menibus A., Hamard E., Lecompte T., 2020. Hygrothermal properties of light-earth building materials. Journal of Building Engineering 29, 101134.

Evola G., Marletta L., Sicurella F., Tanasiev V., 2013. Combining thermal inertia, insulation and ventilation strategies for improving indoor thermal summer comfort. In Proceedings of the 34th AIVC. Athens.

Guo R., Hu Y., Liu M., Heiselberg P., 2019. Influence of design parameters on the night ventilation performance in office buildings based on sensitivity analysis. Sustainable Cities and Society 50, 101661.

Hema C., Messan A., Lawane A., Van Moeseke G., 2020. Impact of the Design of Walls Made of Compressed Earth Blocks on the Thermal Comfort of Housing in Hot Climate. Buildings 10(9),157.

Rupp R.F., Giraldo Vásquez N., Lamberts R., 2015. A review of human thermal comfort in the built environment. Energy and Buildings 105, 178–205.

Lauzet N., Colinart T., Musy M., Lapray K., 2021. Selecting extreme weather file to assess overheating in residential building. Journal of Physics: Conference Series 2069(1), 012231.

Verbeke S., Audenaert A., 2018. Thermal inertia in buildings: A review of impacts across climate and building use. Renewable and Sustainable Energy Reviews 82, 2300–2318.

6th International Conference on Building Energy and Environment
Eindhoven University of Technology, The Netherlands
6 - 10 July 2025

Human thermal responses and preferences during climate transitions

Pei-Lun Fang [1], Wen-Mei Shih [2], Ruey-Lung Hwang [3], Kuo-Tsang Huang [4]

[1] *Department of Bioenvironmental Systems Engineering, National Taiwan University, Taipei, Taiwan, r13622035@ntu.edu.tw*
[2] *Department of Refrigeration, Air-Conditioning and Energy Engineering, National Chin-Yi University of Technology, Taichung, Taiwan, shihwenmei@gmail.com*
[3] *Department of Industrial Technology Education, National Kaohsiung Normal University, Kaohsiung, Taiwan, rueylung@nknu.edu.tw*
[4] *Department of Bioenvironmental Systems Engineering, National Taiwan University, Taipei, Taiwan, huangkt@ntu.edu.tw*

SUMMARY
This study investigates the thermal responses and adaptive behaviors of the human body during seasonal transitions in Taiwan. The research employs objective physical measurements and subjective thermal questionnaire surveys to analyze the effects of short-term thermal history on thermal perception and comfort. The study period encompasses two transitional seasons: the warming period (January to August) and the cooling period (July to the following February). The results reveal a significant asymmetry in thermal sensitivity between the warming and cooling transition processes, influenced by prior thermal experiences. During the warming period, clothing adjustments exhibit a certain lag, whereas during the cooling period, adjustments are relatively prompt, reflecting a heightened sensitivity of residents to cooling environments. This study highlights the importance of thermal history on thermal perception and adaptive behavior, emphasizing the need to fully consider its effects during seasonal transitions between warm and cold periods.

Keywords: Climate Transitions, Thermal Comfort, Psychological Adaptation, Universal Thermal Climate Index.

1. INTRODUCITON

The outdoor thermal environment is directly related to thermal comfort. During the transition between warm and cold conditions, the previous thermal conditions experienced by residents, i.e. the thermal history, plays a crucial role in influencing their thermal responses and preferences (Brager & de Dear, 1998). Brychkov et al. suggested that thermal history can be divided into long-term and short-term thermal history (Brychkov et al., 2018). Jowkar et al. defined long-term thermal history as the climatic influence of people's place of residence over many years or an entire season, while short-term thermal history refers to the effects of daily thermal exposure over shorter time scales, ranging from weeks, days, and hours to even seconds (Jowkar et al., 2020). In recent years, the impact of thermal history on thermal comfort has attracted significant attention. Additionally, personal factors such as clothing insulation, psychological factors, and cultural aspects also significantly affect subjective perceptions of thermal comfort (Zhang et al., 2010).

Xie et al. explored outdoor thermal comfort among Hong Kong residents using a questionnaire survey, proposing the interactive effects between seasonal thermal history changes and thermal comfort criteria (Xie et al., 2019). Hwang et al. combining field questionnaire surveys with

environmental physical measurements, discussing on how short-term thermal history affects the thermal perception of pedestrians walking on sidewalks (Hwang et al., 2022). Hwang et al. also assessed the transitional spaces between outdoor and indoor environments, investigating the thermal sensation of individuals experiencing abrupt temperature changes and confirming that thermal comfort in these spaces is closely related to prior thermal exposure (Hwang et al., 2008). Lam et al. conducted outdoor thermal comfort surveys in Guangzhou, Zhuhai, and Melbourne, analyzing the interaction of long-term and short-term thermal histories on outdoor thermal comfort as well as examining the influence of prior exposure environments across different climate zones (Lam et al., 2021).

Previous studies have extensively explored the relationships and effects among thermal history, thermal adaptation, and thermal perception. However, relatively little analysis has focused on changes in thermal history during transitions between warm and cold outdoor climates. This study aims to examine the impact of short-term thermal history on dynamic changes in thermal perception during these transitions. Furthermore, this study investigates the driving mechanisms of thermal adaptive behaviors, explores how thermal history affects the inertia of clothing adjustment behaviors, and reveals residents' responses to thermal stress during outdoor cold-to-warm climate transitions.

2. METHOD

2.1. Physical measurement and subjective survey

The physical microclimate measurement and the subjective thermal perception questionnaire investigation was simultaneously conducted in university campuses, parks, and other locations in Taichung City, central Taiwan. Each survey session lasted 8 hours, from 9:00 AM to 5:00 PM. All surveys were conducted on days with favorable weather, avoiding strong winds or rain. Meteorological parameters measured includes air temperature, relative humidity, wind speed, and globe temperature. The questionnaire consisted of two parts to collect the following information: (1) Basic participant information, including clothing insulation, gender, age, height, weight, and long-term place of residence; (2) Questions related to thermal perception, designed to understand participants' thermal sensations in outdoor environments. Thermal perception was assessed based on the ASHRAE classification, using a 7-point scale, including thermal perception levels of cold, cool, slightly cool, neutral, slightly warm, warm, and hot (Standard, 1992).

2.2. Data Analysis

To explore the relationship between climate transitions (especially seasonal changes from warm to cold or cold to warm) and human thermal responses, as well as to evaluate the influence of thermal history and behavioral adaptation on thermal comfort. This study utilizes the weather variation recorded in the TMY3 weather data of Taichung City (TAIWAN) as the basis for seasonal transition classification. As shown in Figure 1, the weather data are divided into two weather transition periods: the warming period, which refers to the period from the coldest month gradually warming to the hottest month (January to August); and the cooling period, which refers to the period from the hottest month gradually cooling to the coldest month (July to February of the following year). Based on this transitional weather classification, the study analyzes the experimental data to investigate the characteristics of residents' thermal perceptions and adaptive behaviors during the outdoor environment's warm-to-cold and cold-to-warm transition processes.

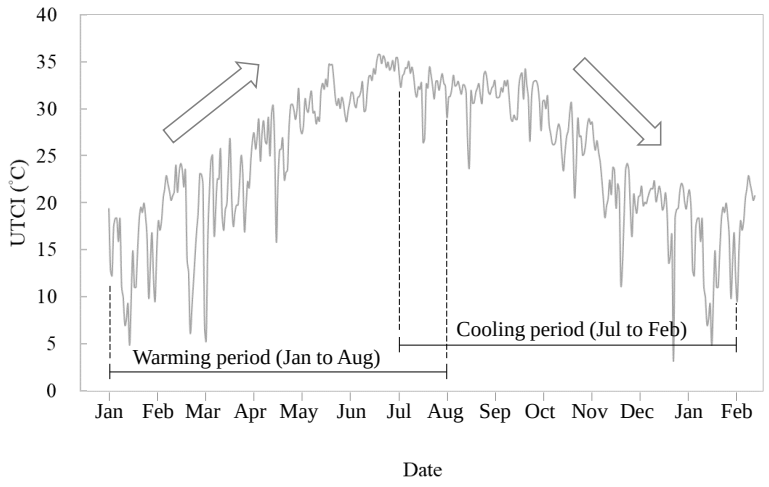

Figure 1. Seasonal transition group for cold-to-warm and warm-to-cold environments

The Universal Thermal Climate Index (UTCI) was used as an indicator to evaluate outdoor thermal comfort. The UTCI is a biometeorological index developed by a team of multidisciplinary experts to describe the thermal stress experienced by the human body in real environments, considering factors such as air temperature, mean radiant temperature, wind speed, and humidity. The metabolic rate in the UTCI multi-node model (Fiala et al., 2012) is assumed to be a constant value of 2.3 Met, which is similar to the metabolic rate of a person walking outdoors at a speed of 1.1 m/s (Bröde et al., 2012). Due to its comprehensiveness and applicability, the localized UTCI scale model has been developed in Taiwan (Chen et al., 2025) and many other countries, becoming one of the most widely used indicators in the field of outdoor thermal comfort assessment.

To understand the participants' responses to varying environmental thermal stimuli during questionnaire completion, this study analyzes the transition temperatures associated with each thermal sensation vote (TSV) based on a substantial dataset of participant's TSVs collected during climatic transitions. The transition temperature is defined as "the temperature at which the maximum number of people change their vote from one thermal sensation to the next." As shown in Table 1, six types of responses can be listed using the seven-point TSV thermal sensation voting scale (Nicol et al., 2012; Xie et al., 2019), by dividing the TSV data into two groups. In the third row of Table 1 as an example, Group 1 refers to participants who consider "colder than neutral," while Group 2 refers to those who consider "neutral to warm."Ballantynre et al. proposed the use of probability analysis for thermal perception analysis (Ballantyne et al., 1977). By treating thermal stimuli as the independent variable and thermal sensation as the dependent variable in binary logistic regression analysis, as shown in formula (1). Logistic regression can effectively describe how the probability of response changes with thermal stimuli, and the likelihood of transition is established as a linear relationship between the two variables, as shown in formulas (2) and (3). The S-shaped curve obtained from the binary response logistic probability fitting model using P and (1-P) represents the transition temperature at the point where the probability equals 50%, which is the threshold temperature corresponding to the TSV transition from 0 to 1. The temperature change between the two transition temperatures defines the thermal sensation range (Ballantyne et al., 1977).

Table 1. Example of thermal sensation vote combination.

Group1 (P)	Group2 (1-P)	Criteria for Group
P(-3)	P(-2)+P(-1)+P(0)+P(+1)+P(+2)+P(+3)	P(TSV≧-2)
P (-3)+P(-2)	P(-1)+P(0)+P(+1)+P(+2)+P(+3)	P(TSV≧-1)
P (-3)+P(-2)+P(-1)	P(0)+P(+1)+P(+2)+P(+3)	P(TSV≧0)
P (-3)+P(-2)+P(-1)+P(0)	P(+1)+P(+2)+P(+3)	P(TSV≧+1)
P (-3)+P(-2)+P(-1)+P(0)+P(+1)	P(+2)+P(+3)	P(TSV≧+2)
P (-3)+P(-2)+P(-1)+P(0)+P(+1)+P(+2)	P(+3)	P(TSV≧+3)

$$P = f(\beta_0 + \beta_1 x) \tag{1}$$

$$Logit\ P = ln\left[\frac{P}{1-P}\right] = \beta_0 + \beta_1 x \tag{2}$$

$$P = \frac{\exp(\beta_0 + \beta_1 x)}{1 + \exp(\beta_0 + \beta_1 x)} \tag{3}$$

Where P represents the probability of response to a stimulus, as the cumulative distribution function; β_0, β_1, are constants; x is UTCI.

3. RESULTS AND DISCUSSION

3.1. Questionnaire investigation results

Figure 2 shows significant changes in outdoor thermal conditions during the transition periods, encompassing a wide range of climate conditions. In both transition seasons, the UTCI ranged from 1°C to 49°C. During the warming period, the mean UTCI was 28.44°C, while during the cooling period, it was 28.37°C. A total of 12,872 valid responses were collected during the entire experimental period, with 7,326 responses during the warming period and 10,353 responses during the cooling period. As the UTCI increased, the TSV gradually rose from -3 to 3, showing high consistency across both seasons. Notably, when the UTCI exceeded 31°C, the mean UTCI during the cooling period was lower than that during the warming period, with most TSV values concentrated between 1 and 2. The TSV distribution for both periods when UTCI was below 17°C showed smaller differences, but it was observed that the mean UTCI during the warming period was higher than that during the cooling period. Between the UTCI range of 19°C to 31°C, the TSV distribution was wide.

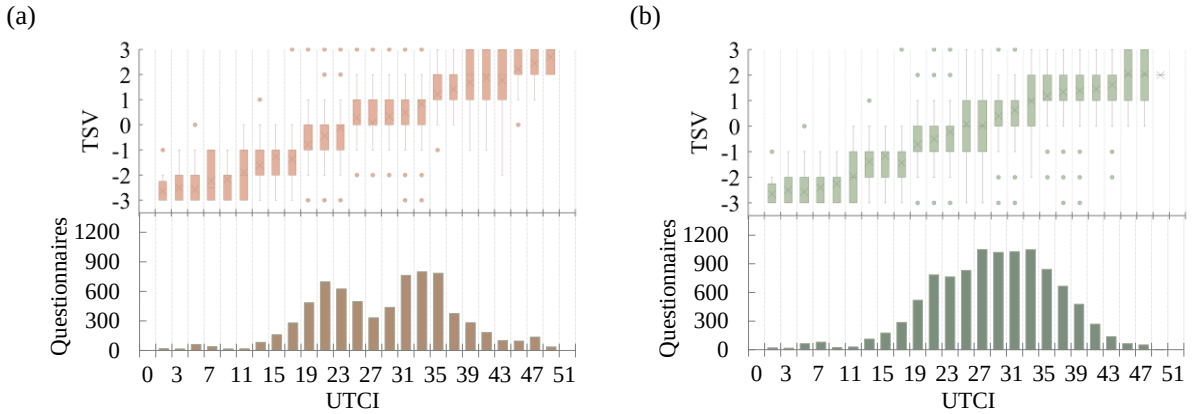

Figure 2. Distribution of thermal sensation votes (a) during the warming period, (b) during the cooling period.

3.2 Clothing Adaptation Behavior

Clothing adjustment is a key adaptive behavior people use to maintain thermal comfort in outdoor environments. As shown in Figure 3, the distribution of clothing insulation values during the experimental period is primarily concentrated between 0.35 and 1.8, with mean values ranging from approximately 0.35 to 1.0. When the UTCI exceeds 30°C, the mean clothing insulation value is below 0.6 and remains stable, indicating that even in hot environments, individuals maintain a minimum level of clothing, demonstrating limited capacity for further clothing reduction. In cold environments, a stable upper limit of clothing insulation was not observed; individuals adjusted their clothing freely according to the decreasing temperatures to adapt to the progressively cooler conditions. In Figure 3, data from the coldest months (January-February) and the hottest months (July-August) are distinguished by light gray and light yellow dots, respectively. The transition periods from cold to warm (March-June) and from warm to cold (September-December) are represented by orange and blue dots, as shown in Figure 3. Regression analysis revealed that the linear slope of clothing insulation during the warming period is -0.0129, while during the cooling period, the slope is -0.0165. This indicates a faster rate of clothing insulation change during the cooling period than during the warming period. This result suggests that under Taiwan's hot and humid climate, individuals exhibit greater sensitivity to cold weather after prolonged adaptation to hot conditions. During the cooling period, as the weather transitions from warm to cold, individuals tend to increase their clothing more rapidly. Additionally, when the UTCI is the same, individuals are influenced by their thermal history and tend to delay taking off their clothing. Thus, for a given UTCI, thermal history influences individuals to delay clothing removal, resulting in higher clothing insulation values during the warming period compared to the cooling period.

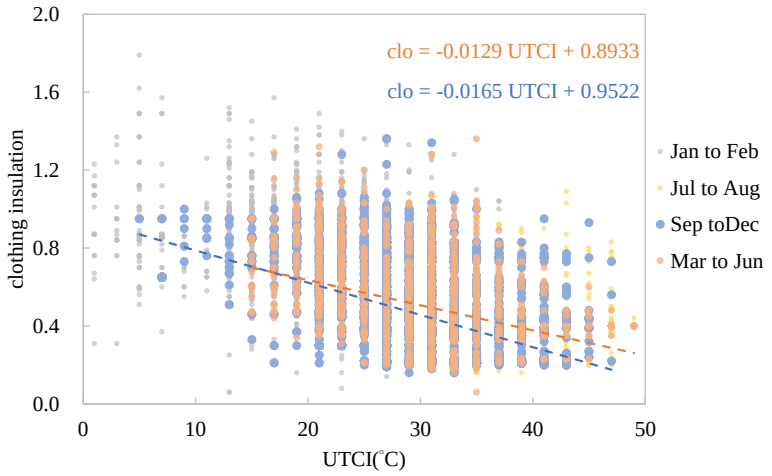

Figure 3. Trend of clothing amount variation with outdoor UTCI changes

3.3 Transition temperatures during the two periods

Figures 4 (a) and (b) show that the range of transition temperatures spans from 6.4°C to 45.4°C during the warming period and from 5.3°C to 48.0°C during the cooling period, with transition temperatures in the latter period generally exceeding those in the former. Among all thermal sensation values (TSVs), the neutral sensation (TSV=0) exhibits the broadest temperature range. As UTCI increases or decreases, it reflects that the more extreme the thermal environment, the narrower the temperature range. Focusing on the transition between warm and cold environments,

it is observed that in a progressively warming environment, the thermal sensation range for TSV = -2 is only 6.3°C (from 6.4°C to 12.7°C) when the TSV changes from -3 to -1. This represents the narrowest range observed during the warming process, suggesting that individuals, having experiencing a prolonged cold season, develop an anticipatory expectation of warming. Consequently, they exhibit heightened sensitivity to thermal conditions exceeding their prior thermal experience.

In contrast, during the cooling period, when TSV changes from 3 to 1, the transition temperature ranges from 48.0°C to 40.2°C. Although individuals may also anticipate a gradually cooling environment, for those with prolonged exposure to hot and humid climates, the influence of their established thermal history necessitates a more substantial cooling effect for the environment to be perceived as cool. This phenomenon confirms that sensitivity to hot and cold environments is influenced by factors such as thermal history, psychological expectations, and clothing adjustments, and further demonstrates an asymmetry in thermal sensations.

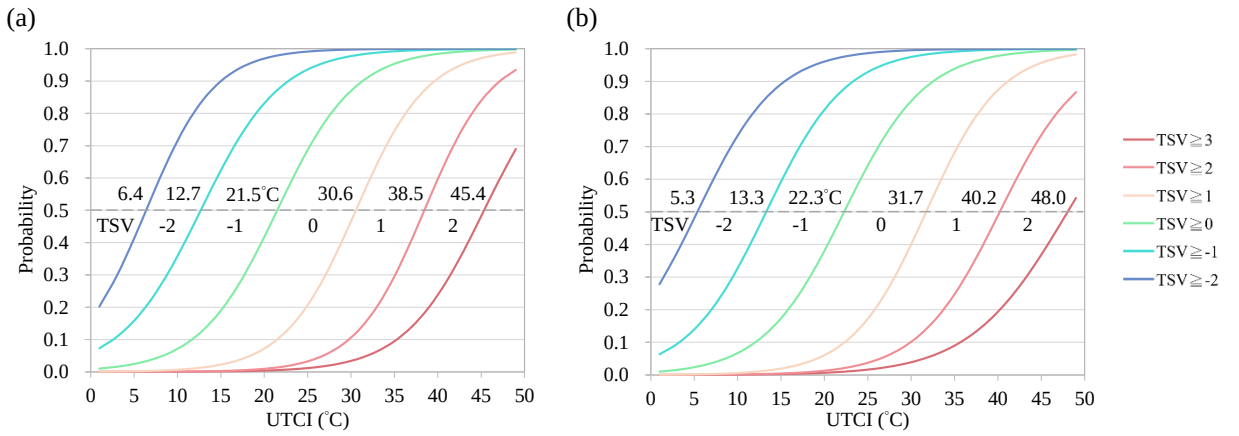

Figure 4. (a) Warming phase, (b) Cooling phase ordinal logistic regression fitting curves for the changes in thermal sensation

3. 4 Relationship between clothing insulation and transition temperature

Environmental changes not only directly affect individuals' thermal perception but also interact with adaptive behaviors, thereby influencing thermal comfort. As shown in Figure 5, during the warming period, the mean clothing insulation across all thermal sensation ranges is higher than that during the cooling period. Comparing the transition temperatures between the two periods reveals that the transition temperature during the warming period is lower than that during the cooling period. This finding suggests that the higher clothing insulation during the warming period may lead individuals to experience greater thermal discomfort as the weather becomes increasingly hot. Conversely, during the cooling period, the reduced clothing insulation may exacerbate cold discomfort as ambient temperatures decrease. Furthermore, it is noteworthy that in hot environments (TSV > 1), the clothing-based adaptation is limited, with little difference in the thermal sensation range at TSV = 2 between the two periods. Despite the reduction of clothing insulation to a mean clothing insulation of 0.4 during the warming period, the impact of prior thermal discomfort resulting from neutral-to-warming conditions leads to a 1.7°C higher transition temperature during the warming period (40.2°C - 38.5°C). Conversely, in cold environments, clothing insulation does not reach a limit, and the adaptive capacity is comparatively greater. Clothing adaptation has a greater effect on the thermal sensation range at TSV = -2, with a higher

clothing insulation during the warming period exacerbating thermal discomfort from warming conditions and resulting in lower transition temperatures. During the cooling period, despite the influence of prior discomfort from neutral-to-cooling thermal history, the increase in clothing insulation to a mean of 0.85 is sufficient to mitigate cold discomfort, resulting in a transition temperature during the cooling period that is only 0.6°C higher than that during the warming period (13.3°C - 12.7°C). This analysis not only highlights the differences and contributions of clothing behavior in thermal adaptation during cold-to-warm and warm-to-cold transitions but also emphasizes the significant impact of thermal history on individuals' thermal perception and adaptive behaviors.

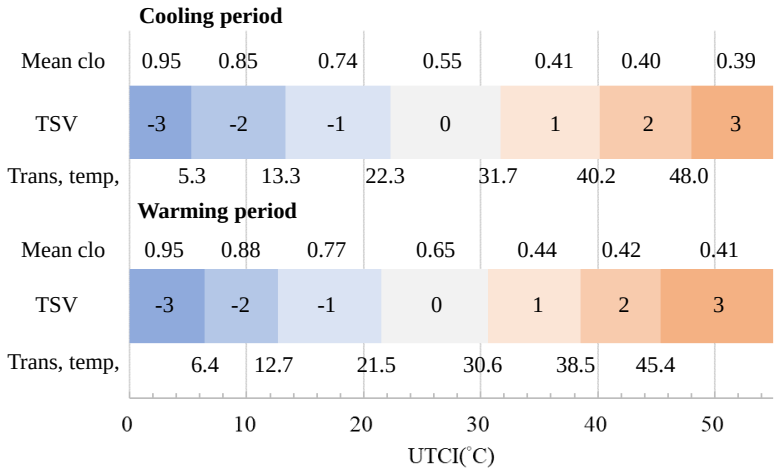

Figure 5. Thermal sensation range and mean clothing volume

4. CONCLUSION

This study, through analysis of outdoor microclimate measurements and subjective questionnaire surveys, elucidates the dynamic role of thermal history during the warming and cooling periods of temperature transitions. The influence of short-term thermal history on individuals' thermal perception and adaptive behavior during seasonal transitions is also investigated. The principal findings are as follows:

- This study confirms that short-term thermal history significantly affects individuals' thermal perception and adaptive behavior, particularly during seasonal transitions, where its influence on thermal comfort exhibit dynamic changes.
- Thermal perception during the warming and cooling periods is asymmetric, with transition temperatures influenced by thermal history. Specifically, thermal perception during the warming period is generally lower than that during the cooling period.
- During the warming period, individuals exhibit inertia influenced by thermal history, tending to delay reducing clothing insulation; conversely, during the cooling period, a delay in increasing clothing insulation is observed. In hot environments, the capacity for clothing adjustment is limited, whereas in cold environments, clothing adjustments are more flexible, indicating differences in adaptation to environmental changes.

REFERENCES

Ballantyne, E. R., Hill, R. K., & Spencer, J. W., 1977. Probit analysis of thermal sensation assessments. International Journal of Biometeorology 21(1), 29-43.

Brager, G. S., & de Dear, R. J., 1998. Thermal adaptation in the built environment: A literature review. Energy and Buildings 27(1), 83-96.

Bröde, P., Fiala, D., Blazejczyk, K., Holmér, I., Jendritzky, G., Kampmann, B., Tinz, B., & Havenith, G., 2012. Deriving the operational procedure for the Universal Thermal Climate Index (UTCI). International Journal of Biometeorology 56(3), 481-494.

Brychkov, D., Garb, Y., & Pearlmutter, D., 2018. The influence of climatocultural background on outdoor thermal perception. International Journal of Biometeorology 62(10), 1873-1886.

Chen, W.-A., Fang, P.-L., & Hwang, R.-L., 2025. Calibrating the UTCI scale for hot and humid climates through comprehensive year-round field surveys to improve the adaptability. Urban Climate 59, 102267.

Fiala, D., Havenith, G., Bröde, P., Kampmann, B., & Jendritzky, G., 2012. UTCI-Fiala multi-node model of human heat transfer and temperature regulation. International Journal of Biometeorology 56(3), 429-441.

Hwang, R. L., Weng, Y. T., & Huang, K. T., 2022. Considering transient UTCI and thermal discomfort footprint simultaneously to develop dynamic thermal comfort models for pedestrians in a hot-and-humid climate. Building and Environment 222, 109410.

Hwang, R. L., Yang, K. H., Chen, C. P., & Wang, S. T., 2008. Subjective responses and comfort reception in transitional spaces for guests versus staff. Building and Environment 43(12), 2013-2021.

Jowkar, M., de Dear, R., & Brusey, J., 2020. Influence of long-term thermal history on thermal comfort and preference. Energy and Buildings 210, 109685.

Lam, C. K. C., Gao, Y., Yang, H., Chen, T., Zhang, Y., Ou, C., & Hang, J., 2021. Interactive effect between long-term and short-term thermal history on outdoor thermal comfort: Comparison between Guangzhou, Zhuhai, and Melbourne. Science of the Total Environment 760, 144141.

Nicol, F., Humphreys, M., & Roaf, S., 2012. Adaptive thermal comfort: Principles and practice.

Standard, A., 1992. Thermal environmental conditions for human occupancy. ANSI/ASHRAE 55.

Taiwan, I. C. D. I. Typical meteorological year.

Xie, Y., Liu, J., Huang, T., Li, J., Niu, J., Mak, C. M., & Lee, T.-C., 2019. Outdoor thermal sensation and logistic regression analysis of comfort range of meteorological parameters in Hong Kong. Building and Environment 155, 175-186.

Zhang, H., Arens, E., Huizenga, C., & Han, T., 2010. Thermal sensation and comfort models for non-uniform and transient environments: Part I: Local sensation of individual body parts. Building and Environment 45(2), 380-388.

Building Acoustics & Lighting (13:30-15:00 h)

6th International Conference on Building Energy and Environment
Eindhoven University of Technology, The Netherlands
6 - 10 July 2025

Study on lightscape perception of Chongqing Historical and Cultural Districts: Taking Longmenhao Old Street as an example

Yaoxi Liu [1], Haijing Huang [1, 2], Miao Li [1], Xintang Deng [1], Lin Hu [1]

[1]*Chongqing University, Chongqing, China, 1003434637@qq.com*
[2] *Key Laboratory of New Technology for Construction of Cites in Mountain Area, Chongqing, China*

SUMMARY
This study explores "lightscape" perception in Longmenhao Old Street, Chongqing. Six key sites were analyzed through lightwalk and questionnaires based on 18 perception indicators. Results show that tourists prefer traditional architecture, interactive natural light, and landmark features, while commercial clutter and mismatched facilities negatively impact perception. Strong correlations were found between preference and visual indicators like scenic quality and spatial diversity. The findings highlight the need to enhance visual appeal and spatial layering in historical street renewal.

Keywords: Longmenhao Old Street, Lightscape, Lightwalk, Perception.

1. INSTRUCTIONS

In the process of urban evolution, Historical and Cultural Districts face many challenges. On the one hand, some districts are at risk of destruction and disappearance, and urgently need protection; On the other hand, from a development perspective, the material and intangible cultural heritage of the district should be maintained; And at the policy level, it actively guides Historical and Cultural Districts to move towards a direction conducive to urban cultural development, which coincides with the current "city walk" trend of people's enthusiasm for characteristic cultural spaces. Chongqing Historical and Cultural Districts, with their profound historical accumulation, rich cultural resources, and unique street and alley spaces shaped by mountainous terrain, have extremely high research value. As an important aspect of public perception, Lightscape can deepen people's understanding of the history, culture, and spatial charm of the districts, effectively enhance the aesthetic value of districts, and inject vitality into the protection, inheritance, and future development of Historical and Cultural Districts.

2. RESEARCH STATUS

2.1. Current Status of Research on Historical and Cultural Districts

The research object and scope of Historical and Cultural Districts have mainly developed from the protection of individual historical buildings to traditional architectural complexes with historical significance (Jing, 2022). Then, economic factors have been included in the consideration of protection policies (Liu, 2021). Based on this, scholars have coincidentally studied the overall situation of Historical and Cultural Districts from the perspective of urban planning. Hossain explored the ways of planning activities for historic districts and emphasized

the rational preservation of their structure, cultural heritage, and overall environment (Hossain, 2013). Tutkboni analysed and proposed various impacts of newly built urban districts on historic districts (Shehata,2022). Ren Huan studied the mountainous street and alley spaces of Liziba Old Street, Chongqing, exploring the traditional views and cultural characteristics that reflect regional customs (Ren, 2017). In order to further study the elements and values of Historical and Cultural Districts, scholars have conducted evaluation analysis. Yu Hongxia conducted a decentralized assessment of several indicators of the architectural environment when studying the value assessment system of Qingdao Historical and Cultural Districts (Yu et al., 2014). Wang Haobin constructed an evaluation index system for the quality of tourism experience in Historical and Cultural Districts (Wang, 2023). After completing the analysis of the district environment, the focus of research gradually shifted to people's perception. For example, Taketo Naoi analysed tourists' evaluation of the authenticity of historical urban areas (Naoi, 2004). In terms of soundscape, Zhou Min (Zhou, 2015), Liu Jiang (Liu et al., 2019) conducted sound walks and fixed-point surveys in various historical districts. In terms of lightscape, Chen Ranpeng conducted a lightscape study on the Xiguan historical area in Guangzhou, emphasizing the importance of light-visual elements in improving satisfaction and artistic conception (Chen, 2021). In terms of visual perception, Meysam studied the impact of the visual preference dimension of historic urban areas on urban heritage protection (Najd et al., 2015). From the perspective of comprehensive perception, Yu Hui took the Zhongshan Road Historical and Cultural District in Shenyang as the research object, studied the current status of the district in terms of the five senses of vision, hearing, smell, taste, and touch, and proposed to create a "multi-sensory" experience environment (Yu et al., 2023).

2.2. Current Status of Research on Lightscape

In 2017, Wu Shuoxian, an academician of the Chinese Academy of Sciences, first proposed the concept of "lightscape", which refers to landscapes that cause strong visual impressions mainly due to light sources, light and shadows, and their changes (Wu, 2017). Except China, scholars in other countries have conducted little studies on lightscape, and more focus on studying light environment and lighting. At present, the research on lightscape is mainly concentrated in three aspects. First, scholars Bian Yu (Bian et al., 2020), Wu Jihong (Wu, 2022), and Li Yating (Li et al., 2023) separately have sorted out lightscape from three perspectives: ancient Chinese literature and classics, Chinese classical folk scenes, and natural images, and summarized the techniques of lightscape creation. Second, many Chinese scholars have conducted lightscape analysis and application in spaces such as buildings (Qiu et al., 2017), gardens (Qiu et al., 2018), squares (Qiu et al., 2020), historical districts (Chen, 2021), and campuses (Qiu et al., 2022). Among them, Chen Ranpeng (Chen, 2021) explored the lightscape creation strategy for Xiguan historical area in Guangzhou, and proposed balancing the old and new designs and optimizing the light colour and brightness to match the environment. Finally, scholars emphasize the importance of using light to integrate health elements into design.

In general, there is little research on lightscape in Historical and Cultural Districts, especially for Chongqing, a city with a unique historical and cultural background and mountainous features. The research on lightscape perception in its historical and cultural districts is of great significance for understanding the public's perception and evaluation of urban space. Incorporating light as a new perspective into its planning and protection design will also have a positive effect on the heritage protection work within the districts.

3. MATERIALS AND METHODS

3.1. Overview of the Lightscape in Longmenhao Old Street

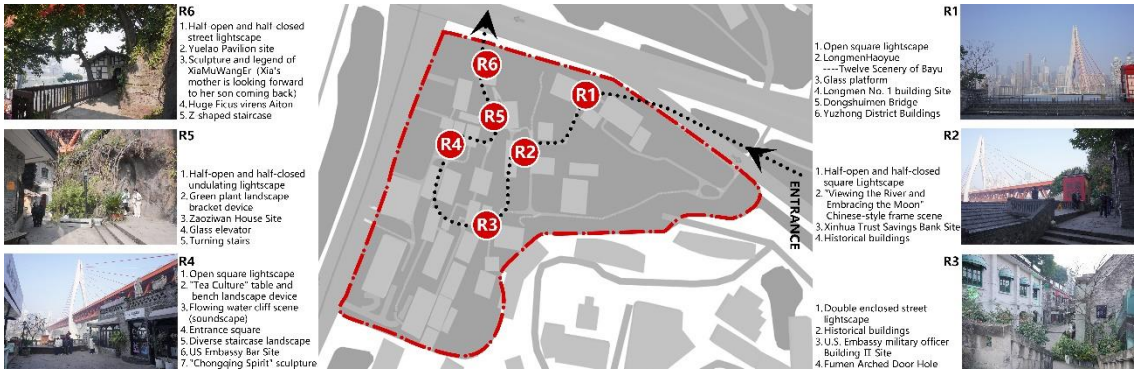

Figure 1. Overview of Lightscape Site

Longmenhao Old Street is located in the Nan'an District of Chongqing and is one of the most well-preserved historical and cultural Districts in the city's main urban area. Based on preliminary research, six representative sites within the street were selected as evaluation sites for lightscape perception, which include famous attractions and key pedestrian nodes. The sites are numbered from R1 to R6 according to the typical order. On-site photos and the main features of each lightscape site are shown in Figure 1.

3.2. Lightwalk Questionnaire Design

In order to fully understand tourists' perception and evaluation of lightscape, a structured questionnaire was designed, consisting of three parts. The first part collects basic information, including gender, educational background, etc. The second part focuses on lightscape evaluation: (1) participants indicate the lightscape elements liked and disliked at each site; (2)Score the 18 lightscape perception indicators using a 5-point Likert scale; (3)The third part addresses overall preference, in which each participant selects their favorite lightscape site from among R1 to R6.

3.3. Participant Selection and Implementation of the Lightwalk Survey

The "Lightwalk" survey recruited 27 health participants, aged between 18 and 27 years old. The survey was arranged on sunny days on weekdays, guided by 3 researchers from Chongqing University. Participants followed the lightscape map of the six lightscape sites (R1-R6) as shown in Figure 1. At each site, participants stayed for 5 to 20 minutes to fully experience the lightscape characteristics, and fill out the questionnaire based on their individual perceptions (Figure 2 - Figure 3). A total of 27 questionnaires were collected at each site, resulting in 216 valid responses overall.

Figure 2. On-site photo 1

Figure 3. On-site photo 2

4. RESULTS

This chapter explores the relationship between the characteristics of different lightscape sites in Longmenhao Old Street and tourists' preferences. It further investigates the weight and impact pathways of 18 lightscape perception indicators in perceptual evaluation.

4.1. Analysis of Preferred and Non-Preferred Lightscape Types

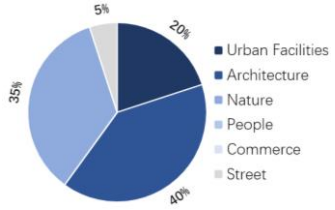

Figure 4. Preferred lightscape type

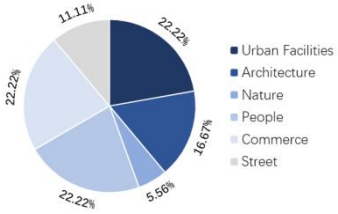

Figure 5. Non-preferred lightscape types

Figure 6. Disliked lightscape word cloud

Survey results indicate that the most preferred types of lightscape respondents are architecture, natural landscape and urban facilities(Figure 4). On the contrary, the least favored types include commercial elements, human activities, and certain urban facilities (Figure 5).

Further analyze the favorite lightscape of R1-R6 sites (Figure 7):

(1) Areas with a historical architecture generally received higher evaluations. For example, historical buildings with traditional elements (sloped roofs, gray bricks, and framed views, etc.) are more popular among tourists, which indicates that the tangible expression of traditional culture significantly enhances lightscape perception.

(2) In terms of natural lightscapes, dynamic scenes involving strong light interaction—such as water reflections and shaking tree shadows—elicited strong emotional resonance from visitors. Accompanying soundscapes (e.g., flowing water, wind) further contributed to an immersive experience.

(3) Landmark urban facilities with strong regional characteristics, such as the Dongshuimen Bridge, also received high ratings. Its distinctive form and vivid color made it a visual focus. And lightscape elements involving the bridge were consistently among the most favored.

Figure 7. Top 3 Favorite Lightscape Elements at R1–R6 Sites

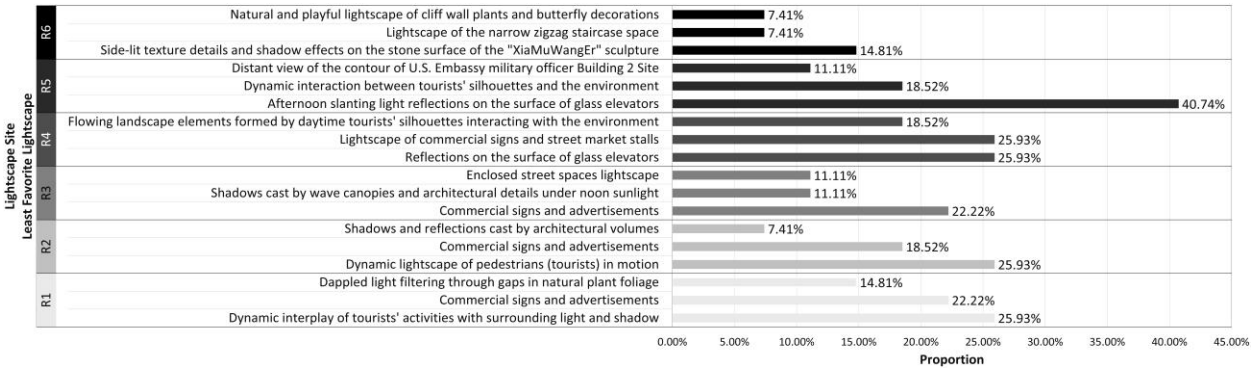

Figure 8. Least Favorite Lightscape Elements at R1–R6 Sites

According to the word cloud of "disliked lightscape" (Figure 6), commercial advertisements and related activities were identified as the primary sources of disturbance, which include signage, advertising boards, and street stall markets, etc.; Secondly, the gathering and activities of high-density people also significantly affect quality of the lightscape experience. Together, these factors reflect that excessive commercialization and dynamic visual disturbances tend to undermine tourists' perception of the lightscape. Moreover, inconsistent urban facilities and improper light treatments are frequently mentioned, such as glass elevators that produce strong reflections under sunlight, strong shadows formed by strong midday light, and landscape devices that do not match the historical atmosphere (Figure 8). These elements weaken the overall quality of the lightscape experience of visitors to varying degrees.

4.2. Analysis of Lightscape Indicator Scores at Each Point

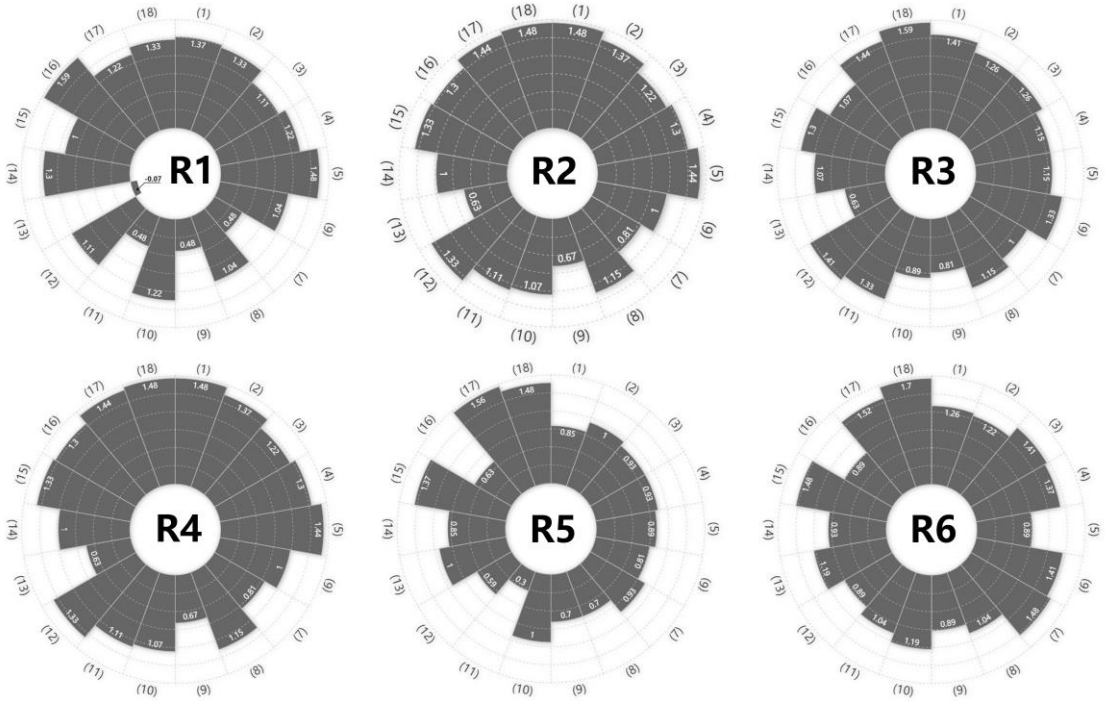

Figure 9. Radar Chart of Average Scores for Lightscape Indicators at R1–R6

This study established 18 lightscape perception indicators, covering multiple dimensions including lightscape, nature, space, history, culture, aesthetics and mountain. The 18 indicators and corresponding numbers are shown in Table 1. The scores of 6 lightscape sites on each indicator were analyzed (Figure 9), and the results were as follows:
(1) R1's advantages are high Cleanliness and Visual Openness. The disadvantages are low Comfort, sense of Change and Nature. The overall assessment is that the space is visually open but provides a rather plain experience. So it is advisable to enhance the landscape layering and natural vegetation.
(2) The advantages of R2 are beautiful Scenery, high scores in Attractiveness, Satisfaction, and Characteristics. While in terms of Coordination and Nature are poor. The overall assessment is that it has strong visual appeal but lacks natural elements and spatial coherence.
(3) R3 excels in Historicity and Cultural Identity, but has lower scores in Color Harmony and Distinctiveness. In general, R3 conveys a strong cultural atmosphere, but color coordination should be improved.
(4) R4 has high Cultural Identity and Spatial Diversity. While the disadvantages are poor Attractiveness and Satisfaction. Overall, the cultural atmosphere is well expressed but lacks significant visual attraction.
(5) The advantage indicators of R5 are that there are many Natures and Undulation Degree, but it has lower scores in Scenic Quality, Satisfaction, Distinctiveness, and Cleanliness. Comprehensive evaluation shows that although they have natural terrain advantages, the overall landscape quality is relatively low, and landscape creation and spatial integration should be strengthened. Overall assessment is that although the site benefits from natural terrain, the overall landscape quality is inadequate and requires enhanced spatial organization and visual design.
(6) R6 has high scores in Pleasantness, Harmony, Comfort Level, Spatial Diversity, and Layers Perception, but with a moderate performance in Cultural Identity and Distinctiveness. In general, R6 offers the best overall spatial experience, but the cultural depth and uniqueness could be further enhanced.

4.3. Correlation Analysis Between Lightscape Indicators and Favorite Site

In order to explore the degree of influence of each lightscape indicator on tourists' preferences, this paper uses Pearson's correlation analysis method to calculate the correlation coefficient between the 18 indicators and the selection frequency of the "favorite site". The results are shown in Table 1:

Table 1. Correlation Analysis Between Indicators and Favorite Lightscape Site

Number	Indicator	Correlation Coefficient(r)	Strength of Correlation	Explanation
(1)	Scenic Quality	0.82	Strong(+)	The level of ligtscape beauty directly affects tourist preferences.
(2)	Attractiveness	0.78	Strong(+)	Interactive and iconic designs significantly improve selection rates.
(3)	Pleasantness	-0.05	Weak (-)	No significant association.
(4)	Satisfaction	0.27	Weak (+)	Tourist satisfaction weakly correlates with selection behavior.
(5)	Distinctiveness	-0.15	Weak (-)	Unique styles may not be sufficiently perceived.
(6)	Harmony	0.65	Moderate(+)	Harmony among lightscape elements has a moderate impact.

(7)	Comfort Level	0.09	Weak (+)	Comfort has little impact on selection behavior.
(8)	Affection Degree	-0.21	Weak (-)	Slight contradiction with selection rates.
(9)	Change Perception	0.25	Weak (+)	Dynamic lighting effects are not clearly perceived.
(10)	Color Harmony	0.47	Weak (+)	Color combinations have limited influence on preferences.
(11)	Historicity	0.12	Weak (+)	Tourists prioritize visual appeal over historical value.
(12)	Cultural Identity	0.19	Weak (+)	Cultural attributes have little influence on preferences.
(13)	Naturalness	-0.58	Moderate (-)	Artificial designs may be more popular.
(14)	Cleanliness	0.31	Weak (+)	Cleanliness is not a core factor.
(15)	Spatial Diversity	0.72	Strong(+)	Diversified spatial forms enhance visitor interest.
(16)	Visual Openness	0.44	Weak (+)	Open sightlines play a minor role.
(17)	Undulation Degree	0.29	Weak (+)	The gap of terrain elevation differences have minimal impact.
(18)	Layers Perception	0.75	Strong(+)	The three-dimensional effects are key drivers.

(1) Strongly positive correlated indicators ($|r| \geqslant 0.7$):
Scenic Quality, Attractiveness, Layers Perception, and Spatial Diversity show strong positive correlations with the frequency of being selected as the favorite lightscape site. This indicates that tourists' preferences are highly influenced by visual aesthetics, terrain hierarchy , and spatial organization.
(2) Moderately correlated indicators ($0.5 \leqslant |r| < 0.7$):
Indicators such as Harmony and Naturalness have a certain degree of influence but are not decisive factors. Notably, Naturalness shows a negative correlation with preference (e.g., R1 had a negative score for Naturalness yet was still well-liked), suggesting that in highly artificial environments, carefully designed artificial elements may be more appealing.
(3) Weakly correlated indicators ($|r| < 0.5$):
Traditional evaluation dimensions such as Historicity, Cleanliness, and Cultural Identity have relatively little impact on visitors' choices. This suggests that contemporary tourists place greater value on immediate spatial experiences rather than historical or cultural context.

5. CONCLUSION AND OUTLOOK

5.1. Research Conclusions

Based on the theory of lightscape perception, this study took Longmenhao Old Street in Chongqing as a case study. Six representative sites (R1–R6) were selected for lightwalk experiments and questionnaire surveys. A systematic analysis was conducted on visitor preferences regarding different types of lightscape and the role of 18 perception indicators in shaping the visitor experience. The main conclusions are as follows:
(1) Preferred lightscape types are primarily concentrated in three categories: architectural scenes with historical and cultural imagery, natural scenes that strongly interact with light elements, and landmark urban facilities. These reflect visitors' high sensitivity to visual aesthetics, cultural identity, and spatial rhythm.
(2) Main sources of disturbance include commercial advertisements, poorly integrated modern facilities (such as glass elevators), and overcrowding. These negative lightscape elements significantly disrupt the spatial atmosphere and perceived quality, suggesting the need for stricter management of commercial elements and the spatial scale of facilities during future

redevelopment.
(3) R6, the highest-rated site, demonstrated comprehensive advantages in spatial layering, comfort, and harmony, offering a model for effective lightscape enhancement. In contrast, R5 received the lowest scores across several indicators and urgently requires improvements in landscape quality and cleanliness.

Future research can expand to include more historical districts in Chongqing, explore night-time lightscape perception, and integrate multi-sensory elements such as soundscapes to deepen understanding of visitor experiences.

REFERENCES

Bian Y., Liu L., Huang C., 2020. Lightscape in A Dream ofRed Mansions and lts Enlightenment. South Architecture (04), 100-105.

Chen R. Research on lightscape of historic areas in Xiguan, Guangzhou. Master's thesis, South China University of Technology, 2021.

Hossain G M A B., 2013. Historical imprints of Panam Nagar. In: International Conference Built Heritage 2013 - Monitoring Conservation Management, pp. 401-407.

Jing Y. Visual Landscape Optimization ofChongqing's Historical and Cultural Districts Based on SBE Method. Master's thesis, Southwest University, 2022.

Li Y., Qiu J., 2023. Analysis of Moon Lightscape Configuration in Traditional Chinese Gardens. Landscape Architecture 30(04),130-136.

Liu J., Yang L., Zhang X., 2019. Research on the Relationship between Soundscape Perception and Landscape Evaluation in Historical Block: A Case Study in the Three Lanes and Seven Alleys in Fuzhou. Chinese Landscape Architecture (01),35-39.

Liu Y. Light art involved in Historical District -- a case study of Yidu ancient town in Chongqing. Master's thesis, Sichuan Fine Arts Institute, 2021.

Najd M D., Ismail N A., Maulan et al., 2015. Visual preference dimensions of historic urban areas: The determinants for urban heritage conservation. Habitat International 49, 115-125.

Naoi T., 2004. Visitors' evaluation of a historical district: The roles of authenticity and manipulation. Tourism and Hospitality Research 5(1),45-63.

Qiu J., Chen J., Li Y., 2020. Evaluation of Lightscape in Guangzhou Huacheng Square. South Architecture (03),94-100.

Qiu J., Li Y., 2018. Lightscapt in Chinese Traditional Garden. Chinese Landscape Architecture 34(05),136-139.

Qiu J., Wei T., Li Y., 2022. A Preliminary Study on Comprehensive Evaluation ofUniversity Campus Lightscape -- A Case of South China University of Technology(Wushan Campus). South Architecture (12),83-92.

Qiu J., Wu S., 2017. Lightscape and Architecture. Architectural Journal (09),115-118.

Ren H, 2017. Characteristics of typical vertical profile of mountainous street in chongoing traditional style area from the perspective of typology -- a case study of liziba traditional scenic area in yuzhong. In: Proceedings of Urban Development and Planning 2017, pp.1536-1540.

Shehata A M., 2022. Current trends in urban heritage conservation: Medieval historic Arab city centers. Sustainability 14(2): 607.

Wang H. Research on the evaluation of tourism experience quality of historical and cultural block based on the embodied theory. Master's thesis, Shenyang Normal University, 2023.

Wu J. Lightscape features of Lantern Festival Venues and the Subjective Evaluation -- Examples of Three Spatial Types in the Southern China. Master's thesis, South China University of Technology, 2022.

Wu S., 2017. Main Points of Lightscape. South Architecture (03), 4-6.

Yu H., Luan X., 2014. Evaluation on historic and cultural blocks in qingdao and strategies for sustainable development. City Planning Review, (3), 65-69.

Yu H., Wang Y., 2023. Research on the renewal of Historical and Cultural Blocks based on sensory experience. Low Temperature Architecture Technology 45.11, 24-28.

Zhou M., 2015. The urban soundscapes of historic conservation areas in mountainous cities: a case stuty in Cigikou, Chongqing. Art & Design (07),136-137.

6th International Conference on Building Energy and Environment
Eindhoven University of Technology, The Netherlands
6 - 10 July 2025

Senses versus Sensors; A measurement tool to enhance students' comprehension of the indoor environmental quality.

Mariëlle P.J. Aarts [1], Twan A.J. van Hooff [2], Constant C.J.M. Hak[3], Maarten C.J. Hornikx[4]

[1]*Eindhoven University of Technology, Unit Building Physics and Services, Eindhoven, The Netherlands,* M.P.J.Aarts@tue.nl
[2] *Eindhoven University of Technology, Unit Building Physics and Services, Eindhoven, The Netherlands,* T.A.J.V.Hooff@tue.nl
[3]*Eindhoven University of Technology, Unit Building Physics and Services, Eindhoven, The Netherlands,* C.C.J.M.Hak@tue.nl
[4]*Eindhoven University of Technology, Unit Building Physics and Services, Eindhoven, The Netherlands,* M.C.J.Hornikx@tue.nl

SUMMARY
To enhance students' understanding of Indoor Environmental Quality (IEQ), a measurement tool was developed for use in the educational program at Eindhoven University of Technology (TU/e) in the Netherlands. The tool includes sensors to measure air temperature, relative humidity, illuminance, and sound pressure level—factors perceivable by humans. It was designed to be inexpensive, suitable for instant and continuous measurements, robust for student use, compatible with Android and iOS, and capable of local data storage. The "SvS" (Senses versus Sensors) device was created, and following a prototype phase, 300 units were produced. The SvS device was used twice in a first-year bachelor's course at TU/e. After the course, 82% of students reported that the device improved their understanding of IEQ. The sensors were calibrated, and all perform accurately within the normal ranges, except for the light sensor which requires a correction factor of 1.5.

Keywords: Indoor Environmental Quality, education, measurement device

1. INTRODUCTION

As professors at the department of the Built Environment at Eindhoven University of Technology (TU/e) working on Building Physics, we considered it an essential skill for future architects and building engineers to be able to fully comprehend the concept of Indoor Environmental Quality (IEQ). In that sense, we were convinced that only learning the theory and the quantitative values given in, for example building standards, codes, or regulations, is not sufficient. These students will be the ones who in their future professions will have to consider and balance many aspects, among which energy, sustainability and the user's needs. While currently, the building process and buildings have their focus on energy and sustainability, we should not forget that the reason we as human beings build is to facilitate the user's needs. We also know that users spend 90% of their time indoors (e.g. Klepeis et al., 2001; Awbi 2003; WHO 2014), meaning that a good IEQ is essential for the quality of a building; a poor IEQ leads to reduced comfort, health and productivity. We also noticed that Architecture students and Building Engineering students often struggle to grasp the practical applications of typically used aspects to identify IEQ, finding it difficult to discern normal or significant values.
Therefore, we decided to develop a measurement device for all students enrolled in the bachelor program Architecture, Urbanism, and Building Science (AUBS) to use. The device should measure

typical values characteristic of various aspects of Indoor Environmental Quality (IEQ), enabling students to connect their own perceptions (senses) to measurable data (sensors). IEQ encompasses factors such as air quality, temperature, light, and sound, which influence occupant comfort, health, and energy use in buildings. Since air quality is key component of IEQ, we chose to measure relative humidity (RH) because it is easier for humans to perceive than CO_2 or PM concentrations. The measurement device should be paired with a software application (app), providing a hands-on method that enhances students' understanding and integration of these factors into their building designs. By bridging the gap between theoretical knowledge and practical application, this initiative also aims to inspire students to pursue advanced studies in building physics, addressing the growing demand for specialists in this field.

2. METHODOLOGY

2.1 Device requirements

At the start of this project, we explored existing devices for student use. Our initial aim was to develop a smartphone application that would utilize the phone's built-in sensors. This approach offered significant advantages: students would have a personal measurement device readily available, and app maintenance and distribution would be simple and sustainable. However, this option proved impractical due to the wide variability of smartphone sensors (van Duijnhoven et al., 2023) and the challenge of accurately measuring environmental temperature with a device that generates its own heat. Therefore, we decided to develop an external device equipped with four sensors. To minimize costs, we created an app that connects to the device to read sensor data. While momentary measurements are useful, incorporating a logging function to store time series data would further enhance students' understanding of the variability of these environmental values. Therefore, the development requirements were:

1. Sensors for measuring illuminance, sound pressure level, air temperature, and relative humidity;
2. Small device that should be carried in a bag;
3. The device should allow to measure real time (momentarily) and as a data logger (continuously);
4. An app should be developed to read real time measurements and to program the logging schedule for continuous measurements;
5. Powered by internal batteries and by an external power unit (e.g. power bank) or the regular power net;
6. Data should not be stored on the smart phone and should be transferable to a computer for analysis;
7. The device should be robust and intuitive to use;
8. The price for the students should be low (preferably under € 25).

2.2 Development procedure

With the specifications given, the TU/e Equipment and Prototype Center (EPC) developed the first version of the device (version 1, see Figure 1). This version contained a small digital display to be used for real time measurements.

Due to the high costs, the size, and the low visibility of the display, the display function was removed and added to the app. During the development, several setbacks had to be overcome. An important one was that the development of an app for an iOS driven device (iPhone) needs approval from Apple. This was achieved via the board of the University.

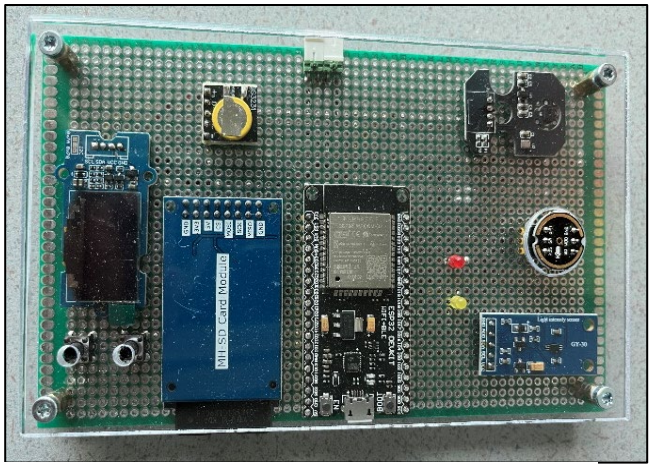

Figure 1 First version of the SvS device (version 1)

Another consideration was the placement of the sensors to ensure they were not obstructed, as this could affect the measurements, while also protecting them from external elements such as dirt, handling, or being tossed into bags. This led to the situation where the light sensor and the microphone are placed on top of the device, while the air temperature and relative humidity sensors are 'isolated' and placed at the bottom of the device. Ten devices of this version were produced (version 2, see Figure 2) and used for testing the design and usability in a pilot test among seven bachelor students.

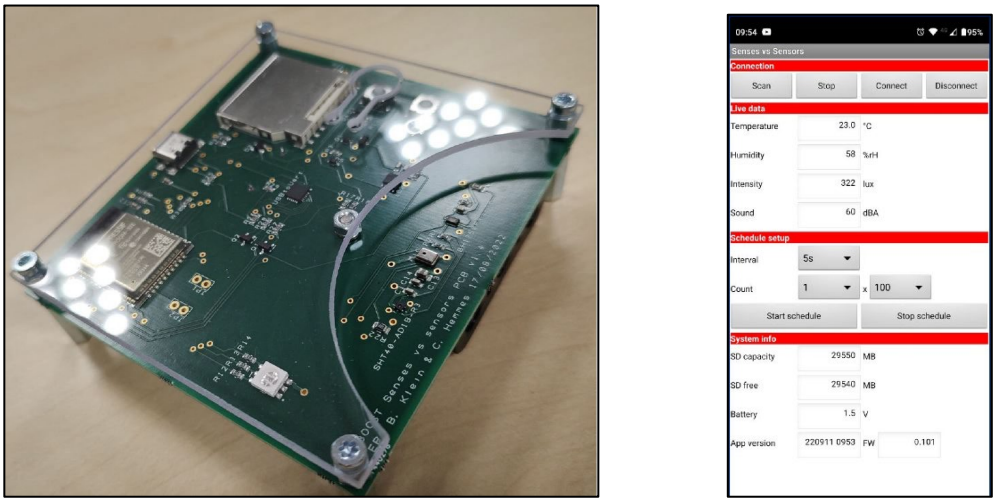

Figure 2 Version 2 of the SvS device (left) and the app (right)

This process led to relevant practical insights, such as the size of the device, the battery life span, the connectivity, and the design.
With these insights, the final version (version 3) of the SvS device was developed as well as the app applicable for people with Android and with iOS smartphones (see Figure 3). After the first round of usage in education, 295 students used the device and also this version was evaluated.

Initially, the selected sensors were identified based on their price, availability and the specified range of accuracy. In a later stage they were calibrated and software wise adjusted. To validate the quality of the sensors the SvS devices (version 3) were calibrated. The calibration results for the four different sensors and both student evaluations are presented in this paper.

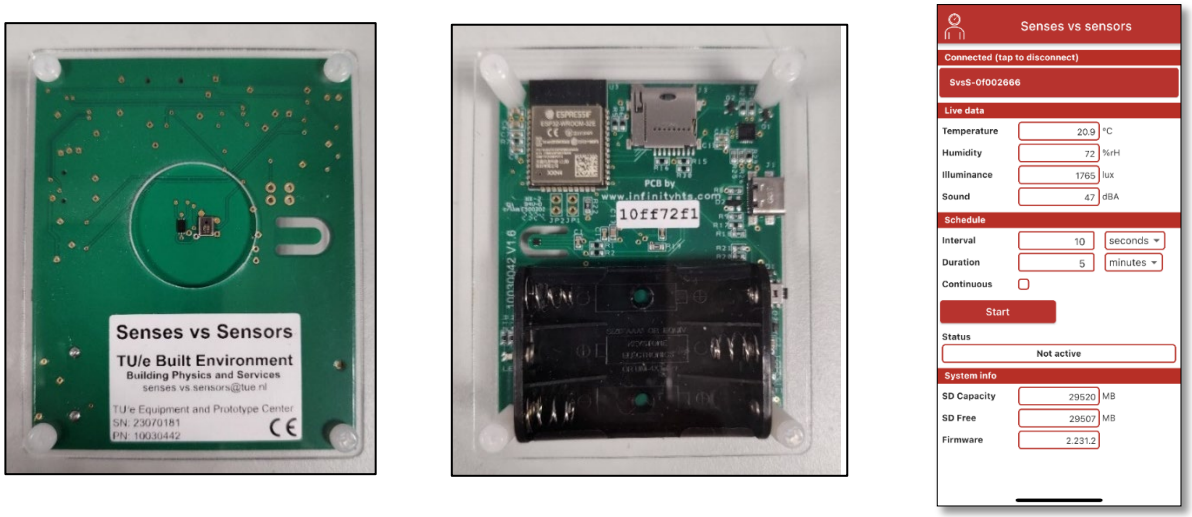

Figure 3 Picture of the SvS device (version 3) front (left), back (middle) and the app (right). Device size is 8.2*6.8*2.0 cm^3

To assess the SvS device and the app, student evaluations were organized in the bachelor program of our department. The two evaluations are outlined in paragraph 2.3 and 2.4 and the calibration is introduced in paragraph 2.5.

2.3 Student evaluation on design and usability of the SvS device (version 2)

To test how students experienced the device, a pilot was conducted among seven bachelor students who followed the third-year bachelor course, *Building Physics and Building Services Engineering*, mandatory for AUBS. These students (3 male, 4 female) were recruited via an announcement on the course page. For the testing purpose, ten devices of the second version were manufactured as well as the first working version of the app. Since the app was only available for Android at that time, students with other smartphones could use an Android phone from our laboratory. The students were given an assignment to measure both real-time values as well as to use the logging function for 24 hours. After one week of use, students provided insights and feedback through an online survey with 19 mostly open-ended questions on the usability of the device. To gather the most comprehensive feedback, the survey results were discussed in a group session with all students, a student assistant, and the project leader.

2.4 Student evaluation on the applicability of the SvS device (version 3) for the intended learning goal.

The SvS device was used in an assignment for the first-year mandatory bachelor course *Healthy and Sustainable Living Environments* in the Architecture, Urbanism, and Building Sciences program. In this group assignment (two students per group), students used the device to measure real-time conditions in their own dwelling and predict values based on their perceptions. They

were also asked to log data for at least 48 hours and explain any differences. The results had to be presented in graphs and be discussed within each group. A total of 295 students used version 3 of the device. To gather feedback, an online survey was conducted during the last lecture using Mentimeter (Mentimeter, n.d.). The survey, focusing on the device's usage and the course's learning objectives, received responses from 35-46 students (not all students answered every question).

2.5 Calibration of the SvS devices, version 3

Since we were interested to know the quality of the sensors, ten randomly selected devices of the SvS were calibrated. See specifications of the sensors in Table 1

Table 1 Specification of the used sensors in the SvS device

Aspect	Sensor type	Manufacturer	Type	Specified range
Illuminance	Ambient light sensor	ROHM Semiconductor	BH1750FVI	1-65535 lx
Sound pressure level	Omnidirectional MEMSmicrophone	CUI Devices	CMM-4030D-261-I2S-TR	38-120dB, 100-10.000 Hz
Air temperature Relative Humidity	Combined air temperature and RH sensor	SENSIRION	SHT4x	-40-125°C 0-100%

For calibrating the illuminance, an Ulbricht Sphere was used (uku 1600) with 12V halogen incandescent lamps, and an Illuminance Spectrophotometer (Konica Minolta, CL-500A). The sound pressure level was measured in a diffuse field measurement room of the TUE Acoustics Lab, using an omnidirectional sound source (Brüel & Kjaer, OmniPower Sound Source Type 4292-L, Acoustics Engineering Power Amplifier and noise generator Type Amphion). For temperature and RH, we used a climate chamber (Memmert, type ICH260) in combination with two research grade air temperature and relative humidity Probes (Vaisala, type HMP1).

3. RESULTS

In this paragraph the results of both student evaluations are presented as well as the results from the calibration.

3.1 Results student evaluation on design and usability of the SvS device (version 2)

In total seven students used the device for one week. The results from the questionnaires indicated potential improvements of the SvS device related to the manual and the process of connecting the device, the logging function, the size of the device (too big), and the pricing (should be less than € 20 if they would need to buy it). Also, a special casing was needed to protect the device and the blinking light indicating that the logging was active, was too bright. As additional IEQ indicators, they would prefer the option to measure air quality (e.g. CO_2 or PM concentrations). The students were pleased with all the different features, the look of the device ('what you see is what you get'), the options for both logging and real-time measurements, and the IEQ insights it provided to them. Most students would have liked to have such a device at the beginning of their studies. The insights obtained from this survey led to an adjustment in the size (half the size and as consequence battery pack of 3* AAA), improvement of the app (more intuitive), reducing the brightness of the blinking LED, and adding a case to the device. In September 2023, a total of 300 SvS devices (version 3) were produced and implemented in our educational program.

3.2 Results student evaluation on the applicability of the SvS device (version 3) for the intended learning goal.

Since we wanted to know more about how students experienced the SvS device and whether it contributed to their comprehension of IEQ in buildings, a survey was conducted during the final lecture of the course *Healthy and Sustainable Living Environments,* leading to 35-46 respondents. The results showed that 50% of the students encountered some technical difficulties, however, these were all solved along the way. These difficulties were related to the connectivity and limited life span of the batteries. In addition, 75% of the technical problems were not related to the device, but with experienced problems when working with Microsoft Excel for processing the logged data. When asking for their gained insights, 82% indicated that using the device added to their comprehension of IEQ aspects. Although the students considered all four aspects insightful, illuminance was considered most insightful (30%). When asked if they would like to use the SvS device more often, 60% answered positively and 45% would like to buy the device (average suggested price € 22).

Some of the results led to an improved assignment in the following year, i.e. a short instruction on how to work with MS Excel to process the measurement data and dimming of the blinking. Also, some problems occurred with the limited lifespan of the batteries. Therefore, we decided to discourage the use of batteries but suggest using an external power supply when possible.

3.3 Calibration of the SvS devices

3.3.1 Illuminance

By using the Ulbricht sphere, the linearity of the results was tested against a calibrated device. In addition to the 'no light' situation, four light conditions with a similar spectral power distribution (SPD) were tested. The light sources were halogen incandescent lamps. From the graph in Figure 4, the linearity is near to perfect (R^2=1) but the SvS largely underestimates the illuminance by a factor of 1.5 (calibration factor y = 1.5x-1.6). An explanation is that the illuminance sensor is not omnidirectional and therefore also not cosine corrected. This means that predominantly, the illuminance incident to the device is measured and much less towards the other angles.

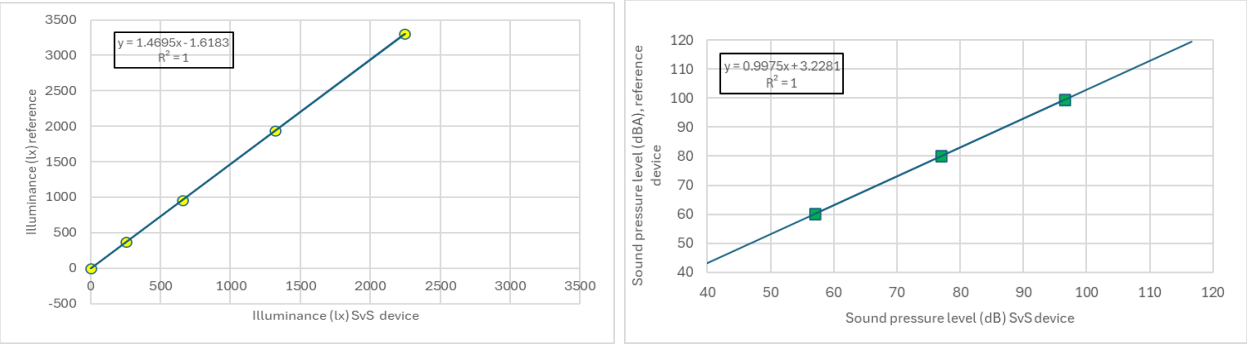

Figure 4 Calibration of the illuminance (left) and sound pressure level (right)

3.3.2 Sound pressure level

In the acoustic room with an omnidirectional sound source, the responses of the SvS device are compared to a calibrated measurement device for three different white noise levels. In addition, a fourth level is introduced, namely the 'no sound' situation where only background noise is

available. Since the minimum threshold for the SvS device is 38 dB, this value is not included in the graph. From the graph (Figure 4) both values align within 3dB ($y = 1.0x - 3.2$, $R^2 = 1$). It must be noted that the response of the SvS device closely aligns with the A-weighted values for white noise, indicating the human perception correction.

3.3.3 Air temperature and Relative Humidity (RH)

Since air temperature and RH are closely related, these will be discussed in one paragraph. In the climate cabinet, temperatures between 12-32 °C and RH between 28-77 % were assessed.
In Figure 5 the differences between the SvS device and the reference device are given over time. Since the SvS requires a few minutes to stabilize, the data after stabilization are used. When calculating the differences, ignoring the peaks due to stabilization, the SvS device slightly underestimates the air temperature by 0.3 °C ($y = 1.0x + 0.3$, $R^2 = 1.0$), while the RH is slightly overestimated by 8.3 % ($y = 1.1x – 8.3$, $R^2 = 1.0$).

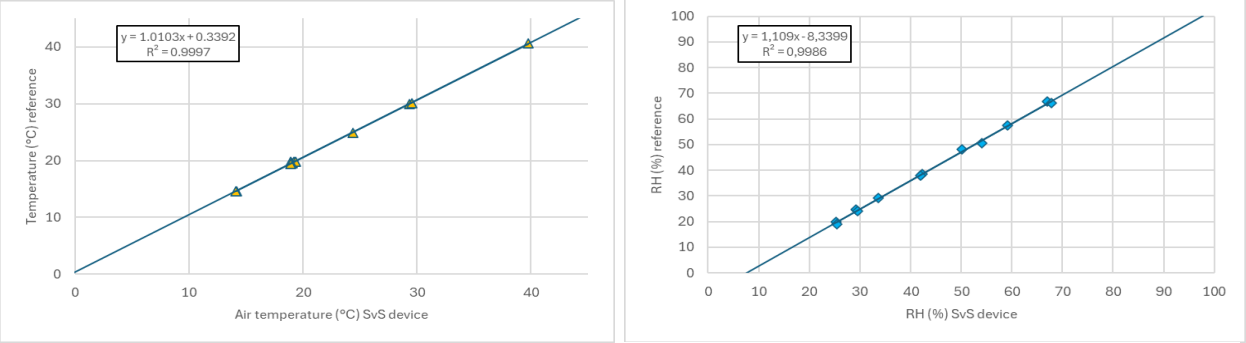

Figure 5 Difference between the SvS device and the calibrated reference device over time. Air temperature (left); and the RH (right)

4. CONCLUSIONS

The device is sufficiently robust to be used in education, meeting the envisioned learning outcome as to contribute to a better understanding of IEQ and the related measurable values. The device is sufficiently user friendly, and the user instructions are of such quality that additional teacher support is hardly required. The sensors perform very well with only minor differences for temperature (underestimation of 0.3 °C), RH (overestimation of 8.3 %) and sound level (underestimation of 3 dB). The difference in illuminance is a factor of 1.5, which can be explained by the absence of a 'cosine diffuser' in the sensor. For the next version, adding sensors to assess the air quality (e.g. CO_2 sensor) is considered as well as improved versions of the sensors, especially the light sensor. A contract for maintenance is needed to check the functioning and performance of the app on new smartphones and with new updates of mobile operating systems. To make the device more accessible, the option to make it cheaper, the sensor quality better, making the specifications of the device open, and the maintenance less time-consuming will be explored.

ACKNOWLEDGEMENTS

This project was supported by the TU/e BOOST! funding. We want to thank Kees Hemmes from the TU/e Equipment and Prototyping Center (EPC) for developing the device and the app and his inexhaustible dedication to solving any potential issue. In addition, we want to thank the Building Physics and Services lab for their help in calibrating and handling the SvS devices. Finally, we want to thank Rijn Jo Kersten for calibrating the different devices.

REFERENCES

Awbi H.B. Ventilation of buildings. Spon Press, London, UK, 2003

Klepeis N., Nelson W., Ott W., Robinson J.P., Tsang A.M., Switzer P., Behar J.V., Hern S.C., Engelmann W.H., 2001. The National Human Activity Pattern Survey (NHAPS): a resource for assessing exposure to environmental pollutants. J Expo Sci Environ Epidemiol.11, 231–252. https://doi.org/10.1038/sj.jea.7500165

Mentimeter. (n.d.). Mentimeter [Web-based interactive feedback software]. https://www.mentimeter.com/

van Duijnhoven J., Aarts M.P.J., Mardaljevic J., 2023. Illuminance readings from thirteen smartphones: measurement accuracy and applicability. In: Proceedings of the 30th Session of the CIE Ljubljana, Slovenia, September 15 – 23, 2023 Volume 1 – Part 2. CIE, 1020-1029

World Health Organization. Regional Office for Europe, 2014. Combined or multiple exposure to health stressors in indoor built environments: an evidence-based review prepared for the WHO training workshop "Multiple environmental exposures and risks": 16–18 October 2013, Bonn, Germany.World Health Organization. Regional Office for Europe.https://iris.who.int/handle/10665/350495

6th International Conference on Building Energy and Environment
Eindhoven University of Technology, The Netherlands
6 - 10 July 2025

Indoor glare control of automatic shading system by exterior daylight measurement

TSANG, Ernest Kin-wai [1], AGHIMIEN, Emmanuel Imuetinyan [2], LI, Shuyang [3]

[1]*Department of Construction and Quality Management, Hong Kong Metropolitan University, Homantin, Hong Kong SAR, ekwtsang@hkmu.edu.hk*
[2]*School of Architecture, The University of Utah, Utah, USA, emmanuel.aghimien@utah.edu*
[3]*Department of Construction and Quality Management, Hong Kong Metropolitan University, Homantin, Hong Kong SAR, shyali@hkmu.edu.hk*

SUMMARY
Modern residential and commercial buildings often feature automatic shading devices (ASDs). However, these systems frequently underperform and are often manually overridden. This issue arises mainly because current ASD control systems focus primarily on reducing cooling energy and enhancing indoor thermal comfort by blocking solar radiation. Typically, these systems monitor outdoor irradiance, activating shades only when specific thresholds are reached. In addition to energy conservation, ASDs also aim to ensure visual comfort for occupants. Glare is traditionally measured using indicators like daylight glare potential (DGP) and daylight glare index (DGI), which require computational analysis of wide-angle indoor images. This necessitates installing several cameras indoors, leading to significant drawbacks: it disrupts interior layouts and limits the connection between indoor and outdoor environments when shades are deployed. Consequently, a more comprehensive control algorithm for ASDs is essential. This study aims to establish the relationship between indoor glare indicators and external climatic conditions. Field measurements were conducted, utilizing cameras and illuminance meters within a model room to evaluate glare. Additional meters will be placed with fisheye lenses to monitor outdoor daylight conditions. Random forest (RF) is a good tool in predicting the indoor glare levels while the use of traditional pattern recognition approach by convolutional neural networks (CNN) might not be a good solution and more works is required.

Keywords: Automatic shading control system, daylight glare control, sky image.

1. INTRODUCTION

Natural lighting is one of the crucial elements in modern green architectural designs. It provides a healthy indoor environment and offers an enormous amount of energy-saving opportunities through the adoption of daylight-linked lighting control (DLLC) systems. A good daylighting design admits the maximum amount of natural light without compromising visual comfort. Most designers are interested in daylight availability rather than visual comfort. Hirning et al. (2014) collected 493 responses from a survey conducted in Brisbane and found that 49% of occupants reported that uncomfortable glare was found in green buildings equipped with automatic shading devices (ASDs) control. A poorly installed and commissioned ASDs control system affects both occupants sitting in the perimeter zones and the interior zones. Both the design and installation of ASD control should not reduce the functionalities of the DLLC system or sacrifice human visual comfort.

Automatic shading device control and the DLLC are two major systems in daylighting designs. The DLLC aims at reducing lighting energy consumption and maintaining suitable lighting levels. While ASD control prevents excessive glare and cooling load, it should not worsen the indoor

daylight availability. Unlike DLLC can use both open- and closed-loop controls, ASD control usually uses open-loop controls only (Jain and Grag, 2018). Common controlling parameters for ASD control are indoor temperature, cooling and heating loads, outdoor daylight level, glare and solar irradiance. When a shading device is switched on, the connection between the indoor and outdoor is lost due to blockage of glazings by shading devices. Hence, feedback (closed-loop) control cannot be formed. Meerbeek et al. (2014) used vertical illuminance as a threshold to switch the blind on and off which can minimize the number of switching. However, the performance of the control device could not fulfil occupants' expectations since occupants tend to operate shading devices depending on weather conditions, the demand for sunshine and the prevention excessive of glare. Hence, a shading control links glare and climatic parameters is needed.

Recently, high dynamic range (HDR) imaging techniques have been widely adopted for glare evaluation. Camera sensor has a dynamic range of 7-8 exposure values (EV) which is far less than 14-16 EVs for human eyes. To study indoor daylight measurement, 20 EVs or higher are needed. HDR image comprises images with different EVs. Well-prepared HDR images have been widely used to assess discomfort glare (Wolska and Sawicki, 2020). Hirning et al. (2014), Jakubiec et al. (2015) and Jakubiec & Reinhart (2015) reported that different types of glare index perform nearly the same but have their own limitations. Mahić et al. (2017) also showed that luminance values correlate well with occupant responses. A RADIANCE build-in program, "evalglare" calculates different glare indices such as daylight glare index (DGI) and daylight glare potential (DGP) from HDR images.

This study aims to develop a method for determining the interior glare level by exterior weather and solar geometrical relationship. The study will form a basis for filling the gap in current ASD controlling system responses to indoor visual comfort environments when the shading systems are actuated.

2. METHODOLOGIES

This study is mainly focused on developing the relationship between the outdoor parameters and the glare and illuminance levels. In this section, the details of the experimental setup, glare index calculation and the training of machine learning are presented.

2.1. Case studies

A low-rise residential building was selected for the field measurement. One of the reasons for selecting a low-rise building instead of a high-rise one is that the building is under single ownership and hence, measurement can be performed in the room and on the roof. The building being studied is a three-storey height residential building located in the countryside of Hong Kong.

Figure 1 shows the site layout plan. As indicated on the plan, the residential block was in Shatin, New Territories. The window is facing west-southwest viewing an open car park with around 120° free of heavy obstruction.

(a) (b)

Figure 1. Location plan (a) and exterior fisheye view (b) of measuring location.

2.1.1. Experimental setup

Figure 2 depicts the plan and section of the room together with the equipment setup. The measured room is approximately 2.3m (W) x 4.74m(L) x 2.3m (H) and is located on the second floor. Inside the room, 2 locations were selected namely 1 and 2. Those two locations are near the room are located far from the windows as it can represent indoor environment with high contrast in term of luminance distribution. Location 1 is in about 75% depth of the room. Location 2 is in the middle of the room. At each point, one camera and one illuminance meter were mounted facing vertically toward the window direction. The focal length of each camera is set to about 24mm equivalate in 135-film format to capture wide-angle images. Minolta T-10MA was used to measure the vertical illuminance and two cameras, Nikon Z 8 and Pentax Q were used to capture photos in the room. On the windows, another Minolta T-10MA was also used to measure the outdoor vertical illuminance. While an Insta360 X4 camera was used to capture the High dynamic range image of the vertical outdoor view. Similarly, another Insta 360 X4 and illuminance meter were installed on the roof to capture horizontal illuminance and sky images. The surface reflectances within the room were measured by Minolta Spectrophotometer CM-25cG.The spectrophotometer measures the reflectance between wavelengths from 360nm to 740 nm covering the near-infrared, visible light and ultraviolet regions. The transmittance of the window was measured by an illuminance meter T-10MA according to Fontoynont (1999). The relevant reflectance and transmittance are shown in Table 1. In general, the surface of the room has a light colour but the transmittance of the window is a little low making the room look gloomy. Inside the room, there are some windows for installing air conditioning units and ventilation purposes. Those small windows were covered by an opaque surface during measurement.

Table 1. Room surface characteristics

Item	Reflectance / Transmittance
Ceiling	70.47%
Wall	76.34%
Floor	18.34%
Window	13.39%

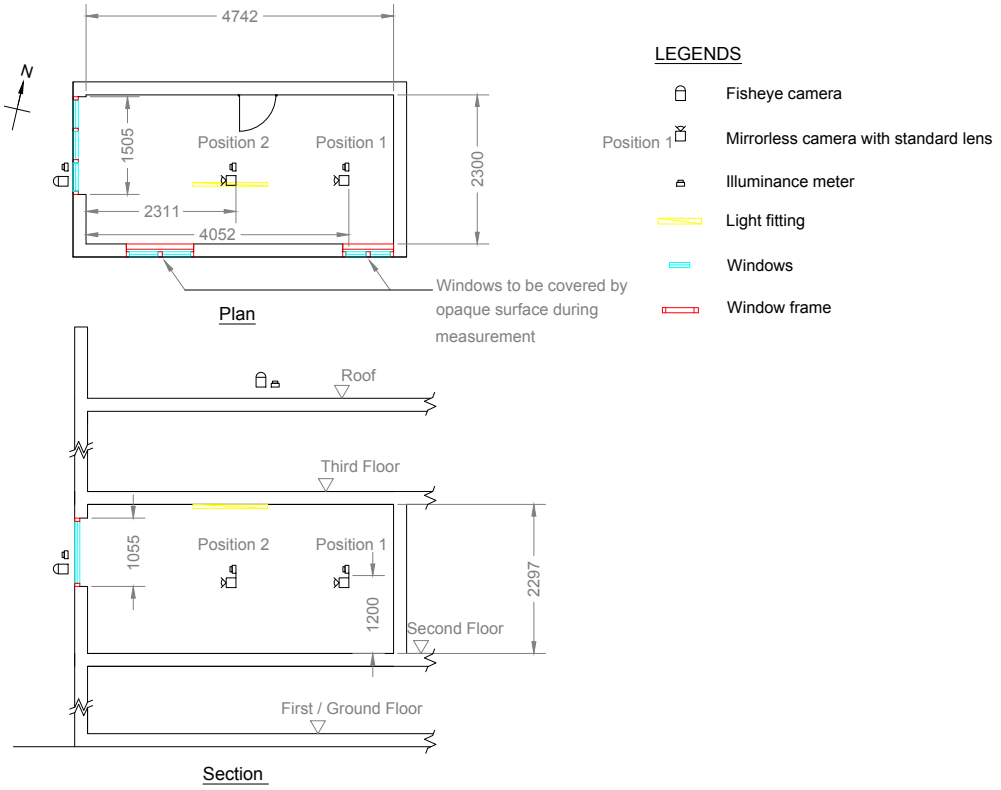

Figure 2. Plan and section of studied room and arrangement of measuring equipment.

2.2. Glare Measurement

One of the aims of shading control is to limit the glare and hence an adequate method for determining the glare is needed. This section outlines the method of glare measurement and calculation. There are several indicators quantifying degree of glare, among all of them, Daylight glare index (DGI) has better reflection on high contrast environment (Quek et al., 2021). DGI is calculated according to Eq. (1) and it is commonly used in determining glare related to daylighting applications.

$$\mathrm{DGI} = \frac{10\ log \sum_{i=0}^{n} 0.478\left(L_s^{1.6} \times \Omega^{0.8}\right)}{L_b + 0.07 \times \omega^{0.5} \times L_s} \quad (1)$$

Where,

L_s = luminance of glare source (cd/m^2)

Ω = solid angle subtense of the source at the eye of the observer modified for the effect of position of the observer in relation to the glare source (sr)

ω = solid angle of the source at the eye of the observer (sr)

L_b = luminance of the background (cd/m^2)

n, i = total and current number of light sources

Bellia et al. (2008) compared a few glare indexes and listed the degree of perceived glare as Table 4. The classifications are as follows: 'Below 16 – unaware'; '16 to 20 – perceptible'; '20 to 22 – acceptable'; '22 to 24 – between acceptable and discomfort'; '24 to 28 – discomfort'; 'over 28 – intolerable'. The British Standard Institution (2017) stated that a DGI of 22 should be set as the threshold for activating of shading device. Although the DGI is commonly referred to in many standards and guidebooks, however, the measurement of glare is extremely complicated (Wolaks and Sawicki, 2020). In reference to Eq. (1)., it can find that many instruments and precious location setting up are needed. And it makes using these complicated setups in field measurement is infeasible. With the advancement of digital cameras in the late 80s, Rea and Jeffrey (1990) suggest using digital devices to conduct fast and practical measurements in assessing the indoor visual environment.

In this study, two cameras as described in 2.1.1 were used to analyze the indoor visual environment. Both cameras were calibrated according to Wolska and Sawiociki (2020). The aperture and shooting mode of these cameras were set to f/14 and aperture priority. The auto exposure bracketing was set to ±2 EV. A total of 5 pictures were captured for each set of measurements and these pictures were combined into HDR images with Photoshop. Glare sources were identified by the "evalglare" program in RADIANCE. Finally, the information was passed to the Aftab Glare Analysis program to calculate the DGI.

2.3 Machine learning training approach

The measurements were conducted from December 2024 to Feb 2025 and 7-day measurements were conducted. However, the winter of Hong Kong is dominated by clear skies and nearly clear skies which makes the current study can only cover a few sky conditions and low solar altitude situation. After applying quality control to the weather and indoor measurement data (Li et al., 2008), there were about 100 sets of valid data for this analysis.

2.3.1. Modelling with outdoor illuminance data and relative solar position by random forest

Over the years, machine learning (ML) models have gained traction as a preferred approach for daylight prediction due to their high accuracy when compared to conventional regression models (Ayoub, 2019). In particular, ensemble models which combine several ML models to build a single and more powerful model than its original constituents have been widely explored (Mohammed and Kora, 2023). Compared with the traditional decision tree process, random forest (RF) can build the decision tree on a random sample of data and provide an average result. RF is a tree ensemble that grows several decision trees for reducing the variance and bias of a model which was used in this study. Ensemble models are known for their efficiency and ability to prevent overfitting (Khan et al., 2024). Previous studies have shown that RF has a strong learning ability, and the model is robust enough to handle regression problems (Ao et al., 2019). Due to the nature of RF, it is still one of the most commonly used machine learning methods in study fields related to climate and weather (Rozante et al., 2023; Wen et al., 2024).

Four (4) RF models for the DGI and indoor vertical illuminance were proposed. The model inputs were vertical illuminance at the window, horizontal illuminance on the roof, solar altitude, relative solar azimuth, and scattering angle. Each RF model predicts the middle and rear DGI and indoor vertical illuminance, respectively. For model development, the split data were separately scaled

using the min-max method to prevent data leakage. Then a splitting ratio of 80 to 20% dividing the data into training and testing datasets. Also, the Grid search method was used to optimize the model. Finally, the model was assessed using correlation of determination (R^2), and % root mean square error (%RMSE).

2.3.2. Modelling with outdoor illuminance data, relative solar position and outdoor images by convolutional neural networks

Computer vision is one of the research directions of deep learning and it can be used for image processing tasks, like image classification, image segmentation, and object detection (Lecun et al., 2015). For daylight predictions, reference planes are evenly divided into grids thereby becoming an array of data. Such divisions are like an image structure composed of pixels, making it possible to apply such models in daylighting analysis (He et al., 2021). Specifically, convolutional neural networks (CNN) have enhanced research in computer vision. CNN can make mostly correct assumptions about image data, and it requires fewer connections and parameters than traditional neural networks (Krizhevsky et al., 2012). Moreso, they can extract features from geometries and construct non-linear models to predict the required daylight performance metrics (He et al., 2021). Therefore, in this study, CNN was adopted to handle the image data of the daylighting from the sky and through the window. Two CNN models were proposed for the mid (Position 2) and rear (Position 1) DGI. The structure of both models was the same with the major difference being in the output file. For a model, the structure consists of numerical inputs made up of the outdoor vertical and horizontal illuminance, solar altitude, relative solar azimuth, and scattering angle. While the image inputs were daylight illuminance from the roof and the window captured by the fisheye camera lens. All numerical data were scaled using the Min-Max method while the images were rescaled to 32 by 32 pixels before normalizing between 0 to 1. The image input layer accepts inputs with a shape of 32, 32, and 6 which represent the pixel height, width and channels, respectively. Also, the CNN had three convolutional layers and a RELU activation function was used. The size of the filters for the three convolutional layers were 32, 64 and 64, respectively. Furthermore, a 64-neuron dense layer was used together with a RELU activation function and cross-validation of the data was also conducted to prevent overfitting. Importantly, the model was split into training and testing datasets using a ratio 80 to 20% and Adam optimizer was used to optimize the process. Unfortunately, this method seems not able to reproduce the data for indoor vertical illuminance values, further works are required in coming studies.

3. ANALYSIS AND DISCUSSION

The training and testing results for the ML including the RF and CNN modeling are presented in Table 2. The result is generally considered as good in terms of field measurement data. In general, it is very interesting that the use of RF approach which without any image as input provides a better result than the CNN approach. Only under the mid of the room, the use of CNN slightly outperforms the RF approach. One of the reasons is that RF using multi-model structure seems more appropriate in selecting different set of equations in determining the DGI values. Unfortunately, normal RF approach cannot use images as input directly, hence adding additional input parameters seems cannot improve or maintain the same accuracy. Another reason may be the pictures were taken in auto exposure mode. This approach is acceptable in predicting glare as glare is a sensation of relative luminance. However, for acting as input features in ANN, undefined relative values might often misleading. Furthermore, during the resizing pre-process, the resized pictures were suffered from a lost in picture's Exif data. Hence, the use of sky image not only

could not provide additional weather information, but more noises for modeling training was introduced.

Table 2. Performance of random forest model in predicting indoor DGI and illuminance level

		RF				CNN			
		Training set		Testing set		Training set		Testing set	
		r^2	%RMSE	r^2	%RMSE	r^2	%RMSE	r^2	%RMSE
Position 1 (Rear of the room)	DGI	0.905	12.09%	0.887	6.28%	0.020	24.81%	0.095	29.43%
	Vertical illuminance	0.951	20.22%	0.873	15.10%				
Position 2 (Middle of the room)	DGI	0.848	6.18%	0.259	12.19%	0.104	12.68%	0.033	11.20%
	Vertical illuminance	0.991	6.36%	0.644	36.87%				

Comparing the DGI and illuminance data, the ability of RF in predicting the DGI is far better than the illuminance values. It may due to the order of magnitude for DGI is smaller than that of the vertical illuminance. Hence smaller errors were recorded for DGI compared with illuminance values. While the RF model performs better in the rear part of the room (Position 1) than the middle of the room (Position 2). A plausible explanation is that the view of exterior environment from the rear part of room is smaller than that of the middle of the room then the variations of DGI and illuminance values in the rear part is larger. For example, the DGI in Position 1 is ranged from 1.23 to 25.52 while the range is 15.47 to 31.52 for Position 2.

3. CONCLUSIONS AND FUTURE WORKS

In this study, a field study is conducted to study the feasibility of estimating the indoor glare and interior illuminance by climatic parameters. It is found that using the random forest can estimate the indoor DGI and vertical illuminance based on real-time weather data and basic solar geometrical relationship. Additional feasibility study on employing sky and obstruction images were carried out. CNN, a commonly used tools for pattern recognition was employed. Unfortunately, basic CNN models cannot further improve the accuracy of the ANN model and sometimes, it introduces noises in model training. With this technique, it is expected that the use of ML (especially RF) can fulfill the gap that ASD controller cannot have any feedback when the shading devices is lower down.

This work is an improvement work for the ASD controlling system. Even the performance of using CNN in predicting DGI or indoor illuminance seems not promising, however, there are still some improvements work can be done by using multi-modality model. Works such as appropriate number of pixels in the image, changing the angle of view in fisheye view image, including Exif information as input to better represent the daylight climate. Apart from imaging aspect, indoor glare index is highly affected by indoor environment. Both natural and artificial lights are presented inside normal occupied space. It makes the prediction of glare is harder. Needless to say, the difficulty will be increase if the DLLC controller is incorporated. To have a completed picture,

more scale-model & field measurements and simulation works are required.

ACKNOWLEDGEMENTS

Work described was fully supported by a Faculty Development Scheme from the Research Grant Council of HKSAR [Project no. UGC/FDS16/E07/23] and Research Matching Grant Scheme from the Research Grant Council of HKSAR [Ref. no. 2021/3006]. The authors would also like to express their thanks to student helpers, Mr. Chris K.S. IM, Mr. Philip P.F. KONG, Phelim C.Y. LAI and Mr. Jackson W.Y. WONG for conducting field measurement. The authors would like to thank the late Prof Danny Li who was Co-I of one of the research projects and giving valuable advice to the authors.

REFERENCES

Ao, Y., Li, H., Zhu, L., Ali, S., Yang, Z. 2019. The linear random forest algorithm and its advantages in machine learning assisted logging regression modelling. Journal of Petroleum Science and Engineering 174, 776-789.

Ayoub, M. 2019. 100 Years of daylighting: A chronological review of daylight prediction and calculation methods. Solar Energy 194, 360 – 390.

Bellia, L., Cesarano, A., Iuliano, G.F., Spada, G., 2008. Daylight glare: a review of discomfort indexes, in: In Proceedings of Visual Quality and Energy Efficiency in Indoor Lighting: Today for Tomorrow, Rome, Italy.

Fontoynont M, editor. Daylight performance of buildings. New York: ROUTLEDGE; 2017.

He, Q., Li, Z., Gao, W., Chen, H., Wu, X., Cheng, X., Lin, B., 2021. Predictive models for daylight performance of general floorplans based on CNN and GAN: A proof-of-concept study. Building and Environment 206, 108346.

Hirning, M.B., Isoardi, G.L., Cowling, I., 2014. Discomfort glare in open plan green buildings. Energy and Buildings 70, 427–440.

Jain, S., Garg, V., 2018. A review of open loop control strategies for shades, blinds and integrated lighting by use of real-time daylight prediction methods. Building and Environment 135, 352–364.

Jakubiec, J.A., Reinhart, C.F., 2016. A Concept for Predicting Occupants' Long-Term Visual Comfort within Daylit Spaces. LEUKOS 12, 185–202.

Khan, A., Chaudhari, O., Chandra, R. 2024. A Review of Ensemble Learning and Data Augmentation Models for Class Imbalanced Problems: Combination, Implementation and Evaluation. Expert Systems with Applications 244,122778.

Krizhevsky, A., Sutskever, I., Hinton, G.E., 2017. ImageNet classification with deep convolutional neural networks. Commun. ACM 60, 84–90.

LeCun, Y., Bengio, Y., Hinton, G., 2015. Deep learning. Nature 521, 436–444.

Li, D.H.W., Lam, T.N.T., Cheung, K.L., Tang, H.L., 2008. An analysis of luminous efficacies under the CIE standard skies. Renewable Energy 33, 2357–2365.

Mahić, A., Galicinao, K., Van Den Wymelenberg, K., 2017. A pilot daylighting field study: Testing the usefulness of laboratory-derived luminance-based metrics for building design and control. Building and Environment 113, 78–91.

Meerbeek, B., Kulve, M., Gritti, T., Aarts, M., van Loenen, E., Aarts, E., 2014. Building automation and perceived control: A field study on motorized exterior blinds in Dutch offices. Building and Environment 79, 66–77.

Mohammed, A., Kora, R. 2023. A Comprehensive Review on Ensemble Deep Learning: Opportunities and Challenges. Journal of King Saud University –Computer and Information Sciences 35, 757- 774.

Quek, G., Wienold, J., Khanie, M.S., Erell, E., Kaftan, E., Tzempelikos, A., Konstantzos, I., Christoffersen, J., Kuhn, T., Andersen, M., 2021. Comparing performance of discomfort glare metrics in high and low adaptation levels. Building and Environment 206, 108335. https://doi.org/10.1016/j.buildenv.2021.108335

Rea, M.S., Jeffrey, I.G., 1990. A New Luminance and Image Analysis System for Lighting and Vision I. Equipment and Calibration. Journal of the Illuminating Engineering Society 19, 64–72.

Rozante, J.R., Ramirez, E., Ramirez, D., Rozante, G., 2023. Improved frost forecast using machine learning methods. Artificial Intelligence in Geosciences 4, 164–181. https://doi.org/10.1016/j.aiig.2023.10.001

The British Standards Institution, 2017. Energy performance of buildings – energy needs for heating and cooling, internal temperatures and sensible and latent heat loads: Part1 Calculation Procedures (No. BS EN ISO 52016-1:2017). The British Standards Institution, London, UK.

Wen, Q.H., Wan, D., Dong, Q., Yan, Y., Zhang, P., 2024. Improved freezing rain forecast using machine learning. Weather and Climate Extremes 44, 100690.

Wolska, A., Sawicki, D., 2020. Practical application of HDRI for discomfort glare assessment at indoor workplaces. Measurement 151, 107179.

6th International Conference on Building Energy and Environment
Eindhoven University of Technology, The Netherlands
6 - 10 July 2025

Evaluation of implicit data collection methods for accuracy, reliability and energy efficiency

Sascha Hammes [1], Johannes Weninger [2], Simon Beck [1], Maximilian Dick [2], Andreas Frei [1], Philipp Zech [3], Rainer Pfluger [1]

[1]*University of Innsbruck, Unit of Energy Efficient Building, Innsbruck, Austria, sascha.hammes@uibk.ac.at, simon.beck@uibk.ac.at, andreas.frei@uibk.ac.at, rainer.pfluger@uibk.ac.at*
[2]*Bartenbach GmbH, research & development, Wattens, Austria, johannes.weninger@bartenbach.com, maximilian.dick@bartenbach.com*
[3]*University of Innsbruck, Department of Computer Science, Innsbruck, Austria, philipp.zech@uibk.ac.at*

SUMMARY
Despite existing energy efficiency measures, the building sector is responsible for around 30-40% of global energy demand. Sensors can help to improve energy efficiency. However, their use involves additional energy consumption, complex hardware installations and therefore critical installation and operating costs, all of which become more important as additional or higher resolution information is collected. Implicit sensing methods, like Bluetooth detection or computer activity, can provide occupancy data without the use of dedicated sensors. To demonstrate the benefits of implicit sensing in terms of energy efficiency, reliability and accuracy, a technical-functional system evaluation was conducted with 60 participants as part of a structured laboratory study. The results of the study show that a passive approach can provide sufficiently accurate information to maintain overall control reliability without the need to install additional sensors. The detection methods were evaluated for user acceptance via a questionnaire.

Keywords: Sensor technology, occupancy detection, implicit detection, user acceptance.

1. INTRODUCTION

To achieve the current energy policy goals, it is essential not only to transition to renewable energy sources but also to improve the energy efficiency of existing consumers (Byun et al., 2013). In the building sector, particularly regarding artificial lighting, there is significant potential as 20% to 45% of electrical energy consumption in commercial buildings are due to lighting (Madias et al., 2016). In addition, reducing lighting energy consumption can also reduce internal heat gains, which in turn reduces a building's cooling load (Ryckaert et al., 2010). This indirect effect means that lighting energy savings contribute to overall energy efficiency and climate targets not only directly, but also indirectly. There is also great potential for heating, ventilation and air conditioning (HVAC) to contribute to climate goals by improving the energy efficiency of these technical systems. In commercial buildings, controls and sensors are primarily used to achieve energy savings in lighting and HVAC. One possibility is to use illuminance sensors to regulate artificial light depending on the availability of daylight. A central approach is the occupancy-based control of lighting and HVAC systems, which only activates devices when the room is actually being used. Compared to manual controls, occupancy-based solutions achieve on average around 30% higher energy savings for lighting, regardless of building type and application scenario (Galasiu et al., 2007). The combination of daylight and occupancy controls reduces running costs while maintaining comfort and supporting sustainability.

Information about real occupancy patterns at the workplace can also be used for further energy efficiency measures, such as deriving optimised user distributions in offices with zoned lighting concepts (Hammes et al., 2022), or as a basis for evaluating the comfort and health of occupants. In order to take user-related influences on energy performance into account and to meet user-related comfort requirements in the best possible way, a high resolution of occupancy data at the workplace proves to be essential (Hammes et al., 2024). Occupancy data is therefore considered to be one of the key variables for the success of set control strategies. The role of occupancy detection for lighting controls and for controls of other building actuators was already investigated in multiple reviews (Salimi and Hammad, 2019; Shen et al., 2017).

Occupancy control is usually based on passive infrared sensors (PIR), as the hardware costs are low and implementation is simple. The disadvantage is the need for a direct line of sight (Guo et al., 2010). CO_2 sensors offer the possibility of deducing the number of occupants in a room in addition to receiving binary information. However, there is a certain inertia associated with CO_2 sensors, which prevents real-time detection capability, as well as interference from unmonitored ventilation (Salman et al., 2024). Camera systems offer high resolution, but associated applications for occupancy detection are computationally intensive, usually lead to low acceptance in terms of data protection and require a direct line of sight (Salimi and Hammad, 2019; Salman et al., 2024).

Ultimately, occupancy detection in these approaches is always linked to the use of dedicated sensors, which usually have permanent energy consumption. Standby times rarely exist. Therefore, it should be checked first whether net energy savings during operation justify the use of additional hardware and the associated grey energy. The energy consumption of sensor-based lighting control systems can outweigh the energy savings, especially in individual offices with high user absence (Gentile et al., 2014). In addition, these sensors are associated with other costs and require maintenance (Salman et al., 2024). The alternative use of wireless sensor networks and energy harvesters shows great potential for energy-efficient operation (Hidalgo-Leon et al., 2022).

Implicit detection methods are another promising solution. Existing hardware is used to derive occupancy information. This includes timestamp clocks as well as computer activities (e.g., via keyboard and mouse tracking) and network activities (e.g., WiFi and Bluetooth-based detection of mobile devices). A conceptual approach to live-position detection of Bluetooth Low Energy (BLE) devices is offered by (Daniş et al., 2023). The framework is based on a hidden Markov model that uses Received Signal Strength Indicator (RSSI) data and heuristically modelled movements to determine positions from sequential RSSI measurements using probabilistic filtering. A hybrid approach to locating building occupants using WiFi and BLE networks is provided by Chen et al. (2019). The system integrates a conventional k-nearest neighbour positioning algorithm with a stochastic random walk algorithm to derive high-resolution occupancy data. The challenges of implicit detection methods are efficient algorithms, data semantics, interoperability, privacy, and reliability in wireless communication (Shen et al., 2017).

The use of implicit recording methods theoretically offers the possibility of recording additional application-relevant information without the use of dedicated sensors or direct user input, e.g., testing of health-effective light doses. It has also been shown that interaction speeds with the mouse and keyboard can provide information on fatigue (Natnithikarat et al., 2019). The objective of the study is to investigate whether implicit detection methods can provide a practical, reliable and

accepted alternative to conventional sensor-based occupancy detection. The use of implicit occupancy detection methods was therefore evaluated as part of a structured laboratory study.

2. METHODOLOGY

2.1. Study Design

For the structured laboratory study, an approximately 30 m² corner office at the University of Innsbruck was set up so that 4 people could carry out typical office activities at the same time (Fig 1a). The study stations were located in the corner of each side of the table. The personal computers (PC) in the center of each desk, shown in Fig. 1a, were used exclusively for monitoring and conducting the study and were not occupied by study personnel during the testing phase.

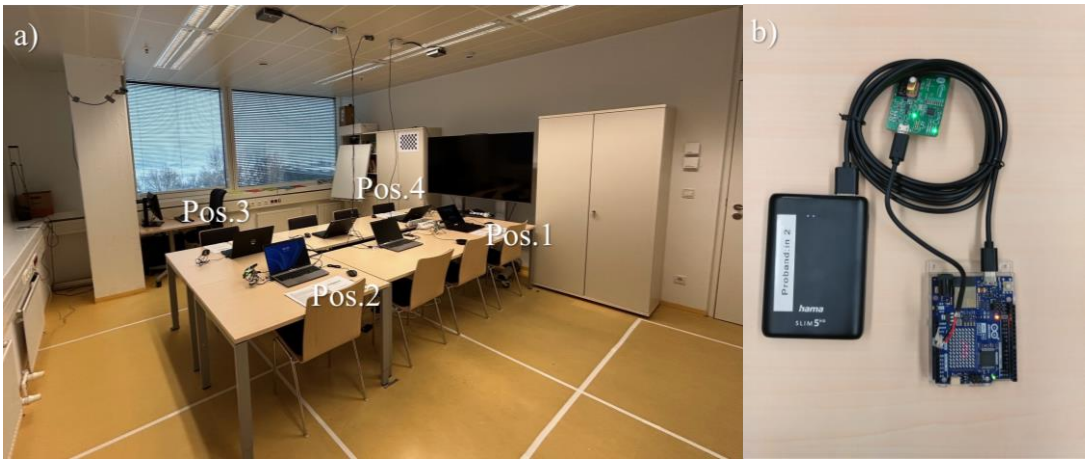

Figure 1. a) Display of the study site, occupied by a maximum of 4 participants at the same time. b) A Bluetooth device that the study participants carried in their pockets, which tracked their movements.

Four different tasks were defined to simulate typical office work: Task A required participants to type a given text, simulating screen and desk work. In Task B, participants had to watch a video that simulated passive PC work, such as online meetings. Task C required participants to sort sheets of paper. This required directional movement around the room. Task D simulated absence. This required the participants to leave the room. The order of the tasks was randomly assigned to each participant to reflect all possible task combinations. Each person completed a total of 16 tasks, lasting 3 minutes each. All tasks occur equally frequently. There was a 10-second transition period between tasks to prepare for the next one. Task changes were automatically indicated by an acoustic signal and automatically recorded. The controlled study setting represents the ground truth for evaluating the accuracy of implicit recording methods.

To avoid distortions due to individual behaviour and to ensure the reliability and validity of the data, the group size was chosen accordingly to ensure a representative sample (Rosenthal and Rosnow, 2008). 60 people took part in the present study (40 female, 20 male). Of these, 44 were students, 13 had a professional focus on office work and 3 had no focus on office work. A total of 17 sessions took place (12 sessions with 4 people and 5 sessions with 2-3 people). The study was conducted from 29 November 2024 to 6 December 2024.

A Python-based desktop app that mimics a time clock was installed on the study laptops at the

workstations. A graphical user interface made it possible to choose between ‘Come’ and ‘Leave’ with a button click (required for Task D). In addition, a self-written Python script was used to implement mouse and keyboard tracking (Python 3.12). The primary libraries used were pynput (version 1.7.7) and requests (version 2.32.3). All measurement data collected during the measurement campaign was saved including a timestamp in an InfluxDB. BLE devices were taken out of the room by the study participants when performing Task D (Fig. 1b) to track movement. The RSSI of the known device addresses was collected using a Python script (Python version 3.10.12, Bleak library version 0.22.3) and was also stored with a timestamp in another InfluxDB. RSSI-based passive detection uses the received signal strength of BLE devices as an indicator for occupancy detection. The RSSI decreases with distance in this case from the operating laptop in the middle of the workplaces. Limits for RSSI with devices in the room are in the range of less than -80dBm. RSSIs correspond to an integer measurement of a received radio signal that follows the IEEE 802.11 standard (Chen et al., 2019). All measurements were carried out with high resolution in time steps of a few seconds. This resolution is also the basis for the analysis.

The implicit methods were evaluated in terms of accuracy and reliability. Accuracy represents the percentage of correctly identified presences and absences in relation to the task-specific ground truth (presence at the workplace for tasks A and B; absence for tasks C and D). The 50% split in the ground truth for accuracy is to avoid favouring any sensor technology. Reliability reflects the consistency of occupancy detection for a technology within a specific task.

2.2. User Acceptance and Ethics

The participants also completed a questionnaire (Limesurvey, version 3.22.4+200212), in which they rated the acceptance of various occupancy detection technologies. Selected results on implicit detection methods from the questionnaire are presented in this study. There are 53 complete responses to the questionnaire. On average, participants took 5:52 minutes to complete the questionnaire. In the case of Likert-type questions, care was taken to ensure a symmetrical distribution of complementary characteristics. To avoid bias in the answers due to their predetermined order, the order of the answers was randomized for ranking questions and closed questions with a fixed choice option. Participants were usually given the option of selecting 'not assessable' to avoid biased responses.

All participants took part in the study voluntarily. The study participants were informed in advance about the purpose of the study and were free to leave the study at any time. None of the study participants chose this option. All participants signed an informed consent before participation and were compensated with €30 for full participation in the study. All aspects of data protection were considered when conducting the study.

3. RESULTS

3.1. Accuracy and Reliability

Compared to ground truth, occupancy detection at the workplace via RSSI measurement has an overall accuracy of (52.91±6.64) % across all tasks and users. The virtual time clock (desktop app) achieves (64.85±2.17) %, the mouse and keyboard tracking (63.28±3.58) % accuracy. In combination via logical-or linking with the desktop app, BLE tracking can achieve (52.16±3.32) % accuracy and BLE tracking with mouse & keyboard tracking (52.96±4.01) %. The PC-related

applications can achieve (58.31±1.76) % in combination. All three variants together in logical-or linkage achieve an accuracy of (52.17±3.04) %. Fig. 2a shows the accuracies depending on the task. The reliability of the occupancy detection is shown in Fig. 2b. The consistency of the values obtained is always high (Fig. 2b), regardless of whether the value is correct or not (Fig. 2a).

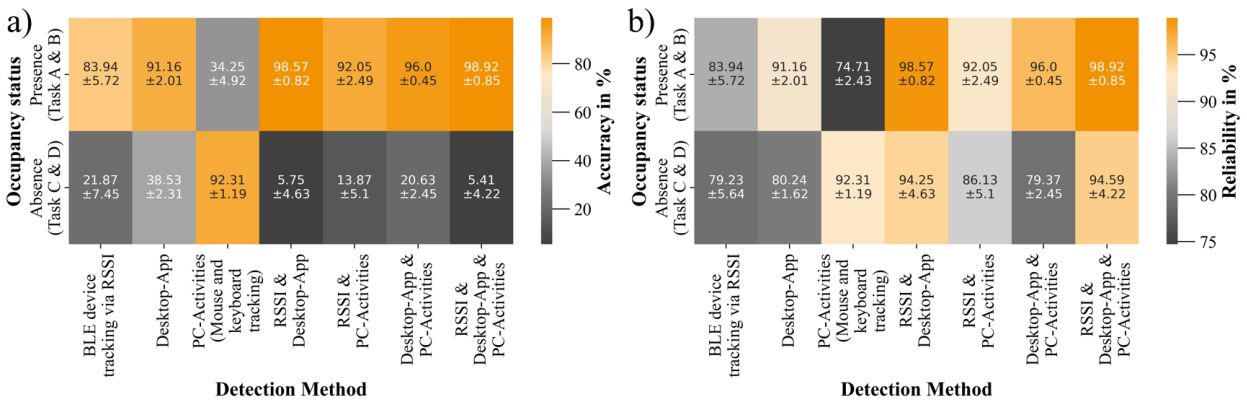

Figure 2. a) Accuracy of occupancy detection at the workplace and b) reliability of occupancy detection of the implicit detection methods as a function of the tasks (Task A: active PC work, Task B: passive PC work, Task C: movement in the room, Task D: leaving the room).

While deviations between the study participants are balanced out by the sample size (Rosenthal and Rosnow, 2008), slight deviations can in principle occur in the BLE device detection with regard to the position, even though the receiver PC was positioned as centrally as possible. This results in an accuracy (total of absence and presence) of 62.40% for BLE device detection at position 1, 51.46% at position 2, 49.10% at position 3 and 48.51% at position 4 (see positions in Fig. 1a). There were no position-dependent influences for the other recording methods.

False negatives, i.e., incorrectly recognised absences, are the biggest obstacle to a satisfactory technology implementation, as they can have a disruptive effect on the user experience. Tab. 1 therefore shows the proportion of correct detections, false absences and incorrect attendances across all users and tasks in relation to attendance at the workplace (attendance Task A & B and absence Task C & D). While the study participants always took the BLE devices with them during Task D, there was a frequent operating error with the virtual time clock via the desktop app. It could be observed that leaving and returning to the work space was not indicated properly 22 times and 13 times, respectively.

Table 1. Identified false absences and false presences at the workplace in relation to the ground truth.

Detection method	Correct detection	False absence	False presence
BLE device tracking (via RSSI)	52.91%	8.03%	39.06%
Desktop-App	64.85%	4.42%	30.73%
Mouse & keyboard tracking	63.28%	32.87%	3.85%

3.2 Questionnaire

The recording of workplace-centred information proves to be valuable in ensuring that the technical building systems are controlled as energy-efficiently as possible and that user-related comfort requirements are implemented in the best possible way (Hammes et al., 2022, 2024). Collecting workplace-centred information via wall and ceiling mounting can prove to be complex

or involve the use of technologies that meet with low acceptance, such as cameras (Salimi and Hammad, 2019). In the questionnaire, most people also find the use of cameras indoors unacceptable (Fig. 3). It can be seen that visible sensors positioned close to the workplace meet with a low level of acceptance compared to wall and ceiling mounting (Fig. 4). Implicit sensors, as non-physically dedicated recording devices, can be excluded from this category as they are primarily background processes in existing IT infrastructure. The time clock as a desktop app shows a comparatively high level of acceptance compared to other sensor types (Fig. 3). Mouse and keyboard tracking is viewed rather critically, although 32% of participants had no knowledge of implicit detection methods and 45% had heard of them but knew no details. Only 23% were aware of this technology.

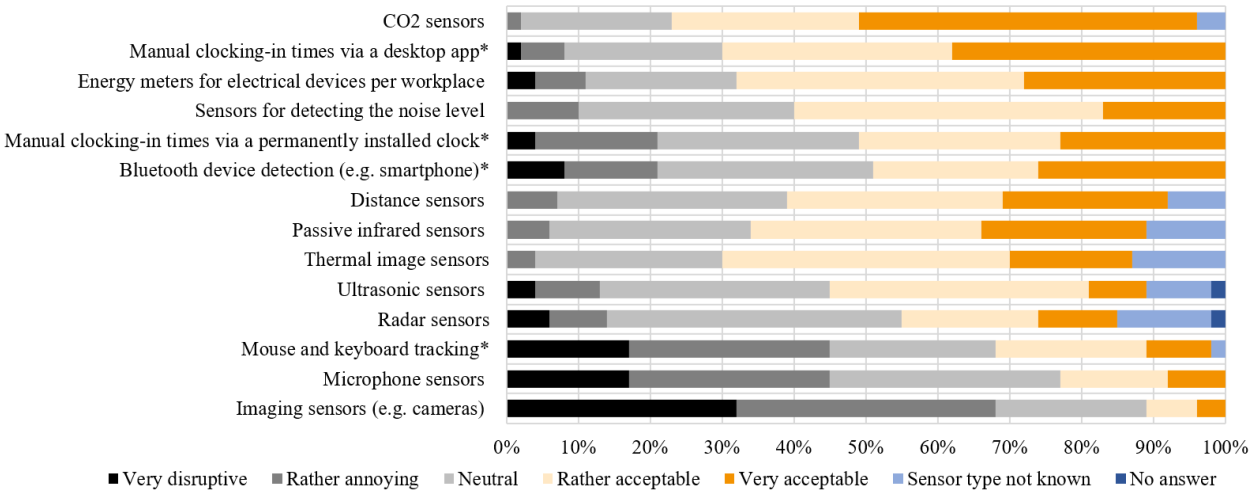

Figure 3. Feedback from study participants on the question of how acceptable they find the use of individual sensor technologies in indoor spaces (Question type: 5-point Likert scale). The implicit recording methods relevant to the study are marked with *.

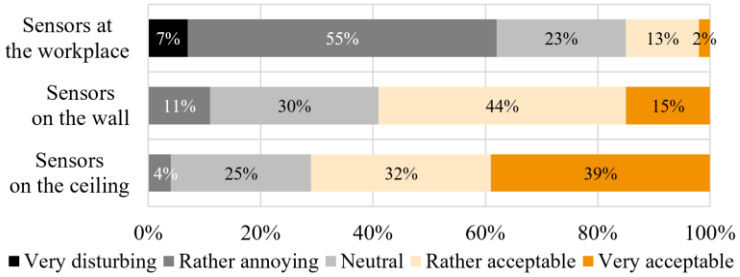

Figure 4. Feedback from participants on the question of how they rate visible sensors in indoor spaces (Question type: 5-point Likert scale).

4. DISCUSSION

4.1 Reflection and implication of the results

The results show that BLE device tracking via RSSI delivers the lowest accuracy. With Bluetooth device detection, reflections, refraction and scattering in particular can strongly influence the signal strength. Room size, building materials and interior of the building and the presence of obstacles, such as uncontrolled extraneous movements, can have a detrimental effect on detection

accuracy (Salman et al., 2024). Applying device detection in practice can be difficult because people use multiple Bluetooth devices, Bluetooth is often turned off, or the occupant does not have a device with them. An approach that takes advantage of both Bluetooth and Wi-Fi networks could maximise positioning accuracy. Determining a suitable Bluetooth signal strength threshold to infer presence poses a significant challenge. Complex and dynamic characteristics compromise the use of a fixed threshold, such as the study setting with numerous obstacles and high dynamics due to the study design. Salman et al., (2024) present a self-adaptive system based on WiFi for occupancy monitoring and thus without the use of dedicated sensors. In particular, it is based on a data mining algorithm for cluster analysis (DBSCAN algorithm) to ensure self-adaptation of the control limit threshold for dynamic environments. Based on the increase in WiFi-based infrastructure, such approaches to occupancy detection are gaining in importance.

BLE detection and the desktop app display the comparable data, so the combination has the same uncertainties. Mouse and keyboard tracking shows high accuracy in absence detection at workstation level and the desktop app in terms of presence detection. The desktop app is also rated with high acceptance (Fig. 3). By combining these implicit methods, accuracy and reliability can be significantly improved overall (Fig. 2). While they were logically OR-linked in this study, future research should investigate whether a rule-based linking of the technologies could further improve reliability. This is because the recorded interactions with the desktop application and the mouse and keyboard tracking provide reliable evidence of presence at the time of interaction compared to many other technologies. This creates an accurate ground truth, whereas many comparable sensors generally operate with the risk of false absences and presences. It should be noted that no interaction with the PC does not provide verified absence. The media used for implicit data collection also has the great advantage of already being present and being able to communicate due to another primary reason for use (Shen et al., 2017), which saves energy and costs as no dedicated sensors are required. The results from Fig. 2a show improvements in accuracy by combining the methods with regard to presence detection and this with high reliability Fig. 2b. Although the accuracy of absence detection is consistent across all methods and combinations, with the exception of mouse and keyboard tracking, it does not sufficiently represent the correct target value, which is evident from the high reliability.

4.2 Limitations

The study setting is limited to office applications. Further investigations are necessary to validate the data for other applications. The signal-based processing of work tasks was used as ground truth. Even if the degree of error was reduced by transition times, the tasks are not necessarily carried out at the exact times. This can lead to unwanted pauses, particularly in Task A, the PC work. A remedy could be a switch-off time, analogous to PIR sensor technology (Guo et al., 2010), which reduces false-off rates during mouse and keyboard tracking, e.g., according to the methodology of Hammes et al., (2021), in order to derive the cumulative probability of the minimum absence duration from periods of inactivity.

Although multiple Bluetooth receivers can be used to locate the position in the room, this study is limited to recording the Boolean presence status at the workstation in order to maintain comparability between the different recording methods. While limited accuracy was achieved using RSSI in the given study setting, its use in other scenarios, such as larger rooms with fewer obstacles, should be tested.

5. CONCLUSION

Implicit occupancy detection offers the potential for acceptable accuracy, lower costs and lower energy consumption compared to conventional explicit concepts. A combination of several implicit detection methods may prove beneficial to capture presences for the control system. The results of the study show that while attendances are correctly captured with high consistency, absences do not achieve sufficient accuracy. Direct processing of the information in compliance with data protection regulations is considered a suitable option. Implicit occupancy detection is used not only to optimise artificial lighting, but also to control HVAC systems.

ACKNOWLEDGEMENTS

The research leading to these results has received funding from the Austrian Research Promotion Agency (FFG) under Grant Agreement No.: 910225, BOREALIS.

REFERENCES

Byun, J., Hong, I., Lee, B., Park, S., 2013. Intelligent household LED lighting system considering energy efficiency and user satisfaction. IEEE Trans. Consumer Electron. 59, 70–76.

Chen, J., Chen, H., Luo, X., 2019. Collecting building occupancy data of high resolution based on WiFi and BLE network. Automation in Construction 102, 183–194.

Daniş, F.S., Ersoy, C., Cemgil, A.T., 2023. Probabilistic indoor tracking of Bluetooth Low-Energy beacons. Performance Evaluation 162, 102374.

Galasiu, A.D., Newsham, G.R., Suvagau, C., Sander, D.M., 2007. Energy Saving Lighting Control Systems for Open-Plan Offices: A Field Study. LEUKOS 4, 7–29.

Gentile, N., Laike, T., Dubois, M.-C., 2014. Lighting Control Systems in Peripheral Offices Rooms at High Latitude: Measurements of Electricity Savings and Users Preferences. Energy Procedia 57, 1987–1996.

Guo, X., Tiller, D., Henze, G., Waters, C., 2010. The performance of occupancy-based lighting control systems: A review. Lighting Research & Technology 42, 415–431.

Hammes, S., Geisler-Moroder, D., Hauer, M., Weninger, J., Obleitner, M., Miller, J., Plörer, D., Van Karsbergen, V., Weitlaner, R., Pfluger, R., 2024. Concepts of user-centred lighting controls for office applications: A systematic literature review. Building and Environment 254, 111321.

Hammes, S., Weninger, J., Geisler‐Moroder, D., Pfluger, R., Pohl, W., 2021. Reduzierung des Kunstlichteinsatzes durch Anpassung der Nachlaufzeit an individuelle Anwesenheitsmuster. Bauphysik 43, 50‐64.

Hammes, S., Weninger, J., Pfluger, R., Pohl, W., 2022. Take the Right Seat: The Influence of Occupancy Schemes on Performance Indicators of Lighting in Open Plan Offices. Energies 15, 3378.

Hidalgo-Leon, R., Urquizo, J., Silva, C.E., Silva-Leon, J., Wu, J., Singh, P., Soriano, G., 2022. Powering nodes of wireless sensor networks with energy harvesters for intelligent buildings: A review. Energy Reports 8, 3809–3826.

Madias, E.-N.D., Kontaxis, P.A., Topalis, F.V., 2016. Application of multi-objective genetic algorithms to interior lighting optimization. Energy and Buildings 125, 66–74.

Natnithikarat, S., Lamyai, S., Leelaarporn, P., Kunaseth, N., Autthasan, P., Wisutthisen, T., Wilaiprasitporn, T., 2019. Drowsiness Detection for Office-based Workload with Mouse and Keyboard Data. In: 12th Biomedical Engineering International Conference (BMEiCON), Ubon Ratchathani, Thailand, 2019, pp. 1-4.

Rosenthal, R., Rosnow, R.L., 2008. Essentials of behavioral research: methods and data analysis, 3. ed. ed, McGraw-Hill higher education. McGraw-Hill, Boston.

Ryckaert, W.R., Lootens, C., Geldof, J., Hanselaer, P., 2010. Criteria for energy efficient lighting in buildings. Energy Build. 42, 341–347.

Salimi, S., Hammad, A., 2019. Critical review and research roadmap of office building energy management based on occupancy monitoring. Energy and Buildings 182, 214–241.

Salman, M., Caceres-Najarro, L.A., Seo, Y.-D., Noh, Y., 2024. WiSOM: WiFi-enabled self-adaptive system for monitoring the occupancy in smart buildings. Energy 294, 130420.

Shen, W., Newsham, G., Gunay, B., 2017. Leveraging existing occupancy-related data for optimal control of commercial office buildings: A review. Advanced Engineering Informatics 33, 230–242.

Pandemic and Epidemic (13:30-15:00 h)

6th International Conference on Building Energy and Environment
Eindhoven University of Technology, The Netherlands
6 - 10 July 2025

Contribution of airborne microorganisms to surface contamination in hospital environments

W. Hiwar[1], M-F King[1], I. Clifton[2]. L. A. Fletcher[1] & C.J. Noakes[1]

1. School of Civil Engineering, University of Leeds, UK
2. Department of Respiratory Medicine, St. James's Hospital, Leeds, UK.

SUMMARY

The contribution of airborne microorganisms to surface bioburden in indoor environments is an important factor in infection control and hygiene. This study conducted air and surface microbiological sampling in a 4-bed naturally ventilated respiratory ward to measure total aerobic colony count (ACC) and to identify the present of *Staphylococcus spp*. Results show a positive strong significant relationship between airborne ACC and *Staphylococcus spp* r=70 (0.60-.078), p=<0.001, n=120. A linear regression equation to describe surface microbial load ($cfu.cm^{-2}.h^{-1}$) based on the airborne microbial load ($cfu.m^{-3}$) showed the contribution of the airborne microorganisms to the total surface load was 65% ± 18 after cleaning. This study provides valuable insights into the relationship between airborne microorganisms and surface contamination, with implications for improving hygiene practices in hospitals.

Keywords: Airborne Microorganisms, Surface Bioburden, Hospital Infection Control, Ventilation and Microbial Load Deposition.

1 INTRODUCTION

Airborne microorganisms are removed through ventilation or deposition onto surfaces, and the number of deposited microorganisms over a period of time correlates to the number of airborne microorganisms. A qualitative link between air and surface microbes has been shown as a percentage of positive sampling. More recently, researchers found a tenuous quantitative correlation of *P.aeruginosa* and total fungal load in the air and on surfaces (Bonnal 2015). However, a study on the total fungal flora and *Aspergillus spp* shows no significant correlation between airborne fungal and surface fungal (Gheith 2015). The quantitative relationship between microorganisms measured through active and passive sampling is still unclear and needs to be supported with empirical evidence. Despite the number of studies that have sampled the hospital environment, there have been few attempts to evaluate any relationships between microorganisms in the air and on surfaces. This study measures the transient relationships between air and surface bioburden in a hospital ward to: (i) to investigate the quantitative relationships between both airborne aerobic colony count (ACC) and *Staphylococcus spp*, hospital environment; (ii) to provide a mathematical model that relates airborne microorganisms' concentration and surface load; and (iii) to quantify the contribution of airborne microorganism load on the surface load in the healthcare environment.

2 METHODOLOGY

The study was performed in a 4-bed adult respiratory ward in a hospital in Leeds (in England) during February (17th and 21st) and March (3rd and 10th) 2020, from 8:00 am to 4:00 pm. The ward is naturally ventilated, bed occupancy ranges from 75 – 100%, each patient is nursed on a 1:1 basis. Domestic and near-patient sites are cleaned once daily around 12:00 midday.

Active air sampling was performed using a single-stage impactor Microbio MB2 bioaerosol sampler (Fred Parrett, UK) at an airflow of 100 l/min and placed between beds at 1.5 m height. Air was sampled onto Tryptone Soya Agar plate (TSA) (Oxoid, UK) to determine an Aerobic Colony Count (ACC) and onto Mannitol Salt Agar plate (MSA) (Oxoid, UK) for *Staphylococcus spp* for 5 minutes every 15 minutes. For passive air sampling, two TSA and two MSA agar settle plates (90 mm) were placed on a 1 m high trolley that is 0.75 m away from the active sampler and at the center between the four beds. Passive sampling was performed every 30 minutes for ACC and every 1 hour for *Staphylococcus spp*, for the first day and then every 30 minutes for the rest of three study days. ACC and *Staphylococcus* spp were the most interesting target for researchers as it is related to the standard hygiene recommendations (Dancer 2004). Surface screening was performed using 55 mm contact plates at five high hand-touch surfaces (bedside cabinet, overbed table, patient's note, right side bed rail and left side bed rail). Screening was carried out in the morning (9:00) and in the evening (16:00) to allow comparison with previous work (Dancer 2004).

Pearson's correlation assessed the relationship between airborne ACC and Staphylococcus spp., reporting r and 95% CI for precision. Significance was set at $p<0.05$, with $p<0.001$ highly significant. Analyses were conducted in R 4.4.2. To quantify the contribution of airborne microorganism load on the surface load, we compared the accumulated deposited load on petri dishes (12pm-4pm) with the surface evening screening using contact plates (at 4pm). The loss rate of airborne microorganisms due to deposition onto floor surfaces ($\lambda_{d.f}$) can be calculated according to equation.

$$\lambda_{d.f} = \frac{C_{sf}\, A_f}{C\, V} \qquad 1$$

Where C_{sf} is the deposited microorganisms' concentration on the floor ($cfu.m^{-2}.h^{-1}$). A_f is the surface area of the floor (m^2). and V is the volume of the room (m^3). Most standard hospital wards are rectangular rooms with uniform height so A_f/V is equal to 1/H, where H is the height of the room.

3 RESULTS

Figure 1 shows time-series data for active and passive samples over the 4 days. Across all samples the average concentration of airborne ACC and *Staphylococcus spp*. were 196 ± 103 and 158±86 cfu.m^{-3}, respectively, and there is a positive strong significant relationship between airborne ACC and *Staphylococcus Spp* r=70 (0.60-.078), p=<0.001, n=120. The average concentration of airborne deposited microbial concentration measured as ACC and *Staphylococcus spp*. were 18±10 (cfu. Plate^{-1} .h^{-1}) and 8±6 (cfu. Plate^{-1}.h^{-1}) respectively. The mean of $\lambda_{d,f}$ calculated from the sample data is 3.38 (h^{-1}) and 1.97 (h^{-1}) for ACC and *Staphylococcus spp.*, respectively **(Figure 2).**

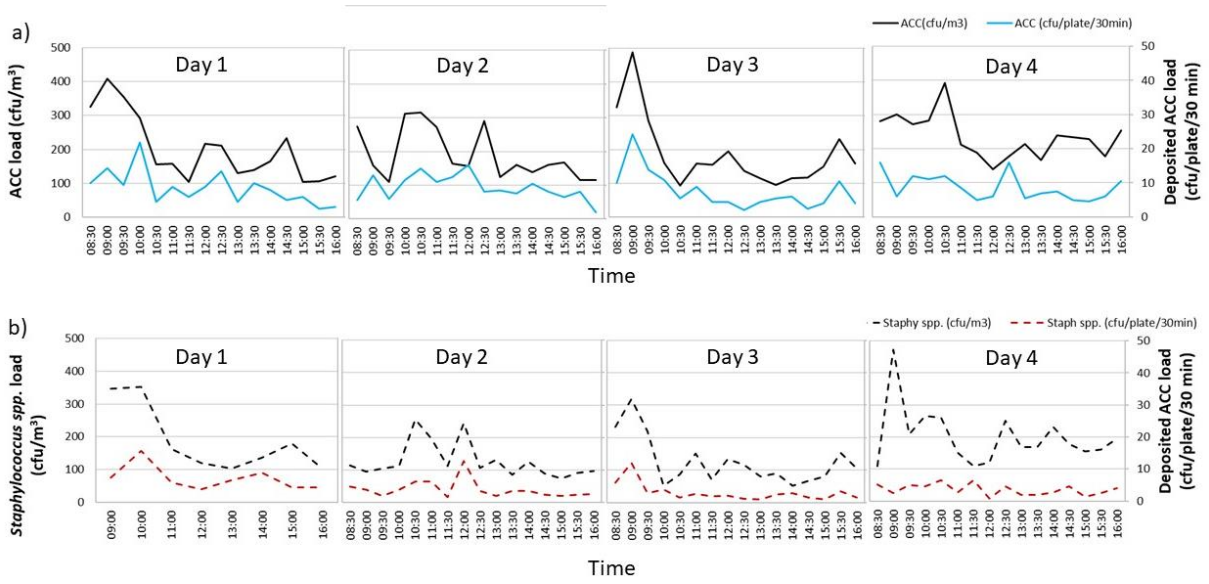

Figure 1: Active and passive air sampling results for four days on the time series a) microbial concentration measured as ACC and b) *Staphylococcus spp.* load.

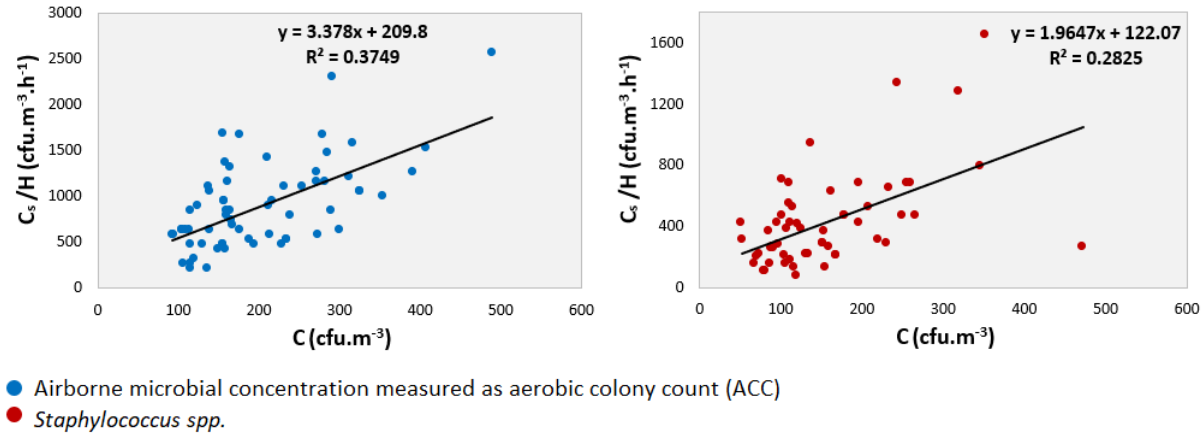

Figure 2: The scatter plot of the concentration of microorganisms on Petri dishes divided by the room height against the mean indoor airborne microorganism's concentration $\lambda_{d,f}$.

The contribution of the airborne microorganism load to the total surface load was calculated based on the passive samples and the surface screening data to be 65% ± 18% (range 39% - 82%) for the first four hours after cleaning (**Table 1**).

4- DISCUSSION AND CONCLUSIONS

This research establishes a quantitative evaluation of airborne microorganisms that influence surface contamination in healthcare facilities with natural ventilation. Airborne microorganisms maintained a strong positive relationship to surface contamination. A high percentage of surface contamination (65% ± 18%) comes from deposited airborne microorganisms. The average concentration of airborne deposited microbial concentration measured as ACC and *Staphylococcus spp*. were 18±10 (cfu. Plate^{-1} .h^{-1}) and 8±6 (cfu. Plate^{-1}.h^{-1}) respectively.

Table 1: The contribution of airborne ACC on surface contamination in a four-bed ward for 4 hours (12 pm - 4 pm).

	Day 1	Day 2	Day 3	Day 4	Average
	mean ± SD (Min-Max), sample size				
Surface ($cfu/cm^2/4h$)	1.49 ± 1.04 (0 - 4.08), n=20	0.83 ± 1.05 (0 - 3.62), n=20	1.58 ± 1.19 (0.25 - 4.46), n=20	0.99 ± 0.94 (0.25 -2.99), n=16	1.36 ± 1.07 (0 - 4.46), n=75
Petri dishes ($cfu/cm^2/4h$)	0.83	0.93	0.62	0.98	0.7
Contribution	56%	82%	39%	82%	65% ± 18% (39% - 82%)

Different microorganism deposition rates existed probably because the particles showed various sizes and airborne characteristics. ACC tends to deposit faster because of its wider microbial content and larger particle groups. The rates at which microorganisms deposit change based on ventilation conditions as well as ward occupancy. A limitation is that the study lacks time-series data on the transient relationship between airborne and surface microbial load, with considerations to the presence and activity level of patients and healthcare workers. Overall, the study demonstrates the potential to develop quantitative correlations between air and surface microorganisms which support the approach for using surface screening as a broader hygiene marker (Smith, et al. 2018). Future research should include monitoring tools or interval time series monitoring such as AMPAS (automatic multiplate passive air sampler, (Hiwar, et al. 2022) to maintain continuous microbial measurement capabilities. Improved time-sensitive monitoring of microorganisms in healthcare environments is likely to be important for better infection prevention systems (Smith, et al. 2018).

REFERENCES

Bonnal, C., Leleu, C., Brugière, O., Chochillon, C., Porcher, R., Boelle, P. Y., ... & Derouin, F. 2015. "Relationship between fungal colonisation of the respiratory tract in lung transplant recipients and fungal contamination of the hospital environment." *PLoS One* 10 (12): 0144044.

Carvalho, S., C. Melo, and B. & Gontijo-Filho, P. Melo. 2007. "Hospital surface contamination in wards occupied by patients infected with MRSA or MSSA in a Brazilian university hospital." *Journal of Basic and Applied Pharmaceutical Sciences* 28 (2): 159–163.

Dancer, S.J. 2004. "How do we assess hospital cleaning? A proposal for microbiological standards for surface hygiene in hospitals." *Journal of Hospital Infection* 56 (1): 10-15.

Gheith, S., Ranque, S., Bannour, W., Ben Youssef, Y., Khelif, A., Ben Said, M., ... & Saghrouni, F. 2015. "Hospital environment fungal contamination and aspergillosis risk in acute leukaemia patients in Sousse (Tunisia)." *Mycoses* 58 (6): 337-342.

Hiwar, W., M. F. King, H. Kharrufa, E. Tidswell, and L. A., & Noakes, C. J. Fletcher. 2022. "The impact of ventilation rate on reducing the microorganisms load in the air and on surfaces in a room-sized chamber." *Indoor air* 32 (11): 13161.

Smith, J., C. E. Adams, M. F. King, C. J. Noakes, and C., & Dancer, S. J. Robertson. 2018. "Is there an association between airborne and surface microbes in the critical care environment?" *Journal of Hospital Infection* 100 (3): 123-129.

6th International Conference on Building Energy and Environment
Eindhoven University of Technology, The Netherlands
6 - 10 July 2025

Impact of gender, mask usage, and speaking on aerosol emissions in a controlled chamber environment

Arya Toghraei [1], Djordje Romanic [2]

[1]*Department of Atmospheric and Oceanic Sciences, Faculty of Science, McGill University, Montreal, Quebec, Canada, arya.toghraei@mail.mcgill.ca*
[2]*Department of Atmospheric and Oceanic Sciences, Faculty of Science, McGill University, Montreal, Quebec, Canada, djordje.romanic@mcgill.ca*

SUMMARY
Understanding the emission and persistence of aerosols in enclosed spaces is critical for mitigating airborne transmission of pathogens. In this controlled chamber experiment (volume = 12 m³), six graduate students (three males, three females) performed four 20-minute tasks: natural breathing and reading aloud, each with and without a surgical mask. Aerosol concentrations (ranging from 0.25–33 µm) were recorded every 6 seconds using a GRIMM 11D spectrometer placed 1 m from the participant. Data were segmented into 3.4-minute intervals and analysed using weighted least squares regression and a mixed-effects model at the 5% significance level. Results indicate that speaking increases aerosol emissions by 26% compared to breathing ($p < 0.001$) and that mask usage reduces emissions by 63% ($p < 0.001$). Moreover, male participants produced 38% more aerosols than females, though this difference was not significant ($p = 0.079$). These findings underscore the importance of integrated mitigation strategies to manage indoor air quality and reduce transmission risks effectively.

Keywords: Airborne Transmission, Respiratory Aerosols, COVID-19

1. INTRODUCTION

Respiratory aerosols, generated through breathing, speaking, and coughing, stay suspended in the air for longer periods compared to larger droplets, which fall quickly due to gravity. This makes them particularly important when considering airborne disease transmission. Studies have confirmed that viruses such as SARS-CoV-2 can spread through aerosols, remaining in the air for extended durations and traveling significant distances, increasing the likelihood of inhalation and infection (Chia et al., 2020; Green et al., 2023). Accurately quantifying individual aerosol emissions in enclosed spaces remains a significant challenge, as the total aerosol level depends on multiple factors, including individual variation in emissions, room ventilation, and particle interaction with the surrounding air (Nicas et al., 2005; Zhang & Bluyssen, 2022).

Most current methods measure exhaled aerosols at the source, typically just a few centimetres from the mouth. While this provides useful data on particle size and concentration, it does not account for the behaviour of aerosols after exhalation. Once released, these particles undergo evaporation, mix with ambient air, and interact with airflow patterns, all of which influence their airborne lifetime and spatial distribution (Asadi et al., 2020; Morawska & Cao, 2020). Consequently, direct measurement of aerosol persistence and accumulation in indoor spaces is necessary for a more accurate estimation of exposure risk (Chia et al., 2020).

This study focuses on respiratory aerosols in a controlled environment, specifically examining the effects of mask usage, gender, and speaking. Instead of just measuring exhaled particles near the source, it considers how aerosols accumulate and persist in the air over time. This approach allows for a better assessment of how much each individual contributes to the overall aerosol concentration and provides insight into effective airborne disease mitigation strategies. Additionally, recent research highlights that individual differences in aerosol production can be substantial. Some individuals, referred to as "superemitters" consistently release orders of magnitude more particles than others during the same expiratory activities (Asadi et al., 2020; Gregson et al., 2021).

2. METHODOLOGY

2.1. Experimental Setup

The controlled chamber experiments were conducted in a sealed chamber designed to minimize external influences on aerosol dispersion. The chamber, measuring 3 m × 2 m × 2 m with a total volume of 12 m^3, was constructed using structural lumber and enclosed with heavy-duty clear plastic sheeting to ensure airtight conditions. This setup provided a controlled environment, free from external airflow and ambient particulate matter, allowing for accurate aerosol emission assessments.

Participants containing of 3 male students and 3 female students completed four experimental scenarios: natural breathing (unmasked), speaking (unmasked), breathing (masked), and speaking (masked). All participants submitted consent forms approved by the McGill University Ethics Committee. In speaking scenarios, the participants were asked to read "The Rainbow Passage", a standardized script widely used in voice studies, ensuring consistency in phonation effort across experiments. Each experiment scenario lasted 20 minutes, followed by a 15-minute air exchange period. Figure 1 shows a photograph of an experiment session with a participant.

Figure 1. Photograph of an ongoing session.

To ensure consistent conditions between different experiment scenarios, an IQAir HealthPro air purifier equipped with high-efficiency particulate air (HEPA) filtration system was placed inside the chamber. This system removed residual aerosols between sessions, restoring the background concentration to below 50 particles per Liter (P/L) within 15 minutes. Continuous monitoring of temperature, relative humidity and carbon dioxide (CO_2) concentrations was conducted using TSI AirAssure 8144-6 and 8144-2 sensors. Aerosol measurements were performed using a GRIMM 11D aerosol spectrometer, positioned 1 m from the participants. This instrument recorded real-time size-resolved aerosol concentrations every 6 s, covering 31 size bins ranging from 0.253 µm to 35.15 µm. The spectrometer detection limit is 50 P/L for small aerosols and 10 P/L for larger particles. Figure 2 shows the experimental setup and plan view of the controlled chamber.

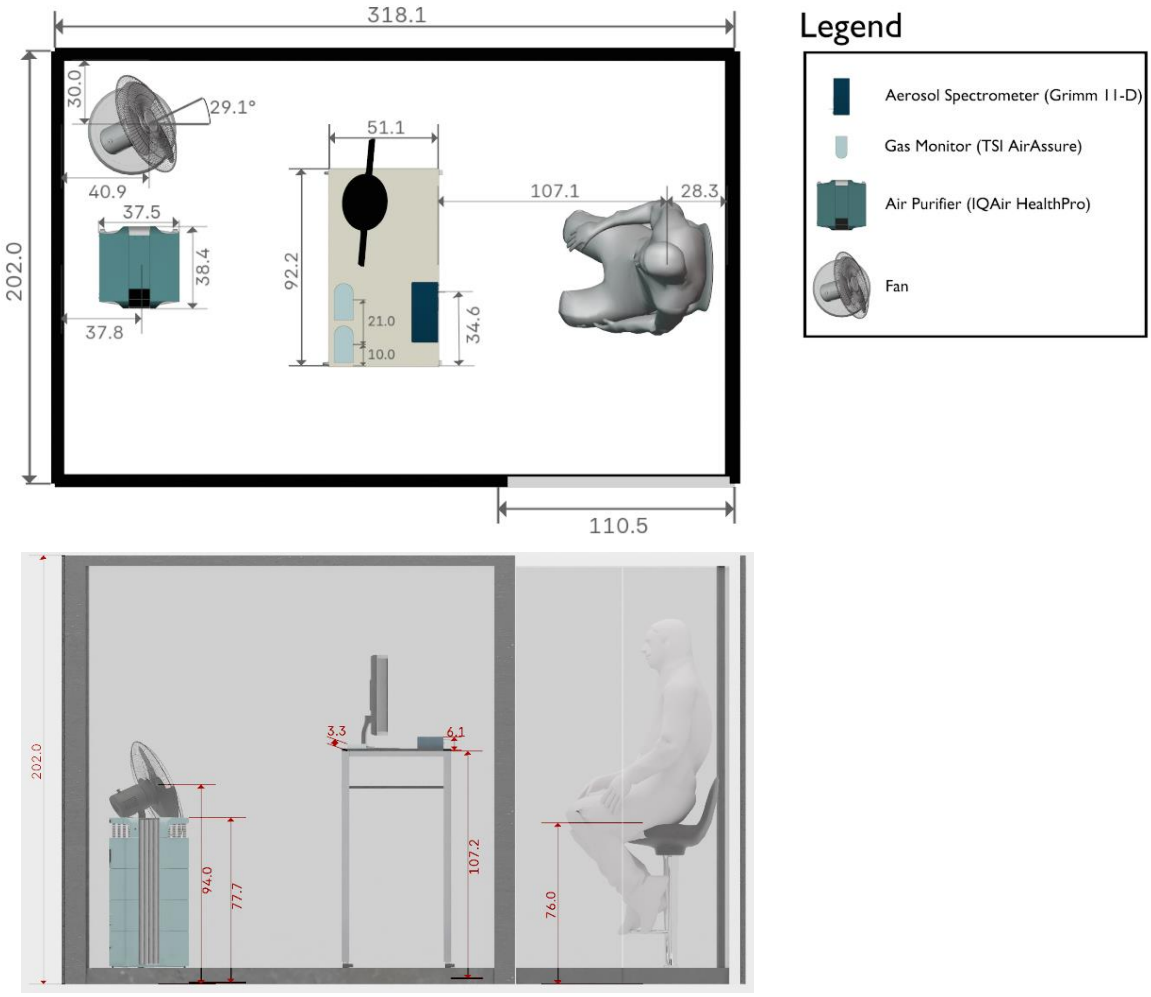

Figure 2. Experimental setup and plan view (top) and sideview (bottom) of the controlled chamber. Dimensions are in cm.

2.2. Data Analysis

Aerosol concentration data were collected continuously throughout each experimental session and divided into six intervals of 3.4 minutes each to capture short-term fluctuations. Before analysis, the raw concentration data were log-transformed to stabilize variance and allow for the interpretation of model coefficients in terms of relative percentage changes rather than absolute

differences. Baseline corrections were applied to each participant's dataset to ensure that aerosol emissions were analysed independently of the conditions from previous experimental scenarios.

To analyse how aerosol concentrations changed over time, weighted least squares (WLS) regression was first applied to estimate trends in aerosol increase and decay, accounting for measurement uncertainty across different particle sizes. A linear mixed-effects model was then used to quantify the effects of mask usage, speaking, and gender on aerosol emissions while controlling for time. In this model, mask condition (with mask versus without mask) and activity type (breathing versus speaking) were treated as fixed effects, while time-dependency was modelled as a random effect, incorporating random intercepts and slopes for each participant group. Interaction terms were included to determine whether the effects of speaking and mask usage simply added together or if they influenced each other in a more complex way.

To improve the reliability of effect size estimates, bootstrap resampling (1,000 iterations) was performed to generate robust 95% confidence intervals. All statistical tests were two-tailed, and significance level was set at $p < 0.05$.

3. RESULTS

Figure 3 displays the mean aerosol concentration (aggregated across all particle sizes) for each condition, stratified by gender and activity type. Error bars indicate measurement precision, rather than inter-participant variability. In all experimental conditions, aerosol concentrations increased over time. Speaking produced higher aerosol emissions than breathing under the same mask condition, confirming that speech-generated aerosols contribute to airborne particle levels. However, aerosol concentration trends for breathing without a mask were comparable to those observed for speaking with a mask, suggesting that wearing a mask during speaking effectively reduces aerosol emissions to levels similar to breathing without a mask.

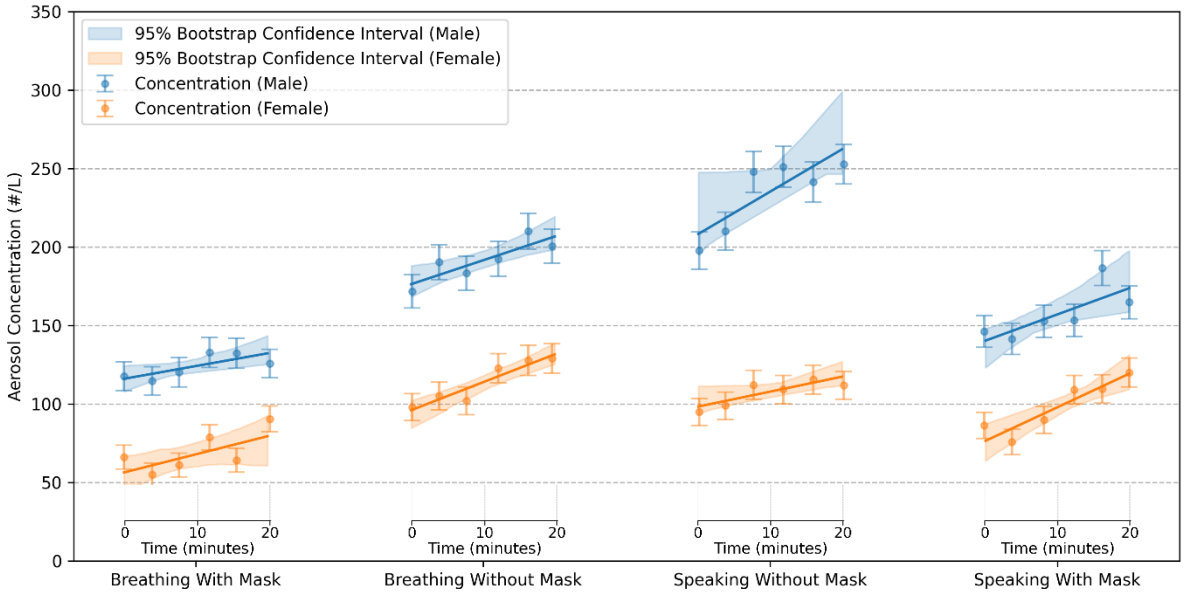

Figure 3. Aerosol concentration (#/Liter) for males and females across four activities (breathing and speaking,

with and without surgical masks). Each activity lasts 20 min and is divided into 6 intervals, with each data point representing the average aerosol concentration over a time interval. Trend lines fitted using Weighted Least Squares show changes in aerosol concentration over time, error bars indicate measurement precision, and shaded regions represent 95% bootstrap confidence intervals for the trend lines.

The data also indicate that male participants exhibited higher aerosol emissions on average compared to female participants. To quantify the effects of each experimental variable while controlling for time, a linear mixed-effects model was applied to the log-transformed aerosol concentration data. The results from this model are presented in Table 1.

Table 1. Mixed-Effects Model Regression Results.

Variable	Coefficient	Std. Error	z-value	p-value	95% Cl
Intercept	4.109	0.225	18.295	<0.001	(3.669, 4.550)
Without Mask (vs. With Mask)	0.490	0.039	12.575	<0.001	(0.414, 0.567)
Speaking (vs. Breathing)	0.230	0.048	4.807	<0.001	(0.136, 0.323)
Male (vs. Female)	0.324	0.184	1.758	0.079	(–0.037, 0.686)
Without Mask × Speaking Interaction	–0.241	0.055	–4.371	<0.001	(–0.349, –0.133)
Speaking × Male Interaction	0.112	0.055	2.029	0.042	(0.004, 0.220)
Time (Scaled)	0.495	0.175	2.826	0.005	(0.152, 0.838)

The estimates for percentage changes were derived by exponentiating the regression coefficients and expressing them as relative differences. The coefficient for "Without Mask" condition is 0.490 ($p < 0.001$), which translates to an estimated 63.28% increase in aerosol concentration when a mask is not worn. Similarly, the coefficient for "Speaking" condition is 0.230 ($p < 0.001$), corresponding to a 25.80% increase in aerosol emissions when participants engage in speech rather than passive breathing. While the coefficient for "Male" is 0.324 ($p = 0.079$), suggesting a 38.31% increase in aerosol emissions for male participants, this effect does not reach significance level ($p > 0.05$), meaning the gender-based differences observed may not be entirely generalizable.

There is a significant negative interaction between "Without Mask" and "Speaking" (–0.241, $p < 0.001$), indicating that the combined effect of not wearing a mask and speaking is less than the sum of their individual effects. In other words, while both factors increase aerosol emissions, their combined effect is not simply additive. Additionally, the interaction between "Speaking" and "Male" (0.112, $p = 0.042$) suggests that male participants experience a further increase in aerosol emissions when speaking.

The model also identifies time as a significant predictor of aerosol concentration. The coefficient for time (0.495, $p = 0.005$) translates to a 64.01% increase in aerosol concentration per unit increase in the time scale, confirming that emissions accumulate over time.

These findings highlight that mask usage and speech activity play dominant roles in determining aerosol emission levels. The interactions indicate that the combined effects of these factors are not strictly additive, suggesting a more complex relationship between speaking and the protective effects of masking. The time-dependent increase in aerosol concentration underscores the importance of extended exposure periods in indoor environments, particularly in settings where masks are not worn.

Figure 4 shows the size distribution of aerosols during the breathing without mask scenario, based on the number concentrations averaged across all participants. The size distribution, presented on

a logarithmic scale, reveals a primary peak below the detection limit of the instrument (<0.25 µm) and a secondary peak at approximately 2.5 µm. This pattern is consistent with previous studies reporting a primary mode at around 0.5 µm or within the 0.2–0.5 µm range (Bagheri et al., 2021; Holmgren et al., 2010). The observed shift to smaller diameters could be due to particle evaporation or interactions with indoor air, which alter the size distribution of respiratory aerosols after being exhaled into the room environment.

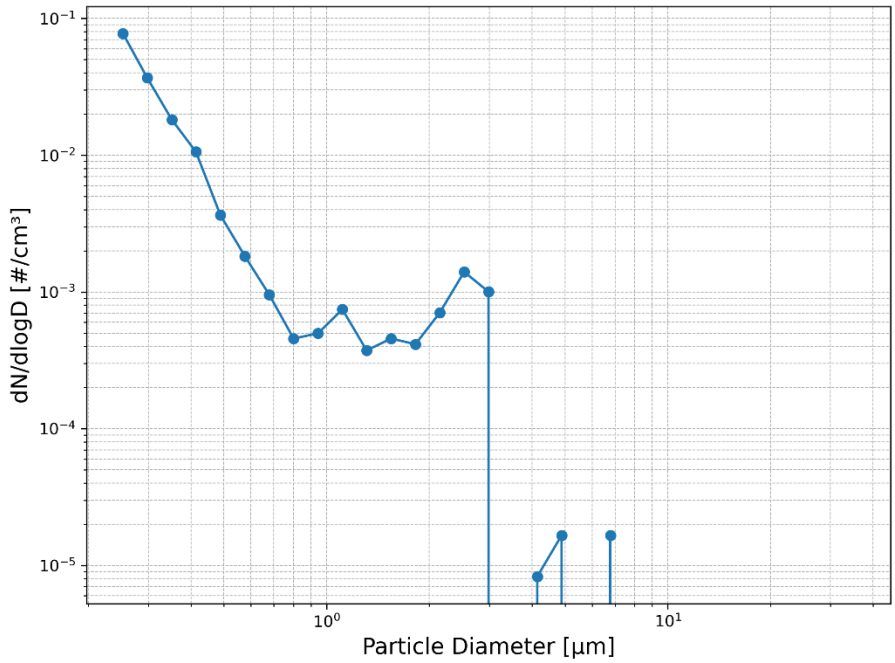

Figure 4. Size distribution of aerosols during the breathing without mask scenario, based on number concentration averaged across all participants

The secondary peak at 2.5 µm aligns with findings by Morawska et al. (2009), who identified a similar peak at approximately 4 µm in the log-normal size distribution of exhaled particles. The difference in peak location can be attributed to the fact that Morawska's study involved direct measurement of exhaled droplets, whereas the present study assessed particles that had interacted with indoor air over time. The shift toward smaller particle sizes suggests that processes such as evaporation and aerosol aging may influence the persistence and transformation of exhaled particles in indoor settings.

4. Conclusions

This study provides quantitative evidence on how mask usage, speech activity, and gender influence aerosol emissions in a controlled indoor environment. The results demonstrate that speaking increases aerosol concentration by approximately 26% compared to breathing, while not wearing a mask leads to a 63% increase in emissions. The interaction between these factors suggests that the combined effect of speaking without a mask is not strictly additive, implying a complex relationship between speech-driven aerosol generation and the protective role of masks.

Although male participants emitted, on average, 38% more aerosols than female participants, this

difference was not statistically significant at the 5% level. However, the interaction between speaking and male gender suggests that men may experience a greater increase in aerosol emissions when speaking, potentially due to physiological differences in vocalization. These findings suggest that gender-related variability should be considered in exposure assessments, though further research with larger sample sizes is needed to confirm this trend.

Aerosol concentrations increased steadily over time, confirming that particles accumulate in enclosed spaces when ventilation is limited. This reinforces the need to consider not just emission rates but also how long aerosols persist in indoor environments. Without adequate air exchange, even relatively low emission rates can lead to significant aerosol buildup over time, especially in settings where multiple people are present for extended periods.

These findings highlight the importance of masking and ventilation as complementary strategies for managing indoor air quality. While masks effectively reduce emissions at the source, ventilation plays a key role in preventing long-term accumulation. Future studies should investigate how these patterns hold in real-world environments with varying ventilation rates, larger populations, and different types of face coverings, particularly in shared indoor spaces where exposure risk is highest.

REFERENCES

Asadi, S., Bouvier, N., Wexler, A. S., & Ristenpart, W. D., 2020. The coronavirus pandemic and aerosols: Does COVID-19 transmit via expiratory particles? Aerosol Science and Technology 54.

Bagheri, G., Schlenczek, O., Turco, L., Thiede, B., Stieger, K., Kosub, J.-M., Pöhlker, M. L., Pöhlker, C., Moláček, J., Scheithauer, S., & Bodenschatz, E., 2021. Exhaled particles from nanometre to millimetre and their origin in the human respiratory tract. medRxiv, 2021.2010.2001.21264333.

Chia, P. Y., Coleman, K. K., Tan, Y. K., Ong, S. W. X., Gum, M., Lau, S. K., Lim, X. F., Lim, A. S., Sutjipto, S., Lee, P. H., Son, T. T., Young, B. E., Milton, D. K., Gray, G. C., Schuster, S., Barkham, T., De, P. P., Vasoo, S., Chan, M., . . . Moses, D., 2020. Detection of air and surface contamination by SARS-CoV-2 in hospital rooms of infected patients. Nature Communications 11.

Green, D., Cooper, N., de Silva, C., Bahl, P., Bhattacharjee, S., Mahmoud, M. M. A., Doolan, C., & Raina Macintyre, C., 2023. Demonstrating the most effective interventions to improve classroom air quality. What novel in situ tests of real-world conditions show is still missing in our guidance. Environmental Research: Health 1.

Gregson, F. K. A., Watson, N. A., Orton, C. M., Haddrell, A. E., McCarthy, L. P., Finnie, T. J. R., Gent, N., Donaldson, G. C., Shah, P. L., Calder, J. D., Bzdek, B. R., Costello, D., & Reid, J. P., 2021. Comparing aerosol concentrations and particle size distributions generated by singing, speaking and breathing. Aerosol Science and Technology 55.

Holmgren, H., Ljungström, E., Almstrand, A.-C., Bake, B., & Olin, A.-C., 2010. Size distribution of exhaled particles in the range from 0.01 to 2.0μm. Journal of Aerosol Science 41, 439-446.

Morawska, L., & Cao, J., 2020. Airborne transmission of SARS-CoV-2: The world should face the reality. Environment International 139.

Morawska, L., Johnson, G. R., Ristovski, Z. D., Hargreaves, M., Mengersen, K., Corbett, S., Chao, C. Y. H., Li, Y., & Katoshevski, D., 2009. Size distribution and sites of origin of droplets expelled from the human respiratory tract during expiratory activities. Journal of Aerosol Science 40.

Nicas, M., Nazaroff, W. W., & Hubbard, A., 2005. Toward understanding the risk of secondary airborne infection: emission of respirable pathogens. Journal of Occupational and Environmental Hygiene 2, 143-154.

Zhang, D., & Bluyssen, P. M., 2022. Exploring the possibility of using CO2 as a proxy for exhaled particles to predict the risk of indoor exposure to pathogens. Indoor and Built Environment.

6th International Conference on Building Energy and Environment
Eindhoven University of Technology, The Netherlands
6 - 10 July 2025

Development of an objective evaluation method of odor reduction performance of air purifiers

Jing Xu [1], Junjie Liu [2], Min Xue [3], Junjie He [4]

[1] *Tianjin Key Laboratory of Indoor Air Environmental Quality Control, Tianjin, China, xu_jing@tju.edu.cn*
[2] *Tianjin Key Laboratory of Indoor Air Environmental Quality Control, Tianjin, China, jjliu@tju.edu.cn*
[3] *Tianjin Key Laboratory of Indoor Air Environmental Quality Control, Tianjin, China, xuem@tju.edu.cn*
[4] *Tianjin Key Laboratory of Indoor Air Environmental Quality Control, Tianjin, China, junjie_he@tju.edu.cn*

SUMMARY

Indoor volatile organic compounds (VOCs) not only include formaldehyde, toluene, etc. which are harmful to human health, but also include odor-producing compounds, causing smell discomfort to occupants. Decorated wooden panels are one of the main sources of indoor VOCs, but the odor components released by them are not clear. In the study, acetic acid and hexanal were utilized as odor compounds, and actual material samples of odor emission sources were employed. An environmental chamber was used to assess the odor reduction capabilities of air purifiers. By leveraging Weber-Fechner's law, a correlation was established between odor concentration and perceived intensity. Additionally, the study analyzed the impact of air purifiers on reducing odor intensity and introduced a novel general odor purification performance index. Propose a subjective-objective hybrid evaluation method to establish a connection between the objective indicators of the air purifier and the subjective odor evaluation of personnel.

Keywords: Odor intensity, Indoor air quality (IAQ), Purification efficiency, VOCs.

1 INTRODUCTION

As awareness about indoor air quality grows, the need for creating a comfortable and healthy indoor environment has become increasingly important. Indoor volatile organic compounds (VOCs), acknowledged for their elevated levels and potential health risks, have drawn significant attention. Common sources of VOCs include decorative materials such as wood, adhesives, and paints, which can emit harmful substances like formaldehyde and benzene (Dong et al., 2019). While measures such as source control and mechanical ventilation techniques have succeeded in reducing VOCs concentrations below the threatening levels; however, indoor odor problems persist, especially during renovation processes (Liu et al., 2024). Odors are not just unpleasant; they can initiate adverse health reactions including emotional stress, respiratory issues, and cognitive impairments.

Despite the prevalence of air purifiers in mitigating indoor pollutants, especially in newly renovated spaces, their effectiveness varies based on their technology – ranging from adsorption and catalytic oxidation to plasma treatments. However, the challenge remains in establishing a standard method to evaluate their performance on odor-causing VOCs. Current market indicators like the total volatile organic compound (TVOC) removal rate are too broad, failing to specify which VOCs are reduced and not directly correlating with changes in odor intensity. This lack of

specificity in TVOC measures calls for more targeted research for odor removal.

2 METHOD

The evaluation of the removal effect of air purifiers on pollutants in current standards is limited to objective indicators. Especially in a real environment, odors have companionship and hybridity characteristics, and it is difficult to establish a connection between objective indicators of individual odors and subjective evaluations of a specific environmental odor by personnel. We propose a new method to establish a connection between the objective indicators of the air purifier and the subjective odor evaluation of personnel. Using personnel odor recognition experiments to obtain personnel stimulation calculation models for various elemental odor substances, and establishing a comprehensive odor intensity model (Wang et al., 2023). Moreover, monitoring and evaluating the effectiveness of air purifiers on odors by detecting typical irritants and establishing a connection between subjective and objective indicators.

2.1 Air purifier and experimental setup

Table 1 shows the details of the PACs measured. The air purifier tested was fitted with a composite filter that sandwiched granular coconut shell activated carbon (average particle size: 0.3 mm) between the HEPA filter media. The surface of activated carbon is treated with chemical reagents to improve the adsorption performance of formaldehyde. The manufacturer did not provide details of the surface modification. The air purifier with multiple purification technologies is used for the purification experiment of odor compounds released by the medium density fiberboard (MDF).

Table 1. Basic information on the tested air purifier in the laboratory

Sample No.	Filter information					Rated Airflow (m^3/h)	CADR (m^3/h)	
	Size (mm)	Number	Pleat Number	Filtering Area (m^2)	Rating & Materials		HCHO	TVOC
Air purifier[a]	Φ280×180	2	200	2.88×2	activated carbon	800	300	/

[a] Equipped with amino acid aldehyde removal crystals and negative ion purification technology.

The experimental system consists of two parts: an environmental chamber with accessories, and a sampling and analyzing system. The environmental chamber used in the experiment was built following the requirements of the Chinese national standard GB18801-2022, and the volume of the environmental chamber was 30 m^3. The surface of the environmental chamber (6 sides of the wall and the ground) is composed of stainless-steel boards, to avoid the deposition or chemical reaction of gaseous compounds on the surface of the environmental chamber, which endangers the health of the experimenters and increases the experimental error. Next to the environmental chamber is the observation room, one of which is equipped with transparent glass as an observation window. Figure 1 provides a schematic diagram of the environmental chambers for the experiment (Figures 1a, b). In the center of the environmental chamber (3.5m×3.4m×2.5m), Air conditioners are placed to control the temperature and humidity in the cabin. Table 2 shows the environmental conditions of the chamber used for the experiment. Throughout the test, the temperature and relative humidity of the environmental chamber were recorded by an automatic recorder (HOBO, Onset, USA). Before testing, indoor surfaces were scrubbed with deionized water and air-dried in

ventilation mode. When the indoor and outdoor air properties were balanced, the valves in all sampling pipes were sealed and the background concentration of gaseous pollutants was measured.

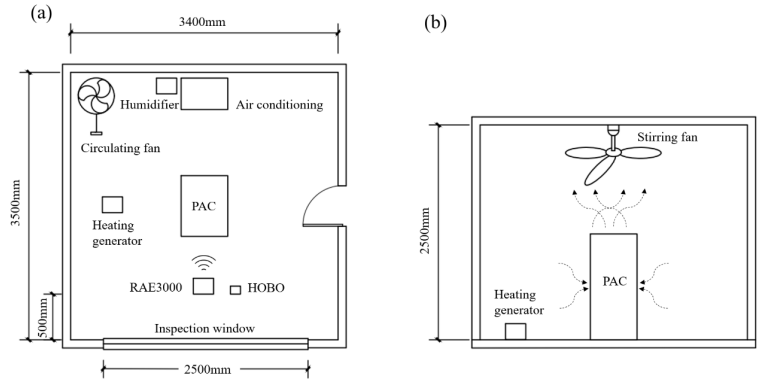

Figure 1. Experimental setup for the odor purification experiments: (a) top view with samples and (b) front view with samples

Table 2. Full scale chamber environmental conditions for air purifier performance tests.

Specification	Set point values	Measured values mean (SD)[a]
Temperature	23±1℃	23℃ (0.0)
Relative Humidity	50%±10%	53.2% (2.1)
Air exchange rate	≤0.05h-1	0.047 (0.003)
Air mixing	>80%	100%[b]

[a] SD: standard deviation
[b] No standard deviation because of single-value data

2.2 VOCs emissions

Medium-density fiberboard, which is widely used in building decoration, is the main sources of indoor VOCs. Acetic acid, hexanal, and pentanal were found to be odor compounds common to these materials. As one of the main compounds released by human skin, acetic acid is commonly present in indoor environments. At the same time, acetic acid and hexanal have a low threshold value of exposure, which are easy to cause poor perceived air quality. According to the above characteristics, acetic acid and hexanal were used as typical odor compounds in building materials to carry out the pollutant purification experiment.

The medium density fiberboard (MDF) stored for two years, which released pollutants at a slow stable rate, was utilized to simulate the release of odorous VOCs from building materials in residential environments. Compared with the high-release state of the newly renovated building, the slow-release state of the decoration board accounts for a higher proportion of the actual building life cycle. Therefore, it is more practical to select MDF that has been aged for two years to test the purification performance. Six MDF panels with dimensions of 2.4 m×1.2 m × 0.015 m was evenly arranged in the environmental chamber, and the air purifier was placed in the middle of chamber. The loading rate of the panels in the environmental chamber is 1.17 m^2/m^3, which is close to the arrangement of materials in the actual building interior.

2.3 Sniffing Discrimination Experiments

A cohort of four odor evaluators (gender-balanced; 2 males, 2 females) aged 20-26 years, in good health and without a history of smoking or olfactory impairments, were recruited from the university campus. The evaluators underwent a rigorous training program adhering to the ISO12219-7 standard, spanning four sessions within a month. Odor intensity (OI) assessments were conducted utilizing a standardized 6-point scale methodology. To represent varying odor intensities, aqueous solutions of 1-butanol were prepared at distinct concentrations, as guided by previous research, with detailed parameters outlined in Table S1. According to the ISO13725 standard, the experimental environment was carefully controlled, ensuring an odorless room with constant ventilation and a temperature maintained at 23 ± 2° C. The test room was devoid of any non-essential items capable of emitting odors.

Odor evaluation and compound characterization were performed using GC-O-MS. The operating principle of GC-O-MS is shown in Figure 2. The Supelco tube was installed on the thermal desorption instrument of the GC-O-MS. Before odor evaluation, a blank Supelco tube was run to rinse the VOC impurities trapped in the GC-O-MS to eliminate background errors. The qualitative method is the same as that of GC-MS. Some VOCs took a long time to elute from the column, for example, acetic acid eluted between 7.56 and 8.08 min. In the characterization of odor compounds, the allowable deviation between the time of smelling the odor and the retention time was ± 0.1 min.

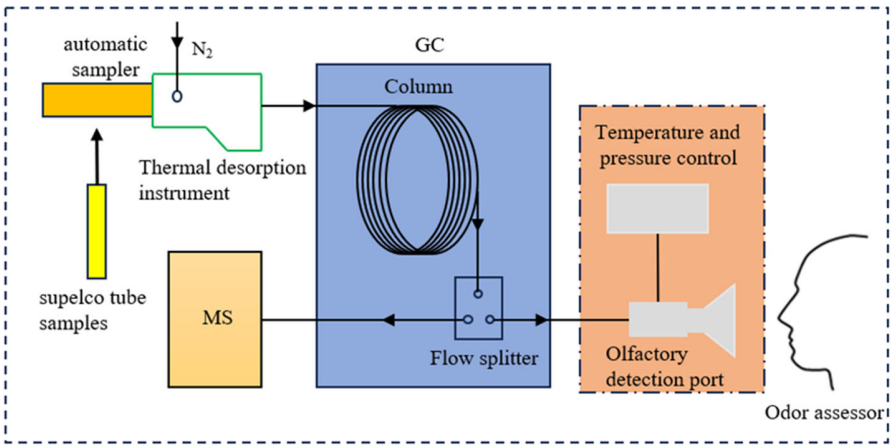

Figure 2. Schematic diagram of the operation of GC-O-MS.

Preceding the experiment, evaluators were instructed to abstain from pungent odor sources, including perfumes and strongly flavored foods, for 24 hours. Upon arrival, participants acclimatized to the test environment for 5 minutes prior to analysis, with each sample assessment taking approximately 45 minutes. To mitigate olfactory fatigue, evaluators alternated sniffing sessions in three 15-minute cycles, as detailed in Table S2. During the formal experiment, evaluators sniffed through a designated olfactory port and promptly recorded the retention time (RT), odor intensity (OI), and odor descriptors (such as rubber, fruity, cucumber, sour, rosin) upon perception. Following this, the OI values were averaged across all evaluators' scores. The odor

threshold was defined as the concentration at which at least 50% of the evaluators could detect the odor, with the presence of the odor being confirmed if detected by two or more evaluators.

2.4 Experimental Procedure

The purification experiment of odor compounds released by the plate was divided into two stages: gas release and purification. After the initial environment of the environmental chamber was adjusted, 6 MDF boards were evenly placed in the chamber, the circulating fan and stirring fan were turned on, and the environmental chamber was sealed for 8 h. The purification phase was divided into 4 steps and lasted 120 minutes as show in Figure 3. First, turned off the stirring fan and proceed to the initial 20-minute concentration sampling. After that, turned on the air purifier and took 3 concentration samples in a row for 20 minutes each, according to the Chinese national standard GB/T 18801–2022.

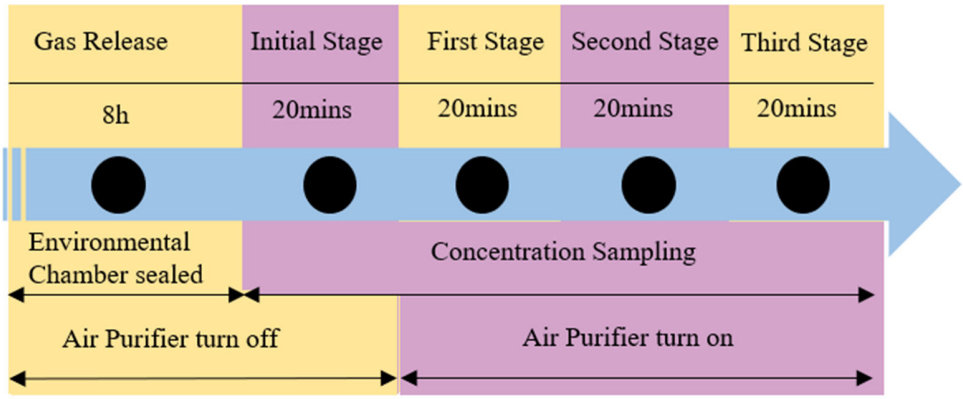

Figure 3. Sampling in the concentration of odor compounds at each stage

In both natural attenuation and total attenuation experiments, the variation of pollutant concentration with time conforms to the trend of exponential function, as shown in Eq. (1).

$$C_t = C_0 e^{-kt} \quad (1)$$

Where, t is time, min, C_0 is the concentration of gaseous pollutants at the initial moment in ppm, C_t is the concentration of gaseous pollutants at time t in ppm and k is the pollutant concentration attenuation index in min^{-1}.

Ventilation efficiency η defined as the ratio of the amount of air involved in diluting pollutants to the amount of ventilation sent into the room, expressed by Eq. (2). In this study, we used the evaluation formula of ventilation efficiency to evaluate the purification performance of air purifiers.

$$\eta = \frac{CADR}{Q} \quad (2)$$

Where, η is the purification efficiency of the air purifier and Q is the circulating air volume of the air purifier in m^3/h.

Due to the limited number of data points for offline sampling, CADR cannot be calculated, so the purification effect is evaluated by the concentration purification efficiency index, and the definition of concentration purification efficiency η' is shown in Eq. (3).

$$\eta' = \frac{C_0 - C_t}{C_0} \quad (3)$$

Where, η' is the purification efficiency of pollutants at time t, C_t is pollutant concentration at time t and C_0 is a concentration of contaminants at the initial moment

Weber-Fechner's law is one of the most widely used concentration-odor intensity transformation models and is, therefore, the model that is the focus of this study. Based on the Weber-Fechner law, this study proposes to evaluate the odor purification performance of air purifiers by using odor intensity reduction ΔOI index. Based on the GC-MS results of the actual odor activity value OAV_i of the panel, combined with the sensory evaluation results as per our previous study, to obtain a constant a_i, the odor intensity (OI_i) and odor intensity reduction (ΔOI) can be obtained, and finally, the comprehensive odor intensity SOI of the mixed gas can be obtained .

$$OAV_i = \frac{C_i}{C_{Ti}} \quad (4)$$

$$OI_i = a_i log OAV_i + b_i \quad (5)$$

$$\Delta OI = OI' - OI'' \quad (6)$$

$$SOI = log \sum 10^{OIi} \quad (7)$$

3 RESULT

3.1 Purification effect of odor compounds released from the MDF boards

The offline analysis method was used to obtain the average concentration over four time periods. The concentration changes of the odor compounds detected in the experiment are shown in Figure 4, and the concentration values of the compounds have been subtracted from the background concentrations in the environmental chamber. The odor compounds detected in this experiment included acetic acid, toluene, and hexanal, and there may still be compounds with odor but concentrations below the detection limit of GC-MS instruments, which cannot be characterized. Toluene concentrations below the odor threshold concentration do not produce odor in the environmental chamber, but toluene remains a potential odor compound when the loading rate of the material increases, so the variation in toluene concentration is listed here.

In Figure 4, the concentrations of the three odor compounds showed a decreasing trend when the purifier was turned on. The initial concentration of acetic acid was 8.51 μg/m^3, and after 40 minutes, the concentration of acetic acid decreased to 0.03 μg/m^3, and the purification efficiency was 99.6%. The initial concentrations of toluene and hexanal were 23.45 μg/m^3 and 25.86 μg/m^3, respectively, and the concentration purification efficiency η' after 1 h was 64.5% and 40.0%.

Filters are typically tested for efficiency and lifetime using ppm levels of contaminants. The initial concentration of VOCs detected in the environmental chamber was very low compared to the initial concentration of the compound used in the single-pass efficiency of the filter or the test of the air purifier CADR. The purification efficiency of the filter varies with the initial concentration, so it is of little significance to compare the purification efficiency at different initial test concentrations. The experimental object in this research is a two-year MDF with a load factor of 1.17 m^2/m^3. The experimental conditions are in accord with the real residential buildings, which can better reflect the actual odor compound purification effect. This is instructive for the establishment of a test method for the odor purification performance of air purifiers. In the next

step of the study, it was necessary to use panels with updated production times to simulate the odor emission conditions of newly renovated buildings.

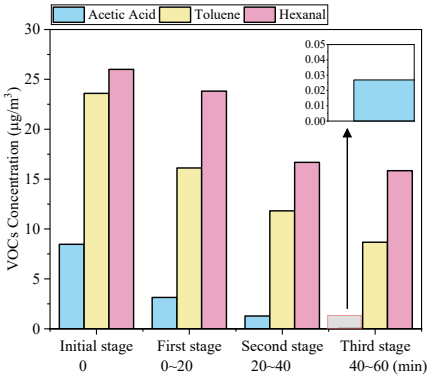

Figure 4. Changes in the concentration of odor compounds at each stage

3.2 Reduction in odor intensity

It is important to note that the Weber-Fechner law applies to moderately intensive stimuli. For compounds with a concentration equal to the odor threshold, it has been assumed that bi=0.5. This is because the odor threshold concentration is defined as the concentration at which 50% of the group members perceive a faint odor and others do not, so the theoretical odor intensity OI should be 0.5, i.e., 0.5 for bi. To obtain the coefficient a_i of Weber-Fechner's law, an odor evaluator must evaluate the odor at the scene. Detailed data on this can be found in Table S3. According to the principle of the GC-O-MS instrument, the odor evaluator smells the gas after the gas in the gas bag is concentrated 40 times more at the olfactory port, and the compound concentration corresponding to the odor intensity given by the odor evaluator can be calculated. According to Eq. (5), the odor data are fitted to obtain the coefficient a_i of Weber-Fechner law. There are 6 data points for both acetic acid and hexanal, and the concentration of toluene in the purification experiment does not contribute to the odor, so no fitting is done here. Figure 5 show the fitting results of acetic acid and hexanal. The fitting correlation coefficients R^2 of acetic acid and hexanal were 0.998 and 0.981, respectively, which were higher than 0.98, indicating that the fitting effect was good. The transition relationship between acetic acid and hexanal concentrations and odor intensity is as follows in Equations 8 and 9:

$$OI_{Acetic\ acid} = 1.9375 * logOAV_{Acetic\ acid} + 0.5 \quad (8)$$

$$OI_{Hexanal} = 0.8832 * logOAV_{Hexanal} + 0.5 \quad (9)$$

By substituting the concentrations of acetic acid and hexanal detected in the environmental chamber, respectively, the corresponding odor intensity can be calculated. The odor intensities of acetic acid and hexanal at different stages are shown in Figure 6. The initial odor intensity of acetic acid released by MDF is 1.33, indicating a weak odor. After turning on the air purifier, the odor intensity of acetic acid gradually decreased, and after 1 hour, the odor intensity of acetic acid decreased to 0. The initial odor intensity of hexanal released by MDF was 1.66, and the odor intensity of hexanal slowly decreased after 1 h operation of the air purifier. From the perspective of odor characteristics, the sour taste characteristics of acetic acid gradually decreased to 0 after

the air purifier was turned on for 1 h, and the grassy flavor characteristics of hexanal changed slightly. In this study, the odor intensity reduction ΔOI index was proposed to evaluate the odor purification performance of air purifiers.

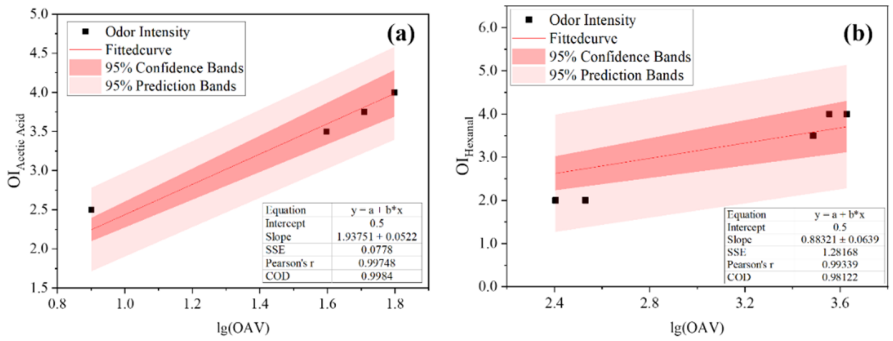

Figure 5. Linear fitting results of logOAV and OI of (a) acetic acid and (b) hexanal

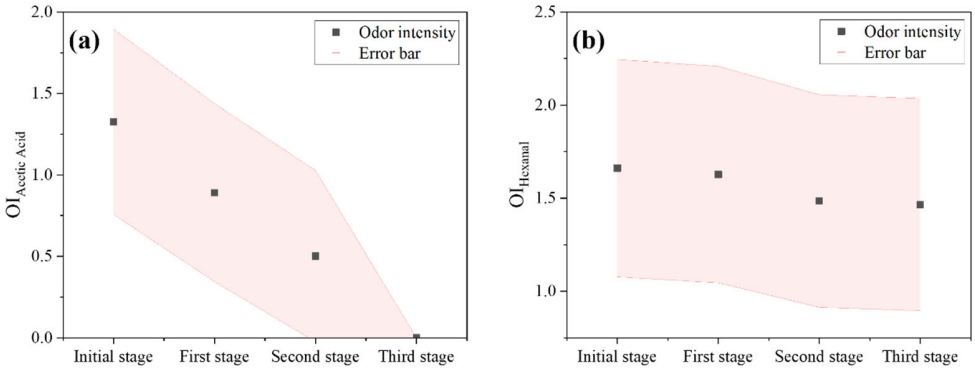

Figure 6. Changes in odor intensity when the air purifier is turned on (a) in acetic acid and (b) hexanal odor intensity

It should be noted that the odor intensity calculated in Figure 5 and Figure 6 is at a weak stage, and the accuracy of the prediction of the Weber-Fechner law at this stage needs to be verified. The main goal of this study is to preliminarily explore the evaluation method of odor purification performance, and the analysis of the applicability scope of the model will be carried out in future research. This study provides reference directions for the establishment of an evaluation method for the purification odor performance of air purifiers. In addition, according to the experimental results, it is recommended to increase the intensity of the air release source based on this experiment to achieve more accurate odor intensity prediction when evaluating the odor purification effect of the air purifier on the MDF.

REFERENCES

Chen H., et al., 2024. Two-parameter C-history method: A fast and accurate method for determining the characteristic parameters of formaldehyde/VOC early-stage emissions from building materials. The Science of the total environment946,174218-174218.

Caron F., et al.,2020. Behaviour of individual VOCs in indoor environments: How ventilation affects emission from materials. Atmospheric Environment 243 .

Dong H., et al., 2019. Identification and analysis of odor-active substances from PVC-overlaid MDF. Environmental Science And Pollution Research 26 , 20769-20779.

6th International Conference on Building Energy and Environment
Eindhoven University of Technology, The Netherlands
6 - 10 July 2025

Effects of twist wind on outdoor air temperature and wind comfort under solar radiation

Wenxin Li [1], Cheuk Ming Mak [1,*]

[1]*Department of Building Environment and Energy Engineering, The Hong Kong Polytechnic University, Hong Kong, China, wenxinn.li@connect.polyu.hk*
[1,*] *Department of Building Environment and Energy Engineering, The Hong Kong Polytechnic University, Hong Kong, China, cheuk-ming.mak@polyu.edu.hk*

SUMMARY
This study used a wind tunnel experiment to measure the flow field under conventional and twist wind profiles and employed steady Reynold-Averaged Navier-Stoke equations with standard $k-\varepsilon$ model, coupled with the discrete ordinate (DO) model to investigate the impact of twist wind on wind environment and air temperature around two prevalent building configurations: tandem and side-by-side arrangements. The results indicated that the twist wind can generate asymmetrical flow fields around both the tandem and side-by-side arrangements, with the effects of twisting flows being more pronounced in densely urbanized areas characterized by narrow street widths. The twist winds have cooling effects on air temperature because the weakened downwash flow is unable to resist the buoyancy flow, thus facilitating the rise of heated air within the street canyon.

Keywords: Twist wind profile, Computation fluid dynamic, Pedestrian-level wind comfort, Air temperature.

1. GENERAL INSTRUCTIONS

As urbanization progresses, the urban heat island (UHI) effect has become increasingly pronounced, leading to a yearly rise in temperatures across an expanding number of regions (Perkins-Kirkpatrick and Lewis, 2020). An increasing body of research has focused on strategies to reduce urban temperatures, mitigate the heat island effect, create comfortable pedestrian wind and thermal environments, and promote outdoor activities among residents (Weerasuriya, et al., 2020). In addition, an uncomfortable thermal environment tends to encourage residents to remain indoors during hot weather, thereby leading to a significant increase in energy consumption due to the use of air conditioning (Giridharan and Emmanuel, 2018). Hence, investigating the impact of architectural design on urban wind and thermal environments holds significant importance.

As the scarcity of land resources becomes increasingly apparent, an expanding number of structures are being constructed not only within urban centers but also in proximity to mountainous regions. This trend is particularly pronounced in cities characterized by their mountainous terrain, such as Hong Kong and Chongqing. For buildings situated in these areas, the influence of the wind field exhibits significant differences compared to that observed in flat terrains, this phenomenon has been addressed in the previous literature (Yuan, et al., 2023). Twisted wind profile (TWP), defined as the variation in wind direction along the vertical axis due to terrain effects, has been extensively examined in prior research. The complex topography in mountainous areas has been proven to induce helical wind patterns, therefore affecting the ventilation, structural stability, and

pollutant dispersion. Through wind tunnel experiments, Tse, et al., (2017) successfully simulated twist wind using twist vanes and discovered that it significantly influences the position of the downstream low wind velocity areas. Yuan, et al., (2022) conducted RANS simulations to examine the modification of the flow field under twisted winds while considering horizontal homogeneity. They concluded that the asymmetry in the flow field is influenced by the twist angle varying with height. Therefore, the flow characteristics under the conventional wind profile (CWP) and twist wind profile (TWP) exhibit significant differences and warrant further investigation.

Nowadays, the Computation Fluid Dynamics (CFD) approach has emerged as a robust and indispensable tool for investigating wind flow patterns and air temperature distributions within street canyons (Toparlar, et al., 2015). The thermal forcing plays a crucial role in determining the flow field structures within street canyons (Hang, et al., 2024). Li, et al., (2020) highlighted the significance of modelling the solar radiation in urban wind and thermal environments, noting that solar radiation serves as the primary thermal forcing in urban areas. In this study, the Discrete Ordinate (DO) model in FLUENT was utilized to simulate solar radiation and sunlight exposure. The pedestrian-level wind environment and air temperature around two distinct building configurations (tandem and side-by-side arrangements with varying gaps) were simulated using the steady Reynolds-Averaged Navier-Stokes (RANS) equations with standard $k-\varepsilon$ turbulence models.

2. METHODS

2.1. Wind tunnel experiments

The wind tunnel experiment was conducted in the Aerodynamics and Acoustic Facility (AAF) at the Hong Kong University of Science and Technology. The twisted wind profile has been replicated by the twist vanes, which induce varied wind directions along the vertical axis. The maximum twist angle at ground level was measured to be 25° (Figure 1). The pedestrian-level wind velocity was measured using the KANOMAX Model 0965-07 anemometer at a height of 1 cm above ground level across 72 distinct locations (Li, et al., 2024).

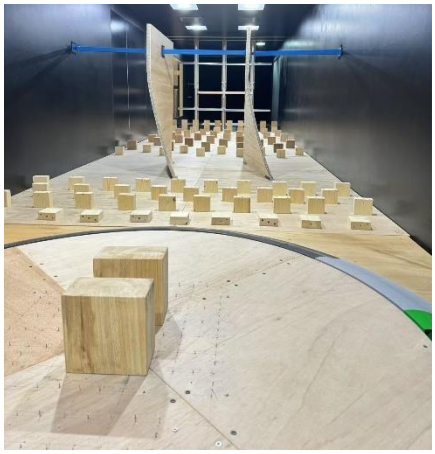

Figure 1. Inside view of wind tunnel experiment.

2.2. CFD simulations

The inlet conditions, encompassing wind velocity, turbulence intensity, and twist angle profile, were consistent with the data obtained from the wind tunnel experiment (Figure 2). The distances from the building edges to the computational domain boundaries (inlet, lateral, outlet, and top) were set at 5 *H*, 5 *H*, 15 *H*, and 5 *H*, respectively (Table 1). The boundary conditions for the computational domain are detailed in Table 2. Lateral 1 and lateral 2 were modified to velocity inlets under TWP conditions to accurately simulate the twisted wind profile phenomenon. The reference velocity is determined to be 7.23 m/s at a building height of 600 mm, while TWP 25 represents the twist wind profile where the maximum twist angle measured at the ground level is 25 degrees.

In this study, various configurations of neighboring buildings, including tandem and side-by-side arrangements, were simulated to represent the diverse building layouts commonly found in urban environments. The flow field under conventional wind profile (CWP) and twist wind profile (TWP) were simulated using the steady Reynold-Averaged Navier-Stoke equations with standard $k-\varepsilon$ models. Air temperature was evaluated under realistic solar radiation conditions, which were simulated using the Discrete Ordinate (DO) model in FLUENT, the radiation simulations were conducted at LSTs (local solar times) of 1500 LST (3. p.m) on a summer day in Hong Kong. This time was selected to simulate the hottest period of the day in Hong Kong, representing the most severe conditions.

$$u_{(z)} = \frac{u^*_{ABL}}{\kappa} \ln\left(\frac{z+z_0}{z_0}\right) \quad (1)$$

$$\theta_{(z)} = \theta_0 \exp\left(\alpha \times z/\beta\right) \quad (2)$$

$$v_{(z)} = u_{(z)} \tan\left(\theta_{(z)}\right) \quad (3)$$

$$k_{(z)} = \frac{3}{2}\left(I_{(z)} u_{(z)}\right)^2 \quad (4)$$

$$\varepsilon_{(z)} = \sqrt{C_\mu} k_{(z)} \sqrt{\left(\frac{\partial u}{\partial z}\right)^2 + \left(\frac{\partial v}{\partial z}\right)^2} \quad (5)$$

where frictional velocity u^*_{ABL} =0.37 m/s; dynamic roughness height z_0 =0.00025 m; von Karman constant κ =0.4187 and the model constant C_μ =0.09; $\theta_{(z)}$ is the twist angle along the vertical height; θ_0 is the yaw angle measured at the lowest height; The constants α and β, derived from the line fitted to the twist angle profile of the incident flow, were –3.06 and 1.43 respectively. The turbulence intensity profile ($I_{(z)}$) was obtained by fitting the wind tunnel data and the inlet turbulence kinetic energy ($k_{(z)}$) was derived from Blocken, et al., 2012. The inlet turbulence dissipation rate ($\varepsilon_{(z)}$) can be calculated based on the above Equations. The pedestrian-level wind environment was assessed based on the mean wind velocity ratio (*MVR*), which is defined as the mean wind velocity at the pedestrian level height (z=2 m) and the wind velocity at the reference height (z=200 m in prototype scale). The air temperature near the tandem and side-by-side building arrangement was presented by T-T_{ref}, where T_{ref}=273.15 K.

Table 1. Computational domain size for varied test cases.

Cases	H_{domain}	L_{domain}	D_{domain}
SBS1	2.4	8.1	4.7
SBS2	2.4	8.1	4.9
SBS3	2.4	8.1	5.1
Tandem1	2.4	8.3	4.3
Tandem2	2.4	8.5	4.3
Tandem3	2.4	8.7	4.3

Table 2. Boundary conditions for the computational domain.

Location	CWP	TWP
Inlet	Velocity inlet	Velocity inlet
Lateral 1	Symmetry	Velocity inlet
Lateral 2	Symmetry	Velocity inlet
Outlet	Outflow	Outflow
Top	Free slip	Free slip
Ground	No-slip wall	No-slip wall

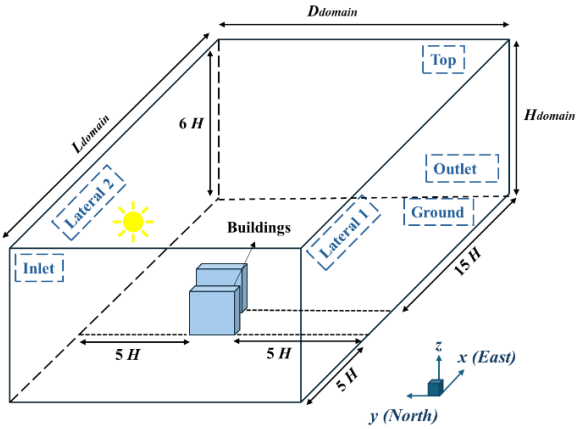

(a)

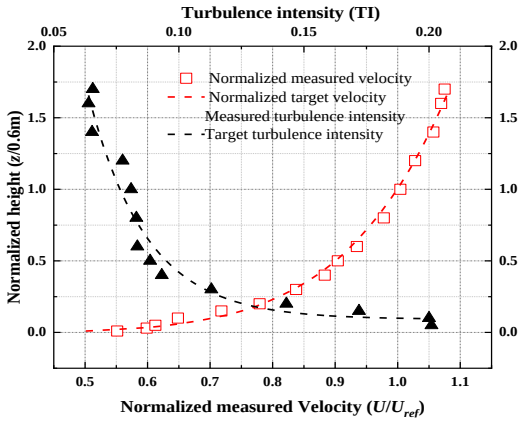

(b)

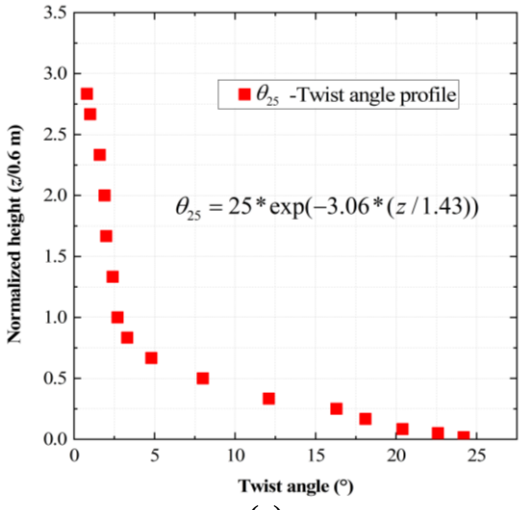

(c)

Figure 2. (a) Computational domain, (b) Wind and turbulence intensity profile, and (c) Twist wind profile.

3. RESULTS

3.1 Grid sensitivity test and Validation

The mesh was a structured hexahedral mesh generated by ANSYS ICEM CFD using the blocking technique. Grid sensitivity was evaluated for three distinct grid arrangements: Coarse (minimum cell size of 4 mm), Medium (minimum cell size of 2 mm), and Fine (minimum cell size of 1 mm). The number of cells was 1,649,376, 3,425,424, and 4,931,538 for coarse, medium, and fine cell sizes, respectively. These arrangements were compared, and the computational results between the medium and fine grid arrangements exhibit negligible differences (Figure 3). The medium mesh was selected for optimal balance between computational resource utilization and simulation accuracy. The simulation results were compared with the wind tunnel results at several different horizontal lines (x=-0.225 m, 0 m, 0.075 m, 0.31 m, 0.385 m, and 0.535 m). While high consistency was observed in most regions, discrepancies were noted in the location of wake areas relative to wind tunnel experiment results (Figure 4). This is due to the well-known drawback of RANS models in predicting the wind conditions in the building wake (Yoshie, et al., 2007). The temperature simulation results were compared with the reference data and agreed with the on-site measurement results (Idczak, et al., 2006) in Table 3.

Table 3. Comparison of the wall temperature between CFD and on-site measurement.

Location	On-site measurements (Idczak, et al., 2006)		Present study	
	0800 LST	1600 LST	0800 LST	1600 LST
x/H=0.21	21.4 ℃	29.2 ℃	21.7 ℃	29.5 ℃
x/H=0.84	24.9 ℃	28.9 ℃	23.8 ℃	28.6 ℃

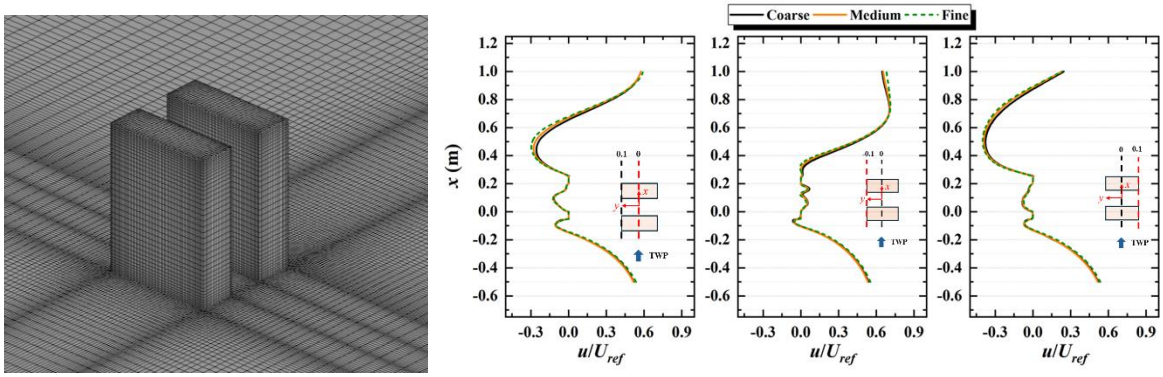

(a) (b)

Figure 3. (a) Mesh arrangements (medium arrangement as an example) and (b) Grid sensitivity test results for u/U_{ref} along three horizontal lines under TWP 25.

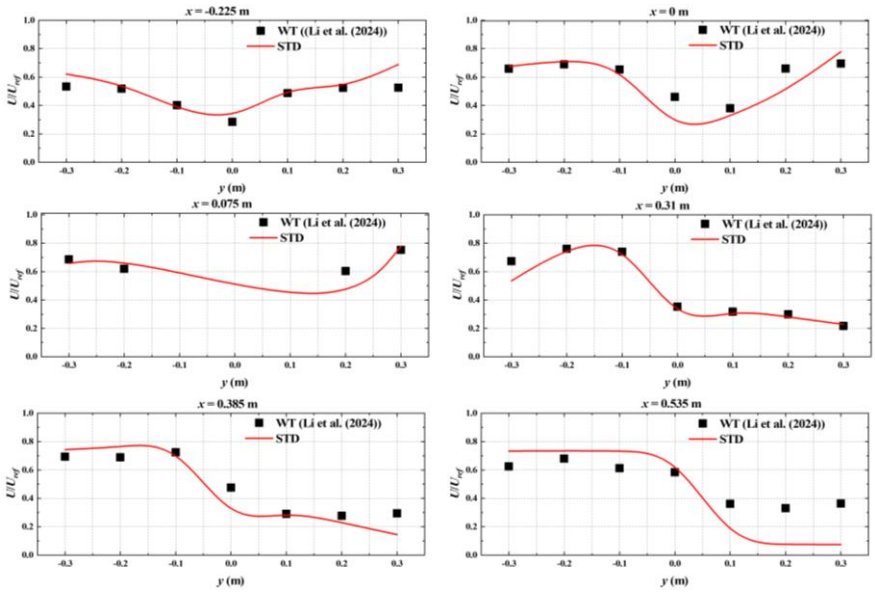

Figure 4. Comparison of the U/U_{ref} results between the CFD and the wind tunnel experiment results under TWP.

3.2 Effect of twist wind on wind comfort

Figure 5 describes the flow field distribution under CWP and TWP for varied building configurations. The twisted wind affects the creation of an asymmetrical flow field distribution around building arrays. For the side-by-side arrangement of the building array, when the gap spacing is small (SBS1), vortices behind the two buildings tend to interact with each other. Conversely, when the gap spacing exceeds the building widths, the two buildings behave as independent entities, each with its own inclined flow field. In addition, when the gap spacing is small, the Venturi effect was observed. The corner vortex on the right side of the building tends to be located downstream of the passages due to the acceleration phenomenon. This indicates that the influence of twist winds is more pronounced in narrow building arrangements. The twisted wind clearly enhances the vortex shedding on the side surface in the direction of its approaching flow. Upon analyzing adjacent structures with varying inter-building distances, it becomes apparent that the wider the spacing between buildings, the more accurately the deviation angle aligns with the wind's angle of incidence.

For the tandem arrangement, the wind velocity magnitude was lower than that in the flow field surrounding the side-by-side arrangement due to the wake effect caused by the upstream buildings. With the increasing gap between buildings, a vortex was observed in the passage between the two structures, and its intensity increases as the building separation widens under TWP conditions.

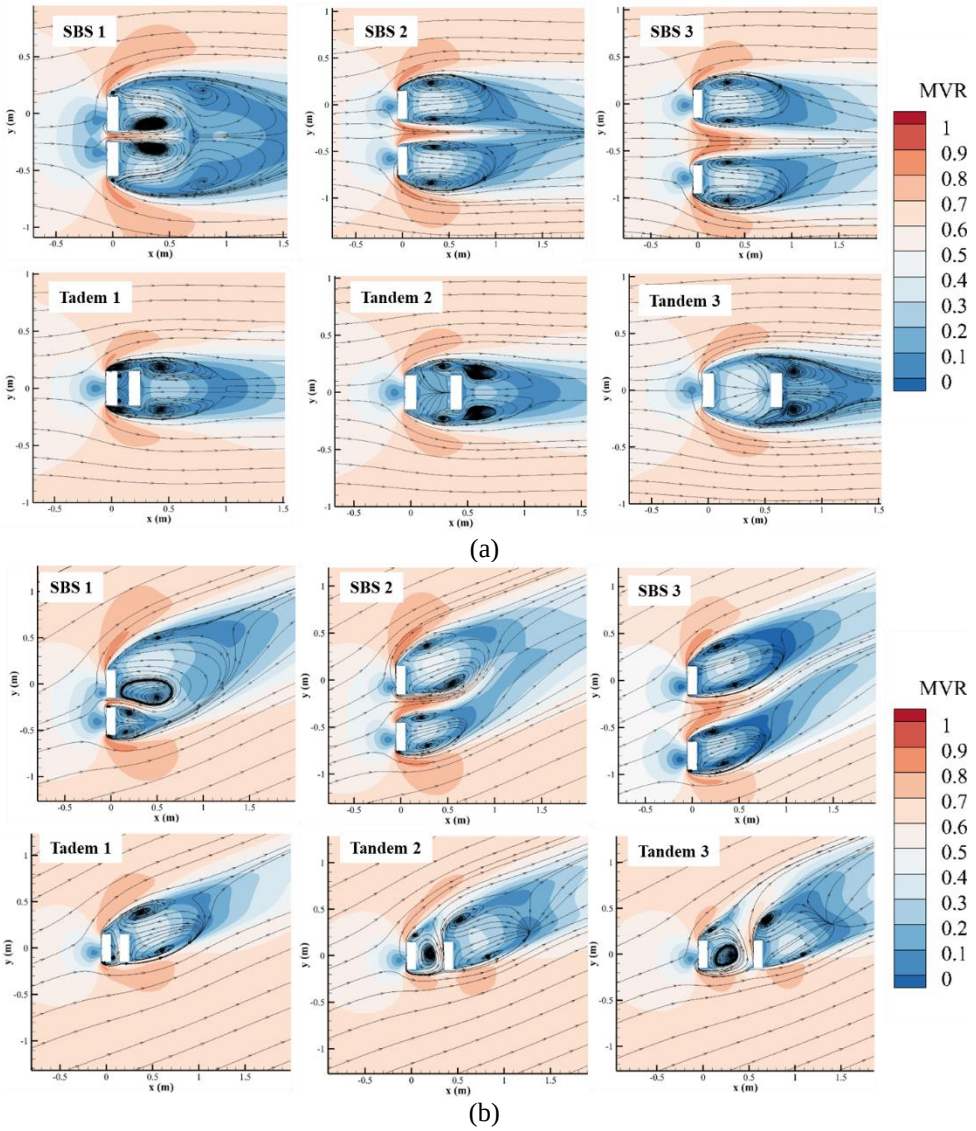

Figure 5. *MVR* distribution at the horizontal plane (z=0.01 m) under (a) CWP and (b) TWP.

3.3 Effect of twist wind on air temperature

Twisted winds can significantly alter the air temperature in the passages between two buildings, with more noticeable changes occurring in tandem arrangements compared to side-by-side arrangements (Figure 6 and Figure 7). For side-by-side arrangements, unlike the symmetric temperature distribution observed under CWP, the air with higher temperatures tends to flow toward the approaching twist wind directions. This phenomenon was more pronounced with narrower gaps between the two buildings. For buildings in tandem arrangement, high temperatures were observed near the leeward façade under CWP due to direct solar radiation. However, under TWP, high temperatures were observed near the windward façade because the weakened downwash flow cannot effectively counteract the buoyancy flow. The impact of twist wind on air temperature distribution was more significant in buildings arranged in tandem compared to those arranged side-by-side.

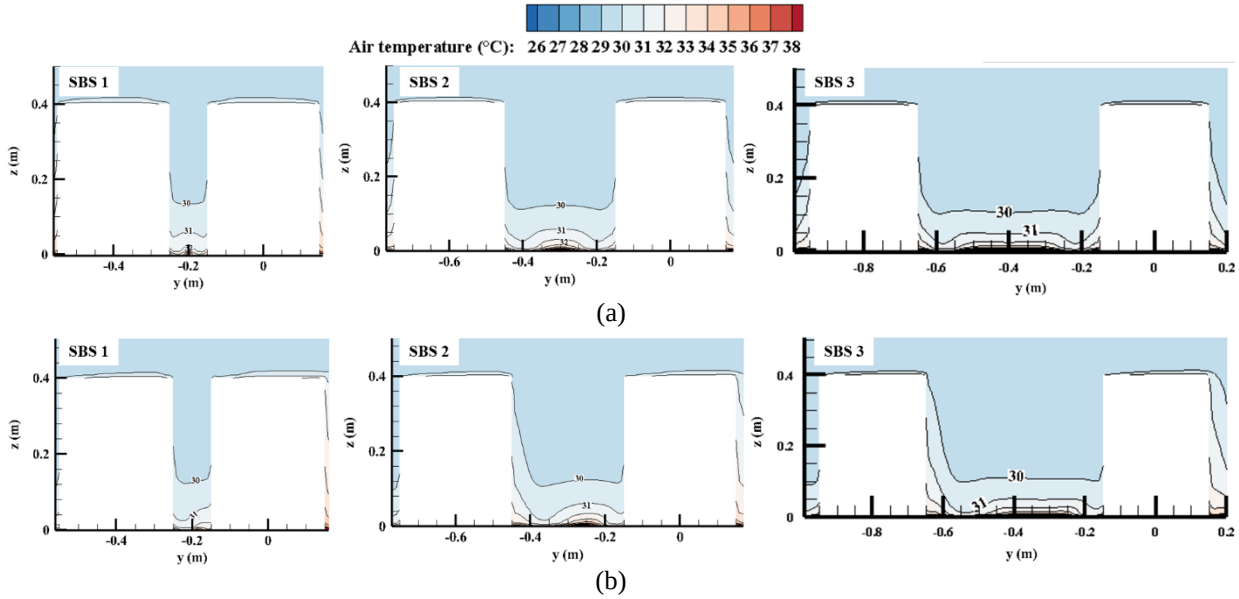

Figure 6. Air temperature contour in the vertical plane at x=0 for the side-by-side arrangement under (a) CWP and (b) TWP.

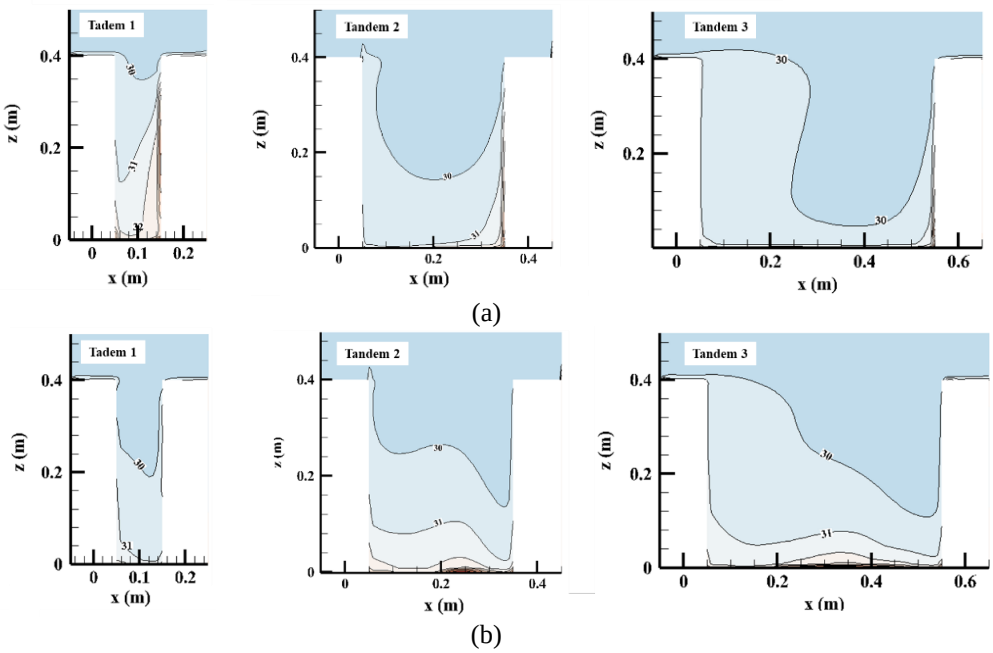

Figure 7. Air temperature contour in the vertical plane at y=0 for tandem arrangement under (a) CWP and (b) TWP.

4. CONCLUSION

CFD simulations were conducted to investigate the impact of twist wind on pedestrian wind

environment and air temperature around two commonly observed building configurations: tandem and side-by-side arrangements. The results demonstrate that the twist generates an asymmetrical flow field, enhancing the corner stream in the direction of the approaching twisted wind flow while weakening the corner stream on the opposite side of the building. For the side-by-side building configuration, the effect of twist winds is more pronounced with narrow spacing. When the building gap exceeds twice the building depth, the two buildings behave as independent structures, and complete vortex shedding phenomena are observed behind each building. For the tandem building arrangement, the inclined corner flow of the upstream building tends to be redirected into the passages between the two tandem buildings, forming a significant counterclockwise street canyon vortex. The twist wind altered the air temperature distribution within the street canyon. The weakened downwash flow was unable to counteract the buoyancy-driven flow, thereby facilitating the removal of heated air from within the street canyon.

ACKNOWLEDGEMENTS

This work was supported by a grant from the Research Grants Council of Hong Kong Special Administrative Region, China (Project No. T22-504/21-R). The authors of this paper would like to express their gratitude to the staff of AAF in HKUST for supporting the wind tunnel experiment.

REFERENCE

S. E. Perkins-Kirkpatrick,S. C. Lewis, 2020. Increasing Trends in Regional Heatwaves, Nat Commun. **11** (1) 3357.

A. U. Weerasuriya, X. Zhang, B. Lu, K. T. Tse,C.-H. Liu, 2020. Optimizing Lift-up Design to Maximize Pedestrian Wind and Thermal Comfort in 'Hot-Calm' and 'Cold-Windy' Climates, Sustainable Cities and Society. **58**.

R. Giridharan,R. Emmanuel, 2018. The Impact of Urban Compactness, Comfort Strategies and Energy Consumption on Tropical Urban Heat Island Intensity: A Review, Sustainable Cities and Society. **40** 677-687.

Y. Yuan, B. Yan, X. Zhou, Q. Yang, M. Wei, Y. He, X. Zhou,X. Li, 2023. Twisted-Wind Effect on the Aerodynamic Force Acting on Varying Side-Ratios Tall Buildings, Journal of Wind Engineering and Industrial Aerodynamics. **240**.

K. T. Tse, A. U. Weerasuriya, X. Zhang, S. Li,K. C. S. Kwok, 2017. Pedestrian-Level Wind Environment around Isolated Buildings under the Influence of Twisted Wind Flows, Journal of Wind Engineering and Industrial Aerodynamics. **162** 12-23.

Y. Yuan, B. Yan, X. Zhou, Q. Yang, G. Huang, Y. He,J. Yan, 2022. Rans Simulations of Aerodynamic Forces on a Tall Building under Twisted Winds Considering Horizontal Homogeneity, Journal of Building Engineering. **54**.

Y. Toparlar, B. Blocken, P. Vos, G. J. F. van Heijst, W. D. Janssen, T. van Hooff, H. Montazeri,H. J. P. Timmermans, 2015. Cfd Simulation and Validation of Urban Microclimate: A Case Study for Bergpolder Zuid, Rotterdam, Building and Environment. **83** 79-90.

J. Hang, Q. Li, Y. Du, J. Feng, J. Hua,B. Zhao, 2024. Effects of Arcade Design on Wind and Thermal Environment inside an Idealized 2d Urban Canyon with Realistic Solar Heating, Building and Environment. **254**.

Z. Li, H. Zhang, C.-Y. Wen, A.-S. Yang,Y.-H. Juan, 2020. Effects of Height-Asymmetric Street Canyon Configurations on Outdoor Air Temperature and Air Quality, Building and Environment. **183**.

W. Li, C. M. Mak, Y. Fu, C. Cai, K. T. Tse, J. Niu,S. H. Y. Wong, 2024. Pedestrian-Level Wind Environment Surrounding Two Tandem Non-Identical Height Elevated Buildings under the Influence of Twisted Wind Flows, Sustainable Cities and Society.

B. Blocken, W. D. Janssen,T. van Hooff, 2012. Cfd Simulation for Pedestrian Wind Comfort and Wind Safety in Urban Areas: General Decision Framework and Case Study for the Eindhoven University Campus, Environmental Modelling & Software. **30** 15-34.

R. Yoshie, A. Mochida, Y. Tominaga, H. Kataoka, K. Harimoto, T. Nozu,T. Shirasawa, 2007. Cooperative Project for Cfd Prediction of Pedestrian Wind Environment in the Architectural Institute of Japan, Journal of Wind Engineering and Industrial Aerodynamics. **95** (9-11) 1551-1578.

M. Idczak, P. Mestayer, J.-M. Rosant, J.-F. Sini,M. Violleau, 2006. Micrometeorological Measurements in a Street Canyon During the Joint Atreus-Picada Experiment, Boundary-Layer Meteorology. **124** (1) 25-41.

6th International Conference on Building Energy and Environment
Eindhoven University of Technology, The Netherlands
6 - 10 July 2025

How large should urban green spaces be to mitigate urban heat? — A study based on the threshold value of efficiency perspective

Qi Li [1,2], Qiong Li [1,2], Sisi Chen [1,2]

[1] *School of Architecture, South China University of Technology, Guangzhou 510640*

[2] *State Key Laboratory of Subtropical Building and Urban Science, South China University of Technology, Guangzhou 510640*

ABSTRACT

Is bigger always better when it comes to urban green spaces (UGS)? How large should urban green spaces be to effectively mitigate urban heat? This study develops a temperature and humidity regulation model for UGS, exploring the optimal size from the perspective of the threshold value of efficiency (TVoE) required to counteract heat from upwind built-up areas. The results show that TVoE for green spaces to effectively mitigate urban heat is around 1000 m. As the building density in the upwind built-up area increases, the required size of the UGS also increases. The TVoE is generally higher at night, indicating a reduced cooling effect during nighttime. The analysis of heat index (HI) levels shows that UGS can significantly reduce extreme heat conditions (Danger levels) and increase more comfortable temperature ranges (Caution levels), especially near UGS boundaries. However, they may also slightly increase extreme danger levels in areas with lower building densities. This research provides theoretical support for the strategic planning and management of urban green spaces, helping cities better adapt to the challenges of climate change.

Keywords: Urban green space, Threshold value of efficiency, Cooling effect

1 INTRODUCTION

Urban greening is considered a highly promising measure for improving the urban heat environment (Wong et al., 2021), with vegetated urban green spaces (UGS) exhibiting higher cooling efficiency (Kumar et al., 2024). At both micro and macro scales, UGS can alleviate the negative impacts of the urban heat island by altering the surface energy balance (Zölch et al., 2024). The cool island effect created by UGS, along with the infiltration of cool air into surrounding urbanized areas, plays a key role in improving local thermal environments and enhancing human thermal comfort (Bie et al., 2020).

The role of UGS as a "regulator" of the urban microclimate has been confirmed by numerous studies (Hwang et al., 2015; Algretawee et al., 2019). Previous studies have shown a nonlinear relationship between the size of the UGS and cooling intensity (Monteiro et al., 2016). So how big does the UGS need to be in order to effectively regulate the urban microclimate? Yu et al. (Yu et al., 2017) proposed the concept of the threshold value of efficiency (TVoE) from the perspectives of "law of diminishing marginal utility". TVoE considers the trade-offs that exist between the size of the UGS and the cooling effect from the principle of cost-effectiveness (Yang et al., 2020). TVoE has been applied in several studies to determine the minimum size required for UGS to sustain the cooling effect (Fan et al., 2019).

These studies typically determine the TVoE at the UGS size in terms of the cooling effect of the UGS on the surrounding built-up area, and are primarily focused on satellite imagery-based surface temperatures (LST). However, remote sensing of LST is not applicable to capture the effects of UGS on air temperature and pedestrian-scale thermal climate (Sun et al., 2015). How large does UGS need to be as a "buffer" against heat in upwind built-up areas? This study will base on the numerical modeling to determine the TVoE of the UGS that resists heat from the upwind built-up area from the perspective of the UGS cooling the air temperature.

2 METHODOLOGY

2.1 STUDY AREA AND BACKGROUND CLIMATE

This study was conducted in Guangzhou, Guangdong province, China (22.3°N to 24.1°N, 112.8°E to 114.2°E). Guangzhou is a megacity in southern China with a population of over 18 million, and classified as Cfa (C: warm temperate; f: fully humid; a: hot summer) (Chen et al., 2023) according to Köppen Geiger climate classification, Guangzhou.

Meteorological data above the urban canopy were collected from a weather station installed on the roof of the Building Energy and Environment Laboratory at South China University of Technology, as shown in Figure 1. This weather station will provide data on solar radiation, long-wave radiation, air temperature, relative humidity, wind speed, and rainfall above the urban canopy. Meteorological data within the urban canopy were provided by a Bowen station located in an unmanaged green space at the South China University of Technology, as shown in Figure 1. The Bowen station will provide air temperature, relative humidity, and soil water content within the urban canopy. The distance between the two sites is about 350m.

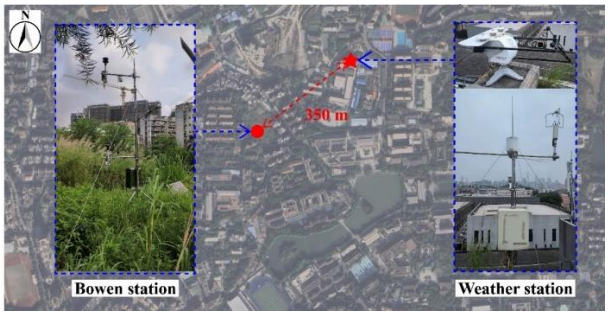

Figure 1. Study area and weather station

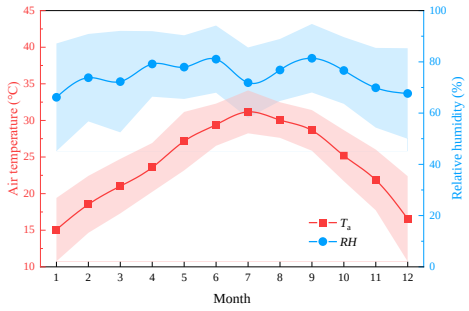

Figure 2. Background climate

The monthly variations of air temperature and relative humidity in urban canopy are shown in Figure 2. The average monthly maximum air temperature is observed from June to August, while the average monthly minimum air temperature is recorded from December to February. The warm period, comprising June, July, and August, is defined as the three months with the average monthly maximum air temperature.

2.2 MODEL DESCRIPTION

We developed the Upark model for the common vertical composition of "trees + shrubs + soil" in the UGS. The Upark model considers the vertical combination of "trees + shrubs + soil" and its effects on radiative transfer, turbulent energy exchange, and ET. The Upark model solves the energy and hydrology budget to calculate the air temperature, surface temperatures of vegetation leave and soil, and relative humidity. The tree canyon air space is subdivided into two layers. T_a and RH are calculated at the tree crown layer and human height layer, and the modeled energy and water vapor fluxes.

The air temperature is obtained by solving the energy budget. The energy balance equations (Equations 1 and 2) are solved separately for the tree crown layer and human height layer to calculate the air temperatures at the tree crown layer (T_{at}) and human height layer ($T_{a1.5}$):

$$QH_{atm} + QH_{1.5\to t} + QH_t + QH_{adv} = 0 \quad (1) \qquad QH_{t\to 1.5} + QH_{sh} + QH_s + QH_{adv1.5} = 0 \quad (2)$$

where QH_{atm} is the turbulent exchange of sensible heat flux between the atmosphere above the tree crown and tree crown layer (W m^{-2}); $QH_{1.5\to t}$ and $QH_{t\to 1.5}$ are the turbulent exchange of sensible heat fluxes between the tree crown layer and human height layer (W m^{-2}), where the direction of heat flux is the opposite, $QH_{1.5\to t} = -QH_{t\to 1.5}$; QH_t, QH_{sh}, and QH_s are the sensible heat fluxes from tree, shrub, and soil (W m^{-2}), respectively; and QH_{adv} and $QH_{adv1.5}$ are the sensible heat transport

by advection at the tree crown layer and human height layer (W m^{-2}), respectively.

$$T_{a1.5} = \frac{\left[T_{at} + \left(\frac{R_{nsh} - LE_{sh}}{\rho c_p} + \frac{R_{ns} - LE_s - G}{\rho c_p} + \frac{T_{r1.5}}{r_a^{adv1.5}}\right) r_a^{1.5t}\right] r_a^{adv1.5}}{r_a^{1.5t} + r_a^{adv1.5}} \quad (3)$$

where $T_{a1.5}$ is air temperature at 1.5 m above ground (°C); T_{at} is air temperature at the tree crown layer (°C); R_{nsh}, and R_{ns} are the net radiant fluxes for the shrub, and soil (W m^{-2}); LE_{sh}, and LE_s are the latent heat fluxes for the tree, shrub and soil (W·m^{-2}) calculated by the three-layer model (Li et al, 2024); $T_{r1.5}$ are the air temperatures near the UGS at 1.5 m above ground (°C), calculated using the UT&C model (Meili et al, 2020); $r_a^{adv1.5}$ is the resistances of sensible heat transport by advection at 1.5 m above ground (s m^{-1}); $r_a^{1.5t}$ is the aerodynamic resistances from 1.5 m to the tree crown (s m^{-1}); G is the soil heat flux (W m^{-2}).

The specific humidity of air is obtained by solving the water vapor budget. The water vapor balance equations (Equations 4 and 5) for the tree crown layer and human height layer are solved to calculate the specific humidity of the tree crown layer (q_{at}) and human height layer ($q_{a1.5}$):

$$QE_{atm} + QE_{1.5\to t} + QE_t + QE_{adv} = 0 \quad (4) \qquad QE_{t\to 1.5} + QE_{sh} + QE_s + QE_{adv1.5} = 0 \quad (5)$$

where QE_{atm} is the turbulent exchange of water vapor flux between the atmosphere above the tree crown and tree crown layer (kg m^{-2} s^{-1}); $QE_{1.5\to t}$ and $QE_{t\to 1.5}$ are the turbulent exchange of water vapor flux between the tree crown layer and human height layer (kg m^{-2} s^{-1}), respectively; QE_t, QE_{sh}, and QE_s are the water vapor flux from tree, shrub, and soil (kg m^{-2} s^{-1}); and QE_{adv} and $QE_{adv1.5}$ are the water vapor transport by advection at the tree crown layer and human height layer (kg m^{-2} s^{-1}).

The specific humidity is calculated based on air temperature and relative humidity:

$$q_{sat}(T_i) = 0.622\frac{e_{sat}(T_i)}{p_{atm} - 0.378e_{sat}(T_i)} \quad (6) \qquad e_{sat}(T_i) = 0.611\exp\left(\frac{17.27T_i}{T_i + 237.3}\right) \quad (7)$$

where i represents the tree crown layer or human height layer; $q_{sat}(T_i)$ is the saturated specific humidity at location i (kg kg^{-1}); T_i is the air temperature at location i (°C); RH_i is the relative humidity at location i (%); $e_{sat}(T_i)$ is the saturation vapor pressure at temperature T_i (kPa) calculated by using the Clausius–Clapeyron relation (Brutsaert, 2023); and p_{atm} is the atmospheric pressure (kPa).

The relative humidity is calculated based on the specific humidity:

$$RH_{1.5} = \frac{q_{a1.5}}{q_{sat}(T_{a1.5})} \times 100 \quad (8)$$

where $RH_{1.5}$ is the relative humidity at 1.5 m above ground (%); $q_{a1.5}$ is the specific humidity at 1.5 m above ground (kg kg^{-1}); and $q_{sat}(T_{a1.5})$ is the saturated specific humidity at 1.5 m above ground (kg kg^{-1}).

2.3 CASE SETTING

Based on the urban morphology classification of 141,375 urban blocks in 63 major cities in China, the primary urban block types in Chinese cities are predominantly medium-rise, high-density areas (3 < number of floors < 7, building density > 0.25) (Long et al. 2019). Specifically, in Guangzhou, medium-rise high-density (33%), low-rise high-density (number of floors < 3, building density > 0.25; 27%), and high-rise high-density areas (number of floors > 7, building density > 0.25; 22%) dominate. In this study, the buildings in the upwind urbanized area are modeled with six floors, each having a floor height of 3 m, resulting in a building height (h_b) of 18 m. Additionally, the building density in most urban blocks in China ranges between 0.22 and 0.52 (Long et al. 2019). To account for the impact of varying building densities, this study sets the

building density (ρ_b) between 0.2 and 0.6. The building width (w_b) is set at 10 m. The road width (w_r) under different conditions is calculated based on ρ_b and w_b, $w_r = w_b/\rho_b - w_b$.

The built-up area will be simulated using the UT&C model (Meili et al, 2020), with material parameters configured as shown in Table 1.

Table 1. Parameters in the UT&C model.

Parameter description	Values	Parameter description	Values
α_g, albedo of ground (-)	0.2	E_t, emissivity of tree canopy (-)	0.95
α_w, albedo of wall (-)	0.35	λ_g, thermal conductivity of impervious ground (W K^{-1} m^{-1})	1.2
α_t, albedo of tree canopy (-)	0.2	λ_w, thermal conductivity of wall (W K^{-1} m^{-1})	0.57
E_g, emissivity of ground (-)	0.95	Cv_g, volumetric heat capacity of impervious ground (MJ K^{-1} m^{-3})	1.5
E_w, emissivity of wall (-)	0.95	Cv_w, volumetric heat capacity of wall (MJ K^{-1} m^{-3})	1.0

The UGS in this study consisted of trees and shrubs. The morphological parameters of trees and shrubs were derived from field measurements conducted in a small park on the Wushan Campus of South China University of Technology. Specifically, the heights of trees and shrubs were set at 15 m and 0.6 m, respectively, with corresponding leaf area indices of 4.5 m^2 m^{-2} and 3.5 m^2 m^{-2}. The size of the UGS (windward distance) was varied from 100 m to 2000 m. The UGS microclimate model is described below, with temperature and humidity data calculated by the UT&C model for the built-up area serving as boundary conditions for advection source terms.

2.4 THRESHOLD VALUE OF EFFICIENCY (TVOE)

The TVoE is a metric designed from a cost perspective to evaluate the trade-off between microclimate regulation efficiency and the size of UGS (Epstein et al. 2017). In the microclimate regulation efficiency curve, the cooling and humidifying effects initially increase significantly as the scale of UGS expands. However, beyond a certain point, the growth in cooling and humidifying effects becomes marginal with further increases in UGS size. This critical point, referred to as the TVoE, is defined as the point where the slope of the microclimate regulation curve equals 1 or -1, as illustrated in Figure 3. To calculate the TVoE: First, the variables (air temperature/relative humidity and UGS scale) are non-dimensionalized. The non-dimensionalized data are then fitted to a function to determine the microclimate regulation efficiency curve and identify the point where the slope equals 1 or -1. Finally, the identified point is re-dimensionalized to determine the TVoE.

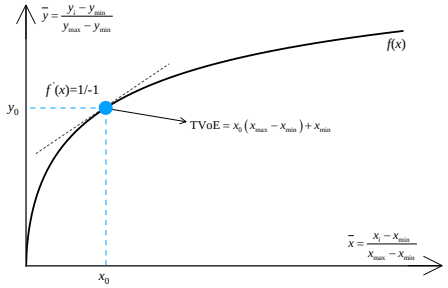

Figure 3. Schematic diagram of TVoE.

3 RESULTS AND DISCUSSION

3.1 AIR TEMPERATURE IN THE UGS AND THE TVOE

During the daytime in the warm period (defined as the period when the monthly mean hourly solar radiation exceeds 15 W m^{-2}, corresponding to 7:00~19:00), the relationship between air temperature and distance from the UGS boundary is shown in Figure 4(a). The solid lines represent the average air temperature under five different building density cases, with the shaded areas indicating ±1.5 standard errors (SE). As the distance from the UGS boundary increases, air temperature decreases rapidly at first but gradually stabilizes. Within the initial 100 m from the UGS boundary, the temperature decreases by 0.9 ℃~1.3 ℃, while at 2000 m, the reduction is only

0.003 ℃~0.01 ℃. This indicates that UGS has an optimal threshold for mitigating heat from surrounding built-up areas.

The cooling effect of UGS is also influenced by the building density (ρ_b) of the upwind built-up area. At a distance of 100 m from the UGS boundary, the temperature difference between the cases of ρ_b = 0.6 and ρ_b = 0.2 is 1.3 ℃, whereas at 2000 m, the difference is only 0.05 ℃. This suggests that the area near the UGS boundary is more affected by the urban morphology of the upwind built-up area. At 100 m, UGS in the ρ_b = 0.6 case exhibits a higher cooling effect of 1.3 ℃. This is because the high-density built-up area (ρ_b = 0.6) provides warmer and drier air, which enhances the transpiration effect of vegetation within the UGS.

Following the method outlined in Section 2.4 for determining the TVoE, the trade-off value of UGS in mitigating heat from upwind built-up areas was identified, excluding fitting formulas with R^2 < 0.8 and anomalous TVoE values, as shown by the boxplot in Figure 4(a). The TVoE exhibits some variability due to background climate conditions but is relatively concentrated. For the ρ_b = 0.2 case, 10%~90% of TVoE values range from 482 m to 644 m. Higher building density cases result in higher TVoE values, indicating that larger UGS scales are needed to mitigate heat. However, the differences between TVoE values under varying building density cases are relatively small, with averages ranging from 569 m to 617 m and medians between 565 m and 606 m. A value of 600 m is selected as the TVoE for mitigating heat from upwind built-up areas. At this distance, air temperature decreases by 2.2 ℃~3.3 ℃, with differences between cases of up to 0.6 ℃.

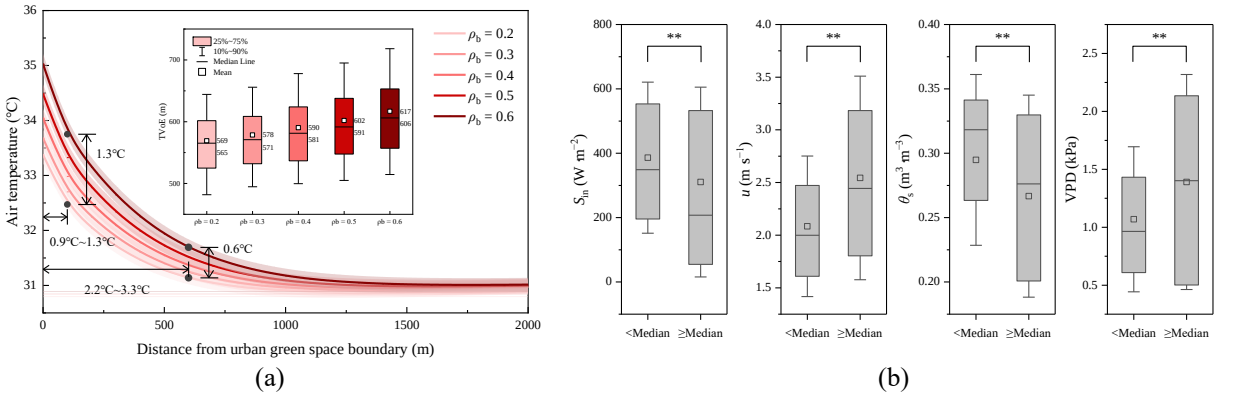

Figure 4. Daytime urban green space mitigation of hot air in upwind built-up areas. (a) changes in air temperature and TVoE within urban green spaces; (b) impact of background meteorological conditions on TVoE.

The TVoE values were divided into two groups based on the median: TVoE < Median and TVoE ≥ Median. A Mann-Whitney U test was conducted to analyze whether the background climate conditions differed significantly between the two groups, as shown in Figure 4(b). The results revealed that solar radiation and soil moisture content were significantly higher for TVoE < Median compared to TVoE ≥ Median ($P<0.01$). Higher solar radiation and soil moisture content promote vegetation transpiration, which enhances cooling effects, leading to lower TVoE values under such background climate conditions. Conversely, wind speed was significantly higher for TVoE ≥ Median compared to TVoE < Median ($P<0.01$). Under higher wind speeds, advection effects become more pronounced, making UGS more susceptible to the influence of upwind built-up areas, thereby resulting in higher TVoE values. It is noteworthy that the vapor pressure deficit (VPD) for TVoE ≥ Median was also significantly higher than for TVoE < Median ($P<0.01$). Although higher VPD generally enhances vegetation transpiration, similar to solar radiation and soil moisture, thereby promoting cooling effects, the VPD in this study represents that of the upwind built-up area. This elevated VPD near the UGS boundary facilitates transpiration in vegetation located in the first 100 m grid of the UGS, leading to more pronounced cooling and

humidifying effects in this zone. Given that the model considers the influence of preceding grids on subsequent grids, stronger cooling and humidifying effects in the initial grid reduce the VPD in subsequent grids. This reduction weakens vegetation transpiration, resulting in higher TVoE values under such conditions.

During the nighttime in the warm period, the TVoE of UGS in resisting heat from upwind built-up areas is shown in Figure 5. Similar to daytime conditions, upwind built-up areas with higher building densities exhibit higher TVoE values. However, the influence of building density on TVoE is more pronounced at night compared to during the day. The average TVoE values at night range between 720 m and 928 m, with a difference of 208 m, whereas the daytime difference is only 48 m. The median TVoE values at night range between 669 m and 919 m, with a difference of 250 m, compared to a daytime difference of 41 m. Due to reduced transpiration by vegetation at night, the TVoE values for nighttime temperatures in UGS are higher than during the day. The difference in average TVoE values between day and night across various building density cases is between 151 m and 311 m, with median differences ranging from 104 m to 313 m. This is particularly evident in the case of a building density of 0.6, where the day-night disparity in TVoE is more significant.

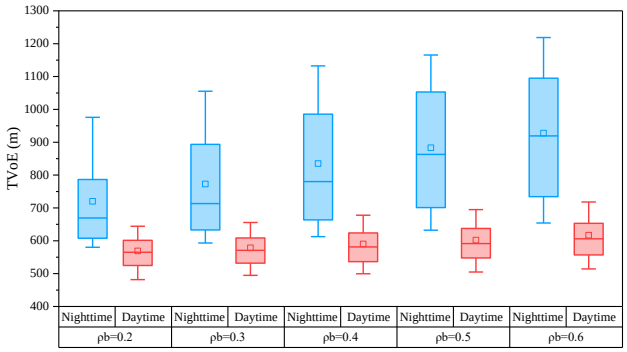

Figure 5. Efficiency thresholds for mitigating hot air from upwind built-up areas in urban green spaces during daytime and nighttime.

3.2 HEAT INDEX OF THE UGS

The analysis indicates that UGS have significant potential for mitigating heat, especially in areas near the boundaries of UGS. This capability is beneficial for reducing heat exposure and improving the outdoor thermal environment. However, RH is also a critical factor influencing thermal comfort. Unfortunately, while UGS rapidly cooling air temperature, this phase is also accompanied by a sharp increase in RH, which may negatively impact the outdoor thermal environment. To evaluate the combined effects of air temperature and RH on human thermal comfort, we selected the heat index (HI) for analysis. HI is an indicator used to assess the risk of heat exposure, which accounts for the combined effects of air temperature and RH, thereby quantifying the human perception of temperature. The HI is a function of T_a and RH. The formula to calculate HI is commonly given as:

$$\begin{aligned} HI = {} & -8.784695 + 1.61139411 \times T_a + 2.338549 \times RH - 0.14611605 \times T_a \times RH - 1.2308094 \times 10^{-2} \times T_a^2 \\ & -1.6424828 \times 10^{-2} \times RH^2 + 2.2211732 \times 10^{-3} \times T_a^2 \times RH + 7.2546 \times 10^{-4} \times T_a \times RH^2 - 3.582 \times 10^{-6} \times T_a^2 \times RH^2 \end{aligned} \quad (10)$$

HI is classified according to Ref. (Blazejczyk et al. 2012), as shown in Table 2.

Table 2. Classification of HI levels.

Classification	Caution	Extreme caution	Danger	Extreme danger
Extreme caution	27–32 ℃	32–41 ℃	41–54 ℃	≥54 ℃

The daytime distribution of HI levels is shown in Figure 6(a). In all five cases, instances of HI < 27 ℃ were observed, but the duration was limited to a maximum of 8 hours, accounting for

only 0.7% of the total warm period daytime hours (1196 hours). Among all HI levels, the Danger category (41 ℃~54 ℃) had the highest proportion, exceeding 50% in all cases, followed by the Extreme Caution category (32 ℃~41 ℃), which accounted for 20%–30%. This highlights the harsh outdoor thermal environment in Guangzhou during the warm period. UGS significantly mitigate the outdoor thermal environment, primarily by reducing the proportion of the Danger category. At a distance of 0 m from the urban green space boundary, the proportion of Danger ranged from 66% to 69%. This proportion decreased to 58%~63% at the thermal vegetation offset effect (TVoE, 600 m) and further dropped to 52%~53% at 2000 m. However, the proportion of Extreme Caution increased correspondingly, particularly under the case with a building density of 0.6. Unfortunately, urban green spaces also increased the proportion of the Extreme Danger category, especially under the building density case of 0.2, where the proportion rose from 1% to 11% at a distance of 2000 m from the green space boundary.

The nighttime distribution of HI levels is shown in Figure 6(b). The frequency of HI < 27 ℃ was slightly higher at night than during the daytime, with a maximum duration of 26 hours, accounting for 2.6% of the total nighttime hours (1012 hours). At night, HI levels predominantly fell within the Extreme Caution category, accounting for 70%–80%, reflecting a pronounced "hot night" phenomenon in Guangzhou. Urban green spaces primarily reduced the proportion of the Extreme Caution category and increased the proportion of the Caution category (27 ℃~32 ℃). Across the five cases, at a distance of 2000 m from the green space boundary, the Caution category increased by 12%~13%, while at the TVoE, the proportion increased by 7%~9%. However, urban green spaces also slightly increased the proportion of the Danger category, though the increment was relatively small. UGS effectively reduce HI levels and contribute positively to improving the outdoor thermal environment. However, it is important to note that the rapid cooling effect of urban green spaces is accompanied by a rapid increase in RH, which may lead to intensified heat stress.

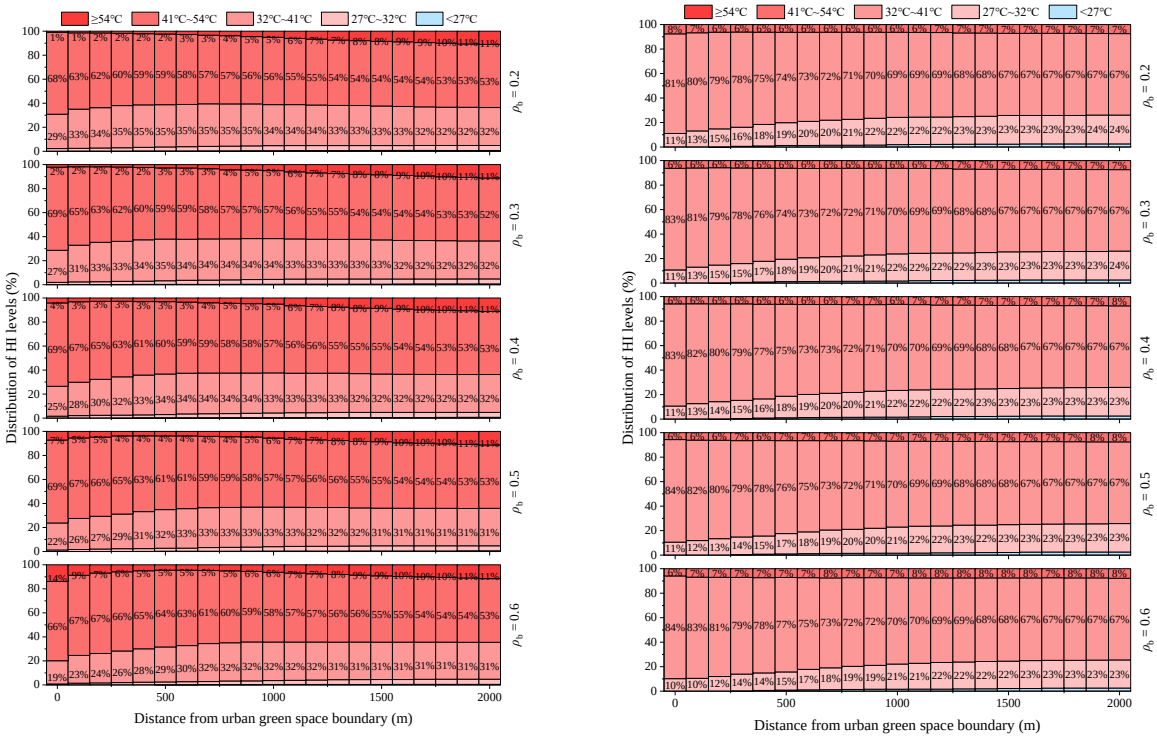

(a) (b)

Figure 6. The distribution of HI levels. (a) daytime; (b) nighttime.

4 CONCLUSION

Urban green spaces (UGS) play a crucial role in mitigating urban heat, with the cooling effect being most pronounced near the UGS boundary. The optimal threshold for UGS to effectively counteract heat from surrounding built-up areas is around 600 m. At this distance, air temperature decreases by 2.2 ℃–3.3 ℃, with variations of up to 0.6 ℃ depending on building density. The cooling effect is more effective during the day, with average temperature differences between high-density (ρ_b = 0.6) and low-density (ρ_b = 0.2) areas reaching up to 1.3 ℃ at 100 m, while the difference decreases to 0.05 ℃ at 2000 m. The TVoE values for mitigating heat range from 482 m to 644 m for lower-density areas, while they range from 569 m to 617 m in higher-density areas. At night, the TVoE increases by 151 m to 311 m compared to daytime values, with higher building densities contributing to more significant differences. Additionally, UGS reduce the proportion of extreme heat (Danger levels) from 66%–69% at 0 m to 52%–53% at 2000 m. However, in low-density areas, UGS may slightly increase the proportion of extreme danger levels.

REFERENCE

Algretawee, H., Rayburg, S., & Neave, M. 2019. Estimating the effect of park proximity to the central of Melbourne city on Urban Heat Island (UHI) relative to Land Surface Temperature (LST). Ecological engineering, 138, 374-390.

Bie, Q., Xie, Y., Wang, X., et al. (2020). Understanding the attributes of the dual oasis effect in an arid region using remote sensing and observational data. Ecosystem Health and Sustainability, 6(1), 1696153.

Blazejczyk, K., Epstein, Y., Jendritzky, G., et al. 2012. Comparison of UTCI to selected thermal indices. International Journal of Biometeorology, 56, 515-535.

Brutsaert, W. 2023. Hydrology. Cambridge university press.

Chen, G., Chen, Y., Tan, X., et al. 2023. Assessing the urban heat island effect of different local climate zones in Guangzhou, China. Building and Environment, 244, 110770.

Epstein, S. A., Lee, S. M., Katzenstein, A. S., et al. 2017. Air-quality implications of widespread adoption of cool roofs on ozone and particulate matter in southern California. Proceedings of the National Academy of Sciences, 114(34), 8991-8996.

Fan, H., Yu, Z., Yang, G., et al. 2019. How to cool hot-humid (Asian) cities with urban trees? An optimal landscape size perspective. Agricultural and Forest Meteorology, 265, 338-348.

Hwang, Y. H., Lum, Q. J. G., & Chan, Y. K. D. 2015. Micro-scale thermal performance of tropical urban parks in Singapore. Building and Environment, 94, 467-476.

Kumar, P., Debele, S. E., Khalili, S., et al. 2024. Urban heat mitigation by green and blue infrastructure: Drivers, effectiveness, and future needs. The Innovation, 5(2).

Li, Q., Li, Q., Mi, J., & Wu, H. 2024. A Three-Layer Evapotranspiration Model Considering the Vertical Structure of Urban Green Spaces. Urban Forestry & Urban Greening, 128389.

Long, Y., Li, P., & Hou, J. 2019. Three-Dimensional Urban Form at the Street Block Level for Major Cities in China. Shanghai Urban Planning Review, 3, 10-15.

Meili, N., Manoli, G., Burlando, P., et al. 2020. An urban ecohydrological model to quantify the effect of vegetation on urban climate and hydrology (UT&C v1. 0). Geoscientific Model Development, 13(1), 335-362.

Monteiro, M. V., Doick, K. J., Handley, P., & Peace, A. 2016. The impact of greenspace size on the extent of local nocturnal air temperature cooling in London. Urban Forestry & Urban Greening, 16, 160-169.

Sun, H., Chen, Y., & Zhan, W. 2015. Comparing surface-and canopy-layer urban heat islands over Beijing using MODIS data. International Journal of Remote Sensing, 36(21), 5448-5465.

Wong, N. H., Tan, C. L., Kolokotsa, D. D., & Takebayashi, H. 2021. Greenery as a mitigation and adaptation strategy to urban heat. Nature Reviews Earth & Environment, 2(3), 166-181.

Yang, G., Yu, Z., Jørgensen, G., & Vejre, H. 2020. How can urban blue-green space be planned for climate adaption in high-latitude cities? A seasonal perspective. Sustainable Cities and Society, 53, 101932.

Yu, Z., Guo, X., Jørgensen, G., & Vejre, H. 2017. How can urban green spaces be planned for climate adaptation in subtropical cities?. Ecological Indicators, 82, 152-162.

Zölch, T., Maderspacher, J., Wamsler, C., & Pauleit, S. 2016. Using green infrastructure for urban climate-proofing: An evaluation of heat mitigation measures at the micro-scale. Urban Forestry & Urban Greening, 20, 305-316.

6th International Conference on Building Energy and Environment

Eindhoven University of Technology, The Netherlands

6 - 10 July 2025

Assessing urban microclimate for sustainable planning: A multi-scale modelling approach in Lecce (Italy)

Francesco Giangrande [1], Gianluca Pappaccogli [1], Antonio Esposito [1], Rohinton Emmanuel [2], Riccardo Buccolieri [1]

[1]Dipartimento di Scienze e Tecnologie Biologiche ed Ambientali, University of Salento, Lecce, 73100, Italy, francesco.giangrande@unisalento.it; gianluca.pappaccogli@unisalento.it; antonio.esposito@unisalento.it; riccardo.buccolieri@unisalento.it

[2]Built Environment Asset Management Centre, Glasgow Caledonian University, Cowcaddens Rd, Glasgow G41 0BA, UK, Rohinton.Emmanuel@gcu.ac.uk

SUMMARY

This study evaluates urban microclimates using a modelling chain that integrates the MLUCM BEP+BEM parameterization with the ENVI-met CFD model. A case study in a residential district of Lecce, Italy, examines three simulation scenarios with varying meteorological inputs. Cases 1 and 2 use urban meteorological station data, while Case 3 employs outputs from the MLUCM BEP+BEM model. Results indicate that Case 3 effectively captures daily temperature trends, improving accuracy in built-up areas, though discrepancies persist in open spaces. The study confirms that enhanced urban parameterization improves microclimate simulations but highlights challenges in spatial variability. This approach provides a scalable framework for assessing urban microclimates and evaluating climate mitigation strategies.

Keywords: Urban Microclimate, MLUCM BEP+BEM, ENVI-met.

1. GENERAL INSTRUCTIONS

Cities are facing extreme heat phenomena such as Heat Waves (HWs), exacerbated by the Urban Heat Island (UHI) which is linked to issues such as thermal discomfort and various health problems (Oke, 2017; McRae et al., 2020). These effects are caused by the urban geometry composed of tall buildings, limited green areas and a dense urban fabric (Pappaccogli et al., 2018). Mitigating these effects through urban planning is difficult, especially due to the complexity of the interaction between the built urban environment and the surrounding atmosphere (McRae et al., 2020). In this context, numerical models capture key urban effects by linking urban geometry characteristics with energy, mass, and momentum exchanges within the Urban Boundary Layer (UBL). These models, known as Urban Climate Models (UCMs), are used to simulate the coupled evolution of atmospheric and urban surface climates. They are conventionally classified into micro/local-scale and mesoscale models, though they can be coupled, with one being used to provide boundary

conditions for the other. Computational Fluid Dynamics (CFD) models, for example, simulate airflow around obstacles at the micro/local scale, while mesoscale UCMs focus on the evolution of the UBL due to interactions with the underlying urban surface. The domain of mesoscale models extends both vertically into the Atmospheric Boundary Layer (ABL) and horizontally beyond the city edge, with grid cells typically between hundreds of metres to 1km.

This study aims to analyse the microclimate of a typical Mediterranean city, Lecce (southern Italy), using a modelling approach that bridges mesoscale dynamics and microscale effects. To achieve this, a modelling chain is proposed, integrating the ENVI-met model with data from ground meteorological stations and the recently released MLUCM BEP+BEM urban parameterization scheme. BEP+BEM scheme coupled with a 1-D column model of the urban canopy flow, describes the vertical arrangement of the urban fabric considering the distribution of heat, humidity and momentum sources in the urban canopy but also provides a perspective on the urban energy balance by estimating the internal energy consumption of buildings through heating and cooling (Pappaccogli et al., 2024). The modelling chain, combining MLUCM BEP+BEM with ENVI-met, assesses whether mesoscale model outputs can replace in-situ observations as inputs for CFD models to better represent urban microclimates. This approach enhances microclimate modelling through result validation while ensuring scalability for broader applications.

2. METHODOLOGY

2.1. Study area

The study area is in the city of Lecce (southern Italy), specifically in the San Pio district. Lecce (UTM coordinates: 40°21.0’7.24” N, 18°10.0’8.9” E) is a city of about 95,000 inhabitants (http://demo.istat.it/pop2019/index.html), and is situated on a flat territory approximately 40-50m above sea level (Fig. 1a). The city experiences a warm Mediterranean climate, classified as Csa according to the Köppen–Geiger system. The urban morphology of the San Pio district consists primarily of two- to three-story buildings and narrow street canyons (Gatto et al., 2020). The area is predominantly residential buildings, with some schools and a few commercial establishments. Urban green spaces are limited, while private green areas are prevalent. Impervious surfaces, which cover a larger area than green spaces mainly consist of concrete sidewalks, asphalt roads and parking lots. Temperature and humidity measurements are recorded by a waterproof data-logger (Tinytag Plus 2-TGP-4505, Gemini Data Loggers Ltd., Chichester, West Sussex, UK), which is equipped with air temperature and relative humidity probes with an accuracy of ±0.3°C and ±3%, respectively, at 25°C. The thermo-hygrometer is installed approximately 4m above ground level on the balcony exposed to SE, surrounding a small concrete-paved square (Fig. 1b). Here, numerous trees, primarily *Quercus ilex* L. and *Pinus pinea* L., ranging from 5 to 8m in height and planted in flowerbeds with sandy-clayey soil. The measurements recorded by the thermo-hygrometer are used to validate the output meteorological results from the microclimate simulations performed with ENVI-met.

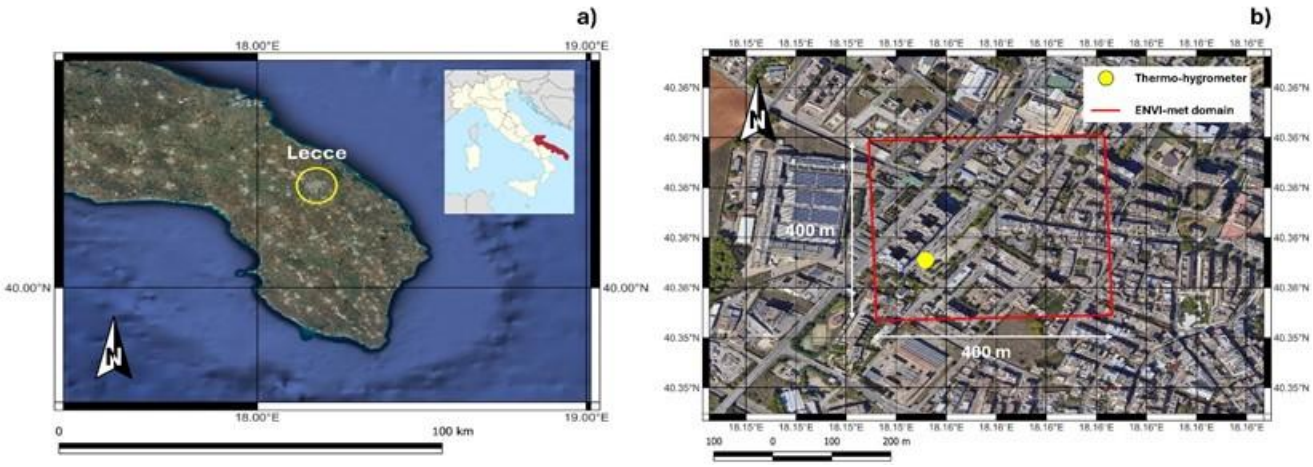

Figure 1. a) Salento Peninsula. b) Study area with the 400 x 400 m domain represented and the position of the thermo-hygrometer.

2.2. Meteorological data and modelling setup in ENVI-met

Meteorological data were collected from two stations in Lecce. The Ateneo station, operated by Fondazione OMD Osservatorio Meteo Milano Duomo, is located 11m above ground level (40°21'22.22"N, 18°10'4.59"E) and records temperature, relative humidity, wind speed and direction, and precipitation. The ARPA station, managed by Environmental Protection Regional Agency, is positioned 13ms above ground level (40°20'44"N, 18°10'37"E) and measures solar radiation. The two stations are 1.1km and 2.2km away from the study area in the E and SE directions, respectively. Measurements from 15 July to 15 August 2024 were processed to obtain a mean daily cycle of a typical summer day for each meteorological variable based on data recorded at 30-minute intervals. These processed data were then used as meteorolgical input for ENVI-met 5.1.0. August 1st was selected as the representative day of the chosen period; the first 6 hours were considered as initialization time (spin up). A geometric model of the 400 × 400 m study area was created in QGIS and imported into ENVI-met, where the grid was set to 225 × 225 × 35 cells, with a resolution of 2 m and 5 nesting grids (Fig. 2). A 10% telescoping factor was applied from ground level, extending the model domain to a maximum height of 160 m. The tallest building (30m), leaves a vertical gap of 130 m between its top and the model upper boundary, ensuring sufficient space above the urban area. Three simulation cases with different meteorological inputs were analyzed, and their output results were compared (Table 1). The roughness length (z_0) was set to 1m for all cases. Case 1 used measurements only from the "Ateneo" station; Case 2 used measurements from both the "Ateneo" and "ARPA" stations; and Case 3 used meteorological data provided by the MLUCM BEP+BEM model.

Table 1. Three simulation cases using different ENVI-met meteorological inputs.

Case	ENVI-met meteorological input
1	Air temperature (°C); Relative humidity (%); Wind speed (m/s); Wind direction (°); Precipitation (mm)
2	Air temperature (°C); Relative humidity (%); Wind speed (m/s); Wind direction (°); Precipitation (mm); Downward short-wave radiation (W/m^2)

3	Direct downward short-wave radiation (W/m^2); Diffuse downward short-wave radiation (W/m^2); Downward long-wave radiation (W/m^2); Air temperature (°C); Relative humidity (%); Wind speed (m/s); Wind direction (°); Precipitation (mm)

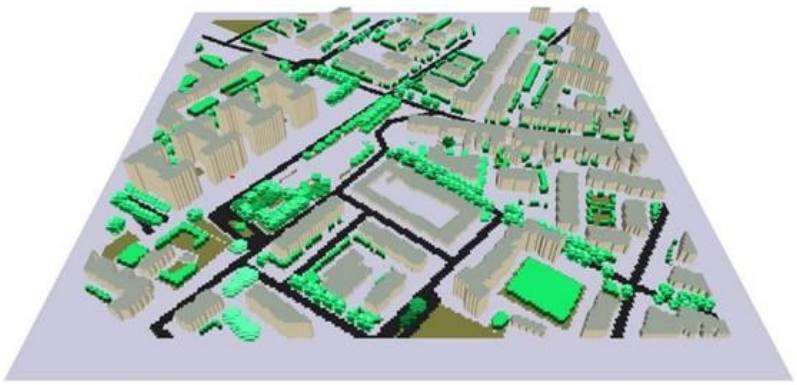

Figure 2. 3D model reconstruction in ENVI-met.

2.3. MLUCM BEP+BEM and ENVI-met model chain

The methodology involves the use of a modelling chain consisting of the recently released MLUCM BEP+BEM urban parameterization model (Pappaccogli et al., 2025) and the ENVI-met neighborhood-scale CFD model (Fig. 3). MLUCM BEP+BEM incorporates the vertical turbulent diffusion scheme of Santiago and Martilli (2010) with the Building Effect Parameterization (BEP, Martilli et al., 2002) and the Building Energy Model (BEM, Salamanca et al., 2009). It features improved turbulent length scales and eddy diffusivity coefficients that account for atmospheric stability, along with a detailed representation of urban vegetation, including green spaces and street trees. Designed for offline applications, the model maintains low computational demands, making it well-suited for independent simulations, coupling with climate projections or ERA5 reanalysis. The MLUCM BEP+BEM properly describes the vertical layout of the urban fabric considering the distribution of heat, humidity and moment sources throughout the urban canopy layer. The model also estimates energy consumption within buildings for both cooling/heating systems, providing a comprehensive perspective on the urban energy balance at neighborhood scale. ENVI-met is a CFD (Computational Fluid Dynamics) model that simulates at high spatial (0.5-10m grids) and temporal (10s) resolutions. The meteorological inputs required for the initial and boundary conditions of ENVI-met can come from observations at a nearby site or from a mesoscale meteorological model such as Weather Research and Forecasting (WRF) model (McRae et al., 2020).

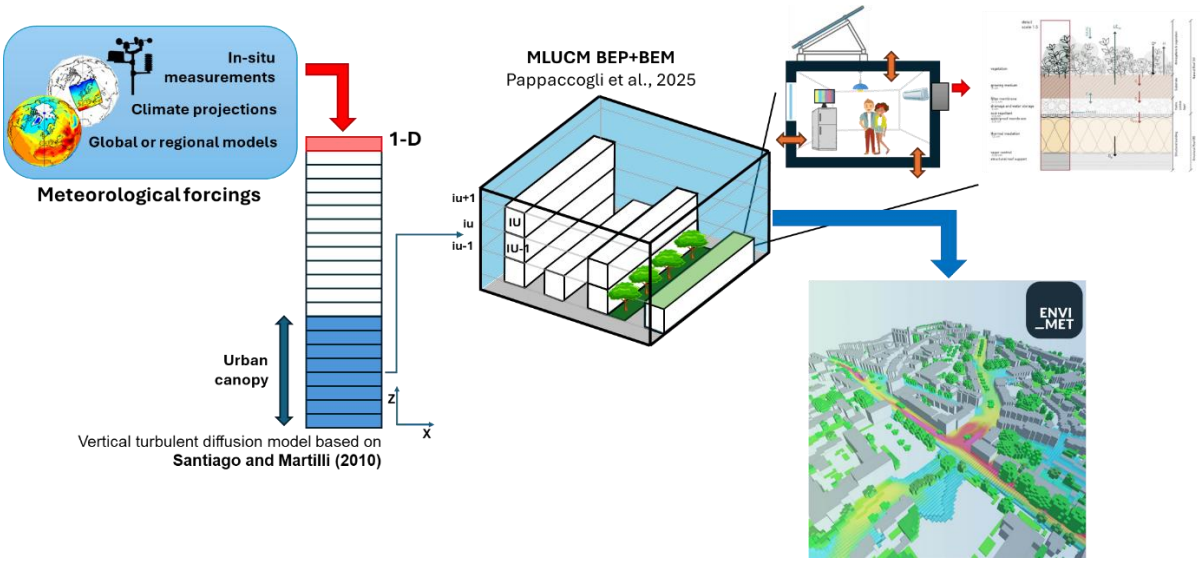

Figure 3. Modelling chain composed by: ERA5 reanalysis or climate projections data, MLUCM BEP+BEM/ENVI-met model.

3. RESULTS

3.1. Model forcings and observations

Fig. 4 shows the profiles of the meteorological forcings used as input in ENVI-met for the three simulated cases. In all cases a north-westerly wind was set for the wind direction and the absence of precipitation. The values of all input variables are every 30 minutes, as required by ENVI-met. In Fig. 4a the temperature values for case 1 and 2 are slightly lower than case 3 for most of the day except for the early morning hours (from about 06:00 LT to 10:00 LT). The comparison shows that the output values of the MLUCM BEP+BEM model (case 3) are similar to the input values coming from the data of the Ateneo station. The profiles of cases 1, 2 and 3 reach a maximum at 14:00 LT of 32.94°C and 33.63°C, respectively; cases 1 and 2 have a minimum of 25.53°C at 04:00 LT while case 3 has a minimum of 26.12°C at 05:00 LT.

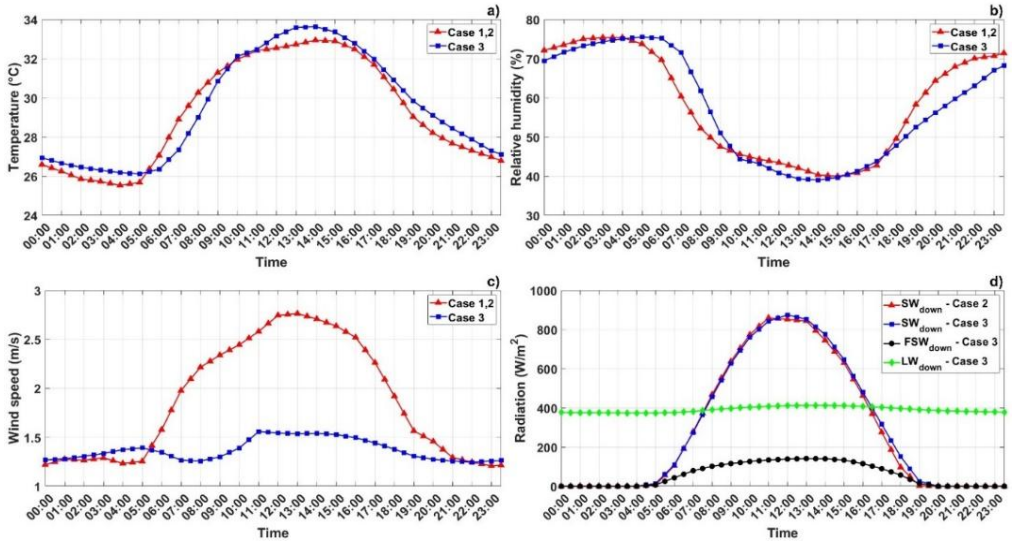

Figure 4. ENVI-met input meteorological forcing profiles based on daily pattern obtained from the selected period for the three cases every 30 minutes. a) Air temperature (°C); b) Relative humidity (%); c) Wind speed (m/s); d) Radiative components.

Relative humidity profiles (Fig. 4b) are similar during the daytime, reaching their minimum in the central hours and their maximum at night, ranging between 40% and 70%. Slight discrepancies occur in the early morning (05:00 LT – 09:00 LT) and evening (06:00 LT – 00:00 LT), corresponding to air temperature variations. Fig. 4c highlights a difference in wind intensity between 06:00 LT and 08:00 LT, particularly during midday. In cases 1 and 2, wind speed peaks at around 3 m/s, whereas in case 3, it is roughly half that value. In contrast, wind speeds between 21:00 LT and 05:00 LT are similar across all cases. These discrepancies arise from differences in data sources: cases 1 and 2 use data from the Ateneo station, representing wind intensity at roof level, while case 3, based on MLUCM BEP+BEM data, accounts for drag effects caused by buildings in the study domain, despite being taken at the same vertical level. Fig. 4d shows different radiative components used as input for cases 2 and 3. The SWdown profiles for cases 2 and 3 are very similar, with a maximum of about 860 W/m^2 at noon, whereas FSWdown reaches values of around 140 W/m^2 during the central hours, while LWdown assumes values between 376 W/m^2 and 412 W/m^2.

3.2. Analysis of modelling outputs

Fig. 5 presents a comparison between the simulation results from ENVI-met and the observed temperature and relative humidity recorded by the thermo-hygrometer. The observed temperatures are higher than three simulated cases from 00:00 LT to 09:00 LT, while they are significantly lower during the central hours (11:00 LT-17:00 LT), when the differences between simulations and observations vary on average between 1.31°C (case 1), 0.84°C (case 2) e 1.43°C (case 3). After 18:00 LT, temperature differences are minimal, with observed values falling between case 3 (highest) and cases 1 and 2 (lowest). In cases 1 and 2, these discrepancies remain small during the early nighttime hours, while in case 3, they progressively reduce and disappear by midnight.

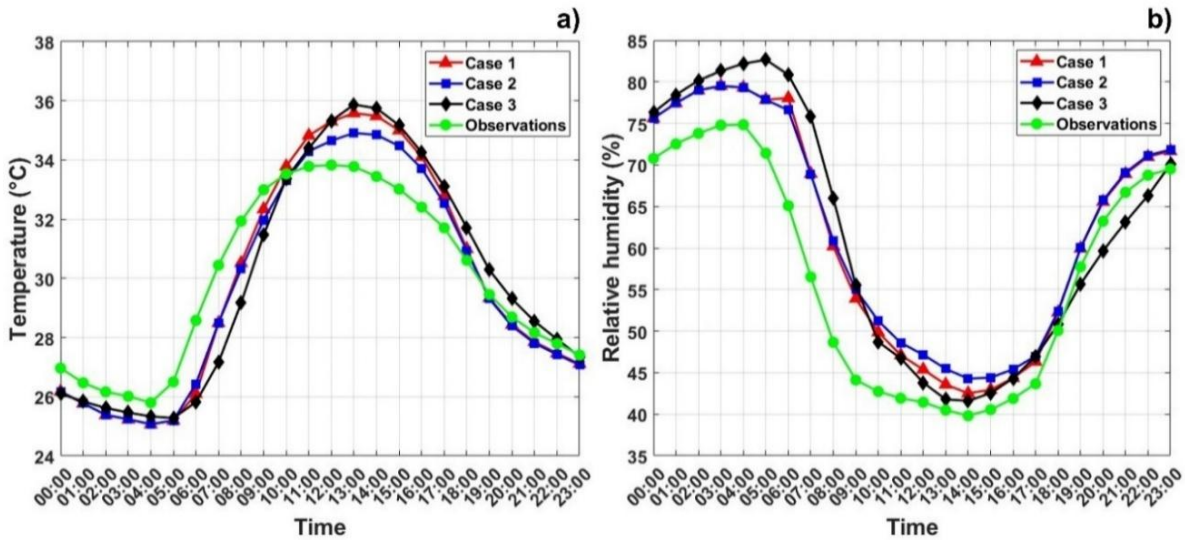

Figure 5. Air temperature (a) and relative humidity (b) profiles obtained from the three simulated cases compared with the observations.

It is worth pointing out that the rapid rise in temperatures observed during the early morning hours is probably due to the positioning of the thermo-hygrometer, which is located to the south-facing wall of the building. Similarly, temperatures decrease more rapidly due to the shading of the area surrounding the building, which is reflected in a peak temperature at 12 noon (average of 33.9°C). To quantitatively assess the model's performance, the mean error (BIAS) and root-mean-square error (RMSE) were calculated. As shown in Tab. 2, case 1 exhibits the lowest RMSE, indicating the smallest overall error. However, it also has the most negative BIAS, suggesting a greater tendency to underestimate values. In contrast, case 3 has the highest RMSE but a BIAS close to zero, meaning that despite discrepancies in daily minimum and maximum values, it accurately captures the overall daily temperature trend on average.

Table 2. RMSE and BIAS for the three cases.

	Temperature (°C)		Relative humidity (%)	
Case	RMSE	BIAS	RMSE	BIAS
1	1.23	-0.05	6.02	5.01
2	1.04	-0.24	6.38	5.53
3	1.54	0.01	7.93	5.01

In Fig. 5b the observed relative humidity (RH) values are lower than the three simulated cases from 00:00 LT to 13:00 LT, while they become similar from 13:00 LT to 23:00 LT, ranging between 40% to 75%. From 00:00 LT to 09:00 LT the observed values are lower than the three simulated cases on average of 7% (case 1 and 2) and 11% (case 3), whereas the three profiles are similar for the rest of the day. Tab. 2 reports for RH a lower RMSE value for case 1 and a higher one for case 3. The BIAS values are around 5% for all three cases, which means that the simulated results tend to overestimate the observations.

Fig. 6 illustrates the differences in air temperature simulations between case 2 and case 3 at pedestrian level (2m above ground). This analysis compares case 2, which best matches the observed measurements, with case 3 to assess the similarity of model results at 04:00 LT (Fig. 6a) and 13:00 LT (Fig. 6b), corresponding to the minimum and maximum air temperature values, respectively. At 04:00 LT, smaller differences are observed in a limited portion of the study area, ranging from -0.30 °C to over -0.16 °C, while the rest of the domain exhibits more pronounced discrepancies. In this period, case 3 generally shows higher temperatures than case 2, bringing its values closer to the observations. At 13:00 LT, smaller differences are found in the southern part of the domain (ranging from -0.88°C to -0.56°C), while more significant discrepancies appear towards the northern edge (exceeding -1.00 °C). According to the mean daily pattern, larger differences occur during this hour (13:00 LT) due to notable variations in input temperature and wind speed intensity. Notably, both during the day and at night, temperature differences are smaller in areas with taller buildings and street canyons. This suggests that the MLUCM BEP+BEM meteorological forcings are more representative of denser urban environments.

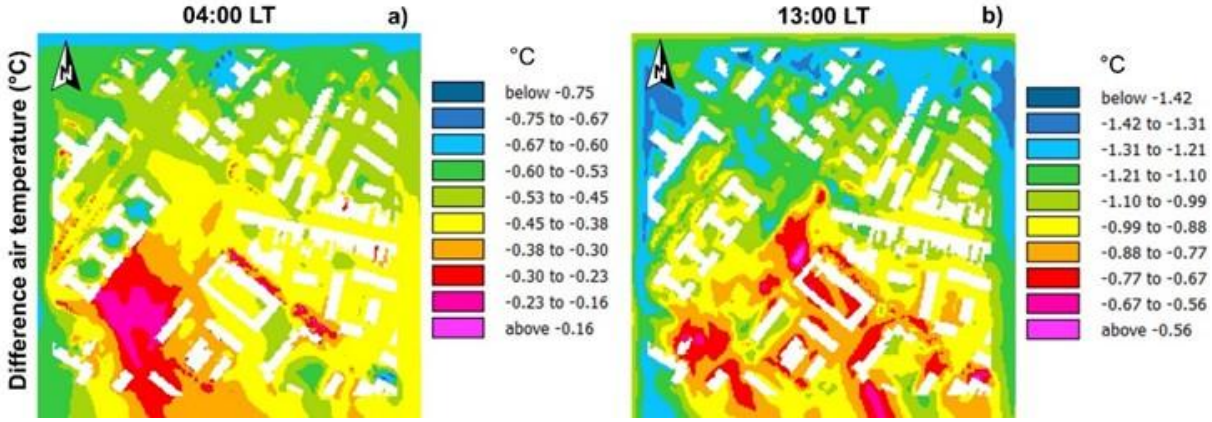

Figure 6. Difference in air temperature at 2m a.g.l. simulations between case 2 - case 3 for 04:00 LT (a) and for 13:00 LT (b).

4. CONCLUSIONS

This study emphasizes the importance of integrating different modelling approaches to improve urban microclimate simulations. By coupling the MLUCM BEP+BEM parameterization with the ENVI-met model, it assessed whether a mesoscale-based model can replace in-situ observations. The case study in Lecce demonstrated the potential of this modelling chain to capture summertime climate dynamics. Among the simulations, case 3 produced a temperature trend closest to observations. Wind speed and radiative inputs affected accuracy, with case 3 better accounting for building-induced drag in dense areas. Despite advancements, challenges remain in capturing microclimatic variability, requiring refined input data and model parameters. While the current results may not fully isolate the added value of MLUCM BEP+BEM compared to other modelling approaches, this urban parameterization enabled a more realistic representation of building energy exchanges and urban morphology. Future work will aim to better quantify its comparative benefits through targeted analyses and complementary indicators. The study provides a scalable approach for analysing extreme heat events and improving urban climate resilience.

ACKNOWLEDGEMENTS
F.G. acknowledges the financial support of the (i) PNRR ITINERIS IR0000032—Missione 4, Componente 2, Investimento 3.1 “Fondo per la realizzazione di un sistema integrato di infrastrutture di ricerca e innovazione” funded by European Union – NextGenerationEU (CUP B53C22002150006). The Ateneo meteorological data refer to the Lecce weather station of the ClimateNetwork® operated by Fondazione OMD.

REFERENCES

Gatto E., Buccolieri R., Aarrevaara Eeva, Ippolito F., Rohinton E., Perronace L., Santiago J., 2020. Impact of Urban Vegetation on Outdoor Thermal Comfort: Comparison between a Mediterranean City (Lecce, Italy) and a Northern European City (Lahti, Finland). Forests 11, 228.

Gohil K., Jin M., 2019. Validation and Improvement of the WRF Building Environment Parametrization (BEP) Urban Scheme. Climate 7, 109.

Martilli A., Clappier A., Rotach M. W., 2002. An urban surface exchange parameterisation for mesoscale models, Boundary Layer Meteorology, 104, 261–304.

McRae I., Freedman F., Rivera A., Li X., Dou J., Cruz I., Ren C., Dronova I., Fraker H., Bornstein R., 2020. Integration of the WUDAPT, WRF, and ENVI-met models to simulate extreme daytime temperature mitigation strategies in San Jose, California. Building and Environment 184, 107180.

Miao, S., Chen F., LeMone M.A., Tewari M., Li Q., Wang Y. 2009. An observational and modeling study of characteristics of urban heat island and boundary layer structures in Beijing. Journal of Applied Meterology and Climatology 48, 484–501.

Oke T.R., Mills G., Christen A., Voogt J.A. 2017. Urban Climates. Cambridge University Press.

Papangelis, G., M. Tombrou, A. Dandou, T. Kontos, 2012. An urban green planning approach utilizing the Weather Research and Forecasting (WRF) modeling system. A case study of Athens, Greece. Landscape Urban Planning 105, 174–83.

Pappaccogli G., Giovannini L., Cappelletti F., Zardi D., 2018. Challenges in the application of a WRF/Urban-TRNSYS model chain for estimating the cooling demand of buildings: A case study in Bolzano (Italy). Science and Technology for the Built Environment 24, 1-34.

Pappaccogli G., Zonato A., Martilli A., Buccolieri R., Lionello P., 2024. The Implementation of the BEP+BEM Offline Parameterization Scheme: Exploring Urban Dynamics through Climatic Projections, EGU General Assembly 2024, Vienna, Austria, 14–19 Apr 2024, EGU24-6308

Pappaccogli G., Zonato A., Martilli A., Buccolieri R., Lionello P., 2025 MLUCM BEP+BEM: An offline one-dimensional Multi-Layer Urban Canopy Model based on the BEP+BEM Scheme, EGUsphere [preprint], https://doi.org/10.5194/egusphere-2025-219.

Santiago J., Martilli A., 2010. A dynamic urban canopy parameterization for mesoscale models based on computational fluid dynamics Reynolds-averaged Navier–Stokes microscale simulations, Boundary Layer Meteorology 137, 417–439.

Wang X., Chen F., Wu Z., Zhang M., Tewari M., Guenther A., Wiedinmyer C., 2009. Impacts of weather conditions modified by urban expansion on surface ozone: Comparison between the Pearl River Delta and Yangtze River Delta regions. Advances in Atmospheric Science 26, 962–72.

Occupant-Centric Building Design and Controls (13:30-15:00 h)

6th International Conference on Building Energy and Environment
Eindhoven University of Technology, The Netherlands
6 - 10 July 2025

Identifying occupant showering behaviors for energy consumption using a mixed-qualitative approach

Dadi Zhang[1], Ling-Tim Wong [2], Kwok-Wai Mui [3]

[1] *The Hong Kong Polytechnic University, Hong Kong, China, Beee-dadi.zhang@polyu.edu.hk*
[2] *The Hong Kong Polytechnic University, Hong Kong, China, ling-tim.wong@polyu.edu.hk*
[3]*The Hong Kong Polytechnic University, Hong Kong, China, horace.mui@polyu.edu.hk*

ABSTRACT

Buildings account for a significant portion of overall energy consumption, especially in urban areas with high-density residential structures like Hong Kong. Reducing energy usage in residential buildings is a key objective in pursuing carbon neutrality. Statistics show that over 20% of household energy consumption is attributed to hot water systems, highlighting substantial opportunities for energy conservation during showering activities. Therefore, understanding occupants' showering behavior and mitigating energy consumption during showering is essential. This study employed a mixed-methods investigation that included a discrete choice experiment and collages making of ideal showering scenarios to explore the showering behaviors of occupants, particularly their comfort requirements. Twenty-one subjects, aged 19 to 70, participated in the focus group and completed the discrete choice experiment. Both qualitative and quantitative data (including transcripts of the focus group discussions) were analyzed using SPSS and QDA Miner Lite, respectively. The results indicated that participants prioritized thermal sensation, making air temperature the most influential factor in their showering setting preferences. Additionally, water flow rate and showering duration also significantly impacted their decisions. These findings provide empirical support for using visual methods in showering environment research, facilitating a deeper understanding of the diverse showering behavioral patterns related to energy consumption and comfort. Furthermore, the insights gained from this study offer evidence for designing customized bathroom environments that meet the specific needs of occupants, ultimately reducing energy consumption while maintaining thermal comfort.

Keywords: Showering behaviour, shower room environment, showering thermal comfort.

1. INTRODUCTION

Buildings account for significant global energy consumption, especially in densely populated urban areas like Hong Kong. According to statistics, buildings consume over 90% of Hong Kong's electricity, which corresponds to approximately 60% of the region's carbon emissions (Wang et al., 2018). A survey on showering behavior revealed that residents in Hong Kong shower an average of 1.4 times per day, significantly higher than in other parts of the world. The government report showed that domestic freshwater consumption constitutes 54% of the total water usage in Hong Kong (Water Supplies Department, 2014), with more than 40% of this being used for

showering (Water Supplies Department, 2020). Additionally, Wan and Yik (2004) found that electricity consumption for water heaters accounts for nearly half of the total electricity used per household. These findings highlight the considerable potential for energy savings during shower times in Hong Kong.

Occupants' behaviour, especially their interactions with building systems, is one of the crucial factors that influence the energy consumption of buildings (Ebuy et al., 2023). Previous studies demonstrated a significant correlation between occupant habits and energy consumption, highlighting the need for tailored energy efficiency measures (Ahmed et al., 2023). However, most of these studies focused on adjusting HAVC or lighting systems (Liu & Gou, 2024). Very little research has focused on the specific context of showering behaviours and their impact on energy consumption. Moreover, occupant behaviour is often unpredictable, leading to fluctuations in energy use and thermal comfort levels (Yan et al., 2023).

Understanding the patterns of occupant showering behaviours is crucial for developing effective strategies to reduce water and energy usage, thereby contributing to sustainability efforts in urban environments. Therefore, this study aims to investigate building occupants' showering behaviours to identify key patterns influencing energy consumption and water usage. By analyzing these patterns, this study seeks to provide empirical support for designing customized bathroom environments that meet the specific needs of occupants and actionable suggestions for encouraging occupants to change their showering behaviour towards a more sustainable lifestyle, ultimately reducing the overall environmental impact of residential and commercial buildings.

2. METHODS

2.1 Study design and preparation

A mixed-methods approach was employed in this study, incorporating both qualitative and quantitative data collection techniques, namely, Focus Group Discussion (FGD) and Discrete Choice Experiment (DCE). Before the FGD, a sensitization process was implemented to prepare participants for the discussion. Following the methods outlined in a previous study by Otize et al. (2022), all participants received a package 7-8 days before the FGD. This package included a hygrothermograph, a booklet, a pen, and stickers with words related to comfort in showering. Participants were asked to engage in several weekly daily activities, including self-introductions, completing a questionnaire survey about their showering preferences, describing a comfortable showering experience, etc. These preparatory activities aimed to help participants reflect on and explore the features of their showering behaviour.

2.2 Focus group discussion

The FGD was held in a multi-functional room at The Hong Kong Polytechnic University. Participants were divided into groups of 5 to 6 individuals. Two researchers facilitated the discussion: one served as the moderator while the other took notes and photographs. The focus group comprised five parts: introduction, discrete choice experiment (DCE) regarding showering preferences, sharing experiences related to comfort in showering, collage creation, and the presentation of the collages. The entire process lasted approximately one hour (see Figure 1). During the experience sharing and presentations, participants' voices were recorded. After the

introduction, participants were asked to sign a consent form, which informed them that their voices would be recorded and assured them that the data would remain confidential and used solely for this study.

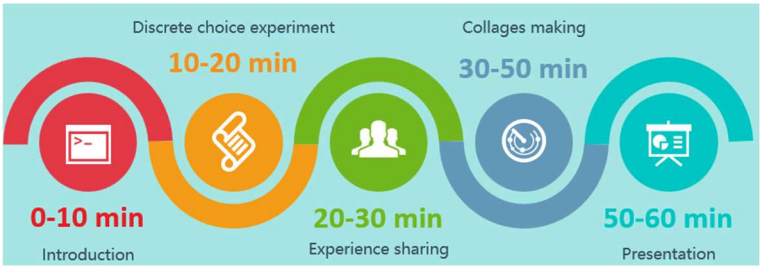

Figure 1. Focus group flow chart.

The discrete choice experiment (DCE) is similar to the questionnaire used during the sensitization phase and validates the questionnaire design. The DCE aimed to elicit participants' preferences regarding showering settings without asking them directly. This experiment selected eight showering scenario pairs based on four factors: water temperature, air temperature, water flow rate, and showering time, each having two levels. The occupants' annual energy bills and thermal sensations during the undressing and showering periods in the scenarios were calculated. To enhance participants' understanding, five factors—undressing thermal sensation, showering thermal sensation, water flow rate, showering time, and estimated annual energy bills—were utilized in both the questionnaire and the DCE (see Figure 2). Participants were then asked to select their preferred option between the paired choices.

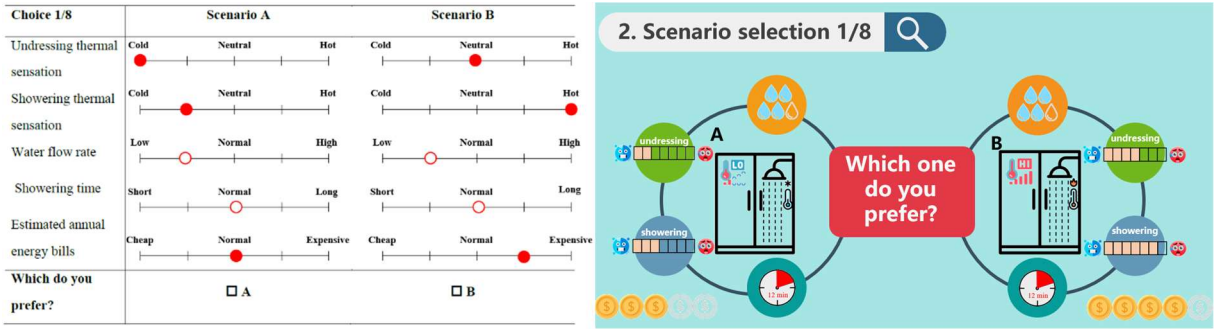

a) Questionnaire b) Discrete Choice Experiment

Figure 2. Examples of questions used in the Questionnaire and Discrete Choice Experiment.

For the collage-making activity, participants were provided with an A3 cardboard canvas and various materials, including newspapers, magazines, colored papers with different textures, washi tapes, and paper-cutting and joining tools. The materials were consistent across all groups. Participants were instructed to use these materials to make a collage about their ideal showering environment within a 20-minute timeframe. During the collage-making process, they were not allowed to communicate. After all the participants completed the collage-making, they were invited to present their artwork in a two-minute presentation.

2.3 Data analysis

All the quantitative data, including demographics, questionnaires, and DCE, were imported into SPSS and analyzed using four steps. First, descriptive statistics of frequency and percentage were performed to understand the general information of the participants. Then, paired-sample t-tests were conducted to compare the questionnaire and the DCE results. Third, a series of chi-square tests were conducted to test the impacts of the four variables on participants' preferences regarding showering settings. Lastly, the effects of participants' characteristics on their choices were evaluated using independent t-tests and Chi-square tests. It is worth noting that considering the relatively small sample size, the significance threshold for the statistical analyses was set as 0.1 in this study.

For the audio data collected during the FGD, this study only focused on the explanations provided during the collage-making presentations (i.e., the last ten minutes of the FGD). All recordings were transcribed verbatim in Microsoft Word files and subsequently imported into the QDA Miner Lite v3.0. Each participant was treated as a separate case. Then, these data were analyzed using content analysis as proposed by Kuckartz (2019). Specifically, the main text was coded according to a coding scheme that included several categories and codes.

3. RESULTS AND DISCUSSION

3.1 Descriptive Results

Twenty-one subjects participated in this focus group study, averaging 42.2 years (SD = 18.8) old. Their information is shown in Table 1. The majority of participants were female (67%), single (76%), and reported being in good health (67%). The highest level of education achieved varied among participants: 14% had a high school diploma, 19% held a bachelor's degree, 38% had a master's degree, and 19% possessed a doctoral degree. Most participants lived with others (67%), and their household sizes varied: 33% had a living area of less than 200 square feet, 38% had a living area between 200 and 500 square feet, and 29% had a living area between 500 and 700 square feet.

Table 1. Participants' general information.

Variables	Categories	n(%)
Gender	Female	14 (67%)
	Male	7 (33%)
Health	Excellent	2 (9.5%)
	Good	6 (28.6%)
	Fair	12 (57.1%)
	Poor	1 (4.8%)
Highest education	High school	3 (14%)
	Bachelor	4 (19%)
	Master	8 (38%)
	Doctor	4 (19%)
Martial status	Single	19 (76%)
	Married/cohabiting	4 (19%)
Live alone	Yes	7(33%)
	No	14 (67%)
House area	<200 sf	7 (33%)
	200-500	8 (38%)
	500-700	6 (29%)

Showering duration	<10 min	8 (38%)
	10-15	5 (24%)
	15-20	6 (29%)
	20-25	2 (9.5%)
Age*	23-76	42.2 (18.8)
Shower times per week*	1-10	6.9 (1.8)

* Continuous variables presented in min-max, mean (S.D.).

Participants' showering behaviors also varied: 38% took showers lasting less than 10 minutes, 24% took showers lasting 10-15 minutes, 29% took showers lasting 15-20 minutes, and 9.5% took showers lasting 20-25 minutes. On average, they showered 6.9 times per week (SD = 1.8), with most reporting seven showers per week. Notably, one participant showered once a week, while two reported showering ten times per week.

3.2 Impacts on showering setting preferences

According to the comparison between the questionnaire's choice selection results and the focus group ($\chi^2 = 45.9, p < 0.001$), participants' answers to these two question sets were closely related. Among the 168 selections (21 participants* 8 questions), 128 (76.2%) were the same. This consistency suggests the reliability of the responses. During the focus group, questions were fully explained to ensure participants understood the concepts. Consequently, this study focused on the data collected during the FGD.

Table 2. Comparison between results collected during the questionnaires and focus groups.

NO.	**Questionnaire**		**Focus Group**		χ^2**(p)**
	A	B	A	B	
1	29%	71%	38%	62%	**7.29 (0.007)**
2	19%	81%	48%	52%	**5.44 (0.02)**
3	71%	29%	62%	38%	**2.91 (0.088)**
4	38%	62%	29%	71%	**7.29 (0.007)**
5	86%	14%	81%	19%	0.46 (0.489)
6	71%	29%	52%	48%	**4.30 (0.038)**
7	52%	48%	62%	38%	**8.24 (0.004)**
8	48%	52%	52%	48%	**5.84 (0.016)**

Note: the significant results (p<0.1) are marked in bold.

The collected data were used to check the relationships between participants' choices and the four tested variables. As indicated in Table 3, air temperature, water flow rate, and showering duration emerged as the key factors influencing participants' preferences. Specifically, participants favored relatively higher air temperatures, lower water flow rates, and longer showering durations. In contrast, water temperature did not significantly impact their decisions.

Table 3. Relationships between participants' choice and four tested variables.

	Tw		Ta		Water flow rate		Showering duration	
	Low (36 ℃)	High (40 ℃)	Low (24 ℃)	High (28 ℃)	Low (0.13 kg/s)	High (0.17kg/s)	Short (12 min)	Long (16 min)
Selected	50%	50%	43.5%	56.5%	55.4%	44.6%	45.2%	54.8%
χ^2(p)	0.00 (1.000)		**5.762 (0.016)**		**3.86 (0.050)**		**3.05 (0.081)**	

Note: the significant results (p<0.1) are marked in bold.

Moreover, this finding also aligns with participants' importance ranking (see Table 4). According to the collected data, participants valued showering thermal sensation the most, followed by water flow rate, showering duration, and undressing thermal sensation, while energy bill was the least important factor that might influence their decision.

Table 4. Importance ranking of the variables that might influence showering comfort and energy consumption.

	1st	2nd	3rd	4th	5th
Undressing thermal sensation	14.3	4.8	19.0	**42.9**	
Showering thermal sensation	**61.9**	23.8	4.8	9.5	
Water flow rate	14.3	**47.6**	28.6		9.5
Showering duration	4.8	9.5	**33.3**	38.1	14.3
Energy bills	4.8	14.3	14.3	9.5	**57.1**

Note: the most selected options are marked in bold.

Besides the showering setting-related variables, the impacts of participants' characteristics (as shown in Table 1) were also tested. However, none of the investigated personal information significantly impacted participants' decision-making, probably due to the small sample size.

3.3 The ideal showering environment

Based on the collages created by the participants and their explanations, a coding system was developed that consisted of seven categories: Visual, Acoustic, IAQ, Thermal, Feeling, Decoration, and Others. Each category included two to eight codes. In total, 27 codes were used in the content analysis. The frequencies of 23 codes (except for those only appeared once), as they appeared in the recordings, are presented in Figure 3.

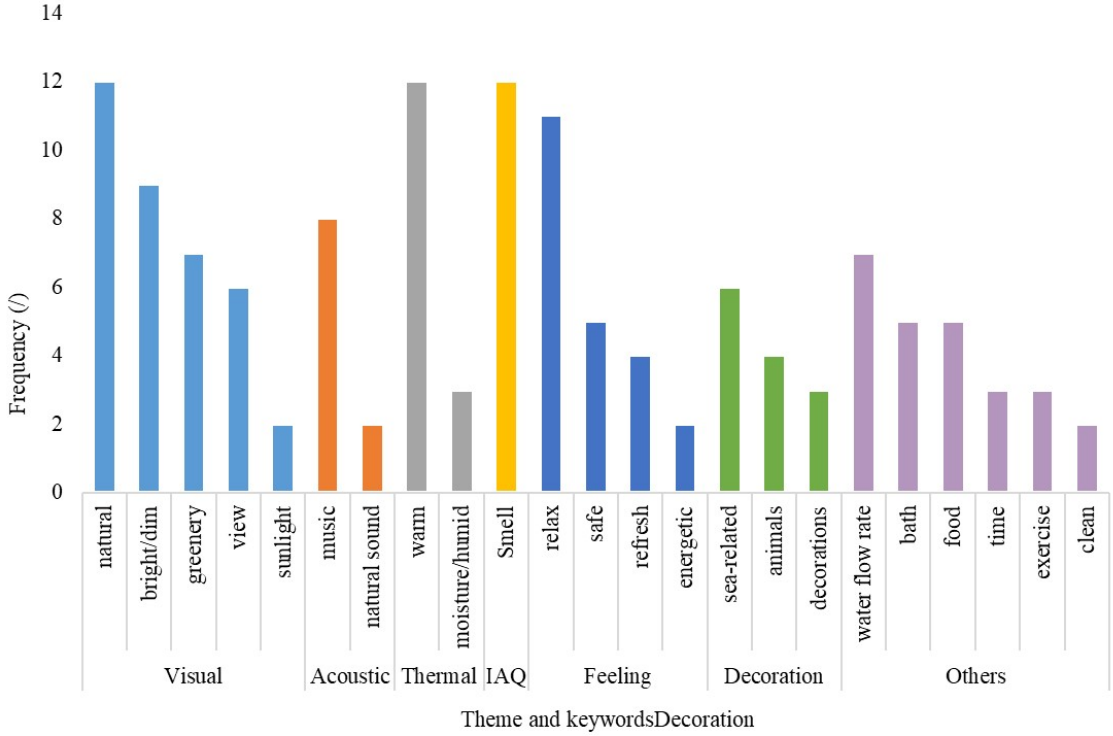

Figure 3. Frequency of the keywords appeared in the participants' focus group discussions.

As illustrated in Figure 3, the visual category was the most frequently mentioned, with 36% of participants discussing aspects related to visuals. Within this category, "natural" was the most commonly used keyword, with 12 participants expressing a preference for natural surroundings, environments, or decorations. Other frequently mentioned keywords included "smell" and "warm", with 12 participants indicating a desire for fragrance in their bathrooms, most favoring citrus or floral scents. Additionally, 12 participants specified their temperature preferences, with a majority seeking a neutral environment—neither too hot nor too cold. The term "relax" was also prevalent, as 11 participants expressed a desire for a relaxing atmosphere, with one participant using this term four times during the presentation. Beyond these commonly mentioned requirements, over 30% of participants articulated specific lighting and background music needs.

The analysis suggests that participants' awareness of energy conservation during showering is insufficient, as most did not prioritize energy bills associated with showering. The result might be attributed to the relatively low energy consumption during showering. Increased advocacy and education on energy-saving practices are recommended. Furthermore, these results indicated that air temperature was the primary factor influencing participants' preferences. However, according to a previous study, air temperature was less critical for energy consumption than water temperature and flow rates (Zhang et al., 2023). Therefore, it is suggested to maintain a relatively high air temperature while keeping water temperatures and flow rates lower to save energy and ensure comfort during showering.

Regarding the bathroom design, improvement should focus on several key elements. First, maintaining a comfortable air temperature is crucial, possibly through adjustable heating systems. Incorporating natural decor, such as greenery or nature-inspired artwork, can create a calming environment. Installing a speaker system that plays soothing music when the shower is in use adds to the relaxing atmosphere. Aromatherapy options, like built-in diffusers with popular scents such as citrus and floral, can elevate the sensory experience. Lastly, adjustable lighting allows users to customize the ambience, catering to different moods and preferences. These features collectively enhance the showering experience by making it more personalized and enjoyable.

3.4 The application of collage-making

The combination of FGD and collage-making proved to be an effective approach to identify occupants' nuance showering behaviour and preferences. Compared with traditional investigation methods, this visualization method could reveal deeper and latent insights that are important to occupants' ideal showering environment and experience. For example, natural-related decorations, as one of the most frequently mentioned keywords in participants' collages and presentations, were not prioritized by the researchers and rarely investigated in previous related studies. Additionally, this method could help designers to convey abstract ideas into practical solutions. For instance, most participants mentioned relaxed environment, which is quite abstract and hard to realize. However, at the meantime, most of them included fruits/floral scents and background music in their collages. This provided detailed and practical guidance for creating a comfort and relaxed showering environment and covered the gap between user experience and practical bathroom design.

4. CONCLUSION

Showering behavior and bathroom design affect occupants' thermal comfort and building energy consumption. Focus group studies incorporating discrete choice experiments and collage-making activities were conducted to understand these impacts and identify the optimal showering environment. Quantitative and qualitative analyses were performed using SPSS and QDA Miner Lite. The results revealed that air temperature, water flow rate, and showering duration significantly influenced participants' preferences for showering settings. Participants preferred relatively higher air temperatures, lower water flow rates, and longer showering durations, suggesting that comfort is a key determinant in their choices.

Additionally, the qualitative data highlighted that most participants desired natural decorations, soothing music, and pleasant fragrances in their bathrooms. Specifically, keywords such as "natural," "warm," and "relax" were frequently mentioned, indicating a strong inclination towards creating a calming and inviting atmosphere. These findings provide valuable insights for future bathroom design, applicable to residential settings and the hospitality industry, such as hotels or public shower houses. By integrating elements that enhance thermal comfort and aesthetic appeal, designers can create showering environments that cater to users' preferences, ultimately promoting well-being and satisfaction. Furthermore, optimizing water flow and temperature settings can significantly contribute to energy savings during showering.

5. ACKNOWLEDGEMENTS

This research was supported by grants from the Research Grants Council of the Hong Kong Special Administrative Region, China (Project no. 15217221, PolyU P0037773/ Q86B) and the Policy Research Centre for Innovation and Technology (PReCIT) Seed Funding Scheme of the Hong Kong Polytechnic University (Project ID: P0043831).

6. REFERENCES

Ahmed, O., Sezer, N., Ouf, M., Wang, L. (Leon), & Hassan, I. G. (2023). State-of-the-art review of occupant behavior modeling and implementation in building performance simulation. *Renewable and Sustainable Energy Reviews*, *185*, 113558. https://doi.org/10.1016/j.rser.2023.113558

Ebuy, H. T., Bril El Haouzi, H., Benelmir, R., & Pannequin, R. (2023). Occupant Behavior Impact on Building Sustainability Performance: A Literature Review. In *Sustainability (Switzerland)* (Vol. 15, Issue 3). MDPI. https://doi.org/10.3390/su15032440

Liu, X., & Gou, Z. (2024). Occupant-centric HVAC and window control: A reinforcement learning model for enhancing indoor thermal comfort and energy efficiency. *Building and Environment*, *250*, 111197. https://doi.org/10.1016/j.buildenv.2024.111197

Ortiz, M. A., Kim, D. H., & Bluyssen, P. M. (2022). Substantiation of home occupant archetypes with the use of generative techniques: analysis and results of focus groups. *Intelligent Buildings International*, *14*(2), 239–257. https://doi.org/10.1080/17508975.2020.1747381

Wan, K. S. Y., & Yik, F. W. H. (2004). Building design and energy end-use characteristics of high-rise residential buildings in Hong Kong. *Applied Energy*, *78*(1), 19–36. https://doi.org/10.1016/S0306-2619(03)00103-X

Wang, J., Yu, C., & Pan, W. (2018). Life cycle energy of high-rise office buildings in Hong Kong. *Energy and Buildings*, *167*, 152–164. https://doi.org/10.1016/j.enbuild.2018.02.038

Water Supplies Department. (2014). *Combat Against Climate Change: Exploit new water resources and foster water conservation culture*.

Water Supplies Department. (2020). *Virtual Water*. The Government of the Hong Kong Special Administrative Region. https://www.waterconservation.gov.hk/en/why-save-water/virtual-water/index.html

Yan, B., Yang, W., He, F., & Zeng, W. (2023). Occupant behavior impact in buildings and the artificial intelligence-based techniques and data-driven approach solutions. *Renewable and Sustainable Energy Reviews*, *184*, 113372. https://doi.org/10.1016/j.rser.2023.113372

Zhang, D., Mui, K.-W., & Wong, L.-T. (2023). Establishing the Relationship between Occupants' Thermal Behavior and Energy Consumption during Showering. *Buildings*, *13*(5), 1300. https://doi.org/10.3390/buildings13051300

6th International Conference on Building Energy and Environment
Eindhoven University of Technology, The Netherlands
6 - 10 July 2025

Impact of Router Placement on Wi-Fi-Based Human Detection

Reza Daneshazarian [1], Jeffrey Siegel [2], Seungjae Lee [3]

[1]*University of Toronto, Toronto, Canada, reza.daneshazarian@utoronto.ca*
[2] *University of Toronto, Toronto, Canada, jeffrey.siegel@utoronto.ca*
[3] *University of Toronto, Toronto, Canada, sjae.lee@utoronto.ca*

SUMMARY
Wi-Fi networks can be used for human detection, but their accuracy depends on optimized router placement and configuration to minimize interference. Human sensing involves tracking spatio-temporal data, such as location, movement, or actions like gestures and falls. This study investigates different router placements in studio apartments and one-bedroom spaces with obstacles like walls. The goal is to analyze signal coverage while assessing the interference from other devices. An experimental approach is used, employing Wi-Fi routers and signal measurement devices to map signal distribution and identify areas where human presence impacts signal strength. Physical interference is measured and integrated into Python workflows to quantify disturbances affecting detection accuracy. These metrics help evaluate router placement for reliable data collection and network stability. This study shows how router placement affects signal behaviour and human detection, ensuring accurate sensing and efficient network performance in various indoor environments.

Keywords: Wi-Fi sensing, Human detection, Interference minimization.

1. INTRODUCTION

Wi-Fi-based human detection is gaining attention for smart buildings, security, and indoor environmental quality (IEQ) monitoring (Wang, Wang, and Liu 2024). Unlike cameras or motion sensors, which can be intrusive and expensive, Wi-Fi sensing offers a cost-effective, non-intrusive alternative using existing infrastructure (Ahmad, Ullah, and Choi 2024). However, router placement and configuration significantly impact detection accuracy, as signal interference, obstacles, and environmental factors can distort readings. This study examines how different router placements affect stationary human detection, aiming to enhance occupant localization and improve thermal comfort, energy efficiency, and air quality.

Most research in Wi-Fi sensing has focused on movement detection and gesture recognition, often neglecting the role of router placement in stationary human detection (Ma, Zhou, and Wang 2020). While Channel State Information (CSI) has been used for presence tracking, its connection to building science applications like HVAC optimization and IEQ enhancement remains underexplored. This study fills that gap by experimentally analyzing router placement effects in an indoor setting, showing that Wi-Fi can serve as a reliable occupancy sensing tool.

Accurate human detection enables dynamic HVAC control and ventilation optimization, reducing energy waste and ensuring healthier indoor environments. By optimizing router placement, Wi-Fi sensing can be integrated into smart buildings, making indoor spaces more efficient, adaptive, and sustainable.

2. METHODOLOGY

2.1.Experimental Setup

This study was conducted in a 3×5×2.5 m enclosed room, designed to evaluate the impact of human presence on Wi-Fi signal propagation. The experiment involved a Wi-Fi transmitter (Raspberry Pi 4) and a receiver (ASUS RT-AC86U), which were tested under two placement configurations. In the Entrance-Wall configuration, the receiver was positioned at (0, 1.5) m, near the entrance, while the transmitter was placed at (5, 1.5) m, along the opposite wall. This configuration aimed to simulate a conventional router placement scenario often found in indoor spaces (Fig 1). In contrast, the Diagonal configuration placed the transmitter at (0, 3) m and the receiver at (5, 0) m, forming a diagonal orientation across the room (Fig 1). The goal of this setup was to observe how alternative router positioning might affect signal distribution and human detection capabilities. A single individual was instructed to stand stationary for two minutes at nine predefined locations (nodes) distributed evenly throughout the room. These positions were selected to assess the impact of human presence on signal strength variations. The stationary nature of the individual allowed for the isolation of signal disturbances caused by the occupant's presence rather than movement, providing a controlled dataset for analysis.

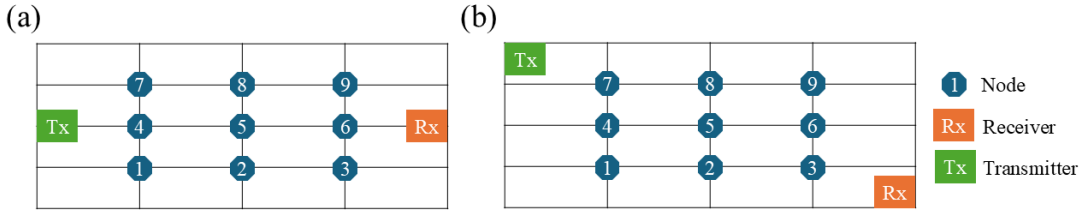

Figure 1. Room layout with nodes (a) Entrance-Wall, and (b) Diagonal configurations.

2.2.Data collection and processing

To evaluate the effects of human presence on Wi-Fi signal propagation, CSI data was continuously recorded during each test scenario. CSI measurements were collected for each of the nine stationary positions, capturing variations in signal behavior as the individual moved between predefined nodes. CSI recordings captured fine-grained fluctuations in signal strength, phase shifts, and multipath effects, which are essential for detecting human presence and its impact on wireless propagation. The primary focus of the data analysis was on identifying signal disruptions, attenuation effects, and fluctuations in CSI values across different node locations and router placements. identifying signal disruptions, attenuation effects, and fluctuations in CSI values across different node locations and router placements.

3. RESULTS

The CSI magnitude data across different node positions for the Entrance-Wall and Diagonal configurations reveal variations in signal strength, attenuation, and multipath effects, all of which influence human detection accuracy. Wi-Fi signals interaction with obstacles, reflections, and router placement, affecting localization and sensing reliability can be defined by analyzing the CSI values. The multipath effect occurs when Wi-Fi signals reflect off obstacles (e.g., walls, furniture) causing variations in CSI values that affect signal stability and human detection. Figure 2 presents the average CSI magnitudes at different nodes for both configurations, demonstrating how placement impacts signal reception. In the Entrance-Wall configuration, the highest CSI values

were recorded at Nodes 1 (1120), 2 (1050), and 7 (1078), suggesting strong signal reception due to their proximity to the transmitter or receiver. In contrast, Node 4 exhibited the lowest CSI value (280), indicating significant attenuation likely caused by physical obstructions. This reduction in signal strength results from barriers or human presence blocking the direct line-of-sight transmission. Meanwhile, Nodes 5 (490) and 6 (350) displayed moderate CSI values, suggesting partial obstruction or distance-related signal loss. The fluctuations in CSI values suggest multipath effects, where signals reflect off walls and objects, contributing to variations in signal strength. In the Diagonal configuration, the highest CSI values were recorded at Nodes 1 (1260) and 9 (1330), indicating stronger signal reception at room extremes. This could be attributed to broader coverage and constructive interference from reflected signals. However, Nodes 3 (280) and 7 (210) experienced the lowest CSI values, highlighting severe attenuation in these regions. The sharp drop at Node 7 suggests strong obstruction or destructive interference, where multipath reflections canceled out the direct signal. Moderate CSI values at Nodes 4 (854), 5 (602), and 6 (910) indicate that multipath reflections reinforced rather than attenuated the signal. Comparing both configurations, the Diagonal setup provided stronger coverage at extreme points but suffered from major signal loss at Nodes 3 and 7. The Entrance-Wall setup exhibited more stable high CSI values but experienced a drop at Node 4, suggesting obstructions weakened the signal. The greater variability in the Diagonal configuration suggests that multipath effects were more pronounced, leading to unpredictable CSI fluctuations. CSI drops at specific nodes indicate human presence or obstacles affecting signal transmission, making Wi-Fi a useful tool for occupancy detection. Router placement impacts detection accuracy, with the Entrance-Wall setup offering more stable CSI values but being sensitive to localized obstructions, while the Diagonal setup provides broader coverage but requires optimization to reduce signal loss.

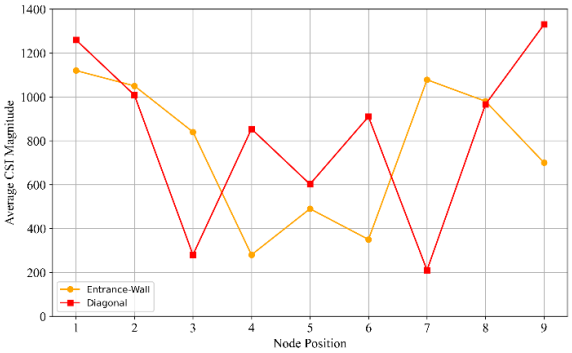

Figure 2. Average CSI magnitude at different nodes in Entrance-Wall and Diagonal configurations.

Table 1 provides an analysis of phase shift variations across different node positions in Diagonal configuration, highlighting deviations caused by the presence of an occupant. The baseline phase represents normal signal conditions in an unoccupied room. The raw phase data captures fluctuations in phase values due to environmental factors and the human presence at Node 4. A large deviation is observed at Node 4, confirming the occupant's presence. Moderate deviations at Node 7 suggest that the occupant’s presence also affects nearby positions due to multipath effects. All other nodes exhibit small or minimal deviations, indicating that they are likely unoccupied. The classification of a 0.1 difference as minimal, small, or moderate depends on the magnitude of the baseline phase value—when the baseline is large (e.g., ±2.5), a 0.1 change is minor, but when the baseline is small (e.g., 0.3), the same change is proportionally larger. Thus, "minimal

deviation" is used when the change is insignificant compared to the baseline, "small deviation" when slightly more noticeable, and "moderate deviation" when the change is significant relative to a small baseline.

Table1. Interpretation of phase shift variation at different nodes

Node	Baseline Phase (rad)	Raw Phase Data (rad)	Interpretation
1	-2.5	-2.4	Small deviation, likely unoccupied
2	1.2	1.1	Minimal deviation, likely unoccupied
3	-2.8	-2.7	Small deviation, likely unoccupied
4	-1	0.8	Large deviation, occupant present
5	-0.7	-0.6	Small deviation, likely unoccupied
6	2	2.1	Minimal deviation, likely unoccupied
7	0.3	0.2	Moderate deviation, occupant nearby
8	0.5	0.4	Minimal deviation, likely unoccupied
9	1.8	1.7	Small deviation, likely unoccupied

4. CONCLUSIONS

This study demonstrated the impact of Wi-Fi router placement on human detection accuracy using Channel State Information (CSI). The results highlight how different placement configurations influence signal reception, attenuation, and multipath effects, ultimately affecting occupancy detection reliability. The entrance-wall configuration provided more stable CSI values, making it suitable for detecting stationary occupants in predefined areas. However, it was more sensitive to localized obstructions, as seen in the attenuation at Node 4. On the other hand, the diagonal configuration offered broader coverage, achieving higher CSI values at room extremes (Nodes 1 and 9), but suffered from greater variability and signal loss at certain locations, particularly at Nodes 3 and 7. The study also explored phase shift variations to enhance human presence detection. The analysis showed that large deviations in phase data, particularly at Node 4, confirmed occupant presence, while moderate deviations at Node 7 suggested the influence of multipath effects on nearby positions. These findings validate the feasibility of using Wi-Fi-based phase shift analysis for non-intrusive and cost-effective occupancy detection in indoor environments. Overall, the results emphasize the critical role of router placement in optimizing Wi-Fi sensing applications for smart buildings. While entrance-wall placement is preferable for stable and localized occupancy detection, diagonal placement may be beneficial for larger area coverage but requires optimization to mitigate signal loss.

ACKNOWLEDGEMENTS

This research was supported by the Natural Sciences and Engineering Research Council of Canada (NSERC, RGPIN-2022-04453 and PDF-587559-2024).

REFERENCES

Ahmad, Iftikhar, Arif Ullah, and Wooyeol Choi. 2024. “WiFi-Based Human Sensing with Deep Learning: Recent Advances, Challenges, and Opportunities.” *IEEE Open Journal of the Communications Society* 5(July):3595–3623.

Ma, Y, G Zhou, and S Wang. 2020. “WiFi Sensing with Channel State Information: A Survey.” *ACM Computing Surveys* 52(3).

Wang, Siyang, Lin Wang, and Wenyuan Liu. 2024. “Feature Decoupling and Regeneration towards Wifi-Based Human Activity Recognition.” *Pattern Recognition* 153: 110480.

6th International Conference on Building Energy and Environment
Eindhoven University of Technology, The Netherlands
6 - 10 July 2025

A computer vision-based model for occupancy detection using low-resolution thermal images

Xue Cui [1], Vincent Gbouna Zakka [2], Minhyun Lee [3],

[1]*Department of Building and Real Estate, The Hong Kong Polytechnic University, Hong Kong, China, xue.cui@connect.polyu.hk*
[2] *College of Engineering and Physical Sciences, Aston University, United Kingdom, vzakk22@aston.ac.uk*
[3] *Department of Building and Real Estate, Research Institute for Smart Energy (RISE), The Hong Kong Polytechnic University, Hong Kong, China, minhyun.lee@polyu.edu.hk*

SUMMARY
Occupancy plays an essential role in influencing the energy consumption and operation of heating, ventilation, and air conditioning (HVAC) systems. Traditional HVAC typically operate on fixed schedules without considering occupancy. Advanced occupant-centric control (OCC) adopted occupancy status in regulating HVAC operations. RGB images combined with computer vision (CV) techniques are widely used for occupancy detection, however, the detailed facial and body features they capture raise significant privacy concerns. Low-resolution thermal images offer a non-invasive solution that mitigates privacy issues. The study developed an occupancy detection model utilizing low-resolution thermal images and CV techniques, where transfer learning was applied to fine-tune the You Only Look Once version 5 (YOLOv5) model. The developed model ultimately achieved satisfactory performance, with $precision$, $recall$, $mAP50$, and $mAP50-95$ values approaching 1.000. The contributions of this model lie not only in mitigating privacy concerns but also in reducing computing resource demands.

Keywords: occupant-centric building control, HVAC system, computer vision, face detection

1. INTRODUCTION

The building sector is responsible for 34% of global energy consumption (United Nations Environment Programme, 2024). Heating, ventilation, and air conditioning (HVAC) systems are the most energy-intensive systems in buildings, accounting for 38% of building energy consumption (González-Torres et al., 2022). Existing HVAC systems usually operate on fixed schedules, easily causing over-conditioning (Wu et al., 2024). Occupant-centric control (OCC) has emerged as an advanced strategy to address this issue by utilizing actual occupant information to control HVAC operations. Among various occupant-related factors, occupancy plays an essential role in determining the on/off status of HVAC systems. Studies have shown that integrating occupancy into HVAC operations can achieve an energy-saving ratio between 19% and 44% (Pang et al., 2020), demonstrating the significant benefits of leveraging occupancy for HVAC control.

Incorporating occupancy into HVAC operations begins with occupancy detection, which forms the essential foundation. Existing studies primarily rely on passive infrared, radio frequency signal technology, cameras, environmental sensors, Wi-Fi, and Bluetooth for occupancy detection (Ding et al., 2022). Passive infrared, radio frequency signal technology, and environmental sensors are relatively easy to deploy (Ding et al., 2022). However, passive infrared is unable to detect static people and multi-occupant scenarios, and has a limited detection range (Choi et al., 2021; Ding et al., 2022). Radio frequency signal technology is highly sensitive to indoor electromagnetic conditions (Ding et al., 2022), while environmental sensors (e.g., CO_2 sensors) often experience

delay issues when detecting occupancy (Choi et al., 2021). Wi-Fi and Bluetooth are efficient and convenient, however, their connection points do not always match the actual number of occupants (Ding et al., 2022). Cameras offer high accuracy in detecting occupancy and can immediately track changes in occupants (Choi et al., 2021; Ding et al., 2022), in particular, computer vision (CV) techniques are commonly applied to images for occupancy detection (Choi et al., 2021).

Many existing CV-based occupancy detection models employ Red, Green, and Blue (RGB) images for detecting occupancy. Tien et al. (2020b) applied a convolutional neural network to images to detect occupancy activity, achieving an average detection accuracy of 80.62%. Similarly, Choi et al. (2021) integrated a CV-based occupancy-centric counting method into the HVAC and lighting systems in two offices, achieving a 10.2% energy reduction. Overall, CV-based occupancy detection models commonly achieve high accuracy while contributing to building energy savings. However, most of these studies rely on high-resolution RGB images, which raise significant privacy concerns since the detailed facial and body features of occupants are captured (Choi et al., 2021). In addition, the high-resolution nature of RGB images requires high computing power and memory capacity (O'Mahony et al., 2020). To address this challenge, it is crucial to conserve computing resources when developing a CV-based occupancy detection model. Here, low-resolution thermal images provide an effective option since they not only mitigate privacy concerns but also reduce processing demands.

In summary, existing occupancy detection models reveal two main research gaps. First, most occupancy detection approaches based on passive infrared, radio frequency signal technology, environmental sensors, Wi-Fi, and Bluetooth, encounter significant limitations in practical applications. Second, the use of RGB images for occupancy detection raises privacy concerns and requires high computing resources. To address these gaps, this study aims to develop an occupancy detection model leveraging low-resolution thermal images and CV techniques. The novelty lies in its non-invasive nature and ability to mitigate privacy concerns, making it more psychologically acceptable to occupants. Furthermore, it reduces the requirement for computing resources, enhancing its practicality for real-world building environments.

2. METHODOLOGY

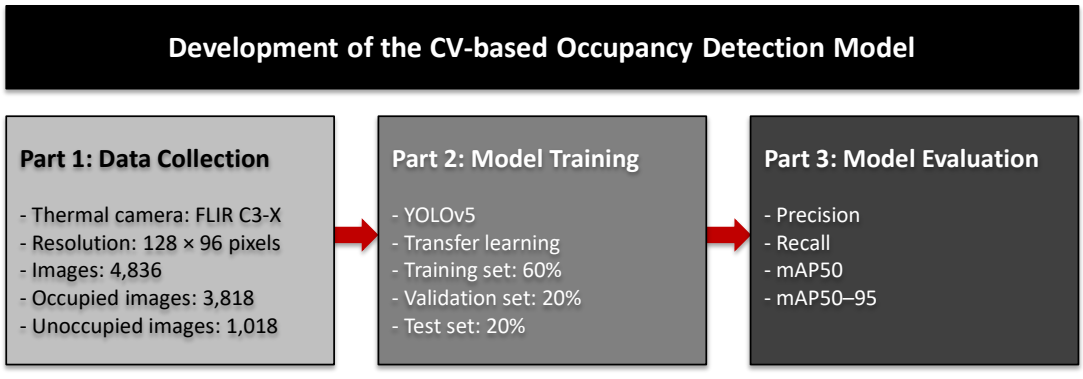

Figure 1. The methodological framework for developing the CV-based occupancy detection model.

Figure 1 illustrates the methodological framework for developing the CV-based occupancy detection model, consisting of three main parts: (1) data collection, which involves gathering sufficient low-resolution thermal images under occupied and unoccupied scenarios; (2) model

training, where transfer learning is applied to fine-tune the You Only Look Once version 5 (YOLOv5) model using the collected thermal images; and (3) model evaluation, which assesses the reliability of the developed model based on four metrics.

2.1. Data collection

Occupant thermal images were collected in a single-person office at The Hong Kong Polytechnic University on 8 August 2024. To simulate a realistic working environment, a single occupant performed typical computer-based tasks following their natural working habits, without any prescribed activity schedule or arrangement. Thermal images were captured using a FLIR C3-X compact thermal camera, featuring a low-resolution of 128 × 96 pixels ("FLIR C3-X Compact Thermal Camera with Cloud Connectivity and Wi-Fi | Teledyne FLIR," 2024). The camera was mounted on the upper bezel of the computer monitor and connected to the computer via USB. To ensure sufficient data collection, thermal images were automatically captured at 10-second intervals using radiometric streaming through the FLIR Desktop Atlas SDK. By the end of the day, a total of 4,836 thermal images were collected, comprising 3,818 images with the occupant present and 1,018 without, resulting in an occupied-to-unoccupied ratio of 3.75.

2.2 Model training

The study initially employed the YOLOv5 model to detect occupant faces since it demonstrates efficient and robust performance in this field (Jeoung et al., 2023). However, the publicly available YOLOv5 model produced unsatisfactory detection results when applied to the low-resolution thermal images collected in this study. This result may be attributed to the YOLOv5 model being pretrained on the Common Objects in Context (COCO) dataset (Choi et al., 2021), which offers limited exposure to low-resolution thermal images. Consequently, the pretrained YOLOv5 model likely struggled to capture the distinctive features of occupant faces in low-resolution thermal images, resulting in its suboptimal detection performance.

To improve the detection accuracy of the YOLOv5 model on low-resolution thermal images, an end-to-end transfer learning approach was employed. In this approach, the original YOLOv5 weights were fine-tuned using a curated dataset of low-resolution thermal images. Unlike traditional transfer learning methods that freeze early layers to retain generic feature representations, this approach involved fine-tuning the entire model. The layers of YOLOv5 were retrained on the curated dataset of low-resolution thermal images. This end-to-end retraining ensured that the model adapted comprehensively to the specific characteristics of thermal images, such as reduced resolution, lack of color information, and distinct thermal patterns.

LabelImg, a graphical image annotation tool, was utilized to label face bounding boxes in the thermal images ("HumanSignal/labelImg," 2024). The annotations were saved in YOLO-compatible .txt files, capturing the coordinates of the labeled bounding boxes ("HumanSignal/labelImg," 2024). All thermal images containing occupants were labeled, while annotation files for unoccupied images were left blank. After completing the annotation process, the thermal images and their corresponding annotation files were randomly split into a training subset (60%), a validation subset (20%), and a test subset (20%) for model training. Table 1 presents the sample sizes for each subset, with the occupied-to-unoccupied ratio in each subset matching the overall dataset ratio of 3.75.

Table 1. Sample sizes for the training, validation, and test subsets.

Subset	Thermal images		Annotation labels		Occupied-to-unoccupied ratio
	Occupied	Unoccupied	Occupied	Unoccupied	
Training	2290	610	2290	610	
Validation	764	204	764	204	3.75
Test	764	204	764	204	

2.3 Model evaluation

To evaluate the reliability of the trained model, the test subset was employed to assess detection performance under unseen scenarios. In this evaluation, it is essential to set an appropriate confidence threshold, as detection accuracy is highly sensitive to this parameter (Choi et al., 2022). Specifically, only objects with confidence scores exceeding the threshold are detected, while those below it are ignored (Choi et al., 2022). Thus, a low confidence threshold raises the likelihood of falsely detecting non-occupant objects, while a high confidence threshold increases the risk of missing true occupants (Choi et al., 2022). Following prior studies (Sohn et al., 2020; Xiao et al., 2021), this study adopted a confidence threshold of 0.9 to ensure robust detection performance. In addition, four criteria were used to assess the model performance, including $precision$, $recall$, $mAP50$, and $mAP50-95$. $Precision$ and $recall$, derived from $true\ positive\ (TP)$, $false\ positive\ (FP)$, and $false\ negative\ (FN)$, are defined by equations (1) and (2) ("formula of Box(P R mAP50 mAP50-95) Issue #9221," 2024). $mAP50$ and $mAP50-95$ are based on $average\ precision\ (AP)$ calculated at specific Intersection over Union (IoU) thresholds ("formula of Box(P R mAP50 mAP50-95) Issue #9221," 2024). $mAP50$ calculates the AP at an IoU threshold of 50%, while $mAP50-95$ provides a stricter assessment by averaging the AP across IoU thresholds ranging from 50% to 95% in 5% increments ("formula of Box(P R mAP50 mAP50-95) Issue #9221," 2024). Higher values across these four criteria indicate better model performance ("What is Box(P R mAP50 mAP50-95)?," 2024).

$$Precision = \frac{TP}{TP + FP} \tag{1}$$

$$Recall = \frac{TP}{TP + FN} \tag{2}$$

3. RESULTS AND DISCUSSION

3.1. Description of thermal images

As indicated in section 2.1, a total of 4,836 thermal images were collected. Figure 2 presents representative thermal images under occupied and unoccupied scenarios. Specifically, Figure 2(a) depicts the most typical unoccupied condition, while Figure 2(b)-(j) illustrate various occupied scenarios. Among these, Figure 2(b) shows the most typical occupied condition, featuring a frontal face view. Figure 2(c)-(d) display partial face visibility, Figure 2(e)-(g) show the face obscured by a hand or bottle, and Figure 2(h)-(j) present side-face views with varying head orientations. Notably, the diversity of head orientations, occupant gestures, and the limited visibility of occupant faces in these thermal images poses significant challenges for developing an effective occupancy detection model, as further discussed in section 3.3.

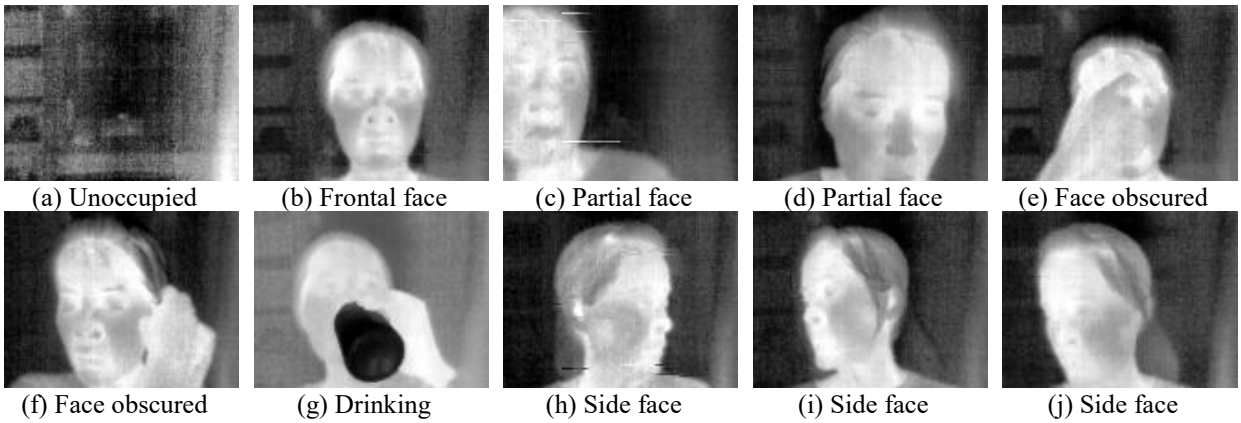

Figure 2. Representative thermal images featuring occupied and unoccupied scenarios.

3.2. Evaluation of model performance

Figure 3 illustrates the training curves of $precision$, $recall$, $mAP50$, and $mAP50-95$ of the model on the validation subset across 250 epochs. $Precision$ quickly converged to nearly 1.000, while $recall$ gradually stabilized around 1.000 despite minor fluctuations. Similarly, $mAP50$ rapidly stabilized near 0.995, and $mAP50-95$ progressively converged to approximately 0.980, demonstrating the robust detection capabilities of the model across varying IoU thresholds. As described in section 2.3, the study evaluated the model performance on the test subset. Table 2 summarizes the results of the four evaluation criteria on the test subset. Overall, the model performed excellently on the test subset, achieving a $precision$ of 1.000, $recall$ of 0.984, $mAP50$ of 0.991, and $mAP50-95$ of 0.975. These consistently high scores indicate the strong accuracy and generalizability of the developed occupancy detection model under unseen scenarios.

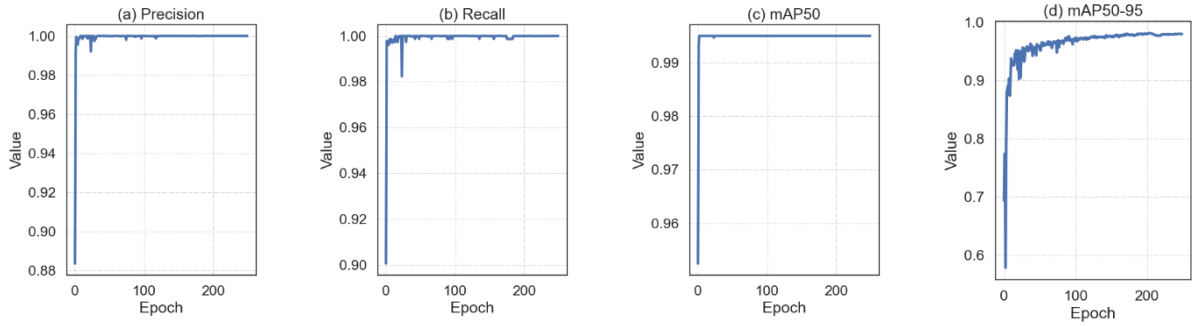

Figure 3. Training curves of $precision$, $recall$, $mAP50$, and $mAP50-95$ of the model on the validation subset across 250 epochs.

Table 2. Results of four evaluation criteria on the test subset.

	$Precision$	$Recall$	$mAP50$	$mAP50-95$
On the test subset	1.000	0.984	0.991	0.975

To ensure the reliability of the developed occupancy detection model, the study compared its performance with other similar CV-based detection models reported in previous studies. $Precision$ and $recall$ were selected as the key comparison criteria since they are widely used to evaluate model performance in this field. Table 3 summarizes the comparison results of $precision$ and $recall$ of the developed model and other similar CV-based detection models

from previous studies. The prior models examined in Table 3 primarily focus on detecting occupant activities (such as sitting, standing, and walking), the on/off status of the personal computer monitor, the open/closed status of windows, and worker tracking in off-site construction. The $precision$ of these CV-based models ranges from 0.864 to 0.987, while their $recall$ ranges from 0.828 to 0.967. By comparison, the occupancy detection model developed in this study achieved a $precision$ of 1.000 and a $recall$ of 0.984, exceeding the highest values reported among the examined models. These findings highlight the superior performance and reliability of the developed model in detecting occupancy.

Table 3. The comparison results of $precision$ and $recall$ of the occupancy detection model developed in this study and other similar CV-based detection models in previous studies.

	Detection target	*Precision*	*Recall*
This study	**Occupancy**	**1.000**	**0.984**
(Tien et al., 2020a)	Occupant activity	0.932	0.930
	Personal computer monitor _ on	0.914	0.860
(Tien et al., 2022)	Occupant activity _ sitting	0.925	0.891
	Occupant activity _ standing	0.906	0.828
	Occupant activity _ walking	0.864	0.927
	Window open	0.962	0.909
(Xiao et al., 2022)	Worker tracking in off-site construction	0.987	0.967

3.3. Analysis of occupancy detection

Figure 4 presents the actual and detected occupancy curves on the test subset. The model successfully detects the majority of occupancy states, with only a few exceptions. Specifically, out of 968 thermal images in the test subset, only 12 occupied images were not detected. Figure 5 presents the detection results for representative thermal images, corresponding to the scenarios shown in Figure 2. As seen in Figure 5(b)-(f) and Figure 5(j), the model correctly detects occupancy even under challenging conditions such as partial face visibility, side-face views, and faces obscured by a hand. In contrast, Figure 5(g)-(i) show three occupied scenarios that the model failed to detect. In these cases, although the room was indeed occupied, the model incorrectly identified it as unoccupied. This misclassification is likely due to the limited visibility of the occupant face, as specific head orientations (e.g., side-face views) and occupant gestures (e.g., drinking) do not provide sufficient visual information for the model to capture, leading to incorrect identification. These observations suggest that head orientations, occupant gestures, and face visibility play a significant role in influencing the model detection performance.

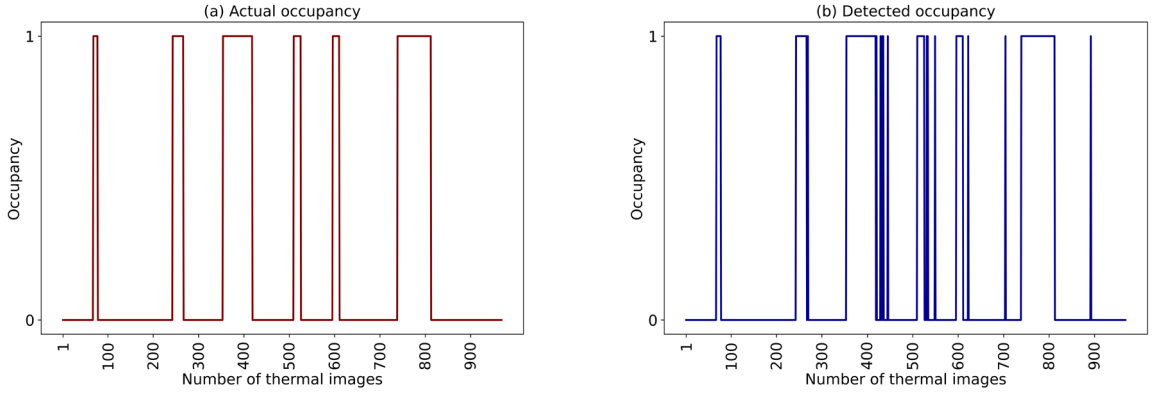

Figure 4. Actual and detected occupancy curves on the test subset.

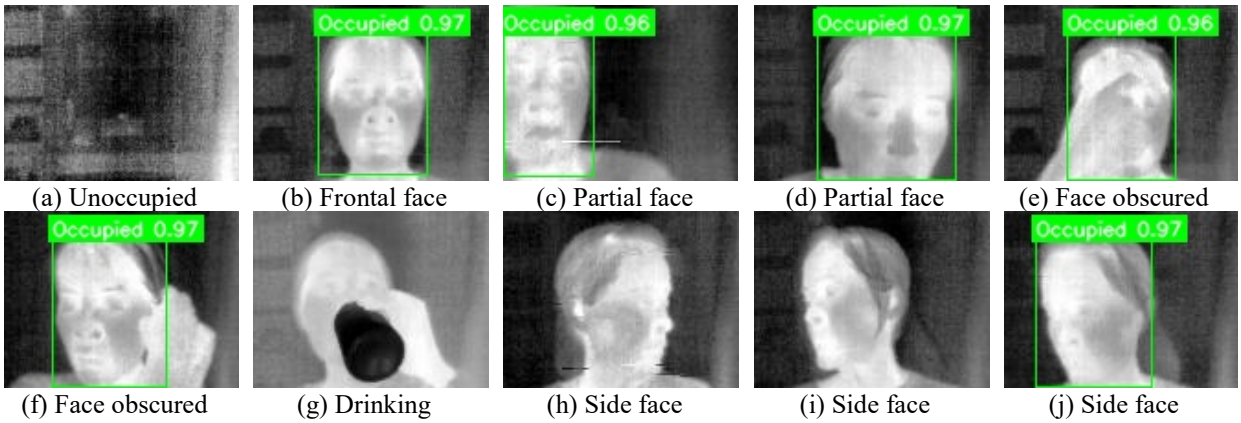

(a) Unoccupied (b) Frontal face (c) Partial face (d) Partial face (e) Face obscured

(f) Face obscured (g) Drinking (h) Side face (i) Side face (j) Side face

Figure 5. Detection results of representative thermal images corresponding to Figure 2.

4. CONCLUSION

Occupancy plays an essential role in influencing the energy consumption and operational status of HVAC systems. OCC system has become increasingly recognized in HVAC management since it utilizes actual occupant information to optimize system operation. Reliable occupancy detection is a fundamental requirement for developing an effective OCC system, as it directly determines the on/off status of HVAC equipment. However, most existing CV-based detection models rely on RGB images, which can raise privacy concerns and require high computing resources. To address these challenges, the study developed an occupancy detection model based on low-resolution thermal images combined with CV techniques. A total of 4,836 thermal images were collected for model development, ultimately achieving $precision$, $recall$, $mAP50$, and $mAP50-95$ values close to 1.000 on the test subset. Furthermore, the detection results reveal that head orientations, occupant gestures, and face visibility significantly affect the model performance.

The developed occupancy detection model demonstrates exceptional accuracy, making it highly suitable for integration into OCC systems to determine the on/off status of HVAC systems and potentially achieve energy savings. Additionally, its non-invasive design effectively addresses privacy concerns, enhancing psychological acceptability among building occupants. The use of low-resolution thermal images also reduces the demands on computing resources, thereby improving the practicality and applicability of the model in real-world building environments. The study acknowledges a limitation that most thermal images collected in this study predominantly capture frontal face views, which may not fully represent diverse real-world scenarios. Model accuracy tends to decrease when processing thermal images with varied head orientations, occupant gestures, or limited face visibility. However, these conditions are commonly encountered in practice. To address this, future research should focus on enhancing the model robustness when detecting thermal images with incomplete or minimally visible occupant faces, heads, bodies, and diverse orientations and gestures, thereby further improving its reliability and adaptability across a wide range of real-world applications.

ACKNOWLEDGEMENTS

This work was supported by the PhD Student Stipend and Seed Funding for Competitive Projects from the Department of Building and Real Estate at The Hong Kong Polytechnic University.

REFERENCES

Choi, H., Lee, J., Yi, Y., Na, H., Kang, K., Kim, T., 2022. Deep vision-based occupancy counting: Experimental performance evaluation and implementation of ventilation control. Building and Environment 223, 109496. https://doi.org/10.1016/j.buildenv.2022.109496

Choi, H., Um, C.Y., Kang, K., Kim, H., Kim, T., 2021. Application of vision-based occupancy counting method using deep learning and performance analysis. Energy and Buildings 252, 111389. https://doi.org/10.1016/j.enbuild.2021.111389

Ding, Y., Han, S., Tian, Z., Yao, J., Chen, W., Zhang, Q., 2022. Review on occupancy detection and prediction in building simulation. Build. Simul. 15, 333–356. https://doi.org/10.1007/s12273-021-0813-8

FLIR C3-X Compact Thermal Camera with Cloud Connectivity and Wi-Fi | Teledyne FLIR [WWW Document], 2024. URL https://www.flir.asia/products/c3-x/?vertical=condition+monitoring&segment=solutions&srsltid=AfmBOorRFysotltrIrUQfXbVcTGmP7igmJvBIlw9DbXCf8WkyY74lVtQ (accessed 12.25.24).

formula of Box(P R mAP50 mAP50-95) Issue #9221 [WWW Document], 2024. . GitHub. URL https://github.com/ultralytics/ultralytics/issues/9221 (accessed 5.2.25).

González-Torres, M., Pérez-Lombard, L., Coronel, J.F., Maestre, I.R., Yan, D., 2022. A review on buildings energy information: Trends, end-uses, fuels and drivers. Energy Reports 8, 626–637. https://doi.org/10.1016/j.egyr.2021.11.280

HumanSignal/labelImg [WWW Document], 2024. URL https://github.com/HumanSignal/labelImg (accessed 12.5.24).

Jeoung, J., Jung, S., Hong, T., Lee, M., Koo, C., 2023. Thermal comfort prediction based on automated extraction of skin temperature of face component on thermal image. Energy and Buildings 298, 113495. https://doi.org/10.1016/j.enbuild.2023.113495

O'Mahony, N., Campbell, S., Carvalho, A., Harapanahalli, S., Hernandez, G.V., Krpalkova, L., Riordan, D., Walsh, J., 2020. Deep Learning vs. Traditional Computer Vision, in: Arai, K., Kapoor, S. (Eds.), Advances in Computer Vision, Advances in Intelligent Systems and Computing. Springer International Publishing, Cham, pp. 128–144. https://doi.org/10.1007/978-3-030-17795-9_10

Pang, Z., Chen, Y., Zhang, J., O'Neill, Z., Cheng, H., Dong, B., 2020. Nationwide HVAC energy-saving potential quantification for office buildings with occupant-centric controls in various climates. Applied Energy 279, 115727. https://doi.org/10.1016/j.apenergy.2020.115727

Sohn, K., Zhang, Z., Li, C.-L., Zhang, H., Lee, C.-Y., Pfister, T., 2020. A Simple Semi-Supervised Learning Framework for Object Detection. https://doi.org/10.48550/arXiv.2005.04757

Tien, P.W., Wei, S., Calautit, J., 2020a. A Computer Vision-Based Occupancy and Equipment Usage Detection Approach for Reducing Building Energy Demand. Energies 14, 156. https://doi.org/10.3390/en14010156

Tien, P.W., Wei, S., Calautit, J.K., Darkwa, J., Wood, C., 2022. Real-time monitoring of occupancy activities and window opening within buildings using an integrated deep learning-based approach for reducing energy demand. Applied Energy 308, 118336. https://doi.org/10.1016/j.apenergy.2021.118336

Tien, P.W., Wei, S., Calautit, J.K., Darkwa, J., Wood, C., 2020b. A vision-based deep learning approach for the detection and prediction of occupancy heat emissions for demand-driven control solutions. Energy and Buildings 226, 110386. https://doi.org/10.1016/j.enbuild.2020.110386

United Nations Environment Programme, 2024. 2023 Global Status Report for Buildings and Construction: Beyond foundations - Mainstreaming sustainable solutions to cut emissions from the buildings sector. United Nations Environment Programme. https://doi.org/10.59117/20.500.11822/45095

What is Box(P R mAP50 mAP50-95)? [WWW Document], 2024. . GitHub. URL https://github.com/ultralytics/ultralytics/issues/9446 (accessed 12.26.24).

Wu, Z., Zhang, W., Tang, R., Wang, H., Korolija, I., 2024. Reinforcement learning in building controls: A comparative study of algorithms considering model availability and policy representation. Journal of Building Engineering 90, 109497. https://doi.org/10.1016/j.jobe.2024.109497

Xiao, B., Xiao, H., Wang, J., Chen, Y., 2022. Vision-based method for tracking workers by integrating deep learning instance segmentation in off-site construction. Automation in Construction 136, 104148. https://doi.org/10.1016/j.autcon.2022.104148

Xiao, B., Zhang, Y., Chen, Y., Yin, X., 2021. A semi-supervised learning detection method for vision-based monitoring of construction sites by integrating teacher-student networks and data augmentation. Advanced Engineering Informatics 50, 101372. https://doi.org/10.1016/j.aei.2021.101372

6th International Conference on Building Energy and Environment
Eindhoven University of Technology, The Netherlands
6 - 10 July 2025

Towards a data-driven heat emergency alert system based on measured and simulated indoor temperatures and window ratios

Ulrike Passe [1], Negar Salahi [2], Kimia Sharifi[1]

[1]*Iowa State University, Ames, USA, upasse@iastate.edu*
[2]*University of Texas at Arlington, Arlington, USA, nxs4282@mavs.uta.edu*

ABSTRACT
Extreme heat events, the most lethal weather condition in the United States, are increasing and pose significant risks to vulnerable populations such as elderly and low-income residents. Vulnerability is exacerbated in homes lacking adequate cooling systems. In the Capitol East neighbourhood in Des Moines, Iowa 50-60% of homes lack central air conditioning. Indoor temperature in buildings without active cooling vary significantly during the summer heat, however, gathering real-time temperature data is challenging due to dynamic factors within and around a building. Developing machine learning-based model predictions could enhance and personalize heat emergency management by predicting real-time indoor temperatures. This system could mitigate dangers associated with excessive heat for residents of homes without AC across the U.S. To ensure the accuracy of the machine learning (ML) model, training and validation are needed. This paper presents the first step towards a predictive indoor dry bulb temperature model based on data collected from buildings in the study area during the summer of 2023 using the Energy Plus-based plugin Climate Studio. To assess the influence of building variables, windows to wall ratios of 5% and 10% were simulated and compared with measured data. for some homes, simulated temperatures were higher than measured for both 10% and 5% WWR. Conversely, in buildings with lower simulated temperatures than measured for both WWR levels, 5% WWR showed lower temperatures than 10%.

Keywords: Indoor Temperature Prediction, Thermal simulation, Extreme Heat Emergency Management

INTRODUCTION

Extreme heat is the deadliest type of weather in the United States (US) and disproportionately affects vulnerable populations (Donegan 2019). Called the ‘silent killer’ by health experts (TNC 2019, Voelkel et al. 2018) due to its gradual and invisible nature, extreme heat is especially dangerous for the elderly (Hajat et al. 2007) and low-income residents who are less likely to have centralized or adequate home cooling. The Fourth US National Climate Assessment predicts that extreme heat events will increase markedly with significant threat to human health (Angel et al. 2018). The frequency of high humidity/dew point days, which cause a 10–30% increase in daily human mortality by the fifth day at > 90°F are also predicted to increase (Kalkstein 2014). Lack of central air-conditioning (US EIA 2015) and the impact of urban heat island (UHI) effects caused by urban density and lack of tree canopy can create dangerous indoor living conditions. This impact is exacerbated in residences of low-income neighborhoods (Hoffman 2020).

To address the dangers of excessive heat, many public health authorities use a Heat Health Warning System (HHWS) to raise public awareness. However, HHWS alerts are based on dynamics of large air mass weather conditions that lack spatial and temporal specificity (Sheridan 2018). While HHWS predictions are based on outdoor conditions, most heat stress illnesses are occurring indoors and differ significantly based on context (Kuras et al. 2017).

This study is part of *CommHeat*, funded by the US National Science Foundation's Smart and Connected Communities program (2023-2025 # 2226880). *CommHeat* develops a community-focused microclimate-informed indoor heat emergency alert system that will enhance and personalize community heat-related emergency management capacity. The framework combines data collection from residents and community partners in a low-income neighborhood of a US Midwestern city. Ultimately the project will develop scientific machine learning (SciML) approaches to reliably predict heat flux and human response to support vulnerable community residents and stakeholders during extreme heat events in identifying which homes and residents might be at risk of overheating.

Indoor temperature directly affects occupants' thermal comfort; however, gathering real-time temperature data during an extreme event is challenging due to privacy concerns. Developing a machine learning-based system based on dynamic factors within a building's indoor environment could enhance and personalize heat-related emergency management by predicting real-time indoor temperatures. This system could mitigate dangers associated with excessive heat for residents of homes without AC across the U.S. A major challenge in developing a ML model based on field-collected temperature data is that the collected data does not yet account for changes in climate patterns, as they are trained and tested using data from a current period. The Earth is becoming warmer compared to the past (Wang et al. 2023), and this trend is expected to continue. As a result, temperature data collected during the summer of 2023 may not be sufficient to predict future indoor temperatures during summer and seasons may shift. Simulating indoor temperatures in buildings presents a promising solution, as it allows for the generation of temperature data for any desired future period. By using simulated indoor temperature data, an ML model can be trained to reflect future conditions more accurately. However, a key challenge in this approach lies in the accuracy of the simulations, which can be affected by various input parameters. Among these, the window-to-wall ratio is a critical factor influencing indoor temperature. Thus, to ensure the accuracy of the ML model, training and validation are needed. Window to Wall Ratios have been identified as a major factor to assess building cooling loads (Li et al. 2021). The aim of this study is to assess relationship between window-to-wall ratios of 5% and 10% and the indoor dry-bulb temperature variation inside the buildings. This analysis will help adjust the simulated temperature to match field-collected data, ensuring validation for developing the machine learning algorithm.

2. METHODOLOGY

This study presents the first step to develop predictive indoor dry bulb temperature model based on data collected from eight houses and one apartment unit in an inner city neighbourhood of a midwestern city in the US with the Köppen Climate Classification subtype of hot summer continental climate (Des Moines, Iowa Köppen Climate Classification, 2024). The data was collected during the summer of 2023. The methodology for this study is separated into three phases: thermal simulation of houses, comparison of simulated data with in-field collected data, and identification of parameters to align simulated data with collected data (Figure 1).

2.1 Phase 1 (Thermal simulation of houses)

In the initial phase of this study, the EnergyPlus Weather EPW file containing TMY3 data was downloaded from (EnergyPlus, 2025). The dry bulb temperature, relative humidity, wind speed, and wind direction values in the TMY3 file were updated with measurements recorded during the summer (from July 24, 2023, to September 13, 2023) at one-hour intervals. The data was collected

using a ClimaVue 50 weather station by Campbell Scientific in close vicinity of the houses. This modified EPW file was then utilized for thermal simulations in ClimateStudio. Climate Studio, a specialized plugin for the Rhinoceros 3D platform using EnergyPlus and Radiance as modelling engine (Solemma, 2025) was employed for building energy and lighting simulations.

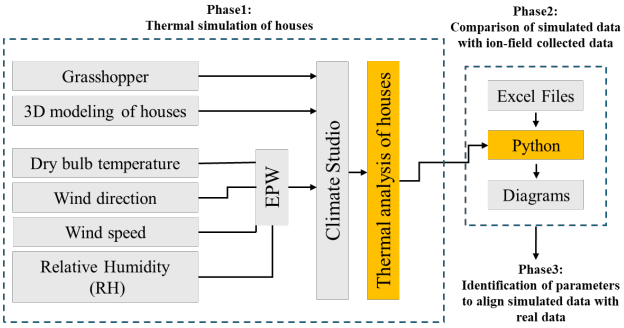

Figure 1. Flowchart of the study illustrating its three phases: (1) thermal simulation of houses, (2) Comparison of simulated data with in-field collected data, and (3) Identification of parameters to align simulated data with real data.

For the thermal simulation, five of the houses were first modelled and simulated within the Rhino environment. In the absence of precise dimensional data for the buildings, a parametric 3D model was created using the Grasshopper plugin (Simply Rhino, 2025) environment based on publicly available geospatial data. Grasshopper is a Rhino based plugin for visual programming and parametric design tool. In this script, the window-to-wall ratio and the dimensions of the buildings are controlled with adjusting sliders. All individual 3D models of the buildings were created using a Grasshopper script as illustrated in Figure 2. Another script (Figure 3) was used to calculate the window-to-wall ratio.

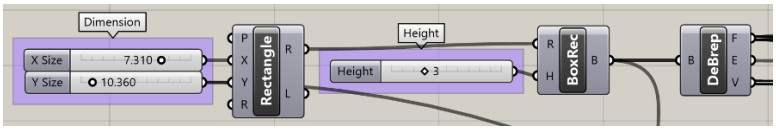

Figure 2. The script used for 3D modelling in Grasshopper

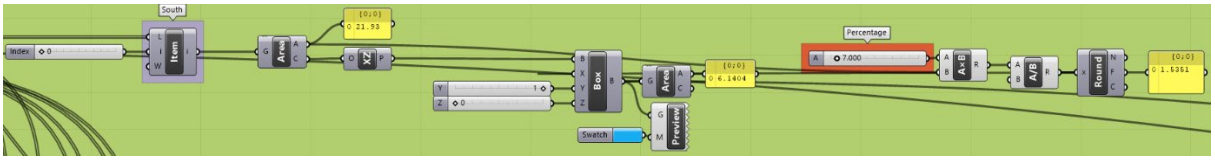

Figure 3. The script used for the window modelling

Table1. The properties of the materials used in the thermal simulations of the buildings

Buildings features	U-value W/ $(\boldsymbol{m^2.k})$	Thermal capacitance kJ/k/$\boldsymbol{m^2}$
Roof	0.23	95.64
Exterior facade	0.06	80.77
Slab	0.29	394.98
Ground slab	1.53	1833.56

Then, the estimated dimensions of each of the buildings was extracted from the GIS (Geographic Information System) files of Polk County Iowa. Each 3D model was used for the thermal simulation. Then, Climate Studio was used to simulate the temperature inside the houses. The material used for the simulation was adjusted to residential building template material (Table1) prepared for the inner city neighborhood in a previous project which used the Urban Modelling Interface (MIT Sustainable Design Lab, 2025.).

2.2 Phase 2 (comparison of simulated data with in-field collected data)

In the second phase indoor temperature of houses was recorded using Onset Hobo sensors during the warm months, from July 24, 2023, to September 13, 2023. These sensors were installed near the windows to measure the indoor temperature every ten minutes. The temperature hourly data obtained from the simulation was then compared with the data collected from the sensors.

Then, the simulated indoor temperatures were compared with the data collected from sensors installed inside the buildings to determine the alignment between the simulation results and the field-measured temperature data for the nine houses. All buildings are named alphabetically for easy comparison with each other and to keep locations anonymous as was promised to the residents (Table 2). Since multiple factors influence the simulation of indoor temperatures, such as internal loads, occupancy schedules, infiltration rates, and window-to-wall ratios, discrepancies were observed between the simulated results and the field data. Among these factors, the window-to-wall ratio was identified as having a significant impact on indoor temperatures.

Table 2. The building's geometric features used for the simulation

Houses used for the simulation				
House A	Unit B	House C	House D	House E
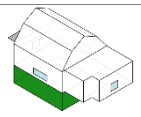	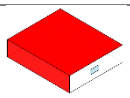	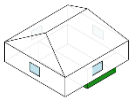	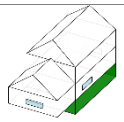	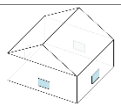

2.3 Phase 3 (identification of parameters to align simulated data with real data)

The final phase of the study focuses on identifying a pattern that could convert thermal data extracted from the simulations of five houses located in the inner-city neighborhood into measured data. To achieve this, two different window-to-wall ratios of 10% and 5% were selected for each direction in the thermal simulation of each house (Figure 3), with the goal of finding a correlation to modify the pattern of the houses' internal temperature. To determine the correlation, the simulated data was subtracted from the measured data, and the resulting differences were analyzed for both WWR 10% and 5% scenarios. Additionally, for each scenario, the number of instances where the temperature difference was less than 1°C was calculated and evaluated.

3. RESULTS

The simulated temperatures were measured during three periods of time. July 24 to July 31, August 1 to August 31, and September 1 to September 13.

3.1. The comparison of the July data

According to the simulation results with a 5% window-to-wall ratio in July for Unit B and House D, 75% and 56% of the time, the predicted interior dry bulb temperature was lower than the

measured temperature from the sensors installed inside the building. Among the times when the simulated temperature was lower than the measured temperature for Unit B, 23% of the time, the difference of simulated data and sensors extracted data was less than 1°C (Figure 4).
However, for the 10% window-to-wall ratio, 56% of the simulated temperature data was lower than the data obtained from the sensors. Of this, 30% had a temperature difference of less than 1°C (Figure 4).

In contrast, for Unit B, 55% of the time, the dry bulb temperature data collected during July was higher than the simulated temperature with a 5% window-to-wall ratio. Among these instances, 22% of the time, the difference was less than 1°C. The pattern observed with the 10% window-to-wall ratio followed a similar trend in temperature fluctuations but with different percentages of change. 51% of the time, the simulated data was lower than the real data, with 22% of this data showing a difference of less than 1°C. The simulated temperatures for House A and House C were generally higher than the collected data in July when considering the WWR of 5% and 10%. This increase was more pronounced for the 10% WWR in both cases. Among the instances where the simulated temperature exceeded the real temperature for the 10% WWR, building C showed a temperature difference of less than 1°C in 26% of the cases, whereas House A showed this result only 3% of the time. All the simulated data was higher than the real collected data for the House E both with 10% and 5% WWR (Figure 4).

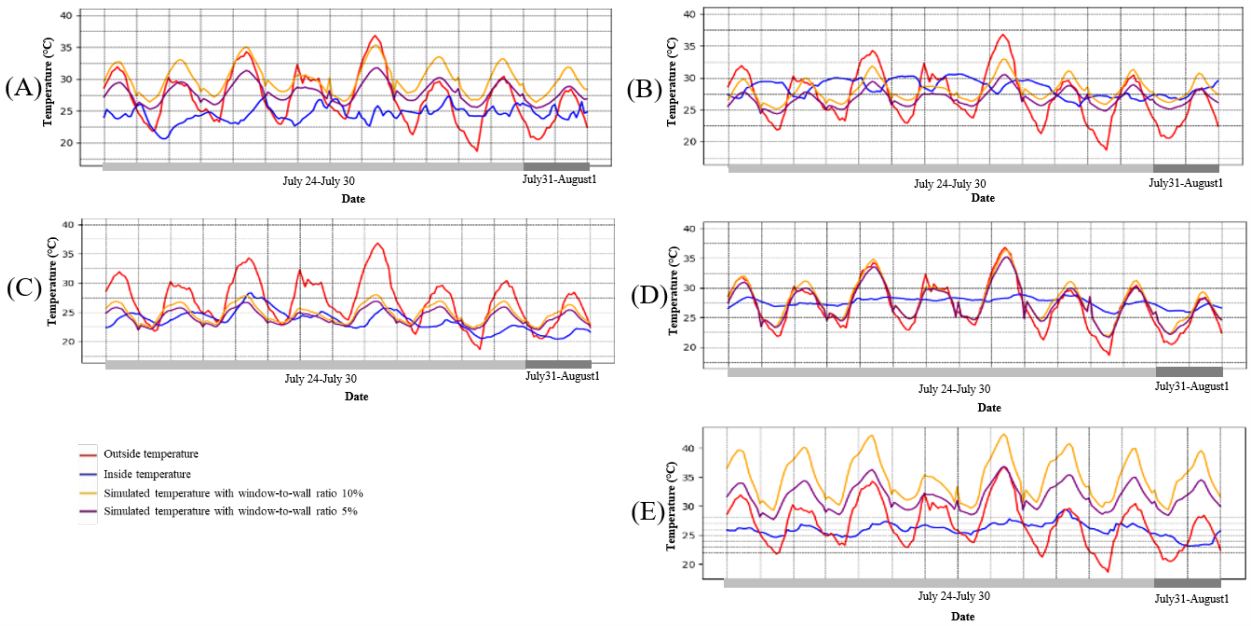

Figure 4. Thermal simulation results from July 24 to July 31:
A: House A, B: Unit B, C: House C, D: House D, E: House E

3.2. The comparison of the August data

However, the results from August showed that the temperature measured by sensors inside three out of the five houses (A, C, and E) was lower than the simulated data for most of the time. In contrast, the temperatures in the B and D Houses displayed a different pattern, with both 5% and 10% window-to-wall ratios (WWR). A similar pattern was observed in the three buildings, House A, C and E. In these buildings, the simulated temperatures with both 5% and 10% WWR were generally higher than the real data collected most of the time (Figure 5).

For House C, the simulated temperature was 58% times higher than the real with a 5% WWR, and it increased to 68% with a 10% WWR. The temperature difference between the simulated and real temperatures was within 1°C for 68% of the time, with 5% WWR in building C (Figure 5). However, when the WWR increased to 10%, this percentage dropped to 18%. Building A exhibited a higher temperature difference, with a simulated increase of 86% for a similar WWR. 15% of the time, the simulated temperature was within 1°C of the actual temperature. Additionally, 14% of the time, the simulated temperature was lower than the real temperature, and 48% of the time, the temperature difference was less than 1°C. The simulated temperature results for building E with a 5% WWR were higher than the real data 97% of the time. Of these instances, 78% showed a temperature difference of less than 1°C between the real and simulated temperatures. For the 10% WWR, all the simulated data were higher than the real data, and none of the temperature differences were less than 1°C. House D and B followed a similar pattern. In these buildings, the simulated temperature was higher than the real temperature when considering a 10% WWR; however, for the 5% WWR, the real data was higher than the simulated temperature (Figure 5).

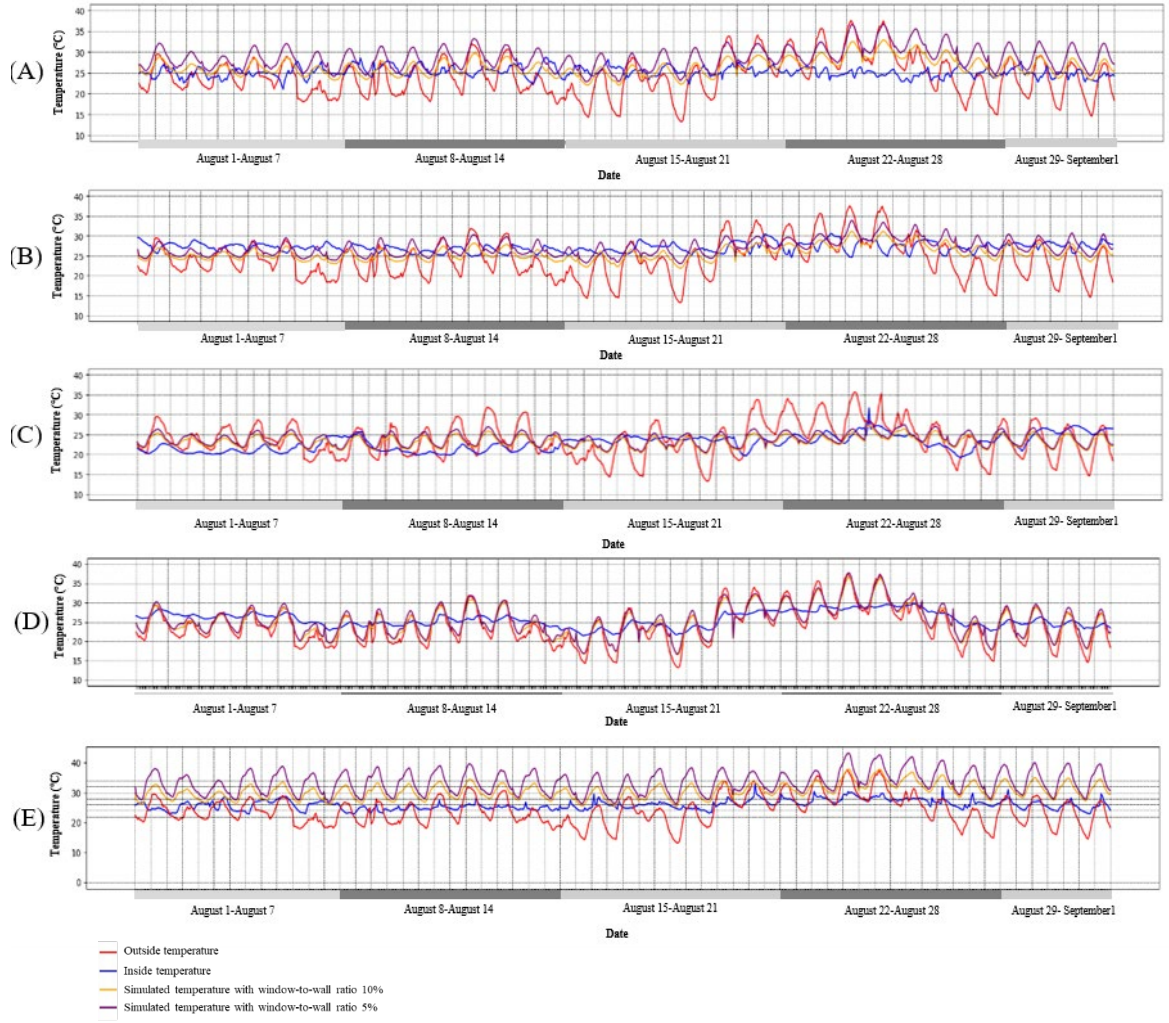

Figure 5. Thermal simulation results from August1 to August 31:
A: House A, B: Unit B, C: House C, D: House D, E: House E

3.3. The comparison for the September data

According to the simulation data from September for Houses B, C, and D, the simulated temperatures were generally lower than the measured temperatures for both 5% and 10% WWR (Figure 6). However, for all these buildings with a 5% WWR, the simulated temperatures were higher than the measured temperatures most of the time. For House C, the simulated temperature was lower than the real temperature in 39% of times, and in 40% of those instances, the difference was less than 1°C when considering both the 5% and 10% WWR. Similarly, building D showed that 23% of the time, the difference between the simulated and measured temperatures was less than 1°C (Figure 6).

In House A, the simulated temperature was higher than the measured temperature 51% of the time for a 5% WWR and 71% of the time for a 10% WWR. In most of these instances (60%), the difference between the simulated and real temperatures was less than 1°C. However, for building E with a 5% WWR, the simulated temperature was lower than the measured temperature 68% of the time. In contrast, for the 10% WWR, the simulated temperature was higher than the real temperature 93% of the time (Figure 6).

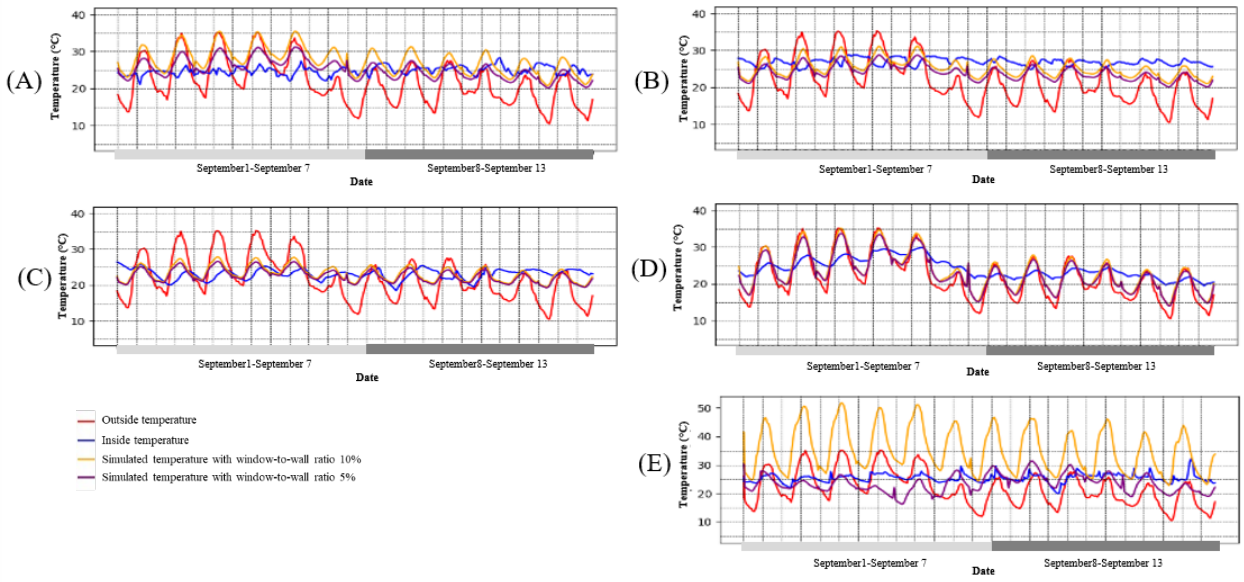

Figure 6. Thermal simulation results from September1 to September 13:
A: House A, B: Unit B, C: House C, D: House D, E: House E

DISCUSSION AND CONCLUSION

The analysis of the thermal data from simulations and real measurements of the five buildings in this inner-city neighborhood over three months revealed significant insights into the relationship between window-to-wall ratios (WWR) and internal temperature patterns. According to the results achieved from the simulation, the window-to-wall (WWR) ratio had different effects on the buildings' interior temperatures, and this effect followed a distinct pattern for each month. The results from the three months showed that in some buildings, the simulated temperature was higher than the measured temperature for both 10% and 5% WWR; in these buildings, the 10% WWR resulted in a higher simulated temperature than the 5%. In buildings where the simulated

temperature was lower than the real temperature for both 10% and 5% WWR, the 5% WWR showed a lower simulated temperature compared to the 10% WWR. Thus, while considered a major factor, the WWR cannot be the only factor to determine indoor temperature. Thus, other external factors will also need to be assessed in the next steps to develop the SciML model. Therefore, the next step in this project will be to include further factors, such as interior equipment and lighting loads, as well as external vegetation and trees, still need to be studied for their impact on indoor temperature in future work.

ACKNOWLEDGEMENT

This work was supported by the US National Science Foundation, Award # 2226880. Any opinions, findings, and conclusions or recommendations expressed in this material are those of the author(s) and do not necessarily reflect the views of the National Science Foundation.

REFERENCES

Angel, J., C. Swanston, B.M. Boustead, K.C. Conlon, K.R. Hall, J.L. Jorns, K.E. Kunkel, M.C. Lemos, B. Lofgren, T.A. Ontl, J. Posey, K. Stone, G. Takle, and D. Todey, 2018: Midwest. In Impacts, Risks, and Adaptation in the United States: Fourth National Climate Assessment, Volume II [Reidmiller, D.R., C.W. Avery, D.R. Easterling, K.E. Kunkel, K.L.M. Lewis, T.K. Maycock, and B.C. Stewart (eds.)]. U.S. Global Change Research Program, Washington, DC, USA, pp. 872–940. doi: 10.7930/NCA4.2018.CH21

Des Moines, Iowa Köppen Climate Classification (Weatherbase). (2024). Retrieved January 31, 2025, https://www.weatherbase.com/weather/weathersummary.php3?s=64527&cityname=Des+Moines,+Iowa,+United+States+of+America.

Donegan, B. (2019). The Top Cause of Weather Fatalities in Your Area May Surprise You. Retrieved August 1, 2020, from https://weather.com/safety/news/2019-09-17-top-cause-weather-fatalities-nws-cwa-united-states-map

Hajat, S., Kovats, R. S., & Lachowycz, K. (2007). Heat-related and cold-related deaths in England and Wales: who is at risk?. Occupational and environmental medicine, 64(2), 93-100. https://doi.org/10.1136/oem.2006.029017

Hoffman, J. S., Shandas, V., & Pendleton, N. (2020). The effects of historical housing policies on resident exposure to intra-urban heat: A study of 108 US urban areas. Climate, 8(1), 12. https://doi.org/10.3390/cli8010012

Kalkstein, L. (2014, November). An evaluation of air mass trends and a determination of changing weather/health responses in Polk County, Iowa [Presentation]. Polk County Health Department.

Kuras, E. R., Richardson, M. B., Calkins, M. M., Ebi, K. L., Hess, J. J., Kintziger, K. W., … & Hondula, D. M. (2017). Opportunities and challenges for personal heat exposure research. Environmental health perspectives, 125(8), 085001.

Li J, Zheng B, Bedra KB, Li Z, Chen X. Evaluating the Effect of Window-to-Wall Ratios on Cooling-Energy Demand on a Typical Summer Day. Int J Environ Res Public Health. 2021 Aug 9;18(16):8411. doi: 10.3390/ijerph18168411. PMID: 34444161; PMCID: PMC8393238.

MIT Sustainable Design Lab. (2025.). *UMI – Urban modeling interface*. Retrieved January 31, 2025, from https://web.mit.edu/sustainabledesignlab/projects/umi/index.html

Sheridan, S. (2018). Spatial Synoptic Classification. Kent State University Department of Geography. Retrieved August 18, 2019, from http://sheridan.geog.kent.edu/ssc.html

Solemma. (2025). *Climate Studio*. Retrieved, January 31, 2024, from https://www.solemma.com/climatestudio.

Simply Rhino. (2025). *Grasshopper - 3D modelling software*. Retrieved January 31, 2025, from https://simplyrhino.co.uk/3d-modelling-software/grasshopper.

The Nature Conservancy (TNC) (2019) The Green Heart Project; https://www.nature.org/en-us/about-us/where-we-work/united-states/kentucky/stories-in-kentucky/green-heart-project/ Last accessed: 02.22.2021

U.S. Energy Information Administration (EIA). (2015). Table HC 7.5: Table HC7.5 Air conditioning in U.S. homes by household income. Retrieved August 27, 2019, from https://www.eia.gov/consumption/residential/data/2015/hc/php/hc7.5.php

Voelkel, J., Hellman, D., Sakuma, R., & Shandas, V. (2018). Assessing vulnerability to urban heat: A study of disproportionate heat exposure and access to refuge by socio-demographic status in Portland, Oregon. International journal of environmental research and public health, 15(4), 640.

Wang, L., Wang, L., Li, Y., & Wang, J. (2023). A century-long analysis of global warming and Earth temperature using a random walk with drift approach. Decision Analytics Journal, 7, 100237. https://doi.org/10.1016/j.dajour.2023.100237

6th International Conference on Building Energy and Environment
Eindhoven University of Technology, The Netherlands
6 - 10 July 2025

Rethinking Retrofit Approaches: Evaluating the Impact of Occupant Heating Practices on Efficiency and Costs

Carolina Recart [1], Iris Loche[1], Lenneke Kuijer[2], Roel Loonen[1]

[1]*Department of Built Environment, Eindhoven University of Technology, Eindhoven, the Netherlands,* *c.a.recart.zapata@tue.nl*
[2]*Department of Industrial Design, Eindhoven University of Technology, Eindhoven, the Netherlands*

SUMMARY

This study evaluates the interaction effects between heating practices, such as adjusting indoor setpoint temperatures, and the calculated energy-saving potential highlighting opportunities to rethink the scale and effectiveness of retrofit strategies. Advanced energy simulations were conducted for a typical terraced house, using three different setpoint temperatures during the heating season to assess their impact on the energy performance of three retrofit scenarios: singular measures, moderate interventions, and deep retrofits. Results show that reducing setpoint temperatures alone decreased energy demand up to 45%. Additionally, the performance of deep energy retrofits was significantly diminished under lower setpoint temperatures. This finding suggests that for households with low indoor temperature settings the benefits of deep retrofits may be outweighed by their implementation costs. These results highlight the importance of considering occupant heating habits when designing retrofit strategies to optimize energy savings and improve decision-making processes.

Keywords: Heating practices, Building modelling, Energy retrofitting

1. INTRODUCTION

Deep energy retrofits have become a widely adopted strategy to enhance building performance in response to the climate crisis. While energy renovation projects in Europe progress, concerns persist about achieving climate goals within the necessary timeframe and at a reasonable cost (Eyre et al., 2023; Filippidou et al., 2018). Retrofits primarily focus on technological optimizations, such as insulation upgrades, ventilation improvements, and installation of new heating systems. However, these measures often fail to deliver the anticipated energy savings, resulting in an "energy performance gap" (Giandomenico et al., 2022).

Occupant behavior is a critical contributor to this gap, since it is hard to predict but also significantly influences a building's energy performance (Gram-Hanssen & Georg, 2018). As building envelopes and energy systems are optimized, the impact of occupant behaviour becomes even more critical (Hu et al., 2023). Yet, renovation projects rarely account for the diversity of occupant practices. Instead, they typically rely on assumptions of standardized occupancy patterns based on average energy use and heating habits (Marshall et al., 2016; Van Moeseke et al., 2024). This "one-size-fits-all" approach neglects the dynamic interplay between retrofit measures and occupant behavior, limiting the effectiveness of energy renovations (Levesque et al., 2019).

Occupant heating habits, such as the use of adjusted setpoint temperatures, can significantly impact overall energy use in buildings (Du et al., 2019; Recart et al., 2025). Studies have demonstrated

that small changes to indoor temperatures can yield significant energy savings without compromising comfort (Hoyt et al., 2015). Nevertheless, reducing indoor temperatures as a strategy to lower energy demand is often overlooked. A common argument against this approach is the concern that indoor temperatures below 18-20°C may lead to unhealthy and uncomfortable conditions (Ortiz et al., 2017). However, emerging research has challenged this assumption, demonstrating that thermal comfort can be achieved across a broader range of temperatures (Chappells, 2010; van Marken Lichtenbelt et al., 2017). For instance, Schellen et al. (2010) showed that both young adults and elderly individuals can tolerate thermal variations between 17°C and 25°C across seasons. Similarly, Van Moeseke et al. (2024) found that systematically lowering setpoint temperatures from 19°C to 15°C, combined with the use of personal insulation and heating strategies resulted in significant long-term adaptation and achieved average energy savings of 50%.

By incorporating occupant heating practices into the energy retrofit decision-making process, there is an opportunity to rethink the scale and effectiveness of energy retrofitting projects. This study investigates the potential for reducing energy demand and associated costs by integrating heating practices that extend beyond traditional comfort assumptions. In this context, we examine the potential for energy demand reduction and the associated economic implications of three different levels of energy retrofit implementation, each considering different indoor temperature scenarios.

2. METHODS

In this study, we conducted building simulations to evaluate how considering a broader range of heating habits influences the performance of energy retrofit measures. The case study focused on a standard Dutch terraced house, which constitutes approximately 40% of the residential building stock (Ministerie van Binnenlandse Zaken en Koninkrijksrelaties (BZK), 2022). For the Dutch terraced house, the exterior wall assemblies were defined as double brick walls, the floors as concrete slabs, and the roof as a pitched structure with moderate insulation. The building consists of three floors, two of which are conditioned: the ground floor and the first floor, while the second floor remains free-floating. The house is mid-row, featuring adiabatic partitions on both sides, with its main façade oriented south (See Figure 1).

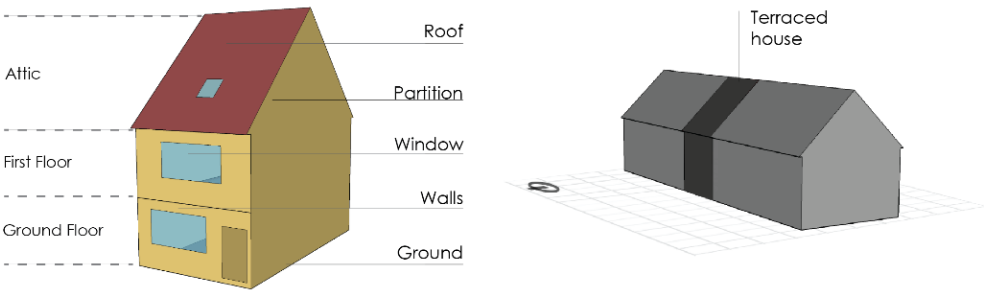

Figure 1: Terraced house - Left: schematic perspective illustrating its ground floor, first floor, and attic. Right: Schematic representation showing its spatial position.

2.1. Occupant's heating practices and general assumptions

To estimate the influence of occupant's heating practices on building energy performance, we intentionally included a broad range of occupant's heating habits, some of which deviate from traditional comfort norms. Our focus was on the adjusting setpoint and setback temperature during heating season, defined as October 1st to May 31st. We assumed full occupancy, with the ground floor used for daily activities and the first floor designated for sleeping As a benchmark, we use a setpoint of 20°C (standard) during occupied hours with a setback of 16°C for unoccupied hours. To represent a wider range of heating habits, we included two additional setpoint schemes: 18°C (SP18) and 15°C (SP15) during occupied hours, with corresponding setbacks of 14°C and 11°C for unoccupied hours as illustrated in Figure 2.

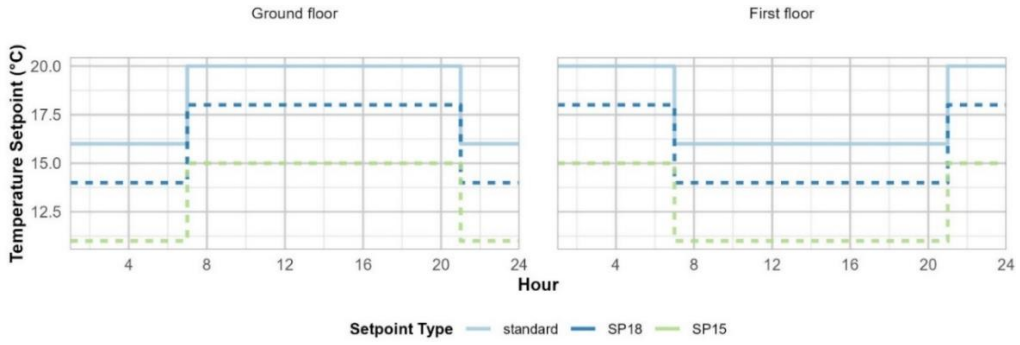

Figure 2: Daily setpoint temperatures The continuous line represents the reference setpoint, while the dashed lines indicate the temperature reduction.

2.2. Energy retrofit measures

To evaluate the impact of energy retrofitting, we introduced a series of measures aimed at improving the home's thermal performance, including single, moderate, and deep retrofits, as illustrated in Table 1: single retrofits (SR), which focus on specific thermal improvements such as walls, roofs, and windows; moderate retrofits (MR), which involve broader upgrades targeting multiple components of the building envelope; and deep retrofits (DR), which comprise comprehensive measures that significantly disrupt daily life. In total, we tested eight different strategies, each combined with various heating practices to assess their effectiveness.

Table 1: Existing conditions and energy retrofit measures for the three intervention levels

Intervention level	**No renovation**	**Single Retrofit (SR)**			**Moderate Retrofit (MR)**			**Deep Retrofit (DR)**	
Renovation measure	**Existing condition**	**SR1**	**SR2**	**SR3**	**MR1**	**MR2**	**MR3**	**DR1**	**DR2**
Walls (m^2 K/W)	0.690	2.237		-	2.237	2.237	2.237	6.250	6.250
Roof (m^2 K/W)	1.718	-	-	-	5.650	5.650	5.650	8.264	8.264
Windows (W/m^2K)	5.894	-	2.665	-	-	2.665	2.665	0.687	0.687
Partition (m^2K/W)	0.610	-	-	-	-	-	-	-	-
Ground Floor (m^2K/W)	0.758	-	-	-	-	-	-	-	-
Infiltration (ach)	0.7	-	-	0.1	-	-	0.3	-	0.1
Mechanical ventilation with heat recovery	-	-	-	-	-	-	-	80% efficiency	80% efficiency

2.3. Building simulation

The simulation model was developed using DesignBuilder v7, integrated with EnergyPlus 9.4, to represent the case study and quantify heating energy demand. We use weather data from De Bilt, the Netherlands, that provided hourly inputs for temperature, humidity, and solar radiation, all synchronized with the simulation's 10-minute time step (NEN, 2018).

2.4. Key performance indicators (KPIs)

The KPIs for evaluating energy efficiency correspond to annual space heating demand (kWh/year), expressed as percentage reduction (%). Additionally, to estimate the operational costs for each retrofit package, we applied a fixed gas price to the energy demands simulated in the study. Initial investment costs were sourced from the Kostenkentallen database, which offers detailed pricing information for various retrofit measures, including building envelope upgrades, ventilation systems, and heating systems (RVO, 2024). We calculated the simple payback periods by considering both operational cost savings and initial investments for all proposed packages, and the net present value (NPV) over a 30-year period, assuming a 5% discount rate.

3. RESULTS

3.1. Energy demand reductions

The assessment approach used in this study resulted in the development of eight renovation packages based on three different setpoint temperature profiles: Standard, SP18, and SP15. The findings shown in Figure 3, reveal that adjusting setpoint temperatures significantly impacts heating load reduction. Specifically, adopting the SP15 setpoint profile can reduce heating loads by up to 45%, while the SP18 scheme achieves a 20% reduction compared to the reference case.

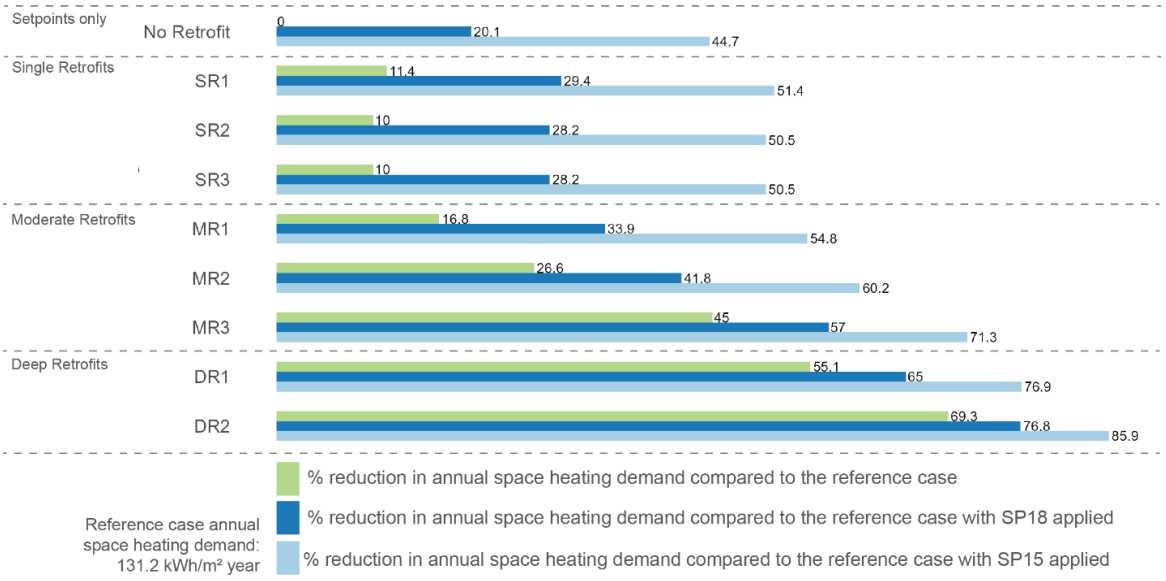

Figure 3: Energy demands reduction for retrofit packages across different setpoint temperature scenarios

The results showed that the reduction in energy demand achieved with SP18 is comparable to the outcomes of moderate retrofit packages MR1 and MR2, which yielded reductions of 17% and 27%, respectively. For single retrofits, such as cavity insulation (SR1), window upgrades (SR2), and infiltration reduction (SR3), energy savings were slightly more, ranging between 28% and 29%.

Deep energy retrofits, which include envelope improvements and mechanical ventilation with heat recovery, showed significant energy reductions, with DR1 and DR2 achieving reductions of 65% and 69%, respectively. Notably, the SP15 setpoint scheme showed the largest energy savings across all retrofit categories, even when applied to less intensive retrofit measures. For instance, single retrofit measures under the SP15 scheme achieved savings of approximately 50%, outperforming some moderate and deep retrofits using either the Standard or SP18 profiles.

3.2. Economic assessment

The payback analysis highlights a preference for implementing moderate or single retrofit measures compared to deep energy retrofits (see Figure 4). Single retrofits, such as SR1, SR2, and SR3, require lower initial investments and demonstrate shorter payback periods along with more favorable NPV. In contrast, as investment levels increase with packages like MR3, DR1, and DR2, payback periods are longer, and NPV decline, showing lower returns for higher-cost retrofits. Notably, the SP15 setpoint scheme achieved significant energy demand reductions and resulted in higher NPV across all retrofit categories. In contrasts, the SP18 profile yielded better NPV than the Standard setpoint profile, particularly for single and moderate retrofits. Despite their substantial energy-saving potential, deep retrofits may not be financially viable due to their high costs and long payback periods.

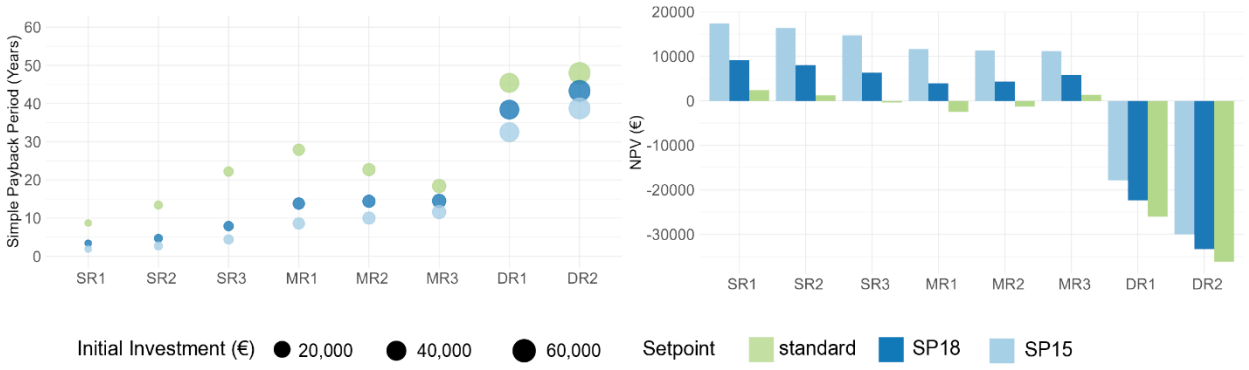

Figure 4: Left: simply payback period. Right: Net Present Value (NPV) for all retrofit packages.

4. CONCLUSIONS

This study aimed to quantify the impact of three different levels of energy retrofit implementation (single, moderate, and deep) while considering distinct heating practices to evaluate their potential for reducing energy demand and associated economic implications. By incorporating a broader range of heating habits into the retrofit decision-making process, the study highlights the opportunity to reassess the scale and design of retrofit measures. Tailoring retrofit projects to

account for heating practices can lead to solutions that are both energy-efficient and economically viable while considering the efficient use of materials and labor.
The results showed that single and moderate retrofits were the most cost-effective strategies, offering shorter payback periods and favourable NPV. These findings suggest that modest investments can achieve energy savings comparable to more extensive retrofits when combined with lower setpoints, making them practical options for budget-conscious households.

In contrast, deep retrofits, despite their significant energy-saving potential, were not financially viable due to high upfront costs and extended payback periods. This emphasizes the importance of balancing energy savings with economic feasibility. This extent of this study was limited to heating season. Additionally, we did not include thermal comfort analysis since the main focus was to explore possibilities beyond standard comfort parameters, as existing models are mainly calibrated for office settings rather than domestic buildings. Future research should build on this approach by exploring tensions between lowering setpoints, energy justice and comfort practices, and incorporating CO2 emissions of retrofit measures into the comparison.

ACKNOWLEDGEMENTS
This work was supported by the BeHeaT (Built Environment Heat Transition) program, funded by the Eindhoven Institute for Renewable Energy Systems (EIRES) at the Eindhoven University of Technology.

REFERENCES
Chappells, H. (2010). Comfort, well-being and the socio-technical dynamics of everyday life. *Intelligent Buildings International*, *2*(4), 286–298. https://doi.org/10.3763/inbi.2010.0003

Du, C., Li, B., Yu, W., Liu, H., & Yao, R. (2019). Energy flexibility for heating and cooling based on seasonal occupant thermal adaptation in mixed-mode residential buildings. *Energy*, *189*, 116339. https://doi.org/10.1016/J.ENERGY.2019.116339

Eyre, N., Fawcett, T., Topouzi, M., Killip, G., Oreszczyn, T., Jenkinson, K., & Rosenow, J. (2023). Fabric first: is it still the right approach? *Buildings and Cities*, *4*(1), 965–972. https://doi.org/10.5334/bc.388

Filippidou, F., Sandberg, N. H., Sartori, I., Nieboer, N., Vestrum, M. I., Næss, J. S., & Brattebø, H. (2018). Energy renovation rates in the Netherlands – comparing long and short term prediction methods. In *Architecture and the Built Environment*. TU Delft OPEN. https://doi.org/10.59490/abe.2018.14.3553

Giandomenico, L., Papineau, M., & Rivers, N. (2022). A Systematic Review of Energy Efficiency Home Retrofit Evaluation Studies. *Annual Review of Resource Economics*, *14*(1), 689–708. https://doi.org/10.1146/annurev-resource-111920-124353

Gram-Hanssen, K., & Georg, S. (2018). Energy performance gaps: promises, people, practices. *Building Research & Information*, *46*(1), 1–9. https://doi.org/10.1080/09613218.2017.1356127

Hoyt, T., Arens, E., & Zhang, H. (2015). Extending air temperature setpoints: Simulated energy savings and design considerations for new and retrofit buildings. *Building and Environment*, *88*, 89–96. https://doi.org/10.1016/J.BUILDENV.2014.09.010

Hu, S., Zhou, X., Yan, D., Guo, F., Hong, T., & Jiang, Y. (2023). A systematic review of building energy sufficiency towards energy and climate targets. *Renewable and Sustainable Energy Reviews*, *181*, 113316. https://doi.org/10.1016/J.RSER.2023.113316

Levesque, A., Pietzcker, R. C., & Luderer, G. (2019). Halving energy demand from buildings: The impact of low consumption practices. *Technological Forecasting and Social Change*, *146*, 253–266. https://doi.org/10.1016/J.TECHFORE.2019.04.025

Marshall, E., Steinberger, J. K., Dupont, V., & Foxon, T. J. (2016). Combining energy efficiency measure approaches and occupancy patterns in building modelling in the UK residential context. *Energy and Buildings*, *111*, 98–108. https://doi.org/10.1016/J.ENBUILD.2015.11.039

Ministerie van Binnenlandse Zaken en Koninkrijksrelaties (BZK). (2022). *Energiemodule woON 2018*. Ministerie van Binnenlandse Zaken en Koninkrijksrelaties. https://data.overheid.nl/dataset/woon#panel-description

NEN. (2018). *Hygrothermische eigenschappen van gebouwen - Referentieklimaatgegevens*.

Ortiz, M. A., Kurvers, S. R., & Bluyssen, P. M. (2017). A review of comfort, health, and energy use: Understanding daily energy use and wellbeing for the development of a new approach to study comfort. *Energy and Buildings*, *152*, 323–335. https://doi.org/10.1016/J.ENBUILD.2017.07.060

Recart, C., Loche, I., Kuijer, L., & Loonen, R. (2025). Quantifying energy efficiency potential in existing residential buildings: integrating heating practices into energy retrofit projects. *CLIMA 2025: Decarbonized, Healthy and Energy Conscious Buildings in Future Climates*.

RVO. (2024). *Kostenkentallen* . https://regelhulpenvoorbedrijven.nl/kostenkentallen/

Schellen, L., van Marken Lichtenbelt, W. D., Loomans, M. G. L. C., Toftum, J., & De Wit, M. H. (2010). Differences between young adults and elderly in thermal comfort, productivity, and thermal physiology in response to a moderate temperature drift and a steady-state condition. *Indoor Air*, *20*(4), 273–283.

van Marken Lichtenbelt, W., Hanssen, M., Pallubinsky, H., Kingma, B., & Schellen, L. (2017). Healthy excursions outside the thermal comfort zone. *Building Research and Information*, *45*(7). https://doi.org/10.1080/09613218.2017.1307647

Van Moeseke, G., De Grave, D., Anciaux, A., Sobczak, J., & Wallenborn, G. (2024). New insights into thermal comfort sufficiency in dwellings. *Buildings & Cities*, *5*(1). https://doi.org/10.5334/bc.444

6th International Conference on Building Energy and Environment
Eindhoven University of Technology, The Netherlands
6 - 10 July 2025

Earthquake damage condition to reinforced concrete building envelope system

Chu-Tsen Liao [1], Wen-I Liao [2], Chien-Kuo Chiu [3], Heui-Yung Chang [4], Chi-Ming Lai [5], Yu-Han Pai [6]

[1] *National Taiwan University of Science and Technology, Taipei, Taiwan, liaoct@mail.ntust.edu.tw*
[2] *National Taipei University of Technology, Taipei, Taiwan, wiliao@ntut.edu.tw*
[3] *National Taiwan University of Science and Technology, Taipei, Taiwan, ckchiu@mail.ntust.edu.tw*
[4] *National Chung Hsing University, Taichung, Taiwan, hychang586@dragon.nchu.edu.tw*
[5] *National Cheng Kung University, Tainan, Taiwan, cmlai@mail.ncku.edu.tw*
[6] *National Taipei University of Technology, Taipei, Taiwan, yuhan900103@gmail.com*

SUMMARY
Reinforced concrete (RC) buildings in Taiwan usually use tile as a construction finish material. The wet construction of an RC building envelope wall system consists of cement mortar, adhesive, and tiles. The layers are about 3 cm in size and could protect the RC. However, large and small earthquakes can cause varying degrees of damage to buildings. When earthquakes damage the exterior wall system, its ability to protect the building is reduced.
In this study, we set the thrust force as a seismic force to two RC specimens and controlled the story drift ratio from 0% to 0.750%. The purpose of the study is to define the condition of the exterior wall system of the RC building after an earthquake. Low and high specimen wall sizes are 180×150cm and 70×240cm. A comprehensive analysis of crack characteristics and tile adhesive strength was conducted through the failure process of the wall systems.

Keywords: envelope wall system, wet construction, earthquake damage, adhesive strength

1. INTRODUCTION

An integrated building is constructed with a structural framework enveloped by an outer shell. The building envelope system protects the building structure from external environmental impacts, thereby ensuring the building's durability. Taiwan, located on the Pacific Ring of Fire, frequently experiences tectonic movements that cause earthquakes. Large and small earthquakes can cause varying degrees of damage to buildings, with seismic zones experiencing more damage. When the building envelope system is damaged, its ability to protect the building is reduced. While previous earthquake damage assessments have primarily focused on building structures, our research emphasizes the importance of building envelope systems in addressing durability issues.

Taiwan has high temperatures and humidity, and the exterior walls of reinforced concrete (RC) buildings often use tiles as building envelope materials. The building envelope used in the wet construction process typically involves several steps, including the structural framework, cement mortar layer, waterproofing layer, and adhesive layer, depending on the requirements of the construction companies. This study conducts cyclic thrust experiments on walls to observe the location of shear cracks during the displacement process and the width of the maximum and residual cracks. The research aims to identify the key factors influencing the pull-off strength of building envelope material.

2. EXPERIMENTAL PROGRAM

The tile installation consists of the following steps: structural layer, cement mortar layer, and adhesive layer. (Figure 1) The tile size is 4.5 × 9.5 cm. Two specimens have dimensions of 180 × 150 cm (code name: 1815) and 70 × 240 cm (code name: 0724). The tile pull-off areas of specimen 1815 are divided into five zones along the diagonal, including left, right, upper, lower, and diagonal sections. Each zone contains nine pull-off test positions, totaling 48 pull-off test positions across the entire wall. (Figure 2) Taking the left zone as an example, it is divided into three sections from bottom to top: sections 1, 2, and 3, each having three pull-off test positions. During the first cycle of 0.000% drift ratio, the pull-off test is conducted in section 1; at 0.375%, the test is conducted in section 2; and at 0.750%, the test is conducted in section 3.

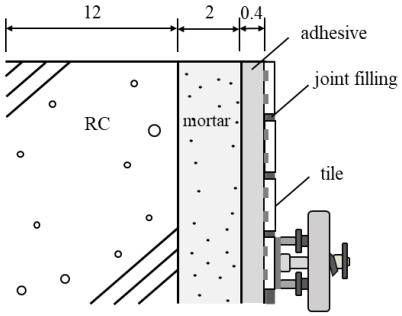

Figure 1. Diagram of the wall section and pull-off testing machine (Unit: cm)

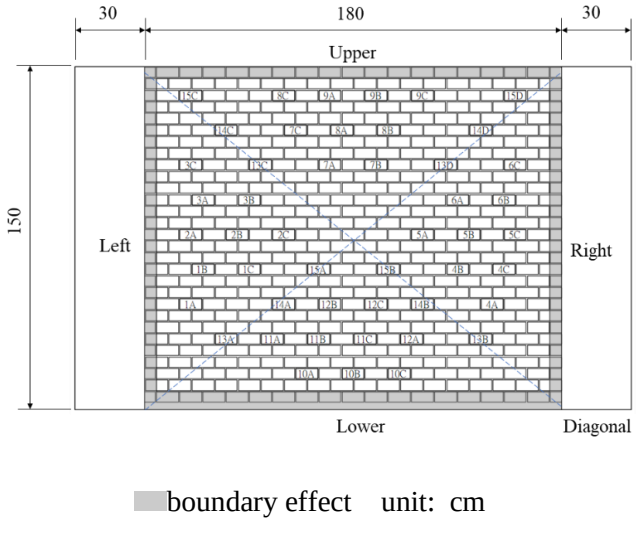

Figure 2. Specimen 1814 plan

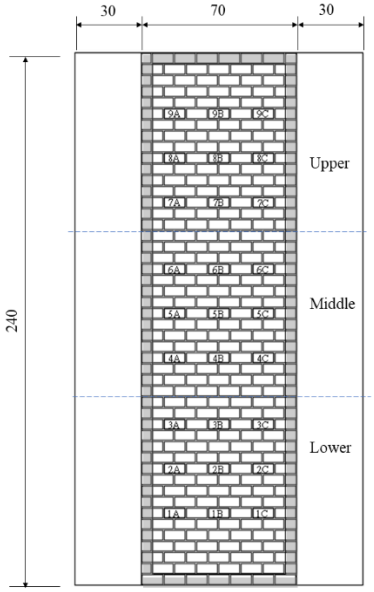

Figure 3. Specimen 0724 plan

The tile pull-off areas of specimen 0724 are divided into three zones, including upper, middle, and lower sections. Each zone contains nine pull-off test positions, totaling 27 pull-off test positions across the entire wall. (Figure 3) Taking the lower zone as an example, it is divided into three sections from bottom to top: sections 1, 2, and 3, each having three pull-off test positions. During the first cycle of 0.000% drift ratio, the pull-off test is conducted in sections 1- 1A,1B, and 1C; at 0.375%, the test is conducted in sections 2- 2A,2B, and 2C; and at 0.750%, the test is conducted in sections 3- 3A,3B, and 3C.

This study involves a cyclic thrust experiment, where the specimen undergoes repeated lateral thrust. The rift ratio (%) is calculated using the displacement (cm) parameter, as shown in Equation (1). In this equation, Δh represents the displacement between the original center of the specimen and the displaced position after thrust, and H denotes the height of the specimen.

$$(\text{Drift Ratio}) = \frac{\Delta_h}{\mathrm{H}} \quad (1)$$

Zone 1, 4, 7, 10, and 13 of 1815 are designated the control group before the main loading. During the first cycle at a drift ratio of 0.375% (displacement of 0.675 cm), pull-off tests are conducted in zones 2, 5, 8, 11, and 14. During the first cycle at a drift ratio of 0.750% (displacement of 1.350 cm), pull-off tests are conducted in zones 3, 6, 9, 12, and 15. (Table 1)

Table 1. Experimental setup

Specimen	Aspect Ratio (cm)	Drift ratio (%) of cyclic thrust experiments	Drift ratio (%) for pull-off testing	Pull-off test zones
1815	180 ×150	From 0.000% to 0.750%	0%	1(Left)、4(R)、7(U)、10(Lower)、13(D)
			0.375%	2(Left)、5(R)、8(U)、11(Lower)、14(D)
			0.750%	3(Left)、6(R)、9(U)、12(Lower)、15(D)
0724	70 ×240	From 0.000% to 0.750%	0%	1(Lower)、4(M)、7(U)
			0.375%	2(Lower)、5(M)、8(U)
			0.750%	3(Lower)、6(M)、9(U)

3. TEST RESULTS

3.1. Pull-off strength and crack width of specimen 1815

Before conducting the thrust experiment, 16 data for pull-off strength were obtained from different zones. The highest strength was 5.97 kN in 4C, while the lowest was 2.20 kN in 13C. At a drift ratio of 0.125% with a displacement of 0.225 cm, the first cycle produced flexural cracks of 0.20 mm and shear cracks of 0.40 mm. When returning to zero in the first cycle, the flexural crack width was 0.03 mm, and the shear crack width was 0.10 mm. (Figure 4, Table 2)

At a drift ratio of 0.375% with a displacement of 0.675 cm, the first cycle produced flexural cracks of 0.20 mm and shear cracks of 1.30 mm. When returning to zero in the first cycle and thrust of 1612.23 kN, the flexural crack width was 0.10 mm, and the shear crack width was 0.50 mm. Three tiles had already fallen off during the pull-off test, resulting in 13 data. The maximum pull-off strength was 5.20 kN in 11B, while the minimum was 0.81 kN in 11A.(Figure 5, Table 2)

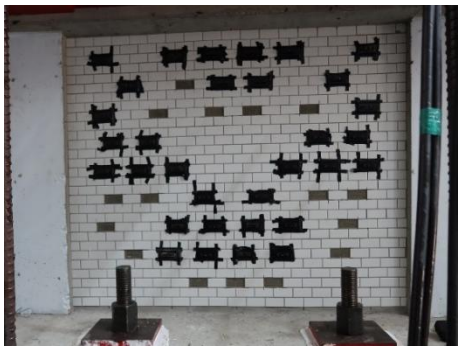

(a) Specimen photo

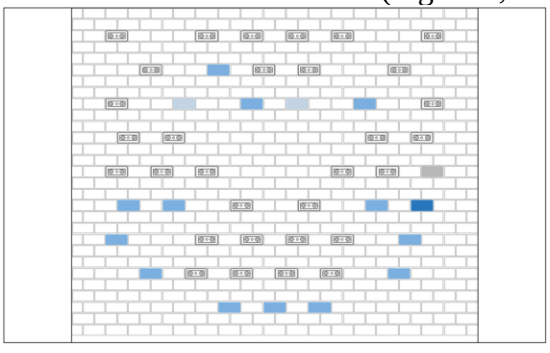

(b) Damage record

Figure 4. 1815-1 Drift ratio 0.000%

At a drift ratio of 0.750% with a displacement of 1.350 cm, the first cycle produced flexural cracks of 0.60 mm and shear cracks of 3.00 mm. When returning to zero in the first cycle and thrust of 2029.17 kN, the flexural crack width was 0.20 mm, and the shear crack width was 1.25 mm. Eight tiles had already fallen off during the pull-off test, resulting in 8 data. The maximum pull-off strength was 4.75 kN in 9B; the minimum was 0.34 kN in 12A. During the third cycle, the wall was destroyed, and the failure strength was 1362.4 kN. (Figure 6, Table 2)

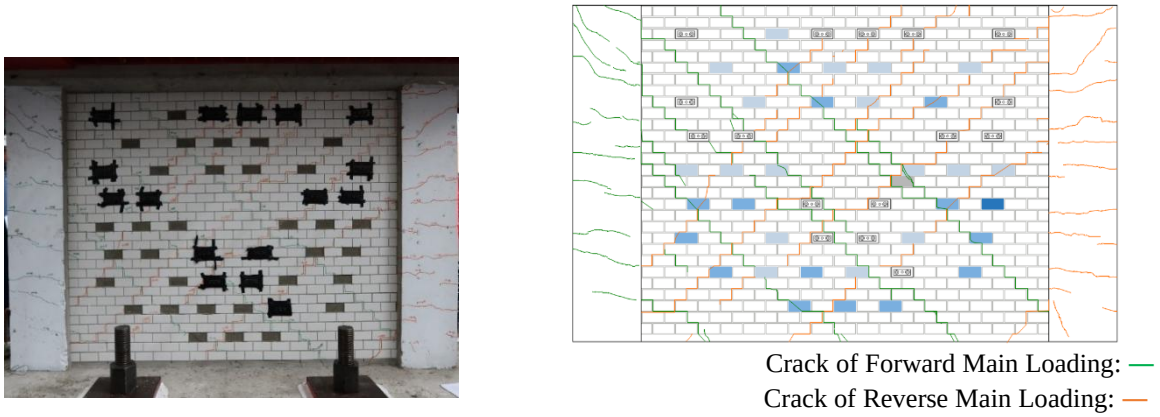

(a) Specimen photo (b) Damage record

Figure 5. 1815-1 Drift ratio 0.375%

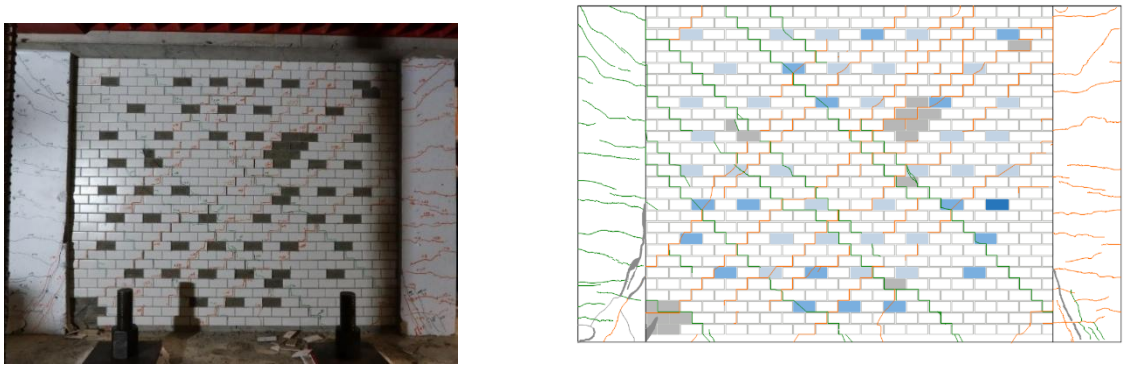

(a) Specimen photo (b) Damage record

Figure 6. 1815-1 Drift ratio 0.750%

Table 2. Crack and Strength Record for 1815 Cyclic Thrust Experiments

Zone	Drift ratio (%)	Displacement (cm)	Cycle		Maximum crack width (mm) flexural (Horizontal, vertical)	Maximum crack width (mm) shear (Diagonal)	Residual cracks width(mm) flexural (Horizontal, vertical)	Residual cracks width(mm) shear (Diagonal)	Pull-off Test Strength(kN) A	B	C	D
1									3.45	5.56	5.69	
4									3.20	3.72	5.97	
7	0.000	0.000	none		–	–	–	–	4.01	0.89	5.26	–
10									5.59	4.07	4.73	
13									3.44	4.47	2.20	3.58
all	0.125	0.225	1	+	0.20	0.40	0.03	0.10		–		
				-	0.25	0.45						
			3	+	0.25	0.55	0.05	0.15		–		
				-	0.25	0.55						
all	0.250	0.450	1	+	0.30	0.65	0.08	0.25		–		
				-	0.30	0.75						

			3	+	0.35	0.85	0.10	0.30			–		
				-	0.30	0.65							
2				+	0.20	1.30			1.69	N	N		
5									2.21	0.86	N		
8			1				0.10	0.50	N	2.11	1.27		–
11	0.375	0.675		-	0.40	1.20			0.34	5.20	2.11		
14									1.54	0.76	2.56	0.55	
all			3	+	0.30	1.40	0.10	0.55			–		
				-	0.40	1.50							
all	0.500	0.900	1	+	0.40	4.00	0.15	0.60			–		
				-	0.45	1.70							
			3	+	0.30	1.50	0.15	2.20			–		
				-	0.45	3.50							
3				+	0.60	3.00			N	N	1.54		
6									N	1.45	N		
9	0.750	1.350	1				0.20	1.25	N	4.75	N		–
12				-	0.40	3.50			0.34	0.61	N		
15									0.46	0.81	N	4.12	

3.2. Pull-off strength and crack width of specimen 0724

Before conducting the thrust experiment, 9 data points for pull-off strength were obtained from different zones. The highest strength was 9.77 kN in 1A, while the lowest was 4.72 kN in 7B. At a drift ratio of 0.125% with a displacement of 0.3375 cm, the first cycle produced flexural cracks of 0.10 mm and shear cracks of 0.05 mm. When returning to zero in the first cycle, the flexural crack width was 0.015 mm, and the shear crack width was 0.01 mm.(Figure 7-8, Table 3)

At a drift ratio of 0.375% with a displacement of 1.0125 cm, the first cycle produced flexural cracks of 0.15 mm and shear cracks of 0.30 mm. When returning to zero in the first cycle and thrust of 594.41 kN, the flexural crack width was 0.03 mm, and the shear crack width was 0.06 mm. The maximum pull-off strength was 6.79 kN in 8B, while the minimum was 0.74 kN in 2B. (Figure 7-8, Table 3)

At a drift ratio of 0.750% with a displacement of 2.025 cm, the first cycle produced flexural cracks of 0.35 mm and shear cracks of 0.35 mm. When returning to zero in the first cycle and thrust of 778.35 kN, the flexural crack width was 0.04 mm, and the shear crack width was 0.06 mm. The maximum pull-off strength was 6.41 kN in 9A; the minimum was 0.52 kN in 6C. (Figure 7-8, Table 3)

Figure 7. 0724 Specimen photo - Drift ratio 0.000%(Left), 0.375%(Middle), 0.750%(Right)

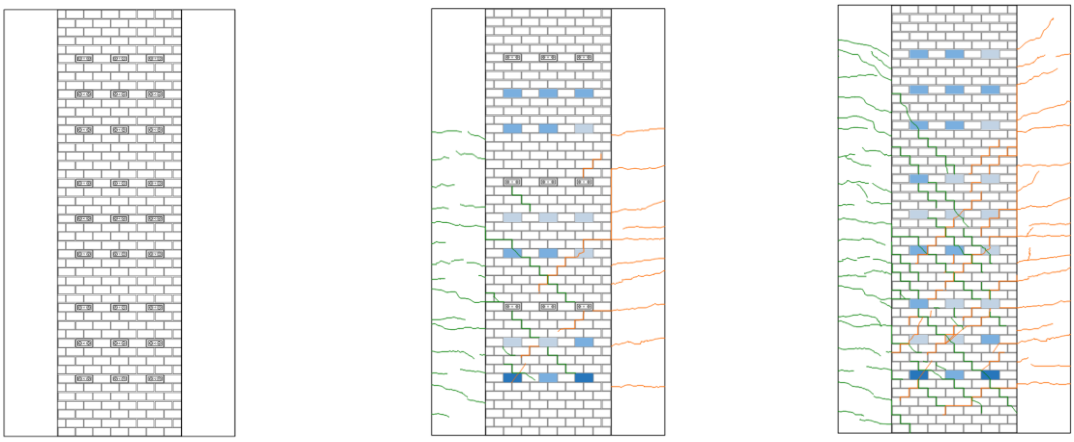

Crack of Forward Main Loading: — Crack of Reverse Main Loading: —

Figure 8. 0.24 Damage record - Drift ratio 0.000%(Left), 0.375%(Middle), 0.750%(Right)

Table 3. Crack and Strength Record for 1815 Cyclic Thrust Experiments

Zone	Drift ratio (%)	Displacement (cm)	Cycle		Maximum crack width (mm)		Residual cracks width (mm)		Pull-off Test Strength(kN)		
					flexural (Horizontal, vertical)	flexural (Horizontal, vertical)	flexural (Horizontal, vertical)	shear (Diagonal)	A	B	C
1 4 7	0.000	0.0000	none		–	–	–	–	9.77 8.04 5.89	7.84 6.03 4.72	8.49 3.60 3.56
all	0.125	0.3375	1	+ -	0.10 0.15	0.05 0.05	–	–		–	
			3	+ -	– –	– –	0.015	0.01			
all	0.250	0.6750	1	+ -	0.15 0.20	0.20 0.20	–	–		–	
			3	+ -	– –	– –	0.02	0.03			
2 5 8 all	0.375	1.0125	1	+ -	0.15 0.40 0.15	0.30 0.30 0.30	–	–	3.03 2.49 4.64	0.74 3.45 6.79	4.40 2.71 5.37
			3	+ -	– –	– –	0.03	0.06		–	
all	0.500	1.3500	1	+ -	0.20 0.40	0.35 0.30	–	–		–	
			3	+ -	– –	– –	0.03	0.04			
3 6 9 all	0.750	2.0250	1	+ -	0.35 0.35 0.35	0.35 0.35 0.35	–	–	4.47 4.27 6.41	2.87 0.53 6.39	1.31 0.52 3.77
			3	+ -	– –	– –	0.04	0.06		–	
all	1.000	2.7000	1	+ -	1.70 0.40	0.40 0.40	–	–		–	
			3	+ -	– –	– –	0.65	0.08			
all	1.250	–	1	+ -	2.90 2.00	0.30 0.45	–	–		–	
			3	+ -	– –	– –	0.95	0.10			
all	1.500	–	1	+ -	2.20 3.50	0.20 0.60	–	–		–	

			3	+	–	–	0.75	0.25		
				-	–	–				
all	2.000	–	1	+	3.50	0.30	–	–	–	
				-	2.20	1.00				
			3	+	–	–	1.30	0.65		
				-	–	–				

Table 4. Average strength of Pull-off tests

	1815 Cyclic Thrust Experiments						0724 Cyclic Thrust Experiments					
Drift Ratio	0.000%		0.375%		0.750%		0.000%		0.375%		0.750%	
Displacement (cm)			0.675		1.350				1.0125		2.0250	
Maximum displacement force (kN)			1612.23		2029.17				594.41		778.35	
	Area	kN	Area	kN	Area	kN	Area	kN	Area	kN	Area	kN
Left	1	4.90	2	1.69	3	1.54	–	–	–	–	–	–
Right	4	4.30	5	1.54	6	1.45	–	–	–	–	–	–
Upper	7	3.39	8	1.69	9	4.75	7	4.72	8	5.60	9	5.52
Lower	10	4.80	11	2.55	12	0.48	1	8.70	2	2.72	3	2.88
Diagonal	13	3.42	14	1.35	15	1.80	–	–	–	–	–	–
Middle	–	–	–	–	–	–	4	5.89	5	2.88	6	1.77
Average		4.16		1.76		2.00		6.44		3.74		3.39

Table 4 presents the average pull-off strengths of walls 1815 and 0724. For wall, 1815:The average strengths of the left zone at drift ratios 0.000%, 0.375%, and 0.750% are 4.90 kN, 1.69 kN, and 1.54 kN. The right zones are 4.30 kN, 1.54 kN, and 1.45 kN. The upper zones are 3.39 kN, 1.69 kN, and 4.75 kN. The lower zones are 4.80 kN, 2.55 kN, and 0.48 kN. The diagonal zones are 3.42 kN, 1.35 kN, and 1.80 kN. The average strengths across all regions are 4.16 kN, 1.76 kN, and 2.00 kN. At 0.375%, the highest pull-off strength, 5.20 kN, occurred at location 11B, where no surrounding cracks were observed. The strength at a drift ratio of 0.375% was reduced by 2.36 times compared to 0.000%. At 0.750%, the reduction was less pronounced. This was due to locations 9B and 15D maintaining high strengths of 4.75 kN and 4.12 kN despite unidirectional cracks caused by shear forces.

For wall 0724:The average strengths of the upper zone at drift ratios 0.000%, 0.375%, and 0.750% are 4.72 kN, 5.60 kN, and 5.52 kN. The middle zones are 5.89 kN, 2.88 kN, and 1.77 kN. The lower zones are 8.70 kN, 2.72 kN, and 2.88 kN. The average strengths across all regions are 6.44 kN, 3.74 kN, and 3.39 kN. At a drift ratio of 0.375%, the highest pull-off strength, 6.79 kN, occurred in the upper zone at location 8B, with no surrounding cracks observed. The strength at 0.375% was reduced by 1.72 times compared to 0.000%. At a drift ratio of 0.750%, the reduction factor was 1.90 compared to 0.000%. The highest pull-off strength at 0.750% was 6.41 kN in the upper zone at location 9A.

4. CONCLUSION

This study conducted Cyclic Thrust Experiments on walls with different drift ratios to observe the shear crack locations, the widths of the maximum and residual cracks, and the displacement process. The influence of cracks caused by seismic loading on pull-off strength was analyzed. The key conclusions are as follows:

4.1. Crack Characteristics

Most of the cracks formed along the grout of the tiles. As the thrust increases, the width and the number of cracks increase. In wall 1815, drift ratios of 0.125%, 0.375%, and 0.750%, the residual shear cracks increased from 0.10 mm, 0.50 mm to 1.25 mm, while the maximum cracks were 0.45 mm, 1.20 mm, and 3.50 mm. In wall 0724, drift ratios of 0.125%, 0.375%, and 0.750%, the residual shear cracks increased from 0.01 mm, 0.06 mm to 0.06 mm, while the maximum cracks were 0.05 mm, 0.30 mm, and 0.35 mm. The residual cracks in the shear direction of the two walls differ by a factor of 10.

Cracks that pass through behind the tiles will affect pull-off strength. For example, a drift ratio of 0.375% in wall 1815,11B, which had no cracks, showed the highest strength at 5.20 kN. 11A, with forward and reverse shear cracks passing through, had the lowest strength at 0.34 kN.

At location 2B of wall 0724, both forward and reverse directional cracks intersect, resulting in the lowest strength of 0.74 kN. In contrast, at location 8B, no cracks are present, and the highest strength of 6.79 kN is recorded. At a drift ratio of 0.750%, the overall strength generally decreases. For wall 1815, location 9B has the highest strength of 4.75 kN, with only unidirectional cracks appearing along the grooves (Figure 9.a). For wall 0724, location 9A, with no intersecting cracks, achieves the highest strength of 6.41 kN. (Figure 9.b)

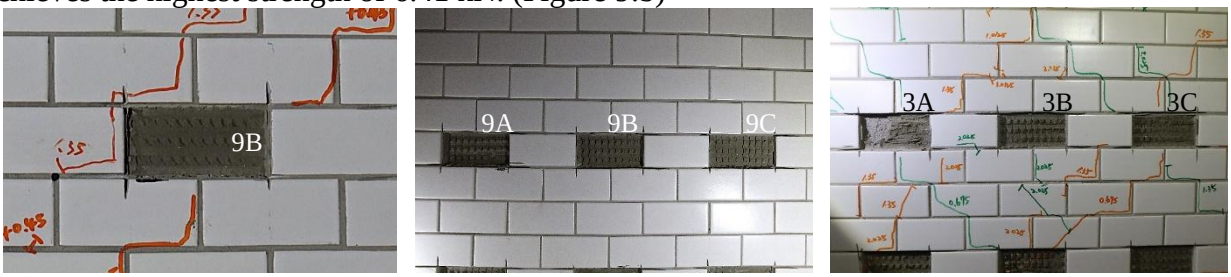

(a) 1815:9B (b) 0724:9A 9B 9C 0724:3A 3B 3C

Figure 9. Drift Ratio 0.750% Cycle1 Maximum pulling force position

4.2. The pull-off strength differences between shear short walls and flexure tall walls

Cyclic Thrust Experiments caused X-shaped shear diagonal cracks on the 1815 short wall. At a drift ratio of 0.375%, the strength decreased by 2.36 compared to 0.000%. At 0.375%, 4 tile specimens had already fallen off the wall surface; by 0.750%, 8 tile specimens had fallen off.

Cyclic lateral loading caused flexural cracks on the 0724 tall wall, concentrated at the bottom of the specimen. At a drift ratio of 0.375%, the strength decreased by 1.72 compared to 0.000%. During the pull-off test at a drift ratio of 0.750%, the upper zone (e.g., 9A, 9B, 9C) exhibited the highest pull-off strength, with no cracks (Figure 9.b). In contrast, the lower zone (e.g., 3A, 3B, 3C) showed significant intersecting bidirectional cracks (Figure 9.c).

At a drift ratio of 0.375%, the strength of the short wall decreased significantly compared to the tall wall. Both walls showed noticeable strength reduction at 0.375%, but no further reduction occurred at 0.750%.

According to the National Standards of the Republic of China, the adhesion strength is 2.565 kN. For wall 0724, only the strength in Zone 6 at 0.750% fell below the standard value, while all other average strengths exceeded the standard. In contrast, the average strength of wall 1815 at 0.375% was 1.45 times lower than the standard value. During the experiment, the surface tiles on the tall wall retained their adhesive strength and did not fall off, resulting in an overall higher average pull-off strength than the short wall.

ACKNOWLEDGEMENTS

This study was supported by the National Science and Technology Council (NSTC) of the Republic of China (ROC in Taiwan through Project No. NSTC 112-2625-M-011-006 -

REFERENCES

Chu-Tsen Liao, Chih-Chieh Lin, Min-Ju Lu and Meng-Hsiu Chang, 2023. Research on the Proportion and Strength of Joint Filler Materials for External Wall Tiles, Key Engineering Materials, Vol. 970, pp. 87-92.

Yagi Shotaro, Teramoto, Atsushi, Yeow Trevor, Seike Tsuyoshi, Kusunoki Koichi, and Nakamura Izumi, 2021. Validating Resilient Detailing of Japanese Ceilings, Windows, and Wall Tiles Using an E-defense Shake-table Test, Journal of Earthquake Engineering, Vol. 26, Issue 16, pp. 8525-8551.

Wen-I Liao, Fang-Fei Lin, Syuan-Jhen Chen, Yu-Ze Chen, 2025. Experimental and Simulation Study on the Residual Seismic Performance of Low-Rise Earthquake-Damaged Reinforced Concrete Walls, Structural Engineering, Vol. 40, No. 1, pp. 51-68.

Advancing Personalized Environmental Control Systems (PECS): Performance, Design, and User Experience (13:30-15:00 h)

6th International Conference on Building Energy and Environment
Eindhoven University of Technology, The Netherlands
6 - 10 July 2025

PECS Performance Evaluation: Simulation methods and metrics

Douaa Al-Assaad[1,2], Jianlei Niu[3]
[1]KU Leuven, Gent, Belgium, douaa.al-assaad@kuleuven.be, [2]TU Eindhoven, Eindhoven, the Netherlands
[3]The Hong Kong Polytechnic University, Hong Kong, China, jian-lei.niu@polyu.edu.hk

SUMMARY
The building sector faces challenges in balancing occupant comfort and resource efficiency. Indoor environmental quality (IEQ) systems often regulate entire spaces, including unoccupied areas, leading to resource waste and unguaranteed comfort. This has spurred the development of personalized environmental control systems (PECS), which adjust IEQ conditions to individual occupants' needs, enhancing comfort while potentially reducing energy use through effective design and operation. PECS have been studied using simulation and experimental methods, with their performance reported using diverse methods metrics. In this study, the results from a literature review conducted in the framework of IEA EBC's Annex 87 (Subtask D) on PECS will be presented. The objective of the review is to give an overview of different PECS performance simulation evaluation methods (building simulations, computational fluid dynamics), approaches and KPIs used to assess thermal comfort & IAQ.
Keywords: personalized ventilation, CFD simulations, experiments, key performance indicators

1. REVIEW METHODOLOGY AND OVERVIEW OF STUDIES

This review was carried out following the Preferred Reporting Items for Systematic Reviews and Meta-Analyses (PRISMA) statement. An extensive literature search was conducted, targeting publications from 1990 to 2023. Databases searched include namely Web of Science, ScienceDirect, PubMed and Scopus. Keywords were grouped into three levels: (i) general context ("built environment", "indoor environment", "occupant", "human", "user", "system", "HVAC"), (ii) PECS-specific terms ("personal", "personalized", "individual", "micro", "local", "centric", "portable"), and (iii) evaluation methods ("simulations", "computational fluid dynamics", "chamber studies", "lab studies", "field studies", "experiment"). An extensive number of potential publications was obtained, out of which studies unrelated to PECS or typically encountered indoor environmental conditions were excluded yielding a total of 302 papers. From the final pool of selected papers, the studies were classified depending on the adopted PECS evaluation method(s): a) Building simulations (BS), b) Computational fluid dynamics (CFD) studies, c) chamber or lab studies (CS) and c) field studies (FS) and relevant methodological elements were extracted. CS was the most common method (174 studies) used in the literature, followed by CFD (81 studies), BS (30 studies) and finally FS (17 studies). In this work, BS and CFD studies will be highlighted. PECSs were further classified into thermal management PECS regulating only the body's heat loss mechanisms "thermal PECS". When additionally regulating IAQ, they were referred to as "thermal+IAQ PECS". Moreover, the mobility of the PECS was defined and used in the classification. Building attached PECS refers to devices that are integrated within the building envelope. Semi-detached refers to PECS that have more degrees of freedom in certain planes and can be attached to the furniture. Detached PECS refer to PECS that are portable and independent from the building. Other refers to vehicles or aircrafts.

Figure 1 illustrates the chronological progression of simulation studies on PECS. Since 2010, there has been a notable rise in studies using Building Simulation (BS) and Computational Fluid Dynamics (CFD). Notably, no IAQ-only PECS were assessed using BS, likely due to the typical assumption of uniform zonal conditions, which limits BS's ability to evaluate air quality. Detached

thermal PECS became a common focus in BS studies from 2017, with a peak in 2022. CFD, offering detailed insights into temperature and airflow in microenvironments, was used more frequently than BS. Throughout the years, building-attached or semi-detached PECS addressing both thermal and IAQ control were consistently studied. Most of these involved ceiling- or desk-mounted personalized ventilation systems delivering conditioned outdoor air.

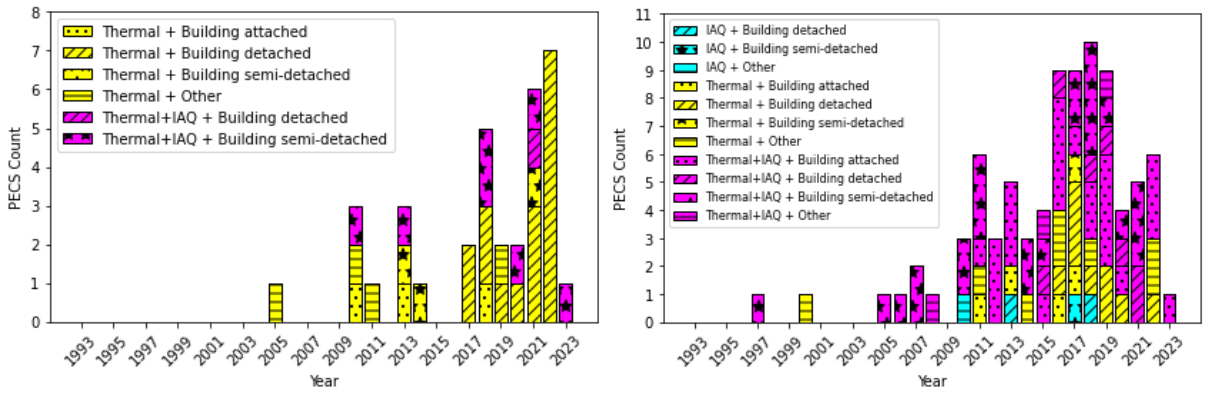

Figure 1. Illustration of the chronological evolution of PECSs' simulation studies: BS (left), CFD (right)

1.1 Building simulations

Three different approaches were identified in the literature to integrate PECSs into BS tools: direct, collaborative and custom. Direct approaches model PECSs and its operation directly into the computational domain in the building simulation tool. **Figure 2** presents the use of these methods to simulate the different types of PECS. Direct approaches were possible with tools such as IES-VE and IDA-ICE and were used for thermal chairs (Shahzad et al., 2018) (thermal, building detached PECS) and personalized ventilation (PV) (Lipczynska et al., 2021) (thermal+IAQ, building semi-detached PECS). These tools allow for some degree of spatial granularity when simulating PECS. However, their accuracy was not proven as validation studies were either not conducted or conducted without the presence of PECS. Collaborative approaches model used BS tools (Modelica, Energy plus, etc.) to model the building and its general systems and couple the PECS externally as a boundary condition. They were used mainly for building detached thermal PECS (e.g., desk fans, thermal chairs, foot heaters, heated furniture). This was done via coupling with thermoregulation models (Boudier & Hoffmann, 2022)or PECSs' performance curves (Veselý et al., 2019). Collaborative methods did not consider the interaction between the PECS and the background environment. The limitations associated with the first two methods gave rise to the final integration method – the custom method; where authors develop their own code of the building its systems and the PECS. These codes differ in their level of space discretization. The simplest ones divide the space into two interacting zones: an occupied zone with PECS and the second zone representing the rest of the space and more complex codes discretize the macroclimate and microclimate control volumes into multi-layers (Al Assaad et al., 2018; Jain & Shorey, 2015). Thus, custom codes consider the interaction between the PECS and the background environment. They were the most consistently used method across all PECS types.

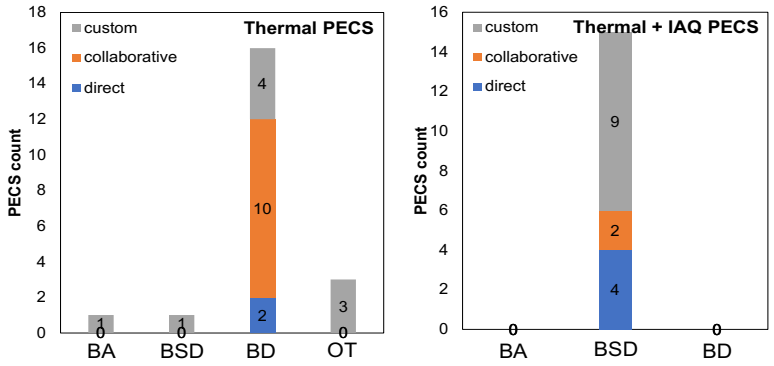

Figure 2. Different integration methods of building attached (BA), building semi-detached (BSD), building detached (BD) and other (OT) (i.e., vehicles) thermal and thermal+IAQ PECS into BS.

Figure 3 illustrates the different approaches used to assess thermal comfort using BS. 3 approaches were mainly used. The most common one was to couple the BS model with thermophysiological models (AUB (Salloum et al., 2005), Tanabe (Takahashi et al., 2021)) and sensation/comfort models (Zhang's (Zhang et al., 2010a)). The outputs were a thermal sensation and comfort votes on a 9 pt scale assessed for cases with and without PECS. This approach was used for building detached thermal PECS and semi-detached thermal+IAQ PECS in tandem with custom and collaborative methods. The second most used approach was the PMV/PPD used across all PECS types and for all three integration methods. However, its implementation was not always clarified. Finally, the third approach was via subjective experiments conducted in climatic chambers or field tests. Other approaches used include the adaptive comfort model, regression equations for thermal comfort derived from the first approach, and temperature and RH(%) levels falling within certain ranges. For IAQ, it was only assessed in two studies on PV (Al Assaad et al., 2018; Harrouz et al., 2023) using custom integration approaches as BS tools were meant for thermal/energy simulations. In these custom codes, the species' transport equations were solved and key performance indicators such as the ventilation effectiveness and CO_2 removal rates from the indoor air were calculated.

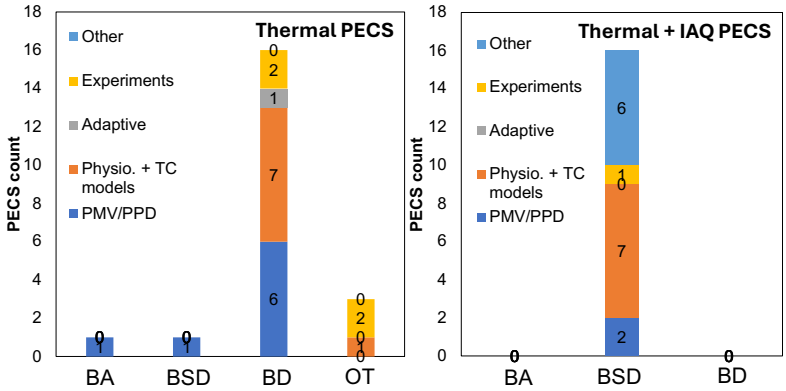

Figure 3. Comfort evaluation methods of building attached (BA), building semi-detached (BSD), building detached (BD) and other (OT) (i.e., vehicles) thermal and thermal+IAQ PECS using BS

1.2 CFD simulations

Computational fluid dynamics (CFD) serves as a powerful tool offering a detailed visual analysis of the performance of PECS in indoor built environments. Ensuring high-quality simulations requires a well-managed numerical modelling process accounting for the geometry including the

computational thermal manikin (CTM), grid generation and refinement, turbulence models, numerical schemes and boundary conditions. Implementation of realistic CTM with humanoid shapes guarantees an accurate prediction of the convective heat transfer between the body surface and ambient environment, radiant heat transfer between the body and walls and the buoyancy driven thermal plume. **Table 1** presents the adopted mesh types/metrics and CTM types in PECS CFD studies. In the PECS literature, only Reynolds-Averaged Navier-Stokes (RANS) models have been used, due to their balance between computational efficiency and accuracy. Among these, the most commonly used was the Re-Normalization Group (RNG) k–ε model (30%), followed by the realizable k–ε model (18%), the standard k–ε model (10%), the shear stress transport (SST) k–ω model (6%), the Reynolds Stress Model (RSM) (3%)—often combined with Lagrangian particle tracking—and the zero-equation model (1%). Notably, 15% of studies did not report the airflow model used, while 19% provided only partial information (e.g., referring simply to a "k–ε model"). From the 81 main studies, 62 validate with their own experimental data from climatic chamber experiments or field tests, 12 validate from published experimental data sets in the literature and 7 studies do not mention any validation.

Table 1. Adopted mesh types and mesh metrics in PECS CFD studies

Mesh type	**(%) of studies***
Hexahedral structured	14%
Tetrahedral/polyhedral unstructured	43%
Hybrid	8%
Mesh metrics	**(%) of studies**
Skewness	Only 26% report 1 or 2 of these metrics
Aspect ratio	
Orthogonality	
Grid growth rate	
Mesh sensitivity analysis	40%
CTM	**(%) of studies**
realistic	54%
simplified	21%
rectangular	15%
single segment	10%

**35% of studies do not detail their adopted mesh*

In the literature, different methods were adopted to assess the thermal comfort performance of PECS. The methods varied in complexity and were not particularly motivated by the specific PECS type. The coupling of physiological models as done in (Gao et al., 2006), (Zhang (Zhang et al., 2010b), Radtherm software including the Fiala model (Fiala et al., 2001), AUB (Al-Othmani et al., 2008; Salloum et al., 2005)) and Zhang's thermal sensation and comfort models (Zhang et al., 2010c) with CFD models were the most common method for all PECS types. The coupling was often clearly laid out in the studies with explanatory flow charts. The second approach was to use psychological rational models such as the PMV/PPD, standard effective temperature (SET) and equivalent temperature (ET) at segmental level. In the latter, the studies do not detail all the necessary inputs to calculate these quantities. Few studies on convective-based PECS additionally assess the DR, turbulence and airflow fluctuation frequencies (Conceição & Awbi, 2021). All CFD studies utilize temperature and velocity contours to further support their conclusions. To study the

IAQ performance of PECS, studies can be classified depending on their scope into 3 main categories:
C1: Studies assessing IAQ performance with respect to non-infectious exogenous or endogenous pollutants/**C2:** Studies assessing the ability of the PECS in protecting occupants from cross contamination due to exposure to infectious aerosols & **C3:** Studies that assess IAQ indirectly via air renewal metrics that evaluate the amount of clean air delivered to the occupant. Note that some studies can belong to multiple categories. **Figure 4** shows the used KPIs for IAQ assessment and occurrence frequency per category and PECS type. The intake fraction (iF) (i.e., ratio of mass inhaled over mass emitted) was the most used KPI across all study scopes followed by the normalized concentration. The ventilation effectiveness was the second most used KPI for C1.

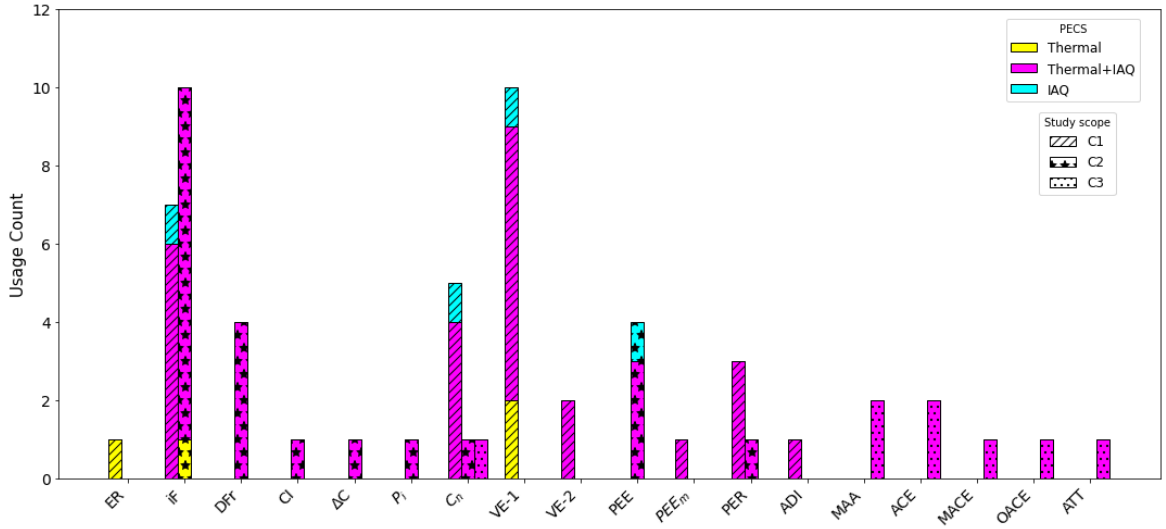

Figure 4. Usage count of KPIs used in CFD studies per PECS type and study scope (C1, C2, C3)

3. CONCLUSION

Building energy simulation tools offer significant advantages in modelling and optimizing PECSs, particularly given the limited market availability of such systems. However, several limitations remain, particularly concerning model accuracy and the lack of validation, as opposed to CFD analysis. On the other hand, CFD requires careful selection of simulation time steps, mesh refinement, and convergence criteria, all of which ensure numerical stability and reliability. In terms of methods and KPIs, various methods exist with no specific selection criteria. Currently, in the literature, there are no standardized ways in which PECSs' performance could be assessed and reported. Future work should focus on formulating such guidelines and recommendations for both researchers and practionners.

ACKNOWLEDGEMENTS

This study is performed within the framework of the International Energy Agency - Energy in Buildings and Communities Program (IEA-EBC) Annex 87 "Energy and Indoor Environmental Quality Performance of Personalized Environmental Control Systems". This work has been supported by the FWO junior postdoctoral fellowship number 1272224N for the project "Performance of resilient personalized environmental control systems (r-PECS) in non-residential buildings".

REFERENCES

Al Assaad, D., (2018). A simplified personalized and displacement ventilation model for predicting passive contaminant spread in office spaces, Energy conversion and management
Al-Othmani, M., (2008). A multi-segmented human bioheat model for transient and asymmetric radiative environments. International Journal of Heat and Mass Transfer
Boudier, K., & Hoffmann, S. (2022). Analysis of the Potential of Decentralized Heating and Cooling Systems to Improve Thermal Comfort and Reduce Energy Consumption through an Adaptive Building Controller, Energies
Conceição, E., & Awbi, H. (2021). Evaluation of Integral Effect of Thermal Comfort, Air Quality and Draught Risk for Desks Equipped with Personalized Ventilation Systems. Energies
Fiala, D., (2001). Computer prediction of human thermoregulatory and temperature responses to a wide range of environmental conditions. International Journal of Biometeorology
Gao, N., Niu, J., (2006). Coupling CFD and human body thermoregulation model for the assessment of personalized ventilation, HVAC&R research
Harrouz, J. P., (2023). Personalized ventilation with embedded air treatment system for simultaneous cooling and sorption-based carbon and humidity capture. Energy Conversion and Management
Jain, M (2018) Using personal environmental comfort systems to mitigate the impact of occupancy prediction errors on HVAC performance, Energy Informatics
Lipczynska, A., (2021). The energy-saving potential of chilled ceilings combined with personalized ventilation. Energies
Salloum, M., (2005). A new transient bio-heat model of the human body. Heat Transfer Summer Conference
Shahzad, S., (2018). Advanced personal comfort system (APCS) for the workplace: A review and case study, Energy & Buildings
Takahashi, Y., (2021). Thermoregulation model JOS-3 with new open source code. Energy and Buildings
Veselý, M., (2019). Energy performance of personalized heating: Numerical case study for a medium sized office building including different envelope qualities and climates, Journal of Building engineering
Zhang, H., (2010a). Thermal sensation and comfort models for non-uniform and transient environments, part II: Local comfort of individual body parts. Building and Environment
Zhang, H., (2010b). Thermal sensation and comfort models for non-uniform and transient environments, part III: Whole-body sensation and comfort. Building and Environment
Zhang, H., (2010c). Thermal sensation and comfort models for non-uniform and transient environments, part III: Whole-body sensation and comfort. Building and Environment

6th International Conference on Building Energy and Environment
Eindhoven University of Technology, The Netherlands
6 - 10 July 2025

Personalized Environmental Control Systems (PECS): Novel classification of devices enhancing thermal comfort

Dolaana Khovalyg [1], Jun Shinoda [2], Mariya P. Bivolarova [3]

[1]*École polytechnique fédérale de Lausanne (EPFL), Lausanne, Switzerland, dolaana.khovalyg@epfl.ch*
[2]*Technical University of Denmark, Kongens Lyngby, Denmark, junshi@dtu.dk*
[3]*Technical University of Denmark, Kongens Lyngby, Denmark, mbiv@dtu.dk*

SUMMARY
Personalized Environmental Control Systems (PECS) provide individualized thermal comfort by conditioning a person's immediate surroundings rather than the entire space, offering a shift toward occupant-centered building operation. While the existing classification of PECS concerning thermal comfort focused on design aspects and heat transfer methods, this study, part of the IEA EBC Annex 87 international project, introduces a novel framework categorizing PECS by their mobility and thermal functionality. The classification includes *building attached, building semi-detached*, *building detac*hed, *wearables*, and *others*, with building-detached devices being the most common and versatile in providing a better thermal environment compared to the conventional approach. These devices typically heat extremities and cool the back and neck, while the head requires both for optimal comfort. Combining different PECS types can effectively enhance comfort across a wide range of background temperatures. Therefore, this new classification offers a deeper understanding of personalized device designs that enhance personal thermal comfort.

Keywords: thermal environment, personalized environmental comfort systems, PECS, heating and cooling, mobility.

1. INTRODUCTION

Personalized Environmental Control Systems (PECS) offer the benefit of adjusting the immediate environment around an individual based on their preferences rather than conditioning an entire room (Shinoda et al., 2024). This marks a shift in building operations, emphasizing personalized, occupant-centered comfort instead of conditioning spaces that may often be unoccupied. Over the past decades, extensive research has been conducted on PECS aimed at enhancing thermal comfort. Understanding which devices can effectively provide comfort to individuals is crucial. Several studies, including those by Veselý & Zeller (2014), Rawal et al. (2022), Song et al. (2022), and Luo et al. (2022), have systematically reviewed various personalized devices, evaluating their comfort and energy performance. However, previous classifications of thermal devices have primarily focused on design aspects (e.g., seat, foot heater, garment) and heat transfer methods (e.g., convection, radiation). This study presents findings from a systematic literature review on PECS conducted within the IEA EBC Annex 87 international project. It introduces a novel classification framework that categorizes PECS based on their *mobility* and *thermal functionality*, providing deeper insights into the types of personalized devices that can enhance thermal comfort and their applicable environmental conditions.

2. METHODOLOGY

A systematic literature review on thermal and indoor air quality-related PECS was conducted as part of IEA EBC Annex 87, using Scopus, Taylor & Francis, PubMed, Google Scholar, and Web of Science, with a focus on peer-reviewed publications in English. After several screening stages,

342 original publications related to thermal comfort and indoor air quality (IAQ) were identified, with 166 specifically examining the thermal aspects of PECS involving human participants. Among 203 test conditions from these papers, 115 reported improved thermal environments compared to conventional heating and cooling. Per convention developed within IEA EBC Annex 87, the PECS devices were categorized into 5 types: (i) *building detached* (attached to the building and immobile), (ii) *building semi-detached* (mobile but requires connection to the building by ducts or pipes), (iii) *building detached* (mobile and can be positioned freely in a room), (iv) *wearables* (attached to the human body), and (iv) *others* (related to other applications beyond buildings). Additionally, their thermal functionality was categorized into three types: heating only, cooling only, and both heating and cooling. This study focuses on devices that improve thermal environments, emphasizing their *mobility*, *thermal functionality*, applicable *background conditions* (air temperature), and targeted *body parts*.

3. RESULTS AND DISCUSSION

An overview of PECS devices that enhance thermal environments compared to traditional heating and cooling methods is shown in Figures 1–4. Figure 1 shows the distribution of PECS types, while Figure 2 presents their distribution across different background air temperatures, highlighting thermal functionality and type. Figure 3 focuses on specific design details, and Figure 4 outlines the cases where the combination of PECS were deployed.

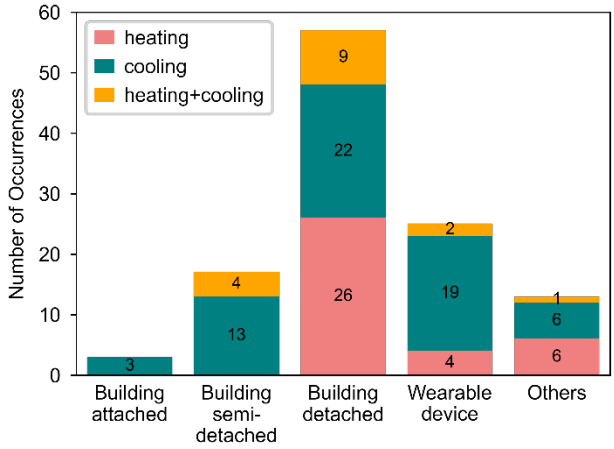

Figure 1. Overview of PECS devices providing better thermal environment per category of device type

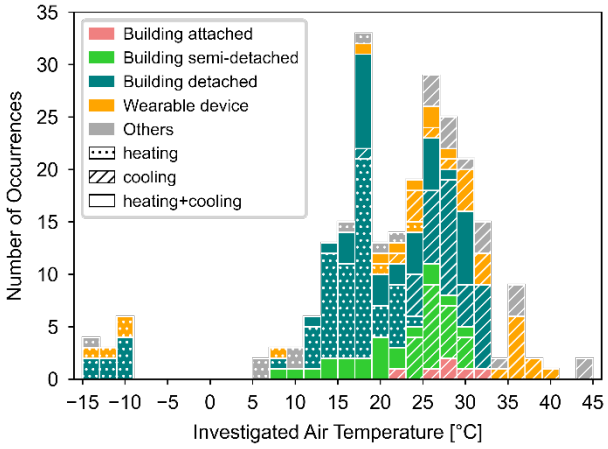

Figure 2. Range of background air temperatures tested for different types of PECS

Building detached devices occur as beneficial ones most often (50%), followed by *wearables* (22%) and *building semi-detached* ones (15%). *Building attached* devices, such as ceiling fans and air nozzles, are among the least represented, accounting for only 3% of the total. Similarly, devices categorized as *others* (e.g., car seats) make up 11%. In contrast, as shown in Figure 3, there is significantly greater diversity in the designs of *building detached* devices, highlighting a broader range of options within this category of PECS. Among specific categories, chair-based solutions (*building detached* devices) are the most frequently used for providing a better thermal environment. Interestingly, the combination of different types of PECS is the most common and effective approach for achieving an improved thermal environment, often surpassing the performance of individual PECS types. These are combinations of devices, as shown in Figure 4,

that target both core body parts and extremities, such as a heated chair and a foot warmer, a heated desk and a floor mat, or a fan and cooling desk panel.

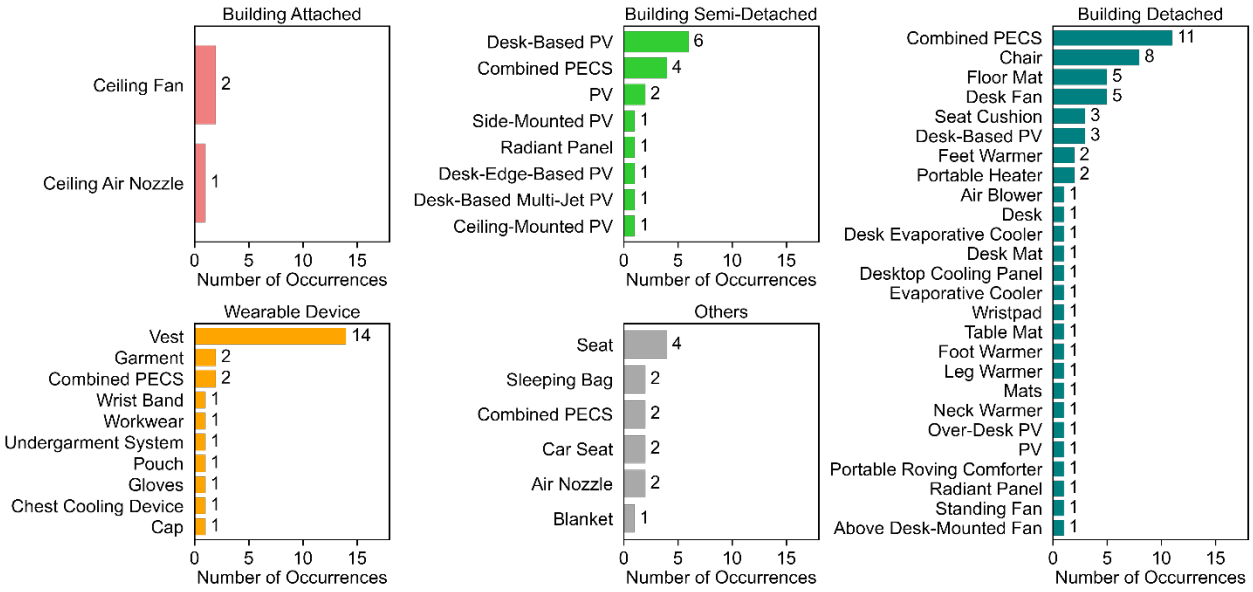

Figure 3. Frequency of studied PECS devices that provide improved comfort (PV – personalized ventilation)

The analysis of the functionality of PECS and their operational background air temperature range shown in Figure 2 further reveal the following:

- **Cooling application:** The operational range of PECS for cooling spans from as low as 18°C to as high as 45°C, with most usage occurring within the 25-33°C range. At air temperatures exceeding 33°C, wearable devices such as cooling garments and vests are predominantly utilized for outdoor work environments. Within the 21-33°C range, more typical for indoor application, building attached devices for cooling are less common compared to the building detached and semi-detached PECS.
- **Heating application**: The use of the heating function of PECS can be split into two distinct ranges: (i) sub-zero air temperatures (-15…-10°C) representing outdoor conditions and (ii) air temperatures that are typical indoors (5-30°C). Mobile devices and wearables are commonly used for outdoor applications, while building-detached PECS are more often employed indoors, particularly in the 17-19°C range.
- **Heating and cooling application**: While many PECS are designed for specific thermal applications (either heating or cooling), a few types can serve both functions. These include mainly chairs and convective systems such as air blowers.

The list of body parts shown in Figure 5 reveals that the extremities (e.g., as feet, hands, arms, thighs, and legs) were the most frequently studied body parts for local thermal sensation in heating scenarios, while the back and neck were primarily examined in cooling scenarios. This trend aligns with the understanding that cold discomfort in the extremities significantly impacts overall comfort, while cooling core body areas is essential for preventing overheating and regulating core body temperature (Gagge et al., 1967). Interestingly, the head was studied almost equally in both heating and cooling scenarios, emphasizing its important role in maintaining thermal comfort.

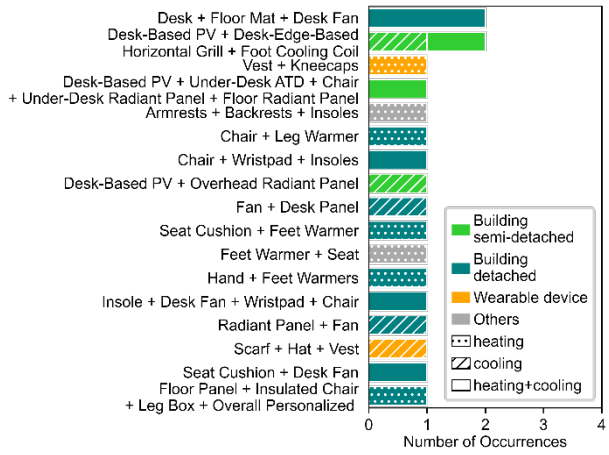

Figure 4. Overview of the combination of PECS providing better thermal environment

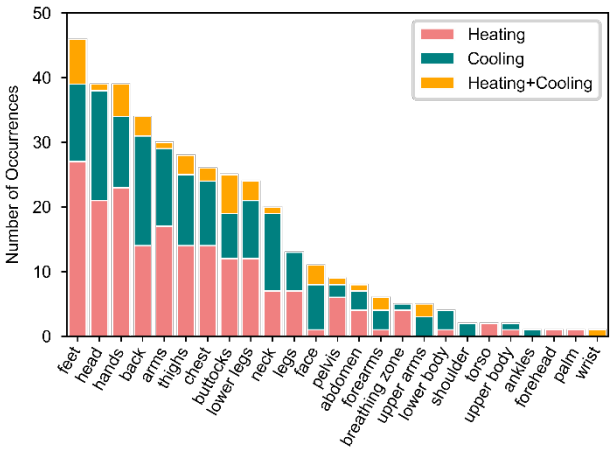

Figure 5. Body parts examined using PECS for local thermal sensation in heating and cooling cases

4. CONCLUSION

This work introduces a new classification of PECS (Personal Environmental Control Systems) based on their mobility relative to buildings, categorizing them as *building-detached*, *semi-detached*, *mobile detached*, *wearables*, and *others*. Building-detached devices are the most common and diverse, addressing different body parts in various settings - typically heating extremities and cooling the back and neck, while the head requires both for comfort. Combining PECS types, like heated chairs with foot warmers, effectively improves thermal comfort across a wide range of background temperatures. Some PECS can function to provide both cooling and heating, but often using different mechanisms (e.g., conductive heating and convective cooling in chairs, etc.). Further research into more quantitative analysis on the level of thermal comfort improvement in the proposed classification is ongoing, aiming to better understand the effectiveness of different types of PECS designs.

ACKNOWLEDGEMENTS

We thank all contributors to IEA EBC Annex 87 who participated in the systematic literature review within Thermal and IAQ domains and took part in different phases of the review process.

REFERENCES

Shinoda J., Bogatu D-I., Watanabe F., Yosuke K., Olesen B.W., Kazanci O.B., 2024. Performance evaluation of a multi-functional personalized environemntal control system (PECS) prototype. Building and Environment 252, 111260

Veselý M., Zeller W., 2014. Personalized conditioning and its impact on thermal comfort and energy performance - A review. Renewable and Sustainable Energy Reviews 34, pp.401-408.

Rawal R., Schweiker M., Kazanci O.B.,Vardhan V., Jin Q., Duanmu L. 2020. Personal comfort systems: A review on comfort, energy, and economics. Energy and Buildings 214, 109858.

Song W., Zhang Z., Chen Z., Wang F., Yang B. 2022. Thermal comfort and energy performance of personal comfort systems (PCS): A systematic review and meta-analysis. Energy and Buildings 256, 111747.

Luo W., Kramer R., de Kort Y., van Marken Lichtenbelt W. 2022. Effectiveness of personal comfort systems on whole-body thermal comfort - A systematic review on which body segments to target. Energy and Buildings 256, 111766.

Gagge A.P., Stolwijk J.A. J., Hardy J.D., Comfort and thermal sensations and associated physiological responces at various ambient temperatures. Environmental Research,Vol.1, 1, pp.1-20.

6th International Conference on Building Energy and Environment
Eindhoven University of Technology, The Netherlands
6 - 10 July 2025

On the users' comfort and operation in office environments equipped with PECS: insights from living lab study

Ilaria Pigliautile [1,2], Martina Botticelli [3], Agnese Chiucchiù[2], Fiorella Lauro [3], Veronica Martins Gnecco [4], Anna Laura Pisello [2,4], Michele Zinzi [3]

[1] *Department of Theoretical and Applied Sciences, eCampus University, Novedrate (CO), Italy, ilaria.pigliautile@uniecampus.it*
[2] *EAPLAB at CIRIAF, University of Perugia, Perugia, Italy*
[3] *Energy Technologies and Renewables Department - ENEA, Rome, Italy*
[4] *Engineering Department, University of Perugia, Perugia, Italy*

SUMMARY
Personalized Environmental Control Systems (PECSs) manage individuals' surroundings with limited energy use. This study evaluates user acceptance and perceived comfort of a thermal (360 W fan heater) and visual (12 W task lamp) PECS in two living-lab office environments in central Italy, both permanently equipped to monitor environmental parameters at room level and at each workstation. Twenty-four occupants participated in the study. The experimental design comprised three scenarios: a reference without PECS, a PECSs scenario with participants controlling their surroundings exclusively via PECSs, and a mixed scenario where both PECSs and background systems were available to final users. The campaign last 4 working weeks with participants providing their environmental sensation, satisfaction, and preferences by answering an online questionnaire administered twice-a-day for a total of 447 datapoints. Overall, the scenario combining the usage of PECS and background systems was the most appreciated configuration, especially considering the thermal environment.

Keywords:Personalized Environmental Control System, PECS operation, PECS control, Office environment.

1. INTRODUCTION

Occupants' environmental dissatisfaction is common in shared spaces due to standard system design and regulation aimed to accomplish the response of the average person, neglecting individual preferences and diversity (Parkinson, et al. 2023). Moreover, building systems addressing the environmental management at room-level can contribute to energy waste: to lit or condition the thermal environment of an entire room often leads to excessive energy consumption, especially when only a portion of the space is in use. Personalized Environmental Control Systems (PECS) offer a promising solution to both challenges by improving individual comfort while reducing energy consumption (Godithi, et al. 2019). The localized PECS approach enhances occupant satisfaction by catering to personal preferences while minimizing energy use since PECS generally operate with limited power to address specific areas rather than big volumes.
Heating PECS include air sleeves, heating seats, foot heaters, local radiative heating devices, among others. A review paper screened 77 projects, and it was found a very high energy saving potential, even if real-case applications resulted in a high variability of the results (Rawal, et al.

2020). Personalized lighting is also relevant since visual tasks can vary significantly in the same working/living environment. The combination of general with local lighting solutions may increase users productivity and ensure energy savings. Energy savings up to 40% were found in a study where local lighting was combined with lower general illuminance levels in (Logadòttir, et al. 2014). Visual PECS can be desktop-based luminaries, as well as ad-hoc and locally operated dynamic lighting systems.
Despite the concept and the first device date back to more than 40 years ago (Madsen e Saxhof 1977), PECS are not yet extensively applied in practice and there is limited evidence of their application in real case studies accounting for users' feedback. This study, developed in the framework of IEA EBC Annex 87 project on Energy and Indoor Environmental Quality Performance of Personalised Environmental Control Systems (IEA-EBC 2021), aims to fill this gap by observing the adoption of both thermal and lighting PECS in two office living-labs environments.

2. MATERIALS AND METHODS

The aim of this research is to evaluate the potential of thermal and lighting PECS in enhancing occupants' environmental perception in real office settings and to gather user feedback on PECS functionality. This will help assess the overall acceptability of introducing PECS in contexts where room-based regulation systems are predominantly used. To this aim, the same experimental protocol was implemented in two office living-labs in central Italy over a four-week period in winter 2025. The protocol included an environmental monitoring setup for continuous data collection at both room and workstation levels. Additionally, it involved an environmental perception survey, to be completed twice a day by participants, and a PECS operational feedback survey, to be completed once at the end of the study. This paper focuses solely on the survey results, while the analysis of environmental data will be presented in future works.

2.2 Living Labs

This section describes the two living-labs involved in the research providing a general overview of their characteristics as well as a presentation of the occupants' sample in terms of size and experimental scenarios distribution.

2.2.1. EAPL^{2}AB (LL1)

The EAPL^{2}AB comprises 10 offices on the first floor of the two-story Interuniversity Research Centre on Pollution and Environment "Mauro Felli" (CIRIAF) building in Perugia, central Italy. The city is in *Cfa* (humid subtropical) climate according to the Köppen-Geiger international climate classification. Details about building structure and thermal properties of the opaque and transparent components of the envelope can be checked in (Pisello, et al. 2016). All the LL1 offices present similar dimensions (4x4x2.9 m) and are equipped with the same HVAC and lighting system. HVAC is centralized but each room has its thermostat so that occupants can adjust the setpoint $\pm$3 °C from the target temperature. The lighting system includes four lighting fixtures (57 × 57 cm) made by four fluorescent tube light each. The environmental conditions are continuously monitored thanks to a Wireless Sensors Network infrastructure described in detail in (Pisello, et al. 2016). Three out of 10 LL1 offices were involved in this study, all North-East facing, with 2 or 3 occupants each. Overall, 7 occupants took part to the study and they were subsequently exposed to three scenarios: the reference configuration with only background systems (LL1_Room) lasting 1 week, the PECS configuration with lighting and thermal management limited to the adoption of

the introduced PECSs (LL1_PECS) lasting 2 weeks, and the mixed scenario with both PECSs and background systems available to final users (LL1_Mixed), lasting 1 week.

2.2.2. ENEA Living Lab (LL2)

The ENEA Living Lab (LL2) is on the second floor of an office building located in the Casaccia Research Centre in the northern outskirts of Rome, *Csa* (Mediterranean) climate, according to the Koppen classification. The living-lab consists of 11 rooms: 7 west oriented and 4 facing east. The rooms are 3.90m wide, 4.34m deep and 3.2m high. The LL2 has one floor above and one below at the same temperature, thus the thermal exchange with the outdoor environment takes place only through the facades. Each office is equipped with room air conditioning unit, providing space heating and cooling energy services interdependently at room level. LL2 is equipped with a smart energy management system able to control and monitor several functions of the building. A detailed description of the LL2 features can be found in (Zinzi e Chiesa 2023). 17 occupants were involved in this study, 7 assigned to private offices and the remaining in shared spaces with at least one colleague. Due to organizational constraints, it was not possible to limit the control of occupants to the room background system, therefore, in LL2 only two scenarios were tested: the reference configuration with only background systems (LL2_Room) and the mixed scenario with both PECSs and background systems available to final users (LL2_Mixed). Among participants, 3 experienced the LL2_Room and 9 the LL2_Mixed configurations for the entire duration of the campaign. The remaining 5 participants experienced both.

2.3 PECS

The PECS for lighting consist of desk led lamps, whose position, generally above the PC monitor, is set by the single user according to their preferences. The product choice was a compromise between cost and characteristics of the lamp. A relevant feature is the possibility of modulating the power in 11 levels with 12W as maximum electric power absorption; in addition, the light colour has five modes between 3000K and 6000K.

The PECS for heating is a fan heather, chosen as a good compromise between cost and performance. The device dimensions are: 150mm width, 100mm depth and 175mm height; this size makes it easy to be placed and moved on the desk depending on the user's need. The electric power absorption is 360 W constant and, unfortunately, it is not possible to modulate the power; conversely, it is possible to move the air outlet grid to properly direct the flow.

2.4 Surveys

2.4.1. Environmental perception survey

The implemented questionnaire adapts the ASHRAE procedures defined in (ASHRAE 2013) to collect right-here-right-now responses of the occupants in both thermal and visual domains. Questions are limited to sensation (5 points), satisfaction (5 points), and preference (3 points) to reduce participants' fatigue and keep their engagement high by avoiding an excessive number of questions and time to compile. The perception survey had to be filled via web twice a day: in the morning and the afternoon.

2.4.2. PECS operative feedback survey

The PECS operative feedback survey was distributed to participants that experienced the PECS scenario just once, at the end of the campaign. Questions were structured in order to focus on how people interact with PECS taking advantage of the adjustable settings and limited target areas, as

reported in Table 1.
Finally, any potential PECS limitation was further explored giving the chance to provide an open-ended list of faced challenges while using PECS.

Table 1. PECS operative feedback survey structure

PECS type	Question	Answer options
Lighting	Do you change the lamp orientation to enhance your comfort?	Never Sometimes Often Always
	Do you use the function to adjust the light intensity?	
	Do you use the function to adjust the light colour temperature?	
	Do you keep both the table lamp and ambient lights on?	
	Do you find the lamp control buttons easy to use?	Not at all Slightly easy to use Moderately easy to use Absolutely yes
Thermal	Do you change the fan's position during the day to ensure maximum comfort?	Never Sometimes Often Always
	Do you use the knob to adjust the airflow speed?	
	Do you ever keep both the fan and the air conditioner on, with the set-point higher than the one configured?	
	Do you find the heating fan easy to use?	Not at all Slightly easy to use Moderately easy to use Absolutely yes

3. RESULTS

3.1 Environmental perception

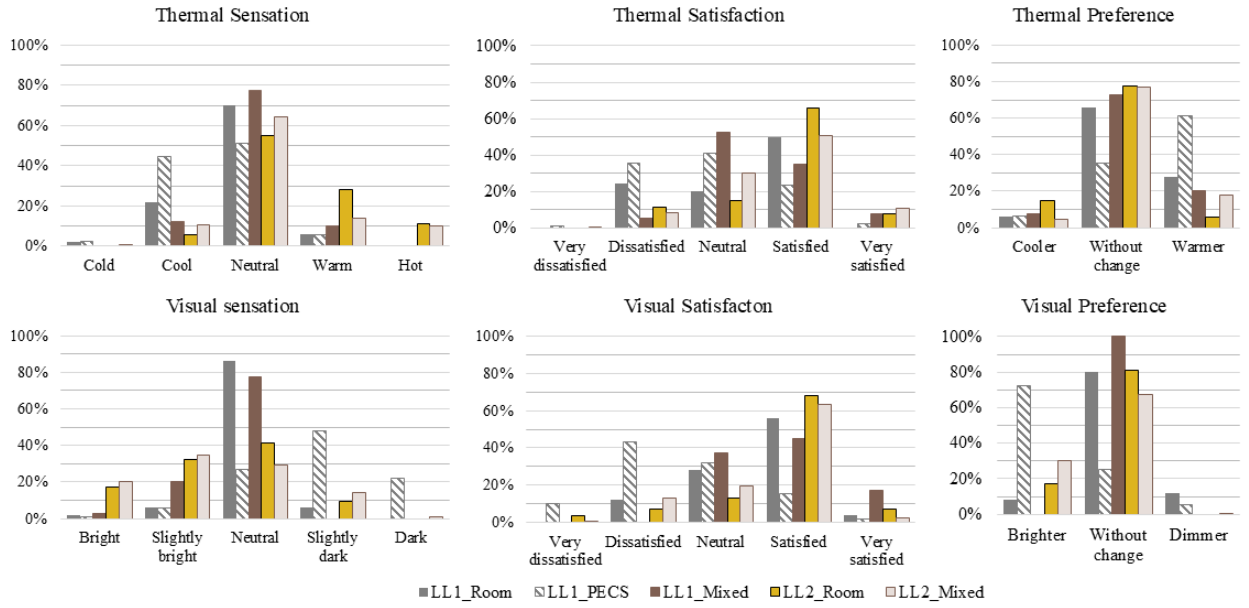

Figure 1. Environmental perception responses across scenarios and living-labs

Results are summarized in Figure 1. Focusing on responses pertaining to the thermal domain, the Mixed scenario received the highest percentage of perceived neutral thermal sensation for both LL1 (78%) and LL2 (64%). This scenario also had the highest share of "Very satisfied" votes for the thermal environment. However, on average, the Room configuration (without PECS) achieved

the highest satisfaction score in LL2, i.e. 0.70 against 0.63 of LL2_Mixed. The PECS-only scenario, evaluated only in LL1, received the lowest ratings, i.e., average thermal sensation and satisfaction of -0.42 and –0.10, respectively, with 61% of participants seeking for warmer conditions. Notably, 6% of collected environmental feedback in LL2 preferred a cooler environment, 39% of reported thermal sensation votes for the LL2_Room scenario described warm-to-hot thermal sensations, compared to 24% of the LL2_Mixed configuration.
Concerning the visual domain, the Room scenario showed the highest frequency of neutral sensation votes in both LL1 (86%) and LL2 (42%). Nevertheless, the Mixed scenario received the highest satisfaction score in LL1 (0.80) while the PECS-only scenario, experienced in LL1, received the most negative feedback in terms of visual perception, including the only average sensation leaning toward the darker side of the visual sensation scale (+0.82).

3.2 PECS operative feedback

Here only feedback from participants involved in PECS and Mixed scenarios are analysed without distinctions between LL1 and LL2 samples. The desk lamp's light intensity was the most frequently adjusted setting among the tested PECS, with 15% of participants reporting they adjusted it "Always" and another 10% doing so "Often." For the thermal PECS, the airflow speed of the fan heater was the most commonly modified setting. In contrast, the positions of both the desk lamp and the portable fan heater were rarely adjusted. Specifically, 40% of users reported "Never" changing the desk lamp's position, while 53% said the same for the portable fan heater. Overall, feedback on ease of use showed that both PECS were considered moderately to absolutely easy to use by all participants. Only 5% of the sample found the thermal PECS "Slightly easy to use." Under Mixed scenario, 80% of participants never switched on simultaneously both PECS and background systems a percentage that decrease down to 50% considering the lighting system.

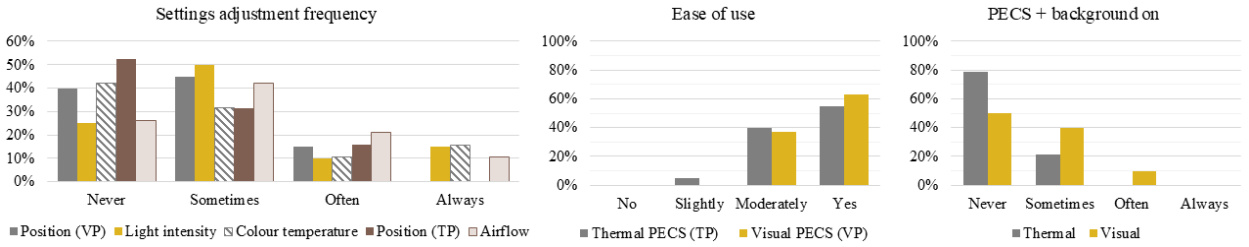

Figure 2. PECS users feedback on settings adjustment frequency and ease of use.

In the following, the main challenges and limitations of the adopted PECS are presented, as reported by LL1 participants immediately after experiencing the PECS-only scenario.
Regarding the desk lamp, 5 out of 7 participants mentioned the discomfort of working in a dark environment. Three of them further explained that although the desk lamp adequately illuminated the working area, the intense contrast with the dark surroundings results in uncomfortable conditions. One participant noted that even the combination of daylight and the desk lamp was insufficient to create a comfortable environment. Another issue highlighted by 2 participants concerned the sensitivity of the control buttons: one found them too much sensitive, while the other felt they were not sensitive enough. Additional challenges mentioned by individual participants included an excessive number of light colour temperature options (quote: *…a lot, I can't find the right one*) and the light position, which was too close to the eyes.
Feedback on the fan heater revealed that 3 participants reported no issues. However, 2 participants

expressed dissatisfaction with the PECS operation settings, citing limited functionalities and automatic, unexpected shutdowns. Additionally, 2 out of 7 users found the thermal environment inadequate, describing it as too cold, especially in the morning (…*when entering the room and the system is off, it takes too much time to reach the desired thermal conditions*). One of these users also noted that directing the heat flux towards the head was extremely uncomfortable.

4. CONCLUSIONS

Thermal and visual PECS were distributed in two office living-labs. Occupants feedback about their thermal perception and PECS operative settings were collected for four-weeks in winter, 2025. Throughout the experiment, three scenarios were investigated: without PECS, a PECS-only scenario, and a mixed-scenario characterized by the availability of PECS in addition to background system control. Findings highlight that the mixed scenario was the most appreciated one by participants while relying just upon PECS is not enough to achieve comfortable conditions. Therefore, to meet the dual goal of occupants' environmental satisfaction and building energy savings, to develop smart control is crucial to not compromise sustainability. Relevant settings to be adjusted at personal level to meet requirements that may change over time can be the intensity of light for the desk lamp and the airflow speed for convection-based PECS heater.

Outcomes are going to be further analysed combining collected perceptual votes with observed environmental conditions to identify optimal ranges of PECS use as stand-alone or supportive system to the common room-based regulation. Moreover, energy consumptions observed for the three scenarios are going to be compared to clarify PECS energy saving potentials.

ACKNOWLEDGEMENTS

The activity was conducted within the IEA-EBC Annex 87 framework. The University of Perugia research group thank the EU-Horizon programme supporting their research through the project SONATA (GA 101137507).

REFERENCES

1. ASHRAE. 2013. "ANSI/ASHRAE 55-THERMAL ENVIRONMENTAL CONDITIONS FOR HUMAN OCCUPANCY." ATLANTA, GA, USA.

Godithi, Sam Babu, Enna Sachdeva, Vishal Garg, Richard Brown, Christian Kohler, and Rajan Rawal. 2019. "A review of advances for thermal and visual comfort controls in personal environmental control (PEC) systems." *Intelligent Buildings International* 11 (2): 75-104. doi:10.1080/17508975.2018.1543179.

IEA-EBC. 2021. *Annex 87 - Energy and Indoor Environmental Quality Performance of Personalised Environmental Control Systems.* https://annex87.iea-ebc.org/.

Logadòttir, Asta, Rahimi Ardkapan Siamak, Johnsen Kjeld, Baadsgaard Signe, Dam-Hansen Castern, Anders Thorseth, and Hakan Johansson. 2014. "Energy Efficient Task Light: Final Report for PSO 344-059."

Madsen, Thomas Lund, and Bjarne Saxhof. 1977. "An unconventional method for reduction of the energy consumption for heating of buildings." *Second International CIB Symposium on Energy Conservation in the Built Environment.*

Parkinson, Thomas, Stefano Schiavon, Jungsoo Kim, and Giovanni Betti. 2023. "Common sources of occupant dissatisfaction with workspace environments in 600 office buildings." *Buildings&Cities* 4 (1): 17–35. doi:10.5334/bc.274.

Pisello, Anna Laura, Veronica Castaldo, Cristina Piselli, Claudia Fabiani, and Franco Cotana. 2016. "How peers' personal attitudes affect indoor microclimate and energy need in an institutional building: Results from a continuous monitoring campaign in summer and winter conditions." *Energy and Buildings* 126: 485-497. doi:10.1016/j.enbuild.2016.05.053.

Rawal, Rajan, Marcel Schweiker, Ongun Berek Kazanci, Vishnu Vardhan, Quan Jin, and Lin Duanmu. 2020. "Personal comfort systems: A review on comfort, energy, and economics." *Energy and Buildings* 214: 109858. doi:10.1016/j.enbuild.2020.109858.

Zinzi, Michele, and Giacomo Chiesa. 2023. "Living lab testing report." Deliverable D4.3, EU-Horizon Project E-DYCE, GA 893945.

Health and Indoor Air Quality, Ventilation (15:30-17:00 h)

6th International Conference on Building Energy and Environment
Eindhoven University of Technology, The Netherlands
6 - 10 July 2025

Computational fluid-particle dynamics simulations to predict particle aspiration and deposition efficiencies in a monkey airway model

Yuichiro Suda [1], Kazuki Kuga [2], Kazuhide Ito [3]

[1]*Kyushu University, Fukuoka, Japan, suda@kyudai.jp*
[2]*Kyushu university, Fukuoka, Japan, kuga@kyudai.jp*
[3]*Kyushu University, Fukuoka, Japan, ito@kyudai.jp*

SUMMARY
Dose-response data from laboratory animals are commonly extrapolated to assess human health risks associated with inhalation exposure to contaminants. However, the availability of *in vivo* data is limited because of animal protection and ethical considerations. Although monkey-based experiments represent a suitable alternative to human exposure studies, the characteristics of particle transport and deposition in monkey airways remain poorly understood. Furthermore, the external shape of the nasal cavity in the upper airway differs between humans and monkeys, which may result in differences in particle aspiration efficiency. The objective of this study was to predict the efficiencies of particle deposition and aspiration in the airways of monkeys during inhalation using computational fluid-particle dynamics. We developed a numerical airway model that reproduces the detailed geometry from the nasal cavity to the 33rd generation bronchial tubes.

Keywords: Computational fluid-particle dynamics, Monkey airway model, Particle deposition, Aspiration efficiency.

1. INTRODUCTION

The behavior of inhaled substances within the respiratory system, including the nasal cavity, airways, bronchi, and lungs, is essential for the development of inhaled pharmaceuticals such as anti-coronavirus therapeutics and drugs for managing bronchial asthma. Additionally, the atmosphere contains a wide variety of substances, ranging from gaseous compounds, such as volatile organic compounds (VOCs), to aerosol particles, such as pollen, which can be transported and absorbed into the body through respiration. Inhalation toxicity studies involving humans have ethical limitations, necessitating alternative approaches. These approaches often involve extrapolating the results from animal experiments to humans or performing experiments using artificial respiratory models. Among animal models, nonhuman primates, particularly rhesus macaques, are highly effective surrogates because of their high physiological similarity to humans. In this study, computational fluid-particle dynamics (CFPD) was employed to develop numerical monkey airway models capable of predicting particle deposition and aspiration efficiency during respiration. A highly detailed numerical airway model was constructed by replicating bronchial structures up to the 33rd generation. Furthermore, we investigated the impact of various factors, including breathing volume, particle size distribution, and airway geometry, on particle deposition within the respiratory tract.

2. MATERIALS AND METHODS

The geometric model of the rhesus macaque respiratory tract was constructed based on a study by

Corley et al., who utilized computed tomography (CT) imaging of the upper airway, spanning from the nasal cavity to the larynx, and magnetic resonance imaging (MRI) of the trachea and lungs. These images were derived from a silicone cast of a 6-month-old male rhesus macaque weighing 1.3 kg, as shown in Fig. 1. To accurately capture the transport behavior of particles from the indoor environment to the respiratory system, this study incorporated a spherical breathing zone integrated with the face features. To construct a computationally suitable airway model for CFD analysis, ANSYS/SpaceClaim software was used for segmentation and geometric repair. Furthermore, the mass flow rate to each lung lobe was preliminarily determined using a model with 48 million cells (Fig. 1b), in which a pressure outlet boundary condition was applied at the airway edge (Fig. 1a: gray zone). ANSYS Fluent was used for fluid and particle dynamics simulations. The Reynolds-averaged Navier-Stokes (RANS) equations were solved to predict airflow patterns under steady-state and transient breathing conditions. A second-order upwind discretization was applied to all governing equations in conjunction with the semi-implicit pressure-linked equation (SIMPLE) algorithm for numerical stability and accuracy. Particle simulations were applied one-way coupling Lagrangian discrete-phase model. To ensure a wide-ranging prediction of particle deposition across microscale sizes, eleven representative particle sizes were selected, ranging from 1 to 80 μm. Moreover, particle density was set to 1,000 kg/m^3. The breathing cycle was constructed based on the experimental results of Karel et al., with a ventilation volume (tidal volume) of 13.13 mL. The computational results for the macaque model were compared with those of a human model (Kuga et al. 2024) to validate the feasibility of the simulation.

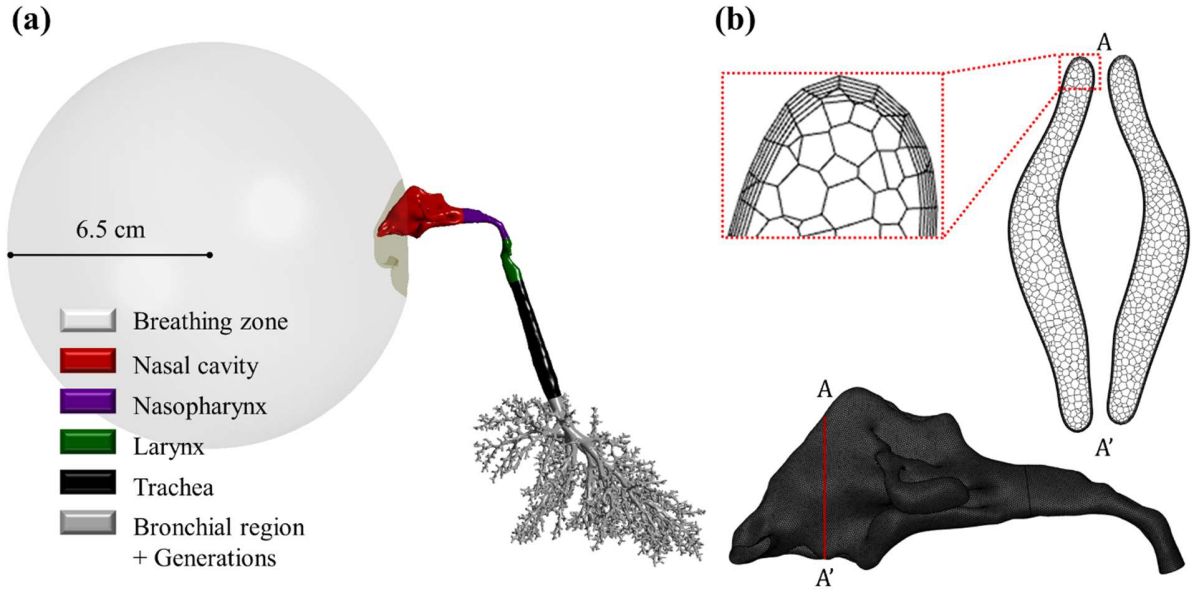

Figure 1. Overview of the constructed computed tomography-based models of the (a) rhesus macaque airway geometry and (b) computational mesh of the monkey nasal passage.

3. RESULTS AND DISCUSSIONS

3.1. Comparison of particle aspiration efficiency between monkey and human

The aspiration efficiency is defined as the ratio of the concentration of inhaled particles to the

concentration of particles in the ambient environment. Fig. 2 presents the various aspiration efficiency datasets plotted against different particle sizes. The particle aspiration efficiency of the monkey exhibited high values for the 1–20 μm particle size range, showing good agreement with the human model. On the other hand, a sharp decline was observed in the 40–50 μm particle size range for the monkey. This was likely because the simulation was conducted under isothermal conditions, which neglected the thermal plume around the body and might reduce the particle aspiration efficiency in the micrometers that are significantly affected by gravitational settling. In summary, the simulation results of the smaller particles demonstrated sufficient agreement with the human model, whereas larger particle sizes, which were significantly influenced by gravitational sedimentation, presented opportunities for further investigation.

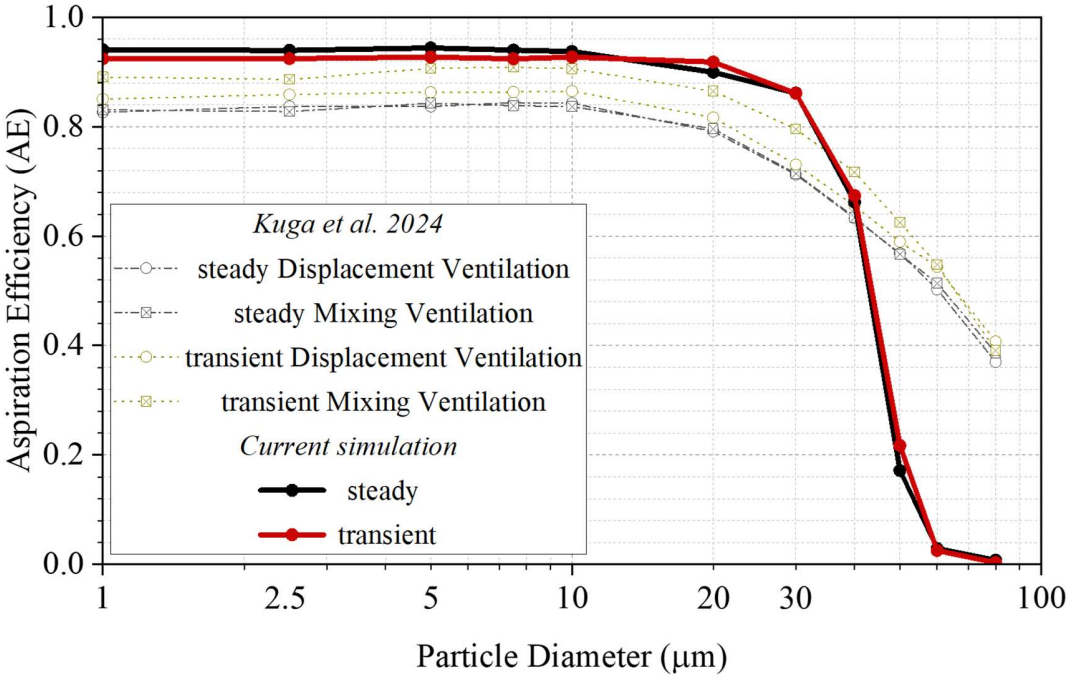

Figure 2. Comparison of aspiration efficiency as a function of particle size between the present study in the monkey model and previous simulations in the human model by Kuga et al.

3.2. Particle deposition efficiency in the monkey respiratory tract

Fig. 3 illustrates the visualization of the deposited particle distribution within the airways of the monkey model under steady inhalation (Fig. 3a) and transient breathing conditions (Fig. 3b). The figure also shows the percentage of particles deposited in each region relative to the total number of particles inhaled through the nostrils. A comparison of the three particle sizes confirmed that 5 μm particles showed the highest deposition rate across all regions. Additionally, analysis of different breathing conditions showed that unsteady breathing, including exhalation, resulted in a higher deposition rate in the upper airway. This suggests that in more realistic scenarios, the upper airway regions, particularly the nasal cavity and pharyngeal areas, are more susceptible to the effects of microparticles, which requires further investigation. A similar trend was observed in a previous study in humans, further supporting the high similarity between the nasal structures of rhesus macaques and humans. Furthermore, the detailed model of the lower airways used in this study enabled the observation of microparticle deposition, which was previously difficult to detect.

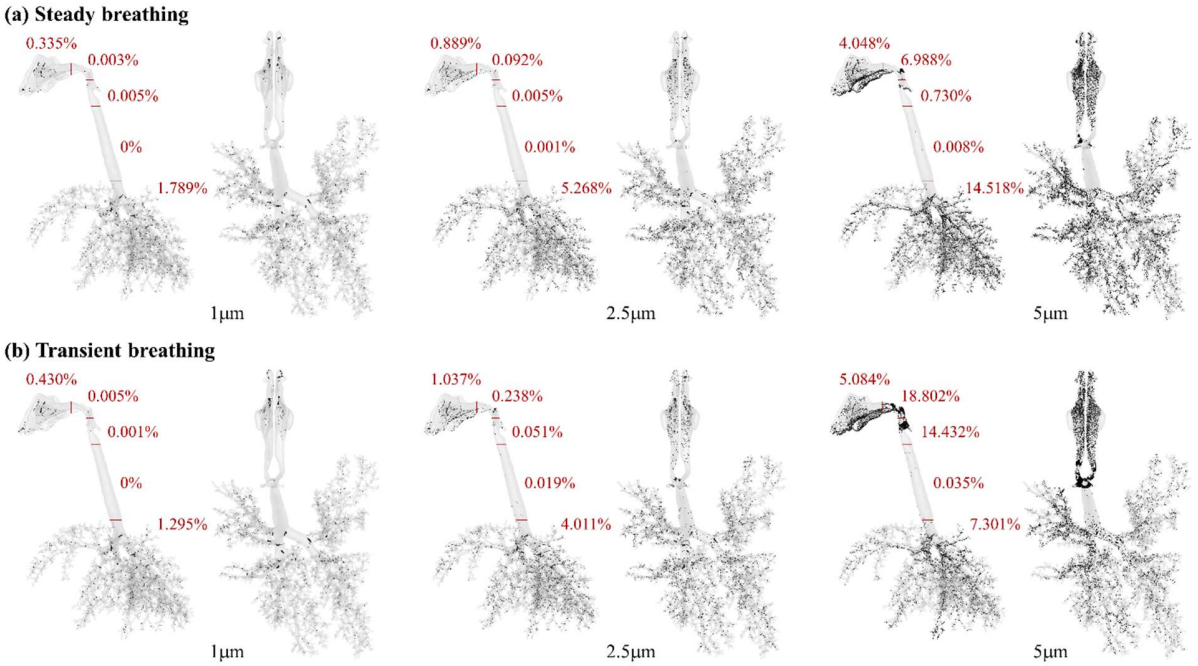

Figure 3. Deposition distribution of different inhaled particle sizes during (a) steady breathing and (b) at the end of transient breathing cycles, viewed from an isometric and superior perspective.

4. CONCLUSIONS

In the present study, detailed monkey airway models were used to simulate particle inhalation under steady and transient breathing conditions. The results obtained using the developed airway models agreed well with human data for the microparticles analyzed in this study. Furthermore, the models were effective tools for predicting particle deposition patterns, particularly for fine particles, which are traditionally challenging to analyze. The observed similarities in the deposition efficiency with human models, coupled with the unique characteristics of the monkey model, provide valuable insights into the roles of anatomical variations in respiratory mechanics and particle behavior. These insights are not only critical for advancing the understanding of respiratory diseases but also show potential for improving therapeutic strategies, such as targeted drug delivery systems.

ACKNOWLEDGEMENTS

This study was partially funded by the FOREST program of JST, Japan (JPMJFR225R), JSPS KAKENHI (JP 25H00409, JP 22K18300, JP 22K14371), Health, Labour and Welfare Policy Research Grants (JP 24KD2001), and MEXT as a “Program for Promoting Research on the Supercomputer Fugaku” (JPMXP1020210316).

REFERENCES

Karel, L., & Weston, R. E. (1946). Respiration in Macaca mulatta (Rhesus monkey). *Proceedings of the Society for Experimental Biology and Medicine*, *61*(3), 291-296.

Corley, R. A., Kabilan, S., Kuprat, A. P., Carson, J. P., Minard, K. R., Jacob, R. E., ... & Einstein, D. R. (2012). Comparative computational modeling of airflows and vapor dosimetry in the respiratory tracts of rat, monkey, and human. *Toxicological Sciences*, *128*(2), 500-516.

Kuga, K., Kizuka, R., Abouelhamd, I. M., & Ito, K. (2024). Aspiration efficiency and respiratory tract deposition of indoor suspended micro-particles during steady and transient breathings. *Building and Environment*, *249*, 111114.

6th International Conference on Building Energy and Environment
Eindhoven University of Technology, The Netherlands
6 - 10 July 2025

High-accuracy and real-time prediction of non-isothermal indoor environment via neural networks with a novel activation function

Xuesong Hu [1], Ruibin Li [1], Tianle Chen [1], Naiping Gao [1,*]

[1]*Tongji University, Shanghai, China, gaonaiping@tongji.edu.cn*

ABSTRACT
Neural networks, combined with computational fluid dynamics, are among the most widely employed approaches for optimizing indoor temperature and velocity distributions. The selection of activation functions in a neural network significantly influences prediction accuracy. This study introduces a novel activation function, Leaky-Sigmoid, featuring tunable parameters (α, β), to enhance the prediction accuracy of neural networks in indoor environments. The results show that the neural networks based on Leaky-Sigmoid can predict airflow and temperature within 2 milliseconds, with an average relative error of only 2%. Moreover, the proposed networks employing Leaky-Sigmoid outperform existing models in reducing prediction errors for temperature by 19.47% and 9.10% in B3 and B5, and for velocity by 11.74% and 5.43% in B3 and C2. Lastly, the derivatives of the activation functions play a crucial role in determining the prediction accuracy. In conclusion, the Leaky-Sigmoid activation function offers substantial improvements in prediction in indoor environments.

Keywords: Neural networks, Computational fluid dynamics, Indoor environment, Activation function

1. INTRODUCTION

Artificial intelligence (AI), as a key driver of social development, has made significant advancements in fields such as autonomous driving (Grigorescu et al., 2020), image recognition (Krizhevsky et al., 2017), and various other areas. In the context of the built environment, the rapid prediction of physical parameters, the solution of partial differential equations (PDEs) (Li et al., 2021), and the acceleration of computational fluid dynamics (CFD) techniques (Obiols-Sales et al., 2020) have emerged as increasingly prominent research topics. Compared to traditional CFD methods, AI, particularly neural networks, offers a distinct advantage in terms of computational speed and efficiency. Some studies focus on the internal structure of neural networks to explore their contributions to CFD calculations. For instance, Zhou et al. (2021) examine the impact of various data preprocessing methods on prediction accuracy and conclude that data preprocessing plays a crucial role in ensuring the accuracy of indoor flow field predictions. They also find that different preprocessing approaches produce similar performance in forecasting indoor airflow. Additionally, the activation functions used between the layers of a neural network are essential components of the network's architecture. However, the mechanisms by which these activation functions affect prediction results in the field of built environment remain unclear.

Activation functions are nonlinear functions designed to enhance the network's fitting ability to capture complex patterns within neural networks. The most commonly used activation functions include Sigmoid (Cybenko, 1988), ReLU (Glorot et al., 2011), and Leaky-ReLU (Maas et al., 2013), among others. While these functions are widely applied across various tasks, their inherent

limitations cannot be ignored. For instance, the Sigmoid activation function was prone to the vanishing gradient problem (Bengio et al., 1994), which occurs during the backpropagation process and hinders effective learning in deep networks. To address this issue, the ReLU activation function (Bengio et al., 1994) was introduced, offering a simple and computationally efficient solution. However, ReLU's tendency to produce 'dead neurons'—caused by its zero output for non-positive inputs—can result in inactive neurons that fail to contribute to the training process. The Leaky-ReLU activation function partially mitigated this issue by allowing a small gradient for negative inputs. Nevertheless, its prediction accuracy is sometimes lower than that of the standard ReLU. Therefore, these limitations highlight the need for improved activation functions that enhance accuracy, stability, and generalization capabilities.

In this paper, a novel activation function, Leaky-Sigmoid, is proposed to enhance the nonlinear characteristics of ReLU-based functions while mitigating the gradient vanishing issue inherent in the Sigmoid function. To evaluate its effectiveness, we compare conventional activation functions (ReLU, Leaky-ReLU, and Sigmoid) with the proposed Leaky-Sigmoid in terms of prediction accuracy and efficiency, utilizing the same input data and network architecture for consistency. Numerical experiments show that a network configuration utilizing the Leaky-Sigmoid activate functions achieves superior prediction results under specific conditions.

2. METHODS

2.1. Settings for the Physics Model

With regard to the case settings, a three-dimensional room is considered here, as illustrated in Fig. 1 (a), with dimensions of 6.00 m, 2.44 m, and 2.44 m in the x-, y-, and z- directions. The supply air temperature is varied from 20 ℃ to 35 ℃, with an interval of 5 ℃. The supply air velocity is varied from 4.00 m/s to 6.25 m/s, with an interval of 0.75 m/s. The heat generation is set from 100 W, 200 W, and 300 W. Other boundaries are set to insulated walls. Consequently, a total of 48 cases are contained in the training database. Meanwhile, 2 cases that are never contained in the training database are set for the testing database, such as (27 ℃, 4.30 m/s, 173 W) and (32 ℃, 5.10 m/s, 230 W). All cases are assumed to be in a steady condition. The CFD simulations are run using the Fluent 2022R1 on a Windows server with a 12th Gen Inter(R) Core(TM) i9-12900K CPU.

All the prediction processes are divided into two steps. The first step is named the ‘K-fold training step’, and the second step is named the ‘true testing step’. In the first step, the 6-fold cross-validation is used for the stability of the training process. Above 48 cases in the training database, 40 cases are used for training datasets, named ‘K-train’, and another 8 cases are used for validation datasets, named ‘K-valid’. In the second step, all of the 48 cases are used for the training dataset, named ‘train’, and the 2 cases in the testing database are used for the testing dataset, named ‘test’.

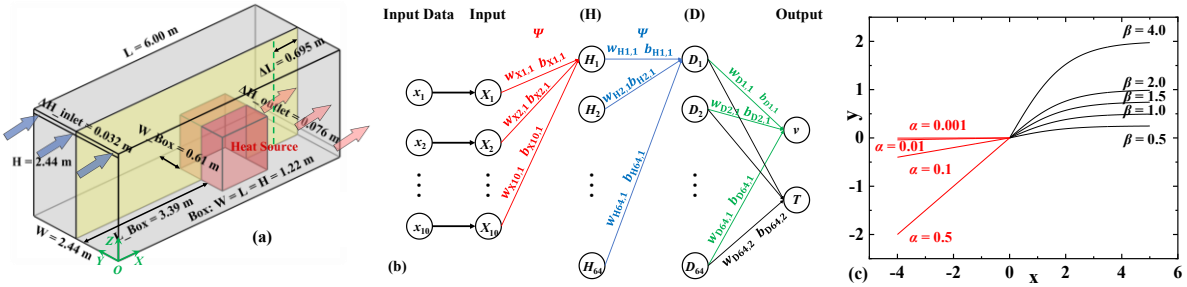

Figure. 1 The detailed information on the geometry and the neural network. (a) Geometrical model of mixing ventilation in a non-isothermal room. The cross-section examined in this study is the yellow darkened zone in the figure (y = 1.22 m). The selected monitoring line is indicated by the green dashed line (x = 5.305 m). (b) The structure of MLP in this paper. (H) is the first hidden layer and (D) is the second hidden layer, with 64 neurons in each. Ψ is the activation function for each layer. This paper is analyzed from $w_{X1,1}$ in the discussion. (c) Leaky-Sigmoid activation functions and the images of different α and β. α = 0.001, 0.01, 0.1, 0.5. β = 0.5, 1.0, 1.5, 2.0, 4.0.

2.2. Settings for Neural Networks

In this study, a neural network named multiple perceptrons (MLP) is adopted to predict the airflow and temperature distribution simultaneously. The detailed structure is shown in Fig. 1 (b), containing one input layer, two hidden layers, and one output layer. There are 64 neurons in each hidden layer. The input layer contains inlet velocity, inlet temperature, heat source's producing capacity, horizontal coordinates of the grid center, vertical coordinates of the grid center, distance of each coordinate from the inlet, distance of each coordinate from the center of the heat source, velocity coupling parameters, temperature coupling parameters, and the angle. The output parameters are velocity and temperature at each coordinate location. In the neural networks, the learning rate and the training epochs are set at 0.001 and 2500.

2.3. Settings for Activation Functions

Activation functions are necessary structures between two adjacent layers for predicting complex nonlinear features. In this study, a novel activation function called Leaky-Sigmoid is introduced. For the Leaky-Sigmoid activation functions, a variable slope (denoted as α) is introduced to the negative axis, and a scaling factor (denoted as β) is applied to the positive axis. The detailed number codes and images are shown in Table 1 and Fig. 1 (c).

$$LS(x) = \begin{cases} \alpha x, & x \le 0 \\ \beta\left(\frac{1}{1+e^{-x}} - 0.5\right), & x > 0 \end{cases} \quad (1)$$

Table 1. The detailed number codes for different combinations of α and β

Existing	Coding	α	β	Coding	α	β	Coding	α	β	Coding	α	β	Coding
ReLU	R		0.5	A1		0.5	B1		0.5	C1		0.5	D1
			1.0	A2		1.0	B2		1.0	C2		1.0	D2
Leaky-ReLU	L	0.001	1.5	A3	0.01	1.5	B3	0.1	1.5	C3	0.5	1.5	D3
			2.0	A4		2.0	B4		2.0	C4		2.0	D4
Sigmoid	S		4.0	A5		4.0	B5		4.0	C5		4.0	D5

3. RESULTS

3.1. Prediction Accuracy in Training and Testing Datasets

3.1.1. Evolution of model errors

In this section, the root mean square errors (RMSE) of velocity and temperature distributions are separately analyzed. Specifically, Fig. 2 (a) shows the temperature RMSE of all of the cases. In Groups A, B, and C, the T-RMSEs of training and validating results tend to decrease as β increases. This trend is more pronounced in Group C. The prediction accuracy of MLP improves with the increase of β. In terms of nonlinearity, β parameter is the scaling factor that controls the nonlinear components of the Leaky-Sigmoid activation function. This component shows a more pronounced nonlinear approximation in contrast to the linear component controlled by α. Consequently, adjusting β can enhance the ability to fit the nonlinear data in MLP. In terms of backpropagation, the computation in MLP is based on the Chain Rule. These parameters are derived through backpropagation, influenced by the multilayer neurons and activation functions, during the process of updating the weight parameters. The scaling factor β enlarges the derivative range, thereby increasing the extent of nonlinear mapping. In Group D, RMSE improves with increasing β, reaching its maximum at D3. However, the gradient vanishing issue causes computation disruption in the D5 case. This indicates that α imposes a stronger constraint on the range of RMSE than β, with β serving to fine-tune the network's performance within that range.

In Groups A, B, C, and D, most cases achieve accuracy levels comparable to those of conventional activation functions. In the test datasets, the T-RMSEs in A5, B3, and B5 are 4.05%, 7.97%, and 7.20% lower, respectively, compared to the network using the ReLU activation function. Furthermore, the v-RMSE distribution patterns of the v-train and v-K-train results shown in Fig. 2 (b) closely resemble those of the T-RMSE curves. The v-RMSEs in the test datasets are 1.97%, 5.95%, and 6.61% lower than the results obtained using Leaky-ReLU in A5, B3, and B5.

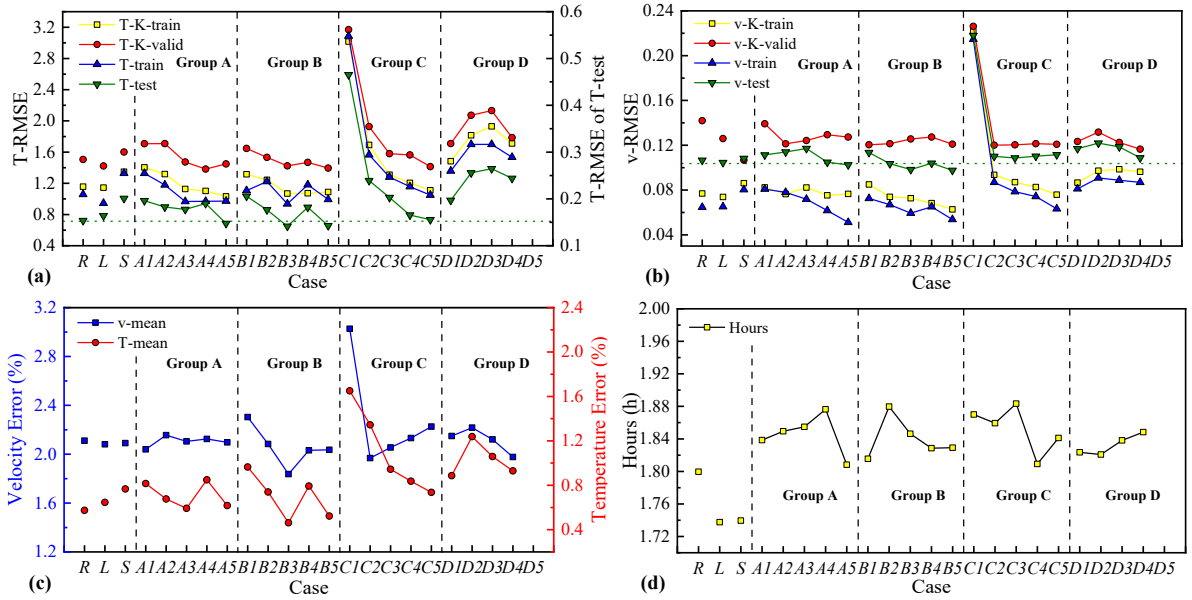

Figure. 2 Comparison of the Leaky-Sigmoid and conventional activation functions in terms of RMSE, relative errors, and training time with variables α and β. (a) RMSE of temperature. (b) RMSE of velocity. (c) Relative errors of test datasets. The yellow squares represent the v/T-K-train and the red circles for the v/T-K-valid, the blue positive triangles represent the v/T-train, and the green inverted triangles for the v/T-test in (a) and (b). (d) Training time comparison of the conventional activation functions and others with various combinations of α and β when

computing the same epochs. The equation of RMSE is $\sqrt{\frac{1}{N}\sum_{i=1}^{n}(y - y_{pred})^2}$. Where y is the CFD result, y_{pred} is the prediction result. N is the number of the coordinates.

The absolute values of RMSEs have limitations in accurately representing the true error of the test datasets, providing only a rough analysis of forecasting trends. Therefore, the relative error is employed to compare the prediction accuracy across the test datasets. The detailed prediction results are shown in Fig. 2 (c). The relative error of temperature shows lower deviations compared to those of velocity distribution, likely due to the lower complication of the data distribution.

The relative errors for temperature are generally lower than those for velocity, as the larger range of absolute values for temperature in the denominator compared to velocity. The relative errors for temperature in B3 and B5 are 19.47% and 9.10% lower, respectively, compared to the results from the ReLU activation function. For the velocity, the results of B3 and C2 are 11.74% and 5.43% lower compared to the Leaky-ReLU activation function. The detailed information is shown in Fig. 2 (c). The overall trend shows that prediction accuracy improves as β increases in each group.

3.1.2. Overall data distributions

Although there are overall analyses of the temperature and velocity results, the detailed prediction distribution remains unclear. These are crucial for analyzing the prediction characteristics of neural networks with different activation functions. As shown in Fig. 3 (a), all temperature results with different activation functions underestimate $T_{MAX\text{-}CFD}$. In Groups A, B, and C, the prediction results of temperature display more centralized trends as β increases within each group. The temperature distributions of A5, B3, B5, and C5 are most comparable to the CFD simulation.

When predicting the temperature data in the top 1%, MLPs tend to be conservative, leading to prediction values that are less dispersed compared to the CFD simulation. As β increases within each group, the range of temperature predictions more closely aligns with the CFD simulation for 1.75%–98.25% of the data, with the exception of Group D. These findings suggest that MLPs can better capture the patterns of data distributions as β increases. Additionally, MLPs are effective at predicting the velocity distributions. Furthermore, data with small gradients, such as velocity distributions, are predicted with higher accuracy, as shown in Fig. 3 (b).

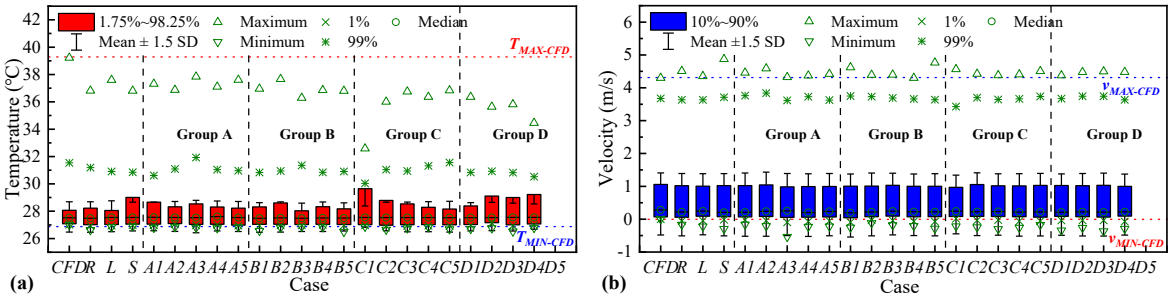

Figure. 3 The overall distribution of temperature and velocity prediction data for conventional activation functions and Leaky-Sigmoid activation functions with different α and β combinations. (a) Overall data distribution of temperature. (b) Overall data distribution of velocity. The Δ and ▽ are the maximum and the minimum values in each predicted data (velocity or temperature distribution). The * is the 1st or 99th percent of the data sequentially.

3.1.3. Local data distributions

To examine the detailed information in the key regions, some local data are extracted as shown in Fig. 4. The overall predicted temperature curves for the Leaky-Sigmoid activation functions show zigzag patterns when $\alpha \geq 0.1$ (Group C). The temperature distribution becomes progressively more unstable as α increases, displaying unexplained inflection points, especially when $\alpha \geq 0.1$. These inflection points also appear in MLPs with conventional activation functions, providing strong evidence of the absence of physical constraints in neural networks. In Groups A and B, the prediction results have a higher accuracy compared to other groups. As α increases, the MLP's prediction for the velocity range shows little variation, whereas the temperature predictions become relatively more discrete. Significant fluctuations in the temperature distribution occur only near the heat source, indicating that the activation functions may lack the sensitivity required to accurately predict data distributions in regions with high variability. Additionally, MLPs can force-fit the data and accurately capture the magnitudes of velocity and temperature, regardless of the activation function used. However, it is important to recognize that this forced-fitting approach disregards objective physical patterns and relies solely on a data-driven perspective. Enhancements could be realized by implementing more sophisticated deep learning approaches that incorporate various data pre-processing techniques.

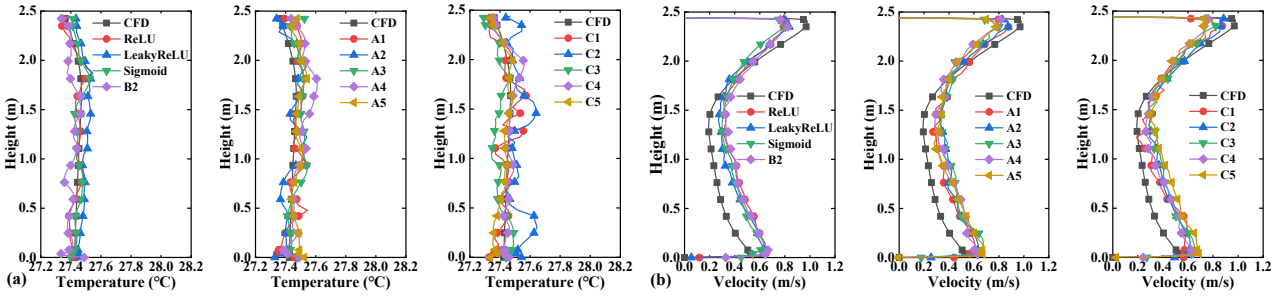

Figure. 4 Local data distribution for temperature and velocity predicted by CFD simulation, conventional activation functions, and MLPs employing Leaky-Sigmoid activation functions with various combinations of α and β at x = 5.305 m. (a) Distribution of temperature at the monitoring line. (b) Distribution of velocity at the monitoring line.

3.2. Prediction Efficiency in Training and Testing Datasets

As shown in Fig. 2 (d), within each group, the computation time is relatively shorter when β assumes a higher value. Group D is not significantly representative due to its dispersion conditions ($\alpha = 0.5, \beta = 4.0$). The average training time for the Leaky-Sigmoid activation functions is 2.4%, 6.1%, and 6.0% slower than that of the ReLU, Leaky-ReLU, and Sigmoid activation functions, respectively, when computed over the same number of epochs. The prediction time for each activation function is approximately 2 milliseconds, which is one millionth of the time required by the CFD simulations.

4. DISCUSSION

This section aims to explain the principles governing Leaky-Sigmoid activation functions through theoretical analyses, using the MLP neural network as an example, as shown in Fig. 1 (b). The formula for the total loss function is presented below. For ease of analysis, the loss ($E_{partial}$) of temperature and velocity are considered separately at each coordinate point in this derivation.

$$E_{total} = \frac{1}{N}\sum_{i=1}^{N}\left[(v_i - \tilde{v}_i)^2 + \left(T_i - \tilde{T}_i\right)^2\right] \quad (2)$$

$$E_{partial} = \left[(v - \tilde{v})^2 + \left(T - \tilde{T}\right)^2\right] \quad (3)$$

$$\frac{\partial E_{partial}}{\partial w_{X1,1}} = 2\left[(v - \tilde{v}) \cdot w_{D1,1} + \left(T - \tilde{T}\right) \cdot w_{D1,2}\right] \cdot \Psi'\left(H_1 \cdot w_{H1,1} + b_{H1,1}\right) \cdot w_{H1,1} \cdot \Psi'\left(X_1 \cdot w_{X1,1} + b_{X1,1}\right) \cdot X_1 \quad (4)$$

$$w_{X1,1}{}^{+} = w_{X1,1} - \eta \cdot \frac{\partial E_{partial}}{\partial w_{X1,1}} \quad (5)$$

In the formula, i is the index of the input data (i.e., the coordinate point index, i = 1, ..., N with N = 48 × 4733 = 227184), v_i, T_i are the real values obtained from the CFD simulation, while $\tilde{v}_i$, $\tilde{T}_i$ are the prediction values from the MLP. The physical meaning of $\frac{\partial E}{\partial w}$ is the amount of the resultant change in E when w changes, w^+ is the weight after the gradient update, and w is the weight before the gradient update. η represents the learning rate.

Eq. 5 provides the generic formula used in the above derivation to solve $w_{X1,1}$. In this network, the derivative of the Sigmoid activation function appears twice, such as $\sigma(t)\left(1 - \sigma(t)\right)$ $(t = H_1 \cdot w_{H1,1} + b_{H1,1}$, $H_1 = \sigma(\varphi))$, and $\sigma(\varphi)\left(1 - \sigma(\varphi)\right)$ $(\varphi = X_1 \cdot w_{X1,1} + b_{X1,1})$. The derivative of the Leaky-Sigmoid activation function is $\beta \cdot \sigma(t')\left(1 - \sigma(t')\right)$ $(t' = H_1' \cdot w_{H1,1} + b_{H1,1}$, $H_1' = \beta \cdot (\sigma(\varphi) - 0.5))$ and $\beta \cdot \sigma(\varphi)\left(1 - \sigma(\varphi)\right)$ $(\varphi = X_1 \cdot w_{X1,1} + b_{X1,1})$.
When $x > 0$,

$$\Psi'\left(H_1 \cdot w_{H1,1} + b_{H1,1}\right) \cdot \Psi'\left(X_1 \cdot w_{X1,1} + b_{X1,1}\right) = \beta^2 \cdot \sigma(t')\left(1 - \sigma(t')\right) \cdot \sigma(\varphi)\left(1 - \sigma(\varphi)\right) \quad (6)$$

When $x \leq 0$,

$$\Psi'\left(H_1 \cdot w_{H1,1} + b_{H1,1}\right) \cdot \Psi'\left(X_1 \cdot w_{X1,1} + b_{X1,1}\right) = \alpha^2 \quad (7)$$

When other parameters remain constant, the weights of the networks with the Leaky-Sigmoid activation functions update more quickly with larger β values, indicating a larger step size in the gradient update. As a result, each iteration of the neural network gets more information, thereby increasing the prediction accuracy. Furthermore, when x ≤ 0, the derivative of the Leaky-Sigmoid activations becomes quite low, determined by the constant α^2. Given the variance in the distribution of input data and the randomness of the initial weights, the variable including X and H_1, will alternate between positive and negative during the backpropagation process. The loss will fluctuate as the magnitude of the weight update increases or decreases with each gradient computation when α and β induce 'instantaneous switching' during the training process. This phenomenon causes the loss to fluctuate more widely as β increases, explaining the oscillations observed in some monitoring lines. Therefore, a higher β accelerates the speed of weight updates, increasing the prediction accuracy. Selecting the appropriate values necessitates thorough testing and multiple rounds of debugging. Indeed, determining the optimal value β requires careful consideration of several factors, including weight initialization, network architecture, and data distribution, among others.

5. CONCLUSIONS

In this study, the performance of the Leaky-Sigmoid activation functions is detailedly evaluated by prediction accuracy and efficiency. Additionally, this study aims to understand the basic patterns underlying Leaky-Sigmoid activation functions through theoretical analysis. The main conclusions are as follows.

1) MLP can quickly predict the temperature and velocity distributions in a mixing ventilation room. To some extent, it can serve as a substitute for CFD simulation in real-time predictions of temperature and velocity distributions within a specific range of boundary conditions, achieving a relative error of approximately 2% compared to CFD simulations. The prediction time is merely 2 milliseconds, representing just one millionth of the time required by the CFD simulations.

2) In terms of training accuracy, the Leaky-Sigmoid activation functions are better than conventional activation functions in B3 and B5. When α is low, the RMSE and relative error of the neural networks during the same epoch steadily decrease as β increases, producing a gradual improvement in training accuracy. The relative errors for temperature in B3 and B5 are 19.47% and 9.10% lower, respectively, compared to the results from the ReLU activation function.

3) The specific formula of the activation functions significantly impacts both the rate of weight updates in the neural networks and the prediction accuracy. The amplitude of the oscillations in prediction results slightly increases as β increases. Additionally, it is crucial to consider the initialization of weights, as well as the width and number of layers within neural networks. Each neural network has an appropriate set of activation functions. Fixed activation functions are merely a compromise for accuracy and convenience.

ACKNOWLEDGEMENTS

This work was supported by the National Key Research and Development Program of China (NO.2023YFC3805304-2) and International Cooperation project of Science and Technology Commission of Shanghai Municipality (NO.22200711400).

REFERENCES

Bengio Y., Simard P., Frasconi P., 1994. Learning long-term dependencies with gradient descent is difficult. IEEE transactions on neural networks 5, 157-166.

Cybenko G. Continuous valued neural networks with two hidden layers are sufficient, University of Illinois at Urbana-Champaign. Center for Supercomputing Research and Development, 1988.

Glorot X., Bordes A., Bengio Y., 2011. Deep sparse rectifier neural networks. In: Proceedings of the fourteenth international conference on artificial intelligence and statistics, Lauderdale, Vol. 15, pp. 315-323.

Grigorescu S., Trasnea B., Cocias T., Macesanu G., 2020. A survey of deep learning techniques for autonomous driving. Journal of Field Robotics 37, 362-386.

Krizhevsky A., Sutskever I., Hinton G.E., 2017. ImageNet classification with deep convolutional neural networks. Communications of the ACM 60, 84-90.

Li Z., Kovachki N., Azizzadenesheli K., Liu B., Bhattacharya K., Stuart A., 2021. Fourier neural operator for parametric partial differential equations. arXiv preprint arXiv, 2010.08895.

Maas A., Hannun A., Ng A., 2013. Rectifier nonlinearities improve neural network acoustic models. In: Proceedings of the 30th International Conference on International Conference on Machine Learning – ICML'13, Georgia, Vol. 30, pp. 3.

Obiols-Sales O., Vishnu A., Malaya N., Chandramowliswharan A., 2020. CFDNet: A deep learning-based accelerator for fluid simulations. In: Proceedings of the 34th ACM international conference on supercomputing – ICS '20, Barcelona, Vol. 3, pp. 1-12.

Zhou Q., Ooka R., 2020. Influence of data preprocessing on neural network performance for reproducing CFD simulations of non-isothermal indoor airflow distribution. Energy and Buildings 230, 110525.

6th International Conference on Building Energy and Environment
Eindhoven University of Technology, The Netherlands
6 - 10 July 2025

The influence of cascading airflow paths on the performance of a residential exhaust ventilation system

Van Thillo Jitse[1], Zakarya Kabbara[2], Jorens Sandy[3], Verhaert Ivan[4]

[1] *University of Antwerp, Antwerp, Belgium, jitse.vanthillo@uantwerpen.be*
[2] *University of Antwerp, Antwerp, Belgium, zakarya.kabbara@uantwerpen.be*
[3] *University of Antwerp, Antwerp, Belgium, sandy.jorens@uantwerpen.be*
[4] *University of Antwerp, Antwerp, Belgium, ivan.verhaert@uantwerpen.be*

SUMMARY

Managing airflow paths in residential buildings is essential for indoor air quality (IAQ), occupant comfort, and energy efficiency. While ventilation rates and system types often get attention, airflow path configuration remains underexplored. This study uses Modelica-based simulations to assess three strategies: direct exhaust, cascading, and extended cascading systems, under varying occupancy scenarios.

In direct exhaust, each room is ventilated separately, ensuring good local air quality but at higher energy costs. Cascading systems guide air from one room to another, reducing total airflow needs while maintaining IAQ. The extended cascading system furthers this by routing air through multiple zones, achieving similar IAQ with lower airflow rates and energy use.

Results show all systems maintain acceptable CO_2 levels, but extended cascading offers the best energy performance, cutting consumption by up to 30% without sacrificing comfort. The findings highlight the value of optimizing airflow paths, especially in renovation projects.

Keywords: residential ventilation, cascading ventilation, air quality, energy efficiency

1. INTRODUCTION

The residential ventilation market has faced significant challenges due to evolving consumer demands, stricter regulations, and climate goals. The building sector contributes approximately 36% of total CO_2 emissions in the European Union, highlighting its role in sustainability efforts (Economidou et al., 2020). Improving energy efficiency in buildings has become a priority, leading to tighter regulations such as the Energy Performance of Buildings Directive (EPBD). However, renovation rates remain insufficient to meet climate targets (Filippidou et al., 2016; Sandberg et al., 2016).

Deep renovations, which enhance insulation and reduce air leakage, significantly lower energy consumption (Kurnitski et al., 2014). However, increased airtightness also reduces natural airflow, negatively impacting indoor air quality (IAQ). Effective ventilation systems are essential for

maintaining acceptable IAQ levels and mitigating health risks, including Sick Building Syndrome (SBS) and Building-Related Illness (BRI) (EPA, 1991).

Beyond health, ventilation plays a critical role in reducing airborne disease transmission, as underscored by the COVID-19 pandemic. However, many systems designed for regulatory compliance fail to ensure adequate IAQ in practice, highlighting the need for performance-based design approaches. The 2022 energy crisis further emphasized the importance of energy-efficient solutions, as rising energy costs pressured households to reduce consumption. Renovation projects face additional technical and economic challenges when integrating modern ventilation systems into existing structures.

Three primary ventilation systems exist, each with distinct benefits and limitations (Zaniboni and Albatici, 2022). Natural ventilation depends on wind and buoyancy but is weather-dependent. Mechanical exhaust ventilation improves airflow control using a fan but requires ductwork and additional energy. Mechanical balanced ventilation provides precise airflow control and heat recovery but is complex to install. The optimal system choice depends on building constraints, climate, and occupant behavior.

A key determinant of ventilation efficiency is airflow path design, which influences both energy use and IAQ. Series connections between rooms can reduce fresh air requirements and simplify ductwork but may compromise air quality in downstream spaces. Fewer exhaust points lower costs but challenge uniform air distribution. These trade-offs are particularly relevant in renovations, where flexibility and adaptability are crucial.

This paper explores airflow path optimization for energy-efficient and effective ventilation in residential buildings, with a focus on renovation challenges. By examining the relationship between airflow configurations, IAQ, and energy use, this research aims to optimize ventilation design to balance sustainability and occupant well-being.

2. METHOD

The aim of this paper is to explore multiple variants of an exhaust ventilation system by examining different airflow paths and pressure drops across components, and to compare their performance in terms of indoor air quality (IAQ) and energy consumption. Extended airflow paths can offer energy benefits due to reduced overall airflow rates but may negatively impact IAQ. To evaluate the performance of the various ventilation systems, a simulation framework is required.

2.1. Building Model

For this research, a virtual building model is created using the Modelica modelling language. This equation-based language enables the modelling of building physics and allows for transient simulations. The building model is based on the IDEAS library, developed by KU Leuven (Jorissen et al., 2018). This library includes pre-made and validated sub-models (e.g., walls, windows) that can be used to construct a zonal model representing the building. The model assumes that the air in each zone is well-mixed, meaning air quality is considered uniform throughout the zone. A similar approach is used for temperature, however, thermal stack models are implemented to account for air movement caused by temperature differences. This concept is also applied to model infiltration,

specifically by placing two cracks at different heights in the wall. The dimensions of these cracks are based on the building's airtightness. Additionally, the outdoor environment (e.g., wind speed, temperature, humidity) is defined by a weather file, which varies over time and location. This weather file is also used to calculate wind pressure on the facades.

2.2. CO_2 Concentration

Carbon dioxide (CO_2) is a widely used indicator for ventilation performance, particularly due to its strong link with human activity, a relevance highlighted during the COVID-19 pandemic. Although CO_2 itself poses minimal direct health risks at typical indoor levels (requiring >10,000 ppm for extended periods to be harmful), it often co-occurs with other bio-effluents such as odours and ammonia that affect comfort and health (Fanger et al., 1988; Zhang et al., 2017). Elevated concentrations have been associated with reduced cognitive performance and sleep quality, reinforcing its role as a practical proxy for IAQ (Satish et al., 2012; Strøm-Tejsen et al., 2016).

Because of its strong correlation with occupancy, CO_2 is particularly relevant in occupied spaces. In contrast, IAQ in unoccupied zones is more influenced by emissions from materials or ventilation systems. This study follows the NBN EN 13779 standard, targeting the IDA 3 "acceptable" category, with CO_2 levels maintained below 800 ppm.

To model realistic conditions, CO_2 production is based on occupant behavior, using a metabolic-rate-based formula that links activity to emission rates (Persily and Jonge, 2017). This enables a detailed assessment of system performance under dynamic occupancy.

2.3. Humidity

Humidity is a critical factor in IAQ, significantly influencing occupant health, comfort, and building durability. High humidity encourages mould growth, which can damage furniture, pose health risks, and diminish indoor aesthetics. Conversely, low humidity may lead to nasal, throat, and eye irritation, highlighting the importance of maintaining stable humidity levels. Humidity is typically expressed as absolute humidity (g/kg) or relative humidity (RH). While absolute humidity measures moisture content regardless of temperature, relative humidity, which is more relevant to human perception, varies with temperature.

Comfort standards for indoor environments are usually based on RH, with an optimal range of 30–70% (Wolkoff, 2018; Wolkoff et al., 2021). Values below this range can cause discomfort, such as dry eyes and sore throats, while levels above 70% RH increase the likelihood of mould growth. At near 100% RH, condensation becomes inevitable, potentially causing water damage. The humidity model used in this study, similar to the CO_2 model, is linked to occupant metabolic activity (Poirier et al., 2021).

2.4. Energy Losses

Besides IAQ, energy use is the second key performance indicator for ventilation systems. The primary energy losses are thermal, resulting from the temperature difference between indoor and outdoor air. In winter, cold outdoor air increases heating demand, while in summer, warm outdoor air raises cooling needs. The extent of these losses depends on the mass flow rate of ventilated air and the temperature differential.

Thermal comfort is characterized by the operative temperature, which combines air temperature and mean radiant temperature. Achieving universal thermal comfort is complex due to variations in individual preferences, clothing, activity levels, humidity, and draft sensitivity. Fanger's Predicted Mean Vote (PMV) model, based on activity and clothing levels, is widely used (as per ISO 7730:2005), although adaptive comfort models suggest that occupants can adapt to different temperatures. For simplicity and comparability, a fixed indoor temperature of 21°C is assumed for all zones year-round, in line with EPB approaches. To fully capture the ventilation system's impact, heating and cooling losses are computed for an idealized HVAC system in each zone.

Additionally, the energy used by the ventilation fan to overcome pressure differences is included. While fan energy is generally an order of magnitude lower than thermal losses, it is still factored into the simulations.

3. CASE STUDY

3.1. The Building

For the case study, a two-story, free-standing building representative of a typical Flemish (Belgian) house is selected. This specific building geometry and structure were developed during the GEBOU-EL2EP study (Verbeeck and Hens, 2007). In this research, the building is divided into four zones with distinct functions: the downstairs living and kitchen area, and the upstairs night zone and adjacent bathroom. The zones are fully enclosed by walls, windows, floors, and ceilings modelled using the IDEAS library, enabling realistic simulation of heat losses through the building envelope.

The building is not perfectly airtight, and leakage through the walls allows for (un)intended airflow caused by buoyancy and wind pressure. Wind pressure on each façade is calculated using coefficients from AIVC for a low-rise building surrounded by obstructions equivalent to half the building's height (Liddament, 1996). A historical weather file from central Belgium is used to drive the model.

3.2. Occupancy

To simulate realistic internal loads, four virtual occupants and their associated impacts (i.e., moisture, heat, and CO_2) are modelled. Each occupant follows an individual schedule generated by the EROB model (Event-based Residential Occupant Behaviour model) (Verbruggen, 2021). This deterministic model produces unique behavioral profiles for the entire simulation period, resulting in a realistic load profile that enables performance comparison between ventilation system configurations.

3.3. Airflow Rate

Current practice in residential ventilation design is guided by national standards specifying mandatory airflow rates. In Belgium, the NBN D-50-001 standard defines design criteria for residential ventilation systems. It calculates the required airflow based on available floor space, assigning 3.6 m^3/h per square meter in rooms where occupants are regularly present. Additionally, the standard prescribes minimum and maximum airflow rates for specific room types (e.g., kitchen, bathroom). These rates are used in this case study. For the night zone, an equivalent of three bedrooms is assumed (see Table 1). When air is cascaded from one room to another, the highest required flow

rate among the rooms is used and carried through the rooms with lower ventilation demands.

Two control strategies are applied in the simulations: a fixed airflow rate controller and a simple rule-based controller. The fixed airflow rate controller allows comparison of the airflow paths without the influence of adaptive controls. The rule-based controller adjusts fan speed, and thereby total airflow rate, based on indoor pollution loads (i.e., humidity and CO_2). It can reduce airflow to 10% of the design rate when loads are low. When a threshold is exceeded, 400 ppm above outdoor CO_2 concentration or 70% relative humidity, the airflow increases to the nominal value, and decreases again when values fall below 350 ppm or 50%, respectively.

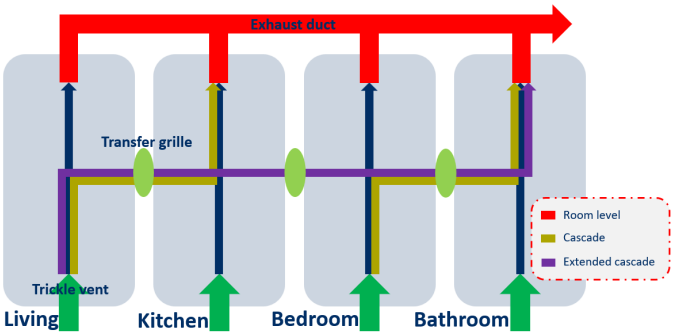

Figure 1. Illustration of the different airflow paths through the house. Red and green arrows indicate the exhaust ducts and trickle vents; the green oval represents a low-pressure-drop transfer grille.

Zone	Airflow Rate $[m^3/h]$
Living	150
Kitchen	66
Bedrooms	150
Bathroom	50

Table 1. Necessary airflow rates for each zone according to NBN D-50-001.

3.4. Ventilation System Design

Given the increased demand for renovation-oriented ventilation systems that ensure healthy IAQ regardless of outdoor conditions, this study focuses on mechanical exhaust ventilation. Three system variants are simulated:

- **Room-based ventilation system:** Each room has an independent supply and exhaust, allowing individual airflow control during the design phase.
- **Cascading ventilation system:** Fresh air is introduced into one room (typically the living room or bedroom) and cascades to another (e.g., kitchen or bathroom) for extraction, reducing total airflow without compromising IAQ.
- **Extended cascading ventilation system:** Air cascades continuously through all rooms, from a trickle vent as the supply to a single extraction point. This further reduces airflow needs, however, it does not align with regulations that require air from wet rooms (e.g., kitchen, toilet, bathroom) to be extracted directly rather than passed through to other rooms.

4. RESULTS AND DISCUSSION

The simulation results of the three ventilation systems under both fixed and adaptive control strategies are evaluated in terms of IAQ and energy consumption, fig. 2 and fig. 3 present the performance metrics for each case. To ensure clear interpretation, time spent outside the target air

quality zone is expressed in hours during which at least one zone exceeds the threshold. If multiple zones exceed the threshold simultaneously, this is multiplied accordingly. CO_2 is quantified as the duration exceeding 400 ppm above outdoor levels, while humidity is evaluated as the time spent below 30% or above 70% relative humidity—both of which indicate potential discomfort or risk.

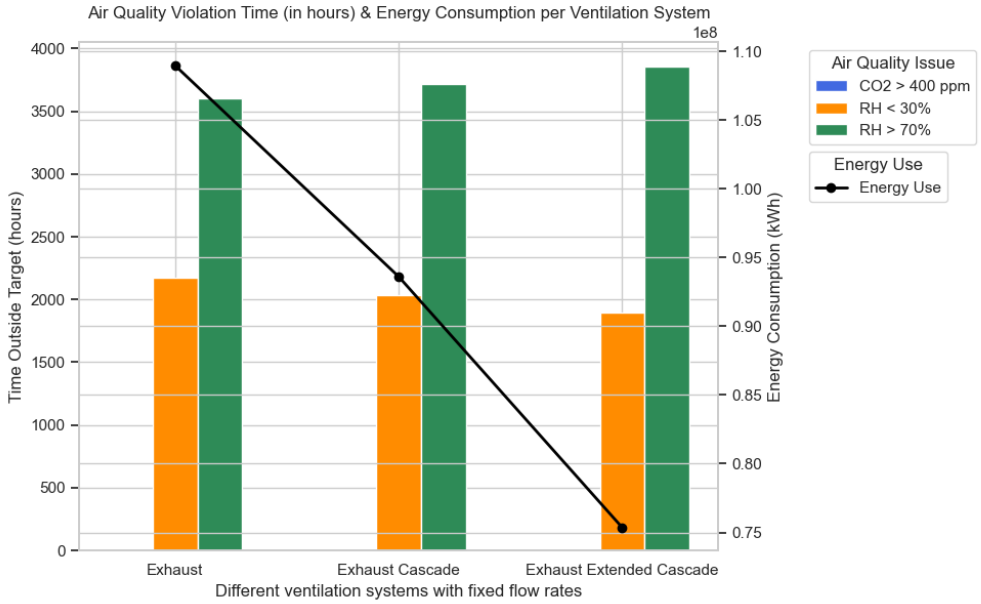

Figure 2. Summary of air quality performance and total energy use for the three ventilation systems with fixed flow rate.

A key observation is that under fixed airflow conditions, all systems maintained CO_2 concentrations within acceptable limits. However, under the rule-based control strategy, only the direct exhaust system consistently kept CO_2 below the threshold. The cascading and extended cascading systems exceeded the threshold for 54 and 485 hours, respectively. This outcome aligns with expectations, as the extended cascading system operates with the lowest airflow. Moreover, since air passes sequentially through multiple rooms, any exceedance in the first zone (e.g., the living room) is propagated downstream, compounding the total hours above threshold.

Humidity trends follow a similar pattern for both control strategies. The direct exhaust system recorded the fewest hours above 70% RH, followed by the cascading and extended cascading systems. Conversely, the extended cascading system performed best in terms of avoiding low humidity (<30%). Comparing the two control strategies, the fixed flow rate slightly outperforms the adaptive strategy for low humidity control, while high humidity exposure remains similar.

One of the major advantages of the extended cascading system is its energy efficiency, primarily due to reduced heating losses. While cooling demand increases slightly, likely due to diminished ventilative cooling in warmer periods, the total energy use is still lower. Among the flow path types, the adaptive direct exhaust configuration achieved the lowest energy use, while the extended cascading system with rule-based control used more energy than its fixed counterpart. This suggests that although adaptive control reduces airflow, it may also limit natural cooling opportunities, thereby increasing mechanical cooling demand.

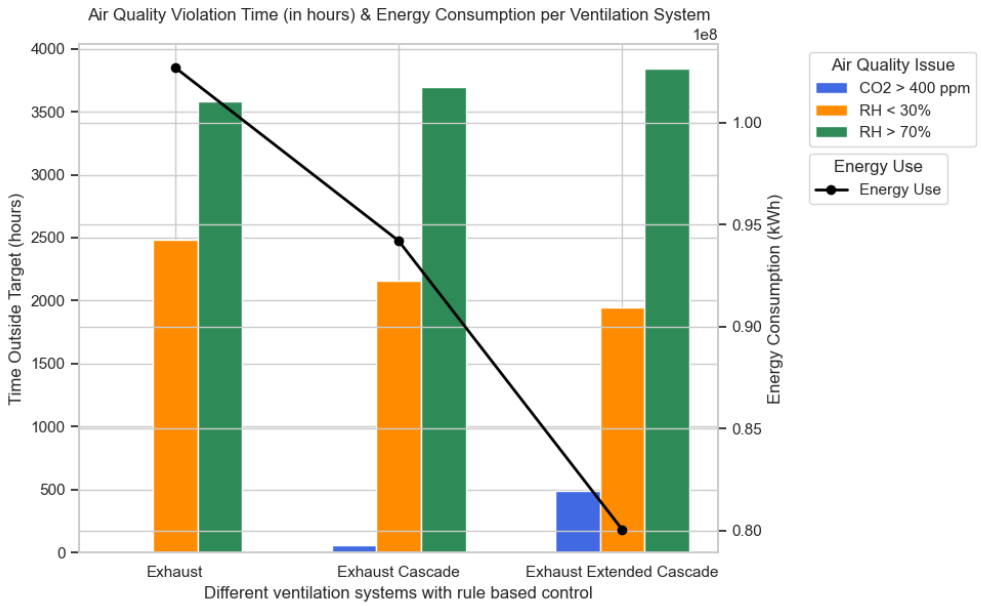

Figure 3. Summary of air quality performance and total energy use for the three ventilation systems with adaptive flow rate due to a rule based controller.

A notable limitation of this study is the absence of advanced control algorithms for both the ventilation and HVAC systems. For example, the current setup could cause simultaneous heating at night and cooling during the day. Incorporating more intelligent control strategies, such as model predictive control (MPC), that respond to occupancy and weather patterns could further reduce energy consumption and improve comfort.

5. CONCLUSION

This study evaluated three residential ventilation strategies, direct exhaust, cascading, and extended cascading systems, under both fixed and adaptive airflow control, using a simulation-based approach. All systems successfully maintained acceptable CO_2 levels under fixed flow rates, even for a two-person occupancy scenario. However, high airflow rates required to meet air quality demands led to increased energy consumption, particularly during colder periods due to heating needs. Cascading airflow through rooms emerged as a potential strategy to reduce total airflow and energy use, while still maintaining IAQ.

Humidity control proved more challenging, particularly during unoccupied periods when conditions were primarily driven by outdoor weather. While these conditions may not directly impact occupant comfort significantly, sustained high humidity poses a risk for condensation and mould growth, affecting both IAQ and building durability.

The extended cascading system demonstrated strong potential for energy savings, up to 30% compared to other systems, while maintaining competitive air quality performance. Results also indicate that airflow configuration alone is not sufficient, the interaction between control strategy and airflow path plays a critical role in balancing IAQ and energy performance.

This study focused on static airflow paths and a limited set of performance indicators. Nevertheless, the benefits of optimized airflow design are clear. Future work should explore dynamic or flexible airflow configurations that respond to occupant needs in real-time. To enable this, intelligent control systems capable of assessing IAQ and energy metrics must be integrated. Additionally, more advanced HVAC control strategies should be considered to avoid unnecessary heating or cooling and to further improve overall system efficiency.

ACKNOWLEDGMENTS

This work has been supported by the Flemish Agency for Innovation and Entrepreneurship (VLAIO) Flux50 cSBO project 'NudgeFlow' (HBC.2023.0488).

REFERENCES

Economidou M., Todeschi V., Bertoldi P., D'Agostino D., Zangheri P., and Castellazzi L., Oct. 2020. Review of 50 Years of EU Energy Efficiency Policies for Buildings. Energy and Buildings 225, 110322.

EPA, Feb. 1991. *Sick Building Syndrome*.

Fanger P. O., Lauridsen J., Bluyssen P., and Clausen G., Apr. 1988. Air Pollution Sources in Offices and Assembly Halls, Quantified by the Olf Unit. Energy and Buildings 12, 7–19.

Filippidou F., Nieboer N., and Visscher H., Nov. 2016. Energy Efficiency Measures Implemented in the Dutch Non-Profit Housing Sector. Energy and Buildings. Towards an Energy Efficient European Housing Stock: Monitoring, Mapping and Modelling Retrofitting Processes 132, 107–116.

Jorissen F., Reynders G., Baetens R., Picard D., Saelens D., and Helsen L., 2018. Implementation and Verification of the IDEAS Building Energy Simulation Library. Journal of Building Performance Simulation 11 (6), 669–688.

Kurnitski J., Kuusk K., Tark T., Uutar A., Kalamees T., and Pikas E., June 2014. Energy and Investment Intensity of Integrated Renovation and 2030 Cost Optimal Savings. Energy and Buildings 75, 51–59.

Liddament M. W., 1996. A Guide to Energy Efficient Ventilation. Technical Note / AIC. Air Infiltration and Ventilation Centre, Coventry.

Persily A. and Jonge L., 2017. Carbon Dioxide Generation Rates for Building Occupants. Indoor Air 27, 868–879.

Poirier B., Guyot G., Geoffroy H., Woloszyn M., Ondarts M., and Gonze E., Oct. 1, 2021. Pollutants Emission Scenarios for Residential Ventilation Performance Assessment. A Review. Journal of Building Engineering 42, 102488.

Sandberg N. H., Sartori I., Heidrich O., Dawson R., Dascalaki E., Dimitriou S., Vimm-r T., Filippidou F., Stegnar G., Šijanec Zavrl M., and Brattebø H., Nov. 2016. Dynamic Building Stock Modelling: Application to 11 European Countries to Support the Energy Efficiency and Retrofit Ambitions of the EU. Energy and Buildings 132, 26–38.

Satish U., Mendell M. J., Shekhar K., Hotchi T., Sullivan D., Streufert S., and Fisk W. J., Dec. 2012. Is CO2 an Indoor Pollutant? Direct Effects of Low-to-Moderate CO2 Concentrations on Human Decision-Making Performance. Environmental Health Perspectives 120, 1671–1677.

Strøm-Tejsen P., Zukowska D., Wargocki P., and Wyon D. P., 2016. The Effects of Bedroom Air Quality on Sleep and Next-Day Performance. Indoor Air 26, 679–686.

Verbeeck G. and Hens H., 2007. Optimisation of Extremely Low Energy Residential Buildings - KU Leuven. phdthesis, KULeuven.

Verbruggen S., Sept. 2021. Window Use Habits as an Example of Habitual Occupant Behaviour in Residential Buildings. phdthesis, Gent University, Gent.

Wolkoff P., Apr. 1, 2018. Indoor Air Humidity, Air Quality, and Health – An Overview. International Journal of Hygiene and Environmental Health 221, 376–390.

Wolkoff P., Azuma K., and Carrer P., Apr. 1, 2021. Health, Work Performance, and Risk of Infection in Office-like Environments: The Role of Indoor Temperature, Air Humidity, and Ventilation. International Journal of Hygiene and Environmental Health 233, 113709.

Zaniboni L. and Albatici R., Nov. 2022. Natural and Mechanical Ventilation Concepts for Indoor Comfort and Well-Being with a Sustainable Design Perspective: A Systematic Review. Buildings 12 (11), 1983.

Zhang X., Wargocki P., and Lian Z., 2017. Physiological Responses during Exposure to Carbon Dioxide and Bioeffluents at Levels Typically Occurring Indoors. Indoor Air 27, 65–77.

6th International Conference on Building Energy and Environment
Eindhoven University of Technology, The Netherlands
6 - 10 July 2025

Health in the Built Environment: A lifelong goal

Helianthe S.M. Kort[1], Henk W. Brink[2], Marcel G.L.C. Loomans[1]

[1]*Eindhoven University of Technology, Eindhoven, The Netherlands,*
[2]*Research Group Facility Management, Research Centre for Built Environment NoorderRuimte, Hanze University of Applied Sciences, Groningen, The Netherlands,*
h.s.m.kort@tue.nl, h.w.brink@pl.hanze.nl, m.g.l.c.loomans@tue.nl

SUMMARY
Creating healthy building environments is highly relevant in cities that face growing populations, climate change, mobility challenges, and the risk of crises such as a pandemic. Society increasingly values sustainable environments that support the functionality of buildings for their users. Adding value to the environment goes beyond sustainability for energy savings or circularity. Building engineers should be (more) aware of the impact of the built environment on building users, their performance at work, school, and home, and their health and well-being. Addressing the cross-cutting health issue in the built environment requires multidisciplinary research to find design, construction, and technology solutions for societal challenges. In line with the above context, the paper presents several examples of research studies illustrating the position of health in research executed by the Health in the Built Environment Community at the Department of Built Environment at Eindhoven University of Technology.

Keywords: Public Health, Indoor Air Quality, Human Performance, Climate Change.

1. THE RELEVANCE OF HEALTH IN THE BUILT ENVIRONMENT

Examining health in the built environment has to be preceded by understanding health. Health is not merely the absence of disease or infirmity but also includes complete physical, mental, and social well-being, as stated by the WHO constitution (WHO, 2005). In addition to this, we have to realize that health also relates to (self) managing or coping with a chronic disorder or NCD (Non-Communicable Disease). The WHO indicates that NCDs account for nearly 75% of deaths in the WHO European Region, which includes the Netherlands (WHO, 2020). Cardiovascular diseases and cancers are the leading causes of premature mortality in the region.

So we could argue that to examine health there are two tracks to follow. One is indicated as the health continuum, which comprises the route of being healthy, obtaining a disease, and having diagnostic examinations, after which there is treatment in the hospital or at home, eventually followed by rehabilitation. The other track contains self-managing or coping with one or multiple chronic disorders. NCDs usually are treated by pharmacological interventions (medication and or therapy, information, and lifestyle advice). These tracks can have an individual approach or a public health approach.

The central mission of the Dutch Ministry of Health, Welfare, and Sport (VWS) is aiming that in 2040 all Dutch citizens will live at least five years longer in good health, and the health disparities between the lowest and highest socioeconomic groups will have decreased by 30%."The mission has five objectives: Promoting Healthy Lifestyles, Improving Access to Care, Supporting People

with Chronic Diseases, Focusing on Dementia Care, Improving care and support for people with dementia and their families, and Reducing Health Inequalities (Ministerie VWS, 2023).

All objectives except the objective of improving Access to Care entail the Built Environment. The Built Environment includes elements like buildings and their services. Building façades connect Indoor Environmental Quality (IEQ) to outdoor environmental quality as well as city design, including walking and cycling paths and parks, which are crucial for promoting healthy lifestyles, enhancing quality of care, supporting mental health, and encouraging physical activity. This illustrates that the built environment could be used as a passive non-pharmacological intervention aiming at both public health as well as individual health and well-being. The application domains are broad, from home to school, work, leisure facilities, hospital, and long-term and residential care. Target groups can be all citizens, children, young people, aging adults, as well as those who take care professionally or voluntarily for someone with a care demand. Alongside understanding health, it's essential to have a deep knowledge of the target group to assess the impact of the built environment or to develop effective solutions.

There are current knowledge gaps where the needs and perceptions of target groups are often not well understood. Additionally, building environment requirements frequently overlook individuals with health problems or NCDs. Existing guidelines for the built environment do not always align well with understanding their impact on health. More research is needed to better align these guidelines with health benefits.

In the following paragraphs, a narrative of various studies tries to illustrate the above statements, considering the life course of children to older adults, including those who provide professional care when needed. Studies selected are aligned to the life course and are studies executed by the Health in the Built Environment Community at the Department of Built Environment at Eindhoven University of Technology.

2. CHILDREN AT PRESCHOOL AND YOUNG PEOPLE AT SCHOOLS

Children at preschool or daycare centers are not the easiest target group since they cannot voice their needs about the built environment. Nevertheless, highly interesting and extensive studies have been executed, focusing on the Indoor Air Quality (IAQ) in Dutch daycare centers and on the effect of the indoor environment on learning outcomes in higher education classrooms. Education is seen as a relevant prevention of health problems.

2.1. VOCs emission, ventilation, and health risks at daycare centers

This research by Zheng et al. focused on sources of indoor air contamination, such as emissions of Volatile Organic Compounds (VOCs) from materials and daycare center activities, and the effectiveness of ventilation in bedrooms to mitigate exposure to such contaminants. Analyses of VOC emissions from arts and crafts and cleaning activities representative of daycare centers demonstrated that there are clear differences between the products used (Zheng et al., 2024). Although the emission rates appear to be generally acceptable for adults, very young babies may be exposed to a health risk from such emissions. This shows the importance of considering the specific target group in the analysis.

With regard to ventilation, the study showed that in Dutch daycare centers the ventilation in the

sleeping rooms is inadequate (Zheng et al., 2023a,b). This is due to the type of beds used in such centers. They do not allow effective ventilation, which may result in unfavorable IAQ conditions for the baby or toddler, e.g., due to emissions from mattresses. The results would favor a rethinking of the design of bedrooms and beds for daycare centers. A design improvement with local ventilation was proposed (Zheng et al., 2025).

2.2. Indoor Environment Quality influencing the academic performance

The most important role for school management is to provide an optimal school climate that represents virtually every aspect of the school experience. This includes the quality of teaching and learning, school-community relationships, school organization, and the institutional and structural features of the school environment (Wang & Degol, 2016). A positive school climate is associated with students' healthy development and the retention of lecturers and can even have a predictive value for the academic performance of students (Cohen et al., 2009).

To improve the effectiveness of this climate, it is essential to create an optimal learning environment. This requires, among other things, appropriate ventilation, heating and air conditioning, ample forms of lighting, necessary acoustical control, and upkeep of maintenance (Wang & Degol, 2016). Evidence reveals that optimal indoor environmental conditions improve students' comfort, health, well-being, and performance (Brink et al., 2021). Four major factors – acoustic environment, lighting, thermal environment, and indoor air quality (IAQ) – determine the indoor environmental quality (IEQ) in school buildings (Frontczak & Wargocki, 2011). Although evidence is piling up, revealing individual contributions of IEQ factors (Brink et al., 2021), evidence which reveals the combined and interaction effects of two or more IEQ factors on students in educational settings is limited (Torresin et al., 2018).

To contribute to the understanding of combined and interaction effects, in future studies, the influence of multiple IEQ factors on students' health, well-being, and performance will be examined. The first results have come available from such studies (Brink et al. 2023), addressing the combination of acoustics, light, and air quality. By extending such research, we aim to gain more in-depth knowledge about how the indoor environment can contribute to an optimal school climate.

3. ADOLESCENTS IN THEIR WORK ENVIRONMENT

3.1. The office environment, work performance, and mental health

Multiple studies worldwide have been executed studying the effects of IEQ on office workers' work performance and mental health. Less explored are the positive health-related, also called salutogenic, aspects on office workers. One promising salutogenic aspect is sound masking in office environments to mitigate distractions and reduce mental health issues. Also, biophilic design elements in office environments positively influence psychological and cognitive responses (Bergefurt, 2023). In addition, other aspects of IEQ, such as lighting, air quality, and thermal comfort, also influence office workers' satisfaction and, consequently, their perception of health. Office workers' satisfaction with privacy, daylight, views outside, and artificial light are highly interconnected, indicating a complex mechanism influenced by multiple variables (Bergefurt et al., 2022).

Earlier research indicated that the lighting conditions experienced by office workers fluctuate throughout the day, with notable peaks in the morning and around lunchtime. Large individual differences in personal light conditions may occur depending on work schedule, traveling to work, sleep behaviour, and preferences. Office workers who worked full-time were less advantaged in their light exposure than those working part-time and spending most time away from the office (van Duijnhoven et al., 2021). Most offices are shared environments, yet office workers often wish to have control over their workspace. Greater perceived control of the indoor environment enhances comfort while impacting the incidence of sick building symptoms positively (Boerstra et al., 2013).

3.2. The care environment and job performance challenges

Healthcare professionals in hospitals and long-term care facilities encounter performance issues related to the IEQ. Hospitals can be likened to a micro city. You need to navigate from one point to another while concentrating on tasks that require either cognitive or physical effort. Remembering to execute tasks becomes even challenging during the day. Nurses may have tasks related to a certain event or related to a time or location (Patient A has to be at location B at time C). In many cases, tasks are interrupted, and remembering to proceed with the execution of the tasks is called the prospective memory. Reinten demonstrated that the PM load of nurses increased during the first 30 minutes of their shift due to distractions, which could be attributed to sound-task interference (Reinten, 2020).

In hospitals, temperature settings were perceived as slightly warm discomfort. Nurses have to wear the obligatory uniform. In hospital wards, temperatures reaching up to 25°C can cause warm discomfort. The optimal thermal sensation for nursing staff tends to be on the cooler side of the scale (Derks et al., 2018). Nurses working in operational theatres also perceive thermal comfort issues. A case study, along with perception data, revealed that within a surgical team, the anaesthesiology assistant reported significantly more complaints compared to other team members. Nurses often perceive their hands and arms as cold due to drafts, whereas surgeons generally report fewer complaints (Jacobs, et al., 2019). Another challenging environment in hospitals concerns the medication room, although nurses do not complain about the lighting. The lighting in one of the medication rooms was below 200 lux at desk level, which is inadequate for performing visual tasks (Aarts et al., 2018).

Despite the dedication and heartfelt efforts of most care staff, working in nursing homes comes with its own set of challenges. Challenges in the built environment include light conditions. Lighting conditions in nursing homes are managed by care staff, particularly in communal areas. Sinoo's studies revealed that out of seven nursing homes where illuminance levels were measured in communal areas and corridors, only one met the threshold values of 750 lx for communal areas and 200 lx for corridors. Additionally, in 90% of the measurements taken in the central or rear parts of common rooms, the limit for horizontal illuminance was not met. Horizontal illuminance at the window met the threshold in 41% of cases (Sinoo, 2016). These measurements were taken in winter (2010), indicating that care professionals need to be especially vigilant during this period to ensure residents receive adequate exposure to (day)light for both visual tasks and maintaining a healthy day/night rhythm.

4. OLDER PEOPLE AT HOME AND IN LONG-TERM CARE FACILITIES

4.1. Older people ageing-in-place

Ageing in place is a concept that allows older adults to remain in their own homes as they age, even if their health and mobility change. Home refers to the unit, the community, the street and the social network. Aging in place also involves having access to care, as well as living in an age-friendly city or neighborhood and a supportive home environment (Raymundo et al., 2024).

General functional and mental decline restricts older people to age-in-place. As people age, many prefer to continue living in their (family) homes, and most countries support this preference through health policies aimed at ageing citizens. Policies alone do not help. Knowledge of risks and validated interventions are needed to support ageing citizens. Interventions could be on a city level, comprising the design of walking and cycling pathways, as well as the position of parks for leisure activities and social connections and the distance to public transportation and facilities. Vitality as loneliness can be mediated by the vicinity of green spaces resulting in physical activities (van den Berg et al., 2019).

In general, it is known that environmental adaptations and improvements and the use of assistive technologies support the independence of older people and increase their quality of life (Lansley et al., 2004). Therefore, more in-depth knowledge is needed about the effect of the built environment on supporting ageing in place.

Older people will experience mental and functional decline. Also, visual decline due to biological ageing and eye or NCDs-related pathologies will occur. The ageing eyes will result in dry-eye symptoms, which could be compensated by medication (eye drops) and interventions in the indoor environment (van Tilborg et al., 2017). Interventions in the indoor environment include maintaining optimal humidity levels, which can help reduce tear evaporation. Minimizing direct airflow from fans or air conditioning units can prevent the exacerbation of dry eye symptoms as well (van Tilborg et al., 2015).
Dry eye symptoms could limit work performance. In another domain, we also see changing requirements regarding thermal comfort due to age and frailty (Schellen et al., 2010; Zhou et al., 2024).

A major issue in ageing-in-place concerns the risk of falls due to eye aging. The anatomy and function of the eye will change over the course of life. A relevant eye function is contrast sensitivity, which discriminates two luminance levels and helps to detect objects in the environment. It also relates to past occurrences of falls and predicts future falls (Saftari et al., 2028). Understanding this relationship in combination with the knowledge of the visual acuity of the ageing eye, the home environment layout, and light conditions will contribute to design solutions for ageing-in-place.

4.2. Indoor environment quality and sleep when having dementia

People with dementia do not always voice their wishes and needs. We have to realize, though, that there are many manifestations of dementia and a majority of people living with dementia (PlwD) are active within their functional and mental capacity. They accommodate strategies to cope with the challenges (Huizenga et al., 2022). Still, they face many challenges in the Built Environment.

A major challenge when having dementia is sleep. This has been identified as a primary reason

for moving people to long-term care facilities. Over time, dementia progresses and will affect sleep disturbance, resulting in displaying challenging behaviors that contribute to increasing the care load of their family carers. Previous studies have shown that non-pharmacological interventions comprising improvement of the IAQ can positively influence sleep quality and next-day performance of older people and youngsters, respectively (Strøm-Tejsen et al., 2016; van der Veen et al., 2021; Mishra et al., 2018). In a future study, the influence of this and other domains of the indoor environment on PlwD will be examined to gain more in-depth knowledge of sleep problems when having dementia and to give directions to design and system solutions.

5. CONCLUSION

Research in the combined domain of health and the built environment addresses developing solutions for several societal challenges over the life course. In addition, gaining competencies in different methodologies and approaches will be a prerequisite. This, however, may not be feasible for most research projects due to time constraints. Therefore, multidisciplinary teams will need to rely on trust, respect, and recognition of each other's expertise.

ACKNOWLEDGEMENTS

We extend our gratitude to all current and past Health in Built Environment Community researchers for their contributions to this interdisciplinary field.

REFERENCES

Aarts, M. P. J., & Kort, H. S. M. (2018). Lighting conditions in hospital medication rooms and nurses appraisal. In Healthy Buildings 2017 Europe, 2-5 July 2017, Lublin, Poland Article ID0118

van den Berg, M. M., van Poppel, M., van Kamp, I., Ruijsbroek, A., Triguero-Mas, M., Gidlow, C., Nieuwenhuijsen, M. J., Gražulevičiene, R., van Mechelen, W., Kruize, H., & Maas, J. (2019). Do Physical Activity, Social Cohesion, and Loneliness Mediate the Association Between Time Spent Visiting Green Space and Mental Health? Environment and Behavior, 51(2), 144-166. https://doi.org/10.1177/0013916517738563

Bergefurt, L., Weijs-Perrée, M., Appel-Meulenbroek, R., Arentze, T., & de Kort, Y. (2022). Satisfaction with activity-support and physical home-workspace characteristics in relation to mental health during the COVID-19 pandemic. Journal of Environmental Psychology, 81. https://doi.org/10.1016/j.jenvp.2022.101826

Bergefurt, A. G. M. (2023). The physical workplace as a resource for mental health: A salutogenic approach to a mentally healthy workplace design at home and at the office. [Dissertatie 1 (Onderzoek TU/e / Promotie TU/e), Built Environment]. Eindhoven University of Technology.

Boerstra, A. C., Beuker, T., Loomans, M. G. L. C., Hensen, J. L. M. 2013. Impact of available and perceived control on comfort and health in European offices. Architectural Science Review, 56(1), 30-41. https://doi.org/10.1080/00038628.2012.744298

Brink, H., Krijnen, W. P., Loomans, M. G. L. C., Mobach, M. P., Kort, H. S. M. 2023. Positive effects of indoor environmental conditions on students and their performance in higher education classrooms: A between-groups experiment. Science of the Total Environment, 869, Article 161813. https://doi.org/10.1016/j.scitotenv.2023.161813

Brink, H. W., Loomans, M. G. L. C., Mobach, M. P., & Kort, H. S. M. (2021). Classrooms' indoor environmental conditions affecting the academic achievement of students and teachers in higher education: A systematic literature review. *Indoor Air*, 31(2), 405–425. https://doi.org/https://doi.org/10.1111/ina.12745

Derks, M. T. H., Mishra, A. K., Loomans, M. G. L. C., & Kort, H. S. M. (2018). Understanding thermal comfort perception of nurses in a hospital ward work environment. Building and Environment, 140, 119-127. https://doi.org/10.1016/j.buildenv.2018.05.039

van Duijnhoven, J., Aarts, M. P. J., van den Heuvel, E. R., & Kort, H. S. M. (2021). Personal lighting conditions of office workers: An exploratory field study. Lighting Research and Technology, 53(4), 285-310. https://doi.org/10.1177/1477153520976940

Frontczak, M., & Wargocki, P. (2011). Literature survey on how different factors influence human comfort in indoor environments. *Building and Environment*, 46(4), 922–937. https://doi.org/https://doi.org/10.1016/j.buildenv.2010.10.021

Huizenga J, Scheffelaar A, Fruijtier A, Wilken JP, Bleijenberg N, Van Regenmortel T. Everyday Experiences of People Living with Mild Cognitive Impairment or Dementia: A Scoping Review. International Journal of Environmental Research and Public Health. 2022; 19(17):10828. https://doi.org/10.3390/ijerph191710828

Jacobs, I. M., Loomans, M., Hensen Centnerová, L., Krombeen, M., & Kort, H. (2019). Thermal comfort in operating theatres for different types of ventilation systems. REHVA Journal, 2019(February), 34-39

Lansley P, McCreadie C, Tinker A. (2004). Can adapting the homes of older people and providing assistive technology pay its way? Age Ageing, 33(6), 571- 576. https://doi.org/10.1093/ageing/afh190

Ministerie VWS Volksgezondheid, Welzijn en Sport (2023) https://www.health-holland.com/sites/default/files/downloads/Missiedocument%20Gezondheid%20en%20Zorg%202024-2027.pdf

Mishra, A. K., van Ruitenbeek, A. M., Loomans, M. G. L. C., Kort, H. S. M. 2018. Window/door opening-mediated bedroom ventilation and its impact on sleep quality of healthy, young adults. Indoor Air, 28(2), 339-351. https://doi.org/10.1111/ina.12435

Raymundo, T. M., Lorenzi, L., Huisman, E., Bet, P., Facioli, M. S. B., Medola, F. O., Bernardo, L. D., Castro, P. C., & Kort, H. (2024). Ageing in place and dementia: A scoping review identifying preconditions and Gerontechnology participation domains. Gerontechnology, 23(1), 1-13. https://doi.org/10.4017/gt.2024.23.1.843.06

Reinten, J. (2020). Exploring the effect of the sound environment on nurses' task performance: an applied approach focusing on prospective memory. [Phd Thesis 1 (Research TU/e / Graduation TU/e), Built Environment]. Technische Universiteit Eindhoven.

Saftari, L.N., Kwon, OS. Ageing vision and falls: a review. J Physiol Anthropol 37, 11 (2018). https://doi.org/10.1186/s40101-018-0170-1

Schellen, L., Marken Lichtenbelt, van, W. D., Loomans, M. G. L. C., Toftum, J., Wit, de, M. H. 2010. Differences between young adults and elderly in thermal comfort, productivity, and thermal physiology in response to a moderate temperature drift and a steady-state condition. Indoor Air, 20(4), 273-283. https://doi.org/10.1111/j.1600-0668.2010.00657.x

Sinoo, M. M. (2016). Light conditions in nursing homes : visual comfort and visual functioning of residents. [Phd Thesis 1 (Research TU/e / Graduation TU/e), Built Environment]. Technische Universiteit Eindhoven

Strøm-Tejsen, P., Zukowska, D., Wargocki, P., & Wyon, D. P. (2016). The effects of bedroom air quality on sleep and next-day performance. Indoor Air, 26(5), 679–686.

van Tilborg, M. A., Kort, H., Murphy, P., & Evans, K. (2015). The influence of dry eye and office environment on visual functioning. In C. Sik-Lányi, E.-J. Hoogerwerf, K. Miesenberger, & P. Cudd (Eds.), Assistive Technology (pp. 427-431). (Studies in Health Technology and Informatics; Vol. 217). IOS Press. https://doi.org/10.3233/978-1-61499-566-1-427

van Tilborg, M. M. A., Kort, H. S. M., & Murphy, P. J. (2017). Specialist report: Dry eye disease and aging. Gerontechnology, 16(4), 211-217. https://doi.org/10.4017/gt.2017.16.4.002.00

Torresin, S., Pernigotto, G., Cappelletti, F., & Gasparella, A. (2018). Combined effects of environmental factors on human perception and objective performance: A review of experimental laboratory works. *Indoor Air*, 28(4), 525–538. https://doi.org/10.1111/ina.12457

van der Veen, K. S., Loomans, M. G. L. C., Kort, H. S. M., Vink, P. R. 2021. The relation between indoor air quality in a bedroom and sleep quality of ageing adults. Healthy Buildings 2021-Europe.

Wang, M., & Degol, J. L. (2016). School Climate: a Review of the Construct, Measurement, and Impact on Student Outcomes. *Educational Psychology Review*, 28(2), 315–352. https://doi.org/https://doi.org/10.1007/s10648-015-9319-1

WHO (2005). https://www.who.int/about/governance/constitution retrieved on February 19, 2025

WHO (2020) https://www.who.int/europe/tools-and-toolkits/noncommunicable-diseases-%28ncd%29-dashboard retrieved on February 19, 2025

Zheng, H., Csemezová, J., Loomans, M., Walker, S., Gauvin, F., Zeiler, W. 2024. Species profile of volatile organic compounds emission and health risk assessment from typical indoor events in daycare centers. Science of the Total Environment, 918, Article 170734. https://doi.org/10.1016/j.scitotenv.2024.170734

Zheng, H., Wang, Z., Loomans, M., Walker, S., Zeiler, W. 2023a. Bedroom ventilation performance in daycare centers under three typical ventilation strategies. Building and Environment, 243, Article 110634.https://doi.org/10.1016/j.buildenv.2023.110634

Zheng, H., Wang, Z., Loomans, M., Walker, S., Zeiler, W.2023b. Bed-level ventilation conditions in daycare centers. Building and Environment, 243, Article 110638. https://doi.org/10.1016/j.buildenv.2023.110638

Zheng, H., Loomans, M. G. L. C., Walker, S. S. W., Wang, Z., Zeiler, W. 2025. Breathing Better: Evaluating the Impact of Personalized Ventilation in Daycare Baby Beds. In P. Wouters, A. Janssens, & M. Kapsalaki (Eds.), 44th AIVC Conference, 12th TightVent Conference, 10th venticool Conference: Retrofitting the Building Stock: Challenges and Opportunities for Indoor Environmental Quality (pp. 21-30). Air Infiltration and Ventilation Centre (AIVC).

Zhou, H., Kort, H. S. M., Loomans, M. G. L. C., Tran, T. H., Wei, S., Zhang, Y., Wang, Y., Shi, W., Zhou, S., & Yu, W. (2024). Lab study on the physiological thermoregulatory abilities of older people with different frailty levels. Building and Environment, 266, Article 112130. https://doi.org/10.1016/j.buildenv.2024.112130

Building Renewables, Solar Buildings and Smart Grid (15:30-17:00 h)

Performance Evaluation of a Nano-composite PCM-integrated Solar Collection System for Space Heating

Yuetian Liu[1], Jiaheng Yu[1], Guoying Xu[1] and Xiaolin Wang[2]

[1]*School of Energy and Environment, Southeast University, Nanjing, China, xugy@seu.edu.cn*
[2]*School of Engineering, University of Tasmania, Australia, xiaolin.wang@utas.edu.au*

SUMMARY

Integrating solar heating system with building envelopes has become an effective means of realizing energy savings and carbon emission reduction in the built environment. However, the traditional passive solar collector walls are limited by inadequate heating regulation and seasonal operation. This study proposes a modular solar collection and storage component integrated with light-absorbing nano-composite phase change materials (NPCMs) that, when combined with existing building walls, can provide flexible solar heating. The NPCM-integrated solar heating system was experimentally investigated for its performance in solar thermal collection and storage as well as space heating. The results indicate that the nano-composite PCM-integrated solar collection system has advantages to achieve higher heating stability. The maximum instantaneous thermal efficiency of the component reaches 78.94%. The ventilation rate of 1.0 m/s resulted in an enhancement of the heating performance of the solar collector-conditioner wall, enabling the wall to maintain a set temperature of 20 ℃ for a duration of 13 hours.

Keywords: Nano-composite PCM; the NPCM-integrated solar collection component; solar heating and ventilation

1. INTRODUCTION

Building energy consumption accounts for a large proportion of global energy use. Therefore, implementing energy-saving measures is essential for reducing carbon emissions. The integration of solar energy into building practices offers a promising approach for decreasing both building energy consumption and associated emissions (Bosu et al. 2023). Passive solar buildings, such as those equipped with Trombe walls (TW), are cost-effective and well-suited for cold climates (Lan et al. 2022;).The application of TW technology mitigates heating demands. The renowned Trombe wall, designed by French architect Felix Trombe (Xue et al. 2010), is the archetypal heat-collecting wall that passively captures solar energy for heating purposes. Subsequent research has focused on refining and enhancing this concept through advancements in wall materials and optimization of structural designs (Corasaniti et al. 2017). Nonetheless, challenges persist with Trombe walls, such as inconsistent heating performance during winter and potential overheating issues in summer conditions (Xiao et al. 2024).

On the other hand, extensive research has been conducted on the incorporation of phase change materials (PCMs) into building fabric, such as walls and roofs. The integration of PCM in building structures enhances thermal capacity, stabilizes indoor temperature, and consequently reduces the total annual cooling and heating loads. Wu et al. (2024) investigated a composite phase-change material comprising three phase-change substances. Their findings revealed that the application of this material resulted in a significant reduction

in temperature fluctuations, achieving a decrease of 31.91% during winter and 54.51% during summer. While prior research has made significant advancements in optimizing PCM wall structures and materials (e.g., enhancing thermal conductivity and phase-change enthalpy), traditional passive solar collector walls or PCM walls are constrained by inadequate heating regulation, seasonal operation constraints, and challenges in retrofitting existing buildings. Additionally, issues such as peeling of solar collector coating, delayed response to thermal regulation are prevalent, and the solar energy utilization efficiency need improved (Askari et al. 2023).

In this paper, a modular solar thermal storage component is proposed, which uses light-absorbing nano-composite phase change material (NPCM) inside. Combined with the existing building walls and other envelope structures, the air supply volume can be flexibly adjusted according to the indoor load, so as to realize the integration of solar collection-heat storage and heating ventilation and reduce the building heating energy consumption and carbon emission.

2. METHODS

2.1. System description

Fig. 1 shows the schematic configuration of the NPCM-integrated solar collection component and its applications in building heating. The solar collection component consists of double insulating glazing, NPCM thermal storage layer, plate metal, air channel. The baseplate is enclosed by the wall to form an air channel.

The NPCM absorbs solar radiation and converts it into thermal energy, which is stored as sensible and latent heat. As the indoor return air or outdoor fresh air flows through the channel, it is heated by the NPCM attached to the inside surface of the metal corrugated baseplate. Subsequently, this warmed air is circulated into the room for space heating.

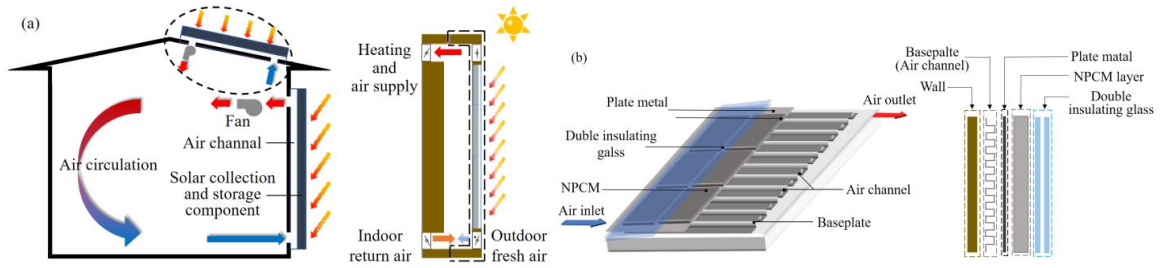

Figure 1. (a) Schematic configuration of the NPCM-integrated solar heating system in building applications, (b) Structure of the NPCM-integrated solar collection component

As shown in Fig. 2, the operation of the system can be divided into four different modes via the precise adjustment of the channel valve, namely: (a) space heating mode; (b) insulation mode, (c)Ventilation and heat insulation mode; (d) The optional mode for water heating. The optional water heating mode can significantly contribute to reducing energy consumption for domestic hot water production during periods when space heating is not required.

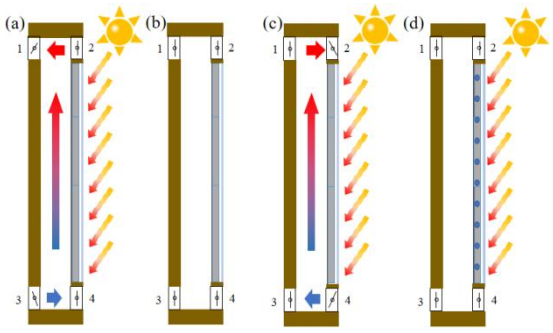

Figure 2. Operation modes: (a) Space heating mode, (b) Insulation mode, (c)Ventilation and heat insulation mode, (d) The optional mode for water heating

2.2. Experiments

To evaluate the heat transfer performance of the NPCM-integrated solar collection component across various operating conditions and parameters, a solar thermal performance test platform was developed. This platform consists of a temperature control system, a NPCM-integrated solar collection component ($0.8m^2$) and a data acquisition system. The experimental setup are shown in Fig. 3.

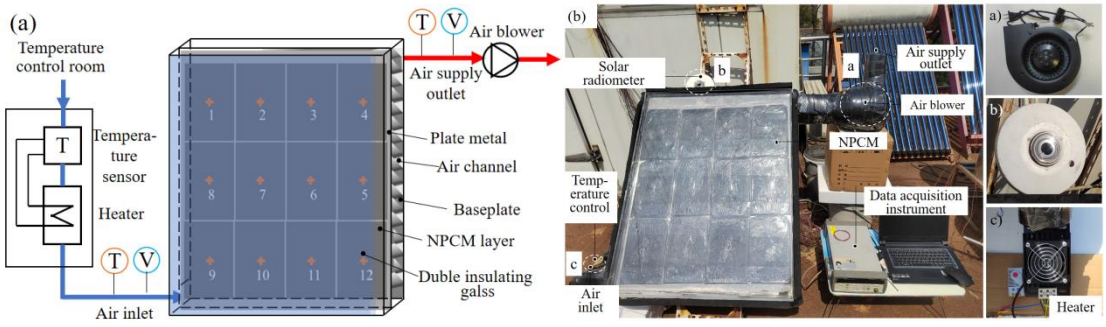

Figure 3. (a) Schematic layout of measurement points, (b) Experimental setup

As shown in Fig. 3, 12 temperature measurement points were uniformly distributed across the central region of the NPCM-integrated solar collection component. Each air inlet and outlet was equipped with temperature and wind speed measurement points to monitor internal temperature variations within the system. The arrangement and nomenclature of the temperature measurement points are illustrated in Fig. 3(a). T_{air} and T_{PCM} were measured using T-type thermocouples (accuracy: ±0.2 ℃, range: -200℃ to 350 ℃). Wind speeds at the inlet and outlet of the channel were measured using a hot-wire anemometer (accuracy: ± 0.1 m/s, range: 0.05 m/s to 50 m/s).

This study aims to enhance light absorption by developing NPCM incorporating graphene. The prepared 0.01 wt% NPCM exhibits both high energy storage density and excellent photothermal conversion performance. The physical properties of the prepared 0.01 wt% NPCM are listed in Table 1.

Table 1. Physical parameters of 0.01%wt% NPCM.

Parameters	Solid	Liquid

Phase change temperature, T/(℃)	51-61	
Latent heat, h/(kJ/kg)	171	
Thermal conductivity, λ[W/(m·℃)]	0.258	0.165
Density, ρ/(kg/m3)	915	880
Absorption Coefficient, Ka/(m-1)	650	350
absorptivity	0.9999	0.9991

2.3. Theoretical Modeling

In the space heating mode, the instantaneous collector efficiency of the NPCM-integrated solar collection component is defined as the ratio of (the daily heat supply to the room (Q_{air}) + the heat stored in the NPCM (Q_{pcm}) to the daily cumulative solar irradiation, as shown in Eq. (1).

$$\eta_i = \frac{Q_{pcm}+Q_{air}}{Q_{sun}} \tag{1}$$

The heat transfer process of collecting wall is shown in Fig. 4, including phase transition and temperature rise of PCM, convection heat transfer inside ventilation holes and conduction heat transfer in PCM. The heat balance equation is expressed in Eq. (2).

$$Q_{sun} = Q_{loss}+Q_{pcm}+Q_{air}+Q_{in} \tag{2}$$

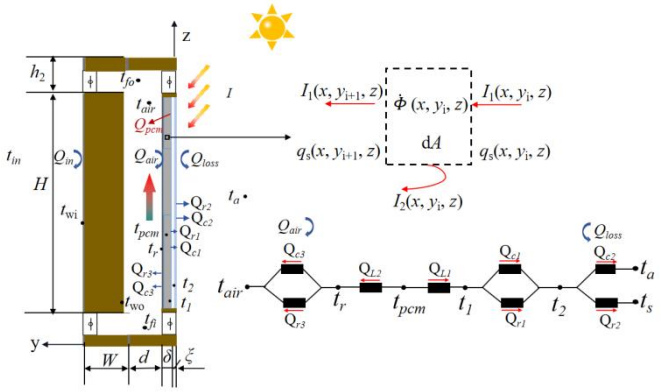

Figure 4. Schematic diagram of heat transfer process for the collecting wall.

The heat exchange amount from the wall to ventilation channel(Q_{air}) is calculated by Eq. (3) .

$$Q_{air} = \int_{\tau_0}^{\tau} h_{ch}A_r(t_r - t_{air})\,d\tau + \int_{\tau_0}^{\tau} \sigma\varepsilon A_r\left(t_r^4 - t_{air}^4\right)d\tau \tag{3}$$

Where h_{ch} is the heat transfer coefficient of the heat transfer surface of the air flow channel, W/(m^2·℃); A_r is the total area of the metal plate in the air flow channel, m^2; t_r, t_{air} are the temperature of the metal plate and the temperature of the air in the air flow channel, ℃; τ is the time.

The heat converted by NPCM from solar radiation (Q_{sun}) and heat stored in NPCM(Q_{pcm}) is

calculated by Eq. (4), (5) respectively.

$$Q_{\text{sun}} = \int_{\tau_0}^{\tau} A_{\text{c}} I \alpha_{\text{nf}} \, d\tau \tag{4}$$

$$Q_{\text{pcm}} = m_{\text{pcm}} c_{\text{pcm}} (t_{\text{i}} - t_{\text{ini}}) + m_{\text{pcm}} + \beta L \tag{5}$$

Where A_{c} is the total lighting area, m^2; α_{nf} is the percentage of radiation absorption of light-absorbing PCM; I is the total solar radiation acting on the outer surface of double insulating glass, W/m^2; t_{ini} is the initial temperature of the NPCM, ℃; t_{i} is the instantaneous temperature of the NPCM at i, ℃; L is the latent heat of phase change of the NPCM, J/kg; and β_{i} is the liquid phase rate of the NPCM at i.

The heat lost to the environment(Q_{loss}) and heat conducted into the room(Q_{in}) is calculated by Eq.(6).(7) respectively.

$$Q_{\text{loss}} = \int_{\tau_0}^{\tau} h_{\text{out}} A_{\text{c}} (t_2 - t_a) \, d\tau + \int_{\tau_0}^{\tau} \sigma \varepsilon A_{\text{c}} \frac{\nu_{\text{fi}} + \nu_{\text{fo}}}{2} (t_2^4 - t_{\text{a}}^4) \, d\tau \tag{6}$$

$$Q_{in} = \int_{\tau_0}^{\tau} h_{in} A_w (t_{wi} - t_{in}) \, d\tau \tag{7}$$

Where h_{out}, h_{in} are the surface heat transfer coefficients of the external wall surface and the internal wall surface, respectively, $\text{W/(m}^2\cdot\text{℃)}$; A_{w} is the internal surface area of the existing wall, m^2; t_2, t_{wi} are the temperature of the external wall surface of the double glazing and the temperature of the internal wall surface of the wall, respectively, ℃; t_{a} is the ambient temperature, ℃; ε is the emissivity of the external wall surface.

3. RESULTS

3.1 Thermal performance of t the NPCM-integrated solar collection component

Fig. 5(a) depicts the variations in outdoor solar radiation intensity and ambient temperature. The period from 13:12 to 17:00 is identified as the heat-release stage, during which the stored heat in the NPCM is released for heating due to the weakened solar radiation. The average ambient temperature measured 13.3 ℃ during the heat-collection phase and 11.5 ℃ during the heat-release phase. The experiment employed a constant air volume heating operation, with an airflow rate of 0.024 m^3/s.

Fig. 5(b) illustrates the temperature variations at the measurement points within the NPCM during the experiment. In the storage-heating phase, the NPCM's temperature rises as it absorbs solar radiation. When the temperature zone reached 51 - 61 ℃ , the heating mode changes to latent heat storage, resulting in a slow temperature rise. After the complete phase change, the heating rate accelerates once more. During the release-heating phase, the NPCM's temperature decreases due to heat exchange with air in the channel. Furthermore, horizontal temperature stratification occurs within the component. The air enters the channel at a lower temperature. As it exchanges heat with the NPCM, the air's temperature rises, diminishing the temperature difference between the air and the NPCM. As a result, the heat exchange intensity is reduced on the outlet side compared to the inlet side.

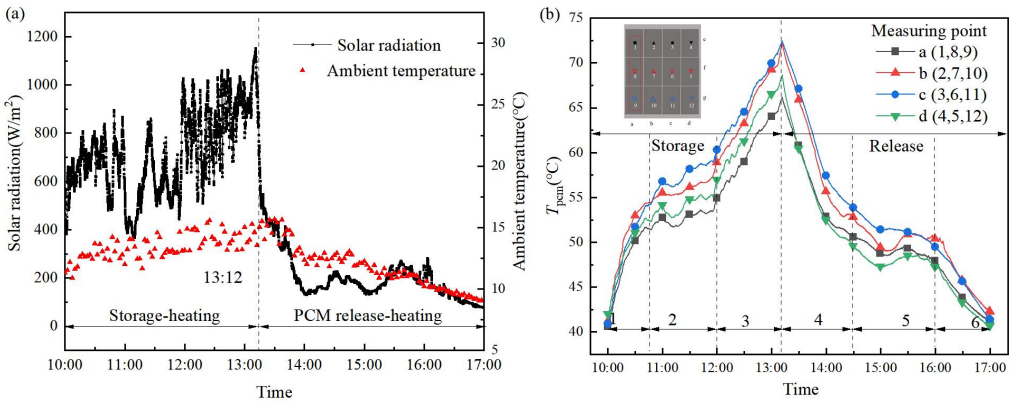

Figure 5. (a)The change in outdoor solar radiation intensity and ambient temperature, (b)Temperature variations of of NPCM at different measuring points

Fig. 6 depicts the solar radiation intensity (Q_{sun}) and heat supply (Q_{air}) across different time periods. The effective output energy of the NPCM-integrated solar collection component with a lighting area of 0.8 m^2 is 6.43 MJ (accounting for about 72.4% of the received solar radiation), which improves the stability of solar heating. Among them, the heat supply in the heat storage section is 3.52 MJ (with a heating power of 305.6 W), and the heat supply in the heat release section of the PCM is 2.90 MJ (with a heating power of 212 W). Notably, due to significant fluctuations in solar radiation, the collector and heating performance varies greatly across different time periods. For instance, the supply air temperature difference before 14:00 can reach 15.4 ℃, with the maximum supply air temperature approaching 40 ℃. However, after 14:00, the heating temperature is mostly below 25 ℃.

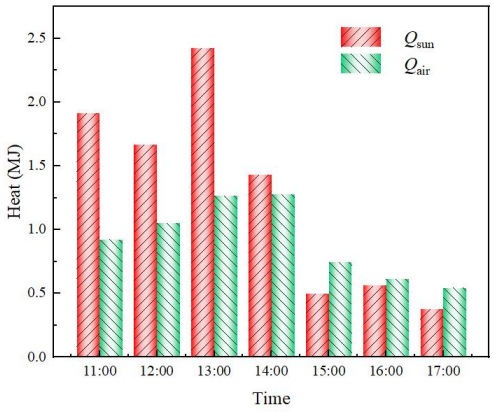

Figure 6. The comparison of Q_{air} and Q_{sun}

3.2 The influence of ventilation rate on the heating

We analyzed the heating performance for a 24 m^2 room with an 18 m^2 NPCM-integrated solar collection component integrated into the south wall. Using DEST software and data from a typical winter day, the room's daily energy load is approximately 130 MJ. The target indoor temperature is 20 ℃, with an air supply rate of 450 m^3 /h. The impact of ventilation speed on heating performance was investigated by systematically altering its rate.

It can be observed from Fig. 7(a) that the supply air temperature decreases as the ventilation rate increases under typical meteorological conditions. At low ventilation rates, the retention time is extended, which facilitates sufficient heat exchange; however, the

intensity of heat exchange remains relatively low, thereby limiting heat removal by the air at the runner side and allowing for predominant accumulation of absorbed heat in the NPCM.

Fig. 7(b) depicts cumulative heat supply over time for different ventilation rates. The dotted line represents the cumulative heat supply required to maintain a set temperature of 20 ℃ within the room. The duration required for indoor temperatures to reach set points varies with different ventilation speeds. The time required for the room temperature to reach the set point when the ventilation speed is 0.6 m/s, 1.0 m/s, 1.4 m/s and 1.8 m/s, respectively, is 19:00 to 01:00 (the following day), respectively. The heating period is guaranteed to last for a minimum of six hours, 13 hours, 14 hours and 15 hours.

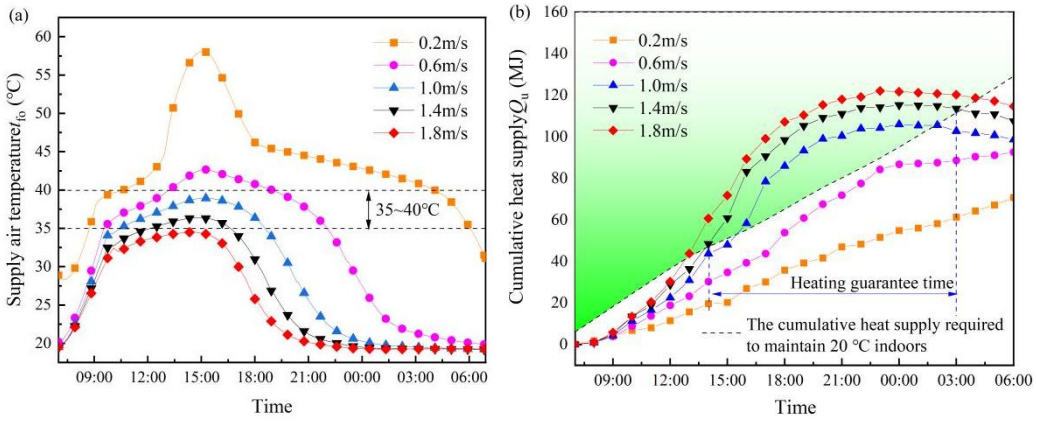

Figure 7. (a) Supply air temperature at different ventilation rates, (b) Variation of heat supply at different ventilation rates over time

Fig. 8 illustrates the daily heat supply and thermal efficiency at various ventilation rates. It is evident that as the ventilation rate increases, there is a corresponding rise in the daily heat supply to the room, average daily thermal efficiency, and guaranteed heating rate, which facilitates greater heat transfer into the room. When the ventilation rate was decreased from 1.8 m/s to 0.2 m/s, all three parameters-daily heat supply, average daily thermal efficiency, and guaranteed heating rate—experienced an approximate reduction of 35.1%.

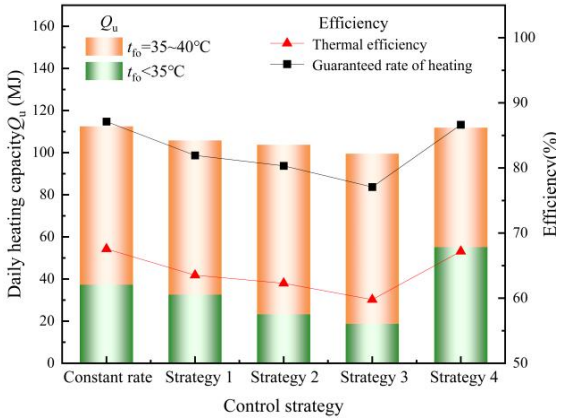

Figure 8. Daily heating capacity and thermal efficiency at different ventilation speeds

At a ventilation speed of 1.0 m/s, the solar collector-storage ventilated thermal wall

demonstrates exceptional heating performance; specifically, it provides a daily heat supply of 112.6 MJ along with an average daily thermal efficiency of 67.6% and a heating guarantee rate of 87.2%. Under these conditions, indoor spaces are capable of achieving a set temperature of 20 ℃ for up to 13 hours.

4. Conclusions

This study proposed a the NPCM-integrated solar collection component integrating solar energy and PCM, and investigated its thermal performance, with a focus on winter heating. The main conclusions drawn in this study are as follows:

During the heating experiment of the NPCM-integrated solar collection component, the maximum instantaneous collector efficiency reached 78.94%. This component delivered 6.43 MJ of heat, accounting for approximately 72.4% of the received solar radiation. Specifically, the storage-heating phase contributed 3.52 MJ (heating power: 305.6 W), while the release-heating phase supplied 2.90 MJ (heating power: 305.6 W), collectively enhancing the stability of solar-assisted heating. When the ventilation speed of the solar collector wall is 1.0m /s, the heating performance is excellent. Its daily heating capacity, daily average thermal efficiency and heating guarantee rate are 112.5MJ, 67.6% and 90.0% respectively, and the room can reach the set temperature of 20 ℃ 13 h.

Compared to traditional systems, the NPCM-integrated solar collection component offers higher heating stability and solar energy utilization efficiency. Its modular design allows for effective adjustment of heat storage and release according to indoor thermal demands.

ACKNOWLEDGEMENTS

This work is financially supported by the National Key Research and Developlment Plan Project of China (2022YFE0208600) and the National Natural Science Foundation of China (No. 52276179), and Natural Science Foundation of Jiangsu Province [grant number BK20231425].

REFERENCES

Bosu I, Mahmoud H, Ookawara S, Hassan H. Applied single and hybrid solar energy techniques for building energy consumption and thermal comfort: a comprehensive review. Energy. 2023; 259: 188 - 228.

Lan X, Qin LC, Wu SY. Proposal and application of comprehensive thermal comfort evaluation model in heating seasons for buildings with solar Trombe wall. Appl Therm Eng. 2022; 213: 118774.

Xue Y, Chen C, Li QQ. Study on the effect of composite phase - change thermal storage wall materials applied to solar greenhouse. North Horticulture. 2010; 222(15): 6 - 11.

Corasaniti S, Manni L, Russo F, et al. Numerical simulation of modified Trombe - Michel Walls with exergy and energy analysis. Heat Mass Tran. 2017; 88: 269 - 276.

Xiao YL, Yang QL, Fei F, Li K, Jiang YJ, Zhang YW, Fukuda H, Ma QS. Review of Trombe wall technology: Trends in optimization. Renewable and Sustainable Energy Reviews. 2024; 200: 114503.

Wu W, Li WZ, Han HB, Xu MJ, Lu EH, et al. Advanced thermal energy storage made of a ternary CPCM with two phase change temperatures in building walls. Energy and Buildings. 2024; 318: 114445.

Mu Y, Li M. Synthesis of novel form - stable composite phase change materials with modified graphene aerogel for solar energy conversion and storage. Solar Energy Materials and Solar Cells. 2019; 191: 466 - 475.

Askari M, Jahangir MH. Evaluation of thermal performance and energy efficiency of a Trombe wall improved with dual phase change materials. Energy. 2023; 284: 128587.

6th International Conference on Building Energy and Environment
Eindhoven University of Technology, The Netherlands
6 - 10 July 2025

Comparative life cycle carbon emission assessment of a residential building: a case study of Cambodia

Makara Long [1,4], Virak Han [2], Pierre Leclercq [3], Sigrid Reiter [4]

[1]*Research and Innovation Center, Institute of Technology of Cambodia, Phnom Penh, Cambodia, makara.long@doct.uliege.be & makara_long@gsc.itc.edu.kh*
[2]*Faculty of Civil Engineering, Institute of Technology of Cambodia, Phnom Penh, Cambodia, virak@itc.edu.kh*
[3]*LUCiD, University of Liège, Liège, Belgium, pierre.leclercq@uliege.be*
[4]*LEMA, University of Liège, Liège, Belgium, sigrid.reiter@uliege.be*

SUMMARY
This paper studies life cycle assessment (LCA) of a townhouse in Cambodia as a case study and compares carbon emission (CE) of green building scenarios generated with two types of LCA: screening and simplified. The research methodology is based on the building modelled in SimaPro software using ecoinvent 3 databases to assess life cycle CE of case study and different selected scenarios. The simplified LCA result show that the building produced a CE of 1276 kg CO_2-eq/m^2 and the average difference between the screening result and that of the simplified LCA is 2.8%, ranging from 1.9% to 4.9% according to the design scenario studied. The combination of the four tested strategies reduced the building's CE by 42% compared to the existing house. The results show the potential for integrating LCA into green building design in Cambodia. The screening LCA can be a useful tool to pre-size the GHG emissions produced by building and test different decarbonization options during the design stage.

Keywords: carbon footprint, screening LCA, residential building.

1. INTRODUCTION

In Cambodia, with a rising urban population and a construction sector growing at 18.1% between 2014 and 2019, GHG emissions from buildings are expected to increase rapidly (GGGI, 2021). To minimize the environmental impact (EI) of the building sector and promote green building design, the approach of LCA helps estimate the EI generated by a building throughout its whole life cycle. While the building LCA has reached an advanced stage of development in many developed countries, there remains a considerable need to enhance its adoption in developing countries, especially in Southeast Asia (Jayawardana et al., 2023). LCA has recently been introduced in Cambodia, primarily applied to sectors such as hydropower plants, cement production plants, and food production system to assess the EI, emissions to air pollution, and CO_2 emissions, respectively (Chhun et al., 2021; Chea et al., 2022; Hor et al., 2021). However, the application of LCA to buildings has not yet been implemented in the country. This study constitutes a valuable innovation for the local construction sector, providing a representative benchmark for developing green building guidelines and a practical method for simplifying LCA.

The ISO 14040 describes principles and framework of LCA and ISO 14044 describe the requirements and guidelines of LCA (ISO, 2006a; ISO 2006b). The European Standards for LCA of buildings: EN 15978 and EN 15804 provide guidance on how to apply LCA to buildings, divide the life cycles of building into five stages, define system boundaries, and allocation methods (CEN,

2012a; CEN, 2012b). Architects and planning professionals recognized LCA in supporting decision-making process in building design and assisting in materials selection (Mateus et al., 2011). Decisions made during the early design stages critically determine a building's EI, and LCA helps designers, faced with many decisions, choose those that are significant regarding the building's EI (Basbagill et al., 2013).

For building LCA, there are two types of simplification to facilitate the completion of a LCA study, used by stakeholder and practitioners for the early design stage of a building: screening and simplified LCA (Wittstock et al., 2012). The simplified LCA was conducted to obtain a more detailed and thorough assessment compared to the screening LCA. Full LCA can be hardly accomplished since it is time-consuming and resource-intensive, and often faces a lack of data, so that it is recommended to use simplification in LCA (Hochschorner et al., 2003; Gradin et al., 2021). The simplification of LCA methods is essential if practitioners aim to include environmental aspects in an early stage of product development and improvement.

SimaPro software is particularly suitable for estimating the global warming potential (GWP) of a building during production phase and is considered the most widely used LCA database-software combination in the building sector (Gu et al., 2024; Emami et al., 2019). The software includes several databases, among which ecoinvent is the most widely utilized in building sector. Furthermore, SimaPro allows users to modify input data to reflect regional conditions not explicitly included in the default database options. The environmental LCA of a single house in India was modeled in SimaPro using the ecoinvent database, which integrated the European Life Cycle Database (Pinky and Palaniappan, 2012). A similar study, analysing the EI of a residential building in Malaysia, was conducted using LCA in SimaPro and the Malaysian Life Cycle Inventory Database, adapted from ecoinvent database (Abd Rashid et al., 2017).

2. METHODOLOGY

An LCA model was developed and analysed using SimaPro V9.4.0.2 software due to its popularity and leading LCA software used as a decision tool (Herrmann et al., 2015). The ecoinvent 3 database is selected to model the inventory of the housing unit, considering all inputs of material manufacturing (gradle-to-gate) and energy involved in life cycles, as no database specific to materials in Cambodia has yet been developed. This database was chosen for the study due to its status as the largest transparent unit-process Life Cycle Inventory database globally, distinguished by its integrity, usability, and completeness (Wernet et al., 2016; Martínez-Rocamora et al., 2016). The CE in this study is the amount of GHG produced throughout the building life cycle and it was calculated in kg CO_2-eq/m^2.

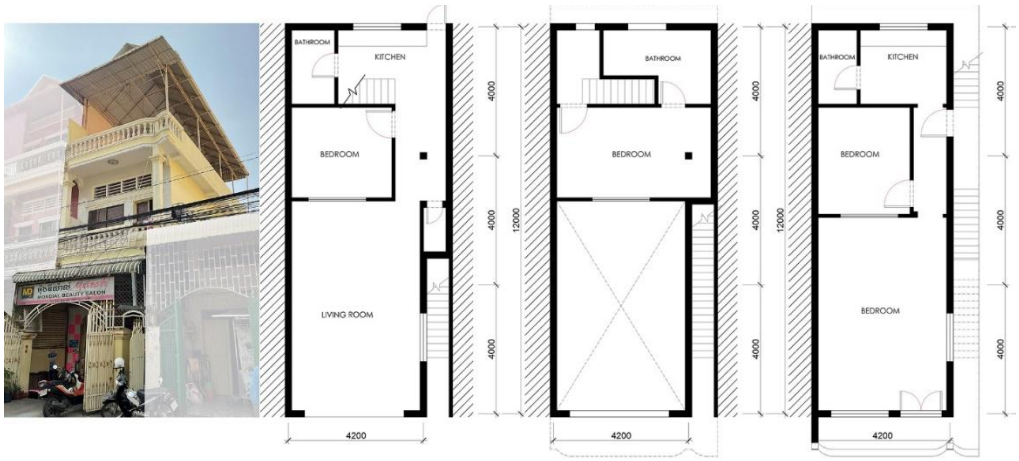

Figure 1. Streetview photo and floor plans of the building case study.

The selected building case study is a three-storey townhouse with a gross floor area (GFA) of 157 m^2 as shown in Fig. 1 and located in Cambodia, a hot and humid tropical climate. The construction techniques and materials are common in Cambodia: reinforced concrete structural frames and brick masonry walls without insulation. The annual electricity and water consumption is 6,480 kWh and 1,200,000 liters. The case study was selected based on the fact that this housing type is mostly built in urban areas, an important part of current city development and suitable for the Cambodian context (Taing et al., 2023; Khoan et al., 2022). The number of constructions this townhouse type increased by more than 34% from 2020 to 2021 in Cambodia (Choun et al., 2022).

This study follows the LCA method standardised by ISO 14040 and 14044 standards, using the screening and simplified LCA based on EN 15978, which includes four stages as follows: goal and scope definition, life cycle inventory, life cycle impact assessment, interpretation. The two simplification types of LCA studies are applied on the one hand to the reference building, selected as a case study, and on the other hand to five environmental improvement strategies described below.

2.1. Goal and scope definition

The goal of this study was to evaluate the CE of a townhouse in Cambodia using two types of LCA: screening and simplified LCA, taking into account the production and use phase within specific system boundaries as shown in Table 1. Other LCA impact categories were not considered, as there is an urgent need for research on embodied carbon in developing countries, where the CE is the most widely recognized emission indicator (Nawarathna et al., 2021). Additionally, the selected impact method focuses exclusively on CO_2 emissions. The construction and end of life phase were not taken into account due to the study's system boundary, building's data, and references limitation. Although waste processing and disposal are defined as mandatory modules, they were excluded from the assessment due to the absence of data and information regarding the building's end of life phase. Neglecting the end of life phase is acceptable because their impacts are very low compared to the CE on its entire life cycle (Sharma et al., 2011). The building functional unit selected was 1 m^2 of GFA and its lifespan assumed to be 50 years as recognized in building industry (Abd Rashid and Yusoff, 2015).

Table 1. Life cycle phases to be considered for screening and simplified LCA type (based on EN 15978).

Production			Const-ruction		Use							End of life				Benefits and loads beyond the system boundaries
A1	A2	A3	A4	A5	B1	B2	B3	B4	B5	B6	B7	C1	C2	C3	C4	D
Raw material acquisition**	Transportation**	Manufacturing**	Transportation to the site	Construction and installation	Use	Maintenance	Repair	Replacement*	Refurbishment	Operational energy use**	Operational water use	Demolition	Transportation	Waste processing*	Disposal*	Reuse, recovery or recycling potential

Legend:
* Mandatory for simplified LCA
** Mandatory for screening and simplified LCA
☐ System boundary

2.2. Life cycle inventory (LCI)

2.2.1 Production phase

The inputs for the production phase were obtained from on-site measurements and survey with house owner. Following detailed measurements of each building component, the construction materials used for each component were estimated with the assistance of construction engineers, as no technical drawings or plans were available for the building. The ratio of each building material's component was divided per m^2 of GFA. The LCI data for the production phase were modelled by calculating the detailed build-up elements of the building components, and are presented in Table 2.

Table 2. LCI of materials in production phase.

Components	Materials	Amount	Unit	Ratio (kg/m^2 or m^3/m^2)
Internal walls	Ceramic tile	1225.35	kg	7.80
	Clay brick	2839.2	kg	18.08
	Cement mortar	2028	kg	12.92
	Base plaster	930	kg	5.92
External walls	Ceramic tile	1278.83	kg	8.15
	Clay brick	14196	kg	90.42
	Cement mortar	5371	kg	34.21
	Base plaster	2580	kg	16.43
Structures (slab, column, and beam)	Ceramic tile	4761.40	kg	30.33
	Normal concrete	31.75	m^3	0.20
	Reinforcing steel	2715.28	kg	17.29
	Base plaster	1670	kg	10.64
	Cement mortar	716.22	kg	4.56
Stairs	Steel	69	kg	0.44
	Alkyd paint	2.5	kg	0.02
	Normal concrete	1.36	m^3	0.01
	Reinforcing steel	16.74	kg	0.11
Roof shelter	Zinc	300	kg	1.91
	Steel	412.80	kg	2.63
Doors	Polyvinylchloride	27	kg	0.17
	Wood	4.8	m^2	0.03

	Alkyd paint	3.2	kg	0.02
	Steel	92	kg	0.59
	Coated flat glass	30.8	kg	0.20
Windows	Aluminum frame	4.95	m^2	0.03
	Coated flat glass	84.24	kg	0.54
	Steel	200.82	kg	1.28
	Alkyd paint	3.6	kg	0.02

The main building components to be considered in the screening LCA included exterior walls, windows, roof and floor slab, and load-bearing walls and structure (Hollberg, 2016). For simplified LCA, foundations, interior walls, building services, and finishing are added to the components listed in the screening LCA.

The transportation of virgin materials to the factory gate was taken into account in the production phase and the average distance per trip was assumed to be 130 kilometers (Decorte et al., 2020).

2.2.2. Use phase

The inputs for the use phase were obtained from bills of electricity and water consumption given by the house owner. Electricity is the only form of energy consumed during the building's use phase, as no active mechanical systems are installed. It is mainly used for cooling (electrical and ceiling fan), lighting, and appliances. Energy for water heating is not required, as hot water is not provided within the building. The electricity and water consumption were modelled by the total amount of electricity (kWh) and water (kg) consumed per year, multiplied by 50 years and expressed by m^2 of GFA. The CE associated with these operational phases were calculated based on the embodied emissions resulting from the building operation, included electricity and water use.

Maintenance inputs were modelled based on the potential of replacement, reapplying, and change of each component. Painting, windows, and solar PV panels were considered in the use phase maintenance. The replacement of roofing materials, floor tiles, and electrical and plumbing fixtures was not included. The number of replacements in 50 years of painting and windows are 4 times and 1 time, respectively (Abd Rashid et al., 2017; Ortiz-Rodríguez et al., 2010). The used PV panels will be replaced 1 time in 50 years due to their lifetime of 25 years (Chowdhury et al., 2020). The CE calculation for this phase accounts for all modules within the production phase of the selected components.

2.3. Life cycle impact assessment (LCIA)

The CE of the case study were assessed using the IPCC 2021 GWP100 method considering and quantifying only the Global Warming Potential indicator for a timeframe of 100 years (GWP100) with climate change factors of IPCC (PRé Sustainability-SimaPro, 2023).

2.4. Interpretation

The LCIA results were interpreted according to the goal and scope of the study and made it possible to identify the significant potential of improvements of the studied scenarios.

2.5. Building studied scenarios

The studied scenarios were designed to reduce the CE of the case study and other residential buildings in Cambodia. LCA modelling of the scenarios applied to the case study are carried out

and analysed, following the same methodological framework as for the existing house's LCA. The description and aim of each scenario are listed in Table 3.

Table 3. Building studied scenarios and their descriptions.

Scenario	Description
Reference	• Existing situation of the building case study
Strategy 1: removing unnecessary materials	• Removing ceramic tiles from the external walls and steel bars from exterior windows and doors, aiming to minimize the excessive materials consumption for decoration
Strategy 2: using environmental manufacturing and bio-based materials	• Replacing of normal reinforced concrete by lean concrete and aluminum window frames by wooden frames
Strategy 3: using lightweight timber frames	• Replacing brick masonry walls by lightweight timber frames for the external walls only
Strategy 4: installing solar PV panels	• Implementing the solar panels on the existing roof shelter, generating solar energy that cover about 51% of the annual energy consumption. This value was calculated based on the installation of 24 solar panels, each with a power output of 380 W and an efficiency of 20%, at a location receiving an average of 5 peak sun hours per day.
Strategy 5: combined strategy	• Combination of the four studied strategies to find the potential of improvement and green building solutions

3. RESULTS

Fig. 2 shows the CE comparison of the reference and four studied scenarios corresponding to the production phase by building component. The following scenarios, reference, strategy 1, strategy 2, strategy 3, and strategy 4, accounted for 175, 170, 148, 140, and 188 kg CO_2-eq/m^2 in the production stage, respectively. Among all scenarios, strategy 3 shared a lower CE than others while strategy 4 generated a higher emission.

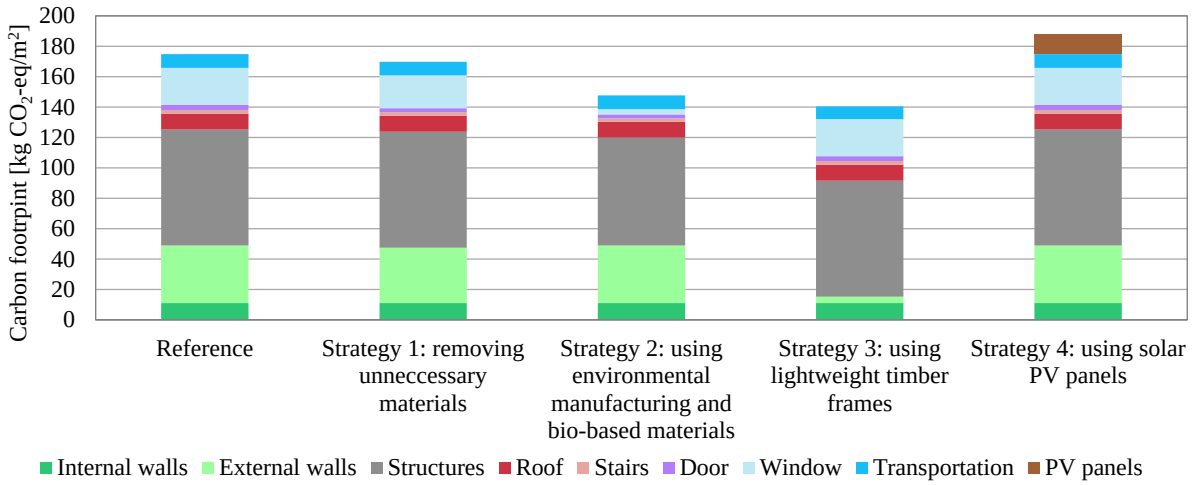

Figure 2. Carbon emission of the reference and four studied scenarios during the production phase, presented by building component.

In the reference scenario, the structure (floor slab, column, and beam) was the dominant contributor to CE, external wall ranked second, and windows ranked third compared to other components. The 35%, 22%, and 14% were shared to the total CE by the structure, external walls, and windows, respectively. Strategy 1, aiming to remove ceramic tiles from interior of the external walls, gives a slight reduction of 3% compared to the reference scenario. While strategy 2, using lean concrete in place of normal concrete and using wooden window frames in place of aluminium frames, gives a reduction of 16% compared to the reference and reduces significantly the impact of windows on the total CE. Strategy 3 replacing the masonry external walls by lightweight timber frames brings a reduction of 20% compared to the reference. This strategy generates a significant improvement in the CE of external walls and shifts its rank from the second most influential to a less dominant position. However, strategy 4, implementing solar PV panels on the roof, led to an increase of approximately 7% in CE compared to the reference.

Fig. 3 presents the overall CE comparison of the reference and four studied scenarios, calculated using screening LCA and simplified LCA. The reference scenario showed a CE of 1248 and 1276 kg CO_2-eq/m^2 for the screening and simplified LCA, respectively, with a 2.2% difference. For strategy 1, CE were 1244 (screening LCA) and 1271 kg CO_2-eq/m^2 (simplified LCA), yielding a 2.2% difference. Strategy 2 showed CE of 1226 (screening) and 1249 kg CO_2-eq/m^2 (simplified), resulting in a 1.9% difference. In strategy 3, total CE were 1214 (screening) and 1242 kg CO_2-eq/m^2 (simplified), with a 2.3% difference. Strategy 4 resulted in CE of 794 (screening) and 835 kg CO_2-eq/m^2 (simplified), with a 4.9% difference. Overall, the differences between the screening and simplified LCA across all scenarios ranged from 1.9% to 4.9%.

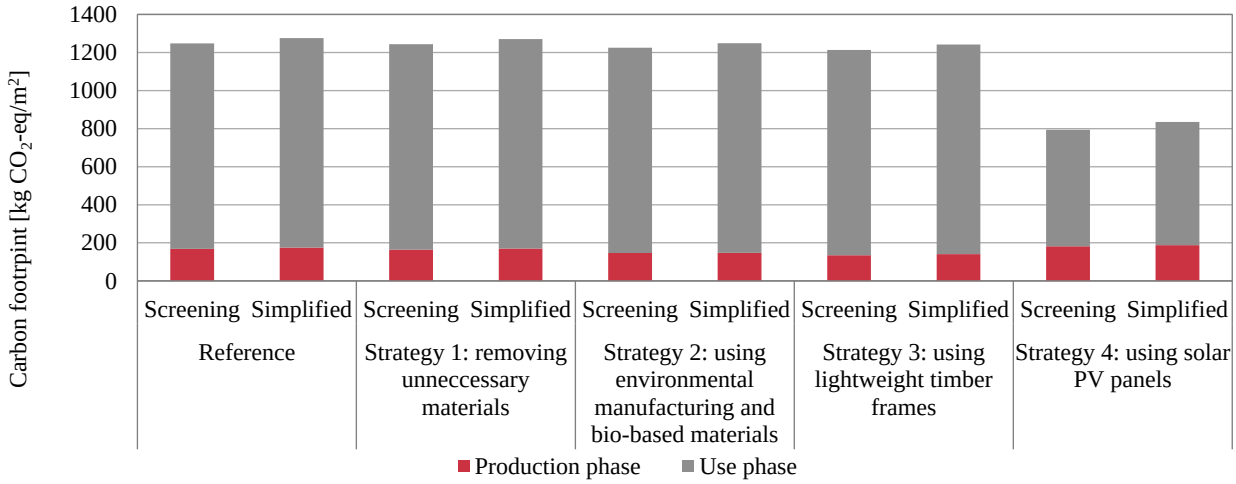

Figure 3. Carbon emission results comparison based on all the scenarios by two types of LCA.

Using screening LCA, the results of strategy 1, strategy 2, strategy 3, and strategy 4 accounted for 0.35%, 1.79%, 2.75% and 36.39% reduction in CE compared to the reference, respectively. Using simplified LCA, these scenarios accounted for 0.39%, 2.13%, 2.69%, and 34.57% reduction in CE compared to the reference, respectively. Thus, there is about 1% to 2% difference between CE reduction percentage results from the screening and simplified LCA of the reference and studied scenarios comparison. Strategy 4 generated a significantly greater reduction in CE than the other strategies.

Fig. 4 presents the overall CE comparison of the refence and combined scenarios using the screening and simplified LCA methodologies. The combination of four strategies demonstrates a significant reduction in total life cycle CE, approximately 42% of the reference building's CE. The combined strategy showed a total CE of 722 and 749 kg CO_2-eq/m^2 for the screening and simplified LCA, respectively, with a 3.6% difference. The combined strategy generates overall 42.13% and 41.67% less CE compared to the reference scenario, resulted from screening and simplified LCA, respectively.

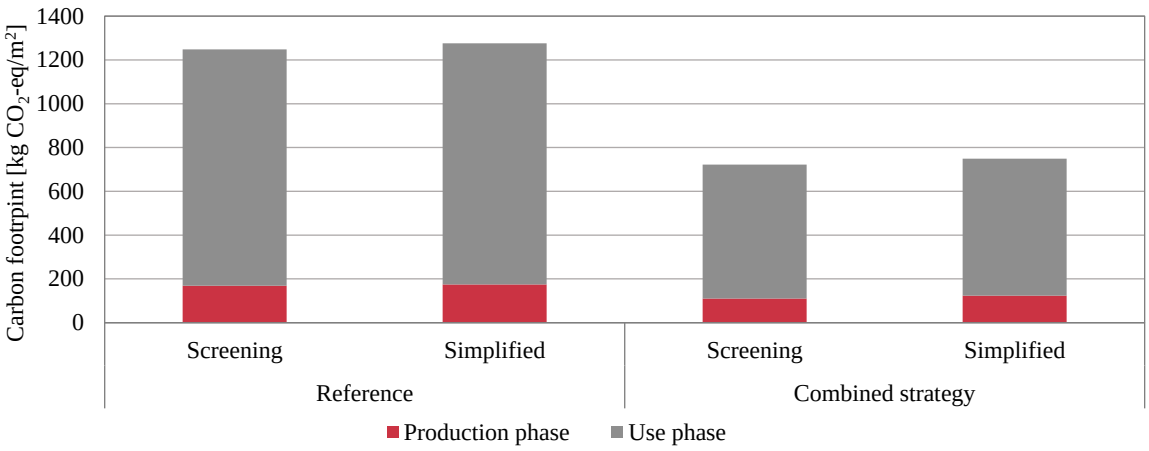

Figure 4. Carbon emission results comparison based on the reference and combined strategy.

4. DISCUSSION

The studied townhouse in Cambodia generates the highest CE during the use phase which is similar to other residential building case studies in Southeast Asia (Abd Rashid et al., 2017; Le et al., 2021) and in other developing countries (Morsi et al., 2020). Strategy 4 implementing solar PV panels is a particularly relevant solution for buildings in Southeast Asia, as there is significant potential for renewable solar energy resources in this region (Lai et al., 2023). Incorporating a broader range of energy conservation measures in future research, such as building envelope improvements, energy-efficient electrical appliances, behavioural controls, and advanced technologies, could provide valuable insights. In terms of production phase, the scenarios of removing unnecessary materials and using more environmental manufacturing and biogenic materials show a significant reduction of CE and reflect the needed effort to select more sustainable materials and minimize materials consumption to achieve sustainable building in Cambodia (Durdyev et al., 2018). However, the main drivers of the significantly reduced CE for the combined strategy are primarily related to use phase, followed by the production phase.

This study compares the CE result of the reference and combined strategy to results from the literature review on building LCA in Southeast Asia and in Egypt, another developing country, by phases of life cycle included in the LCA and its entire lifespan, as shown in Fig. 5. The CE of these cases: Morsi et al. (2020), Le et al. (2021), and Abd Rashid et al. (2017) varied at 1062, 1335, and 3327 kg CO_2-eq/m^2, respectively. The reference result of this study calculated by the simplified LCA is 1276 kg CO_2-eq/m^2, which is comparable to the case of Le et al. (2021) in Vietnam, while the other cases produced a lower and higher emission. However, the second design scenario using greener materials in the study of Le et al. (2021) produced 834 kg CO_2-eq/m^2 of CE based on

production and use phase, which is a higher CE reduction than the combination of the first 3 strategies related to greener materials in this study, but is a lower CE reduction than the combined strategy of this study considering greener materials and PV panels, which produces 749 kg CO_2-eq/m^2. The different CE results of all scenarios from the screening and simplified LCA studies vary minorly in a range from 1.9% to 4.9%, representing a slight difference. With these percentage values, the results of a screening LCA are reliable and results from these two types of LCA simplification are comparable.

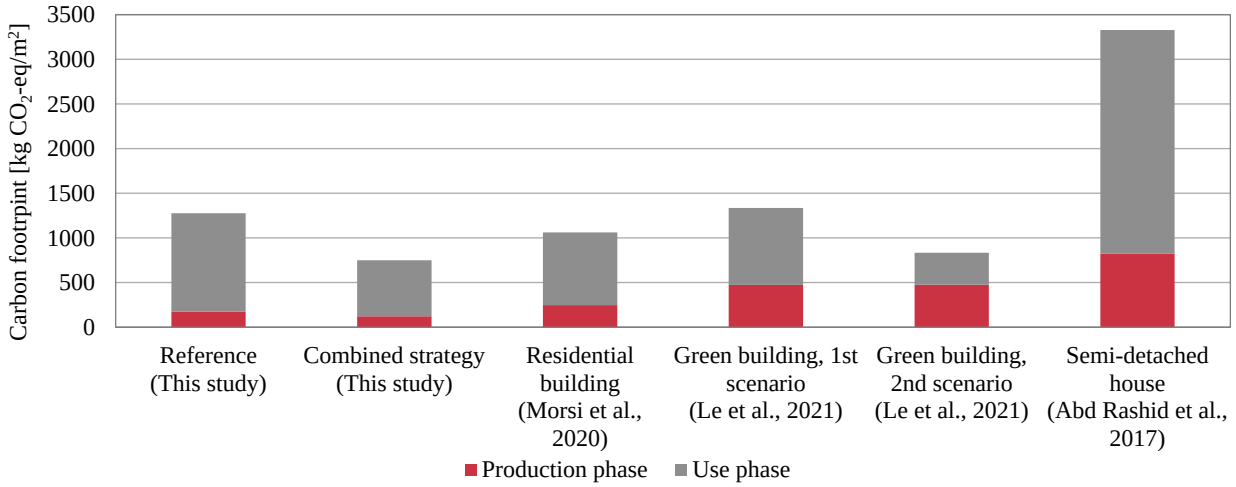

Figure 5. Carbon emission results comparison of this case study in Cambodia with other LCA studies.

The limitations of this study are related to assumptions made regarding the materials database, system boundaries, and the assessment of only a single impact category. It would be valuable to test the results obtained using the same regional database or other LCA software for comparison. Moreover, mandatory modules for the end of life phase were not included due to the lack of data on all activities and energy consumption during the building's demolition. The end of life phase of buildings is becoming critical in circular economy policies aimed at extending building service life and promoting component reuse or recycling (Giorgi et al. 2018). While using a single impact indicator may be sufficient for a specific study, it is not recommended for the holistic optimization of building designs, as it may result in suboptimal solutions (Hollberg, 2016).

5. CONCLUSION

The average difference between results of the screening and simplified LCA studies is 2.8% according to the results comparison from 6 different scenarios. All studied scenarios show a different reduction value of CE. Strategy 3 using lightweight timber frames walls in place of masonry walls presents the highest CE reduction during the production phase with approximately 20% of CE reduction during the building's production phase, while strategy 4 presents about 36% CE reduction in terms of overall life cycle compared to the reference. The combined strategy allows a significant reduction of 42% throughout its life cycle compared to the existing house. The results of this study demonstrate the potential of integrating the life cycle perspective into green buildings design in Cambodia and highlight the best strategies that should be used for future renovation and design of new residential buildings. Furthermore, this study proves that a screening LCA is a useful tool to pre-size the GHG emissions produced by a building and test different

decarbonization design options during the building design phase. However, the future study should study several environmental impacts to check the variability and accuracy of the screening LCA results concerning the total building environmental footprint compared to those of a simplified LCA.

ACKNOWLEDGEMENTS

The authors would like to thank the building owner who allowed and contributed to the building data collection process. We extend our thanks and appreciation to ARES – COMBOdIA project for funding and supporting this research. This research is carried out by three research laboratories: LEMA & LUCiD – ULiège and RIC – ITC.

REFERENCES

Abd Rashid A.F., Yusoff S., 2015. A review of life cycle assessment method for building industry. Renewable and Sustainable Energy Reviews 45, pp. 244-248.

Abd Rashid A.F., Idris J., Yusoff S., 2017. Environmental impact analysis on residential building in Malaysia using life cycle assessment. Sustainability 9, 329.

Basbagill J., Flager F., Lepech M., Fischer M., 2013. Application of life-cycle assessment to early stage building design for reduced embodied environmental impacts. Building and Environment 60, pp. 81-92.

CEN (European Commitee for Standardization), EN 15978:2012 Sustainability of construction works - Assessment of environmental performance of buildings - Calculation method, 2012a.

CEN (European Committee for Standardization), EN 15804:2012 Sustainability of construction works. Environmental product declarations. Core rules for the product category of construction products, 2012b.

Chea C., Ket P., Taing L., Kong S., Um D., Taing C., Or C., Aun S., Hang L., 2022. Life-Cycle Impact Assessment of Air Emissions from a Cement Production Plants in Cambodia. Open Journal of Air Pollution 11, pp. 85-99.

Chhun B., Bonnet S., Gheewala S.H., 2021. Life cycle assessment of the Kamchay hydropower plant in Cambodia. Journal of Sustainable Energy & Environment 12, pp. 23-33.

Choun P., Heang V., Vongchanh K., Chan S., 2024. Simulation of energy consumption for different types of walls and colour for a residential building, case study: Phnom Penh city, Cambodia. Malaysian Journal of Science and Advanced Technology 4, pp. 448-455.

Chowdhury M.S., Rahman K.S., Chowdhury T., Nuthammachot N., Techato K., Akhtaruzzaman M., Tiong S.K., Sopian K., Amin N., 2020. An overview of solar photovoltaic panels' end-of-life material recycling. Energy Strategy Reviews 27, 100431.

Decorte Y., Steeman M., Krämer U.B., Struck C., Lange K., Zander B., de Haan A., 2020. Upscaling the housing renovation market through far-reaching industrialization. In: Proceeding of the BEYOND 2020 – World Sustainable Built Environment conference, Vol. 588, 032041.

Durdyev S., Zavadskas E.K., Thurnell D., Banaitis A., Ihtiyar A., 2018. Sustainable Construction Industry in Cambodia: Awareness, Drivers and Barriers. Sustainability 10, 392.

Emami N., Heinonen J., Marteinsson B., Säynäjoki A., Junnonen J.-M., Laine J., Junnila S., 2019. A Life Cycle Assessment of Two Residential Buildings Using Two Different LCA Database-Software Combinations: Recognizing Uniformities and Inconsistencies. Buildings 9(1), 20.

Giorgi S., Lavagna, M., Campioli A., 2018. Life Cycle Assessment of Building End of Life. In: Proceedings of the 12th Italian LCA Network Conference Life Cycle Thinking in Decision-Making for Sustainability: From Public Policies to Private Businesses, Messina, pp. 30-38.

Global Green Growth Institute (GGGI), 2021. Cambodia Country Planning Framework 2021-2025 (CPF). Seoul, Republic of Korea. GGGI.

Gradin K.T., Björklund A., 2021. The common understanding of simplification approaches in published LCA studies—a review and mapping. The International Journal of Life Cycle Assessment 26, pp. 50-63.

Gu C., Gu H., Gong M., Blackadar J., Zahabi N., 2024. Comparison of using two LCA software programs to assess the environmental impacts of two institutional buildings. Sustainable Structures 4(1), 000034.

Herrmann I.T., Moltesen A., 2015. Does it matter which Life Cycle Assessment (LCA) tool you choose? – a comparative assessment of SimaPro and GaBi. Jounral of Cleaner Production 86, pp. 163-169.

Hochschorner E., Finnveden G., 2003. Evaluation of Two Simplified Life Cycle Assessment Methods. The International Journal of Life Cycle Assessment 8(3), pp. 119-128.

Hollberg A., 2016. Parametric Life Cycle Assessment: Introducing a time-efficient method for environemntal building design optimization. Ph.D. thesis, Bauhaus-Universität Weimar.

Hor R., Ly P., Putra A.S., Ishizaki R., Ahamed T., Noguchi R., 2021. Estimation of Carbon Dioxide Emissions from

a Traditional Nutrient-Rich Cambodian Diet Food Production System Using Life Cycle Assessment. Sustainability 13(7), 3660.
ISO (International Organization for Standardization), 2006a. ISO 14040:2006 Environmental Management—Life Cycle Assessment—Principles and Framework. Geneva, Switzerland.
ISO (International Organization for Standardization), 2006b. ISO 14044:2006 Environmental Management—Life Cycle Assessment—Requirements and guidelines, Geneva, Switzerland.
Jayawardana J, Sandanayake M, Jayasinghe J.A.S.C, Kulatunga A.K., Zhang G., 2023. A comparative life cycle assessment of prefabricated and traditional construction – A case of a developing country. Journal of Building Engineering 72, 106550.
Khoan P., Tirapas C., 2022. A survey of Phnom Penh apartment shophouses' conditions for future housing adaptability revitalization in Phnom Penh. In: Proceedings of the World Building Congress 2022, Vol. 1101.
Lai F., Zhou J., Lu L., Hasanuzzaman M., Yuan Y., 2023. Green building technologies in Southeast Asia: A review. Sustainable Energy Technologies and Assessments 55, 102946.
Le D.L., Nguyen T.Q., Huu K.D., 2021. Life Cycle Carbon Dioxide Emissions Assessment in the Design Phase: A Case of a Green Building in Vietnam. Engineering Journal 25(7), pp. 121-133.
Martínez-Rocamora A., Solís-Guzmán J., Marrero M., 2016. LCA databases focused on construction materials: A review. Renewable and Sustainable Energy Reviews 58, pp. 565-573.
Mateus R., Bragança L., 2011. Life-Cycle Assessment of Residential Buildings. In: Proceedings of the International Conference Sustainability of Constructions – Towards a better built environment, Innsbruck, pp. 255-262.
Morsi D.M.A., Ismaeel W.S.E., Abd El-Hamed A.E., 2020. Life cycle assessment of a residential building in Egypt: A case study. In: Proceeding of the 13th International Conference on Civil and Architecture Engineering (ICCAE-13), Bristol, Vol. 974, 012028.
Nawarathna A., Alwan Z., Gledson B., Fernando N., 2021. Embodied carbon in commercial office buildings: Lessons learned from Sri Lanka. Journal of Building Engineering 42, 102441
Ortiz-Rodríguez O., Castells F., Sonnemann G., 2010. Life cycle assessment of two dwellings: One in Spain, a developed country, and one in Colombia, a country under development. Science of The Total Environment 408(12), pp. 2435-2443.
Pinky L., Palaniappan S.M.R.S., 2012. Application of Life Cycle Assessment for a Residential Building Construction. In: RILM Publications SARL of the International Symposium on Life Cycle Assessment and Construction – Civil engineering and buildings, pp. 213-222.
PRé Sustainability-SimaPro, SimaPro database manual – Methods library. PRé Sustainability, 2023.
Sharma A., Saxena A., Sethi M., Shree V., Varun G., 2011. Life cycle assessment of buildings: A review. Renewable and Sustainable Energy Reviews 15(1), pp. 871-875.
Taing K., Andre P., Leclercq P., 2023. Analysis of thermal performance of naturally ventilated residential building in tropical climate: case study of Phnom Penh, Cambodia. In: Proceedings of the 2nd ASEAN International Conference on Energy and Environment, Phnom Penh, Vol. 1199, 012038.
Wernet G., Bauer C., Steubing B., Reinhard J., Moreno-Ruiz E., Weidema B., 2016. The ecoinvent database version 3 (part I): overview and methodology. International Journal of Life Cycle Assessment 21, pp. 1218-1230.
Wittstock B., Gantner J., Lenz K., Saunders T., Anderson J., Carter C., Gyetvai Z., Kreißig J., Braune A., Lasvaux S., Bosdevigie B., Bazzana M., Schiopu N., Jayr E., Nibel S., Chevalier J., Hans J., Fullana-i-Palmer P., Gazulla C., Mundy J., Barrow-Williams T., Sjöström C., 2012. EeBGuide Guidance Document Part B: BUILDINGS, European Commission.

6th International Conference on Building Energy and Environment
Eindhoven University of Technology, The Netherlands
6 - 10 July 2025

The study of the impact of different land development on the street-block thermal environment in the Asia medium-sized city： A case study in tropical city, Taiwan

Jou-Man Huang [1]

[1]*Department of Landscape Architecture, National Chiayi University, Taiwan 60004; jouman@mail.ncyu.edu.com*

SUMMARY
The urban climate has seriously deteriorated with population urbanization and global climate change. The most obvious impact is the Urban Heat Island effect (UHI). In Taiwan, it was even found that in the tropical, medium-sized city of Chiayi, UHI intensity was comparable to that in large cities (4.1°C) in 2018. Therefore, this study selected Chiayi City as the object, using the CFD tool - ENVI-met to simulate land-use development types on the impacts of the thermal environment and comfort. As a result, we obtained three important conclusions：(1) The existing undeveloped environment (forest land) had a better thermal environment of 8~10°C cooler than the street in air temperature and PET. (2) Regardless of the type of development, the overall thermal environment of the block (air temperature, MRT, PET) deteriorates, with parking lot development being the most serious. (3) This research shows the importance of establishing urban development control regulations.

Keywords: urban heat island (UHI), ENVI-met, thermal environment, land-use.

1. INTRODUCTION

The urban climate has seriously deteriorated with population urbanization and global climate change (Oke, 1987; Akbari et al.,1992; Brown et al., 1995; Givoni, 1997; Kim et al.,2021). The most obvious impact is the Urban Heat Island effect (UHI). In Taiwan, a study of the Taipei area in 1999 found that heat island intensity was 1~2 °C (Lin et al., 1999) higher than that of the Tokyo area in Japan, a high-latitude country (Ministry of the Environment, Japan, 2000). In the summer of 2012, Taipei also experienced high temperatures above 38°C for three days (https://codis.cwa.gov.tw/StationData). In 2018, it was even found that in the tropical region, a medium-sized city-Chiayi City, its UHI intensity was comparable to that in large cities (4.1℃) (Huang et al., 2020). Hence, these indicated that the deterioration of the thermal environment in Taiwan cities is one of the urgent issues. Past studies on land development and thermal environment have mostly focused on the discussion of land use or land cover (LULC) (Patel et al., 2024) , and have mainly explored the differences in thermal environment based on the current status of different land use or land cover (Shen et al., 2022; Salan et al., 2024). There has been little research that explored the land development process and responded to the regulatory controls on urban land development. In addition, the methods used by these research were mostly remote sensing image analysis (Salan et al., 2024). Even some studies that use CFD as a tool almost focused on the impacts caused by different green spaces, building configurations, and building forms (Sodoudi et al., 2018; Mansouri st al, 2025). Few studies discussed the land development process that occurs in cities. This process is an issue that each city will encounter at the source of urban development. However, due to the lack of scientific verification, urban governments have

forgotten that the urban environment, especially the climate and thermal environment, can be changed from the source. Therefore, this study selected tropical, medium-sized Chiayi City as the research object, using the CFD tool - ENVI-met to simulate land-use development types on the impacts of the thermal environment. It is hoped that this study could enable government agencies for urban land development management to realize the importance of source management and establish relevant regulations to mitigate the damage caused by human development.

2. MATERAL AND MOTHED

2.1. Research Area

Chiayi City has entered a rapid growth phase since 2016, due to the entry of a chain movie studio and shopping mall (January 2016) and the development of the Huzai Nei Redevelopment Area (193.49 ha) in December of the same year. It has attracted a large number of people from neighbouring counties and cities to travel back and forth or migrate. In addition to a significant increase in the number of vehicles on the main connecting roads, urban land has also begun to be rapidly developed due to this trend. As shown in Figure 1, according to the aerial photos of Chiayi City in 2014, 2018, and 2022, the undeveloped land in the city (Figure 1(a)) was mostly woodland or grassy wasteland; and after 2016, in response to the rapid development of the city, many lands were first developed into concrete parking lots (Figure 1(b)) to obtain greater economic benefits. Later, if there was enough capital or resells it to the developer, it will be developed into 4F townhouses (a common residential development form in secondary cities of Taiwan, Figure 1(c)) or buildings with more than 7 floors (mostly commercial development).

(a) Woodland or grassy wasteland (b) Converted to concrete parking lots (c) Converted to residential buildings

Figure 1. Example of land development changes in residential areas of Chiayi City (2014~2022)

2.2. Setting of the Simulation Area

According to data from the Chiayi City Urban Planning Information Query System (https://landuse.chiayi.gov.tw/chyiurdweb/), the blocks in Chiayi City are generally divided by roads larger than 20m, the block size is approximately 400m×400m, the road width within the block is 12m, and the average size of individual urban planning land use zones is approximately 73m×73m. Therefore, the simulation area was set to 400m×400m. The surrounding streets were 20m wide, the size of the development site was 80m×80m, and the set to a 4F townhouse form. The streets in the area were evenly divided into 12~14m widths in accordance with the total grid size, which can be divided into 16 sites in total (Figure 2(a)). In addition, in order to understand the impact of different urban developments on the surrounding thermal environment during urban development, the four sites in central were set as the change areas of development type and development degree (the red dotted area in Figure 2(a)), and the original land type was woodland (including fruit tree or woodland) (Figure 2(b)). The 3D settings of development type and development ratio

configurations are shown in Table 1. The floor area ratio and building coverage ratio settings of 4F-Buildings (L2) and 7F-Buildings (L3) were set based on the Chiayi City Urban Planning Detailed Plan regulations in 2015.

2.3. Explored Variables and Research Design

This study mainly discussed the following two items: (1) Type of land development and (2) Degree of development. In terms of the development type, as mentioned above, this paper mainly discussed three common land development types in Chiayi City, a secondary city in Taiwan: (1) parking lots, (2) 4F-Buildings, and (3) 7F-Buildings. They represented the types of land development used for parking in response to urban transportation/economic needs, directly developed into 4-story buildings of residential (or mixed residential and commercial) use and developed into residential or commercial buildings (7-story buildings), respectively. In terms of development degree, in order to understand the impact of different development levels on the surrounding thermal environment, the development ratios were set 4 kinds: 25% (R1), 50% (R2), 75% (R3), and 100% (R4). The distribution of development locations is shown in Table 1.

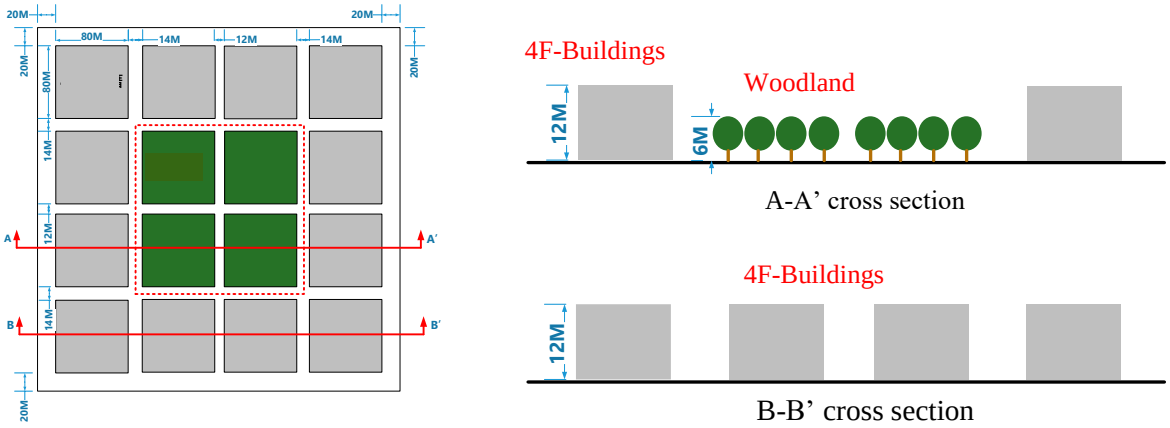

(a) Floor plan (----Land-use/Land development type change area)

(b) Cross section

Figure 2. Basic spatial model settings of the simulation area

2.4. Simulation Scenarios and Space Setting

According to the setting in explored variables and research design of Section 2.3, there were 13 simulation schemes as shown in Figure 3. Among them, B0 represents the current situation before development, and the three development types were further divided into four development ratios, resulting in a total of 12 development scenarios. The detailed space setting of three development types is shown in Table 1.

3. RESULT

3.1. Undeveloped situation (B0)

The overall thermal environment of the block before development had a minimum air temperature of 35.04℃ in the woodland area, and a maximum air temperature of 42.78℃ almost distributed on streets parallel to the wind direction without any building shade. The overall average air temperature of the block was 38.75℃. Regarding MRT (Mean Radiant Temperature), the highest was 75.64℃ in the road area, followed by the east side of the building, which can drop to about 55℃, and the lowest was 32.68℃ in the undeveloped area. The overall average MRT of the block is 60.81℃, which was a very hot radiation environment. In terms of comfort index, PET, the lowest value was 36.46℃ in the woodland area, which

was a hot degree with a cold or hot feeling; the highest value was 52.23℃ in the street area on the west sides of the building, and the street area was almost 48.40℃, which was a very hot degree with a cold or hot feeling. The overall average PET of the block was 46.65℃, which was very hot.

Table 1. Space setting list on the type and ratio of development

Items	Parking lots(L1)	4F-Buildings (L2)*[1]	7F-Buildings (L3)*[2]
Development Type (80m×80m Site)	Concrete Pavement	4F-Buildings (60%) Space (40%)	7F-Buildings (50%) Space (50%)
Ratio and Arrangement*[3]	25% (R1)	50% (R2)	75% (R3) 100% (R4)

*1、2：According to the regulation of Chiayi City Urban Planning Detailed Plan in 2015, the building coverage ratio and the floor area ratio of Residential-Use 3 are 60% and 240%, respectively, and Commercial-Use 2 are 70% and 350%.
*3：The red area is presented as developed, and the green area is presented as undeveloped.

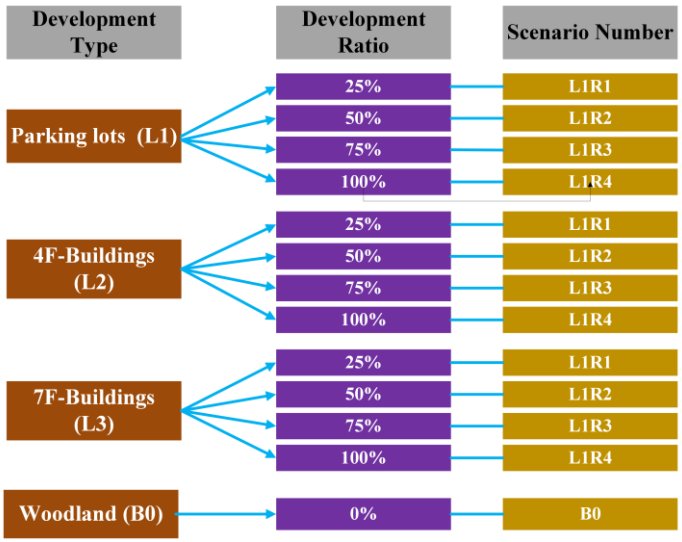

Figure 3. Simulation scenarios

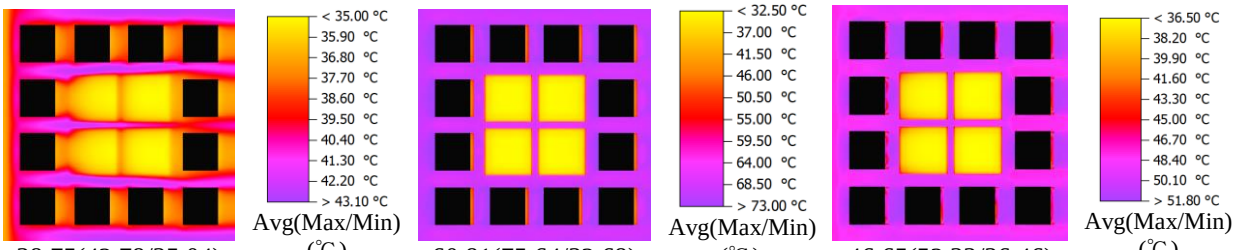

38.75(42.78/35.04) (a) AT
60.81(75.64/32.68) (b) MRT
46.65(52.33/36.46) (c) PET

Figure 4. The simulation results of the thermal environment in an undeveloped scenario (B0).

3.2. Comparison of air temperature (AT) between each scheme and the undeveloped scheme

As shown in Figure 5, in the parking lot development type (L1), as the development ratio increased, the average AT of the block increased, and the increase rate also increased equal times with the development ratio. For example, when the development ratio was 25%, it was 0.46℃, and when the development ratio became 75% (3 times), it also became 3 times to 1.37℃. The maximum warming scheme was 1.83℃ of 100% development. At the same time, when there were two continuous areas developed in parallel wind directions (L1R2~L1R4), the maximum AT increased by about 1.6~1.7℃. There was a similar trend in the 4F-residential development type (L2), and the increase also increased equal times with the development rate. The maximum warming scenario was 0.97℃ of 100% development, which was only about 1/2 of L1. At the same time, when there were two consecutive areas developed in parallel wind direction, the maximum AT increased by about 0.5~0.6℃, which was 1/3 of L1. The 7F-buildings (L3) development type also had the same trend as the above two types. The maximum hot scheme was 0.92℃ of 100% development, close to the L2 increasing value. At the same time, when there were two continuous areas developed in parallel wind directions, the maximum AT increased by about 0.9~1.1℃, which was 2/3 of L1. If we focus on the changes in the core area, we can find that whether it was developed into a parking lot, 4F-buildings or 7F-buildings, the average AT increasing in the core area was about twice that of the overall block.

3.3. Comparison of MRT between each scheme and the undeveloped scheme

As shown in Figure 6, in the parking lot development type (L1), the MRT increased rapidly by about 38℃ (L1R1) with the development. At the same time, the larger the development ratio, the larger the area where the MRT increases in the block, resulting in the average MRT of the block increasing to a maximum of 8.75℃. If we focus on the core development area, MRT increased to as much as 27.19℃. In the 4F-residential development type (L2), there was also a trend of increasing on average MRT of the block with the increase of development rate, but the increase was smaller than that of L1, about 1/2 of that. It was worth noting that when there were two continuous areas developed, there was a small MRT lowering area on the east side of the buildings in the development zone, which was about 2℃ lower (the blue area of L2R2~L2R4 in Figure 7). The development type of 7F-buildings (L3) also showed the same trend as the L2 type. The increase was also about 1/2 of L1 but slightly increased by about 0.2~0.4℃ compared to L2. If we focus on the changes in the core area, we can find that whether it was developed into any of the three types, the average MRT increase in the core area was about 3 times that of the overall block. Notably, the L2R4 and L3R4 areas even had increased by as much as 4.5 times.

3.4. Comparison of PET between each scheme and the undeveloped scheme

As shown in Figure 7, in the parking lot development type (L1), as the development ratio increased, the overall comfort index, PET, of the block increased, and the increase rate also increased equal times with the development ratio, the maximum increase was 2.84℃ of 100% development. In the 4F-residential development type (L2), there was also a trend of average PET increase with the development ratio increased, and the increase rate also increased equal times with the development rate. The maximum increase was 1.52℃ of 100% development, which is only about 1/2 of L1. The development type of 7F-buildings (L3) also showed the same trend as the other two types. The maximum warming scheme was 1.58℃ of 100% development, close to the increased value of L2. If we focus on the changes in the core areas, we can find that whether it was developed into

any of the three types, the average PET increase in the core area was about 3 times that of the overall block. Notably, the L2R4 and L3R4 even had increased by as much as 4 times.

4. CONCLUSION

As a result, we obtained the following important conclusions of five：

- The undeveloped area (woodland) had a better thermal environment, compared with the street AT of 42.78°C, it was reduced by about 8°C to 35.04°C. PET was also reduced by about 12°C to 36.46°C from 48.40°C of the street.
- Regardless of the development type, the block's overall thermal environment (AT, MRT, PET) all deteriorated.
- Among the three types of land development, the parking-lot development type had the most serious impact, with the deterioration of AT, MRT, and PET being twice that of the 4F-buildings and 7F-buildings development types.
- In the core blocks of the development area, no matter which development method was used, it all caused a more serious deterioration than the thermal environment of the overall block, with the deterioration by up to 2 times in AT and up to 3~4.5 times in MRT and PET.
- It is obvious that the undeveloped environment (woodland) had a better thermal environment. Any development method will cause serious deterioration of the thermal environment. Therefore, establishing relevant land development control regulations to prevent is a solution to improve the urban thermal environment.

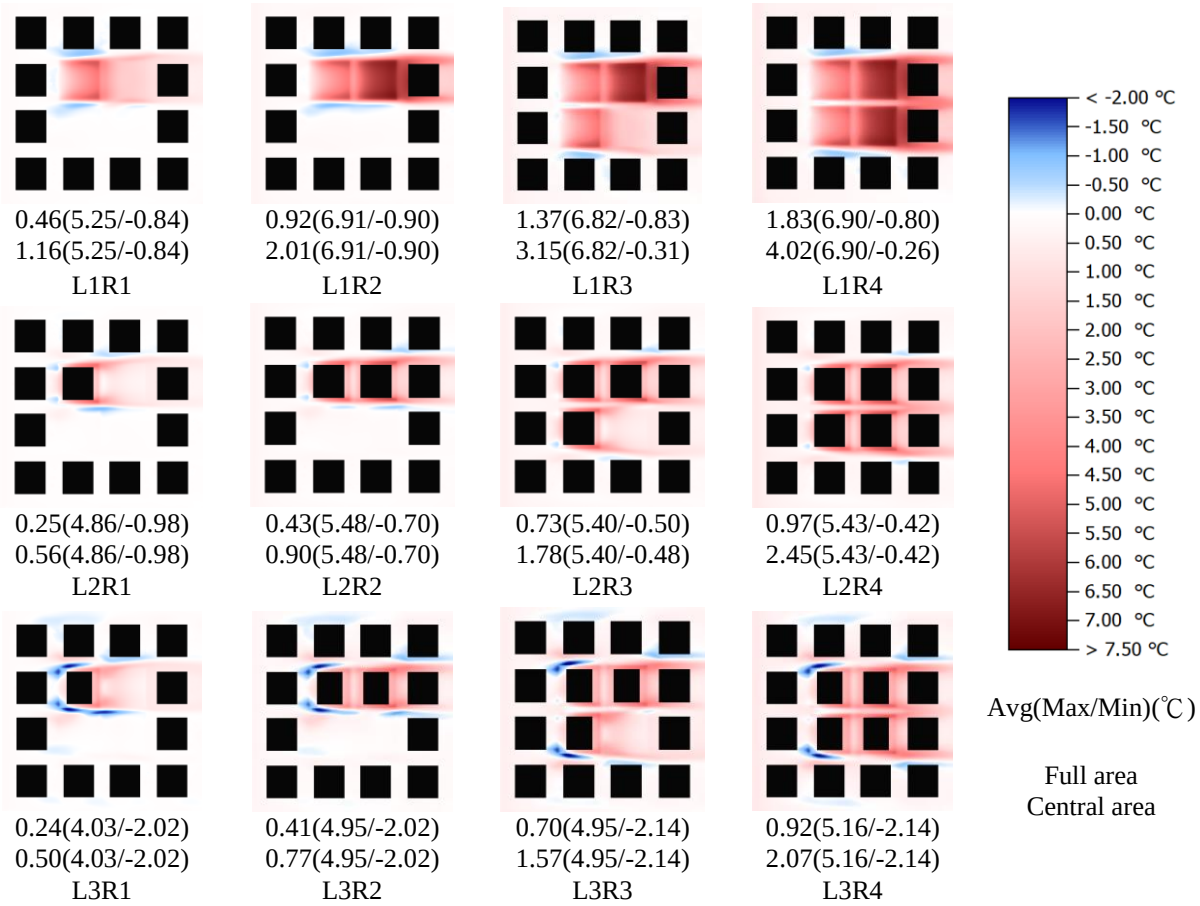

Figure 5. The difference of AT between each scenario and B0 (LxRx – B0)

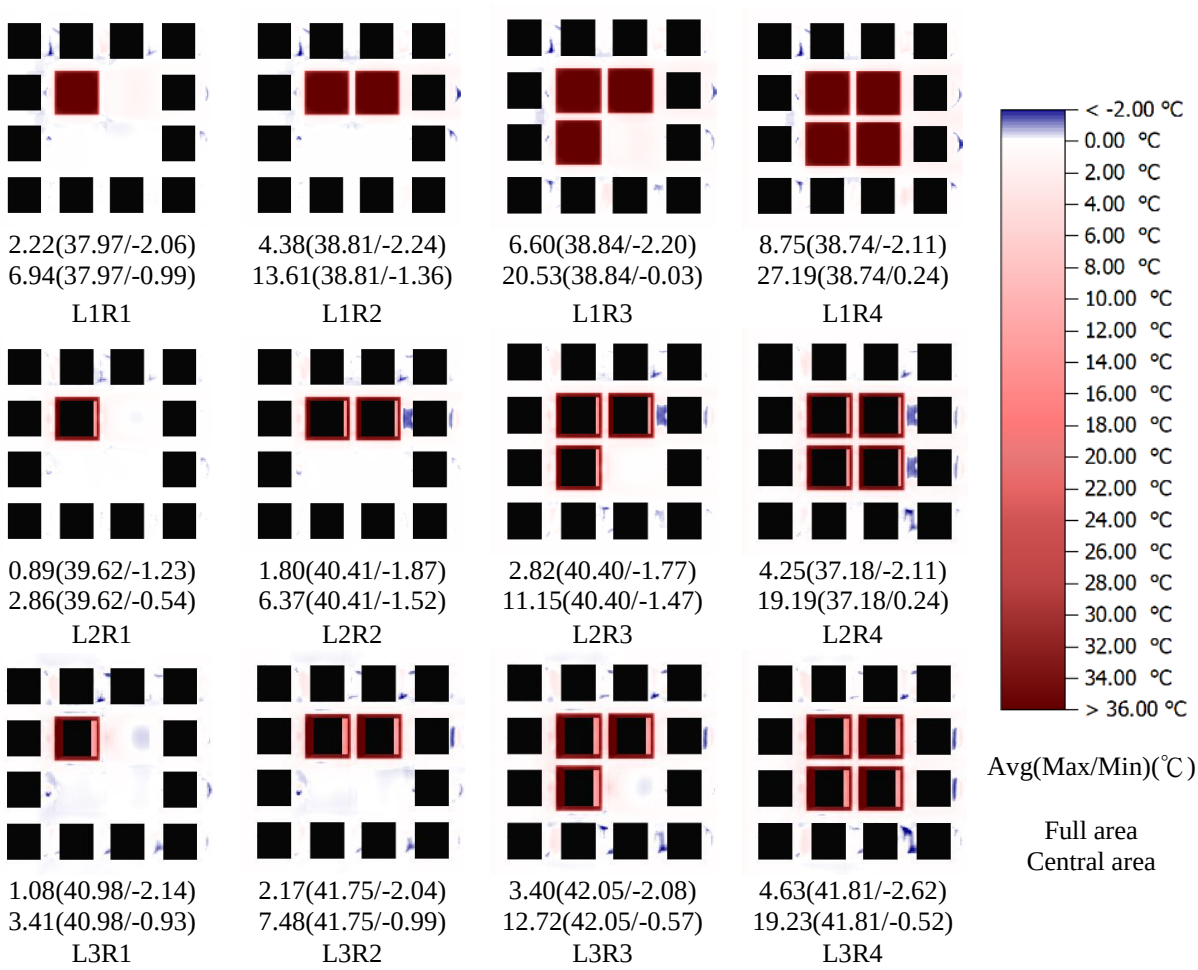

Figure 6. The difference of MRT between each scenario and B0 (LxRx – B0)

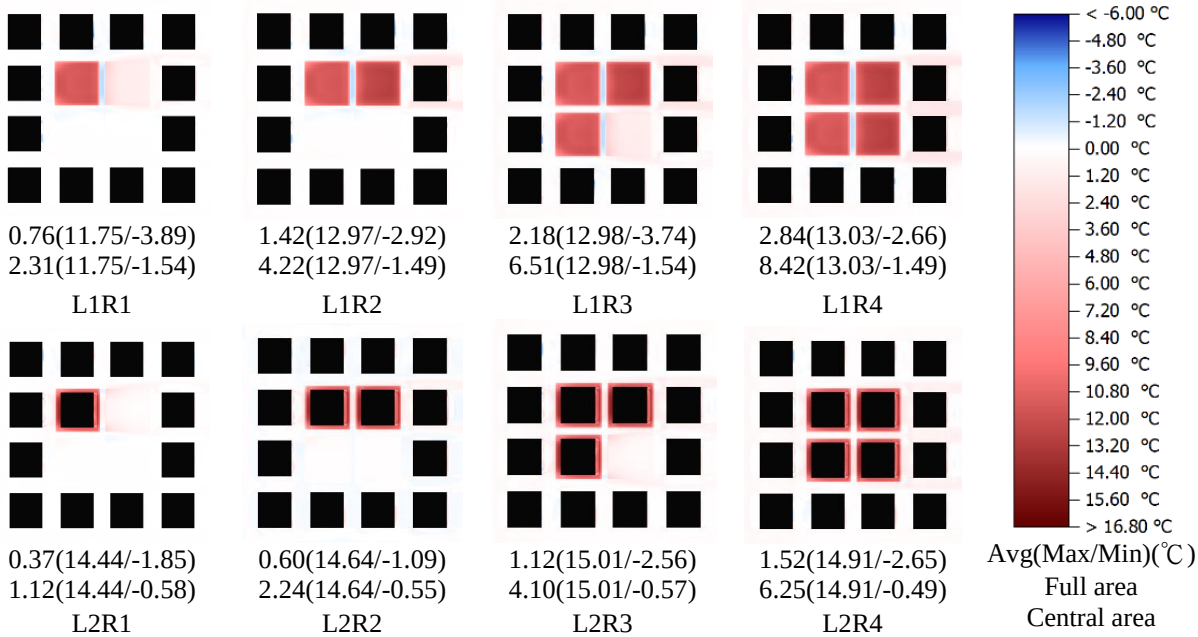

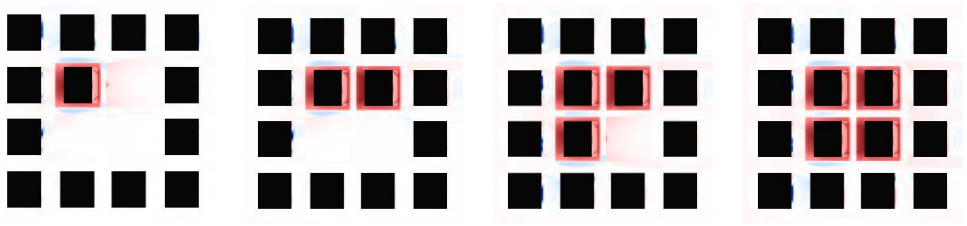

0.38(14.83/-5.47)	0.73(15.27/-5.91)	1.17(15.25/-5.48)	1.58(15.29/-5.49)
1.19(14.83/-1.44)	2.44(15.27/-1.44)	4.24(15.25/-1.43)	6.23(15.29/-1.43)
L3R1	L3R2	L3R3	L3R4

Figure 7. The difference of PET between each scenario and B0 (LxRx – B0)

ACKNOWLEDGEMENTS

The support for this study received from the National Science and Technology Council, Taiwan, through grant no. NSTC 113-2221-E-415-003 - is gratefully acknowledged.

REFERENCES

Akbari H., Davis S., Dorsano S., Huang J., Winnett S. Cooling Our Communities: A Guidebook on Tree Planting and Light-Colored Surfacing. USA. United Nations Environmental Protection Agency, Office of Policy Analysis, Climate Change Division Press, 1992.

Brown R.D., Terry J.G. Microclimatic Landscape Design: Creating Thermal Comfort and Energy Efficiency. New York, USA. John Wiley & Sons Press, 1995.

Chiayi City Urban Planning Information Query System, Taiwan. https://landuse.chiayi.gov.tw/chyiurdweb/

Climate Observation Data Inquire Service, Central Weather Administration, Taiwan. https://codis.cwa.gov.tw/StationData

Givoni B. Climate Consideration in Building and Urban Design. New York, USA. John Wiley & Sons Press, 1997.

Huang J-M., Chang H-Y., Wang Y-S., 2020. Spatiotemporal Changes in the Built Environment Characteristics and Urban Heat Island Effect in a Medium-Sized City, Chiayi City, Taiwan. Sustainability 12(1), 365.

Kim S.W., Brown R.D., 2021. Urban heat island (UHI) variations within a city boundary: a systematic literature review. Renew. Sust. Energ. Rev. 148, 111256.

Lin H.T., Lee K.P., Chen K.T., Lin L.J., Kuo H.C., Chen T.C., 1999. Experimental Analyses of Urban Heat Island Effects of the Four Metropolitan Cities in Taiwan(I)—The Comparision of the Heat Island Intensities Between Taiwan and the World Cities. J. Archit. 31, 51–73. (In Chinese)

Mansouri S.T., Zarghami E., 2025. Investigating the effect of the physical layout of the architecture of high-rise buildings, residential complexes, and urban heat islands. Energy and Built Environment 6(1), 1-17.

Ministry of the Environment, Japan, 2000. Report on the Analysis of the Actual Conditions of the Heat Island Phenomenon and the Ideal Countermeasures (Expanded Edition). (In Japanese)

Oke T.R. Boundary Layer Climates 2nd ed. London, UK. Routledge Press, 1987.

Patel S., Indraganti M., Jawarneh R.N., 2024. A comprehensive systematic review: Impact of Land Use/ Land Cover (LULC) on Land Surface Temperatures (LST) and outdoor thermal comfort. Building and Environment 249, 111130.

Salan M.S.A., Bhuiyan M.A.H., 2024. Estimating impacts of micro-scale land use/land cover change on urban thermal comfort zone in Rajshahi, Bangladesh: A GIS and remote sensing based approach. Urban Climate 58,102187.

Shen Z., Xu X., Xu S., Sun D., 2022. A comparative study of land development patterns and regional thermal environments (RTEs) in typical urban agglomerations of China and America: A case study of Beijing-Tianjin-Hebei (BTH) and Boswash. Science of The Total Environment 803,149735.

Sodoudi S., Zhang H., Chi X., Müller F., Li H., 2018. The influence of spatial configuration of green areas on microclimate and thermal comfort. Urban Forestry and Urban Greening 34, 85-96.

6th International Conference on Building Energy and Environment
Eindhoven University of Technology, The Netherlands
6 - 10 July 2025

Data-driven characterization of thermal dynamics in PV curtain walls using grey-box modeling

Xiang Zhang [1,2], Diego Van Heurck[3], Dirk Saelens[3,4]

[1]*Architecture, The Design School, Arizona State University, Tempe, AZ, United States, jason.zhang@asu.edu*
[2]*School of Sustainable Engineering and the Built Environment, Arizona State University, Tempe, AZ, United States*
[3]*Department of Civil Engineering, Building Physics and Sustainable Design, Kasteelpark Arenberg 40, Heverlee 3001, Belgium*
[4] *EnergyVille, Thor Park 8310, Genk 3600, Belgium*

ABSTRACT

In response to the climate change crisis, building-integrated photovoltaics (BIPV) has proven to be a promising technology for harnessing renewable solar energy to reduce buildings' operational carbon emissions. As widely reported, the overheating issue of BIPV systems (e.g., PV surface temperatures reaching 50-60°C), caused by the hot weather and abundant solar radiation, can significantly reduce their electrical power generation efficiency. Thus, it is important to predict and manage PV surface temperatures to enhance the electrical generation efficiency of BIPV. Using on-site data of PV systems, such as outer/inner surface temperatures of PV panel, dry-bulb air temperature, and wind speed, to train statistical models for predicting PV surface temperature is a promising approach. This work used on-site data to train grey-box models to characterize the thermal dynamics of PV panels, as grey-box modeling combines the strengths of white- and black-box models. It allows predictions with a good balance of physical interpretation and predictive accuracy, using limited on-site data. Based on a case study of a naturally ventilated BIPV curtain wall under real climate conditions, installed on a test building in Leuven, Belgium, this work initially demonstrated that the proposed grey-box models can effectively characterize and predict the thermal dynamics of BIPV system. When applied to a new test dataset, the trained grey-box model predicts the PV panel temperature closely following the measured profile, with prediction errors ranging from –3°C to +2°C under daily PV panel temperature variations between 10°C and 70°C. This study only explored a one-state grey-box model; future work could investigate two- or multi-state grey-box models for a more precise characterization of the BIPV thermal dynamics.

Keywords: Building-integrated photovoltaics (BIPV), solar radiation, grey-box model, in-situ data, statistical modeling

INTRODUCTION

The building operational energy accounts for 30% of global final energy consumption and 26% of global energy-related carbon dioxide emissions [1]. In addition to minimizing energy consumption through enhanced building energy efficiency, enhancing the share of solar renewable energy is essential for mitigating global greenhouse gas (GHG) emissions. Building-integrated photovoltaics (BIPV) have proven to be a promising technology for harnessing renewable (solar) energy, reducing building operational carbon emissions, by up to 50% in a case reported in [2]. Among the four categories of building-integrated photovoltaic (BIPV) systems, PV-wall, PV-roof, PV-window, and

PV-shading [3], the PV-roof product remains the most widely implemented option. However, limited rooftop space may be insufficient to meet a building's energy demands fully. Therefore, PV walls are attracting increasing interest, as building façades (i.e., exterior walls) typically have a larger surface area than rooftops, offering greater potential for electrical energy generation. In addition, the operating temperature of photovoltaic (PV) modules significantly impacts their performance and electrical power generation efficiency [4]. For instance, the electrical power production efficiency of crystalline silicon PV cells decreases by approximately 0.5% for every 1°C rise in PV cell temperature [5]. Currently, the three main types of modeling approaches, are white-box, black-box, and grey-box modeling [6], or physics-based, data-driven, and hybrid models [4]. Most existing studies predominantly rely on either white-box models (e.g., simulation tools) or black-box models (e.g., artificial neural networks). However, white-box models require extensive input data [7], whereas black-box models lack the physical interpretability of the parameters involved in the model, making them more applicable to power generation forecasting [8]. The grey-box model (also known as a hybrid model) integrates the advantages of both approaches, leveraging limited on-site data to balance predictive accuracy and physical interpretability. Therefore, this project aims to develop a grey-box model for forecasting BIPV performance, with an emphasis on modeling and predicting PV module operating temperature and output electrical power generation. The grey-box model proposed in this study combines experimental data with theoretical insights into the underlying physical processes, yielding a simple yet accurate model with physical interpretations of the parameters. The experimental data is collected from measurements of a real-world BIPV application, specifically a curtain wall system integrated into the façade of a test building located in Leuven, Belgium.

CASE STUDY

2.1 BIPV Curtain Wall in Vliet test building

A testbed has been set up on a BIPV curtain wall installed in the Vliet test building (50.88°N, 4.7°E) [9], located in Leuven, Belgium. This full-size BIPV curtain wall, developed by KU Leuven/EnergyVille [10], is positioned at the far left of the BIPV façade of the Vliet test building, as shown in **Figure 1**.

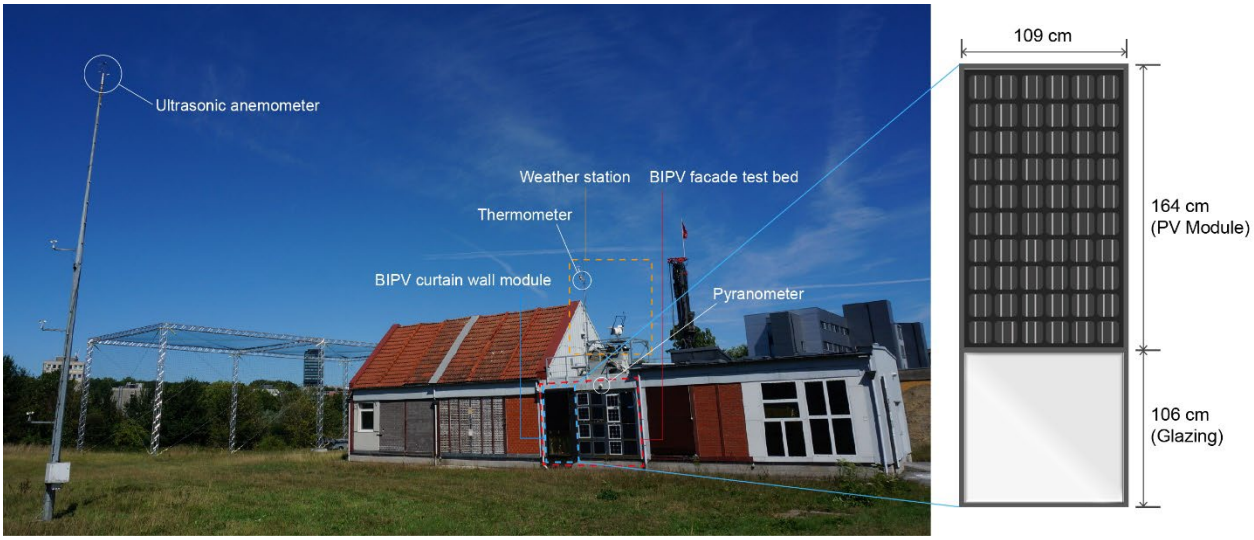

Figure 1. Vliet test building in Leuven. Belgium, with BIPV curtain wall testbed.

The curtain wall's upper section incorporates the PV module, while the bottom section consists of a triple-glazed argon window to allow sunlight into the building (**Figure 1**). The PV module consists of 60 monocrystalline silicon solar cells encapsulated in a transparent EVA layer on the front and a black EVA layer on the back. Table 1 summarizes the characteristics of the PV module used in the BIPV curtain wall.

Table 1. Main characteristics of PV modules used in the curtain wall.

Peak power (P^{STC})	244 W_p
PV module area (A_{PV})	1.09×1.64 m2
Efficiency at standard test conditions η^{STC}	13.6 %
Power temperature coefficient (μ)	0.42 %/K

2.2 PV Curtain Wall Temperature and Weather Data Monitoring

The curtain wall features four ventilation apertures on both the top and bottom sections of its sides, shown in **Figure 2**. Each aperture, with a diameter of 1 cm, allows a limited amount of ambient air to circulate within the air cavity behind the PV module. The upper section of the PV curtain consists of three layers, from exterior to interior: the PV module (Layer 1), followed by a 0.07 m air cavity, a 0.15 m mineral wool insulation layer (Layer 2), and finally, a plywood panel (Layer 3). Each of these layers is equipped with 12 type-T surface contact thermocouples, which record temperature data every second. **Figure 2** illustrates the thermocouple locations, marked as yellow dots, with the thermocouples attached to the back side of the PV module in Layer 1 and the front sides of Layers 2 and 3. In addition to temperature data, global solar irradiance, ambient dry-bulb air temperature, wind speed, and wind direction are also collected. Vertical global solar irradiance on the BIPV facade is measured every 10 seconds by a pyranometer positioned on the facade (**Figure 1**).

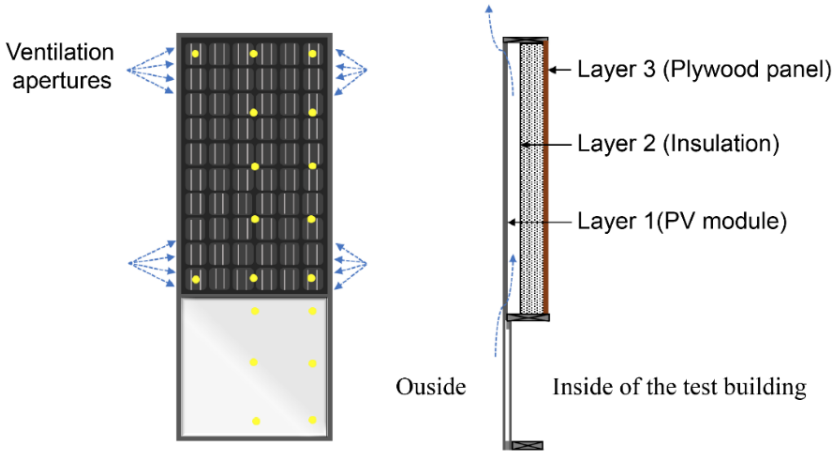

Figure 2. Curtain wall ventilation apertures and placement of thermocouples (left), section with layers (right)

Ambient air temperature is recorded every minute by a thermometer in the weather station on the rooftop of the Vliet test building (**Figure 1**). The ultrasonic anemometer located 10 meters above ground next to the test building, shown in **Figure 1**, records both wind speed and direction every 5 minutes. The readers refer to Ref. for a more detailed description of the measurement campaign. The measurements were performed over a one-year period (2019–2020), and the raw data were pre-processed and averaged into 10-minute time intervals. Moreover, two datasets are constructed as training and test datasets, referred to as Dataset 1 and Dataset 2, respectively. Their key characteristics

are summarized in Table 2. Dataset 1 is used for grey-box model training and identification, while Dataset 2 is used to validate the PV panel temperature prediction capability of the grey-box model trained and selected based on Dataset 1.

Table 2. Two pre-constructed datasets used in this study and their key features.

No.	Role	Period	Length	Sky conditions	Wind speed	Wind direction
1	Training dataset	22-27 March	6 days	clear	0.1-6.5 m/s	Leeward
2	Test dataset	20-23 April	4 days	(near) clear	0.1-6.1 m/s	Mixed

GREY-BOX MODELING

3.1 Brief Introduction of Grey-box Modeling and forward selection

In brief, a grey-box model comprises two types of equations: system equation(s) and measurement equation(s). The system equation(s) are constructed based on physical knowledge. These models estimate system parameters by fitting the model to observed data using the maximum likelihood estimation (MLE) method. In this study, forward selection is employed to determine the appropriate model complexity, starting with the simplest one-state model and progressively increasing its complexity step by step. At each step, the performance is evaluated and compared based on the values of the Log-Likelihood, Akaike Information Criterion (AIC), and Bayesian Information Criterion (BIC). Readers are referred to [11] for more details on grey-box modeling and the application of forward selection. The grey-box modeling process is executed using the Continuous Time Stochastic Modeling package in R (CTSM-R).

3.2 Heat Transfer and Energy Balance of the PV Curtain Wall

To construct the system equation(s) of grey-box models for the PV Curtain Wall, **Figure 3** visualizes the different energy/heat flux flows based on a horizontally elongated cross-section of the PV curtain wall.

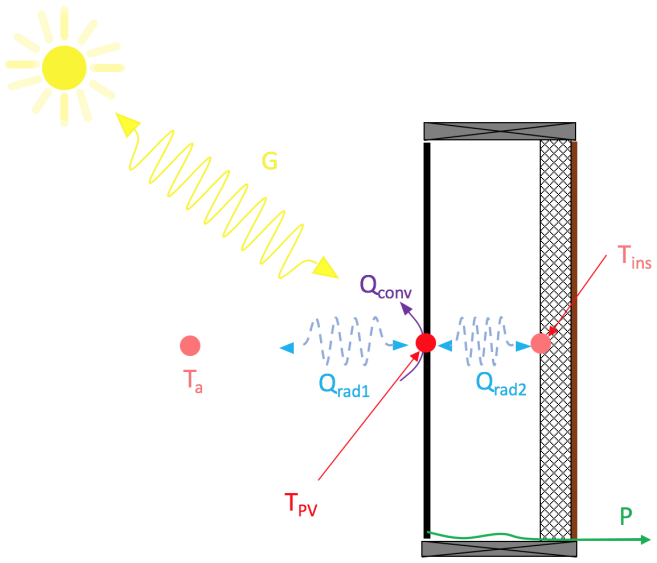

Figure 3. Energy balance and heat transfer diagram of the PV curtain wall.

3.3 Simplest Grey-box Model (T_{PV})

Based on the heat transfer and energy balance visualized in **Figure 3**, the simplest stochastic differential equation that characterizes the energy balance is Eq. (1). where C_{PV} is the heat capacity of the PV module and σ_1 an unknown model parameter characterizing the diffusion term, not to be confused with the Stefan-Boltzmann constant (σ). The observation equation is simply defined as Eq. (2). T_{PV} represents the average temperature of the solar panel, as a system state, determined by the enegy balance of the PV curtain wall. Irradiance on the PV panel (G; in W/m^2) is the system's only energy input and $(\tau\alpha)A_{PV}G$ represents the portion of solar irradiance absorbed by the PV curtain wall, where $\tau\alpha$ [-] is the absorption coefficient of solar irradiance, and A_{PV} (in m^2) is the area size of PV panel. P denotes the DC output power of the PV module.

$$C_{PV}dT_{PV} = \Big[(\tau\alpha)A_{PV}G - P - \sigma\varepsilon_{PV}A_{PV}(T_{PV}^4 - T_a^4) - \frac{\sigma A_{PV}}{1/\varepsilon_{PV}+1/\varepsilon_{ins}-1}(T_{PV}^4 - T_{ins}^4) - h_{c,e}A_{PV}(T_{PV} - T_a)\Big]dt + \sigma_1 d\omega_1 \quad (1)$$

$$T_{PV_m} = T_{PV} + e_1 \quad (2)$$

As shown in Figure 3, the radiative heat transfer from the front surface of the PV panel to the exterior is denoted as Q_{rad1} and is expressed as $\sigma\varepsilon_{PV}A_{PV}(T_{PV}^4 - T_a^4)$ in Eq. (1), under the assumption of considering the environment as a black body ($\varepsilon = 1$). ε_{PV} signifies the long-wave emissivity, set to 0.9 in this case for the EVA cover layer, and T_a referes to the temperature of the surrounding environment as perceived by the front surface of PV panel. Similarly, the radiative heat transfer from the back surface of the PV panel to the insulation layer is denoted as $Q_{rad2}\ [W]$ and estimated by Eq. (3) . It is simplified in Eq. (1) as $\frac{\sigma A_{PV}}{1/\varepsilon_{PV}+1/\varepsilon_{ins}-1}(T_{PV}^4 - T_{ins}^4)$. Specifically, the PV panel and insulation layer have the same area ($A_{PV} = A_{ins}$) and the view factor between the two surfaces is set to 1 ($F = 1$) since the distance separating them (0.07 m) is two orders of magnitude smaller than the length of the surface sides (1.09 m).

$$Q_{rad2} = \frac{\sigma\,(T_{PV}^4 - T_{ins}^4)}{\frac{1-\varepsilon_{PV}}{\varepsilon_{PV}A_{PV}} + \frac{1}{A_{PV}F} + \frac{1-\varepsilon_{ins}}{\varepsilon_{ins}A_{ins}}} \quad (3)$$

The convection-based heat exchange between the PV panel and the ambient air is expressed as $h_{c,e}A_{PV}(T_{PV} - T_a)$ in Eq. (1), where $h_{c,e}$ [W/m^{2}K] is the convective heat transfer coefficient between the PV panel and ambient air.

Building on the simplest T_{PV} model, further refinements were made to increase the complexity of the grey-box model candidates and better capture the actual thermal performance of the PV system. This study explored three approaches: (1) incorporating the incidence angle modifier (IAM); (2) accounting for the effect of wind; and 3) separating the exterior environment into sky and ground parts when modeling radiative heat transfer from between the front surface of the PV panel and the exterior environment. The three approaches lead to three more grey-box model candidates.

3.4 Inclusion of Incidence Angle Modifier (IAM) in T_{PV} Model ($T_{PV}IAM$)

The incidence angle of solar irradiance (i.e., the angle between the normal to the surface and the incoming irradiance) significantly impacts the absorption ratio of solar irradiance, as the amount of radiation reflected from the PV panel increases with the incidence angle. This effect can be

incorporated by using the incidence angle modifier (IAM), which is defined as the ratio of the irradiance absorbed by the cell at incidence angle θ_s to the irradiance absorbed by the cell at normal incidence [12], as Eq. (4), where $(\tau\alpha)_{\theta_s}$ and $(\tau\alpha)_n$ represent the fraction of solar irradiance absorbed by the cells at incidence angle θ_s and normal incidence representatively.

$$IAM = \frac{(\tau\alpha)_{\theta_s}}{(\tau\alpha)_n} \tag{4}$$

3.5 Inclusion of wind effect in T_{PV} Model ($T_{PV}W$)

Instead of treating $h_{c,e}$ as a constant value, based on the T_{PV} model, the $T_{PV}W$ further consider the impact of wind on the convective heat transfer coefficient $h_{c,e}$ via Eq. (5).

$$h_{c,e} = C_1(W)^{C_2} \tag{4}$$

Where *W* denotes the wind speed measured by ultrasonic anemometer located 10 meters above ground , as shown in **Figure 1** and C_1 and C_2 are treated as unknown parameters and will be estimated through data fitting.

3.6 Differentiation between sky and ground in T_{PV} Model ($T_{PV}Sky$)

As discussed, the T_{PV} model treats the exterior environment in aggregate, represented soley by the ambient air temperature T_a, and it models the radiative heat transfer from the front surface of the PV panel to the exterior (Q_{rad1}) as $\sigma\varepsilon_{PV}A_{PV}(T_{PV}^4 - T_a^4)$. The Q_{rad1} can be further refined by differentiating between radiation to the ground and to the sky separately in Eq. (5), leading to an expanded $T_{PV}Sky$ model.

$$Q_{rad1} = F_{gnd}\left(T_{PV}^4 - T_{gnd}^4\right) + F_{sky}\left(T_{PV}^4 - T_{sky}^4\right) \tag{5}$$

The view factors of the PV panel to the ground and sky denoted as F_{gnd} and F_{sky} respectively, are given by Eqs. (6-7), and β represents the inclination angle of the PV module (i.e., the angle between the PV panel and the horizontal), which is 90º in this case. In addition, the ground temperature (T_{gnd}) is assumed to be equal to the ambient air temperature (T_a), while the sky tempeature is treated as an unknown parameter, similar to C_1 and C_2.

$$F_{gnd} = (1 - cos\ (\beta))/2 \tag{6}$$
$$F_{sky} = (1 + cos\ (\beta))/2 \tag{7}$$

RESULTS

4.1 Forward selection results

As discussed in Section 3.1, forward selection is used to identify the most suitable single-state model, starting from the simplest T_{PV} model and step-by-step increasing its complexity by incorporating one or more of the approaches outlined in Sections 3.4–3.6. In brief, forward selection requires that each successful extension of the grey-box model results in an increased log-likelihood value and reduced AIC and BIC values, continuing until no further extension yields a significantly better fit (i.e., no

substantial increase in log-likelihood). The model selection process is visualized in **Figure 4**. The $T_{PV}WSky$ model is identified as the best-fitting model for Dataset 1 in this study. It builds upon the T_{PV} model but incorporates the effect of wind and separates the environmental impacts into sky and ground components. The $T_{PV}WSky$ incroporates Eqs. (4-5) to extend Eq. (1) as Eq. (8). The parameters C_{PV}, T_{sky}, C_1, C_2 and σ_1 are treated as unknowns to be estimated through data fitting. Specifically, the $T_{PV}WSky$ is composed of Eq. (8) and Eq. (2).

$$C_{PV}dT_{PV} = \Big[(\tau\alpha)A_{PV}G - P - \sigma\varepsilon_{PV}A_{PV}(T_{PV}^4 - T_a^4) - \frac{\sigma A_{PV}}{1/\varepsilon_{PV}+1/\varepsilon_{ins}-1}(T_{PV}^4 - T_{ins}^4) - h_{c,e}A_{PV}(T_{PV} - T_a)\Big]dt + \sigma_1 d\omega_1 \quad (8)$$

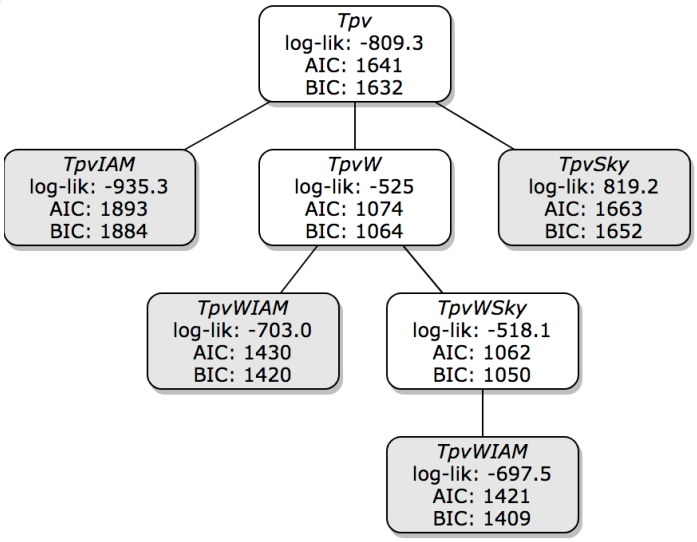

Figure 4. Summary model selection process for the first-order model

4.2 Model prediction performance using test dataset

To validate the general T_{PV} prediction capability of the trained $T_{PV}WSky$ model (based on the training dataset, Dataset 1), the model is applied to predict T_{PV} dynamics using weather data from the test dataset (Dataset 2). The input data for the $T_{PV}WSky$ model include solar irradiance, wind speed, and ambient air temperature, covering the period from April 20 to April 23, 2020. **Figure 5** shows promising T_{PV} prediction results, demonstrating that the model can reasonably predict and capture the key daily dynamics of PV panel temperature. As shown in Figure 5, the simulated temperatures follow the measured profile closely, with prediction errors ranging from –3°C to +2°C, which is acceptable in practice, considering the peak PV temperature exceeds 50°C, even approaching 70°C during this specific four-day period.

DISCUSSION AND CONCLUSION

This pilot study initially revealed the promising performance of grey-box models in predicting PV surface temperature, which plays a crucial role in estimating electrical power generation. The proposed grey-box model, trained on one dataset, was able to predict PV panel temperature dynamics with acceptable accuracy on a new test dataset collected from the same PV system during a different period. The predicted PV panel temperatures closely followed the measured temperature profile, with prediction errors ranging from –3°C to +2°C, under daily variations between 10°C and 70°C. While

this study focused on a one-state grey-box model, future research could explore two- or multi-state models to achieve a more accurate representation of BIPV thermal behavior. Additionally, future work could extend the grey-box modeling approach to predict electrical power generation.

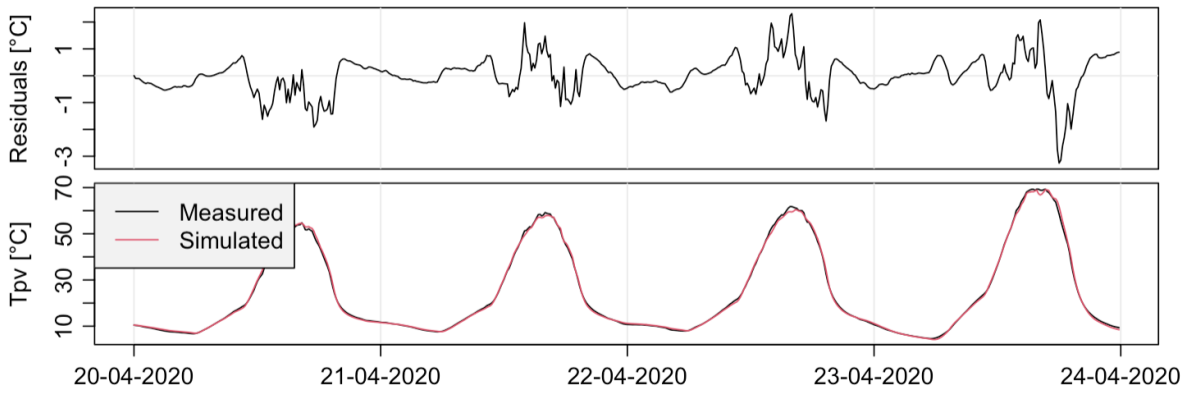

Figure 5. Prediction of PV panel tempeature (T_{PV}) with $T_{PV}WSky$ model for the test dataset (Dataset 2).

References

[1] International Energy Agency, Tracking Clean Energy Progress 2023 – Analysis, IEA (2023). https://www.iea.org/reports/tracking-clean-energy-progress-2023.

[2] G. Happle, Z. Shi, S. Hsieh, B. Ong, J.A. Fonseca, A. Schlueter, Identifying carbon emission reduction potentials of BIPV in high-density cities in Southeast Asia, Journal of Physics: Conference Series 1343 (2019) 012077. https://doi.org/10.1088/1742-6596/1343/1/012077.

[3] X. Zhang, S.-K. Lau, S.S.Y. Lau, Y. Zhao, Photovoltaic integrated shading devices (PVSDs): A review, Solar Energy 170 (2018) 947–968. https://doi.org/10.1016/j.solener.2018.05.067.

[4] L. O. Santos, F. A. A. Souza, C. O. Carvalho Filho, P. C. M. Carvalho, T. AlSkaif, R. I. S. Pereira, Hybrid Modeling for Photovoltaic Module Operating Temperature Estimation, IEEE Journal of Photovoltaics 14 (2024) 488–496. https://doi.org/10.1109/JPHOTOV.2024.3372328.

[5] M.M. Fouad, L.A. Shihata, E.I. Morgan, An integrated review of factors influencing the perfomance of photovoltaic panels, Renewable and Sustainable Energy Reviews 80 (2017) 1499–1511. https://doi.org/10.1016/j.rser.2017.05.141.

[6] X. Zhang, C. Rasmussen, D. Saelens, S. Roels, Time-dependent solar aperture estimation of a building: Comparing grey-box and white-box approaches, Renewable and Sustainable Energy Reviews 161 (2022) 112337. https://doi.org/10.1016/j.rser.2022.112337.

[7] J.E. Goncalves, T. van Hooff, D. Saelens, A physics-based high-resolution BIPV model for building performance simulations, Solar Energy 204 (2020) 585–599. https://doi.org/10.1016/j.solener.2020.04.057.

[8] P. Li, K. Zhou, X. Lu, S. Yang, A hybrid deep learning model for short-term PV power forecasting, Applied Energy 259 (2020) 114216. https://doi.org/10.1016/j.apenergy.2019.114216.

[9] S. Roels, M. Deurinck, The effect of a reflective underlay on the global thermal behaviour of pitched roofs, Building and Environment 46 (2011) 134–143. https://doi.org/10.1016/j.buildenv.2010.07.005.

[10] J.E. Gonçalves, H. Montazeri, T. van Hooff, D. Saelens, Performance of building integrated photovoltaic facades: Impact of exterior convective heat transfer, Applied Energy 287 (2021) 116538. https://doi.org/10.1016/j.apenergy.2021.116538.

[11] P. Bacher, H. Madsen, Identifying suitable models for the heat dynamics of buildings, Energy and Buildings 43 (2011) 1511–1522. https://doi.org/10.1016/j.enbuild.2011.02.005.

[12] S.A. Kalogirou, Chapter 9 - photovoltaic systems, in: Solar Energy Engineering: Processes and Systems, Academic Press, Boston, 2014: pp. 481–540.

Building Mechanical System and Controls (15:30-17:00 h)

6th International Conference on Building Energy and Environment
Eindhoven University of Technology, The Netherlands
6 - 10 July 2025

Data-driven modelling and automated optimization of multi-chiller sequencing

Qiwei Qin [1], Etienne Saloux [1]

[1]*CanmetENERGY, Natural Ressources Canada, Varennes, QC, Canada*

SUMMARY
Central cooling systems are commonly used in medium and large commercial buildings, but their energy-intensive nature necessitates efficient operation, particularly in multi-chiller sequencing. While research has focused on theoretical simulations and data-driven methods, practical deployment faces challenges such as limited sensors, computational constraints, and chiller performance degradation over time. This study proposes an automated, data-driven methodology for optimizing multi-chiller sequencing based on real measurements. Performance curves are derived using historical operational data and used in an optimization routine that identifies the most energy-efficient combination of chillers to operate. This optimal sequencing can then be integrated into existing control systems using simple control sequences, facilitating scalability and field deployment. This approach minimizes electricity use of the cooling system, including chillers, circulation pumps, and water tower fans. The method has been applied to two large buildings and results showed that electricity use was reduced by 9% and 15%. By dynamically adapting to load changes, it demonstrates the potential for sustainable, reliable, and automated building energy management.

Keywords: Multi chillers; cooling system; data-driven; energy efficiency; modelling; sequencing.

1. INTRODUCTION

Improving building controls could help reduce energy use by up to 30% with simple payback periods of around 2 years while cooling energy is projected to become predominant (Saloux et al., 2023). Central cooling systems are commonly used in medium and large commercial buildings, but their energy-intensive nature necessitates efficient operation (Liu et al., 2017). Optimal chiller sequencing can lower energy consumption of chiller while meeting building cooling load demand (Sun et al., 2009). Research has extensively focused on optimal chiller sequencing; for instance, based on theoretical simulations by using different optimization algorithms such as dynamic programming (Li et al., 2024), generic pattern search optimization algorithm (Faulkner et al., 2024) and Lagrangian method (Chang, 2004). However, challenges such as limited sensor availability, computational demands, and the inevitable performance degradation of chillers over time hinder widespread adoption. Data-driven models, which are based on sub-hourly data from building automation systems, provide an opportunity for improving existing building controls (Saloux and Zhang, 2023). These models could be used to derive data-driven rule-based controls, which are much easier to implement in existing building.

This study addresses these challenges by presenting an automated, data-driven methodology for optimizing multi-chiller sequencing based on real-world measurements. Performance curves are derived from historical operational data and are leveraged to identify the most energy-efficient combination of chillers. Furthermore, the proposed methodology not only minimizes the central cooling plant electricity use but also addresses the switching between chillers. The proposed

approach is applied to two commercial and institutional buildings and achieves significant energy efficiency improvements. By streamlining complex processes, this approach bridges the gap between theoretical methodologies and real-world applications, making optimal chiller sequencing more accessible and scalable for widespread adoption in buildings.

2. METHODS: AUTOMATED MULTI-CHILLER SEQUENCING OPTIMIZATION

A typical central chilled water system which is commonly used in medium to large commercial or institutional buildings is shown in Fig. 1 (*ASHRAE Handbook: HVAC Systems and Equipment*, 2008). To ensure redundancy and flexibility, multiple chillers are connected in parallel and a decoupler pipe is used to bypass the chiller when necessary. Primary pumps maintain constant refrigerant flow through the chillers, while variable-speed secondary pumps distribute chilled water throughout the building. In the condenser loop, constant-speed pumps reject heat via cooling towers or air condensers. The efficiency of chillers varies at cooling conditions and makes optimal sequencing critical. This study presents an automated approach for equipment mapping, data cleaning, performance modeling, and chiller sequencing. It also evaluates model accuracy and potential savings. These capabilities are integrated into a Python-based tool, under development.

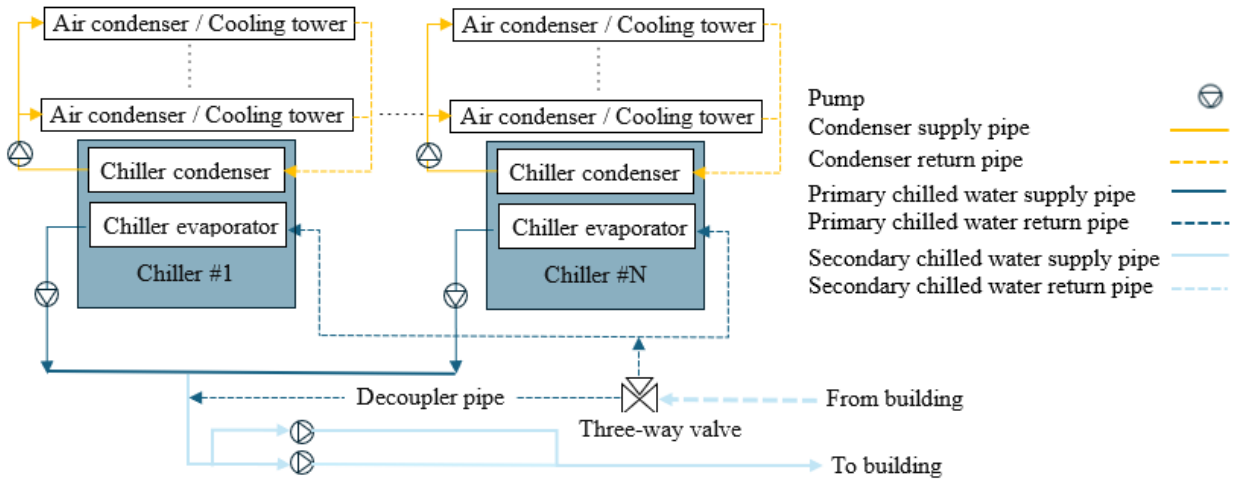

Figure 1. Schematic of a typical chilled water system, equipped with multiple chillers.

2.1 Equipment variable mapping and data cleaning

Users are required to provide basic plant information (e.g. number of chillers, nominal capacities) and sub-hourly operational data. This information is processed as follows:

1. *Data resampling*: Data is averaged at hourly intervals for deriving performance curve.
2. *Data filtering*: Cooling load is calculated using temperature difference and flow rate. To reduce noise and uncertainty, minimum threshold values below which the data is removed are used for temperature difference and flowrate, and for electric power. This threshold can be specified by the user or automatically calculated (5^{th} percentile for temperature difference and flowrate; 5% of nominal capacity for electric power).
3. *Chiller combination identification*: The operational status of each chiller (on/off) is automatically determined using electric power minimum threshold values, and combinations of chillers are identified using IDs. To remove transient operation for

deriving performance curves, for each point, the combination of chillers must have been in operation for a user-defined duration and must remain in operation for the same period. This period is set to 1 hour by default. To ensure sufficient data points, only combinations that have been in operation for a minimum number of hours are kept (default: 50 hours).

2.2 Data-driven part-load ratio performance curves

Chiller performance is primarily influenced by evaporator and condenser temperatures, as well as building cooling load. Including variables such as outdoor air temperature, humidity, or condenser inlet (air, water) temperature could improve model accuracy but may introduce practical constraints. Indeed, it may yield to more complex chiller sequencing strategies, reducing interpretability and making practical implementation more complex while possibly causing more chiller switches. Moreover, modelling might leverage more advanced black-box techniques, possibly causing overfitting while performance under extrapolation conditions might be more difficult to assess. To balance model accuracy and real-world applicability, this study adopts cooling load as the sole input variable – a commonly accepted simplification in many data-driven modeling efforts (Saloux and Zhang, 2023). While it may not capture all nuances of chiller performance under varying weather conditions, it allows for a scalable, low-cost, and practical solution facilitating implementation and large-scale adoption.

Two definitions of Coefficient of Performance (COP) are considered for determining the optimal chiller sequencing. COP_{ch} evaluates the energy consumption of the chillers only whereas COP_{sys} tackles the cooling system and accounts for chillers along with auxiliary equipment (pumps, fans):

$$COP_{ch}(t) = \frac{\dot{Q}_{cooling}}{\sum_i \dot{W}_{ch,i}} \quad \text{Eq.(1)}$$

$$COP_{sys}(t) = \frac{\dot{Q}_{cooling}}{\sum_i \dot{W}_{ch,i} + \sum_j \dot{W}_{pp,j} + \sum_k \dot{W}_{fan,k}} \quad \text{Eq.(2)}$$

where $\dot{W}_{ch,i}$ is the electric power of the i^{th} chiller in the considered combination. For the cooling system COP, $\dot{W}_{pp,j}$ is the electric power of the j^{th} pump and $\dot{W}_{fan,k}$ is the electric power of the k^{th} fan of cooling towers and air condensers. Therefore, the cooling system COP is calculated by considering all chillers and auxiliary equipment and is then filtered for each chiller combination. In theory, the equipment that is not related to a specific combination of chillers should be excluded from the calculations (e.g. the pump related to chiller #1 should not be in operation if chiller #1 is not in operation). However, in practice, it becomes cumbersome to automatically gather connection details between the different components from users and to identify the exact multi-chiller system configuration. Therefore, Eq. (2) is used and may potentially account for the operation of equipment not related to a specific chiller combination. Data-driven performance curves are determined by plotting chiller COP or cooling system COP as a function of building cooling load. Users can select linear, quadratic, or cubic models. Furthermore, for each combination, datasets are randomly divided into training (80%) and validation (20%). These models are evaluated and compared based on the coefficient of determination (R^2) and the coefficient of variation of the root mean square error (CV-RMSE). Models are automatically selected using a default metric as shown in Eq. (3), which balances model accuracy and complexity whereas users can also select the most appropriate model for each combination.

$$R^2_{adjust} = R^2 - \lambda p \quad \text{Eq.(3)}$$

where R^2 is the coefficient of determination and p is the number of parameters in the model (2 for linear model; 3 for quadratic; 4 for cubic). $\lambda > 0$ is a factor used to penalize model complexity; the penalty is set as 1.5% after trial and error.

2.3 Chiller sequencing strategy

The proposed chiller sequencing strategy optimizes cooling system energy efficiency using data-driven performance curves while minimizing equipment wear and tear:

1. *Curve fitting for each combination*: performance curves are derived for all possible chiller combinations using linear, quadratic or cubic models (Section 2.2). The combination of chillers in operation for particular loads is determined based on historical operational data. To avoid questionable values, a given combination cannot provide more cooling than the sum of 110% of the nominal capacity of each chiller. This additional 10% accounts for potentially favorable operating conditions. Similarly, a combination cannot provide less cooling than 15% of the nominal capacity of each chiller.
2. *Maximizing COP and minimizing chiller status changes*: the cooling load range is divided into 100 intervals. The strategy prioritizes energy efficiency, and the highest COP is identified for each interval; any combinations showing values higher than 97% of the highest COP are considered as optimum candidates. When multiple combinations are possible, the one with minimal chiller status changes (compared with the previous hour) is selected to enhance equipment stability.
3. *Deriving optimal control sequences*: The final output identifies threshold values indicating the switch from one combination to another. To avoid frequent switch around thresholds, a deadband of 5% is applied (e.g., a 100-kW threshold triggers a switch to a new combination at 105 kW if the cooling load increases and 95 kW if the cooling load decreases). This deadband represents the trade-off between chiller switch number and energy savings (a larger value may reduce the number of switches but also the COP).

While more complex approaches (e.g. controlling chillers, fans and pumps individually), chiller models (e.g. considering additional modelling techniques and/or variables such as temperatures) and optimization routines can be found in the literature, this method prioritizes simplicity, requires minimal data while ensuring practical adoption and scalability across multi-chiller systems.

2.4 Performance evaluation

The chiller sequencing strategy is evaluated based on cooling system electricity use, peak power, and energy costs, the number of chiller switches and the number of operating hours for each chiller. The building cooling load remains unchanged. COP models are used to estimate electricity use. For the reference case, chiller combinations were extracted from operational data.

3. CASE STUDY BUILDINGS

The approach was tested for two commercial buildings. The first building is a 36,000 m^2, 11-floor commercial building equipped with two air-cooled chillers connected to two air condensers and one water-cooled chiller connected to two wet cooling towers. The second building is a 33,000 m^2, 3-floor institutional building equipped with 5 water-cooled chillers and 5 wet-cooling towers. Both

buildings are located in the Montréal area, Canada. The data was available from Jun 1 to Aug 30, 2023 for building #1 and May 1 to Sep 13, 2021 for building #2. Electricity cost is assumed to be CAD 4.339 c/kWh. For building #1, all required measurements were obtained from the control system or electric power spot measurements. However, for building #2, chiller power was estimated from % RLA readings, while pump power was calculated from on/off status and nominal capacity, which is suitable for constant-speed pumps but not variable-speed ones. Nonetheless, variable speed pumps are in operation regardless of chiller combinations and might not affect the optimal sequencing. Therefore, supply pump powers are neglected for modelling chiller performance curve to avoid adding uncertainty.

4. RESULTS: MODEL ACCURACY AND ENERGY SAVINGS

This section discusses electricity use distribution, model accuracy and expected savings; results are presented side-by-side for both buildings to highlight differences between case studies.

4.1 Cooling system electricity use distribution

The cooling system electricity use distribution shown in Fig. 2 is a critical indicator of energy usage patterns and system efficiency. For both buildings, chillers account for the largest share (53-55%) of electricity use, which underscores the importance of optimizing the operation of chillers, but also auxiliary equipment, to maximize system efficiency. Moreover, significant differences are observed for auxiliary equipment electricity use, which can be explained by energy efficiency levels. Building #1 primarily relies on air-cooled towers, which are generally less efficient than cooling towers (15.3% vs. 8.1%); a similar observation can be made for condenser pumps (14.0% vs. 12.8%). For chilled water pumps, the contribution varies between 17.1% and 24.3% but energy use is overestimated for building #2 (variable speed pump on/off was used, see Section 3).

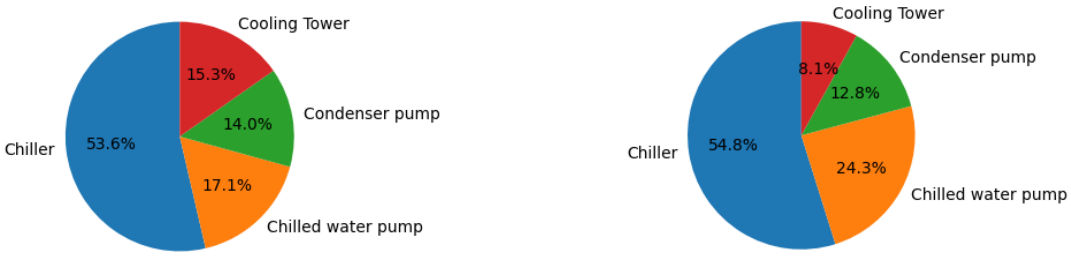

Figure 2. Cooling system electricity use distribution for building #1 (left) and #2 (right). Cooling towers account for air condensers and wet water towers; chilled water pump represents primary and secondary pumps.

4.2 Accuracy of performance curves

Fig. 3 shows performance curves for both buildings. With three chillers, 7 combinations are in theory possible for building #1, but only four have been in operation for more than 50 hours. Although identical, chillers #2 and #3 (air-cooled screw chillers) show slight differences in performance. Chiller #1 (water-cooled centrifugal chiller) is expected to be more efficient than #2-3 but real-world data indicate lower performance, revealing potential inefficiencies and the importance of empirical analysis. For building #2, with 5 chillers, only 18 chiller combinations were observed out of 31 possible ones, and just 10 showed a minimum operation of 50 hours, highlighting the impact of operational constraints or system limitations. Chillers #4-5 are smaller units for low loads, while chillers #1-3 are identical but chiller #3 demonstrates higher efficiency. Fig. 3 also complements Fig. 2 by emphasizing differences between chiller COP and system COP, especially at low loads where auxiliary equipment has a significant impact. Tables 1 and 2

summarize model accuracy metrics (R^2, CV-RMSE) for all chiller combinations. Models are considered calibrated when $R^2 > 75\%$ and CV-RMSE < 30%, although these thresholds are not necessarily suitable for data-driven models (Saloux, 2025). While CV-RMSE ranges between 4-19%, R^2 falls below 70% for 6 (system COP) and 10 (chiller COP) combinations, and can be as low as 2%, indicating low COP variations with cooling load.

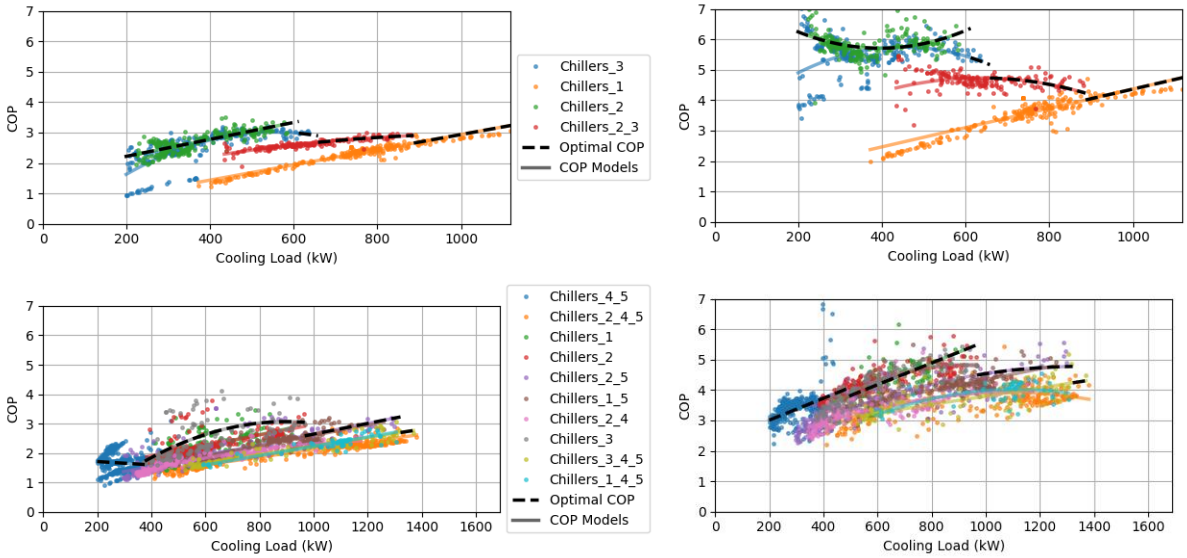

Figure 3. Measurements (dots), COP model (solid line) and optimal COP (dashed line) of different combinations of chillers based on system COP (left) and chiller COP (right) for building #1 (top) and building #2 (bottom).

Table 1. Model accuracy metrics for system COP (left) and chiller COP (right) for building #1.

Combination	Model	R^2	CV-RMSE
#3	Quadratic	62%	16%
#1	Linear	95%	5%
#2	Linear	63%	8%
#2-#3	Quadratic	80%	4%

Combination	Model	R^2	CV-RMSE
#3	Quadratic	20%	12%
#1	Linear	83%	8%
#2	Quadratic	7%	8%
#2-#3	Quadratic	33%	7%

Table 2. Model accuracy metrics for system COP (left) and chiller COP (right) for building #2.

Combination	Model	R^2	CV-RMSE
#4-#5	Linear	2%	18%
#2-#4-#5	Linear	89%	8%
#1	Linear	36%	13%
#2	Linear	44%	14%
#2-#5	Linear	70%	16%
#1-#5	Linear	73%	9%
#2 #4	Quadratic	88%	7%
#3	Quadratic	48%	19%
#3-#4-#5	Linear	85%	8%
#1 #4 #5	Linear	85%	6%

Combination	Model	R^2	CV-RMSE
#4-#5	Linear	13%	17%
#2-#4-#5	Quadratic	57%	9%
#1	Linear	64%	7%
#2	Quadratic	70%	6%
#2-#5	Quadratic	78%	10%
#1-#5	Linear	55%	8%
#2 #4	Quadratic	60%	10%
#3	Quadratic	83%	6%
#3-#4-#5	Linear	51%	10%
#1 #4 #5	Quadratic	55%	7%

4.3 Chiller sequencing strategy

Based on the optimal COP presented in Section 4.2, Table 3 outlines the optimal chiller sequencing using chiller on/off as a function of cooling load. As discussed in Section 2, threshold values are implemented with deadbands to improve operational efficiency (cooling system COP) while

minimizing chiller switches, and reducing equipment wear and tear. For building #1, chiller #2 should be used at low cooling loads due to its higher efficiency while chiller #3 should be employed for a small load range before running both chillers #2-3 at higher loads. Chiller #1 is less efficient and is only used when chillers #2-3 cannot meet the demand. For building #2, chillers #4-5 are used at low cooling loads and are assisted by chillers #2 and #3 for higher loads; chiller #1 is never in operation.

Table 3. Chiller sequencing strategy for building #1 (left) and building #2 (right) based on optimal system COP, with thresholds for decreasing and increasing cooling load (kW) and chiller on (green) and off (red).

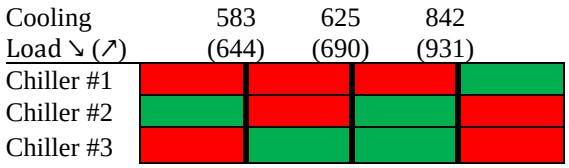

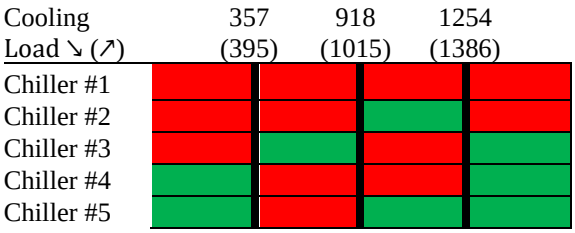

4.4 Performance evaluation

Table 4 shows the performance of the optimal chiller sequencing strategy. Energy savings of 9% and 15% are obtained for building #1 and #2, ultimately translating into similar cost savings, whereas the electric power peak remains unchanged. These results may be achieved by switching more or less between chillers (-51% to +30%) and by prioritizing higher-efficiency chillers (#2 for building #1; #3 for building #2), which may eventually impact equipment longevity. It shows some potential for better balancing energy efficiency and equipment lifespan in the objective function.

Table 4: Performance comparison of reference and optimal chiller sequencing for buildings #1 and #2.

	Building #1		Building #2	
	Reference	Optimal	Reference	Optimal
Seasonal system COP (-)	2.28	2.49 (+0.21)	2.1	2.48 (+0.38)
Electricity consumption (MWh)	338	309 (-9%)	989	838 (-15%)
Cooling system electric peak (kW)	396	396 (-)	588	588 (-)
Energy costs (CAD)	14,655	13,408 (-9%)	42,913	36,361 (-15%)
Number of chiller switches	472	213 (-55%)	1084	1400 (+30%)
Number of operating hours for each chiller	#1: 336 #2: 681 #3: 679	#1: 38 #2: 2048 #3: 367	#1: 904 #2: 1371 #3: 440 #4: 1638 #5: 2053	#1: 0 #2: 502 #3: 2130 #4: 678 #5: 1180

5. DISCUSSION: PRACTICAL CHALLENGES AND LESSONS LEARNED

The development of the proposed chiller sequencing strategy as an automated process introduces several practical challenges. One major issue is the variability in plant configurations, with diverse design and control capabilities. To address this, the approach relies on high-level information (e.g., type and number of components), though this may lead to inaccurate performance estimates due to auxiliary equipment interactions (e.g., a cooling tower pump operating with air-cooled chillers). Another challenge is data availability and quality—key variables such as electric power are often missing and must be estimated using %RLA, manufacturer specs, or spot measurements. While data postprocessing is automated (Section 2.1), manual efforts may be needed when results deviate from expectations. Finally, integration into existing control systems as a supervisory layer raises

additional issues, such as code modifications and legacy system compatibility. Furthermore, since the strategy reflects historical data, it must be updated regularly to capture equipment degradation or operational changes.

Despite these challenges, the strategy was validated using historical datasets, providing a reasonable estimate of expected savings. Implementation is ongoing in one case study building, alongside the development of a user-friendly tool for broader deployment. A key takeaway is that simplicity is essential for scalability and operator acceptance—supervisory strategies are preferred over those requiring full control of all components. Additionally, the use of data-driven performance curves has revealed performance deviations; for instance, chiller #1 in building #1 underperformed due to rust buildup, while anomalies in chillers #4 and #5 in building #2 suggested operational issues. Such curves offer potential for fault detection, performance tracking, and predictive maintenance (Saloux and Zhang, 2023).

6. CONCLUSIONS AND FUTURE WORK

This study demonstrates the feasibility and effectiveness of an automated data-driven chiller sequencing. This strategy has been applied to two buildings and demonstrated significant energy savings while ensuring a reasonable number of chiller switches, highlighting both energy and operational benefits. This approach leverages operational data and balances simplicity and accuracy, which makes it practical for field implementation and large-scale adoption, bridging the gap between theoretical work and practical usage. Future work can focus on the integration of new plant configurations (heat recovery between high and low temperature networks; water-based free cooling), the improvement of models, objective functions and optimization routines, and the development of predictive control strategies to improve performance. Field implementation is also critical to identify and address implementation barriers.

ACKNOWLEDGEMENTS

The financial support of Natural Resources Canada through the Office of Energy Research and Development (OERD) and the Greening Government Fund (GGF) is gratefully acknowledged.

REFERENCES

American Society of Heating Refrigerating and Air-Conditioning Engineers, 2008. ASHRAE Handbook: HVAC Systems and Equipment.

Chang, Y.-C., 2004. A novel energy conservation method—optimal chiller loading. Electr. Power Syst. Res. 69, 221–226.

Faulkner, C.A., Shi, C., Ho, J., Ildiri, N., Zuo, W., 2024. Developing Near Optimal Control Sequences for Chiller Plants with Water-side Economizers: A Case Study in a Warm and Marine Climate, in: Proceedings of SimBuild Conference 2024, IBPSA-USA Building Simulation Conference. IBPSA-USA, Denver, Colorado, pp. 178–184.

Li, Shuhao, Li, Siqi, Wang, Z., 2024. Accelerating chiller sequencing using dynamic programming. Energy Build. 325, 115037.

Liu, Z., Tan, H., Luo, D., Yu, G., Li, J., Li, Z., 2017. Optimal chiller sequencing control in an office building considering the variation of chiller maximum cooling capacity. Energy Build. 140, 430–442.

Saloux, E., 2025. Exploring building performance evaluation methods to estimate energy savings following field implementation. Build. Environ. 269, 112346.

Saloux, E., Zhang, K., 2023. Data-Driven Model-Based Control Strategies to Improve the Cooling Performance of Commercial and Institutional Buildings. Buildings 13.

Saloux, E., Zhang, K., Candanedo, J.A., 2023. A Critical Perspective on Current Research Trends in Building Operation: Pressing Challenges and Promising Opportunities. Buildings 13.

Sun, Y., Wang, S., Huang, G., 2009. Chiller sequencing control with enhanced robustness for energy efficient operation. Energy Build. 41, 1246–1255.

6th International Conference on Building Energy and Environment
Eindhoven University of Technology, The Netherlands
6 - 10 July 2025

Adaptive Fuzzy Logic Control for Optimizing HVAC Setpoints to Enhance Energy Efficiency in Urban Buildings

Mojtaba Safdari[1], Mohammad Al Janaideh[2], Kamran Siddiqui[3], Amir A. Aliabadi[1]

[1] *School of Engineering, University of Guelph, Guelph, Ontario, Canada, msafdari@uoguelph.ca*
[2] *School of Engineering, University of Guelph, Guelph, Ontario, Canada, maljanai@uoguelph.ca*
[3] *Department of Mechanical and Materials Engineering, Western University, London, Ontario, Canada, ksiddiq@uwo.ca*
[1] *School of Engineering, University of Guelph, Guelph, Ontario, Canada, aaliabad@uoguelph.ca*

ABSTRACT

This paper presents a Weather-Responsive Fuzzy Control (WRFC) strategy to dynamically adjust temperature and humidity setpoints for energy-efficient HVAC operation in urban buildings. WRFC integrates external weather data, electricity prices, and occupancy levels to adapt HVAC setpoints, aligning indoor conditions with outdoor temperature and humidity variations. Using a Fuzzy Logic Controller (FLC), a control variable (w) is calculated to optimize setpoints, balancing energy use and occupant comfort. Compared to fixed setpoint strategies, WRFC significantly reduces heating and humidification demands, especially under high Air Changes per Hour (ACH) conditions. While cooling and dehumidification demands increase in summer, WRFC achieves annual energy savings of 274 [kW-hr m^{-2} $year^{-1}$] for a typical residential house. Sensitivity analysis highlights WRFC's effectiveness across diverse building types, particularly older and less airtight structures. These results demonstrate that weather-responsive setpoint control enhances HVAC sustainability and energy efficiency in urban environments.

Keywords: Building Energy Modeling, Fuzzy Control, Sensible and Latent Loads.

INTRODUCTION

The growing need for energy-efficient technologies underscores the importance of optimizing Heating, Ventilation, and Air Conditioning (HVAC) systems, which are major energy consumers and vital for maintaining indoor comfort and health. Temperature and humidity, the most critical parameters for Indoor Environmental Quality (IEQ) and thermal comfort must be carefully managed. Proper control prevents damage to buildings and HVAC equipment while adapting operations to occupancy and external conditions . Setpoint control, which involves maintaining target temperature and humidity levels, plays a key role in HVAC performance. Optimizing these setpoints allows operators to reduce energy use without compromising indoor conditions [5].

Control strategies for building energy management include On/Off, PID, MPC, and FLC . PID and On/Off are simple but struggle with nonlinearities and tuning issues. MPC is more advanced but limited by high computational demands. FLC handles uncertainties and nonlinearities effectively, making it suitable for dynamic environments. Hybrid methods like Fuzzy-PID and NN-MPC com-

bine strengths to improve performance. Recent works [3] show FLC's potential in energy-efficient temperature and humidity control [4].

Most existing controllers and smart building research focus on systems that adjust setpoints based on occupancy detection [10]. These systems often overlook other environmental factors. The concept of a physically intelligent building that adapts setpoints based on occupancy, outdoor conditions, electricity pricing, and latent heat remains under explored, but it could significantly enhance energy efficiency and comfort. Traditional HVAC control strategies typically rely on fixed setpoints, missing opportunities to use favorable outdoor conditions and reduce HVAC loads.

This study proposes a Weather-Responsive Fuzzy Control (WRFC) strategy that dynamically adjusts temperature and humidity setpoints using real-time data, including outdoor conditions, occupancy, and electricity prices. WRFC continuously adapts to optimize HVAC performance in both peak occupancy and energy-saving modes, reducing energy use while maintaining comfort. It integrates both sensible and latent loads, improving energy efficiency and occupant comfort, advancing HVAC setpoint decision-making and creating a physically intelligent building.

1. METHODOLOGY

1.1. Model Description

This study simulates urban physics using the Vertical City Weather Generator (VCWG v3.0.0), a multi-physics model that integrates processes for momentum, heat, humidity, and water exchanges through urban surfaces, soil, and the atmosphere. VCWG uses models like the Resistance Capacitance thermal network, Navier-Stokes transport, and Monin-Obukhov Similarity Theory (MOST) [1] to predict urban climate and building performance. For weather boundary conditions, the Vatic Weather File Generator (VWFG v1.0.0) provides data using the ERA5 datasets. VCWG's results for a base building were validated against real-world data from London, Ontario [9]. This paper extends the model by integrating a Fuzzy Logic Controller (FLC) and running it for Toronto in 2020. For more details, refer to earlier publications [7, 2, 8].

Figure 1 shows the arrangement of single detached residential buildings considered in this study. Such houses are prevalent in North America and account for 52.6% and 64% of residential building stock in Canada and the United States, respectively. The building features for each city are based on common codes and standards such as the National Energy Code of Canada for Buildings (NECB), the American Society of Heating, Refrigerating and Air-Conditioning Engineers (ASHRAE) 62.1, ASHRAE 62.2, ASHRAE 90.1, and ASHRAE 90.2.

1.2. Weather-Responsive Fuzzy Control (WRFC)

This study introduces a novel real-time control strategy known as Weather-Adaptive Fuzzy Control (WRFC), designed to dynamically manage indoor temperature and humidity setpoints within a building. This method has been integrated with the VCWG software according to the flowchart in figure 3. The core principle of this method is to closely track external conditions and adjust the indoor setpoint accordingly whenever feasible. For instance, when outdoor conditions fall outside the human comfort range but occupancy levels are low, the system gradually adjusts the indoor setpoint to align with the outdoor temperature or humidity, provided it remains within predefined setback limits. Conversely, if outdoor conditions are within the comfort zone, the indoor setpoint

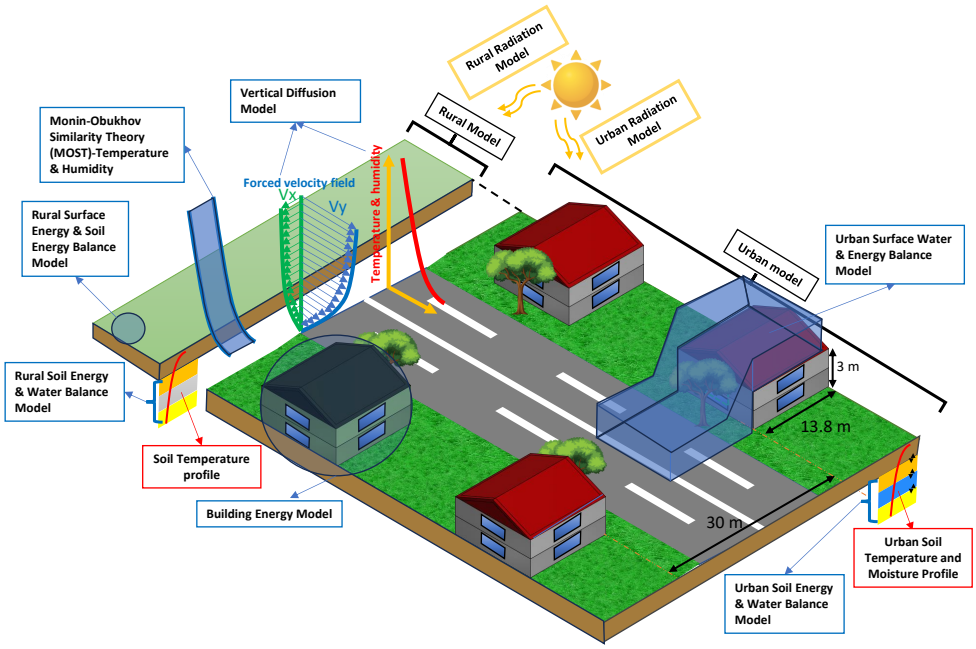

Figure 1. Illustration of the Vertical City Weather Generator (VCWG v3.0.0) model and the constituent sub-models.

is maintained in close proximity to the external conditions to eliminate the need for HVAC system operation. A basic description of the algorithm can be found in the flowchart in Figures 3 and 8. Another innovative aspect of this approach involves an integration of a fuzzy inference system that uses linguistic variables to evaluate the impact of external, uncontrollable factors, enabling a more refined and adaptive control of indoor environmental conditions for higher energy savings. The comfort ranges are defined in Figure 2 for humidity and temperature. It should also be noted that the basic thermostat mode for cooling setpoint is 27 °C and for heating setpoint is 22 °C.

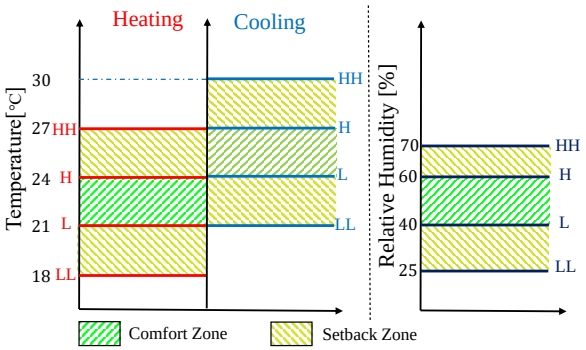

Figure 2. Illustration of the comfort and setback ranged for indoor temperature and humidity.

According to the FLC process diagram illustrated in the Figure 3 which follows Mamdani's Fuzzy Inference System (FIS) [6] the controller employs FLC to determine the w parameter, which governs the adaptation of setpoints by creating an adjustment value based on current input values.

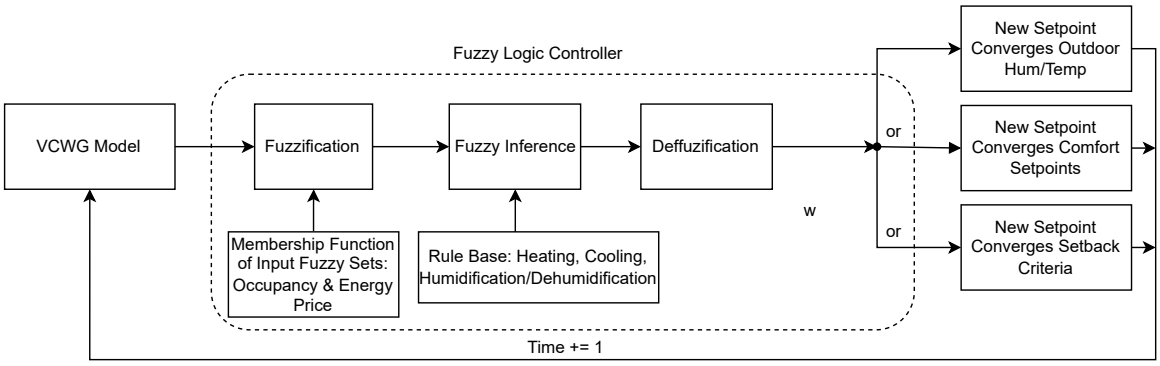

Figure 3. Flowchart illustrating the integration of the Weather-Adaptive Fuzzy Control (WRFC) with the Vertical City Weather Generator (VCWG) software

To do so, first the system uses predefined membership functions to assess the input's degree of membership. The controller uses two fuzzy variables as occupancy level [Person m^{-2}], and time of day [hr]. It is assumed in this study that three persons are living in a residential detached house of 100 m^2 with membership functions defined for low, medium, and high that any density more than 0.03 Person m^{-2} would be considered as a high occupancy level. For electricity price we have used the Time-Of-Use (TOU) pricing scheme in Ontario, Canada, as an example reflecting different electricity costs during different periods of the day and season. It is important to note that the differences in electricity prices between Winter and Summer, as well as between weekdays and weekends, have been accounted for in this study. These two inputs, with their respective levels in Figures 4 and 5, are mapped using trapezoidal and triangular membership functions to capture the varying degrees of occupancy and TOU.

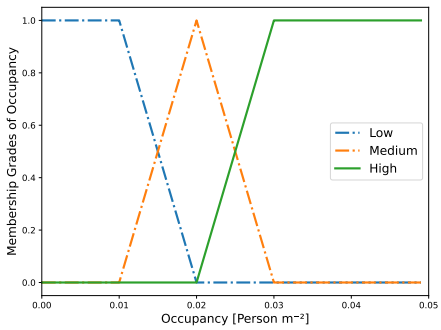

Figure 4. Fuzzy membership functions for the occupancy variable in the building.

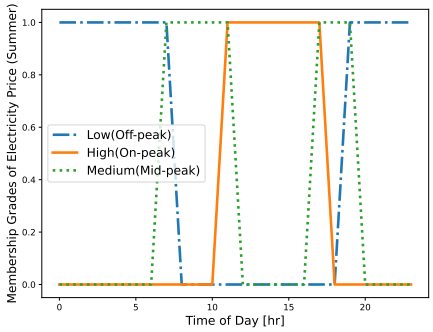

Figure 5. Fuzzy membership functions for the price variable in Summer.

Following the fuzzy inference process, we apply the fuzzy rules defined in Table 1 to the fuzzified input variables (electricity price and occupancy level) to determine the output variable w. These rules differentiate between weekday and weekend strategies for the Summer and Winter. Specifically, weekend rules do not account for electricity price fluctuations since rates remain constant throughout the day and night. In contrast, heating and humidification rules are not dependent on electricity price fluctuations, as these processes utilize natural gas in the HVAC system. Given

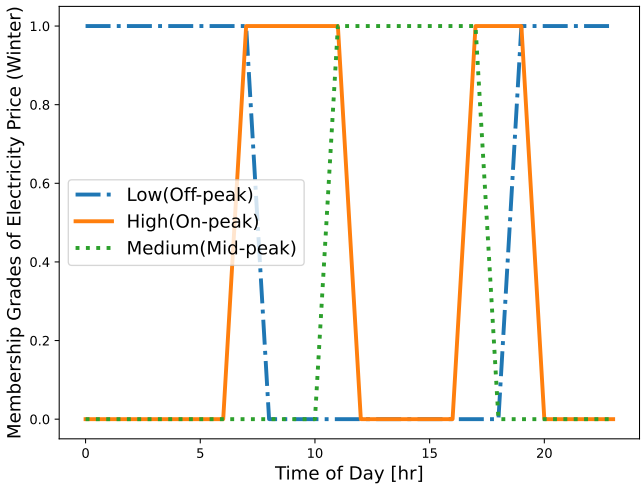

Figure 6. Fuzzy membership functions for the price variable in Winter

that gas prices remain constant throughout the day and night in Canada, gas price has not been considered a fuzzy input for these processes. Conversely, cooling and dehumidification require a refrigeration cycle, and thus electricity, so the corresponding rules depend on electricity price. In this table N means the setpoints should converge to outdoor condition, P means the setpoints should converge to comfort levels, and Z means no change.

Regarding Table 1 for cooling during weekdays, when occupancy is low and electricity price is low, medium, or high, the system should attempt to converge to the outdoor conditions, which is likely higher than the indoor and comfort setpoints. This corresponds to the linguistic variable N in our rule definition. In this scenario, energy efficiency takes precedence over comfort considerations when occupancy is low. Subsequently, when occupancy is medium and the price is low, the system converges to the comfort level P, while a medium price results in no change Z, and a high price increases convergence to the outdoor level N. Finally, high occupancy with low, medium, and high prices prompts convergence to the comfort level P. It should be noted that in this study Max operator has been used for decision-making process [11]. With the Max operation method, the output value for the linguistic variables corresponds directly to the highest activation levels.

In this step, the fuzzy outputs obtained earlier are converted into a crisp value (w) that can be utilized to adjust the setpoints.

The fuzzy output membership function employed in this study is a triangular membership function designed to calculate w, which controls the heating, cooling, humidification, or dehumidification setpoints (Figure 7). It includes three categories: N, Z, and P, ensuring a consistent and adaptable control strategy across all of these processes. The P and N values of these membership functions determine whether the smart setpoint should follow outdoor conditions or adhere to predefined comfort setpoints, dynamically adjusting the setpoints based on real-time input data.

The defuzzification process utilizes the centroid method, also known as the center of gravity or center of area method, to compute a specific numerical output for the w variable (Figure 8).

Table 1. Combined rules for HVAC adjustments based on occupancy presence, electricity price, and day type (weekdays and weekends): N: Converging to outdoor, Z: No change, P: Converging to comfort setpoint

Function	Day Type	Occupancy	Electricity Price	w Adjustment
Cooling/Dehumidification	Weekday	Low	Low	N
		Low	Medium	N
		Low	High	N
		Medium	Low	P
		Medium	Medium	Z
		Medium	High	N
		High	Low	P
		High	Medium	P
		High	High	P
	Weekend	Low	-	N
		Medium	-	Z
		High	-	P
Heating/Humidification	All Days	Low	-	N
		Medium	-	Z
		High	-	P

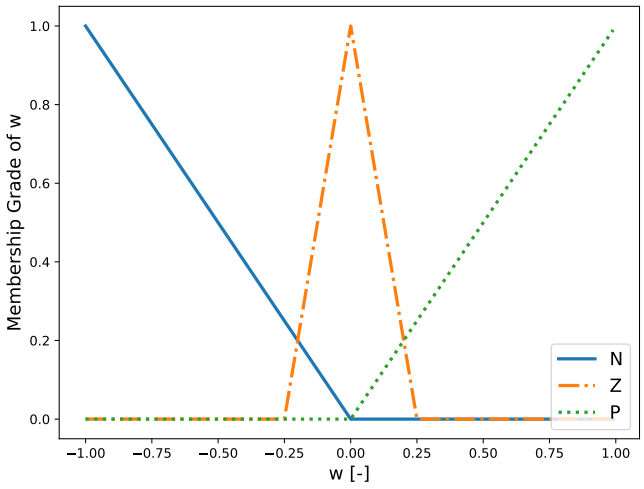

Figure 7. Fuzzy membership functions for temperature and humidity setpoints' adjustments. Both temperature and humidity adjustments use similar membership functions categorized into Negative (N), Zero (Z), and Positive (P) to guide the control of HVAC system setpoints.

2. RESULTS AND DISCUSSION

2.1. Performance of the Weather-Responsive Fuzzy Control (WRFC)

The model was run for a full year with a runtime of about 30 minutes on a single CPU, demonstrating its efficiency for a comprehensive urban physics simulation. Results for selected months with Air Changes per Hour (ACH) set at 1.5 hr^{-1} highlight its operation.

In May, a shoulder season with mixed heating, cooling, and neutral modes, the system's response is complex. Figure 9 (a) shows temperature behavior, while Figure 9 (b) illustrates the corresponding sensible heating and cooling loads. Early in the month, the system predominantly heats the building, keeping indoor temperatures within the comfort and setback thresholds (blue lines) during high occupancy. As outdoor temperatures rise later in the month, the system occasionally

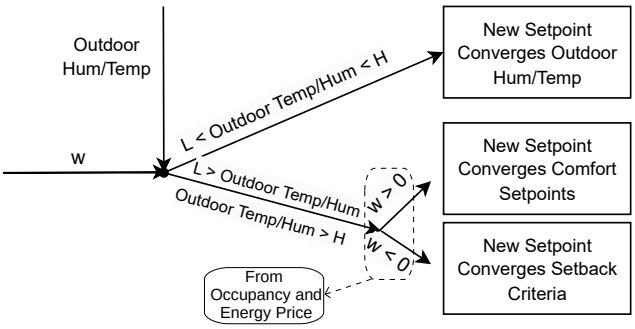

Figure 8. Decision tree illustrating how a value of w forces the smart setpoint to move toward comfort or outdoor conditions by adjusting the setpoint accordingly.

enters neutral mode, requiring no heating or cooling, with indoor temperatures naturally aligning within the comfort zone. When occupancy is low, indoor temperatures are allowed to drift outside comfort limits, prioritizing energy efficiency.

The system dynamically adjusts to outdoor temperature fluctuations. Around 700 hr, the outdoor temperature rises to 28°C, and the indoor temperature aligns with the comfort range (L to H). As outdoor temperatures exceed the H threshold, indoor conditions follow until occupancy increases, prompting the system to maintain comfort. This adaptive behavior repeats, balancing comfort and energy efficiency.

Smart humidity control also adapts effectively to dynamic conditions. Figure 10 (a) shows relative humidity (RH) behavior, while Figure 10 (b) displays humidification and dehumidification loads. When outdoor RH exceeds comfort thresholds, indoor RH adjusts to conserve energy during low occupancy. Conversely, when conditions demand, the system prioritizes comfort by maintaining indoor RH within acceptable ranges, showcasing its flexibility in balancing efficiency and comfort.

3. CONCLUSION

This study evaluated the impact of smart thermostat and humidistat configurations on building energy efficiency, focusing on seasonal variations in heating, cooling, humidification, and dehumidification under different air change rates (ACH). By integrating a Fuzzy Logic Control (FLC) system into the Vertical City Weather Generator (VCWG v3.0.0), we simulated a detached residential building in Toronto over a full year (2020). The findings highlight both the potential and the limitations of dynamic setpoint adjustments based on environmental, occupancy, and energy price inputs.

- Smart control yielded significant energy savings, reducing heating loads by up to 132.8 [kW-hr m^{-2} $year^{-1}$] during colder months and saving 141.5 [kW-hr m^{-2} $year^{-1}$] for humidification by aligning indoor relative humidity (RH) with outdoor conditions, particularly in leakier buildings.
- During peak summer months, cooling demand increased by 31.4 [kW-hr m^{-2} $year^{-1}$], and dehumidification demand rose by 5.3 [kW-hr m^{-2} $year^{-1}$], due to fluctuations and higher mass loads. These results indicate reduced effectiveness of the smart control in warm sea-

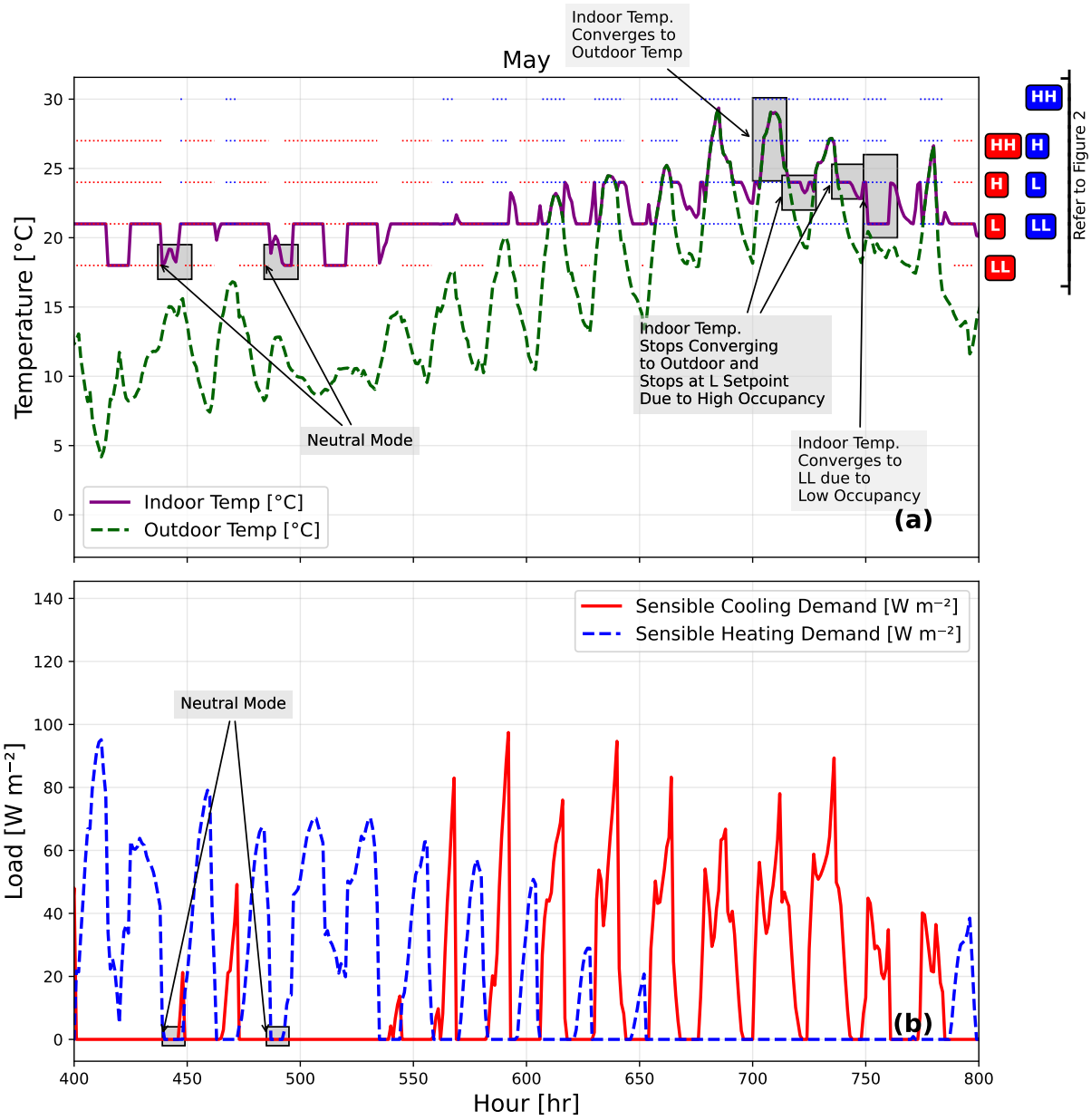

Figure 9. (a) Indoor temperature variations and (b) sensible heating and cooling load variations, both for May, showing the system's response to occupancy changes, electricity prices, and outdoor conditions.

sons.

- Year-round smart control achieved a net saving of 237 [kW-hr m^{-2} $year^{-1}$]. A hybrid approach, disabling smart features in summer, increased savings to 274 [kW-hr m^{-2} $year^{-1}$], demonstrating the advantages of a seasonal, adaptive strategy.
- Unlike conventional systems requiring airtightness, this approach proved effective in older, leakier buildings, reducing energy loads through better air exchange management.

In summary, while the smart control strategy excelled in heating and humidification, challenges

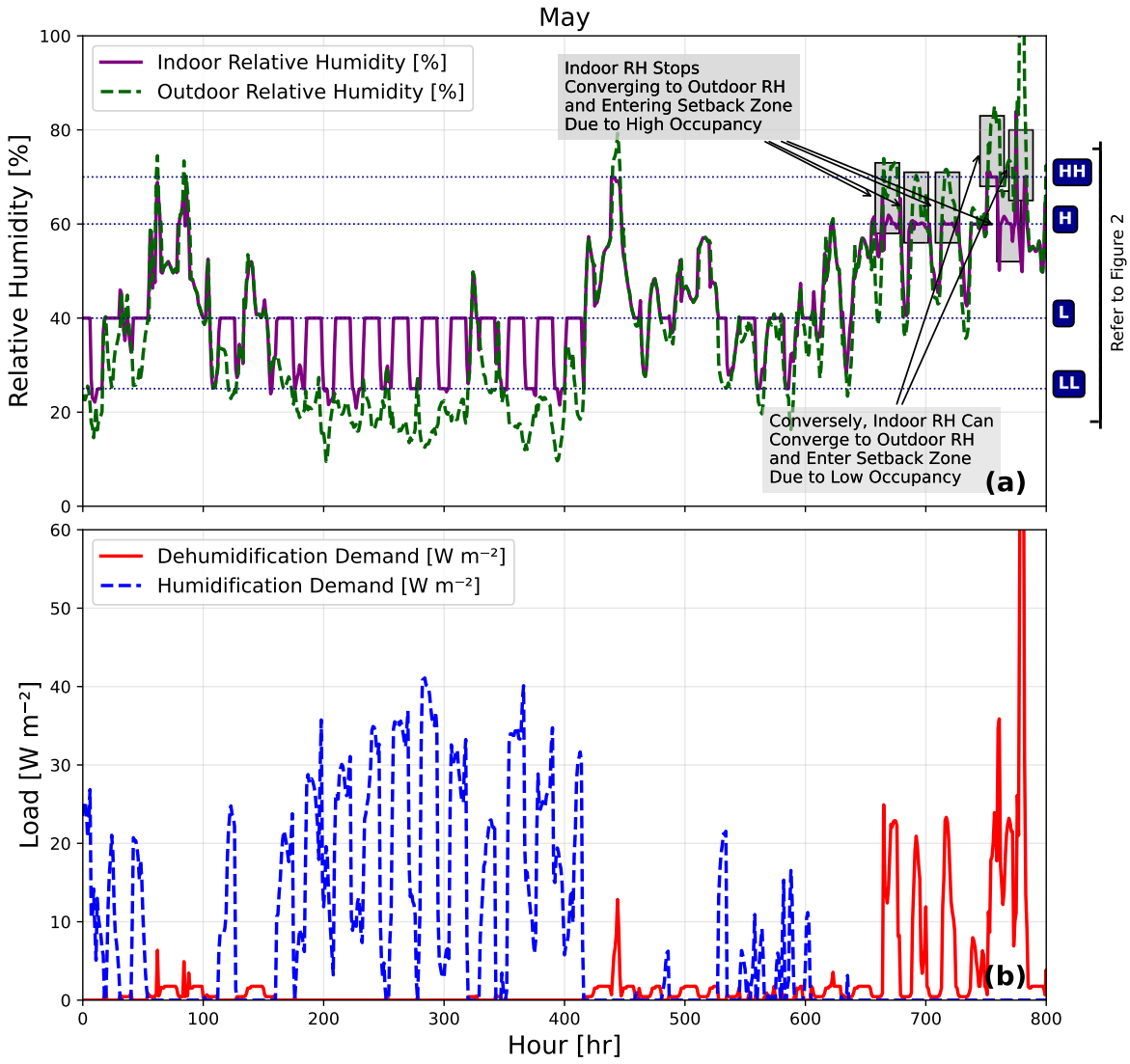

Figure 10. (a) Indoor RH variations and (b) latent (Humidification/Dehumidification) load variations, both for May, showing the system's response to occupancy changes, electricity prices, and outdoor conditions.

in cooling and dehumidification suggest the value of a hybrid approach, applying smart features selectively by season. This adaptable strategy enhances energy efficiency in diverse building types and supports sustainable HVAC energy management. Future research could extend these findings to other climate zones and building configurations.

REFERENCES

[1] A. A. Aliabadi. *Turbulence: A Fundamental Approach for Scientists and Engineers*. Springer, Cham, 2022.

[2] Amir A. Aliabadi, Xuan Chen, Jiachuan Yang, Ali Madadizadeh, and Kamran Siddiqui. Retrofit optimization of building systems for future climates using an urban physics model. *Building and Environment*, 243:110655, 2023.

[3] Russell James P Barte, Trexil O Querimit, and Jocelyn F Villaverde. Automatic Temperature and Humidity Control System for Tarantula Terrarium Using Fuzzy Logic Algorithm. In *2023 15th International Conference on Computer and Automation Engineering (ICCAE)*, pages 463–468, Piscataway, 2023. IEEE.

[4] Ali Beheshtikhoo, Mahdi Pourgholi, and Iman Khazaee. Design of type-2 fuzzy logic controller in a smart home energy management system with a combination of renewable energy and an electric vehicle. *Journal of Building Engineering*, 68:106097, 2023.

[5] Poul O Fanger. *Thermal comfort. Analysis and applications in environmental engineering.* 1970.

[6] E. H. Mamdani. Application of fuzzy algorithms for control of simple dynamic plant. In *Proceedings of the Institution of Electrical Engineers*, volume 121, pages 1585–1588, London, 1974. Institution of Engineering and Technology (IET).

[7] Mohsen Moradi, E. Scott Krayenhoff, and Amir A. Aliabadi. A comprehensive indoor–outdoor urban climate model with hydrology: The Vertical City Weather Generator (VCWG v2.0.0). *Building and Environment*, 207:108406, 2022.

[8] Mojtaba Safdari, Rouhollah Ahmadi, and Sadegh Sadeghzadeh. Numerical and experimental investigation on electric vehicles battery thermal management under New European Driving Cycle. *Applied Energy*, 315:119026, 2022.

[9] Mojtaba Safdari, Kadeem Dennis, Bahram Gharabaghi, Kamran Siddiqui, and Amir A. Aliabadi. Implications of latent and sensible building energy loads using natural ventilation. *Journal of Building Engineering*, 96:110447, 2024.

[10] Bing Su and Shengwei Wang. An agent-based distributed real-time optimal control strategy for building hvac systems for applications in the context of future iot-based smart sensor networks. *Applied Energy*, 274:115322, 2020.

[11] Woei Wan Tan and Teck Wee Chua. Uncertain rule-based fuzzy logic systems: introduction and new directions (mendel, jm; 2001)[book review]. *IEEE Computational intelligence magazine*, 2(1):72–73, 2007.

6th International Conference on Building Energy and Environment
Eindhoven University of Technology, The Netherlands
6 - 10 July 2025

Finite-time thermodynamics analysis of solution regeneration for frost-free air-source heat pump

Liutao Zhu [1], Xiaosong Zhang [1, 2*], Shifang Huang [1, 2*]

[1]*School of energy and environment, Southeast University, Nanjing, China, zlt@seu.edu,cn*
[2]*MOE Engineering Research Center of Building Energy Equipment and Environment, Nanjing 210096, China, shifang_huang@seu.edu.cn*

SUMMARY
The regeneration process of frost-free air-source heat pumps (FFASHPs) consumes energy and affects the overall efficiency of the heat pump. There are numerous studies on different solution regeneration methods, none have clarified their thermodynamic limits, though. This study employs finite-time thermodynamics to study the influence of solution concentration, regeneration ratio, heat source temperature, ambient temperature, heat transfer capacity-to-mass flow coefficient, and internal reversibility coefficient on the minimum regeneration energy. The minimum specific regeneration heat and work are 87.67 and 15.79 kWh/t, respectively, under conditions where heat transfer capacity-to-mass flow coefficient reaches its minimum value. The recommended heat transfer capacity-to-mass flow coefficient is 6. When the total heat transfer capacity-to-mass flow coefficient is 10, the best high temperature-low temperature heat transfer capacity ratio is 0.81, corresponding to a W_{min} of 8.84 kWh/t.

Keywords: frost-free air-source heat pump, antifreeze regeneration, finite- time thermodynamics analysis, thermal regeneration.

1. INTRODUCTION

Heat pumps are considered one of the primary pathways for decarbonizing and electrifying of space heating and cooling due to their capability to effectively utilize low-grade heat sources (J. Zhang et al., 2016; Y. Zhang et al., 2018). Frost-free air-source heat pump (FFASHP), which utilizes a solution circulation between the evaporator and outdoor air to fundamentally solve the frosting problem, is considered to a promising heat pump technology (Lin et al., 2019).

As the solution absorbs latent heat from the air, the condensation of water vapor leads to dilution of the solution and an increase in its freezing point(Huang et al., 2023). There is a risk of freezing when the solution's freezing point approaches the lowest temperature in the system (typically the evaporator temperature) if it is not regenerated promptly. Liang at al. investigated the regeneration performance under three modes and the influence of input heat, outdoor air temperature and humidity(Liang et al., 2014). Huang et al. experimentally investigated the coupled heat and mass transfer characteristics of ethylene glycol solution ADE regeneration process, and the regeneration specific energy consumption (SEC) ranged from 712 kWh/t to 1206 kWh/t(Huang et al.et al., 2018). Song et al. conducted experimental studies on the performance of calcium chloride solution ADE regeneration process, and reported that the SEC ranged from 952 kWh/t to 2778 kWh/t(Song et al., 2019). The most commonly used regeneration method at present is thermal regeneration. There are also many other studies on system optimization of thermal regeneration methods, but there are currently no studies on their thermodynamic limits.

Finite-time thermodynamics (FTT) is an important branch of modern thermodynamics which combines into simple models the most basic concepts of heat transfer, fluid mechanics, and thermodynamics(Andresen et al., 1984). FTT seeks to optimize thermodynamic cycles or processes under conditions of limited time and size, offering a more practical approach to thermodynamic analysis. The concept of FTT was first introduced by Curzon and Ahlborn, who derived the efficiency of a power plant when the output power is maximized(Curzon et al., 1975). This efficiency is lower than the well-known Carnot efficiency, yet it is easier to approach. Due to its strong practical relevance, FTT has been widely applied in various fields(Guo et al., 2021; Sukin et al., 2022; Yaqi et al., 2011). However, in the area of solution regeneration or concentration, there is still a lack of analytical studies from the perspective of FTT. Similar studies have been conducted in the field of separation processes: Berry et al. utilized FTT to analyze thermally driven separation processes, deriving an analytical expression for the minimum average heat consumption in an isothermal heat-source-driven separation process(Orlov & Berry, 1991).

In this study, FTT is applied to derive expressions for the minimum separation heat and work of an internally reversible heat-driven regeneration process. We calculated and investigated the effects of several parameters on the regeneration work of the heat-driven regeneration system. Based on the research results, optimization suggestions for the design of heat-driven antifreeze regeneration systems are proposed.

2. SYSTEM AND DERIVATION

2.1. Internally reversible regeneration system

As shown in Fig. 1 is an internally reversible solution thermal regeneration process. The temperature and pressure of the inlet and outlet solutions are equal, and all processes within the regeneration system are reversible. Assuming the temperatures during heat exchange with the external environment remain constant: the temperature during heat exchange with the heat source is T_1, and the temperature during heat exchange with the environment is T_2. Assuming the heat transfer coefficients at the hot and cold ends of the heat exchangers are fixed values, α_H and α_L, respectively, the heat transfer amounts at the hot and cold ends are as Eq. (1) and Eq. (2).

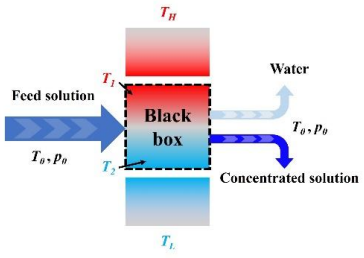

Figure 1. Internally reversible antifreeze thermal regeneration system

$$Q_H = \alpha_H(T_H - T_1) \tag{1}$$

$$Q_L = \alpha_L(T_2 - T_L) \tag{2}$$

Where T_H and T_L represent the temperatures of the heat source and the cold source, respectively, with T_L assumed to be equal to the ambient temperature T_0 in this study. According to the first and second law of thermodynamics:

$$Q_H - Q_L = \dot{m}_w h_w + \dot{m}_c h_c - \dot{m}_f h_f \tag{3}$$

$$\frac{Q_H}{T_1} - \frac{Q_L}{T_2} = \dot{m}_w s_w + \dot{m}_c s_c - \dot{m}_f s_f \tag{4}$$

Where $\dot{m}$ is the mass flow rate, h is the specific enthalpy, and s is the specific entropy. The subscripts w, c and f represent water, the regenerated concentrated solution, and the feed solution, respectively. We define enthalpy flow and entropy the following:

$$\dot{H} = \dot{m}_w h_w + \dot{m}_c h_c - \dot{m}_f h_f \tag{5}$$

$$\dot{S} = \dot{m}_w s_w + \dot{m}_c s_c - \dot{m}_f s_f \tag{6}$$

2.2. Derivation of the minimum regeneration heat

Our goal is to first obtain the minimum value of Q_H, denoted as Q_{min}, for a given regeneration process, where m_f, x_f, and r are fixed. By constructing the Lagrange function Eq. (7), the problem is transformed into finding the minimum value of the function. Substituting Eq. (1) and Eq. (2) into Eq. (7) yields Eq. (8).

$$L = Q_H - \lambda\left(\frac{Q_H}{T_1} - \frac{Q_L}{T_2} - \dot{S}\right) - l(Q_H - Q_L - \dot{H}) \tag{7}$$

$$L = -\alpha_H\left(l - 1 + \frac{\lambda}{T_1}\right)(T_H - T_1) + \alpha_L\left(l + \frac{\lambda}{T_2}\right)(T_2 - T_L) + \lambda\,\dot{S} + l\,\dot{H} \tag{8}$$

First, by optimizing T_1 and T_2, we obtain:

$$L_{\min}\ (\lambda,\ l)\ = -\alpha_H\left[\sqrt{T_H(l-1)} - \sqrt{-\lambda}\right]^2 - \alpha_L\left[\sqrt{T_L\,l} - \sqrt{-\lambda}\right]^2 + \lambda\,\dot{S} + l\,\dot{H} \tag{9}$$

Next, we obtain the optimized λ by taking the partial derivative of L with respect to λ, which satisfies Eq. (8). It is evident that $\hat{\lambda} < 0$.

$$\sqrt{-\hat{\lambda}} = \frac{\alpha_H\sqrt{T_H(l-1)} + \alpha_L\sqrt{T_L\,l}}{\alpha_H + \alpha_L + \dot{S}} \tag{10}$$

Then we have:

$$L_{\min}\ (l)\ = -\alpha_H \left[\sqrt{T_H(l-1)} - \sqrt{-\hat{\lambda}}\right]^2 - \alpha_L \left[\sqrt{T_L\, l} - \sqrt{-\hat{\lambda}}\right]^2 + \hat{\lambda}\,\dot{S} + l\,\dot{H} \tag{11}$$

Finally, we take the derivative of L with respect to l, and obtain:

$$\frac{dL_{min}(l)}{dl} = -2\,\alpha_H \left[\sqrt{T_H(l-1)} - \sqrt{-\hat{\lambda}}\right]\left[\frac{T_H}{2\sqrt{T_H(l-1)}} - \frac{d\sqrt{-\hat{\lambda}}}{dl}\right] - 2\,\alpha_L \left[\sqrt{T_L l} - \sqrt{-\hat{\lambda}}\right]\left[\frac{T_L}{2\sqrt{T_L l}} - \frac{d\sqrt{-\hat{\lambda}}}{dl}\right] - 2\sqrt{-\hat{\lambda}}\,\dot{S}\frac{d\sqrt{-\hat{\lambda}}}{dl} + \dot{H} \tag{12}$$

It is evident that $l > 1$. As l approaches 1, equation (12) tends to negative infinity; as l approaches positive infinity, equation (12) becomes greater than 0. Therefore, equation (11) must have an extremum. Setting equation (12) equal to 0, the optimized l can be obtained using numerical methods, and by substituting this value into equation (11), Q_{min} can be determined. Then we can determine specific energy consumption (SEC), including specific heat consumption and specific work consumption:

$$q_{min} = \frac{Q_{min}}{\dot{m}_w} \tag{13}$$

$$w_{min} = q_{min}\,(1 - \frac{T_0}{T_H}) \tag{14}$$

We define:

$$\theta_H = \frac{\alpha_H}{\dot{m}_f} \tag{15}$$

$$\theta_L = \frac{\alpha_L}{\dot{m}_f} \tag{16}$$

2.3. Parameters

This study investigates the effects of feed solution concentration, regeneration ratio, heat source temperature, ambient temperature, and θ on regeneration performance. The basic parameter settings are shown in Table 1.

Table 1. Basic parameter settings.

X_f (%)	r	T_H (K)	T_L (K)	θ_H (J/(kg·K))	θ_L (J/(kg·K))
0.19	0.05	333.15	273.15	10	10

3. RESULTS AND DISSCUSSION

As shown in Fig. 2(a), the derivative of $L_{\min}$ with respect to l is monotonically increasing, with at most one zero point. When a zero point exists, $L_{\min}$ first decreases and then increases, indicating the presence of a minimum value. This validates the soundness of our derivation. Fig. 2(b) illustrates some solutions for l and λ under different θ values based on the fundamental parameters.

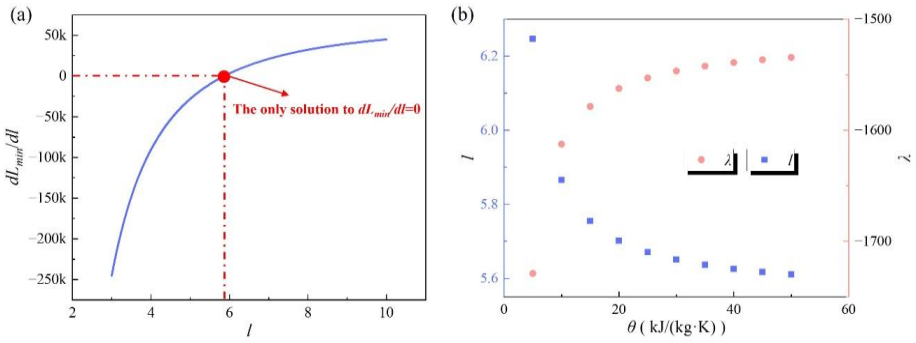

Figure 2. Partial solutions for l and λ

3.1. Influence of feed solution concentration

As shown in Fig. 3(a), q_{min} and w_{min} increase significantly with the rise in feed solution concentration. This is in accordance with general knowledge: the higher the solution concentration, the more difficult the regeneration process. Fig. 3(b) shows how the temperature differences at the hot and cold ends of the heat exchanger change with the solution concentration. The required temperature difference for heat exchange becomes larger as the concentration increases.

3.2. Influence of regeneration ratio

As shown in Fig. 3(c), as the regeneration ratio increases, both q_{min} and w_{min} increase to some extent. When the regeneration ratio increases from 0.0001 to 0.1, the minimum regeneration heat and work increase by approximately 19%. This is because, with the increase in the regeneration ratio, the solution concentration gradually rises, making regeneration more difficult.

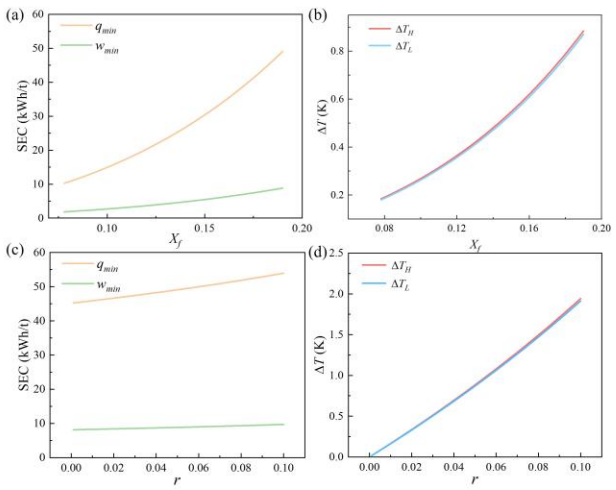

Figure 3. Influence of X_f and r

3.3. Influence of heat source temperature

It can be observed form Fig. 4(a) that as the heat source temperature increases, q_{min} initially decreases rapidly, then more slowly. However, w_{min} remains nearly unchanged. This suggests that

while increasing the heat source temperature reduces the heat demand, it comes at the cost of raising the energy quality, and fundamentally, no true energy savings are achieved in thermodynamic terms. The temperature differences for heat transfer decrease as the heat source temperature rises as shown in Fig. 4(b).

3.4. Influence of ambient temperature

Fig. 4(c) shows that q_{min} increases with the rise in ambient temperature, while the minimum regeneration work remains almost unchanged. Since the temperature of the heat source is fixed, although the ambient temperature has little effect on energy efficiency from a thermodynamic perspective, it suggests less energy costs under lower ambient temperature. The temperature differences for heat transfer increase as the heat source temperature rises as shown in Fig. 4(d).

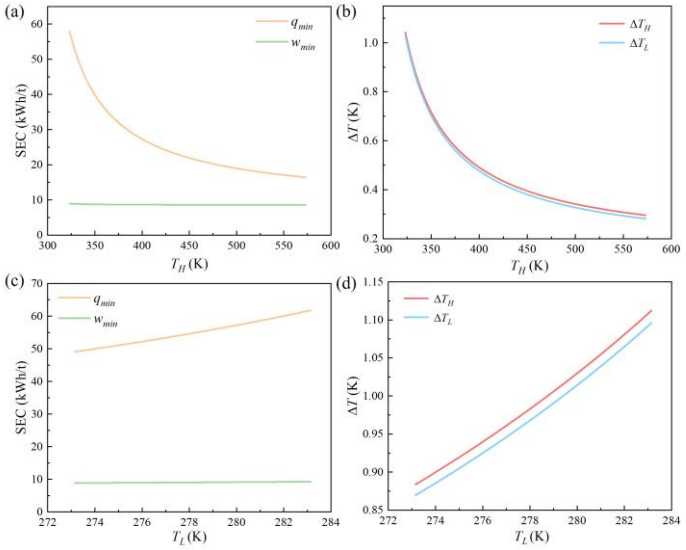

Figure 4. Influence of T_H and T_L

3.5. Influence of heat transfer capacity-mass flow coefficient

Fig. 5(a) shows that as θ increases, both q_{min} and w_{min} exhibit a rapid decrease followed by a slower decline. This is because a larger θ implies a relatively smaller solution flow rate, a larger heat exchange area, and a stronger system reversibility. However, q_{min} and w_{min} will not decrease indefinitely. As θ approaches infinity, w_{min} approaches a critical value, rather than zero. This critical value should correspond to the minimum regeneration work for a reversible process. This is because an infinite θ implies an infinitely small solution flow rate and an infinitely large heat exchange area. From Fig. 5(b), it can be seen that at this point, the temperature difference for heat exchange gradually approaches zero, indicating that the regeneration process is fully reversible. Additionally, under the given regeneration requirements and environmental parameters, θ has a minimum boundary value. This means that a certain flow rate imposes a minimum requirement for the heat exchange capacity of the equipment, or a device with a certain heat exchange capacity can only accommodate a maximum solution flow rate. Under the basic parameters used in this study, the minimum value of θ is 1.15, corresponding to a q_{min} and w_{min} of 87.67 and 15.79 kWh/t, respectively. After θ reaches a certain value, further increases in θ will cause minimal changes in the minimum separation heat and work. If we define the thermodynamic perfection as:

$$\eta = \frac{W_{th}}{W_{min}} \tag{17}$$

Where w_{th} is the minimum separation work for a reversible process, i.e., the value of w_{min} when θ approaches infinity. Under the basic operating conditions of this study, when θ reaches 6, η reaches approximately 95%. The θ corresponding to η = 95% is referred to as the recommended θ_{rec} in this study.

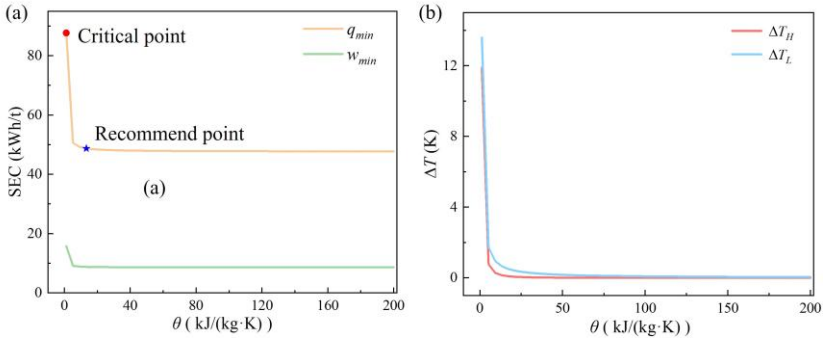

Figure 5. Influence of θ

3.5. Influence of θ_H/θ_L

Fig. 6 shows that as θ_H/θ_L increases, W_{min} first decreases and then increases. There exists an optimal ratio at which W_{min} reaches its minimum. In this study, the optimal ratio is 0.81, corresponding to a W_{min} of 8.84 kWh/t.

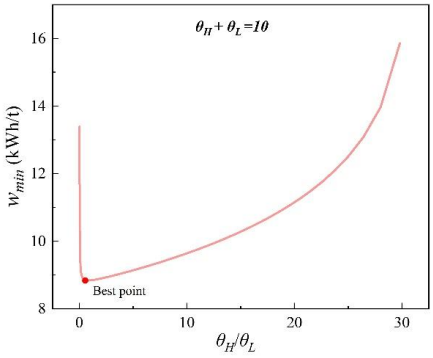

Figure 6. Influence of θ_H/θ_L

4. CONCLUSION

This study utilized finite-time thermodynamics to derive expressions for the minimum separation heat and work of an internally reversible heat-driven antifreeze regeneration process. The results show that the minimum specific regeneration heat and work are 87.67 and 15.79 kWh/t, respectively, under conditions where heat transfer capacity-to-mass flow coefficient reaches its minimum value. The recommended heat

transfer capacity-to-mass flow coefficient is 6. When the total heat transfer capacity-to-mass flow coefficient is 10, the best high temperature-low temperature heat transfer capacity ratio is 0.81, corresponding to a Wmin of 8.84 kWh/t.

ACKNOWLEDGEMENTS

The research described in this paper is supported by the National Natural Science Foundation of China (No. 52206005).

REFERENCES

Andresen, B., Berry, R. S., Ondrechen, M. J., & Salamon, P. (1984). Thermodynamics for processes in finite time. *Accounts of Chemical Research*, *17*(8), 266–271.

Curzon, F. L., & Ahlborn, B. (1975). Efficiency of a Carnot engine at maximum power output. *American Journal of Physics*, *43*(1), 22–24.

Guo, H., Xu, Y., Zhang, X., Zhu, Y., & Chen, H. (2021). Finite-time thermodynamics modeling and analysis on compressed air energy storage systems with thermal storage. *Renewable and Sustainable Energy Reviews*, *138*, 110656.

Huang, S., Lv, Z., Zhang, X., & Liang, C. (2018). Experimental investigation on heat and mass transfer in heating tower solution regeneration using packing tower. *Energy and Buildings*, *164*, 77–86.

Huang, S., Yu, H., Zhang, M., Qu, H., Wang, L., Zhang, C., Yuan, Y., & Zhang, X. (2023). Advances, challenges and outlooks in frost-free air-source heat pumps: A comprehensive review from materials, components to systems. *Applied Thermal Engineering*, *234*, 121163. https://doi.org/10.1016/j.applthermaleng.2023.121163

Liang, C., Wen, X., Liu, C., & Zhang, X. (2014). Performance analysis and experimental study of heat-source tower solution regeneration. *Energy Conversion and Management*, *85*, 596–602. https://doi.org/10.1016/j.enconman.2014.05.020

Lin, Y., Wang, W., Sun, Y., Liu, J., & Deng, S. (2019). A field study on the effects of outdoor coil fouling at different ambient air temperatures on the operating performances of a space cooling ASHP unit. *Energy and Buildings*, *183*, 639–649.

Orlov, V. N., & Berry, R. S. (1991). Estimation of minimal heat consumption for heat-driven separation processes via methods of finite-time thermodynamics. *The Journal of Physical Chemistry*, *95*(14), 5624–5628.

Song, P., Xiao, H., Wang, B., Shi, W., Li, X., & Zhang, G. (2019). Experimental investigation of the regeneration performance of an internally heated regenerator used for heating tower solution regeneration. *Energy Conversion and Management*, *189*, 184–194. https://doi.org/10.1016/j.enconman.2019.03.089

Sukin, I., Tsirlin, A., & Andresen, B. (2022). Finite-time thermodynamics: Multistage separation processes consuming mechanical energy. *Chemical Engineering Science*, *248*, 117250.

Toth, A. J. (2020). Modelling and Optimisation of Multi-Stage Flash Distillation and Reverse Osmosis for Desalination of Saline Process Wastewater Sources. *MEMBRANES*, *10*(10). https://doi.org/10.3390/membranes10100265

Wen, X., Cao, X., Yu, P., & Yu, J. (2018). Experimental Research on a Novel Solution Regeneration System for Heat Source Tower Based on Vacuum Boiling and Condensation. *ES Energy & Environment*, *2*, Article 2. https://doi.org/10.30919/esee8c175

Xiao, H., Song, P., Wang, B., Li, Z., Shi, W., Yang, Z., Li, X., Huang, Y., & Liang, Z. (2021). Experimental investigation of a heat-source tower heat pump with self-regenerator using subcooling heat. *Energy and Buildings*, *240*, 110858. https://doi.org/10.1016/j.enbuild.2021.110858

Yaqi, L., Yaling, H., & Weiwei, W. (2011). Optimization of solar-powered Stirling heat engine with finite-time thermodynamics. *Renewable energy*, *36*(1), 421–427.

Zhang, J., Zhang, H.-H., He, Y.-L., & Tao, W.-Q. (2016). A comprehensive review on advances and applications of industrial heat pumps based on the practices in China. *Applied Energy*, *178*, 800–825.

Zhang, Y., Zhang, G., Zhang, A., Jin, Y., Ru, R., & Tian, M. (2018). Frosting phenomenon and frost-free technology of outdoor air heat exchanger for an air-source heat pump system in China: An analysis and review. *Energies*, *11*(10), 2642.

6th International Conference on Building Energy and Environment
Eindhoven University of Technology, The Netherlands
6 - 10 July 2025

Stochastic assessment requirements for unsteady ventilation flow patterns

Jelle Laverge [1], Merel Decleyre [1], Lisa Corneillie [1], Klaas De Jonge [1]

[1]*Ghent Univeristy, Gent, Belgium, jelle.laverge@ugent.be*

SUMMARY
The evolution of ventilation systems toward "smart" designs aims to enhance indoor air quality (IAQ) while minimizing energy consumption and costs. Traditional design standards use predefined airflow rates, but recent advancements advocate for performance-based approaches, as outlined in the proposed CEN standard prEN 15665. Smart ventilation systems dynamically adjust airflow based on factors like occupancy and environmental conditions. Advanced controllers with self-learning features, such as grey-box model predictive controllers (MPCs), outperform conventional proportional controls but necessitate the use of stochastic assessment methods and convergence-based performance indicators, which assess system behavior over time. In this paper, we propose the use of convergence based performance indicators the assessment of smart ventilation as a way to address this. This approach offers computational efficiency and addresses the complexities introduced by self-learning algorithms. For regulatory applications, convergence assessments must consider confidence intervals and sensitivity of the performance indicators to low frequencies in the input parameters. This approach can enhance the accuracy and neutrality of ventilation performance assessment while reducing simulation times by up to 90%.

Keywords: Ventilation, IAQ, Assessment, Criteria, Performance based design

1. INTRODUCTION

The primary goal of the ventilation system is to insure good IAQ through replacing indoor air with (hopefully) cleaner outdoor air. In currently applicable design standards, such the European EN 16798-1 and EN 16798-3, this is generally translated in requirements for applying a known supply or extraction flow rate in the individual rooms of the building or to the full building, with or without transfer between the rooms. Adding additional transfers is often called extended cascade ventilation (Rojas et al., 2015) and adds some complexity in estimating the exposure of the occupants, but does not fundamentally affect the design strategy of a known airflow directed through the building as if it were a duct system.

Only in recent years have efforts from the scientific community to define, implement and test ‘smart’ ventilation led to the adoption of more performance-based rating methods to assess ventilation design and performance (Guyot et al., 2019). The AIVC definition of smart ventilation (Durier et al., 2018) is relatively long, but starts as follows:

> *"Smart ventilation is a process to continually adjust the ventilation system in time, and optionally by location, to provide the desired IAQ benefits while minimizing energy consumption, utility bills and other non-IAQ costs (such as thermal discomfort or noise).*

A smart ventilation system adjusts ventilation rates in time or by location in a building to be responsive to one or more of the following: occupancy, outdoor thermal and air quality conditions, electricity grid needs, direct sensing of contaminants, operation of other air moving and air cleaning systems. "

Typical implementations of 'smart' ventilation only partially exploit the potential for 'smartness' put forward in this definition allows and only add proportional control to the predefined flow pattern from the design standards (Guyot et al., 2018).

In an effort to embrace more ambitious renderings of what smart ventilation could be, the proposal for a new CEN design standard for residential ventilation systems prEN 15665 defines 3 steps within the performance assessment method step of the performance-based design process: 1) Select a calculation level, 2) Describe the relevant features, and 3) Select an appropriate calculation method and run the calculations. This paper addresses the question of the appropriate calculation method and calculation level for systems with advanced controllers.

2. ASSESSMENT REQUIREMENTS

For the 'appropriate calculation method', the most advanced options in literature typically use multi-zone airflow simulation with 1 or more (using Monte-Carlo techniques) fixed weather and occupancy profiles (Laverge, 2011). Such simulations show that, in multi-zone ventilation systems typical for residential settings, the intended flow pattern regularly breaks down due to the impact of wind and thermal buoyancy. Advanced controllers, like grey-box MPCs, have been shown to have superior performance to typical proportional rule based controlers in such conditions (Merema al., 2022) and, provided the appropriate actuators are available, can change flow paths through the flow network in response to the changing ventilation needs.

The grey-box nature of existing optimal controllers and the increasing popularity of the inclusion of self-learning algorithms in control loops (eg. Zou et al., 2024), introduces fundamentally new features to the process and poses a challenge to the selection of the appropriate calculation method for regulatory purposes. A fundamental requirement for a regulatory assessment procedure is that it does not provide an advantage to a particular (type of) system that is not a reflection of a real feature of the system (avoiding bias or 'technological neutrality' of the assessment method). As the repetition of known boundary conditions (weather data) and excitations (occupancy patterns) in existing methods can easily be picked up by self-learning algorithms, the appropriate assessment methods needs to be inherently stochastic in nature. This, however, requires fundamentally rethinking the current *best practices* of performance assessment for smart ventilation and IAQ management more broadly. A fundamental step towards this is moving to stochastic assessment methods.

In addition to moving towards stochastic inputs, like stochastic user profiles (Verbruggen et al., 2019) and synthetic weather files (Jia et al., 2024), the checking of the satisfaction of the set IAQ criteria, required moving to a convergence based assessment rather than a deterministic threshold, because the obtained performance metrics will be affected by the stochastic variation in conditions. The simulation then needs to be run until the selected performance indicators have converged. In this paper, we analyse the feasibility of convergence based performance indicators.

3. ANALYSIS AND DISCUSSION

As shown in Figure 1, this is typically reached relatively soon in simulations ran over one year or heating season. The figure shows the convergence of the average exposure of 4 occupants to carbon dioxide in a single family apartment in Belgium in a simulation of 1 heating season spanning from September to April, at 477, 615, 407 and 439 ppm respectively. All modeling assumptions used can be found in report of the 'Freduc' study (Caillou et al. 2014).

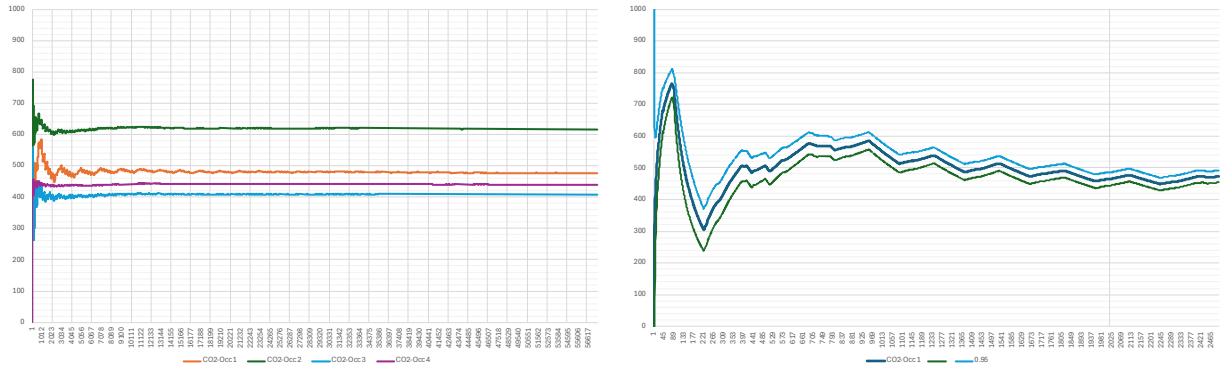

Figure 1. Convergence of average exposure to CO_2 (ppmvol) of 4 occupants in a traditional deterministic simulation over 1 heating season (left) and the confidence interval around the mean for occupant 1 over slightly more than 1 weeek (right).

It is clear that convergence of this particular performance indicator is reached relatively quick. After 6 weeks (grid lines in the graph), all values have effectively converged. If ranking of the occupants is the objective of the analysis (Sarrazin et al., 2016), then this is already the case after 2 weeks. This analysis shows that moving towards a convergence based assessment could not only provide an answer to the challenge of assessing self-learning controls, but could also provide substantial computational savings over traditional simulation methods, in this case by a factor of 8-20, depending on the selected performance indicator and convergence metric.

At the same time, the results also show that the average exposure of occupant 1 is strongly affected by weekly disturbance in the occupancy pattern, the regular occurrence of the weekend for a full-time working adult in the repeating fixed occupancy pattern as shown in Figure 2. (left), leading to an underestimation of the confidence interval around the mean early in the early stages of the convergence. Although several of the weather variable included in the analysis have frequence components with a much longer period than the occupancy pattern (think of temperatures that typically follow a one-year cycle and therefore will only converge after several years, see Figure 2.), these components do not seem to affect the convergence of the selected performance indicator. In this particular case, this means we need to use both the confidence interval and the value of the performance indicator when assessing convergence.

The sampling of the input parameters could be optimized to facilitate faster convergence provided that this does not affect the behavior of the system that is being assessed. A stochastic assessment framework for IAQ management systems should therefore include an analysis of the dominant frequencies in the input variables as well as a sensitivity analysis of the selected performance indicators to the input parameters.

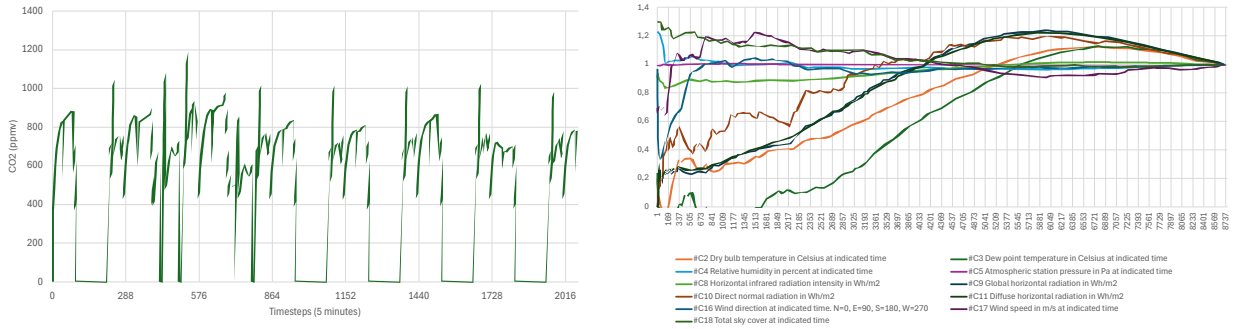

Figure 2. Time series of the exposure of occupant 1 to carbon dioxide (ppmvol) over 1 week (left). Convergence of normalised average values of the weather variables in the weather input file of the simulation over 1 year (right).

5. CONCLUSIONS

In this abstract, we have argued that the advent of MPC and self-learning controls in smart ventilation and other IAQ management applications introduces the need for stochastic simulation methods in a regulatory framework. We proposed the use of convergence based performance indicators and demonstrated that it is important to consider both the confidence interval and the value of the performance indicator when assessing convergence. Finally, our findings suggest that moving to stochastic assessment methods could reduce computation times by at least one order of magnitude.

ACKNOWLEDGEMENTS
This work is funded by Flux50/VLAIO under grant n° HBC.2023.0488

REFERENCES

Caillou, S., Heijmans, N., Laverge, J., Janssens, A., 2014, Methode de calcul PER: Factuers de réduction pour la ventilation à la demande, rapport freduc, marché public IBGE-BIM n°2012/E12-627, BBRI, Brussels

Durier, F., Carrié, R., Sherman, M., 2018. What is smart ventilation? AIVC, VIP 38.

Guyot, G., Sherman, M., Walker, I., 2018. Smart ventilation energy and indoor air quality performance in residential buildings: A review. Energy and Buildings 165 (15), 416-430.

Guyot, G., Walker, I., Sherman, M., 2019. Performance based approaches in standards and regulations for smart ventilation in residential buildings: a summary review. International Journal of Ventilation 18 (2), 96-112.

Jiao, Z., Yuan, J., Farnham, C., Emura, K., 2024. Multivariate stochastic generation of meteorological data for building simulation through interdependent meteorological processes. Sci Rep 14, 24927

Laverge, J., Van Den Bossche, N., Heijmans, N., Janssens, A,. 2011. Energy saving potential and repercussions on indoor air quality of demand controlled residential ventilation strategies. Building and Environment 46 (7), 1497-1503.

Merema, B., Saelens, D., Breesch, H., 2022. Demonstration of an MPC framework for all-air systems in non-residential buildings, Building and Environment 217, 109053

Rojas, G., Pfluger, R., Feist, W., 2015. Cascade ventilation—Air exchange efficiency in living rooms without separate supply air. Energy and Buildings 100 (1), 27-33.

Sarrazin, F., Pianosi, F., Wagener, T., 2016. Global Sensitivity Analysis of environmental models: Convergence and validation. Environmental Modelling & Software 79, 135-152.

Verbruggen, S., Laverge, J., Delghust, M., Janssens, A., Stochastic occupant behaviour model : impact on residential energy use. in: Proceedings of Building Simulation 2019: 16th Conference of the International Building Performance Simulation Association (IBPSA), vol 16. pp. 2310-2317

Zou, M., Huang, W., Jin, J., Hu, B., Liu, Z., 2024. Deep spatio-temporal feature fusion learning for multi-step building cooling load forecasting. Energy and Buildings 322, 114735.

Smart Buildings and Smart Cities (15:30-17:00 h)

6th International Conference on Building Energy and Environment
Eindhoven University of Technology, The Netherlands
6 - 10 July 2025

Enhanced building-specific heat load prediction with limited information through an automated zoning algorithm

Kevin Waiz[1], Jacob Estevam Schmiedt [1], Jana Stengler[1], Bernhard Hoffschmidt[1,2]

[1]*Institute of Solar Research, German Aerospace Center (DLR), Jülich, Germany, kevin.waiz@dlr.de*
[2]*Chair of Solar Components, RWTH Aachen University, Germany*

SUMMARY
In urban development, buildings have a key influence on energy use and sustainability. Therefore, accurate building energy demand predictions are required to design climate neutral energy systems. GML models, common for city-scale energy simulations in Europe, often lack detailed building information about architecture and construction. This study addresses the challenge of predicting heat load profiles for buildings with limited available data, especially those characterized by multiple thermal zones and various use types. A Multizone Assignment Algorithm (MZA) is developed to improve load prediction by defining zoning strategies using the concept of Binary Space Partitioning (BSP). The MZA integrates an automated zoning approach, embedded into the TEASER-AixLib framework for seamless energy simulation. By incorporating adjacency relations and interzonal heat transfer, the methodology improves prediction accuracy while requiring minimal manual input. This novel approach accelerates and simplifies district-scale simulations, providing important insights into how different areas within buildings interact and improving the operation of energy systems with limited initial data.

Keywords: CityGML, heating demand simulation, zoning strategies

1. INTRODUCTION

Buildings account for up to 40 % of global energy demand, significantly contributing to climate change (Statista, 2022). Improving energy efficiency in buildings is crucial for sustainable development, with heat demand prediction playing a central role in optimizing design and operation. Thermal simulations often rely on public GML files, classified into Levels of Detail (LoD) that range from simple footprints (LoD0) to detailed volumetric models (LoD3) (Biljecki et al., 2016). However, most municipal data is typically limited to rudimentary information, resulting in reduced prediction accuracy and compromised thermal simulation quality.

Despite the frequent lack of information, there are approaches aimed at improving the accuracy of predictions. In addition to the estimation of material properties of the facade or the enrichment of building models with information from aerial images, the assumed structure within the building envelope also plays a decisive role. For example, unheated partial areas or heat transitions between neighboring zones influence the heat demand of a building. Through inadequate or inappropriate zoning techniques this results in deviations of up to 15 % for a single zone (Jansen et al., 2021; Kühn et al., 2024). In addition, the high diversity of occupancy profiles and, in this context, the behavior of the residents significantly influences energy consumption patterns. Not only do heat transitions into unheated neighboring zones affect the heat demand, but also heat exchanges between apartments and floors arise due to user-controlled setpoint temperatures. Hence, the decomposition of a single-zone model into a multi-zone model is suggested and has already been

addressed in other works. Some approaches address this challenge by focusing on the expansive generation and zoning of interior floor plans. For instance, Lopes et al. (2010) present a flexible method for generating procedural interior room layouts that accommodate various building types, including those with multiple floors. In contrast, Dogan et al. (2016) and Johari et al. (2022) concentrate on subdividing larger buildings into subzones, both recommending detailed zoning for varying usage profiles.

In contrast to these advancements, many existing approaches do not adequately address the complexities introduced by multiple thermal zones and diverse usage types on a larger scale for multi-family houses or apartment blocks. Due to the lack of information, a time-consuming multiple zone modeling is not considered, leading to inaccuracies in energy demand predictions. This work addresses these challenges by enhancing heat demand estimation through an automated zoning algorithm, even when detailed architectural information is lacking. The methodology focuses on an automated heuristic approach that can generate individual apartments within multi-family buildings while adhering to predefined constraints. Although manual zoning and perimeter-core zoning have been integrated into the framework, the emphasis in the present study is on the automated zoning method.

2. METHODOLOGY

2.1. Data aggregation and preprocessing

In this work, we combine geodata from OpenStreetMap (OSM) (2024) with CityGML data (Remmen et al., 2016) as input in order to obtain detailed information about the buildings. The integration of OSM data enables the supplementation of the information contained in CityGML, specifically by using attributes such as building and roof type in OSM or the address point of a building. In addition, we integrate further data (Blanco et al., 2023), enriching the dataset per building with additional information, such as the classification of buildings into construction year typologies. The systematic analysis and processing of these combined sources ensures a consistent and sufficient database for subsequent applications.

In order to reduce the computational effort and limit the number of possible solutions, a discretization of the building floor area is necessary. We carried out this reduction of the solution space using the Binary Space Partitioning (BSP) algorithm (H. Fuchs et al., 1980). This approach enables an automatic subdivision of the base surface up to a predefined granularity, efficiently dividing the solution space into smaller, manageable, and convex hyperplanes called leaves. The outcome is a recursive data structure in the form of a tree, as shown in Fig. 1.

Finally, further information is aggregated per leaf, such as direct neighboring leaves or connections to the outer edge of the building, which are essential for the functionality of the proposed methods and the placement of staircases. The latter is important for two reasons: Firstly, an unheated staircase influences the energy demand of a building and its individual zones, and secondly, the placement creates additional constraints that facilitate the automatic zoning. Consequently, the staircase for a building is aligned based on the address point and orthogonal to the nearest possible external wall. The dimensions of the staircase are currently determined by a proportion of the floor area and with respect to the standards (DIN 18065, 2011), but future iterations will adjust them according to the year of construction and building type.

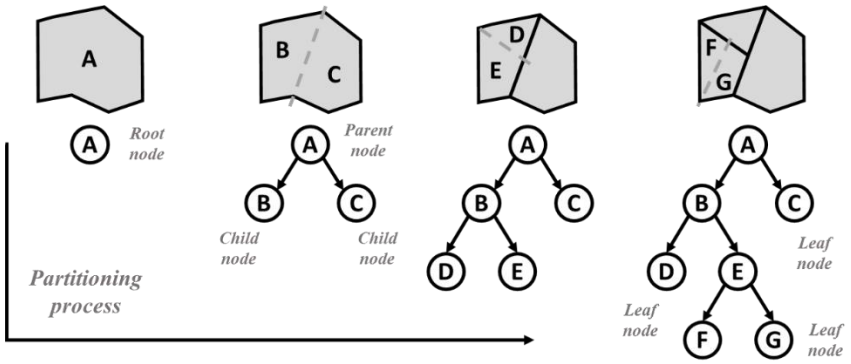

Figure 1. Partitioning process of a Binary Space Partitioning (BSP) tree with leaves as final partitions

2.2. Automatic zoning

The heuristic zoning algorithm presented here is based on a combination of random seed placement and subsequent regional allocation of areas, under adherence to predefined constraints. In the first step, the seeds — i.e., starting points — are generated along polygon boundaries. These boundaries correspond to the partition wall between the stairwell and the rest of the floor area along which the starting points are positioned. Each starting point represents a required zone per floor. The number of zones or apartments to be determined per building and per floor is derived from databases, using either the average apartment size or a predefined number of households per building volume (Census, 2011; Destatis, 2023). Subsequently, up to a defined iteration limit, a procedure with uniform spacing of the starting points is carried out. Beyond a certain threshold, random placements within or along the boundary line are allowed. For each iteration, all leaves are assigned to the nearest sub-area using a breadth-first search method, where multiple seeds act simultaneously in a queue. The subareas grow in parallel, assigning neighboring leaves (connected by an adjacency list) to the subarea that "captures" them first, which is comparable to the method described by Loga et al. (2016).

As soon as all leaves have been assigned, a constraints check is carried out to ensure minimum requirements are met. These relate to the number of leaves bordering the stairwell and an external facade in each sub-area or a maximum permissible deviation of the individual subarea areas from the specified average value. An assignment is only considered valid if these conditions are met.

$$Z = P_{\text{total}} + \alpha(\max(A_{\text{subarea}}) - \min(A_{\text{subarea}})) \quad (1)$$

The final step involves postprocessing to reduce local irregularities at the boundaries and smooth out potential "jagged patterns" in the subareas. For this purpose, each leaf is evaluated in the context of its neighborhood, where the majority subarea is determined based on the adjacent leaves. If flipping the respective leaf into this dominant subarea is feasible without violating global constraints, the adjustment is executed. Overall, this methodology combines a heuristic, random-based approach with multi-criteria evaluation and a local smoothing algorithm. It is primarily designed for an accelerated process and simpler building floor plans. However, for more complex geometries and additional boundary conditions, such as window positions specified in an LoD3 standard, a different algorithm is currently under development. This algorithm will employ graph partitioning to address the optimization problem.

2.3 Enrichment and simulation

For the thermal simulation of buildings, the methodology presented in 2.2 is embedded in the TEASER framework (Remmen et al., 2018) and the Modelica library AixLib (Müller et al., 2016). TEASER, a Python-based program, automates the parametrization of building models according to VDI 6007-1 (2015) and utilizes data such as construction type, year, and material properties derived from the German TABULA typology (Loga et al., 2016). Additionally, features such as the set temperature and the usage conditions of each zone are defined. Through its interface with AixLib, the model is converted into a Reduced-Order Model (ROM), which represents thermally conductive components using resistance-capacitance (RC) elements. To allow heat exchange between zones, we follow the approach of Groesdonk et al. (2023), which extends the ROM by adding an additional RC element per zone. This enables the simulation of interzonal heat transfer in cases of temperature differences or adjacent unheated zones. If the building model lacks window information, window areas are determined by considering wall-to-window ratios from the TABULA database and the available external walls, taking adjacent buildings into account. Furthermore, internal gains can be provided via an external model for residential energy consumption as an alternative to the standardized approach. The LoadProfileGenerator (LPG) (Pflugradt et al., 2022) determines profiles for occupants, machinery, or lighting based on Markov chains, allowing a more accurate representation of human behavior and the associated internal gains. The LPG simulates the activities of individual households, which we then distribute across the zones, allowing us to assign each household to a specific subarea. Fig. 2 provides an overview of the study's workflow.

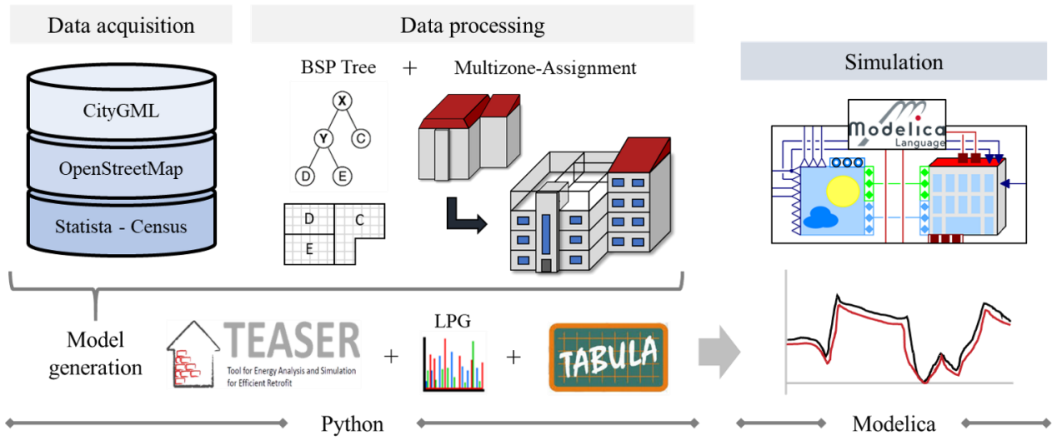

Figure 2. Schematic overview of the process.

3. FIRST RESULTS AND DISCUSSION

The partitions shown in Fig. 3 represent the results of applying the previously discussed sequence of methods for automatic zoning. We processed the GML models of three different apartment blocks (A-C) and three different apartment buildings (D-F). Additionally, a second version was created for each floor plan (specified as "-2"), either generating a predefined number of partial areas or applying a different weighting factor for the objective function. All samples were generated with a total of 200 iterations for the assignment of leaves, as determined through experiments. Increasing the number of iterations beyond this value does not generally improve results, while reducing it, for structures such as in example C, fails to produce sufficiently valid

results for satisfactory zoning (e.g., isolated inclusions). The algorithm demonstrates its ability to produce consistent zonings for most base areas. The equality of areas is preserved across all samples, although certain zone boundaries tend to exhibit irregularities. These include narrow elements, as observed in A-1 and B-1, as well as unsatisfactory handling of the "jagged pattern," as seen in F-1 and E-2. The postprocessing step requires further refinement to better identify and adapt these cases more effectively and accurately.

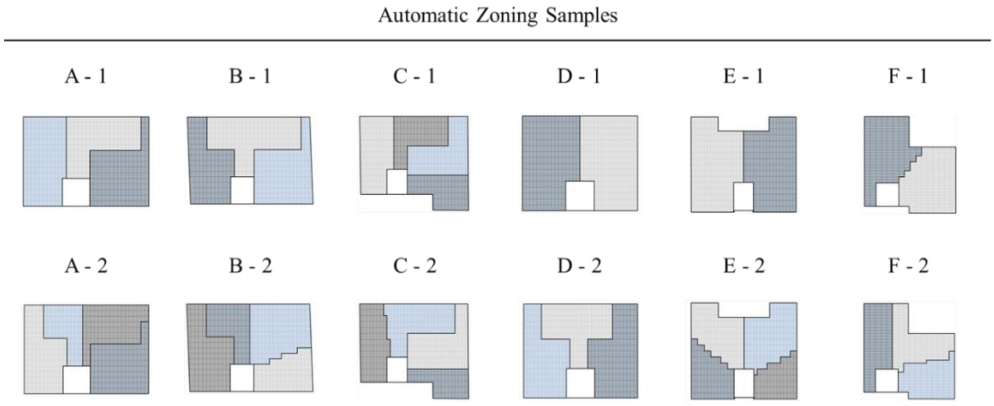

Figure 3. Results for the automatic zoning process for six different floor plans (staircase in white) with $\alpha = 2.0$ (except for C - 2 ($\alpha = 1.0$)) and predefined number of subareas for "-2".

Although the advantages of zoning with dynamic occupancy profiles and variable setpoints per dwelling have been extensively discussed in other studies (see, e.g., Kühn et al. (2024) for a detailed analysis of zoning effects and LoD variation), the results of a dynamic thermal simulation for the building depicted in Fig. 3 (E-1) are presented in Fig. 4-6. We simulated a total of four variants: Variant Multizone A corresponds to the partitioned building with an unheated stairwell, Multizone B includes a heated stairwell, Variant C incorporates usage profiles from the LPG with an unheated stairwell, and the final variant represents a single-zone model. For the weather data, a Test Reference Year (TRY) for the city of Aachen from 2015 was used. Unless otherwise specified, a setpoint temperature of 20 °C was assumed for all zones. An ideally operating heater was modeled for all variants, combined with a standard construction type from the Tabula database. An ideal cooler was not considered, since we primarily focus on the heating demand. The modeling (data acquisition and processing) as well as the simulation were executed on an i7-1370P CPU (1.90 GHz, RAM 16 GB). The figures show that the Multizone models exhibit a heat demand curve with an increased number of steep demand peaks. Notable peaks, particularly around midday, are clearly visible, whereas the single-zone model does not display these peaks to the same extent. It is evident that the single-zone model has the lowest annual heat demand of all versions. This may be attributed to the Reduced-Order Model for larger buildings, which tends to underestimate the internal mass of the building, thereby reducing the heat demand (see also Jansen et al., 2021). Additionally, significant differences in simulation time are apparent. While the modeling remains below 20 seconds for all models, the simulation time for the Multizone model, including heat transfer, increases substantially up to 750 %. This can pose challenges when simulating a large number of buildings. Nonetheless, considering the Multizone model offers advantages for scenarios with varying occupancy profiles and setpoints.

It accounts more accurately for demand peaks and provides a more precise representation of

dynamic processes (as demonstrated in variant C), both of which are critical for the design and operation of an energy system, such as ensuring sufficient capacity during high-demand periods in winter when heating requirements significantly increase. It is evident that the individual zones contribute not only differently to the peak demand during colder periods (see Fig. 5) but also, particularly on summer days (Fig. 6), to an increased overall heat demand. The zoning also indicates that cooling specific areas is becoming more important due to a spread in overheating zones. Temperatures exceeding 28 °C are reached for certain zones, while in the single-zone model, values above 25 °C are rarely found during the same period.

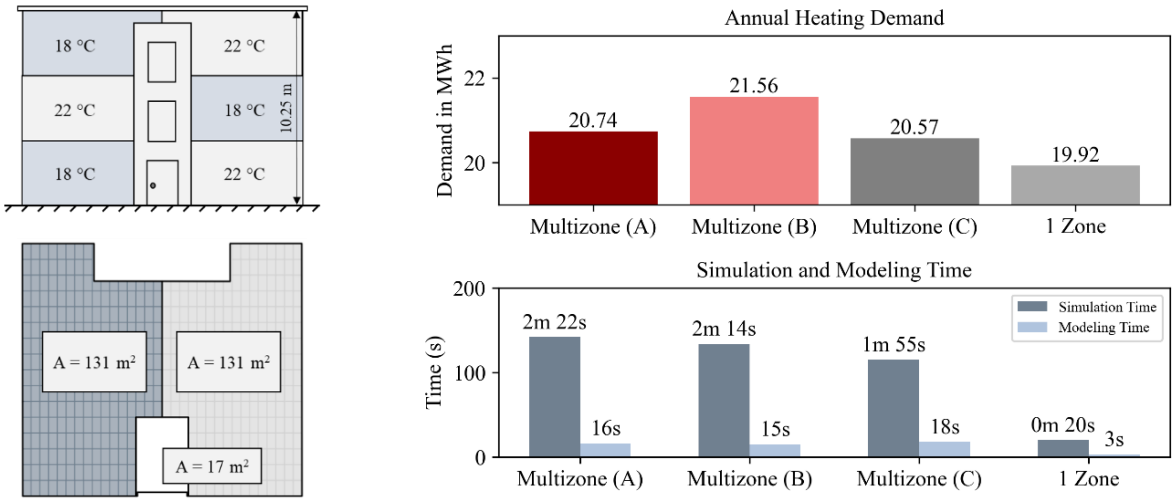

Figure 4. Front and top view of the building with varying set temperatures (left), annual heating demand, simulation and modeling time (right).

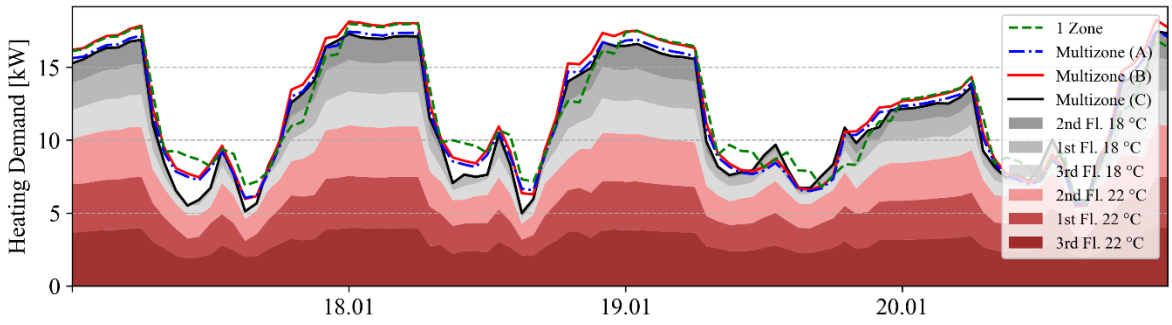

Figure 5. Heating demand comparison over a four-day time span for four different variants and stacked heating demand for the Multizone (C). Multizone (C) demand contributions are ordered from highest (dark red) to lowest (dark gray).

Regarding the zoning methodology and its functionality, some additional points require discussion. There are regional and age-related differences in the layout and construction of apartment buildings, including variations in staircase and corridor dimensions, as well as differences in apartment size and orientation. These assumptions must be carefully considered, as they significantly influence the simulation results. Furthermore, the most advantageous granularity of the zones must be considered in terms of the trade-off between accuracy and effort. While

Jansen et al. have already analyzed this for an office building, they, like Kühn et al., refer only to more complex models as a reference. However, a comprehensive examination and validation of this aspect for residential buildings using real measurement data remains open and should be pursued in the future. Moreover, the location of the stairwell can vary, potentially being positioned away from the street-facing side or located in a corner of the building.

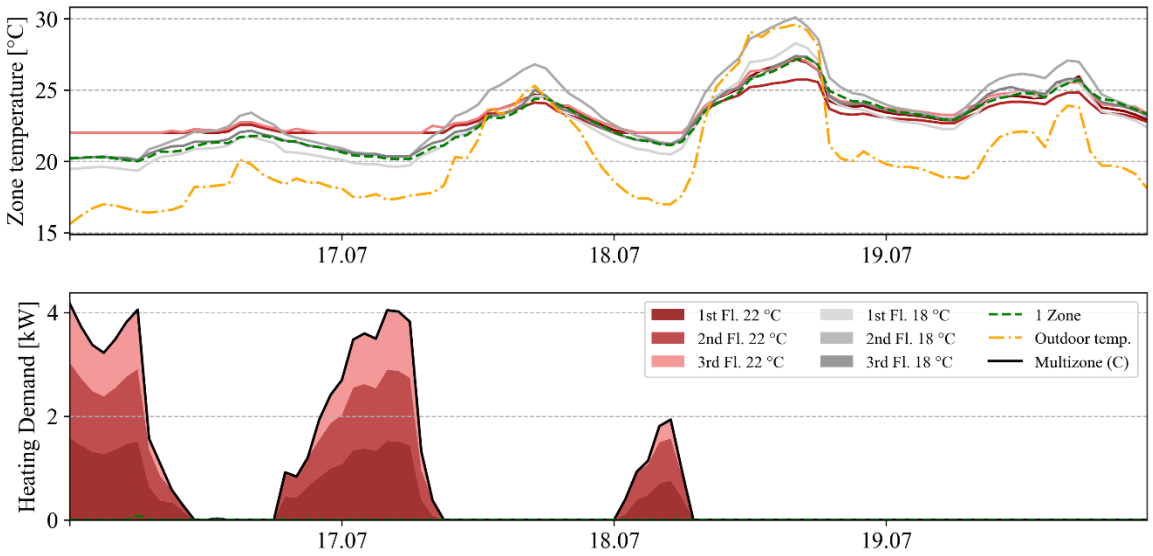

Figure 6. Zone temperature curves (above) and heating demand comparison over a four-day time span Multizone (C) and single zone (below).

These variations affect the zoning configuration and may distort heat demand results. Large apartment blocks present a significant challenge due to the increased number of apartments, which substantially raises simulation effort. Additionally, LoD2 models lack window areas in their GML data, leading to inaccuracies when assigning windows to walls that do not actually have them. Addressing this issue without image evaluations is not feasible.

4. CONCLUSION AND FUTURE WORK

This study focuses on the automatic partitioning of building models into individual residential units to improve heat load calculations. The Multizone Assignment Algorithm utilizes open-source data to enhance building models and is integrated into a thermal simulation environment within the TEASER-AixLib framework. The methodology is primarily designed for analyzing heat demand in smaller areas or specific applications, rather than large districts or entire cities. From a computational perspective, the single-zone model is the most resource-efficient option for large-scale observations. In contrast, the zoning approach targets small to medium-sized districts emphasizing dynamic factors like varying temperature setpoints and diverse occupancy profiles. This methodology aims to simplify building partitioning, especially when architectural data is limited, allowing users to model and parameterize buildings more easily. Future enhancements could include synergies with other algorithms, such as refurbishment status recognition or weather-related factors. Application scenarios may involve energy efficiency assessments for retrofitting buildings or demand response strategies for managing peak loads in urban planning. Further work

will primarily focus on refining the methodology's structure and conducting extensive validation using real buildings. Additionally, an export function for the generated models is planned, enabling not only the preservation of model configurations but also ensuring applicability beyond the scope presented in this study.

REFERENCES

Biljecki F., Ledoux H., and Stoter J., 2016. An improved LOD specification for 3D building models. Computers, Environment and Urban Systems 59, 25–37.

Blanco L., Aditya M., Schiricke B., and Hoffschmidt B., Sept. 4–6, 2023. Classification of building properties from the German census data for energy analyses purposes. Proceedings of Building Simulation 2023: 18th Conference of IBPSA. International Building Performance Simulation Association (IBPSA). Shanghai, China.

Census, 2011. Zensus 2011 – Gebäude und Wohnungen. Zugriff am 9. Januar 2025.

Destatis, 2023. Wohnungsbestand in Deutschland nach Wohngebäudetypen. Zugriff am 9. Januar 2025.

DIN 18065, Mar. 2011. Gebäudetreppen – Begriffe, Messregeln, Hauptmaße. Stand 03-2011. Berlin, Germany: Deutsches Institut für Normung (DIN).

Dogan T., Reinhart C., and Michalatos P., 2016. Autozoner: An algorithm for automatic thermal zoning of buildings with unknown interior space definitions. Journal of Building Performance Simulation 9, 187–201.

Fuchs H., Kedem Z. M., and Naylor B. F., 1980. On visible surface generation by a priori tree structures. Proceedings of Proceedings of the 7th Annual Conference on Computer Graphics and Interactive Techniques, SIGGRAPH 1980, 124–133.

Groesdonk P., Jansen D., Estevam Schmiedt J., and Hoffschmidt B., 2023. Integration of Heat Flow through Borders between Neighbored Zones in AixLib's Reduced-Order Model. Proceedings of Proceedings of the CESBP Central European Symposium on Building Physics and BauSIM 2023. Fraunhofer IRB Verlag, Germany.

Jansen D., Richter V., Lopez D. C., Mehrfeld P., Frisch J., Müller D., and Treeck C. van, 2021. Examination of Reduced Order Building Models with Different Zoning Strategies to Simulate Larger Non-Residential Buildings Based on BIM as Single Source of Truth. Proceedings of Proceedings of the 14th International Modelica Conference. Modelica Association and Linköping University Electronic Press, Linköping, Sweden, 665–672.

Johari F., Munkhammar J., Shadram F., and Widén J., 2022. Evaluation of simplified building energy models for urban-scale energy analysis of buildings. Building and Environment 211, 108684.

Kühn L., Zoumba B., Spratte T., Maier L., and Müller D., 2024. Level of Detail in Dynamic Simulation Models – a Comparison for Multi-Family Houses. Proceedings of Proceedings of BauSim 2024: 8th German-Austrian IBPSA Conference. Acknowledgment: Funded by the German Federal Ministry for Economic Affairs and Climate Action (BMWK, reference 01255249/1). Aachen, Germany.

Loga T., Stein B., and Diefenbach N., 2016. TABULA building typologies in 20 European countries—Making energyrelated features of residential building stocks comparable. Energy and Buildings 132, 4–12.

Lopes R., Tutenel T., Smelik R. M., Kraker K. J. de, and Bidarra R., 2010. A Constrained Growth Method for Procedural Floor Plan Generation. Proceedings of Proceedings of the GAME-ON 2010 Conference. EUROSIS. EUROSISETI, Leicester, United Kingdom, 11–18.

Müller D., Lauster M., Constantin A., Fuchs M., and Remmen P., 2016. AixLib – An Open-Source Modelica Library within the IEA-EBC Annex 60 Framework. Proceedings of CESBP Central European Symposium on Building Physics and BauSIM 2016. RWTH Aachen University, Dresden, Germany, 3–10.

OpenStreetMap (OSM), 2024. Planet dump retrieved from https://planet.osm.org. https://www.openstreetmap. org.

Pflugradt N., Stenzel P., Kotzur L., and Stolten D., 2022. LoadProfileGenerator: An Agent-Based Behavior Simulation for Generating Residential Load Profiles. Journal of Open Source Software 7, 3574.

Remmen P., Lauster M., Mans M., Fuchs M., Osterhage T., and Müller D., 2018. TEASER: An open tool for urban energy modelling of building stocks. Journal of Building Performance Simulation 11, 84–98.

Remmen P., Lauster M., Mans M., Osterhage T., and Müller D., Sept. 2016. CityGML Import and Export for Dynamic Building Performance Simulation in Modelica. Proceedings of

Statista, 2022. Greenhouse gas (GHG) emissions of the building sector in Germany from 1990 to 2020, by building type. https://www.statista.com/statistics/1297313/ghg-emissions-by-buildings-in-germanyby-type/. Accessed: 2024-12-16.

VDI 6007-1, June 2015. Calculation of transient thermal response of rooms and buildings - Modelling of rooms (Berechnung des instationären thermischen Verhaltens von Räumen und Gebäuden - Modellbildung von Räumen). Düsseldorf, Germany: Verein Deutscher Ingenieure (VDI)

6th International Conference on Building Energy and Environment
Eindhoven University of Technology, The Netherlands
6 - 10 July 2025

Characteristics and phytoremediation mechanism of atmospheric polycyclic aromatic hydrocarbons in the roadside environment of Beijing

Shili Tian[1], Qingyang Liu[2], Ming Yang[1], Zheng Yang[3], Yanju Liu[1,*]

[1] *Institute of Analysis and Testing, Beijing Academy of Science and Technology (Beijing Center for Physical and Chemical Analysis), Beijing, China, liuyanju@bcpca.ac.cn*
[2] *College of Biology and the Environment, Nanjing Forestry University, Nanjing, China, nfu@nifu.edu.cn*
[3]*Beijing Milu Ecological Research Center, Beijing 100076, China, 3180400016@cas.edu.cn*

SUMMARY
Polycyclic aromatic hydrocarbons (PAHs) are known for their high toxicity and pose significant threats to human health, with vehicular traffic being a prominent source. Between October 2021 and September 2022, a comprehensive study was carried out along Beijing's roadside. The findings indicated that during winter, the concentration of PAHs in $PM_{2.1}$ peaked at 35.3 ng m^{-3}. Moreover, the leaves of 20 plant species exhibited diverse PAH levels, and it was observed that low-molecular-weight PAHs were more abundantly present in plant leaves of *Rosa chinensis* Jacq. Leaves were exposed to 0.1 μg $L^{-1}$and 5 μg L^{-1} PAHs for seven days, with de-ionized water serving as the control. The results demonstrated that the 5 μg L^{-1} treatment led to pronounced gene expression changes across seven pathways. In contrast, the environmentally relevant concentrations of PAHs had minimal effects on the leaves of *R. chinensis*. Collectively, these findings provide strong evidence in support of leveraging terrestrial trees to mitigate PAH pollution.
Keywords: ambient PAHs; roadside environment; phytoremediation mechanism

1. INTRODUCTION

Polycyclic aromatic hydrocarbons (PAHs), characterized by their teratogenic, carcinogenic, and mutagenic properties as recognized by the World Health Organization (WHO)(Cave et al. 2016), primarily emanate from the incomplete combustion of fossil fuels and hydrogen-containing materials such as wood, crop residues, and tobacco. Mobile sources, biomass combustion, and coal burning constitute the principal emission pathways(Wang et al. 2017). Notably, China's PAHs emissions account for approximately 20% of the global total. In North China, the mean annual particulate BaP (a paradigmatic PAHs) concentrations range from 1.1 to 14.3 ng m^{-3}, surpassing the WHO-recommended threshold of 1.0 ng m^{-3}(Shen 2019), thereby posing significant risks to public health and eliciting ecological toxicological impacts on the ecosystem.

The ecological remediation approach, leveraging trees and plant leaves, has emerged as a cost-effective and sustainable means to attenuate the high-toxicity PAHs in the ambient milieu. Trees function as sieves for PAHs, while plant leaves can be regarded as reactors for their removal. Prior investigations have demonstrated substantial air pollutant removal capacities. For instance, in 55 cities across the United States, trees were estimated to eliminate approximately 710,000 tons of air pollutants, inclusive of NO_2, SO_2, and particulate-bound contaminants(Nowak, Ellis and Greenfield 2022). Based on 150 field studies spanning 15 countries from 1960 to 2016, plant leaves were found to absorb around 1.71 ± 0.05 g m^{-2} of particulate air pollutants per week(Corada et al. 2020). Research on PAHs accumulation in species such as *Quercus palustris* and *Pinus nigra* has

elucidated correlations between leaf PAHs concentrations and ambient air, with discernible variations in PAHs levels contingent upon tree age and seasonal fluctuations(Fellet et al. 2016). The epicuticular waxes of leaves are deemed pivotal in PAHs sequestration.
The majority of PAHs ingress plant leaves via stomatal openings, wherein lipid constituents within the waxes engage in adsorptive interactions with ambient PAHs. Subsequently, the adsorbed PAHs traverse the leaf surface through the stomata and translocate to the internal leaf tissues. Previous studies have also documented the PAHs-mitigating capabilities of trees and the mechanisms underlying PAHs entry into leaf tissues(De Nicola et al. 2017). However, the toxicological ramifications of PAHs on plant leaves during their migration from the ambient environment to the internal tissues remain relatively understudied. The present study endeavors to bridge this knowledge gap by employing whole-transcriptome analysis to scrutinize the responses of plant leaves upon exposure to environmentally relevant and elevated levels of PAHs. By doing so, this research will amass evidence regarding the physiological and pathological responses of plants to ambient PAHs, thereby augmenting our comprehension of the plant-PAHs interplay and the potential of ecological remediation strategies.

2. MATERIALS AND METHODS

2.1. Sampling collection

Samples were collected from October 1, 2021, to September 30, 2022. The sampler was placed 1.5 m above the ground on the side road of the West Third Ring Road, within a commercial and cultural area. There were many roads in the vicinity, but no significant primary PAHs sources like industrial ones within several kilometers. Its proximity to the main urban highways made it suitable for representing a roadside environment.
An 8-stage sampler (Andersen Series 20-800, Cleves, USA) with cutoff points from 0.43 to 9.0 μm was operated at a flow rate of 28.3 L^{-1} min for 48 hours to collect size-resolved particles. Over 70% of the samples could detect the target PAHs compounds within 48 hours. A total of 35 sets of samples were collected on quartz fiber filters. Before sampling, the filters were preheated at 450°C for 2 hours to remove organic substances.
In July 2022, leaves of 20 tree species were collected along Beijing's West Third Ring Highway. For each species, three similar-sized and aged healthy trees were chosen. Around 100 leaves per set were gathered from the highway-facing side, placed in polyethylene bags, and transported to a 4°C laboratory for further study.

2.2 Chemical analyses

Mixed standards of 24 PAHs at 500 mg L^{-1} were used for a stock standard solution for PAHs quantification in leaves and particles, which includes naphthalene, acenaphthylene, acenaphthene, fluorine, phenanthrene, anthracene, fluoranthene, pyrene, benzo(a)anthracene, chrysene, benzo(b)fluoranthene, benzo(k)fluoranthene, benzo(e)pyrene, indeno(1,2,3-cd)pyrene, dibenzo(a,h)anthracene, benzo(g,h,i)perylene, benzo(c)phenanthrene, 7,12-dimethylbenz(a)anthracene, benzo(j)fluoranthene, benzo(e)pyrene, 3-methylcholanthrene, picene, dibenzo(a,l)pyrene, and dibenzo(a,i)pyrene. Two substitutes including 2-fluorophenyl and terphenyl-d14 concentrated at 4000 mg L^{-1} were adopted to evaluate the efficiencies of extraction

processes. A solution of five compounds including naphthalene-d8, acenaphthene-d10, phenanthrened10, chrysene-d12, and perylene-d12 at 4000 mg L^{-1} was selected as the internal standard.

2.3 Exposure experiments

One-year-old healthy *Rosa chinensis* Jacq. were selected and planted in 15-cm pots with a 12L:12D photoperiod. Three groups were set: control, low ($0.1 \mu g L^{-1}$), and high ($5\ \mu g L^{-1}$) concentration exposure groups. The exposure reagent was a mixture of 16 commonly detected PAHs. Different concentration solutions were prepared. Considering leaves contain methanol (10-26.8 $\mu g\ g^{-1}$), the methanol levels in the exposure groups (about $25 \mu L\ L^{-1}$ and $0.5\ \mu L\ L^{-1}$ respectively) had negligible impacts on leaf physiology. Each group had 4 replicates. Leaves were washed with de-ionized water before the experiment. The exposure groups were sprayed with corresponding PAHs concentrations daily, while the control group used de-ionized water on similar leaves. Daily measurements of chlorophyll, water content, and nitrogen in leaves were averaged. Given the PAHs half-life on leaves, the experiment was conducted at 18-20°C and 40%-50% humidity for 7 days. Then, 5 g of leaves from each low and high-concentration group were collected and stored at -80°C for transcriptomic sequencing.

2.4 Transcriptome sequencing and bioinformatic analyses

The RNA Nano 6000 Kit was used to assess the quantity and integrity of leaf RNA. Starting with total RNA, through steps like mRNA purification, fragmentation, cDNA synthesis, end treatment, adapter ligation, fragment screening, PCR, and product purification, 150 bp paired-end reads were generated on the Illumina Novaseq platform.
Raw data were processed by fastp software to obtain high-quality data for subsequent analyses. The reference genome files were downloaded, and Hisat2 was used for alignment. StringTie assembled the reads, Counts counted, and FPKM was calculated to evaluate gene expression. DESeq2 analyzed differential genes, and the p-values were corrected. Genes with an adjusted $p \leq 0.05$ were considered differentially expressed. The cluster Profiler R package was used to test the enrichment of differential genes in KEGG pathways.

3. RESULTS AND DISCUSSION

3.1. Seasonal variation in PAHs

The mean levels of 24 species of PAHs in fine particles ($PM_{2.1}$) exhibited obvious seasonal variations (Fig. 1), with the greatest found in winter (35.3 ± 14.6 ng m^{-3}), followed by autumn (16.0 ± 6.1 ng m^{-3}), spring (15.3 ± 4.6 ng m^{-3}), and summer (6.5 ± 1.8 ng m^{-3}). The seasonal trends of average PAHs concentrations in coarse particles ($PM_{2.1-9}$) differ from those of $PM_{2.1}$ slightly. The highest concentration of PAHs was detected in winter (20.5 ± 10.3 ng m^{-3}), followed by spring (16.5 ± 7.4 ng m^{-3}), autumn (7.1 ± 5.2 ng m^{-3}), and summer (6.8 ± 4.5 ng m^{-3}). The high concentrations of PAHs in coarse particles in spring may be related to the high concentration of dust in spring. The seasonal trends in PAHs mainly resulted from variations in emission sources and changes in meteorological conditions. Compared to previous studies in Beijing, the

concentrations of PAHs in fine particles in winter were lower relative to the results reported during the periods from 2013 and 2018(Li et al. 2022). The reduction in concentrations of PAHs implied the effectiveness of pollution prevention strategies in Beijing.

From the perspective of PAHs with different benzene rings, concentrations of low molecular-weight PAHs (2–3 ring, LMW PAHs) and middle molecular-weight (4 ring, MMW PAHs) PAHs in fine particles followed the order of winter > spring > autumn > summer, while concentrations of high molecular-weight PAHs (5–6 ring, HMW PAHs) were higher in autumn and winter compared to those in spring and summer. HMW PAHs (29.0–45.7%) and MMW PAHs (22.0–36.3%) were the main PAHs compounds during the cold period, while LMW PAHs (47.9–57.5%) dominated the PAHs mixture during the warm period. LMW PAHs in coarse particles exhibited the highest concentrations in spring, followed by winter, summer, and autumn. However, MMW PAHs showed the highest concentration in winter, followed by spring, summer, and autumn. Notably, the levels of HMW PAHs were found to be greater in autumn and winter than in spring and summer. The contributions of LMW PAHs (36.9–71.9%) to total PAHs in coarse particles were higher than that of MMW and HMW PAHs in all seasons.

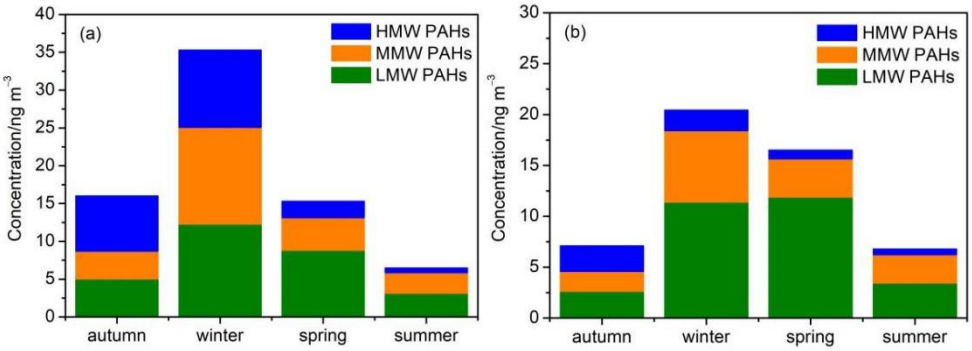

Figure 1. Concentrations of PAHs in $PM_{2.1}$ (a) and $PM_{2.1–9}$ (b)
(Note: originated from Tian *et al.*, Atmosphere, 2024, 15, 346, Figure 1)

3.2. Differences in the accumulation of PAHs across plant species

The highest concentration of total PAHs was found to be 68.4 ng g^{-1} in the leaves of *Ginkgo biloba* L., followed by *Viburnum sargentii* (67.1 ng g^{-1}), *Robinia pseudoacacia* (65.9 ng g^{-1}), *Platanus* × *acerifolia* (58.1 ng g^{-1}), *Sophora japonica* (54.1 ng g^{-1}), *Populus tomentosa* (53.1 ng g^{-1}), *Salix matsudana* (48.4 ng g^{-1}), *Salix babylonica* (47.8 ng g^{-1}), *Ailanthus altissima* (43.7 ng g^{-1}), *Broussonetia papyrifera* (43.2 ng g^{-1}), *Lonicera maackii* (42.1 ng $g^{-}1$), *Paulownia fortune* (40.9 ng g^{-1}), *Fraxinus chinensis* (40.7 ng g^{-1}), *Acer mono* (38.6 ng g^{-1}), *Ulmus pumila* (36.7 ng g^{-1}), *Prunus triloba* (35.7 ng g^{-1}), *Prunus cerasifera* (32.7 ng g^{-1}), *Chaenomeles speciosa* (26.7 ng g^{-1}), *Jasminum nudiflorum* (23 ng g^{-1}), and *Prunus persica* (12.4 ng g^{-1}) (Fig. 2).

The adsorption amounts of PAHs on leaves are associated with several environmental factors (Klingberg et al. 2022). Among 20 trees, the occurrences of naphthalene, fluorene, fluoranthene, and pyrene were detected in the leaves of 20 trees with an average concentration in the range of 2.0–7.8 ng g^{-1}, while most PAHs congeners, including acenaphthylene, acenaphthene, anthracene, benzo(g,h,i)perylene, benzo(c)phenanthrene, benz(a)anthracene, benzo(k)fluoranthene, 7,12-dimethylbenz(a)anthracene, benzo(j)fluoranthene, benz(e)pyrene, perylene, 3-methylcholanthrene, dibenz(a,h)anthracene, picene, benzo(g,h,i)pery, dibenz(a,l) pyrene, dibenz(a,e)pyrene, coronene, dibenz(a,i)pyrene, and dibenz(a,h)pyrene, were not detected (<0.5

ng g^{-1}) in the leaves of 20 trees. The highest number of detected species of PAHs congeners was eleven in an individual tree among 20 species of trees, while the lowest number of detected species of PAHs congeners was five in the leaves of *Prunus persica*. The contribution of low-ring (i.e., the sum of two-ring and three-ring) PAHs accounted for the total PAHs in the range from 37% to 71%, while medium-ring (i.e., four-ring) and high-ring PAHs (i.e., the sum of five-ring and six-ring) contributed to the total PAHs ranging from 20% to 47% and from 5% to 13%, respectively (Fig. 2).

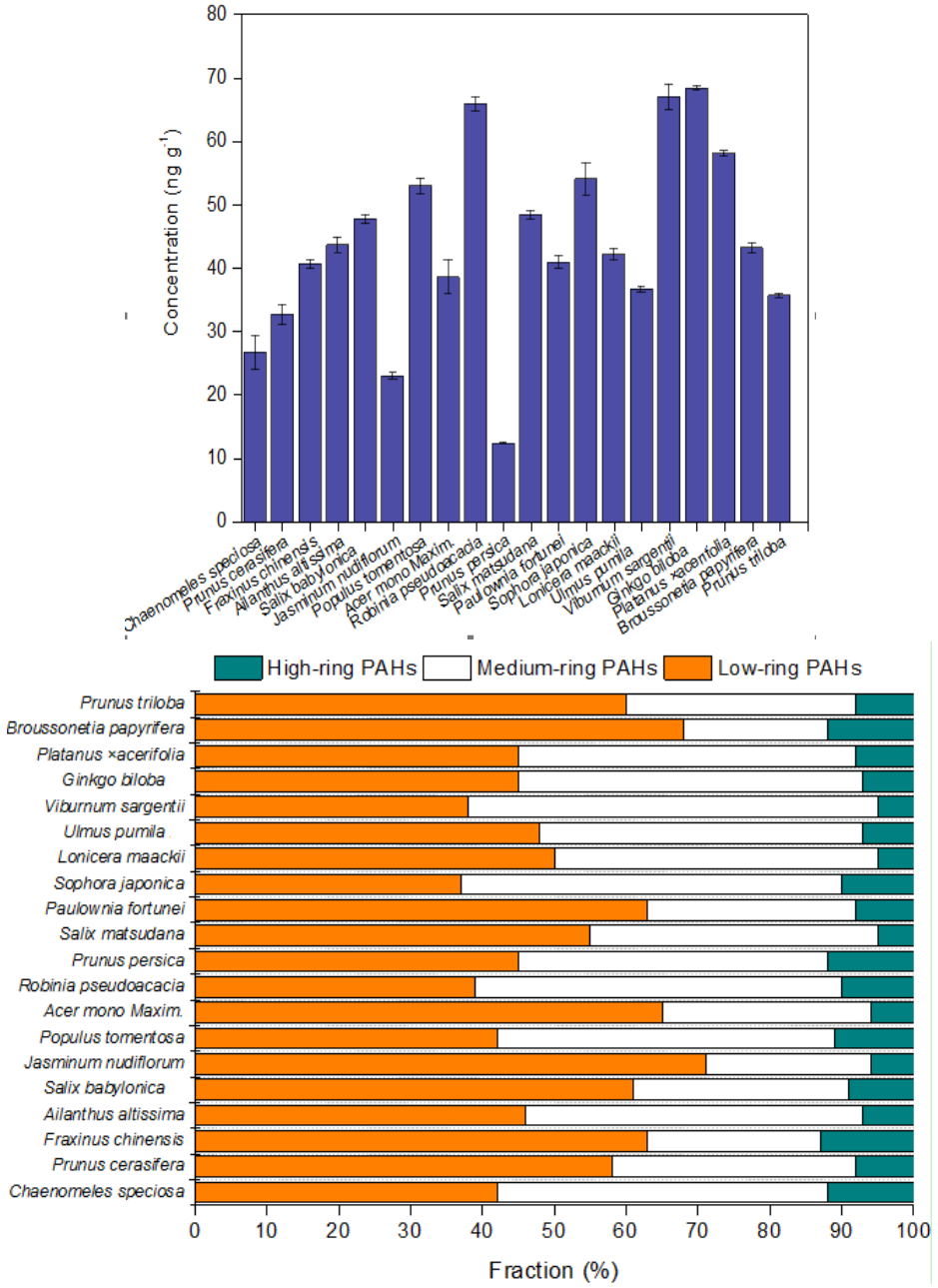

Figure 2. Concentrations of PAHs in 20 tree leaves

(Note: originated from Yang *et al.*, Atmosphere, 2024, 15, 1165, Figure 1 and Figure 2)

3.3. Differentially expressed genes

We used the concentrations of individual PAHs at 5 μg L^{-1} to investigate the responses of leaves under exposure to PAHs at a high concentration. As shown in Fig.3, significant differences in expressed genes were observed after 7 days of exposure between the high-concentration exposure group and the control group. The numbers of upregulated and downregulated genes of the high-concentration exposure group relative to the control group were 1150 and 5502, respectively. It is noteworthy that the concentrations of individual PAHs in the exposure group were much higher than the levels of individual PAHs at the environmentally relevant concentration in this study(Tian et al. 2019). After exposure to individual PAHs at 0.1 μg L^{-1} for seven days, differences in expressed genes between the low-concentration exposure group and the control group were found to be insignificant. The numbers of upregulated and downregulated genes were 112 and 195, respectively.

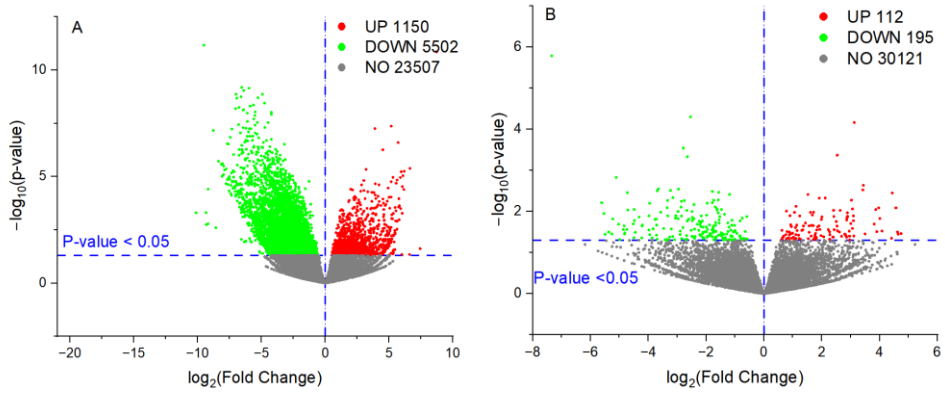

Figure 3. Number of upregulated and downregulated genes for high-concentration exposure group relative to the control (**A**) and low-concentration exposure group relative to the control (**B**)
(Note: originated from Tian *et al.*, Toxics, 2023, 11, 610, Figure 2)

3.4. KEGG enrichment analysis

Subsequently, we performed KEGG enrichment analysis to show which genes or pathways that the differentially expressed gene cluster was in. KEGG is a comprehensive database that integrates genome, chemistry and system function information(Sangwan et al. 2013). A padj of less than 0.05 was used as the threshold for significant enrichment. For the comparison between the high-concentration exposure and the control group, significant differentially expressed genes were assigned into seven main pathways, which included flavone and flavonol biosynthesis, glyoxylate and dicarboxylate metabolism, RNA polymerase, ribosome biogenesis in eukaryotes, porphyrin metabolism, photosynthesis-antenna proteins and photosynthesis (Fig.4).
In contrast, there were no significant differentially expressed genes in the KEGG enrichment analysis between the low-concentration exposure group and the control group (Fig. 4). In general, the gene transcription levels obtained from the KEGG enrichment analysis exhibited a similar pattern and degree of alterations in comparison to the physiological results, thereby demonstrating that the responses of leaves to exposure to PAHs at environmentally relevant concentrations were negligible.

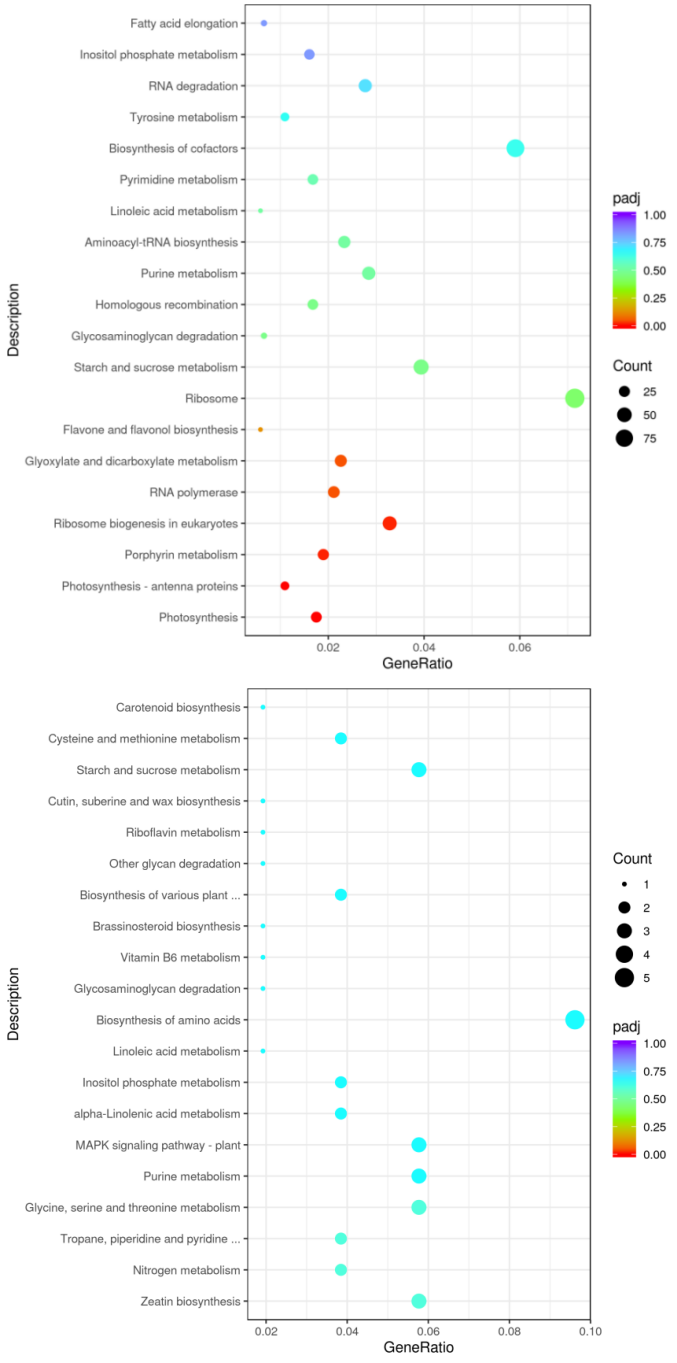

Figure 4. KEGG enrichment analysis of high and low-concentration exposure group relative to the control group. Scatter plot of KEGG enrichment, showing all pathways significantly enriched ($p < 0.05$) in each module （Note: originated from Tian *et al.*, Toxics, 2023, 11, 610, Figure 3 and Figure 4）

4. CONCLUSIONS

In this study, 24 species of PAHs in size-segregated particles and 20 species of plant leaves at the roadside environment of Beijing were observed. The levels of total PAHs across 20 tree species ranged from 12.4 ng g^{-1} to 68.4 ng g^{-1}. After exposure to PAHs at 5 μg L^{-1}, significant differences in the gene transcription levels of the leaves of *Rosa chinensis* Jacq. were observed relative to the

control group. These significant differentially expressed genes pertain to seven main pathways, which are flavone and flavonol biosynthesis, glyoxylate and dicarboxylate metabolism, RNA polymerase, ribosome biogenesis in eukaryotes, porphyrin metabolism, photosynthesis-antenna proteins, and photosynthesis. On the contrary, environmentally relevant concentrations of PAHs had no significant effect on the physiological parameters and gene transcription levels of the leaves of *Rosa chinensis* Jacq. during the 7-day exposure period in this study. Our results illustrate that exposure to ambient PAHs may have a negligible impact on the leaves of terrestrial plants at gene transcription levels. The findings of our study highlight the important roles of terrestrial plants in regulating ambient PAHs.

ACKNOWLEDGEMENTS

This work was supported by the Beijing Natural Science Foundation (8232025 and 8222044) and the Beijing Academy of Science and Technology Innovation Project (23CA005-05).

REFERENCES

Cave, M. R., J. Wragg, R. Thomas, G. Wills & F. Evans] (2016) A review of the current state of the art of physiologically-based tests for measuring human dermal in vitro bioavailability of polycyclic aromatic hydrocarbons (PAH) in soil. *Journal of Hazardous Materials*.

Corada, K., H. Woodward, H. Alaraj, C. M. Collins & A. D. Nazelle (2020) A systematic review of the leaf traits considered to contribute to removal of airborne particulate matter pollution in urban areas - ScienceDirect. *Environmental Pollution*.

De Nicola, F., E. Concha Grana, P. Lopez Mahia, S. Muniategui Lorenzo, D. Prada Rodriguez, R. Retuerto, A. Carballeira, J. R. Aboal & J. Angel Fernandez (2017) Evergreen or deciduous trees for capturing PAHs from ambient air? A case study. *Environmental Pollution,* 221**,** 276-284.

Fellet, G., F. Poscic, S. Licen, L. Marchiol, R. Musetti, A. Tolloi, P. Barbieri & G. Zerbi (2016) PAHs accumulation on leaves of six evergreen urban shrubs: A field experiment. *Atmospheric Pollution Research***,** S130910421630023X.

Klingberg, J., B. Strandberg, H. Sjman, M. Taube, G. Wallin & H. Pleijel (2022) Polycyclic aromatic hydrocarbon (PAH) accumulation in Quercus palustris and Pinus nigra in the urban landscape of Gothenburg, Sweden. *The Science of the total environment,* 805**,** 150163.

Li, Y., X. Bai, Y. Ren, R. Gao, Y. Ji, Y. Wang & H. Li (2022) PAHs and nitro-PAHs in urban Beijing from 2017 to 2018: Characteristics, sources, transformation mechanism and risk assessment. *Journal of Hazardous Materials,* 436**,** 129143.

Nowak, D. J., A. Ellis & E. J. Greenfield (2022) The disparity in tree cover and ecosystem service values among redlining classes in the United States. *Landscape and Urban Planning,* 221**,** 104370-.

Sangwan, R. S., S. Tripathi, J. Singh, L. K. Narnoliya & N. S. Sangwan (2013) De novo sequencing and assembly of Centella asiatica leaf transcriptome for mapping of structural, functional and regulatory genes with special reference to secondary metabolism. *Gene,* 525**,** 58-76.

Shen, J. T., Shu (2019) Improving regulations on residential emissions and non-criteria hazardous contaminants-Insights from a field campaign on ambient PM and PAHs in North China Plain. *Environmental science & policy,* 92.

Tian, L., S. Yin, Y. Ma, H. Kang, X. Zhang, H. Tan, H. Meng & C. Liu (2019) Impact factor assessment of the uptake and accumulation of polycyclic aromatic hydrocarbons by plant leaves: Morphological characteristics have the greatest impact - ScienceDirect. *Science of The Total Environment,* 652**,** 1149-1155.

Wang, X., C. P. Meyer, F. Reisen, M. Keywood, P. K. Thai, D. W. Hawker, J. Powell & J. F. Mueller (2017) Emission Factors for Selected Semivolatile Organic Chemicals from Burning of Tropical Biomass Fuels and Estimation of Annual Australian Emissions. *Environmental Science and Technology,* 51**,** 9644-9652.

COBEE

6th International Conference on Building Energy and Environment
Eindhoven University of Technology, The Netherlands
6 - 10 July 2025

Building a Digital Hydro Twin for Capturing Stakeholders Perspectives for Flood Resilience

Özgün Balaban[1], Erica Arango Patino[2], Ranjith Soman[2], Pieter Pauwels[1]

[1] *Eindhoven University of Technology, Eindhoven, the Netherlands, o.balaban@tue.nl p.pauwels@tue.nl*
[2] *Delft University of Technology, Delft, the Netherlands, e.a.arango@tudelft.nl r.soman@tudelft.nl*

SUMMARY
Climate change and rapid urbanization have increased the risk of urban flooding, creating challenges for cities such as Rotterdam and Chennai. To address these flood threats and improve urban resilience, this study focusses on the construction of an urban digital twin under the Resilient Hydro Twin (RHT) project. RHT is designed to support decision-makers and urban planners in enhancing flood preparedness and response strategies. The platform features interactive visualizations and a web-based dashboard, enabling users to analyse flood scenarios, assess blue-green infrastructure strategies and soft adaptation measures, and contribute to data-driven policy decisions. Initial results indicate that the system may improve collaboration, enhances data accessibility, and facilitates participatory flood risk management. This work-in-progress research highlights the potential of digital twins in fostering interdisciplinary flood resilience strategies.

Keywords: digital twin, flood simulation, urban resilience, stakeholder participation

1. INTRODUCTION

Urban flooding is an increasingly critical challenge as climate change accelerates the frequency and intensity of extreme weather events (Pour et al., 2020). This challenge is particularly critical for vulnerable cities such as Rotterdam and Chennai, where flood control has been a vital concern for centuries due to their geographic and climatic conditions. Rotterdam, as a low-lying delta city, has historically relied on advanced flood management systems such as the Delta Works to mitigate risks (Klijn et al., 2015), while Chennai faces recurrent urban flooding exacerbated by rapid urbanization and monsoon variability, necessitating improved drainage and water governance (Singh et al., 2023). With rapid urbanization, cities face growing exposure to flood risks, highlighting the need for more advanced flood management strategies that integrate real-time data, predictive modelling, and stakeholder engagement.

Traditional flood risk assessment methods rely heavily on hydrological models and static flood maps, often lacking the dynamic capabilities required for proactive decision-making (Ward et al., 2015). Recent advancements in digital twin technology offer an opportunity to transform urban flood resilience by providing a data-driven, interactive, and continuously updating representation of flood risk scenarios (Batty, 2018; Dembski et al., 2019). Digital twins allow the integration

of multi-source data, such as hydrological models, GIS, BIM, and real-time IoT sensor networks, facilitating real-time monitoring and improved collaboration between stakeholders.

Despite the potential of digital twins in flood risk management, significant challenges remain in ensuring effective stakeholder participation, data integration, and system scalability (Ge and Qin, 2025). Many existing flood models are designed primarily for hydrologists and engineers, often requiring specialised knowledge that limits accessibility for policymakers, urban planners, emergency responders, and the general public (Gralepois, 2020). In addition, integrating heterogeneous data sets, including real-time hydrological monitoring, urban infrastructure data, and behavioural flood models, remains a complex technical challenge (Yan et al., 2025). Addressing these challenges requires a system that not only improves predictive accuracy but also enhances multi-stakeholder engagement by making flood risk data more transparent, interactive, and actionable.

In these contexts, the Resilient Hydro Twin (RHT) project aims to explore how the implementation of a digital twin in water disaster management can enhance the overall urban resilience of a city. This will be achieved through the development and integration of a digital twin, stakeholder cooperation, and resilience building strategies. This paper presents RHT, which is designed to bridge the gap between data-driven flood modelling and stakeholder-driven decision making. Built on a modular architecture, the system will induce hydrological simulations, GIS-based flood mapping, and infrastructure analysis. This approach enables different user groups to interact with flood risk data according to their specific needs. The platform aims to facilitate collaborative decision making by allowing stakeholders to visualise flood scenarios, run predictive simulations, and explore alternative mitigation strategies based on blue-green infrastructure, soft adaptation measures, and adaptive planning solutions.

This study focusses primarily on the role of stakeholder participation in the development and deployment of the RHT platform. In particular, it emphasises the identification of relevant stakeholders involved in urban flood resilience and the systemic listing of their user and software requirements. By engaging multiple stakeholders from the outset, the platform aims to provide a more inclusive and accessible decision support system that extends beyond technical experts to include policymaker and urban planners.

The early results of the implementation suggest that the system facilitates improved collaboration by reducing disciplinary silos, enhancing data accessibility, and providing interactive tools for flood risk assessment. The following sections detail the methodology used to define stakeholder requirements and develop the system architecture, discuss preliminary results on user engagement, and outline future directions. By addressing both the technical and participatory challenges of digital twin applications in flood resilience, this study aims to advance the role of data-driven decision making in urban flood risk management.

2. METHODOLOGY

This study adopts a multi-phased methodological approach to guide the development of the Resilient Hydro Twin (RHT) platform. The process begins with the identification of relevant stakeholders engaged in urban flood resilience, followed by the gathering of user and software require-

ments, the design of a modular system architecture, and iterative co-design activities for platform refinement. The methodology emphasizes stakeholder-centered design, technical feasibility, and system scalability to ensure the platform's adaptability in real-world contexts.

2.1. Stakeholder identification

The identification of stakeholders formed the foundational step in the development of the Resilient Hydro Twin (RHT) platform. Recognising that flood resilience involves a wide array of actors with varying roles and responsibilities, the research adopted a structured approach to stakeholder mapping. The stakeholders were initially identified through a series of collaborative workshops involving consortium partners and domain experts. These sessions aimed to determine the actors involved in flood resilience efforts. To complement this, brainstorming sessions were held to refine and categorise stakeholders based on thematic areas such as planning, hydrological modelling, infrastructure management, and governance. Then a dedicated stakeholder mapping document was developed in collaboration with the project partners. This document systematically linked stakeholder groups to specific components and activities of the RHT project, enabling a clear understanding of their relevance and expected interactions with the platform.

2.2. Determining the User and Software Requirements

Following stakeholder identification, the next phase involved the systematic gathering of user requirements and the finding out the corresponding software requirements. User needs were gathered through workshops conducted during the early stages of the project. To ensure that the platform met the real-world expectations of its users, user stories were collected during these workshops. These user stories captured narrative scenarios describing how different actors intended to interact with the system, what problems they aimed to solve, and what kinds of outcomes they expected. These needs were classified into functional domains relevant to the core aims of the RHT platform, including traffic modelling, semantic city modelling, hydrological simulations, blue-green infrastructure planning, and stakeholder engagement.

The translation of user needs into concrete software requirements was guided by participatory design principles. Functional requirements were defined to describe specific capabilities the platform must offer to support each stakeholder group. Concurrently, non-functional requirements were identified to address broader system qualities such as interoperability, scalability, usability, and security. The MoSCoW prioritization method (Must-have, Should-have, Could-have, Won't-have) was employed to evaluate the relative importance of each requirement, ensuring that platform development was aligned with stakeholder priorities and constraints (Clegg and Barker, 1994).

2.3. System architecture

A modular system architecture (Figure 1) was designed to ensure flexibility, scalability, and maintainability within the RHT platform. The system is built using Django, a Python-based framework widely used for developing scalable and maintainable web applications. Django follows the Model-View-Template (MVT) architecture, organising the platform's logic into distinct layers to improve data management, request handling, and user interaction.

At the core of Django's architecture, the model represents the data structure and business logic, defining the entities and relationships stored in the database. The view layer is responsible for pro-

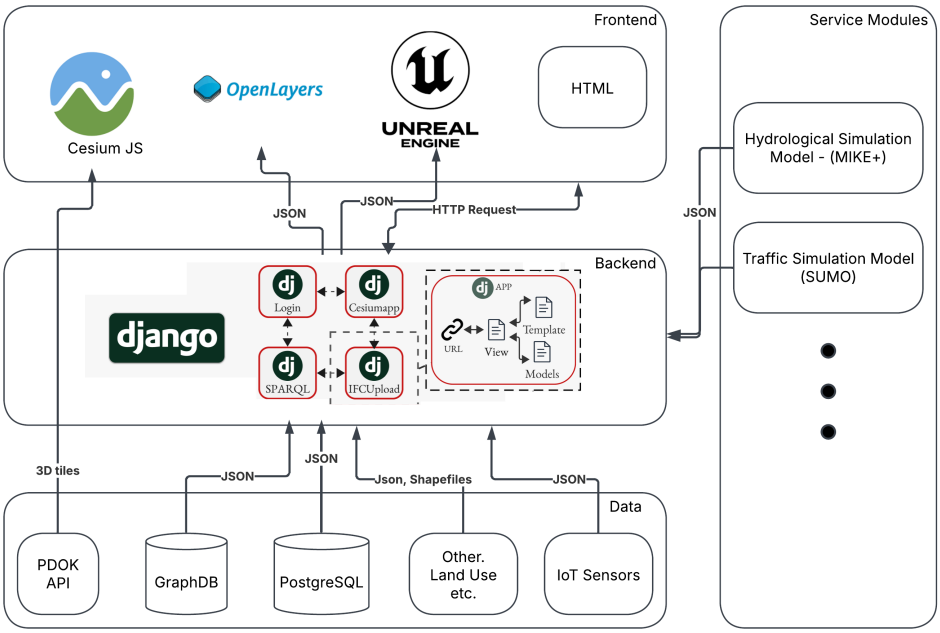

Figure 1. System Architecture.

cessing user requests, interacting with models, and generating appropriate responses. Views are defined as Python functions or classes, managing data retrieval, computation, and user authentication. The template layer is used for rendering dynamic HTML content, ensuring that users receive real-time updates and interactive visualisations. In Django-based applications, when a user makes a request, Django's URL resolver matches the request to the correct view function, which then queries the database, processes the logic, and renders the appropriate template. This structured flow ensures that the platform remains efficient and user-friendly, catering to multiple stakeholders with varying levels of technical expertise.

To ensure scalability, the platform follows a modular structure, where different applications are developed as independent units, each handling a specific functionality. Within the RHT, these modules correspond to key functional areas, such as traffic modelling, hydrological simulations, semantic city modelling, and blue-green infrastructure planning. Each module contains its own models, views, templates, and APIs, allowing for independent development, testing, and integration.

A PostgreSQL database stores foundational data, including login credentials, land use information, and GIS datasets. A graph database manages semantic relationships, enabling advanced data integration and querying. In addition, the system is designed to connect with various external APIs, such as PDOK which is an open data API of the Netherlands for geospatial data and IoT sensor networks, ensuring seamless data retrieval and dynamic flood prediction capabilities.

For front-end visualisation, Django integrates with CesiumJS to provide 3D geospatial mapping and with openlayers for 2D maps with GIS features, allowing urban planners, researchers, and

policymakers to interact with real-time flood scenarios. Additionally, RESTful APIs are implemented using Django REST Framework (DRF) to enable external system integration, allowing data exchange with hydrological modelling tools, GIS platforms, and urban planning dashboards.

3. RESULTS AND DISCUSSION

3.1. Stakeholder Groups and Platform Interaction

A key outcome of the early development phase of the RHT platform was the systematic identification and classification of stakeholders engaged in urban flood resilience. Stakeholders were grouped into five major categories: infrastructure engineers, water management agencies, urban planners, policymakers, and the general public. Each group demonstrated distinct functional needs and varying levels of technical expertise, necessitating tailored interfaces and access levels within the platform. Table 1 summarizes the functional focus and expected platform interactions for each group.

Table 1. Overview of RHT Stakeholders and their Platform Needs

Stakeholder Group	Functional Focus	Platform Needs and Interactions
Infrastructure Engineers	Traffic modelling during flood events	Simulate traffic disruptions, test evacuation scenarios, modify network parameters
Water Management Agencies	Hydrological modeling and drainage performance	Integrate and calibrate hydrological models, process real-time sensor data, run flood simulations
Urban Planner	Blue-green infrastructure and spatial planning	Evaluate nature-based adaptation strategies, conduct spatial analysis, integrate planning scenarios
Policymakers	Governance, regulation, and stakeholder coordination	Access regulatory scenarios, visualize historical and projected flood data, facilitate public engagement
General Public	Risk awareness and emergency readiness	View simple dashboards, receive flood alerts, understand neighborhood-specific flood risk

Functional requirements are collected after the review of user stories and they are structured around the core domains of the platform, including traffic modelling, semantic city modelling, hydrological simulations, blue-green infrastructure planning, and stakeholder engagement. These requirements are summarized in Table 2. In parallel, a comprehensive set of non-functional requirements was established to address system-level performance, data integration standards, and user experience criteria. These include aspects such as interoperability, scalability, usability, and security—essential for ensuring the platform's long-term adaptability and accessibility for users with varying technical backgrounds. These are presented in Table 3.

The resulting stakeholder-system relationships were also visualized through a platform use case diagram (Figure 2), which illustrates the key interactions between each stakeholder group and the functional modules they access. By aligning technical development with clearly articulated stakeholder narratives and requirements, the RHT platform advances a participatory and user-informed approach to digital twin system design. This ensures that the resulting tool remains relevant, functional, and inclusive for a broad spectrum of end users engaged in urban flood resilience planning and response.

3.2. Initial Results

The initial implementation of the platform has focused on stakeholder engagement workflows and collaborative data sharing. A preliminary version of the system has been deployed for internal

Table 2. Functional Requirements

Functional Area	Requirement Description	MoSCoW Priority
Traffic Modelling	The system shall integrate real-time traffic models to calculate the impact of flood events to road network.	Must have
	The system shall allow engineers to modify parameters and simulate different traffic scenarios.	Should-have
Semantic City Modelling	The platform shall integrate GIS and BIM data to create a structured urban flood risk model.	Must-have
	Users shall be able to query semantic city models.	Should-have
	Users shall be able to visualize flood defences in 3D.	Could-have
Hydrological Model Integration	The system shall integrate existing hydrological and hydraulic simulation models.	Must -have
	The system shall support real-time hydrological data input and processing from IoT sensors.	Could-have
	The platform shall allow users to run flood simulations and visualize projected inundation.	Could-have
Blue-Green Infrastructure Planning	The system shall allow urban planners to analyse flood mitigation strategies using blue-green infrastructure models.	Should-have
	Users shall be able to compare different nature-based flood adaptation strategies.	Should-have
Governance & Stakeholder Collaboration	The platform shall support multi-user collaboration, allowing different stakeholders to contribute to the Resilient Hydro Twin application.	Must-have
	The system shall include a stakeholder feedback module for collecting public insights on flood resilience measures.	Could-have

Table 3. Non-functional Requirements

Category	Requirement Description	MoSCoW Priority
Interoperability	The platform shall support open standards (e.g., IFC, CityGML) to ensure compatibility with external GIS and BIM systems.	Must-have
	The system shall allow exporting flood simulation results in commonly used formats such as GeoJSON.	Must-have
Scalability	The system shall be scalable to accommodate change in the scale of flood-prone areas without major architectural changes.	Should-have
	The system shall support integration with additional data sources, including external hydrological models and real-time APIs.	Must-have
Usability	The platform shall provide an intuitive, user-friendly interface for stakeholders with varying levels of technical expertise.	Must-have
Security	The system shall enforce role-based access control to prevent unauthorized access to sensitive data.	Must-have

testing. The early results indicate that the system has the potential to improve interdisciplinary collaboration by allowing stakeholders to work with a shared data environment. In addition to improving cross collaboration, the platform has enhanced stakeholder interaction and accessibility. The use of web-based interactive dashboards will make it easier for non-technical users, such as policymakers and community representatives, to engage with flood risk data. Public stakeholders can check flood risks and increase their awareness and readiness for an emergency.

Although the system provides a robust framework for stakeholder collaboration, several challenges remain in data integration and user adoption. Integrating heterogeneous datasets, including hydrological models, GIS layers, and sensor data, has proven complex. Furthermore, the need for increased automation in data preprocessing and scenario-based decision support was highlighted. The early findings suggest that the Resilient Hydro Twin has the potential to improve cross-sector collaboration and decision-making in urban flood resilience. However, several areas require further refinement. Expanding stakeholder participation will be a priority in future iterations of the platform, involving broader engagement workshops to gather more diverse feedback from local governments, environmental agencies and the private sector. Efforts are also underway enhance-

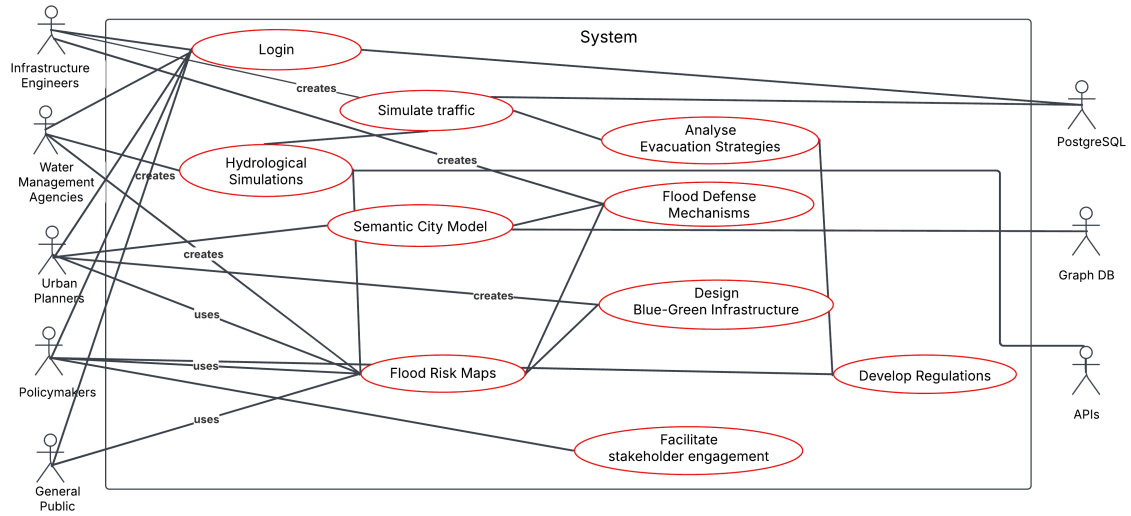

Figure 2. Use case diagram.

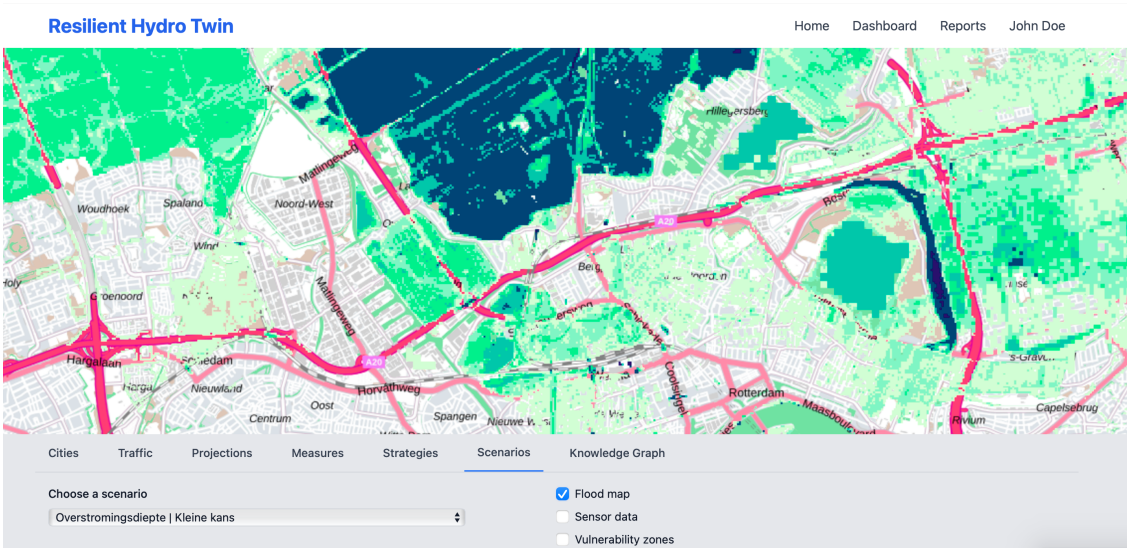

Figure 3. Screenshot of the Resilient Hydro Twin (RHT) platform interface.

ments in decision-support features will allow policymakers to evaluate different flood mitigation strategies and assess the long-term implications of policy decisions.

Overall, RHT can serve as a valuable tool for collaborative flood risk assessment and has the potential to transform stakeholder engagement in urban flood resilience planning. Future work will focus on refining system usability and improving data integration pipelines.

4. CONCLUSIONS

This paper presented the ongoing development of a Resilient Hydro Twin platform designed to enhance urban flood resilience through improved stakeholder engagement and data integration.

The system architecture was developed with a modular approach, allowing various stakeholders to interact with flood risk data through a shared and accessible platform. The integration of GIS, BIM, hydrological models, and sensor networks has demonstrated potential in fostering interdisciplinary collaboration and supporting data-driven decision-making in flood risk management.

The preliminary results suggest that the platform facilitates more effective collaboration by providing a centralized system where different user groups can access, analyze, and contribute to flood-related data. However, challenges remain, particularly in ensuring seamless integration of heterogeneous datasets, hydrological and hydraulic simulation capabilities, and making the system more user-friendly for a diverse set of users.

As this is an ongoing study, future work will focus on completing the functional and non-functional requirements as discussed previously. In addition, more engagement with stakeholders will be conducted through participatory workshops and pilot studies to assess the usability and effectiveness of the platform in real-world scenarios. The expansion of decision-support functionalities will be a priority, ensuring that policymakers can effectively evaluate the impact of different flood mitigation strategies. By addressing these challenges, the RHT aims to become a comprehensive decision-support tool that enhances flood resilience through interdisciplinary collaboration, and stakeholder-driven decision-making.

ACKNOWLEDGMENTS

This work was also supported by the Dutch Research Council (NWO) and the Department of Science & Technology, India (DST), through the Merian Fund under Grant No. 482.482.302.

REFERENCES

Batty M., 2018. Digital twins. Environment and Planning B: Urban Analytics and City Science 45, 817–820.

Clegg D. and Barker R., 1994. Case Method Fast-Track: A Rad Approach. Addison-Wesley Longman Publishing Co., Inc., USA.

Dembski F., Wössner U., and Letzgus M., Sept. 2019. The Digital Twin Tackling Urban Challenges with Models, Spatial Analysis and Numerical Simulations in Immersive Virtual Environments.

Ge C. and Qin S., 2025. Urban flooding digital twin system framework. Systems Science & Control Engineering 13, 2460432.

Gralepois M., 2020. What Can We Learn from Planning Instruments in Flood Prevention? Comparative Illustration to Highlight the Challenges of Governance in Europe. Water 12.

Klijn F., Kreibich H., Moel H. de, and Penning-Rowsell E., Aug. 2015. Adaptive flood risk management planning based on a comprehensive flood risk conceptualisation. Mitigation and Adaptation Strategies for Global Change 20, 845–864.

Pour S. H., Wahab A. K. A., Shahid S., Asaduzzaman M., and Dewan A., 2020. Low impact development techniques to mitigate the impacts of climate-change-induced urban floods: Current trends, issues and challenges. Sustainable Cities and Society 62, 102373.

Singh H., Nielsen M., and Greatrex H., 2023. Causes, impacts, and mitigation strategies of urban pluvial floods in India: A systematic review. International Journal of Disaster Risk Reduction 93, 103751.

Ward P. J., Jongman B., Salamon P., Simpson A., Bates P., De Groeve T., Muis S., Perez E. C. de, Rudari R., Trigg M. A., and Winsemius H. C., Aug. 2015. Usefulness and limitations of global flood risk models. Nature Climate Change 5, 712–715.

Yan J., Lu Q., Li N., and Pitt M., 2025. Developing Data Requirements for City-Level Digital Twins: Stakeholder Perspective. Journal of Management in Engineering 41, 04024068.

6th International Conference on Building Energy and Environment
Eindhoven University of Technology, The Netherlands
6 - 10 July 2025

Improved data preprocessing for secondary network heating load prediction

Bingyang Zhang [1], Tianle Chen [1], Xuesong Hu [1], Yuanyuan Liu [1], Naiping Gao [1,*]

[1] *Tongji University, Shanghai, China, gaonaiping@tongji.edu.cn*

SUMMARY
Accurate heating load prediction is crucial for the meticulous management of heating station. Data-driven heating load prediction techniques have garnered significant attention due to its promising application prospects. High-quality historical input data is the key prerequisites for improving model prediction accuracy. Taking a floor radiant heating system as the case, this paper applies Singular Spectrum Analysis to decompose the original heating load, removing noise components with the cumulative feature contribution rate of less than 9.2%. Then the improved quartile method is employed to identify outliers in the denoised reconstructed time series. Finally, the back propagation neural network (BPNN) is adopted to establish an hourly heating load prediction model. The results show that compared with the original data processed using the traditional quartile method, the load prediction accuracy can be significantly improved by Singular Spectrum Analysis and the improved quartile method, with the root mean square error (RMSE) reduced by 51.0%.

Keywords: Secondary heating load prediction, Singular spectrum analysis, Improved quartile method.

1. INTRODUCTION

District heating system is an important part of the urban energy infrastructure. According to statistics (Center TUBE, 2021), the total urban heating area in China reaches 15.2 billion m^2, and the heating energy consumption is 213 million tons of standard coal, accounting for 30% of the total building energy consumption. With the application of building management systems, the large amount of data obtained from the management platform helps to build data-driven models for load prediction (Fan et al., 2020). The accurate load prediction technique can realize personalized and meticulous regulation of the district heating system, and reduce the system energy consumption by improving the energy efficiency. High-quality historical input data can ensure the load prediction accuracy of the data-driven model. To improve the quality of the input data, the data decomposition and outlier identification of the original data have been investigated by many researchers. The Empirical Mode Decomposition (EMD), proposed in 1998, can decompose the signal with the intrinsic mode function (Huang et al., 1998). Deng and Jin used EMD to decompose the electric load into the stochastic, periodic, and trend components, removing the redundant components by analyzing the characteristics of each sub-signal (Deng & Jin, 2018). Then the Variational Mode Decomposition (VMD) was proposed to in 2014, and it was found that using this algorithm to decompose the data can effectively improve the prediction accuracy. (Dragomiretskiy, 2014; Sun et al., 2019). However, these decomposition methods typically require manually setting the number of components or modes, and an excessive or insufficient number will affect the decomposition accuracy. Recently, Singular Spectrum Analysis（SSA）has been widely applied to time series as it does not require the assumption of parametric models and stationarity conditions. While most current research focuses on power load decomposition, there

are relatively few studies on the secondary heating load (Stratigakos et al., 2021). In terms of outlier identification, various methods have currently been proposed such as the quartile method, 3σ criterion, and t-test criterion, etc. (Frigge et al., 1989; Xue et al., 2017). However, these traditional methods usually focus on the mathematical level and lack integration with domain-specific knowledge for more effective identification. Based on the research gaps, this paper applies Singular Spectrum Analysis to decompose the original heating load time series, and then proposes a novel improved quartile method incorporating the professional background knowledge for more precise outlier identification. Finally, taking the secondary heating system of Tianjin, China as an example, an hourly heating load prediction model is built based on the back propagation neural network (BPNN) algorithm to validate the effectiveness of the adopted load decomposition and outlier identification methods.

2. METHOD

2.1 Singular Spectrum Analysis

Singular Spectrum Analysis (SSA) is a decomposition method with simple operation and excellent decomposition effect. It can extract trend items, period items and residual items from time series. Since it does not require the assumption of parametric models and stationarity conditions, it has been well applied to time series. SSA embeds, decomposes, groups, and diagonally averages the studied time series.

2.1.1. Embedding

The original time series $X = (x_1, x_2, \dots, x_N)$ is transformed into a K-dimensional vector matrix, where each vector has a length of L. N is the length of the one-dimensional time series, and the transformed matrix is shown in Eq. (1).

$$X = [x_1, x_2, \dots, x_K] = (x_{ij})_{i,j=1}^{L,K} = \begin{bmatrix} x_1 & \cdots & x_K \\ \vdots & \ddots & \vdots \\ x_L & \cdots & x_N \end{bmatrix} \quad (1)$$

Here, L represents the window length, with a range of $2 \leq L \leq N/2$, $L \leq K$, $L = N - K + 1$

2.1.2. Decomposition

The transformed matrix is processed using Singular Value Decomposition (SVD). Due to the difficulty of direct matrix manipulation, covariance matrix S is constructed according to Eq. (2) and Eq. (3).

$$S = XX^T \quad (2)$$

$$X = X_1 + X_1 + \cdots + X_L \quad (3)$$

Here, $X_i = \sqrt{\lambda_i} U_i V_i^T$, $\lambda_i, \lambda_i, \dots, \lambda_L$ is the eigenvalue of S, the corresponding orthogonal vector is $u_1, u_2, \dots, u_L$, and $\lambda_1 \geq \lambda_2 \geq \cdots \geq \lambda_L \geq 0$.

2.1.3. Grouping

Divide all L components into m mutually exclusive groups $I_1, I_2, \dots I_m$, let $I = \{i_1, i_2, \dots, i_p\}$, corresponding to the composite matrix $X_I = X_{i1} + X_{i2} + \cdots + X_{ip}$, then the matrix X is expressed as Eq. (4)

$$X = X_{I1} + X_{I1} + \cdots + X_{Im} \tag{4}$$

2.1.4. Diagonal averaging

Transforming X_{ij} in Eq. (4) into a sequence of length N. Define Y as a matrix with L rows and K columns, where the elements are represented by y_{ij} for $1 \le i \le K$ and $1 \le j \le K$. The diagonal averaging can be expressed through Eq. (5).

$$y = \begin{cases} \frac{1}{k}\sum_{m=1}^{k} y_{m,k-m+1}, & 1 \le k \le L^* \\ \frac{1}{L^*}\sum_{m=1}^{L^*} y_{m,k-m+1}, & L^* \le k \le K^* \\ \frac{1}{N-k+1}\sum_{m=k-K^*+1}^{N-K^*+1} y_{m,k-m+1}, & K^* \le k \le N \end{cases} \tag{5}$$

For singular spectrum analysis, the trend term, period term, and residual term are determined based on the finally calculated eigenvalues of each signal component. Generally speaking, trend items and period items include more than 80% of the main information of the original load series.

2.2 The Quartile Method

Identifying and eliminating outlier data is an important means to improve the quality of sample data. The traditional quartile method usually identifies the outlier data from the whole dataset and performs well in small to medium-sized sample datasets with a lower percentage of outliers. The relevant calculation formulas are shown in Eq. (6), Eq. (7) and Eq. (8).

$$IQR = Q_3 - Q_1 \tag{6}$$
$$P_L = Q_1 - 1.5IQR \tag{7}$$
$$P_U = Q_3 + 1.5IQR \tag{8}$$

Where Q_1 and Q_3 represent the lower and the upper quartile, respectively; *IQR* represents the interquartile range; P_L and P_U represent the lower and the upper boundary, respectively.

The heating system monitoring data spans an entire season and exhibits high volatility and seasonal variability. It typically contains tens of thousands of records, which can be considered a medium to large-sized dataset. In such cases, the traditional quartile method may fail to accurately identify outliers. Given that there is a strong negative correlation between the heating load and the outdoor temperature, this paper proposes an improved quartile method for fine-cleaning of the heating data. The heating load data is divided into several intervals based on the outdoor temperature with 1°C increments, and each interval is calculated individually in quartile method.

2.3 Machine Learning Algorithm and Evaluation Indices

The BPNN algorithm is often used in heating demand prediction and have good performance. The learning process of the BPNN model can be mainly divided into two stages: information forward propagation and error back propagation, which can realize highly nonlinear mapping. The basic learning principle of BPNN model is the gradient descent method, and its core idea is to minimize the total error by adjusting the weights and thresholds of the network connection. In this paper the mean absolute error (MAE), the root mean square error (RMSE), and the determination coefficient (R^2) are used to evaluate the performance of the prediction model. MAE, RMSE, and R^2 are calculated according to Eq. (9), Eq. (10), and Eq. (11).

$$MAE = \frac{1}{n}\sum_{i=1}^{n}|y_i - \hat{y}_i| \quad (9)$$

$$RMSE = \sqrt{\frac{1}{n}\sum_{i=1}^{n}(y_i - \hat{y}_i)} \quad (10)$$

$$R^2 = \frac{\sum_{i=1}^{n}(\hat{y}_i - y_i)^2}{\sum_{i=1}^{n}(\bar{y}_i - y_i)^2} \quad (11)$$

Where n represents the sample size, $\hat{y}_i$ represents the true value, y_i represents the predicted value, $\bar{y}_i$ represents the average value of the true value.

3. DATA PREPROCESSING RESULTS

3.1 Case Information and Data

In this study, a secondary heating system in Tianjin, China is selected as the case. The system is for residential customers, with a heating area of about 80,000 square meters. The heating system operates in a quality-regulated mode, maintaining a nearly constant flow rate. The heating terminal adopts floor radiant. The design outdoor temperature in winter is -7℃, and the design secondary supply/return temperature is 50/40℃. By the smart heating platform and meteorological stations, this paper collected secondary heating system operation data and outdoor meteorological parameter data from November 10, 2022 to March 9, 2023. The collected data include secondary heating load, secondary supply/return temperature, indoor temperature, outdoor air temperature, air velocity, and solar radiation intensity.

3.2 Decomposition of Heating Load

Affected by the monitoring devices and the variation of the outdoor parameters, the heating load is characterized by high volatility and strong instability. This paper adopts the singular spectrum analysis to decompose the heating load, and a total of 27 days from February 2, 2023 to February 28, 2023 (with a large variation in heating load) were selected for analysis. The embedding window length is 12, resulting in 12 sub-signals. Fig. 1 illustrates the sub-signals of the heating load after SSA decomposition. Table 1 presents the specific feature values for each sub-signal.

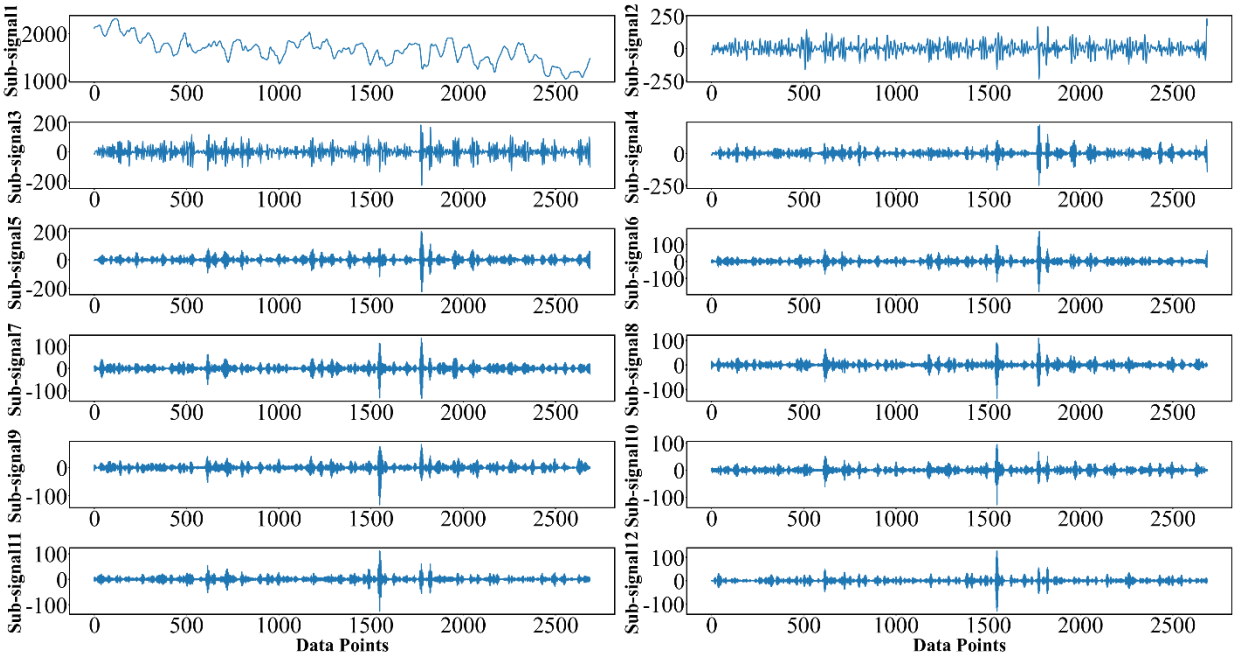

Figure 1. Sub-signals of heating load decomposed by SSA.

Table 1. Feature values and variance contribution rates of sub-signals

Number	Feature Value	Variance Contribution Rate	Cumulative Variance Contribution Rate
1	298085.73	82.72	82.72
2	11552.82	3.21	85.93
3	9880.12	2.74	88.67
4	7880.46	2.19	90.86
5	6498.52	1.80	92.66
6	5197.62	1.44	94.11
7	4506.02	1.25	95.36
8	3970.93	1.10	96.46
9	3494.38	0.97	97.43
10	3266.29	0.91	98.33
11	3031.61	0.84	99.18
12	2968.91	0.82	100.00

According to the Table 1 and Fig. 1, the sub-signal 1 is considered a trend component, which has the highest variance contribution rate of 82.72%, providing a reasonably accurate reflection of the original load trend. The sub-signals 2 to 4 are considered periodic components, with the range of 3. 21% to 2.19%. From the 5th sub-signal, the contribution rate of features begins to level off, indicating a slow change in feature values. Consequently, sub-signals 5 to 12 are considered residual components.

This paper selects the top 4 sub-signals as the reconstruction time series with the cumulative feature contribution greater than 90%, while eliminates the noisy data with the cumulative feature contributions less than 9.2%. The comparison of the heating load time series before and after processing is shown in Fig. 2. It can be found that the reconstructed time series presents clear non-linearity and smoothness, which can better reflect the trend and periodicity of data.

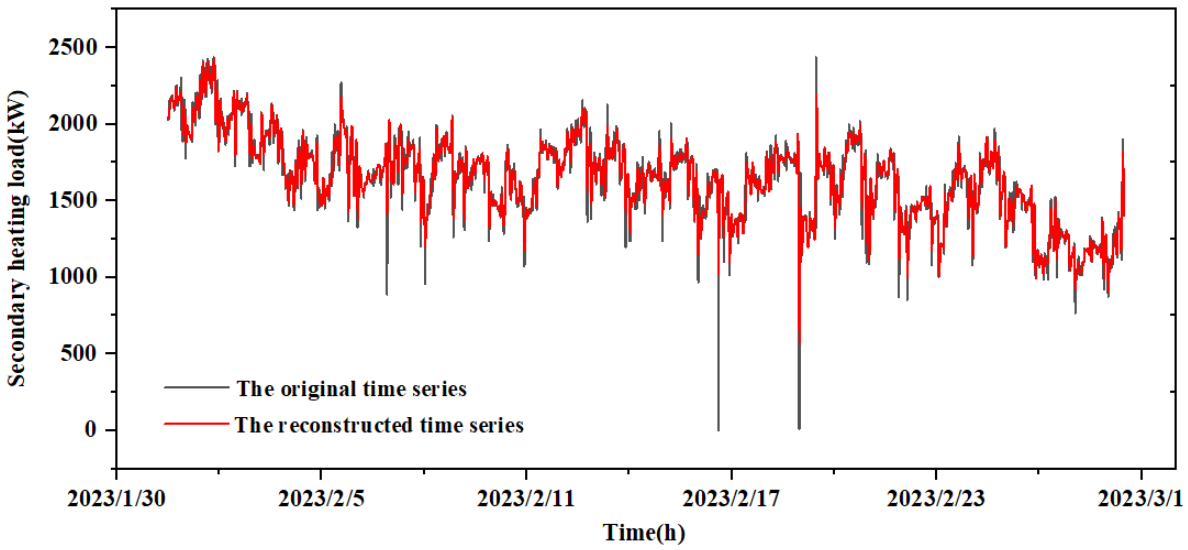

Figure 2. Comparison of the heating load time series before and after processing.

3.3 Identification of Outlier Data

This section focuses on identifying outliers in the hourly heating load data using the two quartile

methods mentioned in Section 2.2. A total of 2735 records from the whole heating season were selected for analysis. Fig. 3 and Fig. 4 show the identification results under the traditional quartile and improved quartile method, respectively.

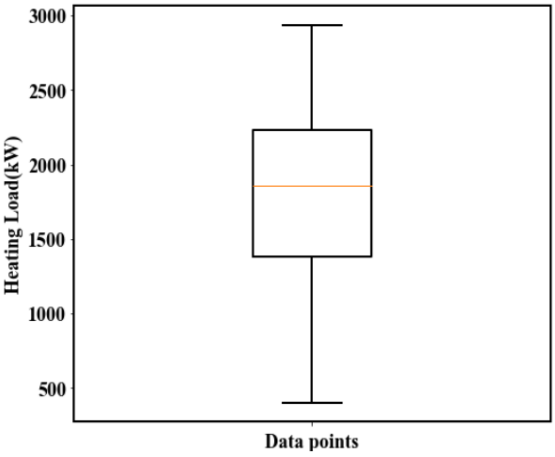

Figure 3. Identification result of traditional quartile.

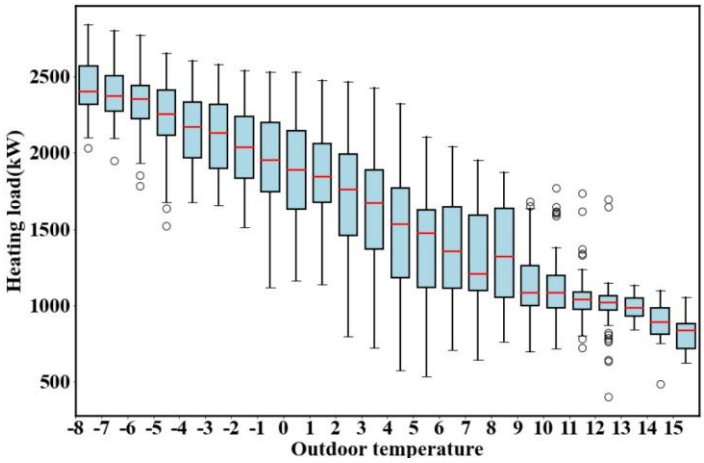

Figure 4. Identification result of improved quartile.

As shown in Fig. 3, there are no outliers identified by the traditional quartile method. A possible explanation is that the selected dataset is a medium to large-sized dataset with the high volatility and seasonal variability, where the traditional quartile method fails to identify the outliers.

For the improved quartile method, the heating load is divided into 23 intervals based on the outdoor temperature with 1°C increments, and each interval belongs to small and medium-sized sample datasets. Fig. 4 shows that the median of the boxplot overall presents a decreasing trend as the outdoor temperature increases, which indicates there is a negative correlation between the outdoor temperature and the heating load. The outliers exceeding the upper and lower boundaries of the boxplot are indicated by black circles in Fig. 4. It can be evidently observed that there are a few outliers in the heating load below the lower boundary when the outdoor temperature is lower than -3°C, and a larger number of outliers exceeding the upper and lower boundaries when the outdoor temperature is higher than 9°C. Further analysis reveals that most of these outliers are distributed at the end of the heating season, a period when the outdoor temperature fluctuations greatly, leading to an increased instability of the heating system, making it susceptible to outliers. In conclusion, the outliers can be effectively identified by using improved quartile method.

4. MODEL VALIDATION AND RESULTS

4.1 Selection of Input Feature Variables

For a defined building, the secondary heating load is influenced by both heating parameters and indoor and outdoor air parameters, specifically the secondary supply temperature (T_g), secondary return temperature (T_h), indoor temperature (T_{in}), outdoor air temperature (T_{air}), solar radiation (S), and wind speed (V_w). Due to the thermal inertia of the building and the thermal delay of the radiant floor heating system, heat dissipation from the heating system to the room is influenced not only by the current heating load but also by the historical load. Moreover, this paper selects the historical supply/return temperatures to reflect the heating system thermal delay, and the historical indoor and outdoor parameters to consider the influence of building thermal inertia. Further considering

that the delay time of ground heat transfer is generally longer than that of building envelope heat transfer, the heating load prediction also needs to consider the outdoor parameters of multiple future moments, which can be obtained from meteorological forecasts. In this paper, L^t is the predicted heating load at the moment t. L^{t-i} and L^{t+i} represent the moment of i hour ahead and after moment t, respectively, and the other variables are expressed in the same way. Finally, this paper uses the Spearman rank correlation coefficient to calculate the correlation between the heating load and various variables, the 47 variables with strong correlation are input feature variables, as shown in Table 2.

Table 2. The input feature variables

Feature categories	Feature variable symbols	Range of i values
Secondary heating load	L^{t-i}	$i = 1 \ldots 6$
Secondary supply temperature	T_g^{t-i}	$i = 1 \ldots 6$
Secondary return temperature	T_h^{t-i}	$i = 1 \ldots 6$
Indoor temperature	T_{in}^{t-i}	$i = 0 \ldots 1$
Outdoor air temperature	$T_{air}^{t\pm i}$	$i = 0 \ldots 4$
Solar radiation intensity	$S^{t\pm i}$	$i = 0 \ldots 4$
Wind speed	$V_w^{t\pm i}$	$i = 0 \ldots 4$

4.2 Comparison of Load Prediction Results

This section uses the BPNN algorithm to compare the load prediction results under the two different inputs. Input_1 is the original data processed by the traditional quartile method, and input_2 is the original data processed by the singular spectrum analysis and improved quartile method. The data from February 22 to February 28, 2023 is selected as the test set, while the rest as the training set. Fig. 5 shows the prediction results of the 2 groups inputs under the BPNN model, respectively. And the performance of the models is summarized in Table 3.

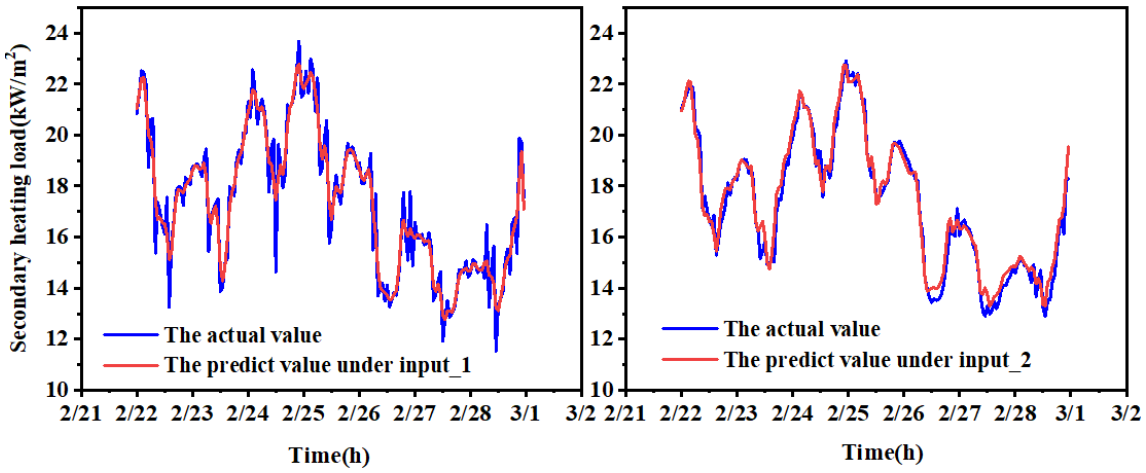

Figure 5. Prediction results of BPNN models.

Table 3. The performance of the models

Input data	MAE (℃)	RMSE (℃)	R^2
Input_1	0.930	1.301	0.792
Input_2	0.456	0.588	0.960

Fig. 5 and Table 3 show that the model based on the input_2 achieves higher prediction accuracy with an RMSE of 0.456℃. Compared to the model based on input_1, the MAE value decreased by 54.8% and the R^2 value increased by 21.2%. This indicates that the noise and outliers of the original data will affect the model prediction performance, and the prediction accuracy can be significantly improved through singular spectrum analysis and improved quartile method.

5. Conclusions

The energy saving of urban heating systems is crucial to achieving the dual-carbon goals, and secondary network heating load prediction plays a key role in the operation and regulation of heating systems. This study focuses on the hourly heating load prediction based on the improved data preprocessing method, mainly includes Singular Spectrum Analysis and an improved quartile method. The specific conclusions are as follows:

The Singular Spectrum Analysis algorithm is applied to decompose the secondary network heating system monitoring load data, removing noisy data with the cumulative feature contributions less than 9.2%. The comparison results show that the reconstructed time series presents clear non-linearity and smoothness, which can better reflect the trend and periodicity of the load data. In terms of outlier identification, compared with the traditional quartile method, the improved quartile method can effectively identify outliers and improve the quality of the data. Further comparison shows that the accuracy of heating load prediction can be significantly improved through Singular Spectrum Analysis and the improved quartile method, with the RMSE reduced by 51.0% for the BPNN model. In conclusion, data preprocessing is essential for building high-precision data-driven models. The results of this paper can guide the fine operation of heating system, promoting the development of green buildings and energy-saving technologies.

ACKNOWLEDGEMENTS

This work was supported by the National Key Research and Development Program of China (NO.2023YFC3805304-2) and International Cooperation project of Science and Technology Commission of Shanghai Municipality (NO.22200711400).

REFERENCES

Center TUBE. Annual report on China building energy efficiency. Tsinghua University Building Energy Research Center, China: Construction Industry Publishing House, 2021.

Deng A., Jin M., 2018. Time-scale feature extraction based on EMD and its application on short-term power load forecasting. Application Research of Computers 35 (10), 2952-2955.

Dragomiretskiy K., Zosso D., 2014. Variational mode decomposition. IEEE Transactions on Signal Processing 62 (3), 531-544.

Fan C., Sun Y.J., Xiao F., Ma J., Lee D.S., Wang J.Y., Tseng Y.C., 2020. Statistical investigations of transfer learning-based methodology for short-term building energy predictions. Applied Energy 262, 114499.

Frigge M., Hoaglin D.C., Iglewicz B., 1989. Some Implementations of the Boxplot. The American Statistician 43 (1), 50-54.

Huang N.E., Shen Z., Long S.R., Wu M.L.C., Shih H.H., Zheng Q.N., Yen N.C., Tung C.C., Liu H.H., 1998.The empirical mode decomposition and the Hilbert spectrum for nonlinear and non-stationary time series analysis. Proceedings of the Royal Society of London. Series A: Mathematical, Physical and Engineering Sciences 454 (1971), 903-995.

Sun J., Xing H.Y., Wu J.J., 2019. Sea clutter hybrid denoising algorithm based on VMD. In: Proceedings of 2019 14th IEEE International Conference on Electronic Measurement & Instruments (ICEMI), China, pp. 551-558.

Stratigakos A., Bachoumis A., Vita V., Zafiropoulos E., 2021. Short-Term Net Load Forecasting with Singular Spectrum Analysis and LSTM Neural Networks. Energies 14, 4107.

Xue P.N., Zhou Z.G., Fang X.M., Chen X., Liu L., Liu Y.W.,Liu J., 2017. Fault detection and operation optimization in district heating substations based on data mining techniques. Applied Energy 205, 926-940.

6th International Conference on Building Energy and Environment
Eindhoven University of Technology, The Netherlands
6 - 10 July 2025

Development of a preliminary life cycle cost assessment tool for Building Automation and Control Systems in office buildings: The B•CLIC project

Jasmine Meysman[1], Lukas Vandenbogaerde[1], Sophie van Roosmale[1], Stijn Verbeke[1,2,3], Amaryllis Audenaert[1]

[1] *University of Antwerp Faculty of Applied Engineering, Antwerp, Belgium, jasmine.meysman@uantwerpen.be*
[2] *Vlaamse Instelling voor Technologisch Onderzoek (VITO), Belgium*
[3] *EnergyVille, Genk, Belgium*

SUMMARY
To meet global climate goals by 2050, policies such as the European Energy Performance of Buildings Directive focus on enhancing building energy performance. Traditionally, this involved improving building envelopes and technical systems. Recently, smart building technologies, such as Building Automation and Control Systems (BACS), have gained attention for optimizing energy performance and occupant comfort. However, BACS adoption faces challenges, including high initial investment, uncertain returns, and concerns about component reliability and vendor lock-in. The B•CLIC project aimed to bring data-driven scientific insights on the benefits of BACS in office buildings, enabling stakeholders to make well informed investment decisions beforehand. This is done through the development of a novel proof-of-concept tool that allows stakeholders to compare the life cycle cost of different BACS scenarios in early design stages. Although the current version of the tool has some important limitations, the results look promising and the feedback from stakeholders shows its usefulness.

Keywords: Building Automation, Life Cycle Cost Assessment, Energy simulations, office buildings

1. INTRODUCTION

To meet global climate goals by 2050, national and international policies, such as the European Energy Performance of Buildings Directive, are increasingly focusing on enhancing the energy performance of buildings by reducing energy usage and subsequent emissions (The European Parliament and the Council of the European Union, 2024). Traditionally, this has involved improving the envelope and increasing the efficiency of technical building systems. More recently, there has been growing awareness of the potential of smart building technologies, such as Building Automation and Control Systems (BACS), to optimize energy performance and occupant comfort. This shift is supported by the revised European Directive on Performance of Buildings (The European Parliament and the Council of the European Union, 2024).

Despite their potential, the adoption of BACS is hindered by perceived drawbacks. The initial investment can be substantial, and the return on investment is often uncertain. Additionally, there is a lack of information on the service life of components, reliability, and the risk of vendor lock-in, which increases the investment risk (Sophie van Roosmale et al., 2024). The B•CLIC project aimed to bring data-driven scientific insights on the benefits of BACS in office buildings, enabling stakeholders to make well informed investment decisions in early design stages. This was achieved through the development of a novel life cycle cost assessment tool that includes innovative energy

simulation data and a probabilistic approach to maintenance costs. This article describes the methodology behind this novel tool and shares preliminary results.

2. STATE OF THE ART

2.1 Building Automation and Control systems

BACS are defined as systems that comprise products, software and engineering services for automatic controls, monitoring, optimization, operation, human intervention and management integrated in buildings with the aim of ensuring energy efficient, safe and cost-effective building operations and services (European Commission et al., 2021; Van Thillo et al., 2022; L. Vandenbogaerde et al., 2023). According to the EN ISO 52120-1:2022 standard, BACS can be classified in seven main control functions: Heating control, cooling control, ventilation and air conditioning control, lighting control, blind control, domestic hot water (DHW) control and technical home and building management (Bureau for standardisation, 2022). In this study, only five of these functions will be considered: heating, cooling, ventilation, lighting and blind control.

2.2 Life cycle cost assessment

Investments in BACS can be very substantial due to the inherent complexity of these systems (S. van Roosmale et al., 2024). Therefore, it is crucial for investors and other stakeholders to have a comprehensive understanding of initial investments, expected costs, and anticipated returns. A widely used methodology for assessing these aspects is Life Cycle Cost Analysis (LCCA), which evaluates all costs associated with constructing, owning, operating, maintaining, and disposing of a building or asset (Fuller & Petersen, 1996).). The specific LCCA methodology for the assessment of buildings and construction is established in several standards such as the ISO 15686-5:2021 standard (International Standards Organisation, 2021), NIST (Fuller, 2016) or the ASTM standard (ASTM, 2011). These standards are often generic to accommodate a wide range of building and construction project types.

The LCCA methodology framework includes costs related to initial investment (IC), operations (OP), maintenance (MC), and end-of-life (EoL) (Fuller & Petersen, 1996; Islam et al., 2015). Initial investment costs encompass all expenses related to design, planning, permits, construction, acquisition, and installation of BACS. Operational costs include day-to-day expenses such as energy and other consumables. Maintenance costs, which can be periodic (e.g., daily, weekly, monthly, yearly) or ad-hoc, cover all expenses necessary to keep the system operational, including both scheduled and unscheduled maintenance actions. EoL costs pertain to disassembly, demolition, and disposal, including labour, transport, and waste disposal. Depending on the system boundaries, EoL costs may also include recycling, reconditioning, or refurbishing. Future costs must be discounted to present value (PV) to account for the time value of money. An overview of the LCCA formula is provided:

$$LCCA = IC + OP_{PV} + MC_{PV} + EoL_{PV} \quad (1)$$

3. METHODOLOGY

The objective of the B•CLIC project was to develop an enhanced methodology for assessing the life cycle cost of Building Automation and Control Systems (BACS) in office buildings, allowing

investors to make well informed investment decisions early on in the design stage. This methodology integrates two innovative approaches: the creation of a toolchain to evaluate the energy savings potential of BACS in office buildings, and a novel Life Cycle Cost Analysis (LCCA) methodology that addresses specific challenges and pitfalls of BACS applications, such as component service life, reliability, and uncertain return on investment. These approaches were combined into a preliminary tool that enables stakeholders to evaluate BACS investments ex ante. The tool was implemented using Python. In the following sections, the general functioning of the tool will be addressed, and both the novel tool chain for energy simulations and the novel LCCA methodology will be explained.

3.1 Preliminary tool to assess BACS investments

The tool allows stakeholders to simulate and compare different BACS scenario's, based on different sets of predefined characteristics. In a first step, stakeholders determine the case parameters: a building typology is specified, and case-specific parameters are determined. In total the impact of ±27.000 different combinations can effortlessly be studied, with for each set of combinations a specific energy profile that is simulated through the novel toolchain discussed in section 3.2. Based on the selected case and simulated energy profile, a specific LCCA is performed following the newly developed probabilistic method, which is elaborated on in section 3.3.
In the B•CLIC project, four distinct base building typologies were identified to represent typical office building configurations. Figure 1 provides an overview of these four typologies, highlighting their most distinguishable characteristics. All typologies are situated within the climate zone of Brussels, Belgium.

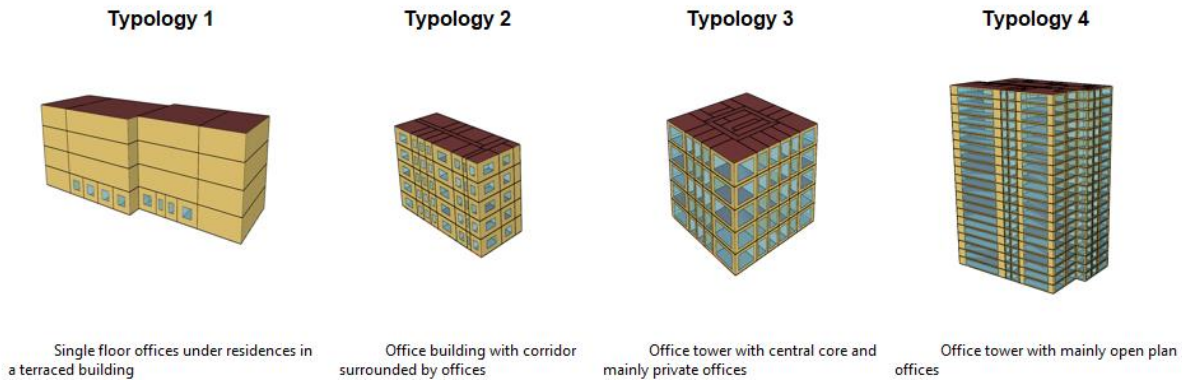

Figure 1. Overview of office building typologies as included in the B•CLIC project

In addition to selecting the building typology, it is necessary to specify several general characteristics of the office building that influence its energy performance. This can be done for selected characteristic through a dropdown menu, which is included in parentheses: Window-to-wall ratio (20%-50%-80%), Building envelope characteristics (Passive Building, EPB 2006 demands[1], Pre-EPB demands), internal gains (LED lighting and energy-efficiency equipment vs. non-LED and low energy-efficiency equipment), Main heating generator (Fuel, Boiler-non-condensing, Boiler-condensing, heath pump air to water, heath pump ground to water) and main cooling generator (Chiller-air cooled, Chiller-water cooled, heath pump air to water, heat pump

[1] The Flemish government imposed a maximum K-Value of K45 for office buildings between 2006 and 2009

ground to water).

After specifying its general characteristics, it is necessary to specify the current and desired status of BACS in the studied office building, in order to compare a business-as-usual LCCA scenario and a future BACS LCCA scenario. This comparison allows for the calculation of savings and return on investment. For these scenarios, the following parameters have to be specified: heating and cooling system automation (Central thermostat with fixed or setback temperature, Room thermostat with fixed or setback temperature), free cooling system automation (manual window control – no heat recovery, Free cooling – heat recovery), ventilation system automation level (High constant flow, time control flow, CO2 level based flow), lighting system automation level (manual – no dimming, manual – no dimming-sweeping signal, Occupancy on/off - Off with sufficient daylight, Occupancy on/off - Daylight dimming) and sun shading system automation (no shading, Manual Control, Automated based on irradiance, Automated considering lighting and cooling loads). After specifying all characteristics, energy requirements for both business-as-usual and BACS scenarios are simulated and LCCA is calculated. In the following sections both the novel toolchain for the energy savings assessment and the novel LCCA methodology is explained.

3.2 Novel toolchain for energy savings assessment

EnergyPlus[2] is used as simulation engine to assess the potential of the aforementioned BACS functionalities in 4 typologies. Python is used to implement the behavioural impact of occupants in operating windows, shades and lights, and to implement the functions of BACS. This resulted in ±27,000 unique cases where the electricity, heating and cooling demand is simulated in a multizone dynamic thermal simulation for a full year at a subhourly timestep. Due to the time-consuming simulation process, the simulations are not carried out live, but processed prior and fed into the database of the B•CLIC tool. As a further elaboration of the novel toolchain does not fall within the scope of this paper, readers are encouraged to consult L. Vandenbogaerde et al. (2025).

3.3 Novel Life Cycle Cost Assessment methodology

In this section, an overview of the LCCA methodology is given based on the different components of the assessment-methodology. A lifespan of 20 years was considered and a discount rate of five percent (European Commission, 2024) was included in all future cost calculations.

3.2.1 Initial costs

The initial costs of Building Automation and Control Systems (BACS) can vary significantly between buildings, primarily depending on the level of automation and the types of BACS implemented. To estimate the initial investment costs for both current and desired BACS systems, a comprehensive inventory of the required BACS components was created. This inventory includes, but is not limited to, sensors, switches, cables, valves, and actuators. These components are considered brand-independent, meaning no specific brand names are included. For each component type, an average cost was determined based on the building material cost indexes for the Flanders region in 2024 (ASPEN Architecten & Ingenieurs, 2024). Additionally, a statistical lifespan for each component was established based on regulations, academic literature, and technical sheets from manufacturers (i.a. Belany et al., 2021; European Parliament & Council of the European Union, 2024; Richter et al., 2019; Verhelst et al., 2017; Zhang & Cai, 2014)

[2] https://energyplus.net/

Using the case characteristics outlined in Section 3.1, a list of components (including both types and quantities) was compiled from the inventory, allowing for the calculation of the initial cost.

3.2.2 Operational costs

Operational costs are those costs that occur to ensure the operation of BAC-systems on a daily basis. In this model, the main operational costs are energy costs considered to run the different BACS. In the current version these are limited to electricity costs only. For the proof-of-concept version of this tool, electricity costs are set on an arbitrary fixed rate of €0.15/kWh (Eurostat, 2024), with energy consumption derived from the energy simulations presented in section 3.2. To account for potential increases in energy prices, an annual escalation rate of two percent (Eurostat, 2024) has been incorporated into the model

3.2.3 Maintenance costs

Maintenance costs comprise all costs pertaining to the maintenance of BACS, whether it is considered reactive, proactive or preventive, planned or unplanned. The main cost of maintenance is considered to be the replacement cost of hardware. In traditional LCCA of buildings, the expected lifespan is typically well known because of ample records of historic performance data. Many components of BACS however have a much shorter expected life time compares to other construction products, and empirical data is scarce and scattered. Furthermore, as BACS can be very complex systems, consisting of hundreds of components, it is likely that some components will fail before their predicted functional life expectancy. For some critical subsystems, failure of one component can affect the operation of the BACS system as a whole. Therefore, the B•CLIC project introduces a probabilistic method to estimate life span of BAC systems. The current version of the tool incorporates Monte Carlo simulations in order to predict the life span of individual components in the business-as-usual and future scenarios. For each component type, a specific probability distribution was developed based on the statistical lifespans described in section 3.2.1. These probability distributions are used as input for the Monte Carlo simulations that simulate the life spans of each component in the simulated system, resulting in a more scattered cost profile than in LCCAs of conventional building materials, which represents a real life scenario for BACS more closely.

3.2.4 End-of-life costs

In the current model, no end-of-life-costs are included. Determining end-of-life costs of BACS can be quite challenging, as of the components are integrated in the building in such a way that removal would require drastic actions. Conversely, some components such as copper wire or electronic waste can generate a positive cashflow at the end of life. Given this complexity and expected limited net impact on the discounted life cycle costs, end-of-life costs (or profits) are currently not included in the proof-of-concept model.

4. RESULTS

The results from the LCCA methodology explained in section 3.3 entail both an overview of life cycle costs for a business-as-usual scenario, where no changes to BACS are made in the next 20 years except for maintenance replacements of components, and a desired future BACS scenario, under the same conditions. This allows stakeholders to compare the life cycle costs of the two BACS scenarios, in order to determine the potential benefits and costs of both scenarios in an early

stage. This would enable stakeholders to test different future BACS scenarios and, compared to their current BACS status, determine which BACS investments could result in the highest return on investment, before major design decisions and commitments have to be made.
The tool returns a set of different graphical overviews, as can be seen in figure 2. On the left diagram, an overview is given for both scenarios based on cost category. This allows stakeholders to visualise investment estimates and simulated operational costs to evaluate the potential return on investment. In the right diagram, the cumulative life cycle costs over the 20-year life span are shown. This gives stakeholders a clear idea of when an investment in BACS will start paying off, and whether this payback time is acceptable or not.

Figure 2 displays the results of a case pertaining an office building following Typology 4, studying the impact of lighting automation on life cycle costs under ceteris paribus conditions. In the business-as-usual scenario, lights are manually controlled, and no dimming function is present. In the desired BACS scenario, lights are automatically controlled based on zone occupancy and daylight dimming is active. In this example, the investment in the smart lighting system pays of in the operational phase: the electricity consumption is significantly lower than in the business-as-usual scenario, and after approximately seven years, the life cycle cost of the desired BACS scenario is already lower than the business-as-usual scenario. Given the limitations to the current methodology (as discussed in section 5), the absolute numbers should be interpreted with caution. Nevertheless, this example shows the potential and usefulness of the tool for different stakeholders.

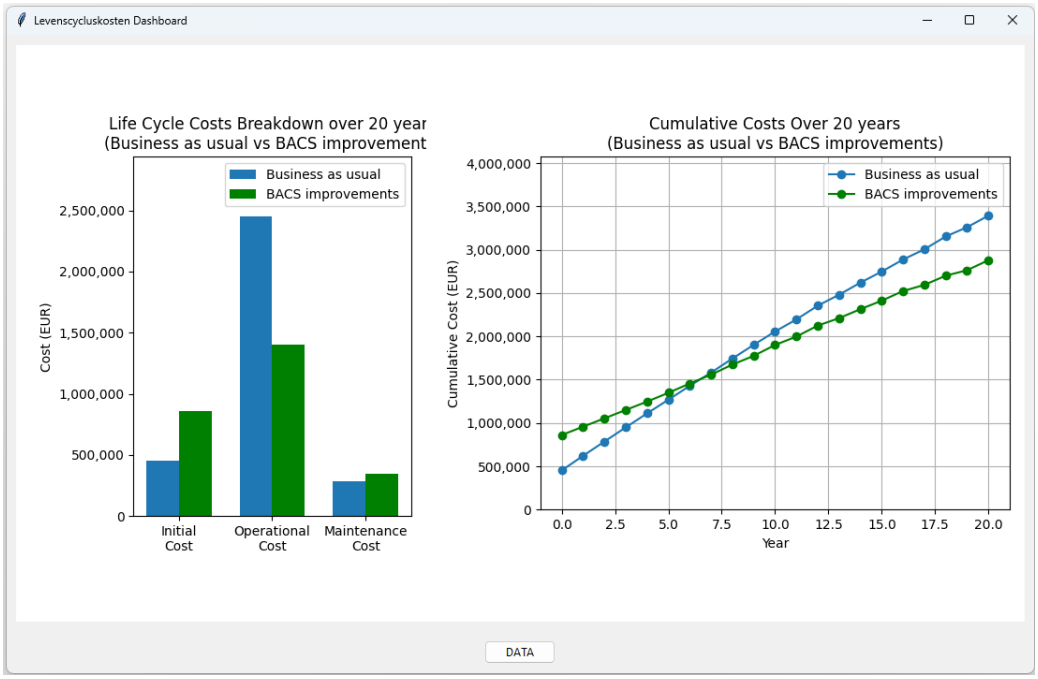

Figure 2. The B•CLIC tool returns different graphical interfaces

5. LIMITATIONS, DISCUSSION AND FUTURE RESEARCH

The current tool, still in its proof-of-concept phase, has several limitations, including the exclusion

of energy consumption from heating and cooling, which would enhance model accuracy. It also lacks labor cost data for installation, operation, and maintenance of BACS, and uses fixed economic parameters over a 20-year period, which should be adjustable for relevance. These issues are currently being worked on, to increase the overall accuracy and usefulness. The maintenance cost calculation in the Life Cycle Cost Analysis (LCCA) methodology relies on limited theoretical data for Monte Carlo simulations, needing more real-life data for accuracy. Additionally, data protection by producers and high costs of data extraction pose challenges.

Early feedback from stakeholders on the proof-of-concept tool was promising, as its usefulness is very apparent. However, the tool's accuracy heavily depends on the quantity and quality of the included data. Therefore, developing a robust data-gathering strategy for these systems in the long term is crucial to benefit from data-based models.

To tackle this last problem, a new research project is planned, in cooperation with different stakeholders within the building automatization ecosystem: Building owners, BACS producers, integrators, etc. with the aim of developing said robust data gathering strategy and including more real-life data into the current model. Furthermore, this research project will allow for more insight into the needs of stakeholders when it comes to BACS project evaluation, improving the usability of the current tool.

6. CONCLUSIONS

The aim of the B•CLIC project was to develop a novel LCCA tool including innovative energy simulation data and a probabilistic approach to maintenance costs, to enable stakeholders to make well informed decisions on BACS investments in early design stages. While the current tool is only a proof-of-concept, it shows great promise for various stakeholders. It allows different stakeholders to evaluate the life cycle costs of BACS in office buildings for current business-as-usual and future desired scenarios. However, currently there are still important limitations to the model, that influence the accuracy of the results, that must be addressed in the further development of the tool. This includes but is not limited to the further integration of real-life data in the probability distributions for life spans of components. To conclude, this methodology and tool not only provide a robust framework for evaluating BACS but also pave the way for future innovations in the field. By addressing different cost categories comprehensively, this work ensures informed decision-making and promotes the efficient use of resources, ultimately contributing to the advancement of sustainable office building.

REFERENCES

ASPEN Architecten & Ingenieurs. (2024). *Aspen Index: Prijsinformatie voor alle aannemingswerken 2024 ASPEN Architecten & Ingenieurs*. ASPEN Architecten & Ingenieurs.

ASTM. (2011). Standard Practice for Measuring Life-Cycle Costs of Buildings and Building Systems. In *Annual Book of ASTM Standards: Vol. i* (Issue Reapproved 2010, pp. 1–19). https://doi.org/10.1520/E0917-17E01

Belany, P., Hrabovsky, P., & Kolkova, Z. (2021). Combination of lighting retrofit and life cycle cost analysis for energy efficiency improvement in buildings. *Energy Reports*, *7*, 2470–2483. https://doi.org/10.1016/j.egyr.2021.04.044

Bureau for standardisation. (2022). *ISO 52120-1:2022* (p. 107). Nationaal Bureau voor Normalisatie.

European Commission. (2024). *Discount rates in European Union for 2023* (Issue 271, p. 2008).

European Commission, Van Tichelen, P., Verbeke, S., Yixiao, M., Ectors, D., McCullough, A., Nuttall, C., & Waide,

P. (2021). *Ecodesign preparatory study for Building Automation and Control Systems (BACS) : implementing the Ecodesign Working Plan 2016 -2019 : final report*. https://op.europa.eu/en/publication-detail/-/publication/974eacea-e5aa-11ed-a05c-01aa75ed71a1/

European Parliament, & Council of the European Union. (2024). Regulation (EU) 2024/1781 of the European Parliament and of the Council of 13 June 2024 establishing a framework for the setting of ecodesign requirements for sustainable products, amending Directive (EU) 2020/1828 and Regulation (EU) 2023/1542 and repeal. *Official Journal of the European Union*, *L 223*, 1–42. http://data.europa.eu/eli/reg/2024/1781/oj

Eurostat. (2024). *Electricity prices for non-household consumers - bi-annual data (from 2007 onwards)*. Eurostat. https://ec.europa.eu/eurostat/databrowser/view/nrg_pc_205/default/table?lang=en&category=nrg.nrg_price.nrg_pc

Fuller, S. K. (2016). *Life-Cycle Cost Analysis (LCCA)* (pp. 1–6). National Institute of Standards and Technology. http://www.nist.gov/index.html

Fuller, S. K., & Petersen, S. R. (1996). Life-Cycle Costing Manual for the Federal Energy Management Program. In *NIST Handbook 135* (1995th ed., Issue 135). U.S. Department of Commerce.

International Standards Organisation. (2021). *NBN EN ISO 15686-5:2021 - Buildings and constructed assets - service life planning - part 5: Life Cycle Costing* (p. 54). https://www.nbn.be/shop/en/standard/nbn-en-15804-2012-a2-2019_33774/#%0Ahttps://www.nbn.be/shop/en/standard/nbn-en-iso-52016-1-2017~565443/

Islam, H., Jollands, M., & Setunge, S. (2015). Life cycle assessment and life cycle cost implication of residential buildings - A review. *Renewable and Sustainable Energy Reviews*, *42*, 129–140. https://doi.org/10.1016/j.rser.2014.10.006

Richter, J. L., Van Buskirk, R., Dalhammar, C., & Bennich, P. (2019). Optimal durability in least life cycle cost methods: the case of LED lamps. *Energy Efficiency*, *12*(1), 107–121. https://doi.org/10.1007/s12053-018-9662-4

The European Parliament and the Council of the European Union. (2024). Directive (EU) 2024/1275 of the European Parliament and of the Council of 24 April 2024 on the energy performance of buildings. *Official Journal of the European Union*, *1275*, 1–68. https://eur-lex.europa.eu/legal-content/EN/TXT/PDF/?uri=CELEX:52021DC0550&from=EN

van Roosmale, S., Hellinckx, P., Meysman, J., Verbeke, S., & Audenaert, A. (2024). Building automation and control systems for office buildings: Technical insights for effective facility management - A literature review. *Journal of Building Engineering*, *97*(November 2023), 110943. https://doi.org/10.1016/j.jobe.2024.110943

van Roosmale, Sophie, Audenaert, A., & Meysman, J. (2024). Understanding the opportunities and challenges of building automation and control systems to support facility management – an extensive literature review. *Facilities*, *42*(7–8), 677–693. https://doi.org/10.1108/F-05-2023-0042

Van Thillo, L., Verbeke, S., & Audenaert, A. (2022). The potential of building automation and control systems to lower the energy demand in residential buildings: A review of their performance and influencing parameters. *Renewable and Sustainable Energy Reviews*, *158*(February 2021), 112099. https://doi.org/10.1016/j.rser.2022.112099

Vandenbogaerde, L., Verbeke, S., & Audenaert, A. (2023). Optimizing building energy consumption in office buildings: A review of building automation and control systems and factors influencing energy savings. *Journal of Building Engineering*, *76*(July), 107233. https://doi.org/10.1016/j.jobe.2023.107233

Vandenbogaerde, Lukas, Meysman, J., Audenaert, A., & Verbeke, S. (2025). Case study assessment of the energy performance of emission control in office buildings. *6th International Conference on Building Energy and Environment (COBEE 2025)*, *July*.

Verhelst, J., Ham, G. Van, Saelens, D., & Helsen, L. (2017). Economic impact of persistent sensor and actuator faults in concrete core activated office buildings. *Energy and Buildings*, *142*, 111–127. https://doi.org/10.1016/j.enbuild.2017.02.052

Zhang, Y., & Cai, M. (2014). Overall life cycle comprehensive assessment of pneumatic and electric actuator. *Chinese Journal of Mechanical Engineering (English Edition)*, *27*(3), 584–594. https://doi.org/10.3901/CJME.2014.03.584

Integrated building design using performance simulation tools - Skillset training and capability building in a studio setting (15:30-17:00 h)

6th International Conference on Building Energy and Environment
Eindhoven University of Technology, The Netherlands
6 - 10 July 2025

Integrated building design using performance simulation tools - Skillset training and capability building in a studio setting

POH Hee Joo[1], CHONG Adrian[2], Chandra SEKHAR[3]

Department of the Built Environment, College of Design and Engineering, NUS, Singapore, bdgphj@nus.edu.sg
[2]Department of the Built Environment, College of Design and Engineering, NUS, Singapore, adrian.chong@nus.edu.sg
[3]Department of the Built Environment, College of Design and Engineering, NUS, Singapore, bdgscs@nus.edu.sg

SUMMARY
High performing buildings are a consequence of an integrated design approach with a good understanding of the building science domain coupled with the ability to quantitatively evaluate performance at various stages of the design process. This paper aims to share the pedagogy of such a graduate course of our MSc (Building Performance and Sustainability) program, focusing on Green Building Integration and Evaluation Studio. It is offered as a two-semester studio-based course that synthesizes the theoretical and practical aspects of building performance and detailed design development, bringing sustainable design concepts and elements to the forefront. The students are exposed to performance evaluation and simulation tools such as SpaceCLAIM, ANSYS Meshing, ANSYS-FLUENT, Rhino, Design Builder and EnergyPlus. The need for sustainable design and its integration into a holistic performing building will be a key principle of studio learning. Design decision support using simulation tools will be brought to life in a studio environment in the realization of holistic sustainable buildings. Simulation tools will be used for thermal, ventilation, IAQ, daylighting and building energy analysis. Current sustainable building assessment techniques will be applied. During semester 1 (13 weeks), students work on two individual assignments, namely application of CFD in Natural Ventilation Modelling and familiarization with BES tool. In Semester 2, students work in small groups on the design and development of an actual project on a site in Singapore. It involves the evolution of the design to lead to a high performing building using Building Performance & Simulation (BPS) tools to guide the design development process. Since its inception in 2010 and as envisioned then, this course has been pivotal in strengthening our graduates' future career path to become qualified Environmental Sustainable Design (ESD) consultants in the built environment profession.

Keywords: Building Performance and Simulation, CFD Applications in Built Environment, Green Development, Building Energy Analysis and Simulation

1. INTRODUCTION

The global urgency to address climate change and promote environmental sustainability has significantly transformed the priorities of the built environment sector. In response, academic institutions have a pivotal role in cultivating a new generation of building professionals who are equipped with the interdisciplinary skills and knowledge to design, evaluate, and deliver high-performance sustainable buildings. While conventional design education often emphasizes aesthetic and functional aspects, there remains a critical need to integrate building performance evaluation and sustainability principles into the architectural and engineering design pedagogy. The challenge lies in effectively bridging the gap between theoretical learning and practical application, especially through simulation-based design processes that reflect real-world complexities.

A growing body of literature advocates for the incorporation of performance-based design education into architectural and engineering curricula. Studies highlight the importance of

embedding Building Performance Simulation (BPS) tools in design studios to enable students to evaluate energy efficiency, thermal comfort, natural ventilation, indoor air quality (IAQ), and daylighting performance (Hansen and Lambert, 2019; Zhai, 2020; Mirzaei, 2022). However, existing pedagogical approaches often fall short in ensuring students develop a deep, iterative understanding of how to use simulation data to inform design decisions in a holistic and integrated manner. Furthermore, most reported case studies are limited to singular aspects of performance—typically building energy or daylighting—rather than demonstrating a comprehensive, multi-domain evaluation across the building lifecycle.

In the context of Southeast Asia's tropical climate and the policy direction set by national green building certification schemes such as Singapore's BCA Green Mark, there is a pressing demand for graduates who are not only familiar with sustainability frameworks, but also competent in using advanced digital tools to support performance-driven design. Despite this, limited academic publications have documented how postgraduate design studios in this region are responding to this need through innovative pedagogical strategies.

To address this knowledge gap, this paper presents the pedagogy and studio-based learning structure of the National University of Singapore (NUS) *Master of Science in Building Performance and Sustainability* (MSc BPS), specifically focusing on the course BPS5112 – *Green Building Integration and Evaluation Studio*. This two-semester course exemplifies how a performance-driven studio can serve as an effective educational platform to merge sustainable design principles with simulation-informed decision making. The course exposes students to a suite of performance evaluation tools—such as SpaceCLAIM, ANSYS Meshing, ANSYS Fluent, Rhino, DesignBuilder, and EnergyPlus, - and guides them through a structured progression from individual analytical tasks to collaborative real-site design development projects.

The primary objective of this paper is to share the methodology, structure, and learning outcomes of BPS5112, emphasizing how simulation tools are applied across multiple sustainability dimensions. It aims to demonstrate how this pedagogical model fosters critical thinking, technical competence, and professional readiness among students aspiring to become Environmental Sustainable Design (ESD) consultants. In doing so, the paper contributes to the discourse on effective pedagogy for sustainable building education and provides a reference model for other academic institutions seeking to enhance their curricula in the face of growing sustainability imperatives.

2. METHODOLOGY

The BPS5112 course adopts a studio-based learning methodology structured over two semesters, combining individual analytical tasks with collaborative project-based learning. The first semester emphasizes foundational skills through targeted assignments focused on computational modelling and performance evaluation. The second semester transitions into integrative group work on an actual project site in Singapore, enabling students to apply simulation tools in iterative design development. Students are guided through a design-thinking process grounded in sustainability principles, where feedback loops between design intent, simulation results, and performance goals are emphasized. This hands-on approach fosters critical inquiry, teamwork, and professional-level competency in sustainable building design.

Further description about student's training on BPS tools and Design Brief of the studio project are illustrated as below.

2.1. Training on Computational Fluid Dynamics (CFD) tool

Students are trained to use CFD simulation tool (ANSYS-FLUENT) in order to perform ventilation simulation modelling and analysis and ensure good natural ventilation within the functional unit. They must complete the individual assignment. The Intended Learning Outcomes (ILO) of this CFD assignment are 1) To ensure CFD quality control and fulfil check list for the building aerodynamics and natural ventilation study, 2) To analyze the CFD result and perform a series of modified/improved design iteration for GM building natural ventilation design. The assignment comprises two work scopes as listed below.

Firstly, students should ensure good wind flow simulation can be obtained from CFD modelling work through benchmarking studies. They can choose any two (2) of the following test cases for their benchmarking study. The literature data of the test case are given to students.

1. Wind flow around single buildings
2. Wind Flow Over 2 Buildings; with one smaller building in front of the big building
3. Urban Street Canyon Flow; with wind flow regime at three different H/W
4. Urban Like Flow Around Building Blocks
5. Venturi Effect In Between Buildings; Wind Flow Over V Shape channel between two buildings

Secondly, students are expected to use the established CFD methodology from the first part to perform CFD Natural Ventilation studies for the actual building, either residential or non-residential unit type. The Non-Residential Building type includes *hospitals, industrial facilities, hawker centres, sports facilities, commercial atriums and schools.* They should follow the Green Building certification criteria (e.g. Singapore BCA Green Mark Platinum GM Version 2021 or equivalent standard) to assist the natural ventilation analysis for their project. The project work scopes should include firstly baseline design case (1 geometry); and followed by improved design cases (another geometry is required). Each simulation case is subjected to one (1) prevailing wind condition (either Northerly or Southerly wind). Students can plan for computational domain with maximum site development area of 100m x 100m, subjected to computer resource availability. Plot ratio can be approximated necessarily. Existing building layout can be obtained from google map and on-site observation (for building height). Building geometry entities can be imported from SketchUp, AutoCAD 2D/3D, 3D Studio Max or BIM-REVIT. Alternatively, students can also plan for the new building with their own drawing or derive the necessary info from work experience or literature paper. In this CFD assignment, students are also encouraged to follow the CFD quality control checklist adopted in Singapore BCA CFD Guidelines Green Mark Platinum GM Version 2021 (Poh et. al, 2019) to ensure the CFD Natural Ventilation results fulfill the modelling fidelity and accuracy standard.

2.2. Training on Building Energy Simulation (BES) tool

The aim of the BES assignment is to familiarize student with building performance modelling and simulation. The Intended Learning Outcomes (ILO) of this BES assignment is to evaluate student's ability to quantify building performance using simulation tools. The proposed location for the assignment is the current building at Department of the Built Environment (DBE) on NUS campus. The building shall have a floor area of approximately 6,000m2 ± 5%. Student must use perimeter/core zoning where the depth of the perimeter zone does not exceed 1.5 times the floor-to-floor height. The submission requirement for this BES assignment is listed below.

1. Perform a climate analysis by reviewing the local climate information. The climate analysis should include the following:

a. Dry-bulb temperature
b. Relative humidity or wet-bulb temperature
c. Wind speed and direction
d. Insolation

2. Analyse and discuss the effects of the following on building energy use and peak cooling load:
    a. Building geometry and orientation.
    b. Window-to-wall ratio (by orientation) and shading options.
    c. Envelope thermal performance.
    d. Effects of the above three parametric variations on the subsequent cooling energy consumption. Student can assume a generic cooling system using the DesignBuilder simple HVAC template.

The ETTV does not need to be considered in this assignment. However, internal loads and their corresponding schedules, and ACMV schedule (On/Off) should follow the baseline standards specified in Green Mark 2021 Energy Modelling Guideline.

3. Provide a clear and concise report of BES study. The report should include Study objectives, Model inputs (including assumptions) and the corresponding sources/references, Results and discussion.

2.3. Design Brief of Studio Project

The proposed location is the empty land located at typical site in Singapore, which is assumed to be developed as **a mixed-use district comprising educational institute, commercial and business park uses**. The maximum allowable GFA for the development is limited to 80,000 sqm (+/- 10%). Students are required to develop a design for a mixed-use development comprising the following components:

- Offices (40% of NFA)
- Retail, food & beverage shops (20% of NFA)
- Educational & childcare centre (40% of NFA)

Students must consider the following attributes while developing the design of the above building:

a. Passive design principles and system solutions that achieve a minimum of 20% reduction in cooling load compared to baseline building that is based on the Singapore Green Mark 2021 Energy Modelling Guideline.
b. At least 25% and not more than 40% of the total GFA to be naturally and/or hybrid ventilated (without cooling). The remaining GFA is to be air-conditioned.
c. Achieve 80% energy savings based on SLE criteria compared to 2005 codes.
d. There is no cap on the overall building energy use derived from renewable sources.

In support of Singapore Green Building Masterplan's (SGBMP) 80-80-80 by 2030 targets, the project shall aim to achieve the following objective:

1. Super Low Energy (SLE) Certification: Demonstrate compliance with the SLE certification under Green Mark 2021, specifically through Pathway 3 as detailed in the Green Mark 2021 energy efficiency standard,
2. Explore innovative technologies and solutions to exceed the minimum 60% energy savings threshold (compared to 2005 codes) required for SLE certification to achieve 80% energy savings. Student can consider both passive and active strategies. Building performance simulation should be used to evaluate the feasibility of the proposed solution, ensuring that additional energy savings do not compromise thermal comfort or other total building performance mandates.

The environmental building analysis shall include but not limited to bioclimatic analysis, sun-path analysis, wind analysis, solar radiation and insolation analysis, daylight and glare analysis, energy modelling, weather protection, rain penetration, building orientation, natural and mechanical ventilation strategies, etc.

CFD indoor environmental modelling should also be carried out to exploit the innovative component on both active and passive design. Students are required to develop a design solution through an integrated design and engineering approach using performance evaluation tools (such as CFD and energy simulation tools), which shows a holistic appreciation on sustainability issues. Every individual in the group should make a specific contribution towards one or more aspects of the studio project. The design shall demonstrate adequate considerations for the latest version of Singapore BCA GM2021 in terms of Energy Efficiency, Resilience, Health and Wellbeing and Intelligence.

All groups are expected to carry out a thorough solar modelling including daylighting evaluation of the office spaces, CFD simulation and studies for habitable naturally ventilated spaces, complete energy modelling that includes detailed ACMV modelling with appropriate thermal zoning, and a Green Mark score card evaluation for the project.

There are three main stages of evaluation for the project:

1. Concept design stage – During this stage, each group is expected to develop a design idea identifying the key performance mandates that they want to achieve through their design and set targets for spatial, thermal, acoustic, indoor air quality, visual & building integrity.
2. Design evaluation stage – During this stage, the group is required to demonstrate a thorough simulation of the concept taken through evaluation of parameters to demonstrate that their design achieves the set targets during the earlier stage. A refinement of the targets is allowed at this stage.
3. Final design stage – This would be a consolidated outcome of the entire semester's work and for this final design submission, students are required to submit a group report. One A1 e-poster can be used to explain the design supported with simulation images and graphics.

<u>Deliverables for 3 stages:</u>

Stage 1 – Design Target & Concept design which includes Preliminary massing, Site level studies – wind analysis, solar modelling and over shadowing by adjacent buildings, Preliminary evaluation of energy end uses and demand characteristics that affect building conceptual design that are tied to the form and architecture of the building, Sustainability thrust area – case studies or examples to demonstrate key ideas or concepts, Conceptual idea for the active systems proposed for the project and Targets and performance matrix

Stage 2 – Design evaluation stage which includes Site plan, Ground floor plan, typical office, retail, childcare centre plan, Massing level studies – floor plate daylighting, massing and heat gain performance, 3D model for simulation, Massing studies for wind flow and CFD, Indoor environmental modelling for both active and passive designs, Develop and evaluate load reduction strategies, Estimate annual energy and demand impacts of active system options, Design integration and optimisation, CFD and energy simulations (where available), Green Mark evaluation with recommended ideas and Relevant Green Mark calculations.

Stage 3 – Final design stage to include 1 x A1 e-poster, Rendered perspective of design, Floor plans, Site plan, Roof plan, Final simulation results of energy modelling, daylighting, facade study, CFD study and Final Green Mark score card

3. RESULTS

The selective results from student's studio project are shown below. For brevity, they are presented here without further illustration. More details to be shared during the COBEE 2025 symposium.

3.1. Design Targets & Concept Design

Figure 1 shows the design target comprise the spatial, thermal, acoustic, IAQ, visual and building integrity aspects of total building performance.

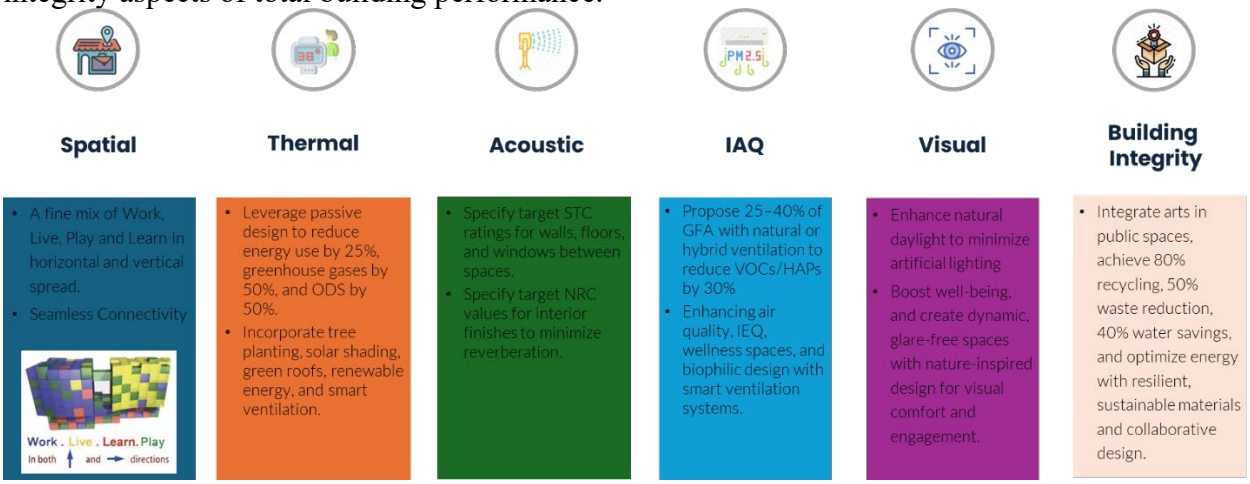

Figure 1. Total Building Performance Target.

Figure 2 shows the massing concept with three design options, namely 1) 4 isolated blocks with podium, 2) 5 isolated blocks with low level connectivity and 3) 4 isolated blocks with high level connectivity.

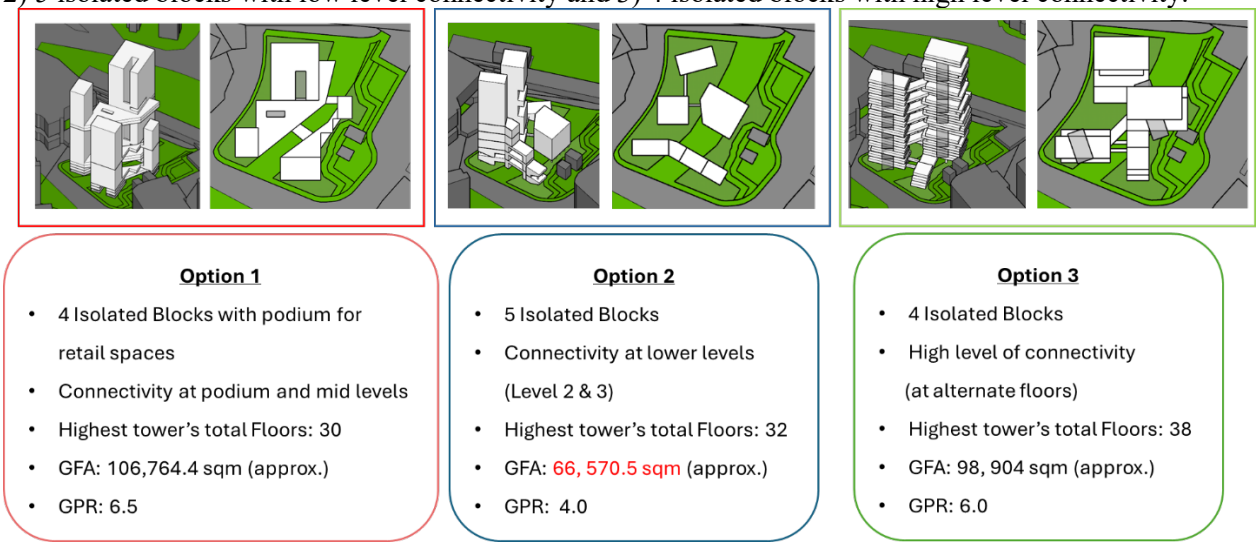

Figure 2. Massing Concept with Three Design Options.

3.2. Design Evaluation

After the concept design, the studio team proceed to the design evaluation stage with the key refinement indicators as illustrated in Figure 3.

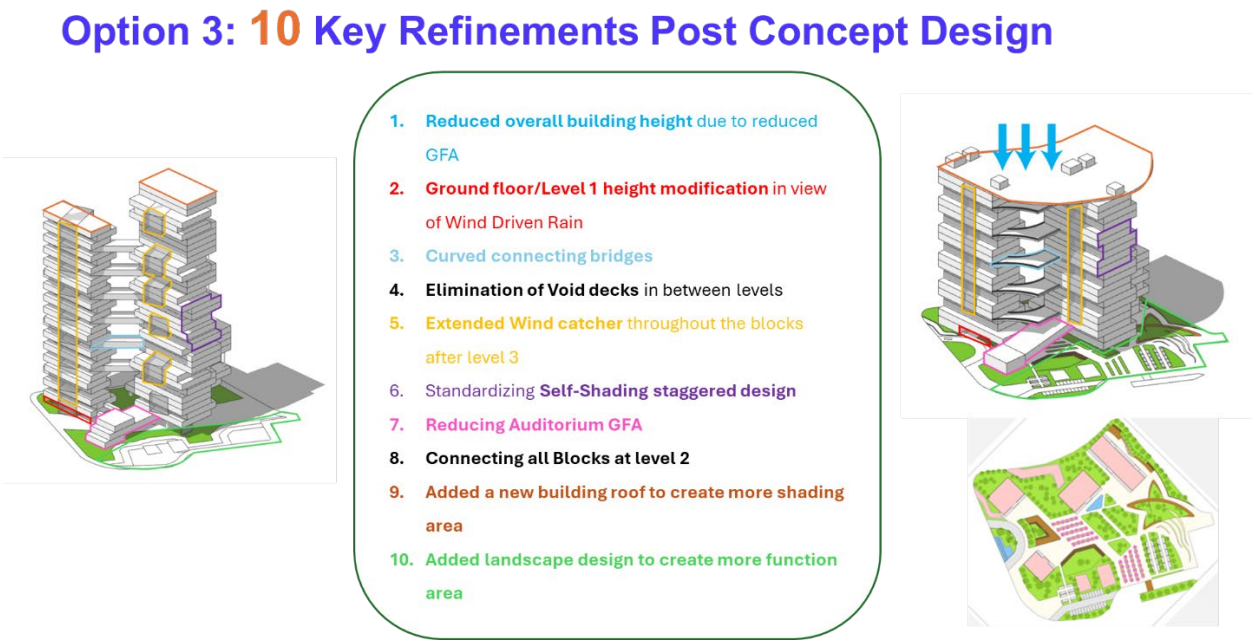

Figure 3. Key Refinements Post Concept Design.

3.3. Final Design

The final design with rendered perspective and simulation results of energy modelling, daylighting and CFD study is shown in Figure 4.

Figure 4. Final Design after evaluating with BPS tools.

4. CONCLUSIONS

Since August 2010, the BPS5112 Green Building Integration and Evaluation Studio has been a compulsory course in the NUS Master of Science in Building Performance and Sustainability programme, providing comprehensive training to nearly 500 graduate students. It serves as a pedagogical model that effectively integrates sustainable design principles with performance-based simulation tools. By combining theoretical knowledge with real-world application, the course empowers students to make informed design decisions that align with environmental performance goals. Through iterative learning, hands-on simulation training, and collaboration on actual projects, students gain the technical proficiency and critical thinking skills necessary for future roles as Environmental Sustainable Design (ESD) consultants. This studio experience underscores the value of simulation-driven education in shaping the next generation of built environment professionals committed to sustainability and performance excellence.

ACKNOWLEDGEMENTS

Authors would like to acknowledge BPS5112 students' contribution, in particular Mr. Ng Jing Xian and Mr. Ang Kok Kiong, along with Mr. Ian Tan Eng Kiong, Ms. Lyu Jiachen, Mr. Ng Jing Xian, Ms. Patil Tanaya Amar, Ms. Patnala Reena Sri, Ms. Si Wenqing, Mr. Wilfred Leung Wei Lit. These students are part of this course in AY24/25 and are sharing their results in the paper. We are also grateful to our Teaching Assistants (TAs), namely Xiang Yeyu, Liu Puyang, Lin Subin, Ting Shi An, Sicheng Zhan, Siyu Cheng, Yue Lei, Kazuki Horikoshi and Zhang Yiting for their invaluable support to the students during the coursework.

REFERENCES

Jan L.M. Hensen & Roberto Lamberts (2019). *Building Performance Simulation for Design and Operation*, 2nd Ed. (Routledge, Taylor & Francis Group)

Zhai, Zhiqiang (John). (2020). *Computational Fluid Dynamics for Built and Natural Environments*, 1st Ed. (Springer Verlag, Singapore)

Mirzaei, Parham A. (2022). *Computational Fluid Dynamics and Energy Modelling in Buildings: Fundamentals and Applications*, 1st Ed. (John Wiley & Sons Ltd)

POH, Hee Joo; CHIU, Pao-Hsiung; OOI, Chin Chun; RAGHAVAN, Venugopalan; WAN, Yee Ming, Stephen; XU, Xiangguo, George; LI, Ruixin; Leong-Kok, Su-Ming, Development of GM2015 Computational Fluid Dynamics (CFD) Methodology for Naturally-ventilated Non-residential Buildings (NRB) in Singapore , (2019) IOP Conf. Ser.: Earth Environ. Sci. 238 012079. https://iopscience.iop.org/article/10.1088/1755-1315/238/1/012079

Singapore BCA Green Mark 2021 CFD Modelling Guideline, https://www1.bca.gov.sg/docs/default-source/docs-corp-buildsg/sustainability/20210909_cfd-guideline_r1.pdf

Singapore BCA Green Mark 2021 Energy Modelling Guideline, https://www1.bca.gov.sg/docs/default-source/docs-corp-buildsg/sustainability/20210909_energy-modelling-guideline_r1.pdf

COBEE 2025 – Proceedings

WEDNESDAY

Advanced Modeling and Building Simulations (11:00-12:30 h)

6th International Conference on Building Energy and Environment
Eindhoven University of Technology, The Netherlands
6 - 10 July 2025

Two-stage adjoint-shape optimization of a duct network to reduce flow resistance and realize identical flow rate distribution

Zhaoyu Yao [1], Tengfei (Tim) Zhang [1,2], Feng Wang [3*]

[1]*School of Environmental Science and Engineering, Tianjin University, Tianjin, China*
[2]*Department of Civil Engineering, Dalian University of Technology, Dalian, China*
[3]*Department of Building Environment and Energy Engineering, The Hong Kong Polytechnic University, Hung Hom, Hong Kong, China*

SUMMARY
Duct network with multiple branch ducts is widely used to distribute conditioned air to some indoor spaces. Reducing flow resistance while assuring the identical flow rate to each branch duct is needed. However, these dual objectives may conflict between each other. This investigation proposed to adopt a two-stage shape optimization to realize the both objectives: in the first stage the flow resistance is minimized by optimizing the geometric shapes without addressing the requirement of identical airflow rate in each duct; in the second stage, the airflow rate in each duct is adjusted. A duct network containing one main duct and four arc-shaped branch ducts are optimally designed. The designed duct network was manufactured by the 3D printing for measurement. The obtained results reveal that the flow resistance was reduced by at least 30% after the design while achieving the nearly identical airflow rate in each branch duct.

Keywords: Duct network, adjoint shape optimization, flow resistance, identical flow rate distribution, energy saving

1. INTRODUCTION

For long enclosed space like an aircraft cabin, train compartment, and coach, the conditioned air is commonly supplied into the internal space by a ductwork with many branch ducts. Commonly the airflow rate in each branch duct shall be nearly identical to minimize the undesired longitudinal airflow. The current practice adds some flow resistances, such as baffles or restrictors, to hydraulically balance the airflow rate in each branch duct. This inevitably leads the increased energy consumption and louder noise. It is viable to adopt the guide vanes (Yin et al., 2021) or shape optimization (Tian et al., 2024) to reduce the flow resistance. The optimization algorithms, such as genetic algorithms (Simpson et al., 1994; Dandy et al., 1996), simulated annealing method (Cunha et al., 1999), harmonic search (Geem et al., 2002), and Dijkstra's algorithm (Gunawan, et al., 2021), etc., have been proposed to improve the ductwork design. These practices concentrate to the sole goal to reduce the flow resistance. So far, no research optimizes the duct geometry to reduce flow resistance while assuring the identical airflow rate to each branch duct. This research proposes a two-stage adjoint-shape optimization to achieve the dual goals. Note that these dual goals may contradict with each other during the design.

2. METHODS

A simplified network with multi-branch ducts as shown in Fig. 1(a) is investigated. This duct network contains a main duct with two transitions in the duct diameter and four arc-shaped branch

ducts. The main duct has a total length of 59 cm. Each branch duct has an inner diameter of 15 mm and is separated from the adjacent duct(s) with 160 mm. The inner diameter of the entrance section of the main duct is 28 mm. The diameter is reduced to 21 mm between the two middle branch ducts. The main duct is finally narrowed to 15 mm, as the same size of the branch ducts. The rated total airflow rate through the main duct is 25.31 m³/h. When optimizing the geometric design, the total airflow rate, the inner diameter of the main duct at the entrance, and the inner diameter of the branch duct exits are fixed, while the remaining geometry is adjustable.

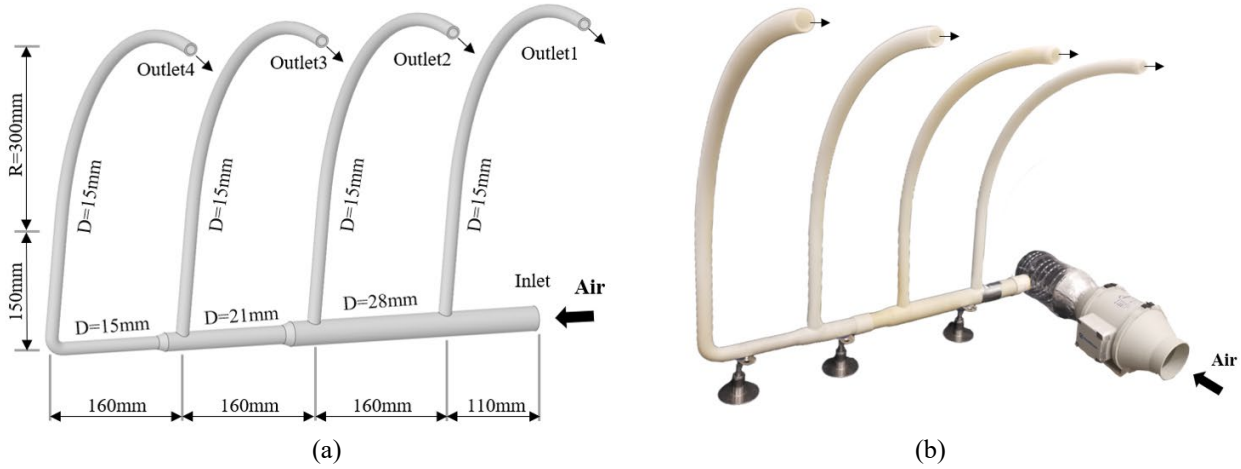

(a) (b)

Figure 1. A duct network for optimal geometric design: (a) initial geometric model, (b) picture of the optimally designed duct network for measurement.

A two-stage optimization strategy is utilized: in the first stage the flow resistance is minimized without considering the requirement of identical airflow rate in each duct; in the second stage, the airflow rate in each duct is adjusted to approach identity with the optimized geometry in the first stage as the input. The two design objectives are defined as:

$$J_1 = \frac{P_{\text{Outlet}-i}}{P_{\text{Inlet}}} = \frac{\int p_{\text{Outlet}-i} dS}{\int dS} \Big/ \frac{\int p_{\text{Inlet}} dS}{\int dS} \tag{1}$$

$$J_2 = \frac{\sum_{i=1}^{n} \left| Q_{\text{Outlet}-i} - Q_{\text{Average}} \right|^2}{n} = \frac{\sum_{i=1}^{n} \left| \int q_{\text{Outlet}-i} dS - \frac{\sum_{i=1}^{n} \int q_{\text{Outlet}-i} dS}{n} \right|^2}{n} \tag{2}$$

where J_1 and J_2 are the design objective in the first and second stage, respectively, P represents the surface-average total pressure (relative pressure), p is the local total pressure (relative pressure) per unit area, S denotes the cross-sectional area, Q is the airflow rate, q is the airflow rate per unit surface, n represents the total number of branch ducts, and i denotes the branch duct index. The design tries to minimize both J_1 and J_2.

The steady-state flow in the duct network was resolved by the Reynolds-averaged Navier-Stokes (RANS) modeling with the Realizable k-ε turbulence model and the Menter-Lechor wall treatment in Ansys Fluent. All of the physical variables were discretized by the second-order upwind scheme. The pressure and velocity were coupled by the SIMPLE algorithm. The discrete adjoint method

(Liu et al., 2023) was employed to guide the duct geometry adjustment based on the sensitivity of the objective functions. The convergence criterion for adjoint equations was defined as the adjoint residuals below 10^{-3}. A total of $200 \times 100 \times 50$ control points were adopted and the geometric modifications were implemented using the mesh morphing technique based on the Bernstein polynomials and B-spline function. The design was continued until the residuals of both J_1 and J_2 are below 10^{-3}.

The optimally designed prototype was manufactured by the 3D printing with the interior surfaces polished for measurement of the performance, as shown in Fig. 1 (b). A fan pumped the outside air into the plenum connecting to the main duct. The airflow rate in each branch duct and the total flow resistance through the whole duct network were measured by a Pitot tube (model: LPT-03-300; Yiou, China). The fan energy consumption was recorded by a power meter (model: DL333501C; Deli, China) to examine the energy saving. The noise was measured by a sound level meter (model: HS6288B; Hongsheng, China). In addition to the designed airflow rate of 25.20 m³/h, other total airflow rates were also tested, including 8.25, 12.52, 19.24, and 33.89 m³/h, respectively. This was to evaluate the robustness of the optimal design.

3. RESULTS AND DISCUSSION

Fig. 2(a) presents the optimally designed geometric shape of the duct network. After the optimal design, the transitions in the diameter of the main duct along the flow direction were still maintained. The major geometric shape adjustment lied in the Tee ducts and the elbow, which were evolved into irregular shapes. Fig. 2(b) presents distribution of the total pressure across the middle cross-section in surrounding of the main duct. The maximum total pressure inside the main duct has been reduced from 193.0 Pa in the initial design to 111.9 Pa in the optimal design. The pressures near the Tee ducts have been minimized significantly.

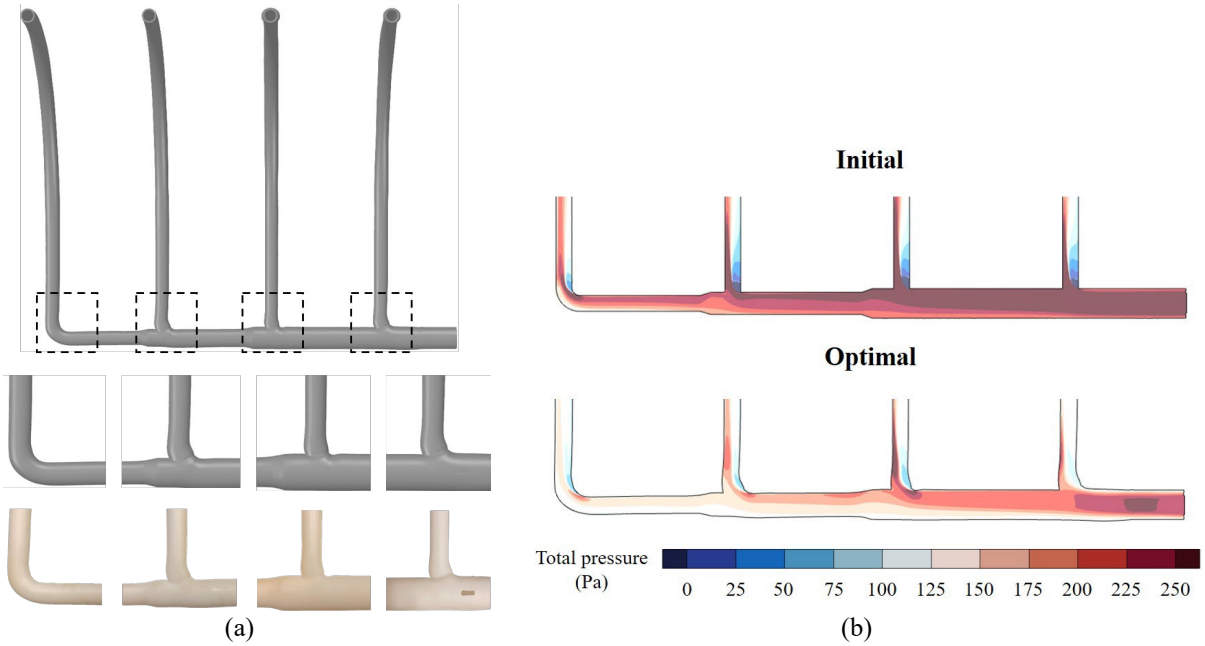

Figure 2. Optimally designed duct network: (a) geometric shape of the final optimal design, (b) comparison of the total pressure distribution across the middle cross-section in surrounding to the main duct between the initial design

and the final optimal design.

Fig. 3(a) shows comparison of the measured total pressure difference between the initial design and the final optimal design under different total ventilation rates. Under the ventilation rate of 25.31 m³/h, the total pressure was reduced by 75.2 Pa after the optimal design and the pressure reduction rate was 41.02%. Fig. 3(a) also shows the total pressure reduction ratio increases with the ventilation rate for the ventilation rates between 8.25 and 19.24 m³/h. The pressure reduction ratio is nearly identical for the ventilation rates between 19.24 and 33.89 m³/h. The total pressure reduction ratio ranges from 30.81% to 41.02%. Fig. 3(b) shows that the standard deviation of the airflow rate in each branch duct is reduced from 0.28 m³/h to 0.11 m³/h under the rated ventilation rate of 25.31 m³/h. The flow homogeneity has been increased by 18.68% to 61.93% among the tested ventilation rates. The varying trend of the fan energy consumption resembles the total pressure difference as shown in Fig. 3(c). The fan power consumption reduction ranges from 15.04% to 31.72%. Fig. 3(d) shows the design can also reduce the noise level by 3.4-4.8 dB, mainly because the rotational speed of the fan is slowed down with the reduced flow resistance.

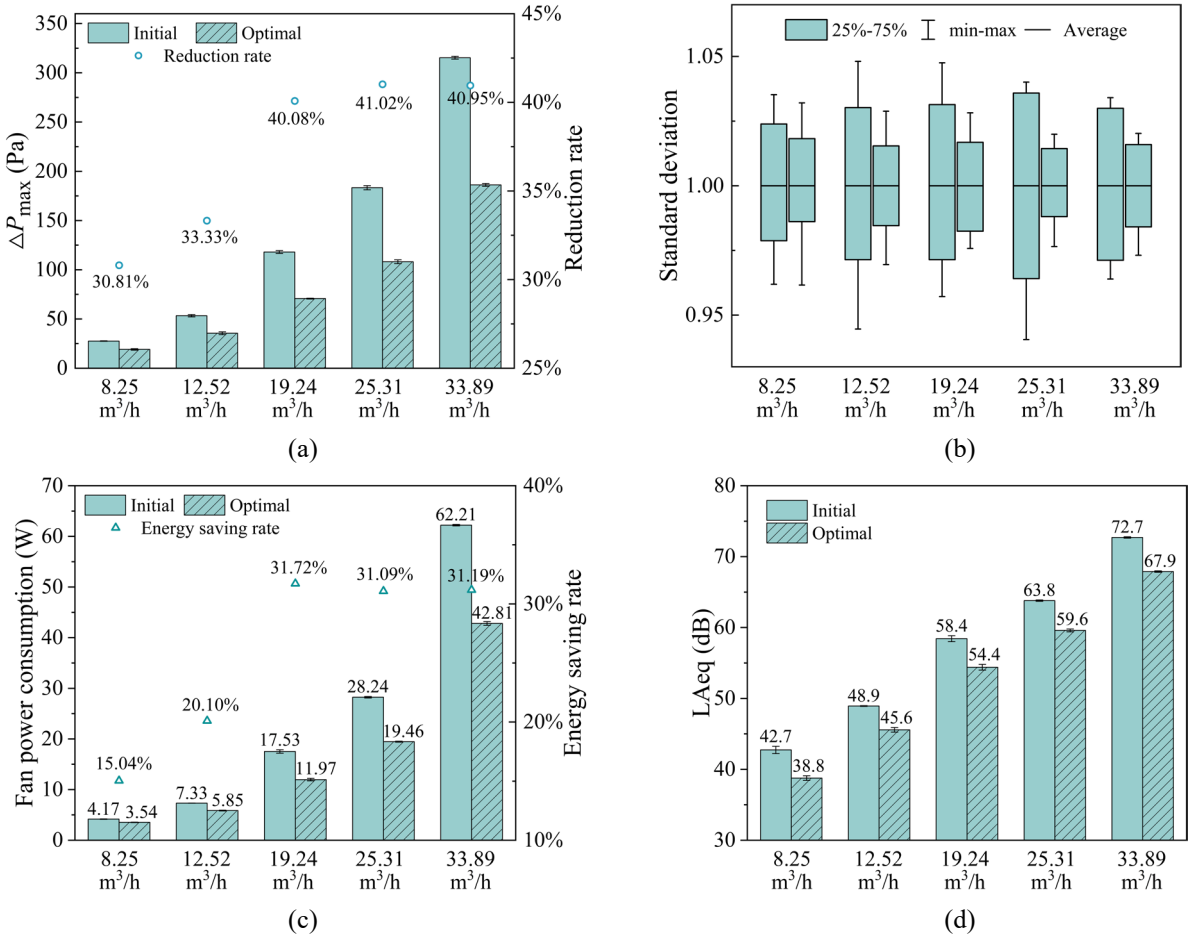

Figure 3. Performance of the final optimized ductwork under different total ventilation rates: (a) total flow resistance and the total resistance reduction rate, (b) homogeneity of the flow rate distribution evaluated by standard deviation of the ratio of the flow rate in each branch duct to the average flow rate, (c) fan power consumption and the energy saving rate, (d) noise level (LAeq).

These improvements are primarily attributed to the geometric optimization that refrain the vortex

development mainly in the Tee ducts and elbow. However, the optimal design also results in 4% increase of the total surface area, which requires slightly more investment in the materials.

4. CONCLUSIONS

As compared with the conventional duct network without carrying out the optimal geometric design, the optimally designed duct network improves the airflow rate homogeneity by at least 18.68%, while lowering the total flow resistance by no less than 30.81%. The monitored fan energy consumption of the new design was at least 15.04% less. Although the geometric design is carried out under the rated total ventilation rate, the optimally designed duct network performs robustly well in other smaller or larger ventilation rates. This justified that the proposed two-stage adjoint-shape design is very promising to enhance the duct network performance.

REFERENCES

Dandy, G. C., A. R. Simpson, and L. J. Murphy, n.d.,1996, An Improved Genetic Algorithm for Pipe Network Optimization: Water Resources Research, v. 32, no. 2, p. 449-458.

Cunha, M. da, and J. Sousa, n.d.,1999, Water Distribution Network Design Optimization: Simulated Annealing Approach: Journal of Water Resources Planning and Management, v. 125, no. 4, p. 205-214.

Geem, Z. W., J. H. Kim, and G. V. Loganathan, 2002, Harmony Search Optimization: Application to Pipe Network Design: International Journal of Modelling and Simulation, v. 22, no. 2, p. 125–133.

Gunawan, Allessandro Setyo Anggito Utomo, F. Fariz, and S. A. Lambang, 2021, Reduction of Drag Resistance by Pressure Drop in Pipeline with 3-Dimensional Design Optimization: Journal of Advanced Research in Fluid Mechanics and Thermal Sciences, v. 83, no. 2, p. 44–53.

Liu, F., H. Chen, H. Yuan, T. (Tim) Zhang, and W. Liu, 2023, Shape optimization of the exhaust hood in machining workshops by a discrete adjoint method: Building and Environment, v. 244, p. 110764.

Tian, Y., 2023, Low-resistance local components design method based on topology optimization: A case study of a duct tee: Building and Environment, v.244, p. 110823.

Simpson, A. R., G. C. Dandy, and L. J. Murphy, 1994, Genetic Algorithms Compared to Other Techniques for Pipe Optimization: Journal of Water Resources Planning and Management, v. 120, no. 4, p. 423–443.

Yin, Y., A. Li, X. Wen, J. Zhang, X. Zhang, J. Guo, J. Li, W. Zhang, and J. Che, 2022, Resistance reduction of an elbow with a guide vane based on the field synergy principle and viscous dissipation analysis: Journal of Building Engineering, v. 54, p. 104649.

6th International Conference on Building Energy and Environment
Eindhoven University of Technology, The Netherlands
6 - 10 July 2025

Evaluation of model reliability for digital twin frameworks

Alireza Ghadertootoonchi [1], Seungjae Lee [2]

[1]*University of Toronto, Toronto, Canada, a.ghadertootoonchi@mail.utoronto.ca*
[2]*University of Toronto, Toronto, Canada, sjae.lee@utoronto.ca*

SUMMARY
Buildings are responsible for one-third of global energy consumption and greenhouse gas emissions. A major part of building energy consumption is related to HVAC systems which aim to provide thermal comfort. Hence, improving the efficiency of HVAC systems using optimization and fault detection techniques is crucial not only to mitigate climate change but also to satisfy occupant needs. To achieve the best performance, an accurate model is often required. Previous studies have highlighted potential limitations focusing on error minimization for model evaluation. This study (i) introduces the concept of reliability as a complementary criterion and (ii) analyzes its importance in building energy modeling using the concept of k-fold cross validation. To this end, models of a water-cooled chiller are developed and compared considering reliability. The results suggest that in addition to training accuracy, reliability is another important factor to consider in model selection and evaluation processes.

Keywords: Digital twin, Data-driven modelling, Model evaluation, Building energy system

1. INTRODUCTION

Buildings are major energy consumers and greenhouse gas emitters, with these issues worsening due to climate change, urbanization, and population growth (International Energy Agency (IEA), 2018). A positive feedback loop exists where increased energy use worsens climate change, further driving energy demand (UNEP, 2023). Breaking this cycle while satisfying occupant comfort needs requires improving HVAC efficiency, as these systems are a major energy consumer in buildings (Zhao et al., 2013)(Borja-Conde et al., 2024). The concept of digital twins, the creation of models for synchronized simulation with their target systems (Huang et al., 2022), provides opportunities to enable advanced optimization and fault detection strategies for improved HVAC efficiency(Pau et al., 2019). However, model evaluation and selection for digital twinning is still an active area of research (Mihai et al., 2022).

The majority of the previous studies in building system modeling primarily focus on minimizing prediction error (i.e., improving accuracy). Previous literature suggests that reliability could be another criterion besides accuracy (Newrzella et al., 2022). Reliability refers to a model's ability to produce consistent and stable outputs when deployed in real-world scenarios. A reliable model performs with low variability when encountering new but similar data to what it was trained on. (Cordeiro-Costas et al., 2023). Reliability is not necessarily aligned with accuracy. For instance, a model might achieve high overall accuracy but generate highly variable predictions for different operating conditions which shows low reliability. Reliability is used in fields such as finance (Ata & Hazim, 2020), medicine (Wang et al., 2023), and Chemistry (Naef, 2015), where it is quantified by measuring the variability of validation error metrics in K-fold cross-validation (KFCV) (Edgar Ceh-Varela et al., 2024).

This study highlights an opportunity to enhance model selection and evaluation processes in the

field of building energy modeling. By analyzing the impact of reliability, the study demonstrates that it is a crucial factor in determining which model should be implemented.

2. METHODOLOGY

Previous studies have often used the standard deviation of K number of validation errors from KFCV to evaluate reliability. A reliable model, which performs with low variability and high stability, exhibits a low standard deviation. This indicates that no matter which part of the dataset the model is exposed to, it provides consistent performance (Vorotyntsev et al., 2021).

To assess the importance of quantifying model reliability in the field of building energy modelling, a water-cooled chiller dataset (Zhang et al., 2022) is used. The aim is to predict the chiller's COP using condenser and evaporator inlet and outlet temperatures, along with water flow rates as input variables. To achieve the goal, 500 single-layer neural networks with random hyperparameters are constructed. Random hyperparameters and their range are shown in Table 1.

Table 1. Range of random hyperparameter values

	number of first layer neurons	activation function	L_2 regularization	Initial Learning rate	β_1	β_2
Range of random value	[10,100]	Logistic – Relu - Tanh	$[10^{-6}, 10^{-2}]$	$[10^{-6}, 10^{-2}]$	[0.85,0.99]	[0.85,0.999]

Models are then trained and validated using 10-fold cross validation. One fold is considered as the test and is not observed during the CV process. Nine folds entered the CV process and the means and standard deviations of the RMSE of the validation folds are obtained. Next, these values are compared and analysed to determine whether they affect the model's performance on the test data.

3. RESULTS AND DISCUSSION

Following the methodology results in 500 trained models, each with different mean and standard deviation for the RMSE of the validation folds as shown in Figure 1.

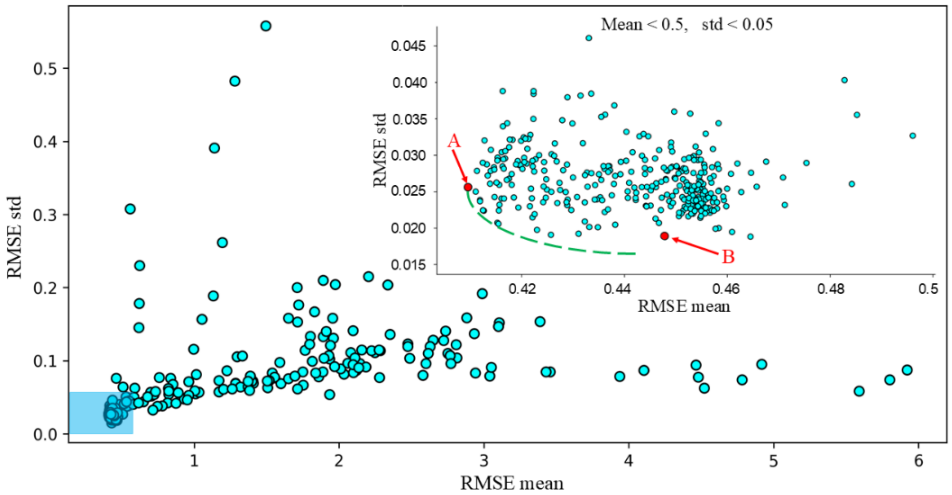

Figure 1. Mean and std of validation RMSEs (inner Figure shows the sky-blue area with mean < 0.5 and std < 0.05)

As Figure 1 shows, the relationship between the mean and standard deviation is not linear meaning that minimizing the mean does not result in the minimum standard deviation. In some cases, models have a close mean value but different standard deviations. In addition, the green line in the

inner figure resembles the Pareto frontier that can be obtained using bi-objective optimization. To analyse whether there is a difference in test performance between these models, points A, which has the minimum mean, and B, which has the minimum standard deviation, are selected for further investigation. The parameters of these models are shown in Table 2.

Table 2. Hyperparameters of model A and B

	number of first layer neurons	activation function	L_2 regularization	Initial Learning rate	β_1	β_2
Model A	47	Relu	0.0062689	0.00934	0.9496	0.9591
Model B	74	Tanh	0.0022579	0.00932	0.9619	0.9034

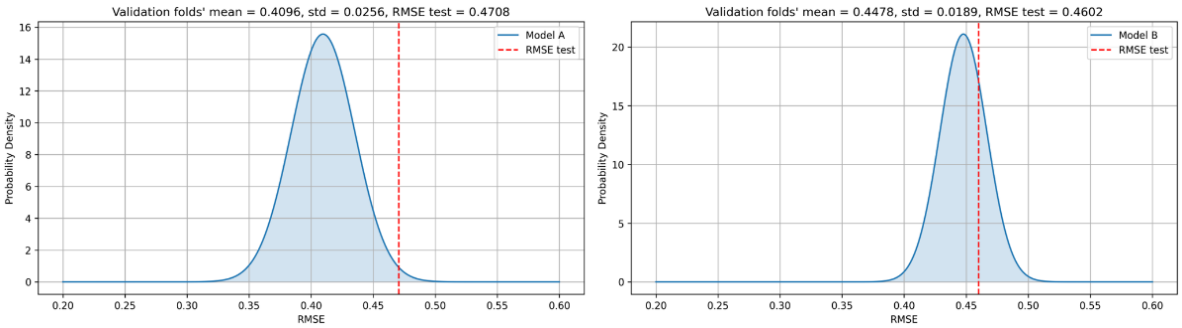

Figure 2. Comparing the test performance of models A and B with their validation error distribution

Figure 2 compares the test performance of these two models with validation error distribution. As can be seen, model B has a considerably lower bias, and the test error is closer to the expectation. Also, model A underestimated the error and provided an optimistically biased result which is aligned with the findings of previous studies in other fields (Pohjankukka et al., 2017)(Leinonen et al., 2024). In addition, absolute RMSE is also lower (0.46 vs. 0.47). Although the results do not guarantee that lower bias is always observed when minimizing standard deviation, it provides evidence indicating that ignoring reliability in model evaluation and selection process results in losing valuable information.

4. CONCLUSION

The present study investigated whether reliability is an effective criterion in model selection and evaluation. For this purpose, 500 single-layer neural networks with random hyperparameters are constructed to predict the COP of a real-world water-cooled chiller. Next, the models' performance is evaluated using KFCV, and the mean and standard deviation of the validation RMSE for each model are obtained. The results show that the mean and standard deviation do not always align, so minimizing the mean does not minimize the standard deviation. Thus, ignoring reliability and focusing only on average performance leads to the loss of useful information. For future research, a bi-objective hyperparameter tuning algorithm will be developed to find Pareto optimal solutions and evaluate test performance across these solutions. In addition, the performance of other machine learning algorithms will be analysed.

ACKNOWLEDGEMENTS

This research was supported by The Ontario Centre of Innovation (Grant OCI# 35202) and PLC Group Inc.

REFERENCES

Ata, O., & Hazim, L. (2020). Comparative analysis of different distributions dataset by using data mining techniques

on credit card fraud detection. *Tehnicki Vjesnik*, *27*(2), 618–626. https://doi.org/10.17559/TV-20180427091048

Borja-Conde, J. A., Nadales, J. M., Ordonez, J. G., Fele, F., & Limon, D. (2024). Efficient management of HVAC systems through coordinated operation of parallel chiller units: An economic predictive control approach. *Energy and Buildings*, *304*(December 2023), 113879. https://doi.org/10.1016/j.enbuild.2023.113879

Cordeiro-Costas, M., Villanueva, D., Eguía-Oller, P., Martínez-Comesaña, M., & Ramos, S. (2023). Load Forecasting with Machine Learning and Deep Learning Methods. In *Applied Sciences* (Vol. 13, Issue 13). https://doi.org/10.3390/app13137933

Edgar Ceh-Varela, Maes, L., & Sarbagya Ratna Shakya. (2024). Machine Learning Analysis of Factors Contributing to Diabetes Development. *Cloud Computing and Data Science*, *5*(1), 157–182. https://doi.org/10.37256/ccds.5120243751

Huang, Z. F., Soh, K. Y., Islam, M. R., & Chua, K. J. (2022). Digital twin driven life-cycle operation optimization for combined cooling heating and power-cold energy recovery (CCHP-CER) system. *Applied Energy*, *324*(July), 119774. https://doi.org/10.1016/j.apenergy.2022.119774

International Energy Agency (IEA). (2018). *The Future of Cooling: Opportunities for Energy-Efficient Air Conditioning. Paris, France: International Energy Agency*. 92. https://iea.blob.core.windows.net/assets/0bb45525-277f-4c9c-8d0c-9c0cb5e7d525/The_Future_of_Cooling.pdf

Leinonen, T., Wong, D., Wahab, A., Nadarajah, R., Kaisti, M., & Airola, A. (2024). *Empirical investigation of multi-source cross-validation in clinical machine learning*. http://arxiv.org/abs/2403.15012

Mihai, S., Yaqoob, M., Hung, D. V, Davis, W., Towakel, P., Raza, M., Karamanoglu, M., Barn, B., Shetve, D., Prasad, R. V, Venkataraman, H., Trestian, R., & Nguyen, H. X. (2022). Digital Twins: A Survey on Enabling Technologies, Challenges, Trends and Future Prospects. *IEEE Communications Surveys & Tutorials*, *24*(4), 2255–2291. https://doi.org/10.1109/COMST.2022.3208773

Naef, R. (2015). A Generally Applicable Computer Algorithm Based on the Group Additivity Method for the Calculation of Seven Molecular Descriptors: Heat of Combustion, LogPO/W, LogS, Refractivity, Polarizability, Toxicity and LogBB of Organic Compounds; Scope and Limits of Applicability. In *Molecules* (Vol. 20, Issue 10, pp. 18279–18351). https://doi.org/10.3390/molecules201018279

Newrzella, S. R., Franklin, D. W., & Haider, S. (2022). Three-Dimension Digital Twin Reference Architecture Model for Functionality, Dependability, and Life Cycle Development Across Industries. *IEEE Access*, *10*, 95390–95410. https://doi.org/10.1109/ACCESS.2022.3202941

Niu, K., Guo, J., Pan, Y., Gao, X., Peng, X., Li, N., & Li, H. (2020). Multichannel Deep Attention Neural Networks for the Classification of Autism Spectrum Disorder Using Neuroimaging and Personal Characteristic Data. *Complexity*, *2020*(1), 1357853. https://doi.org/https://doi.org/10.1155/2020/1357853

Pau, M., Cremer, J. L., Ponci, F., & Monti, A. (2019). *Day-Ahead Scheduling of Electric Heat Pumps for Peak Shaving in Distribution Grids BT - Smart Cities, Green Technologies, and Intelligent Transport Systems* (B. Donnellan, C. Klein, M. Helfert, O. Gusikhin, & A. Pascoal (eds.); pp. 27–51). Springer International Publishing.

Pohjankukka, J., Pahikkala, T., Nevalainen, P., & Heikkonen, J. (2017). Estimating the prediction performance of spatial models via spatial k-fold cross validation. *International Journal of Geographical Information Science*, *31*(10), 2001–2019. https://doi.org/10.1080/13658816.2017.1346255

UNEP. (2023). *Air conditioners fuel the climate crisis*. UNEP. https://www.unep.org/news-and-stories/story/air-conditioners-fuel-climate-crisis-can-nature-help

Vorotyntsev, P., Gordienko, Y., Alienin, O., Rokovyi, O., & Stirenko, S. (2021). Satellite Image Segmentation Using Deep Learning for Deforestation Detection. *2021 IEEE 3rd Ukraine Conference on Electrical and Computer Engineering (UKRCON)*, 226–231. https://doi.org/10.1109/UKRCON53503.2021.9575783

Wang, J., Khan, M. A., Wang, S., & Zhang, Y. (2023). SNSVM: SqueezeNet-Guided SVM for Breast Cancer Diagnosis. In *Computers, Materials \& Continua* (Vol. 76, Issue 2). https://doi.org/10.32604/cmc.2023.041191

Yu, H., Zhang, T., Chen, L., & Tao, W. Q. (2023). Refrigeration equipment model construction based in data center cooling station. *International Journal of Green Energy*, *20*(15), 1741–1749. https://doi.org/10.1080/15435075.2023.2194374

Zhang, B., You, S., Wang, S., Ding, X., Wang, C., & Gao, Y. (2022). From laboratory to on-site operation: Reevaluation of empirically based electric water chiller models. *Building Simulation*, *15*(2), 213–232. https://doi.org/10.1007/s12273-021-0797-4

Zhao, L., Cai, W., Ding, X., & Chang, W. (2013). Model-based optimization for vapor compression refrigeration cycle. *Energy*, *55*, 392–402. https://doi.org/https://doi.org/10.1016/j.energy.2013.02.071

6th International Conference on Building Energy and Environment
Eindhoven University of Technology, The Netherlands
6 - 10 July 2025

Fast building performance simulation method for evaluating renovation strategies of terraced houses in the Netherlands

Chaobo Zhang*, Pieter-Jan Hoes, Ruqian Zhang

Department of the Built Environment, Eindhoven University of Technology, Eindhoven, the Netherlands
**Corresponding author. E-mail address: c.zhang5@tue.nl*

SUMMARY
A fast building performance simulation method is proposed for evaluating renovation strategies of Dutch terraced houses. It utilizes limited EnergyPlus simulation data generated by data sampling to train surrogate models. Two data sampling approaches (simple random sampling (SRS) and Latin hypercube sampling (LHS)) and three data-driven models (multiple linear regression, extreme gradient boosting, and artificial neural network (ANN)) are investigated. A Dutch terraced house is applied for performance verification. The results show that surrogate models trained with simulation samples from LHS achieve accuracy similar to those trained with samples from SRS. Furthermore, it is found that limited simulation data (400 samples) are sufficient to train an accurate surrogate model. ANN is the most accurate model in simulating indoor air temperatures (R^2 = 0.99, *MAE* = 0.12 ºC) and thermal loads (R^2 = 0.95, *MAE* = 700 W). The computational time of ANN accounts for only 0.03% of that of EnergyPlus.

Keywords: machine learning, surrogate model, building performance simulation, building renovation.

1. INTRODUCTION

Building performance simulation (BPS) offers a cost-effective mean to evaluate building renovation strategies. There are two main modeling approaches: data-driven and physics-based. Data-driven models depend on high-resolution measured data from buildings (e.g., indoor air temperatures and energy consumption). However, the availability of such data is often limited, restricting the application of these models. Physics-based models, on the other hand, can simulate high-resolution dynamic performance of individual buildings without relying on measured data. They can provide reliable simulation outcomes based on general building information (e.g., location, geometry, and construction details), making them powerful tools for decision-making. Nevertheless, physics-based models typically result in high computational loads (Hong et al., 2020). When assessing renovation strategies for large neighborhoods (e.g., in the Netherlands, a typical neighborhood could encompass 1,500 houses with a variety of building typologies, building shapes and construction years), this computational demand becomes impractical. The challenge increases when investigating a wide range of renovation strategies per house, including the performance robustness of each strategy under different occupant behavior and climate change scenarios. The computational load becomes even more pressing when also evaluating neighborhood-scale energy system strategies, such as district heating or local energy communities that involve sharing and matching of electricity production and demand. Consequently, developing efficient methods to accelerate BPS is both necessary and important.

A promising solution is developing data-driven surrogate models based on physics-based models. These surrogate models are trained using a limited set of simulation data generated by the physics-

based models. Once trained, they can rapidly estimate the simulation results of physics-based models with acceptable accuracy. Surrogate models have been successfully applied in various areas, including urban building energy simulation, building energy model calibration, and optimization studies for building design and renovation. For instance, Pan et al. (2024) developed a long short-term memory-based surrogate model for hourly electricity consumption simulation of urban-scale buildings. This model reduced the simulation time by 90% while maintaining an accuracy of over 90%. Herbinger et al. (2023) used a limited set of simulation data from physics-based models to train artificial neural network (ANN) models. These trained ANN models were then utilized to calibrate unknown building model parameters, providing accurate parameter calibration with short calibration times. Yigit (2021) proposed a surrogate model based on gradient boosting machine to optimize envelope insulation retrofit strategies for residential buildings, revealing optimal design strategies with fast optimization speeds. Lu et al. (2024) developed a graph convolutional networks-based surrogate model to quantify the uncertainty of building design loads, reducing the computational time from 331 hours to 30 seconds compared to physics-based models. Sharif and Hammad (2019) trained an ANN model as a surrogate model to optimize building renovation strategies, reducing the optimization time by 99% compared to physics-based models while achieving similar optimization results.

Surrogate models thus show great potential for accelerating BPS. In the context of neighborhood-scale building and energy system renovation strategies, the surrogate models must reliably generate hourly simulation results based on the physics-based models. These hourly results are needed for calculating several relevant performance indicators. For instance, the hourly indoor air temperatures are needed to calculate summer overheating risks and the hourly energy demand is required for evaluating local energy matching and sharing strategies. However, few studies have explored the effectiveness of surrogate models in this context. Key questions that need to be addressed are: What are the most suitable data-driven surrogate models for this purpose? What data sampling approaches are appropriate for training the models? What is the appropriate sample size for physics-based models to ensure the accuracy of surrogate models? How much computational time can surrogate models save in practice?

This paper aims to address these questions through a case study of a Dutch terraced house using EnergyPlus simulation data. Specifically, it compares the performance of three widely used data-driven models: multiple linear regression (MLR), extreme gradient boosting (XGBoost), and ANN. Additionally, this study evaluates two common data sampling approaches: simple random sampling (SRS) and Latin hypercube sampling (LHS). This paper also provides valuable insights into generating simulation samples and training surrogate models to support fast and accurate performance evaluations.

2. METHODOLOGY

Figure 1 illustrates the surrogate model development process. The process consists of two steps: physics-based model sampling and surrogate model training. The first step aims to generate a limited set of EnergyPlus simulation samples. The second step focuses on training a surrogate model based on these samples. Further details on these steps are provided in Sections 2.1 and 2.2.

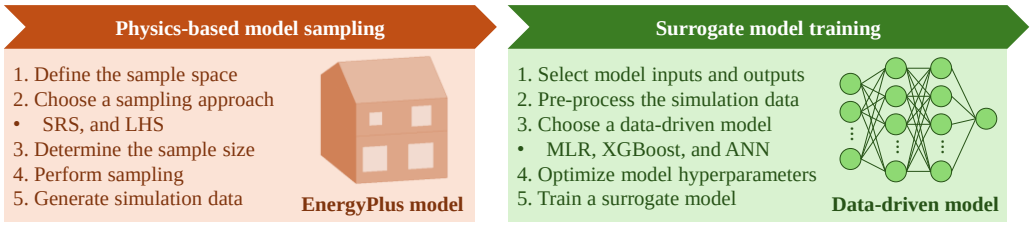

Figure 1. Flowchart of the surrogate model development process.

2.1 Physics-based model sampling

The first sub-step is to define the sample space. In this study, the sample space for variables influencing building renovation performance is defined. Key variables should be related to, but are not limited to, building geometry, occupant behavior, building insulation, and space heating.

Then, it is necessary to select a suitable sampling approach. SRS and LHS are two commonly used approaches for the surrogate models of BPS (Zhang, 2021). SRS is a basic approach where each variable value is chosen independently and has an equal chance of being selected. This approach is easy to implement. However, it might require a large sample size to fully capture the variability of multiple variables. LHS is a stratified sampling approach designed to ensure that each variable is sampled efficiently within its space. It maintains good coverage of the multi-variable space.

After that, the sample size is determined, and the selected sampling approach is used to generate the required number of samples. Finally, EnergyPlus is used to generate the data for the samples.

2.2 Surrogate model training

The first sub-step is to determine the model inputs and outputs. Relevant key performance indicators (KPIs) for evaluating building renovation strategies include thermal comfort, overheating/underheating hours, peak thermal loads, operational CO_2 emissions and operational costs. Hourly indoor air temperatures and thermal loads are needed to calculate these KPIs. Therefore, the outputs of the surrogate model in this study focus on those variables. The inputs are factors related to building geometry, occupant behavior, building insulation, and space heating.

Then, the simulation data of the inputs and outputs should be pre-processed to enhance the accuracy of the surrogate models. Max-min normalization is applied to scale both the inputs and outputs to the same range of 0 to 1. This reduces the impact of varying magnitudes between them.

Next, a suitable data-driven model should be selected for developing a surrogate model. MLR, XGBoost, and ANN are three commonly used data-driven models for building energy modeling (Zhao et al., 2022). MLR is used to learn the linear relationship between inputs and outputs. It is easy to implement and interpret, while it usually shows low accuracy. XGBoost is one of the most powerful ensemble learning models, known for its high accuracy and fast computation speed. As for ANN, it is a widely used machine learning model in this domain. This model excels at capturing non-linear relationships between inputs and outputs, resulting in high accuracy.

After that, the hyperparameters of the data-driven models are optimized, which plays a crucial role in enhancing the model accuracy. Grid search is applied for hyperparameter optimization. It involves systematically searching through a manually specified subset of hyperparameters to find

the best combination that maximizes the model accuracy on the validation datasets. Finally, the surrogate models with the best hyperparameters are trained using the EnergyPlus simulation data.

3. RESULTS

3.1 Case study overview

This case study focusses on a terraced house located in Eindhoven, the Netherlands. Space heating is provided on the first and second floors, while the attic is not heated. DesignBuilder is used to define the geometry and zoning of this house (see Figure 2). Subsequently, an EnergyPlus model is created using DesignBuilder, and Python is employed to run this model with different configurations in batches for generating hourly simulation data. Hourly weather data for Eindhoven in 2019 are collected from the Dutch meteorological institute for use in the simulations.

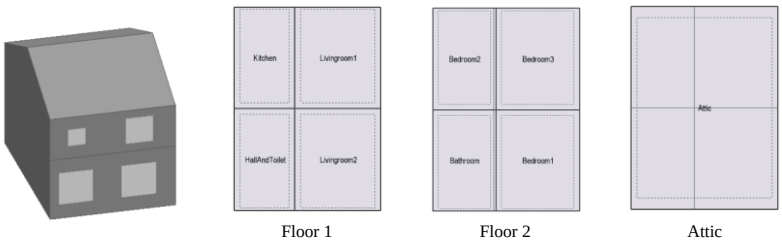

Figure 2. Geometry and zoning of the terraced house used for performance verification.

The configurations are sampled from the sample space listed in Tables 1-4. The sample space encompasses four types of variables affecting the renovation performance: building geometry (orientation and boundary condition), occupant behavior (occupancy schedule, indoor air heating setpoints, ventilation rate, and solar shading), space heating (hot water supply temperature and radiator renovation status), and building insulation (infiltration rate, Rc-values of floors/walls/roofs, and U-values of windows/doors). The rated heating capacity of each radiator in a zone is selected based on the renovation status and the rated heating capacities of radiators available in the Netherlands (https://radiatorendiscounter.nl/). The design heating load for the zone is calculated by EnergyPlus. If the radiator is not renovated, its rated heating capacity is determined by selecting the available rated heating capacity (at a 75 °C supply temperature) that is closest to the design heating load. If the radiator is renovated, its rated heating capacity is determined by selecting the available rated heating capacity (at the sampled supply temperature) that is closest to the design heating load. Two sampling approaches are compared: SRS and LHS. Each approach generates 1,000 variations of the building model for training the surrogate models. Additionally, 500 variations are randomly generated to verify the performance of trained surrogate model; note that these variations are different from the 2,000 variations in the training samples. Two commonly used accuracy metrics, i.e., R^2 and mean absolute error (*MAE*), are used for verification.

Table 1. Sample space related to the renovation of Dutch terraced houses.

No.	Variable	Unit	Space	Source
1	Orientation	-	North, south, east, west	-
2	Boundary condition	-	Between, corner	-
3	Occupancy schedule	-	Refer to Table 2	VLA, 2018
4	Indoor air heating setpoint	-	Refer to Table 3	BZK and CBS, 2019
5	Ventilation rate	-	Refer to Table 4	BZK and CBS, 2019
6	Solar shading	-	Refer to Table 4	BZK and CBS, 2019

7	Hot water supply temperature	ºC	45, 55, 75	Lund et al., 2018
8	Radiator renovation status	-	Renovated, not renovated	-
9	Rc-value of ground floors	$(m^2.K)/W$	0.15, 0.17, 0.52, 2.5, 3.5	RVO, 2023
10	Rc-value of walls	$(m^2.K)/W$	0.35, 0.43, 1.3, 1.7, 2.5, 4.5	RVO, 2023
11	Rc-value of roofs	$(m^2.K)/W$	0.35, 0.72, 0.86, 1.3, 2.5, 3.5, 6.0	RVO, 2023
12	U-value of windows	$W/(m^2.K)$	1.1, 2.8, 5.8	RVO, 2023
13	U-value of doors	$W/(m^2.K)$	1.4, 3.4	RVO, 2023
14	Infiltration rate	$dm^3/(s.m^2)$	[0.1, 3]	Bramiana et al., 2016

Table 2. Occupancy schedules for three typical Dutch families.

Family	Occupant	Occupancy schedule
Family 1	Adult (working)	**Workday: Bedroom:** 0:00-6:00, 23:00-0:00; **Living room:** 6:30-7:00, 18:00-18:45, 19:30-22:45; **Kitchen:** 6:15-6:30, 18:45-19:30; **Bathroom:** 6:00-6:15, 22:45-23:00 **Weekend: Bedroom:** 0:00-8:00, 23:00-0:00; **Living room:** 8:30-11:00, 14:00-18:45, 19:30-22:45; **Kitchen:** 8:15-8:30, 18:45-19:30; **Bathroom:** 8:00-8:15, 22:45-23:00
Family 2	Adult (staying at home)	**Bedroom:** 0:00-8:00, 23:00-0:00; **Living room:** 8:30-11:00, 14:00-18:45, 19:30-22:45; **Kitchen:** 8:15-8:30, 18:45-19:30; **Bathroom:** 8:00-8:15, 22:45-23:00
	Adult (staying at home)	**Bedroom:** 0:00-8:00, 23:00-0:00; **Living room:** 8:30-11:00, 14:00-22:45; **Kitchen:** 8:15-8:30; **Bathroom:** 8:00-8:15, 22:45-23:00
Family 3	Adult (working)	**Workday: Bedroom 1:** 0:00-6:00, 23:00-0:00; **Living room:** 6:30-7:00, 18:00-22:45; **Kitchen:** 6:15-6:30; **Bathroom:** 6:00-6:15, 22:45-23:00 **Weekend: Bedroom 1:** 0:00-8:00, 23:00-0:00; **Living room:** 8:30-11:00, 14:00-22:45; **Kitchen:** 8:15-8:30; **Bathroom:** 8:00-8:15, 22:45-23:00
	Adult (staying at home)	**Workday: Bedroom 1:** 0:00-6:00, 23:00-0:00; **Living room:** 7:00-11:00, 14:00-18:45, 19:30-22:45; **Kitchen:** 6:15-7:00, 18:45-19:30; **Bathroom:** 6:00-6:15, 22:45-23:00 **Weekend: Bedroom 1:** 0:00-8:00, 23:00-0:00; **Living room:** 8:30-11:00, 14:00-18:45, 19:30-22:45; **Kitchen:** 8:15-8:30, 18:45-19:30; **Bathroom:** 8:00-8:15, 22:45-23:00
	Three-year kid (staying at home)	**Workday: Bedroom 2:** 0:00-7:30, 19:15-0:00; **Living room:** 8:00-11:00, 14:00-19:00; **Kitchen:** 7:45-8:00; **Bathroom:** 7:30-7:45, 19:00-19:15 **Weekend: Bedroom 2:** 0:00-9:00, 20:15-0:00; **Living room:** 9:30-11:00, 14:00-20:00; **Kitchen:** 9:15-9:30; **Bathroom:** 9:00-9:15, 20:00-20:15
	Ten-year kid (going to school)	**Workday: Bedroom 3:** 0:00-7:15, 20:15-0:00; **Living room:** 7:45-8:00, 18:00-20:00; **Kitchen:** 7:30-7:45; **Bathroom:** 7:15-7:30, 20:00-20:15 **Weekend: Bedroom 3:** 0:00-9:00, 21:15-0:00; **Living room:** 9:30-11:00, 14:00-21:00; **Kitchen:** 9:15-9:30; **Bathroom:** 9:00-9:15, 21:00-21:15

Table 3. Typical indoor air heating setpoint schedules (ºC) for Dutch buildings.

Schedule No.	0:00-6:00	7:00-9:00	10:00-12:00	13:00-15:00	16:00-18:00	19:00-23:00
1	17.5	19	19	19	19.5	20
2	20.5	20.5	20.5	20.5	20.5	21
3	15	15.5	19.5	19.5	20	20
4	15	19.5	19.5	19.5	19.5	20
5	17	20.5	21	21.5	21.5	21.5
6	15.5	17.5	16.5	16.5	17.5	19.5

Table 4. Typical ventilation and solar shading control strategies for Dutch buildings.

Control type	No.	Strategy description
Ventilation	1	The ventilation rate is maintained at a low level of 0.75 $m^3/(h.m^2)$.
	2	The ventilation rate is maintained at a mid level of 1.50 $m^3/(h.m^2)$.
	3	The ventilation rate is maintained at a low level of 0.75 $m^3/(h{\cdot}m^2)$ when the house is unoccupied. When the house is occupied, the ventilation rate increases to a moderate level of 1.50 $m^3/(h{\cdot}m^2)$.
Shading control	1	No solar shading.
	2	External shading is used when the indoor air temperature exceeds 22 ºC, and the solar irradiance on windows surpasses 200 W/m^2. Otherwise, it remains inactive.
	3	External shading is used when the house is occupied, the indoor air temperature exceeds 24 ºC, and the solar irradiance on windows surpasses 300 W/m^2. Otherwise, it remains inactive.
	4	External shading is used from May to September, and not used in other months.

Three data-driven models are investigated in this case study (MLR, XGBoost, and ANN). The outputs are the hourly average indoor air temperatures on the 1st and 2nd floors, and the hourly building thermal load. The inputs for these outputs are listed in Table 5. The hyperparameter optimization space for XGBoost and ANN is shown in Table 6. For hyperparameter optimization, 75% of the training data are utilized to train the surrogate models, and the rest of the data are applied to evaluate hyperparameter combinations.

Table 5. Inputs of the surrogate models for hourly indoor air temperature and hourly thermal load simulation.

Input	Output		
	Hourly indoor air temperature on the 1st floor	Hourly indoor air temperature on the 2nd floor	Hourly thermal load
Orientation	Yes	Yes	Yes
Boundary condition	Yes	Yes	Yes
Indoor air heating setpoint	Yes	Yes	Yes
Hot water supply temperature	Yes	Yes	Yes
Radiator renovation status	Yes	Yes	-
Rc-value of ground floors	Yes	Yes	Yes
Rc-value of walls	Yes	Yes	Yes
Rc-value of roofs	Yes	Yes	Yes
U-value of windows	Yes	Yes	Yes
U-value of doors	Yes	Yes	Yes
Infiltration rate on the 1st floor	Yes	-	-
Infiltration rate on the 2nd floor	-	Yes	-
Infiltration rate of the house	-	-	Yes
Ventilation rate on the 1st floor	Yes	-	-
Ventilation rate on the 2nd floor	-	Yes	-
Ventilation rate of the house	-	-	Yes
Outdoor air temperature	Yes	Yes	Yes
Solar radiation	Yes	Yes	Yes
Solar shading status	Yes	Yes	Yes

Table 6. Search range for hyperparameter optimization.

Model	Hyperparameter	Search range
XGBoost	Number of trees	20, 40, 60, 80, 100, 120, 140, 160, 180, 200
	Learning rate	1, 0.5, 0.1, 0.05, 0.01
ANN	Number of hidden layers	1, 2, 3, 4, 5
	Activation function	ReLU, sigmoid, tanh
	Number of nodes in hidden layers	15, 20, 25, 30

3.2 Simulation accuracy of surrogate models

Figure 3 illustrates the accuracy of MLR, XGBoost, and ANN in simulating hourly indoor air temperatures and hourly thermal loads with different training sample sizes generated using LHS and SRS. According to the results, the three models trained using the samples generated by LHS exhibit similar accuracy to those trained using the samples generated by SRS. The main reason might be that most inputs are independent of each other. Additionally, the accuracy of the three models improves when increasing the sample size, however the accuracy no longer improves significantly when the training sample size reaches 400. This indicates that limited simulation data are sufficient to develop an accurate surrogate model. ANN demonstrates the highest accuracy among the three models. With a sample size of 400, it shows a R^2 of 0.99 for the indoor air temperature and a R^2 of 0.95 for thermal load. Moreover, it shows a *MAE* of 0.12 ºC for the indoor air temperature and a *MAE* of 700 W for the thermal load.

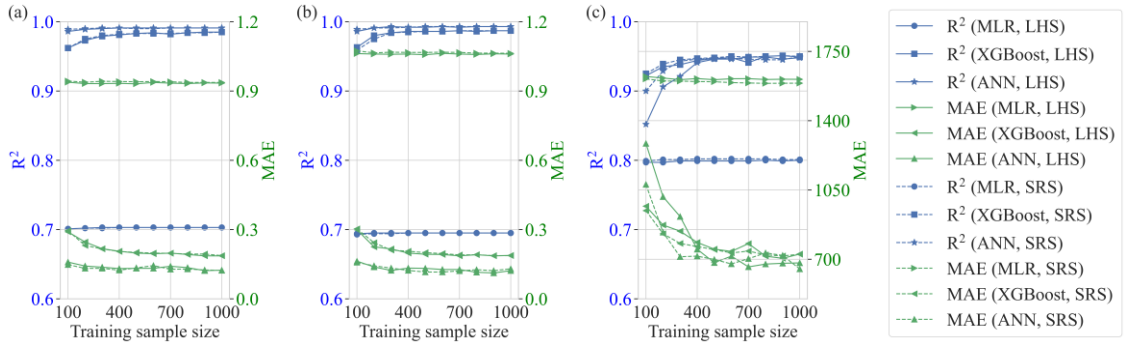

Figure 3. Accuracy of MLR, XGBoost, and ANN with different training sample sizes for the (a) hourly indoor air temperature on the 1st floor, (b) hourly indoor air temperature on the 2nd floor, and (c) hourly thermal load.

Figure 4 illustrates the ANN prediction results (400 LHS training samples) and EnergyPlus simulation results in six building variations with different occupant behavior. These variations are derived from the same base variation, with only one behavior modified in each variation. As shown, ANN results closely match those of EnergyPlus. Figures 4 (a) and (d) show the results on Feb. 1st for two variations with high and low heating setpoints (schedules 5 and 6 in Table 3), respectively. An increase in the setpoint significantly increases the heating load in winter. Figures 4 (b) and (e) illustrate the results on Aug. 1st for two variations with low and high ventilation rates (No. 1 and 2 strategies in Table 4), respectively. Increasing the ventilation rate slightly lowers the indoor air temperatures and cooling load in summer. Figures 4 (c) and (f) present the results on Jul. 22nd for two variations without and with solar shading (No. 1 and 2 strategies in Table 4), respectively. Solar shading significantly reduces the indoor air temperatures and cooling load in summer. Given the high accuracy of the ANN model, its prediction results are reliable for calculating specific KPIs such as thermal comfort hours, overheating hours, underheating hours, and peak thermal loads.

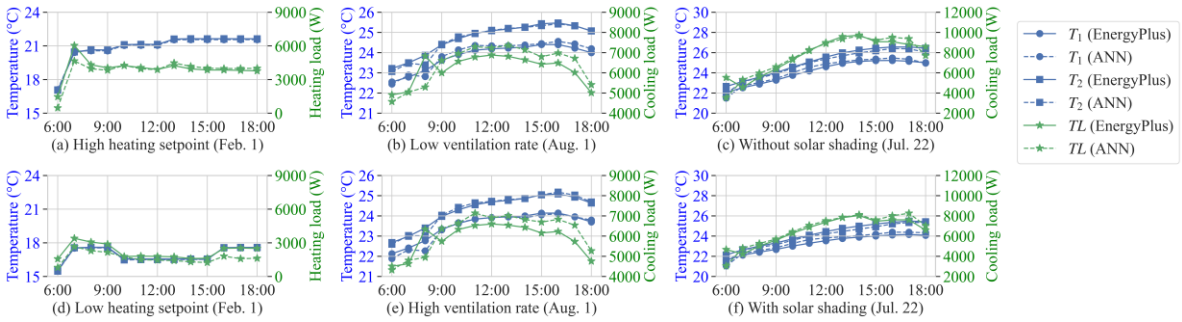

Figure 4. ANN results vs. EnergyPlus results for the hourly indoor air temperatures on the 1st floor (T_1) and 2nd floor (T_2), and the hourly thermal load (TL) in six building variations.

3.2 Simulation time of surrogate models

A laptop with a 2.3 GHz Intel Core i7-11800H processor is selected as the computational tool in this case study. The training time for the ANN surrogate model with a sample size of 400 is 25.9 min, while the simulation time is 0.01 s per simulation. As for EnergyPlus, its simulation time is 30.4 s per simulation. This implies that using surrogate models can reduce the simulation time by 99.97% when evaluating building renovation strategies in this case study.

4. CONCLUSIONS

This paper proposes a fast BPS method that can be used to evaluate large numbers of renovation strategies for terraced houses in a neighborhood. The basic idea is to train surrogate models using a limited dataset of EnergyPlus hourly simulation results for each relevant house. The simulation performance of surrogate models is verified and demonstrated for one terraced house in this study. In future research, the surrogate models will be applied to optimize renovation strategies for a variety of terraced houses in a neighborhood.

The results show that the surrogate models trained with simulation samples generated using Latin hypercube sampling demonstrate similar accuracy to those trained with samples produced by simple random sampling. Additionally, it is found that limited simulation data (sample size of 400) are sufficient for training an accurate surrogate model. Among three widely used data-driven models, artificial neural networks exhibit the highest accuracy in simulating indoor air temperatures (R^2 = 0.99 and MAE = 0.12 ºC) and building thermal loads (R^2 = 0.95 and MAE = 700 W). Regarding the computational time, it is shown that using surrogate models can reduce the simulation time by 99.97% compared to using EnergyPlus.

ACKNOWLEDGEMENTS

This work is supported by the project from Urban Development Initiative (No. 10030737).

REFERENCES

Bramiana C.N., Entrop A.G., Halman, J.I.M., 2016. Relationships between Building Characteristics and Airtightness of Dutch Dwellings. Energy Procedia 96, 580–591.

Herbinger F., Vandenhof C., Kummert M., 2023. Building energy model calibration using a surrogate neural network. Energy and Buildings 289, 113057.

Hong T., Chen Y., Luo X., et al., 2020. Ten questions on urban building energy modeling. Building and Environment 168, 106508.

Lu J., Zheng Z., Zhang C., et al., 2024. Graph convolutional networks-based method for uncertainty quantification of building design loads. Building Simulation.

Lund H., Østergaard P.A., Chang M., et al., 2018. The status of 4th generation district heating: Research and results. Energy 164, 147–159.

Ministerie van Binnenlandse Zaken en Koninkrijksrelaties (BZK), Centraal Bureau voor de Statistiek (CBS). WoON2018energie: release 1.0–Energiemodule WoON2018. Data Station Social Sciences and Humanities, 2019.

Pan X., Xu Y., Hong T., 2024. Surrogate modelling for urban building energy simulation based on the bidirectional long short-term memory model. Journal of Building Performance Simulation 0, 1–19.

RVO, Voorbeeldwoningen 2022 bestaande bouw. Den Haag, The Netherlands: Rijksdienst voor Ondernemend Nederland (RVO), 2023.

Sharif S.A., Hammad A., 2019. Developing surrogate ANN for selecting near-optimal building energy renovation methods considering energy consumption, LCC and LCA. Journal of Building Engineering 25, 100790.

VLA, VLA methodiek gelijkwaardigheid voor energiebesparende ventilatieoplossingen in woningen. Vereniging Leveranciers Luchttechnische Apparaten (VLA), 2018.

Yigit S., 2021. A machine-learning-based method for thermal design optimization of residential buildings in highly urbanized areas of Turkey. Journal of Building Engineering 38, 102225.

Zhang L., Plathottam S., Reyna J., et al., 2021. High-resolution hourly surrogate modeling framework for physics-based large-scale building stock modeling. Sustainable Cities and Society 75, 103292.

Zhao Y., Zhang C., Zhang Y., et al., 2022. A review of data mining technologies in building energy systems: Load prediction, pattern identification, fault detection and diagnosis. Energy and Built Environment 1, 149–164.

COBEE

6th International Conference on Building Energy and Environment
Eindhoven University of Technology, The Netherlands
6 - 10 July 2025

Fast and batch generation of orthogonal hexahedral grid for CFD analysis in built environments

Zhenyu Sun[1], Qingwei Miao[2], Wei Liu[1]

[1] *Tianjin Key Laboratory of Indoor Air Environmental Quality Control, School of Environmental Science and Engineering, Tianjin University, Tianjin, China, weiliu@tju.edu.cn*

[2] *District Heating Engineering Technology Research Center of North China Municipal Engineering Design and Research Institute Co., Ltd.*

SUMMARY

In built environments, typical flow features such as wall-bounded flow and flow over flat surfaces can be well simulated with a hexahedral grid. In addition, under the same grid size, the use of hexahedral mesh better controls the overall number of grid cells. However, in the generation of a hexahedral mesh, connectivity modifications propagate through the mesh, resulting in a complex spatial partition of blocks. To address this complexity, the tool can automatically generate blocks for uniform grids by inputting characteristic coordinates and global grid size. It also supports the input of the first layer grid size, growth rate, and maximum grid size to automatically generate sub-blocks further for non-uniform grids. The definition of a boundary only requires inputting the diagonal coordinates of the surface. Additionally, the tool can automatically check the correctness of the definition of boundary parts. The tool will be open source on GitHub.

Keywords: indoor airflow, outdoor airflow, OpenFOAM, Structured mesh

1. INTRODUCTION

The mesh in a computational fluid dynamics (CFD) analysis is used to discretize a computational domain into numbers of control volumes, on which the conservation of mass, momentum, and energy is applied. Mesh generation can take up to about 40%-60% of the total time spent on a CFD mission (Liu et al., 2022). This is because a mesh should first be able to accurately describe the geometry of a computational domain. Besides, the mesh should be fine enough to capture the flow features or minimize the truncation error, and should not be too fine since beyond a certain level of refinement, the accuracy of the results does not improve significantly. Further, a smooth transition from small-scale grid to large-scale grid is needed as the discretized governing equations are solved dependently.

When generating a mesh, the choice of grid type is critical for optimizing computational accuracy, speed, and memory usage. The orthogonal hexahedral grid is widely favored for its high computational accuracy (Sarrate Ramos et al., 2014; Wang et al., 2021), excellent convergence properties (Baker et al., 2020; Liu et al., 2022), and efficient space-filling capabilities (Katz and Sankaran,

2011). It is commonly used in both indoor airflow simulations (Sheng et al., 2023; Yuan, Xu, et al., 2020) and outdoor wind field studies (S. Chen et al., 2024; Lin et al., 2024). For instance, Wang et al. (Wang et al., 2021) demonstrated that the hexahedral orthogonal mesh outperforms other grid types in terms of accuracy in outdoor wind field simulations. Similarly, Li et al. (Li and Okaze, 2024) found that hexahedral meshes provided better accuracy than polyhedral meshes when simulating flow over building arrays in various boundary layers. Duan et al. (Duan et al., 2015) also concluded that hexahedral grids were the most accurate for CFD simulations of air distribution in aircraft cabins, offering better control over grid size and simplifying grid independence analysis.

Several tools can generate hexahedral grids, such as ANSYS Meshing, ANSYS Fluent Meshing, ICEM CFD (Fluent, ANSYS, 2020), GAMBIT (ANSYS, Inc., 2009), StarCCM+ (CD-adapco, 2016), `blockMesh`, and `snappyHexMesh` (Jasak et al., 2007). While these tools can generate tetrahedral meshes for complex geometries, the quality of hexahedral grids varies. Tools like ANSYS Meshing, Fluent Meshing, ICEM CFD, and `snappyHexMesh` use octree algorithms to refine the grid progressively, generating hexahedral-dominant grids. However, this method struggles with complex geometries and may not generate sufficiently fine grids near boundaries. Some tools, such as ICEM CFD and GAMBIT, can create fully hexahedral grids, but these require manual geometry partitioning, making the process time-consuming. `blockMesh` in OpenFOAM can generate fully hexahedral grids for simple geometries but requires manual input, making it impractical for more complex shapes. In general, generating fully hexahedral grids involves complex spatial partitioning and manual geometry handling, which can be challenging for intricate structures.

Based on the challenges mentioned above, this study developed a scripting tool based on `blockMesh` that can automatically output the point, block, and boundary required by `blockMeshDict` through inputting typical geometric data and meshing parameters.

2. METHOD

The process starts with deriving characteristic points from the digital model as shown in Fig. 1, then the global block partitioning is automatically generated. Subsequently, the framework is able to generate either uniform or non-uniform grid per user's specification. For a uniform grid, a global grid size is needed. For an non-uniform grid, user needs to specify the corresponding mesh parameters. At last, boundary parts are defined, and the tool uses a staggered addition method to automatically check whether the boundary parts are correctly defined.

2.1. Geometry to Blocks

A geometric model consisting solely of orthogonal bodies can always be described as cubic volume $\mathbf{V}$ with cubic volumes $\mathbf{V}_i$ subtracted from it and rectangular surfaces $\mathbf{S}_i$ carved on volumes. Then the corresponding computation domain could be reproduced by characteristic points including two diagonal points of $\mathbf{V}$, two diagonal points of each $\mathbf{V}_i$, and two diagonal points of each $\mathbf{S}_i$.

Based on these characteristic points, sort the coordinate values in each direction to obtain n_x, n_y, and n_z different coordinates in x, y, and z directions, respectively. Using these coordinates, the volume $\mathbf{V}$ is partitioned into a total of $(n_x-1)\times(n_y-1)\times(n_z-1)$ blocks. Then, based on the characteristic points of $\mathbf{V}_i$, blocks inside $\mathbf{V}_i$ are deleted. The remaining blocks represent the computation domain.

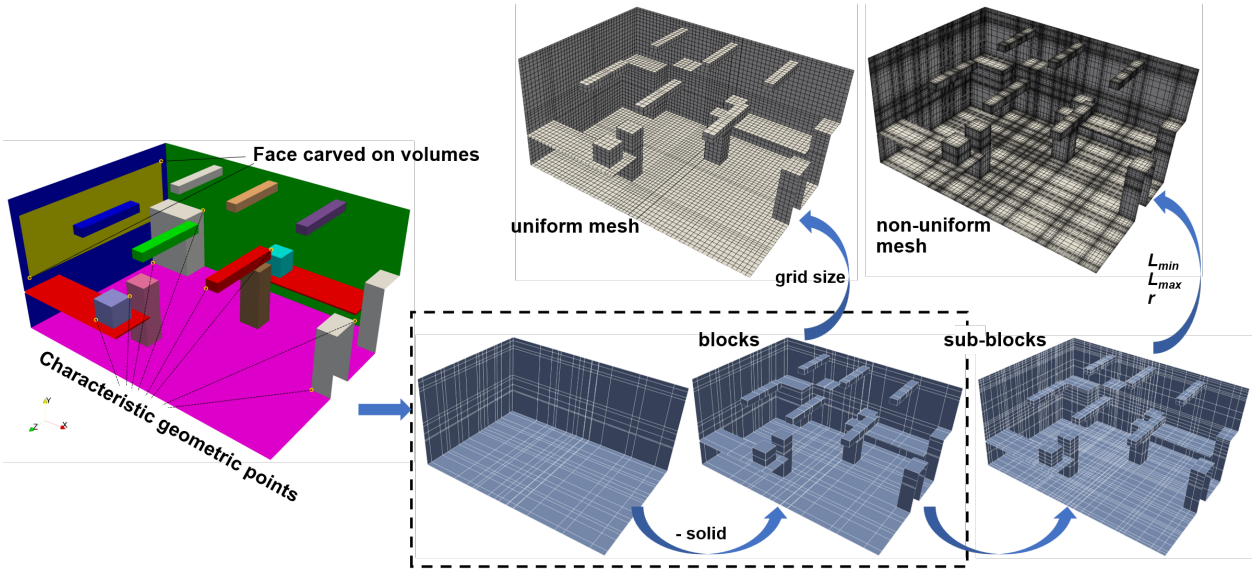

Figure 1. From geometry to block and mesh

2.2. Grid

For a uniform grid, the above block partition does not need to change. With a user specified global grid size, the number of grid cells is calculated based on the size of each block, which serves as the parameter for simpleGrading with a mesh growth rate of 1 in `blockMeshDict`.

In most scenarios, a non-uniform grid is needed. For built environments, fine grid is applied in the near-wall region where the gradient of air velocity and temperature could be large and coarse grid in those regions away from walls. Then a user needs to specify the minimum grid size $L_{\min}$, grid growth rate $r \in (1,2)$, and maximum grid size $L_{\max}$. To create such a grid, each of the aforementioned blocks may need to be further partitioned into sub-blocks. This is because the simpleGrading in `blockMesh` only allows grid size growth in one direction. Referring to Table 1, in either x, y, or z dimension, if the block length L_B is within the range $(0, 4 \times L_{min}]$, further partition is not needed and $N_u = [\frac{L_B}{L_{min}}]$ uniform grids are applied in this dimension. If $L_B > 4 \times L_{min}$, the grid size starts with L_{min} at the two ends and grows with rate r to the middle. If the maximum grid size L_{max} cannot be or is just reached, the block is divided into two sub-blocks in this dimension, with the mesh size growing from both ends towards the middle. The criterion for the division is that $L_B \leq 2D$, where the length D is determined by Eq. (1). The growth from L_{min} to L_{max} with rate r needs N_n grid cells determined by Eq. (2). If $L_B > 2D$, the block in this dimension is divided into three sub-blocks, with the two side sub-blocks having length D, and the middle sub-block using uniform grids with size L_{max}. Please note that sub-blocks generated in this section are temporary and will not affect the subsequent *Boundary parts* and *Boundary check*.

$$D = \frac{L_{max} - L_{min}}{r - 1} \tag{1}$$

$$N_n = [\log_r \frac{L_{max}}{L_{min}}] \tag{2}$$

Table 1. Number of sub-blocks for different block lengths.

Range of block length L_B	Number of sub-blocks
$(0, 4 \times L_{min}]$	1
$(4 \times L_{min}, 2 \times D]$	2
$(2 \times D, \infty)$	3

2.3. Boundary Parts

Using n_x, n_y, n_z different coordinates in x, y and z directions, there are a total of $n_x \times (n_y - 1) \times (n_z - 1)$, $(n_x - 1) \times n_y \times (n_z - 1)$ and $(n_x - 1) \times (n_y - 1) \times n_z$ faces perpendicular to the x, y, and z axes, respectively. Among these faces, those adjacent to only one block are boundary faces to be partitioned, while the remaining faces are internal faces of either fluid or solid regions and do not require boundary partitioning.

Each boundary to be defined can always be represented as a rectangle $\mathbf{R}$ with several rectangles $\mathbf{R}_j$ subtracted from it. Using the two diagonal points of $\mathbf{R}$ and $\mathbf{R}_j$, all faces within $\mathbf{R}$ can be defined, while faces within $\mathbf{R}_j$ will be skipped. Please note that $\mathbf{R}_j$ is an optional parameter. For a complete rectangular boundary part, $\mathbf{R}_j$ is not needed. Additionally, $\mathbf{R}_j$ does not need to be entirely within $\mathbf{R}$ because only the overlapped surfaces of $\mathbf{R}$ and $\mathbf{R}_j$ are skipped when defining a boundary part.

2.4. Boundary Check

To succinctly introduce the boundary check process, Fig. 2 presents a schematic diagram for a two-dimensional geometry. After partitioning the computational domain, a second rank tensor $\mathbf{B}$ of dimensions $\langle (n_x - 1), (n_y - 1) \rangle$ composed of 0 and 1 is defined. This tensor corresponds to the blocks, indicating that 1 represents a fluid domain where there is a block, and 0 represents a solid domain where there is no block. For checking cell faces perpendicular to the x axis, a column of zeros is added to the left side and right side of $\mathbf{B}$ that generates two new tensors $\mathbf{B}_{x-}$ and $\mathbf{B}_{x+}$, respectively. The dimension of $\mathbf{B}_{x-}$ and $\mathbf{B}_{x+}$ is $\langle n_x, (n_y - 1) \rangle$. The addition of $\mathbf{B}_{x-}$ and $\mathbf{B}_{x+}$ creates a new tensor $\mathbf{F}_x^*$. The same approach generates a new tensor $\mathbf{F}_y^*$ for cell faces perpendicular to the y axis. By mapping $\mathbf{F}_x^*$ and $\mathbf{F}_y^*$ to the cell faces, each cell face is assigned a value that can be either 0, 1 or 2. For a three-dimensional geometry, $\mathbf{B}$ will be a third rank tensor, and it will yield tensors $\mathbf{F}_x^*$, $\mathbf{F}_y^*$ and $\mathbf{F}_z^*$ for cell faces perpendicular to the x, y, and z axes, respectively. This process can be described by Eqs. (3, 4, and 5).

$$\mathbf{F}_x^* = \mathbf{B}_{x-} + \mathbf{B}_{x+} = \left[\ 0 \ \middle|\ \mathbf{B}\ \right] + \left[\ \mathbf{B} \ \middle|\ 0\ \right] \in \mathbb{R}^{n_x \times (n_y - 1) \times (n_z - 1)} \tag{3}$$

$$\mathbf{F}_y^* = \mathbf{B}_{y-} + \mathbf{B}_{y+} = \left[\ 0 \ \middle|\ \mathbf{B}^T\ \right]^T + \left[\ \mathbf{B}^T \ \middle|\ 0\ \right]^T \in \mathbb{R}^{(n_x - 1) \times n_y \times (n_z - 1)} \tag{4}$$

$$\mathbf{F}_z^* = \mathbf{B}_{z-} + \mathbf{B}_{z+} = \left[\ 0 \ \middle|\ \mathbf{B}^{\{T,\cdot\}}\ \right]^{\{T,\cdot\}} + \left[\ \mathbf{B}^{\{T,\cdot\}} \ \middle|\ 0\ \right]^{\{T,\cdot\}} \in \mathbb{R}^{(n_x - 1) \times (n_y - 1) \times n_z} \tag{5}$$

For each element within the tensor $\mathbf{F}_x^*$, $\mathbf{F}_y^*$ and $\mathbf{F}_z^*$, if it is 0, it indicates that the face is not adjacent to any blocks and does not belong to a boundary part. If the element is 1, it indicates that the face

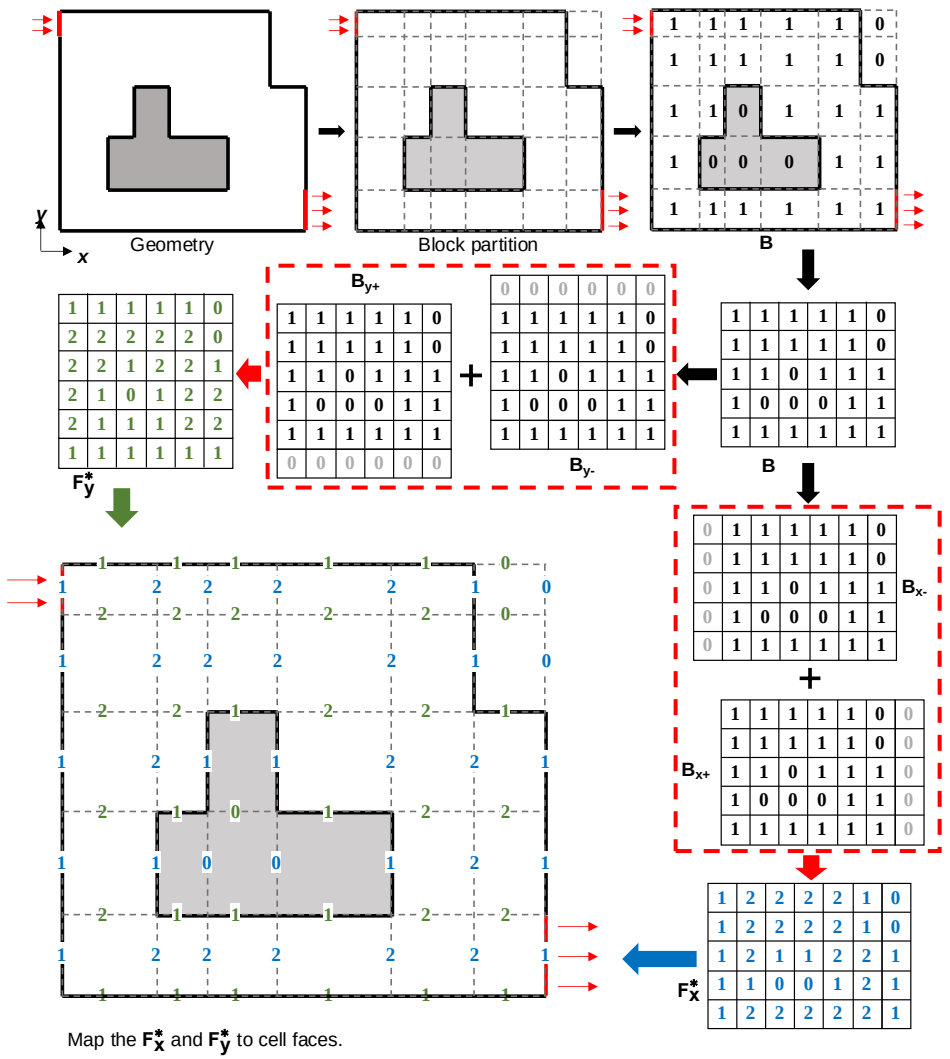

Figure 2. Boundary check: step 1

is adjacent to only one block and requires the definition of boundary parts. If the element is 2, it indicates that the face is adjacent to two blocks and is an internal face within the fluid domain.

Based on the diagonal points in section *Boundary parts*, the tool will generate three tensors $\mathbf{F}_x^{**}$, $\mathbf{F}_y^{**}$, and $\mathbf{F}_z^{**}$ of the same size as $\mathbf{F}_x^{*}$, $\mathbf{F}_y^{*}$, and $\mathbf{F}_z^{*}$, each composed of 0 and 1. In $\mathbf{F}_x^{**}$, a value of 1 indicates that the face belongs to the boundary, while a value of 0 indicates that the face does not belong to the boundary. Then the addition of $\mathbf{F}_x^{**}$ and $\mathbf{F}_x^{*}$ leads to $\mathbf{F}_x$. For this process, Fig. 3 provides a schematic diagram for a two-dimensional geometry. Similar operations are performed for $\mathbf{F}_y^{*}$ and $\mathbf{F}_z^{*}$. This process can be represented by the Eqs. (6, 7, and 8).

$$\mathbf{F}_x = \mathbf{F}_x^{*} + \mathbf{F}_x^{**} \tag{6}$$

$$\mathbf{F}_y = \mathbf{F}_y^{*} + \mathbf{F}_y^{**} \tag{7}$$

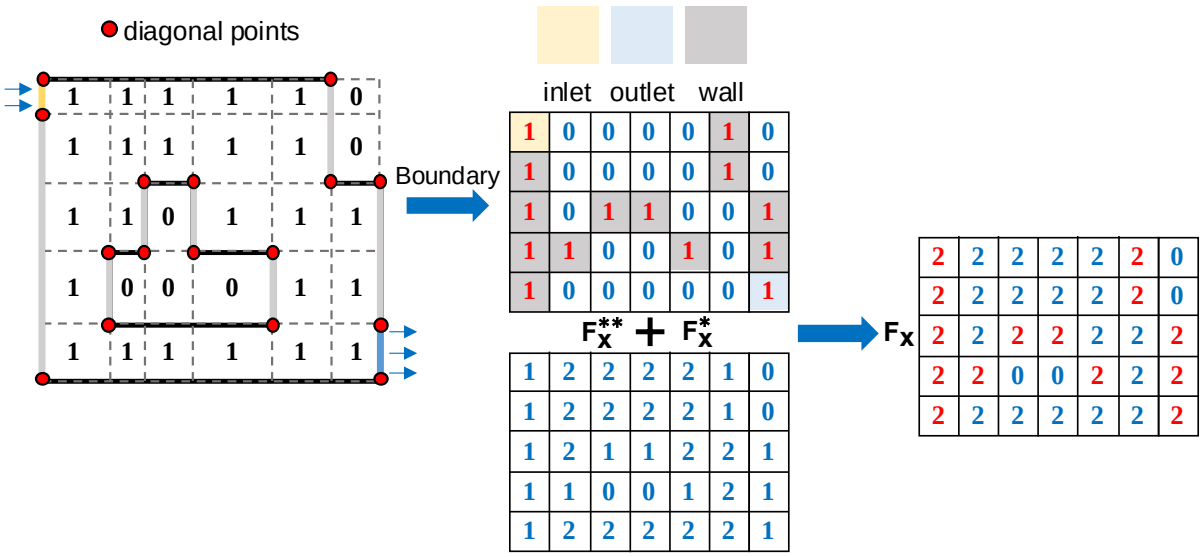

Figure 3. Boundary check: step 2

$$\mathbf{F}_z = \mathbf{F}_z^* + \mathbf{F}_z^{**} \tag{8}$$

If the elements that were 0 or 2 in the tensors $\mathbf{F}_x^*$, $\mathbf{F}_y^*$ and $\mathbf{F}_z^*$ remain unchanged in $\mathbf{F}_x$, $\mathbf{F}_y$ and $\mathbf{F}_z$, and the original 1 become 2, the boundary parts are correctly defined. Otherwise, there is an error and the reason and position for the error will be given. Table 2 gives the reasons for error in defining boundary parts.

Table 2. Reasons for error in defining boundary parts

Element in $\mathbf{F}_x^*$, $\mathbf{F}_y^*$ and $\mathbf{F}_z^*$	Element in $\mathbf{F}_x$, $\mathbf{F}_y$ and $\mathbf{F}_z$	Reasons for error
$=0$	>0	This face is an internal face of a solid domain and cannot be defined.
$=1$	$=1$	This face has not been assigned to any boundary parts.
$=1$	>2	This face is defined in multiple boundary parts.
$=2$	>2	This face is an internal face of the fluid domain and cannot be defined.

3. RESULTS

This study firstly tests the mesh tool using an office model (5.16 m $\times$ 3.65 m $\times$ 2.43 m) (Yuan, Q. Chen, et al., 1999). The fluid domain is formed by subtracting furniture, including two people, two computers, two tables, six lamps, and one diffuser. The room is meshed into a uniform grid and a non-uniform grid. For the uniform grid, with a grid size of 0.1m (Fig. 4a), the grid number is $59 \times 30 \times 44$. For the non-uniform grid, with $L_{min} = 0.01$ m, $L_{max} = 0.2$ m, and $r = 2$, the grid number is $131 \times 70 \times 132$, with finer grids near the walls (Fig. 4b).

The second case is a high-rise slab building with a height of 27 m, which has 9 floors with a floor height of 3 m, and the total construction area is 10,459 m². Fig. 5 shows the floor plan of the building, with four suites on each floor.

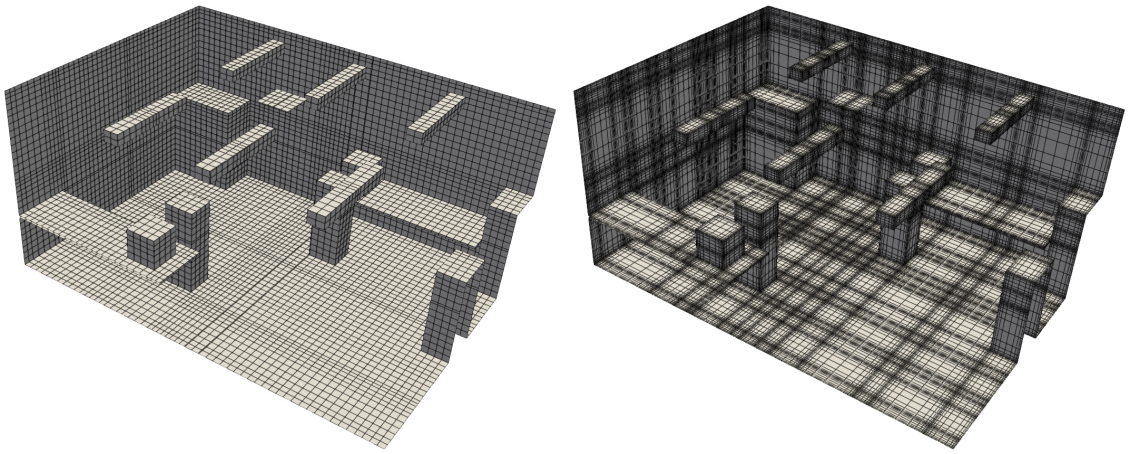

(a) Uniform mesh (grid size 0.1 m)

(b) Non-uniform grid ($L_{min} = 0.01$ m, $L_{max} = 0.2$ m, and $r = 2$)

Figure 4. Block partition and grid generation for an office with displacement ventilation.

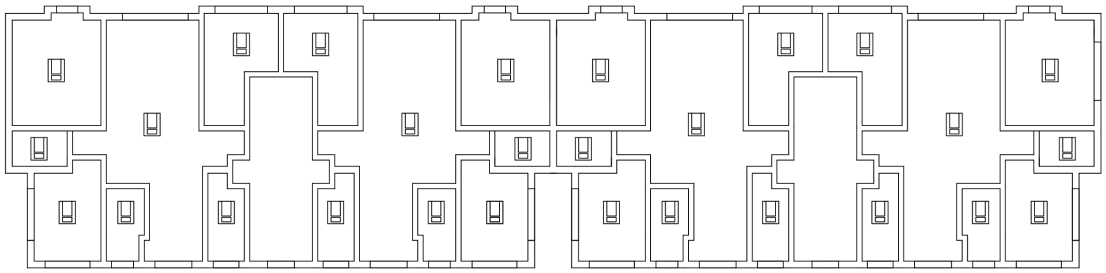

Figure 5. Floor plan of the building

Based on the building plan, in the mesh tool, walls and windows are treated as rectangular obstacles for input. Windows can be optionally included to simulate their opening or closing states. The characteristic points only require the diagonal coordinates of the computational domain and obstacles. Fig. 6a and 6b give the isometric and front view of the grid on the external surface of the building.

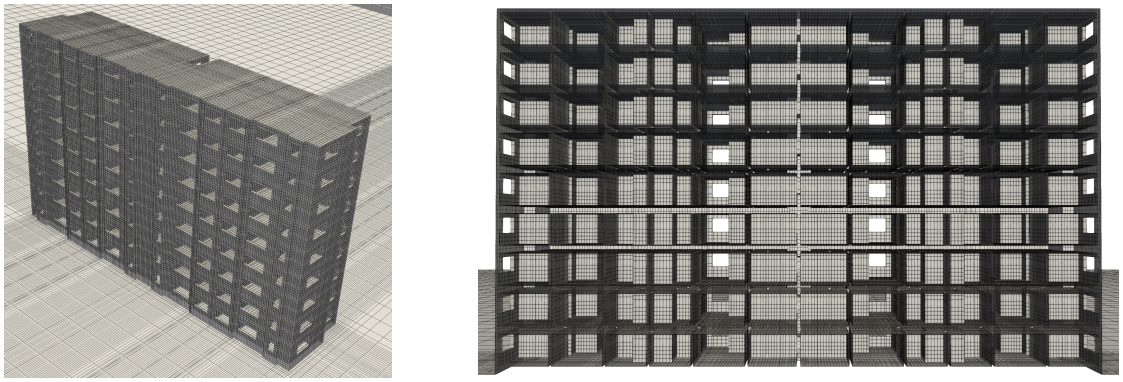

(a) Isometric view

(b) Front view

Figure 6. Grid of the nine-story high-rise slab building with $L_{min} = 0.3$ m, $L_{max} = 3$ m, and $r = 2$ m.

4. CONCLUSION

This study developed a mesh tool based on the `blockMesh` utility from the open source CFD program OpenFOAM. The tool is able to generate fully hexahedral grid with either uniform or non-uniform grid. Users only need to input the information of geometry, boundary parts, and global grid size. For the geometry, two diagonal points of all orthogonal bodies are needed. For the grid size, uniform grid needs a global size and non-uniform grid needs a minimum grid size, maximum grid size, and growth rate. The mesh tool conducts boundary check to ensure the correct definition of boundary parts. Case 1 is a typical office with displacement ventilation and case 2 is an outdoor case with detailed building internal configurations. The mesh tool and the two cases will be made open source on GitHub.

ACKNOWLEDGMENTS

This work was supported by the National Key R&D Program of the Ministry of Science and Technology, China, on "National Quality Infrastructure (NQI)" (Grant No. 2023YFF0613101).

REFERENCES

CD-adapco, 2016. *STAR-CCM+ 11.0 User Guide*. Available at https://www.cd-adapco.com. CD-adapco, Inc. New York, USA.

ANSYS, Inc., 2009. *GAMBIT*. Version 2.4.6, available at https://www.ansys.com.

Baker N., Kelly G., and O'Sullivan P. D., 2020. A grid convergence index study of mesh style effect on the accuracy of the numerical results for an indoor airflow profile. International Journal of Ventilation 19, 300–314.

Chen S., Fan Z., He L., Ma S., and Liu J., 2024. Ventilation benefit assessment of space organization design for'L'type inner corridor buildings. Building and Environment 253, 111327.

Duan R., Liu W., Xu L., Huang Y., Shen X., Lin C.-H., Liu J., Chen Q., and Sasanapuri B., 2015. Mesh type and number for the CFD simulations of air distribution in an aircraft cabin. Numerical heat transfer, part B: fundamentals 67, 489–506.

Fluent, ANSYS, 2020. R2 User's Manual; ANSYS. Inc.: Canonsburg, PA, USA.

Jasak H., Jemcov A., Tukovic Z., et al., 2007. OpenFOAM: A C++ library for complex physics simulations. Proceedings of International workshop on coupled methods in numerical dynamics. Vol. 1000. Dubrovnik, Croatia), 1–20.

Katz A. and Sankaran V., 2011. Mesh quality effects on the accuracy of CFD solutions on unstructured meshes. Journal of Computational Physics 230, 7670–7686.

Li Y. and Okaze T., 2024. Application of polyhedral meshes in large-eddy simulation of building array flow fields within neutral and unstable boundary layers. Building and Environment 263, 111846.

Lin P., Hao Q., Lau S. S. Y., and Wei Q., 2024. Impact of unit type and configuration on indoor natural ventilation performance of high-rise, high-density residential buildings in Hong Kong. Building and Environment, 112444.

Liu Y., Long Z., and Liu W., 2022. A semi-empirical mesh strategy for CFD simulation of indoor airflow. Indoor and Built Environment 31, 2240–2256.

Sarrate Ramos J., Ruiz-Gironés E., and Roca Navarro F. J., 2014. Unstructured and semi-structured hexahedral mesh generation methods. Computational Technology Reviews 10, 35–64.

Sheng S., Yamanaka T., and Kobayashi T., 2023. Heating and ventilation performance investigation of a novel linear slot diffuser with adaptive outlet area for near window applications. Building and Environment 244, 110813.

Wang W., Cao Y., and Okaze T., 2021. Comparison of hexahedral, tetrahedral and polyhedral cells for reproducing the wind field around an isolated building by LES. Building and Environment 195, 107717.

Yuan X., Xu X., Liu J., Pan Y., Kosonen R., and Gao Y., 2020. Improvement in airflow and temperature distribution with an in-rack UFAD system at a high-density data center. Building and Environment 168, 106495.

Yuan X., Chen Q., Glicksman L. R., et al., 1999. Measurements and computations of room airflow with displacement ventilation. ASHRAE Transactions.

6th International Conference on Building Energy and Environment
Eindhoven University of Technology, The Netherlands
6 - 10 July 2025

Reducing Energy Poverty Through Energy-Efficient Interventions at a National Scale in Households

Afshin Saeedian[1*], Lorna Fitzsimons[2], James McGrath[3], James O'Donnell[4], Reihaneh Aghamolaei[5]

[1]*School of Mechanical & Manufacturing Engineering, Faculty of Engineering and Computing, Dublin City University, Dublin, Ireland, afshin.saeedian2@mail.dcu.ie*
[2]*School of Mechanical & Manufacturing Engineering, Faculty of Engineering and Computing, Dublin City University, Dublin, Ireland, lorna.fitzsimons@dcu.ie*
[3]*Department of Experimental Physics, Faculty of Science & Engineering, Maynooth University, Co. Kildare, Ireland, James.McGrath@mu.ie*
[4]*School of Mechanical and Materials Engineering and UCD Energy, University College Dublin, Dublin, Ireland, james.odonnell@ucd.ie*
[5]*School of Mechanical & Manufacturing Engineering, Faculty of Engineering and Computing, Dublin City University, Dublin, Ireland, reihaneh.aghamolaei@dcu.ie*

SUMMARY
Energy poverty is a critical issue impacting numerous households globally, where rising energy costs and inefficient buildings exacerbate the problem. Existing studies often overlook the broader impact of energy efficiency interventions, such as how many individuals can be lifted out of energy poverty. This study investigates the impact of building envelope improvements and lighting control systems on reducing energy poverty risks at a national scale. By considering the socio-economic context, including household income, and applying an energy poverty indicator based on the 10% threshold, the research explores how specific energy efficiency measures, such as insulation upgrades and daylight-responsive lighting, can alleviate the financial burden of high energy costs. A case study of the archetype demonstrates how these interventions reduce the proportion of energy-poor households. The results indicate that, with the proposed enhancements, fewer households fall below the 10% energy expenditure threshold, offering promising solutions to combat energy poverty. These findings underscore the importance of targeted building interventions and the role of socio-economic factors in shaping energy poverty outcomes.

Keywords: Energy efficiency, Building Envelope, Energy poverty, Lighting control, Energy retrofit.

1. INTRODUCTION

Energy poverty appears in various forms and can be evaluated through several commonly used methods. These include subjective indicators, which focus on household perceptions of comfort and affordability; expenditure-based approaches, which evaluate energy costs relative to income; and multi-dimensional indicators, which integrate multiple factors to capture the multidimensional nature of energy poverty (Siksnelyte-Butkiene et al., 2021). One of the earliest and most widely used measures is the 10% indicator, which defines a household as energy-poor if its energy expenses exceed 10% of total income. While simple and widely adopted, this approach has been criticized for not accounting for variations in income levels and energy needs (Al Kez et al., 2024).

Energy poverty significantly affects daily life, limiting access to basic needs such as warmth and electricity, which are essential for improving living standards, health, education, and productivity (Halkos and Gkampoura, 2021). This issue is a significant societal issue impacting millions of households across Europe and globally. Europe faces harsh winters and rising energy costs, posing significant challenges for its population. In 2021, 7% of Europeans struggled to keep their homes warm, a figure that increased to 9.3% in 2022 and 10.6% in 2023 (Teixeira et al., 2024, Filippidou et al., 2024). Moreover, recent findings from the U.S. Energy Information Administration indicate that approximately one-third of households in the United States face energy poverty (Batlle et al., 2024). A 2022 report by Ireland's ESRI revealed that 29% of households (approximately 415,000 homes) were affected, with vulnerable groups disproportionately impacted. If energy prices rise further, up to 43% of households could face energy poverty, highlighting the need to identify those most at risk (Barrett et al., 2022). Addressing energy poverty requires a multi-faceted approach, including energy efficiency improvements, behavioural interventions, financial support, renewable energy integration, and policy reforms. Initiatives like the US Weatherization Assistance Program (WAP), the Energy Poverty Observatory (EPOV), and Ireland's Warmer Homes Scheme provide funding for energy-efficient upgrades, reducing energy costs for low-income households (Heller et al., 2024). Integrating climate-focused policies with energy poverty objectives ensures comprehensive and equitable outcomes, as evidenced by cross-country analyses (Belaid et al., 2023). Studies have demonstrated that behavioural interventions can lead to reductions in household energy consumption (Dietz et al., 2009, Composto and Weber, 2022). Enhancing energy efficiency in affordable housing can significantly reduce energy costs for low-income households, thereby alleviating energy poverty (Shwashreh et al., 2024). Despite growing research on energy poverty, less than 10% of studies address poor building conditions—a key contributor to high energy costs (Fabbri, 2024). Poorly constructed buildings with inadequate insulation and inefficient systems exacerbate energy poverty for low-income families (Fabbri, 2024). Retrofitting measures, such as insulation, airtightness, Passivhaus windows, solar PV, and mechanical ventilation with heat recovery (MVHR) systems, can significantly mitigate these issues. For instance, a case study housing retrofit in England reduced energy costs by 89%, fuel consumption decreased from 1,581 kWh to 550 kWh, representing 65% reduction, and improved indoor temperatures from 6 °C to 19.27 °C in winter (Shwashreh et al., 2024). Building envelope insulation, particularly using cost-efficient prefabricated panels, has been identified as a long-term solution to energy poverty in Italian social housing, offering significant heating cost reductions. Structural upgrades, such as facade insulation, could cut energy poverty by 30%, outperforming temporary subsidies (Fabbri et al., 2023). The effectiveness of these measures varies with energy prices, income, and rent levels (Fabbri et al., 2023). Such interventions highlight the economic and indoor environmental benefits of addressing poor building conditions alongside energy poverty alleviation strategies. However, despite these recent interesting findings, some limitations in these studies remain. The research by Shwashreh, Taki, and Kagioglou (2024) is constrained by its focus on a single case study, limiting the generalizability of findings to other regions or building archetypes. Similarly, Fabbri et al. (2023) primarily explore insulation strategies without integrating complementary measures, such as advanced artificial lighting performance. These gaps highlight the need for more comprehensive frameworks that address household's energy poverty, integrate advanced modelling techniques, and control devices for artificial lighting. Moreover, the

studies mentioned do not account for the number of individuals who would benefit from reducing energy poverty, which is a crucial aspect when assessing the broader impact of such interventions. By addressing some of these gaps, this paper aims to provide a robust approach to mitigating energy poverty through integrated strategies that align structural improvements with socioeconomic realities.

2. METHODOLOGY

This study aims to develop a comprehensive framework for evaluating and potentially mitigating energy poverty through integrated household energy enhancements and interventions at a national scale. The effectiveness of interventions is evaluated by analyzing their potential for energy savings, which in turn determines their impact on reducing energy poverty. The methodology involves three core phases as detailed below, which are also shown in Fig. 1:

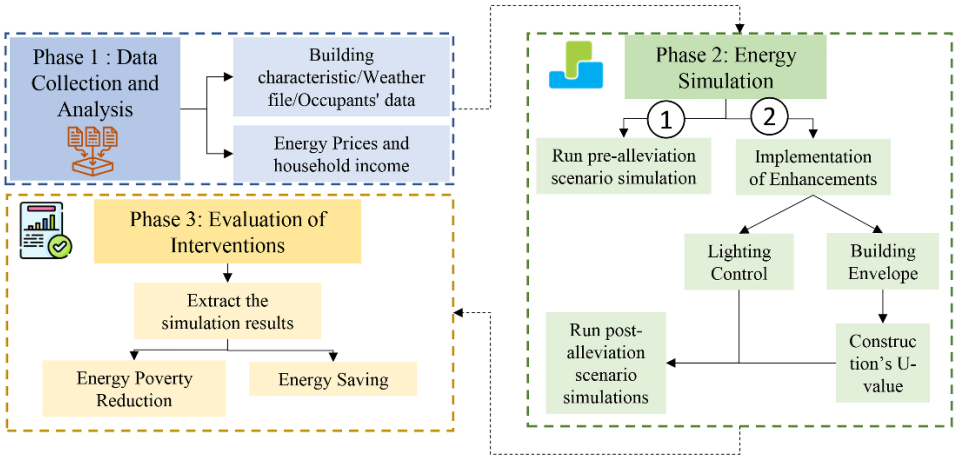

Figure 1. Comprehensive Methodology for Energy Savings and Addressing Energy Poverty

2.1. Phase 1: Data Collection and Analysis

Data collection focused on capturing quantitative variables influencing household energy consumption and expenditure. The key components include:

- Household characteristics: information related to a two-story, 4-bedroom, detached house in Ireland was extracted from a previous study (Egan et al., 2018);
- A relevant, updated weather file was added to the pre-retrofit archetype, and the building envelope for this archetype was assessed in terms of thermal performance and compliance with Irish standards.
- Energy Pricing and Socioeconomic Data: household income data from 2022, obtained from the Central Statistics Office (CSO), and 2024 energy pricing data from the Sustainable Energy Authority of Ireland (SEAI) were utilized in the analyses.

Detailed explanations for both components are provided in Section 3.

2.2. Phase 2: Energy Simulation

This section focuses on simulating the pre-retrofit and post-retrofit scenarios for the archetype to

evaluate building energy consumption. Simulation modelling was conducted using the DesignBuilder software tool. The process included creating a virtual representation of the case study, incorporating relevant parameters and constraints. The energy intervention includes envelope enhancements and daylight-responsive lighting control systems. Envelope enhancements focused on improved insulation and energy-efficient windows. Building regulations specify maximum allowable U-values for renovated or repurposed dwellings: 0.16 W/m²·K for pitched roofs with ceiling insulation and for ceilings, 0.35 W/m²·K for external walls, and 1.6 W/m²·K for external windows and doors (Building Regulation, 2022). Daylight-responsive lighting control systems, as encouraged by the Technical Guidance Document L 2022, optimize energy efficiency in Irish buildings by dynamically adjusting artificial lighting based on natural daylight availability (Building Regulation, 2022, SEAI, 2017). These systems dim or switch off lights when natural light is sufficient, ensuring functionality at a consistent workplace height of 0.8 meters. As a result, the building's energy efficiency strategies were implemented, with each step conducted independently rather than incrementally. The retrofit process started with insulating the external wall using sprayed polyurethane foam in the air gap layer (U-value: 0.338 W/m²·K). Next, the semi-exposed ceiling and pitched roof were insulated with 12 cm and 8 cm layers of polyurethane foam, reaching U-values of 0.165 W/m²·K and 0.150 W/m²·K, respectively. Triple-clear glazing with argon-filled gaps (U-value: 1.620 W/m²·K) was used to upgrade the windows, and the external door was also insulated with foam (U-value: 0.800 W/m²·K). Daylight-responsive lighting systems automatically adjust artificial lighting based on the amount of natural light available. Finally, all of these measures were integrated into a holistic approach to enhance the building's energy performance.

Table 1. Energy Poverty Actions in each step

	Construction	Intervention	Thermal Conductivity	U value (W/m2-k)
Step 1	External Wall	Sprayed Polyurethane Foam in the Air Gap	0.022	0.338
Step 2	Semi-Exposed Ceiling	Apply a 12 cm layer of Polyurethane Foam on the outer face	0.022	0.165
	Pitched Roof (Unoccupied)	Apply an 8 cm layer of Polyurethane Foam on the inner face	0.022	0.150
Step 3	External Window	Triple-clear glazing with a 3 mm pane thickness and a 13 mm argon-filled gap	-	1.620
	External Door	Sprayed Polyurethane Foam in the Air Gap	0.03	0.800
Step 4	Lighting Control			
Step 5	Combination of Steps 1 to 4			

2.3. Phase 3: Evaluation of Interventions

The effectiveness of energy renovation interventions was assessed using a comprehensive analysis of two key aspects of energy performance: energy savings and energy poverty mitigation. Simulated reductions in electricity and gas consumption were calculated to determine the overall energy savings achieved. Additionally, using the 10% indicator, the study assessed how many individuals fell below the energy poverty threshold and examined the reduction in the number of people affected by energy poverty relative to the pre-retrofit archetype.

3. CASE STUDY

A two-story detached, four-bedroom dwelling in Dublin's climate was selected as a case study in this research. According to Ireland's Census of Population 2016, there were 715,133 occupied detached houses, representing approximately 42% of all occupied dwellings at that time. Additionally, around 25% of occupied dwellings in Ireland had four bedrooms (CSO, 2017). Fig. 2 illustrates the layout of spaces in the detached house under study, with the relevant area given for each space.

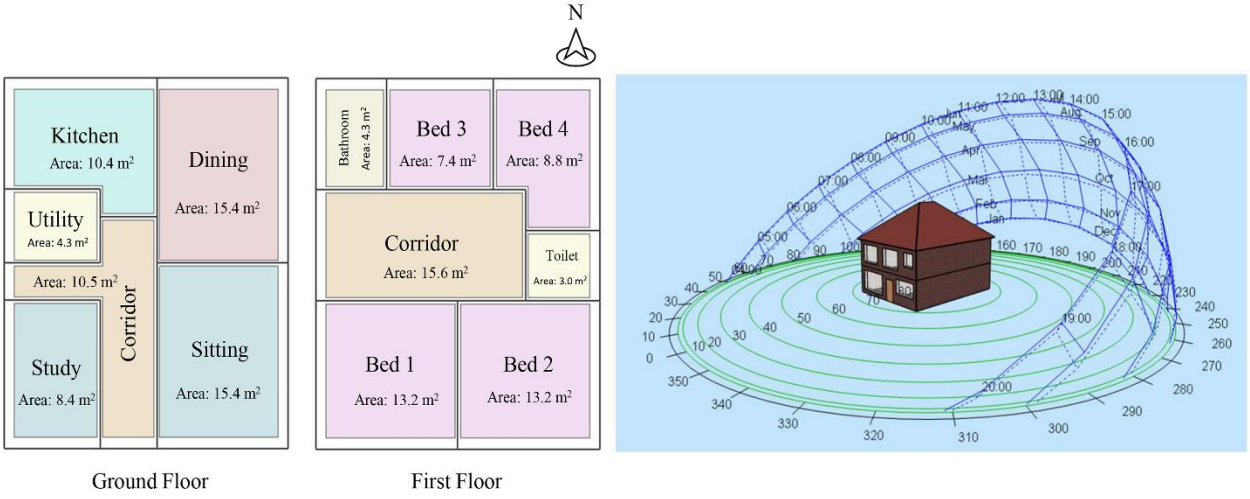

Figure 2. Detached building's space layout

As discussed in Section 2, energy pricing and household income levels were incorporated to assess the economic implications of the proposed interventions. As of the first half of 2024, the average electricity price for households in Ireland, including VAT, was approximately €0.354 per kilowatt-hour (kWh); for natural gas, the average price, including VAT, was €0.128 per kilowatt-hour (kWh), according to the Sustainable Energy Authority of Ireland (SEAI, 2024). According to the CSO, the median annual disposable household income in 2022 was €41,823, with significant variation across economic sectors and regions (CSO, 2022). The year 2022 was specifically chosen for this analysis due to the availability of highly detailed income data, allowing for an in-depth examination of income distribution and its relationship to energy poverty. Comparable datasets for 2023 and 2024 are either not yet available or lack the same level of granularity, making 2022 the most suitable reference point for this study. The granular analysis is crucial for evaluating energy poverty in this research because it is essential to recognize people who are living in 4-bedroom houses.

4. RESULTS

4.1. Archetype Simulation: Energy Consumption, Bills, and Poverty Assessment

The results of the simulations are shown in Table 2. The pre-retrofit archetype consumes 3,030.20

kWh/year for electricity and 24,097.91 kWh/year for gas. Based on calculations using the building's energy consumption and current energy prices (€0.354 per kWh for electricity and €0.128 per kWh for gas, including VAT), the annual energy cost amounts to €4,157.23. When assessed using the 10% energy poverty indicator, this represents approximately 10% of the average annual disposable income of an Irish citizen, which is €41,823 (CSO, 2022). According to the Individualised Gross Income Distribution report, 2,646,440 individuals out of a total population of 3,859,076 earn less than €40,000 annually (Revenue Commissioners, 2022). However, given that the selected building was designed for larger families (currently or previously), the analysis specifically focuses on individuals responsible for household expenses. These include married couples (both earning or one earning), widows, and widowers. The same report indicates that 1,099,382 individuals out of 1,832,859 people in these categories earn below €40,000 annually, accounting for 59.98% of this group (Revenue Commissioners, 2022). These findings underscore the critical need for targeted energy efficiency measures to reduce energy poverty, especially for vulnerable households in Ireland.

4.2. Effectiveness of Energy Efficiency Interventions

According to Table 2, the energy consumption analysis clearly illustrates the impact of each intervention on energy consumption. Initially, Step 1 (External Wall Enhancement) reduced gas consumption by 1,245.46 kWh/year, with electricity consumption remaining unaffected. Step 2 (Roof Insulation) reduced gas consumption by 2,783.59 kWh/year, maintaining the same level of electricity consumption. Following this, Step 3 (Window and Door Improvements) achieved the most significant gas reduction of 6,056.94 kWh/year, again without impacting electricity. In contrast, Step 4 (Lighting Control) led to a reduction of electricity consumption by 385.681 kWh/year, though it slightly increased gas consumption by 291.6 kWh/year. Ultimately, Step 5, which integrates all the previous interventions, delivered the most substantial reduction in both electricity and gas consumption, lowering electricity to 2,644.52 kWh/year and gas to 13,680.76 kWh/year, thereby showcasing the greatest overall energy savings. This combined approach clearly shows how integrating multiple energy-saving measures leads to better outcome.

4.3. Energy Poverty Reduction

Table 2 provides a comprehensive overview of energy consumption and cost reductions achieved through each intervention step, highlighting their impact on reducing energy poverty. Step 1, focused on External Wall Enhancement, achieved a modest 3.83% reduction, bringing the bill to €3,997.81/year. Building on this, Step 2, which addressed Semi-Exposed Ceiling and Pitched Roof Insulation, delivered a more notable reduction of 8.57%, lowering the bill further to €3,800.93/year. Step 3, targeting External Window and External Door Improvements, marked a significant turning point with an 18.65% decrease, reducing the bill to €3,381.94/year. Additionally, Step 4, which introduced Lighting Control, resulted in a smaller reduction of 2.39%, causing a slight decrease in the bill to €4,058.02/year. Finally, Step 5, combining all interventions, achieved the most substantial impact with a 35.36% reduction, lowering the energy bill to €2,687.30/year. Collectively, assuming that people can get free grants, these interventions played a critical role in addressing energy poverty by making energy bills more affordable and reducing the minimum income required to cover them. While Steps 1, 2, and 4 successfully eased the

financial burden on households, the income range classifications defined by the Revenue Commissioners limit the ability to precisely quantify the number of individuals lifted out of energy poverty by these measures. Nonetheless, their positive impact on vulnerable households remains clear. Step 3 emerged as particularly impactful, reducing the number of individuals affected by energy poverty by 131,141. The cumulative benefits of all interventions became most evident in Step 5, where the number of individuals affected by energy poverty decreased by 363,381 people. This underscores the effectiveness of integrated strategies in enhancing energy affordability and alleviating financial strain, providing a robust framework for future policymaking.

Table 2. Comparison of each step in reducing the energy bill

Intervention	Energy Consumption (kWh/year)		Energy bill (€/year)	Energy bill Reduction (%)
	Electricity	Gas		
Pre-retrofit Archetype	3,030.20	24,097.91	4,157.23	-
Step 1: External Wall	3,030.20	22,852.45	3,997.81	3.83
Step 2: Semi-Exposed Ceiling and Pitched Roof	3,030.20	21,314.32	3,800.93	8.57
Step 3: External Window and External Door	3,030.20	18,040.97	3,381.94	18.65
Step 4: Lighting Control	2,644.52	24,389.51	4,058.02	2.39
Step 5: Combination of Steps 1 to 4	2,644.52	13,680.76	2,687.30	35.36

These results are particularly relevant when considered alongside national funding schemes such as SEAI's grant programmes, which can cover up to 80% of retrofit costs for eligible homes (SEAI, 2025). For example, the Individual Energy Upgrade Grants offer up to €3,200 for retrofitting works, such as insulating cavity walls and ceilings (SEAI, 2025), making the interventions more financially accessible. With reduced utility bills, the payback period for households becomes significantly shorter, further strengthening the case for large-scale policy support.

5. DISCUSSION AND CONCLUSION

This study helps to fill an important gap in the literature, as previous studies did not quantify how many individuals directly benefit from such building interventions. For instance, Shwashreh et al. (2024) and Fabbri et al. (2023) provide valuable insights into retrofit impacts in the UK and Italian social housing contexts, respectively. However, their analyses are either limited to single-case studies or lack integration of complementary measures and socio-economic scaling. In contrast, the present study not only combines building envelope and lighting-control interventions but also uniquely quantifies the number of individuals lifted out of energy poverty at a national scale, an aspect that has not been addressed in previous literature. This is specifically discussed in Section 4.3 and detailed in Table 2, where we demonstrate that integrated interventions can reduce the number of energy-poor individuals by over 360,000.

This study shows that upgrading the building envelope and adding daylight-based lighting controls can significantly reduce household energy use and lower the share of homes falling below the 10% energy poverty threshold across Ireland. Specifically, the analysis shows that this approach reduced the number of income-earning individuals responsible for household expenses experiencing energy poverty by 33.05%, from 1,099,382 to 736,001. Additionally, the stepwise comparison of interventions supports scalable analysis of individual and combined retrofit

packages. These findings underscore the value of national retrofit grant schemes (e.g., SEAI) in improving affordability and uptake, while also providing actionable insights for policymakers seeking to advance both energy efficiency and social equity. Future work should explore the scalability of these interventions across various housing types and assess the potential for integrating more interventions, such as renewable energy sources and heating systems, to further enhance energy resilience.

REFERENCES

AL KEZ, D., FOLEY, A., LOWANS, C. & DEL RIO, D. F. 2024. Energy poverty assessment: Indicators and implications for developing and developed countries. *Energy Conversion and Management,* 307**,** 118324.

BARRETT, M., FARRELL, N. & ROANTREE, B. 2022. Energy poverty and deprivation in Ireland. Research Series.

BATLLE, C., HELLER, P., KNITTEL, C. & SCHITTEKATTE, T. 2024. US federal resource allocations are inconsistent with concentrations of energy poverty. *Science Advances,* 10**,** eadp8183.

BELAID, F., HEJAZI, M., KAMBOJ, P. & YILMAZ, F. 2023. *Implications of climate policy on energy poverty*, King Abdullah Petroleum Studies and Research Center.

BUILDING REGULATION 2022. Building Regulations, Technical Guidance Document L , Conservation of Fuel and Energy – Buildings other than Dwellings. *In:* DEPARTMENT OF HOUSING, L. G. A. H. (ed.). Government of Ireland.

COMPOSTO, J. W. & WEBER, E. U. 2022. Effectiveness of behavioural interventions to reduce household energy demand: a scoping review. *Environmental Research Letters,* 17**,** 063005.

CSO 2017. Central Statistics Office. Census of Population 2016, Profile 1 – Housing in Ireland. Dublin: CSO.

CSO 2022. Earnings Analysis Using Administrative Data Sources 2022. *In:* (CSO), C. S. O. (ed.).

DIETZ, T., GARDNER, G. T., GILLIGAN, J., STERN, P. C. & VANDENBERGH, M. P. 2009. Household actions can provide a behavioral wedge to rapidly reduce US carbon emissions. *Proceedings of the national academy of sciences,* 106**,** 18452-18456.

EGAN, J., FINN, D., SOARES, P. H. D., BAUMANN, V. A. R., AGHAMOLAEI, R., BEAGON, P., NEU, O., PALLONETTO, F. & O'DONNELL, J. 2018. Definition of a useful minimal-set of accurately-specified input data for Building Energy Performance Simulation. *Energy and Buildings,* 165**,** 172-183.

FABBRI, K. 2024. Energy Poverty and Poor Buildings: A Brief Literature Review to Promote New Topics for Future Studies. *Sustainability,* 16**,** 9638.

FABBRI, K., MARCHI, L., ANTONINI, E. & GASPARI, J. 2023. Exploring the Role of Building Envelope in Reducing Energy Poverty Risk: A Case Study on Italian Social Housing. *Energies,* 16**,** 8093.

FILIPPIDOU, F., KOKKINOS, C., CHEILAS, P., TSIARAS, S., VRONTISI, Z., CHEIKH, N., TORRES, P., YING LEE, L., VAN DER STEEN, E. & LIVRAGHI, S. 2024. Study on optimisation of energy poverty indicators collected at EU and national level.

HALKOS, G. E. & GKAMPOURA, E.-C. 2021. Coping with energy poverty: Measurements, drivers, impacts, and solutions. *Energies,* 14**,** 2807.

HELLER, P., SCHITTEKATTE, T. & BATLLE, C. 2024. EU and US Approaches to Address Energy Poverty: Classifying and Evaluating Design Strategies.

REVENUE COMMISSIONERS 2022. Individualised Gross Income Distribution. *In:* COMMISSIONERS, R. (ed.).

SEAI 2017. Energy Efficient LED Lighting. Sustainable Energy Authority of Ireland.

SEAI 2025. Individual Energy Upgrades Grants.

SEAI, S. E. A. O. I.-. 2024. Electricity and Gas Prices for Irish Households - 2024.

SHWASHREH, L., TAKI, A. & KAGIOGLOU, M. 2024. Retrofit Strategies for Alleviating Fuel Poverty and Improving Subjective Well-Being in the UK's Social Housing. *Buildings,* 14**,** 316.

SIKSNELYTE-BUTKIENE, I., STREIMIKIENE, D., LEKAVICIUS, V. & BALEZENTIS, T. 2021. Energy poverty indicators: A systematic literature review and comprehensive analysis of integrity. *Sustainable Cities and Society,* 67**,** 102756.

TEIXEIRA, I., FERREIRA, A. C., RODRIGUES, N. & TEIXEIRA, S. 2024. Energy poverty and its indicators: A multidimensional framework from literature. *Energies,* 17**,** 3445.

6th International Conference on Building Energy and Environment
Eindhoven University of Technology, The Netherlands
6 - 10 July 2025

Performance improvement of airflow distribution and contamination control for a biotech cleanroom

Rahmadi Aulia Pramudantoro[1], Chu-Cheng Wei[1], Bowo Yuli Prasetyo[2], Parisya Premiera Rosulindo[2], Fu-Jen Wang[1]

[1] *Department of Refrigeration, Air Conditioning and Energy Engineering, National Chin-Yi University of Technology, Taichung, Taiwan, fjwang@ncut.edu.tw*
[2]*Department of Refrigeration and Air Conditioning Engineering, Politeknik Negeri Bandung, Bandung, Indonesia*

SUMMARY
Cleanrooms are widely used in many industries such as semiconductor, bio-tech, microelectronics, pharmaceuticals, and nanotechnology. However, pharmaceutical industries (such as vaccine production) need a critical clean environment and contamination control is always a vital concern for the manufacturing process. This study investigates a bio-tech cleanroom through a comprehensive field measurement and numerical analysis. Computational fluid dynamics (CFD) simulation was also conducted to validate the numerical results and to identify strategies for performance improvement of a bio-tech cleanroom. The results reveal that based on cleanroom standard of ISO and PIC/S, the field test results conform to the design specification satisfactorily after the necessary adjusting. Higher air change rate per hour (ACH) results in a higher cleanness level. Room pressurization conforms to the design specification and all HEPA filters have been tested extensively. Performance improvement through CFD can be obtained through the layout arrangement for supply and return air grille. Airflow patterns improve contamination control through optimizing the ACH and supply air face velocity of HEPA filters extensively.

Keywords: biotechnology, cleanroom, field measurement, numerical simulation, contamination

1. INTRODUCTION

With the development of technology industries nowadays, the need for a better cleanrooms design has been increase especially in bio-tech industries. This increasing demand that could be related with a larger number of semiconductor industry, research laboratory, bio-tech, microelectronics, pharmaceutical, and nanotechnology. Cleanroom are classified according to the number and size of particle permitted per volume of air within a specific amount of time. There are three levels of condition (occupancy states) for testing and characterizing the performance of cleanrooms: as-built; at-rest; and operational. Standards such as ISO (2015, 2019) and GMP (2007) pertain to the cleanroom and associated environments. Industries require specific environment to prevent contamination because the manufacturing process or products are sensitive to indoor environmental parameters such as temperature, relative humidity, airborne particles, room pressurization, and illumination (Yang, 2007). To achieve these requirements, cleanrooms are designed and built to control these environmental parameters.

Field measurement tests are essential to assure the cleanroom performs satisfactorily and achieves the contamination standards (Yang, 2021). Additionally, it has been reported that contamination cannot be completely eliminated, thus targeted monitoring should involve reviewing data for trends (Sandle, 2015). Testing results form the basis for validating cleanroom performance.

Furthermore, Computational fluid dynamics (CFD) represent an important tool to do simulation especially in the HVAC field like predicting of airflow pattern in a cleanroom and its ability to remove airborne particles (Tung, 2009). Otherwise to full scale ventilation performance test, the CFD methods is cheaper and less interfering than the traditional experimental test and it allows to investigate different case and solution without intrusive the original case (Sun, 2010). Some CFD studies of indoor ventilation systems have been already carried out, Memarzadeh et. al. (2002) have used CFD to represent that unidirectional flow conditions are the best option for an operating room through of controlling the risk of contamination. Srebric et al. (2008) have demonstrated the accuracy of CFD simulation is depend on the considered obstacles in the room, e.g., occupants, equipment, the appropriate settings of boundary condition and numerical simulation parameters like heat flux and contaminant source.

This study investigates the indoor environment parameter for a bio-tech clean-room through comprehensive field measurement test to verify the effectiveness of the cleanroom system. The experimental data were analysed and validated with the numerical simulation in order to find the improvement strategy for a better approach design.

2. METHODOLOGIES

2.1. System Description

The layout of the investigated bio-tech cleanroom is displayed in Figure 1. The HVAC system for this cleanroom uses central air conditioning. Supply air was distributed from air handling unit (AHU) through ducts and high efficiency particulate air (HEPA) filters above the cleanroom. A regulating damper is installed in each room to adjust airflow rate. The field measurement test was conducted for all of main room process. The dimensions of the cleanroom are 15.4 m (length), 16.35 m (width), and 2.8 m (height), with a total volume of 524.2 m^3. Based on ISO 14644, this clean-room has a cleanliness level of 10,000 and 100,000 (Grade C and D). Total of the grade C cleanroom is equipped with 10 pieces of small HEPA filters (0.6 m × 0.6 m) and 10 pieces of large HEPA filters (1.2 m × 0.6 m) at the filtration efficiency over 99.97% (above 0.5 μm). The grade C room is used for a main manufacturing process such as weighing room, material storage, mixing raw material and take a material sample from bio-safety cabinet and fume hood. The grade D clean room is equipped with 2 pieces of small HEPA filters. The Grade D room is used for garbing and hand washing. The last room is a changing room for personnel and this room is equipped with 3 pieces of small HEPA filters.

2.2. Field Measurement Test

This study examined the indoor environmental parameters of the investigated bio-tech cleanroom during an unoccupied (at-rest) period. After inspection, the next step was validating the data using numerical simulation. All of the experiments were done during a construction of this factory. The tests for field measurement are as follows:

1. Airflow Rate

A contamination control is the primary purpose of the cleanroom. A way of contamination control by a controlled the air supply system. A TSI model 8380 was employed to monitor the velocity of each HEPA. To get the air flow rate, measure a HEPA dimension. After that, measure the air supply velocity with an apparatus and cover the hood to HEPA.

2. HEPA Leak Test

To qualify as HEPA the air filter must remove at least 99.97% of all airborne particles greater than

0.5µm in diameter from the air that passes through it. Poly Alpha Olefin (PAO) testing is a very quick process that tests the integrity of the High Efficiency Particulate Air (HEPA) filter using PAO solutions in their operational conditions. These tests generate a gas type smoke and then generate gas particles that will be greater than 0.5 micrometres. The test will certify the HEPA filter is fully functioning and there is no leakage or damage. PAO tests were conducted as well with an ATI TDA-2H photometers. The schematic of HEPA leak test is shown in Figure 2.

3. Particle Counts

The most important test used to ensure a cleanroom is working correctly is the measurement of the airborne particle concentration. A particle counter is used to count particles in the air of a cleanroom. A measurement of particle counts was performed with Beckman Counter model 3413 particle counter, sensitive to particles larger than 0.5 µm. The sampling flow rate for particle counter operated at 28.3 l/min (1 ft3/min) with sampling period 1 minute.

4. Room Pressurization

A cleanroom must have sufficient clean air supplied to dilute and remove the air-borne contamination generated within the room. A pressure is critical to the proper functioning of the clean room, the pressure test should be established in order to determine that the clean room can set-up a stable pressure difference between the environment to avoid a cross-contamination. A TSI model 9555-P digital manometer was be used to monitor the pressure difference of the bio-tech cleanroom. There are 10 measurement point and 3 times of measuring at each measurement point.

5. Temperature and Relative Humidity

Temperatures is required for comfort, precision measuring equipment, the handling of sensitive products, and compounds or ingredients. Humidity control is the most complex parameters because this parameter can make a big impact for personal comfort and a product. Too high humidity can encourage the growth of bacteria and microbes and corroding sensitive metals whether in products or equipment. There are 25 measurement point and 3 times of measuring at each measurement point. The variation of temperature and humidity were recorded by TSI model 9555-P.

(a) (b)

Figure 1. Layout of the investigated bio-tech cleanroom; (a) HEPA location; (b) particle counts measurement point.

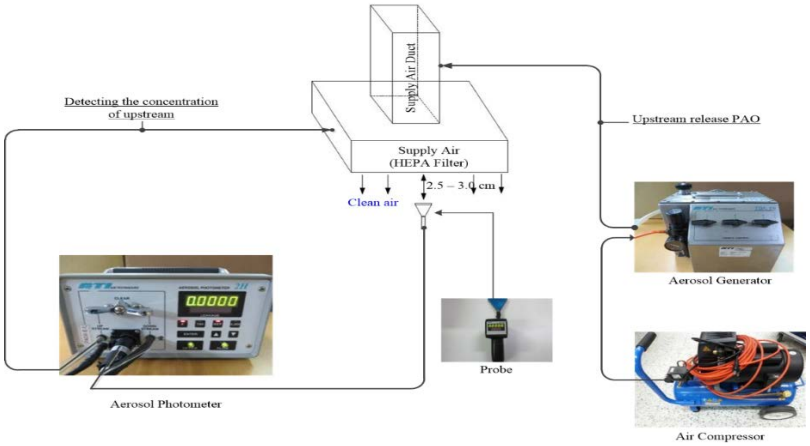

Figure 2. Schematic diagram of HEPA leak test apparatus.

Table 1. Typical input parameters of building for building simulation.

Apparatus Model	Operative range	Accuracy
TSI-8380	0.125 - 12.5 (m/s)	3%
ATI TDA-2H	0.0001%-100ug/L	1%
Beckman Counter 3413	0.3, 0.5, 1, 3, 5, 10 µm	5%
	-3735 ~ +3735 Pa	1 Pa
TSI-9555-P	-10 ~ 60 (℃),	0.3℃
	0 - 100 (%RH)	3%RH

2.3. Numerical Simulation

The 3D model of the investigated bio-tech cleanroom is shown in Figure 3. Some manufacturing machines were sketched in the layout as well. The main process clean-room of Grade C is chosen to be the research object. The geometry of the research object according on the actual size. The dimension of the investigated cleanroom is at length of 11.0 m, width of 8.25 m, height of 2.8 m, and total area of this cleanroom 90.75 m3. Total of the investigated bio-tech cleanroom is equipped with nine pieces of HEPA filters and two return air grilles. The dimension of HEPA is at length of 1.2 m and width of 0.6 m then the dimension of the return air grille is at length of 0.6 m and width of 0.3 m. This investigated bio-tech cleanroom is used for main manufacturing process such as weighing room, material storage, mixing a raw material, and take a material sample from bio-safety cabinet.

The computational fluid dynamics (CFD) simulation has been proven to be powerful tool and efficient in airflow distribution and concentration profile case. In this study, steady state numerical simulation has been carried out using Ansys Fluent Workbench version 2020 R2. The solution of simulation analysis is divided into two categories, the steady-state and unsteady state (transient) solution. This research will be carried out in two phases stage of the simulation. The first stage is for airflow distribution simulation analysis, it has been simulated with steady-state solution. The coupling iterative calculation for this stage is solved by SIMPLE (Semi-Implicit Method for Pressure Linked Equations) method. The second stage is the exclusion of the contamination airborne analysis with unsteady solution (transient) to simulate. The simulation time is 450 second with time step size is 0.25 second. The numerical method is used to establish the difference equation for the finite-volume method. The coupling iterative calculation is solved by PISO (Pressure Implicit with Splitting of Operator) method. The residual value is set to 10-6. The contamination airborne is set at the species model used species transport with carbon-monoxide as

a mixture material. The CO2 concentration in the outdoor atmosphere is about 400 ppm, which will be used as the concentration value for supply air from HEPA. The initial contaminant concentration in the bio-tech cleanroom is set to 3,000 ppm.

The performance improvement strategy was proposed and analysed by numerical simulation. The temperature and velocity of the HEPA filters have been measured through field measurement test to provide reliable measurement data as the boundary condition of CFD simulation. Furthermore, all of the boundary conditions for solution domain were clearly defined according to the actual field measurement tests data to carry out the accurate solutions. The heat flux from machine is based on the machine specification. The boundary condition for numerical simulation is displayed in Table 2. Numerical simulation of different approaches to improve performance of the bio-tech cleanroom was conducted and assessed comprehensively.

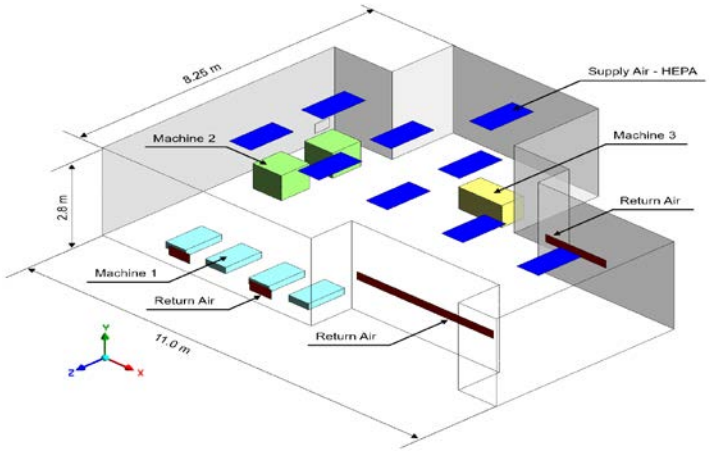

Figure 3. Computational model of the investigated bio-tech cleanroom

Table 2. Boundary condition for numerical simulation.

Parameters	Type	Value
Supply Air	Velocity Inlet	Velocity: 0.205 m/s Temperature: 19.2°C
Return Air	Pressure Outlet	Pressure: -8.2 Pa Temperature: 24°C
Machine 1	Wall	Heat Flux: 20 W/m^2
Machine 2	Wall	Heat Flux: 30 W/m^2
Machine 3	Wall	Heat Flux: 35 W/m^2

3. RESULTS AND DISCUSSION

3.1. Experimental Results

The experiments on the bio-tech cleanroom were conducted under at-rest occupancy conditions. Field measurement were carried out for all room. In this study will focus only on Ether Treatment room for numerical simulation. HEPA leakage testing is necessary to ensure the HVAC system in a good condition. Figure 4 (a) represent the field measurement data of a HEPA leak test. HEPA filter must remove at least 99.97% of all airborne particles greater than 0.5 micrometres. The leak test was performed twice and the maximum permissible leak-age should be 0.01%.

The indoor environmental condition design including temperature are maintained at 20±5°C,

relative humidity at 40-60%, and pressure at -5 Pa. The experimental data shows a good in the range of acceptance with temperature between 20.5°C - 21.6°C, relative humidity 54.2% - 55.4%, and pressure at -8.2 Pa. The bio-tech cleanroom is classified into Grade C which the particle size at 0.5µm should be less than 325,000 pcs/m3 and 5µm less than 2,900 pcs/m3 in at-rest occupancy state condition. The airflow rate for Grade C should be greater than 20 ACH and for Grade D should be greater than 10 ACH. As shown in Figure 4 (b), the results are appropriate with the standard. A higher particle counts occurs in the main process room because of production machines but still less than the standard. A higher airflow rate also is about 41 ACH occurs in the Grade C rooms. The increasing of ACH may increase the cleanliness level in a room.

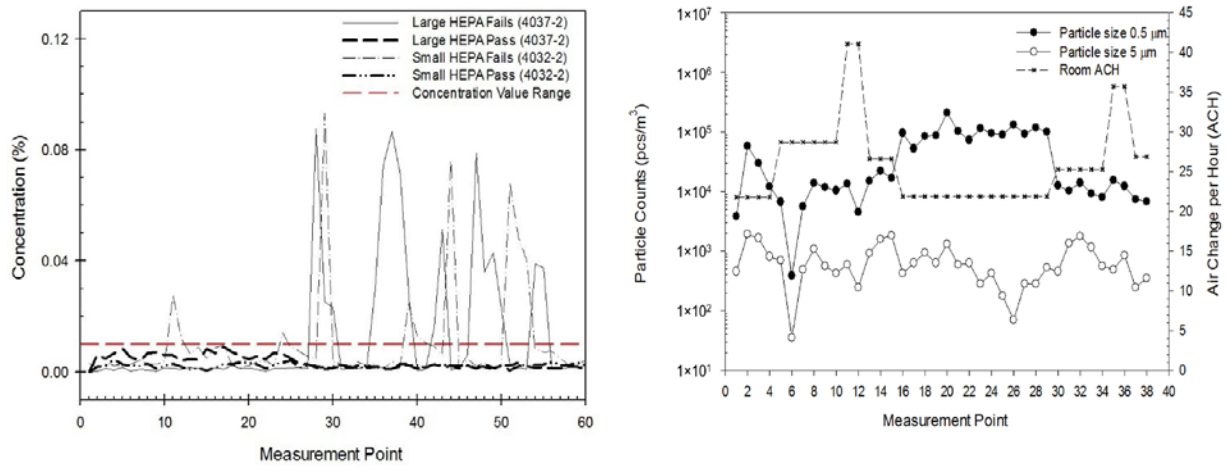

(a) (b)

Figure 4. Field measurement test; (a) particle counts and ACH; (b) HEPA leak test

3.2. Validation

During the simulation process, the parameters could change the level of accuracy. As the number of elements in the mesh will increase the accuracy of the simulation results. However, this requires a long time and sufficient resources. In this research, there are four sets of grids number are selected to verify accuracy of simulation, 280,064 grids, 310,013 grids, 530,127 grids, and 630,75 grids. Moreover, increasing the number of grids makes the simulation results more precise and effectively reduce required time to simulate. In this research, the grid number of 530,127 is chosen as a follow-up numerical simulation of the grid number. The numerical simulation has been conducted to validate the field measurement result. As a main production room is used for a numerical simulation in this case. The error rate result of the temperature between numerical simulation and field test are less from 8% and for error rate of the velocity is less than 9%.

3.3. Numerical Simulation Results

In order to increase the performance improvement and contamination control, a higher velocity or ventilation rate is increased to 0.25 m/s and 0.3 m/s respectively and analysed numerically. Temperature will be reached quickly with higher ventilation rate. Not only the temperature desire level, but also a higher cleanliness level will increase. Figure5 shows the results of velocity, temperature, and concentration distribution in each case. Increasing face velocity improved airflow distribution, reaching the corners of the cleanroom.

The temperature data collected were conducted at the height of 1.4 m above the floor for both field measurement test and numerical simulation. The total of 7-point measurement were recorded and

analysed. The effect of increasing face velocity result in a distributed temperature. The point 1 in the case 1 has a higher temperature around 24°C, it is located upper the position of machine 2. While in the point 6 and point 7 have a lower temperature around 20°C. In that area have no heat flux from machine, so the temperature could result in a lower than others point. By increasing the face velocity, the temperature could result in more distributed and lower, especially in the point 2 near the heat flux generated area.

Contamination control is one of way for improving and maintaining the cleanliness level in the bio-tech cleanroom. The contaminant concentration in bio-tech clean-room is displayed in three-dimensional plane at the height of 1.4 m above the floor in the time condition at 450 seconds. The high contaminant concentration in case 1 is happened around the monitoring point 1, point 3, and point 5. It was showed that the contaminant concentration is around 700 ppm in the monitoring point 3. In addition, it also shows the accumulation of contamination at the corner of bio-tech cleanroom, the reason of the air distribution is not evenly distributed to cleanroom especially to the corner. Face velocity of the HEPA or supply air grille did not distribute to the outer part or corner and may cause the contamination residue due to the return air pattern between the return air is open. In the area that more airflow was distributed evenly such as monitoring point 6 and point 7 has better performance of contamination removal.

Another assessment, ventilation efficiency is the ratio between contaminant concentration in the occupied spaces and the concentration in the exhaust air. It is a measure of how effectively the air present in a space is replaced by fresh air from the ventilation system. Table 3 depicts the results of the ventilation efficiency in different case study. The lower concentration in the cleanroom result in a higher ventilation efficiency. Case 3 has the highest ventilation efficiency with 96.55% efficiency. While, case 1 and case 2 result in 85.47% and 90.42% of efficiency.

Table 3. Ventilation efficiency results

Case Study	Concentration Average (ppm)	Concentration at Supply Air (ppm)	Concentration at Outlet Air (ppm)	Ventilation Efficiency (%)
Case 1	579	400	553	85.47
Case 2	494	400	485	90.42
Case 3	458	400	456	96.55

4. CONCLUSIONS

The following conclusions may be drawn:

- All indoor environmental conditions met the design specifications in the experiments. However, some location result in a higher concentration generated.
- The numerical simulation was conducted in different face velocity which to analysed a better concentration distribution. Case 3 with a higher ventilation rate result in a lower concentration.
- Increasing face velocity resulted in lower pressurization in each case, but still within the acceptable range.
- The lower concentration in the cleanroom result in a higher ventilation efficiency. Case 3 has the highest ventilation efficiency with 96.55% efficiency. While, case 1 and case 2 have efficiency of 85.47% and 90.42% respectively.

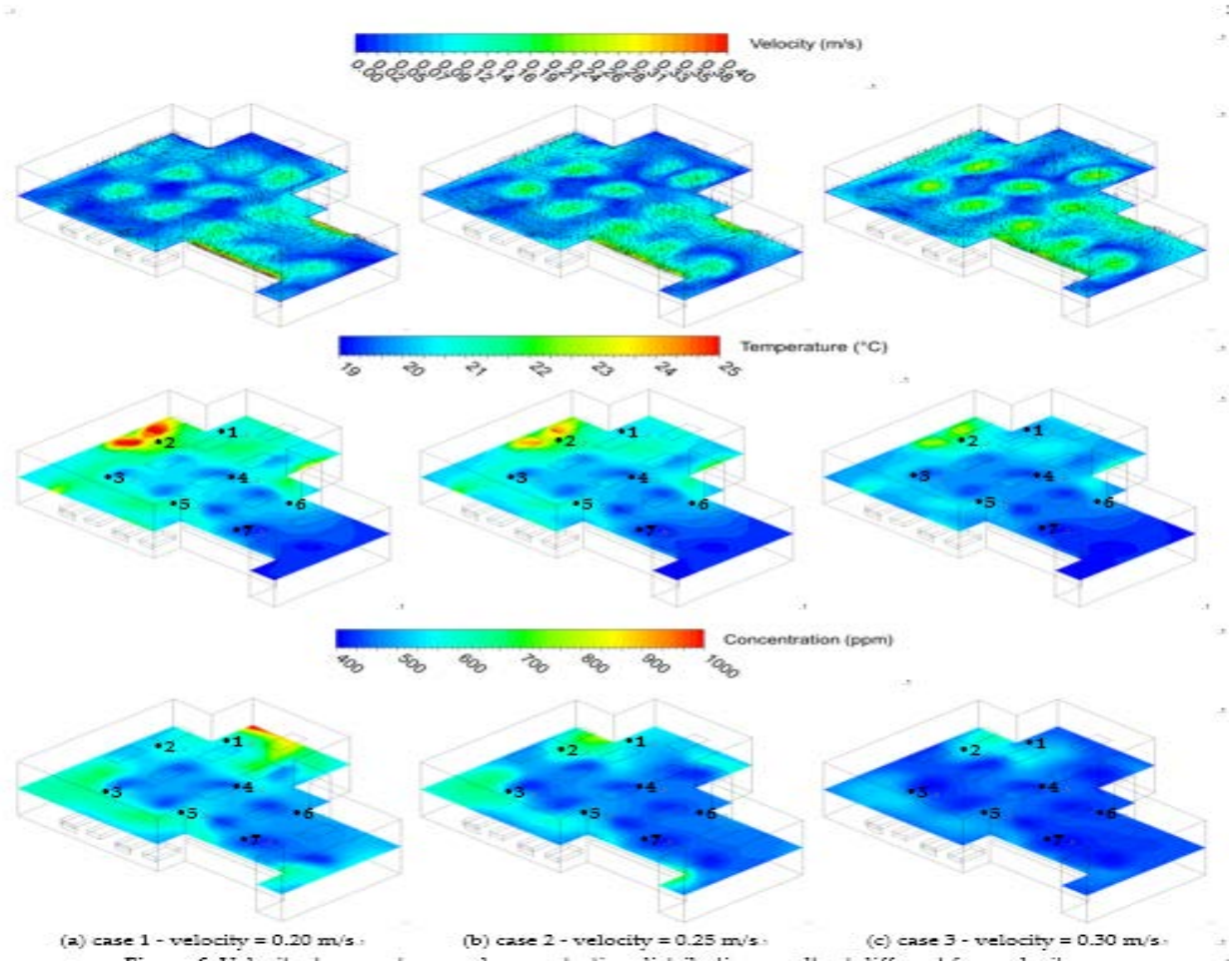

Figure 5. Velocity, temperature, and concentration distribution results at different face velocity

REFERENCES

International Organization for Standard (ISO). ISO 14644-1, Cleanroom and associate controlled environments-Part 1: Classification of air cleanliness. The Institute of Environmental Sciences and Technology (IEST), 5005 Newport Drive, Suite 506, Rolling Meadows, IL 60008, USA, 2015.

International Organization for Standardization (ISO). ISO 14644-3, Cleanrooms and associate controlled environments—Part 3: Test methods. The Institute of Environmental Sciences and Technology (IEST), 5005 Newport Drive, Suite 506, Rolling Meadows, IL 60008-3841, USA, 2019.

International Organization for Standardization (ISO). ISO 22716, Good Manufacturing Practices (GMP) Guidelines on Good Manufacturing Practices. The Institute of Environmental Sciences and Technology (IEST), 5005 Newport Drive, Suite 506, Rolling Meadows, IL 60008-3841, USA, 2007.

Memarzadeh F.; Manning, A.P. Comparison of operating room ventilation systems in the protection of the surgical site. ASHRAE Trans. 2002, 108, 1-13.

Sun Z.; Wang, S. A CFD-based test method for control of indoor environment and space ventilation. Build. Environ. 2010, 45, 1441-1447.

Srebric, J.; Vukovic, V.; He, G.; Yang, X. CFD boundary conditions for contaminant dispersion, heat transfer and airflow simulations around human occupants in indoor environments. Build. Environ. 2008, 43, 294-303.

Tung Y.C.; Shih Y.C.; Hu, S.C. Numerical study on the dispersion of airborne contaminants from an isolation room in the case of door opening. Appl. Therm. Eng. 2009, 29, 1544-1551.

Yang L.; Gan, C.E. Costing small cleanrooms. Build. Environ. 2007, 42, 743-751.

Yang Z.; Hao Y.; Shi W.; Shao X.; Dong X.; Cheng X.; Li X.; Ma X. Field test of pharmaceutical cleanroom cleanliness subject to multiple disturbance factors. J. Build. Eng. 2021, 42, 103083.

6th International Conference on Building Energy and Environment
Eindhoven University of Technology, The Netherlands
6 - 10 July 2025

Building Integrated Photovoltaic system coupled with latent thermal energy storage in the campaign for innovative passive cooling technology

Miroslav Čekon[1,2], Rossella Cottone[2,3], Ondřej Šikula[1,4], Richard Slávik[1,5], Peter Matiašovský[1]

[1]*Slovak Academy of Science, Institute of Construction and Architecture, Bratislava, Slovakia, miroslav.cekon@savba.sk; ondrej.sikula@savba.sk; richard.slavik@savba.sk; peter.matiasovsky@savba.sk*
[2]*Slovak University of Technology in Bratislava, Faculty of Civil Engineering, Bratislava, Slovakia, miroslav.cekon@stuba.sk; rossella.cottone@stuba.sk*
[3]*KU Leuven, Department of Architecture, Campus Brussels and Ghent, Brussels, Belgium, rossella.cottone@kuleuven.be*
[4]*Brno University of Technology, Faculty of Civil Engineering Brno, Czechia, ondrej.sikula@vut.cz*
[5]*Mendel University in Brno, Faculty of Forestry and Wood Technology, Brno, Czechia, richard.slavik@mendelu.cz*

SUMMARY
This study introduces innovative passive cooling technology for latent thermal energy storage systems (TES) using Phase Change Materials (PCMs), aimed at improving the operational performance of BiPV façade systems under dynamic conditions. The focus was to investigate and compare different passive BiPV cooling principles at the back of the PV module. Specifically, the present concept employs two innovative high-content PCM incorporated systems. First by integrating a honeycomb structure with microencapsulated PCM (mPCM) and second using a PCM composite panel. The operational performance of the proposed systems has been evaluated to assess the efficiency of these two innovative PCM configurations. A comparative investigation was conducted using numerical computational methods. Multidimensional, non-stationary heat transfer was solved using the control volume method, while the thermal effect of the phase change was modelled using the effective thermal capacity method. Accordingly, the heat conduction effect for sufficient thermal stratification inside the PCM was investigated.

Keywords: Building integrated Photovoltaic, Phase change material, numerical simulation, operational performance.

1. INTRODUCTION

According to projections by the Energy Information Administration (EIA, 2023), global energy demand is expected to increase by 50% by 2050. Buildings currently account for approximately one-third of global energy consumption and greenhouse gas (GHG) emissions, a share that is anticipated to grow as the International Energy Agency predicts building energy consumption will double by 2050, exacerbating environmental challenges. Increasing energy efficiency and the use of renewable solar energy could be one way to reduce greenhouse gas emissions. Recently, a wide range of novel façade solutions directly utilizing the potential of solar energy gains has been described. Photovoltaic (PV) systems for building integration (BiPV) have a relevant contribution to the field of solar energy exploitation in building energy performance. However, novel building materials and components need to possess the ability to dynamically adjust their physical properties and energy performance in response to environmental stimuli.

BiPV integrated into the building envelope, represents an established solution to address current

challenges (Singh et al., 2021). Meanwhile, integrating phase change materials (PCM) within building components still emerges as a promising and innovative approach (Cunha et al., 2016). In BiPV systems, a portion of the solar radiation is converted into electricity, while part of it is absorbed by the system leading to an increase in operating temperature and a consequent decrease in both efficiency and lifespan (Sohani et al., 2022). To address this, different cooling strategies have been implemented and investigated by the scientific community, with the integration of passive cooling using PCM standing out as particularly effective. Indeed, coupling BiPVs with PCM not only reduce overheating of BiPVs, but also improves the generation of renewable energy, bridge the gap between demand and supply, reduce peak consumption and enhances indoor thermal comfort (Chinnaiyan et al., 2022). Different BiPV-PCM solutions have been investigated to reduce the operating temperature and store excess thermal energy by integrating a PCM layer on the back side of the BiPV module. These include PCM plastic bags (Fayaz et al., 2019), biochar derived from water hyacinth impregnated with PCM (Das et al., 2021), and PCM matrix with expanded graphite (Karthikeyan et al., 2020), demonstrating how the integration of a BiPV system with an appropriate PCM module has high potential and is extremely valuable.

This work investigates and compares the performance of a passive cooling system with two different PCM modules on the back of the PV. The first involves a previously studied technology (Lai & Hokoi, 2014; Wang et al., 2018) based on a honeycomb structure incorporating mPCM. The second introduces an innovative technology that utilises a novel PCM-impregnated panel (Cottone et al., 2025). In particular, the operational performance of both design proposals was evaluated and compared using numerical calculation methods of a validated simulation model. This comparative analysis aims to evaluate their effectiveness in reducing operating temperatures, storing excess thermal energy, and enhancing the overall performance of BiPV systems.

1.1 Problem statement and research relevance

The application of a honeycomb structure has been shown to have a direct impact on the improvement of PV cooling and solar energy absorption efficiency of the PCM. However, this method is associated with a significant leakage problem of PCM (solid/liquid transition). Therefore, in this study, two configurations of PCM systems were utilised, a micro-capsulated PCM (mPCM) used for numerical validation using experimental campaign (Čurpek et al., 2025) and novel composite system (Cottone et al., 2025) to compare both technologies. Honeycomb has been demonstrated to facilitate effective heat conduction enhancement, thereby preventing thermal stratification within the PCM. Furthermore, the PCM ensures that the BiPV module operates at a reduced temperature and that the time lag of the peak load is increased. This study also provides insights into performance prediction using numerical simulations to identify thermo-responsive reactions for novel BiPV PCM facades (Čurpek et al., 2023). Numerical complexity of thermo-responsive mechanisms in both modelling and simulation is of a relevant significance to reliable predicting the operational performance of BiPV coupled with PCMs (Čurpek & Čekon, 2022). The development of numerical simulation models may allow comprehensive analyses, as well as optimization of the novel TES system for real applications (Čorić et al., 2025).

2. METHODOLOGY

First, the validation of a model is demonstrated for the purpose of modelling and simulating a BiPV/PCM experimental prototype. Second, the capability of real and modelled performance is

analysed to theoretically describe the thermal performance of the BiPV/PCM façade model. Finally, the material parameters of the new composite PCM system are used for the simulation of the thermal performance of the new BiPV/PCM façade model.

2.1. Materials and methods

An experimental investigation was carried out in summer using an outdoor test cell for two scenarios (case A and case B in Figure 1), and the measurement results were used to validate numerical calculation models. An integrated model was developed to simulate the thermal performance of the BiPV façade systems within which summer boundary conditions were implemented. The performance of three unventilated façade configurations was compared. Specifically, case A was an experimental honeycomb-based without PCM, case B experimental honeycomb-based filled with mPCM, and case C simulated new composite PCM system. This approach enabled the thermal characterisation of BiPV/PCM systems to be reliably obtained from the simulation to identify the theoretical performance for novel BiPV/PCM façade configurations.

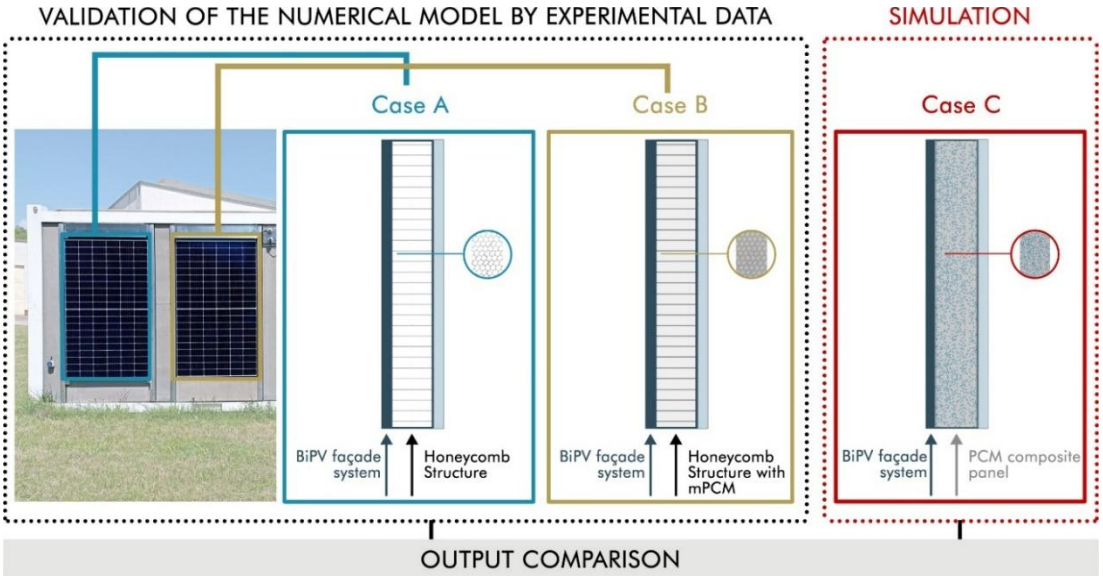

Figure 1. Test cell and design strategies of two BiPV/PCM concepts, experimental (A and B) and numerical (C)

2.1.1. Experimental study

The experimental campaign focused on the assessment of the operational performance of the reference BiPV (case A) and the proposed BIPV/T-mPCM façade (case B) under real-world conditions. For the façade application, the honeycomb is sandwiched between two layers of the rear of the BiPV panel and cement-bonded particleboard, as shown in Figure 1. The honeycomb structure consists of an aluminium with a hexagonal cell size of 9 mm and a thickness of 30 mm. The cavities for test case B were filled with mPCM (type MPCM 37D), a melting point of 37 °C and a heat of fusion of 190 J/g. The specific heat capacity (Figure 2) required for numerical calculations for two PCMs integrated in BiPV facades (experimental mPCM37 and simulated R35HC+CS) was measured using differential scanning calorimetry.

The day used in this study is characterised by incident solar radiation of a 600 W/m^2 with outdoor air temperatures of up to 23 °C and 12 °C minimum. Climate response of typical BiPV facades

can reach PV operating temperature up to 52 °C. According to experimental results, the cooling effect of the PCM in the honeycomb structure behind the BiPV can provide a reduction of 10 K in the afternoon peaks compared to a honeycomb PV façade without PCM.

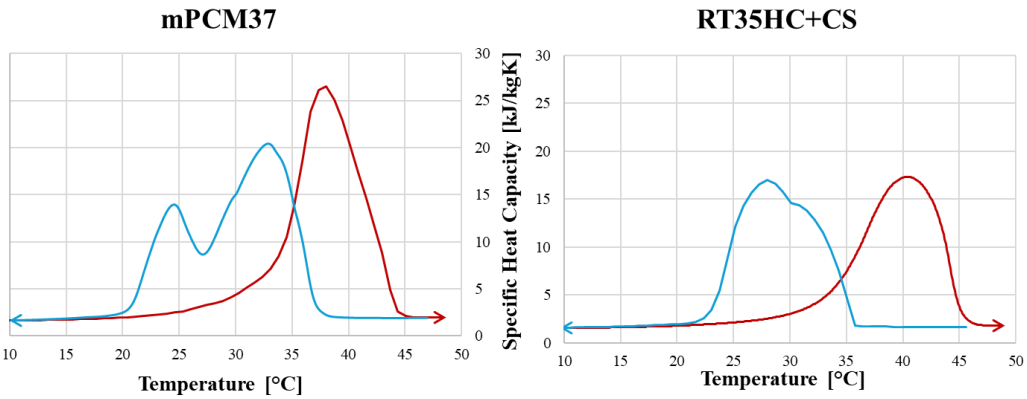

Figure 2. Specific heat capacity of two PCMs used, microencapsulated mPCM37 and RT35HC composite system

2.1.2. Numerical validation and optimization

The numerical modelling and simulation are based on the following assumptions: the influence of natural convection of the liquid phase of the PCM on heat transfer is neglected and only non-stationary heat conduction is considered in a 2D rotationally symmetric computational domain with Dirichlet, Robin + Neumann and adiabatic boundary conditions (Figure 3). The numerical model is based on an implicit solution by the finite volume method implemented on a structured computational grid in CalA 4.0 software (Sikula & Plasek, 2015). The Gauss-Seidel iterative method with convergence criterion 1E-5 is used to solve the model. Detailed materials parameters used in numerical simulations are presented in Table 1.

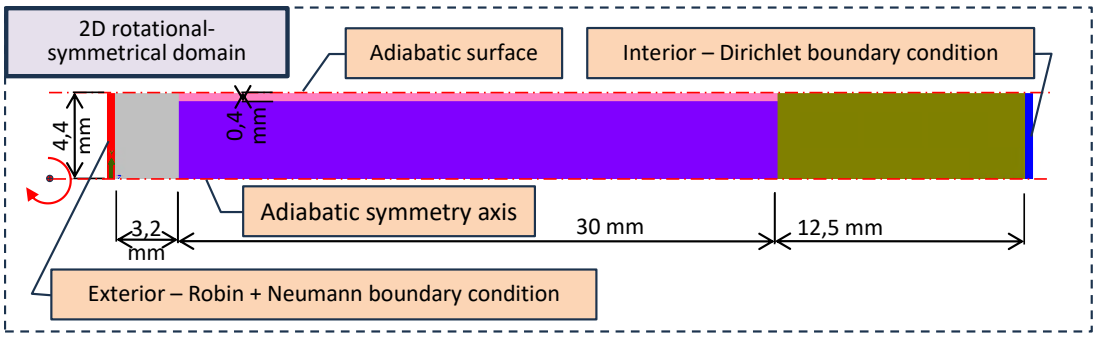

Figure 3. Numerical simulation model and basic assumptions used

Table 1. Materials parameters used in calculations.

Materials	Thickness mm	Density kg/m^3	Specific Heat J/(kg.K)	Therm. conductivity W/(m.K)
Photovoltaic panel	3.2	2330	677	11 (effective)
Aluminum	0.05 (0.8)	900	56	200 (12.5 effective)
Air cavity in honeycomb	30	1.15	1010	0.0624 (effective)
mPCM microencapsulated	30	485	$c_{eff} = f(T)$ Fig. 2	0.2
PCM panel composite system	30	830	$c_{eff} = f(T)$ Fig. 2	0.2
Cement-bonded particleboard	12.5	1200	1580	0.35

In the model, the measured net heat flux, including the both short- and long-wave radiation from the surroundings of the tested façade, is applied to the external boundary condition, and the measured surface temperature is applied to the interior boundary condition. The model validation was performed on both cases A and B. Based on the results, a new case C with a composite panel was then calculated to evaluate the suitability of this new component solution for PV cooling.

3. RESULTS AND DISCUSSION

The results presented in Figure 4 show all measured, validated and optimized data. In general, good agreement in the results was obtained for both the case without PCM (case A) and the model with mPCM (case B). The strong correlation between the experimental measurements and the simulation predictions underscores the reliability of the modelling approach and validates the efficacy of integrating PCM into photovoltaic façade systems.

According to results (see Figure 4, left), the data illustrates a notable reduction in peak temperatures by approximately 8 K when mPCM is utilized, in contrast to the system without PCM. This decrease in peak temperature is indicative of the PCM's effectiveness in absorbing excess thermal energy during periods of high solar irradiance. By transitioning from a solid to a liquid state, the mPCM absorbs heat, thereby mitigating the temperature spikes that typically occur during peak sun hours. This thermal buffering effect is essential for maintaining a stable indoor environment and reducing the thermal load on building HVAC systems. Additionally, the analysis reveals a delay of approximately 1.5 hours in the occurrence of peak temperatures when mPCM is employed. This delay is crucial for optimizing energy management strategies, as it allows for a more gradual release of stored thermal energy during the evening hours. Consequently, the building component can maintain a more consistent temperature profile, reducing the need for mechanical cooling during peak demand times. This delay not only enhances occupant comfort but also contributes to energy savings by shifting the load away from peak energy pricing periods, further underscoring the economic advantages of incorporating PCM into building design.

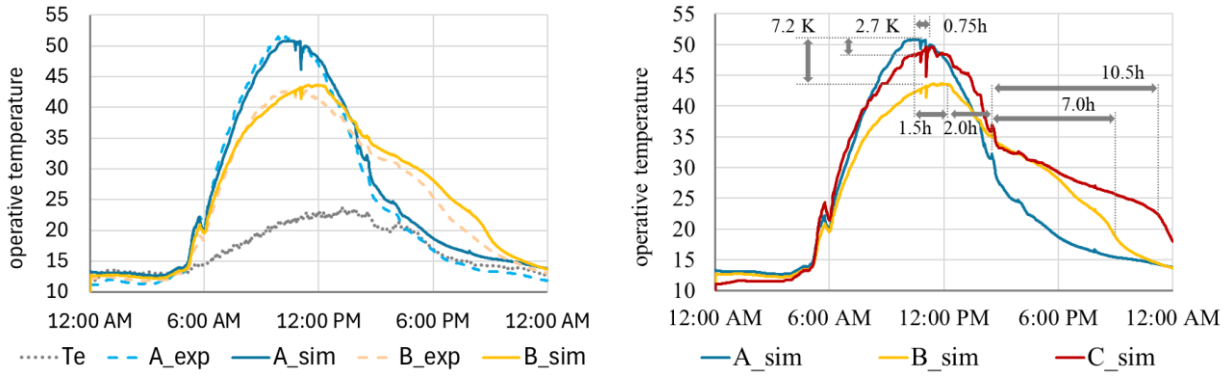

Figure 4. Numerically validated results for case A and B on the left side, comparison between all simulated cases including the new composite system with integrated PCM

The experimental and numerical results (case A and B) validate the premise that PCM can effectively manage thermal energy within building envelopes, thereby optimizing the operational efficiency of BiPV systems. The observed improvements obtained numerically in thermal performance (operative temperature difference around 7 K) can be attributed to the inherent

properties of PCM, particularly its high latent heat capacity and the ability to absorb and release heat during phase transitions. On the contrary, the results presented for optimisation purposes (case C) using the newly developed RT35HC composite system (Fig. 4, right) show that its efficiency decreases significantly and that a reduction in peak temperatures by a maximum of 3 K is theoretically achieved. In addition, the time lag between two modelled PCM systems is more than 3 hours during the night. This indicates that increasing the thermal conductivity of the PCM system is very important to ensure a proper efficiency, and the suitability of new composite system application needs to be further investigated to improve its overall performance.

4. CONCLUSION

In this study, numerical calculations were conducted to identify the thermal performance of a photovoltaic façade system enhanced with Phase Change Material (PCM) of two different configurations. This innovative approach aims to enhance the energy efficiency and thermal comfort of building-integrated photovoltaic (BiPV) systems. The primary focus of this research was first to validate simulation models that predict the latent thermal energy storage capabilities of PCM. To achieve this, experimental data obtained from real-world tests were utilized, which served as a benchmark for assessing the accuracy of our theoretical models. The results of this study indicate a strong correlation between the measured data and the predictions made by used simulation models for both experimental configurations used. This alignment underscores the reliability of used modeling approach and its applicability in real-world scenarios.

However, the theoretical results from the optimization tests with the new composite system reveal some limitations, as the system exhibited a smaller reduction in peak temperature and a longer time lag compared to the mPCM system. This suggests that while the new composite system shows potential, improvements in thermal conductivity are necessary to enhance its overall efficiency. Therefore, further research and development are essential to explore and optimize the performance of composite PCM systems, ensuring they can effectively compete with existing mPCM solutions in building design applications. Overall, these findings underscore the importance of PCM in enhancing the operational efficiency of building-integrated photovoltaic systems and contribute to the ongoing pursuit of sustainable and energy-efficient architectural solutions. Future studies may explore further configurations and material compositions to optimize the performance of PCM in diverse climatic conditions, paving the way for broader adoption of this technology in the building.

ACKNOWLEDGEMENTS

This research was supported by Scientific Grant Agency of the Ministry of Education, Science, Research and Sport of the Slovak Republic, project VEGA 2/0145/24, and from the European Union's Horizon Europe research & innovation programme under the HORIZON-MSCA-2021-DN-01 grant agreement No. 101072598 – "ActaReBuild". The authors would like to thank M. Žemlička and J. Čurpek for their technical assistance during the construction of the experiment at the Institute of Construction and Architecture of the Slovak Academy of Sciences.

REFERENCES

Chinnaiyan, V. K., Patil, C. K., Patil, M. M., Baviskar, P. R., Karthick, A., Selvakumar, P., & Rajkumar, S. (2022). Review on application of phase change material for BIPV system. *Materials Today: Proceedings*, *59*, 1243–1248.

Cottone, R., Čekon, M., Glorieux, C., Fantucci, S., Čurpek, J., Slávik, R., & Rychtáriková, M. (2025). Investigation of Phase Change Material Impregnation in a Highly Porous Structure. In U. Berardi (Ed.), *Multiphysics and Multiscale Building Physics* (pp. 455–460). Springer Nature Singapore.

Cunha, S., Lima, M., & Aguiar, J. B. (2016). Influence of adding phase change materials on the physical and mechanical properties of cement mortars. *Construction and Building Materials*, *127*, 1–10.

Čurpek, J., & Čekon, M. (2022). Building performance simulation of a photovoltaic façade enhanced with latent heat storage: Model validation and power generation prediction. *Journal of Energy Storage*, *56*, 106143.

Čurpek, J., Čekon, M., Šikula, O., & Slávik, R. (2023). Thermodynamic responses of adaptive mechanisms in BiPV façade systems coupled with latent thermal energy storage. *Energy and Buildings*, *279*, 112665.

Čurpek, J., Čekon, M., Slávik, R., Kómar, L., & Matiašovský, P. (2025). Outdoor Performance of a Photovoltaic Façade System Enhanced with Microencapsulated Phase Change Material Embedded in a Honeycomb Structure. In U. Berardi (Ed.), Multiphysics and Multiscale Building Physics (pp. 589–595). Springer Nature Singapore.

Čorić, I., Nižetić, S., Jurčević, M., Bošnjak, J., Čoko, D., Arici, M., & Papadopoulos, A. (2025). An overview of passive cooling techniques using phase change materials for photovoltaic panels: A focus on numerical simulation techniques. 55th International HVAC&R Congress and Exhibition, 55(1), 239-247.

Das, D., Bordoloi, U., Kamble, A. D., Muigai, H. H., Pai, R. K., & Kalita, P. (2021). Performance investigation of a rectangular spiral flow PV/T collector with a novel form-stable composite material. *Applied Thermal Engineering*, *182*, 116035.

EIA. (2023). *International Energy Outlook 2023*. https://www.eia.gov/outlooks/ieo/pdf/IEO2023_Narrative.pdf

Fayaz, H., Rahim, N. A., Hasanuzzaman, M., Rivai, A., & Nasrin, R. (2019). Numerical and outdoor real time experimental investigation of performance of PCM based PVT system. *Solar Energy*, *179*, 135–150.

Karthikeyan, V., Sirisamphanwong, C., Sukchai, S., Sahoo, S. K., & Wongwuttanasatian, T. (2020). Reducing PV module temperature with radiation based PV module incorporating composite phase change material. *Journal of Energy Storage*, *29*, 101346.

Lai, C., & Hokoi, S. (2014). Thermal performance of an aluminum honeycomb wallboard incorporating microencapsulated PCM. *Energy and Buildings*, *73*, 37–47.

Sikula, O., & Plasek, J. (2015). *Software CalA 4.0 (Calculation Area). Version 4.0 Education*.

Singh, D., Kumar Gautam, A., & Chaudhary, R. (2021). Application of phase change material in building integrated photovoltaics: A review. *Materials Today: Proceedings*, *45*, 4624–4628.

Sohani, A., Dehnavi, A., Sayyaadi, H., Hoseinzadeh, S., Goodarzi, E., Garcia, D. A., & Groppi, D. (2022). The real-time dynamic multi-objective optimization of a building integrated photovoltaic thermal (BIPV/T) system enhanced by phase change materials. *Journal of Energy Storage*, *46*, 103777.

Wang, S.-M., Matiašovský, P., Mihálka, P., & Lai, C.-M. (2018). Experimental investigation of the daily thermal performance of a mPCM honeycomb wallboard. *Energy and Buildings*, *159*, 419–425.

Urban microclimate & Pollutant dispersion (11:00-12:30 h)

6th International Conference on Building Energy and Environment
Eindhoven University of Technology, The Netherlands
6 - 10 July 2025

Characterization of the flow around a model low-rise house in the presence of a deciduous tree

Ryan Aziz [1], Kamran Siddiqui [2]

[1]*Western University, London, Canada, jaziz22@uwo.ca*
[2]*Western University, London, Canada, ksiddiq@uwo.ca*

SUMMARY
Buildings are often surrounded by trees that influence the airflow patterns around the building and hence, the external energy exchange. The present study reports the airflow behaviour around a model house in the presence of a model deciduous tree using particle image velocimetry (PIV). The investigation aims to characterize the flow behaviour at different tree positioning with respect to a house under foliated and defoliated conditions. The results show that the location of the tree impacts airflow patterns. The presence and absence of foliage also has recognizable influence on the airflow behaviour. Generally, when the distance of the tree from the house increases, the turbulence in the separated shear layer from the leading edge of the house slightly increases. In general, the tree without foliage induced slightly more turbulence along the house. These changes in airflow around the house indicate an alteration in the external energy exchange of the house.

INTRODUCTION

Trees are a common feature in the surroundings of buildings. However, the effect of trees on the airflow around buildings is not well understood. A deeper insight into the flow alteration due to trees is vital for understanding the impact that trees have on the external energy exchange of buildings. A noteworthy aspect of deciduous trees is that they do not have foliage in winter in many regions and hence, the impact of such a tree on the airflow around a building has seasonal variation. Such behavior has not been extensively investigated. A better understanding of how trees affect airflow around a building can lead to improved understanding of building energy use and improved building energy modelling.

Limited research work has been reported on the impact of trees on the airflow around buildings. A numerical study investigated how coniferous trees in a shelterbelt alter the convective effect of wind, and the effect that the shelterbelt has on shading. The study observed a reduction in the heating requirements of a low-rise office building in Scotland when a tree shelterbelt was present (Liu & Harris, 2008). These shelterbelts are not typical of many houses where trees are typically placed without wind breaking in mind. A recent study by Li et al. (2024) has numerically investigated the impact that tree morphology and leaf area density have on the air blockage. The effect of trees on wind-comfort levels in high rise building environments was simulated. It was concluded that in such an environment, building arrangement is the main contributor to comfort level. It was also shown that trees can reduce wind speeds, but when near a building corner, trees had limited impact because of flow acceleration past corners (Kubilay et al., 2024). Manickathan et al. (2018) investigated various scale model trees in a low turbulence wind tunnel including trees lacking foliage, and natural trees. Particle image velocimetry (PIV) was used to measure the velocity field and loads cells were used to determine tree drag coefficients. These models featured

reconfiguration. The study found that the defoliated trees have lower drag coefficients than those with foliage. PIV and drag coefficient data revealed that the defoliated trees investigated had minimally influenced the flow when compared to trees with foliage. It was also found from PIV that some model trees exhibited very similar wake structure to natural trees. Another study conducted wind tunnel experiments to analyze how trees at differing growth stages in street canyons affect outdoor pedestrian level temperature. A model street canyon was heated, and temperatures at the pedestrian level were found to be cooler with the presence of trees for moderate heat conditions, but not extreme heat. Generally, trees were found to increase street canyon temperature. In this study, however, heat reduction from shading was not considered, which is significant (Zhao et al., 2023).

Limited knowledge on how the presence of trees alters airflow around a building is known. The present paper is focused on a detailed characterization of airflow around a model-scale two-story house in the presence of a tree to investigate how the presence of a tree alters the flow behaviour around the house. A specific focus is on the impact of a deciduous tree with and without foliage on the airflow around the house. It also in investigates the effect of the distance and position of a tree relative to a house has on the airflow behaviour around the house. Aziz & Siddiqui (2024) previously reported the mean and turbulent flow behaviour around a house in the presence of a tree, but only with foliage present, and without altering the distance from the house.

METHODOLOGY

All experiments were conducted using a closed loop wind tunnel with low turbulence at Western University. The test section is composed of transparent acrylic walls. The test section is 122cm long, with a square cross section perpendicular to the airflow of 46cm × 46cm. The test section features removable testing plates and removable side panels. All experiments were run with a freestream velocity of 10.0m/s.

A model house with a scale of 1:65 was constructed to represent an idealized two-story house with a height of 10cm, length of 19.5cm, and width of 13cm. The slope of the roof is 6:12 (26.6 degrees). The house was manufactured using an FDM 3D printer using a dark filament to reduce reflections. The model house was fastened from the inside to a testing plate. The testing plate was covered in black foil and black tape to reduce reflections from the bottom of test section.

A deciduous style tree was manufactured using an FDM 3D printer. The tree was designed using a 3D L-system (Lindenmayer system) approach. L-system can be used to represent organic growth patterns (Chan et al., 2020; Prusinkiewicz, 1990). The model tree has a height of 7cm, and the crown has a diameter of 9cm, located 2cm from bottom of a cylindrical trunk. Tree foliage consisted of sisal fiber, however a correlation to leaf area index has not been determined (Gromke & Ruck, 2008). A packing density of sisal fiber similar to that of Gromke & Ruck (2008) was used. Fig. 1 shows the model tree with and without foliage. The foliage makes up the crown with a volume of approximately 180cm^3. The foliage had a mass of 1.3g, resulting in a packing density of around 7g/dm^3. All experiments were conducted with and without tree foliage.

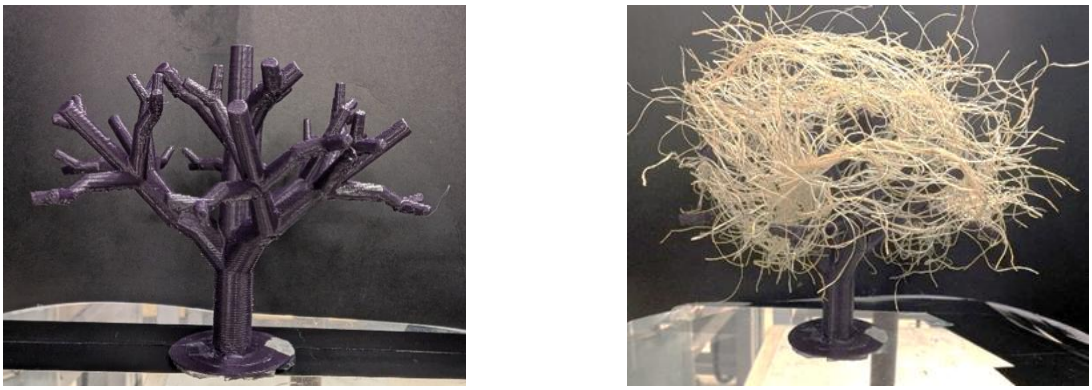

Defoliated tree | Tree with sisal fiber foliage

Figure 1. Model tree configurations

The house was positioned so the long side (L) was perpendicular to the wind direction. Three positions of the tree in relation to the house were considered. The tree was positioned L/4 distance from the side (W) of the house and three distances upstream from the house. All layouts are shown in Fig. 2.

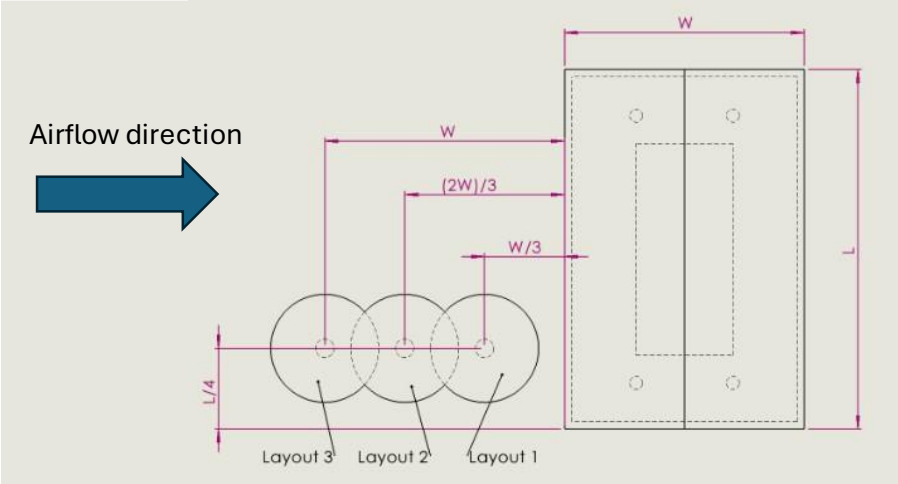

Figure 2. Tree and house layouts

Particle image velocimetry (PIV) was used to measure the velocity of the airflow around the model tree and the model house. A schematic of the PIV setup can be seen in Fig. 3. The PIV system included a dual-cavity 120 mJ Nd:YAG laser illuminating at 15Hz per cavity. The laser emitted through a cylindrical lens creating a flat sheet parallel to the ground and 5cm above the bottom of the test section. Two 12-Megapixel (4096x3072 pixel) CMOS sensor cameras (Flare, IO Industries) were used overhead to allow for a wider field of view and to capture enough seeding detail. Both cameras used lenses with 60mm focal length (60mm f/2.8 Micro-NIKKOR AF-D, Nikon) set to f/8 with an APS-C size sensor.

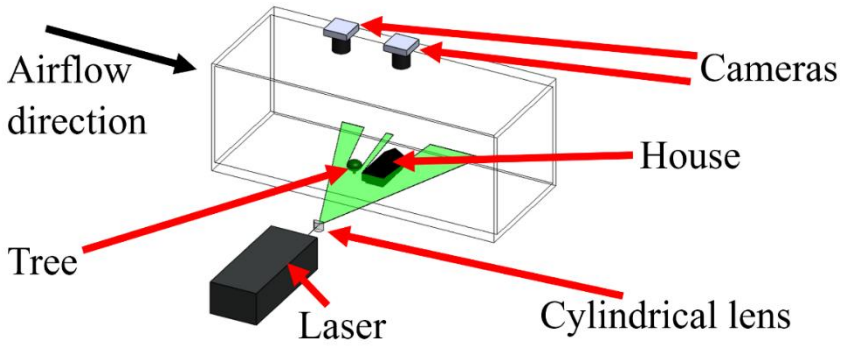

Figure 3. PIV Setup

The cameras were synchronized, and images were recorded at 30 frames per second (image pairs at 15 frames per second) using CoreView software. A digital pulse generator was used to synchronize laser pulses with camera frames. The first frame in the image pair used 200μs shutter speed, and the second used automatic exposure to determine shutter speed. The camera sensor planes were parallel to ground and 68cm above the laser sheet. The position of the camera was moved to capture different areas of interest. Images were taken over one-minute periods, that is, 1800 images were taken for each one-minute run resulting in 900 image pairs. The time delay between the laser pulses in each image pair was 60μs.

The instantaneous velocity fields were computed by cross correlating image pairs using an in-house algorithm running in the MATLAB environment. For cross correlation, the size of the interrogation window was set to 32 pixels, and the size of the search window was set to 64 pixels. The velocity vectors were interpolated onto a regular grid with 32 pixels spacing using AGW interpolation scheme. As the laser sheet was illuminated from one side, it created shadows of the tree and the house (see Fig. 3), creating erroneous vectors in the dark regions. Therefore, masking was implemented for each layout to eliminate any data in the dark regions or from the regions where the exposure was too high or too low. A local medial filter was used to detect and correct spurious vectors (which were typically very few). The uncertainty in the PIV velocity vectors was estimated using the methodology presented in (Cowen & Monismith, 1997; Prasad et al., 1992). The maximum uncertainty in the velocity for all experiments was estimated to be ±0.13m/s or 1.3% of the free stream velocity. The mean velocities were computed by time-averaging instantaneous velocity data over the one-minute duration. Turbulent velocity fields were obtained by subtracting the mean velocity field from each instantaneous velocity field. The turbulent kinetic energy (TKE) was computed from the two-dimensional turbulent velocity fields.

RESULTS

The effect of the tree on the airflow around the house was characterized through mean velocity and turbulent kinetic energy (TKE), for all layouts.

For layout 1, where the tree was positioned upstream and closest to the house (W/3 distance from the front of the house as seen Fig. 2), the colormaps of the mean velocity field are illustrated in

Fig. 4 for both foliated and defoliated cases. The plots show that the presence of the tree caused the flow acceleration on the side, which is expected due to the mass conservation. The flow acceleration is found to be relatively stronger in the foliated case, which is likely due to the higher flow resistance caused by the foliage. The results also show that in the absence of the foliage, the flow separation region on the side of the house was suppressed. Downstream from the house, the characteristic wake region is visible. The comparison between the foliage and no foliage cases shows that the mean flow behaviour in this wake region has negligible difference. The results also reveal the flow separation occurring at the leading edge of the house on the upstream side. The TKE plots in Fig. 5 show that the turbulent flow structure is relatively similar for both cases, however, the turbulence along the side of the house and in the wake region is relatively stronger in the absence of the foliage. This indicates that the convective heat transfer on the exterior side of the building is impacted by the absence of the foliage.

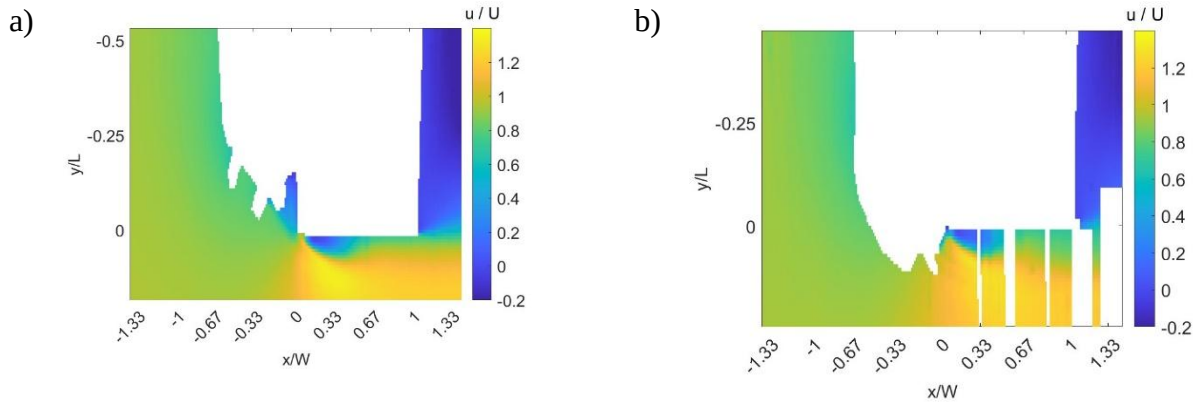

Figure 4. Contours of normalized average streamwise velocity for layout 1. For the coordinate system, the origin is located at the left upstream corner of house. a) defoliated tree b) foliated tree

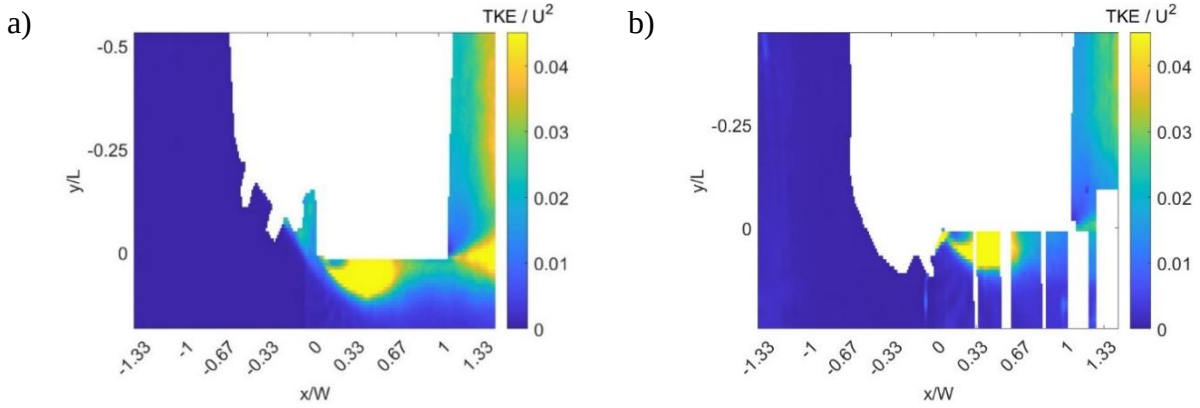

Figure 5. Contours of normalized average TKE for layout 1. For the coordinate system, the origin is located at the left upstream corner of house. a) defoliated tree b) foliated tree

Fig. 6 shows the mean velocity field as the tree was positioned further upstream of the house at a distance of 2W/3. The results show the presence of a wake behind the tree (defoliated case), as expected, covering the entire region between the tree and the house. Such measurements were not

possible for the foliage case due to the extent of the foliage, covering that region. The comparison between the two cases shows that similar to the Layout 1, the flow separation on the side of the house was suppressed in the absence of the foliage. The results also show that the wake region downstream from the house Fig. 6 is not altered significantly by the presence of foliage in the tree compared with the case without foliage. The TKE plots in Fig. 7 show a relatively similar structure of the turbulent flow along the side and in the downstream wake region, with a slightly higher turbulence in the absence of the foliage. Strong turbulence in the wake of the tree is also visible, as expected.

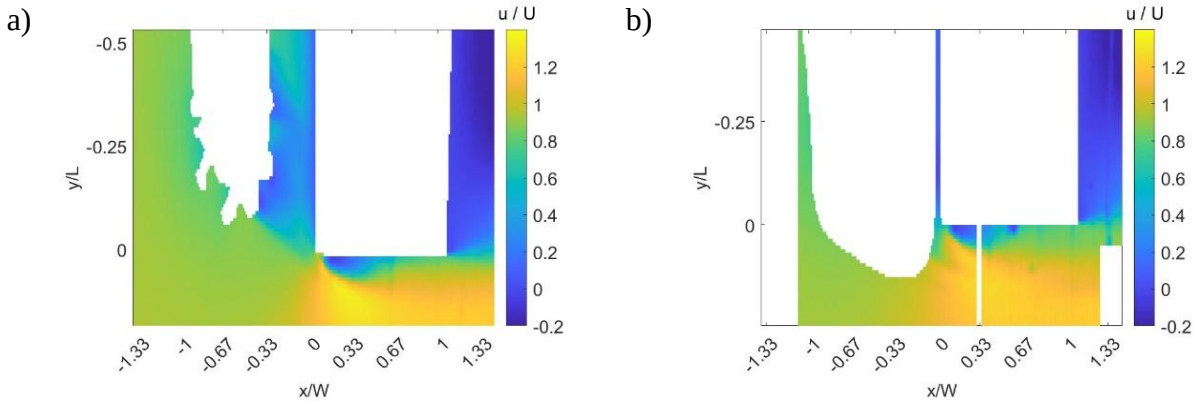

Figure 6. Contours of normalized average streamwise velocity for layout 2. For the coordinate system, the origin is located at the left upstream corner of house. a) defoliated tree b) foliated tree

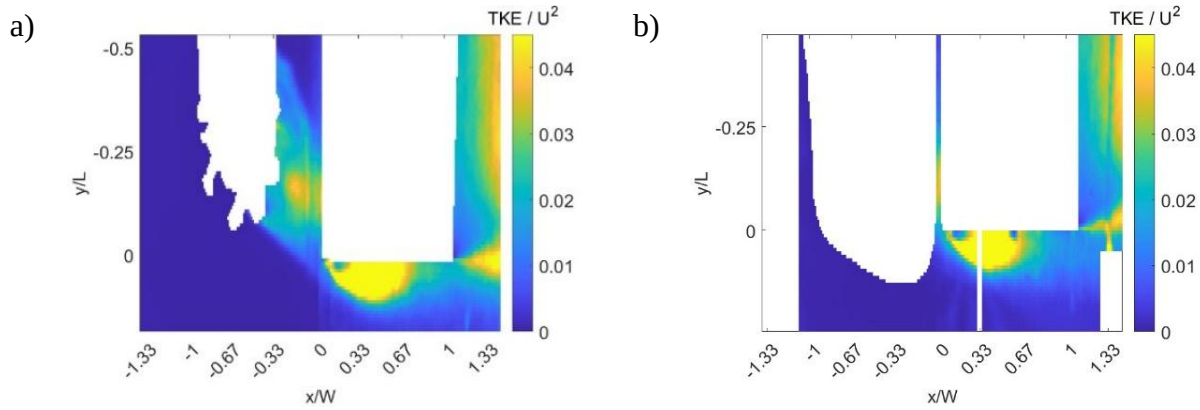

Figure 7. Contours of normalized average TKE for layout 2. For the coordinate system, the origin is located at the left upstream corner of house. a) defoliated tree b) foliated tree

For layout 3, when the tree is farthest from the house at the distance of W, differences in the flow behaviour in the wake of the tree are observed in the presence and absence of the foliage. The mean velocity fields in Fig. 8 show localized wake regions immediately downstream from the tree in the defoliated case, which are expected to be induced by the defoliated branches of the tree. However, in the foliated case, a uniform wake is observed behind the tree. Similar to the other cases, in the absence of the foliage, the flow separation on the side of the house was suppressed. The TKE plots in Fig. 9 show stronger turbulence behind the tree in the defoliated case, which was

extended over a relatively wider region. The results also show that the turbulence magnitudes on the side and behind the house are relatively higher in the absence of the foliage and extended over a wider region.

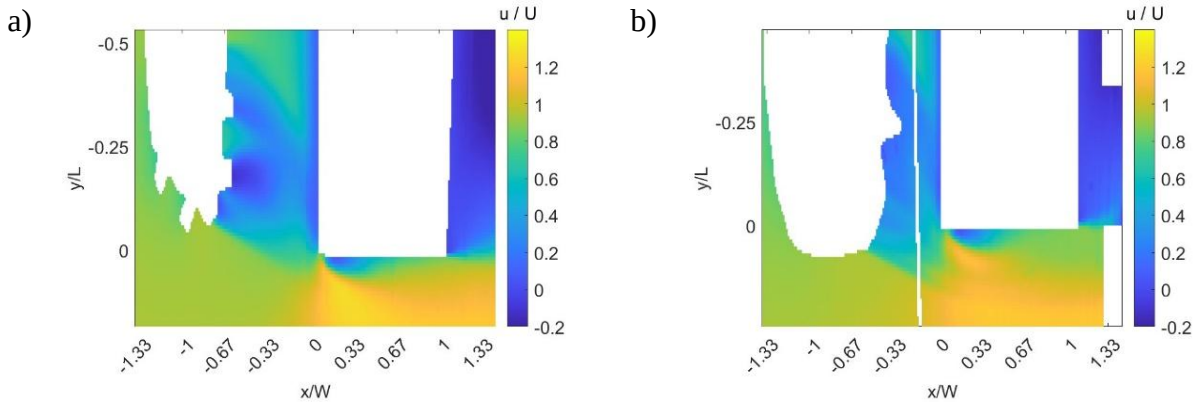

Figure 8. Contours of normalized average streamwise velocity for layout 3. For the coordinate system, the origin is located at the left upstream corner of house. a) defoliated tree b) foliated tree

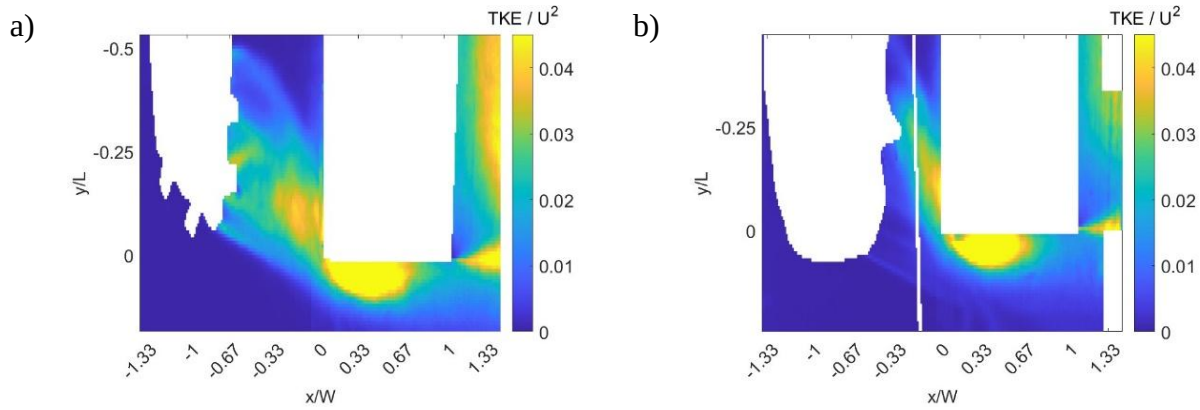

Figure 9. Contours of normalized average TKE velocity for layout 3. For the coordinate system, the origin is located at the left upstream corner of house. a) defoliated tree b) foliated tree

Comparing the characteristics of the airflow between layouts, it is observed that as the tree moves farther away from the house in the upstream direction, a non-uniform wake region is established between the tree and the house, when the tree is defoliated. The presence of the tree upstream of the house also causes the flow acceleration on the side of the house, which is relatively stronger in the absence of the foliage. The TKE plots show that the turbulence behind the tree becomes relatively stronger as the location of the tree is moved further upstream of the house. In the absence of the foliage, the turbulence becomes relatively stronger on the side of the house and in the wake of the house.

CONCLUSIONS

The present study investigated the influence of tree foliage on the flow around a house for different tree locations. Particle image velocimetry was used to characterize the two-dimensional mean and

turbulent airflow fields. The results show that when a tree is located upstream of a building, the flow accelerates on the side. Where the flow reattaches to the wall downstream, the flow is more turbulent is this region in the presence of the defoliated tree. The air was found to be more turbulent in the wake of the defoliated tree that in the wake of the tree with foliage. When comparing the distance of the tree from the upstream side of the house, the separated shear layer size and turbulence increases slightly as the distance of the tree from the house increases. The results from this study show that as a tree defoliates in the colder season, it alters the airflow behaviour around the house and hence alters the external building energy exchange.

REFERENCES

Aziz, R., & Siddiqui, K. (2024). *Investigation of the Impact of Trees on Building's External Energy Exchange* [Conference]. International Mechanical Engineering Congress and Exposition (IMECE), Portland, Oregan, U.S.A. https://imece.secure-platform.com/a/solicitations/236/sessiongallery/17944/application/150311

Chan, W.-L., Eng, Y., Ge, Z., Lim, C. W. C., Gobeawan, L., Poh, H. J., Wise, D. J., Burcham, D. C., Lee, D., Cui, Y., & Khoo, B. C. (2020). Wind Loading on Scaled Down Fractal Tree Models of Major Urban Tree Species in Singapore. *Forests*, *11*(8), 803. https://doi.org/10.3390/f11080803

Cowen, E. A., & Monismith, S. G. (1997). A hybrid digital particle tracking velocimetry technique. *Experiments in Fluids*, *22*(3), 199–211. https://doi.org/10.1007/s003480050038

Gromke, C., & Ruck, B. (2008). Aerodynamic modelling of trees for small-scale wind tunnel studies. *Forestry*, *81*(3), 243–258. https://doi.org/10.1093/forestry/cpn027

Kubilay, A., Rubin, A., Derome, D., & Carmeliet, J. (2024). Wind-comfort assessment in cities undergoing densification with high-rise buildings remediated by urban trees. *Journal of Wind Engineering and Industrial Aerodynamics*, *249*, 105721-. https://doi.org/10.1016/j.jweia.2024.105721

Li, R., Zhao, Y., Wang, L., Niu, J., Shi, X., & Gao, N. (2024). Numerical investigation of the blockage effect of trees on airflow distributions in a wind tunnel. *Building and Environment*, *263*, 111848-. https://doi.org/10.1016/j.buildenv.2024.111848

Liu, Y., & Harris, D. J. (2008). Effects of shelterbelt trees on reducing heating-energy consumption of office buildings in Scotland. *Applied Energy*, *85*(2), 115–127. https://doi.org/10.1016/j.apenergy.2007.06.008

Manickathan, L., Defraeye, T., Allegrini, J., Derome, D., & Carmeliet, J. (2018). Comparative study of flow field and drag coefficient of model and small natural trees in a wind tunnel. *Urban Forestry & Urban Greening*, *35*, 230–239. https://doi.org/10.1016/j.ufug.2018.09.011

Prasad, A. K., Adrian, R. J., Landreth, C. C., & Offutt, P. W. (1992). Effect of resolution on the speed and accuracy of particle image velocimetry interrogation. *Experiments in Fluids*, *13*(2–3), 105–116. https://doi.org/10.1007/bf00218156

Prusinkiewicz, P. (with Lindenmayer, A.). (1990). *The algorithmic beauty of plants*. Springer-Verlag.

Zhao, Y., Li, H., Bardhan, R., Kubilay, A., Li, Q., & Carmeliet, J. (2023). The time-evolving impact of tree size on nighttime street canyon microclimate: Wind tunnel modeling of aerodynamic effects and heat removal. *Urban Climate*, *49*, 101528. https://doi.org/10.1016/j.uclim.2023.101528

6th International Conference on Building Energy and Environment
Eindhoven University of Technology, The Netherlands
6 - 10 July 2025

Analysis of urban wind conditions and wildfire smoke dispersion for downtown Montréal using computational fluid dynamics

Quinn Dyer-Hawes [1], Djordje Romanic [1], Yi Huang [1], John R. Gyakum[1], Peter Douglas[2]

[1]*Department of Atmospheric and Oceanic Sciences, McGill University, Montréal, Canada, quinn.dyer-hawes@mail.mcgill.ca*
[2]*Department of Earth and Planetary Sciences and Geotop Research Centre, McGill University, Montréal, Canada*

SUMMARY
Computational fluid dynamics is used to simulate urban wind conditions and wildfire smoke dispersion in the city of Montréal. A case study for the day of July 17, 2023, in Montréal is used, which was characterized by moderate southwest winds and significant amounts of wildfire smoke. Steady-state RANS simulations testing the standard k-ε and Shear Stress Transport (SST) k-ω model as well as different values of turbulent Schmidt number are validated against lidar, anemometer, and air quality monitoring station measurements. Both models predict the urban boundary layer winds, although the SST k-ω model fails to capture some complex urban dynamics. The wind flow is analyzed to address issues of wind comfort. Wildfire smoke dispersion dynamics are also investigated, and an optimum value of 0.6 for the turbulent Schmidt number is found. The resulting smoke distributions throughout the city reveal areas prone to worse air quality.

Keywords: computational fluid dynamics, urban wind conditions, pollutant dispersion, wildfire smoke.

1. INTRODUCTION

The wind conditions found in cities significantly affect the daily lives and comfort of urban residents. Strongly connected with this are issues of air quality and pollution. With over half of the world's population living in cities (Ritchie et al., 2024), it is vitally important to study how atmospheric flow affects urban air quality. Smoke from wildfires is increasingly becoming a concern as it is often transported by the wind into cities. Exposure to wildfire smoke can be very harmful, causing eye and respiratory irritation, the exacerbation of preexisting lung diseases, and even death (Liu et al., 2015). As climate change begins to increase the frequency of wildfires, their detrimental effects on urban air quality will only amplify (Abatzoglou & Williams, 2016).

Micro-scale urban wind and dispersion dynamics can be investigated using multiple approaches, such as field measurements and wind tunnel experiments. Recently, the approach of using computational fluid dynamics (CFD) has shown to provide many benefits over previous methods. CFD, which works by numerically solving simplified versions of the Navier-Stokes equations, provides predictions of the wind field and pollutant concentrations at every location within the domain, whereas in-situ and wind tunnel measurements are limited to discrete locations. CFD simulations also give control over meteorological conditions, useful in predicting and modelling events that have not yet occurred. Instead, field measurements and wind tunnel tests often serve as the necessary initial and boundary conditions for running CFD models.

CFD models use one of two main approaches, either large eddy simulation (LES) or Reynolds-averaged Navier-Stokes (RANS) simulations. While LES provides time-dependent simulated fields and resolves large-scale turbulence, RANS models parameterize all scales of turbulence and provide only the time-averaged, mean flow. The potential increased accuracy of LES is offset by significantly higher computational expense and complexity, resulting in the frequent use of RANS in industry and research (Blocken 2018). The technique of RANS is also supported by more robust best practice guidelines, preventing incorrect model initializations common with the higher complexity of LES. However, RANS simulations do require the selection of turbulence model, which can have a large effect on the accuracy of the simulations. No one turbulence model is appropriate for all scenarios, and as such, multiple must be tested (Franke et al. 2007). Among the most frequently used are the standard k-ε and the Shear Stress Transport (SST) k-ω models, both of which have been shown provide accurate simulations of pollutant dispersion in various circumstances (Gousseau et al. 2010; Tominaga & Stathopoulos 2007; Wang & McNamara 2006). In particular, the standard k-ε model is known to overestimate turbulent kinetic energy (TKE) at a building's windward edge (Tominaga & Stathopoulos 2007), for which the SST k-ω was introduced to correct, but this model is known to poorly predict flow in the wake regions of buildings (Wang & McNamara 2006). This research aims to test the accuracy of these two turbulence models in predicting wind flow and wildfire smoke dispersion in downtown Montréal. An additional RANS model parameter that is tested is the turbulent Schmidt number, Sc_t, which further affects the model's prediction of pollutant concentration. This parameter can vary between 0.2 and 1.3, with the optimum value dependent on the characteristic flow structures (Tominaga & Stathopoulos 2007). This study's goal is to validate a RANS based numerical model testing multiple turbulence models and turbulent Schmidt numbers for urban wind flow and wildfire smoke dispersion in downtown Montréal. The model's predictions are compared against anemometer, lidar, and air quality monitoring station measurements in the city center. The wind field and smoke distribution are analyzed to investigate urban wind comfort and air quality issues.

2. METHODOLOGY

This study simulates the conditions of July 17, 2023, for downtown Montréal, which experiences moderate southwest flow transporting significant amounts of wildfire smoke into the city. Canada's wildfire season was its worst on record in 2023 (Copernicus 2024), and Montréal saw many similar days of decreased air quality due to wildfire smoke. Here, $PM_{2.5}$ (particulate matter with a diameter of less than 2.5 μm) is used as a proxy for wildfire smoke concentration as it constitutes over 90% of the mass within the smoke (Vicente et al. 2013) and is more chemically stable than other components of wildfire smoke (Atkinson 2000). Weather and air quality monitoring stations at the Montréal-Pierre Elliott Trudeau International Airport (45.4678°N, 73.7417°W) were for the boundary conditions of wind speed and direction and $PM_{2.5}$ concentration. Eight hours (15:00–22:00 UTC) were simulated, representing the time period during which the wildfire smoke peaked inside the domain and began to dissipate.

Validation of the model is done using an anemometer at the McTavish Reservoir (45.5047°N, 73.5792°W) and a lidar on the roof of McGill University's Burnside Hall (45.5047°N, 73.5751°W) for predictions of wind speed and direction, and an air quality monitoring station downtown (45.5122°N, 73.5667°W) for predictions of $PM_{2.5}$ concentrations. Lidar, standing for light detection and ranging, can serve as a more complete validation tool for CFD models than

the more common anemometers, as lidars are able to measure wind velocities across many different heights. This provides much more detail as to the vertical structure of urban wind flow. While lidars have been frequently deployed in investigations of the urban boundary layer (Drew et al. 2013), their use in validating CFD models is still limited.

The numerical model is run using the open-source CFD software OpenFOAM. The mesh was created using OpenFOAM's SnappyHexMesh and includes explicitly modeled buildings and topography. Designed following best practice guidelines (Frank et al. 2007), the domain measures 10 × 8 × 1.7 km and was mesh using three different grid resolutions to ensure grid independence. The medium resolution mesh, consisting of 80 million cells, was used in all simulations for its accuracy and reduced computational expense. Details of the computational domain are shown in Fig. 1. Inlet wind profiles are assigned with the approach of Richards and Hoxey (1993), with the wind speed given by:

$$U_h = \frac{u_*}{\kappa} \ln\left(\frac{z+z_0}{z_0}\right), \quad (1)$$

where u_* is the friction velocity found with the 10 m height airport reference velocities, κ is the von Kármán constant of 0.41, and z_0 is the roughness length estimated from the Wieringa updated Davenport classification system (1992). TKE is assumed to be constant with height according to:

$$k = \frac{u_*^2}{\sqrt{C_\mu}}, \quad (2)$$

where C_μ is a model constant equal to 0.09. Finally, for the standard *k*-*ε* model the profile of TKE dissipation rate is given as:

$$\varepsilon = \frac{u_*^3}{\kappa(z+z_0)}, \quad (3)$$

while in the case of the SST *k*-*ω* model the profile of specific turbulent dissipation rate is given by (Wilcox 2006):

$$\omega = \frac{\varepsilon}{C_\mu k}. \quad (4)$$

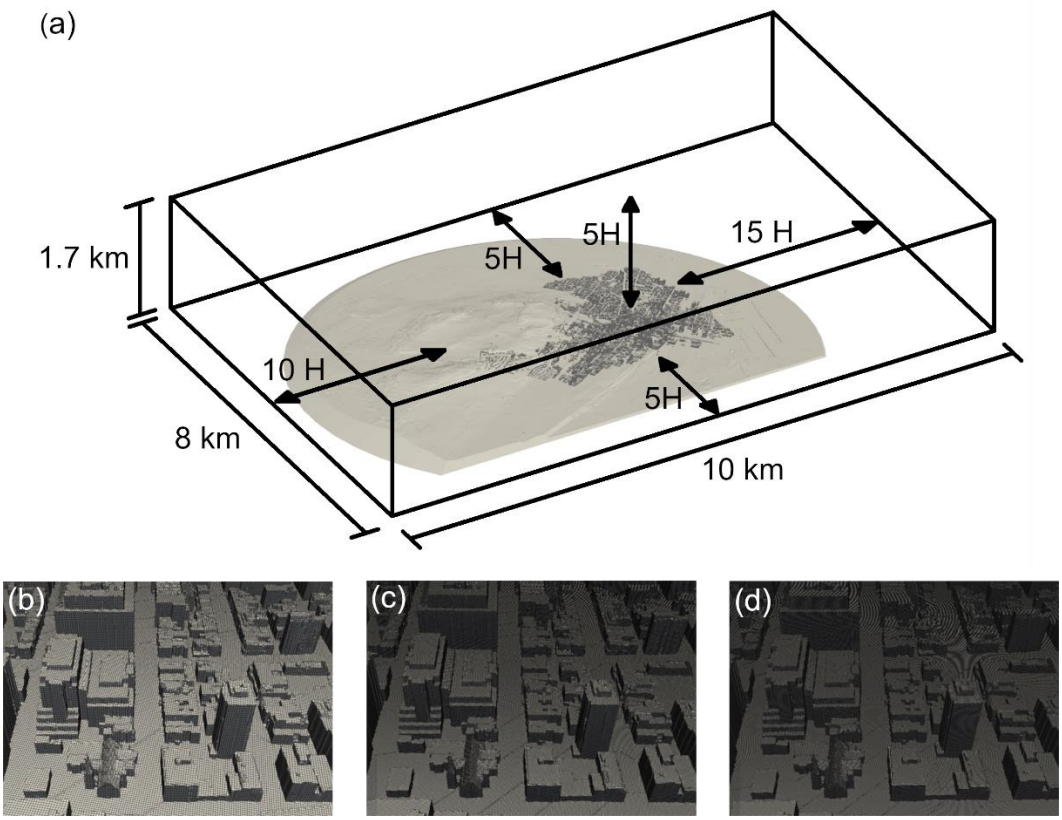

Figure 1. (a) Computational domain dimensions. (b) Coarse grid resolution. (c) Medium grid resolution. (d) Fine grid resolution.

The solver simpleFoam was used, which assumes incompressible flow, first finding the converged wind field, and then a modified version including turbulent diffusion and scalar transport was used to simulate the wildfire smoke dispersion. During these simulations, the value of Sc_t was varied between 0.4 and 1 to investigate its effects on the wildfire smoke dispersion.

3. RESULTS

The predicted wind speeds by the two turbulence models are first compared to the 20-minute averaged lidar wind speeds (Fig. 2). This comparison shows good agreement by the models across many of the hours, with the *k*-ε and SST *k*-ω models performing similarly. The characteristic logarithmic profile of ABL flow is well captured at the lower altitudes for which this profile is the proper representation of the boundary layer. Later in the day (Fig. 2e-h), with the development of the mixing and residual layer responsible for more complex dynamics, the models provide less accurate predictions of wind speed. The models' predictions of wind speed and direction at the McTavish weather station are shown in Fig. 3, from which can be seen that at this location the SST *k*-ω model significantly underpredicts the wind speed while the *k*-ε model shows much better agreement with an average error of only 13.2%. This is found to be the result of the SST *k*-ω model's difficulty in simulating wake reattachment length.

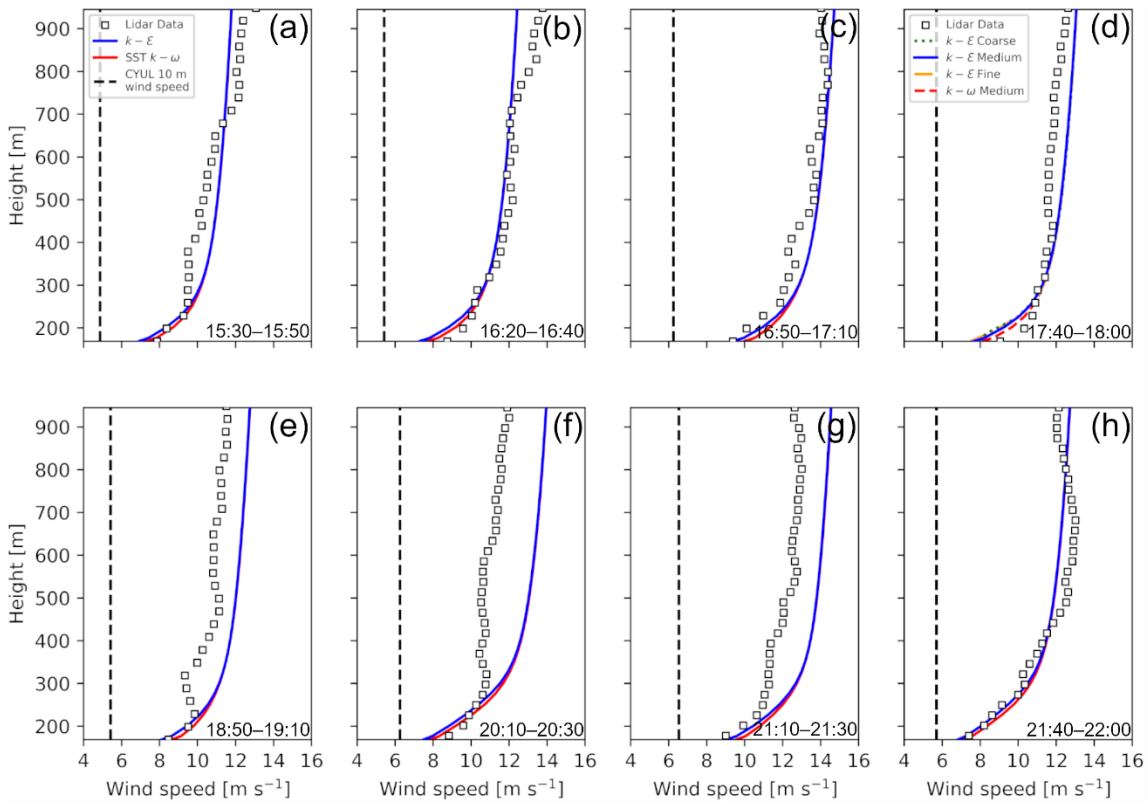

Figure 2. Modeled and lidar measured wind speeds for the averaging periods indicated in the bottom right of each subplot.

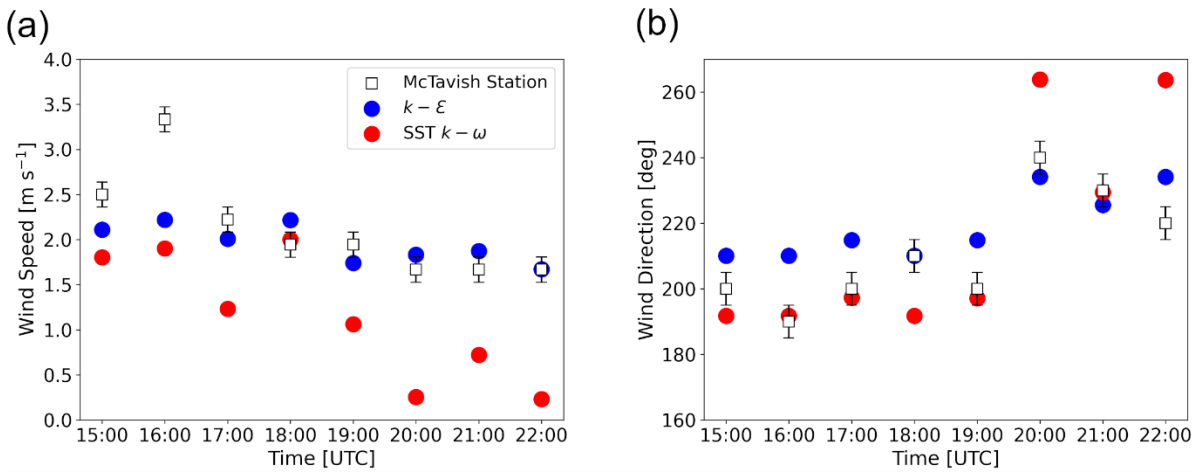

Figure 3. Modeled and anemometer measured (a) wind speed and (b) wind direction.

The validated numerical model is able to investigate features of the urban wind flow such as wind comfort and implications for air quality. Figure 4 show the wind speeds 1.75 m above ground level predicted by the standard *k-ε* model for 18:00 UTC. Most of the city experiences low wind speeds, partly due to the mountain of Mount Royal blocking higher wind speeds. Two

areas in the city are found to be susceptible to higher wind speeds, potentially causing uncomfortable pedestrian level wind conditions. The first is found in the south of the domain where the city's tallest buildings are located. Across many of the hours simulated, wind speeds here approach and exceed 5 m s^{-1}, the threshold beyond which winds pose a danger to those with reduced mobility and the elderly (Blocken & Carmeliet 2004). Another location in the eastern part of the city, near both a metro station (Sherbrooke) and retirement home, also experience high pedestrian level wind speeds, affecting both commuters and those susceptible to being injured by strong wind. Both locations are in regions where tall buildings force the strong winds aloft down to the ground, emphasizing the importance of this consideration when designing new high-rises to decrease uncomfortable and dangerous wind conditions.

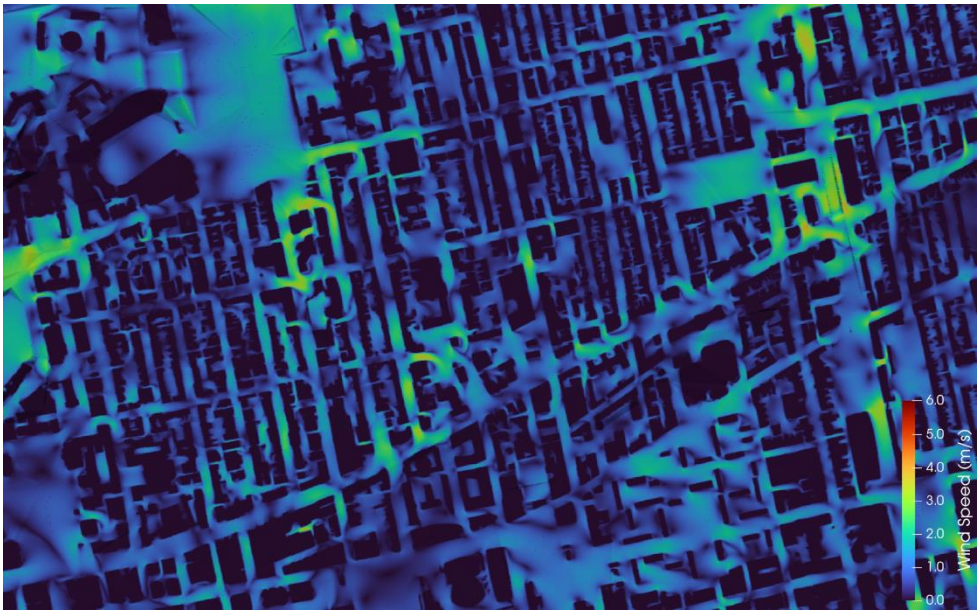

Figure 4. Standard *k-ε* model predicted wind speeds 1.75 m above ground level at 18:00 UTC

After the converged wind fields are found, wildfire smoke is introduced into the domain, which then dispersed throughout the city. Figure 6. shows the predicted concentration of $PM_{2.5}$ with different values of Sc_t. The best agreement with the air quality monitoring station is achieved with Sc_t = 0.6, which is on the higher end of previously derived values (Gousseau et al. 2010) but aligns well with a study by Toja-Silva et al. (2017) investigating urban dispersion characteristics. This value of Sc_t = 0.6 was then also test using the SST *k-ω* model, and a similar level of accuracy to the standard *k-ε* model was found. The characteristics of the smoke dispersion is also investigated by analyzing the smoke's spatial distribution throughout the city. Figure 5 shows the concentration of $PM_{2.5}$ for two separate hours at the heights of 1.75 and 30 m above ground level. Heightened concentrations of smoke are found near the base of the mountain where wind speeds are lower and decreased natural ventilation. Conversely, a region of lower elevation and sparser urban density exhibits lower concentrations due to the higher wind speeds. These local differences in smoke concentrations point to the complex dispersion dynamics of urban regions. They also suggest particular areas of cities may be more or less susceptible to decreased air quality, which could affect the long-term health of city residents.

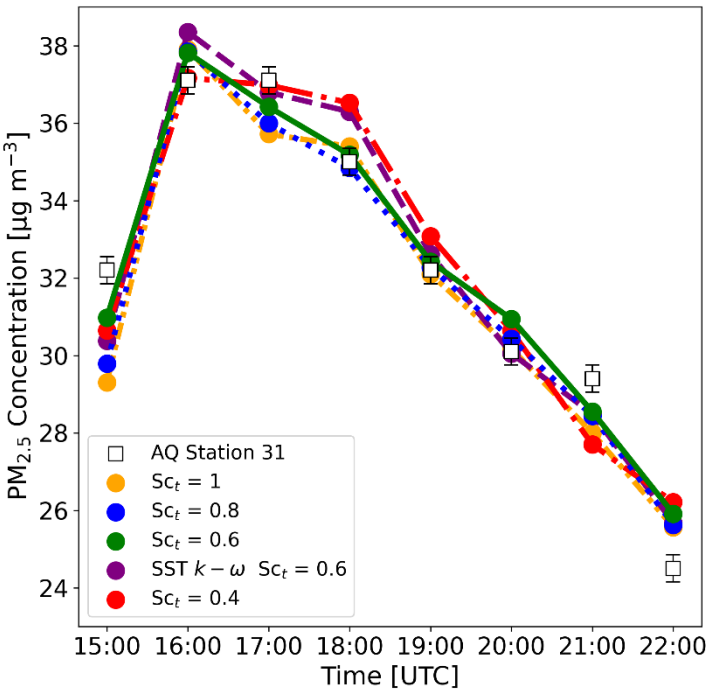

Figure 5. Model predictions of $PM_{2.5}$ using different values of Sc_t compared with air quality monitoring station measurements.

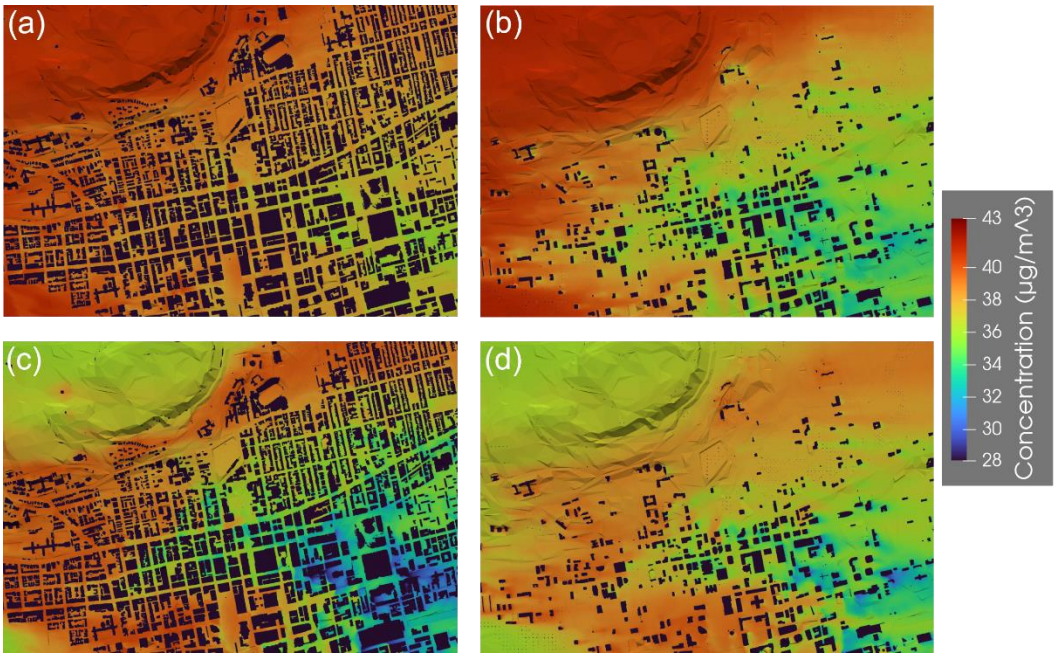

Figure 6. Predicted $PM_{2.5}$ concentrations for 16:00 UTC (a) 1.75 m above ground level and (b) 30 m above ground level and for 18:00 UTC (c) 1.75 m above ground level and (d) 30 m above ground level.

4. CONCLUSIONS

Urban wind flow and dispersion characteristics in the downtown region of Montréal on the day of July 17, 2023, were simulated, validating two turbulence models and choice of turbulent Schmidt number. Lidar measurements are shown to provide valuable validation data for urban CFD models. The standard k-ε model with Sc_t = 0.6 was found to be highly accurate in simulating both the wind field and smoke concentrations. The validated model was then used to analyze issues related to wind comfort and air quality.

ACKNOWLEDGEMENTS

This work was supported by the Government of Canada (Environment and Climate Change Canada Grant: EDF-CA-2021i022).

REFERENCES

Abatzoglou, J. T., Williams, A. P., 2016. Impact of anthropogenic climate change on wildfire across western US forests. Proceedings of the National Academy of Sciences of the United States of America 113, 11770-11775. https://doi.org/10.1073/pnas.1607171113.

Atkinson, R., 2000. Atmospheric chemistry of VOCs and NO_x. Atmospheric Environment 34, 2063-2101. https://doi.org/10.1016/S1352-2310(99)00460-4.

Blocken, B., Carmeliet, J., 2004. Pedestrian wind environment around buildings: literature review and practical examples. Journal of Building Physics 28, 107-159. https://doi.org/10.1177/1097196304044396.

Blocken, B., 2018. LES over RANS in building simulation for outdoor and indoor applications: A foregone conclusion? Building Simulation 11, 821-870. https://doi.org/10.1007/s12273-018-0459-3.

Copernicus, 2024. Copernicus: Canada produced 23% of the global wildfire carbon emissions for 2023. https://atmosphere.copernicus.eu/copernicus-canada-produced-23-global-wildfire-carbon-emissions-2023.

Drew, D. R., Barlow, J. F., Lane, S. E., 2013. Observations of wind speed profiles over Greater London, UK, using a Doppler lidar. Journal of Wind Engineering and Indusrial Aerodynamics 121, 98-105. https://doi.org/10.1016/j.jweia.2013.07.019.

Franke, J., Hellsten, A., Schlünzen, H., Carissimo, B., 2007. Best Practice Guideline for the CFD simulation of flows in the urban environment. COST Office.

Gousseau, P., Blocken, B., Stathopoulos, T., van Heijst, G. J. F., 2010. CFD simulation of near-field pollutant dispersion on a high-resolution grid: a case study by LES and RANS for a building group in downtown Montreal. Atmospheric Environment 45, 428-438. https://doi.org/10.1016/j.atmosenv.2010.09.065.

Liu, J. C., Pereira, G., Uhl, S. A., Bravo, M. A., Bell, M. L., 2015. A systematic review of the physical health impacts from non-occupational exposure to wildfire smoke. Environmental Research 136, 120-132. https://doi.org/10.1016/j.envres.2014.10.015

Richards, P. J., Hoxey, R. P., 1993. Appropriate boundary conditions for computational wind engineering models using the k-ϵ turbulence model. Journal of Wind Engineering and Industrial Aerodynamics 46-47, 145-153. https://doi.org/10.1016/0167-6105(93)90124-7.

Ritchie, H., Samborska, V., Roser, M., 2024. Urbanization. https://ourworldindata.org/urbanization.

Toja-Silva, F., Chen, J., Hachinger, S., Hase, F., 2017. CFD simulation of CO2 dispersion from urban thermal power plant: analysis of turbulent Schmidt number and comparison with Gaussian plume model and measurements. Journal of Wind Engineering and Industrial Aerodynamics 169, 177-193. https://doi.org/10.1016/j.jweia.2017.07.015.

Tominaga, Y., Stathopoulos, T., 2007. Turbulent Schmidt numbers for CFD analysis with various types of flowfield. Atmospheric Environment 41, 8091-8099. https://doi.org/10.1016/j.atmosenv.2007.06.054.

Vicente, A., Alves, C., Calvo, A. I., Fernandes, A. P., Nunes, T., Monteiro, C., Almeida, S. M., Pio, C., 2013. Emission factors and detailed chemical composition of smoke particles from the 2010 wildfire season. Atmospheric Environment 71, 295-303. https://doi.org/10.1016/j.atmosenv.2013.01.062.

Wang, X., McNamara, K. F., 2006. Evaluation of CFD simulation using RANS turbulence models for building effects on pollutant dispersion. Environmental Fluid Mechanics 6, 181-202. https://doi.org/10.1007/s10652-005-5656-9.

Wieringa, J., 1992. Updating the Davenport roughness classification. Journal of Wind Engineering and Industrial Aerodynamics 41, 357-368. https://doi.org/10.1016/0167-6105(92)90434-C.

Wilcox, D. C. Turbulence Modeling for CFD. La Cañada, California, United States of America. DCW Industries Inc. 2006.

6th International Conference on Building Energy and Environment
Eindhoven University of Technology, The Netherlands
6 - 10 July 2025

A numerical study of urban canyon flow under surface heating: Comparing wall-modelled and wall-resolved LES across scales

Xing ZHENG [1], Pu GONG[1], Lemei LI [1,2]
[1]*Department of Architecture and Civil Engineering, City University of Hong Kong, Hong Kong, China, lemeili2-c@my.cityu.edu.hk, x.zheng@cityu.edu.hk*
[2]*School of Architecture & Fine Art, Dalian University of Technology, Dalian, China, llm@mail.dlut.edu.cn*

SUMMARY
Large Eddy Simulation (LES) has been widely used to investigate urban airflow and heat removal processes. Due to the high computational costs associated with implicit filtering in LES, wall-modelled (WM) LES is often preferred over wall-resolved (WR) LES. However, the effectiveness of LES-WM for canyon flow under surface heating has not been thoroughly explored. This study assesses the performance of both WMLES and WRLES for reproducing the flow and temperature fields in a street canyon model with surface heating in a wind tunnel. Three computational grids with different resolutions, i.e., n/δ = 40, 10, and 2.5, are generated. WRLES is conducted with the grid with n/δ=40, and WRLES is conducted for all three grids. WRLES and WMLES with n/δ = 40 and n/δ = 10 demonstrate relative good agreement with the experiment, in terms of velocity, turbulent kinetic energy, and air temperature. In contrast, the WMLES simulation at n/δ = 2.5, significantly underpredicts the turbulent kinetic energy and overpredicts the air temperature near the heated wall.

Keywords: Best practice recommendations, Large-eddy simulation; Buoyancy flow; Surface heating

1. INTRODUCTION

Understanding the airflow patterns and dissipation of heat from building surfaces is critical for addressing urban heat islands, which exacerbate energy consumption, public health risks, and thermal comfort issues in cities. Large Eddy Simulation (LES) is commonly used to examine the aerodynamics and heat removal from the building surfaces. Due to the high computational costs associated with implicit filtering in LES for flows at relatively high Reynolds numbers, (WM) LES is often preferred over wall-resolved (WR) LES (Chew et al. 2018, Iousef et al. 2023). However, the effectiveness of WMLES for such applications has not been thoroughly explored. Therefore, this study assesses the performance of both WMLES and WRLES for reproducing the flow and temperature fields within a street canyon model with surface heating in a wind tunnel.

2. METHODOLOGY

2.1. Description of the wind tunnel experiment

The wind tunnel experiment conducted at the University of Surrey examined the effects of local heating on flow dynamics in a street canyon (Marucci and Carpentieri 2019). Each of the building models that form the street canyon measures 0.166 m in height (H), 0.166 m in width, and 2.490 m in length. Electric heating mats were utilized to achieve local heating to the windward and leeward walls. Velocity measurements were performed using a two-component laser-Doppler

anemometer. Air temperatures were measured using a calibrated fast-response cold-wire probe. The reference wind speed (U_{ref} = 0.65 m/s) was recorded upstream of the canyon model. In the experiment, different heating conditions were examined. The present validation study takes the condition of windward wall heating under a neutral boundary layer.

2.2. COMPUTATIONAL SETTING AND PARAMETERS

The LES simulations are performed with OpenFOAM-v2012. The computational domain and boundary conditions follow the setups in the wind tunnel. Synthetic turbulence at the inlet is generated using the digital filter method (Xie and Castro 2008), which modifies the inlet velocity profiles by incorporating the Reynolds stress tensor, length scale, and white noise. As shown in Fig 1., three computational grids with different resolutions are generated, i.e., n/δ = 40, 10, and 2.5. Note that n represents the number of cells used to discretize the turbulence boundary layer thickness $\delta = H/2$ (Mukha et al. 2019). Only the grid n/δ = 40 is used for the WRLES. WMLES is conducted using the three computational grids. All WMLES simulations employ Spalding's law (Spalding and others 1961), which is valid for the wall region of $0 \leq y^+ \leq 350$:

$$y^+ = u^+ + e^{-\kappa B}\left[e^{-\kappa u^+} - 1 - \kappa u^+ - \frac{1}{2}(\kappa u^+)^2 - \frac{1}{6}(\kappa u^+)^3\right]$$

After the simulation reaches statistical steadiness, the sampling is taken from 81 seconds following (Qin et al. 2024).

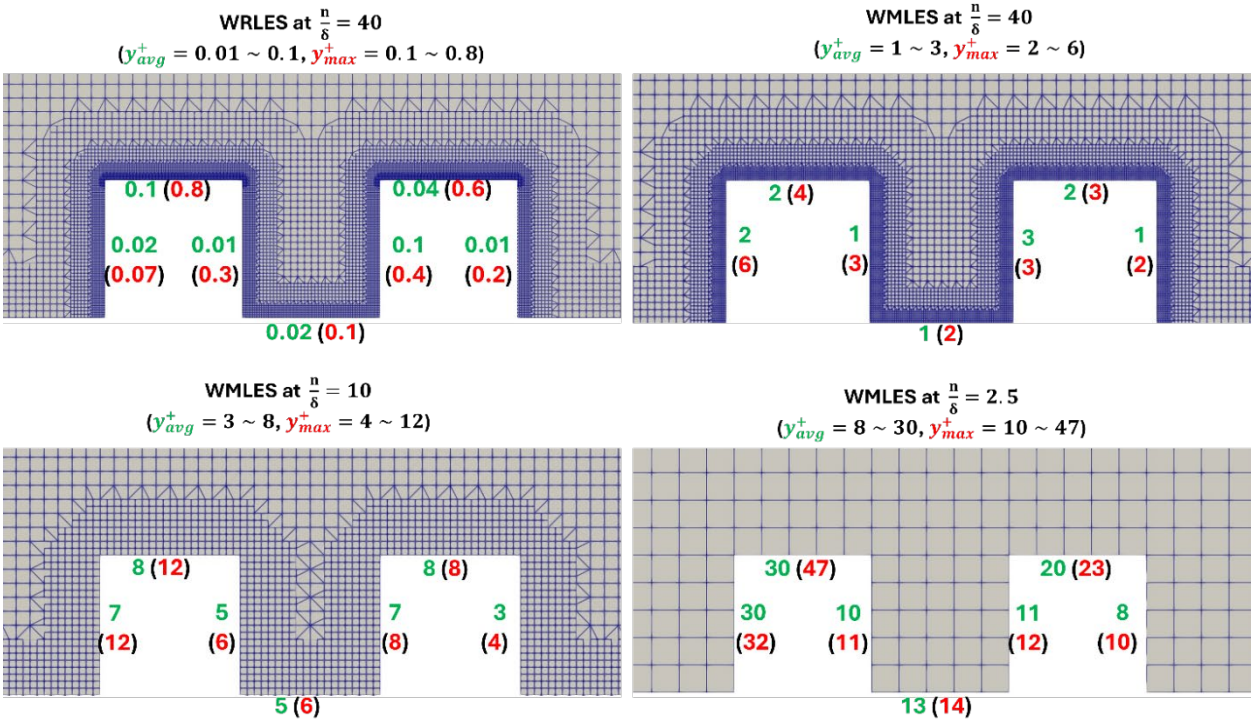

Figure 1. Area-averaged y⁺ values (y^+_{avg}, numbers in **green** color), area-maximum y⁺ values (y^+_{max}, numbers in **red** color), and the grid configurations of WRLES simulation at n/δ=40 and WMLES simulations at n/δ=40, 10, and 2.5 for the street canyon with the heated windward wall.

3. RESULTS

3.1. Wind flow and pollutant field

At a grid resolution of $n/\delta = 40$, WRLES simulation shows a y^+_{avg} ranging from 0.01-0.1, and y^+_{max} ranging from 0.1 to 0.8. These y^+ values indicate an adequate resolution of the boundary layer. All three WMLES simulations demonstrate y^+ values ranging from 0 to 350, indicating that the grid resolution is suitable for modeling turbulence in the boundary layer. It should be noted that WRLES simulation at $n/\delta = 40$ and WMLES simulation at $n/\delta = 40$ yield different y^+ values, probably due to different predictions for the velocity close to the wall.

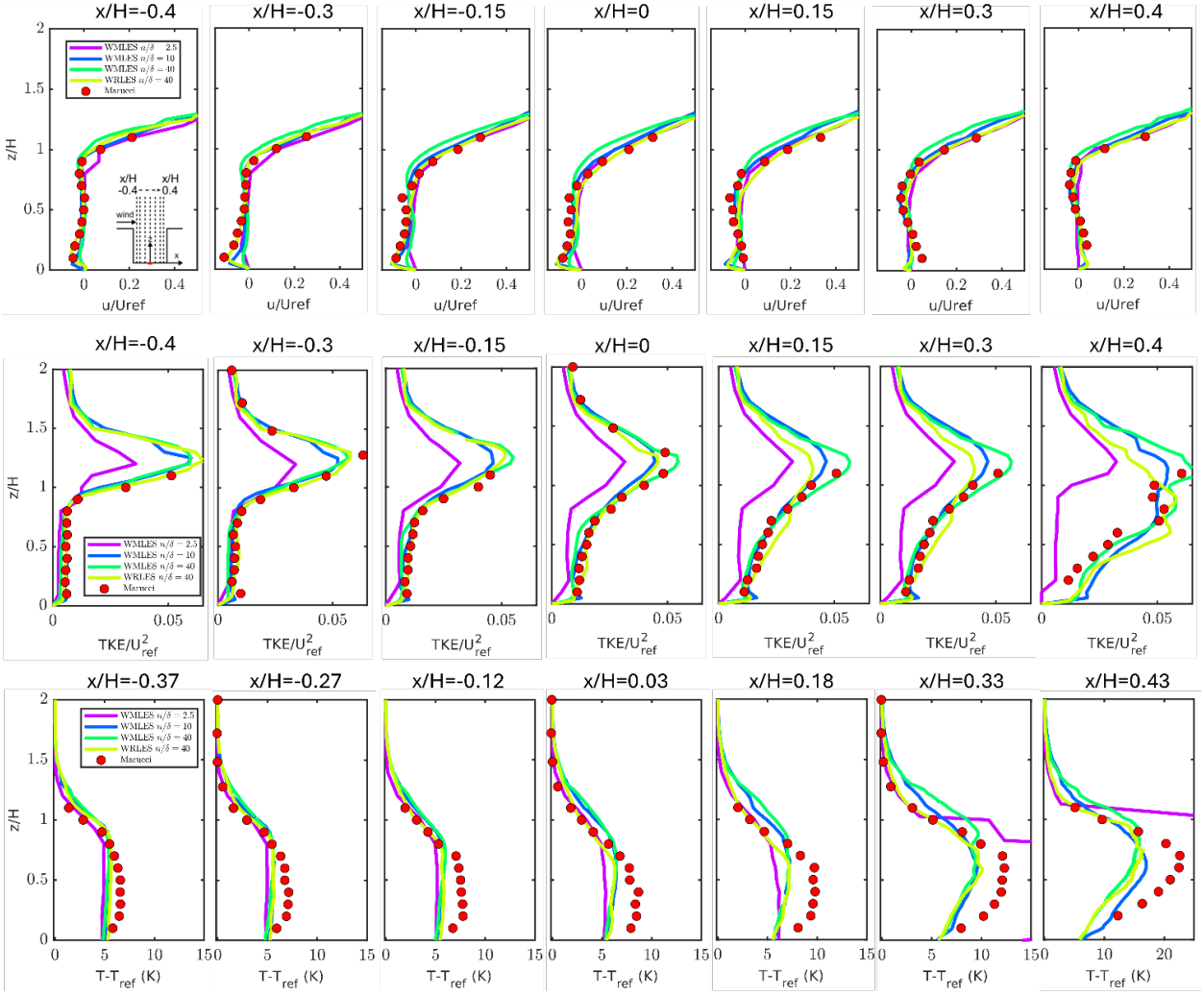

Figure 2. Comparison of the vertical profiles of (top) normalized streamwise velocity, (mid) normalized turbulence kinetic energy, and (bottom) relative temperature (T-T_{ref}) at different x values in the center section (y=0) between the wind tunnel experiment, WRLES simulation with n/δ =40 and WMLES simulations with n/δ =40, 10 and 2.5 replicating this experiment for a street canyon with heated windward wall

For the vertical profiles of the normalized streamwise velocity (see the top row in Fig. 2), WRLES simulation with n/δ = 40 and WMLES simulation with n/δ = 40 and n/δ = 10 demonstrate good agreement with the experiment. In contrast, the WMLES simulation at n/δ = 2.5 does not capture the flow in the anti-stream direction at ground level (0 < z/H < 0.2) at some locations, e.g., x/H = -0.15 or x/H = 0. For the vertical profiles of the normalized turbulence kinetic energy (see the middle row in Fig. 2), WRLES with n/δ = 40 and WMLES with n/δ = 40 and n/δ = 10 maintain consistency with the experiment by accurately capturing the TKE in the shear layer above the canyon within the range 1 < z/H < 1.5. In contrast, WMLES simulation with n/δ = 2.5 underpredicts the TKE in this region. For the

vertical profiles of the relative temperature, the WRLES simulation with n/δ = 40 and the WMLES simulations with n/δ = 40 and n/δ = 10 captures the shape of the profile, with an underprediction of less than 3K within the height range of 0.3<z/H<0.6. However, WMLES with n/δ = 2.5 significantly overpredicts air temperature near the heated wall, given that the big cell occupies the near wall region.

The results of the intermediate and full-scale simulations will be presented at the conference.

ACKNOWLEDGEMENTS
The numerical simulation for this article was supported by the supercomputing service platform called Paratera HPC Cloud.

REFERENCES
Chew, L. W., Glicksman, L. R., and Norford, L. K. (2018), "Buoyant flows in street canyons: Comparison of RANS and LES at reduced and full scales," Building and Environment, 146, 77–87.
Marucci, D., and Carpentieri, M. (2019), "Effect of local and upwind stratification on flow and dispersion inside and above a bi-dimensional street canyon," Building and Environment, 156, 74–88.
Mukha, T., Rezaeiravesh, S., and Liefvendahl, M. (2019), "A library for wall-modelled large-eddy simulation based on OpenFOAM technology," Computer Physics Communications, 239, 204–224.
Qin, P., Ricci, A., and Blocken, B. (2024), "On the accuracy of idealized sources in CFD simulations of pollutant dispersion in an urban street canyon," Building and Environment, 265.
Spalding, D. B., and others (1961), "A single formula for the law of the wall," Journal of Applied mechanics, 28, 455–458.
Xie, Z. T., and Castro, I. P. (2008), "Efficient generation of inflow conditions for large eddy simulation of street-scale flows," Flow, Turbulence and Combustion, 81, 449–470.

6th International Conference on Building Energy and Environment
Eindhoven University of Technology, The Netherlands
6 - 10 July 2025

Impact of 2D/3D built environments on block-scale urban thermal comfort – a case from Xi'an, China

Xukun Yan [1], Yupeng Wang [2]

[1] *School of Human Settlement and Civil Engineering, Xi'an Jiaotong University, Xi'an, China, xukun_yan@stu.xjtu.edu.cn*
[2] *School of Human Settlement and Civil Engineering, Xi'an Jiaotong University, Xi'an, China, wang-yupeng@xjtu.edu.cn*

SUMMARY
Optimizing the built environment is essential for mitigating the adverse effects of extreme heat events; however, comprehensive studies on the impact of 2D and 3D built environment morphology on local thermal comfort remain scarce. This study focuses on Xi'an, China, and aims to assess the influence of morphology indicators by: 1) quantifying urban thermal comfort using the modified temperature-humidity index (MTHI), and 2) applying boosted regression trees (BRT). The results indicate that: (1) 71.27% of blocks in the study area experience uncomfortable thermal conditions, (2) the normalized difference vegetation index (NDVI) is the primary factor influencing MTHI, and (3) the 2D built environment is most strongly associated with the thermal environment during hot summer. These findings provide a quantitative foundation for enhancing urban thermal comfort and promoting sustainable development through modifications to the built environment.

Keywords: thermal comfort, multi-dimensional urban factors, boosted regression tree (BRT).

1. INTRODUCTION

Urban heat island (UHI) effect and rapid urbanization are increasing the frequency of extreme heat events worldwide, with the United Nations Environment Program (UNEP) projecting that by 2050, 1.6 billion urban dwellers will experience extreme heat. This escalating heat presents significant risks to infrastructure, public health, and mortality. The World Health Organization (WHO) estimates that, between 2030 and 2050, extreme heat will result in 250,000 deaths annually, primarily due to heat-related illnesses, heart failure, and respiratory complications, with the elderly being particularly vulnerable. Studies from Europe, the United States, China, and Japan have consistently shown that older populations bear the highest risk during extreme heat events (Ballester et al. 2023; Carr, Falchetta, and Sue Wing 2024; Chen et al. 2023; Zeng, Baptista, and Kakinuma 2024). Given this alarming trend, there is an urgent need for urban adaptation strategies to mitigate the impacts of climate change.

Research leveraging remote sensing and field measurements has demonstrated a clear connection between urban planning and thermal characteristics. Urban green infrastructure such as parks, have been shown to provide a cooling effect that helps reduce urban heat (Zhou et al. 2022). In contrast, high building and road densities are typically associated with elevated land surface temperatures (LST) (Xu et al. 2024). Furthermore, land use types, such as industrial areas, are often warmer due to the heat generated by infrastructure and activities (Su et al. 2021). With increasing urban verticalization, the impact of 3D urban structures on the thermal environment is gaining more

attention (Yuan et al. 2024). Research has indicated that building heights and street canyon configurations (e.g., openness and orientation) can influence temperature distribution at the street level (Han et al. 2023; Ali-Toudert and Mayer 2006). Additionally, compact urban spaces with higher floor area ratios tend to lower LST (Luo et al. 2023), while shadows from vertical structures (such as buildings and trees) can block solar radiation, improving thermal comfort (Park, Guldmann, and Liu 2021). These 3D characteristics, along with traditional 2D urban features, provide new insights into how the built environment affects urban heat dynamics.

Temperature is a key indicator of thermal exposure, and numerous studies have explored the impact of urban morphology on surface and air temperatures. However, thermal comfort is not only influenced by temperature but also by humidity, which plays a crucial role in how heat is perceived (Liu, Zhang, and Deng 2016). Indices that combine temperature and humidity, such as the discomfort index (DI), physiological equivalent temperature (PET), and the Universal Thermal Climate Index (UTCI), offer a more comprehensive and sensitive measure of thermal comfort, reflecting the combined effects of heat and moisture on the human body (Thom 1959; Bröde et al. 2012; Höppe 1999). These indices provide a more accurate assessment of urban microclimates, yet few studies have comprehensively examined the impact of 2D and 3D built environment variables on urban thermal comfort using temperature and humidity indices.

To address these research gaps, this study integrates thermal discomfort data and 2D and 3D built environment variables to analyze the spatial distribution of urban thermal comfort and the impact of urban built environment on it. The main objective is to identify how multidimensional built environment indicators can enhance thermal comfort, promote equitable heat mitigation, and inform climate adaptation urban planning policies.

2. MATERIALS AND METHODS

2.1. Study area

The study area (34°11′–34°22′ N, 108°47′–109°06′ E, Fig. 1a) is located in the central region of Xi'an, covering 45,734.37 ha and enclosed by the Xi’an Bypass Highway. As a pivotal city in Northwest China, Xi'an is characterized by rapid urbanization and a high population density and also faces considerable heat challenges, with the Xi'an Weather Station reporting an average of 43 days in 2023 when temperatures surpassed 35°C. Given these conditions, there is a pressing need for research on thermal comfort during extreme heat events in the region.

2.2. Datasets

The datasets used in this study include remote sensing images with a 30-meter spatial resolution from Landsat8 TIRS satellite, as well as data from the Shuttle Radar Topography Mission (SRTM), the Advanced Land Observing Satellite (ALOS), and building and road network data from AutoNavi Map and Baidu Map Street View images, both primarily captured in 2020. The study is carried out in two main stages.

First, urban thermal comfort is assessed at the block level using the modified temperature-humidity index (MTHI). MTHI values are derived from LST and normalized difference moisture index (NDMI), calculated using Landsat 8 imagery acquired on August 2, 2021 (https://glovis.usgs.gov/, path 127, row 36, cloud cover: 5.41%). On this observation day, typical summer conditions were

recorded, with a maximum temperature of 39°C, no precipitation, and light breezes classified as force 2 within the study area. Secondly, this study explores the relationship between three environmental indicators (MTHI, LST and NDMI) and environmental variables affecting urban thermal comfort. The 2D built environment indicators of cities, derived from city maps and remote sensing images, have long been important references for urban planning studies. However, digital elevation models (DEMs) and 360° street images captured through panoramic photographs now offer a more multidimensional perspective for urban studies. STRM (https://glovis.usgs.gov/) is a globally unique terrain dataset that provides uniform, consistent and high-resolution imagery (Yang, Meng, and Zhang 2011), while the ALOS (https://www.eorc.jaxa.jp/) offers the most accurate global-scale elevation data available (Nikolakopoulos 2020).

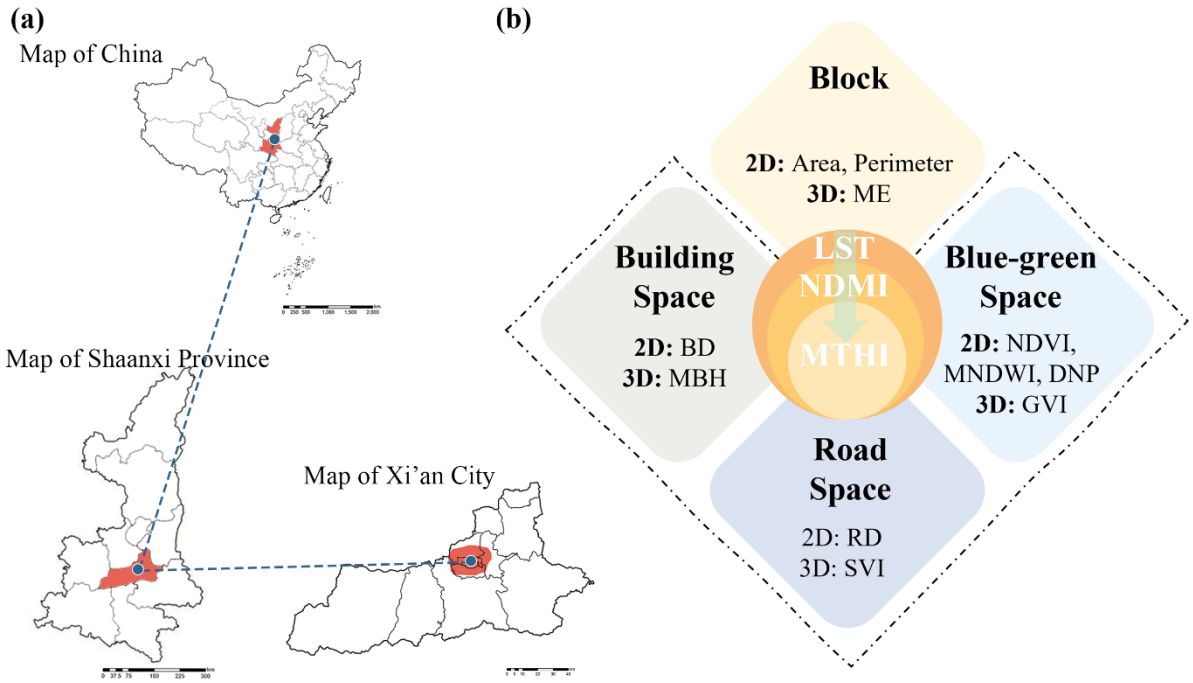

Figure 1. (a) The location of the study area and (b) indicators used in the study.

2.3. Quantification of urban thermal comfort

Quantifying urban thermal comfort and exposure requires consideration of both temperature and humidity, as the latter significantly influences human thermal comfort. The DI, based on dry-bulb (Td) and wet-bulb (Tw) temperatures, is a widely used thermal comfort metric (Thom 1959). This concept evolved into the temperature-humidity index (THI), which relies on air temperature (AT) and relative humidity (RH) (Nieuwolt 1977):

$$THI(℃) = 1.8 \times AT + 32 - 0.55 \times (1 - 0.01 \times RH) \times (1.8 \times AT - 26) \quad (1)$$

However, thermal comfort studies based on meteorological data are constrained in urban contexts due to sparse observation networks. For instance, Xi'an has only one state-run weather station (Jinghe Weather Station) near the central city. To address this limitation, a modified method using remote sensing data has been developed, substituting LST for AT and NDMI for RH. This approach, known as the MTHI, has proven reliable (Zeng et al. 2024; Feng et al. 2020):

$$MTHI(℃) = 1.8 \times LST + 32 - 0.55 \times (1 - NDMI) \times (1.8 \times LST - 26) \quad (2)$$

To validate the MTHI method for Xi'an, we compared three-day AT and RH data from Jinghe National Weather Station with LST and NDMI values derived from Landsat 8 imagery (July 28, August 13, and August 28, 2019). The computed THI and MTHI showed strong correlations (average $R^2 = 0.986$). Following THI's thermal comfort grading, MTHI values were normalized as:

$$TI = \frac{MTHI - MTHI_{mean}}{MTHI_{mean}} \quad (3)$$

where TI represents the normalized MTHI, and $MTHI_{mean}$ is the average MTHI value in the study area. Based on standard deviation, thermal comfort was classified into five levels, with lower TI values indicating higher summer comfort (Table 1) (Feng et al. 2020).

Table 1. Thermal comfort grading in summer.

Thermal comfort grading	Rang of TI value	Meaning (Relatively)
1	$TI \leq -1.5a$	More comfortable
2	$-1.5a < TI \leq -0.5a$	Comfortable
3	$-0.5a < TI \leq 0.5a$	Less comfortable
4	$0.5a < TI \leq 1.5a$	Uncomfortable
5	$1.5a < TI$	More uncomfortable

a is the standard deviation of TI.

2.4. Indictors of built environment

In this study, MTHI, LST and NDMI were used as the dependent variable, while 2D and 3D built environment indicators served as independent variables. This approach enabled a comprehensive analysis of the built environment's multifaceted impact on urban thermal comfort. The independent variables were extracted from four primary spatial dimensions: block morphology, architectural space, blue-green space, and road space (Fig. 1b).

For block morphology, key variables such as block area, perimeter, and mean elevation (ME)—accounting for buildings, greenery, and other structures—were considered. In the building space, building density (BD) and mean building height (MBH) were included as critical descriptors. For blue-green and street spaces, data from Baidu Maps Street View were incorporated. Using Python, we crawled 14,213 panoramic data points, each comprising four 90° segmented images (0°–90°, 90°–180°, 180°–270°, and 270°–360°). Semantic segmentation techniques, trained with the Cityscapes dataset (Cordts et al. 2016) , were applied to calculate the pixel occupancy for greenery and sky in these images. The Green View Index (GVI) and Sky View Index (SVI) were then derived as the average of the four images at each point. Additional blue-green space indicators included the normalized difference vegetation index (NDVI), the modified normalized difference water index (MNDWI), and the distance to the nearest park (DNP). For road space, road density (RD) was calculated. Table 2 summarizes the definitions and units of these built environment indicators.

Table 2. Built environment (2D/3D) indicators.

Type	Indicator	Definition / Equation	Unit
2D	Area	Total area of the block	ha
	Perimeter	Total perimeter of the block	km

	BD	$BD = \frac{S_{building}}{Area}$	
	NDVI	$NDVI = \frac{NIR - RED}{NIR + RED}$	
	MNDWI	$MNDWI = \frac{GREEN - SWIR}{GREEN + SWIR}$	
	DNP	Spatial distance from nearest park boundaries	m
	RD	$RD = \frac{L}{Area}$	
3D	ME	$ME = DSM - DEM$	m
	MBH	$MBH = \frac{V_{building}}{S_{building}}$	m
	GVI	$GVI = \frac{\sum_{i=1}^{4} Greenery\ Pixels}{\sum_{i=1}^{4} Total\ Pixels}$	
	SVI	$SVI = \frac{\sum_{i=1}^{4} Sky\ Pixels}{\sum_{i=1}^{4} Total\ Pixels}$	

Here, $S_{building}$ and $V_{building}$ represent the building footprint and volume, respectively; L is the total length of roads classified as level 3 or higher within the block. NIR, RED, GREEN and SWIR are near-infrared, red, green and short-wave infrared spectrum values of Landsat image. Elevation data, including DEM and digital surface model (DSM), were sourced from SRTM and ALOS, respectively.

2.5. Boosted regression trees

The boosted regression tree (BRT) method, a robust machine learning approach, is well-suited for analysing complex, multidimensional, non-linear data. It is particularly effective in addressing the intricate relationships between urban morphological features and thermal comfort (Elith, Leathwick, and Hastie 2008). In this study, the BRT model was implemented using the 'dismo' package and the 'gbm' function in R. The model examines the effects of multiple independent variables on the dependent variables—MTHI, LST, and NDMI—by iteratively constructing a series of decision trees. To interpret the results, partial dependence plots were generated to visualize the marginal effects of the five most influential variables, providing a quantitative means to understand the relationships between urban environmental characteristics and thermal comfort. The BRT model parameters were configured as follows: a learning rate of 0.01, a bag fraction of 0.5, a tree complexity of 5, and 10-fold cross-validation.

3. RESULTS AND DISSCUSION

3.1. Thermal comfort in Xi'an

The data of MTHI in the central area of Xi'an around 11:19 a.m. local time are shown in Fig. 2a and the average value (range) of MTHI is 35.89 °C (25.58 to 51.43 °C), respectively. The results show that lower MTHI is mainly concentrated in urban parks and large water bodies, etc., while higher MTHI is predominantly found in dense residential areas and industrial areas. This demonstrates that blue-green spaces effectively mitigate urban extreme heat events, while human activities and urban impermeable surfaces significantly degrade the urban thermal environment. Of the 1848 blocks, only 79 (4.27%) are more comfortable, 452 (24.46%) are comfortable, 744 (40.30%) are less comfortable, 435 (23.54%) as uncomfortable, and 138 (7.47%) as extremely uncomfortable. With over 70% of the city's blocks experiencing discomfort during extreme heat

events, addressing the thermal environment issue is crucial.

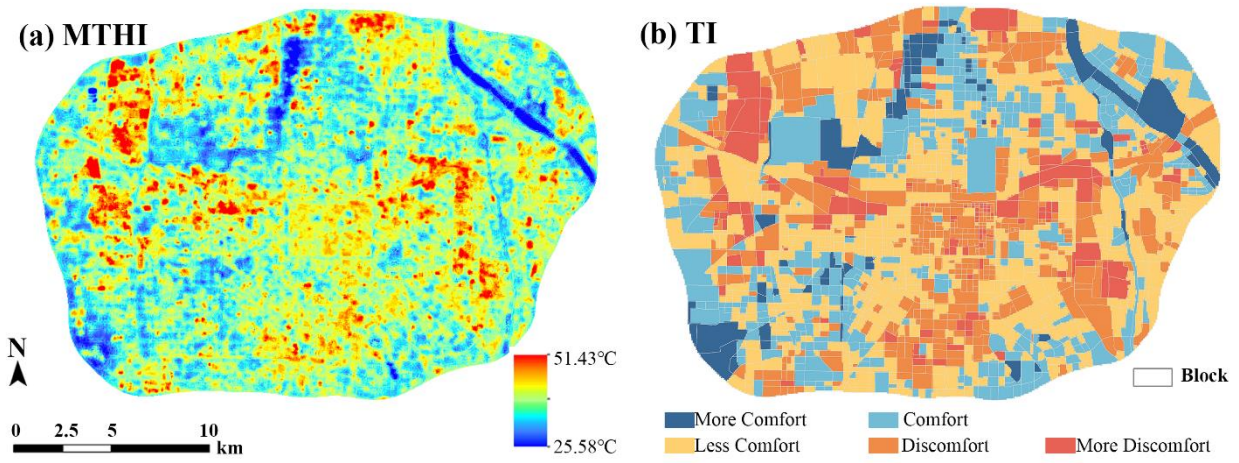

Figure 2. The spatial distribution of (a) MTHI and (b) TI.

3.2. Relative contributions of 2D/3D built environment

According to the fitted BRT model, the relative contributions of the indicators on LST, NDMI and MTHI are shown in Figure 3, with the sum of the contributions of all indicators equal to 100. Since the correlation between NDMI and NDVI exceeded 0.8, NDVI is excluded from the contribution of the indicators on NDMI. In LST, NDVI has the highest contribution of 48.54%, which is significantly higher than other indicators. In NDMI, MNDWI and BD held a contribution of 32.48% and 18.14% respectively, while the rest of the indicators had a relatively small effect on NDMI. Panel (c) shows the relative contributions to MTHI, where BD and NDVI are the highest contributors, each accounting for 21.17% and 20.42%. This underscores that both the built environment and vegetation have a major impact on modifying thermal conditions and heat perception. The results show that 2D indicators, such as BD, NDVI and MNDWI, contribute significantly to all three variables. This indicates that the influence of 2D indicators on thermal comfort is still greater than that of 3D indicators. Meanwhile, the relative contributions of building height (MBH) are 8.13%, 5.11%, and 10.04% for LST, NDMI, and MTHI, respectively, making it the next most significant factor following the previous 2D indicators. This suggests that the influence of 3D environmental indicators on thermal comfort should not be overlooked. It maintains a stable negative correlation with LST and MTHI, providing a cooling effect due to the shading caused by high buildings. Finally, the relative contributions of block morphological indicators, such as perimeter and area, are minimal and show similar trends across all three variables. In addition to considering 2D and 3D perspectives, the contribution of blue-green space indicators to all three variables is significantly greater, with all showing a negative correlation. This suggests that land cover significantly impacts thermal comfort, and that green spaces and water bodies should be effectively utilized in urban design to mitigate urban heat.

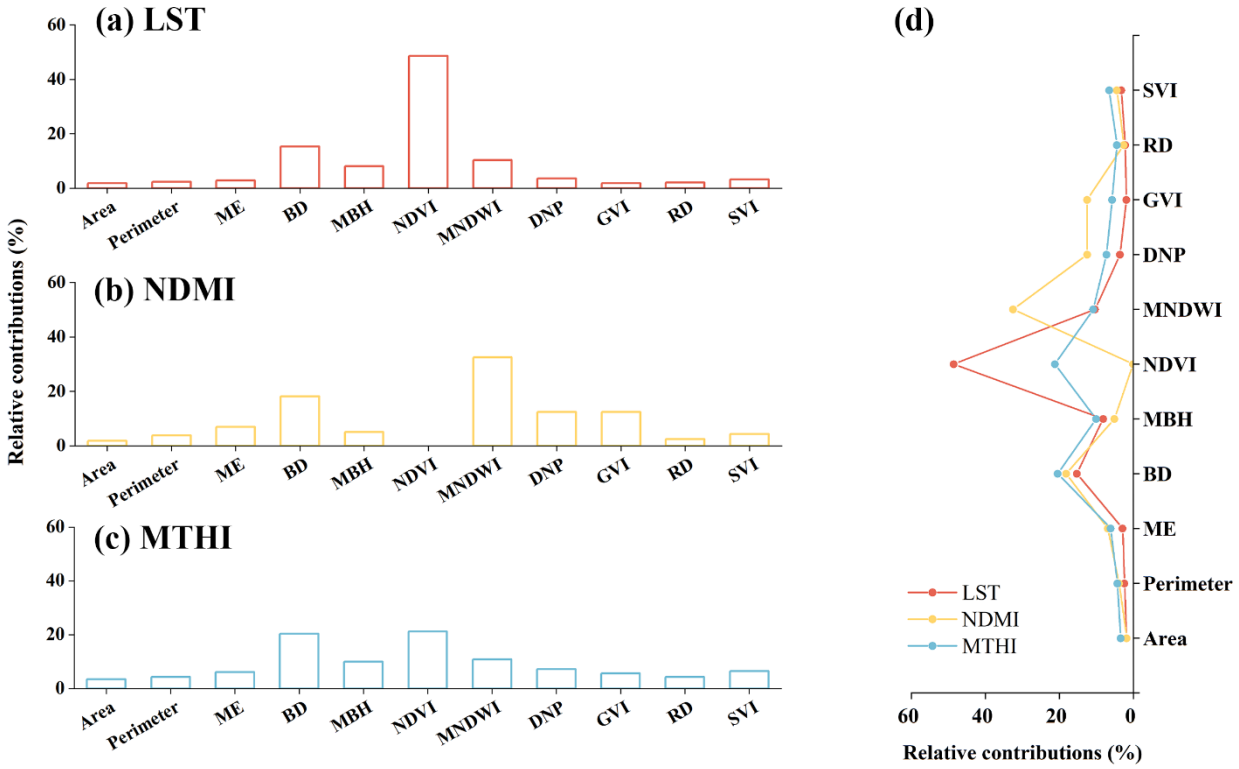

Figure 3. Relative contributions of the selected indicators on the (a) LST, (b) NDMI, (c) MTHI and with (d) comparisons.

4. CONCLUSION

This paper takes Xi'an as the study area, with blocks as the smallest study unit, based on data from Landsat 8, AMAP, etc. and BRT to explore the current thermal comfort conditions in the city and assess the impacts of 2D/3D urban morphology. The key findings are as follows: (1) Over 70% of blocks experience thermal discomfort, highlighting the urgent need for effective thermal mitigation measures. (2) Considering the average impact of 2D/3D indicators on LST, NDMI and MTHI, the three 2D indicators, NDVI, BD and MNDWI, are the most important indicators. In terms of their relative impact, the order of importance is as follows: blue-green space > building space > road space > block pattern. The findings of this study contribute to the understanding of the relationship between 2D and 3D urban morphology and thermal comfort, providing practical recommendations for mitigating UHI effect through rational urban planning.

ACKNOWLEDGEMENTS

This research was funded by the National Natural Science Foundation of China, grant number 52350610262.

REFERENCES

Ali-Toudert, Fazia, and Helmut Mayer. 2006. 'Numerical study on the effects of aspect ratio and orientation of an urban street canyon on outdoor thermal comfort in hot and dry climate', *Building and Environment*, 41: 94-108.

Ballester, Joan, Marcos Quijal-Zamorano, Raúl Fernando Méndez Turrubiates, Ferran Pegenaute, François R Herrmann, Jean Marie Robine, Xavier Basagaña, Cathryn Tonne, Josep M Antó, and Hicham Achebak. 2023. 'Heat-related mortality in Europe during the summer of 2022', *Nature medicine*, 29: 1857-66.

Bröde, Peter, Dusan Fiala, Krzysztof Błażejczyk, Ingvar Holmér, Gerd Jendritzky, Bernhard Kampmann, Birger Tinz, and George Havenith. 2012. 'Deriving the operational procedure for the Universal Thermal Climate Index (UTCI)', *International journal of biometeorology*, 56: 481-94.

Carr, Deborah, Giacomo Falchetta, and Ian Sue Wing. 2024. 'Population aging and heat exposure in the 21st century: Which US regions are at greatest risk and why?', *The Gerontologist*, 64: gnad050.

Chen, Mingxing, Liangkan Chen, Yuan Zhou, Maogui Hu, Yanpeng Jiang, Dapeng Huang, Yinghua Gong, and Yue Xian. 2023. 'Rising vulnerability of compound risk inequality to ageing and extreme heatwave exposure in global cities', *npj Urban Sustainability*, 3: 38.

Cordts, Marius, Mohamed Omran, Sebastian Ramos, Timo Rehfeld, Markus Enzweiler, Rodrigo Benenson, Uwe Franke, Stefan Roth, and Bernt Schiele. 2016. "The cityscapes dataset for semantic urban scene understanding." In *Proceedings of the IEEE conference on computer vision and pattern recognition*, 3213-23.

Elith, Jane, John R Leathwick, and Trevor Hastie. 2008. 'A working guide to boosted regression trees', *Journal of animal ecology*, 77: 802-13.

Feng, Li, Menmen Zhao, Yanan Zhou, Liujun Zhu, and Huihui Tian. 2020. 'The seasonal and annual impacts of landscape patterns on the urban thermal comfort using Landsat', *Ecological Indicators*, 110: 105798.

Han, Sijia, Hao Hou, Ronald C Estoque, Yaoyao Zheng, Chuhui Shen, Yuji Murayama, Jing Pan, Ben Wang, and Tangao Hu. 2023. 'Seasonal effects of urban morphology on land surface temperature in a three-dimensional perspective: A case study in Hangzhou, China', *Building and Environment*, 228: 109913.

Höppe, Peter. 1999. 'The physiological equivalent temperature–a universal index for the biometeorological assessment of the thermal environment', *International journal of biometeorology*, 43: 71-75.

Liu, Weiwei, Yingxia Zhang, and Qihong Deng. 2016. 'The effects of urban microclimate on outdoor thermal sensation and neutral temperature in hot-summer and cold-winter climate', *Energy and buildings*, 128: 190-97.

Luo, Pinyang, Bingjie Yu, Pengfei Li, Pengpeng Liang, Yuan Liang, and Linchuan Yang. 2023. 'How 2D and 3D built environments impact urban surface temperature under extreme heat: A study in Chengdu, China', *Building and Environment*, 231: 110035.

Nieuwolt, Simon. 1977. *Tropical climatology: an introduction to the climates of the low latitudes* (Wiley London).

Nikolakopoulos, Konstantinos G. 2020. 'Accuracy assessment of ALOS AW3D30 DSM and comparison to ALOS PRISM DSM created with classical photogrammetric techniques', *European Journal of Remote Sensing*, 53: 39-52.

Park, Yujin, Jean-Michel Guldmann, and Desheng Liu. 2021. 'Impacts of tree and building shades on the urban heat island: Combining remote sensing, 3D digital city and spatial regression approaches', *Computers, Environment and Urban Systems*, 88: 101655.

Su, Hangying, Guifeng Han, Lin Li, and Hongqiao Qin. 2021. 'The impact of macro-scale urban form on land surface temperature: An empirical study based on climate zone, urban size and industrial structure in China', *Sustainable Cities and Society*, 74: 103217.

Thom, Earl Crabill. 1959. 'The discomfort index', *Weatherwise*, 12: 57-61.

Xu, Duo, Yiquan Wang, Dian Zhou, Yupeng Wang, Qian Zhang, and Yujun Yang. 2024. 'Influences of urban spatial factors on surface urban heat island effect and its spatial heterogeneity: A case study of Xi'an', *Building and Environment*, 248: 111072.

Yang, Liping, Xingmin Meng, and Xiaoqiang Zhang. 2011. 'SRTM DEM and its application advances', *International journal of remote sensing*, 32: 3875-96.

Yuan, Bo, Liang Zhou, Fengning Hu, and Chunzhu Wei. 2024. 'Effects of 2D/3D urban morphology on land surface temperature: Contribution, response, and interaction', *Urban Climate*, 53: 101791.

Zeng, Ming, Emerson Augusto Baptista, and Kaoru Kakinuma. 2024. 'Heat impacts on an aging society: a spatio-temporal analysis of heatstroke deaths in Japan', *Environmental Research Communications*, 6: 115003.

Zeng, Peng, Dachuan Shi, Yaoyi Liu, Tian Tian, Yue Che, and Marco Helbich. 2024. 'Parks may not be effective enough to improve the thermal environment in Shanghai (China) as our modified H3SFCA method suggests', *Building and Environment*: 111291.

Zhou, Yi, Haile Zhao, Sicheng Mao, Guoliang Zhang, Yulin Jin, Yuchao Luo, Wei Huo, Zhihua Pan, Pingli An, and Fei Lun. 2022. 'Studies on urban park cooling effects and their driving factors in China: Considering 276 cities under different climate zones', *Building and Environment*, 222: 109441.

6th International Conference on Building Energy and Environment
Eindhoven University of Technology, The Netherlands
6 - 10 July 2025

Air Curtain Performance in Controlling Pollutant Dispersion during Vehicle Unloading in Semi-Open Industrial Buildings

Wenzhi Nie[1], Yu Liao[1], Gaoju Song[2], Yujie Chu[1], Jianlin Liu[1,*]

[1] *College of Environmental Science and Engineering, Donghua University, Shanghai, China, jianlin.liu@dhu.edu.cn*
[2]*Sippr Engineering Group Co., Ltd., Zhengzhou, China*

ABSTRACT
The dispersion of dust during vehicle unloading in semi-open industrial buildings poses environmental and health risks. This study aims to evaluate the potential of air curtains as a solution for this issue. To validate the used turbulence model and numerical methods, comparisons are made with wind tunnel experimental results. Furthermore, a 1:30 scale model of a semi-open industrial building is subsequently established to assess the impact of air curtains at varying flow speed (6, 8, 10, 12, 14, 16 and 18 m/s) and flow angles (0°, 5°, 10° and 15°) on pollutant leakage. Results show that as the air curtain flow speed increases from 6 m/s to 14 m/s, the control efficiency rises from -41.12% to 98.10%. Meanwhile, further increases of flow speed show a slight decrease in efficiency, down to 97.18%. This study provides preliminary insights into the application of air curtains in semi-open industrial buildings.

Keywords: Semi-open industrial building, Air curtain, Pollutant control, CFD simulation.

1. INTRODUCTION

Dust pollution is a prevalent issue in both global industrial sectors and urban environments, with significant adverse impacts on ecological systems, human health, and economic development (Guo et al. 2022). With studies showing that inhalable particles such as PM_{10} and $PM_{2.5}$, which are highly mobile and persist in the air for extended periods, present a higher inhalation risk for workers near the building and residents in downwind areas (Li et al. 2024). The primary sources of these particles are industrial material handling processes, including loading, transportation and unloading. This is particularly concerning during unloading operations, where dust and particulate matter are stirred up and can be carried downstream by wind, posing a significant health risk to workers. Therefore, addressing dust pollution in such production scenarios is critical.

Controlling pollutants within enclosed spaces during production appears to be the simplest and most effective approach. However, semi-open industrial buildings are commonly used in these industries for material unloading operations (Liu et al. 2022; Chu et al. 2024). Unlike fully enclosed structures, these buildings typically lack walls on one side, allowing dust generated inside to be easily affected by external wind, resulting in the dispersion of pollutants into the surrounding environment. Previous studies have demonstrated that semi-open building designs can hinder air circulation, leading to the accumulation of pollutants. As a dust suppression technology, air curtains have been widely applied in mining faces (Zhang et al. 2022), tunnel construction, and other fields (Chen et al. 2021). Wang et al.(2021) proposed a local ventilation system that combines push-pull ventilation with an air curtain. The study showed that increasing the air curtain jet velocity effectively reduces pollutant leakage from aircraft painting factories. Additionally, there

remains a lack of in-depth investigation into the performance and optimization of air curtains in semi-open industrial buildings, which presents a unique challenge due to the unpredictable nature of wind and the dynamic characteristics of the unloading process. Furthermore, the effects of air curtain performance parameters (e.g., angle and velocity) on controlling pollutant dispersion during material unloading in semi-open industrial buildings have not been thoroughly studied.
This study aims to evaluate the performance of air curtains in controlling pollutant dispersion during vehicle unloading in semi-open industrial buildings. To analyze the effects of different parameters on the dust suppression performance of the air curtain under outdoor natural wind conditions, this study employs numerical simulation. The key parameters of air curtain in the model include the jet velocity (6 m/s, 8 m/s, 10 m/s, 12 m/s, 14 m/s, 16 m/s and 18 m/s), the jet angle (0°, 5°, 10° and 15°). This study provides preliminary insights into the application of air curtain in semi-open industrial buildings for improving air quality in the surroundings.

2.METHODOLOGY

2.1 Turbulence model

In this study, the RNG k-ε model was employed to simulate the characteristics of dust control by air curtains during unloading operations at a single semi-open industrial building. For an isothermal turbulent process, an additional term in the ε equation makes the model particularly suitable for strained and swirling flows, enabling effective performance prediction in low Reynolds number flows and near-wall regions. The governing equations are as follows:

$$\frac{\partial \overline{u_i}}{\partial x_i} = 0 \tag{1}$$

$$\frac{\partial \left(\rho \overline{u_i u_j}\right)}{\partial x_i} = -\frac{\partial p}{\partial x_i} + \frac{\partial}{\partial x_j}\left[\mu\left(\frac{\partial u_i}{\partial x_j} + \frac{\partial u_j}{\partial x_i}\right)\right] + \frac{\partial}{\partial x_j}\left(-\rho \overline{u_i' u_j'}\right) \tag{2}$$

where the velocity components of x and y direction were u_i and u_j, respectively; the ρ, μ and $-\rho \overline{u_i' u_j'}$ were the air density, dynamic viscosity and Reynolds stress, respectively. The local mass fraction of each species Y_S, was predicted by solving a convection diffusion equation for the species in Eq. (3):

$$\frac{\partial}{\partial x_i}\left(\rho_m u_i Y_S\right) = \frac{\partial}{\partial x_j}\left[\left(\rho_m D + \frac{\mu}{s_c}\right)\frac{\partial Y_S}{\partial x_j}\right] \tag{3}$$

where ρ_m was the density of the mixture, D was the mass diffusion coefficient for the species in the mixture, and s_c was the turbulent Schmidt number (the default s_c was 0.7 for RNG k-ε model). The mass fraction Y_S could be converted to the volume concentration C by the Eq. (4):

$$Y_S = \frac{C\rho_S}{C\rho_S + (1-C)\rho} \tag{4}$$

where ρ_S was the tracer gas density.

2.2 CASE DESCRIPTION

The building had a height (H) of 0.2 m and a 1:1:1 aspect ratio ($L \times W \times H$), with a scale factor of 1:30. The silo had a vertical depth of 0.1 m (0.5H) and a bottom width of 0.1 m. Part of the silo's bottom was left open to simulate a connection to the transportation chamber below, although the chamber itself was not modeled. The pollutant source, being generated by vehicle unloading, was simplified and located on a quarter of the silo's side wall. The air curtain's length matched the building's width, with an outlet width and height of 0.02 m × 0.02 m, and an air outlet width of

0.006 m. The models were placed in a computational domain with dimensions of 21H × 11H × 6H (length × width × height), where H denoted the height of the semi-open industrial building (Figure. 1(a)). The upstream and lateral boundaries of the computational domain were positioned 5H from the building, while the downstream boundary was set at 15H from the building's leeward wall. Three measurement lines (Lines A, B, and C) were set to capture pollutant concentration levels around the building, which is critical for assessing pollutant dispersion and evaluating the effectiveness of the air curtain in controlling pollutant spread (Figure. 1(b)).

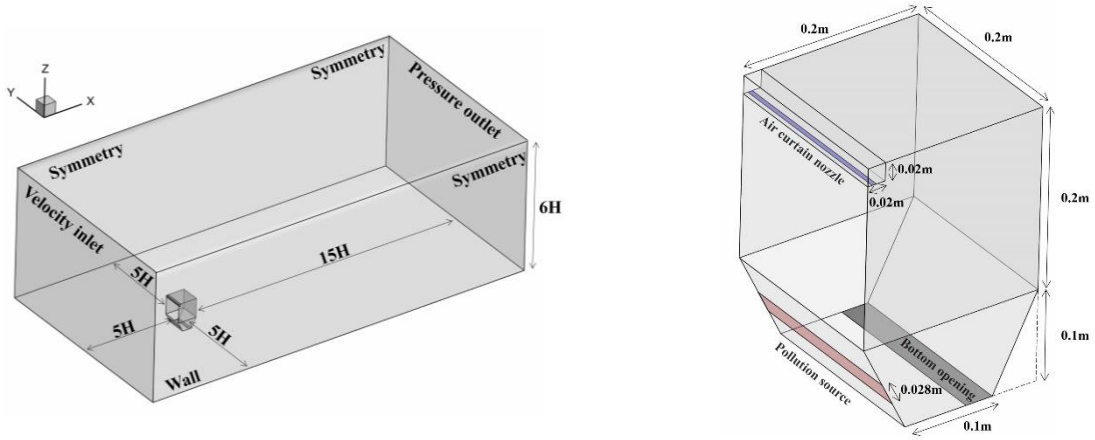

(a) (b)

Figure 1. Detail model information of test cases: (a) computational domain and boundary conditions, (b) semi-open building model.

A total of 11scenarios were modelled, each incorporating different influencing parameters: air curtain jet velocity and air curtain jet angle. Detailed information on these scenarios is provided in Table 1.

Table 1 Detailed parameter setting information for 11 cases.

Case No.	Air curtain Jet velocity (m/s)	Air curtain Jet angle (°)	Change Parameters
1	\	\	Basic case
2	6	0	
3	8	0	
4	10	0	
5	12	0	Jet velocity
6	14	0	
7	16	0	
8	18	0	
9	12	5	
10	12	10	Jet angle
11	12	15	

2.3 BOUNDARY CONDITIONS

In the test cases, the inlet wind profile was described using a power-law equation: $u_z = u_{ref} \times (\frac{z}{z_{ref}})^{\alpha}$, where u_z was the mean wind velocity at height z (m/s), $u_{ref} = 4.5$ m/s was the

reference mean wind velocity at the building reference height z_{ref} = 0.2 m, and $\alpha = 0.1$ was the power-law exponent. The ground and building wall boundaries were specified as no-slip wall boundaries. Two near-wall treatment methods were used: enhanced wall treatment for grids with y+ values around 5, and the standard wall function for grids with y+ values above 35. The silo bottom opening and the computational domain outlet were set as pressure outlets, while the side and top boundaries were assigned symmetric boundary conditions, with a normal velocity of zero. Pollutant concentrations at different locations were scaled as the dimensionless concentration $K_c = \frac{c^* U_{ref}^* H^2}{C^* Q_l}$, where c was the pollutant concentration, U_{ref} was the reference mean wind velocity at the building height, H was the building height, C was the pollutant source concentration (1,000,000 ppm), and Q_l was the pollutant source release rate. Before further analysis of the simulated cases, the used turbulence model and numerical methods are compared with the wind tunnel experimental results (Yang et al.2019), which show the wind around the building, considering the interaction between the air curtain and outdoor wind. Slight differences are shown between the simulated and experimental results.

3. RESULTS

3.1 EFFECTS OF AIR CURTAIN JET VELOCITY

In Figure 2, both the dimensionless mean wind velocity and the time-averaged streamlines on the *x*-*z* plane are displayed for four distinct air curtain outlet velocities. The results reveal that as the air curtain velocity increases, the flow field distribution on the building's leeward side remains similar, with primary differences observed within the interior of the semi-open building. As shown in Figure 2(a), when the air curtain velocity is 6 m/s, the air curtain exhibits the weakest resistance to interference and cannot block the incoming flow. The air curtain airflow divides the interior space into two sections: an upper section with a counter clockwise vortex and a lower section with a smaller clockwise vortex. In Case 4 (Figure. 2(b)), when the air curtain velocity is increased to 10 m/s, the air curtain's resistance to interference improves somewhat, though it still does not fully prevent external airflow infiltration, and the vortex below the air curtain disappears. When the air curtain velocity increases from 10 m/s to 14 m/s (Figure. 2(c)), the velocity of the air curtain reaching the ground exceeds 5 m/s, enabling it to block most of the external airflow. Due to the Coanda effect, a large counter clockwise vortex forms inside the building. Further increasing the air curtain velocity to 18 m/s (Figure. 2(d)) does not produce significant changes in the internal flow field, though more airflow exits through the building's bottom opening.

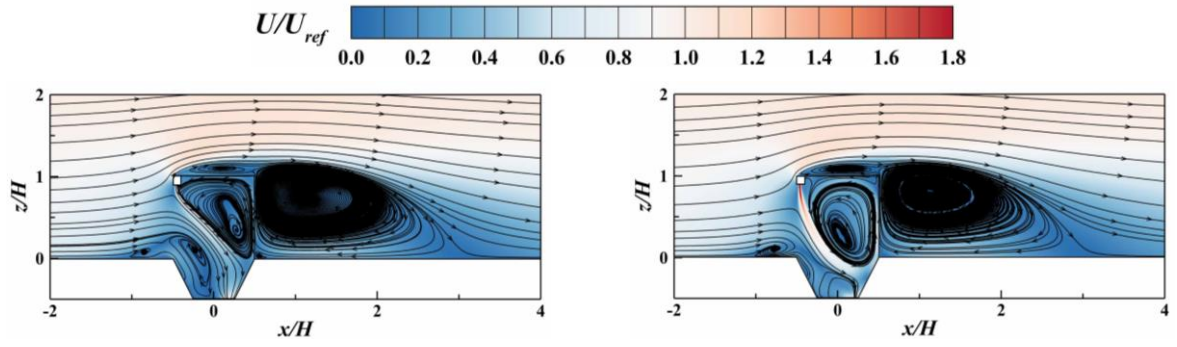

(a) (b)

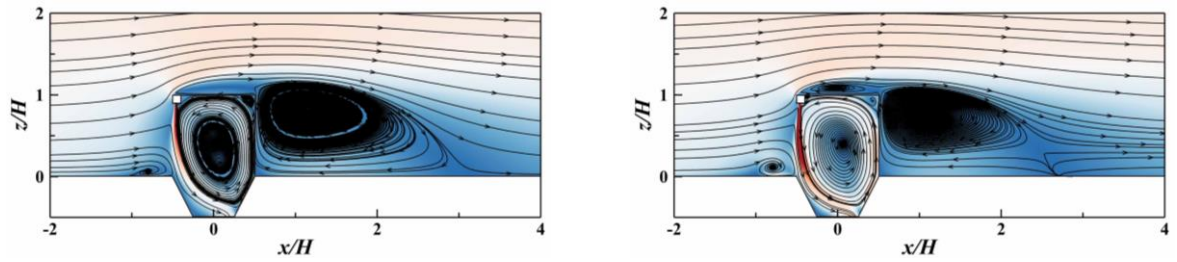

(c) (d)

Figure 2. Normalized mean wind velocities of four typical jet velocities on the *x*-*z* plane at *y* = 0 for: (a) Case 2 (6 m/s), (b) Case 4 (10 m/s), (c) Case 6 (14 m/s) and (d) Case 8 (18 m/s).

Figure 3 displays the dimensionless mean concentration distribution contours on the *x*-*z* plane for four different air curtain outlet velocities. It is evident from the figure that the amount of pollutant escaping decreases as the air curtain velocity increases, indicating a negative correlation. Specifically, when the air curtain velocity is 6 m/s (Figure. 3(a)), high concentrations of pollutants still accumulate on the windward side of the building, promoting pollutant accumulation at the bottom of the silo. As the velocity increases to 10 m/s, the vertical dispersion of pollutants on the windward side of the building is significantly reduced, while the pollutant concentration within the building gradually extends to the roof level (Figure. 3(b)). Figure 3(c) illustrates the pollutant dispersion when the air curtain velocity is set to 14 m/s, where the air curtain effectively isolates the indoor and outdoor environments, with almost no pollutants diffusing outside through the building opening. When the velocity increases further to 18 m/s (Figure. 3(d)), the proportion of the high-concentration pollutant accumulation zone at the bottom of the silo continues to decrease, indicating that more pollutants are being directed toward the bottom opening and expelled by the air curtain.

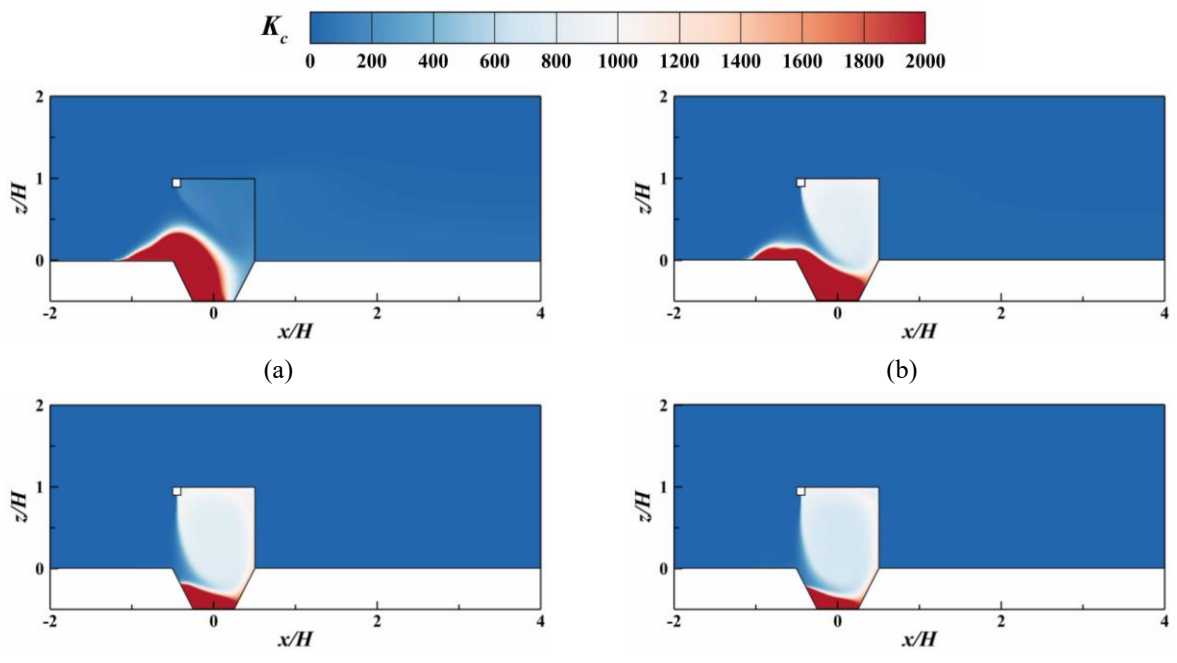

(a) (b)

(c) (d)

Figure 3. Normalized pollutant concentration of four typical jet velocities on the *x*-*z* plane at *y* = 0 for: (a) Case 2

(6 m/s), (b) Case 4 (10 m/s), (c) Case 6 (14 m/s) and (d) Case 8 (18 m/s).

3.2 EFFECTS OF AIR CURTAIN JET ANGLE

The contours of the dimensionless mean concentration distribution on the *x*-*z* plane for air curtain velocities of 12 m/s (the intermediate jet velocity between the minimum and maximum values) and outlet angles of 5°, 10° and 15° (Case 9 – 11, Table 1) are illustrated in Figure 4. A comparison of the three cases reveals that all air curtain angles help to suppress pollutant dispersion. At an angle of 5° (Figure. 4(a)), the pollutant concentration inside the building is higher compared to 10° (Figure. 4(b)) and 15° (Figure. 4(c)), indicating that this setting does not direct most pollutants toward the bottom opening. Due to internal vortices, pollutants are contained within the building, circulating internally. When the angle increases to 10°, the airflow from the end of the air curtain aligns with the bottom opening of the silo, allowing some pollutants to exit through the opening and reducing the internal pollutant concentration. However, the air curtain with an angle of 15° fails to direct pollutants toward the bottom opening effectively, resulting in a slight increase in pollutant concentration within the building. Therefore, when the air curtain jet velocity is 12 m/s, the jet angle of 10° is a good choice to control pollutant effectively.

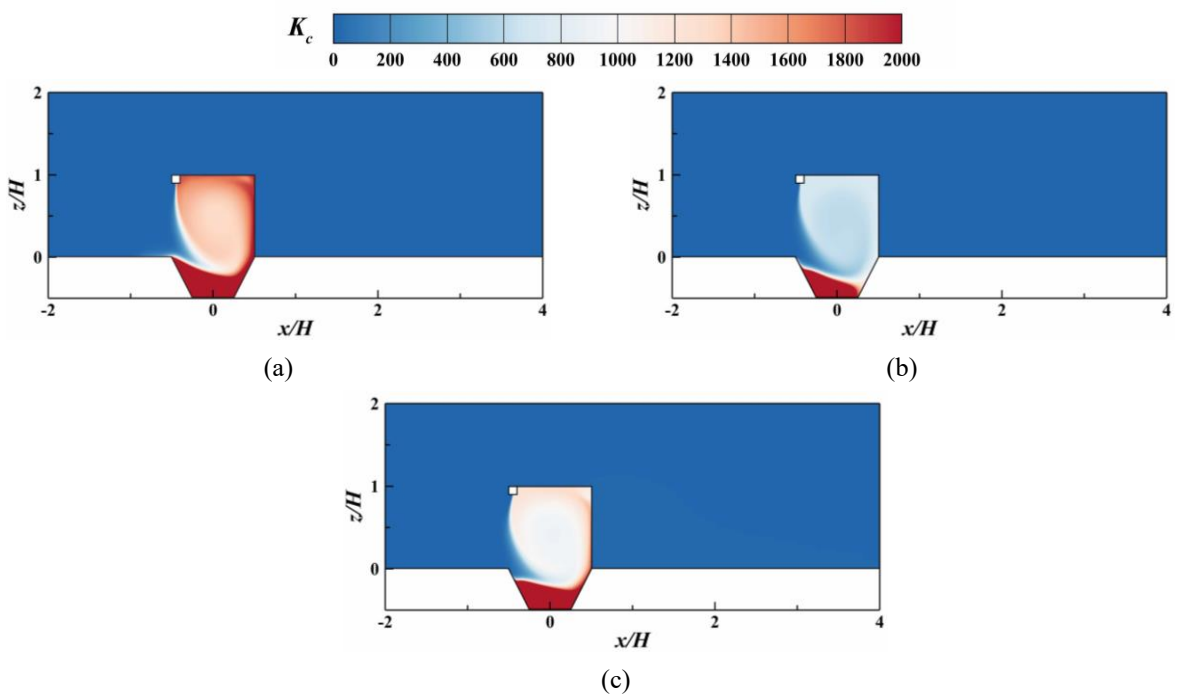

Figure 4. Normalized pollutant concentration of three jet angles on the *x*-*z* plane at $y = 0$ for: (a) Case 9 (5°), (b) Case 10 (10°) and (c) Case 11 (15°).

4.CONCLUSIONS

This study examined the effectiveness of air curtains in controlling pollutant dispersion during vehicle unloading in semi-open industrial buildings, and quantitatively assessed the influence of various air curtain parameters on the control performance. Based on the results presented in the previous analysis, the following conclusions can be drawn. Optimizing the air curtain's jet velocity and jet angle is crucial to its performance; however, this optimization effect can reach a saturation point. When the velocity exceeds a certain threshold (14 m/s) or the outlet angle exceeds a specific

range (10°), the control effect of the air curtain no longer significantly improves.

ACKNOWLEDGEMENTS

The work described in this paper was supported by the National Natural Science Foundation of China (52278094, 52008079).

REFERENCES

Chen T, Cao S, Wang J, et al. (2021). Influences of the optimized air curtain at subway entrance to reduce the ingress of outdoor airborne particles. *Energy and Buildings*, 244: 111028.

Chu Y, Liu J, Zhang Y, et al. (2024). Pedestrian-level wind driven pollutant dispersion and exposure risk during vehicle unloading around a semi-open industrial building. *Journal of Building Engineering*, 95: 110302.

Guo P, Tian W, Li H (2022). Dynamic health risk assessment model for construction dust hazards in the reuse of industrial buildings. *Building and Environment*, 210: 108736.

Li J, Hua C, Ma L, et al. (2024). Key drivers of the oxidative potential of PM2.5 in Beijing in the context of air quality improvement from 2018 to 2022. *Environment International*, 187: 108724.

Liu J, Zheng R, Zhong J, et al. (2022). Dust dispersion around a semi-open industrial building: assessing effects of wind and induced airflow. *Journal of Safety and Environment*, 22: 3370-3378.

Yang S, Alrawashdeh H, Zhang C, et al. (2019). Wind effects on air curtain performance at building entrances, *Building and Environent*, 151: 75-87.

Wang J, Huo Q, Zhang T, et al. (2021). Performance evaluation for a coupled push–pull ventilation and air curtain system to restrict pollutant dispersion in a factory building. *Journal of Building Engineering*, 43: 103164.

Zhang F, Lu Y, Wang Y, et al. (2022). Study on air curtain cooperative spray dust removal in heading face based on swirl theory. *Journal of Environmental Chemical Engineering*, 10: 108892.

Health and Indoor Air Quality, Ventilation (11:00-12:30 h)

6th International Conference on Building Energy and Environment
Eindhoven University of Technology, The Netherlands
6 - 10 July 2025

The performance of cooling, dehumidify, and air clean via heat pump system in the Bus Stop to reduce the urban island effect

M. C. Jeffery. Lee [1], Y. M. Fang [1], Christoph Mitterer [2], Hartwig. M. Künzel [3]

[1]*Department of Interior Design, National Taichung University of Science and Technology, Taichung 40401, Taiwan, MCJL@nutc.edu.tw*
[2]*Fraunhofer-Gesellschaft, International Business Development, Hansastraße 27c, 80686 München, Germany, christoph.mitterer@zv.fraunhofer.de*
[3]*Department of Hygrothermics, Fraunhofer Institute for Building Physics, Fraunhofer Straße 10, 83626 Valley Germany, hartwig.kuenzel@ibp.fraunhofer.de*

SUMMARY
Substantial waste heat generated by transportation and air-conditioning significantly increases urban temperatures, contributing to severe urban heat island effects. Although existing mitigation measures are limited, a novel smart-controlled Chilled Waterfall Wall (CWW), equipped with a heat pump, was developed to simultaneously reduce ambient temperature and humidity while filtering dust and particulate matter ($PM_{2.5}$). The system was pilot-tested within a practical prototype in the laboratory. In addition, it was integrated with a vegetative wall irrigated by cascading water, creating smaller, distributed cooling nodes strategically positioned throughout the urban area. A Building Integrated Photovoltaic (BIPV) folding panel installed atop the bus shelter captures solar energy, providing additional electrical support while maximizing natural daylight. The lower section of this panel includes a rainwater harvesting inlet, which collects rainwater after dust filtration and UV sterilization, storing the purified water in two insulated tanks beneath the bus shelter. Despite its effectiveness, the initial tests revealed notable challenges including water evaporation loss and biofilm maintenance concerns within the recycling system. A prototype measuring 1 m × 1 m × 2.1 m was constructed in a controlled environmental chamber to evaluate performance metrics. Results demonstrated that flow rates between 300 L/hr and 500 L/hr achieved an average temperature reduction of 4.2°C and a humidity reduction from 75% to 60% within 30 minutes. Furthermore, $PM_{2.5}$ concentration dropped significantly from 120 μg/m³ to 60 μg/m³, effectively halving airborne dust concentration compared to untreated control scenarios. Future studies will concentrate on enhancing water circulation efficiency and exploring durable photovoltaic materials suited for diverse climatic regions, further optimizing this innovative urban cooling technology

Keywords: Chilled Waterfall Wall, cooling, dehumidify, air clean, heat pump system, urban island effect.

1. GENERAL INSTRUCTIONS

Waste heat emissions from urban traffic and air-conditioning systems, along with impermeable pavements, contribute significantly to the urban heat island effect (UHIE) and deteriorating air quality. During scorching summers, the frequent occurrence of heatstroke or dizziness among citizens waiting at bus stops has become a critical issue in tropical and subtropical metropolitan areas. To address this challenge, the Chilled Waterfall Wall (CWW) integrated with a water-source heat pump has been developed (Lee, 2023a). The CWW employs chilled water to create a waterfall that effectively reduces ambient temperature. Additionally, since the temperature of the chilled water is below the dew point, the CWW simultaneously removes moisture from the air, providing dehumidification. Furthermore, due to thermodynamic principles, hot air carrying particle matters naturally moves toward the cooler waterfall, where the particle matters are captured and flushed

down, thereby purifying the air. The captured particle matter is subsequently filtered, and the recycled chilled water is sterilized by UV light, ensuring continuous water quality within the system.

As the urban heat island effect (UHIE) becomes increasingly severe in tropical and subtropical metropolitan regions, the construction of large-scale infrastructure to reduce urban temperatures requires substantial financial investment. However, by connecting smaller cooling nodes dispersed through bus shelters in an urban area, it becomes possible to significantly improve the local microclimate, mitigating the urban heat island effect, air pollution, and sudden urban flooding by collecting and distributing heavy rainfall. This decentralized approach offers promising potential for the development of sustainable cities (Figure 1, Lee, 2023b). The design concept for integrating the Chilled Waterfall Wall (CWW) system with bus shelters has been developed and is illustrated in Figure 2 (Lee, 2023c). This study demonstrates the effectiveness of the CWW-integrated bus shelter system by highlighting its capacity for cooling, dehumidification, and dust removal.

Figure 1. Connect bus stops to solve troubles

Figure 2. The design concept for integrating the CWW system with bus shelters

2. PROTOTYPE TEST

The prototype was experimentally tested under four different flow conditions (no water flow, 300 liters/hour, 500 liters/hour, and 700 liters/hour) in a laboratory setting to evaluate optimal performance for controlling hygrothermal conditions and air quality in hot and humid environments. A Chilled Waterfall Wall (CWW) was installed on a surface measuring 1.00 m × 1.60 m, supplied with chilled water maintained at approximately 8–9°C by a water-source heat pump to reduce overall energy consumption, as illustrated in Figure 3. For experimental measurements, a closed, insulated test chamber with dimensions of 1 m (length) × 1 m (width) × 2.1 m (height) was established to examine the CWW's performance at varying water flow rates, as depicted in Figure 4.

The measure sensors were setup in the both sides of heat pump to measure the chilled water (T_{cw}) and heated water temperature (T_{Hw}), the water temperature in the sink (the bottom) of CWW (T_w), chilled water flow rate (Q_{cw}), heated water flow rate (Q_{Hw}), the chilled water pressure (P_{cw}), and heated water pressure (P_{Hw}). All sensors were connected to data logger to evaluate the efficiency of water flow rate between CWW and heat pump. Three different heights of measured points in 0.6m,1.1m, and 1.7m at 0.5m far from CWW for the air temperature and relative humidity referred by ASHRAE Standard 55 (ASHRAE, 2013). The particulate matter in diameter 2.5μm ($PM_{2.5}$) was measured by TSI Quest EVM-7 for air quality. A heat source (heater), a humidifier, and ten burning incenses were setup to check the performance at cooling, dehumidify, and the air cleaning

for testing the performance of CWW.

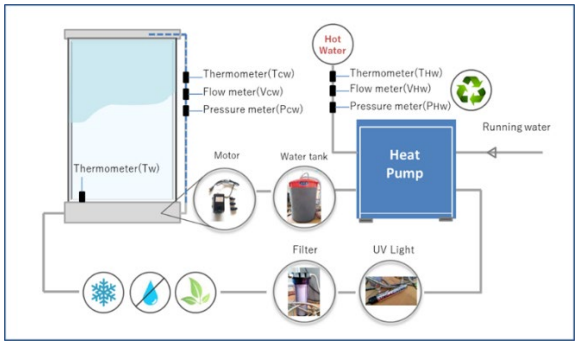

Figure 3. CWW as an air conditioner, air cleaner, dehumidifier and water heater with a heat pump

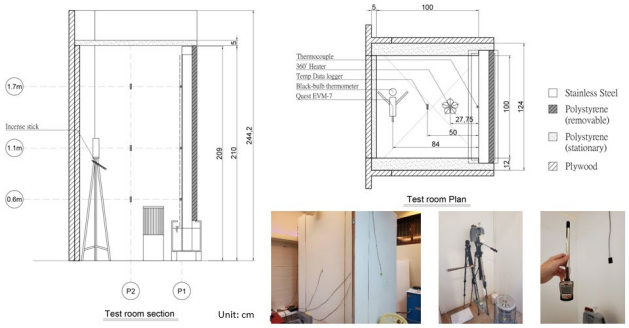

Figure 4. The experiment design scheme and the sensors setup in the test chamber

3. RESULTS AND DISCUSSION

As shown in Figure 5, the air temperature measured at a height of 1.1 m with a water flow rate of 300 L/hr demonstrated superior performance compared to other conditions, providing a similar cooling effect while consuming less energy in hot climates. Furthermore, as depicted in Figure 6, the chilled water temperature consistently decreased, stabilizing at approximately 16°C. This resulted in a significant ambient temperature reduction ranging from 6°C to 8°C.

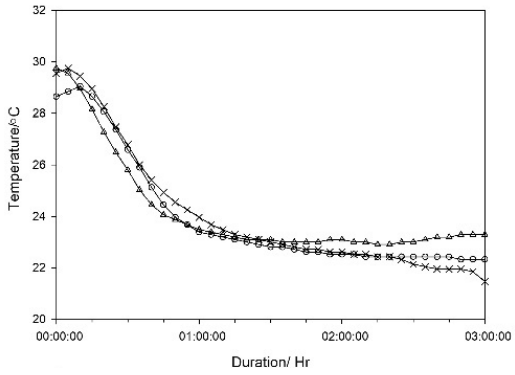

Figure 5. The ambient temperature various

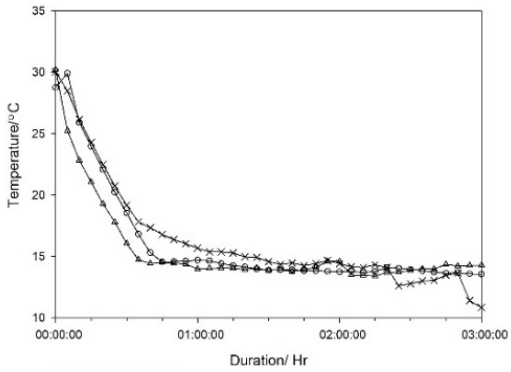

Figure 6. The chilled water temperature various

A humidifier vapored 100 ml moisture into the test chamber for 2 hours then turned on the heat pump for waterfall flowing on the CWW (marked as red line), the measured results in different height as shown in Figure 7. It presented the damp was slowly increasing in the begin 2 hours, the humidity was dropped when the chilled waterfall staring. However, the moisture still went up when the chilled water falling around the flow rate at 300 l/hour. The reason would be the chilled water suddenly raised the temperature to increase the ambient temperature and it could absorb more damp till the saturation.

The efficiency of particulate matter removal at different water flow rates was tested by burning a consistent quantity of incense inside the chamber, fully consumed in approximately 50 minutes. As shown in Figure 8, the concentration of PM2.5 (initially around 120 μg/m³) decreased more rapidly when the CWW was operational compared to when it was inactive.

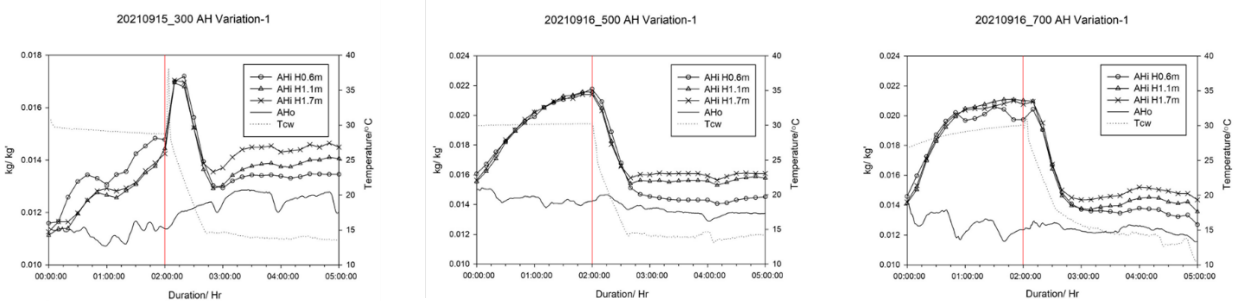

Figure 7. The dehumidify efficiency in each test

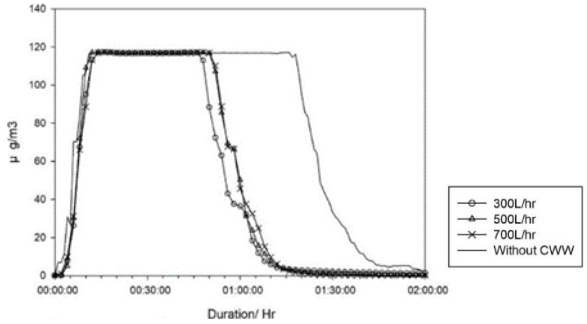

Figure 8. The concentration reduction of in each test

Overall, these test results clearly demonstrate the effectiveness of the CWW in cooling, dehumidifying, and removing airborne particulates. Integrating the CWW system into the design of bus shelters can effectively mitigate the urban heat island effect and improve air quality by efficiently removing airborne dust.

4. CONCLUSION

The test results confirmed that the CWW has effective performance in cooling, dehumidifying, and dust removal. Additionally, the use of a water-source heat pump enhances energy efficiency, enabling successful integration of the CWW with bus shelters. Besides the integrated design considerations, the control of water flow and the efficiency of the heat pump are crucial factors. Incorporating a solar-assisted heat pump system in the future could further improve energy savings.

ACKNOWLEDGEMENTS

The author thanks the members of Fraunhofer IBP (Germany) to collaborate with the technical, and also thanks the support by National Taichung University of Science and Technology (Taiwan).

REFERENCES

ASHRAE, ANSI/ASHRAE 55-Thermal Environmental Conditions for Human Occupancy. Atlanta, GA, USA: American Society of Heating, Refrigerating and Air-Conditioning Engineers (ASHRAE), 2013.

M.C. Lee, Hartwig Künzel, Christoph Mitterer, (2023a) Water-flow cooling and heating air-conditioning system with clean air function, ROC Invention Patent, I798566, 2023.04-2040.07

Meng-Chieh Jeffrey Lee, (2023b) Smart self-sufficient bus stops with cooling, dehumidify, and air clean via heat pump system for reducing the urban island effect, 13th International Symposium on Environmentally Conscious Design and Inverse Manufacturing, EcoDesign 2023 (2023. 11.29-12.1, Nara, Japan)

Meng-Chieh, Jeffrey Lee, (2023c) Bus stop design with chilled waterfall wall for cooling, dehumidify, and air clean, ICSDII 2023 (2023. 11.15-18, Taichung, Taiwan)

6th International Conference on Building Energy and Environment
Eindhoven University of Technology, The Netherlands
6 - 10 July 2025

Graduate student office measurements of aerosol concentrations and size distributions

Arya Toghraei [1], Djordje Romanic [2]

[1]*Department of Atmospheric and Oceanic Sciences, Faculty of Science, McGill University, Montreal, Quebec, Canada, arya.toghraei@mail.mcgill.ca*
[2]*Department of Atmospheric and Oceanic Sciences, Faculty of Science, McGill University, Montreal, Quebec, Canada, djordje.romanic@mcgill.ca*

SUMMARY
Maintaining indoor air quality in shared spaces requires understanding how ventilation, air purification, and human presence influence aerosol concentrations and CO_2 levels. This study examined these factors in a graduate student office (volume = 31.2 m³) across controlled scenarios with and without ventilation and air purification. Results show that occupancy led to a sharp increase in both $PM_{2.5}$ and CO_2, with the most pronounced rise occurring when ventilation was off. Ventilation effectively reduced CO_2 levels but introduced outdoor particles, leading to higher $PM_{2.5}$ concentrations compared to air purification alone. The air purifier significantly lowered aerosol concentrations, particularly for the smallest particles. Size distribution analysis confirmed a bimodal pattern, with a secondary peak around 2.5 µm when occupants were present. These findings reinforce the importance of combining ventilation and air purification, as filtration alone provided the most effective aerosol reduction while ventilation was essential for CO_2 removal.

Keywords: Indoor Air Quality, Aerosol Size Distribution, Ventilation, Air Purifying

1. INTRODUCTION

Indoor air quality (IAQ) is a key factor in maintaining the health and productivity of individuals working in shared spaces such as graduate student offices. Fine aerosols like $PM_{2.5}$ and gases such as carbon dioxide (CO_2) serve as important indicators of IAQ because they reflect both human activity and the effectiveness of ventilation systems. Previous research has shown that the presence of occupants can significantly influence aerosol levels through both direct respiratory emissions and the resuspension of settled particles (Chatoutsidou et al., 2015; Hussein et al., 2006). These processes can lead to fluctuations in particle levels throughout the day, affecting both air quality and exposure risks.

Understanding aerosol size distribution is as important as measuring their overall concentration. Smaller particles (particulate matter $PM_{0.1}$–PM_1) can stay suspended in the air for long periods and penetrate deep into the lungs, while larger ones ($PM_{2.5}$–PM_{10}) settle faster but can still contribute to indoor exposure. Indoor environments often show a bimodal size distribution, with one peak in the submicron range another at larger sizes due to resuspension from surfaces and occupant movement (Ogulei et al., 2006). Recognizing these patterns helps in designing better strategies to control exposure.

Effective IAQ management typically relies on a combination of mechanical ventilation and air purification. While ventilation is essential for maintaining acceptable CO_2 levels and reducing

airborne particles, in some cases, it can also introduce outdoor pollutants or fail to eliminate fine aerosols effectively (Felgueiras et al., 2022). Air purifiers equipped with high-efficiency particulate air (HEPA) filters can efficiently reduce particle concentrations but do not lower CO_2 levels, which are more directly linked to occupancy and air exchange rates (Aldekheel et al., 2022). This means that a combination of strategies is often necessary to maintain good air quality in occupied spaces.

This study investigates how ventilation rates, air purification, mask usage, and occupancy affect aerosol concentrations and size distributions in a graduate student office. By analysing $PM_{2.5}$ and CO_2 trends across different scenarios, this study aims to examine how these factors shape IAQ in real-world conditions.

2. METHODOLOGY

2.1. Experimental Setup

The study was conducted in a graduate student office at Burnside Hall, McGill University, with a volume of 31.2 m³ (4.3 m × 2.9 m × 2.5 m). The room was equipped with a displacement ventilation system, where air was supplied through floor vents and exhausted through ceiling outlets, providing an air change rate (ACH) of 8.1 h^{-1}. An air purifier with HEPA filtration was also used, operating at 7.0 h^{-1}.

Four graduate students participated, each submitting consent forms approved by the McGill University Ethics Committee. Experimental conditions varied based on ventilation status (on/off), air purifier usage (on/off), mask-wearing, and occupancy level (participants present or absent). Each scenario lasted 30 minutes, ensuring sufficient time to observe aerosol trends under different conditions. Aerosol concentrations were measured using a GRIMM 11D aerosol spectrometer, positioned centrally in the room to capture most representative values, while CO_2 levels were recorded using a TSI AirAssure 8144-6 sensor. Figure 1 illustrates the experiment setup and measurement configuration within the office space.

2.2. Data Analysis

Aerosol concentrations were continuously recorded at 6 s intervals using the GRIMM 11D spectrometer, with $PM_{2.5}$ and number concentrations extracted for analysis. Environmental parameters, including CO_2 concentrations, were measured every 1 minute using the TSI AirAssure 8144-6 sensor. To remove short-term fluctuations and retain long-term trends, a low-pass Butterworth filter was applied to both datasets.

For aerosol data, a cutoff frequency of 0.11 cycles per minute was selected, meaning variations occurring over periods shorter than ~9.1 minutes were filtered out. Given the 6 s sampling interval, this ensured that only gradual changes in $PM_{2.5}$ concentrations were retained, removing high-frequency noise. Similarly, for environmental data, a cutoff frequency of 0.23 cycles per minute was used, filtering out fluctuations shorter than ~4.35 minutes. Since CO_2 concentrations were recorded every 1 minute, this filtering method preserved meaningful long-term variations while eliminating transient fluctuations.

In addition to total $PM_{2.5}$ concentrations, aerosol size distributions were analysed across 31 size

bins ranging from 0.253 to 35.15 µm. By comparing size-resolved aerosol concentrations under different experimental conditions, we evaluated how ventilation, air purification, and mask usage influenced the distribution of fine and coarse particles in the indoor environment.

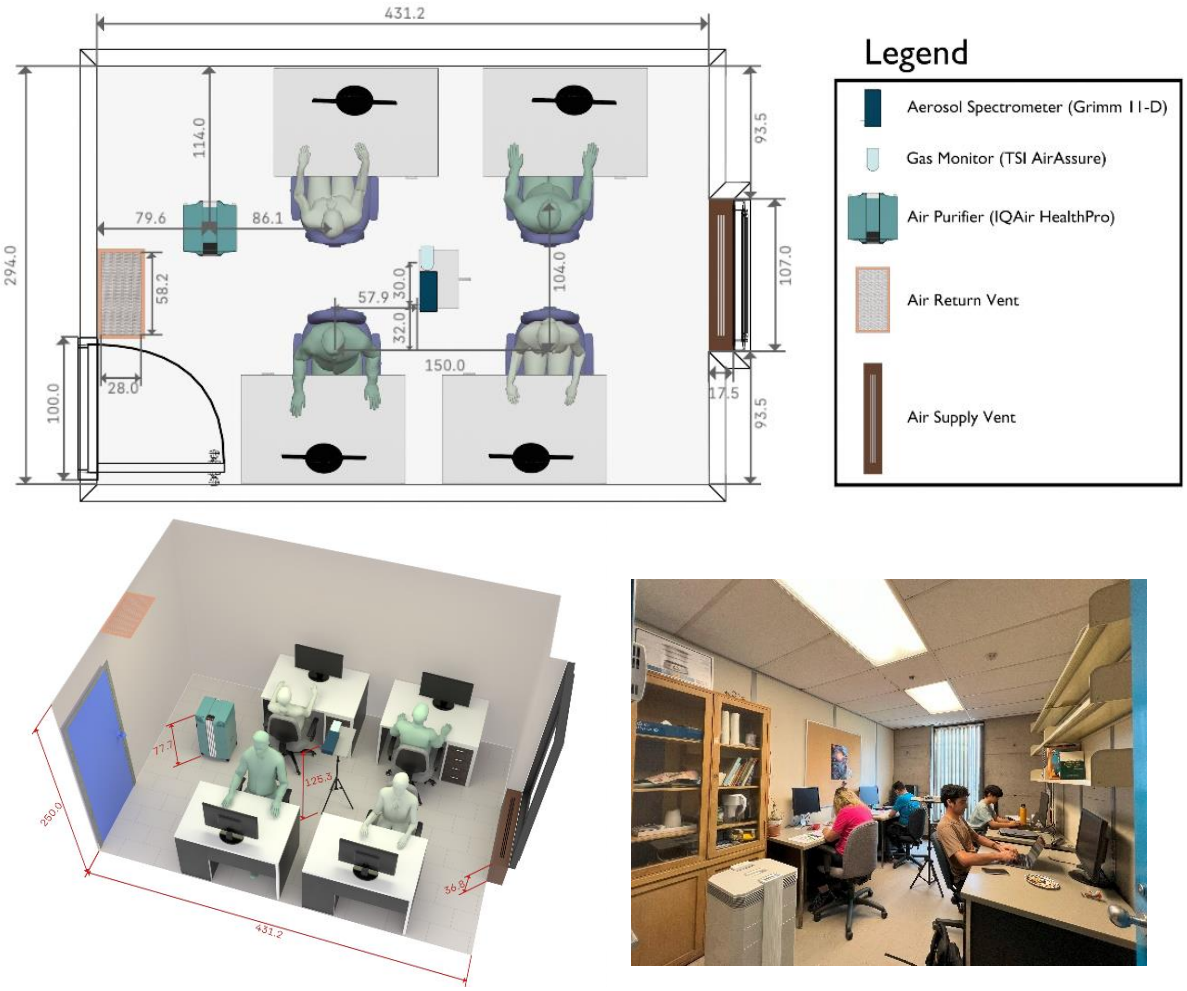

Figure 1. a) Experimental setup and plan view, b) sideview of the office and c) a photograph of the experiment. Dimensions are in cm.

3. RESULTS

3.1. Trends in $PM_{2.5}$ and CO_2 Concentrations

Figure 2 shows the temporal variation of $PM_{2.5}$ (top) and CO_2 (bottom) concentrations across different occupancy and mask conditions. The small spikes at the start of each segment correspond to door openings and closings, so the analysis focuses on the remaining 25 minutes of each period. During the initial unoccupied phase (red shading), both $PM_{2.5}$ and CO_2 remain stable, with CO_2 at approximately 450 ppm and $PM_{2.5}$ around 0.6 $\mu g/m^3$, representing background levels with minimal indoor sources.

When occupants enter without masks (green shading), both CO_2 and $PM_{2.5}$ begin to increase. CO_2 rises gradually due to respiration, reaching approximately 800 ppm in ventilated conditions and exceeding 1600 ppm when ventilation is off. $PM_{2.5}$ also increases, surpassing 1 $\mu g/m^3$ in the absence of ventilation, indicating a combination of respiratory emissions and resuspension of particles from activity in the room. The lower slope observed when masks are worn (blue shading) suggests that respiratory emissions play a significant role in aerosol accumulation.

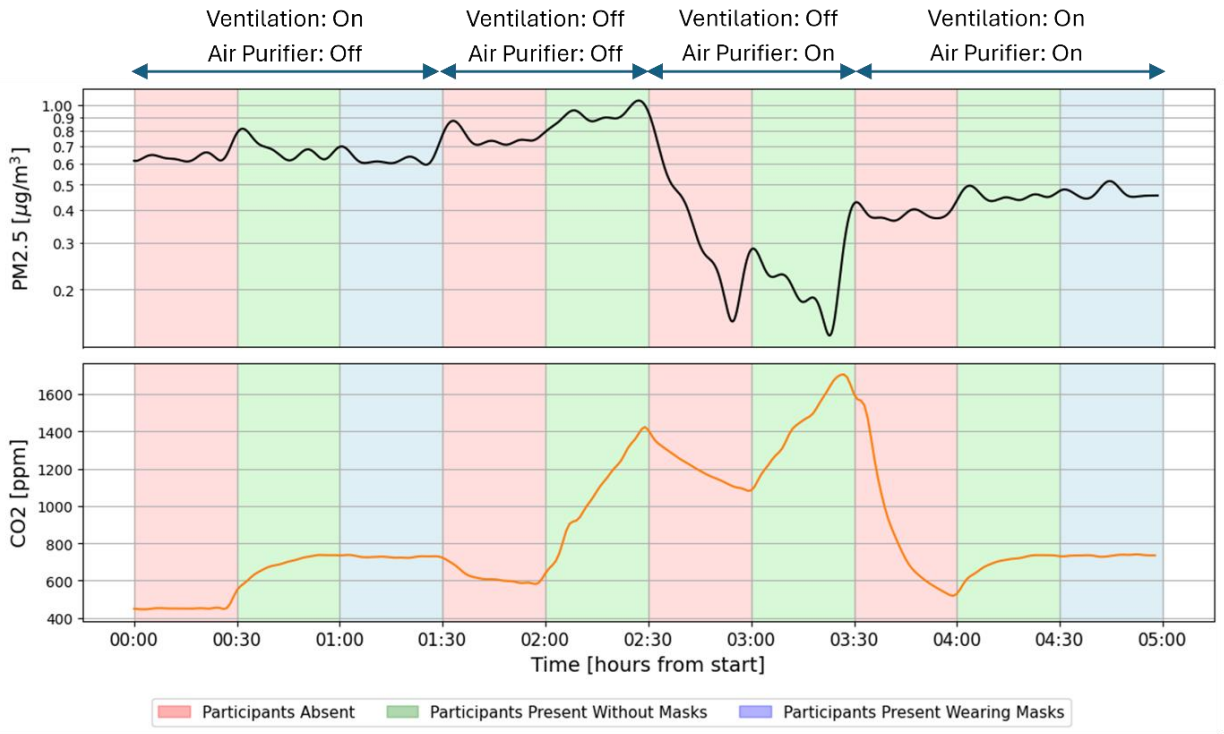

Figure 2. $PM_{2.5}$ ($\mu g/m^3$) and CO_2 (ppm) concentrations over time since the start of the experiment. The $PM_{2.5}$ scale is logarithmic. Periods when the ventilation and air purifier were on or off are indicated at the top of the figure. Occupancy is represented by colored highlights for each 30-minute period.

The air purifier significantly reduces $PM_{2.5}$ concentrations, bringing them below 0.2 $\mu g/m^3$. However, it does not affect CO_2 levels, emphasizing that filtration removes aerosols but does not affect exhaled gases. Notably, even when occupants remain in the room, the purifier lowers $PM_{2.5}$ although some particles persist.

A key observation is the effect of reintroducing ventilation after the air has been purified. While CO_2 concentrations return to background levels within approximately 30 minutes, $PM_{2.5}$ increases again, stabilizing around 0.45 $\mu g/m^3$, higher than with the purifier alone but lower than with ventilation alone. This pattern suggests that outdoor air introduces additional particles while simultaneously diluting CO_2. The results highlight the complementary roles of ventilation and air purification in controlling indoor air quality, with air purifiers more effective at reducing aerosols and ventilation critical for controlling CO_2 buildup.

3.2. Aerosol Size Distributions Across Different Scenarios

Figure 3 presents two heatmaps showing the temporal evolution of aerosol size distribution throughout the experiment based on number concentration (bottom) and mass concentration (top). These heatmaps highlight different aspects of aerosol dynamics: the number-based distribution (d*N*/dlog*D*) emphasizes smaller particles, which dominate in count but contribute less to total mass, whereas the mass-based distribution (d*M*/dlog*D*) reflects the greater influence of larger particles, which, despite being fewer, account for most of the particulate mass.

During the initial unoccupied period, both distributions remain relatively stable, with low concentrations across all size ranges. Once participants enter without masks, a gradual increase in particle concentrations is observed, particularly in the larger size range (>2.5 µm) in both the number-based and mass-based plots. This suggests that resuspension from movement is a primary contributor to coarse particle generation, rather than direct respiratory emissions. The buildup is more pronounced when ventilation is turned off, where accumulation occurs across the entire size spectrum, indicating reduced particle removal efficiency in the absence of air exchange.

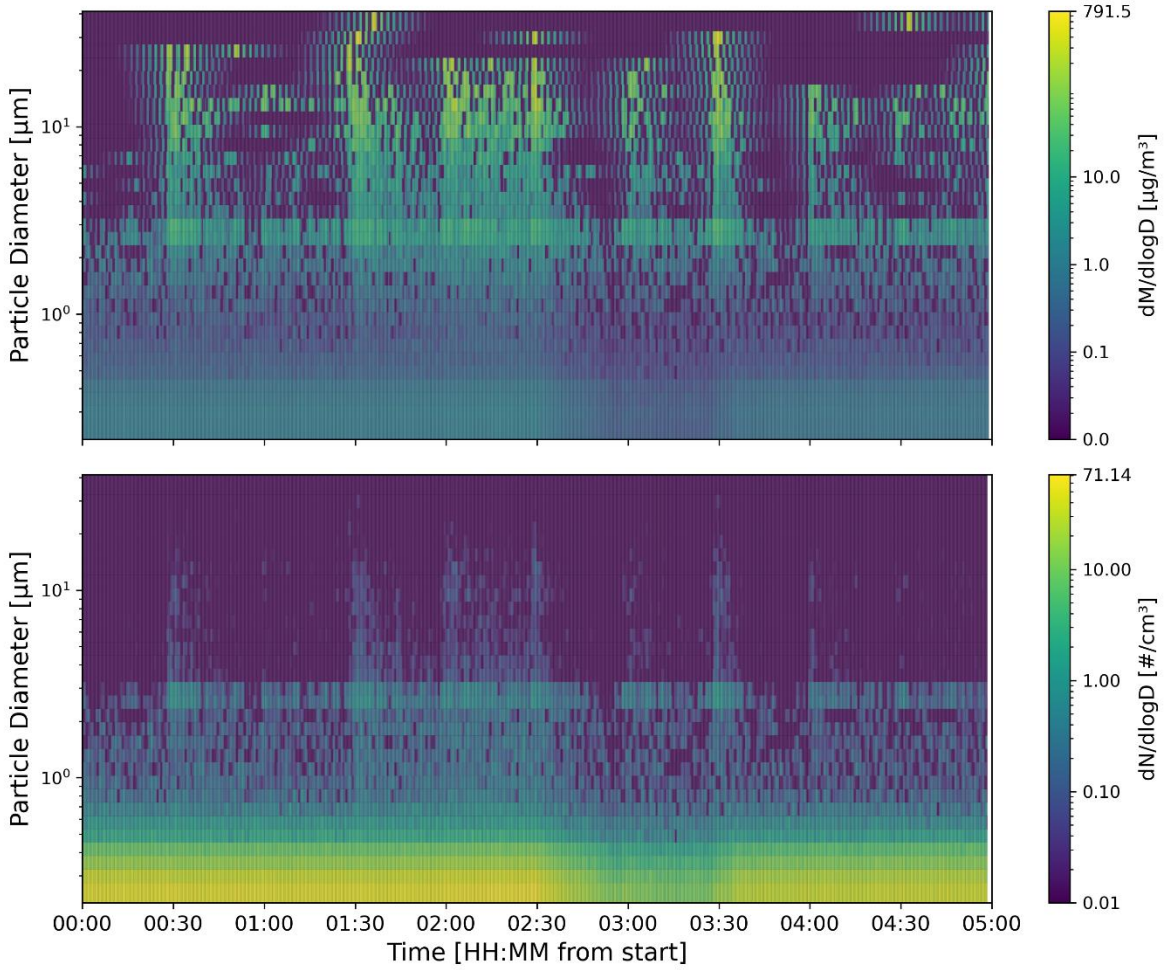

Figure 3. Temporal evolution of aerosol size distribution throughout the experiment in terms of (top) mass concentration (d*M*/dlog*D*) and (bottom) number concentration (d*N*/dlog*D*). The y-axis represents particle diameter (µm), divided into 31 logarithmically spaced bins ranging from 0.253 to 35.15 µm. Warmer colors indicate higher values.

When the air purifier is activated, a significant reduction in particle concentrations is observed across all sizes, but the effect is particularly strong in the submicron range. This suggests that HEPA filtration effectively removes finer particles, which remain airborne for longer periods, while larger particles settle more rapidly. After air purification, reintroducing ventilation leads to an increase in particle levels. This suggests that outdoor air intake is a source of additional particles, particularly in the smallest particle diameter range, counteracting the air purifier's effect.

A consistent feature throughout the experiment is the presence of a bimodal size distribution, with a primary peak in the submicron range and a secondary peak around 2.5 µm. These peaks are more pronounced in scenarios where occupants were present, reinforcing the role of human activity in shaping indoor aerosol dynamics. The persistence of these modes indicates that respiratory emissions primarily contribute to the finer fraction, while resuspension and environmental factors drive the coarser mode.

To better assess the impact of ventilation and air purification on aerosol size distribution, four specific scenarios were chosen, each representing different air controlling conditions while participants were present and unmasked, as shown in Figure 4. These scenarios were selected to isolate the effects of ventilation and air filtration separately, as well as in combination, and to compare them against a background condition where no participants were present. Size distributions were plotted based on the averaged data over the 25-minute period of each scenario.

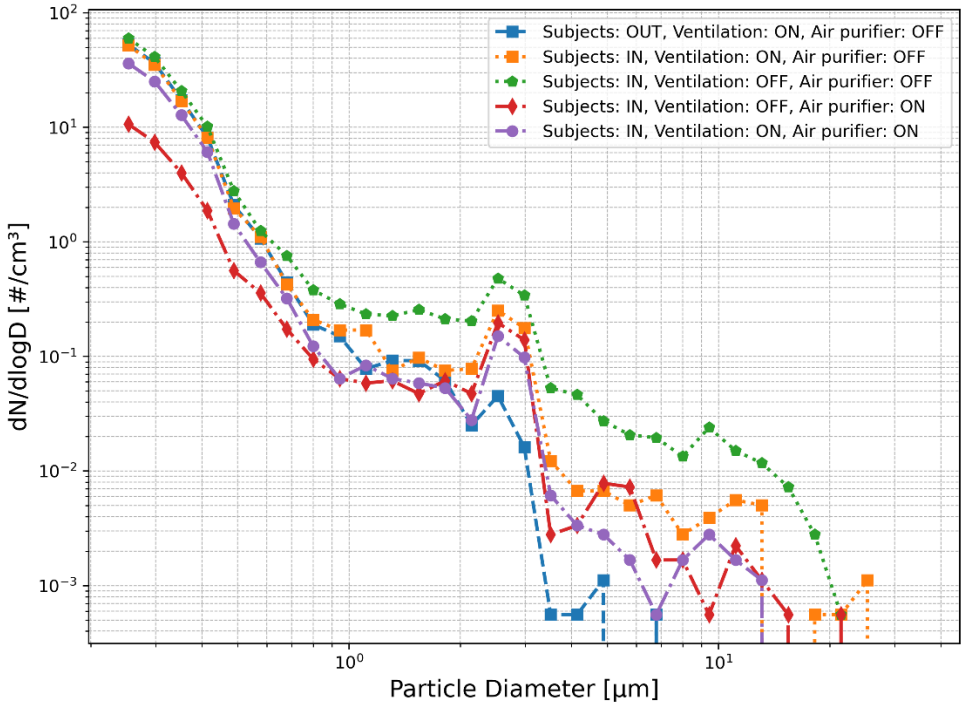

Figure 4. Number-based aerosol size distribution averaged over 25 minutes for five scenarios. The x-axis represents particle diameter (µm) on a logarithmic scale, and the y-axis shows dN/dlog$D$ on logarithmic scale.

The background scenario (blue line) serves as a reference, representing the particle concentrations when the room was unoccupied and the ventilation was on. The scenario where participants were

present with both ventilation and the air purifier turned off (green line) captures the maximum aerosol accumulation, as no removal mechanisms were active, allowing both respiratory emissions and resuspended particles to build up. The ventilation-only condition (orange line) isolates the effect of ventilation air exchange, showing how mechanical airflow influences particle removal without additional filtration. The air purifier-only scenario (red line) examines the impact of HEPA filtration without the potential particle influx from outdoor air. Finally, the combined ventilation and air purifier scenario (purple line) demonstrates the interaction between these two mitigation strategies.

A clear peak around 2.5 μm is present across all conditions with participants, while it is much less pronounced in the background scenario, highlighting that this size range is associated with human activity. The air purifier shows a strong effect in reducing submicron particles, while for particles larger than 1 μm, its performance aligns closely with the ventilation-only and combined scenarios. The green line, which represents the scenario where both air purifier and ventilation were off, consistently shows the highest particle concentrations at all sizes, particularly in the larger size range. This confirms that without ventilation or purification, aerosols build up and remain in the indoor environment, while using either strategy effectively reduces larger particles. These scenarios offer a clear comparison of the impact of different mitigation strategies.

4. Conclusions

This study demonstrates how occupancy, ventilation, and air purification influence aerosol concentrations and CO_2 levels in an indoor environment. $PM_{2.5}$ and CO_2 both increase with human presence, though their behaviours differ. CO_2 rises steadily due to exhalation, while $PM_{2.5}$ levels fluctuate more sharply, particularly when ventilation is off. The impact of masks is evident in reducing aerosol concentrations but does not affect CO_2. Air purification is highly effective at lowering aerosol levels, particularly for submicron particles, yet has no influence on CO_2. Notably, reintroducing ventilation after air purification results in a slight increase in $PM_{2.5}$ concentrations, likely due to outdoor air intake.

The size distribution analysis provides further insights into aerosol behaviour under different conditions. The bimodal nature of the distribution is consistent across scenarios, with a primary peak in the submicron range and a secondary peak around 2.5 μm, which appears in occupied periods. This suggests that fine aerosols originate primarily from respiratory emissions, while the larger peak likely results from resuspension and coarse respiratory droplets. The air purifier effectively reduces particle concentrations across all sizes but has the most pronounced effect on smaller aerosols. Ventilation plays a more complex role, effectively diluting CO_2 but also capable of introducing outdoor particle.

These results emphasize the importance of a balanced approach to indoor air quality management. Ventilation and air purification each address different aspects of air quality, and their combined use, along with wearing masks, provides the most effective strategy for minimizing harmful indoor air effects. Future research should explore how these mitigation strategies interact in indoor environments with varying ventilation rates and occupancy patterns.

REFERENCES

Aldekheel, M., Altuwayjiri, A., Tohidi, R., Jalali Farahani, V., & Sioutas, C., 2022. The Role of Portable Air Purifiers and Effective Ventilation in Improving Indoor Air Quality in University Classrooms. International Journal of Environmental Research and Public Health 19.

Chatoutsidou, S. E., Ondráček, J., Tesar, O., Tørseth, K., Ždímal, V., & Lazaridis, M., 2015. Indoor/outdoor particulate matter number and mass concentration in modern offices. Building and Environment 92.

Felgueiras, F., Mourão, Z., Moreira, A., & Gabriel, M. F., 2022. A systematic review of ventilation conditions and airborne particulate matter levels in urban offices. Indoor Air 32.

Hussein, T., Glytsos, T., Ondráček, J., Dohányosová, P., Ždímal, V., Hämeri, K., Lazaridis, M., Smolík, J., & Kulmala, M., 2006. Particle size characterization and emission rates during indoor activities in a house. Atmospheric Environment 40.

Ogulei, D., Hopke, P. K., & Wallace, L. A., 2006. Analysis of indoor particle size distributions in an occupied townhouse using positive matrix factorization. Indoor Air 16.

6th International Conference on Building Energy and Environment
Eindhoven University of Technology, The Netherlands
6 - 10 July 2025

Optimizing Ventilation System Simulations with Compressed Weather Data Using Fast Fourier Transform

Merel Decleyre [1,2], Klaas De Jonge [3], Jelle Laverge [4]

[1]*Ghent University, Ghent, Belgium, merel.decleyre@ugent.be*
[2]*FWO, Brussels, Belgium, merel.decleyre@ugent.be*
[3]*Ghent University, Ghent, Belgium, klaas.dejonge@ugent.be*
[4]*Ghent University, Ghent, Belgium, jelle.laverge@ugent.be*

SUMMARY
A key challenge in optimal performance-based design of ventilation systems is the need to accurately assess its performance under varying conditions, such as fluctuating weather patterns, occupancy behaviour, and the layout of the dwelling. Achieving this requires numerous evaluations, which are computationally unfeasible with traditional simulation-based methods.
This study addresses this challenge by exploring methods to reduce the computational load, specifically focusing on filtering and compressing input data using Fast Fourier Transform (FFT) analysis.
Typical input variables for building simulation models can be approximated using a limited set of frequencies, or by a distribution of discrete events. This principle is demonstrated using dry-bulb air temperature as a case study. By identifying and isolating dominant frequencies, the proposed method simplifies weather input data, thereby reducing simulation time while preserving the complexity of the underlying white-box building model. The approach increases simulation speed while maintaining appropriate accuracy in system performance evaluations.

Keywords: simulation, performance assessment, Fast Fourier Transform (FFT), indoor air quality

1. INTRODUCTION

This research is conducted within the framework of the NudgeFlow project, which aims to develop a decentralized ventilation system that leverages natural airflow within dwellings. By dynamically optimizing airflow patterns in response to real-time ventilation needs and environmental factors (e.g., wind, temperature gradients, and outdoor pollutants), the NudgeFlow system aims to minimize mechanical energy use. This represents a departure from conventional prescriptive ventilation designs, aligning with a global shift toward performance-based design methodologies.

This paradigm shift is evident in initiatives like the harm-based indoor air quality (IAQ) procedure proposed as an alternative compliance method for ASHRAE Standard 62.2, as well as the anticipated updates in European ventilation design standards (e.g., EN 16798-1-3 and EN 15665).

The primary challenge in developing performance-based ventilation systems, including the NudgeFlow system, lies in evaluating performance under variable conditions such as fluctuating weather patterns, diverse occupancy behaviours, and varied dwelling layouts. Performance-based workflows necessitate iterative assessments.

Traditionally the performance is assessed using Monte Carlo sensitivity analyses. It relies on running multi-zone airflow simulations, using an extensive number of fixed weather and occupancy profiles (Laverge et al., 2011). While effective for evaluating individual ventilation configurations, this approach is computationally intensive, requiring supercomputers to manage the high volume of variations involved. As a result, it is impractical for use in design optimization workflows. The main challenges include the lengthy computation times required for dynamic building simulations and the vast number of simulations necessary to achieve performance convergence.

Existing strategies to reduce computational loads have included optimizing solver choices, streamlining model structures, and minimizing events (Jorissen et al., 2018; Tiller, 2001). However, these approaches focus primarily on the simulation process itself. This paper takes a different approach by simplifying input signals, specifically weather data, to improve computational efficiency.

This study explores the application of Fourier Transform (FT) techniques to compress weather input data, with two primary objectives:

1. Signal Reconstruction: Using FT to reconstruct continuous input signals that minimize simulation events in variable timestep solvers, such as those used in Dymola (Modelica).
2. Frequency Filtering: Identifying and retaining dominant frequencies in weather patterns to streamline signal reconstruction while preserving the dominant dynamics of the input data.

2. METHODOLOGY

As a first step this research transforms the dry-bulb air temperature to the frequency domain. Since this data is commonly represented using time series without discrete changes, it is well suited for performing a discrete Fourier transform (DFT).

The accuracy and speed of simulations using the simplified signal input for the dry bulb temperature will be tested using Modelica in Dymola. The preprocessing of the weather data is done in python using the NumPy package. The results are then integrated into a Modelica model and tested using existing building models.

2.1. Weather data analysis with FFT

The Fast Fourier Transform (FFT) is an efficient algorithm to perform the Discrete Fourier Transform (DFT), that translates a finite sequence of data samples, in this case the dry-bulb air temperature measurements, into the frequency domain, using Equation 1. This transformation represents the original signal as a sum of sine and cosine waves, each with a specific frequency, amplitude, and phase.

$$F_k = \sum_{n=0}^{N-1} \left(f_n \cdot e^{-i2\pi \frac{k}{N} n} \right) \quad (1)$$

When applied to real-valued data, the FFT yields a series of complex coefficients that encode both amplitude and the phase of each frequency component. These complex numbers F_k, can be

decomposed into their real and imaginary parts as shown in Equation 2.

$$F_k = \mathrm{Re}(F_k) + \ Im(F_k) \tag{2}$$

Using the preprogrammed FFT function of NumPy, gives insight into the dominant frequencies present in the dry-bulb temperature. When assessing the power spectrum of the dry-bulb temperature of a typical meteorological year (TMY) for Brussels 2001-2020, two main frequencies stand out: 3.17E-8 Hz and 1.16E-5 Hz. These correspond to periodicities of one year and one day, respectively (Figure 1), reflecting the expected variations in outdoor air temperature.

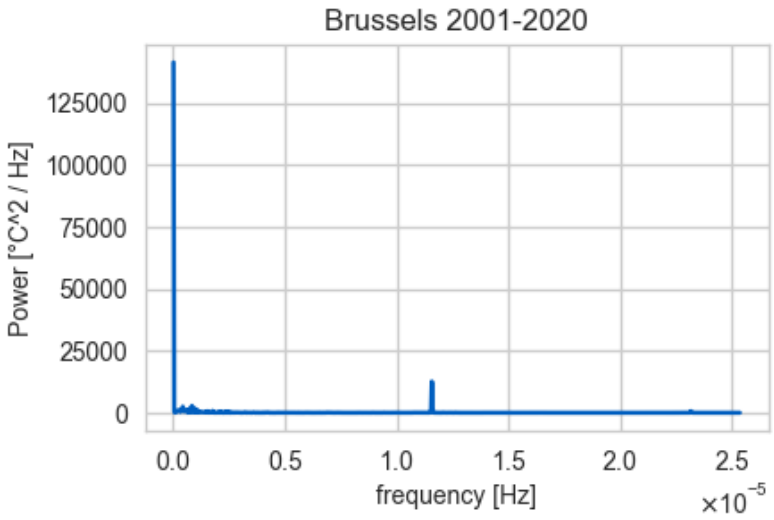

Figure 1 Power spectrum of dry-bulb temperature from TMY Brussels 2001-2020

A new model was developed in Modelica to reconstruct the temperature signal from the output of the FFT. This model reads the complex FFT output and uses it to reconstruct the original time-domain temperature signal based on Equation 3. Euler's formula (Equation 4) is applied to express the complex exponential terms as a sum of sines and cosines (Equation 5). This approach enables the generation of a continuous approximation of the original temperature time series, with the flexibility to incorporate a variable number of frequency components.

$$f_n = \frac{1}{N}\sum_{k=0}^{N-1}\left(F_k \cdot \ e^{i2\pi \frac{k}{T} n}\right) \tag{3}$$

$$e^{i\theta} = \cos\theta \ + i\sin\theta \tag{4}$$

$$f_n = \frac{1}{N}\cdot \sum_{k=0}^{N-1}(\mathrm{Re}(F_k) \ \cdot \cos(\frac{2\pi kn}{N}) \ - \ Im(F_k) \ \cdot \sin(\frac{2\pi kn}{N})) \tag{5}$$

2.2. Preliminary Impact on Simulation Speed and Accuracy

The proposed method was evaluated on six typical meteorological years (TMY) for two locations in Belgium: Brussels and Ghent. These TMYs were assembled in the context of the IEA EBC Annex 80, following the ISO EN 15927-4 standard (Machard et al., 2024). For each of the cities there are three TMY files spanning different time periods. The period 2001-2020 represents historical measured data while the periods 2041-2060 and 2081-2100 represent future climates under the Representative Concentration Pathway (RCP) 8.5.

The choice for TMY format weather data was made, as it aligns well with the IDEAS Modelica library, preventing the need to add additional information or extensive transformations on the file format. Secondly, in the generation of TMY files, the dry-bulb air temperature is considered as a primary parameter, as opposed to e.g. wind speed.

The dry-bulb temperature is reconstructed by progressively adding frequencies, starting with the one with the highest spectral power and sequentially including those with the next largest spectral powers in descending order. The Root Mean Square Error (RMSE) of each reconstructed signal follows a logarithmic relationship with the number of included frequencies.

The simulation speed of signal reconstruction is compared to reading the dry-bulb temperature time series using the 'CombiTimeTable' block from the Modelica Standard Library, which mimics how weather data is typically processed in an IDEAS simulation. The results show a reduction in CPU time for the reconstructed signal when using up to 86–100 frequencies. However, adding more frequencies slows down the simulation speed beyond the reference time series approach.

3. CASE: TWIN HOUSES

3.1. Model Description

The Twin Houses model, part of the IDEAS library, is used to test the impact of the proposed method. This model is based on the Twin House experiment conducted as part of the IEA EBC Annex 58 project (Strachan et al., 2016) and has been validated against experimental measurements. Additionally, the Twin Houses model was chosen because it has been extensively tested for validating the accuracy of the IDEAS library (Jorissen et al., 2018).

The experimental setup and corresponding model implementation follow a structured sequence. Initially, the indoor temperature is stabilized at a constant 30°C. This is followed by a phase in which a pseudo-random sequence of heat injections is applied. Subsequently, the system is re-initialized by restoring a stable indoor temperature. Finally, the experiment concludes with a free-floating period, allowing the building to cool down naturally without external interventions.

The model consists of seven thermal zones: the living room, corridor, bathroom, bedroom, kitchen, doorway, and parent bedroom. Each zone incorporates detailed representations of thermal and airflow dynamics, making it well-suited for evaluating ventilation system performance.

To enhance the applicability of this method for assessing ventilation system performance, a minor modification was made to the original model. Specifically, the supply air temperature was directly

linked to outdoor temperature profiles. In the initial configuration, the ventilation model used measured air temperatures for the ventilation air, while the rest of the model relied on a weather file. This adjustment created a more consistent approach to weather data integration, enabling a more accurate evaluation of the impact of simplified weather input data on indoor temperature conditions.

3.2.Testing Process

For the simulations, weather data is sourced from the six TMY files described above, with the option to substitute the dry-bulb temperature with a reconstructed signal using FFT. The number of frequencies that are included in the reconstructed signal varies between 2 and the maximum of 4380 on a logarithmic scale, as the initial testing showed drastic improvement in accuracy for the first additional frequencies. The simulations run using the original TMY input for the dry-bulb temperature are used to benchmark the accuracy and simulation speed of the simulations using the FFT-based reconstructions.

Experiment 1, building 1 is simulated from day 213 to day 297, encompassing all phases of the experimental setup: initialization, heating, re-initialization, and free-floating. The built-in Dassl solver was used with the standard 0.0001 tolerance (Petzold, 1982). The initial 14 days serve as an initialisation period for the simulation. During the heating and free-floating phases, the Root Mean Square Error (RMSE) and Mean Bias Error (MBE) are evaluated for the temperature of both the living room and the kitchen.

4. RESULTS

Figure 2 presents the RMSE values calculated for the free float period in both the living room and the kitchen across the six tested TMY files. The living room exhibits a higher RMSE compared to the kitchen, which can be attributed to its direct supply of outdoor air. This increased exposure to external temperature fluctuations leads to greater deviations in simulated indoor temperature, as reflected in the RMSE values.

The impact of the ventilation on the error is further validated by analysing the RMSE results from the original IDEAS simulation, where ventilation is not linked to outdoor air temperature but instead to measured temperatures. In these tests, RMSE values remain below 0.6K across all cases. This reinforces the observation that it is crucial to include the effects of a direct link to the outdoor air temperature through ventilation when opting for a filtered temperature input. When aiming for the same accuracy a simulation that includes ventilation will need a more detailed input, in this case more frequencies.

The heating period shows similar trends compared to the free float period, with slightly lower RMSE values recorded. In all cases the coefficient of variation of the RMSE (cvRMSE) remains within the limits outlined in ASHRAE Guideline 14-2002 across all tested frequency ranges. The mean bias error (MBE) for both periods remains consistently centered around zero, indicating no intrinsic bias in the model's predictions. Additionally, the normalized mean bias error (NMBE) consistently falls below the 10% threshold of the ASHRAE Guideline 14-2002 when more than 10 frequencies are considered. It is important to note that this ASHRAE guideline is designed for use in whole-year simulations, meaning that these results should be interpreted as an indication of

model performance rather than a definitive validation of compliance.

Overall, the results indicate that adding more frequencies initially has a significant impact on accuracy, but the effect diminishes as additional frequencies are introduced. This trend supports the approach of sequentially incorporating frequencies based on their respective power contribution.

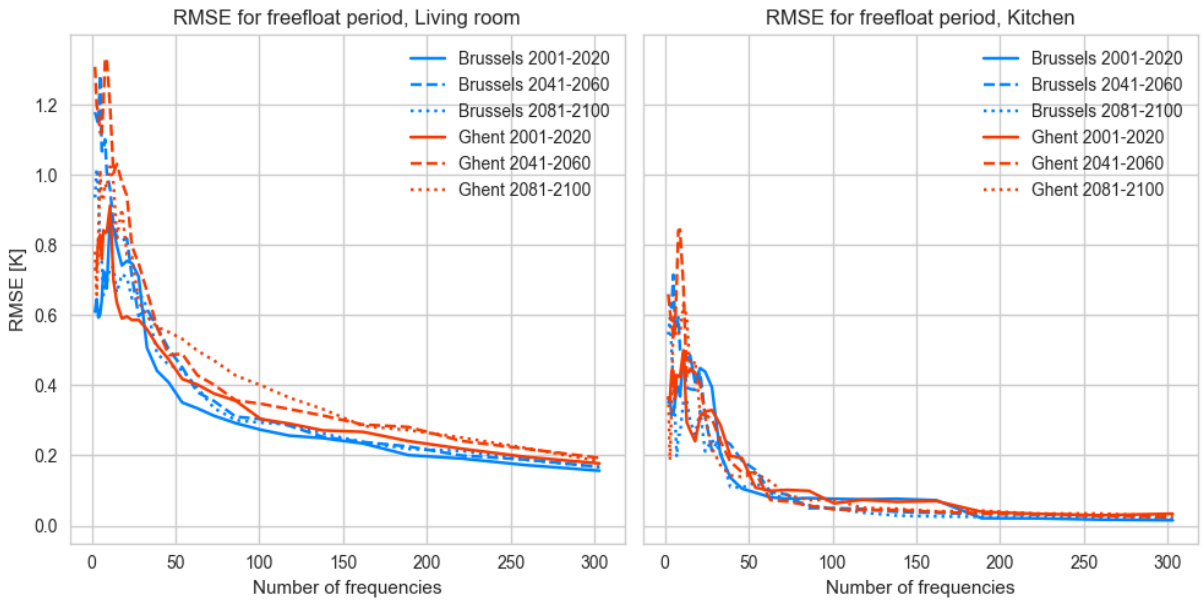

Figure 2 RMSE values computed between the default IDEAS model results and the model using reconstructed signals with varying frequency amounts, during the free float period (days 262 to 297), for both the living room and kitchen.

To evaluate computational efficiency, the CPU time for each simulation is recorded and averaged over five simulation runs. The speed of the baseline IDEAS simulation using TMY files is then compared to simulations using the reconstructed FFT signal. As illustrated in Figure 3, simulation speed decreases progressively as more frequencies are introduced. For the TMY Brussels dataset (2001–2020), no additional speed gains are observed beyond 101 frequencies, whereas for the TMY Ghent dataset (2041–2060), the tipping point occurs at 486 frequencies. The remaining cases fall within this range, demonstrating a varying impact of frequency count on computational performance.

When applying this method to enhance simulation speed, a trade-off must be considered between accuracy and computational efficiency. Using 21 frequencies, the RMSE falls below 1K across all tested cases, while simulation time is improved by 11.1% on average. Increasing the number of frequencies to 54, further reduces the RMSE below 0.5K while still maintaining a notable speedup of 9.6%. The most accurate results that can be achieved without compromising simulation speed occur at 259 frequencies, where the RMSE values range between 0.157K and 0.193K. This indicates that beyond this point, further improvements in accuracy come at the expense of increased computational cost, when compared to the default IDEAS simulation.

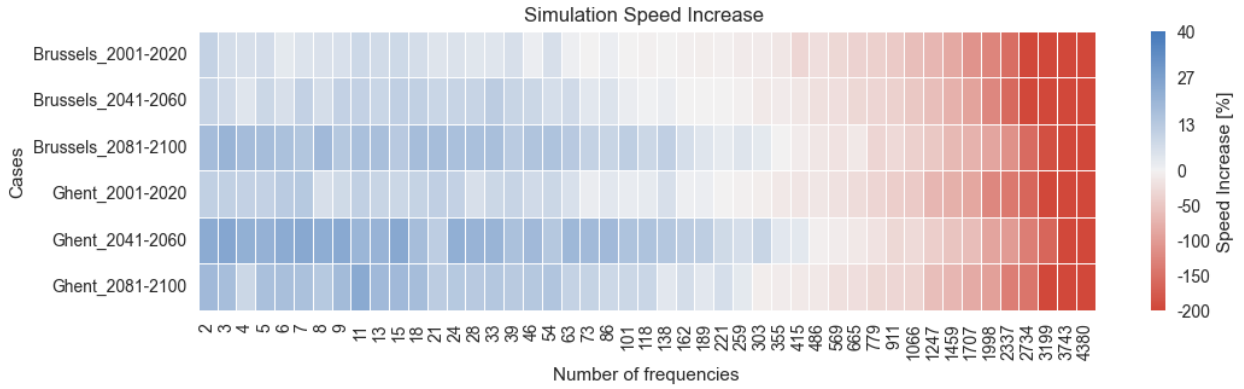

Figure 3 Simulation speed improvement with varying frequencies compared to the default IDEAS model, analyzed on a case-by-case basis.

5. DISCUSSION

When comparing the RMSE results from the simulation incorporating ventilation linked to outdoor air with the original simulation that used measured air temperatures for ventilation, the original simulations exhibited significantly lower RMSE values. This finding emphasizes the crucial role of ventilation in the accuracy of indoor climate modelling and highlights the necessity of incorporating higher frequency components when assessing the impact of ventilation on indoor temperature fluctuations. Neglecting these higher frequencies could lead to an oversimplification of the dynamic interactions within the indoor environment. However, the inclusion of higher frequencies also increases computational complexity, thereby partially limiting the potential for further acceleration of the simulations.

In this setup, only one input signal was considered: the dry-bulb temperature. Expanding this method to all weather data inputs could further enhance simulation speed. However, the simulation time is strongly influenced by the syntax and modeling methods used in Modelica. Additionally, different signals may require distinct filtering thresholds to ensure sufficient simulation accuracy. This would necessitate either further preliminary research into the reconstructed signals and the dominant frequencies affecting specific buildings or a reduction in overall filtering potential. Investigating which frequencies most influence the thermal dynamics of buildings, based on factors such as thermal mass, construction build-up, and ventilation strategy, could enable a more targeted filtering approach. These insights may lead to adaptive filtering strategies that preserve accuracy while enhancing simulation efficiency.

6. CONCLUSIONS

In conclusion, the results of this study demonstrate the effectiveness of using frequency-based signal filtering to enhance simulation speed while maintaining a high level of accuracy in indoor climate modeling. A reduction of 10% in simulation time is achievable with minimal impact on RMSE. The addition of more frequencies initially improves the model's performance, with significant reductions in RMSE and MBE as the number of frequencies increases. However, this improvement in accuracy diminishes as additional frequencies are added, highlighting the need to balance accuracy with computational efficiency.

These findings suggest that the method offers a viable approach for reducing simulation time without significantly sacrificing accuracy, making it a valuable tool for optimizing building performance simulations. However, careful consideration must be given to the trade-offs between accuracy and computational resources, especially when scaling the method to larger, more complex simulations. Expanding this approach to include additional weather data inputs and refining filtering thresholds may further enhance both simulation speed and accuracy, offering a promising direction for future research in this field.

ACKNOWLEDGEMENTS

The author would like to acknowledge FWO and Ghent University, respectively, for supporting and hosting the work she does in her role as SB PhD fellow at FWO (1S27725N). This work has been supported by the Flemish Agency for Innovation and Entrepreneurship (VLAIO) Flux50 cSBO project 'NudgeFlow' (HBC.2023.0488)

REFERENCES

Jorissen, F., Reynders, G., Baetens, R., Picard, D., Saelens, D., & Helsen, L. (2018). Implementation and verification of the IDEAS building energy simulation library. *Journal of Building Performance Simulation*, *11*(6), 669–688. https://doi.org/10.1080/19401493.2018.1428361

Laverge, J., Van Den Bossche, N., Heijmans, N., & Janssens, A. (2011). Energy saving potential and repercussions on indoor air quality of demand controlled residential ventilation strategies. *Building and Environment*, *46*(7), 1497–1503. https://doi.org/10.1016/j.buildenv.2011.01.023

Machard, A., Salvati, A., P. Tootkaboni, M., Gaur, A., Zou, J., Wang, L. L., Baba, F., Ge, H., Bre, F., Bozonnet, E., Corrado, V., Luo, X., Levinson, R., Lee, S. H., Hong, T., Salles Olinger, M., Machado, R. M. E. S., Da Guarda, E. L. A., Veiga, R. K., … Holzer, P. (2024). Typical and extreme weather datasets for studying the resilience of buildings to climate change and heatwaves. *Scientific Data*, *11*(1), 531. https://doi.org/10.1038/s41597-024-03319-8

Petzold, L. R. (1982). *A Description of Dassl: A Differential/Algebraic System Solver*.

Strachan, P., Svehla, K., Heusler, I., & Kersken, M. (2016). Whole model empirical validation on a full-scale building. *Journal of Building Performance Simulation*, *9*(4), 331–350. https://doi.org/10.1080/19401493.2015.1064480

Tiller, M. (2001). *Introduction to Physical Modeling with Modelica* (2nd ed.). Kluwer academic publishers.

6th International Conference on Building Energy and Environment
Eindhoven University of Technology, The Netherlands
6 - 10 July 2025

Study on optimal sensor placement for indoor air pollution monitoring based on inverse analysis with adjoint concentration

Hideki Kikumoto [1], Hongyuan Jia [2]

[1]*Institue of Industrial Science, The University of Tokyo, Tokyo, Japan, kkmt@iis.u-tokyo.ac.jp*
[2]*Institue of Industrial Science, The University of Tokyo, Tokyo, Japan, jhy@iis.u-tokyo.ac.jp*

SUMMARY
Ensuring accurate indoor air pollution monitoring is essential for maintaining human health and comfort, especially as pollutant sources are often dynamic. This study proposes a method for optimizing the placement of a single air pollution sensor in an indoor environment. This method utilizes inverse analysis with adjoint concentrations, which enables efficient analysis of the spatially averaged concentration of a given evaluation area for arbitrary pollutant source locations. By leveraging this, we presented an optimal sensor location and an algorithm for exploration. A numerical experiment was conducted in an isothermal airflow field within a 2-dimensional indoor model to validate the applicability of the proposed method. A single optimal sensor was identified among the candidates as the position with adjoint concentration values highly correlated with the evaluation region's values. Furthermore, we discuss the optimal location of each sensor from the perspective of its sensitivity to pollutant emissions using adjoint concentration distributions.

Keywords: air quality, sensor placement, optimization, inverse analysis.

1. INTRODUCTION

Indoor air pollution significantly affects the health and comfort of occupants. In recent years, environmental sensors have been increasingly installed in indoor spaces to enable advanced monitoring and control of indoor air quality as well as the efficient operation of ventilation and air conditioning systems (Mylonas et al., 2019; Wang et al., 2023). However, the sensor's position significantly affects the monitoring quality (Yun & Licina, 2023). Studies have been conducted to identify the sudden generation of hazardous substances in indoor environments and optimize the placement of sensors (Chen & Wen, 2008; Zeng et al., 2020). However, enough consideration has not been given to monitoring substances that are always present in the environment but whose concentration distribution changes dynamically. Some studies have been proposed for optimal sensor placement utilizing CFD (computational fluid dynamics) simulation and heuristic optimization (Mousavi et al., 2017). However, these approaches often require prior knowledge or assumption of specific emission scenarios or involve high computational costs. Therefore, for spatially heterogeneous target variables such as pollutant concentration fields, methodologies are needed to assess how well sensor measurements represent the spatial characteristics and to guide sensor placement accordingly.

In addition, the locations and intensities of pollutant sources are diverse in the indoor environment, making it inefficient to perform a forward analysis for all possible scenarios. Conversely, adjoint concentrations enable the efficient analysis of pollutant concentrations within the evaluation area

and sensor measurements across various pollutant source conditions, and they have been applied to identify unknown pollutant sources outdoors and indoors (Jia & Kikumoto, 2022; Keats et al., 2007; Pudykiewicz, 1998; Wang et al., 2022). Therefore, in this study, we aim to develop a method for optimizing sensor placement for concentration monitoring for generally existing indoor pollutants based on inverse analysis using the adjoint concentration. The optimized sensor location is expected to be robust or, on average, closely matches the average concentration of the evaluation area under scenarios where pollutants are probabilistically generated from various places.

2. PROBLEM STATEMENT AND ASSUMPTIONS

Consider a single-ventilated indoor space (room) where a steady airflow is established through constant ventilation. Within this space, an air pollutant is generated, which is the subject of monitoring. The objective of this study involves evaluating the spatially averaged concentration of this pollutant within a designated evaluation area as a representative value of the air quality of the room. To realize this, a single concentration sensor is installed in the room, and its placement must be optimized such that the sensor's reading closely approximates the actual spatially averaged concentration within the evaluation area. We assume that although the pollutant emission rate is unknown, its intensity remains constant. Additionally, for simplicity, we exclude the effects of changes in airflow due to variations in pollutant source conditions or ventilation and focus on monitoring the pollutant concentration passively transported under constant airflow conditions.

3. SPATIALLY AVERAGED POLLUTANT CONCENTRATION FROM THE PERSPECTIVE OF ADJOINT CONCENTRATION

This section first introduces the concept of adjoint concentration and its mathematical foundation. Then, we explain how it is utilized to compute spatially averaged concentrations and guide sensor placement optimization under uncertain pollutant emission scenarios.

3.1. Overview of Adjoint Concentration and Duality Relationship

In a steady turbulent dispersion field, when the point source of a pollutant is located at $\mathbf{x}_\mathrm{s}$, its concentration at position $\mathbf{x}$ can be denoted as $C(\mathbf{x}|\mathbf{x}_\mathrm{s})$ and transport equation is expressed as:

$$\nabla \cdot (\mathbf{U}C - \Gamma \nabla C) = q_\mathrm{s}\delta(\mathbf{x} - \mathbf{x}_\mathrm{s}) \tag{1}$$

where $\mathbf{U}$ denotes the mean velocity vector, Γ denotes the effective diffusion coefficient of the concentration, and q_s denotes the emission intensity of the pollutant. In a steady turbulent field, the adjoint concentration is defined as the concentration $C^*(\mathbf{x}|\mathbf{x}_\mathrm{r})$ of a hypothetical tracer released at receptor location $\mathbf{x}_\mathrm{r}$ with an intensity of q_r in a reversed mean flow field, as shown in Fig. 1. The transport equation for the adjoint concentration is:

$$\nabla \cdot (-\mathbf{U}C^* - \Gamma \nabla C^*) = q_\mathrm{r}\delta(\mathbf{x} - \mathbf{x}_\mathrm{r}) \tag{2}$$

The pollutant and adjoint concentrations satisfy the duality relationship (Pudykiewicz, 1998):

$$q_\mathrm{r}C(\mathbf{x}_\mathrm{r}|\mathbf{x}_\mathrm{s}) = q_\mathrm{s}C^*(\mathbf{x}_\mathrm{s}|\mathbf{x}_\mathrm{r}) \tag{3}$$

This relationship implies that once the distribution of C^* is determined, concentration C at $\mathbf{x}_\mathrm{r}$

for any $\mathbf{x}_s$ and q_s can be immediately calculated as $C = q_s C^*(\mathbf{x}_s|\mathbf{x}_r)/q_r$, provided that the flow field remains unchanged. Typically, the number of potential pollutant source locations (N) is much larger than the number of receptor locations (e.g., person or sensor) (M), i.e., $N \gg M$. Therefore, using adjoint concentrations requires fewer analyses and is more efficient.

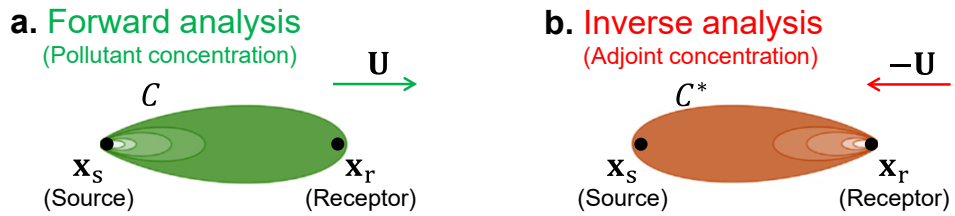

Figure 1. Conceptual diagram of forward (pollutant concentration) and inverse (adjoint concentration) analysis.

3.2. Spatially Averaged Pollutant Concentration Represented using Adjoint Concentration

In a target room noted as Ω_∞, one of the indicators representing the pollutant concentration to which occupants are exposed is the spatially averaged concentration within an evaluation region Ω_o ($\in \Omega_\infty$), such as a living area. Let the spatially averaged value f_o of any function $f(\mathbf{x})$ over Ω_o be defined as follows:

$$f_o = \frac{1}{V_o}\int_{\Omega_\infty} \phi_o f \mathrm{d}\mathbf{x} = \frac{1}{V_o}\int_{\Omega_o} f \mathrm{d}\mathbf{x} \quad \text{where} \quad \phi_o(\mathbf{x}) = \begin{cases} 1 & \mathbf{x} \in \Omega_o \\ 0 & \mathbf{x} \notin \Omega_o \end{cases}, \; V_o = \int_{\Omega_\infty} \phi_o \mathrm{d}\mathbf{x} = \int_{\Omega_o} \mathrm{d}\mathbf{x} \tag{4}$$

Here, let $\mathbf{x}_r$ be an arbitrary position within Ω_o. If a pollutant source with strength q_s is located at $\mathbf{x}_s$, the spatially averaged concentration $C_o|_{\mathbf{x}_s}$ of the pollutant in Ω_o can be expressed as:

$$C_o|_{\mathbf{x}_s} = \frac{1}{V_o}\int_{\Omega_o} C(\mathbf{x}_r|\mathbf{x}_s)\mathrm{d}\mathbf{x}_r \tag{5}$$

Applying the duality relationship in Eq. (3), $C_o|_{\mathbf{x}_s}$ in Eq. (5) can also be expressed using the adjoint concentration as:

$$C_o|_{\mathbf{x}_s} = \frac{q_s}{q_r V_o}\int_{\Omega_o} C^*(\mathbf{x}_s|\mathbf{x}_r)\mathrm{d}\mathbf{x}_r = \frac{q_s}{q_r} C_o^*(\mathbf{x}_s) \quad \text{where} \quad C_o^*(\mathbf{x}) = \frac{1}{V_o}\int_{\Omega_o} C^*(\mathbf{x}|\mathbf{x}_r)\mathrm{d}\mathbf{x}_r \tag{6}$$

The transport equation for $C_o^*(\mathbf{x})$ can be derived by applying an averaging operation, as shown in Eq. (4), with respect to $\mathbf{x}_r$ on both sides of Eq. (2) yields:

$$\nabla \cdot (-\mathbf{U}C_o^* - \Gamma \nabla C_o^*) = \frac{q_r}{V_o}\phi_o(\mathbf{x}) \tag{7}$$

Thus, once distribution $C_o^*(\mathbf{x})$ of the adjoint concentration with the source term $q_r/V_o \cdot \phi_o(\mathbf{x})$ is calculated using Eq. (7), the spatially averaged concentration $C_o|_{\mathbf{x}_s}$ in the evaluation region can be obtained from Eq. (6) for any point source ($\mathbf{x}_s$, q_s), as long as the flow field remains constant.

4. OPTIMIZATION METHOD FOR SINGLE SENSOR PLACEMENT USING ADJOINT CONCENTRATION

4.1. Definition of Optimal Sensor Location

In this study, we consider a scenario in which a single sensor is installed in a room to measure the concentration of a target pollutant. The goal involves identifying the sensor position that provides measurements that closely match the spatially averaged concentration $C_o|_{\mathbf{x}_s}$ within the evaluation region, considering probabilistic pollutant emissions from various locations $\mathbf{x}_s$.

The concentrations in the evaluation region and sensor location are proportional to q_s. Thus, q_s does not influence the optimal sensor position for passively transported pollutants. From Eq. (6), $C_o|_{\mathbf{x}_s}$ can be replaced with $C_o^*(\mathbf{x}_s)$. Furthermore, for a specific sensor location $\mathbf{x}_{r'}$, the adjoint concentration $C^*(\mathbf{x}|\mathbf{x}_{r'})$ can be evaluated using Eq. (2) (with $\mathbf{x}_r$ replaced by $\mathbf{x}_{r'}$). Therefore, if the potential emission region of the contaminant is Ω_s ($\in \Omega_\infty$), the optimal sensor location $\mathbf{x}_{opt}$ can be defined as:

$$\mathbf{x}_{opt} = \arg\max_{\mathbf{x}_{r'}} \mathrm{cor}(C^*(\mathbf{x}|\mathbf{x}_{r'}), C_o^*(\mathbf{x})|\mathbf{x} \in \Omega_s) \tag{8}$$

This implies that the adjoint concentration $C^*(\mathbf{x}|\mathbf{x}_{r'})$ at the sensor placed at $\mathbf{x}_{opt}$ exhibits the highest spatial correlation (cor) with $C_o^*(\mathbf{x})$ within Ω_s. Based on the duality relationship, this is equivalent to ensuring a high correlation between the sensor's measured concentration and spatially averaged concentration in the evaluation region. Additionally, by performing correlation analysis and obtaining a linear regression line (with slope α and intercept β) to estimate $C_o^*(\mathbf{x})$ from $C^*(\mathbf{x}|\mathbf{x}_{r'})$, the spatially averaged concentration C_o in the evaluation region can be accurately estimated from the sensor measurement C_{opt} at the optimal location as follows:

$$\hat{C}_o = \alpha \cdot C_{opt} + \beta \tag{9}$$

4.2. Algorithm for Searching the Optimal Sensor Location

Based on the approach presented in the previous section, we propose an algorithm for identifying the optimal sensor location, as outlined in Table 1. The optimal sensor location is selected from a predefined set of discrete and finite candidate positions (Steps 4 and 7 of Table 1) for practical considerations.

5. OVERVIEW OF CASE STUDY

A case study was conducted to evaluate the effectiveness of the proposed sensor location optimization method introduced in the previous section. As an initial investigation, the problem is simplified by employing an isothermal airflow field within a two-dimensional indoor space model termed the IEA Annex 20 model, which has been widely used as a benchmark for CFD analyses (Ito et al., 2015; Lemaire et al., 1993; Nielsen, 1990). As shown in Fig. 2, the indoor space model (Ω_∞) has a height of H (= 3.0 m) and a width of $3H$. It is continuously ventilated through an inlet with a height of $0.056H$ and an outlet with a height of $0.16H$, maintaining a steady airflow.

Two scenarios are considered for the pollutant concentration evaluation region (Ω_o). Scenario 1: The evaluation region covers the entire indoor space ($\Omega_{o1} = \Omega_\infty$). Scenario 2: The evaluation region is restricted to the central part of the room ($\Omega_{o2} = \{x \in [H, 2H], z \in [H/3, 2H/3]\}$), representing the breathing zone of an occupant situated near the center of the room.

Table 1. Algorithm for searching the optimal sensor location and constructing the estimation model for spatially averaged concentration.

Step 1. Definition of the target indoor space: Define room Ω_∞.
Step 2. Definition of the evaluation region for pollutant concentration: Define the evaluation region $\Omega_\mathrm{o}(\in \Omega_\infty)$, such as the living area, where pollutant concentration will be monitored.
Step 3. Analysis of adjoint concentration in the evaluation region: Using CFD analysis and following equation (Eq. (7)), obtain distribution of $C_\mathrm{o}^*(\mathbf{x})$ in Ω_∞: $\nabla\cdot(-\mathbf{U}C_\mathrm{o}^* - \Gamma\nabla C_\mathrm{o}^*) = q_\mathrm{r}/V_\mathrm{o}\cdot\phi_\mathrm{o}(\mathbf{x})$
Step 4. Definition of candidate sensor locations: Define M candidate sensor locations $\{\mathbf{x}_{\mathrm{r}',i}\vert i=1,\dots,M\}$.
Step 5. Analysis of adjoint concentration at candidate sensor locations: For each candidate sensor location $\mathbf{x}_{\mathrm{r}',i}$, use CFD analysis and the following equation (Eq. (2)) to obtain the distribution of $C_i^*(\mathbf{x}) = C^*(\mathbf{x}\vert\mathbf{x}_{\mathrm{r}',i})$: $\nabla\cdot(-\mathbf{U}C_i^* - \Gamma\nabla C_i^*) = q_\mathrm{r}\delta(\mathbf{x}-\mathbf{x}_{\mathrm{r}',i})$
Step 6. Definition of potential pollutant emission region: Define the potential emission region Ω_s $(\in\Omega_\infty)$.
Step 7. Selection of the optimal sensor location: Among the M candidate locations, identify $C_i^*(\mathbf{x})$ that shows the highest correlation with $C_\mathrm{o}^*(\mathbf{x})$ in its spatial distribution over Ω_s. The corresponding sensor location is designated as the optimal location $\mathbf{x}_\mathrm{opt}$.
Step 8. Construction of the estimation model for spatially averaged concentration: Using the least squares method, construct a linear regression model (slope α, intercept β) to estimate $C_\mathrm{o}^*(\mathbf{x})$ from $C^*(\mathbf{x}\vert\mathbf{x}_\mathrm{opt})$ in Ω_s.
Step 9. Estimation of spatially averaged concentration in the evaluation region: Estimate the spatially averaged concentration $\hat{C}_\mathrm{o}$ in the evaluation region using the sensor measurement C_opt at $\mathbf{x}_\mathrm{opt}$ and the following equation (Eq. (9)): $\hat{C}_\mathrm{o} = \alpha\cdot C_\mathrm{opt} + \beta$

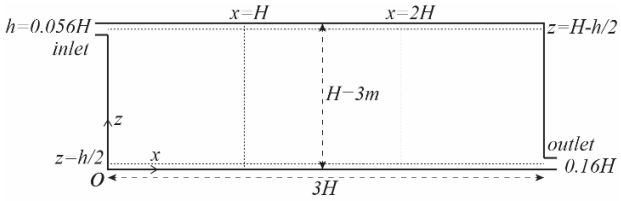

Figure 2. IEA Annex 20 indoor space model.

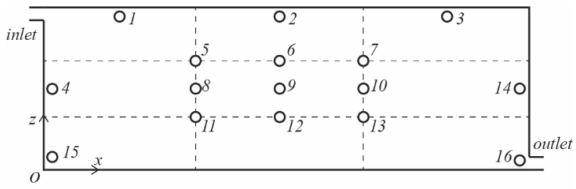

Figure 3. Candidate sensor positions and numbers.

Table 2. CFD analysis methods and boundary conditions.

Turbulence model	Steady RANS (Standard k-ε model)
Mesh number	5643 (= 99 (x) × 57 (z))
Schemes	Advection term: QUICK scheme; Others: bounded central scheme
Inlet	$U = 0.455$ m/s $(= U_{ref})$; $k = 3/2\cdot(U_{ref}\times 0.1)^2$; $\varepsilon = C_\mu^{3/4}k^{3/2}/l$; $l = h/10$; $C_\mu = 0.09$; C^*: zero-gradient; C: fixed value (= 0)
Outlet	Flow: zero-gradient; C^*: fixed value (= 0); C: zero-gradient
Wall	Flow: wall function; C^*, C: zero-gradient
Source	C^*, C: Const. emission rate (= 1 s^{-1})
Schmidt number	Schmidt number = 1.0; Turbulent Schmidt number = 0.7

Fig. 3 shows the candidate positions for sensor placement ($\mathbf{x}_{\mathrm{r}',i}$). A total of 16 (= M) candidate positions were considered, including areas near the ceiling, walls, and center of the room. As potential pollutant emission regions, $\Omega_\mathrm{s} = \Omega_\infty$ (pollutants are emitted uniformly from the entire room) is assumed for simplicity. The CFD analysis of airflow and concentrations in the indoor space model (Fig. 2) was conducted using OpenFOAM v2106 with transport equations for the adjoint concentrations and other implemented variables. To perform dispersion analysis in a

steady-state turbulent field, the standard k–ε turbulence model was used. Further details of the CFD analysis are listed in Table 2.

6. RESULTS OF CFD ANALYSIS

First, the mean flow field within the room was calculated using CFD. The velocity streamlines are shown in Fig. 4. Air entering through the inlet flowed along the ceiling, struck the right wall, and exited through the outlet. This indicates that a primary ventilation pathway was formed near the ceiling, whereas a recirculation flow developed on the right side of the room. Dispersion analysis is conducted based on the flow field, and the resulting average concentration distributions are shown in Fig. 5. Low concentrations are observed along the ventilation pathway near the inlet.

The adjoint concentration fields for the pollutant concentration evaluation region and candidate sensor locations were calculated. The adjoint concentration represents the pollutant concentration response in the evaluation region or sensor location if a point source of pollution is present at that location. The results for the evaluation regions Ω_{o1} (entire room), Ω_{o2} (central part of the room), and selected sensor positions (No. 2, 9, 15) are shown in Fig. 6. In Ω_{o1}, the averaged concentration is highly sensitive to the influence of sources located in the left lower part of the space, while Ω_{o2} is more susceptible to concentrations from central emissions. Pollutants in ventilation pathways are rapidly transported, limiting the response of Ω_{o1} and Ω_{o2} to sources appearing in these areas. Sensors located near the walls (No. 1–3, 14, and 16) in the ventilation pathways constantly receive fresh air and are influenced only by nearby sources. However, sensors in the room's central area, such as No. 9, primarily detect emissions originating from the center. Moreover, given the low ventilation efficiency in the lower-left corner of the room, the response area of sensor No. 15 is restricted to a small range, making it less sensitive to emissions from other locations.

7. OPTIMIZATION RESULTS FOR SENSOR PLACEMENT

In scenarios where emission conditions are unknown, the spatial correlation between the adjoint concentration fields of each candidate sensor location and monitoring evaluation region were calculated using the following equation (refer also to Eq. (8)), where subscript i denotes the i-th candidate sensor location.

$$R_{\Omega_o}(i) = \mathrm{cor}(C_i^*(\mathbf{x}), C_o^*(\mathbf{x}) | \mathbf{x} \in \Omega_s) \tag{10}$$

The results of the correlation calculations are presented in Table 3. Based on these results, under the assumption that emission conditions are unknown in advance, optimal sensor locations corresponding to evaluation regions Ω_{o1} (entire indoor space) and Ω_{o2} (central area of the room), were determined as No. 11 and No. 9, respectively. Furthermore, it was observed that the results for the sensors in the central region (No. 5–13) were similar. In Fig. 6, it can be inferred that the responsiveness of sensors located in well-ventilated areas (No. 2 and 14) is low, resulting in lower $R_{\Omega_{o1}}$ and $R_{\Omega_{o2}}$ values. Furthermore, due to the high concentration of the adjoint concentration field around the sensor in the corner (No. 15), its relationship with Ω_{o2} was found to be negligible. Although sensors are often placed near exhaust outlets to monitor indoor air environments, the results in Table 3 indicate that sensor No. 16 has a correlation coefficient of approximately 0.3 with any of the evaluation regions.

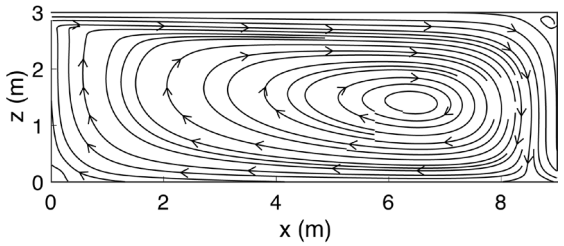

Figure 4. Streamlines of the mean velocity field obtained via CFD analysis.

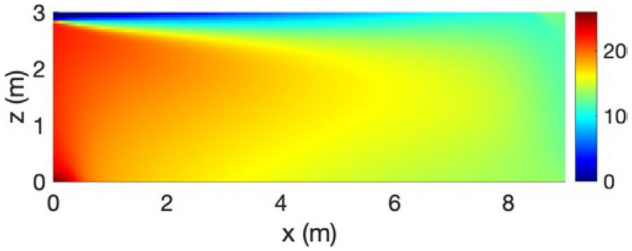

Figure 5. Average concentration distribution resulting from uniform emission in the emission region.

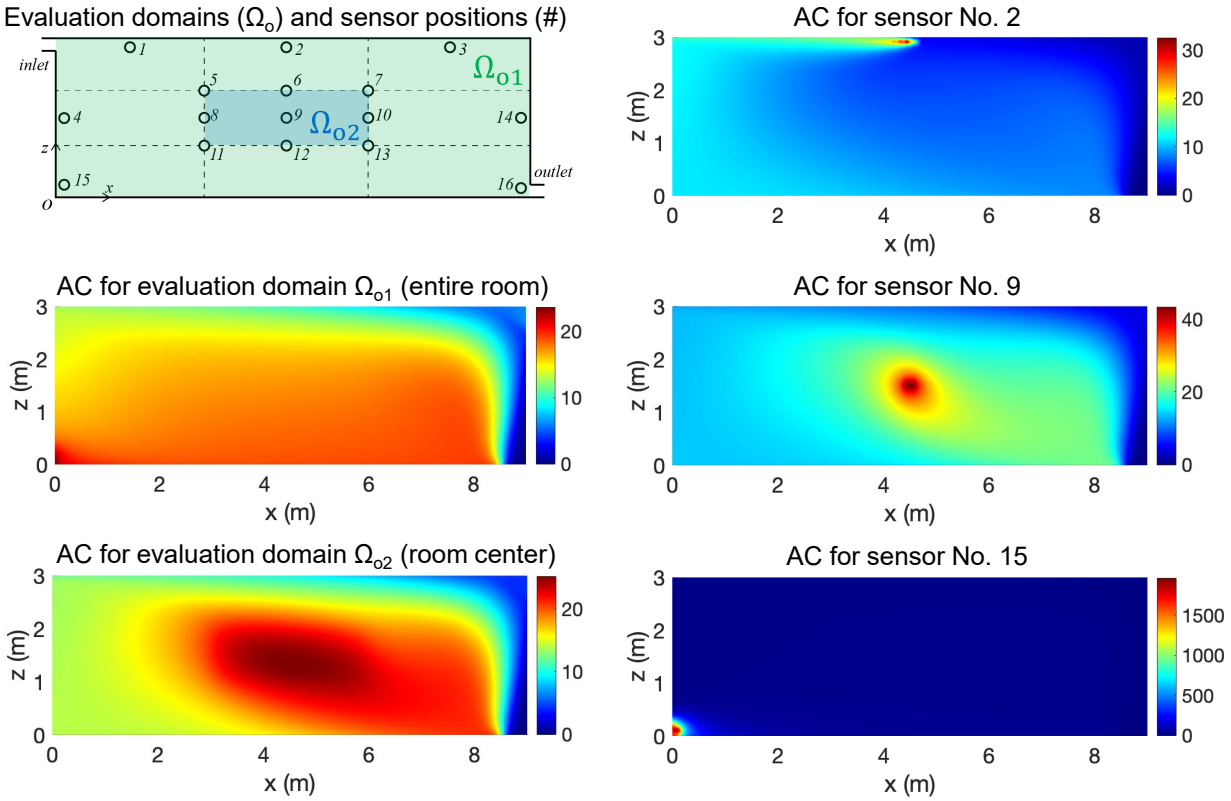

Figure 6. Distributions of adjoint concentration (AC) for evaluation domains (Ω_{o1}: entire room (green area); Ω_{o2}: room center (blue area)) and representative sensor positions (No. 2, 9, 15) in a 2-dimensional indoor model

Table 3. Results of spatial correlation of adjoint concentrations between each sensor and evaluation regions.

Sensor No.	x (m)	z (m)	$R_{\Omega_{o1}}$	$R_{\Omega_{o2}}$	Sensor No.	x (m)	z (m)	$R_{\Omega_{o1}}$	$R_{\Omega_{o2}}$
1	1.5	2.9	0.41	0.12	9	4.5	1.5	0.79	0.97
2	4.5	2.9	0.55	0.25	10	6	1.5	0.77	0.87
3	7.5	2.9	0.54	0.36	11	3	1	0.81	0.88
4	0.1	1.5	0.51	0.17	12	4.5	1	0.79	0.94
5	3	2	0.77	0.78	13	6	1	0.76	0.83
6	4.5	2	0.80	0.94	14	8.9	1.5	0.05	-0.03
7	6	2	0.80	0.90	15	0.1	0.1	0.20	0.00
8	3	1.5	0.79	0.86	16	8.9	0.1	0.29	0.28

8. CONCLUSIONS

This study proposed a method to optimize single-sensor placement for indoor air pollution monitoring using CFD-based inverse analysis with adjoint concentrations. The method identifies sensor locations that robustly estimate the average pollutant concentration in a target area under uncertain emission conditions. A case study in a two-dimensional indoor space demonstrated its effectiveness: Sensor No. 11 (entire room) and Sensor No. 9 (central area) achieved high correlation coefficients of 0.81 and 0.97, respectively. Conversely, Sensor No. 16 near the exhaust outlet showed a low correlation of 0.29 (entire room) and 0.28 (central area), highlighting the limitations of typical placement strategies. Future work will extend this approach to more diverse emission scenarios, three-dimensional spaces, multi-sensor systems, etc., toward practical applicability in real buildings.

ACKNOWLEDGEMENTS

This research is part of a study conducted with the support of the Global Activity Support Program for Young Researchers at the University of Tokyo. JSPS KAKENHI (Grant Number 24K21642) partially supported this research.

REFERENCES

Chen, Y. L., & Wen, J. (2008). Sensor system design for building indoor air protection. *Building and Environment*, *43*(7), 1278-1285. https://doi.org/10.1016/j.buildenv.2007.03.011

Ito, K., et al. (2015). CFD Benchmark Tests for Indoor Environmental Problems: Part 1 Isothermal/Non-Isothermal Flow in 2D and 3D Room Model. *International Journal of Architectural Engineering Technology*, *2*(1), 01-22. https://doi.org/10.15377/2409-9821.2015.02.01.1

Jia, H., & Kikumoto, H. (2022). Sensor configuration optimization based on the entropy of adjoint concentration distribution for stochastic source term estimation in urban environment. *Sustainable Cities and Society*, *79*, 103726. https://doi.org/10.1016/j.scs.2022.103726

Keats, A., Yee, E., & Lien, F.-S. (2007). Bayesian inference for source determination with applications to a complex urban environment. *Atmospheric Environment*, *41*(3), 465-479. https://doi.org/10.1016/j.atmosenv.2006.08.044

Lemaire, A. D., et al. (1993). *Room Air and Contaminant Flow, Evaluation of Computational Methods: Subtask-1 Summary Report*. TNO Building and Construction Research,. https://www.iea-ebc.org/Data/publications/EBC_Annex_20_room_air_and.pdf

Mousavi, M. S., et al. (2017). Design of a correlated validated CFD and genetic algorithm model for optimized sensors placement for indoor air quality monitoring. *Heat and Mass Transfer*, *54*(2), 509-521. https://doi.org/10.1007/s00231-017-2138-9

Mylonas, A., et al. (2019). Capabilities and limitations of wireless CO2, temperature and relative humidity sensors. *Building and Environment*, *154*, 362-374. https://doi.org/10.1016/j.buildenv.2019.03.012

Nielsen, P. V. (1990). *Specification of a Two-Dimensional Test Case: (IEA)* (Gul Serie, Issue. A. U. Institut for Bygningsteknik. https://vbn.aau.dk/en/publications/specification-of-a-two-dimensional-test-case-iea

Pudykiewicz, J. A. (1998). Application of adjoint tracer transport equations for evaluating source parameters. *Atmospheric Environment*, *32*(17), 3039-3050. https://doi.org/10.1016/s1352-2310(97)00480-9

Wang, F., Zhou, X., & Kikumoto, H. (2022). Improvement of optimization methods in indoor time-variant source parameters estimation combining unsteady adjoint equations and flow field information. *Building and Environment*, *226*, 109710. https://doi.org/10.1016/j.buildenv.2022.109710

Wang, J., et al. (2023). Quantifying the dynamic characteristics of indoor air pollution using real-time sensors: Current status and future implication. *Environment International*, *175*, 107934. https://doi.org/10.1016/j.envint.2023.107934

Yun, S., & Licina, D. (2023). Optimal sensor placement for personal inhalation exposure detection in static and dynamic office environments. *Building and Environment*, *241*, 110459. https://doi.org/10.1016/j.buildenv.2023.110459

Zeng, L., et al. (2020). Markov-chain-based probabilistic approach to optimize sensor network against deliberately released pollutants in buildings with ventilation systems. *Building and Environment*, *168*, 106534. https://doi.org/10.1016/j.buildenv.2019.106534

6th International Conference on Building Energy and Environment
Eindhoven University of Technology, The Netherlands
6 - 10 July 2025

Associations between indoor and outdoor size-resolved particulate matter in urban Beijing: chemical composition, source and health risk

Shili Tian[1], Qingyang Liu[2], Liang Luo[3] and Yanju Liu [1,*]

1 Institute of Analysis and Testing, Beijing Academy of Science and Technology (Beijing Center for Physical and Chemical Analysis), Beijing, China, liuyanju@bcpca.ac.cn
2 College of Biology and the Environment, Nanjing Forestry University, Nanjing, China, nfu@nifu.edu.cn
3 Department of Chemistry, Capital Normal University, Beijing, China, info@cnu.edu.cn

SUMMARY
Ventilation may lead to a deterioration in indoor air quality in urban environments located close to roads. Comprehending the disparities in chemical compositions of size-resolved particulate matter (PM) between indoor and outdoor settings is crucial for evaluating associated health effects. In this study, indoor and outdoor size-resolved PM was collected from an office in Beijing in summer and winter. The levels of $PM_{2.1}$ and $PM_{2.1–9}$ mass were higher outdoors than they were indoors. The size distributions of mass concentrations were shown to be bimodal, peaking at 0.43–0.65 μm and 4.7–5.8 μm, respectively. The most abundant chemicals were organic matter, nitrate, and sulfate for $PM_{2.1}$ and organic matter, crustal materials, and nitrate for $PM_{2.1\text{-}9}$. We found higher percentages of sulfate, nitrate, ammonium, elemental carbon, and heavy metals in smaller-size fractions of PM. Additionally, positive matrix factorization showed that biomass burning, secondary inorganic aerosol, coal combustion, dust, traffic, and industrial pollution were the main sources of PM during the study period. The greatest non-carcinogenic and carcinogenic hazards were found at 0.43–0.65 μm in summer and 2.1–3.3 μm in winter. Our results indicate that size-resolved PM of ambient origin may infiltrate buildings near roads to varying degrees, resulting in negative health effects.

Keywords: indoor and outdoor; health risk assessment; size distributions

1. INTRODUCTION

Particulate matter (PM) is a significant air pollutant with adverse health impacts. Studies have associated short-term PM exposure with increased morbidity and mortality (Weber, 2020). Understanding its size distributions and chemical compositions is essential for health effect assessment (Tian el al., 2014), as large particles influence deposition in the respiratory tract and chemical components contribute to toxicity, with heavy metals being of particular concern. The determination of chemical species in size-resolved fractions of PM is central in evaluating the health impacts associated with exposure to airborne particles (Enyoh et al., 2020).

For urban dwellers, indoor environments are a major source of PM inhalation, yet the relationship between outdoor and indoor air quality remains unclear. In urban environments, researchers have investigated PM sources and associated health risks outdoors, but the possible impacts of outdoor air pollution on indoor air quality are not yet well understood. Regarding the potential health risks associated with the ventilation of outdoor air pollution (Liu et al., 2024), two questions should be addressed separately. Firstly, we must distinguish the differences in the size fractions and chemical components of indoor and outdoor PM, as they may originate from different sources (Morawska et al., 2017). Then, since the size fractions for indoor and outdoor

PM may vary, assessments of potential health effects can guide the development of air pollution control policies for indoor and outdoor environments (Nassikaset al., 2024).
Quantifying source contributions to size-resolved PM aids in emission management. While outdoor pollution is regulated, indoor pollution control is lacking (Huang et al., 2014). The receptor model, such as PMF, has been widely used worldwide to estimate the source contributions of PM in the absence of inputs from a local source profile (Dao et al., 2022). Prior studies have focused on the estimation of source contributions to indoor and outdoor PM in single-size fractions (Huang et al., 2023), but there have been an inadequate number of quantitative studies on source contributions to size-resolved PM collected from indoor and outdoor air.
This study evaluates mass concentrations, chemical compositions, sources, and health implications of indoor and outdoor size-segregated aerosols in Beijing, aiming to provide insights into the outdoor-indoor air quality relationship and support emission remediation strategies.

2. MATERIALS AND METHODS

2.1 Sample collection

This study focused on an office in Beijing, located near a residential area close to the 3rd Ring Road. The outdoor sampling site was positioned at approximately 15 m above the ground on the office building roof, while the indoor site was within a 10-square-meter office furnished with four computers, a printer, a refrigerator, and an air conditioner. Four people worked in the office on weekdays. In summer, the windows were open, and the air conditioner was operational during the day. The area had no neighboring industrial pollution sources, and sampling was conducted during two periods: 5 - 25 July 2020 (summer) and 5 - 31 January 2021 (winter).
Two nine-stage particle samplers (Andersen Series 20-800, USA) were utilized to simultaneously collect indoor and outdoor size-segregated airborne particles at a flow rate of 28.3 L min^{-1}, targeting nine particle sizes (0.43 - 9.0 μm). Quartz fiber filters were used for water-soluble ions, organic carbon, and elemental carbon analysis, while cellulose filters were for elemental concentration quantification. Samples were collected for 24 - 48 h, yielding 14 sets in summer and 18 sets in winter.

2.2 Chemical Analyses

For water-soluble ion analysis, a quarter (7 cm^2) of each quartz filter was added to 25 mL of de-ionized water and ultrasonically extracted for 30 min at room temperature. The extract was then filtered through a 0.22 μm filter before measuring the levels of water-soluble ions including Na^+, NH_4^+, K^+, Mg^{2+}, Ca^{2+}, Cl^-, NO_3^-, and SO_4^{2-} using an ICS-90 ion chromatograph. The ions' limits of detection were less than 0.02 μg m^{-3} when the injection volume was 100 μL. The thermal/optical carbon aerosol analyzer (DRI Model 2001A) was used to determine organic carbon and elemental carbon levels. For trace element measurement, 7 cm^2 of the cellulose membrane was digested with a mixture of HNO_3, H_2O_2, and HF, and the levels of 19 trace elements included Na, Mg, Al, K, Ca, V, Cr, Mn, Fe, Co, Ni, Cu, Zn, Mo, As, Cd, Sb, Ba, and Pb, were measured using an Agilent 7500ce inductively coupled plasma mass spectrometer.

2.3 PMF Model

EPA-PMF 5.0 was employed to apportion sources for PM, with concentrations and uncertainty of the above chemical species in size fractions of <0.43, 0.43–0.65, 0.65–1.1, 1.1–2.1, 2.1–3.3, 3.3–4.7, 4.7–5.8, and 5.8–9 μm as input. We calculated the uncertainty of the concentration data using the following equations.

We used Equation (1) to calculate the uncertainty when the measured level was lower than or equal to the detection limit (MDL) for the analytical method.

$$\text{Uncertainty} = 5/6 \times \text{MDL} \quad (1)$$

We used the following calculation Equation (2) when the concentration was higher than the detection limit (MDL) for the analytical method.

$$\text{Unc} = \sqrt{(Errorfraction \times concentration)^2 + (0.5 \times MDL)^2} \quad (2)$$

3. RESULTS AND DISCUSSION

3.1. Mass Concentrations

Fine particles (<2.1 μm) and coarse particles (2.1-9.0 μm) were considered as proxies for $PM_{2.5}$ and PM_{10}, respectively, due to sampler limitations. A significant linear correlation was observed between $PM_{2.1}$ and $PM_{2.5}$ ($R^2 = 0.89$, $p < 0.05$), and between PM_9 and PM_{10} ($R^2 = 0.87$, $p < 0.05$). $PM_{2.1}$ and $PM_{2.1–9}$ concentrations were generally lower indoors, except for $PM_{2.1–9}$ in summer, indicating that major indoor sources different from those outdoors were responsible for the coarse particles in summer offices. Winter had higher $PM_{2.1}$ but lower $PM_{2.1–9}$ compared to summer. During haze days (defined as PM2.5 > 35 μg m^{-3}), both indoor and outdoor particle levels substantially increased compared to clear days.

The size distribution of mass concentration (Fig. 1) showed a bimodal pattern, with peaks at 0.43–0.65 μm (fine mode) and 4.7–5.8 μm. Notably, for outdoor particles, the fine-mode peak shifted to larger sizes on haze days in both seasons. The indoor/outdoor (I/O) ratios were generally below 1 across most size ranges in both seasons, except for some coarse fractions (2.1–3.3 μm and 3.3–4.7 μm). The I/O ratio was highest in the 2.1–4.7 μm range, potentially due to elevated human activity indoors. This ratio was also affected by the penetration efficiency of particles and the protection of the building envelope from coarser outdoor particles.

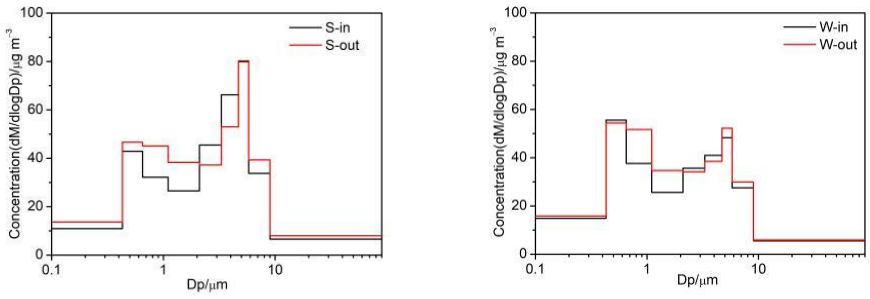

Figure 1. Size distributions of the mass concentrations of both inside and outside particles.

3.2 Chemical components of PM

PM chemical components were grouped into eight categories (Fig. 2): sulfate, nitrate, ammonium, chlorine, organic matter (OM), elemental carbon (EC), crustal materials (CM), and heavy metals (HM). OM and sulfate-nitrate-ammonium (SNA) dominated the $PM_{2.1}$ mass, accounting for over 76.6% of the total. The fraction of SNA was higher in outdoor $PM_{2.1}$, suggesting more secondary particle formation outdoors. In contrast, the fraction of OM was lower outdoors, indicating indoor sources of OM. High contributions of CM and OM were observed in $PM_{2.1–9}$, accounting for 30.3%~40.2% and 24.3%~54.0% of the total $PM_{2.1-9}$ mass, respectively. The undetermined fraction for $PM_{2.1}$ and $PM_{2.1–9}$ ranged from 1.4% to 8.8%, potentially due to oxide species, heteroatoms, water molecules, and undetermined mineral components.

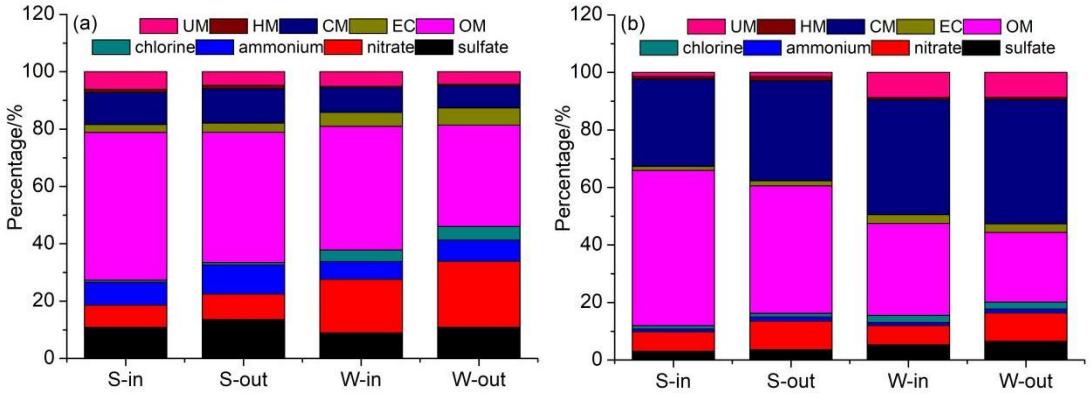

Figure 2. Average mass closure for the indoor and outdoor samples of (**a**) $PM_{2.1}$ and (**b**) $PM_{2.1–9}$.

The mean concentrations of water-soluble ions were higher in winter (28.8 μg m^{-3} indoors and 36.9 μg m^{-3} outdoors) compared to summer (18.8 μg m^{-3} indoors and 25.0 μg m^{-3} outdoors). SNA contributed to 69.5% - 74.4% of water-soluble ions in $PM_{2.1}$ and 25.7% - 48.4% in $PM_{2.1-9}$. The concentrations of SO_4^{2-}, NO_3^-, and NH_4^+ were higher in indoor $PM_{2.1}$ and $PM_{2.1–9}$. During haze days, the accumulation of SNA occurred both indoors and outdoors. The sulfur oxidation ratio (SOR) and nitrogen oxidation ratio (NOR) were positively correlated with relative humidity (RH) in winter. The size distribution of SNA was bimodal, with the fine-mode maximum shifting to larger sizes on haze days for outdoor particles.The acidity and alkalinity of PM, evaluated by the equivalent ratio of cations to anions ($R_{C/A}$), showed that outdoor PM was more acidic. The $R_{C/A}$ values ranged from 0.9 to 3.3, with the lowest ratios in the 1.1–2.1 μm size fraction.

OC and EC concentrations varied seasonally and between indoor and outdoor. In summer, indoor OC and EC in $PM_{2.1}$ and $PM_{2.1–9}$ were slightly lower than outdoors, while the opposite was true for OC in $PM_{2.1–9}$. In winter, indoor OC was slightly higher, and EC was lower than outdoors. During haze days, the average concentrations of OC and EC in $PM_{2.1}$ and $PM_{2.1–9}$ increased. The size distribution of carbonaceous constituents was bimodal or trimodal, with the fine-mode maximum shifting to larger sizes on haze days for outdoor OC, likely due to the hygroscopic growth of ultrafine particles and the secondary formation of secondary organic carbon.

I/O ratios for CM and HM were <1 in both $PM_{2.1}$ and$PM_{2.1–9}$, indicating dominant outdoor contributions. Haze days showed higher CM and HM concentrations than clear days, with fine-mode CM ($R_{H/C}$: 1.28–2.30) accumulating more than coarse-mode (1.11–1.84), while HM exhibited accumulation in both modes ($PM_{2.1}$: 1.30–1.61; $PM_{2.1–9}$: 1.35–2.11). Size distributions

of CM and HM displayed bimodal peaks: fine mode (0.43–1.1 μm) and coarse mode (3.3–5.8 μm). Outdoor HM fine-mode peaks shifted from 0.43–0.65 μm (clear days) to 0.65–1.1 μm (haze days), suggesting hygroscopic growth or secondary formation, but indoor particles showed no such shift. These findings highlight outdoor sources as major contributors to indoor pollution, with haze enhancing fine-particle accumulation.

3.3 Source Apportionment

Six sources of PM were identified through positive matrix factorization (PMF) analysis: biomass burning, secondary inorganic aerosols (SIA), coal combustion, dust, traffic, and industrial pollution. These sources accounted for 91.3%- 99.0% of $PM_{2.1}$ and 90.7% - 98.4% of $PM_{2.1–9}$ (Fig. 3).

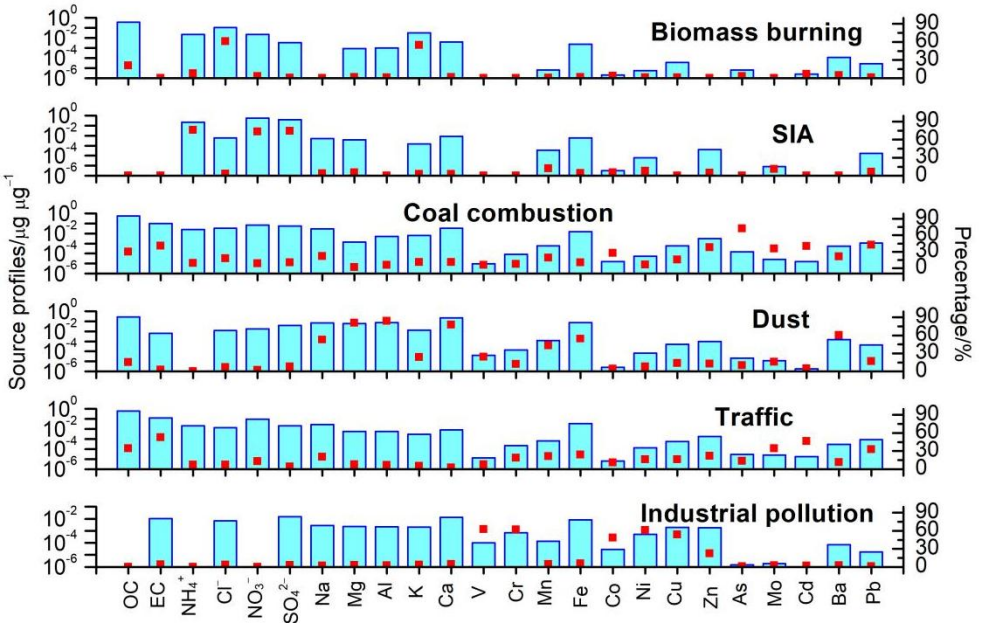

Figure 3. The profiles of each source and the apportioned percentages of species for each source.

The first source, biomass burning, was represented by the high Cl^- (61.1%), K (54.7%), which is an excellent tracer of aerosols from biomass burning, and OC (20.6%) contents. Their contributions to indoor and outdoor $PM_{2.1}$ in winter were 4.9% and 5.2%, which were slightly higher than their 3.6% and 3.3% contributions to $PM_{2.1–9}$. This finding is consistent with previous studies (Cheng et al., 2014). The greater contributions to $PM_{2.1}$ and $PM_{2.1–9}$ were found in summer (6.6% and 6.9% to indoor and outdoor $PM_{2.1}$ and 7.5% and 7.7% to $PM_{2.1–9}$), demonstrating an obvious seasonality.

The second source was SIA, which was characterized by significant amounts of SO_4^{2-} (74.4%), NO_3^- (73.1%), and NH_4^+ (75.7%). SNA represented the dominant composition of secondary inorganic aerosols. SNA was mainly formed through the photochemistry and heterogeneous processes of gaseous precursors (SO_2, NO_x, and NH_3). Their contributions to indoor and outdoor $PM_{2.1}$ in winter were 32.1% and 39.2%, which were significantly greater than their 13.7% and 18.6% contributions to $PM_{2.1–9}$. The contributions of SIA to both $PM_{2.1}$ and $PM_{2.1–9}$ revealed

significant seasonal trends, with lower concentrations observed in summer (27.8% and 34.2% to indoor and outdoor $PM_{2.1}$ and 13.0% and 15.4% to $PM_{2.1–9}$).
The third source, coal combustion, was represented by elevated As (72.4%), Pb (42.2%), Cd (40.1%), EC (40.5%), Zn (37.8%), Mo (35.8%), Co (27.5%), and OC (30.0%) concentrations . As is an excellent tracer of aerosols from coal combustion. Coal combustion is one of the main sources of primary OC and EC. Moreover, Pb, Cd, Zn, Mo, and Co are present in coal combustion. The contributions of this source to indoor and outdoor $PM_{2.1}$ in winter were 19.3% and 20.6%. Besides the contribution to $PM_{2.1}$, coal combustion contributed significantly to $PM_{2.1–9}$ (21.4% and 21.9% to indoor and outdoor $PM_{2.1-9}$). The contributions of coal combustion to $PM_{2.1}$ and $PM_{2.1–9}$ showed the obvious seasonal pattern of winter > summer (17.2% and 17.4% to indoor and outdoor $PM_{2.1}$ and 20.1% and 20.5% to $PM_{2.1–9}$).
The fourth source was dust, which were characterized by significant amounts of crustal elements, such as Al (83.9%), Mg (80.9%), Ca (77.9%), Ba (60.4%), Fe (54.3%), Na (52.7%), and Mn (40.3%). The OC content was close to 15.2%, and these high levels suggest resuspended dust. Thus, this source possibly mixes desert/loess dust, anthropogenic construction dust, fugitive dust, and resuspended road dust. The contributions of this source to indoor and outdoor $PM_{2.1}$ in winter were 8.6% and 7.8%, which were significantly lower than the 32.0% and 35.2% contributions to $PM_{2.1–9}$. Its fraction of both $PM_{2.1}$ and $PM_{2.1–9}$ showed significant seasonal trends, with lower concentrations found in summer (9.2% and 9.9% to indoor and outdoor $PM_{2.1}$ and 26.3% and 29.8% to $PM_{2.1–9}$).
The fifth source, traffic, was characterized by elevated EC (52.7%), Cd (46.3%), Mo (34.4%), OC (34.2%), Pb (32.7%), Fe (23.9%), Zn (21.9%), and Mn (21.2%) concentrations. The contributions of this source to indoor and outdoor $PM_{2.1}$ in winter were 22.6% and 21.8%. These aerosol species are all enriched in vehicular and/or waste incineration emissions. EC primarily arises from engines; Zn, Fe, and Mn are found in tailpipe emissions; and OC, Pb, Cd, and Mo are present in motor and fuel oil combustion. In addition to its contributions to $PM_{2.1}$, traffic significantly contributed to $PM_{2.1–9}$ (17.5% and 16.6% to indoor and outdoor $PM_{2.1–9}$). The contributions of traffic to $PM_{2.1}$ and $PM_{2.1–9}$ exhibited the similar seasonal pattern of winter < summer (24.5% and 22.9% to indoor and outdoor $PM_{2.1}$ and 19.2% and 18.7% to $PM_{2.1–9}$).
The sixth source was industrial pollution, which were characterized by significant amounts of V (62.6%), Cr (61.8%), Ni (61.1%), Cu (53.6%), Co (48.6%), and Zn (22.6%); this source may be related to smelters and the metallurgical industries. The contributions of this source to indoor and outdoor $PM_{2.1}$ in winter were 4.2% and 4.4%, which were slightly higher than the 2.5% and 2.8% contributions to $PM_{2.1–9}$. Its fractions of both $PM_{2.1}$ and $PM_{2.1–9}$ indicated significant seasonal trends, with higher contributions found in summer (5.9% and 6.2% to indoor and outdoor $PM_{2.1}$ and 4.6% and 3.9% to $PM_{2.1–9}$).

3.4 Possible human health implications

The non-carcinogenic and carcinogenic risks of toxic elements were calculated, considering both indoor and outdoor exposures. The total HQ values in PM_9 and TSP during both summer and winter were higher than unity, indicating notable non-carcinogenic risks from these elements. For estimating the risks of individual elements, the HQ values for Ni were found to be greater than those of other elements, and the HQ values for Ni in PM_9 and TSP in winter were higher than 1. This indicates that Ni in PM_9 and TSP poses significant non-carcinogenic risks to human health during winter. Similarly, the total CR values in $PM_{2.1}$, PM_9, and TSP during both summer and winter were greater compared with the acceptable limit of 1.0×10^{-6}, indicating the potential

carcinogenic risks caused by these elements. Additionally, the CR values of Co in PM_9 and TSP in summer, Co and Ni in PM_9 and TSP in winter, and Pb in $PM_{2.1}$, and PM_9 and TSP during winter were located between 1.0×10^{-6} and 1.0×10^{-4}, indicating potential the carcinogenic risks caused by these elements.

Fig. 4 shows the non-carcinogenic and carcinogenic risks and relative proportions of toxic elements in different size fractions. The HQ values of different elements follow the order Ni > Mn > Al > Cd > Co in both summer and winter. Generally, the highest non-carcinogenic risks were observed at 0.43–0.65 μm in summer and 2.1–3.3 μm in winter. The CR values of different elements follow the order Co > Pb > Ni > Cd in both summer and winter. The highest carcinogenic risks were also observed at 0.43–0.65 μm in summer and 2.1–3.3 μm in winter. These results indicate that we cannot ignore the non-carcinogenic and carcinogenic risks caused by coarse particles.

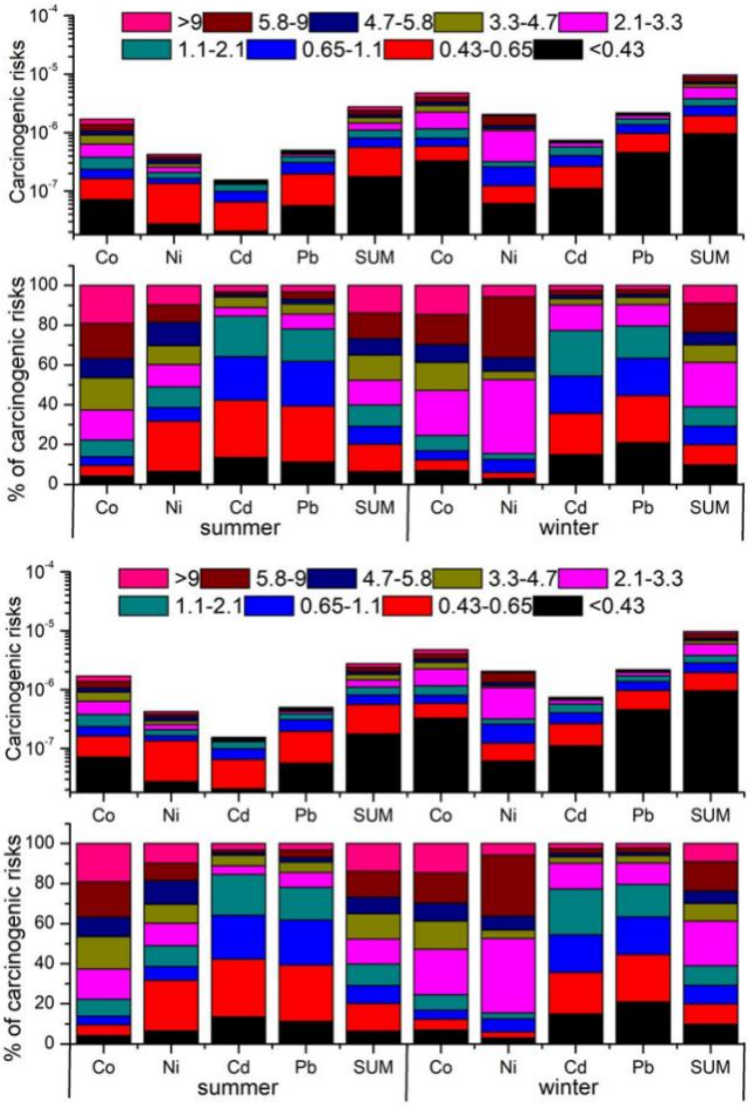

Figure 4. Non-carcinogenic and carcinogenic risks and relative proportions of toxic elements in different size fractions.

4. CONCLUSIONS

This study compared indoor and outdoor size-resolved particles in urban Beijing. Results showed that $PM_{2.1}$ and $PM_{2.1–9}$ concentrations were usually lower indoors but increased during haze. The size distribution was bimodal. OM and SNA dominated $PM_{2.1}$, while CM and OM were significant in $PM_{2.1–9}$. The source apportionment results indicated that biomass burning (4.9%~6.9% to $PM_{2.1}$ and 3.3%~7.7% to $PM_{2.1-9}$), SIA (4.9%~6.9% to $PM_{2.1}$ and 3.3%~7.7% to $PM_{2.1–9}$), coal combustion (4.9%~6.9% to $PM_{2.1}$ and 3.3%~7.7% to $PM_{2.1–9}$), dust (4.9%~6.9% to $PM_{2.1}$ and 3.3%~7.7% to $PM_{2.1–9}$), traffic (4.9%~6.9% to $PM_{2.1}$ and 3.3%~7.7% to $PM_{2.1–9}$), and industrial pollution (4.9%~6.9% to $PM_{2.1}$ and 3.3%~7.7% to $PM_{2.1–9}$) were the main sources of PM during the study period. Toxic elements in PM_9 and TSP exhibited non-carcinogenic risks, and those in $PM_{2.1}$, PM_9, and TSP had potential carcinogenic risks. The highest non-carcinogenic and carcinogenic risks were observed at 0.43–0.65 μm in summer and 2.1–3.3 μm in winter. However, the study had limitations, such as a single sampling location and small volume. Future studies should further explore the associations between indoor and outdoor particles.

ACKNOWLEDGEMENTS

This study was supported by Beijing Natural Science Foundation (8222044 and 8232025), the National Natural Science Foundation of China (No. 41807311) and the Beijing Academy of Science and Technology Innovation Foster (24CB003-05).

REFERENCES

Cheng, Y.; Engling, G.; He, K.-b.; Duan, F.-k.; Du, Z.-y.; Ma, Y.-l.; Liang, L.-l.; Lu, Z.-f.; Liu, J.-m.; Zheng, M.; et al. The characteristics of Beijing aerosol during two distinct episodes: Impacts of biomass burning and fireworks. Environ. Pollut. 2014, 185, 149–157.

Dao, X.; Di, S.; Zhang, X.; Gao, P.; Wang, L.; Yan, L.; Tang, G.; He, L.; Krafft, T.; Zhang, F., Composition and sources of particulate matter in the Beijing-Tianjin-Hebei region and its surrounding areas during the heating season. Chemosphere 2022, 291, 132779.

Enyoh, C. E.; Verla, A. W.; Qingyue, W.; Ohiagu, F. O.; Chowdhury, A. H.; Enyoh, E. C.; Chowdhury, T.; Verla, E. N.; Chinwendu, U. P., An overview of emerging pollutants in air: Method of analysis and potential public health concern from human environmental exposure. Trends Environ. Anal. Chem. 2020, 28, e00107.

Huang, R. J.; Zhang, Y. L.; Bozzetti, C.; Ho, K. F.; Cao, J. J.; Han, Y. M.; Daellenbach, K. R.; Slowik, J. G.; Platt, S. M.; Canonaco, F.; et al. High secondary aerosol contribution to particulate pollution during haze events in China. Nature 2014, 514, 218–222.

Huang, R. J.; Zhang, Y. L.; Bozzetti, C.; Ho, K. F.; Cao, J. J.; Han, Y. M.; Daellenbach, K. R.; Slowik, J. G.; Platt, S. M.; Canonaco, F.; Source apportionment of fine particulate matter at a megacity in China, using an improved regularization supervised PMF model. Sci. Total Environ. 2023, 879, 163198.

Liu, X.; Xue, Q.; Tian, Y.; Jia, B.; Chen, R.; Huo, R.; Wang, X.; Feng, Y., Potential toxic components in size-resolved particles and gas from residential combustion: Emission factor and health risk. Environ. Int. 2024, 185, 108551.

Morawska, L.; Ayoko, G. A.; Bae, G. N.; Buonanno, G.; Chao, C. Y. H.; Clifford, S.; Fu, S. C.; Hänninen, O.; He, C.; Isaxon, C.; et al. Airborne particles in indoor environment of homes, schools, offices and aged care facilities: The main routes of exposure. Environ. Int. 2017, 108, 75–83.

Nassikas, N. J.; McCormack, M. C.; Ewart, G.; Balmes, J. R.; Bond, T. C.; Brigham, E.; Cromar, K.; Goldstein, A. H.; Hicks, A.; Hopke, P. K.; et al. Indoor Air Sources of Outdoor Air Pollution: Health Consequences, Policy, and Recommendations: An Official American Thoracic Society Workshop Report. Ann. Am. Thorac. Soc. 2024, 21, 365–376.

Tian, S.; Pan, Y.; Liu, Z.; Wen, T.; Wang, Y., Size-resolved aerosol chemical analysis of extreme haze pollution events during early 2013 in urban Beijing, China. J. Hazard. Mater. 2014, 279, 452–460.

Weber, R. A map of potentially harmful aerosols in Europe. Nature 2020, 587, 369–370.10.

6th International Conference on Building Energy and Environment
Eindhoven University of Technology, The Netherlands
6 - 10 July 2025

Formaldehyde removal test of Metal Organic Frameworks in the environmental chamber

Weihui Liang [1], Shan Guo [1], Menghao Qin [2]

[1]*School of Architecture and Urban Planning, Nanjing University, Nanjing, China, e-mail: liangwh@nju.edu.cn*
[2]*Department of Environmental and Resource Engineering, Technical University of Denmark, Denmark, e-mail: menqin@dtu.dk*

SUMMARY
Formaldehyde is a prevalent indoor pollutant with well-documented adverse health effects. Recent advancements in metal-organic frameworks (MOFs) have demonstrated their ability to efficiently and reversibly capture formaldehyde, with minimal energy penalties for subsequent regeneration. In this study, we evaluated the formaldehyde removal efficiency of a newly developed MOF (Al-3.5-PDA/MOF-303), activated carbons, and MnOx catalysts in a 500 L airtight environmental chamber. The removal efficiencies were found to be 96.0% for Al-3.5-PDA, 44.8% for activated carbons, and 92.6% for MnOx catalysts. Additionally, formaldehyde emissions from medium density fiberboard (MDF) were measured in a 100 L environmental chamber both in the presence and absence of Al-3.5-PDA. Under continuous emission conditions, the average removal rate of Al-3.5-PDA was approximately 66%, which is lower than that observed under static conditions. Notably, Al-3.5-PDA exhibited consistently stable performance for formaldehyde removal over a 150-hour testing period.

Keywords: dynamic environmental chamber, material emissions, activated carbons, MnOx catalysts, Al-3.5-PDA

1. INTRODUCTION

Maintaining optimal indoor air quality (IAQ) is crucial due to its significant impact on human health, productivity, and overall well-being (Lizana et al., 2020; Oh et al., 2019). Among the various indoor pollutants, formaldehyde is of particular concern. Formaldehyde is released from a wide array of sources, including building materials, furniture, and household products (Salthammer, 2019). Prolonged exposure to formaldehyde has been associated with numerous adverse health effects, such as respiratory irritation, nasal cancer, and leukemia (IARC, 2012; Tang et al., 2009). Consequently, research into formaldehyde and effective mitigation strategies is essential for enhancing indoor air quality and safeguarding public health.

Purification techniques have been widely utilized for formaldehyde removal (Wang et al., 2023). The effectiveness of purification in reducing formaldehyde levels is primarily due to its ability to significantly decrease indoor formaldehyde concentrations through advanced air purification technologies, such as activated carbon adsorption, photocatalysis, manganese oxides (MnOx), and negative ion generation (Law et al., 2024; Zhao et al., 2022). Despite their widespread use, these conventional purification methods are constrained by limitations in efficiency, selectivity, and energy consumption (Zhang et al., 2017). Recent developments in metal-organic frameworks (MOFs) have highlighted their potential for reversible formaldehyde capture. Nevertheless, existing MOFs still face challenges, including inadequate water stability, competitive adsorption under humid conditions, and high energy requirements for regeneration (Vikrant et al., 2019;

Wang et al., 2016). For example, amine-functionalized MOFs like UiO-66-NH_2 require regeneration temperatures above 130°C (Vikrant et al., 2019). These limitations emphasize the necessity for designing MOFs with optimized architectures that ensure high selectivity, stability, and energy-efficient regeneration processes.

More recently, a novel pyrazole-based aluminum MOF, Al-3.5-PDA (MOF-303), has shown remarkable potential for efficiently capturing formaldehyde in a reversible manner with minimal energy requirements for regeneration (Sadovnik et al., 2024). Unlike traditional MOFs, Al-3.5-PDA exhibits a hybrid architecture consisting of infinite Al(III)-hydroxyl chains and 3,5-pyrazoledicarboxylate ligands, forming one-dimensional microporous channels (6 Å) with accessible pyrazole groups (Fathieh et al., 2018; Sadovnik et al., 2024). This unique structure enables synergistic chemisorption via dual hydrogen bonding between formaldehyde and the framework's μ_2-OH and pyrazole moieties, achieving an unprecedented adsorption capacity of 5 $mmol \cdot g^{-1}$ under humid conditions (90% RH). Notably, Al-3.5-PDA demonstrates negligible formaldehyde desorption below 50 °C and can be regenerated through water washing at ambient temperature, thereby eliminating energy-intensive thermal processes. Furthermore, its hydrophobic pores and tailored active sites provide exceptional selectivity against co-contaminants such as toluene and CO_2, surpassing amine-functionalized MOFs and activated carbons (Sadovnik et al., 2024).

However, comparative studies assessing the effectiveness of different purification technologies remain scarce. Furthermore, since building materials are major sources of formaldehyde emissions, it is essential to evaluate whether newly developed Al-3.5-PDA can effectively remove formaldehyde under continuous emissions from these materials. Herein, we first compare the performance of Al-3.5-PDA with activated carbons and MnOx catalysts in a 500 L airtight environmental chamber under static conditions. Subsequently, formaldehyde emissions from medium density fiberboard (MDF) were measured in a 100 L environmental chamber both in the presence and absence of Al-3.5-PDA to assess its removal efficiency under continuous emission scenarios. The results of this study offer significant insights into the formaldehyde removal capabilities of the newly developed Al-3.5-PDA material when applied in indoor environments.

2. MATERIAL AND METHODS

2.1 The tested materials

The activated carbon utilized in this study was procured from Nanjing Wanqing Chemical Glass Instrument Co., Ltd., with a particle size of 20−50 mesh. The active manganese decomposition sheets were sourced from Nanjing Yujie Environmental Technology Co., Ltd., under the product patent number ZL 2013 1 0139928.3. These sheets are composed of high-molecular-weight polyethylene terephthalate fibers serving as the carrier, onto which MnOx crystals are loaded. The fiber diameter is approximately 15−20 μm, and the specific surface area of the MnOx particles is 202.89 m^2/g, with pore diameters predominantly ranging from 4 to 6 nm. Each sheet measures 125 mm × 180 mm. The Al-3.5-PDA was synthesized using cellulose fibers and nano-fibrillated cellulose (NFC) as carriers, impregnated with MOF particles Al-3,5-PDA. This material comprises helical AlO4(OH)2 chains and 3,5-pyrazoledicarboxylate ligands, forming one-dimensional channels with a diameter of approximately 0.7 nm, a specific surface area (BET) of about 1343 m^2/g, and a porosity of 0.49 cm^3/g. Detailed information regarding the preparation method of this

Al-3.5-PDA can be found in US Patent US 20230001380A1. The paper membrane has dimensions of 200 mm × 200 mm and a mass of 12.0 g. Images of each material are presented in Figure 1.

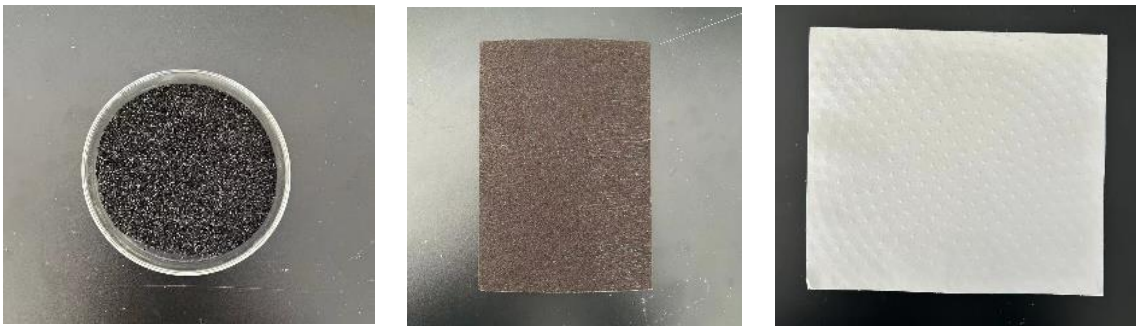

Figure 1. The images of the (a) activated carbons, (b) MnOx catalysts, and (c) Al-3.5-PDA materials used in the experiments.

Prior to the experiment, both the Al-3.5-PDA and activated carbon samples must undergo activation in a vacuum drying oven. By applying heat and vacuum extraction, impurities adsorbed within the pores of the samples are effectively desorbed. Specifically, the Al-3.5-PDA was activated at 102°C under a vacuum of 800-850 mbar for 5 hours. For the activated carbon particles, the activation process involved exposure to 102°C under a vacuum of 500 mbar for 16 hours. When reused after adsorption, the Al-3.5-PDA needs to be regenerated at 102°C under a vacuum of 500 mbar for 16 hours. In all experiments, a consistent mass of 12 grams was used for each material.

2.2 The static tests

The formaldehyde removal efficiency of the three materials under static conditions was evaluated in a 500 L (780 mm × 800 mm × 800 mm) airtight environmental chamber maintained at a constant temperature of 25°C. The natural decay rate of formaldehyde in the chamber, in the absence of any test materials, was determined to be 0.013 h^{-1}. To achieve a high initial formaldehyde concentration, 2.5 mL of a 1000 mg/L formaldehyde standard solution was evenly dispensed into a glass dish positioned centrally within the chamber. A small heating pad placed beneath the glass dish was activated for 30 minutes to expedite the evaporation of the formaldehyde solution. Subsequently, the circulating fan within the chamber was turned on, and the formaldehyde solution was allowed to volatilize for an additional 2 hours. Once complete volatilization was confirmed, the initial formaldehyde concentration in the chamber was measured using the 3-methyl-2-benzothiazolinone hydrazide (MBTH) spectrophotometric method as recommended by Chinese national standard (GB/T 18204.26, 2002). The chamber door was then opened, and the test material was promptly placed on the stainless steel shelf at the center of the chamber before closing the door again. Formaldehyde concentrations were periodically sampled at the chamber outlet using a QC-3 pump (Beijing Institute of Labor Protection) operating at a flow rate of 0.3 L/min for 5 minutes. Measurements were conducted twice for each material to validate the robustness of the results.

2.3 The environmental chamber tests

A medium-density fiberboard (MDF) sample measuring 200 mm × 200 mm × 30 mm was initially evaluated in a 100 L dynamic environmental chamber at 23°C, 50% relative humidity, and an air

exchange rate of 1 h^{-1} for 150 hours to investigate the dynamic emission characteristics of the material. Subsequently, a second sample from the same MDF batch was tested under identical conditions in the presence of Al-3.5-PDA. By comparing formaldehyde concentrations between these two scenarios, the dynamic formaldehyde removal efficiency of Al-3.5-PDA in response to continuous emissions from building materials could be assessed.

2.4 Quality control and assurance

To determine formaldehyde concentrations, 0.4 mL of a 10 g/L ferric ammonium sulfate solution was added to the sampling tube. The tube was shaken and then incubated for 15 min, during which formaldehyde reacted with MBTH to form a blue cationic dye. The absorbance was measured at 630 nm using a spectrophotometer (Unic 7200, China). Formaldehyde quantification was performed based on standard calibration, yielding a calibration curve with ten data points and $R^2 > 0.99$. The detection limit of this method was 0.056 μg, and the recovery rate of formaldehyde ranged from 90% to 105%.

3. RESULTS AND DISCUSSIONS

3.1 Results of the static tests

The decay pattern of formaldehyde concentration and the removal efficiency of activated carbons, MnOx catalysts, and Al-3.5-PDA in static testing conditions are shown in Figure 2. There were some differences in concentrations between repeat measurements due to variations in the initial formaldehyde concentration in the chamber and the sampling time points throughout the measurement process. However, by comparing the removal rates at the same time points, the differences remained within 5% for most of the measurements, indicating the good repeatability of the experimental results.

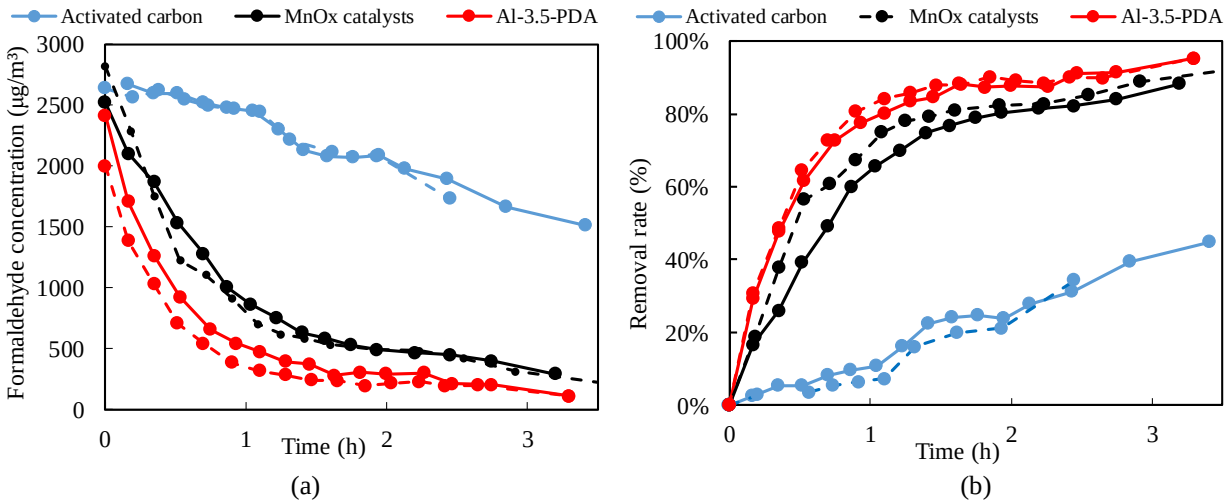

Figure 2. (a) The decay pattern of formaldehyde concentration and (b) the removal efficiency of activated carbon, MnOx, and Al-3.5-PDA in static testing conditions. The dashed and solid lines represent the two repeated measurements for each material.

In the presence of MnOx catalysts and Al-3.5-PDA, the formaldehyde concentration within the chamber decreased rapidly before stabilizing at a relatively low level. Specifically, one hour after introducing Al-3.5-PDA, the formaldehyde concentration dropped from an initial 2416.0 μg/m³ to

477.4 μg/m³, representing a reduction of 1938.6 μg/m³ (79.8%). The concentration then gradually decreased further, reaching 112.78 μg/m³ after 3.3 hours. Similarly, in the presence of MnOx catalysts, the formaldehyde concentration also decreased rapidly; one hour after introduction, it fell from an initial 2818.3 μg/m³ to 704.3 μg/m³, representing a reduction of 2114.0 μg/m³ (75.0%). After 3.6 hours of MnOx catalysts introduction, the concentration had further decreased to 208.0 μg/m³. In contrast, the rate of decrease was more gradual with activated carbons. The initial formaldehyde concentration was 2741.9 μg/m³ and decreased to 2449.9 μg/m³ one hour after introducing the activated carbons, representing a reduction of only 292.0 μg/m³ (10.6%). By 3.4 hours into the test, the concentration had decreased to 1513.78 μg/m³.

The removal rate of the materials was determined by comparing the concentration decay to the initial concentration. As illustrated in the figure, both Al-3.5-PDA and MnOx catalysts exhibited rapid increases in formaldehyde removal rates at the onset of the experiment, followed by gradual stabilization. Among the three materials, Al-3.5-PDA achieved the highest formaldehyde removal rate of 96.0% at 3.3 hours, demonstrating its superior performance in formaldehyde purification under static conditions. The trend for MnOx catalysts was similar to that of Al-3.5-PDA, with a removal rate of 92.6% at 3.6 hours, indicating effective purification albeit at a slightly slower rate compared to Al-3.5-PDA. In contrast, the formaldehyde removal rate of activated carbons increased steadily but at a relatively slower pace throughout the entire testing period, reaching 44.8% at 3.4 hours.

3.2 Results of the environmental chamber tests

Formaldehyde concentration in the dynamic environmental chamber of MDF with and without Al-3.5-PDA is illustrated in Figure 3. The presence of Al-3.5-PDA did not significantly alter the overall trend of formaldehyde concentration changes within the chamber, although it notably influenced the concentration levels. In both cases, formaldehyde concentration initially increased rapidly before stabilizing at a relatively constant level. However, during the later stages of emission, the formaldehyde concentration without Al-3.5-PDA exceeded 600 μg/m³, while with Al-3.5-PDA, it was maintained at approximately 200 μg/m³. This indicates that Al-3.5-PDA demonstrates effective formaldehyde adsorption capacity under dynamic testing conditions, maintaining a consistently stable adsorption rate. The removal rate of Al-3.5-PDA under this scenario was calculated by the concentration decay to that without Al-3.5-PDA. It could be figured out that the removal rate was between 60−70% during the dynamic testing, with an average value of 66%.

Overall, the formaldehyde removal rate of the Al-3.5-PDA in dynamic testing is lower than that observed in static testing. In static conditions, the environmental chamber remains sealed, enabling the Al-3.5-PDA to achieve prolonged and thorough contact with formaldehyde, thereby maximizing adsorption. Conversely, in dynamic testing, formaldehyde emission and adsorption occur concurrently. When the adsorption rate of the Al-3.5-PDA for formaldehyde is slower than the emission rate from the MDF, it becomes challenging to effectively reduce the formaldehyde concentration within the chamber, leading to a reduced removal rate in dynamic testing.

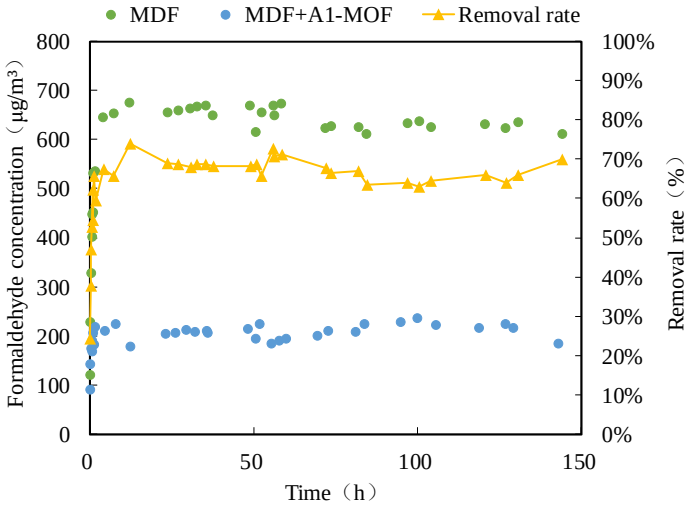

Figure 3. The variations of formaldehyde concentration and the removal efficiency of Al-3.5-PDA in dynamic environmental chamber testing conditions.

3.3 Limitation

While this study confirms the superior formaldehyde removal performance of Al-3.5-PDA, several limitations must be acknowledged to guide future research and practical deployment. First, the synthesis of Al-3.5-PDA depends on hydrothermal conditions and pyrazole dicarboxylate ligands, which may result in higher material costs compared to conventional activated carbons. Therefore, scalable production methods should be investigated to reduce manufacturing expenses. Second, although laboratory tests have shown high efficiency in controlled environments, integrating Al-3.5-PDA into real-world applications such as heating, ventilation, and air conditioning (HVAC) systems or portable air purifiers presents challenges, including optimizing pressure drop for MOF-coated filters and ensuring stability under fluctuating humidity and temperature conditions. Third, while Al-3.5-PDA demonstrates regenerability through water washing, its long-term cyclability (>10 cycles) in complex indoor environments—exposed to mixed pollutants such as volatile organic compounds (VOCs) and particulate matter—has yet to be tested. Future studies should focus on conducting field trials and performing cost-benefit analyses compared to commercial adsorbents to bridge the gap between laboratory innovation and industrial adoption. Addressing these limitations will enhance the potential of Al-3.5-PDA as a sustainable and energy-efficient solution for indoor air purification.

4. CONCLUSION

In this study, we assessed the formaldehyde removal efficiency of a newly developed MOF, activated carbons, and MnOx catalysts within a 500 L sealed environmental chamber. The results indicated that Al-3.5-PDA and MnOx catalysts achieved a removal efficiency of 96.0% and 92.6%, markedly higher than the 44.8% for activated carbons. Additionally, formaldehyde emissions from MDF were measured in a 100 L environmental chamber both in the presence and absence of Al-3.5-PDA. Under continuous emission conditions, Al-3.5-PDA maintained an average removal rate of approximately 66%, which is relatively lower compared to its performance under static conditions.

REFERENCES

Fathieh, F., Kalmutzki, M.J., Kapustin, E.A., Waller, P.J., Yang, J., Yaghi, O.M., 2018. Practical water production from desert air. Science Advances 4, 1–9. https://doi.org/10.1126/sciadv.aat3198

GB/T 18204.26-2000, 2002. Methods for determination of formaldehyde in air of public places.

IARC, 2012. Agents Classified by the IARC Monographs , Volumes 1 – 104. IARC Monographs 7, 1–25. https://doi.org/10.1007/s13398-014-0173-7.2

Law, C.K., Lai, J.H.K., Ma, X.D., Sze-To, G.N., 2024. Enhancing indoor air quality: Examination of formaldehyde adsorption efficiency of portable air cleaner fitted with chemically-treated activated carbon filters. Building and Environment 263, 111823. https://doi.org/10.1016/j.buildenv.2024.111823

Lizana, J., Almeida, S.M., Serrano-Jiménez, A., Becerra, J.A., Gil-Báez, M., Barrios-Padura, A., Chacartegui, R., 2020. Contribution of indoor microenvironments to the daily inhaled dose of air pollutants in children. The importance of bedrooms. Building and Environment 183, 107188. https://doi.org/10.1016/j.buildenv.2020.107188

Oh, H.J., Jeong, N.N., Sohn, J.R., Kim, J., 2019. Personal exposure to indoor aerosols as actual concern: Perceived indoor and outdoor air quality, and health performances. Building and Environment 165, 106403. https://doi.org/10.1016/j.buildenv.2019.106403

Sadovnik, N., Lyu, P., Nouar, F., Muschi, M., Qin, M., Maurin, G., Serre, C., Daturi, M., 2024. Metal-organic frameworks based on pyrazolates for the selective and efficient capture of formaldehyde. Nature Communications 15, 1–12. https://doi.org/10.1038/s41467-024-53572-z

Salthammer, T., 2019. Formaldehyde sources, formaldehyde concentrations and air exchange rates in European housings. Building and Environment 150, 219–232. https://doi.org/10.1016/j.buildenv.2018.12.042

Tang, X., Bai, Y., Duong, A., Smith, M.T., Li, L., Zhang, L., 2009. Formaldehyde in China: Production, consumption, exposure levels, and health effects. Environment International 35, 1210–1224. https://doi.org/10.1016/j.envint.2009.06.002

Vikrant, K., Cho, M., Khan, A., Kim, K.H., Ahn, W.S., Kwon, E.E., 2019. Adsorption properties of advanced functional materials against gaseous formaldehyde. Environmental Research 178, 108672. https://doi.org/10.1016/j.envres.2019.108672

Wang, Q., Li, L., Hong, Y., Zhai, Q., He, Y., 2023. Novel insights into indoor air purification capability of microalgae: characterization using multiple air quality parameters and comparison with common methods. Environmental Science and Pollution Research 30, 49829–49839. https://doi.org/10.1007/s11356-023-25799-8

Wang, Z., Wang, W., Jiang, D., Zhang, L., Zheng, Y., 2016. Diamine-appended metal-organic frameworks: Enhanced formaldehyde-vapor adsorption capacity, superior recyclability and water resistibility. Dalton Transactions 45, 11306–11311. https://doi.org/10.1039/c6dt01696k

Zhang, X., Gao, B., Elise, A., Cao, C., Li, Y., 2017. Adsorption of VOCs onto engineered carbon materials : A review. Journal of Hazardous Materials 338, 102–123. https://doi.org/10.1016/j.jhazmat.2017.05.013

Zhao, L., Niu, S., Niu, X., Chen, T., Wang, Y., Li, L., Huang, F., Wu, H., Mo, L., Zhang, M., 2022. Manganese Oxide Minerals from the Xiangtan Manganese Deposit in South China and Their Application in Formaldehyde Removal. Minerals 12. https://doi.org/10.3390/min12050552

6th International Conference on Building Energy and Environment
Eindhoven University of Technology, The Netherlands
6 - 10 July 2025

Enhancing vapor pressure deficit (VPD) control in cold-climate greenhouses: a simulation approach for improved plant growth

Mohammed Sarmouk[1], Hachimi Fellouah[1], Sébastien Poncet[1], Gilbert Larochelle Martin[2]

[1]*Université de Sherbooke, Sherbrooke, Canada, mohammed.sarmouk@usherbrooke.ca*
[2]*Laboratoire des technologies de l'énergie, Hydro-Québec, Shawinigan, Canada*

SUMMARY
This study investigates the impact of VPD regulation strategies on energy consumption in a commercial tomato greenhouse in Quebec, Canada. Three scenarios are simulated: Natural ventilation (NV) only, combined NV and mechanical dehumidification (MD), and MD only. Results show that while MD significantly improves VPD stability (75.27% satisfaction), it substantially increases energy consumption (1878.15 kWh/m²) compared to NV only (427.31 kWh/m²). The combined NV and MD strategy achieves a balance, improving VPD satisfaction (61.19%) with a moderate energy increase (1320.76 kWh/m²). This study highlights the critical trade-off between VPD control precision and energy efficiency, emphasizing the need for optimized control strategies and renewable energy integration for sustainable greenhouse operations in cold climates.

Keywords: VPD control, TRNSYS, Greenhouse, Regulation

1. INTRODUCTION

In recent years, controlled environment agriculture, particularly in greenhouses, has become a key strategy for optimizing crop productivity, especially for high-value crops like tomatoes. By controlling parameters such as temperature, humidity, ventilation, and vapor pressure deficit (VPD), greenhouses can create optimal growing conditions that enhance both crop quality and yield (Kempkes et al., 2017). However, while greenhouse environments are designed to support crop growth, balancing these environmental parameters can be energy-intensive, especially in cold-climate regions such as Quebec. Maintaining VPD within its optimal range, around 0.5 to 1.2 kPa is critical for maximizing plant transpiration and nutrient transport (Rahman et al., 2021; Shamshiri et al., 2018), while reducing disease risks that arise from excessive humidity or low VPD conditions (De Halleux & Gauthier, 1998).

Recent studies highlight the importance of VPD control in enhancing crop productivity and optimizing resource use in greenhouse environments. Gates et al. (Gates et al., 1998) developed strategies to implement VPD control for plant propagation, demonstrating how simultaneous manipulation of air temperature and humidity could be effectively achieved using low-cost chambers, with methods and logic applicable to broader systems. Lu et al. (Lu et al., 2015) studied the effects of a fogging system for VPD control during the winter season in greenhouses, showing that reducing VPD from 1.4 to 0.8 kPa enhanced tomato plant growth, stomatal function, and photosynthetic rates, ultimately increasing biomass and yield by 17.3% and 12.3%, respectively. Similarly, Zhang et al. (Zhang et al., 2017) explored VPD regulation to reduce plant water stress and improve water productivity in tomato plants, finding a 19.9% reduction in cumulative transpiration and significant improvements in irrigation water use efficiency, with yield gains of

up to 39.1% under low-VPD treatments. Noh and Lee (Noh & Lee, 2022) investigated VPD regulation with automated fogging systems, observing significant improvements in total yield, fruit count, and commercial yield—up to 89%—especially in crops grown in coconut fiber. These works collectively underscored the critical role of precise VPD management in achieving better plant growth, resource efficiency, and crop yield, forming the basis for advancing VPD-focused climate control strategies in modern greenhouses.

Despite advances in greenhouse climate control technologies, gaps remain in understanding the influence of VPD management on energy consumption. Existing research has often overlooked the direct impact of enhanced VPD control strategies on energy use. This gap is especially evident in cold regions, where greenhouse operations must contend with both extreme external temperatures and the challenge of maintaining humidity levels without excessively increasing heating energy demands.

Addressing these concerns, the present research focuses on evaluating the impact of VPD regulation on energy consumption, particularly through the development of a user-defined TRNSYS type for VPD control. This paper aims to fill this gap by analyzing and comparing different scenarios of VPD regulation in greenhouses, providing insights into both the energy demands and the cost implications of improving climate control precision.

2. METHODOLOGY

2.1. Greenhouse description

The data utilized in this study were obtained from a commercial greenhouse located in Saint-Jérôme, Quebec, Canada (45.77° N, 73.96° W). This facility, “Serres Royales”, is a specialized tomato-growing greenhouse consisting of eight connected spans. Each span measures 7.62 m in width, 121.92 m in length, and 6.40 m in height, resulting in a total cultivated area of approximately 5200 m^2 and a volumetric capacity of 50,000 m^3 (Fig. 1). The plant density is maintained at 2.8 plants per square meter to optimize growth conditions.

Dedicated to tomato production, the greenhouse operates from January to late November, capturing data across a range of climatic variations. To maintain a consistent and controlled temperature, radiant heating pipes are installed between each pair of plant rows within every span. This placement allows for uniform heat distribution and ensures optimal growing conditions throughout the cultivation period.

The greenhouse’s structure integrates a thermally efficient design, including a double-layer polyethylene roof with a 10 cm insulating air gap, enhancing energy conservation. The side walls combine polycarbonate panels for high light transmission and durability, while the lower portions consist of a polyurethane core enclosed between two metal sheets, offering superior insulation and mechanical strength.

For natural ventilation (NV) and humidity management, the greenhouse employs a mid-roof ventilation system. Each span is equipped with two automated roof panels that open partially or fully based on specific temperature and relative humidity thresholds. This ventilation setup ensures cooling and dehumidification when internal conditions exceed preset limits.

2.2. TRNSYS Model

The simulation framework for this study builds on a previously validated TRNSYS model developed to replicate the microclimatic dynamics of the studied greenhouse. The model considers one span out of eight to reduce computational time, with validation confirming satisfactory results

for this approach. It incorporates critical processes such as heating, CO_2 enrichment, condensation, and crop evapotranspiration, with the latter implemented using a custom TRNSYS type based on the Stanghellini model (Stanghellini, 1987). NV was integrated into the system through coupling with CONTAM, enabling precise modeling of airflow dynamics. The model's validation, performed in accordance with ASHRAE guidelines (Garrett & New, 2016), demonstrated its ability to accurately predict greenhouse environmental conditions under various scenarios.

Figure 1. Greenhouse dimensions.

For this study, the TRNSYS model was enhanced by integrating new features to assess VPD regulation. A new user-defined type was developed to implement a control strategy prioritizing NV over mechanical dehumidification (MD), combining energy efficiency with effective VPD control. A cooling coil system was added to represent a dehumidifier, selected with an airflow rate of 21 000 cfm, corresponding to the maximum ventilation rate in greenhouses of 0.01 $m^3/s/m^2$ (Jackson & Darby). The optimal temperature range, encompassing both day and night conditions, was set dynamically by agronomists between 14°C and 26°C which aligns with (Ruiz-Nieves et al., 2021). Fogging needs were evaluated and incorporated directly into the Type 56 model as a humidity gain, eliminating reliance on a separate humidifier type.
All simulations were conducted using hourly experimental weather data collected for the year 2022. This dataset provided a comprehensive representation of ambient conditions for the studied greenhouse, capturing the variability of environmental parameters across a complete annual cycle. By leveraging this extended and validated TRNSYS model, the study investigates the performance of the proposed control strategy across three scenarios, as detailed in the subsequent sections.

2.3 VPD control strategy Type development

The developed control strategy for this study operates based on a hierarchical logic designed to manage VPD effectively in the greenhouse while optimizing energy use. The strategy dynamically adjusts NV and MD depending on both indoor and outdoor environmental conditions, incorporating a precise interaction between temperature, humidity, and the operational states of the greenhouse systems. The Type controller takes as parameters VPDmin (0.5 kPa), VPDmax (1.2 kPa), Lock-ON (15 min) and Lock-OFF (15 min) which are the minimum and maximum optimal VPD values and the minimum run times for the ON and OFF operation cycles of the dehumidifier, respectively. Parameters have fixed values during the simulation but can be changed

by the user prior to the simulation. The Type considers as inputs, indoor parameters such temperature, relative humidity, absolute humidity, VPD, and the predefined ventilation setpoint set by agronomists. Outdoor parameters, such as temperature, relative humidity, and absolute humidity, serve as real-time inputs influencing the control logic. The outputs from the Type are ventilation signal, dehumidifier signal, relative humidity setpoint for dehumidifiers, and absolute humidity difference used for fogging.

The control process begins by assessing whether NV can be used to reduce humidity. The logic works as follows:
The vents are first activated if the indoor temperature exceeds the predefined ventilation setpoint and if outdoor conditions are suitable (i.e., outdoor temperature and VPD fall within an acceptable range). Vents open incrementally by 10%. The temperature is monitored for 1 hour following this opening (this duration can be adjusted by the user). If, after one hour, the temperature has not decreased or if the external temperature remains higher than indoor conditions, the vents are closed, and the dehumidifier signal is activated. To avoid "cold ventilation", the rapid entry of cold air causing temperature drops that affect plant transpiration, NV is avoided when the indoor temperature falls below 8°C, and vent opening is limited to 10% when the temperature is below 12°C. If NV is deemed ineffective, dehumidifiers are switched on to maintain the optimal indoor conditions.

An important aspect of this strategy is the dynamic adjustment of the relative humidity setpoint for the dehumidifier, based on the VPD. The strategy uses TRNSYS's moist air properties function to calculate the relative humidity at each timestep (5-minute step for simulation accuracy):

$$\begin{Bmatrix} if\ \ VPD < VPDmin\ \ \ Then\ RH_{set} = f(T_{in}, VPDmin) \\ \\ if\ VPD > VPDmax\ \ Then\ \ AH_{diff} = AH_{set} - AH_{int} \\ with\ \ AH_{set} = \ f(T_{in}, VPDmin) \end{Bmatrix}$$

The resultant humidity gain is added to Type 56 in the TRNSYS model, reflecting an increase in humidity within the greenhouse.

For accurate simulation of indoor climate dynamics, the model operates at a time-step of 5 minutes. This provides sufficient resolution for tracking rapid changes in temperature, humidity, and VPD, as well as for effective control of both NV and MD.

To evaluate the performance of the developed control strategy and its impact on maintaining optimal VPD, three distinct scenarios were simulated:

1- Scenario (a): NV only;
2- Scenario (b): Combined NV and MD;
3- Scenario (c): MD only;

3. RESULTS

3.1 Controller performance

Table 1 presents the monthly average, standard deviation, and minimum values of VPD across the three scenarios. While the average VPD remains within the optimal range ([0.5–1.2 kPa]) for all scenarios, the standard deviation is highest in Scenario (a) and decreases progressively in Scenarios (b) and (c). This trend highlights the increasing effectiveness of the control strategy in stabilizing VPD.

The minimum VPD values frequently reach 0 kPa, indicating periods of high relative humidity and potential condensation. However, in months where minimum VPD is above 0, the values increase noticeably with Scenarios (b) and (c), suggesting the positive impact of dehumidification in preventing saturation.

Additionally, the monthly percentage of time where VPD = 0 is relatively low across all scenarios but shows a clear decline in Scenarios (b) and (c). This further emphasizes the role of the control strategy and dehumidification in reducing excessive humidity and mitigating condensation risks.

Table 1. Monthly VPD Average (± standard deviation) and minimum.

	VPD (kPa)								
	Scenario (a)			*Scenario (b)*			*Scenario (c)*		
Month	*Average*	*Minimum*	*% VPD=0*	*Average*	*Minimum*	*% VPD=0*	*Average*	*Minimum*	*% VPD=0*
Jan	1.03 ± 0.24	0.00	0.01	1.03 ± 0.21	0.00	0.01	1.03 ± 0.21	0.00	0.01
Feb	1.01 ± 0.23	0.30	-	0.97 ± 0.21	0.50	-	0.97 ± 0.21	0.50	-
Mar	0.79 ± 0.27	0.12	-	0.82 ± 0.20	0.47	-	0.81 ± 0.20	0.49	-
Apr	0.63 ± 0.22	0.03	-	0.80 ± 0.26	0.30	-	0.70 ± 0.14	0.40	-
May	0.65 ± 0.46	0.00	4.61	0.67 ± 0.34	0.00	4.16	0.68 ± 0.17	0.00	0.17
Jun	0.56 ± 0.50	0.00	9.78	0.52 ± 0.33	0.00	6.49	0.65 ± 0.16	0.00	0.46
Jul	0.73 ± 0.58	0.00	7.14	0.50 ± 0.34	0.00	10.34	0.58 ± 0.20	0.00	2.67
Aug	0.55 ± 0.53	0.00	10.27	0.45 ± 0.34	0.00	13.56	0.60 ± 0.20	0.00	2.76
Sep	0.49 ± 0.45	0.00	6.053	0.58 ± 0.33	0.00	5.06	0.70 ± 0.18	0.00	1.14
Oct	0.55 ± 0.33	0.00	1.9	0.75 ± 0.31	0.00	1.11	0.73 ± 0.16	0.00	0.08
Nov	0.82 ± 0.36	0.00	0.62	0.89 ± 0.32	0.00	0.10	0.86 ± 0.27	0.06	-

Fig. 2 illustrates psychrometric behavior across three scenarios. Scenario (a), relying solely on NV, achieves 43.85% VPD satisfaction but lacks precision, leading to high variability. Scenario (b), combining NV with MD, improves satisfaction to 61.19% by mitigating NV's limitations, particularly when external air is unsuitable for dehumidification or cooling. MD enhances control, reducing VPD fluctuations. Scenario (c), using only MD, achieves the highest satisfaction at 75.27%, as cooling coils precisely regulate moisture independent of external conditions. While MD minimizes thermal stress and eliminates "cold ventilation" risks, it demands more energy, bypassing NV’s passive dehumidification potential. The data clustering below 26°C in (b) and (c) further highlights MD’s effectiveness in stabilizing VPD and reducing plant stress.

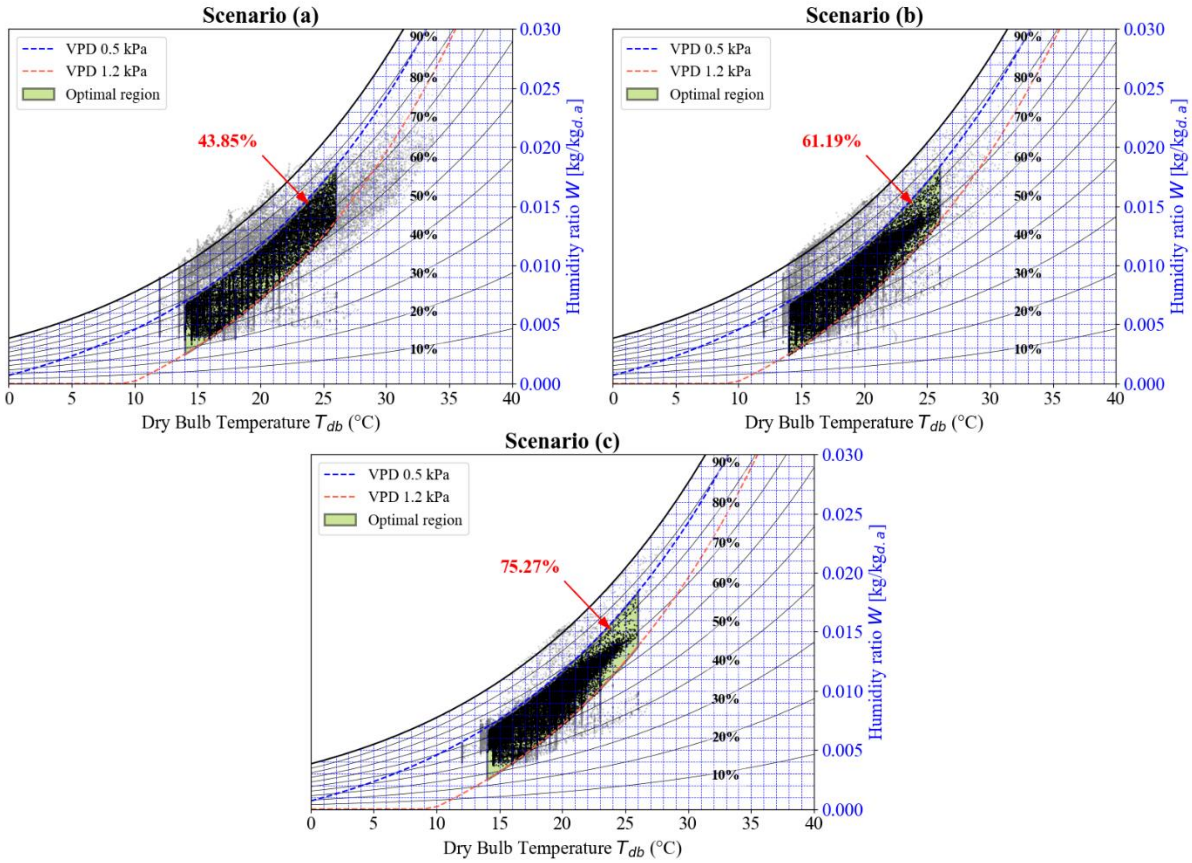

Figure 2. VPD distribution and optimal ranges for the 3 scenarios.

3.2 Energy use

Fig. 3 presents the energy consumption breakdown for heating and dehumidification across scenarios. In scenario (a), energy use is solely for heating, as no MD is involved. Despite lower total consumption, the lack of precise moisture control results in fewer optimal VPD values, potentially impacting yield and quality.

Scenario (b) introduces MD, increasing energy demand compared to (a), but remains more efficient than (c) by prioritizing NV when conditions allow. The dynamic RH setpoint ensures MD operates only as needed, reducing unnecessary energy use while improving environmental stability.

Scenario (c) has the highest energy consumption, relying entirely on MD for humidity control. While this ensures optimal VPD, it eliminates passive energy savings from NV, increasing operational costs and sustainability concerns. The rise in heating demand in (b) and (c) stems from MD's cooling effect, which requires additional heating to maintain suitable temperatures.

The energy use outlined in Table 2 shows that introducing mechanical dehumidifiers (as in scenarios b and c) drastically increases energy consumption, primarily due to the associated cooling and reheating demands to counter the dehumidification process. Transitioning from scenario (a) to scenario (b) increases energy consumption from 427 kWh/m² to 1320 kWh/m², tripling the energy use. Moving from scenario (b) to scenario (c) raises energy use further to

1878.15 kWh/m², an additional 42.3% increase. This suggests that improving VPD control leads to higher energy consumption, with diminishing returns in energy efficiency, thus resulting in increased operational costs. Based on the calculated energy use per percentage of VPD satisfaction, using Scenario (a) as the baseline, Scenario (b) shows 11.83 kWh/m²/%, while Scenario (c) uses 15.2 kWh/m²/%. This highlights that both Scenario (b) and Scenario (c) result in considerably higher energy consumption compared to Scenario (a), which relies solely on NV.

When estimating the operational costs based on Hydro-Québec's Tarif général G, the costs are 1267.2 $/ % for scenario (b) and 1627.7 $/ % for scenario (c).

This reinforces the finding that while precision control strategies like dehumidification and heating improve VPD satisfaction, they come at a significantly higher operational cost.

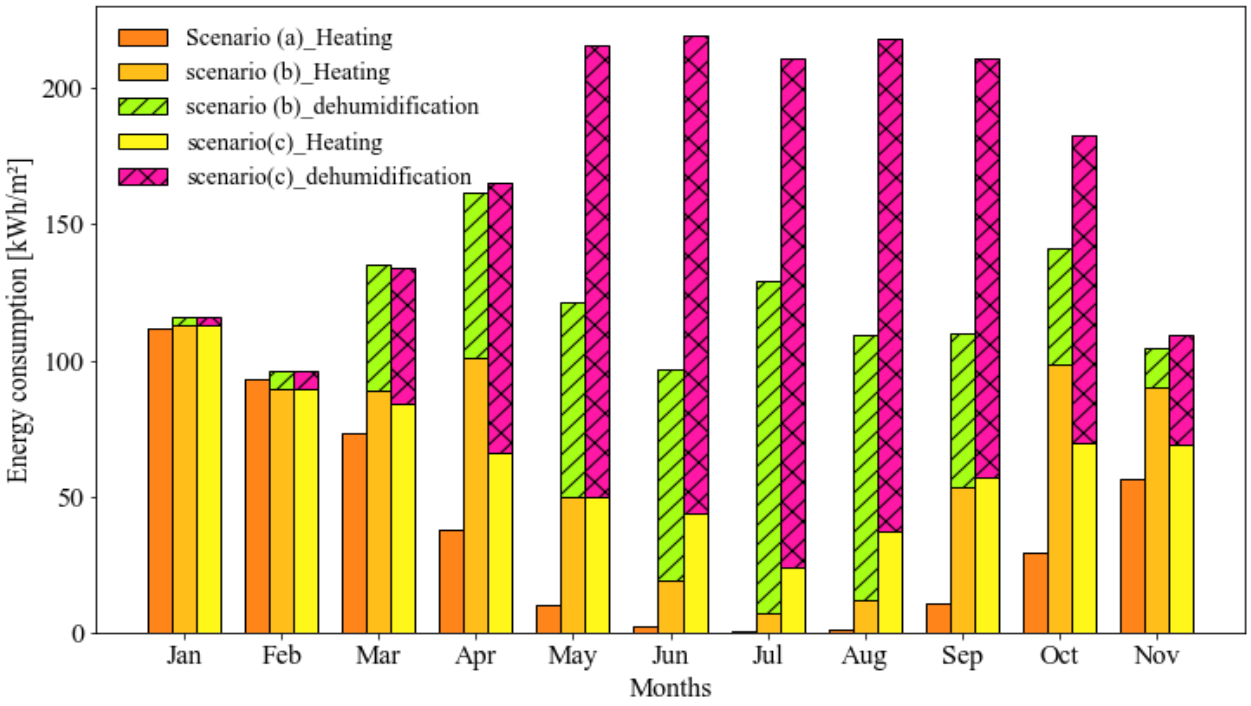

Figure 3. Monthly heating and dehumidification energy use comparison.

Table 2. Monthly and total energy consumption for the 3 scenarios.

	Energy consumption [kWh/m²]		
Month	Scenario (a)	Scenario (b)	Scenario (c)
January	111.65	115.90	116.10
February	93.39	95.87	95.87
March	73.22	135.12	134.05
April	37.88	161.51	165.00
May	10.28	121.47	215.68
June	2.30	96.49	219.12
July	0.63	129.17	211.09
August	1.26	109.30	218.08
September	10.82	110.15	211.07
October	29.21	141.29	182.88
November	56.68	104.50	109.20
Total	**427.31**	**1 320.76**	**1 878.15**

4. CONCLUSION

This study investigated the impact of VPD regulation on energy consumption in a commercial greenhouse. Three scenarios were simulated: NV only (43.85% VPD satisfaction), combined NV and MD (61.19% VPD satisfaction), and MD only (75.27% VPD satisfaction). While MD significantly improved VPD stability, it substantially increased energy consumption. The combined NV and MD strategy, prioritizing NV, achieved a balance, tripling energy use compared to NV only (427 kWh/m²) to 1320 kWh/m², while MD further increased it to 1878.15 kWh/m². This translates to operational costs of 1267.2 $/% and 1627.7 $/% for scenarios (b) and (c), respectively, compared to scenario (a).

Implementing advanced control algorithms, such as predictive control, could further refine the balance between energy use and environmental stability, reducing unnecessary dehumidification and heating demands.

ACKNOWLEDGMENTS

The authors would like to thank the support of Hydro-Québec, Serres Royales, Abri Végétal, Copeland Canada Inc., Atis Énergie and CETAB+ through the NSERC Alliance (ALLRP 565628-21) and Innovéé Innovation en Énergie Électrique (PSO-2104) grants established in 2021 at Université de Sherbrooke.

REFERENCES

De Halleux, D., & Gauthier, L. (1998). Energy Consumption Due to Dehumidification of Greenhouses under Northern Latitudes. *Journal of Agricultural Engineering Research*, *69*(1), 35–42. https://doi.org/10.1006/jaer.1997.0221

Garrett, A., & New, J. R. (2016). *Suitability of ASHRAE guideline 14 metrics for calibration*. Oak Ridge National Lab.(ORNL), Oak Ridge, TN (United States).

Gates, R. S., Zolnier, S., & Buxton, J. (1998). Vapor Pressure Deficit Control Strategies for Plant Production. *IFAC Proceedings Volumes*, *31*(12), 271–276. https://doi.org/10.1016/S1474-6670(17)36076-7

Jackson, H.A. & Darby, D. E. *La ventilation des serres*. Canada - Service de plans, M-6704. https://www.agrireseau.net/documents/Document_93708.pdf

Kempkes, F., De Zwart, H. F., Munoz, P., Montero, J. I., Baptista, F. J., Giuffrida, F., Gilli, C., Stepowska, A., & Stanghellini, C. (2017). Heating and dehumidification in production greenhouses at northern latitudes: Energy use. *Acta Horticulturae*, *1164*, 445–452. https://doi.org/10.17660/ActaHortic.2017.1164.58

Lu, N., Nukaya, T., Kamimura, T., Zhang, D., Kurimoto, I., Takagaki, M., Maruo, T., Kozai, T., & Yamori, W. (2015). Control of vapor pressure deficit (VPD) in greenhouse enhanced tomato growth and productivity during the winter season. *Scientia Horticulturae*, *197*, 17–23. https://doi.org/10.1016/j.scienta.2015.11.001

Noh, H., & Lee, J. (2022). The Effect of Vapor Pressure Deficit Regulation on the Growth of Tomato Plants Grown in Different Planting Environments. *Applied Sciences*, *12*(7), 3667. https://doi.org/10.3390/app12073667

Rahman, M. S., Guo, H., & Han, J. (2021). Dehumidification requirement modelling and control strategy for greenhouses in cold regions. *Computers and Electronics in Agriculture*, *187*, 106264. https://doi.org/10.1016/j.compag.2021.106264

Ruiz-Nieves, J. M., Ayala-Garay, O. J., Serra, V., Dumont, D., Vercambre, G., Génard, M., & Gautier, H. (2021). The effects of diurnal temperature rise on tomato fruit quality. Can the management of the greenhouse climate mitigate such effects? *Scientia Horticulturae*, *278*, 109836. https://doi.org/10.1016/j.scienta.2020.109836

Shamshiri, R. R., Jones, J. W., Thorp, K. R., Ahmad, D., Man, H. C., & Taheri, S. (2018). Review of optimum temperature, humidity, and vapour pressure deficit for microclimate evaluation and control in greenhouse cultivation of tomato: A review. *International Agrophysics*, *32*(2), 287–302. https://doi.org/10.1515/intag-2017-0005

Stanghellini, C. 1953-. (1987). *Transpiration of greenhouse crops: An aid to climate management* [Instituut voor Mechanisatie, Arbeid en Gebouwen]. WorldCat.org.

Zhang, D., Du, Q., Zhang, Z., Jiao, X., Song, X., & Li, J. (2017). Vapour pressure deficit control in relation to water transport and water productivity in greenhouse tomato production during summer. *Scientific Reports*, *7*(1), 43461. https://doi.org/10.1038/srep43461

Climate Change and multi hazard risk assessment (11:00-12:30 h)

6th International Conference on Building Energy and Environment
Eindhoven University of Technology, The Netherlands
6 - 10 July 2025

Evaluating pre-cooling for mitigating indoor overheating in residential buildings during heatwaves with power outages

Xue Liu [1], Yi Wu [2], Hao Tang [3], Da Yan [2]

[1] *School of Architecture, Southwest Jiaotong University, Chengdu, 611756, China*
[2] *Building Energy Research Center, School of Architecture, Tsinghua University, Beijing 100084, China*
[3] *Institute of Smart City and Intelligent Transportation, Southwest Jiaotong University, Chengdu, 611756, China*

SUMMARY
Due to climate change, extreme hot and cold weather events are becoming more frequent, intense, and prolonged. Pre-cooling has been suggested as a feasible solution, few studies have explored its potential to mitigate indoor overheating during heatwaves coinciding with power outages. In this study, an optimized pre-cooling strategy was developed using Bayesian Optimization to thermostat setpoint schedule by minimizing electricity cost and thermal discomfort. Two rule-based pre-cooling strategies and one baseline cooling strategy with no pre-cooling were compared. A prototype residential building was used to evaluate the performance of precooling strategies under a five-day heatwave scenario in Chengdu in 2022, coinciding with scheduled power outages. The results demonstrate that the optimized pre-cooling strategy can reduce approximately 78% of PMV exceedance hours compared to the rule-based strategies. Although its total electricity consumption was higher than that of the baseline and rule-based strategies, the optimized strategy achieved comparable or even lower electricity costs. This study highlights the potential of cost-effective pre-cooling strategies to enhance thermal resilience under extreme weather coincided with power outage.

Keywords: heatwave, pre-cooling, Bayesian Optimization, thermal resilience

1. INTRODUCTION

With climate change, extreme heatwaves have become more frequent, longer, and intense. The frequency of extreme heat events is projected to increase by 5–10 times by the end of the twenty-first century (Luber et al., 2008). The heatwave events have significant adverse effects on human health, energy consumption, and the economic, especially in light of projections indicating that the intensity and severity of climate change-related events will continue to escalate (Seneviratne et al. 2021). In addition, when a heatwave event occurs, the sustained abnormally high temperatures will lead to a surge in cooling electricity demand, resulting in power supply shortages and even grid failures. In the summer of 2022, the southwest region of China experienced unprecedented and prolonged heatwave, exceeding any observed in at least the past 63 years (Liang et al. 2024). This led to a historical peak in electricity demand. Due to power outages, many residential buildings had to suspend or limit air conditioning (AC) usage due to power outage, significantly increasing the heat risks for building occupants.

To enhance thermal resilience during heatwaves, pre-cooling can be an effective strategy to mitigate indoor overheating and reduce peak cooling electricity demand in buildings. This approach is typically implemented within the context of demand response (DR), achieved by lowering the thermostat setpoint below the conventional cooling setpoint before peak hours (Yin et al. 2010). During this period, the building's thermal mass stores cooling energy, which is then

gradually released during peak hours. This process allows for an increase in the cooling setpoint, helping to reduce peak cooling demand.

Numerous studies have been conducted to explore the performance of pre-cooling techniques in reducing power consumption and energy costs in buildings. Turner et al. evaluated the potential of pre-cooling to shift peak electricity loads during peak periods in residential buildings across 12 US climate zones (Turner et al., 2015). In their study, the optimal pre-cooling result was achieved with a 5-hour pre-cooling time and a setpoint temperature of 23.3°C, which shifted more than 75% of the peak load. Chen et al. conducted an experimental study to investigate the effects of a pre-cooling strategy, with the indoor temperature set to 22°C from 1:00 a.m. until it reached 26°C when DR occurred (Chen et al. 2020). The results indicated that chillers could be turned off for approximately 90 minutes without affecting thermal comfort. More recently, several studies have developed optimized pre-cooling control strategies to determine the optimal cooling setpoint schedule, aiming to maximize the trade-off between thermal comfort and energy costs (Wang et al. 2023; Zeng et al. 2022).

Previous studies have primarily focused on the effectiveness of pre-cooling strategies within the context of DR programs, aiming to reduce electricity load during peak hours, with air conditioning systems always in operation. Few studies, however, have explored the use of pre-cooling strategies in residential buildings to enhance thermal resilience during heatwave coincided with a power outage. In this context, pre-cooling is defined as lowering the indoor air temperature a few degrees below the conventional cooling setpoint prior to a power outage. The objective of this study is to mitigate the indoor overheating risks without increasing energy cost burden by implementing pre-cooling strategy. An optimized precooling strategy was developed using a Bayesian Optimization algorithm to determine the optimal setpoint and the starting time for pre-cooling. A prototype residential building located in Chengdu, China, was selected as the case study to evaluate the effectiveness of the proposed strategy based on simulation work.

2. METHODOLOGY

The aim of this study is to investigate the effect of pre-cooling strategies on reducing indoor overheating during extreme heatwaves combined with a power outage in a residential building. An optimized strategy is developed using Bayesian Optimization, which determines the optimal cooling setpoint and precooling start time by minimizing a composite objective function. The overview of methodology is shown in Fig. 1.

2.1. Weather data

In 2022, Chengdu experienced a long duration and intense heat wave from August 8 to August 24, marking the most severe heat wave events since 1961. To explore the impact of pre-cooling strategies under heat waves conditions, hourly weather data from August 8 to 12 were collected, when the daily maximum temperature exceeds 35℃. The meteorological data are from the ERA5 (the European Center Reanalysis version 5) dataset, which is the fifth generation of the Global Climate Reanalysis dataset produced by the European Centre for Medium-Range Weather Forecasts (ECMWF 2024). This dataset includes meteorological parameters such as atmospheric variables, radiative variables, precipitation variables, and offers meteorological information with a spatial resolution of 0.25° × 0.25° (about 31 km × 31 km) and an hourly temporal resolution.

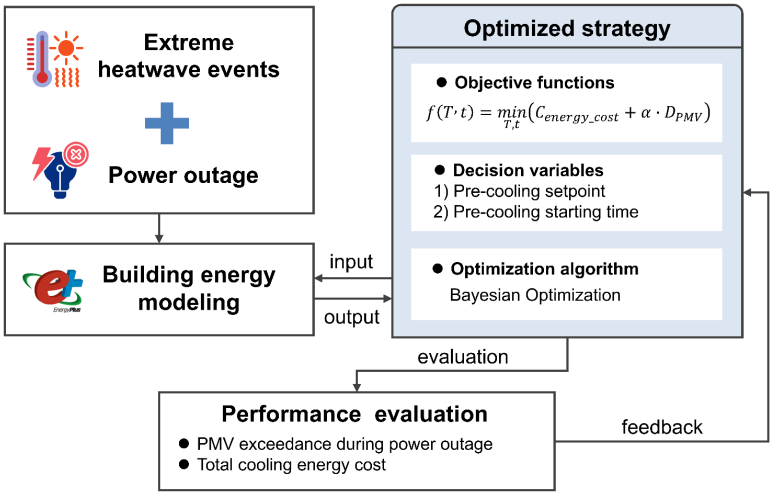

Figure 1. Overview of the methodology.

2.2. Building energy model

This study used a prototype high-rise residential building in Chengdu, China, where the climate zone is hot summer and cold winter. The building has a total floor area of 10,261 m^2 and includes 24 floors. The building geometry model is shown in Fig. 2. The case building consists of several types of zones, including residential bedrooms, living rooms, kitchen, and bathrooms. However, only the bedrooms and living rooms are equipped with air conditioners. In this study, a test living room located in the northwest corner of the standard floor was selected to evaluate the performance of the pre-cooling strategies. Solar radiation can enter into the room through exterior windows. The building envelope thermal properties were set based on the national standard of building energy efficiency of residential building released in 2010. The operating schedules of each household were determined based on the prototype building introduced in a previous study (Liu et al. 2024). Table 1 lists the key simulation parameters.

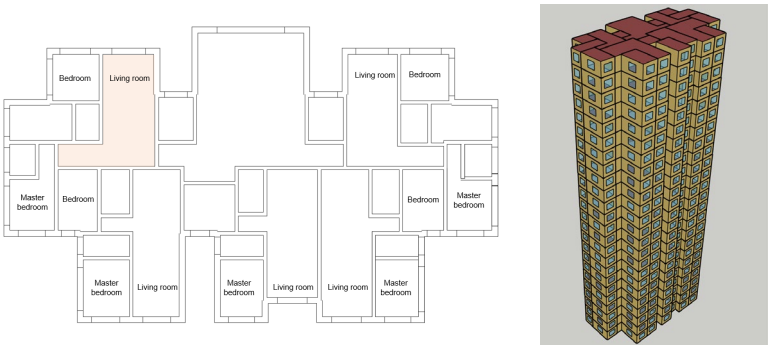

Figure 2. Building geometric model.

Table 1. Key parameters for building energy modeling.

Parameters	Value
Average window-to-wall ratio	0.27
U-value of exterior wall /W/(m^2·K)	0.8
U-factor exterior window /W/ (m^2·K)	3.0
U-value of roof /W/ (m^2·K)	1.0
Window SHGC	0.3

Lighting power density /W/m^2	5.0
Equipment power density /W/m^2	9.0
Air conditioner COP	2.75
Infiltration /ACH	0.6

The AC capacity for each conditioned room was autosized using the EnergyPlus model, as actual equipment capacity data was unavailable. Once the AC capacities were determined, pre-cooling strategies were implemented based on these capacities. Furthermore, the internal thermal mass was set by using *InternalMass* object and *ZoneCapacitanceMultiplier:ResearchSpecial* object recommended by a previous study (Chen et al. 2022). The setting of internal thermal mass was 196 kJ/(m^2·K), and the surface area was 2 times of the floor area. The Zone Capacitance Multiplier C_T was set as 2.

To calibrate the building energy model, the hourly indoor air temperature of a living room in Chengdu was recorded from October 15th to November 15th, during which the room operated in free-running mode. The root mean square error (RMSE) of the calibration was 0.8°C, which is below the required 1.5°C threshold (Donovan et al., 2019).

2.3. Pre-cooling strategies

The pre-cooling strategies were applied to a real five-day heatwave event that coincided with a power outage in 2022. The power outage during the heatwave occurred from 7:00 a.m. to 1:00 p.m., which was reported by the website of Sichuan Power Grid Corporation and sourced from its official website.

2.3.1. Optimized strategy

To optimize the pre-cooling strategy of a residential thermal zone during summer mornings, a multi-objective optimization problem was formulated aimed at minimizing energy costs and thermal discomfort. The decision variables include the pre-cooling setpoint temperature and the pre-cooling start time. Once pre-cooling began, the air conditioner operated continuously until the power outage began, maintaining a constant thermostat setpoint to maximize thermal storage. The optimization was implemented using a simulation-based approach integrated with EnergyPlus. The objective function is defined as:

$$f(T,t) = \min_{T,t}(C_{energy_cost} + \alpha \cdot D_{PMV}) \quad (1)$$

Where T and t are decision variables; T denotes the pre-cooling temperature setpoint (°C), constrained between 20.0°C and 26.0°C, with a resolution of 0.5°C; t represents the start time of pre-cooling, ranging from 1:00 a.m. to 7:00 a.m., with a resolution of 0.5 hour; C_{energy_cost} is the total electricity cost (in CNY) during the heatwave event, calculated based on hourly time-of-use (TOU) pricing; D_{PMV} is the accumulated thermal discomfort defined as the sum of the predicted mean vote (PMV) exceedances above 0.7 during 7:00 a.m. – 1:00 p.m.; α is a weighting factor to normalize the discomfort penalty relative to energy cost. In this study, α was set to 0.1, as the typical magnitude of D_{PMV} was approximately ten times greater than that of C_{energy_cost}. Regarding the cooling electricity cost, it is calculated based on the real-time TOU tariff in Chengdu during the summer of 2022. The off-peak rate of 0.239 CNY/kWh is applied from 23:00 to 7:00. A mid-peak rate of 0.497 CNY/kWh is used during 7:00–14:00 and 21:00–23:00. The on-peak period, corresponding to the highest rate of 0.754 CNY/kWh, occurs between 14:00 and 21:00.

Given the high computational cost of dynamic building energy simulations, Bayesian Optimization (BO) was adopted to efficiently search for the optimal decision variables. BO is well suited for problems involving expensive black-box functions, as it builds a probabilistic surrogate model of the objective function. This study employed BO algorithm using Gaussian Process regression as the surrogate model and the Expected Improvement acquisition function for sampling. In this study, BayesianOptimization Python package was utilized for implementing BO algorithm. The BO process was initialized with 20 randomly sampled points to fit the initial surrogate model. Subsequent iterations used the EI acquisition function to propose the next input combination, which was then evaluated by running an EnergyPlus simulation and calculating the corresponding objective value. This study conducted 100 iterations in total to determine the decision variables.

2.3.3. Benchmarking of the optimized precooling strategy

Two rule-based setpoint temperature scenarios were designed as benchmarks for evaluating the optimized precooling strategy, as illustrated in Fig. 3. Scenario 1 adopted a rule-based pre-cooling schedule in which the AC operated from 0:00 a.m. to 7:00 a.m. with a cooling setpoint of 24°C. Scenario 2 used a schedule from 3:00 a.m. to 7:00 a.m. with a setpoint of 20°C. The Baseline scenario represents a situation with no pre-cooling, where the AC operates from 1:00 p.m. to 9:00 p.m. with a cooling setpoint of 25°C. The optimized strategy identified through BO algorithm operated AC from 0:00 a.m. to 7:00 a.m., with a cooling setpoint of 21.5°C.

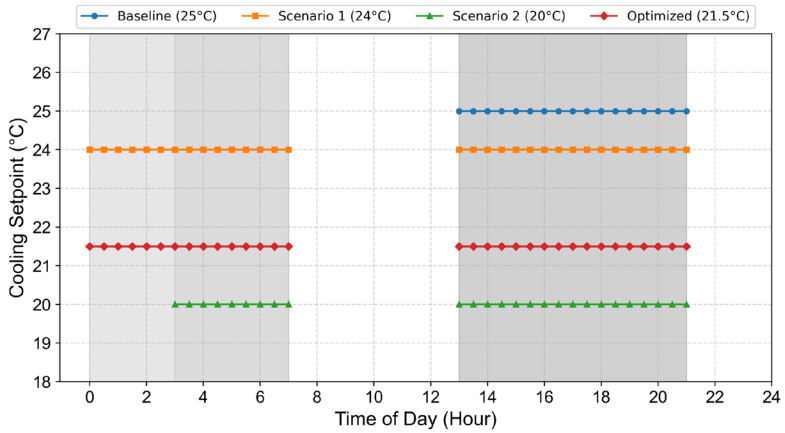

Figure 3. The schedules of four cooling strategies. The gray shade areas indicate the periods when AC is on, while unshaded areas indicate it is off.

3. RESULTS AND DISCUSSION

3.1. Indoor air temperature and overheating

Fig. 4 demonstrates the indoor air temperature profiles under four different cooling strategies during the heatwave. During each day, a power outage occurred from 7:00 a.m. to 1:00 p.m., during which no active cooling was available. As shown in the figure, the baseline strategy results in a significant temperature rise during the outage period, with peak indoor temperatures exceeding 28°C. In contrast, the optimized strategy successfully mitigates this temperature rise through effective the nighttime pre-cooling, maintaining indoor temperatures below 27°C during the outage periods. Scenario 1 and Scenario 2, which represent rule-based pre-cooling strategies, provide partial mitigation but are less effective than the optimized approach. These results indicate the potential of the optimized pre-cooling strategy in enhancing thermal resilience during heatwave coinciding with power outages.

It can also be noted that, although the pre-cooling setpoint for Scenario 2 was 20°C, the indoor air temperature did not consistently reach this setpoint and only approached approximately 22°C. This is mainly because the room air conditioning equipment was selected based on a set temperature of 25°C under typical meteorological conditions, without considering heatwave scenarios. As a result, during the heatwave events in this study, the capacity of the room air conditioning equipment was insufficient to quickly cool the living room.

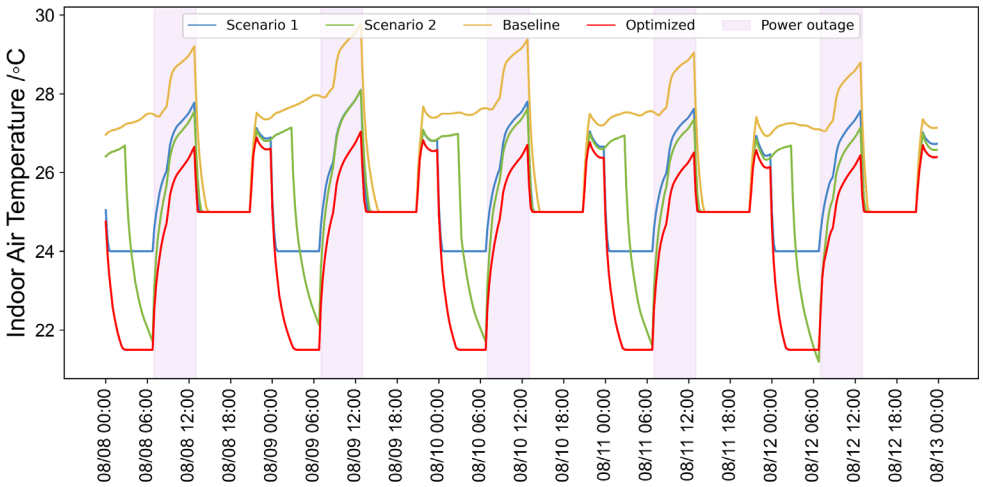

Figure 4. The indoor air temperature of the four cooling strategies during the heatwave.

Table 2 summarizes the accumulated thermal discomfort during the heatwave, measured as the total number of hours in which the predicted mean vote (PMV) exceeded the comfort threshold. The baseline scenario exhibits the highest level of discomfort, with 32 hours of exceedance. In contrast, Scenario 1 and Scenario 2 reduces the exceedance hours to 19 and 17, respectively, indicating an improvement in indoor thermal comfort. Notably, the optimized strategy demonstrates the best performance, reducing PMV exceedance to only 3 hours, which corresponds to an approximate 78% reduction compared to the rule-based strategies and 87% reduction compared to the baseline. This result highlights the effectiveness of the optimization-based approach in significantly enhancing indoor thermal conditions during extreme heat events.

Table 2. Indoor overheating risks of the four strategies.

Strategy	Hours of PMV exceedance
Scenario 1	19
Scenario 2	17
Baseline	32
Optimized	3

3.2. Energy consumption and cost

The hourly cooling electricity consumption profiles of the four cooling strategies was shown in Fig. 5, and the total electricity consumption and cost during the heatwave were also calculated and given in Table 3. In pre-cooling scenarios, two peaks in electricity consumption occur: one during the night and the other during the daytime. The night peak corresponds to the start of the pre-

cooling process, while the daytime peak marks the initiation of cooling after the power outage. The baseline strategy shows the highest cooling electricity during afternoon hours, primarily due to the accumulation of indoor heat gain. Scenario 1 and Scenario 2 achieve partial load shifting to earlier hours, thereby reducing peak demand during outage recovery periods. The optimized strategy has the lowest electricity consumption during the afternoon, indicating a more effective utilization of building thermal inertia.

Regarding cooling electricity consumption, although the baseline scenario exhibits the lowest total energy use of 21.8 kWh, its electricity cost is not the lowest due to the concentration of AC operating during more expensive mid- and peak-price periods. In contrast, the electricity cost of Scenario 1, 2 and optimized strategy are 14.9, 16.2 and 15.0CNY, respectively, indicating that the implementation of pre-cooling strategies does not lead to a significant increase in cooling electricity expenses. This is because the optimized strategy takes advantage of lower TOU electricity prices by shifting the cooling load to nighttime hours.

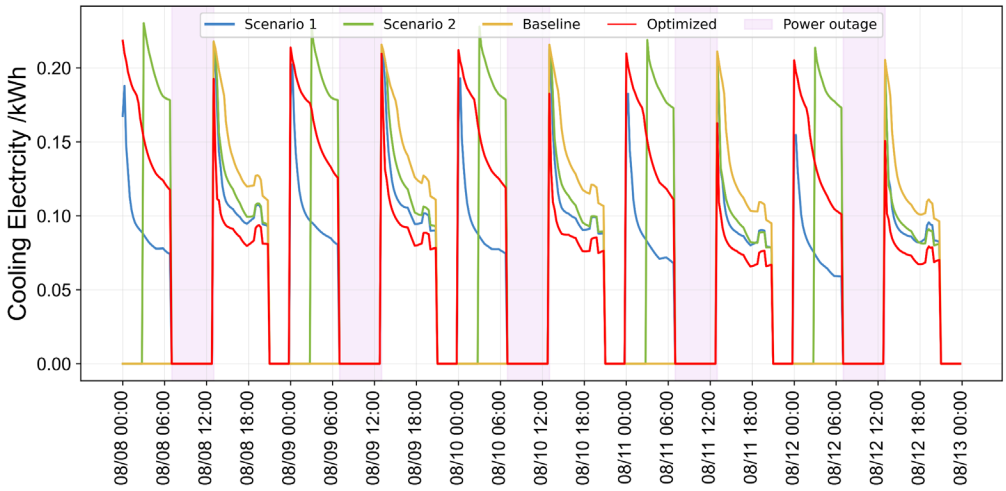

Figure 5. The cooling consumption of the four cooling scenarios during the heatwave.

Table 3. Electricity consumption and cost of the four strategies.

Scenario	Electricity consumption (kWh)	Electricity cost (CNY)
Scenario 1	30.0	14.9
Scenario 2	33.2	16.2
Baseline	21.8	15.4
Optimized	35.4	15.0

4. CONCLUSIONS

This study evaluated the performance of the optimized pre-cooling strategy developed by Bayesian Optimization algorithm, focusing on their impacts on indoor thermal comfort, electricity consumption, and cost. Two rule-based pre-cooling strategies and one baseline strategy with no pre-cooling were used as benchmarks. A prototype residential building in Chengdu, under a real five-day heatwave coincided with a power outage, was selected as a case study. Results showed

that the optimized strategy significantly outperformed the other cooling strategies, reducing PMV exceedance hours by approximately 78% compared to the rule-based precooling strategies and by 87% compared to the baseline, without increasing the energy cost burden. Although its total electricity consumption was higher than that of the baseline and rule-based strategies, the optimized strategy achieved comparable or even lower electricity costs by shifting cooling load to nighttime hours. These findings highlight the potential of the optimized pre-cooling strategy in improving the thermal resilience of residential cooling systems under extreme heatwaves.
Future work will explore the integration of passive design strategies with pre-cooling to further enhance and evaluate its potential for mitigating indoor overheating.

REFERENCES

Chen, Yongbao, Peng Xu, Zhe Chen, Hongxin Wang, Huajing Sha, Ying Ji, Yongming Zhang, Qiang Dou, and Sheng Wang. 2020. "Experimental Investigation of Demand Response Potential of Buildings: Combined Passive Thermal Mass and Active Storage." *Applied Energy* 280:115956. https://doi.org/https://doi.org/10.1016/j.apenergy.2020.115956.

Chen, Zhelun, Jin Wen, Steven T Bushby, L James Lo, Zheng O Neill, W Vance Payne, Amanda Pertzborn, et al. 2022. "An Analysis of the Hybrid Internal Mass Modeling Approach in EnergyPlus." *12th ESim Building Simulation Conference, Ottawa, Canada*.

ECMWF. 2024. "Introduction of ERA5 Dataset." European Centre for Medium-Range Weather Forecasts. 2024. https://www.ecmwf.int/en/forecasts/dataset/ecmwf-reanalysis-v5.

Liang, Wenjun, Chenhao Li, Yifan Wu, Meng Zou, Xian Zhu, Wenjie Dong, John C Moore, et al. 2024. "Anthropogenic Forcing and Subtropical Anticyclonic Drivers of the August 2022 Heatwave in China." *Weather and Climate Extremes* 45:100707. https://doi.org/https://doi.org/10.1016/j.wace.2024.100707.

Liu, Xue, Zhaoru Liu, Yi Wu, Shan Hu, Fan Bu, Jingjing An, Xin Zhou, and Da Yan. 2024. "A Novel Quantitative Method of Heatwave Classification for Building Resilience Analysis." *Sustainable Cities and Society* 112:105603. https://doi.org/https://doi.org/10.1016/j.scs.2024.105603.

Luber, George, and Michael McGeehin. 2008. "Climate Change and Extreme Heat Events." *American Journal of Preventive Medicine* 35 (5): 429–35. https://doi.org/https://doi.org/10.1016/j.amepre.2008.08.021.

O' Donovan, Adam, Paul D O' Sullivan, and Michael D Murphy. 2019. "Predicting Air Temperatures in a Naturally Ventilated Nearly Zero Energy Building: Calibration, Validation, Analysis and Approaches." *Applied Energy* 250:991–1010. https://doi.org/https://doi.org/10.1016/j.apenergy.2019.04.082.

Seneviratne, S.I., X. Zhang, M. Adnan, W. Badi, C. Dereczynski, A. Di Luca, S. Ghosh, et al. 2021. *Weather and Climate Extreme Events in a Changing Climate, In Climate Change 2021: The Physical Science Basis*. Cambridge University Press. https://www.ipcc.ch/report/ar6/wg1/ch apter/chapter-11/.

Turner, W J N, I S Walker, and J Roux. 2015. "Peak Load Reductions: Electric Load Shifting with Mechanical Pre-Cooling of Residential Buildings with Low Thermal Mass." *Energy* 82:1057–67. https://doi.org/https://doi.org/10.1016/j.energy.2015.02.011.

Wang, Jiewei, Ziqing Wei, Yikang Zhu, Chunyuan Zheng, Bin Li, and Xiaoqiang Zhai. 2023. "Demand Response via Optimal Pre-Cooling Combined with Temperature Reset Strategy for Air Conditioning System: A Case Study of Office Building." *Energy* 282:128751. https://doi.org/https://doi.org/10.1016/j.energy.2023.128751.

Yin, Rongxin, Peng Xu, Mary Ann Piette, and Sila Kiliccote. 2010. "Study on Auto-DR and Pre-Cooling of Commercial Buildings with Thermal Mass in California." *Energy and Buildings* 42 (7): 967–75. https://doi.org/https://doi.org/10.1016/j.enbuild.2010.01.008.

Zeng, Zhaoyun, Wanni Zhang, Kaiyu Sun, Max Wei, and Tianzhen Hong. 2022. "Investigation of Pre-Cooling as a Recommended Measure to Improve Residential Buildings' Thermal Resilience during Heat Waves." *Building and Environment* 210:108694. https://doi.org/https://doi.org/10.1016/j.buildenv.2021.108694.

ACKNOWLEDGEMENTS

This research was supported by National Natural Science Foundation of China (Grant Number: 52408132 and 52308100), Fundamental Research Funds for the Central Universities (Grant Number: 2682024CX072 and 2682024CX071).

6th International Conference on Building Energy and Environment
Eindhoven University of Technology, The Netherlands
6 - 10 July 2025

URBAN GENERATION: optimising the design of NBS for climate change adaptation

Francesca Mosca [1], Katia Perini [2]

[1]*University of Genoa, Genoa, Italy, francesca.mosca@edu.unige.it*
[1]*University of Genoa, Genoa, Italy, katia.perini@unige.it*

SUMMARY
Urban areas are facing different challenges related to the increase in population, land use and greenhouse gases emissions. The subsequent environmental degradation requires the implementation of a new set of planning and design strategies to improve liveability and reduce the vulnerability of cities. Nature-based Solutions (NBS) constitute one of the most promising strategies among the regenerative tools currently available. The occurrence of the urban heat island effect is one of the most relevant challenges, due to the direct impact on ecosystems and on human health. NBS can play a key role in improving urban microclimatic conditions due to their capacity to provide shade and the evapotranspiration processes, driven by the radiative properties of plants. The URBAN GENERATION project aims to develop a computational design approach to optimise the definition of mitigation and adaptation to climate change, particularly concerning the reduction of the urban heat island effect.

Keywords: climate adaptation, nature-based solutions, design optimisation.

EXTENDED ABSTRACT

Introduction

The urban environment is characterized by several challenges due to anthropic activities, on top of which climate change is widely recognized as one of the most critical aspects (Rosenzweig et al., 2018). In addition, the effects of climate change are constantly increasing over time, resulting in extreme events and related high vulnerability for urban infrastructures and citizens (Füssel et al., 2017). Urban areas main challenges include vulnerability to climate change effects and the increase in the frequency and entity of extreme events, as well as reduced ecosystem health and related ecosystem services production, and the environmental harm they themselves cause (Thomas et al., 2019). The urban heat island effect and the increase in global temperatures is particularly relevant, due to the consequent increase in energy consumption for cooling and the heat-related risks for human health (Jain et al., 2022).
Given the relevance of the topic, design and planning solutions should focus on the implementation of adaptation strategies to improve the liveability of urban areas. Nature-based solutions (NBS), defined as solutions inspired by nature and its processes (Castellar et al., 2021), play a crucial role in climate change adaptation and enhancing the overall environmental quality of densely populated urban areas (Mosca et al., 2023). In order to ensure the effectiveness of NBS, it is particularly important to measure and quantify their site-specific performances (Kamari et al., 2021). Different methods can be applied, such as field measurement, however, computational tools constitute one of the most promising methods, due to the potential application at early design stages and without

the need for real mock-ups, allowing the quantification of the performance before the construction of the design solution (Peters & Peters, 2018).
Several simulation and computational tools have been developed during the last years to allow designers to assess the performances of buildings and NBS in terms of energy consumption but also in terms of impact on microclimate (Manso et al., 2021; Perini et al., 2022). However, a systematic approach to understand and evaluate the synergies and trade-offs between the urban context and different design solutions in terms of climate change mitigation and adaptation is still missing.
The URBAN GENERATION project aims at developing a comprehensive design approach to include both mitigation and adaptation strategies into urban and building design processes to optimise the performance of different design solutions.
Focusing on the support of NBS in achieving climate change adaptation in terms of microclimate regulation, an operative methodology has been defined, to provide designers and policy makers knowledge and tools to optimise the performance of their solutions (Perini & Mosca, 2024).

Methodology
In order to develop and test the design approach, we simulate a wide range of NBS in different urban contexts/scales, being able to quantify the effects of vegetation on microclimate to improve thermal comfort (adaptation action) and, consequently, reduce the energy consumption of buildings (mitigation action). Firstly, we focus on urban canyon to generalize the results; it is defined as a theoretical flat site, with two standard buildings and an empty area in between. Secondly, a set of NBS well-known for their microclimatic performance are selected and modelled (Fig. 1): in particular, groups of trees with different crown shapes (spherical, conical, vase, columnar and vertical oval crowns) and dimensional order (1st class height >16m, 2nd class height 10m<h<16m, 3rd class height h<10m). Specifically, trees have been selected as the most relevant land-media NBS in terms of microclimate regulation according to literature (Mosca et al., 2025).

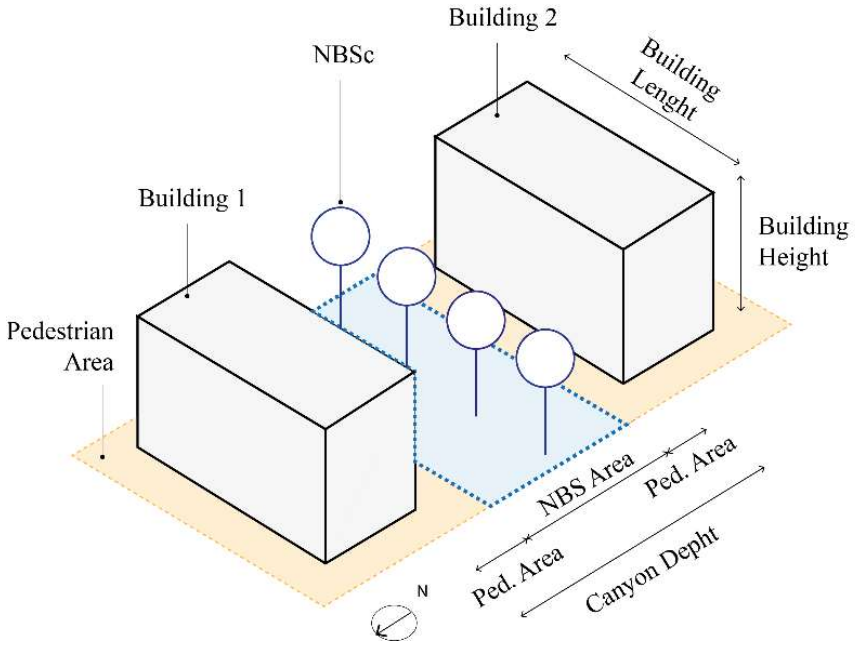

Figure 1. Definition of Urban Canyon and NBS parameters for the simulations.

By varying the geometrical parameters and NBS types, we can identify correlations between NBS performances and urban canyon configuration. To do so, the methodology includes an optimization process running on a wide range of simulations to support the design process focused on microclimate regulation. The workflow takes into account also the role of NBS cooling capacity in reducing energy consumption for air conditioning.

Results and future developments

Currently, 16 configurations of NBS type and trees typologies are simulated for two case studies cities in Italy, considering different geographical and climatic conditions (Genoa and Turin). The NBS and urban canyon configurations simulated are the same for both locations, while latitude and weather parameters vary. Fig. 2 shows the operative workflow and the related application on one of the configurations defined. The results from each package of simulations are exported as .csv files, collecting output data related to each configuration. In particular, the most relevant parameters are related to the NBS features (e.g. type and number of trees) and microclimatic conditions (e.g. Mean Radiant Temperature and percentage of shading provided on the urban canyon). Based on the results, a database made of the output data is build and used for a multi-objective optimization process, which aims at identifying the most performing NBS configuration in relation to the urban canyon geometry.

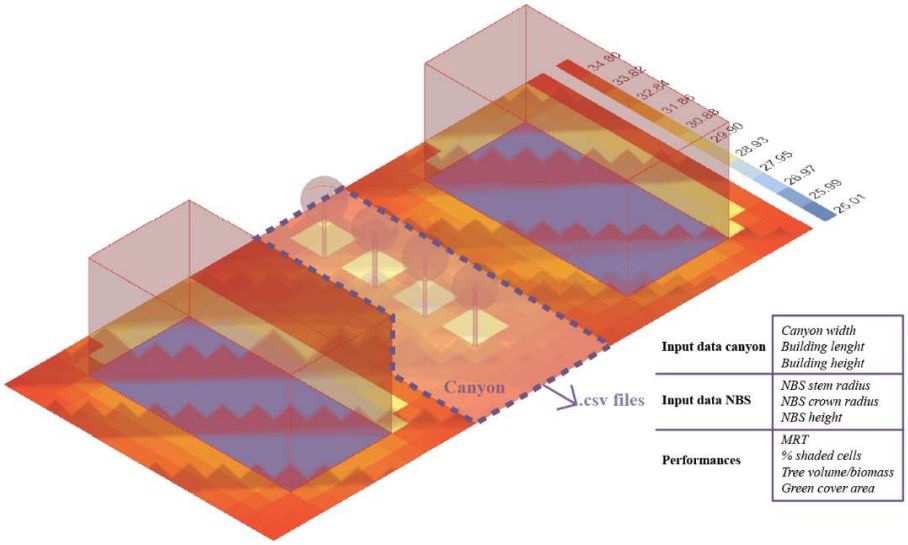

Figure 2. Example of simulation output and related data for the optimization.

The potentials and limitations of the selected tool has been widely deepen in literature, however, the main aim of this experiment is to reduce the need for CFD simulations at early design stages, allowing the definition of the best-performing NBS configuration depending on geographical and climatic conditions. Future developments include the application of the methodology to more sites/cities to acquire data on the microclimatic performances of NBS in relation to different geographical and climatic conditions. Based on the results from this study, a set of correlations

between urban conditions and NBS can be derived and generalized, through the use of machine-learning methodologies (linear regression, random forest). This approach will allow informing the urban design process without the need to run specific microclimatic simulations, supporting urban policies for climate change adaptation.

ACKNOWLEDGEMENTS

The presented research is part of the URBAN GENERATION project (PRIN PNRR 2022 program - CUP D53D23020090001), funded by the Italian Research Ministry. The project consortium consists of researchers from University of Genoa, Polytechnic School of Turin and the CIMA Research Foundation.

REFERENCES

Aronson, M. F., Lepczyk, C. A., Evans, K. L., Goddard, M. A., Lerman, S. B., MacIvor, J. S., Nilon, C. H., & Vargo, T. (2017). Biodiversity in the city: Key challenges for urban green space management. Frontiers in Ecology and the Environment, 15(4), 189–196. https://doi.org/10.1002/fee.1480

Castellar, J. A. C., Popartan, L. A., Pueyo-Ros, J., Atanasova, N., Langergraber, G., Säumel, I., Corominas, L., Comas, J., & Acuña, V. (2021). Nature-based solutions in the urban context: Terminology, classification and scoring for urban challenges and ecosystem services. Science of The Total Environment, 779, 146237. https://doi.org/10.1016/j.scitotenv.2021.146237

Füssel, H.-M., Kristensen, P., Jol, André., Marx, A., & Hildén, M. (2017). Climate change, impacts and vulnerability in Europe 2016: An indicator-based report. Publications Office of the European Union.

Jain, R., Brar, T. S., & Kamal, M. A. (2022). Environmental Impact and Mitigation Benefits of Urban Heat Island Effect: A Systematic Review. Architecture Engineering and Science, 3(4), 230. https://doi.org/10.32629/aes.v3i3.1008

Kamari, A., Jensen, S. R., Petersen, S., & Kirkegaard, P. H. (2021). SUSTAINABILITY KEY PERFORMANCE INDICATORS' (KPIs) ASSESSMENT AND VISUALIZATION AIMED AT ARCHITECTS IN (EARLY) RENOVATION DESIGN PROCESSES. Nordic Journal of Architectural Research, 33(2), 41–80. Scopus.

Manso, M., Teotónio, I., Silva, C. M., & Cruz, C. O. (2021). Green roof and green wall benefits and costs: A review of the quantitative evidence. Renewable and Sustainable Energy Reviews, 135, 110111. https://doi.org/10.1016/j.rser.2020.110111

Mosca, F., Canepa, M., & Perini, K. (2023). Strategies for adaptation to and mitigation of climate change: Key performance indicators to assess nature-based solutions performances. Urban Climate, 49, 101580. https://doi.org/10.1016/j.uclim.2023.101580

Mosca, F., Calbi, M., Roccotiello, E., & Perini, K. (2025). A computational approach to assess the effects of ecological building envelopes on outdoor thermal comfort. Sustainable Cities and Society, 106170. https://doi.org/10.1016/j.scs.2025.106170

Perini, K., Calise, C., Castellari, P., & Roccotiello, E. (2022). Microclimatic and Environmental Improvement in a Mediterranean City through the Regeneration of an Area with Nature-Based Solutions: A Case Study. Sustainability, 14(10), 5847. https://doi.org/10.3390/su14105847

Perini, K., & Mosca, F. (2024). A Computational Design Approach for Climate Change Adaptation and UHI Mitigation. In F. Calabrò, L. Madureira, F. C. Morabito, & M. J. Piñeira Mantiñán (Eds.), Networks, Markets & People (Vol. 1189, pp. 98–105). Springer Nature Switzerland. https://doi.org/10.1007/978-3-031-74723-6_8

Peters, B., & Peters, T. (2018). Computing the environment: Digital design tools for simulation and visualisation of sustainable architecture. Wiley.

Rosenzweig, C., Solecki, W. D., Romero-Lankao, P., Mehrotra, S., Dhakal, S., & Ibrahim, S. A. (2018). Climate Change and Cities: Second Assessment Report of the Urban Climate Change Research Network. Cambridge University Press.

Thomas, K., Hardy, R. D., Lazrus, H., Mendez, M., Orlove, B., Rivera-Collazo, I., Roberts, J. T., Rockman, M., Warner, B. P., & Winthrop, R. (2019). Explaining differential vulnerability to climate change: A social science review. WIREs Climate Change, 10(2), e565. https://doi.org/10.1002/wcc.565

6th International Conference on Building Energy and Environment
Eindhoven University of Technology, The Netherlands
6 - 10 July 2025

Numerical risk assessment of first and second-hand exposure to group 1 hazardous chemicals generated by e-cigarette smoking using coupled CFD-PBPK model

Kazuki Kuga [1], Kazuhide Ito [2]

[1]*Kyushu University, Kasuga, Japan, kuga@kyudai.jp*
[2]*Kyushu University, Kasuga, Japan, ito@kyudai.jp*

SUMMARY
Electronic cigarettes (e-cigarettes) are considered less harmful than conventional cigarettes due to the absence of combustion; however, harmful chemical substances are generated during vaporization. This study employed a numerical airway model replicating the geometry from the nasal and oral cavities to the 13th bronchial bifurcation, integrating computational fluid dynamics (CFD) with a physiologically based pharmacokinetic (PBPK) model. The study quantitatively analyzed first-hand exposure during inhalation, the dispersion of exhaled chemicals in indoor environments, and second-hand exposure to non-smokers. Formaldehyde, acetaldehyde, acrolein, benzene, toluene, glycerol, and nicotine were examined. The findings revealed varying deposition rates in the upper airways, with nasal exhalation increasing absorption by 4-9%. Second-hand exposure was affected by spatial positioning and airflow patterns, emphasizing the need for further assessment of e-cigarette-related health risks.
Keywords: CFD, PBPK, e-cigarette, numerical airway model.

1. INTRODUCTION

Electronic cigarettes (e-cigarettes) have gained significant attention worldwide due to the misconception that they are safe for human health in terms of first-, second-, and third-hand exposure to smoking. E-cigarettes are portable devices designed to vaporize "e-liquid," which contains various chemicals. While they do not rely on tobacco combustion, they are often perceived as less harmful than traditional smoking. However, despite the non-combustion process, the vapor they produce can still contain pollutants resulting from chemical reactions in the e-liquid. Beyond the direct inhalation associated with first-hand smoking, the exhaled vapor from e-cigarette users introduces a new source of pollutants that can impact indoor air quality. As a result, developing a numerical prediction method to assess the health risks of e-cigarette vapor exposure in both the human respiratory tract (first-hand exposure) and indoor environments (second-hand exposure) is critical. This study aims to provide a qualitative and quantitative evaluation of e-cigarette vapor exposure in the human respiratory tract using coupled CFD–PBPK analysis.

2. METHODOLOGY

2.1. Numerical Airway model and Room model

A numerical airway model was developed based on the CT data of a 30-year-old male, accurately replicating the geometry from the nasal and oral cavities to the 13th bronchial bifurcation (Corley et al., 2021, Kabilan et al., 2016). The model consisted of 273 bronchial outlets, ensuring detailed anatomical representation. A high-resolution mesh was created to maintain wall unit y+ values

below 1, optimizing accuracy in CFD simulations. To simulate e-cigarette inhalation, a circular opening with 8.0 mm diameter was placed at the mouth opening. The model enabled the analysis of inhaled pollutant distribution and deposition dynamics, providing a foundation for integrating the PBPK model. A scenario involving secondary exposure was simulated by integrating the numerical airway model into a simplified indoor environment. This indoor space was modeled as a room with a volume of 27 m^3, where two numerical human models (Computational Simulated Persons, CSPs) were positioned facing each other to replicate a typical face-to-face interaction scenario. This setup allowed for the evaluation of pollutant transport from the initial inhalation of e-cigarette vapor through exhalation and dispersion within the indoor space and finally to the secondary exposure of the non-smoking individual. The room was designed with displacement ventilation, featuring two openings: an inlet at the upper front wall and an outlet at the lower rear wall, both measuring 0.3 m × 0.3 m.

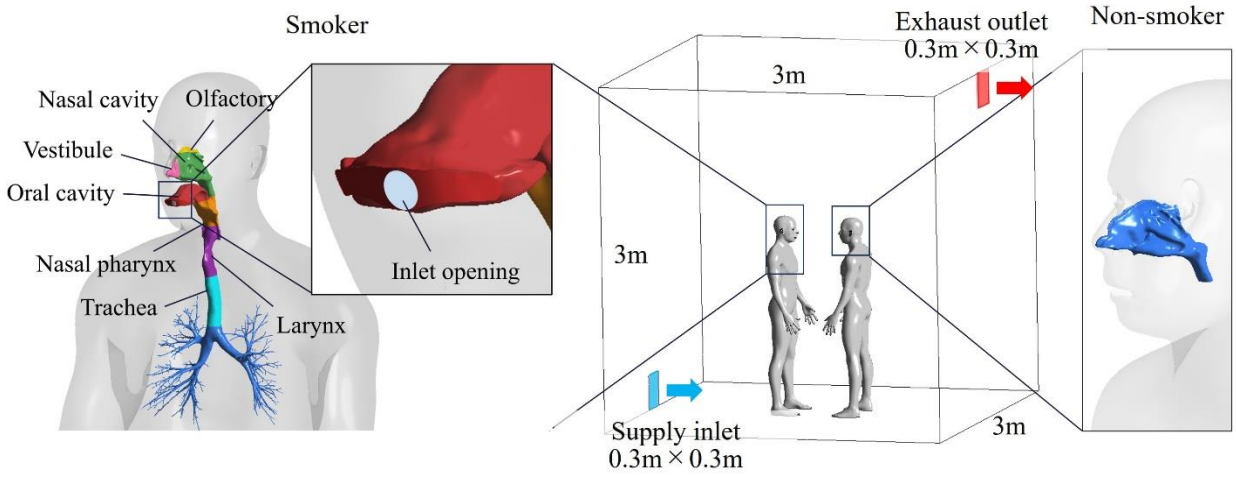

Figure 1. Numerical airway model and room model

2.2. Coupled CFD-PBPK model

The PBPK model was incorporated to simulate the diffusion of inhaled pollutants across the mucus layer, epithelial cells, and subepithelial tissues. Seven key pollutants—formaldehyde, acetaldehyde, acrolein, benzene, toluene, glycerol, and nicotine—were analyzed. The model accounted for chemical absorption through airway walls, enhancing the understanding of pollutant retention and translocation within respiratory tissues. The PBPK model was integrated into the airway geometry, allowing coupled CFD-PBPK simulations to evaluate pollutant behavior under different inhalation and exhalation conditions. The concept and governing equations of the coupled CFD-PBPK analyses are shown in Figure 2.

2.3. Setup for Numerical Simulation of First and Second-hand Exposure

Primary exposure analysis was conducted using only the numerical airway model to simulate the inhalation and exhalation of e-cigarette aerosols. The inhaled concentrations of the selected pollutants were set as follows: formaldehyde (0.70 μg/mL), acetaldehyde (0.22 μg/mL), acrolein (0.02 μg/mL), benzene (1.6 × 10 μg/mL), toluene (3.1 × 10 μg/mL), glycerol (33.2 μg/mL), and nicotine (0.27 μg/mL). During exhalation, it was assumed that the air returning from the lungs to the bronchial region was completely free of pollutants. The CFD-PBPK model was applied to the

airway walls, and simulations were performed for two exhalation methods: oral exhalation and nasal exhalation. The spatial distribution of pollutant concentrations within the airway during exhalation was analyzed accordingly. For the second-hand exposure analysis in the room, fresh air was supplied at a velocity of 0.05 m/s. To account for human thermal effects, each CSP was equipped with Fanger's thermo-regulation model. Furthermore, PBPK models were applied not only to the airway walls but also to the skin and ocular surfaces of the CSPs to evaluate the absorption of pollutants through these additional exposure pathways. Simultaneous simulations of inhalation, dermal, and ocular exposure were performed to provide a comprehensive assessment of the diffusion and absorption dynamics of e-cigarette vapor in the room.

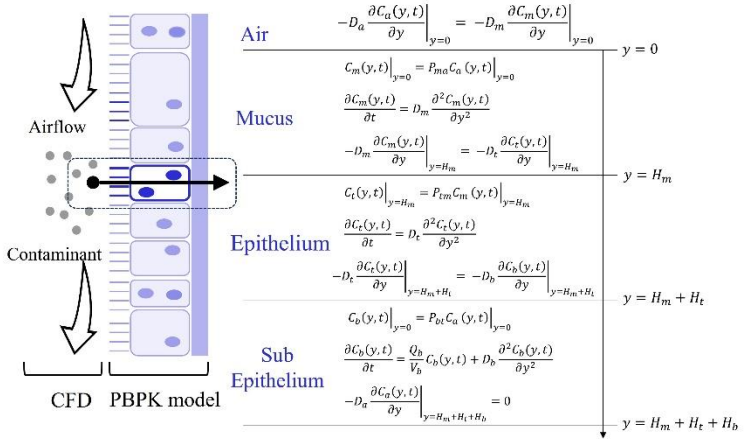

Figure 2. Concept of coupled CFD-PBPK model

3. RESULTS AND DISCUSSIONS

Fig. 3a shows the normalized concentration distributions of formaldehyde, nicotine, and acrolein within the airway model at the end of inhalation. The concentration distributions were found to be heterogeneous, with noticeable differences in deposition near the oral cavity and pharyngeal region depending on the pollutant. This indicates that each pollutant exhibited distinct upper airway distributions due to variations in adsorption along the mucosal surfaces. The absorption rates of all pollutants into the airway walls, calculated as the ratio of absorbed mass to inhaled mass, are shown in Fig. 3b. The results reveal that nasal exhalation led to an increase in absorption rates by approximately 4–9% for all pollutants compared to oral exhalation. This increase is attributed to the elevated absorption flux into the nasal mucosal surfaces during exhalation, which enhances retention within the nasal cavity. The initial indoor airflow field in the exposure risk analysis incorporating the CSPs is shown in Fig. 3c. Since displacement ventilation was assumed in this analysis, thermal plumes formed around the human body. This thermal environment significantly influenced the transport and dispersion of exhaled pollutants in the indoor space. The temporal variation of formaldehyde concentration exhaled by the smoker is illustrated in Fig. 3d. The exhaled pollutants were diluted in the ambient air and reached the chest area of the facing nonsmoker within approximately 2.5 seconds. Subsequently, the pollutants were lifted into the breathing zone of the nonsmoker due to the thermal plume generated by body heat. Previous studies on secondary exposure have often assumed that pollutants exhaled from the oral cavity travel directly from the smoker's mouth to the nonsmoker. However, in this study, by incorporating realistic oral cavity geometry and conducting a continuous analysis from primary to secondary exposure, it was observed that the exhaled pollutants were initially transported diagonally downward due to the specific shape of the oral cavity.

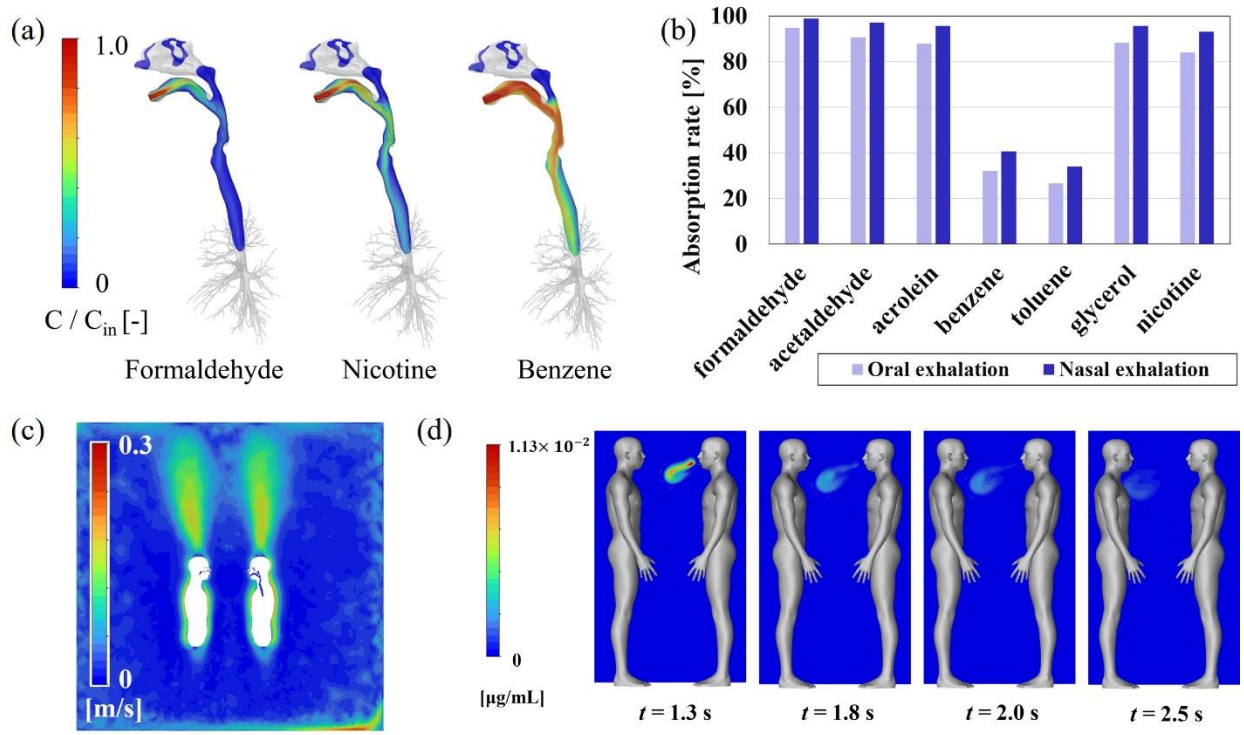

Figure 3. (a) Normalized concentration distribution of pollutants within the numerical airway model at the end of inhalation, (b) the absorption rates of all pollutants into the airway walls, (c) the initial indoor airflow field, and (d) the temporal variation of formaldehyde concentration exhaled by the smoker

4. CONCLUSIONS

This study integrated CFD and PBPK modeling to quantitatively assess e-cigarette-related exposure risks. First-hand exposure analysis demonstrated that pollutant deposition varies based on chemical properties and inhalation pathways. Second-hand exposure assessment confirmed that pollutant dispersion and absorption depend on spatial arrangement, ventilation, and exhalation methods. Comparisons with previous studies (Kuga et al., 2020) suggest that inhalation exposure among non-smokers is significantly influenced by airflow patterns and the relative positioning of smokers. These findings contribute to understanding the health risks associated with e-cigarette use and emphasize the need for further research on exposure mitigation strategies.

ACKNOWLEDGEMENTS

This study was partially funded by Japan Science and Technology (JST), CREST Japan (JP 20356547), FOREST program from JST, Japan (JPMJFR225R) and JSPS KAKENHI (JP 24KK0094, JP 22H00237, JP 22K18300, JP 22K14371), and MEXT as "Program for Promoting Researches on the Supercomputer Fugaku" (JPMXP1020210316).

REFERENCES

Corley et al. New approach methodology for assessing inhalation risks of a contact respiratory cytotoxicant: Computational fluid dynamics-based aerosol dosimetry modeling for cross-species and in vitro comparisons. Toxicological Sciences. 2021;182(2), 243-259.

Kabilan et al. Computational fluid dynamics modeling of Bacillus anthracis spore deposition in rabbit and human respiratory airways. Journal of Aerosol Science. 2016; 99, 64-77.

Kuga et al, A numerical investigation of the potential effects of e-cigarette smoking on local tissue dosimetry and the deterioration of indoor air quality, Indoor Air. 2020;30:1018–1038.

6th International Conference on Building Energy and Environment
Eindhoven University of Technology, The Netherlands
6 - 10 July 2025

Objective measurement of pedestrian thermal comfort within footbridges in Hong Kong during hot weather

Lan Chen [1], Cheuk Ming Mak [1]

[1]*Department of Building Environment and Energy Engineering, The Hong Kong Polytechnic University, Hong Kong, China, landy.chen@connect.polyu.hk*
[1]*Department of Building Environment and Energy Engineering, The Hong Kong Polytechnic University, Hong Kong, China, cheuk-ming.mak@polyu.edu.hk*

SUMMARY

To ease traffic congestion and improve walkability, densely populated cities have put more emphasis on developing footbridge systems. Given the shortage of thermal comfort research on footbridges, this study measured the daytime thermal environments and evaluated pedestrian thermal comfort using the physiological equivalent temperature (PET) across nine urban footbridges in Hong Kong on very hot days. Compared to open footbridges, covered footbridges showed more stable and cooler microclimates, averagely decreasing T_a, T_g, and T_{mrt} by 1.2 ℃, 7.2 ℃, and 16.7 ℃, respectively. Pedestrians walking on covered footbridges (mean PET = 34.8 ℃) generally feel "slightly warm" in contrast to "hot" at open footbridges (mean PET = 44.7 ℃). Simultaneous comparisons further revealed that the maximum PET reduction reached 11.4 ℃ under the glass cover, extending to 16.4 ℃ under the metal cover. This study highlights the significance of overhead covers in improving thermal comfort on footbridges during hot weather.

Keywords: Outdoor thermal comfort, Pedestrian bridge, Elevated walkway, Walkable city

1. INTRODUCTION

High traffic volume has been a common scene across global cities. The resulting traffic congestion and safety risks are impeding sustainable urban development. One of the effective strategies for tackling such traffic problems is to grade separate pedestrians from vehicles by constructing flyovers, footbridges, and subways. Unlike flyovers, footbridges are designed solely for pedestrians, allowing them to cross the roads without regard to vehicles. This can considerably reduce traffic accidents, improve traffic mobility, and enhance road safety (Highways Department, 2024). In addition to the traditional perpendicular form, footbridges can be parallel to the street with functions that give way for vehicular traffic and decrease ground pedestrian flow. Beyond traffic-related functions, urban planners are giving footbridges more landscaping, recreational, and commercial value (Rotmeyer, 2006). Given the aforementioned benefits, footbridges prevail increasingly in densely populated cities.

Walkability is widely perceived as a key component of sustainable urban development because a walkable neighborhood is lively, environmentally friendly, equitable, exercise-inducing, and conducive to social interaction (Forsyth, 2015; Kim et al., 2024). Consequently, walkability is gaining prominence in high-density cities (Moreno et al., 2021). The widespread of footbridges caters to the planning vision of walkable cities. Although the exact definition of walkability is still debatable, walking safety and comfort are considered essential factors. Pedestrians are more likely

to incorporate walking into their daily routines when they feel the walking environment is comfortable. Evidence shows that thermal comfort has a crucial effect on pedestrian comfort and walking preference (Lee et al., 2020). However, few studies have considered the role of thermal comfort on footbridges' walkability.

In summer, footbridges can either be thermally uncomfortable or become locally cooling hubs (Chen et al., 2024; Yang et al., 2016), which leads to a contrary walking experience. Considering the correlation between walkability and thermal conditions, it is worth investigating thermal comfort on footbridges and exploring influential factors, especially for hot and humid cities prone to strong heat stress. Therefore, the objectives of this study are to measure the thermal environment on footbridges, evaluate pedestrian thermal comfort using a well-recognized thermal comfort index, and analyze the effects of cover type.

2. METHODS

Hong Kong is a typically densely populated city, with a land population density of 6,910 people per km^2 in mid-2023 (GovHK, 2024). By June 2024, it has constructed over 1,000 footbridges on grounds of road safety and pedestrian walkability (Highways Department, 2024). Influenced by the subtropical monsoon, Hong Kong features prolonged hot and humid summers (*Cwa* in Köppen-Geiger climate classification). The average daily maximum temperature (T_{max}) exceeds 28 ℃ during May and October. Nine footbridges with different overhead covers, located in dense districts (> 40,000 people per km^2), were selected for pedestrian thermal comfort measurement. The measuring sites are named according to their covered conditions: uncovered or open (O1, O2, and O3), concrete-covered (C1 and C2), glass-covered (G1, G2, and G3), and metal-covered (M1 and M2). Note that O1 and G2 are located on two sides of a footbridge. Photos of measuring footbridges are presented in Figure 1.

Figure 1. Photos of measuring footbridges.

During the measurements, air temperature (T_a), relative humidity (RH), and wind speed (v) were measured using the mobile weather station (model: HY-WDS9, accuracy: ±0.5 ℃, ±3%, ±2%),

while globe temperature was collected by the black globe thermometer (model: WBGT-2010SD, accuracy: ±0.6 ℃). The equipment was fixed on a solid tripod, with the highest ultrasonic sensors 1.5 m above the footbridge's floor. The Observatory will issue a "very hot" weather warning to remind the public to take precautions against heat stroke when T_a is predicted to reach 33 ℃ or above. Given the health risks under such hot conditions, it is crucial to investigate pedestrian thermal comfort on footbridges. So, measurements were conducted during the daytime on eight very hot days, generally lasting seven to eight hours between 9:30 and 17:30. Table 1 shows the official weather information on measuring days (Hong Kong Observatory, n.d.-b), during which the daily average T_a and RH were around 30 ℃ and 76%, respectively.

Table 1. Weather conditions on measuring days provided by the HKO (T_{min} is the daily minimum temperature).

Date (dd/mm)	Site	T_{max}−T_{min} (℃)	T_a (℃)	RH (%)	v (m/s)	Sunlight (h)	Global solar radiation (MJ/m^2)
13/July	G1	33.8−27.7	30.7	61−92	2.22	8.9	22.58
24/Aug	C2	34.3−28.1	30.2	57−93	2.33	11.0	24.94
25/Aug	G2/O1	33.7−28.0	30.1	57−87	2.36	9.0	23.41
26/Aug	M1/O2	33.8−28.4	30.3	56−88	2.58	11.2	25.98
27/Aug	O3	34.1−28.5	30.6	57−86	2.61	11.1	25.08
3/Sep	M2	33.5−25.5	30.2	67−94	1.75	8.3	17.86
12/Sep	C1	32.2−27.7	29.8	65−90	2.06	9.8	21.77
19-Sep	G3	33.6−28.7	30.2	65−84	3.44	9.4	20.41

This study adopted physiological equivalent temperature (PET) to evaluate pedestrian thermal comfort because of its high recognition and wide application in outdoor thermal comfort research. RayMan Pro 3.1 was used to calculate PET by inputting meteorological data and individual information (Matzarakis, 2007, 2010). Mean radiation temperature (T_{mrt}) was first calculated from T_g using Eq. (1) and then adjusted to another T_{mrt} based on six-directional radiation flux densities using Eq. (2) (Li et al., 2022). The age, height, weight, clothing insulation, and metabolic rate of pedestrians were assumed to be 25 years old, 1.75 m, 70 kg, 0.4 clo, and 100 W, respectively (Huang et al., 2017; Chen et al., 2024).

$$T_{mrt} = \left[\left(T_g + 273.15\right)^4 + \frac{1.10\times10^8\times v^{0.6}\times(T_g - T_a)}{\varepsilon D^{0.4}}\right]^{0.25} - 273.15 \quad (1)$$

$$T_{mrt}(six-directional) = (T_{mrt}(T_g) + 3.6986)/1.1383 \quad (2)$$

Where the black globe diameter (D) is 0.075 m; the back globe emissivity (ε) is set as 0.95.

3. RESULTS

3.1. Overview of microclimate and thermal comfort conditions

Table 2 statistically describes 1-minute-averaged T_a, RH, v, and T_g and 15-minute-averaged T_{mrt} and PET at ten footbridge sites. During the daytime, the mean T_a and RH at open footbridge sites were 32.68 ℃−33.68 ℃ (average = 33.07 ℃) and 53.49%−59.53% (average = 56.69%), respectively; the mean T_a and RH at covered footbridge sites were 30.99 ℃−32.60 ℃ (average = 31.91 ℃) and 58.91%−67.11% (average = 64.07%), respectively. On average, covered footbridge sites exhibited lower mean T_a but higher mean RH compared to open ones. In the context of the officially reported T_{max} being 33.65±0.56 ℃, open footbridge sites had an average maximum T_a of 35.13 ℃, higher than 33.54 ℃ measured at covered footbridge sites. Regarding wind speed, the

lowest mean v of 0.26 m/s occurred at site M2 due to its footbridge sidewalls being installed with metal panels approximately 2 m high; Site G1 had the highest mean v of 1.72 m/s, which can be attributed to its proximity to the coast.

Concerning received radiation, the average maximum T_g at open footbridge sites measured 48.14 ℃, exceeding those at glass-covered, concrete-covered, and metal-covered footbridge sites by approximately 10.1 ℃, 12.2 ℃, and 11.6 ℃, respectively; the average maximum T_{mrt} at open footbridge sites reached 68.05 ℃, surpassing values at glass-covered, concrete-covered, and metal-covered footbridge sites by 18.5 ℃, 24.9 ℃, and 28.8 ℃, respectively. According to the standard deviations, T_g and T_{mrt} fluctuated within a small range at covered footbridge sites, while evident variations appeared at open footbridge sites. On average, open footbridge sites had a mean T_g of 41.48 ℃ and a mean T_{mrt} of 56.50 ℃, which were 7.2 ℃ and 16.7 ℃ higher than those at covered footbridge sites, respectively. In particular, sites G1, G2, and C1 had higher maximum T_{mrt} (> 50 ℃) above the average of covered sites. The reason was that the sunlight could slant down from the open sidewall under specific solar altitudes.

As a result of high temperature and strong radiation, open footbridge sites' maximum and mean PET exceeded 50 ℃ and 41 ℃, respectively. The overhead cover exhibited a remarkable cooling effect on PET, resulting in an average PET of 34.80 ℃ at covered footbridge sites. Specifically, site O3 had the highest PET (maximum = 52.3 ℃ and mean = 48.57 ℃); site O2 had the lowest mean PET of 41.45 ℃ among open footbridge sites due to its small sky view factor; sites G1 and G2 had higher maximum PET (> 40 ℃) compared to the remaining covered sites.

Table 2. Overview of measuring microclimate and thermal comfort variables.

Measuring variables		Open/Uncovered			Glass-covered			Concrete-covered		Metal-covered	
		O1	O2	O3	G1	G2	G3	C1	C2	M1	M2
T_a (℃)	Max	34.62	35.27	35.49	33.04	34.45	32.19	32.69	34.32	33.83	34.29
	Min	30.32	30.56	30.67	30.62	29.94	29.92	29.44	30.17	30.75	31.01
	Mean	32.86	32.68	33.68	31.94	32.52	30.99	31.15	31.97	32.17	32.60
	Deviation	1.09	1.33	1.07	0.54	1.08	0.47	0.74	0.89	0.86	0.98
RH (%)	Max	68.94	70.31	66.58	75.00	71.47	72.77	74.86	76.34	68.03	67.83
	Min	46.71	45.47	46.17	57.91	47.96	62.22	62.10	52.68	50.32	55.69
	Mean	57.06	59.53	53.49	66.69	58.91	67.11	66.91	65.69	60.39	62.82
	Deviation	5.45	7.61	4.71	3.56	5.84	2.48	2.76	5.39	5.72	2.37
v (m/s)	Max	2.18	2.21	2.15	3.84	2.64	2.90	3.94	3.67	2.37	1.19
	Min	0.05	0.09	0.09	0.41	0.20	0.41	0.07	0.21	0.10	0.01
	Mean	1.13	0.89	0.90	1.72	1.28	1.59	1.49	1.51	1.00	0.26
	Deviation	0.35	0.41	0.38	0.55	0.41	0.42	0.79	0.77	0.46	0.22
T_g (℃)	Max	46.04	48.99	49.39	38.33	41.20	34.65	35.88	35.45	36.59	36.55
	Min	32.90	32.87	35.73	32.72	32.75	31.25	31.54	31.40	32.51	32.30
	Mean	40.63	39.22	44.60	35.34	36.66	33.01	33.59	33.10	34.24	34.17
	Deviation	3.82	5.34	3.26	1.25	1.82	0.77	0.95	0.93	1.08	1.00
T_{mrt} (℃)	Max	67.52	68.88	67.74	51.65	55.58	41.49	50.92	37.33	41.16	37.28
	Min	35.04	36.20	39.47	39.26	34.91	34.92	36.16	33.68	35.09	33.45
	Mean	56.45	50.53	62.53	44.95	46.34	38.67	39.95	35.76	38.25	34.92
	Deviation	11.02	12.29	7.50	2.75	5.71	1.80	2.91	0.80	1.82	1.02
PET (℃)	Max	50.50	52.00	52.30	40.20	44.10	34.90	37.20	35.20	36.80	36.20
	Min	33.10	33.30	36.60	33.90	32.90	31.00	31.30	30.20	32.50	32.80
	Mean	44.15	41.45	48.57	36.70	38.40	33.01	33.85	32.85	34.59	34.21
	Deviation	5.73	7.18	4.15	1.78	2.71	1.12	1.31	1.32	1.33	0.98

3.2. Simultaneous comparison between open and covered footbridge sites

3.2.1. Open site vs. glass-covered site

Figure 2 compares temporal variations of T_a, RH, v, T_g, T_{mrt}, and PET between open site O1 and glass-covered site G2. Statistically significant inter-site differences ($p < 0.01$) were found in T_a, RH, T_g, T_{mrt}, and PET via Mann-Whitney U tests and in v through the independent samples t-test. Figure 2(a) illustrates that the two sites exhibited nearly parallel variation trends in T_a and RH, though with distinct mean values. The T_a differences ranged from -0.11 ℃ to 0.86 ℃ (mean = 0.34 ℃), while RH differences varied between -3.76% and -0.01% (mean = -1.85%). So, site O1 demonstrated significantly higher mean T_a but lower mean RH compared to site G2 during daytime measurements. Furthermore, both sites had highly variable wind speeds, maintaining fluctuations around 1 m/s (Figure 2(b)). The inter-site v difference (range: -1.01 to 0.59 m/s) yielded a mean value of -0.15 m/s, indicating a higher wind speed at site G2 compared to site O1. Regarding T_g, the measured inter-site differentials varied from -0.13 ℃ to 8.47 ℃, averaging 3.96 ℃. The T_g curve of site O1 predominantly exceeded site G2's curve except after 15:33 when diminishing solar radiation caused the two curves to approximate convergence. The T_{mrt} comparison revealed more distinct differences between the sites, with the maximum and mean inter-site differentials reaching 21.63 ℃ and 10.11 ℃, respectively (Figure 2(c)). Consistent with T_g, T_{mrt} patterns of sites O1 and G2 nearly merged during the late afternoon (15:45−17:00) when T_{mrt} differences were below 1 ℃. Owing to the above microclimate differentials, site O1 exhibited significantly higher PET than site G2 during daytime measurements (Figure 2(d)). In particular, the PET differences varied from 2.6 ℃ to 11.4 ℃ (mean = 7.11 ℃) at pre-15: 45, narrowing to < 1 ℃ at post-15: 45.

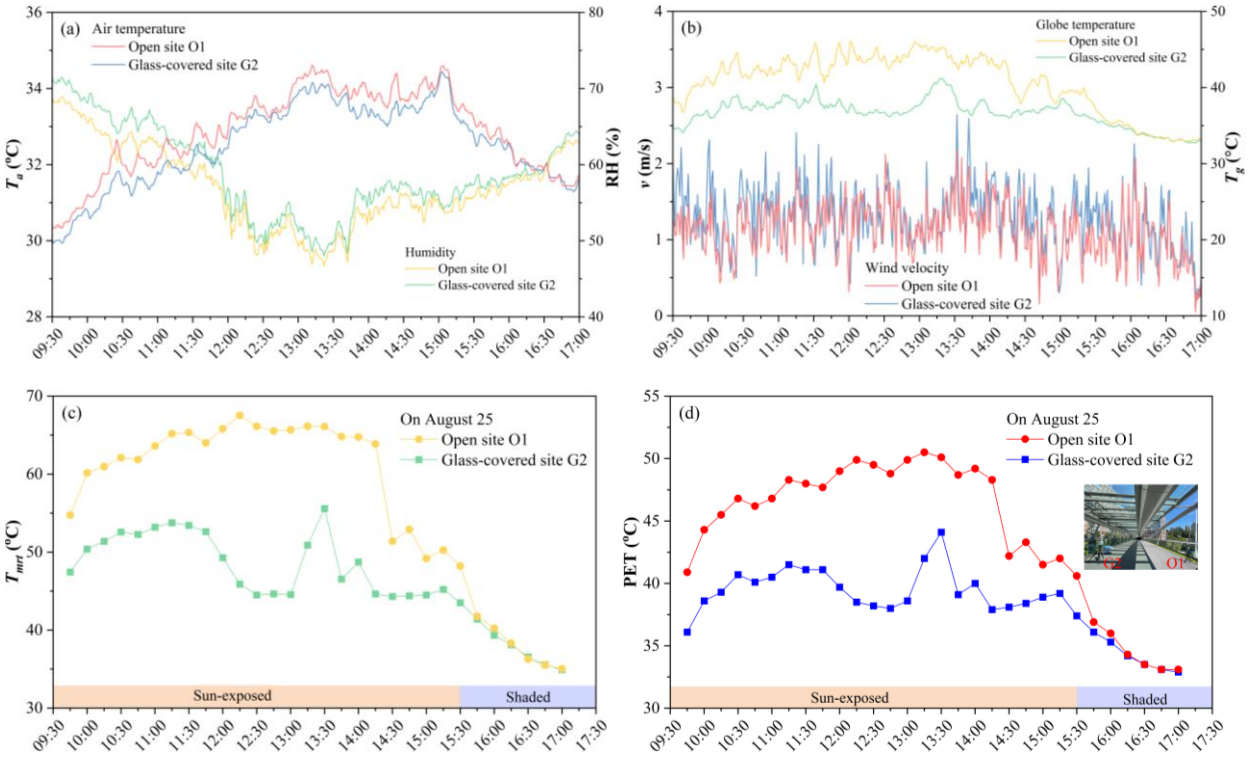

Figure 2. Variations of microclimate and thermal comfort variables at sites O1 and G2 on August 25th.

3.2.2. Open site vs. metal-covered site

Figure 3 shows temporal comparisons of T_a, RH, v, T_g, T_{mrt}, and PET between open site O2 and

metal-covered site M1. Mann-Whitney U tests revealed statistically significant differences ($p < 0.01$) for T_a, v, T_g, T_{mrt}, and PET between the two sites, while no statistically significant difference ($p > 0.05$) was found for RH. In terms of T_a (Figure 3(a)), site O2 showed apparently higher values than site M1 during direct solar radiation exposure (10:55−14:00). However, site O2's temperature superiority diminished and reversed in the mid-to-late afternoon after shaded. Inter-site T_a differences ranged from -0.97 ℃ to 2.45 ℃, with an average of 0.51 ℃ higher at site O2. RH displayed a nearly inverse trend to T_a, with inter-site differences ranging from -6.51% to 6.07%, averaging 0.86% higher at site M1. Wind speed presented high fluctuation at both sites (Figure 3(b)). Site M1 recorded 0.11 m/s higher v than site O2 on average, with inter-site differences varying between -1.97 m/s and 1.60 m/s. Regarding T_g (Figure 3(b)), site O2 exhibited rapid increases during solar exposure and sharp declines when shaded, while site M1 maintained stable values around 34 ℃. The T_g differences peaked at 14.06 ℃ and reached a minimum of -0.36 ℃, with a daytime average difference of 4.98 ℃. Figure 3(c) illustrates that site O2 remained consistently higher T_{mrt} than site M1, with a mean T_{mrt} difference of 12.28 ℃. During sun exposure, T_{mrt} differences ranged from 12.09 ℃ to 29.38 ℃, but eventually dropped to approximately 1 ℃ in the shade. Consequently, PET values at site O2 averaged 6.87 ℃ higher than at site M1, with maximum and minimum differences of 16.4 ℃ and 0.2 ℃, respectively (Figure 3(d)).

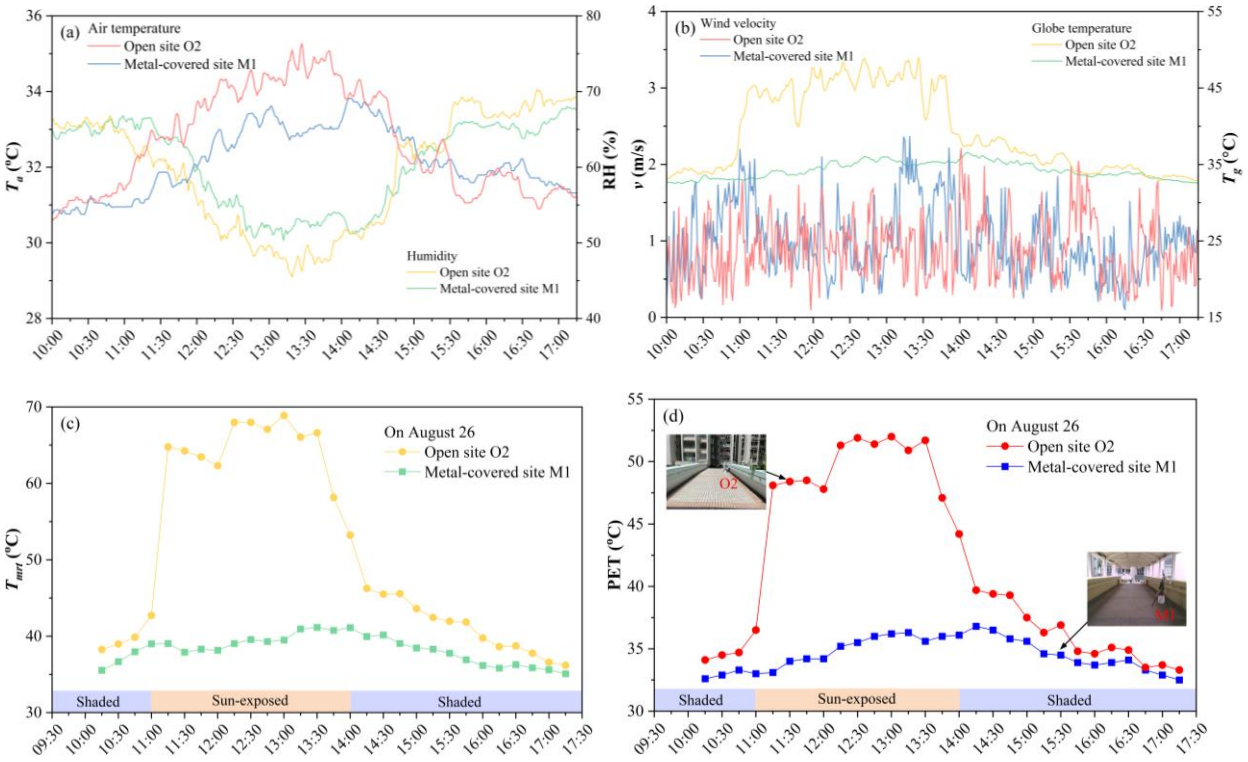

Figure 3. Variations of microclimate and thermal comfort variables at sites O2 and M1 on August 26th.

4. DISCUSSION

This study measured daytime microclimate and thermal comfort on footbridges and compared the performance of different covered conditions (open, glass-covered, metal-covered, and concrete-covered). The results reveal that covered footbridges generally provide lower daytime T_a, T_g, and

T_{mrt} but higher RH than open footbridges on very hot summer days, irrespective of the cover types. The average reductions in mean T_a, T_g, and T_{mrt} were approximately 1.2 ℃, 7.2 ℃, and 16.7 ℃, respectively, indicating the cooling effect of overhead covers on footbridges' thermal environment. The cooling magnitude is comparable to previous findings on other shading strategies in Hong Kong (Cheung & Jim, 2018; Lee et al., 2020; Ouyang et al., 2024). In contrast to thermal-related parameters, wind speed results are more prone to other factors rather than solar radiation. Distinct v differences (up to 1.5 m/s) existed among covered footbridges, highlighting the significance of open and semi-open sidewalls in footbridges' ventilation.

Concerning thermal comfort, pedestrians walking on open footbridges (mean PET = 41.5−48.6 ℃) are likely to feel "warm to hot" and suffer moderate to strong heat stress in contrast to "slightly warm" sensation and slight heat stress on the covered footbridges (mean PET = 32.9−38.4 ℃), referring to the correlation between PET level and thermal sensation class in Hong Kong (Huang et al., 2017; Lee et al., 2020). On average, covered footbridges could cool mean PET by 9.9 ℃ compared to open footbridges. Such remarkable heat stress mitigation is of great significance on hot days, especially for hot and humid cities where high humidity exaggerates thermal discomfort. Simultaneous comparisons (open vs. glass-covered and open vs. metal-covered) provide further evidence for the overhead cover's cooling effect. Compared with the open side, the glass-covered side could maximally cool T_a, T_g, T_{mrt}, and PET by 0.9 ℃, 8.5 ℃, 21.6 ℃, and 11.4 ℃, respectively (Figure 2). The metal cover shows more powerful cooling performances, decreasing T_a, T_g, T_{mrt}, and PET by up to 2.4 ℃, 14.1 ℃, 29.4 ℃, and 16.4 ℃ (Figure 3). Overall, considering summer thermal comfort, covered footbridges are recommended in Hong Kong.

This study focuses on summer daytime measurements due to pedestrians being more vulnerable to high heat exposure during this period. However, nighttime results may be opposite due to radiative cooling (Cheung & Jim, 2018) and seasonal variation can also influence the results. Moreover, the footbridge's geometric dimension, orientation, street aspect ratio, and vegetation may influence the microclimate and pedestrian thermal comfort (Chen et al., 2024), deserving in-depth research in the future. Furthermore, Lam et al. (2023) reported that concrete, aluminum, and PVC covers exhibit superior cooling effects over glass covers and the glass cover's performance depends on its transparency. More controlled studies are necessary to explore the effects of cover materials on footbridges' microclimate and thermal comfort. Last, thermal comfort assessment is limited to objective measurement, PET model, and uniform pedestrian data. Further questionnaire surveys are needed to validate PET results and investigate the effects of non-physical factors.

5. CONCLUSION

This study conducted on-site measurements on nine urban footbridges with four covered conditions in Hong Kong during very hot summer days. Daytime microclimates and pedestrian thermal comfort were statistically analyzed. The main findings are summarized as follows:

- During daytime measurements, all overhead covers demonstrate exceptional performance in blocking solar radiation, resulting in more stable and cooler thermal environments for covered footbridges compared to open ones. The average reductions in T_a, T_g, and T_{mrt} were approximately 1.2 ℃, 7.2 ℃, and 16.7 ℃, respectively.
- The daytime average PETs at open and covered footbridges were 44.7 ℃ and 34.8 ℃, respectively. Therefore, pedestrians using open footbridges are liable to feel hot and endure strong heat stress, whereas those on covered footbridges typically feel slightly warm and

experience slight heat stress.

- Simultaneous measurements between open and covered footbridges indicated that the maximum cooling effect on T_a, T_g, T_{mrt}, and PET reached 0.9 ℃, 8.5 ℃, 21.6 ℃, and 11.4 ℃ under the glass cover, and increased to 2.5 ℃, 14.1 ℃, 29.4 ℃, and 16.4 ℃ under the metal cover.

This study extends the scope of outdoor thermal comfort research to skywalk environments and demonstrates the efficacy of covered footbridges in mitigating heat stress and improving thermal comfort on hot days, offering valuable insights into the development of walkable cities in humid subtropical climates.

ACKNOWLEDGEMENTS

This study was supported by the Research Grants Council of the Hong Kong Special Administrative Region, China [Grant No. T22-504/21-R] and the Postdoc Matching Fund Scheme of The Hong Kong Polytechnic University [No. 1-W34Y]. The authors would like to thank the lab technician and students for their assistance during measurements.

REFERENCES

Chen, L., Mak, C. M., Hang, J., & Dai, Y., 2024. Influence of elevated walkways on outdoor thermal comfort in hot-humid climates based on on-site measurement and CFD modeling. Sustainable Cities and Society, 100.

Cheung, P. K., & Jim, C. Y., 2018. Comparing the cooling effects of a tree and a concrete shelter using PET and UTCI. Building and Environment, 130, 49–61.

Forsyth, A., 2015. What is a walkable place? The walkability debate in urban design. URBAN DESIGN International, 20(4), 274–292.

GovHK., 2024. Hong Kong – the Facts. https://www.gov.hk/en/about/abouthk/facts.htm

Highways Department., 2024. Footbridges and Subways of Hong Kong. https://www.hyd.gov.hk/en/information_corner/hyd_factsheets/doc/e_Footbridges_and_Subways.pdf

Hong Kong Observatory., n.d.-b. Climatological information services: Daily exact. https://www.hko.gov.hk/en/cis/climat.htm

Huang, T., Li, J., Xie, Y., Niu, J., & Mak, C. M., 2017. Simultaneous environmental parameter monitoring and human subject survey regarding outdoor thermal comfort and its modelling. Building and Environment, 125, 502–514.

Kim, Y., Yeo, H., & Lim, L., 2024. Sustainable, walkable cities for the elderly: Identification of the built environment for walkability by activity purpose. Sustainable Cities and Society, 100, 105004.

Lam, C. K. C., Weng, J., Liu, K., & Hang, J., 2023. The effects of shading devices on outdoor thermal and visual comfort in Southern China during summer. Building and Environment, 228, 109743.

Lee, L. S. H., Cheung, P. K., Fung, C. K. W., & Jim, C. Y., 2020. Improving street walkability: Biometeorological assessment of artificial-partial shade structures in summer sunny conditions. International Journal of Biometeorology, 64(4), 547–560.

Li, J., Niu, J., Huang, T., & Mak, C. M., 2022. Dynamic effects of frequent step changes in outdoor microclimate environments on thermal sensation and dissatisfaction of pedestrian during summer. Sustainable Cities and Society, 79, 103670.

Matzarakis, A., 2007. Modelling Radiation fluxes in simple and complex environments – Application of the RayMan model. International Journal of Biometeorology, 51, 12.

Matzarakis, A., 2010. Modelling Radiation fluxes in simple and complex environments – Basics of the RayMan model. International Journal of Biometeorology, 54, 9.

Moreno, C., Allam, Z., Chabaud, D., Gall, C., & Pratlong, F., 2021. Introducing the "15-minute city": Sustainability, resilience and place identity in future post-pandemic cities. Smart Cities, 4(1), 93–111.

Ouyang, W., Ren, G., Tan, Z., Li, Y., & Ren, C., 2024. Natural shading vs. artificial shading: A comparative analysis of their cooling efficacy in extreme hot weather. Urban Climate, 55, 101870.

Rotmeyer, J., 2006. Can elevated pedestrian walkways be sustainable? The Sustainable City IV: Urban Regeneration and Sustainability.

Yang, F., Qian, F., & Zhao, W., 2016. Towards a Climate-Responsive Vertical Pedestrian System: An Empirical Study on an Elevated Walkway in Shanghai China. Sustainability, 8(8), 744.

Health in the built environment: an integral approach to address societal challenges (11:00-12:30 h)

6th International Conference on Building Energy and Environment
Eindhoven University of Technology, The Netherlands
6 - 10 July 2025

The impact of lighting and indoor air quality conditions on students' well-being in higher education: a full factorial design approach

H.W. Brink[1], W.P. Krijnen[2,3], M.G.L.C. Loomans[4], M.P. Mobach[1,5], H.S.M. Kort[4,6]

[1] *Research Group Facility Management, Research Centre for Built Environment NoorderRuimte, Hanze University of Applied Sciences, Groningen, The Netherlands, h.w.brink@pl.hanze.nl*
[2] *Research Group Healthy Ageing, Allied Health Care and Nursing, Hanze University of Applied Sciences, Groningen, The Netherlands*
[3] *Faculty of Mathematics and Natural Sciences, University of Groningen, Groningen, The Netherlands*
[4] *Department of the Built Environment, Building Healthy Environments for Future Users, Eindhoven University of Technology, The Netherlands*
[5] *Research Group Spatial Environment and the User, Research Centre Mission Zero, The Hague University of Applied Sciences, The Netherlands*
[6] *Research Group Technology for Healthcare Innovations, Research Centre Sustainable and Healthy Living, Utrecht University of Applied Sciences, The Netherlands*

SUMMARY
This study examines the impact of moderate and high lighting and indoor air quality (IAQ) conditions on students' well-being during a regular academic course in higher education. To determine the precise contribution of these two indoor environmental factors, students' perceptions of their well-being were examined with the Positive and Negative Affect, Basic Emotional Process, and Karolinska Sleepiness Scale. Data were collected from 83 students, resulting in 285 responses, distributed across four combinations of moderate and high IAQ conditions, resp. > 800 ppm ≤ 950 ppm carbon dioxide (CO_2) and < 800 ppm CO_2, and moderate and high horizontal illuminance (HI) levels, resp. 500 lx and 750 lx. The results indicated that high HI levels did not enhance students' perceived well-being compared to moderate levels. However, high IAQ conditions significantly contributes to students' well-being, compared to moderate conditions. Interaction effects between the two factors were observed at moderate conditions.

Keywords: emotional response, horizontal illuminance, higher education, indoor environmental quality.

1. INTRODUCTION

The growing emphasis on the well-being of higher education students has highlighted the significance of indoor environment research within educational buildings (Makaremi et al., 2024). Students' well-being is essential for fostering a supportive and effective learning environment in higher education and enhancing academic performance (Chaudhry et al., 2024). Evidence reveals that there is a relation between the indoor environmental quality (IEQ) and students' well-being (Brink et al., 2021). Four major factors – acoustic environment, lighting, thermal environment, and indoor air quality (IAQ) – determine the indoor environmental quality (IEQ) in schools (Frontczak & Wargocki, 2011), which may impact students' well-being.

In 2005 Mendell and Heath (2005) conducted a literature study that suggested that certain indoor air quality and thermal conditions found in schools adversely affect occupants' well-being. Furthermore, Frontczak and Wargocki (2011) stated that humans are subject to multiple environmental factors simultaneously, and that interactions among these can impact their perception and performance. Interactions between IEQ factors were observed by Kim and De Dear (2012), who developed a model to determine interaction effects and the existence of a hierarchy

among IEQ factors in an office environment. However, whether this model is applicable in an educational setting has not yet been studied to the best of our knowledge.

To determine what is known about the combined effects of environmental factors on the perceived IEQ and human performance, Torresin et al. (2018) performed a literature review. This study revealed combinations of IEQ factors that were studied and interaction effects between IEQ factors were identified. However, studies which examined multiple IEQ factors in an educational setting are limited. Furthermore, no studies have been found dealing with the interaction effects of indoor air quality and lighting conditions.

To contribute to the understanding of interaction effects and hierarchy between IEQ factors in higher education, this study focuses on the effects of two factors: horizontal illuminance (HI) level and ventilation rate representing lighting and IAQ respectively. And by doing so, this study provides more knowledge about the effect of simultaneously improving lighting and IAQ conditions on students' well-being in higher education. Additionally, when examining the impact of IEQ factors on students, it is essential to consider individual differences in students' subjective responses to identical indoor environments (Frontczak & Wargocki, 2011). These differences include individual characteristics (e.g., gender, age), building features (e.g., use, spatial qualities), or the outdoor climate, including seasonal changes and therefore daylight entrance and air quality. This study includes relevant individual differences when studying the influence of IEQ factors on students in higher education.

Specific lighting and IAQ quality conditions for this study were derived from Dutch guidelines for school buildings. These guidelines list three quality classes (A, B and C) addressing the four major IEQ parameters (RVO, 2021). When building or renovating schools in The Netherlands, school management may choose between quality classes A, B or C. To support this decision-making process, this study compares quality class A and B requirements for HI levels (HI ~750 vs ~500 lx), and IAQ (≤800 ppm vs > 800 ppm ≤ 950 ppm CO_2). The objective of this study is to answer the following research question: What is the impact, expressed as main and interaction effects, of increasing HI level from 500 to 750 lx and improving indoor air quality (IAQ) from CO_2 concentrations above 800 ppm but below 950 ppm to concentrations below 800 ppm CO_2 on students' perceived well-being during a regular academic course?

2. METHOD

2.1 Practical setting

The experiment was performed from the 20th of November till the 20th of December 2023. In this study, 32 male and 51 female freshmen, aged 19±1.7, participated in six campaigns, while following their regular academic classes. These first-year students were selected for the study, because they were lay persons and not yet versed in building physics. The study was performed in a classroom of the Hanze University of Applied Sciences (UAS) School of Future Environments, the Netherlands. The classroom's size is 10,641 x 7,041 mm, the reverberation time of the classroom is 0.4s at 250-2k Hertz, and the classroom is orientated west-south-west (53.24077N, 6.53106E). To prevent daylight entry during the experiment, the awnings on the outside of the windows were kept closed during the experiment.

The classroom was fitted with thirteen ETAP U3352 lighting armatures with a color temperature of 5000K and a color rendering index of 80. The lighting system is equipped with a dimmer and the HI at lecturer's desk was adjusted to meet the specified value before the start of every lecture. Lecturers were instructed not to adjust the illuminance level during the lecture. Furthermore, the classroom is equipped with a heating, ventilation, and air conditioning (HVAC) system. This system consisted of a combined air handling unit, including fixed plate heat exchangers and F7 filters, with a capacity of 3500 m^3/h, which results in a maximum ventilation rate of 16 l/s per person at a maximum of 30 persons. Furthermore, an air-cooled heat pump of 25

kW is installed. Using this system, both air temperature and air quality – defined by air temperature and maximum concentration of CO_2 – can be regulated in the classroom by entering the desired values into the control system. Figure 1 shows two pictures of the interior of the classroom.

Figure 1 Visual appearance of the classroom's interior. The left photo shows the classroom from the lecturer's perspective, the right photo shows the students' perspective

In approximately the middle of the classroom, a Delta Ohm HD32.3TCA Thermal Microclimate sensor, ACCREDIA calibrated, which was placed at a height of 1.1 meters. This device recorded every minute the actual air temperature (t_a), globe temperature (t_g), relative humidity (RH), CO_2, particulate matter (PM_{10}) and total volatile organic compounds (VOC). Figure 2 shows the layout of the classroom and technical details of the HVAC system.

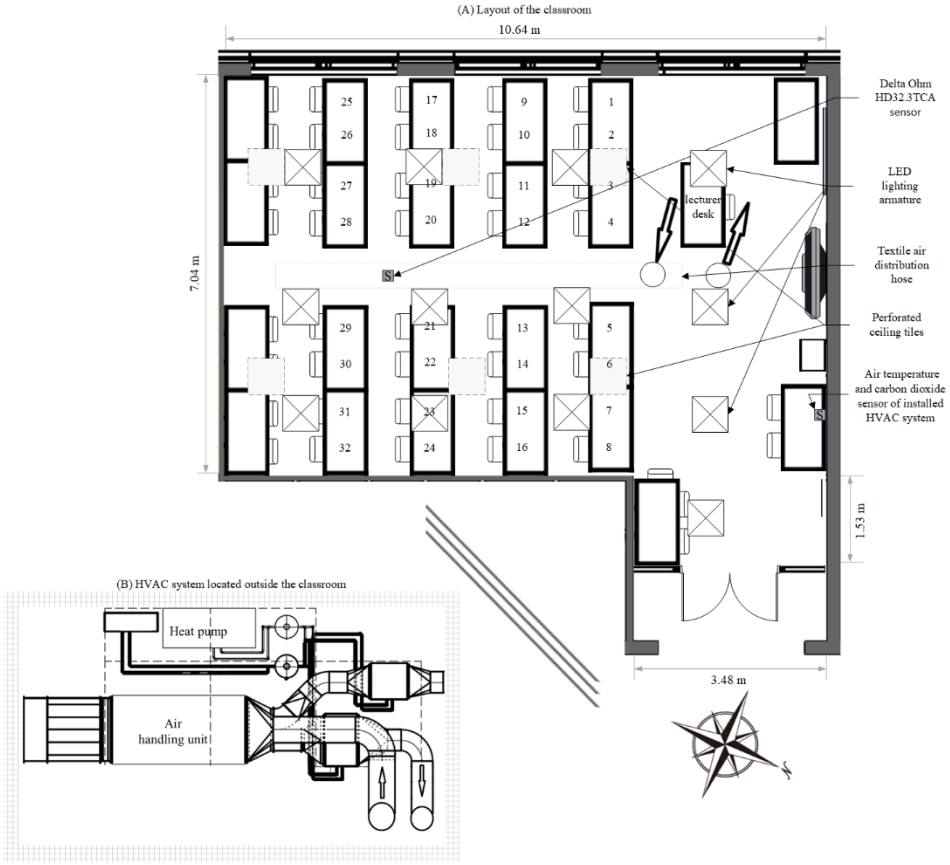

Figure 2 Layout of the classroom including the orientation (A) and technical details of the heating, ventilation, and air conditioning (HVAC) system (B)

2.2 Data collection of the actual indoor environmental quality and students' well-being

At the beginning of each lecture, the desired concentration of CO_2 (<800 ppm or > 800 ppm ≤ 950 ppm CO_2) was set in the CO_2 controlled ventilation system. Additionally, the desired HI level at the lecturer's task area was set to either 750 lx or 500 lx. The average HI level at the students' task area corresponded to that of the lecturer's task area, with a variation of approximately ±50 lx.

Students' well-being was measured with a questionnaire consisted of general items age, gender, table number, and self-reported hours of sleep before participation. Student well-being was examined with the Basic Emotional Process Scale (BEPS), which measures students' perceived levels of activation, orientation, evaluation and control (Gentile et al., 2018; Kuller, 1991). Furthermore, students reported their well-being using the Positive And Negative Affects Scale (PANAS) (Gentile et al., 2018; Watson et al., 1988). And finally, students had to rate their sleepiness in relation to their alertness using the Karolinska Sleepiness Scale (KSS) (Choi et al., 2019; Åkerstedt & Gillberg, 1990).

As a final step to enable the application of the questionnaire, all questions and statements were translated into Dutch by the authors. To validate, these questions and statements were then translated back into English by a professional translator. This translation was compared to the original English approach, differences were discussed with the translator and, if necessary, the Dutch translation of the question or statement was adjusted.

2.3 Data collection procedure

The final study design was approved by Hanze UAS' Ethical Committee (No. T2023.040). Before their participation, the students received a general outline of the study and its objective, which was to assess the quality of the classroom. All students who participated in this study signed an informed consent form. The students could end their participation in the study without any consequences and at any time. However, none of the students requested to do so or to have their data removed. The type of lecture was a tutorial, in which the lecturer gave a presentation about basic management principles. The duration of the lecture was approximately 90 minutes.

Four groups of freshmen and two lecturers (X, Y) participated in the experiment. The lecturers involved consecutively gave two lectures to two groups (A-D). For example, an involved lecturer gave a lecture on Wednesday from 8:30 a.m. to 10:00 a.m. Shortly after this first lecture, the same lecturer gave a lecture from 10:30 a.m. to 12:00 a.m. The lecturers were instructed to give the same lecture both times and were not informed which conditions were created in the classroom.

Before the experiment, students were randomly assigned to a group, initially with approximately 27 students each. All lectures were given from Tuesday to Friday and on the same day and approximately the same time for each group and in the same classroom (Figure 1). All four groups were at least one time exposed to the four tested high – moderate lighting and IAQ conditions. To complete the factorial design, all six possible combinations of high – moderate conditions were evaluated. This full-factorial design allows us to examine the main effects of, as well as the interaction effects between the two factors: HI and IAQ. Table 1 provides an overview of all conditions evaluated and six possible contrasts between the four different conditions examined during the experiment.

Table 1 Overview of study design with 4 groups of approximately 27 students and 2 lecturers over the 6 runs

	Condition			
Lecture (week)	group A lecturer X	group B lecturer X	group C lecturer Y	group D lecturer Y
1 (2)	IAQ_h - HI_m [2]	IAQ_m - HI_m [1]	IAQ_h - HI_m [2]	IAQ_m - HI_m [1]
2 (2)	IAQ_h - HI_h [4]	IAQ_m - HI_h [3]	IAQ_h - HI_h [4]	IAQ_m - HI_h [3]

3 (3)	IAQ_m - HI_m[1]	IAQ_m - HI_h[3]	IAQ_m - HI_m[1]	IAQ_m - HI_h[3]
4 (4)	IAQ_m - HI_h[3]	IAQ_h - HI_m[2]	IAQ_h - HI_m[2]	IAQ_m - HI_h[3]
5 (5)	IAQ_h - HI_m[2]	IAQ_h - HI_h[4]	IAQ_h - HI_m[2]	IAQ_h - HI_h[4]
6 (6)	IAQ_h - HI_h[4]	IAQ_m - HI_m[1]	IAQ_h - HI_h[4]	IAQ_m - HI_m[1]

[1] > 800 ppm ≤ 950 ppm CO_2, E_{hor} 500 lx; [2] ≤ 800 ppm CO_2, E_{hor} 500 lx; [3] > 800 ppm ≤ 950 ppm CO_2, E_{hor} 750 lx; [4] ≤ 800 ppm CO_2, E_{hor} 750 lx; $_m$= moderate quality condition; $_h$= high quality condition

At the end of the lecture, after approximately 90 minutes, the lecturer left the classroom, and the researcher entered asking the students to participate in the study. The degree of participation was high, reaching approximately 90% of all students present.

2.4 Data and statical analysis

To analyze the main and interaction effects of the two IEQ factors, first, mean scale values were calculated for the Positive Affect and Negative Affect Scales (PANAS), Basic Emotional Process Scales (BEPS) (Gentile et al., 2018; Kuller, 1991). Next, mixed-effects linear models (LMMs) were computed with a student specific random intercept to determine the main and interaction effects. These models include the main effects of the factors. Multiple LMMs were conducted to evaluate the students' responses under the varying conditions of the factors HI and IAQ. Student responses were statistically corrected for the moderators gender, the number of hours of sleep before participation, and distance to the lecturer (the latter being derived from their seating position) (Gentile et al., 2018; Norbäck et al., 2013). In addition, the LMMs were controlled for individual student level by random intercept. Therefore, the composed models account for both fixed effects which are consistent across individuals and random effects which capture individual variability. Furthermore, the models were computed with a general unstructured covariance matrix dealing with the dependent repeated measurements in the design. Main and interaction effects were considered statistically significant at a *p*-value <.05.

The factors HI and IAQ were considered as the independent factors in all LMMs. Those LLMs which revealed significant effects were verified by the significance of the LMM parameters' estimated by robust LMMs (Yohai et al., 1991). When these robust analyses led to a different conclusion regarding the estimated coefficient (β) beyond the first decimal, this is reported. The LMM function in the linear mixed-effects models package (lme4) in R version 3.5.0 (R Foundation for Statistical Computing, 192 Vienna, Austria) and IBM SPSS Statistics Version 28.0.0.0 (190) were used for statistical analyses.

3. RESULTS

3.1 Participation and actual indoor environmental conditions

From 83 students, 285 responses were collected and analyzed. Attendance at the lectures was not mandatory, resulting in fluctuating attendance rates and an unequal distribution of responses across the four combinations of moderate-high HI and IAQ conditions. As a result of the low number of students present in the classroom and minimum ventilation flow rate of the HVAC system, the desired moderate indoor air quality (IAQ) was not achieved in some runs. Consequently, all responses were classified based on the actual conditions observed. During the experiment, the outside temperature was 5.5°C (min 1.8– max 9.8°C). Table 2 presents an overview of the number of students who participated in the experiment and the actual classroom conditions during the four combinations of moderate-high HI and IAQ conditions. The IEQ factors temperature and relative humidity were similar in the four conditions tested, see Table 2. Moreover, the two lecturers involved gave the lectures in all four experimental conditions and in the same classroom.

Therefore, the perceived thermal and acoustic comfort of the students during the experiment was assumed to be similar and these factors were not included in the statistical models.

Table 2 Overview of preset and actual indoor environmental conditions during the experimental runs

C	n	% ♀	Setp. E_{hor} [lx]	Setp. CO_2 [ppm]	Avg. CO_2 (min-max) [ppm]	Avg. t_a (min-max) [°C]	Avg. t_g (min-max) [°C]	Avg. RH (min-max) [%]	Avg. VOC (min-max) index	Avg. PM_{10} (min-max) [µg/m³]
1	55	73	500	>800 <950	865 (651-1036)	21.3 (20.2-22.1)	19.9 (19.9-21.5)	44.4 (42.5-46.0)	217 (106-350)	2.6 (0.25-15.8)
2	96	69	500	<800	668 (547-790)	21.3 (20.8-22.1)	21.0 (20.4-21.6)	40.6 (38.3-42.6)	206 (94-364)	3.0 (0.5-20.7)
3	32	66	750	>800 <950	836 (558-943)	21.2 (20.6-21.7)	20.4 (20.3-21.4)	31.6 (29.6-33.2)	192 (111-328)	3.0 (0.5-17.9)
4	102	69	750	<800	627 (511-749)	21.0 (20.5-21.7)	20.2 (20.1-21.1)	37.5 (35.6-39.7)	159 (64-356)	2.6 (0.6-16.7)

C: experimental condition; n: number of participants; E_{hor}: horizontal illuminance; CO_2: carbon dioxide; t_a: air temperature; t_g: globe temperature; RH: relative humidity; VOC: volatile organic compounds; PM: particulate matter

3.2 Main effects of the factors IAQ and HI

With regard to the research question, whether increasing HI levels from 500 to 750 lx and improving IAQ from CO_2 concentrations between 800 and 950 ppm and CO_2 concentrations below 800 ppm impacts students' perceived well-being, LMMs were computed with the four basic emotional process scales (BEPS), i.e., level of activation, orientation, evaluation and control, as outcome variables and the factors HI and IAQ as predictor variables. Additionally, the variables gender, the estimated number of hours of sleep before participation, and distance to the lecturer were included as covariates in the LMMs. The factor HI did not affect students' perceived level of activation, orientation, evaluation, and control. However, the factor IAQ affected students' perceived level of activation (β=0.34; t(277)=4.16; p=.000), evaluation (β=0.10; t(277)=2.19; p=.029), orientation (β=0.15; t(277)=2.45; p=.015), and control (β=0.14; t(277)=2.32; p=.021). Furthermore, the activation, evaluation, and orientation LMMs revealed an effect of gender; males scored higher on these scales. The activation model revealed an effect of number of hours of sleep, more hours of sleep led to a higher score on these scales.

Furthermore, LMMs were computed with the PANAS. Neither the factor HI nor the factor IAQ affected students' negative affect scale (NAS) scores. And although HI also did not affect students' positive affect scale (PAS) score, the factor IAQ did affect students PAS score (β=2.60; t(278)=3.28; p=.001). Additionally, this model revealed an effect of gender (males scored higher). Furthermore, this model revealed an effect of number of hours of sleep; more hours of sleep led to a higher score on this scale.

The factor HI did not affect students' scores on the KSS. However, the factor IAQ affected students' scores on the KSS (β=0.53; t(277)=2.58; p=.010). Furthermore, this LMM revealed an effect of gender, males scored more alert; and an effect of the number of hours of sleep, more hours of sleep led to a higher perceived level of alertness. **Figure 3** shows all mean scores on BEPS, PANAS, and KSS at high and moderate IAQ and HI levels.

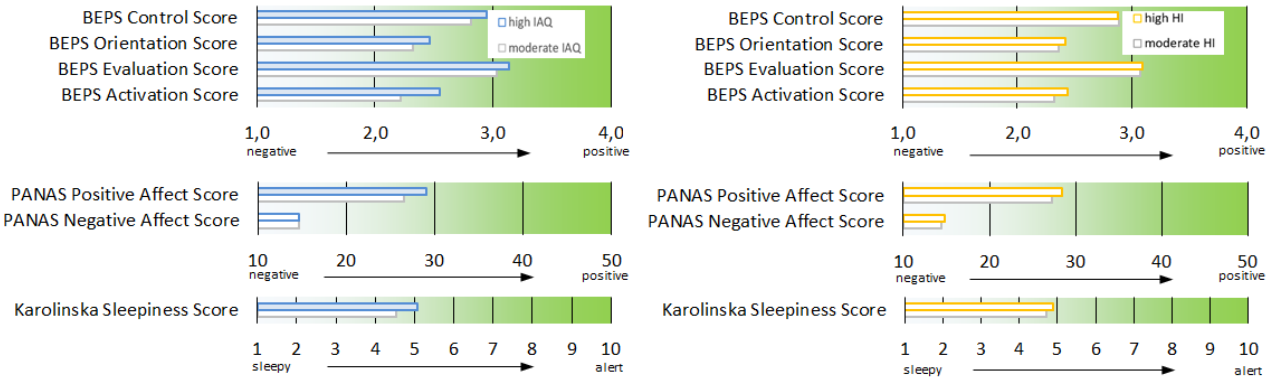

Figure 3 Mean scores on BEPS, PANAS, and KSS at high and moderate indoor air quality (IAQ) and horizontal illuminance (HI) levels. Shading of the bar is applied when the effect of the factor is significant (p<0.05).

3.3 Interaction effects of the factors IAQ and HI

To determine interaction effects between the factors IAQ and HI, LMMs were computed with the four basic emotional process scales (BEPS), i.e., level of activation, orientation, evaluation, and control, PANAS and KSS as outcome variables and the factors HI and IAQ as predictor variables. Additionally, the variables gender, the estimated number of hours of sleep before participation, and distance to the lecturer were included as covariates in the LMMs. Significant two-way interactions only occurred at moderate IAQ and moderate HI levels in LMMs activation (β=0.33; t(279)=3.10; p=.002), evaluation (β=0.12; t(279)=2.05; p=.041), and orientation (β=0.20; t(279)=2.70; p=.007).

5. DISCUSSION

The single and combined effects of lighting conditions measured by Horizontal illuminance on the lectures desk and IAQ in higher educational settings are critical factors influencing both the quality of teaching and learning, as well as students' well-being. Individually, optimal lighting conditions have been shown to enhance visual comfort, reduce eye strain, and improve students' level of concentration (Brink et al., 2021). Similarly, good IAQ, characterized by adequate ventilation and low levels of pollutants, is essential for maintaining students' health, reducing absenteeism, and enhancing cognitive performance (Brink et al., 2021).

Although a relationship between illuminance level and students' IAQ sensation votes was earlier reported by Jiang and Yang (2011) and Pittana et al. (2022), Torresin et al. (2018) concluded that the interaction between illumination and air freshness and odor perception is not very clear. Furthermore, no evidence is available that examines the interaction effect of the IEQ factors lighting and IAQ conditions on students in higher education (Brink et al., 2021; Torresin et al. 2018). This study tries to fill in this gap. And although Du et al. (2020) reported that studies that examine IAQ conditions with CO2 concentrations between 600 and 1100 ppm do not provide unequivocal evidence, our study reveals multiple significant effects of high IAQ conditions (CO_2 < 800 ppm) on students' perceived well-being, compared to moderate (800 < CO_2 < 950 ppm), this study shows a significant positive effect of high IAQ conditions on students' well-being, compared to moderate conditions. This finding highlights the importance of good IAQ conditions in higher education classrooms. Achieving this requires the installation of CO_2-controlled ventilation systems, which have been shown to have positive effects, as previously reported by Norbäck et al. (2013). Additionally, it is important to maintain CO_2 concentrations below 800 ppm during use.

In this study, lighting is only measured via HI. Other lighting factors, such as color temperature or exposure to natural daylight, that affect personal lighting conditions were not examined (Van Duijnhoven et al., 2021). Although limited evidence is available about different lighting systems (Gentile et al., 2018), future research may focus more on how other lighting factors affect student well-being. Furthermore, in previous work, authors reported an effect of HI on students' responses under moderate IAQ conditions; however, this effect was not observed under high IAQ conditions (Brink et al., 2023). However, in this study the factor HI did not affect students' well-being although an interaction effect of moderate HI and IAQ on students' well-being was observed.

6. CONCLUSION

This study examined the impact of enhanced lighting (horizontal illuminance at the lecturers desk) and indoor air quality measured via CO2 as a proxy on students in higher education. With a full-factorial experimental design, the effect of quality class A and B requirements of Dutch guidelines for school buildings for horizontal illuminance levels, respectively 750 and 500 lux at lecturer's desk, and indoor air quality, respectively $CO_2 \leq 800$ ppm and $800 < CO_2 < 950$ ppm. This effect was examined during a tutorial, as part of a regular academic course, with a duration of 1.5 hr. The findings indicate that high indoor air quality conditions have a positive effect on students' well-being, compared to moderate conditions. Furthermore, in this study at high indoor air quality conditions, moderate or high horizontal illuminance levels do not impact students' well-being, whereas at moderate indoor air quality conditions they do.

7. REFERENCES

Åkerstedt, T., & Gillberg, M. (1990). Subjective and objective sleepiness in the active individual. *International Journal of Neuroscience, 52*(1-2), 29–37. https://doi.org/10.3109/00207459008994241

Brink, H. W., Krijnen, W. P., Loomans, M. G. L. C., Mobach, M. P., & Kort, H. S. M. (2023). Positive effects of indoor environmental conditions on students and their performance in higher education classrooms: A between-groups experiment. *Science of the Total Environment, 869*, 161813. https://doi.org/10.1016/j.scitotenv.2023.161813

Brink, H. W., Loomans, M. G. L. C., Mobach, M. P., & Kort, H. S. M. (2021). Classrooms' indoor environmental conditions affecting the academic achievement of students and teachers in higher education: A systematic literature review. *Indoor Air, 31*(2), 405–425. https://doi.org/10.1111/ina.12745

Chaudhry, S., Tandon, A., Shinde, S., & Bhattacharya, A. (2024). Student psychological well-being in higher education: The role of internal team environment, institutional, friends and family support and academic engagement. *Plos One, 19*(1), e0297508. https://doi.org/10.1371/journal.pone.0297508

Choi, K., Shin, C., Kim, T., Chung, H. J., & Suk, H. J. (2019). Awakening effects of blue-enriched morning light exposure on university students' physiological and subjective responses. *Scientific Reports, 9*(1), 1–8. https://doi.org/10.1038/s41598-018-36791-5

Du, B., Tandoc, M. C., Mack, M. L., & Siegel, J. A. (2020). Indoor CO2 concentrations and cognitive function: A critical review. *Indoor Air, 30*(6), 1067–1082. 10.1111/ina.12706

Frontczak, M., & Wargocki, P. (2011). Literature survey on how different factors influence human comfort in indoor environments. *Building and Environment, 46*(4), 922–937. https://doi.org/10.1016/j.buildenv.2010.10.021

Gentile, N., Goven, T., Laike, T., & Sjoberg, K. (2018). A field study of fluorescent and LED classroom lighting. *Lighting Research & Technology, 50*(4), 631–650. https://doi.org/10.1177/1477153516675911

Jiang, J. T., & Yang, C. Z. (2011). Investigation of the subjective evaluation of indoor illumination level on perceived air quality. Paper presented at the *7th International Symposium on Heating, Ventilating and Air Conditioning, Proceedings of ISHVAC 2011,* 453–458.

Kim, J., & de Dear, R. (2012). Nonlinear relationships between individual IEQ factors and overall workspace satisfaction. *Building and Environment, 49*, 33–40. https://doi.org/10.1016/j.buildenv.2011.09.022

Kuller, R. (1991). Environmental assessment from a neuropsychological perspective. In T. Garling, & G. W. Evans (Eds.), *Environment, Cognition, and Action: An Integrated Approach* (pp. 78–95). Oxford University Press.

Makaremi, N., Yildirim, S., Morgan, G. T., Touchie, M. F., Jakubiec, J. A., & Robinson, J. B. (2024). Impact of classroom environment on student wellbeing in higher education: Review and future directions. *Building and Environment, 265*, 111958. https://doi.org/10.1016/j.buildenv.2024.111958

Mendell, M. J., & Heath, G. A. (2005). Do indoor pollutants and thermal conditions in schools influence student performance? A critical review of the literature. *Indoor Air, 15*(1), 27–52. https://doi.org/10.1111/j.1600-0668.2004.00320.x

Norbäck, D., Nordström, K., & Zhao, Z. (2013). Carbon dioxide (CO2) demand-controlled ventilation in university computer classrooms and possible effects on headache, fatigue and perceived indoor environment: an intervention study. *International Archives of Occupational and Environmental Health, 86*(2), 199–209. https://doi.org/10.1007/s00420-012-0756-6

Pittana, I., Morandi, F., Cappelletti, F., & Gasparella, A. (2022). Investigating the quality of the correlation between indoor environmental factors and human perception. Paper presented at the I*nternational High Performance Buildings Conference*

RVO. (2021). *Programma van Eisen Frisse Scholen 2021.* Utrecht: Rijksdienst voor Ondernemend Nederland. https://www.rvo.nl/sites/default/files/2021/06/PvE-Frisse-Scholen-2021.pdf

Torresin, S., Pernigotto, G., Cappelletti, F., & Gasparella, A. (2018). Combined effects of environmental factors on human perception and objective performance: A review of experimental laboratory works. *Indoor Air, 28*(4), 525–538. https://doi.org/10.1111/ina.12457

Van Duijnhoven, J. &., Aarts, M. P. J., Van den Heuvel, E. R. &., & Kort, H. S. M. (2021). The identification of variables influencing personal lighting conditions of office workers. L*ighting Research & Technology*, *53*(6), 527–541. https://doi.org/10.1177/1477153520976950

Watson, D., Clark, L. A., & Tellegen, A. (1988). Development and validation of brief measures of positive and negative affect: the PANAS scales. *Journal of Personality and Social Psychology, 54*(6), 1063. https://doi.org/10.1037/0022-3514.54.6.1063

Zhao, Y., & Li, D. (2023). Multi-domain indoor environmental quality in buildings: A review of their interaction and combined effects on occupant satisfaction. *Building and Environment, 228*, 109844. https://doi.org/10.1016/j.buildenv.2022.109844

ACKNOWLEDGEMENTS

The authors would like to thank the Institute of Future Environments of the Hanze UAS for giving permission and organizing this research project. Also, the authors are grateful to the involved students and lecturers, both for their contribution to this study and for their hospitality that allowed our presence during the lectures.

Wind Engineering & Aerodynamics (13:30-15:00 h)

6th International Conference on Building Energy and Environment
Eindhoven University of Technology, The Netherlands
6 - 10 July 2025

Urban wind energy: A comprehensive experimental study through Building-Integrated Wind Turbines

Payam Gholamalipour*, Ted Stathopoulos, Hua Ge and Murad Aldoum

Department of Building, Civil, and Environmental Engineering, Concordia University, Montreal, Quebec, Canada
**Corresponding email: payam.gholamalipour@mail.concordia.ca*

SUMMARY
Building-Integrated Wind Turbines (BIWTs) present a promising renewable alternative in urban areas, offering potential sustainable energy production directly where it is consumed. However, the performance of BIWTs is influenced by the complex turbulent wind flow patterns caused by urban environments. This study investigates the performance of both Horizontal Axis Wind Turbines (HAWTs) and Vertical Axis Wind Turbines (VAWTs). First, the performance is measured in wind-tunnel (WT) conditions, focusing on the impact of various parameters such as wind speeds, directions, and upstream roughness. These controlled tests aim to replicate diverse urban environments and compare the outputs with the manufacturer's nominal performance values. The second phase involves real-world testing on Concordia University's Future Buildings Laboratory (FBL) rooftop, assessing the wind BIWTs' long-term performance in complex urban wind environments. Consequently, this study provides valuable insights into optimizing BIWT installations and improving the efficiency of urban wind energy systems.

Keywords: Urban wind energy, Building Integrated Wind Turbine (BIWT), Wind-tunnel and field measurements.

1. INTRUDUCTION

The growing demand for localized energy generation to reduce transmission costs and power losses has increased interest in urban wind energy solutions. Wind power in urban settings offers a promising low-cost renewable alternative to conventional wind power (turbines in open wind farms) and demonstrates significant potential for development (Campbell et al., 2009). BIWTs are categorized based on the axis of rotation into two types: Horizontal Axis Wind Turbines (HAWTs) and Vertical Axis Wind Turbines (VAWTs). HAWTs have demonstrated higher effectiveness for large-scale energy production compared to VAWTs. However, VAWTs offer greater flexibility in installation, particularly on rooftops or building sides.

Unlike turbines situated in open wind farms, BIWTs' output is influenced by diverse factors. Key parameters affecting BIWT performance include wind speed, wind direction, installation height and location, building geometry, roof shape, surrounding obstacles, urban density, urban layout, and the type of BIWT (Juan et al., 2021). These variables can significantly impact BIWT's efficiency, making the effective positioning of BIWTs a challenge in urban areas. For instance, the shape of the roof is a significant factor influencing wind flow patterns and turbulence intensities. The accelerated wind velocity near the building roof can result in up to 56% more power output compared to a free-standing wind turbine (Abohela et al., 2013). Another example is a CFD-based study that examines both buildings and BIWTs on rooftops. The study shows that selecting the optimal BIWT installation location, building geometry, and BIWT type (e.g., number of blades) can lead to an increase in the power coefficient from 0.043 to 0.24 (Larin et al., 2016). However,

a poor installation choice can lead to zero energy output even in high-wind conditions (Toja-Silva et al., 2013). Therefore, despite extensive investigations into BIWTs, the complexity of urban airflow, turbulence characteristics, and the numerous influential parameters mean that much remains unknown and is still under investigation (Rezaei and Paraschivoiu, 2023; Stathopoulos et al., 2018; Vranešević et al., 2022). In this study, a comprehensive investigation of BIWTs was conducted under both fixed conditions in WT and real-world field measurements to better understand the impact of various geometrical parameters, wind flow pattern, and turbulence characteristics in urban areas.

2. WIND-TUNNEL (WT) MEASUREMENTS

The inflow profiles are measured for four wind speeds, at a location 1.2 m upstream of the BIWTs within WT. **Fig. 1** shows the dimensionless profiles of simulated Atmospheric Boundary Layer (ABL) inflow velocity, $\frac{\bar{U}(z)}{\bar{U}_{max}}[-]$, and Turbulent Kinetic Energy (TKE), $\frac{k(z)}{\bar{U}_{max}^2}[-] = \frac{1}{2}\frac{(\bar{U}^2 I_u^2+\bar{V}^2 I_v^2+\bar{W}^2 I_w^2)}{\bar{U}_{max}^2}$, in which $I_{u,v,w}$ (measured as %) is the turbulence intensity. The streamwise mean velocity increases with height from the WT floor up to 0.7 m before decreasing due to the effect of the WT ceiling. $\overline{U}_{max}$, measured at the height of 0.7, is 6.2, 10.8, 12.3 and 13.1 m/s for Low, Mid_1, Mid_2, and High wind speeds, respectively. Roughness cubes of varying sizes were placed over a 6-meter section of WT, starting 2.4 m upstream of the BIWTs. The TKE exhibits high values near the floor due to surface roughness and the carpet, decreases up to a height of 0.9 m, and then slightly increases. Moreover, the inflow profile with higher streamwise velocity corresponds to higher TKE.

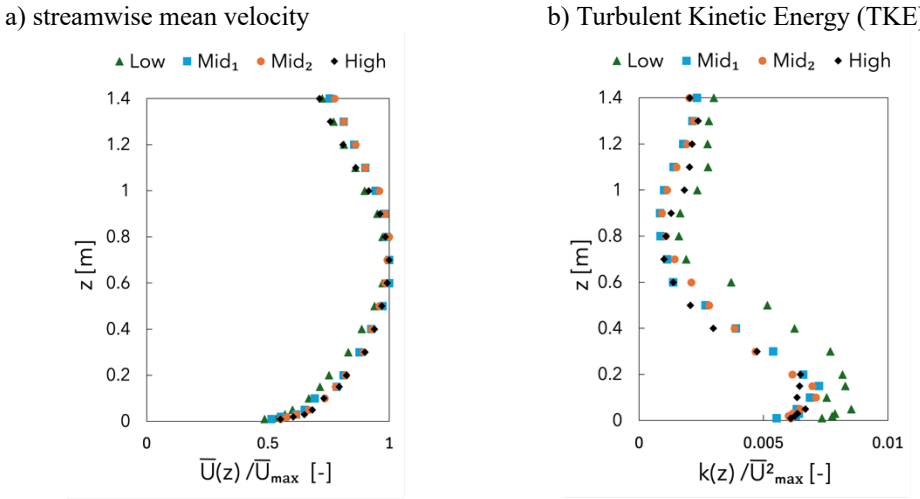

Figure 1. Dimensionless inflow ABL profiles, measured at Concordia University's wind-tunnel

Figs. 2a and 2c show the HAWT and VAWT installed in Concordia University's wind-tunnel. Both wind turbines used in this study were purchased from Leading Edge Power, and details regarding their dimensions and manufacturing specifications are available in the company manuals (Leading Edge Power, LE-300 Turbine Installation & Operation Guide; LE-v150 & LE-v150 Extreme & LE-v150 Extreme Storm Installation & Operation Guide, 2025). The blockage ratios for the HAWT and VAWT are 7% and 9%, respectively, based on the WT cross-section dimensions of $W \times H$=1.8×1.7 m^2. Higher blockage ratios (>5%) lead to the acceleration of wind flow around BIWTs, potentially leading to discrepancies in power output results. **Figs. 2b and 2d**

present the power output comparisons between the nominal and measured values at various wind speeds. For the VAWT, the effects of different wind directions, i.e., front, side, and back, were also studied. The swept areas of the HAWT and VAWT begin at heights of 0.187 m and 0.1 m above the WT floor, respectively. Thus, the average streamwise velocities impacting the turbine blades were calculated specifically within these swept areas. For the HAWT, the average velocities are $\overline{U}_{ave} = 5.60, 10.17, 11.60$ and 12.24 m/s. For the VAWT, the corresponding average velocities are $\overline{U}_{ave} = 5.54, 10.06, 11.49,$ and 12.17 m/s, shown in **Fig. 1**. The best performance of VAWT is observed for front wind directions (lower discrepancy) and the worst for side wind directions.

a) HAWT in wind-tunnel

b) HAWT power output comparisons

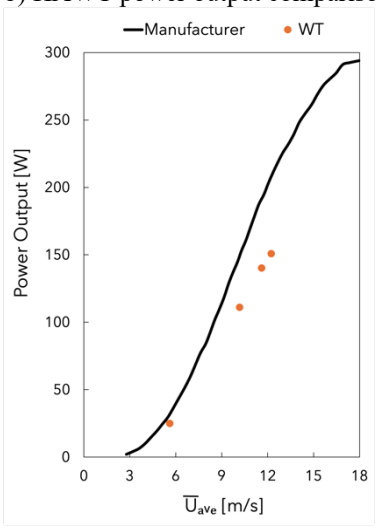

c) VAWT in wind-tunnel

d) VAWT power output comparisons

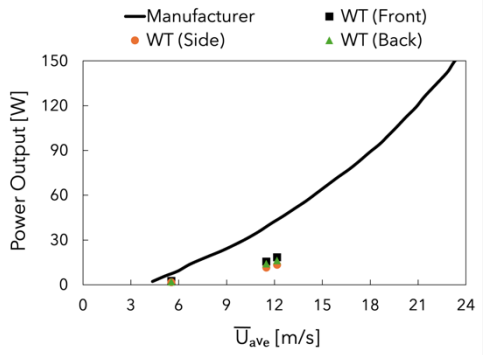

Figure 2. Power output comparisons between wind-tunnel measurements and available manufacturer data

3 FIELD MEASUREMENTS

Fig. 3a shows Concordia University's Future Building Laboratory (FBL) located on the Loyola Campus. Additional information regarding the size and location of the FBL can be found on the Concordia University Website. Preliminary wind measurement data has already been collected from a station on the roof of the FBL, which will be used to optimize the installation process for the BIWTs. **Fig. 3b** presents the wind direction distribution (in %) for the year of 2024, excluding a few days of data loss, highlighting the predominant wind directions from the N, SSE and WSW. **Fig. 3c** shows nine years of wind direction distribution, measured at Dorval/Lac Saint-Louis weather station in Montreal to compare and verify the local measurements (Al-Quraan et al., 2016).

a) Future Buildings Laboratory (FBL) b) FBL in year 2024 (%) c) Montreal from 2007 to 2016 (%)

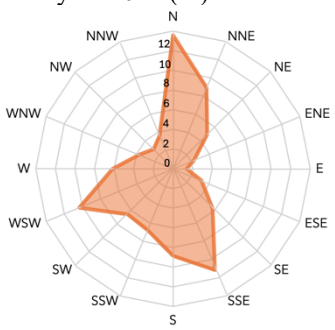

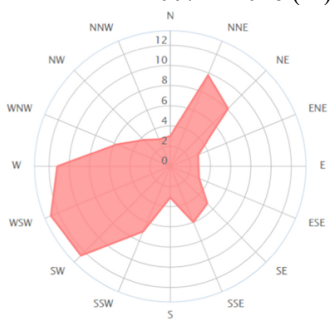

Figure 3. Wind rose comparison between measurements on the roof of Concordia University's FBL in year 2024 and Dorval/Lac Saint-Louis weather station in Montreal from 2007 to 2016 (Al-Quraan et al., 2016)

4. CONCLUSIONS

- Horizontal and vertical axis wind turbines (HAWT and VAWT) were tested in Concordia University's wind-tunnel under controlled conditions with fixed wind speeds and directions. The measurements show that HAWT power output aligns more closely with the nominal values provided by the manufacturer compared to VAWT, particularly under side wind direction. The discrepancies may be due to the higher blockage ratios (7% and 9%).
- The preliminary wind measurements from the weather station on the FBL's roof provide essential information for optimizing the installation of the BIWTs, including their location, height, and orientation.

REFERENCES

Abohela, I., Hamza, N., Dudek, S., 2013. Effect of roof shape, wind direction, building height and urban configuration on the energy yield and positioning of roof mounted wind turbines. Renew Energy 50, 1106–1118.

Al-Quraan, A., Stathopoulos, T., Pillay, P., 2016. Comparison of wind tunnel and on site measurements for urban wind energy estimation of potential yield. Journal of Wind Engineering and Industrial Aerodynamics 158, 1-10.

Campbell, N., Harries, A., Stankovic, S., 2009. Urban wind energy. Urban Wind Energy 1–189.

Juan, Y.H., Wen, C.Y., Li, Z., Yang, A.S., 2021. Impacts of urban morphology on improving urban wind energy potential for generic high-rise building arrays. Appl Energy 299, 117304.

Larin, P., Paraschivoiu, M., Aygun, C., 2016. CFD based synergistic analysis of wind turbines for roof mounted integration. Journal of Wind Engineering and Industrial Aerodynamics 156, 1–13.

Leading Edge Power, LE-300 Turbine Installation & Operation Guide, Leading Edge Power, [Online]. Available: https://www.leadingedgepower.com/documents/GA-LETU-007-LE300-User-Manual.pdf [Accessed: Feb. 6, 2025].

Leading Edge Power, LE-v150 & LE-v150 Extreme & LE-v150 Extreme Storm Installation & Operation Guide, Leading Edge Power, [Online]. Available: https://www.leadingedgepower.com/documents/GA-LETU-013-LE-v150-&-LE-v150-Ex-User-Manual.pdf [Accessed: Feb. 6, 2025].

Rezaei, F., Paraschivoiu, M., 2023. Computational study of the effect of building height on the performance of roof-mounted VAWT. Journal of Wind Engineering and Industrial Aerodynamics 241, 105540.

Stathopoulos, T., Alrawashdeh, H., Al-Quraan, A., Blocken, B., Dilimulati, A., Paraschivoiu, M., Pilay, P., 2018. Urban wind energy: Some views on potential and challenges. Journal of Wind Engineering and Industrial Aerodynamics 179, 146–157.

Toja-Silva, F., Colmenar-Santos, A., Castro-Gil, M., 2013. Urban wind energy exploitation systems: Behaviour under multidirectional flow conditions—Opportunities and challenges. Renewable and Sustainable Energy Reviews 24, 364–378.

Vranešević, K.K., Vita, G., Bordas, S.P.A., Glumac, A.Š., 2022. Furthering knowledge on the flow pattern around high-rise buildings: LES investigation of the wind energy potential. Journal of Wind Engineering and Industrial Aerodynamics 226, 105029.

6th International Conference on Building Energy and Environment
Eindhoven University of Technology, The Netherlands
6 - 10 July 2025

Numerical evaluation of atmospheric wind load on buildings through small-scale downscaling of extreme weather event

Petros Ampatzidis[1], Bidesh Sengupta[1], Francesco De Martin[1], Andrea Zonato[2], Andrea Petronio[3], Carlo Cintolesi[1], Silvana Di Sabatino[1]

[1] *University of Bologna, Bologna, Italy, Email address*
[2] *Koninklijk Nederlands Meteorologisch Instituut, De Bilt, The Netherlands*
[3] *National Institute of Oceanography and Applied Geophysics - OGS, Trieste, Italy*

SUMMARY
Extreme winds pose high risks for the loss of functionality of structures, which is not yet well studied and incorporated into risk analyses. This work aims to quantify the impact of intense winds on buildings, focusing on the case study of the Cattinara Public Hospital in Trieste (Italy). The hospital stands on an isolated hill exposed to strong local winds, e.g. the Bora. A powerful storm event (which occurred in winter 2012) was numerically reproduced on the city scale using the Weather Research and Forecast (WRF) model. Subsequently, a statistical downscaling procedure was used to set up high-resolution simulations with computational fluid dynamics models. The weather-informed Reynolds-Averaged Navier-Stokes simulations reproduced the local wind dynamics and a detailed estimation of atmospheric load on the hospital compound. Beyond the specific case study, the work proposes a general methodology for estimating the impact of extreme winds on structures by numerical downscaling at very high resolution.

Keywords: Extreme Weather Events, Downscaling strategies, Environmental Fluid Dynamics.

1. INTRODUCTION

Extreme weather events are expected to increase in intensity and frequency due to ongoing climate change. These include highly energetic thunderstorms, which can strongly impact assets and socio-economic activities. Specifically, the last decade has seen several extreme wind events that have resulted in significant damage to infrastructure, e.g. building roofs, power grids, warehouses, window glass and frames. Although the structural stability of infrastructures and buildings is hardly at risk, intense winds can produce extensive damage and loss of functionality, (Pastori and Mazzucchelli, 2023), which become critical when it comes to key socio-economic infrastructures such as hospitals, transport networks, energy distribution and communications. Despite this, the assessment of the risks from extreme wind events is still not properly included in the emergency and risk mitigation plans developed by infrastructure managers. This is also because realistic wind load estimation at the building scale is complex and challenging: it requires accurate numerical modelling of the local terrain topography, building area morphology, and the reproduction of atmospheric dynamics and turbulence, which play a key role in the estimation of the wind impact (Dagnew and

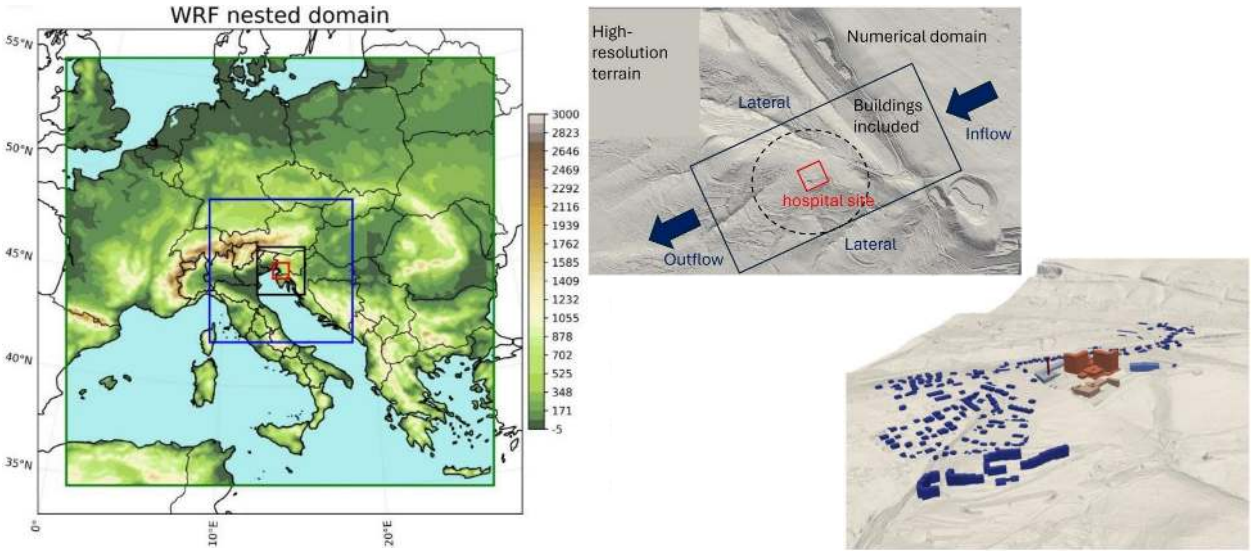

Figure 1. The case study of Cattinara public hospital in Trieste, Italy. Left panel, nested domains for WRF simulations; Right panels, an overview of the simulation domain including complex topography and major buildings of the areas.

Bitsuamlak, 2013). Such elements cannot be reproduced with a single tool, but require the coordinated and complementary use of multiple simulation models covering the variety of spatial and temporal scales that characterise the problem. This issue is here addressed by implementing and applying to a real-world case, a (general) numerical downscaling strategy that aims to reproduce the realistic atmospheric load on buildings by transporting information from the meteorological scale to the very small, local, building scale.

2. METHODOLOGY

The work focusses on the case study of the Cattinara Public Hospital in Trieste (Italy), which is taken as a representative of a relatively tall building and is regularly exposed to strong local wind (the Bora wind) characterised by high intensity and strong gusts. Specifically, a particular extreme event of strong Bora wind (registered in February 2012) has been selected to be numerically reproduced and analysed. Wind velocity is the main meteorological variable used to estimate the atmospheric load on building facades, quantified as the surface pressure load. An additional element that can increase the load is the wind-driven rain, which can be included through semi-empirical relations. The wind dynamics at the building scale is obtained through a chain of numerical simulations and different scales, strategically linked together (Figure **??**): the meteorological simulations have been carried out to reproduce the selected extreme event using the Weather Forecast and Research (WRF) model - version 4.5.1 (Zonato et al., 2022). Three nesting domains have been used to obtain a horizontal resolution in the Cattinara area of 333 m. A sensitivity study has been carried out on different submodels and schemes, and the simulation results have been evaluated against measured data available from the public Environmental Protection Regional Agency (ARPAFVG) of the Trieste region. The WRF simulations allowed us to characterise the mesoscale dynamics of the Bora wind. Raynolds-Averaged Navier-Stokes (RANS) simulations at a very high

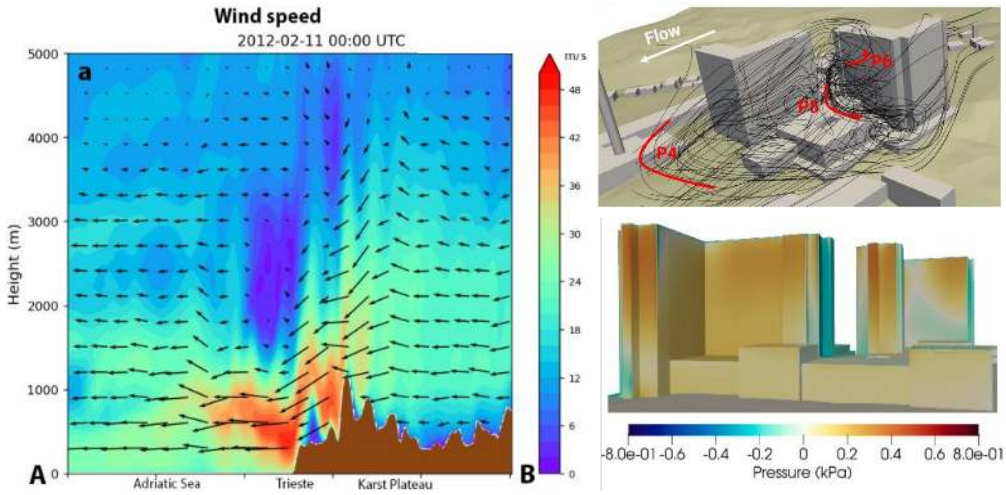

Figure 2. Statistical downscaling of wind dynamics from mesoscale to building scales. Left panel, wind speed from WRF simulation at the area of the city of Trieste (vertical section); Right panels, channelling effect between the hospital towers and recirculation region in the downwind yard (top panel), and pressure coefficient distribution on building surfaces.

resolution around the hospital compound are used to reconstruct the turbulent wind field at the building scale—for the numerical approach, see e.g. Ampatzidis et al., 2024. The simulation code is the open-source software OpenFOAM and the domain dimensions are $37H \times 33H \times 15H$ in the streamwise, spanwise and vertical directions, with respect to the prevalent wind direction and the hospital height $H = 54$ m. The complex terrain topography is reproduced together with the secondary buildings around the hospital within a distance of 300 m. The computational mesh is composed of around 50×10^6 cells and the cell height at the hospital facades is 0.6 m to ensure a direct resolution of the wall-boundary layer, while elsewhere wall functions are applied.

3. DISCUSSION AND FINAL REMARKS

Three simulations with different inflow conditions are carried out: (1) uniform inflow condition, the inflow is very simplified and consists of a constant wind value; (2) log-law inflow, where the inflow wind has a theoretical profile of an atmospheric boundary layer; (3) WRF-informed inflow, using the first- and second-order statistics of wind velocity and key atmospherical variables (wind velocity, direction, turbulent kinetic energy) derived from WRF simulations. The comparison between the three simulations provides information about the effects and features reproduced by realistic boundary conditions with respect to the simplified ones and allows to evaluate the loss of accuracy when simplified conditions are used.

WRF simulations satisfactory reproduce the extreme weather event selected and highlight the synoptic drivers of the Bora wind: it was generated by the difference of pressure between the Adriatic Sea and the Balkans (see Figure 2-left panel). Results provide velocity statistics at the inflow boundary for the high-resolved simulations. RANS simulations show that the uniform inflow condition results in an oversimplification of the system and overestimates the atmospheric load on buildings while not correctly reproducing several features of the general wind circulation. In par-

ticular, the interaction with the complex topography is not properly reproduced, which affects the overall simulation results. The log-law and WRF-informed inflow show similar results in terms of wind load on the hospital buildings, but the global circulation exhibits different features (see Figure 2-right panel). This is mainly due to the presence of a vertical velocity component in the WRF-informed inflow, which interacts with the complex terrain. The effect of the local topography on the circulation and intensity of the winds is analysed, together with the influence of the building morphology in accentuating or not the wind impact (e.g. triggering channelling effects that locally increased the speeds, or generating recirculation and stagnation zones - Figure 2-right panel).

In short, the atmospheric load on buildings is highly dependent on specific local topography and building area morphology, as well as contingent weather conditions. Hence, deriving a universal conclusion about the effects of local topography and building morphology on wind circulation and intensity is a challenging goal which has not been explored here. However, the work proposes and applies a general methodology for estimating the impact of extreme winds on structures by numerical downscaling at very high resolution. The loss of functionality risk estimation is not directly addressed in this work, but the outcome of the simulations serves as input for such an estimation.

ACKNOWLEDGMENTS

This study is funded by the Horizon Europe RISKADAPT project (grant no. 101093939). The authors acknowledge the use of computational resources from the Open Physics Hub at the Dept of Physics and Astronomy "Augusto Righi" at the University of Bologna (Italy).

REFERENCES

Ampatzidis P., Cintolesi C., Di Sabatino S., and Kershaw T., 2024. Blue space effects on urban flow and pollution dispersion in a stable atmosphere. Urban Climate 55, 101898.

Dagnew A. and Bitsuamlak G. T., 2013. Computational evaluation of wind loads on buildings: a review. Wind Struct 16, 629–660.

Pastori S. and Mazzucchelli E. S., 2023. "Climate Change and Extreme Wind Events: Overview and Perspectives for a Resilient Built Environment". Proceedings of *Urban Transition*. Ed. by M. Wallhagen and M. Cehlin. IntechOpen, Rijeka. Chap. 9.

Zonato A., Martilli A., Jimenez P. A., Dudhia J., Zardi D., and Giovannini L., 2022. A new K–ε turbulence parameterization for mesoscale meteorological models. Monthly Weather Review 150, 2157–2174.

6th International Conference on Building Energy and Environment
Eindhoven University of Technology, The Netherlands
6 - 10 July 2025

Large eddy simulations of downburst propagation in urban environments

Mohammad Hadavi [1], Djordje Romanic [1]

[1] *Department of Atmospheric and Oceanic Sciences, Faculty of Science, McGill University, Montreal, Canada*
mohammad.hadavi@mail.mcgill.ca, djordje.romanic@mcgill.ca

SUMMARY
Downbursts are damaging downdrafts of negatively buoyant air generated within thunderstorms. Their intense winds near the ground pose significant risks to urban safety. Previous studies have mainly focused on isolated downburst-like winds or the propagation of atmospheric boundary layer (ABL) winds in cities. Consequently, the interaction between downbursts, ABL winds, and urban geometries remains relatively underexplored. This study employs large eddy simulations (LES) based on the Smagorinsky model to fill this gap. The simulations are validated against experimental studies through two scenarios: one involving ABL winds in urban environments and the other focusing on isolated downburst-like winds. The results indicate that the channelling effect causes wind speeds at pedestrian level to exceed the downburst centerline velocity. Although the spatially averaged velocity in urban areas is generally lower than in open terrain, the high-intensity winds persist over a greater vertical distance. This exacerbates the impact of downburst outflows on the built environment.

Keywords: Downburst, Urban environment, LES, Experiment.

1. INTRODUCTION

Downbursts are negatively buoyant air currents generated within thunderstorms that impinge upon the surface and spread radially (Hjelmfelt, 1988). Their high-intensity, transient, and spatially localized winds distinguish them from typical atmospheric boundary layer (ABL) winds. During these events, wind gusts can exceed 60 m s^{-1} at heights of 50 to 120 m above ground level, endangering both natural and built environments (Solari, 2020). The hazardous nature of downbursts is particularly pronounced in urban areas, where complex interactions with buildings can amplify localized wind speeds.

Collecting data on downbursts in urban areas is challenging due to their sudden onset, non-stationary nature, and the complexities of city environments. Furthermore, weather radars, a standard meteorological tool for observing near-surface flow fields in downbursts, cannot measure winds in urban areas due to ground clutter from buildings and other urban structures that interfere with radar signals. This results in limited full-scale data with sufficient spatiotemporal resolution. Wind tunnel measurements also encounter financial (Hangan et al., 2017) and physical constraints when simulating various configurations. Computational Fluid Dynamics (CFD) offers a valuable alternative for gaining insights into full-field flow characteristics, complementing experimental data. With advancements in computational resources, large eddy simulations (LES) are increasingly utilized. LES provides accurate results by resolving a significant portion of turbulent eddies within the entire spectrum of the turbulent kinetic energy fluctuations. This is essential for understanding the highly turbulent flow of downburst propagation (Aboshosha, 2015).

Several techniques exist to simulate downburst-like (DB) winds. One common method is the impinging jet (IJ), which is a turbulent, axisymmetric air jet that strikes the ground perpendicularly and spreads radially. This approach is well-regarded in wind engineering (McConville et al., 2009) for its effectiveness in replicating key dynamic features of a downburst outflow, including primary and secondary vortices.

Previous studies have extensively examined the effects of ABL winds in urban environments (Ricci and Blocken, 2020; Hadavi and Pasdarshahri, 2021). The dynamics of isolated DB winds in empty chambers are also well-documented (Romanic and Hangan, 2020; Žužul et al., 2024). However, the interaction between downburst winds, ABL winds, and urban areas remains relatively underexplored. This gap is particularly critical given the projected increase in the frequency and intensity of thunderstorms (Rädler et al., 2019) alongside rising urbanization (Uttara et al., 2012). Therefore, this research focuses on the propagation of a downburst-like wind within a representative urban setting under the influence of a background ABL wind.

2. METHODOLOGY

2.1. Case scenarios

This study considered two validation cases. First, the behavior of ABL winds in an urban environment was validated using wind tunnel measurements. A case from the Architectural Institute of Japan (AIJ) database (Tominaga et al., 2008) was selected to represent a typical idealized urban neighborhood. This case is referred to as "ABL validation" in this paper. Second, an isolated IJ without ABL and buildings was numerically simulated, and the results were compared against various experimental and numerical studies. This case is termed "IJ validation" in the present study. The validated simulations were then used to investigate the interactions of ABL and DB winds with the idealized urban environment.

2.2. LES simulations

The unsteady-state and isothermal LES simulations based on the Smagorinsky model were performed using the pimpleFoam solver from the OpenFOAM v2306 open-source CFD library (Ricci, 2024). The snappyHexMesh utility was used to generate a hexahedron-based unstructured mesh from a background grid. Details on the grid refinement are provided in the following subsections. The Courant–Friedrichs–Lewy number was kept below 0.5 throughout all simulations. A ratio of resolved turbulent kinetic energy (k_{res}) to total turbulent kinetic energy (k_{tot}) above 80% was maintained (Pope, 2001).

2.2.1. ABL validation

The idealized urban neighborhood consists of a grid of nine cubic building blocks (H_{Urban}=0.2 m). A refined uniform cell size of H_{Urban}/10=0.02 m was used for the target region (Fig. 1). The cells were kept as uniform as possible across the entire domain, with a stretching ratio below 1.05. This resulted in a grid of ~9.3 million cells. No-slip conditions were specified at the top, ground, sides, and building facades, while a zero-static gauge pressure was set at the outlet; the inlet ABL profile was imposed based on the wind tunnel data. The near-surface flow was modeled using Spalding's universal law of the wall.

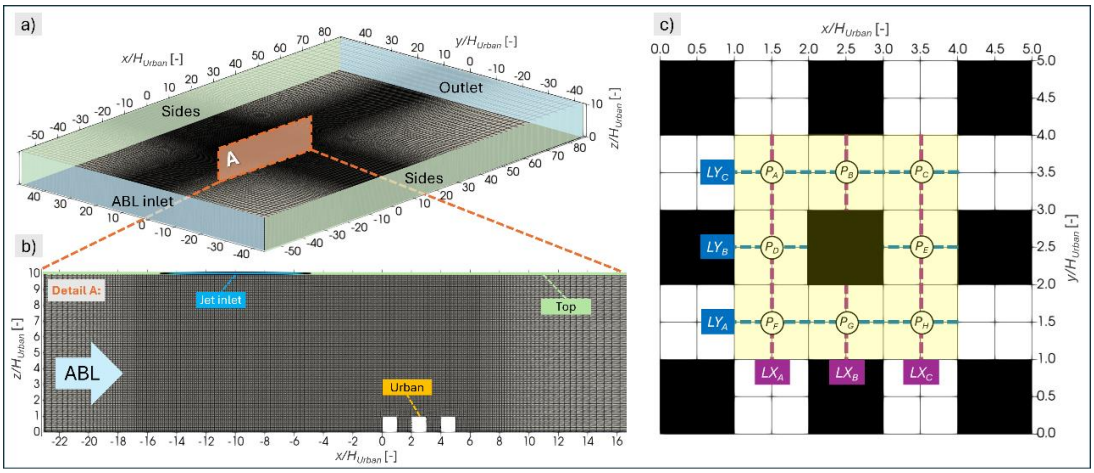

Figure 1. (a-b) Computational domain with the details of mesh refinement in the target region and boundary indications. The same computational grid was used for the ABL validation case and the ABL+DB scenario. c) Geometry of the urban neighbourhood. Results will be presented along the indicated lines. The yellow shaded region is designated for calculating the spatially averaged velocity within the urban area.

2.2.2. IJ validation

Figure 2 illustrates the dimensions, boundary conditions, and grid resolution of the IJ validation case. The jet has a diameter of D=0.0381 m, a height of 2D, and a downdraft centerline velocity of 7.9 m s^{-1} (Kim and Hangan, 2007). To optimize computational resources, half of the IJ was simulated, assuming axisymmetric behavior (Kim and Hangan, 2007). The cell size was refined to 0.0002 m near the ground surface and within the downdraft region, gradually increasing with a ratio of ~1.04 throughout the entire domain.

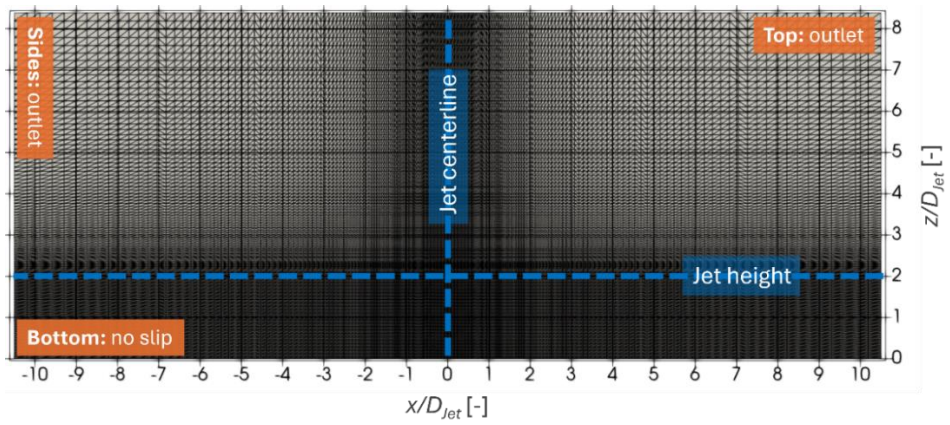

Figure 2. A cross-section of the computational domain for the IJ validation case at the jet centerline, showing the boundaries and mesh refinement details. The dimensions are based on the work of Kim and Hangan (2007).

2.2.3. Main case studies

A DB wind was modeled using a jet with a height and diameter of 2 m and a centerline velocity (w_{jet}) of 10 m s^{-1}. The urban area was located at a distance of one diameter from the jet centerline (Fig. 1b), i.e., a region of expected maximum radial velocity. With a spatial scale of 1:200, this study simulates a small microburst with a height and diameter of 400 m (Romanic et al., 2020),

impacting a mid-rise urban neighborhood with a height of 40 m in reality. For normalization, the urban height was used as the reference, with $U_{Urban} = U(H_{Urban})$, where U_{Urban} denotes the velocity of the ABL flow in the empty chamber.

The computational domain is identical to that used in the ABL validation case. This domain was developed through preliminary simulations to ensure the DB flow evolves without boundary interference. We observed that the size of the domain influences the flow, particularly upstream of the touchdown point (not shown due to space constraints). Moreover, the jet is injected directly at the top of the domain without employing a bell-mouth or nozzle geometry. This approach was selected because preliminary simulations indicated that the nozzle geometry disrupted the flow and created turbulent eddies, which affected the near-building flow. These disturbances were undesirable, as the focus is solely on the impact of the jet flow.

The non-dimensional distance from the wall (y^+) values across the ground ranged from ~2 in the stagnation region to ~218 in areas of highest radial velocity. These values fluctuated over time due to the passage of turbulent structures. For urban blocks, the minimum y^+ value was ~5, while the maximum reached ~306.

The LES simulations were conducted in three phases over a total duration of 14 s. In Phase 1 (0–4.5 s), the jet inflow is turned off, allowing the ABL flow to develop within the domain. Phase 2 (5–9 s) introduces a jet velocity of 10 m s^{-1}. In Phase 3 (9.5–14 s), the jet inflow is turned off again to replicate the dissipation stage. A uniformFixedValue boundary condition was applied, with a 0.5-second interval between each phase to allow for smooth transitions in velocity from 0 to 10 m s^{-1} and back.

3. RESULTS

3.1. Validation cases

Figure 3 presents the comparison between wind tunnel measurements and LES results of the ABL wind across three lines within the urban environment. The LES simulations effectively reproduce the flow characteristics in the open gaps between buildings and the wake regions behind them.

Figure 4a presents the IJ validation results as a vertical profile of horizontal velocity. The instantaneous maximum radial velocity profile extracted from the LES simulations aligns well with previous experimental and numerical studies. A discrepancy is noted with the field measurements from JAWS data (Hjelmfelt, 1988), which could be attributed to the influence of the ABL winds and cloud motion in the real environment. Moreover, the specific spatial location of real data collection, including radial distance and azimuth relative to the downburst centerline, is often not documented. Additionally, the peak velocity occurs at a slightly higher elevation in our LES simulations compared to some other profiles (e.g., Mason and Wood, 2004). This difference could be due to the small scale adopted for the simulations, potentially overestimating the outflow thickness. The formation of the primary vortex, as shown in Fig. 4b, is consistent with what is observed in nature. This occurrence is caused by Kelvin-Helmholtz instability, which arises from the shear between the still ambient air and the strong downward jet flow.

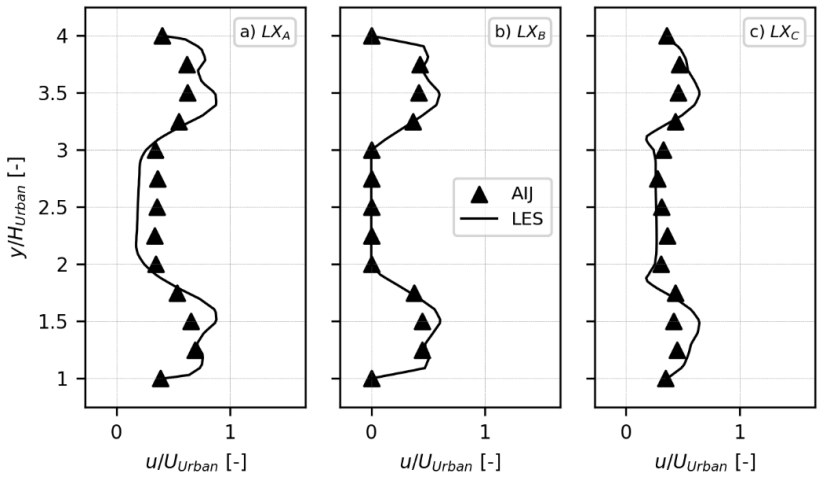

Figure 3. Results of the ABL validation case. (a-c) Comparison of experimental (AIJ) and LES results at z/H_{Urban}=0.1, across three horizontal lines of LX_A, LX_B, and LX_C. Refer to Fig. 1c for the location of these lines. The LES results are based on a cumulative average over 5 seconds following the initial transition period.

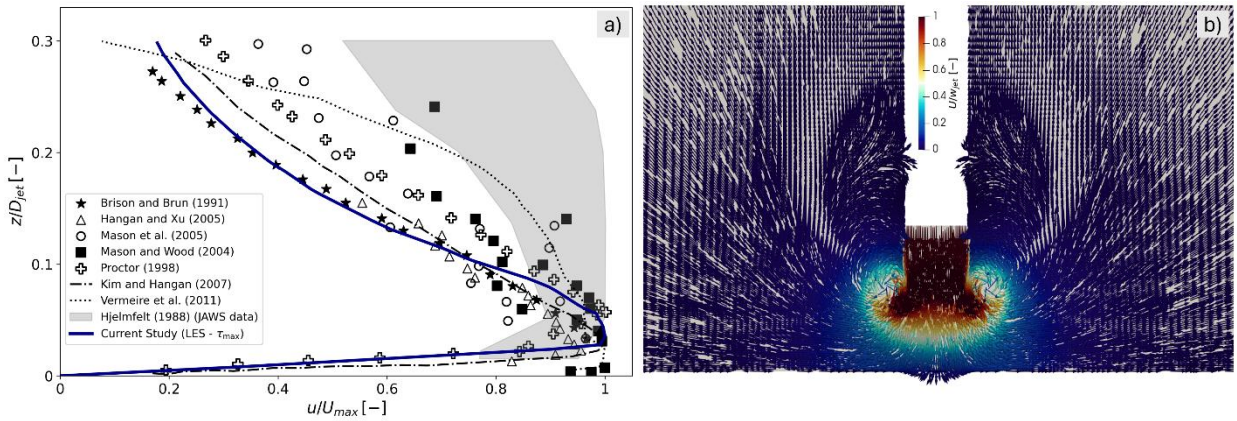

Figure 4. Results of the IJ validation case. a) Comparison of the instantaneous maximum radial velocity profile from LES with several studies. b) Generation of the primary vortex after jet release.

3.2. Main case studies

Figure 5 illustrates the wind flow variations along horizontal lines at heights z/H_{urban}=0.1, 0.5, 1, 2 for the ABL+DB scenario in both open terrain (i.e., non-buildings) and the urban environment. The profiles correspond to the time step when maximum radial velocity occurred in the open terrain scenario. As expected, recirculation zones behind buildings show the lowest wind speeds. In contrast, the channelling effect in unshielded areas between urban blocks accelerates wind speeds. These speeds exceed those in the non-urban case and even w_{jet}, worsening the impact of the downburst outflow on the built environment. This effect is most pronounced at the first and second roads. Farther downstream from the jet impingement, even unshaded locations experience a decrease in wind speeds (Fig. 5f, h), due to turbulent eddies generated by the DB propagation.

The maximum wind speed rises with height (Fig. 5c, e, g) as the impact of surface friction decreases and the ABL intensifies. In the open terrain scenario, wind speed peaks at z/H_{urban}=0.5 (Fig. 5e) before declining at higher elevations, indicating the gust front thickness. Above the urban

area (Fig. 5a), wind speeds along LX_A, LX_B, and the non-urban case are similar that shows the disappeared urban impact. However, behind the second row of buildings (LX_C), an intense peak occurs before a sharp velocity drop. This observation indicates that flow characteristics differ between the first and second roads. On the other hand, LY_A and LY_C show consistent patterns at all heights, pointing out nearly symmetrical wind flow behavior parallel to ABL and DB winds. Finally, the increase (Fig. 5b) and decrease (Fig. 5h) in wind speeds along LY_A and LY_C after y/H_{urban} ≈2.5 result from vortical structures generated downstream of the jet. This pattern is also seen in the non-urban case. An attached video at the end of this paper further visualizes the time evolution of turbulent eddies during the propagation and dissipation of downbursts in both open terrain and urban environments.

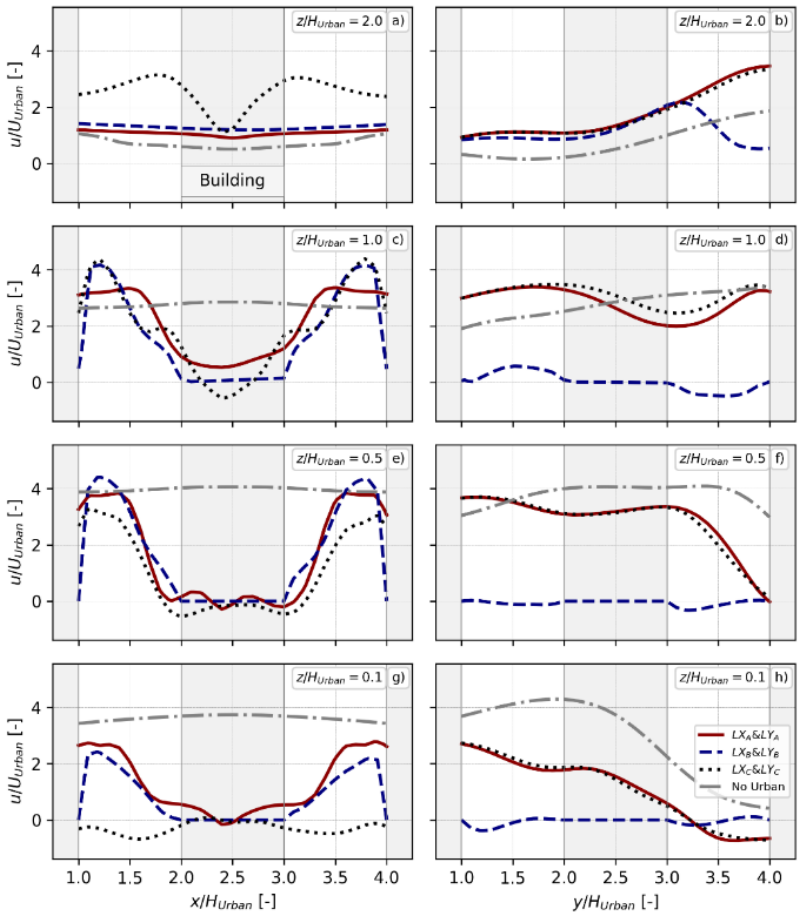

Figure 5. Horizontal wind speed variations along several lines between the urban blocks at four heights: z/H_{Urban}= (a-b) 2; (c-d) 1; (e-f) 0.5; (g-h) 0.1. The profiles correspond to the time step when the maximum radial velocity was recorded in the open terrain scenario. The left and right columns compare wind speeds along the LX and LY lines, respectively; refer to Fig. 1c for the line locations. The building locations in the urban area are shaded in grey. The profiles for the non-urban case are extracted at LX_B and LY_B.

Figure 6 depicts the vertical profile of horizontal wind, spatially averaged across the urban area. In the ABL case (Fig. 6a), a logarithmic wind profile is evident within the urban canopy layer, consistent with previous studies (Macdonald, 2000; Di Sabatino et al., 2008). The profiles for open terrain and urban cases exhibit similarities in DB propagation alone (Fig. 6b). However, mean wind speeds in the urban case are lower due to the inclusion of low-velocity wake regions in the

spatial averaging. Notably, while the non-urban case displays a typical nose-shape profile, the urban environment maintains the high-intensity winds over a greater vertical extent (Fig. 6c). This results in higher wind pressure on structures at elevated heights, exacerbating the vulnerability of the built environment to downbursts.

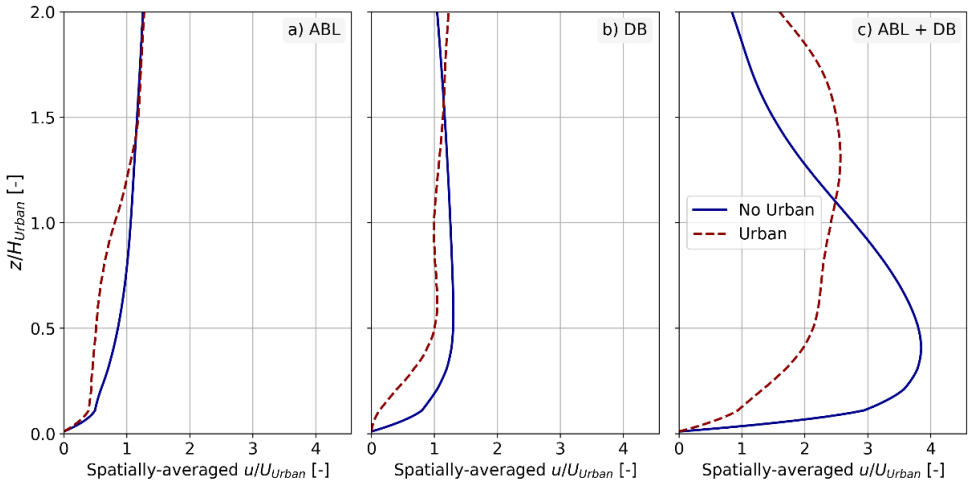

Figure 6. Vertical profiles of spatially averaged horizontal velocity for the scenarios of a) ABL, b) DB, and c) ABL+DB propagations in both open terrain and the urban area. The horizontal velocity is averaged at each vertical level within the area shown in Fig. 1c.

4. CONCLUSIONS

Downbursts are strong downdrafts of negatively buoyant air that descend from thunderstorms and impact the Earth's surface. They generate powerful outflows of intense winds close to the ground, posing risks to human safety and structures. This study explores a relatively underexplored topic in this field: the interaction between downburst winds, background atmospheric boundary layer (ABL) winds, and an idealized urban environment. We conducted large eddy simulations (LES) based on the Smagorinsky model. The simulations were validated against experimental studies through two cases: ABL propagation in an urban environment and an isolated downburst-like wind.

The results reveal that the channelling effect in unshielded areas between urban blocks accelerates wind speeds, surpassing those in the non-urban scenario and even the downburst centerline velocity. Additionally, we observed nearly symmetrical wind flow behaviour parallel to ABL and downburst winds at all heights within the urban neighbourhood. While spatially averaged wind velocities are lower in urban areas due to the inclusion of low-velocity wake regions, the urban environment maintains high-intensity winds over a greater vertical extent. Consequently, aerodynamic loads escalate at higher elevations, making urban infrastructure more susceptible to downburst wind damage.

ACKNOWLEDGEMENTS

The authors thank the Digital Research Alliance of Canada for providing access to supercomputer clusters used for running the LES simulations. We acknowledge the financial support of the Natural Sciences and Engineering Research Council of Canada (NSERC) through Discovery Grant

RGPIN-2021-02651. We appreciate the funding provided by the Fonds de recherche du Québec – Nature et technologies (FRQNT) through a Doctoral Research Scholarship. We also extend our gratitude to McGill University for their support through a Lorne Trottier Science Accelerator Fellowship.

REFERENCES

Aboshosha, H., Bitsuamlak, G. and El Damatty, A., 2015. Turbulence characterization of downbursts using LES. Journal of Wind Engineering and Industrial Aerodynamics 136, pp.44-61.

Di Sabatino, S., Solazzo, E., Paradisi, P. and Britter, R., 2008. A simple model for spatially-averaged wind profiles within and above an urban canopy. Boundary-layer meteorology 127, pp. 131-151.

Hadavi, M. and Pasdarshahri, H., 2021. Impacts of urban buildings on microclimate and cooling systems efficiency: Coupled CFD and BES simulations. Sustainable Cities and Society 67, p.102740.

Hangan, H., Refan, M., Jubayer, C., Romanic, D., Parvu, D., LoTufo, J. and Costache, A., 2017. Novel techniques in wind engineering. Journal of Wind Engineering and Industrial Aerodynamics 171, pp. 12-33.

Hjelmfelt, M.R., 1988. Structure and life cycle of microburst outflows observed in Colorado. Journal of Applied Meteorology and Climatology, 27(8), pp. 900-927.

Kim, J. and Hangan, H., 2007. Numerical simulations of impinging jets with application to downbursts. Journal of wind engineering and industrial aerodynamics, 95(4), pp. 279-298.

Macdonald, R.W., 2000. Modelling the mean velocity profile in the urban canopy layer. Boundary-Layer Meteorology 97, pp. 25-45.

McConville, A.C., Sterling, M. and Baker, C.J., 2009. The physical simulation of thunderstorm downbursts using an impinging jet. Wind and structures, 12(2), p.133.

Pope, S.B., 2001. Turbulent flows. Measurement Science and Technology, 12(11), pp. 2020-2021.

Rädler, A.T., Groenemeijer, P.H., Faust, E., Sausen, R. and Púčik, T., 2019. Frequency of severe thunderstorms across Europe expected to increase in the 21st century due to rising instability. npj Climate and Atmospheric Science, 2(1), p.30.

Ricci, A., 2024. Review of OpenFOAM applications in the computational wind engineering: from wind environment to wind structural engineering. Meccanica, pp.1-41.

Ricci, A. and Blocken, B., 2020. On the reliability of the 3D steady RANS approach in predicting microscale wind conditions in seaport areas: The case of the IJmuiden sea lock. Journal of Wind Engineering and Industrial Aerodynamics 207, 104437.

Romanic, D. and Hangan, H., 2020. Experimental investigation of the interaction between near-surface atmospheric boundary layer winds and downburst outflows. Journal of Wind Engineering and Industrial Aerodynamics 205, p.104323.

Romanic, D., Nicolini, E., Hangan, H., Burlando, M. and Solari, G., 2020. A novel approach to scaling experimentally produced downburst-like impinging jet outflows. Journal of Wind Engineering and Industrial Aerodynamics 196, p.104025.

Solari, G., 2020. Thunderstorm downbursts and wind loading of structures: Progress and prospect. Frontiers in built environment 6, p.63.

Tominaga, Y., Mochida, A., Yoshie, R., Kataoka, H., Nozu, T., Yoshikawa, M. and Shirasawa, T., 2008. AIJ guidelines for practical applications of CFD to pedestrian wind environment around buildings. Journal of wind engineering and industrial aerodynamics, 96(10-11), pp.1749-1761.

Uttara, S., Bhuvandas, N. and Aggarwal, V., 2012. Impacts of urbanization on environment. International Journal of Research in Engineering and Applied Sciences, 2(2), pp.1637-1645.

Žužul, J., Ricci, A., Burlando, M., Blocken, B. and Solari, G., 2024. Vortex dynamics and radial outflow velocity evolution in downburst-like winds. Computers & Fluids 283, 106393.

SUPPLEMENTARY MATERIAL

The following video visualizes the interactions between downburst and ABL winds over time in both open terrain and urban environments. Please note that only a portion of the domain, specifically the target region, is shown. The horizontal cross-sections are at mid-building height. The wind profile on the right corresponds to P_A (see Fig. 1c), as also indicated by a black star at the beginning of the video. The normalized time (τ) is defined as $\tau = t.f_s$ where f_s is the vortex passage frequency based on the Strouhal number.

Video link (Google Drive)

6th International Conference on Building Energy and Environment
Eindhoven University of Technology, The Netherlands
6 - 10 July 2025

The effects of downslope winds on complex built environments: A case study of Genoa port

Ivana Ivančić [1], Alessio Ricci [1,2], Massimiliano Burlando [3], Djordje Romanic [4], Branko Grisogono [5], Hrvoje Kozmar [5]

[1]*University School for Advanced Studies IUSS, Pavia, Italy, ivana.ivancic@iusspavia.it, alessio.ricci@iusspavia.it*
[2]*Eindhoven University of Technology, Eindhoven, the Netherlands, a.ricci@tue.nl*
[3]*University of Genoa, Genoa, Italy, massimiliano.burlando@unige.it*
[4]*McGill University, Montreal, Canada, djordje.romanic@mcgill.ca*
[5]*University of Zagreb, Zagreb, Croatia, branko.grisogono@gfz.hr, hkozmar@fsb.hr*

SUMMARY
Proper management of the port areas is hugely influenced by the wind conditions. While impact of neutrally stratified atmospheric boundary layer (ABL) wind on port infrastructures and ships has been investigated, less attention was given to extreme winds like downbursts, tornados and downslope winds. Downslope winds (DW) similarly to other extreme winds are characterized by high velocity near the ground, where port infrastructures are deployed. In this paper preliminary results of Computational Fluid Dynamics (CFD) simulations and LiDAR measurements of DW are compared for the case study in the port of Genoa, showing nose shape vertical velocity profile obtained both by measurements and CFD simulations.

Keywords: CFD, LiDAR measurements, risk exposure, port areas

1. INTRODUCTION

Ports are hubs for international trade and play a crucial role for the economy of countries. However, port areas as well as coastal areas are highly exposed to extreme meteorological phenomena, especially winds (Castillo et al., 2024). Extreme winds can cause accidents in port areas as well as pose risks to human life (Zhang et al., 2015). Most commonly used international standards and codes are based on neutrally stratified ABL winds. In case of neutral stratification, ABL winds are characterized by lower mean velocities near the ground compared to other extreme winds like thunderstorm downbursts, tornados, downslope winds (DW). Despite the great efforts made by the wind engineering community in the recent years to understand downbursts and tornados (e.g. Solari et al., 2020), less attention has been given to DWs. DWs typically develop when air flows over high mountains and falls down along steep lee slopes accelerating because of the negative buoyancy (Fig. 1a). This wind is known to occur all over the world with different local names like Alpine Foehn, Rocky Mountain Chinook, Croatian Bora (e.g. Kozmar et al., 2012; Durran, 2014; Lepri et al., 2015). In Liguria, Italy, specific DWs can occur when the wind blows from the north of Apennines and Maritime Alps towards the Ligurian Sea. The DW is driven by the large-scale pressure gradient directed from the colder continental air toward warmer air above the Ligurian Sea (Burlando et al., 2017). Understanding the nature of DWs is vital for improvement of existing formulations for wind provisions on port structures, which will help to safeguard the port

operations. This manuscript describes part of the first stage of a PhD project which started in early 2024 with the aim to provide port stakeholders with practical tools to better manage the safety of port areas. CFD simulations, LiDAR scanner and profiler measurements are carried out on DW, and a preliminary comparison in terms of vertical wind profiles is provided. It is worth mentioning that even though DWs were extensively studied by atmospheric scientists and simulated with weather forecast models, to the best of the author's knowledge they have never been simulated by means of CFD techniques with focus on their effect on the urban environment.

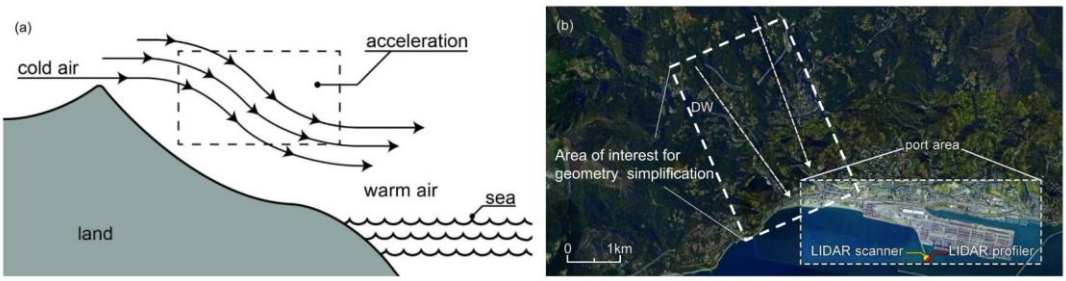

Figure 1. a) Schematic view of DW. b) Aerial view of the port of Genoa with the LiDAR scanner and LiDAR profiler positions with the indication of DW approaching direction and area of interest for construction and simplification of geometry

2. METHODOLOGY

2.1. LiDAR measurements

In the Turchino valley, situated in the western part of Genoa city, DW occurring during the winter period are much stronger than those occurring during other seasons. Therefore, measurements in the port of Genoa are carried out in the winter season using the LiDAR scanner WindCube 400S and LiDAR profiler WindCube-V2. The LIDAR scanner operates in a range of 14 km and a gate resolution set to 75 m, while the LiDAR profiler measures at 12 levels from 40 to 250 m above the sea level. LiDAR stations are situated at the end of the quay, which is a suitable position for measuring DWs approaching from the Turchino valley and nearby valleys towards the sea (Fig. 1b). The LiDAR profiler can provide wind velocity and turbulence intensity at 12 different levels above the sea level allowing for the reconstruction of a vertical profile. The LiDAR scanner can provide the wind velocity field in terms of radial velocity ensuring at this stage a qualitative understanding of the 3D flow field and a preliminary comparison with wind velocity contours obtained by CFD. In this paper only data obtained by the LiDAR profiler are shown.

2.2. CFD simulation

Steady Reynolds-averaged Navier-Stokes (RANS) simulations were performed on a simplified 2.5D computational domain (Fig. 2a). Simplification of the Genoa region was performed in two steps. Firstly, the 3D geometry of Genoa's region was used to obtain characteristic slopes of the terrain orography by “slicing” the area of interest and saving the coordinates of each characteristic slope. Secondly, coordinates of characteristic slopes were imported in opensource software Blender for simplification (Fig. 2a). The computational grid was constructed with the *blockMesh* utility of the opensource code OpenFOAM (Fig 2b). The boundary conditions are shown in Fig 2c. At the inlet face, a log-law mean velocity profile was imposed to reproduce neutral ABL wind.

The aerodynamic roughness length (z_0) was assumed equal to 0.05 m with reference velocity of 5 m/s at of 660 m above the sea level. Temperature at the inlet was set according to the thermal gradient of dry adiabatic lapse rate (i.e. 10 K/km), with surface temperature equal to 16°C. No slip conditions were imposed on the walls with z_0 = 0.05 m for mountain and z_0 = 0.0002 m for the sea. The *buoyantBoussinesqSimpleFoam* solver, with *k-ε* turbulence model was used.

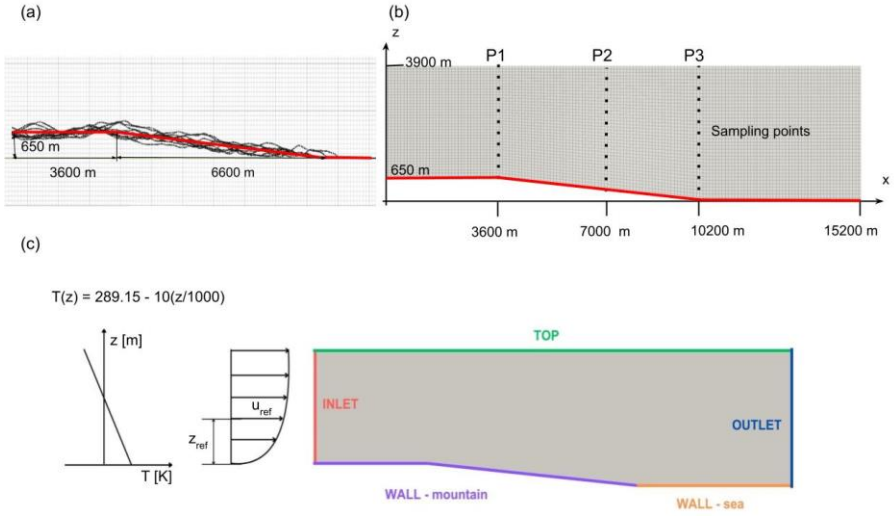

Figure 2. a) Characteristic slopes obtained from the area of interest (see Fig 1b); b) 2.5 D computational domain and grid with the indication of sampling positions for the vertical profiles of the mean wind velocity; c) Boundary conditions imposed on the domain

3. RESULTS AND CONCLUDING REMARKS

Fig 3a shows the development of the vertical profile of mean velocity at three positions (P1, P2, P3): beginning, middle, and end of the slope upstream the coastline (see also Fig. 2b). The velocity profiles are normalized with the maximum velocity (U_{max}) measured/simulated at each sampling point. In general, Fig. 3 shows a significant development of the mean velocity profile, from a standard neutral ABL profile (inlet) to a vertical nose-shape profile typical of DWs (outlet). This nose shape is certainly caused by the temperature gradient and gravity force further emphasized by the nature of the slope. Considering the high level of simplifications introduced in the computational model, the first qualitative comparison of CFD and LiDAR in terms of vertical profiles showed a good agreement between 40 and 250 m. Additional results will be shown during the presentation.

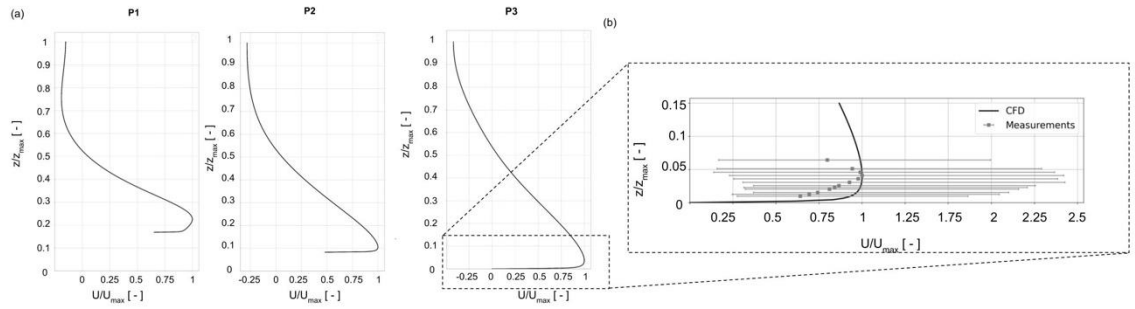

Figure 3. a) Development of the DW nose shape profile at the three positions P1, P2 and P3 (see also Fig. 2b); b)

Comparison of LiDAR and CFD profiles in terms of mean velocity at position P3.

ACKNOWLEDGEMENTS

This study was developed while attending the PhD programme in Sustainable Development And Climate Change at the University School for Advanced Studies IUSS Pavia, Cycle XXXIX, with the support of a scholarship financed by the Ministerial Decree no. 351 of 9 April 2022, based on the NRRP - funded by the European Union - NextGenerationEU - Mission 4 "Education and Research", Component 1 "Enhancement of the offer of educational services: from nurseries to universities"- Investment 4.1 "Extension of the number of research doctorates and innovative doctorates for public administration and cultural heritage".

REFERENCES

Burlando, M., Tizzi, M., Solari, G., 2017. Characteristics of downslope winds in the Liguria Region. Wind and Structures Vol. 24, pp. 613-635.

Castillo, A. P. P., Heranza, J. C. M., 2024. A review of wind impact on container port operations: current technologies, strategies and future perspectives. Procedia Computer Science Vol. 251, pp. 783-788.

Zhang, Y., Lam, J. S.L.,2015. Estimating the economic losses of port disruption due to extreme wind events. Ocean & Coastal management Vol. 116, pp. 300-310.

Durran, D.R., 2014. Encyclopaedia of Atmospheric Sciences. 2nd ed., Academic press, 69-74.

Kozmar, H., Butler, K., Kareem, A., 2012. Transient cross-wind aerodynamic loads on a generic vehicle due to bora gusts. Journal of Wind Engineering and Industrial Aerodynamics 73-84.

Lepri, P., Večenaj, Ž., Kozmar, H., Grisogono, B., 2015. Near-ground turbulence of the Bora wind in summertime. Journal of Wind Engineering and Industrial Aerodynamics 345-357.

Solari, G., Burlando, M., Repetto, M. P., 2020. Detection, simulation, modelling and loading of thunderstorm outflow to design wind-safer and cost-efficient structures. Journal of Wind Engineering and Industrial Aerodynamics 200, 104142.

6th International Conference on Building Energy and Environment
Eindhoven University of Technology, The Netherlands
6 - 10 July 2025

Influence of Upstream Fetch for Environmental Wind Engineering Applications

Jianhan Yu [1,2,3], Ted Stathopoulos [1], Mingshui Li [2]

[1] *Centre for Zero Energy Buildings Studies, Department of Building, Civil and Environmental Engineering, Concordia University, Montreal, Quebec, Canada H3G 1M8*
[2]*Research Centre for Wind Engineering, Southwest Jiaotong University, Chengdu, Sichuan, 610031, China*
[3]*School of Architecture, Southwest Jiaotong University, Chengdu, Sichuan, 610031, China*

SUMMARY
With the rapid urbanization process, there is a growing concern regarding the wind environment in suburban and urban regions. The purpose of this study is to investigate the influence of the upstream fetch length on environmental wind engineering issues, such as the pedestrian level wind (PLW) and the wind comfort assessment around newly built buildings. The suburban region of Westmount in Montreal and the urban area of Kowloon in Hong Kong are selected for case studies. The investigation has been experimental and results were obtained from two atmospheric boundary layer wind tunnels. The results indicate that the upstream fetch length that influences the PLW estimation in suburban areas is as short as 200 m and in urban areas is as short as 450 m, as illustrated in Figure 1. For the wind comfort assessment of a newly building, an upstream fetch length of 100 m from the building site can be utilized depending on the criteria used.

Keywords: environmental wind engineering, upstream exposure, pedestrian level wind.

1. CASE STUDIES

1.1 Westmount, Montreal

The Westmount, Montreal case study is distinguished by sparsely distributed, low- to mid-rise buildings. To analyze the impact of upstream exposure on environmental wind flows, three upstream fetch lengths of 100 m, 200 m, and 300 m are utilized, as indicated by the red circles in Figure 1. Within this region, a proposed building is positioned at the center, marked by a red rectangle.

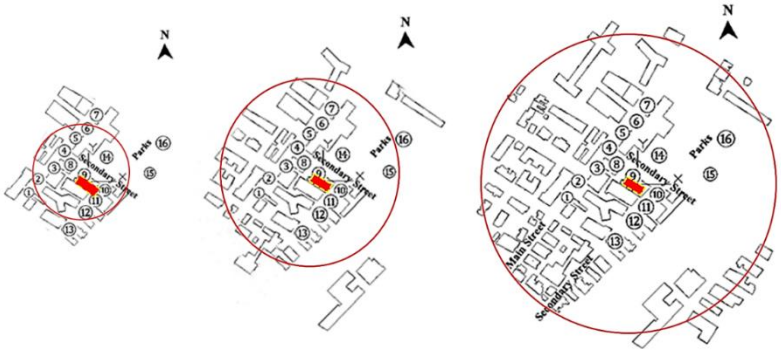

(a) Fetch length of 100 m (b) Fetch length of 200 m (c) Fetch length of 300 m

Figure. 1 Investigated area with varying lengths of upstream fetch.

1.2 Kowloon, Hong Kong

Kowloon, Hong Kong exemplifies a typical urban exposure characterized by heavily distributed high-rise buildings. This case study is chosen for evaluating the wind environment around existing buildings, with a specific focus on the wind velocity of pedestrian height within the inside circle with a radius of 450 m. Notably, the two most critical wind directions, W and E, have been identified. As the E wind direction faces the open sea, a wind direction of 260° is adopted to explore the impact of upstream urban exposure on the PLW, which extends up to 3,300 m in this wind direction, as depicted in Figure 2. In this study, fifty observation locations uniformly distributed in this area are selected.

Figure 2. Observation locations and upstream fetch length in investigated wind direction

2. EXPERIMENTAL METHOD

Experimentation of Westmount, Montreal was conducted at the wind tunnel of Concordia University in Montreal, Canada. The model is scaled down at a ratio of 1:400 with a blockage ratio of 3%, which is maintained below the 5% threshold recommended by (ASCE 49, 2021). The Reynolds number during the test exceeds 4.3×10^4, meeting the requirement for Reynolds number independence. Figure 3 shows a photo of this experimental model in the wind tunnel. PLW velocities were measured at 0.005 m above the floor in the reduced scale model, representing 2 m of the pedestrian height in full scale.

The experimental study of Kowloon, Hong Kong was conducted at the XNJD-3 wind tunnel of Southwest Jiaotong University. Considering the wind tunnel size and model dimensions, the scaling down of model is set at 1:800. Figure 4 shows a picture of the experimental model of Kowloon. The models were manufactured from foam, and finer details which have a minimal impact on PLW were eliminated. Only the wind direction of 260° was explored in this case study. Wind velocities were observed at a level of 0.0025 m in the tests, aligned with 2 m of full scale.

Figure 3. Experimental study of Westmount, Montreal.

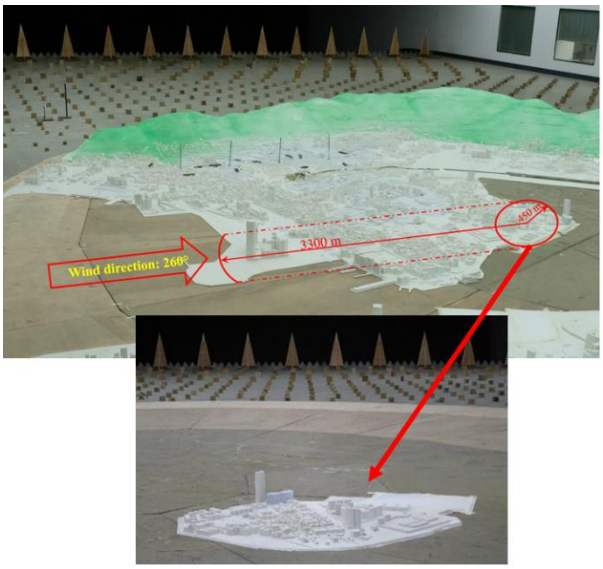

Figure 4. Experimental study of Kowloon, Hong Kong.

3. IMPACT OF UPSTREAM FETCH ON ENVIRONMENTAL APPLICATIONS

Figure 5 shows the differences of wind velocities of at pedestrian level with upstream fetch lengths of 100 m versus 200 m, as well as 200 m versus 300 m of suburban exposure. The figures indicate that the differences in the results between the upstream fetch length of 200 m *versus* 300 m are considerably smaller than the results between those of 100 m *versus* 200 m, although there are significant deviations in the parts with lower wind speeds, say less than 2 m/s. In the study of pedestrian wind environments, more attention is paid to the effects caused by higher wind speeds. This implies that the variation of velocity at pedestrian height stabilizes as the fetch length increases. The results demonstrate that the upstream fetch length of 200 m can be adopted for the wind comfort assessment of a proposed building in a typical suburban exposure.

The comparative analysis of PLW velocities across various upstream fetch lengths of urban exposure is presented in Figure 6. Clearly, while PLW velocity exhibits slight sensitivity to different upstream fetch lengths, the deviations at the majority of observation points between upstream fetch lengths of 450 m and 3,300 m remain within the 30% range. This indicates that assessing the wind comfort in urban exposure with consideration for an upstream fetch of 450 m

is reliable, as deviations within this range are deemed acceptable. However, It is essential to extend the analysis to figure out the minimum upstream fetch length impacting PLW velocity in urban exposure.

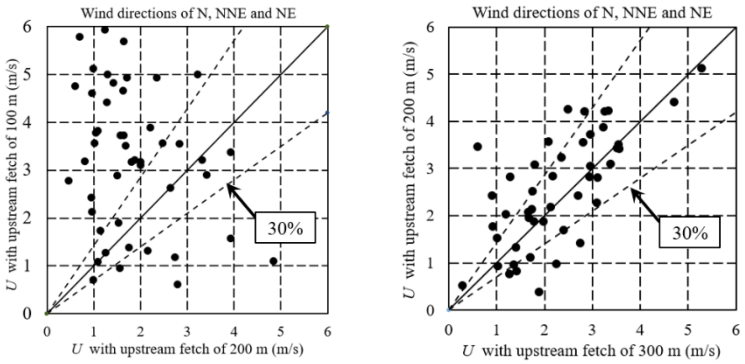

(a) 100 m versus 200 m. (b) 200 m versus 300 m.

Figure 5. Comparison of PLW velocities. Dashed lines denote 30% deviations.

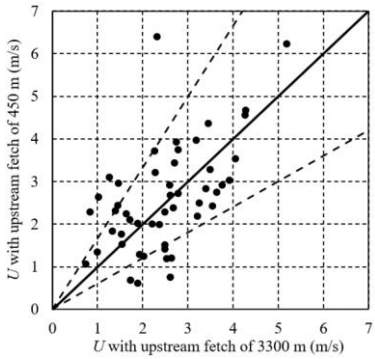

Figure 6. Comparison of wind velocities at pedestrian height. Dashed lines denote 30% deviations.

4. CONCLUSIONS

This study investigates the influence of the upstream fetch length on environmental wind engineering issues by experimental. The suburban region of Westmount in Montreal and the urban area of Kowloon in Hong Kong are selected for case studies. The results indicate that the upstream fetch length that influences the PLW estimation in suburban areas is as short as 200 m and in urban areas is as short as 450 m.

ACKNOWLEDGEMENTS

The authors acknowledge the Natural Sciences and Engineering Research Council of Canada (NSERC) through a Discovery grant to the second author.

REFERENCES

Wieringa, J. 1992. Updating the Davenport roughness classification, Journal of Wind Engineering and Industrial Aerodynamics, 41 (1-3), 357-368.

Yu, J., Stathopoulos, T., & Li, M. 2023. Exposure factors and their specifications in current wind codes and standards. Journal of Building Engineering, 107207.

6th International Conference on Building Energy and Environment
Eindhoven University of Technology, The Netherlands
6 - 10 July 2025

High-fidelity digital twin model of a large-scale complex environment for CFD simulations of wind and temperature

Žužul Josip [1], Ricci Alessio [2,3], Burlando Massimiliano [1]

[1]*University of Genoa, Genoa, Italy, josip.zuzul@edu.unige.it , massimiliano.burlando@unige.it*
[2]*University School for Advanced Studies IUSS, Pavia, Italy, alessio.ricci@iusspavia.it*
[3]*Eindhoven University of Technology, Eindhoven, the Netherlands, a.ricci@tue.nl*

SUMMARY
For over a decade, computational fluid dynamics (CFD) has been essential in urban physics and wind engineering, tackling topics like pedestrian wind comfort, pollutant dispersion, and structural wind loads. These studies demand detailed modeling of complex landscapes as mountains, forests, and water bodies. While CFD can provide accurate results, generating geometries and grids for such environments poses significant challenges. Input geometry simplification, in particular, plays a key role in the success of the reconstruction. This study proposes an innovative high-fidelity digital twin modeling approach for the generation of complex environments. A digital twin model of Genoa municipality, Italy, was used to investigate the wind flow in the urban boundary layer by means of steady-state Reynolds-averaged Navier-Stokes (RANS) simulations. Hazard maps for extreme winds and temperatures are the ultimate goal of this work, aiming at improving the safety management and risk awareness during adverse weather.

Keywords: digital twin, RANS simulations, complex environment, wind, temperature, hazard map.

1. INTRODUCTION

Computational Fluid Dynamics (CFD) simulations have become a cornerstone for exploring urban physics and wind engineering phenomena at mesoscale levels, addressing topics such as pedestrian wind comfort, air pollutant dispersion, urban heat effects, and structural wind loads. At the mesoscale, such investigations could also involve the construction of digital twins - virtual replicas of intricate natural and built environments. Yet, developing a digital twin for expansive urban areas remains a formidable challenge, sparking growing attention from the research community in recent years (e.g. Alemayehu and Bitsuamlak, 2022; Pađen et al., 2022; Žužul et al., 2024). Despite progress, a comprehensive framework for accurate digital twin creation and mesh generation in complex settings is still lacking. These models often encompass diverse terrain features - hills, water surfaces, and vegetation - where topography introduces notable complexity. However, it is the detailed representation of the built infrastructure that proves most pivotal to the success of digital twin development. The relevance of specific geometric features depends heavily on the study's scale and objectives, with some details being vital for certain applications yet negligible for others. As a result, geometrical simplifications are frequently employed to facilitate automated reconstruction of large urban areas, a step critical for effective mesh generation. Striking the right balance in simplification is essential, as excessive reduction can alter the simulated flow field significantly (Ricci et al., 2017). Additionally, as urban scales expand, computational limitations endure, requiring geometry simplifications to control the total size of the computational mesh, while carefully balancing the retention of adequate details to fulfil the objectives of the analysis.

This study will outline key considerations, practical recommendations, and propose a systematic process for automating digital twin development in CFD wind engineering studies. An application of this approach is provided through the automated 3D geometry reconstruction of Genoa municipality, Italy, a coastal city of roughly 600,000 people, framed by sea and mountains.

2. DIGITAL TWIN CREATION FOR CFD APPLICATIONS

The framework for constructing a digital twin begins with meticulous geometry preparation, treating the built infrastructure and terrain topography as distinct entities. This approach aligns with the methodology of the City4CFD tool (Pađen et al., 2022) and forms the foundation of the procedure proposed in this study. The process starts with acquiring and pre-processing terrain topography data for the area of interest. As mentioned above, the large-scale city of Genoa (Italy) spanning 37 × 18 km², was selected. A high-resolution digital terrain model (DTM) with 1 m resolution was smoothed using a 50 × 50 m² moving window to mitigate outliers from measurement uncertainties. However, irregular topography at the domain boundaries can still hinder successful CFD simulations. To address this, the artificial buffering technique was used, extending the terrain outward to ensure a smooth transition to the far-field elevation (set at sea level, $z = 0$ m). This buffering adopts a two-zone strategy inspired by Žužul et al. (2024): (*i*) an inner buffer, where the terrain surface is smoothed by solving the Laplace equation, and (*ii*) an outer buffer, fixed at a constant elevation of 0 m. The resulting terrain data is then exported as a point cloud for subsequent processing.

The built infrastructure data, represented as polygons with assigned heights (in GeoJSON format), required additional simplification due to the complex and irregular shapes typical of Mediterranean coastal cities. Direct reconstruction proved impractical, prompting a series of simplification steps. Buildings shorter than 5 m or with roof areas below 25 m² were excluded. The Ramer-Douglas-Peucker algorithm (Douglas and Peucker, 1973) was applied to reduce the number of points defining each building's footprint. Additionally, buildings within 2 m of one another were merged to eliminate narrow gaps and passages, enhancing mesh quality. These simplified building polygons were then converted into a stereolithography (STL) file using OpenSCAD (2024). The entire terrain and building preparation workflow are automated via an in-house Python script, producing a CFD-ready geometry representation, as illustrated in Fig. 1.

The prepared terrain point cloud and building STL files were then processed through the City4CFD tool Pađen et al. (2022), an essential component of the digital twin generation workflow that corrects persistent triangulation errors and ensures seamless topological connectivity between buildings and terrain. With the computational domain boundaries established, generating a computational mesh becomes feasible. The mesh was created using `cfMesh`, an automated meshing library available in `OpenFOAM`. To manage the scale of Genoa's digital twin and excessive RAM memory requirements during the mesh generation process, the domain was divided into eight distinct subdomains, each meshed individually. The subdomains were subsequently combined to form a final computational mesh comprising of about 600 million cells in total. Although the grid-sensitivity study was not conducted due to the large scale of the case, it was created following the standards established in the community. This robust digital twin enables high-fidelity CFD simulations of atmospheric wind flows over large-scale complex environments.

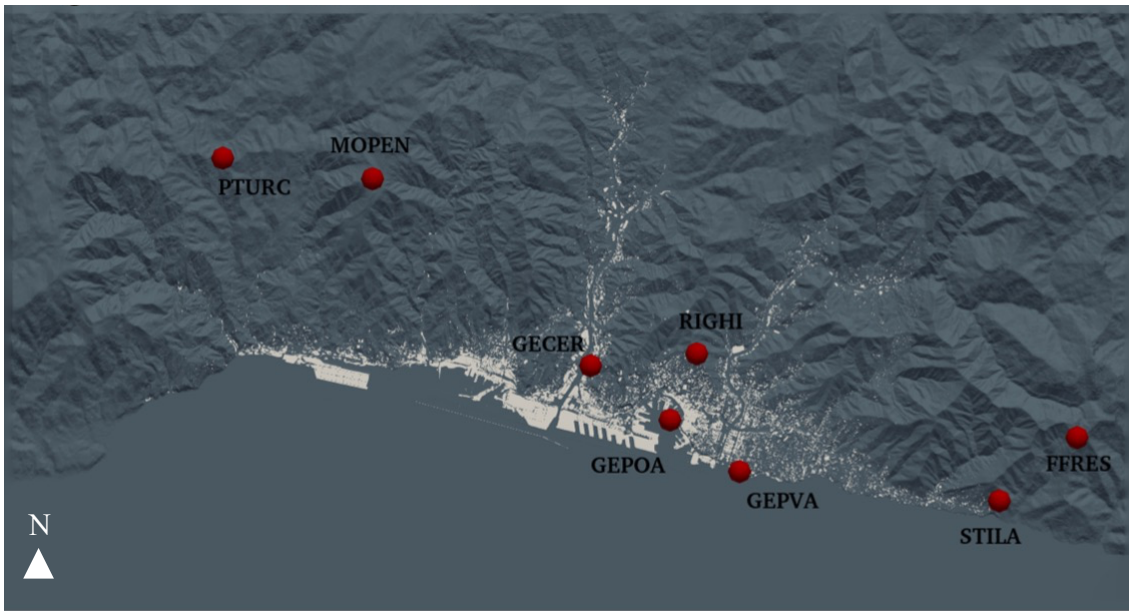

Figure 1. The target complex domain covering a 37 × 18 km^2 area around Genoa, including the reconstructed buildings and infrastructures. Red dots indicate meteorological stations collecting data for validation of CFD results and wind hazard map generation.

3. RESULTS

A 3D steady RANS approach coupled to realizable k-ε turbulence model was used to conduct simulations for 12 reference wind directions (i.e. $\alpha = 15°, 45°, \ldots, 345°$) under neutrally stratified atmospheric boundary layer (ABL) wind conditions. The ABL was based on the measurements taken at the nearby airport. The aerodynamic roughness lengths (z_0) were assigned as follows: 0.0002 m for the sea surface ($z_{0,\text{sea}}$), 0.4 m for rural regions ($z_{0,\text{rural}}$), and 0.8 m for urban zones ($z_{0,\text{urban}}$). Fig. 2 illustrates key aspects of the study: a side-by-side comparison of the computational mesh (Fig. 2a) with the expansive, the complex orography of Genoa municipality (Fig. 2b), alongside detailed wind velocity contours overlaid with velocity vectors in a horizontal plane at 30 m above sea level. These results focus on the western sector of Genoa for a wind direction of $\alpha = 225°$, as depicted in Fig. 2c and Fig. 2d, highlighting the realistic flow patterns achieved. Since the research goal is to generate wind hazard maps through statistical modelling, the RANS simulations used as an input are considered sufficiently accurate for that purpose.

5. CONCLUSIONS AND PROSPECTS

This study presents insights gained from an ongoing research on automating geometry preparation to streamline the development of digital twins and mesh generation for large-scale, high-fidelity urban areas in complex terrain. Successful handling such cases requires balancing of multiple factors, with geometry preparation and simplification emerging as a key element in accurate domain reconstruction. Employing these simplification techniques and presented workflow based on the automatic mesh generator `cfMesh` and CFD library `OpenFOAM` were found to be robust and optimal for generating meshes and obtaining wind field results in wind engineering applications. This framework enhances the efficiency and feasibility of large-scale simulations, contributing to more accurate and accessible modeling in urban physics and wind engineering.

Going forward, the CFD results will be first validated by comparison with the anemometric measurements taken through the network of about 35 meteorological stations belonging to the Municipality of Genoa installed within the urban canopy, and then combined with measured meteorological data to generate wind hazard maps. These maps will improve the capacity to predict and mitigate wind-related challenges in cities with diverse atmospheric conditions. In the near future, the simulations will also incorporate temperature fields, enabling the creation of hazard maps for extreme temperatures.

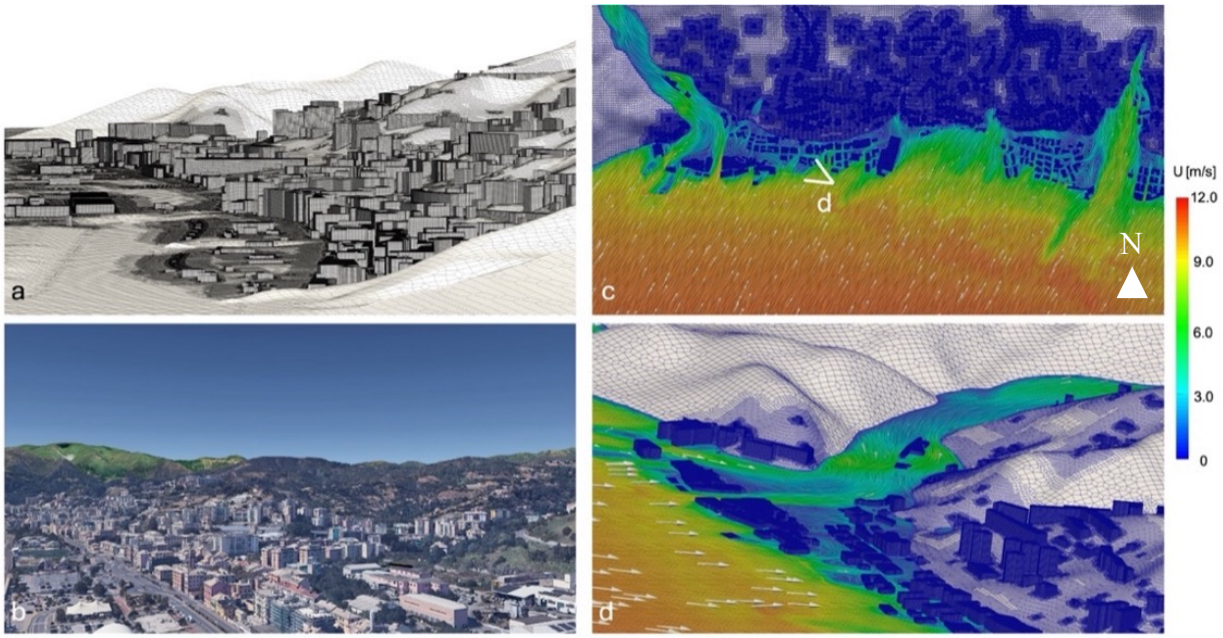

Figure 2. Comparison of the computational grid with the large-scale complex environment of Genoa (a-b); computational grid overlaid with wind velocity contours at 30 m above sea level (c-d).

ACKNOWLEDGEMENTS

This study was funded by ADAPTNOW Project—"ADAPTation Capacity Strengthening for Highly Affected and Exposed Territories in the Alps NOW" (Grant No. ASP0100048). ADAPTNOW is co-financed by the European Regional Development Fund through the Interreg Alpine Space programme. The authors also acknowledge the support of the Municipality of Genoa (Italy) in providing the relevant datasets used in the framework of this research study. The authors acknowledge the support of the Italian supercomputing center CINECA for providing access to their High-Performance Computing (HPC) facilities needed to carry out the research presented in this paper.

REFERENCES

Alemayehu, T.F. and Bitsuamlak, G.T., 2022. Autonomous urban topology generation for urban flow modelling. Sustainable Cities and Society, 87, 104181.

Douglas, D.H. and Peucker, T.K., 1973. Algorithms for the reduction of the number of points required to represent a digitized line or its caricature. The Canadian Cartographer 10(2), 112–122.

OpenSCAD, 2024. The Programmers Solid 3D CAD Modeller. https://openscad.org.

Pađen, I., García-Sánchez, C., and Ledoux, H., 2022. Towards Automatic Reconstruction of 3D City Models Tailored for Urban Flow Simulations. Frontiers in Built Environment, 8.

Ricci, A., Kalkman, I., Blocken, B., Burlando, M., Freda, A., and Repetto, M. P., 2017. Local-scale forcing effects on wind flows in an urban environment: Impact of geometrical simplifications. Journal of Wind Engineering and Industrial Aerodynamics, 170, 238- 255.

Žužul, J., Ricci, A., and Burlando, M., 2024. An automated geometry generation procedure for CWE applications in OpenFOAM: the case study of a thunderstorm downburst moving over Genoa city. Meccanica.

Thermal Comfort (13:30-15:00 h)

6th International Conference on Building Energy and Environment
Eindhoven University of Technology, The Netherlands
6 - 10 July 2025

Development of Condensation-free Personalized Radiant cooling Technique

Gongsheng HUANG[1*], Yuying LIANG[1,2]

[1]*Department of Architecture and Civil Engineering, City University of Hong Kong, Hong Kong, China*
[2]*School of Automation, Guangdong Polytechnic Normal University, Guangzhou 510665, China*
gongsheng.huang@cityu.edu.hk; Yuying.Liang@my.cityu.edu.hk

SUMMARY

This paper presents a condensation-free personalized radiant cooling (CF-PRC) technique, aiming at creating a "cooling oasis" in hot (indoor) ambient environments using two condensation-free radiant cooling boards (CF-PRCBs) placed on both sides of an occupant. Each board has a membrane with high infrared transmittance to seal a layer of dry air to separate the radiant cooling surface from the air-contact surface, enabling the use of a low radiant cooling temperature (such as 5°C) to enhance the cooling power of the boards (>100 W/m^2) without increasing condensation risk. We investigated the thermal performance of the cooling oasis when the cooling boards have different configurations, such as board size and cooling temperature, through numerical and experimental studies. We found that the PRCB pair can efficiently reduce the local operative temperature, local mean radiant temperature and local air temperature of the microthermal environment and thus form "cooling oasis" within a hot ambient environment. In a warm ambient environment (such as $T_{amb} = 28$°C), the CF-PRCB with the dimension of 1m × 0.7m could achieve a thermoneutral state using a radiant cooling tempreature around 10°C. The insights gained from this study provide valuable guidance for the design and operation of the CF-PRC technique, especially when considering energy-efficient and user-centric built environments.

Keywords: Personalized radiant cooling, condensation-free, cooling oasis, hot and humid climates.

1. Introduction

Indoor space cooling for thermal comfort is energy intensive (Garimella et al. 2022), motivating much effort from scientists and engineers to understand the mechanism to achieve thermal comfort and develop measures to improve the energy efficiency of cooling systems (Fanger 1967; Booten et al. 2021). Variant techniques have been developed for indoor cooling, and these techniques are categorized into air-cooling and radiant cooling. The former achieves thermal comfort mainly through the regulation of indoor air temperature, while the latter is mainly through the regulation of mean radiant temperature (MRT). Both can be used to create a global thermal-comfort indoor environment in the form of a "one-fits-all" system or a local thermal-comfort indoor environment in the form of a personalized comfort system (PCS) (ANSI/ASHRAE Standard 55-2023; Xie et al. 2020). Compared with a "one-fits-all" system, a PCS has been considered an efficient technique to save energy in conditioning a large-scale indoor space, especially when this space is partially occupied (Kim et al. 2018, Vesely et al. 2014). This is because a PCS for cooling enables the use of higher ambient temperature (e.g., 28°C) than "one-fits-all" systems (e.g., 24°C). Imanari et al (1999) shows that a PCS could increase the ambient temperature by 4.2°C compared with a "one-fits-all" cooling system under the same thermal conditions. This increment might lead to

significant energy saving as the increase of 1°C could save energy by ~3% (Zhang et al., 2015).

Generally, there are two types of systems that can be used to achieve personal cooling comfort: personalized ventilation (PV) systems and personalized radiant cooling (PRC) systems. A PV system creates a comfortable microthermal environment for occupants using a high airflow rate (Niu et al. 2007; Yang et al. 2010; Kalma et al. 2013). Since PV systems should be placed close to occupants, the cool air with a high velocity will produce a cold-draft and noise. This unwanted local thermal discomfort could hardly be avoided when using PV systems. Thus, PRC systems have been proposed to overcome the limitations of PV systems. PRC systems inherit the merits of a radiant cooling system that is installed on the ceiling in the form of radiant cooling panels, such as lower noises, smaller vertical temperature differences, and less draft risk (Rhee et al. 2015; 2017). Similar to PV systems, PRC systems should be installed close to users. However, unlike PV systems, PRC systems utilize radiant cooling surfaces to provide a cooling sensation rather than relying on high-speed cold air.

There are different designs of PRC systems in literature, including radiant cooling cubicle reported by Garg et al. (2017) and radiant cooling desk by He et al. (2017). However, these designs do not directly deal with the condensation problem but require that the radiant cooling surface temperature should be kept above dew-point temperature to avoid condensation. Therefore, these designs suffer from very limited cooling power. Membrane-assisted radiant cooling technology has been proposed to increase the cooling power of radiant cooling systems while avoiding condensation risk, which provides a fundamental solution to the condensation problem (Morse 1963; Teitelbaum et al. 2020; Zhang et al. 2021; Liang et al. 2021; 2022). Their studies show that when low-density polyethylene (LDPE), which has an average transmittance of 0.82 for the infrared radiation between 2-22μm, is used as the membrane, the cooling panel can provide a cooling power of 110 W/m^2 using the radiant cooling temperature of 5°C without condensation.

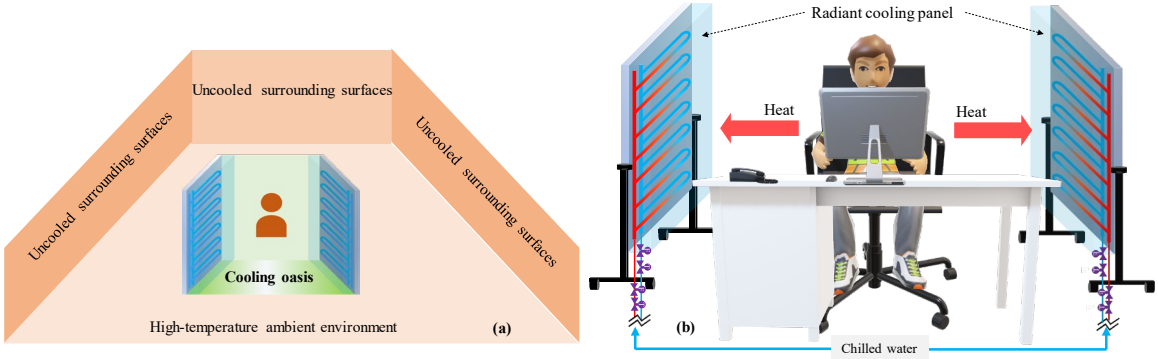

Figure 1. (a) The concept of 'cooling oasis' in a hot ambient environment; (b) the developed personalized radiant cooling technique (Liang et al. 2024)

Motivated by the above works, we propose a condensation-free PRC (CF-PRC) technique, aiming at creating a comfortable microthermal environment, or "cooling oasis", within warm/hot ambient environments through enhanced radiative rather than convective heat exchange. The concept of the cooling oasis is shown in Figure 1(a). The CF-PRC system consists of two CF-personalized radiant cooling boards (or CF-PRCB pair), installed on the right and left-hand side of the occupant, shown in Figure 1(b). The radiant cooling surface of the CF-PRCB pair is cooled to a preferable temperature using the chilled water from a chiller plant, and the occupant disposes of the body heat directly to the PRCB pair mainly through radiant heat

exchange. Our previous works explore the fundamental issues of CF-PRCBs, such as heat transfer modelling, thermal comfort survey and energy performance (Liang et al., 2024; 2025). In this paper, we will investigate the thermal environment created by a CF-PRCB pair with three different dimensions and demonstrate their capability in creating comfort thermal conditions within warm/hot ambient environments.

2. THERMAL ENVIRONMENT MODELLING

The structure of the CF-PRCB is given in Figure 2(a). The radiant cooling surface is coated with a high emissivity material (such as graphene-composite carbon nanotube with emissivity of 0.95) and a set of chilled water capillaries is fixed on a wooden board behind the radiant surface. An insulation layer is fixed on the other side of the wooden board to prevent cooling loss. A 10cm-air layer is sealed by an LDPE membrane to provide enough thermal resistance for the heat exchange between the air-contract and the radiant cooling surface to maintain a high temperature at the air-contact surface to prevent condensation. In application, a CF-PRCB pair could be installed for each workstation in a large office to create an individually preferable microthermal instead of cooling down the whole office; and individual CF-PRCB pairs should be switched on or off as simple as a desk lamp.

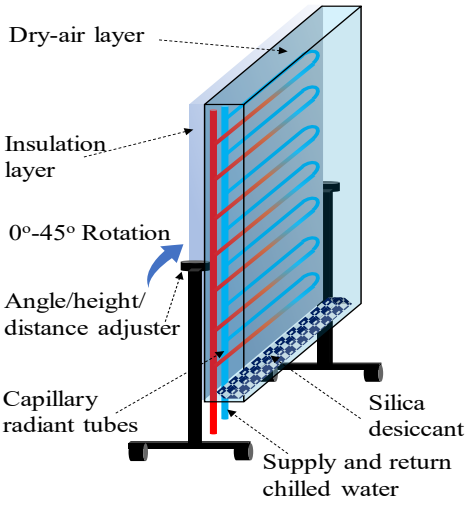

Figure 2. The structure of the CF-PRCB in the test chamber.

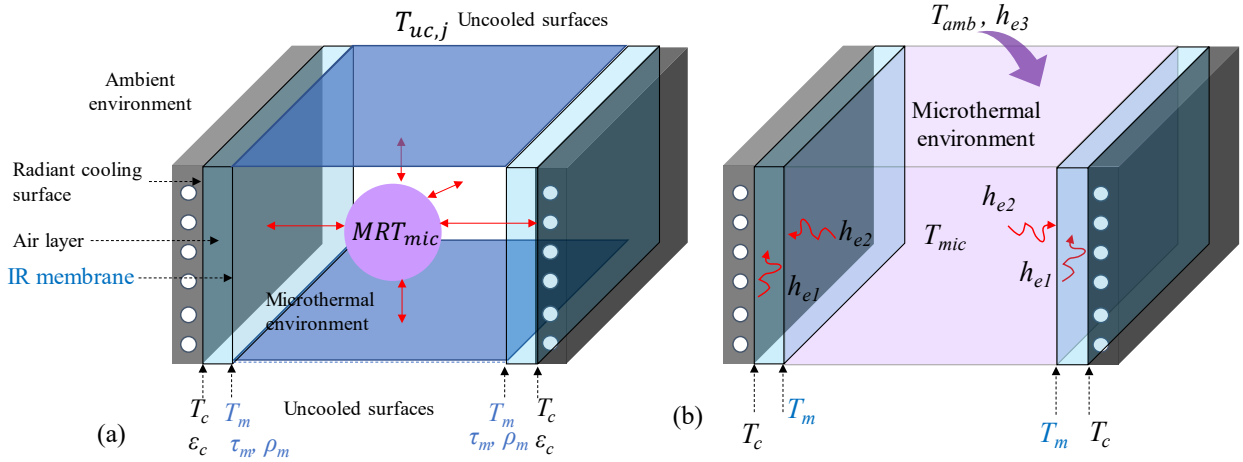

Figure 3. Microthermal environment modelling for the microthermal environment: (a) radiant heat transfer; (b) convective heat transfer.

The microthermal environment model for the CF-PRCB pair is developed based on the assumption that an imaginary cuboid, formed by the CF-PRCB pair and four imaginary boundary surfaces (as shown in Figure 3a), can isolate the microthermal environment from the surrounding ambient environment. The virtual boundary surfaces facilitate heat transfer through radiation and convection between the microthermal environment and the ambient environment, as illustrated in Figures 3a and 3b, respectively. Additionally, the two LDPE membranes, being semi-transparent, allow heat transfer between the radiant cooling surfaces and the microthermal environment.

Given the size of the CF-PRCBs and the distance between the CF-PRCB pair, the local mean radiant temperature MRT_{mic}, the local air temperature T_{mic}, and the membrane temperature (T_m) are estimated as follows. MRT_{mic} is given by Eqn. (1):

$$MRT_{mic}^4 = (2\varepsilon_c ERT_c^4 F_{P\to RCP} + \sum_{j=1}^{n_{uc}} \varepsilon_j T_{uc,j}^4 F_{P\to uc,j})/\varepsilon_o \quad (1)$$

where ε_c is the emissivity of the radiant cooling surface; ε_o is the uniform emissivity of the enclosure surface; $F_{P\to RCP}$ is the angle factor between the occupant and the radiant cooling surfaces; $T_{uc,j}$ is the temperature of the j^{th} uncooled surrounding surface; and $F_{P\to uc,j}$ is the angle factor between the occupant and the j^{th} uncooled surface. ERT_c is the equivalent temperature of the radiant cooling surfaces, defined as the temperature of a PRCB without the membrane and the dry-air layer that could provide the same cooling power by the membrane-integrated PRCB with the radiant cooling temperature of T_c. ERT_c can be calculated using the algorithm detailed in the supplement notes in (Liang et al. 2024).

Assuming the local air temperature of the microthermal environment is homogenous, we calculate the local air temperature T_{mic} and membrane temperature T_m using Eqns. (2) and (3)

$$T_{mic} = \frac{h_{e2}A_{e2}}{h_{e2}A_{e2}+h_{e3}A_{e3}} T_m + \frac{h_{e3}A_{e3}}{h_{e2}A_{e2}+h_{e3}A_{e3}} T_{amb} \quad (2)$$

$$T_m = \frac{h_{e1}}{h_{e1}+h_{e2}} T_c + \frac{h_{e2}}{h_{e1}+h_{e2}} T_{mic} \quad (3)$$

where $A_{e1} = A_{e2} = A_1 + A_6$, $A_{e3} = A_2 + A_3 + A_4 + A_5$; and A_1, A_6 are the left and the right area of the membrane surface, respectively, $A_1 = A_6$; A_2, A_3, A_4, A_5 represent the area of the virtual boundary in the microthermal environment, for the two side, bottom surface, and upper surfaces, respectively. The coefficients h_{e1}, h_{e2} and h_{e3} in Eqs. (2) and (3) should be known before the calculation and they can be identified using experimental data (Liang et al. 2024).

To validate the environmental model, a test rig was setup in a controllable environment chamber (9m × 5.4m × 2.4m), shown in Fig. 4, where the ambient air temperature and relative humidity (RH) were controlled by electric heaters and humidity regulators. Two PRCBs (0.7m × 1m each) were placed 1.2m apart, accommodating the arm length of a 175 cm tall person. The bottom edges were 0.4m above the floor, with the center height at 0.9m, targeting cooling for the upper body of a seated person. Swema test equipment and Lutron recorders measured air velocity and temperature at various heights (0.1, 0.6, 0.9, 1.1, and 1.7m), black globe temperature (0.9m) and relative humidity (0.9m).

Figure 4. Experiment setup, where a mannikin was placed between two CF-PRCBs

3. RESULTS AND ANALYSIS

3.1 Microthermal environment analysis

Table 1 summarized the main temperatures of the ambient environment, including T_{amb}, *MRT* and T_{op}, before and after the CF-PRC system was switched on. Even when the heaters were fully off, the ambient environment was "warm" or slightly "hot" and outside of the generally thermal comfortable range (T_{op} = 24 - 26ºC) defined by ANSI/ASHRAE Standard 55-2023. Table 1 also showed that the CF-PRC system had a limited capacity to affect the ambient environment. Even if the radiant cooling temperature was as low as 5ºC, the ambient environment was not significantly affected. For example, there was only 0.3ºC in the air temperature difference before and after the PRC system was on. At each scenario, the radiant cooling temperature T_c was controlled and stabilized at 5, 10, 15, and 20°C. The local air temperature T_{mic}, the local *MRT* and the local operative temperature $T_{mic,op}$ at different T_c were recorded and listed in Table 2. These data were used to validate the model briefly introduced in Section 2, where we compared the membrane temperature, local air temperature and local MRT from the experiment with those calculated using the models. All absolute errors were less than 0.5°C and we thus conclude our model in Section 2 is accurate and reliable.

Table 1. Main variables of the ambient environment.

Scenario (Electrical heater)	before PRC system on			after PRC system on (with $T_c = 5$°C)		
	T_{amb}(°C)	*MRT* (°C)	T_{op} (°C)	T_{amb}(ºC)	*MRT* (ºC)	T_{op} (ºC)
1 (Fully on)	31.3	31.3	31.3	31.0	30.9	30.9
2 (Half on)	29.2	29.5	29.4	29.2	29.3	29.3
3 (Full off)	27.7	27.7	27.7	27.4	27.4	27.4

Table 2. Main variables of the microthermal environment created by the CF-PRCB pair (1m × 0.7m).

Radiant cooling temperature	Scenario 1	Scenario 2	Scenario 3
	$MRT_{mic}, T_{mic}, T_{mic,op}$	$MRT_{mic}, T_{mic}, T_{mic,op}$	$MRT_{mic}, T_{mic}, T_{mic,op}$
$T_c = 20$°C	29.9, 30.0, 29.9	28.7, 28.7, 28.7	26.3, 26.7, 26.5
$T_c = 15$°C	29.2, 29.7, 29.4	27.9, 28.3, 28.1	25.5, 26.4, 25.9
$T_c = 10$°C	28.4, 29.4, 28.8	27.3, 28.0, 27.6	24.7, 26.1, 25.2
$T_c = 5$°C	27.8, 29.1, 28.3	26.7, 27.6, 27.1	24.2, 25.9, 24.9

Note: all the temperatures are in degree Celsius (°C)

The CF-PPRCB pair can significantly reduce the local MRT through radiative heat exchange with the radiant cooling surface, as shown in Table 2. For example, when the radiant cooling temperature of the PRCB pair was 5ºC, the local MRT was lowered from 31.3ºC, 29.5ºC and 27.7ºC to 27.8ºC, 26.7ºC and 24.2ºC, with the decrease of 3.5ºC, 2.8ºC and 3.4ºC in Scenarios 1, 2 and 3respectively. Using the data generated from the validated environment model, the local MRT for different sizes of the CF-PRCB boards can be estimated by

$$MRT_{mic} = 0.125T_c + 0.875T_{ew}, \text{ for } 1m \times 0.7m \quad (4a)$$

$$MRT_{mic} = 0.188T_c + 0.812T_{ew}, \text{ for } 1m \times 1.0m \quad (4b)$$

$$MRT_{mic} = 0.229T_c + 0.771T_{ew}, \text{ for } 1m \times 1.2m \quad (4c)$$

where T_{ew} is the equivalent uncooled surface temperature. The weighting factor associated with T_c indicates the significance of T_c contributing to the local MRT of the microthermal environment. A higher value means more contribution. Comparing the weighting factor in Eqns. (4a)-(4c), we can find that a larger CF-PRCB has a stronger capability to regulate the local MRT. For example, when the ambient temperature is 31.3ºC and $T_c = 5$ºC, the local MRT for the CF-

PRCB is 27.8ºC, which will be decreased to 26.4ºC when the board becomes 1m × 1.2m.

The CF-PRCB pair reduced the local air temperature through the heat exchange with the membrane surface. As shown in Table 2, the local air temperature was lowered from 31.3ºC, 29.2ºC and 27.7ºC to 29.1ºC, 27.6ºC and 25.9ºC, with the decrease of 2.2ºC, 1.6ºC and 1.8ºC by the PRCB pair with 5ºC, being around 2ºC. This reduction was not significant, indicating that the PRCB pair had a limited capacity in adjusting local air temperature of the microthermal environment. This could also be explained using the formular derived through fitting the data from the model:

$$T_{mic} = 0.076T_c + 0.924T_{amb} \text{ , for } 1m \times 0.7m \quad (5a)$$
$$T_{mic} = 0.112T_c + 0.888T_{amb} \text{ , for } 1m \times 1.0m \quad (5b)$$
$$T_{mic} = 0.120T_c + 0.880T_{amb} \text{ , for } 1m \times 1.2m \quad (5c)$$

Here the weighting factor for T_c was only 0.076 for the CF-PRCB pair with 1m × 0.7m, much smaller than the weighting factor for $T_{amb}(0.924)$. This shows that the local temperature was mainly affected by the ambient temperature. A large PRCB should enhance the contribution of T_c to T_{mic}. For example, when the PRCB was enlarged from 1 m × 0.7 m to 1 m × 1 m and 1 m × 1.2 m, the weighting factor for T_c was increased to 0.112 and 0.120 respectively. Compared Eqns. (4a)-(4c) with Eqn. (5a)-5(c), the PRCB pair has a stronger capability to regulate the local MRT than the local air temperature.

Table 2 also shows the local operative temperature $T_{mic,op}$ of the microthermal environment when T_c was 5ºC, 10ºC, 15ºC, and 20ºC under the ambient temperature of 31.3ºC, 29.2ºC and 27.7ºC respectively. It shows that the CF-PRCB pair can efficiently reduce the operative temperature. Using the data generated from our environment model, $T_{mic,op}$ is approximated by

$$T_{mic,op} = 0.611\, MRT_{mic} + 0.389\, T_{mic}, \text{ for } 1m \times 0.7m \quad (6a)$$
$$T_{mic,op} = 0.616\, MRT_{mic} + 0.384\, T_{mic}, \text{ for } 1m \times 1.0m \quad (6b)$$
$$T_{mic,op} = 0.618\, MRT_{mic} + 0.382\, T_{mic}, \text{ for } 1m \times 1.2m \quad (6c)$$

The coefficient α (0.611), much larger than β (0.389), indicating that the contribution of the local MRT to the local operative temperature is higher than that of the local air. When enlarging the PRCBs' size, the coefficient for MRT_{mic} and T_{mic} was not significantly changed.

3.2 Operation guideline

As CF-PRCB pair is used to create comfortable environment preferred individually, we first investigate the thermal comfort of the microthermal environment created by the PRCB pair through a comfort survey. To simplify the analysis, we focused on a common office scenario, where the metabolic rate was assumed to be 1.2 met and clothing insulation at 0.5 clo. A total of 24 participants were invited to provide feedback on their thermal sensation within the thermal environment generated by the PRCB pair. The radiant cooling temperatures were set at 5°C (cold), 10°C (moderate), and 15°C (cool), while the ambient temperatures were 28°C (warm) and 30°C (hot). The comfort survey was designed in accordance with the established procedure outlined in the ANSI/ASHRAE Standard 55-2023. Using the available 1008 data sets, the TSV in the microthermal environment created by the PRCB pair was estimated by

$$TSV = 0.063T_c + 0.414T_{amb} - 12.28 \quad (7)$$

Based on this equation, we calculated the radiant cooling temperature range for the CF-PRCB pair with the dimension of 1 × 0.7m, 1 × 1.0m, 1 × 1.2m repectively when we use $TSV = \pm 0.5$ as the criterion for the individual thermal comfort. The results are shown in Figure 5(a) for $T_{amb} = 28$°C and Figure 5(b) for $T_{amb} = 30$°C. The radiant cooling tempreatgure for the CF-PRCB pair with the dimension of 1 × 0.7m should be adjusted inside (3.0, 18.9)°C for $T_{amb} = 28$°C and (-10.2, 5.7) °C for T_{amb}= 30°C. The thermoneutral state was achieved at $T_c = 10.9$°C for $T_{amb} = 28$°C and at $T_c = -2.2$°C for $T_{amb} = 30$°C. In the current practice of chiller plants, the chilled water supply with a temperature below 3°C is not practical. Therefore, the PRCB pair with the dimension of 1 × 0.7 m could not be used to achieve general thermal comfort when the ambient temperature was higher than 28°C. The radiant cooling tempreatgure for the CF-PRCB pair with the dimension of 1 × 1.0m should be adjusted inside (11.9, 23.9)°C for $T_{amb} = 28$°C and (1.8, 13.8)°C for T_{amb}= 30°C. The thermoneutral state can be achieved at $T_c = 17.9$°C for $T_{amb} = 28$°C and at $T_c = 7.8$°C for $T_{amb} = 30$°C. When the CF-PRCB pair with the dimension of 1 × 1.2m is used, the radiant cooling tempreatgure should be adjusted inside (14.4, 24.6)°C for $T_{amb} = 28$°C and (6.1, 16.2)°C for T_{amb}= 30°C. The thermoneutral state can be achieved at $T_c = 19.5$°C for $T_{amb} = 28$°C and at $T_c = 11.1$°C for $T_{amb} = 30$°C. Both can can achieve the thermoneutral state at a feasible chilled water supply temperature above 3°C.

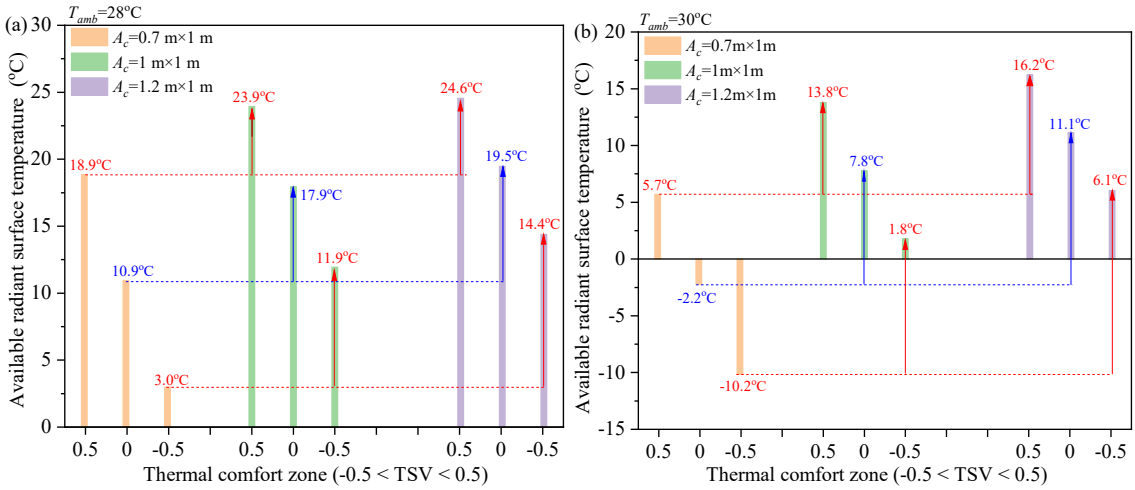

Figure 5. Radiant cooling temperature fulfilling the requirement of (-0.5 < *TSV* < 0.5) when the PRCB with different sizes was used for (a) $T_{amb} = 28$°C and (b) for $T_{amb} = 30$°C.

4. CONCLUSIONS

We have demonstrated that the proposed CF-PRC system can create a comfortable microthermal environment for occupants by adjusting board size and cooling temperature. The main conclusions are listed below:

- The PRCB pair can efficiently reduce the local operative temperature, local mean radiant temperature and local air temperature of the microthermal environment and thus form "cooling oasis" within a hot ambient environment. A larger PRCB has a stronger capability to regulate the microthermal environment.
- The thermal comfort created by microthermal environment can be estimated by $TSV = 0.063T_c + 0.414T_{amb} - 12.28$. In a warm ambient environment (such as $T_{amb} = 28$°C), the CF-PRCB with the dimension of 1m × 0.7m achieved a thermoneutral state using a radiant cooling tempreature around 10°C . However, if the ambient temperature is higher, such as

$T_{amb} = 30$°C, a large PRCB pair should be used.

Acknowledgement

The research work presented in this paper was supported by a grant from the Research Grants Council of the Hong Kong Special Administrative Region, China (Project No. 11212919).

References

ANSI/ASHRAE Standard 55-2023, Thermal Environmental Conditions for Human occupancy.

Booten C., Rao P., Rapp V., Jackson R., Prasher R., Theoretical minimum thermal load in buildings *Joule* 5, 24–46, 2021.

Fanger, P.O. (1967). Calculation of thermal comfort: introduction of a basic comfort equation. *ASHRAE Trans* 73, III.4.1–III.4.20.

Garg R., Khare V.R., Mathur J., Garg V., Performance evaluation of personalized radiant conditioning system for cooling mode. Proceedings of the 15th IBPSA Conference, 2728-2734, San Francisco, USA, Aug. 7-9, 2017.

Garimella S., Lockyear K., et al., Realistic pathways to decarbonization of building energy systems, *Joule* 6, 956–971, 2022.

Griefahn B., Mehnert P., Bröde P. and Forsthoff A., Working in moderate cold: a possible risk to health. *Journal of occupational health* 39 (1997) 36-44.

He Y., Li N., He M., He D., Using radiant cooling desk for maintaining comfort in hot environment. *Energy and Buildings* 145 (2017) 144-154.

Imanari T., Omori T. and Bogaki K., Thermal comfort and energy consumption of the radiant ceiling panel system: Comparison with the conventional all-air system, *Energy and buildings*, 30 (2) (1999) 167-175.

Kalma F., Kalma T, Alternative personalized ventilation. *Energy and Buildings* 65 (2013) 37-44.

Kim J., Schiavon S., Brager G., Personal comfort models – A new paradigm in thermal comfort for occupant centric environmental control. *Building and Environment* 132 (2018) 114-124.

Liang Y.Y., Wu H.J., et al., Local thermal environment and thermal comfort of a novel low-temperature radiant structure using CFD simulation. *Energy and Buildings* 308 (2024) 114007.

Liang Y.Y., Zhang N., *et al.*, Thermal environment and thermal comfort built by decoupled radiant cooling units with low radiant cooling temperature. *Building and Environment* 206 (2021) 108342.

Liang Y.Y., Zhang N., *et al.*, Radiative cooling oases for condensation-free personal cooling in ambient environment. *Cell Reports Physical Science* 11 (2024) 102265.

Morse R., Radiant cooling. *Architectural Science Review* 6 (1963) 50–53.

Niu J., Gao N.P., Ma P., Zuo H., Experimental study on a chair-based personalized ventilation system. *Building and Environment* 42 (2007) 913-925.

Rhee K.N., Kim K.W., A 50 year review of basic and applied research in radiant heating and cooling systems for the built environment. *Building and Environment* 91 (2015) 166-190.

Rhee K.N., Olesen B.W., Kim K.W., Ten questions about radiant heating and cooling systems. *Building and Environment* 112 (2017) 367-381.

Teitelbaum E., Chen K.W., Dorit Aviv D., et al., Membrane-assisted radiant cooling for expanding thermal comfort zones globally without air conditioning. *PNAS* 117 (2020) 21162–21169.

Vesely M., Zeiler W., Personalized conditioning and its impact on thermal comfort and energy performance – A review. *Renewable and Sustainable Energy Reviews* 34 (2014) 401-408.

Xia Y., Niu J., Zhao R. and Burnett J., Effects of turbulent air on human thermal sensations in a warm isothermal environment. *Indoor air* 10 (2000) 289-296.

Xie J., Li H., Li C., Zhang J. and Luo M., Review on occupant-centric thermal comfort sensing, predicting, and controlling. *Energy and Buildings* 226 (2020) 110392.

Yang B., Sekhar C., Melikov A.K., Ceiling mounted personalized ventilation system in hot and humid climate—an energy analysis. *Energy and Buildings* 42 (2010) 2304-2308.

Zhang H., Arens E. and Zhai Y., A review of the corrective power of personal comfort systems in non-neutral ambient environments. *Building and Environment* 91 (2015) 15-41.

Zhang N., Liang Y., *et al.*, Heat transfer modeling and analysis of air-layer integrated radiant cooling unit. *Applied Thermal Engineering* 194 (2021) 117086.

Zhang N., Wan H., et al., Principle and application of air-layer integrated radiant cooling unit under hot and humid climates, *Cell Reports Physical Science* 4 (2023) 101268.

6th International Conference on Building Energy and Environment
Eindhoven University of Technology, The Netherlands
6 - 10 July 2025

Measured hygrothermal behavior of occupied straw bale building

Jordy Rabetanetiarimanana[1], Soizic Gibeaux[1], Thibaut Lecompte[1], Thibaut Colinart[1]

[1] *Univ. Bretagne Sud, UMR CNRS 6027, IRDL, F-56100 Lorient, France, thibaut.colinart@univ-ubs.fr*

SUMMARY

This paper presents a long-term monitoring study performed on an occupied timber-frame building in which straw bales are used as wall and roof filling. Temperature and relative humidity are measured in ten locations within straw bale walls with different orientations. The monitoring took place over three years to capture seasonal variations and plausible temporal evolution of hygrothermal behavior and durability. In addition, indoor air quality parameters (temperature, relative humidity, CO2 concentration) are measured in an open living room and a landing. The results showed that the average indoor temperature and relative humidity are 20°C and 60%rh, respectively. In summer, a phase shift of 3 hours and a damping of 11% are observed accross the walls. This case study confirms the potential of straw bale low-energy construction in providing thermal comfort fabric while minimizing the whole-life carbon of buildings. Regarding durability, mold growth is suspected only on the north-facing wall, an area less exposed to solar radiation.

Keywords: Relative humidity, hygrothermal comfort, mold growth, case study

1. INTRODUCTION

In recent years, low-carbon construction has emerged as an essential approach to mitigate the environmental impacts and energy demands of the construction sector. Bio-based materials such as straw, bamboo, and wood are increasingly used to decarbonize the construction sector. Straw was first used in construction around 1880 in Nebraska (D'Alessandro et al., 2017) and reemerged in the 1980s (Wall et al., 2012). In France, the first straw bale house was built in 1921 (Douzane et al., 2016). In the last decades, straw bale construction has gained attention and the advantages of this bio-based material have been recognized (Douzane et al., 2016). First, straw is cheap and easily accessible. In France, the national harvestable straw potential was estimated at 25 million tons in 2020. In addition, the use of straw in construction is a means of valorizing through recycling (Ashour et al., 2011; Wall et al., 2012). Besides, straw has also interesting thermal properties, such as low thermal conductivity. Depending on the orientation of straw stems to the heat flux and on density, the thermal conductivity ranges between 0.05 W/mK (D'Alessandro et al., 2017), 0.0723 W/mK (Douzane et al., 2016), 0.0939 W/mK (Gallegos-Ortega et al., 2017). These values are, of course, higher than those of conventional insulation materials (XPS, EPS, glass wool), but straw is prepared in the form of bale with thicknesses ensuring high thermal resistance (Chen et al.,

2024). This conditioning implies straw bales to be used mainly as infill materials in timber-framed buildings (Rota Font et al., 2024).

In the last two decades, numerous studies aimed to evaluate the hygrothermal behavior and/or the thermal performance of such buildings. (Ashour et al., 2011) monitored temperature and relative humidity within the building envelope of a straw bales timber-framed house in Bavaria, Germany, over a period of 450 hours. The results show that the straw walls attenuate extreme temperature peaks on the outside and that the migration of relative humidity from the outside to the inside of the straw is very slow (a difference of 3.4% to 2.5% after 400 hours). (Douzane et al., 2016) then studied the thermal and hygric performance of a house in Picardie, France, over 14 months. The results show that the indoor temperature stabilises between 20°C and 25°C in both summer and winter. Despite fluctuations in the outdoor RH, the indoor RH varies only between 40% and 60%. Analysis of the data recorded in the south façade in summer shows that there is a phase shift of 6h and a damping of 91%. For the north facade, the straw RH remains around 40% at 500mm depth, even for an outdoor RH of 100%. Last, comfort analysis based on the Bragger model combined with the Fauconnier model (Fauconnier, 1992) shows a level of discomfort of 26% to 32% for a level of satisfaction of 80% and 90%. Similarly, the work carried out by (Miljan et al., 2017) highlighted that straw bale walls can be used in an area with a harsh winter, such as Estonia. In Tecate, Mexico, (Gallegos-Ortega et al., 2017) monitored a building for 66 days in the summer. The result indicated a damping of 93.6% and a phase shift of 9.12h. Once again, a building envelope made of straw bales can provide comfort for the occupants, with the indoor temperature stabilizing at around 25°C whereas the outdoor temperature varies between 14 and 28°C.

Regarding the durability of straw walls, (Chen et al., 2024) mentioned that the great thickness of walls may lead to mold problems, particularly in cold, wet environments. Nevertheless, a visual inspection of the inside of the straw bale wall performed by (Thomson and Walker, 2014) after three years of service life showed no visible signs of decay in their experimental cell located in Liskeard Cornwall, United Kingdom, an area exposed to heavy rainfall. Besides, their laboratory analyses also highlighted that cyclical condition (28 days with high humidity and 14 days in a dry environment) does not compromise durability.

The number of case studies on a straw building is unfortunately limited and lasts for short periods that are not long enough to understand their long-term hygrothermal behavior and performance in view of validating their broader adoption. Note that when walls are monitored, only one orientation is considered in each study. In this view, this article describes the three-year monitoring of an occupied timber-frame building with straw-bale walls in Vannes, France, under real-life conditions. The aim is to verify the long-term hygrothermal performance and also to analyse the durability of the straw wall.

2. METHODOLOGY

2.1. Description of case study building and of its monitoring

The studied building is a two-floor family house built in 2021 near the city of Vannes (west coast of France, characterized by an oceanic climate). The building is 15.5 m long and 8.5 m wide and

has a living area of 140 m^2. The building is oriented in the E-W direction and windows are mainly oriented in the south façade. The building's walls and roof are made with 37 cm thick straw bales as an insulation layer. Their design is shown in Fig.1b. The wall and roof have U-value of 0.11 and 0.207 $W.m^{-2}.K^{-1}$ respectively. Last, heating system and controlled mechanical ventilation without heat recovery are installed.

Ten temperature and relative humidity sensors (S-THB-M008 from HOBO connected to HOBO Micro Stations H21-002) are embedded in the building envelope to assess the hygrothermal behavior and durability of the straw. Here, all wall orientations are investigated, which is the originality of the work. Sensor positions in the wall and roof are shown in Fig.1a. A weather station (made with HOBO sensors) monitors outdoor conditions just around the building (air temperature and relative humidity, wind speed and direction, global horizontal irradiance). In addition, one could access data from a weather station located 5 km from the studied building. Tow HOBO MX1102 logger provides measurements of indoor temperature and relative humidity, CO2 concentration in an open living room and in a landing. All data are recorded every 15 min. The experimental campaign started at the end of building construction (in July 2021) and was carried out for 3 years (until July 2024). During this period, the dwelling is occupied by a 4-person family. As usual for long-term experiments, some measurement problems arise during the monitoring period and some data are missing due to data acquisition failure and power outage, particularly for indoor ambient data.

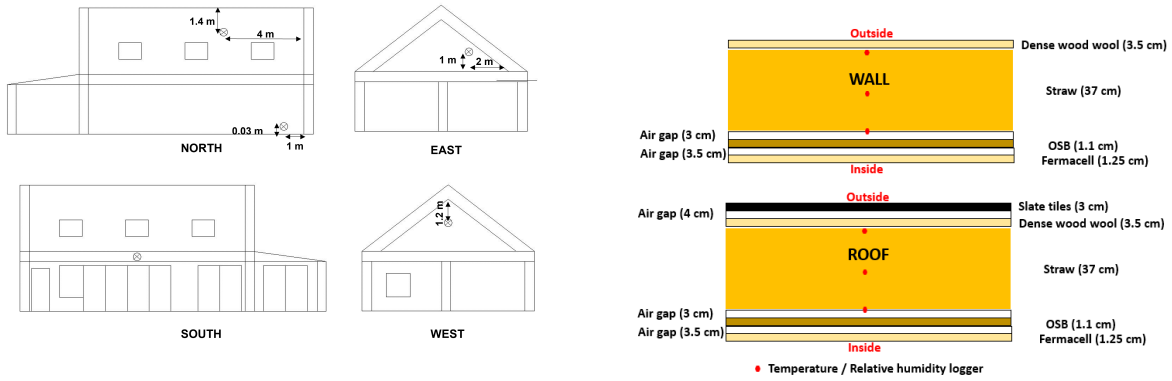

(a) **(b)**

Figure 1. Sensors positions in the wall (a) and view of wall and roof design (b)

2.2. Methods of analysis

The temperature and relative humidity variations are analyzed during the monitoring period. Then, the phase shift and damping rate of the straw bale wall are calculated in order to highlight its thermal performance. Last, mold growth risk is broadly evaluated by comparing temperature and relative humidity measured locally to isopleth defining critical conditions for mold growth. Here, the Fraunhofer Institute's isopleth curve (Eq(1)) is used (Sedlbauer et al., 2011).

$$RH_{critical} = 0.0001 \times T^3 + 0.0286 \times T^2 - 1.817 \times T + 100 \quad (1)$$

The time of wetness TOW is defined as the cumulated time when critical conditions are exceeded. Nevertheless, TOW criteria do not account for the mold decline during unfavorable conditions. To

overcome this limit and refine mold growth evaluation, mold growth is predicted through M index defined in the VTT model (Viitanen et al., 2011). The M index, which varies from 0 to 6, measures the level of mold growth.

3. RESULTS

3.1. Hygrothermal performance of building

Fig.2a illustrates the mean daily outdoor and first-floor indoor temperatures and relative humidities recorded from August 2022 and December 2023. Indoor temperature is stable around 20.2°C, whereas outside it varies between -1°C in winter and 25.7°C in summer. Regarding relative humidity, the value stabilizes around 60% despite strong fluctuations outside. When focusing on the period between June 2022 and October 2022, the indoor environment remains relatively stable (with an average of 22,5 °C) despite the large variations in outdoor temperature (up to 37 °C). Fig.2b compares the evolution of outdoor vapor pressure with the one measured in landing. The later is often higher of about 0.01 atm than outdoor vapor pressure during winter (December-March). Heating increases the indoor temperature, which in turn raises the vapor pressure. In July, outdoor vapor pressure slightly exceeds the indoor one. This indicates a migration of water vapor from inside to outside during winter and punctually in the opposite direction during summer.

Since occupancy could not be assessed, evaluation of hygrothermal comfort using psychrometric chart or adaptive models in occupancy is not possible. Nevertheless, the evolution of indoor temperature and relative humidity let us think that hygrothermal comfort could be achieved. This is confirmed by the occupants during an interview. The questionnaires, prepared by students, address thermal comfort (temperature perception and degree of discomfort), visual comfort (satisfaction with natural lighting), and indoor air quality (perception of dry or humid air, and the presence of unpleasant odours).

This hygrothermal comfort is notably achieved during the summer when straw bale walls can mitigate high outdoor temperature peaks. For example, in July 2022, outdoor temperature reaches 41°C, compared to 27.5°C indoors. It is due, among other thermal phenomena, to the thermal inertia of the building envelope. Phase shift and damping are evaluated during this period as shown in Fig.3. A phase shift of approximately 3 hours and a damping rate of 11.8% are noted between outdoor and indoor temperatures. This result is lower than what is reported in the literature. For example, (Douzane et al., 2016) report a phase shift of 7 hours and damping of 9%. Similarly, (Gallegos-Ortega et al., 2017) observe a phase shift of 9.12 hours and a damping of 6.4% during the summer period in a straw bale house in Mexico. These differences can be explained by different strategies for managing solar radiation and ventilation.

3.2. Hygrothermal performance of straw bale walls

Fig.4a and Fig.4b show the evolution of temperature and vapor pressure at different depths of the west-oriented wall, respectively. One observes that, during the night until noon, T and pv decrease with a gradient directed inward. Once solar radiation reaches the west wall, T and pv start rising from noon and reach their maximum around 10 PM. The amplitude of T and pv variations depends logically on the position of the sensor: the highest amplitude is observed close to outdoors. This highlights the possibility of straw bale to dampen and shift solicitation. For this west-oriented wall,

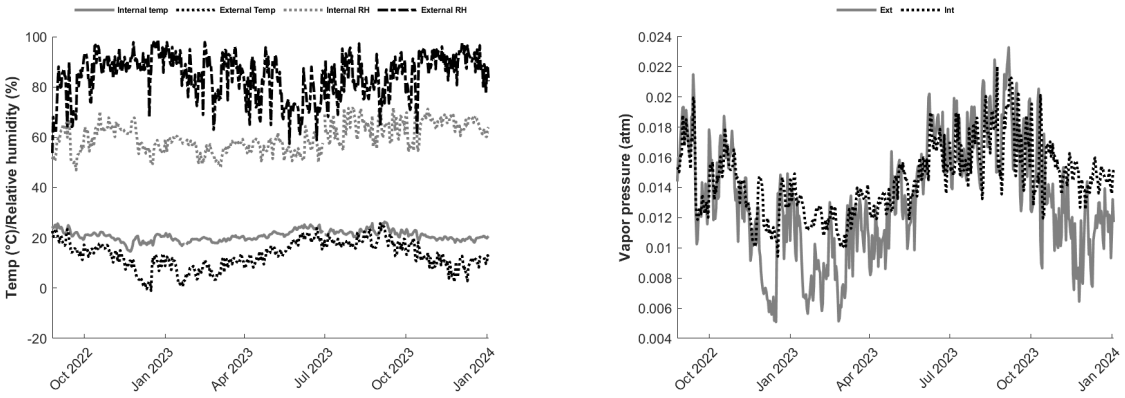

(a) **(b)**

Figure 2. Evolution of outdoor and indoor temperatures and relative humidities (a) and of vapor pressure (b)

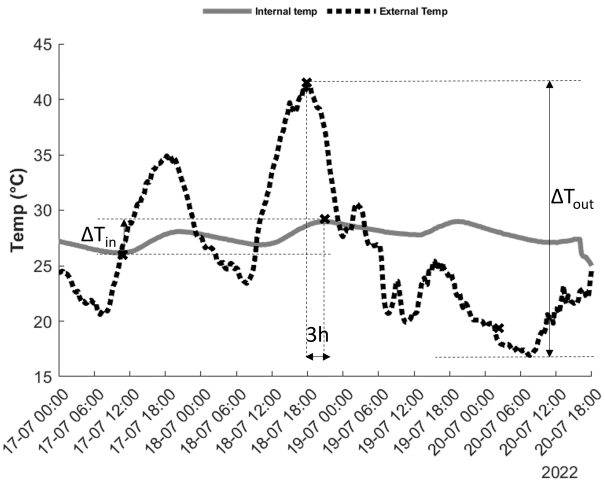

Figure 3. Evaluation of phase shift and damping during 3 days in summer 2022

dampening and time shift are about 50.4% and 2.25h for T and 45.5% and 3.75h for pv. These results are almost in line with the ones predicted with the EN ISO 13786 standard (3.88h and 9.1% damping). Regarding vapor pressure, the behavior is mainly driven by temperature variations as the relative humidity does not vary to a large extent. Close to outdoor, relative humidity increases suddenly in line with temperature increase, highlighting local evaporation of moisture adsorbed by straw (Colinart et al., 2017). Nevertheless, this vapor does not have time to flow elsewhere in the straw bale and is re-adsorbed locally by straw once temperature decreases. When analyzing the data for the north and south-oriented walls, one comes to a time shift of 1.25h and 8.25h, respectively, and damping of 35%. These values differ significantly from the theoretical ones. Nevertheless, the sensors of these walls are located at single positions (close to the floor for the north wall and just above the windows for the south wall - see Fig.1a) where the assumption required by EN ISO 13786 does not prevail. For the south wall, the strong solar radiation and the local thermal bridges may influence the analysis. For the north wall, high humidity levels are noted, modifying the thermal properties of straw and involving enhanced coupling between heat and moisture transfer.

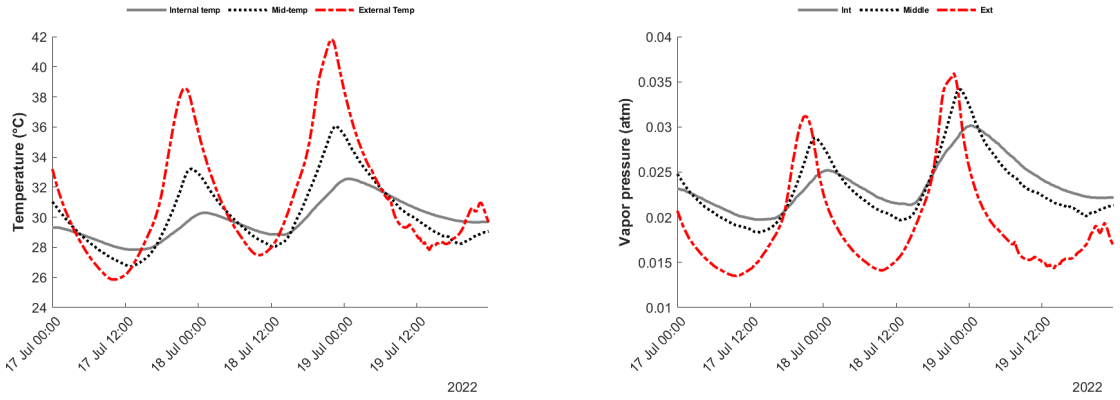

(a) **(b)**

Figure 4. Evolution of the temperatures (a) and vapor pressure (b) accros the west-oriented wall

3.3. Mold growth risk analysis

The durability of a straw wall depends on the type of environment it is used in. Therefore, it is essential to compare the relative humidity measured at different locations with the critical relative humidity evaluated with the measured temperature for each timestep. An example of comparison is shown in Fig.5a for one sensor located in the north wall at the straw–exterior cladding interface. The exceedance occurs for more than a third of the year. The air trapped in the wall is often saturated with humidity or close to saturation. Consequently, for years 1, 2, and 3, the time of wetness TOW is 126 days, 150 days, and 290 days, respectively. This process encourages the growth of mold on the straw and also damages the timber-framed structure. According to Fig.5b, the mold index M increases from 0 and to 3.5 after three years. (Johansson et al., 2013) indicate that even in an environment unfavorable to growth, spores and certain fungal structures do not disappear and can resume colonizing surfaces when humidity levels rise again. This is demonstrated in our situation, where the arrival of summer is not enough to decline mold, which keeps growing every year. Such M index indicates 10 to 50% coverage of mold if the material is directly in contact with air. For interfaces and surfaces which are not in direct contact with the interior air, (Viitanen et al., 2011) suggest to use M index as the threshold above which the mold growth risk is not acceptable. For instance, (Marincioni and Bradshaw, 2023) suggest that $M > 2$ represent a possible risk and requires further assessment, while $M > 3$ should be avoided. These conservative values were recommended to support safe design.

(Thomson and Walker, 2014) used the isopleth curve to see how often the critical moisture threshold was exceeded. Their results indicate that for a point in the mold growth zone, the measured MC is equal to 28.4%, although no signs of decomposition are visible. However, according to the literature, mold growth begins at a MC > 20% or RH > 70%. Hence, in our case, a visual inspection is planned in the coming months to confirm or rule out the presence of mold at this location. Note that this location is the most critical in the building: the north wall is logically not exposed to solar radiation and the bottom of the wall is very close to vegetation, which hinders air convection, maintains higher outdoor relative humidity levels and, thus, prevent the wall's drying out.

For the west facade, a lower exceedance is observed, resulting in mold index M of 0.02 at the end of the studied period (Fig.5c). For all other facades, no risk is noted, highlighting the durability of

the walls.

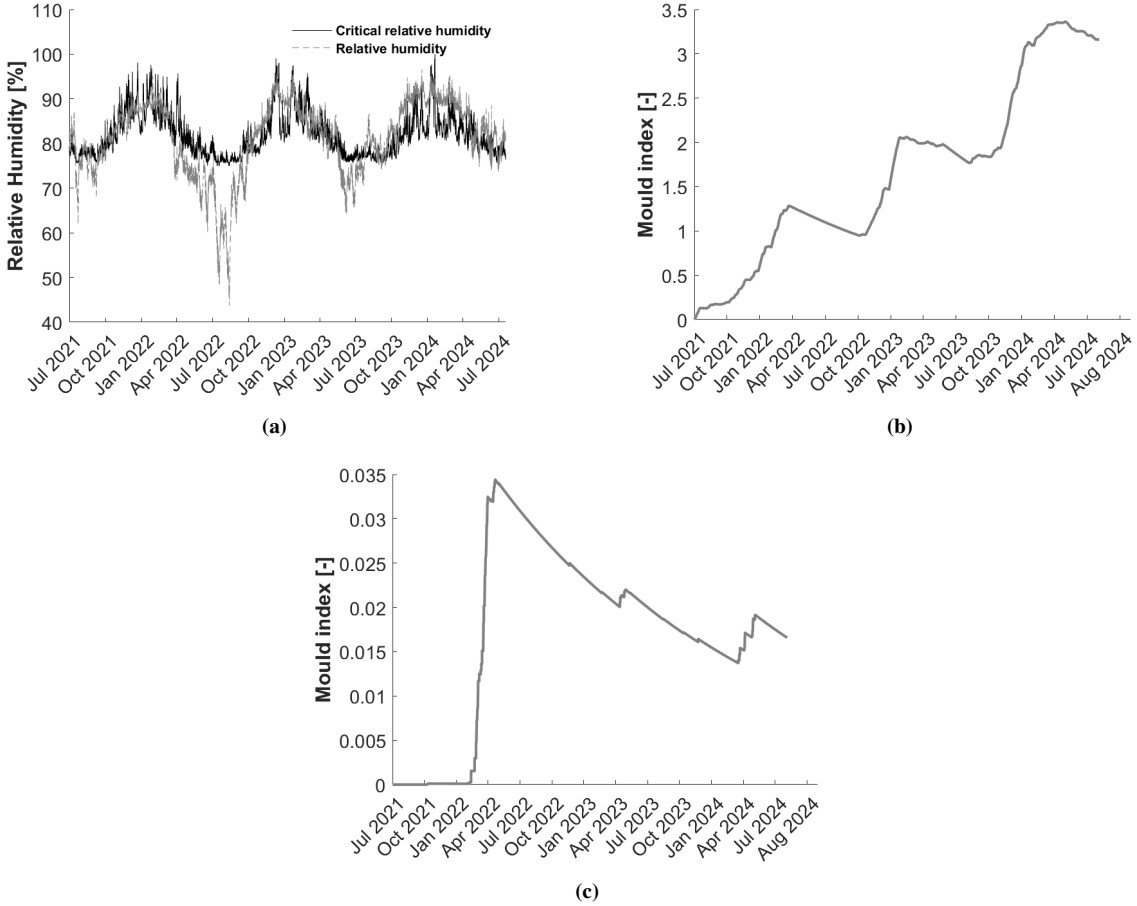

Figure 5. Evolution of relative humidity in the North (a) and of Mold Growth Index in the North (b) and the middle of the western wall (c)

4. CONCLUSION

This study analyzed the hygrothermal behavior and the durability of a straw bale house using sensors embedded within the walls or located in the room. The collected data, representing three years of monitoring, have been analyzed. Results have shown that hygrothermal comfort is achieved in the building, even during heat waves. Among other reasons, this is due to the thermal inertia of the building envelope, which allows damping and shifting of the heat wave within the current section of the walls. Nevertheless, the contribution of specific parts of the wall becomes more significant and requires specific attention. This is particularly the case for the shaded bottom part of the north façade, where high relative humidity levels are noted. High levels of mold are expected according to the VTT model. The water infiltration issue at the base of the wall, combined with the excessive vegetation near the wall, could be responsible for this phenomenon. Visual inspection are planned to confirm or not this risk. Further works will focus on modelling the hygrothermal behavior of this house, first at the wall scale and then at the building scale.

REFERENCES

Ashour T., Georg H., and Wu W., 2011. Performance of straw bale wall: A case of study. Energy and Buildings 43, 1960–1967.

Chen Y., Wang X. A., Li D., Rodrigue D., and Gosselin L., 2024. Hygrothermal performance of straw bales split-insulation wall assembly in cold and humid climates. Energy and Buildings 307, 113974.

Colinart T., Glouannec P., Bendouma M., and Chauvelon P., 2017. Temperature dependence of sorption isotherm of hygroscopic building materials. Part 2: Influence on hygrothermal behavior of hemp concrete. Energy and Buildings 152, 42–51.

D'Alessandro F., Bianchi F., Baldinelli G., Rotili A., and Schiavoni S., 2017. Straw bale constructions: Laboratory, in field and numerical assessment of energy and environmental performance. Journal of Building Engineering 11, 56–68.

Douzane O., Promis G., Roucoult J.-M., Le A.-D. T., and Langlet T., 2016. Hygrothermal performance of a straw bale building: In situ and laboratory investigations. Journal of Building Engineering 8, 91–98.

Fauconnier R., 1992. L'action de l'humidite de l'air sur la sante dans les bâtiments tertiaires. Environmental science.

Gallegos-Ortega R., Magaña-Guzmán T., Reyes-López J. A., and Romero-Hernández M. S., 2017. Thermal behavior of a straw bale building from data obtained in situ. A case in Northwestern México. Building and Environment 124, 336–341.

Johansson P., Bok G., and Ekstrand-Tobin A., 2013. The effect of cyclic moisture and temperature on mould growth on wood compared to steady state conditions. Building and Environment 65, 178–184.

Marincioni V. and Bradshaw F., 2023. A long-term monitoring study on the thermal comfort and durability of a straw bale Passivhaus cottage. Proceedings of E3S Web of Conferences. Vol. 396. EDP Sciences, 01065.

Miljan M.-J., Allikmäe R., Jürgenson A., Miljan M., and Miljan J., 2017. Hygrothermal Behaviour of the Timber-Framed Sauna with Straw-Bale Walls. CIVIL ENGINEERING 17, 124.

Rota Font F., Ciriano Nogales Y., Temes Mendoza D., Vallbé Mumbrú M., Barbeta Solà G., and De Felipe Blanch J. J., 2024. In-Situ Thermal Performance of Straw Bale Building in Relation to Fiber Orientation.

Sedlbauer K., Hofbauer W., Krueger N., Mayer F., and Breuer K., 2011. Material specific isopleth-systems as valuable tools for the assessment of the durability of building materials against mould infestation-the" isopleth-traffic light".

Thomson A. and Walker P., 2014. Durability characteristics of straw bales in building envelopes. Construction and Building Materials 68, 135–141.

Viitanen H., Ojanen T., Peuhkuri R., Vinha J., Lähdesmäki K., and Salminen K., 2011. Mould growth modelling to evaluate durability of materials. Proceedings of 12th International Conference on Durability of Building Materials and Components, XII DBMC. FEUP Edições, 409–416.

Wall K., Walker P., Gross C., White C., and Mander T., 2012. Development and testing of a prototype straw bale house. Proceedings of the Institution of Civil Engineers-Construction Materials 165, 377–384.

6th International Conference on Building Energy and Environment
Eindhoven University of Technology, The Netherlands
6 - 10 July 2025

Investigating and quantifying the Impact of Non-thermal Factor Influences on Thermal Sensation

Jiawei Wang [1], Jianong Li [1], Jianlei Niu [1]

Department of Building Environment and Energy Engineering, The Hong Kong Polytechnic University, Hunghom, Kowloon, Hong Kong, China

SUMMARY
In transition season, studying how non-thermal factors affect people's thermal sensation is crucial for optimizing public outdoor spaces (POS) design. Field measurements in Jordan Valley Park and Lok Wah Estate revealed a 5 mPET °C difference in thermal comfort due to age distribution and building shape. A Non-Thermal Factor Coefficient (NTFC_TSV) was developed to relate non-thermal factors to Thermal Sensation Votes (TSV), showing significant influence within comfort ranges. These results stress the need to account for both thermal and non-thermal factors in POS design for improved POS users' thermal comfort.

Keywords: Public outdoor space; Thermal sensation; Non-thermal factor

1. GENERAL INSTRUCTIONS

More than half of the world's population now lives in cities. With rapid urbanization and a soaring urban population, public outdoor spaces (POS) are becoming more valuable (Huang et al., 2020). POS offers people opportunities to relax and do some activities, which is crucial in maintaining citizens' physical and mental health. Therefore, Improving the quality and comfort of POS while attracting and encouraging citizens to participate in outdoor activities are the ultimate goals of urban design (Marcus & Francis, 1997).

Local microclimate conditions in urban areas, such as air temperature, wind speed, and mean radiant temperature significantly affect people's thermal comfort and behavior (Wang et al., 2025). In previous research, researchers have sought to encourage people to enjoy the outdoor environment by identifying thermal comfort ranges in which people's thermal sensation vote is -0.5 to 0.5 (Li & Liu, 2020). Findings vary across different regions, with studies in Tianjin indicating an mPET range of 11–24°C (Lai et al., 2014), in Changsha reporting 24–31°C (Yang et al., 2013), in Hong Kong identifying 27–29°C (Ng & Cheng, 2012), in Taiwan finding a range of 21.3–28.4°C (Lin, 2009).

On the other hand, according to recent studies, thermal factors are not the only factor that affects people's thermal sensitivity, and non-thermal factors also play a significant role (Li et al., 2023). Li et al. found that specific attributes of POS within communities, such as accessibility and visual factors, influence residents' heat acceptance (Li et al., 2024). Wang et al. discovered that the function of POS affects the thermal thresholds of elderly POS users (Wang et al., 2025). Therefore, understanding and quantifying the role of non-thermal factors in people's thermal sensitivity will provide valuable insights for future urban design.

This study aims to investigate the thermal comfort range of different types of POS and proposes a method to quantify and assess the influence of non-thermal factors on people's thermal sensitivity. The findings of this research will provide valuable insights for urban designers, helping them understand users' activities and preferred thermal environments across different types of POS.

2. METHODOLOGY

2.1. Study Site

Figure 1. Study sites: POS in Lok Wah Estate (LH_E) and POS in Jordan Valley Park (JV_P)

In this study, five POS are selected, three of which are from Lok Wah Estate (LH_E) and two of which are from Jordan Valley Park (JV_P), the pictures of POS are shown in Fig. 1.

2.2 Field Study

The field study includes microclimate measurement, passive observation, and the questionnaire survey, the experiment time was 9:00 to 17:30 from December 8th, 2023 to April 20th,2024 in LH_E and JV_P. The equipment. The collected environment parameters by the mini-weather station include air temperature (T_a), wind speed (v), black globe temperature (T_g), and relative humidity (RH), the instrument collects weather data every second, Figure. 2 shows the detailed information of the mini-weather station. During the measurement of microclimates at POS, student assistants conduct questionnaire surveys in the POS area. The surveys include ASHRAE 7-point thermal sensation vote (TSV) and 5-point thermal comfort vote (TCV).

Specifications of mini-weather station and globe thermometer

Meteorological parameter	Instrument	Measuring Range	Accuracy	Resolution
Air temperature	HY-WDS	-40°C-+80°C	±0.5°C	0.1°C
Relative humidity		0-100%	±2%	0.1
Wind speed		0-60m/s	±2%	0.01m/s
Globe temperature	Lutron WBGT-2010SD	0-80°C	±0.6°C	0.1°C

Figure 2. Portable mini weather station and its specifications

2.3 Heat Stress Index

The modified physiologically equivalent temperature(Mpet) is selected to be the thermal comfort indicator. The mPET is calculated based on the linear relationship between mPET and PET under humid conditions as proposed by Lin et al.(Lin et al., 2019), as shown in Eq. (1). PET is calculated using the Rayman software, utilizing weather data collected by a mini-weather station, including Mean Radiant Temperature (Tmrt), Air Temperature (T_a), Wind Speed (v), and Relative Humidity (RH).

$$mPET = 0.888 * PET + 3.5401 \ (R^2 = 0.99) \quad (1)$$

2.4 JOS-3 Model

In this study, the JOS-3 model is used to predict mean skin temperature, which is developed by Takahashi et al. (2020), predicts human physiological responses in diverse thermal conditions. With 83 nodes, it accounts for factors like brown adipose tissue, aging effects, and solar heat gain on the skin. Implemented in Python-3, this open-source model accurately forecasts physiological responses in dynamic thermal settings. Validation against human tests showed enhanced accuracy in heat production and skin temperature predictions across age groups, especially in colder conditions. RMSE values for rectal and mean skin temperatures ranged from 0.12 to 0.38°C and 0.58 to 0.83°C, affirming the model's reliability and utility for further research and applications.

3. RESULTS

3.1 Difference Between POS Users' Thermal Comfort Range in JV_P and LH_E

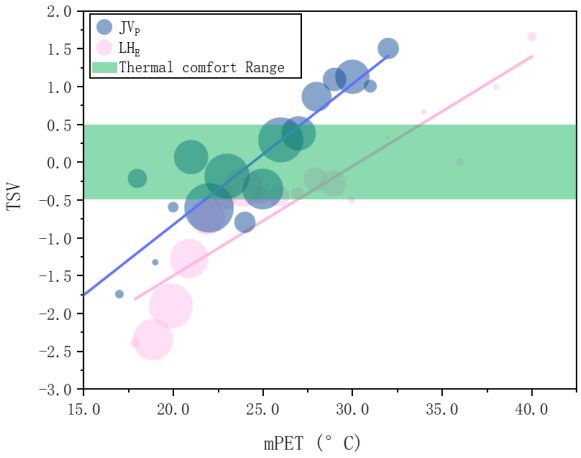

Figure 3. The relationship between the $\overline{mPET}$ which respondents experiencing and their TSV

Figure 3. presents the regression relationship between the Thermal Sensation Vote (TSV) of all respondents in two regions and the corresponding 15-minute average mPET($\overline{mPET}$). The green-shaded area in the figure represents the range where TSV falls between -0.5 and 0.5, which, according to the literature, is regarded as the neutral thermal sensation zone which this interval is defined as the thermal comfort range. The points where TSV = -0.5 and TSV = 0.5 intersect with

the regression curve of TSV and the $mPET$ for both regions indicate that the thermal comfort range in LH_E extends from 26.2°C to 33.5°C, whereas in JV_P, it ranges from 22°C to 26.5°C.

3.1.1 Causes of difference by thermal factor

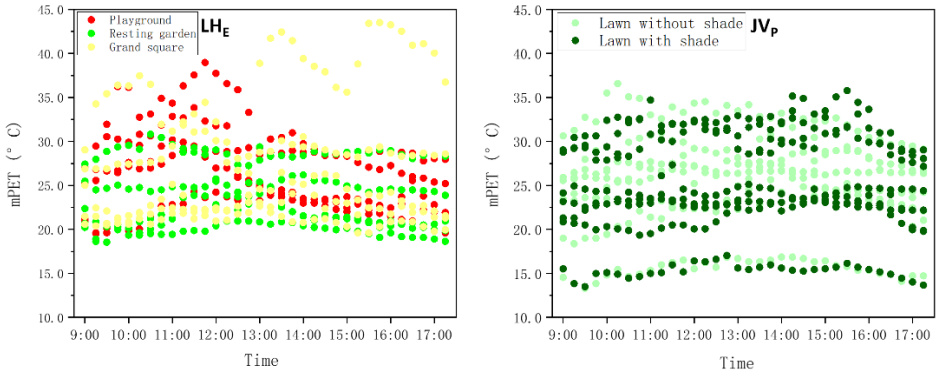

(a) (b)

Figure 4. Variation of pedestrian-level thermal environment mPET from 9:00 to 17:30: (a) LH_E; (b)JV_P

Figure 4. illustrates the distribution of $\overline{mPET}$ across five POS in two regions over a day. The data indicate that LH_E is generally warmer than JV_P, with $\overline{mPET}$ values approximately 7°C higher. This difference can be attributed to the contrasting environments: POS in JV_P is an open area, whereas large residential buildings surround POS in LH_E. As noted in Section 3.1.1, LH_E experiences higher temperatures and lower wind speeds compared to JV_P. Consequently, POS users in LH_E are exposed to a slightly warmer environment, leading to a higher thermal comfort range in this region.

3.1.2 Causes of difference: Non-thermal factor: Age

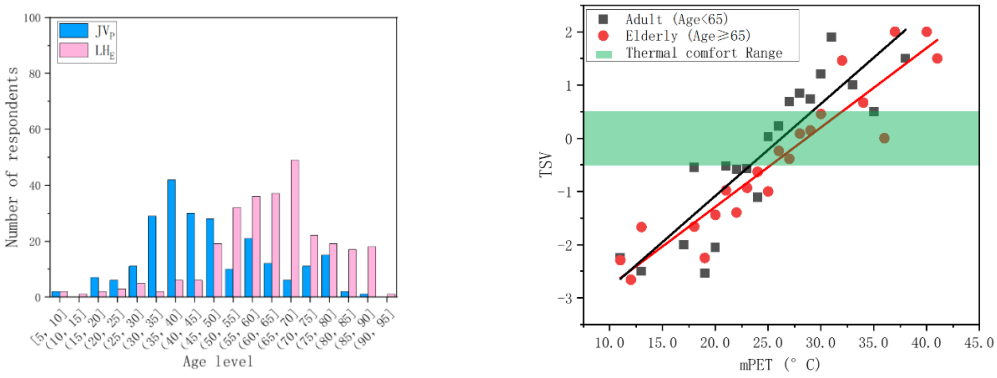

(a) (b)

Figure 5. (a) Histogram of age level in LH_E and JV_P; (b) The relationship between the $\overline{mPET}$ which respondents experiencing and their TSV in the different age group

Figure 5. (a) illustrates the age distribution of randomly selected respondents in the two regions during the questionnaire survey. In LH_E, respondents are primarily concentrated between 65 and 85 years old, with an average age of 73.5 years, whereas in JV_P, respondents are mainly between 35 and 60 years old, with an average age of 45.4 years. Figure 5. (b) presents the relationship and linear regression curve between TSV and $\overline{mPET}$ for elderly individuals (65 years old and older) and adults (under 65 years old), based on the questionnaire survey conducted in the two experimental regions. The thermal comfort range is determined using the same method as previously described. The results indicate that the thermal comfort range for the elderly spans 26.1℃ to 32.5℃, while for non-elderly individuals, it ranges from 22.5℃ to 28.2℃. These findings suggest that during the transition season, for the same $\overline{mPET}$, elderly POS users tend to have a lower TSV, indicating that their thermal comfort range is slightly warmer than that of younger POS users. This implies that the elderly generally prefer a slightly warmer thermal environment. Since the majority of LH_E users are elderly individuals who use POS, and they tend to favor warmer conditions, the overall thermal comfort range in LH_E is higher compared to JV_P.

3.2 Quantify the Impact of Non-thermal Factors on POS Users' Thermal Sensation

Due to the numerous non-thermal factors affecting thermal sensation, it is challenging to quantify the impact of each factor. Therefore, we first focus on the thermal environment experienced by POS users and, based on existing literature, use only thermal factors to predict their TSV. We then compare these predicted values (PTSV) with the real TSV(RTSV) reported by respondents to quantify the influence of non-thermal factors on thermal sensation. To achieve this, we first apply the JOS-3 model to estimate the mean skin temperature of respondents based on their experiencing thermal environment, using a phyton code derived from Takahashi et al. (2021). According to Wang & Hu (2016), mean skin temperature (MST) can be used to predict an individual's current TSV, with distinct prediction formulas for light-level, normal-level, and heavy-level activities, which are detailed in Eq. (2), (3), and (4). The prediction process of PTSV relies solely on microclimate data, making it a theoretical TSV influenced only by thermal factors. Consequently, the difference between PTSV and RTSV reflects the impact of non-thermal factors on thermal sensation. Eq. (5) quantifies this influence, with the abbreviation for the non-thermal factor coefficient impact denoted as NTFC_TSV.

$$Light-level\ activity: TSV = \frac{MST-32.3}{0.69} \quad (2)$$

$$Normal-level\ activity: TSV = \frac{MST-30.7}{0.86} \quad (3)$$

$$Heavy-level\ activity: TSV = \frac{MST-32.8}{1.59} \quad (4)$$

$$RTSV = PTSV * (1 + NTFC_TSV) \quad (5)$$

Figure 5. (a) illustrates the relationship between PTSV and RTSV across three different activity levels, along with their respective regression curves. The regression equations for light-level, normal-level, and heavy-level activities are provided in Eq. (6), (7), and (8), respectively. From

Figure 5. (a), it is evident that during the transition season, RTSV is generally lower than PTSV, indicating that non-thermal factors contribute to a cooler thermal sensation. Additionally, as the metabolic rate of the activity increases, the RTSV of heavy-level activities is consistently lower than that of normal-level activities under the same PTSV, with a difference of approximately 0.8. Compared to light-level activities, as PTSV increases, the gap between the two widens significantly. When PTSV is -2, the difference between light-level and heavy-level RTSV is only 0.1, whereas when PTSV reaches 2, the difference expands to 1.8, highlighting the increasing influence of non-thermal factors at higher heat stress levels.

$$RTSV(Light-level\ activity) = 0.943PTSV - 0.8984 \quad (6)$$

$$RTSV(Normal-level\ activity) = 0.477PTSV - 1.51 \quad (7)$$

$$RTSV(Heavy-level\ activity) = 0.5404PTSV - 2.1374 \quad (8)$$

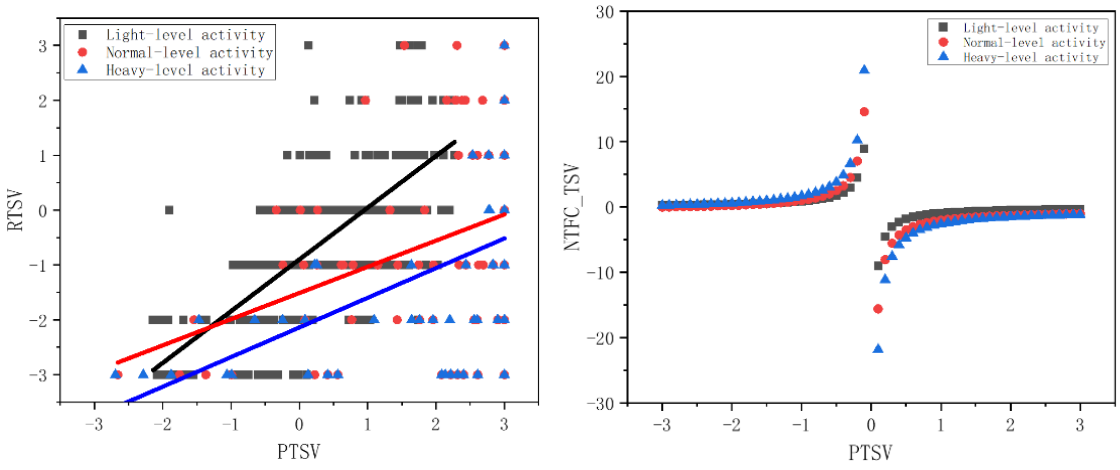

(a) (b)

Figure 6. Sensitivity of PTSV to varying RTSV and NTFC_TSV: (a) PTSV in association with RTSV in three different activity levels; (b) Scatter plot of the relationship between PTSV and NTFC_TSV

Figure 6. (b) shows a hyperbolic relationship between NTFC_TSV and PTSV. As PTSV rises from -3 to 0, NTFC_TSV gradually increases but escalates rapidly near PTSV = -0.5. Conversely, from 0 to 3, it surges from negative infinity, stabilizing around PTSV = 0.5 and approaching 0 at PTSV = 3. This indicates that NTFC_TSV amplifies thermal sensation, making cold environments feel colder and hot environments cooler, leading to actual TSV being lower than predicted. Within the thermal comfort range (-0.5 to 0.5 PTSV), NTFC_TSV has the greatest impact, approaching infinity at PTSV = 0, making true neutrality difficult to achieve. Here, non-thermal factors (e.g., POS function and quality) outweigh thermal influences, as minimal physiological discomfort heightens sensitivity to external conditions. In extreme thermal conditions (PTSV < -0.5 or > 0.5), thermal factors dominate, with NTFC_TSV staying between -5 and 5. Users are more likely to

leave or seek a better environment, and if they stay, TSV fluctuations mainly result from microclimate changes, with non-thermal factors having a reduced effect.

Moreover, different activity levels also influence the magnitude of NTFC_TSV. As PTSV increases, activities with a higher met value experience a more rapid rise in NTFC_TSV. This suggests that during transition seasons, POS users engaged in higher-met activities have a lower TSV than those participating in lower-met activities under the same microclimate. This phenomenon occurs because, in transition seasons, Air temperatures are relatively low. Engaging in high-met activities, such as playing football which is a heavy-level activity induces sweating, which facilitates heat dissipation and makes the environment feel cooler. Additionally, compared to summer, people tend to wear slightly heavier clothing (higher clo values) during transitional seasons. Excessively heavy clothing increases the physical burden of exercise, leading to greater energy expenditure, which in turn results in heightened fatigue and a stronger sensation of cold.

4. CONCLUSIONS

This study explores the differences in thermal comfort range between a park and public housing estates in Hong Kong during the transition season, analyzing the underlying causes from the perspectives of thermal factors, as well as non-thermal factors (age). Furthermore, a method is proposed to quantify the impact of non-thermal factors on TSV. The main conclusions of this study are follows:

(1) The thermal comfort range in JV_P lies between mPET 22°C and 26.5°C, whereas in LH_E, it extends from 26.2°C to 33.5°C. This difference can be attributed to several factors. First, LHE is generally 7°C mPET hotter than JV_P, which influences its thermal comfort range. Second, most POS users in LH_E are elderly, while JV_P is primarily frequented by younger individuals. Given that the thermal comfort range for elderly people is about 4°C higher in mPET than that of younger individuals, this contributes to the observed disparity.

(2) During the transition season, POS users' actual RTSV consistently falls below their predicted PTSV, and this gap widens as activity levels increase. NTFC_TSV plays a significant role in the thermal comfort zone, whereas its influence is less pronounced in extreme cold or hot conditions, where thermal factors become more dominant. Additionally, as activity levels rise, the impact of NTFC_TSV also increases.

REFERENCES

Huang J., Chen Y., Jones P., Hao T., 2022. Heat stress and outdoor activities in open spaces of public housing estates in Hong Kong: A perspective of the elderly community. *Indoor and Built Environment*, 31(6), 1447-1463.

Marcus C.C., Francis C. (Eds.), 1997. *People places: design guidelines for urban open space*. John Wiley & Sons.

Lai D., Guo D., Hou Y., Lin C., Chen Q., 2014. Studies of outdoor thermal comfort in northern China. *Building and Environment*, 77, 110-118.

Yang W., Wong N.H., Zhang G., 2013. A comparative analysis of human thermal conditions in outdoor urban spaces in the summer season in Singapore and Changsha, China. *International Journal of Biometeorology*, 57, 895-907.

Ng E., Cheng V., 2012. Urban human thermal comfort in hot and humid Hong Kong. *Energy and Buildings*, 55, 51-65.

Lin T.P., 2009. Thermal perception, adaptation and attendance in a public square in hot and humid regions. *Building and Environment*, 44(10), 2017-2026.

Wang J., Li J., Niu J., 2025. Assessment of multi-factor influences on elderly usage patterns and heat-stress exposure in neighbourhood public outdoor spaces. *Building and Environment*, 268, 112340.

Li J., Wang J., Niu J., 2023. Elderly residents' uses of fragmented outdoor spaces in public housing estates in Hong Kong—Decoding causality and heat-risk exposure. *Building and Environment*, 245, 110912.

Shade Layout for Urban Walking Routes in Hot Climates: Enhancing Pedestrian Whole-Trip Thermal Comfort

Huihui Zhao[1], Genyu Xu[2], Jiayue Li[1], Lihua Zhao[1], Qinglin Meng[1]

[1] *State Key Laboratory of Subtropical Building and Urban Science, School of Architecture, South China University of Technology, Guangzhou, 510641, China;*

[2] *School of Architecture and Planning, Yunnan University, Kunming, 650550, China.*

Abstract: Against the backdrop of climate warming and urban heat islands, ensuring pedestrian thermal comfort in outdoor walking environments has become a critical aspect of urban design. Although previous research on outdoor thermal environments has frequently emphasized large-scale shadow coverage, it has often overlooked the dynamic thermal perception of pedestrians along specific walking routes. Building on existing experimental results, this study employs theoretical derivations and a dynamic two-node thermoregulation model to analyze shading design strategies for pedestrians' entire walking trip. Key indicators—such as shading coverage ratio along the path, maximum exposure duration of continuous sunlight segments, and average (Sun–Shade) transition frequency—are proposed to optimize spatial shadow distribution. The findings not only enhance thermal comfort for urban pedestrians and encourage walking as a sustainable transportation mode, but also contribute to mitigating carbon emissions and advancing broader urban sustainability goals.

Keywords: *Outdoor walking environment; Whole-trip thermal comfort; Shade design strategy; Urban walkability; Sustainable development.*

1 INTRODUCTION

Frequent walking benefits human health, and accounting for pedestrians' thermal comfort in the design of urban outdoor walking spaces can promote walking and advance urban sustainability (Hanson & Jones, 2015; IPCC, 2023). However, escalating temperatures and the urban heat island effect intensify heat risks (Kim & Brown, 2021), where excessive heat exposure not only diminishes pedestrian comfort but also poses potential safety concerns (Liang et al., 2022). Consequently, improving outdoor thermal conditions to encourage walking has become a critical issue.

Mean Radiant Temperature (MRT) is a key indicator of outdoor thermal comfort, with solar radiation playing a pivotal role: for each 200 W/m² increase in direct solar radiation, pedestrians' thermal sensation and dissatisfaction rise by approximately 0.6 and 30%, respectively (Zhao et al., 2023). Research further shows that under high insolation, pedestrians actively seek shade (Watanabe & Ishii, 2016), and when outdoor UTCI exceeds 40°C, over half of them prefer staying in shaded areas (Watanabe & Ishii, 2016). Thus, shading design for sidewalks is crucial in ensuring outdoor comfort (Turner et al., 2023; Watanabe & Ishii, 2016). Indeed, studies have found that trees, pavilions, and building shadows can reduce PET or UTCI by 9°C to 17°C (Gai et al., 2024). Still, focusing solely on localized shading fails to address the frequent shifts between sunlight and shade during

walking (Zhao et al., 2022). Certain cities recommend a shading coverage of 20% to 80% (David & Babczyk, n.d.; Greater Phoenix Heat Action Planning Guide, 2019), but specifying coverage ratios alone cannot control sun exposure duration (Zhao, Xu, et al., 2024), highlighting the need to optimize shading at the "route" scale. While some scholars have employed multi-layer MRT or treated solar radiation as a "physical workload" (Tomasi et al., 2023), they have not fully considered pedestrians' heat memory biases and dynamic comfort needs. Frequent microclimatic variation can alleviate heat stress, and cumulative heat exposure affects whole-trip thermal perception (Li et al., 2022; Zhao, Zhao, et al., 2024). Earlier foundational studies (Zhao et al., 2023; Zhao, Xu, et al., 2024; Zhao, Zhao, et al., 2024) approached pedestrian thermal comfort from a full-journey perspective. On one hand, their models can directly inform shading designs for specific pedestrian routes by adjusting shade distribution to fulfill dynamic thermal comfort requirements; on the other, they can be applied to entire urban pedestrian networks, integrating meteorological or microclimate data to evaluate walking suitability across varying climates, times, and districts. Nonetheless, no unified set of comprehensive shading indices exists at the pedestrian-path level.

In light of this, promoting urban residents' willingness to walk requires explicit shade control indicators based on pedestrian thermal comfort models. From a "linear" perspective, this study proposes broader shade layout metrics, along with shading control strategies tailored to specific climatic conditions. The primary goal is to establish key path shading criteria that satisfy pedestrians' needs while expanding dynamic thermal comfort research and offering practical guidance for enhancing urban pedestrian environments. This endeavor ultimately aims to provide theoretical underpinnings and practical tools for professionals seeking to improve outdoor walking conditions.

2 METHOD AND RESULT

2.1 Shading Coverage Ratio (R_{shadow}) for Pedestrian Routes

Considering the pedestrian's entire walking trip, the summer shade coverage along paths must exceed a certain proportion to fulfill whole-trip thermal comfort requirements. According to the relationship between pedestrians' whole-trip thermal sensation (TSV_w) and whole-trip percentage dissatisfied (PD_w) in (Zhao, Xu, et al., 2024), when PD_w is capped at 50%, the critical value of TSV_w is approximately 1.91. This value can be viewed as the critical threshold for TSV_w, hereafter referred to as $TSV_{w,critical}$. During a trip, the instantaneous thermal sensation in sunlight ($TSV_{o,sunlight}$) typically surpasses that in shade ($TSV_{o,shadow}$). Consequently, once $TSV_{o,shadow}$ exceeds $TSV_{w,critical}$, the TSV_w under any sunlight conditions is likely to exceed this threshold, becoming a negative thermal experience for pedestrians. Therefore, ensuring pedestrians' whole-trip thermal comfort requires meeting the primary prerequisite expressed in Eq. (1).

$$TSV_{o,shadow} < TSV_{w,critcal} \tag{1}$$

When $TSV_{o,shadow}$ exceeds the critical value, the pedestrian route must maintain 100% shade coverage. Conversely, when $TSV_{o,sunlight}$ does not surpass the critical value, no minimum shade coverage is required. Therefore, this study primarily considers scenarios in which

$TSV_{o,sunlight}$ is greater than $TSV_{w,critical}$, representing most hot and sunny summer conditions. Next, TSV_w reflects pedestrians' whole-trip thermal sensation upon completing a route, yet they may encounter varying levels of heat exposure during walking. Consequently, TSV_o may fluctuate, causing TSV_w to shift between higher values in sunlight areas and lower ones in shaded areas. From a mathematical limit perspective, if the path is divided into as many alternating segments of sunlight and shaded areas as possible, the microclimatic impact in each unit of the route approximates a weighted sum based on shading coverage. Under these conditions, TSV_w comes closest to the weighted sum of $TSV_{o,shadow}$ and $TSV_{o,sunlight}$ according to their respective proportions. In other situations, the longer the continuous sunlight segment, the higher the likelihood that TSV_w, driven by $TSV_{o,sunlight}$, will exceed $TSV_{w,critical}$. Thus, the second condition to ensure TSV_w does not surpass $TSV_{w,critical}$ is that the time- (or distance-) weighted sum of TSV_o across all locations along the route remains below $TSV_{w,critical}$, as stated in Eq. (2).

$$TSV_{o,shadow}R_{shadow} + TSV_{o,sunlight}(1 - R_{shadow}) < TSV_{w,critical} \tag{2}$$

If the difference in pedestrians' thermal sensation when moving from shade to sunlight (ΔTSV_o) is known, then the required shade coverage ratio R_{shadow} under a given climate can be determined by Eq. (3).

$$R_{shadow} > R_{shadow,critial} = \frac{TSV_{o,sunlight} - TSV_{w,critical}}{TSV_{o,sunlight} - TSV_{o,shadow}} = \frac{TSV_{o,sunlight} - TSV_{w,critical}}{\Delta TSV_o} \tag{3}$$

From Eq. (3), once $TSV_{w,critical}$ is specified, substituting the instantaneous thermal sensation values in sunlight and shaded conditions is sufficient for calculation. In general, a person's instantaneous thermal sensation responds rapidly to ambient conditions and stabilizes quickly. Many previous studies have already established correlations between instantaneous thermal sensation and PET or UTCI. Thus, by applying Eq. (3), one can derive the minimum necessary shade coverage for a specific area, where the PET or UTCI values used in the calculation should match typical local parameters, such as the microclimate conditions most frequently encountered during summer daytime.

2.2 Maximum Exposure Duration ($\tau_{sun,lim}$) of Continuous Sunlight Segments

In sunny conditions, pedestrians typically walk along routes where sunlight and shade alternate frequently. Very short periods of sun exposure rarely elicit complaints from most people, but prolonged exposure can worsen their whole-trip thermal sensation and diminish their total walking experience. Therefore, for routes with frequent sun–shade transitions, identifying the upper limit of acceptable sunlight exposure time (or distance) holds significant relevance for outdoor thermal environment design and shading strategies. Figure 1 illustrates a typical example: in summer, a standard human subject (starting from a neutral environment with a neutral initial skin temperature) walks along a street, first passing through a shaded segment, then entering a sunlight segment.

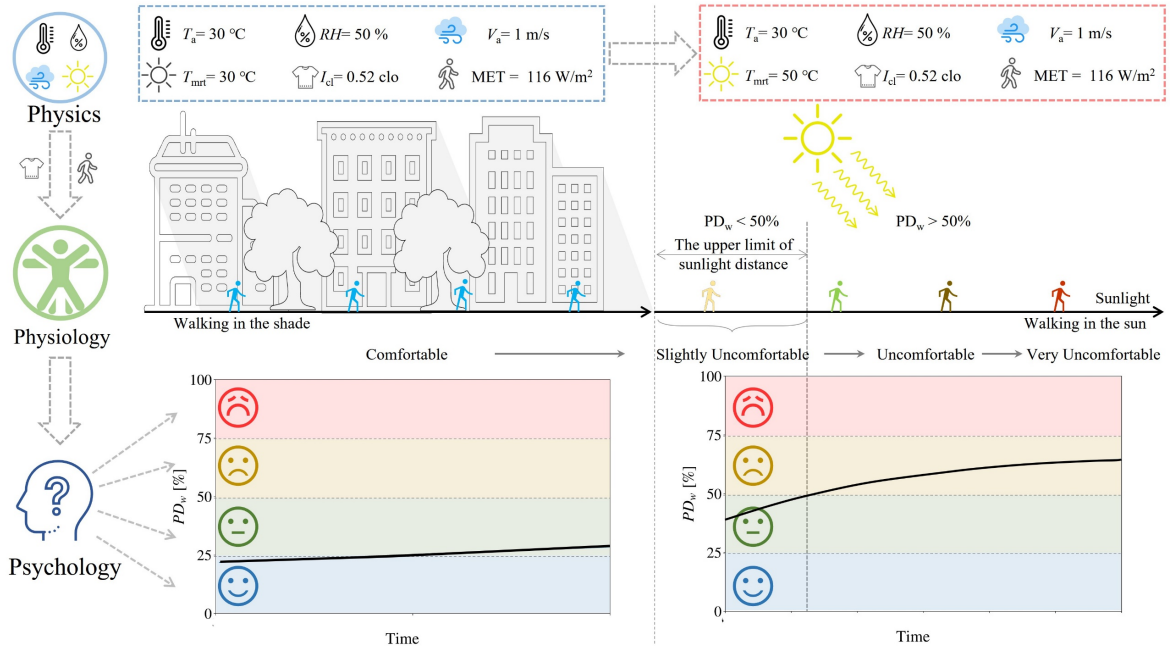

Figure 1. Schematic Illustration of Maximum Exposure Duration of Continuous Sunlight Segments

As shown in Figure 1, even when a route's shading coverage ratio is defined, an extreme adverse case may arise if there is only one continuous sunlight section, causing the pedestrian's TSV_w to reach its maximum in that portion. Hence, constraining the maximum length of uninterrupted sunlight exposure becomes crucial. Because whole-trip thermal comfort can be derived from mean skin temperature ($T_{sk,m}$), skin temperature change rate ($dT_{sk,m}/d\tau$), and stored heat deviating from thermal neutrality (ΔQ_s) (Zhao, Zhao, et al., 2024), and each can be represented as time-dependent functions in a dynamic thermoregulation model, setting an upper threshold for thermal dissatisfaction allows us to determine the continuous sunlight exposure limit necessary to maintain whole-trip pedestrian thermal comfort. By employing the two-node thermoregulation model, one can simulate the dynamic physiological responses and whole-trip thermal comfort of pedestrians in specific environments (Zhao, Zhao, et al., 2024). These simulations yield the temporal change in PD_w during sunlight exposure. If PD_w is set to 50% as the critical value, the model provides the maximum acceptable duration of sun exposure; in combination with walking speed, it then produces the corresponding limit on continuous sunlight distance. Should any urban street segment exceed this limit, pedestrians are likely to experience pronounced thermal discomfort, making additional shading measures essential to reduce prolonged sun exposure.

Previous research indicates that TSV_w represents the sum of contributions from TSV_o, T_{sk}, and ΔQ_s, encompassing both instantaneous and memory-based thermal sensations. Drawing on reference signal theory and time constants, TSV_o, T_{sk}, and ΔQ_s are treated as three distinct subsystems responding to TSV_w. Before entering the sunlight area, each subsystem's thermal sensation approaches $TSV_{o,shadow}$; once stepping into sunlight, each gradually shifts toward $TSV_{o,sunlight}$ at differing rates. At any moment τ, the pedestrian's whole-trip thermal sensation, $TSV_{w,\tau}$, is the weighted sum of these subsystem signals. Consequently, after moving from

shade into sunlight, the evolution of $TSV_{w,\tau}$ over time is described by Eq. (4).

$$TSV_{w,\tau}=TSV_{o,sunlight}-\Delta TSV_o\cdot[w_o\cdot\exp(-\tau/\tau_{c,o})+w_{sk}\cdot\exp(-\tau/\tau_{c,sk})+w_q\cdot\exp(-\tau/\tau_{c,q})] \quad (4)$$

In Eq. (4), w_o, w_{sk}, and w_q are the weighting coefficients corresponding to the TSV_o, $T_{sk,m}$, and ΔQ_s subsystems of TSV_w, respectively. The symbols $\tau_{c,o}$, $\tau_{c,sk}$, and $\tau_{c,q}$ denote the response time constants (in seconds) for each subsystem, while τ represents the walking duration (in seconds) after moving from a shaded area to a sunlight area. $TSV_{w,\tau}$ is the whole-trip thermal sensation at time τ under changing environmental conditions, and ΔTSV_o is the instantaneous difference in thermal sensation when transitioning from shade to sun.

When the human body encounters a sudden environmental change, TSV_o also undergoes a sudden shift and rapidly stabilizes near a certain level, effectively responding immediately to the new environment. Consequently, its corresponding time constant $\tau_{c,o}$ is the smallest (assumed to be 1 s in this study). However, due to the heat storage properties of various bodily tissues and the internal heat transfer process, $T_{sk,m}$ and ΔQ_s do not respond instantaneously. Instead, they gradually approach a stable state as the pedestrian remains in the new environment; their time constants are relatively larger and differ from each other. From the perspective of physiological thermoregulation, $\tau_{c,sk}$, and $\tau_{c,q}$ correlate with the degree of activation in the body's heat-regulating systems under different thermal conditions. By employing a dynamic two-node thermoregulation model, one can simulate the variation of $T_{sk,m}$ and ΔQ_s under abrupt environmental changes and, through regression analysis, estimate each subsystem's time constant. The smaller these time constants are, the quicker TSV_w reaches $TSV_{w,critical}$, making pedestrians more prone to experiencing whole-trip thermal discomfort. Consequently, based on calculations that account for all scenarios, integer minima of 200 s and 400 s are assigned to the $T_{sk,m}$ and ΔQ_s subsystems, respectively.

Let $\tau_{sun,lim}$ be the upper limit of sun exposure time, at which point the pedestrian's whole-trip thermal sensation reaches $TSV_{w,critical}$ Setting $TSV_{w,\tau} = TSV_{w,critical}$ in Eq. (4) and substituting Eq. (3) into Eq. (4) yields the relationship between $\tau_{sun,lim}$ and critical shading coverage ratio ($R_{shadow,critical}$), as shown in Eq. (5).

$$w_o\cdot\exp(-\tau_{sun,lim}/\tau_{c,o})+w_{sk}\cdot\exp(-\tau_{sun,lim}/\tau_{c,sk})+w_q\cdot\exp(-\tau_{sun,lim}/\tau_{c,q})=R_{shadow,critial} \quad (5)$$

Using this approach, one can compute the value of $\tau_{sun,lim}$ under various conditions, as illustrated in Figure 2. It should be noted that Figure 2 only displays the computed results for $\tau_{sun,lim}$ within the range of 0 s to 500 s. Outcomes exceeding 500 s are interpreted as indicating no substantial thermal discomfort during sunlight walking, and such cases are all assumed to have $\tau_{sun,lim}$ = 500 s. The figure shows that when the TSV_o in shaded conditions is higher or when the difference between sunlight and shaded thermal sensations is larger, the acceptable duration of sun exposure diminishes. Therefore, under a specific climatic setting, one may first employ microclimate data and the pedestrian thermal comfort model proposed in this study to estimate $TSV_{o,shadow}$ and $TSV_{o,sunlight}$ in near-steady states. Substituting these into Eqs. (3) and (5) then determines the value of $\tau_{sun,lim}$ for that climatic context.

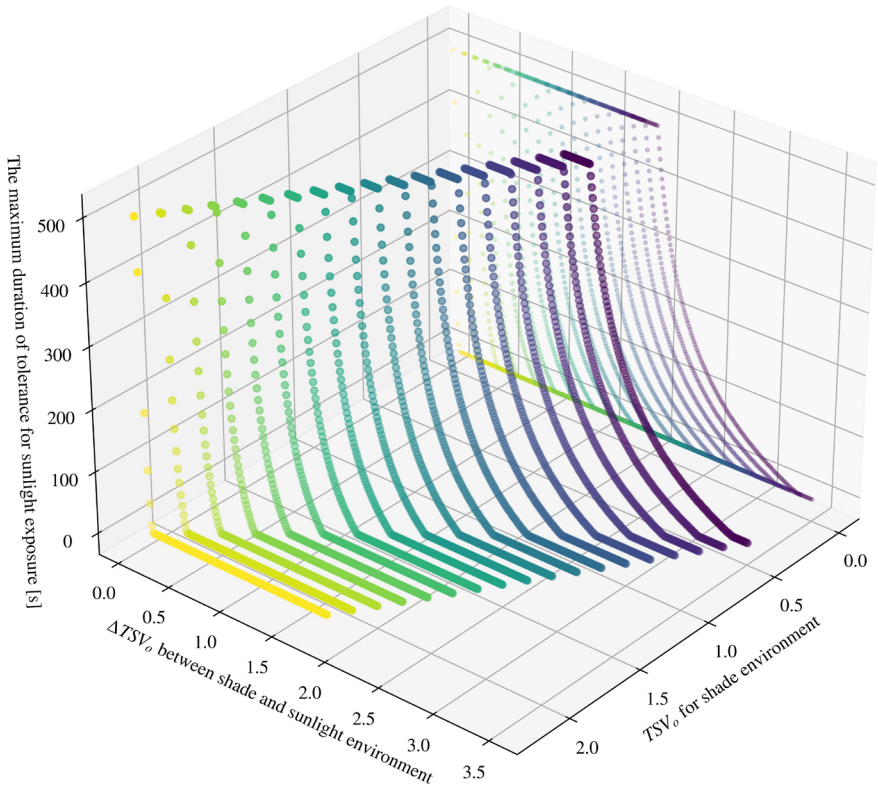

Figure 2. Relationship between the maximum exposure duration and the TSV_o for shade and sunlight environments

2.3 Average frequency of Sun–Shade Transitions (f_{300}) Along Pedestrian Routes

Even if each individual continuous sunlight section along a pedestrian route satisfies the $\tau_{sun,lim}$ constraint, problematic scenarios may still arise if two such sunlight segments are close together and separated by only a short shaded section. In that case, immediately after one sunlight segment—when TSV_w is already elevated—a brief shaded section might not be long enough to lower TSV_w to its original lower level. Thus, an additional constraint must be imposed on the minimum distance of shaded sections separating multiple sunlight segments. Given $\tau_{sun,lim}$ and $R_{shadow,critical}$, one can calculate the minimum required shaded-section duration ($\tau_{shade,lim}$). By treating the sum of $\tau_{sun,lim}$ and $\tau_{shade,lim}$ as the continuous standard observation distance (L_{std}), and then specifying that the shading coverage ratio $R_{shadow,critical}$ must be met within any L_{std}-length interval along the route, it becomes possible to prevent multiple continuous sunlight segments from clustering. Assuming a pedestrian walking speed of v_p, L_{std} is given by Eq. (6).

$$L_{std} = (\tau_{sun,lim} + \tau_{shadow,lim}) \cdot v_p = \frac{\tau_{sun,lim} \cdot v_p}{(1 - R_{shadow,critial})} \tag{6}$$

Once L_{std} is established, the extent of route division by the standard observation distance is defined, so the average frequency of sun–shade transitions per 300 m-long pedestrian route (f_{300}) (Zhao et al., 2022) has a theoretical lower bound specified by Eq. (7).

$$f_{300} > 2 \cdot \frac{300}{\tau_{\text{sun,lim}} \cdot v_{\text{p}} + \frac{\tau_{\text{sun,lim}} \cdot v_{\text{p}}}{(1 - R_{\text{shadow,critial}})} R_{\text{shadow,critial}}} = \frac{600}{L_{\text{std}}} = \frac{600(1 - R_{\text{shadow,critial}})}{\tau_{\text{sun,lim}} \cdot v_{\text{p}}} \quad (7)$$

Eqs. (6) and (7) correspond to environments where high-heat exposure is a concern, and frequent dynamic thermal experiences can effectively prevent the mean skin temperature from reaching higher levels. This helps pedestrians avoid prolonged periods of discomfort, thereby improving their whole-trip walking experience.

In summary, the above approach yields various indicators required to fulfill pedestrian thermal comfort across the entire journey. For noncompliant segments, adding shading devices to increase effective shade coverage or reducing continuous sunlight exposure can enhance thermal comfort. At the neighborhood scale, a GIS-based path shading analysis can characterize sun–shade distribution across pedestrian routes. By assessing the proportion of route segments exceeding threshold values, planners can estimate the level of "heat resistance" for pedestrians during specific time periods, then strategically adjust shade coverage where needed. Reducing the proportion of routes that lead to prolonged thermal discomfort should encourage residents to keep choosing walking as a travel option.

2.4 Limitations and future work

This study focuses on the demand for outdoor shade in hot and humid climates during warmer periods, aiming to guide shade design. It has not yet explored the potential positive effects of sunlight in colder regions or during winter, a limitation that may affect the comprehensiveness of the findings. Future research could investigate adaptive urban shade designs, ideally achieving a dynamic balance of more shade in summer and more sunlight in winter to address diverse climatic needs. Additionally, based on subjective surveys and $TSV_{w,critical}$ calculations in a specific city, this study proposes an analytical framework for local shade layout. However, variations in thermal tolerance and sunlight exposure acceptance across different cities, climates, and urban layouts suggest that the generalizability of the findings requires further validation. Future studies will incorporate multi-regional data to enhance the applicability of conclusions. For urban planning and design, this study offers an analytical approach, enabling planners to assess the shading performance of outdoor pedestrian spaces based on local shade demand indicators and optimize shade facility layouts, such as adding canopies or adjusting green coverage, to improve thermal comfort in pedestrian environments.

3 CONCLUSION

This study, guided by the practical need to ensure thermal comfort throughout pedestrians' whole-trip, proposes a method for analyzing control indicators in path shading design. Under specific climatic conditions, the shading layout must simultaneously satisfy the minimum shading ratio within a standard observation distance, the maximum allowable exposure duration in continuous sunlight segments, and the minimum threshold for shade exposure frequency. These indicators are primarily determined by typical daytime summer climate conditions, as characterized by PET or UTCI in pedestrian spaces. Nevertheless, the present findings represent preliminary inferences, and further research is needed to validate their broader applicability.

ACKNOWLEDGEMENTS

This work is jointly supported by the National Natural Science Foundation of China (No. 52408111), the Guangdong Provincial Natural Science Foundation (2024A1515011415), Key Project of Independent Research Subject, State Key Laboratory of Subtropical Building and Urban Science (No. 2023ZB05).

REFERENCES

David, Y., & Babczyk, U. (n.d.). Open Space Shade Policy Planning Guidelines (TA/9083). Tami Hirsh Architects.

Gai, Z., Yin, H., Kong, F., Su, J., Shen, Z., Sun, H., Yang, S., Liu, H., & Middel, A. (2024). How does Shade Infrastructure Affect Outdoor Thermal Comfort during Hot, Humid Summers? Evidence from Nanjing, China. Building and Environment, 112320.

Greater Phoenix Heat Action Planning Guide. (2019). [Manual]. Arizona State University.

Hanson, S., & Jones, A. (2015). Is there evidence that walking groups have health benefits? A systematic review and meta-analysis. British Journal of Sports Medicine, 49(11), 710–715.

IPCC. (2023). AR6 Synthesis Report: Climate Change 2023.

Kim, S. W., & Brown, R. D. (2021). Urban heat island (UHI) variations within a city boundary: A systematic literature review. Renewable and Sustainable Energy Reviews, 148, 111256.

Li, J., Niu, J., Huang, T., & Mak, C. M. (2022). Dynamic effects of frequent step changes in outdoor microclimate environments on thermal sensation and dissatisfaction of pedestrian during summer. Sustainable Cities and Society, 79, 103670. Scopus.

Liang, M., Min, M., Guo, X., Song, Q., Wang, H., Li, N., Su, W., Liang, Q., Ding, X., Ye, P., Duan, L., & Sun, Y. (2022). The relationship between ambient temperatures and road traffic injuries: A systematic review and meta-analysis. Environmental Science and Pollution Research, 29(33), 50647–50660.

Tomasi, M., Nikolopoulou, M., Giridharan, R., Löve, M., & Ratti, C. (2023). Definition of a maximum threshold of direct solar radiation exposure for pedestrians of diverse walking abilities. International Journal of Biometeorology.

Turner, V. K., Middel, A., & Vanos, J. K. (2023). Shade is an essential solution for hotter cities. Nature, 619(7971), 694–697.

Watanabe, S., & Ishii, J. (2016). Effect of outdoor thermal environment on pedestrians' behavior selecting a shaded area in a humid subtropical region. Building and Environment, 95, 32–41.

Zhao, H., Wang, S., Zhang, Y., Zhao, L., Zhai, Y., Brown, R. D., Jin, L., & Wu, R. (2023). The effect of solar radiation on pedestrian thermal comfort: A climate chamber experiment. Building and Environment, 245, 110869.

Zhao, H., Xu, G., Shi, Y., Li, J., & Zhang, Y. (2022). The characteristics of dynamic and non-uniform thermal radiation experienced by pedestrians in a street canyon. Building and Environment, 222, 109361.

Zhao, H., Xu, G., Shi, Y., Zhai, Y., Zhao, L., & Brown, R. D. (2024). Evaluation of pedestrian thermal comfort from a whole-trip perspective: An outdoor empirical study. Sustainable Cities and Society, 115, 105872.

Zhao, H., Zhao, L., Zhai, Y., Jin, L., Meng, Q., Yan, J., Wu, R., & Brown, R. D. (2024). The impact of dynamic thermal experiences on pedestrian thermal comfort: A whole-trip perspective from laboratory studies. Building and Environment, 258, 111599.

6th International Conference on Building Energy and Environment
Eindhoven University of Technology, The Netherlands
6 - 10 July 2025

Effect of sensations in dominant body part on overall sensation prediction in the CBE comfort model

Junwei Lin, Yongxin Xie, Jianlei Niu

Department of Building Environment and Energy Engineering, The Hong Kong Polytechnic University, Hung Hom, Kowloon, Hong Kong

SUMMARY
Thermal comfort research increasingly targets human responses in non-uniform and transient environments. The CBE comfort model, an advanced multi-nodal prediction tool, was developed to predict local and overall thermal sensations and comforts. In this model, cooling effects on the dominant body parts (back, chest and pelvis) have a dominant influence on overall sensation. However, this prediction logic can lead to prediction errors in real-world scenarios. To quantitatively assess this issue and propose a feasible correction strategy, we conducted field experiments in both indoor and semi-outdoor spaces. The results indicated that the cool sensation in the back affects overall sensation but does not always dominate it. To improve alignment with actual thermal sensation votes, a modified method is proposed for the original dominated cold model. This revised overall sensation calculation method can be incorporated into the original CBE comfort model to increase accuracy in predicting thermal sensation.

Keywords: local sensation, overall sensation, CBE comfort model.

1. INTRODUCTION

To predict human subjective responses more accurately in realistic environments, thermal comfort and sensation research has shifted its focus from the ideal uniform and steady environment to non-uniform and transient conditions (Zhang, 2003; Yang et al., 2024a). Spatially asymmetrical environmental conditions, observed in both indoor and outdoor environments, can result from factors such as temperature stratification, local cooling or heating devices and solar radiation(Zhang, 2003). Temporal non-uniformity also plays a critical role in thermal comfort prediction. During a certain period, dynamic environments and human behaviours contribute to transient thermal comfort and sensation votes (Brager & de Dear, 1998; Jiang et al., 2024; De Dear et al., 2013). Targeting the prediction of human responses to simultaneous non-uniform and transient thermal conditions, a three-part series on thermal sensation and comfort prediction was developed by UC Berkeley (Zhang et al., 2010a, 2010b, 2010c), namely the CBE comfort model.

In this series, Part I developed the local sensation models based on physiological parameters (Zhang et al., 2010a). These models utilize logistic regression functions to link local skin temperatures with thermal sensations. The dynamic term for local sensation is calculated using the derivative of core temperatures and local skin temperatures. After obtaining local thermal sensations, Part II proposed the local comfort calculation models that employ asymmetrical saddle-shaped curves to represent the relationship between local thermal sensations and comfort (Zhang et al., 2010b). Based on the local comfort and sensation results, Part III introduced methods for calculating whole-body comfort and sensations (Zhang et al., 2010c). The authors also published an additional part, Part IV, introducing the smoothing functions (Zhao et al., 2014).

Although these pieced models can better predict the whole-body sensation, the thermal sensation surveys conducted in previous studies observed inaccuracies in prediction (K et al., 2024; Yang et al., 2024b). One of the most significant discrepancies between experimental and calculated overall sensation occurs in cases where the "dominated cold" effect arises. In the original calculation method, cool or cold sensations in dominant body parts, including chest, back and pelvis, are expected to dominate the whole-body sensation. This concept is embedded in one of the pieced models, the opposite-dominated cold model (Zhang et al., 2010c). In this model, if the lowest local sensation in dominant parts is less than or equal to -1, the overall sensation is set to this value. However, this dominant effect appears to be less effective in certain scenarios. Survey results from previous studies showed that under relatively high heat stress, human subjects reported feeling warm or hot even when their dominant body parts were cooled by cooling devices (K et al., 2024; Yang et al., 2024b). Consequently, special attention should be given to the logic of the opposite-dominated cold model.

To address the identified deficiencies, this study aims to refine the original opposite-dominated cold model for overall sensation prediction, targeting more accurate overall sensation predictions. In this study, the experiments under varying thermal conditions were conducted to clarify the influence of the sensations in the dominant body parts on overall sensations and thus provide a basis for subsequent model modifications. Based on the analysis, modified calculation methods were developed to improve the accuracy of the overall sensation predictions when affected by the "dominated cold" effect.

2. METHODOLOGY

In this study, the thermal sensation surveys were conducted at a university campus in Hong Kong, China, from May to September. A total number of 30 human subjects (18 males and 12 females) were recruited to participate in the surveys, with their information details in Table 1. Since the experiments took place during summer in Hong Kong, most subjects wore typical summer clothing with a clothing insulation value of approximately 0.3 clo. The clothing insulation values were derived from tabulated clothing insulation data in the standards (ASHRAE, 2023; ISO, 2009) and the clothing information collected during the experiments.

Table 1. Characteristics of subjects.

	Male	Female	Total
Count	18	12	30
Age (years)	26.3 ± 2.9	27.1 ± 6.6	26.6 ± 4.8
Height (cm)	175.8 ± 5.0	167.1 ± 4.4	172.2 ± 6.4
Weight (kg)	72.1 ± 4.6	59.9 ± 10.0	67.0 ± 9.5
Clothing Insulation (clo)	0.31 ± 0.08	0.34 ± 0.07	0.32 ± 0.08

Each experiment lasted around 35 minutes, including a 10-minute adaptation period and two stages with different exposed conditions lasting 10 and 15 minutes, respectively. These two stages are labelled as Stage 1 and Stage 2. Stage 1 featured relatively constant thermal conditions while in Stage 2, the local cooling was introduced to create the dominated cold. Starting from Stage 1, subjects were asked to continuously report their thermal sensations by completing the questionnaires. The survey included 11 questionnaires, using an extended 9-point thermal sensation scale (Zhang, 2003). The time intervals between each questionnaire ranged from one to four minutes. The entire experimental process and the timing of sensation votes are illustrated in Figure 1. For the first and second questionnaires, subjects only recorded

their overall thermal sensations. Starting from the third questionnaire, recorded just before the local cooling, subjects were required to vote on their thermal sensations for both the whole body and each body part. The analysis of thermal sensation changes focused on questionnaires 3 to 11. Each subject completed the whole procedure one or two times with different experimental settings. The experiment produced 48 sets of data with 528 thermal sensation vote entries (432 entries included values for local body parts).

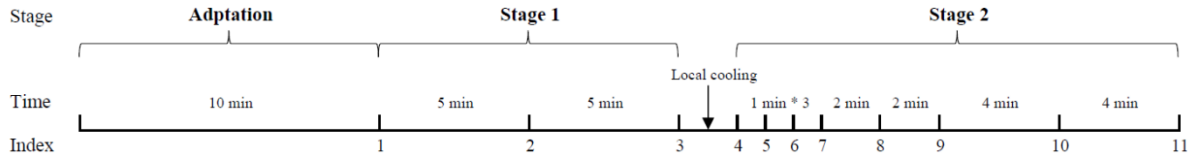

Figure 1. Procedures of the experiment.

To cover both indoor and outdoor conditions, the experiments were conducted in a climate-controlled chamber and a semi-open area. Table 2 presents the settings for four different cases designed for the experiment, consisting of two indoor cases and two outdoor cases. Four types of thermal environments were considered, including slightly cool indoors (set-point temperature: 22.0 °C), slightly warm indoors (set-point temperature: 26.0 °C), and fully and partly shaded outdoor open space with high temperatures (air temperature: 33.7 ± 1.4 °C). The globe temperatures for the fully and partly shaded outdoor cases were 34.4 ± 2.2 °C and 40.1 ± 3.3 °C, respectively. Subjects stayed in these thermal environments for approximately 10 minutes before the local cooling was introduced. The cooling devices were installed on a framework. Subjects were asked to stand with their back to the devices. For the used radiant cooling panels, the setting supply chilled water temperature was 8 °C, and the average panel surface temperature was 14.3 °C (Liang et al., 2024).

Table 2. Configurations of cases set in the experiments.

Case	Condition	Sample Size
1	Indoor (cool)	8
2	Indoor (warm)	8
3	Outdoor (fully shaded)	20
4	Outdoor (partly shaded)	12

3. RESULTS

In the experiment, four cases were designed to examine the possible “dominated cold” effect under different thermal conditions. Figure 2 shows the subjects’ overall thermal sensations during the questionnaires 3 – 11 for different cases (blue lines). When staying indoors and experiencing radiant cooling, the subjects’ average overall sensation decreased by around 1.5 for slightly warm conditions and 0.5 for slightly cool conditions. In the outdoor conditions with mediate and high heat stress (Case 3 and 4), even though the radiant cooling devices can still contribute to a slight decrease in overall sensation, the fluctuations were within 0.5.

Using the local sensations collected in the experiment, the overall sensation can be then predicted based on the CBE models. The predicted results are coloured in orange, distinct from the blue lines which represent the surveyed real overall sensations. The overall sensation predictions in Case 1 showed great agreement with the surveyed data. A larger difference was observed in Case 2 where subjects stayed in slightly warm indoor conditions with local cooling.

For the outdoor cases, the predictions for Case 4 performed well, while those for Case 3 were much less accurate. The predictions in Cases 2 and 3 underestimated the overall sensations and then caused large discrepancies.

The underestimation of overall thermal sensation when using local cooling may be attributed to the consideration of the "dominated-cold" effect. When the back side of the human body, primarily the back in this experiment, was cooled down, its sensations easily reached the threshold for the opposite-dominated cold calculation model. This process, however, may not be suitable for all cases. All four cases in this study which involved local cooling could cause the "dominated-cold" effect. In Case 1, since the differences between room air temperatures and panel surface temperatures were smaller, the radiant cooling was less efficient and thus the discrepancies caused by the "dominated-cold" effect were smaller. Similarly, the predicted sensation results in Case 4 were not affected by this effect, as with high heat stress, the back sensation could not reach the threshold for opposite-dominated cold. However, with mediate heat stress, Case 2 and Case 3 showed the largest differences between predicted and surveyed overall sensations. The underestimation of average overall sensations for Case 2 ranged from 0.1 to 0.7. In Case 3, the discrepancies were even larger, with a maximum bias of 1.1. The real average overall sensations in Case 3 kept at the hot level of around 2 while the predicted results decreased from 2 to 0.5.

Figure 2 illustrates additional lines for local sensations in the dominant part (back) and maximum local sensations. The predicted results in Case 2 and Case 3 were very close to the back sensations, supporting the supposition of the potential misuse of the "dominated-cold" effect. In both Case 2 and Case 3, the maximum local sensations were high, which might explain why the "dominated-cold" effect did not occur.

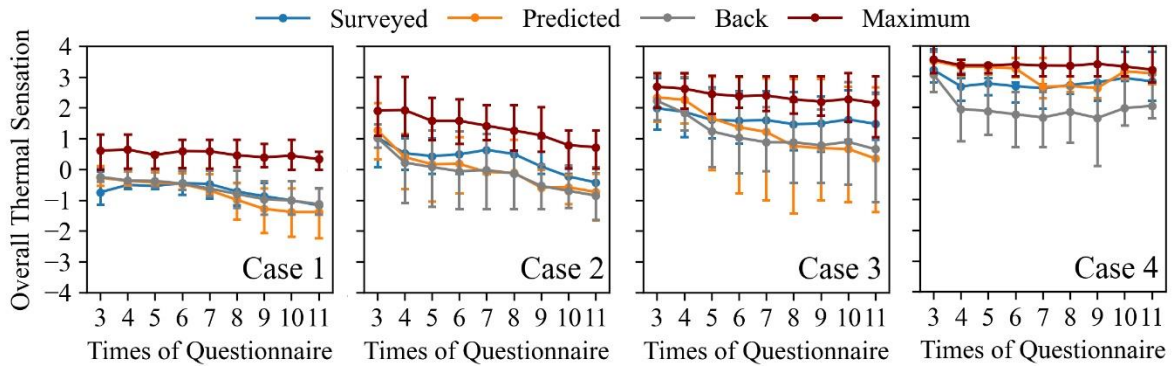

Figure 2. Comparison between surveyed and predicted thermal sensations for different cases.

4. MODIFICATION

The experiment highlighted the need for modifications to the CBE models to improve accuracy. In this section, the causes of inaccurate overall sensation were analysed and the possible solutions to these issues were then proposed. In the original models, the "dominated cold" effect occurs when the sensation group contains at least one positive local sensation. For a sensation group that contains certain local sensations $x_{(i)}$, the calculation of the predicted overall sensation for the opposite-dominated cold model can be expressed as:

$$Y = \min x_{(i),dominant} \quad (1)$$

where Y is the overall sensation and $x_{(i),dominant}$ is the local sensation in the dominant body parts including the pelvis, chest and back. If the lowest sensation in the dominant body part meets the threshold ($\min x_{(i),dominant} \leq -1$), the sensation group falls into the opposite-dominated cold model.

As analysed in Section 3, the predicted overall sensations obtained from the above calculation method were underestimated. Since the inaccuracy was observed when there existed hot or warm local sensations, the possible reason may because the influence of these sensations is overlooked. Among all the pieced models, the opposite cold model, which is similar to the opposite-dominated cold model, can serve as a reference. This model involves the opposite warm modifiers to describe the contribution of the hot or warm local sensations, following the equations:

$$Y = Y_{ex-bigger-group} + F_{warm} \quad (2)$$

$$F_{warm} = \max_1 F_{(i)} + 10\% \times \max_2 F_{(i)} \quad (3)$$

$$F_{(i)} = a_{(i)}\left[\left(Y_{bigger-group} - x_{(i)}\right) - c_{(i)}\right] + b_{(i)} \quad (4)$$

where $Y_{ex-bigger-group}$ and $Y_{bigger-group}$ refer to the overall sensation of the extended bigger group where local sensations $x_{(n)} \leq 1$ and the bigger group where local sensations $x_{(n)} \leq 0$. The calculation of $Y_{ex-bigger-group}$ and $Y_{bigger-group}$ follows the no-opposite calculation methods (the no-opposite high-level warm, high-level cold, low-level warm and low-level cold models). The modifiers $F_{(i)}$ created by opposite warm local sensations in different body parts are combined to generate the combined force F_{warm}. Each warm modifier $F_{(i)}$ is calculated based on the bias between the opposite local sensation and the precalculated overall sensation $Y_{bigger-group}$. The coefficients a, b, and c were defined in Part III (Zhang et al., 2010c).

As a special type of the opposite model, the opposite-dominated model can follow the same logic as other dominated models. To address the underestimation issues, the opposite warm modifier is also incorporated into the calculation of the dominated cold model, as follows:

$$Y = \min x_{(i),dominant} + F_{warm} \quad (5)$$

The modifier F_{warm} is also calculated using Eq. (4) with $\min x_{(i),dominant}$ replacing $Y_{bigger-group}$. The performance of the modified algorithm on the prediction accuracy improvement was evaluated in the next section.

Since the modification of the opposite-dominated cold follows the same logic as the opposite cold model, the sudden jump, when the model transitions across these two models, has been smoothed, as shown in Figure 3. A slight jump remained, which may be attributed to the inconsistency between the value of the lowest local sensation in the dominant part ($\min x_{(i),dominant}$) and the precalculated overall sensation ($Y_{bigger-group}$). A new method is needed to address this issue if the results are required to be fully smoothed.

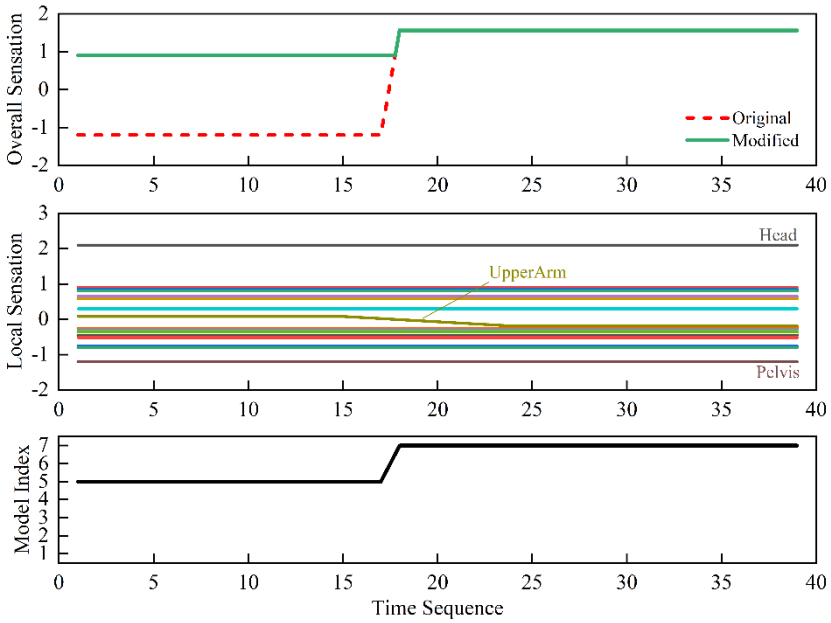

Figure 3 Overall sensation calculation results during the transition from the opposite-dominated cold model and opposite cold model. The upper figure compares the calculated results before and after modification. The middle figure shows local sensations, from top to bottom: head, face, breath, neck, chest, thigh, back, upper arm, lower arm, hands (left and right), legs (left and right), feet (left and right), and pelvis. The lower subfigure shows the model index.

5. VALIDATION

The modified model improved the accuracy of the predictions, as shown in Figure 4. Following the modifications, the predicted overall sensation in Case 2 and Case 3, which previously exhibited the largest discrepancies, aligned more closely with the surveyed overall sensations. This improvement is primarily attributed to the changes in the calculation methods for the dominated cold model. By incorporating additional modifiers generated from hot or warm local sensations, the calculated overall sensations increased, resulting in predictions that more accurately reflected real conditions.

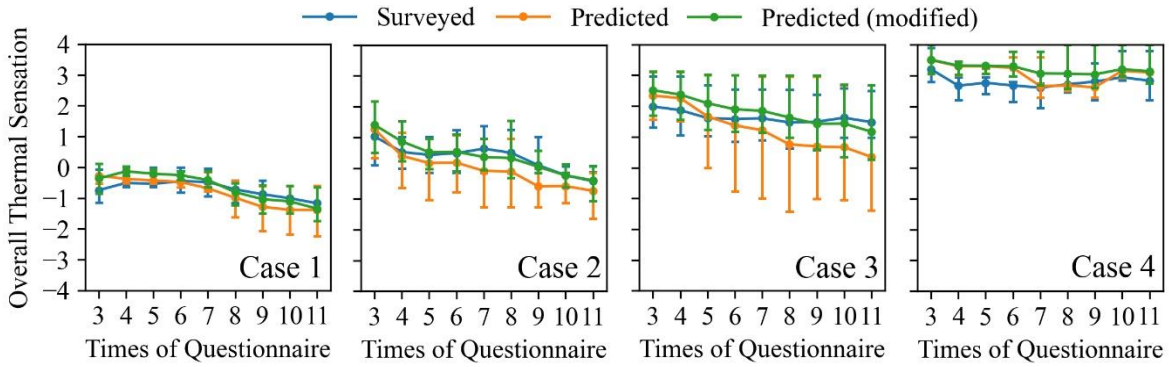

Figure 4. Comparison between surveyed and predicted overall thermal sensations for different cases.

In other cases, the modifications did not significantly impact the calculated values. No notable differences were observed between the overall sensations obtained from the original models and those from the modified models. The slight overestimation of overall sensations in Case 4

when subjects felt hot still remained unsolved even with the modified model. This issue may stem from the coefficients used for calculating warm modifiers. In this study, the coefficients developed for opposite modifiers were also used for the opposite-dominated model, which may not be suitable for all cases. Future investigations could consider developing a new set of coefficients for the modifiers to address this issue.

6. CONCLUSION

In this study, the overall sensation model in the previous papers has been modified and thus improved. Based on experimental data and logical inference, the inaccuracy issues in overall sensation prediction were detected. Modifications to the overall sensation calculation were introduced to resolve the large discrepancies between experimental results and predictions in certain test cases. For the test cases, the inaccuracy was primarily attributed to the consideration of the "dominated cold" effect, which may not always be suitable. By introducing additional modifiers generated from warm or hot sensations, the predicted overall sensations showed much better agreement with those recorded in the experiments. This modification also naturally smoothed the jump when the opposite-dominated cold model transitions to the opposite cold model.

Although the modifications narrowed large discrepancies, slight differences remain when modifiers generated from relatively extreme local sensations influence the whole body. Considerably more work is accordingly needed to optimize the coefficients of these modifiers across various thermal conditions. The modification of the opposite-dominated cold model referred to the logic developed for the opposite cold model, which showed great potential in smoothing the overall sensation results. This unified calculation method may replace the mathematic smoothing methods while maintaining interpretability. Accordingly, in the next step, more underlying patterns of the overall sensations for different local sensation groups should be identified, and further revisions of the models are expected to ensure the overall sensation results are more accurate, smooth and interpretable.

ACKNOWLEDGEMENTS

The work was supported by the Theme-based Research Scheme (Project No. T22-504/21-R) and General Research Fund (Project No. 15204923) of Research Grants Council of the Hong Kong Special Administrative Region, China.

REFERENCES

Zhang H., 2003. Human Thermal Sensation and Comfort in Transient and Non-Uniform Thermal Environments. University of California.

Yang Y., Lyu J., Lian Z., Xie Y., Jiang Y., Lin J., & Niu J., 2024a. Subjective information in thermal comfort evaluation methods: A critical review. Energy and Buildings, 325, 115019.

Brager G. S., & de Dear R. J., 1998. Thermal adaptation in the built environment: a literature review. Energy and Buildings, 27(1), 83-96.

Jiang Y., Xie Y., & Niu J., 2024. Short-term dynamic thermal perception and physiological response to step changes between real-life indoor and outdoor environments. Building and Environment, 251, 111223.

De Dear R. J., Akimoto T., Arens E. A., Brager G., Candido C., Cheong K. W. D., Li B., Nishihara N., Sekhar S. C., Tanabe S., Toftum J., Zhang H., & Zhu Y., 2013. Progress in thermal comfort research over the last twenty years. Indoor Air, 23(6), 442-461.

Zhang H., Arens E., Huizenga C., & Han T., 2010a. Thermal sensation and comfort models for non-uniform and transient environments: Part I: Local sensation of individual body parts. Building and Environment, 45(2), 380-388.

Zhang H., Arens E., Huizenga C., & Han T., 2010b. Thermal sensation and comfort models for non-uniform and transient environments, part II: Local comfort of individual body parts. Building and Environment, 45(2), 389-398.

Zhang H., Arens E., Huizenga C., & Han T., 2010c. Thermal sensation and comfort models for non-uniform and transient environments, part III: Whole-body sensation and comfort. Building and Environment, 45(2), 399-410.

Zhao Y., Zhang H., Arens E. A., & Zhao Q., 2014. Thermal sensation and comfort models for non-uniform and transient environments, part IV: Adaptive neutral setpoints and smoothed whole-body sensation model. Building and Environment, 72, 300-308.

K D., Liang H., Lin J., Xie Y., Yu Y., & Niu J.-l., 2024. Evaluating thermal sensation in outdoor environments - Different methods of coupling CFD and radiation modelling with a human body thermoregulation model. Building and Environment, 266, 112081.

Yang J., Liang Y., Zhong Z., Dharmasastha K., Xie Y., & Niu J.-L., 2024b. Thermal comfort investigation of membrane-assisted radiant cooling in outdoor settings. Sustainable Cities and Society, 113, 105634.

ASHRAE. 2023. ANSI/ASHRAE Standard 55: Thermal environmental conditions for human occupancy. In. Atlanta, GA: American Society of Heating, Refrigerating and Air-Conditioning Engineers.

ISO. 2009. ISO 9920:2009: Ergonomics of the thermal environment—estimation of the thermal insulation and evaporative resistance of a clothing ensemble. In. Geneva, Switzerland: International Organisation for Standardisation.

Liang Y., Yang J., Zhong Z., Xie Y., Dharmasastha K., & Niu J.-L., 2024. Thermal performance and energy efficacy of membrane-assisted radiant cooling outdoors. Sustainable Cities and Society, 114, 105787.

6th International Conference on Building Energy and Environment
Eindhoven University of Technology, The Netherlands
6 - 10 July 2025

The influence of clothing moisture content on heat and moisture transfer between the human body and environment

Cheng Zhao [1], Yichen Yu [1], Jianlei Niu [1]

[1]*Department of Building Environment and Energy Engineering, The Hong Kong Polytechnic University, Hung Hom, Kowloon, Hong Kong*

SUMMARY
Evaporative heat loss is crucial to the human body's energy balance. Various thermal comfort models have been established to analyze the heat and mass transfer between the body and the environment during human sweating, yet the effects of sweat-soaked clothing on heat and moisture transfer remain insufficiently evaluated. This study investigates the thermal and moisture properties of different summer clothing and compares the heat loss of the human body in different sweating states using a sweating thermal manikin. It was found that the evaporative cooling efficiency of the body was suppressed by the soaked clothing as the sweating rate increased, which implies that sweat-soaked garments contribute additional resistance to moisture transfer. Consequently, we observed the dynamic variations in thermal and evaporative resistance of clothing ensembles at different moisture contents. A dynamic heat and moisture transfer model was established by incorporating clothing nodes in the thermal comfort model in detail.

Keywords: Heat and moisture transfer, Clothing model, Thermal comfort.

1. INTRODUCTION

Under warm to hot conditions, evaporative sweating is essential for regulating body temperature (Huizenga et al., 2001; Gagge et al., 2010). Various thermal comfort and clothing models have been developed to assess this process. Gagge's two-node thermo-physiological model was the first to quantify heat and evaporation transfer between the skin and environment, incorporating thermal efficiency and moisture permeation coefficients to calculate heat and moisture transfer through clothing. The more advanced Fiala-UTCI model refined this by detailing heat and mass transfer from the skin to the environment at each body surface and incorporating more precise local thermal and evaporative resistances (McCullough et al., 1985, 1989). The UC Berkeley Thermo-physiological Comfort Model (BTCM), derived from Stolwijk's model (Stolwijk, 1971; Fu et al., 2014), introduced a clothing node that simulates the absorption and desorption processes of clothing. However, both thermal and evaporative resistances of the clothing system remain independent of moisture content, unlike in real conditions where wet clothing alters the air gap between skin and fabric, replacing dry air with water vapor (Mangat et al., 2014). As a result, the overall thermal and hygroscopic properties of wet clothing change significantly, a dynamic process not fully captured by previous models.

This study evaluated the thermal and hygroscopic properties of typical summer clothing and compared the sensible and latent heat losses of the human body in various states of clothing wetness using a sweating thermal manikin. Modification coefficients were proposed to quantify the dynamic variation of thermal and evaporative resistances in varying wetting states. A dynamic heat and moisture transfer model for wetted clothing was developed, enabling the prediction of

temperature and vapor pressure at the clothing nodes during sweating. This model quantifies energy exchange between the skin, soaked clothing, and the environment under heavy sweating conditions, emphasizing the importance of incorporating realistic clothing parameters when assessing thermal comfort in hot and humid environments.

2. METHODS

2.1. Theoretical analysis

The heat exchanges between the skin layers, the environment, and the body's core layers affect the heat stored in the skin, which can be expressed as (Salloum et al., 2007):

$$C_{sk}\frac{dT_{sk}}{dt} = M_{sk} + Q_{co} - Q_l - Q_s + Q_b \quad (1)$$

where C_{sk} is the thermal capacity of the skin, J·K^{-1}; T_{sk} is the skin temperature, K; M_{sk} is the heat production by skin metabolic, W; Q_{co} is the heat transfer from the core layer of the body, W; Q_l represents the latent heat loss on the skin, mainly caused by the sweat evaporation, W; Q_s is the sensible heat loss on the skin, which contains the conduction or convection $Q_{s,c}$, and radiation exchange $Q_{s,r}$ with the environment, W; and Q_b is the heat generated by the skin blood flow, W.

For a clothed body surface, the total thermal resistance and total evaporative resistance were used to represent heat and vapor losses between the skin, clothing, and the environment (Eqs. (2) and (3)), and to use the clothing area coefficient f_{clo} to assess the heat transfer area of the clothing (Eq. (4)).

$$R_{t.t} = R_{t.clo} + \frac{R_{t.a}}{f_{clo}}, \quad (2)$$

$$R_{e.t} = R_{e.clo} + \frac{R_{e.a}}{f_{clo}}, \quad (3)$$

$$f_{clo} = 1 + 1.81R_{t.clo} \quad (4)$$

where $R_{t.t}$ is the total thermal resistance of the clothing, m^2·K·W^{-1}; $R_{e.t}$ is the total evaporative resistance of the clothing, m^2·kPa·W^{-1}; $R_{t.clo}$ is the intrinsic thermal resistance of the clothing, m^2·K·W^{-1}; $R_{e.clo}$ is the intrinsic evaporative resistance of the clothing, m^2·kPa·W^{-1}. The calculated nodes of the heat and moisture transfer are shown in Fig. 1.

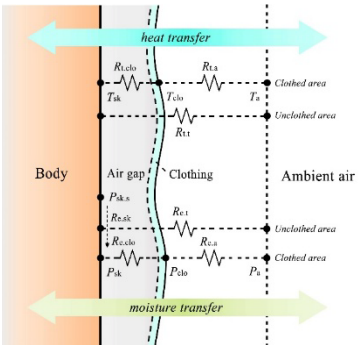

Figure 1. The calculated nodes of the skin-clothing-environment system.

For the calculation of latent heat transfer on the skin, a common method is via the mass balance on the skin surface (Jones et al., 1992). The transfer of moisture from the skin to the environment has two main components: evaporation of sweat and diffusion of moisture through the skin. These two moisture transfer processes can be expressed as Eqs. (5) and (6) (Fiala et al., 2012):

$$\frac{P_{sk}-P_a}{R_{e.a}} = \frac{\lambda_w dM_{sw}}{A_{nude}dt} + \frac{P_{sk.s}-P_{sk}}{R_{e.sk}}, \tag{5}$$

$$\frac{P_{sk}-P_a}{R_{e.t}} = \frac{\lambda_w dM_{sw}}{A_{clothed}dt} + \frac{P_{sk.s}-P_{sk}}{R_{e.sk}} \tag{6}$$

Where λ_w is the enthalpy of vaporization of the water, Wh·g^{-1}; M_{sw} is the mass of the sweat production, g; $R_{e.sk}$ is the evaporative resistance of the skin, which is equal to 0.33 m^2·kPa·W^{-1} for a well-hydrated person (Fu, 1995).

The mass balance methods provide a good assessment of the moisture transfer on the skin both from the unwetted to exactly fully wetted state and for the oversaturation state. According to the mass balance of perspiration between the skin-clothing system, the moisture content absorbed by the clothing M_{clo}, the rate of skin sweat accumulation $\frac{dM_{acc}}{dt}$, and the sweat rate $\frac{dM_{sw}}{dt}$ have the following relationship:

$$\frac{dM_{sw}}{dt} = \frac{dM_{clo}}{dt} + \frac{dM_{acc}}{dt} + \frac{A_{nude}(P_{sk.s}-P_a)}{\lambda_w R_{e.a}} + \frac{A_{clothed}(P_{clo}-P_a)}{\lambda_w R_{e.t}} \tag{7}$$

Sweat on the skin surface will transfer moisture to the clothing in the vapor or liquid state, and the warmer sweat vapor will condense on the surface of the clothing in contact with the clothing and gradually be absorbed by the fabric, which can be described by Eq. (8).

$$\frac{\lambda_w dM_{clo}}{A_{clothed}dt} = \frac{P_{sk.s}-P_{clo}}{R_{e.clo}} - \frac{f_{clo}(P_{clo}-P_a)}{R_{e.a}} \tag{8}$$

Considering the heat stored in the clothing, the heat gain from vapor condensation and sweat absorption, and the evaporative heat loss to the air, the heat transfer of the clothing node can be expressed as:

$$C_{clo}\frac{dT_{clo}}{dt} = A_{clothed}\left(\frac{T_{sk}-T_{clo}}{R_{t.clo}} - \frac{f_{clo}(T_{clo}-T_a)}{R_{t.a}}\right) + \frac{dM_{clo}}{dt}(C_w(T_{sk}-T_{clo}) + H_d) - \frac{A_{clothed}f_{clo}(P_{clo}-P_a)}{R_{e.a}} \tag{9}$$

where H_d is the differential heat of sorption, J·g^{-1} (Hearle, 2008); C_{clo} and C_w are the thermal capacity of the clothing and the water, respectively, J·K^{-1}. Based on Eqs. (8) and (9), the vapor pressure and temperature of the clothing can be derived as follows:

$$P_{clo} = \frac{R_{e.a}P_{sk.s} + f_{clo}R_{e.clo}P_a - R_{e.clo}R_{e.a}\frac{\lambda_w dM_{clo}}{A_{clothed}dt}}{R_{e.a} + f_{clo}R_{e.clo}}, \tag{10}$$

$$T_{clo} = \frac{\left(\frac{dM_{clo}}{dt}(C_w T_{sk} + H_d) - A_{clothed}\frac{f_{clo}(P_{clo}-P_a)}{R_{e.a}}\right)R_{t.clo}R_{t.a} + A_{clothed}(f_{clo}R_{t.clo}T_a + R_{t.a}T_{sk})}{\left(C_w\frac{dM_{clo}}{dt}R_{t.clo} + A_{clothed}\right)R_{t.a} + A_{clothed}f_{clo}R_{t.clo}} \tag{11}$$

The detailed quantification of heat and moisture transfer of clothing during the process of absorbing and releasing sweat can be achieved based on the above formulas.

2.2. Measurements

The experiments were conducted from 2 May to 15 June 2024 at the Wind Tunnel Atmosphere Laboratory, School of Fashion and Textiles, PolyU. The sweating thermal manikin "Walter" was used in this study to investigate the dynamic variation in thermal and moisture properties of clothing ensembles at different moisture content states (Fan et al., 2002). Throughout the measurements, the "Walter" was operated at a constant skin temperature mode, and the skin temperature was set at 34°C to simulate the real human body's temperature in warm to hot conditions. For all measurements, the manikin was placed in an artificial climate chamber to achieve stable boundary conditions (Fig. 2).

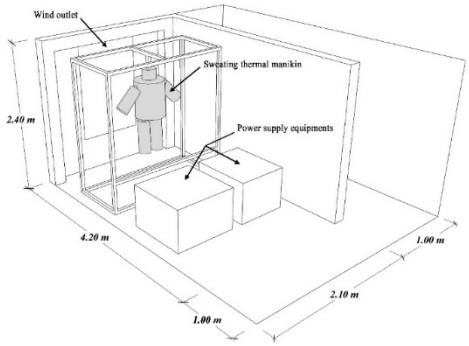

Figure 2. Experimental site and layout.

The ambient temperature and relative humidity of the chamber were set to 21°C and 40%, respectively, to comply with the requirements of the relevant standards (ASTM, 2010, 2016; ISO, 2008) for the measurement of thermal and evaporative resistance of clothing ensembles. Meanwhile, the indoor air velocity was set to 0.2 m/s to provide a natural convection environment. Measurements of the unclothed sweating manikin in this stable environment yielded two basic parameters, the thermal and evaporative resistance of the air boundary layer.

Five different typical summer clothing, namely long-sleeved T-shirts, short-sleeved T-shirts, sleeveless T-shirts, trousers, and shorts, were selected for the measurements. All selected clothing were commercially available (100% cotton) and the dry weight of each clothing was measured after drying using an electronic balance with an accuracy of ±0.02g. More information on different clothing is shown in Table 1.

Table 1. The detailed parameters of the clothing.

Clothing (abbr.)	Content	Length (cm)				Mass (g)	Maximum moisture content (g)
		Length	Chest / Waist	Shoulder / Hip	Sleeve		
Long-sleeved T-shirts (LS)	100% Cotton	75	120	47	60	214.95	253.45
Short-sleeved T-shirts (SS)		76	120	47	25	171.37	210.17
Sleeveless T-shirts (SL)		76	119	-	-	139.28	171.91
Trousers (T)		104	70	114	-	218.98	295.07
Shorts (S)		55	80	122	-	158.92	229.96

Each clothing ensemble was tested with the moisture content level varied from fully dry to saturated wet. For the dry test, clothing ensembles were placed in the drying oven for 2 hours before being worn on the manikin to commence data recording. The non-dried method was to rest the clothing in the artificial climate chamber with 40%RH for more than 8 hours (Koelblen et al., 2017). Another pre-wetting method is to spray deionized water onto the clothing surface directly based on four different water addition gradients of 25%, 50%, 75%, and 100% maximum moisture content. The clothing ensembles were weighed after finishing the tests to obtain the clothing's moisture content.

3. RESULTS

3.1. Sensible and latent heat loss of the human body at different clothing moisture content

Under steady-state conditions, the heating power supplied to the manikin is equal to the total heat loss from the human body (Foda et al., 2016). Thus, the required heating power to maintain a specific skin temperature reflects the corresponding heat loss for different clothing ensembles and moisture contents. Overall heat loss occurs mainly at the sensible heat and latent heat levels, thus the proportion of different heat loss pathways needs to be assessed (Fig. 4).

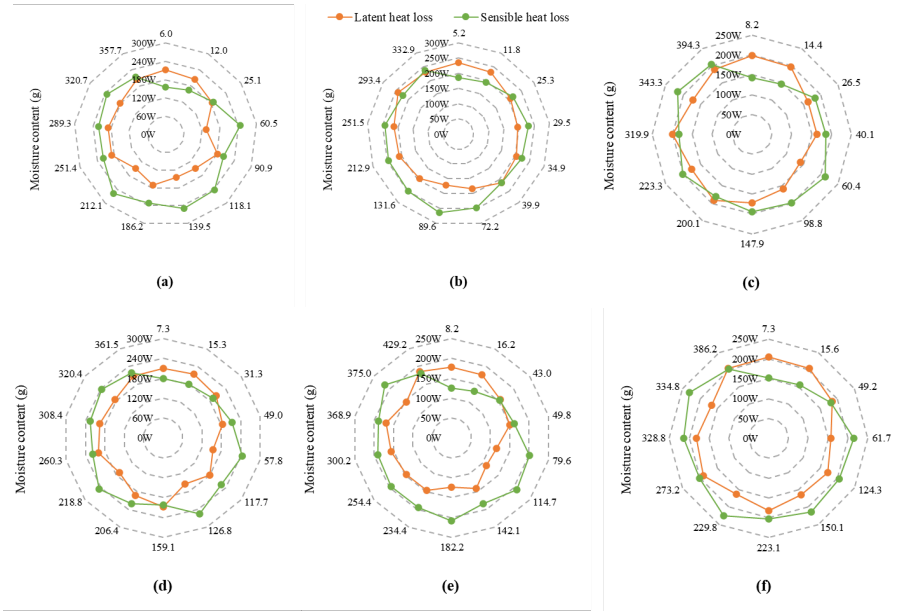

Figure 4. Comparison of the sensible and latent heat loss: (a) SL&T, (b) SL&S, (c) SS&T, (d) SS&S, (e) LS&T, and (f) LS&S.

It can be observed that, except for the two lowest moisture content cases, dry heat loss generally exceeds evaporative heat loss for all clothing ensembles. This suggests that, at lower moisture levels, clothing primarily reduces dry heat loss to minimize overall heat loss. As the moisture content increases, the clothing's ability to prevent dry heat loss significantly diminishes, leading to dry heat loss becoming the dominant heat loss pathway.

3.2. Dynamics of clothing's thermal and evaporative resistance

The thermal and evaporative resistance of clothing represents its ability to limit sensible and latent heat loss, respectively—two key parameters in calculating heat and moisture transfer. To assess these properties under varying clothing moisture content conditions, modifying coefficients were introduced for evaluating thermal resistance, evaporative resistance, and permeation coefficient (Fig. 5).

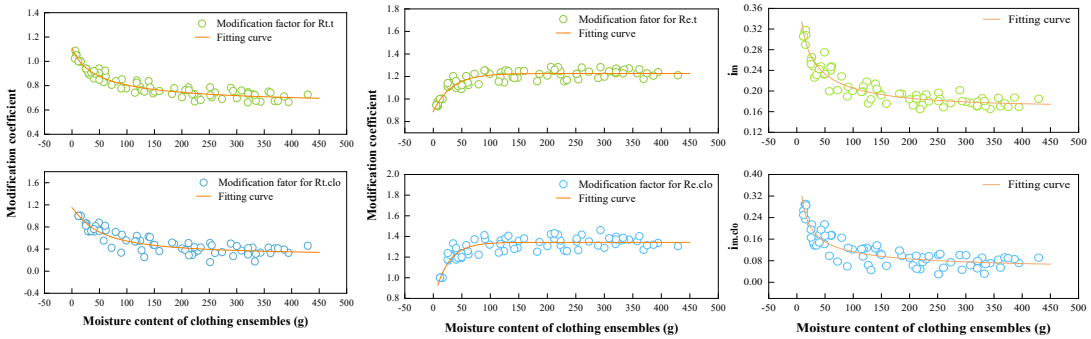

(a) (b) (c)

Figure 5. The proposed modification coefficients for: (a) clothing thermal resistance, (b) clothing evaporative resistance, and (c) clothing permeation coefficients.

The results indicate that both total and intrinsic clothing thermal resistance decreases with increasing moisture content in the clothing ensembles. In the nearly fully wet condition, the total thermal resistance of the six clothing ensembles was reduced by an average of 29.7% compared to the dry ensembles, consistent with the findings of Wang et al. (Wang et al., 2016). Conversely, the evaporative resistance curves exhibit an opposite trend to the thermal resistance curves. Furthermore, the permeation coefficients decreased progressively with increasing moisture content in the clothing ensembles, with a more pronounced reduction observed in the intrinsic permeation coefficients.

The relationship between clothing's moisture content, thermal resistance, evaporative resistance, and permeation coefficient were fitted and summarized in Table 2.

Table 2. Summary of modification coefficients for wetted clothing.

Parameters	Formulas	Fitted equations	R^2
Thermal resistance	$R_{t.wet} = MC_t(M_{clo})R_t$	$MC_{t.t} = 0.637 + \frac{0.472}{1+\left(\frac{M_{clo}}{51.386}\right)^{0.900}}$	0.919
		$MC_{t.clo} = 0.277 + \frac{0.873}{1+\left(\frac{M_{clo}}{49.001}\right)^{1.149}}$	0.813
Evaporative resistance	$R_{e.wet} = MC_e(M_{clo})R_e$	$MC_{e.t} = 1.226 - 0.335 \cdot 0.969^{M_{clo}}$	0.850
		$MC_{e.clo} = 1.343 - 0.571 \cdot 0.960^{M_{clo}}$	0.748
Permeation coefficient	-	$i_m = 0.172\left(1 - exp(-0.006M_{clo})\right)^{-0.224}$	0.895
		$i_{m.clo} = 0.056\left(1 - exp(-0.002M_{clo})\right)^{-0.448}$	0.790

3.3. Heat and moisture transfer modelling for sweat-soaked clothing system

Quantifying heat and moisture transfer at clothing nodes relies on determining the temperature and

vapor pressure parameters of clothing at various moisture contents. The vapor pressure and temperature for six clothing ensembles are presented in Fig. 6.

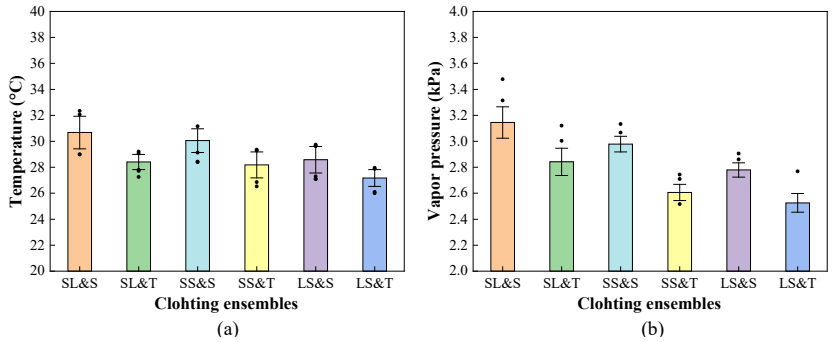

Figure 6. The calculation parameters of different clothing ensembles: (a) temperature, and (b) vapor pressure.

The covering area significantly influences the clothing's temperature and vapor pressure, with larger coverage areas corresponding to lower clothing temperature and vapor pressure. Data indicate that the surface temperature of clothing in an almost fully wet state increased by approximately 1.35°C to 3.34°C compared to dry ensembles, with an average increase of 2.26°C. This finding suggests a sustained temperature rise following moisture adsorption, a trend also observed in studies by Lu et al. (Lu et al., 2016).

4. CONCLUSION

This study explored the thermal and moisture characteristics of sweat-soaked clothing and their influence on heat and moisture transfer between the human body and the environment. As the moisture content of the clothing increased, overall body heat loss was enhanced; however, the evaporative cooling capacity of the body was diminished due to the saturated clothing, resulting in a shift toward sensible heat transfer as the primary mode of heat dissipation. Finally, a dynamic model was developed to quantify the heat and moisture transfer between the skin, soaked clothing, and the surrounding environment under conditions of intense sweating. In regions such as Hong Kong, where high humidity prevails year-round, the rate of sweat evaporation is often slower than sweat production, leading to the saturation of clothing. This condition can increase the evaporative thermal resistance of clothing by up to 20%, significantly inhibiting the body's evaporative cooling efficiency. Therefore, it is critical to incorporate the moisture content of clothing and its associated thermal and evaporative resistances when evaluating outdoor thermal comfort in hot and humid environments.

ACKNOWLEDGEMENTS

The work was supported by the RGC TRS project (No. T22504/21-R).

REFERENCES

American Society for Testing and Materials (ASTM). (2010). Standard test method for measuring the thermal insulation of clothing using a heated manikin. West Conshohocken, PA: American Society for Testing and Materials.

American Society for Testing and Materials (ASTM). (2016). Standard test method for measuring the evaporative resistance of clothing using a sweating manikin.

Fan, J., & Chen, Y. S. (2002). Measurement of clothing thermal insulation and moisture vapour resistance using a novel perspiring fabric thermal manikin. Measurement Science and Technology, 13(7), 1115.
Fiala, D., Havenith, G., Bröde, P., Kampmann, B., & Jendritzky, G. (2012). UTCI-Fiala multi-node model of human heat transfer and temperature regulation. International journal of biometeorology, 56, 429-441.
Foda, E., & Sirén, K. (2016). Evaluating the thermal comfort performance of heating systems using a thermal manikin with human thermoregulatory control. Indoor and Built Environment, 25(1), 191-202.
Fu, G. (1995). 3-D mathematical thermal model for the clothed human. Kansas State University, Kansas, 270.
Fu, M., Yu, T., Zhang, H., Arens, E., Weng, W., & Yuan, H. (2014). A model of heat and moisture transfer through clothing integrated with the UC Berkeley comfort model. Building and environment, 80, 96-104.
Gagge, A. P., & Gonzalez, R. R. (2010). Mechanisms of heat exchange: biophysics and physiology. Comprehensive physiology, 45-84.
Hearle, J. W., & Morton, W. E. (2008). Physical properties of textile fibres. Elsevier.
Huizenga, C., Hui, Z., & Arens, E. (2001). A model of human physiology and comfort for assessing complex thermal environments. Building and Environment, 36(6), 691-699.
ISO 9920:2007. (2008). Ergonomics of the thermal environment. estimation of thermal insulation and water vapour resistance of a clothing ensemble.
Jones, B. W., & Ogawa, Y. (1992). Transient interaction between the human and the thermal environment.
Koelblen, B., Psikuta, A., Bogdan, A., Annaheim, S., & Rossi, R. M. (2017). Comparison of fabric skins for the simulation of sweating on thermal manikins. International journal of biometeorology, 61, 1519-1529.
Lu, Y., Wang, F., Peng, H., Shi, W., & Song, G. (2016). Effect of sweating set rate on clothing real evaporative resistance determined on a sweating thermal manikin in a so-called isothermal condition (T manikin= T a= T r). International journal of biometeorology, 60, 481-488.
Mangat, M. M., & Hes, L. (2014). Thermal resistance of denim fabric under dynamic moist conditions and its investigational confirmation. Fibres & Textiles in Eastern Europe, 22(6 (108)), 101-105.
McCullough EA, Jones BW, Huck J (1985) A comprehensive data base for estimating clothing insulation. ASHRAE Trans 92:2947
McCullough EA, Jones BW, Tamura T (1989) A data base for determining the evaporative resistance of clothing. ASHRAETrans 95:316–328
Salloum, M., Ghaddar, N., & Ghali, K. (2007). A new transient bioheat model of the human body and its integration to clothing models. International journal of thermal sciences, 46(4), 371-384.
Stolwijk, J. A. (1971). A mathematical model of physiological temperature regulation in man (No. NASA-CR-1855). NASA.
Wang, F., Shi, W., Lu, Y., Song, G., Rossi, R. M., & Anaheim, S. (2016). Effects of moisture content and clothing fit on clothing apparent ‘wet’thermal insulation: a thermal manikin study. Textile research journal, 86(1), 57-63.

6th International Conference on Building Energy and Environment Eindhoven University of Technology, The Netherlands
6 - 10 July 2025

A Comprehensive Method for Accurate Assessment of Rooftop Solar Energy Potential in High-Latitude Areas

Nadeem Akhtar [1], Jen-Yu Han [1], Ursula Eicker[2], Kartikay Sharma[2]

[1]*Department of Civil Engineering, National Taiwan University, Taipei, Taiwan (nadeemcivil00@gmail.com & jyhan@ntu.edu.tw)*

[2]*Next-Generation Cities Institute, Concordia University, 2155 Rue Guy, ER-1431.35, Montréal, QC H3H 2L9, Canada (ursula.eicker@concordia.ca & kartikay.sharma@concordia.ca)*

Corresponding Author: Nadeem Akhtar [1]

ABSTRACT

The deployment of rooftop solar photovoltaic (PV) systems is a key strategy for achieving nearly zero-energy buildings (nZEB) and promoting urban sustainability. However, accurately estimating rooftop solar irradiance potential remains challenging due to complex shading effects from surrounding structures and rooftop obstructions, which can lead to significant overestimations in PV capacity. These obstructions, including HVAC units, chimneys, skylights, parapet walls, ventilation shafts, and other mechanical equipment, reduce the usable roof area for PV installations by limiting available space and casting shadows that diminish effective solar exposure. To address these challenges, this research introduces a hybrid approach that integrates Geographic Information Systems (GIS) and deep learning to enhance rooftop solar potential assessments. Currently, a GIS-based shading analysis has been conducted using high-resolution LiDAR data to evaluate inter-building shading effects across 48 buildings in Montreal, Canada, for the year 2023. The findings reveal that neglecting shading can result in an overestimation of rooftop PV capacity by approximately 12.87%, with an estimated annual solar radiation potential of 1.48×10^8 kWh. While GIS-based methods provide a detailed spatial assessment of shading influences, they have challenges in accurately identifying rooftop obstructions. To further refine these assessments, the next phase of this study involves developing a deep learning model for precise rooftop segmentation and obstruction detection. By integrating deep learning with GIS-based methodologies, this approach aims to enhance the accuracy of solar potential estimates, offering a scalable and data-driven solution for urban energy planning. Ultimately, this research supports the development of optimized PV deployment strategies, contributing to the broader goal of sustainable urban energy transitions.

KEYWORDS*: Sustainability, Rooftop Solar Potential, GIS, Shading and Obstacle Effect, Lidar Data, Typical Meteorological Year (TMY),*

1. INTRODUCTION

Urban areas predominantly rely on conventional energy sources such as fossil fuels and coal-fired power plants, contributing significantly to greenhouse gas emissions and accelerating climate change (Emmanuel Augustine Etukudoh et al., 2024; Esfandi et al., 2024; Lang, 2018). In response to these environmental challenges, governments and international organizations have prioritized the transition toward cleaner and more sustainable energy solutions (Agrawal et al., 2024; Ebbin & Ghamarian, 1992; Sharma et al., 2025). The European Union (EU) and other regulatory bodies have introduced stringent energy efficiency targets, emphasizing the development of nearly zero-energy buildings (nZEB) (Lou & Hsieh, 2024; Pisoni et al., 2025). These targets aim to achieve energy-efficient urban infrastructures by minimizing building energy consumption (Sudhakar et al., 2019) and integrating renewable energy technologies such as solar photovoltaics (PVs) (C. Liu et al., 2019). Among various renewable energy sources, solar PV systems are up-and-coming due to their scalability, cost-effectiveness, and minimal environmental footprint (R. Liu et al., 2023). However, the accurate assessment and efficient deployment of rooftop PV systems in urban settings present several challenges, requiring a comprehensive understanding of multiple influencing factors, including solar irradiation levels (Pfeifroth et al., 2018), rooftop characteristics (Sarralde et al., 2015), shading effects from surrounding structures (Zhong & Tong, 2020), and PV panel energy conversion efficiency (Green et al., 2020). The effective deployment of rooftop PV systems depends largely on accurate estimations of solar potential, which are influenced by both environmental and urban morphological factors (Alsuhaibany & Li, 2017; Fakhraian et al., 2021). Solar irradiation levels, which generally decrease with increasing latitude, are further affected by atmospheric conditions, seasonal variations, and the urban heat island effect (Masson et al., 2014; Prasad et al., 2016). The efficiency of rooftop PV panels is not solely dependent on the availability of sunlight; it is also constrained by rooftop obstructions such as water tanks, HVAC systems, lift machine rooms, and parapet walls, as well as the shadowing effects of adjacent buildings (Albatayneh et al., 2022; Zhao et al., 2018). These shading effects can significantly reduce the amount of solar energy received by PV panels, leading to suboptimal energy generation (Vakilinezhad & Ziaee, 2024). While existing solar potential assessment methods have made significant progress in estimating energy output, many fail to account for localized shading effects and rooftop obstructions, leading to overestimations that affect system design and investment decisions (Villa-Ávila et al., 2024).

Several studies have attempted to overcome these challenges through various approaches (Amigó, 2016; Choi et al., 2019). One common method for estimating solar potential involves the use of meteorological station data and satellite-derived solar radiation models (Aliakbarzadeh et al., 2024; Kim et al., 2025; Ordoñez Palacios et al., 2023). Although these methods offer valuable large-scale insights, they lack the spatial resolution necessary for precise urban-level assessments (Baquiran et al., 2020). To address this gap, Geographic Information Systems (GIS) have been widely employed for solar potential mapping, utilizing spatial data to identify optimal photovoltaic (PV) installation sites (Choi et al., 2019). Nevertheless, traditional GIS-based models often rely on simplified assumptions about building heights and rooftop availability, overlooking complex shading interactions that can significantly impact solar energy generation. In response to these shortcomings, recent advancements in remote sensing technologies, particularly Light Detection and Ranging (LiDAR), have substantially improved the accuracy of solar potential assessments (Desthieux et al., 2018). By enabling high-resolution 3D modeling of urban environments, LiDAR data facilitates precise calculations of building heights, rooftop orientations, and inter-building shading effects, thereby enhancing the reliability of solar energy estimations (Prieto et al., 2019). Consequently, the integration of LiDAR with advanced spatial analysis techniques has become indispensable for enhancing the precision and reliability of data-driven urban energy planning.

In addition to GIS and LiDAR-based assessments, artificial intelligence (AI) and deep learning techniques have shown great potential in automating solar potential evaluations (Nadeem et al., 2024). Deep learning models, particularly convolutional neural networks (CNNs), have been employed to identify rooftop features, segment available areas, and predict solar energy output with greater precision (Ding, 2025). These models are trained on diverse datasets that include aerial imagery, LiDAR point clouds, and meteorological data, allowing for robust and adaptive predictions (Rajasundrapandiyanleebanon et al., 2023; Suresh et al., 2020). The integration of deep learning with GIS and LiDAR-based methodologies represents a significant advancement in urban solar energy modeling, offering an efficient and scalable solution for high-accuracy solar potential assessments (Kumar et al., 2024). Despite these technological advancements, high-latitude regions present unique challenges for rooftop solar energy assessments (Jiang, Hou et al., 2024). The lower solar elevation angle in these regions results in longer shadows, making shading effects more pronounced compared to lower-latitude areas. Additionally, seasonal variations lead to significant fluctuations in solar energy availability, requiring more dynamic simulation models to accurately capture these changes. Most existing studies on rooftop solar energy potential have focused on mid-to-low latitude cities, where solar irradiation levels are relatively stable (Zhang et al., 2020). However, a detailed and high-resolution analysis tailored to high-latitude urban environments remains limited. Addressing these challenges is crucial for optimizing solar energy deployment in northern cities, where maximizing energy self-sufficiency is essential for achieving sustainable urban development goals.

This study introduces a novel methodology that integrates deep learning and 3D GIS modeling to accurately assess rooftop solar energy potential in high-latitude urban areas, overcoming the limitations of traditional approaches. The research is structured around several key objectives. The first is to develop a high-resolution framework for rooftop solar energy assessment, which considers localized shading effects and rooftop obstructions using LiDAR-derived 3D urban models. Another objective is to employ deep learning techniques for the automated identification and segmentation of rooftop features, thereby improving the accuracy of available area estimation for photovoltaic (PV) installations. Additionally, the study aims to analyze the temporal variations of solar irradiance on hourly, monthly, and annual scales, ensuring a comprehensive understanding of seasonal energy generation patterns. Although the deep learning model is still in development, its integration is expected to enhance the accuracy of the shading analysis, by enabling the model to more precisely identify complex shading patterns and optimize solar irradiance predictions. Lastly, the methodology will be validated through real-world case studies in Montreal, Canada, a high-latitude city where shading effects significantly influence solar PV performance. This study sets itself apart by introducing a dynamic shading analysis that accounts for the annual trajectory of sun, integrating AI-based image processing with LiDAR data to refine rooftop assessments, and examining high-latitude climatic impacts on solar PV performance. While the deep learning results will be included in future work, the current methodology highlights the significant potential of combining deep learning with traditional shading analysis to improve solar potential estimation. These innovations not only improve the accuracy of solar potential measures but also support urban energy planning and policymaking by enabling informed decisions on PV investments, grid integration, and incentive structures. Ultimately, the research promotes sustainable urban development by facilitating decentralized energy generation and reducing reliance on fossil fuels, while offering a scalable framework for rooftop solar deployment in other high-latitude cities. The findings could significantly advance urban renewable energy solutions and support climate goals. In summary, this study addresses the critical challenges associated with rooftop solar energy assessments in high-latitude regions by introducing an integrated approach that combines deep learning, LiDAR data, and 3D GIS modeling. Although the deep learning

analysis is still being finalized, its anticipated integration will further refine solar potential estimations, contributing to the optimization of PV system placement. The proposed methodology represents a significant step forward in bridging the gap between technological advancements and practical implementation, ultimately driving the adoption of renewable energy solutions in urban environments.

2. METHODOLOGY

The integration of 3D building models in solar energy simulations has become essential for assessing power potential and evaluating receiving areas such as rooftops and facades, significantly contributing to urban development initiatives (Willenborg et al., 2018). Over recent years, research has predominantly focused on maximizing power generation efficiency through angle optimization, often employing solar tracking systems (Romero Rodríguez et al., 2017). Several studies highlight the importance of 3D building models in estimating solar energy potential in urban environments (Bill et al., 2016; Saadaoui et al., 2019; Shirinyan & Petrova-Antonova, 2024; Waqas et al., 2023). However, only a limited number of studies have explored the intersection of solar energy assessment with nearly zero-energy buildings (nZEB) or self-sufficiency, aside from those addressing urban redevelopment or revitalization (Natanian & Auer, 2020). To analyze the impact of shadowing from surrounding buildings on rooftop solar potential, the methodology follows the structured approach illustrated in Figure 1. The process begins with modeling the rooftop structure and determining its tilt and azimuth angle. The solar position, including location and angle, is then considered to evaluate shadow coverage. Based on whether a rooftop section is shaded or not, direct normal irradiation and diffuse horizontal irradiation are calculated accordingly. The final step involves estimating the total radiation received under both shaded and unshaded conditions.

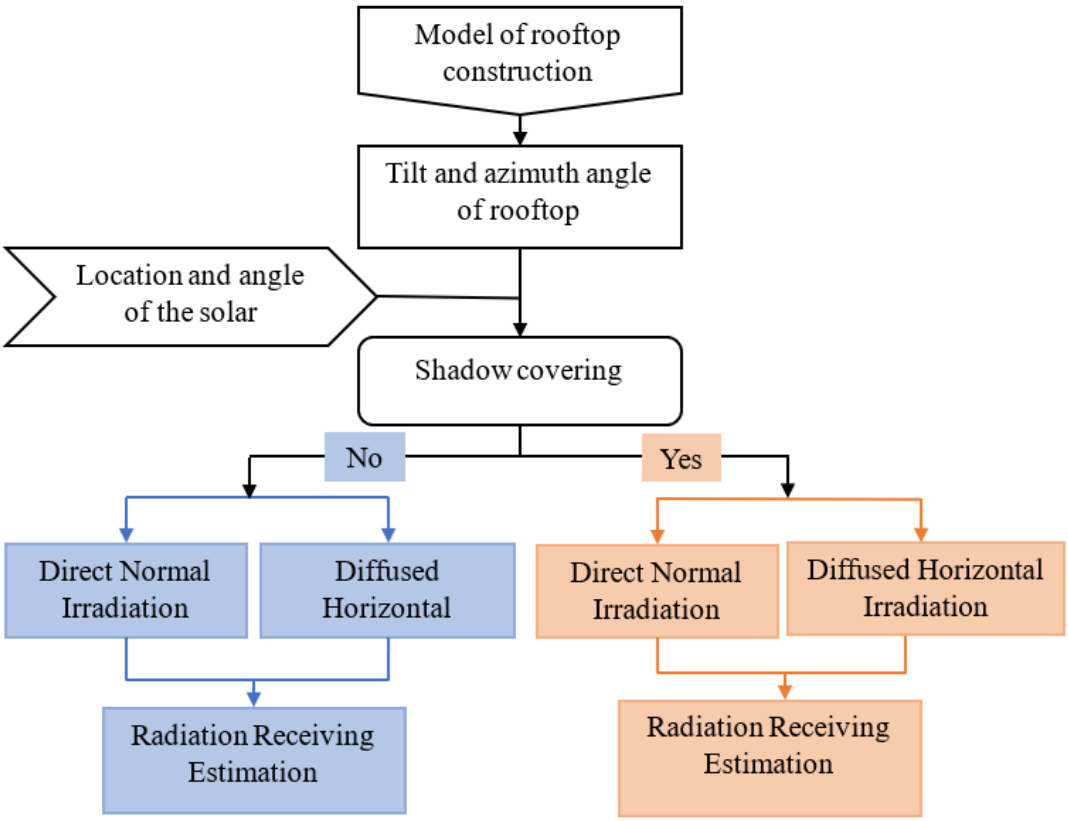

Fig. 01: Methodology Flow Chart

2.1. Study area:

The selected study area is a small urban zone in Montreal, near Place-des-Arts (45.52°N, 73.42°W), characterized by a diverse urban morphology comprising both high-rise and low-rise buildings. This location was strategically chosen due to its architectural heterogeneity, which provides a suitable setting for assessing the impact of overshadowing from taller structures on the rooftop solar irradiance of adjacent low-rise buildings. Situated within a commercial district, the study area consists of 48 buildings with varying architectural configurations, offering a robust dataset for evaluating solar potential in a complex urban environment. This area was specifically selected due to its dense urban fabric and significant solar exposure variations, making it an ideal case for analyzing the challenges and opportunities of rooftop photovoltaic deployment. Understanding how shadowing influences solar energy generation in such settings is essential for developing strategies to enhance urban energy resilience and optimize photovoltaic system placement.

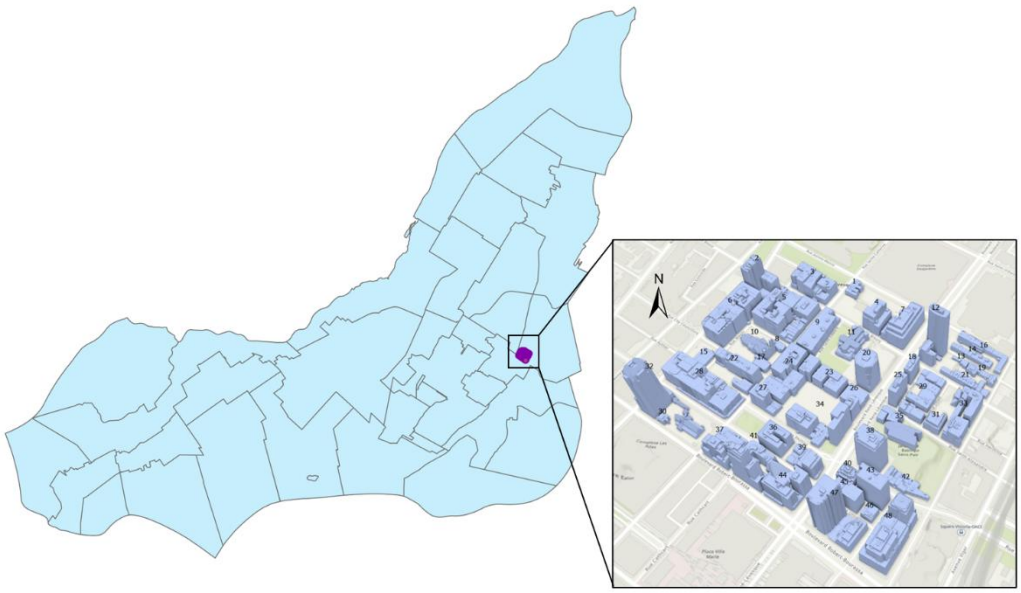

Fig. 02: Geographical scope

2.2. Data Used:

This study utilized three primary data sources: High-resolution Light Detection and Ranging (LiDAR) data, Geographic Information System (GIS) data, and Typical Meteorological Year (TMY) data.

2.2.1. High-resolution LiDAR Data:

LiDAR data was employed to generate detailed 3D models of buildings within the study area. The high-resolution nature of this data allows for precise measurements of building heights and the surrounding structures, which are crucial for performing accurate shading analysis. These measurements enable the study to assess the interaction between buildings and their environment, which is essential for evaluating solar potential.

2.2.2. Geographic Information System (GIS) Data:

GIS data was used to analyze the geographical context and layout of the buildings and their surroundings. This data includes land use information, building footprints, and other relevant geographical features. By leveraging GIS, the study can conduct a comprehensive spatial analysis of the study area, accounting for factors like urban density, terrain, and environmental conditions that influence solar exposure.

2.2.3. Typical Meteorological Year (TMY) Data:

Meteorological data was sourced from the Canadian Weather Year for Energy Calculation (CWEC) using the TMY3 dataset. This dataset provides over 30 years of hourly weather data, including crucial parameters such as direct normal irradiance (DNI), diffuse horizontal irradiance (DHI), global horizontal irradiance (GHI), and solar azimuth angles. These parameters are vital for understanding solar exposure and energy potential, enabling a more accurate assessment of solar power generation. While TMY3 data provides a standardized climatological baseline, its reliance on historical averages may not fully capture extreme weather events or recent climate trends (Wu et al., 2023). For instance, interannual variability in cloud cover or snowfall (critical in high-latitude regions) could introduce ±5–10% uncertainty in irradiance estimates. Future work could integrate multi-year datasets or stochastic weather models to improve robustness.

By integrating these three data sources, the study aims to conduct a comprehensive analysis of the solar potential and shading dynamics in the study area. The methodology consists of two steps: first, extracting detailed building geometries from the LiDAR data, and second, assessing the self-sufficiency potential through the computation of solar irradiance on the rooftops of these buildings. Notably, external TMY3 data was utilized for solar irradiance calculations, rather than relying on built-in ArcMap software data, to improve the accuracy of the solar power potential analysis for the targeted geographic area.

2.3. Building model extraction:

The building model extraction and subsequent analysis were conducted using ArcGIS tools within the ESRI ArcMap environment. In this study, all building data were converted into mesh format with a grid scale of 1 square meter, representing each building's surface as a network of 1m x 1m polygons. This detailed representation allowed for precise modeling of shading effects on solar photovoltaic (PV) performance and ensured compatibility with advanced analytical tools. To assess the slope and orientation of the rooftops for each grid cell, the 3D Analyst Tool in ArcMap was employed, utilizing calculations derived from LiDAR data, building footprint data, and elevation data of adjacent grids from aerial imagery. These calculations were crucial for accurately determining the geometric properties of building surfaces, which were essential for reliable shading analysis (Bayrakci Boz et al., 2015).

$$dy/dx = [(c + 2f + i) - (a + 2d + g)]/(8 \times cellsize) \quad \text{Eq. (1)}$$

$$dz/dy = [(c + 2h + i) - (a + 2b + c)]/(8 \times cellsize) \quad \text{Eq. (2)}$$

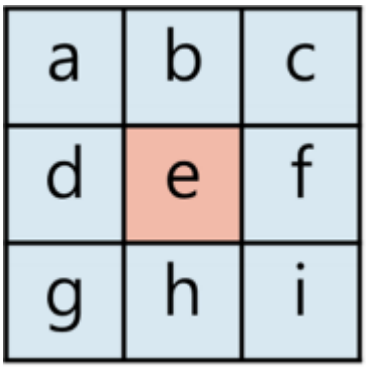

Fig. 3: Illustrating the computation of slope and aspect (Li & Han, 2022)

Eq. (1) and (2) depict the relationship among the x, y, and z axes. Variables 'a' through 'i' denote the altitude of individual grid points. Consequently, the slope and aspect angles can be computed using Eq. (3) and (4).

$$Slope = tan^{-1}\left(\sqrt{(dz/dx)^2 + (dz/dy)^2}\right) \times (180/\pi) \quad \text{Eq. (3)}$$

$$Aspect = tan^{-1}[(dz/dy)/-(dz/dx)] \times (180/\pi) \quad \text{Eq. (4)}$$

By combining slope and orientation data with solar radiation models, we can estimate the amount of sunlight received by each rooftop area throughout the day and year. This solar exposure data enables the calculation of the potential solar energy that photovoltaic (PV) panels can generate when installed on various segments of the rooftop. This research aimed to examine the impact of shadow coverage by developing two simulation scenarios for the buildings: one focusing on the individual building (Scenario A) and the other considering the surrounding structures (Scenario B). Scenario A represents a single building in optimal conditions, free from the influence of neighboring structures, while Scenario B offers a more realistic scenario that accounts for the surrounding environment. The results of Scenario A reflect the isolated conditions of the building, while those of Scenario B represent a broader, more varied context.

After performing the hillshade analysis, the hillshade values, ranging from 0 to 254, were used to calculate solar irradiance. The following formula (Equation 6) was then applied to determine the solar irradiance received at each point:

$$Solar\ irradiance = \left(\frac{Hillshade\ value}{255}\right) * DNI + DHI \quad \text{Eq. (5)}$$

$$GHI = DHI + DNI \times cos\theta \quad \text{Eq. (6)}$$

The comparison of results from both scenarios highlights the impact of shadow coverage on solar irradiance simulations. The percentage difference emphasizes the critical role of accounting for shading in rooftop solar potential assessments. These findings are valuable for optimizing solar panel placement, improving energy yield predictions, and informing urban planning decisions to maximize rooftop solar energy potential in densely built environments. Additionally, this approach can be used to assess the financial viability of solar installations by estimating energy losses due to shading. It also provides a useful tool for architects and urban planners to design buildings and neighborhoods with enhanced solar access, ultimately supporting the development of more sustainable urban energy solutions.

3. RESULTS AND DISCUSSION:

3.1. 3D Visualization Using Digital Elevation Model (DEM) Data:

The LiDAR dataset, sourced from the Government of Quebec's official website, was utilized to generate a 3D model of the selected geographic area, enabling detailed visualization. The process of model generation is illustrated in the diagram below (Figure 04). This 3D model

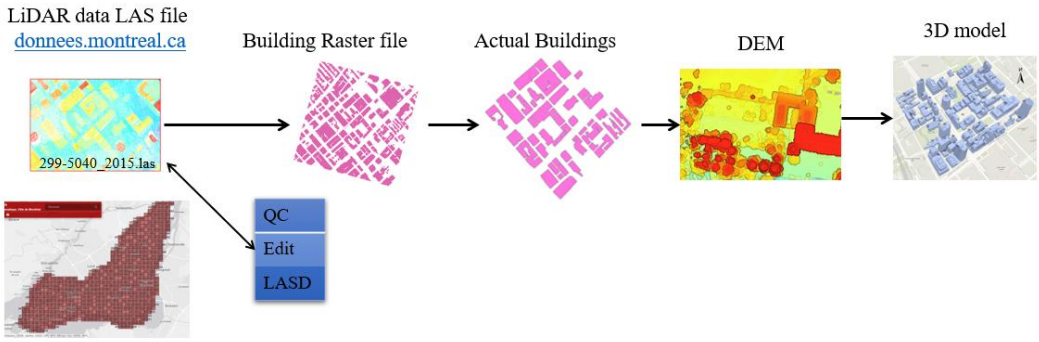

Fig. 4: Flow chart of the 3D building model

offers a clear and detailed representation of the surrounding structures and patterns within the area. The dataset encompasses key attributes for each building, including height, area, and unique identification number, facilitating a comprehensive analysis of individual structures.

3.2. Hillshade analysis:

Hourly data for Direct Normal Irradiance (DNI) and Diffuse Horizontal Irradiance (DHI) from the Canadian Weather Year for Energy Calculation (CWEC) were used for the hillshade analysis, which combined twelve Typical Meteorological Months from up to 30 years of hourly data in the Canadian Weather Energy and Engineering Datasets (CWEEDS). The solar azimuth and altitude for each hour of 2023 were calculated using Python, based on the location's longitude and latitude. Initially, calculations were made for all 8,760 hours in 2023, but after filtering out instances with negative solar altitude, the number of valid hours was reduced to 4,406. The hillshade analysis was performed 4,406 times, adjusting for the changing azimuth and altitude values each hour. Two scenarios were considered: Scenario A, which excluded the effects of surrounding buildings (hillshade analysis without shadow modeling), and Scenario B, which incorporated the influence of nearby buildings (hillshade analysis with shadow modeling). The results from Scenario A established the baseline irradiance without shading effects, while Scenario B highlighted a significant reduction in solar irradiance due to the shadowing effects of nearby structures, emphasizing the importance of considering building shadows in solar energy assessments.

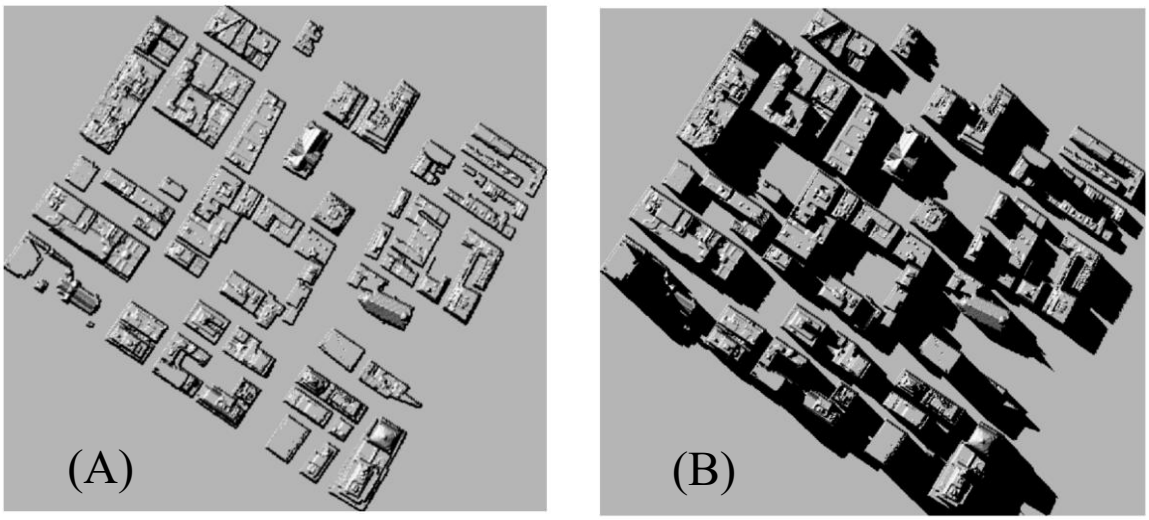

Fig. 5. Solar irradiance scenarios: (A) without shading effects, (B) with shading effects

3.3. Canny Algorithm:

Upon completion of the hillshade analysis for both scenarios, the resulting hillshade raster files were converted into point data. To refine the accuracy of the analysis and remove unnecessary building edges within a one-meter distance, the Canny algorithm was applied. This algorithm was implemented with consideration of the impracticality of parapet areas, ensuring that only significant building features were preserved for subsequent analysis.

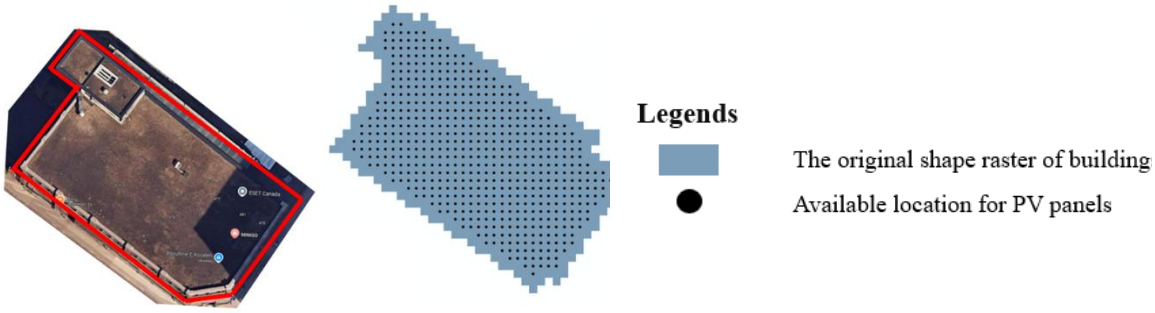

Fig. 6: The example of a feasible area for solar panels by applying the Canny algorithm

3.4. Rooftop solar irradiance simulation:

The solar irradiance received on each building rooftop was calculated, revealing the significant role of shadows in assessing rooftop solar energy potential. As illustrated in Figure 7, consider Building ID 19: in the scenario (a), without considering shadows, the total solar irradiance received by the building is 1.79×10^6kWh. However, when shadows are accounted in the scenario (b), this value decreases to 1.71×10^6kWh. With a total building area of 1,491.67 m², the average solar irradiance is calculated to be $1.20 \times 10^3 \mathrm{kWh/m^2}$. The ratio of irradiance in the shadowed scenario to the unshaded scenario is 95.53%, underscoring the considerable impact of shading on solar energy potential. These findings emphasize the critical need to incorporate shadow analysis in urban planning and building design, particularly for optimizing rooftop solar energy generation.

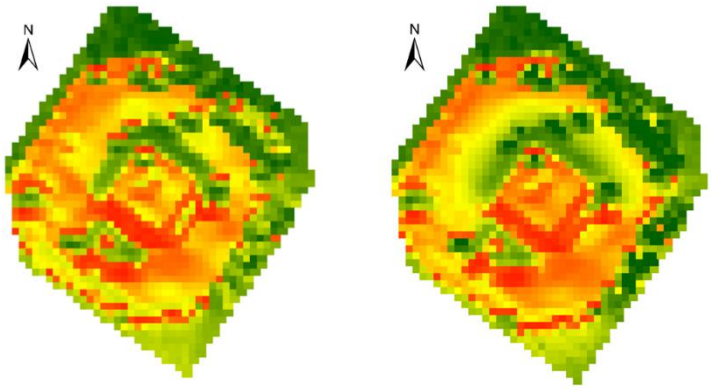

(a) (b)

Fig. 7: Solar irradiance on Building ID 19 (a) without shading and (b) with shading effects

Furthermore, for Building ID 39, the total solar irradiance is 2.62×10^6KWh in the absence of shadows, while it reduces to 1.95×10^6KWh when shadows are considered. The average solar irradiance per square meter for this building is $0.91 \times 10^3 \mathrm{KWh/m^2}$. The ratio of irradiance in the shadowed scenario (Scenario B) to the unshaded scenario (Scenario A) is 74.42% (Figure 8), indicating a notable reduction in solar energy potential due to shadowing.

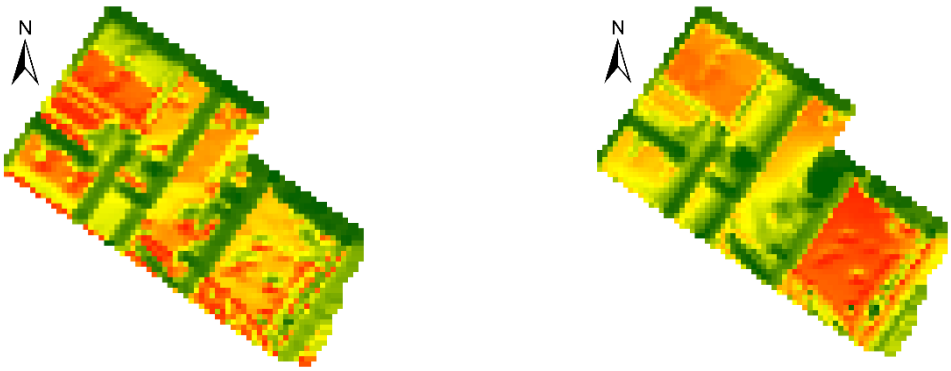

(a) (b)

Fig. 8: Solar irradiance on Building ID 39 (a) without shading and (b) with shading effects

The analysis reveals substantial variations in shading impacts among the buildings studied. Building ID 19 experiences a 4.47% reduction in solar irradiance when accounting for shading effects, decreasing from 1.79×10^6 kWh to 1.71×10^6 kWh. A more pronounced effect is observed for Building ID 39, which shows a 25.58% decline in irradiance, from 2.62×10^6 kWh to 1.95×10^6 kWh. These differential impacts highlight the critical influence of building-specific characteristics and surrounding urban morphology on solar potential. At the aggregate level (Figure 9), Scenario A yields an annual irradiance of 1.48×10^8 kWh (averaging 1.23×10^3 kWh/m^2), while the shading effects of Scenario B reduce this to 87.13% of unshaded potential. This 12.87% overestimation carries material financial implications: assuming a 10 kW PV system with a $2,000/kW installation cost and $0.12/kWh electricity price, the shading-induced energy loss extends the payback period by 15–20% (e.g., 8 years vs. 6.5 years) and reduces the net present value (NPV) by approximately $5,000 over a 25-year lifetime. Such deviations underscore how unmodeled shading effects can distort feasibility studies and undermine investment returns, emphasizing the need for high-resolution assessments in urban solar planning.

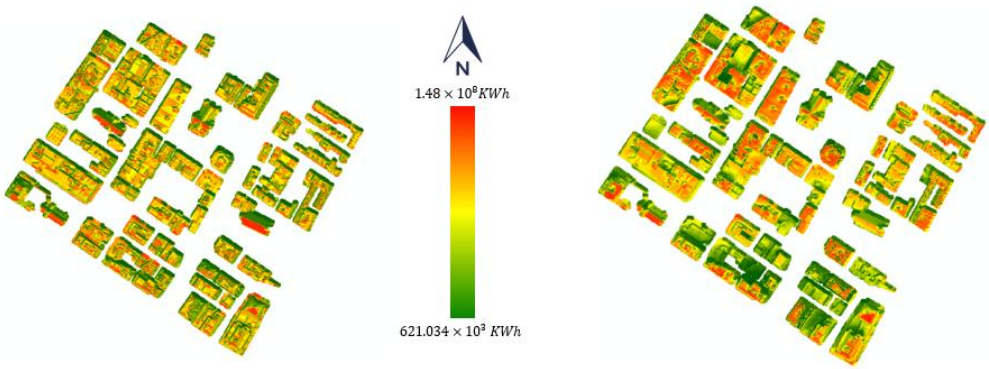

Fig. 9. The yearly distribution of solar irradiance on rooftops in the whole study area

The charts reveal (Figure 10) the substantial effect of shadows on solar irradiance throughout the year. By comparing monthly solar irradiance with and without shadows, it demonstrates a consistent reduction in potential solar energy due to shading. The impact of shadows is most pronounced in January with a 24.49% decrease in irradiance, while May shows the smallest difference at 8.51%, highlighting the variability of shadow effects across different months. This data underscores the importance of incorporating shadow analysis in solar energy assessments to accurately predict and optimize energy generation. The variability in shading effects across different buildings and seasons also emphasizes the need for uncertainty analysis in shadow modeling. Factors such as building height, rooftop features, and

surrounding obstructions can all contribute to variations in shading, which may affect the accuracy of energy predictions. Incorporating sensitivity analysis in future studies would help quantify the degree of uncertainty in shadowing effects, providing a more robust estimation of solar potential. From an urban planning perspective, these findings underscore the necessity of considering shadow impacts in the early stages of building design. Effective mitigation strategies, such as adjusting building orientation and height or implementing green roofs, could significantly enhance rooftop solar energy generation. Additionally, urban planners could focus on reducing shadowing effects by strategically placing solar installations and optimizing building layouts, ensuring maximum sunlight exposure on rooftops.

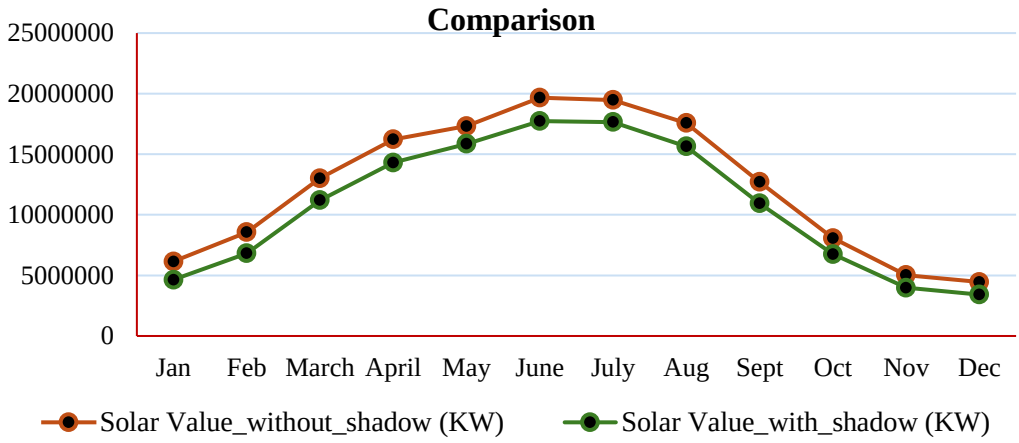

(a)

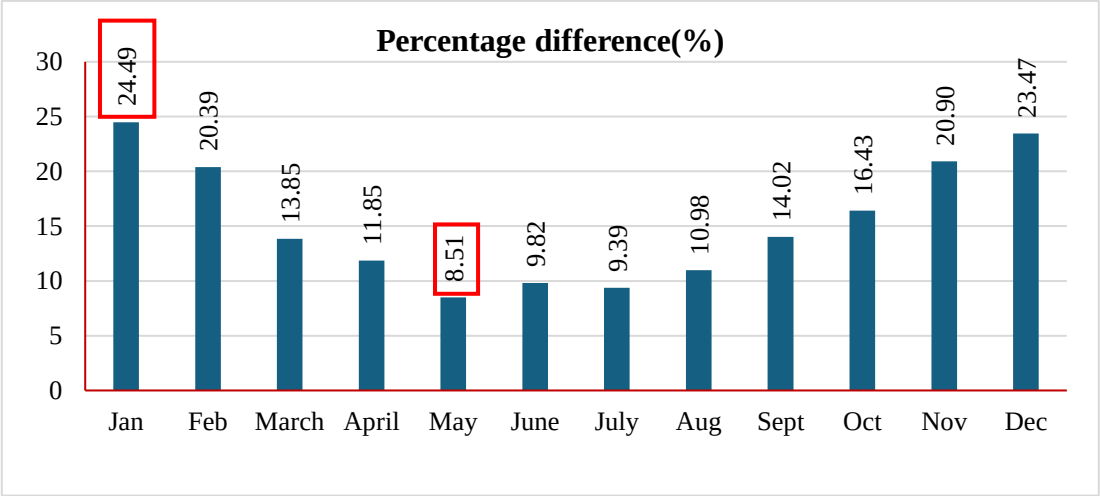

(b)

Fig. 10. The monthly distribution of the solar irradiance on rooftop in the whole study area

4. CONCLUSION & FUTURE WORKS

This study introduced a novel approach for accurately assessing rooftop solar energy potential in high-latitude urban environments by integrating deep learning techniques with LiDAR-derived 3D GIS models. The methodology effectively accounted for complex shading effects, rooftop obstructions, and seasonal solar variations, offering a high-resolution framework for optimizing photovoltaic (PV) installations. By analyzing 48 buildings in Montreal, Canada, the study demonstrated that neglecting shading effects leads to an overestimation of solar potential by 12.87%, highlighting the necessity of precise

shadow modeling in urban energy planning. The findings emphasize the significant influence of building morphology and inter-building shading on rooftop solar performance, particularly in dense urban settings. The simulation results revealed notable variations in solar irradiance across different rooftops, with shadow impacts fluctuating based on building height, surrounding structures, and seasonal sun paths. Monthly analyses further demonstrated that the shadow effect was most pronounced in winter months, whereas summer months exhibited the highest solar potential. These findings provide valuable insights for architects, urban planners, and policymakers, offering a data-driven approach to maximizing rooftop solar energy utilization.

Despite the advancements presented, certain limitations remain. The deep learning-based rooftop segmentation model is still in development, and further refinement is required to enhance its accuracy in detecting usable rooftop areas under varying lighting conditions. Additionally, the study primarily focused on a single geographic region, and its applicability to other high-latitude cities should be further explored. Future work will focus on expanding the deep learning framework by incorporating higher-resolution aerial imagery and diverse urban datasets to improve rooftop feature extraction. Moreover, integrating energy storage and grid-interconnection analysis will allow a more comprehensive evaluation of the feasibility of large-scale solar adoption in urban energy networks. Additionally, further research will explore mitigation strategies for shading effects, such as optimizing PV panel placement and developing dynamic solar tracking mechanisms for rooftop installations. By addressing these future research directions, this study aims to enhance the precision of rooftop solar potential assessments, supporting the transition towards sustainable and energy-efficient urban environments.

REFERENCE

1. Agrawal, K., Sharma, S., Kumar, B., & Verma, P. (2024). Hydrogen an environmental revolution toward clean energy transition: a green concept for current and future perspectives. In *Clean Technologies and Environmental Policy* (Vol. 27, Issue 2). Springer Berlin Heidelberg. https://doi.org/10.1007/s10098-024-03015-6
2. Albatayneh, A., Albadaineh, R., Juaidi, A., Abdallah, R., Zabalo, A., & Manzano-Agugliaro, F. (2022). Enhancing the Energy Efficiency of Buildings by Shading with PV Panels in Semi-Arid Climate Zone. *Sustainability (Switzerland)*, *14*(24), 1–23. https://doi.org/10.3390/su142417040
3. Aliakbarzadeh, Z., Moazenzadeh, R., Mohammadi, B., & Noroozi, Z. G. (2024). On the use of meteorological parameters and satellite image–based indices for improving solar radiation estimation. *Environmental Science and Pollution Research*, *32*(1), 279–297. https://doi.org/10.1007/s11356-024-35743-z
4. Alsuhaibany, Y., & Li, Y. (2017). Estimation of rooftop solar photovoltaic (pv) potential: A systematic literature review and guidelines for future research. *AMCIS 2017 - America's Conference on Information Systems: A Tradition of Innovation*, *2017-Augus*, 1–5.
5. Amigó, L. P. (2016). *Solar Potential Assessment: Comparison Using LiDAR Data and PVsyst*. *June*.
6. Baquiran, A., Javier, T. B., Dalit, R. J., Manuel, J. J., Pacis, D. J., Palchan, D. L., Abana, E., & Daliuag, J.-11. (2020). Mapping of Solar Power Potential Structures Using Geographic Information System. *EnRB) Engineering Research Bulletin*, *8*, 5–9. www.urdc.usl.edu.ph
7. Bayrakci Boz, M., Calvert, K., & R. S. Brownson, J. (2015). An automated model for rooftop PV systems assessment in ArcGIS using LIDAR. *AIMS Energy*, *3*(3), 401–420. https://doi.org/10.3934/energy.2015.3.401
8. Bill, A., Mohajeri, N., & Scartezzini, J. L. (2016). 3D Model for Solar Energy Potential on Buildings from Urban LiDAR Data. *Eurographics Workshop on Urban Data Modelling and Visualisation*, *2016-Decem*, 51–56. https://doi.org/10.2312/udmv.20161420
9. Choi, Y., Suh, J., & Kim, S. M. (2019). GIS-based solar radiation mapping, site evaluation, and potential assessment: A review. In *Applied Sciences (Switzerland)* (Vol. 9, Issue 9). MDPI AG. https://doi.org/10.3390/app9091960
10. Desthieux, G., Carneiro, C., Camponovo, R., Ineichen, P., Morello, E., Boulmier, A., Abdennadher, N., Dervey, S., & Ellert, C. (2018). Solar energy potential assessment on rooftops and facades in large built environments based on lidar data, image processing, and cloud computing. Methodological background, application, and validation in geneva (solar cadaster). *Frontiers in Built Environment*, *4*(March). https://doi.org/10.3389/fbuil.2018.00014
11. Ding, D. (2025). *A Convolutional Neural Network Approach to Predicting the Power Output of a Solar Farm*. 1–7.
12. Ebbin, S., & Ghamarian, A. (1992). Sustainable energy development. *SAE Technical Papers*, *May*. https://doi.org/10.4271/929042
13. Emmanuel Augustine Etukudoh, Zamathula Queen Sikhakhane Nwokediegwu, Aniekan Akpan Umoh, Kenneth Ifeanyi Ibekwe, Valentine Ikenna Ilojianya, & Adedayo Adefemi. (2024). Solar power integration in Urban areas: A review of design innovations and efficiency enhancements. *World Journal of Advanced Research and Reviews*, *21*(1), 1383–1394. https://doi.org/10.30574/wjarr.2024.21.1.0168
14. Esfandi, S., Tayebi, S., Byrne, J., Taminiau, J., Giyahchi, G., & Alavi, S. A. (2024). Smart Cities and Urban Energy Planning: An Advanced Review of Promises and Challenges. *Smart Cities*, *7*(1), 414–444. https://doi.org/10.3390/smartcities7010016
15. Fakhraian, E., Forment, M. A., Dalmau, F. V., Nameni, A., & Guerrero, M. J. C. (2021). Determination of the urban rooftop photovoltaic potential: A state of the art. *Energy Reports*, *7*, 176–185. https://doi.org/10.1016/j.egyr.2021.06.031
16. Green, M. A., Dunlop, E. D., Hohl-Ebinger, J., Yoshita, M., Kopidakis, N., & Hao, X. (2020). Solar cell efficiency tables (version 56). *Progress in Photovoltaics: Research and Applications*, *28*(7), 629–638. https://doi.org/10.1002/pip.3303
17. JIANG, H., Yao, L., BAI, Y., & ZHOU, C. (2024). Assessment of rooftop photovoltaic power generation potentials using multi-source remote sensing data. *National Remote Sensing*

Bulletin, *0*(0), 1–13. https://doi.org/10.11834/jrs.20243440
18. Kim, J., Kim, E., Jung, S., Kim, M., Kim, B., & Kim, S. (2025). Improved Surface Solar Irradiation Estimation Using Satellite Data and Feature Engineering. *Remote Sensing*, *17*(1), 1–30. https://doi.org/10.3390/rs17010065
19. Kumar, A., Dubey, A. K., Segovia Ramírez, I., Muñoz del Río, A., & García Márquez, F. P. (2024). Artificial Intelligence Techniques for the Photovoltaic System: A Systematic Review and Analysis for Evaluation and Benchmarking. *Archives of Computational Methods in Engineering*, 4429–4453. https://doi.org/10.1007/s11831-024-10125-3
20. Lang, G. (2018). Urban energy futures: a comparative analysis. *European Journal of Futures Research*, *6*(1). https://doi.org/10.1186/s40309-018-0146-8
21. Li, S. Y., & Han, J. Y. (2022). The impact of shadow covering on the rooftop solar photovoltaic system for evaluating self-sufficiency rate in the concept of nearly zero energy building. *Sustainable Cities and Society*, *80*. https://doi.org/10.1016/j.scs.2022.103821
22. Liu, C., Xu, W., Li, A., Sun, D., & Huo, H. (2019). Analysis and optimization of load matching in photovoltaic systems for zero energy buildings in different climate zones of China. *Journal of Cleaner Production*, *238*. https://doi.org/10.1016/j.jclepro.2019.117914
23. Liu, R., He, G., Su, Y., Yang, Y., & Ding, D. (2023). Solar energy for low carbon buildings: choice of systems for minimal installation area, cost, and environmental impact. *City and Built Environment*, *1*(1). https://doi.org/10.1007/s44213-023-00019-8
24. Lou, H. L., & Hsieh, S. H. (2024). Towards Zero: A Review on Strategies in Achieving Net-Zero-Energy and Net-Zero-Carbon Buildings. *Sustainability (Switzerland)* , *16*(11). https://doi.org/10.3390/su16114735
25. Masson, V., Bonhomme, M., Salagnac, J. L., Briottet, X., & Lemonsu, A. (2014). Solar panels reduce both global warming and urban heat island. *Frontiers in Environmental Science*, *2*(JUN), 1–10. https://doi.org/10.3389/fenvs.2014.00014
26. Nadeem, A., Hanif, M. F., Naveed, M. S., Hassan, M. T., Gul, M., Husnain, N., & Mi, J. (2024). AI-Driven precision in solar forecasting: Breakthroughs in machine learning and deep learning. *AIMS Geosciences*, *10*(4), 684–734. https://doi.org/10.3934/geosci.2024035
27. Natanian, J., & Auer, T. (2020). Beyond nearly zero energy urban design: A holistic microclimatic energy and environmental quality evaluation workflow. *Sustainable Cities and Society*, *56*. https://doi.org/10.1016/j.scs.2020.102094
28. Ordoñez Palacios, L. E., Bucheli Guerrero, V., & Ordoñez, H. (2023). Integration of satellite imagery and meteorological data to estimate solar radiation using machine learning models. *Journal of Universal Computer Science*, *29*(7), 738–758. https://doi.org/10.3897/jucs.98648
29. Pfeifroth, U., Sanchez-Lorenzo, A., Manara, V., Trentmann, J., & Hollmann, R. (2018). Trends and Variability of Surface Solar Radiation in Europe Based On Surface- and Satellite-Based Data Records. *Journal of Geophysical Research: Atmospheres*, *123*(3), 1735–1754. https://doi.org/10.1002/2017JD027418
30. Pisoni, B., Andrade, B., Antonio, F., Piran, S., Pacheco, D., Miguel, L., Sellitto, A., & Maria, L. (2025). Analysis of methods to transform existing buildings into Nearly Zero Energy Buildings (NZEB). *Energy Efficiency*. https://doi.org/10.1007/s12053-025-10306-4
31. Prasad, B. H. D., Yan, L., & Cheshmehzangi, A. (n.d.). *Lecture Notes in Civil Engineering International Conference on Urban Climate , Sustainability and Urban Design*. https://doi.org/10.1007/978-981-97-8401-1
32. Prieto, I., Izkara, J. L., & Usobiaga, E. (2019). The application of LiDAR data for the solar potential analysis based on urban 3D model. *Remote Sensing*, *11*(20). https://doi.org/10.3390/rs11202348
33. Rajasundrapandiyanleebanon, T., Kumaresan, K., Murugan, S., Subathra, M. S. P., & Sivakumar, M. (2023). Solar Energy Forecasting Using Machine Learning and Deep Learning Techniques. *Archives of Computational Methods in Engineering*, *30*(5), 3059–3079. https://doi.org/10.1007/s11831-023-09893-1
34. Romero Rodríguez, L., Duminil, E., Sánchez Ramos, J., & Eicker, U. (2017). Assessment of the photovoltaic potential at urban level based on 3D city models: A case study and new methodological approach. *Solar Energy*, *146*, 264–275. https://doi.org/10.1016/j.solener.2017.02.043

35. Saadaoui, H., Ghennioui, A., Ikken, B., Rhinane, H., & Maanan, M. (2019). Using GIS and photogrammetry for assessing solar photovoltaic potential on Flat Roofs in urban area case of the city of Ben Guerir / Morocco. *International Archives of the Photogrammetry, Remote Sensing and Spatial Information Sciences - ISPRS Archives*, *42*(4/W12), 155–166. https://doi.org/10.5194/isprs-archives-XLII-4-W12-155-2019
36. Sarralde, J. J., Quinn, D. J., Wiesmann, D., & Steemers, K. (2015). Solar energy and urban morphology: Scenarios for increasing the renewable energy potential of neighbourhoods in London. *Renewable Energy*, *73*, 10–17. https://doi.org/10.1016/j.renene.2014.06.028
37. Sharma, V. K., Monteleone, G., Braccio, G., Anyanwu, C. N., & Aneke, N. N. (2025). A Comprehensive Review of Green Energy Technologies: Towards Sustainable Clean Energy Transition and Global Net-Zero Carbon Emissions. In *Processes* (Vol. 13, Issue 1). https://doi.org/10.3390/pr13010069
38. Shirinyan, E., & Petrova-Antonova, D. (2024). Large-Scale Solar Potential Analysis in a 3D CAD Framework as a Use Case of Urban Digital Twins. *Remote Sensing*, *16*(15). https://doi.org/10.3390/rs16152700
39. Sudhakar, K., Winderla, M., & Priya, S. S. (2019). Net-zero building designs in hot and humid climates: A state-of-art. *Case Studies in Thermal Engineering*, *13*. https://doi.org/10.1016/j.csite.2019.100400
40. Suresh, V., Janik, P., Rezmer, J., & Leonowicz, Z. (2020). Forecasting solar PV output using convolutional neural networks with a sliding window algorithm. *Energies*, *13*(3). https://doi.org/10.3390/en13030723
41. Vakilinezhad, R., & Ziaee, N. (2024). Assessing the combined effect of PV panels' shading and cool materials on building energy loads in different climates. *Environment, Development and Sustainability*, *26*(6), 16201–16221. https://doi.org/10.1007/s10668-023-03293-y
42. Villa-Ávila, E., Arévalo, P., Ochoa-Correa, D., Villa-Ávila, M., Sempértegui-Moscoso, E., & Jurado, F. (2024). A New Methodology for Estimating the Potential for Photovoltaic Electricity Generation on Urban Building Rooftops for Self-Consumption Applications. *Smart Cities*, *7*(6), 3798–3822. https://doi.org/10.3390/smartcities7060146
43. Waqas, H., Jiang, Y., Shang, J., Munir, I., & Khan, F. U. (2023). An Integrated Approach for 3D Solar Potential Assessment at the City Scale. *Remote Sensing*, *15*(23). https://doi.org/10.3390/rs15235616
44. Willenborg, B., Pültz, M., & Kolbe, T. H. (2018). Integration of semantic 3D city models and 3D mesh models for accuracy improvements of solar potential analyses. *International Archives of the Photogrammetry, Remote Sensing and Spatial Information Sciences - ISPRS Archives*, *42*(4/W10), 223–230. https://doi.org/10.5194/isprs-archives-XLII-4-W10-223-2018
45. Wu, Y., An, J., Gui, C., Xiao, C., & Yan, D. (2023). A global typical meteorological year (TMY) database on ERA5 dataset. *Building Simulation*, *16*(6), 1013–1026. https://doi.org/10.1007/s12273-023-1015-3
46. Zhang, Z., Zhong, T., Chen, M., Zhou, Z., Wang, Y., & Zhang, K. (2020). Estimation of Rooftop Solar Potential using Publicly Available Geodata and Deeping Learning. *Energy Proceedings*, *13*. https://doi.org/10.46855/energy-proceedings-7472
47. Zhao, H., Yang, R., & Wang, C. (2018). *The design orientation and shading impacts on rooftop PV economics in the urban environment : a case study in Melbourne , Australia*. 691–699.
48. Zhong, Q., & Tong, D. (2020). Spatial layout optimization for solar photovoltaic (PV) panel installation. *Renewable Energy*, *150*, 1–11. https://doi.org/10.1016/j.renene.2019.12.099

Building Physics, Building Envelope and Materials (13:30-15:00 h)

6th International Conference on Building Energy and Environment
Eindhoven University of Technology, The Netherlands
6 - 10 July 2025

Modelling innovative hygroscopic components for passive control of indoor relative humidity

V. Gentile [1], M. Libralato [2], S. Fantucci[1], M. Perino[1], V. Serra[1]

[1]*TEBE Group, Department of Energy "G. Ferraris", Politecnico di Torino, Turin 10129, Italy, vincenzo.gentile@polito.it*
[2]*Polytechnic Department of Engineering and Architecture, University of Udine, Udine 33100, Italy, michele.libralato@uniud.it*

SUMMARY
Porous building materials control indoor humidity by absorbing and releasing moisture in response to changes in relative humidity and temperature. Recent studies show that incorporating superabsorbent polymers, such as bio-hydrogels, into traditional building materials can increase moisture capacity up to tenfold. However, current testing methods and simulations often neglect temperature effects, which significantly impact water vapor adsorption and moisture diffusion. Water vapor uptake and diffusion follow temperature-dependent behaviours, with adsorption isotherms and diffusivity exhibiting Arrhenius-type relationships. Ignoring temperature fluctuation induced by whether daily cycles, solar heating, or other building-specific factors, can lead to discrepancies between predicted and actual performance. This research develops a methodology to assess hygroscopic materials behaviour under non-isothermal conditions, using dynamic vapor sorption (DVS) analysis and polynomial interpolation. A differential equation model integrates moisture transport with indoor mass and heat balance, enabling real-world performance evaluation through an interactive optimization interface.

Keywords: innovative hygroscopic components, indoor moisture control, hygrothermal modelling.

1. INTRODUCTION

The Porous building materials interact dynamically with ambient air by adjusting their moisture uptake (the mass of adsorbed moisture relative to the dry mass of the material) in response to fluctuations in indoor relative humidity (RH) and temperature (T). Recent research has increasingly focused on identifying more sustainable and hygroscopic material that can buffer indoor RH variations caused by internal loads (Gentile et al. 2024; Zu et al. 2020). This buffering effect is achieved through the ability of buildings material to retain and release moisture, allowing indoor walls, ceilings and other partitioning elements to passively influence indoor RH. Such passive action is particularly valuable in mitigating moisture fluctuations around typical comfort values (RH~50%). The objective of this research field is to enhance indoor thermal comfort and air quality while reducing energy consumption for AC devoted for indoor RH control.

Traditional mineral based building materials used for indoor plasters, such as limestone and gypsum, exhibit moisture uptake values ranging from 0.1 to 2%, depending on the RH of the surrounding air (Yang et al. 2023). These values are relatively insignificant in achieving the dual objective of passive control of indoor comfort and energy savings. Recent experimental studies, however, have demonstrated that incorporating superabsorbent polymers such as alginate bio-hydrogels into conventional building materials like limestone, at mass fractions of 10-30%, can enhance moisture capacity by up to tenfold (Gentile et al. 2023). Other studies have attempted to similarly integrate sorption materials, such as MOF, zeolites and silica gel, into plaster compounds achieving improvements, but with lower magnitude (Qin et al. 2020). The main reason for this

limitation is the intralayer diffusive resistance of moisture, which reduces the active zone of material responding to RH fluctuations. As result, much of the "composite" plaster remains unexploited. In contrast, the introduction of hydrogels creates an interconnected moisture pathway through the material's thickness, effectively overcoming the diffusive resistance inherent in conventional building materials.

Those aspects are critical when simulating behavior of hygroscopic building materials in real environments. Experimental data and tests are essential to properly represent the material properties on simulative tools to understand their response to RH fluctuations and evaluate real effectiveness. The most important information is the equilibrium moisture uptake, typically measured using gravimetric methods, where stepwise changes in RH (while keeping constant temperature) allow for tracking mass variations between different equilibrium states. Depending on the material properties, reaching equilibrium can take several hundreds of hour, and standardized testing methods generally recommend a single testing temperature, typically between 23°C and 25°C. However, as well known in psychrometry, temperature has an intrinsic influence on moisture capacity. For instance, in air, the saturation vapor pressure (Pv_{sat}) of water increases substantially with temperature (e.g., $Pv_{sat} = a * e^{b*T/(T+c)}$).
Similarly, moisture uptake of porous building materials can vary significantly as the air/material equilibrium temperature changes. Despite the critical role of temperature in water vapor adsorption and moisture diffusion, most current testing methodologies and simulation tools for building applications often overlook this influence. Consequently, the common approach is to extrapolate material properties measured at 23-25°C across the broader temperature range encountered in indoor environments throughout the year, typically between 15°C and 35°C.

2. METHOD

2.1. Isothermal and non-isothermal modelling

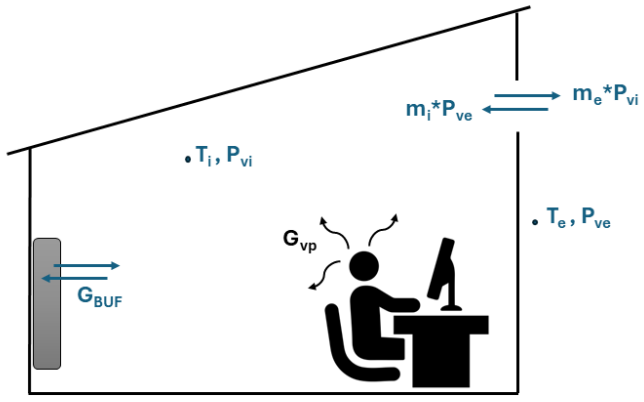

Symbol	Definition	Units
V	*Room volume*	$[m^3]$
A	*Indoor Wall Surfaces*	$[m^2]$
s	*Mortar Thickness*	$[m]$
ACH	*Air changes per hour*	$[h^{-1}]$
W_t	*Mortar moisture uptake*	$[kg_{water}\ kg_{dry}^{-1}]$
$W_{t_{eq}}$	Equilibrium *moisture uptake*	$[kg_{water}\ kg_{dry}^{-1}]$
T_i	*Indoor air temperature*	$[°C]$
P_{v_i}	*Indoor water vapor pressure*	$[Pa]$
T_e	*Outdoor air temperature*	$[°C]$
P_{v_e}	*Outdoor water vapor pressure*	$[Pa]$
x	coordinate normal to the surface	$[m]$
t	*Time*	$[s]$
$D(w_t)$	*Moisture − mortar diffusion coefficient*	$[m^2 s^{-1}]$
G_{BUF}	Type equation here.	$[kg\ s^{-1}]$
G_{VP}	Type equation here.	$[kg\ s^{-1}]$
ρ_d	Type equation here.	$[kg\ m^{-3}]$
LHG	*latent heat gain function of occupant methabolism*	$[W\ person^{-1}]$
n	*Number of occupants*	$[-]$

Figure 1. On the left, a schematic representation of the mass fluxes analyzed in this scenario, along with the equations used to solve the mass balance between building materials, indoor and outdoor air, and the occupant. On the right, the table provides definitions for all symbols and acronyms used.

The scheme in Figure 1 presents a set of differential equations that represent the mass balance between the adsorbing materials present in buildings (e.g., in wall and ceiling plasters) as function of the indoor air at temperature T_i and water vapor pressure Pv_i. The scheme illustrates a scenario in which indoor building materials exchange water vapor with air at a rate G_{BUF}, while the

occupants act as water vapor sources with a generation rate G_{vp}. Additionally, air exchange between indoor and outdoor is considered, where outdoor conditions are defined by T_e and P_{ve}.

$$\begin{cases} \dfrac{\partial w_t(x,t)}{\partial t} = \dfrac{\partial}{\partial x}\left[D(w_t)\cdot\dfrac{\partial w_t(x,t)}{\partial x}\right] \\ \left.\dfrac{\partial w_t(x,t)}{\partial x}\right|_{x=0,t} = 0 \\ w_t(x=+s,t) = W_{t_{eq}}(t) \\ w_t(x,t=0) = w_{t_0} \end{cases} \tag{1}$$

$$\frac{V}{R_v T_i}\frac{\partial P_{v_i}}{\partial t} = \left(P_{v_e} - P_{v_i}\right)\frac{ACH * V}{3600\, R_v T_i} + G_{VP} - G_{BUF} \tag{2}$$

$$G_{BUF} = \frac{\partial w_t}{\partial t} A * s * \rho_d \tag{3}$$

$$G_{VP} = \frac{LHG}{2500}\frac{n}{1000} \tag{4}$$

The system of equation (1) defines the moisture diffusion transport (based on Fick's law) through the material thickness, in relation to the boundary conditions. Boundaries define the initial moisture concentration through material thickness, and also the concentration at the contact layer between air/material. In the hypothesis of a transport mainly constrained by diffusive resistance (hence minimal and neglectable influence from convection on the air side) it is reasonable to consider the persistence of a continuous equilibrium condition on the air/material contact layer. That is, whenever T_i and Pv_i changes over time, this point immediately reaches the equilibrium condition defined by the measured adsorption isotherm. The equations (2) and (3) represent instead the mass balance between air and the hygroscopic component. Equation (4) quantifies the vapor flux generated by internal loads, which depends by the type of occupant metabolic activity (LHG) and the total number of occupants.

Symbol	Definition	Units
W_t	Plaster Moisture Uptake	g_{water}/kg_{dry}
RH	Indoor relative humidity	%
T	Indoor air temperature	°C
D	Plaster Moisture Diffusivity	m^2/s
E_a	Adsorption activation energy	kJ/mol
Mode	shape of the RH solicitation 1-nordtest; 2-sinusoid; 3-skewed sinusoid; 4-triangular; 5-saw; 6-pulse	
t	time	s
RH_{high}	RH upper bound	%
RH_{low}	RH lower	%
duty cycle	$t_{sorption}/(t_{sorption}+t_{desorption})$	-
Period	single cycle duration (24 h for daily)	

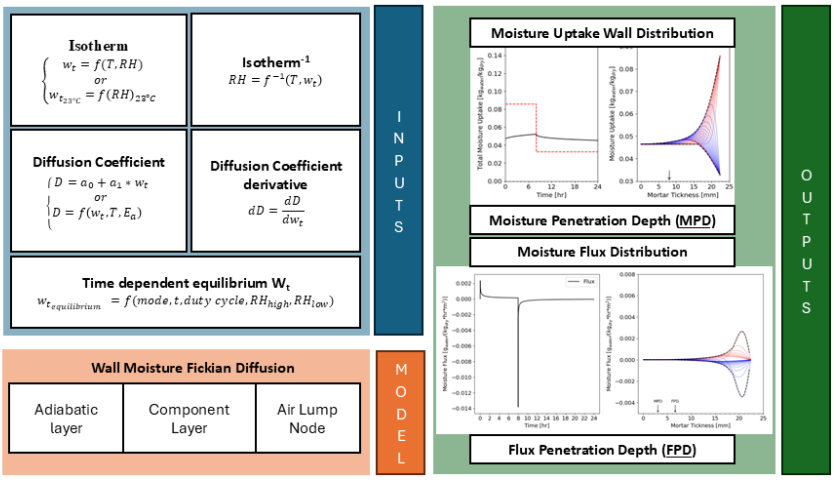

Figure 2. Required inputs and functions for solving moisture diffusion transport through the wall component, along with the outputs that can be derived from the simulation.

The most critical aspect of this set of equations concerns moisture transport through the hygroscopic component, as described in equation (1), particularly how its time derivative hinds the amount of adsorbed or released water vapor. To introduce a dynamic evolution, we implemented a time-dependent function for the equilibrium water uptake ($W_{t_{eq}}$) which updates the boundary condition at the building/air contact layer ($w_t(x = +s, t) = W_{t_{eq}}(t)$) at each time step (around 30-60 seconds). If $W_{t_{eq}}$ change over time due to variation of T_i or P_{vi}, the material reacts dynamically with a diffusive Fickian mass transport. Figure 2 provides a schematic visualization of this approach, in particular the temperature dependence of both inputs required for equation (1): $W_{t_{eq}}$, and the moisture diffusion coefficients (D). As previously mentioned, obtaining the numerical values of these functions requires experimental testing using a DVS analyzer, which measures mass response to stepwise increases in RH and T across the relevant operational range. When temperature dependence is considered, the data can be interpolated using a double-entry polynomial function, as in equation (5), allowing the identification of fitting parameters that describe a family of curves linking temperature (T), relative humidity (RH) and moisture uptake at the equilibrium($W_{t_{eq}}$). However, if temperature influence is neglected, the function simplifies to a single-entry polynomial (eq.6), where RH is the sole independent variable defining equilibrium moisture uptakes.

$$w_t(RH, T) = (d_0 RH^3 + d_1 RH^2 + d_2 RH + d_3) * (d_4 T^3 + d_5 T^2 + d_6 T + d_7) \qquad eq.5$$

$$w_t(RH) = a_0 RH^4 + a_1 RH^3 + a_2 RH^2 + a_3 RH + a_4 \qquad eq.6$$

A similar approach can be applied to moisture diffusivity, especially when temperature dependence is observed. In such cases, the Arrehnius type equation (7) can be used. The fitting parameters for this equation can be determined by interpolating trends from DVS data, using an optimization algorithm (e.g., square root minimization between experimental data and equation (1)).

$$D(w_t, T) = c_0 + c_1 T + c_2\, w_t\, e^{-\frac{E_a\, c_4}{T}} \qquad eq.7$$

$$D(w_t) = b_0 + b_1 w_t \qquad eq.8$$

If experimental data on moisture diffusivity are unavailable, or only a single isotherm has been measured, a simplified approach, such as the one described by equation (8), can be used. For typical building materials, the influence of T on moisture uptake in the interval of 15-35°C is often negligible, as variations in water uptake remain below 1%. In other words, the diffusivity coefficient is assumed to be constant.

The time-dependent variations of those material properties are introduced using a temperature dependent variable over time (which can also be applied to other model inputs). Since the primary focus is building applications, the topology of these functions over time (Figure 3) was chosen to reflect common trends in building physics: *i*) *step function* typical of Nordtest protocols used to evaluate moisture buffering capacity of materials and components (e.g., Moisture Buffering Value) and also representative of occupancy scheduled of tertiary buildings such as offices; *ii*) *sinusoidal function* typical of daily and seasonal temperature fluctuations; *iii) regulated response*, with a triangular or pulse shape, which mimics the temperature control operated by active systems, such as air conditioning units, or impulsive loads that introduce fast and sudden variations of sensible/latent heat into an environment; iv) *occupancy-based variation*, with skewed shape, similar to the step function but with fluctuations that introduce disturbances typical of random

events that generates unpredictable variations in indoor conditions. This pattern is particularly useful for studying the impact of stocastic disturbances on indoor environments.

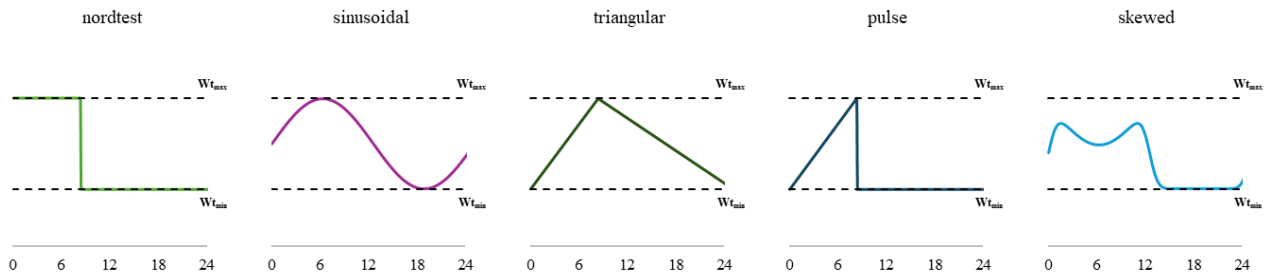

Figure 3. Topology of the forcing function used to simulate the temperature variation over time.

By solving the system of equation (1) to (4) using a forward Euler approach (while the diffusive model relies on iterative resolution algorithm), it becomes possible to obtain the evolution over time of both *Moisture Uptake Distribution* and *Moisture Flux Distribution* (outputs of Figure 2). This analysis is particularly useful for assessing the actual penetration depth in the presence of fluctuations, for example induced by the temperature, this information is essential for determining the optimal thickness of the hygroscopic material/component.

3. RESULTS

3.1. Influence of temperature on moisture exchange with air

For conventional materials, where water uptake variations are in the order of 1% (e.g., concrete, limestone, gypsum), the common approximation of "collapsing" all the adsorption isotherms within the 15-35°C range to a single reference curve at the intermediate value of 25°C does not introduce significant errors (or inaccuracies). The overall mass of water vapor involved in the exchange between the materials and the indoor air is, in these cases, very low.
However, when analyzing innovative, high-performing materials suitably designed to control indoor RH fluctuations, neglecting the influence of temperature can lead to substantial underestimations or overestimations of exchanged water masses. Water vapor adsorption isotherms are intrinsically linked to temperature, and within the typical temperature operational range in building environments, significant variations in moisture uptake at different RH levels can occur. For instance, Figure 4 shows the plot of isotherm function in equation 5 for the lower, the average, and the upper value of the considered range of variation of temperature. It is possible to see that variation of the moisture uptake of about ±30% occurs when the temperature swings between 15°C and 35°C. This effect is observed in both a traditional limestone indoor plaster (Figure 4a), commonly used for building retrofits, and in the same plaster enhanced with hygroscopic calcium alginate beads (Figure 4b). However, in the first case the variation of the moisture uptake is only few grams per kg.

In the first case (limestone) joining the different isotherms at the intermediate value of 25°C generates an error that is in the order of few grams also in the worst case of high RH values (specifically, between 1.6-4 grams when RH ranges between 40 and 95%). On the contrary, using the same approach in the more performing material (Figure 4b), where the enhanced plaster reaches moisture uptake close to 20% at the maximum RH, will induce an error whose is close to 100 grams per each kilos of used material in a room. Comparing this value with the latent load

associated to an occupant seated or doing light work (LHG = 75W) resting mode easily clarify the unacceptability of this approach when for example material is simulated over different seasons of one year.

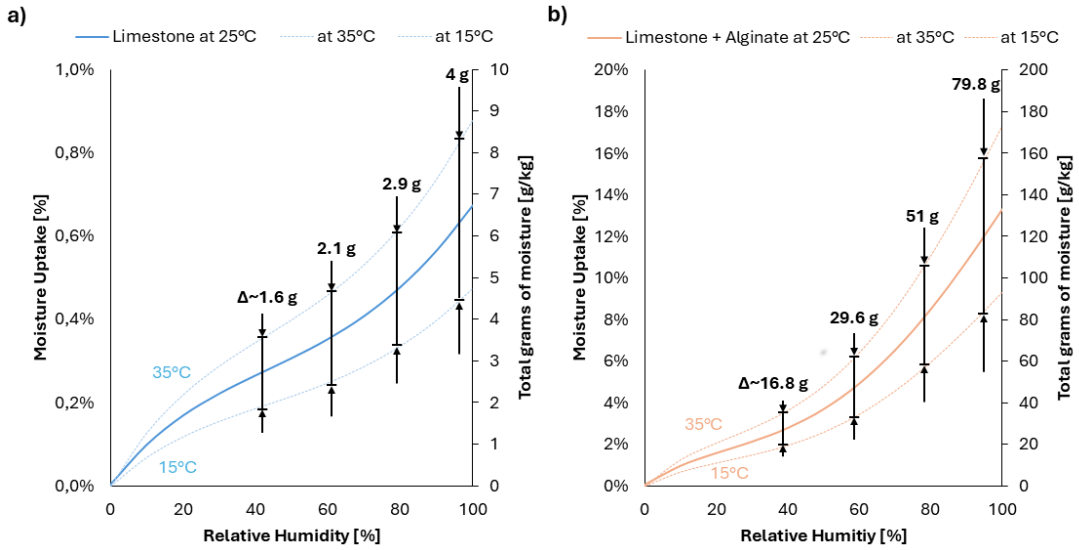

Figure 4. Comparison of equilibrium moisture uptake between unmodified limestone plaster (a) and the same plaster doped with 10% calcium alginate hydrogel beads (b), as the equilibrium temperature varies between 15°C and 35°C (the center, continuous, line correspond to a T=25°C).

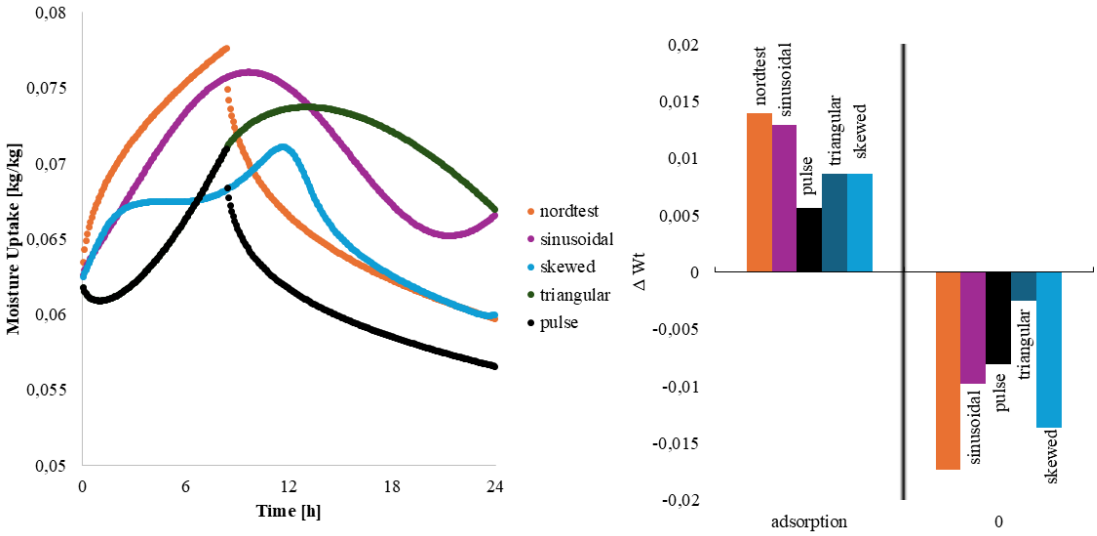

Figure 5. Results of the dynamic model under different temperature forcing functions. The left plot shows the total moisture uptake across the full thickness of the material over time. The right plot presents the total mass of moisture uptake adsorbed and released during the first 8 hours and the last 16 hours of the cycle, respectively.

Figure 5 presents the results the dynamic model related to a daily cycle where RH is maintained constant at 50%, while temperature varies over 24 hours according to the different forcing functions shown in Figure 3. The air change rate is set at 1 h^{-1}, and the room is occupied by a single

person. The plot on the left illustrates the variation in moisture uptake over time under different forcing functions, all applied with an 8/16h duty cycle. Since RH remains constant, temperature fluctuations directly influence vapor pressure variations, shaping the material's response to thermal changes. The response pattern closely follows the shape of the imposed temperature variation. The largest differences between moisture adsorption and desorption occur with the step function (Nordtest). Additionally, some forcing functions lead to a net moisture gain at the end of the 24-hour cycle, while others result in a net loss. This is further clarified in the right plot, where each bar represents the difference in moisture uptake between the start and end of each phase of the cycle (first 8 hours vs. last 16 hours). It is interesting to see that the triangular and sinusoidal functions cause a net increase in moisture content, indicating that at the end of the cycle, the material retains more moisture than at the beginning. Differently, the other shapes of the forcing functions generate a deficit at the end of the day. In general, cycle duration of 24 hours unlikely generate a balanced net mass variation, and the "average" response to a periodic solicitation would require several days to obtain a stable indication.

3. CONCLUSIONS

In conclusion, considering 1 kg of material, this dynamic approach, despite the material not reaching full equilibrium with the surrounding air within each phase, results in moisture variations ranging between ±5 and 15 grams. When extrapolated this information to the entire surface available in the simulated room (3×4×3m³, with 5 out of 6 surfaces covered in the enhanced hygroscopic plaster, totaling 66 m² of exposed surface, a plaster thickness of 2 cm, and a density of 1783 kg/m³), the total moisture exchange between the plaster and indoor air fluctuates between ±11 and 35 kg per cycle. These results highlight the significance of accounting for temperature influence in highly hygroscopic materials and the potential errors introduced when neglecting this factor in long-term simulations.

ACKNOWLEDGEMENTS

This study was possible thanks to the Project "Choisis- Characterisation of Innovative and Sustainable Insulating Solutions", funded within the Italian National Recovery and Resilience Plan (PNRR), Mission 4 – Education and Research- Measure M4C2 – Investment 1.1 PRIN – Research programs of national interest – project code 2022372TM9, CUP F53D23001540006

REFERENCES

Gentile, Vincenzo, Michele Libralato, Stefano Fantucci, Louena Shtrepi, and Giorgia Autretto. 2023. 'Enhancement of the Hygroscopic and Acoustic Properties of Indoor Plasters with a Super Adsorbent Calcium Alginate BioPolymer'. *Journal of Building Engineering* 76 (April): 107147. https://doi.org/10.1016/j.jobe.2023.107147.

Gentile, Vincenzo, Juan Diego Vargas Velasquez, Stefano Fantucci, Giorgia Autretto, Roberta Gabrieli, Pardeep Kumar Gianchandani, Marco Armandi, and Francesco Baino. 2024. '3D-Printed Clay Components with High Surface Area for Passive Indoor Moisture Buffering'. *Journal of Building Engineering* 91 (May): 109631. https://doi.org/10.1016/j.jobe.2024.109631.

Qin, Menghao, Pumin Hou, Zhimin Wu, and Juntao Wang. 2020. 'Precise Humidity Control Materials for Autonomous Regulation of Indoor Moisture'. *Building and Environment* 169 (July 2019): 106581. https://doi.org/10.1016/j.buildenv.2019.106581.

Yang, Zili, Weiyi Zhang, Xi Lin, Qian Xiong, and Qingwen Jiang. 2023. 'Optimization of Minor-LiCl-Modified Gypsum as an Effective Indoor Moisture Buffering Material for Sensitive and Long-Term Humidity Control'. *Building and Environment* 229 (September 2022): 109962. https://doi.org/10.1016/j.buildenv.2022.109962.

Zu, Kan, Menghao Qin, Carsten Rode, and Michele Libralato. 2020. 'Development of a Moisture Buffer Value Model (MBM) for Indoor Moisture Prediction'. *Applied Thermal Engineering* 171 (September 2019): 115096. https://doi.org/10.1016/j.applthermaleng.2020.115096.

6th International Conference on Building Energy and Environment
Eindhoven University of Technology, The Netherlands
6 - 10 July 2025

Research progress on heat and moisture transfer in underground enclosure structure

Qian Xiong [1], Ting Li [2], Lin Zhou [3], Bo Wu [4], Yimin Xiao [5*]

[1]College of Civil Engineering, Chongqing University, China, 202316131108t@stu.cqu.edu.cn
[2]CMCU Engineering Co., Ltd, China, liting@cmcu.cn
[3]CMCU Engineering Co., Ltd, China, zhoulin@cmcu.cn
[4]Shanghai Hua Jian Architecture, Engineering & Consulting Co. Ltd, China, bo_wu@arcplus.com.cn
[5]College of Civil Engineering, Chongqing University, China, xiaoyimin@cqu.edu.cn (Corresponding author)

SUMMARY
The growing demand for human activities has led to increased scale and depth of underground buildings, thereby heightening the need for heat and moisture regulation in their envelopes. Influenced by semi-infinite rock bodies and diverse environmental factors, heat and moisture transfer (HMT) in underground building envelopes presents a complex issue. Firstly, this paper gathers engineering cases and literature related to HMT from Web of Science, expanding the search from both micro and macro perspectives, with a focus on theoretical models, experimental studies, and numerical simulations. Secondly, the literature analysis reviews classical theoretical models of HMT in porous media, predominantly focused on the ground envelope. Finally, the analysis of experimental and numerical simulation studies reveals that experimental studies are scarce and the available numerical models are inadequate. Future research directions encompass understanding the HMT mechanism under multi-factor coupling, enhancing the computational model, and achieving technological breakthroughs in practical applications.

Keywords: Heat and moisture transfer; Underground Enclosure Structure; Environmental Control

1. INTRODUCTION

Amid increasing surface land scarcity, the rational development and utilization of underground space are essential for sustainable urbanization and enhancing urban resilience. Underground space utilization addresses urban land scarcity, traffic congestion, and environmental pollution while also reducing energy consumption, enhancing carbon sinks, and facilitating carbon sequestration (Qin Boyu et al., 2024; Zhao et al., 2016). Progressive urbanization and industrialization have driven the continuous expansion of underground buildings in scale and depth, intensifying environmental regulation challenges. Heat and moisture transfer (HMT) in underground building envelopes is a critical component of internal environmental research. The distinct environmental boundary conditions of underground enclosures result in fundamental differences in their HMT mechanisms compared to aboveground structures. However, the majority of existing studies continue to concentrate on aboveground buildings, resulting in a relative paucity of systematic research and reviews concerning underground enclosures.

Utilizing “underground” and “heat and moisture transfer” as search terms, 33 highly relevant articles were retrieved from the Web of Science database and subsequently clustered using VOSviewer. VOSviewer was used to cluster the articles. As depicted in the keyword distance-density map presented in Fig. 1., research in the field of heat and moisture transfer in underground

enclosure structure primarily concentrates on three salient directions: “environmental factors and material properties” (Chen et al., 2009; Klemczak, 2011; MATSUMOTO, 1995; Shi et al., 2024), “practical engineering problems and moisture transport properties” (Chen et al., 2024; Li et al., 2020; Maliki et al., 2015; Yu et al., 2022; Zhou et al., 2023), and “simulation and analysis of heat and moisture coupling effects” (Chen et al., 2009; Li et al., 2022, 2021; Maliki et al., 2015; Park and Nagai, 2007; Zhao et al., 2020).

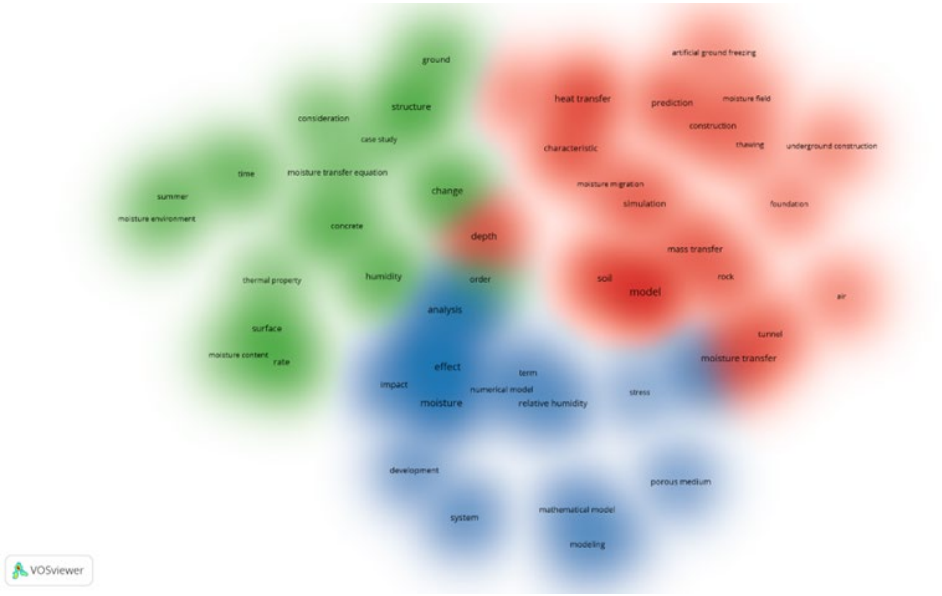

Figure 1. Distance-density view of keywords related to HMT in underground building envelopes.

Given the limited studies on HMT in underground building envelopes, this paper aims to analyze the HMT mechanism from a microscopic materials perspective and summarize research on HMT in practical engineering applications from a macroscopic environmental perspective. The article begins with key research points, expands the search scope, and provides a comprehensive summary of the current research status. The article aims to guide future research on heat and moisture coupling transfer in underground building envelopes and the regulation of underground building environments.

2. MICROSCOPIC PERSPECTIVE: HMT MECHANISM IN POROUS MEDIA

The difference in HMT between underground and surface building envelopes is mainly due to the presence of semi-infinite surrounding rock around underground envelopes (Liu Xichen, 2014) and the influence of complex factors such as burial depth(Liu Xichen, 2014; Stetjukha, 2023)and ground temperature distribution (Wei et al., 2024). The surrounding rock and underground enclosure structures are porous media, and understanding HMT principles within these media is essential for elucidating the formation mechanisms of the heat and moisture environment in underground buildings. The solid part of the porous medium, known as the solid-phase matrix, is distributed throughout the medium. The remaining part constitutes the pore space, which is filled with gas or liquid. Part of the pore space is interconnected (Bear J, 2013). Porous media can be categorized into three types based on moisture content:(1) wet saturated porous media, with pore space entirely filled with liquid; (2) unsaturated porous media, with both liquid and water vapor in

the pore space; and (3) dry saturated porous media, with only water vapor in the pore space. In underground envelope, the most common situation involves HMT in unsaturated porous media. The mathematical models of the coupled HMT process in porous materials are roughly Luikov only theory and Whitaker volume average theory.

2.1 Classical transfer theory

In 1934, Luikov introduced the concept of migration potential, recognizing the interrelation between HMT. Based on this concept, he integrated mass transfer effects into the Fourier heat conduction equation and incorporated heat transfer into the Fick diffusion equation, establishing a two-parameter coupled HMT model for porous media using temperature and volumetric humidity content as variables. Furthermore, he proposed a three-field driven model, where temperature, humidity content, and pressure act as migration potentials (Luikov, 1975). Although Luikov's phenomenological wet migration theory provides a mechanistic and realistic representation of wet migration in porous media, its governing equations rely on complex thermal and humidity parameters that are experimentally challenging to determine, limiting its practical applicability. The Whitaker volume averaging method models porous medium as a virtual continuum by selecting a representative unit cell that is sufficiently large to capture macroscopic transfer phenomena and encompasses all phases of the medium. As a result, the averaged properties and HMT phenomena within this volume are both continuous and representative. This method has become a standard and widely adopted approach for studying HMT in porous media. Furthermore, numerous researchers have extended the Whitaker model to explore various driving mechanisms (Ilic and Turner, 1989; Nasrallah and Perre, 1988; Peishi and Pei, 1989; Wei et al., 1985, 1985). However, the model exhibits several limitations. For instance, the transport and control mechanisms are inadequately described, particularly in expressing the equilibrium relationships among various forces (Liu Xichen, 2014). In porous media, HMT results from the combined action of multiple transport mechanisms. No single theory can comprehensively summarize the HMT behavior of porous media under all conditions. The development of the theory of coupled HMT in porous media has roughly gone through three stages. Initially, the pure vapor diffusion theoretical model dominated. Subsequently, theoretical models that account for evaporation and condensation were introduced. Finally, a comprehensive theoretical model of coupled HMT was developed.

2.2 Thermo-humidity coupled transport theory

In 1957, Philip and De Vries pioneered a dual-field coupling model incorporating temperature and humidity gradients, demonstrating their influence on gas and liquid transport(Liu Xichen, 2014). Luikov later expanded this framework by integrating irreversible thermodynamics, macroscopic conservation laws, and migration potential into heat and moisture transfer (HMT) theory, formulating a dual-drive model driven by temperature and humidity gradients (Liu et al., 2006). Subsequent advancements have refined thermo-humidity coupling models, with extensive research focusing on coupled heat-moisture transfer in porous media, particularly within enclosure structures. The thermo-humidity coupling model proposed by Häupl et al. (1997) correlates temperature and volumetric humidity content, utilizing the hygroscopic equilibrium curve to describe the relationship between pore-space humidity content (per unit volume of liquid water) and relative humidity in porous media. The moisture absorption equilibrium curve of the porous material is illustrated in Fig. 2. N. Mendes(N. Mendes et al., 2002) analyzed the impact of latent heat on thermal conductivity during moisture transfer in building envelopes using the dual-field coupling model by Philip and De Vries. In this model, thermal conductivity, mass transfer

coefficient, and specific heat are expressed as functions of the porous medium's moisture content. The results indicate that gas diffusion and seepage coefficients depend on the porous medium's microstructure and gas properties.

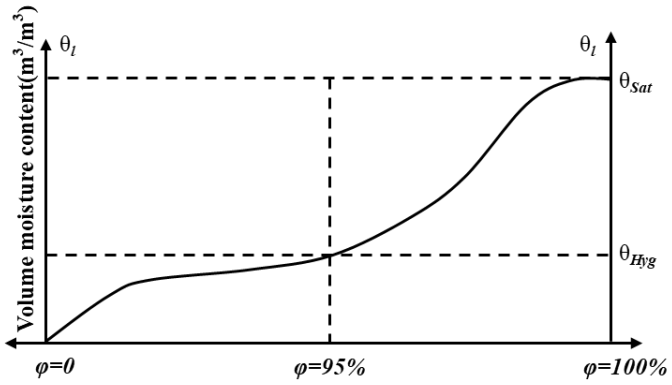

Figure 2. Moisture absorption equilibrium curve of porous materials.

Although more studies have been conducted on the mechanism of HMT in unsaturated porous media, most focus on small-scale porous materials, i.e., HMT over short distances and durations. Additionally, most studies on HMT in enclosure structures concentrate on above-ground buildings, with limited research on underground structures. Since these micro-mechanisms are influenced by boundary conditions, construction methods, and the coupling of multiple factors in the operating environment in macro-engineering applications, the following sections will discuss HMT in enclosure structures from the perspectives of engineering environment regulation and experimental monitoring.

3. MACRO PERSPECTIVE: HEAT AND HUMIDITY ENVIRONMENT CREATION

In addition to research on the heat and humidity coupling mechanism based on material properties, many scholars have also conducted research on HMT in underground buildings for the purpose of environment creation. Yu et al. (Yu et al., 2020) reviewed 107 studies on underground buildings and found that field experimental methods and numerical simulation methods are the primary approaches for studying underground buildings. In this paper, we focus on these two types of research methods and generalize and summarize the studies on HMT in the envelopes of underground buildings.

3.1. Field experiments and parameter testing

3.1.1. HMT of soil, surrounding rock, and lining material (SSL)

Underground buildings are typically surrounded by semi-infinite soil or surrounding rock, and the thermal and moisture properties of these materials significantly influence HMT in underground structures. As early as 1980, Shipp et al. (Shipp et al., 1980) conducted field experiments on heat flux through the walls of underground buildings and the surrounding soil temperatures and moisture content at the University of Minnesota. They highlighted that soil moisture content and surface conditions are key factors affecting soil thermal conductivity, and changes in this coefficient significantly impact heat transfer in the underground building envelope. Around 2000, Japanese scholar Daisuke Ogura (Ogura et al., 2000) conducted a one-year study on HMT

behaviors in underground buildings and their surrounding foundations in Tsu City, Japan. He reached similar conclusions and emphasized that ventilation is an effective means of regulating heat and humidity coupling in underground structures. Zhao et al. (Zhao et al., 2021) conducted a 68-day field monitoring experiment in a typical Nanjing Metro subway section to measure subway tunnel wall temperature (STWT), tunnel air temperature, and wall heat flow. They studied the heat absorption rate (SHAR) of the STWT and surrounding geotechnical soil, as well as their impacts on the subway system's thermal environment and energy consumption. They concluded that train operation, tunnel air temperature, and surrounding geotechnical soil temperature are the primary factors influencing STWT and overall thermal environment and energy consumption. The thermal and moisture characteristics of soil and surrounding rock significantly impact HMT in underground building envelopes. However, due to experimental challenges, field experiments in this area are relatively limited.

The heat and moisture parameters of SSL are crucial for simulating HMT in underground building envelopes, as these materials are predominantly porous media. Since the 1980s, several large-scale testing projects have been conducted in Europe and the United States to investigate the hygric properties of common building materials, including IEA Annex 14 (HENS, 1992), IEA Annex 24 (Canada, 2025), ASHRAE1018-RP (K, 2006), and NRC-IRC MEWS (Walls et al., 2003)35]. These projects have established isothermal moisture absorption and release curves, water retention curves, hygric permeability coefficients, hygric diffusion coefficients, and other hygric parameters for hundreds of porous building materials, forming a comprehensive database to support the simulation of HMT in underground structures. However, these tests have primarily focused on general building materials, with limited specific investigation into the heat and humidity parameters of underground SSL. Further analysis and categorization are still required. In recent years, the China Academy of Building Research and other organizations have actively accumulated data on the hygric properties of porous building materials and have achieved some progress (Feng Chi et al., 2016). However, the current tests on porous materials in China are not yet comprehensive, with limited testing related to the thermal and humidity parameters of SSL. Consequently, a more complete database of thermal and humidity parameters for porous materials has yet to be established.

3.1.2 Exploration of the Interaction between SST and Internal Environment

Excessive moisture is a prevalent issue in the internal environment of underground buildings, and studies on the thermal and humid environments within these structures often necessitate the exploration of dehumidification and moisture prevention strategies. Zhang et al. (Zhang et al., 2017) conducted a one-year field study on two typical underground civil defense works (CADWs) in Beijing. Their research elucidated the mechanisms underlying the thermal and humid environments in these CADWs and provided a foundation for developing appropriate dehumidification solutions. They also emphasized that different types of CADWs necessitate distinct moisture control measures. Ma et al. (Ma et al., 2022) conducted winter and summer tests on the hot and humid environments in three CADWs to characterize the heat and moisture exchange patterns between the underground intake tunnel envelope and the air. Yu et al. (Yu et al., 2022) conducted both short-term and long-term measurements at two subway stations on Tianjin Metro Line 5. They found that while the air temperatures in the stations were relatively stable, the humidity levels varied significantly. Notably, the relative humidity at the platforms was classified as “wet” or “very wet” for 30% of the test duration, indicating a high risk of condensation. Kim et

al. (Kim et al., n.d.) conducted a one-year field study of two typical underground parking lots in Seoul to investigate the phenomenon of moisture condensation and identify the most suitable conditions for condensation prevention. In recent years, with the proliferation of numerical simulation research, fewer studies have focused solely on field experiments. Instead, more research has integrated field experiments with numerical simulations or employed micro-experiments to validate numerical models.

3.2 HMT modeling and numerical simulation of envelope structures

Zhang et al. (Zhang et al., 2010) developed a novel heat-humidity model to describe the coupled HMT process involving water vapor diffusion and liquid water migration in underground building envelopes, based on Philip and De Vries' two-field coupling theory. Liu (Liu Xichen, 2014) established a mathematical model of HMT in an underground plant envelope, using liquid water volumetric moisture content and temperature as driving potentials. He introduced the concept of "cell partitioning" into the solution process for air parameters in longitudinally ventilated, deeply buried underground ducts. He also used coupling as an entry point to investigate the dynamic HMT of the plant envelope, revealing the relationship between air parameters and air temperature. The dynamic HMT of the plant envelope was investigated using coupling as an entry point, revealing the intrinsic connection between air parameters and wall HMT, and proposing a simplified formula for predicting year-round dynamic heat and humidity uptake and discharge of the envelope. Zhong et al. (Zhong et al., 2014) investigated the condensation of basement walls in Chengdu using EnergyPlus simulation software. They proposed condensation is influenced by the combined effects of thermal resistance, air change rate per hour, and heat gain. Huang (Huang, 2023) established a HMT model for underground envelopes using COMSOL Multiphysics software, based on Liu's model and incorporating measured temperature and humidity parameters from Xi'an subway station. He highlighted that an accurate heat and humidity coupling transfer model is crucial for simulating and predicting the heat and humidity distribution in subway station enclosures, as well as for improving air quality and extending the service life of equipment. The primary differences among these models and simulation approaches lie in their specific assumptions. Owing to the complexity of moisture transport theory, which involves multiphase and multilayer pore structures, variable boundary conditions, material properties, and highly nonlinear governing equations, no single model is suitable for all applications. In fact, simpler models, such as Fourier's one-dimensional heat transfer model and Glaser's vapor diffusion model based on Fick's law (Branco et al., 2004), remain popular and widely used in civil engineering.

4. CONCLUSION

This paper systematically reviews the research progress on HMT in underground building envelopes from both microscopic and macroscopic perspectives and obtains the following conclusions:

(1) The HMT process in underground enclosure structures exhibits multiple coupling properties and is influenced by multi-factor coupling, unlike above-ground buildings. Existing simplified or single-phase models are insufficient to accurately reflect this process. A reliable theoretical basis for regulating and designing the underground environment can only be provided by fully considering the pore structure of materials, phase changes, and multi-phase flow characteristics.

(2) Existing engineering practices must enhance the integration of parameter determination and multi-scale numerical simulations. Integrating on-site measurements of underground thermal and humidity environments with microscopic tests can better calibrate and validate model parameters, providing scientific support for optimizing engineering design schemes.

(3) As the potential value of underground buildings in urban complexes, public transportation, and energy utilization becomes more prominent, future research should deeply explore the influence of multi-field coupling (heat, moisture, stress, and chemistry) on the performance of underground structures. Further improving the thermal-humidity coupling model can help achieve energy savings and emission reductions in underground buildings, enhance indoor environmental quality, and meet the needs of sustainable urban development.

REFERENCES

Bear J, 2013. Dynamics of Fluids in Porous Media. Courier Corporation.

Branco, F., Tadeu, A., Simões, N., 2004. Heat conduction across double brick walls via BEM. Build. Environ. 39, 51–58.

Canada, G. of C.N.R.C., 2025. Heat, air and moisture transfer in insulated envelope parts: task 3 material properties: final report - NRC Publications Archive [WWW Document]. URL (accessed 1.15.25).

Chen, X., Zhou, X., Wang, Y., Liang, N., Xu, B., 2024. Study on ambient temperature and humidity in the construction tunnel under the influence of ventilation and hot water gushing. Tunn. Undergr. Space Technol. 143, 105501.

Chen, Y., Zhou, C., Jing, L., 2009. Modeling coupled THM processes of geological porous media with multiphase flow: Theory and validation against laboratory and field scale experiments. Comput. Geotech. 36, 1308–1329.

Feng Chi, Yu xi, Wang Delin, 2016. Determination of wet physical properties of aerated. Civ. Environ. Eng. 38, 125–131.

Häupl P., Grunewald J., Fechner H., Stopp H., 1997. Coupled heat air and moisture transfer in building structures. Int. J. Heat Mass Transf. 40, 1633–1642. The solid part of the porous medium, known as the solid-phase matrix, is distributed throughout the medium. The remaining part constitutes the pore space,

HENS, H., 1992. IEA annex 14: condensation and energy. IEA Annex 14 Condens. Energy 15, 261–273.

Huang Xingjie, 2023. Simulation and application of heat and moisture coupling transfer in the envelope of a subway station in Xi'an, China (Master's Degree). Chang'an University.

Ilic, M., Turner, I.W., 1989. Convective drying of a consolidated slab of wet porous material. Int. J. Heat Mass Transf. 32, 2351–2362.

K, K.M., 2006. A Thermal and Moisture Property Database for Common Building and Insulation Materials. ASHRAE Trans. Am. Soc. Heat. Refrig. Air-Cond. Eng. 112, 485–497.

Kim, H.Y., Chung, M.H., Park, J.C., n.d. Field experiment examining condensation reduction methods based on underground parking lot types. J. Asian Archit. Build. Eng. 0, 1–18.

Klemczak, B., 2011. Prediction of Coupled Heat and Moisture Transfer in Early-Age Massive Concrete Structures. Numer. Heat Transf. Part Appl. 60, 212–233.

Li Y., Yin H., Deng X., Liang L., Zhang Y., Zhai Y., 2022. Simulation study on ventilation design for controlling gaseous pollutants in urban sentry boxes with opening window. Build. Environ. 225, 109642.

Li, Z., Chen, J., Sugimoto, M., Mao, C., 2020. Thermal Behavior in Cross-Passage Construction during Artificial Ground Freezing: Case of Harbin Metro Line. J. Cold Reg. Eng. 34, 05020002.

Li, Z., Xu, Y., Li, R., Jia, M., Wang, Q., Chen, Y., Cai, R., Han, Z., 2021. Impact of the water evaporation on the heat and moisture transfer in a high-temperature underground roadway. Case Stud. Therm. Eng. 28, 101551.

Liu, W., Fan, A., Huang, X., 2006. Theory and Application of Heat and Mass Transfer in Porous Media. Science Press, Beijing.

Liu Xichen, 2014. Formation mechanism of thermal and humid environment of underground hydropower station and energy-saving control strategy (Learned scholar). Chongqing University.

Luikov, A.V., 1975. Systems of differential equations of heat and mass transfer in capillary-porous bodies (review). Int. J. Heat Mass Transf. 18, 1–14.

Ma, M., Chen, J., Xiao, Y., Gao, X., Liu, Y., Yuan, X., 2022. Field tests and analyses of thermal and humidity environment and heating and cooling capacity of air intake tunnels into underground plants. Energy Rep., 2022 The 4th International Conference on Clean Energy and Electrical Systems 8, 665–672.

Maliki M., Laredj N., Missoum H., Bendani K., Naji H., 2015. Numerical modelling of coupled heat, air and moisture transfer in building envelopes. Mech. Ind. 16, 509.
MATSUMOTO, M., 1995. An analysis of heat and moisture behavior of underground space and its surrounding ground under natural condition. J. Archit. Plan. Environ. Eng. 474, 27–36.
Mendes, N., Philippi, P.C., Lamberts, R., 2002. A new mathematical method to solve highly coupled equations of heat and mass transfer in porous media. Int. J. Heat Mass Transf. 45, 509–518.
Nasrallah, S.B., Perre, P., 1988. Detailed study of a model of heat and mass transfer during convective drying of porous media. Int. J. Heat Mass Transf. 31, 957–967.
Ogura, D., Terashima, T., Mizuhata, M., Matsumoto, M., 2000. Field Experiment of Heat and Moisture Behavior of The Underground Space and Its Surrounding Ground. J. Archit. Plan. Trans. AIJ 65, 35–41.
Park, K.-S., Nagai, H., 2007. Study on the Heat Load Characteristics of Underground Structures Part 2.Computational Analysis of the Heat/Moisture Behavior and Heat Load of Underground Structures. J. Asian Archit. Build. Eng. 6, 189–196.
Peishi, C., Pei, D.C.T., 1989. A mathematical model of drying processes. Int. J. Heat Mass Transf. 32, 297–310.
Qin Boyu, Gong Dandan, Chen Zhilong, 2024. The Current Situation, Strategies and Conceptions of Urban Underground Space Development and Utilization in China for Promoting Low-Carbon Development. Tunn. Constr. Engl. Chin. 44, 1337–1355.
Shi, L., Wang, J., Han, X., Wei, W., Guo, Y., Liu, J., 2024. Natural ventilation of underground shelters to improve indoor thermal and moisture environments in the various climates of China. Tunn. Undergr. SPACE Technol. 153, 105916.
Shipp, P.H., Meixel, G.D., Ramsey, J.W., 1980. Analysis and measurement of the thermal behavior of the walls and surrounding soil for a large underground building. Undergr. Space U. K. 5:2.
Stetjukha, V.A., 2023. Energy efficiency of underground structures in harsh climatic conditions. Mag. Civ. Eng. 117, 11710.
Walls, W., Dalgliesh, W., Desmarais, G., Djebbar, R., Kumaran, K., Lacasse, M., Lackey, J., Maref, W., Mukhopadhyaya, P., Nofal, M., Norm, N., Nicholls, M., Quirt, D., Rousseau, M., 2003. Final Report from Task 8 of MEWS Project (T8-03) -.
Wei, C.K., Davis, H.T., Davis, E.A., Gordon, J., 1985. Heat and mass transfer in water-laden sandstone: Microwave heating. AIChE J. 31, 842–848.
Wei, T., Fan, M., Xu, Z., Li, W., Gu, Z., Luo, X., 2024. Assessment of Energy Recovery Potential in Urban Underground Utility Tunnels: A Case Study. BUILDINGS 14, 3113.
Yu, J., Kang, Y., Zhai, Z. (John), 2020. Advances in research for underground buildings: Energy, thermal comfort and indoor air quality. Energy Build. 215, 109916.
Yu, Y., You, S., Zhang, H., Ye, T., Wang, Y., Tang, C., Wei, S., 2022. Measuring and modeling moisture environment in underground metro stations during commissioning stage: A case study. Build. Serv. Eng. Res. Technol. 43, 241–259.
Zhang, H., Liu, J., Li, C., Lian, Z., 2017. Long-term investigation of moisture environment in underground civil air defence work. INDOOR BUILT Environ. 26, 744–757.
Zhang, H.L., Marci, W.M., Fu, X.Z., 2010. Modeling of the hygrothermal absorption and desorption for underground building envelopes. Energy Build. 42, 1215–1219.
Zhao, J.-W., Peng, F.-L., Wang, T.-Q., Zhang, X.-Y., Jiang, B.-N., 2016. Advances in master planning of urban underground space (UUS) in China. Tunn. Undergr. Space Technol., Urban Underground Space: A Growing Imperative Perspectives and Current Research in Planning and Design for Underground Space Use 55, 290–307.
Zhao, P., Li, X., Liu, J., Zhang, D., Qiao, H., 2021. Monitoring and analysis of the subway tunnel wall temperature and surrounding rock/soil heat absorption ratio. Build. Environ. 194, 107657.
Zhao, X., Yang, X., Zhang, H., Lai, H., Wang, X., 2020. An analytical solution for frost heave force by the multifactor of coupled heat and moisture transfer in cold-region tunnels. Cold Reg. Sci. Technol. 175, 103077.
Zhong, H., Feng, Y., 2014. Study on Thermal Resistance of Basement Exterior Wall in Hot Summer and Cold Winter Zone, in: Li, A., Zhu, Y., Li, Y. (Eds.), Proceedings of the 8th International Symposium on Heating, Ventilation and Air Conditioning. Springer, Berlin, Heidelberg, pp. 167–173.
Zhou, J., Zhou, H., Wang, C., Guo, Z., Pei, W., 2023. Analysis of moisture migration, temperature, and pore structure characteristics of the muddy clay column subject to artificial ground freezing based on LF NMR. Tunn. Undergr. Space Technol. 133, 104948.

6th International Conference on Building Energy and Environment
Eindhoven University of Technology, The Netherlands
6 - 10 July 2025

Energy performance of novel low-cost inkjet-printed electrochromic glazing

Martin Tenpierik [1], Zara Huijbregts [1], Thaleia Konstantinou [1], Eleonora Brembilla [1], Alessandra Luna-Navarro [1], Tim Jonathan [2], Spyros Bousios [3]

[1]*Delft University of Technology, Faculty of Architecture and the Built Environment, Department of Architectural Engineering and Technology, Delft, the Netherlands, m.j.tenpierik@tudelft.nl*
[2]*The Green Village, Delft, the Netherlands, tim.jonathan@thegreenvillage.org*
[3]*Brite Solar, Thessaloniki, Greece, sbousios@britesolar.com*

SUMMARY
Rising temperatures are leading to an increase in the cooling demand of buildings. Electrochromic (EC) glazing can be a promising solution for controlling solar heat gains while maintaining outdoor views. This paper presents the results of the monitoring of prototype panels of a novel type of inkjet-printed EC glass under real use and weather conditions in a small office building in the Netherlands. This building contained two identical west-facing meeting rooms of which one was equipped with EC triple glass IGUs and the other with normal triple glass IGUs. Each room was equipped with local heating/cooling units of which the energy use was monitored, and with an extensive environmental sensor network. Sensor and calendar data was fed into an energy balance model for each of the rooms for the entire measurement period, allowing to correct for differences between the two rooms with respect to heat losses and gains and use conditions. The results of the monitoring showed that in the meeting room with EC glass IGUs, the heating demand increased by 34% in Jan.-Mar. 2024 while in Sept. 2023 the cooling demand decreased by 3%. The main reason for the increase in heating demand was found to be the lower g-value of the EC glass IGUs in clear state as compared to the normal IGUs. The almost similar cooling demand was a result of a trade-off between the lower direct solar transmittance of the EC glass IGUs and the heating up of the absorptive layer inside the IGUs. Furthermore, an experiment with participants showed that in general in dark state, satisfaction with view clarity, daylight colour and daylight availability was higher for the EC glass IGUs. In transparent state, no significant difference was perceived between the EC glass IGUs and standard IGUs, except for view clarity.

Keywords: Electrochromic glazing, energy performance, monitoring.

1. INTRODUCTION

Rising temperatures are leading to an increase in the cooling demand and overheating risk of buildings. Dynamic switchable glazing, like Electrochromic (EC) glazing, can be a promising solution for controlling solar heat gains and daylight admittance while maintaining access to outdoor views. By applying a small electric potential, the transparency of the glass can be adjusted to modify the visible light and direct solar transmittance. It can be switched over a range between a clear state with high transmittance, and a tinted state with low transmittance. To produce EC glass, a thin-film EC coating is placed on a glass panel. The coating consists of several layers: at the centre, an ion-conducting electrolyte sandwiched between an active EC layer at one side and a passive counter-electrode layer at the other side. Transparent conductors form the outermost layers (Lee et al., 2006). The thin film deposition can be based on several methods. The selected method affects the production costs and the durability of the end product (Kelly Waskett, 2016). The current high costs hinder the widespread application in buildings. Recently, a cost-effective type of EC glass using inkjet-printing was developed. Its effect on the cooling and heating demand and how it holds under real use and weather conditions is still uncertain.

Several earlier studies have investigated the performance of traditional EC glazing based on field test experiments or energy performance simulations. These studies examined possible energy savings based on different control regimes, environmental conditions or building types (Chambers et al., 2019; Piccolo & Simone, 2015; Papaefthimiou et al., 2006; Li et al., 2023; Klems, 2001); or compared the performance of EC glazing to other solar control devices (Fernandes et al., 2013; Kwee, 2020; Krarti, 2022). One study also included user satisfaction (Kelly Waskett, 2016).

The objectives of the present study, the Windows to the Future project, were: 1) to upscale the production facilities of inkjet-printed EC glazing, 2) to understand and overcome the key bottlenecks when integrating the technology into facades, 3) to understand to what extent the EC glass impacts the cooling and heating demand, as compared to regular high-performance triple glass for office spaces in temperate climates, 4) to explore the satisfaction of the technology by users, and 5) to understand to what extent the EC glass transmits daylight into the workplace and how the colouring of the daylight affects user perception. This paper will mostly address the objective 3 and includes some of the results related to objective 5. More results related to objectives 4 and 5 can be found in Luna-Navarro et al. (2024) and Chiucchiu et al. (2024). The EC glass used in this project was developed by Brite Solar.

2. MATERIALS AND METHODS

2.1. EC glass prototypes

The experiments were done in the OfficeLab at The Green Village on the TU Delft campus, the Netherlands. This building is equipped with HR+++ triple glass with a U-value of 0.6 W/(m^2K), a g-value of 0.48, and a light transmittance (t_{vis}) of 0.73. In the experimental room, the existing insulating glass units (IGUs) were replaced with IGUs with an EC layer. The thermal insulating properties of these IGUs were selected to correspond to the existing triple glazing. Furthermore, the thickness of the new IGUs matched the existing IGUs. The U-value of the EC glass IGU was measured to be 0.60±0.02 W/(m^2K); the light transmittance (t_{vis}) for the clear state between 0.40±0.05 and for the tinted state between 0.08±0.02; and the solar transmittance (t_{sol}) for the clear state 0.18 and for the tinted state 0.004. The software WINDOW was used to assess the g-value of the glass in clear and tinted state, which were respectively 0.35 and 0.34 (if the EC coating is placed on the innermost pane) or 0.26 and 0.04 (if the EC coating is placed on the outermost pane).

Due to the Covid-19 pandemic, the full-scale production line for the EC glass panes was inaccessible. As a result, the EC glass panes had to be produced by a lab printer with much smaller dimensions. The dimensions were therefore limited to 50 x 50 cm. As a consequence, the smaller EC glass panes (two sheets of 3 mm glass with in-between them the active layers) had to be laminated onto a 5 mm glass pane of the full window size (approx. 1 x 2.6 m). This ±11 mm thick glass laminate was used as one of the three glass panes of the IGU. The fixed windows in the façade were subdivided into 12 smaller panes while the operable window was subdivided into 10 panes (Figure 1). Even though the EC glass panes (by lamination) were integrated into a full size triple glass unit, sealing stripes were visible between the smaller EC panes. Table 1 provides the layering of the glass. It is important to mention here that the glass in the fixed windows had the EC glass laminate on the inside while in the operable window it was on the outside. The manufacturer recommended, as a precaution for this experimental version, to place the EC coating on the warm side of the glass to prevent a too low temperature of the coating in winter. However, as sun-shading, the coating should ideally be as close to the outdoor environment as possible.

Table 1. Layering of the triple glass IGUs.

IGU configuration	Existing triple glass IGU	EC glass prototype fixed window	EC glass prototype operable window
Outer pane	6 mm Stratobel laminated 33.1: 3 mm Planibel Clearlite / 0.38 mm PVB clear / 3 mm iplus 1.1. pos.2	5 mm iplus 1.1 (or equal)	11 mm laminated EC glass
Cavity	15 mm argon 90%	13 mm argon	13 mm air
Centre pane	4 mm Planibel Clearlite	5 mm iplus 1.1 (or equal)	5 mm iplus 1.1 (or equal)
Cavity	15 mm argon 90%	13 mm air	13 mm argon
Inner pane	6 mm Stratobel laminated 33.1: 3 mm iplus 1.1. pos.2 / 0.38 mm PVB clear / 3 mm Planibel Clearlite	11 mm laminated EC glass	5 mm iplus 1.1 (or equal)

Figure 1. West façade of the experimental room with EC triple glass IGUs (left) and of the control room with standard triple glass IGUs (right). In the operable window, six of the small panes faced material leakage issues resulting from the lamination process due to improper sealing and could not be used.

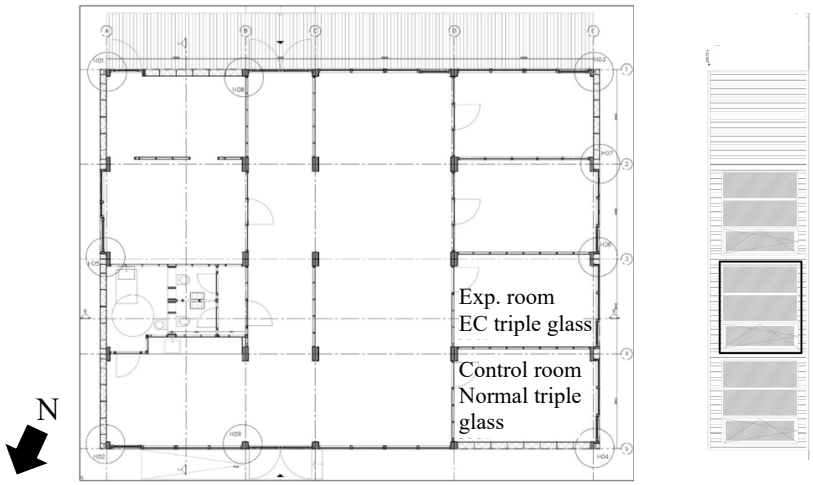

Figure 2. Floor plan and West façade of the OfficeLab. The windows highlighted contain the EC glass IGUs.

2.2. Test rooms set-up

The test building is a lightweight single-storey office building with a timber frame construction. Two similar meeting rooms, with a floor area of 17 m² each, at the western façade are part of the experimental setup: one control room where the original triple glazing is maintained and one experimental room where the original glazing is replaced with the prototype EC glazing (Figure 2). The two rooms have equal window areas with two fixed windows and one operable window.

2.3. Local heating and cooling units

To assess the heating and cooling demand, dedicated local heating / cooling units (portable air conditioner Whirlpool PACW212HP) were placed inside the two rooms and set to the same set-point temperatures (25ºC in cooling mode and 21ºC in heating mode, with a dead band of 1 ºC on both sides, from 3 am till 6 pm). Each unit was connected to a thermostat which was mounted on a wall. The electricity use of the heating / cooling units was measured with SXD10/5 0-10 ampere clip-on CTs attached to the electricity cable of each device and connected to an Eltek GD40A transmitter. The COP for heating was 2.8 and the EER for cooling 2.6.

2.4. Hourly heat balance corrections

The difference between the cumulative heating or cooling output of the local heating / cooling unit inside the two rooms provides an indication of the energy saving potential of the EC glass. However, differences between the two rooms (occupancy, ventilation rates, opening of doors and windows, electric lighting use, infiltration rate, and heat losses in general) will occur. To correct for these effects, a heat balance model was set up for each room for each hour of the full measurement period. This model was fed with data from environmental sensors, the outlook calendar of the rooms and the properties of all surrounding materials. It includes heat transmission through the floor, the roof, the opaque façade, the glass, and the partition walls; infiltration; heat transfer through mechanical ventilation; heat transfer through natural ventilation when the window was open (BLAST model); ventilative heat transfer to the main office when the door was open (stack model); internal heat gains from people, equipment, and lighting; solar heat gains through the glass. The energy use of the air-con unit in the two rooms was then compared and corrected for differences in the heat balance which were not a result of the glass, for every hour of the measurement period. This enabled us to correct for the different position of the rooms (corner versus centred) and differences in use. Also, pyranometers mounted behind the glass of each room ensured that the real solar gains were used in the analysis.

2.5. Sensors and data acquisition system

The meeting rooms and the offices next to them were equipped with multiple sensors to measure environmental variables. The actual monitoring campaign took place from Aug. 15, 2023 till March 31, 2024. Because the OfficeLab was undergoing construction works from April 2024 till Oct./Nov. 2024 the sensors had to be removed. Table 2 provides an overview of the installed sensors. All Eltek transmitters transmitted their data to an Eltek Squirrel RX250 receiver.

Table 2. Overview of installed sensors and transmitters.

Measured property	Sensor	Transmitter	Position
Direct solar transmission through glass	Thies GSM 10.7 pyranometers	Eltek GenII GS-44	behind the glass at 1.1 m above the floor (same height as outdoor one)
Outdoor solar radiation	Thies GSM 10.7 pyranometer	Eltek GenII GS-44	in front of the façade, outdoors, at a height of 1.4 m above the ground
Outdoor weather	Vaisala WXT536D	Eltek TMET	in front of façade at 1.5 m height
Indoor temp. and RH	Eltek GC-10 T and RH sensors and transmitters		at a height of around 1.5 m
Amount and temp. of mechanical air supply	E+E576 air flow sensors thermocouples type T	Eltek GS41AV and GS24 transmitters	inside the supply ducts
Window and door states (open/closed)	magnetic contact sensors	Eltek GenII GC60 transmitters	On openable windows and doors. The doors had automatic closers.
EC glass IGU surface temperature	thermocouples type T	GS24 transmitter	On indoor and outdoor glass surface at a height of approx. 1 m
EC glass IGU heat flux	Hukseflux HFP01	GS44HD transmitter	Same as above

The use of the electric lighting could not be monitored. Lighting use was estimated based on occupancy of the rooms (only then the lights were switched on in reality) and the installed power (65.6 W). The heat gains by equipment were considered small compared to the heat gains by people and lighting and were estimated from the number of people present, assuming 50% of the people brings a laptop with them. Since not everything could be monitored for practical reasons or because of privacy concerns, the following were estimated from the Outlook calendars of the meeting rooms: the time and duration of meetings in the meeting rooms and the number of people present; the time and duration when the flexible partition wall between the two meeting rooms was open.

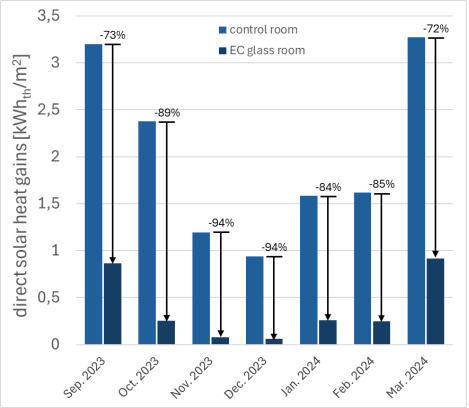

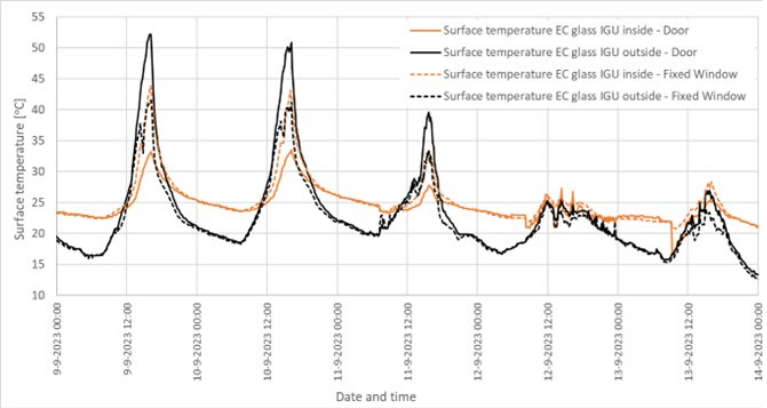

Figure 3 (left). Direct solar heat gains into the EC glass room and control room from Sept. 2023 - March 2024.
Figure 4 (right). Inside and outside surface temperature of the EC glass IGU installed in the middle window (EC coating on glass pane closest to the indoor environment) and in the door (EC coating on glass pane closest to the outdoor environment), for five selected days in September 2023.

3. RESULTS AND DISCUSSION

3.1. Incoming solar radiation and surface temperatures

The direct solar heat gains for the months Sept. 2023 till March 2024 are presented in Figure 3. These results are based on the output of the indoor pyranometers behind the glass and normalised by the floor area of the room. The direct solar gains through the EC glass IGU are much smaller than through the standard IGU. On average, this difference is 81%, with monthly variations from 72-94%. This means that t_{sol} of the EC glass IGU is much smaller than of the standard IGU. However, this does not reflect the difference in total solar heat gains, for which also the indirect component due to absorption and re-emission of heat by the EC coating needs to be considered.
Therefore also the indoor and outdoor surface temperature of the EC glass IGUs were monitored. Figure 4 shows five selected days in September 2023. These measurements show that the absorptive EC coating heats up when exposed to direct solar radiation. During the entire measurement campaign, for the IGU with the EC coating integrated into the glass pane closest to the indoor environment, a peak indoor surface temperature of 49.1 ºC and a peak outdoor surface temperature of 45.7 ºC were measured, but not at the same time. For the IGU with the coating integrated into the glass pane closest to the outdoor environment, a peak indoor surface temperature of 33.5 ºC and a peak outdoor surface temperature of 55.7 ºC were measured, also not at the same time. These high temperatures were recorded when the glass was in tinted state. As a result, the indirect solar gains can be high and, even though the direct solar transmission may be limited, the overall solar heat gain coefficient can still be high.

3.2. Effect of EC glass on heating demand

The months January till March 2024 gave the most reliable data regarding the energy demand for heating. In December 2023, a better air temperature control algorithm was implemented. During these months the heating setpoints were working properly and the average air temperature in both rooms was close to identical, except for January (Figure 6). The heating demand of the room with the EC glass IGU was higher than of the corrected one of the room with the standard IGU, even though the U-value of both were identical. On average, the energy demand for heating in the experimental room was 34% higher than in the control room, with monthly variations from 4-65% (Figure 5). Besides, simulations in the software DesignBuilder v.7 were performed with a calibrated model of the test building and the exact same set-up of the experiment. These simulations showed for a full heating season that the EC glass IGUs increased the heating demand by 12% as compared to the original IGUs, assuming that in winter the glass was in clear state. The main reason for the increased heating demand is that the g-value of the EC glass IGU was lower than of a standard IGU. This reduces the solar heat gains in winter. This effect is stronger than the effect of the heating up of the absorptive layer. Besides, the smaller size EC panels with sealant seals in-between them reduced the 'transparent' area of the glass. The seams covered close to 10% of the glass. The impact of this on the U-value was small because they only appear in the innermost glass pane of the triple glass. However, they did reduce somewhat the direct solar gains.

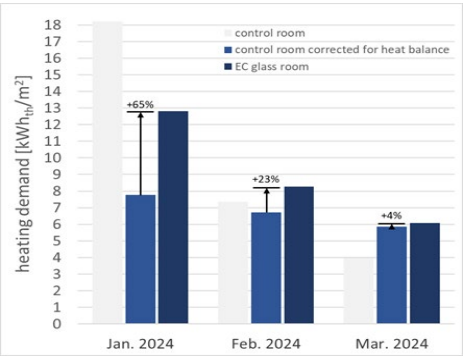

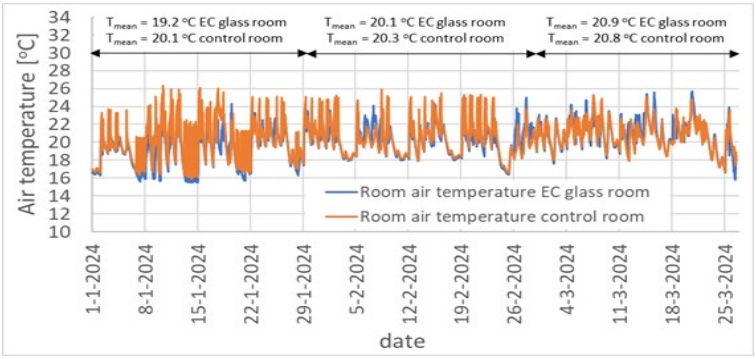

Figure 5 (left). Measured heating demand of the experimental and control room for January till March 2024.
Figure 6 (right). Measured air temperature in the experimental and control room from January till March 2024.

3.3. Effect of EC glass on cooling demand

Unfortunately, no proper monitoring was possible for the summer months because the prototype of the EC glass IGU was only operational from September 2023 onwards and during spring and summer 2024 the test building was undergoing construction works. Luckily, September 2023 had summer-like conditions (av. monthly max. temp. of 23.1ºC). During that month, the cooling demand of the experimental room was similar to that of the control room (Figure 7). A difference of 3% was observed but the absolute value of this difference falls within the measurement uncertainties. Simulations with the calibrated model in DesignBuilder showed that for a full cooling season the EC glass IGUs decreased the energy demand for cooling by 9% as compared to the original IGUs without active sun-shading, and increased the cooling demand by 44% as compared to the original IGUs with active dark outdoor roller blinds (active if solar radiation on façade >125 W/m^2). These results are in line with other studies, albeit slightly lower. For instance, Chambers et al. (2019) found that EC glass could lead to a reduction of 11% in the cooling and lighting demand in Swiss office buildings. Krarti (2022) concluded that EC glass with optimal switching control could lead to an energy reduction of up to 20% for office buildings relative to static glazing. A point of attention in our study are the smaller than full size EC panes and the

resulting sealant seals between the panes. The impact on the cooling demand is difficult to assess because the direct solar transmittance and the temperature of these seams were not measured.

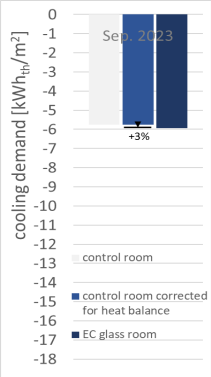

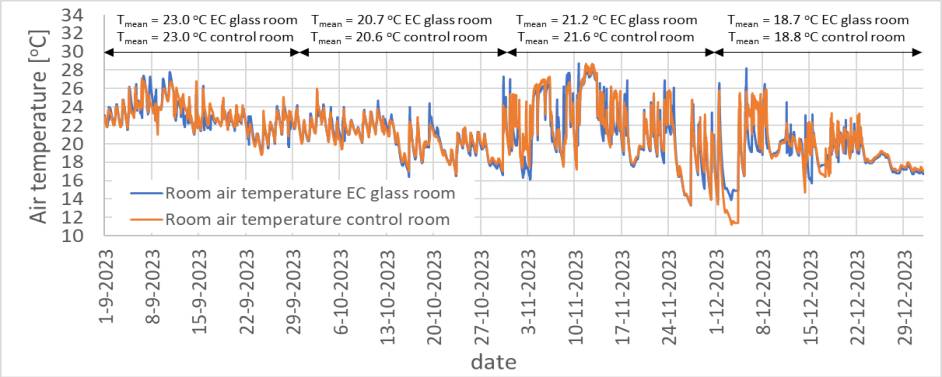

Figure 7 (left). Measured cooling demand of the experimental and control room for September 2023.
Figure 8 (right). Measured air temperature in the experimental and control room from Sept. till Dec. 2023.

4. THERMAL AND VISUAL COMFORT

Besides the extensive monitoring and simulation campaign, an experiment was done as a repeated measures "within subject" study with a total of 38 participants. The participants were spending in total two hours in the two rooms, i.e., the control and the experimental room. They were exposed to different conditions in random order and were working on a reading task. During the first 30 minutes, the EC glass was in clear state in the experimental room or the roller blinds were up in the control room, without sun in the field of view. Then the glazing was tinted or the blinds were lowered for another 30 minutes with the sun in the field of view. Then the glass was bleached and the blinds raised for another 30 minutes. At the end of each 30-minute session, the participants were asked to complete a questionnaire on their perceptions of the visual and thermal environment. The experiment showed that in general in dark state (EC glass tinted or blinds down), satisfaction with view clarity, daylight colour and daylight availability was higher for the EC glass IGUs (Figure 9). In transparent state (EC glass clear or blinds raised), no significant difference was perceived, except for view clarity. Overall, the EC glazing was perceived by the participants as a good alternative to dark roller blinds. More details can be found in Luna-Navarro et al. (2024).

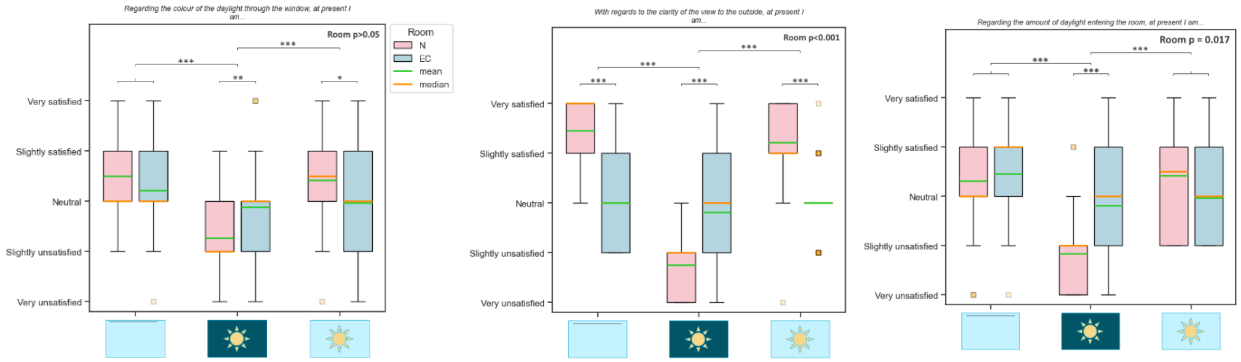

Figure 9. Results from the assessment of the user satisfaction with the visual environment. **left:** satisfaction with the daylight colour in the room; **centre:** satisfaction with view clarity; **right:** satisfaction with the amount of daylight in the room. The level of significance is: * = p-value < 0.05; ** = p-value < 0.01; *** = p-value < 0.001.

5. CONCLUSION

This paper presented some of the results of the Windows to the Future project, a project on the application of low-cost inkjet-printed electrochromic (EC) glazing and focussed on the results of the monitoring campaign. Prototype EC triple glass IGUs were installed in the west façade of a meeting room and the heating and cooling demand of this room were compared to that of a control room with standard triple glass IGUs. The results showed that the EC glass IGUs led to a higher energy demand for heating in winter. This is mainly due to lower solar heat gains through the EC glass. Under summer-like conditions, the energy performance of the EC glass IGUs was found similar to that of the standard IGUs. Even though the EC glass IGUs had much lower direct solar gains, the heating up of the absorptive coating resulted still in high (indirect) solar gains. A key point to mention here is that the EC coating in the triple glass IGUs was placed on the glass pane closest to the indoor environment. For better performance in summer, this coating should be placed on the glass pane closest to the outdoor environment. Besides, a larger dynamic range (especially towards the upper range, i.e. higher transparency) would improve the glass's performance under winter conditions. Also, a controlled experiment with participants showed that in general in dark state, satisfaction with view clarity, daylight colour and daylight availability was higher for the EC glass IGUs. In transparent state, no significant difference was perceived, except for view clarity. Overall, the EC glazing was perceived by the participants as a good alternative to dark roller blinds. Furthermore, future research should increase the length of the monitoring campaign, and test different room orientations and control strategies for the switching of the EC glass, as these were limitations of this study.

ACKNOWLEDGEMENTS

This study was made possible with the support of RVO within the TKI Urban Energy Program (TEUE219006). The authors are also thankful to Si-X for the glass integration and installation.

REFERENCES

Chambers, J., Hollmuller, P., Bouvard, O., Schueler, A., Scartezzini, J.-L., Azar, E., Patel, M. K., 2019. Evaluating the electricity saving potential of electrochromic glazing for cooling and lighting at the scale of the Swiss non-residential national building stock using a Monte Carlo model. Energy 185, 136–147.

Chiucchiu, A., Misuraca, I., Brembilla, E., Pigliautile, I., Tenpierik, M., Pisello, A.L., de la Barra Luegmayer, P.P., Luna-Navarro, A., 2024. Combined Effect of Hot Thermal Conditions and Daylight Transmitted Through Blue Coloured Window Glazing on Human Visual and Thermal Response, In: Proceedings of the conference Comfort at the Extremes 2024, Fundación Visible/ Universidad de Seville/ IUACC/ nceub/ EDIAQI, Seville, Nov. 20-22.

Fernandes, L.L., Lee, E.S., Ward, G.J., 2013. Lighting energy savings potential of split-pane electrochromic windows controlled for daylighting with visual comfort. Energy and Buildings 61, 8–20.

Kelly Waskett, R.. Retrofit Electrochromic Glazing: A longitudinal case study of occupant experience, Ph.D. Thesis, De Montfort University, 2016.

Klems, J.H., 2001. Net energy performance measurements on electrochr. skylights. Energy and Buildings 33, 93–102.

Krarti, M., 2022. Energy performance of control strategies for smart glazed windows applied to office buildings. Journal of Building Engineering 45, 103462.

Kwee, P., Modelling of potential energy savings of solar powered smart windows, M.Sc. Thesis. Delft University of Technology, 2020.

Lee, E.S., Selkowitz, S., Clear, R.D., DiBartolomeo, D.L., Klems, J.H., Fernandes, L.L., Ward, G.J., Inkarojrit, V., Yaxdanian, M., Advancement of Electrochromic Windows. In California Energy Commission, PIER. (Issue Publication number CEC-500-2006-052.), 2006.

Li, Y., Shah, K.W., Li, W., Xiong, T., 2023. Exp. investigation on indoor thermal environment improvement and energy-saving of electrochr. window under Singapore's tropical climate. Journal of Build. Eng. 73(May), 106779.

Luna-Navarro, A., Verbeek, R., Brembilla, E., Huijbregts, Z., Konstantinou, T., Tenpierik, M.J., 2024. User assessment of low-cost inkjet-printed electrochromic glazing, In: Proceedings of the 9th International Building Physics Conference, Toronto Metropolitan University, Toronto, July 25-27.

Papaefthimiou, S., Syrrakou, E., Yianoulis, P., 2006. Energy performance assessment of an electrochromic window. Thin Solid Films 502(1–2), 257–264.

6th International Conference on Building Energy and Environment
Eindhoven University of Technology, The Netherlands
6 - 10 July 2025

Real-Time In-Situ Instrumentation for Multicriteria Building Performance Assessment: New Research Facility Development

Ghizlane El Mahiba [1,2*], Loubna Ait Lahsen [1], Myriam Bahrar [1], Adeline Mélois [3], Imad EL Harraki [2], Mohamed El Mankibi [1]

[1]*Univ Lyon, ENTPE, Ecole Centrale de Lyon, CNRS, LTDS, UMR5513, 69518 Vaulx-en-Velin, France*
[2]*LMAID laboratory, Rabat National School of Mines, Mohamed V University, 10070 Rabat, Morocco*
[3]*CEREMA BPE Research Team, 46, rue Saint Théobald, 38080, L'Isle d'Abeau, France*
**Corresponding author mail: ghizlane.elmahiba@entpe.fr*

SUMMARY
In-situ building performance assessment is a main approach for delivering reliable insights into building operations and hindering environmental phenomena. This paper presents a detailed description of Villa SOBRE, a new full-scale research facility designed upon an existing building for multicriteria in-situ building performance assessments. The facility transformation involved envelope upgrades, advanced systems integration, and real-time monitoring. Over 100 sensors have been implemented to measure indoor and outdoor thermal performance, indoor air quality (IAQ), and energy performance and consumption, providing the building with comprehensive environmental data. Further, controlling mechanical ventilation, heating systems, and glazing alongside real occupancy in-situ simulation promotes building operation dynamics studies. The facility transformation features a new double-skin ventilated facade, advancing natural and hybrid ventilation studies, and inter-room slots for pollutant transport and air filtration research. Through adopting a frugal approach and combining a flexible design with fine instrumentation, the Villa SOBRE facility will provide insights into building multicriteria in-situ assessments, supporting future studies in sustainable new buildings and retrofits.

Keywords: Energy Retrofits, In-Situ Assessment, Building Operation.

1. INTRODUCTION

1.1 Context

Building retrofits have shown a significant capability in upgrading existing buildings' energy performance, accounting for 75% of Europe's building stock, with over 50 % built between 1970 and 1990 (Poel et al. 2007; European Comission 2024). Research within this field extends merely to energy consumption reduction and carbon footprint mitigation toward more comprehensive strategies that promote indoor environmental quality (IEQ), occupants' safety and well-being flexibility, and cost-effectiveness (HEART Project 2020; Pohoryles et al. 2020; Al Dakheel et al. 2024). Building operation assessment is required to prove the implemented strategies. The assessment is often conducted through building modeling or in situ measurement campaigns. However, extensive research has identified a performance gap between simulated and measured data, showing that modeling failed to represent the building's real operation. To foster confidence in numerical models, thorough calibration must be performed to minimize discrepancies in the modeling environment and strengthen its predictive capability (Cuerda et al. 2020; Vivian et al. 2023; Chiesa et al. 2025).On the other hand, in-situ measurement campaigns may be a better method for real performance evaluation, given that they provide direct empirical data accounting for the complexity of environmental conditions. Therefore, in-situ measurements remain crucial, despite ongoing advancements in the modeling techniques. Dedicated testing facilities were

established to enhance the flexibility of in-situ measurement campaigns. These facilities are classified based on their scale and exposure to outdoor conditions, ranging from full-scale test cells and buildings to controlled climate chambers (Berardi 2023). Several studies highlighted these facilities‘ potential and growing interest in real performance evaluation (Ascione et al. 2019; Pisello et al. 2021; Freppel et al. 2022).

1.2 Objectives

Considering the same interest, this paper introduces a new full-scale research facility, designed for building performance multicriteria in-situ assessments. This facility is mainly characterized by the integration of existing building characteristics and the exposure to real outdoor conditions. It will provide real-time monitoring of different performance metrics for building operations through a finely instrumented and flexible testing environment. The transformation process defined in the subsequent sections should enable a range of features, such as:

1) Real-time monitoring of both indoor and outdoor parameters, further the control of glazing, artificial lighting, heating set points, and ventilation rates.
2) Assimilation of different HVAC technologies for comparative analysis and demand-responsive control.
3) Advanced studies on pollutant transport and indoor air quality using inter-room slots and pollutant generators.
4) Experiment with hybrid, active, or natural ventilation strategies, using Double Skin Ventilated Facade and integrated systems.
5) Real occupancy through manual operation, or occupancy behavior modelling through systems control, pollutant generation, carbon dioxide, and humidity injection.

2. VILLA SOBRE AS AN EXISTING BUILDING

2.1 Location and Climate

Villa SOBRE is located on the National School of Public Works (ENTPE) campus in Vaulx-en-Velin, a suburb of Lyon, France (45.46°N,4.55°E), presented in Fig.1.Lyon lies between the Rhône and Saône rivers, influencing its microclimate. It falls within the Cfa/Cfb Köppen-Geiger climate zones and is classified as H1 (northeast) under French building regulation ,which features a temperate climate with warm summers and long, humid winters (Dubreuil 2022; Strohmenger et al. 2024).

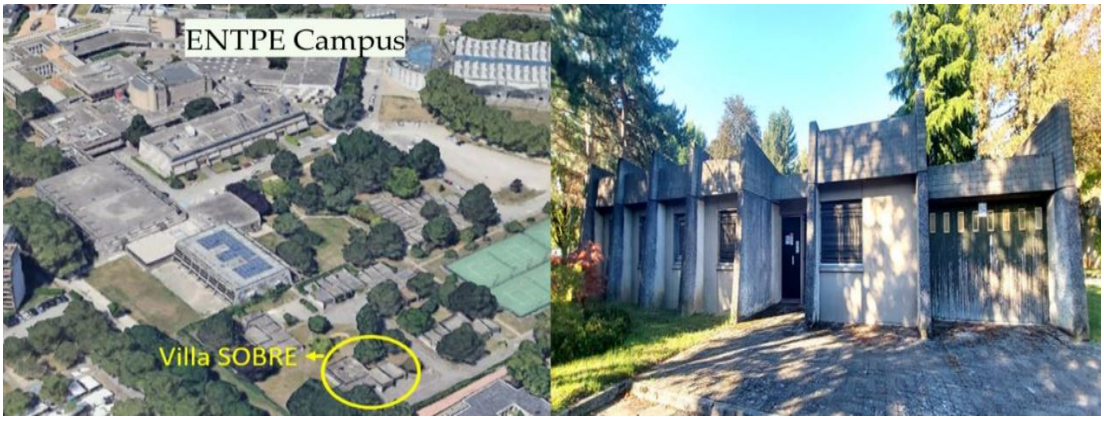

Figure 1. Villa SOBRE location in ENTPE Campus, Vaulx-en-Velin, France

Lyon's historical meteorological data exhibit significant daily thermal fluctuations. The prevailing wind has an azimuth of 340° (-20° from the north), with a monthly average speed of 1- 6 m/s. During the cooling season, temperatures range from 16°C to 27°C, peaking at 36°C with a relative humidity of around 65-70%. Winter temperatures range from 1 to 7°C, dropping extremely to around -7°C. The heating season is characterized by strong wind speeds reaching 17 m/s, and low temperatures with high humidity levels ranging from 76% to 90%, which can lead to significant discomfort and health issues in buildings.

2.2 Building Design & Characteristics

Built in the 1970s as a residential building, Villa SOBRE operated as an experimental site for the Sustainable Construction Research Team at LTDS ENTPE over the past two decades. A 90 m² area, featuring three exposed facades, has been turned into the test facility. The facade walls, partitions, ceiling, and roof are primarily composed of Machefer Concrete, a lightweight material widely used in the 1970s, particularly in the Rhône region. This concrete is composed of metallurgical incineration in various aggregate sizes, combined with lime or cement. (Sadineni et al. 2011; Carnus 2018). The existing doors are wooden, and the windows feature single glazing with metallic frames, each measuring 2.20 m × 1.23 m with a total surface of 2.706 m².

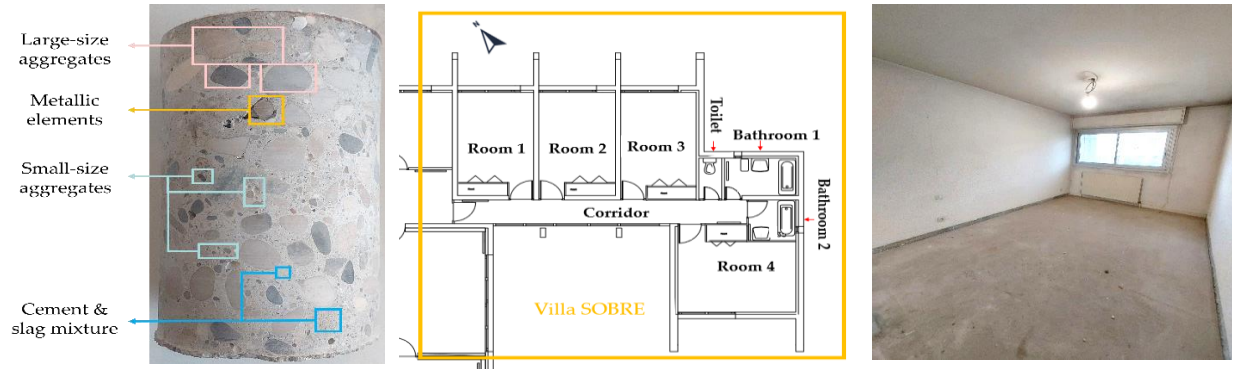

Figure 2. Villa-SOBRE before retrofit: Facade walls sample (**left**), plan view (**middle)**, and indoor rooms (**right**)

2.3 Choice of Retrofit Measures and Systems

The transformation aims to establish a novel experimental research facility that showcases high-performance buildings, applicable to both new constructions and energy retrofitted structures. An initial energy diagnosis using infrared thermography revealed thermal bridges throughout the rooms, localized dampness, cracks, particularly in partition walls, and significant heat loss through window frames. In parallel, the growing interest in multicriteria studies has sparked the importance of IAQ, prompting the design of solutions that control pollutant transfer between spaces and improve the airtightness of the facility components. To address these issues and meet performance objectives, the following measures were considered:

1) Insulation of the facade, ceiling, and floor to enhance the building envelope
2) Upgrading the window systems to reduce thermal losses
3) Improving airtightness, notably through insulated partition walls and airtight doors to enable pollutant transfer studies
4) Adoption of an energy-efficient heating system
5) Integration of a natural ventilation system to explore natural and hybrid ventilation scenarios

2.4 Choice of Sensors

The decision on sensors was guided by the need to gather critical data across multiple performance aspects in the different spaces of the building. The covered metrics are related to the occupant's

thermal comfort perception, indoor air quality, and other operation strategies. Furthermore, accurate boundary condition data were needed for a thorough calibration of building numerical models. Finally, outdoor sensors, comprising the ones measuring meteorological and air quality parameters, were selected to identify the external environmental impact.

2.5 Choice of Strategies

In the absence of occupants, in-situ modelling of occupancy behavior is significant for realistic operation scenarios. This includes opening control, presence patterns, and interactions with building systems such as heating and mechanical ventilation. To replicate real-world scenarios, control strategies were implemented to mimic how occupants typically operate these systems. Moreover, simulated presence needed to account for internal emissions generated by typical occupant activities. Therefore, the integration of emission sources within the building systems was critical to accurately reflect occupant influence on indoor conditions.

3. RESULTS

3.1 Villa SOBRE Envelope after Retrofit

During retrofit, the interior layout was reconfigured, reducing the number of zones from eight to six for space optimization. The new layout features three identical rooms, facing northeast (10.71 m², 25.91 m³ each), a fourth room facing southwest (13.5 m², 32.63 m³), a monitoring room, and a 7.3-meter ventilated façade along the corridor. Structured insulated panels (SIPs) were installed on all indoor walls, floors, and ceilings. SIPs used are a polyurethane core panel sandwiched between two metallic layers. They have been mainly chosen for their high thermal and acoustic insulation, moisture resistance, and specifically for their ease of assembly.(Demharter, 1998;Sadineni et al., 2011;Somarathna et al., 2018).Fig.3 presents Villa SOBRE' 3D view after retrofits and the SIPs application. While the external façades remained unchanged to preserve the original structure, the window area was reduced by approximately 62% through the installation of NF220-certified double-glazed windows, ensuring high standards of thermal and acoustic insulation, air and water tightness, and wind resistance(CSTB 2021). Tables 1 and 2, respectively, list the thermophysical properties of the new walls and the characteristics of the new windows.

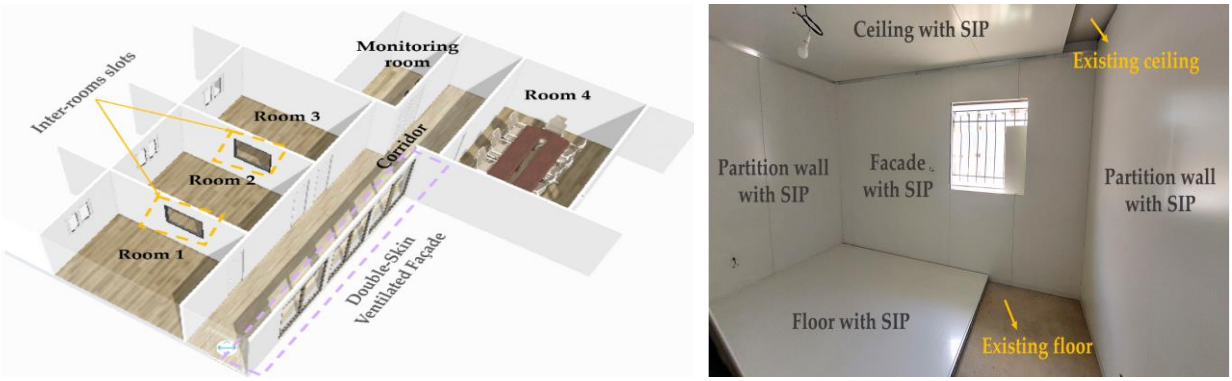

Figure 3. After retrofit 3D design' view (**left**) and the SIPs application on existing walls (**right**)

Table 1. Exterior and partition walls material configuration

	Configuration	Thickness [m]	Thermal conductivity $[W.m^{-1}.K^{-1}]$	Specific heat $[J.kg^{-1}.K^{-1}]$	Density $[kg.m^{-3}]$
Exterior walls	Render (outdoor)	0.01	1	750	800
	Machefer Concrete	0.2	~0.12	~850	~850
	Red brick	0.1	0.83	800	1500

	Plaster (Indoor)	0.01	0.35	1000	1500
	Air gap	0.15	0.02	1005	1.204
	Polyurethane panel	0.08	0.02	800	100
Partition walls	Plaster (Indoor)	0.01	1	750	800
	Machefer Concrete	0.2	~0.12	~850	~850
	Plaster (Indoor)	0.01	0.35	1000	1500
	Polyurethane panel	0.08	0.02	800	100
	Plaster (Indoor)	0.01	1	750	800

Table 2. New windows characteristics

Element	Dimension	Characteristics	Solar transmittance (at 90°) g-value	U value $[\mathbf{W.m^{-2}K^{-1}}]$	Filling gas
Double glazing	1.05 m × 0.98 m; Wsurface= 1.029 m²	4mm-16mm-4mm	0.79	1.2	Argon

For enhanced insulation and airtightness, room doors were replaced with SIP-based cold chamber doors featuring PVC frames and sealing gaskets. Airtightness measures included triple sealing, using polyurethane foam, metallic joint mastic, and gasketed corners to limit air leakage, thermal bridging, noise, and moisture transfer. Additionally, airtight electrical junction boxes were also installed to prevent leakage through the joints.

3.2 Implemented Systems and Strategies

Glazing control is managed by motorized systems: electric chain motors operate the room windows, while a rack-and-pinion motor adjusts the glazed area of the double-skin ventilated facade. Each room is heated by a 2000 W convector regulated through a closed-loop automation system, allowing dynamic power modulation from 0% to 100% to maintain thermal comfort. Fig.4 presents the implemented systems and strategies.

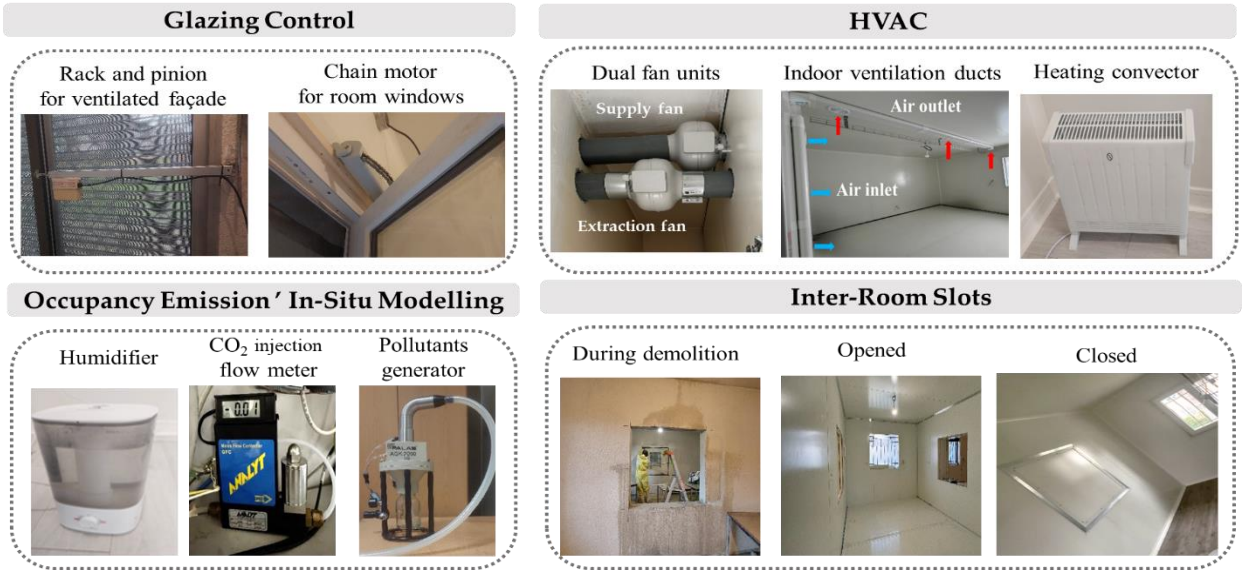

Figure 4. Implemented systems and strategies in Villa SOBRE

Mechanical ventilation relies on two Aldes VC MICRO WATT D125 fans per room (144 m³/h each), one supplying fresh air vertically and the other extracting stale air through top ducts, enabling single or double mechanical ventilation modes. Real occupancy is modeled in-situ, using humidifiers, CO_2 pumps, and flow meters for each room, humidifiers for humidity injection, and an AGK-2000 aerosol generator (5 nm–15 µm) to generate typical airborne pollutants of real

occupant activity, such as VOCs and PMs. Partition walls are modified to include configurable 1m×1m slots designed for experiments on thermal exchange, pollutant transport, and air filtration systems. For natural ventilation integration and investigation of hybrid ventilation strategies, a 7.3m × 2.3m double-skin ventilated facade was implemented in the corridor using SIPs as a second skin with adjusted top and bottom grilles. The double skin ventilated facade is presented in Fig.5.

Figure 5. Double skin ventilated facade (ongoing work)

3.3 Installed Sensors and Data Acquisition

Villa SOBRE has been finely instrumented with over 100 sensors, enabling comprehensive, real-time monitoring for multicriteria assessment of building performance. The monitoring system is categorized into four primary aspects: thermal performance, airflow and ventilation, indoor air quality, and energy use. The sensor's spatial arrangement within rooms is shown on Fig.6. and their specifications are detailed in Table 3.

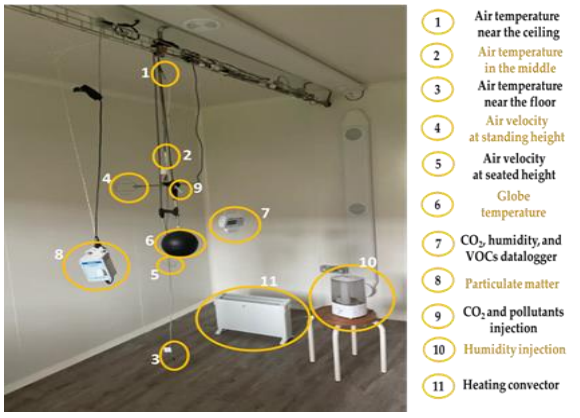

Figure 6. Implemented sensors and systems in rooms

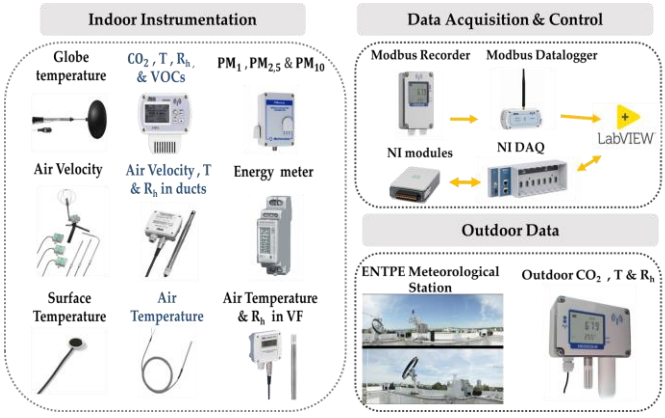

Figure 7. Installed indoor & outdoor sensors, and the data acquisition principle

For thermal monitoring, 33 surface temperature sensors are installed behind SIPs to characterize envelope boundary conditions, along with 4 heat flux sensors to evaluate thermal transmission. Airflow and ventilation are assessed through 14 wind velocity sensors positioned at seated and standing heights within rooms and behind the ventilated facade, 8 duct transmitters measuring air speed, humidity, and temperature to manage ventilation units, and 6 temperature and humidity transmitters for airflow monitoring in the ventilated facade. IAQ monitoring includes 5 particulate matter sensors measuring PM_1, $PM_{2.5}$, and PM_{10}, and 7 wireless data loggers that record humidity, CO_2, and VOC concentrations across the four rooms and central corridor. An outdoor sensor placed at building height measures ambient CO_2, humidity, and temperature, while meteorological

data such as wind speed and direction, and solar irradiation are recorded via the ENTPE weather station. Data acquisition is wireless via MODBUS recorders for giving the possibility of displacing the indoor sensors, except for fixed surface temperature sensors, which are wired through DAQ modules. A custom LabVIEW-based program with a user-friendly interface enables sensor communication, real-time data acquisition, and implementation of control strategies, such as heating setpoint adjustment, glazing opening percentage, and mechanical and occupancy emissions quantification.

Table 3. Characteristics of sensors installed in Villa SOBRE

Sensor type	Parameter	Measurement range	Accuracy
Probe RTD PT100 (SFCAR4F-P12)	Air temperature	-40 to +105 °C	±0.35°C at 100°C
Surface RTD PT100 (SF4F-6-50-P10)	Surface temperature	-40 to +105 °C	±0.35°C at 100°C
Black globe+ RTD PT100 probe (TP875.1.l)	Globe temperature	-30 to +120 °C	±0.1 °C at 0 °C ±0.2 °C at -50 °C ≤ t ≤ 250°C
Active hot wire air speed transmitter (HD403TS2)	Air velocity	0.1 to 5 m/s	± (0.2 m/s +3 % f.s.)
Active air speed transmitter for ducts (HD29371TO1)	Air temperature Air velocity Relative humidity	-10 to +60 °C 0 to 20m/s 0 to 100 % RH	± (0.7 m/s+3% f.s) ± (0.7 m/s+3% f.s) ± (1.5+1.5% f.s)
Dew point transmitter (HD35EDLWH.E)	Dew point temperature Relative humidity Temperature	-20 to +80°C 0 to 100 % RH -40 to+150°C	±0.3°C ±1.5% (0 to 90% RH), ±0.3°C
Wireless data logger (HD35EDG1NBV.E)	Air temperature Dew point temperature Wet bulb temperature Relative humidity Absolute humidity Differential pressure Carbone dioxyde concentration Volatiles compounds concentration	-40 to +105 °C -40 to +105 °C -40 to +105 °C 0 to 100 % RH - ±2000 hPa 0 to 5000 ppm 0 to 500 index	± 0.2 °C (0 to +60 °C) ± (0.2 – 0.05 * T °C) (-40 to 0 °C) - - ±2.5% (0 to 85% RH), ± 3.5% (85 to 100% RH) - ± 1% f.s ± (50 ppm + 3% f.s) -
Particulate matter transmitter-laser diffusion (HD35EDWPM)	PM_1, $PM_{2.5}$, PM_{10} concentration	0 to 1000 µg/m^3 Size 0.3 to 10 µm	-
Wireless Outdoor air quality Datalogger (HD35EDLW1NBTV)	Carbone dioxide Relative humidity Air temperature	0 to 5000 ppm 0 to 100 % RH -40 to+150°C	±(50 ppm+3% f.s) ± 2 %RH ± 0.3 °C (0 to +70 °C)
Energy meter (COUNTIS E03)	Systems electricity consumption		-

6. CONCLUSION & FUTURE WORK

Villa SOBRE (Optimization Systems for Energy Renovated Buildings) is a full-scale facility

devoted to studying buildings' real performance during operation, evaluating advanced integrated systems, analyzing occupant-centric conditions, and developing new approaches for in-situ multicriteria assessment. Its originality lies mainly in the frugal approach adopted for design solutions and flexible design. Moreover, its multizone configuration and structure that showcase the real performance and climatic context of European and French existing building stock. The facility is also designed to remain adaptable for future upgrades and the integration of emerging technologies.

The next phase of work at Villa SOBRE will involve a diagnostic campaign to verify the intended performance outcomes of implemented retrofit measures. This includes infrared thermography, airtightness testing of Villa SOBRE spaces according to ISO 9972, and airtightness evaluation of ventilation ducts following applicable standards. In addition, newly developed HVAC systems from industry partners will be integrated for performance testing and comparative studies. Future developments also anticipate the incorporation of renewable energy systems for approaching Nearly Zero Energy Buildings for energy flexibility research.

REFERENCES

Al Dakheel J, Del Pero C, Leonforte F, et al (2024) Assessing the performance of smart buildings and smart retrofit interventions through key performance indicators: Defining minimum performance thresholds. Energy and Buildings 325:114988.

Ascione F, Borrelli M, De Masi RF, et al (2019) A framework for NZEB design in Mediterranean climate: Design, building and set-up monitoring of a lab-small villa. Solar Energy 184:11–29.

Berardi U (2023) The BeTOP facility for performance testing of building systems. E3S Web of Conf 396:03030.

Carnus B (2018) Machefer de construction : Essais en laboratoire,Cerema Centre-Est

Chiesa G, Pizzuti S, Zinzi M (2025) A new approach to assess the building energy performance gap: Achieving accuracy through field measurements and input data analysis. Journal of Building Engineering 102:111941.

CSTB (2021) NF linked to CSTB certification reference system: PVC and thermal barrier aluminium windows and windows with shutter

Cuerda E, Guerra-Santin O, Sendra JJ, Neila FcoJ (2020) Understanding the performance gap in energy retrofitting: Measured input data for adjusting building simulation models. Energy and Buildings 209:109688.

Demharter A (1998) Polyurethane rigid foam, a proven thermal insulating material for applications between +130°C and −196°C. Cryogenics 38:113–117.

Dubreuil V (2022) Le changement climatique en France illustré par la classification de Köppen. La Météorologie 037.

European Comission D-G for E (2024) In focus: Energy efficient buildings - delivering energy and cost savings for EU citizens. https://energy.ec.europa.eu/news/focus-energy-efficient-buildings-2024-04-16_en. Accessed 7 Feb 2025

Freppel W, Promis G, Tran Le AD, et al (2022) Development of a Novel Experimental Facility to Assess Heating Systems' Behaviour in Buildings. Energies 15:4615.

HEART Project (2020) Holistic Energy and Architectural Retrofit Toolkit | HEART Project | Fact Sheet | H2020. In: CORDIS | European Commission. https://cordis.europa.eu/project/id/768921. Accessed 7 Feb 2025

Pisello AL, Pigliautile I, Andargie M, et al (2021) Test rooms to study human comfort in buildings: A review of controlled experiments and facilities. Renewable and Sustainable Energy Reviews 149:111359.

Poel B, van Cruchten G, Balaras CA (2007) Energy performance assessment of existing dwellings. Energy and Buildings 39:393–403.

Pohoryles DA, Maduta C, Bournas DA, Kouris LA (2020) Energy performance of existing residential buildings in Europe: A novel approach combining energy with seismic retrofitting. Energy and Buildings 223:110024.

Sadineni SB, Madala S, Boehm RF (2011) Passive building energy savings: A review of building envelope components. Renewable and Sustainable Energy Reviews 15:3617–3631.

Somarathna HMCC, Raman SN, Mohotti D, et al (2018) The use of polyurethane for structural and infrastructural engineering applications: A state-of-the-art review. Construction and Building Materials 190:995–1014.

Strohmenger L, Collet L, Andréassian V, et al (2024) Köppen–Geiger climate classification across France based on an ensemble of high-resolution climate projections. Comptes Rendus Géoscience 356:67–82.

Vivian J, Carnieletto L, Cover M, De Carli M (2023) At the roots of the energy performance gap: Analysis of monitored indoor air before and after building retrofits. Building and Environment 246:110914.

6th International Conference on Building Energy and Environment
Eindhoven University of Technology, The Netherlands
6 - 10 July 2025

A Multi-Objective Optimization Algorithm for Building Systems Retrofits

Ali Madadizadeh[1], Kamran Siddiqui[2], Amir A. Aliabadi[1]

[1] *School of Engineering, University of Guelph, Guelph, Ontario, Canada, amadadiz@uoguelph.ca*
[2] *Department of Mechanical and Materials Engineering, Western University, London, Ontario, Canada, ksiddiq@uwo.ca*
[1] *School of Engineering, University of Guelph, Guelph, Ontario, Canada, aaliabad@uoguelph.ca*

ABSTRACT

The building sector accounts for approximately 30-40% of global energy consumption and nearly 40% of Greenhouse Gas (GHG) emissions, making building retrofits essential for achieving significant reductions in energy use and emissions. However, developing effective retrofit strategies requires careful consideration of several critical factors: the economic viability of each retrofit option, local climate, policies, incentives, energy prices, electricity grid emissions intensity, the embodied carbon emissions of materials and processes, and the operational carbon emissions resulting from each retrofit strategy. This study employs a micro-genetic optimization algorithm coupled with the Vertical City Weather Generator (VCWGv1.6.0) urban physics model to identify optimal retrofit strategies for residential buildings in Toronto. The goal is to help homeowners minimize cost, and the associated embodied/operational carbon emissions. The proposed approach offers a framework for sustainable building retrofits that balances energy efficiency, economic viability, and carbon emission reductions simultaneously in the context of evolving policy landscapes.

Keywords: Building Retrofit, Decarbonization, Economics, Micro-Genetic Alborithm (MGA), Optimization.

1. INTRODUCTION

As the global community faces the urgent challenge of mitigating climate change, the building sector has emerged as a critical area for intervention. Buildings are responsible for a significant portion of global Greenhouse Gas (GHG) emissions, both through their operational energy use and the embodied carbon in construction materials. Retrofitting existing building systems presents a unique opportunity to reduce emissions and improve energy efficiency, often at a lower cost and with fewer disruptions compared to new construction. Effective retrofits can address aging infrastructure while incorporating modern, low-carbon technologies that significantly enhance sustainability (Aliabadi et al., 2021; Moradi, 2021; Moradi et al., 2021, 2022; Safdari et al., 2024).

In addition to environmental benefits, cost considerations play a vital role in the adoption of retrofit strategies. The economic viability of retrofit measures is often evaluated through Marginal Cost Analysis (MCA), which compares the cost-effectiveness of various strategies for reducing emissions. Cost-effective retrofitting not only reduces operational and embodied carbon but also en-

hances property values and reduces energy bills, providing a win-win situation for homeowners. Understanding and optimizing these costs is essential to ensure widespread adoption of retrofit solutions (Madadizadeh et al., 2024). Furthermore, a critical aspect of building decarbonization is evaluation of Social Cost of Carbon (SCC) savings achieved through building retrofits. The SCC represents the economic cost of the damages caused by one additional tonne of carbon emissions. By reducing emissions, retrofits contribute to significant SCC savings, which translate into societal benefits.

When considering retrofitting, there are several key aspects to address. The first is carbon emissions savings and the associated environmental benefits, and the second is the cost factor. An effective retrofit strategy should achieve the highest possible emissions savings while minimizing costs or even generating financial returns. To identify the optimal strategy, optimization algorithms are a suitable approach. In particular, Micro-Genetic Algorithm (MGA) is an excellent choice due to its ability to quickly identify quasi-global optimal solutions and their computational efficiency (Aliabadi et al., 2023).

This study investigates the potential of retrofit measures to maximize GHG emissions saving and minimize marginal costs in the residential building sector. Through the application of MGA, we explore optimized retrofit strategies for a typical detached two-storey residential house in Toronto (2020) that balance environmental and economic benefits.

2. METHODOLOGY

2.1. Vertical City Weather Generator (VCWGv1.6.0)

The Vertical City Weather Generator (VCWGv1.6.0) as an urban physics model is used to simulate the performance of residential buildings in Toronto under different retrofit strategies (Fig. 1). VCWGv1.6.0 integrates local weather data, building design parameters, and energy consumption patterns to generate realistic, and high-resolution simulations of building energy use and carbon emissions. The model uses localized climate data for Toronto, accounting for variations in temperature, humidity, wind patterns, and solar radiation over the course of the year 2020. Also, the VCWG model simulates the energy consumption of the building with and without retrofit strategies, considering factors such as thermal insulation, heating and cooling efficiency, and energy consumption patterns. The model calculates both operational carbon (based on energy consumption) and embodied carbon (based on materials used in retrofits) emissions. The total carbon footprint is tracked for each retrofit solution.

2.2. Micro-Genetic Algorithm (MGA)

The Micro-Genetic Algorithm (MGA) is employed to search for optimal retrofit solutions. MGA is a computationally efficient version of traditional genetic algorithms, designed to solve problems involving multiple conflicting objectives. The algorithm operates by evolving a population of potential solutions (5) (representing different retrofit strategies) over a series of generations (5), selecting the best individuals based on the lowest fitness according to the defined objective functions.

The primary goal of this study is to identify retrofit strategies that maximize operational carbon saving ($\mathrm{GHG}_{o,s}$) over $N = 20$ years, embodied carbon emission (GHG_{e}) over $N = 20$ years, and

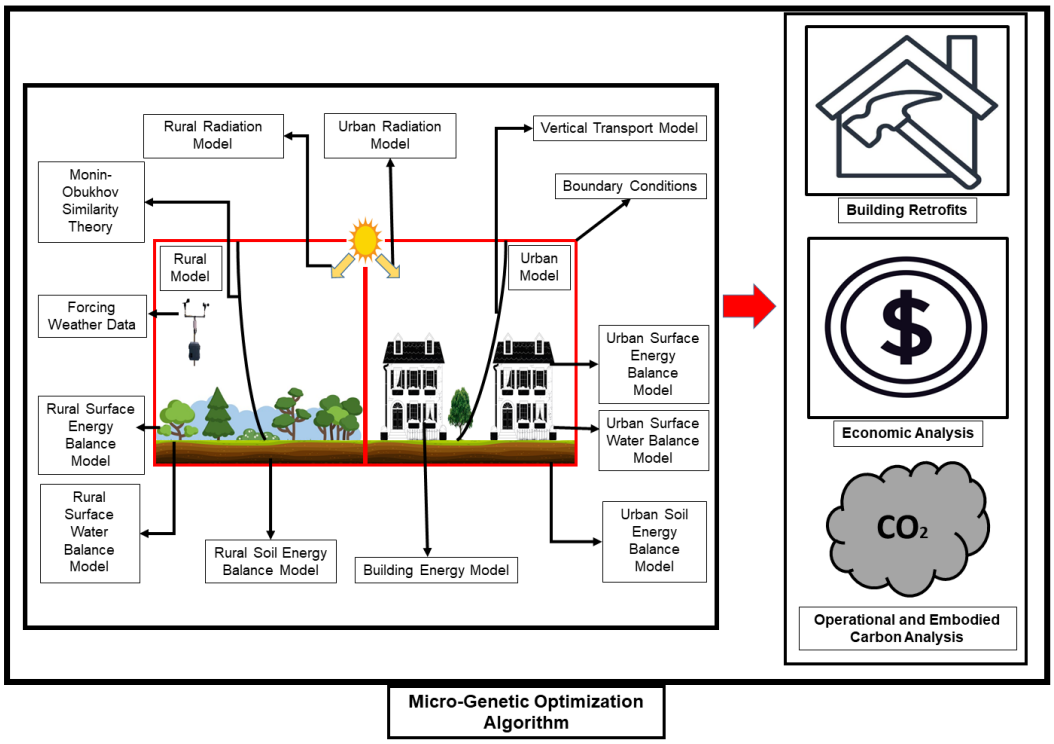

Figure 1. Vertical City Weather Generator (VCWGv1.4.6) and the associated sub-models.

the annualized marginal cost saving (C_s) of each retrofit strategy (Eq. 1). These objectives are considered simultaneously in the optimization process using weighted sum, which is to be minimized:

$$F = -w_{o,s}\frac{\mathrm{GHG}_{o,s}}{\mathrm{GHG}_{0o,s}} + w_e\frac{\mathrm{GHG}_e}{\mathrm{GHG}_{0e}} - w_{C_s}\frac{C_s}{C_{0s}} \tag{1}$$

Since all three objectives are equally important for our analysis, we assign the same weights to each, such that $w_{o,s} = w_e = w_{C,s} = \frac{1}{3}$. $\mathrm{GHG}_{o,s}$ [kg-CO_2], GHG_e [kg-CO_2], and C_{0s} [\$] represent the operational carbon savings, embodied carbon emissions, and marginal annualized cost savings, respectively. These values are derived from the solution of the first iteration of the optimization process. The optimization itself is conducted over a set of retrofit parameters with predefined discrete ranges and intervals, as listed in Table 1.

2.3. Economic analysis

The equations in this section are adapted from Aliabadi et al. (2023). For calculating the annualized cost of residential building retrofits, the following equation is used,

$$C = C_I + C_F + C_E + C_{OM} + L - C_S, \tag{2}$$

Table 1. Optimization variables with minimum value, maximum value, and variation interval: Building Integrated Thermal Energy Storage (BITES), Solar Thermal (ST), Wind Turbine (WT), PhotoVoltaic (PV)

Variables	Minimum	Maximum	Interval
Volume of BITES (V_{bites}) [m^3m^{-2}]	0.01	0.20	0.01
Roof Albedo (α_R)	0.1	0.7	0.05
Working Fluid Flow Rate for ST ($\dot{m}_{\text{st,f}}$) [$\text{kg s}^{-1}\text{m}^{-2}$]	0.0001	0.002	0.0001
Collector Area for ST (A_{st}) [m^2m^{-2}]	0.2	0.6	0.05
Roof Thermal Resistance (R_{roof}) [$\text{m}^2\text{K W}^{-1}$]	5.46	11.5	0.5
Infiltration Rate (V_{inf}) [ACH]	0.5	3.5	0.5
Wall Thermal Resistance (R_{wall}) [$\text{m}^2\text{K W}^{-1}$]	3.6	7	0.5
Ventilation Rate (V_{vent}) [$\text{L s}^{-1}\text{m}^{-2}$]	0.3	0.4	0.05
Glazing Ratio (GR)	0.1	0.4	0.05
Air Flow Rate for ST ($\dot{m}_{\text{he,st}}$) [$\text{kg s}^{-1}\text{m}^{-2}$]	0.001	0.02	0.001
Swept Area of WT (A_{wt}) [m^2m^{-2}]	0.05	0.2	0.05
Solar Heat Gain Coefficient (SHGC)	0.1	0.7	0.1
Collector Area for PV (A_{pv}) [m^2m^{-2}]	0.1	0.6	0.1

where C_I is the annualized initial investment, C_F is the annual fossil fuel cost, C_E is the annualized grid electricity consumption cost, C_{OM} is the annualized operation and maintenance cost, L is the annualized loan cost, C_S is the annualized income from alternative energy system salvage all in [$]. The annualized cost saving is given by:

$$C_s = C_{\text{Base}} - C_{\text{Retrofit}} + SCC_{saving}, \tag{3}$$

where C_{Base} [$] is annualized marginal cost for the base case without any retrofit, $\text{C}_{\text{Retrofit}}$ [$] is annualized marginal cost for each retrofit strategy, and SCC_{saving} is annualized social cost of carbon saving.

2.4. Environmental analysis

The environmental analysis involves the calculation of potential operational GHG emissions savings ($\text{GHG}_{o,s}$) and embodied carbon emission GHG_e through various building retrofit strategies. The embodied carbon emission is the summation of carbon emission of each retrofit strategy as shown in Eq 4:

$$\begin{aligned}\text{GHG}_e = {} & A_{\text{pv}}\text{ECF}_{\text{pv}} + A_{\text{wt}}\text{ECF}_{\text{st}} + V_{\text{BITES}}\text{ECF}_{\text{BITES}} \\ & + A_{\text{st}}\text{ECF}_{\text{st}} + R_{\text{wall}}A_{\text{wall}}\text{ECF}_{\text{Insulation}} \\ & + R_{\text{roof}}A_{\text{roof}}\text{ECF}_{\text{Insulation}} + \alpha_R\text{ECF}_{\text{CoolRoof}}\end{aligned} \tag{4}$$

where embodied carbon factor (ECF) for PV systems (ECF_{pv}) is 50 kg $\text{CO}_2\text{e}\,\text{m}^{-2}$), for wind turbines ($\text{ECF}_{\text{wt}}$) is 100 kg $\text{CO}_2\text{e}\,\text{m}^{-2}$), for the BITES system ($\text{ECF}_{\text{BITES}}$) is 30 kg $\text{CO}_2\text{e}\,\text{m}^{-3}$), and for solar thermal systems (ECF_{st}) is 40 kg $\text{CO}_2\text{e}\,\text{m}^{-2}$). Additionally, the embodied carbon factor for insulation materials ($\text{ECF}_{\text{Insulation}}$) is 10 kg $\text{CO}_2\text{e}\,\text{m}^{-2}$) and for the cool roof ($\text{ECF}_{\text{CoolRoof}}$) is 5 kg $\text{CO}_2\text{e}\,\text{m}^{-2}$).

The operational GHG emissions saving is the summation of GHG saving through a reduction of electricity and fossil fuel consumption. The fuel usage reduction is computed as

$$G_{\text{save}} = [G_{hB} + G_{whB} - (G_h + G_{wh})]A_{bld}N, \tag{5}$$

where G_{hB}, G_{whB}, G_h and G_{wh} [m^3 m^{-2}] are the natural gas usage for the base and retrofitted buildings for space and water heating, respectively. Then, the operational GHG emissions reduction potential in CO_2e associated with gas saving is estimated by,

$$GHG_{G_{\text{save}}} = G_{\text{save}} \rho_G \frac{MW_{\text{CO2}}}{MW_G}, \tag{6}$$

where $\rho_G = 0.669\ \text{kg}_G\ \text{m}^{-3}$ is the density of natural gas, $MW_{\text{CO}_2} = 44\ \text{g}_{\text{CO}_2}\ \text{mole}^{-1}$ is the molecular weight of CO_2, and $MW_G = 16\ \text{g}_G\ \text{mole}^{-1}$ is the molecular weights of natural gas. The electricity usage reduction is computed by,

$$E_{\text{save}} = [E_{cB} + E_{dB} - (E_c + E_h + E_d - E_{pv} - E_{wt})] A_{bld} N, \tag{7}$$

where E_{cB}, E_{dB}, E_c, E_h, and E_d [kW-hr m^{-2}] are the electricity usage for space cooling/heating and domestic appliance in base/retrofitted buildings, and E_{pv} and E_{wt} [kW-hr m^{-2}] are electricity generated by PV and WT, respectively, in the retrofitted building. Then, the GHG emissions reduction potential in CO_2e associated with electricity saving is found as,

$$GHG_{E_{\text{save}}} = E_{\text{save}} EI_E, \tag{8}$$

where $EI_E = 25\ \text{kg}_{\text{CO}_2}\ \text{kW-hr}^{-1}$ is the electricity grid GHG emissions intensity in Toronto in 2020.

3. RESULTS AND DISCUSSION

Fig. 2 illustrates the normalized overall objective function for three runs ((F-min)/(max-min)). It demonstrates that, for all runs, the objective function consistently decreases with each iteration. After more than 30 iterations, the function reaches a stable minimum value, indicating that the optimization process has made progress. This behavior highlights the efficiency of the MGA optimization algorithm in reaching an quasi-optimal solution.

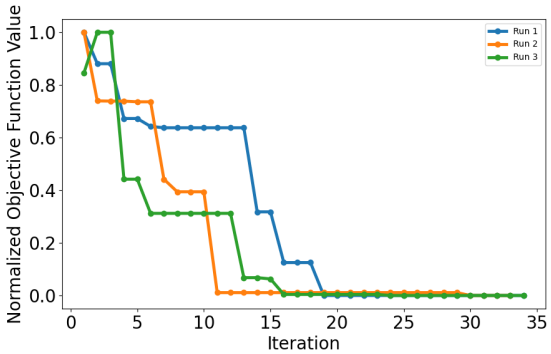

Figure 2. Normalized Best Overall Objective Function.

Table 2 shows best solution values of selected variables for optimization. The comparison between the initial setup of optimization variables (Table 1) and the optimized solutions (Table 2) reveals several key insights into effective retrofit strategies for Toronto. Some variables were maximized. The maximization of photovoltaic collector area (A_{pv}) suggests that integrating solar panels is a highly beneficial strategy for reducing operational carbon emissions, supporting the transition towards sustainable energy. Some variables were minimized, such as ventilation rate (V_{vent}), swept area of wind turbine A_{wt}. Other variables found an optimized value in the middle of their ranges (e.g. solar thermal collector area A_{st}, roof albedo (α_R), the infiltration rate (V_{inf}), Solar Heat Gain Coefficient (SHGC), Glazing Ratio (GR), and volume of BITES). Note that some optimization runs produced values in the entire range for some varaibles (e.g. infiltration rate).

Table 2. Optimized variables for each run

Variable	Run 1	Run 2	Run 3
V_{bites} [$\mathrm{m^3 m^{-2}}$]	5.00e-02	6.00e-02	5.00e-02
α_R	5.00e-01	5.50e-01	4.50e-01
$\dot{m}_{\mathrm{st,f}}$ [$\mathrm{kg\ s^{-1} m^{-2}}$]	5.00e-04	4.00e-04	6.00e-04
A_{st} [$\mathrm{m^2 m^{-2}}$]	2.00e-01	5.00e-01	4.00e-01
R_{roof} [$\mathrm{m^2 K\ W^{-1}}$]	1.146e+01	1.096e+01	6.96e+00
V_{inf} [ACH]	1.50e+00	5.00e-01	3.00e+00
R_{wall} [$\mathrm{m^2 K\ W^{-1}}$]	5.10e+00	5.10e+00	4.60e+00
V_{vent} [$\mathrm{L\ s^{-1} m^{-2}}$]	3.00e-01	3.50e-01	3.00e-01
GR	2.50e-01	4.00e-01	1.50e-01
$\dot{m}_{\mathrm{he,st}}$ [$\mathrm{kg\ s^{-1} m^{-2}}$]	8.00e-03	2.00e-03	1.10e-02
A_{wt} [$\mathrm{m^2 m^{-2}}$]	5.00e-02	5.00e-02	5.00e-02
SHGC	2.00e-01	2.00e-01	1.00e-01
A_{pv} [$\mathrm{m^2 m^{-2}}$]	6.00e-01	6.00e-01	6.00e-01

Fig. 3a demonstrates the process of optimizing operational carbon emissions savings through retrofitting strategies, showcasing the potential benefits for homeowners. Initially, the carbon emissions savings are inconsistent, fluctuating between approximately 120,000 and 130,000 kg-CO_2, indicating instability in the sub-objective function. However, as the optimization progresses, the savings increase and stabilize around 135,000 to 140,000 Kg-CO-2 on average, with reduced variability, reflecting greater reliability and consistency in the solution. For homeowners, this translates into significant carbon emissions reductions, potentially saving an additional 10,000 to 20,000 Kg-CO_2 compared to the sub-optimal initial solution.

Fig. 3b illustrates the embodied carbon emissions associated with retrofit strategies over an optimization process. At the beginning, embodied carbon emission levels are notably high, approximately 18,000 Kg-CO_2. As the optimization progresses, significant reductions are noted, with embodied carbon emissions stabilizing around 9,000 to 10,000 Kg-CO_2. For homeowners, achieving this reduction means cutting embodied carbon emissions by nearly 50% compared to the initial solution.

Fig. 4 shows the marginal annual cost savings achieved through optimized retrofit strategies. For the initial solution, homeowners are subject to significant negative savings (or positive expenses), with losses exceeding $2,500 annually. However, as the optimization process progresses, the annual cost savings improve significantly, eventually stabilizing at approximately $500 per year. This indicates that implementing the optimal retrofit strategies can result in substantial financial benefits, allowing homeowners to save up to $500 annually on operational costs, while enhancing

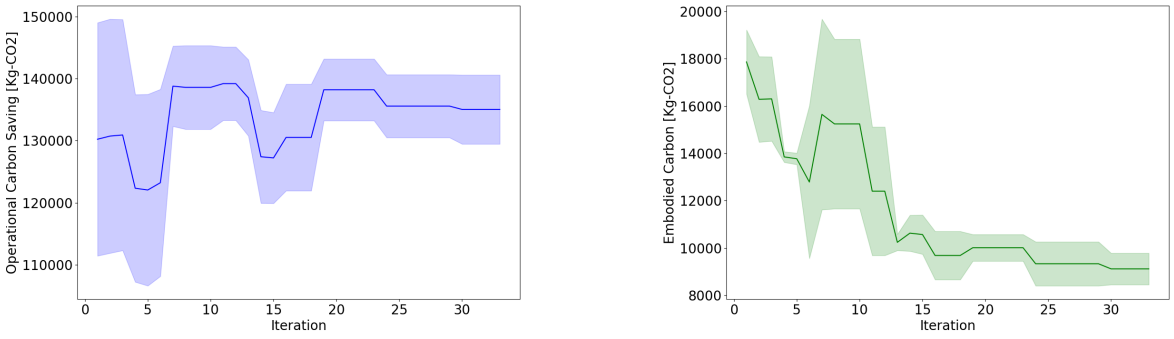

(a) Operational Carbon Saving

(b) Embodied Carbon

Figure 3. Comparison of Operational and Embodied Carbon Savings.

energy efficiency and reducing carbon emissions.

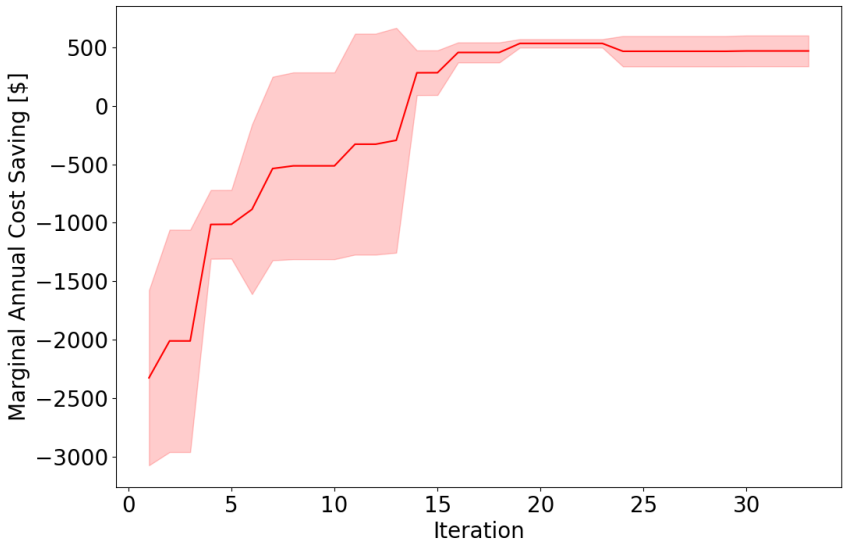

Figure 4. Marginal Annualized Cost Saving.

In addition to optimizing environmental and economic performance, this study also evaluates the savings associated with the SCC for each retrofit strategy. The SCC represents the societal cost of carbon emissions, encompassing the damages caused by climate change, such as extreme weather events, health impacts, and ecosystem destruction. By reducing carbon emissions through retrofits, this study calculates the annualized SCC savings, offering a valuable measure of the broader societal benefits. The reduction in carbon emissions for each retrofit strategy is calculated by comparing the operational and embodied carbon before and after the retrofit. The SCC is derived from existing studies and models that estimate the economic cost per tonne of GHG emissions avoided. Results show that the annualized SCC savings, calculated over 30 iterations, fluctuate between

$1,100 and $1,350. This amount of savings is of great importance as it highlights the potential for reducing the economic impact of emissions on society. The SCC savings underscore the long-term financial and environmental benefits of pursuing greener homes. By finding the optimal retrofit strategy, not only can we reduce emissions and mitigate climate change, but we can also see a financial return on these investments. Such strategies contribute to a more sustainable, resilient society, making the case for sustainable building practices both economically and environmentally beneficial.

4. CONCLUSIONS

The findings highlight the potential of MGA optimization for achieving comprehensive and sustainable building retrofit solutions. By balancing trade-offs between operational carbon emissions savings, embodied carbon emissions caused by retrofitting, and annualized cost savings, the proposed approach demonstrates a practical pathway for reducing upfront environmental impacts while ensuring long-term carbon benefits. Using the VCWG v1.6.0 urban physics model combined with economic analysis tools, the study optimizes retrofit strategies to maximize environmental and financial gains. Results show that retrofitting residential buildings in Toronto can lead to significant carbon emission reductions, up to 140 tonnes over 20 years, while generating annual cost savings of approximately $500. This outcome underscores the dual benefits of reducing carbon emissions and achieving financial savings, replacing high energy expenditures on electricity and gas consumption with sustainable and cost-effective solutions.

References

Aliabadi, A. A., Chen, X., Yang, J., Madadizadeh, A., and Siddiqui, K. (2023). Retrofit optimization of building systems for future climates using an urban physics model. *Building and Environment*, 243:110655.

Aliabadi, A. A., Moradi, M., and Byerlay, R. A. E. (2021). The budgets of turbulence kinetic energy and heat in the urban roughness sublayer. *Environmental Fluid Mechanics*, 21(4):843–884.

Madadizadeh, A., Siddiqui, K., and Aliabadi, A. A. (2024). Review: The Economics Landscape for Building Decarbonization. *Sustainability*, 16(14):6214.

Moradi, M. (2021). *The Vertical City Weather Generator*. PhD thesis, University of Guelph, Guelph.

Moradi, M., Dyer, B., Nazem, A., Nambiar, M. K., Nahian, M. R., Bueno, B., Mackey, C., Vasanthakumar, S., Nazarian, N., Krayenhoff, E. S., Norford, L. K., and Aliabadi, A. A. (2021). The Vertical City Weather Generator (VCWG v1.3.2). *Geosci. Model Dev.*, 14(2):961–984.

Moradi, M., Krayenhoff, E. S., and Aliabadi, A. A. (2022). A comprehensive indoor–outdoor urban climate model with hydrology: The Vertical City Weather Generator (VCWG v2.0.0). *Building and Environment*, 207:108406.

Safdari, M., Dennis, K., Gharabaghi, B., Siddiqui, K., and Aliabadi, A. A. (2024). Implications

of Latent and Sensible Building Energy Loads Using Natural Ventilation. *Journal of Building Engineering*, 96:110447.

6th International Conference on Building Energy and Environment
Eindhoven University of Technology, The Netherlands
6 - 10 July 2025

Comparison of Thermal Response Models for Predicting Overheating Health Risks in High-Temperature Environments

Sisi Chen [1,2], Lihua Zhao [1,2], Qi Li [1,2]

[1] *School of Architecture, South China University of Technology, Guangzhou 510640*
[2] *State Key Laboratory of Subtropical Building and Urban Science, South China University of Technology, Guangzhou 510640*

ABSTRACT

Frequent heatwaves pose significant threats to human health, making the accurate assessment of overheating risks on physiological health and safety in high-temperature environments crucial. Based on previous thermos-physiological experimental data, this study compares the predictive performance of the Two-Node model, JOS-3 model, and Predicted Heat Strain (PHS) model for core temperature, and water loss under various high-temperature conditions. The results show that the JOS-3 model performs best in predicting core temperature, with a root mean square error (RMSE) of 0.17°C. For water loss, the PHS model demonstrates higher accuracy under high metabolic rates but shows significantly increased RMSE in high-radiation and hot-humid environments, where the Two-Node model outperforms it. Overall, the JOS-3 model excels under sedentary and low-to-moderate metabolic conditions, making it suitable for assessing overheating risks in residential and office settings. The PHS model is more applicable for high-metabolic-rate scenarios, such as factory workshops and indoor sports venues. A combined application of the JOS-3 and PHS models can more accurately evaluate overheating risks in outdoor and high-radiation environments. This study provides a basis for selecting appropriate thermal response models to assess overheating health risks in high-temperature environments, contributing to the safety of buildings and urban thermal conditions.
Keywords: Overheating Health Risk, Thermal response models, Core temperature, Water loss

Nomenclatures

T_a	Air temperature [℃]
RH	Relative humidity [%]
MRT	Mean radiation temperature [℃]
V_a	Air velocity [m/s]
Met	Metabolic rate [met]
Clo	Clothing thermal resistance [clo]
T_{cr}	Core temperature [℃]
WL	Water loss [g/m^2]
RMSE	Coefficient of determination

1 INTRODUCTION

In recent years, the frequency and intensity of heatwaves have far exceeded baseline levels of the last century, evolving into a global climate disaster(UN, 2024). Prolonged heat exposure and improper thermoregulation can damage multiple organ systems and disrupt metabolic functions, leading to conditions such as heat-related illnesses (heat cramps, heat exhaustion, heat stroke), dehydration, fluid and electrolyte imbalances, sleep deprivation, cardiovascular diseases, kidney disorders, respiratory disease exacerbation, and even death(Obradovich et al., 2017; Sheridan & Allen, 2018; Winquist et al., 2016). Rapid urbanization has exacerbated the urban heat

island (UHI) effect in China(Yang et al., 2024). The combined impact of heatwaves and UHI has significantly intensified urban overheating issues, severely affecting residents' health, mobility, and safety. This is particularly critical in high-density cities, where heat risks are more pronounced(Ho et al., 2023).

Human tolerance to high temperatures has physiological limits. When a subsystem signals danger, the body enters a state of heat stress. These thermal safety signals primarily include two aspects: body temperature and sweat rate(Weng et al., 2017). In high-temperature environments, the body regulates heat through sweating to maintain metabolic function. However, excessive sweating without adequate fluid replenishment can lead to dehydration. When dehydration exceeds a certain percentage of body weight, various adverse conditions may arise. Additionally, when skin moisture approaches saturation, the body cannot dissipate excess heat through sweating, leading to an increase in core temperature and subsequent heat stress. According to ISO 7933-2023(Ergonomics of the Thermal Environment — Analytical Determination and Interpretation of Heat Stress Using Calculation of the Predicted Heat Strain, 2023), the thermal safety thresholds are defined as a dehydration rate of 3% and a core body temperature of 38°C.

Thermophysiological experiments and mathematical modeling are the two most common methods for studying human thermal responses, each with its advantages and limitations. Experiments provide extensive physiological data but face challenges such as large sample requirements, significant individual variability, risks associated with high-temperature environments, and poor reproducibility. On the other hand, mathematical modeling offers advantages in result reproducibility and flexibility, such as dividing the human body into layers or segments. However, most existing models are developed for moderate-temperature environments, and their applicability to high-temperature conditions remains to be further investigated. This is particularly important for assessing the health risks posed by overheating(Chen et al., 2024).

This study reviews three of the most widely used human thermal response models: the two-node model(Gagge A P et al., 1971), the JOS-3 model(Takahashi et al., 2021), and the Predicted Heat Strain (PHS) model(Ergonomics of the Thermal Environment — Analytical Determination and Interpretation of Heat Stress Using Calculation of the Predicted Heat Strain, 2023). Using data from thermophysiological experiments, the predictive performance of these models was compared under various high-temperature conditions. The applicability of each model was analyzed within specific scenarios, providing recommendations and a scientific basis for selecting an appropriate human thermal response model to accurately assess overheating risks in high-temperature environments.

2 METHODOLOGY

2.1 HUMAN THERMAL REPONSE MODELS

Gagge et al. (Gagge A P et al., 1971)proposed the two-node model, dividing the human body into the skin layer and the core layer. Based on this model, they introduced thermal comfort indices such as Effective Temperature (ET) and Standard Effective Temperature (SET). Due to its simplicity and practicality, Gagge's two-node model is still widely applied in the field of thermal comfort. Numerous researchers have refined components of the two-node model, including skin blood flow, shivering, sweating, and sweat evaporation efficiency(Ji et al., 2021). The development of the Stollwijk multi-node model(Stolwijk J, 1971) marked a significant advancement in the framework of human thermoregulation models, paving the way for more sophisticated multi-node, multi-segment, and non-uniform transient models. Building on Stollwijk's concept, Tanabe(Takahashi et al., 2021) developed the JOS-3 model, which divides the human body into 17 segments and 85 nodes. This model can predict localized core temperature,

skin temperature, and sweating rates while also accounting for the influence of age and gender on thermoregulation.

However, both the two-node and JOS-3 models are primarily applied in thermal comfort research. Their accuracy in assessing overheating risks under extreme heat conditions remains to be verified. To evaluate the risks of heat stress during prolonged work in high-temperature environments, the ISO 7933 standard(Ergonomics of the Thermal Environment — Analytical Determination and Interpretation of Heat Stress Using Calculation of the Predicted Heat Strain, 2023) introduced the PHS model. This model simplifies the two-node framework by predicting sweat rates, cumulative water loss, and changes in core and skin temperatures over time using the virtual sweat rate required to maintain thermal equilibrium. While the PHS model effectively quantifies heat strain in high-metabolic-rate occupational settings, its applicability to daily living environments is yet to be determined.

2.2 THERMOPHYSIOLOGICAL EXPERIMENTS

Thermophysiological experiments typically involve multiple participants undergoing tests in a climate chamber with controlled temperature and humidity. These experiments measure human thermophysiological parameters, such as skin and rectal temperatures, metabolic rate, and sweat production. Drawing on previous thermophysiological studies, this paper summarizes experimental conditions relevant to high-temperature environments in urban walking spaces and indoor buildings, as shown in Table 1. Case 1 to 5 were part of thermophysiological experiments conducted by Ooka's team at the University of Tokyo(Ooka et al., 2010), examining changes in thermophysiological parameters of Japanese university students under varying air temperatures, relative humidity levels, and activity states. Measurements included core temperature, skin temperature, and total body water loss (encompassing respiratory water loss and sweat loss). Case 6-8 were studied by André Dufour in France(Dufour & Candas, 2007), investigating thermophysiological responses across different age groups in high-temperature environments. Case 9-12 were experiments conducted by Stapleton in Canada(Stapleton et al., 2014), focusing on young and older adults under dry and humid heat conditions to examine thermophysiological responses.

Table 1 Thermal Physiological Experiments on Humans in High-Temperature Environments

Case	Subject	Met (met)	Clo (clo)	Environmental parameters				Time (min)
				T_a (℃)	MRT (℃)	RH (%)	V_a (m/s)	
1(Ooka et al., 2010)	Young adults	1	0.3	35	35	50	0.1	60
2(Ooka et al., 2010)	Young adults	2	0.3	35	35	50	0.1	45
3(Ooka et al., 2010)	Young adults	3	0.3	35	35	50	0.1	45
4(Ooka et al., 2010)	Young adults	1	0.3	35	35	70	0.1	60
5(Ooka et al., 2010)	Young adults	1	0.3	40	40	50	0.1	60
6(Dufour & Candas, 2007)	Young males	1	0.08	40	40	40	0.1	90
7(Dufour & Candas, 2007)	Middle-aged males	1	0.08	40	40	40	0.1	90
8(Dufour & Candas, 2007)	Older males	1	0.08	40	40	40	0.1	90
9(Stapleton et al., 2014)	Young adults	1	0.08	36.5	36.5	20	0.1	120
10(Stapleton et al., 2014)	Elderly	1	0.08	36.5	36.5	20	0.1	120
11(Stapleton et al., 2014)	Young adults	1	0.08	36.5	36.5	60	0.1	120
12(Stapleton et al., 2014)	Elderly	1	0.08	36.5	36.5	60	0.1	120

3 RESULT

To compare the accuracy of different models in calculating human thermophysiological parameters under high-temperature conditions, core temperature, and water loss data from

thermophysiological experiments conducted under 12 high-temperature cases were selected for validation. Localized sweat rates were not included, as they are challenging to compute using models and difficult to measure experimentally in isolation. Instead, total body water loss, which can be measured precisely using electronic scales to track body weight changes, was used. This measurement encompasses sweat evaporation and respiratory water vapor loss. Accordingly, only the per-unit-area water loss data from case 1 to 5 were validated, indirectly assessing the models' accuracy in calculating sweat rates. As each condition involved multiple participants, the experimental results shown represent the average physiological parameters of all participants. Similarly, the model calculations were performed using the average physical characteristics of participants as reported in the referenced studies.

3.1 CORE TEMPERATURE

Figure 1 illustrates the comparison between core temperatures predicted by thermoregulatory models and experimental measurements under various high-temperature conditions. Figure 2 presents the root mean square error (RMSE) of core temperature predictions by the JOS-3 model, the two-node model, and the PHS model across different conditions. Based on Figures 1 and 2, except for case 2 and 3, the JOS-3 model demonstrates the highest accuracy among the three thermoregulatory models in predicting core temperature, with RMSE values below 0.5°C for all conditions and an average RMSE below 0.2°C. When participants were engaged in physical activities with higher metabolic rates (case 2 and 3), the JOS-3 model overestimated core temperature compared to experimental results, making it the least accurate model in these scenarios. Additionally, for case 6 through 12, the JOS-3 model exhibited higher prediction accuracy for participants' core temperatures across different age groups compared to the two-node model and the PHS model. This can be attributed to the JOS-3 model's consideration of the effects of aging on metabolic rate. However, its accuracy in predicting core temperature for older adults was generally lower than for younger participants. For the two-node model and the PHS model, the predicted core temperatures were lower than the experimental results in nearly all conditions except for case 2 and 3. The average RMSE for the two-node model was 0.36°C, while that for the PHS model was 0.31°C.

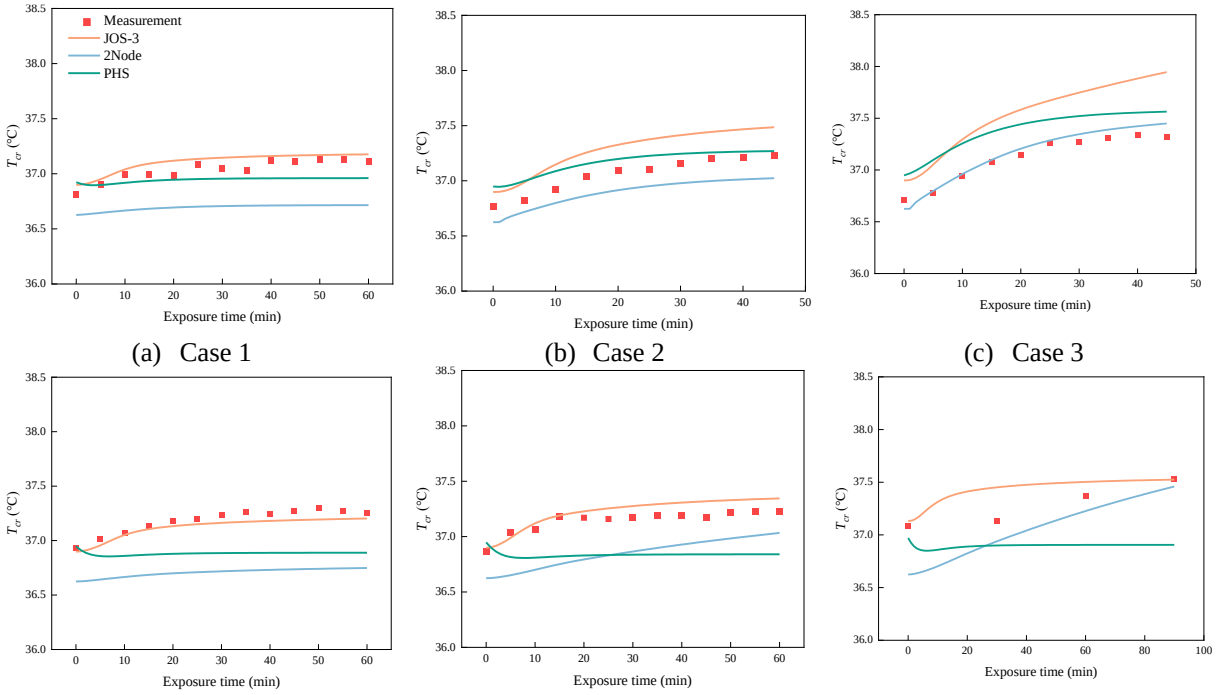

(a) Case 1 (b) Case 2 (c) Case 3

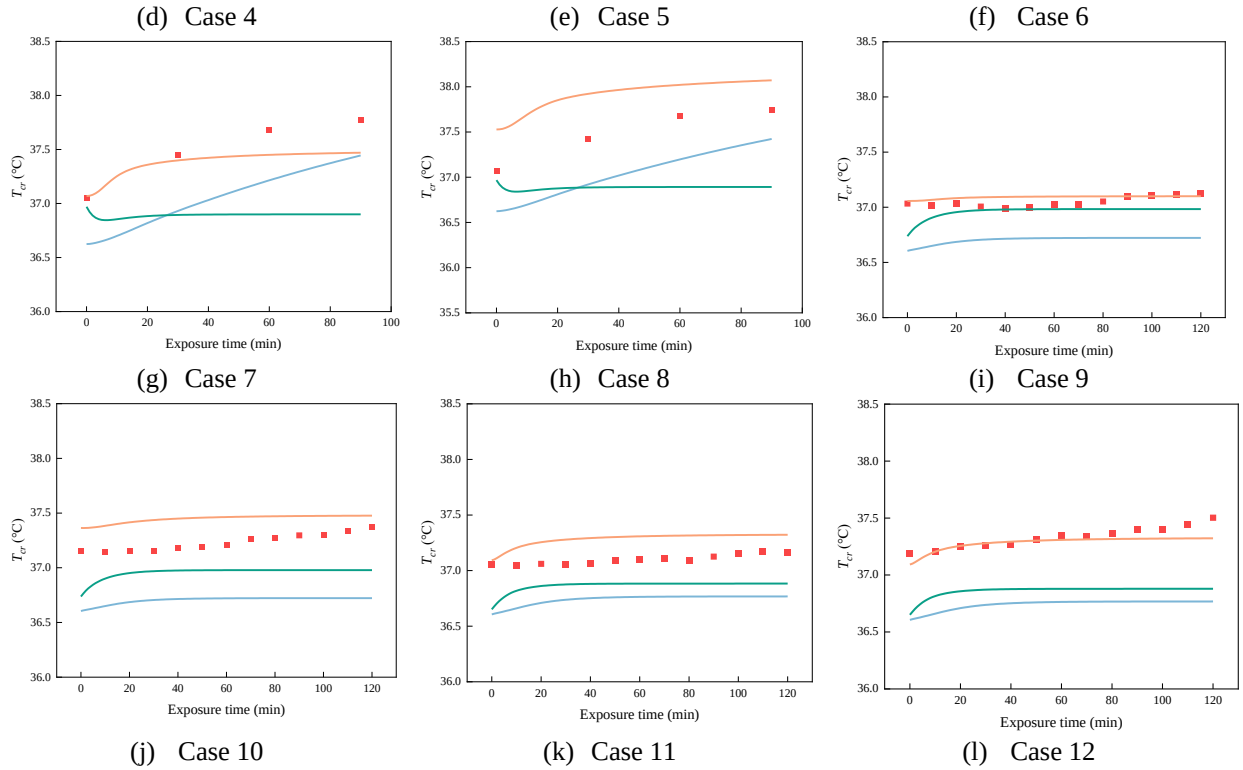

Figure 1. Comparison Between Experimental Results and Model Predictions of Core Temperature

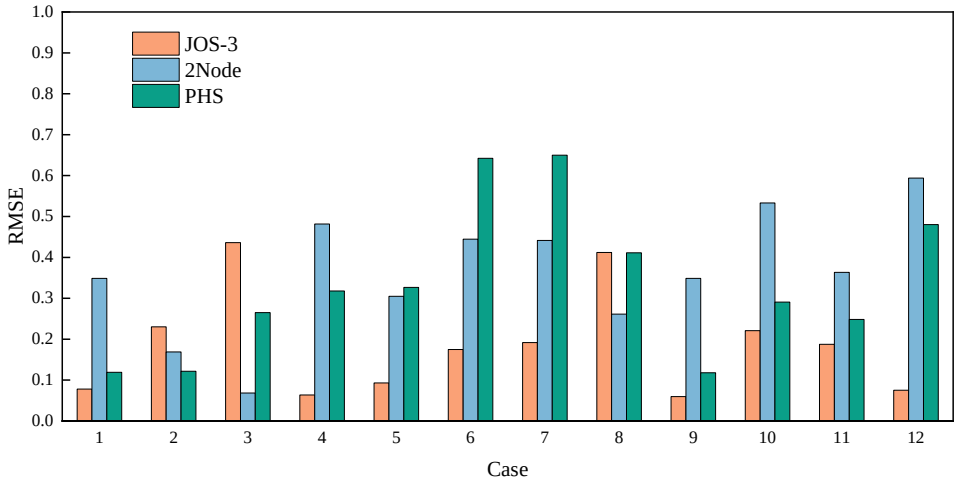

Figure 2. RMSE of Core Temperature Calculations Under High-Temperature Conditions

3.2 WATER LOSS

Figure 3 compares the experimental results of unit area water loss with model calculations, while Figure 4 shows the RMSE statistics of model calculations under different conditions. When the human body is in a sedentary state with a low metabolic rate (corresponding to Conditions 1, 4, and 5), the two-node model demonstrates higher accuracy in calculating water loss, as shown in Figures 3(a), 3(d), and 3(e). When participants are in motion with a higher metabolic rate (corresponding to Conditions 2 and 3), the PHS model provides the most accurate predictions of unit area water loss, while the RMSE for the two-node model and JOS-3 model increases. Particularly, the JOS-3 model significantly underestimates sweat production during physical activity, leading to an overestimation of heat storage in the body. This also explains why the JOS-3 model calculates higher core temperatures compared to measured values, as observed in Figures

1(b)-(c). When T_a and MRT rise to 40°C (case 5), the RMSE of water loss calculations by heat response models increases, especially for the PHS model, which tends to overestimate sweat production in high-temperature, high-radiation environments. This results in underestimating the body's heat storage and core temperature. Comparing Figures 1-4 and contrasting case 1 and 4, as well as case 9, 10 with case 11, 12, it is evident that in humid-heat environments, the accuracy of the PHS model in predicting water loss and core temperature is lower than in dry-heat environments.

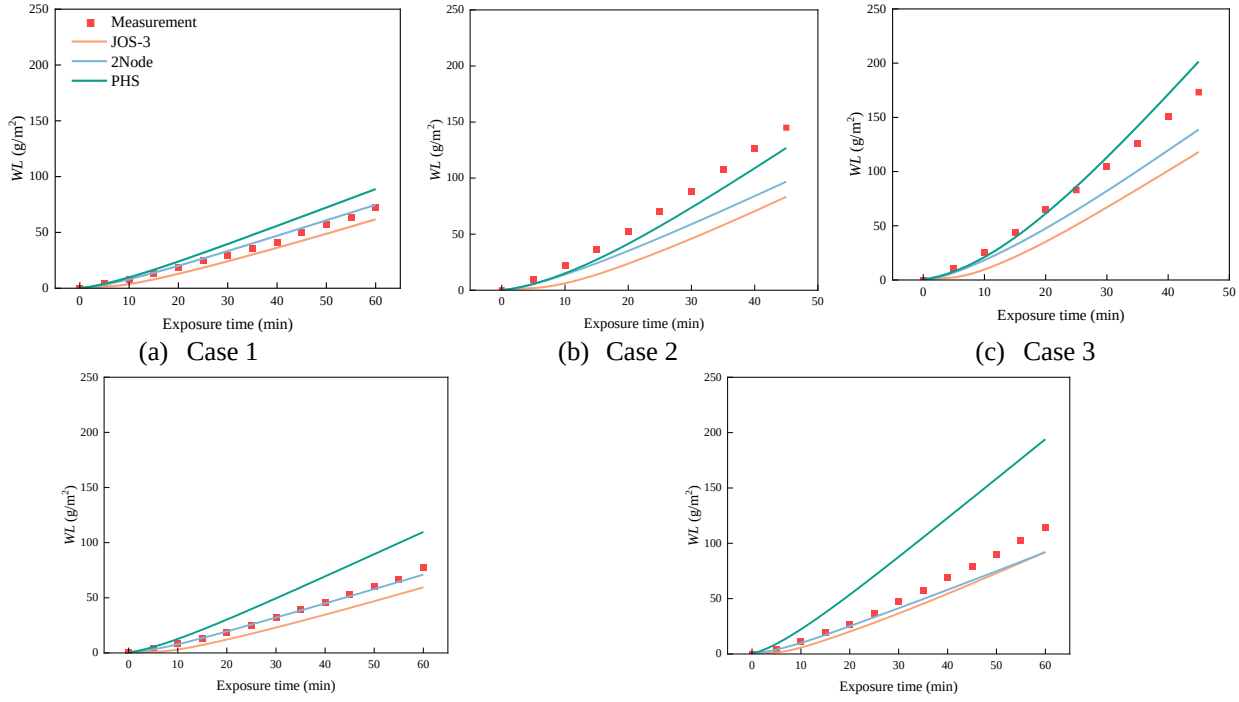

(a) Case 1 (b) Case 2 (c) Case 3

(d) Case 4 (e) Case 5

Figure 3. Comparison Between Experimental Results and Model Predictions of Water loss

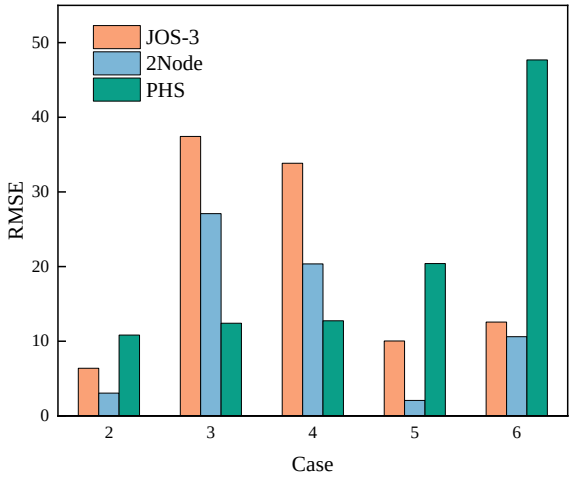

Figure 4. RMSE of Water Loss Calculations Under High-Temperature Conditions

4 DISCUSSION AND CONCLUSION

By comparing experimental results with simulation outputs, the study evaluated the accuracy of the two-node model, JOS-3 model, and PHS model in predicting core temperature and water loss under high-temperature conditions, leading to the following conclusions:

(1) The JOS-3 model achieved an RMSE of 0.17°C, outperforming the PHS model (RMSE: 0.31°C) and the two-node model (RMSE: 0.36°C). Under high-temperature conditions

with elevated metabolic rates, the two-node and PHS models showed higher accuracy in predicting core temperature. In other scenarios, the JOS-3 model demonstrated superior accuracy. Additionally, the JOS-3 model considers the impact of aging on metabolism, resulting in better prediction accuracy for individuals of different age groups.

(2) The PHS model showed high accuracy in estimating water loss under high-temperature conditions with elevated metabolic rates. However, its accuracy significantly declined in high-temperature and high-radiation environments (air temperature and mean radiant temperature reaching 40°C) or hot-humid conditions, where it performed far worse than the two-node model and JOS-3 model.

(3) The JOS-3 model is most accurate under sedentary conditions and low-to-moderate metabolic rates, particularly when accounting for age-related effects. It is suitable for evaluating indoor overheating risks in residential buildings, offices, and nursing homes. The two-node model and PHS model excel in estimating sweat production and core temperature under high metabolic rates, making them appropriate for assessing heat stress risks in factory workers performing high-intensity tasks and in indoor sports venues. For outdoor sports venues and construction sites with high temperatures, intense radiation, and significant physical activity, a combination of the PHS model and JOS-3 model should be used to evaluate overheating risks effectively.

REFERENCE

Chen, S., Zhao, H., Luo, K., Li, Q., Nie, Z., & Zhao, L. (2024). Health risk assessment of residential overheating under the heat waves in Guangzhou. Building and Environment, 266, 112089. https://doi.org/10.1016/j.buildenv.2024.112089

Dufour, A., & Candas, V. (2007). Ageing and thermal responses during passive heat exposure: Sweating and sensory aspects. European Journal of Applied Physiology, 100(1), 19–26. https://doi.org/10.1007/s00421-007-0396-9

Ergonomics of the thermal environment—Analytical determination and interpretation of heat stress using calculation of the predicted heat strain (No. ISO 7933:2023(E)). (2023).

Gagge A P, Stolwijk J A J, & Nishi Y. (1971). An effective temperature scale based on a simple model of human physiological regulatiry response. ASHRAE Transactions, 77(1).

Ho, J. Y., Shi, Y., Lau, K. K. L., Ng, E. Y. Y., Ren, C., & Goggins, W. B. (2023). Urban heat island effect-related mortality under extreme heat and non-extreme heat scenarios: A 2010–2019 case study in Hong Kong. Science of The Total Environment, 858, 159791. https://doi.org/10.1016/j.scitotenv.2022.159791

Ji, L., Laouadi, A., Shu, C., Wang, L., & Lacasse, M. A. (2021). Evaluation and improvement of the thermoregulatory system for the two-node bioheat model. Energy and Buildings, 249, 111235. https://doi.org/10.1016/j.enbuild.2021.111235

Obradovich, N., Migliorini, R., Mednick, S. C., & Fowler, J. H. (2017). Nighttime temperature and human sleep loss in a changing climate. Science Advances, 3(5), e1601555. https://doi.org/10.1126/sciadv.1601555

Ooka, R., Minami, Y., Sakoi, T., Tsuzuki, K., & Rijal, H. B. (2010). Improvement of sweating model in 2-Node Model and its application to thermal safety for hot environments. Building and Environment, 45(7), 1565–1573. https://doi.org/10.1016/j.buildenv.2009.12.012

Sheridan, S. C., & Allen, M. J. (2018). Temporal trends in human vulnerability to excessive heat. Environmental Research Letters, 13(4), 043001. https://doi.org/10.1088/1748-9326/aab214

Stapleton, J. M., Larose, J., Simpson, C., Flouris, A. D., Sigal, R. J., & Kenny, G. P. (2014). Do older adults experience greater thermal strain during heat waves? Applied Physiology, Nutrition, and Metabolism, 39(3), 292–298. https://doi.org/10.1139/apnm-2013-0317

Stolwijk J. (1971). A Mathematical Model of Physiological Temperati Regulation in Man. National Aeronautics and Space Administration.

Takahashi, Y., Nomoto, A., Yoda, S., Hisayama, R., Ogata, M., Ozeki, Y., & Tanabe, S. (2021). Thermoregulation model JOS-3 with new open source code. Energy and Buildings, 231, 110575. https://doi.org/10.1016/j.enbuild.2020.110575

UN. (2024, February 12). WMO confirms 2023 as warmest year on record 'by a huge margin.' https://news.un.org/en/story/2024/01/1145457

Wenguo Weng, Ming Fu, & Jie Yang. (2017). Mechanisms and Safety Assessment of Human Thermal Response in High Temperature Environments. Science Publishing House.

Winquist, A., Grundstein, A., Chang, H. H., Hess, J., & Sarnat, S. E. (2016). Warm season temperatures and emergency department visits in Atlanta, Georgia. Environmental Research, 147, 314–323. https://doi.org/10.1016/j.envres.2016.02.022

Yang, L., Li, Q., Li, Q., Zhao, L., Luo, Z., & Liu, Y. (2024). Different explanations for surface and canopy urban heat island effects in relation to background climate. iScience, 27(3), 108863. https://doi.org/10.1016/j.isci.2024.108863

6th International Conference on Building Energy and Environment
Eindhoven University of Technology, The Netherlands
6 - 10 July 2025

Fire spread and structural fire safety of steel factory buildings

Chi-Wen Lo [1], Chu-Tsen Liao [2], Heui-Yung Chang [3], Chi-Ming Li [4]

[1]*Department of Civil Engineering, National Cheng Kung University, Tainan, Taiwan, Shadow10493@gmail.com*
[2]*Department of Architecture, National Taiwan University of Science and Technology, Taipei, Taiwan, liaoct@mail.ntust.edu.tw*
[3]*Department of Civil Engineering, National Chung Hsing University, Taichung, Taiwan, hychang586@dragon.nchu.edu.tw*
[4]*Department of Civil Engineering, National Cheng Kung University, Tainan, Taiwan, cmlai@mail.ncku.edu.tw*

SUMMARY
As the number of steel structures continues to increase, fire safety of steel buildings has been a subject of lasting interest due to the significantly decrease in steel strength in high temperatures. Therefore, in this study, numerical simulations were carried to explore the fire behaviour of steel factories with high fire loads. Software FDS was used to reconstruct the full-size room-fire scene and obtain the time variation of temperature of indoor air and steel structure. Then, finite element software ANSYS was employed to conduct thermo-solid coupling analysis to analyse the structural behaviour. The properties of structural components and materials set in the simulation works are based on the measured data of common SN490B steel and the recommended values of Eurocode. The results show that the fire spread speed and flashover time will be different depending on the location of the fire source, as well as the intensity of fire load. Extremely high temperature fire smoke accumulates high in space; thus, beams and columns near the roof severely deformed. If firefighters break in to control the fire at this time, the influx of outside air will intensify the fire. The high temperature at this time possibly causes the roof panels and floor panels to collapse, causing serious casualties to people in the factory.

Keywords: fire, room fire, building, steel, flashover.

1. INTRODUCTION

Located on the circum-Pacific seismic belt, Taiwan has seen an increased demand for seismic construction. While light-steel construction is less effective in terms of noise insulation, wind resistance, and leak-proof performance, it offers several advantages, including lower costs, shorter construction periods, shock resistance, and recyclability. These benefits have led to a significant rise in light-steel construction in recent years, gradually replacing traditional reinforced concrete (RC) structures in housing design. According to government statistics, fires occurring in buildings with 1-5 floors account for approximately 90% of all reported incidents. When categorized by building use, fires in warehouses and factories represent about 25% of the total annually. Among the various causes, electrical equipment malfunctions are responsible for around 40% of all fires.

Therefore, in this study, numerical simulations were carried to explore the fire behaviour of steel factories with high fire loads. Software FDS was used to reconstruct the full-size room-fire scene and obtain the time variation of temperature of indoor air and steel structure. Then, finite element software ANSYS was employed to conduct thermo-solid coupling analysis to analyse the structural behaviour.

2. RESEARCH METHOD

2.1. Room fire simulation

The investigated subject is a steel-framed furniture factory with metal exterior walls, as shown in Figure 1, measuring 30m in length, 18m in width, and 9m in height. Each of the two sides is equipped with three sliding windows, each 0.5m wide and 0.75m high. The front of the building features a 3m-wide steel rolling door, which is closed at night but leaves a gap of approximately 10cm. The exterior walls are made of 5cm-wide steel corrugated panels. The flooring consists of 5cm-high steel corrugated panels overlaid with a 5cm-thick wooden layer. The column sections are H-shaped steel profiles, specifically H400×200×8×13mm and H250×125×6×9mm, while all beams are H250×125×6×9mm. All beams and columns are bare steel without any fireproof coating. The steel material used is SN490B, with properties aligned with the values recommended by Eurocode-3 (1995).

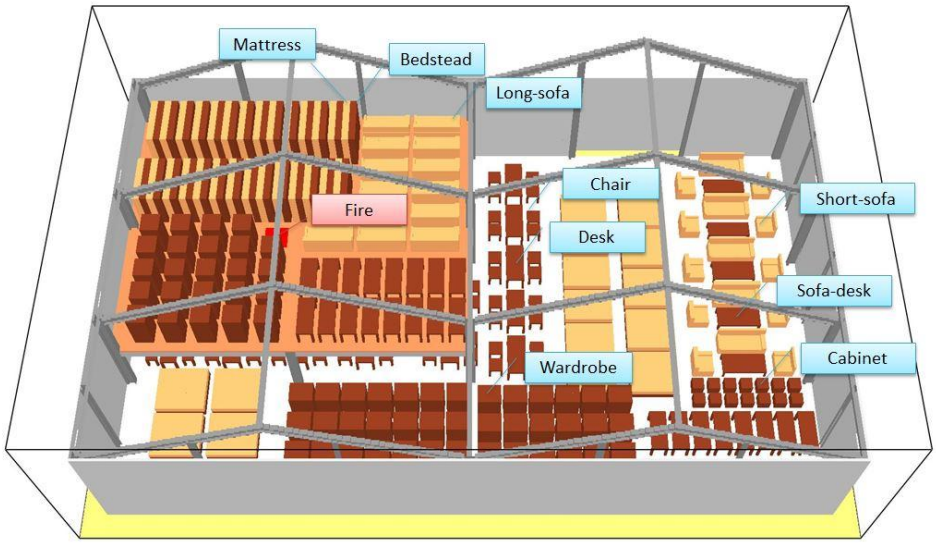

Figure 1. The investigated subject.

The simulation scenario involves an electrical wire short circuit leading to the ignition of a wooden cabinet. The heat release rate (HRR) of the fire source is set based on the burning characteristics of the wooden cabinet and converted into the fire source HRR input for FDS (Fire Dynamics Simulator). The initial simulation conditions include a temperature of 25°C, a relative humidity of 60%, and a simulation duration of 900 seconds.

The ignition point is located on the second-floor slab, where a 1m × 1m fire source replaces the wooden cabinet. The heat release rate per unit area is set at 3000 kW/m², with a maximum HRR of 3000 kW. In the FDS simulation, the HRR rapidly increases during the first 150 seconds and then stabilizes until the simulation ends at 900 seconds.

2.2. Structural behaviour in fires

This study employs the ANSYS transient thermal-structural coupling model for simulation. The analysis involves Thermal Analysis and Nonlinear Structural Analysis. The thermal loading temperature curve is applied to the structure based on the data obtained from the FDS analysis. The material properties are based on the values provided by Luecke (2005) and the European standard Eurocode.

3. RESULTS AND DISCUSSION

The simulation results (Figure 2) show that at 55 seconds, the flames began to spread, expanding the burning area, and the mattress near the fire source had already ignited. By 65 seconds, the mattress and bed frame area were burning. Initially, a large amount of heat energy accumulated on the left side of the roof. Once the heat energy reached a certain threshold, it started to extend toward the right side of the roof (at 65 seconds). Due to the effects of heat transfer through radiation, convection, and conduction, the high-temperature heat flow ignited the flammable furniture below, ultimately causing the entire factory to rapidly become engulfed in flames.

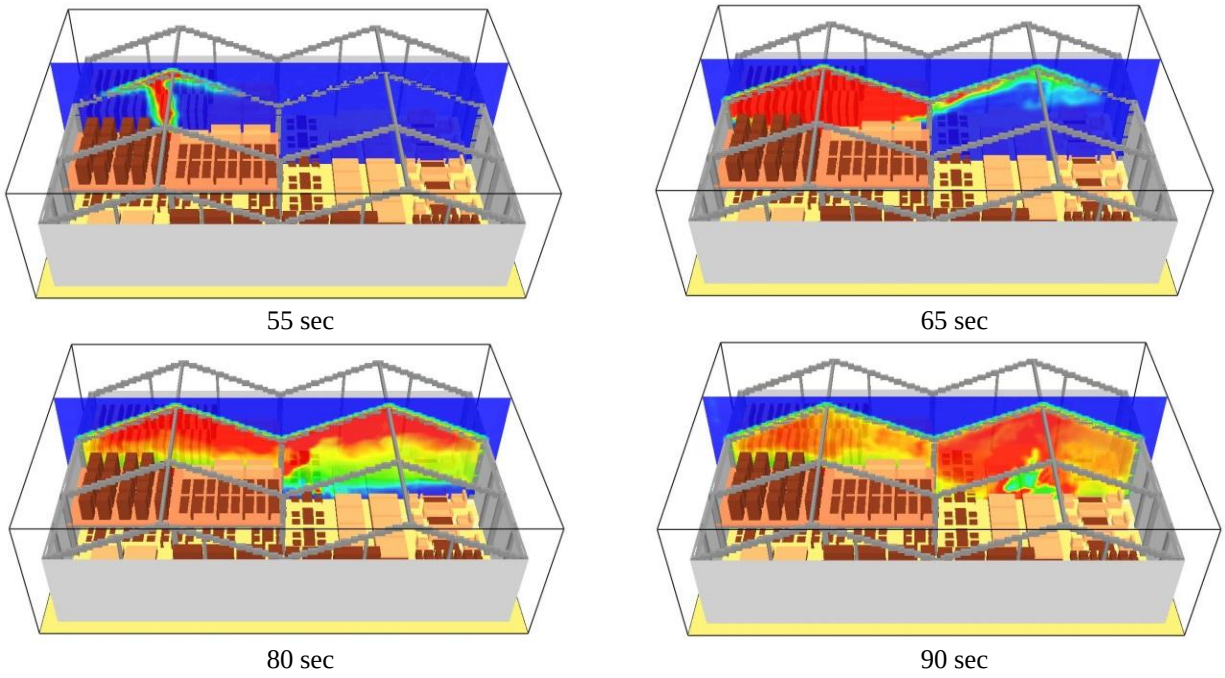

Figure 2. Fire spread (X-Direction).

Temperature measurement points were placed on all beams and columns, and after completing the FDS fire simulation, the measured temperature values were input into ANSYS for thermal analysis. As shown in the figure above, when the fire source begins to burn, the continuously accumulating heat energy causes the beams and columns on the second floor of the left side to rapidly reach high temperatures. As the fire progresses to its fully developed stage, it spreads from the second floor on the left side to the right-side space. In the right-side space, sufficient oxygen and combustible materials fuel extensive burning. The roof beams, subjected to high temperatures, experience thermal expansion as the temperature rises, increasing axial pressure. However, due to restraints at both ends, the beams initially deform in the Y-direction.

With the continued effects of high-temperature softening, axial pressure begins to decrease, leading to increased horizontal deformation of the components. The maximum deformation in the X-direction is 118.78 mm, in the Y-direction is 272.82 mm, and in the Z-direction is 214.51 mm, with an overall maximum total deformation of 273.22 mm. Between 90 and 100 seconds, as the fire reaches its peak intensity, significant deformations can be observed in the upper roof beams and the beams surrounding the second-floor slabs due to high-temperature softening. As shown in

Figure 3, these deformations can potentially lead to structural collapse, resulting in injuries or fatalities for personnel inside the factory.

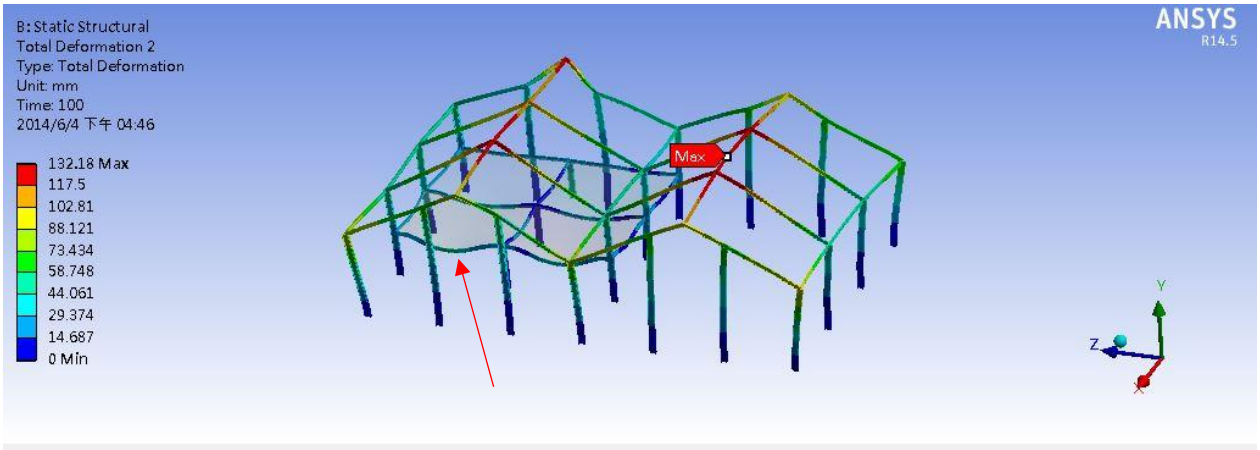

Figure 3. The deformation state of the structure at 100 seconds.

4. CONCLUSION

In the case presented in this study, the space contains a large number of wooden products, making it a high fire load environment. The time required for the fire to progress from the growth stage to the fully developed stage is extremely short. The accumulated heat energy and dense smoke within the factory cannot be effectively vented. If firefighters break in to extinguish the fire during this stage, the influx of air would cause the fire temperature to rise rapidly. The high temperatures would lead to more severe deformations of the beams and columns, potentially resulting in structural collapse, which poses a significant risk of injury or fatality to personnel entering the factory.

REFERENCES

Ansys® Academic Research Mechanical, Release 2021 R1.

Eurocode 3, Design of Steel Structures – Part 1.2: General rules - Structural Fire Design, (ENV1993-1-2), 1995.

National Institute of Standards and Technology, Fire Dynamics Simulator (FDS) Technical Reference Guide, NIST Special Publication 1018-1, 2021. [Online]. Available: https://www.nist.gov

Luecke W.E., McCowan C.N., Banovic S.W., Mechanical Properties of Structural Steels, Federal Building and Fire Safety Investigation of the World Trade Center Disaster, National institute of Standards and Technology, 2005.

6th International Conference on Building Energy and Environment
Eindhoven University of Technology, The Netherlands
6 - 10 July 2025

Explore health risks that the elderly face during heatwaves due to their degraded perceptual responses

Peiyang Du [1], Yongxin Xie [1], Jianlei Niu [1]

[1]*Department of Building Environment and Energy Engineering, The Hong Kong Polytechnic University, Hung Hom, Kowloon, Hong Kong*

SUMMARY
Elderly people are more likely to face heat-related health conditions when exposed to hot weather due to their low sensitivity. However, there is a lack of research in real environments to show the actual heat risks that low sensitivity brings to the elderly. In this study, subjects were asked to exercise on an outdoor treadmill for at a moderate intensity, during which physiological parameters and questionnaire survey were adopted. Results showed that both of the thermal sensation votes and thermal comfort votes of the elderly were higher than the young group, at the same time, the core temperature of the elderly gradually increased to 38°C, indicating that the elderly felt hot but were still comfortable, which means that the elderly had poor thermal sensitivity. The dehydration of the elderly reached 3%, but the thirst votes were lower than 4, indicating that they were not sensitive to their own dehydration status.

Keywords: Outdoor thermal health, High temperature, Senior, Thermal sensitivity.

1. INSTRUCTION

Globally, extreme heatwaves exceeding 40 °C have been recorded in recent years (Calvin et al., 2023). The warming trend in China is expected to accelerate in the future, causing cities in subtropical regions to experience more extreme hot days, posing a significant threat to human health (*Climate Issues to Watch in 2023*, 2022). Heatwaves have been found to increase the hospitalization rate and mortality rate (Conti et al., 2005). The impact of extreme heat is expected to be greater on the vulnerable groups, especially the elderly individuals (Hajat & Kosatky, 2010).

Hong Kong has one of the world's densest populations and limited living space (*Housing in Figures 2024*, 2013), so outdoor public spaces are often used as extensions of private living spaces. According to the previous study, although the Hong Kong Observatory issued "very hot weather warning", many residents still went out for activities, with 44% being elderly (Huang et al., 2022). The elderly group has a higher preference for warm environments than young people, and their thermal sensitivity is attenuated, resulting in the ability for them to remain in a thermally comfortable zone despite being exposed to a certain level of heat stress (Coates et al., 2014). Research has shown that the elderly reduce their activity outdoors only when air temperatures exceed 39°C (Huang et al., 2022). The elderly are less likely to perceive thermal changes than younger people. Therefore, senior individuals are more likely to be exposed to heat-related health risks without being aware of them.

It is a consensus that the elderly have lower thermal sensitivity and higher tolerance to high

temperatures, but there is currently no research that can accurately show the actual heat risks that this low sensitivity brings to the elderly. In addition, most studies are conducted in laboratories and lack experimental data in real environments. Therefore, it is necessary predict the thermal health risks of the elderly under heat stresses based on their subjective reactions and physical conditions, so as to guide the elderly in outdoor activities.

2. METHODOLOGY

2.1. Approach

This experiment was conducted on the outdoor terrace on the sixth floor of Block Z of the Hong Kong Polytechnic University. Nine seniors and three young subjects were recruited through posters distributed within campus, who were healthy and had no chronic diseases such as heart disease, emphysema, and hypertension.

At the beginning of the experiment, subjects were required to sit in the shade outdoors for 20 minutes for adaption. During this period, the subjects had to fill out a basic information questionnaire, including their physical health, exercise habits, etc. The subjects then put on wearable physiological instruments. After relax, the subjects filled out a subjective questionnaire and started walking on a treadmill at a constant speed of 3.5km/h to simulate moderate-intensity exercise. The subjects first walked for 20 minutes under sun exposure, and then walked for 10 minutes in shadings. This step was repeated twice, which meant that the subjects exercised for a total of 60 minutes. During the exercise, the subjects were asked to fill out the questionnaire survey every ten minutes, physiological parameters were measured simultaneously. During the experiment, subjects were told not to drink water as much as possible. The experiment will be terminated if any of the following three situations occur: (1) the subjects' core temperature reached 38.5℃; (2) the elderly's heart rate reached 130bpm or the young's heart rate reached 180bpm for three minutes; (3) the subjects voluntarily requested to stop the experiment. The experimental site is shown in Fig. 1.

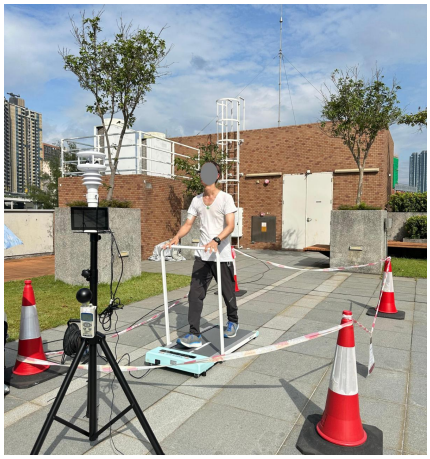

Figure 1. The experiment site.

2.2. Measurements

2.2.1. Physical measurements

The air temperature, relative humidity, wind speed, and wind direction in the shaded environment and the direct sunlight environment were continuously measured by two Mini-weather station (HY-WDS9, HONGYUV, Chengdu, China) during the whole experiment, and the black globe temperature was measured by black bulb thermometer (210SD, LUTRON ELECTRONIC, Coopersburg, USA).

2.2.2. Physiological measurements

Various physiological parameters including core temperature, dehydration status, heart rate, and blood pressure were measured during the experiment. Core temperature (A-166255, greenteg, Rümlang, Zurich), sweat volume (E01, NIX, Boston, USA), and heart rate (DSY-SP-W01F, Delsys, Natick, USA) were tested continuously during the entire experiment using wearable devices, and blood pressure (JPN610T, OMRON, Tokyo, Japan) was tested intermittently 6 times, after resting, after changing exposure conditions during exercise, and before the end of the experiment. The experimental process is shown in Fig 2.

The degree of dehydration of the subject can be expressed by body water loss (BWL). The calculation formula of BWL is as follows:

$$BWL = \frac{m_n - m_w}{m_0} (1)$$

Where m_n represents the total body dehydration of the subject during exercise measured by the wearable device, including sweating and respiratory loss. M_w represents the quantity of water the subject drinks during exercise. M_0 represents the body weights of the subjects before the experiment.

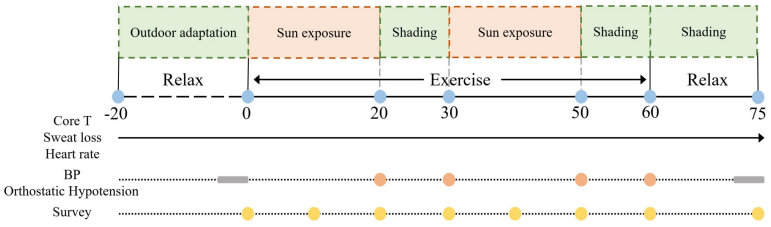

Figure 2. The experimental process.

2.2.3. Subjective measurements

The subjective evaluation was designed for collecting perceptual responses from human subjects, including heat-related and health-related issues. Heat-related questionnaires include thermal sensation vote and thermal comfort vote, both of which used the extended nine-point scale (Xie et al., 2019). The health-related questionnaire was summarized through a survey of heat-related health symptoms, including heat syncope, heat exhaustion, heat stroke, etc. It includes nine questions in total, namely the degree of sweating, thirst, fatigue, muscle cramps, headache, dizziness, palpitations, chest tightness and shortness of breath, and blurred vision of the subjects. Each question is a 10-point scale, with no symptoms (0), mild (1-4), moderate (5-7), and severe (8-10). The four levels of symptoms are described in detail. The subjects need to first select the degree of their symptoms according to the instructions, and then check the corresponding number.

3. RESULTS

3.1. The WBGT during experiments

The experiment was conducted in September 2024, and a total of nine experiments were conducted. The Wet Bulb Globe Temperature (WBGT) is a comprehensive indicators that considered temperature, humidity, solar radiation, and wind speed, evaluating the heat stress under high temperature and humidity. It is globally used to evaluate the heat-health risks of athletes and workers under heat exposure. Fig. 3 shows the WBGT of these nine experiments. It can be found that in each case, the WBGT has two peaks, which are the values in the direct sunlight environment, and the rest of the time are the values in the shadow environment. It can be found that the WBGT in the direct sunlight was basically over 31℃, while the WBGT in the shadings was basically between 28 ℃ and 31℃. According to the guidelines (*Heat Illness Prevention Information: About WBGT*, n.d.), when WBGT exceeds 31℃, it is considered dangerous. Even the elderly may face health risks in the rest room under such conditions, indicating that when subjects exercised under direct sun exposure, the heat stress that they faced was very high. When WBGT is greater than 28℃ and less than 31℃, it is considered a serious warning. It's recommended that everyone avoid direct sunlight when exercising under such conditions, indicating that when subjects exercised in shadings, the heat stress they faced was moderate.

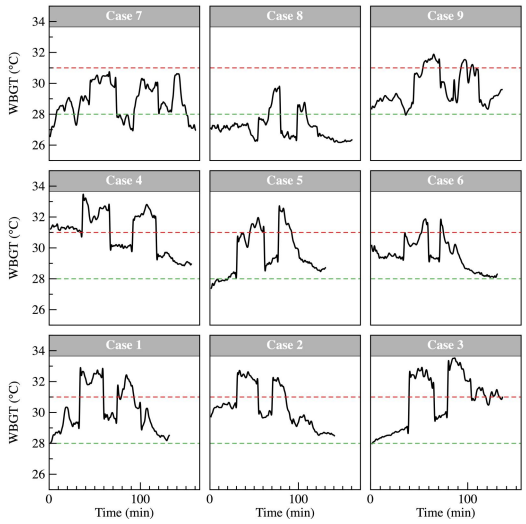

Figure 3. The WBGT during experiments.

3.2. Physiological and psychological responses during experiments

3.2.1. Core temperature and heat-related vote

Fig.4 shows the mean core temperature of both elderly and young group, the shaded area is the error band. It can be seen that after the start of exercise, the core temperature of young people rises faster than that of elderly people, but immediately reaches the threshold of thermoregulation and quickly begins to regulate the body temperature. The core temperature of the elderly

continues to rise during exercise, and the core temperature threshold of thermoregulation is slightly higher than that of young people. And after thermoregulation, their core temperature is still higher than that of young people, approaching 38°C in the later stage of exercise.

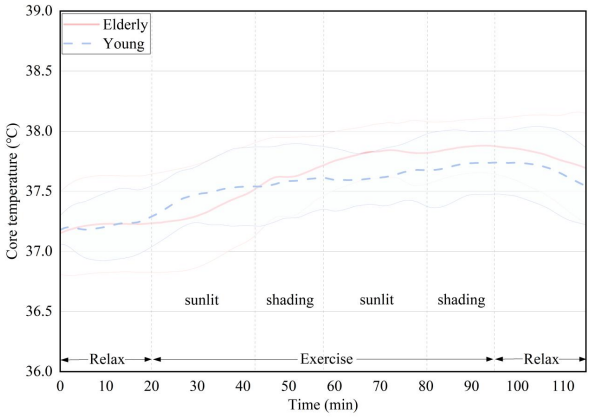

Figure 4. Mean core temperature during experiments.

Fig. 5 and Fig. 6 show the thermal perception votes and thermal comfort votes of the elderly and young people during the experiment respectively. The thermal sensation votes of the elderly and young people were similar, sometimes the elderly's thermal sensation was even higher than the young group, but the thermal comfort votes of the elderly were significantly higher than those of the young people, especially when exercising in direct sunlight. This shows that although the elderly feel that the environment is very hot, they still feel comfortable. It is worth noting that although the core temperature of the elderly was close to 38°C in the later stage of exercise, their thermal comfort voting values were still high, indicating that their thermal sensitivity was poor.

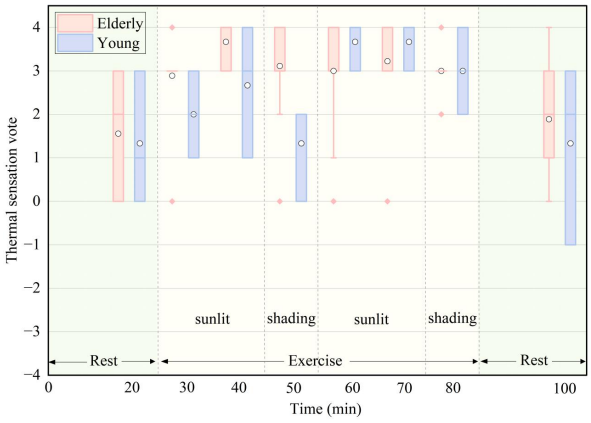

Figure 5. Thermal sensation vote.

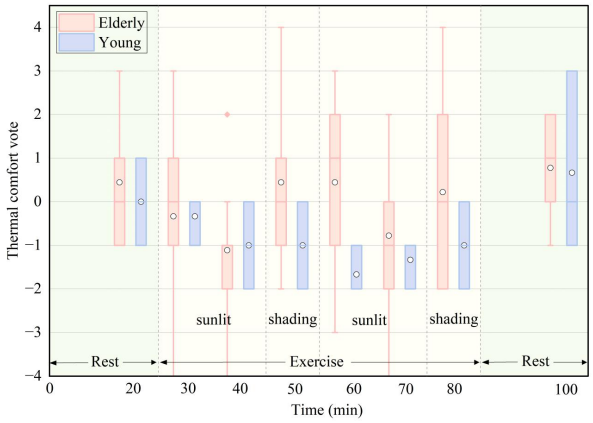

Figure 6. Thermal comfort vote.

3.2.2. Dehydration status and thirsty vote

Fig. 7 shows the degree of dehydration of the elderly and young people during the experiment. It can be found that there is a "scissors gap" between the dehydration of the elderly and the young people, that is, at the beginning of the experiment, the young people sweat more than the elderly, but as the exercise progresses, the elderly sweat significantly more than the young people. This indicated that the elderly's sweating threshold is lower than young group. During the exercise, the body water loss of the elderly reached 2%, and even reached 3% at the end of the experiment, while the body water loss of the young people during the entire experiment was always below 2%, indicating that when doing outdoor exercise under high outdoor heat stress, the risk of dehydration for the elderly is much greater than that for the young.

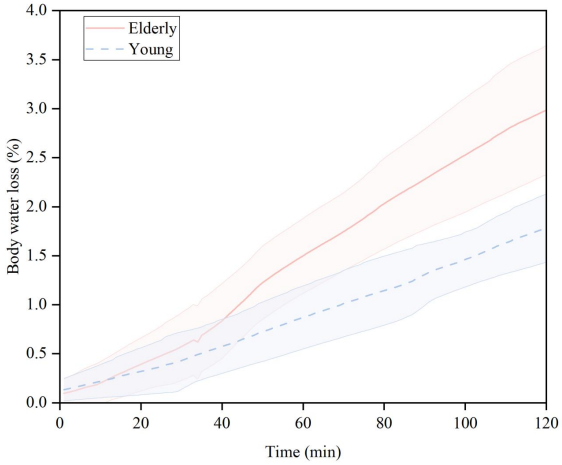

Figure 7. Mean body water loss of different age groups.

Figure 8 shows the thirst votes of the elderly and young people. It can be seen that during the entire experiment, the thirst of the elderly was always lower than that of the young people. As mentioned above, the scale of mild thirst is 1-4, and the scale of moderate thirst is 5-7. During the experiment, the average thirst vote of young people was basically around 4, which was mild thirst, that is, "it's okay not to drink water". In the later stage of exercise, the average thirst vote of young people was close to 5, which was moderate thirst, that is, "realizing that they should drink water, but they can still hold it in." For the elderly, the average thirst vote during the entire

exercise process did not exceed 4, which was mild thirst. After resting after exercise, the thirst even dropped significantly, indicating that the elderly are very insensitive to their own dehydration. The dehydration of the elderly is higher than that of the young, but the thirst vote value is lower than that of the young, which means that the elderly are at risk of dehydration when exercising in high temperatures outdoors because they are unaware of the lack of water.

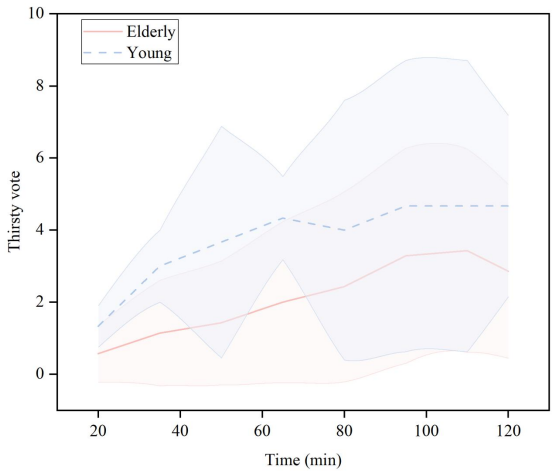

Figure 8. Thirsty vote of different age groups.

4. CONCLUSION

This study aims to investigate the differences in physiological responses and perceptions of the elderly in outdoor high heat stress environments. A total of 12 subjects were recruited to participate in the summer experiment. The subjects were asked to perform moderate-intensity exercise in direct sunlight and shaded environments, and vote on their thermal perception and health-related perceptions at specific time points. At the same time, the subjects' physiological data, including core temperature and sweat rate were collected, and the micro-meteorological station continuously measured the micro-thermal environment. This study shows that the elderly have a delayed perception of their own health status. In the future, the outdoor exposure risk of the elderly will be quantified, and indicators will be further established to regulate the outdoor exercise of the elderly to avoid the occurrence of heat health insurance related problems. The main conclusions are as follows:

(1) The thermal sensation votes of the elderly were similar to those of the young people, but the thermal comfort votes were significantly higher than those of the young people, which means that although the elderly feel hot, they were still comfortable.

(2) The elderly still had a high comfort rating for the thermal environment when their core temperature was dangerous (reach 38 °C), indicating that the elderly is not sensitive to changes of his body temperature.

(3) The sweating threshold of the elderly is lower than the young group. The elderly are more dehydrated than the young, but the thirsty vote of the elderly was always lower than the young group, indicating that the elderly are less sensitive to their own dehydration status and

may not replenish fluid on time, thus put themselves at risk of heat exhaustion.

REFERENCES

Calvin, K., Dasgupta, D., Krinner, G., Mukherji, A., Thorne, P. W., Trisos, C., Romero, J., Aldunce, P., Barrett, K., Blanco, G., Cheung, W. W. L., Connors, S., Denton, F., Diongue-Niang, A., Dodman, D., Garschagen, M., Geden, O., Hayward, B., Jones, C., … Péan, C. (2023). IPCC, 2023: Climate Change 2023: Synthesis Report. Contribution of Working Groups I, II and III to the Sixth Assessment Report of the Intergovernmental Panel on Climate Change [Core Writing Team, H. Lee and J. Romero (eds.)]. IPCC, Geneva, Switzerland. (First). Intergovernmental Panel on Climate Change (IPCC). https://doi.org/10.59327/IPCC/AR6-9789291691647

Climate Issues to Watch in 2023: Toward COP 28 and Faster, More Urgent Climate Action. (2022, December 12). Unfoundation.Org. https://unfoundation.org/blog/post/climate-issues-to-watch-in-2023-toward-cop-28-and-faster-more-urgent-climate-action/

Coates, L., Haynes, K., O'Brien, J., McAneney, J., & de Oliveira, F. D. (2014). Exploring 167 years of vulnerability: An examination of extreme heat events in Australia 1844–2010. Environmental Science & Policy, 42, 33–44. https://doi.org/10.1016/j.envsci.2014.05.003

Conti, S., Meli, P., Minelli, G., Solimini, R., Toccaceli, V., Vichi, M., Beltrano, C., & Perini, L. (2005). Epidemiologic study of mortality during the Summer 2003 heat wave in Italy. Environmental Research, 98(3), 390–399. https://doi.org/10.1016/j.envres.2004.10.009

Hajat, S., & Kosatky, T. (2010). Heat-related mortality: A review and exploration of heterogeneity. Journal of Epidemiology & Community Health, 64(9), 753–760. https://doi.org/10.1136/jech.2009.087999

Heat Illness Prevention Information: About WBGT. (n.d.). Retrieved February 7, 2025, from https://www.wbgt.env.go.jp/en/wbgt.php

Housing in Figures 2024. (2013).

Huang, J., Chen, Y., Jones, P., & Hao, T. (2022). Heat stress and outdoor activities in open spaces of public housing estates in Hong Kong: A perspective of the elderly community. Indoor and Built Environment, 31(6), 1447–1463. https://doi.org/10.1177/1420326X20950448

Xie, Y., Liu, J., Huang, T., Li, J., Niu, J., Mak, C. M., & Lee, T. (2019). Outdoor thermal sensation and logistic regression analysis of comfort range of meteorological parameters in Hong Kong. Building and Environment, 155, 175–186. https://doi.org/10.1016/j.buildenv.2019.03.035

Urban microclimate & Pollutant dispersion (13:30-15:00 h)

6th International Conference on Building Energy and Environment
Eindhoven University of Technology, The Netherlands
6 - 10 July 2025

Transforming air pollution exposure abatement: a vital role for CFD simulations in the implementation of mitigation measures

R. Vervoort [1,2], R. Gijsbers[2], T. van Hooff [1]

[1]*Building Physics and Services, Department of the Built Environment, Eindhoven University of Technology, Eindhoven, the Netherlands, r.p.m.vervoort@tue.nl, t.a.j.v.hooff@tue.nl*

[2]*ENS Clean Air Solutions, Gassel, the Netherlands, r.gijsbers@ens-cleanair.com*

SUMMARY
Rapidly developing societies face environmental challenges, notably air quality issues impacting public health, morbidity, and mortality, with significant socio-economic consequences. The growing awareness of air pollution's adverse effects increases demand for innovative mitigation measures. However, assessing on-site air quality strategies is complex due to fluctuating pollutant concentrations influenced by dynamic environmental factors. Computational fluid dynamics (CFD) simulations offer solutions to these challenges by addressing the limitations of full-scale measurements and enabling systematic scenario analyses. This work demonstrates the practical relevance of CFD simulations using steady Reynolds-averaged Navier-Stokes (RANS) models to study near-field dispersion and particulate matter (PM) mitigation. Despite inherent uncertainties, CFD simulations efficiently provide insights into real-world air pollution issues, supporting clear communication and decision-making. Practical examples highlight how stakeholders utilize these results, emphasizing CFD's vital role in designing effective mitigation strategies.

Keywords: air quality, pollution mitigation, CFD simulations, societal impact.

1. INTRODUCTION

Air pollution is composed of a dynamic mixture of gases and particulate matter (PM). Exposure to PM is widely acknowledged as a health hazard and is considered the main contributor to health effects associated with air pollution (GBD, 2024). A wide body of scientific literature documented positive health-effects and (socio-)economic benefits resulting from air quality improvements (e.g., Laden et al., 2006; Pope et al., 2009; Huang et al., 2018; Schraufnagel et al., 2019). Mitigation of air pollution, particularly PM, is therefore highly significant and of great importance.

Reduction or prevention of air-quality related negative health effects can - evidently - have a positive (socio-)economic impact. Scientific literature reports numerous positive health outcomes correlating to reduction of pollutant concentrations (e.g. Schraufnagel et al., 2019). Tools are available to assess health impact in a simplified way. Usually information is required regarding (spatial distribution of) the population that is being exposed to air pollutants, and evidently detailed spatial quantifications of the latter, to be able to assess the cost-effectiveness of mitigation strategies. Several studies show how geographic information systems can aid in this process (e.g. Bedach et al., 2020). Nevertheless, to calculate the spatial impact of mitigation measures on pollutant concentrations - being the core data for the assessments - additional tools are needed.

Near-field air pollution research can be conducted using either experimental or numerical methods. Experimental work typically involves (full scale) on-site field measurements or reduced scale wind tunnel experiments. Numerical approaches primarily include analytical plume-model based

calculations or computational fluid dynamics (CFD) simulations. Naturally, there are specific reasons to choose one method over the other, depending on the research objectives and constraints. Some advantages and disadvantages can be pivotal in shaping the selection of research methods, effectively ruling out certain approaches. Without delving deeply into the details of all available methods, it can be stated that experimental approaches can sometimes present challenges. For instance, due to scaling constraints it may not be possible to perform wind tunnel tests on complex objects, or it may be impossible to replicate certain key (technological) features. On the other hand, full-scale measurements entail the complexity of dynamic environments, where many conditions may not be controllable (i.e. wind, stratification, pollutant sources, etc.). This can make data interpretation - given a limited number of discrete measurement points - very challenging and occasionally even incomprehensible. As a result, long measurement periods or numerous repetitive tests are often required to achieve research objectives, which can become prohibitively expensive. Such circumstances are generally impractical for engineering practices, where research needs to be systematic and straightforward, avoiding disruptions to ongoing processes.

Testing and optimizing concepts in a 'virtual environment' without the need for expenditure or disruption in practice, could therefore be considered a highly suitable approach for industry. Practitioners often rely on standardized modelling methods to systematically perform scenario analyses (e.g. assessing the effect of mitigation measures). These models - with varying complexity - are mostly based on Gaussian plume and trajectory dispersion methods and operate at meso- (< 200 km) and microscale (< 2 km) levels, but are generally not capable of predicting detailed concentration distributions around (groups of) objects in e.g. an urban environment.

The nature of many engineering tasks related to air pollution (mitigation) often necessitates the use of more advanced, higher spatial-resolution calculation tools, such as CFD. CFD simulations are able to overcome most of the limitations associated with aforementioned methods. This article presents three case studies, with only a brief discussion of the numerical setup in the methodology section. In addition, some further perspective on suitability of quantification methods is given, by briefly addressing some of the experimental work that was done for these case studies. The goal of this manuscript is to illustrate how engineering practice can benefit from the application of CFD.

2. METHODOLOGY

This section outlines the research methodologies adopted. Only the main characteristics are mentioned for the sake of brevity; a detailed description of each distinct case study is not included.

2.1. Numerical

This manuscript presents case studies based on 3D steady RANS analysis in combination with the standard or realizable k-ε turbulence model, using either standard or scalable wall functions. Second-order discretization schemes were adopted for all modeling quantities. Simulations are conducted on highly detailed hybrid grids, partially structured and unstructured, based on manual and automated meshing procedures. The grids were created in accordance with best-practice guidelines (e.g. Franke et al., 2007; Blocken, 2015). Pollutant concentrations are calculated using Eulerian approaches; PM is represented by a passive scalar and modeled with an advection-diffusion equation and standard gradient-diffusion hypothesis, depending on the case, with or without gravitational settling and deposition (method adopted from Chen et al., 2006), using

constant turbulent Schmidt number (Sc_t) of 0.7. Such modeling procedures were previously validated and verified by e.g. Chen et al., (2006), Blocken et al., (2016) and Vervoort et al., (2019).

2.2. Experimental

The presented case studies also involved some on-site experimental activities. Measurements were conducted using 'Grimm EDM-164' high-resolution research-grade optical measurement equipment (Grimm & Eatough, 2009) and weather stations. Local PM concentrations, including particle size distributions, can vary greatly in time and space due to variations in environmental conditions and on-site processes and related emissions. Reference measurement methods rely on data sampling and integration over extended periods, which are not expected to provide a suitable temporal resolution necessary for the case studies presented. Use of low-cost PM sensors was purposely avoided because of the many well-known (potential) issues inherently related to the use of low-cost sensors (e.g. Karagulian et al., 2019; Alfano et al., 2020; Kuula et al. 2020).

3. CASE STUDIES

This paragraph demonstrates how CFD simulations are adopted in the mitigation of real-world air pollution issues. The case studies presented differ significantly in the nature of the pollution problems and situational conditions, covering (1) a bus terminal, (2) an industrial facility and (3) railway works. For each case, the pollution issue is outlined, followed by the rationale for using CFD simulations and a concise summary of key insights.

3.1. Bus terminal

This study focused on a bus terminal, with a capacity of 43 buses, which is being used by approximately 10,000 daily commuters, each spending about 30 minutes per day at the terminal (waiting for buses). In this building, short-term exposure risks are high due to the concentrated amount of people and the buses that emit pollutants in a semi-enclosed volume (empty ~30,000 m^3). To assess possibilities to alleviate exposure risks inside this building, a CFD analysis was conducted including nine high-capacity air purification systems (total ~66,000 m^3/h).

CFD simulations were selected to be the most appropriate method of analysis considering that this involves a highly complex case with a lot of uncontrollable and unregistrable variability, such as (1) moving and parked cars and buses, (2) presence and potential interference by people, and (3) the presence of ceiling-mounted air circulation units for which the control strategy was not clear. In addition, due to the open characteristics of the building and the relatively open upstream wind fetch, high wind-driven ventilation rates and limited percentual mean PM reduction levels are anticipated. All in all, this makes assessment based on full-scale PM measurements (pre- and post-mitigation) unfeasible when long-term measurements (i.e. min. several months) are ruled out.

A multi-scenario analysis was conducted using CFD simulations, covering several critical wind directions, variations in wind speed, and mechanical ventilation settings. The CFD model includes a detailed representation of the bus terminal as well as the main buildings nearby (Fig. 1a-d), which are expected to significantly influence airflow within the terminal (Fig. 1e-f). The study gave clear insight into the spatial performance of the purification units. Anticipated mean PM reductions were presented in the form of 2D contours and zonal quantifications (Fig. 1g-j), which can be adopted in socio-economic impact assessments. Additional suggestions, to improve the local effectiveness

of purification units, such as adapting the building envelope and implementing a targeted control strategy for the existing mechanical ventilation, were provided. Finally, the modeling approach was adopted by Oh et al. (2024) to conduct their own analysis.

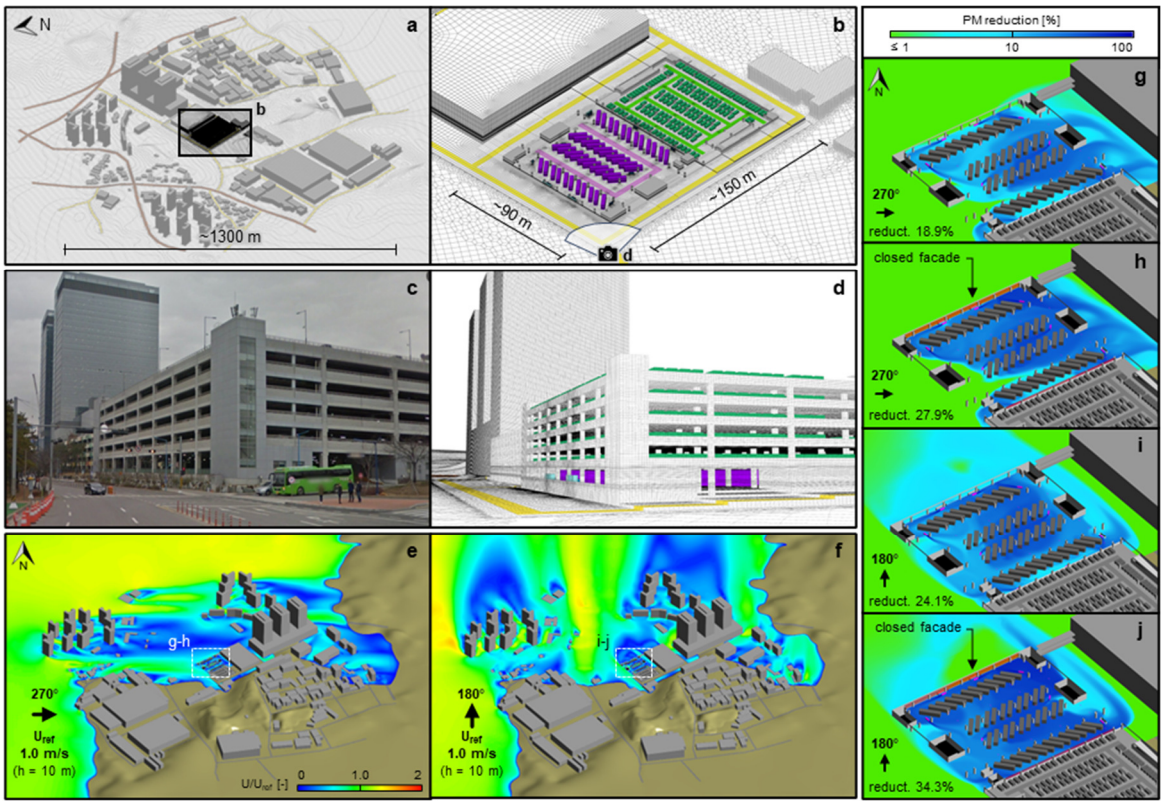

Figure 1. Overview of bus terminal case study: (a-d) computational grid bus station with surroundings, (e-f) flow entire domain for two wind directions and (g-j) PM reduction mitigation measure for two wind directions (g,i) including (h,j) façade adaptation. Contours are shown for the bus station ground floor at 1.1 m height (h = 23.1 m).

3.2. Industrial facility

This study focused on the working environment inside a large industrial facility consisting of several interconnected compartments with a total volume of ~280,000 m^3, partly naturally and partly mechanically ventilated. The scope of the study was to focus on one specific area within one of the sub compartments, where most of the labor takes place (thus exposure risks are most significant), and working processes evidently result in elevated PM concentrations.

Four weeks of full-scale measurements were conducted using four monitors in an attempt to identify the nature of PM-related issues within the facility. Because no permission was granted to install cameras to oversee processes within the facility, personnel were instructed to register the opening of large internal and external doors, working procedures, and any other events that may affect PM concentrations procedures. The measurement campaign and data analysis yielded several key conclusions: PM concentrations exhibited numerous high peaks, with significant variations between locations (Fig. 2a). Various processes across the facility contributed to concentration peaks, with some activities leading to persistently high background levels (Fig. 2b). However, dust-generating actions in the sub-compartment of interest occurred infrequently and were not the sole contributors to high concentrations. The complexity of airflow patterns in and

around the facility made it difficult to identify clear trends from measurement data. Furthermore, manually registering daily activities proved to be insufficiently accurate.

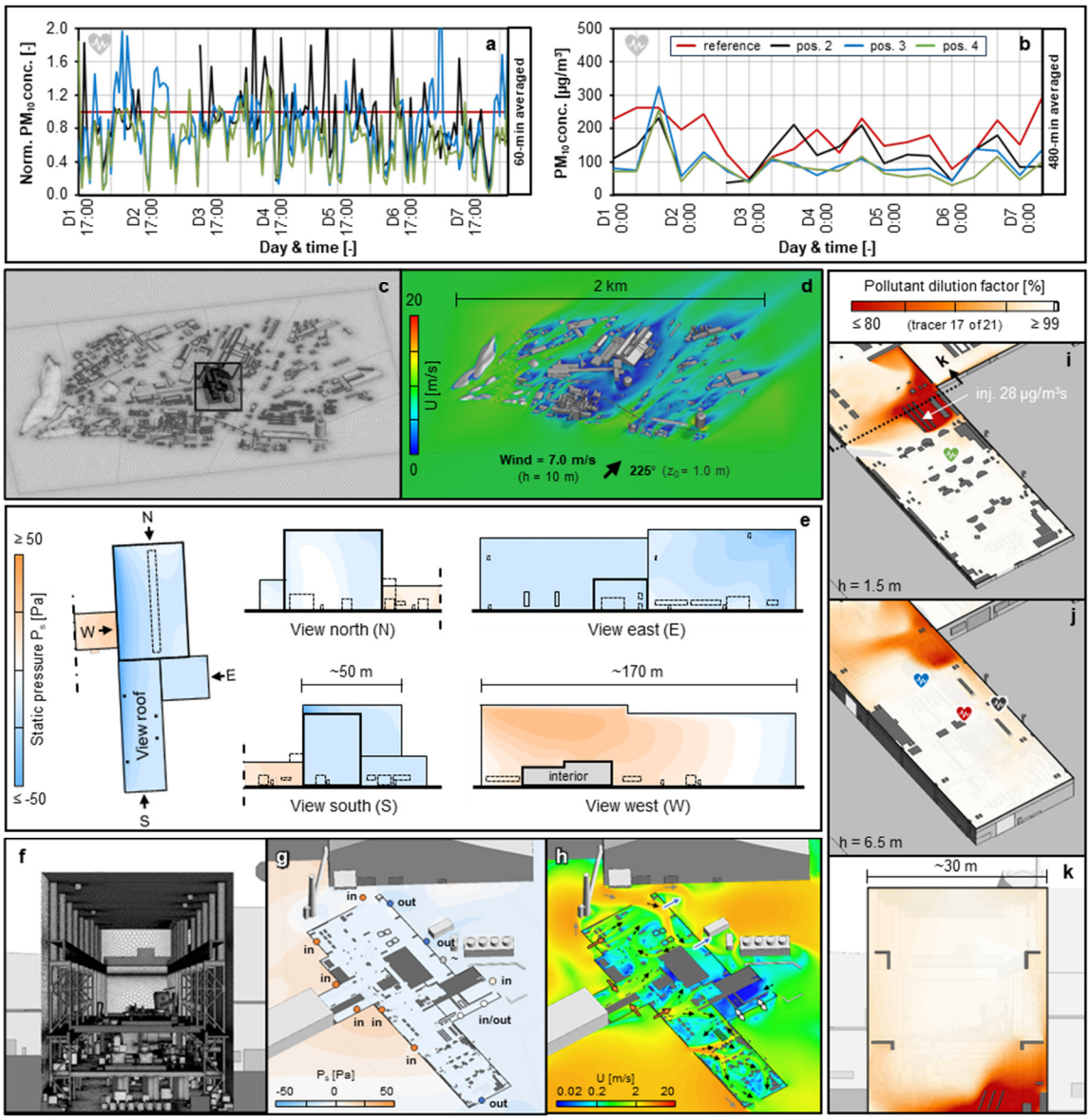

Figure 2. Overview of industrial facility case study: (a-b) One week of PM_{10} concentration measurements at 4 locations; (a) normalized 60-min and (b) absolute 480-min averages (date-time stamp at end of measurement interval), (c) computational grid surroundings, (d) airflow entire domain, (e) pressure faces building of interest, (f) detailed grid building, (g-h) airflow inside building, (i-k) dispersion pattern of one of the tracers injected inside the facility.

Therefore, CFD simulations were employed to gain a better general understanding of site dynamics. The analysis followed a multi-step approach, starting with modeling the airflow and pressure distribution around the building of interest (for a few critical wind directions; Fig. 2c-d). After obtaining information on the pressure distributions at façade openings (Fig. 2e), a more detailed analysis was conducted on the airflow inside the facility (i.e. ventilation effectiveness), considering several critical operational scenarios regarding e.g. mechanical ventilation settings and opening/closing of internal and external doors (Fig. 2f-h). Then several passive pollutant sources

were included at either (1) locations where large amounts of air are displaced or where air exchange occurs between different building compartments, or (2) at locations where employees indicated that a significant amount of dust is likely to be generated. The pollutant source locations were therefore chosen partly generically and partly with specific operational conditions of the facility in mind, primarily to map internal distribution pathways (Fig. 2i-k).

Based on insights from both measurements and CFD simulations, bottlenecks were identified, leading to targeted strategies to reduce PM exposure risks. Solutions ranged from relatively simple interventions, such as policies for workers, building compartmentalization, and optimization of existing building management systems, to more advanced technological interventions.

3.3. Railway works

This study involves a technical intervention to limit PM dispersion during railway works. Most railway tracks are laid on a bed of stones, so-called 'ballast'. However, various materials in this bed of ballast may pose health risks when inhaled, such as respirable crystalline silica (quartz). These risks are particularly high during railway works, as certain processes can erode the material and disperse PM into the surrounding environment (Fig. 3a). This case study involves a machine (SSP 110 SW) which is being used to distribute and profile ballast. A (concept) technological intervention was engineered aimed at limiting dispersion of airborne PM from a brushing compartment by generating a low-pressure zone inside it.

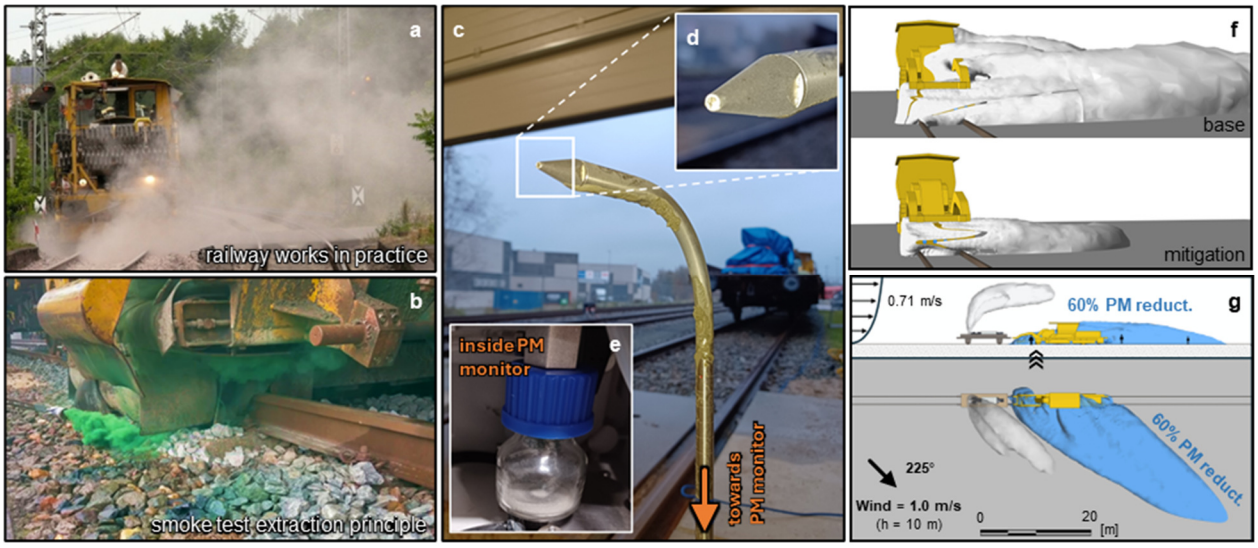

Figure 3. Overview of railway works case study: (a) SSP 110 SW railway works in progress showing the occurrence of a dust 'cloud'; (b) smoke test to assess mitigation extraction principle; (c-e) unsuitable conditions for in-duct isokinetic PM measurements with (c) mud- or cement-like material that deposits on the sampling probe, (d) leading to slippage of the sampling nozzle and (e) sand grain-sized particles accumulation inside the PM monitor (conditions qualified for causing serious damage to equipment); (f-g) indicative figures of CFD analysis effect mitigation measure.

In this case CFD simulations were combined with on-site experiments. Several factors influenced the decision not to rely solely on measurements: (1) The winter measurement period featured low air temperatures and even lower surface temperatures, leading to condensation on metal components and clogging of measurement equipment (Fig. 3c-e); (2) extremely high PM concentrations were present, ranging from a few to tens of mg/m^3, further exacerbates this issue.

(3) The available railway track for testing was limited to 75 meters, making long continuous brushing runs unfeasible (max. 5 min per run). (4) Wind conditions were rather unstable, with high velocities and strong gusts. (5) The available measurement window was restricted to a maximum of 1.5 working days due to scheduled railway works. These challenges, among others, made it difficult to obtain reliable data within the given timeframe.

A few targeted measurements were conducted to characterize (strongly varying) PM particle size distributions to be able to determine the single-pass purification efficiency of the purification chamber. Smoke tests combined with detailed airflow measurements (duct traversing) were performed to identify leaks, determine the total required extraction volume flow rate through multiple extraction openings, and control the respective airflow valves (Fig. 3b). These results were then incorporated into CFD simulations to assess the intervention's impact on the working environment around the machine and to evaluate its effectiveness in limiting the spread of (respirable) PM to the surroundings (Fig. 3f-g).

4. DISCUSSION AND CONCLUSIONS

Conducting full-scale assessments of mitigation measures presents significant challenges. The high costs associated with state-of-the-art equipment, the need for extended measurement periods to capture relevant environmental conditions, and the requirement for mitigation measures to already be in place, all contribute to the complexity of such studies. Additionally, there is a risk of data misinterpretation or a lack of comprehensive understanding of the underlying processes.

The presented case studies highlight the potential of high-resolution numerical analyses, such as CFD simulations, as a cost-effective and systematic alternative to traditional measurement-based assessments. Unlike point-based measurements, which provide limited data at specific locations, CFD simulations offer whole-flow field insights, leading to a more comprehensive overall understanding. It should be noted that the results are subjective to modeling simplifications. Nonetheless, CFD enables a broader perspective, including possibilities for socio-economic impact assessments. While CFD is a powerful tool on its own, it becomes even more valuable when combined with targeted measurements and practical tests, forming a robust methodology for addressing complex environmental engineering challenges

As Blocken (2018) noted, steady RANS simulations remain the workhorse of engineering practice. This article further demonstrates that 3D steady RANS simulations can provide valuable insights into various engineering challenges, particularly in cases where alternative methods - such as measurements or plume models - are either impractical or unsuitable. More computationally intensive approaches, such as large eddy simulation (LES) and Lagrangian particle trajectory modeling, were not feasible for the current case studies due to their scale and complexity. The primary objective of the simulations was to gain general, systematic insights by assessing mean quantities rather than precisely replicating pollution episodes. Given the inherent simplifications of the case studies, the use of higher-fidelity numerical methods would not have been justifiable.

It is important to acknowledge the limitations of the presented case studies, which are inherently linked to the applied numerical methodologies. These limitations are well understood by the authors but fall outside the scope of this manuscript. Nevertheless, CFD simulations have proven

to be a powerful tool for assessing and communicating the potential impact of mitigation strategies. CFD simulations can help bridge the gap between research and practical implementation, offering valuable guidance for reducing air pollution exposure risks in complex real-world scenarios.

ACKNOWLEDGEMENTS

The authors thank Alessio Ricci for his support in grid generation for the bus terminal CFD analysis. They also appreciate the collaboration with Strukton Rail Nederland and ProRail in the railway works case study.

REFERENCES

Alfano, B., Barretta, L., Del Giudice, A., De Vito, S., Di Francia, G., Esposito, E., Formisano, F., Massera, E., Miglietta, M. L., Polichetti, T. (2020). A Review of Low-Cost Particulate Matter Sensors from the Developers' Perspectives. Sensors, 20, 6819.

Badach, J., Voordeckers, D., Nyka, L., van Acker, M. (2020). A framework for Air Quality Management Zones - Useful GIS-based tool for urban planning: Case studies in Antwerp and Gdańsk. Building and Evnrionment, 174.

Blocken, B. (2015). Computational Fluid Dynamics for urban physics: Importance, scales, possibilities, limitations and ten tips and tricks towards accurate and reliable simulations. Building and Environment, 91.

Blocken, B. (2018). LES over RANS in building simulation for outdoor and indoor applications: A foregone conclusion? Building Simulation, 11, 821-870.

Blocken, B., Vervoort, R., van Hooff, T. (2016). Reduction of outdoor particulate matter concentrations by local removal in semi-enclosed parking garages: A preliminary case study for Eindhoven city center. Journal of Wind Engineering and Industrial Aerodynamics, 159, 80-98.

Chen, F., Yu, S.C.M., Lai, A.C.K. (2006). Modeling particle distribution and deposition in indoor environments with a new drift–flux model. Atmospheric Environment, 40, 357-367.

Franke, J., Hellsten, A., Schlünzen, H., Carissimo, B. (2007). Best practice guideline for the CFD simulation of flows in the urban environment. COST Action 732.

GBD 2021 Risk Factors Collaborators (2024). Global burden and strength of evidence for 88 risk factors in 204 countries and 811 subnational locations, 1990-2021: a systematic analysis for the Global Burden of Disease Study 2021. The Lancet, 403, 2162-2203.

Grimm, H., Eatough, D.J. (2009). Aerosol Measurement: The use of optical light scattering for the determination of particulate size distribution, and particulate mass, including the semi-volatile fraction. Journal of the Air & Waste Management Association, 59, 101-107.

Huang, J., Pan, X., Guo, X., Li, G. (2018). Health impact of China's Air Pollution Prevention and Control Action Plan: an analysis of national air quality monitoring and mortality data. The Lancet Planetary Health, 2, 313-323.

Karagulian, F., Gerboles, M., Barbiere, M., Kotsev, A., Lagler, F., Borowiak, A., (2019). Review of sensors for air quality monitoring. EUR 29826 EN, Publications Office of the European Union, Luxembourg, ISBN 978-92-76-09255-1, JRC116534.

Kuula, J., Mäkelä, T., Aurela, M., Teinilä, K., Varjonen, S., González, Ó., Timonen, H. (2020). Laboratory evaluation of particle-size selectivity of optical low-cost particulate matter sensors. Atmospheric Measurement Techniques, 13, 2413-2423.

Laden, F., Schwartz, J., Speizer, F. E., Dockery, D. W. (2006). Reduction in fine particulate air pollution and mortality: Extended follow-up of the Harvard Six Cities study. American journal of respiratory and critical care medicine, 173, 667-672.

Neumann, P.J., Anderson, J.E., Panzer, A.D., Pope, E., D'Cruz, B.N., Kim, D.D., Cohen J.T. (2018). PHP212 - Comparing Cost-Per-Qalys Gained And Cost-Per-Dalys Averted Analyses. Value in Health, 21.

Oh, S., Chang, J., Jeong, J., Yang, D., Ham, D., Kwon, H., Choi, H., Kim, M., Ha, J., Heo, H., Vervoort, R., Lee, H., (2024). Effects of air purifiers and ventilation on particulate matter concentration at semi-outdoor space. Journal of Cleaner Production, 434.

Pope, C.A., 3rd, Ezzati, M., Dockery, D.W. (2009). Fine-particulate air pollution and life expectancy in the United States. The New England journal of medicine, 360, 376-386.

Schraufnagel, D.E., Balmes, J.R., De Matteis, S., Hoffman, B., Kim, W.J., Perez-Padilla, R., Rice, M., Sood, A., Vanker, A., Wuebbles, D.J. (2019). Health Benefits of Air Pollution Reduction. Annals of the American Thoracic Society, 16, 1478-1487.

Vervoort, R., Blocken, B., van Hooff, T. (2019). Reduction of particulate matter concentrations by local removal in a building courtyard: Case study for the Delhi American Embassy School. Science of the Total Environment, 686, 657-680.

6th International Conference on Building Energy and Environment
Eindhoven University of Technology, The Netherlands
6 - 10 July 2025

Numerical investigation of pollutants dispersion characteristics at tunnels in plain and high-altitude areas

Jinxing Li [1], Hongyuan Yang [2], Junjie Liu[3] , Jinjin Pei[4], Xiaoxuan Li[5]

[1]*Tanjin University, Tian Jin, China, Lijinxing@tju.edu.cn*
[2] *Tianjin Municipal Engineering Design & Research Institute, Tian Jin, China,49345440@qq.com*

SUMMARY
In high-altitude tunnels, due to the ambient pressure and density of air being different from those under normal pressure, the pollutant emissions caused by mechanical and electrical equipment varies under different operating conditions. As a result, the diffusion characteristics of pollutants in high-altitude tunnels are different from those in plain areas,and corresponding adjustments need to be made to the pollution sources when studying the ventilation environment in tunnels.The study is based on three-dimensional thermo-hydraulic Computational Fluid Dynamics simulations accounting for the actual fluid flow that occurs in the aforementioned environments, and analyze the diffusion characteristics of pollutants by comparing the pollutant concentrations, diffusion coefficients, and altitude correction factors in tunnels under normal pressure and high altitude.The work also presents novel relationships between pollutant concentration and atmospheric pressure that may be used in the analysis and design of tunnel ventilation system.

Keywords: pollutant dispersion, Plateau tunnel, Numerical simulation.

1. INTRODUCTION

In recent years, with the increase in high-altitude tunnel projects, some studies have begun to focus on the special effects of high-altitude environments on tunnel ventilation. Some studies have revealed the distribution patterns of pollutant concentrations after blasting operations in high-altitude tunnels through on-site monitoring (Zou et al., 2020). Meanwhile, numerical simulation methods have also been widely used to study the pollutant diffusion characteristics in high-altitude tunnels (Huang et al., 2020; Chang et al., 2020). Chang et al. studied the diffusion mechanism of harmful gases by simulating the tunnel flow field under different ventilation modes and derived a ventilation time estimation function.

However, existing studies still have certain limitations. Most studies have focused on the analysis of pollutant diffusion in ventilated tunnels, and relatively few studies have been conducted on the pollutant diffusion characteristics in unventilated single-ended tunnels under altitude changes. On the other hand, although some studies have considered altitude factors, the research on how altitude affects various coefficients and thus affects ventilation volume and ventilation time is not in-depth enough when establishing pollutant diffusion models, lacking a systematic mathematical model to accurately describe this process.

This study aims to fill the above gaps. Through detailed CFD simulations, the variation law of pollutant diffusion characteristics in unventilated single-ended tunnels with the altitude changing from 0km to 4km is deeply studied.

2. MODEL AND BOUNDARY CONDITIONS

The research object is the Huzhu Beishan extra - long tunnel. The altitude of the area where the tunnel is located ranges from 2,815 meters to 3,699 meters, belonging to a high - altitude region. This area has many characteristics such as low air density, low atmospheric pressure, low ambient temperature, low oxygen concentration, and a decline in human body functions. The ventilation environment is importance. During the tunnel construction, the area near the working face is the most polluted and the most difficult to ventilate. Thus, a model is established within a certain distance from the working face to the air supply outlet.

The boundary conditions and relevant parameters need to be set with reference to the real - world environmental conditions. Fluent is used to simulate the diffusion law of polluted gases near the working face. The boundary conditions are set as follows:

(1) Assume that the polluted gases generated during the working process are mainly CO and CO_2 gases, and there are no other pollution sources in the tunnel.(2) The outlet boundary is set as a pressure outlet.(3) For the fixed wall boundary, the working face and the tunnel surface are set as wall boundaries with no slip and no heat exchange.

2.1. GEOMETRIC MODEL AND MESH

According to the tunnel construction design plan, the geometric model for numerical calculation is set up as follows: The tunnel cross-section is a fan-shaped with a radius of 6 m. The tunnel entrance ventilation method is forced ventilation, with the ventilation duct positioned 15 m from the tunnel working face, installed at a height of 4 m, and with a duct diameter of 1.6 m. Fluent software is employed to simulate pollutant diffusion during high-altitude tunnel construction, ignoring the gantry and other special components during the construction period. The three-dimensional modeling software Space Claim is used to create the tunnel geometric model.

For the numerical calculation model of tunnel ventilation, the quality of the mesh significantly impacts simulation results, with structured meshes yielding more accurate simulation outcomes. Fluent Meshing software was used to generate three different mesh densities for the geometric model: Mesh 1 (373,453 elements), Mesh 2 (627,660 elements), and Mesh 3 (976,560 elements). Grid independence tests were conducted for these three different meshes, with results shown in Figure 2.

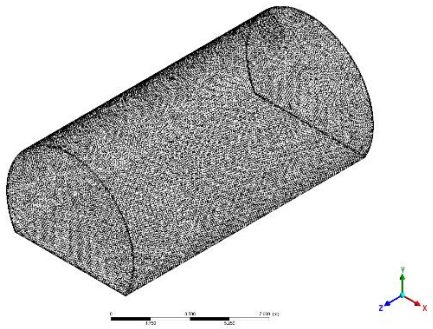

Figure 1. Geometry and face meshing of numerical model.

From Figure 2, it can be observed that the results from Mesh 2 and Mesh 3 are similar, with only Mesh 1 showing slight differences compared to Meshes 2 and 3. However, overall, these differences are relatively minor. Considering both computational performance and mesh quality, Mesh 2 was selected for mesh generation and calculations. When dividing the model mesh, boundary layers were set at the model interfaces to better reflect actual conditions. The final mesh count was 627,660 elements, with good mesh quality that satisfied the computational requirements of this study.

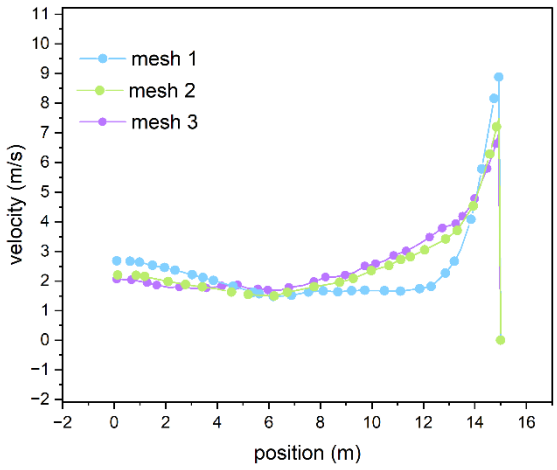

Figure 2. Grid independence.

2.2. BOUNDARY CONDITIONS

In order to carry out effective and reliable numerical simulation, the following assumptions were made in combination with the actual situation (Sun et al., 2018).

(1) The hazardous gases produced by blasting do not have chemical reaction and phase change reaction during diffusion. (2) The air and hazardous gases in the construction tunnel are idealized as three-dimensional viscous incompressible fluids. (3) Assume that all pollution sources release pollutants constantly and there are no other pollution sources in the tunnel. The mathematical model was based on the above.

Continuity equation:

$$\frac{\partial \rho}{\partial t} + \frac{\partial}{\partial x_j}(\rho u_i) = 0 \tag{1}$$

Momentum conservation equation:

$$\frac{\partial u_i}{\partial t} + u_j \frac{\partial u_i}{\partial x_j} = -\frac{1}{\rho}\frac{\partial P}{\partial x_i} + \frac{1}{\rho}\frac{\partial}{\partial x_j}\left[\mu\left(\frac{\partial u_i}{\partial x_j} + \frac{\partial u_j}{\partial x_i}\right)\right] + g_i \beta_T (T - T_0) \tag{2}$$

Energy conservation equation:

$$C_p[\frac{\partial(\rho T)}{\partial t} + u_j \frac{\partial(\rho T)}{\partial x_j}] = \frac{\partial}{\partial x_j}(k \frac{\partial T}{\partial x_j}) + S_T \quad (3)$$

Species transport equation:

$$\frac{\partial(\rho Y_s)}{\partial t} + u_j \frac{\partial(\rho u_i Y_s)}{\partial x_j} = \frac{\partial}{\partial x_j}(\rho D_s \frac{\partial Y_s}{\partial x_j}) + S_{Y_s} \quad (4)$$

Compared with the Standard k-ε model, the Realizable k-ε model improves the calculation of turbulent viscosity and introduces a constraint on the ε equation to ensure that the turbulent normal stresses remain positive, thereby better capturing the characteristics of complex flows. The equations for k and ε are as follows:

$$\frac{\partial(\rho k)}{\partial t} + u_j \frac{\partial(\rho k u_i)}{\partial x_j} = \frac{\partial}{\partial x_j}\left[\left(\mu + \frac{\mu_t}{\sigma_k}\right)\frac{\partial k}{\partial x_j}\right] + G_k - \rho\varepsilon + G_b - Y_M \quad (5)$$

$$\frac{\partial(\rho \varepsilon)}{\partial t} + u_j \frac{\partial(\rho \varepsilon u_i)}{\partial x_j} = \frac{\partial}{\partial x_j}\left[\left(\mu + \frac{\mu_t}{\sigma_\varepsilon}\right)\frac{\partial \varepsilon}{\partial x_j}\right] + C_{1\varepsilon}\frac{\varepsilon}{k}(G_k + C_{3\varepsilon}G_b) - C_{2\varepsilon}\rho\frac{\varepsilon^2}{k} \quad (6)$$

where t is the time; u_i and u_j are the components of the velocity vector, m/s; x_i and x_j are the components of the coordinate system, m; ρ is the density, kg/m³; P is the pressure, Pa; g_i is the acceleration of gravity in i direction, m/s²; T is the temperature, K; μ is the dynamic viscosity, Pa·s; μ_t is the turbulent viscosity, Pa·s; C_p is the specific heat capacity at constant pressure, J/(kg·K); S_{Y_s} is the source term of the s component; Y_s is the mass fraction of the s component.

In this simulation study, we need to use local meteorological data as a reference, and apply relevant formulas to calculate and correct the physical properties of air at different altitudes, including atmospheric pressure, air density, environmental temperature, oxygen content, and other environmental parameters. Since the relationship between atmospheric pressure and altitude is non-linear and air is considered a compressible fluid within a certain height range, the calculation method for atmospheric pressure from sea level to 11 kilometers altitude is as follows:

$$P = 101325 \times (1 - \frac{H}{44329})^{5.2559} \quad (7)$$

where, P is the atmospheric pressure at altitude H, Pa; H is altitude, m.

In high-altitude areas, due to low oxygen concentration, combustion processes are often incomplete, resulting in emission chemical reaction equations that differ from those under standard atmospheric pressure. For diesel engines (commonly used in tunnel construction equipment), the incomplete combustion reaction at high altitudes can be expressed as:

$$C_xH_y + nO_2 \rightarrow aCO_2 + bCO + cH_2O + dC + hHC \quad (8)$$

Where n represents the theoretical amount of oxygen required for complete combustion. Ignoring HC and C emissions, the low oxygen partial pressure in high-altitude regions alters the mixing ratio of fuel and oxygen, leading to an increased CO/CO_2 ratio and higher emissions of unburned

hydrocarbons and particulate matter.

The chemical reaction equations for incomplete combustion are significant for accurately simulating the generation and dispersion of pollutants in high-altitude tunnels. Emission coefficients selected from previous research (Yan et al., 2021) are calculated and input into the CFD model as baseline data for pollution source terms.

The settings of other solvers are shown in Table 1.

Table 1. Major settings in numerical simulation.

Parameter	Values and settings
Time	Steady
Solver type	Pressure- based
Turbulence model	Realizable k-ε
Pressure-Velocity coupling scheme	Couple

3. RESULT

3.1. ANALYSIS OF CO EMISSION PATTERNS

To study the diffusion patterns of polluted gases at different altitudes, the diffusion patterns of polluted gases near the working face were simulated at altitudes of 0 m, 1000 m, 2000 m, 3000 m, and 4000 m respectively, with other conditions and parameters kept unchanged. Due to the variations in environmental parameters, there were differences in the source intensity and distribution of polluted gases. Fig. 2 shows the differences in the source intensity of polluted gases at different altitudes.

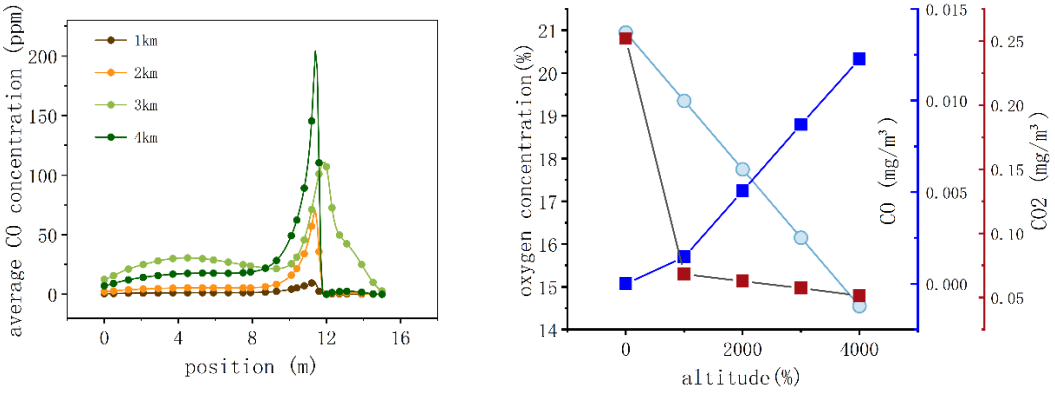

Figure 2. The concentrations of polluted gases at different altitudes.

Due to the changes in the physical properties of gases caused by the increase in altitude, the source intensities of pollutants in different altitude environments are different as calculated. To further study the diffusion levels of the same pollutant source intensity at different altitudes, CFD simulations were carried out. The concentration levels of the polluted gases after the simulations are shown in the Fig. 2 below.

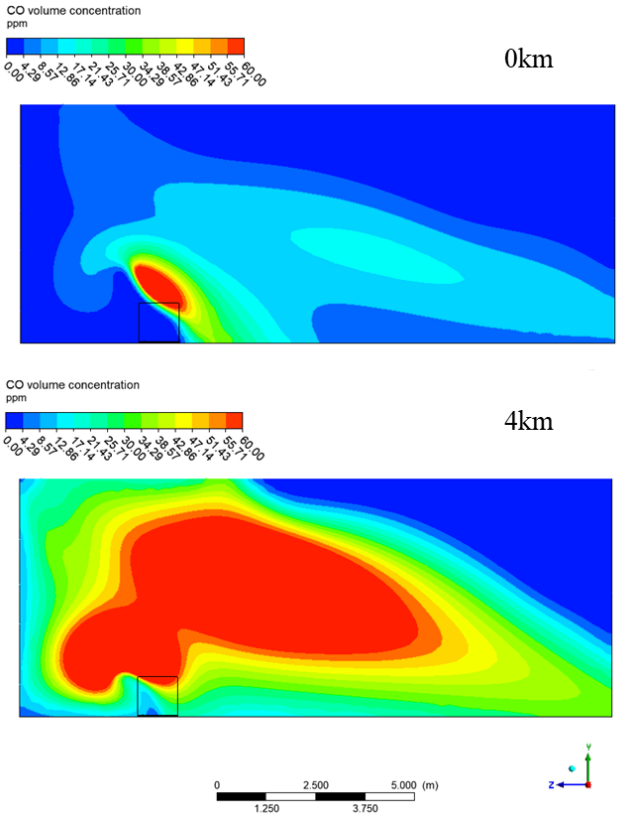

Figure 2. CO concentration distribution.

From the simulation results, even if the source intensity of pollutants remains the same, the concentration distribution of polluted gases varies under different environmental conditions. According to the previous analysis of the mathematical model, such differences are due to the fact that different environments affect the gas diffusion coefficient, thus resulting in differences in the pollutant concentration distribution. By using relevant analysis methods, the correlation between the diffusion coefficient and environmental conditions can be further analyzed.

3.2. ANALYSIS OF THE IMPACT OF ALTITUDE ON CO DIFFUSION

To study the impact of altitude on CO gas diffusion during high-altitude tunnel construction, the variation in tunnel CO mass concentration was calculated for five altitude scenarios (0, 1,000, 2,000, 3,000, and 4,000 meters). All parameters except altitude remained the same. The meteorological parameters used in the study are shown in Table 2.

Table 2. The meteorological parameters.

Altitude (m)	Pressure (Pa)	Air Temperature (℃)	Air Density (kg/m³)
0	101325	15	1.225
1000	89870	8.5	1.112
2000	79500	2	1.007
3000	70110	-4.5	0.909
4000	61640	-11	0.819

As altitude increases, various environmental factors in the atmospheric environment such as air

density, atmospheric pressure, temperature, and humidity will change. Even with the same source intensity, these changes cause the volume of pollutant gases to increase with altitude, resulting in differences in the mass concentration distribution of pollutant gases during the diffusion process in tunnel chambers. The change in atmospheric pressure is the main reason for ventilation differences in high-altitude tunnel areas. Changes in atmospheric pressure alter the static pressure distribution in tunnel chambers, affecting the tunnel's ability to remove pollutants (Cao et al., 2016). Therefore, when studying the impact of altitude changes on CO diffusion in tunnels, temperature and humidity changes are ignored, and only the two main factors of atmospheric pressure and air density are considered.

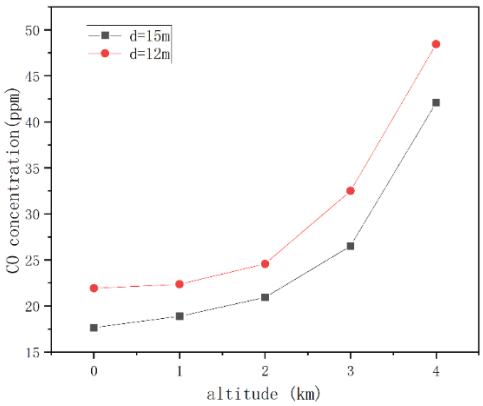

Figure 3. CO concentration at different altitudes.

During the ventilation process, vortex zones form near the tunnel face. Consequently, in the initial stages of CO diffusion, the distribution pattern near the face is highly complex due to the influence of vortices and airflow recirculation. Cross-sections at 12 and 15 meters from the tunnel face are selected to calculate the variation in CO mass concentration at different altitudes, as shown in Figure 3. It is observed that as altitude gradually increases, the CO mass concentration at the same measurement point in the tunnel rises.

To further investigate the relationship between CO mass concentration and altitude during the diffusion process, introduce an altitude-based correction coefficient for CO mass concentration. Under the same ventilation time and distance, assume that the CO mass concentration in a high-altitude tunnel is:

$$C_P = f(C_0,\ P) \tag{9}$$

Where C_P is the CO concentration at altitude p, and P is the atmospheric pressure.

Selecting monitoring planes at 3-meter intervals within the CO diffusion area, recording the average concentration on each plane, and calculating the variation of CO mass concentration with altitude in this region, the results are shown in Table 3.

Table 3. The meteorological parameters.

Altitude (m)	Plane 1	Plane 2	Plane 3	Plane 4	Plane 5
0	2.68	4.78	7.61	10.61	10.63

1000	2.73	4.72	7.30	10.24	7.58
2000	3.02	5.23	8.02	11.19	7.63
3000	4.06	7.17	11.31	15.73	15.54
4000	6.87	18.60	28..41	39.34	48.06

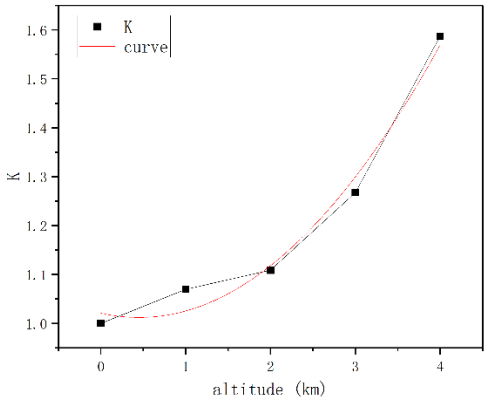

Figure 4. CO concentration at different altitudes.

By fitting the data in Table 3, the fitted curve is shown in Figure 4. It can be seen that the fitting degree R^2 of the equation fitted using the calculation results is greater than 95%, which demonstrates the accuracy of the prediction model. The equation for CO concentration based on altitude during the ventilation and pollution discharge process in tunnels at different altitudes is as follows:

$$\frac{C_P}{C_0} = 1.02071 - 0.03981H + 0.04423H^2 \quad (10)$$

At present, for long-distance tunnels at high altitudes, regulations do not provide clear definitions for ventilation volume and ventilation time. Therefore, the proposed CO concentration correction coefficient based on altitude during the ventilation and pollution discharge process in tunnels at different altitudes can serve as an excellent supplement. It has significant reference and guidance value for the preliminary design of ventilation systems and the estimation of ventilation time during operation in high-altitude areas.

REFERENCES

Huang, R., Shen, X., Wang, B., & Liao, X. (2020). Migration characteristics of CO under forced ventilation after excavation roadway blasting: A case study in a plateau mine. J. Clean. Prod., 267, 122094.

Chang, X., Chai, J., Luo, J., Qin, Y., Xu, Z., & Cao, J. (2020). Tunnel ventilation during construction and diffusion of hazardous gases studied by numerical simulations. Build. Environ., 177, 106902.

Wang, X., Liu, X., Sun, Y., An, J., Zhang, J., & Chen, H. (2009). Construction schedule simulation of a diversion tunnel based on the optimized ventilation time. J. Hazard Mater.

Sun, B., Cheng, W.M., Wang, J.Y., Wang, H., 2018. Effects of turbulent airflow from coal cutting on pollution characteristics of coal dust in fully-mechanized mining face: a case study. J. Clean. Prod. 201, 308–324.

Yan, G., Wang, M., Qin, P., Yan, T., Li, K., Wang, X., & Han, C. (2021). Field measurements of vehicle pollutant emissions in road tunnels at different altitudes. Tunnelling and Underground Space Technology, 118, 104187.

Cao, Z., Yang, Q., & Guo, C. (2016). Migration characteristics of poisonous gas during construction stage in railway tunnels at high altitude areas. Journal of Central South University: Science and Technology, 47(11), 3948-3957.

6th International Conference on Building Energy and Environment
Eindhoven University of Technology, The Netherlands
6 - 10 July 2025

Modeling and validation of convective currents generated by the urban heat island effect using OpenFOAM

Alessia Piazza[1,2], Massimiliano Burlando[3], Girma T. Bitsuamlak[4], Maria Pia Repetto[5]

[1]*University of Genoa, Genoa, Italy, alessia.piazza@edu.unige.it*
[2]*Western University, London ON, Canada, apiazz2@uwo.ca*
[3]*University of Genoa, Genoa, Italy, massimiliano.burlando@unige.it*
[4]*Western University, London ON, Canada, gbitsuam@uwo.ca*
[5]*University of Genoa, Genoa, Italy, maria.pia.repetto@unige.it*

SUMMARY
It is projected that by 2050 70% of the world population will be living in urban areas. Urban Heat Island (UHI) effect is a significant phenomenon that affects urban environments, exacerbating the already elevated temperatures in cities and leading to an increase in illness and mortality. By definition, UHI occurs when urbanized areas experience higher temperature compared to the surrounding. This phenomenon is associated with a closed circulation, characterized by an updraft at the city center and a downdraft at the edge of the circulation. In this study, first a validation of Computational Fluid Dynamics (CFD) simulations of UHI conducted using OpenFOAM is carried out by replicating the set-up of a temperature-controlled water tank experiment reported in Cenedese and Monti, 2003. Then the computational set-up is modified to appropriately conduct a full-scale simulation of convective currents due to UHI in a sample city.

Keywords: UHI effect, urban microclimate, heat transfer, climate change.

1. INTRODUCTION

The Urban Heat Island (UHI) effect is a significant phenomenon that affects urban environments, exacerbating the already elevated temperatures in cities and leading to an increase in illness and mortality (Beniston et al., 2007). By definition, UHI occurs when urbanized areas experience higher temperature compared to the surrounding environment. This is due to a modification in the energy balance accompanying the process of urban development (Oke, 1995). In unstable conditions, during the day, and stable conditions, during the night, and with no concurrent synoptic wind, the circulation associated with UHI effect is described by an updraft inside the city characterized by a convergence at the ground and divergence at the top and by a downdraft that occurs at the edge of circulation, generating a close wind flow.
By the end of the last century, with increasing awareness towards the environment and with the consolidation of the UHI effect as one of the most prominent consequences of urbanization and

climate change (Jamei et al., 2005), the number of studies on UHI and related effects have also increased. Some studies were carried out using numerical simulations (e.g., (Mei et al., 2025; Yoshikado, 1992)) while others were carried out through experimental analysis (e.g., Cenedese and Monti, 2003; Fan et al., 2019; Lu et al., 1997). A water tank model and the natural atmosphere are considered to be thermally similar if equivalent boundary layers occur at equivalent times in both situations (Yuan et al., 2011).
In this study, two different computational domains are being analyzed: the first one will serve as a validation using Cenedese and Monti, 2003 experiments, and therefore the same set-up is reproduced using Computational Fluid Dynamics (CFD). The second one will be a full-scale domain with building clusters. A brief description of the set up will be presented in the methodology and some preliminary outcomes of the study in the section to follow.

2. METHODOLOGY

Computational Fluid Dynamics (CFD) offers a unique opportunity to reproduce complex environmental phenomena at full scale. However, validation is required to prove that reliable and realistic results can be obtained. Accordingly, CFD simulations of the UHI effects experimentally investigated by Cenedese and Monti, 2003 have been carried out as reported in the following sections.

2.1. Experimental set up description

The experiment by Cenedese and Monti (2003) has been carried out using a temperature-controlled water tank of 0.96 m $\times$ 0.30 m $\times$ 0.095 m (respectively along axis x, y and z), as presented in Figure 1. The tank was originally divided in two sections, one representing the sea and the other one the land, but for the purpose of this research the part of the sea is neglected.
The temperature at the top of the tank was maintained at a constant temperature of 46°C (319 K) while on the bottom side a circular-shaped electric heater was place in order to simulate the temperature surplus associated with the UHI. The range of heat flux generated was between 300 $\mathrm{W/m^2}$ and 2000 $\mathrm{W/m^2}$. The temperature of the surrounding ground was maintained constant at temperature of 27°C (300 K) during the noctural simulation and 31°C (304 K) during the diurnal simulation.

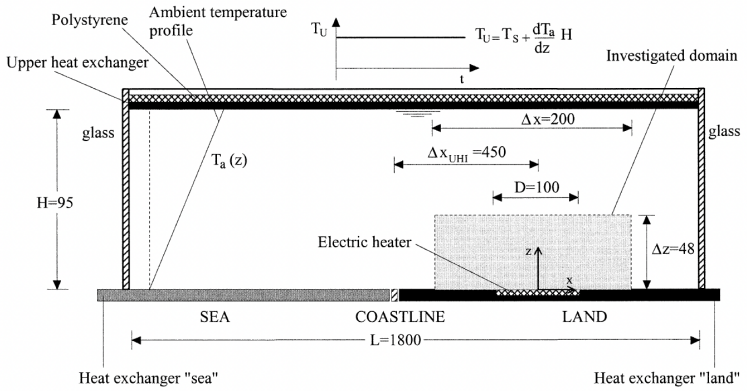

Figure 1. Experimental set up of the water tank. Lengths in mm. From Cenedese and Monti (2003).

2.2. Computational set up description

At first, the experiment of Cenedese and Monti (2003) (only the set up associated with land) is replicated at the same scale using the open source CFD software OpenFOAM (Figure 3a). The solver used for carrying out this simulation is `buoyantBoussinesqSimpleFoam`, based on the Boussinesq assumption. The same boundary conditions are maintained as well: `fixedValue` condition at the top and bottom of the domain, `fixedGradient` for the circular heat exchanger.

In the second part of the study, the domain in scaled by a factor of 10^4 in order to simulate a full-scale condition. Moreover, the fluid is changed from water (with Prandtl number Pr = 6.9, and thermal diffusivity,$\alpha = 0.14 \times 10^{-6} \mathrm{m}^2/\mathrm{s}$) to air (Pr = 0.71, $\alpha = 22.5 \times 10^{-6} \mathrm{m}^2/\mathrm{s}$) in order to represent a real atmospheric boundary layer.

Finally, the circular heater representing the city is replaced with a cluster of buildings corresponding to a neighborhood of the city of Genoa to study how the generated flow by the HIC interacts with the buildings (Figure 3b).

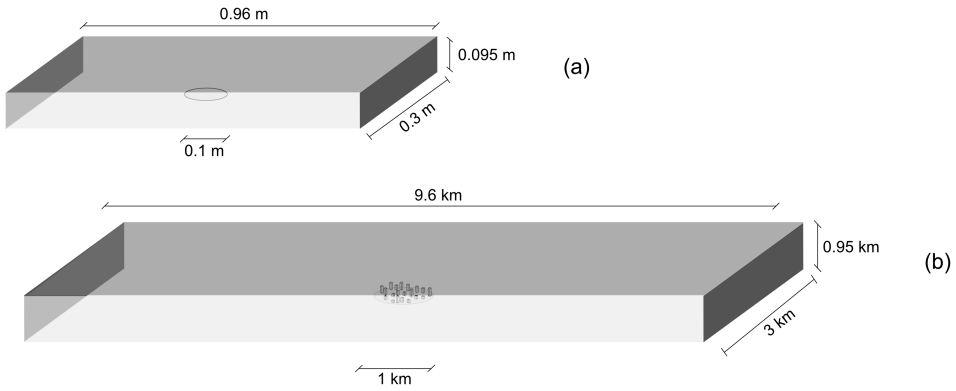

Figure 2. a) Computational domain of the water tank by Cenedese and Monti, 2003 and b) Computational domain full scale.

3. PRELIMINARY RESULTS

The comparison of the Cenedese and Monti (2003) experiment with the CFD shows a good agreement in terms of temperature profiles and flow fields. Figure **??** shows the normalized temperature profiles measured at different distances from the center of the heat exchanger. The profile measured at x/D = 0.75 (external from the circular heat source) shows the least agreement, which is probably related to a limitation of the solver, where conduction between layers is neglected. A good agreement is maintained also in the Heat Island Circulation (HIC) dynamics, where is possible to observe the peculiar shape of the urban heat island (Figure 3).

Further investigations are ongoing for fully evaluating the similarity between the small experimental simulation and the full-scale computational domain and will be presented at the conference.

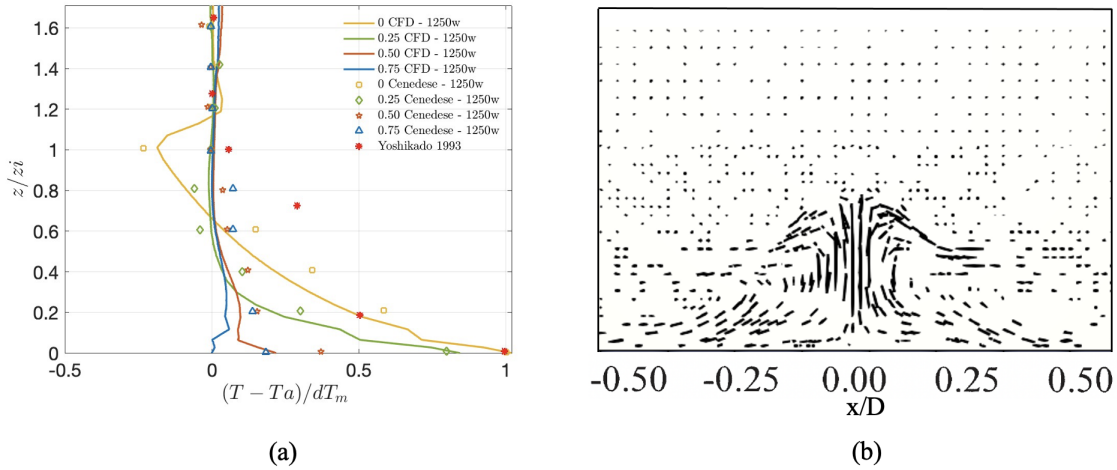

Figure 3. (a) Normalized mean temperature profiles as a function of the radial distance from the UHI center for case with heat flux = $1250W/m^2$ and the vertical displacement z with the mixing height z_i and (b) average velocity vectors for case with heat flux = $1250W/m^2$

ACKNOWLEDGMENTS

This study was partially funded by ADAPTNOW Project – "ADAPTation Capacity Strengthening for Highly Affected and Exposed Territories in the Alps NOW" (Grant No. ASP0100048). ADAPTNOW is co-financed by the European Regional Development Fund through the Interreg Alpine Space programme.

REFERENCES

Beniston M., Stephenson D., and Christensen O. e. a., 2007. Future extreme events in European climate: an exploration of regional climate model projections. JClimatic Change 81, 71–95.

Cenedese A. and Monti P., 2003. Interaction between an Inland Urban Heat Island and a Sea-Breeze flow: A laboratory study. American Metereology Society 42, 1569–1583.

Fan J., Wang Q., Yin S., and Li Y., 2019. Effect of city shape on the urban wind patterns and convective heat transfer in calm and stable background conditions. Building and Environment 162.

Jamei E., Rajagopalan P., Seyedmahmoudian M., and Jamei Y., 2005. Review on the impact of urban geometry and pedestrian level greening on outdoor thermal comfort. Renewable and Sustainable Energy Reviews 54, 1002–1017.

Lu J., Arya S., W. S., and Lawson R., 1997. A Laboratory study of the Urban Heat Island in a calm and stably stratified environment. Part I: Temperature field. American Metereology Society, 1377–1391.

Mei S., Hang J., Fan Y., Yuan C., and Xue Y., 2025. CFD simulation on the wind and thermal environment in urban areas with complex terrain under calm conditions. Sustainable cities and society 118.

Oke T., 1995. The heat island of the urban boundary layer: charcateristics, causes and effects. Wind Climate in Cities, 81–107.

Yoshikado H., 1992. Numerical study of the daytime urban effect and its interaction with the sea breeze. American Metereology Society 31, 1146–1164.

Yuan R., Wu X., Luo T., Liu H., and Sun J., 2011. A review of water tank modeling of the convective atmospheric boundary layer. Journal of Wind Engineering and Industrial Aerodynamics 99, 1099–1114.

6th International Conference on Building Energy and Environment
Eindhoven University of Technology, The Netherlands
6 - 10 July 2025

Spatial Optimization of Roof's Solar Reflectance Index for Urban Heat Island Mitigation in Ahmedabad

Dhruv Varma [1], Rajan Rawal [2], Subham Das [2], Tej Chavda [2]

[1]*Factuly of Technology, CEPT University, Ahmedabad, India, dhruvvarma29@gmail.com*
[2]*CEPT University, Ahmedabad, India, rajanrawal@cept.ac.in*
[2]*CEPT University, Ahmedabad, India, subham.das@cept.ac.in*
[2]*CEPT University, Ahmedabad, India, tej.chavda@cept.ac.in*

SUMMARY
Buildings play a critical role in urban heat stress, particularly in dense metropolitan areas like Ahmedabad. The built environment's thermal properties significantly influence urban microclimate, with roof characteristics being a key factor in heat island mitigation. Using ENVI-met simulation software, three urban sites with varying built cover ratios (BCRs) of 20:80, 35:65, and 50:50 and solar reflectance indices (SRIs) were analysed. The study revealed significant air temperature reduction potential through cool roofs (CR), with the most substantial cooling observed at a 50:50 built cover ratio and a solar reflectance index of 110 (reflectance of 0.85; emittance of 0.95). Peak hour air temperature reductions reached (-)4.24°C, accompanied by space cooling energy demand reductions of up to 19.08%. Cool roofs offer urban planners in India a strategic solution to mitigate urban heat islands, improve public health, and enhance energy efficiency in sustainable city development.

Keywords: Urban Heat Island, Microclimate, Pedestrian Air Temperatures, Energy Consumption.

1. INTRODUCTION

Ahmedabad faces a critical environmental challenge with the Urban Heat Island effect (UHIE), driven by rapid urbanization and extensive construction ("Ahmedabad Records Hottest Day in Century as Mercury Hits 48 Degrees Celcius | Ahmedabad News - The Indian Express," 2016). In 2016, the city recorded its highest ambient air temperature in 100 years at 48°C, highlighting the severity of urban heat issues. UHI emerges from changes in surface energy balance, characterized by lower albedo and higher Bowen ratio compared to natural surfaces (Li et al., 2019). Urban areas absorb more solar radiation, leading to excessive daytime heat and prolonged night-time heat retention (Giridharan et al., 2004; Oke, 1981).

Cool Roofs (referred to as CR) are thermal management systems characterized by high solar reflectance and thermal emittance. They have emerged as a promising mitigation strategy for UHIE (Golden et al., 2007; Khare et al., 2021; Zonato et al., 2021). Direct benefits include significant indoor air temperature reduction, with studies showing potential decreases of 3-4°C (Vellingiri et al., 2020). They directly lower cooling electricity requirements and minimize sensible heat flux, providing immediate thermal comfort improvements (Wang et al., 2022). Co-benefits extend beyond individual building performance. CRs contribute to broader urban thermal management by decreasing outside ambient air temperatures. This improves the efficiency of air conditioning system by decreasing strain on the condensing units in the refrigeration cycle. (Santamouris et al., 2001).

2. PROBLEM STATEMENT

In the heart of Gujarat, Ahmedabad emerges as a microcosm of India's rapid urban transformation, embodying the complex interplay between economic development and environmental sustainability. The city's metamorphosis from the "Manchester of the East" to a diversified economic powerhouse reflects a broader narrative of urban growth that comes with significant ecological challenges. Between 2001 and 2011, the city's population surged by 51%, dramatically outpacing national growth rates. Studies by (Garg et al., 2018) and (Mohammad et al., 2022) reveal that open spaces have diminished by 7%, cropland by 36%, and water bodies by 2%, while built-up areas continue to expand. By 2021, Ahmedabad had lost 1.47km^2 of lakes, the heat sinks and natural stormwater management zones. The city's tree cover of 6.8 m^2 per person falls short of the WHO's 9m^2 recommendation, amplifying UHIE. Future projections are even more alarming: built-up cover is expected to increase by 13.08% by 2030, while cropland is predicted to decrease by 12.54% (Mohammad et al., 2022). With Ahmedabad projected to experience 225 days annually where maximum temperatures exceed 35°C (Mackres et al., 2023), and a Universal Thermal Climate Index (UTCI) above 46 points for 311 out of 365 days (World Bank and CEPT University, 2023), the urgency for innovative cooling solutions becomes paramount. By examining the interaction between CR technologies and Ahmedabad's diverse urban landscapes, this study aims to develop targeted interventions that can simultaneously address urban heat stress, energy efficiency, and sustainable urban development.

3. LITERATURE REVIEW

Elevated temperatures worsen health, energy use, and environmental conditions, intensifying heat waves, straining ecosystems, and worsening air pollution. Ahmedabad's roof area covered 41% of the city in 2020 and is projected to reach 48% by 2030 (Joshi et al., 2022). Conventional dark roofs absorb over 80% of solar radiation, worsening climate warming. CRs along with the appropriate level of insulation, can help cool buildings and cities.

3.1 Conventional Roofs vs Cool Roofs

Surfaces with low albedo absorb more solar radiation, increasing their surface thermal energy. Highly reflective and emissive surfaces remain at a lower surface temperature (ASTM International, 2001). By reflecting the heat-carrying radiation towards the atmosphere, CRs minimize heat absorption and maintain lower surface temperatures. Consequently, the reduced surface temperature of CRs leads to a two-fold benefit. Less heat gets transferred into the building interior via conduction, minimizing the heat gain within the occupied space. As wind flows over the cooler roof surface, the temperature difference between the surface and the surrounding air is minimized. This reduces the driving force for convective heat transfer, further contributing to a cooler ambient environment. The combined effects of selective reflectance and reduced conductive and convective heat transfer result in a cooler surrounding environment and a significant reduction in heat gain within buildings equipped with CRs.

3.2 Impact of Cool roofs on energy consumption

India's energy landscape faces a critical challenge: limited air conditioning penetration (7-9% of housing units) coupled with buildings consuming 33% of total electricity. Projections suggest a dramatic increase from 372 to 4,697 TWh annually by 2047, highlighting the urgent need for energy-efficient solutions. CRs emerge as a promising mitigation strategy. (Rawat & Singh, 2022) found approximately 15% energy savings with an average roof surface temperature reduction of 2.4°C. Microclimate studies provide compelling evidence. (Santamouris et al., 2020) revealed that

integrated reflective materials could reduce peak air temperatures by 2.5–3.0°C during summer. Reflective materials with high SRI values have been shown to reduce land surface temperatures by up to 10°C. The energy-saving potential is significant. (Goldstein et al., 2017) suggest that a 1°C temperature decrease can translate to a 3-6% reduction in cooling electricity demand. In Ahmedabad, (Joshi et al., 2022) estimated annual energy savings of 14.2 kWh per square meter through CR implementation. The effectiveness of CRs extends beyond simple reflectivity. Well-insulated designs outperform conventional roofs, with material composition, thermal emittance, and surface characteristics playing crucial roles in energy efficiency.

4. RESEARCH METHODOLOGY

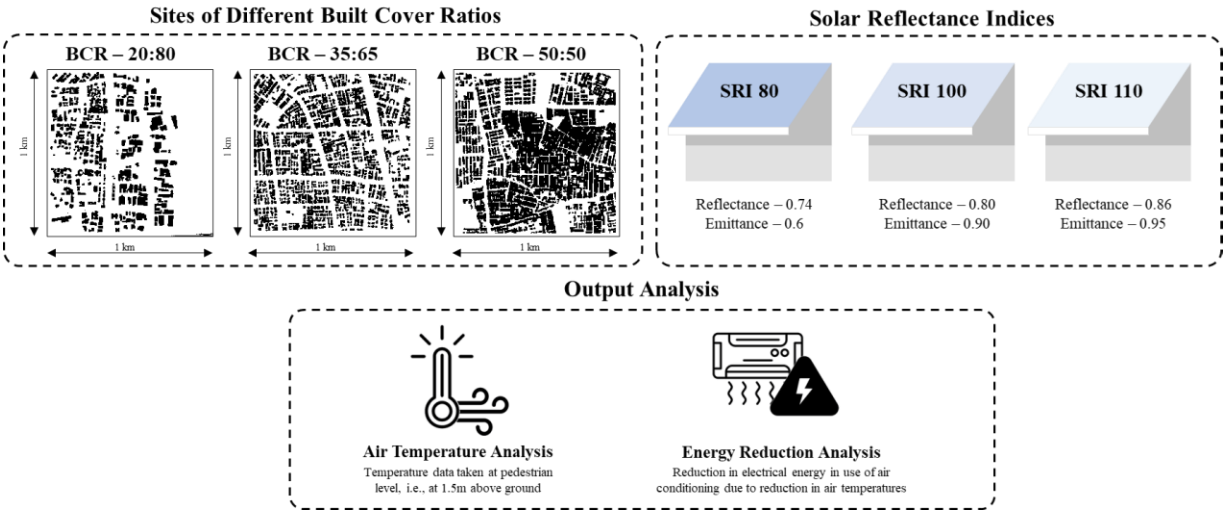

Figure 1. Infographic of methodology for different BCRs and SRIs proposed for the study

To assess the effectiveness of CRs for a reduction in warming due to the heat island effect, several methodologies can be employed. The research involves identifying the built cover ratio of areas for analysis and then identifying the SRI values for implementation on the roofs for modelling. Weather data sourced from the Energy Plus Weather (EPW) file is converted into a forcing file. Subsequently, ENVI-met modelling is conducted, followed by a detailed analysis.

4.1 Site Selection to obtain Built Cover Ratios (BCR)

Table 1. Description of sites with different BCRs chosen for simulation

BCR	20:80	35:65	50:50
Site Map	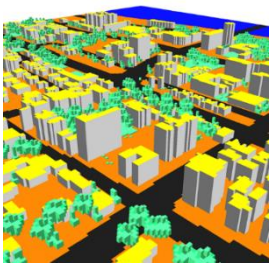	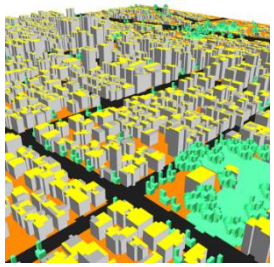	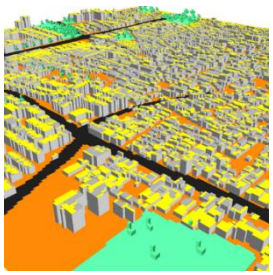
Description	The 1 sq. km. area is part of the Central Business District	The 1 sq. km area comprises a mix of business,	The 1 sq. km area is a mix of businesses, institutions,

	(CBD) of Ahmedabad. It is placed on the Sabarmati riverfront. 60% of the built cover comprises office spaces. The built cover ratio is 20:80, i.e., 20% is built while the remaining 80% is covered by roads and pavements (53%), green cover (9%) and water (18%).	institutional, healthcare and residential areas. The built cover ratio is 35:65, i.e., 35% is covered by built structures while the remaining 65% is covered by roads and pavements (55%) and green cover (10%).	healthcare facilities, and residential neighbourhoods. 50% of the area is covered by buildings, remaining 50% is a mix of roads and pavements (46%), and green cover (4%).

4.2 Modelling and Simulation Inputs

The model is made with the help of shapefile which has been taken from the Centre for Advanced Research in Building Science and Energy (CARBSE) database. The shapefile contains model information regarding the shape of the building, building height from the ground and the precise location of the building. The trees on the site have been marked with the help of Google Earth.

4.2.1 Weather Data

The Energy Plus Weather File (EPW) for Ahmedabad provided a detailed hourly weather data for May 20th (peak day according to Dry Bulb Temperature). A heat transfer lag of about 4 hours is observed between the DBT and the Global Horizontal Radiation. On this day, there is a significant temperature variation of 17°C between the maximum and minimum temperatures, with the maximum reaching 46°C at 5 PM. In contrast, solar radiation peaks at 972 Wh/m² at 1 PM.

4.2.2 Wall and Roof Construction

Energy Conservation Building Code (ECBC) sets out guidelines that define the minimum energy performance standards for buildings in India; considers for roof to be "cool", it must have an SRI of 80 or higher, with a reflectance of at least 0.7 and emittance of 0.75. Ahmedabad's hot and dry climate is considered, and the study explores CR materials with SRI values of 80, 100, and 110 with detailed physical properties given in Table 2.

Table 2. Physical properties of Wall and Roof used for simulations

Building Envelope	Wall	Roof		
SRI	44	80	100	110
Absorptivity	0.6	0.26	0.20	0.15
Reflectance	0.4	0.74	0.80	0.85
Emissivity	0.9	0.60	0.90	0.95
Thickness (m)	0.19	0.4	0.4	0.4
U Value ($W/m^2.K$)	0.4	0.33	0.33	0.33

4.2.3 Trees, Grass, Soil and Road

In modeling the urban environment, indigenous vegetation was selected based on Central Pollution Control Board guidelines (CPCB, 2000). From 200 native Gujarat plant species, three trees were chosen considering height and crown surface area. Grass was selected from the ENVI-met library with a standard height of 0.25m. For soil and road materials, standard ENVI-met library options were utilized. The predominant soil type in Ahmedabad is Loamy, characterized by zero reflectance and 0.9 emissivity, with a non-irrigated surface. The road surface is Asphalt, featuring a reflectance of 0.15 and emissivity of 0.9.

4.3 Limitations

The research methodology reveals limitations in urban thermal performance analysis. By relying exclusively on BCR and neglecting building height considerations, the study potentially oversimplifies thermal dynamics. The restricted dataset, comprising only three sets of BCRs and SRI values, constrains the comprehensiveness of findings. Computational efficiency drove the deliberate exclusion of terrain complexities, with wind parameters standardized at 2m/sec and 270° across simulations. The use of Level of Detail-1 (LOD-1) modelling further restricted granularity, focusing solely on building form while excluding intricate architectural details like fenestration. Additionally, the uniform residential building typology disregards thermal performance variations across different building use categories, potentially limiting the study's broader applicability and insights.

5. RESULTS AND CONCLUSION

All the site scenarios were simulated for the peak day, i.e., May 20th. The air temperatures were extracted for pedestrian level i.e., at 1.5m above ground level. The air temperature values were averaged out for the whole site to analyse the effect of each hour. Sinsel's 2021 study investigated the impact of super CRs on pedestrian-level air temperatures across different urban environments. Current study followed the same framework to extract air temperature data at 1.5m height, which was averaged for further analysis.

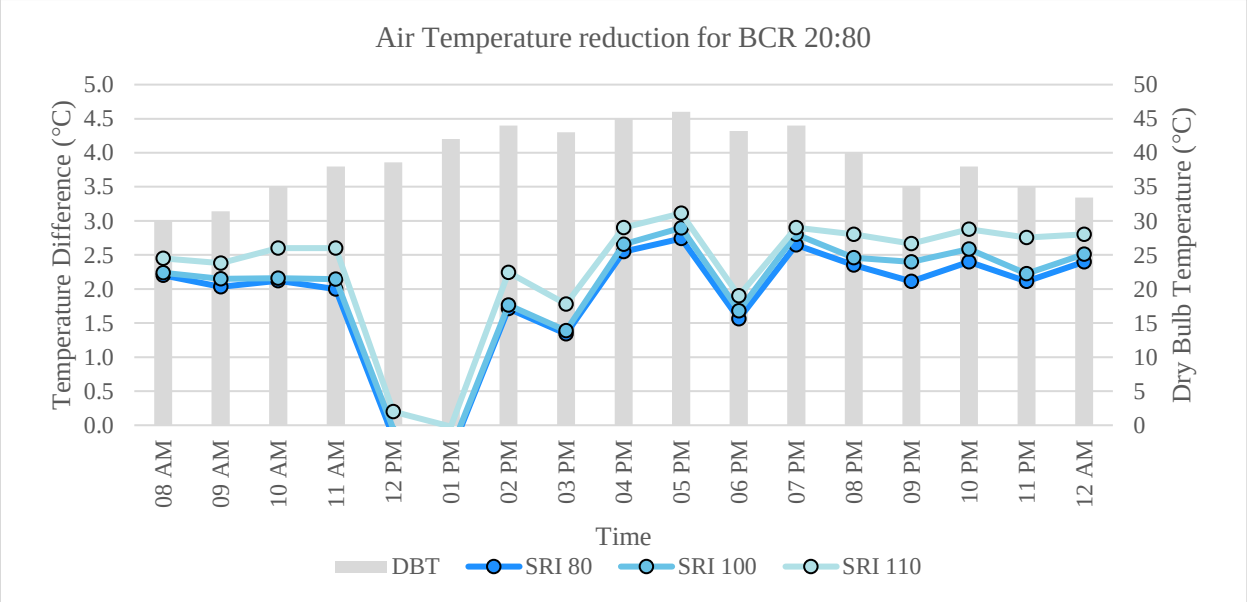

Figure 2. Air temperature reduction for BCR 20:80 and SRI 80,100 and 110

The investigation of air temperature reduction across different BCR scenarios reveals nuanced thermal dynamics influenced by SRI variations. In the BCR 20:80 configuration (Figure 2), the peak DBT hour demonstrated the most modest temperature reduction with SRI 110, achieving a 3.11°C decrease, followed by SRI 100 and SRI 80. Notably, the average air temperatures exhibited negative reductions, indicating temperatures higher than the .epw DBT values during peak solar radiation periods.

Similar thermal behavior was observed in the BCR 35:65 scenario (Figure 3) where the air temperature reduction at peak DBT hour was marginally lower at 2.87°C with SRI 110, again followed by SRI 100 and SRI 80. Unlike the previous case, these reductions remained positive, though diminished around 3 PM near the peak solar radiation timeframe.

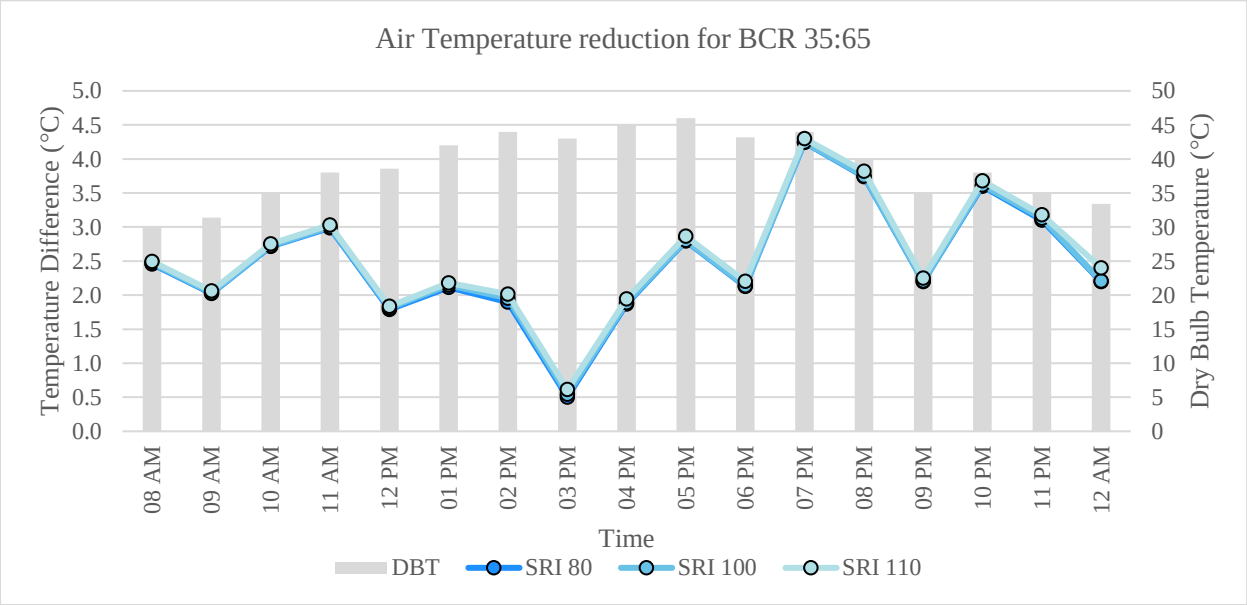

Figure 3. Air temperature reduction for BCR 35:65 and SRI 80,100 and 110

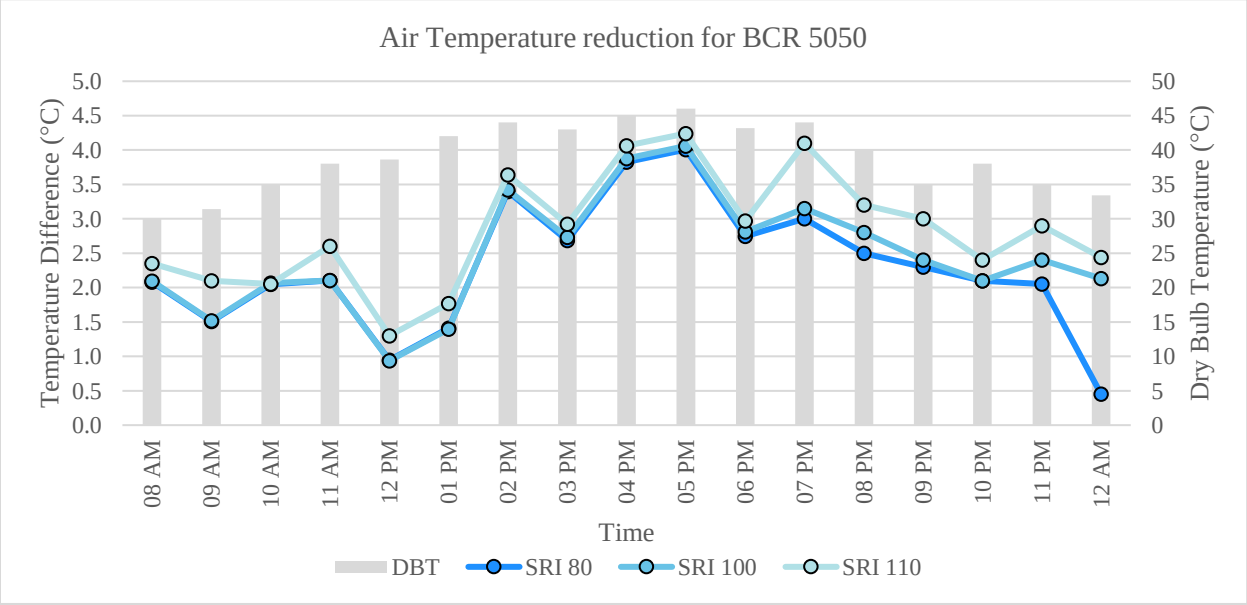

Figure 4. Air temperature reduction for BCR 50:50 and SRI 80,100 and 110

The BCR 50:50 configuration presented comparable thermal characteristics (Figure 4), with the lowest air temperature reduction of 4.24°C occurring with SRI 110. There is a heating effect near peak solar radiation hours, with a discernible temporal lag. Temperature analysis between 8 AM and 12 AM revealed distinct patterns (Figure 5). Minimum temperatures consistently occurred at 8 AM, while maximum temperatures peaked at 5 PM, aligning with the EPW file's peak DBT.

Of particular interest was the observation that the BCR 50:50 scenario exhibited the highest average minimum air temperatures, attributable to its more substantial urban geometric configuration. The finding highlights how urban geometry, solar reflectance, and material choices influence heat dynamics, emphasizing their role in mitigating heat island effects.

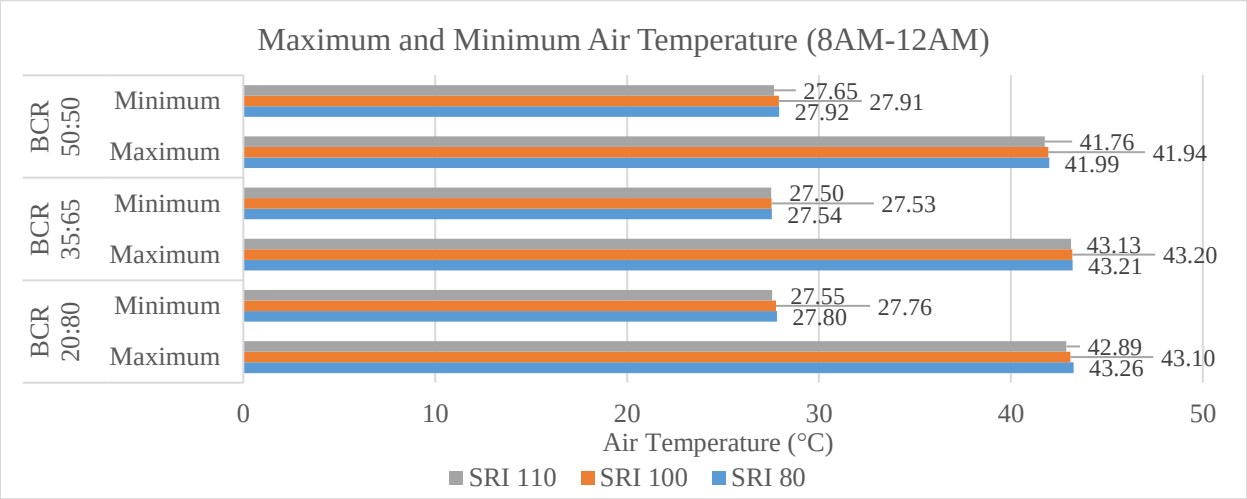

Figure 5. Maximum and minimum Air temperature for different BCR and SRI

The 50:50 BCR with SRI 110 emerges as the optimal case amongst all of the above as this configuration ensures that 50% of the horizontal built surface is covered with high-performance, heat-reflective material. Consider the thermal dynamics: in the 50:50 scenario, half of the horizontal urban surface (roof) becomes a reflective shield against solar radiation. In contrast, the 35:65 ratio limits high-SRI coverage to 35% of horizontal surfaces, while the 20:80 configuration reduces this to 20% horizontal reflective area.

Additionally, the indirect impact of cooler temperatures on cooling loads is noteworthy. An average reduction of 4.5% was considered, leading to a maximum reduction of 19.08% with a BCR of 50:50. Similarly, reductions of 14% and 12.9% were observed for ratios of 20:80 and 35:65, respectively (Figure 5).

6. DISCUSSION

The study provides critical insights into UHI mitigation through innovative material and geometric configurations. By examining the interplay between building coverage ratios and solar reflectance indices, the research reveals nuanced strategies for temperature reduction. The 50:50 BCR and SRI 110 emerged as a promising approach, demonstrating temperature reductions of 2.87°C to 4.24°C and potential cooling energy savings up to 19% in heat-intensive urban environments. The observed temporal lag in heat absorption highlights the complex thermal dynamics of urban surfaces, underscoring the importance of strategic material selection and urban design interventions. Future research should focus on exploring diverse urban contexts, advanced material technologies, and comprehensive green strategies to further enhance urban microclimate management and energy efficiency.

REFERENCES

Ahmedabad records hottest day in century as mercury hits 48 degrees Celcius | Ahmedabad News - The Indian

Express. (2016). *Express News Service*. https://indianexpress.com/article/cities/ahmedabad/ahmedabad-records-hottest-day-in-century-as-mercury-hits-48-degrees-celcius-2809687/

ASTM International. (2001). Standard Practice for Calculating Solar Reflectance Index of Horizontal and Low-Sloped Opaque Surfaces. *ASTM International*, *E 1980*(01), 1–3. www.astm.org

CPCB. (2000). *Guidelines for Developing Greenbelts*.

Garg, A., Avashia, V., & Parihar, S. (2018). *Land use change trends of Indian cities-A Bird's Eye View: Vulnerabilities of unplanned urban growth*. SAGE Publications India Pvt Ltd.

Giridharan, R., Ganesan, S., & Lau, S. S. Y. (2004). Daytime urban heat island effect in high-rise and high-density residential developments in Hong Kong. *Energy and Buildings*, *36*(6), 525–534. https://doi.org/10.1016/J.ENBUILD.2003.12.016

Golden, J. S., Carlson, J., Kaloush, K. E., & Phelan, P. (2007). A comparative study of the thermal and radiative impacts of photovoltaic canopies on pavement surface temperatures. *Solar Energy*, *81*(7), 872–883. https://doi.org/10.1016/J.SOLENER.2006.11.007

Goldstein, E. A., Raman, A. P., & Fan, S. (2017). Sub-ambient non-evaporative fluid cooling with the sky. *Nature Energy*, *2*. https://doi.org/10.1038/NENERGY.2017.143

Joshi, J., Magal, A., Limaye, V. S., Madan, P., Jaiswal, A., Mavalankar, D., & Knowlton, K. (2022). Climate change and 2030 cooling demand in Ahmedabad, India: opportunities for expansion of renewable energy and cool roofs. *Mitigation and Adaptation Strategies for Global Change*, *27*(7), 1–17. https://doi.org/10.1007/S11027-022-10019-4/TABLES/3

Khare, V. R., Vajpai, A., & Gupta, D. (2021). A big picture of urban heat island mitigation strategies and recommendation for India. *Urban Climate*, *37*(May 2020), 100845. https://doi.org/10.1016/j.uclim.2021.100845

Li, H., Zhou, Y., Wang, X., Zhou, X., Zhang, H., & Sodoudi, S. (2019). Quantifying urban heat island intensity and its physical mechanism using WRF/UCM. *Science of The Total Environment*, *650*, 3110–3119. https://doi.org/10.1016/J.SCITOTENV.2018.10.025

Mackres, E., Wong, T., Null, S., Campos, R., & Mehrotra, S. (2023). *The Future of Extreme Heat in Cities: What We Know — and What We Don't*. World Resources Institute.

Mohammad, P., Goswami, A., Chauhan, S., & Nayak, S. (2022). Machine learning algorithm based prediction of land use land cover and land surface temperature changes to characterize the surface urban heat island phenomena over Ahmedabad city, India. *Urban Climate*, *42*(October 2023). https://doi.org/10.1016/j.uclim.2022.101116

Oke, T. R. (1981). Canyon Geometry and the Urban Heat Island. *Journal of Climatology*, *1*, 237–254. doi:10.1002/joc.3370010304

Rawat, M., & Singh, R. N. (2022). A study on the comparative review of cool roof thermal performance in various regions. *Energy and Built Environment*, *3*(3), 327–347. https://doi.org/10.1016/j.enbenv.2021.03.001

Santamouris, M., Paolini, R., Haddad, S., Synnefa, A., Garshasbi, S., Hatvani-Kovacs, G., Gobakis, K., Yenneti, K., Vasilakopoulou, K., Feng, J., Gao, K., Papangelis, G., Dandou, A., Methymaki, G., Portalakis, P., & Tombrou, M. (2020). Heat mitigation technologies can improve sustainability in cities. An holistic experimental and numerical impact assessment of urban overheating and related heat mitigation strategies on energy consumption, indoor comfort, vulnerability and heat-related m. *Energy and Buildings*, *217*, 110002. https://doi.org/10.1016/j.enbuild.2020.110002

Santamouris, M., Papanikolaou, N., Livada, I., Koronakis, I., Georgakis, C., Argiriou, A., & Assimakopoulos, D. N. (2001). On the impact of urban climate on the energy consumption of buildings. *Solar Energy*, *70*(3), 201–216. https://doi.org/10.1016/S0038-092X(00)00095-5

Sinsel, T. (2021). *Advancements and applications of the microclimate model ENVI-met*.

Vellingiri, S., Dutta, P., Singh, S., Sathish, L., Pingle, S., & Brahmbhatt, B. (2020). Combating climate change-induced heat stress: Assessing cool roofs and its impact on the indoor ambient temperature of the households in the Urban slums of Ahmedabad. *Indian Journal of Occupational and Environmental Medicine*, *24*(1), 25. https://doi.org/10.4103/ijoem.IJOEM_120_19

Wang, X., Li, H., & Sodoudi, S. (2022). The effectiveness of cool and green roofs in mitigating urban heat island and improving human thermal comfort. *Building and Environment*, *217*(March), 109082. https://doi.org/10.1016/j.buildenv.2022.109082

World Bank and CEPT University. (2023). *Improving Building-Level Thermal Comfort and Indoor Air Quality in South Asia*.

Zonato, A., Martilli, A., Gutierrez, E., Chen, F., He, C., Barlage, M., Zardi, D., & Giovannini, L. (2021). Exploring the Effects of Rooftop Mitigation Strategies on Urban Temperatures and Energy Consumption. *Journal of Geophysical Research: Atmospheres*, *126*(21), e2021JD035002. https://doi.org/10.1029/2021JD035002

COBEE 2025 – Proceedings

THURSDAY

Advanced Modeling and Building Simulations (11:00-12:30 h)

6th International Conference on Building Energy and Environment
Eindhoven University of Technology, The Netherlands
6 - 10 July 2025

Evaluation and optimization of longitudinal spacing for jet fans in high-altitude, long-distance road tunnels

Yanning Wang [1], Yanan Zhao [2], Jiangang Qiao [1], Rongxin Wang [1], Junjie Liu [2], Peng Xu [1], Zhiyuan Yang [1]

[1]*Tianjin Municipal Engineering Design & Research Institute, Tianjin, China, wyn009@sohu.com*
[2]*Tianjin University, Tianjin, China, zynan@tju.edu.cn*

SUMMARY
This study focuses on the Huzhu Beishan High-Altitude Long Tunnel and leverages CFD simulations to evaluate the velocity field and CO concentration field under jet fan spacings of 150 m, 200 m, 250 m, and 300 m. Incorporating vehicle types and traffic volume data obtained through field surveys, along with the traffic three-phase flow theory, various vehicle distributions were designed to reflect different speeds. The momentum source method was employed to simulate the piston effect of vehicles on the tunnel airflow. Furthermore, vehicle CO emissions were adjusted to account for high-altitude environmental conditions. To validate the simulation results, experimental data from the Yingtian Street Yangtze River Tunnel in Nanjing was used as a benchmark. Through an analysis of the CO concentration distribution, it was determined that a 150m longitudinal spacing for jet fans satisfies the tunnel's air quality requirements.

Keywords: High-Altitude Long Tunnel, Jet Fan, Longitudinal Spacing.

1. INTRODUCTION

Under China's Belt and Road Initiative, the Qinghai-Tibet Plateau region, as a key trade and transportation hub, has experienced significant growth in its road network, accompanied by a notable increase in both vehicular and freight traffic (MOT China, 2022). Considering the unique geological conditions of mountainous regions, long tunnels have progressively become a critical component of modern transportation. Due to the enclosed structure, long tunnels are more prone to accumulating harmful gases, such as vehicle exhaust emissions. Therefore, ventilation systems are essential for diluting pollutant concentrations and ensuring the safe operation of the tunnels. Currently, longitudinal ventilation systems are the preferred solution for ventilation in many ultra-long highway tunnels (PIARC. 2016).

However, in high-altitude regions such as the Qinghai-Tibet Plateau, the reduced air pressure and oxygen concentration can significantly affect engine load and combustion characteristics, thereby influencing vehicle emissions (Wang et al., 2018). Furthermore, the ventilation efficiency of longitudinal ventilation systems depends on the induction and pressurization effects produced by the jet fans. In low-pressure environments, the thrust of jet fan blades is reduced, resulting in a diminished effective working range. Therefore, to ensure optimal performance of the ventilation system, it is essential to investigate the appropriate longitudinal spacing of jet fans. This study focuses on the high-altitude, ultra-long tunnel at Huzhu North Mountain, utilizing field survey data on vehicle types and traffic volumes. Using CFD numerical simulations, the CO concentration

distribution under varying longitudinal spacings of jet fans was assessed. The findings of this study offer valuable insights into the design of jet fan arrangements in high-altitude tunnels.

2. METHODOLOGY

2.1. Model Description

The Huzhu Beishan Extra-Long Tunnel, located on the Jiaxi Highway in Qinghai Province, is a Grade I highway tunnel featuring twin bores and four lanes. The average length of the left and right bores is 11.15 km, and the tunnel is equipped with two ventilation shafts measuring 1.1 km and 1.4 km, respectively. With an altitude of approximately 3 km at both the entrance and exit, it is the second extra-long tunnel in China constructed in a cold, high-altitude region. This tunnel surpasses the previous record held by the Laqi Mountain Tunnel in Qinghai Province (total length of 5.55 km) and is now the longest tunnel in Qinghai Province. The schematic plan of the ventilation design is shown in Fig. 1. To evaluate the ventilation effect of jet fans, the working area of the jet fan closest to the exhaust port of Ventilation Shaft 1 in the left bore was selected for simulation. The area is about 5.92 km away from the tunnel entrance, and the CFD model is shown in Fig. 2.

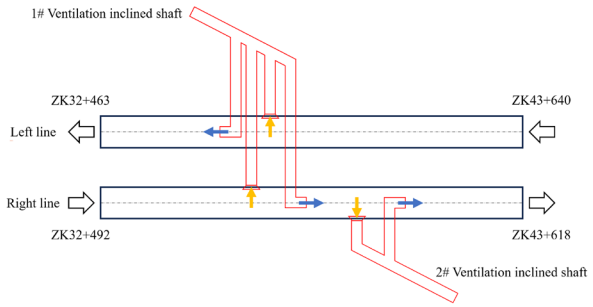

Figure 1. Ventilation Design for the Huzhu Beishan Long Tunnel.

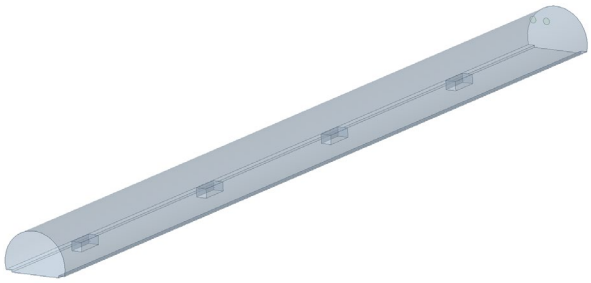

Figure 2. CFD Model.

Based on the traffic volume survey of the road section where the tunnel is located, the equivalent traffic volume, adjusted for the proportion of different vehicle types, is 6,416 PCU/day for the near-term scenario and 17,081 PCU/day for the long-term scenario. The peak-hour traffic volume is estimated to account for 12.5% of the daily traffic volume. According to the three-phase traffic flow theory, four representative vehicle speeds—80 km/h, 60 km/h, 40 km/h, and 20 km/h—are selected to represent distinct traffic conditions. Referencing to the summary of the pollutants emitted by vehicles and their corresponding amounts in China in 2021, carbon monoxide (CO) and

nitrogen oxides (NOx) account for 49.3% and 37.4% of the total emissions, respectively (Zhao et al., 2023). Considering that standard passenger cars are predominantly gasoline-powered, CO is selected as the target pollutant for this study.

2.2. Turbulence Model and Boundary Conditions

This study utilizes the Realizable k-epsilon turbulence model (Shih et al., 1995), which provides notable advancements in the analysis of circular jets and has been validated as an effective approach for simulating tunnel ventilation (Xu et al., 2021).

2.3.1. Environmental characteristics at high altitudes

Air parameters such as atmospheric pressure, temperature, and gas density are changed when the altitude rises. The effects of altitude changes need to be fully considered when designing the simulation of high-altitude tunnels to ensure the credibility of the simulation results. The equation for the variation of atmospheric pressure with altitude can be deduced by considering the temperature variation in the troposphere at altitudes from 0 to 11 km (Jiang et al., 2021):

$$P = P_0 \cdot \left(\frac{T - k\mu gH}{T}\right)^{\frac{1}{kR}} \tag{1}$$

Where P_0 is the standard atmospheric pressure, 101325Pa; μ is the molar mass of air, 29 kg/mol; g is the acceleration of gravity, 9.8 m/s^2; R is the universal gas constant, 8.314 kJ/(kmol·K); T is the temperature, K; H is the altitude, km; $k = \gamma - 1/\gamma R = 0.02268$, where γ is the molar heat capacity ratio.

According to the ideal gas equation of state $PV = mRT/M$, the air density at different air temperatures and pressures can be deduced:

$$\frac{\rho}{\rho_0} = \frac{P}{P_0} \cdot \frac{T_0}{T} \tag{2}$$

Where ρ_0 is the density of air at standard conditions, 1.293 kg/m3.

2.3.2. CO emissions at various vehicle speeds in high-altitude areas

A comprehensive experimental study on vehicle carbon emissions in high-altitude regions was conducted to investigate the CO_2 emission factors of vehicles across different altitudes (2.0–4.5 km), as well as the emission ratios of other gases, including CO and NOx, relative to CO_2 (Jiang et al., 2024).

VSP (Vehicle Specific Power) provides a comprehensive measure of the actual engine load and CO_2 emissions from the motor vehicle. It is the ratio of engine power to vehicle mass, simplified as Eq. (3),

$$VSP = \frac{[A \cdot v + B \cdot v^2 + C \cdot v^3 + (a + g \cdot grade) \cdot v \cdot m]}{m} \tag{3}$$

Where VSP is the instantaneous vehicle specific power (kW/t); v is the instantaneous speed (m/s); a is the instantaneous acceleration rate (m/s^2); $grade$ is the road grade; m is the total vehicle mass (t); A is the rolling resistance coefficient (kW·s/km); B is the friction

coefficient (kW·s^2/km^2); C is the aerodynamic resistance coefficient (kW·s^3/km^3).

At an altitude of 2.5–3.0 km in the Huzhu Beishan Tunnel, the CO_2 emission factor is determined to be 167 g/km. By assuming a standard passenger vehicle mass of 1,500 kg, the VSP values were calculated for four representative vehicle speeds—80 km/h, 60 km/h, 40 km/h, and 20 km/h—along with the corresponding CO emissions. The results are summarized in the Table 1.

Table 1. CO emissions at various vehicle speeds.

Velocity (km/h)	20	40	60	80
VSP (kW/t)	-0.957	-1.914	-2.87	-3.827
CO emission (g/h)	13.74	27.39	45.09	60.12

2.3.3. Vehicle motion model

Vehicles are the primary source of air pollution in tunnels, and their movement exerts a notable influence on tunnel air, commonly referred to as the piston effect. Strictly speaking, vehicle movement is a transient phenomenon. However, under stable traffic conditions, the interaction between vehicles and tunnel air can be approximated as steady-state. The force exerted by an individual vehicle on tunnel air is defined as follows (Lin et al., 2018):

$$F = \frac{\rho}{2} \cdot C_d \cdot (U_{car} - U_t) \cdot |U_{car} - U_t| \cdot A_{car_front} \tag{4}$$

Where C_d is the vehicle drag coefficient, Dimensionless; U_{car} is the vehicle speed, m/s; U_t is the longitudinal average wind speed of tunnel section, m/s; A_{car_front} is the vehicle frontal projected area, m2.

Let N_{real} represent the equivalent number of vehicles (in terms of standard passenger cars) under actual traffic conditions, and N_{geo} denote the number of vehicle geometric models used in the CFD simulation. A vehicle correction factor, f, is introduced, defined as $f = N_{real}/N_{geo}$. Assuming vehicles are uniformly distributed within the tunnel and travel at a constant speed, the influence of an individual vehicle on the tunnel air is expressed in Eq. (5) to Eq. (7).

$$S_{m,x} = \frac{F \cdot f}{V_{car}} \cdot \cos\theta \cdot \cos\varphi \tag{5}$$

$$S_{m,y} = \frac{F \cdot f}{V_{car}} \cdot \cos\theta \cdot \sin\varphi \tag{6}$$

$$S_{m,z} = \frac{F \cdot f}{V_{car}} \cdot \sin\theta \tag{7}$$

Where $S_{m,x}, S_{m,y}, S_{m,z}$ are the momentum source terms of the vehicle in three directions (x, y, z) in the Cartesian Coordinate System; θ and φ are the angles between the vehicle's motion direction and the global coordinate system axes.

The specific boundary conditions are as shown in Table 2. To meet the requirements of simulation accuracy, the first layer of the mesh in the boundary layer was set to 0.01 m to ensure that the y parameter fell between 30 and 300. And coarse, medium, and refined meshes were tested to ensure that the simulation results were independent of the mesh. Ultimately, the maximum size of

the tunnel space is 0.4m, the maximum size of the jet fan surface is 0.05m, and the total number of grids is approximately 5.6 million.

Table 2. The simulation conditions.

Project	Name	Settings
General	Gravity	9.81 m/s^2
	Pressure	70340Pa
	Ambient temperature	293.15K
Materials	Air density	0.834 kg/m3
	CO density	0.809 kg/m3
Boundary Conditions	Tunnel inlet	Velocity-inlet, 3m/s Temperature = 293.15K
	Tunnel outlet	Pressure-outlet
	Tunnel surface	Wall; Temperature=274.5K Roughness heights: 0.008m Roughness constant: 0.02
	Jet fans	Fan; Jet velocity: 35.6m/s
	Vehicle surface	Wall; Insulation Roughness heights: 0.01m Roughness constant: 0.02
	Exhaust tailpipe	Velocity-inlet Temperature = 350K (Song et al., 2019)

3. RESULTS

3.1. Model Validation

To ensure the accuracy of the numerical simulation results, the numerical model was validated through field tests conducted in the Yingtian Street Yangtze River Tunnel. For further details, please consult Reference (Zhao et al., 2022). The validation results as shown in Fig. 3, which indicate that the simulation values exhibit less fluctuation compared to the test values, with the relative error consistently remaining within 15%.

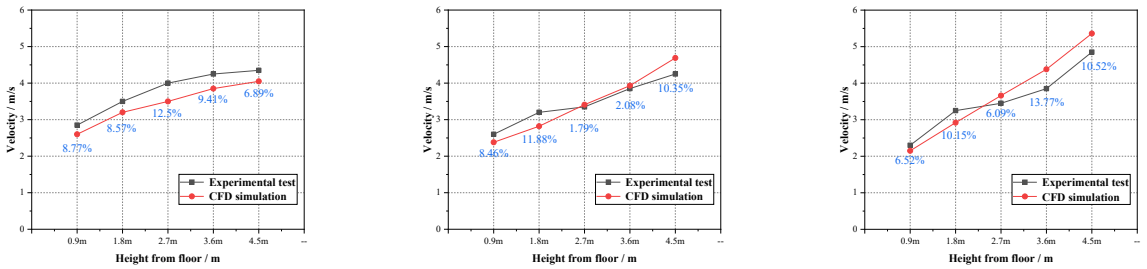

(a) (b) (c)

Figure 3. Vertical velocities at various distances downstream of jet fans: (a) 20 m; (b) 60 m; (c) 100 m.

3.2. CO Concentration Distribution

Initially, the distribution of CO within the tunnel was calculated for different longitudinal spacings of jet fans (150m, 200m, 250m, and 300m) with vehicles traveling at varying speeds. A monitoring plane at a height of 1.2m was selected, and the CO concentration results are presented in Fig. 4. According to tunnel health standards, under normal operating conditions (>20 km/h), the CO

concentration within the tunnel should not exceed 100 cm^3/m^3; during traffic congestion (≤20 km/h), the CO concentration should not exceed 150 cm^3/m^3. Consequently, the maximum value of the following CO distribution contours are based on the design concentration limits specified by the health standards.

The figure illustrates that: (1) In the initial stage of the jet, the convolution range is limited, and the CO concentration near the vehicle exhaust tailpipe is relatively high; (2) As the jet interacts with the surrounding air, the CO dilution effect increases, leading to a reduction in CO concentration; (3) As the jet further develops, its effectiveness diminishes, resulting in a weaker CO dilution effect and the spread of CO around the vehicles; (4) As the longitudinal spacing of the jet fans increases, CO accumulation in the far field intensifies, and the area exceeding health standards expands. Therefore, it is recommended that the longitudinal spacing of jet fans be maintained at 150m.

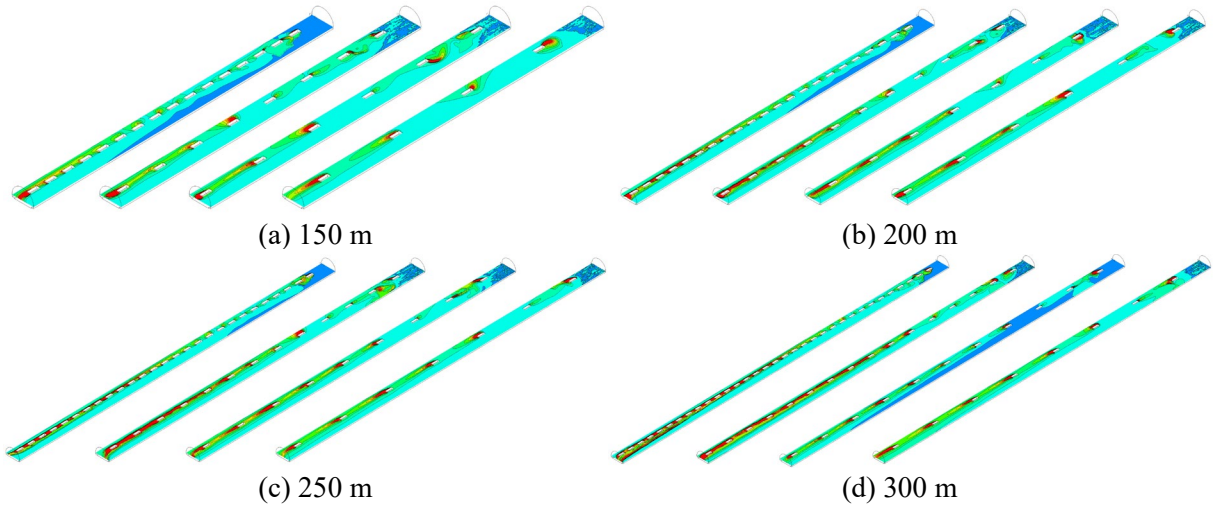

Figure 4. CO Concentration Distribution at Y=1.2m Section at Different Vehicle Speed: (a) 150 m; (b) 200 m; (c) 250 m; (d) 300 m.

3.3. Axial Velocity and Turbulence Intensity of Jet Fan

The fully development of the jet is a crucial condition for ensuring the efficient operation of jet fans. If the longitudinal spacing between fans is insufficient, a uniform flow may not be established within the tunnel, which could adversely affect the performance of subsequent jet fans. Typically, the end of the working section of the jet fan with fully developed has characteristics such as "uniform distribution of cross-sectional velocity and stable turbulence intensity". Fig. 5 and Fig. 6 present the variations in velocity and turbulence intensity along the central axis of the jet fan at a vehicle speed of 20 km/h, under different longitudinal spacings between the jet fans. It can be seen that a longitudinal spacing of 150m is appropriate, enabling the jet to fully develop.

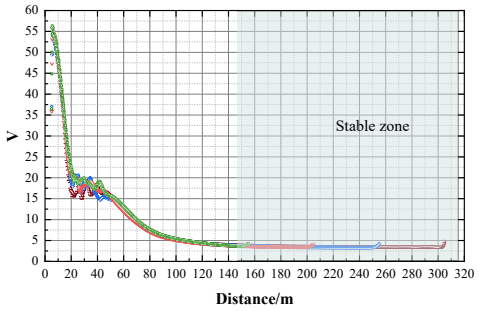

Figure 5. Axial Velocity of Jet Fans at Different Longitudinal Spacing

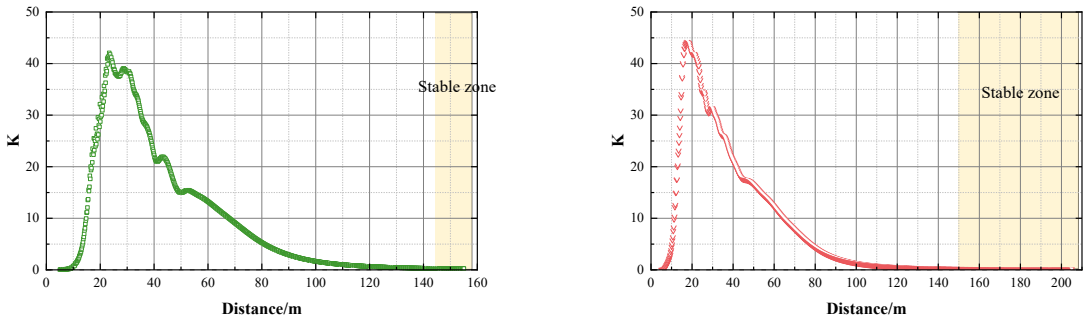

(a) 150 m

(b) 200 m

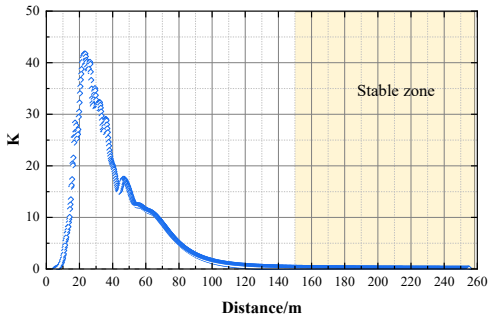

(c) 250 m

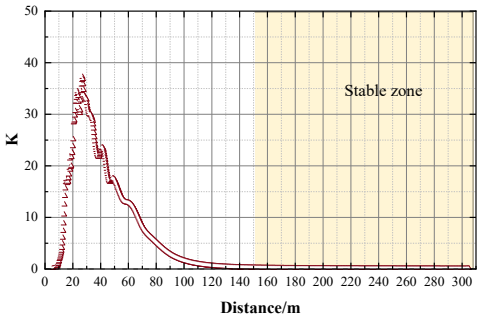

(d) 300 m

Figure 6. Jet Turbulence Kinetic Energy at Different Longitudinal Spacing.

4. CONCLUSIONS

This study calculated the CO concentration distribution within the tunnel under different longitudinal spacings of jet fans and vehicle speeds. By assessing the CO dilution effect, airflow uniformity, and turbulence intensity stability, it is recommended that the fan spacing be set at 150m. This spacing not only meets the health requirements within the tunnel but also ensures the optimal performance of the jet fans.

REFERENCES

Jiang Z., Yang B., Zhang G., Zeng F., Wang Y., 2021. Analysis of dust pollution effect of cutting dust and ventilation control parameters at the heading face in plateau mines. Journal of China Coal Society 46, 2146–2157.

Jiang Z., Wu L., Niu H., Jia Z., Qi Z., Liu Y., Zhang Q., Wang T., Peng J., Mao H., 2024. Investigating the impact of high-altitude on vehicle carbon emissions: A comprehensive on-road driving study. Science of The Total Environment 918, 170671.

Lin Y., Nan S., Chang J., Liu X., Li X., 2018. 3D Numerical Simulation of Ventilation and Purification of Whole Highway Tunnel. Tunnel Construction 38, 232-239.

MOT China (Ministry of Transport of the People's Republic of China) Statistical Bulletin on Development of Transport Industry in 2022.

PIARC. Road tunnels: complex underground road networks [R]. Paris: Technical Committee 3.3 Road Tunnel Operation, 2016: 80.

Shih T.-H., Liou W.W., Shabbir A., Yang Z., Zhu J., 1995. A new k-ε eddy viscosity model for high Reynolds number turbulent flows. Computers & Fluids 24, 227-238.

Song X., Zhao Y., 2019. Numerical investigation of airflow patterns and pollutant dispersions induced by a fleet of vehicles inside road tunnels using dynamic mesh part I: traffic wind evaluation. Atmospheric Environment 212, 208-220.

Wang H., Ge Y., Hao L., Xu X., Tan J., Li J., Wu L., Yang J, Yang D., Peng J., Yang J, Yang R., 2018. The real driving emission characteristics of light-duty diesel vehicle at various altitudes. Atmospheric Environment 191, 126-131.

Xu Z., Wang B., Kong J., Chen T., Liang Y., 2021. Study on the influence of ceiling tunnel angle on the gas shunting efficiency of urban highway tunnel. Case Studies in Thermal Engineering 25, 100888.

Zhao S., Xue P., Xie J., Wang Y., Jiang Z., Liu J., 2022. Optimal pitch angle of jet fans based on air age evaluation for highway tunnel ventilation. Journal of Wind Engineering and Industrial Aerodynamics 228, 105088.

Zhao S., Xie J., Xue P., Wang Y., Jiang Z., Liu J., 2023. Coupling effect of vehicle wake and jet flow on the dispersion characteristics and dilution efficiency of pollutants in urban highway tunnels. Science of The Total Environment 893, 164926.

6th International Conference on Building Energy and Environment
Eindhoven University of Technology, The Netherlands
6 - 10 July 2025

Research of machine learning as CFD surrogate models for rapid prediction of building physical field: A review of methods and status

Tianle Chen [1], Ruibin Li [1], Xuesong Hu [1], Bingyang Zhang [1], Yuanyuan Liu [1], Naiping Gao [1,*]

[1]*Tongji University, Shanghai, China, gaonaiping@tongji.edu.cn*

SUMMARY
The distribution of physical parameters within and around buildings have a significant impact on human health and comfort, highlighting the importance of rapid and accurate prediction of building physical fields. This review focuses on recent advancements in utilizing machine learning (ML) as a surrogate model for computational fluid dynamics (CFD) to predict these fields. First, the study outlines methods for acquiring datasets, discusses the influence of dataset scale on the performance of surrogate model, and presents commonly used techniques for data preprocessing. Next, the review summarizes four types of input features and explores strategies for feature selection. It also reviews the mainstream surrogate models currently employed in research, along with some innovative approaches to modelling. Finally, two major approaches for optimizing built environment based on surrogate models are discussed. This review emphasizes the practical value of ML and provides guidance for its applications in the built environment.

Keywords: Building physical field, Machine learning, Surrogate model

1. INTRODUCTION

The distribution of physical parameters both inside and outside buildings (e.g., air velocity, air temperature, and pollutant concentration) profoundly impacts human health and comfort. Therefore, rapid and accurate prediction of building physical fields is essential for effectively regulating ventilation systems and optimizing building layouts. Computational fluid dynamics (CFD) has become a key tool for simulating complex physical phenomena, such as airflow distribution and thermal transfer. However, CFD simulations require numerous iterative steps to achieve computational convergence, which can be time-consuming.

In recent years, machine learning (ML), a crucial branch of artificial intelligence (AI), has shown potential for achieving rapid and accurate predictions of building physical fields. Current research approaches using ML to accelerate these predictions are mainly divided into two categories: first, as a surrogate model, ML completely replaces traditional numerical simulation methods by constructing a mapping relationship between inputs and outputs, enabling the rapid prediction of environmental parameters (Calzolari & Liu, 2021). Second, ML can enhance numerical simulations by replacing or optimizing specific components, such as improving turbulence modelling (Vinuesa & Brunton, 2022). Compared to surrogate models, auxiliary numerical simulations require more time to compute building physical fields.

The review will focus on strategies for improving the performance of surrogate models, addressing aspects such as dataset acquisition and processing, feature selection, and model innovation. Additionally, this review systematically outlines the practical implementation pathways for

surrogate models in real-world applications.

2. PERFORMANCE IMPROVEMENT OF SURROGATE MODELS

2.1. Dataset

Accurate and comprehensive datasets are fundamental for training ML models. Currently, IoT-based platforms, when equipped with well-calibrated sensors, provide a valuable source for dataset collection (Qu et al., 2023). However, most research still relies on data collected through numerical simulations, and some studies even use data generated by combining multiple software or models (Xu et al., 2023). Additionally, emerging technologies such as computer vision (CV) have proven to significantly enhance data dimensionality and resolution, making them effective tools for gathering information about the built environment (Wang et al., 2024).

Research within specific computational domains has shown that as the number of training samples increases, the prediction error of model gradually decreases. However, when the number of samples reaches a certain critical threshold, further reductions in prediction error become negligible; this threshold can be considered the optimal size (Athavale et al., 2019). Moreover, this review found that in over 80% of studies, the proportion of the training set is not less than 70%, with the 7:3 or 8:2 ratio of training set to test set being commonly used.

Compared to general data, building physical field data typically have larger sizes and higher dimensions. Data preprocessing helps improve the training efficiency of models and can be classified into three types based on their purpose: Firstly, considering the diversity of data distribution in this field, data structure and type conversion, such as normalization, should be performed to make the data more suitable for subsequent analysis. Secondly, raw data often contain outliers and noise, making data cleaning a crucial step in ensuring data quality. Lastly, given that these datasets generally include a vast amount of high-dimensional data, dimensionality reduction techniques can be applied to simplify the dataset. Among these techniques, downsampling is the most used method for data dimensionality reduction. It reduces data complexity by dividing high-resolution grid data obtained from CFD simulations into blocks and calculating the average value of all grid points within each block (Jing et al., 2024).

2.2. Input feature

In the process of constructing ML models, selecting appropriate input features play a pivotal role, as it directly impacts the efficiency of the models. Based on actual needs, the input features used in relevant research can be broadly classified into four categories: boundary conditions, spatial feature points, geometric conditions, and historical physical fields.

When ML is applied to building physical field prediction, the use of boundary conditions as input features has become a widely adopted strategy. Particularly in the context of indoor physical fields, the proportion of boundary conditions exceeds 60%. As shown in Fig. 1(c), common boundary conditions, such as supply air temperature, supply air velocity, and wall temperature. These features reflect the significant impact of indoor environmental control systems and external environmental factors on indoor physical fields. In the case of outdoor physical fields, boundary conditions still play a crucial role, with a usage proportion of 34%. Given that some boundary condition data can be difficult to obtain in real-world situations, the development of sensors offers

a promising direction for ML to reconstruct physical fields in real-time. Sparse physical parameters, monitored by a limited number of sensors, can reflect the state of physical parameters at specific spatial locations. By learning the spatial correlations of the data, ML can predict the entire physical field based on the sparse data measured by fewer sensors. Geometric conditions, which are core elements in building structure and layout, significantly influence the distribution of building physical parameters. While factors like building shape and size have some impact on indoor physical fields, the utilization of building geometric information in indoor physical field prediction remains relatively low. In contrast, for outdoor physical field prediction, the usage percentage of building geometric information reaches 37%, making it the most frequently used type of input features.

Non-time-series models typically rely on the first three types of input features, while time-series models mainly use historical data of physical fields as input. Although this type of data is crucial for prediction, current research employing it for physical field prediction remains relatively scarce. This reflects the limitations of actual related demands and underscores the challenges time-series models face in terms of training difficulty and accuracy.

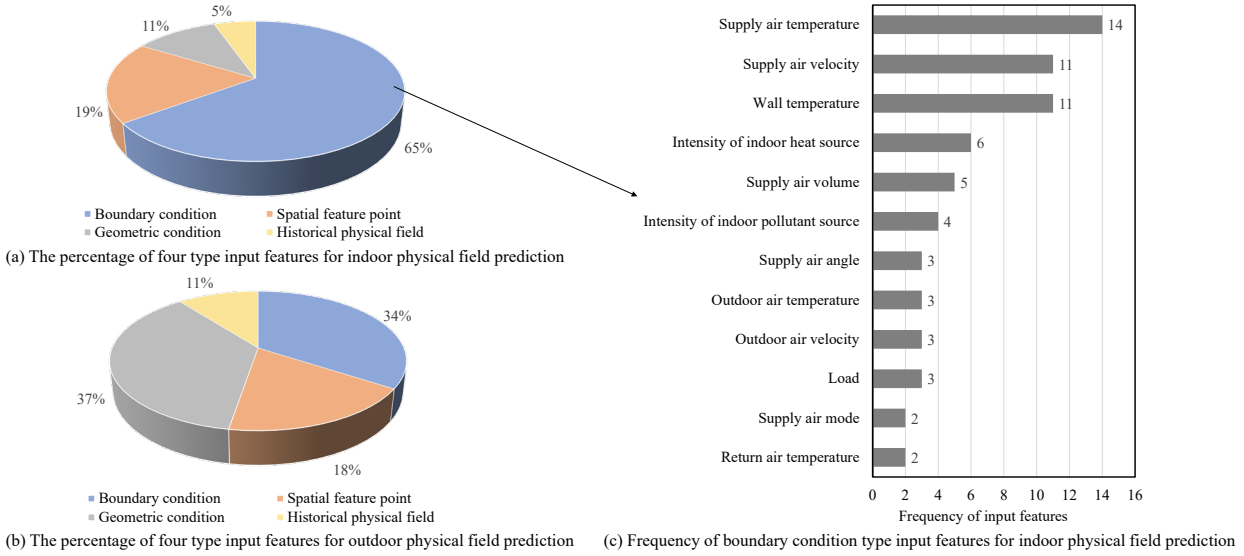

(a) The percentage of four type input features for indoor physical field prediction

(b) The percentage of four type input features for outdoor physical field prediction

(c) Frequency of boundary condition type input features for indoor physical field prediction

Figure 1. The percentage of four type input features and the frequency of boundary condition type input features for indoor physical field prediction.

For selected input features, the key is to ensure their sufficient statistical correlation with the output variables, while avoiding unnecessary features that could increase computational burden. Recursive feature elimination (RFE) and principal component analysis (PCA) are two widely used techniques for feature data processing and analysis, playing important roles in the field of ML. Furthermore, understanding of the importance of individual features and their impact on model predictions is vital for guiding the selection of input features. Correlation analysis is a key method to achieve this goal, focusing on the degree and direction of the relationship between variables. Correlation coefficients, such as Spearman, are commonly used to quantify the strength of association between variables. Additionally, regression analysis is an effective method for revealing interrelationships between variables. Zhang et al. (Zhang et al., 2020) used multivariate regression analysis (MRA) to compare the significance of different variables, successfully

identifying key factors related to the indoor environment and reducing the variable space by 50%.

2.3. Model

From the perspective of the "No Free Lunch" theorem, the average expected performance of various models is equivalent, and no single model can achieve accurate predictions in all scenarios. In the research area of using ML to predict building physical fields, numerous scholars have focused on model comparison and selection tasks.

Due to their exceptional nonlinear processing capabilities and high flexibility in model conversion, artificial neural networks (ANNs) dominate the field of building physical field prediction. Deep learning (DL) models, as an extension of ANNs, achieve efficient processing and learning of complex datasets by constructing deeper neural networks. Among these, models like multilayer perceptron (MLP) and convolutional neural networks (CNNs) are particularly widely used. MLP is illustrated in Fig. 2 with its basic architecture diagram, which consists of input, hidden and output layers, all of which are fully connected. The neurons in each layer are connected to all neurons in the previous layer, with connections between neurons being weighted. Each connection corresponds to a weight value, which represents the signal strength. CNNs are further evolved from MLPs with the help of structures such as convolutional layers, pooling layers and fully connected layers in order to efficiently extract local and global features in images, which is particularly suitable for learning and prediction of physical field data under regular grids.

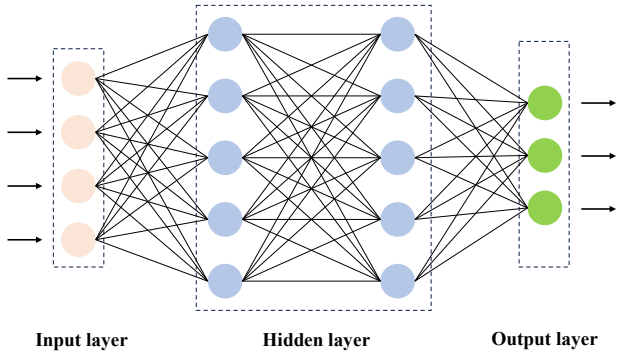

Figure 2. Architecture diagram of MLP with three layers.

Table 1. Advantages, disadvantages, and typical applications of models for building physical field prediction.

Model	Advantages	Disadvantages	Typical applications
MLP	Universal approximation capability for continuous functions via fully-connected layers, suitable for structured data	Parameter count escalates exponentially with input dimensions, struggles with high-dimensional spatial fields	Mapping low-dimensional parameters to scalar physical field outputs
CNN	Spatial feature extraction through local receptive fields and weight sharing, optimal for gridded data	Requires fixed-size inputs, limited adaptability to irregular geometries	Steady-state physical field prediction on regular grids
GAN	High-resolution field generation through adversarial training, complex distribution modeling	Training instability risks, potential physical law violations in generated fields	High-fidelity physical field synthesis
FNO	Spectral-domain global pattern learning with resolution-invariant architecture	Data-intensive operator training requirements, spectral bias towards low-frequency components	Generalizable physical field prediction across complex geometries

With technological advancements, cutting-edge DL models such as generative adversarial networks (GANs) and fourier neural operators (FNOs) have gradually infiltrated the field of built environment. GANs learn and generate samples that approximate the real data distribution through adversarial optimization between a generator and a discriminator. FNOs use Fourier transform to map the data to the frequency domain space, capture the frequency domain features with neural networks, and then invert them back to the time domain to complete the prediction, which is capable of handling input data of different resolutions, and can realise the generalised prediction of the physical field in complex geometries. The advantages, disadvantages and typical application scenarios of each of the above models are shown in Table 1.

After comparation and analysis, innovation at the structural level of the selected models can further enhance their performance in prediction of building physical field. By incorporating attention mechanisms, models can significantly improve their ability to analyse and process key information in input data, thereby enhancing prediction accuracy (Yasuda et al., 2022). Additionally, the concept of hybrid models is increasingly gaining attention in the trend of model development (Prince & Hati, 2021). These models focus on combining the characteristics of multiple models to overcome challenges that a single model cannot address.

3. APPLICATION OF SURROGATE MODLES IN THE FIELD OF BUILT ENVIRONMENT

Fully trained ML models, in addition to demonstrating exceptional performance, enable ultra-fast predictions of physical fields with time resolutions as low as seconds or even milliseconds. This prediction speed represents a significant improvement of three to five orders of magnitude compared to traditional CFD methods (Gao et al., 2024; Zheng & Xu, 2024). With this advantage, ML models can provide strong support for real-time optimization of the built environment.

Two main approaches in current research on built environment optimization based on surrogate models are summarized in Fig. 3. The first approach involves constructing a sufficient dataset to train a surrogate model. Based on this model, a wide range of input parameter combinations are explored under established constraints, and selections are made based on the evaluation values of the objective function. Finally, the rationality of the optimal input parameters is assessed through numerical analysis or experiment. Notably, this approach not only relies on human expertise to intuitively select input features but also incorporates advanced techniques such as optimization algorithms. Essentially, this approach shares roots with the trial-and-error method, but thanks to the efficient prediction capabilities of ML models, the computation time for physical field samples under different input parameters is greatly reduced. Additionally, optimization algorithms replace traditional manual judgment processes, ensuring the accuracy of the final input parameters and enhancing the efficiency of the overall optimization workflow.

The core advantage of the second approach lies in its ability to directly predict optimal parameters without the need for intermediate judgment and adjustment processes. Gao et al. (Gao et al., 2023) utilized their proposed sparse sampling perception network (SSPN) to predict concentration distributions. Subsequently, using these predictions as input, they efficiently derived suitable decontamination strategies through MLP. The latter part of this approach establishes a nonlinear mapping relationship between environmental parameters and design parameters. By accelerating

the prediction of optimal design parameters, this approach effectively shortens the time span of the optimization workflow. However, due to the lack of iterative comparison and adjustment of parameters, as well as strict necessity constraints, its accuracy may be slightly inferior to the first approach (Li et al., 2024). Furthermore, the implementation of this approach depends on a dual-model architecture: one surrogate model for building physical field prediction and another prediction model for optimal design parameter prediction. This means that the cost of collecting and preparing datasets is quite high in the early stages. In contrast, the first approach only requires constructing a dataset for a single model, which can quickly provide necessary samples for the optimization algorithm.

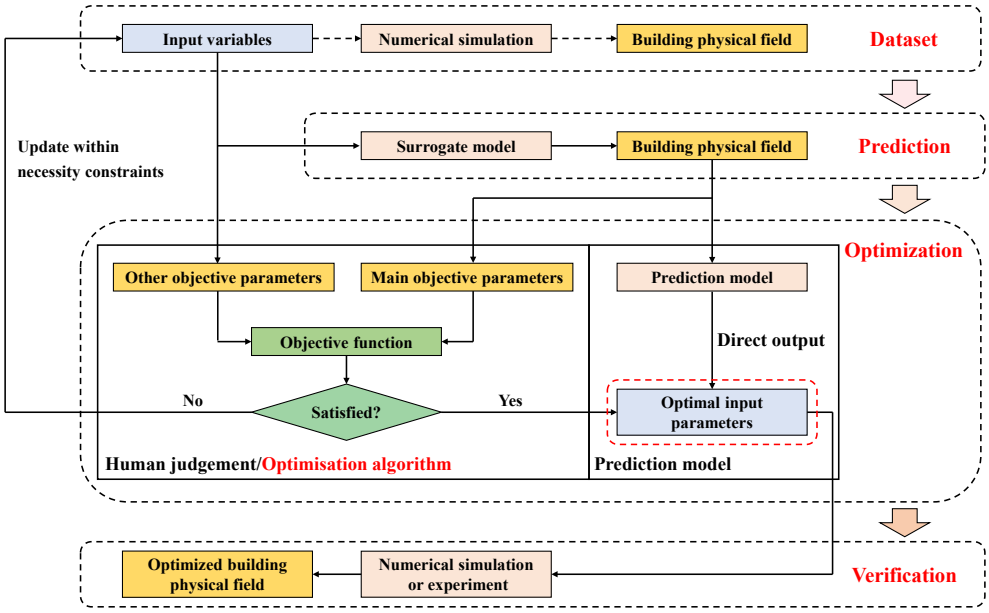

Figure 3. Two major approaches for optimizing built environment based on surrogate models.

As shown in Fig. 4, it is evident that the first approach is currently adopted in most research. Compared to human judgment, more studies combine optimization algorithms and other methods to select the optimal input parameters. In contrast, the second approach has not yet become widespread, with only a few studies attempting to optimize air supply strategies. In terms of surrogate models, ANNs are the preferred choice, although models such as GANs and XGBoost are also used. These surrogate models demonstrate powerful capabilities in simulating building physical fields, providing a foundation for subsequent optimization work. In terms of optimization algorithms, Genetic Algorithms (GAs) are widely used due to their strong global search capabilities and robustness. To further enhance the ability to solve multi-objective optimization problems, the Non-dominated Sorting Genetic Algorithm II (NSGA-II) is used to replace GAs. Additionally, Particle Swarm Optimization (PSO) has also been applied to a certain extent because of its fewer parameters and relatively faster convergence speed. Li et al. (Li et al., 2023) combined the global search capability of PSO with the local fine-tuning ability of the Grey Wolf Optimizer's (GWO), adopting a hybrid PSO-GWO optimization algorithm. This hybrid method exhibits higher optimization performance and a lower computational burden. Besides the optimization algorithms, Reinforcement Learning (RL), which learns optimal strategies through the interaction between agents and the environment, has also attracted attention.

Furthermore, the Sankey diagram reveals that the design parameters of the built environment can be categorized into three types: supply air parameters, layout parameters, and morphological parameters. This indicates that the environment is primarily optimized through three means: control of ventilation system, optimization of building layout, and design of building form.

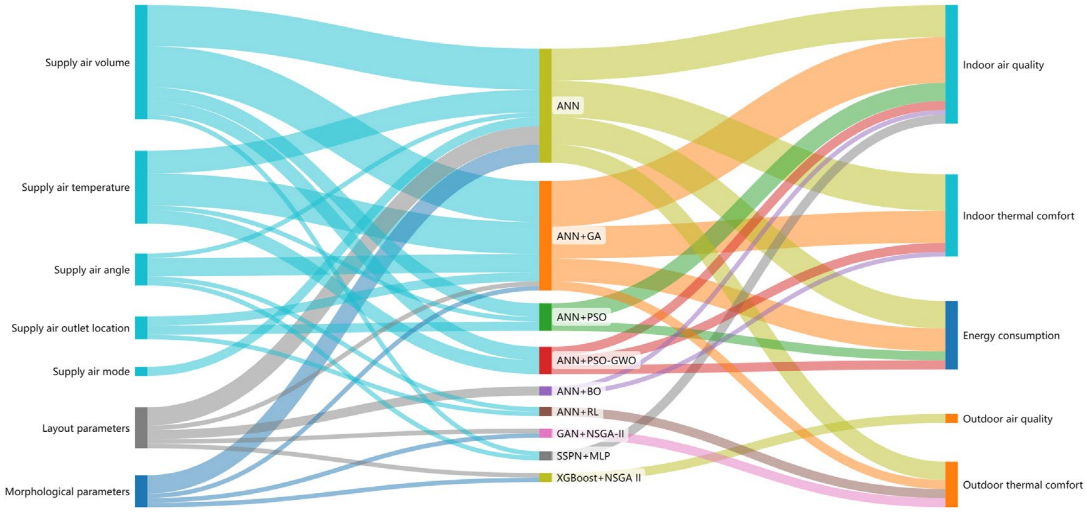

Figure 4. Sankey diagram to show the relationship between different design variables, models and design objectives.

4. DISCUSSION AND FUTURE PERSPECTIVES

ML models with superior performance can serve as an efficient means to rapidly and accurately predict building physical fields, thereby providing a powerful reference for the optimization of built environment. However, the dependence of ML models on large-scale datasets and their generalization ability in practical applications remain significant challenges. In recent years, the rapid development of few-shot learning has offered potential solutions to these problems, primarily through methods such as data augmentation and transfer learning. Data augmentation generates new virtual data from limited real samples to ensure model performance, while transfer learning focuses on leveraging similarities between data, tasks, or models to fine-tune model parameters with a small dataset after training in an existing domain, thereby enabling the application of the model to a new domain. This method allows for the transfer of surrogate models across different building geometric conditions to predict physical fields.

Furthermore, most current ML models make predictions without incorporating any physical prior knowledge, learning solely the mapping relationship between input and output through the training set. Although this approach can effectively avoid the time-consuming process of extracting physical attributes, it may not necessarily adhere to physical laws during computation and sometimes fails to meet the convergence constraints of traditional physical algorithms. Physical Informed Neural Networks (PINNs), as a cutting-edge approach, incorporate key physical characteristics and information into deep learning models. This represents a potential step toward higher-quality predictions and enhances model interpretability.

5. CONCLUSION

This study reviews the research progress on using ML as surrogate models for predicting building physical fields. It analyses key strategies for improving the performance of surrogate models from three perspectives: dataset, input feature, and model. Additionally, the review discusses two major implementation pathways for applying high-performance ML models in practical built environment optimization. However, due to the inherent complexity of building physical fields, surrogate models still face challenges such as high dependence on datasets, insufficient generalization ability, and lack of model interpretability. This review aims to provide guidance for the predictive applications of ML in the field of built environment.

ACKNOWLEDGEMENTS

This work was supported by the National Key Research and Development Program of China (NO.2023YFC3805304-2) and International Cooperation project of Science and Technology Commission of Shanghai Municipality (NO.22200711400).

REFERENCES

Athavale, J., Yoda, M., Joshi, Y., 2019. Comparison of data driven modeling approaches for temperature prediction in data centers. International Journal of Heat and Mass Transfer 135, 1039-1052.

Calzolari, G., Liu, W., 2021. Deep learning to replace, improve, or aid CFD analysis in built environment applications: A review. Building and Environment 206, 108315.

Gao, H., Qian, W., Dong, J., Liu, J., 2024. Rapid prediction of indoor airflow field using operator neural network with small dataset. Building and Environment 251, 111175.

Gao, X., Peng, Y., Yu, M., Hou, Z., 2023. Rapid construction of safe-zone by active flow field control and sparse-sampling-perception-network for public indoor environments suffering from nerve agents. Building and Environment 229, 109961.

Jing, G., Wang, H., Li, X., Wang, G., Yang, Y., 2024. An airflow velocity field reconstruction method with sparse or incomplete data using physics-informed neural network. Journal of Building Engineering 88, 109231.

Li, L., He, Y., Zhang, H., Fung, J. C. H., Lau, A. K. H., 2023. Enhancing IAQ, thermal comfort, and energy efficiency through an adaptive multi-objective particle swarm optimizer-grey wolf optimization algorithm for smart environmental control. Building and Environment 235, 110235.

Li, Y., Pan, Y., Huang, Z., Fu, L., Li, J., Sun, T., Zhu, M., Yuan, X., 2024. Numerical modeling of non-uniform indoor temperature distribution for coordinated air flow control. Journal of Building Engineering 82, 108246.

Prince, Hati, A. S., 2021. A comprehensive review of energy-efficiency of ventilation system using Artificial Intelligence. Renewable and Sustainable Energy Reviews 146, 111153.

Qu, Z., Zhang, Y., Hong, C., Zhang, C., Dai, Z., Zhao, Y., Wu, X., Gao, Y., Jiang, X., Qian, J., Gu, Z., 2023. Temperature forecasting of grain in storage: A multi-output and spatiotemporal approach based on deep learning. Computers and Electronics in Agriculture 208, 107785.

Vinuesa, R., Brunton, S. L., 2022. Enhancing computational fluid dynamics with machine learning. Nature Computational Science 2(6), 358-366.

Wang, J., Jiang, L., Yu, H., Feng, Z., Castaño-Rosa, R., Cao, S., 2024. Computer vision to advance the sensing and control of built environment towards occupant-centric sustainable development: A critical review. Renewable and Sustainable Energy Reviews 192, 114165.

Xu, A., Dong, Y., Sun, Y., Duan, H., Zhang, R., 2023. Thermal comfort performance prediction method using sports center layout images in several cold cities based on CNN. Building and Environment 245, 110917.

Yasuda, Y., Onishi, R., Hirokawa, Y., Kolomenskiy, D., Sugiyama, D., 2022. Super-resolution of near-surface temperature utilizing physical quantities for real-time prediction of urban micrometeorology. Building and Environment 209, 108597.

Zhang, T., Liu, Y., Rao, Y., Li, X., Zhao, Q., 2020. Optimal design of building environment with hybrid genetic algorithm, artificial neural network, multivariate regression analysis and fuzzy logic controller. Building and Environment 175, 106810.

Zheng, Y., Xu, X., 2024. Predicting indoor 3D airflow distribution using artificial neural networks with two different architectures. Energy and Buildings 303, 113841.

6th International Conference on Building Energy and Environment
Eindhoven University of Technology, The Netherlands
6 - 10 July 2025

Phase change materials as complementary retrofit strategy for energy efficiency: A simulation-based comparative analysis

Rafael Alvarez Gutiérrez[1], Amaryllis Audenaert [1], Stijn Verbeke [1,2]

[1]*Energy and Materials in Infrastructure and Buildings (EMIB), Faculty of Applied Engineering, University of Antwerp, Antwerp, Belgium*
[2]*Unit Water and Energy Transition, Flemish Institute for Technical Research (VITO/EnergyVille), Mol, Belgium*
**Corresponding author: rafael.alvarezgutierrez@uantwerpen.be*

SUMMARY
This paper investigates the optimal combination of thermal insulation and phase change materials (PCMs) to retrofit the inside of external walls. Multiple variants of office and residential buildings located in Brussels are analysed by means of dynamic building performance simulations. Findings reveal that, for external wall retrofitting, the building's insulation performance has the greatest impact on energy savings, with PCMs having a more significant effect in lightweight structures. The results substantiate the utility of PCMs as a retrofit measure, particularly in well-insulated office buildings, outperforming adding thermal insulation due to the high internal loads. For interior retrofitting with a maximum thickness of 5 cm, the combination of PCMs and thermal insulation is more effective than insulation alone in most scenarios. This combination effectively balances heating and cooling energy savings, reducing overall energy demand up to 4.8% in the office building and up to 26.7% in the residential building.

Keywords: Phase Change Materials, Retrofit, Energy Efficiency, Dynamic Building Performance Simulations

1. INTRODUCTION

In light of the contemporary challenges of climate change and the energy crisis, Europe strives for a climate-neutral economy with net-zero greenhouse gas emissions by 2050. According to the Energy Performance of Buildings directive, 85% of buildings were built before 2000 and among those, 75% have poor energy performance, highlighting the pressing need for targeted interventions in the building sector (EU 2024/1275, 2024). In response to this challenge, the renovation wave is a key policy initiative to drive the energy efficiency of the building stock to reach the EU targets (Çıldır et al., 2020). This initiative involves the implementation of passive and active retrofit strategies to reduce year-round operating costs and energy use of buildings. Among these strategies, passive solutions enhance the thermal resistance of the building envelope, reducing heat loss to the outside environment and thereby reducing the energy required for cooling and heating (Ibrahim et al., 2024). These strategies - such as incorporating thermal insulation, replacing exterior windows and improving airtightness - are widely adopted practices in the building sector. However, such highly-insulated, airtight buildings can lead to a series of unintended consequences, such as overheating and increased energy demand for cooling during the summer due to heat trapped in the sealed building envelope (Sage-Lauck & Sailor, 2014). In this context, phase change materials (PCMs) have received considerable attention as a promising passive retrofit strategy for buildings. By phase transitioning - typically from solid to liquid in building integrated applications - these

materials can store and release a large amount of latent heat under nearly constant temperatures (i.e. the phase change temperature). Their integration increases the building's thermal storage capacity and stabilizes temperature fluctuations, with the potential to improve thermal comfort and reduce energy demand. In addition, their high energy storage density makes them suitable for reducing construction materials while preserving maximal indoor space, particularly in retrofit scenarios (Al-Absi et al., 2022; Khan et al., 2022). Recent studies using dynamic building performance simulations have demonstrated their influence on the indoor thermal environment of existing buildings. Li et al. reported that depending on the PCMs' location and climate conditions, uncomfortable degree hours were reduced by 24% to 40% (Li et al., 2023). As evidenced by total energy demand reductions of -1.7% to 32.2% reported by various researchers, the effect of PCMs is intrinsically dependent on the boundary conditions of the case study, like building characteristics, climate conditions, PCM characteristics, and location within the building (Abilkhassenova et al., 2023; Mohseni & Tang, 2021; Zhussupbekov et al., 2023).

However, there is a lack of studies investigating PCMs as a complementary retrofit strategy in combination with conventional measures, such as upgrading the thermal envelope. Additionally, current literature on PCMs as retrofitting strategy has primarily focused on analysing their integration in specific individual buildings in the context of their respective climate conditions. This paper goes beyond the state-of-the-art by exploring the potential of PCMs as a complementary retrofit strategy across diverse building contexts, assessing their impact on energy efficiency over a range of building characteristics.

2. RESEARCH METHODOLOGY

A simulation-based approach is designed to evaluate the impact of passive retrofit strategies on the energy performance of two building typologies, including an office building and a detached residential building. The proposed solutions feature a combination of both conventional retrofit strategies, such as enhancing the building envelope by adding thermal insulation, and novel ones by integrating PCMs. The simulation models used in this study are not validated against empirical data; instead, this study adopts a simulation-based comparative analysis to assess the relative impacts of different retrofit interventions on building energy performance. To ensure the accuracy of the results, the assessment is conducted using multi-zone dynamic building performance simulations with EnergyPlus v9.6, a simulation engine validated by the BESTEST evaluation protocol. These models simulate the thermal flows and the resulting energy demand for both cooling and heating. Additionally, the validated "conduction finite difference" (CondFD) and "phase change" models are deployed to simulate the thermal behaviour of PCMs in the building envelope (Tabares-Velasco et al., 2012).

2.1 Description of numeric model

Two reference building models are considered: the top floor of a five-storey office building and a detached residential building, both located in the Belgian city of Brussels. The building models are parametric, allowing for variation in building characteristics and retrofit strategy. This approach makes it possible to investigate the effectiveness of the retrofit strategies across multiple contexts. Figure 1.a illustrates the office building. The top floor, with an area of 1153 m², is divided into 17 different thermal zones by means of internal partitioning. The external walls and roof are subjected to exterior boundary conditions, while the interior floor is subjected to adiabatic conditions as it is

adjacent to the storey below. The detached residential building, illustrated in Figure 1.b, has a floor area of 211 m² and is divided into eight different thermal zones, separated by internal walls. The window-to-wall (WTW) ratio is 40% in all orientations for the office building and 20% for the residential building.

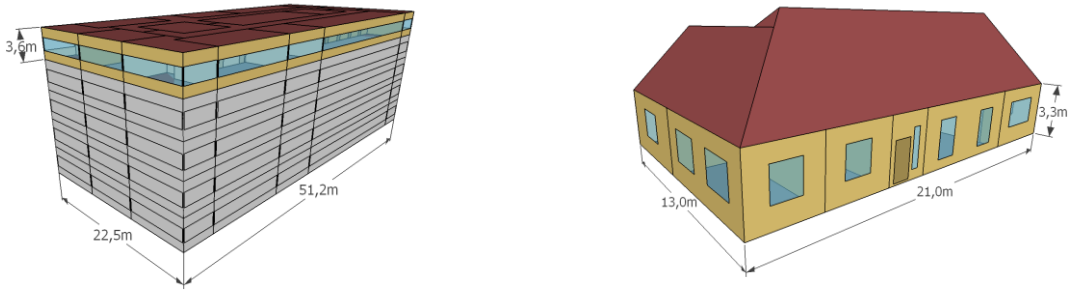

(a) (b)

Figure 1. Buildings examined in the simulation study (a) Office building (b) Residential building

The internal gains of the buildings are considered using the objects "People", "Lights" and "ElectricEquipment" with assumptions based on international standards (ASHRAE 90.1, 2022). Ventilation and infiltration are incorporated with the "Design flow rate" models to comply with the standard for office buildings (ASHRAE 62.1, 2022) and the Belgian residential standard (NBN D 50-001, 1991). Additionally, the "ZoneMixing" object is used to model air mixing occurring between the thermal zones. The HVAC system is modelled using the input object "Ideal Loads Air System", which models the heating or cooling demand as if it were supplied by an ideal system without thermal inertia or efficiency losses. The applied thermostat set-points comply with the thermal comfort category II for air-conditioned zones, as recommended in the relevant standard (NBN EN 16798-1, 2019). The input parameters for the models are summarized in Table 1.

Table 1. Input parameters for numerical model

Parameter	Value for office building	Value for residential building
People	18.58 m²/person	4 occupants
Lights	7.86 W/m²	25 W
Electric equipment	8.07 W/m²	1000 W
Ventilation flow rate	0.0085 m³/s*person	0.001 m³/s*m² (floor area)
Infiltration flow rate	0.0005 m³/s*m² (exterior surface area)	0.0005 m³/s*m² (exterior surface area)
Heating set-point (occupied/unoccupied)	20°C/16°C	20°C/16°C
Cooling set-point (occupied/unoccupied)	26°C/32°C	26°C/32°C

2.2 Input variables of parametric model

Building upon the reference buildings, a parametric model is developed to explore the performance of PCMs as a complementary retrofit strategy across multiple building contexts. This parametric model comprises variations in the original building envelope construction, including a heavyweight structure and a lightweight variant, and 4 variations in thermal performance. The heavyweight structure details a cavity wall, and the lightweight structure features a lightweight steel-framed construction for the office building and a timber-framed structure for the residential building. Table 2 outlines the variation in external wall and roof configurations with different thermal inertia.

Table 2. External wall and roof configuration for heavyweight and lightweight variants (outside to inside layer)

Exterior wall			Exterior roof		
Heavyweight	**Lightweight Steel**	**Lightweight Timber**	**Heavyweight**	**Lightweight Steel**	**Lightweight Timber**
Facade brick 9 cm	Cement render	Wood cladding	Bitumen roofing	Bitumen roofing	Wood cladding roof
Air gap	Rigid thermal insulation	Thermal insulation between timber rafters	Screed 6 cm	Thermal insulation	Thermal insulation between timber rafters
Thermal insulation	Plywood 18 mm	Plaster 10 mm	Thermal insulation	Thermal insulation in steel frame	Plaster 10mm
Hollow brick 13.8 cm	Thermal insulation in steel frame		Concrete slab 15 cm	Plywood 18mm	
Plaster 10 mm	Plaster 10 mm		Plaster 10 mm	Air gap	
				Plaster 10 mm	

For the opaque external constructions, four variations of thermal performance are defined. The constructions are identical, except for the thickness of the thermal insulation layers, which varied to achieve a thermal transmittance (U-value) equal to 1 W/m²K (type: U1), 0.6 W/m²K (type: U0.6), 0.24 W/m²K (type: U0.24) and 0.1 W/m²K (type: U0.1). For each of these variants, distinct window assemblies with varying U-values and solar heat gain coefficient (SHGC) are considered, respectively: single-glazed windows (U = 5 W/m² K, SHGC = 0.8); double-glazed windows (U = 3 W/m² K, SHGC = 0.8); double-glazed window with low-e (U = 1.5 W/m² K, SHGC = 0.5); triple-glazed windows with low-e (U = 1 W/m² K, SHGC = 0.5). These variations cover the range from poorly insulated buildings to those meeting the insulation values suggested for Passive House standards.

2.3 Retrofit measures

In this paper, two different passive retrofit strategies are examined separately and in combination to investigate the impact on the thermal behaviour of the building. For each of the 24 building variants, six combinations of retrofit measures are simulated. The conventional retrofit solution includes enhancing the thermal resistance of the external wall assemblies applying rigid polyurethane foam (PUR) with a thermal conductivity of 0.025 W/mK on the interior part of the external wall, covered with a finishing layer. To complement this conventional strategy, this study investigates the integration of PCMs on the inside of the external walls, also covered with a plaster finishing layer. The PCM selected for this study is the Rubitherm© organic macro-encapsulated PCM, which is commercially available with different melting temperatures and has been widely researched (Al-Absi et al., 2022; Prabhakar et al., 2020). With the aim of reducing cooling loads, the melting temperature of the PCM is selected to be 25°C, closely aligning to the cooling set-point of the building. The thermal conductivity of the PCM is 0.2 W/mK, the specific heat capacity is 2000 J/kgK and the latent heat of fusion is 230 kJ/kg. The thermal behaviour of the PCM is simulated in EnergyPlus with the CondFD solution algorithm. This algorithm follows the temperature-enthalpy function of the material during each iteration of the calculation, and accurately considers the phase change enthalpy and specific heat. The study investigates scenarios where only PUR (5 cm) or PCM (5 cm) is applied, as well as cases where both are combined with a total thickness of 5 cm, complementing each other. These configurations lead to six distinct retrofit combinations, which are simulated for each building variant. In these combined

configurations, the PCM is placed closer to the interior to maximize its heat transfer with the indoor environment. Table 3 gives an overview of the different baseline and retrofitted scenarios, including variable parameters, retrofit options and total number of cases.

Table 3: Overview of baseline and retrofitted scenarios

Scenario	Building typology	Thermal inertia	Thermal performance level	Retrofit options [Insulation-PCM cm]	Number of cases
Baseline	Residential; Office	Lightweight; Heavyweight	U0.1; U0.24; U0.6; U1	None	16
Retrofitted	Idem baseline	Idem baseline	Idem baseline	5-0 ; 4-1 ; 3-2 ; 2-3 ; 1-4 ; 0-5	96

3. RESULTS

The parametric model developed in this study is used to evaluate the performance of various retrofit measures in reducing energy demand and improving thermal conditions across different building contexts. The simulations are conducted for a year, calculating the energy use for heating and cooling. To convert this to electricity demands, the heating energy demand is divided by 3.00 and the cooling demand by 4.10, corresponding to the respective seasonal coefficients of performance (SCOP) for room heating and cooling of an air-to-air heat pump system.

3.1 Retrofitting of building with different construction configurations

In the initial set of simulations, both the office and residential buildings were modelled with heavyweight and lightweight structures, each with four different levels of initial thermal performance, representing 16 variations of business-as-usual cases. These 16 models are the baseline scenarios used as a reference to assess the relative impact of retrofit interventions on the building's energy performance. Subsequently, each building variant is retrofitted through the addition of PCM, PUR or a combination of both at the inner surface of the external walls. This resulted in a total of 112 EnergyPlus simulations conducted (16 baseline scenarios and 96 retrofitted scenarios) of which the energy demand and the indoor thermal environment were analysed. Figure 2 illustrates the reduction in total energy demand after applying the six retrofit measures, compared to the baseline scenarios for each modelled variant of (a) the office and (b) the residential building.

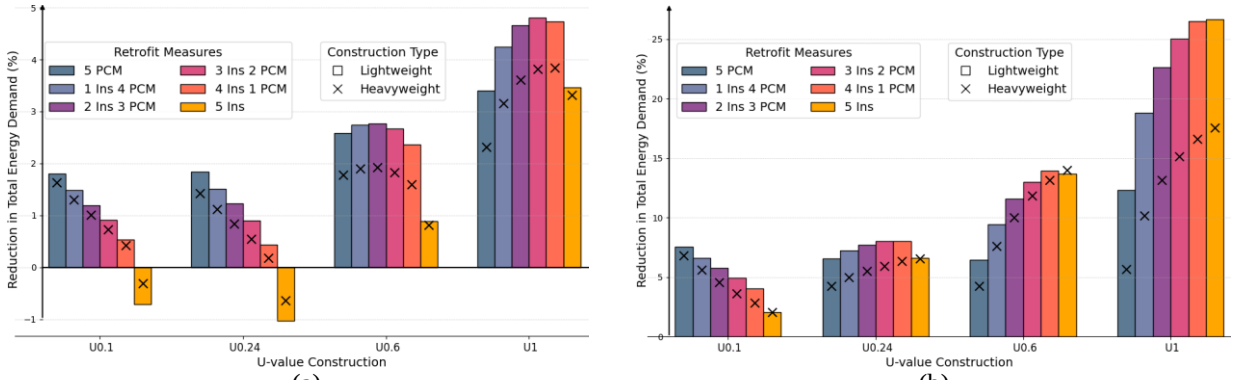

Figure 2. Relative reduction in total energy demand per retrofit measure in (a) Office building (b) Residential building located in Brussels. Bar plots represent results for lightweight buildings, whereas crosses on the graph indicate corresponding results for heavyweight buildings

The results from both graphs reveal that the reduction in total energy demand is significantly dependent on the building characteristics. Notably, the level of initial thermal performance demonstrates the most significant impact on the achieved energy savings, with a similar trend observed in both office and residential buildings. The findings indicate that, in the most effective retrofit configuration, the thickness of the PCM layer increases as the thermal performance of the building improves, while it decreases for lower thermal performance. In poorly insulated buildings, higher energy savings can be achieved by adding insulation, as it is an effective method to lower heating energy demand, which accounts for the largest share of energy demand in such buildings. However, in highly insulated buildings (U0.1) the best retrofit solution features adding 5 cm of PCMs, which contributes to energy savings by reducing the cooling loads. This strategy achieved overall energy savings of 1.4% to 12.3%. Conversely, the addition of insulation in these cases can increase cooling loads due to heat trapped within the building envelope, outweighing the reduction in heating loads. This effect is more pronounced in the office building because of the higher internal loads. In several scenarios, the most effective retrofit solution combines both thermal insulation and PCM, providing a balance in heating and cooling energy savings. This results in total energy savings ranging from 1.4% to 4.8% in the office building and 6.6% to 26.7% in the residential building, demonstrating the potential of PCMs as a complementary retrofit strategy.

Additionally, the findings demonstrate that the impact of adding PCMs is generally greater in lightweight structures than in heavyweight ones, regardless of the initial thermal performance. This can be attributed to the fact that lightweight structures face higher indoor temperature peaks and fluctuations, which can be stabilized through the implementation of PCMs. Figure 3 displays the indoor operative temperature trend of a specific zone of the residential building (U0.24) for 10 summer days. This figure shows the effectiveness of integrating PCMs to reduce indoor temperature peaks in lightweight structures, compared to heavyweight ones.

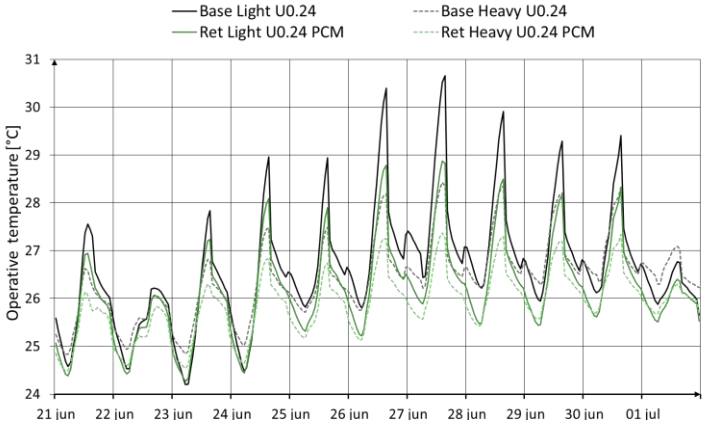

Figure 3. Impact of PCM integration on indoor operative temperature in lightweight and heavyweight building variants (U0.24) of residential building located in Brussels

Overall, the results reveal that energy savings from retrofitting solely with PCMs are relatively low, ranging from 1.4% to 3.4% for the office building and 4.2% to 12.3% in the residential building. These values are consistent with reported energy savings from the literature, ranging from 4.7% to 25.2% (Zhussupbekov et al., 2023), and highlight the need for additional strategies to improve the PCM efficiency, and quantify benefits, such as improvement in thermal comfort.

3.2 Sensitivity to climate conditions

The performance of PCMs is sensitive to the climate where the building is situated. In order to explore the site-specific influence on the retrofit measures, 4 different cities were selected to

represent the most prevailing climates in Europe, according to the Köppen-Geiger classification: Stockholm (cold climate without dry season and warm summer), Brussels (temperate climate without dry season and warm summer), Vienna (temperate climate without dry season and hot summer), and Madrid (temperate climate with dry season, hot summer and cold semi-arid climate). For this analysis, the simulations were restricted to the variants characterized by a lightweight structure and a building envelope U-value of 0.24 W/m² K. The different retrofit measures were evaluated for both buildings across the four cities. The most effective retrofit solution and the associated absolute and relative reductions in total energy demand are outlined in Table 4.

Table 4. Reduction in total energy demand across 4 cities

	Office			**Residential**		
Location	Optimal retrofit solution	Δ [kWh/m²]	Relative [%]	Optimal Retrofit solution	Δ [kWh/m²]	Relative [%]
Stockholm	4 Ins – 1 PCM	0.38	1.63	4 Ins – 1 PCM	1.57	6.44
Brussels	3 Ins – 2 PCM	0.23	1.78	4 Ins – 1 PCM	1.11	8.03
Vienna	3 Ins – 2 PCM	0.27	1.42	3 Ins – 2 PCM	1.16	6.17
Madrid	5 PCM	0.15	0.95	5 PCM	0.89	7.5

The energy savings from retrofitting these buildings are similar in each city, ranging from 1.0% to 1.8% for the office building and 6.2% to 8.0% for the residential building. However, the obtained results reveal a shift in the best retrofit strategy - combination of PCM and insulation - depending on the climate conditions in which the building is simulated. In cooling-dominated cities, such as Madrid, PCMs offer the most effective retrofit solution, while in heating-dominated cities, such as Stockholm, it is preferable to add more insulation and limit the thickness of PCMs to reduce the heating demand. This sensitivity analysis highlights the importance of considering climate conditions when making decisions to retrofit buildings with PCMs and thermal insulation.

4. CONCLUSION

This paper investigates the application of PCMs as complementary retrofit strategy to conventional approaches, specifically the enhancement of external walls through the addition of thermal insulation. To evaluate the performance of the retrofitting measures across different building contexts, a parametric model is developed that includes variations in thermal inertia and thermal performance of the structure, for both an office and a residential building. Dynamic building performance simulations are used to analyse the impact of the different retrofit strategies - adding PCMs and/or thermal insulation to the internal part of the external walls - on energy demand and the indoor thermal environment. The results of this research demonstrate the impact of the building characteristics on the energy savings potential of the retrofit strategies, with the thermal performance having the most significant impact. A similar trend is observed for both residential and office buildings, where higher amounts of PCM are more effective in well-insulated buildings, reducing cooling loads, while thermal insulation performs better in poorly insulated buildings, lowering heating demand. Additionally, the results indicate that the impact of adding PCMs is generally greater in lightweight structures than heavyweight, as they are more effective in mitigating indoor temperature peaks and fluctuations. The results demonstrate the potential of PCMs for building retrofitting, specifically in well-insulated office buildings with high internal loads, where they outperformed adding thermal insulation. When retrofitting the inside of exterior walls with a given maximal thickness of 5 cm, the combination of both thermal insulation and

PCMs consistently reduced energy demand more effectively than thermal insulation in most scenarios. The combination effectively balances heating and cooling energy savings, leading to overall energy savings of up to 4.8% in the office building and up to 26.7% in the residential building. Moreover, the results of the sensitivity analysis highlight the importance of considering boundary conditions, such as climate conditions, when selecting the appropriate retrofit strategy. Future research will extend the analysis including other retrofit strategies, such as shading controls and night ventilation, to assess their synergy with PCM retrofitting and explore additional benefits that PCM can provide in buildings, in particular improving thermal comfort. Moreover, the sensitivity analysis will be expanded to evaluate the performance of the retrofit strategies under future weather scenarios in the context of expected climate change impacts, contributing to the development of more energy-efficient and climate resilient buildings.

ACKNOWLEDGEMENTS

This paper is partly supported through funding from European Union's Horizon Europe research and innovation programme under grant agreement No 101135629, project BIOBUILD.

REFERENCES

Abilkhassenova, Z., Memon, S. A., Ahmad, A., Saurbayeva, A., & Kim, J. (2023). Utilizing the Fanger thermal comfort model to evaluate the thermal, energy, economic, and environmental performance of PCM-integrated buildings in various climate zones worldwide. Energy and Buildings, 297.

Al-Absi, Z. A., Hafizal, M. I. M., & Ismail, M. (2022). Experimental study on the thermal performance of PCM-based panels developed for exterior finishes of building walls. Journal of Building Engineering, 52.

ASHRAE, ASHRAE 62.1-Ventilation and Acceptable Indoor Air Quality, 2022.

ASHRAE, ASHRAE 90.1-Energy Standard for Sites and Buildings Except Low-Rise Residential Buildings, 2022.

Çıldır, A. S., Köktürk, G., & Tokuç, A. (2020). Design approaches for retrofiting offices to reach nearly zero energy: A case study in the Mediterranean climate. Energy for Sustainable Development, 58, 167–181.

Ibrahim, M., Harkouss, F., Biwole, P., Fardoun, F., & Ouldboukhitine, S. (2024). Building retrofitting towards net zero energy: A review. In Energy and Buildings (Vol. 322). Elsevier Ltd.

Khan, M., Khan, M. M., Irfan, M., Ahmad, N., Haq, M. A., Khan, I., & Mousa, M. (2022). Energy performance enhancement of residential buildings in Pakistan by integrating phase change materials in building envelopes. Energy Reports, 8, 9290–9307.

Li, W., Jing, M., Li, R., Gao, J., Zhu, J., & Li, R. (2023). Study of the optimal placement of phase change materials in existing buildings for cooling load reduction - Take the Central Plain of China as an example. Renewable Energy, 209, 71–84.

Mohseni, E., & Tang, W. (2021). Parametric analysis and optimisation of energy efficiency of a lightweight building integrated with different configurations and types of PCM. Renewable Energy, 168, 865–877.

NBN D 50-001-Ventilatievoorzieningen in woongebouwen. (EN: Ventilation systems in residential buildings), 1991.

NBN EN 16798-1-Energy performance of buildings - Ventilation for buildings - Part 1, 2019.

Directive (EU) 2024/1275 of the European Parliament of the council on the energy performance of buildings. (2024). http://data.europa.eu/eli/dir/2024/1275/oj

Prabhakar, M., Saffari, M., de Gracia, A., & Cabeza, L. F. (2020). Improving the energy efficiency of passive PCM system using controlled natural ventilation. Energy and Buildings, 228.

Sage-Lauck, J. S., & Sailor, D. J. (2014). Evaluation of phase change materials for improving thermal comfort in a super-insulated residential building. Energy and Buildings, 79, 32–40.

Tabares-Velasco, P. C., Christensen, C., & Bianchi, M. (2012). Verification and validation of EnergyPlus phase change material model for opaque wall assemblies. Building and Environment, 54, 186–196.

Zhussupbekov, M., Memon, S. A., Khawaja, S. A., Nazir, K., & Kim, J. (2023). Forecasting energy demand of PCM integrated residential buildings: A machine learning approach. Journal of Building Engineering, 70.

6th International Conference on Building Energy and Environment
Eindhoven University of Technology, The Netherlands
6 - 10 July 2025

An experimental and numerical study on daily light integral of vegetation for photovoltaic-green roof in Singapore

Yang He [1], Jianlin Liu [1], Mengmeng Dai [1], Haifeng Cui [2], Zhicheng Duan [1], Mengjie Song [1]

[1]*Donghua University, Shanghai, China, 201620*
[2]*Shanghai Oujing Garden Co., China, 201800*

SUMMARY
Solar radiation plays a crucial role in integrated photovoltaic-green roof (PVGR) systems, but research on the distribution characteristics of solar radiation and photosynthetically active radiation (PAR) or daily light integral (DLI) of vegetation surface under PV shading is limited. To address this gap, a field experiment was conducted in Singapore. The results revealed that on a clear day, the maximum incident solar radiation and PAR on vegetation surface between PV arrays were up to 1136 W/m^2 and 1876.6 μmol/m^2/s, respectively, whereas they were significantly lower below PV panels. Regression analysis demonstrated a highly linear relationship between DLI and solar radiation with an average ratio of 1.799. A numerical model for DLI of vegetations for PVGR was developed, and the effect of PVGR design parameters on the average annual DLI of vegetations was clarified. The findings drawn herein contribute to optimizing PVGR design in terms of selection of plant species.

Keywords: Photovoltaic-green roof, Daily light integral, Solar radiation, Sky view factor

1. INTRODUCTION

In urban areas with limited land, green roofs (Shafique et al., 2020) and photovoltaic (PV) roofs (Ghosh, 2020) are becoming common solutions to meet growing energy demands and address climate change. Green roofs reduce air conditioning energy use through evapotranspiration, shading, and insulation (He et al., 2017), while also mitigating urban heat islands. PV roofs provide shading and have the potential to cover significant energy consumption in certain regions. However, space constraints create competition between these technologies. In recent years, a novel type of roof called PVGR has emerged, which combines both types of roofs together, as shown in Fig. 1. This configuration maximizes roof space, creates synergistic effects, and provides ecological benefits (Talwar et al., 2023). However, poor vegetation design can reduce PV efficiency by obstructing airflow or causing shading (Ogaili and Sailor, 2016). Solar radiation, critical for both PV and green roofs, affects energy balance, photosynthesis, and vegetation growth (Lamnatou and Chemisana, 2013). Accurate solar radiation prediction is essential for optimizing PVGR performance and guiding vegetation selection.

Several methods have been developed to predict solar radiation distribution in PV roofs or PVGR. Fathi and Samer. (2016) introduced a model for multi-row solar fields that accounts for the influence of all rows on the view factors of PV panels, highlighting how design parameters affect radiation distribution. Jahanfar et al. (2020) considered both direct and diffuse solar radiation beneath PV arrays, estimating the sky view factor (SVF) based on a simplified two-dimensional PV panel layout. However, this SVF model only considered the impact of three PV panels on the central point of the vegetated surface below, performing adequately only after calibration for

diffuse solar radiation, which limits its applicability across various weather conditions and PV array configurations.

Figure 1. A example of Photovoltaic-green roof (Ramshani et al., 2020).

Therefore, accurate calculation of SVF serves as a fundamental basis for predicting energy balance in photovoltaic green roofs. The calculation of view factors may be based on (Gupta et al., 2017). Considering the large number of PV arrays and the scalability requirement of the calculation process, this study adopts ray tracing method to reveal the variation pattern of view factors for vegetation surfaces under PV arrays. Photosynthetically active radiation (PAR, 400–700 nm) is essential for plant growth, driving key processes like photosynthesis and transpiration, and influencing urban energy, water, and carbon balance (Wane et al., 2022). Different plant species require varying levels of daily light integral (DLI), such as lettuce (DLI =14.5±4.16 mol/m^2/day) and Kailan (DLI = 47.22 ± 3.48 mol/m^2/day). Therefore, accurate estimation of PAR or DLI is imperative for selecting suitable plant species in PVGR. However, PAR measurements are not commonly available in most weather stations and are rarely conducted within urban built environments. The heterogeneous light environment created by PV arrays above the vegetation surface further poses challenges in selecting suitable plant species. Various methods have been proposed to estimate DLI. One widely used method is based on linear regression between DLI and global solar radiation at different locations (García-Rodríguez et al., 2020). However, this regression model is only applicable for unshaded conditions. For shaded area, considering the varying shading effects of PV arrays across different areas of the vegetation surface and the dynamic characteristics of radiation beneath PV arrays, further validation is required to ensure the accuracy in predicting DLI by SVF.

This paper aims to calculate the SVF of vegetation surface in PVGR and analyze how design factors affect these view factors. Based on the obtained view factors, a solar radiation transfer model for PVGR was developed. Field experiments were conducted to validate the model, and an analysis was performed on the distribution characteristics of solar radiation and DLI with different configurations. The results of this study are expected to provide valuable insights for the advancement of hygrothermal transfer models for PVGR and guide the optimal selection of plant species.

2. METHOD AND MATERIALS

2.1. Solar radiation transfer model of PVGR

Significant heterogeneity of solar radiation has been observed on the vegetation surface of PVGR (Schindler et al., 2016). To facilitate the analysis of distribution, a representative unit of PVGR was selected, as shown in the dotted box in Fig. 2. The PV arrays are assumed to be long enough , so that the solar radiation of the PVGR can be approximated as a two-dimensional distribution. Based on the projection position of the PV array, the vegetation surface is divided into three sub-surfaces: S1, S2 and S3. Additionally, the front and back surfaces of the PV panel are referred to as S4 and S5, respectively. Exposed to solar radiation from the sky, the multiple reflections among S1~S5 need to be taken into account.

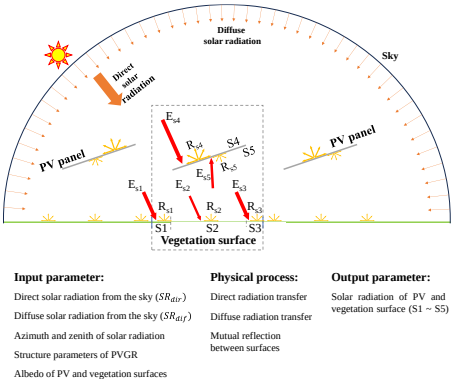

Figure 2. Schematic diagram of solar radiation transfer of PVGR.

In this unit, all the PVGR surfaces are discretized into meshes, and the radiation balance for all the meshes is represented from Eq. (1) to Eq. (5). Incident solar radiation $E_{n,i}$ consists of direct radiation ($D_{n,i}$), diffuse solar radiation from the sky ($R1_{n,i}$) and diffuse solar radiation from other surfaces ($R2_{n,i}$). The Liu and Jordan model (Liu and Jordan, 1960), which assumes isotropic sky diffuse radiation, was used to calculate $R1_{n,i}$. Reflected radiation ($R2_{n,i}$) is determined by the view factor ($VF_{n,i,j}$) and albedo of surfaces, as shown in Eq. (4). The shading factor ($F_{shading,n,i}$) for direct solar radiation is calculated by tracing rays emitted from the mesh center to detect obstructions. By solving Eqs. (1)-(5) simultaneously, the solar radiation for all surfaces can be obtained.

$$E_{n,i} = D_{n,i} + R1_{n,i} + R2_{n,i} \tag{1}$$

$$D_{n,i} = Vec_n \cdot Vec_{solar} \cdot SR_{dir} \cdot F_{shading,n,i} \tag{2}$$

$$R1_{n,i} = VF_{sky,n,i} \cdot SR_{dif} \tag{3}$$

$$R2_{n,i} = \sum_{j=s1}^{s5} E_j \cdot alb_j \cdot VF_{n,i,j} \tag{4}$$

$$E_j = \frac{1}{m}\sum_{k=1}^{k=m} E_{j,k} \tag{5}$$

Where, SR_{dir} and SR_{dif} are measured direct and diffuse radiation, while $F_{shading,n,i} = 1$ is determined based on whether rays intersect PV surfaces. $E_{j,k}$ is the incident solar radiation on mesh k of surface j.

2.2. Field experiment of solar radiation and PAR distribution of PVGR

To investigate the distribution pattern of solar radiation and PAR under PV array and validate the model described in Section 2.1, a field experiment was carried out in Kent Vale, Singapore. As shown in Fig. 3, three arrays of PV panels were installed on the grassland. Each row of PV panels measured 34 cm × 232 cm in size, with a height of 30 cm for the PV array and a gap of 30 cm between each array. The tilt angle of the PV panels was set at 10°, facing southwards. Pyranometers were positioned on both the front and back surface of the PV panel, as well as on the vegetation surface beneath the PV arrays to measure global solar radiation, while PAR sensors were only positioned at vegetation surfaces for measuring photosynthetic light intensity. Additionally, direct and scattered radiation on the horizontal plane were measured using an SPN1 pyranometer from T2 lab at Kent Vale. The field experiment was conducted from 25th Feb. 2022 to 27th Mar. 2022, with a data collection interval of one minute. The detailed specifications of the sensors utilized in this experiment are presented in Table 1.

（1） （2）

Figure 3. Photo of field experiment in Kent vale of Singapore: 1) Solar radiation and DLI measurement of vegetation and PV surfaces; 2) Global solar radiation and diffuse solar radiation measurement at T2 lab of Kent vale.

Table 1 Specifications of sensors used in field experiment.

Parameter	Sensor	Spectral response	Measurement range	Accuracy
Global solar radiation	Onset S-LIB-M003	300-1100nm	0-1280 W/m^2	±5%
PAR	Onset S-LIA-M003	400-700nm	0-2500 umol/m^2/sec	±5%
Diffuse solar radiation	SPN1	400-2700nm	0-2000 W/m^2	±5% for daily integral and ±8 % for hourly averages

3. RESULTS AND ANALYSIS

3.1. Solar radiation and PAR distribution

The measured global solar radiation and diffuse solar radiation on the horizontal plane outside the PV array during seven consecutive non-rainy days from 1st March to 7th March is presented in Fig. 4. And the solar radiation and PAR distribution of PVGR surfaces are presented in Fig. 5, with the annual solar trajectories illustrated in Fig. 5(3). It is evident that the solar radiation received by the back surface of the PV panel and the vegetation surface beneath the PV array was significantly lower compared to that received by the front surface of the PV panel and the vegetation surface between PV arrays, particularly at noon when direct solar radiation was intense. The PAR distribution exhibited a similar pattern. The maximum PAR on the vegetation surface between PV array was approximately 5.2 times higher than the maximum PAR below PV panels, indicating a significant shading effect caused by the PV panels. To examine the correlation between global solar radiation and PAR, a scatter plot of PAR versus solar radiation for all measured points is presented in Fig. 8. It is obvious that both daily averages and hourly averages

show strong and significant linear relationships. And hourly data displays greater variability around the mean compared to daily data, consistent with the findings reported by Tan and Ismail (2016).

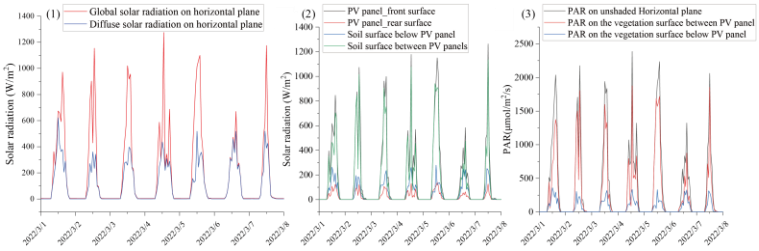

Figure 4. Solar radiation and PAR distribution: 1) Global and diffuse solar radiation on unshaded horizontal plane; 2) Distribution of Solar radiation for PVGR surfaces; 3) PAR of vegetation surface below PV array and unshaded horizontal plane.

To facilitate comparison with previous studies, a linear regression analysis with an intercept of zero is performed on the entire daily dataset collected during experiment, enabling determination of the ratio (R_{PAR}) between daily PAR value (namely DLI) and global solar radiation. The results show that the R_{PAR} value in this study is 1.799, lightly lower than the recommended value of 1.867 by Tan and Ismail (2016). One reason for this discrepancy is that Tan et al. only considered unshaded conditions, where direct solar radiation contributes a large proportion compared to this study. It has been observed that a higher diffuse radiation component leads to a reduction in R_{PAR}, as scattering affects the PAR spectrum more significantly than longer wavelengths.

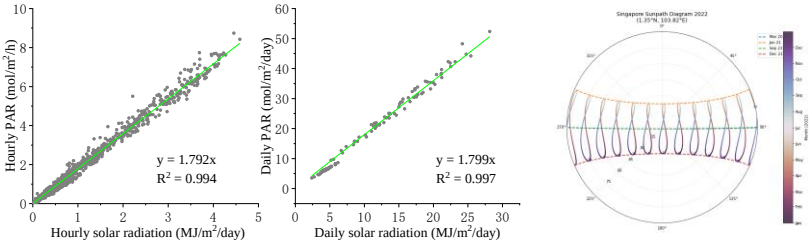

Figure 5. Scatter plot between PAR against solar radiation: 1) Scatter plot of hourly average values; 2) Scatter plot of daily average values; 3) Singapore solar trajectories

3.2. Validation of solar radiation transfer model of PVGR

After inputting the albedos of PV panel and vegetation surface, along with the radiation data (Fig. 4), the solar radiation for different surfaces in PVGR can be simulated based on the model proposed in section 2.1. The albedo values, measured during the field experiment, were 0.1 for the front surface of PV panels, 0.7 for the back surface of PV panels, and 0.24 for the vegetation surface. The comparison between measured and simulated solar radiation (Fig. 6) shows that the model effectively reproduces observed variations. The corresponding RMSE and R^2 are presented in Table 2, demonstrating a high level of efficiency and reliability of the model.

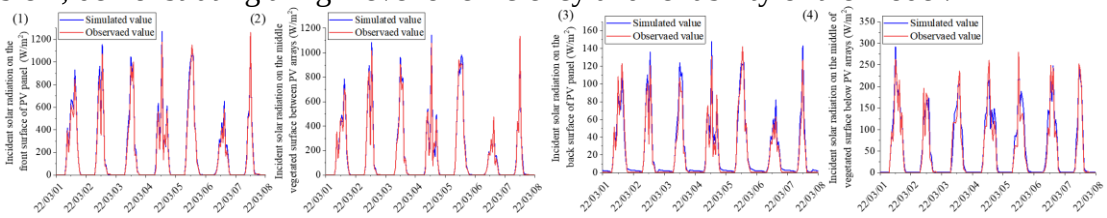

Figure 6. A comparison between measured solar radiation and simulated values on PVGR surfaces: 1) The front surface of PV panel; 2) Vegetated surface between PV arrays; 3) The back surface of PV panel; 4) Vegetated surface below PV panel.

Table 2 RMSE and R^2 for solar radiation simulation of PVGR.

	PV_front	PV_back	Soil_below_PV	Soil_between_PV
RMSE (W/m^2)	51.29	10.36	25.50	37.1
R^2	0.975	0.928	0.895	0.985

3.3. Solar radiation and DLI distribution of vegetation surface

Global and diffuse solar radiation on a horizontal plane were collected at Kent vale in 2021 by T2 lab in Singapore. The measured radiation data were used as input for the solar radiation transfer model in order to analyze the distribution of solar radiation and DLI on vegetation surfaces throughout the entire year. Based on simulation results, the average hourly and total solar radiation is presented in Fig. 7 (1) and Fig. 7 (2), respectively. It is evident that the front surface of PV panels receives the highest solar radiation, while the back surface experiences the lowest levels. As for vegetated surfaces, S1 and S3 exhibit similar levels of solar radiation, with approximately 1.5 times higher than that of S2. Fig. 7 (3) and Fig. 7 (4) illustrates monthly and annual DLI values based on the regression model in section 3.1. During March and September, the solar position is directly above the PV panel, causing significant shading effect that results in low levels of solar radiation for S2. From April to August when the solar position tilts towards to the north hemisphere, S3 receives more direct solar radiation than S1; similarly, when it tilts towards the south hemisphere in other months, S1 receives more direct solar radiation. Throughout the year, DLI of S1~S3 ranges from 10 to 20 $mol/m^2/day$, suitable for crops like *Latuca sativa L.* and *Capsicum annum L.* (Song et al., 2018).

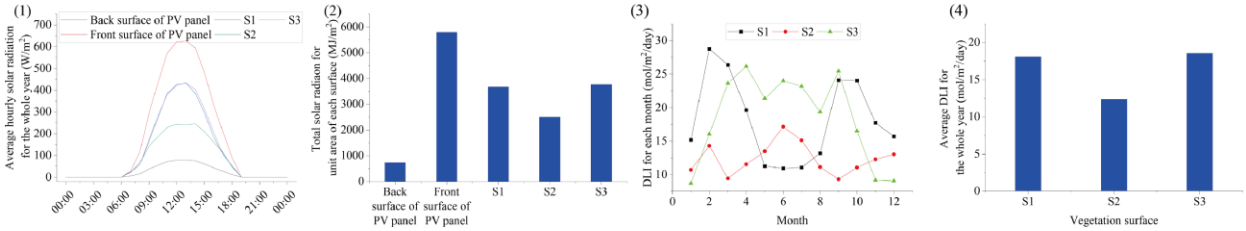

Figure 7. Solar radiation and DLI of PVGR surfaces:1) Average hourly solar radiation of PVGR surfaces for the whole year; 2) Total solar radiation of PVGR surfaces for the whole year; 3) Average DLI of vegetation surfaces for each month; 4) Average DLI of vegetation surfaces for the whole year.

Fig. 8 shows how design parameters of PVGR affect DLI on vegetated surfaces. A higher PV does not impact total incident daylight on vegetated surfaces but can reduce DLI inhomogeneity. The spacing between PV arrays and the width of PV panels primarily influence the DLI of vegetated surfaces by adjusting the coverage ratio of PV panels. Increasing the row space or reducing the width of PV panels can enhance the DLI of vegetated surfaces, but it may also decrease power generation per unit area from PV panels. The impact of tilt angle for PV panels and roof deck on DLI varies for different vegetated surfaces. A larger tilt angle results in a higher DLI for S2, while for S1 and S3, this relationship is non-monotonic due to the combined effect of shading and sky view factors. Given the complex nonlinear relationship between DLI and design parameters of PVGR, specific analyses should be conducted for different configurations to accurately determine the optimal plant species.

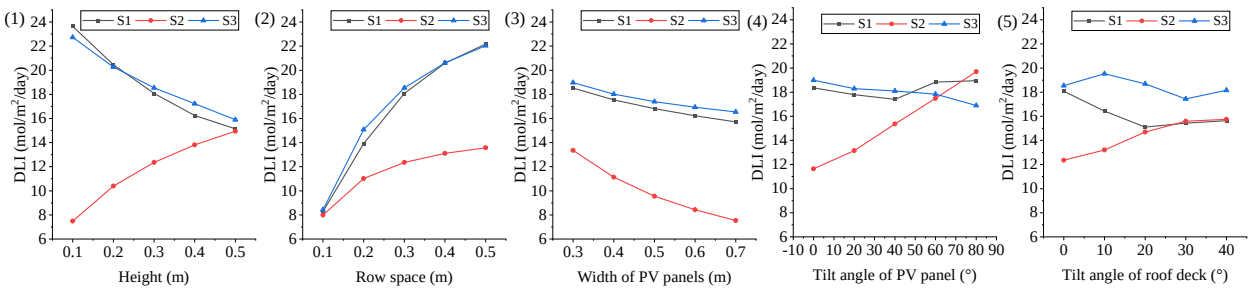

Figure 8. The effect of PVGR parameters on average DLI of vegetations for the whole year: 1) Installation height of PV panel; 2) Row space between PV panels; 3) Width of PV panel; 4) Tilt angle of PV panel; 5) Tilt angle of roof deck.

4. DISCUSSIONS

Accurate prediction of solar radiation distribution lies in the premise of PVGR optimization design. Previous studies usually oversimplified the effect of PV arrays on the SVF of vegetation surface, which weakens the simulation accuracy. While DLI is widely used to select plant species, its prediction under PV shading using the linear relation with SVF has limitations and lacks verification in PVGR scenarios.

To address these gaps, this study proposed a novel solar radiation transfer model for PVGR, incorporating SVF calculated via ray tracing and accounting for multiple radiation reflections. Field experiments revealed a strong linear relationship between DLI and solar radiation under PV arrays, enabling accurate DLI prediction using the regression model developed in this study. A comparison with Tan's DLI model (Tan and Ismail, 2016) for shaded conditions Eq. (6) in Singapore is presented in Table 6. The results show that DLI predicted by Tan's model is higher than that by this study. This discrepancy can be attributed to two key factors: 1) the constrained scenarios and durations of the field experiment by Tan et al., and 2) the inability of the SVF to comprehensively capture the shading impact of PV panels. It is worth noting that, the relationship between DLI and daily solar radiation may vary across different climates and geographical conditions, necessitating the modification of the empirical DLI model when applied in diverse areas.

$$DLI = 31.52 \cdot SVF + 2.9099 \quad (6)$$

Table 6 Comparison of DLI prediction between Tan's model and this study.

	DLI of S1 (mol/m²/day)	DLI of S2 (mol/m²/day)	DLI of S3(mol/m²/day)	Average DLI (mol/m²/day)
Tan's model	19.199	16.690	19.185	18.358
This study	18.079	12.357	18.542	16.326
Error	1.120	4.333	0.643	2.032

5. CONCLUSIONS

This paper focuses on Singapore as the research area, conducting a field experiment and numerical simulation to examine the solar radiation distribution characteristics of PVGR. The following conclusions were drawn:1) The SVF of the vegetation surface is primarily influenced by the installation height of PV panels, row spacing, and the width of PV panels. 2) Under the shading effect of PV panels, a strong linear relationship was observed between solar radiation and DLI of

vegetated surfaces, with a DLI-to-solar-radiation ratio of 1.799. 3) The solar radiation transfer model developed in this study accurately reproduces radiation variations on PVGR surfaces. Notably, a significant difference was found between the DLI between PV arrays and the DLI under PV panels, with the former's average DLI for the entire year being approximately 1.5 times higher than the latter's. 4) DLI on vegetated surfaces is significantly influenced by the design parameters of PVGR, and this effect varies across different configurations.

While this study represents a preliminary exploration, more extensive field measurements and theoretical studies are essential in the future. For instance, optical properties variations of PV and vegetation surfaces in different spectra range should be taken into account, which benefits to improve the simulation accuracy of solar radiation. Besides, the vegetation growth model of different species under PV array should be further explored, which aims to provide accurate structure parameter for PVGR in long-term simulations. Moreover, the optimal layout algorithm of PV array under the constraint of vegetation lighting requirement need to be developed, so that the maximum power generation and vegetation survival can be realized at the same time.

REFERENCES

Fathi, N.Y., Samer, A., 2016. View Factors of Flat Solar Collectors Array in Flat, Inclined, and Step-Like Solar Fields. J. Sol. Energy Eng. 138, 061005.

García-Rodríguez, A., García-Rodríguez, S., Díez-Mediavilla, M., et al., 2020. Photosynthetic Active Radiation, Solar Irradiance and the CIE Standard Sky Classification. Appl. Sci. 10, 8007.

Ghosh, A., 2020. Potential of building integrated and attached/applied photovoltaic (BIPV/BAPV) for adaptive less energy-hungry building's skin: A comprehensive review. J. Clean. Prod. 276, 123343.

Gupta, M.K., Bumtariya, K.J., Shukla, HA., et al., 2017. Methods for Evaluation of Radiation View Factor: A Review. Mater. Today Proc., 5th International Conference of Materials Processing and Characterization (ICMPC 2016) 4, 1236–1243.

He, Y., Yu, H., Ozaki, A., et al., 2017. Influence of plant and soil layer on energy balance and thermal performance of green roof system. Energy 141, 1285–1299.

Jahanfar, A., Drake, J., Gharabaghi, B., et al., 2020. An experimental and modeling study of evapotranspiration from integrated green roof photovoltaic systems. Ecol. Eng. 152, 105767.

Lamnatou, Chr., Chemisana, D., 2013. Solar radiation manipulations and their role in greenhouse claddings: Fresnel lenses, NIR- and UV-blocking materials. Renew. Sustain. Energy Rev. 18, 271–287.

Liu, B.Y.H., Jordan, R.C., 1960. The interrelationship and characteristic distribution of direct, diffuse and total solar radiation. Sol. Energy 4, 1–19.

Ogaili, H., Sailor, D.J., 2016. Measuring the effect of vegetated roofs on the performance of photovoltaic panels in a combined system. J. Sol. Energy Eng. 138.

Ramshani, M., Khojandi, A., Li, X., et al., 2020. Optimal planning of the joint placement of photovoltaic panels and green roofs under climate change uncertainty. Omega 90, 101986.

Shafique, M., Luo, X., Zuo, J., 2020. Photovoltaic-green roofs: A review of benefits, limitations, and trends. Sol. Energy 202, 485–497.

Talwar, P., Verma, N., Khatri, H., et al., 2023. A systematic review of photovoltaic-green roof systems in different climatic conditions focusing on sustainable cities and societies. Sustain. Cities Soc. 98, 104813.

Tan, P.Y., Ismail, M.R.B., 2016. Photosynthetically active radiation and comparison of methods for its estimation in equatorial Singapore. Theor. Appl. Climatol. 123, 873–883.

Wane, O., Ramírez Ceballos, J.A., Ferrera-Cobos, F., et al., 2022. Comparative Analysis of Photosynthetically Active Radiation Models Based on Radiometric Attributes in Mainland Spain. Land 11, 1868.

6th International Conference on Building Energy and Environment
Eindhoven University of Technology, The Netherlands
6 - 10 July 2025

Machine learning based intelligent CFD surrogates for interactive design exploration of built environments)

Usamah Adia[1], Amirul Khan[2], Andrew Sleigh[3], He Wang[4]

[1] *University of Leeds, Leeds, United Kingdom, scuaa@leeds.ac.uk*
[2] *University of Leeds, Leeds, United Kingdom, A.Khan@leeds.ac.uk*
[3] *University of Leeds, Leeds, United Kingdom, p.a.sleigh@leeds.ac.uk*
[4] *UCL Centre of Artificial Intelligence, Department of Computer Science, University College London, London, United Kingdom, he_wang@ucl.ac.uk*

SUMMARY

It is important to incorporate fluid flow early in the design process, it may be difficult to use CFD due to its high computational cost. A way around this is to create a machine learning (ML)-based surrogate model. Once this model has been trained, the surrogate can generate new flow fields for unseen boundary conditions in seconds. ML and reduced order models (ROMs) are coupled to produce these surrogates. Specifically, functional principal component analysis (FPCA) is compared against proper orthogonal decomposition (POD). The results show that flow fields can be predicted for new boundary conditions but there is room for improvement.

Keywords: Built Environment, Reduced Order Modelling, Machine Learning, Indoor Air Quality

1. INTRODUCTION

Understanding the effect of airflow in enclosed/indoor environments is of great interest due to its close relationship to occupant safety, thermal comfort, and energy efficiency. Optimally placed air conditioning could increase the comfort of the inhabitants (Chow, 2022). When this temperature deviates too far from the norm, there can be negative effects such as a decrease in mental performance (Mendell and Heath, 2005). Insufficient ventilation can also cause pollutants to build up such as CO_2 known as stale air, some of the side effects of stale air include nausea, headaches, fatigue and skin/eye irritation (Jansz, 2017). Showing the importance of incorporating fluid flow early into the design process, however, this is impractical with the traditional CFD process as iterating through multiple designs is computationally expensive and takes a significant amount of time. However, creating an ML surrogate is a potential solution. CFD produces a large amount of data that can be used for training. Generating the flow fields for new boundary conditions much faster.

2. GAP IN THE LITERATURE

Although CFD produces a large amount of data that can be leveraged with different ML models, it is not feasible to train a new model for each new case with various geometries and boundary condi-

tions. The goal is to create a more generalisable model using a limited dataset and provide results for multiple geometries/boundary conditions. ROMs have previously been used in many different ML models, including the built environment. Some benefits include decreasing the training time of the model while using less data, however, there is a negative in that accuracy is lost. This is because ROMs extract dominant flow features while losing information on the smaller structures, examples of ROM include POD and FPCA. POD is done by the method of snapshots, where snapshots of a flow-field are used to find the corresponding eigenvectors and the coefficients of the corresponding flow (Sirovich, 1987). These eigenvectors which are known as the principal components are ranked based on most dominant to least dominant. The coefficients then contain the score which are eigenvalues in a diagonal matrix which determine the strength of each component in the reconstruction. Using more components captures a larger range in variation and increases accuracy while decreasing has the opposite effect (Ooi et al., 2021). FPCA is a development of PCA/POD the key difference is the data is treated as a function, the principal components are now eigenfunctions significantly changing the outputs (Shang, 2014). Some of the differences can be seen in table 1, this helps visualise the differences between the two different ROM (Sari et al., 2017) such as the covariance matrix which is now a covariance function that describes the changes between the different eigenfunctions. Past work focuses on using different ML methods to predict the coefficients instead of the components, this allows for some prediction within a set of bounds. An example of this is in Lumet et al., 2025, where POD is used in conjunction with GPR to predict pollutant dispersal, using the GPR to interpolate the coefficients while keeping the original components. However, to produce more generalisable results these components must also be learned by the model,this work focuses on predicting these components with these coefficients.

Table 1. Sample table with shaded background

Element	POD	FPCA
Covariance Matrix	$\mathrm{Cov}(X) = \Sigma_{p\times p}$	$\mathrm{Cov}(X(s),X(t)) = G(s,t)$
Eigen-structures	$v_1, v_2, ..., v_p$	$\varphi_1(t), \varphi_2(t), ...$
Principal Components	$z = (X-\mu, v_k), k = 1,2,...,p$	$\zeta_k = (X-\mu, \varphi_k), k = 1,2,...$

Minimal work has been done on applying FPCA to the built environment. For different cases such as in MRI data, FPCA can recover data more effectively than traditional POD (Viviani et al., 2005). There is a need to test this method for different types of data.

3. METHODOLOGY

The first step was to use Ansys Fluent to generate the data for the model, this is done by creating a script to automate the data generation process. A 2D slice of a room was taken with inlet/outlet conditions being moved through the y-axis. This can be seen in the following figure 1, the reference for the geometry and the boundary conditions are from Hoque and Omar, 2019. Following the data generation different ROMs were applied both POD and FPCA. A GPR using the radial basis function (RBF) kernel was then used to create a model that would predict the components and coefficients for both POD and FPCA. A total of 484 different simulations were used each a different combination of inlet/outlet locations. Experiments were done to determine the best kernel. Once these have been predicted independently, the flow data can be reconstructed to produce a predicted flow field of velocity magnitude for unknown inlet/outlet positions.

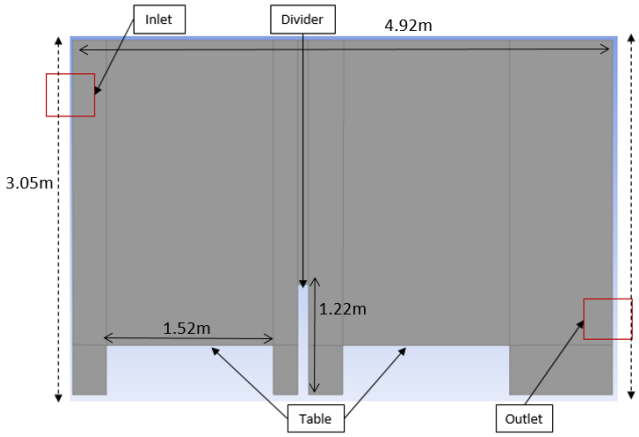

Figure 1. The geometry of the CFD model can be seen which includes the locations of inlet/outlet locations, it is important to note that the dashed lines represent how the inlet/outlet locations move to generate the training data. The inlet and outlet size is This geometry is based on a similar 2D model created by Hoque and Omar, 2019.

4. RESULTS

As previously mentioned, FPCA has been shown to capture a greater range of variations in the data, this can be seen in figure 2 where the first components capture 60% of the variation in the data when compared to POD at only 30%.

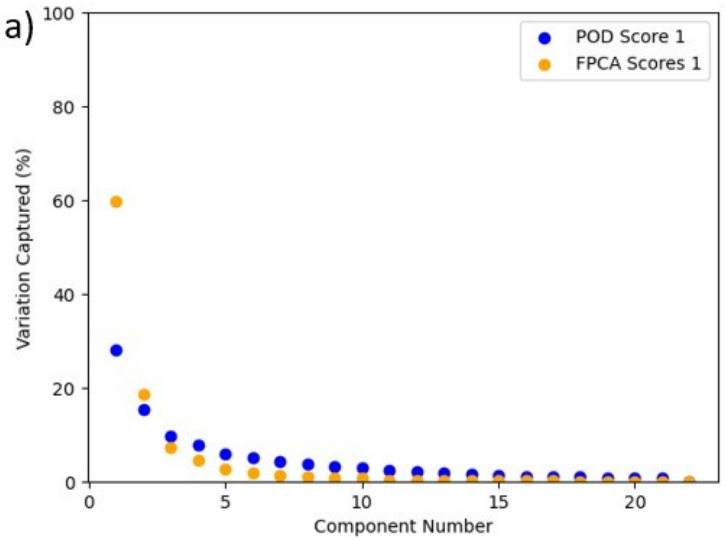

Figure 2. Scatter graphs showing the percentage each mode captures for an inlet location, showing that FPCA captures a larger range of variation with fewer modes.

The results show that it is possible to predict the coefficient and the components for these flow fields using GPR. Once these have been reconstructed, the flow field starts off strong but struggles to develop the flow towards the outlet. This could be due to the fact that the model struggles to predict the later components of FPCA, producing this incorrect flow field. The results show the difference in the flow field prediction when compared to traditional POD as the downwards curve of the flow can be more accurately visualised shown in figure 3. These results use a different number of components but capture a similar amount of variation; this is to directly compare the effectiveness of both models and to determine how they affect the reconstruction.

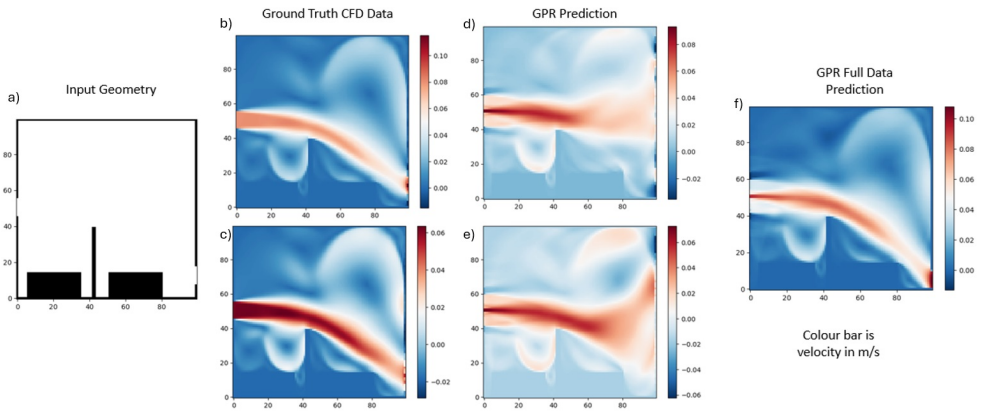

Figure 3. Contour plots comparing the flow field for an inlet position showing a) Inlet position, b) ground truth CFD data after POD reconstruction, c) ground truth CFD data after FPCA reconstruction, d) the GPR prediction using POD data, e) the GPR prediction using FPCA data and f) the GPR prediction for the full data set.

5. CONCLUSION

FPCA can be used to project the flow field in the reduced space captures 87% of the variation using 2 FPCA components compared to POD needing 11 components to reach 86%. 2 POD components only captures 47% of the variation showing the significant change in using FPCA. It also shows that it is more accurate when reconstructing the velocity field, as the distinct flow pattern can be seen, but there is room for improvement as the model struggles towards the outlet.

ACKNOWLEDGMENTS

This work was funded by the UKRI research council.

REFERENCES

Chow D. H., 2022. "Indoor Environmental Quality: Thermal Comfort". Proceedings of *Reference Module in Earth Systems and Environmental Sciences*. Elsevier.

Hoque S. and Omar F. B., 2019. Coupling computational fluid dynamics simulations and statistical moments for designing healthy indoor spaces. International journal of environmental research and public health 16, 800.

Jansz J., 2017. "Sick Building Syndrome". Proceedings of *International Encyclopedia of Public Health (Second Edition)*. Ed. by S. R. Quah. Second Edition. Academic Press, Oxford, pp. 502–505.

Lumet E., Rochoux M. C., Jaravel T., and Lacroix S., 2025. Uncertainty-aware surrogate modeling for urban air pollutant dispersion prediction. Building and Environment 267, 112287.

Mendell M. J. and Heath G. A., 2005. Do indoor pollutants and thermal conditions in schools influence student performance? A critical review of the literature. Indoor Air 15, 27–52.

Ooi C., Le Q. T., Dao M. H., Nguyen V. B., Nguyen H. H., and Ba T., 2021. Modeling transient fluid simulations with proper orthogonal decomposition and machine learning. International Journal for Numerical Methods in Fluids 93, 396–410.

Sari W., Wigena A., and Djuraidah A., Jan. 2017. Quantile regression with functional principal component in statistical downscaling to predict extreme rainfall. 38, 1–9.

Shang H. L., 2014. A survey of functional principal component analysis. AStA Advances in Statistical Analysis 98, 121–142.

Sirovich L., 1987. Turbulence and the dynamics of coherent structures. I. Coherent structures. Quarterly of applied mathematics 45, 561–571.

Viviani R., Grön G., and Spitzer M., 2005. Functional principal component analysis of fMRI data. Human Brain Mapping 24, 109–129.

COBEE

6th International Conference on Building Energy and Environment
Eindhoven University of Technology, The Netherlands
6 - 10 July 2025

Energy retrofitting measures and indoor air: towards a risk assessment methodology for combined exposure

Jaïr Lenssen[1,2], Femke Affourtit-van Driesten[1], Linda van den Berg[1], Rik Bogers[1], Anne Bolders[1], Christine Boomsma[1], Véronique de Bruijn[1], Margot Boshuis-Hilverdink[1], Flemming Cassee[1,2], Fieke Dekkers[1], Christiaan Delmaar[1], Kristina Erdelyi[1], Rosanne Fikke[1], Miriam Gerlofs-Nijland[1], Kyra Herrema[1], Niels Masselink[1], Jordi Minnema[1], Rozemarijn van der Plaats[1], Edith van Putten[1], Marije Reedijk[1], Mirjam Schaap[1], Yvonne Staal[1], Arno Swart[1], Lucie Vermeulen[1]

[1] *RIVM, Bilthoven, Netherlands, jair.lenssen@rivm.nl*
[2] *University Utrecht, Utrecht, Netherlands,*

SUMMARY
This work introduces a project currently underway at RIVM that aims to develop a risk assessment methodology for combined exposure to indoor pollutants following energy retrofits.

In the near future, many homes will be retrofitted to meet the targets on the use of fossil fuels set out by the Dutch Climate Agreement. To assess the impact on indoor air quality and health, we initiated a partnership with housing associations to conduct a measurement campaign, monitoring air quality and occupant behavior before and after renovations. In parallel, we plan to develop quantitative models to estimate the changes in exposure to chemical, microbiological, and radiological agents resulting from these retrofits. Finally, we are exploring methods for integrating the individual health risks associated with exposure to indoor pollutants into a single risk assessment framework.

This work presents the preliminary steps of our study, including a detailed description of our measurement campaign. In addition, we are establishing a network for effective sharing of knowledge with industry and municipal stakeholders.

Keywords: Indoor Air, Retrofitting, Risk assessment, Behavior

1. INTRODUCTION

In 2021, the Dutch government introduced the National Insulation Program (NIP) as part of the Dutch Climate Agreement ('Klimaatakkoord') to make homes more energy efficient. The program aims to provide new insulation to 2.5 million homes - approximately 30% of the total Dutch housing stock - by 2030. Many homes are therefore expected to be retrofitted within the next 5

years, and while reducing housing stock energy demands is critical for sustainability, the large scope of this retrofitting operation has raised questions about its impact indoor air quality. Naively implemented measures may unintentionally worsen indoor air quality (IAQ) (Wang et al., 2022).

Evaluating the potential impacts of energy retrofitting measures (ERM) on indoor air quality is relevant both for public health and public acceptance of these measures. Considerable expertise on the topic exists in relevant domains. However, knowledge gaps remain, making it currently unclear whether robust estimates of net retrofitting effects on IAQ can be achieved. At the Dutch National Institute for Public Health and the Environment (RIVM), the project 'ENABLE' (Energy Transition and Indoor Climate: Towards a risk assessment framework for combined and aggregate exposure.) aims to improve understanding of these effects.

In partnering with housing associations, we are conducting a measurement campaign. During the winters of 2025, indoor environmental factors and airborne chemical, microbiological, and radiological (CBR) pollutants will be monitored in 24 domestic homes, before and after energy retrofits. Multiple efforts have already been made to measure the effects of energy retrofit measures on both sources of and exposure to airborne agents. However, results are difficult to compare due to differences in retrofit measures, measurement equipment, sampling methods, sampling times, building types and occupant behavior (Fisk et al., 2020). To improve comparability and strengthen conclusions, additional research and data collection remain essential. Additionally, we track occupant behavior and perceived indoor air quality, as studies indicate that the user perception of retrofit technologies impact user's implementation (Ortiz et al., 2020).

In addition to measurements, exposure can be estimated with physics-based source-to-dose models. Existing models assess human exposure to chemical substances, biological agents, and radiation in various settings. However, due to the numerous confounding factors that influence indoor pollutant dynamics and exposure, most available models consider highly specified environments. While these detailed models provide valuable insights, they may not always be suitable for determining overall risk. Building on previous research, this study will identify suitable models to estimate occupant exposure before and after retrofitting.

Finally, air quality is often assessed based on the deviation of pollutant concentrations from benchmark values. Instead, we aim to determine air quality from the cumulative health risk of exposure to several indoor pollutants. Such integrated risk estimates are rare, as CBR risk assessments differ significantly in health endpoints and metrics. For example, chemical risk assessments follow the EFSA guidelines on grouping approaches, radon risks are based on a combination of biokinetic models for airways and epidemiological studies, and microbiological hazards use quantitative microbial risk assessment (QMRA) (Committee et al., 2019; ICRP, 2017; UN, 2020). In our proposed case study, we provide an overview of these methodological differences and explore the feasibility of combining them in a single framework. The results of our exposure analyzes, both from the measurement campaign and from our quantitative model, serve as input for this case study.

2. METHODOLOGY

2.1. Recruitment of participating homes

We partnered with housing associations to find 24 domestic homes undergoing substantial energy retrofits. The houses were built around 50-60 years ago, share similar layouts with 90 to 110 m^2 floor area, and sit on sand soil without crawl spaces. Retrofit measures include the following:

- Adding blown-in mineral wool cavity insulation to existing glass wool insulation and repair mortar joints.
- Replacement of windows with HR++ glass and new wooden frames.
- Installing a new 55mm PIR-insulated roof with new tiling.
- The predominantly naturally controlled ventilation system is replaced with a central heat recovery system and sensor or manually controlled mixing fans in each room. The mixing fan moves air from rooms with high CO_2 concentrations to the hallway, relying on the raised pressure gradient to draw in fresh air.
- Maintaining existing gas stoves.

2.2. Monitoring of indoor air

A summary of the indoor environmental factors and pollutants monitored is presented in Table 1. Before starting the measurement, all participants complete surveys on the perceived state of the home environment and their habits. In addition, participants will be asked about occupancy, activity levels, notable indoor activities and perceived indoor air quality levels three times a day.

Table 1. Summary of monitored indoor air parameters, and sampling methodology employed.

Parameter	Sampling method	Sampling location	Sampling time
Active, Continuous Measurements			
Temperature	MF52A NTC Thermistor	L, K, MB, B	2 Weeks (1 min intervals)
Humidity	Sensirion SHT4x	L, K, MB, B	2 Weeks (1 min intervals)
CO_2	SenseAir S88	L, K, MB, B	2 Weeks (1 min intervals)
TVOC, NO_X	Sensirion SGP41	L, K, MB, B	2 Weeks (1 min intervals)
PM 1.0, 2.5, 10	Cubic PM2012B	L, K, MB, B	2 Weeks (1 min intervals)
Noise	ACOEM CUBE, Classe 1	Indoor (L)	2 Weeks
	Munisense NP9, Classe 2	Outdoor	2 Weeks
	Unclassified[a]	Outdoor	2 Weeks
Integrated-Time Measurements			
Radon	Radonova Radtrak[3]	L	2 Months
General VOC (incl. BTEX)	VOC Chek 575 Passive Sampler	L	2 Weeks (passive)
General VOC (TO-15 screening)	Silonite Canisters	L	2 Weeks (active)
Formaldehyde	UME[x] 100 Passive Samplers	L	2 Weeks (passive)
Aspergillus Fumigatus	Polystyrene petri dish[b]; qPCR	MB, B	3 Weeks (passive)

[a] DIY noise sensor, design by sensor.community, [b] growth-medium-free,
L = Living room, K = Kitchen, MB = Master Bedroom, B = Bathroom

2.3. Review of source-to-dose models

To control the influence of confounding factors, such as occupant behavior, we propose evaluating exposure in pairs of pre- & post-retrofit homes. This approach helps isolate the effects of energy retrofits on indoor air quality. We will review the available physics-based source-to-dose models and determine, through a multitude of selection criteria, which are the best suited to estimate indoor exposure variations due to energy retrofitting interventions.

2.4. Risk Assessment

In our proposed case study, for each of the respective CBR fields, we characterize the health risk from exposure to an illustrative common indoor pollutant to highlight contrasts and commonalities. These will be; Formaldehyde, commonly found in building materials and household products, is classified as a human carcinogen and can cause irritation of the eyes, nose, and throat; Aspergillus fumigatus, a well-known biological hazard, releases airborne conidia (spores) that can lead to severe lung infections; And Radon (Rn-222), a radioactive noble gas naturally occurring in soil and certain building materials, which is also classified as a carcinogen.

3. DISCUSSION

As part of the ENABLE project, we measured indoor environmental factors and airborne pollutants of 24 domestic homes. This measurement campaign is the first in a series of two, with the next round scheduled for the winter of 2025/2026.

The planned measurement campaign includes a relatively small number of homes, which may limit statistical significance. However, it is expected to provide valuable information on the measurability of different agents in the indoor environment, as well as the significance of observed differences before and after retrofitting interventions. Through this campaign, we aim to assess the feasibility and identify key focus areas for future larger-scale studies.

Furthermore, this project explores the feasibility of integrating risk estimates of exposure to CBR agents. However, combined exposure to stressors from different CBR agents could lead to health effects that are not simply the aggregate risk of individual agents. Such interactions between stressors could introduce errors in our risk assessment. Future work of the ENABLE project will include *in vitro* experiments to investigate these interactions.

Although in its early stages, the project has established a network of researchers, industry partners, and municipal stakeholders. Researchers and stakeholders interested in contributing to the ENABLE project are encouraged to contact us.

REFERENCES

Committee E. S., More S. J., Bampidis V., Benford D., Bennekou S. H., Bragard C., Halldorsson T. I., Hernández-Jerez A. F., Koutsoumanis K., Naegeli H., Schlatter J. R., Silano V., Nielsen S. S., Schrenk D., Turck D., Younes M., Benfenati E., Castle L., Cedergreen N., Hardy A., Laskowski R., Leblanc J. C., Kortenkamp A., Ragas A., Posthuma L., Svendsen C., Solecki R., Testai E., Dujardin B., Kass G. E., Manini P., Jeddi M. Z., Dorne J.-L. C., and Hogstrand C., 2019. Guidance on harmonised methodologies for human health, animal health and ecological risk assessment of combined exposure to multiple chemicals. EFSA Journal 17, e05634.

Fisk W. J., Singer B. C., and Chan W. R., 2020. Association of residential energy efficiency retrofits with indoor environmental quality, comfort, and health: A review of empirical data. Building and Environment 180, 107067.

ICRP, 2017. Occupational intakes of radionuclides: Part 3. ICRP.

Ortiz M., Itard L., and Bluyssen P. M., 2020. Indoor environmental quality related risk factors with energy-efficient retrofitting of housing: A literature review. Energy and Buildings 221, 110102.

UN, 2020. Annex B, Lung cancer from exposure to radon. United Nations Scientific Committee.

Wang C., Wang J., and Norbäck D., 2022. A systematic review of associations between energy use, fuel poverty, energy efficiency improvements and health. International Journal of Environmental Research and Public Health 19, 7393.

6th International Conference on Building Energy and Environment
Eindhoven University of Technology, The Netherlands
6 - 10 July 2025

Comparison of causal discovery algorithms for climate and building factors: case study on synthetic data

Han Gyeong Chu [1], Hye-Gi Kim[2] , Deuk-Woo Kim [3]

[1]*Korea institute of Civil Engineering and Building Technology, Goyang-si, South Korea, hankyon0122@kict.re.kr*
[2]*Korea Institute of Civil Engineering and Building Technology, Goyang-si, South Korea, kimhyegi@kict.re.kr*
[3]*Korea Institute of Civil Engineering and Building Technology, Goyang-si, South Korea, deukwookim@kict.re.kr*
corresponding author

SUMMARY
Climate change and carbon emissions have emerged as critical environmental issues worldwide, with the building sector being a major source of carbon emissions. Therefore, it is necessary to predict and benchmark energy consumption considering climatic factors and building elements to achieve energy savings. However, existing methods for analyzing energy consumption factors focus only on the primary influence between input and output variables, highlighting the need for additional approaches to analyze relationships among variables. This study explores the application of causal discovery methods to analyze relationships between climatic factors and building elements. Using synthetic data, the performance of the Peter-Clark (PC) and Fast Causal Inference (FCI) algorithms was compared. The results indicate that while the PC algorithm identifies simple associations, it struggles with hidden confounders. In contrast, the FCI algorithm effectively detects both associations and hidden confounding effects. The study highlights the importance of domain knowledge and suggests future work on diverse data scenarios and algorithm comparisons.

Keywords: Causal discovery, Peter-Clark algorithm, Fast causal inference algorithm, synthetic data

1. INTRODUCION

Climate change and carbon emissions have emerged as critical environmental issues worldwide, with the building sector being a major source of carbon emissions. Consequently, research is being conducted to develop and predict energy usage models that consider various design elements of buildings and climatic conditions. In particular, South Korea is collecting building and energy data for energy benchmarking and analyzing the impact of climate and building factors on the Energy Use Intensity (EUI) (Kim et al., 2019). However, existing data-driven modeling and analysis approaches heavily depend on the expertise of professionals in model construction, and primarily focus on one-dimensional sensitivity analyses between input and output variables. As a result, it is challenging to include and analyze factors related to the interdependencies among variables or hard-to-predict elements, such as occupant behavior, within these models.

Causal discovery is an approach used to identify and understand the causal relationships among variables based on a dataset (Spirtes et al., 2000). By discovering these causal structures, it enables to move beyond simple correlations, providing evidence into the data's inherent dependencies and improving the accuracy of predictive models and decision-making processes (Eberhardt, 2017). Therefore, in this paper, the relationship between solar radiation and building cooling energy consumption was analyzed and compared using the widely used causal discovery methods, the

Peter-Clark (PC) and Fast Causal Inference (FCI) algorithms, on synthetic data. The experiment consists of the following three steps: 1) synthetic data generation. 2) causal discovery using PC and FCI algorithm. 3) compare result and analysis.

2. METHOD

Causal discovery algorithms can be classified into two types: constraint-based and score-based. The constraint-based approach verifies the independence between variables through conditional independence constraints and constructs the graph accordingly. The score-based approach generates a number of candidate causal graphs and selects the graphs with the highest scores. In this study, we conducted research using the PC and FCI algorithms, which are part of the constraint-based methods.

The PC algorithm (Spirtes et al., 2001) is an approach that discovers causal structures under the assumption that no unobserved confounders exist. The process consists of the following steps: 1) It starts by assuming that all variables are connected with edges. 2) It then tests for independence between each pair of variables, removing edges where independence is confirmed to complete the structure. 3) Finally, it determines the direction of influence for the remaining edges to finalize the causal graph. Since the algorithm assumes no unobserved confounders, it may face difficulties in accurately identifying relationships between variables when hidden confounding factors are present. Additionally, as the algorithm focuses primarily on detecting conditional independence, the direction of causal influence may not always be clearly established. The FCI algorithm (Spirtes et al., 2001) is similar to the PC algorithm but operates under the assumption of unobserved confounders, making it applicable when some or all confounding variables are not observed. The procedure of edge removal and initial structure formation is similar to that of the PC algorithm. However, unlike the PC algorithm, the FCI algorithm further incorporates potential hidden confounders when orienting the edges.

As an example of causal discovery with two algorithms, an analysis and comparison were conducted on 1,000 sample data generated based on Eq. (1)–(5). To compare the differences between the two algorithms, a confound factor H was introduced, which can represent factors such as occupants in the building sector. X, Y, Z, and W are observable factors, which may correspond to variables like outdoor temperature and wall insulation. The confound factor H was designed to influence Y together with X, while also affecting Z, which in turn influences W. Subsequently, causal discovery was performed on the data for X, Y, Z, and W, excluding H. The PC and FCI algorithms were implemented using the Python causal-learn package (Zheng et al., 2024). For the independence verification method, the default Fisher's Z conditional independence test was applied, and the significance level of individual partial correlation tests (alpha) was set to the default value of 0.05.

$$H = uniform[0, 2] \quad (1)$$
$$X = uniform[0, 1] \quad (2)$$
$$Y = 0.4 \times X + H + normal[0, 0.8] \quad (3)$$
$$Z = 0.5 \times H + normal[0, 0.6] \quad (4)$$
$$W = 0.2 \times Z + normal[0, 0.9] \quad (5)$$

Fig 1 shows the analysis results of the sample data using the PC and FCI algorithms. Fig 1(a)

represents the ground truth structure designed for the test, illustrating the causal relationships when the confound factor H is observed. In the case of the PC algorithm, it successfully identified the causal influence of X on Y, but failed to account for the confound factor, leading to the incorrect inference that Z has a direct influence on Y (Fig 1(b)). Additionally, the algorithm detected an association between Z and W, but was unable to determine the direction of the relationship.

In contrast, the FCI algorithm identified the influence of X on Y while also suggesting the presence of a hidden confounding factor (Fig 1(c)). Additionally, the relationship between Z and W indicates weak causal evidence; however, unlike the ground truth, it is inferred that the influence flows from W to Z. In such cases, the graph estimation process can be improved by incorporating domain knowledge (Shen et al., 2020).

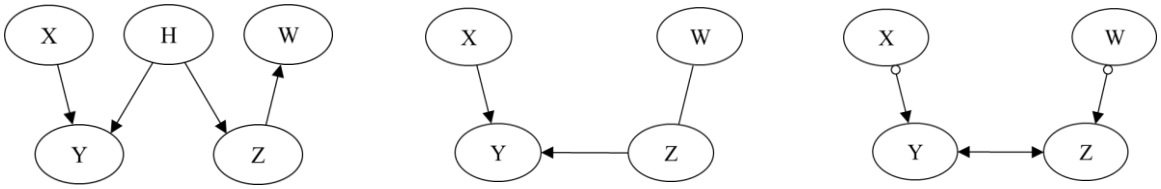

(a) ground truth (b) PC (c) FCI

Figure 1. Compare of PC and FCI algorithms

3. RESULTS

In this study, causal discovery was conducted to analyze the relationships between climatic and building factors. Since real-world data contains many uncertainties, a simplified and interpretable structure was designed to generate and utilize synthetic data. The synthetic dataset consists of the sol-air temperature (T_{sol}), the relevant climatic factors (outdoor temperature T_{out}, global solar irradiance I, and extra infrared radiation Q_{ir}), and a building-related factor, solar radiation absorptivity α. The sampling ranges for each variable are presented in Eq. (6)–(9) in the form of [mean, standard deviation], and the sol-air temperature was calculated using Eq. (10). Using these variables, 1,000 samples of synthetic data were generated. To illustrate the difference in interpretation between the PC and FCI algorithms, extra infrared radiation was treated as a hidden confounder, and causal discovery was applied to a dataset in which this variable was excluded.

$$T_{out} = normal[26, 3] \quad (6)$$
$$\alpha = normal[0.5, 0.2] \quad (7)$$
$$I = normal[100, 10] \quad (8)$$
$$Q_{ir} = normal[10, 2] \quad (9)$$
$$T_{sol} = T_{out} + (\alpha \times I - Q_{ir}) \div 4 + uniform[0, 1] \quad (10)$$

Fig 2 shows the results of causal discovery performed using the PC and FCI algorithms, assuming extra infrared radiation (Q_{ir}) as a hidden confounder in the synthetic data. The independence verification method and the significance level of individual partial correlation tests are the same as those described in Section 2. The results indicate that both the PC and FCI algorithms consistently identified T_{out}, α, and I as variables influencing T_{sol}. However, since the FCI algorithm accounts for hidden confounders, the results also imply the presence of an unobserved confounding factor, even though these variables are shown to affect T_{sol} (Fig 2(b)).

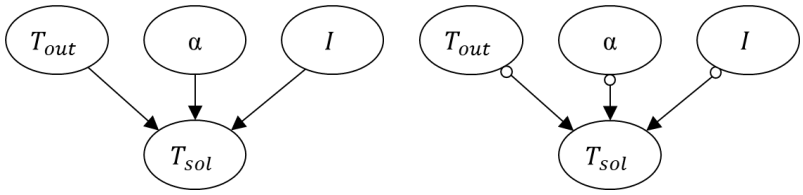

(a) PC (b) FCI

Figure 2. Compare of PC and FCI algorithms with synthetic data

4. CONCLUSION

In this paper, a pilot study was conducted on the causal discovery approach to identify the relationships between climatic factors and building elements. Synthetic data were generated, and analyses were performed using the PC and FCI algorithms, with the results compared. The findings revealed that in the presence of hidden confounding variables, the PC algorithm provides information on simple associations, whereas the FCI algorithm offers insights into both associations and the presence of hidden confounding factors.

However, the PC algorithm is advantageous when the relationships between input variables are clear, suggesting the need to analyze various scenarios beyond the one assumed in this study. Additionally, incorporating domain knowledge can enhance causal discovery compared to relying solely on data.

For future work, we plan to compare the performance of the PC, FCI, and other algorithms across more diverse data scenarios, as well as analyze the impact of integrating domain knowledge on causal discovery outcomes.

ACKNOWLEDGEMENTS

This work is supported by the Korea Agency for Infrastructure Technology Advancement(KAIA) grant funded by the Ministry of Land, Infrastructure and Transport (Grant RS-2023-00244769, Development of a data framework for integrating building energy datasets and applications to accelerate carbon neutrality in the building sector).

REFERENCES

Kim, D. W., Kim, Y. M., & Lee, S. E. 2019. Development of an energy benchmarking database based on cost-effective energy performance indicators: Case study on public buildings in South Korea. Energy and Buildings, 191, 104-116.

Eberhardt, F. 2017. Introduction to the foundations of causal discovery. International Journal of Data Science and Analytics, 3, 81-91.

Shen X., Ma S., Vemuri P., Simon G., 2020. Challenges and opportunities with causal discovery algorithms: application to Alzheimer's pathophysiology. Scientific Reports, 10(1), 2975.

Spirtes, P., Glymour, C., Scheines, R., Kauffman, S., Aimale, V., & Wimberly, F. 2000. Constructing Bayesian network models of gene expression networks from microarray data.

Spirtes, P., Glymour, C., & Scheines, R. 2001. Causation, prediction, and search. MIT press.

Zheng, Y., Huang, B., Chen, W., Ramsey, J., Gong, M., Cai, R., ... & Zhang, K. 2024. Causal-learn: Causal discovery in python. Journal of Machine Learning Research, 25(60), 1-8.

Smart Buildings and Smart Cities (11:00-12:30 h)

6th International Conference on Building Energy and Environment
Eindhoven University of Technology, The Netherlands
6 - 10 July 2025

LPWAN based IoT Architecture for Distributed Energy Monitoring in Deep Indoor Environments

Christof Röhrig[1] and Benz Cramer[1]

[1] *Dortmund University of Applied Sciences and Arts, Institute for the Digital Transformation of Application and Living Domains (IDiAL), Otto-Hahn-Str. 23, 44227 Dortmund, Germany*
christof.roehrig@fh-dortmund.de

SUMMERY
Continuous energy monitoring is essential for identifying potential savings and predicting the energy requirements of buildings. Energy meters are often located in underground spaces that are difficult to reach with wireless technology. This paper presents an experimental study comparing different Low Power Wide Area Networks (LPWAN) technologies in terms of building penetration and radio coverage. The technologies Low Power Long Range Wide Area Networks (LoRaWAN®), Narrow Band Internet of Things (NB-IoT), Sigfox 0G and Wireless Smart Ubiquitous Networks (Wi-SUN®) are evaluated experimentally.

It also proposes a distributed hybrid IoT architecture that combines multiple LPWAN technologies using an abstraction layer to optimize cost and coverage. Communication is message-based using the publish-subscribe messaging pattern. It is implemented using the MQTT protocol. The abstraction layer decodes the proprietary binary data and converts it to a normalized JSON format.

Keywords: energy monitoring, smart buildings, smart metering, LPWAN

1. INTRODUCTION

The Dortmund University of Applied Sciences and Arts operates more than a dozen university buildings spread across the city of Dortmund. These buildings are heated and air conditioned using various forms of energy: District heating and cooling networks, gas and electricity. The energy meters are located in underground rooms and energy supply tunnels that are difficult to reach with wireless technology. Continuous energy monitoring is essential for identifying potential savings and for adaptive model predictive heating control of buildings (Wan et al., 2023). The paper presents an experimental study that compares different LPWAN (Low Power Wide Area Networks) technologies in terms of building penetration and radio coverage. These LPWAN technologies differ in terms of topology (star, mesh), power consumption, link budget, radio coverage and radio range. The experiments will be carried out in various university buildings and in a district heating and cooling tunnel linking several buildings on the campus (see Fig 1 (a)).

Furthermore, the paper proposes a distributed hybrid IoT architecture that combines different LPWAN technologies to optimize cost and coverage. The architecture connects existing energy

meters and sub-meters with different interfaces (M-Bus, Pulse, SML) via multiple LPWAN radio technologies to the IoT middleware.

2. PROBLEM DEFINITION AND METHODICAL APPROACH

This research compares four LPWAN radio technologies for smart metering applications in deep indoor and underground environments. The aim of the research is to investigate the building penetration loss (BPL) of different radio technologies in real-life scenarios. An empirical evaluation is chosen using a pre-installed radio infrastructure. The measurements are performed with inexpensive off-the-shelf equipment. We focus on measuring the BPL without considering the power consumption of the equipment.

We consider two scenarios: In the first scenario, the radio infrastructure, such as gateways (GWs) and base stations (BSs), is installed inside the building. Radio waves propagate through walls and ceilings. It is assumed that the energy meters are located in the basement of the buildings. In the second scenario, the wireless infrastructure is installed outdoors. The radio waves propagate through the windows or the exterior wall into the building (Outdoor to Indoor, O2I). Theoretical path loss models for indoor environments and O2I penetration can be found in (ITU-R, 2015) and (3GPP, 2024) respectively. It is very difficult to calculate the BPL based only on theoretical models because radio waves propagate in different ways in the building due to reflections and diffraction. Especially in deep indoor and underground scenarios such as basements and tunnels, the real signal path and thus the entire link budget is too complex to be accurately represented by a linear model (Malarski et al., 2019).

Therefore, we chose an empirical experimental evaluation where the received signal strength indicator (RSSI) is measured at outdoor measurement points (MPs) at ground level and then compared with the RSSI measured at indoor MPs on the first floor and underground MPs in basements and a tunnel (see Fig. 1 (a)). The BPL is calculated from these measurements and compared between the different radio technologies.

3. RELATED WORK

LPWAN technologies have received increased attention in recent years. They are characterized by their long range and low power consumption. LPWAN technologies known for their good building penetration include LoRaWAN®, NB-IoT, Sigfox 0G and Wi-SUN®. Kadusic et al. (2022) provides an overview of LoRaWAN®, NB-IoT and Sigfox and the characteristics of these radio technologies. Hoo et al. (2023) compares Wi-SUN® with LoRaWAN® and NB-IoT. The main application is a building management system. Naumann and Oelers (2021) compares the energy consumption and the link budget of NB-IoT, LoRaWAN® and Sigfox based on theoretical models.

Roosipuu et al. (2023) investigates the use of NB-IoT for monitoring and control of smart urban drainage systems. Different depths of devices in manholes are investigated. Persia et al. (2017) presents a connectivity analysis of NB-IoT and LoRaWAN® for smart grid applications in outdoor, indoor and deep indoor environments. Tangsunantham and Pirak (2022) presents an experimental evaluation of Wi-SUN® for advanced metering in smart grids. Thrane et al. (2020) presents an experimental evaluation of an NB-IoT propagation model for deep indoor scenarios. The measurement campaign was conducted in a system of long underground tunnels.

4. TECHNOLOGY OVERVIEW

LPWAN technologies known for good building penetration operate in the sub-GHz spectrum and include LoRaWAN®, NB-IoT, Sigfox 0G and Wi-SUN®. LoRaWAN®, Sigfox 0G and Wi-SUN®operate in the unlicensed spectrum of 868 MHz in Europe, while NB-IoT operates in the licensed spectrum of 800 MHz (band 20) or 900 MHz (band 8) in Europe. To ensure fair use of the unlicensed spectrum, each device is limited in transmit power and duty cycle (DC). In the 868 MHz band, the transmit power is normally limited to 14 dBm (25 mW) and a DC of 0.1%, except in the G1 band (868.0 - 868.6 MHz) where a DC of 1% is allowed and the G3 band (869.4 - 869.65 MHz) where a transmit power of 27 dBm (500 mW) and a DC of 10% is allowed. The G3 band is typically used for downlink (DL) messages where a BS is connected to many devices and transmits at high power. In contrast, quality of service can be guaranteed in the licensed spectrum, where the mobile network operator (MNO) controls the use of the spectrum an the DC is not limited.

The proprietary Sigfox 0G radio technology was developed by the French company Sigfox S.A. (now owned by UnaBiz). It uses Ultra Narrow-band (UNB), achieves long range and requires low power. The Sigfox 0G network is based on a star topology and requires a local 0G network operator to carry the traffic generated. In Europe, Sigfox 0G is using the G1 band for the UL and the G3 band for the DL. Sigfox supports up to 140 uplink (UL, from device to BS) and 4 DL messages per day, each carrying a payload of 12 bytes and 8 bytes respectively, at a data rate of 0.1 kbit⁄s. Sigfox 0G subscription cost is 10 € per year for one device and 140 UL, 4 DL messages per day (Heliot Europe).

LoRaWAN® is based on the proprietary LoRa radio technology developed by Scemtech. LoRaWAN® defines the communication protocol and system architecture and is managed by the open LoRa Alliance. It can achieve data rates between 0.25 kbit⁄s and 11 kbit⁄s in Europe. The payload of the messages can be from 51 to 222 bytes in Europe depending on the data rate. The number of messages is limited by the DC regulations in Europe and may be even lower due to restrictions by the LoRaWAN® network operator. The Things Network's (TTN) fair use policy limits a device's airtime to 30 s per day. LoRaWAN® networks can be operated by a network operator, a community such as TTN, or self-deployed. LoRaWAN® thus offers a high degree of flexibility for the end user.

Wi-SUN® is based on the open IEEE 802.15.4g/e standards. Unlike other LPWAN technologies, it offers mesh and multi-hop features for enhanced reliability and range. In addition to low power consumption and long range, it offers lower latency and higher data rate up to 300 kbit⁄s compared to the other LPWAN technologies. The downside of Wi-SUN® is the lower link budget and therefore lower range and building penetration, and the lack of off-the-shelf devices for the end user. The target applications of Wi-SUN® are in the field of building automation (Hoo et al., 2023).

NB-IoT operates in licensed spectrum and is standardized by the 3rd Generation Partnership Project (3GPP) as LTE Cat-NB1 and -NB2. It is only available through MNOs. Implementing NB-IoT is cost effective as it is based on existing cellular infrastructure. Compared to other LPWAN technologies that operate in unlicensed spectrum, the transmit power and DC are not limited by regulation. Therefore, the link budget is higher, resulting in better building penetration. The downside is higher power consumption. NB-IoT offers data rates of up to 62 kbit⁄s in Cat NB1 and up to 159 kbit⁄s in Cat NB2 in the UL and up to 26 kbit⁄s and 127 kbit⁄s respectively in the DL. Applications are typically low throughput, delay tolerant and low mobility. Examples are smart

meters and remote sensors. The cost of the subscription is 11 € for a SIM card, 500 MByte for 10 years (1NCE).

Table 1 compares the key parameters of the technologies. The link budget is the maximum possible path loss from transmitter to receiver. A high value is important for penetrating underground environments. The values are taken from (Naumann and Oelers, 2021) and the data sheets of the experimental equipment in Table 2.

Table 1. Comparison of different LPWAN technologies (Europe)

Technology	LoRaWAN®	Sigfox	NB-IoT	Wi-SUN®
Topology	star	star	star	mesh
Band in MHz	868	868	800 / 900	868
Tx power GW in dBm	14 / 27*	27	23	14
Tx power device in dBm	14	14	23	14
Rx sensitivity GW in dBm	-140	-144	-131	-120
Rx sensitivity device in dBm	-136	-132	-131	-120
link budget+ UL in dB	154	158	154	134
link budget+ DL in dB	150 / 163*	159	154	134
price of module	9€	9€	12€	20€
annual subscription cost	-	10€	1-2€	-
Device availability	++	0	+	- -

* depending on the frequency of use, + without antenna gain (0dBi)

5. EXPERIMENTAL EVALUATION OF LPWAN TECHNOLOGIES

5.1. Experimental setup

An area of the campus consisting of several challenging buildings for building penetration was chosen as the experimental environment (see Fig 1 (a)). We use several off-the-shelf devices for the experiments (see Table 2). Since there are no end-user Wi-SUN® devices available, we use a development kit from Silicon Labs. This equipment does not provide an accurate measurement of RSSI, but is intended to provide an estimate of building penetration with real devices.

Table 2. Devices used in experiments

Device	LPS8	DLOS8	LoRa E5 mini	SIM7020E	MKR FOX	SLWSTK6007A
type	GW	GW	device	device	device	dev kit
manufacturer	Dragino	Dragino	Seeed	Simcom	Arduino	Silicon Labs
radio chip	SX1308	SX1301	STM32WLE	MT2625	ATAB8520E	EFR32MG12
technology	LoRa	LoRa	LoRa	NB-IoT	Sigfox	Wi-SUN®
band MHz	868	868	868	900 / 800	868	868
Tx pow. / dBm	14 / 20	14 / 27	14	23	13	14
Rx sen. / dBm	-140	-140	-136.5	-131	-132	-120

5.2. Indoor experimental evaluation of LoRaWAN® and Wi-SUN®

In the first measurement campaign, we compare LoRaWAN® with Wi-SUN®. The experiments are performed in building 2, where the LoRaWAN® gateway GW2 (LPS8) is placed on the first

floor near a window. Measurements are made on different floors and in the basement to measure the penetration loss of the ceilings. With LoRaWAN® it is possible to reach every floor of the building up to the 3rd floor and even the basement. Penetration loss is 10 dB for each ceiling upstairs and 55 dB to the basement.

With Wi-SUN® it was only possible to penetrate two ceilings. The basement could not be reached with this technology. In general, it was not possible to establish a stable connection when the RSSI was lower than -95 dBm. Due to the relatively low link budget, building penetration is not Wi-SUN®'s strength. Rather, its strengths lie in high data throughput and low latency.

5.3. O2I penetration of LoRaWAN®, Sigfox OG and NB-IoT

Fig. 1 (a) shows the experimental area at the campus Emil-Figge-Str. in Dortmund. The outdoor MPs are named O1, O2, O3 and are located between the buildings. The indoor MPs I1-I4 are located on the first floors in the entrance halls of the buildings. The MPs in the basements of the buildings are labeled B1-B4. There are two MPs in the energy supply tunnel, T1 and T2. T1 is placed under an emergency manhole of the tunnel, T2 is placed directly at the heat meters. Two LoRaWAN® gateways are placed in the area. The outdoor gateway GW1 (DLOS8) is placed on the roof of building 1, while the indoor gateway GW2 (LPS8) is placed inside on the first floor near a window. Both gateways are preinstalled and not placed for this work.

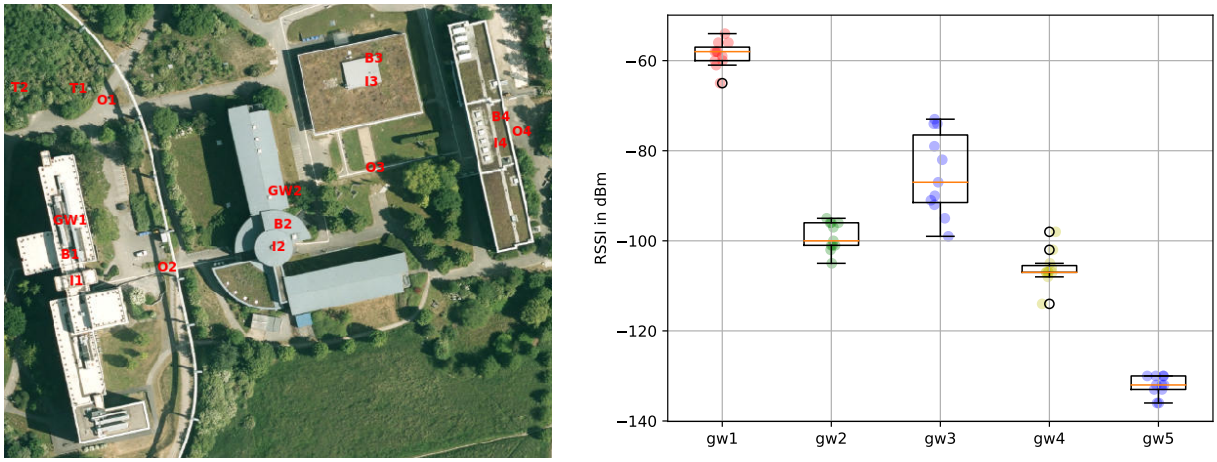

(a) (b)

Figure 1. (a) Experimental area at campus Emil-Figge-Str. with measurement points marked in red (b) LoRaWAN®RSSI values of Gateways at measurement point O2

At each MP, several measurements are made for each radio technology except Wi-SUN®. The results are shown in Table 3. For LoRaWAN®, the reported RSSI fluctuates a lot. Fig. 1 (b) shows the fluctuation of the RSSI reported by the gateways. The values are not normally distributed and have outliers. The RSSI values in the figure are reported by four gateways receiving the messages from a device at O2. The RSSI values in the Table 3 are the medians of the measurements at the indicated MP. In this challenging environment, Sigfox 0G was unable to reach the basements of the buildings (except B2 and B4) and the energy supply tunnel. LoRaWAN® can reach the basements and the tunnel except for MP T2, which has a greater distance to the emergency manhole than T1. Two MNOs with different frequency bands are evaluated. Vodafone (NB Vo) uses band 20 (800 MHz) for NB-IoT, while Deutsche Telekom (NB DT) uses band 8 (900 MHz). The RSSI values for NB-IoT are measured DL and are obtained directly from the NB-IoT

modem using AT commands. The UL RSSI values for LoRaWAN® are obtained from the TTN back-end. The DL RSSI is obtained from the device using AT commands. The Sigfox 0G RSSI values are measures UL at the BS and reported by the Sigfox back-end system.

Table 3. RSSI values in dBm for LoRaWAN® (LW), NB-IoT (NB) and Sigfox

MP	LW UL	LW DL	NB DT	NB Vo	Sigfox
O1	-72	-68.5	-66	-77	-96.5
O2	-58	-61	-66	-74	-94
O3	-57	-55	-63	-73	-101
O4	-83.5	-84	-64	-74	-100
I1	-81	-78.5	-74	-84.5	-111
I2	-87	-90	-85	-90	-116.5
I3	-102	-102.5	-90	-99	-127
I4	-93	-94	-77	-81	-114
B1	-101	-106	-95	-116	-
B2	-111	-110	-97	-112	-137
B3	-114	-115	-110	-111	-
B4	-111	-106	-85	-94	-124
T1	-116	-112	-107	-114	-
T2	-	-	-112	-118	-

To compare the BPL of different LPWAN technologies, the RSSI of the indoor MPs is subtracted from the RSSI of the nearest outdoor MP. Table 4 compares the BPL for each indoor MP.

Table 4. Calculated O2I BPL from nearest outdoor MP to indoor MP in dB

	I1	B1	I2	B2	I3	B3	I4	B4	T1	T2
LoRaWAN® UL	23	43	29	54	45	57	9.5	27.5	44	-
LoRaWAN® DL	17.5	45	29	55	47.5	60	10	22	43.5	-
Sigfox 0G	14.5	-	22.5	43	26	-	13	23	-	-
NB-IoT DT B8	8	29	22	34	27	47	13	21	41	48
NB-IoT Vo B20	10.5	42	17	39	26	38	7	20	39	45

Due to measurement inaccuracies, these values are not exact and it is not possible to rank the performance of the technologies in terms of BPL. In addition, the LoRaWAN® GWs adjust the transmit power depending on the RSSI, so the BPL in the DL may be too low.

The BPL depends more on the signal path than on the LPWAN technology used. The LoRaWAN® GW1 is placed on top of building 1, the signal has to travel through all ceilings to reach the first floor and the basement. Therefore the BPL of I1 and B1 is much higher for LoRaWAN®compared to NB-IoT and Sigfox 0G. The basement of building 4 is underground on the west side and above ground on the east side. The signal of LoRaWAN® comes from the west, that of NB-IoT and Sigfox 0G come from the east, so the BPL of LoRaWAN® is much larger than that of NB-IoT and Sigfox 0G. The Sigfox 0G BS is much further away than the LoRaWAN® GWs. The angle of entry into the buildings is therefore significantly flatter compared to LoRaWAN® and the BPL is in a similar range to NB-IoT.

From the measured values it can be concluded that the angle at which the signal enters the building, and therefore the position of the GW and BS, has a greater influence on BPL than the technology used. This means that if the LPWAN infrastructure is unknown, the suitability of a LPWAN technology must be determined by measurements. However, the measured values can be used to determine the order of magnitude of BPL to be expected. It is clear to see that the MPs in the basements have a very high BPL of up to 60 dB for LoRaWAN®, which means that the signal is attenuated by a factor of 10^6.

6. LPWAN ARCHITECTURE

There are many reasons to choose a LPWAN technology. In addition to range and building penetration, cost, availability of devices and infrastructure play a major role. In addition, technologies are constantly evolving. Technologies such as Wi-SUN®, which are not widely used today, may become more prevalent in the future, while other technologies such as Sigfox may become less important. In particular, the market for LPWAN energy monitoring devices is changing rapidly. Even if a separate LoRaWAN® infrastructure is operated, it is usually cheaper to use an NB-IoT device than to install a separate LoRaWAN® gateway for a single device if there is no LoRaWAN® coverage at the device's location. For this reason, a hybrid and modular

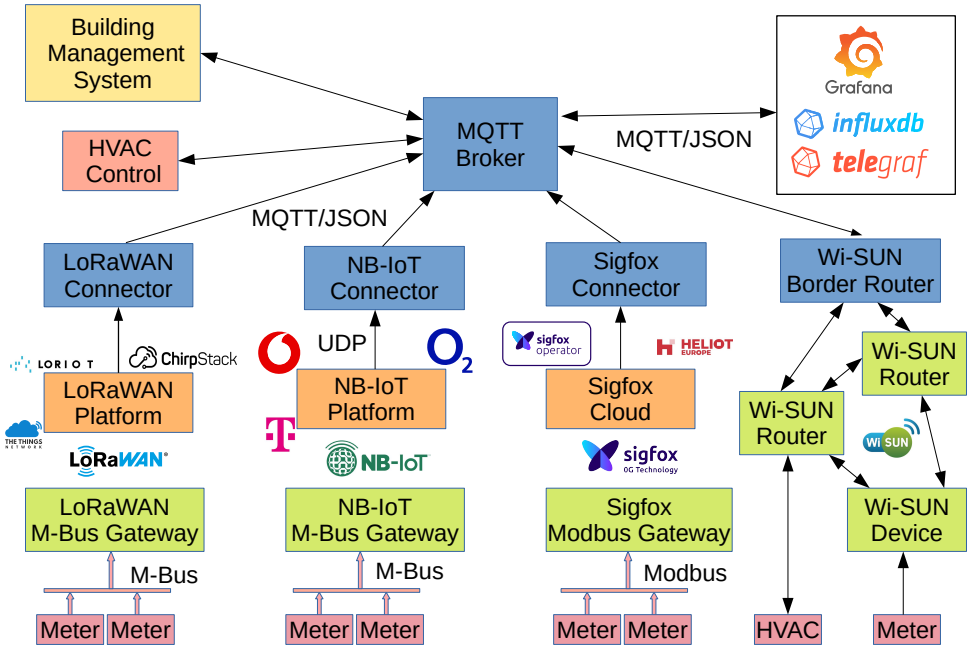

Figure 2. Proposed architecture for energy monitoring and control

architecture is proposed in which multiple LPWAN technologies can be integrated (see Fig. 2). The communication is message based and uses the publish-subscribe messaging pattern. It is implemented using the MQTT protocol. Multiple devices such as meters are connected to a MQTT broker via software connectors. The software connectors provide an abstraction layer for LPWAN technologies with a common interface based on MQTT and JSON.

The architecture connects existing energy meters and sub-meters with different interfaces to the IoT middleware via multiple LPWAN radio technologies. The district heating and cooling meters provide an M-Bus interface, while the gas meters provide only pulses to be counted. Energy data from different sources and technologies is transmitted over different wireless technologies. A connector for each technology receives the energy data over the Internet, decodes the binary

data, and converts it to a normalized JSON format. The energy data is then published to a MQTT broker, which acts as a central hub in the system. The data is stored in a time series database for later analysis and visualization in a web front-end.

7. CONCLUSIONS

The paper presents an experimental evaluation of four LPWAN technologies in deep indoor environments. LoRaWAN® and NB-IoT show better building penetration than Sigfox 0G and Wi-SUN®. By using licensed radio bands and automatic retransmission in case of packet loss, NB-IoT offers higher reliability compared to other LPWAN technologies. Compared to NB-IoT, LoRaWAN® has the advantage of lower power consumption, greater flexibility in the choice of infrastructure, and a wider range of devices available for energy monitoring. Wi-SUN® may become more important in the future due to its mesh topology. However, there are currently no energy monitoring devices available for use in Europe. Furthermore, Wi-SUN® has the lowest building penetration compared to the other LPWAN technologies considered. Sigfox 0G generally offers a high link budget and therefore the potential for high building penetration, but only two out of four basements are reached in the experimental evaluation. This is likely due to the low density of Sigfox BSs in the area studied.

A hybrid and modular architecture for energy monitoring has been proposed that can integrate multiple LPWAN technologies. The architecture has been implemented and tested for LoRaWAN® and NB-IoT. It is successfully used for energy monitoring in several buildings at the Dortmund University of Applied Sciences and Arts.

REFERENCES

3GPP, 2024. Study on channel model for frequencies from 0.5 to 100 GHz. 3GPP TR 38.901 version 18.0.0.

Hoo F., Lim Tan F. S., Ching Bon Chan R., Waszecki P., Keoh S. L., Kiat Seow C., Li M., Cao Q., and Sum C. S., 2023. 5G-Wi-SUN for Building Management System. Proceedings of 2023 6th International Conference on Applied Computational Intelligence in Information Systems (ACIIS), 1–6.

ITU-R, 2015. Propagation data and prediction methods for the planning of indoor radiocommunication systems and radio local area networks in the frequency range 300 MHz to 100 GHz. P Series Radiowave propagation, Recommendation ITU-R.

Kadusic E., Ruland C., Hadzajlic N., and Zivic N., 2022. The factors for choosing among NB-IoT, LoRaWAN, and Sigfox radio communication technologies for IoT networking. Proceedings of 2022 International Conference on Connected Systems & Intelligence (CSI), 1–5.

Malarski K. M., Thrane J., Bech M. G., Macheta K., Christiansen H. L., Petersen M. N., and Ruepp S., 2019. Investigation of Deep Indoor NB-IoT Propagation Attenuation. Proceedings of 2019 IEEE 90th Vehicular Technology Conference (VTC2019-Fall), 1–5.

Naumann H. and Oelers W., 2021. *LPWAN Comparison – Low Energy Consumption with NB-IoT, LoRaWAN and Sigfox*.

Persia S., Carciofi C., and Faccioli M., 2017. NB-IoT and LoRA connectivity analysis for M2M/IoT smart grids applications. Proceedings of 2017 AEIT International Annual Conference, 1–6.

Roosipuu P., Annus I., Kuusik A., Kändler N., and Alam M. M., July 2023. Monitoring and control of smart urban drainage systems using NB-IoT cellular sensor networks. Water Science and Technology 88, 339–354.

Tangsunantham N. and Pirak C., 2022. Experimental Performance Analysis of Wi-SUN Channel Modelling Applied to Smart Grid Applications. Energies 15.

Thrane J., Malarski K. M., Christiansen H. L., and Ruepp S., 2020. Experimental Evaluation of Empirical NB-IoT Propagation Modelling in a Deep-Indoor Scenario. Proceedings of GLOBECOM 2020 - 2020 IEEE Global Communications Conference, 1–6.

Wan L., Dai X., Welfonder T., Petrova E., and Pauwels P., Sept. 2023. Semi-automated thermal envelope model setup for adaptive model predictive control with event-triggered system identification. Proceedings of Building Simulation 2023: 18th Conference of IBPSA. Vol. 18. Building Simulation. IBPSA, Shanghai, China, 3664–3671.

6th International Conference on Building Energy and Environment
Eindhoven University of Technology, The Netherlands
6 - 10 July 2025

DataNet: Introducing a Korean project on integrating multifaceted datasets for evidence-based building performance analysis

Hye-Gi Kim[1], Hyery Shin[2], Ki-Uhn Ahn[3], Han Gyeong Chu[4], Deuk-Woo Kim[5]

[1]*Korea Institute of Civil Engineering and Building Technology, Goyang-si, South Korea, kimhyegi@kict.re.kr*
[2]*Korea Institute of Civil Engineering and Building Technology, Goyang-si, South Korea, hyeryshin@kict.re.kr*
[3]*Korea Institute of Civil Engineering and Building Technology, Goyang-si, South Korea, ahnkiuhn@kict.re.kr*
[4]*Korea Institute of Civil Engineering and Building Technology, Goyang-si, South Korea, hankyon0122@kict.re.kr*
[5]*Korea Institute of Civil Engineering and Building Technology, Goyang-si, South Korea, deukwookim@kict.re.kr*
corresponding author

SUMMARY
Recently, several administrative registration datasets have become public or partially accessible, including building registries, monthly energy billing information, building footprint polygons, business registration data, ministry-maintained facilities data, and weather data. However, from a building analysis perspective, these datasets remain fragmented as they are by-products of administrative processes not originally designed for integration. This paper introduces the *DataNet* project, which aims to integrate multifaceted building energy datasets nationwide in South Korea. The main objectives are to establish a national data framework that accelerates the transition to carbon neutrality in the building sector, and to support more effective, evidence-based performance analysis. In this project, the building registry serves as a reference base, with other datasets linked through addresses and associated attributes, such as building or business names. To date, we have collected and linked 13 of the 19 targeted datasets. This paper presents the overall framework, data categories, spatial and temporal resolutions, and linkage approach.

Keywords: data framework, linked data, carbon neutrality, evidence-based, performance gap

1. INTRODUCTION

As a cornerstone initiative to support evidence-based decision making in Korea's decarbonization strategy, the *DataNet* project was launched in April 2023, with a four-year timeline extending through December 2026. This collaborative endeavor brings together approximately 130 researchers and experts from 16 institutions across the country. The project is structured into four distinct work packages: (1) development of multi-faceted data linkage technologies, (2) design of unstructured data informatization techniques, (3) establishment of building energy consumption performance evaluation methodologies, and (4) construction of an Integrated Building Energy Database (I-BED) system and preparation of a utilization framework. This paper focuses specifically on the first work package — the result of multi-faceted data linkage — which has been the primary focus during the initial two years (2023-2024) of the project. The paper explains the data identification, collection, and linking approaches at a nationwide scale, along with an overview of the constructed 13 datasets.

Carbon neutrality achievement in the building sector faces considerable complexity due to the scale of existing building stock, which numbers approximately 7 million buildings in South Korea.

While most policies and regulations focus on large buildings, new constructions, and energy-efficient buildings, small buildings (less than 1,000 ㎡), which account for more than 90% of existing building stock, remain overlooked in energy and GHG emissions management. Kim et al. (2019), Ahn et al. (2022), Kim et al. (2022) and Kim et al. (2024) highlighted this South Korean challenge and proposed a cost-effective approach to address it. The management of these buildings is particularly challenging due to limited data availability. Addressing these underserved areas is critical for achieving carbon neutrality in the building sector in an equitable manner. To support this goal, the *DataNet* project focuses on building-level benchmarking, aiming to establish appropriate baseline consumption patterns and identify inefficient buildings at a nationwide scale.

The IEA EBC Annex 53 framework identifies six primary factors: climate, building envelope, building services and energy systems, building operation and maintenance, occupants' activities and behavior, and indoor environmental quality (Yoshino et al. 2017). The *DataNet* project extends this framework by adding two additional factors and further subdividing total energy consumption by source and usage. These factors can be categorized into eight main groups: (1) weather factors (temperature, humidity, solar radiation), (2) building physical factors (form, shape, size, thermal properties, window-to-wall ratio), (3) system factors (system load, efficiency, specifications), (4) building type factors (primary space use categories), (5) operational and activity factors (number of workers, operating hours), (6) social factors (age, gender, behavior patterns), (7) demographic factors, and (8) neighboring factors (Figure 1). These various factors are essential for ensuring equitable energy benchmarking.

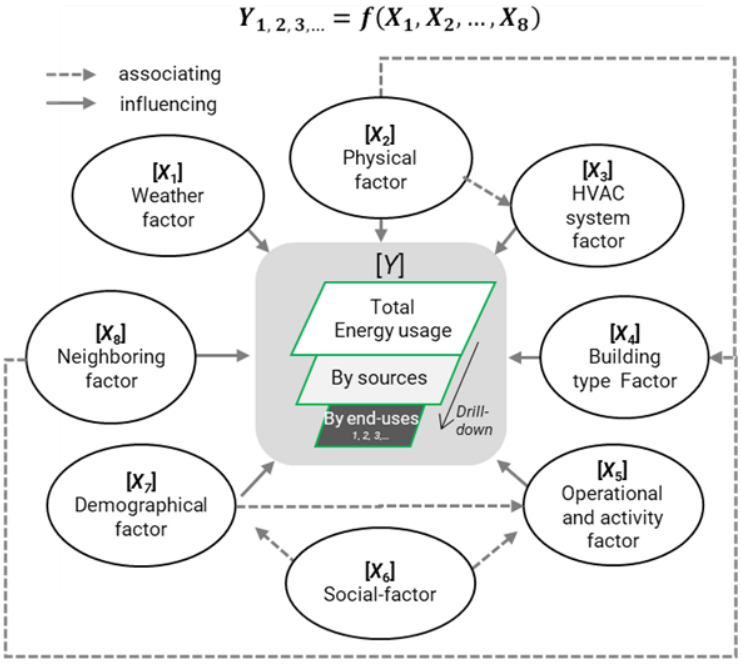

Figure 1. Conceptual diagram illustrating the association between multi-faceted factors and energy consumption.

2. DATASETS

Government-held (partially) open data serves as a critical foundation for such analysis, providing extensive coverage and meta-level insights that would be impossible to obtain through individual research efforts. However, these datasets have been independently developed by different

government departments for their specific administrative purposes. For instance, the Ministry of Land, Infrastructure and Transport (MOLIT), Ministry of Health and Welfare (MOHW), and Ministry of Education (MOE) maintain building registration, medical facility information, and educational facilities databases, respectively. This siloed approach to data collection and management has created disconnections that hinder the building-level integration necessary for comprehensive energy performance analysis.

The data identification and selection process consisted of several steps. First, the government-held open datasets were reviewed primarily through the Public Data Portal (www.data.go.kr), which serves as an integrated platform providing multiple datasets from various government departments and agencies. Second, the potential contribution to evidence-based energy benchmarking also was evaluated. Third, the building-level matching capability (data interconnectivity) between siloed instances was assessed using attributes such as building primary key, addresses, or business names. Finally, factors were allocated based on the expanded IEA EBC Annex 53 framework (Figure 1).

Table 1. Overview of identified and collected datasets for building energy benchmarking

	Data Name	Responsible Ministry	Working Progress	Key Information
X_1	Meteorological Observation data	KMA	Done	Regional weather data (temp., RH, solar radiation, etc.)
X_2	Building registry	MOLIT	Done	Address, name, register type, use purpose type, approval date, area, floor info., parking lot, etc.
	Energy Performance Certificates	MOLIT	TBD	Address, name, Grade, simulation info., etc.
	GIS Bldg. footprint data	MOIS	Done	Address, name, number of floors, 2D polygon (shape), etc.
X_3	Mech. equipment maintenance information	MOLIT	TBD	Address, name, field diagnostics for building mechanical equipment
X_4	Cultural facility information part A (Cultural Center, Literature Center)	MCST	Done	Address, name, facility use type, workforce composition information, no. of visitors, operating hours, etc.
	Cultural facility information part B (Libraries, Museums, and Art Galleries)	MCST	Done	*Same as above*
	Medical facility information.	MOHW	Done	Address, name, medical facility class, workforce composition info., no. of beds, operating hours, equipment, etc.
	Higher education facilities information	MOE	Done	University-related statistical information
	K-12 education facility information	MOE	On-going	Elementary/middle/high school-related statistical info.
	Childcare facility information	MOE	On-going	Basic information and current status of childcare centers
X_5	Local administrative business permit data	MOIS	On-going	Permit information for various industries
	Commercial small business information	MSS	TBD	Address and industry data for businesses nationwide
	Apartment management information	MOLIT	TBD	Apartment management fees, energy usage information
	Building historical permit data	MOLIT	TBD	Construction permits, demolition, loss-related information
X_{6-7}	Assessed land value info.	MOLIT	Done	Individual publicly announced land prices
	Resident registration data	MOIS	TBD	Household member information (no. of member, gender, age, etc.)
X_8	GIS Bldg. footprint data *Same as above X_2*	MOIS	Done	2D polygons (shapes) of nearby buildings in a 50-meter buffer around the buildings
	Land use plan info.	MOLIT	TBD	Land use planning information,
	Building 3D geometry data	MOLIT	TBD	3D building form, address, etc.
Y	Monthly energy billing registry	MOLIT	Done	Energy consumption by sources (electricity, gas, district heating)

KMA: Korea Meteorological Administration / MCST: Ministry of Culture, Sports and Tourism / MOE: Ministry of Education / MOHW: Ministry of Health and Welfare / MOIS: Ministry of the Interior and Safety / MOLIT: Ministry of Land, Infrastructure and Transport / MSS: Ministry of SMEs and Startups

2.1 National Building Energy Database as a reference base

The Korea Real Estate Agency has been constructing and maintaining the National Building Energy Integrated Database (NBEID) over the past decade by combining building registry information with building energy consumption billing data (Choi et al., 2017; Ji et al., 2020). The NBEID provides nationwide building-related energy consumption information by integrating two core databases: Building Registry DB, which contains essential building information, and Monthly Energy Billing DB, which records energy usage data (Figure 2). Using the Building Registry DB as a reference base, other datasets were linked according to three matching categories: 1:1 matched, 1:N matched, and unmatched. Figure 3 shows an example matching process from footprint polygon data to a building register (standalone type and complex type).

This database comprises approximately 6.25 billion electricity, gas, and district heating usage records collected from about 50 million individual meters connected to approximately 7.3 million buildings nationwide. This information enables the analysis of energy consumption patterns by meter type across national buildings, providing macro-level insights into energy usage patterns and trends. The *DataNe*t project aims to integrate and link recently released or partially released public data at the building level, utilizing the NBEID and its Building Registry DB as the foundation for data integration.

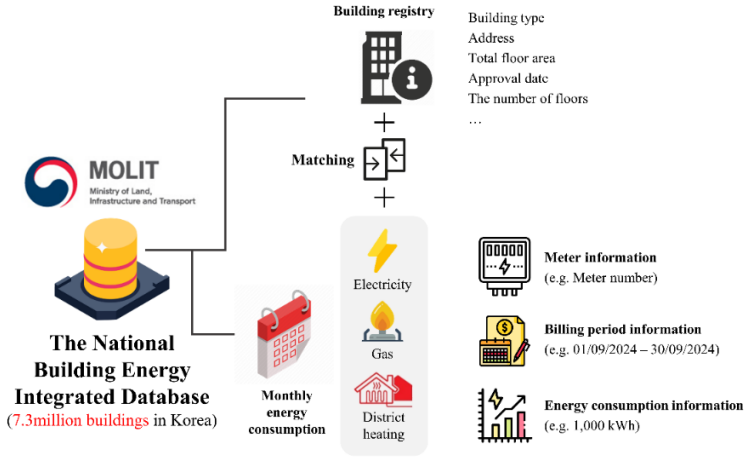

Figure 2. Overview of the National Building Energy Integrated Database

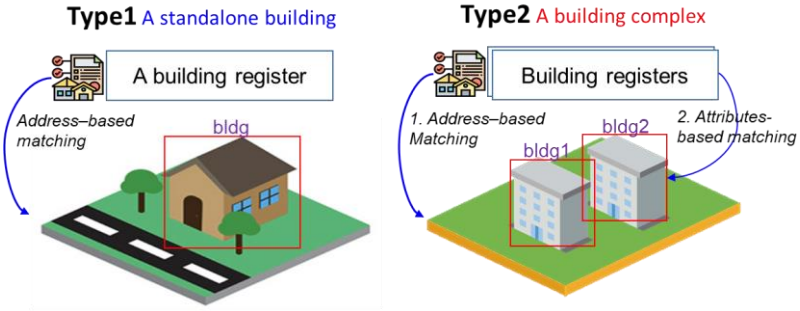

Matching Class	Matching Sub-class	Remark
1:1 Match	Address with bldg. name 1:1 matching	High reliability in matching
	Address only 1:1 matching	
1:N Match	Attribute cross-matching	Medium reliability in matching
	Address code matching	
Un-mappable	Unmappable	Unable to match

Figure 3. Building footprint polygon and registry matching examples for various building configurations within a single land plot

2.2 Data collection with influential factors

The NBEID has numerous applications, such as deriving national-level energy intensity statistics (Kim et al., 2019) and proposing benchmark values for energy benchmarking (MOLIT, 2020). However, from a 'ceteris paribus' perspective, more diverse information is required for energy benchmarking. Based on this perspective, international studies such as Total Energy Use in Buildings (IEA EBC Annex 53) and Building Energy Epidemiology (IEA EBC Annex 70) have been conducted to comprehensively understand building energy consumption patterns (Hamilton et al., 2013; Yoshino et al., 2017). Furthermore, major advanced countries are making efforts to connect building and energy information at the national level under government leadership. Notable examples include Standard Energy Efficiency Data Platform in the United States (Long et al., 2020), the National Energy Efficiency Data Framework in the United Kingdom (DESNZ, 2024), and the Digital Building Logbook (European Commission, 2023) and Building Stock Observatory (European Commission, 2024) in Europe.

From a building perspective, the datasets are completely fragmented, as they are by-products of administrative processes not designed for integration. The research team identified and collected 17 datasets representing fragmented energy consumption influencing factors, as shown in Figure 4. The datasets were classified into 'Common Base' and 'Use-Specific' categories, distinguishing between data that exists commonly across all building types and data that is disclosed specifically according to building use. The reference date for data collection is December 2022, and the energy consumption data spans five years from 2018 to 2022.

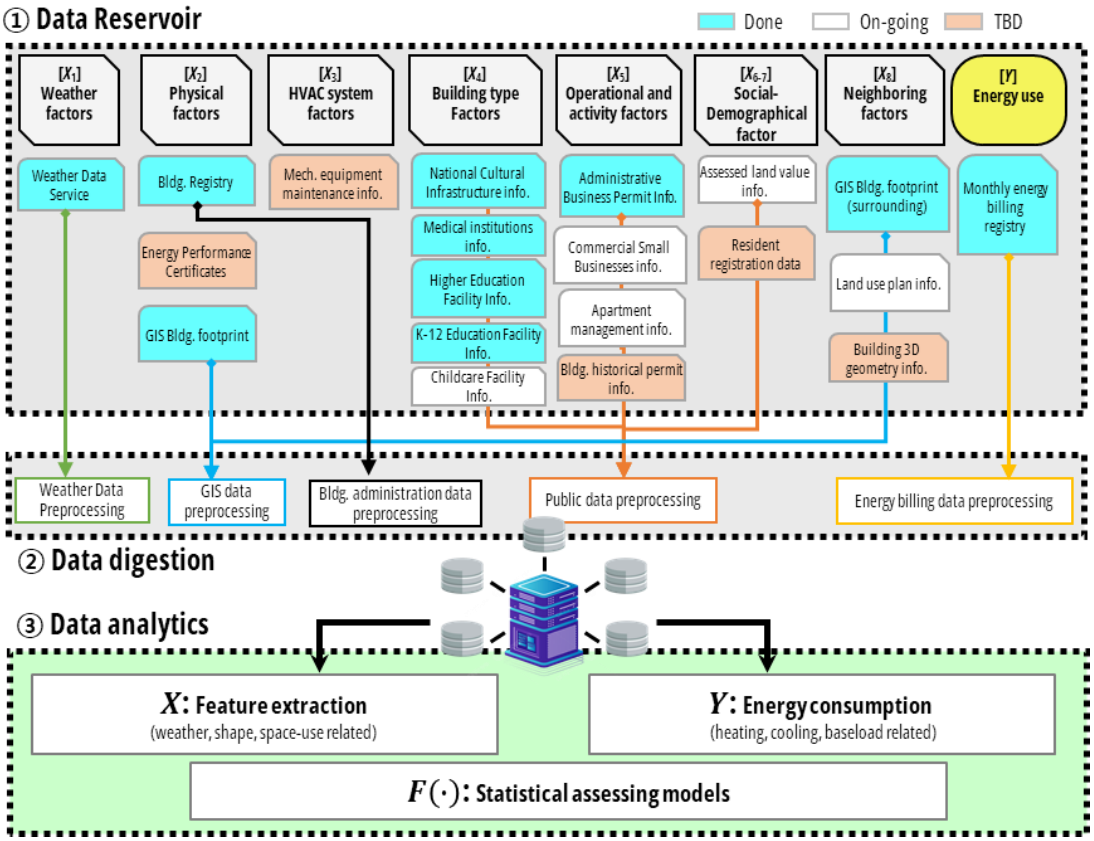

Figure 4. Data integration flowchart

3. SNAPSHOT OF DATASETS

From the established database, energy consumption data were extracted for approximately 590,000 buildings in Seoul, South Korea's capital city (total floor area: 369,027,000 m²). The total energy consumption of 60,459 MWh comprises: electricity: 28,305 MWh (83.0 kWh/m²), city gas: 31,135 MWh (92.6 kWh/m²), district heating: 1,018 MWh (60.7 kWh/m²), total energy intensity: 163.8 kWh/m². These energy flows are visualized in the Sankey diagram (Figure 5), which shows the overall energy distribution by source (left) and highlights cooling energy use (right).

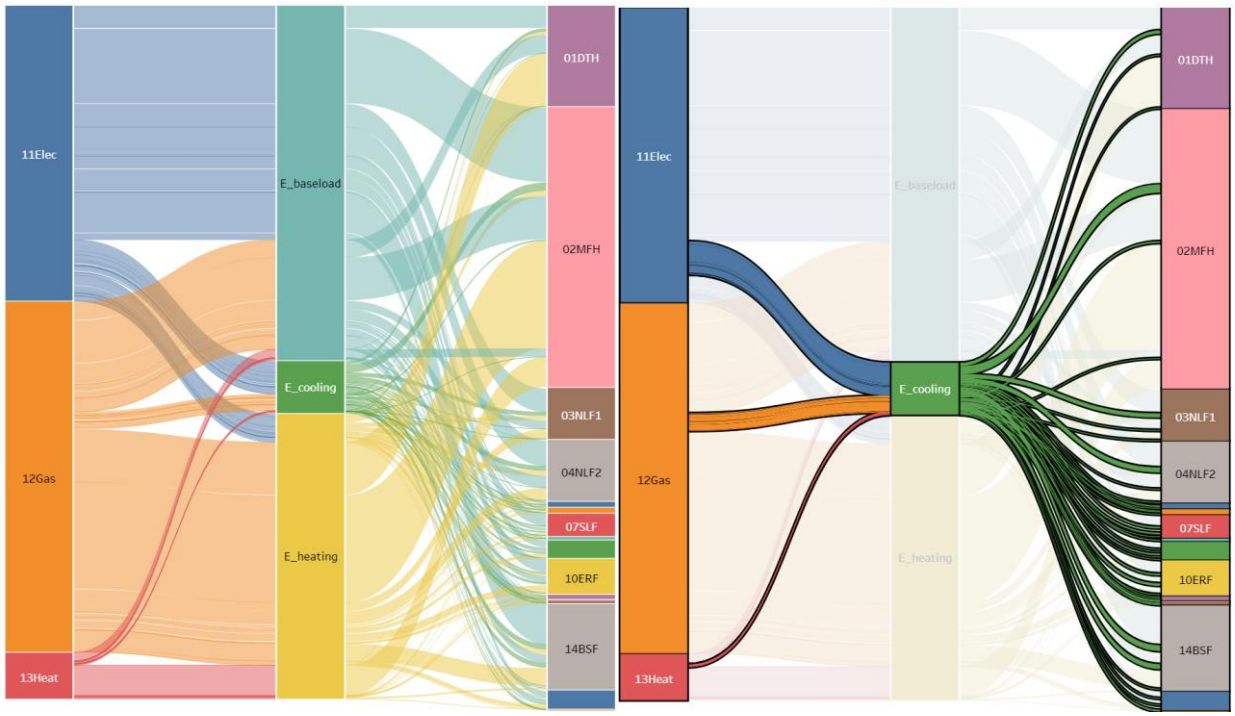

Figure 5. Sankey diagram illustrating energy flows from sources (left) and highlighting cooling energy use (right).

The diagram consists of three main sections: energy sources (left bar) displaying inputs 'Elec' (electricity), 'Gas' (city gas), and 'Heat' (district heating); energy use categories (middle bar) connecting sources to consumption types ('E_baseload', 'E_cooling', 'E_heating'), with flow line thickness indicating energy quantity; and final consumption (right bar) showing building type categories ('01DTH: detached house', '02MFH: multifamily housing', '07SLF: sales facility'). The color coding and flow lines illustrate energy distribution patterns, with 'Gas' primarily serving 'E_heating' (shown in yellow). For cooling energy specifically, electricity ('Elec', shown in blue) serves as the primary source, while gas ('Gas', shown in orange) and district heating ('Heat', shown in red) contribute minimally to cooling demands.

Figure 6 presents a prototype viewer developed for exploring building data status. The viewer comprises six main components: (1) an address search box for locating buildings, (2) building registration information displaying official building data, (3) building floor information with level-by-level usage details, (4) change-point regression analysis results revealing energy use patterns, (5) disaggregated heating and cooling EUI (Energy Use Intensity) data that show detailed energy consumption, and (6) monthly energy consumption by source, illustrating seasonal and temporal trends. In addition, the viewer provides shading information through two features: (7) an

interactive filter that allows users to select a season and cardinal direction to assess building shading performance, and (8) a GIS-based spatial map displaying shading index values for surrounding buildings. For a more detailed and exemplary application of the integrated datasets—particularly regarding the building footprint polygons—please refer to Choi et al. (2025).

Figure 6. Prototype Design of the Data Dashboard for individual buildings

4. DISCUSSION AND CONCLUSION

Regulating building energy performance during the operational phase must be based on data and evidence. Simply targeting high energy-consuming buildings for intensive management and penalties may be unreasonable, as energy consumption is influenced by various contextual factors. Similarly, buildings with large indoor parking areas receiving exclusions or incentives due to low energy use intensity warrants careful reconsideration. In this context, the present study aimed to establish a foundation for comprehensively linking and integrating data on buildings, energy consumption, and their influencing factors. To achieve this objective, 17 datasets were selected based on the building registry. Of these, 13 datasets—including the building registry, road name electronic map building polygons, and local government permit information—were successfully collected, linked, and integrated.

The data integration process presented several technical challenges, including differences in data formats and address systems across government agencies, as well as inconsistencies in data collection cycles and update timelines. To address these challenges, a combined approach using exact matching (1:1 between addresses and the building registry) and partial matching (1:N) techniques was implemented. Additionally, data refinement and processing methods were developed (Kim et al. 2024) to effectively analyze energy consumption characteristics. By linking fragmented datasets at the individual building level, this research aims to establish a methodology

that enables multifaceted assessment of energy consumption patterns, ultimately supporting more informed and accurate evaluations. As this data integration framework matures and becomes standardized, many of the current data linkage challenges are expected to be resolved. Furthermore, if this research contributes to the development of decision-support tools for policymakers, it could facilitate a significant paradigm shift in energy performance evaluation.

ACKNOWLEDGEMENTS

This work is supported by the Korea Agency for Infrastructure Technology Advancement(KAIA) grant funded by the Ministry of Land, Infrastructure and Transport (Grant RS-2023-00244769, Development of a data framework for integrating building energy datasets and applications to accelerate carbon neutrality in the building sector).

REFERENCES

Ahn, K.U., Kim, D.W., Lee, S.E., Chae, C.U., Cho, H.M. (2022). Temporal Segmentation for the Estimation and Benchmarking of Heating and Cooling Energy in Commercial Buildings in Seoul, South Korea. Sustainability, 14(17):11095.

Choi, M.S., O., Seung, Y., Ji, C., & Lee, D.Y. (2017). An Analysis of Residential Building Energy Consumption Using Building Energy Integrated Database - Focused on Building Uses, Regions, Scale and the Year of Construction Completion. Journal of Real Estate Analysis, 3(1), 101-118.

Choi, S ., Yi, DH., Kim, DW., Yoon. S. (2025). Multi-source data fusion-driven urban building energy modeling, Sustainable Cities and Society 123, 106283

DESNZ (2024). NEED - National Energy Efficiency Data-Framework, https://www.gov.uk/government/collections/national-energy-efficiency-data-need-framework, Department for Energy Security & Net Zero, accessed on 11, 2024

European Commission (2023). Technical guidelines for digital building logbooks, 10, Nov. 2023, https://www.ecorys.com/app/uploads/2019/02/DBL-Technical-Guidelines-for-DBLs.pdf

European Commission (2024). EU Building Stock Observatory. https://energy.ec.europa.eu/topics/energy-efficiency/energy-efficient-buildings/eu-building-stock-observatory_en,accessedon 11, 2024

Hamilton, I.G., Summerfield, A.J., Lowe, R., Ruyssevelt, P., Elwell, C.A., & Oreszczyn, T. (2013). Energy epidemiology: a new approach to end-use energy demand research. Building Research Information, 41(4), 482-497.

Ji, C.Y., Choi, M.S., Gwon, O.I., Jung, H.R., & Shin, S.E. (2020). Greenhouse Gas Emissions from Building Sector based on National Building Energy Database. Journal of the Architectural Institute of Korea Structure & Construction, 36(4), 143–152.

Kim, D.W., Kim, Y.M., Lee, S.E. (2019). Development of an energy benchmarking database based on cost-effective energy performance indicators: Case study on public buildings in South Korea, Energy and Buildings 191, 104-116

Kim, D.W., Ahn, K.U., Shin, H., Lee, S.E. (2022). Simplified weather-related building energy disaggregation and change-point regression: Heating and cooling energy use perspective, Buildings 12 (10), 1717

Kim H.G., Lee S.E., Kim D.W, (2024). Impact of calendarization on change-point models, Energy and Buildings. Volume 303, 113803

Long, N., Swindler, A., Bergmann, H., Reagan, A., Held, A., & Longley, J. (2020). "Standardizing City Benchmarking and Reporting: Use Cases in Consolidating Building Data with SEED", 2020 ACEEE Summer Study on Energy Efficiency in Buildings.

MOLIT, (2020). press release, Specific CO2 emissions in Residential Buildings in Republic of Korea (Version 01.0)' UNFCCC Standardized Baseline(ASB0048-2020), Ministry of Land, Infrastructure and Transport, https://m.molit.go.kr/viewer/skin/doc.html?fn=cb68a472ea361564abebb1873db40b03&rs=/viewer/result/20200825. accessed on 11, 2024

Yoshino, H., Hong, T., Nord, N., (2017). IEA EBC annex 53: Total energy use in buildings—Analysis and evaluation methods, Energy and Buildings 152 (1)

6th International Conference on Building Energy and Environment
Eindhoven University of Technology, The Netherlands
6 - 10 July 2025

Application of data-driven techniques for identification of large electricity consumer assets from electricity time series in residential buildings

Mohsen Sharifi [1,2], Jonas Mariën[1,2],Yixiao Ma [1,2]

[1]*VITO, Water and energy transition unit, Mol, Belgium. mohsen.sharifi@vito.be*
[2]*EnergyVille, Genk, Belgium. Yixiao.ma@vito.be*

SUMMARY
Urban Building Energy Models (UBEM) rely on data-driven techniques and offer a structured approach and methods for making informed decisions to reduce the carbon footprint of buildings. Traditionally, UBEM focuses on modelling building structures and simplified representations of heating systems. However, a lack of knowledge about installed solar panels, electric vehicles (EVs), and heat pumps (HPs) can significantly impact the accuracy and effectiveness of these models. Understanding the presence of these assets is crucial for accurately estimating a building's energy use and its potential for decarbonization. This study applies a data-driven method to identify solar panels, EVs, and HPs from residential electricity consumption time-series data for use in UBEM. By analysing large datasets from buildings with varying levels of electricity usage, machine learning algorithms are applied to capture patterns in energy consumption over time. The proposed approach uses historical electricity consumption profiles to predict the presence of these assets, without depending on specific building characteristics. This allows for broader applicability across different building types and locations, even when detailed metadata is unavailable. Several machine learning techniques were compared, and thorough feature engineering was conducted to enhance the model's accuracy. The results demonstrate that the model can achieve an accuracy of over 90%, making it suitable to be sent for more optimization in production phase and prepare for real-world applications. However, future works will explore whether the model requires periodic retraining due to changes in weather conditions, although this effect varies across regions, highlighting the need for localized adjustments in future applications. Moreover, this approach can play a key role in supporting remote energy certification of buildings, making it a valuable tool for energy efficiency assessments.

Keywords: Machine-learning models, time series analysis, electricity smart meter, urban building energy modelling

1. INTRODUCTION

Traditional urban building stock models use urban building energy modelling (UBEM) principles which account for representative buildings (archetypes) to quantify the energy efficiency measures at the building stock level. These models address the heterogeneity in the building morphological characteristics, building age, insulation performance. Hence, these models cannot account for the complete variation in building operations which can cause inaccuracies and uncertainties in the outcomes [Guo et. al, 2025]. The models often lack information about installed photovoltaic (PV) panels and electric vehicles (EV). However, the energy intensive assets such as heat pumps (HP), photovoltaic panel (PV) and electric vehicles (EV) are usually either omitted from these models or studied in post-processing steps. Conventionally, these assets are not among the data available to the researchers conducting urban energy analysis.

The development of smart metering infrastructures has generated rich streams in time series format. Such time series contain hidden information on the type of installed building systems and play a huge role in assessment of operational energy conservation measures. One of the techniques

utilizing these streams is load profile characterization that can generate useful information to enhance building energy modelling and provide metrics to represent patterns and variability of load profiles (Kim et. al, 2023). Such characterizations can be used to identify the kind of electrical appliances and the electric-base heating systems. We utilize these time series and train machine learning models to predict what large consumer electrical assets are installed on a house associated to a time series of electricity consumption. The outcomes provide means for researchers to generate distributions of installed assets in the residential building stock by using large datasets of electricity smart meter.

1.1 State of the art

A variety of data-driven techniques have been adopted in building energy simulations for a variety of applications (Sharifi, 2023).When considering the use of time series of measured building energy use, numerous load profiling frameworks already exist in the literature mainly aimed to classify and identify homogeneous groups of daily load profiles with the aim of load forecasting. Wang et al. (2019) employed a deep learning predictive approach for district scale building energy modelling. The building network was constructed based on correlations between the energy use intensity of buildings, which significantly reduced the computational complexity of the deep learning models for energy dynamic prediction. This study estimated monthly aggregates as the final output and did not consider the time-series dynamics with limited information on installed heating, cooling and ventilation (HVAC) systems. Wei et al. (2021) predicted district heating load using shallow and deep machine learning algorithms that identified the effect of time horizon and historical time-series data on the prediction accuracy. Recent studies (e.g., Hafeez et al., 2020 and Kim et al., 2019) have demonstrated the effectiveness of machine learning techniques in energy including electricity and heating demand forecasting.

1.2 Research question

In this study, we will deploy ML techniques to train models that can predict installed assets such as HPs, EVs, and PVs on a house with given electricity consumption time series. Previous studies have deployed advanced ML techniques to directly forecast demand time series that are mostly used in operation phase. We, on the other hand, aim for using ML techniques to extract extra data from time series to feed into physics-based model in UBEM. As the implication of the work, distribution of installed HPs, EVs, and PVs can be eventually extracted from a large dataset of anonymous electricity demand time series for a region. As previous studies have been developed to serve a different purpose, we aim for extensive research on feature engineering, appropriate models, minimum and maximum required data availability, and check for possibility of model drift. We will also discuss the expected accuracy from the developed models and their possible implications for UBEM.

2. METHODLOGY

This study follows a common structured ML model training framework (Kim et al., 2023), starting with data collection. Labelled electricity consumption time series are imperative to train a model to predict installed EVs, PVs, and HPs from time series. We use a dataset provided by Fluvius which is the grid operator in Flemish region in Belgium (Fluvius, 2024). The time series are anonymous, but they have indication on which large electricity asset has been installed on the associated house. Once the raw data is gathered and cleaned up for analysis, exploratory data

analysis (EDA) is performed to understand distributions, detect anomalies, and identify potential relationships through statistical summaries and visualizations. Following EDA, data cleaning and preprocessing take place to handle missing values, correct inconsistencies, and remove outliers. This step ensures that the data is in a suitable format for modelling, including normalization or standardization if necessary. Once the data is cleaned, feature engineering and selection are applied to create new informative features while eliminating irrelevant or redundant ones that do not contribute to model performance. With the dataset prepared, it is then split into training, validation, and test sets to ensure proper model evaluation. Typically, a common split such as 80%-20% is used in this step, depending on dataset size. The next step involves initial modelling to establish a baseline, where simple models to serve as reference points for further improvement. In this step we use most common existing supervised algorithms for benchmarking. After establishing a baseline, more advanced ML models are trained, and hyperparameter tuning is conducted using grid search. Cross-validation, particularly k-fold cross-validation, is used to ensure generalizability. By that, we can show how much the model is trustable to be used in real applications. Model evaluation is conducted based on relevant performance metrics, such as accuracy in predicting labels, precision-recall, and F1-score as common metrics for classification tasks. Once models are trained and evaluated, model interpretation will be carried out using confusion matrix.

Our approach is generally called time series classification (TSC). Middlehurst et al. (2025) defines TSC as "fitting a model from a continuous, ordered sequence of real valued observations (a time series) to a discrete response variable" after their thorough review on an extensive list of applicable TSC algorithms. They listed and reviewed eight main algorithms that are tabulated in Table 1.

Table 1 Eight main algorithms for time series classification.

Method	Summary	Pros	Cons	Applications	Example Algorithm
Distance-Based	Measures similarity using distance metrics like DTW.	Simple, effective for small datasets.	Computationally expensive for large data.	Pattern recognition, anomaly detection.	KNN-DTW
Feature-Based	Extracts statistical features and applies ML models.	Interpretable, efficient for short series.	May lose temporal dependencies.	Medical signals, finance, monitoring.	Random Forest (RF), XGBoost
Interval-Based	Uses selected time intervals for classification.	Robust, handles long time series well.	Performance depends on interval choice.	Speech, financial forecasting.	Time Series Forest (TSF), RISE
Shapelet-Based	Identifies key patterns (shapelets) for classification.	Interpretable, phase-independent.	Computationally intensive, slow.	ECG analysis, gesture recognition.	Shapelet Transform Classifier (STC)
Dictionary-Based	Converts time series into symbolic representations.	Good for repetitive patterns, scalable.	Loses some temporal order info.	Text mining, speech, DNA analysis.	BOSS, WEASEL
Convolution-Based	Uses convolutional kernels to extract patterns.	Automates feature extraction, accurate.	Needs large data, computationally heavy.	Industry, activity recognition.	ROCKET
Deep Learning-Based	Uses neural networks (CNNs, RNNs, Transformers).	Scales well, learns complex patterns.	Requires large datasets.	Speech, biomedical diagnostics.	ResNet, InceptionTime, LSTMs
Hybrid Approaches	Combines multiple classification models.	High accuracy, leverages multiple methods.	Computationally complex, hard to interpret.	General-purpose, high accuracy TSC.	HIVE-COTE, Hybrid Ensembles

A common challenge to choose the best algorithm is to find the most important features to feed the ML algorithm. Features can be all single datapoints of the time series. This option results an exhaustive search for similarity between time series with the same label. However, this exhaustive search will also result in including datapoints that are not constructive or important in training models, also known as noises. Hence, finding the optimum interval will become another challenge. Advanced algorithms include feature engineering to avoid noise from the dataset. They only take the most important datapoints and their sequence, in case of time series analysis. According to Middlehurst et al. (2025), this step is called series-to vector transformations. In a next step, the transformed time series are ensembled to create a new dataset that only carries the most essential part of the initial dataset, also known as features dataset. The data of features explain the time series in a way that is better understandable for ML algorithms. This step can be a very labor-intensive manual or an automated step. The manual exercise requires a prior knowledge about the system that the data are derived from in addition to the ability to interpret the data itself. This can cause a robust and interpretable model. The automated approach requires less labor work, yet it can result in unstable models and uninterpretable models. Hence, it cannot help in upscaling the models in the given application of this study. Interpretation of the model will help other researchers to develop similar models for their datasets.

Given the computational limitation, high length of available time series, and familiarity with the physics behind the time series, we will use distance-based method. We generate the models using different algorithms for distance-based methods and make initial comparison. We explore the best features to feed to the models during our feature engineering step. The algorithm associated to the best model will be used for hyperparameter tuning using an exhaustive grid search. To provide a robust model to show applicability of the results, we then apply cross-validation by using a variety of different train and test sets to be able to show a realistic accuracy of the model. In cross-validation step, we make multiple folds of the data and each time train and test the model with different folds of the datasets. By that, the model is less prone to be biased by train and test set.

2.1. Dataset and EDA

The datasets used in this study contains 1300 sub-hourly electricity consumption time series (15 minutes time steps) from smart meters in Flemish region published by the grid operator, Fluvius, with open access to public (Fluvius, 2024). There are 300 case studies of each group named as HP+PV (buildings with heat pump and solar panels), EV_noPV (buildings with electric vehicles without heat pumps and without solar panels), EV+PV (buildings with electric vehicles without heat pumps and with solar panels), and Only_PV (buildings with only solar panels). There are also 100 cases without any of these devices installed. Figure 1 presents raw time series of average energy consumption in 15-minute intervals for different categories over the first five days of June 2023. Each line represents a different a building for the same label meaning a group with similar installed assets.

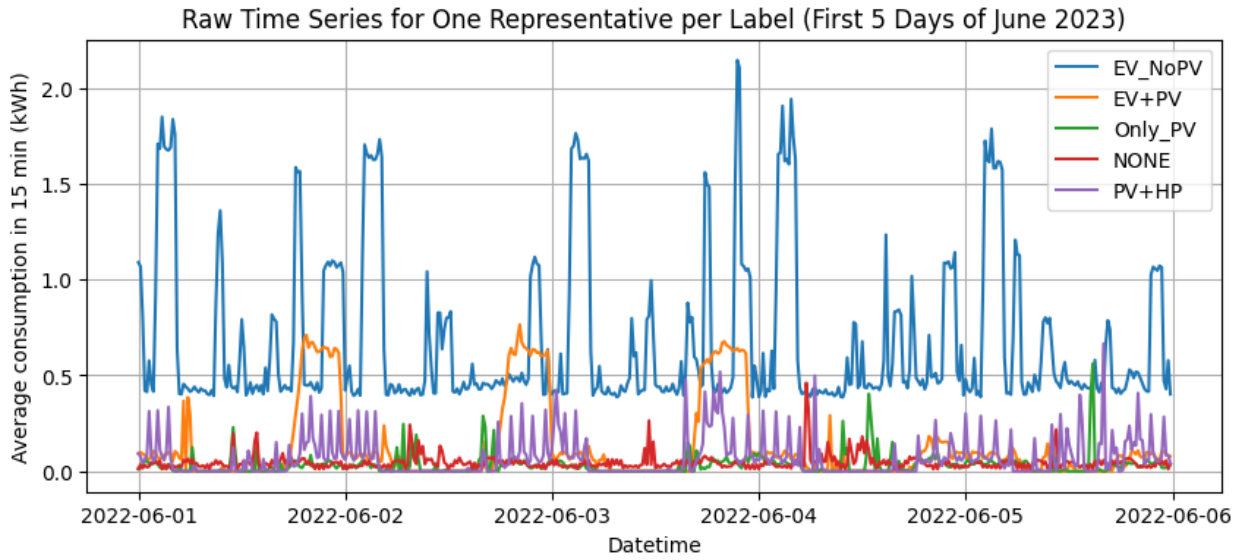

Figure 1 Time series of energy consumption for five different buildings with different labels

Figure 2 visualizes distributions of some initial statistical parameters that also reflect physics of the system and compare them between different groups. Boxplots provide valuable insights for feature engineering and classification. The peak energy consumption (left) and total annual demand (right) could serve as key predictive features for distinguishing between energy user categories. High peaks in EV_NoPV and EV+PV suggest these groups are more energy-intensive in comparions to other groups, making peak demand a strong indicator of EV ownership. The distribution of total energy demand further differentiates users, as Only_PV and NONE have consistently lower consumption.

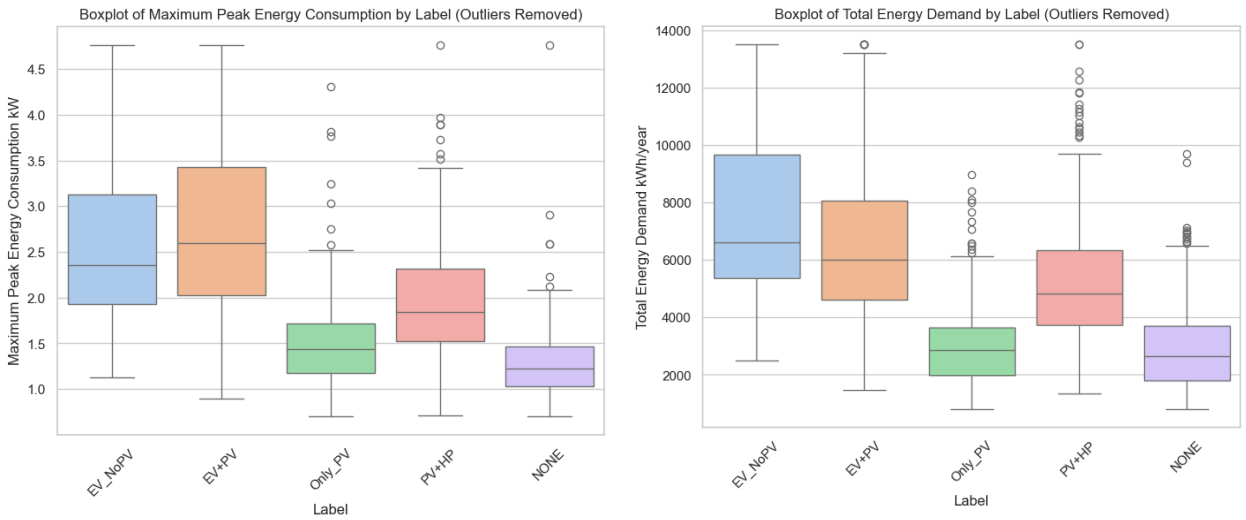

Figure 2 Boxplots depicting maximum peak energy consumption (left) and total yearly energy demand (right) for different labels

3. RESULTS

Searching for the most effective and efficient features is the first step. At this step, we only made

a preliminary comparison to find appropriate features that yield acceptable results with different algorithms. We used nine parameters for the time series in three groups being statistical features, frequency related features, and time series features. In this study, we extracted key statistical features from the electricity consumption time series. The mean that represents typical average energy usage for the building in a month or year. The standard deviation quantifies the variability, indicating fluctuations in consumption over time. The minimum and maximum values provide insight into peak and off-peak energy demand, crucial for detecting extreme usage behaviors. Additionally, skewness measures the asymmetry of the distribution, identifying whether consumption patterns are left- or right-skewed, which is important in distinguishing usage trends across different appliances. Finally, kurtosis assesses the presence of outliers by measuring the heaviness of the distribution tails, helping to detect unusual or extreme energy consumption events. A list of features with their abbreviations used in this study are listed in Table 2.

Table 2 A list of features with their abbreviations used in this

Feature Name	Abbreviation	Description
Mean	Mean	Average energy usage per month or year.
Standard Deviation	Std	Measures variability in energy consumption over time.
Minimum	Min	Lowest energy usage recorded in the time series.
Maximum	Max	Highest energy usage recorded in the time series.
Skewness	Skew	Indicates asymmetry in energy usage distribution.
Kurtosis	Kurtosis	Kurtosis
Summation	Sum	Summation of energy throughout the year

The features can be calculated on any given time interval being annual, monthly, weekly, daily, and even hourly. However, they may become inefficient and appear as noise if the time interval is not long enough. We conducted an exercise to find out appropriate interval for such ML classification application. We first trained models with annual, monthly features as reported in Figure 3 (left monthly, right annual). It is seen in the graph that monthly features, in total 108 features, significantly outperform the models trained with annual features, with 9 features. moreover, Random Forest in both cases stands out as the best algorithm in this application. Then the most important periods were selected from the year and feature for weekly intervals were extracted and used for training to investigate if weekly intervals can improve modelling outcomes. Weekly analysis with 468 features to 180 features did significantly increase model accuracy. Note that this part of the exercise is not documented in this article due to limitation length of the article.

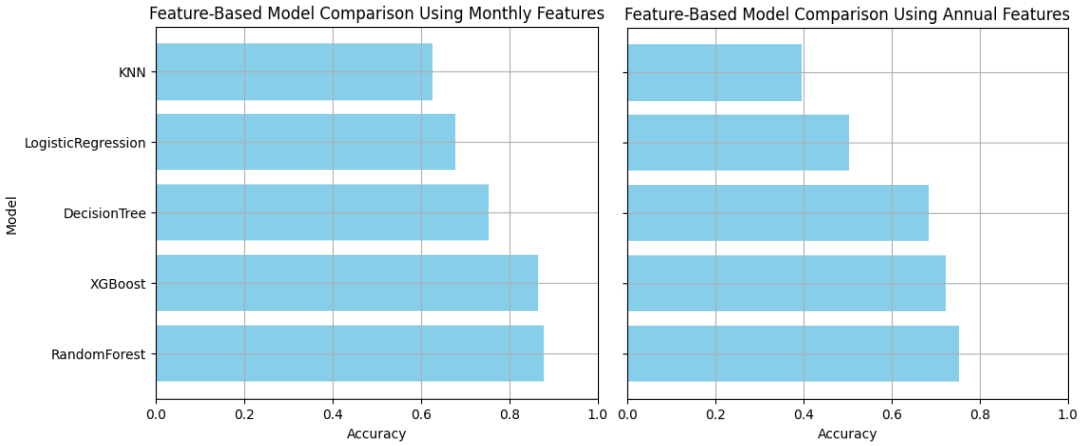

Figure 3 Comparison between different algorithms and different number of features for training ML model. Accuracy refers ratio of correct label prediction to total samples in the test set.

The hyper parameter tuning step improved the model accuracy, 90% in comparison to 85% in initial step. The optimized model was used to predict labels of validation dataset and confusion matrix in figure 4. The confusion matrix for the Random Forest model illustrates the classification performance across five categories: EV+PV, EV_NoPV, NONE, Only_PV, and PV+HP. The diagonal elements represent the number of correctly classified instances for each category, while off-diagonal values indicate misclassifications. PV+HP might have overlapping feature distributions, leading to classification challenges. Overall, the confusion matrix shows that the model performs well in distinguishing the categories, with particularly high accuracy for the "NONE" category. However, some misclassifications occur between EV+PV, Only_PV, and PV+HP. To further continue for production models there are ways to improve the model performance. This includes further feature separation or additional tuning, possibly through more refined feature engineering or hyperparameter adjustments. The general trend suggests that the model can distinguish between distinct groups effectively but struggles slightly when categories share similar characteristics such as PV. Note that Std_M6 means standard deviation the electricity load in month 6 and other features can be read similarly.

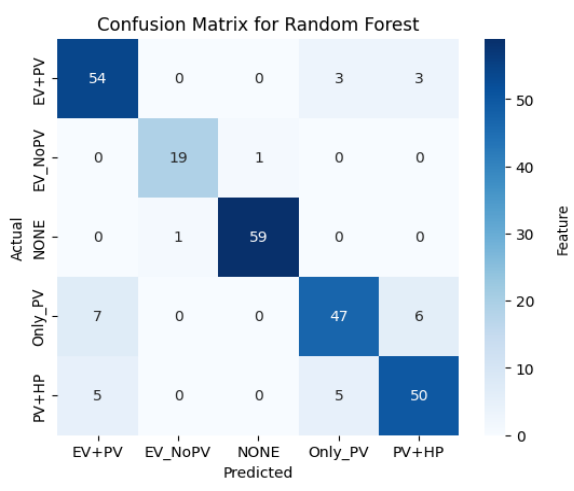

Figure 4 Confusion Matrix for the best model

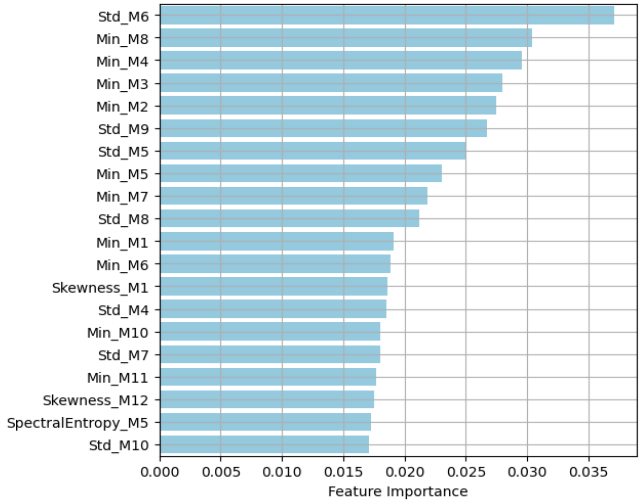

Figure 5 The top 20 most important features for the best model

The cross-validation accuracy averaged 84.33% ± 4.71%, meaning that while the model performs well, there is some variability across different training subsets. The standard deviation of 4.71% suggests moderate fluctuations, indicating that while the model is relatively stable, performance may slightly depend on the data split. Overall, the model demonstrates strong generalization capabilities, particularly excelling in classifying certain categories with high precision and recall.
The bar chart in figure 5 illustrates the top 20 most important features in the Random Forest model, ranked by their feature importance scores. The highest-ranked feature, Std_M6, exhibits the greatest influence on the model's predictions, followed closely by Min_M8, Min_M4, and Min_M3. The distribution of feature importance indicates that both standard deviation (Std) and minimum (Min) statistical measures play a significant role in the model, along with contributions from skewness and spectral entropy. This analysis highlights the key variables driving the model's decision-making process, offering insights into the most relevant factors in the dataset. The results imply significance of statistical features in comparison to frequency-based features. Moreover, it cannot be deducted that only certain months will suffice for training a model in this application. On the other hand, it shows that the model does not require extensive time series with detail that may be in contrast with privacy aspects. Hence, this application can easily be upscaled for use in urban scales. Data providers can simply extract only the statistical parameters and only report those to data users.

4. DISCUSSION

Figure 6 illustrates both normalized time-series signals (left) and their corresponding frequency-based representations (right) for five random buildings with different labels from the dataset. It was previously observed in the results section that statistical features were sufficient for training the model, implying that frequency-based features did not contribute additional information about the labels. To further investigate this, we standardized time series per building and analyzed representative weeks to check whether frequency patterns varied significantly across different labels. The results in these figures suggest two possible conclusions. First, the lack of strong differentiation in frequency-based features across labels indicates that feature-based approaches, such as statistical and temporal metrics, are more effective for classification. Second, this behavior might not be consistent across all the time series, meaning frequency-based patterns may exist but are not generalizable across the entire dataset, limiting their usefulness for model training. Consequently, statistical features remain the primary method for classification, while frequency-domain features do not offer significant improvements in distinguishing between energy consumption behaviors.
An important input to UBEM is installed energy intensive devices in buildings. The provided method will enable energy modelers to generate synthetic data related to large energy consumers only from time series data. These meta data attached to electricity time series will enrich the input data for a more detailed modeling. Detailed models allow for accurate and practical modeling and consequently actionable outcomes.

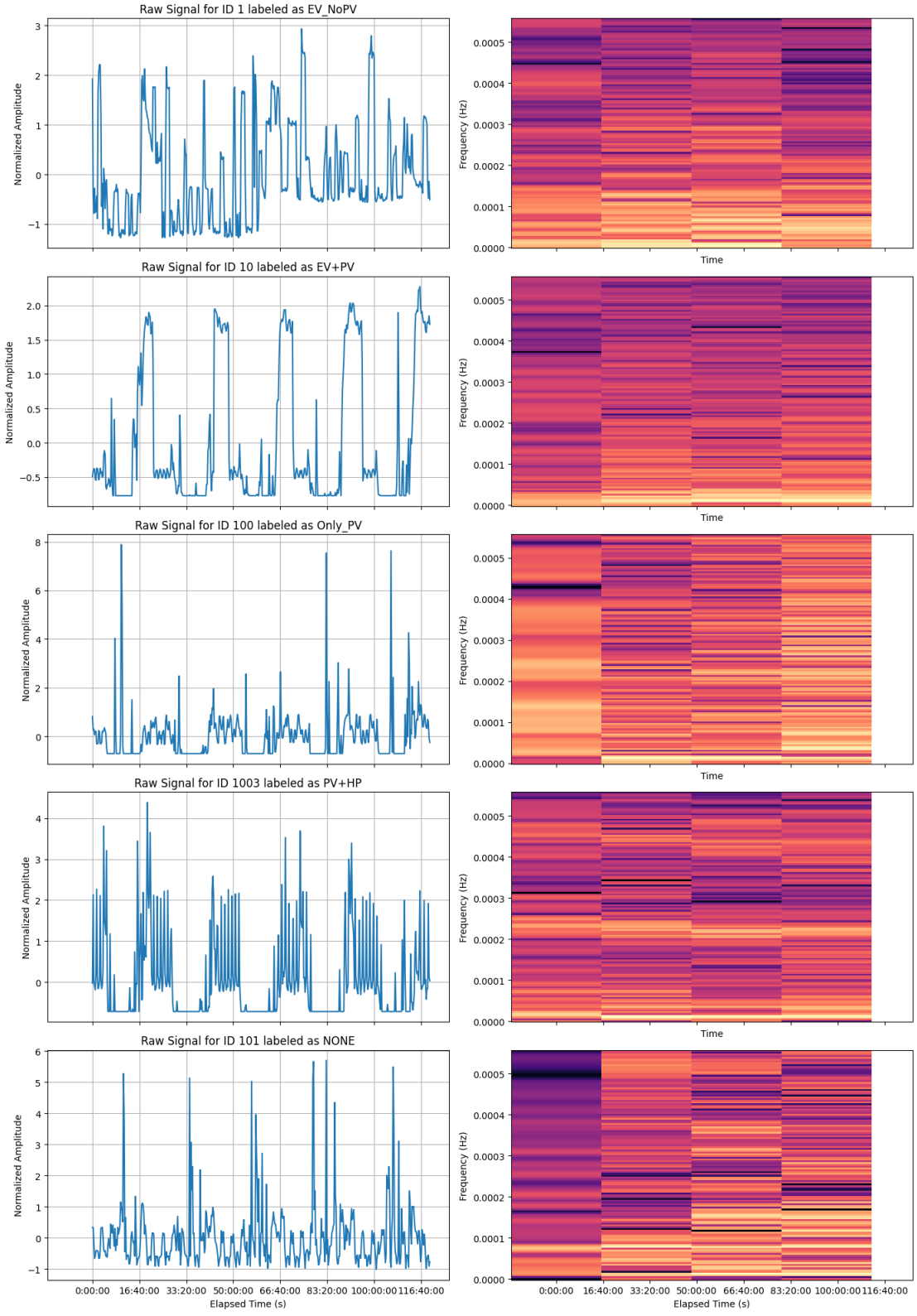

Figure 6 Comparison between raw time-series signals (left) and their corresponding frequency-based representations (right) for different labels.

5. CONCLUSION

This study demonstrated the application of machine learning techniques to identify large electricity-consuming assets, such as solar panels, electric vehicles, and heat pumps, from residential electricity consumption time series. The results showed that statistical features extracted from time series data were highly effective in training the model, achieving an accuracy of over 90%. Frequency-based features, on the other hand, did not provide additional predictive value, indicating that statistical and temporal characteristics are more relevant for classification. The analysis also revealed that monthly features (108 features) significantly improved model performance compared to annual features (9 features), suggesting that a finer temporal resolution enhances predictive accuracy. Additionally, the model demonstrated strong generalization capabilities, although periodic retraining may be required due to seasonal variations. The proposed approach can be instrumental in urban building energy modelling by providing insights into the distribution of high-energy-consuming assets across the residential sector. This can support policymakers and energy providers in optimizing energy management strategies and promoting decarbonization efforts. Future work could explore advanced feature engineering techniques and address potential model drift to further enhance classification accuracy and scalability. An essential input to improve UBEM is the presence of energy-intensive devices in buildings. The proposed method uses electricity time series to generate synthetic metadata for major energy consumers, enhancing model inputs for more detailed and actionable energy simulation outcomes.

ACKNOWLEDGEMENTS

This research was funded by MODERATE project within Horizon Europe research and innovation programme under grant agreement No 101069834. Views and opinions expressed are however those of the author(s) only and do not necessarily reflect those of the European Union or CINEA. Neither the European Union nor the granting authority can be held responsible for.

REFERENCES

Bedi, J. and Toshniwal, D. (2019) 'Deep learning framework to forecast electricity demand', *Applied Energy*, 238, pp. 1312–1326.

Fluvius (2024). https://opendata.fluvius.be/, accessed 11/10/2024.

Guo, R., Shamsi, M. H., Sharifi, M., and Saelens, D. (2024) 'Exploring uncertainty in district heat demand through a probabilistic building characterization approach', *Applied Energy*. https://doi.org/10.1016/j.apenergy.2024.124411.

Hafeez, G., Alimgeer, K.S. and Khan, I. (2020) 'Electric load forecasting based on deep learning and optimized by heuristic algorithm in smart grid', *Applied Energy*, 269, p. 114915.

Kim, H., Park, S., and Kim, S. (2023) 'Time-series clustering and forecasting household electricity demand using smart meter data', *Energy Reports*, 9, pp. 4111–4121. https://doi.org/10.1016/j.egyr.2023.03.042.

Kim, H., Son, H.G. and Kim, S. (2019) 'Short-term electricity load forecasting for institutional buildings', *Energy Reports*, 5, pp. 1270–1280.

Middlehurst, M., Schäfer, P., & Bagnall, A. (2024). Bake off redux: a review and experimental evaluation of recent time series classification algorithms. *Data Mining and Knowledge Discovery, 38(1)*, 1958–2031. https://doi.org/10.1007/s10618-024-01022-1.

Sharifi, M., Kouti, A., Lambie, E., Ma, Y., Boneta, M. F., & Shamsi, M. H. (2023). A Comprehensive Framework for Data-Driven Building End-Use Assessment Utilizing Monitored Operational Parameters. *Energies, 16(20)*, 7132. https://doi.org/10.3390/en16207132.

Wang, W., Hong, T., Xu, X., Chen, J., Liu, Z., & Xu, N. (2019). Forecasting district-scale energy dynamics through integrating building network and long short-term memory learning algorithm. *Applied Energy, 248*, 217–230. https://doi.org/10.1016/j.apenergy.2019.04.085.

Wei, Z., Zhang, T., Yue, B., Ding, Y., Xiao, R., Wang, R. and Zhai, X. (2021) 'Prediction of residential district heating load based on machine learning: A case study', *Energy, 231*, p. 120950. https://doi.org/10.1016/j.energy.2021.120950.

COBEE

6th International Conference on Building Energy and Environment
Eindhoven University of Technology, The Netherlands
6 - 10 July 2025

A proposed peer-to-peer Circular Asset Management System for process planning in modular construction

Benno Felix Fridolin Jochems[1], Gautham Ramana Moorthy[1], Claudia Fecarotti[1], Pieter Pauwels[2]

[1] *Department of Industrial Engineering and Innovation Sciences, Eindhoven University of Technology, Eindhoven, Netherlands, b.f.f.jochems@tue.nl, g.k.ramana.moorthy@tue.nl, c.fecarotti@tue.nl*

[2] *Department of the Built Environment, Eindhoven University of Technology, Eindhoven, Netherlands, p.pauwels@tue.nl*

SUMMARY

As the construction industry is increasingly reducing resource consumption and waste, modular construction (MC) presents a key opportunity for enhancing circularity. Present research, however, has been focused on optimising production processes, instead of enabling efficient reuse of materials and components. This hinders an exploitation of the full potential of MC to create a circular material flow. Since realisation of circular material flows necessitates close collaboration of various stakeholders in the supply chain network, state-of-the-art knowledge on information sharing and circular processes in the construction industry is synthesised from a supply chain perspective. Furthermore, a Circular Asset Management System (CAMS) comprising a Peer-to-Peer information system and digital tools is proposed. This information system is intended to build upon existing information containers and inform digital tools supporting decision making, thus providing the means to track and trace modular components cycling repeatedly through the supply chain.

Keywords: circular economy, modular construction, Circular Asset Management System (CAMS), supply chain

1. INTRODUCTION

The construction sector has been identified as a priority area in the current effort of transitioning to a circular economy (CE) (Giorgi et al., 2022). However, the fragmented nature of the construction supply chain and the lack of suitable information sharing across stakeholders throughout all life-phases of buildings, are among the main barriers towards full implementation of circular strategies (Giorgi et al., 2022). To overcome this, the development of efficient strategies for information sharing among this distributed network of stakeholders is crucial (Hossain et al., 2020), as well as changes in behaviour and viable business models. While the method of prefabricated modular construction offers significant potential for circularity (Iacovidou et al., 2018), challenges regarding the information flow prevail, e.g. availability, quality, machine-interpretability and upkeep of information during operation phase (BAMB, 2017; Kedir et al., 2021). Modular construction, an off-site construction method employing standardised units, was shown to reduce the risk of acci-

dents by 80%, capital cost by10%, wastage by 76% compared to traditional means of construction by removing 90% of on-site activities in favor of digital and industrialised production processes (Abdelmageed and Zayed, 2020). It thus offers economic and environmental benefits "upstream", while generating digital information as a side-product. However, its potential to create a sustainable construction industry will not be exploited until existing modularity and digital information is leveraged throughout the operations stage and at a building's End of Life (EoL) to extend the service life of used products, ultimately resulting in circular material flows (BAMB, 2017; Iacovidou et al., 2018; Kedir et al., 2021). This necessitates close collaboration of various stakeholders and the ability to track and trace products throughout changing ownerships and multiple use cycles. In spite of the increasing digitalisation of the construction sector and a long history of research on such product-specifying data sets, practitioners still lament the lack of a respective digital solution. The objective is to facilitate storage and continuous updating of high-quality information reflecting the journey of individual building components, which can then be shared among a distributed network of stakeholders (BAMB, 2017).

The aim of this paper is to synthesise the state-of-the-art knowledge on improving information sharing and circular processes in the construction industry, as well as propose a framework integrating digital information and decision supporting tools. Although in-depth reviews on specific aspects of the information flow in the construction industry already exist, a link to supply chain networks in modular construction as found in practice is missing. Moreover, there is a lack of concepts for translating theoretical knowledge into action. With this paper, we intend to fill this gap by relating existing knowledge from the scientific literature to a supply chain network for MC as found in practice, and proposing a Circular Asset Management System (CAMS). Furthermore, we do not focus on the relevance of information flow per se, but explicitly highlight its instrumental role when used to support process planning of different activities throughout the life cycles of buildings.

2. METHODOLOGY

A model of the supply chain network serves as a starting point for this study (see Fig. 1, left). We modelled the supply chain according to reports of industrial partners within the research project *Modular Prefabricated Construction* by *TKI Dinalog*, who confirmed concurrence with their practices, and we assume the model to be representative for the MC industry. Based on this model, various activities posing requirements on the information flow are inferred. The observed activities include, but are not limited to: material acquisition, manufacturing (of new, refurbishment of old modules, and mixed assembly from old and new components), transportation, on-site assembly, operation and maintenance, and EoL processing. Regardless of the life cycle phase in which these activities occur, the necessary information exchanges are characterised by requirements that can be grouped in the following themes: structure, storage, and provision of information, as well as respective standards for harmonisation of practices (see Fig. 1, right). The described methodology is illustrated in Fig. 1.

This information, however, only becomes useful if accessed by respective tools to inform said activities. Following a system of systems approach, we dissect the supply chain network into three kinds of layers: an information layer of distributed digital information, a tools layer represent-

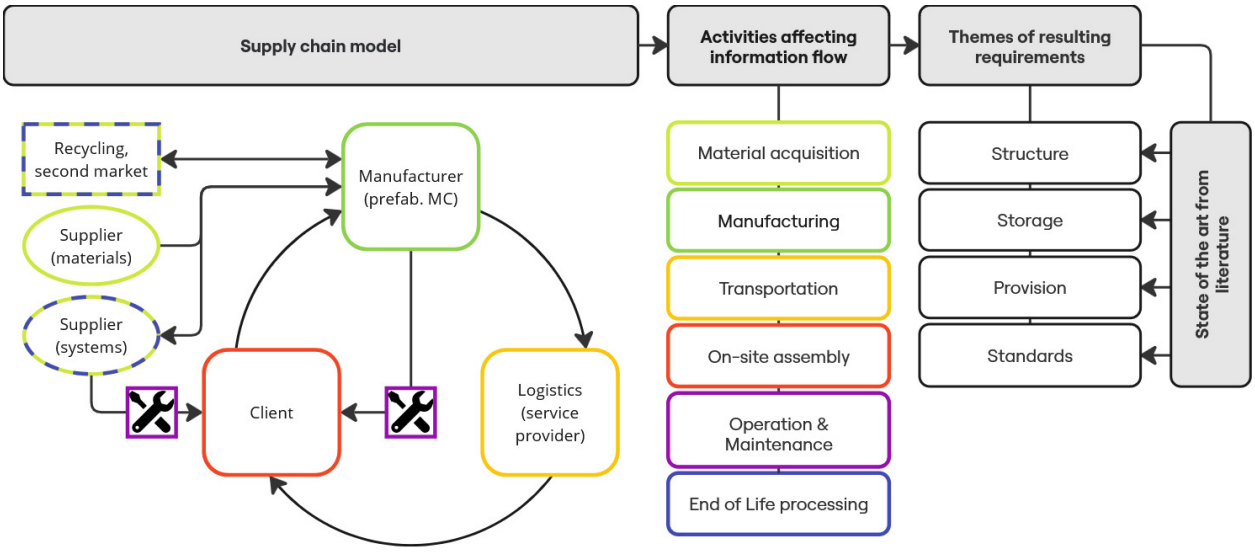

Figure 1. Research methodology: Activities (colour-coded to match elements of the supply chain model) posing requirements on the information flow are inferred from a model of the supply chain network, leading to the synthesis of literature on structure, storage and provision of information, as well as respective standards (own representation).

ing software applications supporting decision making and process optimisation, and the process layer reflecting operational activities of stakeholders. In this system of interdependent systems, the process layer requires information to base decisions on, the information layer feeds the software applications of the tools layer, which finally inform activities of the process layer. Hence, we propose the integration of digital tools with a Peer-to-Peer (P2P) information system, aiming to foster transparency, streamline collaboration, and enhance decision-making capabilities by effectively addressing the challenges of a fragmented linear supply chain and unlocking MC's full potential for realising circular processes.

The information layer and state-of-the-art knowledge in respect to the deducted themes, as gathered from present literature, is presented in the following subsections. The proposed Circular Asset Management System (CAMS), comprising digital tools for optimising processes and streamlining operational flow and the underlying P2P information system, is presented in section 3.

2.1. Information Structure

Material Passports (MP), defined as a digital interface that is specific to a single product and represents a set of information gathered throughout its life cycle (van Capelleveen et al., 2023), have emerged as the dominant concept for structuring and capturing product information in the built environment. Depending on the industry and context, the terms Digital Product Passport (DPP) and Material Passport (specifically common in the built environment) are used interchangeably to describe a data template structuring information such as properties and composition of elements. DPP is used to refer to any passport in the remainder this study, because it aligns more intuitively with the preferred idea of reusing components compared to salvaging them for recycled raw materials, is cross-sectoral and DPPs are backed by a EU regulatory framework (to be elaborated in subsection 2.4). An abundance of research studying DPPs from various perspectives exists, in-

cluding data requirements and their ability to support circular practices. While the comprehensive reviews of van Capelleveen et al. (2023) and Çetin et al. (2023) can be consulted as frameworks on the content of DPPs, it is worth highlighting the need for DPPs to reflect the individual product history (commonly referred to as *track and trace*), as well as transport and storage requirements, so they can support a circular supply chain by informing activities within. Industrialised means of construction, as employed in MC, present a special opportunity to automatically generate DPPs from digital information that is often readily available in existing manufacturing systems and BIM models (Kedir et al., 2021). Since DPPs need to reflect the temporal product history, however, they cannot be treated as static documents but need to capture dynamic data throughout the product's life cycle.

2.2. Information Storage

Projects such as Madaster and Buildings As Material Banks (BAMB) envision a network of information on materials that are currently in use, thus highlighting the need for storing and sharing data (BAMB, 2017). Generally speaking, product information can either be stored in a centralised database (like the Madaster platform), or in a distributed manner in containers related to individual assets (like Asset Information Models). While both approaches are plausible, Sauter et al. (2019) argue against data storage in silos separate from the information owner and in favour of linking distributed sources to establish a distributed network of information. In a small-scale experiment, Byers and de Wolf (2023) experimented with the association of product-specific information to components of a small temporary structure. Struggling with the implementation of dynamic process information, they evolved their system from a relational database to employing a NoSQL database, highlighting the greater flexibility and the ability of their final solution to meet the Create, Read, Update, Delete (CRUD) requirements.

2.3. Information Provision

Information gathered on a specific product needs to become available to a distributed network of stakeholders to inform relevant activities while it cycles through a circular supply chain. Aside from collecting and providing information in a centralised database, the concept of Linked Data (LD) relies on establishing logical connections between pieces of openly published information. The work of Tim Berners-Lee and the World Wide Web Consortium (W3C) serves as a framework for publishing accessible and machine-interpretable Linked Data, highlighting the additional benefit of allowing information that is represented following the Resource Description Framework (RDF) to be searched and queried across platforms (Berners-Lee, 2006). Linked Data relies on ontologies as a common language for the semantic representation of data. Such ontologies for DPPs and asset management data were presented by Kedir et al. (2021) and Polenghi et al. (2021), respectively. Sauter et al. (2019) present ontologies for describing elements necessary for a material exchange between different actors of the supply chain network and for classifying materials, products and activities in the context of circular economy. As a demonstration, the demo Madaster DPP is converted to RDF data using said ontologies.

2.4. Standards

The global Building Information Modelling (BIM) standard ISO 19650 (2018) offers a framework for defining information exchanges. It can thus be used by stakeholders to define requirements on their information exchanges in a specific context. It can be applied to define requirements on the

content and means of information exchanges connected to a circular product flow, but only when involved stakeholders are known. Hence, such an application is possible in the modular construction industry, where stakeholders form a more constant network of lasting business relations, but not feasible in project-based supply chains of traditional construction. ISO 23387 (2020) defines requirements on information exchanges on a technical level, specifying data formats, for example. As part of the US-American National BIM Standard (NBIMS-US)[1], the COBie specification is an example for a standardised data template and schema. The standard defines a minimum set of required data attributes that can be extended to fit national regulations or a user's preferences, focusing on the handover of information for operation and maintenance after conclusion of the production phase. The delivered COBie data (non-graphical), together with a graphical model of the asset, forms what ISO 19650 (2018) defines as an Asset Information Model (AIM). The EU Ecodesign Directive[2], which is applicable to products for the building industry, demands the mandatory introduction of DPPs. The directive thereby foresees DPPs to be stored in a decentralised system by economic operators (such as manufacturers) or service providers (such as Madaster). No such system is available yet, indicating the need for research in this regard. The required content of DPPs is to be defined in ISO 59040 (2025). However, a data template from the leading initiative is already available[3] and depicted in Fig. 2.

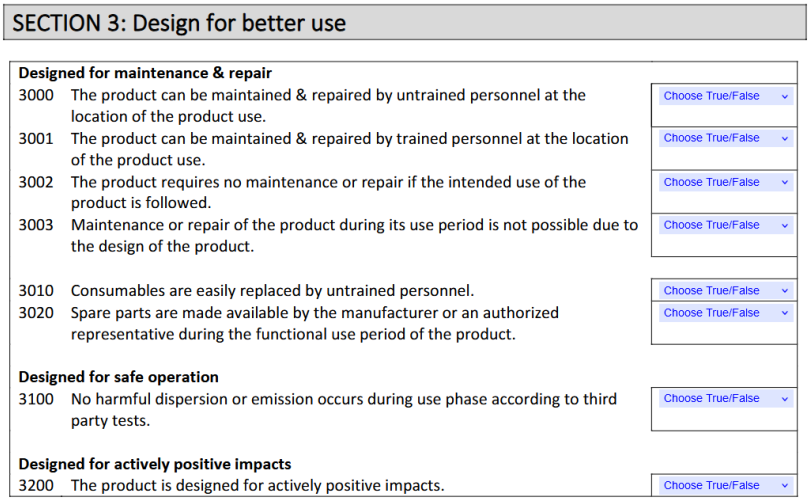

Figure 2. Extract of product passport suggested by PCDS Luxembourg (document created by +ImpaKT Luxembourg for the Ministry of the Economy of Luxembourg)

3. IMPLICATIONS FOR PROCESSES

So far, this paper discussed the information layer necessitated by activities of the supply chain network to feed decision support tools used to improve operational activities. To convert information into an actionable system enabling transformative improvements in operational flows across the MC industry, we propose the integration of digital tools and a Peer-to-Peer (P2P) informa-

[1]NBIMS-US V3 (https://www.nibs.org/nbims/v3, accessed 24.01.2025)
[2]Regulation (EU) 2024/1781 (https://eur-lex.europa.eu/eli/reg/2024/1781/oj/eng, accessed 24.01.2025)
[3]PCDS Luxembourg (https://pcds.lu/pcds-system/, accessed 24.01.2025)

tion system within a Circular Asset Management System (CAMS). The envisioned CAMS system is presented in the following section, while its potential for enhancing collaboration, optimising processes, and streamlining operational flow is discussed.

3.1. A Peer-to-Peer Information System

Various different definitions of "Peer-to-Peer" systems exist, but there seems to be a consensus on the key characteristics: they employ a decentralised architecture of interconnected nodes able to self-organise into a network and adjust to changes to that network, and are used for sharing resources, e.g. information (Staab and Stuckenschmidt, 2006). P2P information systems excel in the actuality of information, because direct referral to the source negates the need to manage changes, as well as the flexibility of the system by allowing sources to be added (Staab and Stuckenschmidt, 2006). In the context of the modular construction industry, the nodes of the proposed P2P information system represent strategic elements of the supply chain and are built on existing systems wherever possible. Manufacturers, suppliers and their respective enterprise information systems come to mind, as well as owners of assets and respective information models; the exact architecture will need to be determined in future research. The proposed system aims to enable direct exchange among trusted stakeholders, thus also providing trust in shared information.

Product passports as the dominant concept for structuring product information have been presented in section 2. As for the acquisition of information from existing systems, it is apparent that the transfer of information from a BIM model (where it is often first generated or collected) to a possible DPP is well understood. Furthermore, requirements on the contents of such a DPP for supporting circular product flows have been researched and reviewed and can thus also be deemed readily available. The upcoming ISO 59040 (2025) standard will harmonise the content of DPPs, which is necessary to allow seamless information exchanges across the industry. However, the data template available at this point is only applicable to a product type (think fridge X of brand Y), but not specific to an individual item (*the* fridge you bought). Consequently, it also does not allow to reflect the service history of a specific component. While the ISO 59040 represents a significant step towards harmonising product information and is yet to be published in its final version, the currently available data template thus fails to address an aspect highlighted as crucial in research: the ability of DPPs to reflect temporal data (Munaro and Tavares, 2021). It is noteworthy, though, that both ISO 59040 and the EU Ecodesign Directive foresee DPPs to be stored de-centrally, supporting the proposed P2P approach. The necessary technology to support establishing a P2P network of linked pieces of openly shared data is available in the form of Linked Data technologies and open data (industry) standards by the W3C. While neither ISO 19650 (2018) nor the related COBie specification address the challenges of tracking and tracing items that might be installed in multiple assets throughout their life cycle, it has been shown that the underlying IFC schema can be utilised to link information from DPPs stored at and provided by a manufacturer (Jochems et al., 2024). STEP files, the most common file format of IFC models, are notoriously difficult to extract and share partial data from, though. Using the JSON format would simplify the exchange of partial model data and dynamic updating of models (Berlo et al., 2021).

3.2. Supporting Decision-Making with a Circular Asset Management System

The purpose of providing information via the proposed P2P system is to inform and enable digital tools to support decision-making and streamlining operations in the supply chain. One of the

core challenges of a circular construction industry is the ability to track and trace products cycling through the supply chain (Hossain et al., 2020). Digital Twins (DT) have the potential to be such a tool that builds upon the information layer to illustrate location and individual history of products, i.e. track and trace components. In the context of this study, DTs will refer to virtual representations of the supply chain and assets within, and serve as an example for the synergy between shared information, digital tools and the support of operational processes. During the production phase, DTs of the supply chain reduce overall transportation and logistics costs by enabling real-time monitoring of material movements, thus improving delivery schedules, minimizing waste, and reducing delays and material damages. In the context of Receiver-Led Consolidation programs for example, such digital integration has demonstrated quantifiable impacts: operational savings for carriers ranging from $376,906 to $1,186,128 per day, a reduction of 33,445 to 104,255 vehicle-miles traveled per day, and per-delivery reductions of approximately 6 miles and 50 minutes (Holguín-Veras and Sánchez-Díaz, 2016). Additionally, DTs provide real-time insights into site conditions and module fitment, enabling the rapid resolution of assembly issues, reducing project delays, and improving coordination. (Opoku et al., 2021). Throughout the operation stage, DTs of built assets enable predictive maintenance by collecting and analysing performance data in real time, extending life of on-site facilities and reducing downtime (Lee et al., 2015). Reaching an asset's EoL, the availability of maintenance histories allows data-driven decisions on further processing of components (e.g. reuse, refurbishment or recycling), maximising the lifespan of modular components (Byers and de Wolf, 2023). Consequently, the combination of digital information and appropriate tools can be said to facilitate the coordination of circular material flows. Hence, we propose the integration of P2P information sharing with decision supporting tools – together forming a Circular Asset Management System (CAMS).

4. CONCLUSION

A model of the supply chain network, based on the observation of industry practices, allowed the identification of several themes of resulting requirements on the information flow within (information structure, storage, provision, and respective standards). Apart from advancing research in these areas (focusing on increasing granularity to include product information specific to individual items and scaling up dynamic information systems to connect data from multiple sources across stakeholders), efforts should be funnelled into closing the gap between theory and practical application. Addressing this, a Circular Asset Management System (CAMS) comprising a Peer-to-Peer information system and digital tools supporting supply chain activities was proposed. This information system is intended to build upon existing information containers, creating a network of nodes representing strategic elements of the supply chain. Digital tools can subsequently access available information, and are aimed to support decision making and provide the means to track and trace modular components cycling repeatedly through the supply chain. In future research, the proposed CAMS is intended to be developed further in terms of architecture of the P2P information system and form of information exchanges, and implemented in practice, eventually.

ACKNOWLEDGMENTS

This research is part of the project *Modular Prefabricated Construction: a circular asset management system for closed-loop supply and logistics chains* by *TKI Dinalog*.

REFERENCES

Abdelmageed S. and Zayed T., 2020. A study of literature in modular integrated construction - Critical review and future directions. Journal of Cleaner Production 277, 124044.

BAMB, 2017. Buildings as Material Banks and the need for innovative Business Models. Buildings As Material Banks, Brussels, BE.

Berlo L. van, Krijnen T., Tauscher H., Liebich T., Kranenburg A. van, and Paasiala P., 2021. Future of the industry foundation classes: towards IFC 5. Proceedings of 38th International Conference of CIB W78. ITC Digital Library, 123–137.

Berners-Lee T., 2006. *Linked Data*. URL: https://www.w3.org/DesignIssues/LinkedData.html (visited on 01/27/2025).

Byers B. and de Wolf C., 2023. QR Code-Based Material Passports for Component Reuse Across Life Cycle Stages in Small-Scale Construction. Circular Economy 1.

Giorgi S., Lavagna M., Wang K., Osmani M., Liu G., and Campioli A., 2022. Drivers and barriers towards circular economy in the building sector: Stakeholder interviews and analysis of five European countries policies and practices. Journal of Cleaner Production 336, 130395.

Holguín-Veras J. and Sánchez-Díaz I., 2016. Freight Demand Management and the Potential of Receiver-Led Consolidation programs. Transportation Research Part A: Policy and Practice 84, 109–130.

Hossain M. U., Ng S. T., Antwi-Afari P., and Amor B., 2020. Circular economy and the construction industry: Existing trends, challenges and prospective framework for sustainable construction. Renewable and Sustainable Energy Reviews 130, 109948.

Iacovidou E., Purnell P., and Lim M. K., 2018. The use of smart technologies in enabling construction components reuse: A viable method or a problem creating solution? Journal of Environmental Management 216, 214–223.

ISO 19650, 2018. Organization and digitization of information about buildings and civil engineering works, including building information modelling (BIM) – Information management using building information modelling. International Standards Organization, Geneva, CH.

ISO 23387, 2020. Building information modelling (BIM) – Data templates for construction objects used in the life cycle of built assets – Concepts and principles. International Standards Organization, Geneva, CH.

ISO 59040, 2025. Circular economy – Product circularity data sheet. International Standards Organization, Geneva, CH.

Jochems B., Johansson P., Kebede R., and Moscati A., 2024. Product Data Provision from Manufacturers to the Construction Industry: A Scoping Literature Review and Case Study Analysis. Proceedings of 41st International Conference of CIB W78. ITC Digital Library.

Kedir F., Bucher D. F., and Hall D. M., 2021. A proposed material passport ontology to enable circularity for industrialized construction. Proceedings of vol. 2. EC3 Conference 2021. European Council on Computing in Construction, 91–98.

Lee J., Bagheri B., and Kao H.-A., 2015. A Cyber-Physical Systems architecture for Industry 4.0-based manufacturing systems. Manufacturing Letters 3, 18–23.

Munaro M. R. and Tavares S. F., 2021. Materials passport's review: challenges and opportunities toward a circular economy building sector. Built Environment Project and Asset Management 11, 767–782.

Opoku D.-G. J., Perera S., Osei-Kyei R., and Rashidi M., 2021. Digital twin application in the construction industry: A literature review. Journal of Building Engineering 40, 102726.

Polenghi A., Acerbi F., Roda I., Macchi M., and Taisch M., 2021. Enterprise information systems interoperability for asset lifecycle management to enhance circular manufacturing. IFAC-PapersOnLine 54, 361–366.

Sauter E., Lemmens R., and Pauwels P., 2019. CEO and CAMO ontologies : a circulation medium for materials in the construction industry. Proceedings of Life-Cycle of Civil Engineering Systems. CRC Press, 1645–1652.

Staab S. and Stuckenschmidt H., 2006. Semantic web and peer-to-peer: decentralized management and exchange of knowledge and information. Springer, Berlin, GER.

van Capelleveen G., Vegter D., Olthaar M., and van Hillegersberg J., 2023. The anatomy of a passport for the circular economy: a conceptual definition, vision and structured literature review. Resources, Conservation & Recycling Advances 17, 200131.

Çetin S., Raghu D., Honic M., Straub A., and Gruis V., 2023. Data requirements and availabilities for material passports: A digitally enabled framework for improving the circularity of existing buildings. Sustainable Production and Consumption 40, 422–437.

Building Physics, Building Envelope and Materials (11:00-12:30 h)

6th International Conference on Building Energy and Environment
Eindhoven University of Technology, The Netherlands
6 - 10 July 2025

Evaluating the Influence of Urban Density on Building Energy Performance and Retrofitting Effectiveness in Various Urban Settings

Mohammad Hamdan [1,2], Hamed Moradi [3], Paria Saadatjoo [4], Mahmoud Murtala [5], Parham Mirzaei [6]

[1]*Department of Architecture, Faculty of Engineering and Design, Middle East University, Amman, Jordan, Mohammad.hamdan@nottingham.ac.uk*
[2]*Department of Architecture and Built Environment, Faculty of Engineering, University of Nottingham, Nottingham, England*
[3]*Department of Construction, Faculty of Architecture and Urban Planning, Shahid Beheshti University, Tehran, Iran, hamy194045@gmail.com*
[4]*Department of Architecture, Faculty of Civil Engineering, University of Tabriz, Tabriz, Iran, paria.saadatjoo@tabrizu.ac.ir*
[5]*Department of Engineering, Aliko Dangote University of Science and Technology, Wudil, Nigeria, mahmoudmurtala@kustwudil.edu.ng*
[6]*Department of Civil and Architectural Engineering - Building Science, Aarhus University, Aarhus, Denmark, parhammir@cae.au.dk*

SUMMARY
Urban Heat Island (UHI) effects have a substantial impact on building energy performance as cities expand, with forecasts estimating that. 70% of the world's population will reside in cities by 2050. While building retrofitting has emerged as a significant method for increasing energy efficiency, current modelling approaches mainly depend on meteorological station data, leaving out complex urban microclimatic variables. This study investigates how building location within an urban neighbourhood impacts retrofit outcomes using ENVI-met 5.6 to generate location-specific meteorological data for five distinct urban density contexts integrated into DesignBuilder 7.3 to assess the impact on energy consumption. The results demonstrate that urban location has significant effects on building energy performance, with consumption ranging from 19% above to 13% below the base scenario under peak summer conditions. Retrofit implementations resulted in a significant 59% reduction in energy consumption in the base case. These findings illustrate the crucial connection between urban morphology and retrofit effectiveness, highlighting the importance of designing location-specific optimisation strategies that consider both building features and urban context.

Keywords: Urban Heat Island, Building Retrofit, Urban Morphology, Building Energy Performance, Computational Fluid Dynamics (CFD).

1. INTRODUCTION

Urbanisation is rapidly increasing, with projections indicating that up to 70% of the world's population will live in cities by 2050 (Organization, 2010). This extraordinary urban development contributes to the Urban Heat Island (UHI) effect, significantly impacting building energy performance and prompting a thorough re-evaluation of energy consumption models (Hamdan et al., 2023; Mombeni & Tariku, 2024). Since the early 2000s, advances in computer technology have allowed for detailed analyses of urban climates (Toparlar et al., 2018), indicating the important effect of the urban wind environment (UWE) on building energy usage. The complex

interactions between wind patterns, heat, and humidity within urban settings substantially shape local microclimates (Jie et al., 2023; Sezer et al., 2023). However, current building energy simulations often depend on rural meteorological data, failing to account for these urban complexities (Vuckovic et al., 2018; Yang et al., 2023). The prevalent use of standardised weather files from non-urban locations introduces significant inaccuracies in energy consumption predictions (Brozovsky et al., 2021). Empirical studies have documented the substantial impacts of UHI on building energy performance. Research in Rome demonstrated that urban areas experience an 18% decrease in heating degree days and a 157% increase in cooling degree days, resulting in significant changes to energy consumption patterns (Zinzi et al., 2018). Similar studies in Beijing revealed urban-rural temperature differences of up to $8°C$ leading to an 11% increase in cooling load and a 16% decrease in heating load (Cui et al., 2017). Recent investigations in Qatar project cooling energy consumption increases of $19 - 33.5\%$ by 2050 (Kamal et al., 2023), while studies in Mediterranean climates forecast cooling demand increases of $37 - 88\%$ (Salvati & Kolokotroni, 2023). The integration of microclimate effects into building energy performance simulations has become imperative for accurate assessment and optimisation (Qiu et al., 2024). This integration enables improved engineering applications and more sustainable building designs while supporting climate resilience goals (Stavrakakis et al., 2021; Tsoka et al., 2021). Advanced simulation methodologies combining CFD with building energy modelling have demonstrated enhanced prediction accuracy, with recent studies showing variations of 3.5% for medium office buildings and 0.5% for high-rise buildings (Feng et al., 2024). Recent studies in New Zealand have demonstrated that urban morphology and UHI effects influence seasonal energy demands, with cooling demand effects of 4.35% in summer and heating demand effects of 2.6% in winter (Jalali et al., 2024). These findings underscore the importance of considering local urban characteristics in building energy assessment and retrofit planning, suggesting that standardised approaches may be suboptimal across different urban contexts. This research systematically investigates the impact of urban morphology on building energy performance and retrofit effectiveness through a comprehensive case study in Amman, Jordan. The study analyses a single residential building positioned across five strategic locations within a dense urban neighbourhood, each representing different urban densities. Using advanced simulation tools - ENVI-met for microclimate analysis and DesignBuilder for energy assessment - the research examines how variations in urban context affect building performance metrics, heat transfer mechanisms, and retrofit outcomes. This integrated approach aims to develop location-specific energy optimisation strategies that consider both building characteristics and urban environmental conditions.

2. METHODOLOGY

A comprehensive methodological framework was used to evaluate the impact of urban morphology on building energy performance and retrofit efficiency in Amman, Jordan. Advanced computational modelling was integrated through a systematic approach encompassing urban context analysis, microclimate simulation, and building energy performance assessment. ENVI-met 5.6 was utilised for comprehensive microclimate modelling, and its computational domain was designed to reflect complex urban interactions. The simulation environment was designed with an ongoing grid resolution of 2m × 2m × 2m, extending vertically to 2.5 times the height of the tallest building to accurately reflect the urban canopy layer. The study evaluated a typical two-story residential building of $450m^2$ as the target building across five urban layouts representing varying density patterns. This systematic approach allowed a detailed examination of how urban

context influences building performance and retrofit outcomes through sequential processes of data collection, simulation, and analysis, thereby providing a strong foundation for better understanding the relationship between urban morphology and building energy efficiency.

2.1 Case Study Area Characteristics

Research was carried out in Amman's Basman neighbourhood (also known as "Dahyat Al-Istiqlal"), a high-traffic region bordered by densely inhabited suburbs. The research region, located at latitude $31.95522° N$ and longitude $35.94503° E$, has around $141{,}423.6\, m^2$ and has heights varying from 890 to 950 meters above sea level (ArabiaWeather, 2024). This location was chosen strategically because it is close (5km) to the official Marka meteorological station, allowing accurate climatic data validation. The district had a variety of urban features, with 132 residential blocks oriented primarily northeast, as shown in Figure 1, which showed the aerial perspective and urban context of the research region.

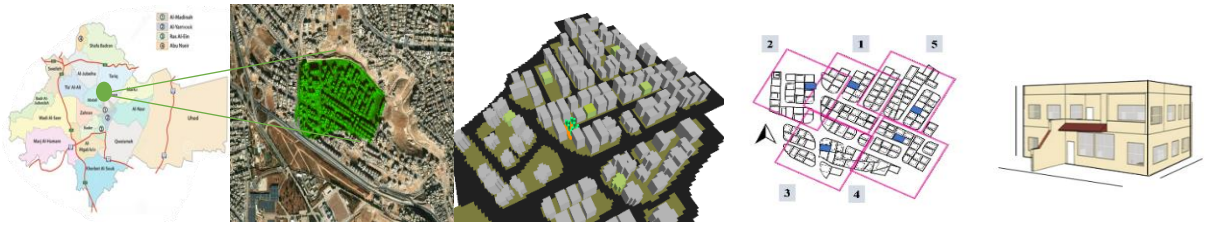

(a) (b) (c) (d) (e)

Figure 1. a) Basman area in Amman map(ArabiaWeather, 2024), b) The map of the target neighbourhood, c) the perspective of the target district, d) the location of five sub-regions, and e) the base case scenario (target building)

Amman's climate was characterised by distinct seasonal patterns, experiencing approximately 320 sunny days annually (Alrwashdeh, 2021). Since 1960, the city's climate has changed significantly, with temperature increases ranging from $0.3°$ to $1.8°C$ in annual maximum temperatures and $0.4°$ to $2.8°C$ in the lowest temperatures (Environment, 2009). Summer temperatures were frequently reported between $28°C$ to $32°C$, whereas winters were occasionally distinguished by snowfall (Potter et al., 2007). A representative two-story residential building with a total area of $450m^2$ was selected as the case study structure. The building's specifications and operational characteristics were detailed in Table 1, which presented comprehensive information about its location, function, envelope properties, and systems.

Table 1. Building energy characteristic settings

Location & Function	Dahyat Al-Istiqlal, Amman (N31°58'23.28", E35°56'28.78"), Residential, 450 m² (Two floors), 9 occupants (0.0156 People/m²)
Envelope Properties	Wall: U = 2.11 W/m²K, (improve: 0.57 W/m²K), Roof: U = 1.02 W/m²K (improve: 0.55 W/m²K), Windows: U = 5.92 W/m²K (improve: 1.59 W/m²K)
HVAC& Temperature	Direct Expansion (DX), Heating: 21°C (setback 12°C), Cooling: 25°C (setback 27°C)
Energy Use	Internal Heat Gains: 2,897 W (peak load), Lighting: 3,260 W (mixed types)

The urban district was systematically divided into five sub-regions, each measuring 200×200 meters, which were selected to represent varying urban densities and morphological

characteristics. Table 2 presents the physical characteristics of these zones, including the number of blocks, occupied and unoccupied areas, and density metrics. This systematic categorisation enabled a detailed analysis of how urban morphology had influenced building performance across different contexts.

Table 2. Physical characteristics of the case study area

Zone	Number of Blocks	Occupied area (m^2)	Unoccupied area (m^2)	O/U	Average Height (m)	Density
1	28	8076.24	31923.75	0.252	11.607	26928.38
2	29	8029.04	31970.95	0.251	11.965	29639.80
3	21	6547.18	33452.81	0.195	11.000	22197.56
4	34	9091.33	30908.66	0.294	12.205	34010.38
5	32	8251.68	31748.31	0.259	12.156	31744.26
Overall	132	39995.49	160004.50	0.249	11.751	…….

2.2 Microclimate-Building Energy Performance Analysis and Coupling Methodology

The research methodology employed a systematic approach to analyse microclimate conditions and their impact on building energy performance. ENVI-met 5.6 was utilised for comprehensive microclimate simulations across each sub-region, with initial simulations conducted using microclimate data from the Marka Airport Meteorological Station for July 26, 2016, identified as the hottest day in the available dataset. The computational domain was configured using the environmental model shown in Figure 2a, which ensured an accurate representation of both the urban neighbourhood and the target building's geometry.

The integration between microclimate simulation and building energy analysis was achieved through a one-way coupling methodology. This process utilised ENVI-met simulation outputs to create modified weather files for each sub-region using the EnergyPlus Weather Converter tool. The coupling mechanism, depicted in Figure 2b, facilitated the incorporation of local microclimate conditions, including temperature profiles, wind velocities, and humidity levels. These detailed environmental parameters were essential for generating accurate weather files for subsequent energy performance simulations.

The simulation phase implemented DesignBuilder 7.3 for comprehensive energy analysis, with parameters calibrated using actual building operational data. This methodological framework, while complex in its implementation, provided a solid framework for understanding the interactions between urban form, microclimate conditions, and building energy consumption patterns. The comprehensive approach enabled a detailed evaluation of how urban morphology influenced building energy performance and retrofit effectiveness across varying urban contexts, ensuring reliable and validated results for the study's objectives.

2.3 Retrofit Scenarios

The retrofit analysis methodology included multiple intervention strategies, which were carefully chosen based on established performance standards and local market availability in Jordan (Shamout, 2018). The comprehensive retrofit approach focused on six key building elements, each optimised for maximum energy performance improvement. Thermal envelope enhancement was achieved through EPS insulation implementation, with thicknesses evaluated between 1-10 centimetres. The thermal bridge mitigation strategy employed metal material solutions, while window performance was upgraded using low-emission double-glazing systems that achieved a U-value of 1.59 W/m²K. External shading was optimised through aluminium devices with depths ranging from 80 to 120 centimetres, complemented by lighting system modernisation that utilised

12w LED fixtures. The domestic hot water system was enhanced through the integration of solar hot water collectors.

The optimisation methodology utilised DesignBuilder's genetic algorithm module to systematically analyse these retrofit combinations. The approach examined multiple parameter combinations using 2,000 comprehensive simulations, considering both performance enhancement potential and practical implementation constraints within the local building context. This stringent optimisation approach ensured that the selected retrofit solutions not only maximised energy efficiency improvements but also remained feasible for real-world application in the Jordanian building market.

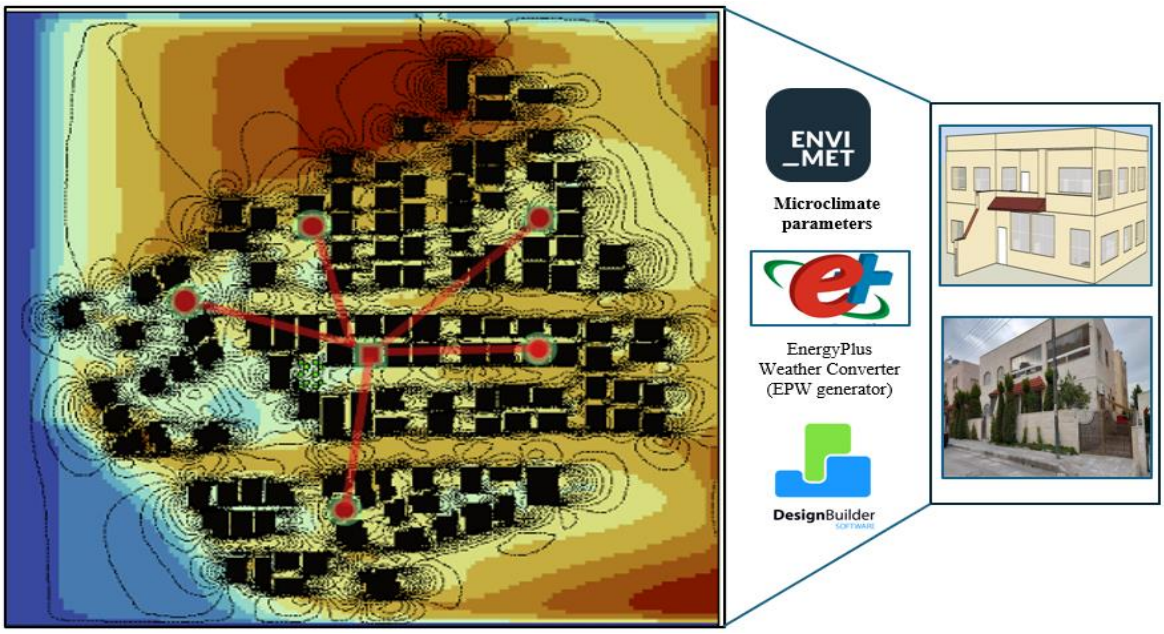

(a) (b) (c)

Figure 2. a) Microclimate neighbourhood model showing building configurations and density patterns, b) coupling methodology diagram, c) target building model

3. RESULT

The results are structured into two main phases. The first phase analyses microclimate variations across different urban densities, including air temperature, relative humidity, wind speed, and long-wave radiation, using CFD simulations. The second phase focuses on the energy performance of the target building, evaluating energy consumption and retrofit effectiveness across five urban locations with varying densities.

3.1 Impact of Urban Density on Microclimate Parameters

The analysis of microclimate parameters across different urban locations demonstrates significant differences influenced by urban density and morphology. As shown in Figure 3a, air temperature variations show a strong connection with urban density patterns, with Location 4 (highest density) exhibiting temperatures up to $2.2°C$ above the base case during peak hours at noon. Conversely, Location 3 (lowest density) records temperatures $1.1°C$ below the base case at the same period, highlighting the substantial impact of urban configuration on local thermal conditions. Relative humidity patterns, illustrated in Figure 3b, show an inverse relationship with urban density. The

highest density location (L4) records humidity levels 9% lower than the base case during peak afternoon hours, while the more open locations (L1 and L5) maintain higher humidity levels, contributing to more moderate microclimate conditions. Wind speed analysis, presented in Figure 3c, demonstrates significant variations across locations, with high-density areas showing reductions of up to 40% in average wind speeds compared to open urban settings.

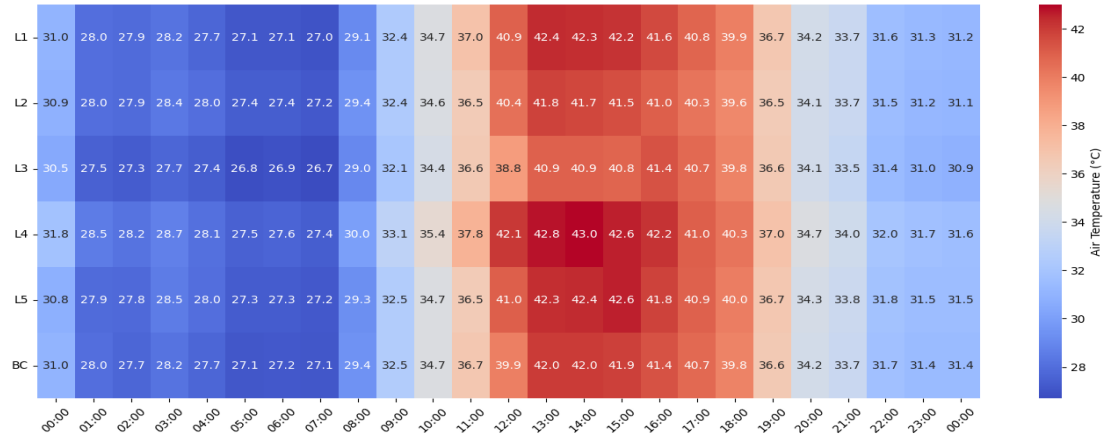

3(a)

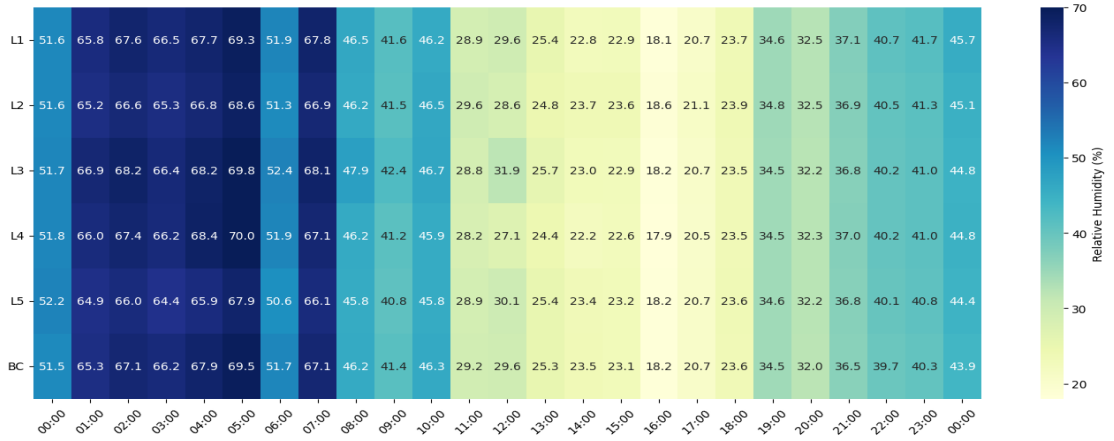

3(b)

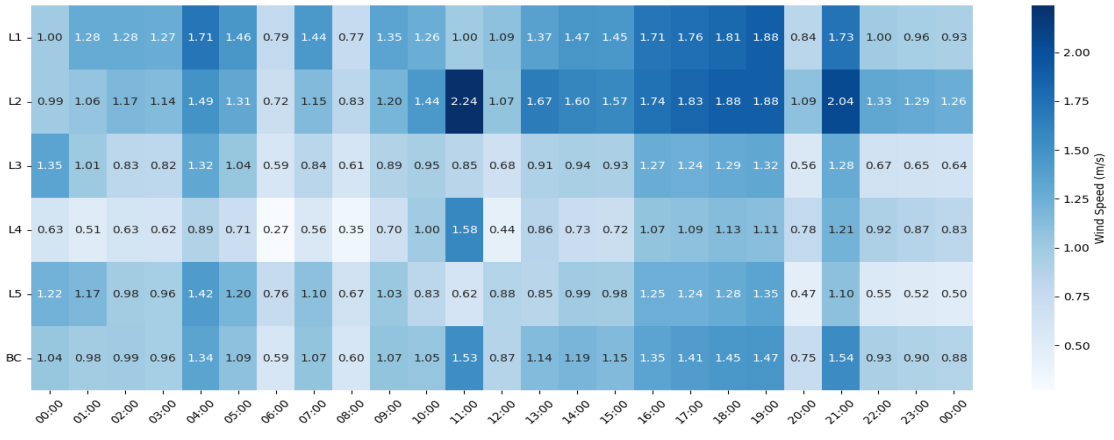

3(c)

Figure 3. a) Air temperature variations across different urban locations, b) relative humidity variations across different urban locations, c) hourly wind speed variations across different urban locations.

3.2 Energy Performance Analysis Across Urban Contexts

The energy consumption analysis shows substantial variations across different urban locations during the hottest day (July 26, 2016). The base case location records a daily energy consumption of $179\ kWh$, while significant variations are observed across other locations. Location 4, characterised by the highest density, demonstrates a 19% increase in energy consumption ($213.01\ kWh$), primarily attributed to reduced wind speeds and increased surface temperatures. In contrast, Location 3, with its more open urban configuration, shows a 13% reduction in energy consumption ($155.73\ kWh$), benefiting from improved natural ventilation and reduced heat island effects.

The impact of urban morphology on retrofit effectiveness is evaluated based on the base case's 59% reduction potential. Location 4's dense urban context limited retrofit effectiveness to approximately 51% improvement (reducing consumption to $104.37\ kWh$), while Location 3's more favourable microclimate conditions enable enhanced retrofit performance, achieving up to 64% reduction (reducing consumption to $56.06\ kWh$). These variations highlight the critical influence of urban morphology on both baseline energy performance and retrofit potential, with denser urban configurations generally showing reduced retrofit effectiveness due to constrained ventilation and increased local heat gain.

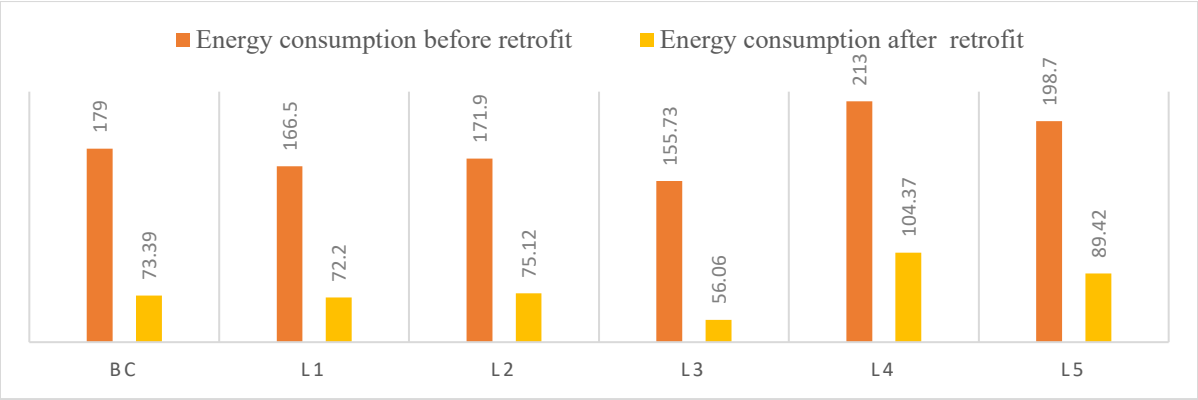

Figure 4. Impact of retrofitting on energy consumption across different urban locations**.**

4. CONCLUSION

This study demonstrated that urban morphology has a crucial impact on building energy performance and retrofit effectiveness in Amman, Jordan. The study found substantial variations in building energy consumption across different urban densities using detailed microclimate and energy analysis, ranging from a 19% rise in high-density blocks to a 13% decrease in more open layouts. The success of retrofit strategies is strongly dependent on the urban context, with high-density areas improving by 51% compared to 64% in more open settings.

These findings highlight the essential function of urban morphology in building energy assessment and retrofit planning. The research concludes that standardised retrofit methods may not be ideal in diverse urban contexts, emphasising the importance of location-specific optimisation strategies that take into consideration both building characteristics and urban conditions. This comprehensive method offers useful information for urban planners and policymakers looking to enhance building energy efficiency in quickly growing cities.

5. REFERENCES

Alrwashdeh, S. S. (2021). Investigation of the energy output from PV panels based on using different orientation systems in Amman-Jordan. *Case Studies in Thermal Engineering*, *28*, 101580.

ArabiaWeather. (2024). https://www.arabiaweather.com/en

Brozovsky, J., Simonsen, A., & Gaitani, N. (2021). Validation of a CFD model for the evaluation of urban microclimate at high latitudes: A case study in Trondheim, Norway. *Building and Environment*, *205*, 108175.

Cui, Y., Yan, D., Hong, T., & Ma, J. (2017). Temporal and spatial characteristics of the urban heat island in Beijing and the impact on building design and energy performance. *Energy*, *130*, 286-297.

Environment, M. o. (2009). *Jordan's Second National Communication to the United Nations Framework Convention on Climate Change (UNFCCC)*.

Feng, W., Chen, J., Yang, Y., Gao, W., Xing, H., & Yu, S. (2024). Multi-objective optimization of morphology for high-rise residential cluster with the regards to energy use and microclimate. *Energy and Buildings*, *319*, 114534.

Hamdan, M., Mirzaei, P., & Gillott, M. (2023). Life Cycle Cost Assessment and Retrofit in Community Scale: A Case Study of Jordan. E3S Web of Conferences,

Jalali, Z., Shamseldin, A. Y., & Ghaffarianhoseini, A. (2024). Urban microclimate impacts on residential building energy demand in Auckland, New Zealand: A climate change perspective. *Urban Climate*, *53*, 101808.

Jie, P., Su, M., Gao, N., Ye, Y., Kuang, X., Chen, J., Li, P., Grunewald, J., Xie, X., & Shi, X. (2023). Impact of urban wind environment on urban building energy: A review of mechanisms and modeling. *Building and Environment*, *245*, 110947.

Kamal, A., Mahfouz, A., Sezer, N., Hassan, I. G., Wang, L. L., & Rahman, M. A. (2023). Investigation of urban heat island and climate change and their combined impact on building cooling demand in the hot and humid climate of Qatar [Article]. *Urban Climate*, *52*, Article 101704. https://doi.org/10.1016/j.uclim.2023.101704

Mombeni, A. G., & Tariku, F. (2024). Urban Heat Island Effect on Building Energy Consumption: ANN Method Application. In *International Association of Building Physics* (pp. 358-363). Springer.

Organization, B. o. t. W. H. (2010). Urbanization and health., *88(4)*, 245–246. . https://doi.org/10.2471/BLT.10.010410

Potter, R. B., Darmame, K., Barham, N., Nortcliff, S., & Mannion, A. (2007). An introduction to the urban geography of Amman, Jordan. *Reading Geographical Papers*, *182*, 1-29.

Qiu, Z., Yong, Q., Wang, J., Liao, L., & Yu, B. (2024). A multi-objective optimization framework for performance-based building design considering the interplay between buildings and urban environments. *Energy Conversion and Management*, *315*, 118793.

Salvati, A., & Kolokotroni, M. (2023). Urban microclimate and climate change impact on the thermal performance and ventilation of multi-family residential buildings. *Energy and Buildings*, *294*, 113224.

Sezer, N., Yoonus, H., Zhan, D., Wang, L. L., Hassan, I. G., & Rahman, M. A. (2023). Urban microclimate and building energy models: A review of the latest progress in coupling strategies. *Renewable and Sustainable Energy Reviews*, *184*, 113577.

Shamout, S. (2018). *Your Guide to Building Envelope Retrofits for Optimising Energy Efficiency Et Thermal Comfort in Jordan*. Jordan GBC.

Stavrakakis, G. M., Katsaprakakis, D. A., & Damasiotis, M. (2021). Basic principles, most common computational tools, and capabilities for building energy and urban microclimate simulations. *Energies*, *14*(20), 6707.

Toparlar, Y., Blocken, B., Maiheu, B., & Van Heijst, G. (2018). Impact of urban microclimate on summertime building cooling demand: A parametric analysis for Antwerp, Belgium. *Applied Energy*, *228*, 852-872.

Tsoka, S., Velikou, K., Tolika, K., & Tsikaloudaki, A. (2021). Evaluating the combined effect of climate change and urban microclimate on buildings' heating and cooling energy demand in a mediterranean city. *Energies*, *14*(18), 5799.

Vuckovic, M., Maleki, A., & Mahdavi, A. (2018). Strategies for development and improvement of the urban fabric: A Vienna case study. *Climate*, *6*(1), 7.

Yang, Y., Gu, Q., Wei, H., Liu, H., Wang, W., & Wei, S. (2023). Transforming and validating urban microclimate data with multi-sourced microclimate datasets for building energy modelling at urban scale. *Energy and Buildings*, *295*, 113318.

Zinzi, M., Carnielo, E., & Mattoni, B. (2018). On the relation between urban climate and energy performance of buildings. A three-years experience in Rome, Italy. *Applied Energy*, *221*, 148-160.

6th International Conference on Building Energy and Environment
Eindhoven University of Technology, The Netherlands
6 - 10 July 2025

The Role of Building Porosity in Enhancing Passive Ventilation in High-Density Urban Street Canyons

Subin LIN[1,2], Jason LEONG[2], Hee Joo POH[1]

[1] *Department of the Built Environment, College of Design and Engineering, National University of Singapore, SDE1, #03-02, 4 Architecture Drive, Singapore 117566s, subin_lin@u.nus.edu*
[2] *Institute of High Performance Computing, Agency for Science, Technology and Research (A*STAR), 1 Fusionopolis Way, 138632, Singapore*

SUMMARY
This study compares buildings with different vertical porosity levels, examining their effects on near-building wind profiles and pedestrian wind velocities, which are critical for ventilation efficiency. We conducted Computational Fluid Dynamics (CFD) simulations using Reynolds-Averaged Navier-Stokes (RANS) equations in ANSYS Fluent to analyze airflow in street canyons. To ensure model reliability, the simulations were validated with experimental data. Results indicate that lower-level porosity, such as Level 1, supports positive ground-level airflow, improving pedestrian-level ventilation without reverse flows. In contrast, higher-level porosity often induces negative ground-level velocities, creating reverse flows that hinder direct ventilation. Smaller porosities are more effective at enhancing ground-level ventilation, while larger porosities improve upper-level airflow. Thus, porosity design should align with specific ventilation needs at different heights. This study highlights the value of integrating building porosity into urban planning to enhance natural ventilation and promote sustainability.

Keywords: Computational Fluid Dynamics (CFD), Building Porosity, Urban Street Canyon

1. INTRODUCTION

Urbanization has intensified built environment density, significantly impacting building energy consumption, air quality, and thermal comfort. High-rise structures disrupt wind patterns, creating stagnation that hinder natural ventilation. Building porosity has emerged as one of the key passive design strategies to enhance airflow, disperse pollutants, and promote sustainable living. Building porosity; through features like permeable facades, void decks, and sky gardens, can facilitate air movement, reduce stagnant zones and improve pedestrian-level ventilation. In tropical cities, where heat and humidity are persistent, building porosity effectively enhances airflow and reduces heat accumulation, and mitigates urban heat, making them essential for sustainable urban environments.

1.1. Problem statement, motivation, and knowledge gap

Building porosity holds significant potential for mitigating urban heat and enhancing passive ventilation, yet it remains under-explored within architectural and engineering fields. Research has historically prioritized other strategies, such as wind catchers, leaving a gap in the systematic study and optimization of building porosity for diverse urban settings. Recent studies

emphasize its critical role in improving natural ventilation and reducing pollutant concentrations, particularly in high-density cities. Despite initial studies on urban microclimates and airflow influenced by building porosity, critical gaps remain in understanding its comprehensive impact on urban airflow patterns and thermal comfort. While prior research has examined street canyon geometry, aspect ratios, and general building configurations on airflow and pollutant dispersion, the specific effects of building porosity—particularly the strategic placement of void decks across different building levels have not been thoroughly investigated. This study employs validated Computational Fluid Dynamics (CFD) simulations to explore the influence of building porosity at varying vertical levels and porosity percentages within urban street canyons (Figure 1). The findings will provide essential insights for optimizing building porosity, and contributing to healthier, more sustainable urban environments.

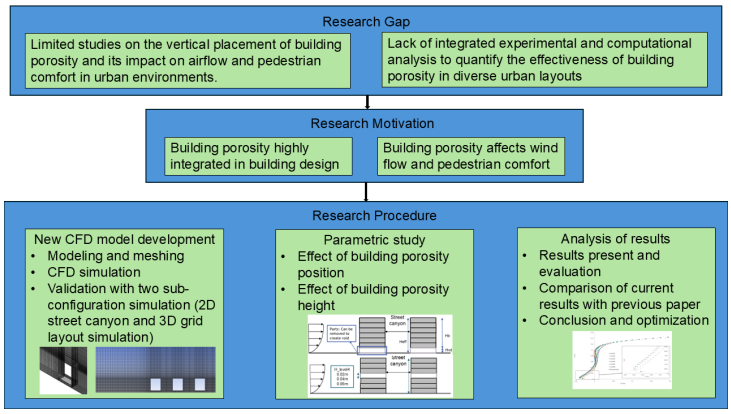

Figure 1. Procedure in this research

2. METHODOLOGY

2.1. Computational domain and grid

CFD simulations were performed at reduced and full scales to ensure the applicability of results to real-world conditions, focusing on achieving Reynolds number independence for accurate flow replication. The computational domain adhered to best practices outlined by Franke et al., 2011 and Tominaga et al., 2008, with upstream and downstream lengths of $5H_{eff}$ and $15H_{eff}$, and a domain height of $5H$ (building model height = 0.14 m). Grid resolution was optimized through sensitivity analysis, details of which are presented in Section 3.1.4.

The grid setup, illustrated in Figure 2 (1), features 2,799,750 hexahedral cells with uniform resolution in the canyon and coarser resolution upstream, above, and downstream. The mesh includes 10 cells per void deck layer, with zero skewness and a maximum expansion ratio of 1.2. These configurations were validated through a mesh sensitivity test to ensure high resolution and reliability of simulation results.

2.2. Boundary conditions

Figure 2 (2) illustrates the boundary conditions applied in this study. A zero normal velocity was imposed on the top surface, while the span-wise (side) surfaces were assigned a stream-wise velocity with a zero-gradient condition. All building walls, including the leeward and windward sides, roofs, and ground surfaces, were subjected to a no-slip boundary condition. The outlet surface was assigned a zero-gradient condition, and atmospheric inlet boundary conditions were applied to the inlet surface, as described in the referenced study Richards and

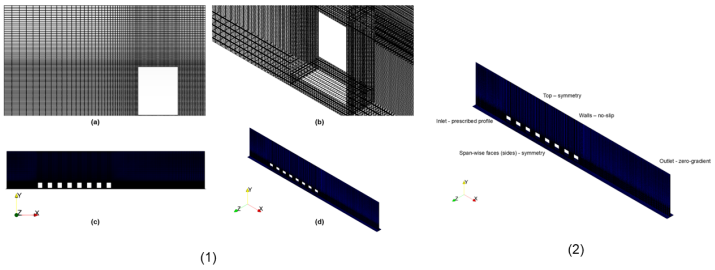

Figure 2. (1) Computational fluid dynamics (CFD) domain mesh: (a) side view of the central plane for the first canyon, (b) 3D view showing only the first canyon, (c) side view of the central plane for the full domain, and (d) 3D view of the central plane for the full domain. (2) CFD domain and boundary conditions for building porosity at level 1 (ground floor), showing the middle plane in the vertical direction (y-axis) and the floor.

Hoxey, 1993. Inlet velocity (U), turbulence kinetic energy (tke), and turbulence dissipation rate (ε) were defined by Equations (1)–(3) below.

$$U = \frac{U_{\text{ref}}}{\kappa} \ln\left(\frac{z+z_0}{z_0}\right) \tag{1}$$

$$tke = \frac{U_*^2}{\sqrt{C_\mu}} \tag{2}$$

$$\varepsilon = \frac{U_*^3}{\kappa(z+z_0)} \tag{3}$$

Where U_* represents the friction velocity calculated using Equation 4, κ is the von Karman's constant (0.41), z is the vertical distance from the ground, z_0 is the surface roughness height, and C_μ is a constant (= 0.09)

$$U = \kappa \frac{U_{(z=z_{ref})}}{\ln\left(\frac{z_{ref}+z_0}{z_0}\right)} \tag{4}$$

Where Equation 1 and Equation 4 can be transformed into a dimensionless velocity profile:

$$\frac{U}{U_{(z=z_{ref})}} = \frac{\ln\left(\frac{z+z_0}{z_0}\right)}{\ln\left(\frac{z_{ref}+z_0}{z_0}\right)} \tag{5}$$

According to previous works from Chew and Norford, 2018, z_0 was set to 0.0002 m, z_{ref} to 0.14, and $U_{(z=z_{ref})}$ to 0.41 m/s for the reduced-scale simulation. For the full-scale simulation, the values were scaled up by a factor of 200, resulting in z_0 = 0.04 and z_{ref} = 28

m. It should be noted that z_0 = 0.04 m corresponds to open terrain, according to the updated Davenport-Wieringa classification Wieringa, 1992. For the full-scale cases, $U_{(z=z_{ref})}$ was set to 2 m/s, consistent with field measurements indicating that a threshold wind speed of 1.5–2 m/s is required to sustain in-canyon vortices.

2.3. Solver settings

All simulations were performed using ANSYS Fluent 2022 R2, employing the steady RANS solver with the standard k-ε turbulence model, chosen for its consistency with experimental results in similar studies. This approach provided a balance between computational accuracy and efficiency. Second-order Gaussian integration with linear interpolation was applied for gradient and divergence schemes, while non-orthogonal corrections were incorporated into the Laplacian schemes. The standard wall function was utilized to enable a coarser mesh, reducing computational costs. Residual tolerances were set to 10^{-5} for all parameters, with convergence achieved when further iterations no longer reduced residuals, in accordance with best practices.

2.4. Mesh independence study

A mesh independence test, illustrated in Figure 3, was performed to ensure that simulation results were not significantly influenced by grid variation. Velocity profiles were extracted from the central vertical plane of the third street canyon, where the void deck is located at the ground floor layer, in accordance with AIJ guidelines Tominaga et al., 2008. Fine and coarse grids were generated using a linear refinement factor of approximately 1.2. The results indicated minimal deviations in U/Uref between the medium and fine grids. Consequently, the medium grid, which satisfied the grid independence test, was selected for the RANS simulations.

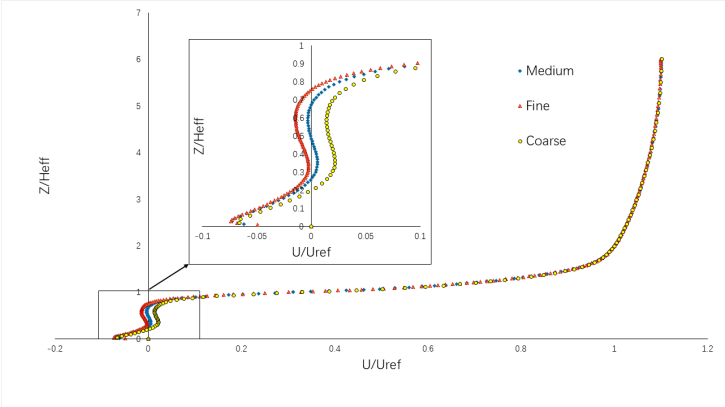

Figure 3. Comparison of normalized stream-wise velocity profiles at three mesh resolutions, extracted along the central vertical plane (y-direction) from the center of the third street canyon in the simulation where the void deck is located on the ground floor layer.

2.5. CFD simulation model

The model comprises seven identical layers, each capable of forming a 0.12 cm high void deck (Figure 4). CFD simulations explore six vertical locations by sequentially positioning the void deck from the ground floor to the sixth layer. This arrangement evaluates the impact of void deck placement on airflow dynamics across the layers.

2.6. Model Validation

To validate the CFD model, a two-step approach was adopted, addressing the absence of experimental data for three-dimensional models with void decks, as recommended by Blocken, 2015. In the first step, two-dimensional buildings with void decks were validated using water channel

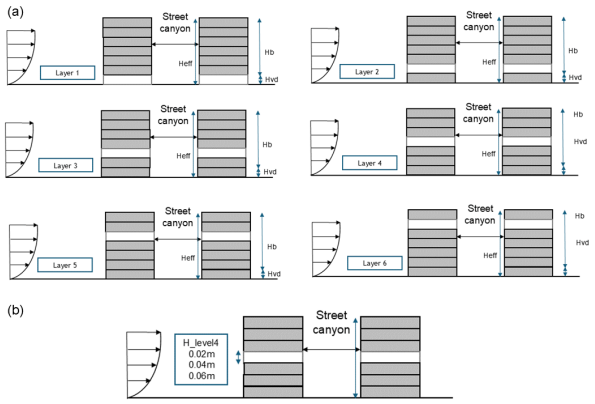

Figure 4. (a) Street canyon with effective height (Heff) formed between two building models, defined by building height (Hb) and void deck height (Hvd). (b) Illustration of level 4 used to analyze varying building porosity heights.

experiments conducted by Chew and Norford, 2018, involving an array of eight lift-up buildings. The second step validated three-dimensional buildings using wind tunnel experiments from Hang et al., 2012, which featured twelve rows of nine rectangular blocks.

For the two-dimensional validation, velocity profiles at the center of canyons 3–6 were compared with experimental data. Figure 5(a) presents the stream-wise velocity profiles at canyon 3, where the buildings feature a void deck height (H_{vd}) of 2 cm and a total effective building height (H_{eff}) of 14 cm. The void decks facilitate airflow penetration near the ground ($z/H_{eff} < 0.14$), with the highest velocity observed in canyon 3, followed by a decreasing trend downstream. The CFD model accurately captures these near-ground flows and the downstream velocity decay. Full-scale simulations, scaled up by a factor of 200, confirm Reynolds number independence, demonstrating the robustness of the results.

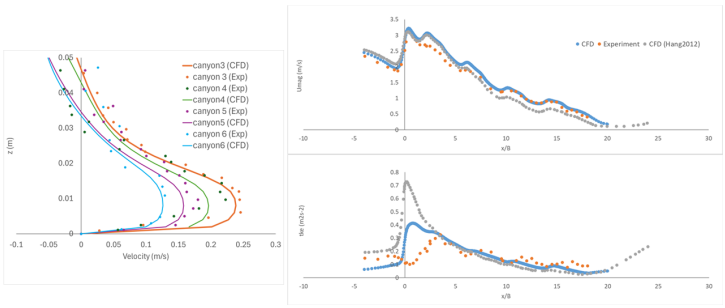

Figure 5. (a) Vertical profiles of stream-wise velocity along the centerlines of the third to sixth canyon, where z denotes the vertical distance from the ground. (b) Top figure: Horizontal profiles of velocity magnitude along the street at an elevation of z/B=1.0, where B represents the building width (B=30mm) in both the wind tunnel experiment and the reduced-scale CFD simulation. The experimental data and dashed-line CFD profiles are sourced from Hang et al., 2012. Bottom figure: Horizontal profiles of turbulence kinetic energy along the street at an elevation of z/B = 1.0.

For the second sub-configuration, Figure 5(b) presents a comparison between CFD results and wind tunnel measurements from Hang et al., 2012 for velocity magnitude and turbulence kinetic

energy (TKE) profiles along the central street between the sixth and seventh building rows at z/B=1.0 (B=30 mm). The CFD predictions show strong agreement with the experimental data, with minor deviations observed in the upstream peak TKE location. The normalized mean-square error (NMSE) values for velocity (0.0106) and TKE (0.2532) fall within the acceptable thresholds defined by Hanna and Chang, 2012, demonstrating the reliability of the CFD simulations in capturing essential flow features. Additionally, CFD results from Hang et al., 2012 are included for further comparison and context.

2.7. Parametric study

This study explores the influence of building porosity on natural ventilation within urban street canyons through two parametric analyses. The first analysis investigates the effect of vertical positioning of porosity, conducting six simulations with openings located at levels 1 through 6 while maintaining a fixed porosity of 100%. The second analysis assesses the impact of porosity height by comparing three configurations with different heights (h, 2h, 3h) at the same vertical position. All configurations ensure a uniform porosity distribution and consistent opening placements across the buildings.

3. RESULT AND DISCUSSION

3.1. Effects of building porosity position

Figure 6(a) presents velocity simulations for the third street canyon, selected for its representative airflow characteristics and minimal surface roughness effects. Ground-level porosity (Layer 1) facilitates steady pedestrian-level airflow without significant reverse flow, thereby improving ventilation and air quality at lower heights. Conversely, higher-level porosities (Layers 4–6) substantially enhance airflow at mid and upper levels but induce reverse flow near the ground, leading to localized stagnation zones and reduced pedestrian-level ventilation efficiency.

The analysis reveals that porosity at the fourth level achieves the highest pedestrian-level velocity (0.0548), whereas porosity at the second level has the least impact (0.0327). These results highlight the critical role of porosity placement in determining ventilation effectiveness. Lower-level porosity promotes direct airflow at pedestrian height, while higher-level porosity improves ventilation at its respective level but may compromise ground-level conditions.

These findings underscore the importance of strategic porosity design to balance improved ventilation at upper levels with maintaining pedestrian comfort and air quality. The study highlights the need to optimize porosity placement in high-rise urban environments to enhance microclimate conditions.

Figure 6(b) depicts velocity profiles (U) as a function of height (z) across street canyon configurations (Canyon 1 to Canyon 7) with porosity positioned at level 4. The main graph illustrates airflow patterns throughout the canyon sequence, while the inset focuses on near-ground velocities ($z<0.06$m), emphasizing pedestrian-level flow dynamics.

Canyon 1 demonstrates the strongest negative velocity near the ground, indicative of pronounced reverse flow or recirculation effects. As airflow progresses through subsequent canyons, these recirculation effects diminish, with reduced negative velocities observed near the ground in Canyons 2 through 7. Above z=0.1m, positive velocities increase, signifying enhanced vertical airflow at higher elevations. From Canyon 4 onward, velocity profiles exhibit minimal

variation, suggesting a reduced influence from upstream conditions.

These results highlight the sequential arrangement of street canyons as a critical factor in urban ventilation. Initial canyons are more prone to recirculation and degraded air quality near the ground, whereas downstream canyons benefit from more stable airflow, leading to improved ventilation and pedestrian comfort. This counterintuitive finding underscores the importance of strategic urban planning to optimize airflow and mitigate pollutant accumulation in densely built environments.

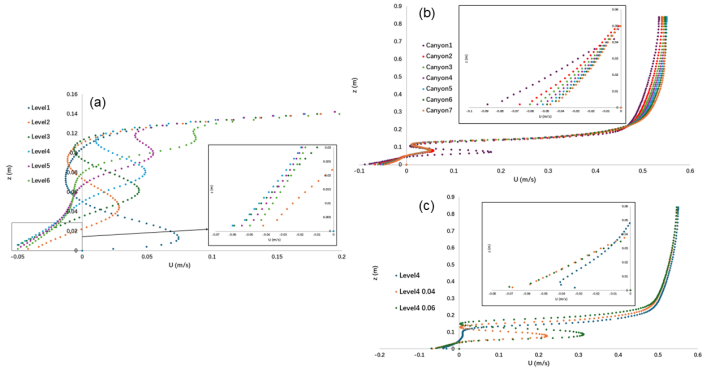

Figure 6. (a) Comparison of stream-wise velocity profiles in the third street canyon for buildings with varying vertical porosity positions, from layer 1 (ground floor) to layer 6. "No porosity" refers to buildings without any porosity. The inset provides a zoomed-in view highlighting near-ground velocity trends. (b) Comparison of stream-wise velocity profiles across all street canyons for buildings with porosity positioned at level 4. The inset focuses on near-ground velocity trends. (c) Comparison of stream-wise velocity profiles for different porosity heights (0.02 m, 0.04 m, and 0.06 m) at level 4 within a street canyon. The inset illustrates near-ground velocity trends.

3.2. Effects of building porosity height

This section investigates the effect of varying porosity heights at Level 4 within a street canyon, focusing on configurations with porosity heights of 0.02 m, 0.04 m, and 0.06 m. Figure 6(c) presents velocity profiles (U) as a function of height (z), highlighting distinct airflow behaviors influenced by porosity height.

Near the ground (z<0.06m), all configurations display negative velocities, indicative of reverse flows. The base "Level 4" configuration exhibits the strongest recirculation effect, while larger porosity heights (0.04 m and 0.06 m) slightly reduce this phenomenon. Above z=0.1m, larger porosity heights enhance airflow, achieving higher velocity magnitudes compared to the base case, thereby improving ventilation at mid and upper levels.

These findings indicate that smaller porosity heights concentrate airflow near the ground, enhancing pedestrian-level ventilation, whereas larger porosity heights promote more uniform airflow distribution across mid and upper elevations. The results emphasize the importance of optimizing porosity height to balance ground-level ventilation with broader airflow improvements within urban street canyons.

4. CONCLUSION

This study investigated the effects of building porosity on passive ventilation in high-rise residential buildings using a combination of experimental data and CFD simulations. The results

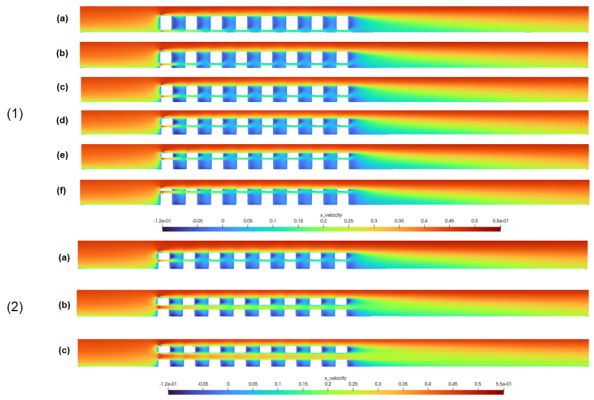

Figure 7. (1) Stream-wise velocity contours at the mid-normal plan (yz-plane at x = 0.25 m) for building porosity located at (a) level 1, (b) level 2, (c) level 3, (d) level 4, (e) level 5, and (f) level 6. (2) Stream-wise velocity contours at the mid-normal plan (yz-plane at x = 0.25 m) for void located at level 4 with (a) 0.02m, (b) 0.04m, and (c) 0.06m

Building porosity location	Canyon	Minimal velocity	Maximal velocity
Level1	line3	-0.0128	0.5467
	line4	-0.0126	0.5504
	line5	-0.01256	0.5520
	line6	-0.01250	0.5504
Level2	line3	-0.0417	0.5460
	line4	-0.0376	0.5495
	line5	-0.0355	0.5505
	line6	-0.0339	0.5486
Level3	line3	-0.0590	0.5458
	line4	-0.0546	0.5492
	line5	-0.0516	0.5500
	line6	-0.0491	0.5481
Level4	line3	-0.0599	0.5459
	line4	-0.0550	0.5494
	line5	-0.0514	0.5504
	line6	-0.0486	0.5504
Level5	line3	-0.0543	0.5460
	line4	-0.0495	0.5495
	line5	-0.0461	0.5510
	line6	-0.0435	0.5493
Level6	line3	-0.0495	0.5460
	line4	-0.0450	0.5497
	line5	-0.0417	0.5513
	line6	-0.0393	0.5500

Table 1. Minimal velocity values, and maximal velocity values for each building porosity level, values extracted from central line (z-direction) of the central canyons (3-6)

demonstrate that the placement of porosity plays a critical role in shaping airflow dynamics. Porosities positioned at higher levels improve ventilation at upper elevations but can generate reverse flows near the ground, potentially compromising street-level ventilation. Conversely, lower-level porosities enhance pedestrian-level airflow by increasing ground-level velocities. These findings underscore the importance of strategic porosity design to achieve a balance between ventilation performance and the sustainability of the urban microclimate.

ACKNOWLEDGMENTS

The authors acknowledge the support of Dr. CHEW Lup Wai for the use of the water tunnel experimental results, as well as Dr. CUI Yondgong and Prof KHOO Boo Cheong for their assistance with the wind tunnel experimental instruments.

REFERENCES

Blocken B., 2015. Computational Fluid Dynamics for Urban Physics: Importance, Scales, Possibilities, Limitations, and Ten Tips and Tricks Towards Accurate and Reliable Simulations. Building and Environment 91, 219–245.

Chew L. W. and Norford L. K., 2018. Pedestrian-Level Wind Speed Enhancement in Urban Street Canyons with Void Decks. Building and Environment 146, 64–76.

Franke J., Hellsten A., Schlünzen K. H., and Carissimo B., 2011. The COST 732 Best Practice Guideline for CFD Simulation of Flows in the Urban Environment: A Summary. International Journal of Environment and Pollution 44, 419–427.

Hang J., Li Y., Sandberg M., Buccolieri R., and Di Sabatino S., 2012. The Influence of Building Height Variability on Pollutant Dispersion and Pedestrian Ventilation in Idealized High-Rise Urban Areas. Building and Environment 56, 346–360.

Hanna S. and Chang J., 2012. Acceptance Criteria for Urban Dispersion Model Evaluation. Meteorology and Atmospheric Physics 116, 133–146.

Richards P. J. and Hoxey R. P., 1993. Appropriate Boundary Conditions for Computational Wind Engineering Models Using the k–ε Turbulence Model. Journal of Wind Engineering and Industrial Aerodynamics 46, 145–153.

Tominaga Y., Mochida A., Yoshie R., Kataoka H., Nozu T., Yoshikawa M., and Shirasawa T., 2008. AIJ Guidelines for Practical Applications of CFD to Pedestrian Wind Environment Around Buildings. Journal of Wind Engineering and Industrial Aerodynamics 96, 1749–1761.

Wieringa J., 1992. Updating the Davenport Roughness Classification. Journal of Wind Engineering and Industrial Aerodynamics 41, 357–368.

6th International Conference on Building Energy and Environment
Eindhoven University of Technology, The Netherlands
6 - 10 July 2025

Elemental leaching behavior of coal ash in concrete production for sustainable building applications

Mahdi Rafieizonooz , Hyounseung Jang , Jimin Kim , Elnaz Khankhaje

Architectural Engineering Program, School of Architecture, Seoul National University of Science and Technology, 232 Gongneung-ro, Gongneung-dong, Nowon-gu, Seoul, 01811, South Korea, mahdirafieizonooz@seoultech.ac.kr , jang@seoultech.ac.kr , jmkim@seoultech.ac.kr , elnazkhankhaje@seoultech.ac.kr

SUMMARY
The use of coal-fired power plant waste materials, such as bottom ash (BA) and fly ash (FA), as substitute by-product in concrete production is gaining momentum. However, a comprehensive understanding of their elemental composition and potential environmental impacts is still needed. This study focuses on evaluating the elemental content (Cu, Hg, and Se) of concrete containing FA and BA, employing tank leaching tests. Results revealed that the leaching of trace elements into the environment remained significantly below regulatory thresholds, supporting the suitability of these materials for construction use. The cumulative mass discharge analysis indicated that the flux-time slope for all three elements was below 0.4, suggesting that surface wash-off was the dominant discharge mechanism for these heavy metals. These findings reinforce previous studies, underscoring the viability of FA and BA as sustainable alternatives in concrete production, contributing to the development of environmentally friendly construction practices.

Keywords: Coal ash, Sustainable concrete, Elemental leaching.

1. INTRODUCTION

As coal-fired power plants continue to play a significant role in energy production, the generation of industrial by-products such as bottom ash (BA) and fly ash (FA) has also increased. Globally, approximately 650–800 million tons of FA and 150–250 million tons of BA are produced annually, posing significant challenges for waste management (Rafieizonooz et al., 2024). In many developing countries, efforts to mitigate the environmental impact of these by-products have led to stricter regulations and the promotion of sustainable alternatives in construction materials. Utilizing FA and BA in concrete production not only addresses waste disposal challenges but also supports sustainable development by reducing the consumption of non-renewable natural resources and mitigating environmental pollution (Pant et al., 2024; Samadi et al., 2024).

The incorporation of FA and BA into concrete has shown promising results, including improved long-term strength, reduced dead weight of structures, and lower carbon dioxide emissions (Rafieizonooz et al., 2017). While FA is predominantly used as a supplementary cementitious material (SCM) and BA as a river sand replacement, the combined use of these materials in

concrete remains underexplored (Abbas et al., 2020). Moreover, the environmental safety of these materials, particularly concerning the leaching of heavy metals such as copper (Cu), mercury (Hg), and selenium (Se), requires further investigation to ensure compliance with environmental standards and minimize potential health risks.

Previous studies have reported varying results regarding the leachability of heavy metals from coal ash materials, influenced by factors such as combustion processes, leaching test methods, and ash handling techniques (Gwenzi & Mupatsi, 2016; W. B. C. Silva et al., 2023). While some studies indicate minimal leaching, others highlight the potential risks associated with trace element diffusion (Pant et al., 2019). To bridge these knowledge gaps, it is crucial to investigate the leaching performance of BA and FA comprehensively, especially when used together in concrete mixtures, to ensure their safe and sustainable application in construction projects.

This study investigates the elemental analysis and leaching performance of FA and BA in concrete using a leaching method: the Semi-Dynamic Tank Leaching Procedure (SDTLP). The leaching mechanisms are derived from the relationship among concentrations of heavy metals and leaching time. This finding aim to demonstrate the feasibility of utilizing coal ash as a sustainable alternative for structural concrete in line with environmental and construction standards.

2. MATERIALS AND METHODS

Ordinary Portland cement (OPC) was used in this study, with an initial setting time of 125 minutes and a final setting time of 210 minutes. Its specific gravity, Blaine surface area, and soundness were 3.15, 3990 cm^2/g, and 1.0 mm, respectively. FA and BA were obtained from the Tang Jun-Bin coal-fired power plant. FA was used as a partial replacement for cement, while BA substituted fine aggregate. The chemical composition of OPC, FA, and BA, as detailed in our previous studies (Rafieizonooz et al., 2016, 2022) indicated that FA primarily contained silica, alumina, and iron oxide, with a combined SiO_2, Al_2O_3, and Fe_2O_3 content of 78.82%, classifying it as Class F according to ASTM C618 & ASTM C618-15 (2012). BA also contained significant amounts of silica, alumina, and iron oxide, with smaller quantities of MgO, SO_2, and CaO. The particle size gradation of BA adhered to ASTM C33 / C33M (2013) standards and was previously reported by the authors. BA's irregular shape and porosity resulted in higher water absorption (11.61%) and lower specific gravity (1.88) compared to river sand (7.4% absorption and 2.62 specific gravity). These characteristics highlight the suitability of BA and FA for sustainable concrete production, considering their physical and chemical properties.

The SDTLP was utilized to assess the leaching behavior of BA, FA, and coal ash concrete (CAC) mixtures. Following the guidelines of U.S. EPA 1315 (2013), three cubic specimens of the CAC mixture (100 mm per side), containing 100% BA as a substitution for river sand and 20% FA as a partial replacement for OPC, were fully immersed in individual 10-L containers. Each container was filled with 5.4 L of purified water to achieve a liquid-to-solid ratio of 9:1 (mL/cm^2) based on the thickness of the monolith. Leachate samples were stored and replaced with fresh purified water at intervals of 2 hours, 1 day, 2 days, 7 days, 14 days, 28 days, 42 days, 49 days, and 63 days. Subsequently, they were acidified to a pH of less than 2 using nitric acid and stored at 4 °C for further analysis using inductively coupled plasma mass spectrometry (E. B. da Silva et al., 2018). At the conclusion of the cumulative mass release, average interval flux, the leaching intervals, and

interval mass for each leaching period were calculated using standard equations provided by Garrabrants et al., (2012) and U.S. EPA 1315, (2013), as outlined in Rafieizonooz et al. (2022). This methodology provided a detailed assessment of the leaching properties and environmental safety of the tested materials.

3. RESULTS AND DISCUSSION

The primary outcomes of the SDTLP test, presenting the total concentrations of all three heavy metals, are summarized in Table 1. These results represent the mean values obtained from three samples of the same mix. The analysis revealed that only trace amounts of Cu, Hg, and Se were detected in all samples, with their concentrations decreasing significantly at later leaching intervals, reaching levels too low to be of concern. The minimal leaching of heavy metals observed for these elements, can be credited to the slow release mechanisms. This behavior likely results from the indirect flow paths between the solid and liquid phases and the encapsulation of heavy metals within the concrete matrix. The encapsulant development within the CAC mixture effectively restricted the mobility of these elements, as previously noted by Cao et al. (2017).

Table 1. Primary results of SDTLP test

Element Code	Tank Leaching Test (µg/L)								
	T01	T02	T03	T04	T05	T06	T07	T08	T09
	2 h	23 h	23 h	5 d	7 d	14 d	14 d	7 d	14 d
Cu	0.548	0.098	0.665	1.588	0.49	0.42	0	0	0
Hg	0	38.213	30.145	43.949	0	0	0	0	0
Se	0.575	0.544	0.097	0.427	0.182	0.23	0.21	0.09	0.12

Based on the initial results of the SDTLP test, Cu, Hg, and Se were identified as key heavy metals for further investigation. The monolithic leaching experiment results provided valuable data to analyze the release mechanisms of these elements from the CAC mixture. Fig. 1. illustrates the diffusion concentrations of Cu, Hg, and Se as a function of leaching time (days). Throughout the leaching intervals, the concentrations of Cu, Hg, and Se remained below 1.588 µg/L, 43.949 µg/L, and 0.575 µg/L, respectively, across all extractions. These findings confirm that the release concentrations of all monitored heavy metals were well within the acceptable limits specified by U.S. EPA 1315, (2013).

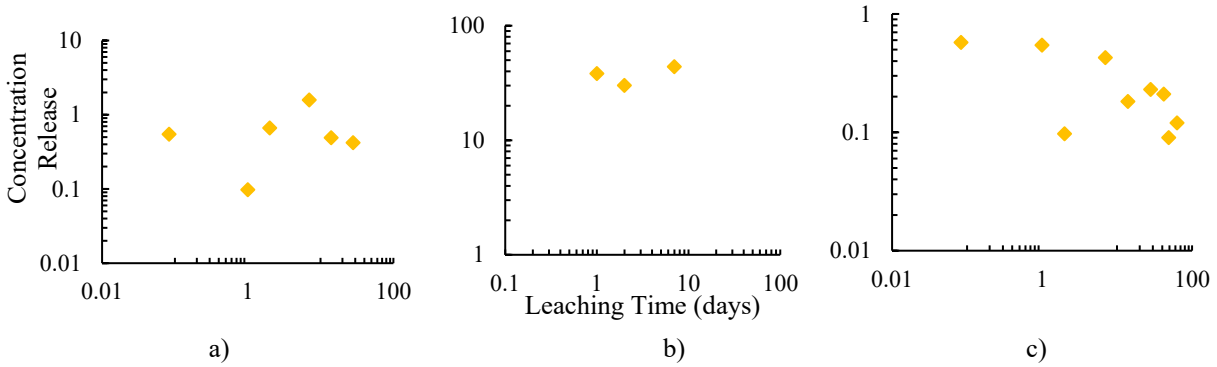

Figure 1. Concentration release of a) Cu, b) Hg, and c) Se versus leaching time

Fig. 2. illustrates the cumulative concentrations of Cu, Hg, and Se in comparison to their respective

standard limits. The data demonstrate that none of the trace elements exceeded the specified standard limitations throughout the entire leaching period. Specifically, the cumulative concentrations at the end of the final interval (63 days) were 0.004 mg/L for Cu, 0.112 mg/L for Hg, and 0.002 mg/L for Se. These values are significantly lower than the standard limitations of 25 mg/L, 0.2 mg/L, and 1.0 mg/L, respectively. These results confirm the environmental safety of the CAC mixture, as the leaching behavior of heavy metals remains well within permissible levels even after prolonged exposure. The minimal leaching of trace elements detected during the sample leaching experiment indicates that these heavy metals were effectively encapsulated and immobilized within the cement paste matrix. This encapsulation can be attributed to the microstructure of the concrete, which prevents the release of heavy metals into the environment. These findings align with previous studies, such as those by Rafieizonooz et al. (2024) and Hayes et al. (2015) which demonstrated that the microstructure of concrete enriched with heavy metals can encapsulate and immobilize these elements.

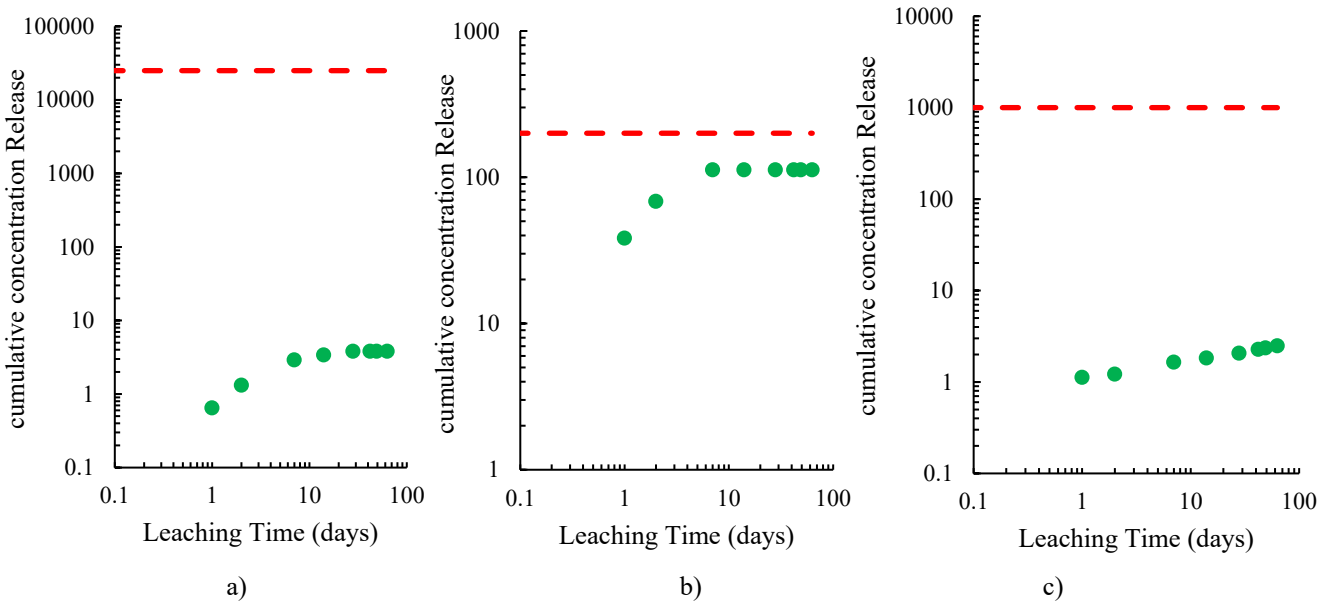

Figure 2. Cumulative concentration release (µg/L) of a) Cu, b) Hg, and c) Se versus leaching time

Fig. 3. illustrates the cumulative mass discharge of trace elements over the leaching period, demonstrating a positive non-linear relationship among the cumulative mass release and cumulative time for the CAC specimens. According to the classification proposed by Goumans et al. (2012), Beard (2002), A. C. Garrabrants et al. (2014), and Rafieizonooz et al. (2024), the release mechanism can be inferred from the slope (s) of log–log plots of cumulative mass discharge versus time. If the slope exceeds 0.8, the mechanism is matrix dissolution; if it falls between 0.8 and 0.4, it is diffusion-controlled release; and if it is below 0.4, the mechanism is dominated by initial surface wash-off. In this study, the calculated slopes for Cu, Hg, and Se were 0.005, 0.115, and 0.003 (mg/m²), respectively—all significantly below 0.4. These results suggest that the primary release mechanism for all the heavy metals was initial surface wash-off. Furthermore, as the experiment progressed, the rate of mass release decreased, confirming that heavy metals were predominantly encapsulated within the concrete matrix.

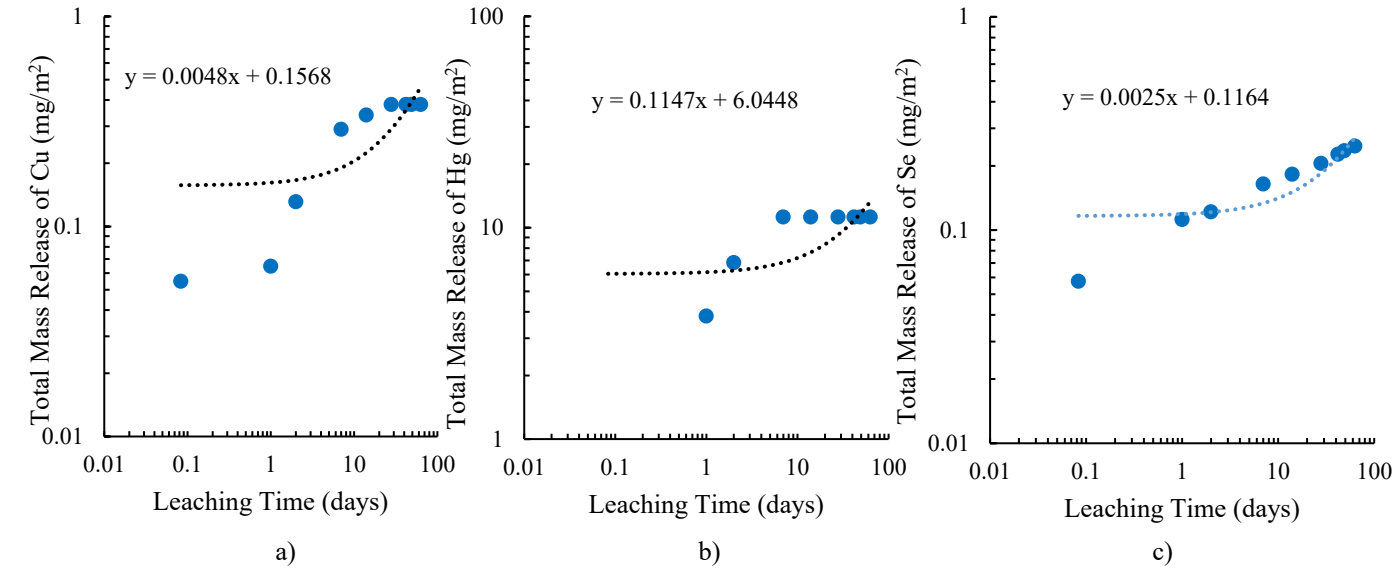

Figure 3. Total Mass Release of a) Cu, b) Hg, and c) Se versus leaching time

The results of the mass interval flux released against test duration, as shown in Fig. 4., further corroborate the findings of this study. The mass interval fluxes of Cu, Hg, and Se on all parts of the exposed surface area of the CAC samples exhibited an inverse linear relationship with leaching time. This trend indicates that as the contact duration increased during successive leaching periods, the mass interval fluxes of all trace elements declined significantly.

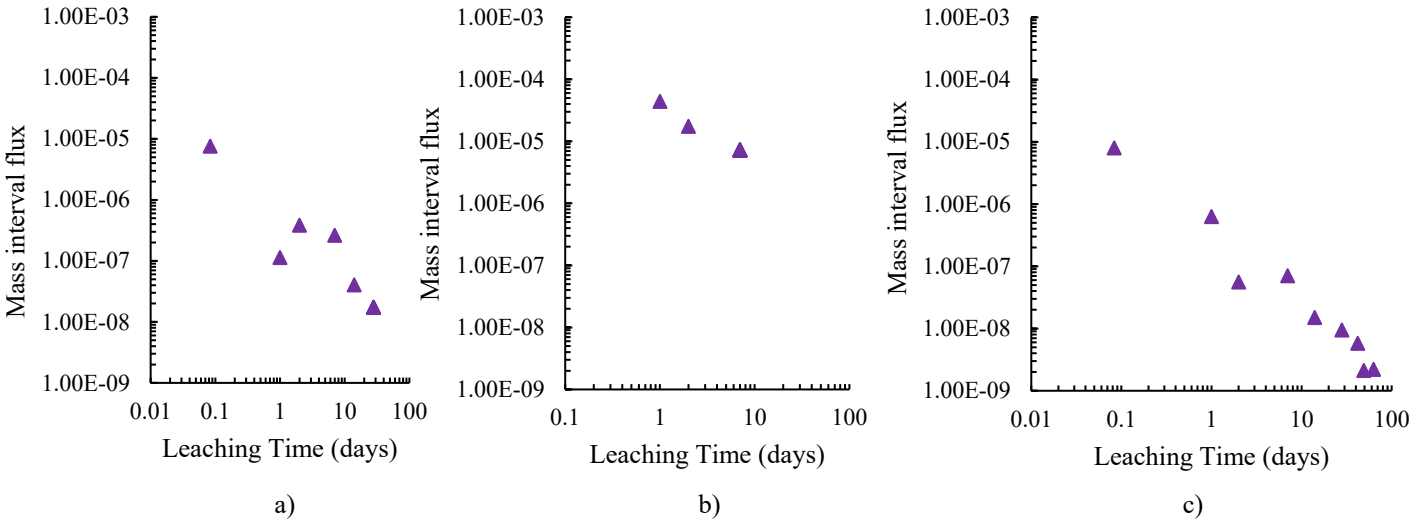

Figure 4. Mass interval flux (mg/m².s) of a) Cu, b) Hg, and c) Se versus leaching time

This observation aligns with the earlier conclusion that the primary leaching mechanism in the CAC mixture is initial surface wash-off. Beyond the initial leaching phase, no significant heavy metal release was detected. These results reinforce the encapsulating ability of the concrete matrix,

effectively preventing further heavy metal discharge during extended immersion periods. In this respect, the microstructure of concrete plays a critical role in the encapsulation of heavy metals by physically entrapping them within its dense matrix and reducing the permeability. Based on the results of the current study, the encapsulation process effectively reduced the leaching of heavy metals under the tested experimental conditions. However, under different environmental conditions—particularly more aggressive or harsh environments—further testing and evaluation are necessary to assess whether heavy metals might gradually accumulate and potentially exceed regulatory limits over extended exposure periods. Considering the results of this study along with previous related works, it can be concluded that utilizing BA and FA from coal-fired power plants contributes to effective waste management and promotes sustainable development. Additionally, it is important to note that these results are based on BA and FA collected from a specific power plant at a particular time. Variations in coal type or combustion conditions can alter the properties of coal ash, potentially leading to different leaching test outcomes. Therefore, continuous leaching testing is essential if these ash materials are to be used in construction applications.

4. RESEARCH GAPS AND RECOMMENDATION

The current study highlights some research gaps that should be addressed in future investigations. One key area is the effect of carbonation on the leaching behavior of heavy metals and trace elements in CAC mixtures. Previous studies, such as Zhang et al. (2022) and Rożek et al. (2019), suggested that carbonation could significantly influence the diffusivity, physical retention, and solubility of these elements; however, its impact remains unexplored in this context. Additionally, while this study used cubic specimens of 100 mm per side, research by Rowe (2005) indicated that increasing material thickness may further reduce the release of heavy metals. The relationship between larger concrete specimens and heavy metal leaching has not been thoroughly investigated. Finally, the leaching behavior of CAC mixtures was assessed under controlled laboratory conditions, but their long-term performance in real-world environments, including exposure to varying pH levels, saline conditions, or cyclic wet-dry scenarios, requires further exploration.

Future studies should address these gaps to enhance the understanding and application of CAC mixtures. Investigating the effects of carbonation and aggressive environment on heavy metal immobilization could provide valuable insights into improving the sustainability of CAC-based materials. Larger specimen sizes should also be studied to optimize material design for practical applications, as thicker structures may demonstrate reduced leaching risks. Additionally, conducting life cycle assessments could offer a holistic view of the environmental and economic benefits of CAC mixtures compared to conventional concrete. Together, these efforts can advance the development of environmentally friendly and durable materials for sustainable construction.

5. CONCLUSION

This study investigated the leaching behavior of heavy metals, including Cu, Hg, and Se, from CAC mixtures using the SDTLP approach. The results demonstrated that the release of these heavy metals remained significantly below the regulatory limits established by U.S. EPA 1315, (2013), indicating the environmental safety of the CAC mixture. The cumulative concentrations of Cu, Hg, and Se after 63 days of immersion were 0.004, 0.112, and 0.002 mg/L, respectively, compared to their standard limits of 25, 0.2, and 1.0 mg/L. The low concentrations observed are attributed to

the encapsulation and immobilization of heavy metals by the cementitious matrix, which hindered their diffusion and solubility in the leachate.

The leaching mechanism was primarily identified as initial surface wash-off, as indicated by the slope values from log-log plots of cumulative mass release versus time, which were below 0.4 for all tested metals. The mass interval flux results further supported this finding, showing a reverse linear relationship between heavy metal flux and leaching time. This behavior confirms that leaching was minimal after the initial surface wash-off phase. The CAC mixture's ability to immobilize heavy metals highlights its potential for sustainable construction applications. Future studies should focus on the effects of carbonation, larger specimen sizes, and real-world environmental conditions to further enhance the understanding and optimization of CAC mixtures for long-term environmental safety and durability.

ACKNOWLEDGEMENTS

This work was supported by the National Research Foundation of Korea (NRF) grant funded by the Korean government (MSIT; Ministry of Science and ICT) [grant numbers NRF- 2022R1A4A3026883, RS-2024-00355862].

REFERENCES

Abbas, S., Arshad, U., Abbass, W., Nehdi, M. L., & Ahmed, A. (2020). Recycling untreated coal bottom ash with added value for mitigating alkali–silica reaction in concrete: A sustainable approach. *Sustainability (Switzerland)*, *12*(24), 1–24. https://doi.org/10.3390/su122410631

ASTM C33 / C33M. (2013). Standard Specification for Concrete Aggregates. *Annual Book of ASTM Standards*, 11. https://doi.org/10.1520/C0033

ASTM C618, & ASTM C618-15. (2012). Standard Specification for Coal Fly Ash and Raw or Calcined Natural Pozzolan for Use. *Annual Book of ASTM Standards*, 3–6. https://doi.org/10.1520/C0618

Beard, J. (2002). A Study of Leaching Tests for Cement Stabilised Waste. *Victoria University of Technology*.

Cao, V. D., Pilehvar, S., Salas-Bringas, C., Szczotok, A. M., Rodriguez, J. F., Carmona, M., Al-Manasir, N., & Kjøniksen, A. L. (2017). Microencapsulated phase change materials for enhancing the thermal performance of Portland cement concrete and geopolymer concrete for passive building applications. *Energy Conversion and Management*, *133*, 56–66. https://doi.org/10.1016/j.enconman.2016.11.061

da Silva, E. B., Li, S., de Oliveira, L. M., Gress, J., Dong, X., Wilkie, A. C., Townsend, T., & Ma, L. Q. (2018). Metal leachability from coal combustion residuals under different pHs and liquid/solid ratios. *Journal of Hazardous Materials*, *341*, 66–74. https://doi.org/10.1016/j.jhazmat.2017.07.010

Garrabrants, A. C., Kosson, D. S., DeLapp, R., & van der Sloot, H. A. (2014). Effect of coal combustion fly ash use in concrete on the mass transport release of constituents of potential concern. *Chemosphere*, *103*, 131–139. https://doi.org/10.1016/j.chemosphere.2013.11.048

Garrabrants, A., Kosson, D., DeLapp, R., Kariher, P., Seignette, P., van der Sloot, H., Stefanski, L., & Baldwin, M. (2012). Interlaboratory Validation of the Leaching Environmental Assessment Framework (LEAF) Method 1314 and Method 1315. *EPA/600/R-12/624*.

Goumans, M., Sloot, H. A. van der., & Aalbers, T. G. (2012). *Environmental aspects of construction with waste materials : proceeding[s] of the International Conference on Environmental Implications of Construction Materials and Technology Developments, Maastricht, the Netherlands, 1-3 June 1994*. 988.

Gwenzi, W., & Mupatsi, N. M. (2016). Evaluation of heavy metal leaching from coal ash-versus conventional concrete monoliths and debris. *Waste Management*, *49*, 114–123. https://doi.org/10.1016/j.wasman.2015.12.029

Hayes, J. B., Wang, J., Roessler, J. G., Ferraro, C. C., Wu, C. Y., Deford, D., & Townsend, T. G. (2015). Evaluation of leaching of trace metals from concrete amended with cement kiln baghouse filter dust. *Resources, Conservation and Recycling*, *94*, 92–98. https://doi.org/10.1016/j.resconrec.2014.11.012

Pant, A., Meena, L., & Desai, V. P. (2024). Environmental sustainability and life cycle assessment of pilot scale application of coal combustion residue as structural fill in mechanically stabilized earth walls. *Journal of Cleaner Production*, *446*, 141422. https://doi.org/10.1016/J.JCLEPRO.2024.141422

Pant, A., Ramana, G. V., Datta, M., & Gupta, S. K. (2019). Coal combustion residue as structural fill material for reinforced soil structures. *Journal of Cleaner Production*, *232*, 417–426. https://doi.org/10.1016/J.JCLEPRO.2019.05.354

Rafieizonooz, M., Khankhaje, E., & Rezania, S. (2022). Assessment of environmental and chemical properties of coal ashes including fly ash and bottom ash, and coal ash concrete. *Journal of Building Engineering*, *49*, 104040. https://doi.org/10.1016/J.JOBE.2022.104040

Rafieizonooz, M., Kim, J. H. J., Khankhaje, E., & Rezania, S. (2024). Leaching behavior of sustainable concrete made with coal ash wastes as replacement of cement and sand. *Environmental Science and Pollution Research*, *31*(52), 61437–61450. https://doi.org/10.1007/S11356-024-35250-1/TABLES/4

Rafieizonooz, M., Mirza, J., Salim, M. R., Hussin, M. W., & Khankhaje, E. (2016). Investigation of coal bottom ash and fly ash in concrete as replacement for sand and cement. *Construction and Building Materials*, *116*, 15–24. https://doi.org/10.1016/j.conbuildmat.2016.04.080

Rafieizonooz, M., Salim, M. R. M. R. M. R., Mirza, J., Hussin, M. W. M. W., Salmiati, Khan, R., & Khankhaje, E. (2017). Toxicity characteristics and durability of concrete containing coal ash as substitute for cement and river sand. *Construction and Building Materials*, *143*, 234–246. https://doi.org/10.1016/j.conbuildmat.2017.03.151

Rowe, R. K. (2005). Long-term performance of contaminant barrier systems. *Géotechnique*, *55*(9), 631–678. https://doi.org/10.1680/geot.2005.55.9.631

Rożek, P., Król, M., & Mozgawa, W. (2019). Solidification/stabilization of municipal solid waste incineration bottom ash via autoclave treatment: Structural and mechanical properties. *Construction and Building Materials*, *202*, 603–613. https://doi.org/10.1016/J.CONBUILDMAT.2019.01.056

Samadi, M., Wong, L. S., G, M., Lim, N. H. A. S., & Ayeni, I. S. (2024). Influence of elevated temperatures on the mechanical behavior of one-part coal ash geopolymer concrete with sodium metasilicate pentahydrate and sodium metasilicate anhydrous as alkaline activators. *Journal of Building Engineering*, 109692. https://doi.org/10.1016/J.JOBE.2024.109692

Silva, W. B. C., Barroso, S. H. A., Cabral, A. E. B., Stefanutti, R., & Picado-Santos, L. G. (2023). Assessment of concrete road paving blocks with coal bottom ash: Physical and mechanical characterization. *Case Studies in Construction Materials*, *18*, e02094. https://doi.org/10.1016/J.CSCM.2023.E02094

U.S. EPA 1315. (2013). *1315 - MASS TRANSFER RATES OF CONSTITUENTS IN MONOLITHIC OR COMPACTED GRANULAR MATERIALS USING A SEMI-DYNAMIC TANK LEACHING PROCEDURE SW-846*. *7345*(January), 1–36.

Zhang, P., Chen, Z., Brown, K. G., Garrabrants, A. C., Delapp, R., Meeussen, J. C. L., van der Sloot, H. A., & Kosson, D. S. (2022). Impact of carbonation on leaching of constituents from a cementitious waste form for treatment of low activity waste at the DOE Hanford site. *Waste Management*, *144*, 431–444. https://doi.org/10.1016/J.WASMAN.2022.04.009

6th International Conference on Building Energy and Environment
Eindhoven University of Technology, The Netherlands
6 - 10 July 2025

Wood species selection and environmental impact assessment for sustainable wood production

Hyeonwoo Jeong [1], Haedeun Park [2], Jiyeong Byeon [3], Seyoun Shin [4], Seong Jin Chang [5*]

[1]*Gyeongsang National University, Jinju, Republic of Korea, hyeonwoo@gnu.ac.kr*
[2]*Gyeongsang National University, Jinju, Republic of Korea, haedeun00@gnu.ac.kr*
[3]*Gyeongsang National University, Jinju, Republic of Korea, byeonjiyeong@gnu.ac.kr*
[4]*Gyeongsang National University, Jinju, Republic of Korea, seyoun@gnu.ac.kr*
[5*]*Gyeongsang National University, Jinju, Republic of Korea, sjc@gnu.ac.kr*

SUMMARY
This study examines reforestation strategies to enhance wood production and carbon sequestration in Korea, addressing the demand for sustainable materials. wood helps reduce building sector emissions due to its low embodied carbon and CO_2 storage. Using multi-criteria analysis, this research identifies optimal tree species based on site index, material properties (specific gravity, weather resistance), and carbon sequestration potential. A Life Cycle Assessment (LCA) evaluates the environmental impact of wood from selected species, analyzing embodied carbon, energy use, and emissions across its entire life cycle, from growth and harvesting to processing, construction, and disposal. The findings support data-driven reforestation, low-carbon wood use, and eco-friendly construction.

Keywords: Domestic wood, Life Cycle Assessment, Wood exterior cladding, Sustainable construction

1. INTRODUCTION

As the demand for sustainable building materials increases, wood has gained attention as a viable alternative to conventional construction materials due to its low embodied carbon and carbon sequestration capacity. However, Korea's post-war reforestation prioritized fast-growing species, leading to a limited supply of structurally suitable wood and a heavy reliance on imports, which undermines the carbon reduction potential of domestic wood resources. Ensuring a stable and sustainable wood supply requires reforestation with tree species optimized for construction applications.

Reforestation plays a crucial role in enhancing carbon sequestration while supporting the long-term viability of wood as a building material. The selection of appropriate tree species significantly impacts wood yield, material properties, and carbon storage capacity. A data-driven approach to species selection can maximize both economic and environmental benefits, contributing to sustainable forest management and climate change mitigation.

This study applies Life Cycle Assessment (LCA) to evaluate the environmental impact of reforested wood, focusing on carbon emissions and storage across different reforestation scenarios to support low-carbon forest management.

2. METHODOLOGY

In this study, a LCA was conducted in accordance with ISO 14040 and ISO 14044 standards established by the International Organization for Standardization (ISO). LCA is a systematic methodology for quantifying inputs and outputs throughout the entire life cycle of a product and assessing the associated environmental impacts.

The life cycle of a building is generally categorized into production, construction, operation, disposal, and regeneration stages. This study specifically evaluates carbon emissions in the production, construction, and operation stages. The scope of the LCA assessment and the specific boundaries considered in this study are shown in Figure 1.

To assess wood production and carbon sequestration in the study area, seven tree species were selected. show in Table 1, the selected species include five coniferous species, Korean red pine, Pitch pine, Japanese black pine, Japanese larch, and Korean pine and two broadleaf species, Sawtooth oak and Mongolian oak.

The carbon absorption capacity of each tree species was estimated using the methodology outlined in the IPCC guidelines, standardized carbon absorption was calculated by applying factors such as wood density, biomass expansion factor, root-to-shoot ratio, and carbon fraction to the periodic annual increment of each species.

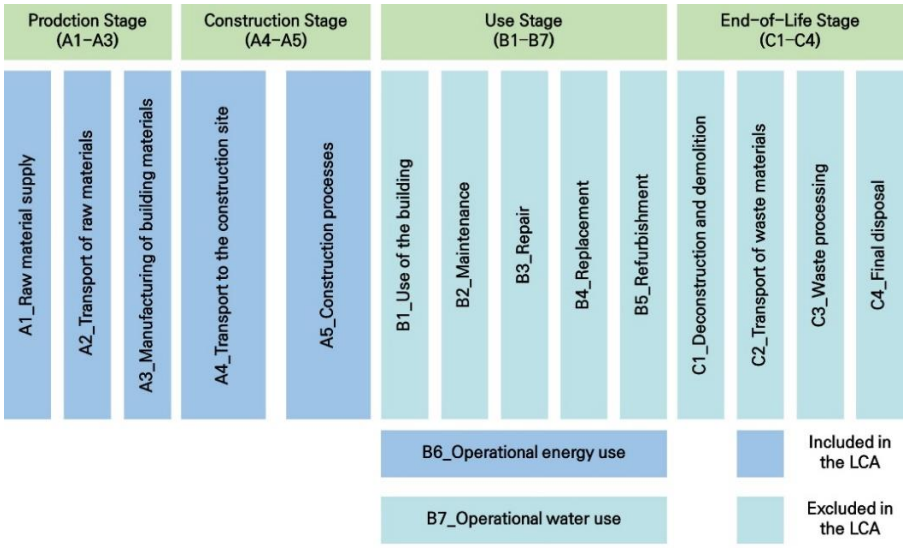

Figure 1. LCA boundaries

Table 1. CO_2 absorption by tree species during their life cycles (Unit: tCO_2/ha/year)

Tree species/ Forest age	10	20	30	40	50	60	70
Korean red pine	3.5	6.9	12.4	6.4	3.3	1.8	1.1
Pitch pine	4.5	13.9	12.4	8.7	5.8	4.1	3.1
Japanese black pine	5.2	10.3	11.5	7.8	5.3	3.8	2.8
Japanese larch	9.1	10.5	9.5	8.5	7.9	7.5	7.2
Korean pine	5.4	11.8	10.8	9.1	7.6	6.5	5.7
Sawtooth oak	11.2	15.9	14.0	12.3	10.9	9.8	8.9
Mongolian oak	8.6	15.0	9.3	8.4	7.5	6.8	6.3

2.1. Study area and suitable wood

The forested area in Yuseong-gu, Daejeon City, which is actively engaged in a wood-friendly city initiative, was selected as the study site. This initiative aims to foster local employment and promote a wood-friendly urban environment by utilizing domestically sourced wood for the construction of wooden streets and buildings. Consequently, cities already implementing wood-friendly urban projects were deemed appropriate for this study.

Among the participating cities, the forests in Yuseong-gu, Daejeon, were selected as the study site due to their extensive forested area within the vicinity of the project. The total forested area in Daejeon spans approximately 781 hectares and is primarily composed of Pitch Pine (41.6%), Mongolian Oak (15.6%), Korean Red Pine (11.6%), Japanese Larch (1.1%), Korean Pine (1.0%), Japanese Black Pine (1.0%), and Sawtooth Oak (0.9%).

To evaluate wood demand in the study area, the wood-friendly city initiative was analyzed, with a particular focus on the development of wood-specialty streets and the promotion of wood utilization in construction. wood -specialty streets incorporate wooden elements such as sculptures, guardrails, benches, and building exteriors, with the latter playing a central role in the project's objectives. Instead of constructing new wooden structures, the initiative primarily emphasizes the integration of wood cladding into existing buildings, thereby increasing the demand for exterior wood materials.

2.2. Configuring the reforestation scenarios

Table 2 shows six reforestation scenarios designed to identify optimal tree species for domestic wood utilization. Alternative 1 (Alt 1) serves as the baseline scenario, representing reforestation without additional selection criteria. Alternative 2 (Alt 2) incorporates species selection based on site index suitability to enhance forest productivity. Alternative 3 (Alt 3) prioritizes species with characteristics favorable for the production of wood exterior cladding. Alternative 4 (Alt 4) emphasizes species selection aimed at maximizing carbon sequestration potential. Alternative 5 (Alt 5) integrates both site index suitability and wood exterior cladding production considerations, reflecting a dual-purpose reforestation strategy. Finally, Alternative 6 (Alt 6) combines site index suitability with carbon sequestration objectives to optimize both forest productivity and climate mitigation benefits.

Table 2. Reforestation considerations for each scenario

Scenario	Considerations of reforestation		
	Site Index	Wood Exterior cladding	Carbon Stock
Alt 1	-	-	-
Alt 2	O	-	-
Alt 3	-	O	-
Alt 4	-	-	O
Alt 5	O	O	-
Alt 6	O	-	O

3. RESULTS AND DISCUSSION

Alt 1 represents the maintenance of existing forests, reflecting the current tree species composition. Alt 2 selected Japanese black pine, Sawtooth oak, and Mongolian oak for reforestation. Alt 3 identified Japanese larch and Mongolian oak. Alt 4 proposed Japanese larch, Sawtooth oak, and Mongolian oak. Alt 5 designated Mongolian oak, while Alt 6 selected Sawtooth oak and Mongolian oak.

Figure 2 shows the production of wood exterior cladding derived from reforestation scenarios in the Daejeon forests. Scenario Alt 3 achieved the highest total wood exterior cladding production at 473.6 m³/ha, representing a 565.1% increase compared to Scenario Alt 1, which produced 71.2 m³/ha. This increase was attributed to the inclusion of Mongolian oak and Japanese larch, which exhibit high suitability for wood exterior cladding production. Scenario Alt 5, emphasizing Mongolian oak, yielded a slightly lower total production of 438.0 m³/ha due to the species' faster growth but lower per-logging yield, highlighting the need to balance growth rates and productivity in reforestation planning.

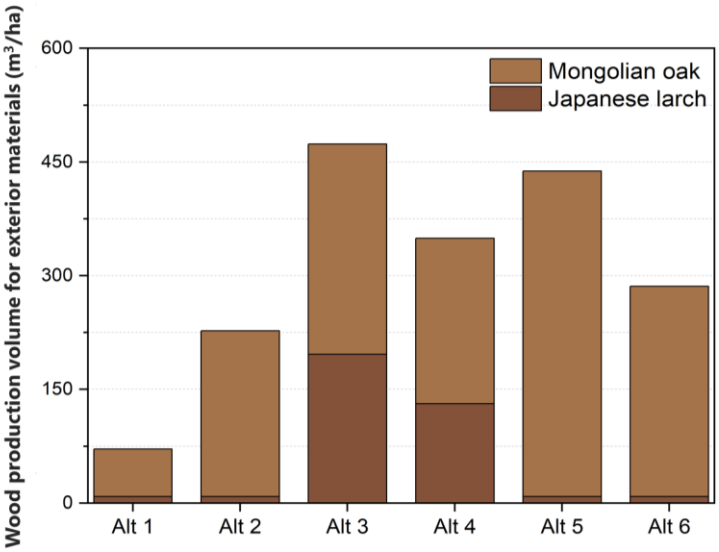

Figure 2. Wood production for wood exterior cladding from 2023 to 2223: Daejeon

ACKNOWLEDGEMENTS

This study was carried out with the support of ´R&D Program for Forest Science Technology (Project No. "RS-2024-00400730)´ provided by Korea Forest Service(Korea Forestry Promotion Institute).

This work was supported by the National Research Foundation of Korea(NRF) grant funded by the Korea government(MSIT) (RS-2025-00519598).

REFERENCES

Julie H, et al. Comparative life cycle assessment of cross laminated timber building and concrete building with special focus on biogenic carbon. Energy and Buildings 254, 111604, 2022.

Wenhuan X, et al. Site-based climate-smart tree species selection for forestation under climate change. Climate Smart Agriculture 1(2), 100019, 2024.

Pedro M, et al. Potential native timber production in tropical forest restoration plantations. Perspectives in Ecology and Conservation. 21(4), 294-301, 2023.

Muhammad H, et al. Deforestation detection and reforestation potential due to natural disasters—A case study of floods. Remote Sensing Applications: Society and Environment, 34, 101188, 2024.

Health and Indoor Air Quality, Ventilation (11:00-12:30 h)

6th International Conference on Building Energy and Environment
Eindhoven University of Technology, The Netherlands
6 - 10 July 2025

A new ventilation efficiency index to evaluate average return time associated with indoor airflow

Ryu Itokazu [1], Kazuki Kuga [2], Kazuhide Ito [2]

[1] *Kyushu University, Kasuga city, Japan, itokazu@kyudai.jp*
[2] *Kyushu University, Kasuga city, Japan, kuga@kyudai.jp*
[3] *Kyushu University, Kasuga city, Japan, ito@kyudai.jp*

SUMMARY
In the ventilation design, we generally determine the ventilation rate assuming well-mixed conditions. However, the assumption of well-mixed conditions is limited because a heterogeneous contaminant concentration field is mostly formed in the indoor environment. One of the main reasons for the heterogeneity of indoor contaminants is the recirculation created by indoor airflow. Therefore, quantitative evaluation using ventilation efficiency indices is effective. In this report, by fusing return probability and travel time, we proposed the average return time concept, which is the time scale of recirculation to a local point. The results show that the average return time was vary depending on source location and airflow. The average staying time of contaminant can include approximately 10% recirculation effect. The recirculation through the shortcut route was confirmed at some locations. By defining the mixing factor at the local point, the intensity of recirculation was evaluated.

Keywords: CFD, Ventilation Efficiency, Return Probability, Travel Time, Average Return Time

1. INTRODUCTION

In ventilation design for controlling indoor heat and contaminants, the ventilation rate is typically determined under the assumption of well-mixed conditions. However, this assumption is inherently limited because indoor environments often exhibit heterogeneous contaminant concentration distributions. One of the primary causes of this heterogeneity is the recirculation created by the indoor airflow. Due to the enclosed nature of indoor spaces, which are characterized by relatively small openings such as supply inlets and exhaust outlets, the airflow field becomes highly complex, often exhibiting multiple recirculation patterns. Recirculation cannot be directly assessed from the flow field alone. To enhance the understanding of recirculation phenomena, Kato et al. (2003) introduced the concept of visitation frequency, which was later refined by Chung et al. (2017) into the return probability concept. Against this background, we extend the discussion and propose a novel ventilation efficiency index, the average return time, which provides a quantitative measure of the timescale of recirculation.

2. VENTILATION EFFICIENCY INDICES

2.1. Return probability (α)

Chung et al. (2017) introduced α and net escape probability (NEP) concept by applying the visitation frequency concept to a control volume (CV). α represents the probability of a contaminant returning to the source domain and is defined as follows:

$$\alpha = \frac{\dot{m}_i}{\dot{m}_o} \tag{1}$$

where, $\dot{m}_i$ and $\dot{m}_o$ are the mass influx and outflux [kg/s] within the source CV, respectively.

2.2. Travel time (TT)

Efthimiou and Bartzis (2011) proposed TT estimation method by using passive/inert and radioactive scalar. The radioactive scalar has same diffusivity and properties as passive/inert scalar, but it has a decay term depending on decay constant (λ) and its own concentration (C_r). Both scalars are generated at the same point and intensity, and, by reading the concentration differences between them as time, TT is evaluated as following equation:

$$TT(\boldsymbol{x}, \boldsymbol{x_0}) = -\frac{1}{\lambda} ln \frac{C}{C_r} \tag{2}$$

where, $\boldsymbol{x_0}$ is source point, $\boldsymbol{x}$ is receptor point and C is passive/inert scalar concentration [kg/m^3].

2.3. Average return time (T_R) concept

TT distribution indicates the average dispersion time of contaminant parcels and, if recirculation is occurred at the source point, TT value at the recirculating region means the average recirculation time sale of contaminants. Therefore, by fusing the concepts of α and TT, we proposed a new ventilation index, average return time, which indicates the time scale for generated contaminants to recirculate back to the source once. By considering the TT value at the inflow and outflow surface, it can be identified. The TT value at the inflow surfaces represents the average travel time of contaminants returning to the source ($\overline{TT}_R$). By applying a geometric series, $\overline{TT}_R$ can be expressed as equation (3). Here, τ_{domain} refers to average staying time of contaminant within the domain. Conversely, the TT value at the outflow surfaces represents the average travel time of the scalar evacuated from the source, denoted as $\overline{TT}_E$ and is defined in equation (4). From equation (3) and (4), T_R can be simply described as equation (5).

$$\overline{TT}_R = \frac{\sum_{n=1}^{\infty}(n\cdot(T_R+\tau_{domain})\cdot\alpha^n)}{\sum_{n=1}^{\infty}\alpha^n} = \frac{T_R+\tau_{domain}}{1-\alpha} \tag{3}$$

$$\overline{TT}_E = \frac{\sum_{n=0}^{\infty}(\tau_{domain}+n\cdot(T_R+\tau_{domain}))(\alpha^n\cdot(1-\alpha))}{\sum_{n=0}^{\infty}((1-\alpha)\alpha^n)} = \frac{\tau_{domain}+\alpha\cdot T_R}{1-\alpha} \tag{4}$$

$$T_R = \overline{TT}_R - \overline{TT}_E \tag{5}$$

Furthermore, by extending this concept to the average staying time of contaminants within the room (τ_{room}), τ_{room} can be decomposed three components: returning to the source, staying within local domain and being direct exhaust from the room, as expressed in equation (6). The scale of τ_{room} can be directly evaluated by using the scale for ventilation efficiency No.1 (SVE1) defined by Kato and Murakami (1988).

$$\tau_{room} = \frac{\sum_{n=0}^{\infty}(T_{DE}+n\cdot(T_R+\tau_{domain}))(\alpha^n\cdot(1-\alpha))}{\sum_{n=0}^{\infty}((1-\alpha)\alpha^n)} = T_{DE} + \frac{\alpha}{1-\alpha}T_R + \frac{\alpha}{1-\alpha}\tau_{domain} \tag{6}$$

3. METHODOLOGY

We conducted isothermal two-dimensional CFD analysis. The incompressible continuity, Reynolds-averaged Navier-Stokes and Scalar transport equations were numerically solved by using ANSYS/Fluent 2023R2 commercial CFD software. The IEA Annex 20 two-dimensional

benchmark test case (Nielsen 1990) was targeted as domain and our geometry is illustrated in Fig. 1. For inflow boundary condition, the inlet velocity (U_{in}) was applied 0.455 [m/s], and turbulent intensity and reference length scale were assumed 10% and one-tenth length scale of the inlet (h/10), respectively. The velocity flow field was initially solved using SIMPLE algorithm, the 2nd order upwind difference scheme for advection term and standard k-ε model. The calculation domain is consisted by an equally spaced structured mesh and the number of grids is 49,120. A mesh independence check was carefully conducted following to previous study (Ito et al., 2015).

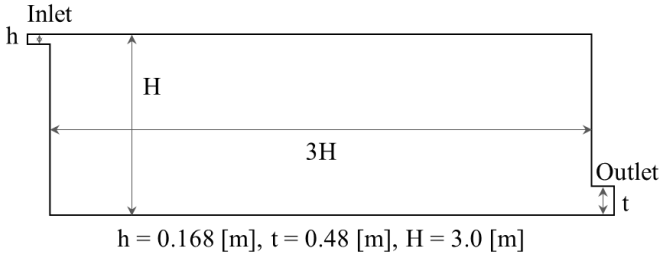

Fig. 1 Two-dimensional geometry of Annex 20 benchmark test (Nielsen 1990)

4. RESULTS AND DISCUSSION

Fig. 2 illustrates the airflow field, with contour values normalized by the inlet velocity and overlaid with streamlines. The air is introduced through the supply inlet located at the ceiling and flows along the indoor walls. Based on the flow field, we coupled it with scalar transport equations to conduct an analysis of the average return time. In this analysis, three points, as shown in Fig. 2, are designated as point sources under separate conditions.

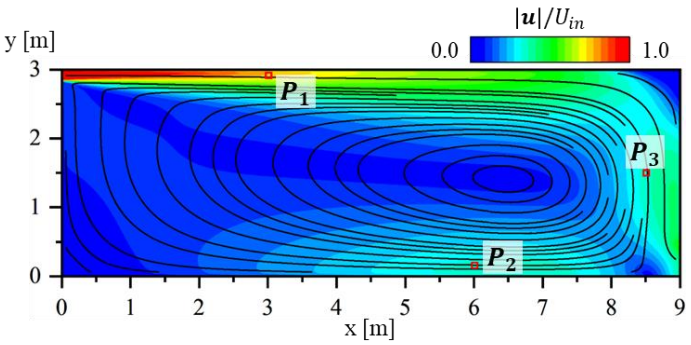

Fig. 3 Airflow field and scalar source descriptions

The results of average return time analysis are summarized in table 1 with all time scales normalized by the nominal time constant (τ_n). Under the condition generated at the P1, the value of T_R is less than τ_{room} and T_{DE}. The contaminants are carried by the main circulation flow, with the majority being discharged directly, while the remaining portion required more time than τ_n to recirculate. On the other hands, under the P2 and P3 conditions, the value of T_R is less than τ_{room} and T_{DE}. This implies contaminants recirculated with the short cut route. Furthermore, by integrating α and T_R indices, the mixing factor (MF) can be newly defined as below:

$$MF = \frac{\alpha}{T_R/\tau_n} \tag{7}$$

This MF value implies the return population of contaminants within the time scale of τ_n with considering both probability and time. The MF value at the P1, P2 and P3 are 0.070, 0.352 and 0.297, respectively. This value directly indicates the intensity of recirculation within the local domain.

Table 1. Results of average return time analysis

	α	$\overline{TT}_R/\tau_n$	$\overline{TT}_E/\tau_n$	T_R/τ_n	τ_{domain}/τ_n	τ_{room}/τ_n	T_{DE}/τ_n
P_1	8.7%	1.38	0.141	1.24	0.020	0.759	0.625
P_2	21.9%	1.04	0.413	0.623	0.187	1.29	0.944
P_3	12.2%	0.721	0.310	0.411	0.222	0.779	0.648

4. CONCLUSION

In this study, by fusing the concept of return probability and travel time, we proposed average return time concept. Considering it with the average staying time of contaminant within the room, we decomposed τ_{room} as three components: recirculation, staying and direct exhaust. By confirming these values, we confirmed the contaminant recirculation behaviour in terms of time. Moreover, we defined mixing factor as the merit indicating the intensity of recirculation. It has the potential to describe the correlation between recirculation and dispersion within the room at a specific local domain or point.

ACKNOWLEDGEMENTS

This study was partially funded by FOREST program from JST, Japan (JPMJFR225R) and JSPS KAKENHI (JP 24KK0094, JP 22H00237, JP 22K18300, JP 22K14371), and MEXT as "Program for Promoting Researches on the Supercomputer Fugaku" (JPMXP1020210316), and Health, Labour and Welfare Policy Research Grants (JP 24KD2001).

REFERENCES

G. C. Efthimiou and J. G. Bartzis., 2011. Atmospheric dispersion and individual exposure of hazardous materials, J Hazard Mater, vol.188, pp. 375–383.

J. Chung., E. Lim., M. Sandberg., K. Ito., 2017. Returning and net escape probabilities of contaminant at a local point in indoor environment, Building and Environment, 125.

K. Ito et al., 2015. CFD Benchmark Tests for Indoor Environmental Problems: Part 1 Isothermal/Non-Isothermal Flow in 2D and 3D Room Model, Int. J. Archit. Eng. Technol., vol. 2, no. 1, Art. no. 1.

P. V. Nielsen., 1990. Specification of two-dimensional test case: (IEA), Institut for Bygningsteknik, Aalborg Universitet, Aalborg.

S. Kato, S. Murakami., 1988. New ventilation efficiency scales based on spatial distribution of contaminant concentration aided by numerical simulation, ASHRAE trans.

S. Kato., K. Ito., S. Murakami., 2003. Analysis of Visitation Frequency through Particle Tracking Method Based on LES and Model experiment. Indoor Air 13, 182–193.

6th International Conference on Building Energy and Environment
Eindhoven University of Technology, The Netherlands
6 - 10 July 2025

Characteristics of temperature distribution under the influence of storage tank layout, air inlet patterns and inflow angle inside a nuclear waste storage plant

Heng Zhou [1], Xiaocheng Song [2], Yu Zhao [1*]

[1] *School of Infrastructure Engineering, Dalian University of Technology, Dalian, China, 2069884839@qq.com*
[2] *Civil and Architectural Engineering College, Dalian University, Dalian, China, songxiaocheng@dlu.edu.cn*
[1] *School of Infrastructure Engineering, Dalian University of Technology, Dalian, China, zhaoyu1220@dlut.edu.cn*

SUMMARY
Due to hourly continuous operation for diluting the large amount of heat induced by the nuclear decay reaction of the waste, ventilation system could consume huge energy inside a nuclear waste storage plant. This study focused on analysing the variation patterns of one of the most important indexes: temperature distribution inside a typical nuclear waste storage plant, when considering of different storage tank layout, air inlet patterns and inflow angle. 16 Computational Fluid Dynamics (CFD) simulation cases determined by the Orthogonal Experimental Design methods when considering several factors including storage tank layout, air inlet patterns and inflow angle were employed. The main heat processes, e.g. conduction, convection and radiation are all included in the simulation. The optimization strategies for the ventilation systems inside the plant were selected from different cases by comparing three key indexes: the maximum wall temperature, the average storage vault internal body temperature and surface-averaged temperature of the nuclear waste storage tank. The results showed that none of the maximum wall surface temperatures exceeded 65°C, that centralized rows would increase local surface temperatures, and that the optimal algorithms were staggered rows of storage tanks with vertical air inlets and outlets located on both sides.

Keywords: nuclear waste storage plant, ventilation, CFD

1. INTRODUCTION

In recent years, energy conservation has become a hot topic, and nuclear energy has gained significant attention due to its clean and efficient characteristics. However, with the global promotion and utilization of nuclear power, the management and storage of nuclear waste have emerged as a challenging issue. In Europe alone (excluding Russia and Slovakia), more than 60,000 tons of nuclear waste are stored (WNWR, 2019). In the United States, 96 operating nuclear power plants have collectively generated over 90,000 tons of nuclear waste (Jacoby, 2020). Currently, research on nuclear waste management has made notable progress. Compared to deep geological storage, repositories are less costly to construct and maintain, and unlike wet storage, they do not require continuous cooling systems or real-time monitoring. Inside storage tanks, nuclear waste releases significant decay heat over a long-term decay process, transferring heat from the inner surface to the outer surface through conduction. The release of decay heat is a continuous and gradual process, unaffected by external changes and without interruptions or power fluctuations. Therefore, each storage tank can be regarded as a constant heat source.

Inside storage repositories, numerous heat sources are arranged in arrays and equipped with a ventilation system featuring downward supply and upward return airflow. Flowing air removes heat through convective heat transfer. The radiative heat transfer between high-temperature heat

sources and wall surfaces is also significant and cannot be neglected. Controlling the wall surface temperature below 65°C (Board, 2001) ensures the structural integrity of the space. The continuous release of decay heat necessitates the long-term operation of the ventilation system, leading to sustained high-load operation of equipment such as fans and motors, which consumes substantial electrical energy. Therefore, studying and optimizing ventilation within storage repositories are essential for improving economic efficiency and ensuring safe storage.

Existing research on repositories primarily employs CFD (Computational Fluid Dynamics) technology, which offers significant advantages in such studies. CFD can accurately simulate complex flow phenomena such as turbulence and natural convection, as well as heat transfer processes including conduction, convection, and radiation. The visualization of temperature and velocity fields facilitates intuitive analysis of fluid flow and heat transfer. Additionally, CFD can replace hazardous and low-tolerance physical experiments, while its flexible parameter adjustment capabilities enhance the efficiency of optimization design. Numerical simulations of repositories predominantly focus on natural convection. Several studies (Chen and Chen, 2021, 2024; Kim et al., 2015; Lin et al., 2024) have used the k-ε turbulence model and the Discrete Ordinates (DO) radiation model, accounting for solar radiation, to investigate velocity and temperature fields within repositories. Lin et al. 2024 demonstrated that the spacing between heat sources affects the radiation view factor but has an insignificant impact on facility temperature. Chen and Chen, 2021, 2024 conducted sensitivity analyses of velocity and temperature fields, examining factors such as the presence of sunlight, windows, fans, and door positions. Their findings indicate that under natural convection, the maximum temperature inside the building does not compromise structural integrity. Kim et al. 2015 optimized repository design through numerical simulation by introducing dimensionless temperature and convection-radiation heat transfer ratios. They analyzed the effects of tank spacing, inlet length, and arrangement patterns on heat transfer, concluding that non-uniform staggered arrangements improve spatial efficiency and ensure thermal safety. Mishra et al. 2022 and Mishra et al. 2025 explored the influence of factors such as inlet position, shape, and duct edge roughness on air velocity and temperature fields, thermal efficiency, and air exchange rates. Ratiko et al. 2018 employed multi-objective optimization, considering thermal safety and cost, to refine repository design, combining numerical simulation with genetic algorithms to determine optimal configurations. Kim et al. 2014 combined the k-ε turbulence model and the Discrete Transfer Radiation Model (DTRM) to simulate repositories of various scales. They constructed a 1/4-scale repository model for experimental validation and evaluated scaling effects using dimensionless temperature, dimensionless residence time, Euler number, and Richardson number.

In summary, numerical simulation studies on repositories have primarily focused on natural convection, with limited analysis combining forced convection and radiation models for large-scale repositories. This study uses a specific repository as a prototype, considering operating conditions where the storage tanks are loaded to one-third of their full capacity. Building on previous research, it examines the effects of tank arrangement, outlet position, and inlet angle on heat transfer efficiency. The k-ε turbulence model and the S2S (Surface-to-Surface) radiation model are employed for CFD simulations, and orthogonal design experiments are used to analyze 16 simulation cases. The significance of this study lies in its ability to provide a detailed analysis of the temperature distribution on wall surfaces, identify the key factors influencing spatial and maximum wall temperatures, and evaluate performance based on standardized temperature metrics. Ultimately, it proposes an optimal energy-saving solution.

2. METHODS

A computational domain including inlets, outlets, and nuclear waste storage tanks was established for numerical simulation, as shown in Figure 1. The internal dimensions of the repository are 15.4 m (length) × 5.4 m (width) × 2.4 m (height). Each storage tank has a diameter of 0.2 m and generates 396 W of heat. The ventilation system adopts a downward supply and upward return configuration. Existing studies have demonstrated that the Realizable k-ε model developed by Shih et al., 1995 has the capability to accurately predict and simulate various flow conditions (Lateb et al., 2013). The model demonstrates good numerical stability and predictive capability when dealing with complex wall boundaries and recirculation regions (Ahmadi-Baloutaki and Aliabadi, 2021). Its precision, computational efficiency, and robustness make it well-suited for indoor environment modeling (Ahmadi-Baloutaki and Aliabadi, 2021). The primary radiative heat transfer in the repository occurs between the high-temperature heat source surfaces and the walls. The S2S (Surface-to-Surface) radiation model, designed to analyze radiative heat transfer between arbitrarily complex surfaces in enclosed spaces, effectively describes this process. The medium filling the space between surfaces is a non-participating medium, meaning it does not absorb, emit, or scatter radiation. The three core governing equations are included in CFD simulations: the continuity, momentum, and energy equations, collectively encapsulated in Eq. (1). The heat transfer equation of S2S radiation model is represented by Eq. (2).

$$\frac{\partial(\rho\phi)}{\partial\tau} + div(\rho U\phi) = div(\Gamma grad\phi) + S \tag{1}$$

where ρ is the fluid density (kg/m^3); ϕ is a general variable that represents the velocity components u (m/s), v (m/s), and w (m/s) in the momentum equation, or temperature T (℃ or K) in the energy equation; τ is the time (s); div indicates divergence; U is the velocity vector; Γ is the generalized diffusion coefficient; grad represents the gradient; and S is the generalized source term.

$$J_k = E_k + \rho_k \sum_{j=1}^{N} F_{kj} J_j \tag{2}$$

Where, J_k represents the total radiation energy leaving surface k, E_k denotes the emissive power of surface k, ρ_k represents the emissivity of surface k, F_{kj} represents the view factor between surfaces k and j, J_j represents the radiation energy emitted from surface j.

Therefore, this study employs the Realizable k-ε model to simulate airflow within the repository and uses the S2S model to simulate the radiative heat transfer process between surfaces.

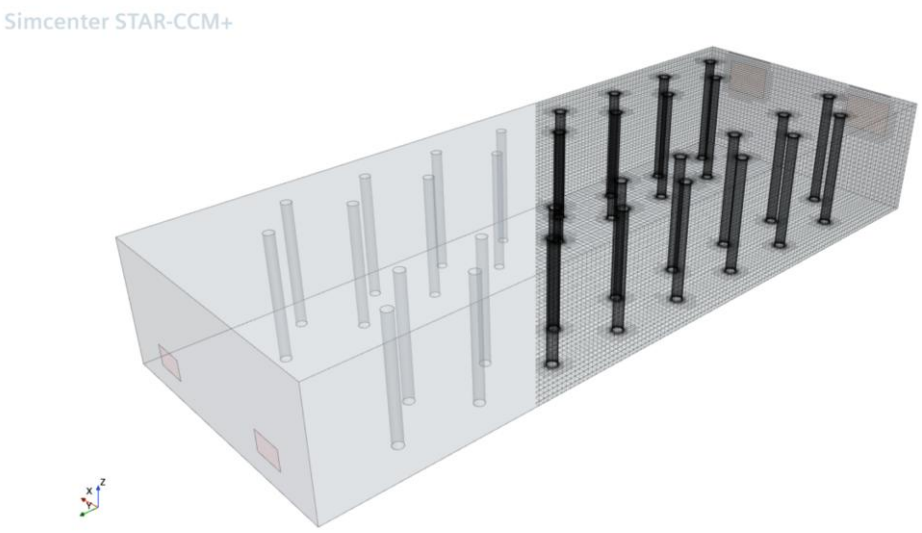

Figure 1. Geometric model diagram

The simulation was conducted using the commercial CFD software STAR-CCM+ 2302. A grid independence test was performed, as shown in Figure 2 a). Considering both the accuracy of the numerical simulation and computational efficiency, a grid size of 846,000 cells was selected for the simulation. During the simulation, it was assumed that the 32 storage tanks act as constant heat sources. The specific boundary types and parameters are listed in table 1. The simulation was performed under steady-state conditions.

Table 1. Boundary condition

Boundary Name	Boundary Type	Parameter	Values
Inlet	Velocity Inlet	Velocity	1.33m/s
		Temperature	18℃
Outlet	Pressure Outlet	-	-
Wall	Wall - Convection	Ambient Temperature	25℃
		Convective Heat Transfer Coefficient	8.7W/m^{2}K
		Surface Emissivity	0.85
Heat Source	Wall - Heat Source	Heat Power	396W
		Surface Emissivity	0.5

In this study, the typical Reynolds number of the airflow within the storage vault is approximately 11,000, indicating a turbulent flow regime. The heat transfer mechanisms primarily involve convective heat exchange between the surface of the storage tanks and the surrounding air, as well as radiative heat transfer between the tanks and the surrounding walls. The gas is assumed to be incompressible, and a gravity model is included to account for buoyancy effects. Due to the relatively large temperature differences in the system, the Boussinesq approximation is not applied. The ideal gas law is used to capture the temperature-dependent density variations, allowing for a more accurate representation of buoyancy-driven flow behavior.

The arrangement of storage tanks within the repository resembles that of a tube bundle heat exchanger. A corresponding model was established and validated against the Zhukauskas empirical correlation for tube bundles:

$$Nu_f = 0.35\left(\frac{S_1}{S_2}\right)^{0.2} Re_f{}^{0.6} Pr_f{}^{0.36}\left(\frac{Pr_f}{Pr_W}\right)^{0.25} \quad (2)$$

Dong et al. 2010 detailed the geometric dimensions and boundary conditions, and the results demonstrated that the numerical model effectively simulates the turbulent heat transfer process. Compared with the SST k-ω model, the simulation results of the Realizable k-ε model show better agreement with Zhukauskas empirical correlations. The model validation error was found to be less than 5% (Figure 2 b)).

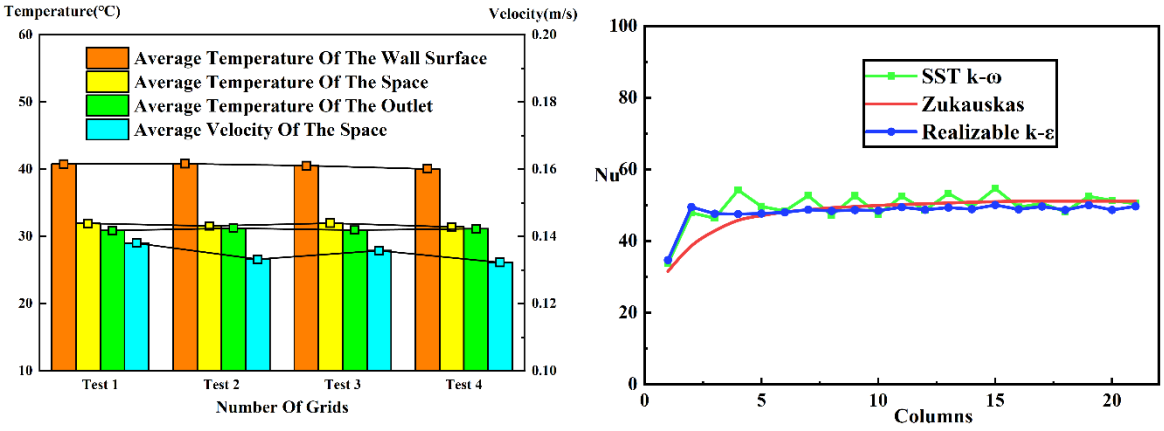

a) Mesh independence test b) Model validation

Figure 2. Mesh independence test and model validation results

The orthogonal experimental design was established with three factors: tank arrangement, outlet position, and inlet angle. A mixed orthogonal experimental table was constructed accordingly (Figure 3.).

No.x	Factor 1 Arrangement Type	Factor 2 Outlet Position	Factor 3 Inlet Angle
1	1	1	1
2	1	2	2
3	1	1	3
4	1	2	1
5	2	1	2
6	2	2	1
7	2	1	1
8	2	2	3
9	3	1	3
10	3	2	1
11	3	1	1
12	3	2	2
13	4	1	1
14	4	2	3
15	4	1	2
16	4	2	1

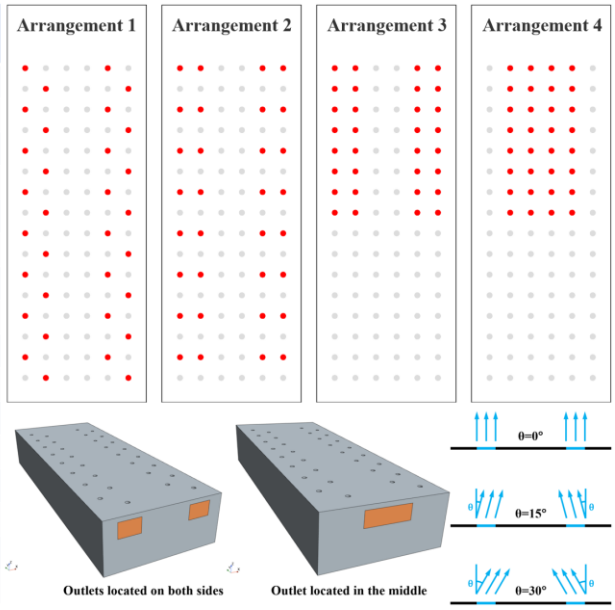

Figure 3. Orthogonal experiment table and influencing factors diagram

3. RESULTS

The Figure 4 display the velocity contour maps of the inlet-outlet diagonal cross-section and the corresponding wall surface temperature contour maps for four typical cases (case 1, case 7, case 11, and case 13).

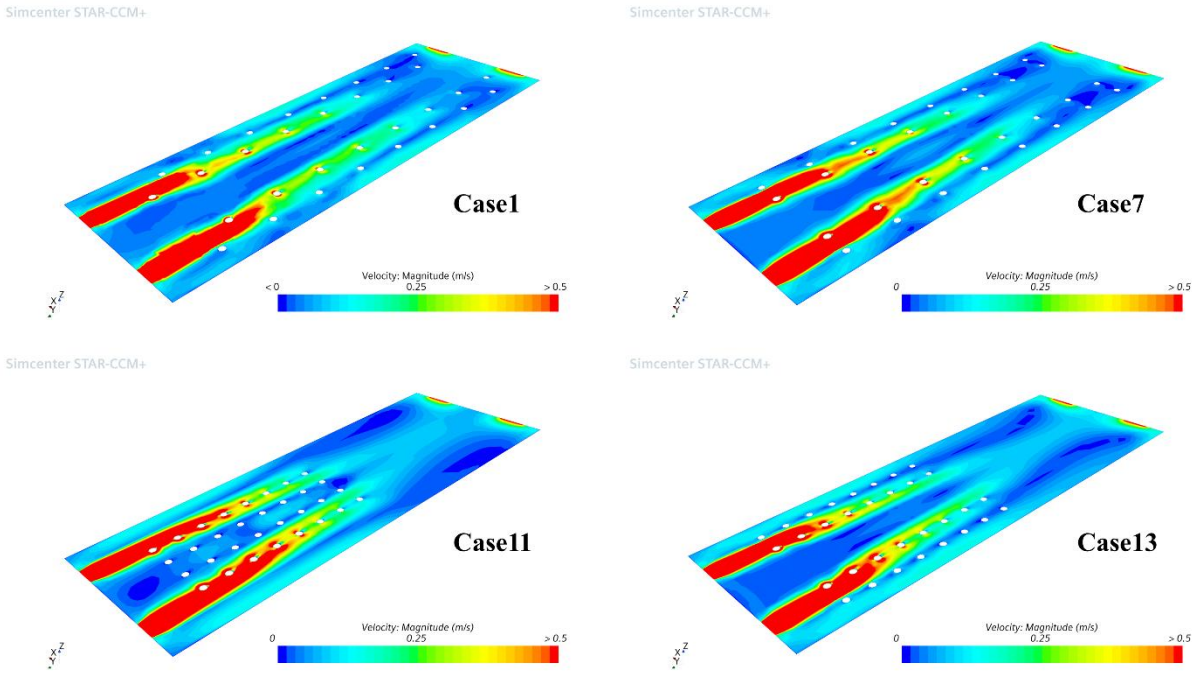

a) Velocity Contour Plot of the Inlet and Outlet Diagonal Section

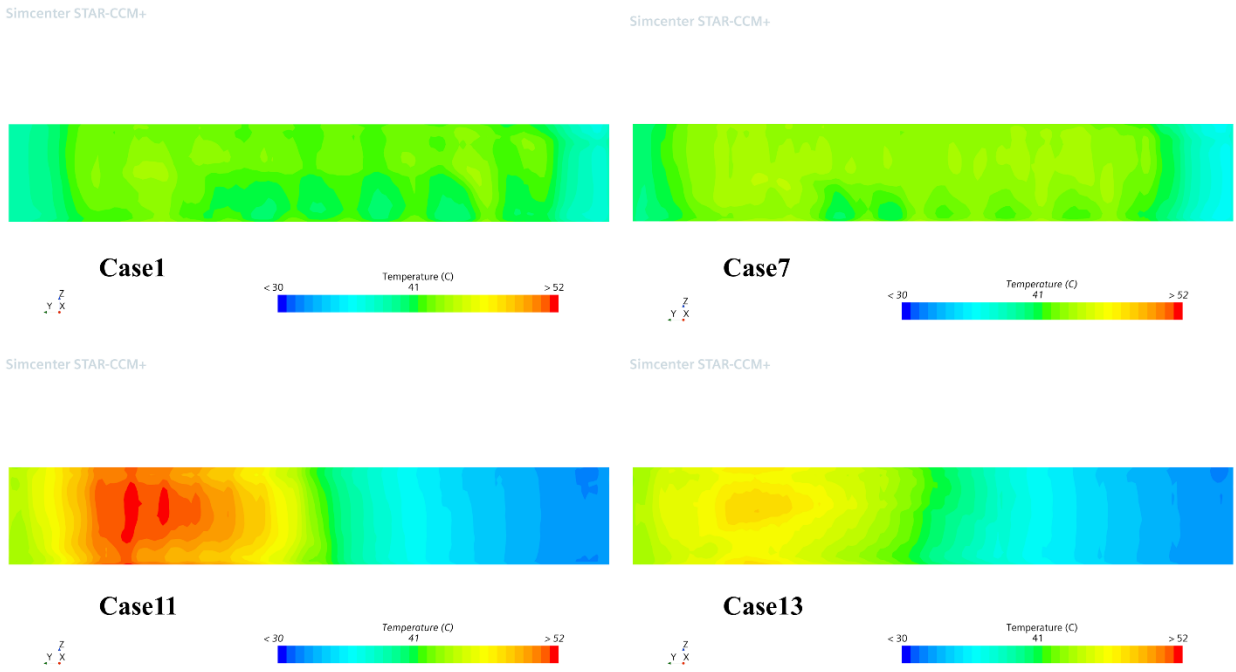

b) Temperature Contour Plot of Wall Surface

Figure 4. Velocity and Temperature of Typical Cases

A range analysis was conducted on the 16 orthogonal experimental cases, and the results indicate that the storage tank arrangement is the most influential factor affecting the maximum wall surface temperature, followed by the inflow angle, while the outlet position has a relatively minor impact. Centralized layouts tend to cause heat accumulation in the central region of the repository, resulting in elevated local wall temperatures. In contrast, staggered or uniformly distributed layouts facilitate better heat exchange between the air and the storage tanks.Due to the combined effects of tank arrangement and inflow angle on the spatial structure of the vault, these two factors significantly influence the temperature of the tank surfaces by shaping the airflow distribution. For the average spatial air temperature, the inflow angle plays the dominant role, as it determines the coverage and penetration of airflow throughout the space.

In summary, the storage tank arrangement governs the locations of local heat accumulation, while the inflow angle determines the overall heat transfer efficiency. The coordinated optimization of these two variables is essential for ensuring thermal safety and achieving energy-efficient operation.

4. DISCUSSION

From the velocity contour maps, it can be observed that due to the tank arrangements, the airflow in uniformly distributed cases (case 1 and case 7) extends further and merges only near the end of the repository. In contrast, for concentrated distributions (case 11 and case 13), the airflow merges in the central part of the repository, with reverse flow occurring along the wall surfaces.

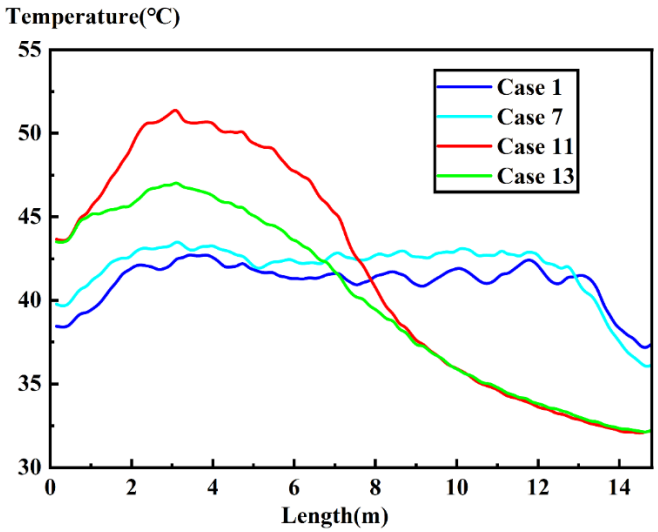

Figure 5. Wall Surface Temperature Distribution of Typical Cases

The simulation results indicate that the wall surface temperature in all cases remains below 65℃. In the uniformly distributed cases (case 1 and case 7), the heat sources closest to the wall are aligned in odd-numbered rows, and the temperature variation between rows 1 and 15 is relatively

stable. The average wall temperature for case 1 is 41.68°C, with a fluctuation of less than 2.6%, while case 7 exhibits a slightly higher average temperature with a fluctuation of 4.2%. Additionally, case 1 shows a wavelike temperature distribution with approximately 8 peaks, attributed to the closer proximity of heat sources in odd-numbered rows to the walls compared to even-numbered rows.

In concentrated distribution cases (case 11 and case 13), heat sources are primarily concentrated in the first eight rows. Compared to case 1, the average wall surface temperature increases by approximately 16.7% and 7.1%, respectively. This difference arises because the heat sources in configuration 4 are more densely located in the central two rows. Between rows 9 and 16, where no heat sources are present, the average wall surface temperature decreases by about 15% compared to configuration 1, with both cases showing nearly identical temperatures.

The maximum wall temperature, average heat source surface temperature, and average spatial temperature for all 16 cases were analyzed and evaluated. Range analysis reveals the following: The position of the outlet has a negligible impact on these temperature metrics. The wall surface maximum temperature is primarily influenced by the arrangement of heat sources, followed by the inlet angle. Both the heat source arrangement and the inlet angle significantly affect the average surface temperature of the heat sources. For the average spatial temperature, the inlet angle has a more pronounced impact.

Using standardized temperature metrics for evaluation, the results indicate that the layouts in case 1 and case 7 are more effective for heat dissipation and reducing wall surface temperatures, while the layouts in case 9 and case 12 perform the worst.

5. CONCLUSIONS

The distribution of wall surface temperatures is closely related to the arrangement of heat sources. For concentrated arrangements (case 11 and case 13), the average temperature in the front rows is 16% and 7% higher than that of the dispersed arrangement, respectively, while the average temperature in the rear rows decreases by 15%.

The arrangement of heat sources has the greatest impact on the maximum wall surface temperature, followed by the inlet angle. Both the arrangement and the inlet angle significantly influence the average surface temperature of the heat sources. However, for the average spatial temperature, the inlet angle has a more pronounced effect.

Using standardized temperature evaluation methods, the 16 cases were assessed. Case 1 exhibited the best performance, followed by cases 4, 7, and 6. Conversely, cases 9 and 12 showed the poorest heat transfer performance and should be avoided under practical operating conditions.

Acknowledgment

This work was sponsored by the National Natural Science Foundation of China (Grant No. 52478080, Grant No. 52408101, and Grant No.52078096), Natural Science Foundation of Liaoning Province (Grant No. 2023-MSBA-023), the fundamental Research funds for the Central Universities (Grant No. DUT24MS023) and 2023 International Exchange Foundation Project of Co-Creation of Excellence Program from Dalian University of Technology (Grant No. DUTIO-ZG-202307).

REFERENCES

Aliabadi, A. A. (2022), 'Turbulence: A Fundamental Approach for Scientists and Engineers', Springer, Cham, ISBN: 978-3-030-95410-9

Ahmadi-Baloutaki, M. & Aliabadi, A. A. (2021), 'A Very Large-Eddy Simulation Model Using a Reductionist Inlet Turbulence Generator and Wall Modeling for Stable Atmospheric Boundary Layers', Fluid Dynamics, 56(3), 413-

432, doi:10.1134/S0015462821020026.
Board, A.E.R., 2001. Design of concrete structures important to safety of nuclear facilities. Safety Standard No. Aerb/Ss/Cse-1.
Chen, B., Chen, Y., 2021. Numerical investigation for the spent fuel storage building design of the chinshan nuclear plant. Prog. Nucl. Energy 135, 11. https://doi.org/10.1016/j.pnucene.2021.103690.
Chen, B., Chen, Y., 2024. Heat transfer analysis for the temporary spent fuel storage of the chinshan nuclear plant. Nucl. Eng. Des. 428, 9. https://doi.org/10.1016/j.nucengdes.2024.113535.
Dong, Q., Ouyang, K., Liu, M., Zhang, L., 2010. Numerical investigation of fluid flow across tube bundles in zukauskas experimental model. Pressure Vessel Technology 27 (1), 21-26. https://doi.org/10.3969/j.issn.1001-4837.2010.01.006.
Jacoby, M., 2020. As nuclear waste piles up, scientists seek the best long-term storage solutions.
Kim, D., Yook, S., Lee, K., 2015. Investigation of radiative and convective heat transfer in storage vaults for improving space efficiency. Int. J. Heat Mass Transf. 80, 301-308. https://doi.org/10.1016/j.ijheatmasstransfer.2014.09.026.
Kim, D., Yook, S., Lee, K., Yu, S., Bang, K., 2014. Scaling method for storage vaults based on thermal-hydraulic characteristics. Nucl. Eng. Des. 275, 242-248. https://doi.org/10.1016/j.nucengdes.2014.04.042.
Lateb, M., Masson, C., Stathopoulos, T., Bedard, C., 2013. Comparison of various types of k -ε models for pollutant emissions around a two-building configuration. J. Wind Eng. Ind. Aerodyn. 115, 9-21. https://doi.org/10.1016/j.jweia.2013.01.001.
Lin, C., Tseng, Y., Lin, K., Chang, Y., Hung, T., Hsu, H., 2024. A numerical investigation of an indoor dry storage facility on heat transfer. Ann. Nucl. Energy 196, 13. https://doi.org/10.1016/j.anucene.2023.110225.
Mishra, V.K., Panda, S.K., Sen, B., Maiya, M.P., Rao, B.P.C., 2022. Numerical analysis of forced convection heat transfer in a nuclear fuel storage vault. Int. J. Therm. Sci. 173, 19. https://doi.org/10.1016/j.ijthermalsci.2021.107429.
Mishra, V.K., Panda, S.K., Sen, B., Samantaray, D., Maiya, M.P., 2025. Potential of thermosyphon for passive cooling of nuclear fuel storage vault. Int. J. Therm. Sci. 208, 15. https://doi.org/10.1016/j.ijthermalsci.2024.109477.
Ratiko, R., Samudera, S.A., Hindami, R., Siahaan, A.T., Naldi, L., Hapsari, D., Mahlia, T.M.I., Nasruddin, N., 2018. Optimization of dry storage for spent fuel from g.a. Siwabessy nuclear research reactor. Int. J. Technol. (1).
Shih, T.H., Liou, W.W., Shabbir, A., Yang, Z.G., Zhu, J., 1995. A new kappa-epsilon eddy viscosity model for high reynolds-number turbulent flows. Comput. Fluids 24 (3), 227-238. https://doi.org/DOI 10.1016/0045-7930(94)00032-T.
WNWR, 2019. The world nuclear waste report 2019 [online].

6th International Conference on Building Energy and Environment
Eindhoven University of Technology, The Netherlands
6 - 10 July 2025

Filter application as air quality improvement strategy for particulate matter

Lisa Corneillie [1], Klaas De Jonge [1], Jelle Laverge [1]

[1]*Ghent University, Ghent, Belgium, lisa.corneillie@ugent.be*

SUMMARY
Particulate matter (PM) is widely recognized as one of the most hazardous pollutants affecting human health and life expectancy, as evidenced by numerous studies. Since individuals spend the majority of their time indoors, reducing indoor exposure to PM is essential for safeguarding overall health. This study utilized dynamic simulations in Dymola to assess the performance of ventilation filters in lowering indoor PM concentrations in a three-bedroom apartment. The findings indicate that maintaining PM levels below the World Health Organization's (WHO) guideline values requires the use of a HEPA filter within the ventilation system, coupled with keeping windows closed. To further mitigate PM generated during cooking, a high-efficiency cooker hood or air purifier can complement the ventilation filter. Additionally, opening nearby windows during cooking can help reduce exposure to PM. However, despite the implementation of filtration systems, the disability-adjusted life years (DALYs) attributed to PM exposure remain three times higher than those associated with other indoor pollutants.

Keywords: Particulate matter, filter performance, indoor air quality, DALY

1. INTRODUCTION

Annually, two million deaths are attributed to particulate matter (PM) inhalation and its associated health effects (Lu et al., 2023). These health effects range from miscarriages and respiratory problems to heart deficiencies and cancer. Given that individuals spend approximately 90% of their time indoors, the majority of these health impacts are linked to indoor PM concentrations (Kim et al., 2023). Air filters can be employed to mitigate exposure to indoor PM; however, questions remain regarding their effectiveness in real-world environments. Laboratory tests of these filters often neglect various parameters that influence indoor PM concentrations, which may lead to an undue sense of security regarding their performance in practical settings. Consequently, the objective of this study is to examine whether filters can sufficiently reduce indoor particulate matter concentrations in a realistic residential environment.

To achieve this goal, a filter component was developed, and an existing multi-zone model was adapted to incorporate particulate matter. Subsequently, a series of simulations was conducted to evaluate the influence of various parameters. The parameters investigated include variable outdoor PM concentrations, the performance of different filter types, the impact of cooking-related PM, demand-based ventilation, and window operation. Finally, the number of disability-adjusted life years (DALYs) per 100 000 individuals resulting from PM2.5 exposure under different scenarios was calculated. This was then compared to the DALYs attributable to other indoor pollutants to assess the significance of particulate matter when a filter is present.

2. METHODOLOGY

To accurately evaluate filter efficiency, it is essential to create a virtual environment specifically designed for this purpose. In this study, dynamic simulations were conducted in Dymola using the Modelica language.

2.1 Filter component

The first step in creating such an environment is modelling a filter component in Dymola. This component was developed based on the current testing standard for high-efficiency filters, NBN EN 1822-1 (2019). Its testing method provides an efficiency curve, and an initial pressure drop. By adhering to this mandatory standard, the model allows comparison of other filters when manufacturers make relevant data available. Applied data is thus treated as potential output data from the testing standard. The filter component can be configured with various PM size fractions and their corresponding filter efficiencies, as derived from the efficiency curve of the testing standard. The number of size fractions can also be adjusted as needed. In this study, four size fractions were used: PM0.1, PM1, PM2.5, and PM10. It is important to note that overlap exists between these size fractions, representing a long-standing research gap in PM guidelines and measured data. Unfortunately, this issue could not be resolved within the scope of this study.

Additional considerations must also be addressed. First, the tested velocity is determined by the manufacturer. Since filter efficiency is highly dependent on velocity, comparing filters evaluated under different velocities presents significant challenges. Second, the humidity condition specified in the testing standard is relatively broad. As humidity influences particle settling rates, variations in humidity could also lead to discrepancies in efficiency. Future updates to the standard should include specified testing velocities to facilitate more consistent comparisons between filters.

The resulting filter component requires the filter efficiency and the initial concentration of pollutants as inputs, and it outputs the remaining particle concentration. The component was validated using data from the Out2In project (Herreweghe et al., 2019).

2.2 Multi-zone model

In the next step, an existing multi-zone model developed in Dymola by De Jonge (2023) was adapted to incorporate particulate matter. To achieve this, PM tracers were added to both the air medium and the outdoor air. Each tracer was assigned a decay rate derived from the literature, ranging from 1.1/h to 151/h. Additionally, the outdoor PM concentrations for the different tracers were made variable. These concentrations were obtained via irCELine.be for PM1, PM2.5, and PM10. For PM0.1, interpolation could be performed; however, due to the unknown size distribution of PM and its significant geographic variability, this approach would not provide an accurate representation of the associated health effects. Using the same data as for PM1 is therefore regarded as a worst-case scenario, assuming all particulate matter within its size fraction belongs to PM0.1. Should more precise data become available in the future, this approach should be revised for greater accuracy.

The overall model represents a three-bedroom apartment with approximately 120 m^3 of living space. The Dymola model is composed of nine separate zones, one for each room, while the communal hallway is excluded. A graphical representation of the model is provided in Fig. 1.

Figure 1. Floorplan of the 3-bedroom apartment.

2.3 Base scenario

To evaluate filter performance within this model, a baseline for comparison must first be established. This baseline scenario assumes the apartment is unoccupied, yet functional as though it were. By making this simplification, particulate matter generated by occupant activities is excluded at this initial stage. Additionally, all windows in the apartment remain closed. Air purification is provided by a mechanical ventilation system with heat recovery (MVHR) operating continuously at a constant flow rate. No filter is included in this ventilation system, and the building is assumed to have good airtightness. The outdoor PM concentrations are sourced from a measuring station in Vilvoorde. The results of this baseline scenario serve as a reference point for the subsequent case studies.

3. CASE STUDIES

In the subsequent phase, several factors influencing indoor PM concentrations were analysed. For each case study, the baseline model was adapted, as necessary. Additionally, various combinations of case studies were simulated. In total, fifteen simulations were conducted, including the baseline scenario. The case studies were categorized into five distinct groups, each addressing a specific influential factor.

3.1 Category A: Variable outdoor concentration

To examine the influence of varying environments within Belgium, three additional sites were selected, each representing distinct surroundings potentially associated with different PM size distributions. These sites included the city center of Ghent, the Antwerp ring road, and a rural area (Moerkerke). The base scenario site was located just outside the Brussels ring road (Vilvoorde).

3.2 Category B: Filter type

Secondly, three filter types with varying efficiencies were evaluated in the developed environment. The efficiencies of a coarse 60% filter and an ePM1 55% filter were derived from data collected during the Out2In research by Buildwise, where filters were evaluated at a face velocity of 0.5 m/s (Herreweghe et al., 2022). The efficiency of an H13 filter was determined using a mathematical approach (Chen et al., 2019) at a velocity of 0.164 m/s. Table 1 provides an overview of the efficiencies used. These filters were subsequently incorporated into the overall multi-zone model, with a filtration efficiency of 10% assumed for O_3 across all filters.

Table 1. Filter efficiencies for each filter type.

Size fraction	Coarse filter *[%]*	ePM1 55% filter *[%]*	H13 filter *[%]*
PM0.1	42.32	53.58	99.95
PM1	40.58	31.07	99.99
PM2.5	50.67	41.26	99.99
PM10	63.99	58.48	99.99

3.3 Category C: Indoor PM source

In the next case study, a family of four was introduced into the apartment. Cooking was identified as the most significant and universal indoor PM source, while smoking, being a lifestyle choice, was excluded. Consequently, a cooking schedule consisting of three basic hot meals was developed as a worst-case scenario, as shown in Table 2. The emissions associated with these meals were linked to the family's occupancy schedule and repeated weekly (O'Leary et al., 2019). To determine the size distribution of cooking-related PM, a lognormal distribution was assumed, with a mode diameter of 0.04 μm and a standard deviation of 0.005 μm (Pikmann et al., 2023). This analysis indicated that nearly all cooking-related PM could be attributed to PM0.1. Based on these findings, a PM source schedule was constructed. The emission rate for lunch was tied to this schedule, and conversion factors were applied to differentiate between the meals. A cooker hood, capable of eliminating 70% of PM emissions directly, was also included in the scenario.

Table 2. Emission rate and duration for the selected meals (Source: O'Leary et al., 2019).

Meal	Average Emission Rate *[μg/min]*	Duration *[minutes]*
Breakfast	220	3.85
Lunch	1900	28
Dinner	3200	17

3.4 Category D: Demand based ventilation

An occupant-based ventilation system was also analyzed. In the selected system, the flow rate is adjusted based on the bathroom's humidity and the kitchen's CO_2 concentration (De Jonge, 2023). However, elevated humidity levels accelerate the settling of particulate matter, which could negatively impact PM concentration.

3.5 Category E: Window opening schedule

The opening of windows introduces additional PM from the outdoor environment. Since a ventilation system equipped with a filter does not alter this concentration, all particles from outside enter the room directly. To assess this influence, a window-opening schedule, detailed in Table 3, was developed, and a window component was modelled using research by Verbruggen et al. (2021). This component applies Phaff's equation, combined with window usage and temperature differences, to simulate airflow through the window.

Table 3. Window types and opening schedules.

Window	number	Type	Opening Winter	Opening Summer
Large window living room	1	Closed	Always closed	Always closed
Small window living room	2	Slide	Always closed	Open 9-5
Window kitchen	3	Turn	Always closed	Always open
Small window bedroom 1	4	Tilted	Open 8-9	Always open
Big window bedroom 1	5	Tilted	Open 8-9	Always open
Window bedroom 2	6	Tilted	Open 8-9	Always open
Window bedroom 3	7	Tilted	Open 8-9	Always open

4. EVALUATION

4.1 WHO target values

All findings are evaluated against the World Health Organization's (WHO) 2021 guideline values for the average annual PM concentration, which emphasizes health impacts. However, the WHO underscores that no safe threshold exists for PM, and concentrations should be minimized as much as possible. The WHO provides guidelines for PM2.5 and PM10, but not for PM1 and PM0.1, so interpolated values were calculated. The used values are shown in Table 4.

Table 4. Guideline values by the WHO, and interpolated values.

Pollutant	Averaging period	Concentration [µg/m³]	Pollutant	Averaging period	Concentration [µg/m³]
PM_{10}	Calendar year	15	PM_1	Calendar year	4
$PM_{2.5}$	Calendar year	5	$PM_{0.1}$	Calendar year	3

4.2 DALYs

The disability-adjusted life years (DALYs) were calculated for several key scenarios, representing the average number of healthy years lost per 100,000 individuals due to premature death or disability caused by pollutant exposure over one year. Due to the availability of effect factors, this analysis includes only PM2.5, excluding PM10. Furthermore, the assessment focuses on the kitchen, where the most significant impact is anticipated. The total DALYs were calculated using Eqs. (1) and (2) (Guyot et al., 2024), employing a time-resolved calculation method for DALYs based on the work of De Jonge (De Jonge & Laverge, 2022):

$$DALYs(t) = \int_{t_0}^{t} \frac{DALYs}{time}(t) \quad (1)$$

$$\frac{DALYs}{time}(t) = EF_{marginal} * IR(t) \quad (2)$$

Here IR(t) represents the intake rate [kg/s], and EF is the effect factor [DALY/kg]. The effect factors for PM2.5 and the other pollutants can be observed in Table 5 (Morantes et al., 2024). The intake rate is determined using Eq. (3).

$$IR(t) = V_{br}(t) * C_{exp}(t) \quad (3)$$

In this equation, $V_{br}(t)$ is the breathing rate over time, assumed to be 16m³/day and $C_{exp}(t)$ is the exposure concentration profile. To construct this profile, the initial worst-case assumption for PM0.1 was replaced with the percentage distribution of the outdoor PM measured in the Out2In study, ensuring no double accounting of concentrations (Herreweghe et al., 2019).

Table 5. Effect factors for various pollutants (Morantes et al., 2024).

Pollutant	EF marginal (median) [DALY/kg]
PM2.5	118.6111
Formaldehyde	18.0351
Ozone	4.2638
Nitrogen dioxide	15.7924
Benzene	0.1268
Toluene	0.0016
Naphthalene	0.6718
Limonene	0.0175

5. SCENARIO ASSESSMENT

5.1 WHO guidelines

For the base scenario, the average annual concentrations of PM exceed the WHO's recommended limits. For PM1 and PM0.1, the averages are approximately 7 µg/m³, compared to the recommended values of 3–4 µg/m³. For PM2.5, the difference with the guideline is around 4 µg/m³ (9 µg/m³ versus a guideline value of 5 µg/m³). For PM10, the difference is minimal. Overall, WHO indoor air quality guideline values are continuously exceeded.

Simulations of indoor PM concentrations under varying outdoor levels revealed that the variation in Belgium is insufficient to significantly influence overall average values. However, minor differences in size distribution are observed based on location. Traffic-heavy areas exhibit higher fine PM levels, while rural areas show elevated concentrations of coarse PM.

The introduction of various air filters had a substantial impact on PM concentrations. Installing an ePM1 filter, designed for smaller particle ranges, effectively reduced concentrations of the most harmful particles to just above the guideline values. However, achieving concentrations below the WHO threshold was only possible with an H13 filter. Adding an indoor PM source, such as cooking, caused a significant increase in the concentration of the smallest particles. High peaks (up to 300 µg/m³ during cooking) were observed, contributing notably to the average concentration. Filters have no effect on these peaks. In comparison to cooking-related PM, the overall reduction in average PM concentration due to filters is minor. Thus, additional source control measures are necessary to mitigate this indoor PM source.

A demand-based ventilation system, adjusted according to occupant activity, significantly increases indoor PM concentrations, particularly in wet rooms. Continuous ventilation systems allow for faster reduction of peak concentrations. A more tailored ventilation schedule, adapted to PM peak periods or integrated with PM sensors, could address this issue. The addition of air exchange through open windows substantially affects indoor air quality. Without a filter, opening windows has little to no effect or a slight positive impact. However, with a filter, the negative impact of window opening increases with the efficiency of the filter. Open windows also function as a source control for cooking-related PM, but if left open for too long, their negative effects outweigh the benefits. Figure 2 summarizes the key scenarios analysed in this study.

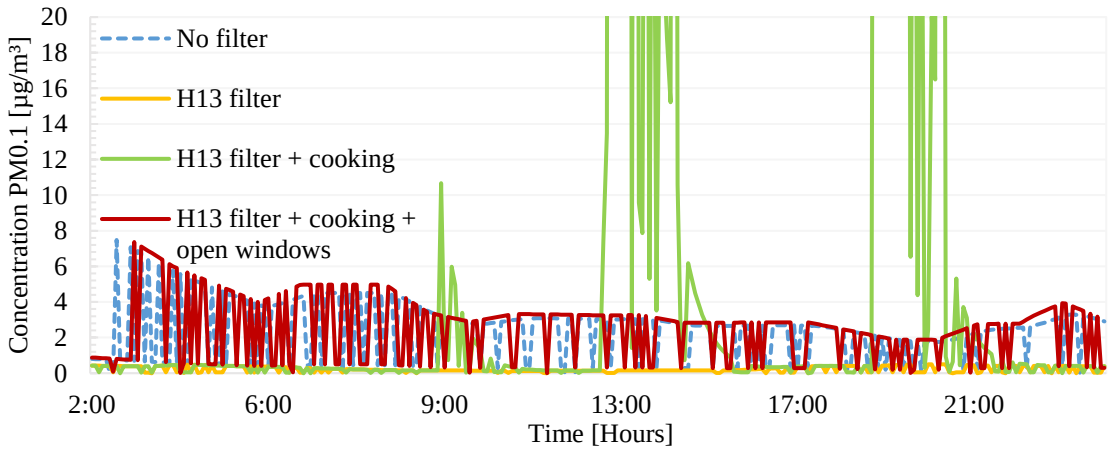

Figure 2. Comparison of daily PM concentration in different scenarios (close-up).

5.2. Health Impact of Mitigation Measures

The calculation of DALYs for PM2.5 in the kitchen across different scenarios demonstrates that air filters can significantly reduce the health impact of particulate matter. Even when cooking and/or window opening occurs, the improvements initiated by a (HEPA) filter remain highly significant in all scenarios. Figure 3 provides a comparative overview of these scenarios. For instance, the inclusion of an H13 filter in the apartment with an indoor source, results in a reduction of 1 300 DALYs.

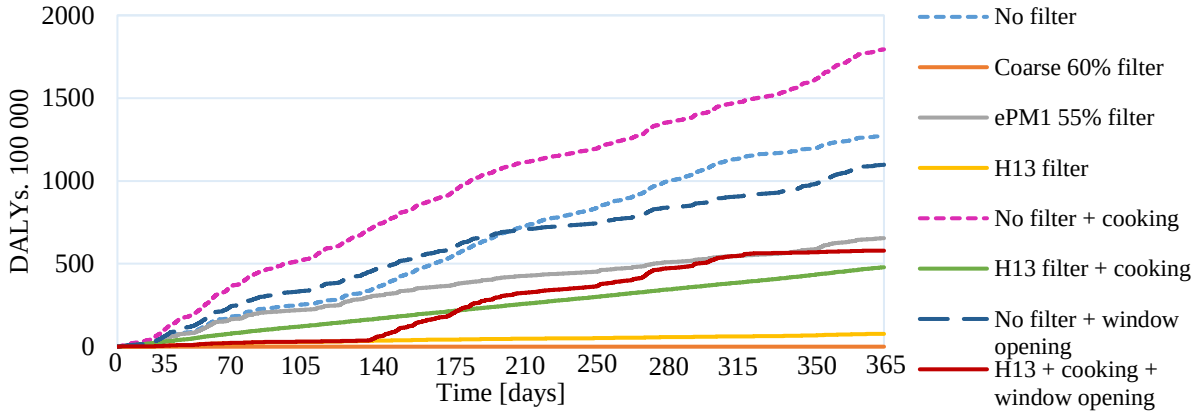

Figure 3. Number of DALYs for PM2.5 in function of the time in the kitchen.

5.3. Other pollutants

The existing multi-zone model includes various other pollutants, such as VOCs, NO_2, and O_3. A DALY assessment for the most realistic scenario—incorporating a filter, occupants, and open windows—highlights the critical importance of particulate matter. The number of DALYs for PM2.5 substantially exceeds those for other pollutants under the same conditions. Apart from PM, NO_2, O_3, and formaldehyde are the most harmful pollutants, as shown in Figure 4.

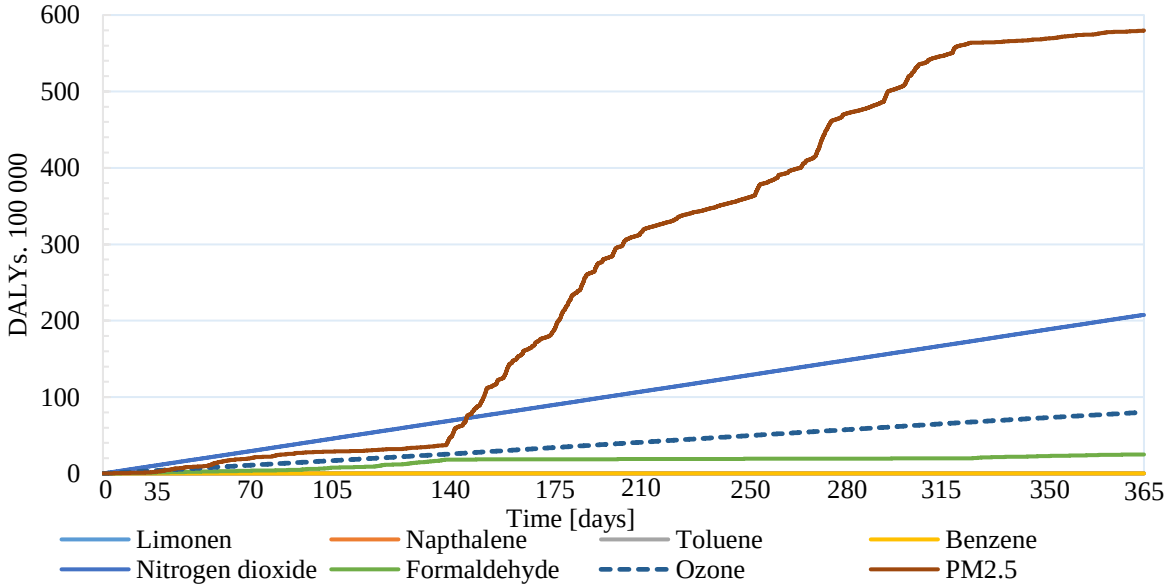

Figure 4. Number of DALYs for various pollutants per 100 000 people in the kitchen.

6. CONCLUSIONS

Particulate matter is a dominant contributor to various adverse health effects. Despite broad consensus on this issue, indoor PM concentrations in an apartment in Belgium, regardless of location, consistently exceed WHO recommendations when no mitigation measures are implemented. Filters offer an effective strategy for improving air quality, but only high-efficiency filters sufficiently reduce concentrations. To maintain their effectiveness in real-world conditions, windows should remain closed as much as possible. Moreover, local PM peaks caused by cooking cannot be offset by filtered air alone. To ensure a healthy environment during meal preparation, implementing local source control measures, such as a high efficiency cooker hood, air cleaners or briefly opening windows, is essential. The evaluated demand-based ventilation strategy proved inadequate, as it failed to reduce peaks quickly enough. Nevertheless, even with a filter in a continuous ventilation system, the DALYs attributable to particulate matter in real-life settings remains significant. Other indoor pollutants pose much less risk to human health. As such, further research into strategies for reducing indoor PM concentrations is essential.

ACKNOWLEDGEMENTS

The author would like to thank Prof. dr. ir. arch. Jelle Laverge and dr. ir. arch. Klaas De Jonge for their guidance throughout the research process. Subsequently the author also would like to thank Joris Van Herreweghe for providing data behind the OUT2IN research project.

REFERENCES

Belias, E., & Licina, D., 2024. European residential ventilation: Investigating the impact on health and energy demand. Energy and Buildings 304, 113839.

Chen, C., Ji, W., & Zhao, B., 2019. Size-dependent efficiencies of ultrafine particle removal of various filter media. Building and Environment 160, 106171.

De Jonge, Klaas, and Jelle Laverge., 2022. Time-Resolved Dynamic Disability Adjusted Life-Years Estimation. Indoor Air 32, no. 11, e13149. https://doi.org/10.1111/ina.13149.

De Jonge K. Holistic performance assessment of residential ventilation systems. Ph.D.thesis, Ghent University, Faculty of Engineering and Architecture, 2023.

Guyot, G., Kolarik, J., Breesch, H., De Jonge, K., Poirier, B., Al Assaad, D., Alonso, M.V. Rating existing smart ventilation strategies (working document - version 28/05/2024).

Herreweghe, J. V., Caillou, S., Haerinck, T., & Dessel, J. V., 2019. Out2In: Impact of filtration and air purification on the penetration of outdoor air pollutants into the indoor environment by ventilation.

Herreweghe, J. V., Caillou, S., Haerinck, T., Graindorge, F., Delmez, C., & Huffel, P. V., 2022. Real-life ventilation filter performance: Final results of an in-depth study.

Kim, M., Jeong, S.-G., Park, J., Kim, S., & Lee, J.-H., 2023. Investigating the impact of relative humidity and air tightness on PM sedimentation and concentration reduction. Building and Environment 241, 110270.

Lu, J., Wu, K., Ma, X., Wei, J., Yuan, Z., Huang, Z., Fan, W., Zhong, Q., Huang, Y., & Wu, X., 2023. Short-term effects of ambient particulate matter (PM1, PM2.5 and PM10) on influenza-like illness in Guangzhou, China. International Journal of Hygiene and Environmental Health 247, 114074.

Morantes, Giobertti, Benjamin Jones, Constanza Molina, and Max H. Sherman., 2024. Harm from Residential Indoor Air Contaminants. Environmental Science & Technology 58, no. 1, 242–57. https://doi.org/10.1021/acs.est.3c07374.

O'Leary, C., Jones, B., Dimitroulopoulou, S., & Hall, I. P., 2019. Setting the standard: The acceptability of kitchen ventilation for the English housing stock. Building and Environment 166, 106417.

Pikmann, J., Drewnick, F., Fachinger, F., & Borrmann, S., 2023. Particulate emissions from cooking activities: Emission factors, emission dynamics, and mass spectrometric analysis for different preparation methods. EGUsphere 1-36.

Technical Committee CEN/TC 195 "Air filters for general air cleaning"., 2009. High efficiency air filters (EPA, HEPA, ULPA) - Part 1 : Classification, performance testing, marking (NBN EN 1822-1).

Verbruggen, S., Janssens, A., & Laverge, J.. Window use habits as an example of habitual occupant behaviour in residential buildings. Ph.D.thesis, Ghent University, Faculty of Engineering and Architecture, 2021.

6th International Conference on Building Energy and Environment
Eindhoven University of Technology, The Netherlands
6 - 10 July 2025

Predicting The Impact of a Formaldehyde Selective Metal-Organic Framework Material on Indoor Air Quality

Zhenlei Liu [1], Jialei Shen [2,3], Rui Zhang [4], Weihui Liang[5], Doyun Won[6], Beverly Guo[7], Wenfeng Huang[7], Jianshun Zhang[7], Nicolas Sadovnik[8], Marco Daturi[8], Christian Serre[9], Menghao Qin[10]

[1]*Building Performance Lab, City University of New York, New York, USA, zliu2@ccny.cuny.edu*
[2]*Department of Civil Construction and Environment Engineering, The University of Alabama at Birmingham, Birmingham, USA, shenj@uab.edu*
[3]*Department of Environmental Health Sciences, The University of Alabama at Birmingham, Birmingham, USA, shenj@uab.edu*
[4]*GTI Energy, Des Plaines, USA, rzhang@gti.energy*
[5]*School of Architecture and Urban Planning, Nanjing University, Nanjing, China, liangwh@nju.edu.cn*
[5] *National Research Council Canada, Ottawa, Canada, Doyun.Won@nrc-cnrc.gc.ca*
[7] *Department of Mechanical Engineering, Syracuse University, Syracuse, USA, bguo@syr.edu, whuang50@syr.edu, jszhang@syr.edu*
[8]*Normandie University, ENSICAEN, UNICAEN, CNRS, Laboratoire Catalyse et Spectrochimie, Caen, France, nicolas.sadovnik@squair.tech, marco.daturi@ensicaen.fr*
[9]*Institut des Matériaux Poreux de Paris, ESPCI Paris, Ecole Normale Supérieure, CNRS, PSL University Paris, France, christian.serre@espci.psl.eu,*
[10] *Department of Environmental and Resource Engineering, Technical University of Denmark, Lyngby 2800, Denmark, menqin@dtu.dk*

SUMMARY
Metal-Organic Framework (MOF) materials present a promising solution to enhance energy efficiency and improve indoor air quality (IAQ) in buildings. This research examines the ability of a MOF material to passively control formaldehyde – a harmful indoor pollutant – by integrating laboratory testing and predictive IAQ modeling.

Laboratory experiments used the microporous Al pyrazole carboxylate, denoted Al-3,5-PDA or MOF-303, that was previously identified as a highly efficient material to capture traces of formaldehyde in air without releasing it before 50°C. The formaldehyde adsorption performance was evaluated in a continuous 28-day small-scale chamber test, followed by a 7-day desorption phase. Tests were performed using an Al-3,5-PDA paper sheet at the formaldehyde concentration of 50 - 500 µg/m^3 to assess the material's adsorption performance. Evaluating of the long-term performance of MOF material in room-scale tests would provide valuable insight into their effectiveness in real-world scenarios. However, due to their high adsorption capacity and the significant cost of experimental specimens, it is too expensive to conduct long-term saturation tests or room-scale implementation. To compensate for the lack of the long-term test data, an IAQ simulation model was developed by integrating the tested adsorption capability via a multizone CONTAM software. This model used the parameters derived from short-term, small-scale tests to simulate large-scale, real-world applications. This model not only can enable more accurate forecasts of effectiveness under various scenarios, but also can reduce the cost to conduct extensive tests.

Simulations were carried out at room scale with interior walls coated with the Al-3,5-PDA. The simulation demonstrated a 47% short-term reduction of formaldehyde levels by coating 10 m^2 of wall surface in a 30 m^3 room at 23 °C and 50% relative humidity. The results confirmed that Al-3,5-PDA's high formaldehyde adsorption capacity, taking 150 days to reach saturation. These findings highlighted the potential of Al-3,5-PDA to effectively adsorb

formaldehyde and reduce ventilation demands, contributing to energy savings and the improvement of IAQ in buildings. This study integrated short-term laboratory data into a scalable IAQ model, providing a cost-effective approach to predict performance of MOF materials in real-world building environments.

Keywords: Metal-Organic Framework, Formaldehyde, Indoor Air Quality, Model-based Testing and Evaluation.

1. INTRODUCTION

Formaldehyde is an indoor air pollutant that commonly found in various household and commercial products such as furniture, textiles, and building materials (Wang and Zhang, 2009; Xu et al., 2012; Zhou et al., 2018). Chronic exposure to formaldehyde can lead to respiratory issues, eye irritation, and cancer risk. This emphasizes both the increased risk within enclosed environments and the importance of effective removal strategies in indoor environments. Although removal is essential, effective technologies for removing formaldehyde in living spaces remain limited.

Metal-Organic Frameworks (MOFs) have emerged as a novel class of materials with significant potential for formaldehyde removal (Achenbach et al., 2025; Vikrant et al., 2019; Wang et al., 2016). This study evaluates Al-3,5-PDA, also known as MOF-303, for its effectiveness in removing formaldehyde from indoor environments. Al-3,5-PDA was shown to exhibit outstanding results in laboratory conditions through breakthrough tests (Sadovnik et al., 2024), single-pass removal efficiency tests (Sadovnik et al., 2024), and small-scale chamber tests (Won et al., 2024) through a unique moderate chemisorption mechanism between the pyrazole and hydroxy moieties decorating its micropores, while not releasing formaldehyde at ambient conditions and being regenerable in water. However, its formaldehyde removal effectiveness in real-world applications remains unproven. Evaluating the long-term performance of Al-3,5-PDA in room-scale tests would provide valuable insight into their real-world effectiveness of formaldehyde removal. However, conducting long-term saturation tests or room-scale implementations can be expensive due to their high adsorption capacity and the significant cost of experimental specimens. To overcome these limitations, this study employs the method of model-based testing and evaluation (Zhang et al., 2019). This study developed an IAQ model by integrating laboratory testing with predictive IAQ modelling. Data from short-term, small-scale tests conducted to evaluate Al-3,5-PDA's performance under specific conditions were used to derive parameters in order to present its long-term performance in controlled environments and large-scale room conditions. This simulation enables us to predict the Al-3,5-PDA’s effectiveness for passive formaldehyde control in actual living spaces, offering crucial insights into its practical applications.

2. LABORATORY TEST

This study focused on deriving the model parameters to represent adsorption dynamics based on the chamber test results. While the detailed methodologies and findings were presented in a prior publication (Won et al., 2024), this section emphasizes the controlled testing approach and data acquisition processes essential for parameter estimation. The laboratory test evaluated the effectiveness of Al-3,5-PDA in adsorbing formaldehyde by using a 50 L sorption test system. The MOF was shaped as a 20 cm by 22.5 cm paper sheet (with a ca. 75 wt % MOF loading), following a green scalable protocol previously reported by some of us (Tignol et al., 2024), that was placed on a sample holder in the chamber so that the formaldehyde gas could be exposed to both surfaces of the sheet. Two distinct formaldehyde concentrations were applied at 23 °C and 50% relative

humidity: 114 μg/m^3 as a low concentration test and 316 μg/m^3 as a high concentration test. This setup aimed to assess how adsorption effectiveness varies under different formaldehyde concentrations. With formaldehyde injected into the chamber, the Al-3,5-PDA was subjected to continuous formaldehyde adsorption for 28 days. After that, the Al-3,5-PDA was allowed to desorb formaldehyde for 7 days by introducing only clean air into the chamber.

3. MATERIAL ADSORPTION MODEL AND IAQ MODEL

Al-3,5-PDA is a water stable and microporous 1D channel hydrophilic MOF material (see Figure 1) that exhibits a unique affinity for formaldehyde based on a chemisorption mechanism recently elucidated (Sadovnik et al., 2024); remarkably, the formaldehyde adsorption is favored in the presence of water. The adsorption processes involved the interplay between adsorption and adsorbate transportation to the surface, with each step potentially limiting the overall adsorption rate. The adsorption behavior of Al-3,5-PDA has been modeled using two distinct frameworks: the Equivalent Diffusion Model (EDM) (Liu et al., 2020) and the Empirical Surface Adsorption Model (ESAM) (Pétigny et al., 2021). The EDM focused on the diffusion of adsorbate molecules through the material's structure, assuming that the process could be effectively represented as a diffusion-controlled process. This model primarily emphasized the ability of the material to transport adsorbate molecules to the adsorption sites, but it did not fully capture the actual adsorption mechanism. The ESAM focuses on the relationship between the surface characteristics of Al-3,5-PDA and its capacity to adsorb formaldehyde. Based on experimental data, this model provided an empirical approach for describing how surface concentration influences the overall adsorption process.

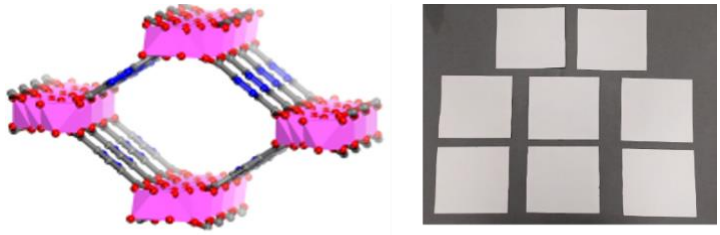

a. Crystal structure of Al-3,5-PDA b. Al-3,5-PDA paper sheet

Figure 1 View of (a) the crystal structure of Al-3,5-PDA. $AlO_4(OH)_2$ octahedra, oxygen, carbon atoms are in pink, red and grey, respectively (hydrogen atoms have been omitted), and (b) tested paper sheet of Al-3,5-PDA.

3.1 EQUVALENT DIFFUSION MODEL

In the EDM, formaldehyde was adsorbed on the Al-3,5-PDA surface, governed by the partition coefficient (K_{ma}), which represented the ratio of the formaldehyde surface concentration ($C_{m,s}$) to the air-material interface concentration (C_s). For the chemisorption, the K_{ma} of Al-3,5-PDA was expected to be significantly higher than that of typical building materials, which relied solely on physical adsorption. Once adsorbed, formaldehyde then diffused deeper into Al-3,5-PDA, governed by the diffusion coefficient (D_m). The EDM assumed that the diffusion rate of formaldehyde within the Al-3,5-PDA was equal to the rate of the chemical reaction, as formaldehyde was removed from the surface. The in-material diffusion process for formaldehyde can be described by Eq. (1).

$$\frac{\partial C_m}{\partial t} = D_m \frac{\partial^2 C_m}{\partial y^2} \tag{1}$$

where C_m was the concentration of formaldehyde in the material (μg/m^3); D_m was the diffusion coefficient of the VOC in the material, which was assumed to be constant (m^2/s); t was the elapsed time (s); y was the vertical coordinate from the centre to the top surface of the material (m).

3.2 EMPERICAL SURFACE ADSORPTION MODEL

The study adopted the ESAM from Pétigny et al., (2021), which was designed to model formaldehyde adsorption by active wall/ceiling materials. The ESAM approach treated sorption as instantaneous process due to its significantly faster timescale compared to mass transfer processes (Pei and Zhang, 2010; Yang et al., 2001), similar to the mechanism observed in formaldehyde chemical adsorption (Pétigny et al., 2021). The equilibrium state could be quantified by a relationship between the adsorbed mass concentration per unit surface area, denoted as M_s, and the gas-phase concentration at the interface, C_s. Testing revealed that the sorption characteristics was represented by a polynomial function (Pétigny et al., 2021), providing a robust framework to understand and model the adsorption process of Al-3,5-PDA.

$$M_s(C_s) = aC_s^2 + bC_s \tag{3}$$

where a and b were constants from the regression analysis of the M_s vs. C_s data obtained from the saturation tests conducted in the small-scale chambers.

3.3 MODEL FOR A SINGLE ZONE

An IAQ model was implemented to predict formaldehyde concentration in a single zone, extending chamber test condition until equilibrium reached, and then incorporated the results into real-life settings. The methodology employed a mass balance equation (Eq. (4)) to model formaldehyde concentration in air, assuming perfect mixing in the single zone. The equation's key principle stated that the rate of change in total formaldehyde mass was equal to the difference between external introduction and exhaust removal, adjusted for surface adsorption. Surface adsorption was considered a sink term influenced by material area and adsorption rate.

$$\mathrm{V}\frac{\partial C_{a,i}}{\partial \mathrm{t}} = \mathrm{Q}\left(C_{a,o} - C_{a,i}\right) - \sum_{1}^{N} A_i \, \mathrm{S_i} \tag{4}$$

where V was the volume of the single zone (m^3); Q was the ventilation flow rate (m^3/s); $C_{a,o}$ was the formaldehyde concentration in the inlet air which was typically equal to the outdoor air concentration in real building scenario (μg/m^3); $C_{a,i}$ was the formaldehyde concentration in the single zone (μg/m^3); A_i was the material surface area of the adsorption sink (m^2); S_i was the adsorption rate of the adsorption sink (μg/(m^2·s)); and N was the total number of adsorption sinks.

The sink term of Al-3,5-PDA was determined by the EDM and the ESAM. The adsorption rate was governed by the convective mass transfer process, which described formaldehyde transports from bulk air to the air-material interface, controlled by the convective mass transfer coefficient and concentration gradient.

$$\mathrm{S_{MOF}} = \mathrm{h_m}\left(\mathrm{C_{a,i}} - \mathrm{C_s}\right) \tag{5}$$

where, h_m was the convective mass transfer coefficient (m/s); $\mathrm{C_i}$ was the concentration of formaldehyde at the interface (μg/m^3). $\mathrm{C_s}$ was correlated to concentration of formaldehyde on the material surface, which can be derived from the EDM and the ESAM.

4. RESULTS

4.1 MODEL PARAMETER ESTIMATION AND ADSORPTION PROCESS ANALYSIS

This study focused on estimating model parameters derived from chamber test results and evaluating how different models reflected the actual adsorption process of formaldehyde onto Al-3,5-PDA. The previous findings provided baseline data for adsorption behavior under controlled conditions (Won et al., 2024). Based on these findings and our previous test data, the results (Figure 2) show that neither low and high concentration test reached Al-3,5-PDA's adsorption capacity. The increase in formaldehyde concentration within the chamber corresponded to a decrease in adsorption rate, highlighting the effect of adsorbed formaldehyde on subsequent adsorption processes.

For the EDM, parameters K_{ma} and D_m were determined through regression analysis, following a methodology outlined by (Liu et al., 2020). The results revealed that K_{ma} values for EDM under low and high concentration tests were 1.47×10^5 and 3.24×10^5 respectively, indicating a significant surface adsorption effect compared with conventional building materials. These findings aligned with the observation that adsorption primarily occurred at the surface due to chemical reactions, leading to a thin adsorbed layer with high capacity. While the D_m values showed a significant difference between the low and high concentration tests, this suggested that the assumed diffusion process did not accurately reflect the actual adsorption behavior. Furthermore, this indicated that, compared with the surface effect, in-material diffusion was not the dominant process governing formaldehyde adsorption on Al-3,5-PDA. Overall, the EDM effectively represented the chamber tests in both the adsorption and desorption phases (Figure 2).

For the ESAM, parameters M_s and C_s were calculated based on chamber test data. The results indicated that parameter a was significantly smaller than b, suggesting that the first-order adsorption-desorption model effectively described early-stage adsorption behavior (Figure 2). The equilibrium constant $K_e = M_s/C_s$ remained relatively constant over the 28-day test period, implying a steady-state condition where adsorption and desorption processes reached the dynamic equilibrium.

4.2 SIMULATION FOR SATURATION CONDITION

Due to the high costs and impracticality of conducting a one-year laboratory test, the EDM was employed to simulate formaldehyde adsorption over extended periods. The results, presented in Figure 3, demonstrated the evolution of formaldehyde concentration under two exposure conditions. Both simulations revealed that the adsorption process followed a characteristic curve where formaldehyde concentration increased over time and approached saturation. Regardless of the initial exposure level, the adsorption exhibited rapid uptake initially, followed by a slower approach towards equilibrium. The findings indicated that both low- and high-exposure concentration conditions led to saturation within approximately one year. These results validated the applicability of diffusion models for long-term predictions and provided valuable insights into practical applications without costly experimental testing. The ability to simulate extended exposure scenarios aided in assessing the long-term effectiveness of adsorptive materials.

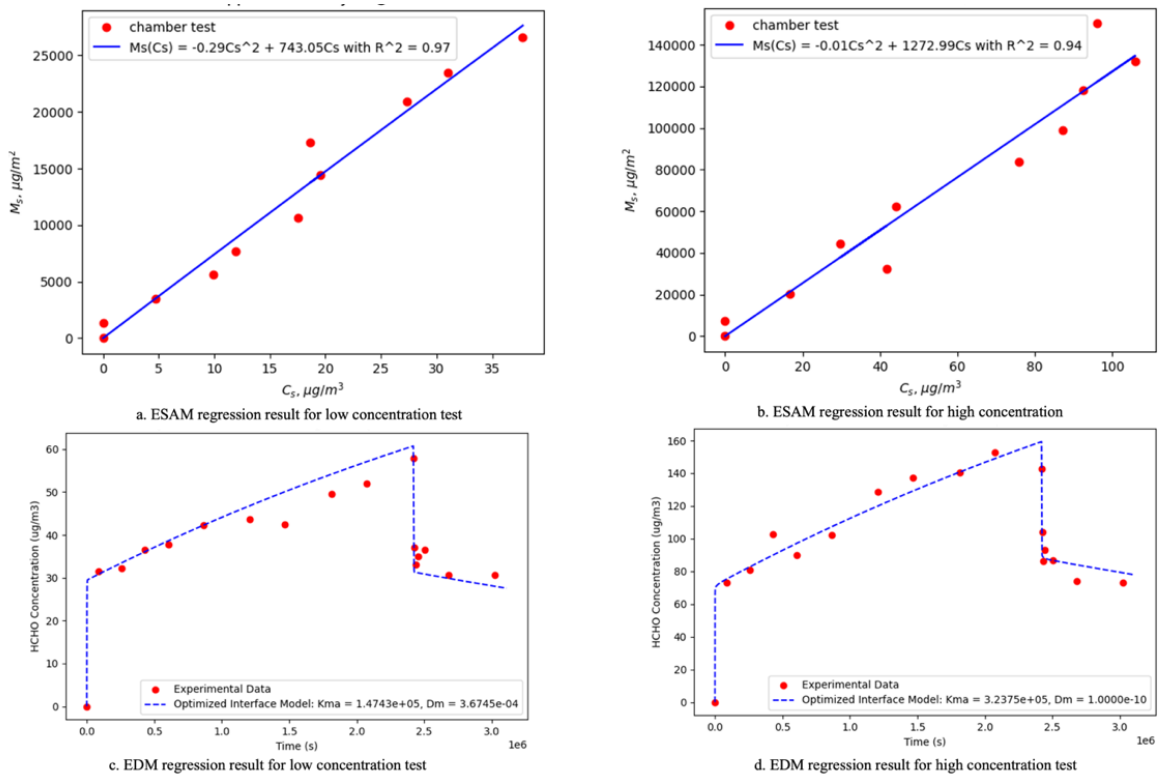

Figure 2 Regression test results of the ESAM and the EDM under low and high formaldehyde concentration tests. (a) Results for ESAM under low concentration test. (b) Results for ESAM under high concentration test. (c) Results for EDM under low concentration test. (d) Results for EDM under high concentration test.

For ESAM, saturation conditions can be determined by solving a quadratic function. The highest surface concentration was achieved at this peak point. By analyzing the total amount of formaldehyde injected, the time required to reach saturation could also be estimated. For low concentrations, this time was approximately 300 days, aligning with EDM results of about one year. However, for high concentrations, ESAM suggested a much longer time of around 13 years, which conflicted with EDM findings. This discrepancy may arise from the limitations of short-term tests in accurately estimating long-term conditions over a year. Further investigation was needed to reconcile these differences and ensure accurate modeling of adsorption processes over various timescales.

4.3 SIMULATION OF Al-3,5-PDA IN A REAL-WORLD INDOOR ENVIRONMENT

This study evaluated the performance of Al-3,5-PDA as a formaldehyde adsorbent in a realistic indoor setting. The simulation replaced a 10 m² gypsum wall with the MOF wallpaper in a 30 m³ room, mimicking a typical small office space. The indoor formaldehyde concentration was set to 32 μg/m³, representing the 95th percentile of residential levels in the United States (United States Environmental Protection Agency, n.d.). Ventilation rate followed ASHRAE 62.1 standards, reflecting normal office conditions with 0.68 air change per hour. The simulation performed at 23 °C and 50% relative humidity, representing typical indoor environment condition. The results in Figure 4 indicated that Al-3,5-PDA effectively reduced formaldehyde levels over time through adsorption. Equilibrium was reached at approximately 150 days, demonstrating Al-3,5-PDA's capacity for sustained formaldehyde mitigation in indoor environments. These findings

highlighted the potential of Al-3,5-PDA as an alternative of conventional gypsum walls, offering a passive and efficient solution for enhancing indoor air quality. The simulation supported the feasibility of using Al-3,5-PDA based materials in real-world applications where extended control of formaldehyde was desired.

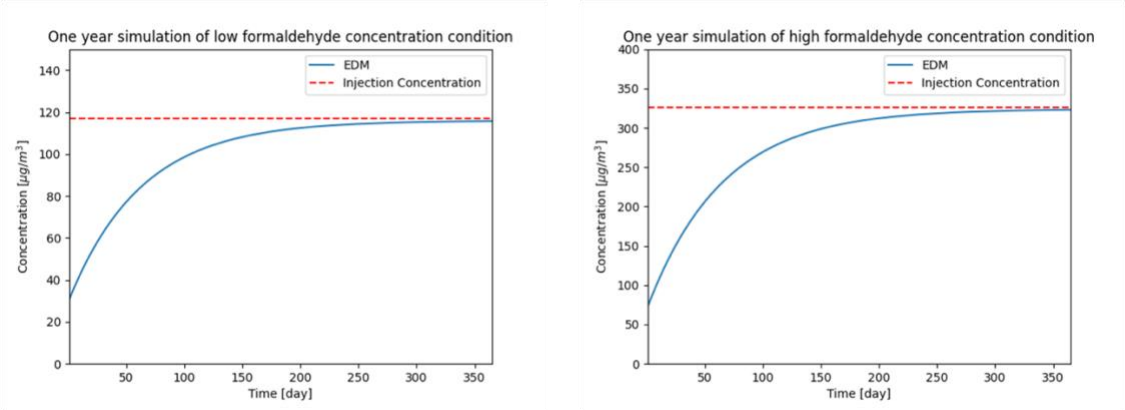

a. Simulation results of EDM for one year under low exposure concentration

b. Simulation results of EDM for one year under high exposure concentration

Figure 3 One-year simulation by EDM of formaldehyde adsorption under low and high concentration

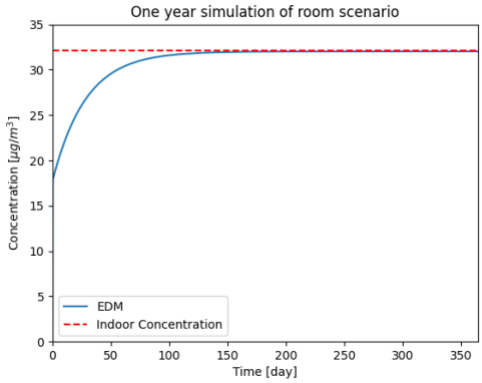

Figure 4 One-year simulation of formaldehyde adsorption in a room scenario

5. CONCLUSION

This study demonstrates the effectiveness of a multi-model approach in enhancing our understanding of adsorption behavior and highlighted the importance of validating models under varied conditions to ensure their reliability in real-world applications. The analysis showed the strengths and limitations of each model. The ESAM, which relied on second-order adsorption characteristic derived from small-scale chamber tests, provided practical predictions for short-term adsorption. However, its reliance on empirical data may lead to inaccurate estimation in longer durations. The EDM, a physics-based approach, offered more generalizable predictions by incorporating mass transport limitations. It was well-suited for capturing complex interactions under conditions beyond those tested in controlled environments, making it more reliable for long-term forecasting. The findings underscored the importance of combining empirical and physics-based models to enhance predictive accuracy and material assessment. It was crucial to ensure reliable results in real-world applications where conditions could vary widely.

This research presented the potential of Al-3,5-PDA (or MOF-303) as an effective adsorbent for

improving indoor air quality. It emphasized the need for comprehensive testing and model validation to ensure accurate predictions. Future studies should focus on scalability, long-term durability, and performance under dynamic environmental conditions to further refine modeling approaches and optimize material implementation in diverse settings.

ACKNOWLEDGEMENTS

This project is part of the IEA EBC Annex 86 Subtask 3 and Annex 92 Subtask C, which focus on smart material as an IAQ management strategy. We would like to thank all participating members and collaborators for their valuable contributions.

REFERENCES

Achenbach, B., Yurdusen, A., Stock, N., Maurin, G., Serre, C., 2025. Synthetic Aspects and Characterization Needs in MOF Chemistry – from Discovery to Applications. Advanced Materials 2411359. https://doi.org/10.1002/adma.202411359

Liu, Z., Nicolai, A., Abadie, M., Qin, M., Grunewald, J., Zhang, J., 2020. Development of a procedure for estimating the parameters of mechanistic VOC emission source models from chamber testing data. Build. Simul. 14, 269–282. https://doi.org/10.1007/s12273-020-0616-3

Pei, J., Zhang, J., 2010. Modeling of sorbent-based gas filters: Development, verification and experimental validation. Build. Simul. 3, 75–86. https://doi.org/10.1007/s12273-010-0309-4

Pétigny, N., Zhang, J., Horner, E., Steady, S., Chenal, M., Mialon, G., Goletto, V., 2021. Indoor air depolluting material: Combining sorption testing and modeling to predict product's service life in real conditions. Building and Environment 202, 107838. https://doi.org/10.1016/j.buildenv.2021.107838

Sadovnik, N., Lyu, P., Nouar, F., Muschi, M., Qin, M., Maurin, G., Serre, C., Daturi, M., 2024. Metal-organic frameworks based on pyrazolates for the selective and efficient capture of formaldehyde. Nat Commun 15, 9456. https://doi.org/10.1038/s41467-024-53572-z

Tignol, P., Pimenta, V., Dupont, A., Carvalho, S., Mohtar, A.A., Inês Severino, M., Nouar, F., Pinto, M.L., Serre, C., Lavédrine, B., 2024. A Versatile Shaping Method of Very-High Loading Porous Solids Paper Adsorbent Composites. Small Methods 8, 2301343. https://doi.org/10.1002/smtd.202301343

United States Environmental Protection Agency, n.d. Summarized Data of the Building Assessment Survey and Evaluation Study.

Vikrant, K., Cho, M., Khan, A., Kim, K.-H., Ahn, W.-S., Kwon, E.E., 2019. Adsorption properties of advanced functional materials against gaseous formaldehyde. Environmental Research 178, 108672. https://doi.org/10.1016/j.envres.2019.108672

Wang, X., Zhang, Y., 2009. A New Method for Determining the Initial Mobile Formaldehyde Concentrations, Partition Coefficients, and Diffusion Coefficients of Dry Building Materials. Journal of the Air & Waste Management Association 59, 819–825. https://doi.org/10.3155/1047-3289.59.7.819

Wang, Z., Wang, W., Jiang, D., Zhang, L., Zheng, Y., 2016. Diamine-appended metal–organic frameworks: enhanced formaldehyde-vapor adsorption capacity, superior recyclability and water resistibility. Dalton Trans. 45, 11306–11311. https://doi.org/10.1039/C6DT01696K

Won, D., Sultani, B.B.F., Guo, B., Huang, W., Liu, Z., Zhang, J., Qin, M., Tignol, P., Sadovnik, N., Nouar, F., Pimenta, V., Daturi, M., Dupont, A.-L., Lavédrine, B., Serre, C., 2024. Collaborative Assessment of a Novel MOF Material for Efficient Removal of Indoor Formaldehyde.

Xu, J., Zhang, J.S., Liu, X., Gao, Z., 2012. Determination of partition and diffusion coefficients of formaldehyde in selected building materials and impact of relative humidity. Journal of the Air & Waste Management Association 62, 671–679. https://doi.org/10.1080/10962247.2012.665812

Yang, X., Chen, Q., Zhang, J.S., An, Y., Zeng, J., Shaw, C.Y., 2001. A mass transfer model for simulating VOC sorption on building materials. Atmospheric Environment 35, 1291–1299. https://doi.org/10.1016/S1352-2310(00)00397-6

Zhang, J., Liu, Z., Guo, B., 2019. Model-based testing and evaluation of VOC emission sources and sinks: theory and application. IOP Conf. Ser.: Mater. Sci. Eng. 609, 042015. https://doi.org/10.1088/1757-899X/609/4/042015

Zhou, X., Liu, Y., Liu, J., 2018. Alternately airtight/ventilated emission method: A universal experimental method for determining the VOC emission characteristic parameters of building materials. Building and Environment 130, 179–189. https://doi.org/10.1016/j.buildenv.2017.12.025

6th International Conference on Building Energy and Environment
Eindhoven University of Technology, The Netherlands
6 - 10 July 2025

Assessing the impact of kitchen layouts and ventilation openings on indoor air quality

Chao-Yen Chang [1], Shou-Wang Chen[2], Ying-Chieh Chan[3],

[1] *Department of Civil Engineering National Taiwan University, Taipei, Taiwan, d05521017@ntu.edu.tw*
[2] *Department of Civil and Construction Engineering Purdue University, IN, USA, chen5330@purdue.edu*
[3] *Department of Civil Engineering National Taiwan University, Taipei, Taiwan, ychan@ntu.edu.tw*

SUMMARY
This study investigates how exhaust hoods and natural ventilation openings contribute to the removal of cooking pollutants and the improvement of indoor air quality in typical Taiwanese kitchens. Using a validated Computational Fluid Dynamics (CFD) model, various scenarios were simulated, including three common kitchen layouts, the effects of opening the front or back doors, and the operation of the exhaust hood. The aim was to evaluate how these different configurations influence indoor air quality during kitchen. The results indicate that different kitchen layouts may slightly impact removal efficiency. Overall, the level of remaining particulate matter is primarily influenced by natural ventilation openings. Layouts which the direction of the two doors is horizontal to the stove direction effectively remove cooking pollutants during the cooking process. It is crucial to minimize disturbances caused by natural ventilation during cooking.

Keywords: Indoor Air Quality, Computational Fluid Dynamic, Kitchen Hood, Natural Ventilation Openings

1. INTRODUCTION

Cooking is a major contributor to the release of volatile compounds and pollutants (Spengler et al., 1983). Without proper ventilation, pollutant levels can rise significantly (Kang et al., 2019). Several studies has shown that using an exhaust hood can effectively reduce the amount of air pollutants produced during cooking (Sun et al., 2021; Lunden et al., 2015; Rim et al., 2012). In most cases, natural make-up air is often used to compensate for air when exhaust hoods are running. This air typically enters through windows and doors. Research has indicated that adequate natural make-up air in the kitchen during cooking can effectively lower pollutant concentrations, though too much ventilation may cause pollutants to spread to adjacent rooms (Liu et al., 2021). This highlights the importance of assessing and analysing indoor airflow and ventilation. However, the impact of kitchen layouts and ventilation openings on indoor air quality has not been thoroughly discussed. This study is using computational fluid dynamics tools to examine how the use of kitchen hoods and ventilation openings affects indoor air quality during cooking. This analysis aims to provide researchers with a deeper understanding of the risks of human exposure to harmful particles and the influence of natural make-up air on indoor air quality.

2. METHODOLOGY

CFD simulations were conducted using ANSYS Fluent (2021 R1) to analyze airflow, heat transfer, and particle motion under transient conditions. The RNG k-ε model was used for turbulence due to its suitability for interior airflow prediction (Eom et al., 2023). Radiation was

modeled with the Discrete Ordinates (DO) model, and particles with the Discrete Phase Model (DPM). For further model details, refer to the ANSYS Fluent user guide.

2.1. CFD model

Figure 1 presents three typical Taiwanese residential kitchen configurations (3.10 m × 2.37 m × 2.27 m), with two doors serving as natural make-up air openings. Case H aligns the doors horizontally with the stove, Case V aligns them vertically, and Case C places them at a cross angle. All kitchen elements were precisely measured and incorporated, with material properties carefully defined. The model includes a stove with heating plates, an exhaust hood with two outlets, and a human model (1.80 m tall) positioned 25 cm from the stove to simulate cooking. Minor structures like small items, pipelines, and wires were simplified to enhance efficiency and improve spatial analysis. Table 1 outlines the boundary conditions for openings, heat sources, and walls. Further model details can be found in Chen et al. (2025).

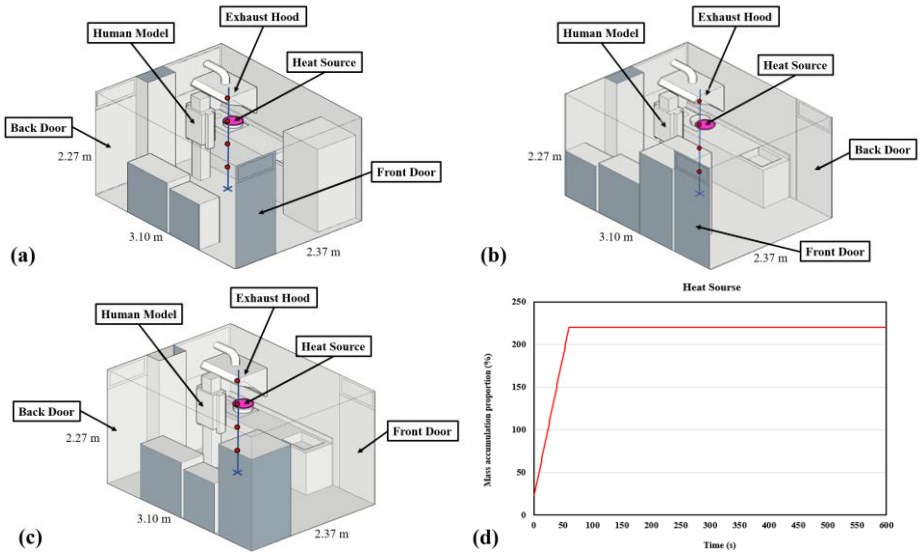

Figure 1. Schematic diagram of the kitchen model: (a) full 3D view (Case H) (b)full 3D view (Case V) (c)full 3D view (Case C) (d) the user defined heating curve for the heat source in simulation cases.

2.2. Case description

This study investigated the effect of natural air openings and the exhaust hood on indoor air quality in a kitchen by comparing simulation results of different scenarios. The evaluation was based on calculating the mass of suspended particulate matter over a fixed 615 seconds transient simulation. Nine cases were analysed to assess differences in pollutant residue levels in the kitchen during cooking, considering the exhaust hood was used and whether the front and back doors were open. Table 1 summarizes the details of the boundary conditions for both open and closed conditions. Table 2 provides detailed information on the simulation cases. In all cases, cooking was performed using a user-defined heat source from 0 to 615 seconds, as shown in Figure 6. During this period, the exhaust hood was in operation, and the front door was open while the back door remained closed, consistent with the validation case.

Table 1. Boundary conditions.

Name	Type	Description
Exhaust hood	Velocity	2.3 m/s
Heat source	Wall / Temperature	20℃ ~ 220℃ (Details in Figure 1 (d))
	Particle / DPM	Diameter: $2.0*10^{-7}$ m Temperature: 220℃ Velocity: 0.1 m/s
Front door	Pressure-inlet for natural ventilation	0 Pa
	Wall / Convection for closing	22.0 ℃
Back door	Pressure-inlet for open conditions	0 Pa
	Wall /Convection for closed condition	16.0 ℃
Window	Wall /Convection	16.0 ℃
Indoor wall	Wall / Convection	22.0 ℃
Outdoor wall	Wall /Convection	16.0 ℃
Human	Wall	36.5 ℃

Table 2. Detailed information about the simulation cases.

Case	0 ~ 615s	
	Front Door	Back Door
Case H1/V1/C1	Close	Open
Case H2/V2/C2	Open	Close
Case H3/V3/C3	Open	Open

3. RESULTS AND DISCUSSIONS

In this study, we simulated 9 cases: three kitchen layouts with three doors situations. Figure 2 shows the mass accumulation proportion of particles during cooking process. The mass accumulation proportion (%) is calculated by taking the highest accumulated particle mass during cooking process as 100%.

3.1. Impact of kitchen layout and natural air openings

Comparing the 9 cases, it can be observed that CaseH, the direction of the two doors is horizontal to the stove, effectively removes cooking pollutants during the cooking process. The mass accumulation proportion of particles in the domain remains below 10%. On the other hand, the CaseV kitchen layout, the direction of the two doors is vertical to the stove, results in poor exhaust efficiency. This is likely due to the airflow path between the two doors being closer to the stove. The airflow significantly affects the particle expulsion efficiency.

Overall, excessive natural ventilation during cooking does not necessarily lead to better pollutant expulsion efficiency, as can be clearly seen in Case V3 and C3. The possible reason is that excessive airflow can interfere with the path of pollutant expulsion from the stove to the exhaust hood, leading to the occurrence of air mixing due to excessive natural ventilation. In addition, if the temperature of the natural ventilation is lower, as seen in Case V1 and C1, it can also result in a reduced pollutant expulsion efficiency from the exhaust hood.

3.2. Limitations

The simulation results have certain limitations. Our study highlights that incoming air directly affects pollutant distribution. We modelled the inlet as a pressure inlet without wind speed, but natural ventilation can be influenced by outdoor wind, which should be considered. Additionally, the presence of individuals alters airflow and pollutant dispersion based on their position and height. Food ingredients also vary, producing different pollutants that affect their spread. These factors should be accounted for in future simulations.

4. CONCLUSION

This study examined the impact of kitchen layouts and natural ventilation openings on indoor air quality using CFD simulations. The results indicate that while kitchen layout influences pollutant removal efficiency, natural ventilation plays a more significant role in determining air quality during cooking. Specifically, configurations where doors align horizontally with the stove enhance pollutant removal, whereas excessive ventilation can disrupt airflow, reducing exhaust efficiency. The findings emphasize the need for a balanced ventilation strategy—ensuring sufficient fresh air intake while minimizing disturbances that may hinder pollutant expulsion. Future studies should incorporate factors such as wind effects on natural ventilation, variations in pollutant characteristics from different cooking methods, and the influence of human presence on airflow dynamics to enhance simulation accuracy and practical applicability.

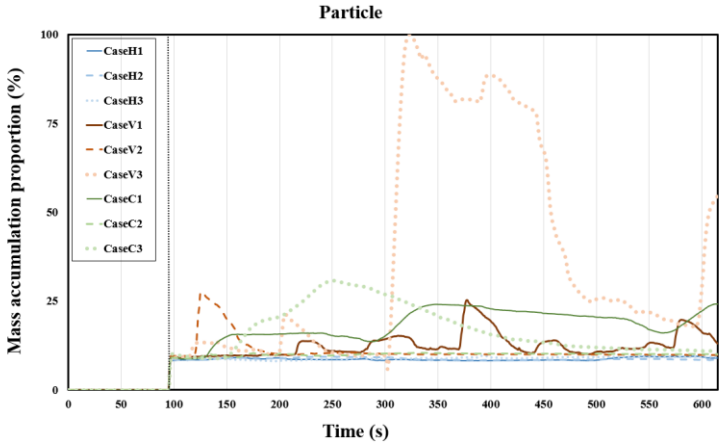

Figure 2. The results of the particle mass accumulation proportion.

ACKNOWLEDGEMENTS

This project is supported by the National Taiwan University Excellence Research Program Core Consortiums - 113L893703.

REFERENCES

Spengler, J.D. and K. Sexton, Indoor air pollution: a public health perspective. Science, 1983. 221(4605): p. 9-17.

Kang, K., H. Kim, D.D. Kim, Y.G. Lee, and T. Kim, Characteristics of cooking-generated PM10 and PM2.5 in residential buildings with different cooking and ventilation types. Science of The Total Environment, 2019. 668: p. 56-66 DOI: https://doi.org/10.1016/j.scitotenv.2019.02.316.

Sun, L. and L.A. Wallace, Residential cooking and use of kitchen ventilation: The impact on exposure. Journal of the Air & Waste Management Association, 2021. 71(7): p. 830-843 DOI: 10.1080/10962247.2020.1823525.

Lunden, M.M., W.W. Delp, and B.C. Singer, Capture efficiency of cooking - related fine and ultrafine particles by residential exhaust hoods. Indoor Air, 2015. 25(1): p. 45-58.

Rim, D., L. Wallace, S. Nabinger, and A. Persily, Reduction of exposure to ultrafine particles by kitchen exhaust hoods: The effects of exhaust flow rates, particle size, and burner position. Science of The Total Environment, 2012. 432: p. 350-356 DOI: https://doi.org/10.1016/j.scitotenv.2012.06.015.

Liu, Y., J. Dong, Y. Wang, W. Zheng, and Y. Jiang, Numerical investigation on the influence of natural make-up air in Chinese-style residential kitchen on indoor environment in a partitioned household. Sustainable Energy Technologies and Assessments, 2021. 46: p. 101244 DOI: https://doi.org/10.1016/j.seta.2021.101244.

Eom, Y.S., D.H. Kang, D. Rim, and M. Yeo, Particle dispersion and removal associated with kitchen range hood and whole house ventilation system. Building and Environment, 2023. 230: p. 109986.

Chen, S.W., C.Y. Chang, and Y.C. Chan, Assessing the impact of kitchen hoods and ventilation openings on indoor air quality post-cooking. Journal of Building Engineering, 2025. 100: p. 111721.